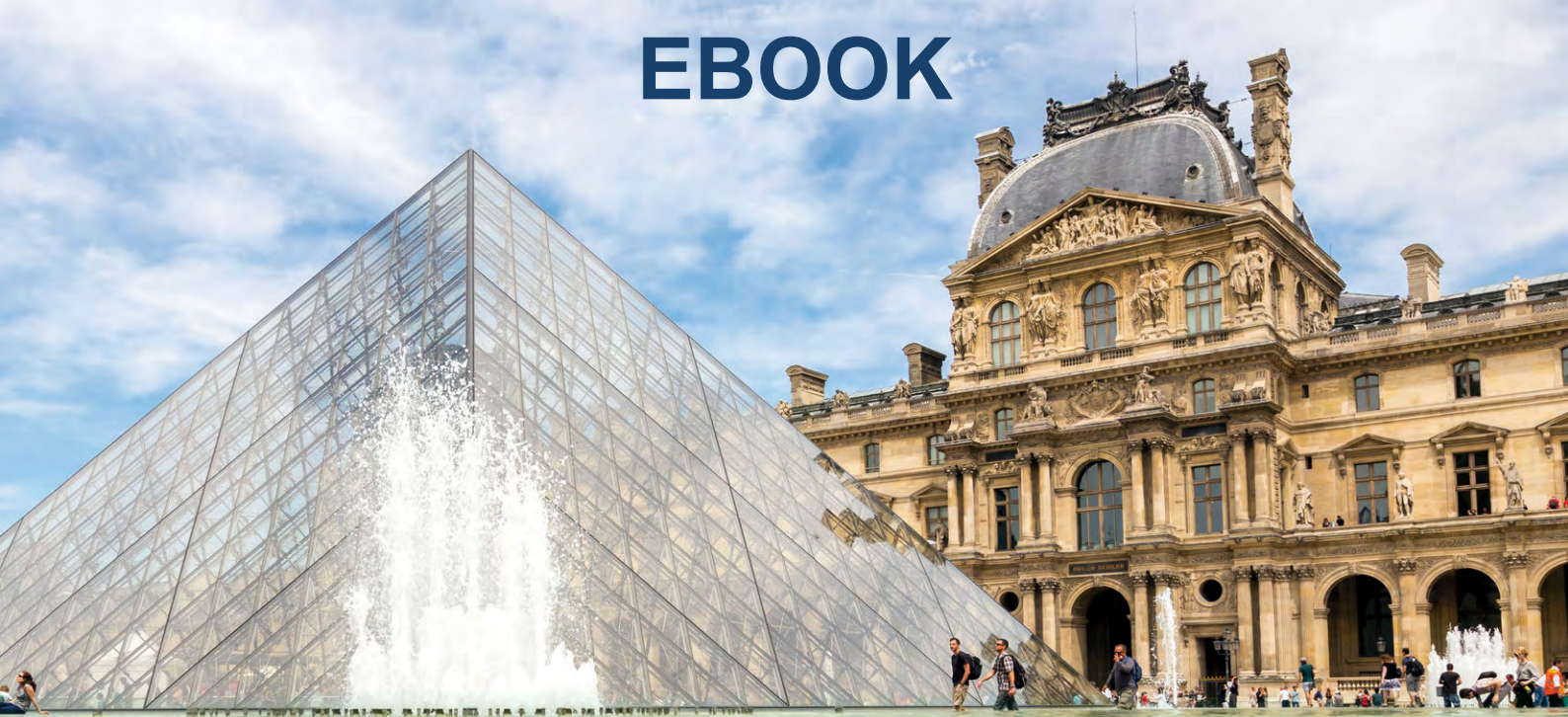




EBOOK



Paris, France, 8-11 July 2019

SMART 2019

9th ECCOMAS Thematic Conference on Smart Structures and Materials

Ayech Benjeddou, Nazih Mechbal and Jean-François Deü (Editors)



**9th ECCOMAS Thematic Conference on
Smart Structures and Materials**

SMART 2019

**Paris, France
July 8 - 11, 2019**

A publication of:

**International Centre for Numerical
Methods in Engineering (CIMNE)**

Barcelona, Spain



First Edition: July 2019

© The Authors

ISBN: 978-84-949194-6-6

Printed by: Artes Gráficas Torres S.L., Huelva 9, 08940 Cornellà de Llobregat,
Spain

TABLE OF CONTENTS

Preface	7
Acknowledgements	9
Summary	11
Contents	13
Lectures	29
Authors Index	1835

PREFACE

This e-book is the edited proceedings of SMART2019, the 9th ECCOMAS *Thematic Conference on Smart Structures and Materials* that held from 8 to 11 July at Paris (France). This biennial (odd years) series, has started in 2003 and progressed successfully over the years. Its earlier editions were located in Poland (2003, 2007), Portugal (2005, 2009, 2015), Germany (2011), Italy (2013) and Spain (2017).

The present edition aimed to: i) increase participants number, ii) raise contributions quality, iii) increase international (non-European) participants, iv) bring industrials, v) involve effectively the scientific committee (SC) in the organization, and vi) provide a good social program. To reach these goals, the SC has been revised according to the earlier edition active members and successful mini-symposia (MS) organizers' responses to a priori 'intended active participation' questionnaire. The general topics, meant for later general sessions (GS), were focused on seven only and hot ones, in the form of MS and Special Sessions (SS), have been introduced with the help of active members of the SC and experts in the suggested up-to-date topics. The technical program resulted in 5 GS, 13 MS and 2 Poster session (PS). In details, 195 contributions were presented in 37 sessions of which are 7 plenary lectures (PL), 28 oral sessions and 2 PS. From these, 176 full papers were submitted in order to be included in the present e-proceedings. Out of the PLs, for which full papers were not expected, this represents ~94% of the 188 talks (170) and Posters (18). Some of the missing 12 papers, related to talks (9) or Posters (3), were expected as they concern industrial (1), Keynote (1) or very late (3) submissions.

SMART2019 was supported by the 3 chairmen's affiliations (Ensam, Le Cnam and Supméca) and by 3 prestigious journals: *Smart Materials and Structures* (SMS), *Journal of Intelligent Material Systems and Structures* (JIMSS) and *Journal of Vibration and Control* (JVC). Presenting authors of a selection of papers from the present e-proceedings will be invited to revise and extend their contributions in order to be potentially published, after the journals regular review processes, in SMART2019 devoted special (JIMSS, JVC) or regular (SMS) issues. The organizers are then very thankful to their affiliations and to the editor-in-chiefs (Daniel J. Inman for JIMSS, Mehdi Ahmadian for JVC and Christopher S. Lynch for SMS) and JIMSS special issues' editor (Norman M. Wereley) for their valuable supports. The present proceedings editors are also very thankful to the authors for their contributions, to the SC active members for their effective involvement, to the MS organizers, chairwomen and chairmen for their help, to Mr. Alessio Bazzanella (CIMNE) for the present proceedings administrative edition, and to the local organization help from Mr. Christophe Canu, our colleagues, Post-Docs and PhDs.

As a closure, the editors wish sincerely that these proceedings will be very useful to academic and industrial researchers, and to engineers in this highly active topic of smart structures and materials.

Ayech BENJEDDOU, Nazih MECHBAL and Jean-François DEÛ (Editors)

ACKNOWLEDGEMENTS

The conference organizers acknowledge the support of the following organizations:



Arts et Métiers – Ensam (Paris Campus)



Conservatoire national des arts et métiers



Supméca

PLENARY SPEAKERS AND MS ORGANIZERS

We would like to thank the Plenary Speakers and the MS Organizers for their help in setting a high level Scientific Programme.

Plenary Speakers: Daniel J. Inman, Christopher S. Lynch, Mehdi Ahmadian, Michael Kyriakopoulos, Farhan Gandhi, Rainer Schweppe and Johannes Riemenschneider.

Minsymposia Organizers: Aurelio Araujo, Olivier Bareille, Tarak Ben Zineb, Andrea Bergamini, Christian Bolzmacher, Álvaro Cunha, Sergio de Rosa, Elke Deckers, Wim Desmet, Christophe Droz, Peter Eberhard, Farhan Gandhi, Jan Holnicki-Szulc, Alexander Humer, Lukasz Jankowski, Michael Krommer, Pawel Kudela, Boris Lossouarn, Theodoros Loutas, Pawel Malinowski, Nazih Mechbal, Filipa Moleiro, Carlos Moutinho, Euripedes Nóbrega, Wieslaw Ostachowicz, Przemyslaw Perlikowski, Marc Rebillat, Oliver Sawodny, Werner Sobek, Malte von Scheven, Norman Wereley, Wael Zaki and Dimitrios Zarouchas.

SUMMARY

MINISYMPOSIA

MS01: Smart & Adaptive Engineering Structures	31
<i>Organized by Malte von Scheven, Werner Sobek, Oliver Sawodny and Peter Eberhard</i>	
MS02: Identification, Control & Structural Health Monitoring of Civil Structures	146
<i>Organized by Carlos Moutinho and Álvaro Cunha</i>	
MS03: Adaptive Mitigation of Dynamically Induced Structural Response	323
<i>Organized by Lukasz Jankowski, Przemyslaw Perlikowski and Jan Holnicki-Szulc</i>	
MS04: Health Monitoring of Advanced Composite Structures	381
<i>Organized by Wiesław Ostachowicz, Paweł Malinowski and Paweł Kudela</i>	
MS05: Morphing Aircraft and Rotorcraft Systems	433
<i>Organized by Farhan Gandhi</i>	
MS06 : Spatial Control of Sound and Vibration	485
<i>Organized by Nazih Mechbal, Marc Rebillat, Euripedes Nobrega and Christian Bolzmacher</i>	
MS07: Modelling and Design of Smart Composite Structures	543
<i>Organized by Aurelio Araujo and Filipa Moleiro</i>	
MS08: Advances in Non-linear Modeling of Smart Materials and Structures	650
<i>Organized by Alexander Humer and Michael Krommer</i>	
MS09: Functional Materials with Multiphysics Coupling and their Applications	787
<i>Organized by Tarak Ben Zineb and Wael Zaki</i>	
MS10: Vibration Mitigation through Electromechanical Couplings	884
<i>Organized by Boris Lossouarn and Andrea Bergamini</i>	
MS11: Smart Design of Periodic Structures	1058
<i>Organized by Christophe Droz, Olivier Bareille, Wim Desmet and Elke Deckers</i>	
MS12: Integrated Prognostic and Health Monitoring of Complex Aeronautical Structures	1189
<i>Organized by Nazih Mechbal, Marc Rebillat, Theodoros Loutas and Dimitrios Zarouchas</i>	
MS14: Magnetorheological Fluids, Devices, and Integrated Adaptive Systems	1270
<i>Organized by Norman Wereley</i>	

GENERAL SESSIONS

GS1: Smart structures	1319
GS2: Smart materials	1377
GS3: Smart systems	1435
GS5: Health monitoring	1501
GS7: Engineering Applications	1622

POSTER SESSIONS

Poster	1671
---------------------	-------------

CONTENTS

MINISYMPOSIA

MS01: Smart & Adaptive Engineering Structures

Organized by Malte von Scheven, Werner Sobek, Oliver Sawodny and Peter Eberhard

An adaptive structure with a metamorphic robotic system	31
<i>M. Pieber and J. Gerstmayr</i>	
Combining Optimal Control and Shape Optimization for an Adaptive Engineering Structure with Parameterized Reduced Order Finite Element Models	43
<i>B. Fröhlich, J.L. Wagner, M. Böhm, O. Sawodny and P. Eberhard</i>	
Condition health monitoring of a suspension strut cap/ upper strut mount using piezoelectric sensor for electro-mechanical impedance technique....	55
<i>S. Moharana and V. S. A</i>	
Dynamic Optimal Control of Building Energy Adapting to External Factors Predictions	65
<i>S. Ben Ayed, D. Kim, J. Borggaard and E. Cliff</i>	
Experimental testing of a small-scale simply supported truss beam that adapts to loads through large shape changes	72
<i>A.P. Reksowardojo, G. Senatore and I. F. C. Smith</i>	
Nonlinear Bending of Functionally Graded Dielectric Composite Plate Reinforced by Graphene Platelets	81
<i>Y. Wang, C. Feng, Z. Zhao and J. Yang</i>	
Nonlinear Modeling and Control of Tension-only Elements in Adaptive Structures	90
<i>J. L. Wagner, M. Boehm and O. Sawodny</i>	
Selected Results on the Development and Testing of Smart Blades Technologies for Wind Turbines.....	102
<i>Z. Montano, S. Opitz, J. Riemenschneider, V. Petrovic, R. Unguran, L. Neuhaus, P. Singh, E. Werthen, C. Balzani and M. Bätge</i>	
Sensor and Actuator Placement in Tensegrity Structures through Cellular Morphogenesis	118
<i>O. Aloui and L. Rhode-Barbarigos</i>	
Simulative Study and Potential Analysis of Inflatable Facade Elements to Balance Environmental Disturbances	125
<i>J. Guenther, M. Oei, N. Harder and O. Sawodny</i>	

Topology optimization of piezoelectric smart structures under active control	137
<i>Z. Jia and X. Zhang</i>	

MS02: Identification, Control & Structural Health Monitoring of Civil Structures

Organized by Carlos Moutinho and Álvaro Cunha

A New Neutral Equilibrium Mechanism Applied to Force Control and its Application	146
<i>M. H. Shih and W. P. Sung</i>	

Active warping control for damping of torsional beam vibrations	158
<i>D. Hoffmeyer and J. Høgsberg</i>	

Assessment of Mode Shapes Based Damage Detection Methods for Building Structures	169
<i>C. M. Chang, H. F. Chiang and J. Y. Chou</i>	

Changes in modal frequencies of a steel plate girder caused by local damage and thermal expansion.....	177
<i>C. W. Kim, T. Hirooka, T. Mimasu, G. Hayashi and Y. Goi</i>	

Contribution to new solutions of instrumentation of Civil Structures for continuous dynamic monitoring	189
<i>C. Moutinho and A. Cunha</i>	

Electromechanical Impedance Method applied to Debonding Identification of NSM FRP Strips in Concrete	200
<i>R. Perera, L. Torres, M. Baena and C. Barris</i>	

Least-squares reverse time migration for flaw characterisation using ultrasonic bulk waves.....	207
<i>J. Rao and Z. Fan</i>	

Multiobjective optimization for identification of a moving load path	215
<i>M. Gawlicki and Ł. Jankowski</i>	

New application of piezoelectric sensors in health monitoring of rocks.....	223
<i>P. Negi, T. Chakraborty and S. Bhalla</i>	

Novel Technique of On-Demand Monitoring of Slider Displacement in Seismic Isolator.....	233
<i>S. Takhirov</i>	

Smart bridge developing based on micro-truss optimization method.....	243
<i>Y. Yokotani, I. Ario, Y. Chikahiro and M. Nakazawa</i>	

Statistical analysis of damage indicators based on ultrasonic testing with embedded piezoelectric transducers	251
<i>A. Deraemaeker, C. Dumoulin, N. Dervilis, E. Cross and K. Worden</i>	
Supervised classification with SCADA data for condition monitoring of wind turbines	263
<i>E. Hoxha, Y. Vidal and F. Pozo</i>	
The use of different modal quantities for identification of damage.....	275
<i>F. Vestroni, J. Ciambella and A. Pau</i>	
Topology optimization approach for dense sensor network distribution over large bridge structures	284
<i>B. Blachowski, P. Tazowski, A. Swiercz and Ł. Jankowski</i>	
Vibration monitoring on a PC girder bridge during a bridge collapse test	291
<i>Y. Kondo, Y. Oshima and C. W. Kim</i>	
Vibration suppression and energy harvesting potential in wind excited buildings equipped with ground floor tuned inerter damper	301
<i>Z. Wang and A. Giaralis</i>	
Vibration-based long-term scour monitoring for an in-service railway bridge	313
<i>K. Yoshitome, C. W. Kim, Y. Goi, S. Kitagawa, M. Shinoda, H. Yao and Y. Hamada</i>	
 MS03: Adaptive Mitigation of Dynamically Induced Structural Response 	
<i>Organized by Lukasz Jankowski, Przemyslaw Perlikowski and Jan Holnicki-Szulc</i>	
An experimental investigation of the Prestress Accumulation Release strategy for local mitigation of structural vibrations.....	323
<i>G. Mikulowski, B. Poplawski and Ł. Jankowski</i>	
Continuously Variable Transmission for Application in Tuned Mass Damper ..	333
<i>M. Lazarek, P. Brzeski and P. Perlikowski</i>	
Inverse Lyapunov based method for semi-active control of energy transfer between vibration modes	345
<i>M. Ostrowski, B. Blachowski, Ł. Jankowski and D. Pisarski</i>	
Semi-active decentralized mitigation of randomly excited vibrations in 2D frame structures.....	357
<i>B. Poplawski, G. Mikulowski and Ł. Jankowski</i>	
SMA-based multi-modal adaptive TMDs: model and tests	364
<i>M. Berardengo, G. Della Porta, S. Manzoni and M. Vanali</i>	

Tuned mass damper with inerter and non-linear damper	373
<i>M. Lazarek, B. Polniak, P. Brzeski and P. Perlikowski</i>	

MS04: Health Monitoring of Advanced Composite Structures

Organized by Wiesław Ostachowicz, Paweł Malinowski and Paweł Kudela

Approaches for localization of damage in composites using propagation of lamb waves	381
<i>K. Balasubramaniam, T. Wandowski and P. Malinowski</i>	

Damage assessment in composite powerboat using electromechanical impedance method	390
<i>W. Ostachowicz, T. Wandowski, P. Malinowski and B. Puchowski</i>	

Damage detection based on multivariate approach: application to aerospace composite structures	402
<i>R. Hadjria and O. D'Almeida</i>	

Effects on bond strength and quality of embedding optical glass fibre sensors in adhesively bonded joints formed by structural film adhesives	409
<i>N. Grundmann, H. Brüning, K. Brune and M. Mayer</i>	

Experimental investigations on the mechanical damage behavior of multifunctional composites with printed electronics	421
<i>M. Linke, T. Genco and R. Lammering</i>	

MS05: Morphing Aircraft and Rotorcraft Systems

Organized by Farhan Gandhi

A novel concept of a modular shape-adaptable sandwich panel able to achieve multiple shapes	433
<i>O. Testoni, A. Bergamini, S. Bodkhe and P. Ermanni</i>	

Analysis of Multifunctional SMA/Piezoelectric/Composite Beam Structure for Morphing and Energy Harvesting	443
<i>N. Mallik</i>	

Integration of the Spiral Pulley Negative Stiffness Mechanism into the FishBAC Morphing Wing	452
<i>C. Wang, J. Zhang, A. Shaw, M. Amoozgar, M. Friswell and B. Woods</i>	

Shape Memory Alloy Actuation Technology for Adaptive Low Boom Supersonic Transports	462
<i>J. Mabe, D. Lagoudas and D. Hartl</i>	

Tailored Nonlinear Negative Stiffness Mechanisms for Linear Motion.....	473
<i>J. Zhang, A. Shaw, C. Wang, M. Amoozgar and M. Friswell</i>	

MS06 : Spatial Control of Sound and Vibration

Organized by Nazih Mechbal, Marc Rebillat, Euripedes Nobrega and Christian Bolzmacher

Adaptable ball-screw inerter for optimal impact absorption	485
<i>R. Faraj, C. Graczykowski, Ł. Jankowski and J. Holnicki-Szulc</i>	

Analysis and Control of Damped Flexible Structures	492
<i>Y. Halevi</i>	

Bending waves focusing in arbitrary shaped plate-like structures: application to spatial audio.....	503
<i>N. Benbara, M. Rébillat and N. Mechbal</i>	

Open-loop transient control of modes for the generation of localized tactile tunable patterns on haptic devices.....	515
<i>C. Giraud-Audine, E. Enferad, F. Giraud, M. Amberg and B. Lemaire-Semail</i>	

Piezoelectric transducer for low frequency sound generation on surface loudspeakers.....	527
<i>C. Bolzmacher, N. Benbara, M. Rebillat and N. Mechbal</i>	

Ultra-Light, Deployable Space-Truss Structures with Dynamic Response Mitigation	537
<i>A. Swiercz and J. Holnicki-Szulc</i>	

MS07: Modelling and Design of Smart Composite Structures

Organized by Aurelio Araujo and Filipa Moleiro

Accurate Characterization of Fluidic Artificial Muscle Force Response for Improved Model Fidelity	543
<i>J. M. Chambers and N. M. Wereley</i>	

ACELAN-COMPOS Package for Finite Element Simulation of Active Composite Materials	551
<i>A. V. Nasedkin</i>	

Application of a Dual PZT Sparse Array with Lamb Wave Mode Decomposition for Damage Localization in an Aluminum Aircraft Wing.....	562
<i>J. R. McCullum, B. Yoo, D. J. Pines and N. M. Wereley</i>	

Bending shape memory process of a fabric-reinforced shape memory polymer composite plate: experimental investigation and numerical simulation	571
<i>P. Fan, W. Chen, J. Gao, G. Fang, F. Peng and Z. Cao</i>	

Design of Electro-Viscoelastic Sandwich Panels for Noise Reduction	580
<i>F. Vieira and A.L. Araujo</i>	
Environmentally-friendly Auxetic Piezoelectric Composites for Additive Manufacturing: Nonlocal and Nonlinear Effects.....	592
<i>A. K. Jagdish, F. C. Buroni, F. Garcia-Sanchez, R. Melnik, L. Rodriguez-Tembleque and A. Saez</i>	
Exact Vibration Analysis of Laminated Piezoelectric Plates through Strong SaS Formulation	599
<i>G. M. Kulikov, N. P. Merkusheva and S. V. Plotnikova</i>	
Multi-dimensional models for the global-local analysis of smart layered structures	610
<i>E. Zappino and E. Carrera</i>	
Optimization of piezoelectric patches with passive shunted damping for noise reduction in sandwich panels	618
<i>A.L. Araujo and J. F. A. Madeira</i>	
Process and Structural Health Monitoring of a "smart" Polymer-Matrix Composite using an in-situ piezoelectric sensor.	628
<i>C. Tuloup, W. Harizi, Z. Aboura, Y. Meyer and K. Khellil</i>	
The development of the prototype of the system for monitoring a stress-strain state of a outlet guide vane with the help of a fiber optical sensors	640
<i>A. Anoshkin, G. Shipunov, A. Voronkov, K. Pelenev, E. Shustova and A. Tikhonova</i>	

MS08: Advances in Non-linear Modeling of Smart Materials and Structures

Organized by Alexander Humer and Michael Krommer

A complete direct approach to electrostrictive polymer plates and shells	650
<i>M. Krommer, E. Hansy-Staudigl and A. Humer</i>	
A scale-adaptive indicator for the simulation of thermomechanically loaded SMA matrix composites	662
<i>M. Praster and S. Klinkel</i>	
Analysis of an energy-based model of the polarization process in ferroelectric materials	674
<i>A.S. Pechstein, M. Meindlhumer and A. Humer</i>	
Application of a microstructural model to simulation of a TiNi beam bending performance and calculation of thickness stress distributions.....	686
<i>A.E. Volkov, M. E. Evard, F. S. Beliaev, N. A. Volkova and P. S. Liulchak</i>	

Assessment of Second Piola-Kirchhoff Stress Tensor in Laminated Piezoelectric Structures through SaS Shell Formulation.....	696
<i>M. G. Kulikov, S. V. Plotnikova, S. A. Mamontov and G. M. Kulikov</i>	
Finite element reduced-order models to predict the geometrically nonlinear dynamics of piezoelectric laminated structures.....	709
<i>A. Givois, O. Thomas and J. F. Deü</i>	
Non-linear Electromechanical Coupling: Large Deformation and Hysteresis	721
<i>A. Humer, A.S. Pechstein, M. Meindlhumer and M. Krommer</i>	
Nonlinear Electromechanical Conversion and Sensory Response of Multi-Stable Piezoelectric Shallow Shells with Piezoelectric Films	730
<i>D. Varelis and D. Saravanos</i>	
Parameter-free optimization of material orientation for high performance composite shell structures	742
<i>M. Shimoda and Y. Muramatsu</i>	
Rate-dependent thermomechanical modelling of entropy changes in superelastic SMA	754
<i>A. Kaup, O. Altay and S. Klinkel</i>	
Shear behaviour of magnetorheological elastomers: viscoelastic and magnetorheological properties	764
<i>A. Bellelli and A. Spaggiari</i>	
Variational inequalities for ferroelectric constitutive modeling	775
<i>M. Meindlhumer, A.S. Pechstein and A. Humer</i>	

MS09: Functional Materials with Multiphysics Coupling and their Applications

Organized by Tarak Ben Zineb and Wael Zaki

A thermomechanically coupled finite-strain constitutive model for Iron-based Shape Memory Alloys accounting for coupling between phase transformation and plastic sliding	787
<i>A. Sallami, W. Khalil, T. Bouraoui and T. Ben Zineb</i>	
Ambient heat-transfer effects on magnetic shape memory alloy actuators	797
<i>S. Zhang, G. Qin and Y. He</i>	
Bending model for laminated composite cantilever beams with multiple embedded shape memory alloy layers	805
<i>W. Zaki and V. Nguyen</i>	

Effect of Cobalt Particle Morphology on Properties of Magnetorheological Elastomers	816
<i>X. Dong, Y. Tong, M. Qi and N. Ma</i>	
Fatigue Analysis of Nitinol Stent Used in Endovascular Aneurysm Repair (EVAR) Considering Anisotropic Aortic Walls	825
<i>R. Jayendiran, B. Nour and A. Ruimi</i>	
Modeling of Fatigue Crack Growth in Shape Memory Materials - Keynote Lecture	837
<i>J. Yaacoub and H. Sehitoglu</i>	
Phenomenological Modeling of Porous Shape Memory Alloys.....	844
<i>G. Ozerim, Z. Moumni and G. Anlas</i>	
Self-heating and fatigue of superelastic shape memory alloy structures.....	855
<i>L. Saint-Sulpice, S. Arbab Chirani, S. Calloch, C. Doudard and V. Legrand</i>	
Sensors integrated inside metal castings verified to respond to force.....	866
<i>R. Carlsson, C. Johansson, L. Elmquist, A. Thore, F. Ahrentorp, M. Törnvall, B. Israelsson, V. Schaller and P. Johannisson</i>	
Study of the pseudoelastic damping behaviour of the Fe-30Mn-6Si-5Cr shape memory alloy	877
<i>M. Megdiche, A. Sallami, F. Thiebaud, T. Bouraoui, T. Ben Zineb and S. A. Chirani</i>	
 MS10: Vibration Mitigation through Electromechanical Couplings	
<i>Organized by Boris Lossouarn and Andrea Bergamini</i>	
A robust calibration procedure for multiple electromechanical shunt absorbers on a flexible structure	884
<i>J. Høgsberg</i>	
Broadband vibration damping of a non-periodic plate by piezoelectric coupling to its electrical analogue	896
<i>R. Darleux, B. Lossouarn and J. F. Deü</i>	
Enhancement of a Dynamic Vibration Absorber by means of an Electromagnetic Shunt Damper.	908
<i>M. Auleley, O. Thomas, C. Giraud-Audine and H. Mahé</i>	
High voltage synthetic inductor in piezoelectric shunt to damp flexible vibrating structures	922
<i>K. Dekemele, P. Van Torre and M. Loccufer</i>	
Hybridization of active control and passive resonant shunt	930
<i>A. Paknejad, G. Raze, G. Zhao, M. Osée, A. Deraemaeker, F. Robert, G. Kerschen and C. Collette</i>	

Integration of piezostacks as frequency dependent stiffness elements in load bearing structures.....	942
<i>J. Schmied and A. Bergamini</i>	
Passive Vibration Damping of Hydrofoils using Resonant Piezoelectric Shunt.....	952
<i>L. Pernod, B. Lossouarn, J. A. Astolfi and J. F. Deü</i>	
Resonant piezoelectric shunt tuning based on the electric current and voltage response to pseudo-random vibration excitation	961
<i>J. F. Toftekær and J. Høgsberg</i>	
Semi-Active Piezoelectric Tuned Mass Damper for Mitigation of Aerodynamic Vibrations in Aircraft Structures	973
<i>K. Georgopoulos-Bosinas, N. A. Chrysochoidis, C. Rekatsinas, Y. Revalor and D. A. Saravanos</i>	
Stick-slip oscillations in an electromechanical system	985
<i>R. Lima and R. Sampaio</i>	
Suppression of delay-induced instabilities of digital piezoelectric vibration absorbers	991
<i>G. Raze, A. Paknejad, G. Zhao, V. Broun, C. Collette and G. Kerschen</i>	
The development of the model of electric analog for electromechanical systems taking into account mechanical losses	1002
<i>D. Oshmarin, N. Sevodina, N. Iurlova and M. Iurlov</i>	
The use of negative capacitances to improve the vibration attenuation of piezoelectric resonant shunt.....	1014
<i>M. Berardengo, S. Manzoni, O. Thomas and M. Vanali</i>	
Theoretical and experimental study of piezoelectric nonlinear resonators for energy harvesting and vibrations control.....	1025
<i>V. Guillot, A. Givois, M. Colin, O. Thomas, A. Ture Savadkoohi and C. H. Lamarque</i>	
Vibration control of smart composite plates using shunted piezoelectric elements	1037
<i>G.K. Tairidis, K. Marakakis, P. Koutsianitis, G. Foutsitzi, J. F. Deü, G. E. Stavroulakis and R. Ohayon</i>	
Vibration mitigation of multiple nonlinear resonances through an analogous piezoelectric network.....	1046
<i>B. Lossouarn, G. Kerschen and J. F. Deü</i>	

MS11: Smart Design of Periodic Structures

Organized by Christophe Droz, Olivier Bareille, Wim Desmet and Elke Deckers

A multi-scale reinforced sandwich panel for vibroacoustic applications: shear transition effects	1058
<i>R. Palumbo, D. Ivanov, C. Droz, F. Scarpa, O. Bareille and M. Ichchou</i>	
A Wave-Based Methodology for the Optimization of Finite 1D Metamaterials	1066
<i>R. Boukadia, E. Deckers, C. Claeys, M. Ichchou and W. Desmet</i>	
Absorption enhancement in poro-elastic materials by mass inclusion, exploiting the mass-spring effect	1076
<i>S. Ahsani, E. Deckers, T. G. Zielinski, Ł. Jankowski, C. Claeys and W. Desmet</i>	
Band diagram and forced response analysis of periodic and quasi-periodic panels	1085
<i>S. Timorian, M. Ouisse, N. Bouhaddi, S. De Rosa and F. Franco</i>	
Decoupling of energy transmission between subsystems of a complex structure	1096
<i>G. Mazzeo, M. Ichchou, G. Petrone, F. Franco and S. De Rosa</i>	
Elastic Energy Transport Leveraging Tunable Topological Structures	1105
<i>D. E. Quadrelli, E. Riva, G. Cazzulani and F. Braghin</i>	
Investigations about the modelling of acoustic properties of periodic porous materials with the shift cell approach	1112
<i>D. Magliacano, M. Ouisse, S. De Rosa, F. Franco and A. Khelif</i>	
On the effect of distributed embedded resonators in curved sandwich panels loaded by turbulent boundary layer	1124
<i>F. Errico, M. Ichchou, S. De Rosa, F. Franco and O. Bareille</i>	
On the structural characterization through k-space methods: assessments and validations	1136
<i>G. Tufano, C. Droz, M. Ichchou, O. Bareille, A. M. Zine, W. Desmet and B. Pluymers</i>	
On the vibration attenuation properties of finite periodic lattices of impact dampers	1146
<i>V. Dertimanis, S. Masri and E. Chatzi</i>	
Parametric analysis of a triple core periodic unit cell including a middle random core	1157
<i>N. Guenfoud, C. Droz, M. Ichchou, O. Bareille, E. Deckers and W. Desmet</i>	
Uncertainties in wave characteristic of one-dimensional periodic media using the fuzzy wave finite element method	1169
<i>R. P. Singh, M. Ichchou, O. Bareille, F. Franco and S. De Rosa</i>	

Wave-diode effect exploiting discretely modulated phononic waveguides	1183
<i>E. Riva, G. Cazzulani, J. Marconi and F. Braghin</i>	

MS12: Integrated Prognostic and Health Monitoring of Complex Aeronautical Structures

Organized by Nazih Mechbal, Marc Rebillat, Theodoros Loutas and Dimitrios Zarouchas

Composite Plate Automatic Damage Isolation Based on Support Vector Machine Classification of Lamb Wave Signals	1189
<i>R. Santos, P. Souza, N. Inocente-Junior and E. Nóbrega</i>	

Damage quantification method in composite materials based on triangulation	1201
<i>W. Briand, M. Rebillat, M. Guskov and N. Mechbal</i>	

Data-Driven Autoregressive Model Identification for Structural Health Monitoring in Anisotropic Composite Plates	1213
<i>S. da Silva, J. Paixão, M. Rébillat and N. Mechbal</i>	

Investigation of nonlinear Lamb wave/damage interaction: numerical and experimental approaches	1224
<i>X. Li, E. Monteiro, M. Rebillat, M. Guskov and N. Mechbal</i>	

Spatial attenuation prediction of Lamb waves in composite materials. ...	1236
<i>S. Guo, M. Rebillat and N. Mechbal</i>	

Strain-Based Damage Assessment on Single-Stiffener Composite Panels	1248
<i>D. Milanoski and T. Loutas</i>	

Structural state awareness of composite structures by blending passive and active acoustic-based health monitoring methods	1260
<i>D. Zarouchas and M. Saeedifar</i>	

MS14: Magnetorheological Fluids, Devices, and Integrated Adaptive Systems

Organized by Norman Wereley

Experimental study on vibration control of a vehicle semi-active suspension with magneto-rheological damper traversing speed bump	1270
<i>M. Yu, X. Du, J. Fu and C. Huang</i>	

Fuzzy-neural control for a magnetorheological elastomer vibration control system with sinusoidal excitations	1281
<i>J. Fu, J. Bai, Z. Yang, Z. Dai, J. Liu and M. Yu</i>	

Interaction between carrier liquid and iron particles in MR-based sealings	1291
<i>C. Hegger and J. Maas</i>	
Multi-axis Magnetorheological Aircraft Seat Suspension	1300
<i>Y.T. Choi, N. M. Wereley and G. Hiemenz</i>	
The Effect of Mesocarbon Microbeads on the Behavior of Magnetorheological Fluid	1312
<i>R. M. Pierce, Y.T. Choi and N. M. Wereley</i>	

GENERAL SESSIONS

GS1: Smart structures

Acoustic energy focusing and band gap structure of robocast ceramic scaffolds	1319
<i>M. Koller, T. Grabec, P. Sedlák, A. Kruisová, B. Román-Manso, M. Belmonte, P. Miranzo and H. Seiner</i>	
Finite Element Reduced Order Model of a Piezoelectric Energy Harvester	1327
<i>R. Aloui, W. Larbi and M. Chouchane</i>	
Influence of viscoelastic elements on the dissipative properties of electro-viscoelastic structures	1337
<i>N. Iurlova, N. Sevodina, D. Oshmarin and M. Iurlov</i>	
On dynamical hierarchical two-dimensional models of multilayer thermoelastic piezoelectric shells	1349
<i>G. Avalishvili and M. Avalishvili</i>	
Plate and shell finite element for piezoelectric patch modelling	1361
<i>O. Polit, M. Ottavio and P. Vidal</i>	
Towards a new generation of soft actuators using phase transition: application to morphable-texture skins and soft grippers	1371
<i>G. Lubineau, R. Chellattoan, N. Bolson and A. Yudhanto</i>	

GS2: Smart materials

Carbon nanotubes modelled as size-dependent nanobeams for mass sensing applications	1377
<i>S. Ceballes, S. Ghaffari, B. Saunders and A. Abdelkefi</i>	
Enhancing damping for composites aerospace structures with piezoelectric and carbon nanoparticles	1389
<i>L. Quiroga Cortes, L. Sanches, L. Barrière, C. Bessaguet, E. Dantras, G. Michon and M. Chevalier</i>	

Investigations on the dynamics and vibrations of carbon nanotubes with multiple deposited nanoparticles	1397
<i>S. Ceballes, D. Furth and A. Abdelkefi</i>	

Large strain measurement method based on dynamic reference in distributed optical fiber	1405
<i>L. Suo and Z. Wu</i>	

Magnetostrictive Composites for Wireless Stress Sensing Applications...	1414
<i>A. Yoffe and D. Shilo</i>	

On the measurement of Giant Magnetostrictive Material properties under mechanical loading	1427
<i>M. Domenjoud, E. Berthelot and L. Daniel</i>	

GS3: Smart systems

Electrostrictive multilayer polymer actuator dimensioning and modelling for continuum snake like robot application	1435
<i>Q. Jacquemin, D. Thuau, E. Monteiro, S. Tencé-Girault and N. Mechbal</i>	

Energy harvesting using a piezoelectric-flexoelectric nanobeam	1446
<i>F. Najar, S. Baroudi and H. Samaali</i>	

Mechatronic robot arm with active vibration absorbers.	1456
<i>Z. Šika, K. Kraus, P. Beneš, J. Krivošej and T. Vyhlídal</i>	

Modeling of smart vibration-based energy harvesters based on the PGD method	1468
<i>M. Infantes, R. Castro-Triguero, P. Vidal, L. Gallimard and O. Polit</i>	

Multi-Section Pneumatic Artificial Muscle Continuum Robot Arm with Ossicle-inspired Structures	1480
<i>T. E. Pillsbury and N. M. Wereley</i>	

Workspace Analysis of Multi-section Continuum Pneumatic Arm	1491
<i>J. Garbuliński and N. M. Wereley</i>	

GS5: Health monitoring

Bayesian Evaluation and Reduction of Economic Risk for Structural Health Monitoring using Weighted Regression.....	1501
<i>A. Iwasaki and S. Shimizu</i>	

Damage localization using controllable inputs: an experimental study ...	1507
<i>B. A. Qadri, M. D. Ulriksen, L. B. Klockmann and P. H. Veis</i>	

Examination of Modal Expansion and Kalman Filtering Techniques for Vibration Estimation.....	1515
<i>M. W. Pedersen, E. K. Andersen, M. D. Ulriksen and L. Damkilde</i>	

Examination of Sensor Distribution Schemes for Vibration Estimation	1527
<i>E. K. Andersen, M. W. Pedersen, M. D. Ulriksen and L. Damkilde</i>	
Fault Localization in Ring Type Structures with a Second-Order Output Spectrum based method	1538
<i>Q. K. Li and X. J. Jing</i>	
Improving efficiency and robustness of SHM techniques based on Lamb wave detection.....	1550
<i>J. Rebufa, G. Jaussaud, F. Claeysen, M. Fournier, M. Logeais, N. Bencheikh, M. Rébillat and M. Guskov</i>	
Material Intrinsic Phenomena Used for Smart Structural Health Monitoring.....	1562
<i>C. Boller, P. Starke, R. Sridaran Venkat, A. Lozák, H. Wu, V. Lyamkin and R. de Acosta</i>	
Modelling of deformation and fracture of composite structures using monitoring data from optical fiber strain sensors	1574
<i>M. Tashkinov and V. Matveenko</i>	
Theoretical and experimental investigation of Lamb waves induced by bonded and debonded piezoelectric actuators in a plate with a delamination	1582
<i>A. Shpak, M. Golub, A. Eremin, I. Mueller, J. Kathol and C. P. Fritzen</i>	
Tubular ultrasonic transducer: MUST with radial excitation versus conventional axial excitation	1594
<i>N. Bencheikh, J. Rebufa and F. Claeysen</i>	
Wind turbine health monitoring based on accelerometer data	1604
<i>Y. Vidal, J. L. Rubias and F. Pozo</i>	
Wireless network monitoring systems for cultural heritage buildings	1612
<i>G. Zini, M. Betti and G. Bartoli</i>	

GS7: Engineering Applications

A New Smart Approach to Monitor Thickness Reduction in Metallic Structures	1622
<i>P. Rizzo, B. Zheng, A. Nasrollahi and H. Jalali</i>	
Development of Control Strategies for Vertical Mobility of Adaptive Telescopic High-altitude Aerostats	1629
<i>C. Graczykowski, L. Knap, J. Holnicki-Szulc and Z. Wołęjsza</i>	
Fluid-structure interaction analysis of a four-bar flapping wing mechanism	1637
<i>C. Beker, A. E. Turgut, K. B. Arikan and D. F. Kurtulus</i>	

Seismic performance of robotic bridge using scissors system	1648
<i>Y. Chikahiro, S. Zenzai, S. Shimizu, I. Ario and M. Nakazawa</i>	

Shape Memory Alloys as pipe joints: applicability as vibration attenuators to drill-strings considering uncertainties	1654
<i>R. Silva, T. Ritto and M. Savi</i>	

The Motions of the Celt on a Horizontal Plane with Viscous Friction.....	1664
<i>M. Munitsyna</i>	

POSTER SESSIONS

Poster

Applicability of Magnetic Hysteresis Models for Predicting the Behaviour of MR Dampers	1671
<i>J. Goldasz, B. Sapiński, Ł. Jastrzębski and M. Kubik</i>	

Comparison of passive and active mitigation devices for vibrations control in slender structures.....	1682
<i>A. Magdaleno, C. Casado, J. M. Soria, E. Pereira, I. M. Diaz and A. Lorenzana</i>	

Eddy Current Damped Interconnection for Mitigation of Internal Pounding for a Seismically-Isolated Building	1694
<i>F. Mazza and R. Labernarda</i>	

Hg(II)-imprinted polymer gels - smart materials for mercury determination and speciation.	1706
<i>I. G. Dakova, T. V. Yordanova , I. Karadjova and M. Karadjov</i>	

Measurement of process-induced strains by embedded fiber-optic strain sensors in composite material	1718
<i>N. Kosheleva, G. Serovaev and A. Shestakov</i>	

Mesosopic Modelling of ZnO Varistors	1726
<i>K. Taylor, E. Gjonaj and H. De Gersem</i>	

Model Predictive Control of a Semi-Active Suspension System Featuring Magnetorheological (MR) Dampers	1738
<i>M. Ngoc, S. B. Choi and G. W. Kim</i>	

Own oscillations of the fragment stands of the sports complex "Arena-Omsk" from the natural background.....	1746
<i>A. Zhivaev and G. Boldyrev</i>	

Research and Development of Circular Pipe Pump using EHD Fluid	1753
<i>T. Tsukiji</i>	

Seismic behaviour of a certain type of Tower Cranes	1760
<i>C. Oliveira and P. Correia</i>	

Self-correcting soil models for numerical simulation of strain rate dependent ice scour in sand	1772
<i>A. Nematzadeh and H. Shiri</i>	
Smart system based on raffinose-coated silver nanoparticles as selective and sensitive optical probe/sorbent for chromium speciation in water samples	1783
<i>P. Vasileva, L. Djerahov and I. Karadjova</i>	
The monitoring system of the Santa Maria di Collemaggio Basilica	1795
<i>R. Alaggio, A. Aloisio, E. Antonacci, L. Di Battista, R. Cirella and M. Fragiaco</i>	
Transparent Sensory Fiber-Reinforced Composites	1812
<i>Y. Caydamli, S. Frick and M. Buchmeiser</i>	
Variable stiffness element based on rheology characteristics of shear thickening fluid	1823
<i>H. Tryggvason, F. Starker, C. Lecompte and F. Jonsdottir</i>	

LECTURES

A SELF-RECONFIGURABLE MECHANISM BASED ON SHAPEABLE TRIANGULAR CELLS

Michael Pieber and Johannes Gerstmayr

Department of Mechatronics

University of Innsbruck

Technikerstraße 13, 6020 Innsbruck, Austria

e-mail: michael.pieber, johannes.gerstmayr@uibk.ac.at,

web page: www.uibk.ac.at/mechatronik/mekt/

Key words: programmable matter, self-reconfigurable system, cellular robots

Abstract. Recently, a new approach for cellular robots has been presented. The single elements of the robot are triangular cells, which can change their shape by means of linear actuators at each edge. The novelty concerns the connection of autonomous cells at their edges rather than at the vertices. In this way, unstructured triangular meshes can be formed. The robot can self-reconfigure and thus can reproduce almost arbitrary planar shapes. The self-reconfigurable system shall serve as a basis for programmable matter. The present paper presents ways to assess and to compensate positioning errors of triangular cells. A mechanical model is developed, which considers compliance of links and joints by introducing axial and bending stiffness of according members of the model. In order to enable a fast computation and an integration of the actuators, a simplified discrete model is developed. A calibration and a comparison with accurate motion and force measurements shows the validity of the model. In the future, an extended model shall be used in order to optimize the mechanical parameters.

1 Introduction

Modular self-reconfigurable mechanisms have been investigated since the 1980s [1]. Self-reconfigurable mechanisms which are able to change their shape autonomously are classified as metamorphic robotic systems [2]. Only few such systems are available and they consist mostly of rigid cubical [3] or spherical [4] cells with an active or passive connection mechanism and are able to self-reconfigure by means of moving around on the other cells. However, these systems can only reconfigure, but not additionally change shape after reconfiguration. Since the development of metamorphic robotic systems, researchers improved the single components of the systems such as actuators, connection mechanisms, electronics and algorithms for self-reconfiguration [5]. Furthermore, spherical cells have been proposed for a possible approach to programmable matter [6], but no concrete areas of application have yet been identified [7].

The present paper deals with a simplified model of an extremely versatile cellular, adaptive and reconfigurable robotic system. The Planar Adaptive Robot with Triangular Structure (PARTS)

[8] goes significantly beyond the technology of existing cellular robots and is intended to be used in a wide range of applications. Considering cell sizes in the range from meters to millimeters, possible applications range from large adaptive and self-constructing scaffolds to small adaptive 'material'. One of the disadvantages of the existing system are the six-bar-linkages, which cause a low stiffness of the cells. In order to determine the stiffness, a test rig was designed which allows the determination of a force-displacement curve by means of two orthogonally applied forces. A mechanical model was developed which takes into account the bending stiffness of the six-bar-linkages. The model is highly important for the further development of the self-reconfigurable system, as it aims to predict the size of positioning errors which can be used to estimate possible connection faults. As compared to earlier works on the triangular cells, positioning errors can be predicted qualitatively given the parameters of a single cell only.

2 A planar cellular robot

The recently developed self-reconfigurable mechanism PARTS with adaptive triangular cells (ATC) and active connection mechanism as shown in Figure 1a), can reconfigure itself autonomously. Specifically, this can be achieved with the advantage that general triangular meshes can be exactly recreated. This is possible because the kinematic rotation axes of the vertices are located outside of the assembly space due to the use of six-bar linkages as shown in Figure 1b). Thus, all polygons with according edge sizes and angle limitations can be built with this method. In contrast to all other existing systems, the above mentioned features of PARTS allow that the whole structure can still move and, e.g., grip something, nearly independent of the reconfiguration of the structure. In other words, the programmable structure PARTS combines self-reconfiguration with adaptronics. Furthermore, programmable matter can be realized if using tetrahedral cells [9] together with miniaturization.

In order to transform the self-reconfigurable mechanism from one to another meshed structure, the cells are moving, e.g., along the outer edges of the current structure, cf. Figure 2. However, the real cells show a significant amount of deformation at the realized joints, such that a deviation of the real mesh from the idealized triangular mesh occurs. As the individual ATCs have no sensors for absolute positioning, the error between actual and target positions should be computed from a calibrated model of the deformable mechanism.

3 Positioning accuracy

The main part of the present contribution concerns the modeling of the cells, specifically of the six-bar-linkage joints as shown in Figure 1b) [8], which lead to a deviation of the real cells as compared to the idealized prescribed movements of the underlying triangular mesh due to compliance, bearing clearances and actuator inaccuracies. A first approach to modeling positioning errors due to compliance, clearance and friction has been based on a simplified mechanical model using elastic trusses of the triangular mesh to predict the positioning errors [8]. To get an accurate prediction of the positioning error, the current model is extended, by modeling every six-bar-linkage with elastic trusses and rods (for bending) and the whole self-reconfiguration mechanism resulting as a multibody system with changing constraints. In the present contribution, the modeling of the joints is improved by means of an additional bending related compliance in the six-bar-linkages. Modeling of bending stiffness follows the finite segment method, which

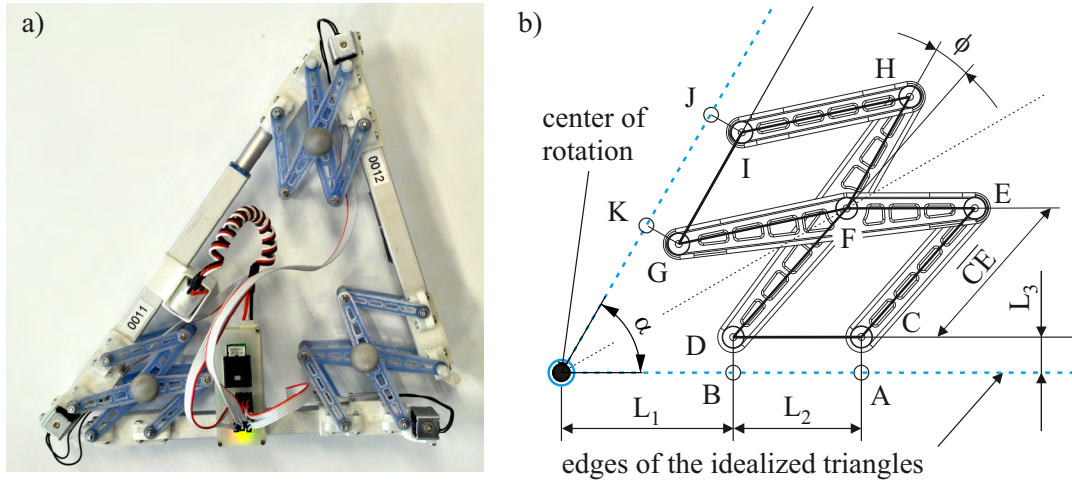


Figure 1: a) Top view of an ATC prototype with six-bar-linkages, electronics and measuring points. b) Schematic representation of a six-bar-linkage with center of rotation outside of the assembly space [8].

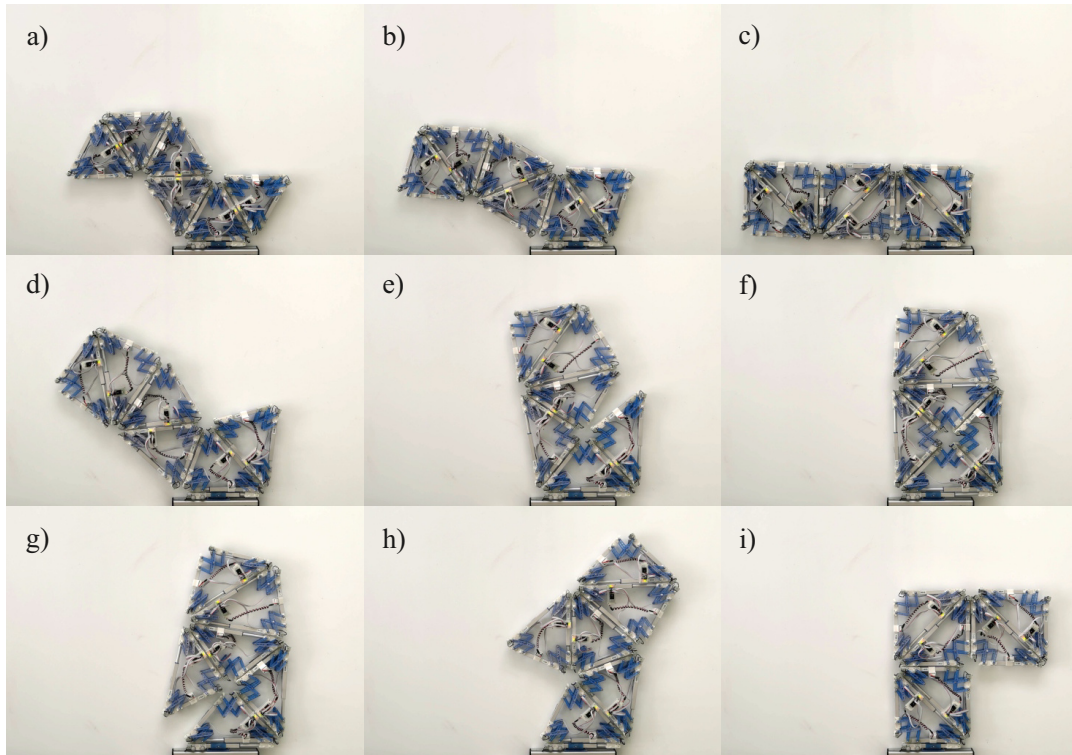


Figure 2: Proof of concept of self reconfiguration of PARTS with six ATCs. Steps a) to i) show the reconfiguration of PARTS by adapting the surrounding ATCs and by releasing and connecting the ATCs at the side edges.

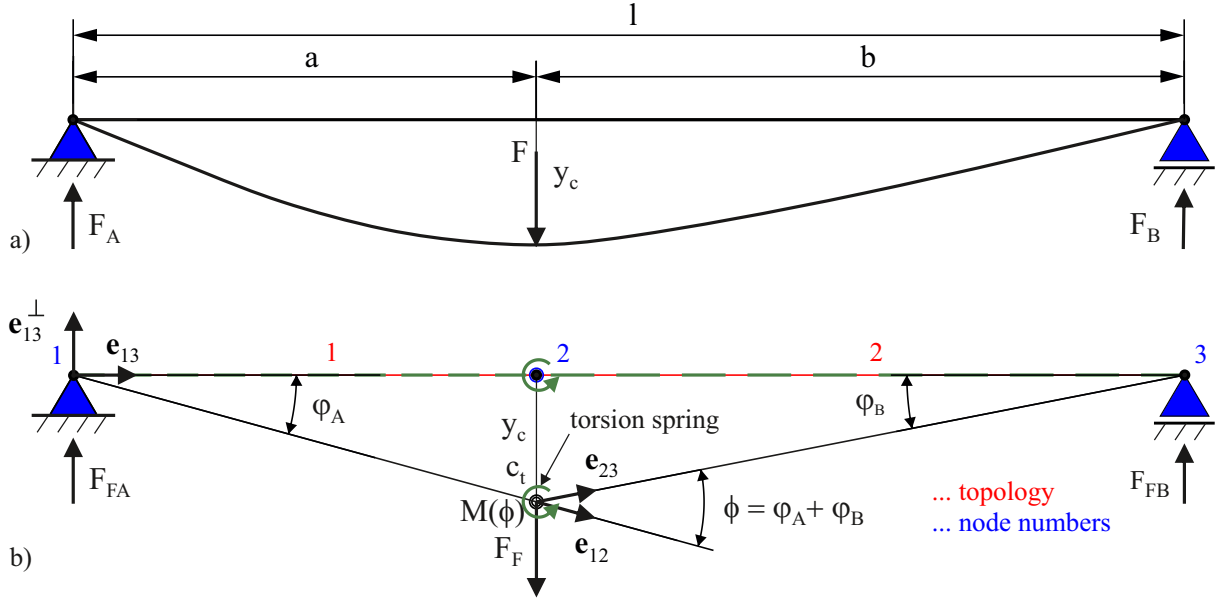


Figure 3: a) Schematic of the deflection of a beam. b) Sketch of a linearized three-point torsion-spring.

allows to use only rigid bodies and springs for the whole model [10].

3.1 Deformation of a beam through bending

Bending stiffness has not been considered within the first model of the ATCs [8], which is why the model error becomes very large with the number of added ATCs. The maximum of the elastic deflection, denoted as y_c , of a simply supported beam loaded at a distance a and b from the support, see Figure 3a), is given by

$$y_c = \frac{Fl^3}{3EI} \frac{a^2 b^2}{l^2} \quad (1)$$

with the force F acting on the beam, the young's modulus E , the area moment of inertia of cross section I and the length l of the beam between the supports. The above formula can be rewritten as

$$F = \frac{3EI}{a^2 b^2} y_c. \quad (2)$$

The supporting forces F_A and F_B are calculated as follows

$$F_A = F \frac{b}{l} \quad \text{and} \quad F_B = F \frac{a}{l}. \quad (3)$$

Modeling of bending stiffness follows the finite segment method, which allows to use only rigid bodies and torsion springs for the whole model as shown in Figure 3b). Note that within the finite segment method, small deformation assumptions of the underlying beam are utilized, but the method could even tackle geometrically nonlinear deformations.

The maximum bending moment of the beam shown in Figure 3a), which is collocated with the point of maximum deflection y_c , is given by

$$M(\phi) = \mathbf{F}_F \cdot \mathbf{e}_{13}^\perp \frac{ab}{l} \quad (4)$$

with

$$\mathbf{F}_F = F \mathbf{e}_{13}^\perp \frac{ab}{l} \quad (5)$$

and the unit vector \mathbf{e}_{13}^\perp perpendicular to \mathbf{e}_{13} . The index gives the direction of the unit vector e.g. from node 1 to node 3, see Figure 3b). In the discrete model Figure 3b), a linearized relation between the deflection y_c and the angle ϕ can be derived. Assuming that the distance $a = b$, the maximum deflection is

$$y_c = \frac{\phi l}{4}. \quad (6)$$

Inserting equation (2) in equation (5) and using equation (6), an according bending stiffness can be derived for the discrete model, see Figure 3b), which is given by

$$M(\phi) = \frac{3EI l}{a^2 b^2} \frac{\phi l}{4} \frac{ab}{l} = \frac{3EI l}{4ab} \phi = c_t \phi. \quad (7)$$

Herein, the torsion stiffness parameter is given by

$$c_t = \frac{3EI l}{4ab}. \quad (8)$$

As our nodal-based model does not include rotations, the angle ϕ_F results from flexible bending as given by the relative displacements of the three nodes, reading

$$\phi_F = \arctan \left(\frac{\mathbf{e}_{12}^\perp \cdot \mathbf{e}_{23}}{\mathbf{e}_{12} \cdot \mathbf{e}_{23}} \right). \quad (9)$$

In order to apply a torque M_F due to (flexible) bending,

$$M_F = c_t \phi_F \quad (10)$$

we apply appropriate forces \mathbf{F}_F , \mathbf{F}_{FA} and \mathbf{F}_{FB} . The force \mathbf{F}_F follows from equation (4),

$$\mathbf{F}_F = M(\phi) \frac{l}{ab} \mathbf{e}_{13}^\perp = c_t \phi_F \frac{l}{ab} \mathbf{e}_{13}^\perp \quad (11)$$

and the forces \mathbf{F}_{FA} and \mathbf{F}_{FB} at the supports are calculated as follows

$$\mathbf{F}_{FA} = \mathbf{F}_F \frac{b}{l} \quad \text{and} \quad \mathbf{F}_{FB} = \mathbf{F}_F \frac{a}{l}. \quad (12)$$

The resulting discrete model is used to approximate the bending effect and is denoted as 'new model' in the experimental results.

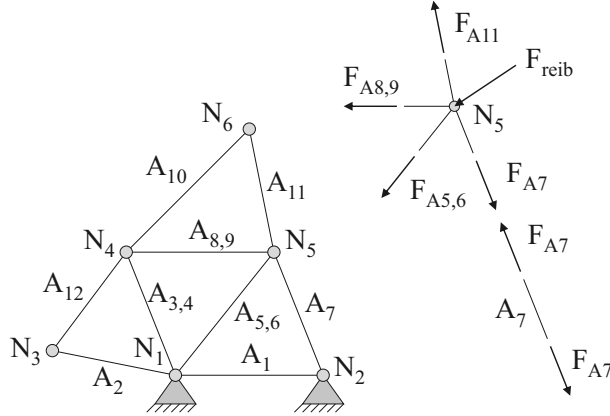


Figure 4: Truss model with friction to represent the edges of the ATC.

3.2 Modeling of positioning errors due to compliance, clearance and friction

In the ATC the parallel six-bar linkage with the two bars DFH and GFE, see Figure 1b), have been identified as components with high compliance and clearance. Clearance is not considered here, because clearance effects will be significantly reduced in the future design with compliant joints. The basic idea of the current truss model with friction is to represent the edges of the ATCs with trusses as shown in Figure 4. Every actuator is represented by means of a truss with stiffness k_A . The friction in this model is based on a spring element and a Coulomb friction element put into series. The values for the simulation are listed in Table 1. For details on the truss model without bending, see [8].

To get an accurate prediction of the positioning error, the current truss model with friction is extended, by modeling every six-bar-linkage with elastic trusses and rods (for bending) as shown in Figure 5a). The modeling of the joints is improved by means of an additional bending related compliance EI in the six-bar-linkages as described above. For the second moment of area I_0 and the area of the C-shaped profile A , the cross-section of the bar CE as shown in Figure 5b) was used. The resulting stiffness parameters of all truss elements, as given in Figure 5b), are listed in Table 1.

4 Laboratory measurements and experiments

Two laboratory scale experiments have been performed. The first experiment with one triangular cell is used to identify the stiffness of a single cell. In particular, the measurements are used to identify the bending stiffness parameter EI for the model as described in Section 3.

The second experiment is carried out with four connected ATCs and detailed measurements are used to validate the model.

4.1 Experiment to identify the bending stiffness parameter

A test bench has been developed, see Figure 6, which allows the precise application of displacements and forces along almost any direction. Within the present setup, one edge is rigidly connected to a ground plate while the opposite vertex of the ATC can freely move on ground.

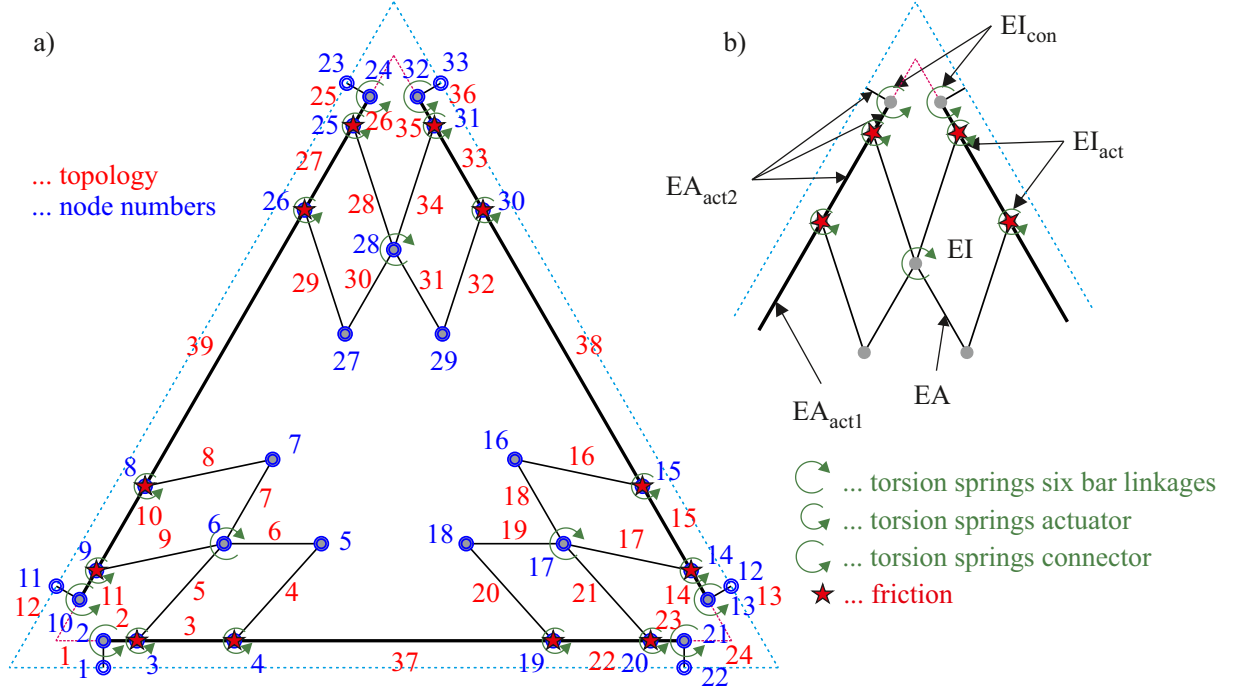


Figure 5: a) Extended truss model with elastic trusses and rods. b) Enlarged representation of one edge.

Table 1: Parameters of the truss model.

parameter	value	unit
actuator stiffness k_A (calibrated)	1.048	N/mm
reference length L_0	229	mm
friction normal force F_N	0.597	N
static friction coefficient (ATC/ground) μ	0.18	–
max. friction force $F_{max} = \mu \cdot F_N$	0.107	N
max. friction spring length d_{max}	2	mm
friction spring constant k_{Fr}	0.054	N/mm
young's modulus VisiJet Navy E	735	N/mm ²
second moment of area of C-shaped profile I_0	84.42	mm ⁴
area of C-shaped profile A	17	mm ²
bending stiffness EI_{act}	$8 \cdot EI$	Nmm ²
bending stiffness EI_{con}	$8 \cdot EI$	Nmm ²
axial stiffness EA_{act1}	$8 \cdot EA$	Nmm ²
axial stiffness EA_{act2}	$8 \cdot EA$	Nmm ²

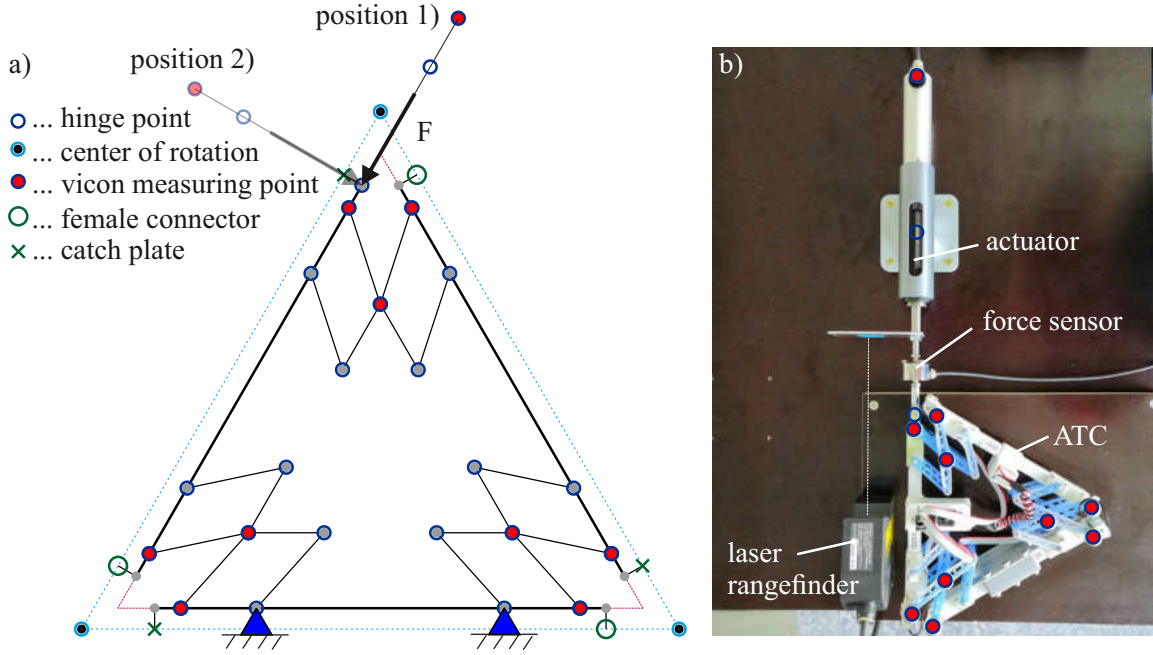


Figure 6: Test bench for measuring force and displacement of an ATC to identify the bending stiffness parameter EI of the model. The actuator is in position 1) in axial direction of the ATC and in position 2) normal to axial direction.

The actuator stroke of the PI 'M-235 High-Resolution Linear Actuator' is prescribed by an according controller with a nominal velocity of 1 mm/s. A force sensor 'U9C' which is attached at the tip of the actuator measures the force along the axis. Note that the center of the actuator can freely rotate using a ball bearing (friction neglected) between the mounting on the base plate and the actuator. The center of gravity of the actuator and the force is carefully balanced such that almost no gravitational force is transferred to the ATC. As the actuator allows no simple synchronization, we measure the actuator displacement with a laser range-finder 'LK-H157'. Two representative orientations of the actuator have been chosen, being the 'axial' direction of the ATC (position 1, tangential to the edge of the ATC) and normal to the first direction (position 2). The diagram of the force path for the two mounting positions is shown in Figure 7a).

Retro-reflective markers were applied to the cells and the relative movements of the markers at given actor strokes were measured with a motion tracking system (Vicon) and compared with the results of the model by an identified force of $f = 14$ N. The location of Vicon measuring points is given in Figure 6a) and also highlighted red in Figure 6b). The error over all Vicon measuring points, which is computed as the distance between measured and computed (model) points, is shown for the two actuator positions in Figure 7b). For model calibration, a factor is used against the nominal bending stiffness EI_0 , which is determined from the material and geometry parameters of the respective arms of the six-bar-linkages. By visual inspection, the optimal bending stiffness parameter is determined as $EI_{opt} = 1.3 EI_0$, which is used in the simulation with the model.

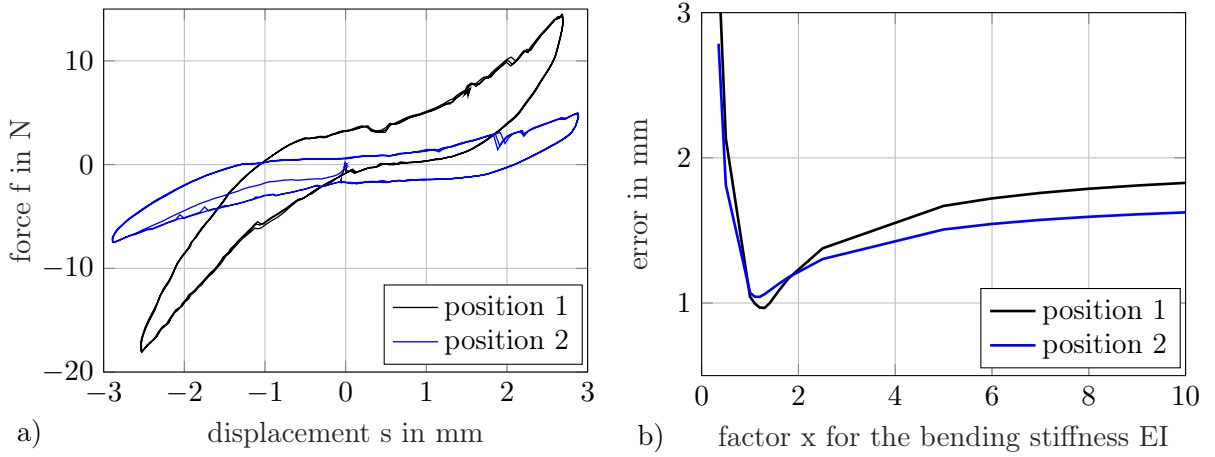


Figure 7: a) Force path diagram for the two measuring positions as shown in Figure 6; b) Error over all measured and calculated points for position 1) (black) and for position 2) (blue).

Table 2: Desired actuator strokes of the first experiment (mm); the strokes are interpolated with 20 mm steps.

step	ATC	act.	stroke	step	ATC	act.	stroke
1)	1	A11	0	4)	1	A11	80
	4	A42	0		4	A42	80
2)	4	A41	80	5)	4	A41	0
3)	1	A13	80	6)	1	A13	0

4.2 Motion tracking experiments

In order to verify the model on a larger scale with four ATCs, the measurement points in Figure 8a) are recorded with the motion tracking system Vicon for every ATC. The desired strokes of the 4 ATC experiment are given in Table 2, which have been prescribed in steps of 20 mm. Figure 8b) shows snapshots of the motion of the real system. The newly developed model is compared against a simpler model [8] in which, however, an adjustment actuator stiffness parameter has been calibrated using the data of the 4 ATC setup itself, while in the present model a reference measurement with one ATC is used. Figure 9b) depicts the distance of the points between measured and desired trajectory and between computed model and desired trajectory. The large deviation between desired (ideal) and real position of point P6 is obviously reduced by the new model. Larger deviations at the beginning of the movement could be attributed to the unknown pre-stress in the system. Concludingly, the model predictions could be used to reduce the positioning errors significantly.

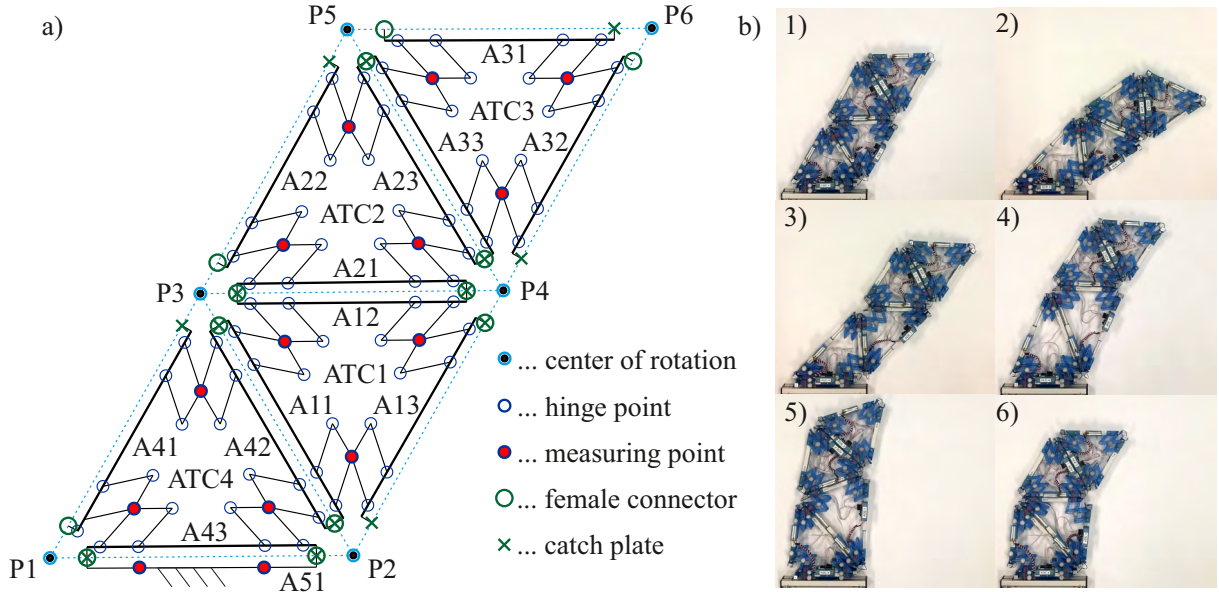


Figure 8: a) Initial position of four ATCs with centre of rotation P1 - P6, parallel six-bar linkages, retroreflective markers (red measuring points), connection mechanism (green) and actuators A11-A51. b) Snapshots of the motion of PARTS for the first experiment, using steps 1) – 6) in Table 2.

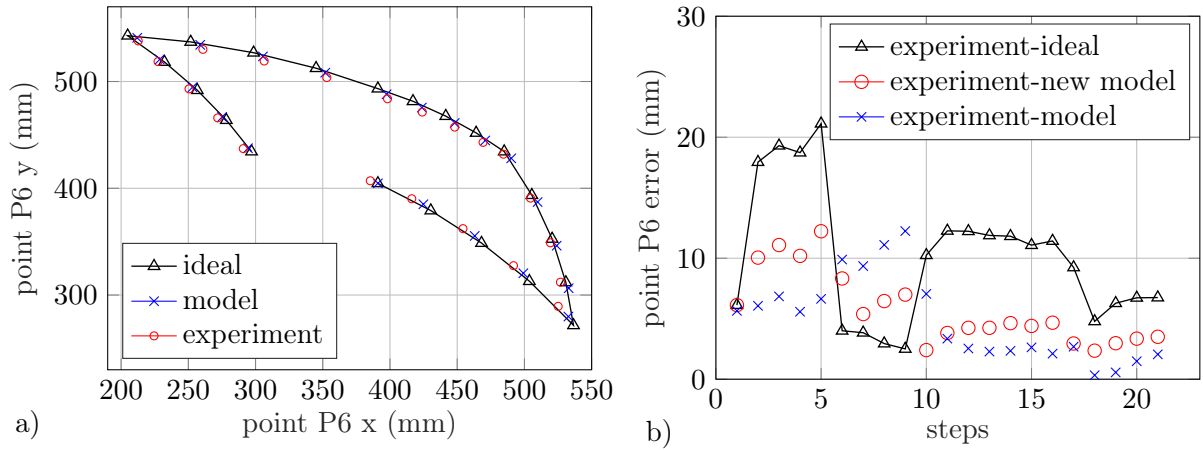


Figure 9: a) Results of the first experiment according to Table 2, showing the desired trajectory, the results of the model and the experiment for the position of P6; b) Evaluation of the position P6 in the first experiment (Table 2), showing the distance between measured (experiment) and desired values as well as between model and desired values.

5 Conclusions

The use of simplified models of the real kinematics of the adaptive self-reconfigurable mechanism delivers the possibility to correct the linear actuators to minimize the positioning errors and to directly set the desired triangular shapes. Furthermore, the laboratory setup opens the possibility to optimize the design and to search for kinematic designs with much higher stiffness. Due to the corrections applied, the general triangular structure based on a given network can be easily programmed, which enables the implementation on an embedded system. A self-reconfiguration algorithm of PARTS is currently under development [11]. At the moment only a static model is considered because motion is slow and dynamic effects are small, which should be extended in further research in order to simulate effects during connection and release. The disruptive potential of the presented adaptive robot is dependent on a realization at the micro-scale, leading to a smart material. Even though such a realization is not expected in the near future, the present approach can be seen as a top-down attempt to obtain a fully programmable matter or a self-healing material.

REFERENCES

- [1] T. Fukuda and S. Nakagawa, “Dynamically reconfigurable robotic system,” *Proceedings. 1988 IEEE International Conference on Robotics and Automation*, pp. 1581–1586, 1988.
- [2] G. Chirikjian, “Kinematics of a metamorphic robotic system,” *Proceedings of the 1994 IEEE International Conference on Robotics and Automation*, pp. 449–455, 1994.
- [3] B. K. An, “EM-Cube: Cube-shaped, self-reconfigurable robots sliding on structure surfaces,” in *Proceedings - IEEE International Conference on Robotics and Automation*, pp. 3149–3155, 2008.
- [4] M. Jorgensen, E. Ostergaard, and H. Lund, “Modular ATRON: modules for a self-reconfigurable robot,” *2004 IEEE/RSJ International Conference on Intelligent Robots and Systems (IROS)*, vol. 2, pp. 2068–2073, 2004.
- [5] A. Brunete, A. Ranganath, S. Segovia, J. P. de Frutos, M. Hernando, and E. Gambao, “Current trends in reconfigurable modular robots design,” *International Journal of Advanced Robotic Systems*, vol. 14, no. 3, pp. 1–21, 2017.
- [6] S. C. Goldstein, S. C. Goldstein, J. D. Campbell, J. D. Campbell, T. C. Mowry, and T. C. Mowry, “Programmable Matter,” *Computer*, vol. 38, no. 6, pp. 99–101, 2005.
- [7] M. Yim, W.-M. Shen, B. Salemi, D. Rus, M. Moll, H. Lipson, and E. Klavins, “Modular Self-reconfigurable Robot Systems: Challenges and Opportunities for the Future,” *IEEE Robotics & Automation Magazine*, vol. 14, no. 1, pp. 43–52, 2007.
- [8] M. Pieber, R. Neurauter, and J. Gerstmayr, “An adaptive robot for building in-plane programmable structures,” *IEEE/RSJ International Conference on Intelligent Robots and Systems*, 2018.

- [9] M. Pieber and J. Gerstmayr, “An adaptive robot with tetrahedral cells,” *The 4th Joint International Conference on Multibody System Dynamics*, pp. 1–15, 2016.
- [10] J. Connelly and R. Huston, “The dynamics of flexible multibody systems: A finite segment approach-I. Theoretical aspects,” *Computers & Structures*, vol. 50, pp. 255–258, jan 1994.
- [11] M. Gerbl, M. Pieber, and J. Gerstmayr, “Reconfiguration of Modular Robots with triangular structure,” *Fifth IFToMM D-A-CH Konferenz 2019*, 2019.

COMBINING OPTIMAL CONTROL AND SHAPE OPTIMIZATION FOR AN ADAPTIVE ENGINEERING STRUCTURE WITH PARAMETERIZED REDUCED ORDER FINITE ELEMENT MODELS

**Benjamin Fröhlich¹, Julia Wagner², Michael Böhm²,
Oliver Sawodny² and Peter Eberhard¹**

¹ Institute of Engineering and Computational Mechanics
University of Stuttgart
Pfaffenwaldring 9, 70569 Stuttgart, Germany
{benjamin.froehlich,peter.eberhard}@itm.uni-stuttgart.de
<http://www.itm.uni-stuttgart.de>

² Institute for System Dynamics
University of Stuttgart
Waldburgstraße 17/19, 70563 Stuttgart, Germany
{julia.wagner,michael.boehm,oliver.sawodny}@isys.uni-stuttgart.de
<http://www.isys.uni-stuttgart.de>

Key words: adaptive engineering structure, moving loads, disturbance compensation, shape optimization, parametric model order reduction

Abstract. This contribution proposes a workflow for simultaneous structural and control design for adaptive engineering structures. It allows to optimize the shape and the control in accordance with each other in order to obtain an overall optimized system. Its main idea is to solve a subordinate optimal control problem in every iteration of a superordinate shape optimization. Additionally, the workflow combines geometrically parameterized finite elements with parametric model order reduction. This allows to conduct the necessary transient simulations during the solution of the optimization problem numerically efficient with models of low order. Next, it enables an efficient sensitivity analysis. An exemplary adaptive engineering structure which diminishes displacements by an actuation is used to illustrate the workflow. In this example, the structure is subjected to a dynamic, moving load. The corresponding actuation is determined by an optimal control law. The objective is to optimize the shape and the control input such that the actuation energy is minimized.

1 INTRODUCTION

The construction sector plays a major role in the worldwide consumption of resources and in the production of emissions, see [9]. In view of limited resources, a decrease of the material consumption and the emissions in the civil engineering sector is, therefore, essential. Adaptive engineering structures are one way to achieve a weight reduction, [11]. It is the idea to combine the actual engineering structure with actuators, sensors, and a control concept to manipulate for example stresses or deformations. Thereby, the load carrying behavior can be improved and a weight reduction of the structure can be achieved.

However, the design of adaptive engineering structures is not a trivial task. It requires to design the structure, the control concept including actuator and sensor placement, see [13], and the control law.

The novel contribution of this paper is a workflow in which both the shape and the control of an adaptive engineering structure are optimized simultaneously. As a result, an adaptive engineering structure is derived in which the shape and the control are optimized in accordance with each other yielding an optimized overall system. Furthermore, the entire simulation and optimization is done using parameterized, reduced order finite element models, see [7]. Including reduced order modeling in the workflow allows very efficient yet accurate reruns of the dynamic, transient simulations and therewith an efficient solution of the simultaneous optimization problem.

This paper is structured as follows. Section 2 describes the adaptive engineering structure used as an illustrative example which is followed by the introduction of the control concept. Simulation results are shown both for the passive and the active structure. Section 3 states the simultaneous shape and control optimization problem and illustrates the proposed optimization workflow. Parametric model order reduction is applied and the optimization problem is solved. The results are interpreted and discussed. The conclusion can be found in Sec. 4.

2 MODELING AND CONTROL OF THE ADAPTIVE ENGINEERING STRUCTURE

This section introduces the adaptive engineering structure which is used as an example in this contribution. The exemplary structure is a simplified model of a bridge. It compensates external loads, for example caused by cars or trains, by an actuation. The structure is first introduced in [12]. For a better understanding, its functionality will be shortly described below.

The structure with material properties and dimensions is illustrated in Fig. 1. The beam-like structure has two supports where the left support constrains displacements in all directions. The right support only constrains displacements in x - and y -direction allowing a horizontal movement of the right support. Two displacement fields, one of the passive, one of the active structure are shown in Fig. 2 for a loading in vertical direction. The passive structure shows clear bending. For the active structure, an actuation force in z -direction is applied at the right support to compensate the bending. It can be seen that the displacement at the loading position is reduced to zero. The displacement along the rest of the structure is also diminished significantly. A more elaborated analysis of this particular adaptive engineering structure including a shape optimization can be found in [7]. However, the authors of [7] only investigate *static* load cases and a *static* compensation. In the following, a *dynamic*, moving load case is considered and transient simulations are conducted. Consequently, the control concept has to be extended to this problem type. First, the governing equations and the modeling of the moving load will be illustrated. Second, an optimal control concept is stated and applied to the structure.

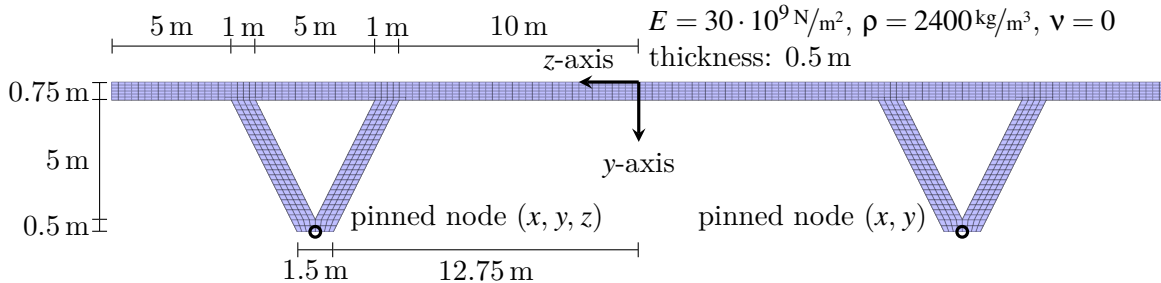


Figure 1: Adaptive structure with pinned nodes (black), the actual element size is two times smaller.

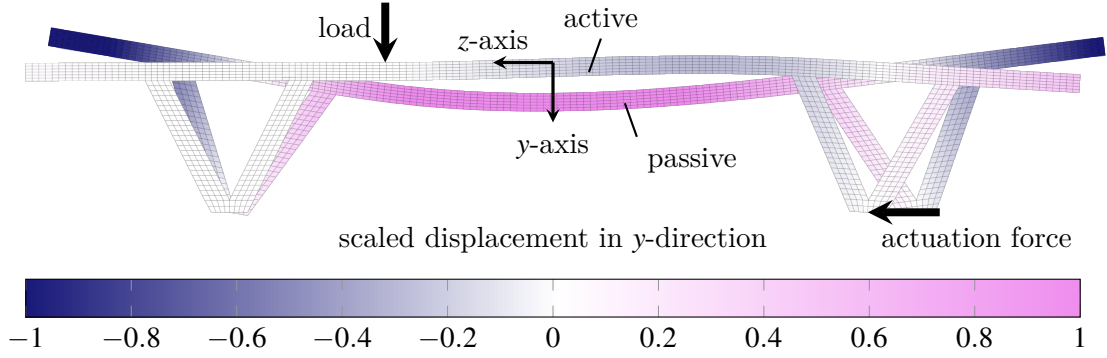


Figure 2: Passive and active structure for an exemplary static loading in y-direction.

2.1 Modeling of the dynamic load case

The structure is discretized with the finite-element-method (FEM), see for example [15], with 5504 hexahedron elements with linear interpolating ansatz functions. This results in a system with 36 200 degrees of freedom. Note that the FEM mesh shown in Figs. 1-2 is a coarse mesh for illustration, the actual mesh size is two times smaller. The dynamic load is modelled as a moving force where its loading position $\eta(t) \in [-21.3\text{ m}, 21.3\text{ m}]$ is a function of time. The load on the structure is written as the product

$$\mathbf{f}_{\text{load}} = \mathbf{e}(\eta(t)) w(t) \quad (1)$$

where the disturbance $w(t) \in \mathbb{R}$ is distributed along the structure with help of the time dependent disturbance input vector $\mathbf{e}(\eta(t))$ as a 1.4 m wide surface load around $\eta(t)$. The control force acting on the right support is written as the product

$$\mathbf{f}_{\text{ctrl}} = \mathbf{b}u(t) \quad (2)$$

with the constant control input vector $\mathbf{b} \in \mathbb{R}^N$ and the control input $u(t) \in \mathbb{R}$. Hence, the governing set of second order differential equations is given as

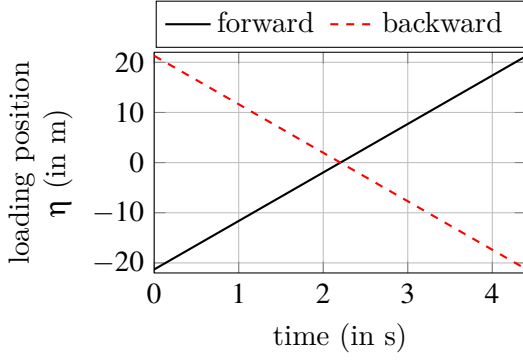
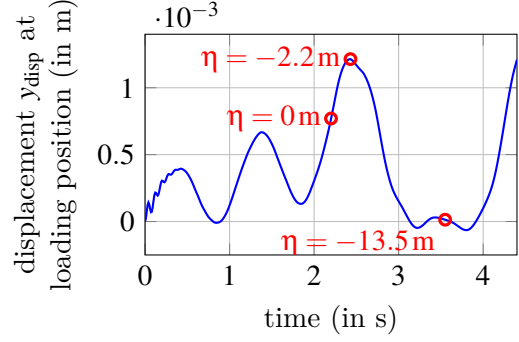
$$\begin{aligned} \mathbf{M}\ddot{\mathbf{q}}(t) + \mathbf{D}\dot{\mathbf{q}}(t) + \mathbf{K}\mathbf{q}(t) &= \mathbf{b}u(t) + \mathbf{e}(\eta(t)) w(t) \\ y_{\text{disp}}(t) &= \mathbf{e}^T(\eta(t)) \mathbf{q}(t) \end{aligned} \quad (3)$$

where $\mathbf{M} \in \mathbb{R}^{N \times N}$, $\mathbf{D} \in \mathbb{R}^{N \times N}$, $\mathbf{K} \in \mathbb{R}^{N \times N}$ are the mass, damping, and stiffness matrix, respectively. The nodal displacements are described by $\mathbf{q} \in \mathbb{R}^N$. Additionally, system (3) includes the system output of interest $y_{\text{disp}}(t)$ describing the displacement in vertical direction at the time dependent loading position $\eta(t)$. In the following, the disturbance force is set to be constant with $w = 1000\text{ kg} \cdot 9.81\text{ m/s}^2 = 9810\text{ N}$. Two loading position trajectories, a forward and a backward trajectory, are considered where both trajectories

$$\eta(t)^{\text{forw,backw}} = \pm 21.3\text{ m} \pm t 9.7\text{ m/s} \quad (4)$$

describe a linear movement with constant velocity, see Fig. 3. The initial conditions are set to zero with $\mathbf{q}(t=0) = \mathbf{0}$ and $\dot{\mathbf{q}}(t=0) = \mathbf{0}$. From now on, the time dependency of $\mathbf{q}(t)$, $u(t)$, $w(t)$, $\eta(t)$ and $y_{\text{disp}}(t)$ will be only written if there is a benefit for the reader.

Solving system (3) in time for the backward loading position trajectory and $u = 0$ yields the displacement y_{disp} of the passive structure, see Fig. 4. The loading position η is marked for some time steps. The displacement y_{disp} increases as the load moves along the structure since the structure becomes more


Figure 3: Trajectories of loading position.

Figure 4: Displacement at loading position for passive structure over time and corresponding z -coordinates of loading position.

flexible for a loading in the center. In the static case, one would expect the maximum displacement for a loading position directly in the center of the structure at $\eta = 0$ m. However, the moving load excites an oscillation such that the maximum displacement of $y_{\text{disp}} \approx 1.21 \cdot 10^{-3}$ m occurs at $t = 2.43$ s at the loading position $\eta = -2.2$ m. Small displacements can be observed when the moving force is acting over the supports, for example at $\eta = 13.5$ m, as the system is stiffer here.

2.2 OPTIMAL CONTROL DESIGN

Assuming the disturbance is known a priori, the input $u(t)$ which minimizes $y_{\text{disp}}(t)$ over the simulation time can be determined by an optimization. In order to do this, system (3) is rewritten in state space notation and discretized in time as

$$\begin{aligned} \mathbf{x}_{k+1} &= \tilde{\mathbf{A}}\mathbf{x}_k + \tilde{\mathbf{b}}u_k + \tilde{\mathbf{e}}_k w_k, \\ y_k &= \tilde{\mathbf{e}}_k^T \mathbf{x}_k \end{aligned} \quad (5)$$

with

$$\tilde{\mathbf{A}} = e^{\mathbf{A}T_s}, \quad \mathbf{A} = \begin{bmatrix} \mathbf{0} & \mathbf{I} \\ -\mathbf{M}^{-1}\mathbf{K} & -\mathbf{M}^{-1}\mathbf{D} \end{bmatrix} \quad (6)$$

and

$$\tilde{\mathbf{e}}_k = \int_0^{T_s} e^{\mathbf{A}(T_s-\tau)} \begin{bmatrix} \mathbf{0} \\ \mathbf{e}(kT_s) \end{bmatrix} d\tau, \quad \tilde{\mathbf{b}} = \int_0^{T_s} e^{\mathbf{A}(T_s-\tau)} \begin{bmatrix} \mathbf{0} \\ \mathbf{b} \end{bmatrix} d\tau. \quad (7)$$

The initial condition is given by $\mathbf{x}_{k=0} = \mathbf{0}$ and the sample time is T_s . The optimization problem can now be formulated as

$$\min J_{\text{ctrl}} = \mathbf{x}_K^T \mathbf{H}_{xx,K} \mathbf{x}_K + \sum_{k=0}^{K-1} \mathbf{x}_k^T \mathbf{H}_{xx,k} \mathbf{x}_k + u_k H_{uu} u_k, \quad \text{subject to system (5)}. \quad (8)$$

Here, K is the number of time steps considered. This means that the time span over which the input u_k is optimized is given by $t_{\text{ctrl}} = KT_s$.

It can be seen that the cost function J_{ctrl} weights and penalizes both the control input u_k and the deviation of the state \mathbf{x}_k from the equilibrium. The weighting matrix H_{uu} is chosen to be constant. In

order to only penalize the displacement at the actual loading position but not the entire state including velocities, the weighting matrix $\mathbf{H}_{xx,k}$ is written as

$$\mathbf{H}_{xx,k} = \tilde{\mathbf{e}}_k H_{xx} \tilde{\mathbf{e}}_k^T \quad (9)$$

such that

$$\mathbf{x}_k^T \mathbf{H}_{xx,k} \mathbf{x}_k = \mathbf{x}_k^T \tilde{\mathbf{e}}_k H_{xx} \tilde{\mathbf{e}}_k^T \mathbf{x}_k = y_{\text{disp},k} H_{xx} y_{\text{disp},k}. \quad (10)$$

The scalar weighting matrix H_{xx} is chosen to be constant, as well. The optimization problem (8) can be analytically solved by backward iteration as depicted in Alg. 1. A more elaborative derivation can be found in [10].

Algorithm 1 Backward iteration

```

1:  $\mathbf{W}_{xx,K} = \mathbf{H}_{xx,K}$ 
2: for  $k = K - 1$  to 0 do
3:    $\mathbf{G}_{xx,k} = \mathbf{H}_{xx,k} + \tilde{\mathbf{A}}^T \mathbf{W}_{xx,k+1} \tilde{\mathbf{A}}$ 
4:    $\mathbf{G}_{xu,k} = \tilde{\mathbf{A}}^T \mathbf{W}_{xx,k+1} \tilde{\mathbf{b}}$ 
5:    $\mathbf{G}_{uu,k} = H_{uu} + \tilde{\mathbf{b}}^T \mathbf{W}_{xx,k+1} \tilde{\mathbf{b}}$ 
6:    $\mathbf{G}_{x,k} = \tilde{\mathbf{A}}^T (\mathbf{W}_{xx,k+1} \tilde{\mathbf{e}}_k w_k + \mathbf{W}_{x,k+1})$ 
7:    $\mathbf{G}_{u,k} = \tilde{\mathbf{b}}^T (\mathbf{W}_{xx,k+1} \tilde{\mathbf{e}}_k w_k + \mathbf{W}_{x,k+1})$ 
8:    $\mathbf{R}_{ux,k} = (\mathbf{G}_{uu,k})^{-1} (\mathbf{G}_{xu,k})^T$ 
9:    $\mathbf{R}_{u,k} = (\mathbf{G}_{uu,k})^{-1} \mathbf{G}_{u,k}$ 
10:   $\mathbf{W}_{xx,k} = \mathbf{G}_{xx,k} - \mathbf{G}_{xu,k} \mathbf{R}_{ux,k}$ 
11:   $\mathbf{W}_{x,k} = \mathbf{G}_{x,k} - \mathbf{G}_{xu,k} \mathbf{R}_{u,k}$ 
12: end for
    
```

The optimal control problem is now solved with Alg. 1. Afterwards, the complete input signal is obtained by forward simulation along with system (5) using the control law $u_k = -\mathbf{R}_{ux,k} \mathbf{x}_k - \mathbf{R}_{u,k}$. The input signal for the backward loading position trajectory is shown in Fig. 5. The corresponding displacement y_{disp} of the controlled structure is illustrated in Fig. 6. The maximum displacement decreases to $y_{\text{disp}} \approx 1.38 \cdot 10^{-4}$ m. The mean displacement over the entire simulation time is also much smaller compared to the mean displacement of the passive structure. The proposed optimal control strategy seems, therefore, to be appropriate for disturbance compensation in this dynamic load case example.

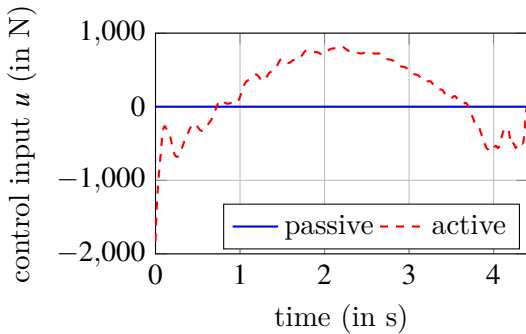


Figure 5: Control input at right support.

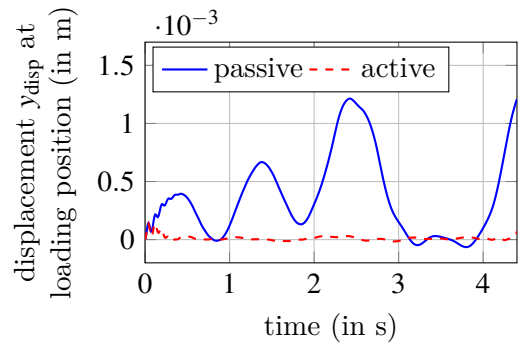


Figure 6: Displacement at loading position for passive and active structure.

3 SIMULTANEOUS CONTROL AND SHAPE DESIGN

This section illustrates the design approach in which the control input and the shape of the adaptive engineering structure are optimized simultaneously. First, the design parameterization and the exemplary optimization problem is stated. Second, parametric model order reduction (PMOR) is applied to enable an efficient computation of the objective function during the optimization. Finally, the simultaneous optimization process will be outlined and numerical results will be shown.

3.1 Formulation of the Optimization Problem

Figure 7 shows the structure where quadratic Bézier curves at the upper part and linear Bézier curves at the supports are added to manipulate its shape. This yields 15 Bézier control points gathered in the parameter vector $\mathbf{p} \in \mathbb{R}^{15}$ which are used to describe the shape parameterization. The objective of this contribution is to optimize the shape of the structure such that the actuator energy for the active control from Sec. 2.2 is minimized. In this particular example, the optimization is conducted for a given loading position trajectory η and a given disturbance w . The actuation energy is both influenced by the control input u and the operating displacement at the right support y_{act} . The latter can be written with the transpose of the control input vector as $y_{\text{act}} = \mathbf{b}^T \mathbf{q}$. The time dependent power output is therefore given as $P(t) = \dot{y}_{\text{act}}(t)u(t)$. It is the goal of this optimization to minimize the integral of the squared power output over the simulation time and thereby to minimize the energy required to run the control. Two loading position trajectories, the forward and the backward trajectory from Fig. 3, are considered to achieve a symmetric load. They are treated in two separate simulations starting with zero initial conditions such that the objective function reads

$$J(\mathbf{p}) = J^{\text{forw}}(\mathbf{p}) + J^{\text{backw}}(\mathbf{p}) = \int_0^{t_{\text{end}}} (\dot{y}_{\text{act}}^{\text{forw}}(t)u^{\text{forw}}(t))^2 dt + \int_0^{t_{\text{end}}} (\dot{y}_{\text{act}}^{\text{backw}}(t)u^{\text{backw}}(t))^2 dt. \quad (11)$$

The optimization problem can therewith be written as

$$\begin{aligned} \min_{\mathbf{p} \in \mathcal{P}} J(\mathbf{p}) &= \min (J^{\text{forw}}(\mathbf{p}) + J^{\text{backw}}(\mathbf{p})) \\ \text{with } \mathcal{P} &:= \{\mathbf{p} \in \mathbb{R}^{15} \mid \mathbf{p}_{\text{lower}} \leq \mathbf{p} \leq \mathbf{p}_{\text{upper}} \mid m(\mathbf{p}) - m(\mathbf{p}_0) \leq 0, c(\mathbf{p}) - c(\mathbf{p}_0) \leq 0\}. \end{aligned} \quad (12)$$

The first nonlinear inequality condition $m(\mathbf{p}) - m(\mathbf{p}_0) \leq 0$ ensures that the mass of the structure $m(\mathbf{p})$ does not exceed the initial mass $m(\mathbf{p}_0)$. The second nonlinear inequality condition $c(\mathbf{p}) - c(\mathbf{p}_0) \leq 0$ guarantees that the mean squared displacement

$$c(\mathbf{p}) = \frac{1}{t_{\text{end}}} \int_0^{t_{\text{end}}} y_{\text{disp}}^2(y) dt \quad (13)$$

at the loading position does not exceed the mean squared displacement at the loading position for the initial geometry. The second inequality $c(\mathbf{p}) - c(\mathbf{p}_0) \leq 0$ is necessary to make sure that the trivial solution with $u(t) = 0$ resulting in a zero actuator energy is excluded from the feasible design space.

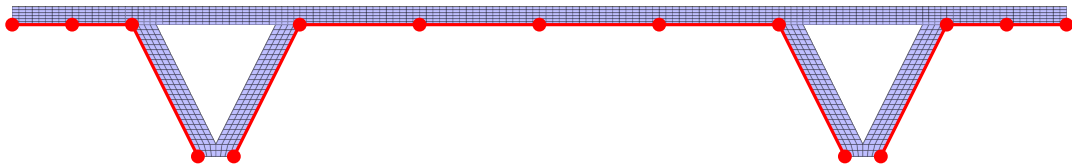


Figure 7: Adaptive structure with Bézier curves (red) and Bézier control points.

3.2 Parametric Model Order Reduction

The shape parameterization introduced in Sec. 3.1 and illustrated in Fig. 7 makes the linear, second order system (3) a linear, *parameter-variant*, second order system

$$\begin{aligned} \mathbf{M}(\mathbf{p})\ddot{\mathbf{q}} + \mathbf{D}(\mathbf{p})\dot{\mathbf{q}} + \mathbf{K}(\mathbf{p})\mathbf{q} &= \mathbf{b}u + \mathbf{e}(\eta)w \\ \mathbf{y} &= [\mathbf{e}(\eta), \mathbf{b}]^T \mathbf{q} \end{aligned} \quad (14)$$

since the system matrices clearly depend on the parameterized geometry. Due to the parameter dependency, the system outputs $\mathbf{y} = [y_{\text{disp}}, y_{\text{act}}]$ implicitly depend on the parameter vector \mathbf{p} as well. This means that the parameter dependent system (14) has to be solved in every iteration of the optimization process. However, the large number of degrees of freedom with $N = 36\,200$ makes the subsequent solution of system (14) numerically expensive. This results in very long and unacceptable computation times to solve the optimization problem.

Parametric model order reduction (PMOR) is an efficient way to overcome this problem. PMOR seeks to replace the parameterized, full order system by a parameterized, reduced order system. For that, the solution is approximated as $\mathbf{q} \approx \mathbf{V}\bar{\mathbf{q}}$ in a lower dimensional subspace \mathcal{V} spanned by the columns of the base $\mathbf{V} \in \mathbb{R}^{N \times n}$ with $n \ll N$, see for example [1, 5]. Inserting the approximation into system (14) and left multiplying with \mathbf{V}^T to perform a Galerkin projection yields the parameterized reduced order system

$$\begin{aligned} \mathbf{V}^T \mathbf{M}(\mathbf{p}) \mathbf{V} \ddot{\bar{\mathbf{q}}} + \mathbf{V}^T \mathbf{D}(\mathbf{p}) \mathbf{V} \dot{\bar{\mathbf{q}}} + \mathbf{V}^T \mathbf{K}(\mathbf{p}) \mathbf{V} \bar{\mathbf{q}} &= \mathbf{V}^T \mathbf{b}u + \mathbf{V}^T \mathbf{e}(\eta)w \\ \bar{\mathbf{y}} &= [\mathbf{e}(\eta), \mathbf{b}]^T \mathbf{V} \bar{\mathbf{q}} \end{aligned} \quad (15)$$

with the reduced system matrices

$$\bar{\mathbf{M}}(\mathbf{p}) = \mathbf{V}^T \mathbf{M}(\mathbf{p}) \mathbf{V}, \quad \bar{\mathbf{D}}(\mathbf{p}) = \mathbf{V}^T \mathbf{D}(\mathbf{p}) \mathbf{V}, \quad \bar{\mathbf{K}}(\mathbf{p}) = \mathbf{V}^T \mathbf{K}(\mathbf{p}) \mathbf{V}, \quad \bar{\mathbf{b}} = \mathbf{V}^T \mathbf{b}, \quad \bar{\mathbf{e}}(\eta) = \mathbf{V}^T \mathbf{e}(\eta).$$

This contribution uses so-called interpolatory projection methods, see [2], to derive the base \mathbf{V} . For that, the transfer behavior from the system inputs to the system outputs of system (14) is described in Laplace domain with the frequency response function

$$\mathbf{H}(s, \mathbf{p}) = [\mathbf{b}, \text{span}(\mathbf{e}(\eta))]^T (s^2 \mathbf{M}(\mathbf{p}) + s \mathbf{D}(\mathbf{p}) + \mathbf{K}(\mathbf{p}))^{-1} [\mathbf{b}, \text{span}(\mathbf{e}(\eta))], \quad (16)$$

where $s \in \mathbb{C}$ denotes the Laplace-variable. Choosing the base

$$\text{span}(\mathbf{V}) = \text{span}([\hat{\sigma}^2 \mathbf{M}(\hat{\mathbf{p}}) + \hat{\sigma} \mathbf{D}(\hat{\mathbf{p}}) + \mathbf{K}(\hat{\mathbf{p}})]^{-1} [\mathbf{b}, \text{span}(\mathbf{e}(\eta))] \mathbf{r}) \quad (17)$$

yields a reduced order system with a reduced order transfer function interpolating the full order transfer function at the frequency expansion point $\hat{\sigma}$ and the parameter expansion point $\hat{\mathbf{p}}$ along the tangential direction \mathbf{r} such that

$$\mathbf{H}(s, \mathbf{p}) \mathbf{r} = \bar{\mathbf{H}}(s, \mathbf{p}) \mathbf{r} \quad \text{for } s = \hat{\sigma}, \quad \mathbf{p} = \hat{\mathbf{p}}. \quad (18)$$

It is also possible to construct a base \mathbf{V} such that the gradient of the reduced order transfer function can be matched to the gradient of the full order transfer function. This property is especially helpful in an optimization context as it allows to preserve sensitivity information in a reduced order model and to conduct a meaningful sensitivity computation with reduced order models. The approximation quality of the parameterized, reduced order model can be further improved by concatenating the result of Eq. (17)

for multiple frequency and parameter expansion tuple $[(\hat{\sigma}_1, \hat{\mathbf{p}}_1), (\hat{\sigma}_2, \hat{\mathbf{p}}_2), \dots]$ in one representative base as

$$\mathbf{V} = \text{span} \left[\left(\hat{\sigma}_1^2 \mathbf{M}(\hat{\mathbf{p}}_1) + \sigma_1 \mathbf{D}(\hat{\mathbf{p}}_1) + \mathbf{K}(\hat{\mathbf{p}}_1) \right)^{-1} [\mathbf{b}, \text{span}(\mathbf{e}(\eta))] \mathbf{r}_1, \right. \\ \left. \left(\hat{\sigma}_2^2 \mathbf{M}(\hat{\mathbf{p}}_2) + \sigma_2 \mathbf{D}(\hat{\mathbf{p}}_2) + \mathbf{K}(\hat{\mathbf{p}}_2) \right)^{-1} [\mathbf{b}, \text{span}(\mathbf{e}(\eta))] \mathbf{r}_2, \dots \right] \quad (19)$$

to ensure interpolation conditions at the tuple $[(\hat{\sigma}_1, \hat{\mathbf{p}}_1), (\hat{\sigma}_2, \hat{\mathbf{p}}_2), \dots]$. The reader is referred to [8, 2, 5, 14, 3] for more details concerning interpolatory projection methods for non-parameterized and parameterized systems. The PMOR in this contribution is done using the MOR-toolbox *Morembs*, see [6].

This contribution uses geometrically parameterized finite elements as presented in [7] for discretization. They allow to derive the system matrices for a parameterized geometry in an affine representation. For example the parameterized, full order stiffness matrix can be explicitly written as

$$\mathbf{K}(\mathbf{p}) = \sum_{m=1}^M \theta_m(\mathbf{p}) \mathbf{K}_m \quad (20)$$

with the scalar weight functions $\theta_m(\mathbf{p})$ and the constant and pre-computable matrices \mathbf{K}_m . Combining the parameterized finite elements from [7] and PMOR has several advantages in an optimization context. Instead of solving the full order system, a reduced order system of much smaller dimension can be solved. Second, the affinely parameterized, reduced system matrices from Eq. (20) can be efficiently evaluated as

$$\tilde{\mathbf{K}}(\mathbf{p}) = \mathbf{V}^T \left(\sum_{m=1}^M \theta_m(\mathbf{p}) \mathbf{K}_m \right) \mathbf{V} = \sum_{m=1}^M \theta_m(\mathbf{p}) \mathbf{V}^T \mathbf{K}_m \mathbf{V} = \sum_{m=1}^M \theta_m(\mathbf{p}) \tilde{\mathbf{K}}_m, \quad (21)$$

where the coefficient matrices $\tilde{\mathbf{K}}_m = \mathbf{V}^T \mathbf{K}_m \mathbf{V}$ are precomputable after the reduction step. Finally, the analytic description of the parameterized system matrices allows to differentiate the system matrices with respect to the parameters and, therefore, enables an efficient sensitivity analysis. In this particular work, 100 frequency and parameter expansion tuples are selected yielding a base with $\mathbf{V} \in \mathbb{R}^{36200 \times 100}$. This means that the parameterized system can be reduced from 36 200 to 100 degrees of freedom.

3.3 Simultaneous Optimization Workflow

The optimal control input signal derived in Sec. 2.2 is based on the system model of the structure in its reference shape described by \mathbf{p}_0 . Hence, it is possible that the input signal $u(t, \mathbf{p}_0)$ is not appropriate to compensate the moving load if the shape of the structure is modified during the iterative solution of the shape optimization problem (12). The control and the shape design should be, therefore, conducted simultaneously.

A possible workflow in which both the control and the shape are optimized is illustrated in Fig. 8. First, the system is modelled to obtain the parameterized, full order system. PMOR is applied to derive the parameterized, reduced order system for which the necessary reruns of the simulation can be performed efficiently during the optimization process. The actual optimization starts with the evaluation of the reduced system matrices for the discrete parameter sample $\tilde{\mathbf{p}}$. The resulting reduced system is used to derive the input signal $u(t, \tilde{\mathbf{p}})$. The controlled system is then simulated to derive $y_{\text{disp}}(t, \tilde{\mathbf{p}})$ and $y_{\text{act}}(t, \tilde{\mathbf{p}})$ and the objective function and the nonlinear inequality conditions are evaluated. The sensitivities are computed using the adjoint variable method, compare [4]. The process is repeated until the optimizer converges. To summarize, the underlying optimal control problem from Eq. (12) is solved in every iteration of the superordinate shape optimization. The control input signal is therefore optimized in accordance with the optimization of the shape yielding an optimized overall system.

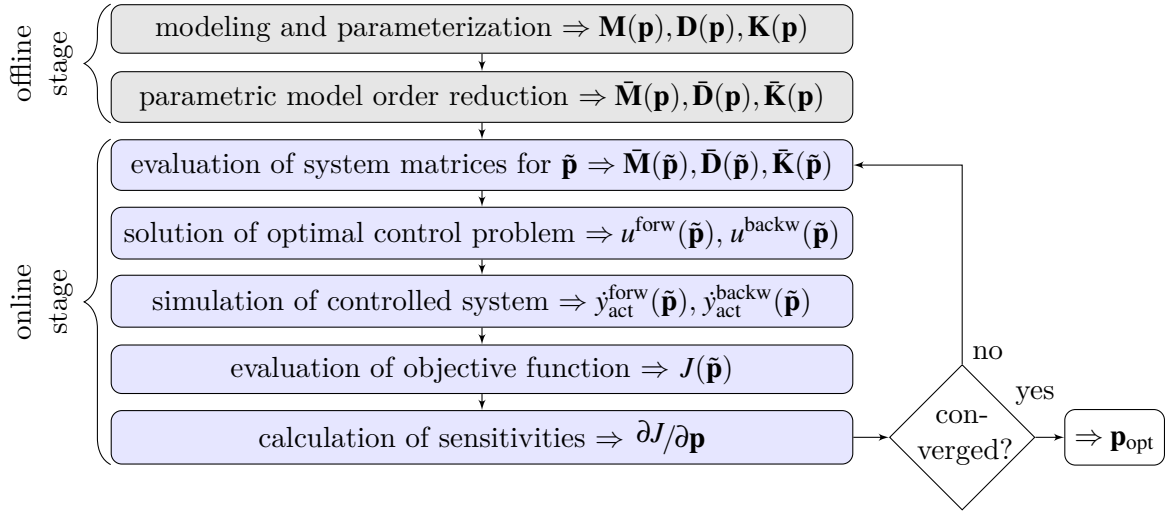


Figure 8: Workflow of simultaneous control and shape optimization.

Note that the workflow in Fig. 8 is separated in two stages. The offline stage (marked grey) covers the model preparation and the reduction. The online stage (marked blue) deals with the actual optimization problem. The computations of the online stage can all be done with the parameterized, reduced order model such that they are numerically cheap to conduct. The computations of the offline part have to be done only once. Therefore, it is possible to re-use the parameterized, reduced order models to solve diverse optimization problems.

3.4 Numerical Results

The optimization problem is now solved according to the previous section with a sequential quadratic programming optimizer. The objective function is $J(\mathbf{p}_0) = 1.06 (\text{Nm})^2/\text{s}$ for the initial design and it is $J(\mathbf{p}_{\text{opt}}) = 0.148 (\text{Nm})^2/\text{s}$ for the optimized design. The corresponding shapes of the structures are shown in Fig. 9. The optimal shape forms a flexible joint in the center. This solid-body like joint allows the structure to act like a kinematic mechanism and to compensate the external disturbances with less activation energy.

The displacements, the optimal control input and the objective function over time are shown in Fig. 10 for the initial and the optimal design for the backward loading position trajectory. In the optimized design, both the mass inequality constraint and the mean displacement inequality constraint are active. The displacements at the loading positions $y_{\text{disp}}^{\text{backw}}$ for the initial and the optimized design show a similar

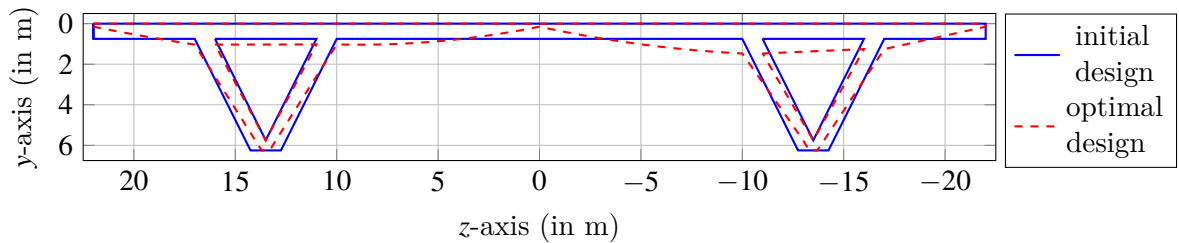


Figure 9: Outer shape of initial and optimal design.

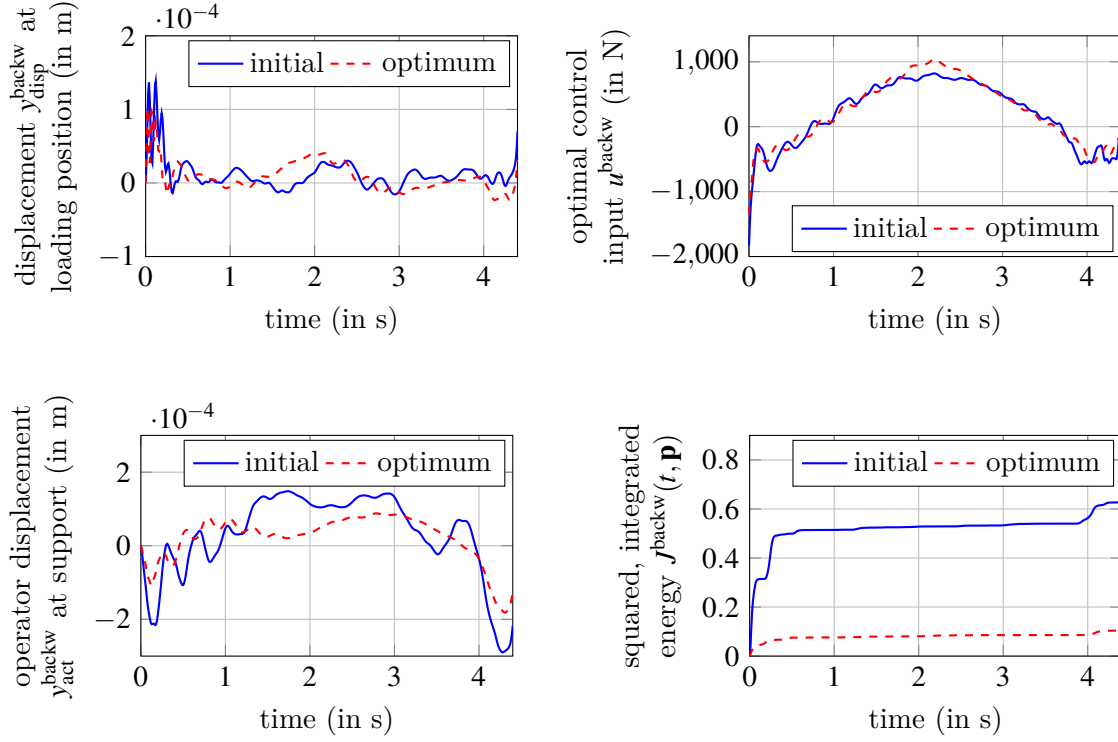


Figure 10: Displacement at loading position and support, control input and objective function over time for initial and optimal design.

behavior confirming that the mean displacement constraint is active. The input signal u^{backw} for the optimized structure shows a similar behavior as for the initial design. In contrast, the required operating displacement $y_{\text{act}}^{\text{backw}}$ is smaller for the optimized design than for the initial design. This is also the reason leading to a much smaller, squared activation energy $J^{\text{backw}}(t, \mathbf{p}) = \int_0^t (\dot{y}_{\text{act}}^{\text{backw}} u^{\text{backw}})^2 dt$.

An interesting fact is that the optimized shape is not symmetric to the y -axis. Instead, the left part of the structure is thinner compared to right part. Conducting the optimization repeatedly for different velocities of the moving load shows that this effect arises less distinct for smaller velocities, see Fig. 11. The smallest velocity of 1.9 m/s describes a more quasi-static load case. Here, the optimal shape becomes almost symmetric to the y -axis. A purely static load case, as in [7], would finally lead to a symmetric optimal shape. It can be shown by investigating the frequency response function, see Fig. 12, that the transfer behavior from the right support to the ends of the structure is indeed symmetric for the static case

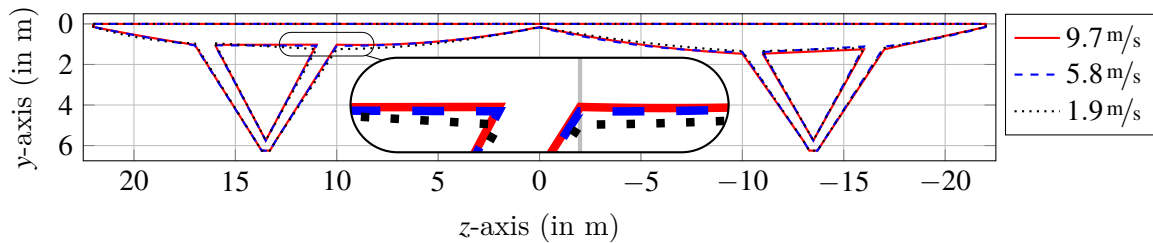


Figure 11: Outer shape of optimized design for different velocities of moving load.

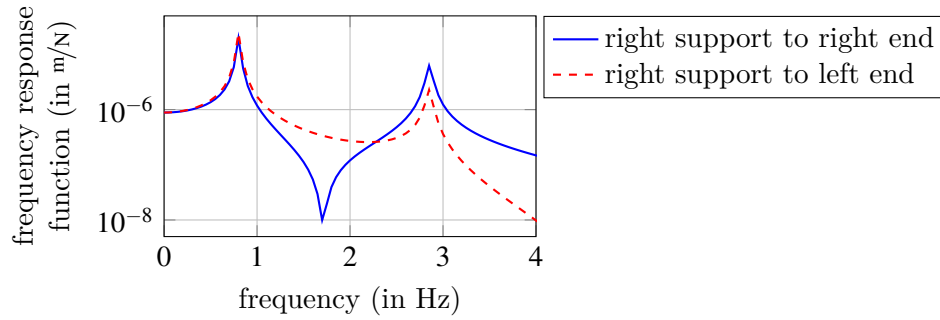


Figure 12: Frequency response function from right support to right and left end of structure.

meaning for a zero exciting frequency. However, for non-zero exciting frequencies the transfer behavior from the right support to the ends of the carrier is not symmetric anymore. This causes the non symmetric optimal shape for the dynamic load case problem.

4 CONCLUSIONS

This article demonstrates the application of adaptive engineering structures as a promising approach to improve the load carrying behavior of classical engineering structures. This is useful for example to save resources or to decrease emissions in the civil engineering sector. To this end, a design approach is suggested supporting engineers in the simultaneous shape and control design for adaptive engineering structures. First, the modeling of a dynamic moving load case for an exemplary structure is described. An optimal control strategy is applied which efficiently compensates the disturbance forces in the dynamic load setup. The optimal control concept is combined with a shape optimization where it is the objective to minimize the actuation energy. For that, an optimization workflow is suggested which both considers the control and the shape design. This is meaningful as it yields an overall system in which the control and the shape are optimized in accordance with each other. Due to the large number of degrees of freedom parametric model order reduction is employed. This allows a significant reduction of the degrees of freedom while retaining the parameter dependency and enables an efficient solution of the optimization problem with reduced order models.

Further research could include the investigation of the robustness of the optimized structure or the simulation of more realistic loading position trajectories and loadings. Furthermore, an interesting topic would be the estimation of unknown loads or unknown loading positions.

ACKNOWLEDGEMENT

The authors gratefully thank the German Research Foundation (DFG) for the support of this research work within the collaborative research center SFB/CRC 1244, "Adaptive Skins and Structures for the Built Environment of Tomorrow" with the projects A06, B01 and B04.

REFERENCES

- [1] ANTOUNAS, A.: Approximation of Large-Scale Dynamical Systems. SIAM, Philadelphia, 2005.
- [2] BAUR, U., BEATTIE, C., BENNER, P., AND GUGERCIN, S.: Interpolatory Projection Methods for Parameterized Model Reduction. SIAM Journal for Scientific Computing 33, pp. 2489–2518, 2009.

- [3] BENNER, P., GUGERCIN, S., AND WILLCOX, K.: A Survey of Projection-Based Model Reduction Methods for Parametric Dynamical Systems. *SIAM Review* 57(4), pp. 483–531, 2015.
- [4] BESTLE, D. AND EBERHARD, P.: Analyzing and Optimizing Multibody Systems. *Mechanics of Structures and Machines* 20, pp. 67–92, 1992.
- [5] FEHR, J.: Automated and Error-controlled Model Reduction in Elastic Multibody Systems. Dissertation, Schriften aus dem Institut für Technische und Numerische Mechanik der Universität Stuttgart, Vol. 21. Shaker Verlag, Aachen, 2011.
- [6] FEHR, J., GRUNERT, D., HOLZWARTH, P., FRÖHLICH, B., WALKER, N., AND EBERHARD, P.: Morembs—A Model Order Reduction Package for Elastic Multibody Systems and Beyond. In Keiper, W., Milde, A., Volkwein, S. (eds.), *Reduced Order Modeling (ROM) for Simulation and Optimization*, Springer Cham, pp. 141–166, 2018.
- [7] FRÖHLICH, B., GADE, J., GEIGER, F., BISCHOFF, M., AND EBERHARD, P.: Geometric Element Parameterization and Parametric Model Order Reduction in Finite Element Based Shape Optimization. *Computational Mechanics* 63(5), pp. 853–868, 2019.
- [8] GUGERCIN, S., ANTOULAS, A., AND BEATTIE, C.: \mathcal{H}_2 Model Reduction for Large-Scale Linear Dynamical Systems. *SIAM Journal on Matrix Analysis and Applications* 30(2), pp. 609–638, 2008.
- [9] OECD: Material Resources, Productivity and the Environment. OECD Publishing, 2015.
- [10] PAPAGEORGIOU, M., LEIBOLD, M. AND BUSS, M.: Optimierung - Statische, dynamische, stochastische Verfahren für die Anwendung (in German). Springer Berlin Heidelberg, 2012.
- [11] SOBEK, W.: Ultraleichtbau (in German). *Stahlbau* 83(11), pp. 784–789, 2014.
- [12] SOBEK, W., TEUFFEL, P., WEILANDT, A., AND LEMAITRE, C.: Adaptive and Lightweight. In *Proceedings of the International Conference on Adaptable Building Structures*, pp. 6–38, 2006.
- [13] WAGNER, J., GADE, J., HEIDINGSFELD, M., GEIGER, F., VON SCHEVEN, M., BÖHM, M., BISCHOFF, M., AND SAWODNY, O.: On Steady-State Disturbance Compensability for Actuator Placement in Adaptive Structures. *at - Automatisierungstechnik* 66, pp. 591–603, 2018.
- [14] WALKER, N., FRÖHLICH, B., AND EBERHARD, P.: Model Order Reduction for Parameter Dependent Substructured Systems using Krylov Subspaces. In *Proceedings of the 9th Vienna Conference on Mathematical Modelling (MATHMOD)*, IFAC-PapersOnLine 51(2), pp. 553–558, 2018.
- [15] ZIENKIEWICZ, O. AND TAYLOR, R.: The Finite Element Method, Vol. 1, 4th ed. McGraw-Hill, London, 1989.

CONDITION HEALTH MONITORING OF A SUSPENSION STRUT CAP/ UPPER STRUT MOUNT USING PIEZOELECTRIC SENSOR FOR ELECTRO-MECHANICAL IMPEDANCE TECHNIQUE

Sumedha Moharana¹ and Vishnu S. A²

¹ Assistant Professor, Department of civil engineering,
Shiv Nadar University, Dadri-201314, Email-sumedha.maharana@snu.edu.in

² Undergraduate Student, Department of civil engineering,
Shiv Nadar University, Dadri-201314, Email- vs558@snu.edu.in

Keywords: Condition Health Monitoring, Structural Health Monitoring, Damage Detection, Suspension strut mount, EMI Technique, FE coupled simulation.

Abstract.

The suspension strut cap is the major component of automobile, which attaches the suspension strut to the vehicle body. In addition, it insulates the tire noise & vibrations from the vehicle for generated due to rough road profile and speed breakers. The suspension cap is mounted at the top of suspension strut, where one side bolts to the vehicle (i.e. cap is directly attached to the body) and the other side to attached to the steering pivots of wheel. So as the vehicle moves and goes over bumps, the up & down impact pushes and pulls at the mount. The caused vibration can be transmitted into the vehicle if routine inspection has not been done and can cause wear and tear in bearing part of the mount (loosening of bolts). The damaged suspension cap can lead to clunking noises, noisy steering, excessive movement, tire alignment etc. Hence, conditional health monitoring of a suspension strut cap is vital in vehicles. For this study, the utilizations of dual sensing mechanism of piezo sensor has made for Structural health monitoring (SHM) technique i.e. Electro-Mechanical Impedance Technique. Different state of damage has been induced by loosening the bolts to different torque range and compared with pristine stage (when bolts are tightened to highest force). The admittance signature are plotted to verify the damage condition raised due self-loosening. The RMSD plots were drawn to quantify the level of damage. Finally the FE coupled simulation has done for the suspension strut mound with surface bonded PZT patch for different damage levels and results are compared with experimental results. The promising results for this study sets a new paradigm for SHM technologies.

1 INTRODUCTION

A Suspension System is essential in an automobile as it provides steering stability and good handling of the vehicle. It also absorbs and counteracts the vibrational forces or shock caused due to the irregularities on the road surface. It consists of a spring which absorbs the energy caused due to the vibration and a strut which consists of a shock absorber (which is a damping

system) to dissipate the absorbed energy. A shock absorber, basically consists of an oil pump which could be either compressed or extended using a piston arrangement. The upper part of the shock absorber is connected the vehicular frame and the lower part is attached the axle, near the wheel. The piston rod of the shock absorber is connected to the upper strut mount through bolt joints, which in turn is connected to the piston, which sits in a tube filled with hydraulic fluid. The Upper Strut Mount used for this study is of the front suspension of MacPherson type, which is the most widely used front suspension system (Earle S. MacPherson in 1947)

Upper Strut mount, also referred to as bearing plate, is an important linking component in the vehicle as it connects the vehicle's suspension system to the body of the vehicle. Strut mounts have to be flexible enough to handle slight angle changes in order to be able to transfer vehicle load to the spring of the suspension system (Huynh et al., 2018). Due to high impulsive loading, brittle failure or small fractures can be observed on the surface of the upper strut mounts. Due to excessive vibrations experienced due the vehicle travelling on a rough road profile, caused the self-loosening of the bolts, which connects the suspension strut to the vehicular body is also termed as a damage criterion for the suspension system. It must be ensured that the bolts remained tightened and maintain the preload conditions (Wang et al., 2013). Also, Failure to replace a worn upper strut mount will cause it to deteriorate very quickly, which will have a knock-on effect to other components, such as the shock absorbers and even the tyres (Huynh et al., 2018).

From the above detailed study, it can be observed that the continuous monitoring of upper strut mount ensure the reduction in maintenance and more passenger safety and comfort. Hence, the authors attempts to monitor the self-lesening effect of bolts on suspension mount for different level lessening state (different torque moment) using piezo sensor for Electro-mechanical impedance technique. For damage quantification statistical interpretation are done. The experimental details and results are discussed in upcoming section.

The process of implementing a damage detection strategy for a civil, mechanical or aerospace infrastructure is known as Structural Health Monitoring (SHM). The damage is defined as changes to the material and/or geometric properties of these systems, including changes to the boundary conditions and system connectivity, which adversely affects the system's performance (Farrar & Worden, 2006). SHM systems are denoted as a reliable system with the ability to detect and interpret adverse changes in a structure due to damage (Kessler et al., 2002). Typically, such a system consists of sensors, actuators, amplifiers and signal conditioning circuit. There are a large variety of methods and evaluation tools used to implement structural health monitoring on a system. (Bhalla, 2004a and 2004b). These methods can be classified as either global or local methods. Global methods study the structure as a whole whereas local methods are used to detect damages in a localized part of the structure. Condition Monitoring is analogous to Structural Health Monitoring, but it addresses to rotating and reciprocating machinery instead of large infrastructures.

2. BASICS OF EMI TECHNIQUE

In general, SHM or damage detection techniques based on the vibration response of the structure can be classified into two categories: model based (which require a model of the structure to start with) and non model based (in which model is not pre requisite). The impedance-based technique belongs to the non model based category. Most of the current work in the impedance based SHM is focused on adapting the EMI technique for application on real world structures. This involves miniaturization of the data acquisition hardware, combination with wireless telemetry and addressing powering issues including energy harvesting techniques.

The basic concept of the EMI technique for SHM is to monitor the integrity of the structure by measuring the electrical admittance via the PZT transducer bonded on the surface of the monitored structure. Because of the direct and the converse piezoelectric effects, any change in the mechanical impedance of the structure caused by damage modifies the electrical admittance of the PZT transducer bonded to it. Usually, the electro-mechanical admittance signature, comprising of the conductance (real part) and the susceptance (imaginary part) is acquired in the healthy condition of the structure and used as the reference baseline for future decisions on structural integrity. Any occurrence of damage on the structure modifies the admittance signature, thereby providing a signal to the end user. Bhalla and Soh (2004a,b) developed a two dimensional piezo-impedance approach based on the concept of effective impedance to model the PZT-structure interaction manifesting active and passive part of coupled admittance signature. Any damage to the structure will cause these characteristics to change and hence changes the structural impedance ($Z_{s,eff}$), which in turn alters the admittance (\bar{Y}) as given by the following expression

$$\bar{Y} = \frac{\bar{I}}{\bar{V}} = G + Bj = 4\omega j \frac{l^2}{h} \left[\frac{\bar{\epsilon}_{33}^T}{\epsilon_{33}^T} - \frac{2d_{31}^2 \bar{Y}^E}{(1-\nu)} + \frac{2d_{31}^2 \bar{Y}^E}{(1-\nu)} \left(\frac{Z_{a,eff}}{Z_{s,eff} + Z_{a,eff}} \right) \left(\frac{\tan kl}{kl} \right) \right] \quad (1)$$

where ω is the angular frequency, l the half-length and h the thickness of the patch, $\bar{\epsilon}_{33}^T = \epsilon_{33}(1 - \delta j)$ the complex piezoelectric permittivity (δ being the dielectric loss factor), $\bar{Y}^E = Y^E(1 + \eta j)$ the complex Young's modulus (η being the mechanical loss factor), $Z_{s,eff}$ and $Z_{a,eff}$ respectively the effective impedances of the structure and the PZT patch and k the wave number. This equation couples the mechanical impedance of the structure with the electrical admittance \bar{Y} , which means that any damage to the structure (change of $Z_{s,eff}$) will reflect itself as change in \bar{Y} . Furthermore, a continuum approach has recently been developed with rigorous inclusion of the bonding effect on the coupled admittance signature (Moharana and Bhalla, 2014, 2015). Recently, the EMI technique has been increasingly tested on civil and mechanical structures (Varadan and Varadan, 2002; Park et al., 2000a, b; Soh et al., 2000; Bhalla, 2001) as well as aerospace structures (Chaudhary et al., 1995; Giurgiutiu, 2000; Giurgiutiu and Zagari, 2002; Ghoshal et al., 2001). Bhalla and Soh (2004a, b) proposed a damage quantification approach, based on identifying the equivalent system parameters from signatures. This approach utilized both real and imaginary components of the signature and paved way for identifying the system parameter from experimental data, enabling parametric damage quantification.

3. EXPERIMENTAL PROCEDURE

A PZT patch is bonded to the surface of the upper strut mount near the bolt connection using high strength epoxy adhesive as shown in Figure 1. The LCR meter is connected to bonded PZT patch. For EMI technique, the PZT patch is excited with 1.41 volt and coupled admittance response has recorded for 30-300kHz through VEE-PRO software.



Fig.1 Experimental set up (a) Suspension strut sample connected to both system and system (b) Digital torque wrench used for loosening bolts

As per the Hyundai specification sheet for suspension strut systems, the upper strut mount nuts have to be fastened by providing torque of 20 Nm for our sample, i.e, the upper strut mount of a Hyundai Accent. So all the nuts were fastened by applying torque of 20 Nm by using a torque wrench and this is considered as the pristine or undamaged state. Five sets of impedance response signatures were recorded by the using the LCR meter to perform the repeatability test of the pristine state. For inducing damages the bolts are loosened to certain torque value as mentioned in Table-1. The coupled admittance signatures were recorded for damaged sates aand compared with pristine values.

Table 1: Different damage level details for the bolt connections.		
Pristine Condition	All bolts tightened to 20 Nm	Intact
Damage Level 1	Bolt 1 $\Delta T = 5$ Nm	Incipient damage
Damage Level 2	Bolt 1 $\Delta T = 10$ Nm	Moderate damage
Damage Level 3	Bolt 1 $\Delta T = 15$ Nm	Severe damage

Statistical quantification methods can be used to detect the changes of the preload in the bolted connections. Two common methods used to quantify damages in the structures or machines are

Correlation Coefficient Deviation (CCD) and Root Mean Square Deviation (RMSD) indices. (Huynh et al., 2018). The CCD can be computed

$$CCD = 1 - \frac{1}{\sigma_Z \sigma_Z^*} E\{[Re(Z(\omega_i) - Re(\bar{Z}))][Re(Z^*(\omega_i) - Re(\bar{Z}^*))]\} \quad (2)$$

where $E[\cdot]$ is the expectation operation; $Z(\omega_i)$ and $Z^*(\omega_i)$ are the impedance responses at the i th frequency value before and after damage, respectively; \bar{Z} and \bar{Z}^* are the mean values of those responses; and σ_Z and σ_Z^* are the standard deviations of the corresponding impedance responses.

The Root Mean Square Deviation (RMSD) index can be computed as

$$RMSD = \sqrt{\sum_{i=1}^n [Z^*(\omega_i) - Z(\omega_i)]^2 / \sum_{i=1}^N [Z(\omega_i)]^2} \quad (5)$$

where n denotes the number of reading

4. RESULTS AND DISCUSSION

For damage identification, conductance signature is more sensitive and widely used for localised SHM techniques. Hence for this study only conductance plot for sensor reading are studied and analysed. The conductance signatures for suspension mount plotted for 30-300 kHz for baseline and damage state (see Fig 2 and Fig 3). The repeatability of sensor signature towards system identification is quite robust, can be seen from Figure 2.

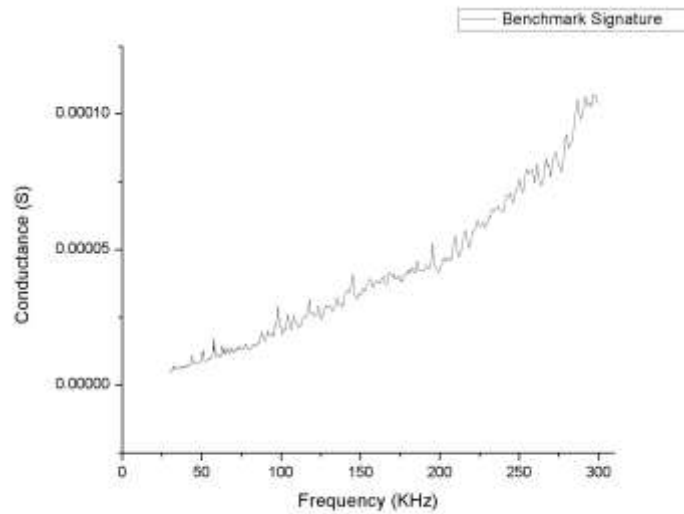


Fig.2 Plot of Conductance versus Frequency in Pristine State

The is shifting resonance peaks and decrease in conductance values in conductance signature of specimen for damage State-3 and State-4, when bolts are loosened to 10Nm and 15Nm torque (see Fig. 3). For better visibility and clarification, closer views of conductance signature for

selective frequency range has plotted in Figure 4. In Figure 4a to 4f, it can be seen that self-loosening effect (loosened to certain torque value) has significantly changed/ shifted the conductance peak values.

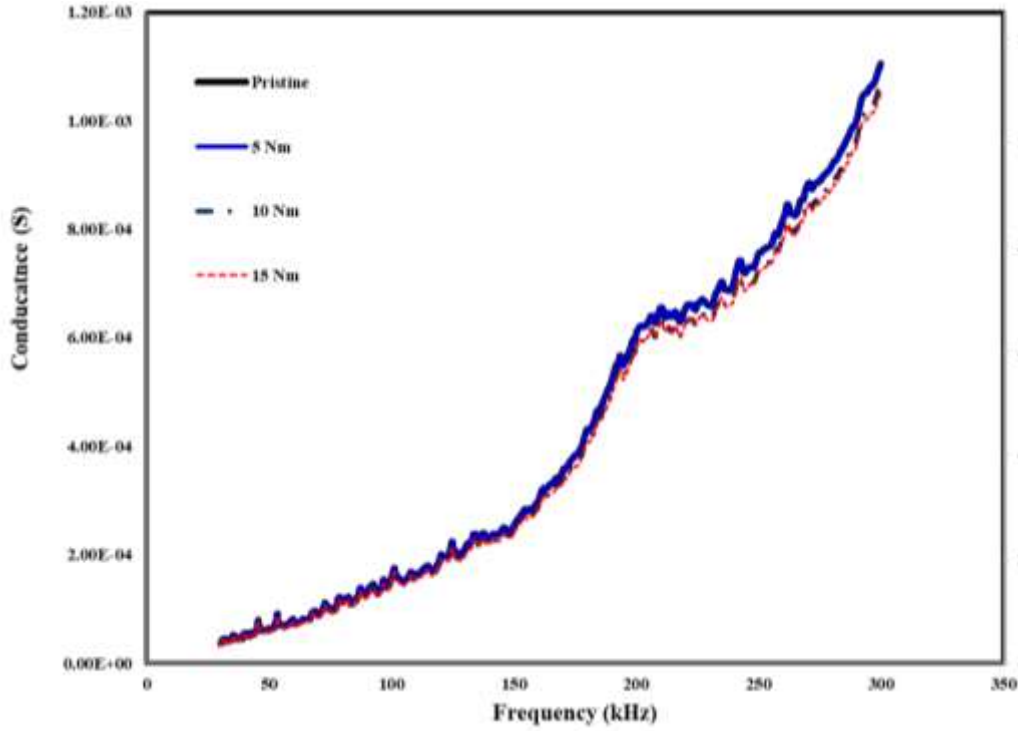
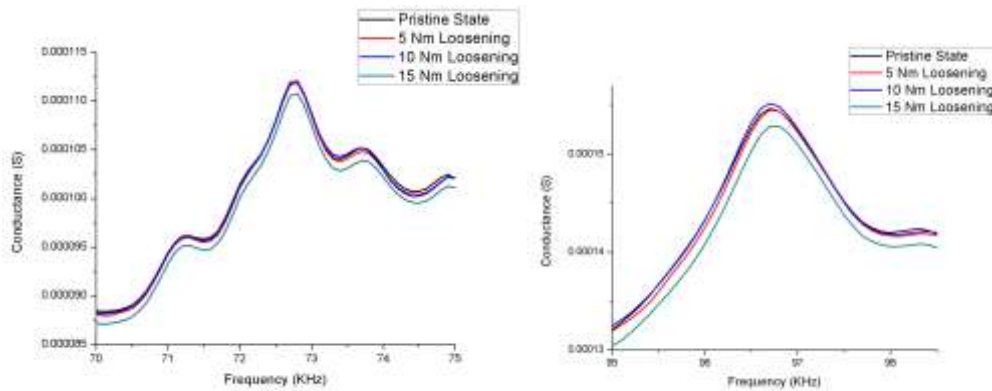
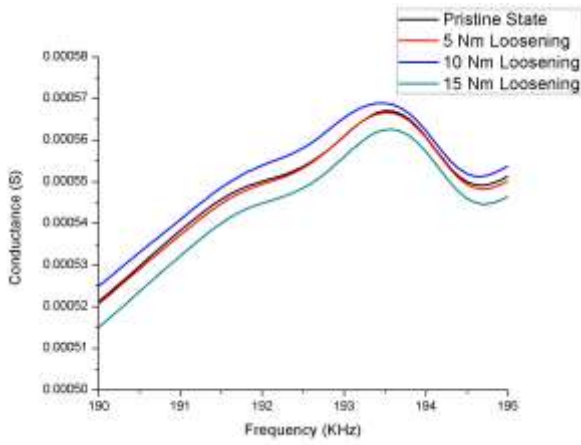


Fig.3 Experimental conductatnce signature (Pristine Vs Damag states)

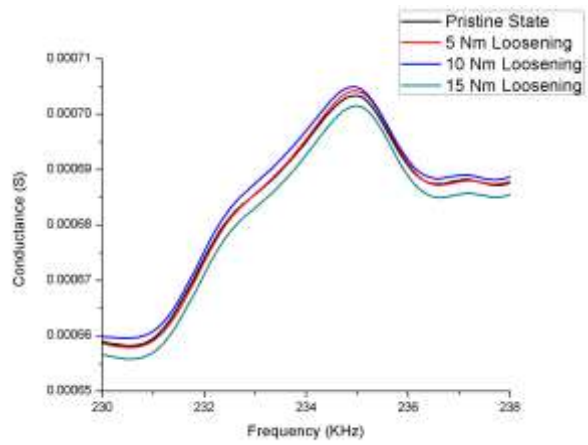


(a) The frequency range of 70-75 kHz

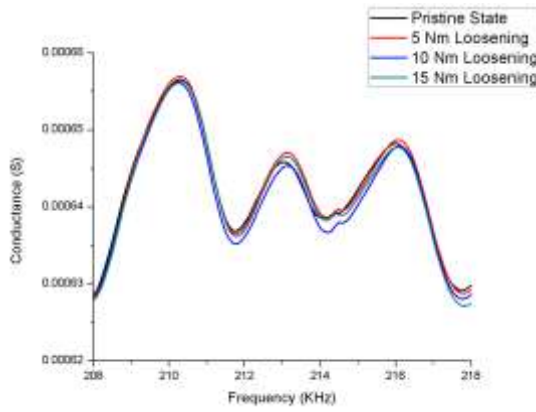
(b) The frequency range of 95-100 kHz



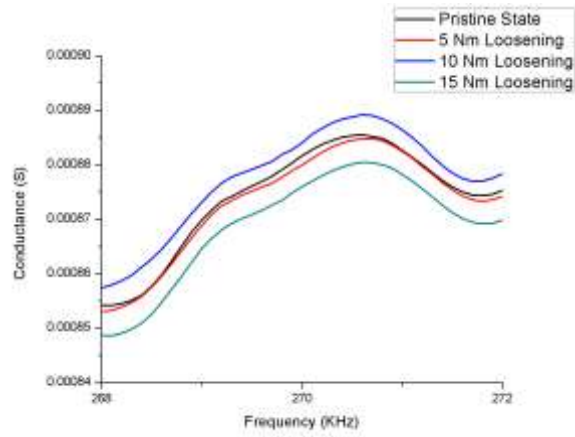
(c) The frequency range of 190-195 kHz



(d) The frequency range of 230-240 kHz



(e) The frequency range of 208-218 kHz



(f) The frequency range of 268-272 kHz

Fig.4 Experimental impedance signatures under bolt-loosening cases obtained from

From Figure 4, it can be concluded that the impedance peaks tend to shift to downwards to the right as bolts are loosened torque values significantly. So, in order to quantify the measured coupled admittance responses, damage-sensitive features were extracted from the impedance data, the correlation coefficient deviation (CCD) and root-mean-square deviation (RMSD) indices. While the CCD index mainly quantifies the frequency shift of the impedance signatures, the RMSD index quantifies both the frequency and magnitude. Figure 5 presents the RMSD and CCD indices that was plotted according to the torque-loss level for all of the loosening cases of Bolt.

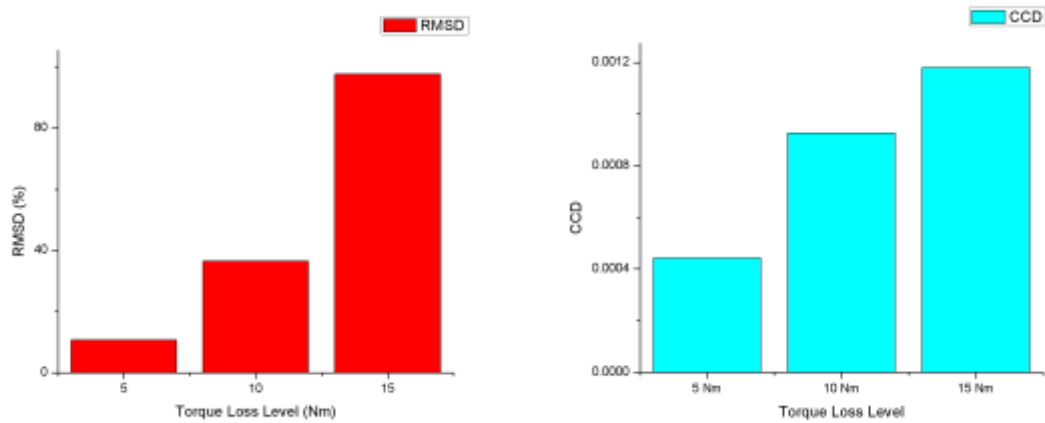


Fig. 5 (a) RMSD Variation for different level of torque loss (b) CCD variation for level of torque loss

The RMSD (%) is plotted against the damage state for clearer understanding of the increasing trend of damage with respect to the preload loss or self-loosening of the bolted connections. The damage progress is plotted against the frequency and the peak conductance value and is shown in Fig.6. We can see that the damage progress is higher at high frequencies and at lower peak conductance values.

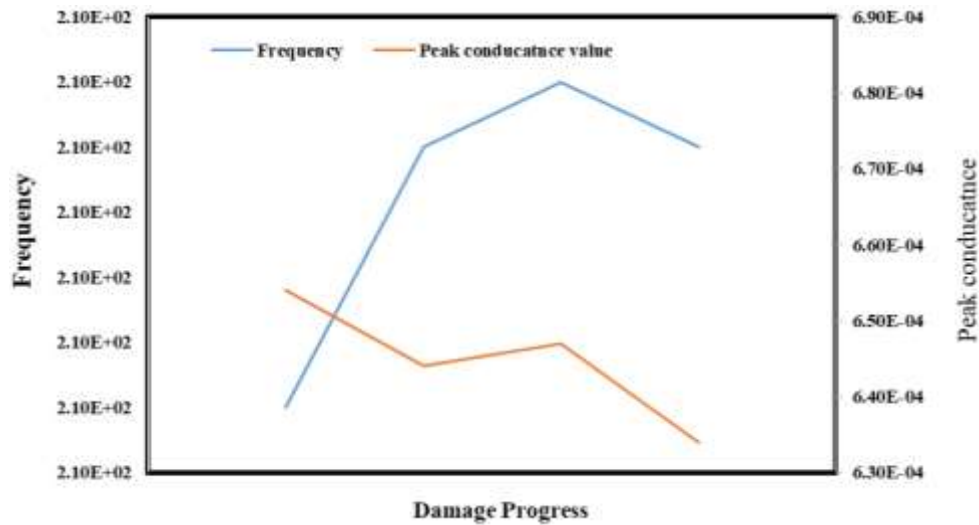


Fig. 6 variation in conductance peak value and frequency with respect to damage progress

6. CONCLUSION

The road roughness leads to excessive vibrations of the suspension system which in turn causes the self-loosening of bolts that connects the suspension strut to the vehicular body through the upper strut mount. This paper comprise the SHM of suspension strut using piezo sensor for the Electro-Mechanical Impedance Technique. The conductance signatures were acquired through impedance analyser for pristine state (tightened to highest torque) and damage state (gradual decrease of torque value for self loosening). The experimental results were compared for both pristine and damaged for comparison and it is found that for increase in loss of torque value there is decrease in conductance peak value and shift in frequency. The statistical quantification of damage has done by evaluation of RMSD and CCD. The results were encouraging and imply with nature of piezo impedance based structural health monitoring.

References

1. Bhalla, S. (2004). A mechanical impedance approach for structural identification, health monitoring and non-destructive evaluation using piezo-impedance transducers (Doctoral dissertation, Nanyang Technological University, School of Civil & Environmental Engineering).
2. Caccese, V., Mewer, R., & Vel, S. S. (2004). Detection of bolt load loss in hybrid composite/metal bolted connections. *Engineering Structures*, 26(7), 895-906.
3. Colombo, D., Gobbi, M., Mastinu, G., & Pennati, M. (2009). Analysis of an unusual McPherson suspension failure. *Engineering Failure Analysis*, 16(3), 1000-1010.
4. Dahil, L. (2017). Effect on the vibration of the suspension system. *Metalurgija*, 56(3-4), 375-378.
5. Dixon, J. C. (2009). *Suspension geometry and computation*. John Wiley & Sons.
6. Farrar, C. R., & Worden, K. (2007). An introduction to structural health monitoring. *Philosophical Transactions: mathematical, physical and engineering sciences*, 303-315.
7. Gillespie, T. D., & Sayers, M. (1981). Role of road roughness in vehicle ride. *Transportation Research Record*, 836, 15-20.
8. Huynh, T. C., Dang, N. L., & Kim, J. T. (2018). Preload Monitoring in Bolted Connection Using Piezoelectric-Based Smart Interface. *Sensors*, 18(9), 2766.
9. ISO 2631-1 (1997) Mechanical vibration and shock—Evaluation of human exposure to whole body vibration—Part 1: General requirements.
10. Jiang, Y., Zhang, M., & Lee, C. H. (2003). A study of early stage self-loosening of bolted joints. *Journal of Mechanical Design*, 125(3), 518-526.
11. Kessler, S. S., Spearing, S. M., Attala, M. J., Cesnik, C. E. S. and Soutis, C. (2002), "Damage Detection in Composite Materials Using Frequency Response Methods", *Composites, Part B: Engineering*, Vol. 33, pp. 87-95.

12. Kjella Ahlin & N.O. Johan Granlund (2002) Relating Road Roughness and Vehicle Speeds to Human Whole-Body Vibration and Exposure Limits, *International Journal of Pavement Engineering*, 3:4, 207-216, DOI: 10.1080/10298430210001701
13. Lengvarský, P., Bocko, J., & Hagara, M. (2013). Modal analysis of titan cantilever beam using ANSYS and SolidWorks. *American Journal of Mechanical Engineering*, 1(7), 271-275.
14. Moharana, S., & Bhalla, S. (2012). Numerical investigations of shear lag effect on PZT-structure interaction: review and application. *Current Science (Bangalore)*, 103(6), 685-696.
15. Park, K., Thomas, N. E., & Wayne Lee, K. (2007). Applicability of the international roughness index as a predictor of asphalt pavement condition. *Journal of Transportation Engineering*, 133(12), 706-709.
16. Sayers, M. W. (1986). The international road roughness experiment: Establishing correlation and a calibration standard for measurements.
17. Wang, T., Song, G., Wang, Z., & Li, Y. (2013). Proof-of-concept study of monitoring bolt connection status using a piezoelectric based active sensing method. *Smart Materials and Structures*, 22(8), 087001. doi:10.1088/0964-1726/22/8/087001
18. Weaver, M. S., Spravsow, D. A., & Carter, R. L. (1994). U.S. Patent No. 5,308,048. Washington, DC: U.S. Patent and Trademark Office.
19. Wollner, A., Lutz, R., & Stautner, R. (2018). U.S. Patent No. 9,969,232. Washington, DC: U.S. Patent and Trademark Office.

DYNAMIC OPTIMAL CONTROL OF ENERGY IN BUILDINGS ADAPTED TO PREDICTIONS OF EXTERNAL FACTORS

Samah Ben Ayed ^{*}, Donghun Kim ^{}, Jeff Borggaard [†] and Eugene Cliff ^{††}**

^{*} Department of Engineering Technology and Surveying Engineering
New Mexico State University
P.O. Box 30001, MSC 3566 Las Cruces, NM 88003
e-mail: benayed@nmsu.edu

^{**} School of Mechanical Engineering
Purdue University
West Lafayette, IN 47907
e-mail: kim1077@purdue.edu

[†] Interdisciplinary Center for Applied Mathematics
Virginia Polytechnic Institute and State University
Wright House West Campus Drive Blacksburg, VA 24061
e-mail: jborggaard@vt.edu

^{††} Interdisciplinary Center for Applied Mathematics
Virginia Polytechnic Institute and State University
Wright House West Campus Drive Blacksburg, VA 24061
e-mail: ecliff@vt.edu

Key words: Smart Buildings, Optimal Control, CFD, Reduced-Order Modeling, Sports Buildings

Abstract. Sports facilities have high energy requirements and therefore, presents a great opportunity for energy savings. In fact, people generate a significant sensible and latent heat because of high activity level and the amount of moisture released through exercising activities and showers. These buildings are more challenging to control because of the specific occupants requirements. In this effort, dynamic control of roof top units subject to external weather predictions is implemented on a case study of a gymnasium. The control model is an an optimal controller based on a reduced order model of CFD simulations of the indoor air, coupled to an envelope model.

1 INTRODUCTION

In 2017, about 40% of total U.S. energy consumption was consumed in residential and commercial buildings [1]. Comprehensive efforts are put in place to optimize the energy use in these buildings. The focus of this paper is on sports facility buildings. This class of buildings features high ventilation rates and cooling power requirements to guarantee the indoor air quality falls within the comfort range of the occupants. Recently, recreational/sports centers have been studied for energy reduction purposes [2, 3, 4, 5].

In sports buildings, adequate control factors like air flow, thermal, and moisture conditions, are crucial since they affect the performance of athletes. These factors are hard to control because of the large spaces. Thus the well-mixed assumption is not realistic because spots may be asymmetric in loading and ventilation. Consequently, a more developed model taking into account the details of the asymmetry in the loads and the provided air is necessary for better control results.

In this work, we investigate the thermal and moisture performance of the HVAC system in a gymnasium for dynamic control purposes. For that, computational Fluid Dynamics (CFD) simulations are performed to capture the thermal fluxes across the building. For that, a linear time-invariant (LTI) model is developed to approximate the input-output behavior observed in computational fluid dynamic (CFD) simulations. Various approaches to couple prediction codes for fluid dynamics and solid conduction have been studied in [6, 7, 8]. Our reduced order model is applied to produce a computationally efficient iterative optimization. Several previous works have used the same method [9, 10, 11].

This modeling approach is now applied to a sports facility where the moisture component is very important. After combining the CFD reduced order model with the envelope model, the Berkeley Library for Optimization Modeling (BLOM) is used to solve the optimization problem of setting the supply RTU temperatures that yield minimum electrical cooling power for the assumed operating conditions. Dynamic control is then implemented to assess the effects of eventual weather variations on the optimal consumed power.

2 CFD MODELING

2.1 Gymnasium geometry and mesh

The gymnasium we studied is located in Knoxville, Tennessee, USA. It is a $30.5\text{ m} \times 22.8\text{ m}$ rectangular area. This open area is cooled using four RTUs, having ceiling-mounted supply vents (at a 6 m height). Each RTU is connected to a wall mounted thermostat placed on the WNW and ESE walls. The short outside wall faces WNW. Other walls of the gymnasium are interior to the building. For the purpose of creating CFD simulations for the space, we define the origin on the floor at the corner of the WNW and NNE walls. 'X' is along the WNW wall, 'Y' is along the NNE wall, and 'Z' is along the ascendant vertical. They are labeled Xmin, Xmax, Ymin and Ymax. For mesh generation, we use the open source software tool, GMSH, developed by C. Geuzaine and J.-F. Remacle [12, 13]. The final geometric configuration of the interior space is described using 310 points, 412 lines, 164 surfaces and 9 volumes. In addition to the three spatial coordinates, each point included a mesh spacing variable that could be used to selectively refine the mesh where needed. The 164 surfaces included the floor, ceiling, and walls but also included a number of internal details such as an elevated track, the entrance doors, 16 diffusers and 4 returns. The final mesh, resulting in approximately 737k tetrahedral cells with 129k vertices (Figure 1), had no cells with worse than a three to one aspect ratio.

2.2 Reduced Order Model

The reduced order model needed for the energy optimization procedure requires the analysis of a specific nominal configuration in which we specify the source terms and the boundary conditions. This nominal configuration is generally chosen based on average operational loads and conditions. The envelope conditions, namely the average wall temperatures, are found from an energy balance taking into account different modes of heat transfer as shown by [7]. The openings to other spaces like the locker and weight rooms are modeled as uniform velocity inlets, with a prescribed temperature and moisture.

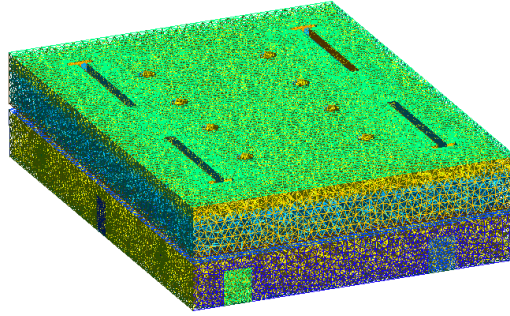


Figure 1: A global view of the mesh

The Ymax wall has two entry doorways. These openings are simulated with a pressure outlet boundary condition and have a prescribed gauge pressure according to the appropriate elevation. Concerning the air supply, each RTU controls two round diffusers of about 0.5 m radius and two 0.6 m x 0.25 m rectangular vents. The air supply from all the round diffusers is at 19.0°C temperature, at 8.0g/kg water vapor mass fraction.

Apart from the boundary conditions specified on the above surfaces, source terms are used to account for the occupants, namely the players on the court and the track, and the audience in the bleachers. The heat source corresponds to that generated by 20 players on the basketball court, 8 supporters on the bleachers, and 2 runners on the track. The occupants' sensible and latent produced loads are adopted from ASHRAE Handbook [14].

The system was subjected to fixed boundary and source conditions chosen to represent a mean condition in the space. FLUENT was run in unsteady mode to simulate more than five hours. Figure 2 shows the mass-averaged temperature over the entire gym space. It proves that the nearly steady state flow is established about half an hour of flow time after the simulation was started. We construct a Linear Time Invariant (LTI) model that approximates the perturbed CFD responses generated by FLUENT simulations as done by [9, 10, 11, 15, 7]. The objective is to reduce the complexity of the CFD simulations to save in computational time, and allow for real-time implementation of a model-based control. The LTI model is written as a first-order state space system in the form

$$\dot{x}(t) = -\frac{1}{\tau}x(t) + bu(t) \quad (1)$$

$$y(t) = Cx(t) + Du(t), \quad (2)$$

The coefficients are obtained through 23 CFD simulations, each one is obtained by assigning a step

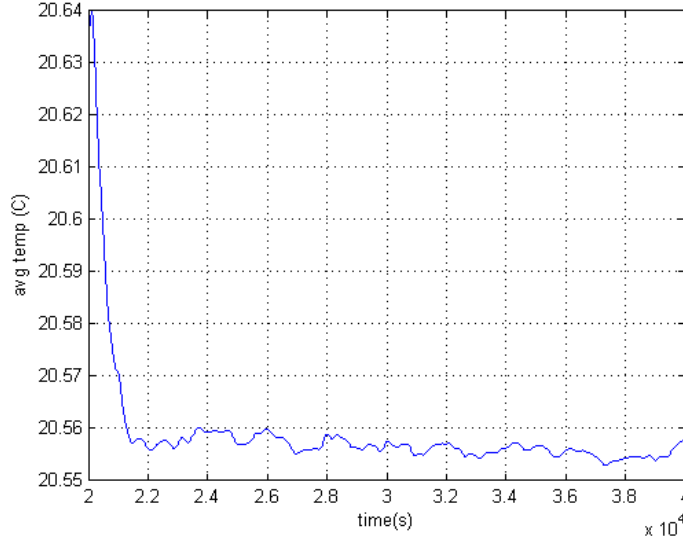


Figure 2: Average temperature

function to the perturbed input. These 23 inputs consist of the wall temperatures, the RTU temperatures, water vapor fraction and mass flow rates, and the occupancy loads. The reactions to these inputs are stored into 44 outputs consisting mainly of the envelope fluxes, the return properties, thermostats temperatures and averaged thermal quantities over different subvolumes. In the state space system, τ and b are respectively the time constant and the scaling factor.

Figure 3 compares the FLUENT data (raw and filtered) to the ROM response. Here the volume averaged temperature of Court 1, which corresponds to the quarter of the court underneath RTU 1, is responding to a 5°C increase in the RTU 1 supply temperature. The first-order ROM response provides a good approximation to the filtered data.

3 DYNAMIC CONTROL

The LTI model developed above is coupled to the dynamics of the envelope model and used to compute the cost function and the comfort constraints (See Figure 4). The coupled model is represented by a single State Space system. For an optimal operation of the facility, we are controlling the RTU supply temperatures $T_{s|i}$ ($i = 1 : 4$). For every other input, we are applying the nominal value to the weather parameters, supply water vapor fractions, supply mass flow rates, and occupancy loads. The model outputs are the return and zone thermodynamic properties in terms of temperature and moisture. Some are required for the cost function and some others are required to formulate the constraints. The cost function is defined as the total power used to run the space cooling under the condition that each of the zones has a set point temperature of 22°C . The cooling power also includes the ventilation load resulting from mixing the recirculated indoor air with sufficient outdoor air 20%.

Then, the total cooling load at each RTU is divided into sensible $Q_{s|i}$ and latent $Q_{l|i}$ loads as shown in the following equations

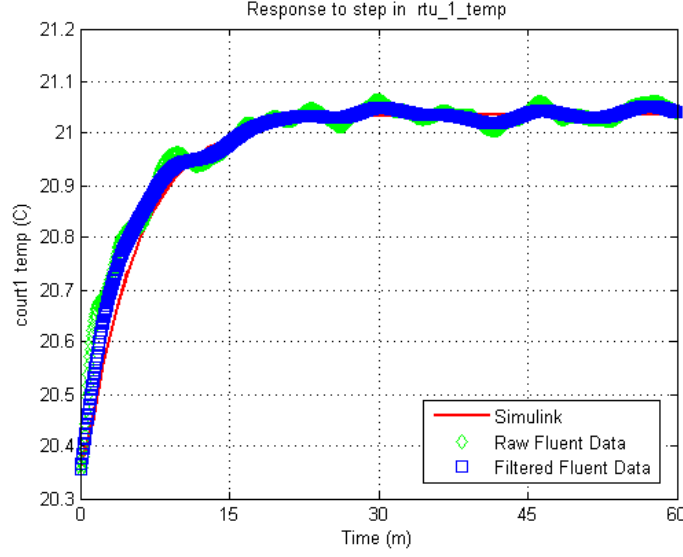


Figure 3: Court 1 temperature response to RTU 1 supply temperature

$$Q_s|_i = C_p \dot{m}_s|_i (T_m|_i - T_s|_i), \quad (3)$$

$$Q_l|_i = L(\dot{m}_r|_i \lambda f_r|_i + \dot{m}_{oa}|_i f_{oa} - f_s \dot{m}_s|_i), \quad (4)$$

$$P_t|_i = \frac{Q_s|_i + Q_l|_i}{cop}. \quad (5)$$

The Berkeley Library for Optimization Modeling BLOM 2.0, which is a MATLAB/SIMULINK based tool, is used to solve the optimization problem over a finite horizon $([0, T])$. Since the tool is restricted to discrete-time dynamics, the continuous state space system is discretized. The optimal control formulation needs to take into account the uncertainties due to the dynamics of the model like the occupants' loads, weather, etc. In this study, the focus is on the external temperature variation. A dynamic control procedure is implemented here. For instance, to launch an optimization at a certain point in time, the weather predictions are updated for the whole time horizon. Naturally, the weather data at a point of time is subject to more error as we approach the end of the time interval. Applying the disturbances to the temperatures in the weather signal: the outdoor air temperature, the ground temperature and the sky air temperature for long wave, and using a maximum error of 10%, we compare two cases. We denote by Method 1, our solution to the optimal control problem for a 12 hour horizon resulting in only one optimization, and by Method 2 an algorithm resulting in a total of 12 optimization problems, and correcting the prediction at each time step. Table 1 shows that the dynamic controller is about 3% more precise in calculating the consumed energy than the optimal controller.

4 CONCLUSIONS

To summarize, a LTI model for the indoor-air is created using Fluent simulations and optimization of model parameters. The interior air model is coupled to the exterior envelope model as an approximation of a Dirichlet-to-Neuman dynamic map. Specifically, the envelope model provides surface temperatures (Dirichlet data) as boundary conditions for the interior fluid dynamics, and the interior-air model provides

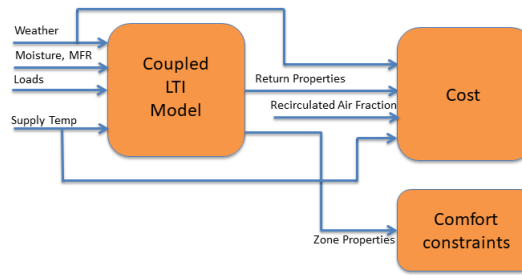


Figure 4: Inputs/Outputs map for control purposes

Table 1: Effects of perturbed weather on total power for a maximum prediction error of 10%.

Weather	error 0	error -10%	error +10%
Method 1 (kJ)	284322	273137	295513
Method 2 (kJ)	284322	283470	285174

resultant wall fluxes (Neuman data) to the envelope. Cooling equipment is also coupled: supply air enters the space at temperature, humidity, flow-rates specified by the equipment (inputs to the indoor-air model) and return air properties are outputs from the model. The output of the reduced-order model is constructed as a nominal steady value plus a perturbation which is realized as a linear time-invariant system. The coupled CFD-ROM/Envelope model is used to study the optimal control problem using BLOM. Dynamic control is also implemented to assess the effects of inaccuracies in weather forecasts.

REFERENCES

- [1] Independent Statistics and Analysis, U.S. Energy Information Administration website.
- [2] M. Schmidt, A. Schlke, A. Venturi, and R. Kurpatov, Predictability of energy characteristics for cooling, ventilation and heating systems in sports facilities, Proceedings of Innovative Smart Grid Technologies Conference (ISGT), IEEE Power and Energy Society, 2015.
- [3] G.M. Revel and M. Arnesano, Measuring overall thermal comfort to balance energy use in sports facilities, Measurement 55, pp 382393, 2014.
- [4] G.M. Revel and M. Arnesano, Perception of the thermal environment in sports facilities through subjective approach, Building and Environment 77, pp 1219, 2014.

- [5] M. Arnesano, G.M. Revel and F. Seri, A tool for the optimal sensor placement to optimize temperature monitoring in large sports spaces, *Automation in Construction* 68, pp 223-234, 2016
- [6] J. Srebric, Q. Chen, Glicksman LG. A coupled airflow-and-energy simulation program for indoor thermal environmental studies. *ASHRAE Transactions* 2000; 106(1): 465-476.
- [7] S. Ben Ayed, D. Kim, J.T. Borggaard and E.M. Cliff, Optimal control of indoor-air cooling in buildings using a reduced order model, *Energy*, 116(1), pp 1191-1204, 2016.
- [8] Z. Zhai, Q. Chen, P. Hayes, and J. Klems. On approaches to couple energy simulations and computational fluid dynamics programs. *Building and Environment* 2000; 37: 857-864.
- [9] J. Borggaard, E. Cliff, and S. Gugercin. Model reduction for indoor-air behavior in control design for energy-efficient buildings. *Proceedings of 2012 ACC* 2012.
- [10] S. Gugercin, A. C. Antoulas, and C. A. Beattie, \mathcal{H}_2 model reduction for large-scale linear dynamical systems. *SIAM J. on Matrix Analysis* 2008;30:609-638
- [11] S. Y. Kung. A new identification and model reduction algorithm via singular value decomposition. *Proc. 12th Asilomar Conf. Circuits, Syst. Comput* 1978.
- [12] C. Geuzaine and J. F. Remacle. Gmsh: a three-dimensional finite element mesh generator with built-in pre- and post-processing facilities. *International Journal for Numerical Methods in Engineering* 79(11), pp. 1309-1331, 2009.
- [13] C. Geuzaine and J.-F. Remacle. *Gmsh Reference Manual for Gmsh 2.8*, 2013.
- [14] 2014 ASHRAE Handbook
- [15] A.J. Mayo and A.C. Antoulas, A framework for the solution of the generalized realization problem, *Linear Algebra and Applications*, pp 634-662, 2007.

EXPERIMENTAL TESTING OF A SMALL-SCALE TRUSS BEAM THAT ADAPTS TO LOADS THROUGH LARGE SHAPE CHANGES

ARKA P. REKSOWARDOJO*, GENNARO SENATORE, IAN F.C. SMITH

Applied Computing and Mechanics Laboratory (IMAC), School of Architecture, Civil and Environmental Engineering (ENAC), Swiss Federal Institute of Technology (EPFL), CH-1015 Lausanne, Switzerland

*e-mail: arka.reksowardojo@epfl.ch

Key words: Adaptive structures, shape control, actuator placement optimization, non-linear force method, structural sensing, structural optimization

Abstract. Adaptive structures can modify their shape and internal forces through sensing and actuation in order to maintain optimal performance under changing actions. Substantial whole-life energy can be saved with respect to traditional passive designs through well-conceived adaptive design strategies; the whole-life energy comprises an embodied part in the material and an operational part for structural adaptation. Controlled large shape changes allows a significant stress redistribution so that the design is not governed by rare and extreme loadings. A design process based on optimization of the structural geometry and actuator placement has been formulated. A method that considers geometric nonlinearity is employed for shape and force control. Experimental testing on a small-scale prototype adaptive structure produced by this design process is presented. The structure is a planar truss. Shape adaptation is achieved through controlled length changes of turnbuckles that replace some of the elements. Stress redistribution through shape adaptation is in good accordance with numerical values, with a minimum Pearson correlation coefficient of 0.86. Results show that stress homogenization through controlled large shape changes is feasible.

1 INTRODUCTION

Civil structures are designed to meet strength and deformation criteria for extreme and thus rarely occurring loads. Consequently, the structural capacity is not fully utilized for most of the service life of the structure. If the structure can counteract the effect of loads through active control, it can be designed to maintain optimal performance as the external load changes [1]. The potential of using adaptation to design structures with a better material utilization has been investigated [2, 3]. A new design criterion for adaptive structures has been introduced [4], which is ‘whole-life’ energy comprising a part embodied in the material and another part for adaptation. Through the methods formulated in [4], it was shown that adaptive structures are more energy efficient than conventional structures. Instead of relying on passive resistance provided by material and form, strategically placed actuators change the shape and internal forces at the occurrence of strong loadings. This way, material embodied energy is reduced at the cost of a small increase in control operational energy. Whole-life energy savings as high as 70% have been achieved for slender structures [5, 6].

Shape optimization is usually employed to optimize the geometry of structures under worst case loadings [7, 8]. When applied to reticular structures, shape optimization can lead to large modifications of nodal coordinates, so that the internal forces are altered significantly [9]. From this process, shapes resembling arch, catenary and lenticular configurations were found to be efficient in terms of material utilization [7]. However, the geometry obtained through these methods is fixed, the structural capacity is only partially utilized under peak demands.

Shape control involving large shape changes has been studied for deployable and tensegrity structures [10, 11]. In this context, however, large shape changes have been achieved through mechanisms based on moving parts. This often results in increased weight of the joints and control complexity [12]. Shape control of reticular structures, which relies mostly on flexibility, has received little attention both theoretically and experimentally. Shape and force control of a reticular adaptive structure has been successfully tested in [13]; however, geometric nonlinearity was not accounted for. Formulations of geometrically non-linear shape and force control exist [14], nonetheless experimental validation is still lacking.

The efficacy of structural adaptation through large shape changes has been studied numerically [15]; a substantial embodied energy savings with respect to structures that are able to adapt through small shape changes was shown to be possible. Though large geometry reconfiguration, the internal forces can be redistributed effectively and thus, the design is not governed by extreme loading. This paper gives details of the experimental testing of a small-scale prototype adaptive structure produced by the methods formulated in [15]. Shape control is achieved through length changes of turnbuckles that replace some of the structural elements. Element stress and nodal displacements are monitored through strain sensors and optimal tracking respectively. Results will inform future research on larger scale adaptive structures.

2 DESIGN METHOD

The design method consists of two parts: (1) optimization of the geometry, internal forces and element cross-section areas to minimize the embodied energy, (2) optimal actuator placement to control the structure into the shapes obtained in (1) through quasi-static, nonlinear geometric shape and force control. The design process is formulated for reticular structures and this study deals only with such structures. Linear actuators are integrated into the structure by replacing selected elements. Figure 1 gives a schematic flowchart of the design process.

The first step of the design process can be thought of as a mapping between external load and target shapes as well as internal forces that are optimized to minimize the embodied energy of the structure. This process is subject to force equilibrium and stress constraints including element buckling. The design variables include the element cross-section areas, which remain constant during control; as well as optimal forces and target shapes for each load case.

The second step of the design process is to obtain an actuator layout that is optimal to control the structure into the target shapes. This is a combinatorial problem and thus, when the number of structural elements is large, a full enumeration is impossible. Instead, optimal actuator placement is carried out using constrained simulated annealing (CSA) [16]. A heuristic based on a measure of efficacy for each element to contribute towards the attainment of the optimal shapes via its length changes [4] is employed to generate the initial candidate solution and to define the neighborhood structure i.e. the set of feasible solutions ‘close’ to the current solution.

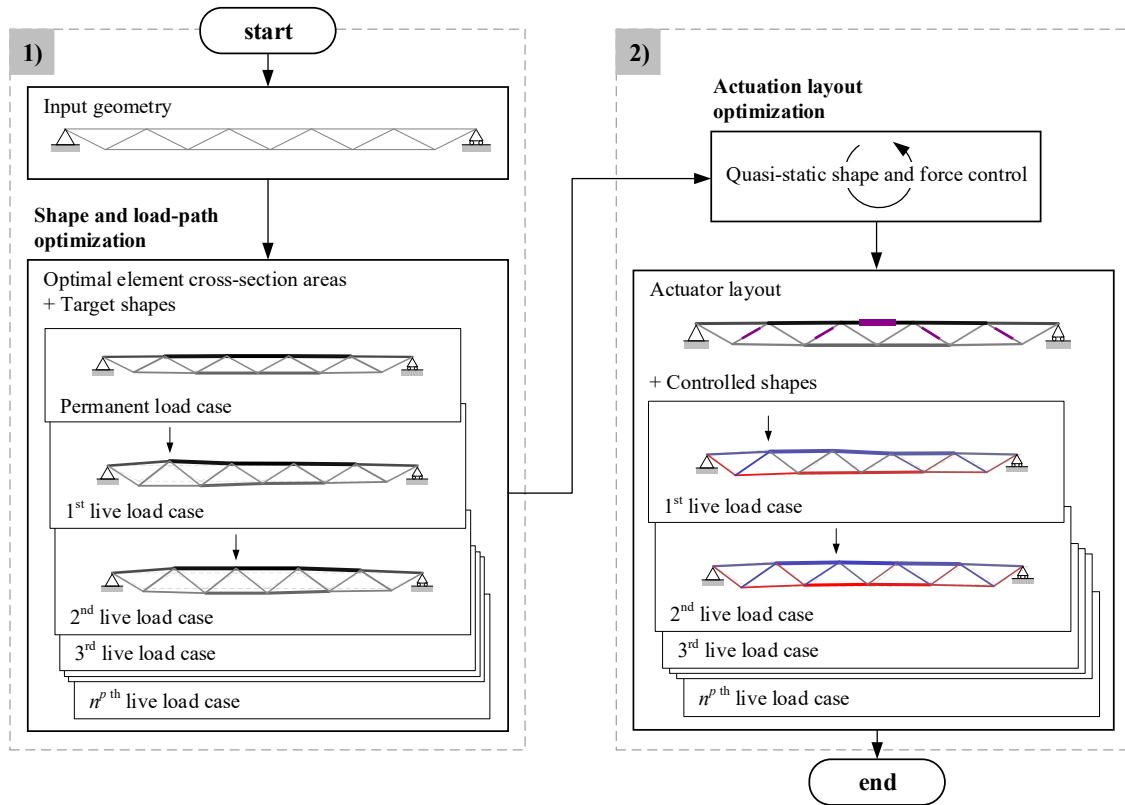


Figure 1: Design method flowchart

The structure has to be controlled through control commands that cause a change of internal forces and nodal displacements which approximate the target ones. Because shape adaptation does not rely on mechanisms with defined kinematics, there are generally infinite solutions to approximate a required shape change through element length changes. A possible strategy is to find the minimum actuator length changes that deform the structure into a required shape. Since large shape changes modify equilibrium conditions, control commands must be computed through an iterative scheme. In this work, shape and force control are implemented using a geometric non-linear force method based on singular value decomposition of the equilibrium matrix [14, 17].

3 NUMERICAL CASE STUDY

The prototype structure tested in this study is a planar simply-supported truss beam which is shown in Figure 2. The truss is thought of as part of a roof system whose lateral stability is assumed to be provided by other means. The structure has a span of 1000 mm and a 20:1 span-to-depth ratio. It consists of 19 elements connected through 11 nodes. All elements have a circular section and are made of aluminum with a Young's modulus of 72.4 GPa.

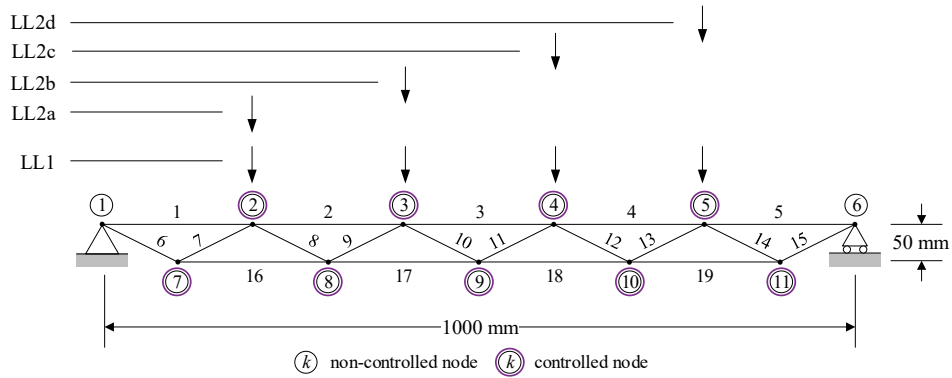


Figure 2: Planar-truss beam

Due to the small scale of this structure, its self-weight is negligible. Two live loads (LL) are considered: (1) a uniformly distributed load of 10 N applied on all top chord nodes (LL1); (2) a moving load of 20 N applied on each node of the top chord in turn (LL2a–LL2d). All nodes except the supports can shift vertically within ± 15 mm. The lower bound for the element radius is set to 1 mm. The first step of the method outlined in Section 2 produces a structure whose embodied energy is reduced by 17% compared to an identical weight-optimized passive structure.

A low number of actuators is generally preferred to reduce monetary cost and control complexity. A minimum number of actuators is determined by applying sequentially the layout optimization process (outlined in Section 2); each time decreasing the number of actuators until no feasible solution can be obtained. Figure 3 shows the layouts obtained for 19, 14, 10, 7, 5 and 4 actuators. No feasible solution (ULS satisfied) can be found for layouts made of less than 5 actuators. The layout shown in Figure 3f is an infeasible solution for 4 actuators; the maximum element demand/capacity ratio is 1.26. With 5 actuators the maximum element demand/capacity ratio is 0.83, and thus this layout was chosen as the optimal actuator layout (Figure 3e). This solution was obtained after 413 iterations at an average of 651 seconds. The global optimality has been verified through a full enumeration (11628 candidate solutions) which has taken approximately 5 hours on an Intel Core i7, 3.60 GHz.

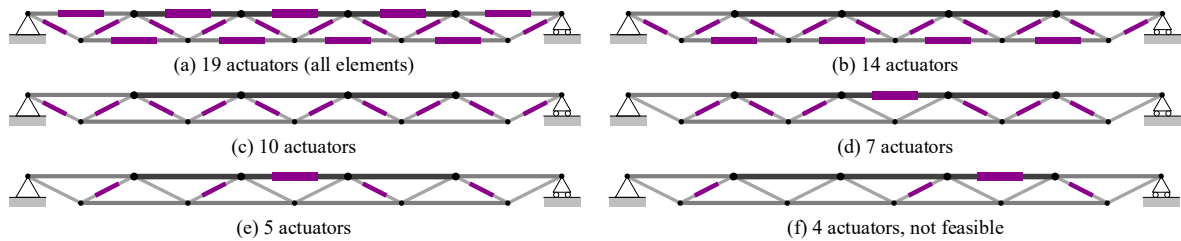


Figure 3: Optimal actuator layouts for 19, 14, 10, 7, 5 and 4 actuators

The optimal shapes obtained in the first part of the design process are shown in Figure 4a. Figure 4b shows the controlled shapes with the element stress mapped onto the geometry. Optimal shapes and controlled shapes are very similar but not identical. There is a maximum distance of 11.8 mm for node 8 between target and controlled shape under LL2b.

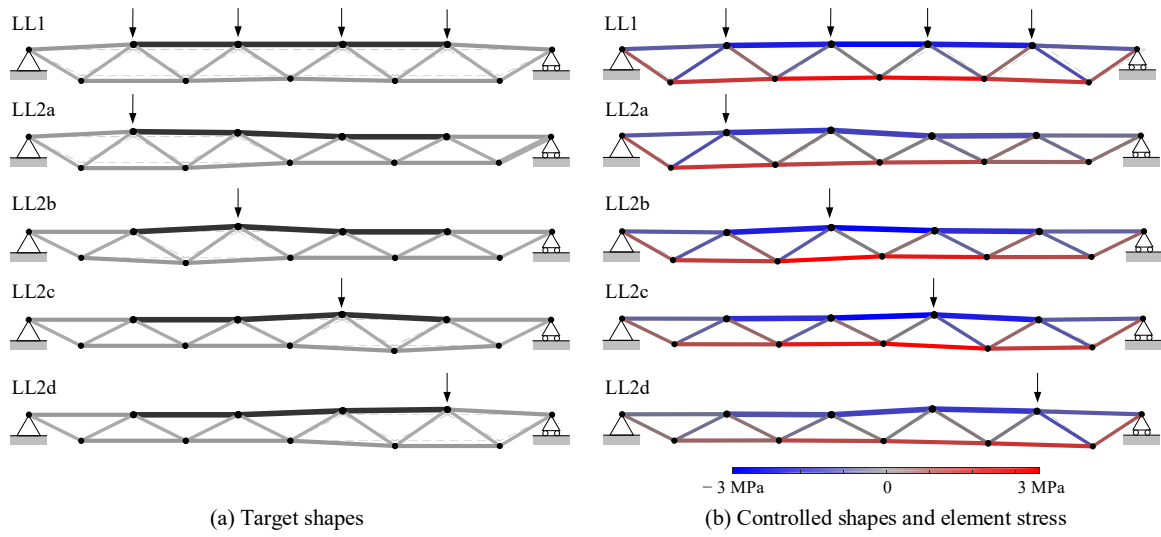


Figure 4: Optimal shapes and controlled shapes

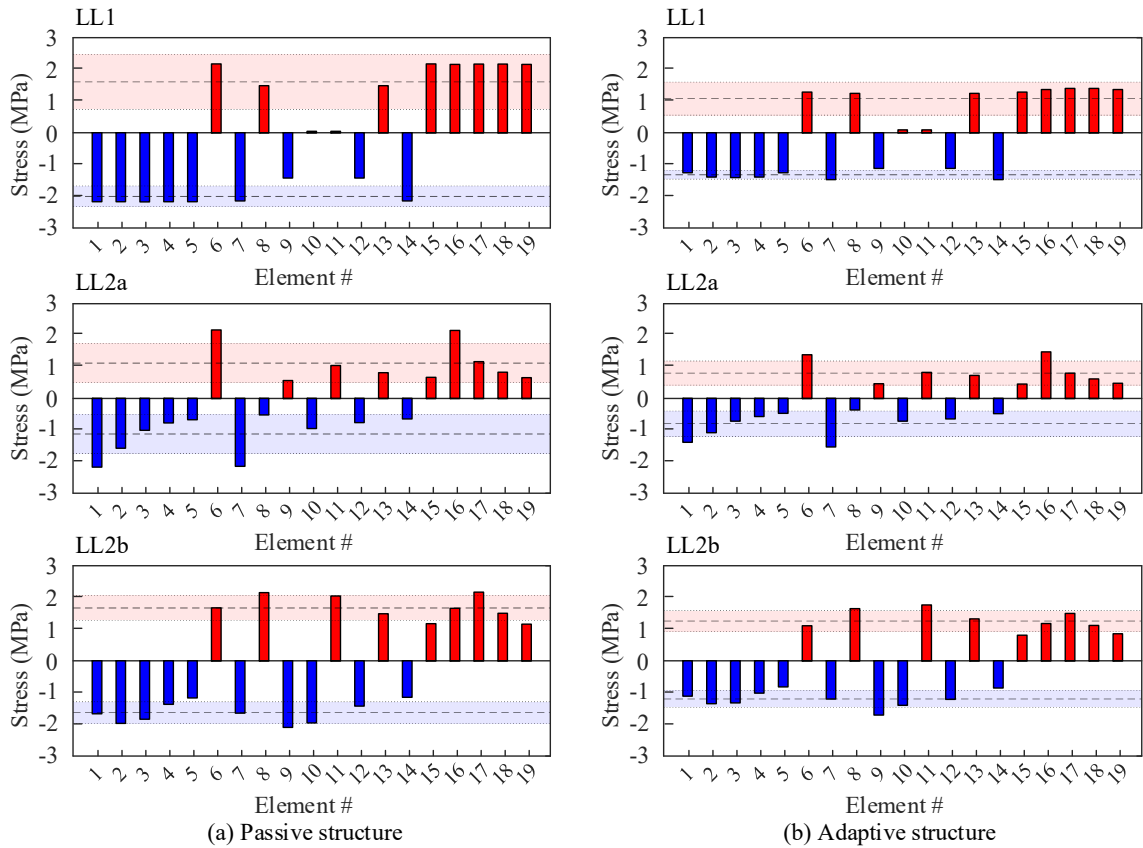


Figure 5: Element stress in passive (a) and adaptive (b) structure

The adaptive solution is compared to an identical weight-optimized passive structure to show stress redistribution through active control. Stress homogenization is understood as a reduction

of magnitude and variability. Figure 5 shows bar charts of the element stress for the passive (a) and adaptive (b) structures. LL2c and LL2d are not shown because they are mirror of LL2b and LL2a. Tensile and compressive stress are indicated in red and blue, respectively. The mean for each data set is shown as a horizontal dashed line. Stress variability is quantified through standard deviation. The width of the shaded band, whose centerline is the mean value of each data set, is twice the standard deviation. The element stress in the adaptive structure is consistently lower than that of the passive structure. The maximum mean reduction for tensile and compressive stress are 33% and 34%, respectively (both in LL1). LL1 and LL2b have the smallest variability through shape control for compressive and tensile stress, respectively. Stress homogenization can be appreciated the most in LL1. The stress of element 8, 9, 12 and 13 remains similar to that of the corresponding elements in the passive structure. However, the stress of element 1~7 and 14~19 decrease. Similarly, in LL2a, the stress of element 6, 7 and 16 decrease significantly while the stress for the other elements remain practically the same. There is no stress reversal between the passive and adaptive structure.

4 EXPERIMENTAL TESTING

A prototype structure was built based on the model described in Section 3. The active elements are five turnbuckles, fitted according to the 5-actuator layout (Figure 4e). The joints are fabricated via additive manufacturing using a polymer-based material with a Young's modulus of 82 MPa. This material was chosen to ease shape reconfiguration, which in this case is manually operated through the turnbuckles.

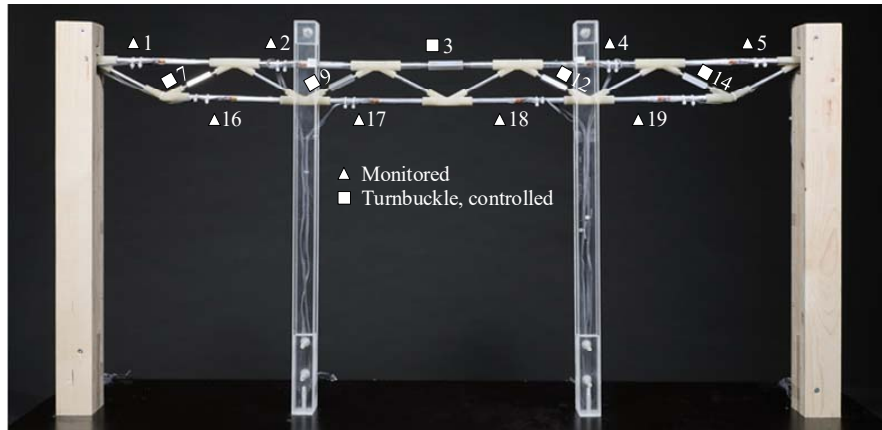


Figure 6: Prototype and supports

Only 8 out of 19 elements are instrumented with strain sensors, namely element 1, 2, 4, 5, 16, 17, 18 and 19 (Figure 6). It was not practical to install strain gauges on the 5 mm diameter bracing elements and on the turnbuckles. The static response under loading is measured and compared to the numerical predictions obtained in Section 3. Element strains and nodal positions are measured before and after shape control. Table 1a gives the maximum Euclidean distance between the nodes of simulated and measured controlled shapes as well as the norm of the shape difference between simulation and measurement.

Table 1: Discrepancy between measurement and simulation

(a) Nodal coordinates

Load case	No load	LL1	LL2a	LL2b	LL2c	LL2d
Norm difference of measurement and simulation (mm)	19.8	21.9	19.6	22.4	23.5	23.4
Max. node distance (mm)	7.9	10.6	11.5	12.2	11.7	12.1

(b) Change of stress

Load case	No load	LL1	LL2a	LL2b	LL2c	LL2d
Pearson correlation measure	-	0.99	0.86	0.93	0.94	0.90

The measured response under shape control is consistent with the numerical predictions (Section 3); an overall reduction of tensile and compressive stress is observed. The reduction is caused by the increase in depth in proximity of point of application of the external load. Table 1b shows the Pearson correlation between measured and predicted change of stress i.e. change before and after control. There is a strong correlation between measurement and prediction for all load cases.

To implement a control system based on the process outlined in Section 2, the external load has to be sensed. This is because a target shape can be computed only after knowing where the load is applied. To infer the external loading, the internal forces and the shape of the structure have to be known. Since only 8 out of 19 elements are instrumented with strain gauges, the forces in non-instrumented elements are obtained through nodal equilibrium. However, it is not possible to compute the force in element 3 through nodal equilibrium because it connects node 3 and 4 where the external load is applied. Instead, the force in element 3 is inferred through linear regression.

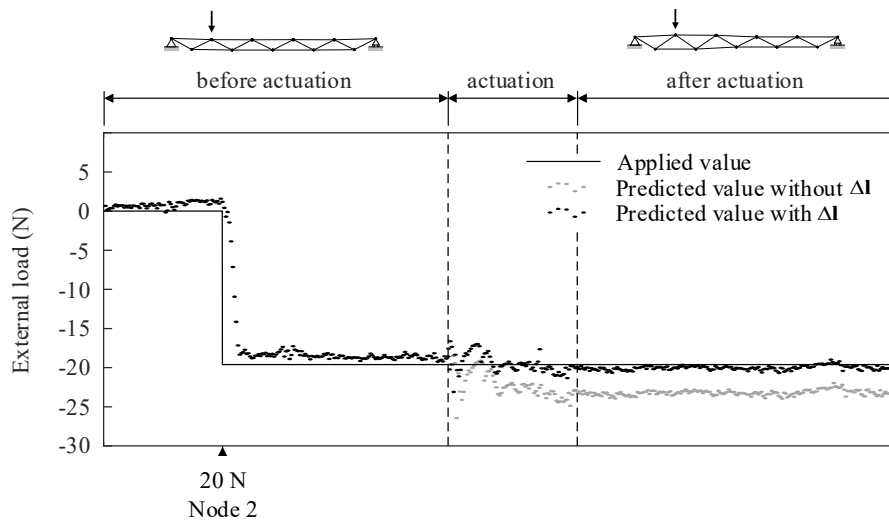
**Figure 7:** External load on node 2 (load case LL2a)

Figure 7 shows the comparison between applied and predicted values for the external load when the structure is subjected to a constant 20 N load on node 2 (LL2a), before and after shape control. Using a linear regression model that considers only internal forces as the independent variables, prediction of the external load was not accurate during and after shape control, with a maximum error of 4 N as shown by the grey scatter plot in Figure 7. Load prediction was more accurate when the length changes were also included in the independent variables in order to obtain the forces in non-instrumented elements. As shown by the black scatter plot in Figure 8, the predicted load is close to the applied one even after shape control with a maximum error of 0.6 N.

5 CONCLUSIONS

The results of this study lead to the following conclusions:

- Experimental testing on a small-scale prototype has demonstrated that stress homogenization through large-shape changes is feasible. This enables an adaptive structure to operate closer to design limits maximizing material utilization and thus saving embodied energy with respect to a passive structure. The maximum mean reduction for tensile and compressive stress are 25% and 32%, respectively.
- The geometrically nonlinear force method offers an efficient way to control the shape of a reticular structure under quasi-static loading as shown by good accordance (Pearson correlation of 0.86) between simulation and measurement.
- Detection of the applied loading is necessary for non-linear shape and force control. The external load was inferred from sparse strain measurements combined by an optical tracking system. The optical system was essential to close the information gap caused by sparse instrumentation, especially in situations where nodal coordinates were varying due to shape control.

Similar conclusions are expected from tests on similar reticular structures designed using the design method outlined in this work. However, it was not possible in this work to appreciate the effect of node stiffness on internal forces and nodal displacements and how this effect behaves with the scale. In addition, the use of machine vision may pose a reliability risk as the monitoring of nodal coordinates may fail when multiple reflective markers are occluded. Future work will involve testing on a larger scale prototype adaptive structure.

REFERENCES

- [1] T. T. Soong, "Active structural Control in Civil Engineering," *Engineering Structures*, vol. 10, no. 4, pp. 74-84, 1988.
- [2] G. P. Cimellaro, T. T. Soong and A. M. Reinhorn, "Optimal Integrated Design of Controlled Structures," in *The 14th World Conference on Earthquake Engineering*, Beijing, 2008.
- [3] W. Sobek and P. Teuffel, "Adaptive Systems in Architecture and Structural Engineering," in *Smart Structures and Materials 2001: Smart Systems for Bridges*, 2001.
- [4] G. Senatore, P. Duffour et P. Winslow, «Synthesis of Minimum Energy Adaptive Structures,» *Structural and Multidisciplinary Optimization*, pp. <https://doi.org/10.1007/s00158-019-02224-8>, 2019.
- [5] G. Senatore, P. Duffour and P. Winslow, "Exploring the Application Domain of Adaptive Structures," *Engineering Structures*, vol. 167, pp. 608-628, 2018.
- [6] G. Senatore, P. Duffour et P. Winslow, «Energy and Cost Analysis of Adaptive Structures: Case Studies,» *Journal of Structural Engineering (ASCE)*, vol. 144, n° %18, p. 04018107, 2018.

- [7] L. Gil and A. Andreu, "Shape and cross-section optimisation of a truss structure," *Computers and Structures*, vol. 79, pp. 681-689, 2001.
- [8] K. Shea and I. F. C. Smith, "Improving Full-Scale Transmission Tower Design through Topology and Shape Optimization," *Structural Engineering*, vol. 132, no. 5, pp. 781-790, 2006.
- [9] B. Descamps and R. F. Coelho, "A lower-bound formulation for the geometry and topology optimization of truss structures under multiple loading," *Structural and Multidisciplinary Optimization*, vol. 48, no. 1, pp. 49-58, 2013.
- [10] G. Tibert, "Deployable Tensegrity Structures for Space Applications," Royal Institute of Technology, Stockholm, 2002.
- [11] N. W. Veuve, S. D. Safei and I. F. C. Smith, "Deployment of a Tensegrity Footbridge," *Journal of Structural Engineering*, vol. 141, no. 11, pp. 1 - 8, 2015.
- [12] L. F. Campanile, "Using compliant and active materials to adapt structural geometry - challenges and good reasons," in *14th International Conference on Adaptive Structures*, Seoul, 2003.
- [13] G. Senatore, P. Duffour, P. Winslow and C. Wise, "Shape control and whole-life energy assessment of an 'infinitely stiff' prototype adaptive structure," *Smart Materials and Structures*, vol. 27, 2018.
- [14] X. Yuan, X. Liang and A. Li, "Shape and force control of prestressed cable-strut structures based on nonlinear force method," *Advances in Structural Engineering*, vol. 19, no. 12, pp. 1917-1926, 2016.
- [15] A. P. Reksowardojo, G. Senatore and I. F. C. Smith, "Actuator layout optimization for adaptive structures performing large shape changes," in *Advanced Computing Strategies for Engineering. EG-ICE 2018. Lecture Notes in Computer Science*, vol 10864, I. F. C. Smith and B. Domer, Eds., Lausanne, Springer, Cham, 2018, pp. 111-129.
- [16] B. Wah and T. Wang, "Constrained simulated annealing with applications in nonlinear continuous constrained global optimization," in *Proceedings 11th International Conference on Tools with Artificial Intelligence*, Chicago, 1999.
- [17] S. Pellegrino, «Structural Computations with The Singular Value Decomposition of the Equilibrium Matrix,» *International Journal of Solids and Structures*, vol. 30, n° 121, pp. 3025-3035, 1993.

NONLINEAR BENDING OF GRAPHENE PLATELETS REINFORCED COMPOSITE PLATE WITH DIELECTRIC PERMITTIVITY

CHUANG FENG^{*}, YU WANG^{*} AND JIE YANG^{*}

^{*} School of Engineering, RMIT University
Bundoora, VIC 3083 Australia
e-mail: chuang.feng@rmit.edu.au

Key words: Nonlinear bending, Dielectric plate, Differential quadrature method, Effective-medium theory.

Abstract. This paper investigates the nonlinear bending of graphene platelets (GPLs) reinforced composite (GPLRC) plate with dielectric permittivity. Effective-medium theory (EMT) is adopted to determine tensile modulus and dielectric while rule of mixture is adopted to determine Poisson's ratio. Governing equations for nonlinear bending of the GPLRC plate are established based on first-order shear deformation plate theory and numerically solved through differential quadrature method (DQM). The dependency of the bending behaviors of the GPLRC plates on the attributes of plate geometry, GPL concentration and electrical field are comprehensively investigated. The analysis reveals that by adjusting several parameters the performances of the GPLRC plate can be designed and actively tuned.

1 INTRODUCTION

The current paper will be the first concentration on nonlinear bending behaviours of graphene reinforced composite plate with considering the dielectric property of the composite material. For case study, PVDF and GPL are chosen as constituent components for the composite plate. The top and bottom surfaces of the plate are coated with conductive paste serving as the compliant electrodes to accommodate the applied electrical voltage. Effective-medium theory (EMT) and rule of mixture will be employed to calculate the composite's material properties as required for structural analysis. Parametric study on the bending of the GPLRC plate is conducted through numerically solving the governing equations, which are derived by first-order shear deformation plate theory taking account of von Kármán geometrical nonlinearity.

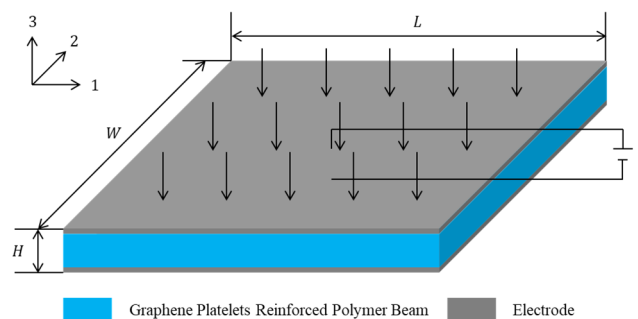


Figure 1 Schematic configuration of GPLRC plate.

2 EFFECTIVE MATERIAL PROPERTIES OF GPLRC

Rule of mixture could determine the effective Poisson's ratio of GPLRC with random and uniform dispersion, as

$$\nu_e = \varphi_m \nu_m + \varphi_f \nu_f \quad (1)$$

where the subscripts “m”, “f” and “e” denote matrix, reinforcing fillers and effective composite, respectively, and ν and φ refer to Poisson's ratio and volume fraction, respectively. In the current paper, the Poisson's ratio of GPL and PVDF are 0.175 and 0.35, respectively.

In the current paper, effective medium theory (EMT) is employed to evaluate the Young's modulus and dielectric permittivity of GPLRC. After some mathematical derivation, the effective property of graphene reinforced composites could be determined by the following scalar equation as

$$\varphi_m \frac{L_m - L_e}{L_m + (1/3)(L_m - L_e)} + \frac{1}{3} \varphi_f \sum_{k=1}^3 \frac{L_k - L_e}{L_e + S_{kk}(L_k - L_e)} = 0 \quad (2)$$

where L_k ($k = 1, 2, 3$) is the component of concerned moduli tensor and S_{kk} ($k = 1, 2, 3$) is the component of Eshelby's tensor of GPL filler in its local coordinate system.

2.1 Effective dielectric permittivity

The moduli components in Eq. (2) can be complex electrical conductivity components of the effective medium. Substituting the corresponding moduli components, one can have

$$\varphi_m \frac{\sigma_m^* - \sigma_e^*}{\sigma_e^* + (1/3)(\sigma_m^* - \sigma_e^*)} + \frac{1}{3} \varphi_f \sum_{k=1}^3 \frac{\sigma_k^* - \sigma_e^*}{\sigma_e^* + S_{kk}(\sigma_k^* - \sigma_e^*)} = 0 \quad (3)$$

where σ^* is the complex electrical conductivity which contains two parts, i.e. $\sigma^* = \sigma + 2\pi f_{AC} \epsilon j$, wherein σ is the DC (direct current) conductivity and the second imaginary term is the AC conductivity with f_{AC} being AC frequency of electrical field and ϵ the dielectric permittivity of the material.

This theory could be improved by taking the imperfect bonding/interaction between reinforcements and matrix into consideration. This is achieved by introducing an interphase surround the filler. As investigated in [1], the effective electrical conductivity and dielectric permittivity of the coated reinforcing fillers, i.e. $\sigma_k^{(c)}$ and $\epsilon_k^{(c)}$, can be estimated by

$$\sigma_k^{(c)} = \sigma_0^{(int)} \left[1 + \frac{(1 - \varphi_{int})(\sigma_k - \sigma_0^{(int)})}{\varphi_{int} S_{kk}(\sigma_k - \sigma_0^{(int)}) + \sigma_0^{(int)}} \right], \quad \epsilon_k^{(c)} = \epsilon_0^{(int)} \left[1 + \frac{(1 - \varphi_{int})(\epsilon_k - \epsilon_0^{(int)})}{\varphi_{int} S_{kk}(\epsilon_k - \epsilon_0^{(int)}) + \epsilon_0^{(int)}} \right] \quad (k = 1, 2, 3) \quad (4)$$

with $\sigma_0^{(int)}$ and $\epsilon_0^{(int)}$ being the electrical conductivity and dielectric permittivity of the interphase, respectively. All the electrical conductivity and dielectric permittivity of the GPL fillers involved in Eq. (3) should be substituted by the ones in Eq. (4). φ_{int} in Eq. (4) denotes the volume fraction of the interphase in the coated GPL, which is

$$\varphi_{int} = 1 - \frac{\frac{4}{3} \pi \left(\frac{t_{GPL}}{2} \right) \left(\frac{D_{GPL}}{2} \right) \left(\frac{D_{GPL}}{2} \right)}{\frac{4}{3} \pi \left(\frac{t_{GPL}}{2} + t_{int} \right) \left(\frac{D_{GPL}}{2} + t_{int} \right) \left(\frac{D_{GPL}}{2} + t_{int} \right)} \quad (5)$$

where t_{int} is the thickness of the interphase.

D

Choosing GPLs and PVDF as the reinforcing fillers and the polymer matrix, respectively, the EMT model on predicting the dielectric permittivity of GPL/PVDF composites was validated by Xia et al. [2].

2.2 Effective elastic modulus

Replacing the parameters with components of stiffness tensor gives the following equation

$$\varphi_m \frac{E_m - E_e}{E_e + (1/3)(E_m - E_e)} + \frac{1}{3} \varphi_f \sum_{k=1}^3 \frac{E_k - E_e}{E_e + S_{kk}(E_k - E_e)} = 0 \quad (6)$$

where E_e is the elastic modulus of the homogeneous GPLRC. Taking the imperfect bonding between fillers and polymer into account, the effective elastic modulus of coated GPL is

$$E_k^{(c)} = E_0^{(int)} \left[1 + \frac{(1 - \varphi_{int})(E_k - E_0^{(int)})}{\varphi_{int} S_{kk}(E_k - E_0^{(int)}) + E_0^{(int)}} \right] \quad k = 1, 2, 3 \quad (7)$$

with $E_0^{(int)}$ being the elastic modulus of the interphase. E_k in Eq. (7) would be substituted by the elastic modulus of coated GPLs. In the current study, the Young's modulus of the PVDF is 1.44 GPa and the in-plane and out-plane Young's modulus of GPL are 1.01 TPa and 101 TPa, respectively. The thickness of the interlayer is 3 nm and the average thickness of GPLs is 50 nm.

3 PROBLEM FORMULATION

Employing first-order plate theory, the displacement field is given as

$$\begin{cases} U_1(X_1, X_2, X_3) = U_1(X_1, X_2, 0) + X_3 \Phi_1(X_1, X_2, 0) \\ U_2(X_1, X_2, X_3) = U_2(X_1, X_2, 0) + X_3 \Phi_2(X_1, X_2, 0) \\ U_3(X_1, X_2, X_3) = U_3(X_1, X_2, 0) \end{cases} \quad (8)$$

where $U_1(X_1, X_2, 0)$, $U_2(X_1, X_2, 0)$ and $U_3(X_1, X_2, 0)$ are the displacement components of the middle plane in X_1 , X_2 and X_3 directions, respectively, $\Phi_1(X_1, X_2, 0)$ and $\Phi_2(X_1, X_2, 0)$ are cross-sectional rotations in the 103 and 203 planes. For convenience, the following conventions would be introduced

$$\begin{aligned} U_1(X_1, X_2, 0) &\equiv U_1, U_2(X_1, X_2, 0) \equiv U_2, U_3(X_1, X_2, 0) \equiv U_3 \\ \Phi_1(X_1, X_2, 0) &\equiv \Phi_1, \Phi_2(X_1, X_2, 0) \equiv \Phi_2 \end{aligned} \quad (9)$$

The strain field could be given by von Kármán geometrical nonlinearity as

$$\begin{Bmatrix} \varepsilon_{11} \\ \varepsilon_{22} \\ \varepsilon_{33} \\ \gamma_{23} \\ \gamma_{13} \\ \gamma_{12} \end{Bmatrix} = \begin{Bmatrix} \varepsilon_{11}^{(0)} \\ \varepsilon_{22}^{(0)} \\ \varepsilon_{33}^{(0)} \\ \gamma_{23}^{(0)} \\ \gamma_{13}^{(0)} \\ \gamma_{12}^{(0)} \end{Bmatrix} + X_3 \begin{Bmatrix} \varepsilon_{11}^{(1)} \\ \varepsilon_{22}^{(1)} \\ \varepsilon_{33}^{(1)} \\ \gamma_{23}^{(1)} \\ \gamma_{13}^{(1)} \\ \gamma_{12}^{(1)} \end{Bmatrix} = \begin{Bmatrix} U_{1,1} + \frac{1}{2} U_{3,1}^2 \\ U_{2,2} + \frac{1}{2} U_{3,2}^2 \\ 0 \\ \Phi_2 + U_{3,2} \\ \Phi_1 + U_{3,1} \\ U_{1,2} + U_{2,1} + U_{3,1} U_{3,2} \end{Bmatrix} + X_3 \begin{Bmatrix} \Phi_{1,1} \\ \Phi_{2,2} \\ 0 \\ 0 \\ 0 \\ \Phi_{1,2} + \Phi_{2,1} \end{Bmatrix} \quad (10)$$

The stress field could be given as

$$\begin{Bmatrix} \sigma_{11} \\ \sigma_{22} \\ \sigma_{33} \\ \tau_{23} \\ \tau_{13} \\ \tau_{12} \end{Bmatrix} = \begin{bmatrix} Q_{11} & Q_{12} & 0 & 0 & 0 & 0 \\ Q_{21} & Q_{22} & 0 & 0 & 0 & 0 \\ 0 & 0 & 0 & 0 & 0 & 0 \\ 0 & 0 & 0 & Q_{44} & 0 & 0 \\ 0 & 0 & 0 & 0 & Q_{55} & 0 \\ 0 & 0 & 0 & 0 & 0 & Q_{66} \end{bmatrix} \begin{Bmatrix} \varepsilon_{11} \\ \varepsilon_{22} \\ \varepsilon_{33} \\ \gamma_{23} \\ \gamma_{13} \\ \gamma_{12} \end{Bmatrix} + \begin{Bmatrix} \varepsilon_{110} \\ \varepsilon_{220} \\ \varepsilon_{330} \\ \gamma_{230} \\ \gamma_{130} \\ \gamma_{120} \end{Bmatrix} - \frac{V^2}{t^2} \varepsilon \begin{Bmatrix} 1 \\ 1 \\ 1 \\ 0 \\ 0 \\ 0 \end{Bmatrix} \quad (11)$$

where $\{\varepsilon_{110} \ \varepsilon_{220} \ \varepsilon_{330} \ \varepsilon_{230} \ \varepsilon_{130} \ \varepsilon_{120}\}^T$ is the prestrain vector, $Q_{ij} (i,j=1,2,4,5,6)$ are the elastic stiffness of the plate given as

$$Q_{11}=Q_{22}=\frac{E}{1-\nu^2}, \quad Q_{12}=Q_{21}=\frac{\nu E}{1-\nu^2}, \quad Q_{44}=Q_{55}=Q_{66}=\frac{E}{2(1+\nu)} \quad (12)$$

The last vector on the right hand side of Eq. (11) denotes the electrostatic stress produced by the voltage due to the dielectric property of the plate. V is the voltage applied across the plate. The voltage applied consists of two parts, i.e. $V = V_{DC} + V_{AC} \sin(2\pi f_{AC} t)$, in which V_{DC} and V_{AC} are the amplitudes of DC and AC voltage, respectively, and f_{AC} is the AC frequency of the voltage in Hertz. Here it should be noted the AC voltage is normally used for actively tuning or periodic excitation and its magnitude is usually much smaller than DC component [3]. Therefore, the magnitude of DC voltage will be used in Eq. (11) to calculate the axial stress.

Integrating the normal and shear stresses over corresponding domains, the internal forces and moment in the plate are derived as

$$\begin{Bmatrix} N_{11} \\ N_{22} \\ N_{33} \\ N_{23} \\ N_{13} \\ N_{12} \end{Bmatrix} = \int_{-\frac{H}{2}}^{\frac{H}{2}} \begin{Bmatrix} \sigma_{11} \\ \sigma_{22} \\ \sigma_{33} \\ \tau_{23} \\ \tau_{13} \\ \tau_{12} \end{Bmatrix} dx_3 = \begin{bmatrix} A_{11} & A_{12} & 0 & 0 & 0 & 0 \\ A_{21} & A_{22} & 0 & 0 & 0 & 0 \\ 0 & 0 & 0 & 0 & 0 & 0 \\ 0 & 0 & 0 & A_{44} & 0 & 0 \\ 0 & 0 & 0 & 0 & A_{55} & 0 \\ 0 & 0 & 0 & 0 & 0 & A_{66} \end{bmatrix} \begin{Bmatrix} \varepsilon_{11}^{(0)} \\ \varepsilon_{22}^{(0)} \\ \varepsilon_{33}^{(0)} \\ \gamma_{23}^{(0)} \\ \gamma_{13}^{(0)} \\ \gamma_{12}^{(0)} \end{Bmatrix} + \begin{Bmatrix} \varepsilon_{110} \\ \varepsilon_{220} \\ \varepsilon_{330} \\ \gamma_{230} \\ \gamma_{130} \\ \gamma_{120} \end{Bmatrix} - \begin{Bmatrix} N_{11}^E \\ N_{22}^E \\ N_{33}^E \\ 0 \\ 0 \\ 0 \end{Bmatrix} \quad (13)$$

$$\begin{Bmatrix} M_{11} \\ M_{22} \\ M_{33} \\ M_{23} \\ M_{13} \\ M_{12} \end{Bmatrix} = \int_{-\frac{H}{2}}^{\frac{H}{2}} X_3 \begin{Bmatrix} \sigma_{11} \\ \sigma_{22} \\ \sigma_{33} \\ \tau_{23} \\ \tau_{13} \\ \tau_{12} \end{Bmatrix} dX_3 = \begin{bmatrix} A_{11} & A_{12} & 0 & 0 & 0 & 0 \\ A_{21} & A_{22} & 0 & 0 & 0 & 0 \\ 0 & 0 & 0 & 0 & 0 & 0 \\ 0 & 0 & 0 & A_{44} & 0 & 0 \\ 0 & 0 & 0 & 0 & A_{55} & 0 \\ 0 & 0 & 0 & 0 & 0 & A_{66} \end{bmatrix} \begin{Bmatrix} \varepsilon_{11}^{(1)} \\ \varepsilon_{22}^{(1)} \\ \varepsilon_{33}^{(1)} \\ \gamma_{23}^{(1)} \\ \gamma_{13}^{(1)} \\ \gamma_{12}^{(1)} \end{Bmatrix} \quad (14)$$

where A_{ij} and D_{ij} are coefficients determined as

$$\begin{aligned} A_{ij} &= \int_{-\frac{H}{2}}^{\frac{H}{2}} Q_{ij} dX_3 \quad (i, j = 1, 2, 3, 6) & A_{ij} &= \int_{-\frac{H}{2}}^{\frac{H}{2}} k_s Q_{ij} dX_3 \quad (i, j = 4, 5) \\ D_{ij} &= \int_{-\frac{H}{2}}^{\frac{H}{2}} X_3^2 Q_{ij} dX_3 \quad (i, j = 1, 2, 3, 4, 5, 6) & N_{11}^E &= N_{22}^E = N_{33}^E = \frac{V^2}{H^2} \varepsilon t \end{aligned} \quad (15)$$

with k_s being the shear correction factor.

Based on energy method, the governing equations for bending of the plate can be obtained with the following boundary conditions:

CCCC:

$$U_1 = U_2 = U_3 = \Phi_1 = \Phi_2 = 0 \quad (X_1, X_2 = 0, 1) \quad (16)$$

SSSS:

$$\begin{aligned} U_1 = U_2 = U_3 = \Phi_2 = 0, D_{11}\Phi_{1,1} + D_{12}\Phi_{2,2} = 0 \quad (X_1 = 0, 1) \\ U_1 = U_2 = U_3 = \Phi_1 = 0, D_{21}\Phi_{1,1} + D_{22}\Phi_{2,2} = 0 \quad (X_2 = 0, 1) \end{aligned} \quad (17)$$

CCSS:

$$\begin{aligned} U_1 = U_2 = U_3 = \Phi_1 = \Phi_2 = 0 \quad (X_1, X_2 = 0) \\ U_1 = U_2 = U_3 = \Phi_2 = 0, D_{11}\Phi_{1,1} + D_{12}\Phi_{2,2} = 0 \quad (X_1 = 1) \\ U_1 = U_2 = U_3 = \Phi_1 = 0, D_{21}\Phi_{1,1} + D_{22}\Phi_{2,2} = 0 \quad (X_2 = 1) \end{aligned} \quad (18)$$

4 SOLUTION

To normalize the governing equations, the following dimensionless quantities are defined

$$\begin{aligned} \{x_1, x_2\} = \left\{ \frac{X_1}{L}, \frac{X_2}{W} \right\}, \{u_1, u_2, u_3\} = \frac{\{U_1, U_2, U_3\}}{H}, \{\varphi_1, \varphi_2\} = \{\Phi_1, \Phi_2\}, q = \frac{Q\eta L}{A_{110}} \\ \{a_{ij}, d_{ij}\} = \left\{ \frac{A_{ij}}{A_{110}}, \frac{D_{ij}}{A_{110}H^2} \right\}, \eta = \frac{L}{H}, \lambda = \frac{L}{W}, \{n_{11}^e, n_{22}^e, n_{33}^e\} = \frac{\{N_{11}^E, N_{22}^E, N_{33}^E\}}{A_{110}} \end{aligned} \quad (19)$$

where A_{110} and I_{10} are the corresponding values of A_{11} and I_1 of plate made of pure polymer, respectively.

The dimensionless governing equations can be solved numerically with the aid of differential quadrature method (DQM). First, the following displacements of the plate and their derivatives are introduced

$$\begin{aligned} \left\{ \begin{aligned} \{u_1, u_2, u_3, \varphi_1, \varphi_2\} &= \sum_{m=1}^M \sum_{n=1}^N l_m(x_1) l_n(x_2) \{u_{1mn}, u_{2mn}, u_{3mn}, \varphi_{1mn}, \varphi_{2mn}\} \\ \left. \frac{\partial^{k_1}}{\partial x_1^{k_1}} \frac{\partial^{k_2}}{\partial x_2^{k_2}} \{u_1, u_2, u_3, \varphi_1, \varphi_2\} \right|_{x_1=x_{1i}, x_2=x_{2j}} &= \sum_{m=1}^M \sum_{n=1}^N C_{im}^{(k_1)} C_{jn}^{(k_2)} \{u_{1mn}, u_{2mn}, u_{3mn}, \varphi_{1mn}, \varphi_{2mn}\} \end{aligned} \right\} \quad (20) \end{aligned}$$

where $\{u_{1mn}, u_{2mn}, u_{3mn}, \varphi_{1mn}, \varphi_{2mn}\}$ is the displacement vector at position $x_1 = x_{1m}$, $x_2 = x_{2n}$, $l_m(x_1)$ and $l_n(x_2)$ are the Lagrange interpolation polynomials and $C_{im}^{(k_1)}$ and $C_{jn}^{(k_2)}$ are the weighting coefficients of the k_1 th derivative at $x_1 = x_{1m}$ and the k_2 th derivative at $x_2 = x_{2n}$, and M and N are the total numbers of grid points distributed along the x_1 and x_2 directions. In present work, the following expression for the distribution of the grid points are used [4]

$$\begin{aligned} x_{1i} &= \frac{1}{2} \left[1 - \cos \frac{\pi(i-1)}{N-1} \right] \quad (i = 1, 2, \dots, M) \\ x_{2j} &= \frac{1}{2} \left[1 - \cos \frac{\pi(j-1)}{N-1} \right] \quad (j = 1, 2, \dots, N) \end{aligned} \quad (21)$$

Substituting Eq. (20) into dimensionless governing equations will yield the discretized governing equations which could be simplified as the following matrix equation

$$[\mathbf{K}_L + \mathbf{K}_{NL}(\mathbf{d})]\mathbf{d} = \mathbf{q} \quad (22)$$

where \mathbf{K}_L denotes linear stiffness matrix, \mathbf{K}_{NL} denotes the nonlinear stiffness matrix depending on displacement vector expressed as

$$\mathbf{d} = \left\{ \left\{ \text{vec}(u_{1ij}) \right\}^T, \left\{ \text{vec}(u_{2ij}) \right\}^T, \left\{ \text{vec}(u_{3ij}) \right\}^T, \left\{ \text{vec}(\varphi_{1ij}) \right\}^T, \left\{ \text{vec}(\varphi_{2ij}) \right\}^T \right\}^T \quad (23)$$

\mathbf{M} denotes mass matrix and \mathbf{q} denotes force vector expressed as

$$\mathbf{q} = \left\{ \left\{ 0 \right\}_{MN}^T, \left\{ 0 \right\}_{MN}^T, \left\{ q(x_i, x_{2j}) \right\}_{MN}^T, \left\{ 0 \right\}_{MN}^T, \left\{ 0 \right\}_{MN}^T \right\}^T \quad (i = 1, 2, \dots, M, j = 1, 2, \dots, N) \quad (24)$$

Eq. (24) can be solved by direct iteration method for nonlinear bending.

5 RESULTS AND DISCUSSION

5.1 Convergence and validation study

Table 1 validates the results of the current method by comparing with those obtained using other methods from literature for an elastic isotropic homogeneous rectangular plates. The present solution is realized for a quadratic plate, with the following parameters: $L = 1$, $W = 1$, $E = 1$, $Q = 1$, $\nu = 0.3$ and three values for the plate thickness: $H = 0.01$, $H = 0.03$, and $H = 0.1$. It is found that present results agree very well with the results from reference

Table 1 Dimensionless deflections of isotropic homogeneous plates

H	Classic [5]	3-D [6]		Ref [7]	Present
		In mid-plane	Average		
0.01	44360.9000	44384.7000	44383.9000	44383.8400	44383.8765
0.03	1643.0000	1650.9400	1650.6600	1650.6460	1650.6578
0.10	44.3609	46.7443	46.6586	46.6548	46.6594

Table 2 presents dimensionless deflection of GPL/PVDF composite plates with different numbers of grid points and boundary conditions. The concentration of GPL in the composites is 1.5 wt%. The dimensions of the plate are $L = W = 0.01\text{m}$ and $H = 0.0005\text{ m}$, respectively. No electrical field are applied on the plate. The initial prestrain are set to be 0.01 in both 1 and 2 directions. The number of grid points M and N in both 1 and 2 directions increases from 5 to

15. It could be concluded that 15 grid points in both 1 and 2 directions are enough for computational accuracy.

Table 2 Dimensionless deflection of GPLRC plate with various boundary conditions

$M=N$	CCCC		SSSS		CCSS	
	Linear	Nonlinear	Linear	Nonlinear	Linear	Nonlinear
5	0.3094	0.3310	0.3769	0.3635	0.3453	0.3388
7	0.2195	0.2163	0.3516	0.3371	0.2760	0.2693
9	0.2226	0.2201	0.3531	0.3386	0.2774	0.2712
11	0.2226	0.2200	0.3530	0.3386	0.2774	0.2712
13	0.2226	0.2200	0.3530	0.3386	0.2774	0.2711
15	0.2226	0.2200	0.3530	0.3386	0.2774	0.2711

5.2 Parametric study

A simply supported GPL/PVDF plate is considered for parametric study. Unless stated otherwise, the size of the plate are $L = W = 0.01\text{m}$ and $H = 0.0005\text{m}$. The prestrain in the 1 and 2 direction are 0.01. The GPL volume fraction is 1.5 wt%. The properties of PVDF are $E_{\text{PVDF}} = 1.44\text{GPa}$, $\nu_{\text{PVDF}} = 0.35$, $\sigma_{\text{PVDF}} = 3.5 \times 10^{-9}\text{S/m}$, $\varepsilon_{\text{PVDF}} = 5 \times 8.85 \times 10^{-12}\text{F/m}$ and the properties of GPL are $E_{\text{GPL}_1} = E_{\text{GPL}_2} = 1010\text{GPa}$, $E_{\text{GPL}_3} = 1010\text{TPa}$, $\nu_{\text{GPL}} = 0.175$, $\sigma_{\text{GPL}_1} = \sigma_{\text{GPL}_2} = 8.32 \times 10^4\text{S/m}$, $\sigma_{\text{GPL}_3} = 83.2\text{S/m}$, $\varepsilon_{\text{GPL}_1} = \varepsilon_{\text{GPL}_2} = 15 \times 8.85 \times 10^{-12}\text{F/m}$, $\varepsilon_{\text{GPL}_3} = 0.6715 \times 8.85 \times 10^{-12}\text{F/m}$.

The plate geometry affects the bending behaviours of GPLRC plate, as presented in Fig. 2. It is found in Fig. 2 the increase of length-to-thickness ratio and the decrease of length-to-width ratio increase the deformation of the plate. The effect of plate geometry on the deflection also depend on the applied electrical voltage and length-to-width ratio.

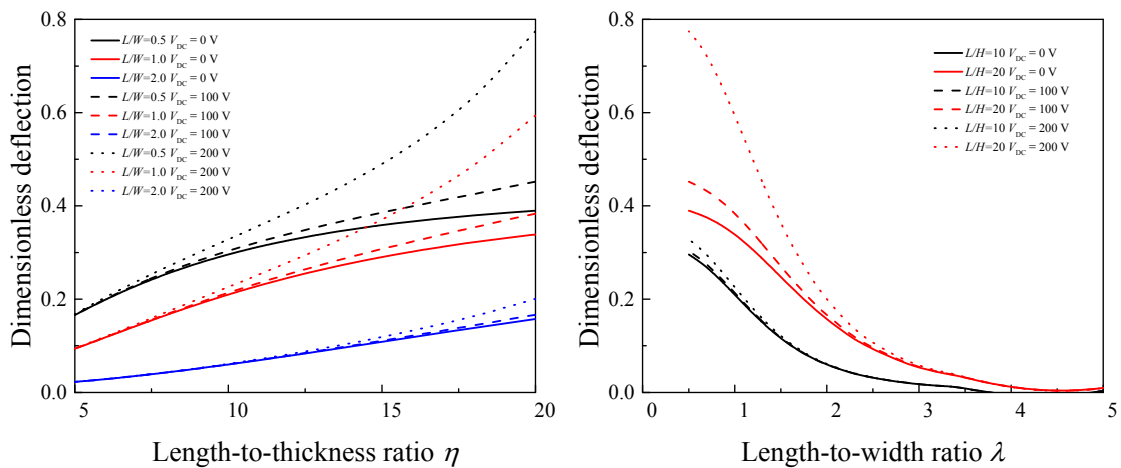


Fig. 2. Variation of dimensionless deflection with thickness of GPL/PVDF plate.

Fig. 3 plots the variation of the dimensionless deflection of the GPL/PVDF plate with the GPL concentration. The decrease of the dimensionless deflection is observed when GPL concentration reaches a critical value, i.e. $f_{\text{GPL}} = 1.1$ wt%. When GPL concentration further increases, the deflection becomes highly dependent on the electrical voltage. Similar trend of the dependency of the deflection on GPL weight fraction is found in Fig. 3. In Fig. 3b, the magnitude of DC voltage is fixed as 100 V while the AC frequency varies from 0 Hz to 10^6 Hz. A snap-through phenomenon is observed for the deflection when the GPL concentration exceeds the critical concentration.

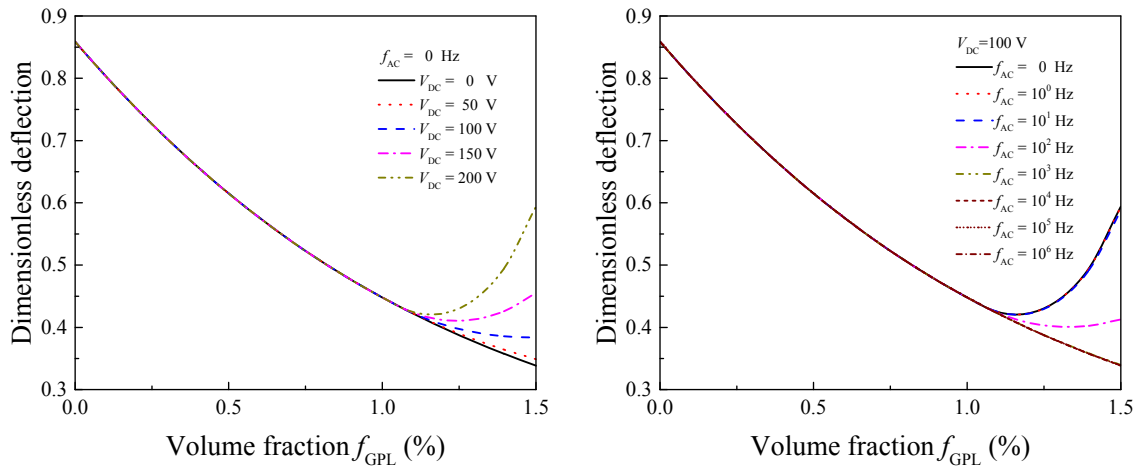


Fig. 3. Variation of dimensionless deflection of GPL/PVDF plate with GPL volume fraction (a) $f_{\text{AC}} = 0$ Hz; (b) $V_{\text{DC}} = 100$ V.

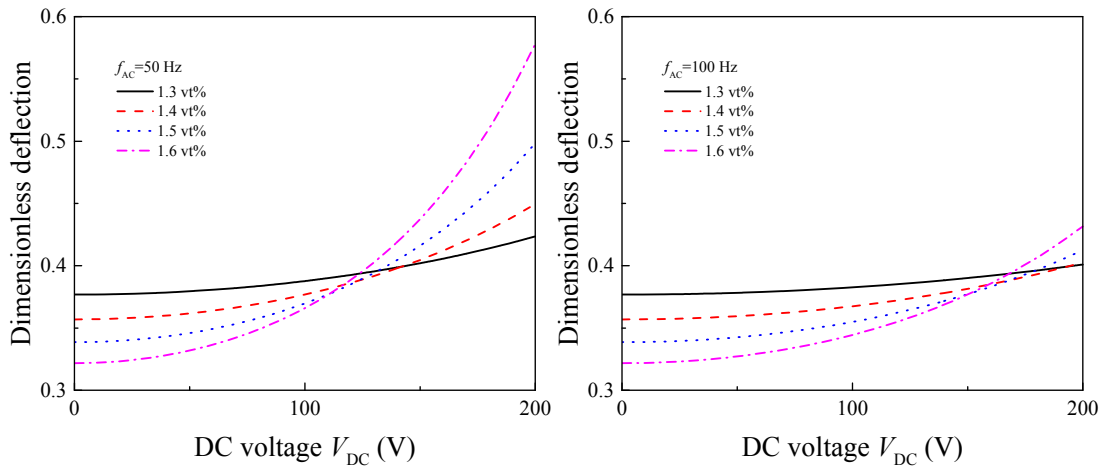


Fig. 4. Variation of dimensionless deflection of GPL/PVDF composite plate with voltage.

Fig. 4 plots the variation of the dimensionless deflection of GPL/PVDF plate with electrical voltage. The dimensionless deflection increases as the electrical voltage grows and the variation of the dimensionless deflection is more evident as the GPL concentration increases. The different of the two figures in figure 4 also indicates that the decrease of AC frequency magnify the effects of DC voltage.

6 CONCLUSIONS

Nonlinear bending of GPLRC dielectric plate are studies by numerically solving governing equations, which are derived based on first-order deformation theory and von Kármán geometrical nonlinearity. The analysis demonstrates that the bending behaviors of the GPL/PVDF plate could be artificially tuned by adjusting several parameters, i.e. plate size, GPL concentration and external electrical field.

REFERENCES

- [1] Y. Wang, J.W. Shan, G.J. Weng, Percolation threshold and electrical conductivity of graphene-based nanocomposites with filler agglomeration and interfacial tunneling, *J Appl Phys*, 118 (2015) 065101.
- [2] X.D. Xia, Y. Wang, Z. Zhong, G.J. Weng, A frequency-dependent theory of electrical conductivity and dielectric permittivity for graphene-polymer nanocomposites, *Carbon*, 111 (2017) 221-230.
- [3] A.H. Nayfeh, M.I. Younis, E.M. Abdel-Rahman, Dynamic pull-in phenomenon in MEMS resonators, *Nonlinear Dynam*, 48 (2006) 153-163.
- [4] X. Wang, *Differential quadrature and differential quadrature based element methods: theory and applications*, Butterworth-Heinemann 2015.
- [5] S.P. Timoshenko, S. Woinowsky-Krieger, *Theory of plates and shells*, McGraw-hill 1959.
- [6] H. Werner, A three - dimensional solution for rectangular plate bending free of transversal normal stresses, *Communications in numerical methods in engineering*, 15 (1999) 295-302.
- [7] A.M. Zenkour, Generalized shear deformation theory for bending analysis of functionally graded plates, *Appl Math Model*, 30 (2006) 67-84.

NONLINEAR MODELING AND CONTROL OF TENSION-ONLY ELEMENTS IN ADAPTIVE STRUCTURES

JULIA L. WAGNER, MICHAEL BÖHM AND OLIVER SAWODNY

Institute for System Dynamics

University of Stuttgart

Waldburgstr. 19 70563, Stuttgart, Germany

e-mail: {wagner, boehm, sawodny}@isys.uni-stuttgart.de, www.isys.uni-stuttgart.de

Key words: Adaptive civil engineering structure, nonlinear modeling, tension-only elements, feedback linearization

Abstract. Adaptive civil engineering structures aim at saving material and energy in the construction and operation of buildings. Such structures incorporate sensors, actuators and a control unit to instantly adapt their response to external dynamic and static loads to guarantee an optimal material utilization all times. These structures are often modeled using a linear approach, however some nonlinear aspects cannot be neglected, but need to be captured by the governing equations. Tension-only elements can bear tension forces but collapse completely under compression. In this contribution, a nonlinear model of a civil engineering structure incorporating tension-only elements is introduced and a model order reduction by means of proper orthogonal decomposition is conducted. The controller design for this nonlinear system is carried out in two steps. First, the closed loop dynamics are forced to follow a linear target dynamic by applying a nonlinear input transformation including a virtual input. Second, this new input is used to control the linear target dynamic with methods from linear control theory with the aim of oscillation damping. The proposed method is applied to an exemplary adaptive high-rise structure. The results illustrate the effectiveness of the introduced control strategy, due to a strong impact of the nonlinearities on the structure's behavior.

1 INTRODUCTION

The introduction of adaptivity in structural engineering enables a way to build lightweight and sustainable and therefore save material in the construction sector by actively influencing the structure. Adaptive engineering structures guarantee their structural stability by combining sensors and actuators with a control unit [21,32]. Therein, a control algorithm processes sensor signals to provide actuator inputs for compensating static and dynamic loads and ensuring a comfortable usage and a secure functioning of the structure. Research in control of adaptive civil engineering structures goes back to the 1970s [37]. Classification of such structures and control approaches can be looked up in [17,33].

Civil engineering structures often make use of tension-only elements, e.g. ropes used as stiffening elements. If such an element is being compressed it gets slack and (temporarily) loses its load bearing behavior and therefore its function in the structure [2]. A high pretension of these elements can prevent slackness. However, if high pretension forces are applied, additional



Figure 1: Rendering of an adaptive high-rise building (right), which will be built on the site of the University of Stuttgart. The left building is the access and supply tower (source: ILEK).

stress is put on the structure, which is not desirable due to the increased need of material and construction costs, which is contrary to our goal of a sustainable and lightweight construction.

Tension-only elements are state-of-the-art in finite element (FE) tools (e.g. ANSYS), however their use results in a loss of linearity. Nevertheless, many control approaches for such large structures are based on linear equations of motion due to its simplicity and the need of low order design models that can easily be derived for linear systems, e. g. by modal transformation [13,28]. Even though this often results in a reasonable control performance, a large number of nonlinear elements might require a nonlinear modeling and control approach to further improve the closed loop system dynamics. However, this impedes the usage of classical workflows, in which linear FE models are extracted and reduced for control design purposes. State-of-the-art light-weight engineering structures typically incorporate a high number of tension-only elements. Despite these local nonlinearities, some of these structures express an almost linear behavior with respect to the global structural modes. Therefore, a proper orthogonal decomposition can be applied to capture the main components of the nonlinear model and to be able to reduce it for simulation and control design purposes.

A lot of research concerning tension-only elements in civil engineering is directed towards tensegrity structures [31]. These consist of tensioned cables and compressed struts. Using activated struts, a control algorithm that manipulate the eigenfrequencies of the structure to minimize vibrations is proposed by [3], whereas in [8] an optimal controller is designed for a tensegrity structure with actuated cables. However, these systems are different to the system in this contribution because the bars in tensegrity structures do not bear bending moments and high pretension of the cables is required.

Structures relying heavily on cable networks can be found in suspension bridges, cable roofs, and transmission lines [19]. The more general concept of tension systems, in addition to cable systems, also includes membranes [5,23]. For modeling and control of single cables, slackness is considered in many contributions [1,14], often in the context of hybrid systems [7]. Hybrid systems are not applicable for the high number of tension-only elements typically found in civil engineering structures, due to the combinatorial explosion of the number of discrete states.

For control of nonlinear system equations, a linearizing input transformation renders the closed-loop dynamics into an integrator chain, an established method in the context of flat systems [11]. The applied control concept is a linearizing input transformation [15,22] forcing

the nonlinear system to the dynamics of a target system. The nonlinear system can then be controlled by controlling the target system with common linear control theory.

To demonstrate the research concerning adaptive civil engineering structures, an experimental adaptive high-rise building will be installed on the site of the University of Stuttgart (see Fig. 1 and details in [36]). A simplified model of this structure's geometry is presented in section 5.1 and used to illustrate the nonlinear effects of tension-only elements and the proposed algorithm.

The main contribution of this article is the modeling and control of nonlinear effects of tension-only elements in the context of adaptive engineering structures, where possibly a high number of tension-only elements can be available. Furthermore, a linearizing input is stated, transforming the nonlinear system into a desired closed-loop target dynamics, which can be controlled with linear control theory.

In the following, the linear model equations are stated in section 2 as the basis for including nonlinear tension-only elements. A nonlinear model order reduction is conducted by means of POD in section 3 and a model for control purposes is derived. In section 4, a linearizing input transformation, which is applied to the nonlinear system, forces the closed-loop system onto a desired target dynamic. Simulation results for the application of the introduced methodology to a numerical high-rise structure are given in section 5.

2 SYSTEM MODELING

This section concerns modeling of linear and nonlinear effects in mechanical structures arising in special civil engineering structures. In the following, the linear equations of motion are introduced as a basis for further nonlinear modeling and for the sake of evaluation and comparison of both model types and the selection of a target system in section 5.

2.1 Linear Equations of Motion

A common technique to model mechanical structures is the application of the finite element method (FEM). This framework discretizes the infinite number of degrees of freedom (DOFs) of flexible structures. The resulting equations of motion with the DOF vector $\mathbf{q}(t) \in \mathbb{R}^n$ are described by the second order differential equation

$$\overline{\mathbf{M}}\ddot{\mathbf{q}}(t) + \overline{\mathbf{D}}\dot{\mathbf{q}}(t) + \overline{\mathbf{K}}\mathbf{q}(t) = \overline{\mathbf{F}}\mathbf{u}(t), \quad t > 0, \quad \mathbf{q}(0) = \mathbf{q}_0, \quad \dot{\mathbf{q}}(0) = \mathbf{q}_1 \quad (1)$$

with the positive definite matrices for mass $\overline{\mathbf{M}} \in \mathbb{R}^{n \times n}$, stiffness $\overline{\mathbf{K}} \in \mathbb{R}^{n \times n}$ and damping $\overline{\mathbf{D}} \in \mathbb{R}^{n \times n}$. Manipulation of the system can be realized by actuator forces $\mathbf{u}(t) \in \mathbb{R}^m$ on the right side of (1). The input matrix $\overline{\mathbf{F}} \in \mathbb{R}^{n \times m}$ distributes these forces among the DOFs. The mass and stiffness matrix are directly obtained by an FE analysis of the underlying structure, whereas the damping matrix is chosen as Rayleigh damping in the following form:

$$\overline{\mathbf{D}} = \alpha_1 \overline{\mathbf{M}} + \alpha_2 \overline{\mathbf{K}}. \quad (2)$$

The coefficients α_1 and α_2 can be determined by experimental identification or from literature. Rayleigh damping is classified as proportional damping, which is accompanied by the advantage that eigenmodes of the model remain unchanged [26, 29].

2.1.1 Modal Analysis

A modal analysis is a powerful tool to characterize and reduce – solely – linear models. Therefore, the harmonic solution $\mathbf{q}(t) = \boldsymbol{\varphi}_i \exp(j\omega_i t)$ is plugged in the undamped system, which

leads to the generalized eigenvalue problem $(\mathbf{K} - \omega_i^2 \mathbf{M})\boldsymbol{\varphi}_i = 0$. The n eigenvalues ω_i represent the oscillation frequencies of the i^{th} eigenmode and the eigenvectors $\boldsymbol{\varphi}_i$ collect the respective mode shape. Equation (1) can be transformed by $\mathbf{q}(t) = \mathbf{\Phi}\boldsymbol{\eta}(t)$ with $\mathbf{\Phi} = [\boldsymbol{\varphi}_1, \dots, \boldsymbol{\varphi}_n]$, where $\boldsymbol{\eta}(t)$ represent the modal amplitudes. This along with left multiplying of (1) by $\mathbf{\Phi}^\top$ yields the modal dynamics:

$$\ddot{\boldsymbol{\eta}}(t) + \mathbf{D}_\eta \dot{\boldsymbol{\eta}}(t) + \mathbf{K}_\eta \boldsymbol{\eta}(t) = \mathbf{F}_\eta \mathbf{u}(t), \quad t > 0, \quad \boldsymbol{\eta}(0) = \mathbf{\Phi}^{-1} \mathbf{q}_0, \quad \dot{\boldsymbol{\eta}}(0) = \mathbf{\Phi}^{-1} \dot{\mathbf{q}}_1. \quad (3)$$

The eigenvector matrix $\mathbf{\Phi}$ is unique besides a scaling factor and therefore normalized such that $\mathbf{\Phi}^\top \mathbf{M} \mathbf{\Phi} = \mathbf{I}$, where \mathbf{I} is the identity matrix. The modal stiffness matrix $\mathbf{K}_\eta = \text{diag}([\omega_1^2, \dots, \omega_n^2])$ is diagonal and includes the squared eigenfrequencies on the main diagonal. Model order reduction can be conducted by applying the transformation above with a reduced set of eigenvectors $\mathbf{\Phi} = [\boldsymbol{\varphi}_1, \dots, \boldsymbol{\varphi}_{n_r}]$.

2.2 Model with Tension-only Elements

In order to model the tension-only elements properly, an adaption of the linear equations of motion is necessary. A qualitative description of the system's behavior shall make the reader comfortable with the effect before the corresponding equations are given. If tension is applied to a tension-only element of the structure, a linear force-displacement relation is assumed (see Fig. 2) and the system can be described as in 2.1. If a tension-only element is at its initial length (or potentially below), the contribution of this element to the stiffness of the structure vanishes. A two-dimensional visualization is given in Fig. 3. The stiffness k of the i^{th} diagonal element for $i = 1, \dots, n_t$ with n_t tension-only elements is given by

$$k_i(\mathbf{q}(t)) = \begin{cases} k_i, & \Delta l_i(\mathbf{q}(t)) \geq 0 \\ 0, & \Delta l_i(\mathbf{q}(t)) < 0 \end{cases} \quad i = 1, \dots, n_t. \quad (4)$$

The absolute length $\Delta l_i(\mathbf{q}(t))$ of a tension-only element i is calculated via the distance of the two nodes the element is attached to. These nodes are referred to as endpoint nodes 1,2. The initial length of a tension-only element equals the initial distance between these nodes: $l_{i,0} = \sqrt{\Delta \mathbf{q}_{i,0}^\top \Delta \mathbf{q}_{i,0}}$ with $\Delta \mathbf{q}_{i,0} = \mathbf{q}_{i,1,0} - \mathbf{q}_{i,2,0}$, where $\mathbf{q}_{i,1,0}$ and $\mathbf{q}_{i,2,0}$ are the initial positions of the endpoint nodes. In the equation of motion, the DOFs $\mathbf{q}(t)$ represent a relative motion around the equilibrium state. The absolute position of a node is given by $\tilde{\mathbf{q}}_{i,1}(t) = \mathbf{q}_{i,1,0} + \mathbf{q}_{i,1}(t)$ and analogously $\tilde{\mathbf{q}}_{i,2}(t) = \mathbf{q}_{i,2,0} + \mathbf{q}_{i,2}(t)$. The relative displacements of the endpoint nodes are a subset of the DOFs vector $\mathbf{q}_{i,1}(t) \subset \mathbf{q}(t)$, respectively $\mathbf{q}_{i,2}(t) \subset \mathbf{q}(t)$. After determining the absolute position of the endpoint nodes, the direction vector between the two nodes is $\Delta \mathbf{q}_i(t) = \tilde{\mathbf{q}}_{i,1}(t) - \tilde{\mathbf{q}}_{i,2}(t)$. The distance between the nodes equals the absolute length of the tension-only element and can be calculated via the scalar product. Subtracting the initial length yields $\Delta l_i(\mathbf{q}(t)) = \sqrt{\Delta \tilde{\mathbf{q}}_i^\top(t) \Delta \tilde{\mathbf{q}}_i(t)} - l_{i,0}$ for evaluating the inequality conditions in (4). Tension-only elements under small pretension can be treated by adjusting $l_{i,0}$ according to the pretension value.

Based on (4), the stiffness matrix is state-dependent and changes to $\mathbf{K}(\mathbf{q}(t))$. The tension-only elements contribute to the stiffness matrix according to the orange graph in Fig. 2 as opposed to a linear stiffness behavior (Fig. 2 gray). Therefore, the stiffness matrix is reassembled in the FE toolchain every time a tension-only element changes in the sense of (4) [6, 30]. The equation for the model with tension-only elements changes to

$$\mathbf{M} \ddot{\mathbf{q}}(t) + \mathbf{D}(\mathbf{q}(t)) \dot{\mathbf{q}}(t) + \mathbf{K}(\mathbf{q}(t)) \mathbf{q}(t) = \mathbf{F} \mathbf{u}(t), \quad t > 0, \quad \mathbf{q}(0) = \mathbf{q}_0, \quad \dot{\mathbf{q}}(0) = \dot{\mathbf{q}}_1, \quad (5)$$

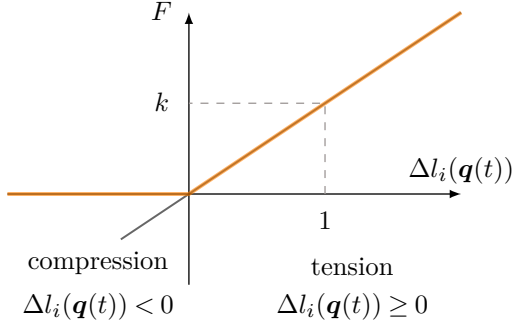


Figure 2: The force in a tension-only element is depicted over the element length (orange). The element force is zero for the element under compression, and linearly increasing with slope k under tension; linear element for comparison (gray).

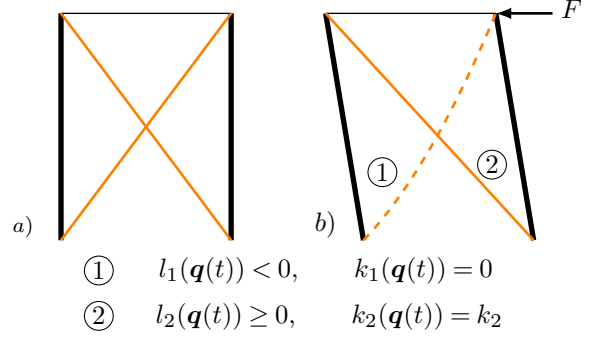


Figure 3: 2D-Sketch with tension-only elements in orange and common linear elements in black. a) Undisplaced structure and b) structure displaced by a force F , which leads to a tension-only element under compression, marked with a dashed line.

with the damping matrix $\mathbf{D}(\mathbf{q}(t)) \in \mathbb{R}^{n \times n}$. It is derived according to (2), where the state-dependency is inherited by $\mathbf{K}(\mathbf{q}(t))$. As can be seen in (5), the mass matrix is equivalent to the linear version because tension-only elements still contribute inertia to the structure. Any effects of a changed mass distribution are assumed to be small and therefore negligible.

3 Proper Orthogonal Decomposition and Model Order Reduction

The kind of systems, introduced in section 2.2, incorporate many local nonlinearities in form of tension-only elements. However, looking at the overall system, almost linear oscillation behavior is observed that motivates the application of proper orthogonal decomposition (POD) for model order reduction and generation of a model for control design. POD is a method to achieve a low-dimensional approximation of a high dimensional space [4]. After the theorem of Eckart-Young-Mirsky, POD is the best low-rank approximation [9, 25] for this task. It is also referred to as Karhunen-Loeve transformation or principal component analysis and is well-established in statistical analysis [24].

The POD is realized by the singular value decomposition, also referred to as the generalization of the eigenvalue problem (see 2.1.1) for rectangular matrices. Performing the singular value decomposition, a general matrix $\mathbf{A} \in \mathbb{R}^{n_1 \times n_2}$ is factorized in three matrices

$$\mathbf{A} = \mathbf{V} \mathbf{\Sigma} \mathbf{W}^* \quad (6)$$

where $\mathbf{V} \in \mathbb{R}^{n_1 \times n_1}$ is a unitary matrix and the columns are the left eigenvectors of \mathbf{A} . $\mathbf{\Sigma} \in \mathbb{R}^{n_1 \times n_2}$ is a diagonal matrix with non-negative real numbers $[\sigma_1, \sigma_2, \dots, \sigma_{\min(n_1, n_2)}]$ on the diagonal, called the singular values of \mathbf{A} . $\mathbf{W}^* \in \mathbb{R}^{n_2 \times n_2}$ is the conjugate transpose matrix of the unitary matrix \mathbf{W} and the column vectors of \mathbf{W} are the linear independent right eigenvectors of \mathbf{A} . If \mathbf{A} is quadratic, the singular values are equal to the squared eigenvalues.

The singular values quantify the importance of a corresponding POD vector for the data set. Therefore, the column vector corresponding to the highest singular value has highest share in the approximation. Selection of $n_r < n$ eigenvectors in the orthonormal POD basis to transform the nonlinear system can be quantified by $\sum_{k=1}^{n_r} \sigma_k^2 / \sum_{k=1}^n \sigma_k^2 > \kappa$, where κ is a defined tolerance. This fraction is referred to as the cumulative energy captured by n_r modes [34]. A physical

interpretation of the POD modes, specifically for mechanical systems, can be found in [10, 20].

POD is a method in model order reduction and can be applied to nonlinear systems. Often, simulation of nonlinear systems is computationally intensive, leading to long simulation times which is even worse in online evaluations for control application. A requirement for the application of POD is the availability of a data set representing the dynamics of a system. In turn, this points out the need of proper data recording. Using the dimensions such that n_2 equals the number of simulation steps and $n_1 = n$, the number of DOFs, the transformation matrix yields $\mathbf{V}_r = [\mathbf{v}_1, \mathbf{v}_2, \dots, \mathbf{v}_{n_r}] \in \mathbb{R}^{n \times n_r}$. A POD is conducted on simulated data set of the nonlinear model (5) which leads to a POD basis \mathbf{V} . The system is reduced by means of a reduced POD basis \mathbf{V}_r under the transformation law $\mathbf{q}(t) = \mathbf{V}_r \boldsymbol{\zeta}(t)$, followed by a left multiplication with \mathbf{V}_r^\top , which yields

$$\begin{aligned} \mathbf{M}_r \ddot{\boldsymbol{\zeta}}(t) + \mathbf{V}_r^\top \mathbf{D}(\mathbf{V}_r \boldsymbol{\zeta}(t)) \mathbf{V}_r \dot{\boldsymbol{\zeta}}(t) + \mathbf{V}_r^\top \mathbf{K}(\mathbf{V}_r \boldsymbol{\zeta}(t)) \mathbf{V}_r \boldsymbol{\zeta}(t) &= \mathbf{F}_r \mathbf{u}(t), \quad t > 0, \\ \boldsymbol{\zeta}(0) &= \mathbf{V}_r^{-1} \mathbf{q}_0, \quad \dot{\boldsymbol{\zeta}}(0) = \mathbf{V}_r^{-1} \mathbf{q}_1. \end{aligned} \quad (7)$$

The coordinates of the nonlinear reduced order model are $\boldsymbol{\zeta}(t) \in \mathbb{R}^{n_r}$. The reduced POD basis \mathbf{V}_r is normalized such that $\mathbf{M}_r = \mathbf{V}_r^\top \mathbf{M} \mathbf{V}_r \approx \mathbf{I} \in \mathbb{R}^{n_r \times n_r}$, with the unit matrix \mathbf{I} . Furthermore, the reduced order input matrix is $\mathbf{F}_r = \mathbf{V}^\top \mathbf{F} \in \mathbb{R}^{n_r \times m}$. As can be seen in (7), the nonlinear evaluation is not eliminated by the transformation and must still be conducted in the original dimensions. For reduction of computation time, the model order reduction with a POD basis is useful despite.

3.1 Design Model for Control

For control design, models of usually low dimension are used, such that the main characteristics of the system can be controlled. Therefore, the complexity in control design and the computation effort remain acceptable. In linear control theory, a modal controller is designed based on the primary modes as can be derived from section 2.1.1 [13]. Higher order modes can be neglected due to a high natural damping of these modes and a limited bandwidth of actuators. However, the selection of the primary modes is delicate and is done based on experience as well as practical relevance and the control engineer must be aware of effects like spillover [16, 28]. This model for control design for the nonlinear system is generated similarly to the reduced order model (7), but a different transformation matrix $\mathbf{V}_c \in \mathbb{R}^{n \times n_c}$ is chosen, where $n_c < n_r < n$ and the transformation law $\mathbf{q}(t) = \mathbf{V}_c \boldsymbol{\zeta}(t)$. The input affine system for control design is now written in general state space form with the state $\mathbf{x} = [\boldsymbol{\zeta}, \dot{\boldsymbol{\zeta}}]^\top$

$$\dot{\mathbf{x}}(t) = \mathbf{f}(\mathbf{x}(t)) + \mathbf{g}(\mathbf{x}(t))\mathbf{u}(t), \quad t > 0, \quad \mathbf{x}(0) = \mathbf{x}_0, \quad (8)$$

$$\mathbf{f}(\mathbf{x}(t)) = \begin{bmatrix} \mathbf{0} & \mathbf{I} \\ -\mathbf{V}_c^\top \mathbf{K}(\mathbf{V}_c \boldsymbol{\zeta}(t)) \mathbf{V}_c & -\mathbf{V}_c^\top \mathbf{D}(\mathbf{V}_c \dot{\boldsymbol{\zeta}}(t)) \mathbf{V}_c \end{bmatrix} \mathbf{x}(t) \quad \text{and} \quad \mathbf{g}(\mathbf{x}(t)) = \mathbf{g} = \begin{bmatrix} \mathbf{0} \\ \mathbf{F}_c \end{bmatrix}. \quad (9)$$

4 CONTROL

A similar behavior between the linearly modeled structure and the nonlinear system is observed. To control nonlinear systems, feedback linearization can be applied, which transforms the system such that a chain of integrators is resulting [11], of which control is fairly simple. This would be an option for the introduced system with tension-only elements, however, due to similarities to linear systems the following approach is proposed. A linearizing input transformation is performed, where the target system is modeled by linear second order equations

of motion. Therefore, the control effort to linearize the system can be kept low because the dynamics of original and target system are similar. The target system is chosen that the desired properties are achieved. A control strategy is applied to the nonlinear system (5) based on the nonlinear model for control design (8).

4.1 Linearizing Input Transformation

In order to control the nonlinear system, a nonlinear input transformation is conducted, which forces the nonlinear system to follow the dynamics of the target system. Under the assumption of local controllability of system (8), a general target system is

$$\dot{\mathbf{x}}(t) = \mathbf{f}_d(\mathbf{x}(t)) + \mathbf{g}_d(\mathbf{x}(t))\mathbf{w}(t), \quad t > 0, \quad \mathbf{x}(0) = \mathbf{x}_0, \quad (10)$$

where a new virtual input $\mathbf{w}(t) \in \mathbb{R}^m$ for the linear target system is defined. For $\mathbf{w}(t) = \mathbf{0}$ the system is required to be stable and show desired decay properties. The target system incorporates desired dynamics and system properties, which are parameters in design. A clever selection of the target system simplifies further control design, e.g. if a linear target system is chosen. The dynamics of the general nonlinear control system (8) are set equal to the dynamics of the target system (10). Solving for the input $\mathbf{u}(t)$ of control system, yields

$$\mathbf{u}(t) = \mathbf{g}^+(\mathbf{x})\left(\mathbf{f}_d(\mathbf{x}(t)) - \mathbf{f}(\mathbf{x}(t))\right) + \mathbf{g}^+(\mathbf{x})\mathbf{g}_d(\mathbf{x}(t))\mathbf{w}(t). \quad (11)$$

If $\mathbf{g}(\mathbf{x})$ is quadratic, the Moore-Penrose pseudo inverse [27] $\mathbf{g}^+(\mathbf{x})$ will be the inverse. This is the case for an equal number of inputs and states, which is generally not valid. Plugging (11) into (8) makes the nonlinear closed-loop system follow the dynamics of the target system. The quality of this approach is highly depending on the pseudo-inverse of $\mathbf{g}(\mathbf{x})$.

4.2 Target System for Mechanical Structures

For the application in structural dynamics, the desired system (10) is chosen as linear second order system in state space form

$$\dot{\mathbf{x}}(t) = \mathbf{f}_d(\mathbf{x}(t)) + \mathbf{g}_d(\mathbf{x}(t))\mathbf{w}(t), \quad t > 0, \quad \mathbf{x}(0) = \mathbf{x}_0, \quad (12)$$

$$\mathbf{f}_d(\mathbf{x}(t)) = \mathbf{A}_d\mathbf{x}(t) = \begin{bmatrix} \mathbf{0} & \mathbf{I} \\ -\mathbf{K}_d & -\mathbf{D}_d \end{bmatrix} \mathbf{x}(t) \quad \text{and} \quad \mathbf{g}_d(\mathbf{x}(t)) = \mathbf{B}_d = \begin{bmatrix} \mathbf{0} \\ \mathbf{F}_d \end{bmatrix} \quad (13)$$

with $\mathbf{f}_d(\mathbf{x}(t)) \in \mathbb{R}^{2n_c}$ and $\mathbf{g}_d(\mathbf{x}(t)) \in \mathbb{R}^{2n_c}$, where the system still shows the structure of a second order mechanical system and \mathbf{A}_d consists of a desired stiffness and damping matrix $\mathbf{K}_d \in \mathbb{R}^{n_c \times n_c}$ and $\mathbf{D}_d \in \mathbb{R}^{n_c \times n_c}$. The structure of system matrix \mathbf{A}_d is Hurwitz [18] and is therefore stable. For control of the linear target system a linear quadratic (LQ) controller is applied as a state feedback [12, 28].

5 NUMERICAL RESULTS

The introduced methodology is applied to an exemplary high-rise structure. The order reduction over the POD basis is evaluated and the POD modes are interpreted physically. A reduced order simulation model is stated and the performance of the control strategy is illustrated.

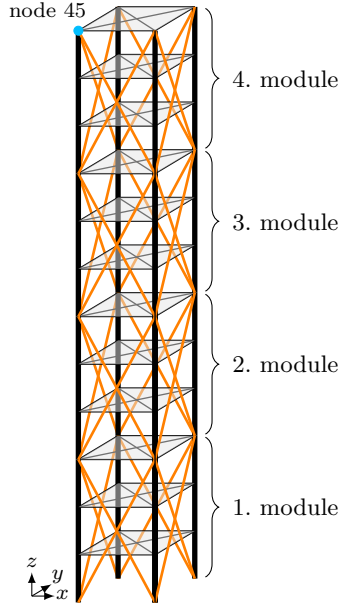


Figure 4: Sketch of the high-rise building with tension-only elements (orange) and the DOF for depiction of results (light blue).

Description	Formula sign	Value	Unit
Density	ρ	7850	kg/m ³
Young's modulus	E	210×10^9	N/m ²
Columns, quadratic hollow profile			
Length	L_v	3	m
Width	w_v	0.3	m
Wall thickness	t_v	0.01	m
Poisson's ratio	ν	0.3	
Horizontal links, 2 rectangular hollow profiles			
Length	L_h	4.75	m
Width	w_h	0.2	m
Height	h_h	0.12	m
Wall thickness	t_h	0.008	m
Horizontal diagonal links			
Length	L_{hd}	6.72	m
Width	h_{hd}	0.01	m
Height	h_{hd}	0.06	m
Diagonal tension-only elements			
Length	L_{vd}	10.18	m
Width	w_{vd}	0.15	m
Height	h_{vd}	0.012	m

Table 1: Geometry and material parameters of the structure.

5.1 High-rise Structure

To illustrate the proposed modeling and control strategy, an adaptive high-rise structure is introduced. This structure (Fig. 1) will be built on the site of the University of Stuttgart and consists of 12 stories, which are summarized in 4 modules comprising 3 stories each. The diagonal bracings are tension-only elements spanning over one module, two on each side, which leads to a total amount of 32 such elements (4 modules with 8 diagonals each). The tension-only elements are realized with flat steel. A sketch of the structure is given in Fig. 4 with tension-only elements in orange. All other elements can withstand compression and tension. The columns in the corner of a story are modeled as beams that are connected by horizontal links on the joints. The horizontal ceilings are approximated by links connecting diagonally opposing nodes. All geometry and material parameters can be taken from Tab. 1. The system incorporates 24 actuators, 8 actuators are in the columns of the lower two modules and the remaining actuators are placed in the diagonal bracings. All diagonals in the first module are equipped with actuators and in the second and third module 4 diagonals elements each [16, 35]. For the linearizing input transformation and the control, the actuators in the columns are used because the effect of the nonlinear bracings is examined in this contribution without interference of actuation. This results in a model with $n = 288$ DOF which are distributed over 48 nodes with 6 DOF each. The DOF at the 4 boundary nodes at the bottom are fixed.

5.2 POD Modes

For the determination of the POD modes by means of (6), the 24 actuators are activated successively with a white noise signal to excite the dynamics of system (5). The POD modes are

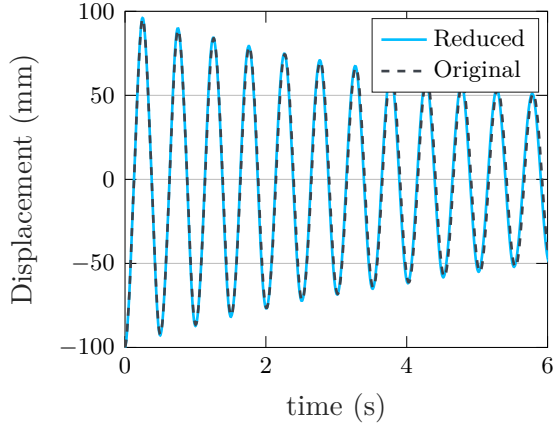


Figure 5: DOF of node 45 at the top left in x -direction of the original nonlinear model (dashed gray) and reduced order (blue) system.

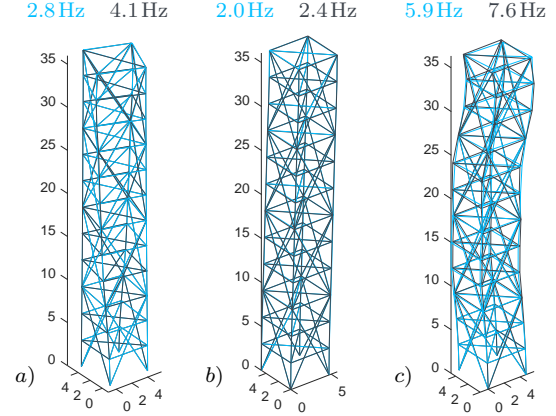


Figure 6: The POD modes of the nonlinear model (blue) are compared to the linear modal modes (gray). a) 1. order torsion mode, b) 1. order bending mode, c) 2. order bending mode.

analyzed regarding their shape with decreasing singular values. The first POD vector represents a first order torsion mode, followed by two first order bending modes. The two bending modes are reasoned in the symmetry of the structure, where one goes in x -direction and the second one in y -direction. The fourth POD vector is the second order torsion mode before two second order bending modes. The shape of the POD modes already indicates similarities to the linear modal analysis. Therefore, the identified POD modes of the nonlinear system are compared to the modal modes of the structure, modeled as a linear system according to (1), where all diagonals are modeled as links, which can bear tension and compression. The comparison results are depicted in Fig. 6, where the frequencies corresponding to the POD modes are determined by fast Fourier transform from the simulation data. Sorting the eigenmodes by increasing frequencies the order of the linear system's modal modes differs from that of the POD modes. In the linear model, both first order bending modes correspond to the lowest eigenfrequencies, followed by the first order torsion mode, two second order bending modes, two third order bending modes and the second order torsional modal mode. The different order regarding mode shapes and frequencies can be explained by the drastically reduced stiffness of the nonlinear model concerning torsional motions. Due to the ineffectiveness of the stiffness component of the tension-only elements under compression, torsion modes get more important, which is captured by the simulation of the nonlinear model. A comparison of the corresponding normalized mode shapes, however, shows high alignment of the POD modes and the modal modes (Fig. 6). Depicted are a) the first order torsion and b) the first and c) second order bending modes in x -direction. As expected, the alignment decreases for higher mode order. However, the good alignment motivates the application of the introduced control approach with linearizing input.

5.3 Reduced Order Simulation Model

The reduced order simulation model is composed of $n_r = 18$ POD modes. This leads to $\kappa = 99.08\%$, which means that the residual modes contribute less than 1% to the cumulative energy with respect to the data set used for the POD analysis. The approximation quality is

illustrated in numerical results in Fig. 5, where the simulation is conducted with a non-zero initial condition. The time series is depicted for node 45 at the top left in x -direction, which is marked in Fig. 4. This node is selected because the largest displacements are found at the top of the building. The data of the full model is depicted in dashed gray needing 49.9s simulation time and the reduced order model in blue with 7.6s. The reduced order model approximates the dynamics of the full model with high accuracy, thus justifying its use to drastically save simulation time of 84%.

5.4 Control Performance

In a first step, the linearizing input (11) is applied to the nonlinear system with the target system (12) as described in section 4. The eight actuators in the columns of the first and second module are used for the linearizing input and control. The model for control design is of order $n_c = 4$, where the first and the second order bending modes are captured in \mathbf{V}_c . The torsional modes are left out because they are not controllable with the selected set of actuators. This selection is justified due to the specific investigation of the nonlinear effect concerning the tension-only elements and the torsion mode is not excited in this numeric experiment.

The target system's matrix \mathbf{A}_d is chosen such that the desired stiffness matrix $\mathbf{K}_d = \frac{1}{4}\mathbf{K}(\mathbf{V}_c\mathbf{0})$ is equal to a quarter of the nonlinear system's stiffness matrix evaluated at zero. The damping matrix is chosen equivalently to $\mathbf{D}_d = \mathbf{D}(\mathbf{V}_c\mathbf{0})$ with increased coefficients in the Rayleigh damping of $\alpha_{1d} = 0.1$ and $\alpha_{2d} = 0.01$. The target input matrix \mathbf{B}_d is set to \mathbf{g} from (9) since there is no nonlinearity in the input and the input affinity of the system can be preserved. The result is illustrated in Fig. 7, where the reduced nonlinear system is shown in dashed gray and the effect of the uncontrolled linearizing input in dark blue, where both times the same initial condition is applied. The system with linearizing input shows an altered oscillation behavior with a decreased oscillation frequency. Due to the increased damping coefficients of the linear target system, the nonlinear system with linearizing input already express a higher damping rate. According to the chosen target matrix, the frequency of the system with linearizing feedback is not a quarter of the original system's frequency because the nonlinearity already leads to decreased oscillation frequencies. Compared to simulating purely the linear target system, small deviations are visible due to the residual modes. With application of the LQ controller the damping of the system is increased further which proofs the effectiveness of the linearizing input transformation. The control algorithm as described in section 4 transforms the nonlinear system to a desired target system with the designed closed-loop dynamics. Thus, control design is simplified drastically through the nonlinear input transformation of such nonlinear systems.

6 CONCLUSION

In this contribution, the nonlinear equations of motion for tension-only elements were derived. A POD was conducted, which captures the main characteristics of the nonlinear system. Properties were compared to the nonlinear system evaluated at zero, where similar behaviors were discovered. The mode shapes of the POD and the eigenmodes are almost equal, whereas the frequencies have changed. The nonlinear system was reduced to achieve acceptable calculation times with high model accordance at the same time. The effect of nonlinearities from tension-only elements have high impact on the systems behavior and need to be considered in modeling. A low dimensional model for control and a linearizing input transformation for the nonlinear model were derived, which drives the system states according to the dynamics of a

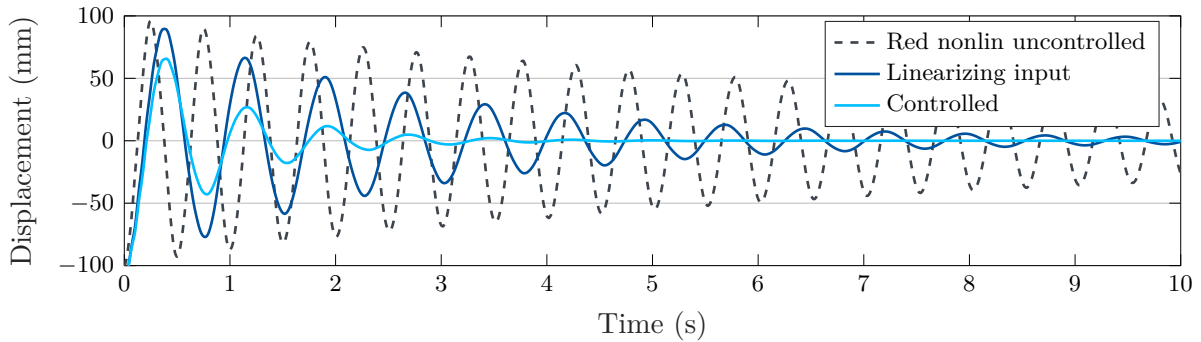


Figure 7: The input-transformed nonlinear system with LQ-controller (light blue) in comparison to the input-transformed nonlinear system without additional feedback control (dark blue) and the original open-loop nonlinear system (gray). The displacement in x -direction of node 45 at the top left is depicted.

linear target system. With this linearizing input, the nonlinear system can simply be controlled by controlling the linear target system, where the wide methods of linear control theory can be applied. The results promise applicability to structures with tension-only elements.

For further research, any other target system or controller can be chosen to achieve a different closed-loop behavior. An integration of actuators in the tension-only elements can be useful to further generalize this method. After construction of the experimental high-rise structure is finished, the presented algorithm will be applied.

ACKNOWLEDGEMENTS

This work is part of the collaborative research center CRC 1244 "Adaptive Skins and Structures for the Built Environment of Tomorrow" funded by the German Research Foundation under grant SFB 1244/1 2017 (B04, A06).

REFERENCES

- [1] M. Ahmadizadeh. Three-dimensional geometrically nonlinear analysis of slack cable structures. *Computers & Structures*, 128:160–169, 2013.
- [2] P. Alart, D. Dureisseix, R. Laniel, and S. Pagano. Wires and cables in some discrete structures of civil engineering. In *6th Eurosim Congress on Modelling and simulation*, 2007.
- [3] N.B.H. Ali and I.F.C. Smith. Dynamic behavior and vibration control of a tensegrity structure. *International Journal of Solids and Structures*, 47(9):1285–1296, 2010.
- [4] F. Bamer and C. Bucher. Application of the proper orthogonal decomposition for linear and nonlinear structures under transient excitations. *Acta Mechanica*, 223(12):2549–2563, 2012.
- [5] M.R. Barnes. Form finding and analysis of tension structures by dynamic relaxation. *International journal of space structures*, 14(2):89–104, 1999.
- [6] M.A. Bhatti. *Advanced topics in finite element analysis of structures: with Mathematica and MATLAB computations*. John Wiley & Sons, Inc., 2006.
- [7] P.J. Cruz, M. Oishi, and R. Fierro. Lift of a cable-suspended load by a quadrotor: A hybrid system approach. In *2015 American Control Conference*, 2015.
- [8] S. Djouadi, R. Motro, J.C. Pons, and B. Crosnier. Active control of tensegrity systems. *Journal of Aerospace Engineering*, 11(2):37–44, 1998.
- [9] C. Eckart and G. Young. The approximation of one matrix by another of lower rank. *Psychometrika*, 1(3):211–218, 1936.
- [10] B.F. Feeny and R. Kappagantu. On the physical interpretation of proper orthogonal modes in vibrations. *Journal of sound and vibration*, 211(4):607–616, 1998.

- [11] M. Fliess, J. Lévine, P. Martin, and P. Rouchon. Flatness and defect of non-linear systems: introductory theory and examples. *International journal of control*, 61(6):1327–1361, 1995.
- [12] O. Föllinger. Regelungstechnik. 8. revised edition. *Hüthig-Verlag, Heidelberg*, 1994.
- [13] W. Gawronski. *Advanced structural dynamics and active control of structures*. Springer Science & Business Media, 2004.
- [14] R.W. Gehle and S.F. Masri. Active control of shallow, slack cable using the parametric control of end tension. *Nonlinear Dynamics*, 17(1):77–94, 1998.
- [15] J. Hauser, S. Sastry, and P. Kokotovic. Nonlinear control via approximate input-output linearization: The ball and beam example. *IEEE transactions on automatic control*, 37(3):392–398, 1992.
- [16] M. Heidingsfeld, P. Rapp, M. Böhm, and O. Sawodny. Gramian-based Actuator Placement with Spillover Reduction for Active Damping of Adaptive Structures. In *Proceedings of the 2017 IEEE/ASME International Conference on Advanced Intelligent Mechatronics*, 2017.
- [17] G. Housner, L.A. Bergman, T.K. Caughey, A.G. Chassiakos, R.O. Claus, S.F. Masri, R.E. Skelton, T.T. Soong, B.F. Spencer, and J.T.P. Yao. Structural Control: Past, Present, and Future. *Journal of engineering mechanics*, 123(9):897–971, 1997.
- [18] A. Hurwitz. Ueber die bedingungen, unter welchen eine gleichung nur wurzeln mit negativen reellen theilen besitzt. *Mathematische Annalen*, 46(2):273–284, 1895.
- [19] H.M. Irvine. *Cable structures*, volume 17. MIT press Cambridge, MA, 1981.
- [20] G. Kerschen, J. Golinval, A.F. Vakakis, and L.A. Bergman. The method of proper orthogonal decomposition for dynamical characterization and order reduction of mechanical systems: an overview. *Nonlinear dynamics*, 41(1-3):147–169, 2005.
- [21] S. Korkmaz. A review of active structural control: challenges for engineering informatics. *Computers & Structures*, 89(23-24):2113–2132, 2011.
- [22] C. Kravaris and M. Soroush. Synthesis of multivariable nonlinear controllers by input/output linearization. *AIChE Journal*, 36(2):249–264, 1990.
- [23] W.J. Lewis. *Tension structures: form and behaviour*. Thomas Telford, 2003.
- [24] Y.C. Liang, H.P. Lee, S.P. Lim, W.Z. Lin, K.H. Lee, and C.G. Wu. Proper orthogonal decomposition and its applications—part i: Theory. *Journal of Sound and vibration*, 252(3):527–544, 2002.
- [25] L. Mirsky. Symmetric gauge functions and unitarily invariant norms. *The quarterly journal of mathematics*, 11(1):50–59, 1960.
- [26] M.E.J. O’Kelly and T.K. Caughey. Classical normal modes in damped linear dynamic systems. *Journal of Applied Mechanics*, 32(3):583–588, 1965.
- [27] R. Penrose. A generalized inverse for matrices. In *Mathematical proc. of the Cambridge philosophical society*, 1955.
- [28] A. Preumont. *Vibration control of active structures*, volume 2. Springer, 1997.
- [29] J.W.S. Baron Rayleigh. *The theory of sound*, volume 2. Macmillan, 1877.
- [30] R. Schwertassek and O. Wallrapp. *Dynamik flexibler Mehrkörpersysteme*. Vieweg, 1998.
- [31] R.E. Skelton, R. Adhikari, J.P. Pinaud, W. Chan, and J.W. Helton. An introduction to the mechanics of tensegrity structures. In *Proceedings of the 40th IEEE conference on decision and control*, 2001.
- [32] W. Sobek and P. Teuffel. Adaptive systems in architecture and structural engineering. *Proc. of SPIE*, 2001.
- [33] B.F. Spencer Jr and S. Nagarajaiah. State of the Art of Structural Control. *Journal of structural engineering*, 129(7):845–856, 2003.
- [34] R. Swischuk, L. Mainini, B. Peherstorfer, and K. Willcox. Projection-based model reduction: Formulations for physics-based machine learning. *Computers & Fluids*, 2018.
- [35] J.L. Wagner, J. Gade, M. Heidingsfeld, F. Geiger, M. von Scheven, M. Böhm, M. Bischoff, and O. Sawodny. On steady-state disturbance compensability for actuator placement in adaptive structures. *at-Automatisierungstechnik*, 66(8):591–603, 2018.
- [36] S. Weidner, C. Kelleter, P. Sternberg, W. Haase, F. Geiger, T. Burghardt, C. Honold, J. Wagner, M. Böhm, M. Bischoff, O. Sawodny, and H. Binz. The implementation of adaptive elements into an experimental high-rise building. *Steel Construction*, 11:109–117, 05 2018.
- [37] J.T.P. Yao. Concept of structural control. *ASCE Journal of the Structural Division*, 98(07):1567–1574, 1972.

SELECTED RESULTS ON THE DEVELOPMENT AND TESTING OF SMART BLADES TECHNOLOGIES FOR WIND TURBINES

**ZHUZHELL M. MONTANO*, STEFFEN OPITZ*, JOHANNES
RIEMENSCHNEIDER*, EDGAR WERTHEN*, MARTIN POHL*, YVES GOVERS**,
JANTO GUNDLACH**, VLAHO PETROVIĆ†, RÓBERT UNGURÁN†, LARS
NEUHAUS†, PIYUSH SINGH†, CLAUDIO BALZANI††, MICHAEL
WENTINGMANN††, AYAN HALDAR††, RAIMUND ROLFES††**

* German Aerospace Center (DLR), Institute of Composite Structures and Adaptive Systems
Lilienthalplatz 7, 38108 Braunschweig, Germany
e-mail: Zhuzhell.MontanoRejas@dlr.de,
web page: <https://www.dlr.de/fa>

** German Aerospace Center (DLR), Institute of Aeroelasticity
Bunsenstr. 10, 37073 Göttingen, Germany
e-mail: Yves.Govers@dlr.de,
web page: <https://www.dlr.de/ae>

† ForWind – Center for Wind Energy Research, Carl von Ossietzky University of Oldenburg
Küppersweg 70, D-26129 Oldenburg, Germany
e-mail: vlaho.petrovic@uni-oldenburg.de,
web page: <https://www.forwind.de/>

†† ForWind – Center for Wind Energy Research, Leibniz University Hannover
Appelstr. 9A, 30167 Hannover, Germany
e-mail: claudio.balzani@iwes.uni-hannover.de,
web page: <https://www.forwind.de/>

Key words: Smart Structures, Wind Energy, Bend-Twist-Coupling, Flaps, Slats

Abstract. Within the frame of the Smart Blades and the SmartBlades2 projects, different technologies for developing smart rotor blades for wind turbines have been developed and are still being studied and tested. These cover the three following technologies: bend-twist coupled rotor blades; rotor blades with trailing edge flaps and rotor blades with leading edge slats. In addition, cross-technology topics that need to be considered for successfully implementing all three technologies as well as for evaluating their performance within a wind turbine system are being studied.

This paper will present an overview of the results of the project focusing in the following:

- Rotor blades with geometrical Bend Twist Coupling (BTC): summary of the blade design and manufacturing processes, summary of the results of modal tests, and selected preliminary results of field tests (on a turbine) with an introduction of a specially developed blade tip sensor for the measurement of the torsional deformation angle at the blade tip.
- Rotor blades with trailing edge flaps: summary of the concept and design of the demonstrator as well as fatigue tests, summary and highlights of the controller design activities, overview of the possibilities for upscaling as well as for developing alternative concepts.
- Rotor blades with leading edge slats: summary of three different concepts and the available results regarding wind tunnel tests as well as controller development with an emphasis on an active and a passive concept.
- Introduction to the evaluation method that will be used for evaluating the different technologies.

1 INTRODUCTION

The use of renewable energies is constantly growing and one of the fastest expanding sectors is wind [1]. In order to satisfy the resulting demand, the tendency in the wind energy sector is going towards building larger rotor blades [2], since the electrical power output that can be generated by a turbine is proportional to the square of the blade's radius. However, increasing the blade's size also means rapidly increasing their weight, proportional to the cube of the blade's radius, and substantially increasing the critical loads at the blade's roots [3].

The Smart Blades and SmartBlades2 projects, funded by the German Federal Ministry for Economic Affairs and Energy (BMWi), explore three different approaches for alleviating these loads increments: using bend-twist coupled rotor blades, using trailing edge flaps and, finally, using leading edge slats. This paper presents an overview of the proposed concepts as well as selected results of the first tests.

2 BEND-TWIST-COUPLED ROTOR BLADES

The first concept focuses on a passive principle that uses geometrical bend-twist coupling. The geometry of the blades allows them to bend and simultaneously twist increasingly across their span when strong wind and loading conditions are present, such as during gusts. This reduces the wind exposed area and angles of attack of the blades, leading to an overall loading reduction. This helps to prevent damage while keeping a high energy yield [4].

2.1 Design and manufacturing

One method for reducing loads along a rotor blade is sweeping. Local sweep variations can decrease heterogenic aerodynamic loading conditions caused by higher loads from effects such as gusts. A parametric study of the blade geometry for an 80 m blade was realized during the Smart Blades project, aiming to achieve an optimal sweep for bend-twist coupling. The parameters taken into account were the vertical displacement of the tip to the pitch axis, the distance of the sweep starting point from the blade root and the projected length of the blade at the pitch axis (Figure 1–Top). Aeroelastic simulations under quasi-static inflow conditions were performed in a discretized blade model (Figure 1–Bottom) to investigate the coupling behavior. A section coupling coefficient calculated by dividing the torsional moment over the flapwise bending moment was introduced to account for the structural coupling effects [5].

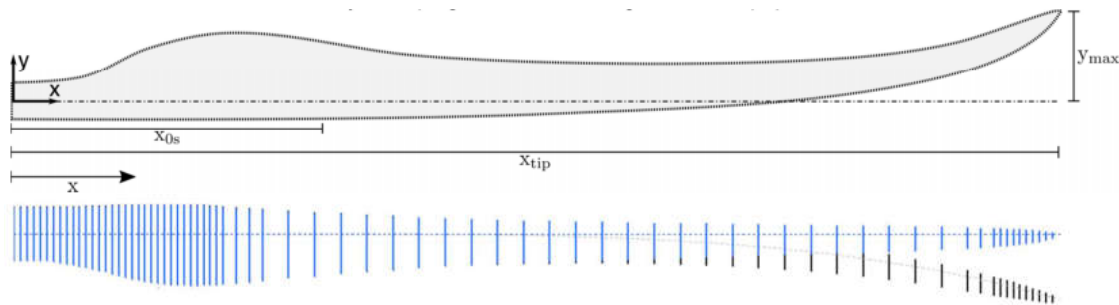


Figure 1: Top: Parameters for the determination of sweep; Bottom: Discretized model of the straight and swept blade [5]

The results were scaled down to a 20 m blade design and focused on manufacturability [6]. At the end of Smart Blades and based on the new design, a Glass Fiber Reinforced Plastic (GFRP) mold with an integrated heating system was built and, during SmartBlades2, used for the production of four blades. The manufacturing process based on a prefabrication concept and followed a semi-shell sandwich construction method: two half shells were individually produced and then fused together to form each blade. Some internal components, such as the spar, consist of sandwich panels that were manufactured separately in a vacuum infusion process and then cut to the designed shapes. Other components, such as the flange, are made of GFRP. For their manufacturing each inlay was pre-cut using a CNC cutter and manually laid in and infused in the appropriate area of the shell tool. For ensuring positioning precision and monitoring the infusion, a laser and a thermographic system were respectively used. The half shells were produced once the prefabrication components were ready. The flange inlays were positioned first and then the two layer outer laminate was laid up. The spar caps and sandwich material, consisting of balsa wood and foam, were then integrated. Once the inner laminate of the blade, which also comprised two layers, had been laid up, the blade halves were vacuum-infused. The final prefabricated part, the base, was then positioned in the shell of the suction

side. In a final step, the pressure and suction sides were bonded to form the finished rotor blade [4].

2.2 Modal tests overview

Once manufactured, all blades were subjected to modal testing and their eigenfrequencies and damping were determined under two different boundary conditions: clamped to a test rig (blade #1) and free-free, hanging on elastic suspensions (all blades). In addition, the modal shapes were measured using a high sensor density array attached to the blades' surfaces. The acquired data is being used for updating self-developed finite element models. To choose an appropriate distribution of the measurement points and excitation locations, a pretest analysis incorporating an FE shell model was carried out. During the modal tests, response signals were recorded via uniaxial accelerometers and force input was provided either by an impulse hammer or through electrodynamic shakers. Table 1: summarizes the eigenfrequency and damping values resulting from the two different test scenarios. Global modes are sorted from lower to higher frequencies as they appear for a clamped rotor blade. The structural dynamic similarity of the three blades can be recognized in the free-free tests results. Furthermore, local eigenforms illustrating cross-sectional vibrations attributed to the deflection of the blade shells could also be identified. Compared to the global results, the local modes correlate poorly with FE predictions [7]. In the forthcoming progress of the project the acquired data will serve as a basis for updating the FE model towards modal parameters.

Table 1: Eigenfrequencies and damping values of blade #1 being clamped to a test rig and arithmetic averages of blades #2 - #4 from free-free tests.

no.	mode description	test rig		free-free		
		eigenfrequency in Hz	damping in %	eigenfrequency in Hz	damping in %	coefficients of variation in %
1	1 st bend. flapwise	2.20	0.29	4.72	0.26	0.2/12.4
2	1 st bend. edgewise	3.07	0.14	9.81	0.38	0.8/26.1
3	2 nd bend. flapwise	6.84	0.41	11.87	0.23	0.6/5.3
4	2 nd bend. edgewise	10.86	0.53	26.68	0.42	0.5/9.5
5	3 rd bend. flapwise	13.57	0.31	20.58	0.36	0.6/8.7
6	1 st torsion	18.78	1.08	17.14	0.56	1.1/3.7
7	4 th bend. flapwise	21.65	0.61	31.21	0.76	0.5/11.4
8	3 rd bend. edgewise	26.49	0.69	48.24	0.65	0.6/22.2
9	5 th bend. flapwise	28.78	0.95	-	-	-
10	2 nd torsion	31.49	1.04	28.69	0.60	0.6/13.0

2.3 Wind turbine tests

In addition to the modal tests, test rig tests (not within the scope of this paper) were performed and turbine tests are being performed. The test rig tests covered extreme loading

testing for different static and dynamic conditions, including fatigue, and were accomplished successfully. The results allowed proceeding towards the turbine tests. The main goal of these is to measure the behavior and performance of the rotor blades under real conditions. Several sensors have been integrated in the blades' structure and on their outer skin to measure their behavior in detail, including strain gauges, torsion sensors, digital image correlation (DIC) foils and a Light Detection and Ranging (LiDAR) system. The Controls Advanced Research Turbine 3 (CART 3) [8] and the National Wind Technology Center (NWTC) [9] site of the National Renewable Energy Laboratory (NREL), where the tests are being performed, are also equipped with a wide range of sensors, allowing obtaining more detailed measurements of the turbine itself as well as of the surrounding environmental conditions.

2.4 Tip pitch Sensor

Even though the blades are instrumented with strain gauges and equipped with an optical deformation measurement system using a stereo camera system, detecting torsion deformation near the tip remains challenging. Strain gauges only detect local strains. Connecting them in Wheatstone bridges and proper calibration allows the measurement of bending and torsion moments at discrete radial positions. To derive the torsion deformation at the tip (θ_{tip}), the moment distribution ($M_t(x)$) needs to be inter- and extrapolated from the discrete measurement locations, divided by the distribution of torsional stiffness ($GI(x)$) and then integrated over the length of the blade - equation $\theta_{tip} = \int_{x_{root}}^{x_{tip}} \frac{M_t(x)}{GI(x)} dx$

(1).

$$\theta_{tip} = \int_{x_{root}}^{x_{tip}} \frac{M_t(x)}{GI(x)} dx \quad (1)$$

This procedure is prone to uncertainties and needs several measurement points as well as a very precise a priori knowledge of the stiffness distribution to deliver accurate results. The optical deformation measurement system installed within the blades cannot measure along the whole length either. The taper of the inner cross section and the elastic deformation of the blades limit the optical markers observability and restrict the measurement range. To solve these problems, an additional sensor capable of detecting torsional motion was developed and placed near the blade tip. The solution is based on a concept developed for active twist helicopter rotor blades [10][11] and was adapted to wind turbine rotor blades.

The new sensor detects rotational accelerations around one rotation axis. An inertia mass is connected to the blade tip via a flexible element. Under acceleration, the mass generates inertia moments that deform the flexible element. The flexible structure is soft in torsion and stiff for all other deformations. The deformation of the flexible element is captured by semiconductor strain gages, which are connected in a Wheatstone bridge that compensates for

temperature and suppresses sensor signals due to unintended deformations (e.g. bending). A tailored design of the inertia mass in combination with static accelerations in the centrifugal field of the rotor allows the detection of static pitch angles. The concept uses the propeller moments that occur in the centrifugal field (Figure 2).

The mass connected to the flexible element at point P consists of two punctual masses m . When the rotor spins with the frequency f_{rotor} , the force F is necessary to counteract the centrifugal force. F has two components: one parallel to the blade, F_{parallel} , and one orthogonal to the blade, $F_{\text{orthogonal}}$. If the pitch angle of the inertia mass, θ_{mass} , is zero, both mass points lie on a plane that is orthogonal to the rotor axis. Consequently, the orthogonal components of the forces do not generate any moment around P. However, if θ_{mass} increases, the mass points move out of the plane that is orthogonal to the rotor axis and contains P, the $F_{\text{orthogonal}}$ components generate a moment around P. This propeller moment deforms the flexible element even in case of static pitch angles.

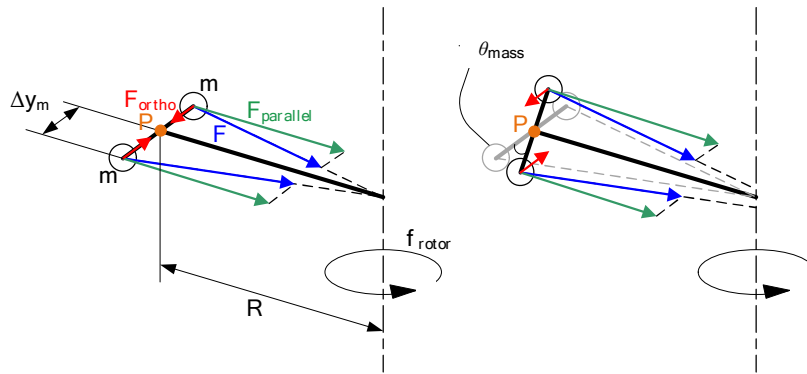


Figure 2: Formation of propeller moments

The location of the sensor near the blade tip brings an increased risk for lightning strike, meaning an electrical conductive connection between the sensor and the blade root needs to be avoided. To fulfill this requirement the sensor was connected with both a fiber optical data and energy transmission system. The system consists of a class 4 laser that couples 2 W of optical power into a fiber optic cable. At the other end of the cable a photovoltaic power converter delivers approx. 500 mW of electrical power, sufficient to operate the sensor and the module that transmits the data to the blade root. Figure 3 shows the major components of the sensor as CAD model and during installation.

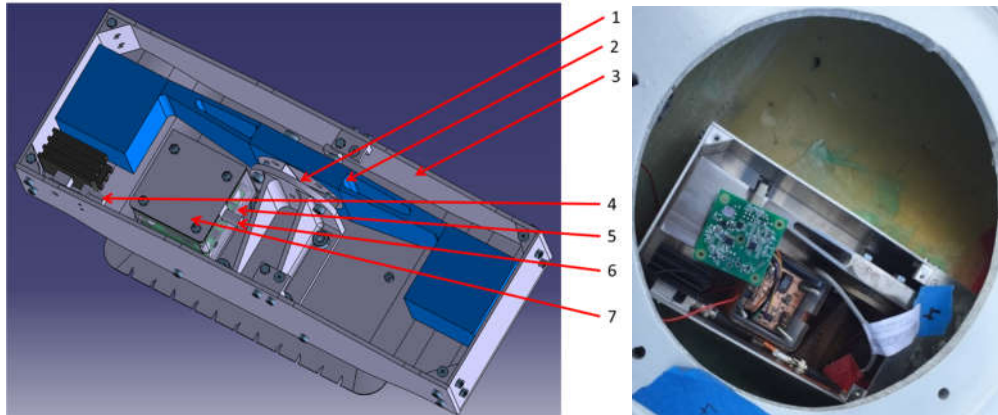


Figure 3: Sensor and its components (left), sensor during integration (right)

The flexible element (1) connects the mass (2) with the blade tip. To protect the sensor from foreign objects, the sensor is capsuled in a housing (3). The photovoltaic power converter (4) provides the power supply for the circuit board that drives the sensor (5) and the data transmission module (6). The latter two are capsuled by the electronic box (7).

3 TRAILING EDGE FLAPS

The second smart blades concept focuses on using trailing edge flaps for active flow control. The flaps function in a similar way to aircraft ailerons, components used to control the aircraft's movement. Even though the aerodynamic effects of trailing edge flaps are very similar, it is important to consider other design aspects for wind turbine rotor blades, such as the rotational operating conditions, maintenance and the environment at low altitudes [3].

3.1 Design concept and demonstrator

A flexible trailing edge structure design was chosen as a solution for the trailing edge flap and was developed during the Smart Blades project. The concept uses a rib like structure with a central support (Figure 4). By pushing or pulling, as the forces F_1 and F_2 show, the structure can be deformed and the desired flap deflection can be achieved, which allows to influence the airflow [3].

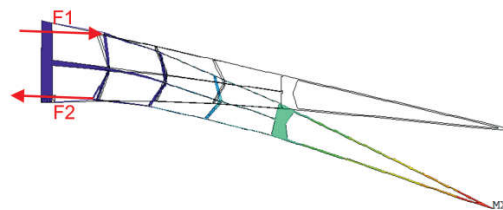


Figure 4: Flexible trailing edge concept [3]

Since the structure is flexible and is destined to morph under aerodynamic loads, the effect of aerodynamic pressure acting on the flap's surface needs to be considered in the structural design phase. An iterative process covering structural and aerodynamic factors was followed. The first step consisted on the creation of a structural model, followed up by the calculation of the actuation induced deflections. Once this done, the aerodynamic pressure distribution of the deflected flap was calculated and input back to the structural model to recalculate loading. The structure was then re-evaluated and optimized. The process stopped when the deflection values remained constant, reaching structural and aerodynamic stability [3].

3.2 Testing of the trailing edge

Three types of tests of the trailing edge flaps have taken place: laboratory tests to analyze its general behavior, fatigue tests and rotational test-rig tests.

The main goal of the laboratory tests was to validate the developed FE models and to demonstrate that the structure could achieve the desired deflection. Angles between -8° and $+12^\circ$ could be measured via DIC. The differences between the deflections expected from the simulations and the experimental results are small (Figure 5 – left). A similar behavior was measured for strain values (Figure 5 – right) [3].

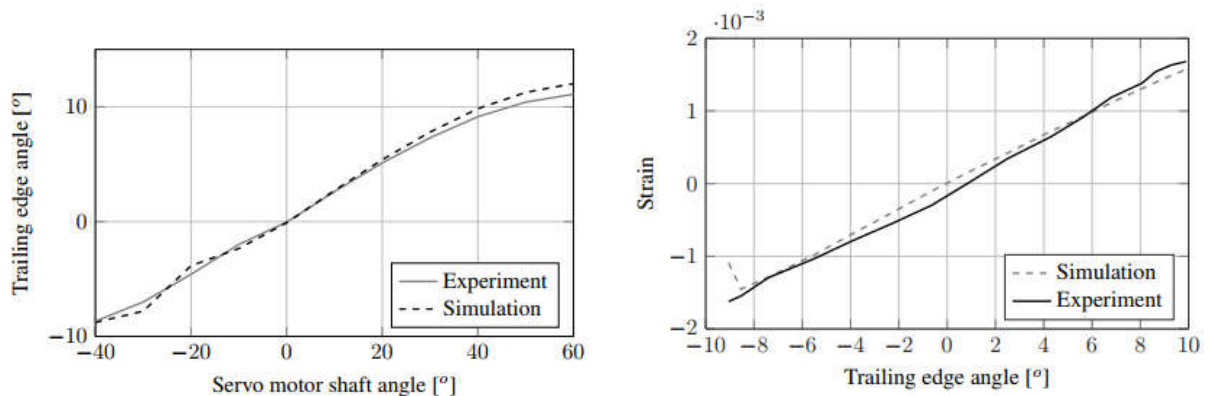


Figure 5: Left: Comparison of simulated and measured trailing edge deflection angle; Right: Comparison of simulated and measured strains [3]

To test the behavior of the structure under realistic conditions, a second demonstrator was designed and built for a measurement campaign on the rotational test bed of the Technical University of Denmark (DTU) (Figure 6). Several sensors were implemented on the demonstrator, including accelerometers, strain gauges and pressure taps. The demonstrator was installed on an adapter airfoil section which was then mounted on DTU's rotational test bed. The goal of the campaign was to measure aerodynamic performance, as well as relevant environmental effects, such as turbulences and centrifugal loads [3]. The measurement campaign was successful and the aerodynamic effects of the flap could be measured. The

results of these tests are not within the scope of this paper.

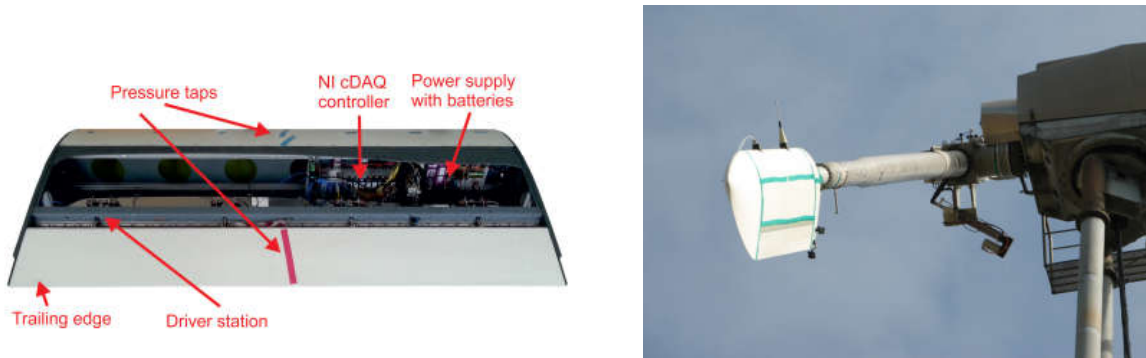


Figure 6: Left: Trailing Edge mounting on Airfoil Section; Right: DTU's rotational test bed with demonstrator mounted [3]

3.3 Flap Controller design and tests

To study control mechanisms for the flap, a model of a movable trailing edge with a 10 m spanwise length was introduced on the blades of a generic three-bladed 7.5 MW wind turbine model with 80 m blades [12]. The chord length of the trailing edge flap is 25 % of the blade's chord length, with 5% flexible and 20% rigid. Deflection angles vary between $\pm 10^\circ$, with a maximum angular rate of $20^\circ/\text{s}$. The pitch angular rate is limited to $3^\circ/\text{s}$ for Individual Pitch Control (IPC). Due to the rotational sampling effect, the blade samples inhomogeneous wind fields with a frequency determined by the rotor speed and the dynamic blade loads are concentrated at multiples of the rotational frequency. IPC is capable of reducing once per revolution (1P) loads [12].

A feedforward-feedback control structure based on the H^∞ loop shaping method [14] was chosen for the study, with a special focus on uncertainty quantification and a robust control performance [15]. Since the flap/blade area ratio is small, the operation is close to the actuator limits and needed to be considered in the controller structure [16]. A series of algorithms with the same baseline controller (REF) for collective pitch and torque control were developed. All additional control loops used flapwise blade root bending moments as a feedback signal: a) individual pitch control acting on 1P (IPC 1P), b) individual flap control acting on 1P (IFC 1P), c) individual flap control acting on 2P (IFC 2P), d) individual flap control acting on 1P and 2P (IFC 1P 2P), and e) individual pitch control acting on 1P and individual flap control acting on 2P (IPC 1P IFC 2P). Time domain simulations were carried out between cut-in wind speed (3 m/s) and cut-out wind speed (25 m/s), using the high fidelity aero-elastic simulation code HAWC2 [17] with the ATEFlap dynamic stall engineering model[18]. The turbulent wind conditions were chosen in accordance with [19], where the turbulence intensity is 41%

at 3 m/s and 15% at 25 m/s. Wind shear and tower shadow were also taken into account and no yaw misalignment was considered. For each wind speed, six 10-minute simulations were carried out, each under different turbulent wind speeds. 1 Hz damage equivalent loads (DEL) were calculated. The obtained DEL were weighted with the Rayleigh probability function with an average wind speed of 10 m/s to determine the lifetime damage equivalent loads.

The power spectral density (PSD) of the flapwise blade root bending moment for the hub height mean wind speed of 13m/s is plotted in Figure 7 (left). It can be seen that 1P and 2P harmonics are the most dominant load components and that all control algorithms are capable of reducing the desired frequencies. Furthermore, the highest load reduction at 1P is achieved with individual pitch control, since it can influence the entire blade. Active flap control only influences parts of the blade and achieves lower reductions at 1P. However, due to its higher dynamics, it is more suitable for reduction of 2P load components. Because of the limited surface and the actuator limitations, the active flap control targeting both 1P and 2P load components (IFC 1P 2P) does not lead to any satisfactory load reductions. The best results can be achieved with IPC targeting 1P loads and individual flap control targeting 2P loads (IPC 1P IFC 2P). The same is valid for the reduction of lifetime damage equivalent loads. Figure 7 (right) summarizes these results for blade root flapwise bending moment, hub yaw and tilt moments and tower top and tower bottom fore-aft and side-side bending moments.

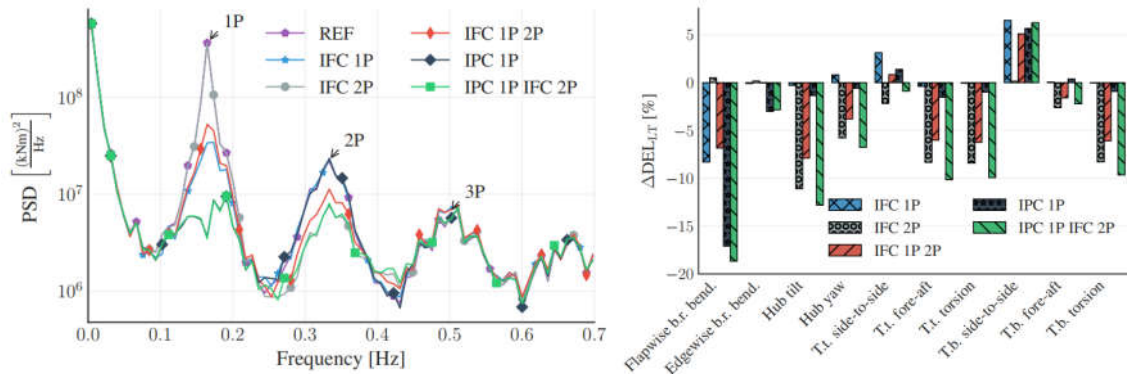


Figure 7: Left: PSD of the flapwise blade root bending moment under different algorithms. Right: Reduction of lifetime damage equivalent loads

3.4 Upscaling Flaps

The SmartBlades2 project is also investigating flap upscaling concepts for their application in larger wind turbines. Different simulation models have been developed and cover overall blade simulation as well as structural optimization. They are also capable of integrating the flap structure and perform sizing and analysis processes. One of the goals of these simulations, as an example, is to find a concept that enables load transmission around the flap

cutout. Some results with this focus are presented in Figure 8. As it can be seen, in comparison to the reference blade [12], the second main spar is shifted in trailing edge direction to the cutout and serves as a connection spar for the flap. The flap cutout lays between 66 m and 75 m in spanwise direction and has a 30% profile depth. Even though the total blade weight increases from 21,7 t to 24,5 t under this configuration, the flap-wise deflection and the induced twist decrease respectively from 11.06 m to 9.95 m and from $0.65^\circ/2.09^\circ$ to $0.61^\circ/-1.54^\circ$. The diminishing values can be explained by the spar cap's area enlargement in blade tip direction. By shifting the rear spar towards the rear edge flap, the chordwise position changes from 40% to 65% of the chord. The absolute spar cap area is therefore increased, leading to a higher flapwise and torsional stiffness and an increment in the overall blade mass. Since the present study does not consider flap aerodynamic forces and moments and the role of the flap is to reduce aerodynamic loads, the total weight could be reduced by considering the complete set of loads.

While this study focuses on the structural aspects, aspects such as costs need to be considered for further development: the total cost of the flap itself and its control mechanism must be lower than the cost reduction that can be achieved by material and weight savings.

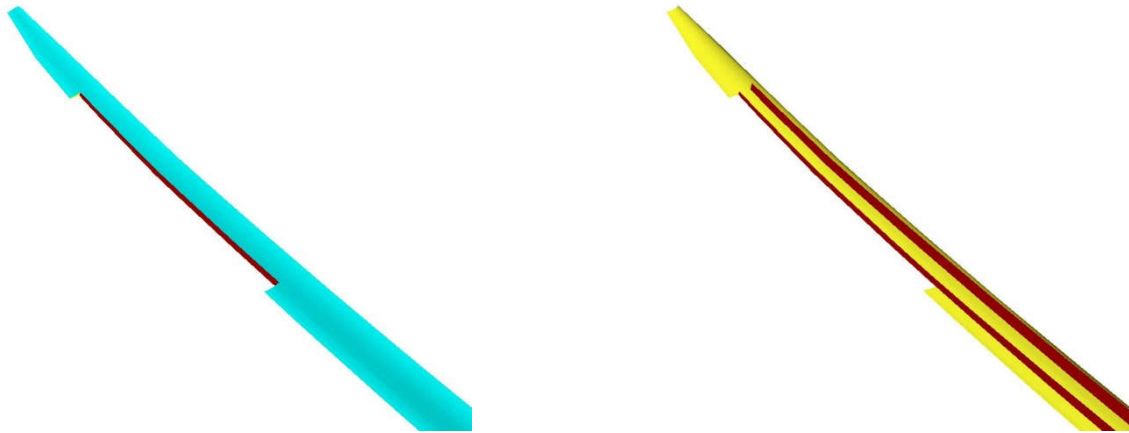


Figure 8: Blade design for the 80m Smart Blade (IWT 7.5 MW) with flap cut-out

3.5 Alternative multistable flap concept overview

Recently, there has been an increased interest in multistable structures. These structures are characterized by two or more stable states with distinct geometrical shapes [20][21] and can remain in these states without requiring any external energy or force input. Force or energy is only required to snap from one shape to another.

A rectangular bistable plate capable of yielding a curved and a flat shape was designed as

an alternative concept for a morphing flap based on [22][23]. The design ensures that the edges of the two stable shapes remain as flat as possible in order to facilitate the flap's embedding. Two sets of actuators were placed on top and bottom of the plate to enable snap-through and snap-back. A nonlinear FE analysis was performed to simulate the proposed concept and a multi-objective non-gradient based optimization was carried out to find the optimal location of the actuators. The objectives were to minimize the snapping voltages while maximizing the curvatures in order to maximize the morphing action. A separate FE analysis was carried out on the optimized rectangular plates to introduce thermal residual stresses. As the plate cools down, it displays a curved stable shape generated by the residual stresses. This curvature defines the flap's deflection angle. The cooled structure can be embedded in its curved form as a deflected flap. Once the voltages are applied to the actuators, strains develop on the plates and they snap to the neutral configuration. When voltage is removed, the flap maintains its new shape. The main advantage of this multi-stability approach is that it obviates the need for a continuous power supply, which is often required in conventional actuation methods.

4 LEADING EDGE SLATS

The third approach for load reduction being investigated within the projects is the use of leading edge slats, particularly for their influence on the aerodynamic behavior of the blades under turbulent inflow conditions. Since turbulences happen at small time scales and because of the large inertia of the blade, turbulences cannot be handled by common pitch control systems. When implemented, these devices allow the airfoil to operate at higher angles of attack, improving its aerodynamic performance compared to an unequipped wind turbine and also help the turbine system to react better against sudden wind changes [24]. Three approaches for this kind of system are being considered: an active, a passive and a rigid one. The active leading edge, as the name says, is actively controlled by a motor. The motor can move the slat in or outwards according to the wind conditions and so change the angle of attack experienced by the blade. The passive concept automatically moves from its retracted to its deployed position by only using the present aerodynamic loads. Finally, the rigid concept stays in a constant rigid position. The gap between the blade and the slat is what allows improving the overall flow conditions.

4.1 Slat controller design and tests

Turbulent wind tunnel tests of a deformable active slat were performed to study the effects of the slat on the blade damage equivalent load due to fast local inflow angle fluctuations [25]. The gap size between the slat trailing edge and the main body of the airfoil could be varied by moving the slat. The aim of the work was to characterize the active slat and to

gauge its initial capabilities under the influence of sinusoidal inflow conditions. It was observed that varying the gap size has an influence on the aerodynamic polars of the airfoil: different aerodynamic coefficients for the same angle of attack could be achieved by moving the slat to different positions and modifying the gap size (Figure 9).

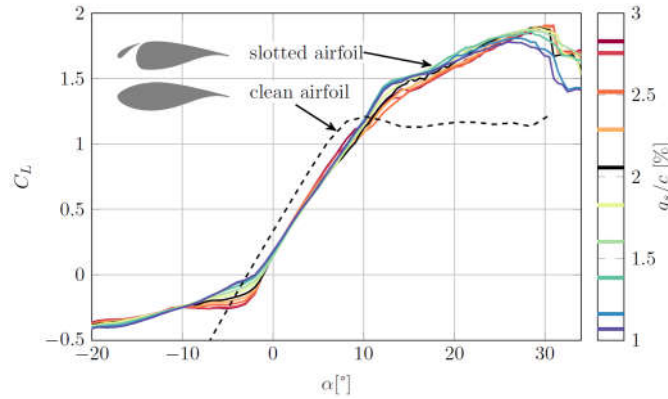


Figure 9: Static lift coefficients C_L for laminar inflow with $Re = 0.6 \times 10^6$ for different gap sizes g_s compared to the clean airfoil without slat [25].

The airfoil was exposed to an inflow with sinusoidal variation of the angle of attack at 5Hz. The amplitude of the inflow angle variation was of 3° . A “TIM control” (Timed Inflow-angle-coupled Motion control) strategy was developed to reduce the resultant fluctuating load. This involved the synchronized variation of the gap size with the wind tunnel’s active grid motion. Measurements for different phase shifts between slat motion and inflow angle fluctuations were performed and as much as 20% of the standard deviation of lift force fluctuation could be reduced compared to the case where the slat wasn’t deployed (Figure 10).

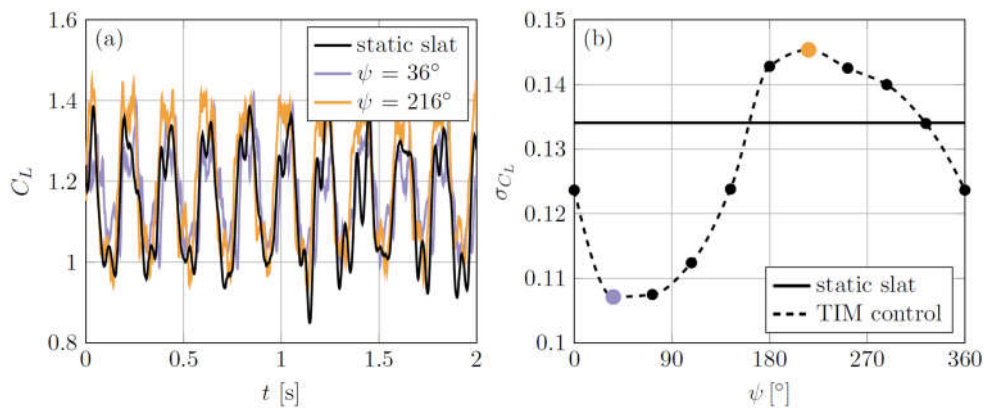


Figure 10: Lift coefficients C_L time series for static slat and TIM controlled slat with phase shifts $\psi = 36^\circ$ and 216° (a) and standard deviation of lift coefficient σ_{C_L} of static slat and TIM controlled slat for different ψ with inflow angle fluctuations (b) [25]

5 TECHNOLOGIES' EVALUATION CONCEPT AND PERSPECTIVES

To compare the performance of the different smart blades technologies, a detailed evaluation is being carried out throughout the project and an economical and a technical assessment according to VDI 2225 [26] is being performed.

The economic performance (P_e) of a technology is based on a comparison of the leveled cost of energy. The included projected costs are calculated using detailed cost models for the reference rotor blade, technology add-ons and the reference wind turbine itself. This way additional material, labor and investment costs as well as differences in annual energy production are taken into account for each technology. Furthermore cost differences occurring from altered operation and maintenance schemes are estimated and implemented in the cost model.

The evaluation of the technical performance (P_t) is done in a utility analysis consisting of 44 criteria, e.g. load reduction, rotor blade mass and reliability. The assessment of the criteria is conducted using customized functions which correlate the respective result with a specific utility value. The resulting utility value is weighted, whereat the weight and the assignment of utility values to certain results are based on a questionnaire handed out to all project partners.

In order to compare the economic and technical performance of the technologies visually P_e and P_t can be normalized and plotted in a diagram as shown in Figure 11.

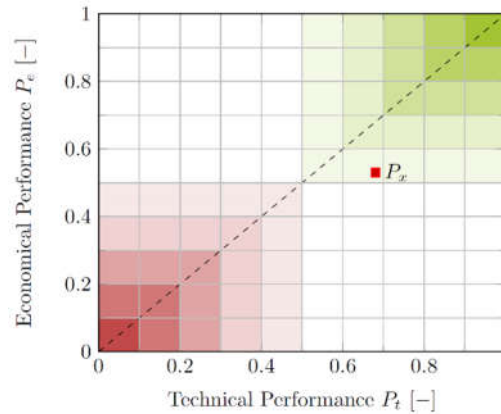


Figure 11: Exemplary visualization of the technical performance, P_t , and economical performance, P_e , of a technology.

So far, each technology has proven its potential within the expected range of the numerical models. In the meantime, validation experiments, such as a field test at the NREL CART3 wind turbine (Section 2.3), are carried out to confirm the results.

11 CONCLUSIONS

Three different approaches for reducing loads in wind turbine blades are being investigated: bend twist coupling, trailing edge flaps and leading edge slats. All three approaches have proven their potential at different scales and under different testing scenarios, such as in test rigs or wind tunnel tests, however further concept development and larger scale tests still need to be performed in order to be able to provide an accurate evaluation of the technologies, especially concerning factors relevant to the industry, such as costs and upscaling. Future work will focus on the detailed results of the projects' tests as well as on the concepts' detailed evaluation based on these results.

AKNOWLEDGEMENTS

This work has been funded by the German Ministry of Economic Affairs and Energy (BMWi) on decision of the German Parliament within the frame of the SmartBlades2 project (funding reference numbers 0324032A-H).

REFERENCES

- [1] International Energy Agency, *Renewables 2018: Analysis and Forecasts to 2023 – Executive Summary*. IEA Publications. Website: www.iea.org, (2018).
- [2] Teßmer, J. and Montano, Z. *Smart Rotors for Cost Efficient Wind Turbines*. Energie: Herausforderungen der Energiewende. Deutsche Physikalische Gesellschaft. Frühjahrstagung des Arbeitskreises Energie, 27.-29. Mär. 2017, Münster, Deutschland. ISBN 978-3-9818197-2-4 (2017).
- [3] Riemenschneider J., Pohl, M. et al. *Smart Trailing Edges for Wind Turbines* (2018). Proceedings of the ASME 2018 Conference on Smart Materials, Adaptive Structures and Intelligent Systems, SMASIS2018, September 10 - 12, 2018, San Antonio, Texas, USA
- [4] Montano, Z., Kühn, M., Daniele E. and Stüve, J. *Bend Twist Coupling on Rotor Blades for Wind Turbines*, *lightweight.design*, Issue 4/2018, Volume 11 / ISSN 1865-4819, p. 46-51 (2018).
- [5] Sevinc, A., Bleich, O. et al. *Parameterized analysis of swept blades regarding bend-twist coupling*, DEWEK 2015: 12th German Wind Energy Conference (2015).
- [6] Bätge, M., Rosemeier, M. et al. *Implementation of Passive Load Reduction in rotor Blade Design*, SmartBlades Conference, 3-4 February, 2016, Stade (2016).
- [7] Gundlach, J. and Govers, Y. *Experimentelle Modalanalyse an einem aeroelastisch optimierten Rotorblatt mit Biege-Torsions-Kopplung im Projekt SmartBlades2* VDI-Berichte 2323 pp 91-104 (2018).
- [8] National Renewable Energy Laboratory (NREL) *NWTC Researchers Field-Test Advanced Control Turbine Systems to Increase Performance, Decrease Structural Loading of Wind Turbines and Plants*, Fact Sheet, NREL/FS-5000-64732 (2015).

- [9] NREL *Field Testing Research at the NWTC*, Fact Sheet, NREL/FS-5000-63355 (2015)
- [10] Opitz, S. *Torsionssensor*. Patent DE102011000054A1 (2012).
- [11] Opitz, S. *Funktionskonforme Sensorintegration in hoch belasteten, adaptiven, umströmten Strukturen*, Dissertation. DLR-Forschungsbericht. DLR-FB--2015-28, ISSN 1434-8454, Deutsches Zentrum für Luft- und Raumfahrt e.V. (2015).
- [12] Sevinc A., Rosemeier, M. et al. *IWES Wind Turbine IWT-7.5-164. Technical report*, Fraunhofer Institute for Wind Energy and Energy System Technology (2014).
- [13] Bossanyi, E. *Individual Blade Pitch Control for Load Reduction*, Wind Energy, vol. 6, pp.119-128, 2003. doi:10.1002/we.76 (2003).
- [14] Duncan C. McFarlane and Glover, K editors. *Robust controller design using normalized coprime factor plant descriptions*, volume 138, Lecture Notes in Control and Information Sciences. Springer-Verlag, Berlin/Heidelberg (1990).
- [15] Ungurán, R., Petrović, V., et al. *Feedback-feedforward individual pitch control design for wind turbines with uncertain measurements*. 2019 American Control Conference (ACC), (2019)
- [16] Ungurán, R., Petrović, V. et al. *Smart rotor control of wind turbines under actuator limitations*. 2019 American Control Conference (ACC), (2019).
- [17] Larsen, T. and Hansen, A. *How 2 HAWC2, the user's manual*. Denmark. Forskningscenter Risoe. Risø-R-1597. Risø National Laboratory, (2012).
- [18] Bergami, L., Riziotis, V. and Gaunaa, M. *Aerodynamic response of an airfoil section undergoing pitch motion and trailing edge flap deflection: a comparison of simulation methods*. Wind Energy, 18(7):1273–1290, (2015).
- [19] IEC. *IEC 61400-1 Wind Turbines - Part 1: Design requirements*. IEC 61400, pages 1–92, (2005).
- [20] Hyer, M. *Some observations on the cured shape of thin unsymmetric laminates*. Journal of Composite Materials, 15(2):175–194, (1981).
- [21] Haldar, A., Reinoso, J. et al. *Thermally induced multistable configurations of variable stiffness composite plates: Semi-analytical and finite element investigation*. Composite Structures, 183:161–175, (2018).
- [22] Arrieta, A., Kuder, I. et al. *Variable stiffness characteristics of embeddable multi-stable composites* Composites Science and Technology, 97:12–18, (2014).
- [23] Haldar, A., Jansen, E. and Rolfes, R. *Analysis of Morphing Trailing Edge Flap with Embedded Multistable Variable Stiffness Laminates*, AIAA Scitech 2019 Forum, AIAA SciTech Forum, (AIAA 2019-0856), (2019).
- [24] Manso Jaume, A. and Wild, J. *Aerodynamic design and optimization of a high-lift device for a wind turbine airfoil* STAB 2015, Projektgruppe/Fachkreis: Numerische Simulation/Windenergie. (2015).
- [25] Neuhaus L, Singh P et al. *Mitigating loads by means of an active slat*, J. Phys: Conf. Ser. 1037 022032, (2018).
- [26] VDI e.V.: *VDI-Richtlinie 2225 Blatt 3: Technisch-wirtschaftliches Konstruieren*. (1998)

SENSOR AND ACTUATOR PLACEMENT IN TENSEGRITY STRUCTURES THROUGH CELLULAR MORPHOGENESIS

OMAR ALOUI^{*}, LANDOLF RHODE-BARBARIGOS[†]

^{*} University of Miami, Dept. of Civil, Architectural & Environmental Engineering
1251 Memorial Dr., McArthur Engineering Bldg, Coral Gables, FL 33146, USA
email: omar.aloui@miami.edu

[†] University of Miami, Dept. of Civil, Architectural & Environmental Engineering
1251 Memorial Dr., McArthur Engineering Bldg, Coral Gables, FL 33146, USA
e-mail: landolfrb@miami.edu

Key words: Tensegrity, Active Structure, Sensor Placement, Actuation, Structural Identification, Structural Control, Cellular Morphogenesis.

Abstract. Tensegrity structures are self-stressed frameworks composed of elements in compression and elements in tension. Their stability is attributed to a state of self-equilibrium in the system. Tensegrity structures are thus statically indeterminate. Many tensegrity systems are also kinematically indeterminate including motions other than the rigid-body motions that can occur without changes in their element lengths (infinitesimal mechanisms). Since not change in element lengths are required, infinitesimal mechanisms have been identified as advantageous control paths. Although tensegrity systems have been proposed for active applications in science and engineering, existing form-finding and design methods do not address or provide any insight regarding sensor and actuator placement in tensegrity structures. In this paper, self-stress and infinitesimal mechanisms are investigated through cellular morphogenesis to identify appropriate sensor and actuator placement strategies.

1 INTRODUCTION

Tensegrity describes a system composed of elements in tension (cables) and compression (struts) in stable state of self-equilibrium [1-2]. Although the concept originates from art work of Kenneth Snelson, it quickly found applications in science, engineering and architecture [3-6]. Tensegrity structures are materially and mechanically efficient structures that can integrate sensors and actuators within their structural elements [2]. They are thus especially advantageous for active applications. However, in most applications, sensors and actuators are placed in tensegrity systems based on engineering judgement resulting to solutions that are closely related to specific applications and contexts. Sensory applications have employed both dynamic and static measurements for structural identification and damage identification in tensegrity structures [7-10], while adaptive application using both active struts and active cables have been proposed [11-13]. Active struts allow tensegrity structures to be stiff for a limited range of configurations, while active cables enable them to remain stable and stiff throughout large shape transformations [14]. Moreover, shape transformations along the directions of infinitesimal

mechanisms (displacements that can occur without changes in the element lengths) have been identified as ideal motion-control paths as no element deformation is required [15]. This paper explores cellular morphogenesis, a bio-inspired generative process for the combined topology identification and form finding of tensegrity structures, as a strategy for identifying advantageous sensor and actuator placement solutions in active tensegrity structures.

2 CELLULAR MORPHOGENESIS

De Guzman and Orden [16] proved that tensegrity structures can be decomposed into elementary units (cells) defined as the complete graphs on $d+2$ nodes with d being the space dimension. Figure 1 illustrates the topology of three-dimensional tensegrity cells. Tensegrity cells have one self-stress state and no infinitesimal mechanism. Aloui et al. [17-18] analytically described the self-stress of tensegrity cells based on their topology and nodal coordinates. Tensegrity structures can thus be seen as multicellular organisms composed of tensegrity cells. Furthermore, in an analogy with biological organisms, starting from a tensegrity cell more complex tensegrity structures can be generated through the multiplication mechanisms of cellular adhesion and fusion. Aloui et al. [17-18] studied the effects of adhesion and fusion on the self-stress of a tensegrity structure being generated through cellular multiplication. They showed that a basis of the self-stress space can be analytically constructed based on the cell topology. Moreover, they showed that with adhesion that represents the gluing of two cell graphs along one or more shared edges and vertices, the number of self-stress states in the composing structure increases, while with fusion which is the removal of one or more of the shared elements between the two cells the number of self-stress states in the composing structure decreases. Consequently, the resulting basis reflects a vector collection of the self-stress states of the constitutive cells and stable sub-structures resulting from their interaction having thus a direct physical interpretation with each state reflecting the contribution of a sub-system of the structure.

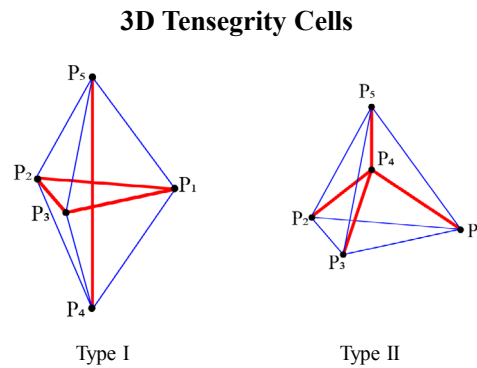


Figure 1: Three-dimensional tensegrity cells

The Simplex (or Triplex) is perhaps the most well-known three-dimensional tensegrity structure. The structure includes 6 nodes, 9 elements in tension and 3 elements in compression in an equilibrium configuration geometrically described by a twisted prism consisting of two equilateral triangular bases rotated by $\frac{\pi}{6}$. Figure 2 illustrates the cellular morphogenesis of the

Simplex as the fusion of tensegrity cells ABCDE and BCDEF, and the removal of elements BD and CE. The combination of the two cells results first into a structure with two self-stress states and no infinitesimal mechanisms which with the removal of elements BD and CE leads to the Simplex structure. The removal of elements BD and CE decreases the number of self-stress states to one creating also one infinitesimal mechanism. The self-stress in the Simplex can thus be obtained through cellular multiplication by identifying a combination of self-stress components that set the self-stress in the elements to be removed equal to zero [19].

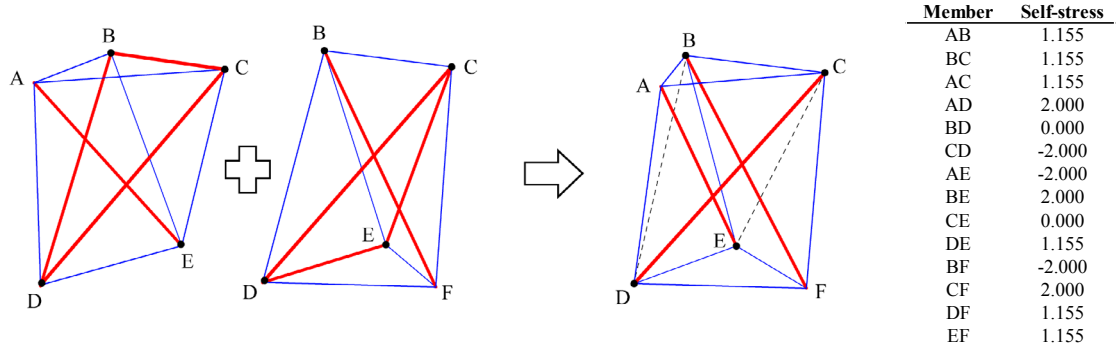


Figure 2: Cellular morphogenesis of a Simplex (dashed lines illustrate removed elements)

The removal of the edges BD and CE during the fusion of the two cells that compose the Simplex introduces an infinitesimal mechanism (Figure 3). This non-trivial infinitesimal mechanism can be described by a direction that is orthogonal to the trivial mechanisms. For a Simplex with unitary height and a triangular base with edge length of $\sqrt{3}$, the direction of the infinitesimal mechanism is described by the nodal displacements:

$$\begin{aligned} \vec{d}_A &= \begin{bmatrix} 0 \\ 1 \\ -0.5 \end{bmatrix} & \vec{d}_B &= \begin{bmatrix} -\sin(\frac{2\pi}{3}) \\ \cos(\frac{2\pi}{3}) \\ -0.5 \end{bmatrix} & \vec{d}_C &= \begin{bmatrix} -\sin(\frac{4\pi}{3}) \\ \cos(\frac{4\pi}{3}) \\ -0.5 \end{bmatrix} & \vec{d}_D &= \begin{bmatrix} \sin(\frac{\pi}{6}) \\ -\cos(\frac{\pi}{6}) \\ 0.5 \end{bmatrix} & \vec{d}_E &= \begin{bmatrix} \sin(\frac{\pi}{6} + \frac{2\pi}{3}) \\ -\cos(\frac{\pi}{6} + \frac{2\pi}{3}) \\ 0.5 \end{bmatrix} & \vec{d}_F &= \begin{bmatrix} \sin(\frac{\pi}{6} + \frac{4\pi}{3}) \\ -\cos(\frac{\pi}{6} + \frac{4\pi}{3}) \\ 0.5 \end{bmatrix} \end{aligned} \quad (1)$$

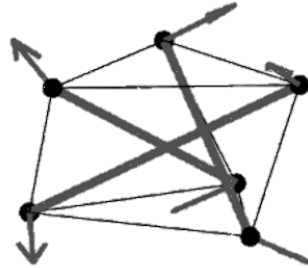


Figure 3: Illustration of the nodal directions of the infinitesimal mechanism in a Simplex

3 SENSOR PLACEMENT AND SELF-STRESS IDENTIFICATION

Structural identification and thus sensor placement in tensegrity systems starts with self-stress identification. The self-stress w in a tensegrity structure corresponds to a solution of the equilibrium in the absence of external loads:

$$Aw = 0 \quad (2)$$

where A is the equilibrium matrix [20]. The set of possible solutions to equation (1) is given by the nullspace of A . The vectors of the basis given by the nullspace of A reflect the self-stress states of the structure and can be grouped to compose the self-stress matrix $= [w_1 \ w_2 \ \dots \ w_s]$ that is by definition full rank. The self-stress in the structure is always a linear combination of the self-stress states. This gives:

$$w = W\alpha \quad (3)$$

where α is a vector of s real coefficients and s is the dimension of self-stress space. Since matrix W is full rank, determining the vector α requires minimum s self-stress values. Consequently, the number of sensors required to characterize the self-stress in a tensegrity structure corresponds to its number of self-stress states s . Following the principles of structural morphogenesis, this number corresponds also to the minimum number of constitutive unicellular sub-structures (cells and stable sub-structures resulting from their interaction) composing the structure as each cell and sub-system composing the structure have one self-stress state. Consequently, for the Simplex, one sensor is enough to characterize its self-stress assuming that the nodal positions are known. The method can be extended for structural identification and damage assessment [21].

4 ACTUATOR PLACEMENT AND CONTROL

Tensegrity structures can be actuated through the integration of active elements (struts and/or cables) with the actuation configuration (number and placement) depending on the topology of the system and the desired change in shape or behavior. However, for applications that require large changes in the length of the elements (large nodal displacements), cable actuation is typically preferred [14]. With cable actuation, a given set of nodal displacements in tensegrity structure can be obtained through a set of cable-length changes applied on different groups of cables. De Guzmán and Orden [16] proved that a node in a tensegrity system in general position can be in a state of self-equilibrium if and only if it has at least four incident members. Consequently, nodal displacements can be expressed as a combination of the change in length of a set of three incident elements with independent directions, which according to de Guzmán and Orden [16] is always satisfied for a system in self-equilibrium. This confirms that to generate any nodal motion in a tensegrity structures, each controlled node should be attached to minimum three active elements.

Let P be a node in a tensegrity structure with PP_1 , PP_2 and PP_3 three incident members to P with independent directions. The displacement at P can be expressed as:

$$\vec{d}_P = \alpha_1 \vec{PP_1} + \alpha_2 \vec{PP_2} + \alpha_3 \vec{PP_3} \quad (4)$$

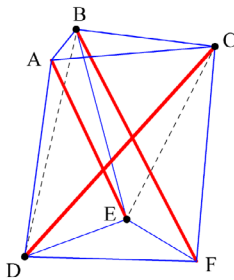
where α_1 , α_2 and α_3 are real coefficients reflecting the motion of the node in each member direction. The displacement of the node in each member direction can be calculated through the projection of d_P in the basis $\beta_P(PP_1, PP_2, PP_3)$. Let M_P be the non-singular matrix described β_P . Then, the coefficients α_1 , α_2 and α_3 can be calculated by:

$$\begin{bmatrix} \alpha_1 \\ \alpha_2 \\ \alpha_3 \end{bmatrix} = M_P^{-1} \vec{d}_P \quad (5)$$

Assuming n nodes P_1, P_2, \dots, P_n are moving in the structure with assigned displacements $d_{P_1}, d_{P_2}, \dots, d_{P_n}$ and the basis matrices $M_{P_1}, M_{P_2}, \dots, M_{P_n}$, the displacements of the nodes along the active elements can be calculated as:

$$\begin{bmatrix} \alpha_{P_1} \\ \alpha_{P_2} \\ \vdots \\ \alpha_{P_n} \end{bmatrix} = \text{blkdiag}(M_{P_1}^{-1}, M_{P_2}^{-1}, \dots, M_{P_n}^{-1}) \begin{bmatrix} d_{P_1} \\ d_{P_2} \\ \vdots \\ d_{P_n} \end{bmatrix} \quad (6)$$

where α_{P_i} is a 3×1 vector of projection coefficients of the displacement d_{P_i} on the basis β_{P_i} and $\text{blkdiag}()$ is the function forming a block diagonal matrix from a set of square matrices. Consequently, any displacement in space including the advantageous paths given by the infinitesimal mechanisms [15] can be decomposed in element-length changes. For a cable-actuated Simplex with only rigid body motions restrained and a desired change in the height of 0.01m, the changes in the length to be applied correspond to:



Cable	Change in length [m]
AB	0.0089
BC	0.0089
AC	0.0089
AD	-0.1000
BE	-0.1000
CF	-0.1000
DE	0.0000
DF	0.0000
EF	0.0000

(7)

5 CONCLUSIONS

Although tensegrity systems have been employed for active applications, there are no widely accepted design guidelines regarding sensor and actuator placement. In this paper, sensor and actuator placement is discussed through cellular morphogenesis highlighting that:

- the number of sensors required to characterize the self-stress in a tensegrity structure corresponds to its number of self-stress states
- the number of sensors required to characterize the self-stress is also given by the minimum number of constitutive unicellular sub-structures composing the structure
- the number of actuators required to control a tensegrity structure depends on the configuration and the desired change in shape or behavior
- nodal displacements can be expressed as a combination of the change in length of a set of three incident elements with independent directions.

The aforementioned statements imply that for an active tensegrity Simplex one sensor and 9 actuators are sufficient.

REFERENCES

- [1] R. Motro, *Tensegrity: Structural Systems for the Future*, Elsevier, 2003.
- [2] R.E. Skelton and M.C. de Oliveira, *Tensegrity Systems*, Springer, 2009.
- [3] D.E. Ingber, N. Wang, D. Stamenovic, Tensegrity, cellular biophysics, and the mechanics of living systems, *Rep. Progr. Phys.* 77 (2014) 046603.
- [4] A.P. Sabelhaus, J. Bruce, K. Caluwaerts, Y. Chen, D. Lu, Y. Liu, A.K. Agogino, V. SunSpiral, A.M. Agogino, Hardware design and testing of SUPERball, a modular tensegrity robot, in: *World Conference of the International Association for Structural Control and Monitoring (6WCSCM)*, Barcelona, Spain, 2014.
- [5] L. Rhode-Barbarigos, N. Bel Hadj Ali, R. Motro, I.F.C. Smith, Design aspects of a deployable tensegrity-hollow-rope footbridge, *Int. J. Space Struct.* 27 (2) (2012) 81–96.
- [6] T. Sterk, Using actuated tensegrity structures to produce a responsive architecture. *ACADIA 2003*, 2003.
- [7] J.F. Dubé, N. Angellier. 2003. Using of tensegrity grid dynamic behavior to identify its self-stress level. *Journal of Constructional Steel Research.* 90 133-9.
- [8] S. Bhalla, R. Panigrahi, A. Gupta. 2013. Damage assessment of tensegrity structures using piezo transducers. *Meccanica.* 48(6) 1465-78.
- [9] B. Adam, I.F.C. Smith. 2007. Self-diagnosis and self-repair of an active tensegrity structure. *Journal of Structural Engineering.* 133(12) 1752-61.
- [10] A.C. Sychterz, I.F.C. Smith. 2018. Using dynamic measurements to detect and locate ruptured cables on a tensegrity structure. *Engineering Structures.* 173 631-42.
- [11] E. Fest, K. Shea, I.F.C. Smith. 2004. Active tensegrity structure, *Journal of Structural Engineering.* 130(10) 1454-65.
- [12] R. Motro, A. Smaili. 2007. Foldable/unfoldable curved tensegrity systems by finite

- mechanism activation, *Journal of The International Association for Shell and Spatial of Structures*. 48(3) 153-160.
- [13] J. Averseng, B. Crosnier. 2004. Static and dynamic control of tensegrity systems, *Journal of the International Association for Shell and Spatial of Structures*. 45(3) 169-174.
- [14] C. Sultan, R.E. Skelton. 2003. Deployment of tensegrity structures, *International Journal of Solids and Structures*. 40(18) 4637-57.
- [15] C. Sultan. 2014. Tensegrity deployment using infinitesimal mechanisms, *International Journal of Solids and Structures*, 51(21–22) 3653-3668.
- [16] de Guzmán M. and Orden D. 2006. From graphs to tensegrity structures: geometric and symbolic approaches, *Publicacions Matemàtiques*, 279-299.
- [17] O. Aloui, D. Orden, L. Rhode-Barbarigos. 2018. Generation of planar tensegrity structures through cellular multiplication. *Applied Mathematical Modelling*. 64 71-92.
- [18] O. Aloui, J. Flores, D. Orden, L. Rhode-Barbarigos. 2019 Cellular morphogenesis of three-dimensional tensegrity structures. *Computer Methods in Applied Mechanics and Engineering*. 346 85-108.
- [19] O. Aloui, J. Flores, L. Rhode-Barbarigos. 2018. Re-discovering the Tensegrity Simplex: decomposition, self-stress analysis and alternative designs, *IASS Symposium 2018 - Creativity in Structural Design*, Boston, USA.
- [20] S. Pellegrino and C.R. Calladine. 1986. Matrix analysis of statically and kinematically indeterminate frameworks. *International Journal of Solids and Structures*. 22(4) 409-428.
- [21] O. Aloui, J. Lin, L. Rhode-Barbarigos. A theoretical framework for sensor placement, structural identification and damage detection in tensegrity structures, *Smart Materials and Structures* (under review)

SIMULATIVE STUDY AND POTENTIAL ANALYSIS OF INFLATABLE FACADE ELEMENTS TO BALANCE ENVIRONMENTAL DISTURBANCES

JANINE GUENTHER*, MARIUS OEI*, NADINE HARDER[†] AND
OLIVER SAWODNY*

*Institute for System Dynamics (ISYS)

University of Stuttgart

Waldburgstraße 19, 70563 Stuttgart, Germany

e-mail: guenther@isys.uni-stuttgart.de, web page: <https://www.isys.uni-stuttgart.de>

[†] Institute for Acoustics and Building Physics (IABP)

University of Stuttgart

Pfaffenwaldring 7, 70569 Stuttgart, Germany

e-mail: nadine.harder@iabp.uni-stuttgart.de - web page: <https://www.iabp.uni-stuttgart.de>

Key words: Adaptive Building Design, Inflatable Membrane Facades, Ultra Light Weight Buildings, ETFE

Abstract. The high thermal mass of conventional buildings is an important factor for maintaining comfortable indoor conditions. The building itself serves as a heat storage and damps the effects of changing outdoor temperatures or varying solar loads. Moving away from heavy-weight to ultra-light-weight buildings allows to rethink the conventional design of facades as sole thermal or noise insulation. Intelligent facade structures with integrated capability for thermal actuation can be used to control indoor conditions in order to reduce the energy demand. Inflatable membrane facades allow for a variation of heat capacity by introducing air and thus increasing the thermal mass of a facade element. This can be used to control the heat exchange between the building interior and the environment depending on the outside conditions. Furthermore, introducing connections between adjacent wall elements enables the transport of thermal energy from one side of the building to another. This allows for intelligent distribution of solar loads by transferring heated air from the south- to the north-facing side of the building.

In this work, a thermal network model of a building using inflatable membrane wall elements is developed. The numerous couplings of element-specific mass and temperature dynamics introduce various effects on the thermal conditions and the related energy demand. The theoretical potential of this type of actuation is determined through a detailed simulative study. Recordings of the temperate climate in Germany are combined with a geometrical solar irradiation model to determine the environmental disturbances. Subsequently, an analysis of different operational conditions is performed to identify the energy saving potential of rewarding use cases. While the energy demand rather depends on system design parameters (e.g. solar absorption), the reduction of radiant temperature asymmetry and demand-oriented heat transfer from unoccupied to occupied zones are promising applications.

1 INTRODUCTION

The growth of the world population creates the need for an increasing amount of living space. This need clashes with the goal of reducing our environmental footprint: today, the European building sector makes up about 50 % of the resource consumption and 42 % of its energy demand [1]. A large portion of the energy that is consumed over the lifecycle of a building is embodied energy. Therefore, one of the primary approaches to both resource and energy consumption reduction is lightweight construction using sustainable materials. The public acceptance of such significant changes constrains their implementation where one driving factor is the occupant's comfort. Hence, it is mandatory for novel building constructions to maintain or even improve the quality of the internal thermal environment compared to conventional building types while reducing the environmental footprint.

The superior indoor comfort of conventional heavy building structures compared to passive lightweight construction is well known, particularly in climates with large daily temperature variations [2, 3]. The lower thermal capacity of light-weight buildings incorporates faster dynamics and results in a more extreme reaction to outside conditions. This leads to a higher energy demand of the heating, ventilation and air conditioning system to ensure the thermal comfort of the occupants. Researchers have devised a number of ways to overcome this limitation, one of which is adaptation of the building's facade to changing environmental conditions. An overview can be found in [4].

Membrane facades are a type of lightweight construction that gained popularity in the past years. They usually consist of fabric or ethylene tetrafluoroethylene (ETFE) films [5]. Membranes made of ETFE can consist of one or more layers and have high light and UV permeability. ETFE offers low soiling due to the smooth surface and low surface tension. Dust and other particles can adhere poorly [6]. It has a low weight and is stable in extreme climatic conditions. A number of exemplary buildings using ETFE cushions are described in [7].

Various efforts have been made to take advantage of the elasticity and durability of membrane materials by introducing adaptivity into the structures. Cardoso et. al. proposed using an electrochromic layer to locally adapt a cushion facade's opacity based on touch-feedback from occupants [8]. Adaptive shading may also be provided by adjusting the inflation of printed multi-layer cushions as described in [5]. Shading and power generation are combined in membrane-integrated photovoltaics, as proposed in [9]. An approach for adaptive membrane facades that is inspired by the human thermoregulatory system are water-filled cushions for active thermal control [10].

In this work, a novel building facade system comprised of inflatable membrane elements is introduced. The facade consists of membrane cushions filled with air. The cushions can be actively inflated or deflated and air can be exchanged between facade elements to achieve varying thermal mass and resistance for each wall and to transport thermal energy. This allows for intelligent distribution of solar loads, e.g. by transferring heated air from the south- to the north-facing side of the building to equalize thermal conditions or transport energy through the building envelope. The following work analyzes the saving potential of this kind of actuation regarding its energy demand for maintaining comfortable conditions. The effect of the inflation state on the building dynamics, the sensitivity to system parameters as well as the impact of air circulation through the facade elements are evaluated for the identification of a meaningful system design and future applications.

Table 1: List of Symbols

Symbol	Description	Value	Unit
A_i	Surface area of i -th wall element	-	m^2
C_{floor}	Heat capacity of floor elements		kJ/K
c_p	Specific heat capacity of moist air	1.020	kJ/kgK
c_a	Specific heat capacity of dry air	1.004	kJ/kgK
c_w	Specific heat capacity of water vapor	1.860	kJ/kgK
d_{mem}	Thickness of membrane	0.5	mm
d_{wall}	Thickness of wall (= inflation state)	1	m
F_{sol}	Solar view factor	-	-
h	Heat transfer coefficient	-	$\text{W/m}^2\text{K}$
I_{dir}	Direct solar radiation	-	$\text{W/m}^2\text{K}$
I_{dif}	Diffuse solar radiation	-	$\text{W/m}^2\text{K}$
m_a	Mass of dry air	-	kg
m_w	Mass of water vapor	-	kg
n_{adj}	Number of adjacent elements of wall or zone	-	-
n_{flow}	Number of connected elements for mass exchange	-	-
R	Thermal resistance	-	$\text{m}^2\text{K/W}$
σ	Stephen-Boltzmann constant	$5.67 \cdot 10^8$	$\text{W/m}^2\text{K}^4$
α	Solar absorption	0.2	-
ϵ	Emissivity of surface	0.8	-
λ_{mem}	Thermal conductivity of membrane	0.24	W/mK

2 MODEL DESCRIPTION

In the following section, the simplified thermal network model is derived based on heat and mass balance equations. The goal is to achieve a quantitative description of the thermal, hygrothermal and energetic effects within the system that allows conclusions about the energy saving potential of the proposed approach. At the same time, the description is kept as simple as possible to achieve a low complexity for the analysis and numerical simulation as well as good interpretability.

2.1 System Description

A schematic representation of the building is given in Figure 1. The sketched two story building is considered in the following analysis where each level consists of one zone which is enclosed by four inflatable wall elements (light shaded). The intermediate floor that separates two zones is considered as ceiling for the lower level and as floor for the upper level simultaneously. The need for a stabilizing floor layer is ignored for simplicity. Each external facade element can be in- or deflated, either by outside air or by exchanging air with adjacent elements. This allows for arbitrary heat transport over the whole building structure. Zones and floors have a constant mass (dark shaded) to avoid a change of the interior volume and consequent implications for the occupants.

Through the described adaptivity, the properties of the membrane facade can be changed. Heat flows can be used selectively to increase the air permeability of the facade to adjust interior

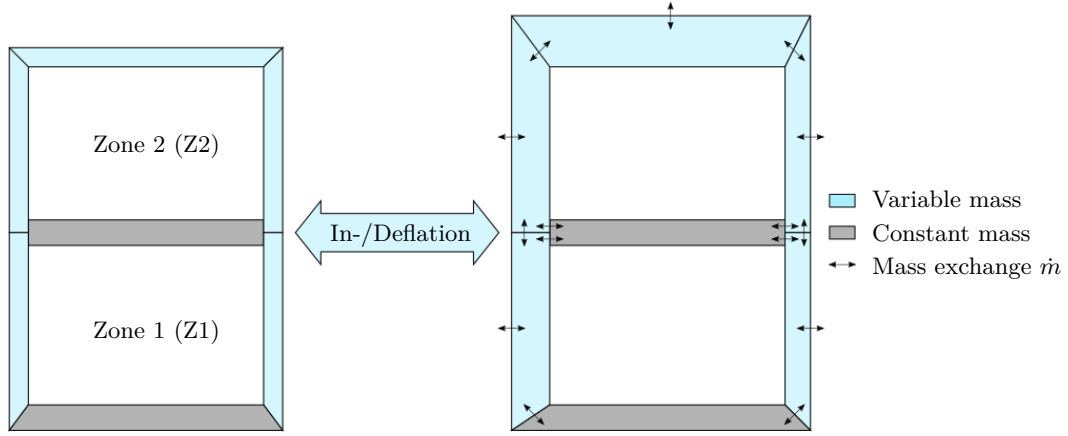


Figure 1: Sketch of inflatable building design for variable insulation state and heat transfer by mass exchange.

surface and room air temperatures. For the following analysis, the material properties of the membrane facade are set based on an exemplary ETFE film as stated in [11] and given in Table 1. It is assumed that a facade element consists of 5 membrane layers with a thickness of 0.2 mm which are cumulated to an inner and outer surface for a simplified reference model. Hence, the total thickness results in $d_{\text{mem}} = 0.5 \text{ mm}$. For further simplification, an opaque membrane without solar transmission is considered.

2.2 Physical Modeling

The dynamic equations to represent the building dynamics are obtained by the heat and mass balance of the facade and zone elements [12] under the assumption of well mixed conditions within the zones and wall components. Each element can be modeled as an air cushion with a temperature T , a mass m and a relative humidity RH . For simpler equations, relative humidity RH is substituted by the mass fraction of water $X_{\text{H}_2\text{O}} = \frac{m_w}{m_w + m_a}$. The temperature and inflation are defined by the heat and mass balance

$$c_p(T, X_{\text{H}_2\text{O}})(m\dot{T} + \dot{m}T) = \sum_{i=1}^{n_{\text{adj}}} \frac{T_i - T}{R_i(T, T_i, \dot{Q}_{\text{sol}})} + \sum_{j=1}^{n_{\text{flow}}} \dot{H}_j + \dot{Q}_{\text{demand}} \quad (1a)$$

$$\dot{m} = \sum_{j=1}^{n_{\text{flow}}} \dot{m}_j \quad (1b)$$

$$\dot{X}_{\text{H}_2\text{O}} = \frac{\dot{m}_w - \dot{m}X_{\text{H}_2\text{O}}}{m} \quad (1c)$$

where c_p is the specific heat capacity of moist air, \dot{H}_j denotes the enthalpy flow due to the mass transfer from or to an adjacent element j , \dot{Q}_{sol} defines the effective solar load and \dot{Q}_{demand} represents the required heating or cooling demand to maintain comfortable indoor temperatures. The j -th enthalpy flow between adjacent wall elements is defined by [13]

$$\dot{H}_j = \dot{m}_j \left(c_a T_j (1 - X_{\text{H}_2\text{O}}) + X_{\text{H}_2\text{O}} \left(c_w T_j + 2501 \frac{\text{kJ}}{\text{kg}} \right) \right), \quad (2)$$

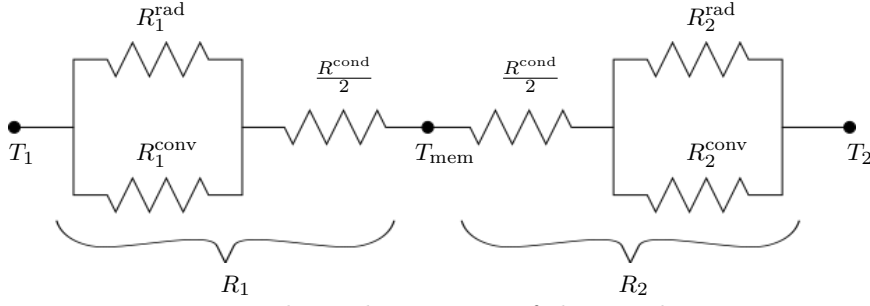


Figure 2: Thermal resistance of the membrane.

where \dot{m}_j denotes the corresponding mass flow and T_j depends on the direction of the flow. The effective solar heat load depends on the sun position as well as direct and diffuse solar radiation:

$$\dot{Q}_{\text{sol}} = F_{\text{sol}} I_{\text{dir}} + I_{\text{dif}}. \quad (3)$$

The view factor F_{sol} is calculated based on the wall's facing angle, the azimuth and elevation of the sun and the absorptivity α as stated in Table 1. Besides mass exchange, heat is transferred by a combined effect of conduction, convection and radiation. These are summarized in the non-linear thermal resistance R_i that is calculated by [14]

$$R_i = \sum_{k=1}^2 \frac{R_{ik}^{\text{conv}} R_{ik}^{\text{rad}}}{R_{ik}^{\text{conv}} + R_{ik}^{\text{rad}}} + R_i^{\text{cond}}, \quad (4)$$

where

$$\begin{aligned} R_i^{\text{cond}} &= \frac{d_{\text{mem}}}{\lambda_{\text{mem}} A_i} \\ R_{ik}^{\text{rad}} &= \frac{1}{h_k^{\text{rad}}(T_{\text{mem}}, T_k) A_i} = \frac{\frac{1}{\epsilon_1} + \frac{1}{\epsilon_2} - 1}{\sigma A_i (T_{\text{mem}}^2 + T_k^2)(T_{\text{mem}} + T_k)} \\ R_{ik}^{\text{conv}} &= \frac{1}{h_k^{\text{conv}}(T_{\text{mem}}, T_k, \dot{Q}_{\text{sol}}) A_i} \\ h_k^{\text{conv}} &= \begin{cases} 1.31 |T_{\text{mem}} - T_k|^{\frac{1}{3}} & \text{for a vertical wall} \\ 1.52 |T_{\text{mem}} - T_k|^{\frac{1}{3}} & \text{for } (\text{floor} \wedge T_{\text{mem}} < T_k) \vee (\text{ceiling} \wedge T_{\text{mem}} > T_k) \\ 0.76 |T_{\text{mem}} - T_k|^{\frac{1}{3}} & \text{for } (\text{floor} \wedge T_{\text{mem}} > T_k) \vee (\text{ceiling} \wedge T_{\text{mem}} < T_k) \end{cases} \\ T_{\text{mem}} &= \frac{R_1(T_{\text{mem}}) R_2(T_{\text{mem}})}{R_1(T_{\text{mem}}) + R_2(T_{\text{mem}})} \left(\frac{T_1}{R_1(T_{\text{mem}})} + \frac{T_2}{R_2(T_{\text{mem}})} + \frac{\alpha}{A_i} \dot{Q}_{\text{sol}} \right). \end{aligned}$$

The convective heat transfer coefficient h_k^{conv} is computed based on the TARP algorithm [15, 16].

The building dynamics are highly influenced by external conditions due to the thin membrane layers without additional insulation. The main impacting factors are outside temperature T_{out} and direct and diffuse solar radiation, I_{dir} and I_{dif} respectively. Solar energy is absorbed by the facade cushions and can either be used as heat source or needs to be removed depending on the required indoor conditions. Although relative humidity changes the heat capacity of the air, simulations showed that the thermal impact is rather low within the occurring humidity range.

3 SIMULATIVE ANALYSIS

The building dynamics are analyzed for different initial inflation states. Multiple simulations based on typical weather conditions in Stuttgart are compared in relation to their energy demand for maintaining comfortable conditions. The applied weather data are taken from the German Weather Service [17]. The desired operative temperature is set to a constant value of $T_{\text{op}}^{\text{des}} = 24^\circ\text{C}$ for simplicity and comparability. This corresponds to a reasonable compromise between comfortable conditions during winter and summer time as well as different clothing levels [18]. The required operative and mean radiant temperature are approximated by [19]

$$T_{\text{op}} = \frac{T_{\text{air}} + T_{\text{mr}}}{2}, \quad T_{\text{mr}} = \frac{\sum_i^{n_{\text{walls}}} A_i T_i}{\sum_i^{n_{\text{walls}}} A_i}. \quad (5)$$

The considered building has a floor area of 10 m by 10 m and a room height of 3 m. The northern facade faces directly to the north such that the building has a clear north (N), east (E), south (S) and west (W) facade which are referred to by the corresponding letter and story number (e.g. N1). The thermal capacity of the floor elements is increased compared to the purely air-filled facade cushions to account for potential interior equipment. Table 2 summarizes the applied system parameter changes that are discussed in the following.

First, the impact of different wall thicknesses is evaluated for typical winter and summer conditions to demonstrate the possible effects and dynamics. The results are given for a period of 48 h and depicted in Figure 3. Comparing the required, time-dependent cooling or heating power for three different inflation states ($d_{\text{wall}} = \{0.1\text{ m}, 1\text{ m}, 10\text{ m}\}$) reveals the potential of changing wall volumes. Generally, a fast response to varying outside conditions and a strong dependency on solar influences can be noted for all setups. Furthermore, the upper zone has a significantly higher energy consumption compared to the lower zone. This is due to the larger external wall area and consequently an increased energy loss through the ceiling/roof. The larger external wall area also implies a lower/higher mean radiant temperature in winter/summer and consequently affects the operative temperature directly. However, only a negligible difference between a wall thickness of 0.1 m and 1 m can be noted on an hourly scale. A notable change of the building dynamics can only be achieved by a high (but presumable physically infeasible) increase to 10 m. The corresponding daily and annual energy demand

$$Q_{\text{demand}}^I = \int_I |\dot{Q}_{\text{demand}}(t)| dt \quad (6)$$

over the examined time interval I is listed in Table 2 and supports the outcome of the graphical analysis. The energy consumption for the first two setups is almost identical. The higher thermal capacity of the walls in setup 3 slows down the building's response and can make better use of the internally stored heat or cold. This effect is even more beneficial during the summer than the winter time due to the damped impact of solar radiation. The lower wall temperatures reduce the zonal mean radiant temperature and hence the impact on the operative temperature as described in (5).

However, instead of increasing the external wall capacity, an opposite change of the internal characteristic, thus decreasing the internal heat capacity, can lead to a similar reduction of the energy consumption. In setup 4, the wall thickness d_{wall} is again set to 1 m while the thermal capacity of the interior is reduced by factor 10 (which corresponds to an air-filled floor element with $d_{\text{wall}} = 1\text{ m}$). Comparing the energy demand of setup 2 and 4 directly shows that heating

Table 2: Energy demand of the inflatable building for different inflation states and system parameter configurations.

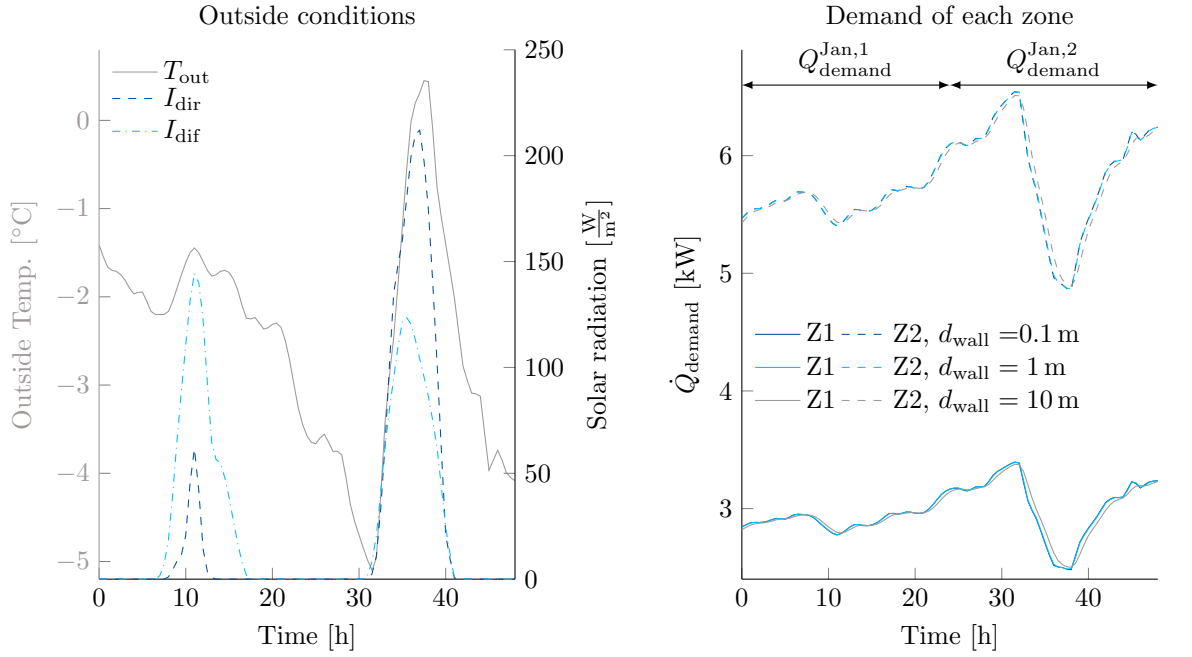
	Setup	Unit	1	2	3	4	5	6	7	8
Config.	d_{wall}	m	0.1	1	10	1	1	1	1	1
	C_{floor}	$\frac{\text{kJ}}{\text{K}}$	1241	1241	1241	124	124	124	124	124
	α	-	0.2	0.2	0.2	0.2	0.8	0.2	0.2	0.2
	d_{mem}	mm	0.5	0.5	0.5	0.5	0.5	5	0.5	0.5
	Mass exchange	-	no	no	no	no	no	no	hor	ver
Energy demand	$Q_{\text{demand}}^{\text{Jan},1}$	kWh	205.41	205.32	204.95	205.16	203.80	198.95	205.17	208.86
	$Q_{\text{demand}}^{\text{Jan},2}$	kWh	213.67	213.72	213.62	213.66	211.37	207.12	213.47	217.43
	$Q_{\text{demand}}^{\text{Jul},1}$	kWh	20.66	20.60	19.46	19.66	27.26	19.36	19.73	20.41
	$Q_{\text{demand}}^{\text{Jul},2}$	kWh	18.77	18.67	18.30	18.59	15.62	18.10	18.48	18.95
	$Q_{\text{demand}}^{\text{year},Z1}$	MWh	12.58	12.58	12.56	12.54	12.23	12.17	12.54	13.54
	$Q_{\text{demand}}^{\text{year},Z2}$	MWh	24.33	24.33	24.31	24.31	23.82	23.67	24.31	24.03
	$Q_{\text{demand}}^{\text{year},Z1+Z2}$	MWh	36.90	36.90	36.87	36.85	36.06	35.84	36.85	37.57

but particularly cooling power is lowered as a result of the smaller internal heat storage. This results in faster dynamics and less required power to keep the desired temperature as shown in Figure 4. Although small variations can be noted, the energy demand is comparable for all facade widths that are within a building-physically meaningful range due to the equal stationary system behavior. Therefore, the impact of other system parameters is further analyzed.

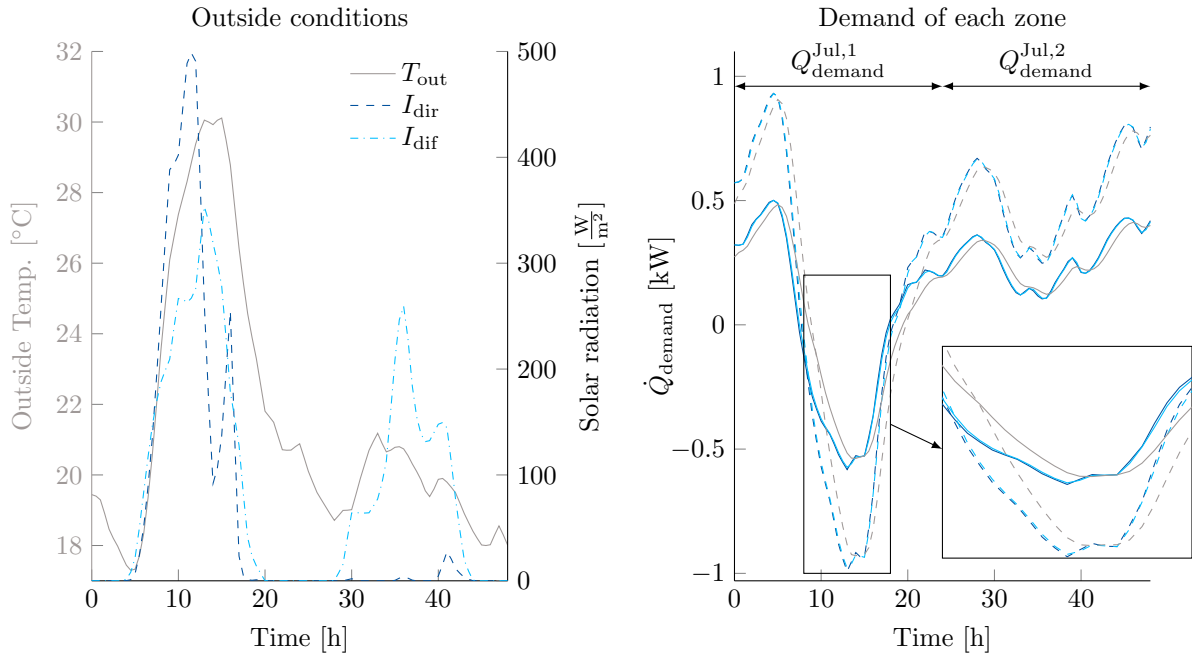
Since solar radiation is a main contributor to the thermal conditions of the light-weight building structure, a higher solar absorption coefficient α leads to a more significant change. The impact of radiation on the operative temperature is clearly demonstrated by the temperature difference between the two zones as shown in Figure 4. Wall temperatures below the desired set-point increase the required air temperature while higher wall temperatures involve lower interior air temperatures. As a consequence, the low wall temperatures during the winter result in a higher temperature set-point ($> 1^\circ\text{C}$) for upper zone (Figure 4a). The smaller temperature differences during the summer time reduce this effect (Figure 4b). Hence, an increase of α to 0.8 according to configuration 5 results in a significant impact on the cooling demand in Figure 4b. The upper zone acts like a greenhouse and requires a very high cooling power due to the considerable temperature increase of the air-filled walls. However, this effect can be beneficially used during winter time to reduce the heating demand by a higher mean radiant temperature and thus operative temperature. This lowers the annual energy consumption because of the higher heating demand on a yearly basis of the considered building location.

For the given modeling assumptions, insulation is only provided by the membrane. Increasing its thickness d_{mem} (or number of layers) directly amplifies the conductive resistance. The resulting system dynamic for $d_{\text{mem}}^{\text{new}} = 10 \cdot d_{\text{mem}}^{\text{old}}$ is also pictured in Figure 4. In particular during the winter time (Figure 4a), the larger insulation is visible as a reduced heating demand due to a smaller heat loss and hence allowing lower wall temperatures. For warmer periods, when the air temperature difference between indoor and outdoor conditions is relatively small, the additional insulation does not result in a notable change of the building dynamics.

So far, only stationary system configurations were analyzed where no mass exchange was

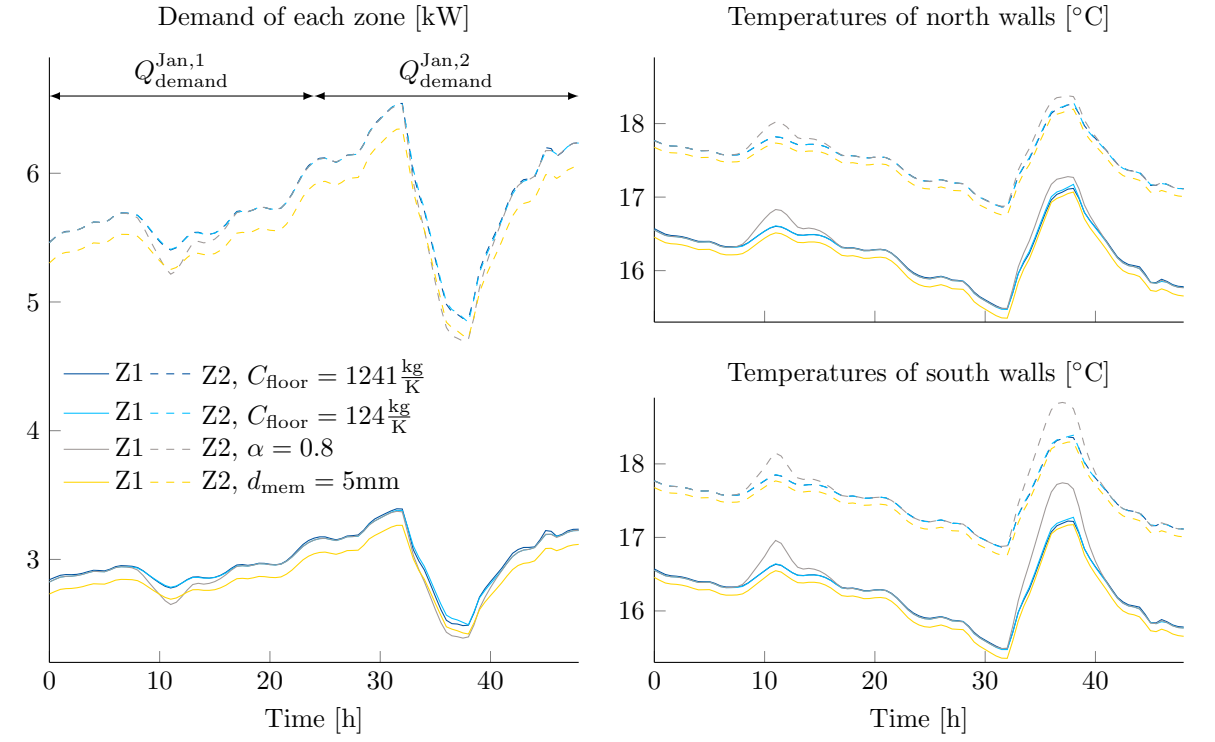


(a) Two days in January.

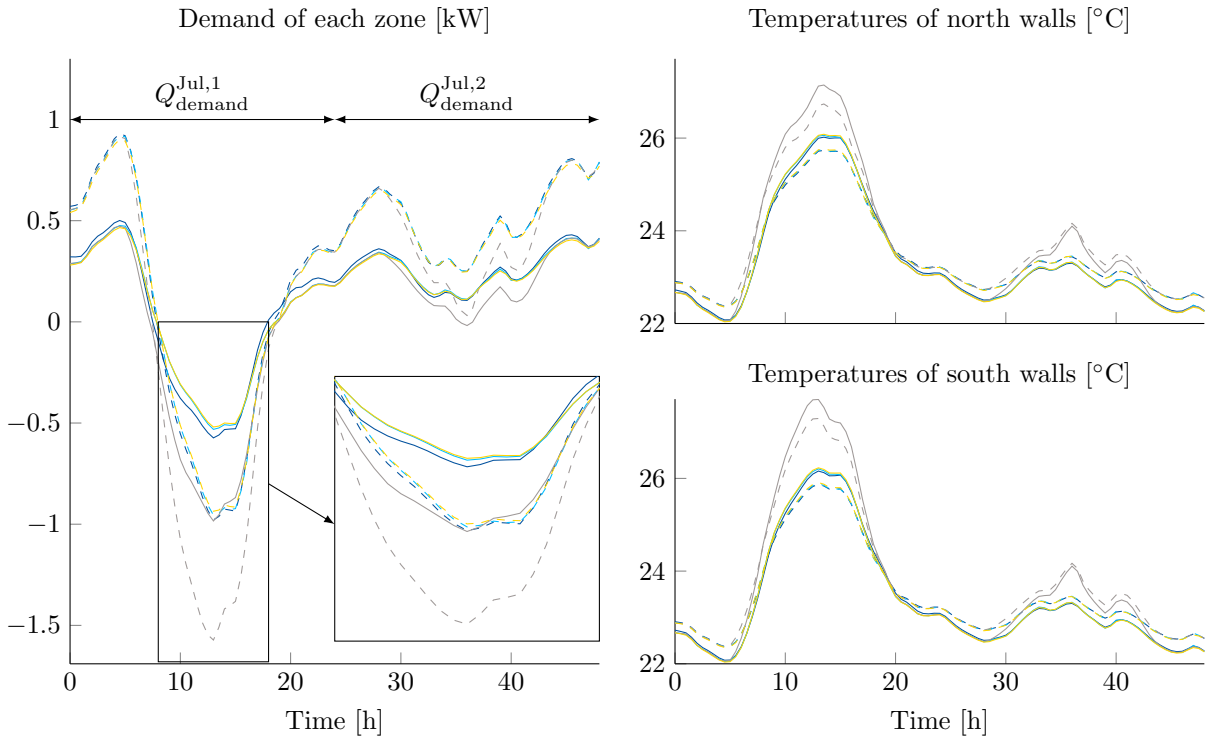


(b) Two days in July.

Figure 3: Effect on energy demand of different air volumes of the facade elements.



(a) Two days in January.



(b) Two days in July.

Figure 4: Effect on energy demand and wall temperatures of varying system parameters.

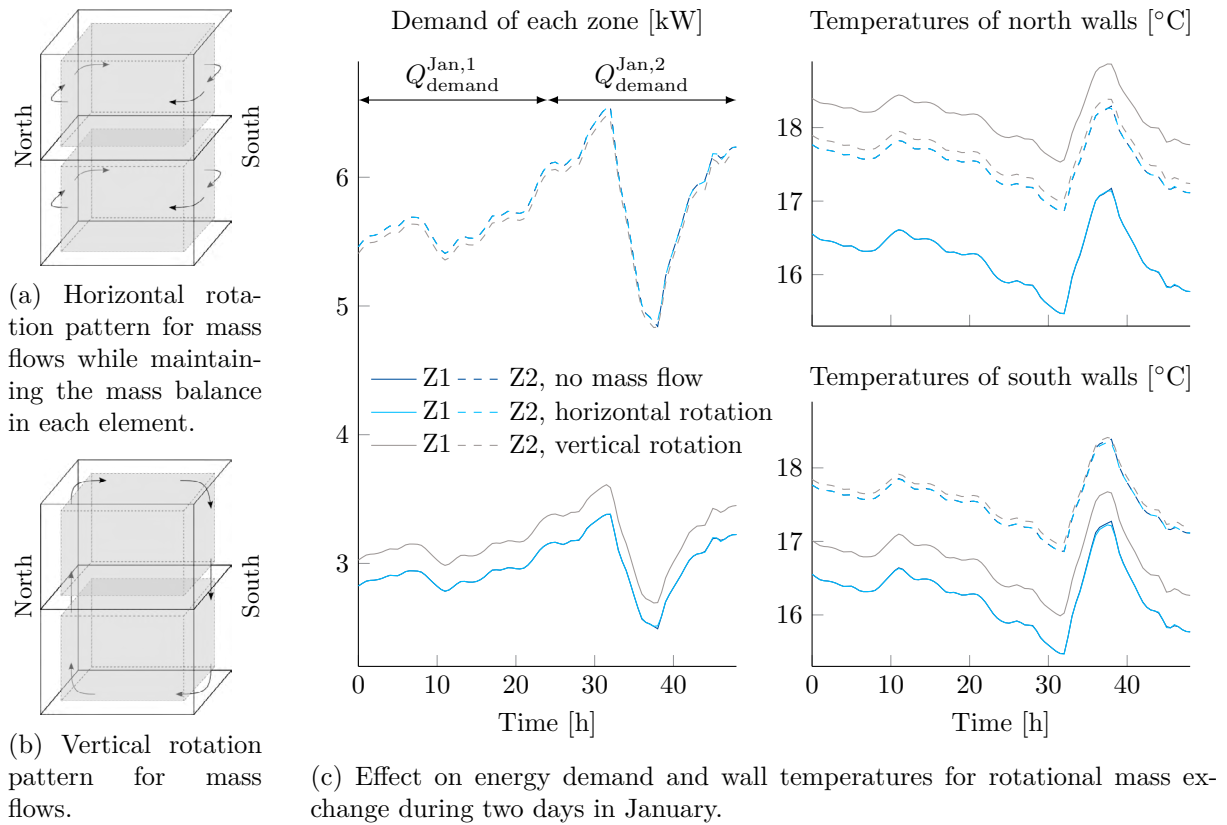


Figure 5: Analysis of the effect of mass exchange between adjacent facade elements.

involved. The impact of air circulation is exemplary analyzed based on two rotational patterns as sketched in Figure 5a and 5b. The resulting power consumption and wall temperatures are shown in Figure 5c. The horizontal mass exchange (Figure 5a) does not change the building dynamics noticeable. Due to the small floor area of the considered building with one zone on each level surrounded by external walls only, the temperature differences between the walls are already relatively small such that an additional mixing does not lead to a significant change. However, a small reduction of the overall energy demand can be achieved.

A larger impact is obvious for the vertical rotation, as pictured in Figure 5b. The rotational mass flow around the building results in an energy exchange between the first and second floor as well as the north and south facade. The air is heated by circulating through the floor and then cooled down on its way around the building. Consequently, the wall N1 is the warmest and S2 the coldest for the simulated winter conditions. The heat transfer from the first to the second level results in a small reduction of the required heating power of the upper zone Z2. However, the consumed heating power of Z1 is increased by a larger amount. This results in a higher energy demand of the building, as stated in Table 2. The detailed results for July are not shown due to smaller effects originating from the lower temperature differences compared to the heating period during winter. Nevertheless, a similar tendency can be noticed for the corresponding energy consumption. In particular the annual demand emphasizes the previous observations. While the consumption of zone 2 can be lowered by approx. 2%, zone 1 requires 8% more energy which leads to a total increase of about 2%.

4 LIMITATIONS AND POTENTIAL

The previous results point to some limitations that are introduced by model assumptions and simplifications. The model approach uses the assumption of perfect mixing within the zones and wall elements. While this is a common assumption for medium-sized spaces, it can entail characteristics which diminish the insulation property of an inflatable facade structure. The perfect-mixing assumption leads to equivalent stationary behavior for all inflation states. A multilayer design, that separates the air volume in several thinner air layers, can reduce convective effects such that the insulation property of air can be used more efficiently. Particularly for the stationary case with still air, conduction should be more dominant and a larger air volume could improve the building's insulation remarkably. As shown by simulation setup 6, this property will have a significant impact on the energy demand.

Moreover, the facade is assumed to be opaque and transmission is completely neglected for the presented results. Using ETFE as facade material allows for bright indoor conditions without adding large-scale glazing. Including this property to the model also changes solar impacts and can lead to lower heating demand during the cold period as indicated by the results for increased solar absorption in setup 5.

Modified results are also possible when internal disturbances, like occupancy, lightning and electrical devices, are considered in the analysis. The prerequisite that all zones must maintain comfortable conditions 24 h per day, is often not necessary and changing occupancy can introduce a great potential. Although the results for vertical mass circulation showed that heat transfer between zones entails energy losses, it could be efficiently used for transferring conditioned air from an unoccupied zone to occupied building sections. A mass exchange can be even more advantageous when considering a larger building with multiple zones on one level, where solar influences have a more local effect on thermal conditions.

Another potential benefit originates from a reduction of radiant temperature asymmetry to improve thermal comfort [19]. Circulating the air and thus equalizing wall temperatures reduces asymmetric conditions and enhances thermal comfort.

5 CONCLUSION

The presented analysis revealed potential but also some problems regarding the use of inflatable membrane facades. While pure inflation does not change the building dynamics significantly, greater impact can be achieved by mass exchange and intelligent selection of system parameters during the design phase. The right choice for a final building setup depends strongly on the building type, utilization and the corresponding occupancy and internal disturbance profiles.

Therefore, further work will analyze the impact of transmission, internal disturbances and varying occupancy as well as different building configurations. Interpreting thermal comfort not only as an operative temperature implies additional potential of this approach.

ACKNOWLEDGMENT

The work described in this paper was conducted in the framework of the Collaborative Research Centre 1244 "Adaptive Skins and Structures for the Built Environment of Tomorrow" funded by the German Research Foundation (DFG - Deutsche Forschungsgemeinschaft). The authors are grateful for the generous financial support and wish to express their gratitude therefor.

REFERENCES

- [1] European Commission, “Roadmap to a resource efficient europe: Com(2011) 571 final,” 2011. [Online]. Available: <https://eur-lex.europa.eu/legal-content/EN/ALL/?uri=CELEX:52011DC0571>
- [2] S. Gauthier, D. Teli, P. James, and S. Stamp, “Are heavyweight buildings more comfortable? the potential of thermal mass in increasing thermal comfort,” *Passive and Low Energy Architecture*, 2017.
- [3] P. J. Hoes, M. Trcka, J. Hensen, and B. Bonnema, “Exploring the optimal thermal mass to investigate the potential of a novel low-energy house concept,” *International Conference for Enhanced Building Operations*, 2010.
- [4] H. Modin, “Adaptive building envelopes,” Master’s Thesis, Chalmers University of Technology, 2014.
- [5] A. Aksamija, *Sustainable Facades: Design Methods for High-Performance Building Envelopes*. Wiley, 2013.
- [6] S. Lehnert, “Innovative Gebäudehüllen. Eigenschaften von ETFE-Folienkissen,” *Deutsche Bauzeitschrift (DBZ)*, vol. 4, 2015.
- [7] J. Cremers, “Energy saving design of membrane building envelopes,” *International Conference on Textile Composites and Inflatable Structures*, 2011.
- [8] D. Cardoso, D. Michaud, L. Sass, and J. Gonzalez, “Soft façade: Steps into the definition of a responsive etfe façade for high-rise buildings,” *Predicting the Future: 25th eCAADe Conference Proceedings*, vol. 2, 2007.
- [9] J. Hu, W. Chen, Y. Liu, B. Zhao, D. Yang, and B. Ge, “Two-layer etfe cushions integrated flexible photovoltaics: Prototype development and thermal performance assessment,” *Energy and Buildings*, vol. 141, pp. 238–246, 2017.
- [10] A. Ganji Kheybari and J. Lam, “Building envelope as heat generator: The impact of water-filled etfe cushion on energy saving and comfort,” *Powerskin*, 2017.
- [11] NOWOFOL® Kunststoffprodukte GmbH & Co. KG, “NOWOFLON® ET 6235 Z-IR ETFE HEAT ABSORBING FILM.” [Online]. Available: <https://www.etfe-film.com/files/etfe/pdf/Product-Information-NOWOFLON-ET-6235-Z-IR.pdf>
- [12] F. P. Incropera, D. P. DeWitt, T. L. Bergman, and A. S. Lavine, *Fundamentals of Heat and Mass Transfer*, 6th ed. Chichester, United Kingdom: John Wiley and Sons Ltd, 2010.
- [13] B. Glück, *Zustands- und Stoffwerte*, 2nd ed. Berlin: Verlag für Bauwesen GmbH, 1991.
- [14] VDI, *VDI-Wärmeatlas*, 11th ed. Berlin, Heidelberg: Springer Berlin Heidelberg, 2013.
- [15] G. N. Walton, *Thermal Analysis Research Program Reference Manual*. National Bureau of Standards (NIST), 1983.
- [16] EnergyPlus. Engineering Reference — EnergyPlus 9.0. Accessed: 2019-04-02. [Online]. Available: <https://bigladdersoftware.com/epx/docs/9-0/engineering-reference>
- [17] Deutscher Wetterdienst (DWD), “CDC OpenData,” 2015. [Online]. Available: https://opendata.dwd.de/climate/{_}environment/CDC/
- [18] ASHRAE, *2017 ASHRAE Handbook - Fundamentals (SI Edition)*, si-edition ed. Atlanta, Georgia: ASHRAE, 2017.
- [19] —, *ANSI/ASHRAE Standard 55-2013: Thermal Environmental Conditions for Human Occupancy*. Atlanta, Georgia: ASHRAE, 2013.

TOPOLOGY OPTIMIZATION OF PIEZOELECTRIC SMART STRUCTURES UNDER CGVF ACTIVE CONTROL

ZHIYUAN JIA, XIAOPENG ZHANG*

* State Key Laboratory of Structural Analysis for Industrial Equipment, Dalian University of Technology, Dalian, China
e-mail: zhangxiaopeng@dlut.edu.cn

Keywords: Topology optimization, Active control, Piezoelectric material structure, Smart structure.

Abstract. Smart structural systems with piezoelectric actuators and sensors are considered as an effective manner to reduce structural vibration for avoiding possible damage of a structure or degradation of system performance. Piezoelectric actuators are often used for providing active damping in the active vibration control system. It is clear that the active control effect can be promoted by optimizing the numbers and positions of piezoelectric actuators. Topology optimization of piezoelectric smart structures has also received increasing attention.

This study presents a topology optimization formulation for optimizing the piezoelectric actuator and sensor layout optimization to suppress the structural dynamic response under active vibration control. The structure is excited by an external harmonic load. For controlling the dynamic response, each sensor patch is connected to a charge amplifier, and the CGVF control algorithm is adopted to convert the sensor output to feedback control voltage in the corresponding actuator patch. Here, the control effect can be treated as active damping of the dynamic system. The structure is discretized with finite element model, and the structural response is evaluated with a time-integration method. In the optimization model, an integral-type performance function in a given time interval is to be minimized. The pseudo-densities of piezoelectric elements (sensor and actuator) with penalization for indicating the presence or absent are taken as design variables. The sensitivity analysis scheme is derived with the adjoint-variable method and the optimization problem is solved with a gradient-based mathematical programming algorithm.

1 INTRODUCTION

Since large vibrations are harmful to structural safety and functionality, many studies have been devoted to the control of structural vibration. According to the control mechanisms, structural vibration control methods can be divided into three categories: active control, passive control, and semi-active control. Herein, the active control approach focuses on reducing the structural vibration by arranging control transducers in the vibrating structure. Active control strategies have been proved effective in reducing the structural vibration level. Many studies on active vibration control of thin-shell structures focus on arranging the spatial distribution of control transducers (e.g. piezoelectric actuator/sensor patches). To achieve the best control

performance, however, finding the optimal layouts of the piezoelectric actuators/sensors patches in accordance with the employed control algorithms becomes highly important.

Optimization of piezoelectric smart structures has received increasing attention. Genetic algorithms^[1], particle swarm optimization algorithms^[2] or other heuristic algorithms^[3], have been used to seek the optimal size and location of piezoelectric actuators. In addition, more and more scholars use the method of topology optimization to study the layout of piezoelectric materials(e.g. Kögl and Silva^[4], Carbonari et al.^[5], Kang et al.^[6], Luo et al.^[7] and Kang and Tong^[8]). Some authors also considered topology optimization of piezoelectric structures under active control. For example, Wang et al.^[9] optimized the distribution of piezoelectric actuators/sensors for suppressing the structural vibration with classical constant gain velocity feedback(CGVF) control and genetic algorithms. Drenckhan et al.^[10] proposed the piezoelectric actuators distribution optimization method in a beam structure. Donoso and Sigmund^[11] studied the mechanism of the piezoelectric bimorph actuators and proposed a parametric optimization method for optimizing the thickness and width profile of the piezoelectric layers.

This paper mainly studies the optimal layout of the piezoelectric sensor layer and actuator layer, which aims at reducing the vibration level of the structure under external harmonic excitation. The classical CGVF control algorithm is adopted as the active control algorithm. The topology optimization problem with the structural dynamic compliance response at the specified harmonic excitation is considered. Numerical examples are given to verify the accuracy and effectiveness of the proposed method.

2 ESTABLISHMENT OF FINITE ELEMENT MODEL

Here, the piezoelectric actuator layer and the sensor layer are attached to the top and bottom surfaces of the host structure (as shown in Figure 1).

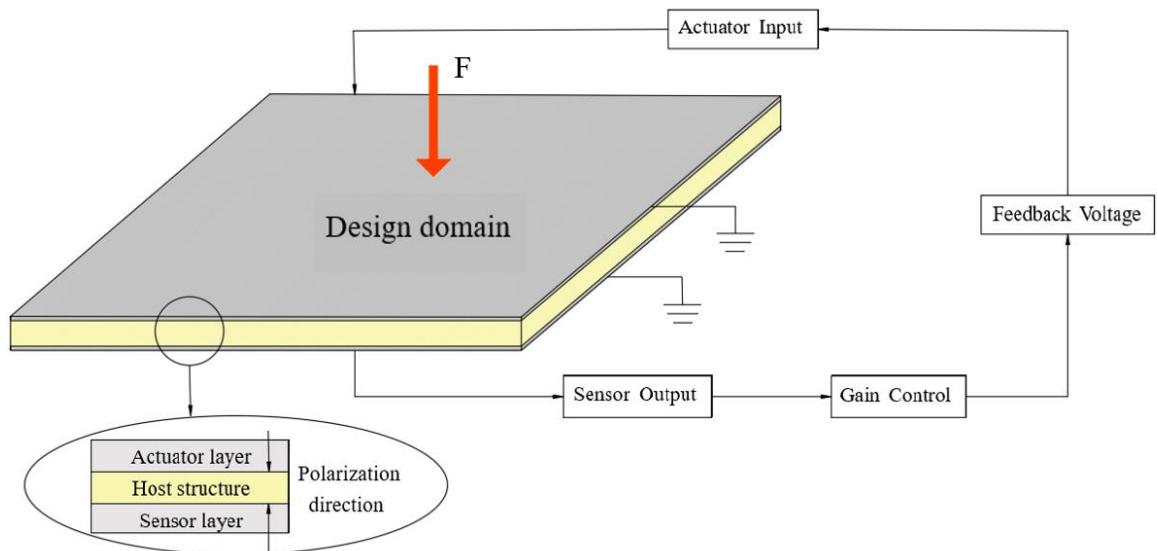


Figure 1: Schematic diagram of active control of laminate structure with surface-attached piezoelectric sensor layer and actuator layer

The mechanical properties of the sensor layer, the actuator layer, and the host layer are considered to be linear elastic. Thus, the constitutive equation for the piezoelectric layer can be written as^[12] $\boldsymbol{\sigma} = \mathbf{D}^E \boldsymbol{\varepsilon} - \mathbf{e}^T \mathbf{E}$. Here, $\boldsymbol{\sigma}$ and $\boldsymbol{\varepsilon}$ are the mechanical stress vector and the mechanical strain vector, respectively; \mathbf{D}^H and \mathbf{D}^E are the elasticity matrices of the host layer and piezoelectric layer, respectively. \mathbf{e} is the piezoelectricity matrix, \mathbf{E} is the vector of electric field.

The electric potential functions are assumed to have linear variations across the thickness of the piezoelectric actuator and sensor layers. The electric voltage in the actuator layer $\boldsymbol{\Phi} = \{\Phi^1, \Phi^2, \dots, \Phi^{N_e}\}^T$. In the active vibration control of plate with piezoelectric layer, the voltage is applied only in the thickness direction. We assume that the electric potential varies linearly across the actuator layer. Thus the electric field vector for the i th actuator patch $\mathbf{E}^i = \{0, 0, -\Phi^i/h\}^T$ ($i=1, 2, \dots, N_e$), h is the thickness of the actuator layer.

We consider the optimal layout of a given volume of piezoelectric material in the actuator and sensor layer. The governing equation of piezoelectric laminate based on finite element discrete can be given as:

$$\mathbf{M}\ddot{\mathbf{y}}(t) + \mathbf{C}\dot{\mathbf{y}}(t) + \mathbf{K}\mathbf{y}(t) = \mathbf{F}(t) + \mathbf{F}_a(t) \quad (1)$$

where $\mathbf{M} \in \mathbf{R}^{n \times n}$, $\mathbf{C} \in \mathbf{R}^{n \times n}$ and $\mathbf{K} \in \mathbf{R}^{n \times n}$ (n is the number of degree of freedom) are the mass matrix, the damping matrix and the stiffness matrix of the whole structure, respectively; $\mathbf{F}(t) = \mathbf{f}e^{i\theta t}$ is the vector of excitation force with a frequency θ and amplitude \mathbf{f} . $\mathbf{F}(t)$ is the vector of time-varying equivalent nodal forces of the piezoelectric actuator that can be express as $\mathbf{F}_a(t) = \mathbf{K}_{u\Phi} \boldsymbol{\Phi}_a(t)$. Here, $\boldsymbol{\Phi}_a(t)$ is the actuator voltage vector and depends on the sensor voltage $\boldsymbol{\Phi}_s(t)$ of the sensor layer; $\mathbf{K}_{u\Phi} = \int_{\Omega} \mathbf{B}_{uu}^T \mathbf{e}^T \mathbf{B}_{u\Phi} d\Omega$ is the structural electromechanical matrix of the actuator layer. \mathbf{B}_{uu} and $\mathbf{B}_{u\Phi}$ are the strain-displacement matrix and the matrix relating the electrical field with the actuation voltage, respectively; and they depend on the geometry of the actuator layer.

3 ACTIVE CONTROL MODEL BASED ON CGVF CONTROL ALGORITHM

In this study, the CGVF control algorithm is adopted to convert the sensor output to feedback control voltage in the corresponding actuator patch. Therefore, the actuator voltage vector $\boldsymbol{\Phi}_a(t)$ can be obtained by using the output sensor voltage $\boldsymbol{\Phi}_s(t)$ as:

$$\boldsymbol{\Phi}_a(t) = -\mathbf{G}_a \boldsymbol{\Phi}_s(t) = -\mathbf{G}_a \mathbf{G}_s \mathbf{K}_{\Phi u} \dot{\mathbf{y}}(t) \quad (2)$$

where \mathbf{G}_a is a constant gain diagonal matrix.

The system equations with active damping can be obtained as:

$$\mathbf{M}\ddot{\mathbf{y}}(t) + (\mathbf{C} + \mathbf{C}_A) \dot{\mathbf{y}}(t) + \mathbf{K}\mathbf{y}(t) = \mathbf{F}(t) \quad (3)$$

where $\mathbf{C}_A = \mathbf{K}_{u\Phi} \mathbf{G}_a \mathbf{G}_s \mathbf{K}_{\Phi u}$ is the active damping matrix.

It is noted that the active damping matrix \mathbf{C}_A is not positive definite and is not symmetric. Thus the damping matrix $(\mathbf{C} + \mathbf{C}_A)$ of the structure is still not a positive definite matrix.

4 TOPOLOGY OPTIMIZATION PROBLEM FORMULATION

We consider the optimal topological layout of the piezoelectric actuator layer and the piezoelectric sensor layer in a piezoelectric laminate structure as shown in Figure 1 with a given volume fraction. Thus, the topology optimization problem can be expressed as:

$$\begin{aligned}
 \min_{\mathbf{x}} \quad & f(\mathbf{x}) = c = \sqrt{(\mathbf{F}^T \mathbf{Y}^R)^2 + (\mathbf{F}^T \mathbf{Y}^I)^2} \\
 \text{s.t.} \quad & (-\theta^2 \mathbf{M} + i\theta(\mathbf{C} + \mathbf{C}_A) + \mathbf{K}) \mathbf{Y} = \mathbf{F} \\
 & \sum_{e=1}^{N_e} x_e V_e - f_v \sum_{e=1}^{N_e} V_e \leq 0 \\
 & 0 < \underline{x} \leq x_e \leq 1 \quad (e = 1, 2, \dots, N_e)
 \end{aligned} \tag{4}$$

Here, the objective function is the dynamic compliance defined by Ma^[13] et al. The vector $\mathbf{x} = \{x_1, x_2, \dots, x_{N_e}\}^T$ collects the element-wise density design variables used to describe the material layout of the piezoelectric actuator layer and sensor layer, N_e denotes the total number of finite elements in the design domain. The symbol f_v denotes the volume fraction ratio, and V_e is the volume of the e th element. The lower bound of the relative density \underline{x} is set as 10^{-6} in this study.

A penalization $p > 1$ on the piezoelectric property is needed to be introduced, the choice of the penalization factors in piezoelectric material topology optimization has been discussed in many studies. Following the suggestion of Noh and Yoon^[14], we set $p = 3$. With this penalization the piezoelectric coefficient matrix of piezoelectric materials and active damping matrix can be written as:

$$\mathbf{e}^{\text{piezo}}(x_e) = x_e^p \mathbf{e} \tag{5}$$

$$\mathbf{C}_A = \sum_{e=1}^{N_e} (x_e)^p \mathbf{K}_{u\Phi}^e \mathbf{G}_a^e \mathbf{G}_s^e \mathbf{K}_{\Phi u}^e \tag{6}$$

5 NUMERICAL EXAMPLES

The optimization program is implemented on the MATLAB platform, and the optimization problem is solved with the globally convergent method of moving asymptotes (GCMMA) for treating highly nonlinear behavior functions in the considered dynamic optimization model.

In all numerical examples, we consider the composite plate as shown in Fig. 1. Here, the host structure (aluminum) has Young's modulus $E^h = 6.9 \times 10^{10} \text{ N/m}^2$, Poisson's ratio $\nu^h = 0.3$, and the mass density $\rho^h = 2700 \text{ Kg/m}^3$; and the properties of the piezoelectric material (PZT) are $E^{\text{piezo}} = 7.1 \times 10^{10} \text{ N/m}^2$, $\nu^{\text{piezo}} = 0.35$ and $\rho^{\text{piezo}} = 5000 \text{ Kg/m}^3$. The

piezoelectric stress coefficients are $e_{31} = e_{32} = -5.2 \text{ C/m}^2$, $e_{33} = 15.1 \text{ C/m}^2$ and $e_{15} = e_{25} = 12.7 \text{ C/m}^2$. The damping coefficients of the host structure are $\alpha = \beta = 5 \times 10^{-4}$. The gain value of the current amplifier is $G_c = 1 \times 10^6 \text{ V/A}$, and the negative feedback control gain is $G_a = 50$.

We first consider the topology optimization of the piezoelectric actuator and sensor layers attached to a cantilever laminate plate, the geometric properties of the plate are $a = 1.5 \text{ m}$, $b = 1 \text{ m}$ and $t_h = 4 \times 10^{-3} \text{ m}$ as shown in Figure 2. The sensor layer and the actuator layer, both with the thickness $t_s = t_a = 0.5 \times 10^{-3} \text{ m}$, are attached to the bottom surface and the top surface of the host structure, respectively. A time-harmonic external force $f(t) = Fe^{i\theta t}$ (with $F = 200 \text{ N}$, $\theta = 2\pi f_p$ and $f_p = 37 \text{ Hz}$) is applied at the midpoint of the free edge. The design domain is discretized by 75×50 uniform-sized four-node Mindlin shell elements.

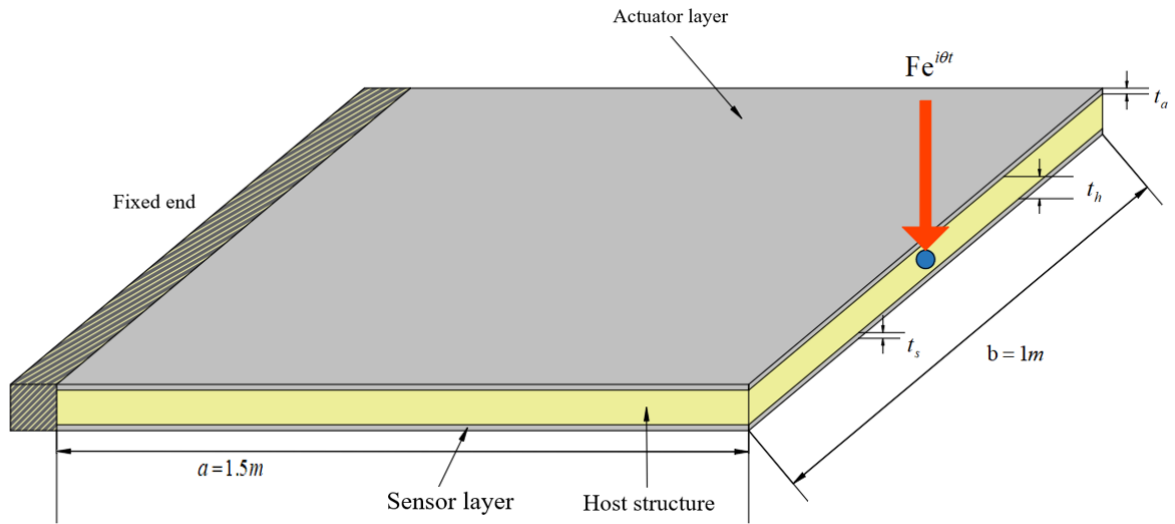


Figure 2: A cantilever plate excited by a time-harmonic load

In the optimization model, the volume fraction ratio of the piezoelectric material in the design domain is restricted by $f_v = 0.5$, and only the first 40 eigenmodes are considered in the computation. The optimization program converges after 65 steps, and its iteration history is shown in Figure 3. The optimal layout of the piezoelectric material is shown in Figure 4. In addition, the active control actuation voltage amplitude applied to the structure is as shown in Figure 5. It can be found that the actively controlled actuation voltage is almost zero in the region without the piezoelectric material.

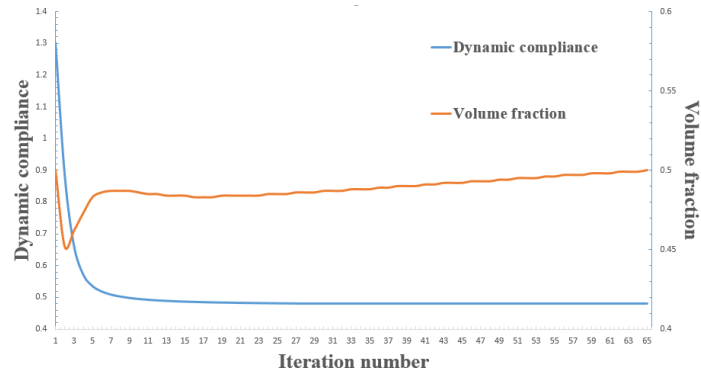


Figure 3: Iteration histories of objective function value and volume fraction ratio

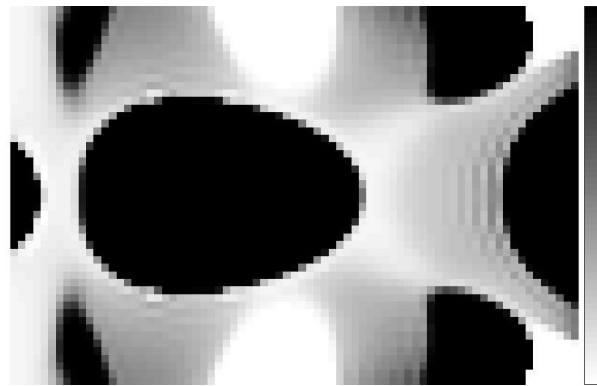


Figure 4: Optimization result of actuator/sensor distribution.

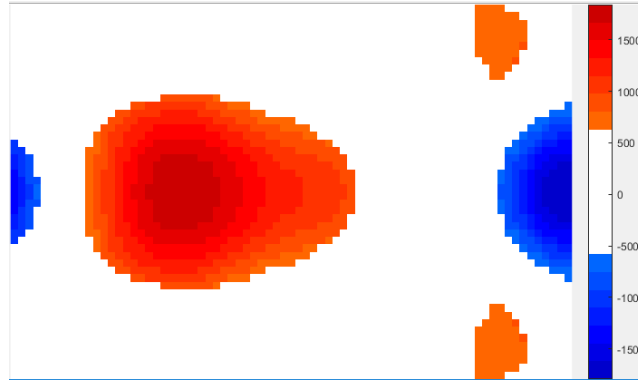


Figure 5: Actuator voltage amplitude distribution for the optimal configuration

To further examine the dynamic performance of the optimized design, we perform the calculation of the structural dynamic compliance for the initial design and optimal design in the excitation frequency range 29-60 Hz, as shown in figure 6. It can be found that, in the excitation range [33, 40] Hz, the dynamic compliance value of the optimal design under active control is

significantly smaller than the value of the initial design, which proves the effectiveness of the proposed optimization model.

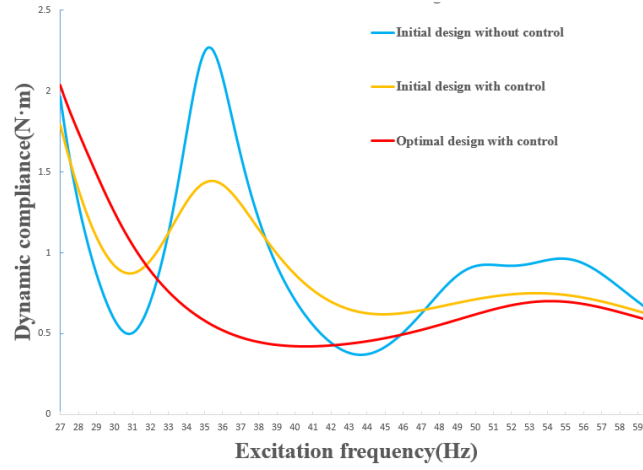
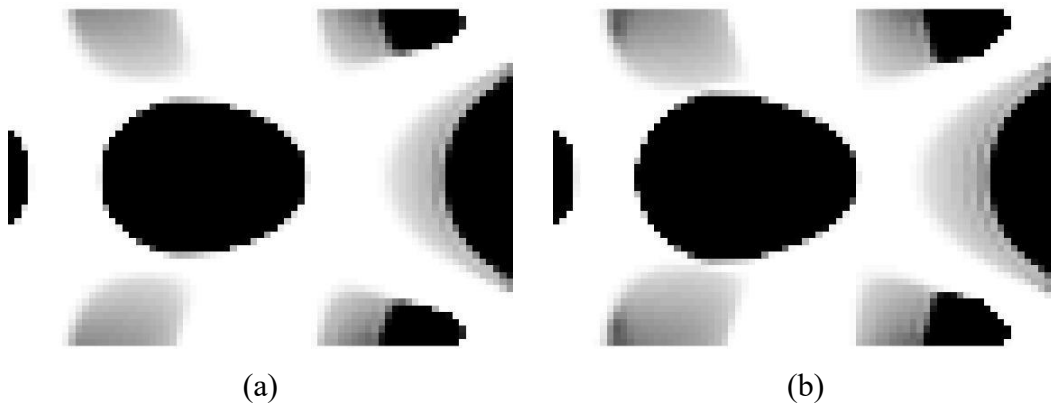


Figure 6: Dynamic compliance sweep in a specified excitation frequency range for the initial design and the optimal design

The effect of volume fraction ratio on the optimization results is also examined. Here we select the same structure and boundary conditions as the previous example, but the volume fraction ratios are taken as $f_v = 0.3, 0.35, 0.4, 0.45$. The optimization results under different volume fraction ratios are shown in Figure 7. It can be seen that as the increasing of the volume fraction ratios, more areas the piezoelectric material occupies, but the shape of the optimization results does not change so much and the topology of the design changes very little.



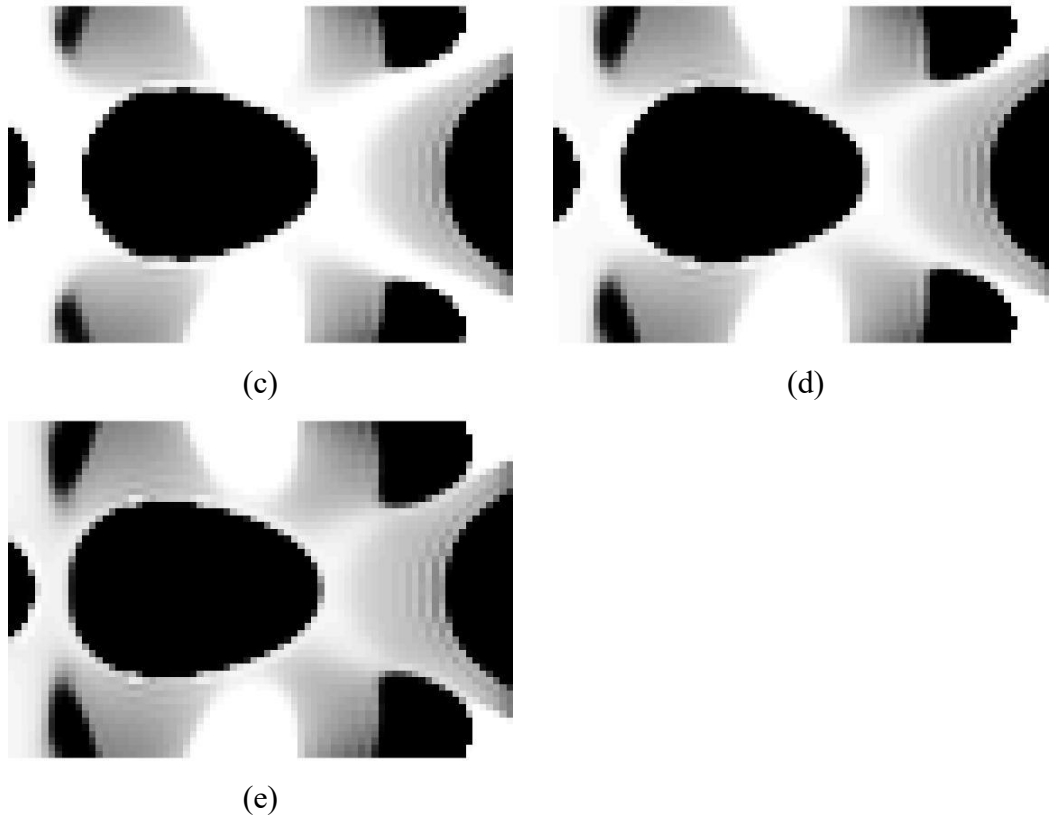


Figure 7: Optimization results for actuator/sensor layers obtained under 37 Hz excitation with different volume fraction ratios. (a) $f_v = 0.3$; (b) $f_v = 0.35$; (c) $f_v = 0.4$; (d) $f_v = 0.45$; (e) $f_v = 0.5$

6 CONCLUSIONS

This study mainly studies the optimal topological layout of piezoelectric laminate based on active control under harmonic excitation. The globally convergent method of moving asymptotes (GCMMA) is employed as the optimizer. In the optimization problem, an artificial piezoelectric material model that simultaneously punishes the piezoelectric material stiffness and the piezoelectric effect are proposed, and dynamic compliance is taken as the objective function in the optimization model. The validity and accuracy of the proposed method are verified by numerical examples. At the same time, it can be found that the dynamic compliance under harmonic excitation can be effectively reduced by topology optimization.

REFERENCES

- [1] Xu B, Jiang JS and Ou JP (2007) Integrated optimization of structural topology and control for piezoelectric smart trusses using genetic algorithm. *Journal of Sound and Vibration* 307: 393-427.
- [2] Zorić ND, Simonović AM, Mitrović ZS, et al. (2013) Optimal vibration control of smart composite beams with optimal size and location of piezoelectric sensing and actuation. *Journal of Intelligent Material Systems and Structures* 24: 499-526.

- [3] Sun D and Tong L (2005) Design optimization of piezoelectric actuator patterns for static shape control of smart plates. *Smart Materials and Structures* 14: 1353-1362.
- [4] Kögl M and Silva ECN (2005) Topology optimization of smart structures: Design of piezoelectric plate and shell actuators. *Smart Materials and Structures* 14: 387-399.
- [5] Carbonari RC, Silva ECN and Nishiwaki S (2007) Optimum placement of piezoelectric material in piezoactuator design. *Smart Materials and Structures* 16: 207-220.
- [6] Kang Z, Wang R and Tong L (2011) Combined optimization of bi-material structural layout and voltage distribution for in-plane piezoelectric actuation. *Computer Methods in Applied Mechanics and Engineering* 200: 1467-1478.
- [7] Luo Z, Gao W and Song C (2010) Design of Multi-phase piezoelectric actuators. *Journal of Intelligent Material Systems and Structures* 21: 1851-1865.
- [8] Kang Z and Tong L (2008) Topology optimization-based distribution design of actuation voltage in static shape control of plates. *Computers and Structures* 86: 1885-1893.
- [9] Wang SY, Tai K and Quek ST (2006) Topology optimization of piezoelectric sensors/actuators for torsional vibration control of composite plates. *Smart Materials and Structures* 15: 253-269.
- [10] Drenckhan J, Lumsdaine A and Parsons M (2008) Topology optimization of a piezoelectric actuator on an elastic beam. *Journal of Intelligent Material Systems and Structures* 19: 445-455.
- [11] Donoso A and Sigmund O (2009) Optimization of piezoelectric bimorph actuators with active damping for static and dynamic loads. *Structural and Multidisciplinary Optimization* 38: 171-183.
- [12] Sodano HA, Park G and Inman D (2004) Estimation of electric charge output for piezoelectric energy harvesting. *Strain* 40: 49-58.
- [13] Ma ZD, Kikuchi N and Hagiwara I (1993) Structural topology and shape optimization for a frequency response problem. *Computational Mechanics* 13: 157-174.
- [14] Noh JY and Yoon GH (2012) Topology optimization of piezoelectric energy harvesting devices considering static and harmonic dynamic loads. *Advances in Engineering Software* 53: 45-60.

A NEW NEUTRAL EQUILIBRIUM MECHANISM APPLIED TO FORCE CONTROL AND ITS APPLICATION

MING-HSIANG SHIH^{*} AND WEN-PEI SUNG[†]

^{*} Department of Civil Engineering
National Chi Nan University
Nan-Tou 545, Taiwan

e-mail: iloveaachen@gmail.com, https://www.ce.ncnu.edu.tw/member/teacher/shih_ming_hsiang.html

[†] Department of Landscape Architecture
National Chin-Yi University of Technology
Taichung 41170, Taiwan
Email: drwpsung@gmail.com

Key words: Neutral Equilibrium Mechanism, Time Delay, Critical Differential Gain, Critical Proportional Gain

Abstract. Earthquake is an inevitable natural disaster. How to improve the seismic resistant capacity of structures is an important issue in the field of seismic engineering research. In this study, a new type of control mechanism, the neutral equilibrium mechanism, is proposed for buildings with insufficient seismic resistance. The neutral equilibrium mechanism is formed by connecting an unstable balance mechanism and a stable balance mechanism in series to achieve the effect of the power amplifier. This mechanism provides a reliable and efficient structural shock absorption with virtually no additional energy supply. This study proposes a prototype of a neutral balance control mechanism and passes functional verification. The experimental results show that the neutral balance mechanism only needs to exert a force of 1/500 of its output force when changing its output size and direction, and does not need to increase the force acting distance, so its power amplification rate has reached 500. With the neutral balance mechanism as the source of control, we then explore how to effectively use this mechanism to control the deformation of structures. Because this mechanism can achieve excellent energy-saving effects, we do not need to consider additional control laws that take into account energy consumption and control effects, such as the optimal control. This study intends to use the PID controller commonly used in automatic control technology because it has good tracking performance and stability. In this study, numerical analysis is used to investigate the effects of Gain coefficient of displacement and Gain coefficient of velocity on control effects and control stability. The analysis results show that the structure will not cause the acceleration amplification effect of the structure when it is subjected to the earthquake force after the installation of the mechanism. In addition, when the velocity gain coefficient and the displacement gain coefficient are larger, the structural displacement response is smaller. However, when the amount of time-delay increases, it may cause divergence of control. The last focus of this paper is to explore the convergence interval of the above two gain coefficients. We found the dimensionless parameters corresponding to these two parameters. When using

the dimensionless parameter, regardless of the mass, natural frequency and damping ratio of the structure, and regardless of the amount of time delay, the convergence interval has its consistency. The mechanism can provide a stable control effect by accurately providing the appropriate speed gain coefficient and displacement gain coefficient. In the future, the mechanism can increase the predictive control to achieve better control effects.

1 INTRODUCTION

The frequency and intensity of earthquakes have gradually increased in recent years. For example, on December 26, 2004, a large earthquake of magnitude 9.0 occurred in Sumatra, Indonesia, which caused a tsunami in South Asia, killing more than 200,000 people. Then, on March 11, 2011, an earthquake occurred in the north-eastern part of Japan, near the Pacific Ocean. With an intensity of 9, it was the most violent earthquake in the past years, causing a severe tsunami that exceeded 10 meters of high waves. A large amount of seawater flooded into coastal areas and washed away a lot of buildings. The number of deaths and missing persons exceeded 20,000, and the economic losses were heavy. Then on September 24, 2013, the magnitude 7.7 earthquake occurred in Pakistan, because the buildings were not earthquake-resistant, causing many buildings to fall, killing 825 people and injuring more than 700 people. In April 2015, a massive earthquake with a magnitude of 7.8 was observed in Nepal. In May of the same year, the 7.3 aftershocks of the earthquake occurred again, causing many casualties. In 2016, there were major earthquakes in Japan's Kumamoto and Fukushima offshore and the Great New Zealand earthquake.

Taiwan is located in the Pacific seismic belt and is at the junction of the Eurasian plate and the Philippine sea plate. There are quite many earthquakes that occur every year. A strong earthquake of 7.3 in the central part of Taiwan occurred 20 years ago, causing buildings and bridges located near the Chegongpu fault that stretched for more than 100 kilometers[1,2]. The Ministry of Science and Technology also announced the "earthquake hazard potential map" in Taiwan. In the next 30 years, the probability of earthquakes with a magnitude of 6.5 or higher in South Taiwan is as high as 64%, and that in East Taiwan is about 20% [3]. Therefore, the threat of earthquakes cannot be ignored. How to improve the earthquake resistance of a large number of old buildings is a subject that must be actively faced.

The basic concept of structural seismic design is: under the premise of not endangering life safety, as long as it meets the principles that the building is easy to repair by small earthquakes, and does not collapse by severe earthquake, some degree of damage is allowable. After the earthquake, some buildings need to be reinforced as soon as possible, so as to avoid more serious damage to the structure or collapse caused by aftershocks after a strong earthquake. How to quickly reinforce components and improve the seismic capacity of such buildings is the main goal of this study. Structural control is an emerging structural reinforcement technology for nearly three decades. Structural control can be divided into passive control (isolation, shock absorption and energy dissipation [4-5]), active control [6-8], and semi-active control [9-11]. This study proposes a new state control mechanism, Neutral Equilibrium Mechanism NEM, which can be applied to active control methods. The mechanism is connected in series with an unstable balance system and a stable balance system to obtain a neutral balance mechanism. This structure, through a cleverly matched connecting rod, spring, and guide rail system, can generate powerful control forces with little energy supply to control the deformation of the

structure under earthquake action.

Firstly, based on the theoretical analysis of the neutral equilibrium mechanism, this paper deduces the design parameters of the mechanism, and designs the prototype of the neutral equilibrium mechanism according to the design parameters, and then verifies the change of the mechanism after the force is applied. By real-time active control, the control force of the mechanism is determined by the displacement, velocity, acceleration and other factors of the structure. Therefore, the neutral equilibrium mechanism is equipped with a PID controller, but the PID controller is subjected to influence of the Gain coefficient of displacement and the Gain coefficient of velocity. Therefore, the dynamic analysis of the structure of the structure is performed to investigate the relationship between the gain coefficients and the damping effect of the neutral equilibrium mechanism. The correlation of the critical Gain coefficient of displacement and velocity and the time delay are also studied.

2 DESIGN CONCEPT OF NEUTRAL EQUILIBRIUM MECHANISM

2.1 Neutral Equilibrium Mechanism

The neutral balance mechanism includes an unstable mechanism, one that has potential energy and releases energy when it loses balance, and a stable spring that stores energy by deformation. In order to maintain the balance of energy, the parameters of the mechanism must be skillfully matched. Based on this, the neutral equilibrium mechanism as shown in Fig. 1 was designed.

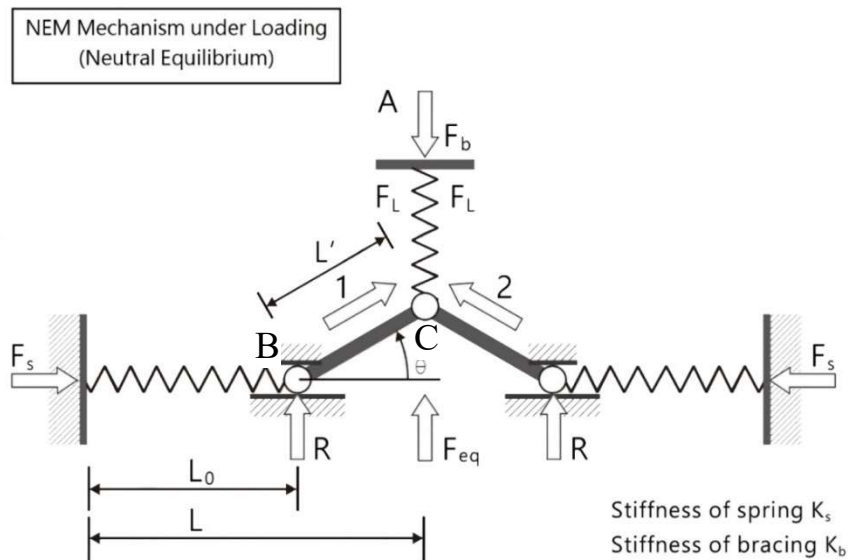


Fig.1 Construction of the Neutral Equilibrium Mechanism

This figure shows the interaction between the mechanism and the structure, and the linear spring element can satisfy this concept. If the linear spring is pressed, it is in an unstable state. Therefore, the structure can be retrofitted with the above unstable mechanism in a statically

stable state, and is connected in series with the structural bracing. When the bracing is under stress, the unstable balance of the linear spring element is broken to exert a force on the structure, and the force can be used to offset the diagonal brace force generated by the deformation of the brace.

The free-body-diagram of the joint B and C in Fig.1 are shown in Fig. 2.

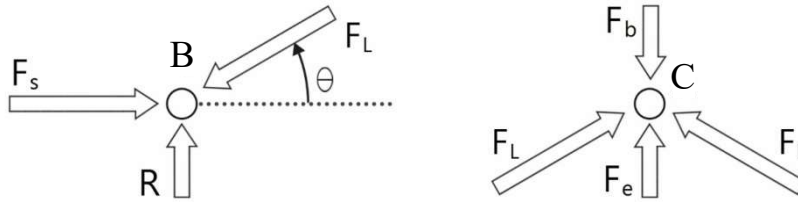


Fig.2 Free-Body Diagram of Joint A and B of NEM in Fig.1.

Take the spring-link free body diagram as shown in Figure 2(a), (b), and take the static balance of point B and C to get the following formula:

For Joint B:

$$\sum F_y = 0 \quad R - F_L \sin \theta = 0 \quad (1)$$

$$\sum F_x = 0 \quad F_L \cos \theta - F_s = 0 \quad (2)$$

Where,

F_L is the axial force of rigid link, F_s is the spring force, and R is the reaction force.

After rearranging the equations,

$$F_s = F_L \cos \theta \quad (3)$$

For joint C:

$$\sum F_y = 0 \quad F_e + 2F_L \sin \theta - F_b = 0 \quad (4)$$

By substituting equation (3) into equation (4) yields:

$$F_e = F_b - 2F_s \tan \theta \quad (5)$$

Where,

F_b is the bracing force in idea state, that no structural displacement exists.

F_e is the actuating force to balance F_b and F_s , the smaller the value, the better, and ideally close to zero.

Assuming θ is equal to 90° , the springs S_1 and S_2 just return to the original length L , that is, when $\theta = 0^\circ$, the compression of the spring is exactly equal to the length L' of the rigid link. So for any angle, θ

$$L' = (L - L_0) \sec \theta \quad (6)$$

Substituting equation (6) into equation $F_e = K_b L' \sin \theta - 2K_s (L - L_0) \tan \theta$ yields,

$$F_e = (K_b - 2K_s) L' \sin \theta \quad (7)$$

When the stiffness of the bracing is exactly two times of the stiffness of springs, as following

$$K_b = 2K_s \quad (8)$$

Then the required actuating force F_e equals to zero. No power supply is required for driving the joint C.

Therefore, a set of parameter values that make the neutral equilibrium mechanism true can be obtained:

- I. The bracing stiffness is equal to 2 times the spring stiffness;
- II. The spring is in an unstressed state when the internal angle θ of the mechanism is equal to zero.

2.2 Force balancing states of the NEM

The change of the force balance of the neutral equilibrium mechanism can be explained by the change of the force behavior in Fig. 3: (1) The horizontal spring reaches the horizontal state, at which time the vertical spring is not deformed and the horizontal spring reaches the maximum compression, but the horizontal resultant force is zero and the vertical spring has no force, so the node driving force is zero, as shown in Figure 3(a); (2) The horizontal spring is deformed and the deformation of the left and right sides is the same and so as the angle, and the vertical spring is deformed. Therefore, the combined force of the horizontal and vertical directions on the node is zero, so the node driving force is still zero, as shown in Fig. 3(b); (3) the horizontal spring reaches the original length without deformation, and the vertical spring reaches the maximum amount of compression. However, because of the angle of the links is perpendicular to the guide of horizontal springs, the resultant force at the intermediate node is zero, so the node driving force is still zero, as shown in Fig. 3(c).

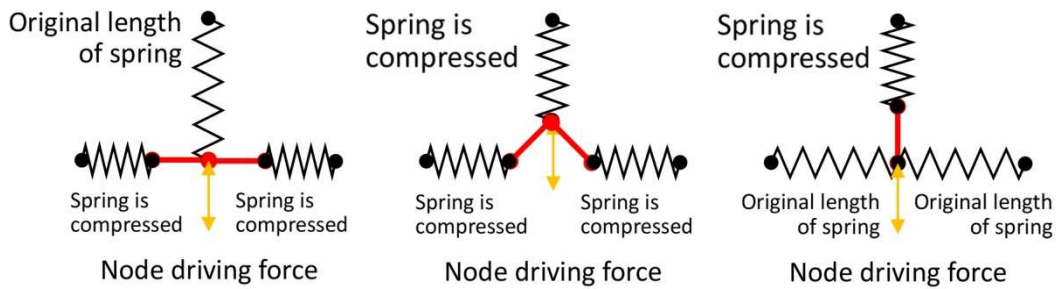


Fig.3 Changing of the equilibrium states

Therefore, to change the output of the vertical spring, it only needs to be based on the magnitude of the seismic force, without the need to provide any driving force to achieve the effect of shock absorption. That is to say, in an ideal state, the control force can be arbitrarily changed without exerting actuating force.

3 CONTROL LAW OF THE NEM ACTUATOR

An active control with NEM can use the common active control law, and this NEM can be said that it does not need to consume a large amount of control energy. Therefore, it is not necessary to pay attention to the control force expenditure, and the deformation of the structure should be minimized, that is, the displacement between the structure and the NEM should be as near to the minimum as possible. Therefore the PID controller is used in the NEM controlled system. That is, using the PID control law to determine the reaction force of the stiffening element, the displacement signal of the structure can be used as the error signal, and the following formula determines the reaction force that the stiffening element should generate, and determines the amount of push/pull displacement of the micro actuator.

3.1 PID Controller

The magnitude of the control force is determined by the displacement, velocity, acceleration, etc. of the structure. The common relationship is as follows:

$$u(t) = G_p x(t) + G_I \int_0^t x(t) dt + G_D \dot{x}(t) \quad (9)$$

Where, $u(t)$ is the control force exerted by bracing, $x(t)$ is the displacement of structure, and G_p, G_I, G_D are the proportional, integral and differential gain respectively.

Changing the gain factor (G_p, G_I, G_D) can change the structural control effect. A relatively large coefficient can achieve a better damping rate, but it can lead to loss of control. The main reason for the loss of control is the “time delay”. The time when the control force occurs always lags behind the time when the control force should occur. The difference between the two is the “time delay”.

This study explores the impact of time delay on NEM and can be modeled using the GENDYN program which is developed in our lab.

The control parameters of the PID controller can be divided into three parts: proportional part P, integral part I, and differential part D. Where: (1) Proportional control term P = error value multiplies with positive constant G_p . When the proportional control gain value increases, there will be a larger output under the same error amount, but if the proportional control gain value is too large, it will make the system unstable. Conversely, if the proportional control gain value is small, the output is small at the same amount of error, so the controller is less sensitive. When external disturbances occur, the control signal may not be large enough to quickly correct the effects of external interference. (2) Integral control term = past error multiplies with positive constant G_I . There are problems such as unavoidable friction and minimum starting command value in the system, causing a residual error to be eliminated by the comparison control. The integral control term is used, and the error is added up to generate a larger control command value, which can eventually eliminate small errors. (3) Differential control term = derivative of error multiplies with positive constant G_D . While the proportional control will cause the system to oscillate back and forth around the predetermined value, applying differential control can eliminate oscillation and improve system stability. When the system parameters are adjusted properly, PID control can be very good, but when the parameter is not carefully adjusted, the

effect will be very poor. The impacts of changes on shock absorption benefits induced by G_p , G_D are discussed in this study.

3.2 Influence of the proportional and differential gain on the displacement of structure

3.2.1 Motion equation

Author's affiliation should be written centered, in 11pt Roman, 12pt below the list of authors. A 12pt space should separate two different affiliations.

A SDOF structure equipped with an active control system can be expressed as the following equation:

$$m\ddot{x}(t) + c\dot{x}(t) + kx(t) = p(t) + u(t) \quad (10)$$

Where, x is structural displacement, m is the mass, c is the damping coefficient, k is the stiffness, $p(t)$ is external force and $u(t)$ is the control force.

When the control force is determined based on PID controller with considering a time delay, the control force $u(t)$ can be expressed as,

$$u(t) = -G_p x(t - \Delta t) - G_D \dot{x}(t - \Delta t) \quad (11)$$

Where, G_p is the proportional gain, G_D is the differential gain and Δt is the time delay.

In case of free vibration, equation (1) can be transformed as,

$$m\ddot{x}(t) + c\dot{x}(t) + G_D \dot{x}(t - \Delta t) + kx(t) + G_p x(t - \Delta t) = 0 \quad (12)$$

3.2.2 Linearized equation of motion

When the amount of time delay is not large, the motion during time interval Δt can be considered as constantly accelerated, and the terms $\dot{x}(t - \Delta t)$ and $x(t - \Delta t)$ can be rewritten as follows:

$$\dot{x}(t - \Delta t) = \dot{x}(t) - \ddot{x}(t) \cdot \Delta t \quad (13)$$

$$x(t - \Delta t) = x(t) - \dot{x}(t) \cdot \Delta t - 0.5\ddot{x}(t)\Delta t^2 \quad (14)$$

Substitute equation (13) and (14) into equation (12), the equation of motion becomes

$$(m - G_D \Delta t - 0.5G_p \Delta t)\ddot{x}(t) + (c + G_D - G_p \Delta t)\dot{x}(t) + (k + G_p)x(t) = 0 \quad (15)$$

It can be seen from equation (15) that the effective mass of the structure is reduced and the structural damping is increased by the differential gain G_D , while the effective mass of the structure and the damping of the structure are reduced by the proportional gain G_p , the stiffness of the structure is increased by G_p . Overall speaking, the effective mass of the structure is reduced and the stiffness of the structure is increased, and the structural damping has the effect of time delay in addition to the influence of G_D and G_p , and does not necessarily increase or decrease. From the results of the above derivation, it can be found that: (1) When G_D and G_p are extremely large, the effective mass of the structure may approach zero, and the frequency

of the structure increases and tends to be unstable. (2) When the time delay is too large, or G_D is too large to reduce the effective mass of the structure and increase the structural frequency, equation (13) and (14) is not applicable, so the above inference is not valid.

4. RESULTS AND DISCUSSIONS OF NUMERICAL SIMULATIONS

When the mechanism proposed by the research institute is used for the damping control of the structure, it is affected by the amount of time delay and the displacement gain coefficient and the speed gain coefficient of the neutral equilibrium mechanism. To explore the effects of these parameters, a numerical simulation of over one million parameter combinations was performed in this study.

In addition to verifying the correctness of the numerical model derived from the equation of motion, this study responds to the corresponding relative displacements of different structural frequencies, damping ratios, frequencies and time delays, and discusses the critical G_D and critical G_p to understand the critical G_p and critical G_D relationship.

4.1 Analysis results

In order to investigate the influence of structural characteristics, time delay, proportional and differential gain on the displacement response of the shear building equipped with NEM, some characteristic responses should be defined. The Displacement response ratio is defined as follows:

$$\text{Displacement Response Ratio} = \frac{\text{The Maximum Relative Displacement of Building under PID Control}}{\text{The Maximum Relative Displacement without Control}}$$

Selected analysis results are shown in Fig.7~8.

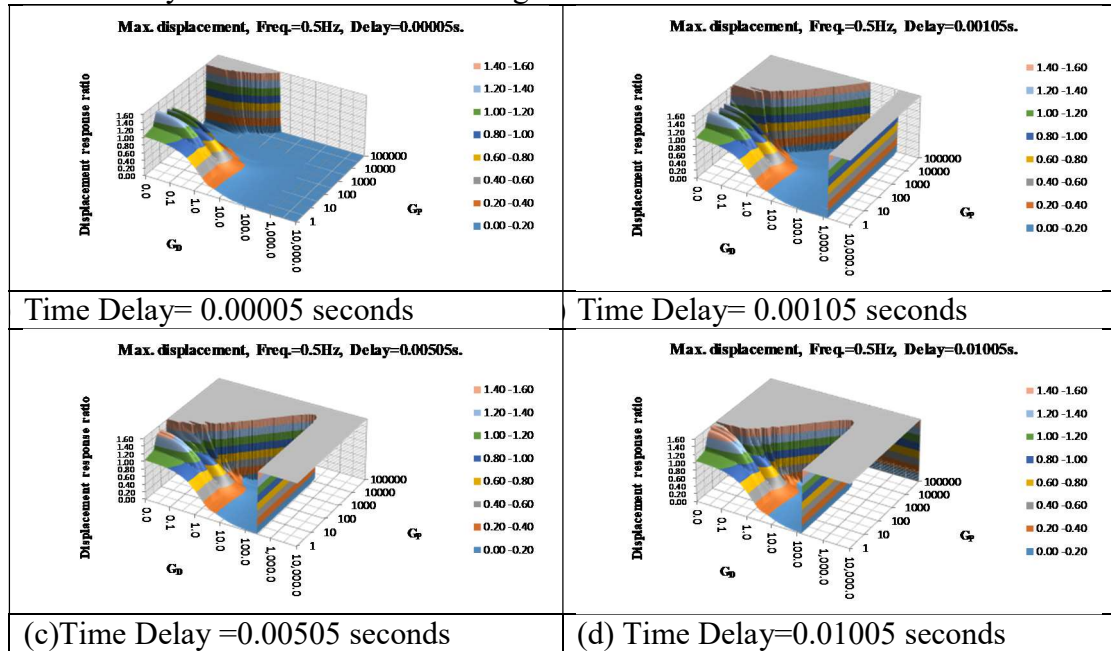


Figure 7. Analysis results of $\xi_0=0.02$, $\omega_n=0.5$ Hz with various time delay and control gains

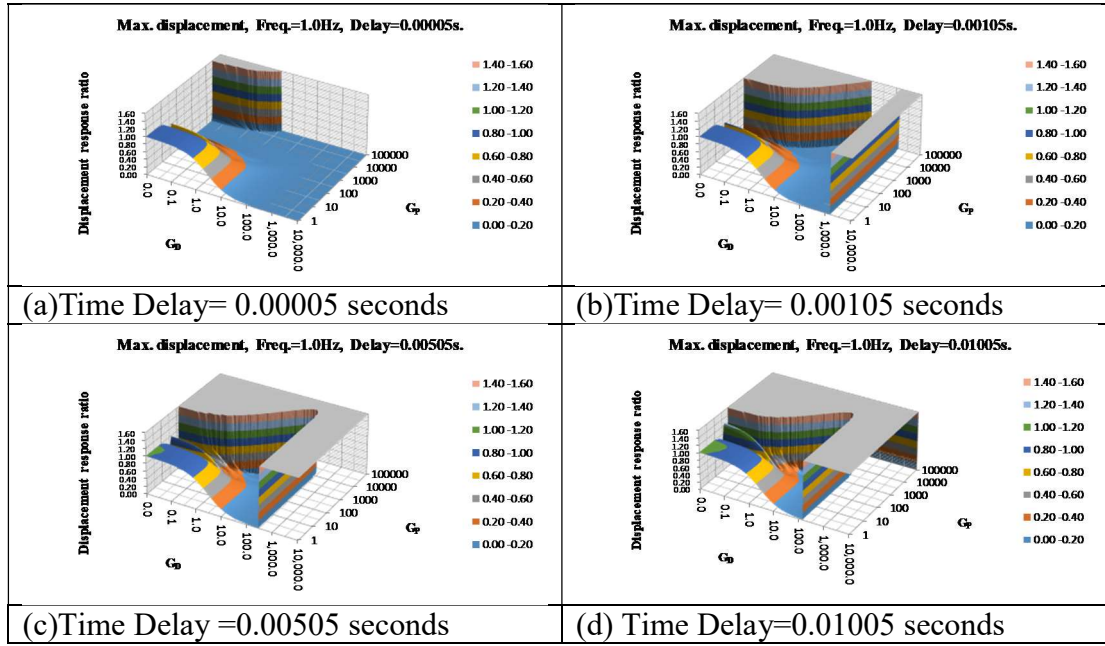


Figure 8. Analysis results of $\xi_0=0.05$, $\omega_n=1.0$ Hz with various time delay and control gains

4.2 Discussion

4.2.1 Performance of reduction of vibration and acceleration response

Comparing the trends in Fig. 7~8, it can be clearly found that when the amount of time delay increases, the interval of G_p and G_d which contribute good damping effect decreases, and even some of the intervals produce amplification benefits, that is, the mechanism fails. The damping ratio of the frame can improve the damping efficiency of the mechanism; when it is known from Fig. 7(a)~8(a) that the time delay is low, as long as the differential gain G_d reaches about 10 or more, the displacement damping effect is very good. But as the natural frequency of the structure increases, the G_d also increases to achieve a good damping effect. If the differential gain coefficient G_d is less than 10, the proportional gain coefficient G_p must be higher than 1000~10000. Comparing Fig. 7 with Fig. 8 it can be found that the damping effect is affected by the time delay when the 1st modal frequency is the same.

The following conclusions can be summarized from Figures 7 and 8:

- (1) When both of the differential gain G_d and the proportional gain G_p are large, the displacement response is small. But when the value G_d and G_p are large and the amount

of time delay increases, it is easy to cause divergence. Therefore, it is necessary to pay attention to the value G_D and G_p to avoid divergence.

- (2) If only the differential gain coefficient is used, i.e. $G_p=0$, the relative displacement of the structure can be effectively reduced. But if the time delay can be precisely controlled, and the simultaneous use of G_D and G_p can achieve better results;
- (3) If G_D exceeds a certain value, it will unconditionally diverge, and this critical value will decrease with the increase of time delay;
- (4) As the differential gain G_D increases, the value G_p can be larger and larger, and good shock absorption can be achieved without causing divergence.

4.2.3 Regression relation of critical G_D and critical G_p

G_p , G_D and time delay are three factors that influence the stability of the system. In this section, we will explore the interaction of the three on the stability interval of the control system. Here, we have a structure with a natural frequency of 1 Hz and a damping ratio of 0.02 as a controlled structure. When the time delay is 0.01005 seconds, the relationship between the critical proportional gain and the differential gain is shown in Fig. 9.

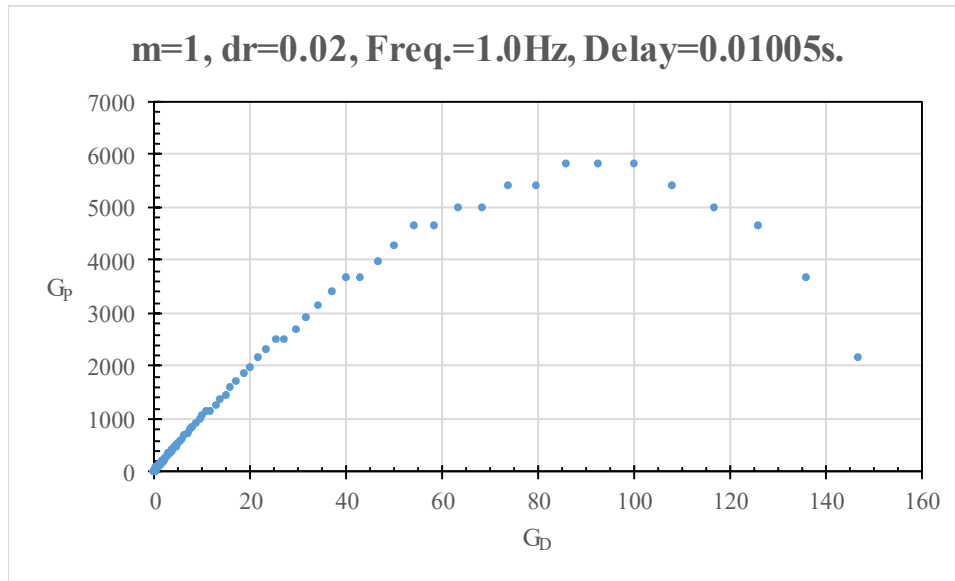


Fig. 9 Relationship of critical proportional gain and critical differential gain for structure with natural frequency = 1.0Hz and damping ratio = 0.02

According to the linear regression results of the effective critical G_p , the regression line formed by the critical G_D and critical G_p has a slope of about $\frac{1}{\Delta t}$ and the intercept is about $\frac{c}{\Delta t}$. The deviations are caused by numerical resolution. The theoretical analysis shows that the

value G_p should also be dimensionless, $\hat{G}_p = \frac{1}{m}(G_p \Delta t^2 - c \Delta t)$, so that the relationship critical G_D and critical can be clearly understood.

After the differential gain and the proportional gain are dimensionless, we find that the relationship between the critical differential gain and the proportional gain of all the analysis results coincides, regardless of structural damping, structural frequency, and time delay. Fig. 10 shows the above relationship.

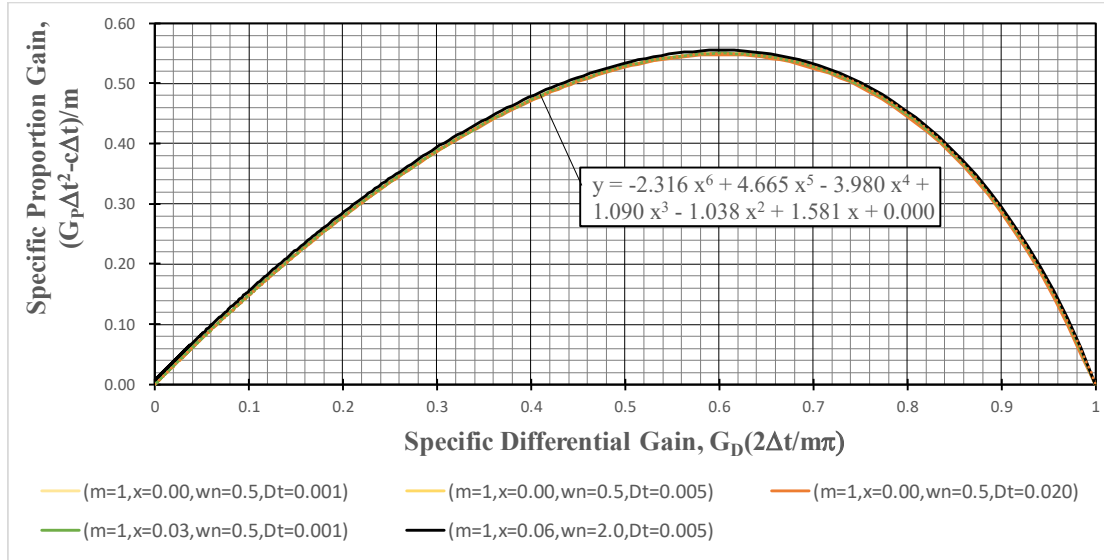


Fig.15 Relation of critical dimensionless proportional and differential gain

5 CONCLUSION

This study uses theoretical and experimental verification and numerical analysis to explore the theoretical assumptions of NEM. The relationship between the critical differential gain and the critical proportional gain is also discussed. The results of the experiment and analysis are summarized as follows:

1. According to theoretical derivation and experimental verification, the condition of this mechanism is that the stiffness of the diagonal bracing is equal to 2 times the spring stiffness; the spring is in an unstressed state when the internal angle θ of the mechanism is equal to zero;
2. By introducing the dimensionless proportional gain, $\hat{G}_p = \frac{1}{m}(G_p \Delta t^2 - c \Delta t)$, and differential gain, $\hat{G}_D = G_D \cdot \frac{2 \cdot \Delta t}{\pi \cdot m}$, all relation curves of the control coincide, regardless of structural mass, stiffness, damping coefficient and among of time delay.
3. NEM can be considered as a power amplification mechanism. When it is mounted on a structure, it can exert shock absorbing efficiency without generating acceleration amplification benefits.
4. NEM is susceptible to the amount of time delay. Stable control effects can be achieved by

accurately providing the appropriate speed gain factor and displacement gain factor. In the future, this organization can increase the predictive control mechanism to achieve better control effects.

REFERENCES

- [1] National Center for Research on Earthquake Engineering, Taiwan, R.O.C., The Investigation of 921 Chi-Chi Earthquake Damages, Reported by NCREE, Taiwan, R.O.C., 1999.
- [2] Sinotech Engineering Consultants, Ltd., “921 Chi-Chi Earthquake Brief Report”, Reported by Sinotech Engineering Consultants, Ltd. Taiwan, R.O.C., 1999.
- [3] <https://zh.wikipedia.org/zh-tw/%E7%B6%AD%E5%86%A0%E9%87%91%E9%BE%8D%E5%A4%A7%E6%A8%93%E5%80%92%E5%A1%8C%E4%BA%8B%E6%95%85>
- [4] Chassiakoes, G. W., et al., “Structural Control : Past Present and Future , “ Journal of Engineering Mechanics, 1997; 123(9): 897-971.
- [5] Yao, J. T. P., “Concept of Structural Control,” Journal of the Structural Division, 1972: 1567-1574.
- [6] Robert, L. C., Willian, R. S. and Gary, P. G., ”Adaptive Structures Dynamics & Control,” by John Wiley & Sons, Inc, 1998.
- [7] Iwata, S., et. el., “Hybrid Earthquake Loading Test (Pseudo-Dynamic Test) of Bi-directional Base Isolation Bearing for A Large Pedestrian Bridge,” 12thWCEE , 2000.
- [8] Jangid, R.S.: Optimum lead–rubber isolation bearings for near-fault motions. Engineering structures. 29(10), 2503-2513(2007).
- [9] Salic, R. B., Garevski, M. A. and Milutinovic, Z. V.: Response of Lead-Rubber Bearing Isolated Structure. The 14th World Conference on Earthquake Engineering. Beijing, China (2008).
- [10] Bridget Cunningham: Using Lead Rubber Bearings in Base Isolation Systems,<https://www.comsol.com/blogs/using-lead-rubber-bearings-in-base-isolation-systems/>(2015)
- [11] Fisco, N. R. and Adeli, H. (2011). Smart structures: Part I - Active and semi-active control, Scientia Iranica. 18(3A), 275-284.

ACTIVE WARPING CONTROL FOR DAMPING OF TORSIONAL BEAM VIBRATIONS

David Hoffmeyer* & Jan Høgsberg

Department of Mechanical Engineering, Technical University of Denmark
Nils Koppels Allé, building 404, DK-2800 Kongens Lyngby, Denmark
e-mail: davhoff@mek.dtu.dk, jhg@mek.dtu.dk, www.dtu.dk

Key words: Torsional beam vibrations, structural dynamics, warping, active control, position feedback, finite element method.

Abstract. This paper considers damping of torsional beam vibrations by active control of the axial warping displacements. A beam element with active positive position feedback (PPF) is set up with an additional flexibility parameter. This arises from partial restraining of warping caused by discrete actuators. The flexibility lowers the frequency associated with an infinite actuator gain and thereby the attainable damping ratio. It is shown how it furthermore affects the stability limit. Results are compared with three-dimensional finite element results, with multiple actuators acting on an end cross-section of the beam. The accuracy of the beam model is justified by an example which shows that substantial damping ratios may be achieved by active warping control.

1 INTRODUCTION

Slender structures like long bridge decks, aircraft wings, wind turbine blades and general thin-walled beams may be prone to vibrations due to loads like wind, traffic etc. If the loads act with an eccentricity relative to the shear center or if the cross-section lacks double symmetry, torsional vibrations may be induced. For some structures the aerodynamic instability phenomenon flutter may occur where flexural and torsional vibrations couple. To potentially avoid flutter or to reduce fatigue stresses, structural mass or accelerations, supplemental damping may be required.

Torsion of thin-walled beams generates out-of-plane, axial warping displacements that are often significant at the boundaries of beams with open cross-sections. Thus, for these types of thin-walled beams the restraining of warping results in an often considerable increase in the natural frequency and change in vibration characteristics as described by Gere [1]. The localized effect of restrained warping is used in [2] to introduce a substantial amount of supplemental damping by applying an energy dissipating boundary condition. In [3] discrete viscous dampers constituting a pure bimoment are placed on the beam cross-section of a three-dimensional finite element model, showing convincing agreement with the governing transcendental equation.

For beams with closed cross-sections or when torsion couples with flexure, viscous dampers may not be sufficient or even practically applicable. Thus, in the present work an active damping concept is used for damping of pure torsional vibrations. A positive position feedback (PPF) [4] signal is passed by a sensor through a simple linear filter to an actuator which produces an active force. The damping

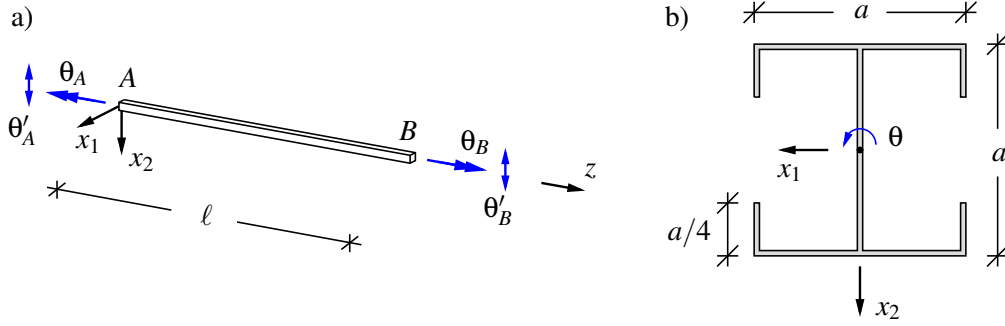


Figure 1: a) beam with degrees-of-freedom and b) thin-walled cross-section with coordinate system.

concept is applied with a beam element and compared with a full three-dimensional finite element (FE) analysis. In an actual structure the actuators are placed as discrete actuators on a beam cross-section, thus only partially restraining the warping. This is associated with an additional flexibility that lowers the frequency obtained when the actuators completely lock - which in control theory typically is referred to as a zero - and thereby also the maximum damping ratio determined as the relative imaginary part of the natural frequency. This flexibility is incorporated into the beam element as a Maxwell-type boundary condition, and is calibrated by dedicated finite element results. The system is solved in state-space form and it is shown that substantial damping ratios may be obtained for the lowest torsional mode. For the position feedback the control gain is limited by stability yielding a gain as derived in [5]. At a certain point the actuator will eliminate the structural stiffness at the location of the actuator and the response becomes unbounded. This limit, however, is based on a static condition and it is shown how the additional flexibility from restraining warping partially affects this limit.

2 STRUCTURAL EQUATIONS

In this section the governing structural equations are presented. First the differential equation governing pure torsion is presented and then the beam is discretized with beam elements, resulting in the governing multi-degree-of-freedom equations.

2.1 Uncoupled torsional vibrations

Consider the beam in Fig. 1a with length ℓ , longitudinal axis z and transverse axes $\{x_1, x_2\}$. For a cross-section like the one in Fig. 1b with double symmetry, the elastic and shear centers coincide and the torsional and flexural vibrations thereby uncouple. The rotation with respect to the shear center is denoted $\theta(t, z)$ and the warping intensity is the spatial derivative of the rotation $\theta'(t, z)$. The differential equation governing pure torsional vibrations may be derived as [1, 3, 6],

$$EI_\psi \theta''''(t, z) - GK\theta''(t, z) - \rho I_\psi \ddot{\theta}(t, z) + \rho J \ddot{\theta}(t, z) = 0 \quad (1)$$

where E is Young's modulus, G is the shear modulus, ρ is the mass density, I_ψ is the warping moment of inertia, K is the torsion stiffness parameter, $(\cdot)' = \partial(\cdot)/\partial z$ denotes partial differentiation with respect to z and $(\cdot) = \partial(\cdot)/\partial t$ denotes partial differentiation with respect to t . The third term is the inertia associated with the axial warping [6] and is often neglected due to its limited importance.

2.2 Discretization with beam elements

The torsion problem is now implemented in a finite element setting and the structure is discretized with beam elements. As pure torsional vibrations are considered the beam element only contains the two torsional degrees-of-freedom as depicted in Fig. 1a, that is the rotation and warping intensity. The four degrees-of-freedom for the beam element are interpolated as,

$$\boldsymbol{\theta} = \mathbf{N} [\boldsymbol{\theta}_A, \ell \boldsymbol{\theta}'_A, \boldsymbol{\theta}_B, \ell \boldsymbol{\theta}'_B]^T \quad (2)$$

where the displacement interpolation array \mathbf{N} contains the Hermitian shape functions,

$$\mathbf{N} = [2s^3 - 3s^2 + 1, s(s-1)^2, -2s^3 + 3s^2, s^2(s-1)] \quad (3)$$

where $s = z/\ell$ is a local element coordinate. The element stiffness matrix \mathbf{K} and mass matrix \mathbf{M} are associated with the elastic and kinetic energy respectively. Setting up the energies and assuming a prismatic beam element leads to the explicit expression for the stiffness matrix

$$\mathbf{K} = EI_\Psi \ell^{-3} \begin{bmatrix} 12 & & & \\ 6 & 4 & & \\ -12 & -6 & 12 & \\ 6 & 2 & -6 & 4 \end{bmatrix} + GK \ell^{-1} \frac{1}{30} \begin{bmatrix} 36 & & & \\ 3 & 4 & & \\ -36 & -3 & 36 & \\ 3 & -1 & -3 & 4 \end{bmatrix} \quad (4)$$

with contributions from homogeneous and inhomogeneous torsion through GK and EI_Ψ respectively. The mass matrix takes a similar form,

$$\mathbf{M} = \rho J \ell \frac{1}{420} \begin{bmatrix} 156 & & & \\ 22 & 42 & & \\ 54 & 13 & 156 & \\ -13 & -3 & -22 & 4 \end{bmatrix} + \rho I_\Psi \ell^{-1} \frac{1}{30} \begin{bmatrix} 36 & & & \\ 3 & 4 & & \\ -36 & -3 & 36 & \\ 3 & -1 & -3 & 4 \end{bmatrix} \quad (5)$$

The first term in (5) contains the torsional inertia and the second term contains the warping inertia. The latter is usually of limited importance and often discarded but may in this format easily be implemented through the submatrices. The local elements are easily assembled and transformed to a global structure [7].

2.3 Multi-degree-of-freedom system

As the model is discretized with beam elements the equations of motion are given in terms of the displacement vector $\mathbf{q}(t)$ of the linear system and the corresponding stiffness matrix \mathbf{K} and mass matrix \mathbf{M} from Section 2.2. Neglecting any inherent structural damping the system has the general form,

$$\mathbf{M} \ddot{\mathbf{q}}(t) + \mathbf{K} \mathbf{q}(t) = -\mathbf{w} B_d(t) \quad (6)$$

where $B_d(t)$ represents the effect of the external actuator on the system in the form of a bimoment [6]. The corresponding connectivity vector \mathbf{w} identifies the point on the structure connected to the actuator for the beam with a single actuator. The vector has the structure $\mathbf{w} = [0, \dots, 1, \dots, 0]^T$ with the single entry defining the degree-of-freedom associated with the actuator.

The actuator is assumed linear and collocated and may be formulated by a frequency transfer function $H(\omega)$ and gain g in the form

$$B_d(t) = g H(\omega) \mathbf{w}^T \mathbf{q}(t) \quad (7)$$

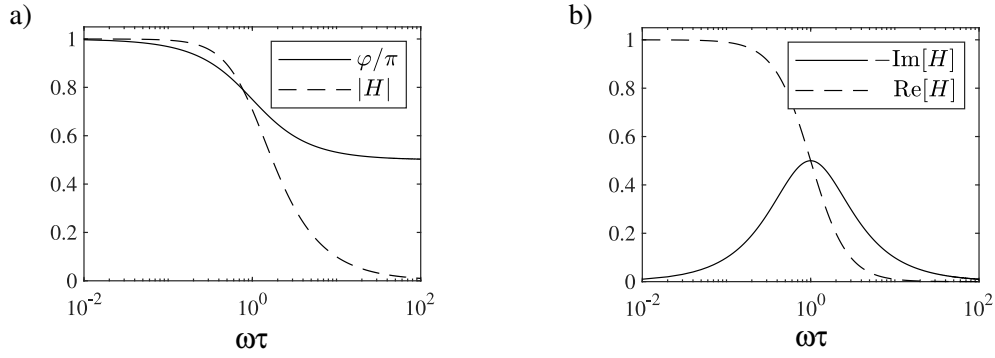


Figure 2: a) magnitude and phase angle and b) real and imaginary part of the transfer function $H(\omega)$.

The frequency function may take several different forms based on the particular control law. By introducing (7) in (6) the equations of motion may be written in the frequency domain as

$$(-\omega_n^2 \mathbf{M} + \mathbf{K} + gH(\omega) \mathbf{w} \mathbf{w}^T) \tilde{\mathbf{q}}_n = \mathbf{0} \quad (8)$$

where $\tilde{(\cdot)}$ indicates the amplitude. If $g = 0$ the actuator does not influence the structure and the solution to the eigenvalue problem in (8) will give real-valued solutions in form of the undamped natural frequencies $\omega_{0,n}$. If, on the other hand, $g \rightarrow \infty$ the actuator will lock and prohibit displacement at its location, whereby the solution to the eigenvalue problem provides the infinitely damped frequencies $\omega_{\infty,n}$, associated with infinite gain. The frequencies ω_0 and ω_∞ are typically denoted pole and zero respectively within control theory.

3 Active control by position feedback

Active control is now introduced by a positive position feedback. The control system detects the axial warping displacement at the end cross-section during the torsional motion, passes it through a simple linear first order filter and feeds it positively back to the structure. The position feedback is deemed appropriate as the warping displacements are small and easily measured by e.g. a piezoelectric sensor or a laser device. The filter is mathematically formulated as [8]

$$B_d(t) + \tau \dot{B}_d(t) = g \theta'_g(t) \quad (9)$$

where $\theta'_g = \mathbf{w}^T \mathbf{q}$ is the displacement at the actuator which in this case constitutes the warping intensity, B_d is the actuator force constituting a bimoment which is energy conjugate to the warping intensity and τ is a filter constant which defines the cut-off frequency at $1/\tau$. Based on the displacement $\theta'_g(t)$ the equivalent actuator force $B_d(t)$ is fed back to the system. The transfer function for the filter in (9) is hereby obtained as

$$gH(\omega) = \frac{g}{1 + i\omega\tau} \quad (10)$$

The corresponding phase angle and magnitude are determined as

$$\tan \varphi = -\omega\tau \quad , \quad |H| = \frac{1}{\sqrt{1 + (\omega\tau)^2}} \quad (11)$$

The phase angle and magnitude are seen in Fig. 2a. This specific filter ensures large damping in the low-frequency range below the cut-off frequency, while attenuating noisy high-frequency components

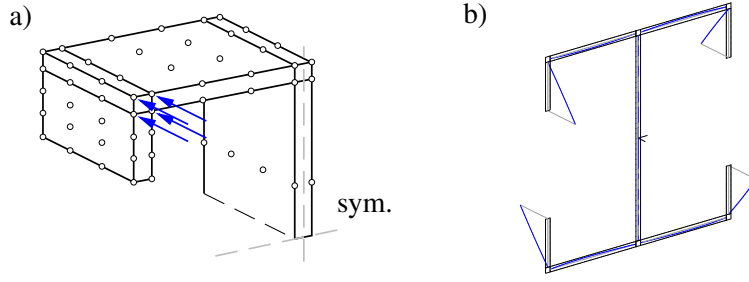


Figure 3: a) quarter cross-section discretized with isoparametric elements and with local actuators and b) altered cross-sectional warping.

which may be badly represented. By the punctured curve in Fig. 2a it is evident that this is achieved as the magnitude of the transfer function vanishes above the cut-off frequency. The major benefit of active control is the possibility of greater damping performance when the actuator leads velocity with a phase angle $\varphi > \pi/2$. Especially in the low-frequency range this filter exhibits a phase angle close to π as indicated by the solid curve, and therefore has a force component in phase with negative stiffness. In order for the actuator to dissipate energy and not amplify the vibrations, it is required that $\text{Im}[gH(\omega)] > 0$. In Fig. 2b the solid curve represent the imaginary part of the transfer function. As this is negative, it means that $g < 0$.

3.1 Warping-restrained flexibility

In practice warping control may be realized by axial actuators, acting on the cross-section as shown in Fig. 3a. In a situation with concentrated axial actuators applied at a cross-section the actuators will only fully restrain the warping displacements at the location of the actuators. At infinitely high gain, i.e. when $g \rightarrow \infty$, the axial movement at the actuator location will be completely prevented. However, the cross-section may still be able to warp in between the actuators and leave an altered warping function as illustrated in Fig. 3b. This is associated with an additional flexibility compared to a fully restrained cross-section [3]. At vanishing damping ($g = 0$) the additional flexibility must however disappear. This additional flexibility may therefore be modelled as a spring in series with the actuator, as seen in Fig. 4. The warping works through the gradient of the angle of twist and therefore so does the spring. It is, however, an artificial spring as it is not physically present, but merely describes the additional flexibility due to the partial warping of the cross-section for $g > 0$. Thereby it may conveniently be modelled as a Maxwell-type boundary condition. The total gradient of the angle of twist, θ'_d , is the sum of the contribution from the actuator and spring as seen in Fig. 4,

$$\theta'_d(t) = \theta'_k(t) + \theta'_g(t) \quad (12)$$

where it works through the actuator bimoment B_d . The bimoment produced by the spring is

$$B_k(t) = k\theta'_k(t) \quad (13)$$

and the bimoment produced by the actuator is given by (9). Introducing (9) and (13) into (12) yields the modified control equation, to be used for calibration of g and identification of the stability limit,

$$\left(\frac{1}{g} + \frac{1}{k}\right) B_d(t) + \frac{\tau}{g} \dot{B}_d(t) = \theta'_d(t) \quad (14)$$

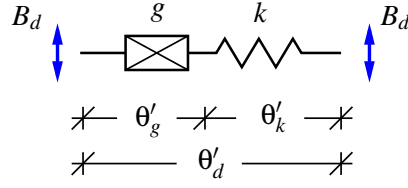


Figure 4: Maxwell-type boundary condition with an active element with gain g in series with a spring with stiffness k .

The determination of k requires in this case knowledge about the actual structure either from a full three-dimensional finite element model, from experiments or from real measurements. The stiffness k in the flexibility format reduces the infinitely damped frequency ω_∞ as the cross-section is now able to warp in between the actuator locations. However, due to the active nature of the actuator there will be a stability limit, see Section 3.3, where the response becomes unbounded. In the complex plane, however, the root locus will trace towards the correct infinitely damped frequency, as the controller equation (14) in the limit describes only the additional flexibility,

$$\left(\frac{1}{g} + \frac{1}{k}\right) B_d(t) + \frac{\tau}{g} \dot{B}_d(t) = \theta'_d \quad \rightarrow \quad B_d(t) = k\theta'_d \quad \text{for } g \rightarrow \infty \quad (15)$$

This means that the structural equations are merely supplemented with a spring, incorporated in flexibility format, when establishing the state-space equations in the following section. The stiffness k is calibrated in the unstable situation where $g \rightarrow \infty$, but this is equivalent with a situation where the actuators are replaced with supports and may thus be used for calibration.

3.2 State-space formulation

The properties of the dynamic system with damping is conveniently demonstrated in the frequency domain. The equations of motion are therefore set up in a state-space format including the feedback force from (14). With the state-vector $\mathbf{z}(t) = [\mathbf{q}(t), \dot{\mathbf{q}}(t), B_d(t)]^T$ the system is

$$\frac{d}{dt} \begin{bmatrix} \mathbf{q}(t) \\ \dot{\mathbf{q}}(t) \\ B_d(t) \end{bmatrix} = \begin{bmatrix} \mathbf{0} & \mathbf{I} & \mathbf{0} \\ -\mathbf{M}^{-1}\mathbf{K} & \mathbf{0} & -\mathbf{M}^{-1}\mathbf{w} \\ g/\tau\mathbf{w}^T & \mathbf{0} & -g/\tau\left(\frac{1}{g} + \frac{1}{k}\right) \end{bmatrix} \begin{bmatrix} \mathbf{q}(t) \\ \dot{\mathbf{q}}(t) \\ B_d(t) \end{bmatrix} \quad (16)$$

where \mathbf{I} is the identity matrix. The presence of the actuator leads to generally complex-valued solutions of ω ,

$$\omega_n = |\omega_n| \left(\sqrt{1 - \zeta_n^2} + i\zeta_n \right) \quad (17)$$

where n denotes the various eigensolutions. The damping ratio is given by the imaginary part of (17) as

$$\zeta_n = \frac{\text{Im}[\omega_n]}{|\omega_n|} \quad (18)$$

The mode shapes obtained from (16) are in general also complex, with the real part representing the physical vibration form and the imaginary part representing the spatial phase shift due to the presence of the energy dissipating actuator.

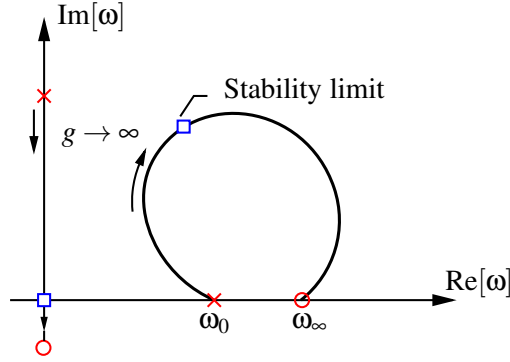


Figure 5: Root locus and indication of the stability limit when the purely imaginary eigenvalue becomes negative.

3.3 Stability and gain limit

When solving (16) varying the gain in the interval $g \in [0; \infty[$ the damped frequency will trace a root locus in the complex plane between the undamped frequency ω_0 and the infinitely damped frequency ω_∞ as shown in Fig. 5. However, as mentioned in Section 3.1 after a certain gain the response becomes unbounded. With a single actuator present, a single eigenvalue will be purely imaginary. Instability occurs when this eigenvalue becomes zero. In order for the response not to become unbounded the stability of the system must therefore be considered. This is mainly to set a limit for the gain g . The stability of the system may be checked with the Routh-Hurwitz criterion. For larger systems this typically requires determination of the Routh arrays and may not be convenient to determine an explicit limit for the gain. An alternative is to write the full system consisting of the structural equations (6) and the controller equation (14) in a block format. The structural equations and controller equation are pre-multiplied with $-gv^{-1}$ where $v = (1 + \frac{g}{k})$, and the original structural displacement vector \mathbf{q} is replaced by the modified set of variables in $\mathbf{q}^* = -gv^{-1}\mathbf{q}$. The equations then take the form

$$\begin{bmatrix} \mathbf{M} & \mathbf{0} \\ \mathbf{0} & 0 \end{bmatrix} \begin{bmatrix} \ddot{\mathbf{q}}^* \\ \ddot{B}_d \end{bmatrix} + \begin{bmatrix} \mathbf{C} & \mathbf{0} \\ \mathbf{0} & -gv^{-2}\tau \end{bmatrix} \begin{bmatrix} \dot{\mathbf{q}}^* \\ \dot{B}_d \end{bmatrix} + \begin{bmatrix} \mathbf{K} & -gv^{-1}\mathbf{w} \\ -gv^{-1}\mathbf{w}^T & -gv^{-1} \end{bmatrix} \begin{bmatrix} \mathbf{q}^* \\ B_d \end{bmatrix} = \begin{bmatrix} \mathbf{0} \\ 0 \end{bmatrix} \quad (19)$$

It is noted that if $|g| < k$ then $v > 0$. The mechanical energy is defined by the first and last matrix. The equivalent mass matrix is always positive semi-definite, and as $\tau > 0$ the equivalent damping matrix will be positive definite if the original structure has positive definite damping and is otherwise positive semi-definite. The stability is therefore entirely governed by the equivalent stiffness matrix and the corresponding reduction in stiffness caused by the actuator with the added warping-restrained flexibility. The potential energy associated with the stiffness matrix can be expressed as

$$V_e = \begin{bmatrix} \mathbf{q}^{*T} & B_d \end{bmatrix} \begin{bmatrix} \mathbf{K} & -gv^{-1}\mathbf{w} \\ -gv^{-1}\mathbf{w}^T & -gv^{-1} \end{bmatrix} \begin{bmatrix} \mathbf{q}^* \\ B_d \end{bmatrix} \quad (20)$$

After some rearranging it takes the form

$$V_e = \frac{1}{2}\mathbf{q}^{*T} [\mathbf{K} + gv^{-1}\mathbf{w}\mathbf{w}^T] \mathbf{q}^* + \frac{1}{2} \left(B_d (gv^{-1})^{1/2} - (gv^{-1})^{1/2} \mathbf{w}^T \mathbf{q}^* \right)^2 - B_d gv^{-1} B_d - \mathbf{q}^{*T} gv^{-1} \mathbf{q}^* \quad (21)$$

The time derivative of this functional is given by the second matrix in (19) as

$$\dot{V}_e = -[\dot{\mathbf{q}}^{*T} \mathbf{C} \dot{\mathbf{q}}^* - \dot{B}_d g v^{-2} \tau \dot{B}_d] \leq 0 \quad (22)$$

The second term in (21) is a quadratic form and thus always positive, while the third and fourth terms are also positive as $g < 0$. Stability is therefore governed by the first term of which the matrix must be positive definite for the combined system to be stable. If the matrix becomes singular it corresponds to the stiffness component of the actuator eliminating the structural stiffness at the location of the actuator and instability occurs. This corresponds to the requirement

$$\det(\mathbf{K} + g v^{-1} \mathbf{w} \mathbf{w}^T) > 0 \quad (23)$$

Thus the matrix in the parentheses must be invertible and the limit of the gain, g_{stab} , may be found by considering the invertibility of the matrix. The result follows from the Sherman-Morrison formula [9] as

$$(\mathbf{K} + g v^{-1} \mathbf{w} \mathbf{w}^T)^{-1} = \mathbf{K}^{-1} - g v^{-1} \mathbf{K}^{-1} \mathbf{w} (1 + g v^{-1} \mathbf{w}^T \mathbf{K}^{-1} \mathbf{w})^{-1} \mathbf{w}^T \mathbf{K}^{-1} \quad (24)$$

When rigid body motion is accounted for, the stiffness matrix will be fully positive definite. Thus, if the term in the parenthesis on the right side of (24) becomes zero, the term may not be inverted. This determines the gain limit as

$$\frac{1}{g_{\text{stab}}} = -\mathbf{w}^T \mathbf{K}^{-1} \mathbf{w} - \frac{1}{k} \quad (25)$$

The above expression leaves a direct way of determining the maximum gain, which is at the same time seen to be negative. A gain that exceeds the above limit will result in an unbounded response.

4 Comparison with a 3D FEM model

The beam model is compared with a full three-dimensional FE model with isoparametric elements. The elements used are bi-cubic-linear elements for flange parts and bi-linear-cubic elements for corners and junctions. For details on the elements and discretization of the beam see [3]. The beam is discretized with 30 length-wise elements, half of them being concentrated over $\ell/25$ of the beam near the end, and a single bi-cubic-linear element per flange part as in Fig. 3a. In the three-dimensional model, actuators are applied in the corners as in Fig. 3a, and as they are placed asymmetrically they are balanced according to [3, 10]. Thus, m actuators are present and the feedback filter now contains several equations written in vector format as

$$\mathbf{f}_d + \tau \dot{\mathbf{f}}_d = \mathbf{G} \mathbf{W}^T \mathbf{q} \quad (26)$$

This equation resembles (9) but without the flexibility k . In order not to damp other modes than those associated with torsion, each connectivity vector \mathbf{w}_j contains contributions from exactly four actuators constituting a pure bimoment. These four actuators are placed symmetrically in the corners with respect to the principal axes of the cross-section in Fig. 1, and thus only one of the four actuators in each corner as indicated in Fig. 6b enters each connectivity vector. Thus the structure is $\mathbf{w}_j = [0, \dots, -\sqrt{1/4}, \sqrt{1/4}, -\sqrt{1/4}, \sqrt{1/4}, \dots, 0]^T$. The collective array $\mathbf{W} = [\mathbf{w}_1, \mathbf{w}_2, \dots, \mathbf{w}_{m/4}]$ contains $m/4$ connectivity vectors and $\mathbf{G} = \text{diag}[g_1, g_2, \dots, g_{m/4}] = g^{3D} \text{diag}[\alpha_1, \alpha_2, \dots, \alpha_{m/4}]$ is a diagonal matrix with all gains. The actuators are in this case not balanced equally due to the asymmetric location of the actuators in Fig. 6. Balancing factors α_j are therefore introduced according to [3] and g^{3D} is a common gain. The stability requirement is derived in the same way as for the beam model with

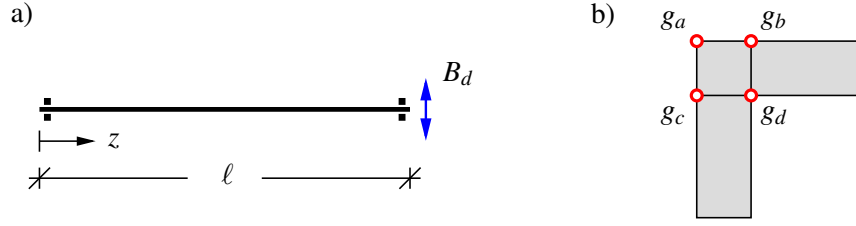


Figure 6: a) 'simple-simple' beam with damping treatment at $z = \ell$ and b) order of actuator gains at cross-section corner.

a single actuator, but the final condition is not an explicit expression for the gain. The following matrix may be derived,

$$\mathbf{H} = \mathbf{G}^{-1} + \mathbf{W}^T \mathbf{K}^{-1} \mathbf{W} \quad (27)$$

which is $m/4 \times m/4$ and will be negative definite for small values of g^{3D} and thereby have all negative eigenvalues $\lambda_i < 0$. Instability occurs exactly when the first eigenvalue of \mathbf{H} becomes positive. As the beam model and three-dimensional model are inherently different, the gain at instability will not be the same as the actuators are tuned differently. However, by setting up the virtual work produced by the actuator in the beam model and the actuators in the three-dimensional model, a conversion factor can be derived as

$$g^{3D} = \frac{g}{\sum_j^m \alpha_j \psi_j^2} \quad (28)$$

where ψ_j is the sector-coordinate of the j 'th actuator. In the next section it will be shown that instability occurs at the same frequency and damping ratio in the two models.

5 Damping of a 'simple-simple' beam

The accuracy of the beam model is now demonstrated by investigating the damping properties of the lowest torsional mode of the 'simple-simple' beam with length ℓ as shown in Fig. 6a. The support conditions restrain rotation but allow warping. The cross-section of the beam is shown in Fig. 1 and has thickness $t = a/40$, Young's modulus $E = 210$ GPa, Poisson's ratio $\nu = 0.3$ and density $\rho = 7850$ kg/m³. The ratio between the cross-section height and the length of the beam is $\ell/a = 30$ and $a = 1$ m, for which the inherent distortion of the cross-section is minimal [3]. The beam model is compared with results from a three-dimensional finite element analysis. In this finite element model four actuators are placed at each corner as shown for a single corner in Fig. 6b, and balanced according to Table 1. This is done in order to avoid unnecessary distortion of the cross-section. For the beam model the first objective is to adjust the infinitely damped frequency ω_∞ to account for the partial restraint of the warping at $z = \ell$. This is done by performing a real analysis of the 3D FE model by solving the full system in (16) with $g \rightarrow \infty$ and afterwards calibrating the flexibility parameter k by a numerical search routine to ensure that the frequency locus terminates at the correct frequency. To create the root locus the gain is varied in the interval $g \in [0; g_{\text{stab}}[$ where the stability limit is given by (25) or (27) for the beam and 3D model respectively.

The root loci for both models are seen in Fig. 7a. The solid line with black circles ($\text{---}, \circ$) are results from the beam model, the red markers ($+$) are results from the 3D model and the blue box marker (\square) indicates the stability limits. Furthermore, the punctured line indicates results for the beam model with $k = \infty$ associated with complete restraint of the warping of the entire cross-section. For comparison,

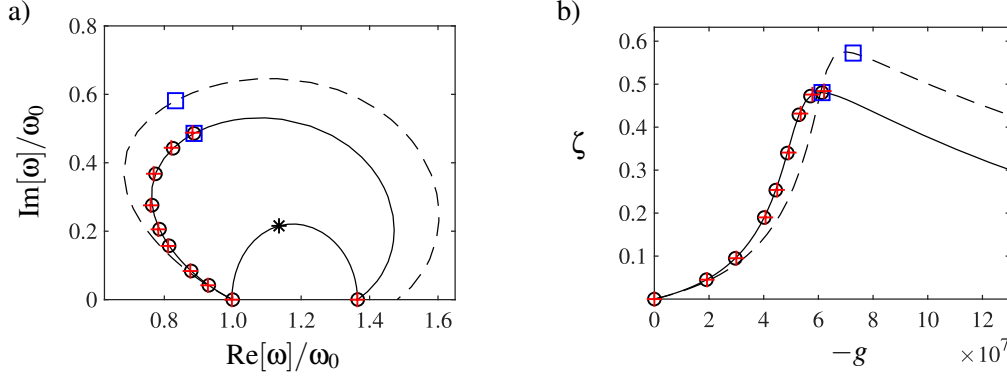


Figure 7: a) root locus and b) damping ratio for the beam analysis (—,○), FE analysis (+), gain limit (□) and $k = \infty$ (---).

the smaller half-circular root locus is with pure viscous damping, and the asterisk (*) indicates optimal tuning. Clearly the partial restraint of the warping associated with the flexibility parameter k given in Table 2 results in a significant difference, lowering the relative frequency increment $(\omega_\infty - \omega_0)/\omega_0$ from 0.481 to 0.365 and the damping ratio at instability from 0.572 to 0.480 for the beam model. The damping ratio as may be seen in Fig. 7b also indicates large damping. The damping ratios at instability and the frequency increments for the two models are very similar as seen in the table, and the small deviation is due to distortional effects in the 3D model, which causes slightly different undamped frequencies ω_0 . Due to the different nature of the two models and actuator configurations, the limit gains g_{stab} and g_{stab}^{3D} are not identical. The factor between these two is $g_{\text{stab}}/g_{\text{stab}}^{3D} = 50.4$ as seen in the table, and this is approximated well with (28) as seen in the last column in the table. Lastly it may be observed that the gain limit for the beam model is higher if not taking the partial warping restraining into account. This may wrongfully lead to instability.

6 CONCLUSION

In this paper a computationally efficient way of investigating the properties of damping the torsional vibrations in a simple beam with active control is considered. A beam element is set up with a single actuator acting on the warping degree-of-freedom. The actuator consists of a simple linear filter in the form of positive position feedback (PPF). It acts on the axial warping displacements, and is on an actual structure placed discretely as a set of actuators constituting a pure bimoment. This partially restrains the warping and allows for an additional flexibility in the beam model. This flexibility lowers the infinitely damped frequency and correspondingly reduces the gain limit at the point of instability. The beam model is compared with a full three-dimensional finite element model which has a set of actuators applied at discrete locations, all constituting pure bimoments. In this way only torsional modes are damped. The system equations are similar to the beam model, and instability is determined by the gain which makes the combined stiffness matrix singular. Considering a simple-simple beam as an example and plotting the root loci and damping ratios, very similar results between the two models are obtained. Only minor

Table 1: Balancing factors.

	g_a	g_b	g_c	g_d
α_j [—]	1.0	7.5	70.0	141.4

Table 2: Results of analysis.

	k	$(\omega_\infty - \omega_0)/\omega_0$	ζ_{stab}	g_{stab}	$g_{\text{stab}}/g_{\text{stab}}^{3D}$	$\sum_j^m \alpha_j \psi_j^2$
Beam model	∞	0.481	0.572	$-7.27 \cdot 10^7$	—	—
	$3.89 \cdot 10^8$	0.365	0.480	$-6.13 \cdot 10^7$	50.4	51.0
3D model	—	0.368	0.484	$-1.22 \cdot 10^6$		

differences are observed, which may be corrected by accounting for the inherent distortion of the three-dimensional model. It is furthermore demonstrated, that the flexibility k is necessary for the beam model to reflect the 3D model. If not included, a gain exceeding the gain limit may wrongfully be chosen. The gain at instability is inherently different in the two models, but may easily be estimated considering the position of the discrete actuators. The benefits with the active filter is clear, as the beam is damped effectively, with a damping ratio of almost $\zeta = 0.5$.

REFERENCES

- [1] Gere, J. M., *Torsional vibrations of Beams of Thin-Walled Open Section*, ASME Journal of Applied Mechanics (1954), vol. 21, no. 4, pp. 381-387.
- [2] Høgsberg, J. & Hoffmeyer, D., *Damping of torsional beam vibrations by control of warping displacement*, Journal of Vibration and Acoustics (2016), vol. 138, DOI: 10.1115/1.4031616.
- [3] Hoffmeyer, D. & Høgsberg, J., *Damping of torsional vibrations in thin-walled beams by viscous bimoments*, Mechanics of Advanced Materials and Structures (2019), DOI: 10.1080/15376494.2019.1567885.
- [4] Fanson, J. L. & Caughey, T. K., *Positive position feedback control for large space structures*, AIAA Journal (1990), vol. 28, no. 4, DOI: 10.2514/3.10451.
- [5] Goh, C. J. & Caughey, T. K., *On the stability problem caused by finite actuator dynamics in the collocated control of large space structures*, International Journal of Control (1985), vol. 41, no. 3, 787-802, DOI: 10.1080/0020718508961163.
- [6] Vlasov, V. Z., *Thin-walled Elastic Beams*, (1961) Israel Program for Scientific Translations, Jerusalem.
- [7] Cook, R. D. et. al., Concepts and Applications of Finite Element Analysis, *John Wiley and Sons*, (2002).
- [8] Høgsberg, J. & Krenk, S., *Linear control strategies for damping of flexible structures*, Journal of Sound and Vibration (2006), 293, pp. 59-77, DOI: 10.1016/j.jsv.2005.09.014.
- [9] Krenk, S. & Høgsberg, J., *Equal modal damping design for a family of resonant vibration control formats*, Journal of Vibration and Control (2012), vol. 19, no. 9, pp. 1294-1315, DOI: 10.1177/1077546312446796.
- [10] Main, J. A. & Krenk, S., *Efficiency and tuning of viscous dampers on discrete systems*, Journal of Sound and Vibration (2005), **286**, pp. 97-122, DOI: 10.1016/j.jsv.2004.09.022.

ASSESSMENT OF MODE SHAPES BASED DAMAGE DETECTION METHODS FOR BUILDING STRUCTURES

CHIA-MING CHANG^{*}, HO-FENG CHIANG^{†1} AND JAU-YU CHOU^{†2}

^{*} Department of Civil Engineering
National Taiwan University/National Center for Research on Earthquake Engineering
Taipei 10617, Taiwan
e-mail: changcm@ntu.edu.tw, web page: <https://sites.google.com/site/cmchanguiuc/>

^{†1} Department of Civil Engineering
National Taiwan University
Taipei 10617, Taiwan
Email: r06521226@ntu.edu.tw

^{†2} Department of Civil Engineering
National Taiwan University
Taipei 10617, Taiwan
Email: d06521008@ntu.edu.tw

Key words: First mode shapes, Damage Detection, Shear-type buildings, Damage localization.

Abstract. Damage of structures can raise concerns about safety issues to users. Minor damage in structures may not be critical to structural safety; however, users may not exactly know the severity of damage in structures. Thus, structural health monitoring (SHM) becomes a strategy that can estimate current performance and safety of structures. Users can be informed regarding the levels and locations of damage in structures before the damage has been turned into a serious problem. To achieve this goal, dynamic characteristics such as natural frequencies and mode shapes can be employed to derive associated damage indices that inform structural integrity. These characteristics are typically obtained from vibrational measurements of structures through operational modal analysis. Then, damage of structures can be diagnosed from mode shapes. Therefore, the objective of this study is to assess multiple mode shapes based methods for the capability of detecting damage levels and locations. First, mode shapes of buildings are numerically calculated. Because the first mode shape is mostly available from operational modal analysis, the mode shape is then employed in all of mode shapes based damage detection methods. The damage detection methods considered in this study include the mode shape curvature method, the bending energy damage index method, the strain energy damage index method, the continuous wavelet transform method based on mode shape curvatures, and the method of changes in the first mode shape slopes. The capability of these methods for damage location detection is investigated, while the sensitivity of damage levels from these methods are also studied to understand the relationship between the derived damage indices and damage severity. Some modifications are made to the existing methods for better representing damage levels. Moreover, multiple damage locations are considered in this study, and these damage locations are assumed to sequentially occur. A detailed comparison among these methods is

carried out. As seen in the numerical results, second derivatives of mode shapes (i.e., mode shape curvatures) can well represent damage of buildings in terms of damage locations and levels.

1 INTRODUCTION

Damage of structures can raise concerns about safety issues to users. Minor damage in structures may not be critical to structural safety; however, users may not exactly know the severity of damage in structures. Thus, structural health monitoring (SHM) becomes a strategy that can estimate current performance and safety of structures. Users can be informed regarding the levels and locations of damage in structures before the damage has been turned into a serious problem.

One of the commonly seen methods in the field of SHM is to regularly obtain dynamic characteristics of structures through operational modal analysis. These dynamic characteristics include natural frequencies, damping ratios, and mode shapes over a number of vibrational modes. If structures suffer some damage or have some defects, these dynamic characteristics will have some changes. These changes provide a source to determine and localize the damage or defects. For examples, cracks which occur in a structure result in decreased stiffness. The decreased stiffness lowers natural frequencies in the first few modes. The mode shapes would have corresponding variations as compared to those of the undamaged structure. If features can be extracted from these changes in natural frequencies and mode shapes, the damage in a single or multiple spot(s) can be determined and localized.

In this research, six mode shapes-based damage detection methods are investigated. The objective of this study is to exploit these methods for damage detection by means of the first mode shapes only. For example, Pandey *et al.* (1991) employed mode shape curvatures to successfully localize damage regions of a structure [1]. Stubbs *et al.* (1995) utilized mode shapes to derive strain energy and computed the energy ratio of a structure before and after the occurrence of damage [2]. This energy ratio can identify the locations of damage [3]. Allemang and Brown (1982) applied mathematical approach to analyzing the relationship between the mode shapes of a structure before and after the occurrence of damage [4]. Lieven and Ewins (1998) advanced this mathematically comparative approach and proposed a coordinate modal assurance method that can improve the accuracy of damage detection using mode shapes [5]. Mallat (1998) facilitated the wavelet transform to find the singular points in mode shapes that can identify damage locations [6]. Zhu *et al.* (2011) found that use of first mode shapes can directly locate damage of a structure by means of the dynamic characteristic equation. All the aforementioned methods are numerically explored in this study for damage detection in terms of occurrence and localization. This numerical example consists of a ten-story shear-type building with two damage scenarios. In each scenario, the damaged story has three levels of reductions in stiffness. By comparing the successfulness, the six damage detection methods are evaluated.

2 DAMAGE DETECTION METHODS

This section briefly introduces six mode-shape based damage detection methods including the mode shape curvature (MSC) method, bending energy damage index (BEDI) method, the

modal assurance criterion (MAC) method, strain energy damage index (SEDI) method, continuous wavelet transform (CWT) method, and the method of changes in the first mode shape slopes (CFMSS).

2.1 Mode shape curvature

The variations of mode shape curvatures are correlated with damaged regions of a structure because curvatures are associated with the bending stiffness of the structure [1]. A mode shape curvature can be presented by

$$\phi''(x) = \frac{M}{E(x)I(x)} = \frac{\phi(x+h) + \phi(x-h) - 2\phi(x)}{h^2} \quad (1)$$

where $\phi''(x)$ denotes the curvature calculated from the mode shapes $\phi(x)$ at location x ; M is the bending moment; $E(x)$ is the Young's Modulus at location x ; $I(x)$ is the moment of inertia; h is the height of each story. If the building has damage, the reduction of $E(x)I(x)$ will result in changes of the mode shape curvatures. The changes can be indicated by

$$MSC_j = \sum_{i=1}^N |\phi''_{i,j}^* - \phi''_{i,j}| \quad (2)$$

where $\phi''_{i,j}$ and $\phi''_{i,j}^*$ are the mode shapes before and after the occurrence of damage; i and j indicates the i -th mode and j -th location in a structure; N is the number of modes of interest.

2.2 Bending energy damage index

The bending energy damage index method calculates a damage index based on the mode shape curvatures [2]. This index can be represented by

$$BEDI = \sum_{i=1}^N \frac{(\sum_{j=1}^m (\phi''_{i,j}^*)^2 + (\phi''_{i,j})^2) \sum_{j=1}^m (\phi''_{i,j})^2}{(\sum_{j=1}^m (\phi''_{i,j})^2 + (\phi''_{i,j}^*)^2) \sum_{j=1}^m (\phi''_{i,j}^*)^2} \quad (3)$$

where $\phi''_{i,j}$ and $\phi''_{i,j}^*$ are the mode shapes before and after the occurrence of damage; i and j indicates the i -th mode and j -th location in a structure; N is the number of modes of interest.

2.3 Modal assurance criterion

The modal assurance criterion is a method to present the correlation between two mode shapes, and this criterion can also provide the information of damage existence [4]. To further detect damage locations, the coordinate modal assurance criterion (COMAC) can be employed [5]. Thus, both MAC and COMAC indices are written by

$$MAC_{i,k} = \frac{|\sum_{j=1}^m (\phi_{i,j} \cdot \phi_{k,j}^*)|^2}{(\sum_{j=1}^m \|\phi_{i,j}\|^2) (\sum_{j=1}^m \|\phi_{k,j}^*\|^2)}, \quad COMAC_j = \frac{|\sum_{i=1}^N (\phi_{i,j} \cdot \phi_{i,j}^*)|^2}{(\sum_{i=1}^N \|\phi_{i,j}\|^2) (\sum_{i=1}^N \|\phi_{i,j}^*\|^2)} \quad (4)$$

where \cdot indicates the dot product of two vectors; i and k represents the i -th and k -th modes; j denotes the j -th locations; m is the total number of stories; N is the number of modes of interest. Moreover, $MAC_{i,k}$ represents the i -th mode shape of the undamaged structure and the k -th mode

shape of the damaged structure. $COMAC_j$ indicates the j -th location with respect to damage levels.

2.4 Strain energy damage index

The strain energy damage index generates the damage index based on the strain energy variations before and after the occurrence of damage in a structure. The stiffness matrix is formed by a shear-type structure, then the strain energy damage index can be derived as

$$\beta_j = \frac{([\phi_i^*]^T [U_j] [\phi_i^*] + \sum_{i=1}^N [\phi_i^*]^T [U_j] [\phi_i^*]) [\phi_i]^T [U_j] [\phi_i]}{([\phi_i]^T [U_j] [\phi_i] + \sum_{i=1}^N [\phi_i]^T [U_j] [\phi_i]) [\phi_i^*]^T [U_j] [\phi_i^*]} \quad (5)$$

where U_j denotes the j -th local stiffness contribution (i.e., the j -th story) with respect to the global stiffness matrix.

2.5 Continuous Wavelet transform

The continuous wavelet transform can present instant frequency components over time [6]. This wavelet transform can be applied to the difference of mode shape slopes before and after the occurrence of damage in a structure such as

$$W\phi'_i(u, s) = \langle \phi'_i, \psi_{u,s} \rangle = \frac{1}{\sqrt{s}} \int_{-\infty}^{+\infty} \phi'_i(x) \psi\left(\frac{x-u}{s}\right) dx \quad (6)$$

where ψ is the mother wavelet function. This position-frequency representation of the difference of the i -th mode shape slopes shows the discontinuousness in high frequencies. To highlight this discontinuousness, a marginal spectrum can be used by accumulating the amplitudes in Eq. (6) over frequencies.

2.6 Changes in the first mode shape slopes

The method of changes in the first mode shape slopes exploits the dynamic characteristic equation to verify that the first mode shape slopes can be a good indication of structural damage [7]. The mode shape slopes are given by

$$CFMSS = \left(\frac{\phi_{1j}^* - \phi_{1(j-1)}^*}{h_j} \right) - \left(\frac{\phi_{1j} - \phi_{1(j-1)}}{h_j} \right) \quad (7)$$

where $\Delta\phi'_{1j}$ represents the difference of the first mode shape slopes at the j -th location. This method is only valid for a cantilever-type structure.

3 NUMERICAL EXAMPLE

In this research, a ten-story shear-type building is employed to evaluate six mode shapes-based damage detection method. For all these methods, only the first mode shape are taken into account to examine performance of damage detection. This building consists of a 100-kg mass, 1 m high, and 15,800-N/m stiffness per story. Two scenarios are considered: a) only the second story has damage and b) both second and fifth stories have damage. Structural damage is mimicked by a stiffness reduction, and three levels of reductions are considered including 15%, 45%, and 75%. Fig. 1 illustrates the damage locations in simulation.

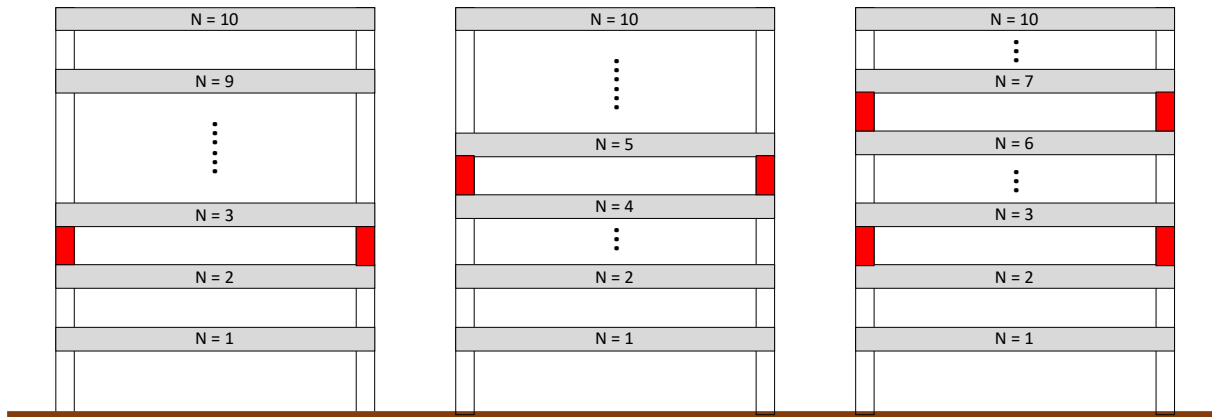


Figure 1: Illustration of two damage scenarios in the ten-story shear-type building

To determine damage locations, each method has a different criterion. The MSC method needs to be normalized by

$$(MSC)_n = MSC / \max(|MSC|) \quad (8)$$

where $\max(MSC)$ denotes the maximum entry in the difference vector of the first mode shape curvatures. When $(MSC)_n$ exceeds 0.5, the damage is viewed to be detectable. In the BEDI method, the building is damaged if the index is greater than 1. In the MAC-COMAC method, if the MAC is lower than 0.7, the structure is viewed to be damaged. Meanwhile, the COMAC is employed to determine the damage locations. The SEDI method assesses damage by the same approach as the BEDI method. In the CWT method, the marginal spectrum is normalized by a norm. Then, the damage location is determined by the normalized marginal spectrum exceeding 0.5. The CFMSS method detects damage when the ratio of the first mode shape slopes is greater than 0.

3.1 Single damage location

As seen in Fig. 1, the single damage location is at the third floor and the fifth floor. Table 1-2 shows the damage detection results for the two scenarios of the single damage location. In this table, 1 means that damage has been detected by the method, while blanks mean that no damage is detected. Most of damage detection methods used in this study is capable of identifying the damage locations except for the MAC-COMAC method. Moreover, the MSC and BEDI methods introduced some faulty detections in the first floor.

Table 1: Damage detection results of a single damage location (3F): 15%, 45%, and 75% stiffness reduction from top to bottom

(Method), 15%	1	2	3	4	5	6	7	8	9	10
MSC		1	1							
BEDI		1	1							
MAC								1	1	
SEDI			1							
CWT			1							
CFMSS			1							

(Method), 45%	1	2	3	4	5	6	7	8	9	10
MSC		1	1							
BEDI		1	1							
MAC								1	1	
SEDI			1							
CWT			1							
CFMSS			1							
(Method), 75%	1	2	3	4	5	6	7	8	9	10
MSC		1	1							
BEDI		1	1							
MAC								1	1	
SEDI			1							
CWT			1							
CFMSS			1							

Table 2: Damage detection results of a single damage location (5F): 15%, 45%, and 75% stiffness reduction from top to bottom

(Method), 15%	1	2	3	4	5	6	7	8	9	10
MSC				1	1					
BEDI					1					
MAC										
SEDI					1					
CWT					1					
CFMSS					1					
(Method), 45%	1	2	3	4	5	6	7	8	9	10
MSC				1	1					
BEDI				1	1					
MAC								1	1	
SEDI					1					
CWT					1					
CFMSS					1					
(Method), 75%	1	2	3	4	5	6	7	8	9	10
MSC				1	1					
BEDI				1	1					
MAC										
SEDI					1					
CWT					1					
CFMSS					1					

3.2 Multiple damage locations

When the building has two damage locations at the third and seventh floors, the results are presented in Table 3. Similarly, 1 means that damage has been detected by the method, while blanks mean that no damage is detected in this table. As seen in the results, the MSC and BEDI methods introduce some faulty detections of damage, while the SEDI, CWT, and CFMSS methods can exactly locate the damage. Therefore, this numerical investigation concludes that the SEDI, CWT, and CFMSS methods are applicable for damage detection of shear-type

buildings based only on the first mode shapes.

Table 3: Damage detection results of multiple single damage locations: 15%, 45%, and 75% stiffness reduction from top to bottom

(Method), 15%	1	2	3	4	5	6	7	8	9	10
MSC		1	1			1	1			
BEDI		1	1				1			
MAC										
SEDI			1				1			
CWT			1				1			
CFMSS			1				1			
(Method), 45%	1	2	3	4	5	6	7	8	9	10
MSC		1	1			1	1			
BEDI		1	1				1			
MAC										
SEDI			1				1			
CWT			1				1			
CFMSS			1				1			
(Method), 75%	1	2	3	4	5	6	7	8	9	10
MSC		1	1			1	1			
BEDI		1	1							
MAC										
SEDI			1			1	1			
CWT			1				1			
CFMSS			1				1			

4 CONCLUSIONS

This study investigated six mode shape-based methods for damage detection of a shear-type building. All these methods included the mode shape curvature method, bending energy damage index method, the modal assurance criterion method, strain energy damage index method, continuous wavelet transform method, and the method of changes in the first mode shape slopes. These methods derived associated indices based on the 1st mode shapes or their derivatives. A shear-type building with two damage scenarios were introduced to evaluate effectiveness of these damage detection methods. As found in the results, most of the methods were able to identify the damage existence and to locate the damage. The SEDI, CWT, and CFMSS methods were capable of providing an accurate indication of damage when only a single damage location occurred. For multiple damage locations, the CWT and CFMSS methods had better performance because other methods could introduce some faulty detections.

ACKNOWLEDGEMENTS

This research is supported by the Ministry of Science and Technology in Taiwan under Grant No. MOST 107-3011-F-009-003. This research is also supported by National Taiwan University under Grant No. NTUCC-108L892502.

REFERENCES

- [1] Pandey, A.K., Biswas, M., and Samman, M.M. Damage detection from changes in curvature mode shapes. *J. Sound Vib* (1991) **145**:321-332.
- [2] Stubbs, N., Kim, J.T., and Arrar, C.R.F. Field verification of a nondestructive damage localization and severity estimation algorithm. *Proc. of the XIII International Modal Analysis Conf* (1995).
- [3] Stubbs, N. and Kim, J.T. Model-uncertainty impact and damage-detection accuracy in plate girder. *ASCE Journal of Structural Engineering*. (1995) 121(10):1409-1417.
- [4] Allemang, R.J. and Brown, D.L. A correlation coefficient for modal vector analysis. *Proc. 1st Int. Modal Anal. Conf* (1982) 110–116.
- [5] Lieven, N.A.J. and Ewins, D.J. Spatial correlation of mode shapes the coordinate modal assurance criterion. *Proc. 6th Int. Modal Anal. Conf* (1988) 690-695.
- [6] Mallat, S. A Wavelet tour of signal processing. *Academic Press* (1998) New York.
- [7] Zhu, H., Li, L., and He, X.Q. Damage detection method for shear buildings using the changes in the first mode shape slopes. *Computers & Structures* (2011) 89:733-743.

CHANGES IN MODAL FREQUENCIES OF A STEEL PLATE GIRDER CAUSED BY LOCAL DAMAGE AND THERMAL EXPANSION

CHUL-WOO KIM¹, TAKUMI HIROOKA¹ TAKUYA MIMASU²
GEN HAYASHI¹ YOSHINAO GOI¹

¹ Department of Civil and Earth Resources Engineering
Graduate School of Engineering, Kyoto University
Katsura Campus, 615-8540, JAPAN

email: kim.chulwoo.5u@kyoto-u.ac.jp, Web page: <http://infra.kuciv.kyoto-u.ac.jp>

² JFE Engineering Corporation
Yokohama headquarters
230-8611 Yokohama, Japan
email: mimasu.takuya.77c@kyoto-u.ac.jp

Key words: Damage Experiment, Local Damage, Steel Plate Girder Bridge, Structural Health Monitoring, Thermal Expansion.

Abstract. This study is intended to investigate how the local damage and varying temperature affect changes in modal frequencies of a steel plate girder bridge. A damage experiment on an actual bridge was conducted, and acceleration responses of the bridge under vehicle loading were monitored. Artificial fatigue cracks were introduced to the lower flange and the web plate near the base plate in the damage experiment. The longitudinal displacement of the bridge at supports were also monitored to investigate structural behaviors of supports under local damage and the varying temperature. Observations showed that frequency of the 1st bending mode increased due to artificial damage though frequencies of the 2nd bending mode and 3rd bending mode decreased. On a finite element model, changes in stiffness of spring which models the cantilever steel pivot bearings at support due to the damage as well as temperature change are considered to examine the reason why the frequency of the first bending mode increased while those of the second and third bending modes decreased. A sensitivity analysis to investigate influences of the changes in the stiffness of the girders and the stiffness of the spring at the support. The sensitivity analysis demonstrated that the changes in the stiffness of the spring at the support resulted in the increase of the first bending frequency.

1 INTRODUCTION

Vibration-based structural health monitoring (SHM) has been developed as one of the efficient ways for maintenance of civil infrastructures including bridges. Many studies for damage detection by means of SHM examined the change in modal parameters of bridges such as frequency, damping ratio and modal shape since changes in these modal parameters are

Table 1: The environmental condition during each damage scenario

Damage Scenario	Time and Date	Weather	Temperature of bridge
INT	17:45-18:45 28th August 2017	Cloudy	28°C
DMG1	13:30-14:30 29th August 2017	Clear	38°C
DMG2	14:45-15:45 29th August 2017	Clear	43°C

relevant to damage or deterioration of bridges [1-3]. One of the typical modal parameters of bridges is the frequency. Modal parameters are identified from vibrations of the bridge.

This study investigates the feasibility of the vibration-based SHM to detect damage on an actual steel plate girder bridge. Especially, changes in frequencies due to fatigue cracks in steel girder near the base plate of supports are examined. Stochastic subspace identification (SSI) is used as a modal identification method [4].

In the finite element (FE) model, an eigenvalue analysis for the bridge is also conducted. For the eigenvalue analysis, structural parameters were calibrated by the model-updating using the identified modal parameters. By comparing the frequencies identified from the vibration responses between the undamaged bridge and damaged bridge, this study investigates the feasibility of damage detection by means of the vibration-based SHM. In addition, the eigenvalue analysis results are also compared to system identification results from experimental data so as to confirm the feasibility of the FE model for the eigenvalue analysis. Reasons of changes in modal parameters for each damage scenario are discussed utilizing results from eigenvalue analysis and sensitivity analysis.

In order to clarify possible reasons for the disagreement in the frequency for the first bending mode between the FE analysis and the field experiment, changes in the structural behaviour associated with each damage scenario are discussed using the displacement and temperature obtained from the field experiment.

2 FIELD EXPERIMENT

The field experiment was conducted on an actual steel plate girder bridge shown in Figure 1, whose span length was 40 m long and width was 4.0 m wide. Figure 1 also shows sensor deployment during the field experiment. Ten accelerometers were installed on the lower flanges of the bridge to measure vertical vibrations. Longitudinal displacements at the both ends of the bridge were measured utilizing displacement sensors. Artificial fatigue cracks (hereafter called artificial damage) at the girder end near the base plate of supports are considered in the experiment by severing the lower flange and the web plate by an Oxyacetylene cutting torch. The location of the artificial damage is on the main girder near the support of upstream-side on Ab1 abutment as shown in Figure 1. The artificial damage comprises two damage levels. One is the lower flange cut (hereafter called DMG1) and the other is the web plate cut (hereafter called DMG2) as seen in Figure 2. The bridge condition before the artificial damage was assumed as the intact condition (hereafter called INT). Types of supports at Ab1 and Ab2 are shown in Figure 3: the Ab1 abutment adopted a line bearing, and the Ab2 abutment adopted a cantilever pivot bearing. It should be noted that the line bearing at the Ab1 abutment was fixed due to corrosion.

Modal parameters of the bridge were identified from the accelerations of the bridge for each bridge condition. The vehicle used for the moving vehicle test was a passenger car and the

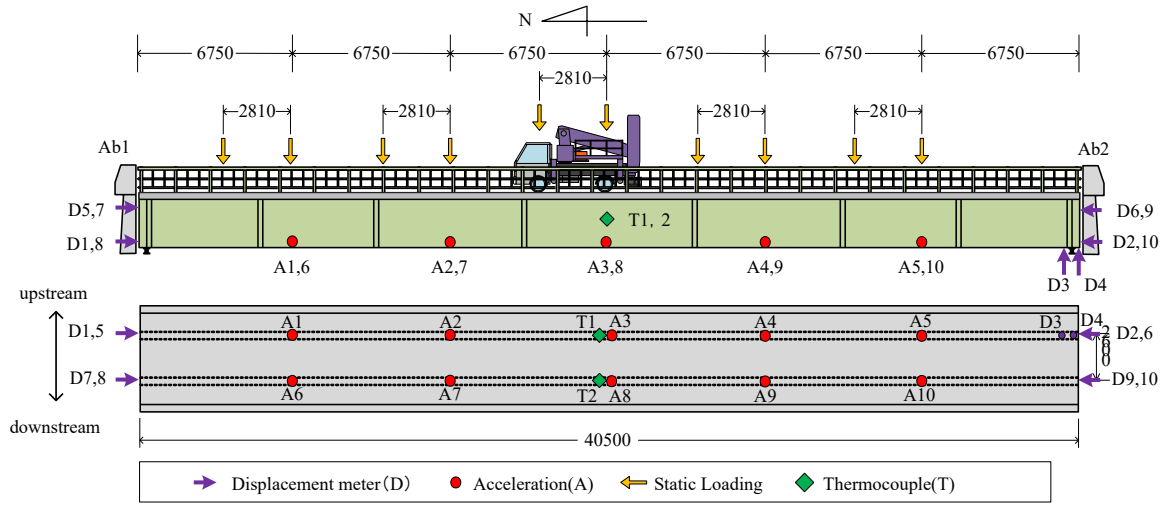


Figure 1: Observation bridge and sensor deployment.



Figure 2: Artificial damage location and each damage scenario.

speed of the car was about 20km/h. The moving vehicle test was conducted 30 round trips for the intact condition, and 15 round trips per damage condition. Sampling rate and length of the vibration data set were 200Hz and 15s, respectively. The environmental condition during the field experiment is summarized in Table 1. Temperatures measured from the thermocouples installed at the center of the plate girder were 28°C, 38°C and 43°C during INT, DMG1 and DMG2 experiments, respectively.

The mechanical properties of the bridge were also examined through static-loading test. The loading was given by a large sized vehicle whose axle weight on front and rear axles were 21.66kN and 54.88kN, respectively. In the loading test, the loading vehicle entered from Ab2 side, and located the rear axle with 6750mm intervals. The loading test was operated two times for each scenario, and each of the displacement was also measured twice. Hereinafter, the averaged displacement is used in discussions.

3 FE MODEL ANALYSIS

To investigate the dynamic characteristics of the bridge, the eigenvalue analysis using the FE model of the bridge was conducted utilizing ABAQUS 6.14. The bridge model, shown in Figure 4, was built based on the documents of periodic inspection and information obtained

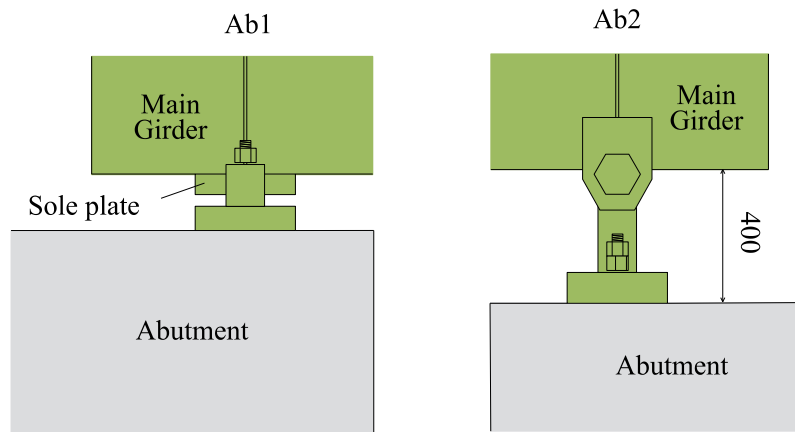


Figure 3: Types of bearing at each support.

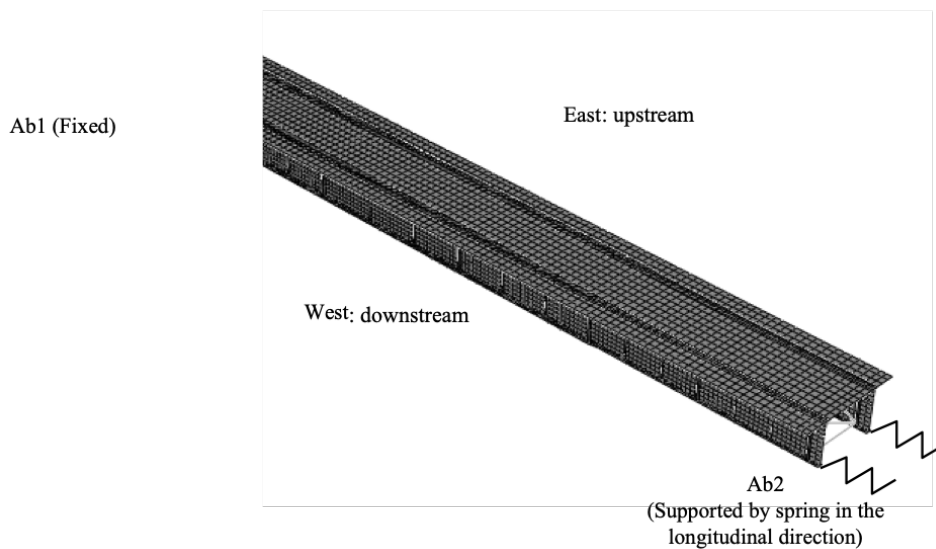


Figure 4: Finite element model.

from the field experiment as the original design documents of this bridge are not available. The concrete deck, main girder, vertical stiffener and horizontal stiffeners were modelled with shell element, and cross frame and lateral bracing were modelled with beam element. According to the results obtained from the static loading test which will be mentioned in Section 4.1, the boundary conditions were given as follows: fixed boundary condition for the Ab1 abutment, and boundary condition with roller supports with elastic longitudinal springs for the Ab2 abutment. As shown in Figure 3, the supports at Ab2 abutment are the cantilever-like steel pivot support which deforms elastically and act as if springs in the longitudinal direction, which is the reason why the longitudinal spring was introduced at the Ab2 in the FE model as seen in Figure 4.

Specific gravities of steel and concrete were assumed as 7.85 and 2.40 respectively. Young's moduli of steel and reinforced concrete were assumed as 210 GPa and 22.02 GPa, respectively.

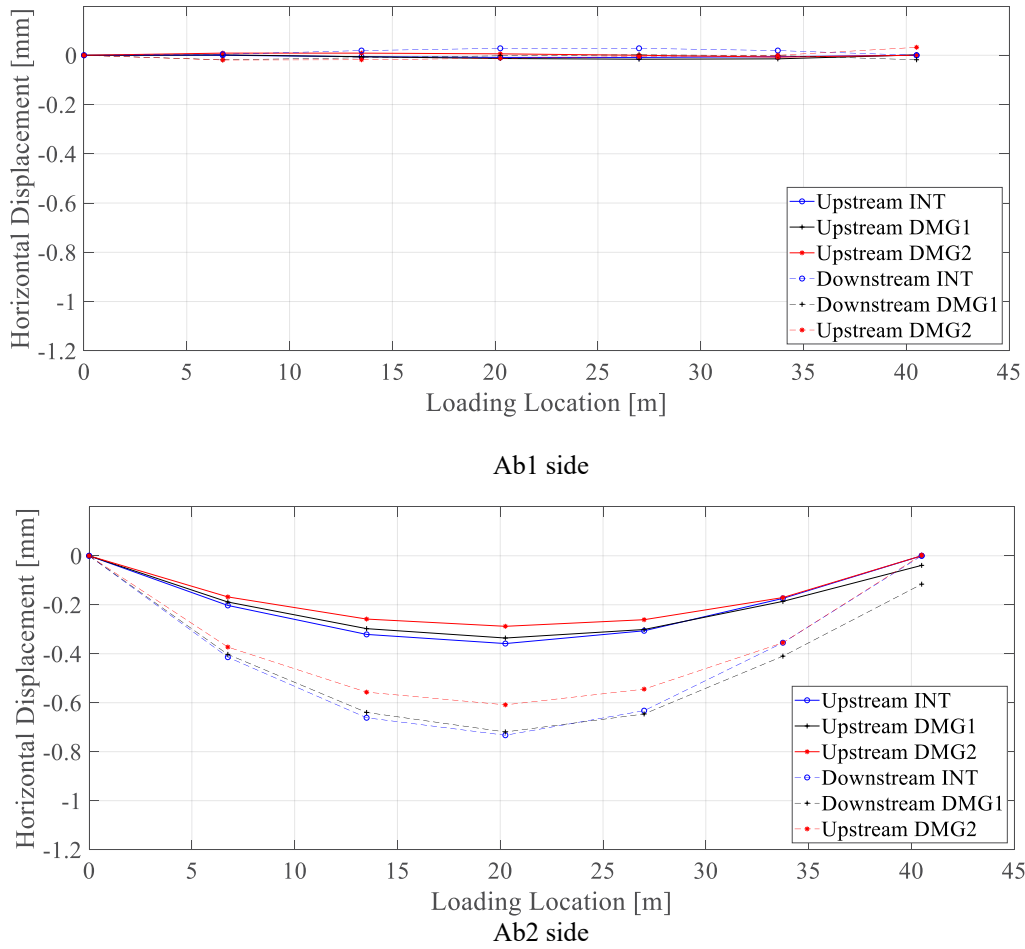


Figure 5: Horizontal displacement of bridge girder at each point.

However, since the bridge model has some differences from the actual bridge due to deterioration and differences between design and construction and so on, the bridge model needs a model updating to calibrate structural parameters of the FE model. The cross entropy (CE) method was applied to update the bridge model so that the eigen frequencies of the FE analysis are fit to those monitored from the actual bridge [5]. The spring constant which idealizes the cantilever steel pivot bearing on Ab2 abutment was also calibrated by means of the model update. The artificial damage was modelled as pseudo cracks in the FE model to realize damage scenarios. This crack was created by removing the connection of elements. The eigenvalue analysis was conducted for each of the damage scenarios. It is noteworthy that, in the model calibration, using the experiment data of INT scenario as reference, the initial finite element model is tuned towards frequencies.

The static longitudinal displacement at the supports is also investigated utilizing the updated FE model for each of the damage scenarios. For the FE analysis, the thermal expansion is evenly considered on each of the elements in the FE model for each damage scenario considering temperature in Table 1. The thermal conductivity of steel and reinforced concrete was assumed

Table 2: Frequency (Hz) and MAC obtained from eigen value analysis (MAC value is in the parenthesis)

	INT	DMG1	DMG2
1 st bending mode	3.13 (-)	3.13 (1.000)	3.11 (0.990)
1 st torsional mode	5.03 (-)	4.97 (1.000)	4.65 (0.989)
2 nd bending mode	9.36 (-)	9.33 (1.000)	9.23 (0.985)
2 nd torsional mode	10.69 (-)	10.66 (0.998)	10.45 (0.917)
3 rd bending mode	22.06 (-)	22.00 (0.999)	21.82 (0.896)

as $45\text{W/m} \cdot \text{K}$ and $1.6\text{W/m} \cdot \text{K}$, respectively. Thermal expansion coefficient of steel and reinforced concrete was assumed as $1.0 \times 10^{-5}/\text{K}$.

4 RESULTS AND DISCUSSION

4.1 Static loading test

To examine static responses of the bridge under vehicle loadings, longitudinal displacements from the static-loading test were examined. Figures 5a and 5b show longitudinal displacements measured at each of the upstream and downstream sides of the girder on Ab1 and Ab2 abutments, respectively. The horizontal axis represents the loading position from the Ab2, and the vertical axis shows the relative displacements taken from the static deformation under the dead load. The displacements adopted in the curves are obtained from the displacement sensors installed nearby the lower flange of each girder at supports (see Figure 1). For each damage scenario, the vehicle loading tests were performed twice, and average displacements are shown in Figure 5.

Figure 5a shows that the supports on Ab1 abutment allows little displacement, while Figure 5b shows that the supports on Ab2 abutment allows longitudinal displacements of the bridge girder. The downstream-side girder showed larger displacements than that of the upstream-side. Focusing on damage scenarios, the relative displacement due to the vehicular loading from the static deformation gets smaller when the damage propagates. This observation will be discussed again in Section 4.3 to clarify why the relative displacement gets smaller when the damage propagates.

4.2 Identified modal properties

The three bending modes and the two torsional modes were stably identified by means of SSI. Histograms of the identified frequencies for each of bridge conditions are shown in Figure 6 with normal distribution fits, where the bin width was chosen as 0.01Hz. The histogram was created utilizing 30 samples of the identified frequencies. The statistical distributions show that frequencies for the 2nd and 3rd bending modes and the 2nd torsional mode tend to decrease as the damage becomes severe, i.e., in the order of INT, DMG1 and DMG2. This result indicates the decrease of bending stiffness of the plate girder due to the artificial damage. However, the frequencies of the 1st bending mode and the 1st torsional mode tend to increase as damage becomes severe. The reasons why the frequencies of these two modes were increased will also be discussed in Section 4.3.

In addition, temperature change on the plate girder is taken into consideration. As shown in Table 1, temperature change was 10°C from INT to DMG1 and 5°C from DMG1 to DMG2

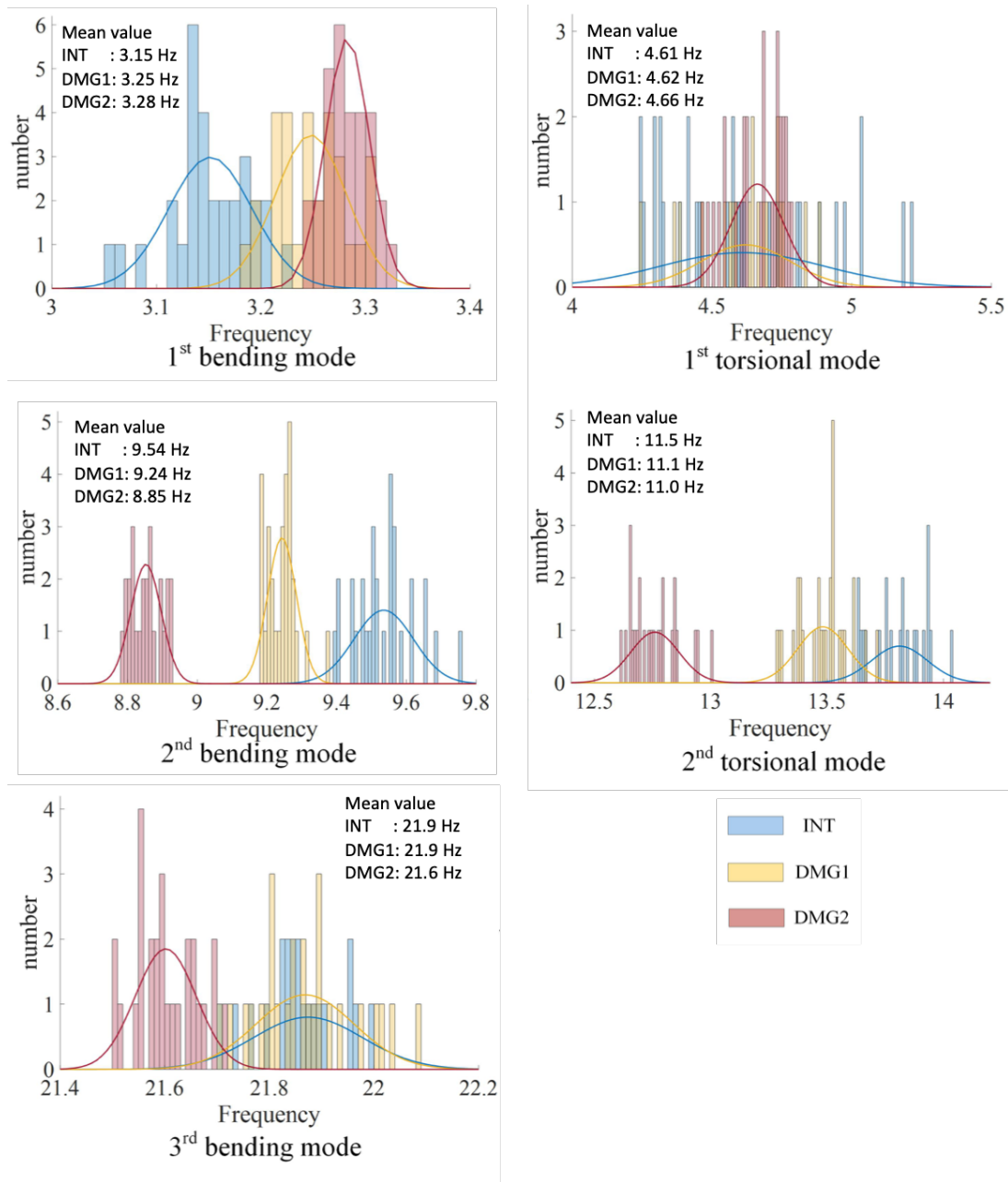


Figure 6: Histograms of identified frequencies associated with bridge condition.

during the field experiment, respectively. However, temperature change was not considered in the eigenvalue analysis in this study.

4.3 Comparison between FE analysis and field experiment

Frequencies and mode shapes from the eigenvalue analysis utilizing the calibrated FE model are compared to those identified from monitoring data. Frequencies obtained from the eigenvalue analysis with the pseudo cracks and values of modal assurance criterion (MAC) are

summarized in Table 2. The spring constant at Ab2 supports was also calibrated referring the frequencies identified in INT. The calibrated FE model of the bridge led to eigen-frequencies of 3.13Hz, 9.36Hz, 22.06Hz, 5.03Hz and 10.69Hz for the 1st, 2nd and 3rd bending modes and 1st and 2nd torsional modes, respectively as shown in Table 2.

MAC values between mode shapes from the eigenvalue analysis and those identified from experimental data were 0.96 for the 2nd torsional mode and more than 0.99 for the other modes. This result means that the mode shapes from the eigenvalue analysis and ones from the experiment were comparable with each other. The frequencies for all modes of the FE analysis decreased as the damage gets severe. The decrease of the 1st bending frequency was much less than the frequencies of the other modes. MAC values for these modes in Table 2 also decreased as the damage gets severe. Changes in the frequencies due to the damage obtained from the eigenvalue analysis showed similar tendency as ones from experiment data except the 1st bending and torsional modes.

Considering the observation of smaller relative longitudinal displacement due to severer damage as seen in Figure 5b that, it can be said that elastic behavior of the pivot bearing becomes stiffer as the damage propagates. In other words, the spring at the support on Ab2 becomes stiffer associate with damage condition. This means the damage might cause not only stiffness reduction on the bridge girder, but also increase stiffness of the spring at the support, so called stiffness hardening effect occurred. However, it should be noted that between damage experiments such as between INT and DMG1 scenarios and DMG1 and DMG2 scenarios temperature changes were observed. Therefore, both damage and temperature should be considered in the discussion for the stiffness hardening effect occurred at the pivot bearing on Ab2 abutment.

To investigate the relationship between the boundary condition and the modal parameters, a sensitivity analysis is performed utilizing the FE model for INT scenario. Figure 7 shows the results of the sensitivity analysis, in which the horizontal axis represents the spring constant for

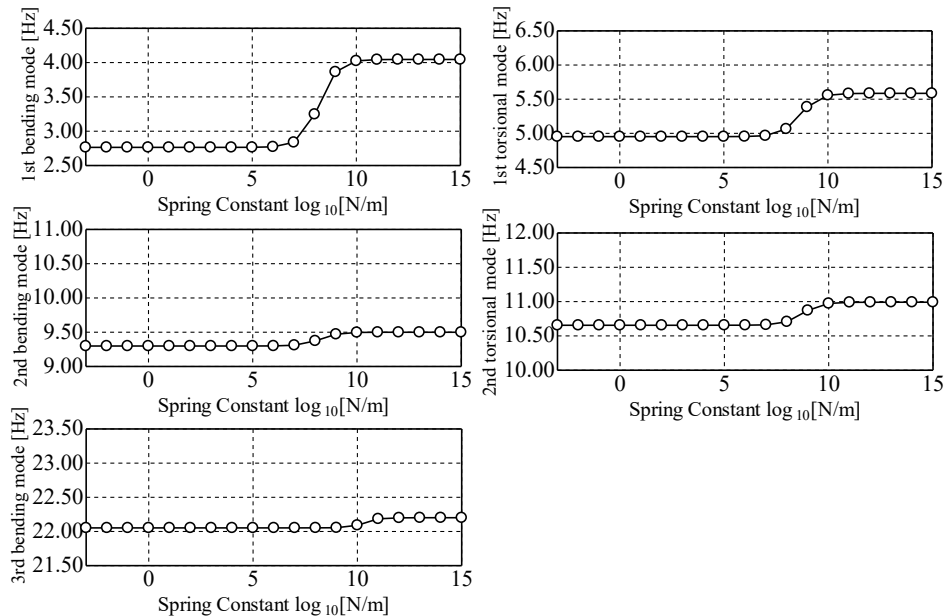


Figure 7: Sensitivity analysis for spring constant at support.

the pivot bearing, and the vertical axis represents each of the modal frequencies. Observations from the sensitivity analysis demonstrated that the spring constant has stronger influences on the change in frequencies of the 1st bending and torsional modes than on the other frequencies. On the other hands, the other modes were strongly influenced by changes in the stiffness of the girder rather than increase of stiffness of the spring at the support. According to the above discussions, the 1st bending and torsional modes were strongly influenced by changes in the boundary condition, rather than changes in stiffness of the girder.

4.4 Structural behavior in longitudinal direction

In this section, longitudinal displacements at girder ends are examined. The relative longitudinal displacements between INT and DMG1 scenarios and DMG1 and DMG2 scenarios are shown in Figure 8 where “D” indicates displacement sensor shown in Figure 1.

Observations from the upstream girder showed that the upper flange elongated due to DMG1 in comparison with the longitudinal displacement under INT condition. Similar trends were observed between DMG1 and DMG2 conditions in the upstream girder. For the downstream girder, a similar trend with that of the upstream girder was observed between INT and DMG1 conditions. However, under the DMG2, the lower flange of the downstream girder on Ab2 abutment was largely elongated than that on the upper flange.

In general, when a damage is propagated on a plate girder, dead load of the bridge increases the deflection of the girder as the stiffness of the girder decreases. Therefore, the upper flange of the girder is expected to compressed when a damage is propagated. Different behaviors were observed in the bridge. One reason might be elongation due to temperature change during the experiment which will be discussed in Section 4.5. For the elongation of the lower flange of the downstream girder on Ab2 abutment under the DMG2, it might be caused by torsional behavior of the bridge under the severe damage DMG2.

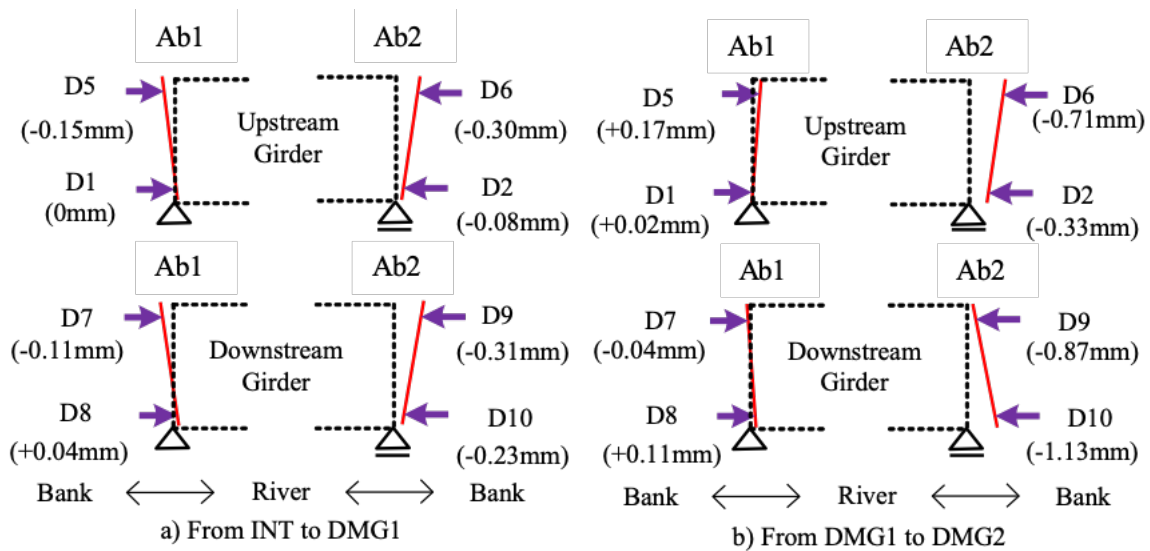


Figure 8: Changes in longitudinal behavior of plate girder bridge associate with damage scenarios.

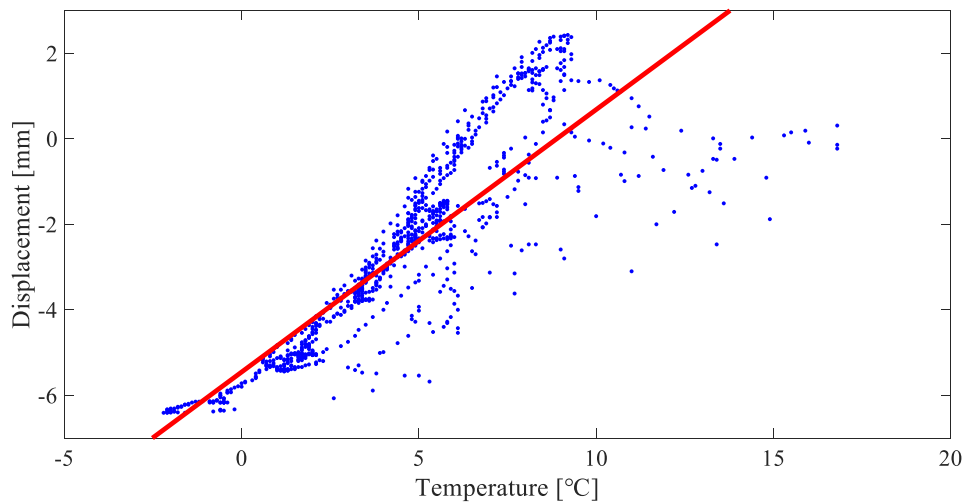


Figure 9: Correlation between temperature and displacement obtained from D2 sensor.

4.5 Thermal expansion

As discussed in Section 4.4, those structural behaviors of the bridge in the longitudinal direction under propagation of damage might be caused by thermal expansion due to the temperature change. There were non-negligible temperature changes between INT scenario and DMG1 scenario as well as between DMG1 scenario and DMG2 scenario as summarized in Table 1. According to the long-term monitoring for this bridge, displacement obtained from D2 sensor showed about 2.5mm changes in the longitudinal direction by changing 5°C as shown in Figure 9. The red line in Figure 9 indicates the linear regression line between temperature change and longitudinal displacement.

In order to investigate the thermal expansion of the bridge, an FE analysis is conducted. In this analysis, temperature changes were 10°C from INT to DMG1 and 5°C from DMG1 to DMG2, and artificial damage for each damage scenario was also considered. The deflection of the bridge from the FE analysis is shown in Figure 10, which shows deflection in upward direction as observed from the field experiment. It is noted that the analytical deflection shapes under the different temperature changes and damage scenarios showed same configuration as seen in Figure 10. This result demonstrated that the thermal expansion affects the structural behavior of the bridge. In addition, the shape after thermal expansion is similar to the end girder shape in Figure 8a, so thermal expansion due to temperature change has more effect on the structural behavior at supports than the artificial damage during DMG1 experiment. However, compared with the end girder shape in Figure 8b, the shape in Figure 10 is so different from the shape in Figure 8b. When it comes to the severe damage such as DMG2, the girder should be much more affected by artificial damage rather than by thermal expansion. Thus, the girder can twist as shown in Figure 8b. On the other hand, such behavior cannot be observed in the FE analysis when DMG2 is propagated. One possible reason for the failure of simulating the structural behavior under DMG2 is that the FE model is not able to simulate different structural

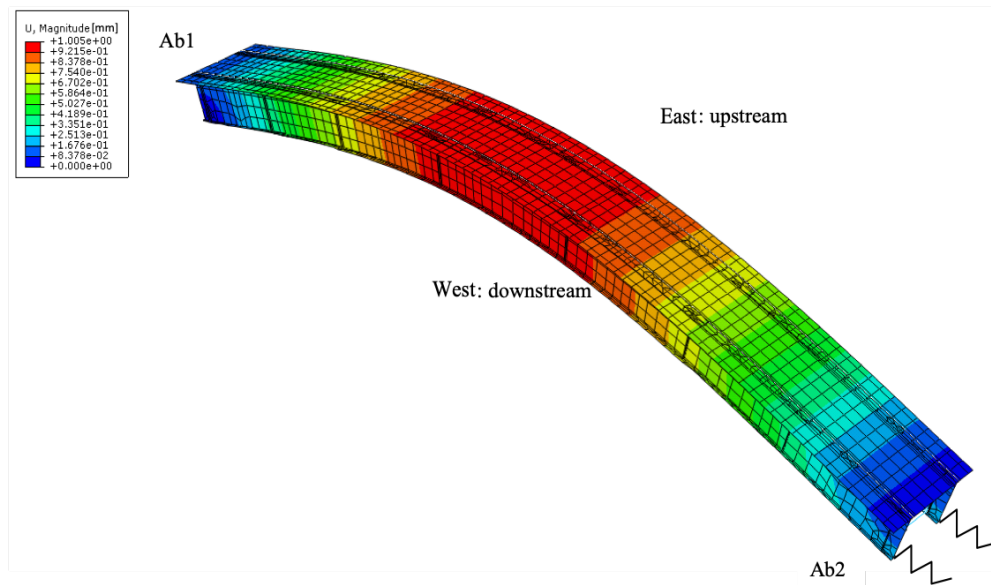


Figure 10: Change in structural behavior due to thermal expansion and artificial damage.

behaviors of the upstream and downstream girders observed in the experiment.

5 CONCLUSIONS

This study investigated feasibility of damage detection of an actual steel plate girder bridge utilizing identified modal parameters from vehicle induced vibrations of the bridge. Especially, the frequency was considered as damage sensitive features of the bridge. In addition, the cause of the frequency changes is considered using results of the static-loading test.

Frequencies identified from the experimental data were changed due to the artificial damage. Frequencies of the 2nd and 3rd bending modes and 2nd torsional mode decreased as the damage gets severe. However, the frequency of the 1st bending and torsional modes increased due to damage.

The FE model is constructed using the results of the static-loading test and the model updating based on the observed frequencies. The eigenvalue analysis utilizing the FE model showed that frequencies for three bending and two torsional modes decreased due to the artificial damage. Tendency of changes in the frequency due to the artificial damage obtained from the eigenvalue analysis were similar to ones from experiment data except the 1st bending and torsional modes.

Observations from this study showed that the 1st bending and torsional modes were strongly influenced by stiffness hardening effect in the cantilevered pivot bearing rather than changes in stiffness of the girder. On the other hand, the other modes were strongly influenced by changes in the stiffness of the girder rather than influence of stiffness hardening effect in the cantilevered pivot bearing.

To investigate the stiffness hardening effect in the cantilevered pivot bearing due to damage, FE analysis adopting spring element as the cantilever pivot bearing and considering thermal expansion was conducted. Comparison of the deflection configurations from FE analysis with

those from the experiment showed that one of the main reasons of the stiffness hardening effect in the cantilevered pivot bearing is thermal expansion due to temperature changes between damage experiments. However, it was unsuccessful to simulate the static behavior under the most severe damage scenario (DMG2) that might be caused by torsional behavior.

The next step for this study is to clarify the static behavior under the most severe damage scenario (DMG2).

ACKNOWLEDGEMENTS

This study is partially sponsored by a Japanese Society for the Promotion of Science (JSPS) Grant-in-Aid for Scientific Research (B) under project No.19H02225, which is greatly appreciated.

REFERENCES

- [1] Chang, K.C. and Kim, C.W. Modal-parameter identification and vibration-based damage detection of a damaged steel truss bridge. *Engineering Structures* (2016) **122**: 156-173.
- [2] Deraemaeker, A., Reynders, E., De, R. G. and Kullaa, J. Vibration-based structural health monitoring using output-only measurements under changing environment, *Mechanical Systems and Signal Processing* (2007) **22**(1): 34-56.
- [3] Zhang, Q.W. Statistical damage identification for bridges using ambient vibration data. *Computers and Structures* (2007) **85**(7-8): 476-485.
- [4] van Overschee, P. and De Moor, B. Subspace algorithms for the stochastic identification problem, *Automatica* (1993) **29**(3): 649-660.
- [5] McGetrick, P.J., Kim, C.W., Gonzalez, A. and O'Brien, E.J. Experimental validation of a drive-by stiffness identification method for damage monitoring. *Structural Health Monitoring* (2015) **14**(4): 347-331.

CONTRIBUTION TO NEW SOLUTIONS OF INSTRUMENTATION OF CIVIL STRUCTURES FOR CONTINUOUS DYNAMIC MONITORING

C. MOUTINHO^{*} AND A. CUNHA^{*}

^{*} CONSTRUCT - ViBest,
Faculty of Engineering (FEUP), University of Porto
R. Dr. Roberto Frias S/N, 4200-465 Porto
e-mail: moutinho@fe.up.pt, acunha@fe.up.pt, www www.fe.up.pt/vibest

Key words: Continuous Dynamic Monitoring, Operational Modal Analysis, Data Acquisition Systems, New Generation of Measurement Systems.

Abstract. This paper describes the work developed by CONSTRUCT – ViBest research group in the area of new solutions of instrumentation of Civil Structures aiming its long term dynamic monitoring. It identifies the main challenges in this area, and focus the discussion around power options and data transmission solutions. The architecture of the developed measurement systems is described, and a few practical examples of monitoring of bridges is presented.

1 INTRODUCTION

The continuous dynamic monitoring of structures is an area that has lately assumed great importance in Civil Engineering. The main reason is related to the subject of Operational Modal Analysis (OMA), which aims to identify the modal parameters of a structure in operating conditions (particularly with regard to natural frequencies, damping ratios and mode shapes) taking into account the measured ambient vibrations at critical points.

In these cases, the measurement of vibrations is performed without disturbing the normal functioning of the structures, which may be implemented in buildings, bridges (railway, roadway, highway), dams and offshore structures. Given the importance of this subject, the Laboratory of Vibrations and Structural Monitoring FEUP (ViBest) has carried out consistent work in this area, both in the development of numerical tools for identifying modal parameters and in the continuous measurement of vibrations in actual structures (see www.fe.up.pt/vibest).

Parallel to this area, ViBest has also developed and implemented vibration measurement techniques that enable to solve specific problems of current systems and to evolve toward a new generation of measurement systems. In particular, the difficulties that are to be overcome include: a) excessive cost of traditional measurement systems; b) excessive dependence on external power supply; c) frequent failures in data acquisition attributed to heavy operating systems; d) difficulty in being physically integrated into structures, taking up too much space and being barely manageable, and; e) when using cables, the number of sensors is limited due to the exponential complexity of the acquisition system.

In contrast, data acquisition systems based microcontrollers and MEM sensors offers the following advantages: a) cost attractive; b) enable wireless solutions; c) autonomous and small size (easily integrated into structures); d) possibility of installation of high number of sensors; e) low power consumption (can run on batteries or solar panels); f) simplicity of functioning and robustness; g) low maintenance, and; h) may be easily customized.

In this context, this paper intends to divulge the instrumentation solutions that have been used by CONSTRUCT - ViBest in the continuous dynamic monitoring of some structures using this technology. The architecture of the developed sensors is described, as well as the power solutions used to guarantee long periods of measurement. In order to illustrate the efficacy of these solutions, a few practical examples of monitoring of bridges is presented.

2 CONTEXT OF THE RESEARCH

The interest of the research in the area of measurement systems emerged from the technological evolution of the last decades in the topic of sensors and data acquisition systems based on microcontrollers. This was encouraged by the easy access to this technology and by the easy access to information available in the internet. In fact, the quantity of tutorials and blogs around this topic is immense.

At same time, researchers who work in actual structures with data acquisition systems, often face many challenges and problems. The lack of robustness of some traditional instrumentation solutions is one of these difficulties. The failure of these systems when working for long periods is not the only cause of that lack of robustness. Sometimes there also external causes like power failures and adverse weather conditions, beyond to other causes of diverse origin. Some data acquisitions systems are also too complex, involving too many cables and connections. The high cost of measurement systems is another factor that hinders the widespread use of these systems in common Civil Structures.

In this context, the objective of the research in this area is to develop instrumentation that meets the following characteristics: i) wireless and compact size, for easy integration and installation in structures; b) robust, allowing the functioning of the system for long periods with no crashes; c) long autonomy; d) flexible, by allowing a variety of different sensors in several mounting schemes; e) accurate, and; f) cost attractive.

The role of these systems is not certainly to substitute the traditional systems. However, there are many applications where these instruments have the same effectiveness as the traditional ones, with additional advantages. In fact, they can simplify the process of installation and operation; they can be custom-made, including the use of 3D printing; maintenance and replacement is facilitated, and; more interesting, their attractive cost may allow the generalization of dynamic monitoring systems in Civil Structures.

Nevertheless, the implementation of these new data acquisition systems also raises some challenges. Particularly with regard to the following issues: a) power supply; b) data transmission; c) reduced energy consumption; d) miniaturization of the systems, and; e) reliability. In this paper, special attention is given to the issue of power supply and data transmission solutions.

Probably the main question about these new systems, most of them base on distributed sensor networks, is how to power them. If they need external electrical energy materialized by a cable, then the wireless functionality do not make any sense. In this case, the power and data

transmission are provided by the physical connection. If they are fully wireless, they need to have a power supply. It's worth to mention that sleep modes in dynamic monitoring are not useful, since the frequency rates are usually high. In addition, many energy-harvesting solutions do not provide enough power for continuous measurement systems.

In parallel to this issue, it is necessary to consider how and how often data is transmitted. It is generally accepted that Civil Engineering structures do not need continuous online observation, with the exception of special cases. Therefore, the continuous data transmission maybe is not useful in the most applications. This will save a lot of energy and will increase autonomy and the robustness of the system. So, it is suggested that data may be accessed by several ways. Probably the most interesting is to access data physically by visiting the structure periodically, say, every 3 or 4 months. This visit is generally needed for inspection of the condition of the whole monitoring system. Data also may be transmitted wirelessly, but in this case it should be selected a limited period of the day to do that. In this case, the wireless connection is established, the data is transmitted, and in the end the wireless is disconnected. This means that the transmission only work for a few minutes each day, saving a lot of power. Another possibility is saving data locally and program the system to send a daily message with some reference parameters in order to check if the acquisition system is functioning properly.

3 DEVELOPED INSTRUMENTATION

In the context of what was said in the previous section, during last years the CONSTRUCT – ViBest research group at FEUP, developed some instrumentation for dynamic monitoring of structures. There are basically two kinds of sensors: those that are powered by batteries, and those that are powered by solar energy.

The earliest developments were based on portable battery-powered devices. In figure 1a) is shown the system here designated by “Portable 1” which was used for the first measurements in 2014, in particular to measure the “lock-in” effect in Luiz I bridge over Douro River in Porto. This device is a little bigger than the size of a credit card, being possible to adapt it to metal structures by powerful magnets. It incorporates a unidirectional MEM accelerometer, antialiasing filters, a 16-BIT ADC and a micro-sd card for saving data. All this hardware is controlled by a 5-V microcontroller powered by one 9-V battery which ensures run time of about 6 hours.

In order to improve system autonomy, another compact system, designated by “Portable 2” was used to measure simultaneously vertical and horizontal vibrations at same section (see Figure 1b). This device, a little smaller than the previous one, also comes with magnets. This model comprises a tri-axis MEM accelerometer, antialiasing filters, independent 16-BIT ADCs and a micro-sd card to save data. Here, the microcontroller is 3.3 V logic level and works with 3 AA batteries allowing the system to work continuously for close to a month. This model is clearly geared to higher periods of measurements.

More recently, these battery-powered devices evolved to a more reduced energy consumption system (“Portable 3”), incorporating a much better tri-axial MEM accelerometer. It uses 3D printing to optimize the shape and space occupied by the device. Figure 2a) represents a very compact model endowed with magnets for fixation to structures, which has an autonomy of 15 days using a battery of 2500 milliamps. The autonomy of these systems may be increased

by adding more batteries. For instance, Figure 2b) represents a model with an autonomy of 6 months using 9 batteries of 3400 milliamps of capacity.

Aiming long periods of data acquisition for enabling the long-term dynamic monitoring of structures, two solar-powered solutions were developed and implemented. The first one (“Solar 1”), was installed in two structures in 2014. It comprises a 10-W 40×28-cm solar panel which

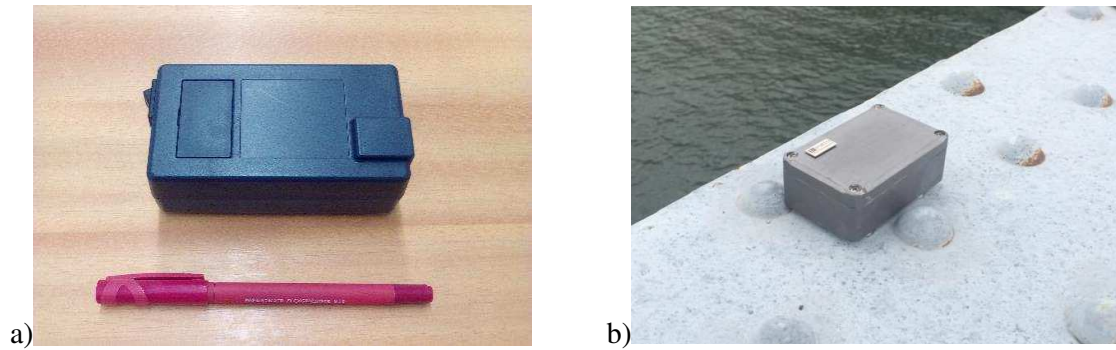


Figure 1: Battery-powered devices: a) “Portable 1” ; b) “Portable 2” measurement system

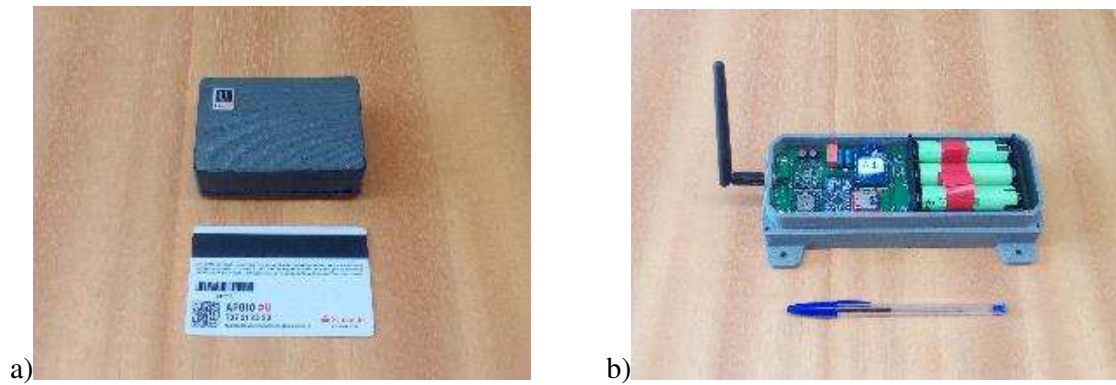


Figure 2: Battery-powered “Portable 3” devices: a) 15 days autonomy ; b) 6 months autonomy

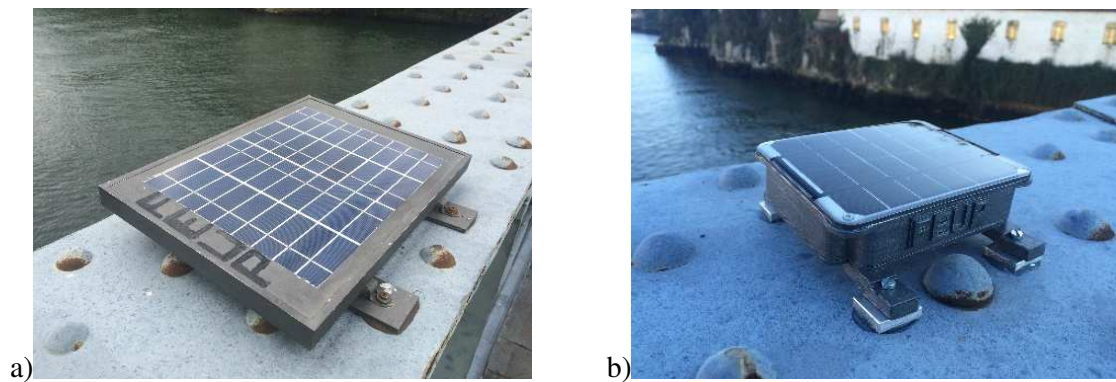


Figure 3: Solar-powered devices: a) “Solar 1” ; b) “Solar 2”

is also used to cover and protect the system against weather conditions (See Figure 3a). The solar controller manages the power to the 5-V acquisition system and, during the daytime, charges $3 \times 12\text{-V}$ batteries to maintain the system working during the night and on cloudy days. The data is acquired by a system integrating a tri-axis MEM accelerometer and is processed using the pieces of hardware described in the other previous devices.

However, “Solar 1” has some issues that needed to be improved upon: i) external dimensions are relatively high, which hinders its integration in the structure; ii) it is inefficient in terms of power consumption because it is based on a 5-V logic level and is powered by 12-V batteries, and; iii) there is no way to check if the system is working properly without being physically accessed. For these reasons, a new version of a solar powered device was developed (“solar 2”). This one is significantly smaller than the previous one (11×14 cm plan view) and the panel has a power of 2W that feeds a 3.3-V system (Figure 3b). The solar controller allows charging a lithium-polymer battery that can run for as much as one week on a single charge. This device consists of a digital tri-axis MEM accelerometer integrating programmable antialiasing filters and programmable ADC frequency rates, and a micro-sd card to save data. In order to monitor the functioning of the acquisition system, this particular model periodically sends a report to an RF serial receiver including the following information: i) device ID; ii) current date and time; iii) current file name; iv) total number of files; v) temperature inside the box, and; vi) battery voltage. This information may be collected locally, for instance, using a smartphone, and allows checking if the system is working properly. Access to the data is only available using a physical connection.

4 EXAMPLES OF MONITORING OF BRIDGES

The first two significant implementations of the developed instrumentation in actual structures are based on solar-powered systems, aiming the long term monitoring of vibrations. One of these structures is a pedestrian bridge located in Porto (Figure 4). It comprises two spans of 30m each, simply supported at the ends with hinges and at mid-length by means of a concrete column. The deck is 3.5 m wide and has an inclination of 6% starting with a lower elevation at the green park and ending in the Transparent Building at a higher level. The cross-section is composed of two lateral steel girders type IPE600, 600 mm high, connected by a secondary steel structure which, in turn, gives support to a wood floor.



Figure 4: General view of the footbridge

Given the “lively” behavior of the structure when subjected to pedestrian loads, it was decided to install a dynamic monitoring system in order to characterize the levels of vibration experienced by this structure during long periods of time [1]. One sensor was adopted and positioned at the mid-span close to the green park at the south-west side. This way, it was possible to install a solar-powered acquisition system similar to “Solar1” described before, by means of a solar panel installed on the outside of the lateral girder (see Figure 5a). The other pieces of hardware are inside a box, which may be accessed using the bridge itself (see Figure 5b). The system produces data files lasting 10 minutes, which results in 144 files or 16.1 MB per day of information, considering a sampling frequency of 40 Hz.

In order to evaluate the autonomy of the solution, Figure 6 shows the periods where valid data exist or do not exist. The horizontal axis represents the total period of 178 days from 5th October 2014 to 31st March 2015, and the vertical axis represents one day divided into 144 intervals of 10 minutes. The failures (dark spots) occurred exclusively due to power issues, especially during the night or on dark days. No problems were detected in the acquisition system itself. This shows that the system worked 90.5% of the time, corresponding to a very good performance of hardware solution, specially taking into account that the acquisition included the winter period.

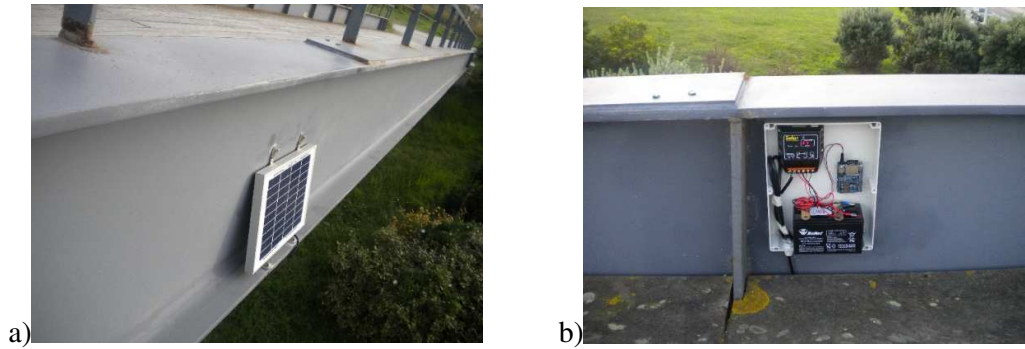


Figure 5: Data acquisition system: a) Solar panel; b) Box with microcontroller, battery and solar controller

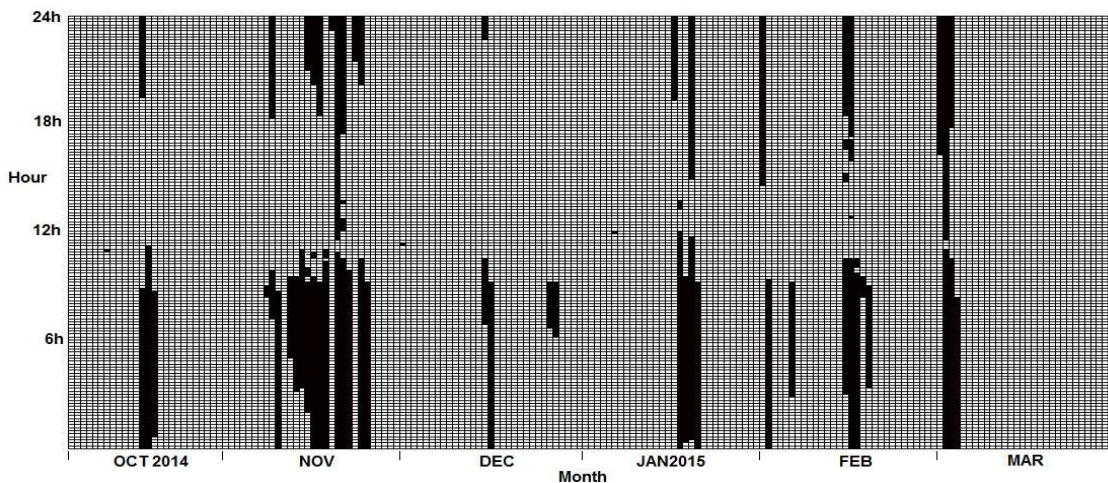


Figure 6: Failures on the signal acquisition detected for 6 months

The data collected by this system allowed characterizing the levels of vibration of the footbridge over time. For instance, Figure 7 shows a map of the amplitude of vibrations during 6 months. It can be seen that the maximum vibration levels induced by pedestrians often reach values between 0.5 and 1.5 m/s^2 approximately, which highlights the “lively” behavior of the structure. In more specific cases, the structure may experience vibration levels higher than 2.5 m/s^2 attributed to intentional resonant loads, inducing intolerable vibrations from the human comfort point of view.

For that reason, it was decided to install two Tuned Mass Dampers (TMDs) to control vibrations of the first vibration mode of the footbridge. The solar-powered system was then updated to include the measurement of four accelerometers and two displacement sensors. Two accelerometers measure the vibration of the footbridge at each side of the deck, and the other two measure the acceleration of the TMD masses. The displacement sensors measure the relative motion between the structure and the TMD masses. By using this instrumentation, it was possible to evaluate the efficiency of the control devices in reducing the vibrations of the structure. Figure 8 represents the maximum vibration levels of the deck before and after the installation of TMDs, where it is clear that TMDs reduced significantly the vibrations associated with the first vibration mode of the structure.

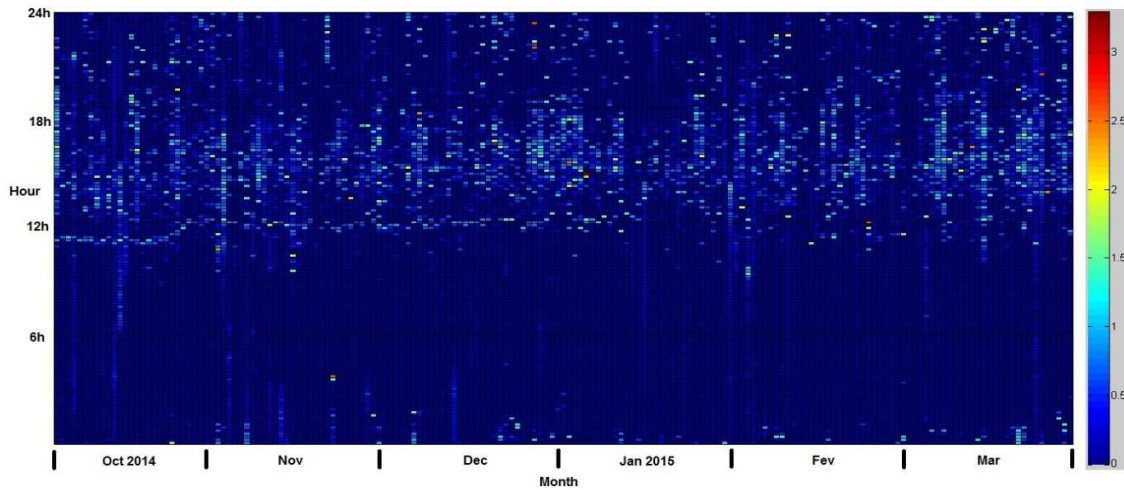


Figure 7: Maximum vibration levels during 6 months

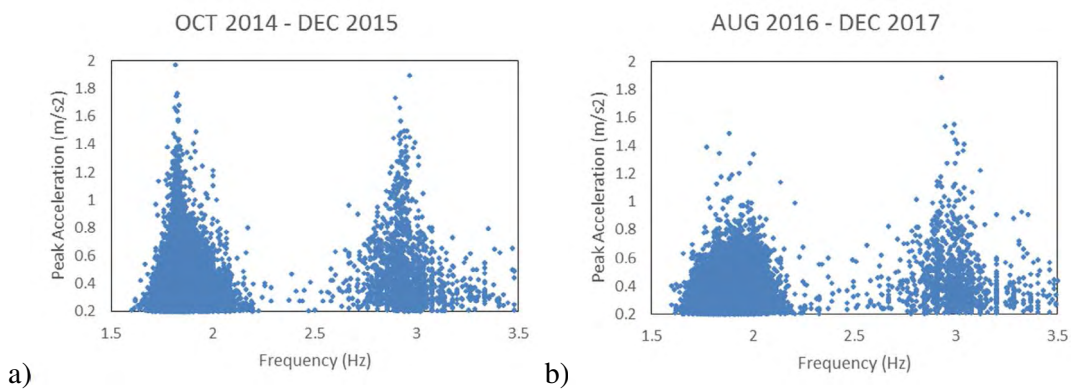


Figure 8: Maximum vibration levels of the footbridge: a) before TMDs; b) after TMDs

The second example of the implementation of solar-powered systems is related to the work developed at Luiz I bridge (Figure 9), which is extensively described in reference [2]. This structure is frequently subjected to extreme events, including crowds of pedestrians walking along the lower and upper deck, as well as pedestrians in athletic races. In the first case, vibrations are lateral and are triggered by a phenomenon known as “lock-in”, characterized by a situation in which a pedestrian crowd, with frequencies randomly distributed around an average value and with random phase shifts, will gradually coordinate at a common frequency (that of the bridge) and enter in phase with the structure motion [3]. In the case of athletic races, the vibrations are essentially vertical, and occur due resonance phenomena between the frequency of the vertical loads directly applied by pedestrians to the pavement and the structure’s natural frequencies.

Because of the unusual levels of vibrations occurred in those situations, there was great interest in installing a dynamic monitoring system in order to quantify those phenomena. Although battery-powered systems have been installed in certain periods, like “Portable 2” devices, this structure has been monitored mainly using solar-powered systems. In particular, “Solar 1” system was used from December 2014 to May 2018, having two “Solar 2” devices measured the vibrations since June 2018.

As an example, figure 10a) shows a time signal of lateral accelerations recorded at mid-span of the lower deck by “Solar 1” system during the feast of St. John 2015. The maximum vibration level reached 0.89m/s^2 , which is which is substantially greater than the recommended maximum value of 0.10m/s^2 . Regarding vertical direction, Figure 10b) shows the measurements made by a “Solar 2” system installed at the lower deck of the bridge. In this case, vibrations reached a maximum value of 3.54 m/s^2 , which is clearly excessive regarding human comfort.



Figure 9: General view of Luiz I bridge

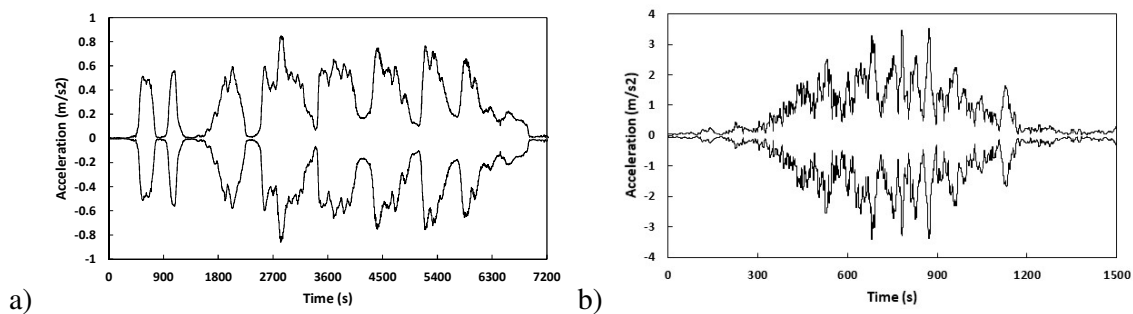


Figure 10: Examples of measurements during extreme events: a) Lateral direction; b) Vertical direction

The use of battery-powered devices in the long term monitoring of structures is relatively more recent. This is because the development of the solution of type “Portable 3” was only finished in 2017. Figure 11a) shows the Arrabida Bridge over Douro River in Porto. It is an arch concrete structure located just down the Luiz I bridge. Since December 2017, two “Portable 3” devices (Figure 11b)) are acquiring dynamic data at Sections S1 and S2 marked in Figure 12. These devices are programed to acquire data in lateral and vertical directions at 60 Hz frequency rate. The batteries allows a continuous functioning for 2 months, which is a period that is adequate to check regularly the condition of the system.

This bridge was studied in past in the context of a rehabilitation that took place in 2003 [4], and since then no dynamic studies were developed. The implementation of this monitoring system is useful to collect data that allow the long term behavior of the structure, as well as to identify modal parameters after the mentioned rehabilitation.

For instance, in Figure 13 the waterfall diagram containing the spectra calculated during one month at section S2 in vertical direction is represented. The natural frequencies can be clearly identified, and the daily variation of some of them, probably due to temperature effects, may be observed. The variation of the traffic intensity may also be noted, which is dependent on the day of the week and the night or day period.

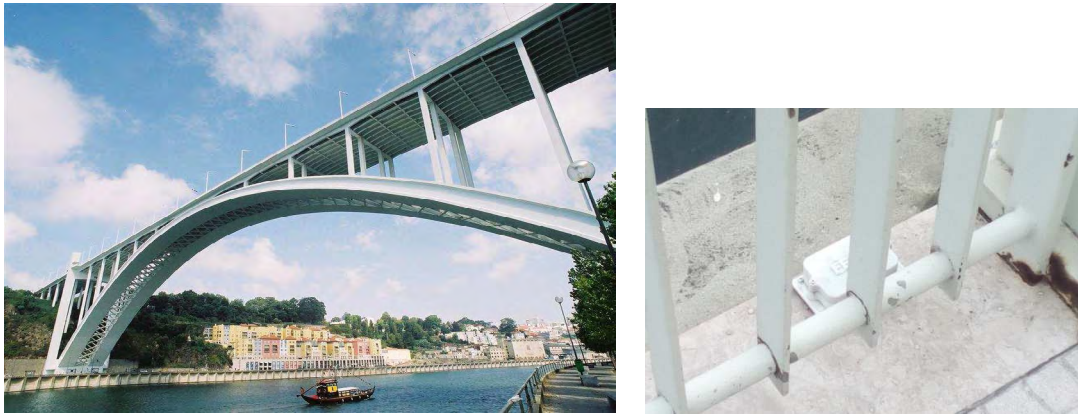


Figure 11: Arrabida Bridge: a) General view; b) Sensor at one measurement section

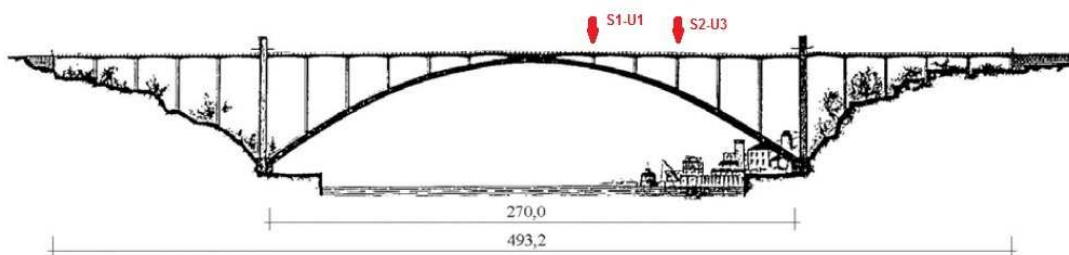


Figure 12: Location of measurement sections over the deck

Another interesting application is the case of the dynamic monitoring of the Ferradosa Railway bridge (Figure 14). Located in Douro, in the north of Portugal, this structure was also submitted to a recent rehabilitation of its concrete piers. The data collected by two “Portable 3” measurement systems located at points 6 and 14 (see Figure 15), will allow understanding how the dynamics of the bridge changed since the previous measurement campaign occurred in 2016 [5].

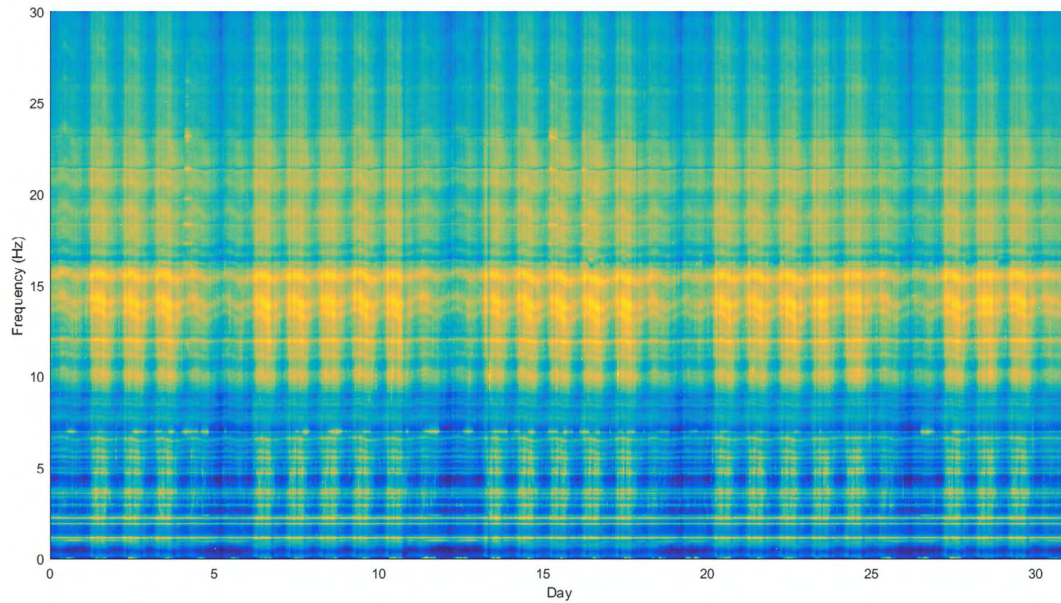


Figure 13: Waterfall diagram during May 2018 – section S2 vertical direction

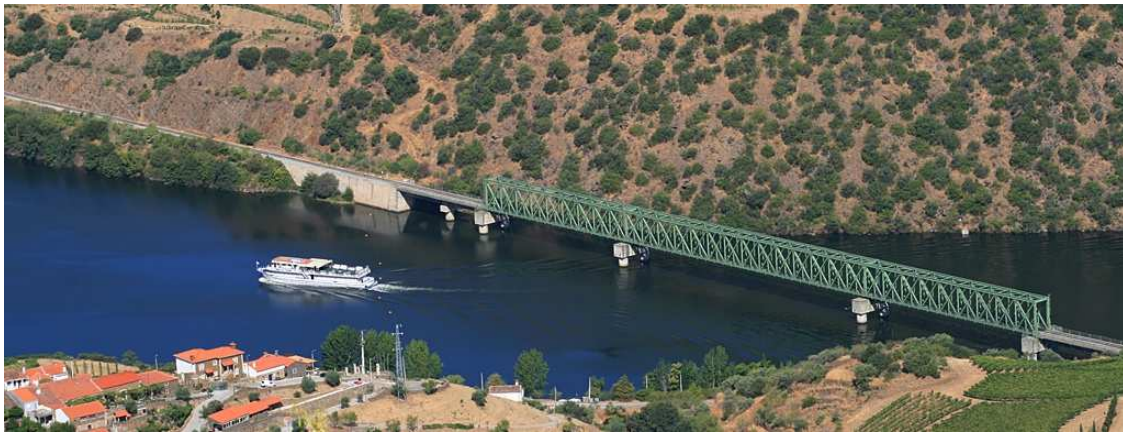


Figure 14: Ferradosa railway bridge

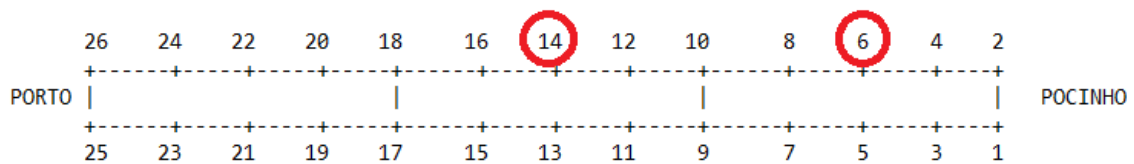


Figure 15: Location of measurement points

5 CONCLUSIONS

This paper describes the work developed at CONSTRUCT – ViBest research group located in FEUP, on the topic of a new generation of dynamic monitoring systems applied to Civil Structures. It was pointed out that some traditional systems have some drawbacks, particularly related to the lack of robustness, complexity, and high cost. In the other hand, simpler systems based on microcontrollers may substitute that classical systems in certain applications, offering some advantages like the ease of installation and operation, less maintenance and attractive cost.

In this context, this document presents several generations of measurement devices based on battery-powered solutions and solar-powered solutions. In any case, the concern in minimizing the power consumption of the systems is always present, aiming longer autonomies. Therefore, the data transmission process needs to be adequate, depending on the objectives of the monitoring.

Some examples demonstrates the utility and the feasibility of using such systems in actual structures. In many practical situations, the results obtained with these systems can be comparable to those obtained with traditional systems.

ACKNOWLEDGEMENT

This work was financially supported by: UID/ECI/04708/2019- CONSTRUCT - Instituto de I&D em Estruturas e Construções funded by national funds through the FCT/MCTES (PIDDAC).

REFERENCES

- [1] Moutinho, C., Magalhães, F. and Caetano, E. Analysis of the vibration levels of a slender footbridge measured by a continuous dynamic monitoring system. 5th ECCOMAS Thematic Conference on Computational Methods in Structural Dynamics and Earthquake Engineering, Crete Island, Greece, (2015).
- [2] Moutinho, C. and Cunha, A. Continuous dynamic monitoring of large human-induced vibrations at the Luiz I Bridge. Submitted to structural control and health monitoring, (2019).
- [3] SÉTRA - service d'Études techniques des routes et autoroutes. Guide méthodologique, Passerelles piétonnes – Évaluation du comportement vibratoire sous l'action des piétons. Ministère des transports de l'équipement du tourisme et de la mer, republique française (2006).
- [4] Rodrigues, J. Stochastic modal identification - Analysis methods and applications in civil engineering structures, PhD thesis, FEUP (2004).
- [5] Henrique, J. numerical modeling and modal characterization of the ferradosa bridge, MSc thesis, FEUP (2016).

ELECTROMECHANICAL IMPEDANCE METHOD APPLIED TO DEBONDING IDENTIFICATION OF NSM FRP STRIPS IN CONCRETE

RICARDO PERERA^{*}, LLUIS TORRES[†], CRISTINA BARRIS[†] AND MARTA BAENA[†]

^{*} Department of Mechanical Engineering
Technical University of Madrid
José Gutiérrez Abascal 2, 28006 Madrid, Spain
e-mail: ricardo.perera@upm.es

[†] Analysis and Advanced Materials for Structural Design (AMADE)
Polytechnic School, University of Girona, Spain
email: lluis.torres@udg.edu

Key words: NSM-FRP RC beams, EMI method, Debonding, Clustering.

Abstract. In the last few decades, strong research efforts have been devoted to the continuous structural condition assessment for the civil engineering infrastructure. Structural Health Monitoring (SHM) traditionally refers to the process of implementing monitoring systems to measure structural responses in real-time and to identify anomalies and/or damage at early stages.

Within the field of strengthening of reinforced concrete (RC) structures with fiber reinforced polymer (FRP) composite materials, some previous studies have been devoted to the identification of damage at their earliest stages on externally bonded (EB) FRP reinforcement. However, until now, to the knowledge of the authors, no previous SHM work was focused on the near surface mounted (NSM) technique using FRP. In the NSM-FRP methodology, the FRP reinforcement is installed into slits cut into the concrete cover using cement mortar or epoxy as bonding materials. Its use has several advantages over the EB FRP technique such as protection, improved bond, better aesthetics and surface preparation; because of it, it has become an attractive method as an effective alternative for strengthening RC structures.

In this work, some relevant cluster-based methods and their adaptation to electromechanical impedance (EMI) based damage detection in NSM FRP strengthened structures SHM are developed.

1 INTRODUCTION

Over the last years, extensive research has been conducted on the strengthening of reinforced concrete (RC) structures using externally bonded fiber-reinforced polymer (FRP) laminates; the technology has also been implemented in a large number of practical projects world-wide and different structural health monitoring (SHM) approaches to identify prematurely the more critical brittle failure modes have also been proposed [1, 2]. More recently, near-surface

mounted (NSM) FRP reinforcement has attracted an increasing amount of research as well as practical applications [3]. In the NSM method, grooves are first cut into the concrete cover of an RC element and the FRP reinforcement is bonded therein with an appropriate groove filler (typically epoxy paste or cement grout). NSM FRP reinforcement has a number of advantages over externally bonded FRP reinforcement, such as more reduced risk of debonding and damage due to accidental impact and vandalism. However, although debonding failures are less likely a problem with NSM FRP compared with externally bonded FRP, they may still significantly limit the efficiency of this technology and, therefore, the implementation of SHM techniques able to detect bar-concrete interfacial debonding at their earliest stages results crucial to avoid catastrophic failures.

SHM based on the electromechanical impedance (EMI) provided by piezoelectric ceramic (PZT) sensor-actuators has been used in numerous applications to detect damage [4-7]. The electrical impedance of the PZT can be directly related to the mechanical impedance of the host structural component where the PZT transducers are attached. Since the structural mechanical impedance will be affected by the presence of structural damage, comparisons of admittance (inverse of impedance) spectra at various times during the service period of the structure can be used as damage indicator. Any change in the spectra might be an indication of a change in the structural integrity. This technique appears to be very interesting for our application since the electrical impedance is measured at high frequencies which means high sensitivity to minor damage as desired for our purpose. Additionally, due to their size and lightness PZT sensors are non-intrusively attached and do not affect the performance of the structure.

Therefore, impedance signatures changes captured with PZTs might be used for debonding identification in NSM FRP reinforcement. The use of different statistical metrics, such as the root mean square deviation (RMSD), might be applied to characterize damage from changes of the impedance signatures. However, the use of a single type of metric for EMI based identification has some limitations regarding damage location and severity. Clustering is an interesting technique within the domain of unsupervised learning which can become very useful for anomaly detection. By using a clustering approach, data points that are similar tend to be grouped in different subsets in such a way that the normal condition of a structure is characterized as clusters and the damage detection strategy is based on an outlier detection approach. Hierarchical clustering analysis has been explored in this work as a tool for debonding detection in RC beams with NSM FRP using the EMI technique.

2 IMPEDANCE-BASED STRUCTURAL HEALTH MONITORING

PZT patches are used as high-frequency actuator/sensors in SHM. Electrical signals from the sensor attached to structure are measured using the coupling effect between the electrical and mechanical impedance of system. Any change in the stiffness of the structure such as damage, material properties, modifies mechanical impedance of structure and consequently affects the electrical impedance of sensor. Therefore, by monitoring the variation of the electrical impedance of the PZT patch, information about the damage of the structure can be obtained.

The impedance signature (or admittance Y) at each sensor is obtained using the one-dimensional analytical model proposed by Liang et al. [8] as follows

$$Y(\omega) = j\omega \frac{b_{PZT} l_{PZT}}{e_{PZT}} (\bar{\epsilon}_{33}^T - \frac{Z_s(\omega)}{Z_s(\omega) + Z_a(\omega)} d_{31}^2 \bar{Y}_{11}^E) \quad (1)$$

where ω is the frequency, d_{31} is the piezoelectric strain constant between the z and x directions at zero stress, $\bar{Y}_{11}^E = Y_{11}^E(1 + \eta i)$ is the complex Young's modulus of the PZT in the 1-1 (x) direction, η denotes the mechanical loss factor $\bar{\epsilon}_{33}^T = \epsilon_{33}^T(1 - \delta j)$ is the complex electric permittivity of the PZT at constant stress, δ is the dielectric loss factor, j is the imaginary unit and b_{PZT} , l_{PZT} and e_{PZT} are the length, the width and the thickness of the PZT sensor, respectively. Furthermore, $Z_a(\omega)$ and $Z_s(\omega)$ represent the mechanical impedances of the PZT and the host structure. The first one depends mainly on the PZT properties. Besides, the mechanical impedance of the structure is computed as follows [6]

$$Z_s(\omega) = j \frac{E_p b_{PZT} d_{31}^2 V(\omega)}{\omega u_s(\omega)} \quad (2)$$

where the axial displacement, $u_s(\omega)$, of the structure in frequency domain is obtained numerically.

Such as observed in Eq.(2), mechanical impedance of a structure is related to the mode functions and natural frequencies of the structure.

Eq.(1) corresponds to a 1D model of PZT and cannot be applied or generalized for all cases. Therefore, we will restrict our study to simplified 1D models.

Conventionally, SHM based on EMI assesses the integrity of a mechanical structure by observing some of the changes in the electromechanical impedance of the PZT between two different stages. For it, a scalar metric such as the root mean square deviation (RMSD) is used

$$RMSD(\%) = \sqrt{\frac{\sum_{i=1}^n [\text{Re}(Z_0(\omega_i)) - \text{Re}(Z_1(\omega_i))]^2}{\sum_{i=1}^n \text{Re}(Z_0(\omega_i))^2}} \cdot 100 \quad (3)$$

where $Z_0(\omega_i)$ is the impedance of the PZT measured at the healthy condition of the structure and $Z_1(\omega_i)$ is the corresponding value at a subsequent stage, which might agree with a post-damage stage, at the i th frequency point; n is the number of frequency points. From Eq.(3), the larger the difference between the baseline reading and the subsequent reading, the greater the value of the RMSD index denoting changes of structural dynamic properties which can be due to damage.

3 CLUSTERING ANALYSIS

Different alternatives exist to perform the clustering. In this work, we will use a hierarchical clustering. By using a hierarchical clustering approach, each one of the different observations is initially treated as a single cluster. Subsequently, using an iterative procedure nearby observations are merged into a new bigger cluster; then, successively, new nearby points are added to the nearest group and so on. In this sense, the algorithm uses a bottom-up or agglomerative strategy. The goal of this strategy is to generate a hierarchy of clusters organized into different levels of membership [9] by using the average-linkage method [10]. The steps to follow with this algorithm are:

- i. Find the similarity or dissimilarity between every pair of objects in the data set. This

- is done by computing the distance between objects.
- ii. Group the objects into a binary, hierarchical cluster tree using their distance as criterion. The clusters generated previously are then linked again by pairs under the same criterion, forming a new hierarchical tree. The procedure is continuously repeated until all the dependencies are established.
 - iii. Cut the hierarchical tree into clusters. A threshold is assigned to each branch of the tree, so that all the objects below that threshold are grouped into the same cluster, which creates a partition of the data.

In the first step, there are several ways to calculate the distances between every pair of objects. In this work, the Euclidean distance has been used

$$d_{st}^2 = (\tilde{x}_s - \tilde{x}_t)(\tilde{x}_s - \tilde{x}_t)' \quad (4)$$

where \tilde{x}_s and \tilde{x}_t are vectors containing different data sets.

4 APPLICATION

4.1 Description of the experimental test

An experimental study was carried out on one NSM-FRP RC specimen. In the test programme performed, the strengthened beam was subjected to a series of four-point increasing static load tests with the purpose of gradually introduce deterioration into the specimen (Figure 1). The material properties were assigned as follows: (a) for concrete, the elastic moduli and the compressive strength were taken to be $E = 26$ GPa and $f_c = 30$ MPa; (b) for steel reinforcement, the elastic moduli and elastic limit were taken to be $E = 210$ GPa and $f_y = 510$ MPa; (c) for the reinforcement, one CFRP bar with $E = 170$ GPa and tensile strength of 2500 MPa was inserted into the concrete cover.

Impedance measurements were captured from an array of eight PZT transducers once the beam has been unloaded after each static test and before loading it again. Two different transducers' types and technologies of integration into the test specimens were applied. Two P-876.A12 DuraAct Patch transducers of dimensions 61 mm x 35 mm x 0.5 mm and six P-876.SP1 transducers of dimensions 16 mm x 13 mm x 0.5 mm, both made by Piceramic, were used [11]. P-876.A12 transducers (PZT1 and PZT2) were bonded directly to the external face of concrete beam (Figure 2). Additionally, from the six smaller transducers, two were attached to the concrete surface (PZT3 and PZT4) while the other four were embedded into the structure by bonding them directly on the FRP bars/laminates (PZT6 to PZT9).

Impedance tests were performed by sweeping a wide frequency band of 10–100 kHz. From the healthy initial stage (D0), five different loading stages were considered (D1 to D5). Before measuring the impedances, the beam was previously unloaded after each loading stage.

4.2 Results

Figure 3 shows the hierarchical trees obtained with the hierarchical clustering analysis for the eight sensors. From this figure, it is clear that, considering their performance during the analysis, five groups of sensors might be defined, PZT1+PZT2, PZT3+PZT4, PZT6+PZT9,

PZT7 and PZT8. The first group, PZT1+PZT2, corresponds to the bigger sensors which are located more distant to the loading points. The variability of these two sensors according to the different damage stages is due to the appearance and growth of the external cracks in the concrete surface. For the second group, PZT3+PZT4, damages D3 and D4 are linked together and clearly distinguished from the remaining damage stages. which means they are identified with a similar severity. It is due the growth of a long crack near to these two sensors in the last two loading stages. For sensors 6 and 9, D5 is distinguished from the previous stages and the remaining damages in this region; additionally, D0 and D1 stages are clustered together and independently of D2, D3 and D4. Big cracks were identified in D5 very close to these sensors. Close to sensor 7, from the second load step, some cracks concentrate and grow progressively with the subsequent load steps. Failure was originated from this area. The area surrounding sensor 8 is, in general, little damaged.

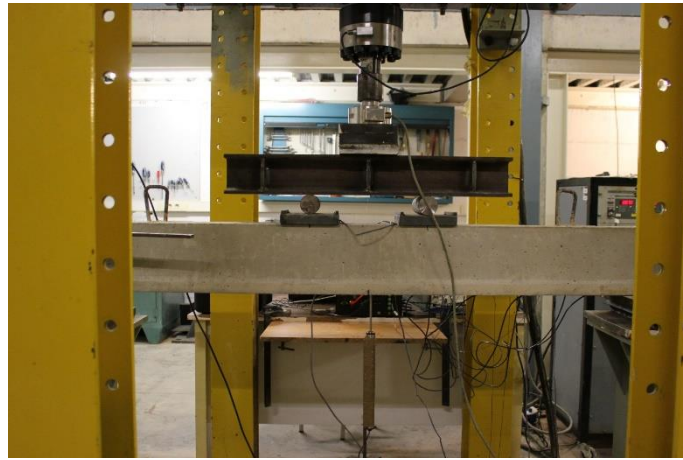


Figure 1: Experimental set-up

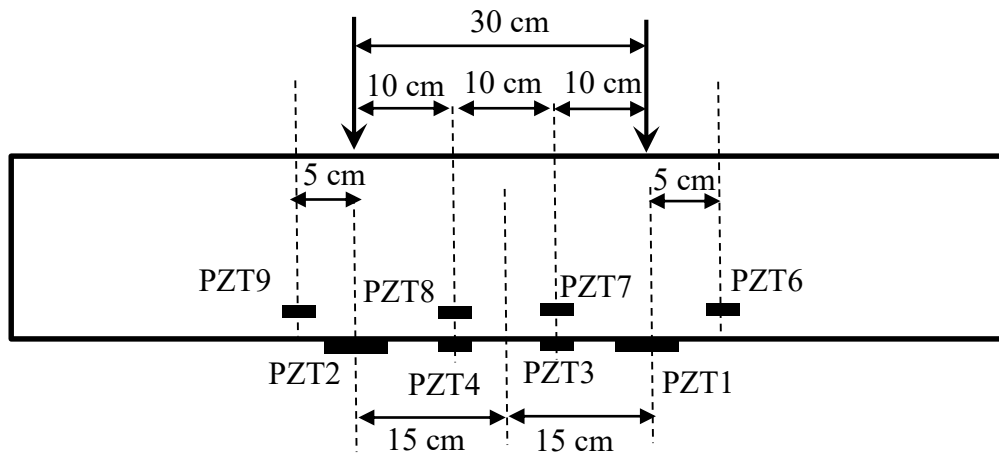


Figure 2: PZT sensor location for the strengthened beam

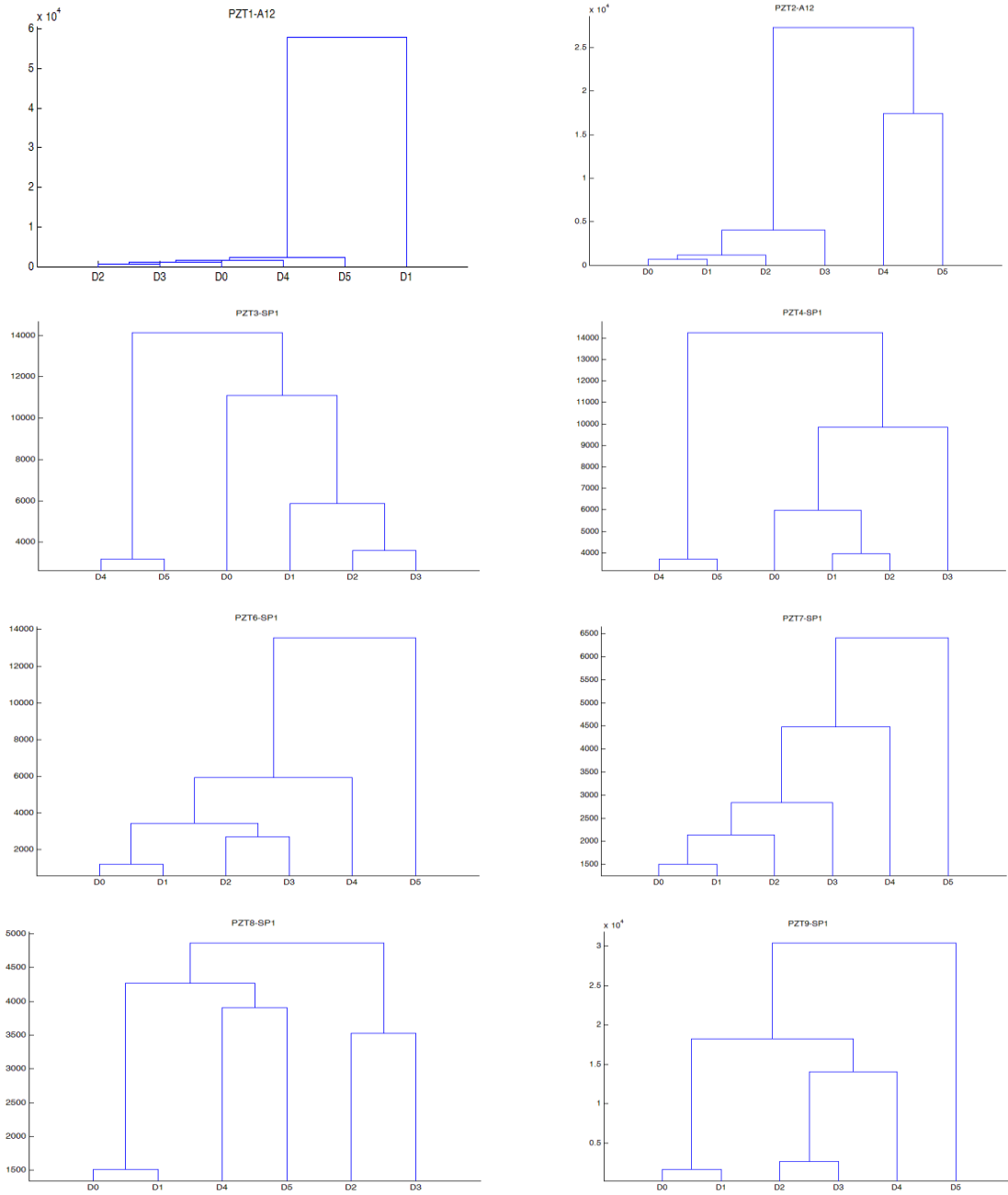


Figure 3: Hierarchical trees

5 CONCLUSIONS

A clustering approach has been proposed to detect brittle debonding in NSM FRP-strengthened RC beams. The approach extracted information from the electromechanical impedance spectrum measured with PZT sensors distributed in different locations of the

inspected beam. The measured information from the entire frequency range is used as the input to a clustering algorithm in order to identify subtle differences between the normal signals and distorted ones. These differences can be associated to abnormal behaviours derived of the appearance of minor damage or debonding. With this method, the evolution of the damage in a complex structure as that used in this work can be tracked in a fast and visual way.

ACKNOWLEDGEMENTS

The writers acknowledge the support for the work reported in this paper from the Spanish Ministry of Science, Innovation and Universities (project BIA2017-84975-C2-1-P).

REFERENCES

- [1] Zienkiewicz, O.C. and Taylor, R.L. *The finite element method*. McGraw Hill, Vol. I., (1989), Vol. II, (1991).
- [2] Idelsohn, S.R. and Oñate, E. Finite element and finite volumes. Two good friends. *Int. J. Num. Meth. Engng* (1994) **37**:3323-3341.
- [1] Sevillano, E.; Sun, R.; Gil, A.; Perera, R. Interfacial crack-induced debonding identification in FRP strengthened RC beams from PZT signatures using hierarchical clustering analysis. *Compos. Part B Eng.* 2016, **87**, 322–335.
- [2] Sun, R.; Sevillano, E.; Perera, R. Identification of intermediate debonding damage in FRP-strengthened RC beams based on a multi-objective updating approach and PZT sensors. *Compos. Part B Eng.* 2017, **109**, 248–258.
- [3] De Lorenzis, L.; Teng, J.G. Near-surface mounted FRP reinforcement: An emerging technique for strengthening structures. *Compos Part B: Eng.* 2007, **38**, 119-143.
- [4] Perera, R.; Pérez, A.; García-Diéguez, M.; Zapico-Valle, J.L. Active wireless system for structural health monitoring applications. *Sensors* 2017, **17**, 2880.
- [5] Min J, Park S, Yun CB, Lee CG, Lee C. Impedance-based structural health monitoring incorporating neural network technique for identification of damage type and severity. *Eng Struct* 2012; **39**:210-220.
- [6] Giurgiutiu V, Zagrai AN, Bao JJ. Piezoelectric wafer embedded active sensors foraging aircraft structural health monitoring. *Struct Health Monit* 2002;**1**:41-61.
- [7] Xu DY, Cheng X, Huang SF, Jiang MH. Identifying technology for structural damage based on the impedance analysis of piezoelectric sensor. *Constr Build Mater* 2010; **24**:2522-2527.
- [8] Liang, C.; Sun, F.P.; Rogers, C.A. Coupled electro-mechanical analysis of adaptative material system-determination of the actuator power consumption and system energy transfer. *J. Intell. Mater. Syst. Struct.* 1994, **5**, 12:20.
- [9] Cai R, Zhang Z, Tung KH, Dai C, Hao Z. A general framework of hierarchical clustering and its applications. *Information Sciences*, 2014, **272**, 29-48.
- [10] Sokal RR, Michener CD. A Statistical Method for Evaluating Systematic Relationships. *The University of Kansas Science Bulletin*, 1958, **38**, 1409-1438.
- [11] PI Piezo Technology. P-876 DuraAct Patch Transducer. Available online:<https://www.piceramic.com/en/products/piezoceramic-actuators/patch-transducers/> (accessed on April 2019).

LEAST-SQUARES REVERSE TIME MIGRATION FOR FLAW CHARACTERISATION USING ULTRASONIC BULK WAVES

J. RAO^{1*} AND Z. FAN²

¹Chair for Computation in Engineering
Technical University of Munich
Arcisstr. 21, 80333, Munich, Germany
* e-mail: jingrao@tum.de

² School of Mechanical and Aerospace Engineering
Nanyang Technological University
50 Nanyang Avenue, Singapore

Key words: Least-squares reverse time migration, ultrasonic imaging, flaw characterization.

Abstract. Accurate detection and characterization of flaws are very important in the assessment of structural integrity of critical structures in aerospace and nuclear industry. In this paper, an effective ultrasonic imaging technique based on least-squares reverse time migration (LSRTM) is developed for imaging flaws. Reverse time migration (RTM) is a powerful wave-equation-based approach and it has the ability to account for rapid spatial velocity variations and to utilize all wavefront information. It is based on cross-correlating the forward wavefield with the back-propagated wavefield scattered from flaws. To achieve images with better quality, the solution can be obtained by iteratively finding an image generating the modeled data which can best match the measured data in a least-squares sense, i.e. least-squares migration (LSM). Combining RTM and LSM, the LSRTM algorithm is applied to the measured data from the virtual experiment and the physical laboratory experiment, and the results show high-quality reconstructed images for flaw identification.

1 INTRODUCTION

Reliable inspection of flaws is very important in the assessment of structural integrity of critical parts in aerospace and nuclear industry. The type, size and shape of the flaw can assist with the prediction of the remaining life of the parts. A lot of ultrasonic non-destructive evaluation techniques have been shown to be useful for characterising flaws [1].

There are different ultrasonic sizing techniques, e.g. amplitude, temporal, inversion and imaging, which have been reviewed in detail in [2]. In this paper, only imaging methods are presented. Ultrasonic imaging is usually based on ultrasonic arrays, which can be operated by using physical beam forming or full matrix capture (FMC), where the data obtained from all source-receiver pairs is captured [3]. With the FMC data, beam forming or focusing can be used in post-processing [4]. For example, the popular post-processing methods can be used to size an embedded flaw with a regular shape by measuring the distance between two tips in a focused image [5], or specular reflections from the surface of the surface-breaking flaw [6]. However, characterizing irregularly shaped flaw remains challenging as singly-scattered, refraction and diffraction waves from the flaw have to be considered.

In this paper, the least-squares reverse time migration (LSRTM) proposed in geophysics [7] is introduced in ultrasonic imaging to size the flaw with irregular shapes. Reverse time migration (RTM) technique is based on a two-way wave equation, which forward extrapolates the wavefield from the source and backward extrapolates the scattered wavefield from the receiver. Extrapolating the time-reversed scattered wavefields by using the finite difference method focuses the wave energy toward damaged regions. With the cross-correlation imaging condition [8], the flaw image can be formed via extrapolation. To reduce the artifacts and improve the quality of the image, least-squares migration (LSM) is proposed to match the amplitudes of the modeled data with the measured data via an iterative inversion scheme [9]. Compared with conventional methods based on the signal diffracted from the flaw tip, the LSRTM algorithm uses the full wavefield with correct amplitude and phase information, and thus it is capable to characterize irregular-shaped flaws.

This paper is organized as follows. The theory of the LSRTM algorithm based on the acoustic approximation is described in Section 2. Finite element modeling and experimental procedures are presented in Section 3. In Section 4, the LSRTM algorithm is applied to the measured data from a virtual experiment as well as a physical laboratory experiment. Conclusions are summarized in Section 5.

2 LEAST-SQUARES REVERSE TIME MIGRATION

The process of reverse-time migration (RTM) contains three steps: (1) the forward wavefield extrapolation from the source, (2) the extrapolation of time-reversed scattered wavefield from the receiver, and (3) imaging using cross-correlation. Details of the three steps are included in [10]. To improve the image quality, the least-squares migration (LSM) is used to match the amplitudes of the modeled data with the measured data. Combining RTM and LSM, the LSRTM algorithm based on 2D acoustic equation in frequency-domain with the constant density is presented in this work.

The forward Born modeling can be compactly given by a matrix-vector multiplication [11]

$$\mathbf{d} = \mathbf{L}\mathbf{m}, \quad (1)$$

where \mathbf{L} is the forward Born modeling operator which linearly relates the reflectivity model \mathbf{m} to the measured scattered data \mathbf{d} . Here, each element of the reflectivity model \mathbf{m}_v can be defined as

$$\mathbf{m}_v(\mathbf{x}) = \frac{\delta v(\mathbf{x})}{v_0(\mathbf{x})}. \quad (2)$$

The migrated reflectivity model \mathbf{m}_{mv} can be calculated by using the adjoint \mathbf{L}^T of the forward Born modeling operator to the measured data \mathbf{d} [12]

$$\mathbf{m}_{mv} = \mathbf{L}_v^T \mathbf{d}, \quad (3)$$

where the adjoint \mathbf{L}_v^T is the migration operator related to velocity.

The aim of LSM is to obtain the reflectivity model \mathbf{m}_v by minimizing the difference between the forward modeled data $\mathbf{L}_v \mathbf{m}_v$ and the measured data \mathbf{d} in a least-squares sense

$$f(\mathbf{m}_v) = \frac{1}{2} \|\mathbf{L}_v \mathbf{m}_v - \mathbf{d}\|^2. \quad (4)$$

The minimum of $f(\mathbf{m}_v)$ is achieved when the reflectivity model \mathbf{m}_v satisfies

$$\mathbf{m}_v = (\mathbf{L}_v^T \mathbf{L}_v)^{-1} \mathbf{m}_{mv}, \quad (5)$$

Table 1: Conjugate gradient approach for solving $\mathbf{H}\delta\mathbf{m}_{v0} = \mathbf{m}_{mv}$.

1. Starting from initial $\delta\mathbf{m}_{v0}$ and setting the residual vector $r_0 = \mathbf{H}\delta\mathbf{m}_{v0} - \mathbf{m}_{mv}$, initial search direction q_0 is set as r_0 , i. e. $q_0 = -r_0$ and $k = 0$.
2. The scalar $\alpha^{(k)}$ is calculated by using the relationship $\alpha^{(k)} = \frac{r^{T(k)}r^{(k)}}{q^{T(k)}\mathbf{H}q^{(k)}}$.
3. The calculation of $\delta\mathbf{m}_v^{(k+1)}$ is expressed as $\delta\mathbf{m}_v^{(k+1)} = \delta\mathbf{m}_v^{(k)} + \alpha^{(k)}q^{(k)}$.
4. Then, the next residual vector $r^{(k+1)}$ is expressed as $r^{(k+1)} = r^{(k)} + \alpha^{(k)}\mathbf{H}q^{(k)}$.
5. The next step is to compute $\beta^{(k+1)}$, which is used to search the next direction $\beta^{(k+1)} = \frac{r^{T(k+1)}r^{(k+1)}}{r^{T(k)}r^{(k)}}$.
6. The next search direction $q^{(k+1)}$ is obtained by using this scalar $\beta^{(k+1)}$, $q^{(k+1)} = -r^{(k+1)} + \beta^{(k+1)}q^{(k)}$.
7. Then, $k = k + 1$, the next scale $\alpha^{(k+1)}$ is computed by using the obtained search direction $q^{(k+1)}$ and this process is repeated.

where $\mathbf{L}_v^T \mathbf{L}_v$ is the migration Green's function (or Hessian matrix \mathbf{H}). The Hessian matrix of $\mathbf{L}^T \mathbf{L}$ or \mathbf{H} is usually not an identity matrix, and the main diagonal elements are nonuniform and the off-diagonal elements are nonzero [13].

Directly solving equation (5) needs to explicitly store the Hessian matrix and calculate its inverse, which is memory-consuming and computationally expensive. Equivalently, \mathbf{m}_v can be iteratively obtained by solving

$$\mathbf{H}\mathbf{m}_v = \mathbf{m}_{mv}, \quad (6)$$

using a conjugate gradient approach. The implementation flowchart is shown in Table 1. In this paper, implementing the frequency domain LSRTM algorithm with constant density depends on the improved scattering-integral method [11]. The forward Born modeling and the adjoint migration model are based on matrix-vector multiplications, which are carried out by accumulating decomposed vector-scalar products without explicitly constructing or storing matrices.

3 TESTING APPROACH

3.1 Finite element simulation

As a first step for validation of the approach instead of a physical experiment, a 'virtual' experiment is conducted. To this end, 2D finite element simulations implemented in ABAQUS are performed in an aluminum sample (longitudinal wave velocity=6190 m/s, density=2700 kg/m³ and Poisson's ratio=0.33) with the dimension of 200 mm \times 50 mm, as shown in Figure 1. Four-node plane strain elements with the size of 0.1 mm are used in the mesh. A flaw with V shape is modeled by removing elements from the mesh. The linear array with 64 elements is placed on the top surface, which are spaced at a fixed pitch of 1.5 mm. A 2-cycle Hann-windowed tone-burst signal with a centre frequency of 2 MHz is excited by the array. The FMC data are collected from this sample.

In this case, the signals from the scattering of the flaw will overlap with the reflection from the backwall, and therefore likely to be shadowed. In the virtual experiment, one possible way of extracting scattered field from the flaw is to obtain the backwall reflection from a flaw-free sample and then subtract it from the overall signal, which is often called the baseline subtraction. However, this way is not practical in real case, and thus another method will be described in the real physical experiment in Section 3.2. It

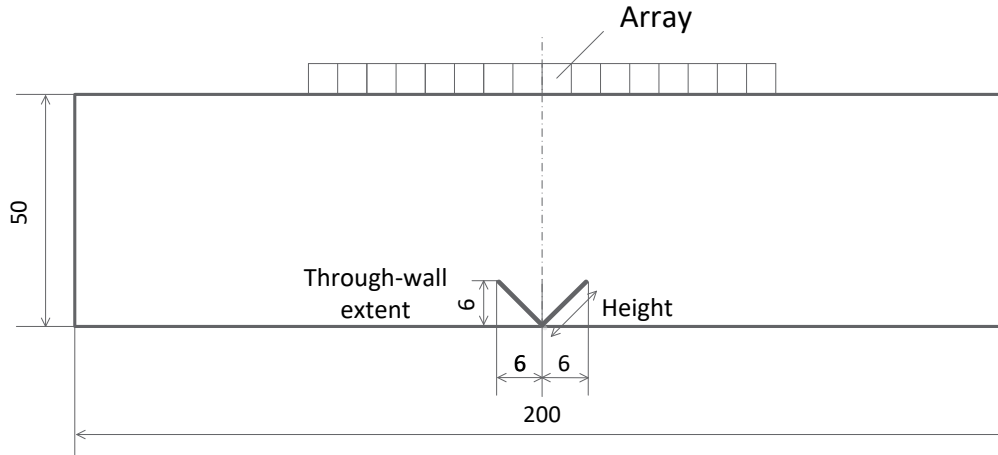


Figure 1: The configuration of an array and a V shaped flaw. The unit is mm.

should be noted that only longitudinal waves are considered in this work, and they can be easily gated from time of arrivals.

3.2 Experimental setup

As a second step for validation a physical experiment is investigated. The experimental setup is shown in Figure 2. The real physical experiment was carried out in a 25 mm thick aluminum block with the height of 50 mm and the width of 200 mm. A V shaped flaw with the width of 1 mm and the through-wall extent of 6 mm was machined in the block, as shown in Figure 2. The ultrasonic array with a central frequency of 2 MHz manufactured by Guangzhou Doppler Electronic Technologies Co., Ltd was used to generate and measure signals. A 5-cycle Hann-windowed tone-burst signal centered at the frequency of 2 MHz was generated from a phased array controller (Lecoeur Electronique, France).

In real inspection, the method of baseline subtraction is not practical because it is not possible to obtain a flaw-free copy of the structure. Therefore, FMC subtraction developed by Zhang *et al.* [14] is used to remove the backwall reflections when flaw signals overlap with backwall reflections. In FMC subtraction, when the element pairs are with the same lateral separation, the length of ray paths of backwall reflections are the same but ray paths of flaw signals are different (see Figure 4(a) in [14]). This means that signals from the backwall have the same arrival time and amplitude compared with the ones from the flaw. Therefore, by subtracting the estimated backwall reflection from the total field, the signal scattered from the flaw can be extracted. Figure 3(a) shows a typical contour plot of the displacement signals measured over all receivers in the aluminum block with the flaw in the physical laboratory experiment. The scattering of longitudinal waves caused by the flaw is separated from the measured signals by removing Rayleigh waves with the gating function and by eliminating backwall reflections with FMC subtraction, as shown in Figure 3(b). The extraction of the flaw signals (see Figure 3(b)) achieved by gating function and FMC subtraction is used in the LSRTM technique to directly image the structure.

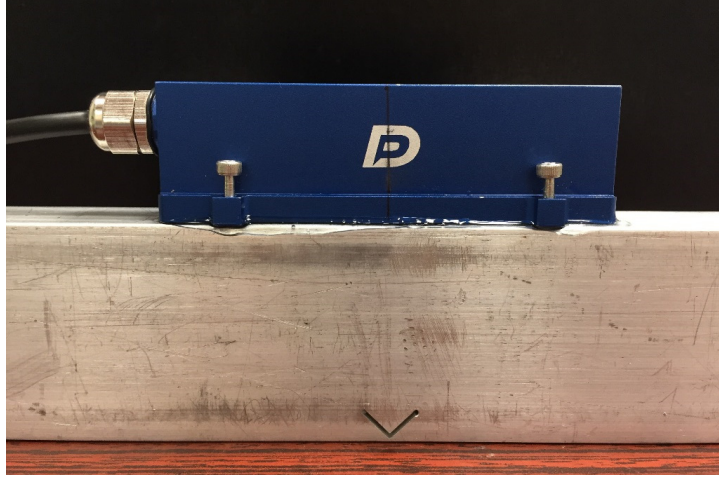


Figure 2: Experimental setup.

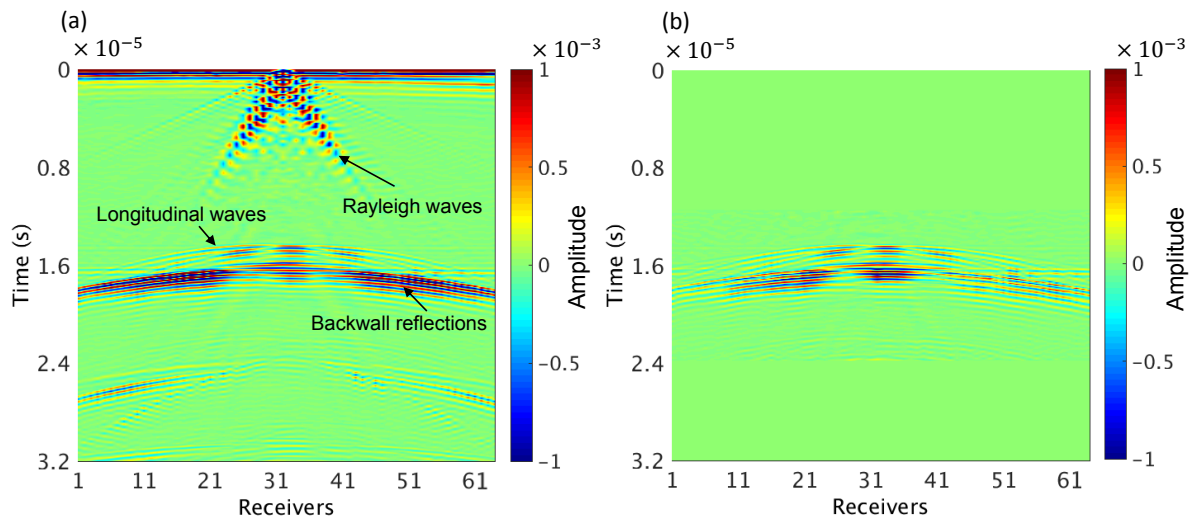


Figure 3: (a) Contour plot of measured displacement excited in the array element 32 shown in Figure 2. (b) Scattered signals caused by the V shaped flaw after time gating and backwall subtraction.

4 RESULTS

The sample with a V shaped flaw is considered in this work, as shown in Figure 1. Post-processing of the LSRTM images after 10 iterations is done by Laplacian filtering, which is applied to suppress low-wavenumber artifacts. Figures 4(a) and (b) show final images obtained from the virtual experiment and the physical laboratory experiment, respectively. The LSRTM algorithm is performed for 15 frequencies from 0.6 MHz to 3.4 MHz in the virtual experiment, and for 8 frequencies from 1.3 MHz to 2.7 MHz in the physical laboratory experiment, with a frequency interval of 0.2 MHz. The forward model is built by using homogeneous background.

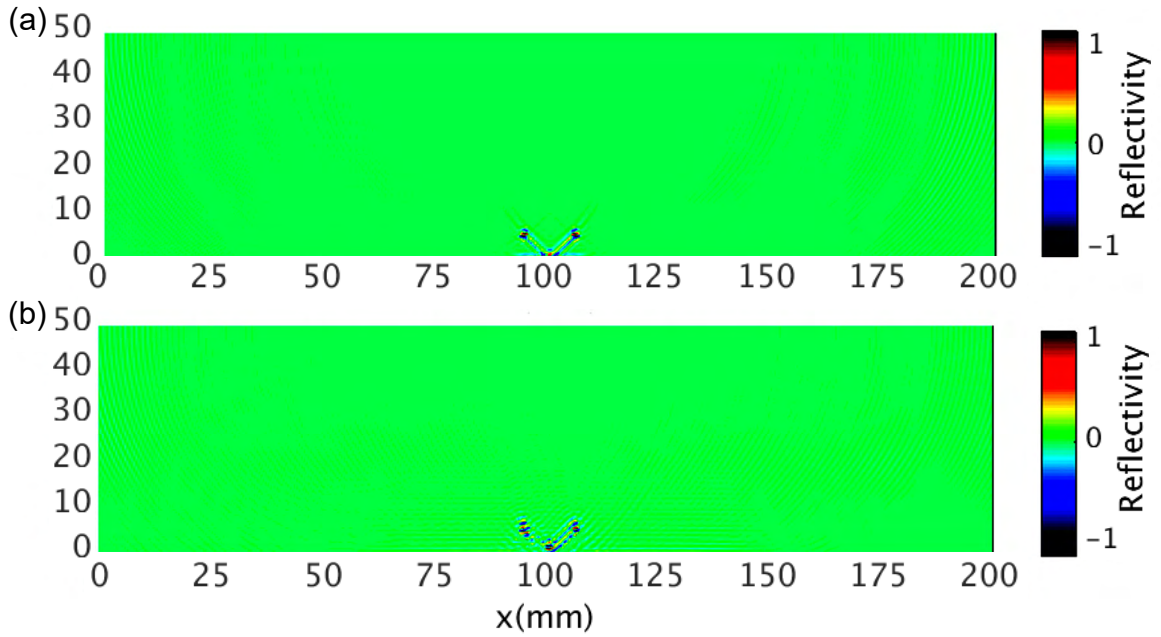


Figure 4: LSRTM images of a V shaped flaw from (a) the virtual experiment and (b) the physical laboratory experiment.

It can be seen from figures that high-quality images are achieved by using LSRTM algorithm, with good reconstruction of the location and the shape of the V shaped flaw in both cases. A clear image is obtained in the virtual experiment, however, the reconstructed width of the flaw is slightly wider than the true model. The reason could be that scattered signals which overlap with mode conversions cannot be accurately separated by using time gating and mode conversions are not considered in the LSRTM algorithm based on the acoustic approximation in this work. In the physical laboratory experiment, the LSRTM image shows a good agreement with the image based on virtual experiment, although some artifacts and wider flaw width are observed. Besides the reason mentioned above, the main reason is the difference between the input waveform used in the LSRTM algorithm and the actual excited waveform in the real physical experiment, which would produce some artifacts to the image. The remaining discrepancy there can be attributed to less frequencies used in the LSRTM imaging from the real physical experiment compared to that from the virtual experiment.

The V shaped flaw was produced in the controlled laboratory environment and have nominal through-

wall extents of 6 mm. The through-wall extent is determined by measuring the vertical distance between the tip and the root of this flaw and is found to be 6.1 mm in the virtual experiment. The through-wall extent is measured to be 6.3 mm from the LSRTM image obtained from the real physical experiment, as shown in Figure 4(b).

5 CONCLUSIONS

In this paper, the least-squares reverse time migration (LSRTM) algorithm is investigated for characterizing irregularly shaped flaw. This algorithm is a two-way wave-equation-based approach and attempts to find the best fit reflectivity model by minimizing the mismatching between the measured and modeled data. The LSRTM has been successfully used in the measured data from the virtual experiment as well as the physical laboratory experiment, and the results have shown good accuracy in determining the size, location and shape of the V shaped flaw.

REFERENCES

- [1] Bai, L., Velichko, A. and Drinkwater, B.W. Ultrasonic characterization of crack-like defects using scattering matrix similarity metrics. *IEEE Trans. Ultrason. Ferroelectr. Freq. Control* (2015) **62**:545–559.
- [2] Felice, M.V. and Fan, Z. Sizing of flaws using ultrasonic bulk wave testing: A review. *Ultrasonics* (2018) **88**:26–42.
- [3] Wilcox, P.D. Ultrasonic arrays in NDE: Beyond the B-scan. *AIP Conference Proceedings* (2013) **1511**:33–50.
- [4] Holmes, C., Drinkwater, B.W. and Wilcox, P.D. Post-processing of the full matrix of ultrasonic transmit/receive array data for non-destructive evaluation. *NDT & E. Int.* (2005) **38**:701–711.
- [5] Holmes, C., Drinkwater, B.W. and Wilcox, P.D. Advanced post-processing for scanned ultrasonic arrays: Application to defect detection and classification in non-destructive evaluation. *Ultrasonics* (2008) **48**:636–642.
- [6] Felice, M.V., Velichko, A. and Wilcox, P.D. Accurate depth measurement of small surface-breaking cracks using an ultrasonic array post-processing technique. *NDT & E. Int.* (2014) **68**:105–112.
- [7] Dai, W., Fowler, P. and Schuster, G.T. Multi-source least-squares reverse time migration. *Geophys. Prospect* (2012) **60**:681–695.
- [8] Claerbout, J.F. Toward a unified theory of reflector mapping. *Geophysics* (1971) **36**:467–481.
- [9] Keys, R. and Weglein, A. Generalized linear inversion and the first Born theory for acoustic media. *J. Math. Phys.* (1983) **24**:1444–1449.
- [10] Baysal, E., Koslo, D.D. and Sherwoods, J.W.C. Reverse time migration. *Geophysics* (1983) **48**:1514–1524.
- [11] Yang, J. Z. and Liu, Y.Z. and Dong, L.G. Least-squares reverse time migration in the presence of density variations. *Geophysics* (2016) **81**:S497–S509.
- [12] Claerbout, J.F. *Earth soundings analysis: Processing versus inversion*. Blackwell Scientific Publications, Cambridge, (1992).

- [13] Chavent, G. and Plessix, R.-E. An optimal true-amplitude least squares prestack depth-migration operator. *Geophysics* (1999) **64**:508–515.
- [14] Zhang, C., Huthwaite, P. and Lowe, M. The application of the factorization method to the subsurface imaging of surface-breaking cracks. *IEEE Trans. Ultrason. Ferroelectr. Freq. Control* (2018) **65**:497–512.

MULTIOBJECTIVE OPTIMIZATION FOR IDENTIFICATION OF A MOVING LOAD PATH

MICHAŁ GAWLICKI AND ŁUKASZ JANKOWSKI

Institute of Fundamental Technological Research
Polish Academy of Sciences
Pawińskiego 5B, 02-106 Warsaw, Poland
e-mail : mgawlic@ippt.pan.pl, ljank@ippt.pan.pl

Key words: Trajectory Identification, Moving Load, Inverse Problem, Structural Health Monitoring, Multicriterial Optimization.

Abstract. This contribution presents an approach for indirect identification of the 2D path of a moving load. A multicriterial formulation is proposed, where one objective function quantifies the mismatch between the measured and the simulated structural response. The second objective function expresses the natural expectation that the paths of moving loads are continuous and relatively smooth, and it expresses thus a certain spline-based measure of the geometric regularity of the path. The Pareto front is determined in a local evolutionary search and used to strike the balance between the response fit and the geometric regularity of the path. The approach is tested in a laboratory experimental setup of a plate loaded by a line-follower robot. It is found that the implementation of the smoothness-based objective has a regularizing influence on the identification results: it reveals and emphasizes the actual geometrical character of the identified paths.

1 INTRODUCTION

This contribution is devoted to the problem of indirect identification of a moving load based on the measured mechanical responses of the loaded structure. In general, such a problem belong to the class of load identification problems, which is an inverse problem that has been intensively studied, and with a certain number of published reviews [1–4]. Load identification problems are typically characterized by

- a very large number of the structural degrees of freedom that can be excited by the moving load and
- a limited number of sensors that are used to measure the response.

In effect, the naïve formulation based on minimization of the norm of the response residuum is underdetermined (that is, there are much more unknowns than equations), and the corresponding identification problem has an infinite number of exact solutions. Therefore, in order to guarantee the uniqueness of the solution, it is typical to limit the generality of the load being considered by assuming that the trajectory of the moving load is known (most often, the problem is reduced to the case of a single vehicle moving over a 1D bridge at a constant velocity [5–7]) and that only the magnitude of the load is a subject to identification.

In contrast, our aim is to identify more general loads, and in particular loads that are freely moving on 1D structures like beams and on 2D structures like plates. In an earlier approach [8],

we have used the sparsity-based optimization [9,10], constrained using the l_1 norm, which guarantees the uniqueness of the solution. It has been found that it is possible to reliably identify the trajectory of transient loads moving on a 1D structure (beam), including its timing (decelerations, stops, accelerations, etc.). For related research, see also [11,12].

In this contribution, the aim is to qualitatively identify the trajectory of a single moving load that excites a 2D structure. To limit the generality of the search space, we notice that 2D trajectories of such loads are expected to be relatively smooth. Therefore, in analogy to the object tracking approaches developed in the computer vision community [13], we use the assumption of smoothness in a multicriterial-type optimization, which weights the norm of the measurement residuum vs. a certain spline-based measure of the smoothness of the interpolated trajectory. Such a formulation allows the apriorical knowledge to be included in the identification process in order to

1. limit the sensitivity of the solution to measurement and modelling errors, and/or
2. account for a limited instrumentation.

In experimental investigations, we have used a 1 m x 1 m plate, loaded by a line follower robot, and instrumented with a limited number of strain gauges. Due to the relatively slow motion of the robot, the quasi-static case is assumed, which allows the computationally costly deconvolution to be avoided.

2 EXPERIMENTAL SETUP

The laboratory experimental setup consists of a pointwise supported, 1 m x 1 m steel plate of 0.5 mm thickness, see Fig. 1. The plate is loaded vertically by a line-follower robot (approx. 0.3 kg) that moves at a constant velocity of approximately 10 cm/s and follows one of the three closed-loop trajectories marked with thick black lines: a square, a circle and a triangle. The mechanical response of the plate is measured with a set of 8 strain gauges (sensors No 2, 3, 5, 6, 8, 9, 11 and 12, as shown in Fig. 1). The sampling frequency of 50 Hz is used.

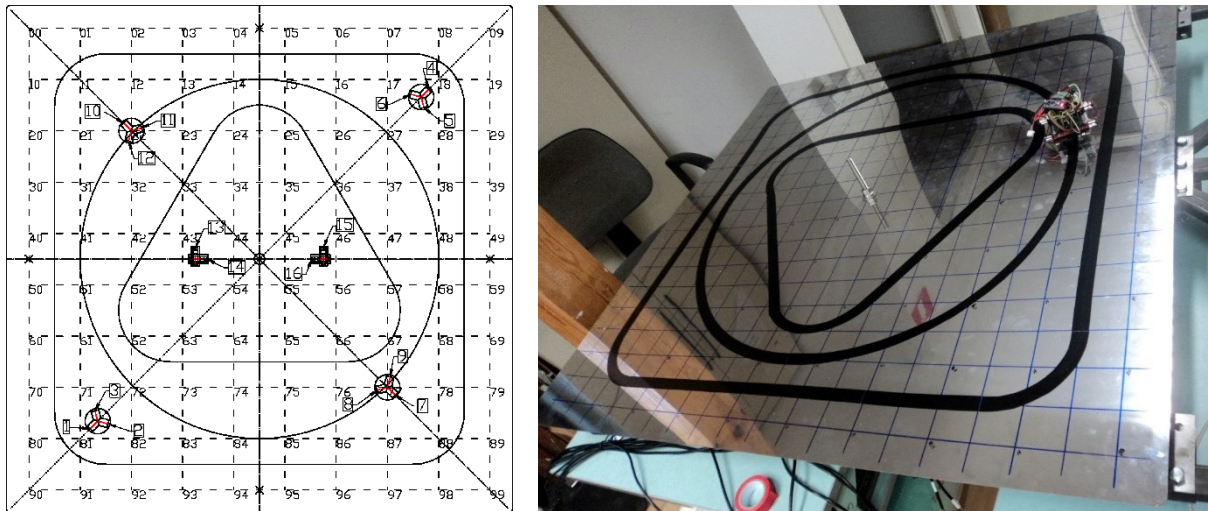


Figure 1: Scheme of the plate (left). The experimental setup (right).

The raw recorded measurements are shown in Fig. 2. As clearly seen from the plots, each path is followed by the robot two times, that the robot follows the respective line approximately two times around the plate.

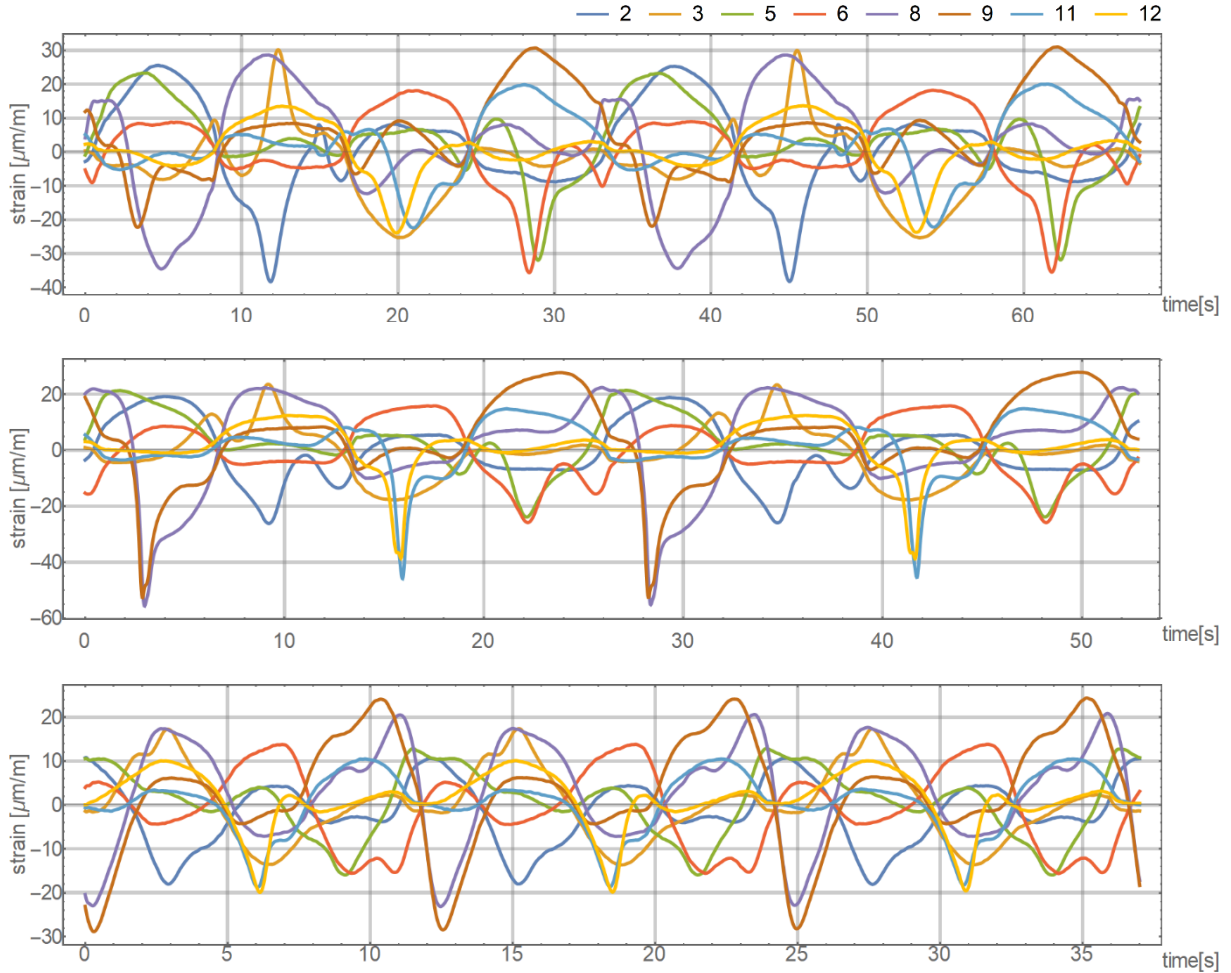


Figure 2: Measurements of the eight strain sensors for the three considered robot paths (top to bottom : the square, the circle, and the triangle).

3 THE INVERSE PROBLEM

Typical formulations of the inverse problem of load identification rely on minimization of the norm of the residuum, which amounts to finding the best fit between the measured response of the structure and its simulated response to the load being identified. Such a structural, response-based objective function is employed also here and described in Section 3.1. However, approaches that are exclusively based on such a formulation suffer often from two problems:

1. *Nonuniqueness of the solution*, which is related to *insufficient instrumentation*: in most practical scenarios there are much more potentially loaded points than sensors, so that the inverse problem has more unknowns than equations and is thus underdetermined.

2. *Ill-conditioning*, that is a large sensitivity of the results to the inaccuracies of the input data, which arise due to inevitable measurement errors and model errors (for example, possible nonlinearities of the sensors in a linear formulation).

Here, the first problem is addressed by the assumption of load sparsity, which is formulated as the requirement that in each time instance the “ l_0 norm” of the load vector equals exactly one, that is that in each time instance the load vector has only one nonzero element. Effectively, it corresponds to the assumption that a single load is being identified. The second problem is addressed by employing a certain apriorical knowledge in a regularization-like approach. Namely, it is noted that the 2D paths (trajectories) of the moving loads are expected to be relatively smooth. A respective, spline-based objective function is proposed to quantify the smoothness of the trajectory, and it is used concurrently with the response-based objective function in a multiobjective optimization problem. These two objective functions are used to form the Pareto front and find the moving load path that strikes the balance between the response fit and the expected characteristics of moving loads.

3.1 Measurement-based objective function

The measurements shown in Fig. 2 are relatively smooth and do not exhibit any apparent transient effects. It suggests that the considered problem has a quasi-static character. Therefore, the response analysis is decoupled with respect to time: the impulse response functions degenerate to points and the operation of deconvolution reduces to a series of simple time point by time point multiplications:

$$\boldsymbol{\varepsilon}(t_i) = \mathbf{B}\mathbf{f}(t_i), \quad i = 1, 2, \dots, N_t \quad (1)$$

where $\boldsymbol{\varepsilon}(t)$ is the 8-element vector of the responses of the strain gauges, as recorded in time instance t , the matrix \mathbf{B} is a compliance matrix reduced to the strain sensors and potential load positions that correspond respectively to its rows and columns, and N_t is the number of the considered time steps. The path of the moving load is discretized to the 100 points numbered 00 to 99 in Fig. 1 (left), and the vector $\mathbf{f}(t)$ collects the corresponding vertical loads in the time instance t . Notice that the elements of the vector $\mathbf{f}(t)$ can be assumed to be nonnegative.

Given the matrix \mathbf{B} and the measurement vectors $\boldsymbol{\varepsilon}(t_i)$, the structural objective function quantifies (in the logarithmic scale) the fit between the expected response and the measurements, as expressed in terms of the squared norm of the residuum vector,

$$F_1(\mathbf{f}) = \ln \sum_{i=1}^{N_t} \|\boldsymbol{\varepsilon}(t_i) - \mathbf{B}\mathbf{f}(t_i)\|^2. \quad (2)$$

3.2 Smoothness-related objective function

The second objective function is employed to enforce the assumption that the paths of the moving load is expected to be smooth. Due to the assumption of sparsity, the vector $\mathbf{f}(t_i)$ for each time instance t_i has only one nonzero element, which corresponds to one of the points numbered 00 to 99 in Fig. 1 (left). Therefore, each point \mathbf{f} of the search space defines a certain 2D path $\mathbf{x}(t_i)$ on the plate, discretized to the time instances t_i and the plate points 00 to 99. The proposed objective function quantifies the smoothness of this path by: (1) calculating a continuous, spline-based interpolation $\mathbf{x}(t) = (x_1(t), x_2(t))$ of the path; (2) computing the

following weighted sum of two terms:

$$F_2(f) = \alpha \int_{t_1}^{t_{N_t}} \ln \left(1 + \frac{(\dot{x}_1 \ddot{x}_2 - \dot{x}_2 \ddot{x}_1)^2}{10^{-3} + (\dot{x}_1^2 + \dot{x}_2^2)^2} \right) dt + \beta \frac{\sqrt{\int_{t_1}^{t_{N_t}} (\|x\| - \int_{t_1}^{t_{N_t}} \|x\| dt)^2 dt}}{\int_{t_1}^{t_{N_t}} \|x\| dt}, \quad (3)$$

which respectively quantify the variability of the angular velocity of the path and the (normalized) variability of its linear velocity. The weights α and β are selected to equalize the mean magnitudes of both terms on a random sample of several hundreds of paths that are near-optimal according to F_1 .

3.3 The optimization procedure

A multiobjective optimization problem is considered, in which both objective functions are minimized concurrently by means of the Pareto front. In the first step, the starting path is determined by minimizing only the structural objective function F_1 . Then, an evolutionary local search is performed: the operation of mutation is defined and extensively used to generate iteratively new search points. In this way, the neighborhood of the starting point is probabilistically explored. In comparison to genetic algorithms, the operation of cross-over is neglected due to the intended local character of the search: a meaningful load path should be relatively smooth, but it must also provide a certain fit to the measurements, and therefore it must be placed in a certain vicinity of the starting point. The employed operation of mutation shifts a small, randomly selected, number of points of the discretized path to their randomly selected neighboring points (for example, point 23 can be shifted to point 34) or a point that provides a slightly better/worse value of the objective function F_1 .

5 EXAMPLE RESULTS

Since the considered case has a quasi-static character, the measurements have been downsampled to one point per 2 seconds, which corresponds to the distance of approximately 20 cm between successive path points and 34, 25 and 29 points for the three considered paths. Figures 3–5 show the computed Pareto fronts and the load paths corresponding to its few selected points, respectively for the three considered paths: the square, the circle and the triangle. The actual paths are shown in Fig. 1 (left).

The results confirm that the proposed smoothness-based objective function has a regularizing influence on the identified load path. In all three cases, the geometric regularity and smoothness of the path are considerably improved. The trajectories that are identified based on the response fit only (case A in each figure) clearly illustrate the detrimental effect of data inaccuracies: even though the considered problem is not underdetermined, the identified paths are highly noisy, which is especially pronounced in case of Fig. 5. Implementation of the smoothness-based objective reveals and emphasizes the actual geometrical character of the identified paths.

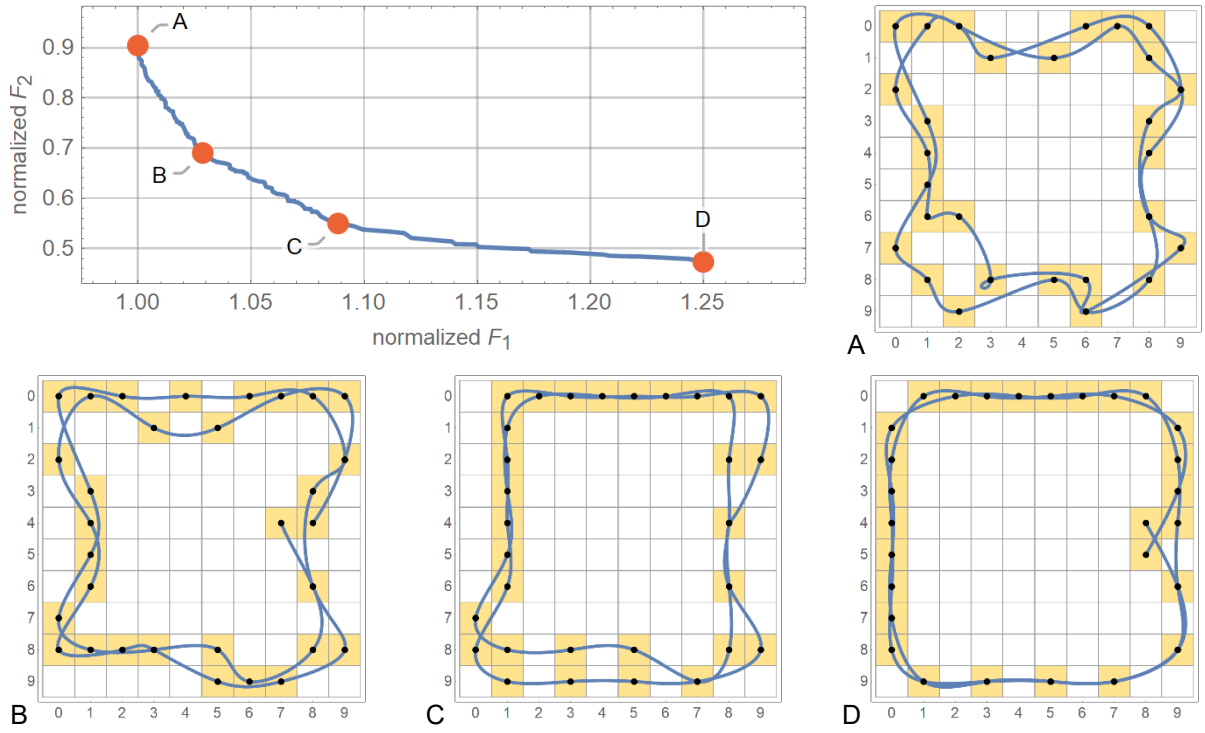


Figure 3: Example identification results: the Pareto front and the identified paths that correspond to its few selected point. The actual path is the square shown in Fig. 1 (left).

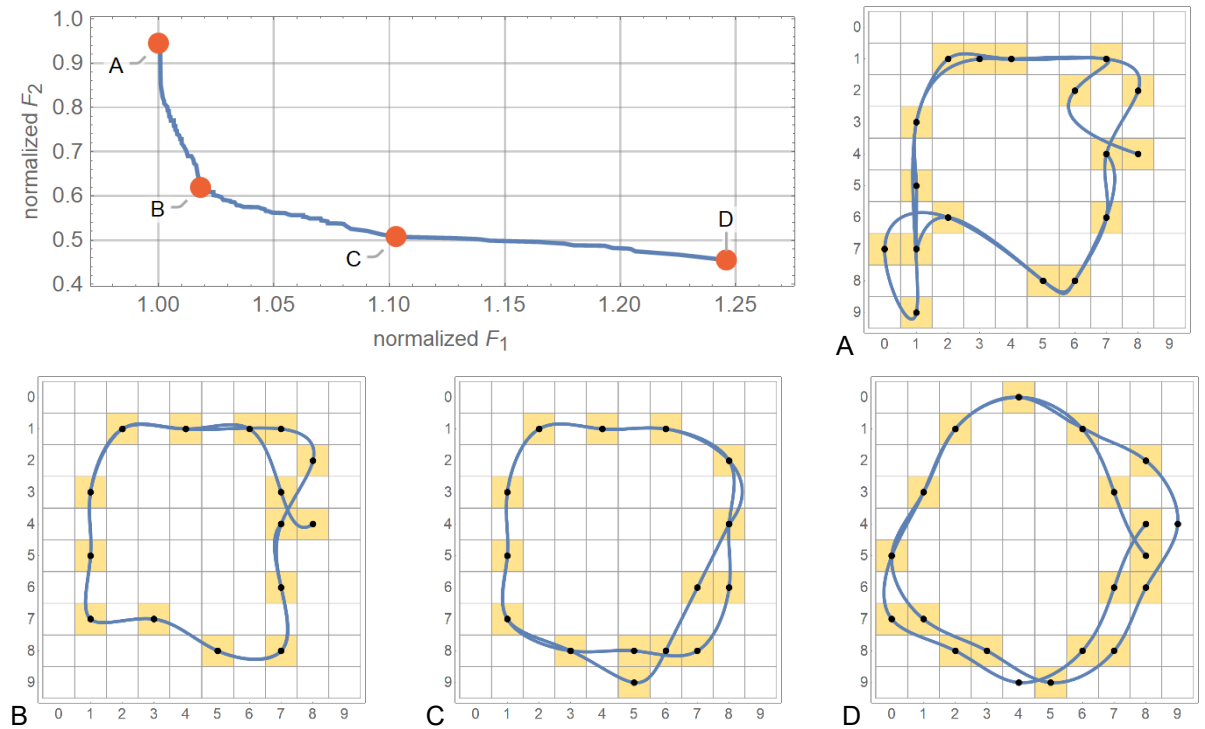


Figure 4: Example identification results: the Pareto front and the identified paths that correspond to its few selected point. The actual path is the circle shown in Fig. 1 (left).

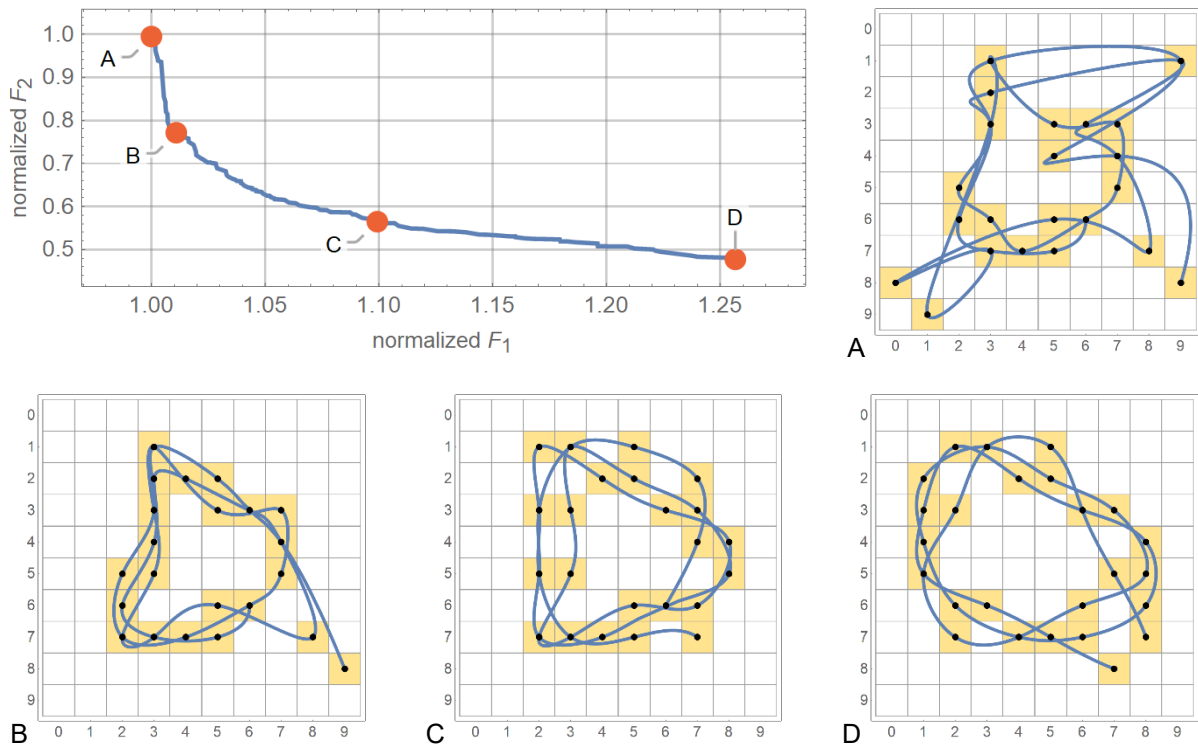


Figure 5: Example identification results: the Pareto front and the identified paths that correspond to its few selected point. The actual path is the triangle shown in Fig. 1 (left).

6 CONCLUSIONS

This contribution proposed a multiobjective approach to indirect identification of 2D paths of moving loads. The formulation employs two objective functions: one is response-based and the other quantifies the geometric regularity of the path. The approach is successfully tested in a laboratory example of a 1 m x 1 m plate loaded by a line-follower robot. The research is ongoing to (1) increase the spatial resolution of the identified paths, to (2) consider multi-load cases, and to (3) automatize the determination of a proper segment on the Pareto front.

ACKNOWLEDGMENTS

The authors gratefully acknowledge the support of the National Science Centre, Poland, granted under the grant agreement DEC-2017/25/B/ST8/01800.

REFERENCES

- [1] Zhu, X.Q. and Law, S.S. Recent developments in inverse problems of vehicle–bridge interaction dynamics. *Journal of Civil Structural Health Monitoring* (2016) **6**(1):107–128.
- [2] Yu, L. and Chan, T.H.T. Recent research on identification of moving loads on bridges. *Journal of Sound and Vibration* (2007) **305**(1–2):3–21.
- [3] Klinkov, M. and Fritzen, C.P. An updated comparison of the force reconstruction methods. *Key Engineering Materials* (2007) **347**:461–466.

- [4] Law, S.S. and Zhu, X.Q. *Moving Loads-Dynamic Analysis and Identification Techniques*. Structures and Infrastructures Book Series. CRC Press, Vol. 8, (2011).
- [5] Wu, S.Q., and S.S. Law. Statistical moving load identification including uncertainty. *Probabilistic Engineering Mechanics* (2012) **29**:70–78.
- [6] Zhang, Q., Jankowski, Ł. and Duan, Z. Simultaneous identification of moving masses and structural damage. *Structural and Multidisciplinary Optimization* (2010) **42**(6):907–922.
- [7] Zhu, X.Q. and Law, S.S. Practical aspects in moving load identification. *Journal of Sound and Vibration* (2002) **258**(1):123–146.
- [8] Gawlicki, M. and Jankowski, Ł. Identification of moving loads using the l_1 norm minimization. *AIP Conference Proceedings* (2018) **1922**:100007.
- [9] Donoho, D.L. Compressed sensing. *IEEE Transactions on Information Theory* (2006) **52**(4):1289–1306.
- [10] Baraniuk, R.G. Compressive sensing. *IEEE Signal Processing Magazine* (2007) **24**(4):118–121.
- [11] Bao, Y., Li, H., Chen, Z., Zhang, F. and Guo, A. Sparse l_1 optimization-based identification approach for the distribution of moving heavy vehicle loads on cable-stayed bridges. *Structural Control and Health Monitoring* (2016) **23**(1):144–155.
- [12] Pan, C.D., Yu, L., Liu, H.L., Chen, Z.P. and Luo, W.F. Moving force identification based on redundant concatenated dictionary and weighted l_1 -norm regularization. *Mechanical Systems and Signal Processing* (2018) **98**:32–49.
- [13] Milan, A., Schindler, K. and Roth, S. Multi-target tracking by discrete-continuous energy minimization. *IEEE Transactions on Pattern Analysis and Machine Intelligence* (2016) **38**(10):2054–2068.

NEW APPLICATION OF PIEZOELECTRIC SENSORS IN HEALTH MONITORING OF ROCKS

PRATEEK NEGI^{*}, TANUSREE CHAKRABORTY[†] AND SURESH BHALLA[#]

^{*} Department of Civil Engineering
Indian Institute of Technology (IIT) Delhi
Hauz Khas New Delhi-110016, India
e-mail: negidynamic@gmail.com

[†] Department of Civil Engineering
Indian Institute of Technology (IIT) Delhi
Hauz Khas New Delhi-110016, India
e-mail: tanusree@civil.iitd.ac.in

[#] Department of Civil Engineering
Indian Institute of Technology (IIT) Delhi
Hauz Khas New Delhi-110016, India
e-mail: sbhalla@civil.iitd.ac.in

Key words: Electro-Mechanical Impedance Technique, Rocks, Structural Health Monitoring, Acoustic Emission.

Abstract. The inspection and maintenance of underground structures built in rocks poses difficulties to the concerned engineers due to the complex behaviour of rocks. Some of the underground regions are inaccessible for the inspection team or might warrant special clearing arrangement, leaving the structure out of service. The complexity of their design, construction and the conditions encountered during service life necessitate the deployment of a dedicated structural health monitoring (SHM) system. It is very crucial to identify the damage in the surrounding rocks in its incipient stage to prevent its further propagation and safeguard the structure built over it. The damage detection in rocks require an efficient SHM system which can monitor them on a regular basis. In the present study, lead zirconium titanate (PZT) patches are used to monitor the condition of rocks under various forms of loadings using electro-mechanical impedance (EMI) technique together with Acoustic Emission (AE) technique. In EMI technique, the vibrations generated by the actuation of PZT patch are sensed by the same PZT patch and is recorded in the form of conductance and susceptance signatures. These signatures can be quantified using root mean square deviation (RMSD) method. The same smart sensors were checked for their potential to be used for AE monitoring of rocks. The AE technique is demonstrated for monitoring acoustic events happening within the rock specimens under uniaxial compressive loading. The study clearly establishes the potential of the EMI and AE technique in detecting and quantifying load induced damages in rocks surrounding the underground structures, opening avenues for its applications in real-life situations.

1 INTRODUCTION

The monitoring of the structures built on rocks or soils requires a timely inspection with the aid of instruments and expert judgment [1]. A structure constructed in rocks or rock mass can fail due to unforeseen geological and weathering conditions or seismic activities. Hence, a continuous systematic health monitoring system is required for timely detection of insipient damages. These damages can be rectified in time instead of letting them progress into a catastrophic failure. Rocks may either fail spontaneously after excavation or may take significant time to fail depending upon its type and surrounding conditions, like overburden pressure.

Health monitoring is a continuous process which is needed at the time of construction and after the operational starting of the structure. A monitoring system should be simple in deployment, should take less time in instrumentation and should cover both accessible and inaccessible areas of the structure. The monitoring methods available are classified into surface and sub-surface methods.

Piezo based sensors are studied extensively for condition monitoring of metallic and concrete structures. However, its applications for SHM of rocks around the underground structures is unexplored yet. The present research aims to explore the potential of piezo sensors in the field of SHM of rocks. The use of smart sensors in condition monitoring of rocks and underground structure has a great possibility. In near future, a smart integrated system can be developed for the automatic monitoring of rocks and structures, especially in remote locations.

2 WORKING PRINCIPLES

This section discusses the working principles of the EMI technique and AE technique in brief.

2.1 The EMI Technique

The underlying principle of EMI method is based on the electro-mechanical interaction between the mechanical impedance of the host structure and the electrical impedance of the piezoelectric sensor which is bonded to the structure. A schematic configuration is shown in Figure 1. The figure shows a square PZT patch that is bonded to the host structure. Here, the data acquisition system excites the PZT patch by sending excitation signals of frequency (ω) and simultaneously measures the corresponding electrical impedance ($Z_E(\omega)$) as the response of the patch. The actuation signals are given as a range of frequency and step interval of frequencies. The electrical impedance signature is acquired in the same frequency range within which the excitation signal is given.

The actuation and sensing behavior of a piezoelectric element can be understood from the following two equations [2]

$$S_j = s_{ji}^E T_i + d_{jm} E_m \quad (1)$$

$$D_m = d_{mj} T_j + \epsilon_{km}^E E_k \quad (2)$$

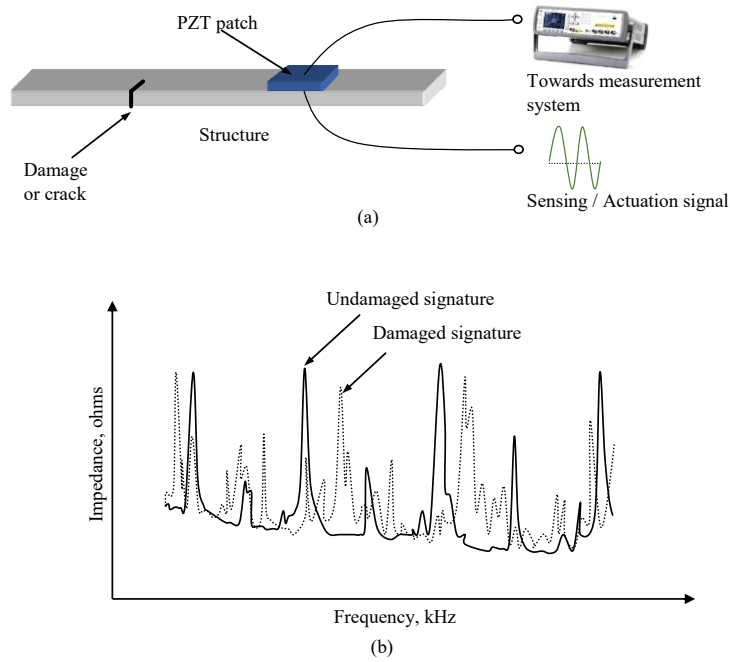


Figure 1: Acquiring EMI signatures of a host structure using PZT patches (a) PZT patch bonded on host structure (b) Impedance signature of the damaged and undamaged structure

The equations (1) and (2) shows the converse and direct piezoelectric effects, where, $[D_m](3 \times 1)$ (C/m²) is the electric displacement vector, $[S_j](6 \times 1)$ is the second order strain tensor, $[E](3 \times 1)$ (V/m) is the applied external electric field vector and $[T](6 \times 1)$ (N/m²) is the stress tensor. Accordingly, $[\epsilon_{km}^E](F/m)$ is dielectric permittivity tensor under constant stress, $[d_{jm}](C/N)$ and $[d_{mj}](m/V)$ is the piezoelectric strain coefficient tensors for direct and converse piezoelectric effects, respectively, and $[s_{ji}^E](m^2/N)$ is the elastic compliance tensor under constant electric field.

In the EMI method, a PZT patch is bonded to the surface of the host structure to be monitored using a high strength epoxy adhesive, as shown in the Figure 1. Electrical terminals are attached to the PZT patch and are then connected to the impedance analyser. The PZT patch can be assumed as a thin axial bar which is vibrating with the host structure. Hence, the mechanical impedance of the structure is the resistance offered to the harmonic vibrations by the PZT patch. Mechanical impedance is a measure for a structure's resistance to movement when subjected to a harmonic force or vibration. It relates the applied force with the velocity of the structure due to the application of the force. The mechanical impedance of a point on a structure is the proportion of the force applied at a point to the subsequent velocity. Mechanical impedance is the opposite of mechanical admittance or mobility. The mechanical impedance is a function of the applied force frequency and can change incredibly over a frequency range. At resonant frequencies, the mechanical impedance is lower. It means less force is expected to cause a

structure to move at a given velocity [3, 4]. Equation (3) shows the relation between the electrical impedance of the PZT patch and the mechanical impedance of the host structure.

$$\bar{Y} = 2\omega j \frac{w_s l_s}{h_E} \left[(\bar{\epsilon}_{33}^T - d_{31}^2 \bar{Y}^E) + \left(\frac{Z_a}{Z + Z_a} \right) d_{31}^2 \bar{Y}^E \left(\frac{\tan \kappa l_s}{\kappa l_s} \right) \right] \quad (3)$$

Here, Z_a is the mechanical impedance of the PZT patch, Z is the mechanical impedance of the host structure. Width length and thickness of the patch is denoted by w , l and h respectively. $\bar{Y}^E = Y^E(1 + \eta j)$ is the complex Young's modulus of elasticity of the PZT patch, d_{31} is the piezoelectric strain coefficient, $\bar{\epsilon}_{33}^T = \epsilon_{33}^T(1 - \delta j)$ is the complex electric permittivity in direction-3 (z) of the piezo material at constant stress and $j = \sqrt{-1}$, η and δ are the mechanical loss factor and the dielectric loss factor of the PZT material, respectively, κ is the wave number, which is dependent on the angular frequency of excitation ω .

So, any variation in the mechanical impedance of the host structure due to any damage or change in the environment reflects a change in the electrical impedance of the PZT patch. Hence, we can visualize any incipient damage in the host structure which is not visible to the naked eyes. In EMI technique the frequency range of excitation is generally in kilohertz (kHz). As the frequencies are very large in comparison to the natural frequency of the structure (which is in the range of 1-100 Hz only), the stress wave generated due to actuation of PZT transducers, are of very small wavelength. Hence, only local structural modes are excited near the PZT patch instead of the global modes. The very high frequency range gives us two advantages. First, small wavelengths can detect incipient damages and second, the sensing zone becomes localized. Hence, we can monitor small crucial areas very well.

2.2 The AE Technique

The same PZT patches can be utilized to acquire AE signals from rocks in a very cost-effective manner. The AE technique is demonstrated for monitoring acoustic events happening within the rock specimens under uniaxial compressive loading. The conventional AE technique has been improved with the advancement in sensor technologies and computing capacities. The present study aims to record acoustic emissions from Kota sandstone rock specimens under unconfined compressive loads. PZT based patches were used as the AE transducers and commercially available sound card of a personal computer (PC) was used for data logging of the AE signals. The proposed technique is found to be very easy and very much cost effective in capturing low frequency AE signals within the targeted range as given by Hardy, 1972 [5] (Figure 2). The recorded data was processed and different AE parameters like the cumulative AE count, the relative energy of the event and the event rate were determined. The results are compared with the conventional stress-strain plots of specimens under uniaxial compressive load.

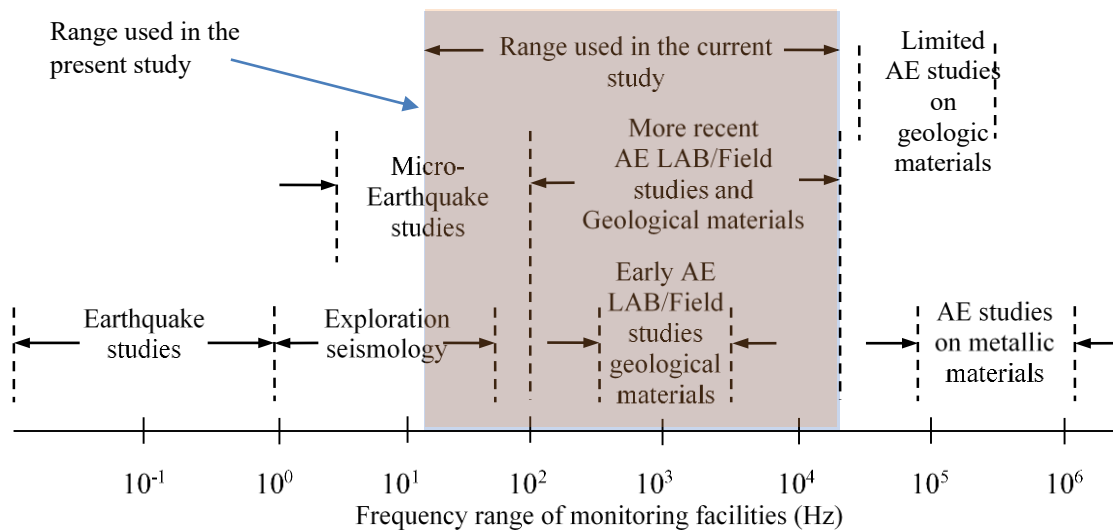


Figure 2: Frequency ranges for various AE and other related studies [5]

The conventional AE equipment are capable of recording AE signals in MHz range which is essential for delicate laboratory studies like monitoring of micro crack propagation. However, for field monitoring the AE system should be economical as more number of sensors are required to cover larger area, must be easy to install and rugged for long duration monitoring.

In the present study the PZT patches were bonded directly on the specimens using epoxy adhesive whereas, in the conventional AE technique, the piezo transducers are bonded using a couplant like natural wax and silicon grease. The use of couplant increases the signal losses by damping the signals. Moreover, no signal conditioner or amplifier were used herein to condition the signals, thus rendering the whole data acquisition process simple and cost effective. A schematic diagram of the acquisition process is shown in Figure 3.

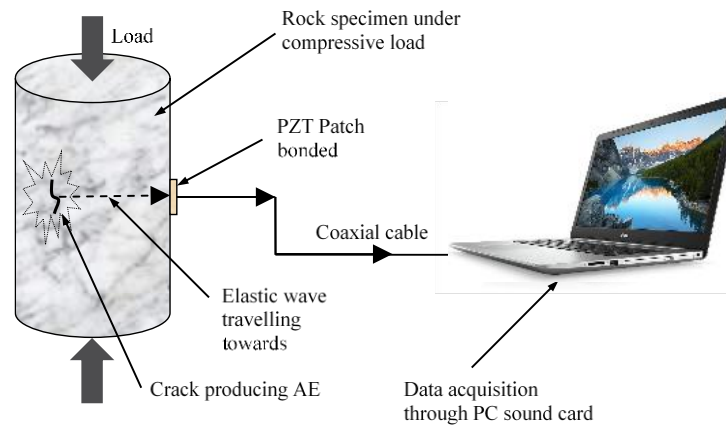


Figure 3: Schematic diagram of AE recording system used in the present study

The frequency range of 16-32 kHz comprises the maximum concentration of AE activities [6]. The present study considers a range of 20-20000 Hz, which falls in the range of AE lab and field studies on geological materials as illustrated in Figure 2. With the latest advancement in data acquisition techniques, AE events in the range of 1-2.5 MHz range, which is more suitable for metals than rocks, can also be recorded. However, the amplitude of such a high frequency signal is very small and occurs in the range of surrounding noise. Liu et al. (2014) tested four different types of rocks *i.e.* granulite, limestone, granite and siltstone, and plotted the energy spectrum coefficient of the AE signals with different frequency ranges, on a wavelet scale [7]. They observed that the energy of the events decreased in a parabolic manner with linear increase in the event frequency. The amplitude of the signal falling under the frequency band of 1.0-2.5 MHz was in the range of 0.02 mV and of those falling under 0-200 kHz were of the order of 2-10 mV, which is nearly 100 times higher than the megahertz amplitudes.

Generally, the data logging is done through multiple channels at moderate to high sampling rate creating a huge volume of data. Multiple sensors are used for the source localization of the AE event. Brantut, et. al. (2014) used multiple sensors for monitoring sandstone specimen under triaxial loading with a constant strain rate of 10^{-5} s^{-1} and under constant stress condition [8]. In order to analyze such a huge volume of data, high speed processing computing with adequate data storage facility is required. The data can be recorded in the raw form, *i.e.* in time vs amplitude form, and can be processed later to compute various parameters like the event rate and the event energy. If the computing capacity of the data logger is fast enough, the AE parameters can be determined simultaneously while recording the AE events. The AE waveform is recorded through an inbuilt analog to digital (A/D) convertor.

The AE application uses the direct piezoelectric effect (sensor application) to acquire the low frequency waves generated due to AE activities (Equation 1). The sensing region for AE activities of a piezo based sensor depends upon the geometry and material of the host structure (rock in the present study) and the nature of the structural discontinuities like pores and fissures. These discontinuities are the main causes of attenuation in the propagation of a stress wave signal [9].

3 EXPERIMENTATION DETAILS AND RESULTS

This section discusses the experimentation details used in condition monitoring of rocks under static and dynamic loading conditions using EMI technique and setup used for acquiring AE signals from rocks using a very cost-effective technique. Cylindrical Kota sandstone specimens of diameter 54 mm and length 108 mm were used in all the studies. The experimental setup used for conducting tests in static and dynamic loading conditions is shown in Figure 4. The conductance signatures were recorded after every loading stage also mentioned here as Load Ratio (LR). A typical variation in the conductance signatures with different load ratios can be seen in Figure 5. The conductance signatures in the range 300-600 kHz are very much capable of capturing the occurrence of damage in both dry and saturated conditions [10]. It is to be noted that this range is specific for the size of PZT used in the study. For larger patches the range is lesser. The change in the position of the peaks in the conductance signatures are the first indicators regarding the development of any damage in the rock. The PZT patches have

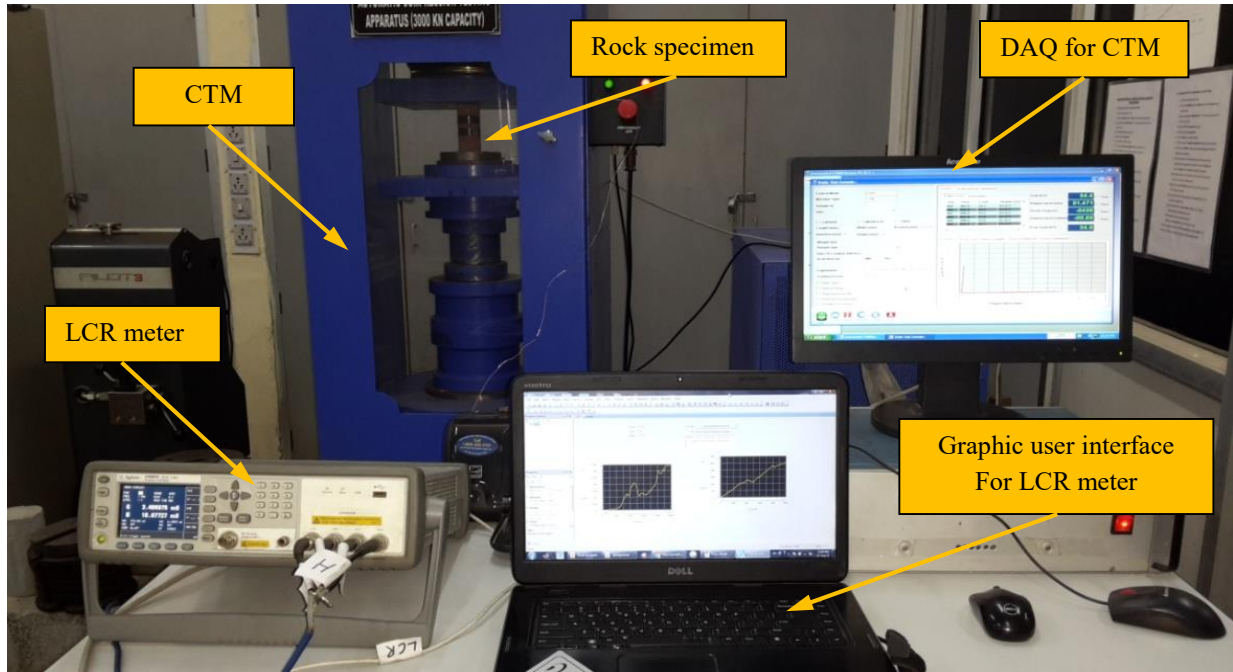


Figure 4: Experimental setup showing compression testing machine and LCR meter for acquiring EMI signatures.

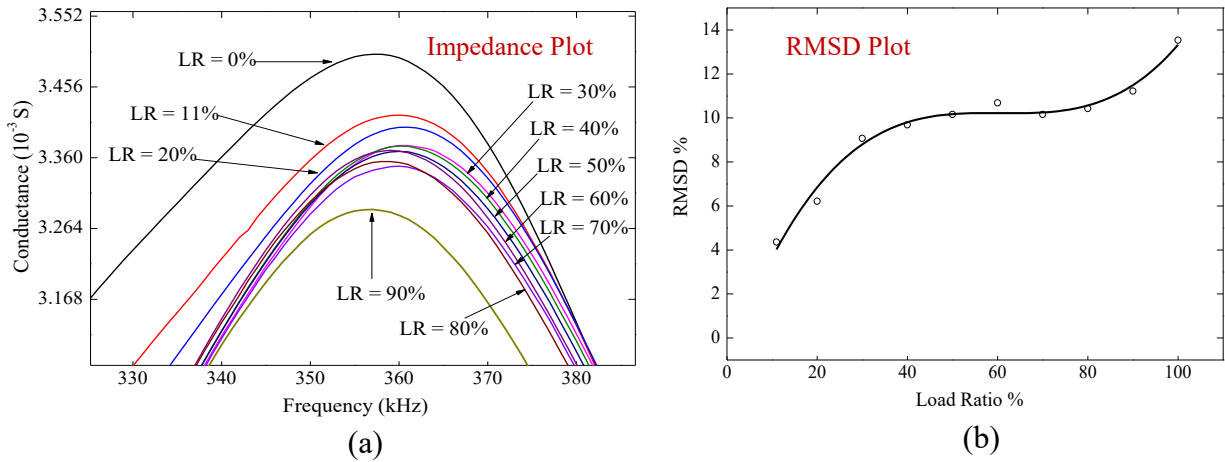


Figure 5: (a) Conductance signatures of rock specimens under different Load Ratio (LR) (b) Non-linear curve fitting for the variation in RMSD with LR

worked properly until the loading reached eighty percent of the peak load value in the dry rock testing and up to hundred percent of peak load in saturated testing conditions. This could be verified based on the consistency of slope in the susceptance signatures. The RMSD index has shown good capability in the quantification of the changes in the conductance signatures and hence damage quantification.

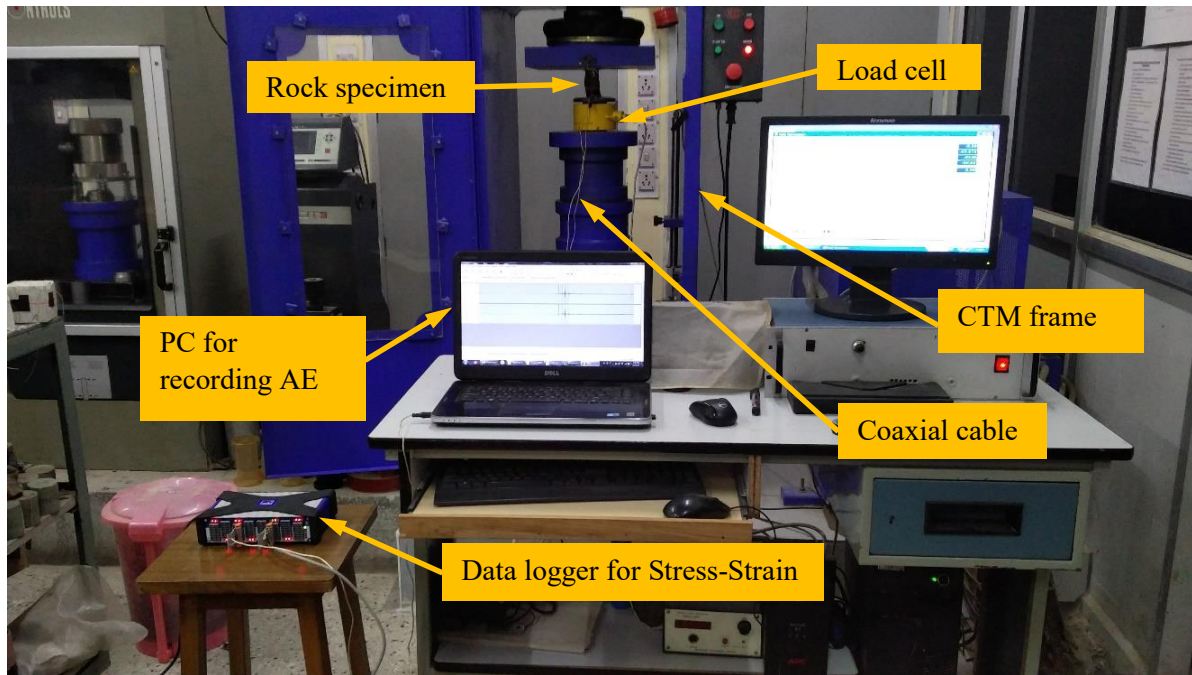


Figure 6: The complete experimental setup for recording acoustic emissions (AE)

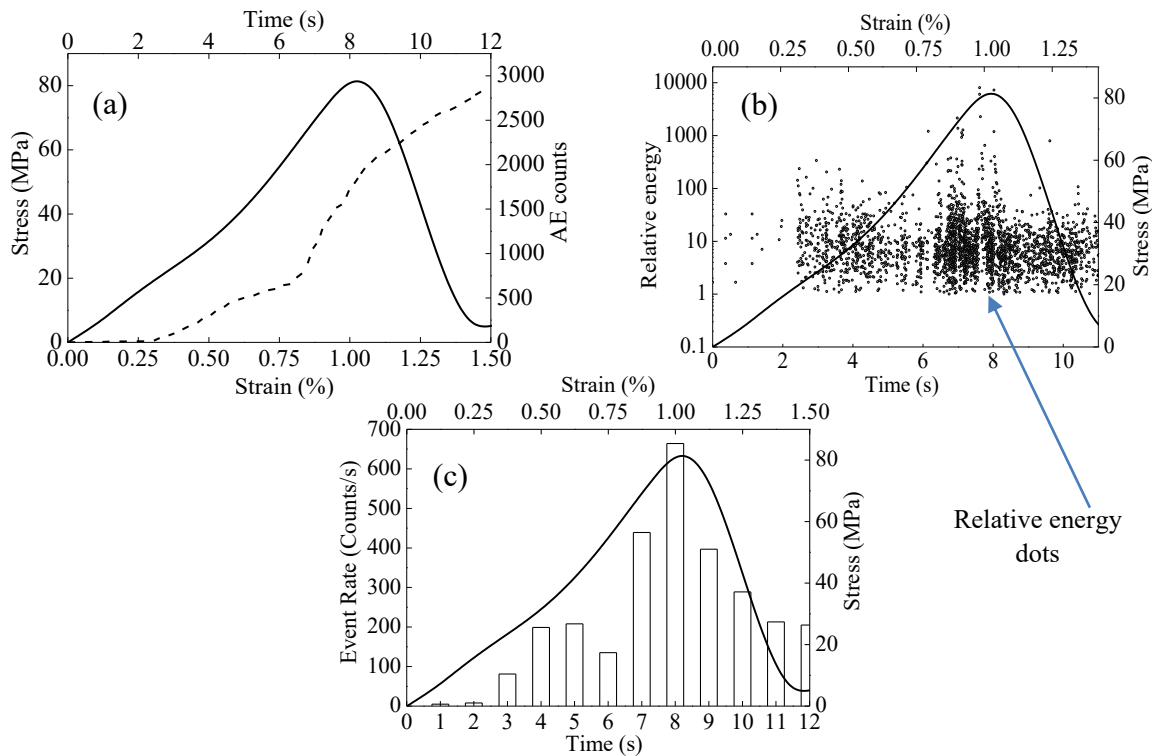


Figure 7: A typical (a) cumulative AE count plot (b) relative energy plot (c) event rate plot

Figure 6 shows the complete experimental setup for acquiring AE signals from the rock specimen under compression. The recorded events were further processed in MATLAB for calculating cumulative event count, relative event energy and event rate. A typical example of recorded parameters is shown in Figure 7. All the parameters are plotted against stress-strain plot of the specimen for better understanding. Based on the test results, it has been found that the PZT patches can record good low frequency AE emissions in rocks. For traditional AE systems, the cost of the complete AE equipment *i.e.* the transducers, data acquisition system, amplifiers, data cables, signal conditioners is around USD 40000-60000. Whereas, the present study needed only PZT patches and a PC with a sound card for data acquisition costing less than USD 1000 including the cost of PC. The cost of traditional AE transducers varies between USD 300-600, whereas the cost of PZT patch is USD 5-15. Further, the cost of the present AE system is subjected to the complexity and nature of the monitoring process. The small patches can be easily instrumented on smaller diameter specimens as less as 38mm, hence are suitable for laboratory demonstration of AE method. Using strong epoxy for bonding the patches provides a dual advantage of less signal attenuation and stable fixity in rough field conditions.

4 CONCLUSIONS

- The EMI technique can be conveniently used as damage monitoring technique in rocks under dry and saturated/ moist underground conditions. Any incipient damage can be detected easily in the initial stage and hence can be taken care of before it advances to a severe condition. The EMI technique can be alongside the conventional monitoring equipment like load cells and extensometers in the initial stage of development for the monitoring of underground structures. There is a huge scope of further research in finding the optimum size of the piezoelectric sensors for extracting more sensitive signatures. There is also a scope of developing a remote monitoring system which can monitor the underground structures remotely in a convenient manner. A standard procedure for using this technique can be developed and then can possibly be followed during construction of the underground structures.
- The PZT patches were found to be good in taking AE signals from rocks under unconfined compressive load. The proposed system aims to drastically reduce overall cost of the whole AE system.
- As sensors were bonded to the rock specimen directly, the emissions have been recorded with a good signal to noise ratio. Once bonded and sealed with epoxy, they are durable and can withstand the rough handling while testing. Hence, they can be used in the site conditions which are generally not suitable for conventional AE sensors.
- The attenuation of the AE signal was negligible as there is absence of air/ couplant in between the host structure and the sensor. The data was recorded straight forward from a PC sound card making the data logging further easier and economical in comparison to the commercially available AE systems.
- As the bonding conditions of every sensor may vary, the acquired data from one specimen testing varies in absolute terms. However, the technique can be further improvised with a higher quality control in bonding the terminals to the PZT patches at manufacturing level.

REFERENCES

- [1] Franklin, J.A. Rock mechanics review: The monitoring of structures in rock, *International Journal of Rock Mechanics and Mining Sciences and Geomechanics* (1977) **14**:163-192.
- [2] IEEE (1987), IEEE standard on piezoelectricity, Std. 176, *IEEE/ANSI*.
- [3] Sabanovic, A. and Ohnishi, K. Motion control systems: Chapter 5, *Wiley Online Library* (2011).
- [4] Gatti, P.L. and Vittorio, L.F. Applied structural and mechanical vibrations, E & FN Sponsored, *Taylor and Francis* (1999).
- [5] Hardy, H.R.Jr. In acoustic emission, ASTM STP 505, *American Society for Testing and Materials*, Philadelphia, (1972) 41-83.
- [6] Suzuki, T., Sasaki, K., Siohara, Z. and Hirota, T. A new approach to the prediction of failure by rock noise, *Fourth International Conference on Strata Control and Rock Mechanics*, Henry Krumb School of Mines, Columbia University, NY, (1964) 99-107.
- [7] Liu, X., Liang, Z., Zhang, Y., Wu, X. and Liao, Z. Acoustic emission signal recognition of different rocks using wavelet transform and artificial neural network, *Shock and Vibration* (2014), 1-14.
- [8] Brantut, N., Heap, M.J., Baud, P. and Meredith, P.G. Rate and strain dependent brittle deformation of rocks, *Journal of Geophysical Research Solid Earth* (2014), **119**:1818-1836, doi:10.1002/2013JB010448.
- [9] Bhalla, S. A mechanical impedance approach for structural identification, health monitoring and nondestructive evaluation using piezo-impedance transducers, *Ph.D. Thesis*, School of Civil and Environmental Engineering, Nanyang Technological University, Singapore (2014), 66-67.
- [10] Negi, P., Chakraborty, T., Bhalla, S. Damage monitoring of dry and saturated rocks using piezo transducers. *ASTM: Journal of Testing and Evaluation* (2017), **45(1)**: 20160158.

NOVEL TECHNIQUE OF ON-DEMAND MONITORING OF SLIDER DISPLACEMENT IN SEISMIC ISOLATOR

SHAKHZOD M. TAKHIROV^{*}

^{*} Eng. Manager of Structures Laboratory, Civil and Environmental Engineering Department,
University of California, Berkeley; 337 Davis Hall, UC Berkeley, Berkeley 94720
e-mail: takhirov@berkeley.edu, www.berkeley.edu

Key words: Friction Pendulum Bearing, Component Testing, Structural Health Monitoring, On-demand Monitoring, Seismic Isolation, Lidar, Laser scanning.

Abstract. Seismic isolation is a common technique used for the protection of structures and equipment from earthquakes. There are several types of devices providing seismic isolation. One of the most popular and commonly used is a friction pendulum bearing (FPB). The main idea behind a FPB is based on sliding movable spherical surfaces in respect to fixed spherical surfaces. A slider in between the surfaces makes this possible. Since there is some friction associated with the slider's performance, the restoring force is not enough to bring the slider to its zero position and as such, there is a possibility of a residual displacement after a seismic event. Monitoring these displacements is essential to ensure that the isolation can still accommodate a displacement demand of a future earthquake. A technique of on-demand monitoring of this displacement is developed in this paper. A short range LiDAR is used and the feasibility of the approach is validated by tracking geometric shapes with precisely known displacements. Due to recent explosive developments of LiDAR and laser scanning technologies driven by demand for collusion detection for autonomous car and robotic industries, the cost of these devices is decreasing dramatically. The device utilized in this approach is competitively priced and allows mass installation on all FPBs used in any particular project without a significant cost increase. In addition, the residual displacements can be measured simultaneously on all devices that allow instantaneous assessment of all FRB after an earthquake. The benefits of this approach are validated in the tests conducted on a full-scale FPB with a full stroke of ± 81.3 cm. The accuracy of the technique developed herein is compared against more accurate conventional instruments and a terrestrial laser scanner.

1 INTRODUCTION

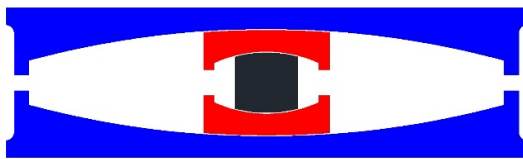
The concept of Smart City is defined as an urban area that utilizes various types of electronic Internet of Things (IoT) sensors to collect data and use these data to manage assets and resources efficiently [1]. The data can be collected from citizens, devices, and assets that is processed and analysed to monitor and manage traffic and transportation systems, power plants, water supply networks, waste management, crime detection, information systems, schools, libraries, hospitals, and other community services. The objective of this paper is to introduce a novel system for monitoring seismic isolators. The seismic isolation is a common technique for

seismic protection of buildings and structures of high importance: hospitals, emergency service buildings, bridges and others. Periodic assessment of the seismic isolators is beneficial for structural integrity of the building and structures, especially right after a major seismic event. This paper presents a discussion of a device enabling this monitoring in near real-time or on-demand configuration. In anticipation of a mass application, it is based on usage of inexpensive 2D LIDAR [2]. A special procedure is developed to access the location of the slider in plane, which was verified by a 3D laser scanner [3]. The data manipulation of all collected point clouds was conducted in a Matlab environment [4].

2 EXPERIMENTAL SETUP FOR COMPONENT TESTING

There are several types of seismic isolation. One of the most commonly used is the Friction Pendulum Bearing (FPB). In the most basic case, the FPB consists of a spherical surface on which a slider slips. Since the radius of the spherical surface is predefined by the design requirement of the isolator, it controls the resonant frequency of the isolator, which is based on a pendulum theory (see [5], for example).

There are several implementations of this basic idea, and the FPB studied in this paper was a representative of the so-called triple FPBs [6]. It consists of two dishes with polished conceived spherical surfaces and a slider pack between them as presented in Figure 1a. In addition, the slider pack consists of two conceived spherical surfaces with a rigid slider inside. This type of isolation provides several advantages. A few advantages are listed here. First, triple FPB is more compact than FPB with a single sliding surface designed for the same seismic displacement demand. Second, due to the presence of several surfaces there is a possibility of having several resonant frequencies of the isolator depending on which surface is involved in the sliding action. Third, due to the presence of several contact surfaces, the overall damping depends on the friction of the slider's liner, which can be selected in the most beneficial way to meet the design requirements of the isolator. The full-scale isolators used in this study are shown in Figure 1b.



a) Schematic drawing



b) Photo of FPBs used in the study

Figure 1: Triple FPB

Since the main mechanism of the FPB is based on friction, there is a possibility of residual

displacement after an earthquake event. The measurement of this displacement in respect to the remaining travel clearance on the sliding surface is important to ensure that the slider's displacement remains within the seismic displacement demand. The monitoring of the precise location of the slider pack is also important for the validation of the theoretical modelling of the FPB's performance (see [7], for example).

A special experimental setup was developed at the University of California, Berkeley to conduct component testing on seismic isolators [8]. A full-scale triple FPB was studied in this setup by imposing incrementally increasing cyclic horizontal displacements while keeping the vertical load constant. The setup was intended for the performance evaluation of FPBs under relatively low vertical load and feasibility study of their application as a seismic isolation of high-voltage equipment. The setup is presented in Figure 2a. To mimic a real-life installation, where the top and bottom dishes remain parallel to each other, a special linear bearing system was introduced to keep the top dish horizontal while allowing its movement up and down as shown in Figure 2b. The bottom dish was attached to a shaking table platform capable of delivering ± 813 mm displacement.

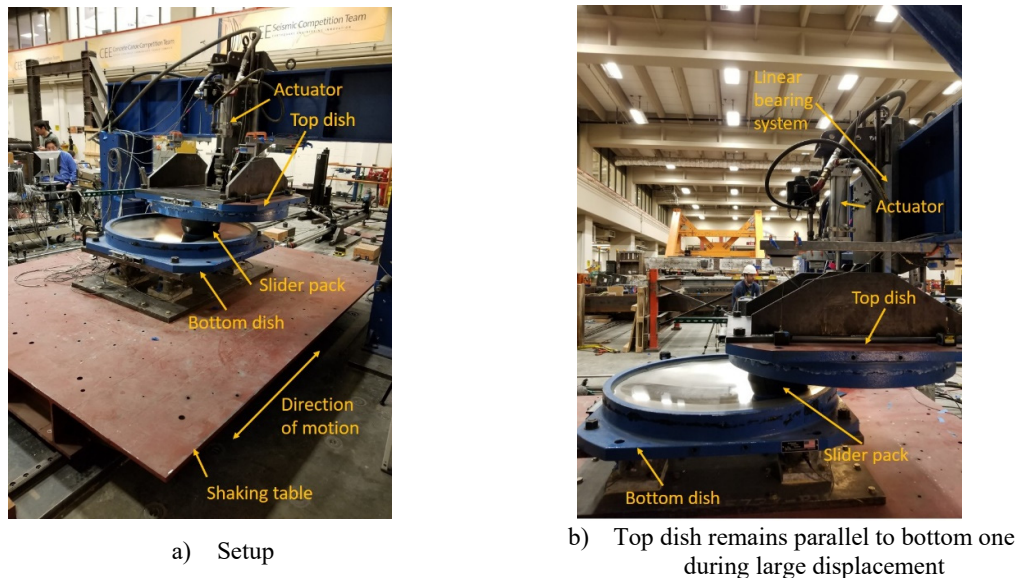


Figure 2: Experimental setup for component tests of full-scale FPBs

In order to study the feasibility of using a 2D scanner for these measurements and their accuracy, the following study was conducted.

3 FEASIBILITY STUDY WITH 2D SCANNER

Prior to the laser scanner measurements on the actual FPB, the 2D LiDAR scanner's performance and accuracy was evaluated in a simple experimental setup inside of a small test room. Objects of different geometry were placed on a linear bearing system as presented in Figure 3. Different cases of geometric shapes were considered: prismatic shapes, globes and cylinders. To study texture and color effects on the results of the laser scanning measurements

the objects were made from different materials: wood, concrete, and spray-painted glass. Some of the examples of the objects used in the study are presented in Figure 3.

Some of the objects remained stationary and were not moved in respect to the 2D scanner. Another object, the so-called movable object, was installed on the carriage of the linear bearing system and was displaced in respect to the stationary object (reference object). The displacements were imposed in an incremental way. The accuracy of the displacements was controlled by high-precision gage blocks [9] as presented in Figure 4. The 2D scanner was used to collect point clouds of all objects at each displacement. The laser scans were conducted from about 0.6 m away from the setup and the laser scanner was not moved during the experiments.

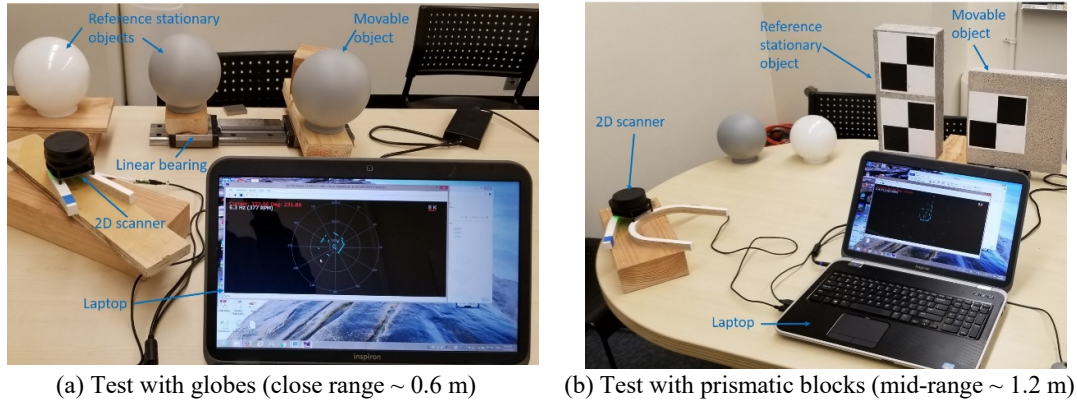


Figure 3: Experimental setup for feasibility study

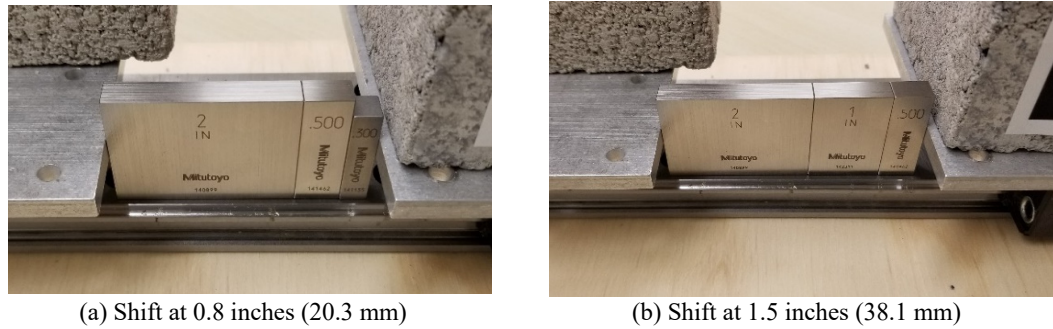


Figure 4: Examples of how the incremental displacement was imposed

Due to the size limitations of the paper, only discussion related to the globes is presented herein. These results were selected for one additional reason, which is as follows. The horizontal sections of the vertically oriented cylinders and globes will result in circles. Since the slider pack of the FPB consists of many cylinders, the approach with globes can be utilized in tracking the position of the slider pack.

A typical point cloud collected in one of the steps of incrementally applied displacements is presented in Figure 5a. It shows the cross section of the test room and objects used in the study. The scanner's location coincides with the origin of the local coordinate system of the scanner. In the case of the globes, each cross section will be a portion of a circle with only the front side collected by the scanner. The rear side will be in a shadow zone and as such, is not visible to

the scanner. The number of the collected points will depend on the proximity of the scanner to the globe and the density of the laser scans. Point clouds for all positions of the movable globe are presented in Figure 5b.

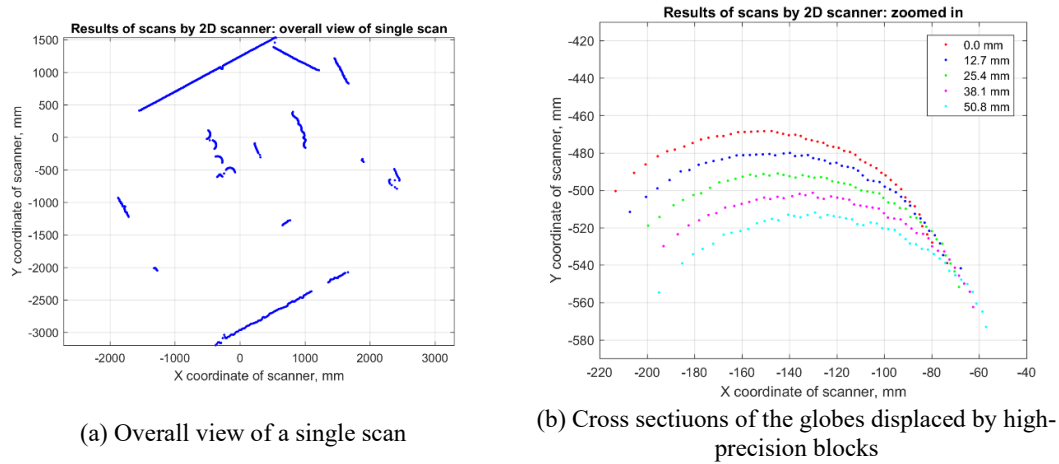


Figure 5: Typical laser scan data

The point clouds of the globe at different displacements were best fitted to circles as presented in Figure 6a. The estimations of the cross sections radii are presented in Figure 6b. The plot also shows the nominal radius of the globe at its center. As can be observed from the plot, there is about 3.5 mm difference between the estimates and the nominal radius. This result has a simple explanation. The radius of the cross section will depend on the elevation of the horizontal section plate and will be close to the nominal radius only at the elevation coinciding with the elevation of the globe's center. All other sections will yield lower estimates. Although originally there was an attempt to scan at the elevation of the globe's center, it was difficult to achieve, resulting in this relatively large difference between the radii.

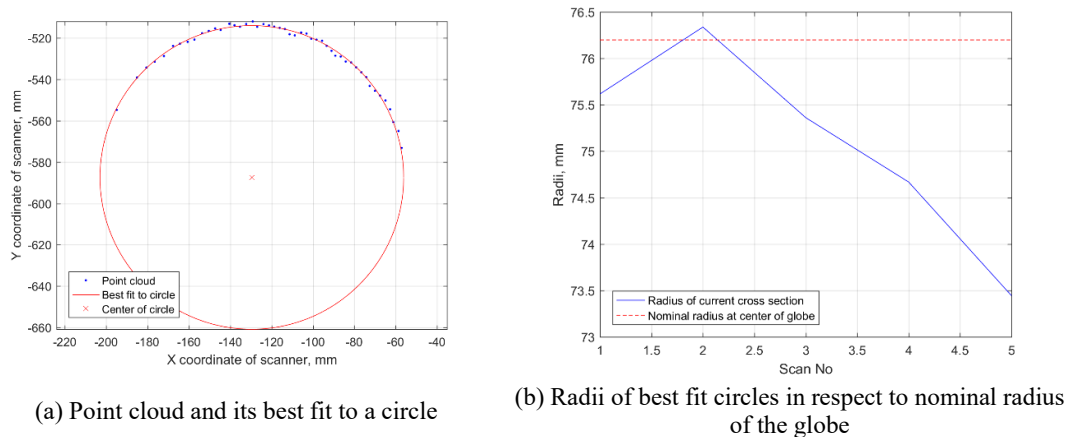
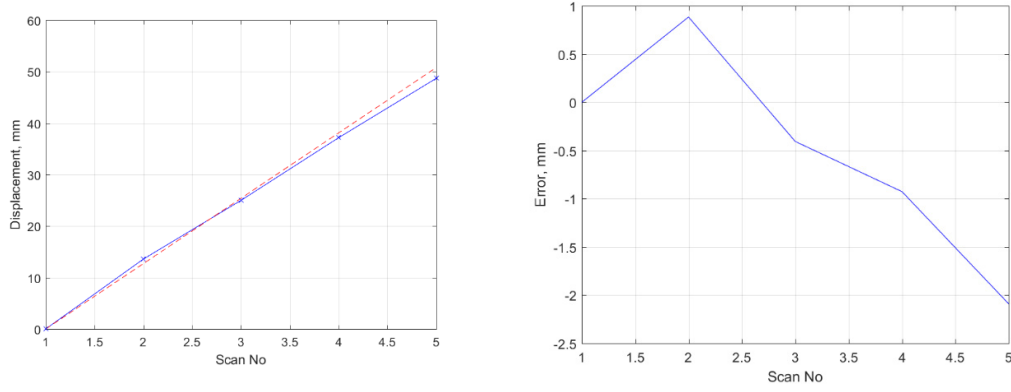


Figure 6: Best fitting of point clouds

An estimate of the circle's centers produced better results, as was expected from the beginning. A comparison between the measured displacement and the estimated location of the

circle's center in respect to its original estimate is presented in Figure 7a. Figure 7b shows an error between the actual displacement and the estimates from the laser scans. As can be observed from the plot, the error does not exceed 2.1 mm, which is considered acceptable for the application of this approach to tracking the slider pack's location inside of FPB.

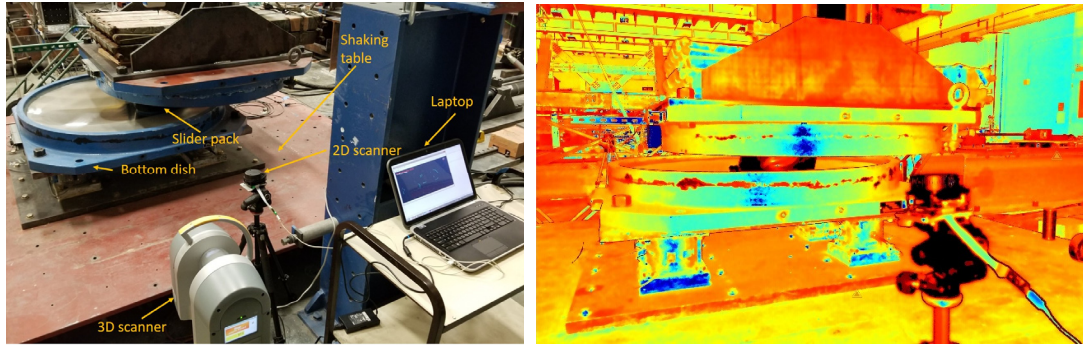


(a) Measured (red) vs. estimated from point clouds (blue) (b) Error between measured and estimated from point clouds

Figure 7: Comparison results for displacements

4 EVALUATION STUDY ON FULL-SCALE FPB

The final evaluation of the approach discussed herein was completed with the utilization of a 3D laser scanner [3]. The point cloud reduction was conducted by using Trimble RealWorks [10] and Cyclone [11]. The 3D scanner and 2D scanner were installed in close proximity to the FPB as presented in Figure 8a. Figure 8b shows the point cloud collected by the 3D scanner.



(a) Setup's photo (b) Point cloud collected by 3D scanner
Figure 8: Experimental setup for final evaluation by comparing 3D scanner and 2D scanner results

As presented in Figure 8, the load to FPB was applied via lead blocks. The shaking table platform was incrementally displaced along a single axis. The displacement was incremented 14 times and the displacement of the shaking table was measured by a position transducer. Displacements of the slider pack were monitored by both the 2D and 3D scanners. Due to size limitations of the paper, only some typical results are presented herein.

The 2D scanner was installed slightly out of plum to make sure that the scanner will capture the rib of the bottom dish and the slider pack. The point cloud of the bottom dish's rib was also collected by the 3D laser scanner. The tests were conducted in a quasi-static setting. The scanners were installed outside of the shaking table and they were stationary during the tests.

Figure 9 presents the results for the best fitting of the point clouds to circles. The point cloud with its best fit for the bottom dish is presented in Figure 9a and the point cloud with its best fit for the slider pack is presented in Figure 9b.

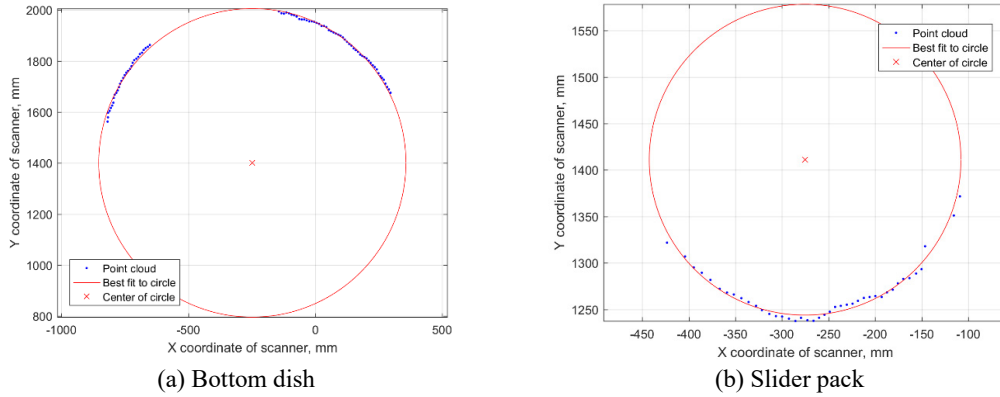


Figure 9: Typical best fits of corresponding point clouds to circles

Figure 10a presents the small variability of a few millimeters in the estimation of the dish's radius and Figure 10b shows the displacement of the bottom dish's center in respect to the top dish. Both results were obtained by utilizing point cloud data of the 2D scanner.

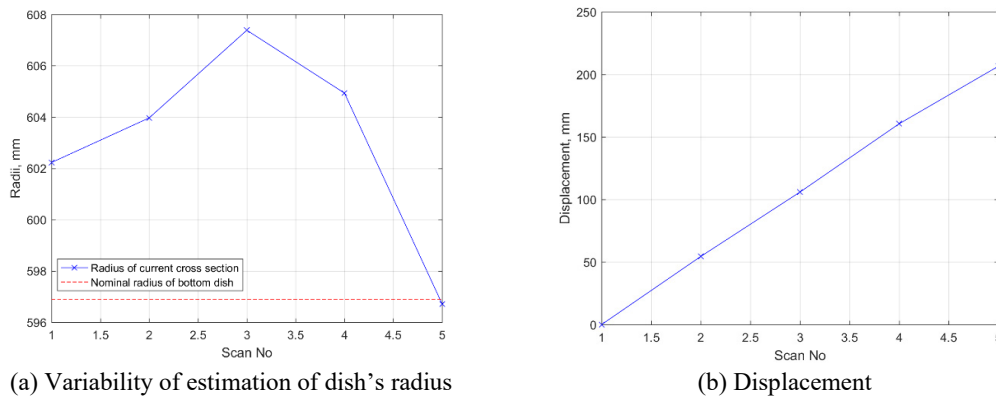


Figure 10: Results of 2D scan data for bottom dish of FPB

Figure 10 shows the comparison of the results from the 3D and 2D scanners. The displacement of the bottom dish is presented in Figure 10a. The displacement is based on the same approach of best fitting the point clouds to circles. In the case of the point cloud collected by the 3D laser scanner, only horizontal slices of the point clouds were considered. The error between the displacements estimated from point clouds of the 3D and 2D scanners are presented in Figure 10b. The latter shows that the error between the two scanners is relatively small and

does not exceed 4 mm. This accuracy is very close to the accuracy measured in the feasibility test conducted on the globes (see Section 3). Hence, the accuracy of the inexpensive 2D scanner is very close to that of the 3D scanner of surveying grade accuracy. The results obtained from the point clouds of the 2D scanner can adequately describe the displacements of the bottom dish.

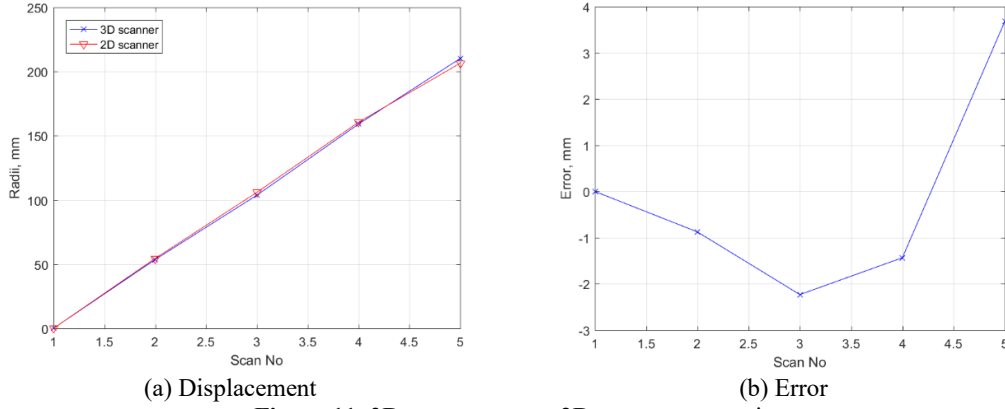


Figure 11: 3D scanner versus 2D scanner comparison

The point cloud of the slider pack captured by the 3D scanner was quite noisy because of its high sensitivity to the black color as presented in Figure 12a. It was noticed earlier [12] when surveyor grade scanners from different manufacturers were compared against each other. On the other hand, the point cloud of the slider pack collected by the 2D scanner had very small variations as shown in Figure 9b. A final comparison showing the slider and bottom dish displacements is presented in Figure 12b. Both displacements were estimated from the point clouds collected by an expensive 2D scanner, which is shown to have about the same accuracy as the 3D laser scanner. The plot presented in Figure 12b shows that the slider's displacement is about two times less than that of the bottom dish. This is related to the fact that the sliding occurs on both spherical surfaces of the top and bottom dishes, which is one of the main features of the triple FPB.

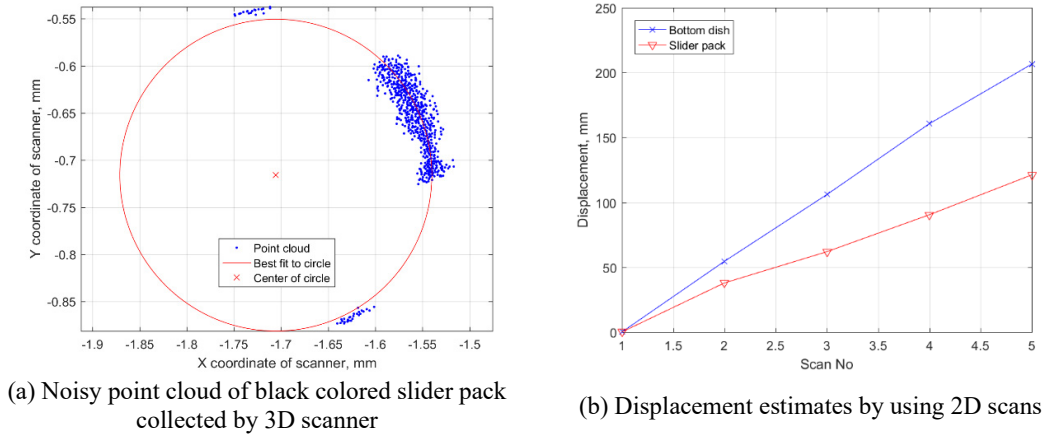


Figure 12: Noisy data of 3D scanner and displacement estimates by using 2D scans

As discussed above, the 2D scanner offers the following advantages. First, it provides an adequate accuracy of the slider pack's position tracking when compared to a 3D laser scanner with a surveyor grade accuracy. Second, it is much more compact and lightweight, which makes it possible for use in permanent installations on a FPB. Third, the price range of the 2D scanner is significantly lower than that of the 3D scanner. The price of a 2D scanner is about 0.2% of the 3D scanner's price. Fourth, low sensitivity of the 2D scanner to the color of the object was observed. Based on all these results, the 2D scanner can be used as one of the sensors in the Smart City's network.

5 CONCLUSIONS

- A smaller sensitivity to the slider's black color was observed for 2D scanner when point clouds from 2D and 3D scanners were compared.
- The approach discussed herein delivers adequate accuracy for monitoring relative dish and slider pack displacements inside of the FPB. Although the advantages of the approach are shown in a static setting, it can be easily extended to a dynamic setting. The sampling rate of the 2D scanner is 10 Hz, which is sufficient for tracking low frequency systems. For example, the FPB used in the study had a frequency close to 0.5 Hz. The approach can be extended to objects of other shapes, which is ongoing.
- Since the approach is based on the utilization of an inexpensive 2D laser scanner with a relatively high sampling rate, it is intended for mass installation to serve as a one of the near-real time sensors in the Smart City network. The approach discussed herein is going to be utilized in a standalone device comprised of a 2D scanner and Arduino [13] or similar boards, which is ongoing.

6 ACKNOWLEDGEMENTS

The work associated with the development of component testing setup for full-scale FPBs was sponsored by the Electric Power Research Institute (EPRI) whose support is greatly appreciated. Special thanks are due to Earthquake Protection Systems for donation of the full-scale FPBs used in the project. The author would like to acknowledge the hard work of the technical staff of Structures Laboratory of Civil and Environmental Engineering (CEE) Department, UC Berkeley: Mr. Matthew Cataleta, Mr. Llyr Griffith, and Mr. Phillip Wong. The 2D laser scanner was provided by 3D Structures along with some additional funding needed for collection of the point clouds, which is greatly appreciated. Technical help by Mr. Martin McDonough (CEE, UC Berkeley) on preparing technical drawings and active participation in testing is greatly appreciated. Special thanks are due to Mr. Bahtiyor Takhirov of Westminster International University in Tashkent (Uzbekistan) for his help on the development of the stand-alone device utilizing the approach discussed in this paper. Special thanks are due to Ms. Holly Halligan of CEE, UC Berkeley for her help with editing the paper.

REFERENCES

- [1] Wikipedia, 2019. https://en.wikipedia.org/wiki/Smart_city.
- [2] Shanghai Slamtec. Co., Ltd, 2018. RPLIDAR A1. Low Cost 360 Degree Laser Range Scanner. Introduction and Datasheet Model: A1M8. 2018-02-05 rev.2.1.

- [3] Trimble Inc. (2016). The Trimble TX6 laser scanner. http://trl.trimble.com/docushare/dsweb/Get/Document-824965/022516-282_TrimbleTX6_DS_US_1016_LR.pdf.
- [4] The MathWorks, Inc., 2016. Matlab Version R2016b.
- [5] Stephen Timoshenko, 1937. Vibration Problems in Engineering, 2nd Edition. New York : D. Van Nostrand, 470 pages.
- [6] Earthquake Protection Systems, 2019. <https://www.earthquakeprotection.com/triple-pendulum>.
- [7] Paul L. Drazin and Sanjay Govindjee, 2017. A Nonlinear Kinetic Model for Multi-Stage Friction Pendulum Systems. PEER Report No. 2017/07. Pacific Earthquake Engineering Research Center, Headquarters at the University of California, Berkeley, October 2017.
- [8] Shakhzod Takhirov, 2019. Updates on EPRI Project Activities at UC Berkeley. Presentation at EPRI meeting. Headquarters of Seattle City Light, April 24th.
- [9] Mitutoyo, 2019. <https://www.mitutoyo.com/wp-content/uploads/2016/09/E-section-Gage-Blocks.pdf>.
- [10] Trimble Inc., 2018. Trimble RealWorks, Version 11.0.
- [11] Leica Geosystems, AG., 2015. Cyclone Version 9.1.
- [12] Jagannath Hiremagalur, Kin S. Yen, Kevin Akin, Triet Bui, Ty A. Lasky, & Bahram Ravani, 2007. Creating Standards and Specifications for the Use of Laser Scanning in Caltrans Projects. AHMCT Research Report, UCD-ARR-07-06-30-01. http://www.dot.ca.gov/newtech/researchreports/reports/2007/final_report_task_0964.pdf
- [13] Arduino, 2019. <https://www.arduino.cc/>.

SMART BRIDGE DEVELOPING BASED ON MICRO-TRUSS OPTIMIZATION METHOD

Y. Yokotani^{*}, I. Ario^{*}, Y. Chikahiro[†] and M. Nakazawa[‡]

^{*} Department of Civil & Environmental Engineering
Hiroshima University
Higashi-hiroshima, Japan
e-mail: m185931@hiroshima-u.ac.jp, mario@hiroshima-u.ac.jp

[†] Department of Water Environment & Civil Engineering
Shinshu University
Nagano, Japan
e-mail: chikahiro@shinshu-u.ac.jp

[‡] Department of Civil Engineering
Tohoku Gakuin University
Tagajo, Japan
e-mail: naka@mail.tohoku-gakuin.ac.jp

Key words: Michell truss problem, Micro-truss method, Topology optimization, Optimum structures

Abstract. The damage and catastrophe to social infrastructures by natural disasters, such as earthquakes, floods, landslides and tsunamis in the world, are serious problems in disaster prevention for the inhabitants of a stricken area. So, we propose the optimum layout designs how to rebuild damaged infrastructure and how to build a new type of rescue system which can be implemented quickly when trying to save lives after an emergency. A design domain on the beam model is optimally formed using micro-trusses for the analysis of a macro-structure. This has the benefit of achieving a more realistic lightweight structure form for repetitive analyses. We presented the modified stiffness matrix method to obtain a solution for the topological optimum structures. The optimisation strategy is based on a fully-stressed design that uses the stiffness of the micro-truss members as design variables. From this structural analysis on the optimum structures using micro-truss model, the smart and deployable bridge Mobilebridge, as the emergency bridge at the time of disaster, is designed.

1 Introduction

Research on the optimum design of a structure has been conventionally performed to optimize the dimensions to determine the ideal sectional area, sectional dimension, member length, etc. of the structural members for given design conditions. Recently, geometry optimization and phase optimization problems for obtaining the ideal shape of a member or structure have been actively investigated. For example, of the available approaches, a homogenization method and a ground structure approach have been proposed. The objective of the homogenization approach is to maximize the stiffness and form design of the structure and to optimally arrange the materials [1]-[3]. The aim of the ground structure

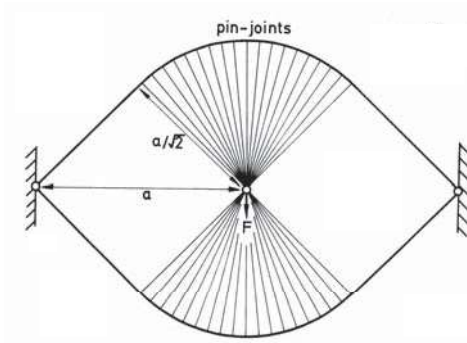


Figure 1: Approximation of Michell's truss using the structure of a finite number of members [9]

method is to minimize compliance (maximize stiffness) by restricting the volume of the structure [4]. However, since these methods are combinatorial optimization problems that involve the determination of which constituent elements of the structure should be combined or removed, there are often no viable solutions.

In addition, there is also active research on the application of emergent methods that can simultaneously produce a large number of viable solutions that exist in a combinatorial optimization problem such as Genetic Algorithms (GA) [5], [6] and Cellular Automata (CA). These studies make it possible to easily generate various phase structures using the simple law or numerical method (local rule) that describe local information. Shape optimization has been extensively studied using such a complicated system. However, these studies have been limited to the basic truss structure optimization problem with a small number of elements, and it is difficult to obtain a stable convergence solution in a large-scale structural model, in addition to the requirement of significant computational complexity.

Further, the evolutionary structural optimization (ESO) method was proposed in the early 1990s to solve a variety of size, shape, and topology optimization problems [7]. The ESO method gradually removes unnecessary or inefficient member from a structure to achieve an optimal design. In addition, the bi-directional evolutionary structural optimization (BESO) method is known as an extension of the ESO method. This method gradually adds necessary or efficient members to the structure at the same time that the inefficient ones are removed to achieve an optimal design [8]. However, these methods sometimes lead to a mesh-dependent solution and a non-convergent solution.

Michell's structure is an example of an optimal design in which the structure transfers the vertical load onto two pinned supports. A schematic representation is shown in **Figure 1** [9]. In 2015, A.V. Pichugin, et al. suggested a new half-plane Michell structure that transmits a uniformly distributed load of infinite horizontal extent to a series of equally spaced pinned supports, and also changed the specified ratio for limiting compressive to tensile stress formed from an arch with vertical hangers attached to a cable-stayed bridge [10]. However, formal proof of optimality of the structure has not yet been demonstrated.

On the other hand, in recent years, the damage and destruction to social infrastructure by natural disasters, such as earthquakes, floods, landslides and tsunamis in the world, are serious problems in disaster prevention for the inhabitants of a stricken area. So, we have to consider how to rebuild damaged infrastructure and how to build a new type of rescue system which can be implemented quickly when trying to save lives after an emergency.

From these backgrounds, we propose the optimum layout designs how to rebuild damaged infrastructure and how to build a new type of rescue system which can be implemented quickly when trying to save lives after an emergency. A design domain on the beam model is optimally formed using micro-trusses

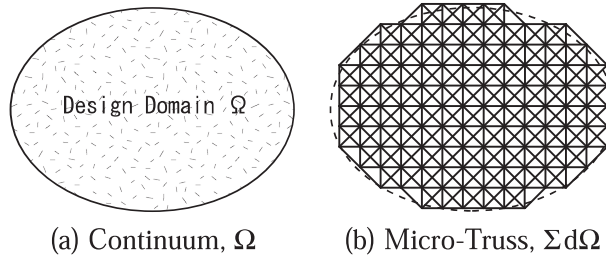


Figure 2: Discretisation of a Continuum

for the analysis of a macro-structure. This has the benefit of achieving a more realistic computational cost for repetitive analyses. We used the modified stiffness matrix method to obtain a solution for the topological optimum structures. The optimisation strategy is based on a fully-stressed design that uses the stiffness of the micro-truss members as design variables. From this structural analysis on the optimum structures using micro-truss model, the smart and deployable bridge “Mobile bridge”, as the emergency bridge at the time of disaster, is designed.

2 OPTIMISATION STRATEGY

2.1 Optimum structure using micro-truss method [11], [12]

We represent the design domain Ω of a continuum by micro-trusses, (1). The discretisation is diagrammatically represented in **Figure 2**, where an example of a continuum **Figure 2(a)** is discretised as **Figure 2(b)**. It is proposed that the behaviour of the domain Ω can be adequately modelled by micro-trusses for large number of unit cells, m , where each micro-truss member represents a pin-jointed linear extensional spring.

$$\Omega = \lim_{d\Omega \rightarrow 0} \sum_{m \in \mathbb{Z}}^{(1/d\Omega) \in \mathbb{Z}} d\Omega^{(m)} \approx \sum_{\substack{m \gg 1 \\ d\Omega \propto 1/m}} d\Omega^{(m)} \propto \sum_{\substack{m \gg 1 \\ x^{(m)} \propto 1/m}} x^{(m)}, \quad m = 1, \dots, M \quad (1)$$

The design variable is the stiffness of the micro-truss members, x and therefore the equilibrium equation can be rewritten as (2).

$$F(u, f, x) = 0 \quad (2)$$

where $x = \{\dots, x^{(m)}, \dots\}^T \in \mathbf{R}^m$.

The goal of optimisation is the fully-stressed design, represented as (3) in a discrete form. The design modification is based on the local stress response, where the stiffness of a member is updated at each load step according to (4).

$$\begin{aligned} \text{Min} \quad & \sum_{m=1}^M \left(\frac{\sigma^{(m)}}{\sigma_{\text{nom}}} - 1 \right)^2 \\ \text{Subject to} \quad & x_{\min} \leq x^{(m)} \leq x_{\max} \end{aligned} \quad (3)$$

where $\sigma = \{\dots, \sigma^{(m)}, \dots\}^T \in \mathbf{R}^m$, σ_{nom} = normal stress and M = total number of micro-cell members. Subscripts, min and max denote the lower and upper bounds, respectively.

$$x_{(v+1)} = \gamma \frac{|\sigma_{(v)}|}{\bar{\sigma}_{(v)}} x_{(v)}, \quad v = 1, 2, \dots \quad (4)$$

where v = iteration number, γ = optimisation rate constant and

$$\bar{\sigma}_{(v)} = \frac{1}{M} \sqrt{\sum_{m=1}^M \left(\sigma_{(v)}^{(m)} \right)^2} \quad (5)$$

After one iteration of design modification, the tangent stiffness matrix is updated and the new equilibrium equation is established for the subsequent load step. The design update is applied at each load step.

2.2 Principle of form formation with the iteration method

While the change of the stiffness is limited to a part of structural system, although it is higher for accuracy of the calculation to carry out structural analysis directly, it is possible for the iteration method to observe “the flow of stress” to get stable solutions for sequential correction of a whole of stiffness. In this paper, the correction of the stiffness matrix is assumed to be a feed-back system of the stress response for each member. This computing process is controlled the amount of stiffness for the finite element satisfied under the equilibrium condition. This method is advantage even though including the large-scale calculation or singular problems.

Now, it is assumed that the equilibrium points $(u, f, x_{(1)})$ are obtained by the method of the loading control and/or displacement control with the configuration of the initial design parameters. The stress in each member is defined as

$$\sigma_{\min} \leq \sigma^{(m)} \leq \sigma_{\max} \quad (6)$$

$$\sigma_{(v)} = W(u_{(v)}) \quad (7)$$

It is the displacement function of each node. Here v is defined as the number of iterations, and $\sigma_{(v)} = \left\{ \dots, \sigma_{(v)}^{(m)}, \dots \right\}^T$ is defined as $u_{(v)} = \left\{ \dots, u_{(v)}^{(m)}, \dots \right\}^T$.

Furthermore, the present design variable (stiffness) $x_{(v)}$ is resolved into $x_{(v+1)}$. A new design variable is also resolved into

$$\begin{aligned} x_{(v+1)} &= F(\gamma, \sigma_{(v)}) \\ &= F(\gamma, W(u_{(v)})) \end{aligned} \quad (8)$$

We ensure that the stiffness matrix is also renewed. F means a function to solve the distribution of stiffness. This result enable us to identify solutions $(u_{(v+1)}, f, x_{(v+1)})$ ¹ from the equilibrium equation.

$$J(u, f, x_{(v+1)}) \tilde{u}_{(v+1)} = \frac{\partial F}{\partial f} \tilde{f} \quad (9)$$

¹Now this solution is defined as displacement vector $u_{(v+1)}$ for weight control.

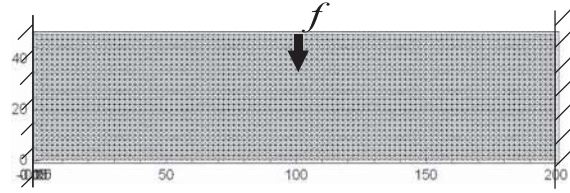


Figure 3: Analytical beam's model with the clamped supports

We substitute this solution into equation (7) and perform a series of repeated calculation, such that the convergence stress and displacement conditions are satisfied. In other words, the nodal displacement and design variable are expressed as

$$\begin{aligned} u_{(v)} &= F(f, x_{(v)}) \\ x_{(v+1)} &= F(\gamma, W(u_{(v)})) \end{aligned} \quad (10)$$

by repeated calculation of the equilibrium equation. If γ , f and W is included, multi-dimensional and multi-feed back of the repeat calculation is expressed as

$$x_{(v+1)} = F(x_{(v)}) = F(F(\cdots F(x_{(1)}))) = F^v(x_{(1)}) \quad (11)$$

We adopt a limited stress condition and variable based on local rules.

3 NUMERICAL RESULTS

3.1 A beam model with the clamped supports

Let us consider the problem of topology optimizing using by the present method of microtruss concept when designing a beam with both-ends fixed model. We consider the discrete model of the design region with a size of 50×200 and mesh division of 25×100 . As shown in **Figure 3**, all nodes of the both sides of the design domein is fixed, and the load position of the vertically downward load was set on the upper side of the beam centre. **Table 1** shows this analysis condition.

The process that needs to be followed step by step to produce the optimum shape is shown in **Figure 4**. **Figure 4** (a)-(d) show the process status from the first step to final shape and stress used by this present method. In this figure, red area shows the compressive members, and blue area shows the tensile members. You can clearly see the shapes determined when balancing compressive (red colour) and tensile (blue colour) members with symmetry. In **Figure 4** (d), we can recognize the final structural frames based on the flow of stress between the load point and the boundary area on which the high stress distribution located at high and low points as far as from the neutral line. And we can carefully see many diagonal members and the triangular substructure. In particular, there are not the horizontal chords at the horizontal positions 50 and 150. If there are only diagonal members in the form of numerical results, and taking all the horizontal members from the structure, the optimized structure can be regarded as a structure compatible with function optimization as a developed structure of the scissors structure.

Figure 5 is the graph shown change in the ratio of the number of necessary members. From this graph, the ratio of the members constituting the final form to the number of initial form is 30.8%. Therefore, about 70% of the number of the initial members could be removed.

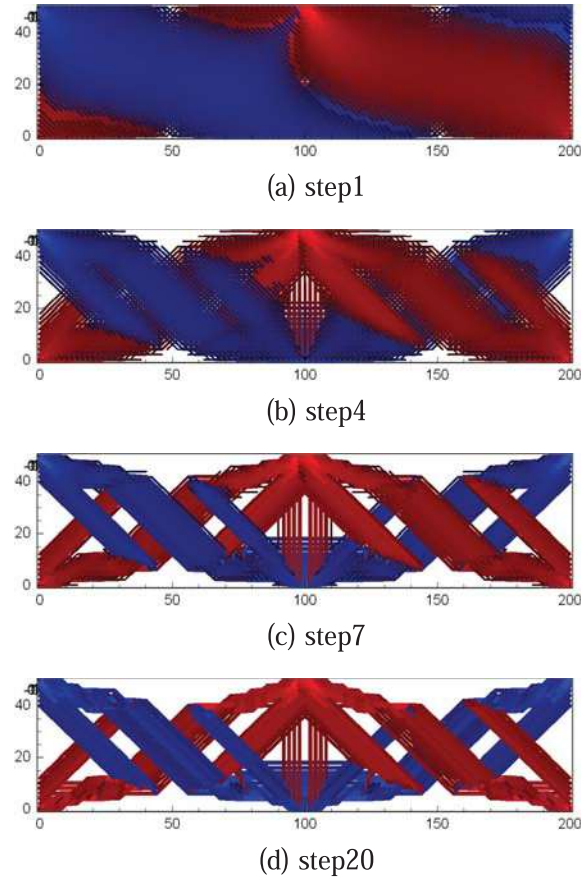


Figure 4: Analytical results produced by the present method

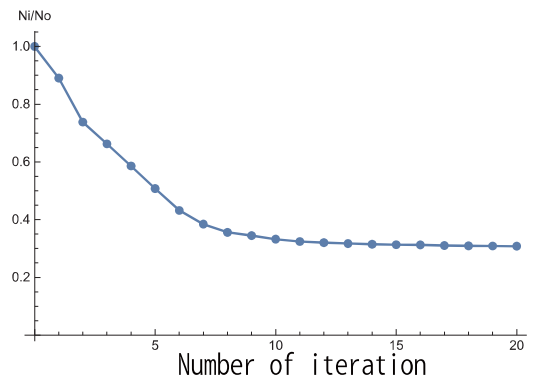


Figure 5: The change of members' ratio

Table 1: Summary of analysis conditions for a model with a size of 50×200

Initial section stiffness	$EA_0 = 1$
Load parameter	$f/EA_0 = 0.001$
Maximum section stiffness	$EA_{\max} = 10.0$
optimisation rate constant	$\gamma = 0.019$

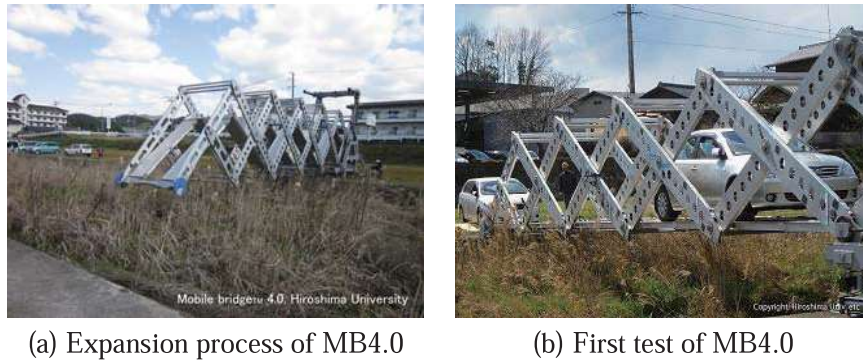


Figure 6: Tests of foldable, movable and deployable bridge “Mobile bridge”

3.2 Mobilebridge of smart bridges

In general, it is known that the upper and lower horizontal members of a truss greatly affect the resistance of the bending moment. In this research, however, the truss was used in a new type of bridge that has only diagonal members and no upper or lower horizontal members as the main frames as shown in **Figure 4(d)**. We considered how to develop and apply a new emergency bridge that can be folded up and ready for deployment by using a truss system. The aim is to use the bridge to restore infrastructure that has been damaged in a disaster. Therefore, we have tried to develop Mobilebridge shown in **Figure 6**. This bridge is based on both the concept of a multi-folding micro-structure and research on structural optimization. However, this structural type of the bridge is based on scissors type contains frame as the units of the pin-rahmen members without truss structure. As the result, it is similar for optimisational shape of this bridge which is available to be deployable. To develop Mobilebridge, we need to develop a way to expand it from a folded state.

For example, we can examine an expandable truss structure in which we replace a beam with a structure that works like a pair of scissors. This is effective from the viewpoint of structural optimization for Michell’s problem. If this scissor structure has enough strength when it is deployed with its own weight, it will not need any horizontal members. However, after it has been expanded it may need to be reinforced to make a completed bridge. In this case, although the horizontal displacement is kept in check owing to both the contact side supports and it keeps its stiffness in a plane, we have to design the bridge so that it has enough stiffness when it moves outside a certain plane without undergoing any large deformation. We believe one effective way to change an unstable structure into a stable structure may be to assemble a three-dimensional truss with a tied cable or tied bar between both of the end supports. This makes it possible to produce an expandable and movable bridge. With the technology used in this bridge system, it is possible to completely and quickly construct a bridge system.

4 CONCLUDING REMARKS

This paper presented a stress based topology optimisation strategy using the large size of micro-truss method. We simplified the continuum using a micro-truss representation in order to reduce the lightweight structure form to a realistic level. The modified stiffness iteration method was implemented for the analysis of multiple bifurcation points. Using the stiffness EA of the micro-truss members as design variables, we modified the stiffness based on the stress ratio. Assuming there is a constant material property, the stiffness EA can be interpreted as the cross-sectional area of micro-truss members, which allows us to understand the optimum solutions. We demonstrated the optimisation strategy through the beam model with the clamped supports. We have obtained the optimum shaped frame with compressive

and tensile area like scissors structure in the beam structure.

From this research, we have proposed the new type of the deployable bridge “Mobilebridge” with scissors structure. This new device is one of the rescue tools for the recovery of a bridge after a disaster. This device is the first bridge type with a scissors structure. In general, some control members are required as in the form of structure optimization in order to statically stabilize the scissors structure. Therefore, we should assemble a three-dimensional truss with a tied cable or tied bar between both of the end supports. This makes it possible to rebuild bridges as fast as possible in the field of engineering.

Acknowledgements

This research is supported by the Grant-in-Aid for Challenging Exploratory Research of the Japan Society for the Promotion of Science (JSPS) KAKENHI Grant Number JP18K18888 in 2018 - 2020.

REFERENCES

- [1] M. P. Bendsoe and N. Kikuchi, Generating Optimal Topologies in Structural Design using a Homogenization Method, *Computer Methods in Applied Mechanics and Engineering*, Vol.71, pp.197-224 (1988).
- [2] K. Suzuki and N. Kikuchi, A homogenization method for shape and topology optimization, *Computer Methods in Applied Mechanics and Engineering*, Vol.93, pp.291-318 (1991).
- [3] R. J. Yang and C. H. Chuang, Optimal topology design using linear programming, *Computer & Structures*, Vol.52, No.2, pp.265-275 (1994).
- [4] Ringertz, U.T., A branch and bound algorithm for topology optimization of truss structures, *Engng. & Optimization*, **10**, pp.111-124 (1986).
- [5] Jenkins, W.M., Towards structural optimization via the genetic algorithm, *Comput & Struct.*, **40**, pp.1312-1327 (1991).
- [6] Ohsaki, M., Genetic algorithm for topology optimization of trusses, *Comput & Struct.*, **57**, pp.219-225 (1995).
- [7] Xie, Y. M. and Steven, G. P., A simple evolutionary procedure for structural optimization, *Comput. Struct.* 49 885-886 (1993).
- [8] Yang, X. Y., Xie, Y. M., Steven, G. P. and Querin, O. M., Bidirectional evolutionary method for stiffness optimization, *AIAA J.* 37 (11), 1483-1488 (1999).
- [9] Michell, A. G. M., The limits of economy of material in framed structures, *Phil. Mag. (Series 6)*, Vol.8, pp.589-597 (1904).
- [10] Pichugin, A. V., Tyas, A., Gilbert, M. and He, L., Optimum structure for a uniform load over multiple spans, *Struct Multidisc Optim*, 52, pp.1041-1050 (2015).
- [11] Ario, I., Tanaka, Y., Nakazawa M., Furukawa Y. and Chikahiro Y., Development of the prototype of a new emergency bridge based on the concept of optimized structure, *J. Struct. Eng.* 64A, 1-12 (2012) (in Japanese).
- [12] Ario I., Nakazawa M., Tanaka Y., Tanikura I. and Ono S., Development of a prototype deployable bridge based on origami skill, *Automation in Construction*, Vol.32, 104- 111 (2013).

STATISTICAL ANALYSIS OF DAMAGE INDICATORS BASED ON ULTRASONIC TESTING WITH EMBEDDED PIEZOELECTRIC TRANSDUCERS

A. DERAEMAER*, C. DUMOULIN*, N. DERVILIS[†], E.J. CROSS[†] AND K.
WORDEN[†]

*Université Libre de Bruxelles - BATir
50 av. F.D. Roosevelt, CP 194/02
B-1050 Brussels, Belgium
e-mail: aderaema@ulb.ac.be, cedumoul@ulb.ac.be

[†] Dynamics Research Group, Department of Mechanical Engineering, University of Sheffield
Mappin Street, Sheffield S1 3JD, UK
e-mail: n.dervilis@sheffield.ac.uk, e.j.cross@sheffield.ac.uk, k.worden@sheffield.ac.uk

Key words: Structural Health Monitoring, Ultrasonic testing, Damage detection, Concrete, Statistical analysis

Abstract. This paper aims at developing a fully automated crack monitoring system for concrete structures, based on embedded piezoelectric transducers. The essential elements of the monitoring system are the embedded transducers, the interrogation unit, the post-processing method, and the determination of a threshold for automated alarm triggering. The paper starts with the description of the sensors and interrogation unit, followed by a presentation of the test setup which consists in a short concrete beam with a pair of embedded piezoelectric transducers subjected to a three-point bending test to induce progressive damage. Continuous monitoring is performed throughout the test and the methodology to compute a damage indicator and compensate for the acoustoelastic effect is described. The last section deals with the determination of the threshold for alarm triggering based on statistical analysis of the damage indicator. Two approaches are compared, the first one which relies on the assumption of normality of the damage indicator, and the second more general one based on extreme value statistics.

1 INTRODUCTION

Concrete is the most widely-used construction material in the world; it is a complex material whose mechanical properties evolve continuously from the time of casting until the end of its lifetime. Over time, when the structure is in-service, the mechanical properties of concrete can deteriorate due to several mechanisms, such as the loss of prestress in prestressed concrete or chemical attacks such as alkali-silica reactions or delayed ettringite formation. In order to ensure the safety of the infrastructure, it is important to be able to assess its state of health. Destructive compressive tests can be performed on sampled cores extracted from the structure. For obvious reasons however, non-destructive techniques are preferable. Among these, the ultrasonic pulse velocity method (UPV) is currently one of the most widely used techniques. This is an established technique described in different national norms including the European

standard *EN 12504-4* [1] and the ASTM norm *C 597 – 02* [2], and used in many commercial systems. The technique consists in exciting the emitter by a short pulse signal and measuring the time of propagation of the wave from the emitter to the receiver. Knowing the distance between the transducers, the velocity of the fastest wave (the compressive wave, also called the *P*-wave) can be measured. The *P*-wave velocity is related to the mechanical properties (Young's modulus and Poisson's ratio) of the concrete and can therefore be used to assess the uniformity and relative quality of concrete [3]; it can also indicate the presence of voids and cracks [4] and can be used to evaluate the setting time in fresh concrete [5].

Over the last ten years, several researchers have studied the possibility of embedding the ultrasonic probes directly inside the concrete [6]. The first and obvious advantage of the technique is the potential automation of ultrasonic monitoring. Additional advantages are an enhanced coupling (without coupling agents) with the concrete for stronger wave generation over longer paths, the protection of the transducers from environmental and accidental attacks, the possibility to perform measurements in the presence of formworks, and an added flexibility of transducer arrangements which allows for direct wave propagation paths. A major requirement with such transducers is however, their low-cost, as they will be lost in the structure.

At ULB-BATir, there has been development of tailored embedded transducers to measure the *P*-wave velocity at early-age [7] and monitor cracking in several laboratory tests [8, 9, 10] (pull-out, three-point bending and compressive tests). In particular, based on the measured received wave, there has been developed a damage indicator able to track the appearance of micro-cracking in concrete. The aim of the present paper is to go one step beyond the definition of the damage indicator by proposing robust techniques to set appropriate thresholds for automated damage detection.

2 SPECIMENS AND MONITORING SYSTEM

Experiments we performed on two short non-reinforced concrete beams in which a pair of transducers had been embedded with a spacing of 14.3 cm. The beams are made of ordinary concrete. The geometry and the components of the beams are given in Table 1.

The embedded transducers have been developed at ULB-BATir and are made of a thin Lead Zirconate Titanate (PZT) patch which is a piezoelectric material [11] and surrounded by several coating materials (Fig. 1).

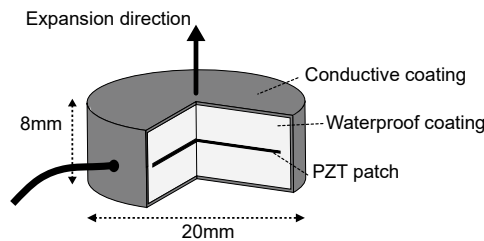
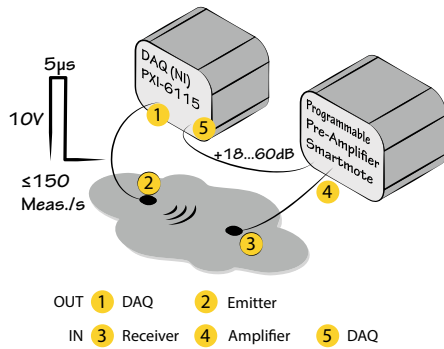


Fig. 1: Embedded piezoelectric transducers designed and manufactured at ULB-BATir.

The ultrasonic monitoring system is described in Fig. 2a; it is composed of a data acquisition board NI

PXI-6115 (10 MHz sampling rate) and a variable-gain preamplifier SmartPre (+18 – 60 dB, band-pass 1 kHz – 1 MHz) designed by SMARTMOTE which are controlled by an in-house program based on the LabView programming environment. The system is able to perform up to 150 ultrasonic measurements per second while the signal which is generated is a short pulse of 5 μ s corresponding to a frequency band up to 200 kHz (–6 dB at 120 kHz). For the present experiments, the ultrasonic measurement rate has been set to 25 Meas./s. The duration of each measurement is 3 ms which allows for a complete attenuation of the ultrasonic wave before the next measurement.

The excitation signal is a low-voltage short pulse (10 V, 5 μ s). Due to the very high measurement rate in this test and the occurrence of damage, some recorded signals are polluted with acoustic emission events which have to be filtered out. Acoustic events are waves generated by the sudden release of energy due to cracking events [12, 13]. In the present study, it was decided to remove these signals from the data, with the procedure described in [10]. This is not problematic as there are enough non-polluted signals due to the very high measurement rate. The measurements which are presented in section 3 correspond to an average of the last 10 sane signals (i.e. without acoustic emission events).



(a) Fast (≤ 150 ultrasonic measurement per second) and low-voltage (≤ 10 V) data acquisition system. (b) Embedded transducers in a prismatic mold.

3 DAMAGE MONITORING

A three-point bending test is performed on one of the two non-reinforced concrete beams after 28 days. An overview of the test setup is shown on Fig. 3. The loading machine is a 200 kN hydraulic jack bending testing machine. The force and the displacement have been recorded on a computer using a National Instruments DAQ system (NI PXI-4461). The vertical displacement at the center of the beam is measured by an inductive displacement transducer (± 5 mm LVDT, HBM W5TK) wired to the DAQ through a specific signal conditioner. The ultrasonic monitoring system is described in Fig. 2a. During the bending test, short low-voltage pulses are sent at regular interval (5 μ s, 10 V, 25 Signals/s).

3.1 Loading Procedure

Since the beam is not reinforced, the maximum load which can be applied is reached at the initiation of the crack. The loading machine is controlled in displacement thanks to an inductive linear displacement transducer (LVDT) as shown in Fig. 3. In order to make sure that the crack is initiating at the center of the beam, a notch of 1 cm of depth is sawed (Fig. 4). The loading procedure and the force-displacement curve are displayed in Fig. 4 where different pictures allow tracking the crack opening. The beam is

Table 1: Composition of the concrete and geometry of the Non-Reinforced Concrete (Mini) Beams

Geometry of the Non-Reinforced Beam		
$L \times l \times h$	cm	$40 \times 10 \times 10$
Distance between transd.	cm	14.3
Concrete components		
CEM I 52.5 N PMES CP2 (Saint Vigor, FR)	kg/m ³	Density 340
Sand 0/4 (Bernières, FR)	kg/m ³	739
Gravel 8/22 (Bernières, FR)	kg/m ³	1072
Total water	kg/m ³	184
Total wet density	kg/m ³	2335
Total dry density	kg/m ³	2250
Mechanical Properties		
Young's Modulus* E_{cm}	GPa	36
Compressive Strength (cube)* $f_{ck,cube}$	MPa	38.04
Compressive Strength (cylinder)* f_{ck}	MPa	30.05
Tensile Strength† f_{ctm}	MPa	$0.3 f_{ck}^{2/3} = 2.89$
Flexural Strength† $f_{ctm,fl}$	MPa	$(1.6 - \frac{h(m)}{1000}) f_{ctm} = 4.63$
Expected Maximum Load†	kN	8.1

* Measured

† Estimated from EUROCODE EN 1992-1-1:2004

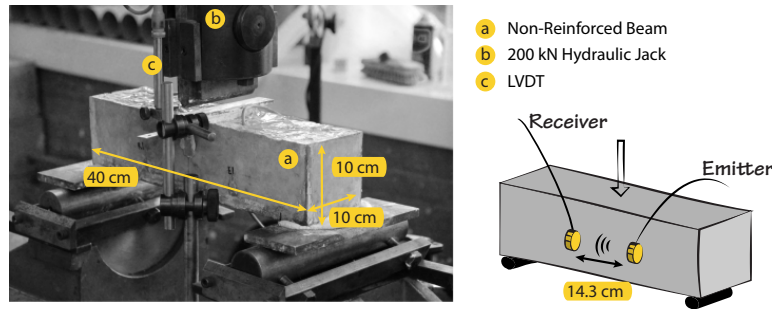


Fig. 3: Overview of the test setup for the bending test. The geometry of the specimen is given in Table 1. The loading machine is a 200 kN hydraulic jack bending testing machine.

unloaded right after the crack visually appears. The different pictures are numbered (from **1** to **3**) in order to relate them to a) the force-displacement and force-time curves in Fig. 4, and b) the evolution of the damage index in Fig. 6. The crack visually appears when the maximum load is already exceeded (see **2** in Fig. 4). It is important to note that the sudden load decreases which can be observed in the loading phase are due to technical features of the loading machine.

3.2 Damage indicator

For real-time monitoring, it is important to be able to distinguish between the effects of damage and operational conditions. As the wave velocity varies due to the appearance of damage as well as changing operational conditions, it is not a robust indicator of damage. The previously-used damage indicator, the early wave damage index, has also been shown to be sensitive to operational conditions [9]. In this paper, the time stretching with DWI [10] is used in order to filter out operational conditions before computing

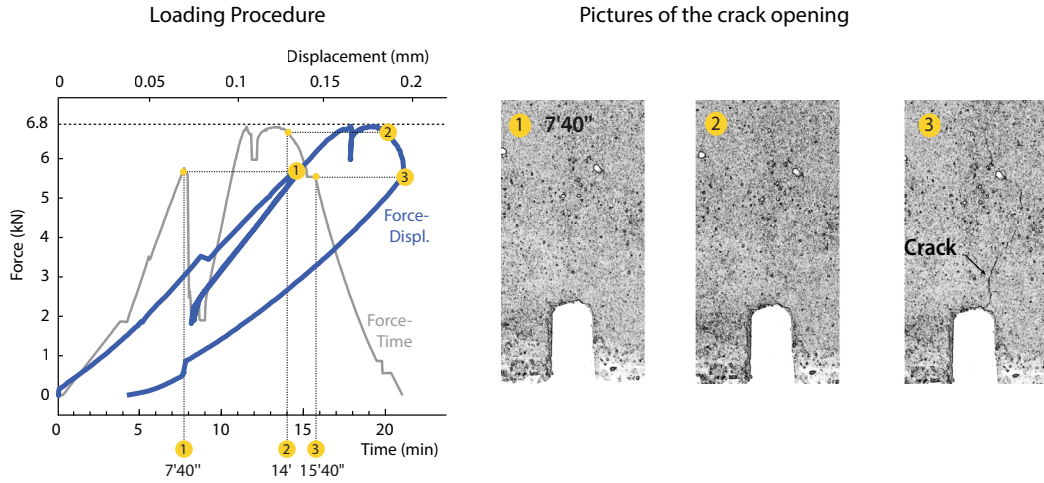


Fig. 4: Loading procedure and force-displacement curve related to the visual appearance of the crack. The three-point bending test is controlled in displacement using a LVDT.

the damage index.

The damage index DI is expressed as

$$DI_j = \sqrt{\frac{\int_{t_1}^{t_2} \left(S_j(t(1 - \epsilon_{max})) - S_0(t) \right)^2 dt}{\int_{t_1}^{t_2} S_0^2(t) dt}} \quad (1)$$

where $S_j(t)$ corresponds to the amplitude of the damaged signal, $S_0(t)$ is the amplitude of the healthy signal, t_1 is the time of arrival of S_0 , and $t_2 - t_1$ corresponds to the duration of the first half-period. This is represented in Fig. 5, where an example of a healthy signal and one with cracking are presented. ϵ_{max} corresponds to the value of time stretching which maximizes the correlation coefficient CC defined by,

$$CC(\epsilon) = \frac{\int_{t_0}^{t_f} S(t) S_0(t(1 + \epsilon)) dt}{\sqrt{\int_{t_0}^{t_f} S^2(t) dt \int_{t_0}^{t_f} S_0^2(t(1 + \epsilon)) dt}} \quad (2)$$

Fig. 6 shows that if no time stretching is applied to the measured signals, the DI is affected by these small velocity changes (see the small increase of the DI around point 1 which can be attributed to the acoustoelastic effect as explained in [10]). Applying time stretching allows removal of the small velocity changes due to operational perturbations, at the cost of a slightly lower sensitivity to the damage. The damage indicators presented in Fig. 6 are obtained after averaging ten ultrasonic signals. This allows to reduce the noise and therefore potentially to increase the sensitivity to damage. In the next section, the methodology to set a robust threshold to distinguish between the healthy and damaged state in an unsupervised manner is discussed. The case where no average is performed on the signals before computing the damage index is also discussed. If no averages are performed, the threshold will most likely be higher and the sensitivity to damage should decrease, but more data is available for the statistical analysis.

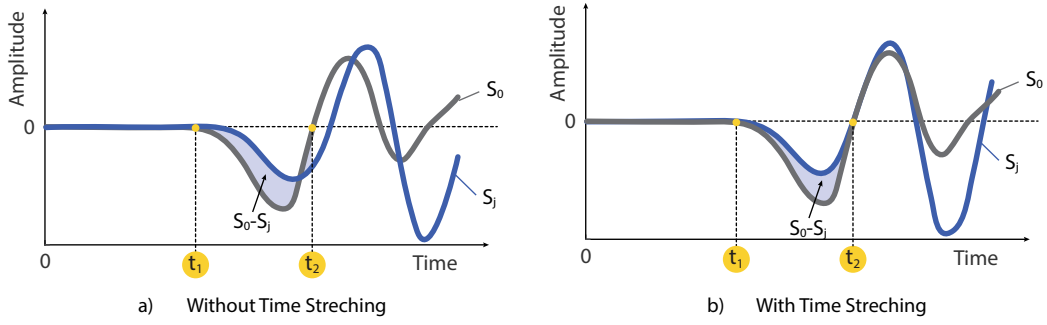


Fig. 5: Example of a healthy and a damaged signal and definition of the quantities used for the computation of the damage index (with and without time stretching).

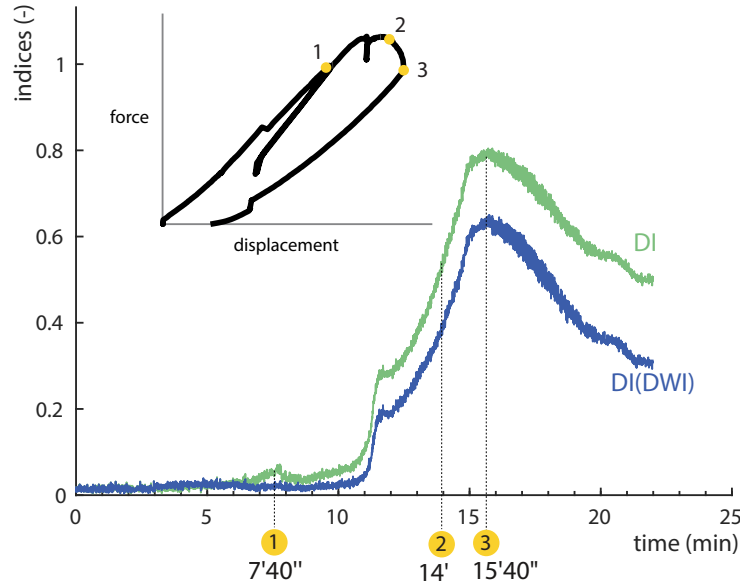


Fig. 6: Evolution of the damage indicator as a function of the time (DWD: direct wave decorrelation, CWD: coda wave decorrelation).

4 Extreme value threshold calculated with differential evolution

The first stage in the analysis is to define an alarm threshold regarding the damage index. Traditionally, the warning levels can be defined by $\bar{n} + a\sigma$, where \bar{n} and σ are respectively the mean and standard deviation of all the values of the novelty index (damage indicator as defined in equation (1)) over the training data. In statistical terms, the parameter a controls the percentage of false-positives. For example, if the distribution is purely Gaussian, then a value of 1.96 will give estimates within warning levels of 95% probability. In this paper, a is set equal to 2.58 giving a 99% confidence limit. In Figures 7, 8, 9 and 10 one can see if the normal/healthy condition of the data as defined before is following a normal distribution. For this reason plots in Figures 7, 8, 9 and 10 show a histogram of values of healthy data and fit a normal density function. Note that as expected, the standard deviation of the data with 10 av-

erages is lower than with no average. It can be seen that the distribution is close to normal but weakly right-skewed with a longer right tail (positive-skew distribution).

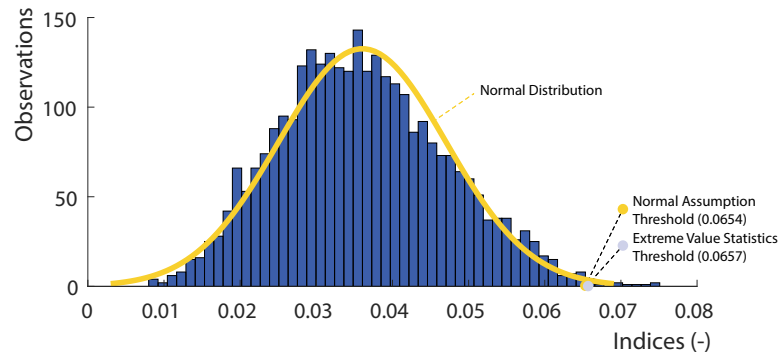


Fig. 7: Histogram with a normal distribution fit of the damage indicator without time stretching (no average).

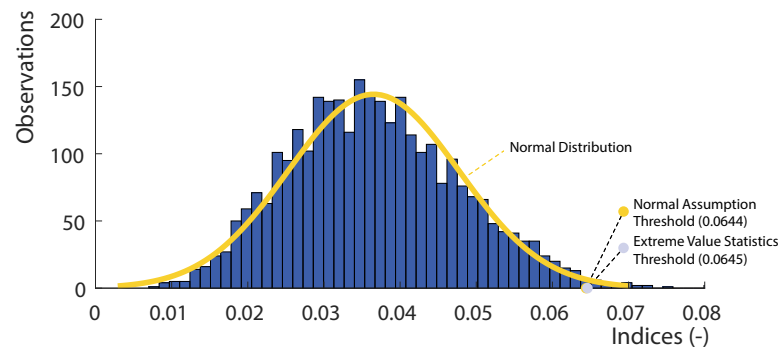


Fig. 8: Histogram with a normal distribution fit of the damage indicator with time stretching (no average).

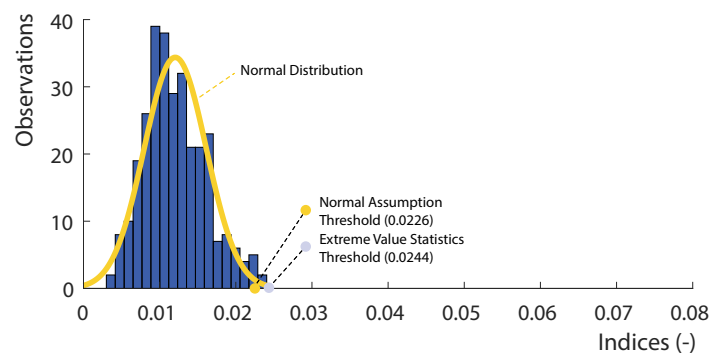


Fig. 9: Histogram with a normal distribution fit of the damage indicator without time stretching (10 averages).

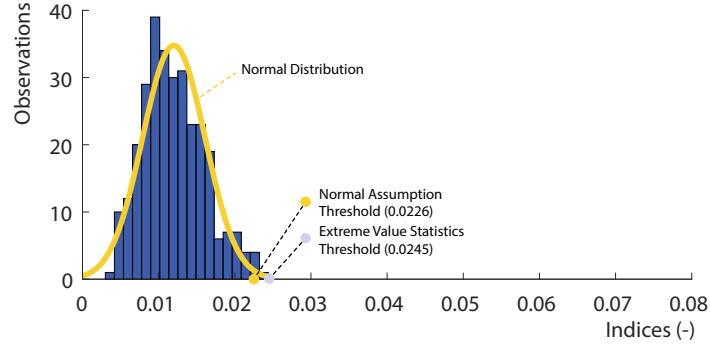


Fig. 10: Histogram with a normal distribution fit of the damage indicator with time stretching (10 averages).

For this reason, extreme value statistics (EVS)[14] was used in order to establish more robust thresholds. The assumption of a Gaussian distribution (chi-square regarding the distances), although very common and very attractive, may not be very appropriate in cases where the problem is concerned with tails of a distribution. In those cases extreme value statistics may be more suitable [15, 16]. In order to study the tails of an arbitrary parent distribution, the maximum of the samples should be used for the right tail and the minimum for the left. According to Fisher and Tippet extreme value theorem (EVT) [17], the induced distribution on the maxima of the samples can only take one of three forms: Gumbel, Weibull, or Frechet [15, 16].

The EVT in statistics is a good analog of the well known central limit theorem (CLT). The core idea of the CLT is that the average of many independently and identically distributed (iid) random variables converges at the end to a normal distribution provided that each random variable has a finite mean and variance. In the exact same sense the EVT is dealing with the central tendency that the maximum of a sample of iid random variables can only converge in distribution to one of three possible distributions as mentioned before. The distribution used here is the Gumbel and it can be seen in equation (3) for the maxima, and (4) for the minima,

$$H(x) = e^{-e^{-\frac{x-\lambda}{\delta}}} \quad (3)$$

$$L(x) = 1 - e^{-e^{-\frac{x-\lambda}{\delta}}} \quad (4)$$

where λ and δ are model parameters to be estimated from the data. It has to be noted that the central point in this study is that in such situations one would fit models to parts of the parent distribution's tails, as they should follow one of the three possible distributions, and identify thus a parametric model. Once the parametric model is obtained, a threshold can be calculated based on the fitted distribution. The chosen approach for the modelling here was differential evolution (DE) [18].

DE belongs to the family of evolution-based algorithms where an initial random population of solutions is propagated through a repeated cycle of mutation and crossover operations until an optimal (or near optimal, according to desired criteria) solution is obtained. The process is explained in more details in [19] and [20]. Naturally, an evolution process needs the calculation of a cost function, which in the particular problem here is to fit a parametric model to a given cumulative distribution function (CDF). A

well known normalised mean squared error, was applied here.

Here, all three distributions were tried, with the Gumbel providing the best results. The parameters of the DE were crossover ratio 0.5, scaling factor in the mutation vectors 0.9 and a population size of 30. A fixed number of maximum generations was set at 100, as it has been noted that the rate of change of MSE was stabilising before actually reaching this number [15, 16]. Figure 11 shows an example of a Gumbel distribution curve-fit after the DE was left to run and fit to the healthy condition data set from the parent distribution.

Figures 12, and 13 show the alarm thresholds when the EVS was used. The level of confidence used was 99 % meaning that 1 % of outliers was expected to be indicated. Results are shown when the evolution of the damage indicator includes two variants, with and without time stretching, in order to compensate for the acoustoelastic effect. The size of the portion of the data from the training test (assumed healthy state) which was used for fitting a Gumbel distribution was set at 10%. Readers should be aware [15, 16] that there can be a difference in the curve-fits with the size of the portion of the data which is used for fitting (something that is expected). In addition in [15, 16] was observed that variability on the curve-fit and the NMSE values can occur when the process is repeated with different random samples. This can be dealt by using a validation set in order to increase the consistency of the selection of the EV parameters. Here the first 60% of the baseline data was used to do the curve-fit.

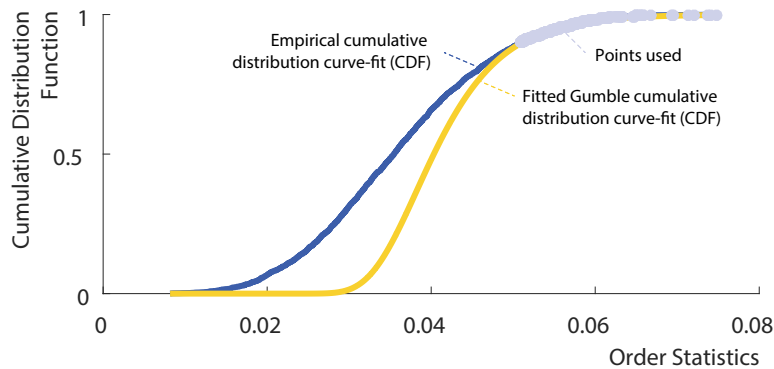


Fig. 11: An example of a Gumbel distribution curve-fit after the Differential Evolution algorithm was left to run, fitting on 10% of data.

It is clear from the figures that time stretching is successful in removing the acoustoelastic effect from the features which is responsible for a high number of false alarms around sample 1000 (10000 without average). When 10 averages are used, this effect can however not be fully removed resulting in a few false alarms before the actual damage occurs. The use of no average results in a higher variance in the data, and therefore this effect is masked and there is no false alarm before the actual damage, but the damage is detected slightly later (around sample 1600 compared to 1500 when averaging is used). This shows that there is a compromise between the noise reduction and the sensitivity to operational condition, as well as to damage.

The approach for the calculation of robust thresholds in the damage index made use of EVS and showed a significant similarity with the assumption of a normal condition threshold. This was expected as the damage index is weakly skewed. However, the approach that was followed here using EVS is

more accurate as there are some heavy tails.

The results shown in this section were presented for thresholds under an assumption of Gaussian statistics and using EVS distributions. It is shown that the EVSs provide the appropriate thresholds for a given confidence level as it nicely fits a Gumbel distribution (see Figure 11).

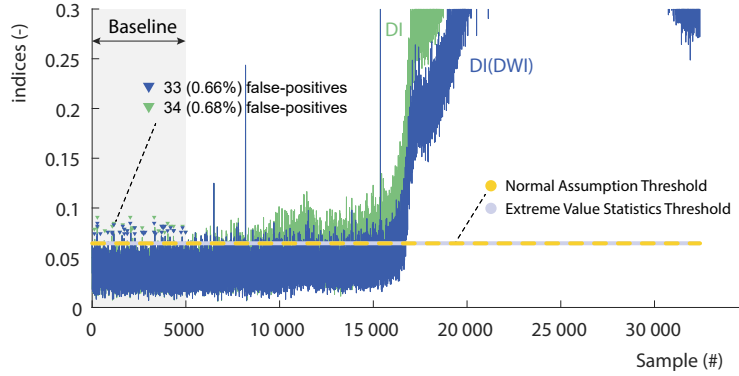


Fig. 12: Alarm threshold of the damage indicator with and without time stretching (no average).

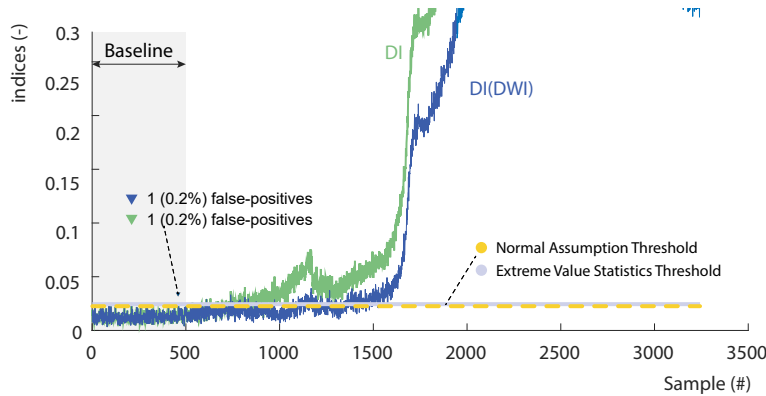


Fig. 13: Alarm threshold of the damage indicator without time stretching (no average).

5 Conclusion

Based on previously obtained results of a crack monitoring system with ultrasonic sensors embedded in a small concrete beam, we have presented a methodology to set a threshold for automated damage detection. The monitoring systems consists in an a pair of transducers embedded in the beam. One of the transducers is used as emitter and the other as receiver. The measured signals are used to build a univariate damage indicator. Due to the very high interrogation rate of the system, the data obtained contains a large number of samples both in the healthy state and during the cracking of the specimen. This allows to perform a sound statistical analysis of the indicator in order to set a meaningful threshold for early damage detection.

Two approaches have been used to determine the value of the threshold: (i) simple threshold based

on the normality assumption and (ii) threshold based on extreme value statistics. The data consists in raw data which is sensitive to the acoustoelastic effect, and data compensated using time stretching in order to remove as much as possible this effect. Due to the fact that the baseline data is shown to follow a distribution very close to normal, extreme value statistics gives very similar results than the ones based on the variance of the baseline data.

Two sets of data are also compared, the first one in which ten averages of the measured signals are used to compute the damage indicator, and the second one where no average is performed on the measured signals. The results show that when averaging is performed, the standard deviation on the baseline is lower, so that damage can be detected earlier, but at the same time, as the acoustoelastic effect is not removed completely, there are a few false positives associated to it. On the other hand, without averaging, the damage is detected slightly later, but the acoustoelastic effect does not cause false alarms as it is mainly covered by the higher noise on the data.

The interesting result of this study is that, at least for the present test, the statistical distribution of the univariate damage indicator is Gaussian, so that extreme value statistics is not essential to set a proper threshold. Further studies will focus on theoretical developments to investigate if this result can be generalized to any type of test using this specific damage indicator.

Acknowledgements

The authors gratefully acknowledge the support of the UK Engineering and Physical Sciences Research Council (EPSRC) through grant reference numbers EP/R003645/1 and EP/S001565/1, the Belgian Fund for Research (F.R.S-F.N.R.S) under the EOS project grant "Interact" (ID 30439691) and the Brussels-Capital Region Fund for Scientific Research and Innovation (INNOVIRIS) under the Launch project grant "TweetCon".

References

- [1] EN 12504-4:2004 (E). Testing concrete. Determination of ultrasonic pulse velocity. *European Standard*, 2004.
- [2] ASTM C597. Standard Test Method for Pulse Velocity Through Concrete. *American Society for Testing and Materials, West Conshohocken, PA, USA.*, pages 1–4, 2016.
- [3] F. Saint-Pierre, A. Philibert, B. Giroux, and P. Rivard. Concrete quality designation based on ultrasonic pulse velocity. *Construction and Building Materials*, (125):1022–1027, 2016.
- [4] BS 1881 - part 203. Testing concrete. Recommendations for measurement of velocity of ultrasonic pulses in concrete. *British Standard*, 1986.
- [5] J. Carette and S. Staquet. Monitoring the setting process of eco-binders by ultrasonic p-wave and s-wave transmission velocity measurement: Mortar vs concrete. *Construction and Building Materials*, (94):32–41, 2016.
- [6] G. Song, H. Gu, Y.L. Mo, T.T.C. Hsu, and H. Dhonde. Concrete structural health monitoring using embedded piezoceramic transducers. *Smart Mater. Struct.*, 16:959–968, 2007.

- [7] Cédric Dumoulin, Grigoris Karaiskos, Jérôme Carette, Stéphanie Staquet, and Arnaud Deraemaeker. Monitoring of the ultrasonic P-wave velocity in early-age concrete with embedded piezoelectric transducers. *Smart Materials and Structures*, 21(4):047001, apr 2012.
- [8] Cédric Dumoulin, Grigoris Karaiskos, J-Y Sener, and Arnaud Deraemaeker. Online monitoring of cracking in concrete structures using embedded piezoelectric transducers. *Smart Materials and Structures*, 23(11):115016, oct 2014.
- [9] Cédric Dumoulin and Arnaud Deraemaeker. Real-time fast ultrasonic monitoring of concrete cracking using embedded piezoelectric transducers. *Smart Materials and Structures*, 26(10):104006, 2017.
- [10] A. Deraemaeker and C. Dumoulin. Embedding ultrasonic transducers in concrete: A lifelong monitoring technology. *Construction and Building Materials*, 194:42–50, 2019.
- [11] Cédric Dumoulin and Arnaud Deraemaeker. Design optimization of embedded ultrasonic transducers for concrete structures assessment. *Ultrasonics*, 79:18–33, aug 2017.
- [12] M. Ohtsu, editor. *Acoustic Emission and Related Non-Destructive Evaluation Techniques in the Fracture Mechanics of Concrete: Fundamentals and Applications*. Woodhead Publishing Series in Civil and Structural Engineering: Number 57. Elsevier, Cambridge, 2015.
- [13] CU Grosse and M Ohtsu. *Acoustic Emission Testing*. Springer Berlin Heidelberg, Berlin, Heidelberg, 2008.
- [14] E. Castillo. *Extreme value theory in engineering*. Academic Press, Inc., 1988.
- [15] Evangelos Papatheou, Nikolaos Dervilis, Andrew E Maguire, Carles Campos, Ifigeneia Antoniadou, and Keith Worden. Performance monitoring of a wind turbine using extreme function theory. *Renewable Energy*, 113:1490–1502, 2017.
- [16] Evangelos Papatheou, Nikolaos Dervilis, Andrew Eoghan Maguire, Ifigeneia Antoniadou, and Keith Worden. A performance monitoring approach for the novel lillgrund offshore wind farm. *IEEE Transactions on Industrial Electronics*, 62(10):6636–6644, 2015.
- [17] R.A. Fisher and L.H.C Tippett. Limiting forms of the frequency distributions of the largest or smallest members of a sample. *Proceedings of the Cambridge Philosophical Society*, 24:180–190, 1928.
- [18] R. Storn and R. Price. Differential evolution – a simple and efficient heuristic for global optimisation over continuous spaces. *Journal of Global Optimization*, 11:341–359, 1997.
- [19] K. Worden, G. Manson, H. Sohn, and C.R. Farrar. Extreme value statistics from differential evolution for damage detection. In *Proceedings of the 23rd International Modal Analysis Conference*, 2005.
- [20] K. Worden, D.W. Allen, H. Sohn, D.W. Stinemat, and C.R. Farrar. Extreme value statistics for damage detection in mechanical structures,. Technical report, Los Alamos National Laboratory LA-13903-MS, 2002.

SUPERVISED CLASSIFICATION WITH SCADA DATA FOR CONDITION MONITORING OF WIND TURBINES

ERVIN HOXHA[†], YOLANDA VIDAL[†] AND FRANCESC POZO[†]

[†] Control, Modeling, Identification and Applications (CoDALab), Department of Mathematics, Escola d'Enginyeria de Barcelona Est (EEBE), Universitat Politècnica de Catalunya (UPC), Campus Diagonal-Besòs (CDB), Eduard Maristany, 16, 08019 Barcelona, Spain
e-mail: ervin.hoxha1990@gmail.com Web page: <http://https://codalab.upc.edu>

Key words: Condition Monitoring, Fault Classification, Wind Turbine, SCADA, Data Based, Machine Learning

Abstract. The reliability requirements of wind turbines have increased significantly in recent years in the search for a lower impact on the cost of energy. In addition, the trend towards larger wind turbines installed in remote locations has significantly increased the cost of repair or replacement of the component. In the wind industry, therefore, condition monitoring is crucial for maximum availability [1]. This contribution makes a review of supervised machine learning classification techniques for wind turbine condition monitoring using only SCADA data already available. That is, without installing extra sensors or costly purpose-built data sensing equipment. Although there has been extensive research into the use of machine learning techniques for wind turbine monitoring, the more recent trend in this type of literature is to focus on a specific WT sub-assembly: the bearings and planetary gearbox [2], the generator and power converter [3], the blades [4], etc. Oil debris systems can detect pitting failures but cannot detect cracking faults. Vibration based systems can detect both pitting and cracking, but most cannot determine the health of components in the planetary section. This work approaches condition monitoring of various wind turbine components (torque actuator, pitch actuator, pitch sensor, and generator speed sensor) with a unique strategy. In particular, for this purpose, a review of supervised machine learning classification techniques is performed and analyzed.

SMART 2019 Conference.

1 INTRODUCTION

Wind energy is a renewable energy, this means that as long as the sun continues to shine we will have wind to generate electricity. Wind energy is also clean and green. At the moment developed countries generate most of their energy from fossil fuels like coal, natural gas and oil. However burning fossil fuels creates green house gases that are through to contribute to the global climate change. In order to make wind energy profitable, the global wind industry has been witnessing an increase in average turbine size over the years. In this regard, offshore wind farms can increase energy production, as bigger wind turbines (WT) can be installed and they take advantage of higher and more uniform wind speeds.

The operation and maintenance of wind turbines is difficult and costly, especially for offshore wind turbines. Thus, condition monitoring is essential to reduce the energy cost. The faults must be anticipated before the break down takes place, and it is crucial to know what type of fault is, and where is it taking place.

Reference [5] reports a wide variety of faults in wind turbines. However, the latest research trend is to target only one specific parts of the wind turbine. For example, reference [6] target condition monitoring approaches of WTs with focus on gearbox, generator, blade, braking system, and rotor. The latest tendency in this type of literature review is to focus on a specific WT sub-assembly: the bearings and planetary gearbox [7], [8]. Reference [9] focuses on the generator and power converter, reference [10] targets the blades, etc. These type of localized strategies require almost always to install extra (an costly) sensors. However, there is already a huge amount of data from the existing sensors in the wind turbine (SCADA-Supervisory Control and Data Acquisition) that could be used for condition monitoring. The reason it is not actually used is that SCADA data is typically recorded at 10-minute intervals to reduce transmitted data bandwidth and storage. This low-frequency resolution negatively affects the diagnosis capabilities, and may hide short-lived events. On the other hand, high-resolution (but feasible) SCADA data should allow the dynamic turbine behavior to be identified with higher fidelity and thus improve detection efficiency. Following what is stated in [1], in this work a research framework is proposed that takes SCADA data with an additional high but feasible (1 s) frequency from the sensors. That is, the only requirement is to increase the frequency rate in the SCADA data from the already available sensors. Thus, this work approaches condition monitoring of various wind turbine components (torque actuator, pitch actuator, pitch sensor, and generator speed sensor) with a unique strategy and using only SCADA data.

Machine learning has been essential in the condition monitoring research arena. For example, application of machine learning method in bridge health monitoring[11], health monitoring of aeroplane structural component based on K-means clustering [12], etc . However, machine learning for condition monitoring of WT is still an incipient research area. In this work different machine learning strategies are used to monitor the condition of a 5 MW wind turbine using only SCADA data and taking into account faults in various WT components (torque actuator, pitch actuator, pitch sensor, and generator speed sensor).

This work is organized as follows. In Section 2, we describe the fault detection and classification methodologies. We discussed and analyzed the results in Section 3. In Section 4, some conclusions about the current challenges and future work are given.

2 FAULT DETECTION AND CLASSIFICATION METHODOLOGIES

2.1 Model overview

The simulated model stated in [13] is utilized in this work. It integrates a 5 MW wind turbine modelled using the FAST software (National Renewable Energy Laboratory, Golden, Colorado, USA), see [14]. The model proposes to simulate the sensors in the block diagram environment Simulink by adding signals from band-limited white noise blocks that are parameterized by noise power to the actual variables provided by the FAST software, see Table 1.

The fault scenarios, that comprehend sensors and actuators, are displayed in Table 2. The interested reader can find a comprehensive description of these faults and their importance in [15].

2.2 Data collection

A total of 260 simulations were conducted in this work: 100 with a healthy WT, and 20 simulations for each studied fault. The simulations have a duration of 400 seconds. Observe that the wind sequence is not used as a known measurement. It is also noteworthy that the data used by the fault detection strategy has a sampling period of 1 second. As noted in the introduction, following what is stated in [1], in this work a research framework is proposed that takes SCADA data with an additional high but feasible (1

Table 1: Available sensors (measured data).

Number	Sensor Type	Symbol	Unit	Noise Power
S1	Generated electrical power	$P_{e,m}$	W	10
S2	Rotor speed	$\omega_{r,m}$	rad/s	104
S3	Generator speed	$\omega_{g,m}$	rad/s	$2 \cdot 10^4$
S4	Generator torque	$\tau_{c,m}$	Nm	0.9
S5	Pitch angle of first blade	$\beta_{1,m}$	deg	$1.5 \cdot 10^3$
S6	Pitch angle of second blade	$\beta_{2,m}$	deg	$1.5 \cdot 10^3$
S7	Pitch angle of third blade	$\beta_{3,m}$	deg	$1 \cdot 10^3$
S8	Tower top fore-aft acceleration	$a_{fa,m}$	m/s^2	$5 \cdot 10^4$
S9	ower top side-to-side acceleration	$a_{ss,m}$	m/s^2	$5 \cdot 10^4$

Table 2: Fault scenarios.

Number	Fault	Type
F1	Pitch actuator (High air content in oil)	Change in system dynamics
F2	Pitch actuator (Pump wear)	Change in system dynamics
F3	Pitch actuator (Hydraulic leakage)	Change in system dynamics
F4	Generator speed sensor	Gain factor (1.2)
F5	Pitch sensor	Stuck value ($\beta_{3,m} = 5$ deg)
F6	Pitch sensor	Stuck value ($\beta_{3,m} = 10$ deg)
F7	Pitch sensor	Gain factor (1.2)
F8	Torque actuator	Offset value (2000 Nm)

second) frequency from the sensors.

2.3 Data reshape

Our goal is to minimize the detection time (T_d) and at the same time to obtain a high accuracy. T_d specifically means the time from when the fault occurs till it is detected. It is proposed to organize the available data from the simulations in samples of only three time steps (this will lead to a detection time of approximately three seconds). In reference [13] the faults detection requirements are given in terms of the sampling time. Fault 8, related to the torque actuator, requires to achieve $T_d < 3s$. This is the fault that requires the fastest detection time. The other faults have a slower dynamic. Fault 1 requires to be diagnosed in less than $8s$ and Faults 4 to 7 require a T_d less than 10 seconds. We will organize our data in 3 time steps. As mentioned before, we used only 400 seconds duration of 260 simulations, from 9 available sensors. Since we will organize the data in 3 time steps, and 400 is not divisible by 3, we will use only 399 seconds. Recall that initially the data was stored as below:

$$\begin{pmatrix} x_{1,1}^{(k)} & x_{1,2}^{(k)} & \dots & x_{1,399}^{(k)} \\ x_{2,1}^{(k)} & x_{2,2}^{(k)} & \dots & x_{2,399}^{(k)} \\ \dots & \dots & \dots & \dots \\ x_{260,1}^{(k)} & x_{260,2}^{(k)} & \dots & x_{260,399}^{(k)} \end{pmatrix} \in M_{260 \times 399}^{(k)}(\mathbb{R}) \quad (1)$$

where k is linked to different sensors $k = 1, 2, 3 \dots 9$, so there is one matrix associated to each sensor. There are 260 simulations, therefore the matrix has 260 rows. In order to minimize the detection time, instead of using this matrix, we reshape the data in a matrix with only 3 columns ($J = 3$):

$$\begin{pmatrix} x_{1,1}^{(k)} & x_{1,2}^{(k)} & x_{1,J}^{(k)} \\ x_{1,J+1}^{(k)} & x_{1,J+2}^{(k)} & x_{1,2J}^{(k)} \\ \vdots & \vdots & \vdots \\ x_{1,400-J+1}^{(k)} & x_{1,400-J+2}^{(k)} & x_{1,399}^{(k)} \\ x_{2,1}^{(k)} & x_{2,2}^{(k)} & x_{2,J}^{(k)} \\ x_{2,J+1}^{(k)} & x_{2,J+2}^{(k)} & x_{2,2J}^{(k)} \\ \vdots & \vdots & \vdots \\ x_{2,400-J+1}^{(k)} & x_{2,400-J+2}^{(k)} & x_{2,399}^{(k)} \\ \vdots & \vdots & \vdots \\ x_{260,1}^{(k)} & x_{260,2}^{(k)} & x_{260,J}^{(k)} \\ x_{260,J+1}^{(k)} & x_{260,J+2}^{(k)} & x_{260,2J}^{(k)} \\ \vdots & \vdots & \vdots \\ x_{260,400-J+1}^{(k)} & x_{260,400-J+2}^{(k)} & x_{260,399}^{(k)} \end{pmatrix} \in \mathcal{M}_{260 \cdot \frac{399}{3} \times 3}^{(k)}(\mathbb{R}), \quad (2)$$

As each sample has 3 seconds, the number of total samples is $I = 260 \cdot \frac{399}{3} = 34580$. Finally, the

matrices coming from all sensors ($k = 1, 2, \dots, 9$) are concatenated to obtain the data matrix X as follows:

$$X = \left(\mathcal{M}^{(1)} | \mathcal{M}^{(2)} | \dots | \mathcal{M}^{(9)} \right)$$

2.4 Preprocess

As the data comes from different sensors and has different magnitudes, it is columnwise normalized. Then, principal component analysis is used to reduce the dimensionality of the data. In this work, the number of principal components is selected based on keeping 99.98% of the variance. In particular, from a total of 27 components, 99.98% of the variance is accomplished by the first 16 components.

2.5 Supervised classifiers

In this work, two well known classifiers have been studied: k -nearest neighbour and support vector machines. It is not the purpose of this work to review these techniques, however the interested reader can find a comprehensive description of these methods in [17] and [18]. In this work, the parameters of both classifiers have been optimized using the 5-fold cross-validation technique. Cross-validation is a resampling procedure used to evaluate machine learning models on a limited data sample. The procedure has a single parameter called k that refers to the number of groups that a given data is to be split into. The choice of k is usually 5 or 10, but there is no formal rule. As k gets larger, the difference in size between the training set and the resampling subsets gets smaller. As this difference decreases, the bias of the technique becomes smaller [19]. In this paper we used 5-fold cross-validation.

3 RESULTS, ANALYSIS, AND DISCUSSION

3.1 k -NN

In order to choose the number of neighbours in k -NN, we test the overall accuracy for different numbers of neighbours. As shown in the Fig. 1, we get the highest accuracy when the number of neighbours is 1. Finally, the results for $k = 1$ and $k = 5$ are shown. Confusion matrices show us a comprehensive decomposition of the error between the true classes and predicted classes, see Figures 2 and 3 (an empty blank square means 0 %). In these matrices, each row represents the instances in a true class while each column represents the instances in a predicted class (by the classifier). In particular, the first row (and first column) is labeled as 0 and corresponds to the healthy case. The next labels (for rows and columns) correspond to each fault (from Fault 1 to Fault 8). From the confusion matrices, the following issues can be highlighted.

When the number of neighbours is $k = 1$ (Fig. 2), the overall accuracy is 95.7 %. In this case, the healthy class has a true positive rate (TPR, the percentage of correctly classified instances) higher than 99% and a false negative rate (FNR, the percentage of incorrectly classified instances) smaller than 1%. Fault 1 (related to the pitch actuator fault with high dynamics) has a TPR of 91% and an FNR of 9%. This FNR percentage was mainly obtained from 2% missing faults, 1% misclassified as Fault 3, 5, 6, 7 or 8, and 6% confusion with Fault 2, which is also a fault located in the pitch actuator. Fault 2, related to pitch actuator (pump wear), has a TPR of 89% and an FNR of 11% . It was misclassified as healthy 4% of the time, 2% of the time it was confused with Fault 1, and 5% of the time it was confused as Fault 3, 5, 6, 7 or 8. Fault 6 (related to the pitch sensor) was the most difficult to be classified, it had a TPR of 88%, 4% was misclassified as Fault 5 (related also to pitch sensor), 3% missing fault, and 5% misclassified as Fault 1,2,3,4,7 or 8. We can see from the confusion matrix that all the Faults, except Fault 2 and Fault 6, have a TPR higher than 91%.

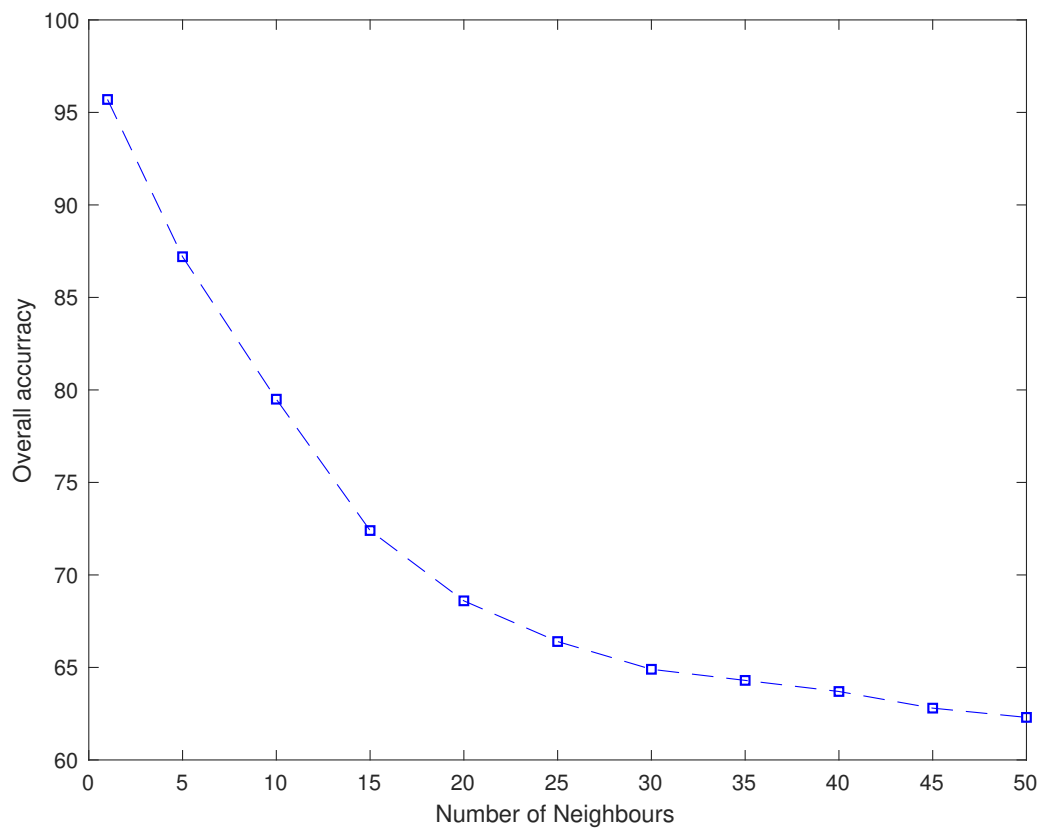


Figure 1: Number of neighbours with respect to overall accuracy.

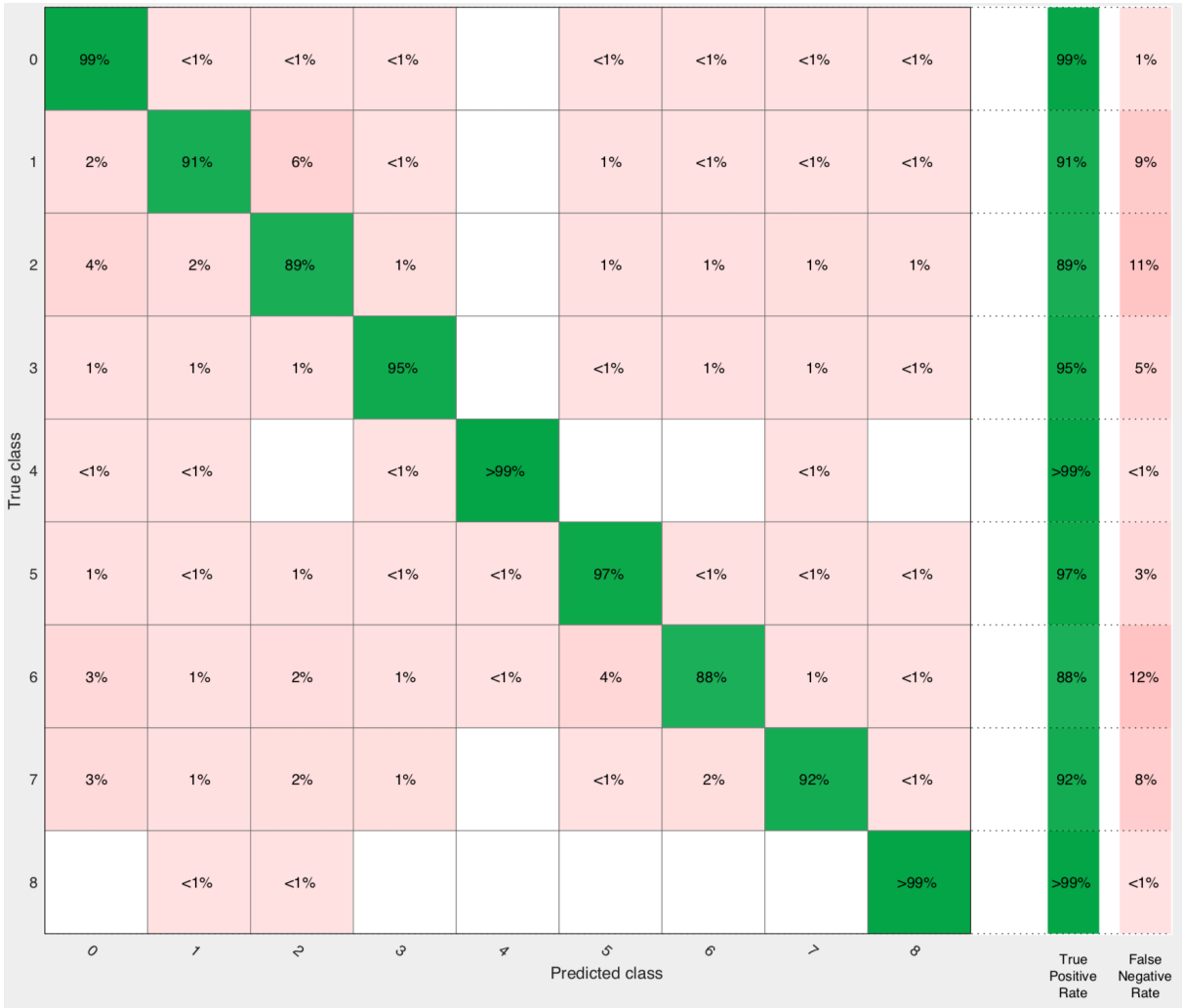


Figure 2: Confusion matrix when the number of neighbours is selected 1

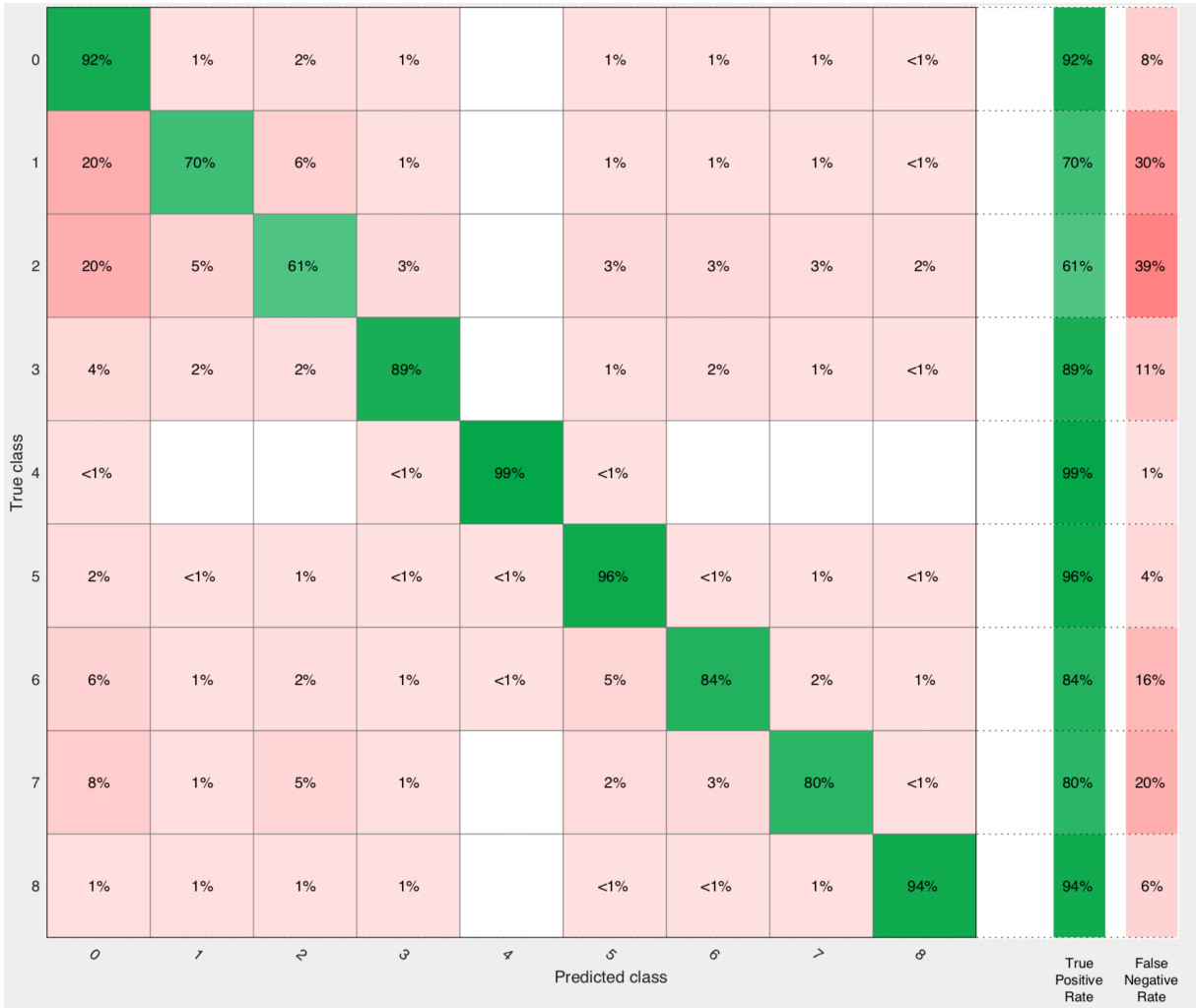


Figure 3: Confusion matrix when the number of neighbours is selected 5

When the number of neighbours is $k = 5$ (Fig. 3), the overall accuracy is 87.2 %. Fault 4 (related to the generator speed sensor) as in the previous case has a TPR of 99%. All the other classes decrease their TPR. The most affected classes are Fault 1 and Fault 2, in particular, Fault 1 decreases its TPR to 70% and Fault 2 to 61%.

3.2 SVM

The 5-fold cross-validation technique is used to select the following parameters: box constraint and kernel scale of the Gaussian kernel, see [20]. The results are presented in Fig. . The highest accuracy is 95% and it is achieved when the kernel scale is equal to 1/4 and the box constraint is 75 or 100.

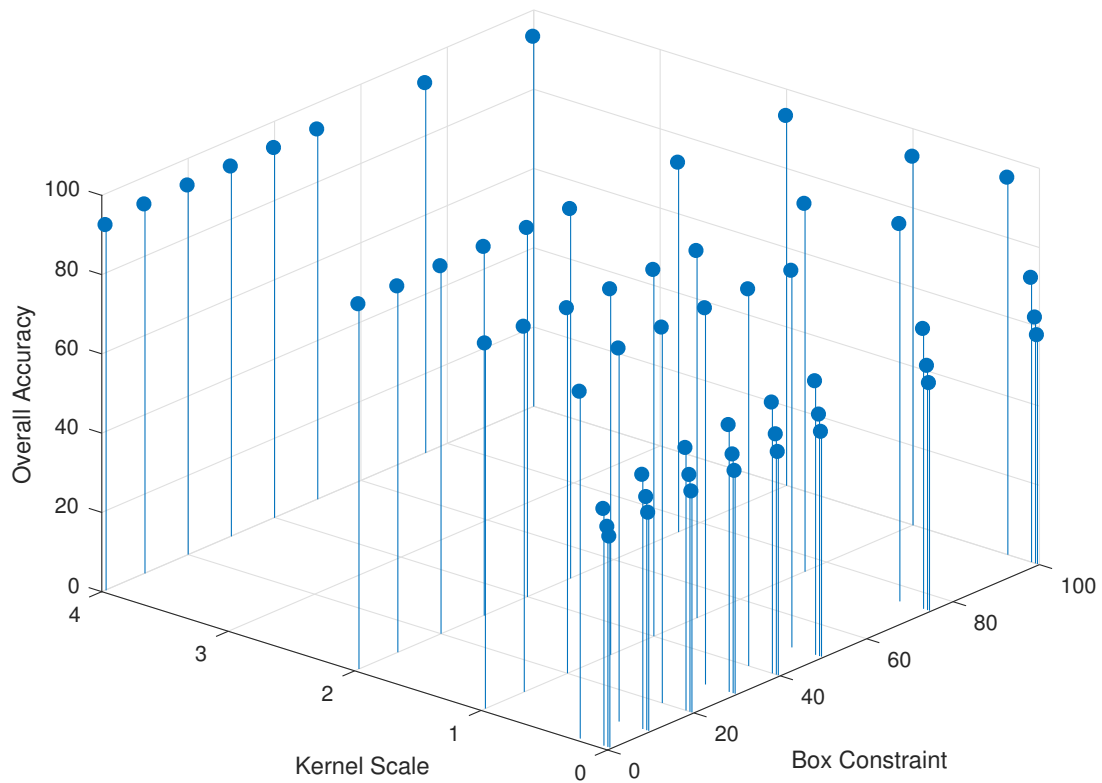


Figure 4: Box constraint value and kernel scale with respect to overall accuracy

Fig. 5 shows the confusion matrix when the box constraint is equal to 75 and the kernels scale is 1/4. In this case Fault 1 (the most difficult to classify) has a TPR of 77%, 17% of the times is misclassified as no fault and 6% is misclassified as Fault 2. Fault 6 has a TPR of 89% and an FNR of 11%. The FNR is mainly obtained from 4% missing fault, 2% misclassified as Fault 2, 3% as Fault 5 and remaining percentage 2% is a misclassification to Fault 1,3,4 or 7. The rest of the faults has a TPR above 90%. Note that Fault 8 has a TPR of 100%.

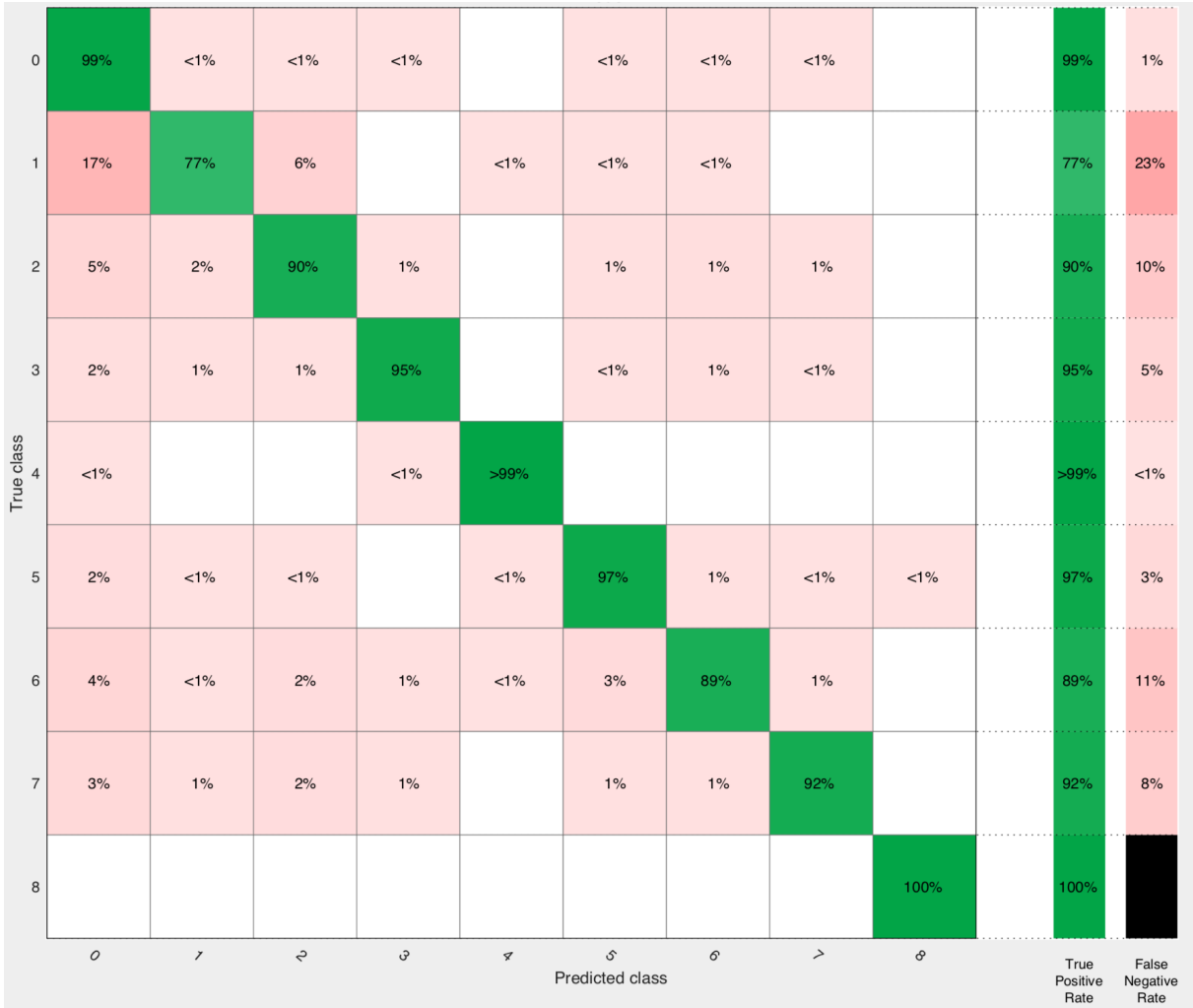


Figure 5: Confusion matrix, SVM with box constraint value 75 and kernel scale 1/4.

4 CONCLUSIONS

In this paper, it was presented a strategy to monitor the condition of a wind turbine. Eight different faults were studied and the model was able to detect and classify the type of the fault. That is, without installing extra sensors or costly purpose-built data sensing equipment. Supervised machine learning classification techniques were essential for wind turbine condition monitoring using only SCADA data already available. Two different classifiers were used, KNN and SVM. It was achieved an overall accuracy of 95.7% when KNN was used and 95% with SVM.

As a future work, we will try to optimise the model, and also include other faults.

REFERENCES

- [1] Y. Vidal, F. Pozo and C. Tutiven, *Wind Turbine Multi-Fault Detection and Classification Based on SCADA Data*, *Energies*, Vol. 11, 3018, (2018).
- [2] S.T. Kandukuri, A. Klausen, H.R. Karimi, H.R. K. G. Robbersmyr, *A review of diagnostics and prognostics of low-speed machinery towards wind turbine farm-level health management* *Renew. Sustain. Energy Rev.*, Vol. 53, 697708, (2016).
- [3] Huang, X. Wu, X. Liu, J. Gao, Y. He, *AOverview of condition monitoring and operation control of electric power conversion systems in direct-drive wind turbines under faults*. *Front. Mech. Eng.*, Vol. 12, 281302, (2017).
- [4] F.X. Ochieng, C.M. Hancock, G.W. Roberts, J. Le Kernec, *A review of ground-based radar as a noncontact sensor for structural health monitoring of in-field wind turbines blades* *Wind Energy*, Vol. 21, 12, (2018).
- [5] Hossain, M.L.; Abu-Siada, A.; Muyeen, S.M. *Methods for Advanced Wind Turbine Condition Monitoring and Early Diagnosis: A Literature Review*. *Energies* 2018, 11, 1309..
- [6] Ahadi, A. *MWind turbine fault diagnosis techniques and related algorithms*. *Int. J. Renew. Energy Res. (IJRER)* 2016, 6, 8089..
- [7] De Azevedo, H.D.M.; Arajo, A.M.; Bouchonneau, N. *A review of wind turbine bearing condition monitoring: State of the art and challenges*. *Renew. Sustain. Energy Rev.* 2016, 56, 368379.
- [8] Kandukuri, S.T.; Klausen, A.; Karimi, H.R.; Robbersmyr, K.G. *A review of diagnostics and prognostics of low-speed machinery towards wind turbine farm-level health management*. *Renew. Sustain. Energy Rev.* 2016, 53, 697708.
- [9] Huang, S.; Wu, X.; Liu, X.; Gao, J.; He, Y. *Overview of condition monitoring and operation control of electric power conversion systems in direct-drive wind turbines under faults*. *Front. Mech. Eng.* 2017, 12, 281302..
- [10] Ochieng, F.X.; Hancock, C.M.; Roberts, G.W.; Le Kernec, J. *AA review of ground-based radar as a noncontact sensor for structural health monitoring of in-field wind turbines blades*. *Wind Energy* 2018..
- [11] Peng, J.; Zhang, S.; Peng, D.; Liang, K. *AApplcation of machine learning method in bridge health monitoring*, 2017.

- [12] Jianguo, C.; Yingyu, W.; Zhonghai, L. ;Liqiu L.; Yun Z.;Guangyan X. *Health monitoring of aero-plane structural component based on K-means clustering*. 2010.
- [13] Odgaard, P.; Johnson, K. *Wind Turbine Fault Diagnosis and Fault Tolerant ControlAn Enhanced Benchmark Challenge*. In *Proceedings of the American Control Conference, Washington, DC, USA, 1719 June 2013*; pp. 16. .
- [14] <https://nwtc.nrel.gov/FAST7>.
- [15] Leahy, K.; Hu, R.L.; Konstantakopoulos, I.C.; Spanos, C.J.; Agogino, A.M.; OSullivan, D.T.J. *Diagnosing and predicting wind turbine faults from SCADA data using support vector machines*. *Int. J. Progn. Health Manag.* 2018, 9, 111 .
- [16] Hong, X.; Xu, Y.; Zhao, G. *LBP-TOP: A Tensor Unfolding Revisit*. In *Proceedings of the Asian Conference on Computer Vision, Taipei, Taiwan, 2024 November*; pp. 513527.
- [17] Cunningham, P.; Delany, S. J. *k-Nearest neighbour classifiers* 2007.
- [18] Evgeniou, T.; Pontil, M. *Support Vector Machines: Theory and Applications*, 2001
- [19] Mulak, P.; Talhar, N. *Analysis of Distance Measures Using K-Nearest Neighbor Algorithm on KDD Dataset* 2013.
- [20] Laouti, N.; Othman, S.; Alamir, M.; Sheibat-Othman, N. *Combination of model-based observer and support vector machines for fault detection of wind turbines*. *Int. J. Autom. Comput.* 2014, 11, 274287.

THE USE OF DIFFERENT MODAL QUANTITIES FOR DAMAGE IDENTIFICATION

FABRIZIO VESTRONI*, JACOPO CIAMBELLA* AND ANNAMARIA PAU†

*Department of Structural and Geotechnical Engineering
Sapienza University of Rome, via Eudossiana 18, 00184 Rome, Italy
email: vestroni@uniroma1.it

†Department of Structural and Geotechnical Engineering
Sapienza University of Rome, via A. Gramsci 53, 00197 Rome, Italy

Key words: Damage Detection, Inverse Problem, Modal Curvatures, Modal Frequencies

Abstract. The problem of identifying small damages in beam-like structures is studied by defining a suitable inverse problem with different modal quantities including frequencies, mode shapes and modal curvatures. With the aim of making a critical analysis of the different approach followed in the literature, we study a prototype problem of a free-free beam with single and multiple damages. The attention is mainly devoted to modal curvatures. It is shown that by making use of a perturbative solution of the equation of motion of a damaged beam, it is possible to obtain a closed form relationship between the modal curvature differences due to damage and the damage distribution itself. This information is added to the contributions of other modal quantities, frequencies and mode shapes, to improve the inverse problem of damage identification and to eliminate possible redundant solutions. On the other side, the variations of the curvature due to damage is concentrated at damage location and this circumstance can lead to difficulties in its detection. The results of the proposed approach are validated by using the results of an experimental campaign carried out by the authors.

1 INTRODUCTION

Vibration-based damage identification techniques have recently been the subject of much research, with particular emphasis on natural frequencies [1, 2]. As a global structural property, they are easily and reliably measured and their variation with damage is clearly monotonic. Unfortunately, due to them being a global characteristic, frequencies offer a modest sensitivity to local damage, mainly when the damage intensity is limited [3]. As such, variations of temperature or humidity could cause changes in frequencies sometimes as large as those induced by damage.

With the increasing availability of more affordable experimental techniques, other modal quantities – modal shapes and modal curvatures – have been the focus of an increasing attention by researchers, with the aim of detecting low intensity damages [4, 5].

In particular, modal curvatures are known to considerably change in the neighbourhood of the damage [6, 7]. However, their evaluation is not simple mainly for two reasons: (i) their variations due to distributed damage could spread over the entire structure [8]; (ii) in the presence of sharp damages, the evaluation of the modal curvature requires sensors placed in close proximity of the damage. For this

reason, this work starts with a critical review of the different approaches for damage identification, with a special focus on those using modal curvatures.

Making use of a perturbative solution of the equation of motion of a damaged beam, it is possible to obtain a closed form relationship between the modal curvature differences due to damage and the damage distribution itself [9]. Such a result suggests that a proper filtering of the modal curvature variations must be carried out for using them in damage localization or in damage assessment techniques when used with other modal quantities, such as frequencies and mode shapes as shown in [10].

The validation of the procedure that makes use of the modal quantities measured by an experimental setup, able to record frequencies, modal shapes and modal curvatures, is performed by means of numerical investigation with pseudo-experimental data and of an experimental laboratory campaign. The experiments deal with a free-free beam. Several damage cases are considered with different intensities. The contribution of using the modal curvature differences in the identification of damage position and intensity is evidenced.

2 MODAL CURVATURES

2.1 Filtering technique

In this section, we briefly review the main results in [8, 9] which concern the localization of damage through modal curvature. The transverse motion of a cracked beam is studied by exploiting the perturbative solution of the dynamic Euler-Bernoulli equation. The procedure is fully described in [8] and very shortly recalled here.

The dimensionless equation governing the i -th transverse mode of a damaged beam is:

$$\frac{d^4\phi_i(x)}{dx^4} - \varepsilon \frac{d^2}{dx^2} \left[\eta(x) \frac{d^2\phi_i(x)}{dx^2} \right] - \omega_i^2 \phi_i^*(x) = 0 \quad (1)$$

where $x = s/L \in [0, 1]$ is the dimensionless abscissa, ε is damage intensity, $\phi(x)$ is the transverse displacement and $\eta(x)$ is a smooth function representing the damage shape, such that $\|\eta(x)\| = 1$. The eigenfunctions ϕ_i and eigenvalues ω_i^2 can be expanded as a power series in terms of ε , i.e.,

$$\phi_i(x) = \tilde{\phi}_i(x) - \varepsilon \bar{\phi}_i(x) + O(\varepsilon^2), \quad \omega_i^2 = \tilde{\omega}_i^2 - \varepsilon \bar{\omega}_i^2 + O(\varepsilon^2) \quad (2)$$

where $\tilde{\phi}_i$ and $\tilde{\omega}_i^2$ are respectively the i th eigenfunction and eigenvalue of the undamaged beam, and $\bar{\phi}_i$ and $\bar{\omega}_i^2$ are their first order variations. By taking into account only the contributions up to the first order in ε , the following system of ordinary differential equations is obtained

$$\text{0-th order:} \quad \frac{d^4\tilde{\phi}_i(x)}{dx^4} - \tilde{\omega}_i^2 \tilde{\phi}_i(x) = 0 \quad (3)$$

$$\text{1-st order:} \quad \frac{d^4\bar{\phi}_i(x)}{dx^4} - \tilde{\omega}_i^2 \bar{\phi}_i(x) = \bar{\omega}_i^2 \tilde{\phi}_i(x) - \frac{d^2\eta_i(x)}{dx^2} \quad (4)$$

where the function $\eta_i(x)$ is the *modal damage shape* weighted through the i th modal curvature, i.e. $\eta_i(x) := \eta(x) d^2\tilde{\phi}_i/dx^2$. Eq.(3) is simply the governing equation of the undamaged system.

The damage shape function $\eta(x)$ can be expressed in terms of the modal quantities of the undamaged system and of the difference between the modal curvature of the damaged and undamaged beams, $\Delta\psi_k$, as in [8], i.e.,

$$\eta_k = -\Delta\psi_k + \frac{\Delta\omega_k^2}{\tilde{\omega}_k^2} \frac{\tilde{\psi}_k}{\|\tilde{\psi}_k\|} + \sum_{l \neq k} \frac{\tilde{\omega}_k^2}{\tilde{\omega}_l^2} \int_0^1 \tilde{\psi}_l^T(x) \Delta\psi_k(x) dx \frac{\tilde{\psi}_l}{\|\tilde{\psi}_l\|^2}, \quad (5)$$

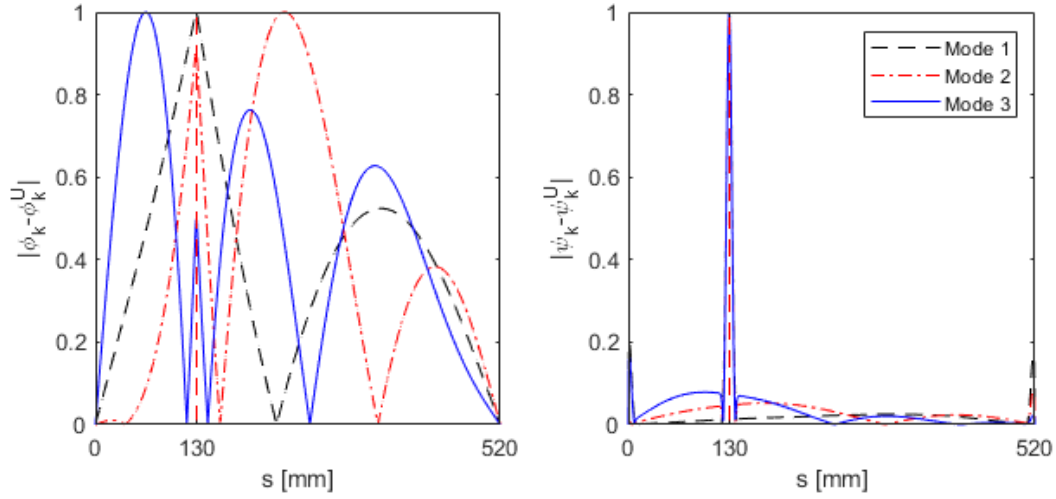


Figure 1: Modal displacement difference (left) between the damaged and undamaged system for the damage case D1 for the first three modes (right). Corresponding modal curvature differences. The dashed red line shows the actual position of the damage.

where $\Delta\omega_k^2 = \tilde{\omega}_k^2 - \omega_k^2$ is the modal frequency variation, between the k -th modal frequency of the undamaged and damaged systems. For the sake of brevity, we have indicated the k -th modal curvature, i.e., the second derivative of the k -th mode shape, as $\psi_k(x) := \phi_k''(x)$.

Equation (5) highlights that the function η_k , i.e., the product of the damage shape with the k -th modal curvature, is, as a matter of fact, the *observable quantity* of the inverse problem based on modal curvatures rather than the modal curvatures themselves. As such, if the damage occurs in a region where the k -th modal curvature vanishes, the damage shape can not be reconstructed from the k -th modal curvature. In addition, Eq. (5) shows that the damage shape can be evaluated only after the k -th modal curvature difference is filtered as that equation suggests; interestingly, all quantities that appear on the right hand side of the equation are indeed easy to measure: $\Delta\psi_k$ is the difference between the k -th modal curvatures of the damaged and undamaged beam, $\Delta\omega_k^2$ is the difference of the corresponding modal frequencies, $\tilde{\psi}_l$ is the l -th undamaged modal curvature divided by its norm $\|\tilde{\psi}_l\|$.

2.2 Numerical evaluation of modal shapes and modal curvatures

In the case of sharp damages, modal curvatures are known to be localized quantities even if not properly filtered. In this respect Fig. 1a shows the first four mode displacement differences obtained by a numerical model of the free-free beam experimentally tested by the authors, whose mechanical and geometric characteristics are shown in Fig. 2 for damage cases D1 (Fig. 3). For the sake of comparison, Fig. 1b shows the corresponding modal curvature differences. It is seen from the figure that multiple peaks appear in the difference when considering modal displacements whereas a more localised information can be extracted from the modal curvature difference. In the case of mode shapes, these peaks are located in a region close to but not correspondent with the actual damage position (represented by a dashed red line). As already pointed out, such a circumstance makes the solely use of eigenmode difference in the damage localization problematic and potentially leading to false indications. However, their use in the objective function together with the eigenfrequencies variation can lead to a more accurate evaluation of the damage parameters with respect to the use of frequencies only.

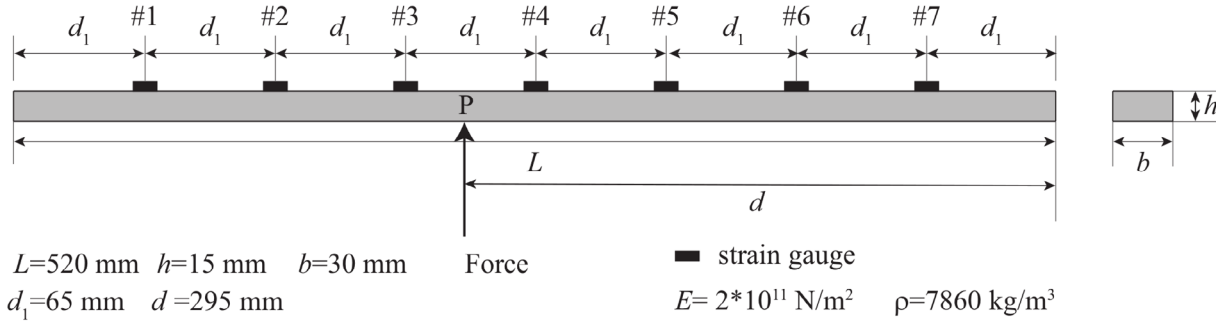


Figure 2: Geometry of the undamaged free-free (FF) beam and steel material properties.

2.3 Experimental evaluation of modal curvatures

Much care must be devoted when extracting modal curvatures from experimental data. When strain gauges are used to measure the structural response, the frequency response function measured at the abscissa s_i for a point force applied at the abscissa s_j is

$$H_{ij}(\omega) = \frac{G_{ij}(\omega)}{G_{jj}(\omega)} \quad (6)$$

where $G_{ij}(\omega)$ is the cross-power spectral density between input and output, and $G_{jj}(\omega)$ is the auto-power spectral density of the input. In particular, when strains are measured, Eq. (6) can be written as:

$$H_{ij}(\omega) = \sum_{k=1}^{\infty} \frac{\psi_k(x_i)\phi_k(x_j)/\rho L \omega^2 \|\phi_k\|^2}{1 - (\omega_k^2 + i\eta_r \omega_k^2)/\omega^2}. \quad (7)$$

The experiments were carried out at the laboratory of the Department of Structural and Geotechnical Engineering, Sapienza University of Rome, on a steel beam whose geometric and mechanical characteristics are reported in Fig. 2. The beam was dynamically excited by a point force generated by an electrodynamic shaker, that was driven by a white noise input signal up to a frequency of 2500/3000 Hz. To measure the proper frequency response function, the input force was recorded with a load cell installed at the base of the shaker stinger, which was realized with a thin steel bar with circular cross section. The response was measured using seven strain gauges equally spaced along the beam axis, in the damaged and undamaged cases.

The investigated damage cases are reported in Figure 3. Case D1 includes a notch localized below the strain gauge #1 with a residual height of the damaged cross-section equal to $h^D = 3h/4$, case D2 has the same localization, but a residual height equal to $h^D = h/2$, case D3 the same damage as D2, plus a second notch of residual height $h^D = 3h/4$ located between strain gauges #5 and #6.

A reduction of natural frequencies with increasing damage is observed. This is shown by the shift of the peaks in Figure 4, which compares the modulus of the frequency response function in terms of strains in the undamaged and damaged (D2) cases. The frequency response function $H_{1P}(f)$ is measured in channel #1 for the forcing function applied at point P. The values of the first four natural frequencies are reported in Table 1 for the undamaged (U), and the three cases of damage under investigation (D1, D2, D3, Figure 3).

Figure 5 shows the modal curvatures for the first four identified modes, in the undamaged and damaged states. Figure 6, which reports the variation of modal curvatures between the undamaged and damaged states, normalized so that the maximum equals one, shows that the local increase in curvature

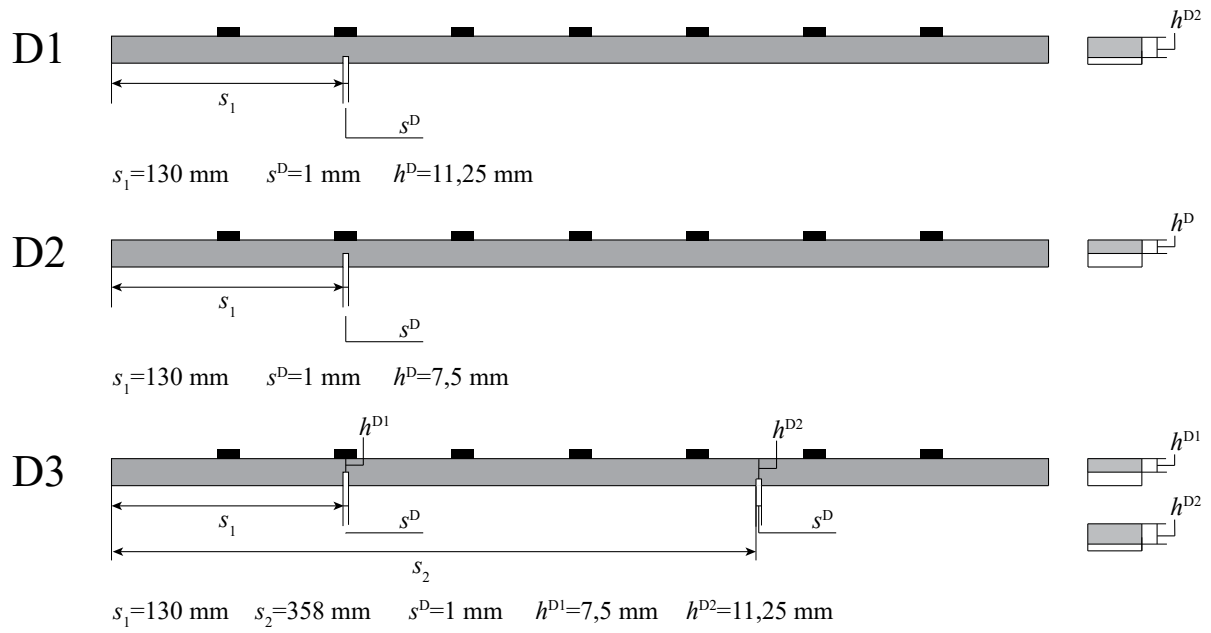


Figure 3: Damage cases for the steel free-free beam.

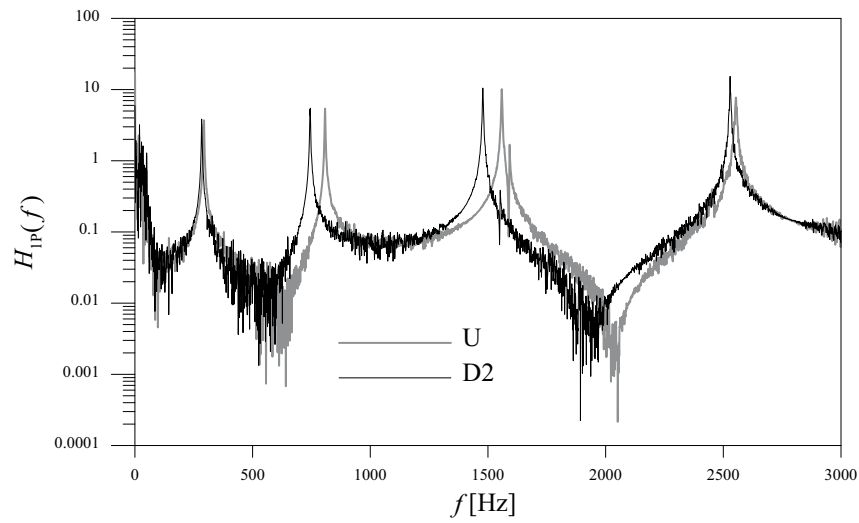


Figure 4: Component H_{1P} of the Frequency Response Function in terms of strains in the undamaged (U) and damaged (D2) cases.

	f_1	f_2	f_3	f_4
U	293	808	1559	2546
D1	292	794	1539	2548
D2	284	744	1478	2535
D3	281	732	1470	2503

Table 1: Natural frequencies in the undamaged and damaged cases [Hz] - FF beam.

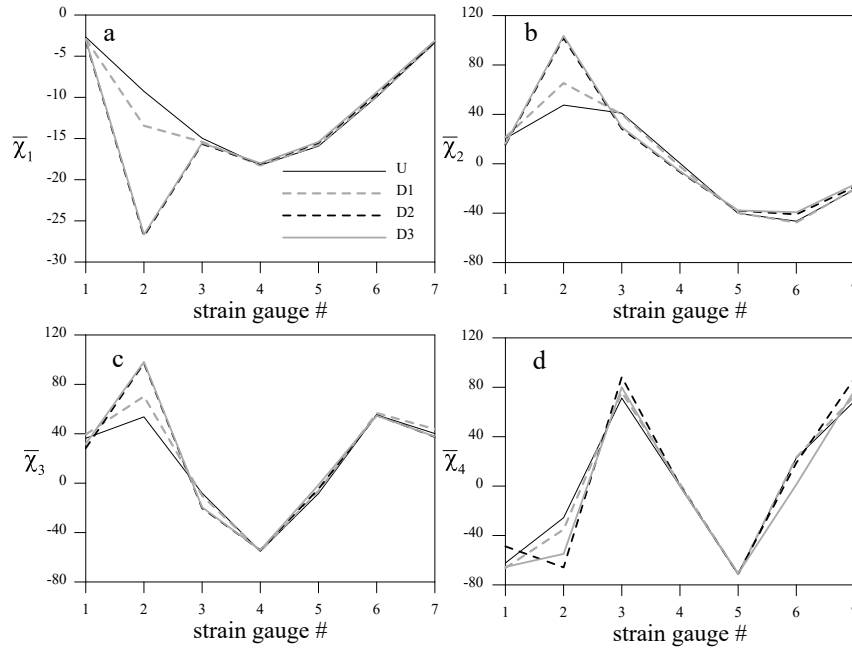


Figure 5: Experimental modal curvatures for the first (a), second (b), third (c), and fourth (d) modes in the undamaged and damaged cases.

where damage is located is very clear when damage is placed just below strain gauge #2 (all cases). On the contrary, when damage is located between strain gauges #5 and #6 (D3), the presence of damage is less evident from the increase in curvature.

3 DAMAGE IDENTIFICATION

The analysis in previous paragraphs has shown that, in case of sharp damages, modal curvature can directly give information on the location of damage. However, the assessment of the damage intensity requires the definition of an inverse problem based on the comparison between the undamaged and damaged state responses. To do that, a finite element model of the beam in Fig. 2 is implemented in Ansys with $n=520$ elements (BEAM 189). The damage is schematically represented as a concentrated

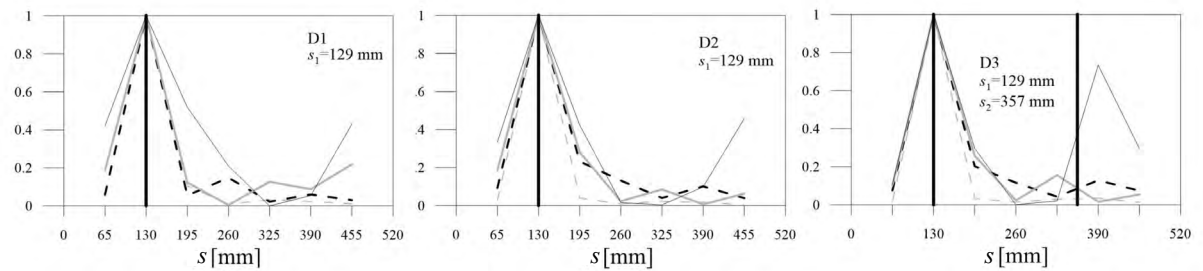


Figure 6: Curvature differences for the three damage states of the FF beam. Mode 1 - dashed grey line; Mode 2 - dashed black line; Mode 3 - grey thick line; Mode 4 - thin grey line.

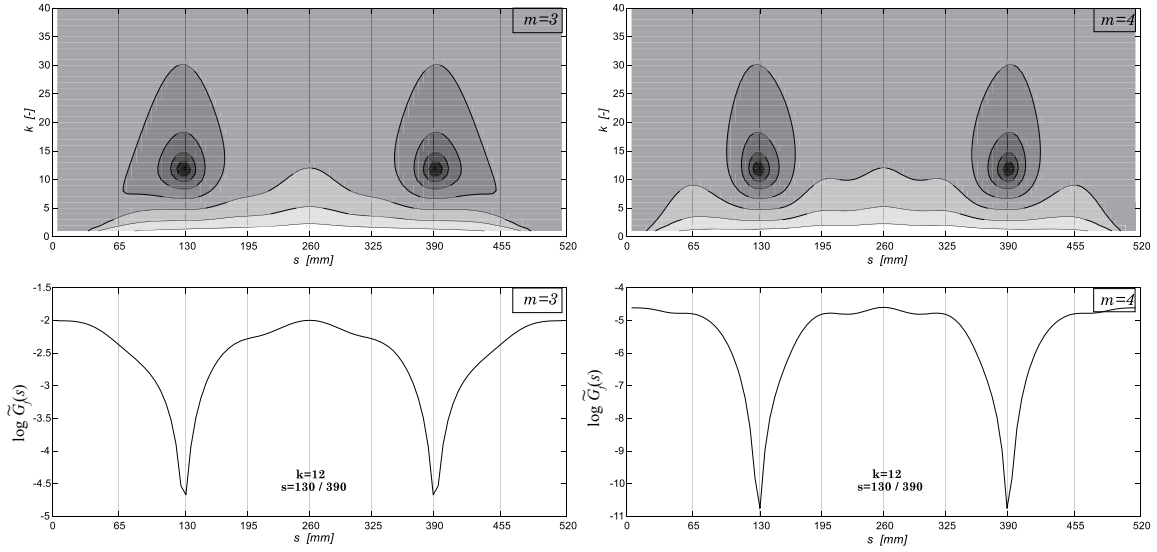


Figure 7: Top line: contour plot of the objective function $G_f(k, s)$ calculated with three (left) and four (right) frequencies in the case of damage D2. Bottom line: function $\tilde{G}_f(k, s)$

spring at position s with dimensionless stiffness $k = \frac{2L}{h^U} \frac{1-\beta}{\beta}$ with $\beta = (EI^U - EI^D)/EI^U$, and EI^U and EI^D respectively the flexural rigidities of the undamaged and damaged cross sections [11]. An optimal estimate of the parameters k and s is obtained by minimizing an objective function which is built as the sum of differences between selected response quantities. As a first step, we consider an objective function which depends only on the first m frequency differences, i.e.,

$$G_f(k, s) = \sum_{i=1}^m \left(\frac{\Delta\omega_i(k, s)}{\omega_i^U} - \frac{\Delta\omega_{ei}}{\omega_{ei}^U} \right)^2 \quad (8)$$

which is the sum of the squares of the differences between the numerical $\Delta\omega_i(k, s)$ and experimental $\Delta\omega_{ei}$ frequency variations between the undamaged and the damaged states, normalized with respect to the frequencies of the undamaged beam, ω_i^U and ω_{ei}^U . Since the $\Delta\omega_i(k, s)$ are not observable in closed-form, they are evaluated at discrete values of k and s , which enables to calculate the function (8) on a grid.

The $G_f(k, s)$ is shown in Fig. 7 (top) by using three ($m=3$) and four ($m=4$) frequencies for the damage case D2; as expected, the function is symmetric with respect to the mid span, since the use of frequencies only cannot distinguish between symmetric locations of damage. The curves on the bottom line are the function $\tilde{G}_f(s)$, which, for each possible damage position, is the minimum of $G_f(k, s)$ with respect to k . The insets in the figure report the values of the parameters s and k at the position of the minimum, to be compared with the real position of the damage $s = 0.130$ and damage parameter $k = 10$. These results show that already with three frequencies a good estimate of the damage position can be achieved despite having a 20% error on the damage intensity.

In order to verify the possible improvement of the identification using modal curvature differences, the following enhanced objective function is considered

$$G_{fc}(k, s) = G_f(k, s) + \alpha G_c(k, s) \quad (9)$$

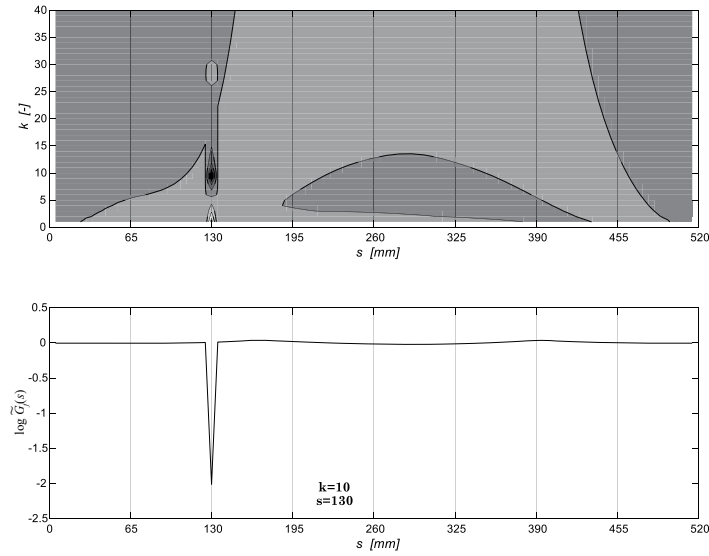


Figure 8: Top line: contour plot of the objective function $G_{fc}(k, s)$ calculated with four frequencies and the first mode curvature difference in the case of damage D2. Bottom line: plot of the function $\tilde{G}_{fc}(s)$.

where α is a positive scaling constant, assumed equal to 0.3 in the present case, and G_c is the function based on the modal curvature differences

$$G_c(k, s) = \sum_{i=1}^n \left(\frac{\Delta\psi_i(k, s)}{\|\psi_i^U\|} - \frac{\Delta\psi_{ei}}{\|\psi_{ei}^U\|} \right)^2 \quad (10)$$

with $\Delta\psi_{ei}$ the experimental modal curvatures and $\Delta\psi_i$ the corresponding numerical value, normalized with respect to the norm of the undamaged modal curvature. Since a robust localization of damage was already obtained with the first modal curvature difference (see Fig. 6), only the first modal curvature is included in the objective function ($n = 1$). The results in Fig. 8 show that the minimum of the enhanced G_{fc} is much sharper and the correct values of the parameter are obtained, confirming the important role played by modal curvatures.

4 CONCLUSIONS

The great part of damage identification techniques used in the literature are based on the differences of the modal frequencies of the damaged and undamaged system. In this work, to enhance the solution of the inverse problem and to have a better estimate of damage parameters, we have examined the use of both frequencies and modal curvatures. The latter have always been considered strictly related to the damage region but some drawbacks have been highlighted:

- modal curvature differences are influenced by the damage distribution in a more significant way than modal shape differences;
- if the damage is extended compared to the characteristic dimensions of the structure, the use of modal curvatures in a damage identification technique requires them to be properly filtered;
- for sharp damages, modal curvature differences are also very sharp and this could make their experimental evaluation difficult.

With reference to an experimental campaign carried out on a free-free beam, we have shown the feasibility of using modal curvature variations, experimentally measured through strain gauges, together with modal frequency variations. For a certain damage scenario, we have compared the results of the identification obtained with an objective function weighing only the modal frequency differences and an enhanced function with both frequency and curvature variations. In the latter case, a more accurate estimate of the damage parameter was achieved and, in addition, the symmetric solution, which can not be distinguished by using only the frequency difference, was eliminated.

5 ACKNOWLEDGEMENTS

The support of Italian MIUR under the grant PRIN–2015, 2015TTJN95, P.I. Fabrizio Vestroni, "Identification and monitoring of complex structural systems" is gratefully acknowledged. The authors thank Giuseppe Marino for his support in carrying out the experiments.

References

- [1] D Montalvao. A Review of Vibration-based Structural Health Monitoring with Special Emphasis on Composite Materials. *Shock Vib.*, 38(4):295–324, 2006.
- [2] Y F Fan, J Zhou, Z Q Hu, and T Zhu. Study on mechanical response of an old reinforced concrete arch bridge. *Struct. Control Hlth.*, 14(6):876–894, 2007.
- [3] F Vestroni and D Capecchi. Damage detection in beam structures based on frequency measurements. *J. Eng. Mech.*, (126):761–768, 2000.
- [4] M Abdel Wahab and G De Roeck. Damage Detection in Bridges Using Modal Curvatures: Application To a Real Damage Scenario. *J. Sound Vib.*, 226(2):217–235, sep 1999.
- [5] D. Anastasopoulos, M. De Smedt, L. Vandewalle, G. De Roeck, and E.P.B. Reynders. Damage identification using modal strains identified from operational fiber-optic bragg grating data. *Struct. Health Monit.*, (2017), in press.
- [6] A K Pandey, M Biswas, and M M Samman. Damage detection from changes in curvature mode shapes. *J. Sound Vib.*, 145(2):321–332, 1991.
- [7] D Dessi and G Camerlengo. Damage identification techniques via modal curvature analysis: Overview and comparison. *Mech. Syst. Signal Pr.*, 52-53:181–205, 2015.
- [8] J Ciambella and F Vestroni. The use of modal curvatures for damage localization in beam-type structures. *J. Sound Vib.*, 340:126–137, 2015.
- [9] J. Ciambella, A. Pau, and F. Vestroni. Modal curvature-based damage localization in weakly damaged continuous beams. *Mech. Syst. Signal Pr.*, 121:171–182, 2019.
- [10] D Capecchi, J Ciambella, A Pau, and F Vestroni. Damage identification in a parabolic arch by means of natural frequencies, modal shapes and curvatures. *Meccanica*, 51(11):2847–2859, 2016.
- [11] A. Pau, A. Greco, and F. Vestroni. Numerical and experimental detection of concentrated damage in a parabolic arch by measured frequency variations. *J. Vib. Control*, 17(4):605–614, 2011.

TOPOLOGY OPTIMIZATION APPROACH FOR DENSE SENSOR NETWORK DISTRIBUTION OVER LARGE BRIDGE STRUCTURES

BARTŁOMIEJ BLACHOWSKI^{*}, PIOTR TAUZOWSKI, ANDRZEJ SWIERCZ
AND ŁUKASZ JANKOWSKI

Institute of Fundamental Technological Research (IPPT PAN)

Polish Academy of Sciences

Pawinskiego 5b, 02-106 Warsaw, Poland

^{*}e-mail: bblach@ippt.pan.pl, www.ippt.pan.pl

Key words: Optimal sensor placement, Structural parameter identification, Topology optimization.

Abstract. Recent progress in sensing technology and measurement techniques allows a growing number of critical infrastructures to be equipped with Structural Health Monitoring (SHM) systems. Sensors in such SHM systems should be placed in a proper way to facilitate extracting valuable information from the structure under investigation. In the case of relatively simple spatial truss structures, sensors can be located with the aid of classical methods such as *Effective Independence (EI) method proposed by Kammer*. However, in the case of large structures, which are intended to be equipped with hundreds if not thousands of sensors, other sensor placement methods may be needed.

The goal of this study is to extend a topology optimization based approach for sensor placement (*proposed originally by Mariani and co-workers*) to the case of real bridge structures represented by finite element models with a few thousand degrees of freedom. Structural topology optimization aims to find the optimum material distribution in order to minimize the mass of the structure while maintaining mechanical properties (load capacity, displacements, etc.). A similar concept can be used to determine the optimal placement of sensors in a structure to identify its dynamic characteristics. The sensor positions are determined in such a way that estimation error of modal coordinates is minimized. The effectiveness of the proposed methodology is demonstrated on an *example of a detailed FE model of a tied-arch bridge*.

1 INTRODUCTION

One of the earliest works on optimal sensor placement (OSP) over a multi-degree of freedom (MDOF) flexible structure was presented by Shah and Udwadia [1]. They proposed time domain sensitivity analysis and its application to sensor placement intended to minimize the error of structural parameter estimation. The second important work in that field was the paper by Kammer [2] introducing the frequently used method called Effective Independence (EFI). The analysis was conducted in modal domain and the concept of Fisher information has been introduced. The EFI method tends to maximize the amount of information in the

measurement signals and it was shown that such a problem is closely related to maximization of the determinant of the Fisher matrix. Next, Cobb and Liebst [3] introduced modal sensitivities into the process of sensor placement optimization. Additionally, they proposed co-linearity metrics for comparing different sensor network configurations. These metrics were used to distribute a sensor network for damage identification in a spatial truss structure. Another interesting concept for optimal sensor placement has been proposed by Papadimitiou [4]. He utilized Bayesian statistical framework for sensor placement over large structures with many DOFs. In particular, information entropy (IE) has been suggested to be efficient in sensor placement for identification of uncertain structural parameters.

All the above mentioned methods treated the problem of sensor placement as a discrete optimization problem, i.e. assumed that candidate locations for a set of sensors, most frequently in form of accelerometers, are discrete variables. An alternative approach has been proposed by Mariani et al. [5]. They formulated sensor placement as continuous optimization and employed numerical methods used in structural topology optimization, where discrete variables are replaced with continuous ones ranging from zero to unity.

A comparison of four different approaches for optimal sensor placement, including: mode shape difference, effective independence, information entropy and modal energy method, has been published by Zhou et al. [6]. A new method for sensor placement based on Virtual Distortion Method has been proposed by the team of Professor Holnicki (Blachowski et al. [7]). In this method, a ranking of sensors has been created and its effectiveness in the selection of optimal sensor locations has been demonstrated on an example of a six-bay planar truss structure. Finally, Blachowski [8] proposed a method for optimal sensor placement and damage identification under sparsity constraints. He applied this method to two engineering examples: one related to a spatial truss girder and the second one to an upper-deck arch bridge.

The purpose of this study is to extend the topology optimization based approach for sensor placement to the case of real bridge structures represented by finite element models with a few thousand degrees of freedom.

2 SENSOR PLACEMENT AS A DISCRETE OPTIMIZATION PROBLEM

Before solving the optimal sensor placement problem, appropriate metrics have to be defined. One of the most frequently used is the determinant of the Fisher information matrix. The basic information about this metric and formulation of the sensor placement as a discrete optimization problem will be briefly recalled in the following two sections.

2.1 Estimation error and metrics for optimal sensor placement

We start the derivation of the topology optimization method for sensor placement with equations representing the response vector of the structure

$$\mathbf{y}(t) = \Phi \boldsymbol{\eta}(t) \quad (1)$$

where $\mathbf{y} \in \mathbb{R}^{n_d}$, $\Phi \in \mathbb{R}^{n_d \times n_m}$ and $\boldsymbol{\eta} \in \mathbb{R}^{n_m}$. Indices n_d and n_m denote the number of DOFs and the number of modes, respectively.

Equation (1) describes structural response in the absence of measurement noise. In reality, however, signals from sensors are always corrupted by noise and the corresponding equations take the following form

$$\mathbf{y}_s(t) = \mathbf{\Phi}_s \boldsymbol{\eta}(t) + \mathbf{w}(t) \quad (2)$$

where $\mathbf{y}_s \in \mathbb{R}^{n_s}$, $\mathbf{\Phi}_s \in \mathbb{R}^{n_s \times n_m}$ and $\mathbf{w} \in \mathbb{R}^{n_s}$. Matrix $\mathbf{\Phi}_s$ denotes measured components of the modal matrix $\mathbf{\Phi}$, vector \mathbf{w} represents measurement errors and index n_s is the number of sensors.

Assuming that the number of sensors is equal to or greater than number of modal coordinates to be identified, i.e. $n_s \geq n_m$, we can determine the least square estimate of modal coordinates using equation (2), namely

$$\tilde{\boldsymbol{\eta}}(t) = (\mathbf{\Phi}_s^T \mathbf{\Phi}_s)^{-1} \mathbf{\Phi}_s^T \mathbf{y}_s(t) = \mathbf{\Phi}_s^+ \mathbf{y}_s(t) \quad (3)$$

where matrix $\mathbf{\Phi}_s^T \mathbf{\Phi}_s$ is called the Fisher information matrix (FIM) and constitutes an essential part of eqn.(3). Using equation (3), an estimate of the structural response can be determined as follows

$$\tilde{\mathbf{y}}(t) = \mathbf{\Phi} \tilde{\boldsymbol{\eta}}(t) = \mathbf{\Phi} \mathbf{\Phi}_s^+ \mathbf{y}_s(t) \quad (4)$$

The difference between the structural response obtained from equation (1) and its estimate from equation (4) gives the estimation error

$$\mathbf{e}(t) = \tilde{\mathbf{y}}(t) - \mathbf{y}(t) = \mathbf{\Phi} \mathbf{\Phi}_s^+ \mathbf{y}_s(t) - \mathbf{\Phi} \mathbf{\Phi}_s^+ [\mathbf{y}_s(t) - \mathbf{w}(t)] = \mathbf{\Phi} \mathbf{\Phi}_s^+ \mathbf{w}(t) \quad (5)$$

and the covariance matrix of the estimation error takes the following form

$$E\{\mathbf{e}(t)\mathbf{e}(t)^T\} = \mathbf{\Phi} \mathbf{\Phi}_s^+ E\{\mathbf{w}(t)\mathbf{w}(t)^T\} (\mathbf{\Phi} \mathbf{\Phi}_s^+)^T \quad (6)$$

Assuming that the components of the measurement noise have zero mean $E\{\mathbf{w}(t)\} = \mathbf{0}$ and uncorrelated covariance matrix $E\{\mathbf{w}(t)\mathbf{w}(t)^T\} = \sigma_w^2 \mathbf{I}$, the above covariance matrix takes the following form

$$E\{\mathbf{e}(t)\mathbf{e}(t)^T\} = \sigma_w^2 \mathbf{\Phi} \mathbf{\Phi}_s^+ (\mathbf{\Phi}_s^+)^T \mathbf{\Phi}^T \quad (7)$$

where σ_w^2 represents the noise variance specific to a selected type of sensors.

From the formula (7) it can be easily observed that by selection of proper measurement locations we can influence the overall estimation error. To compare two different sensor configurations, certain metrics should be defined first. Two such metrics are frequently used in the literature. The first one is based on a trace of the covariance matrix (7)

$$\sigma_{e,avg}^2 = \frac{1}{n_s} \text{trace}(E\{\mathbf{e}(t)\mathbf{e}(t)^T\}) \quad (8)$$

Formula (8) gives information about average estimation error.

The second metric is related to the maximal element on the diagonal of the covariance matrix

$$\sigma_{e,\max}^2 = \max\{\text{diag}(E\{\mathbf{e}(t)\mathbf{e}(t)^T\})\} \quad (9)$$

and corresponds to the component of the response vector with the largest estimation error for a given sensor configuration. The above metrics (eqns. 8 and 9) can be incorporated into the optimization process for finding the best achievable sensor locations.

2.2 Combinatorial methods for optimal sensor placement

The number of ways in which n_s sensor positions can be chosen from among n_d candidate locations is given by the well-known formula

$$\binom{n_d}{n_s} = \frac{n_d!}{n_s!(n_d - n_s)!} \quad (10)$$

This formula shows that in the case of real engineering structures with many degrees of freedom, complete enumeration of possibilities for finding the optimal location of sensors is impractical if not impossible. For that reason a number of approximate methods have been proposed, among which the Effective Independence and Information Entropy methods are the most prominent ones. Both methods are operating in an iterative manner sequentially removing or adding sensors at subsequent iterations. Such an approach related to discrete optimization methods may not be efficient in the case of structures with a large number of degrees of freedom. Therefore, in the next section of this paper, an alternative approach for finding optimal positions of sensors is proposed which assumes that design variables are continuous.

3 THE PROPOSED TOPOLOGY OPTIMIZATION BASED SENSOR PLACEMENT

For the purpose of continuous optimization we introduce the function of sensor density $\rho(\mathbf{x})$, which takes values between 0 and 1. Then, instead of removing individual rows from the full modal matrix we will multiply it by the value of the sensor density function at a given location \mathbf{x}

$$\Phi_s = \text{diag}(\rho(\mathbf{x}))\Phi \quad (11)$$

Using the above relation we can replace the combinatorial problem related to sensor placement with its continuous version. Additionally, depending on the requirements, two continuous formulations are possible.

In the first one the goal is to optimize estimation error under a constraint on the volume (or equivalently - a number) of sensors:

$$\begin{aligned} \text{Minimize } J_1 &= \|E\{\mathbf{e}(t)\mathbf{e}(t)^T\}\| \\ \text{subject to } \int_V \rho(\mathbf{x})dV &\leq \bar{V} \end{aligned} \quad (12)$$

The second formulation aims at minimizing the number of sensors, while limiting the resulting estimation error

$$\begin{aligned} &\text{Minimize} && \mathcal{J}_2 = \int_V \rho(\mathbf{x}) dV \\ &\text{subject to} && \|E\{\mathbf{e}(t)\mathbf{e}(t)^T\}\| \leq \bar{\varepsilon} \end{aligned} \quad (13)$$

4 ILLUSTRATIVE EXAMPLE

4.1 The structure under investigation

The effectiveness of the proposed methodology for optimal sensor placement has been demonstrated on an example of a real tied-arch bridge located in Poland (figure 1). The bridge's main span is 76,6-meter long and consists of an arch box girder supporting the bridge deck using 13 vertical members (hangers). The arch and hangers are made of steel with the following material properties: $E = 210$ GPa, $\nu = 0.2$, $\rho = 7850$ kg/m³. The bridge deck is made of concrete and is additionally supporting a railway track.

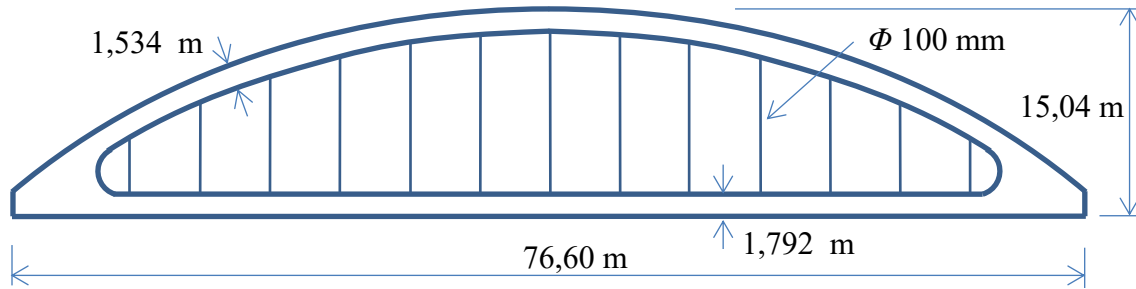


Figure 1: General view of the investigated arch bridge

A numerical model of the bridge was created with the aid of commercial finite element software Abaqus 3DEXPERIENCE R2016x. The model consists of three types of finite elements including brick, shell and beam elements. The total number of finite elements is 68195 and the number of nodes is 76792. The task is to find a distribution of sensors for optimal estimation of the first five modal coordinates of the structure shown in figure 2.

4.2 Optimal sensor distribution

The optimization problem was stated as follows:

$$\begin{aligned} &\text{Maximize} && \det\left((\text{diag}(\rho_i)\Phi)^T(\text{diag}(\rho_i)\Phi)\right) \\ &\text{subject to} && \sum_{e=1}^{n_e} \rho_i \leq n_s, \end{aligned} \quad (14)$$

where ρ_i is the value of the sensor density function at the i -th node's location. The sensor

density function takes values within the range (0,1). The remaining symbols have the following meanings: n_s is the number of sensors, n_e is the number of finite elements. In our approach it is assumed that the sensor density function can be represented as a linear combination of coefficients x_j and y_j together with some prescribed basis functions $\bar{\rho}_{ij}$:

$$\rho_i = \sum_{j=1}^{n_c} x_j \bar{\rho}_{ij}^{(x)} + \sum_{j=1}^{n_c} y_j \bar{\rho}_{ij}^{(y)} \quad (15)$$

where n_c is the number of candidate locations; in this example $n_c = 26$. The design variables for the horizontal and vertical direction are $\mathbf{x} = \{x_1, x_2, \dots, x_{n_c}\}$ and $\mathbf{y} = \{y_1, y_2, \dots, y_{n_c}\}$, respectively.

Each function's value is equal to 1 at nodes connecting vertical hangers with the arch girder and deck of the bridge. The basis function approaches zero at nodes located farther than a certain distance away from the connection.

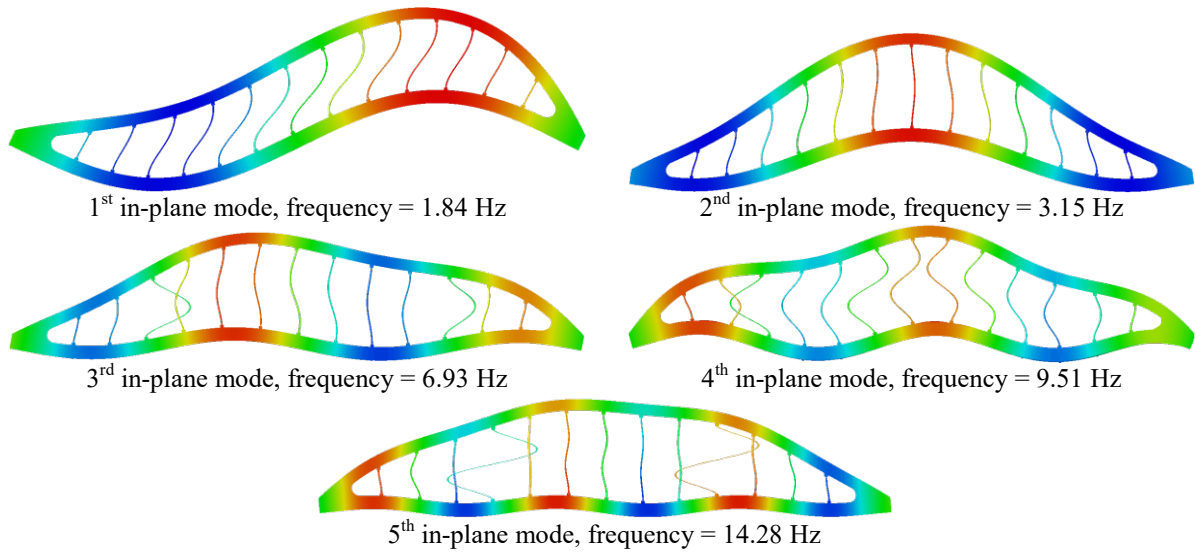


Figure 2: Mode shapes of the investigated arch bridge

The sensor arrangement dedicated to optimal identification of the five modal coordinates described above is presented in figure 3 (red circles in this figure indicate candidate locations).

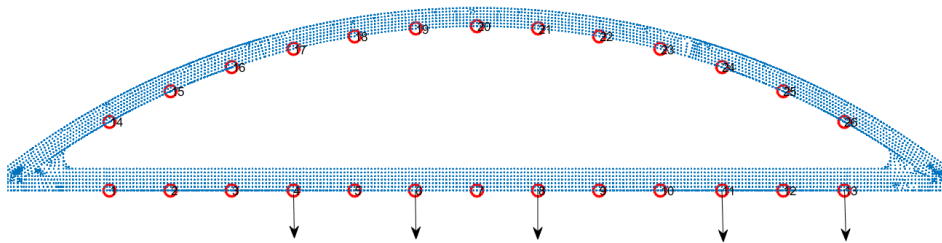


Figure 3: Optimal sensor arrangement for the investigated arch bridge

5 CONCLUSIONS

- In the present study the problem of sensor placement over a large structure with thousands of DOFs has been formulated as continuous optimization similarly to the methods for finding optimal structural topology.
- A real-scale arch bridge had been selected as a numerical example for which the problem of sensor placement for five vibration modes was considered.

ACKNOWLEDGEMENT

The authors gratefully acknowledge the support of the National Science Centre, Poland, granted under grant agreement 2017/25/B/ST8/01800 and of the National Centre for Research and Development, Poland, granted in the framework of the PBS programme (PBS3/B9/36/2015).

REFERENCES

- [1] Shah, P.C., Udawadia, F.E. A Methodology for Optimal Sensor Locations for Identification of Dynamic Systems. *Journal of Applied Mechanics* (1978) **45**(1): 188–196. <https://doi.org/10.1115/1.3424225>
- [2] Kammer, D.C. Sensor placement for on-orbit modal identification and correlation of large space structures. *Journal of Guidance, Control, and Dynamics* (1991), **14**(2): 251–259. <https://doi.org/10.2514/3.20635>
- [3] Cobb, R.G., Liebst, B.S. Sensor Placement and Structural Damage Identification from Minimal Sensor Information. *AIAA Journal* (1997) **35**(2): 369–374. <https://doi.org/10.2514/2.103>
- [4] Papadimitriou, C. Optimal sensor placement methodology for parametric identification of structural systems. *Journal of Sound and Vibration* (2004) **278**(4–5): 923–947. <https://doi.org/10.1016/j.jsv.2003.10.063>
- [5] Mariani, S., Bruggi, M., Caimmi, F., Bendiscioli, P. and Fazio, M.D. Sensor deployment over damage-containing plates: A topology optimization approach. *Journal of Intelligent Material Systems and Structures* (2013) **24**(9): 1105–1122. <https://doi.org/10.1177/1045389X13480570>
- [6] Zhou, K., Wu, Z.Y., Yi, X.H., Zhu, D.P., Narayan, R., Zhao, J. Generic Framework of Sensor Placement Optimization for Structural Health Modeling. *Journal of Computing in Civil Engineering* (2017), **31**(4). [https://doi.org/10.1061/\(ASCE\)CP.1943-5487.0000662](https://doi.org/10.1061/(ASCE)CP.1943-5487.0000662)
- [7] Blachowski, B., Swiercz, A., Jankowski, L. Virtual distortion method based optimal sensor placement for damage identification. *Proceedings of 28th International Conference on Noise and Vibration Engineering (ISMA2018)*, 17-19 September 2018, Leuven, Belgium, 2018.
- [8] Blachowski, B. Modal Sensitivity Based Sensor Placement for Damage Identification Under Sparsity Constraint. *Periodica Polytechnica Civil Engineering* (2019). <https://doi.org/10.3311/PPci.13888>

VIBRATION MONITORING ON A PC BRIDGE DURING A BRIDGE COLLAPSE TEST

YOSUKE KONDO^{*}, YOSHINOBU OSHIMA[†] AND CHUL-WOO KIM^{*}

^{*} Department of Civil and Earth Resources Engineering
Graduate School of Engineering, Kyoto University
Katsura Campus, 615-8540 Kyoto, Japan
e-mail: kim.chulwoo.5u@kyoto-u.ac.jp, <http://infra.kuciv.kyoto-u.ac.jp>

[†] Center for Advanced Engineering Structural Assessment and Research
Public Works Research Institute
305-8516 Tsukuba, Japan
email: y-ooshima@pwri, <https://www.pwri.go.jp/caesar/index-e.html>

Key words: bridge collapse-test; energy capacity; loading capacity; PC girder bridge; vibration monitoring

Abstract. Vibration-based structural health monitoring (SHM) has been successfully applied to damage detection for a specific type of bridges. However, it is still a challenging task to assess structural integrity or structural performance by means of SHM. This study is intended to examine changes in load resistance capacity and modal parameters of an actual PC girder bridge through a bridge collapse-test. In the static loading test, the PC girder bridge was put under several loading and unloading levels until failure. Besides, forced vibration tests from both impact hammer test and moving-vehicle test were carried out along the static loading test in order to assess the changes in the dynamic properties of the PC girder bridge with different health conditions. An energy performance which is a function of energy dissipation and potential energy of the PC bridge is adopted as a feature relevant to structural performance. Observations demonstrated that changes in the frequency of the second bending mode was more strongly correlated with the changes of load resistance capacity than the first bending mode.

1 INTRODUCTION

Prestressed concrete (PC) girder bridges have been constructed since 1970s in Japan, and various damages due to deterioration such as a corrosion of PC tendon have been reported. Many methods have been proposed to evaluate soundness of bridges, and visual inspection is one of the most popular approaches to assess integrity of the PC bridge. In the PC bridge, the compressive stress introduced by the PC tendon cancels the tensile stress generated by applying load, and the crack occurs when the tensile stress reaches crack strength. Occurrence of cracks on the concrete girders is associated with higher possibility of excessive stresses and less margin of strength in the PC bridge.

In addition, damages caused by different phenomena have different effects on load resisting capacity of the PC bridge, and it is desirable to evaluate soundness of the PC bridge not only from external appearance but also from physical index.

Vibration-based structural health monitoring (SHM) thus has been developed as an approach providing physical index on soundness of bridges. Natural frequencies from deteriorated concrete girders have shown to be a sensitive feature for the strength reduction when evaluating the residual strength in bridges with 50 years of service life [1]. At the same time, it rises the likelihood of using natural frequencies as a symptom to be monitored in order to estimate the structural reliability [2]. Literatures also show that the modal damping ratio can be a damage sensitive feature for reinforced and prestressed concrete structures. Moreover, researches indicate that a trend of getting higher value of modal damping ratios with the age of the bridges could be a sign of possible deterioration, which is a strong reason to investigate the relationship between damping parameter and degree of damage [3]. However more evidences are required to validate residual strength models of deteriorating bridges [4] and to prove the link between structural resistance and information for SHM [5].

Inconsistencies between experiment and theoretical models occur due to different reasons that should be clarified [6]. Damage in structures is interpreted as a decay of its mechanical properties, or a decrease in stiffness. However, the tendency of natural frequencies to the development of damage shows an abnormal increase/decrease from one configuration to another, even experimentally [7].

The natural frequency of the first vertical mode showed to rapid decaying tendency, but little change in the damping was observed in the failure process of a PC bridge [1]. It was noticed that the small changes in modal parameters, regardless the large presence of cracks in concrete structures, might be due to the cracks closing by effective prestressing when the structure is unloaded. The decrease of prestressing force should increase the natural frequencies in a concrete element theoretically because a reduction in the axial compressive load would stiffen the element. However, an opposite trend was observed in a PC bridge under test [8] where the frequencies had a small decrement after the decrease of prestress force. Moreover, researches also show that no substantial change was detected in the modal parameters after cutting the prestressing tendons at specific locations of a concrete bridge [9].

This study is intended to examine changes in load resistance capacity and modal parameters of an actual PC girder bridge through a bridge collapse-test. In the static loading test, several loading and unloading levels until failure were considered. Forced vibration tests were carried out along with the static loading test in order to estimate the relationships between modal parameters and structural performance.

2 STATIC LOADING TEST AND VIBRATION TESTS

2.1 Target bridge

Figure 1 shows the target bridge with a static loading device. The bridge is a five-span simply-supported PC girder bridge with four main girders. The length of each span is 34.3 m and width of 7.2 m. 12 pairs of PC steel strand (12 ϕ 7) were utilized as a PC tendon for each girder. The bridge is about 170 m away from the coastline and had been operated over 50 years since its construction. Therefore, chloride attack to the main girder was significant, and cracks of the main girder caused by corrosion of the internal steel rebar and spalling of the concrete

were observed by visual inspection. Figure 2 shows the damage location map of the bridge obtained from the periodic inspection before the experiment. Damage was distributed throughout the span, and exposure of the reinforcing bar due to concrete peeling was observed at three locations. In considering the inspection result, high possibility of reduced load carrying capacity was expected.

2.2 Static loading test

The static loading test was carried out by using two 3000kN center hole type hydraulic jacks installed on the loading beam with a loading block. Figure 3 shows the loading device installed on the PC bridge. The load was given statically and monotonously.

As a reaction device for the static loading, two tendons having a loading capacity of 2500kN for each are anchored to the underground sandstone layer. The applying load was monitored by the load cell and the jack stroke was also monitored during loading. The loading point was set at the span center of the G1 girder shown in Figure 2.

Sensor deploying map is shown in Figure 4. The vertical displacement of each observation



Figure 1 Target bridge.



Figure 3 Loading device.

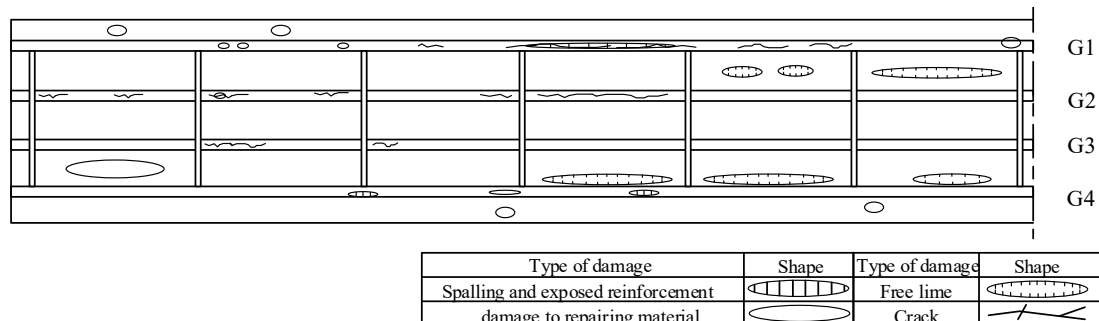


Figure 2 Damage location map.

point was measured by laser displacement meters (LDS-7H, Murakami Giken) and the tape measure type displacement meter (DP-500E, Tokyo Sokki) installed under the girder.

The loading test was conducted over three days, and repeated five stages of loading tests (Loading-1 to Loading-5) until collapse of the upper surface of the loaded PC girder which is assumed as the final state. Loading-1 shows a loading up to 600kN where bending cracks occur to the main girder. Loading-2 shows a loading up to 1200kN which is the yield load of tensile rebars. In Loading-3, as with Loading-2, loading of 1200kN was applied again but the loading was kept for about 2 hours. Loading-4 is loading up to 2400kN which is the failure load predicted in a preliminary structural analysis. Loading-5 was planned to load up to collapse of the upper flange of the loaded PC girder that is the final state, but before the final state, the loading test was terminated under the load of about 3200kN as the jack stroke reaches its admissible length of 50cm prior to the whole collapse of a superstructure. The loading progress is shown in Figure 5 in which “Stage n ” indicates the time of vibration test.

2.3 Vibration test

In order to estimate the vibration characteristics of each state, forced vibration tests were conducted at each unloading state as shown in Figure 5. Stage 1 is the initial state before the

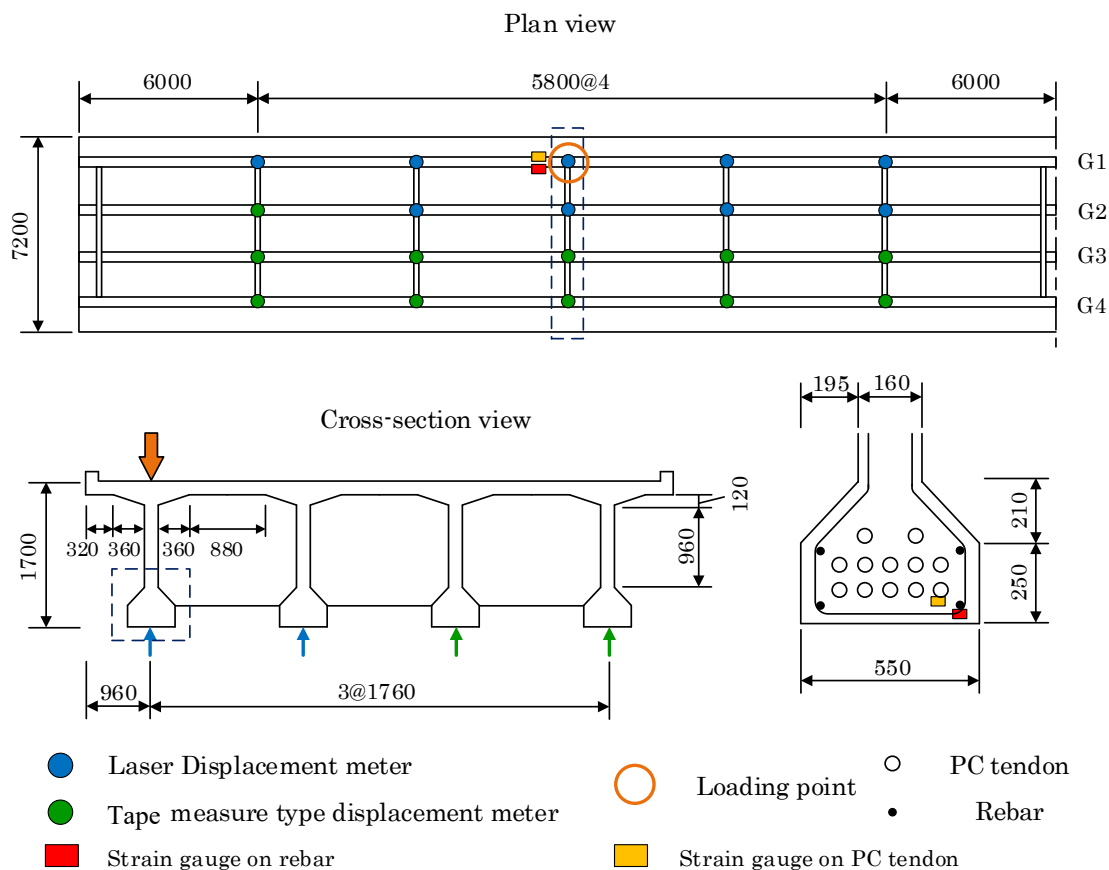


Figure 4 Observation span and location of sensors.

static load test. Stage 2 is the unloaded state after the Loading-1 (600kN) test, and Stage 3 is the unloaded state after the Loading-2 (1200kN) test. Stage 4 is the unloaded state after the Loading-3 test which was the state of being loaded by 1200kN for two hours. Stage 5 indicates the state which was left overnight after the Stage 4. Stage 6 shows the unloaded state of Loading-4 (2400kN). Stage 7 shows the state when it is left overnight after Stage 6. Finally, Stage 8 shows the unloaded state of Loading-5 (3200kN).

Two kinds of vibration tests were carried out. One is the moving-vehicle test which is practical as traffic loads are used as excitation sources without traffic regulation for the experiment. Traffic-induced vibrations of the bridge at each stage are measured by strain gauge type accelerometers (ARS-10A, Tokyo Sokki). The location of accelerometers is shown in Figure 6. As a test vehicle, a heavy vehicle is desirable as it is expected to provide greater excitation force. However, a smaller vehicle, van type vehicle (HIACE, Toyota Motor Corporation), was used because of the restriction of the vehicle passageway due to the static loading device on the bridge. The speed was approximately 30km/h. Three runs for Stage 1, and five runs for other stages were carried out.

Another vibration test is the impact hammer test whose identification accuracy is higher than

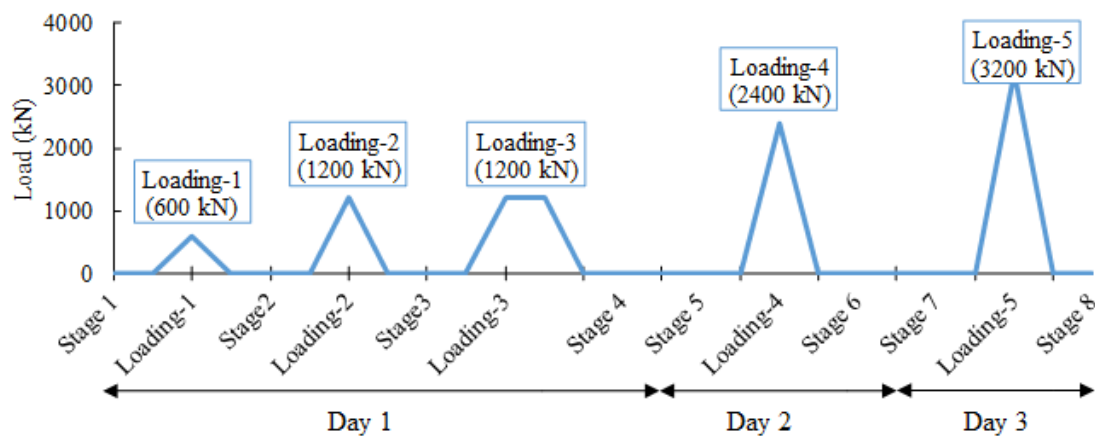


Figure 5 Loading process of the experiment.

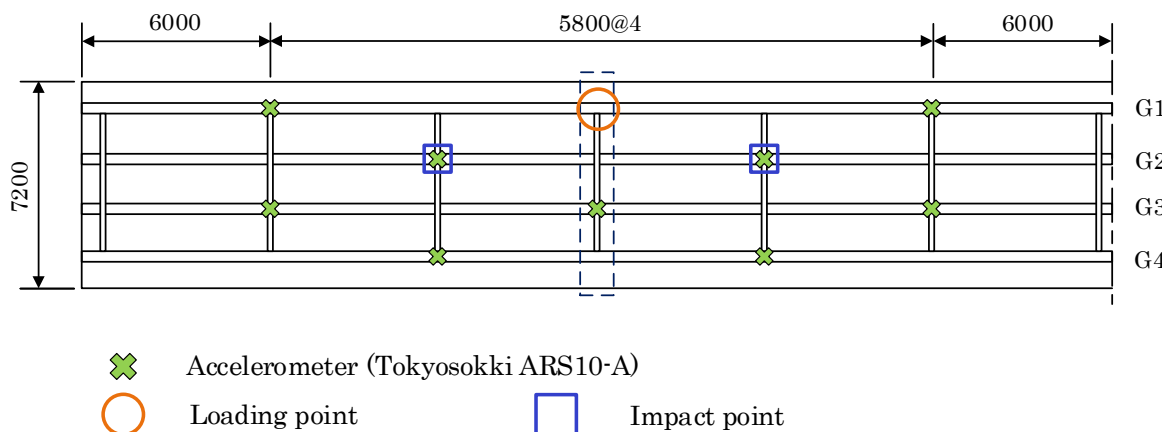


Figure 6 Location of impact points and accelerometers.

that from moving-vehicle test. The equipment used for this test consists of an impact hammer Brüel & Kjær type 8210 – Modal sledge hammer 12 pounds head with a maximum compressive force of 44.4 kN and a sensitivity of 0.225 mV/N. The same accelerometers as moving-vehicle test were used during the impact hammer test. In each stage, the bridge was hit 10 times in each impact point by using two different types of impact tip (medium and tough tips), and the total hitting times was 40 per each stage. The hitting points are also shown in Figure 6.

3 STRUCTURAL PERFORMANCE OF PC BRIDGE

3.1 Load-displacement relation

The load-displacement curve observed at the span center of the G1 girder is shown in Figure 7 in which no clear residual displacement was observed until Loading-3. It indicates the bridge behavior was elastic until Loading-3. After Stage 5, the bridge was loaded up to 2500kN, which is the maximum design load (Loading-4), and unloaded. The maximum design load resulted in the residual displacement of around 16mm. Moreover, when the bridge is reloaded, the load-displacement curve traces the unloading point (point A in Figure 7), which showed enough restoration performance. The gradient of reloading was almost the same as that of the Loading-1 to Loading-4 until the tensile stress is generated at the lower edge of the concrete (point B in Figure 7). This proved that the prestressed force remains in order to keep the entire section effective. Therefore, when the load level is low it can be said that the vibration characteristics are hardly changed as the initial stiffness was about the same as those of Stage 1 to 5. Relationships between structural performance and vibration characteristics are discussed in Section 4.

3.2 Load-strain relation

Load-strain curves of rebar and PC tendon observed near the span center of the G1 girder are shown in Figures 8 and 9 respectively. Figure 8 shows that the load 1100kN in the load-strain curve under Loading-2 (see point C in Figure 8) is close to the yield load calculated by the preliminary analysis, and the behavior also seems to be the yield of the bar. However, the residual displacement after unloading hardly occurred, so this is not an actual yielding. This is because the adhesion force decreases due to the crack development. The same behavior can also be observed in the load-strain curve of PC tendon as shown in Figure 9. From Figure 9, it can be inferred that PC tendon yields at Loading-4 since residual strain occurs. After that, when the strain exceeds 4000 μ at Loading-5, it is considered that the rupture of PC tendon occurs.

3.3 Energy-based bending performance

As performance feature (Z) is introduced to normalize bending performance of PC bridges utilizing the potential energy and energy dissipation in each load step of the experiment. Equation (1) shows the performance feature at n loading stage with function of the energy dissipation (ΔW) and the potential energy (W). The energy dissipation (ΔW) is the enclosed area in the load- displacement graph when the concrete structure is tested in a specific loading-unloading step as shown in Figure 10(a). On the other hand, the potential energy (W), or work applied, is the area below the curve in the same graph, but this time without considering the unloading process as shown in Figure 10(b). Once the dissipated and potential energy are

calculated in a specific stage, the performance Z can be defined as:

$$Z_n = \left(1 - \frac{\Delta W_n}{W_n}\right) \cdot 100 \quad (\%) \quad (1)$$

where, “ n ” represents the loading stage.

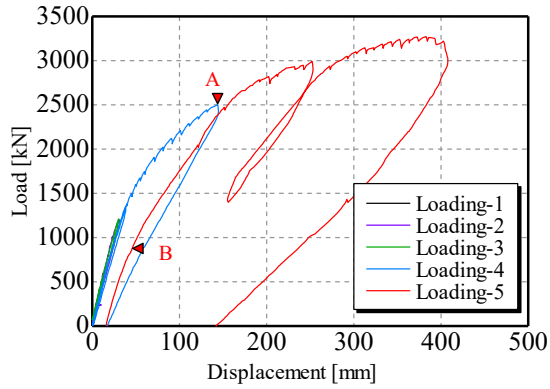


Figure 7 Load vs. displacement curve.

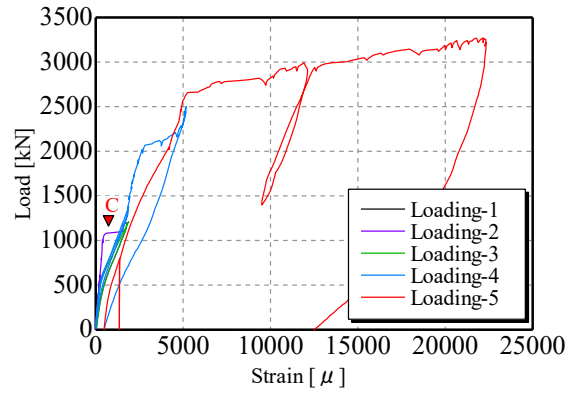


Figure 8 Load vs. strain curve of rebar.

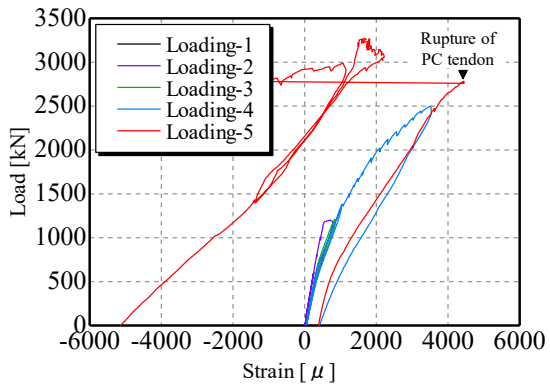


Figure 9 Load vs. strain curve of PC tendon.

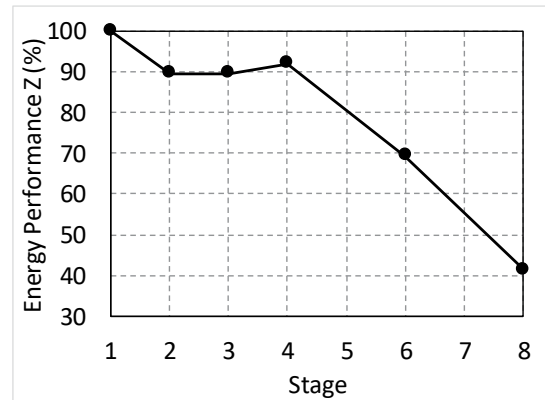


Figure 11 Energy performance w.r.t. stages.

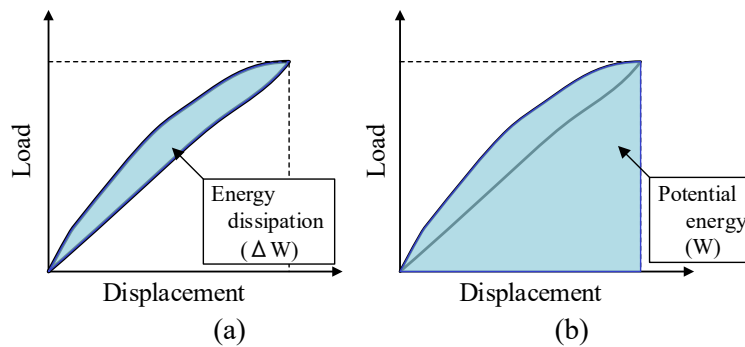


Figure 10 Energy dissipation and potential energy.

When the concrete structure behaves elastically and no damage has occurred, the energy dissipation would be zero and the performance would remain 100%. On the contrary, if damage is introduced or the beam reaches its plastic range, the energy dissipation should be different from zero and the performance feature shows lower value than 100%.

Figure 11 shows the change in the performance with respect to each stage. It can be seen from Figure 11 that the performance Z has been drastically decreased when the static load is larger than the yielding load.

4 MODAL PARAMETERS FROM VIBRAITON TESTS

4.1 Natural frequency and damping ratio

Modal parameters of the PC bridge such as natural frequency and damping ratio are identified from the vibration data as representative vibration characteristics. Stochastic subspace identification (SSI) [10] is adopted as a system identification method for the acceleration response obtained from moving-vehicle test. For vibration data from the impact hammer test, modal parameters are estimated using the frequency response function.

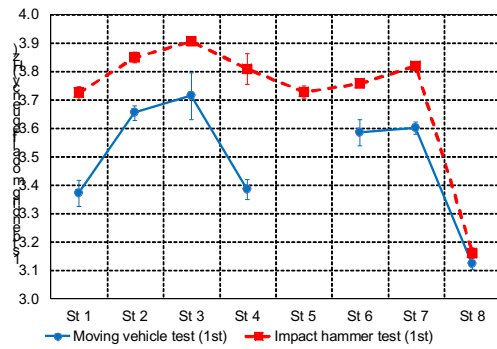
Changes in identified frequencies for the 1st and 2nd bending modes corresponding to structural integrity are plotted in Figure 12 which shows that the frequency for the 2nd bending mode obtained from impact hammer test resulted in stronger relationship with structural integrity. The precision of the natural frequency identified from moving-vehicle test was poor due to the weak excitation.

Figure 13 shows changes in damping ratio corresponding to the 1st and 2nd bending modes. Existing researches [11,12] suggests that decrease of the prestressed force causes increase of damping ratios. Similar phenomena on increase of damping ratio for the 2nd bending mode due to decrease of the prestressed force was observed: the rupture of the PC tendon was confirmed in Stage 8, and the damping ratio for the 2nd bending mode increased as shown in Figure 13. However, change in damping ratio for the 2nd bending mode was unclear comparing to that change in the frequency for the 2nd bending mode.

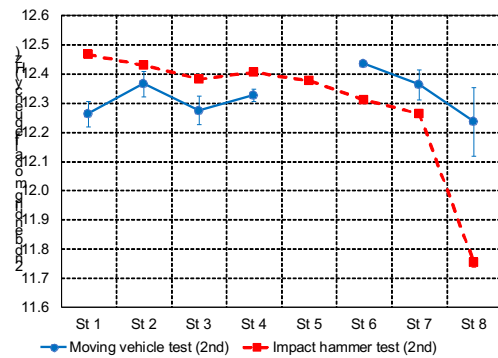
In summary, the frequency for the 2nd bending mode showed stronger relationship with structural integrity of the PC bridge. This result is similar to the PC girder damage experiment in laboratory [13].

4.2 Energy performance and natural frequency

The relationship between changes in energy performance and changes in natural frequency is shown in Figure 14. The natural frequency obtained from impact hammer test is examined as quality of the data from the impact hammer test was better than that from the moving-vehicle test. The dotted line shows a linear regression between frequency and energy performance from Stage 1 to Stage 7. Stage 8 was not considered to the regression since Stage 8 is close to the ultimate condition which rarely occurs in real bridge monitoring. From the linear regression curve, a strong correlation was observed between the 2nd bending modal frequency and the energy performance.

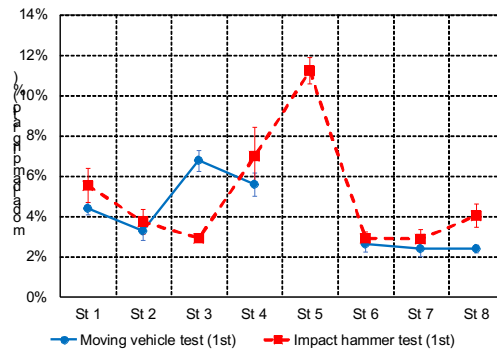


(a) 1st bending mode

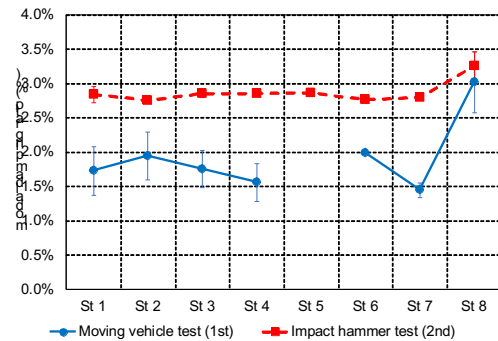


(b) 2nd bending mode

Figure 12 Change in bending modal frequency.

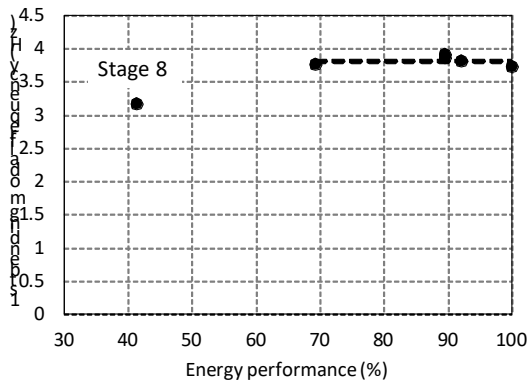


(a) 1st bending mode

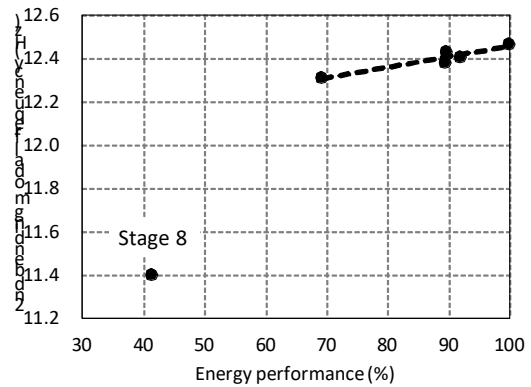


(b) 2nd bending mode

Figure 13 Change in bending modal damping ratio.



(a) 1st bending mode



(b) 2nd bending mode

Figure 14 Energy performance vs. Frequency.

5 CONCLUSIONS

This study investigates the relationship between bridge performance and modal frequencies. In regard to natural frequency, the 2nd bending mode showed stronger correlation with energy

performance than the 1st bending mode. For the damping ratio, the 2nd bending mode showed an increase from Stage 7 to Stage 8 due to the rupture of PC tendon. However, modal damping ratio for the 1st bending mode barely changed from Stage 7 to Stage 8. Observations demonstrated the usefulness of the 2nd bending mode in vibration-based bridge health monitoring of the PC bridge. However, it is still a challenge to estimate the structural performance of the PC bridge from changes in the natural frequency of 2nd bending mode. As a next step for this research, comprehensive investigations on structural performance of the PC bridge will be carried out even utilizing strains measured at concrete and rebar. Moreover, effectiveness of the correlation between the bridge performance and vibration characteristics will be investigated by numerical analysis.

ACKNOWLEDGEMENTS

This study is partially sponsored by a Japanese Society for the Promotion of Science (JSPS) Grant-in-Aid for Scientific Research (B) under project No.19H02225, which is greatly appreciated.

REFERENCES

- [1] Kato, M. and Shimada, S. Vibration of PC bridge during Failure Process. *Journal of Structural Engineering, ASCE*. (1986) **112**(7): 1692-1703.
- [2] Quattrone, A. et al. Vibration tests on dismantled bridge beams and effects of deterioration. *Journal of Physics; Conference Series* **382** (2012) 012059,
- [3] Dammika A. J. et al. An investigation on modal damping ratio as an indicator of invisible damage in PC bridges. *Taylor & Francis Group* (2015) ISBN 978-1-138-00120-6: 404-410.
- [4] Cavell, D. and Waldron, P. A residual strength model for deteriorating post-tensioned concrete bridges. *Computers and Structures* (2001) **79**(4): 361-373.
- [5] Dilena, M. et al. Dynamic identification of a reinforced concrete damaged bridge. *Mechanical Systems and Signal Processing* (2011) **25**(8): 2990-3009.
- [6] Udwadia, F. E. Structural Identification and Damage Detection from Noisy Modal Data. *Journal of Aerospace Engineering* (2005) **18**(3): 179-187.
- [7] Dilena, M. and Morassi, A. Dynamic testing of a damaged bridge. *Mechanical Systems and Signal Processing* (2011) **25**(5): 1485-1507.
- [8] Saiidi, M. et al. Prestress Force Effect on Vibration Frequency of Concrete Bridges. *Journal of Structural Engineering, ASCE*. (1994) **120**(7): 2233-2241.
- [9] Döhler, M. et al. Structural health monitoring with statistical methods during progressive damage test of S101 Bridges. *Engineering Structures* (2014) **69**: 183-193.
- [10] van Overschee, P. and De Moor, B. Subspace Identification for linear Systems. Kluwer Academic Publishers (1996). ISBN 978-1-4613-0465-4
- [11] Miyanaga, K. et al. Monitoring of vibration characteristics of PC bridge and a rupture of PC tendon. *Symposium of Japan Prestressed Concrete Institute*. (2013) **22**: 353-358.
- [12] Kaneko, H. et al. Influence of tendon breaks on structural behavior of concrete beams. *Taylor & Francis Group* (2018) ISBN 978-1-138-73045-8: 1074-1081.
- [13] Luna Vera, O. S., et al. Energy dissipation and absorption capacity influence on modal parameters of a PC girder. *Journal of Physics*. (2017) Conf. series **842**.

VIBRATION SUPPRESSION AND ENERGY HARVESTING POTENTIAL IN WIND EXCITED BUILDINGS EQUIPPED WITH GROUND FLOOR TUNED INERTER DAMPER

ZIXIAO WANG* AND AGATHOKLIS GIARALIS*

* Department of Civil Engineering
City, University of London
Northampton Square, EC1V 0HB, London, UK
e-mail: agathoklis.giaralis.1@city.ac.uk

Key words: Tuned Inerter Damper, Optimal Vibration Control, Energy Harvesting, Weight Reduction Design, Wind Excitation, Vortex Shedding.

Abstract. This paper investigates numerically the potential of ground floor linear tuned inerter damper (TID) to mitigate floor acceleration causing occupants' discomfort in wind-excited multi-storey buildings due to vortex shedding (VS) effects while generating electric energy. To this aim, TID stiffness and damping properties were optimally designed to minimize root mean square (RMS) floor acceleration at the top occupied floor for wide range of fixed inertance values, while an electromagnetic motor (EM), modelled as an ideal damper, was added to endorse energy harvesting capabilities to the TID. Numerical data pertaining to a 15-storey steel moment resisting frame structure with square floor plan, deficient to occupants' comfort (OC) code-prescribed criteria under moderate wind action, are furnished. Wind excitation is by a spatially-correlated across-wind force field accounting for VS effects. It is found that optimally designed ground floor TID can readily meet OC criteria without any structural modification (stiffening) which for the case-study building would require 67% increase of steel weight. It is further shown that increasing EM damping coefficient increases energy harvesting potential at the expense of increased floor accelerations. However, increasing TID inertance enhances *simultaneously* floor acceleration and energy harvesting performance. Hence, it is concluded that it is possible to increase energy generation in ground floor TID-equipped wind-excited multi-storey buildings without necessarily relaxing performance requirements in terms of floor accelerations through judicious changes to EM damping coefficient and/or inertance.

1 INTRODUCTION

Design and construction of slender high-rise buildings in congested modern city centers have been gaining popularity in recent decades mostly due to ever-increasing cost of land associated with urbanization. Satisfying the structural integrity criteria under gravitational and wind design loads at the ultimate limit state is relatively straightforward in such structures using high strength materials and stiff lightweight structural components [1]. However, it is found that slender buildings with rectangular floor plan are prone to excessive oscillations in the across-wind direction (i.e., within the normal plane to the wind direction) due to vortex shedding (VS) effects generated around their corner edges [2]. These oscillations may generate floor

accelerations trespassing occupants' comfort thresholds under moderate wind action (i.e., at the serviceability limit state) [3-4] leading to loss of functionality and to downtime. Increasing the lateral stiffness of VS prone buildings cannot efficiently address serviceability performance associated with floor accelerations [5]. Therefore, dynamic vibration absorbers, with most representative the tuned mass damper (TMD), are widely used in practice for vibration mitigation in wind-excited slender buildings to meet floor accelerations thresholds prescribed by building codes and guidelines [6]. In its simplest form, the classical linear passive TMD comprises an oscillating mass attached towards the building top via linear stiffeners and viscous dampers. Stiffness and damping properties of the TMD are optimally designed/tuned to the dominant building mode shape for fixed attached mass. This provision facilitates the transfer of kinetic energy from the wind-excited building to the TMD secondary mass and, eventually, its dissipation through the dampers. Recently, the potential of TMDs to harvest energy from wind-induced oscillations in slender buildings has been explored by employing electromagnetic motors (EMs) coupled with energy harvesting/storage circuitry to replace viscous dampers in connecting the TMD mass to the host structure [7-8]. In this manner, part of the kinetic energy of the host structure is transformed into usable electric energy instead of being "lost" at the dampers in the form of heat. Moreover, Giaralis and Petrini [9-10] demonstrated that by coupling the TMD with an inerter device in the so-called tuned mass-damper-inerter (TMDI) configuration reduces significantly floor acceleration in tall/slender buildings subject to VS effects for the same attached mass. This improved vibration control efficiency of the TMDI is attributed partly to the mass-amplification effect and partly to higher-modes-damping effect endowed to the TMD by the inerter: a device developing acceleration proportional force by a coefficient termed inertance [11]. Further, Petrini et al. [12] added an EM to the TMDI and showcased significant gains in the available energy for harvesting by varying the inertance and/or the damping property of the TMDI.

Notably, all the above dynamic vibration absorbers are installed towards the top floor of buildings occupying high premium space. To address this issue, herein, the potential of a tuned inerter damper (TID), that is a TMDI with no mass property, [13] installed at the ground floor of wind-excited buildings is explored to mitigate floor accelerations at the upper floors. This consideration is inspired by several studies [13,14,15] demonstrating the high efficiency of ground floor TIDs to control earthquake-induced vibrations in multi-storey buildings. In this work, a ground floor TID is considered for the first time to control wind-induced vibrations. Furthermore, the TID is coupled with an EM to gauge its potential for harvesting energy from wind-induced oscillations. To this aim, a planar dynamical model of a 15-storey benchmark building with square floor plan deficient to floor acceleration thresholds due to VS effects is considered. Attention is focused on quantifying savings in the total weight of the structure achieved by adding a ground floor TID optimally designed for top floor acceleration reduction as opposed to increase the lateral floor stiffness. Additionally, energy harvesting potential is quantified as inertance and EM damping are let to vary.

2 BENCHMARK STRUCTURE AND WIND MODELLING

2.1 Benchmark structure description and reduced order modelling

The benchmark building considered in this paper is a doubly symmetric, 15-storey, 3-bay steel moment resisting frame (MRF) structure with 16.5m-by-16.5m footprint. It totals 49.8m

of height: ground floor is 5.0m high, while the rest of the floors are 3.2m high. The structure comprises four parallel planar MRFs along each principal axis with all beam-to-column joints taken as rigid as shown in Figure 1(a). Columns have hollow square sections with varying outer dimensions and thickness along the building height ranging between 0.48m and 0.32m, and 0.024m to 0.016m respectively. Beams are of various welded wide flange sections with section height and flange width varying between 0.5m and 0.3m, and 0.3m and 0.18m, respectively. Horizontal perfectly rigid diaphragm constraints are imposed at the height of each floor in developing a detailed finite element (FE) linear model of the structure. By deactivating the out-of-plane DOFs, the first three natural frequencies of the building and corresponding modal mass participating ratios in parentheses are 0.548Hz (0.7118), 1.391Hz (0.1675), and 2.342Hz (0.0593). The building is designed to all serviceability and ultimate limit state requirements for static design load combinations including gravitational loads and mean wind component forces acting in the along-wind direction. The required steel tonnage (MRFs self-weight) is 471tons.

To expedite computational work in later sections, a low-order planar dynamic model with 15 degrees of freedom (DOFs) corresponding to the lateral in-plane translations of the rigid slabs is derived from the detailed FE model of the benchmark building using the modal-based procedure detailed in [9]. The 15-DOF model is defined in terms of a diagonal mass matrix, and full damping matrix and stiffness matrices. Building mass including nominal gravitational loads is lumped at each floor as shown in Figure 1(b), while modal damping ratios for the j -th mode are taken as: $\xi_j=1\%$, for $j= 1,2,3$; $\xi_j= 2\%$ for $j= 4,5,6$; $\xi_j= 4\%$ for $j= 7,8,9$; $\xi_j=8\%$ for $j= 10,11,12$; and $\xi_j=16\%$ for $j= 13,14,15$. The first three mode shapes obtained by the detailed FE model and the 15-DOF system match very well as shown in Figure 1(c).

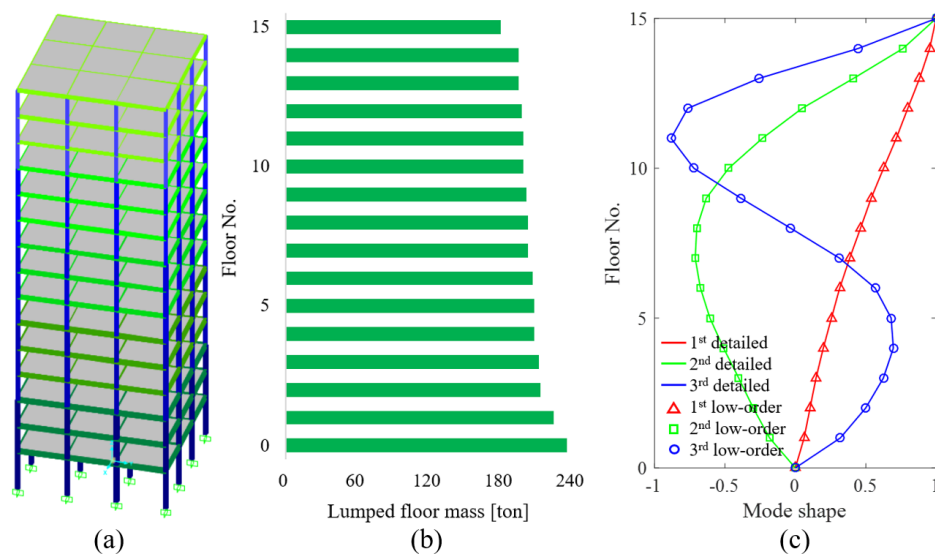


Figure 1: Benchmark building structure: (a) Detailed FE model, (b) lumped floor mass distribution along building height, (c) First three mode shapes obtained by the detailed FE and by the low-order models.

2.2 Across-wind loading model

The input wind action to the 15-storey (15-DOF) low-order model is herein represented by the stochastic across-wind force model developed in [2] for buildings with rectangular footprint.

This wind forcing model is based on experimental data from a comprehensive wind tunnel testing campaign and accounts for both the turbulence and the VS components of the wind force in the across-wind direction, the latter being critical for occupants' comfort. It is defined by a zero-mean stationary Gaussian spatially correlated random field represented in frequency domain by a full power spectral density (PSD) matrix. For the 15-DOF dynamic model, a $\mathbf{S}_{\text{FF}}^{15} \in \mathbb{R}^{15 \times 15}$ wind force PSD matrix is determined upon spatial discretization of the wind random field at each building floor. Throughout this work, the logarithmic mean wind velocity profile of Eurocode 1 [3] is assumed for rough/urban terrain and for a (moderate) basic wind speed of 20m/s (i.e., 10mins mean wind velocity at 10m height above open flat terrain) plotted in Figure 2(a). For this wind profile, wind force PSDs at three different floor slab heights are plotted in Figure 2(b) following [2]. It is seen that the dominant VS frequency increases with floor height. The same happens for the wind force amplitude except from the last floor whose tributary height is only 1.6m. That is, half of the tributary height of typical floors.

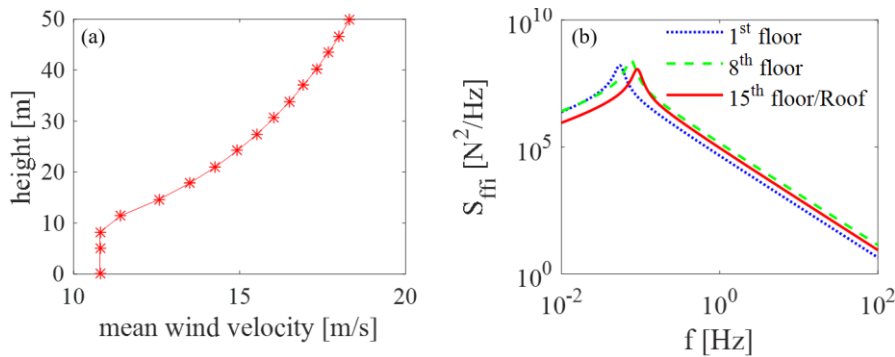


Figure 2: Assumed wind excitation model: (a) mean wind velocity profile, (b) power spectral density functions (PSDs) of across-wind forces acting at different floor levels of the benchmark structure.

2.3 Optimal re-design of benchmark structure for occupants' comfort

Whilst the case-study building in Figure 1 satisfies all requirements for *static* design load combinations, it is found to be deficient for the occupants' comfort serviceability limit state for the wind action defined in Figure 2 according to the ISO Standard 6897 [3] criteria. Figure 3(a) reports the root mean square (RMS) accelerations developing at each floor of the structure (initial structure) along its height together with the ISO 6897 occupants' comfort threshold: it is seen that RMS acceleration is over the threshold at the top two floors.

To this end, the structure is herein re-designed to satisfy the ISO6897 occupants' comfort criteria. This is achieved by using the optimal design method in [16] for MRFs with fixed layout which is based on the optimality criteria (OC) formulation in [17]. The method seeks to minimize the total structural weight while satisfying design constraints including RMS floor acceleration being below the ISO6897 threshold at all floors below the top one (roof) which is not occupied. Figure 3(b) shows the MRF self-weight variation (steel tonnage of lateral load resisting system) throughout the iterations of the optimization starting with the initial deficient design with total weight of 471tons and fundamental frequency 0.548 Hz. The iterative optimization process converges at 786tons of MRF self-weight with fundamental frequency increased to 0.920Hz after 20 design cycles. Consideration of further cycles does not improve much the self-weight. Figure 3(a) plots RMS floor accelerations of the final optimally designed

structure along with the corresponding ISO6897 threshold. The latter has increased since the re-designed structure is stiffer. It is confirmed that in the re-designed structure code-prescribed threshold for RMS floor acceleration is satisfied in all occupied floors, while floor accelerations reduce noticeably compared to the initial structure. However, this is achieved at the expense of using an additional 315tons of steel (i.e., 67% increase of steel tonnage). In following sections, an optimally designed ground floor TID is considered to meet occupants' comfort requirements without without any stiffening of the MRF load-resisting system of the initial structure.

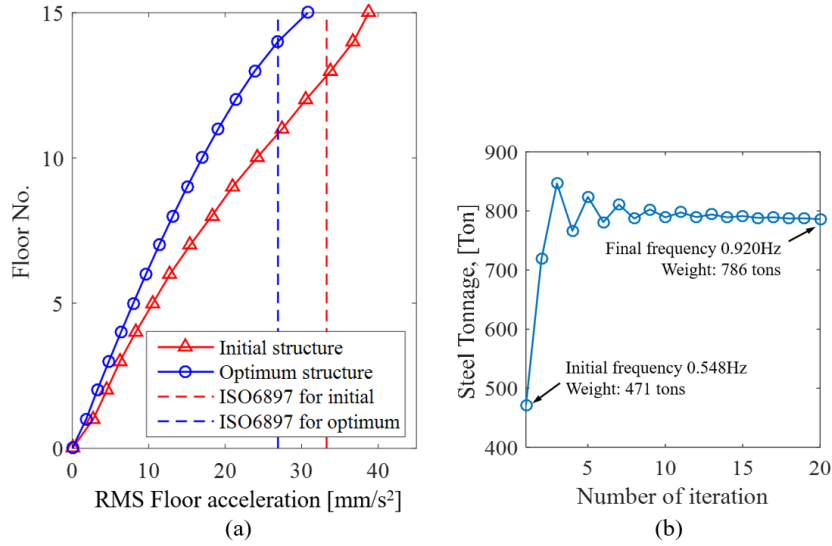


Figure 3: (a) root mean square floor accelerations of initial and optimally re-designed structures with occupants' comfort thresholds (b) Variation of total weight of structure throughout the optimal re-design process.

3 TID-EQUIPPED STRUCTURE AND FREQUENCY-DOMAIN ACROSS-WIND RESPONSE ANALYSIS

The tuned inerter damper (TID) is a linear passive dynamic vibration absorber introduced in [13] for suppressing the lateral motion of seismically excited multi-storey buildings. Herein, a TID installed at the ground floor of the ISO6897 deficient structure in Figure 1 is considered to mitigate wind-induced accelerations in the across-wind direction. TID modelling and its incorporation to the adopted structure is graphically shown in Figure 4(a) depicting the low-order 15-DOF model discussed in section 2.1 as a planar 15-storey frame-like building with lumped floor masses m_k , $k=1,2,\dots,15$, and lateral floor displacements x_k . The TID consists of a visco-elastic link, modelled as a linear spring with k_{TID} stiffness in parallel with a dashpot with damping coefficient c_{TID} , which connects one terminal of an inerter device, highlighted in red in Figure 4(a), with the first building slab. The second inerter terminal is fixed to the ground. The inerter device is idealized by a mechanical element resisting relative acceleration at its two ends through the inertance coefficient b [11]. In this regard, the inerter element force reads as

$$F_b = b\ddot{x}_{TID} \quad (1)$$

where x_{TID} is the lateral TID displacement shown in Figure 4(a) and a dot over a symbol signifies differentiation with respect to time. Therefore, the (control) inerter force depends on the inertance which may be interpreted as a “weightless mass” [11].

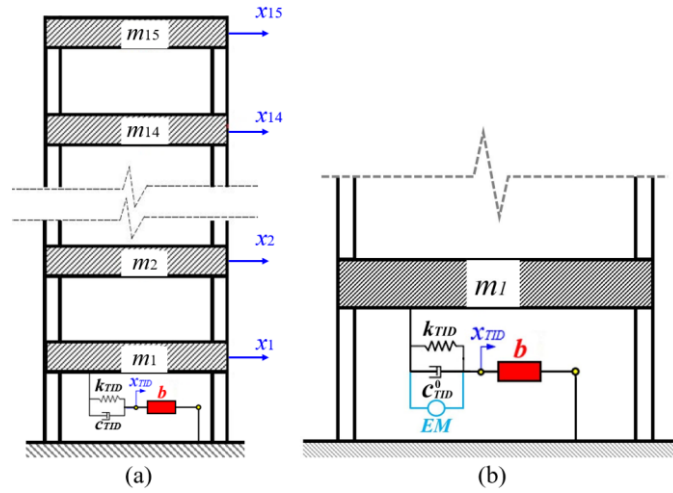


Figure 4: (a) Ground floor TID-equipped lumped-mass planar frame model of the wind-excited case-study building in the across-wind direction, and (b) Considered energy harvesting enabled TID with EM.

In this regard, it is important to note that inertance is readily scalable. Indeed, supplemental damping devices for seismic protection of building structures incorporating inerters with several hundred thousand tons of inertance have been prototyped and experimentally verified in recent years [18]. To shed further light on this issue, consider a commonly used inerter device embodiment employing a rack-and-pinion mechanism to transform the translational motion into rotational motion of a flywheel (i.e., a solid spinning disk) through a gearbox [11]. It can be readily shown that the inertance of such device is given as [19]

$$b = m_f \frac{\gamma_f^2}{\gamma_{pr}^2} \left(\prod_{q=1}^n \frac{r_q^2}{pr_q^2} \right), \quad (2)$$

where m_f and γ_f are the mass and radius of the gyration of the flywheel, respectively, γ_{pr} is the radius of gyration of the flywheel pinion, $r_q/(pr_q)$ is the gearing ratio of the q -th stage/gear of the gearbox with n stages. Clearly, the inertance can be scaled by orders of magnitude through changing the gearing ratios and/or the number of gears. Along these lines, Brzeski et al. [20] demonstrated experimentally the feasibility of inerter devices with continuously varying transmission gearbox, rather than stepped gearing changes, leading to inerters that may achieve any desired inertance value within the gearbox effective range of transmission.

Mathematically, the mass, \mathbf{M} , damping, \mathbf{C} , and stiffness, \mathbf{K} , matrices of the TID-equipped lumped-mass 15-DOF model in Figure 4(a) are given as

$$\mathbf{M} = \begin{bmatrix} b & 0 & 0 & \cdots & 0 & 0 \\ & m_1 & 0 & \cdots & 0 & 0 \\ & & m_2 & \cdots & 0 & 0 \\ & & & \ddots & \vdots & \vdots \\ & & & & m_{14} & 0 \\ & & & & & m_{15} \end{bmatrix}, \quad \mathbf{C} = \begin{bmatrix} c_{\text{TID}} & -c_{\text{TID}} & \cdots & \cdots & 0 & 0 \\ & c_{1,1}+c_{\text{TID}} & c_{1,2} & \cdots & c_{1,14} & c_{1,15} \\ & & c_{2,2} & \cdots & c_{2,14} & c_{2,15} \\ & & & \ddots & \vdots & \vdots \\ & & & & c_{14,14} & c_{14,15} \\ & & & & & c_{15,15} \end{bmatrix}, \quad (3)$$

$$\text{and } \mathbf{K} = \begin{bmatrix} k_{\text{TID}} & -k_{\text{TID}} & \cdots & \cdots & 0 & 0 \\ & k_{1,1}+k_{\text{TID}} & k_{1,2} & \cdots & k_{1,14} & k_{1,15} \\ & & k_{2,2} & \cdots & k_{2,14} & k_{2,15} \\ & & & \ddots & \vdots & \vdots \\ & & & & k_{14,14} & k_{14,15} \\ & & & & & k_{15,15} \end{bmatrix}$$

respectively, where $c_{k,p}$ and $k_{k,p}$ with $k=1,\dots,15$ and $p=1,\dots,15$ are the damping and stiffness coefficients of the low-order 15DOF system representing the benchmark building. Response displacement, velocity, and acceleration PSD matrices of the TID-equipped structure subject to the wind force PSD matrix defined in section 2.2 can be obtained as

$$\mathbf{S}_{\text{xx}}(\omega) = \mathbf{B}(\omega)^* \mathbf{S}_{\text{FF}}(\omega) \mathbf{B}(\omega), \quad \mathbf{S}_{\dot{\text{x}}\dot{\text{x}}}(\omega) = \omega^2 \mathbf{S}_{\text{xx}}(\omega), \quad \text{and} \quad \mathbf{S}_{\ddot{\text{x}}\ddot{\text{x}}}(\omega) = \omega^4 \mathbf{S}_{\text{xx}}(\omega) \quad (4)$$

respectively. In Eq. (4), \mathbf{S}_{FF} is the wind force PSD matrix $\mathbf{S}_{\text{FF}}^{15}$ augmented by an upper zero row and a left-most zero column corresponding to the x_{TID} displacement DOF as the TID is internally housed and not subjected to any wind load. Further, the “*” superscript denotes complex matrix conjugation, and the transfer matrix \mathbf{B} is given as

$$\mathbf{B}(\omega) = [\mathbf{K} - \omega^2 \mathbf{M} + i\omega \mathbf{C}]^{-1} \quad (5)$$

where, $i = \sqrt{-1}$, and the “-1” superscript denotes matrix inversion. The RMS response velocity, and acceleration of the k -th DOF for the TID-equipped structure are obtained as

$$\text{RMS}\{\dot{x}_k\} = \sigma_{\dot{x}_k} = \sqrt{\int_0^{\omega_{\max}} S_{\dot{x}_k \dot{x}_k}(\omega) d\omega} \quad \text{and} \quad \text{RMS}\{\ddot{x}_k\} = \sigma_{\ddot{x}_k} = \sqrt{\int_0^{\omega_{\max}} S_{\ddot{x}_k \ddot{x}_k}(\omega) d\omega} \quad (6)$$

respectively. That is, by integrating the response auto-spectra in the main diagonal of the response velocity and acceleration PSD matrices in Eq. (4) to a cut-off frequency, ω_{\max} , above which the energy of the underlying processes is negligible. Further, the relative RMS velocity between two different DOFs k and j is obtained as

$$\text{RMS}\{\dot{x}_k - \dot{x}_q\} = \sigma_{\dot{x}_{kq}} = \sqrt{\sigma_{\dot{x}_k}^2 + \sigma_{\dot{x}_q}^2 - 2 \int_0^{\omega_{\max}} S_{\dot{x}_k \dot{x}_q}(\omega) d\omega} \quad (7)$$

where the integrand is the response velocity cross-spectra between k and q DOFs.

4 OPTIMAL TID DESIGN FOR VIBRATION CONTROL

In this section, the properties of the ground floor TID in Figure 4(a) are optimally designed to mitigate floor accelerations in multi-storey buildings subject to VS effects associated with

occupants' comfort. To this aim, an optimal design problem is formulated aiming to minimize the RMS floor acceleration of the highest occupied floor taken as the objective function (OF). This is because RMS acceleration increases monotonically with building height in the across-wind direction of typical multi-storey buildings prone to VS effects (see e.g. Figure 3(a)). The problem design variables (DV) are the non-dimensional TID parameters defined as

$$\beta = \frac{b}{M_{tot}}, \quad \nu_{TID} = \frac{\sqrt{k_{TID}/b}}{\omega_1}, \quad \text{and} \quad \xi_{TID} = \frac{c_{TID}}{2\sqrt{k_{TID}b}}, \quad (6)$$

namely, inertance ratio, frequency ratio, and damping ratio, respectively. In the last equation, M_{tot} is the total mass of the building (including design dead and live loads), while ω_1 is the first natural frequency of the uncontrolled (no TID-equipped) structure. The optimization problem is solved numerically using the pattern search algorithm [21] to determine optimal primary DVs frequency ratio, ν_{TID} , and damping ratio, ξ_{TID} , which minimize the OF for fixed building structure, wind excitation, and inertance ratio β treated as secondary DV.

To exemplification of the above TID optimal design problem, Figure 5 furnishes results from application to the 15-storey structure discussed in section 2.1 under the wind force PSD matrix in section 2.2 to minimize $\text{RMS}\{\ddot{x}_{14}\}$ computed by Eq.(6). In doing so, practically meaningful range of values for the primary DVs are searched: ν_{TID} is bounded in the $[0.9, 1.1]$ range based on real-life TMD installations in high-rise buildings tuned to the first natural frequency ω_1 , while ξ_{TID} is bounded in the $[0.0, 0.2]$ range to ensure realistic viscous damping coefficients. Strong convex behavior of the OF on the primary DVs, ν_{TID} - ξ_{TID} , plane is noted with a single global optimal design point readily identified for inertance ratios β ranging within $[0,1]$ interval. For illustration, $\text{RMS}\{\ddot{x}_{14}\}$ surface of the TID-equipped structure normalized by $\text{RMS}\{\ddot{x}_{14}\}$ of the uncontrolled structure is plotted in Figure 5(a) on the ν_{TID} - ξ_{TID} plane for $\beta=0.2$. Further, optimal DV values are plotted in Figure 5(b) as functions of β .

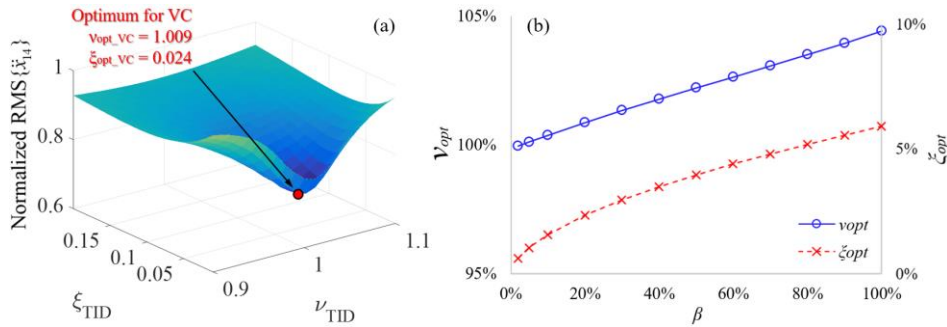


Figure 5: Optimal TID design for structure in Figure 1 subject to wind excitation in Figure 2: (a) Objective function and optimal design point for $\beta=0.20$, and (b) optimal primary DV values with β .

5 PERFORMANCE ASSESSMENT OF OPTIMAL TID-EQUIPPED BENCHMARK STRUCTURE

5.1 Vibration suppression efficiency of ground-floor TID

In this section, the potential of ground-floor TID to satisfy occupants' comfort criteria with no further structural modification in wind-excited multi-storey buildings sensitive to VS effects

is numerically assessed. Attention is focused on demonstrating that ground floor TID can support lightweight slender building designs compliant to occupants' comfort serviceability criteria leading to reduced steel usage. To this aim, optimally designed TIDs obtained as detailed in the previous section are considered for the 15-storey structure of Figure 1 which was found to be deficient to the ISO6897 occupants' comfort criteria, as seen in Figure 3(a), for the moderate across-wind excitation in Figure 2.

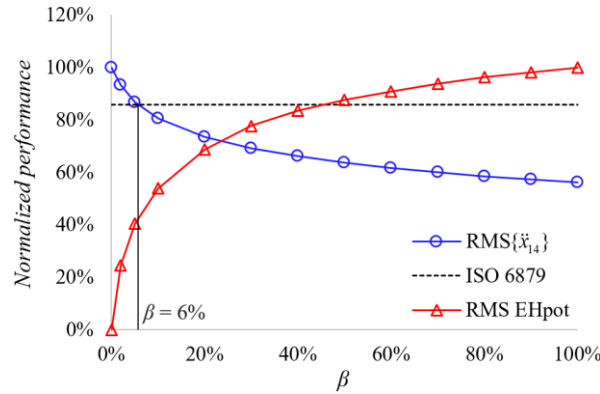


Figure 6: Normalized RMS floor acceleration at penultimate floor and available RMS energy for harvesting for TID-equipped structure in Figure 1 subject to wind forcing of Figure 2.

Figure 6 plots RMS acceleration at the penultimate (last occupied) floor of the optimal TID-controlled structure, $\text{RMS}\{\ddot{x}_{14}\}$, normalized by the corresponding value of the uncontrolled structure, as a function of inertance ratio. In this graph, the limiting case of $\beta = 0$ corresponds to the uncontrolled structure. It is seen that floor acceleration reduces monotonically with the inertance though performance improvement saturates as inertance ratio increases. Notably the inertance values examined in Figure 6 are realistic: even the case of $\beta = 100\%$, which reduces floor acceleration by 44.8% compared to the uncontrolled structure, is achievable. Indeed, this inertance ratio corresponds to inertance $b = M_{\text{tot}} = 3285 \text{ tons}$ which is below the inertance achieved by the hydraulic inerter device discussed in [18]. However, a reduction of 14.2% in 14th floor RMS acceleration is required for the considered benchmark structure to meet ISO6879 occupants' comfort criteria. This is achieved by equipping the initial structure with an optimally tuned TID with $\beta = 6\%$ (or $b = 197 \text{ tons}$), as indicated in Figure 6, without altering in any other way the MRF lateral load-bearing system. Recalling that meeting ISO6879 criteria through structural modification would require 315 tons of additional steel to stiffen the initial MRF if no TID is installed, as discussed in section 2.3, one concludes that optimal ground-floor TID is quite efficient in meeting occupants' comfort criteria in wind excited buildings leading to lightweight designs and material savings.

5.2 Energy harvesting potential for TID with varying inertance and damping coefficient

Having established the benefits of the TID for suppressing floor accelerations in wind-excited tall buildings, the attention is now turned to explore its potential for harvesting energy from wind-borne building oscillations. To this aim, a standard linear translational EM coupled with an energy harvesting (EH) circuit is added in parallel to the visco-elastic TID element as

shown in Figure 4(b). The considered EM consists of a moving magnet travelling within a coil while the EH circuit is equipped with a rectifier to ensure unidirectional electric current flow irrespective of the magnet direction of motion [22]. The resistance of the EM is equal to R_C while EM inductance is negligible for the motion frequencies in the application at hand [22]. Moreover, the EH circuit is assumed to be purely resistive with resistance R_L : a simplification deemed sufficient for the comparative quantification of the available energy for harvesting as TID properties are let to vary (see also [8]). Under the above assumptions, the electromechanical damping coefficient of the EM coupled with the EH circuit is given as [22]

$$c_{EM} = \frac{J^2}{(R_C + R_L)} \quad (8)$$

where J is the magnetic field in the EM with constant flux density, and the resisting damping force contributed by the EM element to the structure in Figure 4 reads as

$$F_{EM} = c_{EM} (\dot{x}_1 - \dot{x}_{TID}) \quad (9)$$

Then, structural analysis to wind excitation remains the same as in section 3 by setting

$$c_{TID} = c_{TID}^0 + c_{EM} \quad (10)$$

where c_{TID}^0 is the TID viscous damping coefficient, as shown in Figure 4(b) and the RMS value of the available energy for harvesting, EHpot, is quantified as

$$\text{RMS}\{\text{EHpot}\} = c_{EM} (\text{RMS}\{\dot{x}_1 - \dot{x}_{TID}\})^2 \quad (11)$$

making use of Eq.(7).

Figure 6 plots the RMS of EHpot for optimal TID-controlled case-study building against the inertance ratio normalized by the value attained for $\beta=1$. In obtaining this data, it is assumed that the EM contributes to half of the (optimal) TID damping, that is, $c_{TID}^0 = c_{EM}$ in Eq.(10), following optimal EH criteria [22]. It is seen that EHpot increases monotonically with inertance and, therefore, increasing inertance is beneficial for both vibration suppression and for energy harvesting in ground floor TID optimally designed for vibration suppression.

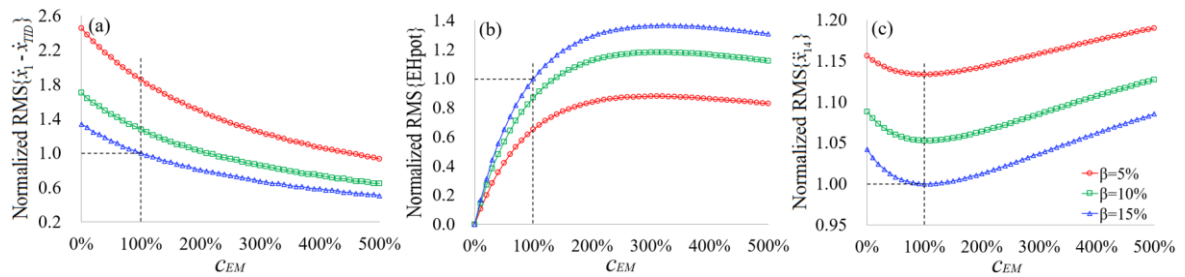


Figure 7: Normalized EH potential and performances of the EH-TID for $v_b = 20\text{m/s}$, $\beta=0.05, 0.10$, and 0.15 , and for (a) RMS relative velocity, (b) RMS EH potential, and (c) RMS acceleration at the last occupiable floor.

Moreover, Figure 7 quantifies RMS EHpot and penultimate RMS floor acceleration for non-optimal TID-equipped structure as c_{EM} in Eq.(9) is let to vary for fixed k_{TID} and c_{TID}^0 , and for three different β values. Values of k_{TID} and c_{TID}^0 are optimal for TID with $\beta=15\%$ and all plotted quantities are normalized to the attained values for this optimal TID design including the value

of c_{EM} . This investigation is motivated by the fact that both the c_{EM} in Eq.(9) and the inertance b in Eq.(2) can vary in a passive-adaptive mode by changes to the EH circuit and to the inerter gearing, respectively. It is seen in Figure 7(b) that c_{EM} increases with c_{EM} until it reaches a plateau due to reduction of $\text{RMS}\{\dot{x}_1 - \dot{x}_2\}^2$ with c_{EM} in Figure 7(a). At the same time, as expected, RMS floor acceleration in Figure 7(c) increases as c_{EM} deviates from its optimal value. Nevertheless, for a fixed, possibly non-optimal, c_{EM} , *simultaneously* enhanced vibration suppression performance and increased EH_{pot} is achieved by increasing inertance. These observations suggest that it is possible to increase energy generation in ground floor TID-equipped wind-excited multi-storey buildings without necessarily relaxing performance requirements in terms of floor accelerations through judicious changes to EM damping coefficient and/or inertance.

6 CONCLUDING REMARKS

The efficacy of a ground floor TID to achieve occupants' comfort performance and to harvest kinetic energy in wind-excited multi-storey buildings susceptible to VS effects has been numerically established. To this aim, a 15-storey steel structure, deficient to occupants' comfort code-prescribed criteria for moderate wind action, has been equipped with optimal TID stiffness and damping properties minimizing floor acceleration in the across-wind direction, being critical for occupants' comfort, for fixed inertance. Further, the TID was coupled with a standard EM modelled as a damper and allowing for energy harvesting. Major conclusions in view of the herein furnished numerical results are: (1) Optimally tuned TID for floor acceleration minimization is a potent retrofitting measure to meet occupants' comfort criteria without structural modifications leading to considerable increase of steel usage (up to 67% increase for the considered structure), (2) Increasing TID inertance is beneficial for both suppressing floor accelerations and for increasing available energy for harvesting in both optimal and non-optimal TID for floor acceleration mitigation, and (3) Increasing the EM damping coefficient increases the available energy for harvesting at the expense of increased floor accelerations. Overall, it is concluded that ground floor TID is a promising dynamic vibration absorber configuration for occupants' comfort criteria which govern the design of slender multi-storey buildings with square floor plan under wind excitation while allows for generating energy from wind-induced building oscillations. Still, further numerical and experimental work is warranted to examine ground-floor TID efficiency for different wind excitation intensity in a performance-based design context and to compare it to alternative widely used solutions such as top-floor TMDs.

REFERENCES

- [1] Taranath, B.S. *Tall Building Design: Steel, Concrete, and Composite Systems*. CRC Press, (2017).
- [2] Liang, S., Liu, S., Li, Q-S., Zhang, L., and Gu, M. *Mathematical model of across-wind dynamic loads on rectangular tall buildings*. *J. Wind Eng. Ind. Aerodyn.* (2002) **90**: 201-251.
- [3] CEN, Eurocode 1: Action on Structures – Part 1-4: General actions – Wind actions. EN 1991-1-4:2005, Comit.
- [4] ISO, Guidelines for the evaluation of the response of occupants of fixed structures to low frequency horizontal motion (0.063 to 1 Hz). ISO Standard 6897 1984, International

Organization of Standardization.

- [5] Ricciardelli, F., Pizzimenti, A.D., and Mattei, M. *Passive and active mass damper control of the response of tall buildings to wind gustiness*. *Eng. Struct.* (2003) **25**: 1199–1209.
- [6] Huang, M-F. *High-rise buildings under multi-hazard environment*. Springer Nature, (2017).
- [7] Tang, X. and Zuo, L. *Simultaneous energy harvesting and vibration control of structures with tuned mass dampers*. *J. Intell. Mater. Syst. Struct.* (2012) **23(18)**: 2117–2127.
- [8] Shen, W., Zhu, S., Xu, Y-L., and Zhu, H-P. *Energy regenerative tuned mass dampers in high-rise buildings*. *Struct. Control Hlth. Monit.* (2018) **25(1)**: e2072.
- [9] Giaralis, A. and Petrini, F. *Wind-induced vibration mitigation in tall buildings using the tuned mass-damper-inerter (TMDI)*. *J. Struct. Eng. ASCE* (2017) **143(9)**: 04017127.
- [10] Giaralis, A. and Petrini, F. *Optimum design of the tuned mass-damper-inerter for serviceability limit state performance in wind-excited tall buildings*. *Procedia Engineering* (2017) **199**: 1773-1778.
- [11] Smith, M.C. *Synthesis of mechanical networks: The Inerter*. *IEEE Transactions on Automatic Control* (2002) **47**: 1648-1662.
- [12] Petrini, F., Wang, Z-X., and Giaralis, A. *Simultaneous vibration suppression and energy harvesting in wind excited tall buildings equipped with the tuned mass damper inerter (TMDI)*. *Proceedings of the 15th Conference of the Italian Association for Wind Engineering- INVENTO*. Springer International Publishing, (2018).
- [13] Lazar, I.F., Neild, S.A., and Wagg D.J. *Using an inerter-based device for structural vibration suppression*. *Earthquake Eng. Struct. Dyn.* (2014) **43(8)**: 1129-1147.
- [14] Zhang, S-Y., Jiang, J-Z., and Neild, S. *Optimal configurations for a linear vibration suppression device in a multi-storey building*. *Struct. Control Hlth. Monit.* (2017) **24(3)**: 1545-2255.
- [15] Giaralis, A. and Taflanidis, A. *Optimal tuned mass-damper-inerter (TMDI) design for seismically excited MDOF structures with model uncertainties based on reliability criteria*. *Struct. Control Hlth. Monit.* (2018) **25(2)**: e2082.
- [16] Chan, C-M. and Chui, J-K-L. *Wind-induced response and serviceability design optimization of tall steel buildings*. *Eng. Struct.* (2006) **28**: 503-513.
- [17] Venkayya, V.B. *Optimality Criteria: a basic multidisciplinary design optimization*. *Comput. Mech.* (1989) **5**: 1-21.
- [18] Nakaminami, S., Kida H., Ikago K., and Inoue N. *Dynamic Testing of a Full-scale Hydraulic Inerter-Damper for the Seismic Protection of Civil Structures*. *7th International Conference on Advances in Experimental Structural Engineering* (2017).
- [19] Marian, L. and Giaralis, A. *The tuned mass-damper-inerter for harmonic vibrations suppression, attached mass reduction, and energy harvesting*. *Smart Structures and Systems* (2017) **19(6)**: 665-678.
- [20] Brzeski, P., Lazarek, M., and Perlikowski, P. *Experimental study of the novel tuned mass damper with inerter which enables changes of inertance*, *J. Sound Vib.* (2017) **404**: 47–57.
- [21] Charles, A. and Dennis Jr., J.E. *Analysis of Generalized Pattern Searches*. *SIAM Journal on Optimization*. (2003) **13(3)**: 889–903.
- [22] Gonzalez-Buelga, A., Clare, L.R., Cammarano, A., Neild, S.A., Burrow, S.G., and Inman, D.J. *An optimised tuned mass damper/harvester device*. *Struct. Control Hlth. Monit.* (2014) **21(8)**:1154-1169.

VIBRATION-BASED LONG-TERM SCOUR MONITORING FOR AN IN-SERVICE RAILWAY BRIDGE

K. YOSHITOME^{*}, C.W. KIM^{*}, Y. GOI^{*}, S. KITAGAWA[†], M. SHINODA[†], H. YAO[†]
AND Y. HAMADA[‡]

^{*} Department of Civil and Earth Resources Engineering
Graduate School of Engineering, Kyoto University
Katsura Campus, 615-8540 Kyoto, Japan
email: kim.chulwoo.5u@kyoto-u.ac.jp, <http://infra.kuciv.kyoto-u.ac.jp>

[†] Product Technology Laboratory
Fuji Electric Co., Ltd.
191-8502, Tokyo Japan
email: kitagawa-shinji@fujielectric.com, <https://www.fujielectric.co.jp/>

[‡] Structural Engineering Office,
West Japan Railway Company
532-0011, Osaka Japan
email: yoshisada-hamada@westjr.co.jp, <https://www.westjr.co.jp/>

Key words: Ambient Vibration, Long-term Monitoring, Railway Bridges, Remote Sensing, Scour Monitoring, System Identification.

Abstract. This study is intended to discuss feasibility of a long-term scour monitoring for an in-service railway bridge by means of a remote microtremor monitoring. In the context of the structural health monitoring, vibration-based approach might be a promising technique for the scour monitoring of railway bridges, as it is well known that changes in the vibration characteristics of the railway bridge pier under scour is obvious. Japanese railway companies make decisions on occurrence of scour investigating changes in a target frequency. Therefore, the impact test on the railway bridge pier to identify changes in frequencies has been adopted as a promising scour detection method in Japan. However, the impact test is a laborious and time-consuming method, and is inapplicable for the real time monitoring to make a proper decision on the train operation control during heavy rains. This study investigates feasibility of vibration-based scour monitoring as an alternative method for the impact test. A railway bridge with high potential of scour was monitored utilizing a smart sensing unit which includes functions of vibration measurement, data processing and remote control. Observations showed that target frequency was slightly decreased under increase of water surface during flood. However, the decreased frequency recovered once water surface level decreased after flood. Scour assessment following a Japanese guideline showed an extremely low probability of scour.

1 INTRODUCTION

Scouring is the erosion of the riverbed caused by fluctuation in the flow of river, turbulence, etc. The number of bridges with scoured piers is increasing due to the deterioration, heavy rain, and the reduction of sediment supply volume [1]. If scouring occurs around the foundation ground, the substructure may settle, incline, or fall, and thus, train operation should be suspended during flood.

Many Japanese railway companies have adopted an impact test on the railway bridge pier as a promising scour detection method focusing on changes in frequencies. However, the impact test is a laborious and time-consuming method, and is inapplicable for the real time monitoring during heavy rains to make a proper decision on the train operation. Therefore, a remote monitoring system and a decision rule to detect scouring are desired.

This study aims to propose a way to monitor scour of piers of railway bridges efficiently and quantitatively without approaching the target bridge especially during flood. A bridge under operation is monitored as a case study. To estimate the natural frequency of the target bridge, accelerometers are installed on the top of the bridge pier and the connected girders for the impact test, and two sensors on the pier top were left for scour monitoring in terms of long-term ambient vibration monitoring. In modal identification of the bridge, this study utilizes time domain method called stochastic subspace identification (SSI) [2,3,4] that is effective for forced vibrations of bridges. Bayesian operational modal analysis (BAYOMA) [5,6,7] is also adopted for the modal identification from microtremor measurement during flood.

2 METHODOLOGY

2.1 Mode Identification by Stochastic Subspace Identification (SSI)

The dynamical system representing the pier vibration is modeled as the following state space model.

$$\mathbf{x}(k+1) = \mathbf{A}\mathbf{x}(k) + \mathbf{w}(k) \quad (1)$$

$$\mathbf{y}(k) = \mathbf{C}\mathbf{x}(k) + \mathbf{v}(k) \quad (2)$$

Therein, $\mathbf{x}(k)$ and $\mathbf{y}(k)$ denote the state of structure and measurement at each time step k , respectively. Also, $\mathbf{w}(k)$ and $\mathbf{v}(k)$ respectively denote the process noise and measurement noise vectors which are assumed to be stationary white noise. System matrix \mathbf{A} comprising modal information is estimated using least-squares method for the minimal prediction error of the state $\mathbf{x}(k)$ given by the forward Kalman filter. The poles of the dynamical system provide modal properties of the dynamical system.

The algorithm for the SSI is described briefly as follows. First, we obtain the projection matrix \mathbf{O}_i , as estimated from Eq. (3).

$$\mathbf{O}_i = \mathbf{Y}_f \mathbf{Y}_p^T (\mathbf{Y}_p \mathbf{Y}_p^T)^\dagger \mathbf{Y}_p \quad (3)$$

Therein $(\cdot)^\dagger$ denotes the Moore-Penrose pseudo-inverse matrix. \mathbf{Y}_f and \mathbf{Y}_p represent the block Hankel matrices of the future and past outputs as shown in Eq. (4) and Eq. (5).

$$\mathbf{Y}_p = \begin{bmatrix} \mathbf{y}(0) & \mathbf{y}(1) & \dots & \mathbf{y}(j-1) \\ \dots & \dots & \dots & \dots \\ \mathbf{y}(i-2) & \mathbf{y}(i-1) & \dots & \mathbf{y}(i+j-3) \\ \mathbf{y}(i-1) & \mathbf{y}(i) & \dots & \mathbf{y}(i+j-2) \end{bmatrix} \quad (4)$$

$$\mathbf{Y}_f = \begin{bmatrix} \mathbf{y}(i) & \mathbf{y}(i+1) & \dots & \mathbf{y}(i+j-1) \\ \dots & \dots & \dots & \dots \\ \mathbf{y}(2i-2) & \mathbf{y}(2i-1) & \dots & \mathbf{y}(2i+j-3) \\ \mathbf{y}(2i-1) & \mathbf{y}(2i) & \dots & \mathbf{y}(2i+j-2) \end{bmatrix} \quad (5)$$

The singular value decomposition (SVD) is then applied to factorize \mathbf{O}_i as follows.

$$\mathbf{O}_i = \mathbf{U}\mathbf{S}\mathbf{V}^T \simeq (\mathbf{U}_1\mathbf{U}_2) \begin{pmatrix} \mathbf{S}_1 & \mathbf{0} \\ \mathbf{0} & \mathbf{0} \end{pmatrix} (\mathbf{V}_1\mathbf{V}_2)^T = \mathbf{U}_1\mathbf{S}_1\mathbf{V}_1^T \quad (6)$$

where, \mathbf{U} and \mathbf{V} are unitary matrices with appropriate size; \mathbf{S} is a diagonal matrix with non-negative elements. The diagonal elements of \mathbf{S} are known as singular values of \mathbf{O}_i . Singular values in \mathbf{S} are listed in descending order. Therefore, the components in $\mathbf{U}_1\mathbf{S}_1\mathbf{V}_1^T$ include most of the information defining the elements in \mathbf{O}_i . Components in $\mathbf{U}_2\mathbf{S}_2\mathbf{V}_2^T$ are regarded as trivial components. The optimal state sequence predicted by the Kalman filter in a least squares sense is obtained as shown below.

$$\mathbf{X}_i = \mathbf{S}_1^{1/2}\mathbf{V}_1^T \quad (7)$$

where $\mathbf{X}_i = [\mathbf{x}(i) \quad \mathbf{x}(i+1) \quad \dots \quad \mathbf{x}(i+j-1)]$.

The system matrices are obtainable from \mathbf{X}_i . The number of poles corresponds to the number of singular values in Eq. (6). In other words, we can extract the modal response of the bridge from the measured acceleration data by the SVD.

2.2 System Identification based on Bayesian Approach

Assume that the acceleration was collected under ambient condition. Let $\{\hat{\mathbf{x}}_j \in R^n: j = 1, \dots, N\}$ denote the measured acceleration data at n degrees of freedom (DOFs) of a structure, abbreviated as $\{\hat{\mathbf{x}}_j\}$, where N is the number of samples collected in the time domain. The j th acceleration response can be modelled as follows:

$$\hat{\mathbf{x}}_j = \check{\mathbf{x}}_j + \mathbf{e}_j \quad (8)$$

where $\check{\mathbf{x}}_j \in R^n$ denotes the model acceleration response; $\mathbf{e}_j \in R^n$ denotes the prediction error between the measured and theoretical responses, mainly consisting of the electronic noise of the data acquisition system, environmental noise and modelling error.

The FFT of $\{\hat{\mathbf{x}}_j\}$ is defined as follows:

$$\hat{F}_k = \sqrt{\frac{2\Delta t}{N}} \sum_{j=1}^N \hat{\mathbf{x}}_j \exp \left[-2\pi i \frac{(j-1)(k-1)}{N} \right] \quad (k = 1, 2, \dots, N) \quad (9)$$

where the FFT corresponds to the frequency $f_k = (k-1)/N\Delta t$ for $k = 2, 3, \dots, N_q$, with $N_q = \text{int}[N/2] + 1$, being the frequency index at the Nyquist frequency, and $\text{int}[\cdot]$ is the integer part; Δt denotes the sampling interval; $i^2 = -1$.

For well-separated or closely spaced modes, they should be included in a series of specified frequency bands. Let D_i denote the FFT data in the i th selected frequency band containing the

possible modes. According to Bayes' Theorem, the posterior PDF of $\boldsymbol{\theta}_i$ for given data, where $\boldsymbol{\theta}_i$ denotes the modal parameters in the i th selected frequency band, can be expressed as:

$$p(\boldsymbol{\theta}_i|D_i) = \frac{p(\boldsymbol{\theta}_i)p(D_i|\boldsymbol{\theta}_i)}{p(D_i)} \quad (10)$$

where $p(D_i|\boldsymbol{\theta}_i)$ is the likelihood function; $p(D_i)$ is a constant; $p(\boldsymbol{\theta}_i)$ is the prior PDF.

The likelihood function $p(D_i|\boldsymbol{\theta}_i)$ can be obtained as follows. Define a vector $\hat{\mathbf{Z}}_{ik} = [\text{Re}\hat{F}_{ik}; \text{Im}\hat{F}_{ik}] \in R^{2n}$ consisting of the real and imaginary parts of the FFT data in the i th selected frequency band at frequency f_k ; Let $D_i = \{\hat{\mathbf{Z}}_{ik}\}$ which includes all the FFT data in the i th selected frequency band. For large N and small Δt , the vector $\hat{\mathbf{Z}}_{ik}$ is shown to be independent at different frequencies and follow a Gaussian distribution with zero means and covariance matrix \mathbf{C}_{ik} . Therefore, the likelihood function $p(D_i|\boldsymbol{\theta}_i)$ in the i th frequency band can be constructed by a Gaussian distribution, i.e.,

$$p(D_i|\boldsymbol{\theta}_i) = \prod_k \frac{1}{(2\pi)^n \det(\mathbf{C}_{ik})^{0.5}} \exp\left[-\frac{1}{2} \hat{\mathbf{Z}}_{ik}^T \mathbf{C}_{ik}^{-1} \hat{\mathbf{Z}}_{ik}\right] \quad (11)$$

in which, $\det(\cdot)$ denotes the determinant; \mathbf{C}_{ik} , the covariance matrix of $\hat{\mathbf{Z}}_{ik}$, is given by

$$\mathbf{C}_{ik} = \frac{1}{2} \begin{bmatrix} \boldsymbol{\Phi}_i & \\ & \boldsymbol{\Phi}_i^T \end{bmatrix} \begin{bmatrix} \text{Re}\mathbf{H}_{ik} & -\text{Im}\mathbf{H}_{ik} \\ \text{Im}\mathbf{H}_{ik} & \text{Re}\mathbf{H}_{ik} \end{bmatrix} \begin{bmatrix} \boldsymbol{\Phi}_i^T \\ \boldsymbol{\Phi}_i \end{bmatrix} + \frac{S_{e_i}}{2} \mathbf{I}_{2n} \quad (12)$$

where $\boldsymbol{\Phi}_i = [\boldsymbol{\Phi}_{i1}, \boldsymbol{\Phi}_{i2}, \dots, \boldsymbol{\Phi}_{im_i}] \in R^{nm_i}$ denotes the mode shape matrix in a selected frequency band; \mathbf{I}_{2n} is an $2n \times 2n$ identify matrix; $S_{e_i} \in R$ is the PSD of prediction error in the i th frequency band; \mathbf{H}_{ik} is a transfer function, whose element can be expressed as:

$$\mathbf{H}_{ik}(u, v) = S_{uv}[(1 - \beta_{iuk}^2) + \mathbf{i}(2\zeta_{iu}\beta_{iuk})]^{-1}[(1 - \beta_{ivk}^2) - \mathbf{i}(2\zeta_{iv}\beta_{ivk})]^{-1} \quad (13)$$

where $\beta_{iuk} = f_{iu}/f_k$; S_{uv} denotes the cross spectral density between the u th and v th modal excitation. Define $\boldsymbol{\theta}_i = \{f_{iu}, \zeta_{iu}, S_{iu}, \boldsymbol{\Phi}_{iu}; u = 1, \dots, m_i, S_{e_i}\}$, where $f_{iu} \in R$ is the u th natural frequency in the i th frequency band; $\zeta_{iu} \in R$ is the u th damping ratio in the i th frequency band; $S_{iu} \in R$ is the u th power spectral density (PSD) of modal force in the i th frequency band; $\boldsymbol{\Phi}_{iu} \in R^n$ is the u th mode shape of the measured DOFs in the i th frequency band; m_i is the number of modes included in the i th frequency band. It is more convenient to write the likelihood function in term of the 'log-likelihood function', i.e.,

$$L(\boldsymbol{\theta}_i) = -\ln p(D_i|\boldsymbol{\theta}_i) \quad (14)$$

$$p(D_i|\boldsymbol{\theta}_i) = \exp[-L(\boldsymbol{\theta}_i)] \quad (15)$$

Note that the log-likelihood function can be well approximated by a second-order Taylor expansion, and so it can be expressed as

$$L(\boldsymbol{\theta}_i) \sim L(\hat{\boldsymbol{\theta}}_i) + \frac{1}{2}(\boldsymbol{\theta}_i - \hat{\boldsymbol{\theta}}_i)^T \hat{\mathbf{H}}_L(\boldsymbol{\theta}_i - \hat{\boldsymbol{\theta}}_i) \quad (16)$$

where $\hat{\mathbf{H}}_L$ denotes the Hessian matrix of $L(\boldsymbol{\theta}_i)$ when the MPV $\hat{\boldsymbol{\theta}}_i$ is evaluated. Substituting (16) into (15), the likelihood function can be given by:

$$p(D_i|\boldsymbol{\theta}_i) \sim \exp\left[-\frac{1}{2}(\boldsymbol{\theta}_i - \hat{\boldsymbol{\theta}}_i)^T \hat{\mathbf{C}}_{\hat{\boldsymbol{\theta}}_i}^{-1}(\boldsymbol{\theta}_i - \hat{\boldsymbol{\theta}}_i)\right] \quad (17)$$

with

$$\hat{\mathbf{C}}_{\theta_i} = \hat{\mathbf{H}}_L^{-1} \quad (18)$$

denotes the covariance matrix of the modal parameters.

The likelihood function in an individual frequency band can be determined according to equation (11). In the damage detection, usually all the possible identifiable modes will be used and the data in all the related frequency bands will be included. Assuming the data in n_b frequency bands are available, the likelihood function considering all these frequency bands can be given by:

$$p(\{D_i\}|\{\theta_i\}) = \prod_{i=1}^{n_b} p(D_i|\theta_i) = \prod_{i=1}^{n_b} \prod_{k=k_{i1}}^{k_{i2}} \frac{1}{(2\pi)^n \det(\mathbf{C}_{ik})^{0.5}} \exp\left[-\frac{1}{2} \hat{\mathbf{z}}_{ik}^T \mathbf{C}_{ik}^{-1} \hat{\mathbf{z}}_{ik}\right] \quad (19)$$

where $\{D_i: i = 1, \dots, n_b\}$ is a collection of the data in all the frequency bands, abbreviated as $\{D_i\}$; $\{\theta_i: i = 1, \dots, n_b\}$ denotes a collection of the modal parameters in all the selected frequency bands, abbreviated as $\{\theta_i\}$; k_{i1} and k_{i2} denotes the start and end frequency indexes in the i th selected frequency band, respectively.

The prior PDF of θ_i can be constructed as follows. The identified modal parameters can be modelled as

$$\hat{\theta}_i = \theta_i + \epsilon_i \quad (20)$$

where θ_i is the theoretical modal parameters and ϵ_i is the prediction error of modal parameters between identified value and theoretical value. Assuming ϵ_i follows a Gaussian distribution, then the prior PDF of θ_i can be given by

$$p(\theta_i) = \frac{1}{(2\pi)^n \det(\mathbf{C}_{\theta_i})^{0.5}} \exp\left[-\frac{1}{2} (\theta_i - \hat{\theta}_i)^T \mathbf{C}_{\theta_i}^{-1} (\theta_i - \hat{\theta}_i)\right] \quad (21)$$

where \mathbf{C}_{θ_i} denotes the covariance matrix of the modal parameters θ_i in the i th frequency band. Since the modal parameters in different frequency bands can be taken to be independent, the prior PDF considering all these frequency bands can be given by:

$$p(\{\theta_i\}) = \prod_{i=1}^{n_b} p(\theta_i) = \prod_{i=1}^{n_b} \frac{1}{(2\pi)^n \det(\mathbf{C}_{\theta_i})^{0.5}} \exp\left[-\frac{1}{2} (\theta_i - \hat{\theta}_i)^T \mathbf{C}_{\theta_i}^{-1} (\theta_i - \hat{\theta}_i)\right] \quad (22)$$

3 TARGET BRIDGE AND MONITORING INFORMATION

The target bridge is a single railway track steel plate girder bridge. The height of target pier is 11m and width is 2.5m. As there is high potential risk of scouring on the target pier, a long-term scour monitoring has been carried out. The photo of the target bridge pier is shown in Figure 1. The elevation and plan views of the target bridge are shown in Figure 2. Eight triaxial sensors were installed on the top of the pier and connecting girders for the impact test as shown in Figure 2 a). All sensors except two sensors installed upstream and downstream of the pier top were removed after the impact test. Two sensors left on the pier top (see Figure 2b) are for the long-term ambient vibration monitoring. The sampling frequency of the measurement was 200Hz. A laser water level meter is installed on the target bridge.



Figure 1: Photo of target bridge pier.

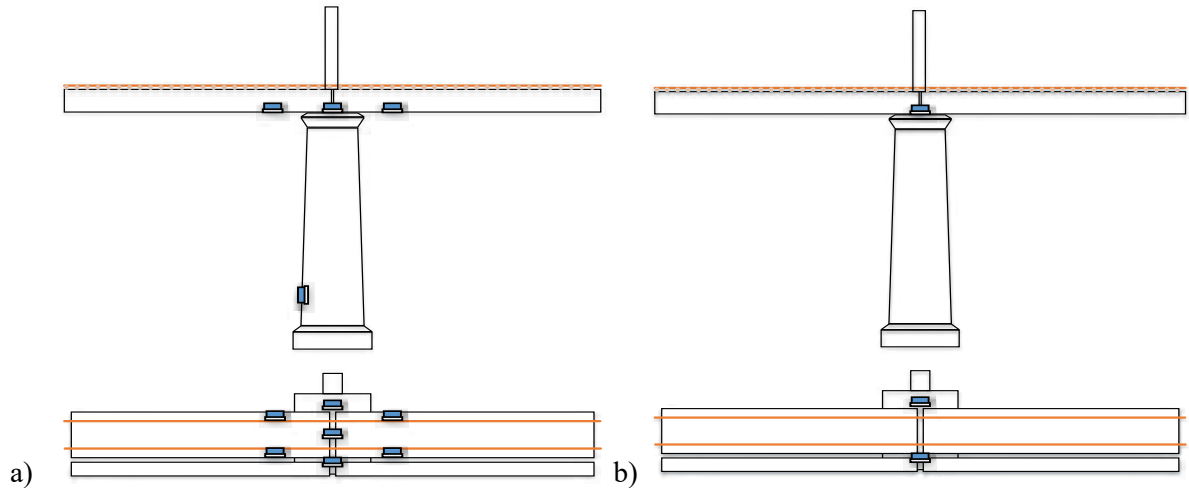


Figure 2: Elevation view and plan view of the acceleration sensor installation position: a) for the impact test, and b) for the long-term ambient vibration monitoring.

4 MODE IDENTIFICATION OF TARGET BRIDGE

Modal characteristics of the bridge pier were identified from the vibration data excited during the impact test. Stability criteria are used to decide stable vibration modes [11]. Figure 3 shows the stabilization diagram (SD) in which the horizontal and vertical axes respectively stand for the frequency and model order. The black dots indicate modal frequencies associated with each model orders. The red circles indicate stably estimated modes that satisfy predefined deviation tolerances of the modal properties, i.e. the natural frequencies, damping ratio, and mode shapes. This study adopted the frequency deviation tolerance of 0.25 Hz, the damping deviation tolerance of 0.1 %, and the lower bound of Modal Assurance Criteria (MAC) of 0.95.

The vertical blue broken lines show dominant modes that appear stably throughout a wide range of model order and satisfy the deviation tolerances. The dominant frequency was identified at 9.2Hz. Figure 4 shows the mode shape of the dominant mode. As shown in Figure 4, this mode shape is relevant to the transversal rocking mode of the pier.

5 SYSTEM IDENTIFICATION DURING FLOOD

On September 30 in 2018, typhoon no.24 was approached and daily precipitation was 114mm, and ambient vibrations monitored on September 30 and October 1 were investigated to identify dominant frequency of the target pier during the flood.

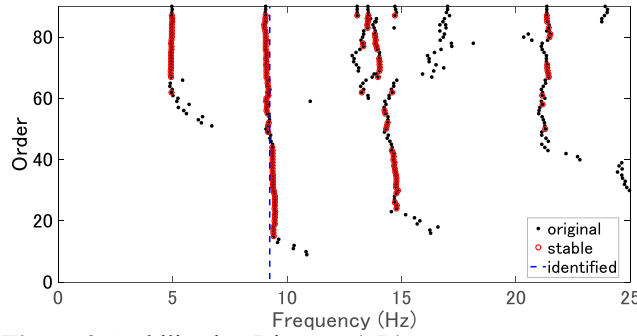


Figure 3: Stabilization Diagram (SD).

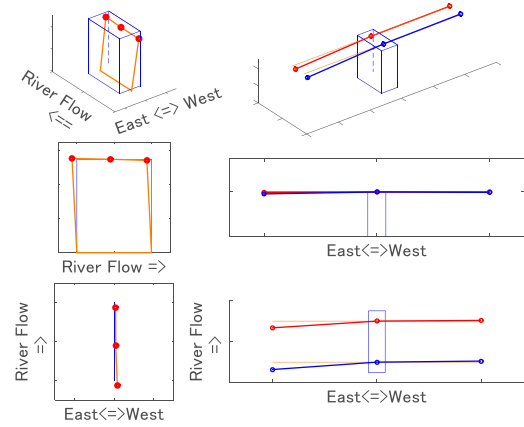


Figure 4: Identified mode shape (9Hz).

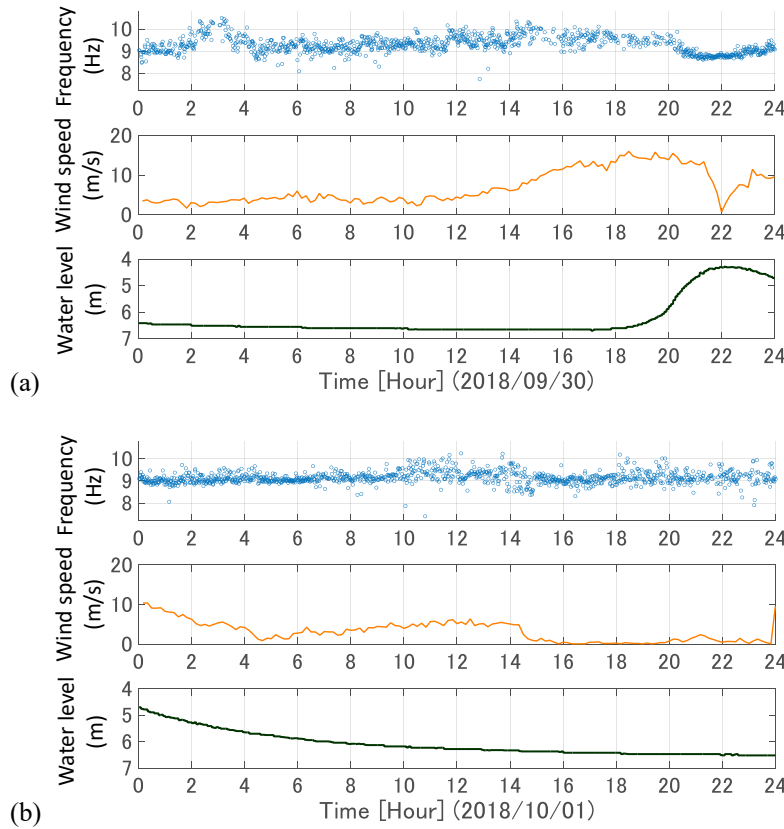


Figure 5: Monitoring data: (a) 30th September 2018; and (b) 1st October 2018.

Plots of the identified frequency per every minute are shown in Figure 5 with observed wind speed and water level. It should be noted that “water level” represents the distance between water surface and lower flange of the bridge girder: i.e. as the water surface goes up, the “water level” gets smaller. In Figure 5, the horizontal axis indicates time, and the vertical axis indicates frequency (Hz), wind speed (m/s), and water level (m) from the top respectively. From 0:00 to

20:00 on September 30 before flood, identified frequencies varied widely between 8.5 Hz and 10 Hz. However, during flood from 20:00 on September 30 to 6:00 on October 1, variation in frequency was quite small. One reason for scattering of identified frequency is the quality of acceleration. Before flood only microtremor measurement whose amplitude was around 0.1 gal was examined. On the other hands during the flood the bridge pier was vibrated by water flows and the maximum amplitude was around 1 gal.

Histograms of identified frequency for different water level are shown in Figure 6. Assuming all distributions follow normal distributions, the mean and variance values are estimated as also seen in Figure 6. The frequency decreases as the water surface level rises (water level decreases), the variance of the identified frequency also decreases. The influence of the additional mass due to flood might be a reason for the decrease of the frequency during flood [12]. The results show that the natural frequency of the bridge pier is identified with high accuracy during the flood condition.

Figure 7 shows that the histogram of identified frequencies during flood: i.e. the water level between 4m and 5m. The blue solid line is the approximate curve of the distribution of the identified frequency. Occurrence of scour during flood is examined following the guideline of Japanese government [13]. The guideline is shown in the Table 1. The soundness index x is calculated by Eq. (23) [13].

$$x = (\text{monitored frequency}) / (\text{frequency of healthy condition}) \quad (23)$$

Table 1: Soundness assessment [13]

Soundness Index x	Category	Assessment
$x \leq 0.70$	A1	Abnormal condition: repair or reinforcement are needed
$0.70 < x \leq 0.85$	A2	Need to check progress of deterioration: <i>e.g.</i> decrease of frequency, etc.
$0.85 < x \leq 1.00$	B	Low possibility of abnormal condition
$1.00 < x$	S	Healthy

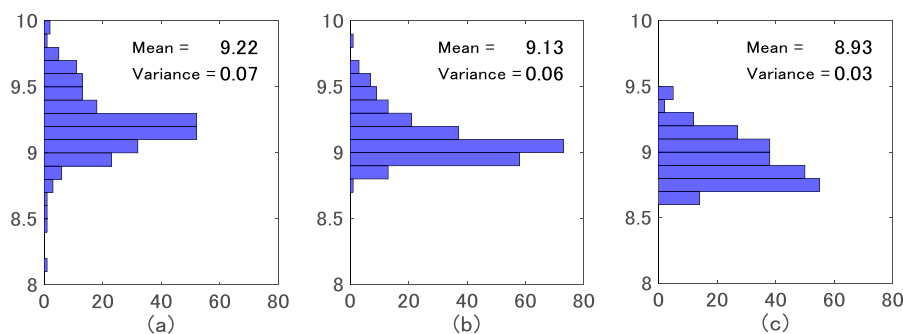


Figure 6: Identified frequency distribution: (a) water level more than 6m (before flood); (b) water level between 5m and 6m; and (c) water level between 4m and 5m (during flood).

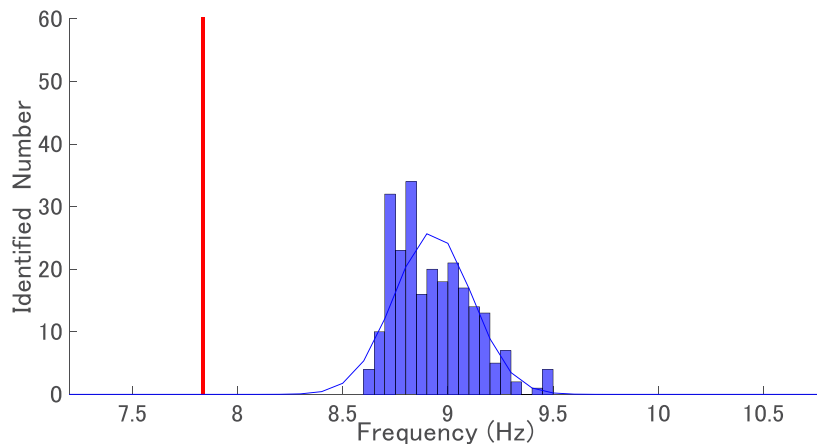


Figure 7: Histogram of identified frequency from ambient vibration (during flood).

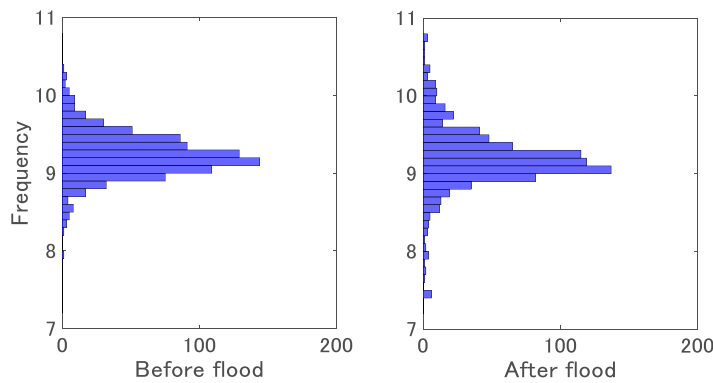


Figure 8: Distribution of natural frequency before and after the flood.

In the guideline, occurrence of scour is decided if it is observed that 85% or less than the natural frequency in the health condition. Therefore, the frequency of 85% of the natural frequency in the health condition is adopted as a threshold of occurrence of scouring. The vertical red solid line in Figure 7 shows 85% of the natural frequency in the healthy condition. It is noted that the mean frequency observed before flood was assumed as healthy condition in scour assessment. The probability of exceeding the threshold was lower than 0.001%, which indicates extremely low possibility of scour occurrence during this flood.

Figure 8 shows the distributions of the identified frequencies before and after the flood. Considering mean values of the identified frequencies 9.23Hz and 9.19Hz for healthy condition and flood condition respectively, the soundness index takes $x = 0.996$ according to Eq. (23), and categorized as B (Low possibility of abnormal condition) according to Table 1. Observations showed low possibility of scouring due to flood.

6 CONCLUSIONS

This study investigates a way of scour detection by means of ambient vibration monitoring of the bridge pier during flood. The natural frequency of the bridge pier was identified with

high accuracy from the ambient vibration during the flood condition. The probability of exceeding the threshold for the scour was lower than 0.001%. Moreover, the soundness index was 0.996 which is categorized as B indicating low possibility of abnormal condition. Observations, thus, demonstrated extremely low possibility of scour occurrence during this flood. This study also demonstrated that it is possible to evaluate scour by using the ambient vibration data during the flood.

ACKNOWLEDGEMENTS

This study is partially sponsored by a Japanese Society for the Promotion of Science (JSPS) Grant-in-Aid for Scientific Research (B) under project No.19H02225, which is greatly appreciated.

REFERENCES

- [1] Keyaki, T. and Suzuki, O. *Development of a new scour detector that enables monitoring of pier soundness*, JR EAST Technical Review-No.27 Special edition paper. (2013) (in Japanese)
- [2] Heylen, W., Lammens, S. and Sas, P. *Modal analysis theory and testing*, K.U. Leuven, Belgium, (1997).
- [3] van Overschee, P. and De Moor, B. *Subspace identification for linear systems*, Kluwer Academic Publishers, (1996).
- [4] Goi, Y. and Kim, C.W. Mode identifiability of a multi-span cable-stayed bridge utilizing stabilization diagram and singular values, *Smart Structures and Systems* (2016) **17**(3):391 - 411.
- [5] Au, S.K. Fast Bayesian FFT method for ambient modal identification with separated modes, *J Eng Mech ASCE* (2011) **137**(3):214-226
- [6] Au, S.K., Zhang, F.L. and Ni, Y.C. Bayesian operational modal analysis: theory, computation, practice, *Computers & Structures* (2013) **126**:3-14.
- [7] Goi, Y., Kim, C.W. and Au., S.K. Investigation of operational modal identification of a cable-stayed bridge based on Bayesian estimation considering stochastic uncertainty, *J. of JSCE A2* (2016) **72**(2):I_751-I_762. (in Japanese)
- [8] Yuen, K.V. and Katafygiotis, L.S. Bayesian Fast Fourier Transform approach for modal updating using ambient data, *Adv Struct Eng.* (2003) **6**(2):81-95.
- [9] Schoukens, J. and Pintelon, R. *Identification of linear systems' a practical guideline for accurate modeling*, London: Pergamon Press, (1991).
- [10] van Overschee, P. and De Moor, B. Subspace algorithms for the stochastic identification problem, *Automatica* (1993) **29**(3): 649-660.
- [11] Chang, K.C. and Kim, C.W. Modal-parameter identification and vibration-based damage detection of a damaged steel truss bridge, *Engineering Structures* (2016) **122**:156-173.
- [12] Samizo, M. *A study on the evaluation of stability of railway bridge piers during the swelling of a river*, PhD Thesis, Kokushikan University, (2014): 126-135. (in Japanese)
- [13] Ministry of Land, Infrastructure, Transport and Tourism, Railway Bureau, *Railway structures maintenance management standard and commentary (structural edition)*, (2007), 169-170. (in Japanese)

AN EXPERIMENTAL INVESTIGATION OF THE PRESTRESS ACCUMULATION RELEASE STRATEGY FOR LOCAL MITIGATION OF STRUCTURAL VIBRATIONS

GRZEGORZ MIKUŁOWSKI, BLAZEJ POPLAWSKI AND ŁUKASZ JANKOWSKI

Institute of Fundamental Technological Research (IPPT),
Polish Academy of Sciences
ul. Pawińskiego 5B, 02-106 Warszawa, Poland
e-mail: ljank@ippt.pan.pl

Key words: Prestress-Accumulation Release, Vibration control, Sensor placement, Semi-active structures, Piezoelectric actuation.

Abstract. This contribution presents an experimental analysis of the control system configuration for a semi-active frame structure. The structure is equipped with a system that implements a Prestress Accumulation Release strategy for mitigation of vibration. A proper distribution of the sensors for monitoring the actual state of the structure is the key factor that determines the overall effectiveness of the applied strategy. The results and findings presented here reveal a set of basic rules dedicated to solving this crucial issue.

1 INTRODUCTION

Prestress Accumulation Release (PAR) is a recently developed control strategy for mitigation of structural vibrations [1,2], which belongs to the class of semi-active control approaches [3]. It utilizes an extremely effective approach, based on the concept of controllable structural constraints, which assumes that it is possible to introduce short lasting modifications of the local effective stiffness of vibrating structures. In practice, the method requires dedicated, semi-actively controllable fuses to be implemented in the structure, which allows local mechanical properties to be modified in a controllable way [4].

The investigations published until now revealed, both numerically and experimentally, a superior effectiveness of the PAR-based vibration control approach, which stems from an optimization procedure and a basic mechanical analysis of the control problem [2]. The experimental verification of the previous results was focused on testing of the control law and on implementing the control algorithm [5], and it prepared the ground for developing a methodology for the optimal distribution of the semi-active fuses within the structure [6].

The idea of the localised control algorithm assumes that internal energy level is monitored locally in a structure and dissipated accordingly [7]. Therefore, it is preferable that the semi-active joints are collocated with the sensors. This is an essential advantage of the concept in comparison to the control systems with the global response monitoring approach. It can be achieved due to the fact that the span of the sensor placement is limited to the direct neighbourhood of the semi-active elements and therefore such a compact installation may be characterised with low complexity and be less expensive. Nonetheless, the exact localisation of

the sensor needs to be determined precisely. The experimental survey presented in this contribution aims at determination of sensors placement of such a type that a system observability is sufficient for the performance of the controller.

2 EXPERIMENTAL INVESTIGATION METHODOLOGY

The examined structure is a frame in a cantilever configuration as depicted schematically in Figure 1. The general dimensions of the frame are 1200 mm length and 300 mm width. The cross-section of the structural members is a square tube 30 mm in height and 15 mm in width. The thickness of the wall is 2 mm. An internal part of the frame is the semi-active member consisting of two joints with an interconnecting element positioned in between. The semi-active member is located between the branches of the structure in a distance of 600 mm from the support, which is half of the total length of the frame. The utilized sensors are strain gauges in a half bridge connection type and configured for measurements of the in-plane bending in the frame members. The coordination system adopted for this investigation is depicted in Figure 1.

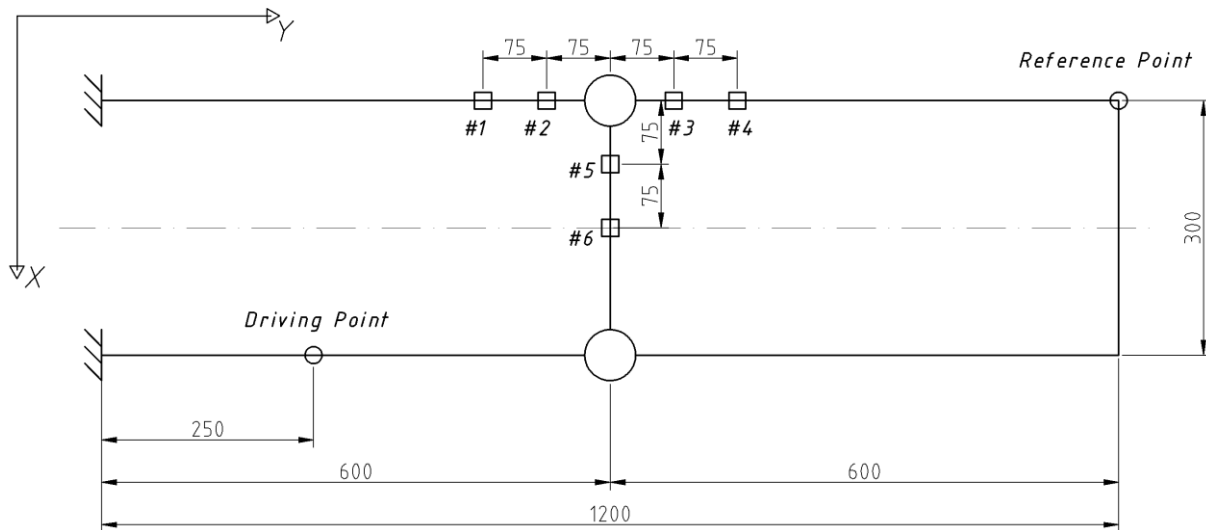


Figure 1: Scheme of the experimental frame and location of sensors #1 – #6

The frame under examination has the eigenfrequencies determined in a spectral testing. The parameters of the structure are given in Table 1.

Table 1: Eigenfrequencies of the in-plane modes

Mode No.	1	2	3
Eigenfrequencies	13.6	38.8	125.3

The testing procedure for this investigation is following. Firstly, six potential sensing locations are determined and evenly distributed on the structure. There are two locations per each of the frame branches, as depicted in Figure 1. Due to symmetry of this particular structure,

the locations are chosen in the neighbourhood of only one of the semi-active joints. Secondly, in order to reveal the sensor locations with satisfactory system observability of the structural eigenfrequencies, spectral tests of the frame in a passive mode (not activated semi-active joints) are carried out. Thirdly, the influence of the sensor location on the overall algorithm effectiveness is assessed by means of quality tests.

The locations of the sensors are evaluated on the basis of the following three criteria:

1. the highest possible level of system observability of the modal vibrational forms exhibited on the structure,
2. the lowest possible level of disturbances created by the semi-active member,
3. a satisfactory level of the overall control procedure quality.

The quality of the vibrational response of the system is tested in a SISO (Single Input Single Output) setup. The FRF accelerance functions are calculated and the resulting amplitudes are compared. The input is a swept sinusoidal force signal in a defined driving location and the output is a vibration level in a defined reference location. The two locations on the structure are determined as constant for the test:

1. Driving Point, which is the point through which vibrational excitation is introduced to the structure by means of a modal shaker (Figure 1).
2. Reference Point, which is the point of acceleration measurement and which is dedicated for assessment of control algorithm quality (Figure 1).

3 RESULTS

The results of the experiments are presented in three groups. The first group introduces the spectral characteristics of the Driving Point and Reference Point. The second group of results presents the spectral responses of the sensors in a passive state of the structure (not activated semi-active joints). The third group reflects how the operation of the activated joints influences

3.1 Spectral characteristics of Driving Point and Reference Point

The quality reference case for the study are accelerance functions (Figure 2) obtained as an effect of an FRF calculation in a passive system. Measurement of acceleration and force is conducted along direction OX (as defined in Figure 1).

The Driving Point response, depicted in colour red in Figure 2, indicates three clear resonances, which suggests that the exciter is connected in a right location to excite the first three in-plane modal forms. The in-plane modal forms are the only properly excited ones in this particular configuration of the experimental setup. It is due to the fact that the signals have been measured in accordance to the chosen excitation direction and measurement direction (OX). The other line on the graph (colour green) depicts the frequency response of the Reference Point, which is positioned on the free tip of the tested frame (Figure 1). The presented FRF graph proves that the Reference Point reflects the mechanical response of the structure in all of the considered in-plane modal forms and can be utilized as a control quality indicator and for assessment purposes.

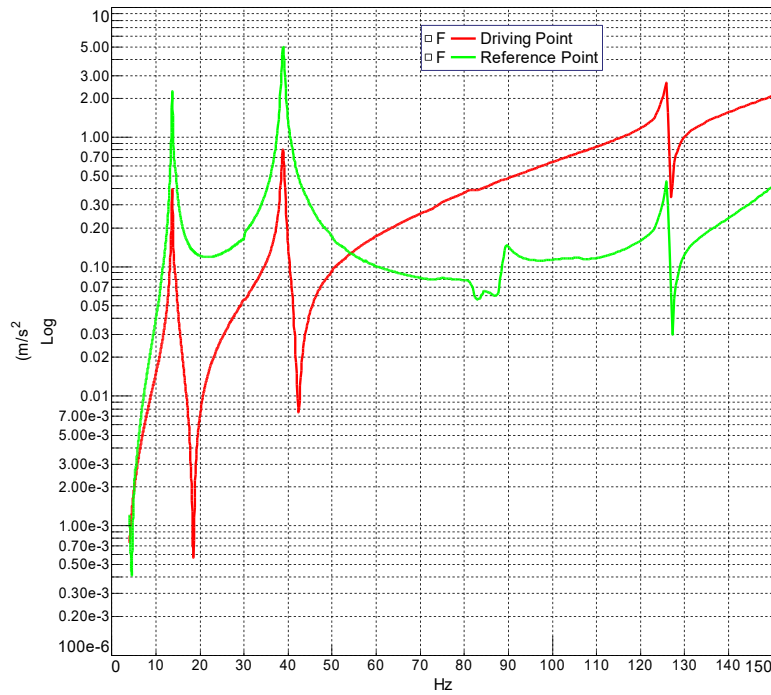


Figure 2: Accelerance functions of the tested system

3.2 Spectral responses of the sensors

Sensor placement is tested on the example of six locations of the strain gauges. The location scheme of the sensors is presented in Figure 1 and denoted as #1 – #6. The sensors are distributed in defined distances from the semi-active node. The graphs in Figures 3–5 present the FRFs of the signals acquired with the particular sensors. The objective of this study is to determine the responsiveness of the particular locations and reflecting it on the FRF graphs. High amplitudes of resonances, exhibited on the particular graphs, indicate that a particular sensor generates a signal, which is characterised by a sufficient SNR (signal to noise ratio) for the control purposes. The criterion for assessing the particular sensor locations is based on the spectral modes observability in the system determined on the basis of the FRF functions. A sufficient location is characterised by a defined level of the FRF amplitude and the threshold is established on level 1 $\mu\text{E}/\text{N}$.

Figure 3 presents the data acquired for locations #1 and #2. These location are characterised by a high observability of the in-plane modes of the structure and therefore satisfy the demands of the system design. Figure 4 depicts the FRFs that characterise the responses in locations #3 and #4, which indicate that both sensor #3 and sensor #4 exhibit lacks in system observability of modes 3rd and 1st respectively. Figure 5 presents that the sensor localised in position #5 allows for observations of all three vibrational modes, which predestines it for adopting in the control system design.

In summary, two locations #2 and #5 seem to exhibit the most favourable features from the point of view of the signal quality. One of them is positioned on the semi-active member of the structure and the other one is positioned on the structural element. Further analysis of the locations is provided in the next section.

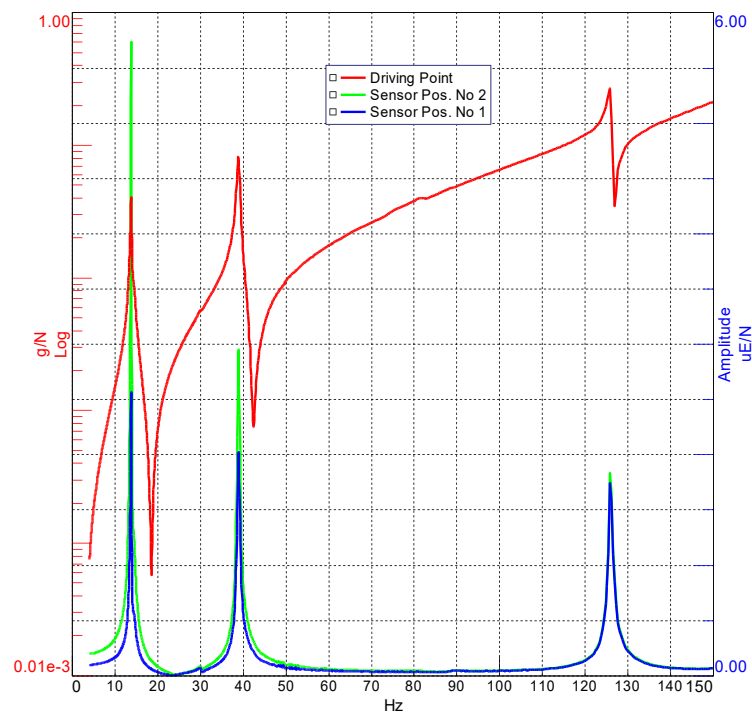


Figure 3: Accelerance functions of the tested system

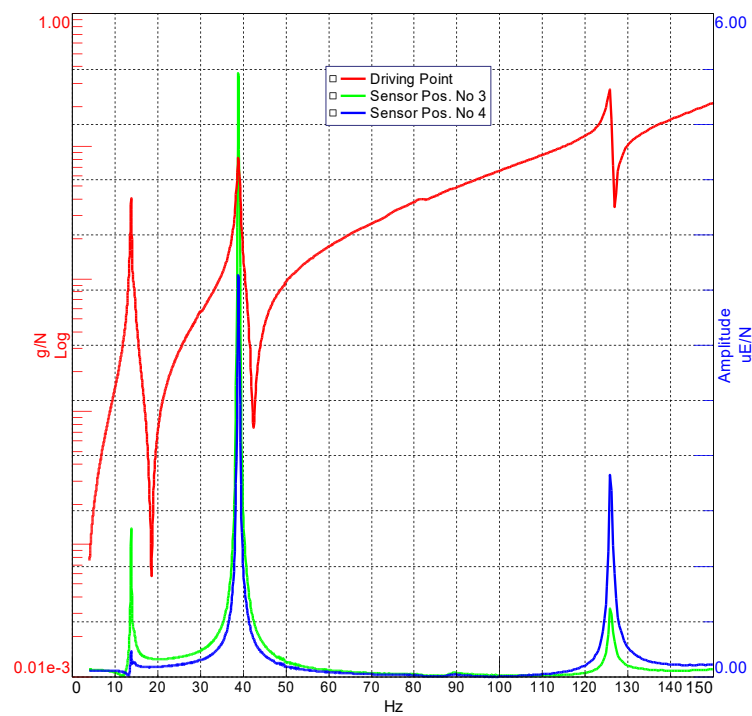


Figure 4: Accelerance functions of the tested system

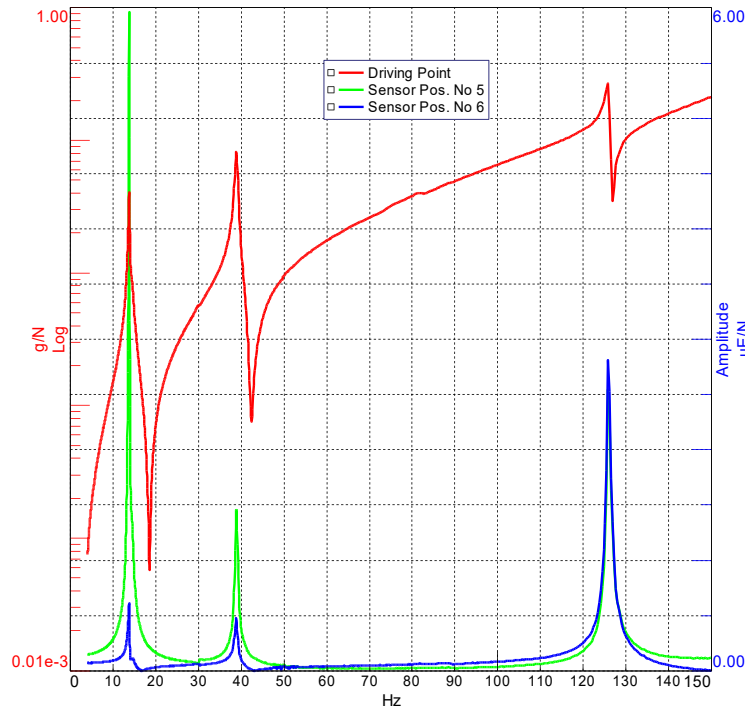


Figure 5: Accelerance functions of the tested system

3.3 Effectiveness of the control procedure

The following section discusses the third group of the results, in which the influence of the activated joints on the structure is studied. The tests are configured in order to carry out an experiment with each of the six tested sensor locations. The experiments are sweep tests of the frame in the control mode. Each experiment is conducted with a specific sensor. The algorithm applied for the test is described in [1] and it follows a rule, in which the joints reduce their torque transmission periodically for a 3 millisecond periods. The time instants for the transmission reduction are determined as the instants of the maximal value of the local internal energy of the structure. The results of the system operation in the controlled mode are presented in Figures 6–8. All of the sensors provide a signal that is functional in the tested control system. The results related to the specific sensors are summarised in Table 2.

Table 2: Accelerance amplitudes under the control procedure

Control case	1 st mode shape			2 nd mode shape		
	Absolute amplitude	Relative amplitude	Gain	Absolute amplitude	Relative amplitude	Gain
	[g/N]	[%]	dB	[g/N]	[%]	dB
Passive	0.187	–	–	0.533	–	–
Controlled with sensor #1	0.026	13.9	-17.1	0.321	60.2	-4.4
Controlled with sensor #2	0.056	29.9	-10.5	0.298	55.9	-5.0
Controlled with sensor #3	0.03	16.0	-15.9	0.304	57.0	-4.9
Controlled with sensor #4	0.044	23.5	-12.6	0.339	63.6	-3.9
Controlled with sensor #5	0.034	18.2	-14.8	0.282	52.9	-5.5
Controlled with sensor #6	0.075	40.1	-7.9	0.243	45.6	-6.8

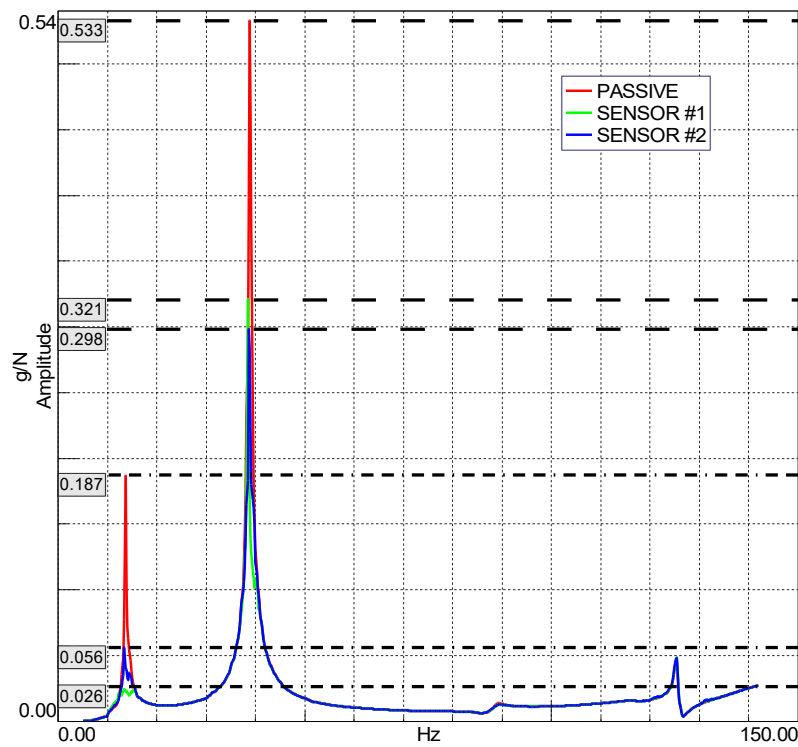


Figure 6: Accelerance function - control based on sensor locations #1 and #2

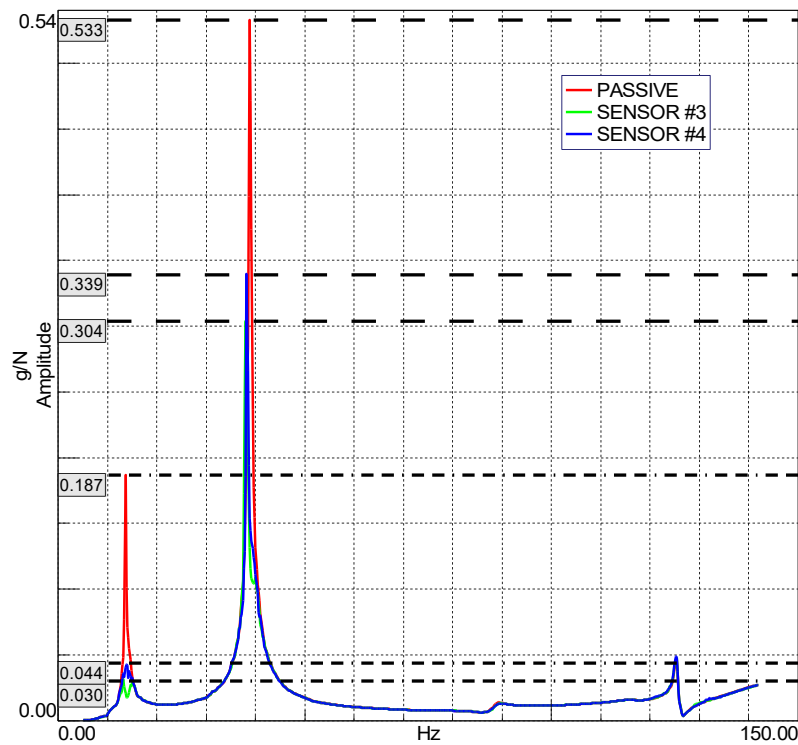


Figure 7: Accelerance function - control based on sensor locations #3 and #4

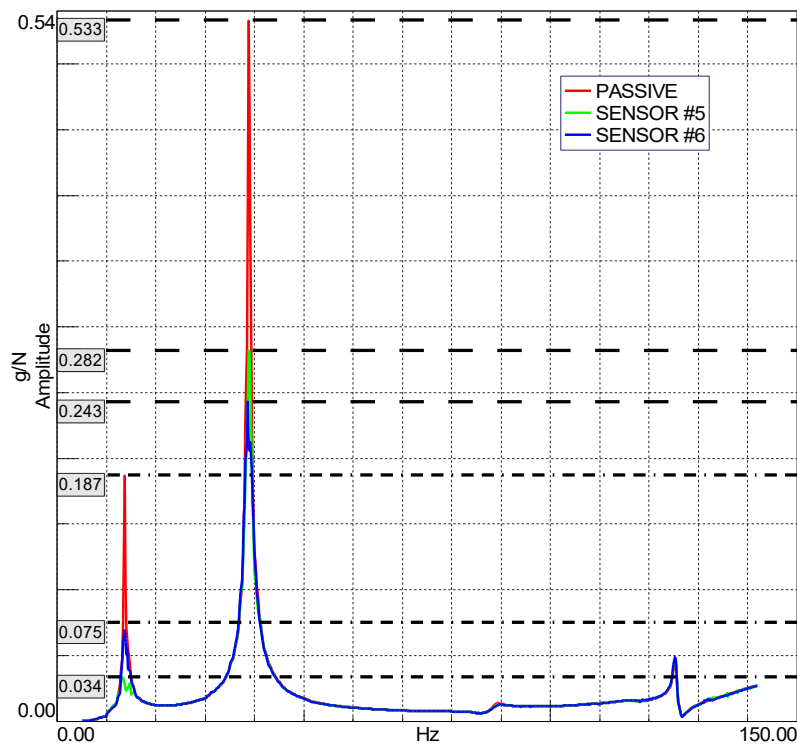


Figure 8: Accelerance function - control based on sensor locations #5 and #6

4 DISCUSSION

Effects of the control system on vibrational response of the structure are noticeable for each of the sensor locations as suggested in the results in Table 2. In most of the cases, the reduction of the accelerance amplitudes is correlated with the quality of the signals generated by the sensors. Sensor locations #1 and #2 both exhibit high system observability of the vibrational modes and in the both cases the amplitude of accelerance is reduced by 17.1 dB and 10.5 dB respectively (Table 2). Contrary to what was expected of the test, the control quality (Figure 6) does not reflect that the sensor location #2 is characterised by a significantly higher system observability level in reference to the sensor location #1 (Figure 3). A possible reason can be that the acquired results are influenced by the stochastic character of the phenomenon. A good correlation between the signal quality and the control results can be observed for the sensor locations #3 and #4. The signal generated in location #4 has low quality for mode no1 and it is reflected in the results of control effects. However, even though the signal acquired seem to be relatively poor in quality, the vibration accelerance amplitude is reduced by 12.6 dB, which indicates a satisfactory level of the control effectiveness. Evidently, lower effectiveness of the control and therefore good correlation with the signal quality can be observed in the case of sensor location #6. The signal quality in location #6 is low for both 1st and 2nd vibration modes of the structure (Figure 5). In contrast, the sensor location #5 exhibits high quality of the signal (Figure 5). This is reflected in the effectiveness of the control procedure. The structure controlled with a system based on sensor location #5 is over 2 times more effective in comparison to location #6. Another important factor is the fact that the semi-active joints

introduce self-vibration during operation. This can disturb the sensor readings in the direct neighbourhood of them. In the analysed case the most endangered sensor location is #5. However, the control effectiveness results disprove this thesis.

5 CONCLUSIONS

The presented results provide a contribution over a specific case, in which a frame is excited in the described, unique, in-plane configuration. That gives a specific results related to the particular configuration of the sensor placement. However, the objective of this work is to derive knowledge about general rules of the sensor placement in the localised control approach. The following clues can be drawn from the conducted research:

1. The basic conclusion coming from the study is that a control system based on the PAR algorithm is sensitive to local distribution of the sensors which makes the study crucial from the point of view of the system preliminary configuration.
2. An improper determination of a sensor location can decrease the effectiveness of the control procedure even by 200%.
3. The system governed by the PAR algorithm exhibits a significant effectiveness of the vibration control (Gain: 13–17 dB).
4. Even suboptimal distribution of the sensors results in an effective vibration reduction, which suggests that the system is robust to slight incorrectness in the final sensors positioning.
5. Vibration induced by the joints by themselves do not interfere with the control input signal and the procedure can be performed successfully.
6. A satisfactory level of correlation is observed between the system observability in the particular locations and the control effectiveness. The method of observability assessment in the sensor locations can be considered as a potential solution in the case of practical implementations.

ACKNOWLEDGMENTS

The authors gratefully acknowledge the support of the National Science Centre, Poland, granted under grant agreements DEC-2017/25/B/ST8/01800 and DEC-2017/26/D/ST8/00883, and the support of the National Centre for Research and Development, Poland, granted in the framework of the TANGO2 programme (TANGO2/341494/NCBR/2017).

REFERENCES

- [1] Mróz, A., Orłowska, A. and Holnicki-Szulc, J. Semi-active damping of vibrations. Prestress Accumulation–Release strategy development. *Shock and Vibration* (2010) **17**:123–136.
- [2] Poplawski, B., Mikułowski, G., Mróz, A. and Jankowski, Ł. Decentralized semi-active damping of free structural vibrations by means of structural nodes with an on/off ability to transmit moments. *Mechanical Systems and Signal Processing* (2018) **100**:926–939.
- [3] Casciati, F., Rodellar, J. and Yildirim, Y. Active and semi-active control of structures—theory and applications: A review of recent advances. *Journal of Intelligent Material Systems and Structures* (2012) **23**(11):1181–1195.

- [4] Mróz, A., Biczysk, J. and Holnicki-Szulc, J. Sterowalne sprzęgło oraz jego zastosowanie [in Polish] (2010) PL Patent No 230890, Instytut Podstawowych Problemów Techniki PAN, Adaptronica Sp. z o.o.
- [5] Mikułowski, G., Popławski, B., Wiszowaty, R., Mróz, A. and Jankowski, Ł. *An investigation on a semi-active damping of forced structural vibrations by means of controllable structural nodes*, ISMA 2018 / USD 2018, International Conference on Noise and Vibration Engineering / International Conference on Uncertainty in Structural Dynamics, September 17–19, Leuven (BE), pp. 189–201, (2018).
- [6] Popławski, B., Mikułowski, G., Pisarski, D., Wiszowaty, R. and Jankowski, Ł. Optimum actuator placement for damping of vibrations using the Prestress–Accumulation Release control approach. *Smart Structures and Systems* (2019) accepted.
- [7] Pisarski, D., Decentralized stabilization of semi-active vibrating structures. *Mechanical Systems and Signal Processing* (2018) **100**:694–705.

CONTINUOUSLY VARIABLE TRANSMISSION FOR APPLICATION IN TUNED MASS DAMPER

MATEUSZ LAZAREK*, PIOTR BRZESKI* AND PRZEMYSŁAW PERLIKOWSKI*

*Division of Dynamics, Lodz University of Technology

Stefanowskiego 1/15

90-924 Lodz, Poland

e-mail: mateusz.lazarek@p.lodz.pl, web page: <http://www.kdm.p.lodz.pl/>

Key words: Continuously Variable Transmission, Mechanical Speed Variator, Inerter, Tuned Mass Damper

Abstract. In this paper we investigate mechanical speed variator for novel tuned mass damper (TMD) application equipped with inerter. In such application inerter consist continuously variable transmission (CVT). Hence the motion of the transmission is oscillatory and we test it for the actual working conditions. We derive the mathematical model of the mechanical speed variator. We analyse the actual transmission ratio, internal motion resistances and identify the inertia of mechanical speed variator components and validate further. We apply actual working conditions and compare the experimental and numerical exciting torques of the CVT. We obtain good agreement between them, hence the proposed model is robust and gives reliable results. Finally, we apply model of the mechanical speed variator into our TMD and propose possible application.

1 INTRODUCTION

The idea of tuned mass dampers (TMD) has more then one hundred years. It is a device designed to reduce undesired oscillations of a structures by addition of a additional body to the system instead of changing its support properties. The first solution was proposed by Frahm in 1909 [1]. The simple device consisted of a mass and a spring. Its natural frequency was tuned to natural frequency of the damped body. Despite impressive performance in resonance and its close neighborhood it was poorly efficient outside the narrow range. The improvement was made by Den Hartog [2] by adding dash-pot between the TMD and damped structure which causes significant increase of TMD efficiency range. Alternative idea concerns interchange the linear spring of TMD by the nonlinear one (with the linear and nonlinear parts of stiffness) [3, 4] or with purely nonlinear characteristic [5, 6, 7]. Further studies led to applications with multiple TMD instead of one [8, 9, 10, 11] able to work with more complex system with multiple natural frequencies. Recently, a novel concept of varying the tuned mass damper natural frequency has been applied using TMD with variable inertia [12, 13].

One of crucial part in solution presented in [13] is continuously variable transmission (CVT). Authors in [14] use belt driven CVT for inertia change. Nowadays CVT is well know transmission design, firstly presented by Leonardo da Vinci. Mechanical designers can select from many realizations of it, following the best type for the chosen application. Currently the most popular types are variable-diameter pulley (VDP), toroidal and speed variators. The first, belt driven transmission consists two pulleys divided into

two sheaves each and a V-belt. Depending on application a steel reinforced rubber V-belt or a chain can be used. Another type is toroidal CVT transmitting power between discs through system of rollers. Transmissions that type can be be partial or full toroidal. Similarly to the belt driven CVTs, efficiency requirements determine the design. The last group are mechanical speed variators. They are designed to provide a variable speed drive. Its main advantage is mechanical and continuously change of the transmission ratio. Such devices are mainly used for production purpose and design to work in specific direction of motion.

According to the main research of our group concerns tuned mass dampers (TMDs) we decided to examine variator as a potential part of a inerter and TMD [13, 14]. We modify CVT produced by Motovario in order reduce internal motion resistance what is a critical factor in case of TMD performance [15, 16]. Considering that type of the CVT as a part of TMD makes difference in operating conditions. Instead of typical one directional motion such application demands bidirectional rotations.

To examine properties of modified variator we create its mathematical model and perform several experimental tests. We study the actual transmission ratio, internal motion resistances and identify the inertia of mechanical speed variator components and validate further. We conduct test with actual working conditions and compare the experimental and numerical exciting torques of the CVT. Obtained good agreement between them, we prove proposed model robustness. We simulate actual working conditions of the mechanical speed variator as a part of complete TMD system. We present results for our laboratory rig showing limitations due to internal motion resistance. Finally, we modify parameters of the damped construction and TMD showing good system performance and proving mechanical speed variator application.

2 INVESTIGATED DEVICE

2.1 Description and model of the modified variator

In this section we introduce the model of the modified CVT produced by Motovario. Our version of this CVT is modified for our specific propose and its properties vary from original one. The schematic model is shown in Fig. 1. The divide is symmetric, hence we draw its half and we neglect all parts that are not involved in the kinematic chain. In panel (a) we show a schematic cross-section of the device with numbering of all parts. Then, in panel (b) we show the front view with geometrical dimensions and we mark all characteristic points. The last panel (c) includes the back view of plate (No. 3). Now let us describe the operation of the device. The output shaft (No. 1f) has velocity ω_1 and it rotates with all parts attached to it (Nos 1a-e). Parts Nos 1a and 1b are internal fixed and mobile tracks respectively. The planet (No. 2) is placed and between them. The necessary pressure to transfer the motion between tracks and planet without slips is ensured by four Belleville springs (No. 1c) which are tensioned in respect to the shaft (No. 1a) via stop ring belleville springs (No. 1d) and Seeger ring (No. 1e). The performed modification concerns reduction amount of Belleville washers by one. The planet (No. 2) is in contact with inertial tracks in point *B* and with external fixed and mobile tracks (Nos. 4a,b) in point *C*. It can rotate in planet bush and slide radially according to paths in the input shaft part No. 3b. One of the external tracks is fixed to the body of CVT (No. 4b) and do not perform any motion. The second external track control gear ratio by its linear movement caused by tension in spring - part No. 4c. Point *C* is a instantaneous center of zero velocity ($V_C = 0.0$ [m/s]). The planet performs the plane motion in respect to external tracks.

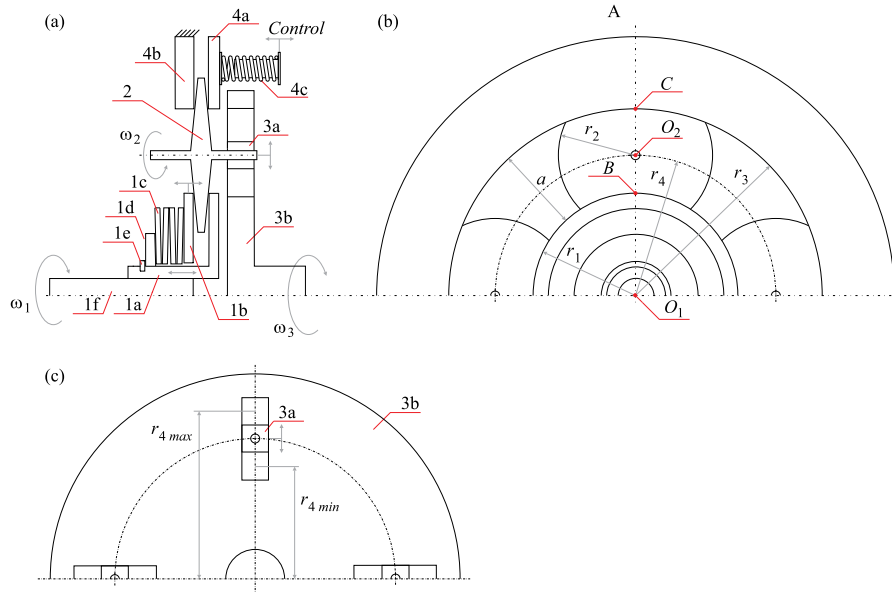


Figure 1: Schematic model of the modified variator.

Now, let us introduce the kinematic relation between all parts of the CVT. The output angular velocity in respect to point O_1 is ω_1 , so $V_B = \omega_1 r_1$. The same velocity can be calculated in respect to point C : $V_B = \omega_2 a$, where $a = (r_3 - r_1)$. This let us calculated the angular velocity of planet: $\omega_2 = \frac{\omega_1 r_1}{a}$. The distance between points C and O_2 is the difference $(r_3 - r_4)$, so the velocity of planet in its center (O_2) is $V_{O_2} = \omega_2 (r_3 - r_4)$. The same velocity has plate (No. 3) $V_{O_2} = \omega_3 r_4$ so the relation between output and input angular velocities are given as follow:

$$\omega_1 = \omega_3 \frac{ar_4}{r_1(r_3 - r_4)} = \omega_3 i, \quad (1)$$

where i is gear ratio. The values of parameters are as follow: $r_1 = 0.0359$, $r_3 = 0.0630$ and r_4 is controlling parameter.

The next step is the dynamical model of the CVT. We assume that the motion is without slips, so the device has one DoF. We divide the moving parts into three groups: input shaft and all connected parts (Nos 1a-f) with total moment of inertia I_1 , planet with moment of inertia I_2 and output shaft with moment of inertia I_3 . The total kinetic energy is as follow:

$$T = \frac{1}{2} I_1 \omega_1^2 + 4 \left(\frac{1}{2} I_2 \omega_2^2 + \frac{1}{2} M_p V_{O_2}^2 \right) + \frac{1}{2} I_3 \omega_3^2 \quad (2)$$

where M_p is mass of planet (there are four planets in the CVT). We use kinematic relations for ω_1 , ω_2 and V_{O_2} to find the equivalent moment of inertia I_{eq} of the system:

$$I_{eq} = I_1 i^2 + 4 \left(I_2 \left(\frac{r_4}{r_3 - r_4} \right)^2 + M_p r_4^2 \right) + I_3. \quad (3)$$

Hence, the equation of motion is as follow:

$$I_{eq} \ddot{\phi}_1 + f(\dot{\phi}) = M_{ext} \quad (4)$$

where $f(\dot{\phi})$ is the internal resistance function which is dependent on the current ratio of the CVT. M_{ext} is external torque applied to the input shaft.

2.2 Laboratory rig

We examine mechanical speed variator in order to find the gear ratio characteristics and value of the inertial motion resistances. While, the first parameter is important from control point of view the second affects overall system performance. Tests are carried out on small laboratory rig designed and build for this particular task. We use structure of the variator (see Fig. 1) and additional parts creating system presented in Fig. 2.

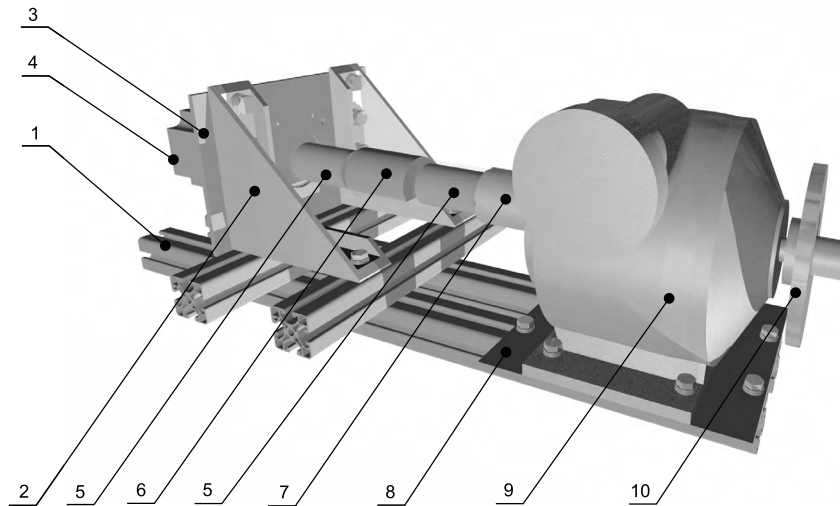


Figure 2: Isometric views of the test rig for the modified CVT (a) project (b) practical realization. Parts presented in the figure: 1 - Supporting profiles, 2 - Angle brackets, 3 - Servo plate, 4 - Servo motor, 5 - Two claw clutches, 6 - Torque sensor, 7 - Sleeve, 8- Motovario supporting plate, 9 - Motovario, 10 - Flywheel.

Therefore, the additional parts are placed on the supporting aluminum profiles (parts Nos. 1) which is a base for an angle brackets (parts Nos. 2) and for a servo plate (part No. 3). Servo motor (part No. 4) is screwed to the servo plate and it drives the CVT with two claw clutches (parts Nos. 5) and torque sensor (part No. 6) mounted between them. The connection between the second clutch and the variator (part No. 9) is realized by the sleeve (part No. 7). Variator is mounted on supporting profiles through supporting plate (part No. 8). At the output shaft of the variator the flywheel (part No. 10) is mounted. The servo motor is driven by a driver controlled from the PLC.

3 TEST OF CVTs CRUCIAL PARAMETERS

3.1 Gear ratio in dependence on rotations of the control knob

Gear ratio for modified variator vary from $1.55[-]$ to $3.15[-]$ achievable with 10 rotations of the control knob. In this case the results are shown in Fig.3 where we can see the nonlinear dependence on angular position of the control knob. Such characteristic exists due to construction of the CVT. Nevertheless there is no hysteresis effect proving transmission robustness and ease in control. According to measured variator parameters we obtain numerical correlation between the control knob rotations and position of r_4 . One can see good correctional between numerical model and the experimental results.

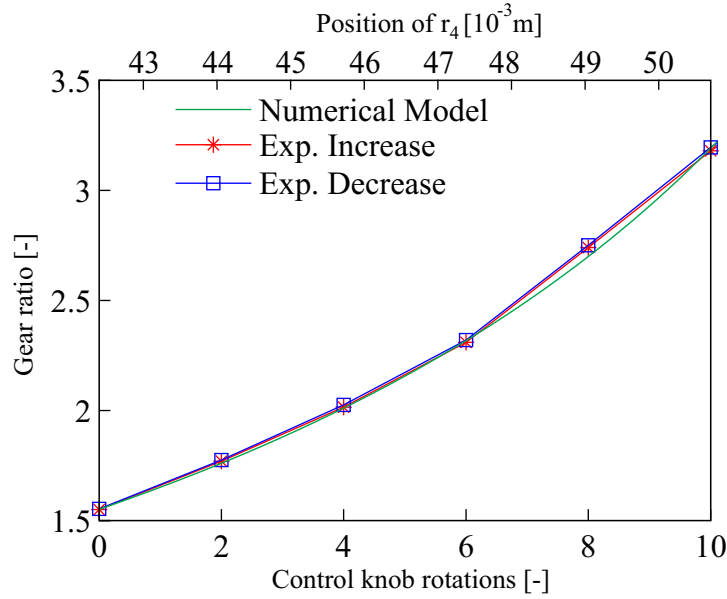


Figure 3: Gear ratio in dependence on rotations of the control knob for the modified variator.

3.2 Internal motion resistance

In next step, we examine the inertial motion's resistance. We choose five specific points equally distributed on the gear ratio characteristic plot. The test rig is equipped with the torque sensor which allows to create the torque versus angular velocity plots. Plots are created with respect to the input velocities of CVTs. In measurements we assume that the input velocity vary in range from -350 [rpm] to 350 [rpm], hence we run the servomotor with constant velocity in counterclockwise and clockwise direction respectively. The internal resistance of the modified variator varies in $\langle 0.8, 2.0 \rangle$ [Nm] range (see Fig. 4). The highest values are observed for low speed of the output shaft and values of internal resistance significantly decrease with increase of the CVT's velocity. The reason of this phenomenon is the oil distribution over the cooperating tracks and planets. The lubrication is achieved by motion of the planets which distribute the oil over all moving elements. In case of the low rotational speed the oil drips into the sump being integral part of the transmission body. According to that the oil cannot be properly distributed to the higher parts of transmission which cause the increase of the internal resistance. Another aspect of observed phenomenon is that the increase of the gear ratio causes the increase of the velocity of the planets and better oil distribution which results in reduce of the resistance. Hence, the general conclusion is that the higher velocity causes better distribution of the oil and decreases the internal resistance.

We also prepare mathematical model of the internal motion resistance. It is formulated as follows:

$$\begin{aligned} & \frac{1}{2} \left(-\frac{2}{\pi} \arctan(10^5 \phi) + 1 \right) (p1 \arctan(p2\phi) + p3) + \\ & \frac{1}{2} \left(\frac{2}{\pi} \arctan(10^5 \phi) + 1 \right) (p4 \arctan(p5\phi) + p6) = f(\phi). \end{aligned} \quad (5)$$

It is based on \arctan function, consists shape parameters, namely from $p1$ to $p6$ and depends from the shaft rotational velocity. It allows different characteristic for negative and positive shaft velocities.

Hence parameters from $p1$ to $p3$ represents negative values of the shaft rotational velocity. Contrary parameters from $p4$ to $p6$ represents positive direction of the shaft rotations. In result we are able to precisely replicate experimental results from laboratory rig. We identify friction parameters according to the model. Tests are carried out for three transmission ratios $i = 1.55 [-]$, $i = 2 [-]$ and $i = 3.15 [-]$. In result, blue curve in Figure 4 is generated. Basing on experimental data we fit internal motion resistance model parameters. In result we obtain a curve fitted to the direction of the shaft velocity. The modeled internal motion resistance model is marked red in Figure 4. For all cases we receive sufficient agreement between the model and the experiment.

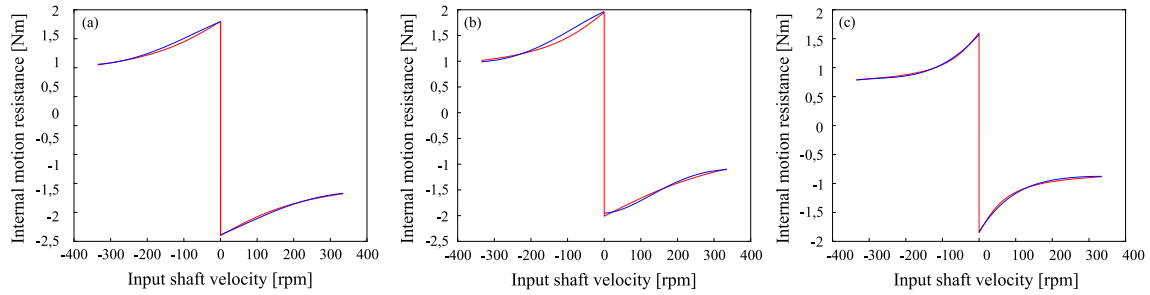


Figure 4: Internal motion resistance as a function of input shaft velocity. Blue curve correspond to experimental data, whereas friction model is marked blue. Three subplots represents gear ratios: (a) $i = 1.55 [-]$, (b) $i = 2 [-]$ and (c) $i = 3.15 [-]$.

3.3 Oscillatory trapezoidal test

The trapezoidal velocity path is controlled with the PLC and the programmed trajectory is presented in Fig. 5. The plot is exemplary, but the values of its parameters given in text correspond to values used in measurements. The motion starts with a small jump to the initial velocity equals $s_0 = 0.3 [\text{rad/s}]$ followed by acceleration to a target speed $s_t = 31.42 [\text{rad/s}]$ in $t_a = 300 [\text{ms}]$. The system performs six rotations (the controlled target value) of the input shaft with constant velocity and decelerates in $t_d = 300 [\text{ms}]$ to the final velocity s_0 . Next stage is a stop followed by change of the rotation direction which takes $t_s = 1 [\text{ms}]$ and is restricted by the motor driver. Then, the same sequence is repeated for the opposite direction of motion.

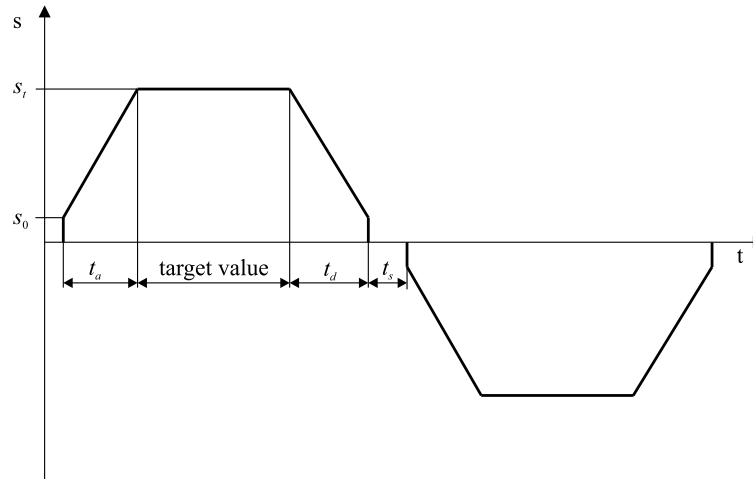


Figure 5: The exemplary trapezoidal velocity path.

We subject to this test transmission for selected transmission ratios. The results obtained for transmission ratio equals to $i = 1.55 [-]$ are presented in Fig. 6. Figure poses three subplots corresponding to the angular positions and the angular velocities of the input and output transmission's shafts marked with blue and red lines respectively. Last subplot presents the torque needed to be applied to achieve the desired velocity path. The diagrams starts during acceleration to the constant negative value of the rotational velocity. Hence it starts with decreasing value of driving torque which levels at constant value equals transmission internal motion resistance. After motion with constant velocity system beginning deceleration stage with reduction of driving torque. Amount of internal motion resistance makes deceleration process too quick and in order to follow velocity path drive controller reacts by adding additional negative torque. After the stop system starts to accelerate to the target speed in clockwise direction which is possible by increase of positive torque. Than, torque stabilizes at target level. We observe minor fluctuations of the velocity during the motion with constant velocity caused by the unbalance of the output shaft. The six rotations are followed by deceleration which leads to the system stop followed by acceleration with negative torque. Presented sequence is repeated in a same way in the second period. We perform same test for transmission ratio equals to $i = 2 [-]$ and $i = 3.15 [-]$. We validate mathematical model, comparing experimental torque-time traces with numerical results. For all transmission ratios we obtain good agreement. Moreover we divide the equivalent moment of inertia into input and output shaft moment of inertia. We use obtained results to study possible application of mechanical speed variator for the TMD.

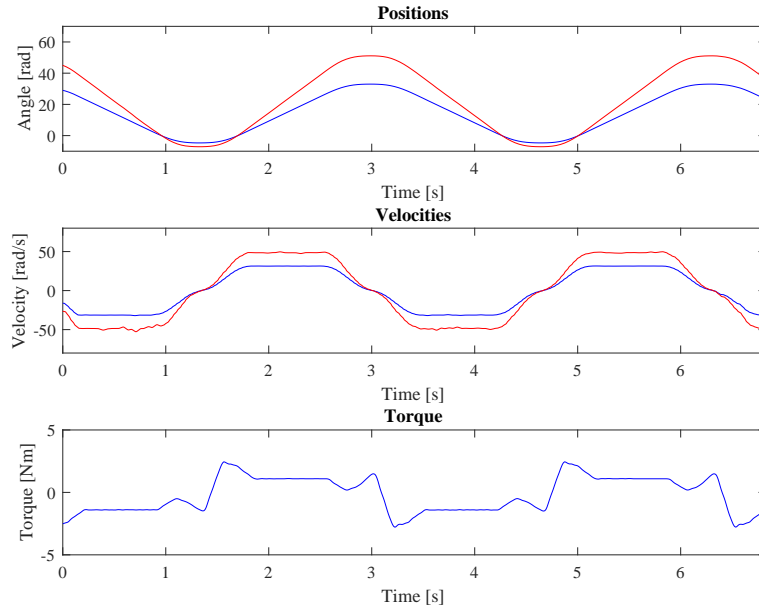


Figure 6: Three subplots represents positions (a), velocities (b) and torque (c) for input (blue) and output (red) transmission shafts in oscillatory motion test. Test is performed with ratio equals to $i = 1.55$ [–] and obtained by trapezoidal forcing.

4 Application of analyzed CVT to TMD

In this section we present application of the studied CVT to TMD with inerter that enables changes of inertance. Inerter is a two terminal device in which force is proportional to the relative acceleration between its ends [17]. Typically, inerter is attached to oscillating bodies. It is a mechanical device where the linear motion is changed into rotational via mechanical gear, hence the energy of vibration is accumulated in the rotating flywheel [18, 19]. In our realization between gear and flywheel we placed CVT, hence we are able to change inertia of inerter. We introduce such device in 2015 [13]. The changes of inertia is realized via change of the gear ratio of the CVT which cause increase or decrease of inertia of the CVT. If we divide the inertia by pitch radius we obtain inertance (I_n [kg]) which is added to total mass of TMD, hence the equivalent mass of TMD is as follow: $(m + I_n)$. Thanks to variable inertance we are able to vary equivalent mass of TMD, thus we are able to change its natural frequency and tune it to current frequency of excitation. In our previous papers we present such TMD with CVT designed in our lab. In this paper we analyze out of shelf CVT with modifications. The main difference in compare to our CVT is larger internal motion resistance, which is crucial to proper operation of TMD (the lower internal motion resistance causes better damping properties). CVT investigated in this paper has approximately two times larger internal motion resistance. In this section we show how it affect damping properties.

4.1 Mathematical model of TMD

In this subsection we present the mathematical model of TMD with inerter attached to damped body presented in Fig. 7. Such system has two DoF and its motion is described by two generalized coordinates: the position of the main oscillator by coordinate x , while the displacement of the TMD by coordinate y . The main oscillator is characterized with the following parameters: M is its mass, K is the stiffness

of the single spring that connects the main mass to the ground, $C = \xi_1 2\sqrt{7KM}$ is the viscous damping coefficient of dash-pot that links mass M and the support and ξ_1 is its damping ratio. The system is forced kinematically via a spring of stiffness K with the displacement $a(t) = A \cos(\omega_e t)$.

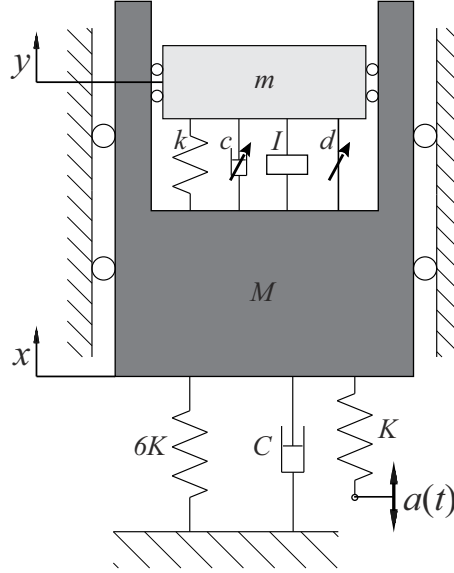


Figure 7: Physical model of the system.

To characterize TMD we use the following parameters values: the moving mass is given by m , the stiffness of the spring that connects it to the main oscillator is described with parameter k . The viscous damper that connect mass m with M is an active device and its damping coefficient $c = \xi_2 2\sqrt{km}$ can be changed according to controlling function. In this study we use two options, i.e., small ($\xi_2 = 0.0222$) and large damping ($\xi_2 = 0.2$). The dry friction force function $f(\dot{\phi})$ corresponds to internal motion resistance of the CVT and for simplicity we use values for $i = 3.15$ [–] (the lowest internal resistance). Inertance $I(i)$ is calculated based on formula ???. Inertia of CVT with flywheel is calculated based on Eq. (3) for ranges of ratio described in subsection 3.1. When we divide inertia by pitch radius $r_p = 0.42$ [m] we obtain the inertance in range $I(i) \in (3.01, 17.2)$ [kg]. Values of other parameters correspond to real existing rig described in our previous papers (see [14, 16]) and are as follow: $M = 102.66$ [kg], $K = 8181.0$ [N/m], $\xi_1 = 0.0041$, $m = 11.26$ [kg], $k = 10448$ [N/m], $A = 0.0148$ [m] and $\omega_e \in (10, 30)$ [rad/s]. To show how proposed device is working for larger total mass of main system and TMD we introduce the scaling factor α . Thus, the dynamics of the system presented in Fig. 7 is governed by the following equations of motion:

$$\alpha M \ddot{x} + \alpha 7Kx + C\dot{x} + \alpha I(i)(\ddot{x} - \ddot{y}) + \alpha k(x - y) + c(\dot{x} - \dot{y}) + f(\dot{\phi}) = \alpha Ka(t), \quad (6)$$

$$\alpha m \ddot{y} - \alpha I(i)(\ddot{x} - \ddot{y}) - \alpha k(x - y) - c(\dot{x} - \dot{y}) - f(\dot{\phi}) = 0. \quad (7)$$

As it easy to see we do not scale internal motion resistance of the CVT because it does not change with change of inetance. Damping coefficients (C and c) are described as factors (ξ_1 and ξ_2) of critical damping, hence they also scale with varying α .

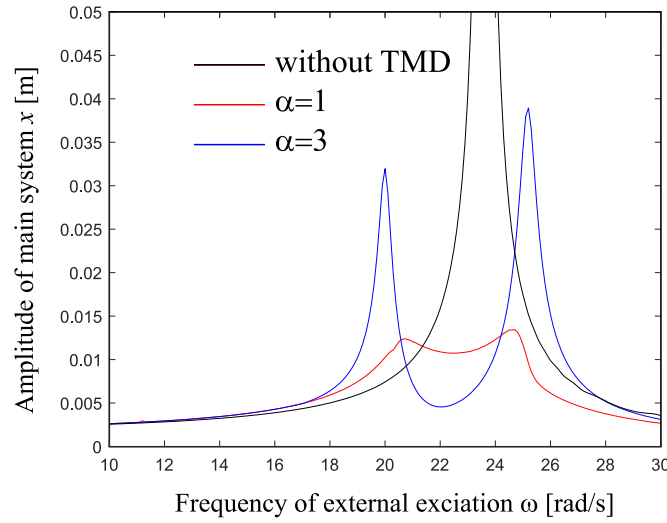


Figure 8: FRCs for different masses of main system.

In Fig. 8 we present the FRCs (frequency response curves) of main body for different configuration of the TMD. In Fig. 8 we present the response of the main system for $\alpha = 1$ without TMD (black line) and with TMD for $\alpha = 1$ (red line) and $\alpha = 3$ (blue line). The inertance for cases with TMD is equal to $I = \alpha \times 10.56 [kg]$. The amplitude for case without TMD reaches $0.255 [m]$ (we cut this plot above $0.05 [m]$ for better visibility). One can see that system with TMD for $\alpha = 1$ reduces amplitude of the main system but the internal motion resistance of the transmission limitates amplitude reduction. TMD with controlled CVT for such configuration is not beneficial in comparison to a classical optimized TMD. Contrary system with TMD for $\alpha = 3$ reduces influence of the internal motion resistance. Hence one can see significant decrease of the amplitude of the main system.

5 CONCLUSIONS

In this paper we show the comprehensive experimental investigations of the CVT. We modify variator produced by Motovario in order to validate it application for the novel TMD [13, 14] which can be tuned to the current frequency of external excitation to efficiently mitigate vibrations. We perform several tests of the CVT to assess its performance and validate its simplified mathematical model. We examine gear ratio in dependence on rotations of the control knob, internal motion resistance and inertias of transmission shafts. We also create mathematical model of the transmission. Identified parameters allow us to validate the prepared model with satisfactory results. Furthermore we implement modeled variator into our model of the TMD. We restricted considered case to constant inertance in order to trace application for the modified TMD. In case of application to the TMD and inerters the internal motion resistance is critical factor. Hence we prove that internal motion resistance in the modified variator is too large for application in our laboratory rig. Nevertheless we show that it is possible to scale the system by three times and obtain proper working conditions. We prove that variator type transmission can be used for damping oscillations of a large constructions with TMDs.

REFERENCES

- [1] H. Frahm. Device for damping vibrations of bodies, 1909.

- [2] J. P. Den Hartog. *Mechanical Vibrations*. McGraw-Hill, New York, 1934.
- [3] R. E. Roberson. Synthesis of a nonlinear dynamic vibration absorber. *Journal of Franklin Institute*, 254:205–220, 1952.
- [4] F. R. Arnold. Steady-state behavior of systems provided with nonlinear dynamic vibration absorbers. *Journal of Applied Mathematics*, 22:487–492, 1955.
- [5] Fotios Georgiades and AF Vakakis. Dynamics of a linear beam with an attached local nonlinear energy sink. *Communications in Nonlinear Science and Numerical Simulation*, 12(5):643–651, 2007.
- [6] A.F. Vakakis, O.V. Gendelman, L.A. Bergman, D.M. McFarland, G. Kerschen, and Y.S. Lee. *Non-linear targeted energy transfer in mechanical and structural systems*, volume 156. Springer, 2008.
- [7] R. Vigié, G. Kerschen, J.C. Golinval, DM McFarland, LA Bergman, AF Vakakis, and N. van de Wouw. Using passive nonlinear targeted energy transfer to stabilize drill-string systems. *Mechanical Systems and Signal Processing*, 23(1):148–169, 2009.
- [8] H. Yamaguchi and N. Harnpornchai. Fundamental characteristics of multiple tuned mass dampers for suppressing harmonically forced oscillations. *Earthquake engineering & structural dynamics*, 22(1):51–62, 1993.
- [9] Masato Abe and Yozo Fujino. Dynamic characterization of multiple tuned mass dampers and some design formulas. *Earthquake engineering & structural dynamics*, 23(8):813–835, 1994.
- [10] Chunxiang Li. Performance of multiple tuned mass dampers for attenuating undesirable oscillations of structures under the ground acceleration. *Earthquake Engineering & Structural Dynamics*, 29(9):1405–1421, 2000.
- [11] Y Yang, J Munoa, and Y Altintas. Optimization of multiple tuned mass dampers to suppress machine tool chatter. *International Journal of Machine Tools and Manufacture*, 50(9):834–842, 2010.
- [12] Michael ZQ Chen, Yinlong Hu, Chanying Li, and Guanrong Chen. Semi-active suspension with semi-active inerter and semi-active damper. *IFAC Proceedings Volumes*, 47(3):11225–11230, 2014.
- [13] P. Brzeski, T. Kapitaniak, and P. Perlikowski. Novel type of tuned mass damper with inerter which enables changes of inertance. *Journal of Sound and Vibration*, 349:56 – 66, 2015.
- [14] P. Brzeski, M. Lazarek, and P. Perlikowski. Experimental study of the novel tuned mass damper with inerter which enables changes of inertance. *Journal of Sound and Vibration*, 2017.
- [15] P. Brzeski and P. Perlikowski. Effects of play and inerter nonlinearities on the performance of tuned mass damper. *Submitted to Nonlinear Dynamics*, 2016.
- [16] M. Lazarek, P. Brzeski, and P. Perlikowski. Design and identification of parameters of tuned mass damper with inerter which enables changes of inertance. *Mechanism and Machine Theory*, 119:161 – 173, 2018.
- [17] M.C. Smith. Synthesis of mechanical networks: the inerter. *Automatic Control, IEEE Transactions on*, 47(10):1648–1662, 2002.

- [18] N.E. Houghton C. Papageorgiou and M.C. Smith. Experimental testing and analysis of inerter devices. *Journal of Dynamic Systems, Measurement, and Control*, 131:011001–11, 2009.
- [19] M.C. Smith and S.J. Swift. Design of passive vehicle suspensions for maximal least damping ratio. *Vehicle System Dynamics*, 54(5):568–584, 2016.

INVERSE LYAPUNOV BASED METHOD FOR SEMI-ACTIVE CONTROL OF ENERGY TRANSFER BETWEEN VIBRATION MODES

MARIUSZ OSTROWSKI*, BARTŁOMIEJ BŁACHOWSKI, ŁUKASZ JANKOWSKI
AND DOMINIK PISARSKI

Institute of Fundamental Technological Research
Polish Academy of Sciences
Pawińskiego 5B, 02-106 Warsaw, Poland

* e-mail: {mostr|bblach|ljank|dpisar}@ippt.pan.pl, web page: <http://www.ippt.pan.pl/en/>

Key words: Modal control, Semi-active control, Lockable joints, Energy harvesting.

Abstract. This contribution proposes a semi-active control approach for a directed energy transfer between structural vibrational modes. The motivation is the intended localization of the vibration energy in a selected mode for the purpose of energy harvesting and mitigation of structural vibrations. The proposed control strategy aims at the instantaneous maximization of the energy transfer to the target mode. It is based on an untypical approach of dynamic structural reconfiguration and implemented using a semi-actively controllable node: a lockable joint. Such a joint, depending on the control signal, can act as a hinge or as a typical frame node. Effectively, it provides thus an on/off ability to control the transfer of bending moments between the adjacent structural elements. The effectiveness of the approach is demonstrated in a numerical example of a plane frame structure.

1 INTRODUCTION

Attenuation of vibrations is a well-known problem [1] with a range of possible optimal control formulations [2]. The topic of vibration reduction by accumulation of the related energy, which is known as energy harvesting, is relatively less explored [3]. Usually, the structural excitation cannot be directly controlled nor easily predicted; it may have a broad frequency spectrum or take the form of rare impulsive shocks that result in free vibrations. The uncertain characteristics of the excitation can affect the efficiency of the energy harvesting process, because the energy-harvesters are usually designed for a single vibration frequency. This problem has motivated the development of a semi-active control strategy that allows the vibration energy to be transferred between selected vibrational modes, so that the energy-harvesters can be efficiently excited.

Controlled energy transfer between vibrational modes can be also used for the related purpose of attenuating the vibrations. Transferring the energy to a mode with a large amplitude at the position of the energy dissipator can speed up the process of vibration reduction. Besides, such an approach can be used to transfer the energy of vibrations to such modes that do not interfere with the intended operation of the structure. The method proposed in this contribution is formulated in a relatively general way, which makes it potentially applicable and implementable with a wide range of semi-active damping devices [4][5][6][7].

This contribution deals with a semi-active control strategy for a directed transfer of the mechanical energy between structural vibration modes. The considered structure is equipped with lockable joints, which enable or disable the transmission of bending moments between the neighbouring structural members in a controlled manner. Such devices have been successfully developed for attenuation of vibrations by stimulating energy transfer to higher-order modes that provide quick material damping [8]. The approach relies on semi-active control, which has several advantages compared to active control, including no need to generate large external control forces. Consequently, as no high-performance power source is required, the strategy is relatively easy to be applied, including large structures [9] and decentralized control [10].

The proposed semi-active control strategy aims to maximize the instantaneous mechanical energy transfer to the target vibrational mode. In the case of free vibrations, the energy of the target mode will increase only at the expense of other modes, which justifies the notion of energy transfer. A mathematical description of the mode mixing and energy transfer between vibrational modes, as well as a respective measurement technique, are proposed. The model is based on coupling the modal equations by coefficients that depend on the control signals, mode shapes and the placement of the lockable joints.

As a demonstrative example, a three-bar frame structure is used. Two different kinds of finite element models of such a structure are analysed: a crude one (with one finite element per beam only) and a refined one (with four elements per beam). The first model is very simple and clearly introduces and illustrates the semi-active control strategy. The second model allows the participation of the higher modes and their influence on the modal energy transfer to be studied. It is shown that the proposed methodology can be used for controlling the modal energy transfer, but a part of the vibration energy is lost due to the inevitable natural material damping of higher modes.

2 SYSTEM DYNAMICS AND CONTROLLABILITY

2.1 Dynamics of a structure with lockable joints

The proposed lockable joint acts as a pin connection, which can be temporarily dynamically locked to transmit the bending moment between the suitable rotational degrees of freedom (DOFs). This concept is illustrated in the Figure 1.

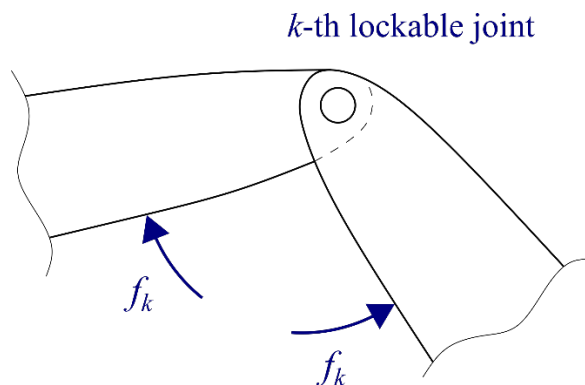


Figure 1: Model of the structural lockable joint in the locked state

In the locked state of the connection, an internal moment f_k of a suitable magnitude acts at the attachment points in order to maintain constant the angle between the joined structural elements.

Assuming small displacements, the structure is described by the linear equation of motion:

$$\mathbf{M}\ddot{\mathbf{q}}(t) + \mathbf{C}_0\dot{\mathbf{q}}(t) + \mathbf{K}\mathbf{q}(t) = \mathbf{L}\mathbf{f}(t) + \mathbf{w}(t) \quad (1)$$

where $\mathbf{q}(t)$ is the vector of the configuration coordinates, \mathbf{M} is the mass matrix, \mathbf{C} is the material damping matrix, \mathbf{K} is the stiffness matrix, $\mathbf{f}(t) = [f_1 \ \cdots \ f_{N_k}]^T$ is the vector of the generalised internal forces at the joined DOFs, \mathbf{L} is the matrix that selects the DOFs for the individual lockable joints, and $\mathbf{w}(t)$ denotes the vector of the external excitation forces. The matrix \mathbf{L} can be expressed in the following form:

$$\mathbf{L} = [\mathbf{L}_1 \ \cdots \ \mathbf{L}_k \ \cdots \ \mathbf{L}_{N_k}] \quad (2)$$

$$\mathbf{L}_k = [0 \ \cdots \ 1 \ \cdots \ 0 \ \cdots \ -1 \ \cdots \ 0]^T$$

where nonzero are only these elements of \mathbf{L}_k that are related to DOFs involved in the k -th lockable joint.

To describe the energy transfer between vibrational modes, modal analysis is performed. The eigenvalue problem for all joints in the unlocked state takes the well-known form

$$(\mathbf{K} - \omega_m^2 \mathbf{M})\boldsymbol{\phi}_m = \mathbf{0} \quad (3)$$

where ω_m is the m -th natural frequency and $\boldsymbol{\phi}_m$ is the corresponding eigenvector. The eigenvectors are collected in the modal matrix $\boldsymbol{\Phi}$ and constitute the basis for the modal coordinates η_m . In the matrix notation

$$\mathbf{q}(t) = \boldsymbol{\Phi}\boldsymbol{\eta}(t), \quad (4)$$

where $\boldsymbol{\eta}(t) = [\eta_1 \ \cdots \ \eta_m \ \cdots \ \eta_{N_m}]^T$ is the vector of the modal coordinates. Additionally, the eigenvectors are normalized with respect to the mass matrix. After substitution of (4) into (1) and a left-side multiplication by $\boldsymbol{\Phi}^T$, the following form of the equation of motion is obtained:

$$\underbrace{\boldsymbol{\Phi}^T \mathbf{M} \boldsymbol{\Phi}}_{\mathbf{I}} \ddot{\boldsymbol{\eta}}(t) + \underbrace{\boldsymbol{\Phi}^T \mathbf{C}_0 \boldsymbol{\Phi}}_{\boldsymbol{\Gamma}_0} \dot{\boldsymbol{\eta}}(t) + \underbrace{\boldsymbol{\Phi}^T \mathbf{K} \boldsymbol{\Phi}}_{\boldsymbol{\Omega}^2} \boldsymbol{\eta}(t) = \underbrace{\boldsymbol{\Phi}^T \mathbf{L}}_{\mathbf{L}_\Phi} \mathbf{f}(t) + \boldsymbol{\Phi}^T \mathbf{w}(t), \quad (5)$$

where \mathbf{I} is the identity matrix, $\boldsymbol{\Gamma}_0$ is the diagonal damping matrix, $\boldsymbol{\Omega}^2$ denotes the diagonal matrix of the squared natural frequencies. Finally, the equation can be expressed as follows:

$$\ddot{\boldsymbol{\eta}}(t) + \boldsymbol{\Gamma}_0 \dot{\boldsymbol{\eta}}(t) + \boldsymbol{\Omega}^2 \boldsymbol{\eta}(t) = \mathbf{L}_\Phi \mathbf{f}(t) + \boldsymbol{\Phi}^T \mathbf{w}(t) \quad (6)$$

2.2 Controllability of modes

A controllability measure is introduced in order to quantify how easily a mode can be controlled. The form of equation (6) allows the controllability measure of vibrational modes to be calculated before employing any joint model or proposing any control law. The controllability measure G_m of the m -th mode is defined as the ℓ_2 norm of the vector contained in the m -th row of the matrix \mathbf{L}_Φ :

$$G_m = \sqrt{\sum_{k=1}^{N_k} l_{\phi m k}^2} = \sqrt{\sum_{k=1}^{N_k} (\boldsymbol{\Phi}_m^T \mathbf{L}_k)^2} \quad (7)$$

The measure G_m is very simple and it provides information about the expected level of modal accelerations for mode m .

2.3 Mechanical model of the lockable joint

Lockable joints are usually friction-based. For the purpose of vibration attenuation, advanced friction models such as the LuGre model are used [7][11]. It is required for proper calculation of the dissipated energy. However, in this contribution, the lockable joints are not intended to dissipate energy, but rather to transfer the energy between the selected modes. The model of the joint considered here can be thus significantly simplified.

The locked state of the joint is modelled by a viscous damper of relative rotations with a large constant. In transient analysis, such a model simulates a rigid connection. The moment f_k in the k -th joint takes thus the form:

$$f_k = u_k c_{MAX} \dot{\phi}_k = -u_k c_{MAX} \mathbf{L}_k^T \dot{\mathbf{q}} \quad (8)$$

where $u_k \in \{0,1\}$ is the control signal that locks or unlocks the k -th lockable joint, c_{MAX} is a large viscous damping coefficient, and $\dot{\phi}_k$ is the relative angular velocity between the DOFs involved in the k -th lockable joint. Taking into account equation (4) and (8), formula (6) takes the following bilinear form:

$$\ddot{\boldsymbol{\eta}} + \boldsymbol{\Gamma}_0 \dot{\boldsymbol{\eta}} + \boldsymbol{\Omega}^2 \boldsymbol{\eta} = - \sum_{k=1}^{N_k} u_k \boldsymbol{\Gamma}_k \dot{\boldsymbol{\eta}} + \boldsymbol{\Phi}^T \mathbf{w} \quad (9)$$

$$\boldsymbol{\Gamma}_k = c_{MAX} \boldsymbol{\Phi}^T \mathbf{L}_k \mathbf{L}_k^T \boldsymbol{\Phi}$$

The terms under the sum in equation (9) couple the modal equations. The equation of motion of the m -th mode reads as follows:

$$\ddot{\eta}_m + 2\mu_m \omega_m \dot{\eta}_m + \omega_m^2 \eta = - \sum_{k,m=1}^{N_k, N_m} u_k \gamma_{mn}^{(k)} \dot{\eta}_n + \sum_{i=1}^{N_i} \phi_{mi} w_i \quad (10)$$

where $\gamma_{mn}^{(k)}$ denotes the m,n -th element of the matrix $\boldsymbol{\Gamma}_k$, and ϕ_{mi} is the i -th element of the m -th eigenvector. Coupling of modal equations by lockable joints allows the mechanical energy to be transferred between selected vibrational modes.

2.4 Energy transfer between the vibration modes

In this section, the physical basics on the modal energy transfer are presented. The total energy of the system V is equal to the sum of the kinetic and strain energies:

$$V = \frac{1}{2} (\dot{\mathbf{q}}^T \mathbf{M} \dot{\mathbf{q}} + \mathbf{q}^T \mathbf{K} \mathbf{q}). \quad (11)$$

Substituting equation (4) into equation (11) the total energy is represented by:

$$V = \frac{1}{2} \left(\dot{\boldsymbol{\eta}}^T \underbrace{\boldsymbol{\Phi}^T \mathbf{M} \boldsymbol{\Phi}}_{\mathbf{I}} \dot{\boldsymbol{\eta}} + \boldsymbol{\eta}^T \underbrace{\boldsymbol{\Phi}^T \mathbf{K} \boldsymbol{\Phi}}_{\boldsymbol{\Omega}^2} \boldsymbol{\eta} \right). \quad (12)$$

The matrices \mathbf{I} and $\boldsymbol{\Omega}^2$ are diagonal, therefore the total energy V is equal to the sum of the energies of each mode:

$$V = \sum_{m=1}^{N_n} V_m = \frac{1}{2} \sum_{m=1}^{N_n} (\dot{\eta}_m^2 + \omega_m^2 \eta_m^2). \quad (13)$$

From (13) it follows that if modal equations are coupled, then any modal energy can increase only at the expense of the other ones. Applying m -th modal energy differentiation its increase represented in watts is obtained:

$$\dot{V}_m = \dot{\eta}_m (\ddot{\eta}_m + \omega_m^2 \eta_m). \quad (14)$$

Respecting equation (10), the terms in brackets in (14) can be replaced by

$$\sum_{i=1}^{N_n} \phi_{mi} w_i - 2\mu_m \omega_m \dot{\eta}_m - \sum_{k,n=1}^{N_k, N_n} u_k \gamma_{mn}^{(k)} \dot{\eta}_n. \quad (15)$$

From (15) it follows that the increase of any m -th mode energy is equal to work performed by external forces reduced by dissipated energy in material damping and modified by term derived from coupling of the modal equations. The last term in (15), caused by modal equations coupling, is equal to the sum of energy transfers from all modes through each joint and is denoted by $\dot{\hat{V}}_m$. It is described in the formula below.

$$\dot{\hat{V}}_m = \sum_{k,n=1}^{N_k, N_n} \dot{\hat{V}}_{mn}^{(k)} = -\dot{\eta}_m \sum_{k,n=1}^{N_k, N_n} u_k \gamma_{mn}^{(k)} \dot{\eta}_n \quad (16)$$

Equation (16) refers to any mode m when vibrational modes are coupled.

Let us denote by p an index of mode selected to maximization. Then, function $\dot{\hat{V}}_p$ described analogously to formula (16) becomes the objective function which is to be maximized at each time instance. It is studied in detail in the following section.

3 INVERSE LYAPUNOV BASED METHOD FOR SEMI-ACTIVE CONTROL

The semi-active control strategy is called “*inverse Lyapunov based method*” since some ingredients of the total energy are to be maximized while traditionally only minimization is pursued. Joint can take two states in the assumed model: locked and unlocked. It follows that the control has the bang-bang form. In the last section, it has been shown that for the free vibration, the energy of a selected mode can increase only at the expense of the others. The controller is of the semi-active type, and thus the energy transfer imposed by maximization of the target mode p cannot destabilize the system [10].

3.1 Instantaneous optimal semi-active control law

The instantaneous optimality has been pursued by maximization p -th modal energy increase at each time instant, namely:

$$\mathbf{u}^* = \arg \max_{\mathbf{u} \in U} \dot{\hat{V}}_p, \quad (17)$$

In (17), p – is the index of maximized mode $\mathbf{u} = [u_k \ \cdots \ u_{N_k}]^T$, $U = \{0,1\}^{N_k}$ – is the set of admissible controls. The substitution of equation (16) into equation (17) yields:

$$\mathbf{u}^* = \arg \min_{\mathbf{u} \in U} \dot{\eta}_m \sum_{k,n=1}^{N_k, N_n} u_k \gamma_{mn}^{(k)} \dot{\eta}_n. \quad (18)$$

Formula (18) can be written in the following matrix form:

$$\mathbf{u} = \arg \min_{\mathbf{u} \in U} \dot{\eta}_p \sum_{k=1}^{N_k} u_k \mathbf{\Gamma}_{k,p\text{-th row}} \dot{\mathbf{\eta}}. \quad (19)$$

From equation (19) it follows that it is profitable to lock the k -th joint when energy transfer through this join is positive. Otherwise, it is supposed to be unlocked:

$$u_k = \begin{cases} 0, & \text{when: } \dot{\eta}_p \mathbf{\Gamma}_{k,p\text{-th row}} \dot{\mathbf{\eta}} > 0 \\ 1, & \text{when: } \dot{\eta}_p \mathbf{\Gamma}_{k,p\text{-th row}} \dot{\mathbf{\eta}} < 0 \end{cases}. \quad (20)$$

The control law as in (20) requires that the modal velocities must be measured globally but each lockable joint can be controlled independently on each other. It is valuable property for large-scale structures, since each joint can have an individual controller.

In general, the matrices $\mathbf{\Gamma}_k$ are coupling all modes. It follows that any joint locked in a suitable instant can excite a broad range of vibrational modes including higher ones. Participation of higher modes can cause high frequency lockable joins switching. Furthermore, in real situation, the actuators in lockable joints may have some time delays, and thus, the control of the higher modes may not be feasible. This problem can be solved by applying the measurement with so called modal filtering, which is required to measure modal velocities. The higher vibration modes can be rejected during this process.

3.2 Measurements – sensor placement and modal filtering

In this section, the method for measurement employing the modal filtering is presented. The modal filtering is used to extract modal velocities from the measured motion of the structure. This technique has been initially proposed by Meirovitch [12] to reduce the effect of observation spillover in actively controlled systems. Mode shapes of the controlled structure need to be known a priori. When a limited number of sensors is used in measurement, the so called spatial aliasing arises of the measured modes with the higher modes [13]. In order to avoid it, in the first step, the sensor placement optimisation should be performed. In the second step, the matrix extracting modes participation from sensor data is designed.

Step I – sensor placement. In this contribution, sensor placement optimization is to select the sensor locations from a candidate set (nodes of the FE mesh) for which the determinant of

the Fisher information matrix achieves the maximum value. This method has been verified in many works, e.g., in modal identification [14] and structural damage identification [15]. Maximization of the norm of the Fisher information matrix minimizes the norm of the covariance matrix of the error between the real values of measured modal coordinates and the estimated ones when gaussian, uncorrelated noise affects the measurement. This property also allows avoiding influence of the higher modes on the accuracy of the measurement. The sensor placement satisfies the following equation:

$$I_S^* = \arg \max_{I_S \subset I_{\text{DOF}}} \det(\hat{\Phi}^T \hat{\Phi}), \quad (21)$$

where $I_S = \{i_1, i_2, \dots, i_S\}$ is the searched set of locations (indices of the FE model DOFs), which is a subset of all possible locations I_{DOF} , S is the number of sensors, $\hat{\Phi} = \hat{\Phi}(i_1, i_2, \dots, i_S)$ is the matrix that contains i_1, i_2, \dots, i_S rows of the modal matrix and the columns related to the measured modes. Matrix $\hat{\Phi}$ for the optimal placement of sensors is denoted by $\hat{\Phi}_{\text{opt}}$.

Step II – weighted matrix design. The weighted matrix \mathbf{F}_ϕ is computed taking into account the orthogonality criteria. The rows of \mathbf{F}_ϕ should be vectors as close to vectors of matrix $\hat{\Phi}_{\text{opt}}$ as possible and they simultaneously should be orthogonal to the eigenvectors of the unmeasured modes (known from the mathematical model). Some compromise is required to satisfy these criteria. The computation is performed in two steps:

1. Solving least-squares problem for each row of the matrix \mathbf{F}_ϕ :

$$\bar{\mathbf{F}}_\phi = \arg \min \left\| \tilde{\Phi}_{\text{opt}}^T \tilde{\mathbf{F}}_\phi^T - \tilde{\mathbf{I}} \right\|_F, \quad (22)$$

where $\tilde{\Phi}_{\text{opt}}$ arises from the matrix $\hat{\Phi}_{\text{opt}}$ by attaching additional columns related to the unmeasured modes, $\tilde{\mathbf{I}}$ is the identity matrix with attached rows of zeros to obtain a proper size, and $\|\cdot\|_F$ is Frobenius norm.

2. Rows of $\bar{\mathbf{F}}_\phi$ are scaled by coefficients to obtain the matrix \mathbf{F}_ϕ that fulfils the condition that each element on the diagonal of $\mathbf{F}_\phi \hat{\Phi}_{\text{opt}}$ is equal to one.

The measured modal velocities $\dot{\mathbf{q}}_M = [\dot{q}_{M1} \ \dots \ \dot{q}_{MN_F}]^T$ are given by:

$$\dot{\mathbf{q}}_M = \mathbf{F}_\phi \underbrace{\tilde{\Phi}_{\text{opt}}}_{\dot{\mathbf{q}}_M} \dot{\mathbf{q}} \quad (23)$$

Here $\dot{\mathbf{q}} = [\dot{q}_{i_1^*} \ \dots \ \dot{q}_{i_S^*}]^T$ is the vector of data collected from sensors, $\{i_1^*, i_2^*, \dots, i_S^*\} = I_S^*$. The control law taking into account the measurement process is as follows:

$$u_k = \begin{cases} 0, & \text{when: } \dot{q}_{Mp} \mathbf{\Gamma}_{k,p\text{-th row}}^M \dot{\mathbf{q}}_M > 0 \\ 1, & \text{when: } \dot{q}_{Mp} \mathbf{\Gamma}_{k,p\text{-th row}}^M \dot{\mathbf{q}}_M < 0 \end{cases} \quad (24)$$

In (24), $\mathbf{\Gamma}_{k,p\text{-th row}}^M$ is of the size $1 \times N_F$.

4 NUMERICAL EXAMPLES

The proposed inverse Lyapunov method for semi-active control has been examined on a three-bar structure. The beams of this structure are connected by means of two lockable joints as demonstrated in Figure 2.

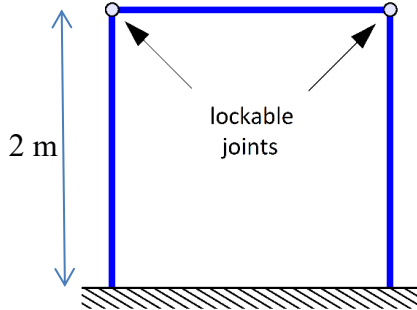


Figure 2: The considered structure with lockable joints

Table 1: Physical parameters of the controlled structure

Young modulus (steel)	E [Pa]	$210 \cdot 10^9$
Material density (steel)	ρ [$kg\ m^{-3}$]	7860
Cross section area (square)	A [m^2]	10^{-4}
Moment of inertia	I [m^4]	$8,33 \cdot 10^{-10}$

The vertical beams are clamped in the ground. For the beam model, we assume small deflections and employ the Euler–Bernoulli beam equation. The assumed parameters of the structure are summarized in table 1.

We consider two FE models of structure. The first one is to justify the semi-active modal control and the second one is to demonstrate the influence of the higher vibration modes on measurement. Each of the presented simulation has been performed by using the Newmark integration method.

4.1 Illustrative 5-DOF FE model

In this example, the model consists of only one FE element per beam to clearly show the basic properties of the presented semi-active control method. The employed finite elements have cubic shape functions. In such a case, the entire model has only five DOFs: 1 horizontal displacement of the top beam and 4 rotational DOFs of beam ends in the lockable joints. There are also 5 vibrational modes which have natural frequencies listed in Table 2 and the shapes shown in Figure 3.

Table 2: Natural frequencies of the considered structure

No.	Natural frequency ω_m [Hz]	Time period T_m [s]
1	1.198	0.835
2	6.504	0.154
3	12.168	0.083
4	13.678	0.073
5	29.804	0.034

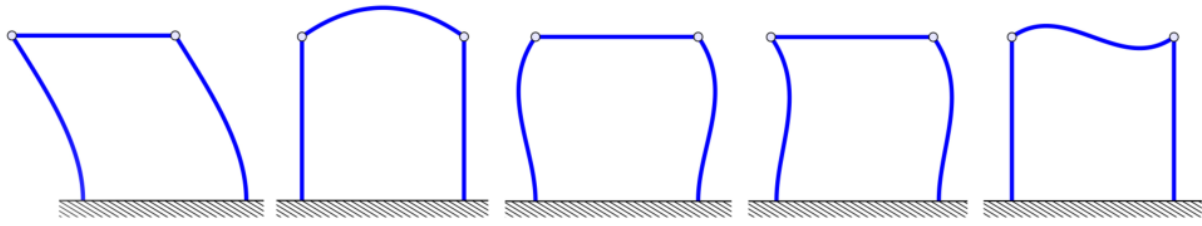


Figure 3: Mode shapes for the 5-DOF model

The controllability measure G_m for each mode is shown in the form of a bar plot in Figure 4.

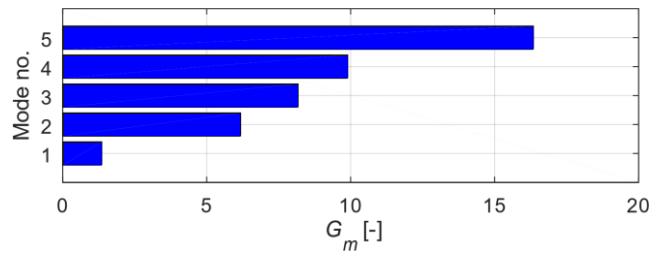


Figure 4: Controllability measure for the modes of the 5-DOF model

The initial condition is defined by the potential (strain) energy: $0.5 J$ in the second mode and $0.5 J$ in the third mode. The case of a free vibration is considered. The fourth vibrational mode is the target mode, with its energy to be maximized. The time histories of the control signals u_k , the modal energies V_m and the modal coordinates η_m are shown in Figure 5.

The first (left) joint is locked immediately at the beginning of the simulation. It results in excitation of all 5 vibrational modes, but after a short time the most pronounced is the target (fourth) mode. Notice that the modal energies change only when at least one joint is locked.

The stepwise changes of the total energy V and the modal energies V_m are the results of a small number of FE elements per beam. A beam with only one relatively massive FE element cannot immediately bend in the way which should follow from the action of the joints; the beam ends rotate thus during joint lock, which results in a slight local energy dissipation. This problem disappears in the model with a finer mesh of FE elements.

4.2 Refined 23-DOF FE model

Next example concerned three-bar structure discretized with 4 elements per beam resulting in 23 DOFs. Damping of 1.5% of critical value for each mode was assumed. First 3 modal velocities were measured with aid of 7 sensors. Measurement signals were subjected to the process of modal filtering. Optimization of sensors placement and filter design was performed according to the procedure described in subsection 3.2.

Numerical simulation of energy transfer has been performed for the structure with initial strain energy of the 2nd mode equal to $1 J$. The structure was released from the initial state performing free vibration. The goal of the control was maximization of energy in the first vibration mode. Time histories of control signals u_k , modal energies V_m and corresponding modal coordinates η_m are shown in Figure 6.

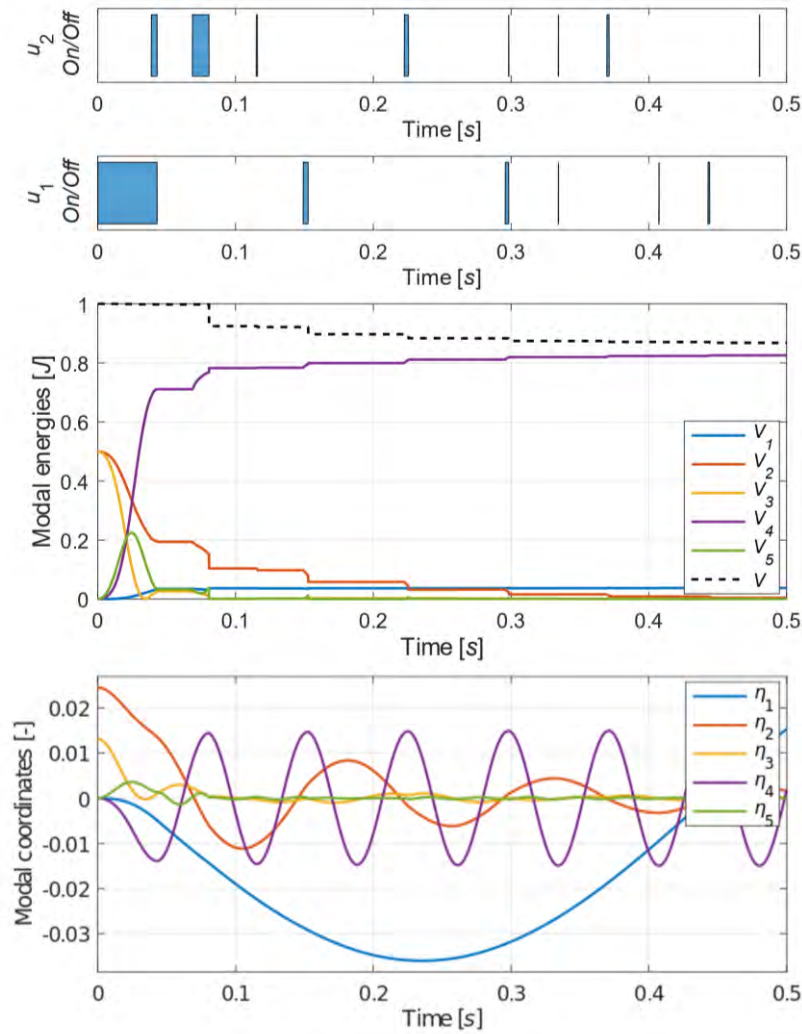


Figure 5: Time histories of the control signals (blue colour means ON), modal energies, modal coordinates

It was assumed that data coming from sensors is not filtered in time domain, so even with modal filtering the influence of higher modes is visible. It resulted in high frequency of oscillation of the control signal. This problem can be avoided by applying e.g. low pass filter or predictor within the control algorithm, which can check averaged energy transfer in finite time horizon and based on this information make decision about locking or unlocking of joint under consideration.

Numerical results in Figure 6 show that presented semi-active modal control is efficient even when limited set of modes is measured – only three modes in this case. It is valuable property for many realistic structures.

Dissipation rate of the total energy V changes during control process, because different modes – with different damping – are excited by lockable joints. This phenomenon is undesirable in the case of energy-harvesters. When targeted mode (the first one) has dominant participation energy dissipation is slower.

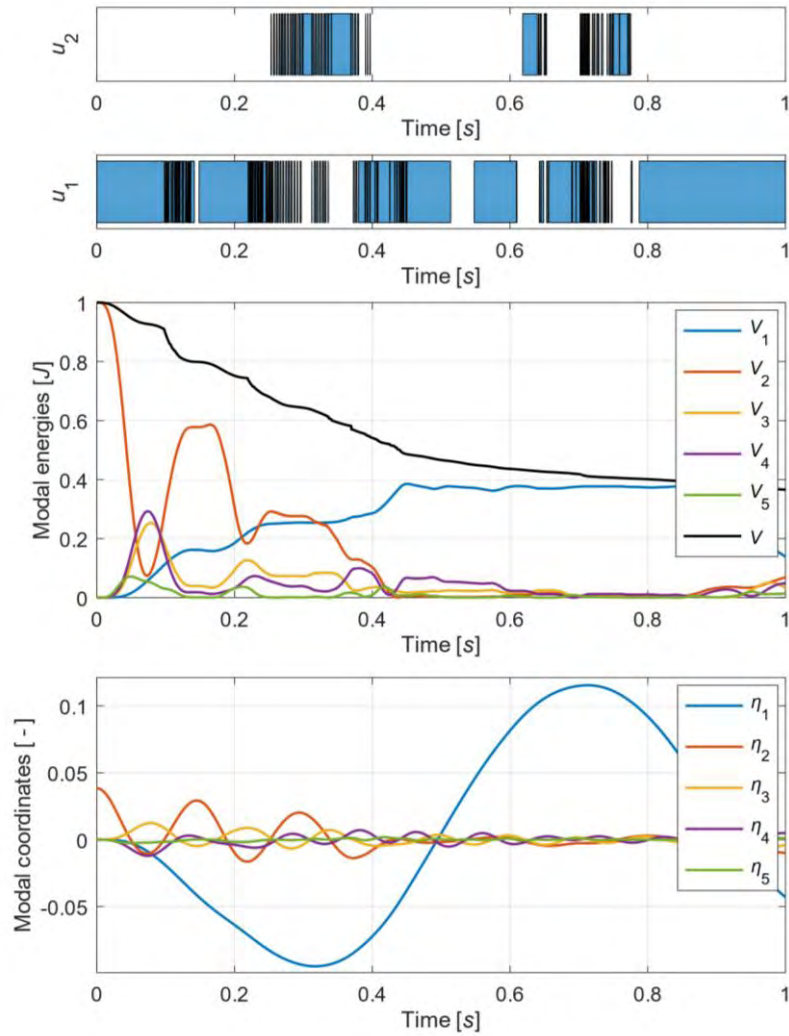


Figure 6: Time histories of the: control signals (blue colour means ON), first five modal energies, first five modal coordinates

5 CONCLUSIONS

This contribution proposes a semi-active control approach for energy transfer between vibrational modes of a frame-like structure. The control method is based on an instantaneous maximization of the momentary energy transfer to the target mode and the other modes. It is implemented by means of a specific actuator that takes the form of a lockable joint, which allows a controllable imposition and configuration of structural constraints. Effectively, such a joint allows the bending moment to be transferred between the adjacent structural elements to be controlled according to the control signal. The work is ongoing mainly to (1) include a more physical models of actuators and to avoid the chattering effect, (2) perform experimental verification, and (3) include energy harvesting devices (dissipators).

ACKNOWLEDGEMENT

The authors gratefully acknowledge the support of the National Science Centre, Poland, granted under grant agreements DEC-2017/25/B/ST8/01800 and DEC-2017/26/D/ST8/00883.

REFERENCES

- [1] Alkhatib, R. and Golnaraghi, M. Active Structural Vibration Control: A Review. *The Shock and Vibration Digest* (2003) **35**:367–383.
- [2] Dhanda, A. and Franklin, G.F. Optimal Control Formulations of Vibration Reduction Problems. *IEEE Transactions on Automatic Control* (2010) **55**(2):378–394.
- [3] Wei, C. and Jing, X. A comprehensive review on vibration energy harvesting: Modelling and realization. *Renewable and Sustainable Energy Reviews* (2017) **74**:1–18.
- [4] Inaudi J.A. Modulated homogeneous friction: a semi-active damping strategy. *Earthquake Engineering & Structural Dynamics* (1997) **26**(3):361–376.
- [5] Muhammad A., Yao, X. and Deng Z. Review of magnetorheological (MR) fluids and its applications in vibration control. *Journal of Marine Science and Application* (2006) **5**(3):17–29.
- [6] Laflamme, S., Taylor, D., Abdellaoui Maane, M. and Connor, J.J. Modified friction device for control of large-scale systems. *Structural Control and Health Monitoring* (2012) **19**(4):548–564.
- [7] Gaul, L. and Nitsche, R. Vibration Control by Interface Dissipation in Semi-Active Joints. *ZAMM – Journal of Applied Mathematics and Mechanics / Zeitschrift für Angewandte Mathematik und Mechanik* (2000) **80**:45–48.
- [8] Poplawski, B., Mikułowski, G., Mróz, A. and Jankowski, Ł. Decentralized semi-active damping of free structural vibrations by means of structural nodes with an on/off ability to transmit moments. *Mechanical Systems and Signal Processing* (2018) **100**:926–939.
- [9] Lu, L.Y. Semi-active modal control for seismic structures with variable friction dampers. *Engineering Structures* (2004) **26**: 437–454.
- [10] Pisarski, D. Decentralized stabilization of semi-active vibrating structures. *Mechanical Systems and Signal Processing* (2018) **100**:694–705.
- [11] Wirnitzer, J., Kistner, A. and Gaul, L. Optimal placement of semi-active joints in large-space truss structures. Proc. SPIE 4697, Smart Structures and Materials 2002: Damping and Isolation (27 June 2002).
- [12] Meirovitch, L. and Baruh, H. Control of self-adjoint distributed-parameter systems. *Journal of Guidance, Control, and Dynamics* (1982) **5**(1):60–66.
- [13] Preumont, A., François, A., Man, P.D. and Piefort, V. Spatial filters in structural control. *Journal of Sound and Vibration* (2003) **265**(1):61–79.
- [14] Stephan, C. Sensor placement for modal identification. *Mechanical Systems and Signal Processing* (2012) **27**(1):461–470.
- [15] Hou, J., Li, Z., Zhang, Q., Zhou, R. and Jankowski, Ł. Optimal placement of virtual masses for structural damage identification. *Sensors* (2019) **19**(2):340.

SEMI-ACTIVE DECENTRALIZED MITIGATION OF RANDOMLY EXCITED VIBRATIONS IN 2D FRAME STRUCTURES

B. POPLAWSKI, G. MIKUŁOWSKI AND Ł. JANKOWSKI

Institute of Fundamental Technological Research, Polish Academy of Sciences

Pawińskiego 5B, 02-106 Warsaw, Poland

e-mail: bpop@ippt.pan.pl, gmikulow@ippt.pan.pl, ljank@ippt.pan.pl

Key words: Semi-active Damping, Vibration Damping, Random Vibration, Forced Vibration

Abstract. Semi-active control systems are investigated for more than 40 years [1, 2], and despite the great progress in this research area, they are still considered to be a complex topic in both theoretical and technical terms. However, their advantages ensure that these control systems remain an extremely attractive subject of scientific and technological development.

In this contribution, we present a semi-active strategy for mitigation of vibration, which utilizes an energy management approach called Prestress-Accumulation Release [3] and is based on controllable activation and removal of selected structural constraints. Here, it is implemented by means of controllable structural nodes of a specific design that allow the transmission of moments between adjacent structural elements to be controlled in an on/off manner. The developed control strategy turned out to be very effective in damping of free structural vibrations of planar frame structures [4]. Extension of the research to other types of vibrations has shown that the proposed control algorithm is versatile and stays efficient in a range of applications and different configurations of the investigated structures. This work is focused on mitigation of vibrations excited by a randomly generated force load.

Decentralization, understood here as controlling the employed actuators based on locally measured structural response [5], results in a decisive reduction of the complexity of the data acquisition and control systems, which is crucial for actual implementations in real structures, and which facilitates an ad hoc reconfiguration and expansion of the control system if necessary. It also provides the possibility of considering selected structural elements as separate energy dissipative devices, which in our approach act effectively as vibration dampers. This feature, provided by the decentralization, enables to take the advantage of two complementary, interrelated mechanisms of material damping: global dissipation of vibration energy by the PAR and local dissipation in single involved elements.

Numerical and experimental analyses indicate a high degree of effectiveness in alleviation of the amplitude of vibrations induced by a random transient force excitation. The proposed control strategy can be thus utilized not only in the case of momentary impulsive loads that result in predominantly free vibrations [4], but also in the case of transient random force excitation. It significantly extends the range of possible modes of operation of a structure equipped with the proposed damping system.

1 INTRODUCTION

The wide range of possible applications and ways of implementation makes semi-active vibration control systems a very attractive subject of engineering and scientific considerations. Such an approach

to control is recently becoming more and more popular, as evidenced by the ever-growing number of publications on the subject. Applications have been studied in a large number of engineering fields, such as suspension bridges [6], vehicle seat suspension [7], seismic response reduction [9], wind turbines under wind, wave and earthquake loads [10], rotating machinery drivetrains [11], landing gears [12], and many others. The technologies used are also diverse, i.e., MR fluids [8], tuned mass dampers [10], MEMS [13], special valves controlling the fluid flow between two absorber chambers [14], etc.

Semi-active vibration damping systems bridge the gap between passive and active damping systems. They make use of active force generation, but only to the extent necessary to enable the structure to adapt itself in a way that would lead to the mitigation of vibration energy. Such a design philosophy causes semi-active vibration damping systems to be generally very reliable. High reliability is a property that brings semi-active systems close to passive systems. The efficiency of a well-designed semi-active vibration damping system can be comparable to the active one, but the main advantage of the semi-active control systems, over the active ones, is their very low demand for the energy. However, these advantages are usually achieved at the cost of a much higher level of the technical and theoretical complexity.

Semi-active control systems typically employ a technique of reconfiguration of the controlled system to achieve the desired dynamic behavior. This could be, for example, a temporary “freezing” of a certain deformation in a selected part of the system in order to resist the inertial forces. Another approach may be to temporarily reconfigure the system to change its mechanical characteristics, such as effective stiffness [3] or, as often related to a change in stiffness, the number of the degrees of freedom.

One of the simplest ways to achieve such a goal is to utilize piezoelectric stacks in bolted joint connections [15]. It allows the normal pressure between the joint interfaces to be controlled so that control of the rotational motion of the structural members can be achieved. The approach pursued here is similar, but the energy dissipation mechanism is focused on global and local dissipation in beams rather than exclusively on local friction-based dissipation in controllable joints. The presented work is focused on vibration mitigation of 2D frame structures with the use of some especially designed semi-active nodes which can switch their state of operation from frame-like to truss-like on demand in a matter of milliseconds. When used in pairs, as joints connecting selected beams to the rest of the structure, they allow the developed control algorithm to be utilized in order to mitigate structural vibrations.

The effectiveness of the proposed algorithm in mitigation of vibrations turned out to be very high for free structural vibrations [4]. This contribution briefly presents the performance of the control algorithm in the case of randomly excited vibrations. Its effectiveness is confirmed both numerically and experimentally.

2 NUMERICAL MODEL OF THE SEMI-ACTIVE NODE

The mathematical model of the semi-active node used to simulate its behavior has been selected based on the criterion of the ease of implementation in numerical calculations. The cost of its simplicity is that its applications are limited to dynamic simulations only.

Numerical model of the considered structure consists of beam finite elements with three degrees of freedom (DOFs) in each node. Typically, the appropriate local DOFs in the coinciding nodes are aggregated to the same global DOF, but in order to create a semi-active node, a different procedure of aggregation is pursued: The translational DOFs are aggregated in the same way as in the typical finite element model; however, the rotational DOFs have to be uncoupled. It is achieved by employing additional rotational DOFs in the nodes that are turned into semi-active ones. In this way, the selected nodes have four global DOFs: two translational and two rotational. The two rotational DOFs are then coupled to each other with a rotational damper with a controllable, high damping coefficient, which

prevents their relative movement in transient, dynamic simulations. The described technique leads to the following equation of motion:

$$\mathbf{M}\ddot{\mathbf{x}}(t) + \left(\mathbf{C} + \sum_{i=1}^N \gamma_i(t) \mathbf{C}_i \right) \dot{\mathbf{x}}(t) + \mathbf{K}\mathbf{x}(t) = \mathbf{f}(t) \quad (1)$$

where \mathbf{M} is the mass matrix of the structure, \mathbf{C} is the damping matrix and \mathbf{K} is the stiffness matrix. All of them include the additional rotational DOFs. The vector of external forces applied to the structure is denoted by \mathbf{f} and γ_i is the control function which is responsible for coupling and uncoupling the rotational DOFs in the i th semi-active node. When γ_i is set to 0, the node is in its truss-like state in which it does not transfer any moments. When γ_i is set to a value large enough, then the semi-active node is in its frame-like state with the maximum moment transfer capability. The matrices \mathbf{C}_i model the rotational relative dampers which in the 2D case are of the following form:

$$\mathbf{L}_i^T \begin{bmatrix} 1 & -1 \\ -1 & 1 \end{bmatrix} \mathbf{L}_i \quad (2)$$

where \mathbf{L}_i are the global–local transformation matrices.

Such an approach does not introduce any non-linearity into the numerical model, which greatly facilitates the theoretical investigations, control and the simulation of the dynamic behavior of the structure.

3 CONTROL ALGORITHM

The control algorithm is designed to mitigate various types of vibrations, such as free vibrations and vibrations excited by a harmonic or a random force. The structures, for which it is best suited, are frames with slender elements, such as the one presented in Figure 1.

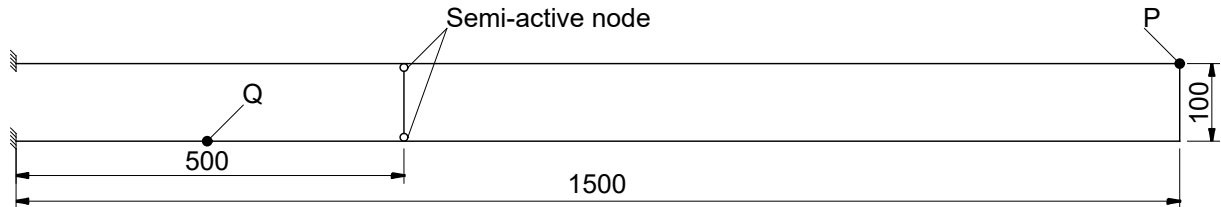


Figure 1: Exemplary frame structure equipped with semi-active nodes

The semi-active nodes are used pairwise, on two ends of selected beams. The control algorithm uses the (strain-based) measurements of the potential energy accumulated in the beams. It indicates the point in time, when the state of operation of the semi-active nodes shall be switched from their default frame-like state to the truss-like state, in which the relative in-plane rotation of the beams joined in the node is temporarily allowed. The switching takes place when the strain energy achieves its local maximum. The energy is measured only locally in selected parts of the controlled structure, for example in the single beam between the nodes.

Such a control strategy is completely local, but it affects the entire structure. Instantaneous local reconfiguration of the structure results in the excitation of the high-frequency vibration modes, which are usually very efficiently damped by means of the standard mechanisms of material damping. The same logic of transferring the energy from low-frequency to high-frequency vibration modes, however at the global level and based on global measurements, was introduced in [16], where it was named the Prestress–Accumulation Release (PAR) strategy.

Knowing the general characteristics of the globally optimal open-loop control, derived with the Pontryagin's minimum principle, which is of the bang-bang type, a heuristic control algorithm has been proposed in [4] for mitigation of vibrations. It can be briefly described in the three simple steps:

1. Semi-active nodes are in their default frame-like state as long as the local strain energy (for example of the involved beam) raises due to the growing deflections of the structure.
2. When the local maximum of the measured energy is achieved, the nodes switch to the truss-like state, in which they do not transfer any moments (only normal and shear forces are transferred).
3. When certain conditions are met, nodes are switched back to their default frame-like state of operation.

The period of time for which the semi-active node stays in truss-like state can be determined on the basis of different conditions. For example, it can be:

1. an arbitrarily set percentage decrease of the strain energy or simply
2. a predetermined period of time.

The first condition seems the most intuitive indicator of the coupling moment of the rotational DOFs in a semi-active node. The condition refers directly to the current state of the controlled object and it can be easily calculated in numerical simulations. However, in the case of a real structure, the condition becomes problematic: the strain energy can be only approximated in terms of the signal obtained from strain gauges, and the high frequency of the induced local vibrations would require a very fast control system. In such a case, the second condition can be used, and it was shown that the control algorithm remains effective over a wide range of time in which the nodes remain open [4]. It can be also utilized as an additional safety condition, in order to avoid long-term weakening of the structure in case of a failure of the data acquisition system. Maintaining the high efficiency of vibration mitigation over a wide range of time period, when the semi-active nodes stay in the truss-like state, in conjunction with the second condition, is very significant for experimental research. Due to some delays in data acquisition and processing, as well as the inertia of piezoelectric stacks and semi-active node casings, the control algorithm is characterized by a certain time shift. Thanks to the aforementioned feature, it is possible to achieve good damping performance even with these control delays.

4 NUMERICAL SIMULATION

Numerical analyses were conducted for the structure presented in Figure 1. It is a slender planar frame, made of steel beams with a cross-section of 5x5 [mm] each, equipped with two semi-active nodes, which make the middle vertical beam a dissipative device. The DOFs of the left-hand side nodes of the frame are fixed, while the exciting force, which is applied at point Q, is a realization of the white noise process with an appropriate amplitude.

The comparison of the results obtained when the control algorithm is activated (controlled, semi-active case) and when it is turned off (passive case) is presented in Figure 2. The graph presents the comparison of the vertical tip displacements in time of the investigated structure (point P in Figure 1). It is clearly visible that the vibration mitigation algorithm is effective even when the exciting force is random. In this case, the mean amplitude of the absolute value of the tip displacement is reduced by almost 25%. The displacement amplitude is reduced, when compared to the passive case, almost in the entire time range of simulation.

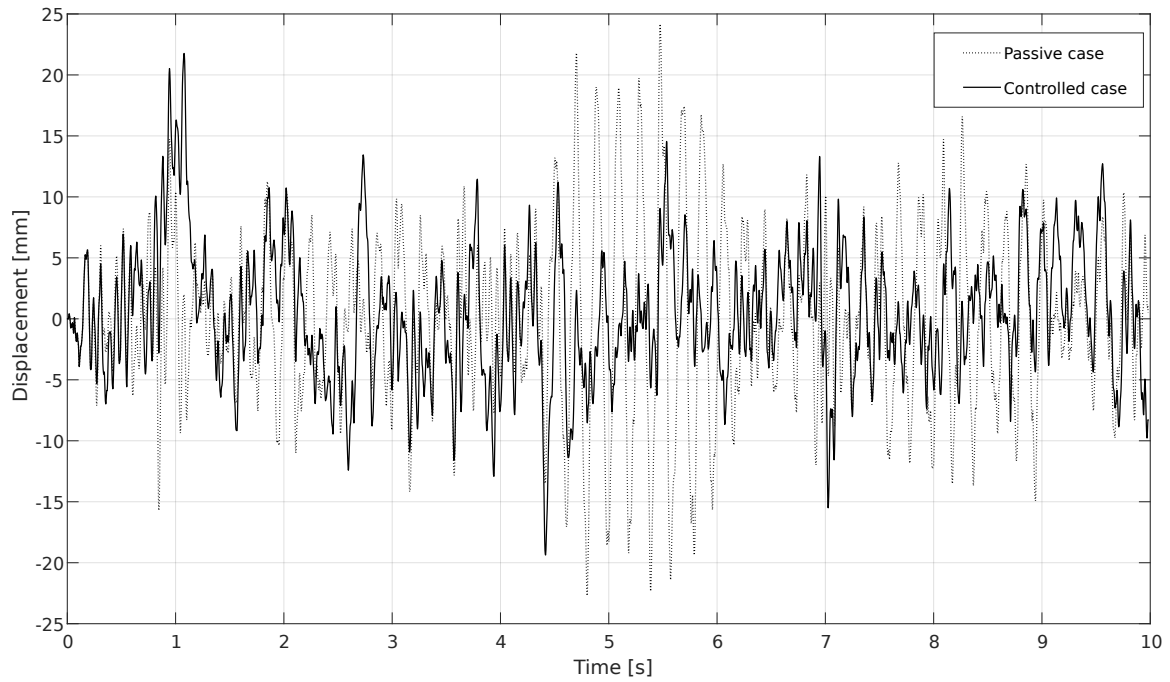


Figure 2: Time courses of the vertical tip displacements of the investigated structure

The results obtained in numerical simulations are very promising. Together with the previously investigated cases of free and harmonic vibrations, they confirm the effectiveness of the proposed control algorithm in a wide variety of structural load conditions.

5 EXPERIMENTAL RESULTS

The effectiveness of the control approach was also studied experimentally. The investigated lab frame structure is presented in Figure 3. The geometry is not exactly the same as in the numerical simulations, but the overall topology resembles the numerical case very closely.

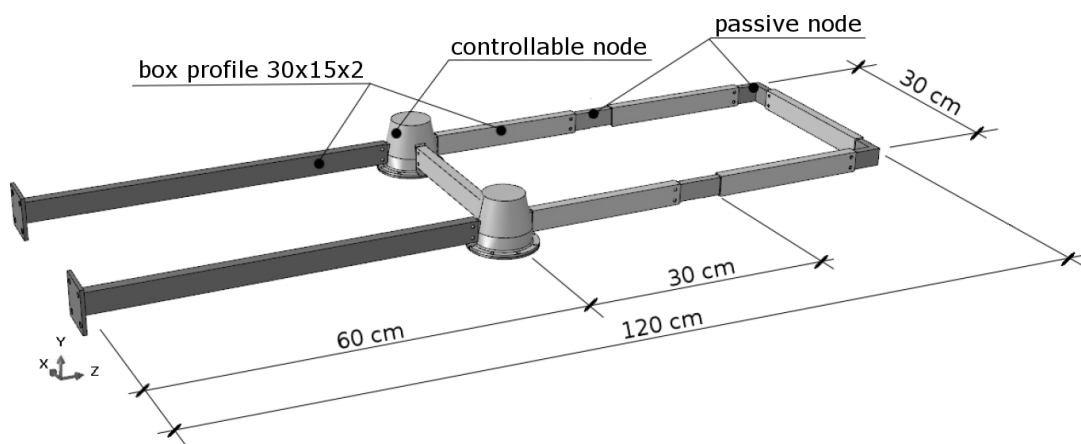


Figure 3: Geometry of the experimental stand

Similarly as in the computer simulation, a random force load is applied in the midpoint of the lower horizontal beam to the left of the semi-active node.

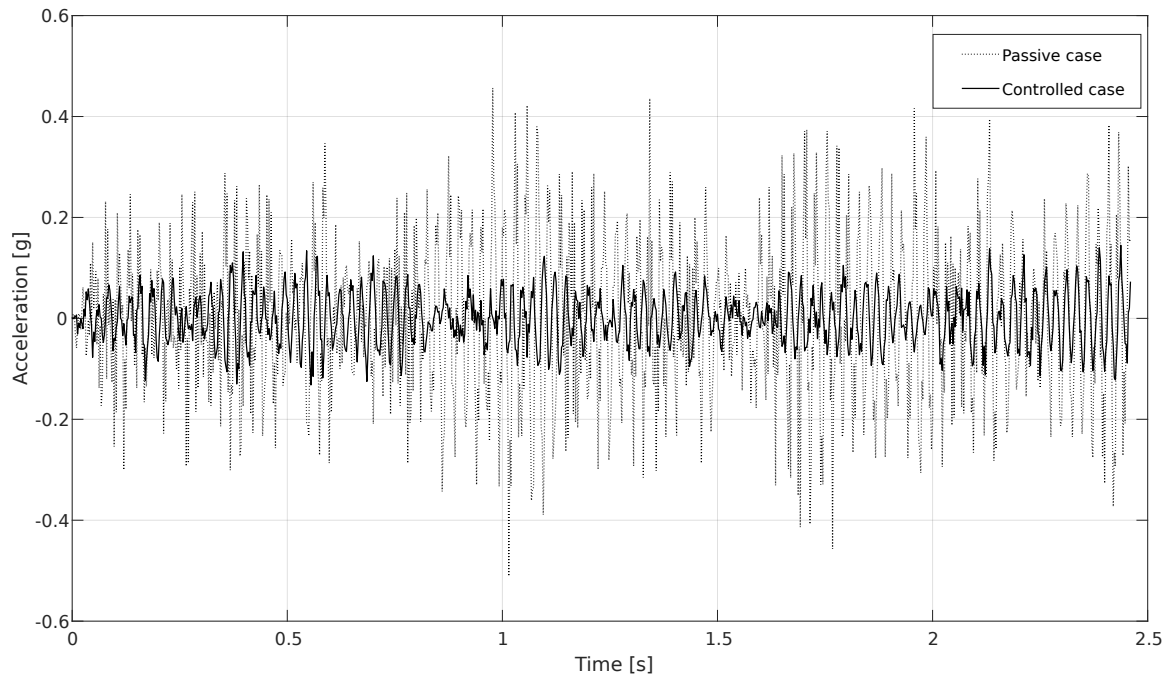


Figure 4: In-plane accelerations of the tip: experimental results

The data presented in Figure 4 are the time courses of the in-plane frame tip accelerations. Even a superficial observation indicates that the obtained result is very good. Application of the control algorithm significantly reduces the tip accelerations in the entire time range. The presented comparison of the dynamic response of the examined real structure is even better than in the numerical analyses.

6 CONCLUSIONS

This work investigates the problem of semi-active mitigation of vibration by local structural reconfiguration. The scope of applicability of a previously proposed control algorithm has been extended to new cases beyond free vibrations. The effectiveness of the proposed algorithm for random force excitation has been confirmed numerically and, more importantly, experimentally.

The results obtained show that the created control algorithm is versatile and at the same time it remains effective in all investigated cases of vibration mitigation. Experimental analyses are promising and allow to believe in successful implementation of such vibration damping systems in real engineering structures.

ACKNOWLEDGMENTS

The authors gratefully acknowledge the support of the National Science Centre, Poland, granted under grant agreements DEC-2017/25/B/ST8/01800 and DEC-2017/26/D/ST8/00883.

REFERENCES

- [1] Hurlebaus, S. and Gaul, L. Smart structure dynamics. *Mechanical Systems and Signal Processing* (2006) **20**:255–281.

- [2] Casciati, F., Rodellar, J. and Yildirim, Y. Active and semi-active control of structures—theory and applications: A review of recent advances. *Journal of Intelligent Material Systems and Structures* (2012) **23**(11):1181–1195.
- [3] Mróz, A., Orłowska, A. and Holnicki-Szulc, J. Semi-active damping of vibrations. Prestress Accumulation-Release strategy development. *Shock and Vibration* (2010) **17**:123–136.
- [4] Poplawski, B., Mikułowski, G., Mróz, A. and Jankowski, Ł. Decentralized semi-active damping of free structural vibrations by means of structural nodes with an on/off ability to transmit moments. *Mechanical Systems and Signal Processing* (2018) **100**:926–939.
- [5] Pisarski, D., Decentralized stabilization of semi-active vibrating structures. *Mechanical Systems and Signal Processing* (2018) **100**:694–705.
- [6] Abdel-Rohman, M. and John, M.J. Control of wind-induced nonlinear oscillations in suspension bridges using a semi-active tuned mass damper. *Journal of Vibration and Control* (2006) **12**(10):1049–1080.
- [7] Ning, D., et al. Vibration control of an energy regenerative seat suspension with variable external resistance. *Mechanical Systems and Signal Processing* (2018) **106**:94–113.
- [8] Weber, F. Semi-active vibration absorber based on real-time controlled MR damper. *Mechanical Systems and Signal Processing* (2014) **46**:272–288.
- [9] Nguyen, X.B., Komatsuzaki, T., Iwata, Y. and Asanuma, H. Modeling and semi-active fuzzy control of magnetorheological elastomer-based isolator for seismic response reduction. *Mechanical Systems and Signal Processing* (2018) **101**:449–466.
- [10] Sun, C. Semi-active control of monopile offshore wind turbines under multi-hazards. *Mechanical Systems and Signal Processing* (2018) **99**:285–305.
- [11] Michajłow, M., Jankowski, Ł., Szolc, T. and Konowrocki, R. Semi-active reduction of vibrations in the mechanical system driven by an electric motor. *Optimal Control Applications & Methods* (2017) **38**(6):922–933.
- [12] Mikułowski, G. and Jankowski, Ł. Adaptive landing gear: Optimum control strategy and potential for improvement. *Shock and Vibration* (2009) **16**(2):175–194.
- [13] Rojas, R.A. and Carcaterra, A. An approach to optimal semi-active control of vibration energy harvesting based on MEMS. *Mechanical Systems and Signal Processing* (2018) **107**:291–316.
- [14] Graczykowski, C. and Faraj, R. Self-adaptive fluid-based absorbers for impact mitigation and vibration damping. *Proceedings of ISMA 2018 – International Conference on Noise and Vibration Engineering and USD 2018 – International Conference on Uncertainty in Structural Dynamics* (2018):217–228.
- [15] Gaul, L., Lenz, J. and Sachau, D. Active damping of space structures by contact pressure control in joints. *Mechanics of Structures and Machines* (1998) **26**(1):81–100.
- [16] Mróz, A., Holnicki-Szulc, J. and Biczuk, J. Prestress Accumulation–Release technique for damping of impact-born vibrations: Application to self-deployable structures. *Mathematical Problems in Engineering* (2015) 720236.

SMA-BASED MULTI-MODAL ADAPTIVE TMDs: MODEL AND TESTS

M. BERARDENGO^{*}, G.E.P. DELLA PORTA[†], S. MANZONI[†] AND M. VANALI^{*}

^{*} Department of Engineering and Architecture
Università degli Studi di Parma
Parco Area delle Scienze 181/A, 43124 Parma, Italy
e-mail: marta.berardengo@unipr.it – marcello.vanali@unipr.it

[†] Department of Mechanical Engineering
Politecnico di Milano
Via La Masa 34, 20156 Milan, Italy
email: stefano.manzoni@polimi.it

Key words: Tuned Mass Damper, Adaptive Control, Smart Structures, Vibrations, Shape Memory Alloys.

Abstract. This paper describes the layout of an innovative adaptive tuned mass damper based on shape memory alloys able to change more than one eigenfrequency at the same time with a given level of independency. Therefore, the adaptive TMD is multi-modal, in the sense that it is able to damp more than one mode of the primary system, and it can also recover the possible changes of the different eigenfrequencies considered for the primary system.

The paper explains how to model such a new device, provides details about how the multi-mode working principle is achieved and, finally, shows the experimental tests which prove the reliability of this type of device.

1 INTRODUCTION

The use of Shape Memory Alloys (SMA) to damp vibrations is a promising approach. Indeed, different SMA-based devices have been proposed in the literature in the last years (e.g. [1–4]) with the aim of attenuating vibrations and different real applications have been shown to be solvable by using SMAs (e.g. [5,6]). Moreover, many research works demonstrated the possibility to develop SMA-based adaptive Tuned Mass Dampers (TMD) able to change their dynamic features thanks to the special and advantageous characteristics of SMAs. This makes possible for the adaptive TMDs to change their dynamics and thus to stay tuned on the primary systems to be damped in case they change their dynamics as well (e.g. due to thermal shifts).

Different layouts of SMA-based adaptive TMDs have been proposed in the literature. The two main configurations proposed were cantilever beams [7–10] and strings with a central mass [11,12]. This work focuses on this latter configuration, whose working principle is described in the next section, because of its advantages:

- it allows changes of its first eigenfrequency (which is the one tuned on the eigenmode of the primary system to be damped) of more than 100% of its initial value;
- it requires low power consumption for the adaptation process;
- it easily allows to couple devices for adapting also the damping (e.g. using eddy-current devices);
- it does not require any special feature for the SMA used.

All the adaptive TMDs relying on the mentioned principles are mono-modal, meaning that they are able to adapt just a single eigenfrequency at time, and thus to damp a single eigenmode of the primary system. The aim of this paper is to show that the layout of adaptive TMD presented in [11,12] can be also used to develop a multi-mode adaptive TMD able to adapt more than one eigenfrequency at the same time with a given level of independency. This would allow to follow the changes of more than one eigenmode of the primary system at the same time.

The structure of this paper is as follows: Section 2 recalls the basics of SMAs and their use in the adaptive TMD presented in [11,12]. Then, Section 3 discusses the layout of the new multi-mode adaptive TMD, together with an introduction about how to model it. Section 4 shows the adaptation capabilities of the new device and Section 5 presents some experimental tests demonstrating the effectiveness and the reliability of the new device.

2 BASICS OF SMA AND THEIR USE IN AN ADAPTIVE TMD

SMA materials can be in three different phases: twinned martensite (TM), detwinned martensite (DM) and austenite (AU) [13]. Once the SMA is stressed over a given stress value at environmental temperature and the transformation from TM to DM is completed, it is then possible to change the shape of the SMA between the strained and unstrained shapes by changing the temperature (temperature-induced transformation) or changing the stress at high temperature (pseudoelasticity) [12,13].

The basic idea behind the work presented in [11,12] is the use of SMA wires with a central mass and elastic elements connecting the SMA wires to the primary system. These springs, together with the mass and the SMA wires, constitute the adaptive TMD (see Figure 1a). When the eigenfrequency of the TMD must be increased, it is possible to heat the SMA wires passing from DM to AU. Hence, the SMA wires undergo to a length decrease, thus causing an increase of the axial load (thanks to the elastic elements) in the wires and, therefore, the eigenfrequency increases. The heating is obtained increasing the current made flow into the SMA wires. Conversely, a decrease of this current allows to pass from AU to DM and, thus, to have a decrease of the eigenfrequency value. More details about this working principle are available in [12].

Relying on this layout, this paper will present how it is possible to extend this working principle in order to make the TMD able to change more than one of its eigenfrequencies with a given level of independency (multi-modal adaptive TMD). This is accomplished in the next sections.

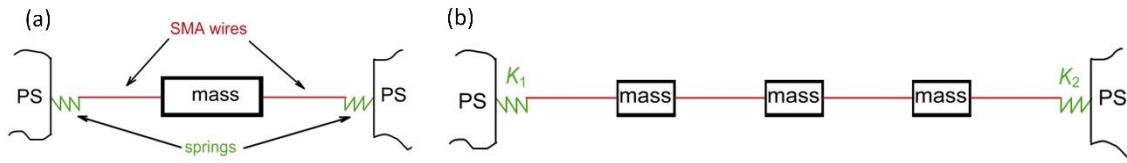


Figure 1: Original adaptive TMD based on SMAs (a) and the new multi-modal adaptive TMD (b). PS means primary system (i.e. the system to be damped).

3 THE MULTI-MODAL ADAPTIVE TMD

If other masses are added to the layout of Figure 1a, a device like that in Figure 1b is obtained. The first modes of this new device (i.e. those with a significant vertical deflection in correspondence of the masses) are those considered here.

If the current flowing in each SMA wire is set independently from that flowing in the other SMA wires, a double effect can be exploited in order to change the eigenfrequencies of the adaptive TMD:

- the axial load into the wires is changed, exactly as previously;
- the geometry of the device is changed. As an example, suppose to start from a configuration where all the wires have the same length (see Figure 1b). Then, the first wire (that on the left side) is heated more than the others. This causes a decrease of its length higher than for the other wires, causing a loss of symmetry of the whole device. Therefore, a change of the device geometry is obtained.

The mentioned double effect is expected to allow for changing two (or more, according to the number of masses used in the device) eigenfrequencies of the adaptive TMD with a given level of independency.

The new multi-modal adaptive TMD can be modelled in order to analyse its behavior and quantify its capability of changing at least two eigenfrequencies with a given level of independency. Such a model must link the input to the TMD (i.e. the currents flowing in the different SMA wires, which are set by a user/controller) and the desired output (i.e. eigenfrequencies and mode shapes of the TMD). This model is, actually, composed by three different models: a thermal model, a model of the material and a dynamic model. They are briefly discussed in the next subsections. More details about the models can be found in [14].

3.1 Thermal model

This model links the current flowing in a wire to its temperature. Such a model, which is written for each of the SMA wires, is based on a power balance which equals that produced by the Joule's effect and that dissipated towards the surrounding environment by means of convection.

3.2 Model of the material

This model takes as input the wire temperatures provided by the thermal model and gives in output the axial stress into the wires and the length of the wires. This is accomplished by

exploiting the one-dimensional (1D) material model [13], in its modified version able to account for partial transformations [12]. The knowledge of the axial stress in the SMA wires allows to estimate also the axial load acting on the whole device. More details about this model can be found in [14].

3.3 Dynamic model

Once the length of the wires and the axial load are known, it is possible to write the equations of motion of the strings (i.e. the SMA wires) with the hypotheses that the masses are concentrated [15] and that the vibration amplitude is small enough to neglect geometrical non-linearity. The solution of the system dynamics leads to the knowledge of the system eigenfrequencies and the related mode shapes. Also in this case, more details on this model are available in [14].

4 SIMULATIONS

This section investigates the performances of the new multi-mode adaptive TMD. At first, an analysis is carried out in order to show how it is possible to change the initial values (i.e. at environmental temperature and with no current flowing in the SMA wires) of the eigenfrequencies of the TMD (see Section 4.1). Then, in Section 4.2, the adaptation capability is investigated, evidencing that it is possible to tune two (or more) different eigenfrequencies of the TMD with a given level of independency by supplying the different wires independently.

4.1 The tuning of the initial eigenfrequency values

It is well known that there are different parameters for tuning the initial values of the TMD eigenfrequencies: an increase of the mass values and of the length of the whole TMD cause a decrease of the eigenfrequency values. The same effect can be also achieved by decreasing the initial axial load in the TMD. The initial axial load can be tuned by changing the elastic constant of the elastic elements connecting the TMD to the primary system (see Figure 1b) [12].

Another factor able to change the initial values of the device eigenfrequencies is the geometry of the device: the eigenfrequencies change by changing the positions of the masses in the TMD (e.g. passing from a symmetric configuration to a non-symmetric one or vice versa).

If the initial percentage change of the eigenfrequencies (named Δ_i , where i indicates the i -th eigenfrequency), caused by a change of the positions of the masses along the TMD, is calculated by using the model described in Section 3, the plot of the percentage changes of two different eigenfrequencies can be obtained. As an example, Figure 2a, Figure 2b and Figure 2c show such a plot for a TMD with two masses in case of equal masses (each dot of the plots is related to given positions of the two masses). These plots reveal that their shapes do not change once the ratio between the masses is kept constant and either the length of the TMD or the mass values are changed. A change of the plot can be obtained by changing the mass ratio [14].

Figure 2 shows that it is possible to have a large number of possible combinations between two different eigenfrequency values tuning the different parameters. Therefore, it is possible to tune the initial values of the eigenfrequencies in order to have tuning between the TMD and the primary system. More details about this analysis can be found in [14].

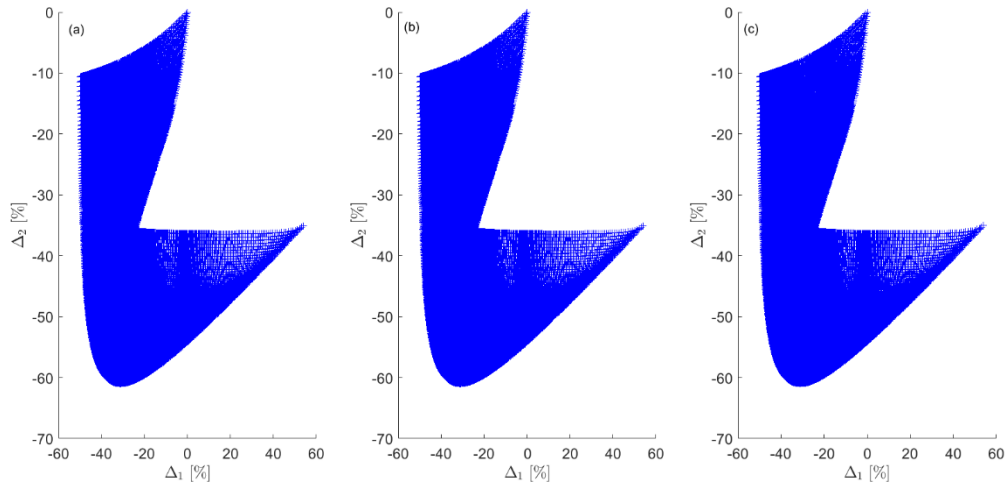


Figure 2: Relationship between Δ_1 and Δ_2 for a TMD with two masses and three wires: length of 20 cm and masses of 100 g (a), length of 40 cm and masses of 100 g (b) and length of 20 cm and masses of 200 g (c). Axial stress into the wires equal to 50 MPa.

4.2 Adaptation capability

This section investigates whether it is possible to have a given level of independency for changing the first eigenfrequencies of the TMD when each of the wires is heated/cooled independently. Simulations, relying on the model of Section 3, were carried out to investigate how different combinations of the temperatures of the wires (e.g. in the case of the mentioned adaptive TMD with two masses, thus having three wires) can change the eigenfrequency values. The percentage change of each eigenfrequency due to temperature changes of the wires are here indicated as Θ_i . Plots like those of Figure 3 are then obtained. The span, which is evident in the middle of the plot, shows that it is possible to have a given level of independency in tuning the first eigenfrequencies of the adaptive TMD. This allows to recover different changes of the corresponding eigenfrequencies of the primary system.

The span evidenced in Figure 3, which is related to the mentioned level of independency, can be changed by changing the SMA material (particularly, changing the value of the current maximum transformation strain [13]), the initial geometrical configuration of the masses (i.e. position of the masses along the whole TMD), the number of the masses and their relative values. A detailed analysis of these effects is available in [14], where it is also shown that the achievable level of independency is enough for real applications.

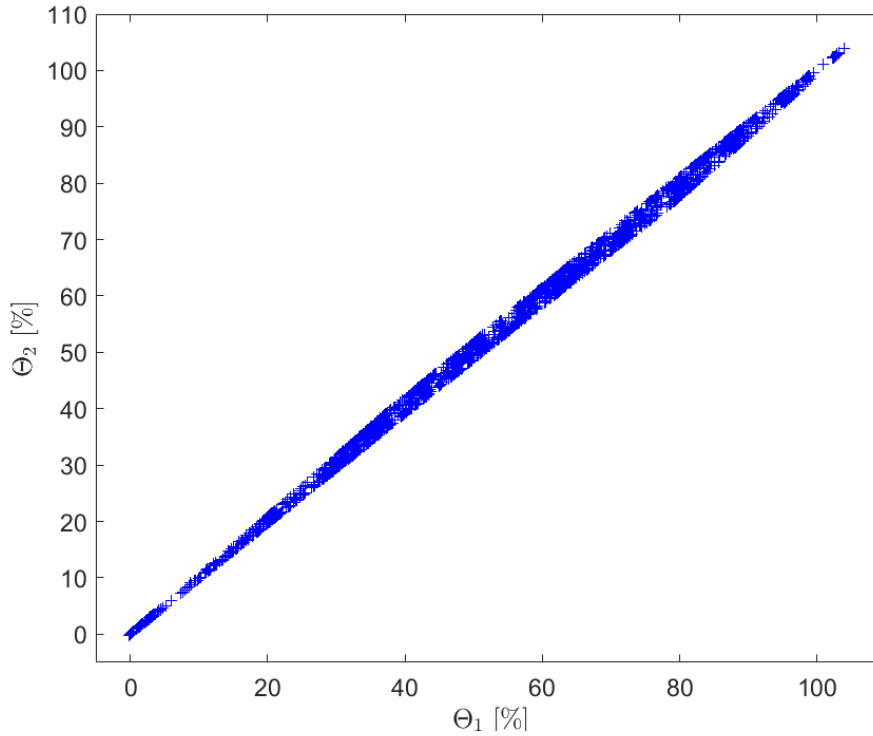


Figure 3: Relationship between Θ_1 and Θ_2 for a TMD with two masses of 100 g, a length of 20 cm and an initial configuration at environmental temperature with the first wire length equal to the 25% of the total TMD length, the central wire with a length equal to the 30% of the total length and the last wire with a length equal to the 45%.

5 EXPERIMENTAL TESTS

A test-set-up was built in order to experimentally validate the possibility of having a given level of independency in tuning two different eigenfrequencies by heating/cooling the different SMA wires of the device independently. A TMD made of three wires and two masses was thus built. The total length of the device was about 35 cm and the two masses had a value of 18 g and 25 g (see Figure 4). The elastic elements were built through cantilever beams. The whole device was excited by means of an electro-dynamic shaker providing a random disturbance. The currents flowing into the wires (and, therefore, the temperatures of the wires) were changed test by test, estimating each time the first two TMD eigenfrequencies (ω_1 and ω_2) by measuring the vibration of the masses with an accelerometer and a laser velocimeter. The experimental results were superimposed to the plot built by using simulations, where many numerical results were reported. The experimental results were in the same area of the plot covered by the numerical results, proving the reliability of the model developed. Furthermore, different experimental points of the plot show the same value for the first eigenfrequency for different values of the second one (e.g. at about 18.75 Hz on the horizontal axis, see Figure 5) and vice versa (e.g. at about 30.8 Hz on the vertical axis, see Figure 5). These results prove that it is actually possible to have a given level of independency in the tuning of at least two different

eigenfrequencies and this makes possible to design and build multi-modal adaptive TMDs based on SMAs.

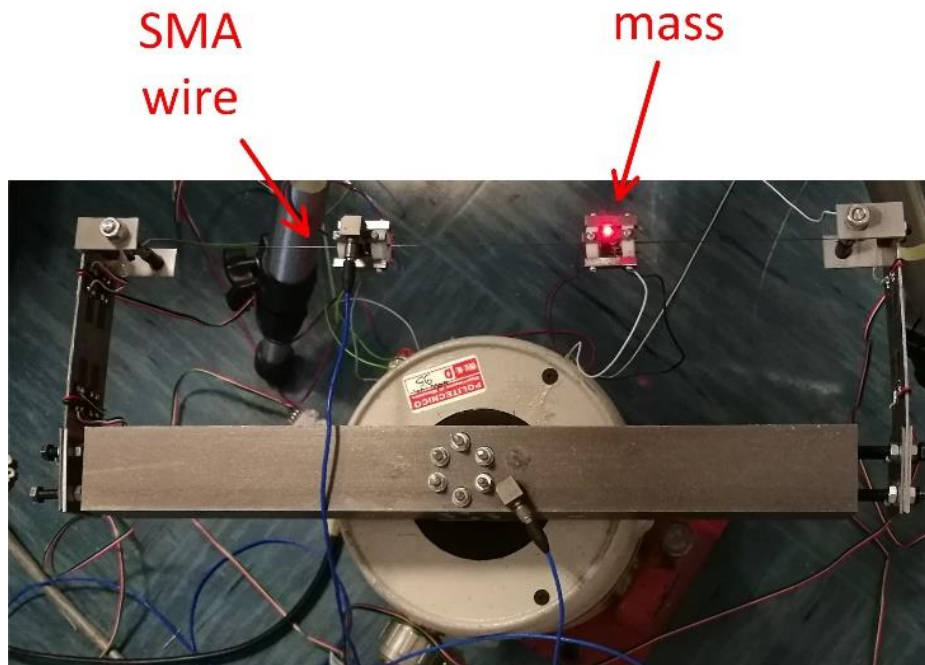


Figure 4: Experimental set-up.

6 CONCLUSIONS

The paper has dealt with the use of SMA wires to build adaptive TMDs able to change with a given level of independency more than one eigenfrequency at the same time thanks to the special features of SMA materials. This allows to build a multi-modal adaptive TMD able to follow the changes of different eigenfrequencies of the primary system in order to avoid mistuning and a worsening of the attenuation performance provided by the TMD.

The layout of this new TMD is based on the use of different masses and SMA wires to build the TMD. Each wire is heated/cooled independently from the others and this allows to obtain the mentioned level of independency.

The effectiveness of the proposed approach is demonstrated experimentally by means of a TMD made from two masses and three SMA wires.

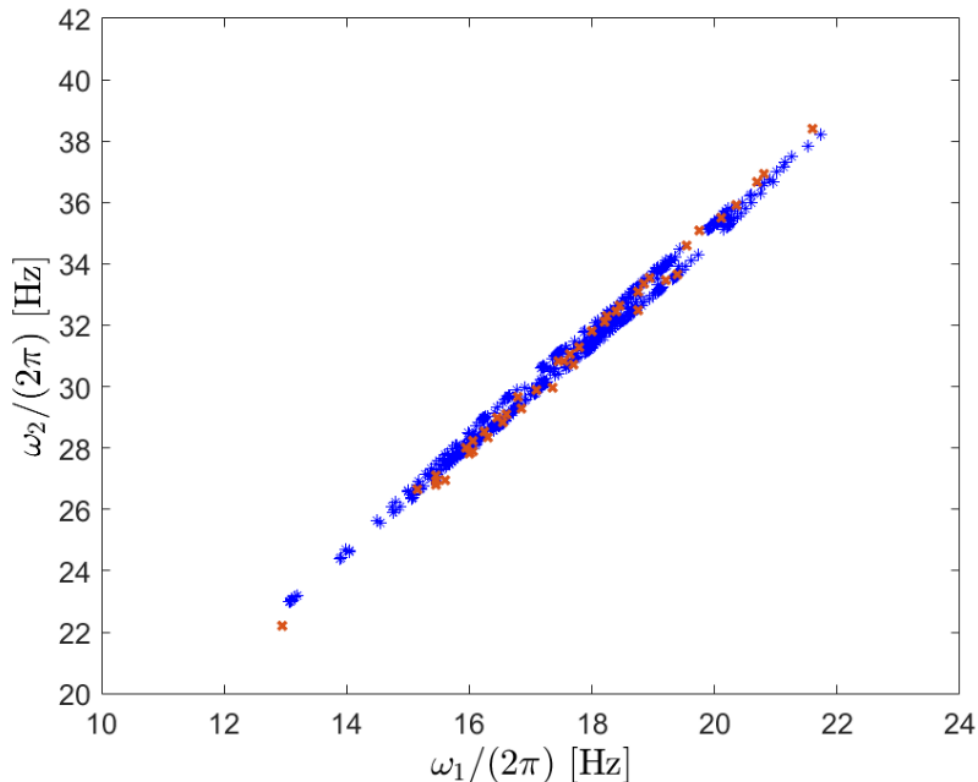


Figure 5: Experimental (red crosses) and numerical (blue asterisks) results.

REFERENCES

- [1] O.E. Ozbulut, C. Mir, M.O. Moroni, M. Sarrazin, P.N. Roschke, A fuzzy model of superelastic shape memory alloys for vibration control in civil engineering applications, *Smart Materials and Structures*. 16 (2007) 818–829. doi:10.1088/0964-1726/16/3/031.
- [2] B. Tiseo, A. Concilio, S. Ameduri, A. Gianvito, A shape memory alloys based tunable dynamic vibration absorber for vibration tonal control, *Journal of Theoretical and Applied Mechanics*. 48 (2010) 135–153.
- [3] M. a. Savi, a. S. De Paula, D.C. Lagoudas, Numerical Investigation of an Adaptive Vibration Absorber Using Shape Memory Alloys, *Journal of Intelligent Material Systems and Structures*. 22 (2010) 67–80. doi:10.1177/1045389X10392612.
- [4] R.A. Aguiar, M.A. Savi, P.M. Pacheco, Experimental investigation of vibration reduction using shape memory alloys, *Journal of Intelligent Material Systems and Structures*. 24 (2012) 247–261. doi:10.1177/1045389X12461696.
- [5] F.A. dos Santos, J. Nunes, Toward an adaptive vibration absorber using shape-memory alloys, for civil engineering applications, *Journal of Intelligent Material Systems and Structures*. 29 (2018) 729–740.
- [6] V. Torra, G. Carreras, S. Casciati, P. Terriault, On the NiTi wires in dampers for stayed cables, *Smart Structures and Systems*. 13 (2014) 353–374.

- doi:10.12989/sss.2014.13.3.353.
- [7] E. Rustighi, M.J. Brennan, B.R. Mace, Real-time control of a shape memory alloy adaptive tuned vibration absorber, *Smart Materials and Structures*. 14 (2005) 1184–1195. doi:10.1088/0964-1726/14/6/011.
 - [8] E. Rustighi, M.J. Brennan, B.R. Mace, A shape memory alloy adaptive tuned vibration absorber: design and implementation, *Smart Materials and Structures*. 14 (2005) 19–28. doi:10.1088/0964-1726/14/1/002.
 - [9] K. Williams, G. Chiu, R. Bernhard, Adaptive-Passive Absorbers Using Shape-Memory Alloys, *Journal of Sound and Vibration*. 249 (2002) 835–848. doi:10.1006/jsvi.2000.3496.
 - [10] K.A. Williams, G.T.-C. Chiu, R.J. Bernhard, Nonlinear control of a shape memory alloy adaptive tuned vibration absorber, *Journal of Sound and Vibration*. 288 (2005) 1131–1155. doi:10.1016/j.jsv.2005.01.018.
 - [11] M. Berardengo, A. Cigada, F. Guanziroli, S. Manzoni, An adaptive tuned mass damper based on shape memory alloys with an extended range of frequency, in: *Proceedings of EESMS 2014 - 2014 IEEE Workshop on Environmental, Energy and Structural Monitoring Systems*, 17-18 September, ISBN: 97814799498922014, Naples (Italy), 2014: pp. 90–95. doi:10.1109/EESMS.2014.6923272.
 - [12] M. Berardengo, A. Cigada, F. Guanziroli, S. Manzoni, Modelling and control of an adaptive tuned mass damper based on shape memory alloys and eddy currents, *Journal of Sound and Vibration*. 349 (2015) 18–38. doi:10.1016/j.jsv.2015.03.036.
 - [13] D.C. Lagoudas, *Shape Memory Alloys: Modeling and Engineering Applications*, Springer, New York, 2008.
 - [14] M. Berardengo, G.E.P. Della Porta, S. Manzoni, M. Vanali, A multi-modal adaptive tuned mass damper based on shape memory alloys, *Journal of Intelligent Material Systems and Structures*. 30 (2019) 536–555. doi:10.1177/1045389X18818388.
 - [15] B.J. Gómez, C.E. Repetto, C.R. Stia, R. Welti, Oscillations of a string with concentrated masses, *European Journal of Physics*. 28 (2007) 961–975. doi:10.1088/0143-0807/28/5/019.

TUNED MASS DAMPER WITH INERTER AND NON-LINEAR DAMPER

MATEUSZ LAZAREK, BARTŁOMIEJ POLNIAK, PIOTR BRZESKI AND
PRZEMYSŁAW PERLIKOWSKI

Division of Dynamics
Lodz University of Technology
90-924 Lodz, Poland

e-mail: przemyslaw.perlikowski@p.lodz.pl, web page: <http://www.perlikowski.kdm.p.lodz.pl/>

Key words: Inerter, non-linear damper, tuned mass damper

Abstract. In this paper we study the dynamics of two degree freedom system, which is consisted of main body and tuned mass damper with inerter (TMDI) and dash-pot with nonlinear damping characteristic. We study influence of non-linear dash-pot on efficiency of proposed device. The non-linear characteristic of the dash-pot is dependent on control parameters which let us change freely its characteristics. To compare response of main system with TMDI with linear and non-linear damper.

1 INTRODUCTION

In this paper, we focus on mitigation of vibrations using a tuned mass damper (TMD). The TMD was patented by Frahm in 1909 [1]. His device is a linear oscillator that consists of a mass and a linear spring with the same natural frequency as the damped system. When both frequencies match, one can avoid the resonance of the main system, but the decrease in the amplitude is observed only around the resonant frequency. There are a lot of modifications of the TMD which lead to the increase in the range of effectiveness. The most fundamental one was the addition of a dash-pot to the TMD [2]. Such TMD can be efficient in much wider range of excitation's frequencies than the Frahm's device. Nowadays, the passive TMDs are used in many systems to mitigate the oscillations, e.g., they prevent damage of buildings due to seismic excitation [3, 4], suppress vibration of tall buildings subjected to wind [5, 6], achieve the best properties of cutting processes [7, 8], decrease vibration of floors or balconies [9, 10], reach stable rotations of rotors [11, 12, 13], stabilize drilling strings [Viguie2009b], etc. Despite the fact that scientists and engineers are working on designing the best passive device, there are also many efforts to improve properties of the TMDs by control (hybrid, semi-active and active systems) [15, 16].

Inerter - introduced in early 2000s by Smith [17] - is a two terminal element which has the property that the force generated at its ends is proportional to the relative acceleration of its terminals. Its constant of proportionality is called inertance and is measured in kilograms. The first studies of this device have been devoted to the possible application as an element of cars' suspensions [17]. It has been shown that oscillations induced by road imperfections and load disturbances can be reduced more effectively using suspensions with inerters. Then, in 2004 Smith and Wang [18] studied several simple passive suspension struts, each containing at most one damper and inerter. The theoretical results are confirmed with experiment showing that suspension layouts with inerter are more effective than classical designs with

dampers and springs only. Wang and Su [19] present how the performance of suspension is influenced by the non-linearities which appear due to inerter's construction including friction, backlash and the elastic effect. They show that the performance benefits are slightly degraded by the inerter non-linearities but still the overall performance of suspension with a nonlinear inerter is better than traditional ones, especially when the stiffness of suspension is large. In 2005 the inerter was profitably used as a part of suspension in Formula 1 racing car under the name of J-damper [20].

In our previous papers we combine TMD with inerter (TMDI) and nonlinear damper and we test its efficiency in comparison to TMDI with linear damper.

2 Non-linear damper

2.1 Model of non-linear damper

Let us introduce the non-linear damper with piecewise quadratic damping characteristic proposed by Y. Starosvetsky i O.V. Gendelman [21]. Such dampers are often considered for hydraulic damping devices [22] that are based on a flow of fluid through orifices in a moving piston. The force in damper is dependent on the square of relative velocity $\dot{X}|X|$ between the terminals of device and is given by following equation:

$$f = \begin{cases} \lambda_1 \dot{X}|\dot{X}|, & \text{if } X < a_{cr} \\ \lambda_2 \dot{X}|\dot{X}|, & \text{if } X > a_{cr} \\ \lambda_2 \geq \lambda_1 \end{cases} \quad (1)$$

where $\lambda_{1,2}$ are damping coefficients and a_{cr} is critical value of deflection $|X|$ for which the damping change its characteristic (rapid increase or decrease of damping coefficient's value). This type of damping characteristics is typical in hydraulic dampers based on the same principle of orifice flow with the addition of semi-active control [23]. It can be realized in the hydraulic dampers containing several on/off orifice valves in a moving piston. State of the valves can change during the work as soon as the piston reaches critical value of deflection a_{cr} that is defined by the designer. When this value is reached, some of the orifices are closed and this results in the increase of damping coefficient. When the piston hits the critical value a_{cr} in the opposite direction, it simply reopens the closed orifices, thus brings the damping coefficient to its original value. The idea behind this type of non-linear damper is simple, but also powerful and with correctly chosen parameters such device can solve the problem of the increase of the amplitude for large deflections.

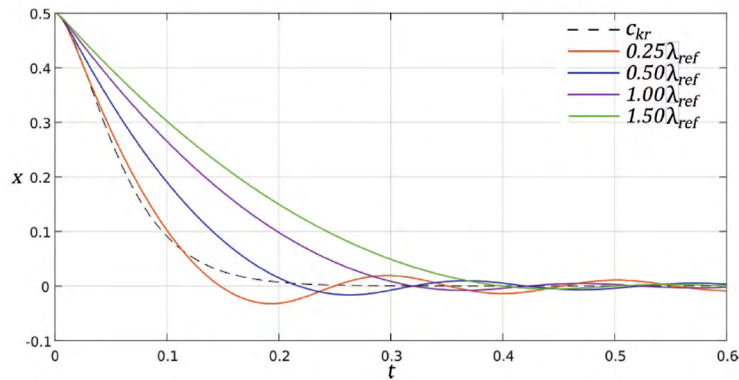


Figure 1: Free response of one DoF system for different values of damping

2.2 Response of one DoF system with nonlinear damper

To compare the response of classical linear damper with considered nonlinear damper we perform simple test on one DoF system. For simplicity we assume $\lambda = \lambda_1 = \lambda_2$. The equation of motion of test system is as follow:

$$m\ddot{x}_1 + kx + c\dot{x}_1 + k(x_1 - x_2) + c\dot{x}_1 + \lambda(\dot{x}_1)|(\dot{x}_1)| = 0, \quad (2)$$

where $m = 10 [kg]$, $k = 9600 [N/m]$. Damping coefficients c and λ are controlling parameters. The critical damping for this system is as follow: $c_{kr}2\sqrt{km}$ and we use as a reference value for $\lambda_{ref} = c_{kr}$ parameter. The results are presented in Fig. 1. The dashed line corresponds to $c = c_{kr}$ and $\lambda = 0$, while continuous lines of different color to $c = 0 [Ns/m]$ and $\lambda = 0.25\lambda_{ref}$, $\lambda = 0.5\lambda_{ref}$, $\lambda = 1.0\lambda_{ref}$, $\lambda = 1.5\lambda_{ref}$ respectively.

As it is easy to see the response of system with nonlinear damper is closest to system with critical damping for $\lambda = 0.25\lambda_{ref}$. For higher values of λ system reaches equilibrium after significantly longer time.

3 Model of the system

In this section we introduce model of the considered system. It is presented in Fig. 2. It consists of two oscillators that can move in vertical direction. The first oscillator is forced by external harmonic excitation. It is used as a model of the structure which vibrations should be mitigated and will be called base oscillator. The second oscillator is connected to the first one and represents the TMD.

The motion of the system is described by two generalized coordinates: the vertical position of the base oscillator by coordinate x_1 , while the vertical displacement of the TMD by coordinate x_2 . The notation of parameters used to characterize the base oscillator is as follows: M is the mass of the oscillator, k_1 and k_2 are the linear and non-linear parts of the base oscillator spring stiffness and its viscous damping coefficient is given by parameter c . To describe the TMD itself we use the following parameters: m is the mass, k describes spring stiffness, c_T is a viscous damping coefficient and I represents the inertance of the inerter. Parameter m describes the total mass of the elements which can perform movement with respect to the base oscillator and will be called the mass of TMD.

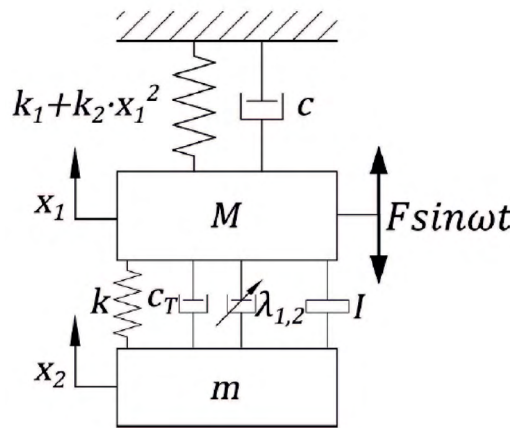


Figure 2: Model of the system

The model of the system is given by:

$$\begin{cases} M\ddot{x}_1 + k_1x_1 + k_2x_1^3 + c\dot{x}_1 + k(x_1 - x_2) + c_T(\dot{x}_1 - \dot{x}_2) + \lambda(\dot{x}_1 - \dot{x}_2)|(\dot{x}_1 - \dot{x}_2)| + \\ + I(\ddot{x}_1 - \ddot{x}_2) = F \sin \omega_0 t \\ m\ddot{x}_2 - k_2(x_1 - x_2) - c_T(\dot{x}_1 - \dot{x}_2) - \lambda(\dot{x}_1 - \dot{x}_2)|(\dot{x}_1 - \dot{x}_2)| - I(\ddot{x}_1 - \ddot{x}_2) = 0. \end{cases} \quad (3)$$

with following parameters: $M = 100 [kg]$, $k_1 = 24000 [N/m]$, $k_2 = 0 [N/m^3]$, $c = 124 [Ns/m]$, $F = 192 [N]$, $m = 10 [kg]$, $k = 9600 [N/m]$, $c_T = 30.98 [Ns/m]$ and I is one of control parameters.

We perform calculations in Auto07p. It is toolbox for continuation of smooth problems, so we had to smooth the damping function by following formula:

$$\lambda = \lambda_2 + (\lambda_2/2 - \lambda_1/2)[\tanh(\gamma(x_1 - x_2 - a_{cr})) - \tanh(\gamma(x_1 - x_2 + a_{cr}))],$$

where $\gamma = 400$.

Then, we rewrite equations to dimensionless form introducing $\tau = \omega_r t$, reference length $l_0 = 1 [m]$ and natural frequency of main body $\omega_r = \sqrt{k_1/M}$:

$$\begin{cases} \ddot{x}'_1 + x'_1 + k_{2D}x'^3_1 + c_D\dot{x}'_1 + k_D(x'_1 - x'_2) + c_{TD}(\dot{x}'_1 - \dot{x}'_2) + \lambda_D(\dot{x}'_1 - \dot{x}'_2)|(\dot{x}'_1 - \dot{x}'_2)| + \\ + I_D(\ddot{x}'_1 - \ddot{x}'_2) = F_D \sin \omega \tau \\ m_D\ddot{x}'_2 - k_{2D}(x'_1 - x'_2) - c_{TD}(\dot{x}'_1 - \dot{x}'_2) - \lambda_D(\dot{x}'_1 - \dot{x}'_2)|(\dot{x}'_1 - \dot{x}'_2)| - I_D(\ddot{x}'_1 - \ddot{x}'_2) = 0. \end{cases} \quad (4)$$

where: $x'_{1,2} = x_{1,2}/l_0$, $\dot{x}'_{1,2} = \dot{x}_{1,2}/l_0\omega_r$, $\ddot{x}'_{1,2} = \ddot{x}_{1,2}/l_0\omega_r^2$, $k_{2D} = k_2l_0^2/M\omega_r^2$, $c_D = c/M\omega_r$, $k_D = kl_0^2/M\omega_r^2$, $c_{TD} = c_T/M\omega_r$, $m_D = m/M$, $F_D = F/Ml_0\omega_r^2$, $\lambda_D = \lambda/M$, $\omega = \omega_0/\omega_r$, $I_D = I/M$. For simplicity primes in dimensionless equations will henceforth be neglected.

4 Results

In this section we present results for obtained for TMD and TMDI with nonlinear and linear dampers.

4.1 Response of TMD with nonlinear damper

Let us study first the influence of nonlinear damper on response of the system mitigated with TMD ($I = 0.0 [kg]$). First we equate values of λ_1 and λ_2 to selected fractions of λ_{ref} . Results are presented in Fig. 3(a). We plot FRC of main body for varying frequency of excitation. Dashed line corresponds to FRC of the system without TMD and continuous lines to FRCs with applied TMD for $\lambda = 0.25\lambda_{ref}$, $\lambda = 0.5\lambda_{ref}$, $\lambda = 1.0\lambda_{ref}$, $\lambda = 1.5\lambda_{ref}$. As we can see for low values of λ we observe similar response as for TMD with linear damper. However, for $\lambda = 1.5\lambda_{ref}$ (large damping) we observe the non-linear trace of FRC (black line). In panel (b) we plotted FRC for optimal values of $\lambda = 0.62\lambda_{ref}$ and $c_{TD} = 0.62$ which corresponds to minimum L_2 norm (optimization procedure is not presented in this paper) for FRC plot. As one can see both FRC are similar, so we can obtain significant reduction of amplitude using both types of dampers.

Next, we fixed damping coefficients $\lambda_1 = 0.05\lambda_{ref}$, $\lambda_2 = 0.6\lambda_{ref}$ and we vary the switching distance a_{cr} . Thus, the damping coefficient is small for small relative amplitude and large for large relative amplitude. In Fig. 4(a) we show response with just nonlinear damping, while in Fig. 4(b) we combine nonlinear damper and linear one ($c_{TD} = 0.02$). In panel (a) we see typical change of response of system damped by TMD with increasing of damping in the system. The interesting observation is in panel (b) where with increase of a_{cr} we see decrease of minimum amplitude in valley while maximum values of amplitude preserve the same.

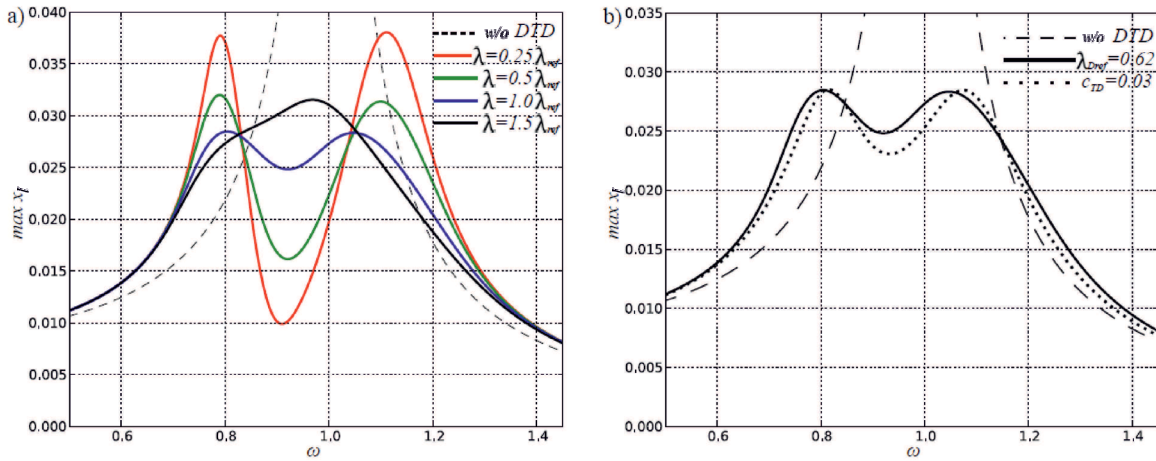


Figure 3: (a) FRC of system for with nonlinear damper and $F_D = 0.008$; $m_D = 0.1$; $c_D = 0.08$; $k_D = 0.08$; $c_{TD} = 0$; $a_{cr} = 0.02$; (b) FRC for system with nonlinear damper $\lambda_1 = \lambda_2 = \lambda_{ref}$ - continuous damper and linear damper $c_{TD} = c_{TDopt}$ - dotted line. Dashed line corresponds to response of the system without TMD.

4.2 Response of TMD inerter

In this subsection we perform calculation for system with TMDI and both types of dampers. We introduce control of inertance to tune natural frequency of TMDI to current frequency of excitation. We change inertance according to formula as follow: $I_D = \frac{k_D}{\omega^2} - m_D$ which changes equivalent mass of the TMDI. For details of this procedure see our previous papers where we preset it in details [24, 25, 26]. Such assumption let us follow response of the main system for varying value of inertance and find minimum amplitude for given equivalent mass of TMDI. In this paper we do not consider control of inertance value, but such theoretical study gives us fast answer about its efficiency. In Fig. 5 we can see four plots and reference dashed line which corresponds to response of the system without TMDI. There are two pairs of lines. In each pair we study TMDI with linear and nonlinear damper. The bottom lines are for low damping coefficients, while top lines for larger values of damping coefficients. As we can see, we obtain the same level of mitigation of vibrations in both cases. Thus, we can use two damper interchangeably.

5 CONCLUSIONS

In this paper we present the properties of TMDI with liner and nonlinear damper. We investigate properties of non-linear damper with piecewise quadratic damping characteristic using one DoF system and compare its free oscillations with response of system with linear viscous damper. Then, we applied TMDI with both types of dampers and we show their FRC plots. Finally, we applied control to inerter which let us change the inertance to tune natural frequency of TMDI to current frequency of excitation. In such configuration obtained FRC have similar amplitude, thus we show that both dampers are comparable. In further studies we will investigate influence of nonlinear damper parameters on response of damped body. We will prepare control algorithm which will change their values based on current state of the system to increase efficiency of TMDI.

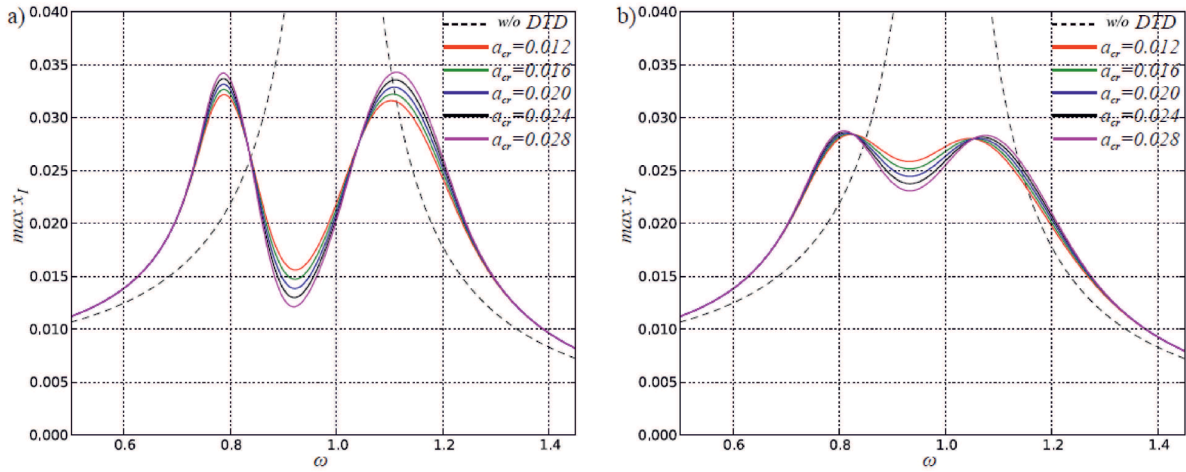


Figure 4: FRC of system for different values of a_{cr} with following parameters of the system: (a) $F_D = 0.008$; $m_D = 0.1$; $c_D = 0.08$; $k_D = 0.08$; $\lambda_1 = 0.05 \lambda_{ref}$, $\lambda_2 = 0.6 \lambda_{ref}$, $c_{TD} = 0$; (b) $F_D = 0.008$; $m_D = 0.1$; $c_D = 0.08$; $k_D = 0.08$; $\lambda_1 = 0.05 \lambda_{ref}$, $\lambda_2 = 0.6 \lambda_{ref}$, $c_{TD} = 0.02$. Dashed line corresponds to response of the system without TMDI.

ACKNOWLEDGMENT

This work has been supported by National Science Centre, Poland - Project No. 2015/17/B/ST8/03325.

REFERENCES

- [1] H. Frahm, Device for damping vibrations of bodies (1909).
- [2] J. P. Den Hartog, Mechanical Vibrations, McGraw-Hill, New York, 1934.
- [3] H. Owji, A. H. N. Shirazi, H. H. Sarvestani, A comparison between a new semi-active tuned mass damper and an active tuned mass damper, *Procedia Engineering* 14 (2011) 2779 – 2787.
- [4] M. M. Ali, K. Sun Moon, Structural developments in tall buildings: Current trends and future prospects, *Architectural Science Review* 50 (2007) 205-223.
- [5] S.-D. Kwon, K.-S. Park, Suppression of bridge flutter using tuned mass dampers based on robust performance design, *Journal of Wind Engineering and Industrial Aerodynamics* 92 (2004) 919-934.
- [6] M. Kitagawa, *Structural Control and Health Monitoring* 11 (2004) 75-90.
- [7] Y. Yang, J. Munoa, Y. Altintas, Optimization of multiple tuned mass dampers to suppress machine tool chatter, *International Journal of Machine Tools and Manufacture* 50 (2010) 834 - 842.
- [8] A. Rashid, C. M. Nicolescu, Design and implementation of tuned viscoelastic dampers for vibration control in milling, *International Journal of Machine Tools and Manufacture* 48 (2008) 1036 - 1053.
- [9] A. Ebrahimpour, R. L. Sack, A review of vibration serviceability criteria for structures, *Computers and Structures* 83 (2005) 2488 - 2494.
- [10] M. Setareh, R. Hanson, Tuned mass dampers for balcony vibration control, *Journal of Structural Engineering* 118 (1992) 723-740.

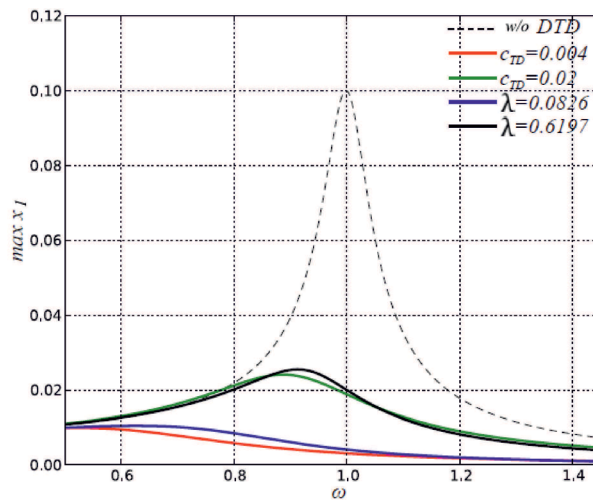


Figure 5: FRC of main systems mitigated with TMDI for two types of damper between main body and TMDI. Inertance is controlled to tune natural frequency of TMDI to current frequency of excitation. Dashed line corresponds to response of the system without TMDI.

- [11] P. Walsh, J. Lamancusa, A variable stiffness vibration absorber for minimization of transient vibrations, *Journal of Sound and Vibration* 158 (2) (1992) 195-211.
- [12] A. Alsuwaiyan, S. Shaw, Performance and dynamics stability of general-path centrifugal pendulum vibration absorbers, *Journal of Sound and Vibration* 252 (2002) 791-815.
- [13] Y. Ishida, Recent development of the passive vibration control method, *Mechanica Systems and Signal Processing* 29 (2012) 2-18.
- [14] R. Viguie, G. Kerschen, J. Golinval, D. McFarland, L. Bergman, A. Vakakis, N. van de Wouw, Using passive nonlinear targeted energy transfer to stabilize drill-string systems, *Mechanical Systems and Signal Processing* 23 (1) (2009) 148-169.
- [15] R. P. Eason, C. Sun, A. J. Dick, S. Nagarajaiah, Attenuation of a linear oscillator using a nonlinear and semi-active tuned mass damper in series, *Journal of Sound and Vibration* 332 (2013) 154-166.
- [16] L. L. Chung, L. Y. Wu, K. H. Lien, H. H. Chen, H. H. Huang, Optimal design of friction pendulum tuned mass damper with varying friction coefficient, *Structural Control and Health Monitoring* 20 (2012) 544-559.
- [17] M. C. Smith, Synthesis of mechanical networks: the inerter, *IEEE Transactions on automatic control* 47 (2002) 1648-1662.
- [18] F.-C. Wang M. C. Smith. Performance benefits in passive vehicle suspensions employing inerters. *Proceedings of the IEEE Conference on Decision and Control*, 3:2258-2263, 2004.
- [19] F.-C. Wang and W.-J. Su. Inerter nonlinearities and the impact on suspension control. In *American Control Conference* (2008) 3245-3250.
- [20] M.Z.Q. Chen, C. Papageorgiou, F. Scheibe, Fu cheng Wang, and M.C. Smith. The missing mechanical circuit element. *Circuits and Systems Magazine, IEEE*, 9 (2009) 10-26.

- [21] Y. Starosvetsky, O. Gendelman, Vibration absorption in systems with a nonlinear energy sink: Nonlinear damping, *Journal of Sound and Vibration* 324 (2009) 916 - 939.
- [22] A.Rittweger, J.Albus, E.Hornung, H.Ory, P.Mourey, Passive damping devices for aerospace structures, *Acta Astronautica* 50 (2002) 597–608.
- [23] A.A. Golafshani, H.R. Mirdamadi, Adaptive control of structures by LMS algorithm: a comparative study, *Structures and Buildings* 152 (2001) 175–191.
- [24] P. Brzeski, T. Kapitaniak, P. Perlikowski, Novel type of tuned mass damper with inerter which enables changes of inertance, *Journal of Sound and Vibration*, 349 (2015) 56-66.
- [25] P. Brzeski, M. Lazarek, P. Perlikowski, Experimental study of the novel tuned mass damper with inerter which enables changes of inertance, *Journal of Sound and Vibration*, 404 (2017) 47-57.
- [26] M. Lazarek, P. Brzeski, P. Perlikowski, Design and modeling of the CVT for adjustable inerter, *Journal of the Franklin Institute* (2018).

APPROACHES FOR LOCALIZATION OF DAMAGE IN COMPOSITES USING PROPAGATION OF LAMB WAVES

Kaleeswaran Balasubramaniam^{*,1, a}, Tomasz Wandowski^{1, b}, Pawel Malinowski^{1, c}

¹
Institute of Fluid Flow Machinery, Polish Academy of Sciences
Department of Mechanics of Intelligent Structures,
Fiszera 14, 80-231, Gdansk, Poland.

Email: ^{a,*} kaleeswaranb@imp.gda.pl, ^b tomaszw@imp.gda.pl, ^c pmalinowski@imp.gda.pl

Web page: <https://www.imp.gda.pl/en/o4/z1/>

Keywords: composites, SHM, numerical simulation, Lamb waves, guided waves

Abstract: Composite materials are now commonly used in various industries ranging from building to space science. The damage analysis in composites is an important task to ensure safe use and prevent failures. Structural health monitoring (SHM) approaches are developed to identify the damage in various structures. This research focuses on the guided wave-based SHM. The guided waves propagate throughout the material and get reflected at the damage or after reaching the boundaries. This is the basis for the damage detection method. The group velocity, RMSD, amplitude variation, the time of flight for the healthy, damage cases are analyzed. The frequency range of 50 kHz is used with a periodic cycle of 5 to analyze the wave pattern over the surface of the composite material. Thus, the change in the signals can be extracted through the developed algorithms and the damage location can be indicated. The studies comprised of scanning laser measurements. A composite GFRP plate with an L-stiffener was studied. The damage localization algorithms are employed for simulated damage in the form of stiffener debonding. The study comprised of analyzing the results from the laser Doppler vibrometer (LDV). The analysis of the LDV results and processing it provides further information about the damage location and its influence on the wave propagation.

1 INTRODUCTION:

Fiber reinforced composite materials are more and more popular in the industry. Such composite structures are lightweight, have large strength and are easy to form. However, they are prone to damage like debonding and delamination very often hidden inside the structure. Therefore the structural state of composite structures needs to be assessed. This allows for increasing the safety of composite structures exploitation. Very popular is the elastic wave propagation method. Many research works towards the development of damage assessment methods for composite structures using elastic wave propagation were published. There was the numerical and experimental study of elastic wave propagation in composite laminate conducted by Gresil, et al [1]. Authors investigated the dispersion curves and wave propagation. This is useful knowledge for the development of elastic wave based damage detection methods for composite structures. Very important is the problem of the debonding in the adhesive joints. Such problems were analyzed with the help of energy propagation RMS methods by Rucka, et al [2]. Gaul, et al [3] paper deals about the surface bonded transducers inspecting a large testing area. The paper is related to early warning maintenance of the structures with the help of built-in sensor network arrangements. LDV helps in the detailed analysis of various anisotropic materials. The interaction of Lamb waves with a T-stiffener has been analyzed by Allen, et al

[4]. Visualization of the damage in the bonding area between the composite plates was analyzed by Sohn, et al [5]. The delamination location between the composite plates was analyzed by Duflo, et al [6]. LDV analysis in the contactless observation in the anisotropic plate was presented by Owens, et al [7]. The damage observation depends on the area of the defect [8] and thus Kehlenbach, et al showed that the numerical and experimental results were analyzed together with it. Use of RMS in damage detection was shown by Radzienski, et al [9]. The delamination detection in the composite plate based on the change in Lamb wave response amplitudes was analyzed by Staszewski, et al [10].

This paper uses guided wave propagation with the help of laser Doppler vibrometer (LDV). The research in this paper focuses on processing the data obtained from the LDV using various methods of analysis guided wave propagation in a composite plate with stiffener.

2 EXPERIMENTAL PROCESS

In this paper, the Lamb wave propagation utilized for bond assessment in the composite plate is analyzed. The plate is of dimension 50x50x0.3 cm³ and includes bonded L-stiffener with a length of 50 cm (figure 1). The plate is made of 12 layers of VV 192T 202 IMP503 prepreg. The L-stiffener is bonded by 3M AF3109 2U bonding agent. The stiffener is not bonded in the middle part with the length 15 cm what simulating its debonding. The piezoelectric transducers (PZT) are attached at 3 different locations. One at the bottom and others to the right and left corner of the plate respectively (figure 1). The LDV with laser heads as shown in figure 2 is used for measuring the guided wave (GW) signals on the flat side of the plate.

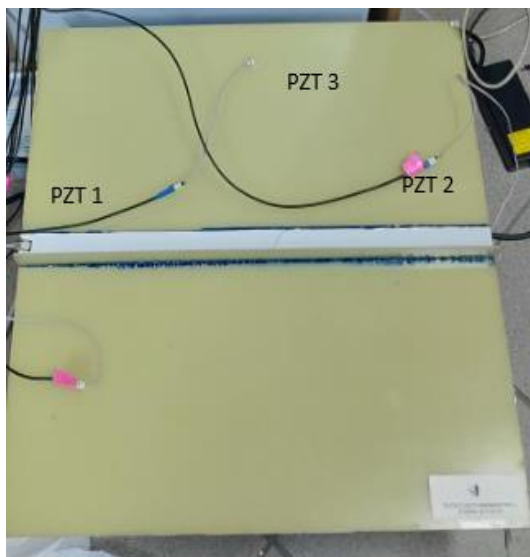


Figure 1: Composite plate and PZT arrangement



Figure 2: Scanning laser heads

2.1 Setup

The elastic wave excitations are performed in 3 PZT across the plate as shown in figure 3.

1. PZT 3 is placed at the bottom of the plate.
2. PZT 2 is placed at the left end of the plate/flat side.
3. PZT 1 is placed at the right end of the plate/stiffened side.

The signals are registered with the help of only one LDV head (an out-of-plane component of velocity). Fine mesh area of about 61503 scanning point where elastic waves are registered is considered in the research. The very dense mesh allows correct space sampling for the shortest wave propagating in the structure.

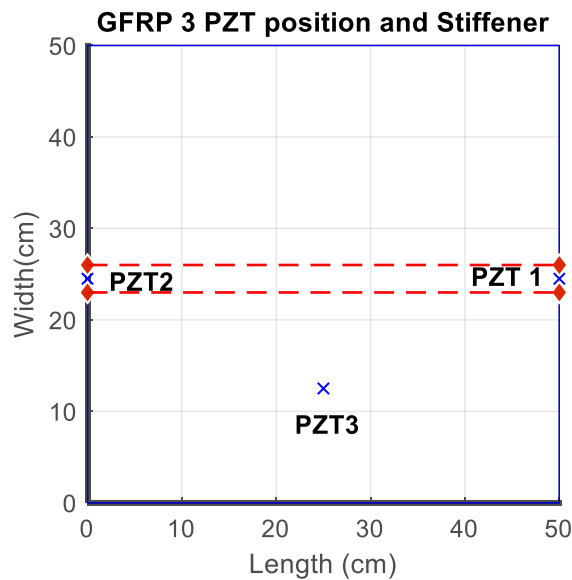


Figure 3: PZT positions – view from the top

3 RESULTS

In the research analysis of the time of arrival (ToF) of the elastic wave is performed. The ToF of the elastic waves is identified based on analyzing the time instances between the wave packets. In this case, the first time instant related to the arrival time of the waves is noted. This is performed by using Hilbert transformation which allows creating the envelope of the signal. Higher the TOF value the larger the time taken for the waves to reach the same set of location. The obtained ToF values help to analyze the changes in the group velocities of the propagating wave modes. In figure 4, the time of arrival of the first wave packet is calculated by identifying the highest peak value (marked in the red spot). In a similar way, the time of arrival for other scanning points is calculated and noted down in table 1.

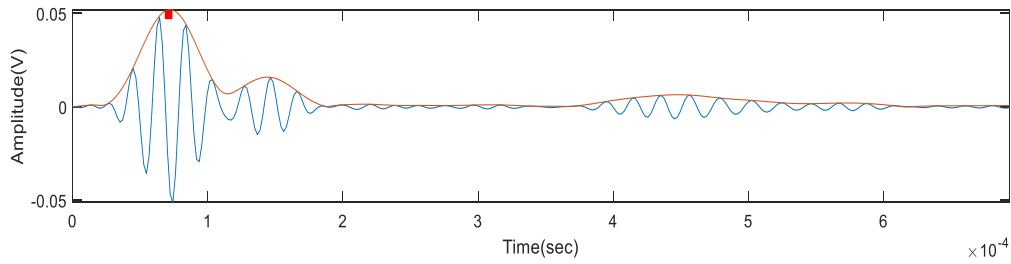


Figure 4: Time of arrival extraction

Figure 5 shows the different snapshots from the animation of the propagation of waves for 50 kHz excitation. At figure 5a the waves get excited from the PZT location to propagate in the plate. Then waves reached the middle stiffener region as shown in figure 5b. At figure 5c the propagating waves reaching the L-stiffener region and starts to separate indicating the region of damage. This is followed by the reflection of the waves after reaching the edges of the composite plate as shown in figure 5d. Table 1 shows the time of the first arrival of waves of various scanning points. It is understood that the time of arrival of the first wave packet is related to fundamental symmetric S0 wave mode which is faster than the fundamental antisymmetric A0 wave mode (also termed as slow waves in general).

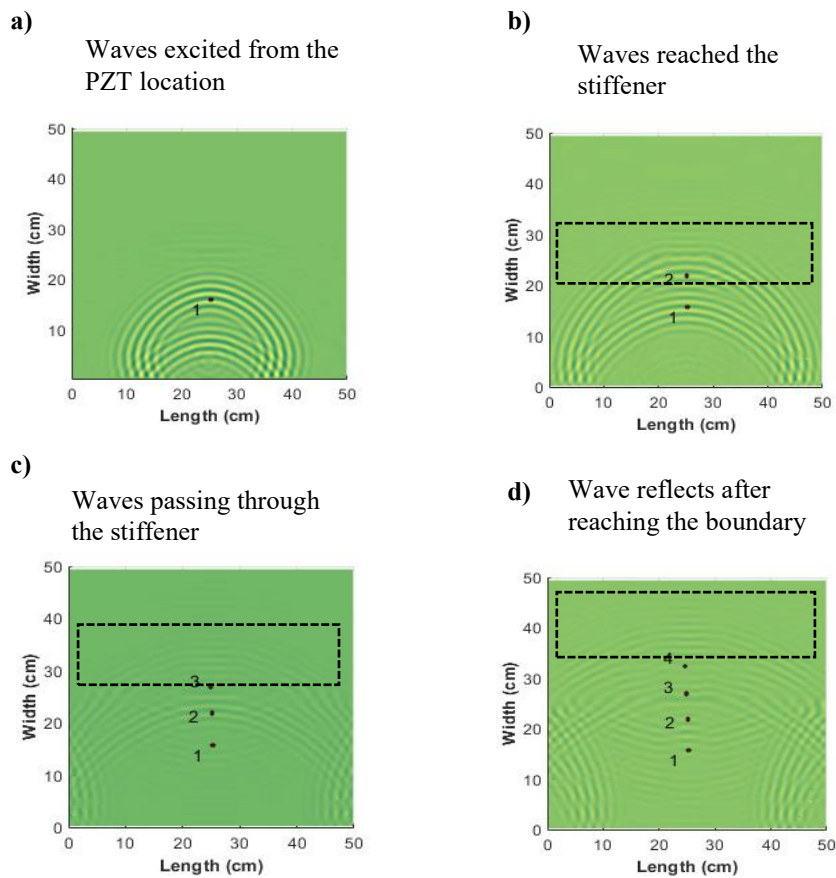


Figure 5: Wave propagation for 50 kHz frequency in an L-stiffened GFRP plate recorded at a) 70 μ s, b) 210 μ s, c) 281 μ s, d) 296 μ s

Point location	First arrival point (μsec)
1	70
2	210
3	281
4	296

Table 1: Time of arrival values of the S0 mode for varying scanning point

3.1 1D plot analysis:

In this section, a one-dimensional analysis is performed. The graphs are plotted by selecting points in two configurations as presented in figure 6a for case 1 and figure 6b for case 2 (focusing on the debonding zone). These analysis are carried out to understand the wave propagation from the results of the LDV measurements at different time points. In this study, the excitation with frequency 50 kHz is applied to PZT 3.

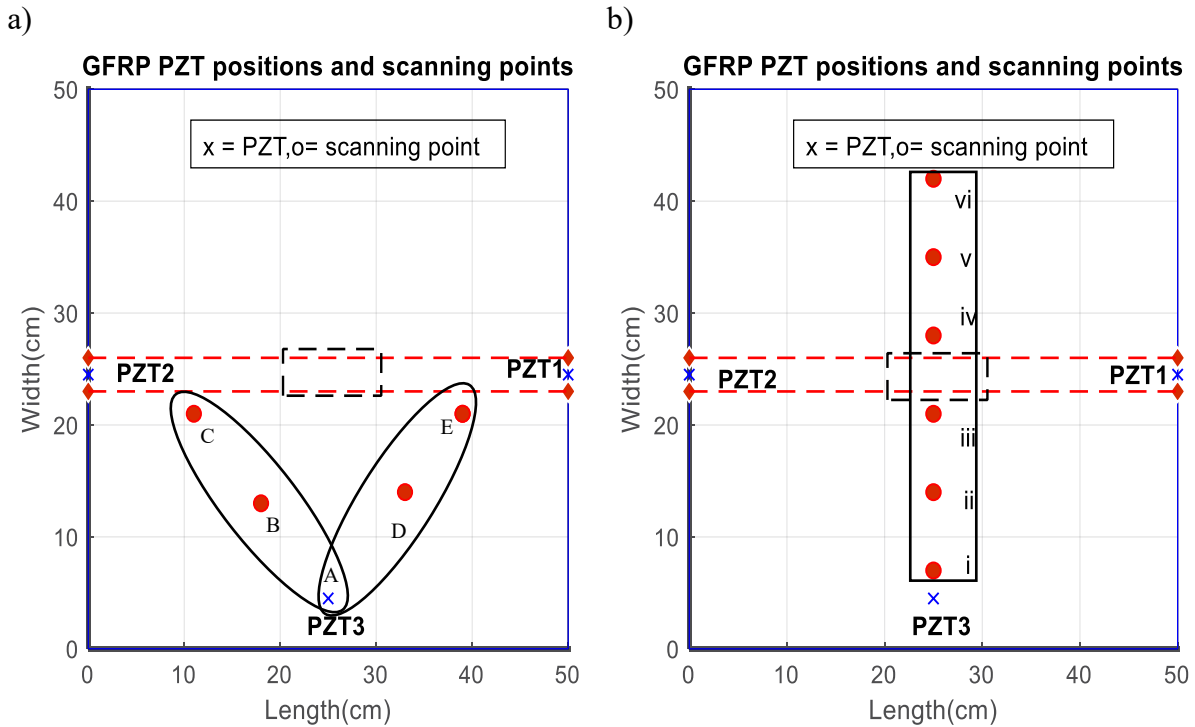
**Figure 6:** Scanning point distribution a) Case 1-angular distribution b) Case 2-linear distribution

Figure 7 indicates the wave propagation for case 2 of points distribution (i-vi) respectively. The case 2 analysis reveals that at the stiffener region which is at the mid-section of the plate occurs larger disruption of the signals indicating the damage region. Figure 7e indicates the wave propagation where it interacts with the stiffener region and passes through it. We have noticed the decrease in the wave amplitude as shown in table 2 is due to structural damping and reflection of the waves after striking the boundary. The case 2 plot informs about the waves and its propagation at various linear paths. We have found the change in the wave pattern happening

in the particular region as shown in figure 7d,e after it passes through the damage stiffener region. Figure 6a case1 is used to understand the propagation of the waves in an angular fashion before the debonding zone. There occurs a change in the amplitude and velocity values before and after the disbond region as shown in table 2 and table 3 respectively.

a) Points	Amplitude difference drop (%)	b) Points	Amplitude difference drop (%)
A-B	83.80	i-ii	54.63
B-C	55.21	ii-iii	38.44
A-D	83.33	iii-iv	75.59
D-E	44.41	iv-v	29.93

Table 2: Amplitude variation a) Case 1-angular distribution b) Case 2-linear distribution

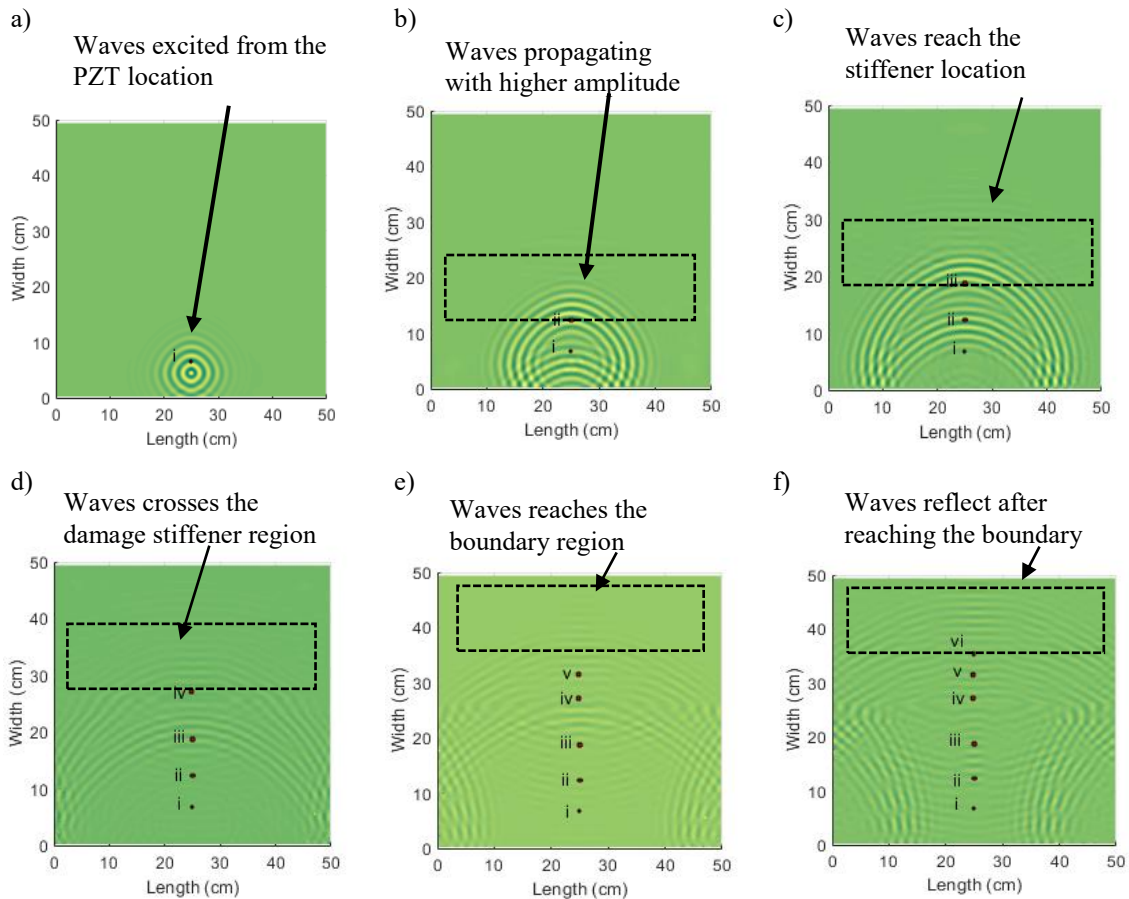


Figure7: Case 2 analyzed at a) 78 μ s, b) 130 μ s, c) 180 μ s, d) 250 μ s, e) 0.29 μ s, and f) 340 μ s

The velocity of the waves is analyzed as shown in table 3. This table shows the result for the case 1 and shows that higher velocity mode S0 mode that propagates from the PZT travels along the line and strikes the debonding region. Thereby an increase in velocity is noted at the path

between points B and C. Also from case 2, the velocity of the waves drops after crossing the debonded stiffener region as shown in points (iii-iv) and then the velocity increases which may be due to higher reflection from the boundary surfaces that results in the overlapping and interfering in the wave movement.

a) Case 1	A-B	B-C	A-D	D-E
Velocity (m/s)	702.459	875	702.459	875

b) Case 2	i-ii	ii-iii	iii-iv	iv-v	v-vi
Velocity (m/s)	1076.26	1328.27	995.73	1790.28	1328.27

Table 3: Velocity distribution a) Case 1-angular distribution b) Case 2-linear distribution

We have also used the root mean square deviation (RMSD) index for signal analysis in this paper [11]. The time signal is limited to 208 μ s to understand the change in the signals before and after the debonded region. Figure 8 is made with the RMSD formulation as shown below in equation (1):

$$RMSD = \sqrt{\sum_{i=1}^N \left(\frac{(a_i - b_i)^2}{(a_i)^2} \right)} \quad (1)$$

where: a - amplitude values for reference scanning point, b - amplitude values for final scanning point, N - no of time samples

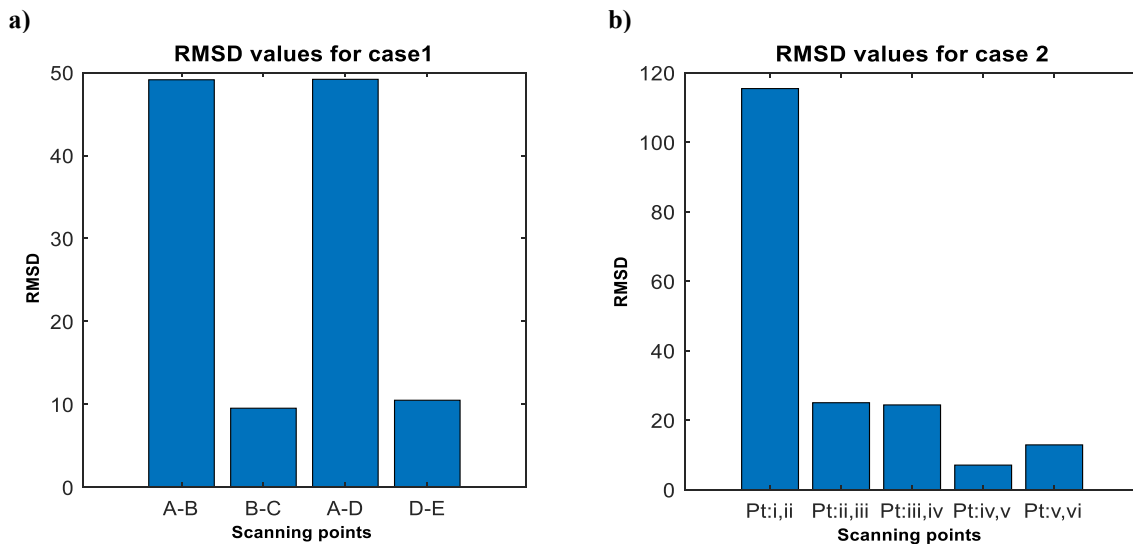


Figure 8: RMSD values a) Case 1-angular distribution b) Case 2-linear distribution

From figure 8a, the RMSD results are analyzed for situation waves have not reached the stiffener region yet. It shows symmetrical values of RMSD index values for two paths of wave propagation. By analysing results presented in figure 8b it could be noted that the RMSD index values drop in a linear fashion and between points i, ii it shows higher wave signal difference. The RMSD values for case 2 do not indicate the influence of the stiffener disbond.

4 CONCLUSION

The paper shows the experimental approach for assessing the influence of stiffener debonding on wave propagation in the composite plate. The methodology is based on analysing the amplitude changes in the wave patterns before it reaches the debonding zone (L-stiffener) and the amplitude change after it crosses the debonding region. The process done may be concluded that the approaches used helps to assess the L-stiffener region. The amplitude gets reduces at the stiffener region indicating a decrease in the energy of the propagating waves. The use of LDV helps in measuring the wave measurements and velocity. In most of the cases, the basic symmetric and antisymmetric modes (A0 and S0) are detected. The excitation signals help to map the damage L-stiffener zone well. The 50 kHz maps the damage region well and thus chosen to be studied further.

The final conclusion is that the amplitude graphs from plotting distributed scanning points help to locate the damage region in the composite plate. The identification of the distributed waves at the L-stiffener region gets identified by the excitation frequency 50 kHz which produce shorter wave movements. These waves pass through the other side of the stiffener and reflect back after touching the boundary.

ACKNOWLEDGMENT:

The authors would like to acknowledge the support funding provided by the National Science Center, Poland under SONATA BIS project titled: Study of piezoelectric sensors placement and their interaction with structural elements (2016/22/E/ST8/00068).

Acknowledgment also provided to Task-CI for allowing the use of computational resources.

REFERENCES

- [1] Gresil, M. Giurgiutiu, V. Guided wave propagation in carbon composite laminate using piezoelectric wafer active sensors. *Proc. of SPIE*. (2013) 86: 1-13.
- [2] Rucka, M. Wojtczak, E and Lachowicz, L. Detection of debonding in adhesive joints using Lamb wave propagation. *MATEC Web of Conferences*, Krynica 2018. (2018) 262: 1-6.
- [3] Gaul, L. Bischoff, S. Sprenger, H. Haag, T. Numerical and experimental investigation of wave propagation. *Eng. Fract. Mech.* (2010) 77: 3532–3540.
- [4] Allen, C. Owens, C. T. Swenson, E. D. Lamb Wave interaction with a T-Joint in Structural Health Monitoring, *Trans Tech Publications*, Stanford. (2011), 2231–2236
- [5] Sohn, H. Dutta, D. Yang, J. Delamination detection in composites through guided wave field image processing, *Compos. Sci. Technol.* (2011) 71: 1250–1256

- [6] Duflo, H. Morvan, B and Izbicki, J.L. Interaction of Lamb waves on bonded composite plates with defects, *Compos. Struct.* (2007)79: 229–233.
- [7] Owens, C. T. Swenson, E. D. and Allen, C. Visualization of Lamb wave interaction with, in: Structural Health Monitoring, Trans Tech Publications, Stanford (2011), 2260–2266.
- [8] Kehlenbach, M. Kohler, B. Cao, X. and Hanselka, H. Numerical and Experimental Investigation of Lamb Wave Interaction with Discontinuities. In Proceedings of the 4th International Workshop on Structural health monitoring: (2003), 421-428.
- [9] Radziński, M. Doliński, Ł. Krawczuk, M. Żak, A and Ostachowicz, W. Application of RMS for damage detection by guided elastic waves. *J. Phys.: Conf.* (2011) 305: 1-10.
- [10] Staszewski, W.J. Mahzan, S. and Traynor, R. Health monitoring of aerospace composite structures. *Composites Science and Technology.* (2009) 69: 1678-85.
- [11] Su, Z.Ye, L. *Identification of damage using Lamb waves*. Vol:48(2009) Springer.

DAMAGE ASSESSMENT IN COMPOSITE POWERBOAT USING ELECTROMECHANICAL IMPEDANCE METHOD

W. OSTACHOWICZ^{*}, T. WANDOWSKI^{*}, P. MALINOWSKI^{*},
B. PUCHOWSKI^{**} AND J. MOLL[†]

^{*} Institute of Fluid-Flow Machinery Polish Academy of Sciences
Fiszera 14, 80-231 Gdansk, Poland
e-mail: wieslaw@imp.gda.pl, web page: <http://www.imp.gda.pl>

^{**} CreeYacht
Platynowa 16, 84-123 Rekowo Gorne, Poland
email: bartosz@creeyacht.pl, web page: <http://www.creeyacht.pl>

[†] Goethe University of Frankfurt am Main,
Max-von-Laue-Straße 1, 60438 Frankfurt am Main, Germany
email: moll@physik.uni-frankfurt.de, web page: <https://www.uni-frankfurt.de/>

Key words: Electromechanical Impedance, Composite Materials, Debonding, Temperature Influence.

Abstract. In this paper authors present results of application of electromechanical impedance (EMI) method based on resistance spectra for damage assessment in composite materials. The EMI method is based on measurements of electrical parameters of piezoelectric transducer bonded on the structure. Due to electromechanical coupling structural changes are seen in electrical characteristics of the piezoelectric transducer. Authors investigated influence of bonding transducer on structural parts with different material and geometrical properties on the resistance spectra. Authors investigated also influence of changing temperature and damage (stiffener debonding) existence on resistance spectra. Results showed that temperature compensation is needed for the purpose of damage detection. Authors proposed temperature compensation algorithm based on signal correlation. Research was conducted for model of structure of composite powerboat. Preliminary measurements were also conducted for the powerboat.

1 INTRODUCTION

Fibre reinforced polymer (FRP) composite structures are very popular in many branches of industry like aviation, automotive and maritime. Application of these materials allows a reduction of weight ensuring high strength to weight factor. Beside the advantages there are also disadvantages related to application of such materials. Important one is related to vulnerability of FRP composites to hidden/barely visible delamination caused by impact loading. Such a hidden damage could cause serious failure of the structure resulting in human injury or even

dead. In order to increase safety of exploitation of FRP composite structures non destructive testing (NDT) or structural health monitoring (SHM) techniques are utilised. Such methods like ultrasound testing (UT) [1], thermography [2], elastic waves propagation [2],[3] and electromechanical impedance [4], [5] are utilised.

The research reported in this paper is related to electromechanical impedance. The authors focused attention on damage detection under the temperature influence for complex composite structures utilised in real maritime structures, i.e. a powerboat. Such structures are manufactured using curved composite laminates with varying thickness, sandwich composite with honeycomb or foam filled and bonded stiffeners. Research was mainly focused on the model of composite structure utilised in powerboat construction. Preliminary research was related to real powerboat. The research that results are presented in this paper is related to development of structural health monitoring system based on electromechanical impedance method for assessment of composite powerboat.

2 ELECTROMECHANICAL IMPEDANCE METHOD

The electromechanical impedance (EMI) method is based on measurements of electrical parameters of piezoelectric transducer coupled with the investigated structure. Due to electromechanical coupling of piezoelectric transducer with the structure the mechanical resonant characteristics of structure could be indentified based on electrical characteristics of piezoelectric transducer. This method is suitable for damage detection and transducer self-diagnosis.

In the research presented in this paper measurements for EMI were realised using impedance analyser HIOKI IM3570 and piezoelectric transducers in the form of discs with diameter 10 mm and thickness 0.5 mm. Transducers were manufactured by NOLIAC using NCE51 piezoelectric material and had a wrap-around electrodes. Spectra of real part of impedance (resistance) were registered in this research.

3 EXPERIMENTAL RESEARCH

Experimental research was related to two objects. First object was a model of composite structure of powerboat (Figure 1). Model includes all the structural features related to real composite powerboat: curved sandwich GFRP honeycomb structure with thickness 4 mm (location of transducer PZT1), composite sandwich of GFRP structure filled with the foam with thickness 12 mm (location of PZT2), bonded stiffeners (e.g. CFRP stiffener with thickness 3mm – location of PZT3).

Second object was composite powerboat. In the Figure 2 the rear part of powerboat including structure where the engine is mounted was shown. This structure was equipped with piezoelectric transducer PZT4. Transducer was located near bolted joints connecting engine to the powerboat.

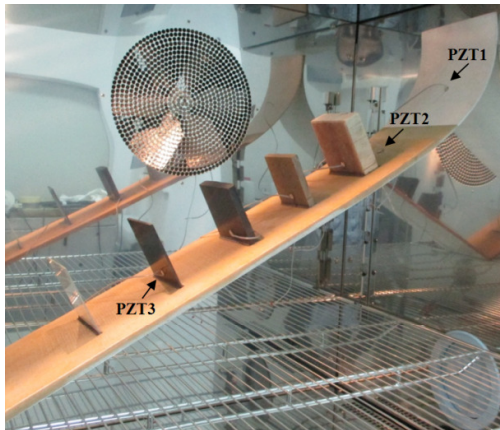


Figure 1: Model of composite structure of powerboat in climate chamber



Figure 2: Demonstrator of composite powerboat

3.1 Influence of structure of EMI characteristics

First step was related to study the influence of bonding of piezoelectric transducer on structures with different material and geometry properties on EMI resistance spectra. All measurements were performed in the room temperature.

In the Figure 3a) resistance spectrum for free (not bonded) piezoelectric transducer was presented. Peak with largest amplitude at frequency 220 kHz is related to radial resonance of transducer which could be estimated using frequency constant of NCE51 piezoelectric material. In the Figure 3b) resistance spectrum for the piezoelectric transducer PZT1 bonded on the curved part of model of composite structure (Figure 1) was presented. Model was installed in the climatic chamber (Figure 1). Influence of bonding on structure is clearly visible. Peak with frequency 220 kHz is much wider and its amplitude was reduced. Frequency of small peak at 500 kHz for free transducer after bonding remains almost the same. Frequency of small peak at 800 kHz for free transducer after bonding increased to about 850 kHz. Additionally after bonding new peak at frequency around 100 kHz could be noticed. In the Figure 4a) magnification of frequency band up to 150 kHz for bonded transducer PZT1 was presented. Peaks related to resonant frequencies of the structure with bonded transducer could be noticed.

In the Figure 3c) resistance spectrum for transducer PZT2 bonded on the thicker part of composite model filled with the foam is presented. There are large peaks about frequencies 250 kHz and 550 kHz and peak at frequency 50 kHz. In the Figure 4b) low frequency region of resistance spectrum was presented. Resonant peaks below frequency 25 kHz have smaller amplitudes than for transducer PZT1.

In the Figure 3d) resistance spectrum for transducer PZT3 bonded on CFRP stiffener (100 mm x 100 mm x 3 mm) bonded to the composite model was presented. Additional peaks in the region about 200 kHz – 350 kHz are visible.

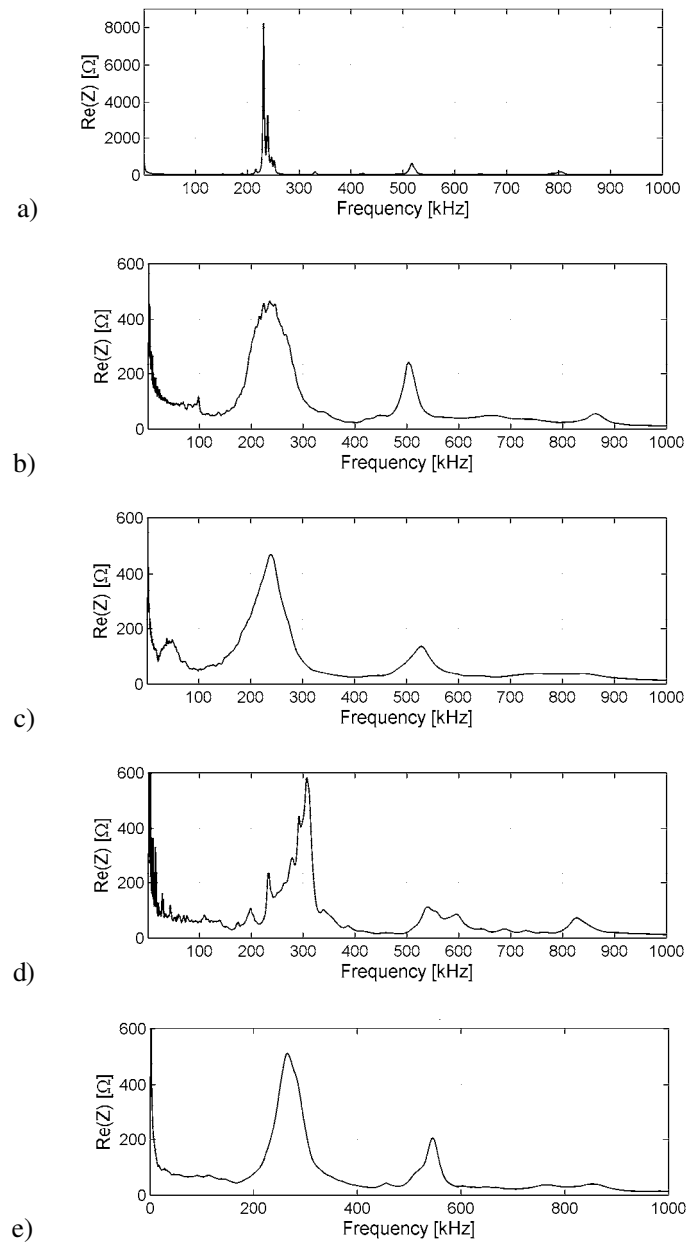


Figure 3: Resistance spectra for piezoelectric transducers: a) free, b) PZT1, c) PZT2, d) PZT3, e) PZT4

Moreover, resonant peaks for frequencies lower than 100 kHz are visible. This could be clearly visible in the Figure 4c). There are clear and strong peaks related to the resonant frequencies of this stiffener.

In the Figure 3e) resistance spectra for transducer PZT4 bonded on the powerboat (Figure 2) was presented. There are two large peaks at frequencies about 250 kHz and 550 kHz. Resonant peaks for frequencies below 150 kHz are clearly visible in Figure 4d). Amplitudes of those peaks are very low. Summarising all presented results, it could be noticed that amplitudes for resonant peaks for frequencies bellow 150 kHz decrease with increase of the thickness of the structure.

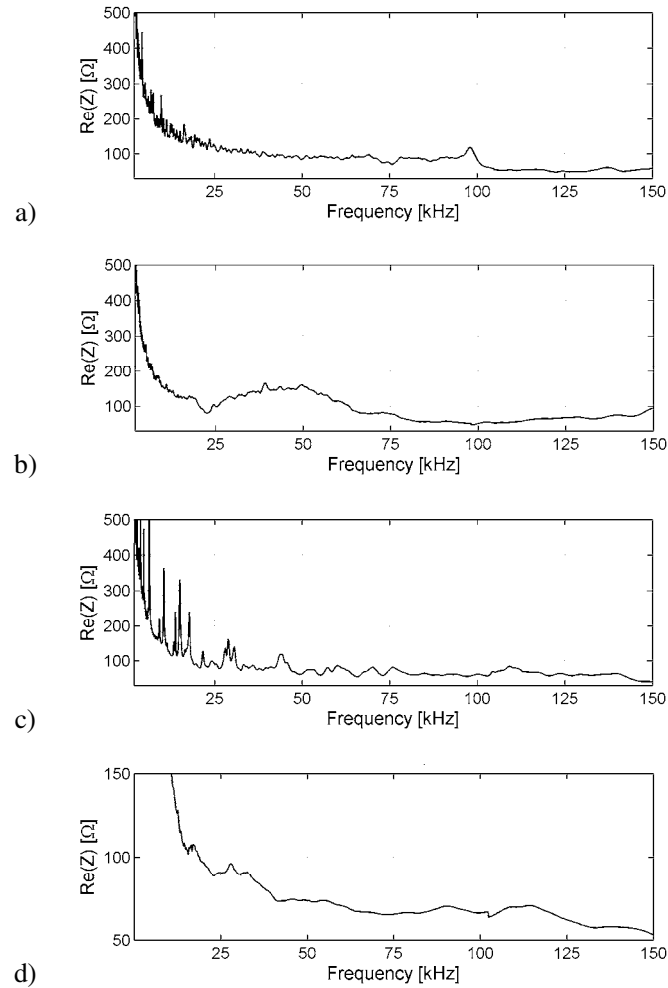


Figure 4: Low frequency region of resistance spectra for piezoelectric transducers:
a) PZT1, b) PZT2, c) PZT3, d) PZT4

3.2 Influence of temperature on EMI characteristics

In next step analysis of influence of changing temperature on resistance spectra for piezoelectric transducer PZT3 bonded on the composite model of structure of powerboat (Figure 1) was investigated. This is very important problem, because changing temperature is source of change of resistance spectra and it can result in false alarms in the SHM systems. Therefore temperature compensation needs to be performed. Measurements for this part of research were performed in climatic chamber under 5 stable temperatures 30, 20, 10, 0 and -10°C .

In the Figure 5 results in the form of resistance spectra for two selected frequency bands were presented. In the Figure 5a) resistance spectra for frequency band 8–17 kHz was presented. As referential resistance spectrum for temperature 30°C is taken. With decreasing temperature resonant peaks shift rightwards. In the Figure 5b) resistance spectrum for frequency range 200–350 kHz was presented. In this case the same effect is observed. Resonant frequencies shift rightwards with decreasing temperature. Such effects were observed in the whole investigated frequency band 1 kHz –1 MHz.

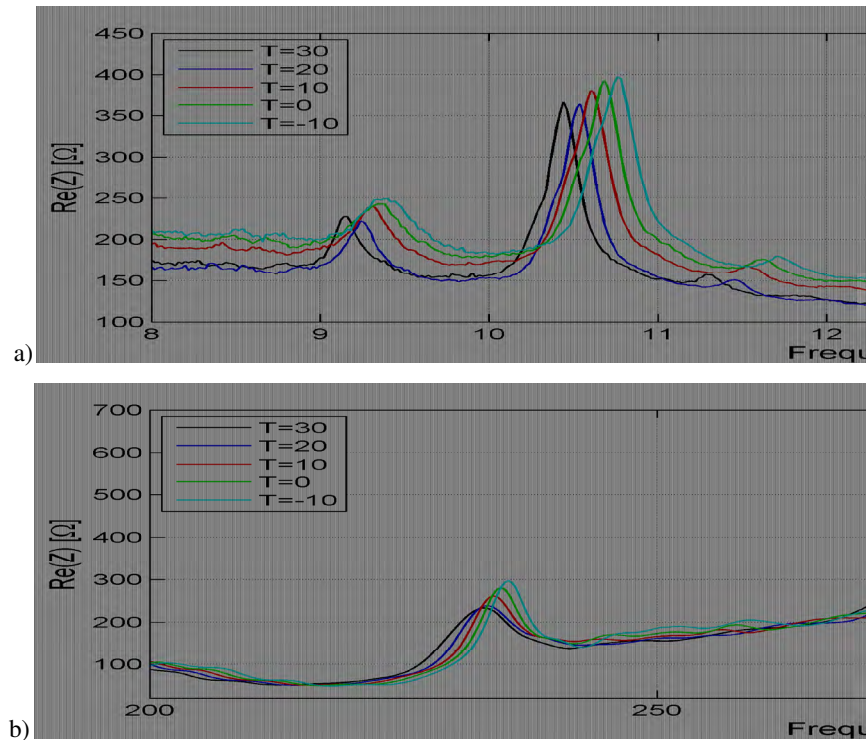


Figure 5: Influence of changing temperature on resistance spectra for frequency band:
a) 8–17 kHz, b) 200–350 kHz

3.3 Influence of debonding on EMI characteristics

Next part of research was related to influence of debonding of CFRP stiffener on resistance spectra. In this case measurements were also taken by transducer PZT3 bonded on the stiffener (Figure 1). Artificial debonding was simulated by 10 mm long cut of bonding layer joining stiffeners with the model (Figure 6).

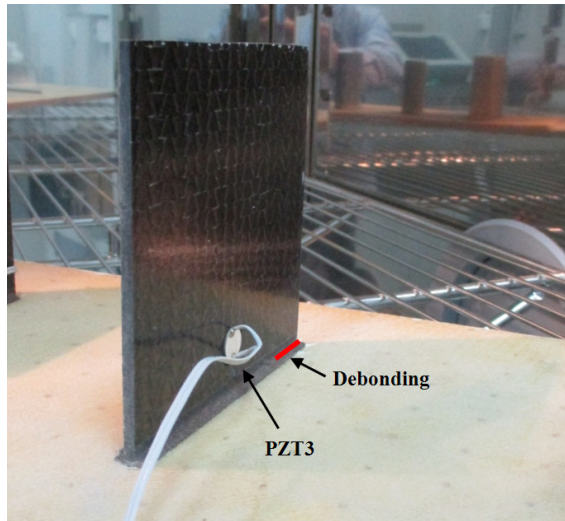


Figure 6: Artificial debonding of stiffener

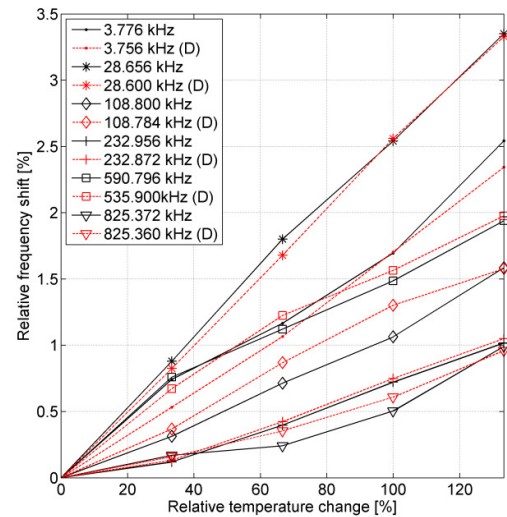


Figure 7: Relative frequency shift as a function of relative temperature change for pristine and damaged structure (D)

Investigations started from analysis of temperature influence on frequency shift for pristine (healthy) and damaged structure. Few resonant peaks were selected from the resistance spectra for both cases. Then the frequency shifts for both cases (pristine and damaged) were extracted taking as a reference spectra gathered at temperature 30 °C. Relative frequency shifts for pristine and damaged structure in the function of relative temperature change are plotted in Figure 7. It could be noticed that relative frequency shifts for pristine and damaged structure differ.

For detailed analysis resonant peak from frequency band 3.6-4 kHz (peak with frequency 3.776 kHz for pristine and 3.756 kHz for damaged structure) was considered. Debonding of the stiffeners caused leftward shift for the selected peak. In Figure 8a) comparison of resistance spectrum for pristine structure (R30) and structure with deboned stiffener (D30) both measured at temperature 30 °C were presented. It could be noticed that in the case of debonding resonant peak was shifted leftwards in respect to the one from healthy structure. In the same figure, also the spectrum for the pristine structure taken at temperature 20 °C was presented. In this case rightwards shift of peak in pristine structure for decreasing temperature is observed. Decrease of temperature by 10 °C for pristine structure caused similar value of frequency shift like debonding but direction of the shift is opposite.

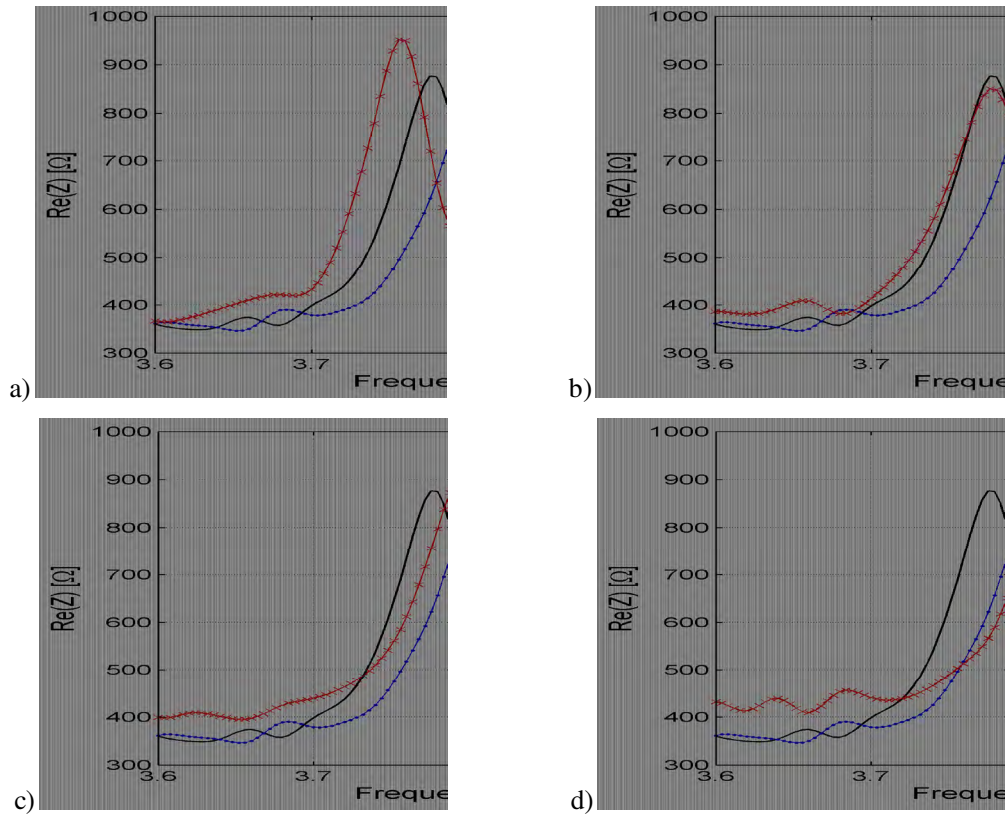


Figure 8: Influence of temperature and debonding on selected resonant peak, deboned stiffener measured at:
a) 30 °C, b) 20 °C, c) 10 °C, d) 0 °C

In the Figure 8b) resistance spectra for pristine structure taken at referential temperature 30 °C (R30) and at temperature 20 °C (R20) are compared with resistance spectrum for deboned structure at temperature 20 °C (D20). It could be noticed that resonant peak for deboned structure measured at decreased temperature 20 °C (D20) has similar frequency to the pristine spectrum taken at referential temperature 30 °C (R30). So a damage indicator based on the shift of resonant peak would not distinguish differences between pristine and damaged structure. Influence of debonding together with decrease of temperature by 10 °C caused that resonant frequencies for pristine and damaged structure are almost the same.

In the Figure 8c) effects of further decrease of temperature for deboned stiffener could be observed. Resistance spectrum for deboned structure at temperature 10 °C (D10) was plotted. Moreover resistance spectra for pristine structure taken at temperatures 30 °C (R30) and 20 °C (R20) were plotted. Resonant peak for deboned structure (D10) was further shifted rightward due to temperature decrease. However, its shift is still lower than for the peak at temperature 20 °C for pristine structure (R20). Further decrease of temperature to 0 °C for deboned structure caused further shift of resonant peak (D0) what is presented in Figure 8d). Resonant peak for deboned structure at temperature 0 °C (D0) is more shifted than resonant peak for pristine structure at temperature 20 °C (R20). This analysis shows that effects of changing temperature need to be compensated for the problem of damage detection.

3.4 Compensation of changing temperature influence

In the purpose of compensation of temperature influence formula (1) is utilised. This allows comparing the correlation of resistance spectra at referential and changed temperature conditions.

$$CCD = 1 - \sum_{i=1}^n \frac{[R(i)_0 - \bar{R}_0] [R(i)_1 - \bar{R}_1]}{\sigma_0 \sigma_1} \quad (1)$$

where: $R(i)_0$ – is the i -th sample of resistance spectrum in signal at referential temperature, $R(i)_1$ – is the i -th sample of temperature influenced resistance spectrum, \bar{R}_0, \bar{R}_1 – mean values of respectively referential and temperature influenced spectra, σ_0, σ_1 – standard deviations for referential and temperature influenced spectra. Temperature influenced resistance spectrum is shifted in such a manner in order to obtained the minimum value of CCD index indicating maximum correlations of the signals. As results frequency shift needed to obtain best match of analyzed signals is registered.

This approach was utilized for resistance spectra including selected resonant peak for pristine structure for temperatures: 20, 10, 0 and -10 °C. In the Figure 9 frequency shift in the function of temperature was plotted for the investigated temperature change.

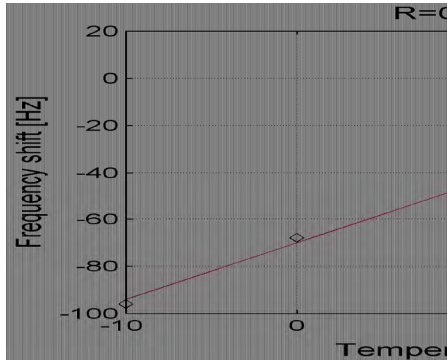


Figure 9: Frequency shift in the function of temperature for pristine structure

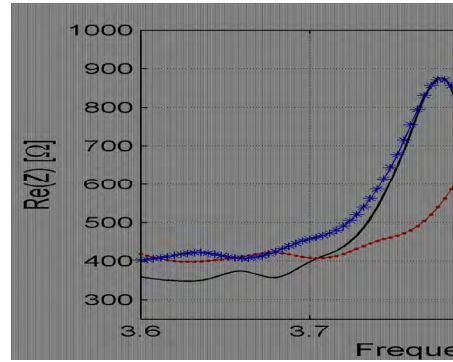


Figure 10: Results of temperature compensation for pristine structure

It could be noticed that this shift is linear for investigated temperature range. In the Figure 10 result of temperature compensation algorithm for selected peak was presented. In this figure spectra for pristine structures taken at temperature 30 °C (R30) and 10 °C (R10) were presented. Frequency shift due to temperature decrease is clearly visible. Moreover, compensated spectrum (RC10->30) which was shifted based on relation presented in Figure 9 was shown. It could be noticed that frequency shift was removed. In the Figure 11a) values of CCD index for comparison of signals for pristine structure at different temperatures were presented. In this case referential resistance spectrum at temperature 30 °C was compared with the spectra taken at temperatures 20, 10, 0 and -10 °C. CCD index values for those cases were marked respectively as R20, R10, R0 and R-10.

In the Figure 11b) results of influence of compensation of temperature change on CCD index were plotted. CCD index values for compensated spectra were marked respectively as RC20->30, RC10->30, RC0->30, RC-10->30. It could be noticed that values of CCD index decreased significantly after the compensation. This indicates the fact that frequency shift caused by temperature change was removed.

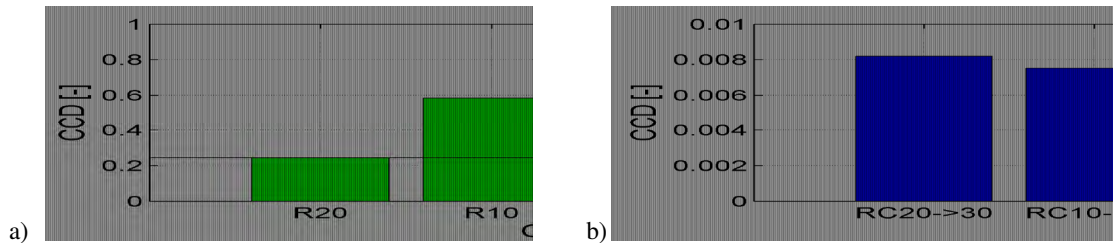


Figure 11: The CCD index values for comparison of referential spectrum with temperature influenced spectra for pristine structure: a) before compensation, b) after compensation (see descriptions in the text)

Then such approach was utilised for the spectra for deboned stiffener registered at different temperatures. In this case spectrum for pristine structure taken at temperature 30 °C was compared with spectra registered at different temperatures for damaged structure. Results in the form of values of CCD index were presented in the Figure 12. First value (R20) is related to comparison with the spectra for pristine structure at temperatures 30 and 20 °C. Next results of comparison were presented of spectrum for pristine structure at temperature 30 °C with spectra for damaged structure at temperatures 50, 30, 20, 10, 0 and -10 °C in the form of CCD index values. Measurement at temperature 50 °C for damaged structure was utilised for the purpose of verification temperature compensation algorithm. CCD index for this case is the largest. Analysing further values of CCD index it could be noticed that decrease temperature to 20 °C for pristine structure has larger influence on CCD than debonding for structure at referential temperature 30 °C. Decreasing the temperature of damaged structure to 20 caused that CCD is even smaller than for temperature 30 °C. Then slightly CCD is increased for temperature 10 °C. In the case of temperature 0 °C CCD value for damaged structure is higher than CCD valued for pristine structure at temperature decreased to 20 °C. This is related to frequency shift of signal due to temperature and debonding discussed in for the Figure 8. In the case of damage structure at temperature -10 °C CCD index further increased. This shows that without temperature compensation correct damage assessment is not possible. Therefore procedure of temperature compensation for spectra taken for damaged structure at different temperatures was performed. In this case frequency shifts for compensation were taken from the case of analysis performed for pristine structure. In the case of temperature 50 °C (lack of spectrum for pristine structure) frequency shift was extrapolated based on linear relation presented in Figure 9. Results of temperature compensation were presented in Figure 12. The CCD index values for compensation cases were marked as DC50->30 – DC-10->30. The values of CCD index for compensated spectra for damaged structure at temperatures: 20, 10, 0, -10 and 50 °C are similar like for damaged structure at 30 °C. It could be noticed that CCD for the case DC50->30 related to damaged structure measured at 50 °C and compensated to 30 °C is much larger than for the rest compensated cases.

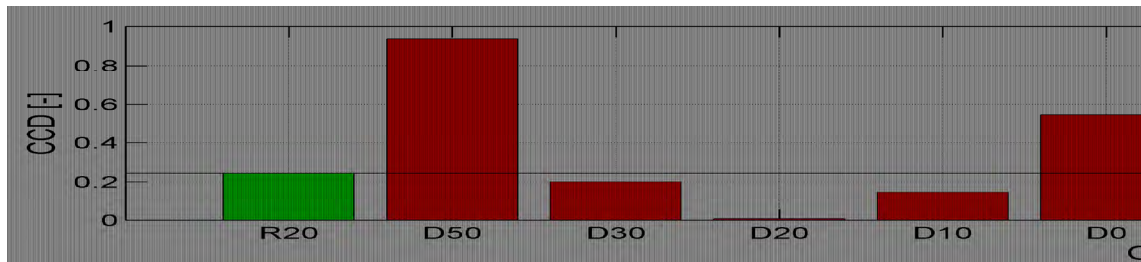


Figure 12: The CCD index values for comparison of referential spectrum with temperature influenced spectra for damaged structure before and after compensation (see descriptions in the text)

In the Figure 13 results of temperature compensation for spectra measured for damaged structures at temperatures 10 and 50 °C were presented. In the Figure 13a) spectra for damaged structure measured at temperatures 30 °C (D30) and 10 °C (D10) were presented. Moreover spectrum measured at temperature 10 °C and compensated to temperature 30 °C was presented. It could be noticed that spectrum after temperature compensation (DC10->30) does not perfectly match the spectrum measured at temperature 30 °C (D30).

The same approach was performed for the spectrum for damaged structure taken at temperature 50 °C. Results are presented in the Figure 13b). In this figure spectra at temperatures 30 °C (D30) and 50 °C (D50) were presented. Moreover, compensated spectrum from 50 °C to 30 °C (DC50->30) was presented. This compensated spectrum also does not match the spectra measured at temperature 30 °C (D30). This could be caused by fact that for compensation frequency shift was extracted from the case of pristine structure. Damage changed slightly the influence of temperature on frequency shift (see Figure 7). This could also be caused by fact that value of frequency shift for temperature 50 °C was extrapolated due to the lack of value of frequency shift for pristine structure.

Moreover, analyzing results in the Figure 13 it could be noticed that decreasing temperature from 30 to 10 °C caused rightward frequency shift (Figure 13a) while increasing temperature from 30 to 50 °C caused leftward shift (Figure 13b).

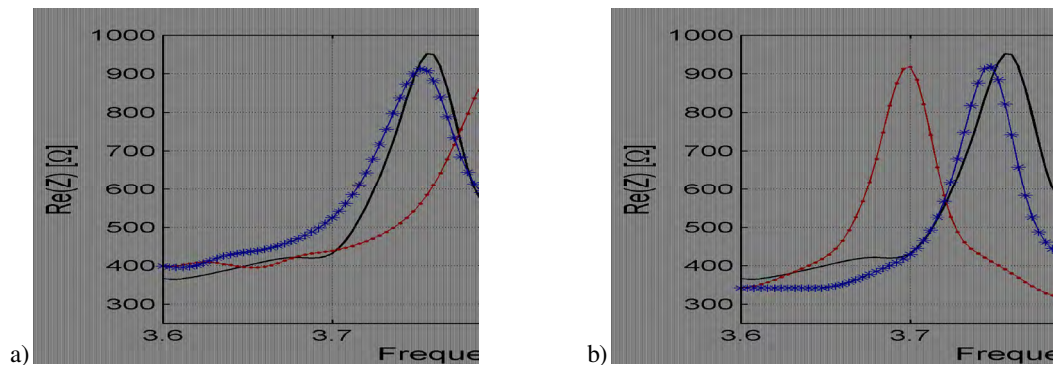


Figure 13: Results of temperature compensation for damaged structure at temperature: a) 10 °C, b) 50 °C

CONCLUSIONS

In this paper influence of bonding of piezoelectric transducer on composite structures with different material and geometrical properties on resistance spectra for EMI method was

discussed. It was noticed that amplitudes of resonant peaks for frequencies below 150 kHz were smaller for the thicker structures.

Detailed analysis of influence of changing temperature on resistance spectra was also investigated. Changing temperature caused leftward shift with decreasing temperatures observed for frequency range 1 kHz – 1 MHz. For selected resonant peak in low frequency range (3.5-4 kHz) linear frequency shift was noticed for the changing temperature. Authors investigated positive and negative temperatures.

Moreover influence of debonding of stiffener on change of resistance spectra was investigated. In this case additional influence of temperature on damaged structure was investigated. It was shown that compensation of changing temperature influence is needed for the purpose of damage detection. Temperature compensation algorithm based on cross-correlation was proposed. Application of this algorithm allowed compensating the influence of temperature.

Further work will be related to similar test for the transducers installed on a powerboat. Measurements will be also carried out on the water in the real operational conditions.

ACKNOWLEDGEMENTS

The authors gratefully acknowledge the financial support of this research by National Centre for Research and Development in Poland (grant: Reliable and Autonomous Monitoring System for Maritime Structures MARTECII/RAMMS/1/2016).

Jochen Moll acknowledges the financial support by the Federal Ministry for Economic Affairs and Energy (grant: 03SX422B).

REFERENCES

- [1] J. Neuenschwander, R. Furrer, A. Roemmeler: Application of air-coupled ultrasonics for the characterization of polymer and polymer-matrix composite samples. *Polym Test*, 56, 379–386, 2016.
- [2] M. Kersemans, E. Verboven, J. Segers, S. Hedayatrasa, W.V. Paepegem: Non-Destructive Testing of Composites by Ultrasound, Local Defect Resonance and Thermography. *MDPI Proc.*, 2(8), 554, 2018.
- [3] Y. Rena, L. Qiu, S. Yuan, Z. Su: A diagnostic imaging approach for online characterization of multi-impact in aircraft composite structures based on a scanning spatial-wavenumber filter of guided wave. *Mech Syst Signal Pr*, 90, 44-63, 2017.
- [4] W.S. Na, J. Baek: A Review of the Piezoelectric Electromechanical Impedance Based Structural Health Monitoring Technique for Engineering Structures. *Sensors (Basel)*, 18(5): 1307, 2018.
- [5] K. Neuenschwander, J. Moll, V. Memmolo, M. Schmidt, M. Bucker: Simultaneous Load and Structural Monitoring of a Carbon Fiber Rudder Stock: Results from a Quasi-Static Tensile Test. *J Intell Mater Syst Struct*, 2018.

DAMAGE DETECTION BASED ON MULTIVARIATE APPROACH: APPLICATION TO AEROSPACE COMPOSITE STRUCTURES

RAFIK HADJRIA*, OSCAR D'ALMEIDA*

*Address: Safran Tech, Safran Sensing System,
Rue des Jeunes Bois, Châteaufort 78114 Magny-Les-Hameaux, France
e-mail: rafik.hadjria@safrangroup.com
oscar.dalmeida@safrangroup.com

Key words: Structural Health Monitoring, Impact testing, Delamination flaw, Principal component analysis, Information theory, Angle between subspaces.

Abstract. Commercial composite aerospace structures are required to be designed and life cycle managed under the damage tolerant principle, while the airworthiness is maintained through the process of scheduled inspection, repair or replacement [1]. In that sense, the scheduled inspection of a structural component is addressed by visual and if needed by non-destructive inspection (NDI) techniques. However, this current practice accounts for more than 27% of the total cost of an aircraft [2], where this cost is mainly due to the high degree of human interaction, and the fact that the structural components which are difficult to access have to be disassembled. To reduce the maintenance cost, Structural Health Monitoring (SHM) has emerged in the inspection strategies, where the health state of the structure is monitored using in-situ sensors [3]. Along with sophisticated data management and multiphysics modeling, the actual state of the structure can be assessed (in sense of reliability), and its remaining useful can be prognosed.

The objective of this study is the development of a damage detection methodology based on principal component analysis, applied to composite coupons that have undergone different impact energies and delaminated area.

2 EXPERIMENTAL SETUP

The test set-up consists of “49” composite coupons of dimensions: $400 \times 400 \times 2$ [mm³]. Six single-lead zirconate titanate (PZT) were surface-mounted on each coupon using an adhesive (cf. Figure 1). The employed PZT emitters/receivers are “10 mm” in diameter and “0.5 mm” in thickness. An SHM hardware/data acquisition were used to carry out the experiments using a pitch-catch setup. A pulse with a duration of 100 μ s was driven the PZT in round-robin mode with sampling frequency acquisition of 5 MHz.

After the baseline signals were recorded on each coupon, impact testing with different energies were carried out in order to obtain different size of delaminated area (cf. Figure 2-3). It is to be noted that impact energies were defined from 8 to 13 J, with different location on the coupons.

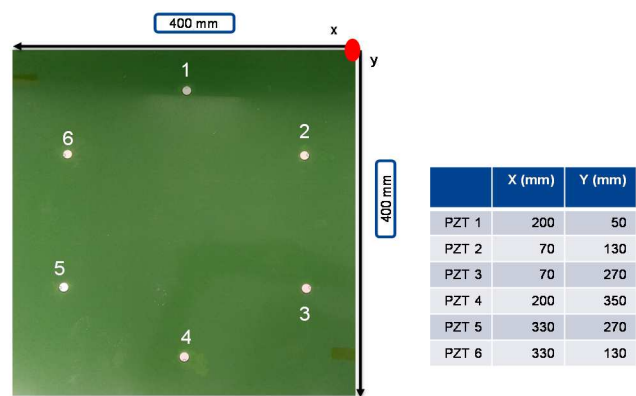


Figure 1: Layout of the PZT sensors/actuators

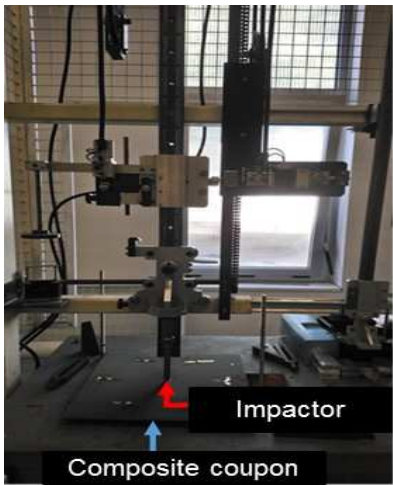


Figure 2: Impact testing set-up

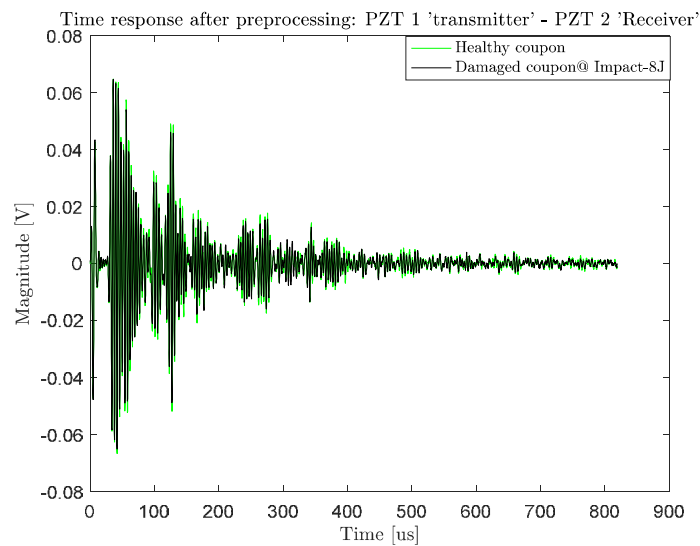


Figure 3: Raw data: healthy and damaged state

3. DAMAGE DETECTION APPROACH

3.1 Blind Source Separation

Let $\underline{\mathbf{y}}(k)$ be a zero mean measurement vector from n_y PZT sensors at time index k :

$$\underline{\mathbf{y}}(k) = [y_1(k) \dots y_{n_y}(k)]^T \quad (1)$$

The measurement matrix $\mathbf{Y} \in \mathbb{R}^{n_y \times N}$ gathering N samples $\underline{\mathbf{y}}(k) (k = 1, \dots, N)$ is defined as follows:

$$\mathbf{Y} = [\underline{\mathbf{y}}(1) \dots \underline{\mathbf{y}}(N)] \quad (2)$$

The linear Blind source separation (BSS) is defined as [4-5]:

$$\underline{\mathbf{y}}(k) = \mathbf{T}\underline{\mathbf{s}}(k) + \underline{\boldsymbol{\epsilon}}(k) \quad (3)$$

where \mathbf{T} is the mixing matrix, $\underline{\mathbf{s}}(k) = [s_1(k) \dots s_{n_y}(k)]^T$ is the sources vector and $\underline{\boldsymbol{\epsilon}}(k) = [\epsilon_1(k) \dots \epsilon_{n_y}(k)]^T$ represents all the uncertainties and perturbation effects (modeling uncertainty and noises). In the present study, we consider the noise-free model (4):

$$\underline{\mathbf{y}}(k) = \mathbf{T}\underline{\mathbf{s}}(k) \quad (4)$$

BSS is an estimation problem, and it is accomplished by finding simultaneously an estimated sources vector $\underline{\hat{\mathbf{s}}}(k)$ and a separation matrix noted \mathbf{W} only from the observed data $\underline{\mathbf{y}}(k)$:

$$\underline{\mathbf{r}}(k) = \underline{\hat{\mathbf{s}}}(k) = \mathbf{W}\underline{\mathbf{y}}(k) \quad (5)$$

where $\underline{\mathbf{r}}(k) = [r_1 \dots r_{n_y}]^T \in \mathbb{R}^{n_y \times 1}$ and $\mathbf{W} \in \mathbb{R}^{n_y \times n_y}$ are respectively the estimated sources vector at instant k and the separation matrix. Equation (5) is called the separation model.

Clearly, without additional assumptions, the BSS problem (equation (5)) is ill-posed. Cardoso [4] has shown that the BSS problem can be resolved using assumptions done on the nature of sources. In this paper, we assume that the sources are temporally identically and independently distributed (*iid*) and Gaussian, which leads to the principal component analysis method.

3.2 Principal component analysis

The separation of sources relies on the basic knowledge of the mutual independence of source components. It is then natural to resolve the BSS problem by minimizing a dependence criterion between these components. In our study, we adopt the mutual information as the separation criterion [5]. From equation (5), the solution is to find the matrix \mathbf{W} , so that the mutual information is zero. In the case where the sources are assumed to follow Gaussian distribution, the mutual information $I(\underline{\mathbf{r}})$ is given by:

$$I(\underline{\mathbf{r}}) = \frac{1}{2} \ln \frac{\prod_{i=1}^{n_y} \sigma_{r_i}^2}{\det(\underline{\Sigma}_{\mathbf{r}})} \quad (6)$$

If the components r_i of the vector $\underline{\mathbf{r}}$ have to be statistically independent, mutual information defined in (6) is equivalent to:

$$I(\underline{\mathbf{r}}) = 0 \quad \Rightarrow \quad \prod_{i=1}^{n_y} \sigma_{r_i}^2 = \det(\underline{\Sigma}_{\mathbf{r}}) \quad (7)$$

Knowing that covariance matrix $\underline{\Sigma}_{\mathbf{r}}$ is symmetric, equality (7) is satisfied if the covariance matrix $\underline{\Sigma}_{\mathbf{r}}$ is diagonal: the sources are uncorrelated and statistically independent. Principal component analysis of a measurement vector $\underline{\mathbf{y}}$ is defined as a pair of matrices $\{\mathbf{P}, \underline{\Lambda}_{\Sigma_{\mathbf{y}}}\}$ such that the covariance matrix $\underline{\Sigma}_{\mathbf{y}}$ is factorized:

$$\underline{\Sigma}_{\mathbf{y}} = \mathbf{P} \underline{\Lambda}_{\Sigma_{\mathbf{y}}} \mathbf{P}^T \quad (8)$$

where $\mathbf{P} = [\underline{\mathbf{p}}_1 \cdots \underline{\mathbf{p}}_{n_y}] \in \mathbb{R}^{n_y \times n_y}$ is the matrix of eigenvectors and $\underline{\Lambda}_{\Sigma_{\mathbf{y}}}$ is the diagonal matrix of eigenvalues. The separation matrix, noted now \mathbf{W}_{PCA} , is given by:

$$\mathbf{W}_{\text{PCA}} = \underline{\Lambda}_{\Sigma_{\mathbf{y}}}^{-\frac{1}{2}} \mathbf{P}^T \quad (9)$$

In order to reduce the number of principal components (PCs), we use the cumulative percent variance (CPV). It is a measure of the percent variance captured by the first n_r PCs:

$$\text{CPV}(n_r) = 100 \frac{\sum_{i=1}^{n_r} \lambda_i}{\sum_{i=1}^{n_y} \lambda_i} \quad (10)$$

3. Damage Index and Results

We seek to detect changes in the structure by monitoring specific features estimated from baseline observation set (referred by the exponent "s") and observation set of an unknown state (referred by the exponent "u"). We note \mathbf{Y}^s , \mathbf{Y}^u , respectively, the measurement matrix of the structure in a healthy and unknown state. To define the feature, we use the separation matrices $\mathbf{W}_{\text{PCA}}^s$ and $\mathbf{W}_{\text{PCA}}^u$. From (9), we have:

$$\mathbf{W}_{\text{PCA}}^s = \underline{\Lambda}_{\Sigma_{\mathbf{y}^s}}^{-\frac{1}{2}} (\mathbf{P}^s)^T \quad (11)$$

$$\mathbf{W}_{\text{PCA}}^u = \underline{\Lambda}_{\Sigma_{\mathbf{y}^u}}^{-\frac{1}{2}} (\mathbf{P}^u)^T \quad (12)$$

Using a fixed CPV, the separating matrix $\mathbf{W}_{\text{PCA}}^s$ and $\mathbf{W}_{\text{PCA}}^u$ can be rewritten as follows [7]:

$$\begin{aligned} \mathbf{W}_{\text{PCA}}^s &= \mathbf{I}_{n_y \times n_y} \mathbf{\Gamma}^s (\mathbf{V}^s)^T = [\mathbf{I}_{n_y \times n_r} \quad \mathbf{I}_{n_y \times (n_y - n_r)}] \begin{bmatrix} \mathbf{\Gamma}_1^s & \mathbf{0} \\ \mathbf{0} & \mathbf{\Gamma}_2^s \end{bmatrix} [\mathbf{V}_1^s \quad \mathbf{V}_2^s]^T \\ &= \mathbf{W}_{\text{PCA1}}^s + \mathbf{W}_{\text{PCA2}}^s \end{aligned} \quad (13)$$

where:

$\mathbf{\Gamma}_1^s = \text{diag}(\sigma_1 \cdots \sigma_{n_r})$, $\mathbf{V}_1^s = [\mathbf{v}_{11}^s \cdots \mathbf{v}_{1n_r}^s] \in \mathbb{R}^{n_y \times n_r}$ and $\mathbf{W}_{\text{PCA1}}^s \in \mathbb{R}^{n_y \times n_y}$ are respectively the matrix of singular values, the matrix of right singular vectors and the separation matrix associated to the principal subspace of the healthy structure.

$\mathbf{\Gamma}_2^s = \text{diag}(\sigma_{n_r+1} \cdots \sigma_{n_y})$, $\mathbf{V}_2^s = [\mathbf{v}_{2(n_r+1)}^s \cdots \mathbf{v}_{2n_y}^s] \in \mathbb{R}^{n_y \times (n_y - n_r)}$ and $\mathbf{W}_{\text{PCA2}}^s \in \mathbb{R}^{n_y \times n_y}$ are respectively the matrix of singular values, the matrix of right singular vectors and the separation matrix associated to the residual subspace of the healthy structure.

In the same way, we define the matrix $\mathbf{W}_{\text{PCA}}^u$ using the following equation:

$$\begin{aligned} \mathbf{W}_{\text{PCA}}^u &= \mathbf{I}_{n_y \times n_y} \mathbf{\Gamma}^u (\mathbf{V}^u)^T = \begin{bmatrix} \mathbf{I}_{n_y \times n_r} & \mathbf{I}_{n_y \times (n_y - n_r)} \end{bmatrix} \begin{bmatrix} \mathbf{\Gamma}_1^u & \mathbf{0} \\ \mathbf{0} & \mathbf{\Gamma}_2^u \end{bmatrix} \begin{bmatrix} \mathbf{V}_1^u & \mathbf{V}_2^u \end{bmatrix}^T \\ &= \mathbf{W}_{\text{PCA1}}^u + \mathbf{W}_{\text{PCA2}}^u \end{aligned} \quad (14)$$

The presence of a damage will modify the measurement matrix \mathbf{Y}^s , and consequently the separation matrix $\mathbf{W}_{\text{PCA}}^u$, compared to the matrix $\mathbf{W}_{\text{PCA}}^s$. Therefore, the subspaces generated by $\mathbf{W}_{\text{PCA}}^u$ are deflected to those of $\mathbf{W}_{\text{PCA}}^s$. The idea here is to monitor changes of specific subspaces. Let, $R\{\mathbf{A}\}$, $R\{\mathbf{A}^T\}$ be respectively the range subspace of a matrix $\mathbf{A} \in \mathbb{R}^{n_y \times n_y}$ and its transpose. $\mathbf{P}_{R\{\mathbf{A}\}}$, $\mathbf{P}_{R\{\mathbf{A}^T\}}$ correspond to the orthogonal projection of the range subspace $R\{\mathbf{A}\}$ and $R\{\mathbf{A}^T\}$. One way to define orthogonal projections is to use SVD, *i.e.*

$$\mathbf{\Gamma} = \mathbf{U}^T \mathbf{A} \mathbf{V} = \text{diag}(\sigma_1 \cdots \sigma_{n_y}) \quad (15)$$

The orthogonal projections $\mathbf{P}_{R\{\mathbf{A}\}}$, $\mathbf{P}_{R\{\mathbf{A}^T\}}$ are respectively defined as follow:

$$\mathbf{P}_{R\{\mathbf{A}\}} = \mathbf{U} \mathbf{U}^T, \mathbf{P}_{R\{\mathbf{A}^T\}} = \mathbf{V} \mathbf{V}^T \quad (16)$$

From the definition of the separating matrices $\mathbf{W}_{\text{PCA}}^s$ and $\mathbf{W}_{\text{PCA}}^u$, the matrix of left singular vectors is equal to the identity matrix:

$$\mathbf{U}^s = \mathbf{U}^u = \mathbf{I}_{n_y} \quad (17)$$

Therefore, no information can be derived from the matrix of left singular vectors, thus we will use the matrix of right singular vectors as a feature. To build our proposed damage index, we will use projections on the transpose of matrices $\mathbf{W}_{\text{PCA1}}^s$ and $\mathbf{W}_{\text{PCA1}}^u$ as a damage feature. This is the subject of the following subsection.

The proposed damage index is based on the calculation of the principal angle vectors between the range subspace of the matrix $(\mathbf{W}_{\text{PCA1}}^s)^T$ and $(\mathbf{W}_{\text{PCA1}}^u)^T$. We note $\underline{\boldsymbol{\varphi}}[R\{(\mathbf{W}_{\text{PCA1}}^u)^T\}, R\{(\mathbf{W}_{\text{PCA1}}^s)^T\}]$, the principal angle vectors between the range subspace $R\{(\mathbf{W}_{\text{PCA1}}^u)^T\}$ and $R\{(\mathbf{W}_{\text{PCA1}}^s)^T\}$. Using the SVD tool, the Euclidean norm of the sinus angle is defined as follow [8-6]:

$$\begin{aligned} \left\| \sin \underline{\boldsymbol{\varphi}}[R\{(\mathbf{W}_{\text{PCA1}}^u)^T\}, R\{(\mathbf{W}_{\text{PCA1}}^s)^T\}] \right\|_2 &= \left\| \mathbf{P}_{R\{(\mathbf{W}_{\text{PCA1}}^s)^T\}^\perp} \mathbf{P}_{R\{(\mathbf{W}_{\text{PCA1}}^u)^T\}} \right\|_2 \\ &= \left\| \left(\mathbf{I}_{n_r} - \mathbf{P}_{R\{(\mathbf{W}_{\text{PCA1}}^s)^T\}} \right) \mathbf{P}_{R\{(\mathbf{W}_{\text{PCA1}}^u)^T\}} \right\|_2 \end{aligned} \quad (18)$$

Let be a smart structure with n_y sensors, and define equations (13), (14) and (18).

Damage could be detected by monitoring the following damage index:

$$DI_{PCA} = \frac{\left\| \sin \underline{\varphi} [R\{(\mathbf{W}_{PCA1}^u)^T\}, R\{(\mathbf{W}_{PCA1}^s)^T\}] \right\|_2}{n_r} \quad (19)$$

where n_r is the number of principal components retained.

Figure 4 depicts the DI behavior in term of impact energies. One can see that there exist a sensitivity of the DI regarding the magnitude of the impact energy.

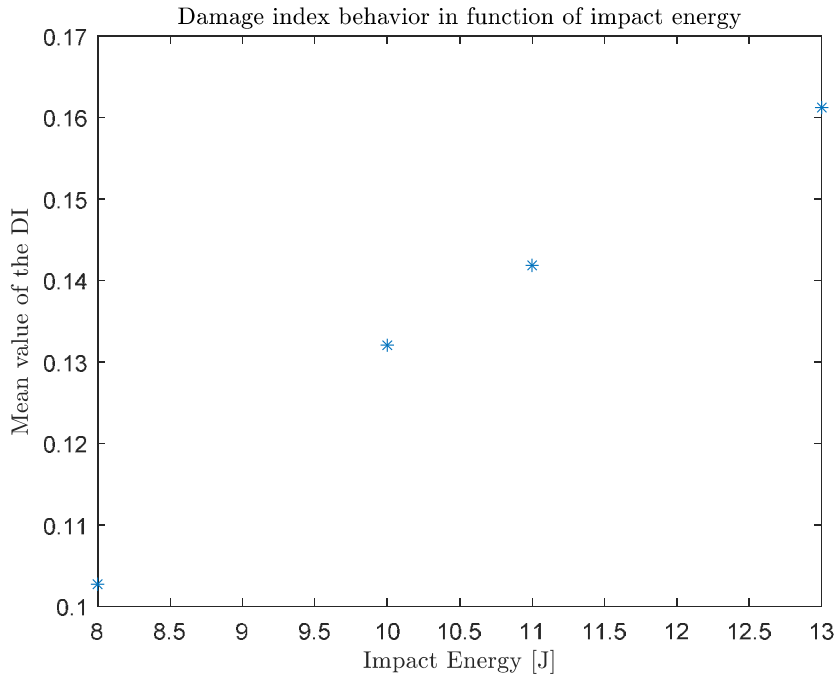


Figure 4: Damage detection results

SUMMARY

The presented paper has addressed a damage detection approach based on principal component analysis, where a damage index based upon the change of the principal angle vectors between subspaces has been proposed. The effectiveness of the proposed approach has been tested on a batch of monolithic composite coupons that have undergone different impact energies and locations with different size of delaminated area. For work under progress, a reliability methodology is underway in order to derive Probability of Detection (POD) for the proposed SHM approach in a fashion that agrees with current nondestructive inspection (NDI) validation requirements.

REFERENCES

- [1] Liddel, P.D., Foote, P (2015) "SHM enabled design: Application to damage tolerance design with bonded composite Joints", *10th International Workshop on Structural Health Monitoring*, Stanford, CA
- [2] Kessler, S.S. "Certifying a structural health monitoring system: Characterizing durability, reliability and longevity". In *Proceedings of the 1st International Forum on Integrated Systems Health Engineering and Management in Aerospace*, Napa, CA, USA, 7–10 November 2005; pp. 7–10.
- [3] ARP6461. "Guidelines for implementation of structural health monitoring on fixed wing aircraft". *Issuing Committee: Aerospace Industry Steering Committee on Structural Health. Publisher: SAE International*.
- [4] Hyvarinen A *et al.* "*Independent component analysis: algorithms and applications*". New York: John Wiley & Sons, 2001.
- [5] Cardoso, J.F "The Three Easy Routes to Independent Component Analysis, Contrasts And Geometry" In: *Proceedings of ICA 2001*. San Diego, USA, 2001.
- [6] Hajrya, R. and Mechbal, N. (2013). "Principal component analysis and perturbation theory based robust damage detection of multifunctional aircraft structure". *Structural Health Monitoring* 12(3), 263-277.
- [7] Golub GH and Van Loan CF. "*Matrix computation*". Baltimore, MD: Johns Hopkins University Press, 1983.
- [8] Davis C and Kahan WM. "The rotation of eigenvectors by a perturbation". *SIAMJ Numer Anal* 1970; 7(1): 1–46.
- [9] Wedin P. "Perturbation bounds in connection with singular value decomposition". *Numer Math* 1972; 12(1): 99–111.

MICROSCOPIC INVESTIGATION AND VISUAL INSPECTION OF THE BONDLINE WHEN EMBEDDING OPTICAL GLASS FIBRES WITH DIFFERENT CLADDING DIAMETERS AND COATING TYPES INTO STRUCTURAL FILM ADHESIVE BONDS BETWEEN CFRP ADHERENTS

NEELE GRUNDMANN^{*}, HAUKE BRÜNING^{*}, KAI BRUNE^{*} AND BERND MAYER^{*}

^{*}Fraunhofer Institute for Manufacturing Technology and Advanced Materials (IFAM)
Wienerstraße 12, 28359 Bremen, Germany
e-mail: neele.grundmann@ifam.fraunhofer.de, www.ifam.fraunhofer.de

Key words: Adhesive Bonding, SHM, FBG, Smart Materials, Bond Thickness, Sensor Position, Polyimide, Acrylate, Epoxy Film Adhesive, High Temperature.

Abstract: The increasing application of CFRP calls for a Structural Health Monitoring (SHM) system for adhesively bonded CFRP joints. Optical glass fibres carrying Fibre Bragg Gratings (FBG) are a promising technology for such a SHM system. This study investigates the effect of embedding optical glass fibres carrying FBGs directly in the adhesive on the adhesive bond quality and the fibre embedding. Embedding the optical glass fibres in the adhesive bond poses the risk of significantly reducing the bond strength. Optical glass fibres with different cladding diameters (50 μm , 80 μm , 125 μm) and coatings (polyimide (3 - 8 μm) and acrylate ($\sim 35 \mu\text{m}$)) are embedded in structural and repair film adhesives. Without embedded optical glass fibres the film adhesives has a bondline thickness of $\sim 90 \mu\text{m}$ (structural) and $\sim 100 \mu\text{m}$ (repair). The influence of embedding optical glass fibres directly in the adhesive is visually inspected in glass-slate adhesive bonds and microscopically investigated in cross-sectional cuts (CFRP adherents). It is found that embedding optical glass fibres with a total diameter $< 100 \mu\text{m}$ (cladding + coating diameter) doesn't increase the number of air inclusions in the adhesive in a visually detectable amount. Also, the adhesive fully encloses embedded optical glass fibres with a total diameter $< 100 \mu\text{m}$. When embedding optical glass fibres with total diameter $\sim 145 \mu\text{m}$ it is found that the structural film adhesive responds with an increased number of air inclusions. It is concluded that the optical glass fibres with total diameter $\sim 200 \mu\text{m}$ (standard telecommunication glass fibre) is too thick for embedding in the tested film adhesives. Furthermore, it is found that polyimide coatings are suited better for embedding in the tested film adhesives than acrylate coatings.

1. INTRODUCTION

The importance of CFRP in aircraft construction has increased over the past years [1]. Adhesive bonding is better suited for joining CFRP materials than conventional joining techniques like riveting or bolting [2,3]. The aeronautic industry however requires high security

standards. Without a method to identify the condition of an adhesive bond in service adhesive bonding will not be approved by the airworthiness authorities for primary aircraft structures [3]. A structural health monitoring (SHM) system to identify the condition and remaining lifetime of an adhesive bond would be a strong support for reaching airworthiness approval. Due to the dimensions and characteristics of optical fibres carrying Fibre Bragg Gratings (FBGs), they are suitable for structural health monitoring in composite adhesive bonds [4,5,6,7,8,9,10,11]. As shown in Fig. 1 an optical glass fibre consists of a very fragile glass core and cladding that are protected by a polymer coating [12]. The FBG sensor itself is a small portion of the glass fibre core with a periodic variation of the effective refractive index that senses fibre elongation and bending [12,13].

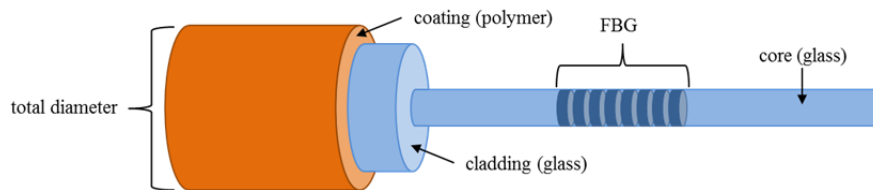


Fig. 1: Schematic sketch of the structure of an optical glass fibre with Fibre Bragg Grating (FBG) (adapted from [14]).

In earlier studies by Jones and Galea [4], Capell et al. [5] and Palaniappan et al. [6,7] the optical fibres carrying the FBGs were embedded in the adherents and standard telecommunication optical glass fibres with a 125 μm cladding diameter were employed. Disbond initiation and crack growth in the adhesive was successfully monitored [5,6,7,8]. In 2014 two studies were published [9, 11] that embedded the optical glass fibre carrying the FBG directly in the adhesive bond. This has the advantage of directly monitoring the stress distribution in the adhesive without signal distorting CFRP layers in between [9]. But embedding the optical fibre directly in the adhesive bears the risk of significantly influencing the bond characteristics and thus strength [10,11]. The intrusive effect of the embedded glass fibre sensor should be minimal. So far, only little attention has been paid to the effect that embedding an optical glass in the adhesive has on the bondline characteristics and quality. Initial investigations were carried out by Da Silva et al. [11] and Canal et al. [10] with SL tensile shear tests. Da Silva et al. [11] investigated the effect of embedding optical glass fibres in SikaForce[®]-7888 L10 adhesive (steel adherents). The authors concluded that embedding optical glass fibres directly in the adhesive can cause a significant reduction of the bond strength. Canal et al. [10] compared the effect of embedding multiplexed FBG arrays in different positions in two component epoxy adhesive Araldite 420 A/B: 1) between the 1st and 2nd CFRP ply, 2) in the adherent-adhesive interface, 3) in the adhesive. No negative effect on joint performance was detected in this study ($n = 4$). Since the possible intrusive effect of embedding optical glass fibres in the adhesive has major impact on reaching airworthiness approval it was decided to pay detailed attention to this problem. In this study, the research is focussed on structural and repair film adhesives commonly used in the aeronautic film industry for bonding load bearing primary structures in the aeronautic industry. Film adhesives pose unique challenges for embedding optical glass fibres. Especially the thin film layer thickness and the fabric carrier in the film adhesive should be

given special attention [15,16]. This paper investigates visually and microscopically the effects of embedding optical glass fibres with different cladding diameters and coatings in structural film adhesive bonds. The visual bondline inspection is performed with the help of transparent glass slate adhesive bonds, the microscopic investigation with cross-sectional cuts from CFRP adhesive bonds. In a consecutive paper the effects of embedding optical glass fibres with different cladding diameters and coatings on the tensile shear strength of structural film adhesive bonds will be investigated and the results will be related to the results from this paper.

The indicators for visually evaluating the bond quality in this study are:

- Fully developed interface between the adhesive and both adherents.
- Even adhesive distribution in the bondline.
- Number of air inclusions in the adhesive.

Air inclusions in the adhesive are related to a significant reduction in bond strength [17]. Bascom and Cottingham [17] discovered a difference in bond strength of up to 30% between specimens with entrapped air in the adhesive in comparison to specimens without entrapped air [17].

The indicators for visually evaluating the fibre embedding in this study are:

- Fibre position in the bondline.
- Full enclosure of the optical glass fibre with adhesive.
- Undamaged fibre and coating after autoclave curing.

The listed factors are critical for the functionality of the FBG sensor.

2. MATERIALS AND METHODS

2.1. Optical glass fibre coatings

The employed fibres are tested with acrylate and polyimide coatings because these are common and commercially available optical glass fibre coatings. Acrylate has a Young's modulus of approximately 100 MPa (compare Tab. 1). It is only deposited on the glass fibre surface and therefore easy to remove [18]. The main drawback is the relatively low thermal stability [19] and distortion of the matrix strain information [18]. Polyimide on the other side has a Young's modulus of approximately 3 GPa, a high thermal stability [20] and is chemically bonded to the glass fibre surface [18]. An advantage is the excellent adhesion of the coating to the glass fibre surface and a relatively precise information transfer from the surrounding host material to the FBG in the glass fibre core [18]. A drawback is the complicated removal of the coating for cleaving and splicing of the fibre [20].

Tab. 1: Comparison of the characteristics of acrylate and polyimide coatings (adapted from [18,19,20]).

Characteristics	Acrylate	Polyimide
Young's modulus	100 MPa	3 GPa
Operating temperature	+85°C/+150°C	+300°C
Bonding to fibre surface	only deposited	chemical bond

2.2. Optical glass fibres

The employed optical glass fibres are manufactured at RISE Acreo Fiberlab (Hudiksvall, Sweden) and have cladding diameters of 50 μm , 80 μm and 125 μm . The protective acrylate or a polyimide coating is applied directly after cooling. Depending on the fibre diameter the acrylate coating is applied with a thickness of 35 – 40 μm , the polyimide with a thickness of 3 – 8 μm . The total fibre diameters resulting from the combination of different cladding diameters and coating types (coating thicknesses) are presented in Tab. 2:

Tab. 2: Glass fibre types employed in this study. Different glass fibre diameters in combination with either polyimide or acrylate coating lead to the listed total fibre diameters.

Glass fibre type	P50	P80	P125	A80	A125
Cladding diameter	50 μm	80 μm	125 μm	80 μm	125 μm
Coating material	Polyimide	Polyimide	Polyimide	Acrylate	Acrylate
Total diameter	54 – 59 μm	95 μm	140 μm	145 μm	200 μm

2.3. Adhesives

The employed adhesives are the industrially available structural film adhesive FM[®] 300K (film thickness: 200 μm) and repair film adhesive FM[®] 300-2M (film thickness: 250 μm) by Cytec Industries Inc. FM[®] 300K is distributed on a wide-open-knit fabric carrier [15]. FM[®] 300-2M is distributed applied on a random matt fabric carrier [16]. The material properties of these film adhesives are stated in the data sheets provided by the manufacturer. The film adhesives are processed and cured according to manufacturer specifications at 121°C (FM[®] 300-2M) and 175°C (FM[®] 300K). After curing the film adhesives have a bondline thickness of ~ 90 μm (FM[®] 300K) and ~ 100 μm (FM[®] 300-2M).

2.4. Glass slate bonds preparation: visual inspection of the adhesive distribution, the number and size of air inclusions and the interface in samples with different embedded optical glass fibres

Specimens are manufactured by bonding two transparent glass slates (100 x 100 x 4 mm) with FM[®] 300-2M and FM[®] 300K film adhesives and embedding one glass fibre per specimen. Specimens are manufactured for all glass fibre diameter and coating combinations. Also, reference specimens without an embedded glass fibre are manufactured. The film adhesive is cut exactly according to the dimensions of the glass slates. The adherents are cleansed with 2-Propanol. After, the pre-cut film adhesive is placed on the lower glass slate (compare Fig. 2). The glass fibre is placed on top of the film adhesive along the centre lines of the glass slate. The second glass slate is placed on top. To achieve an even distribution of the adhesive in the bondline, pressure plates are placed on each specimen. The curing of the specimens takes place in a hot-air autoclave by Scholz Maschinenbau (Coesfeld, Germany) according to the adhesive manufacturer's specifications.

2.5. CFRP slate bonds and cross-sectional cuts preparation: microscopic investigation of the glass fibre position in the bondline and the influence of the glass fibre diameter on the bondline thickness

Specimens are manufactured by bonding two CFRP slates (100 x 100 x 2 mm) with

FM[®] 300-2M and FM[®] 300K film adhesives and embedding one glass fibre per specimen as described in 2.4. Specimens are manufactured for all glass fibre diameter and coating combinations. Also, reference specimens without an embedded glass fibre are manufactured. Deviating from the description in paragraph 2.4 the CFRP specimens are hand sanded prior to bonding and the curing of the specimens takes place under vacuum bagging. Pressure plates are not applied. The cross-sectional cuts are cut from the position indicated by the red dashed line in Fig. 2a with a diamond cutting disc and embedded in two-component epoxy resin EpoFix by Struers GmbH, (Hannover, Germany). The embedded cross-sectional cuts are first grinded with grit sizes ranging from 80 to 4000 and then polished in the following steps: 1. buff MD- Largo, 3 µm suspension + lubricant (300 U/min + 25 N + 3 min); 2. polishing cloth MM414, 1 µm suspension BioDiamant MM 140 (300 U/min + 35 N + 5 min); 3. polishing cloth MD-Chem, 0.25 µm Siliziumoxidsuspension OP-S (150 U/min + 25 N + 2,5 min). Photos are taken with a DMRX Leica light microscope at 25x, 50x, 100x, 200x and 500x magnification.

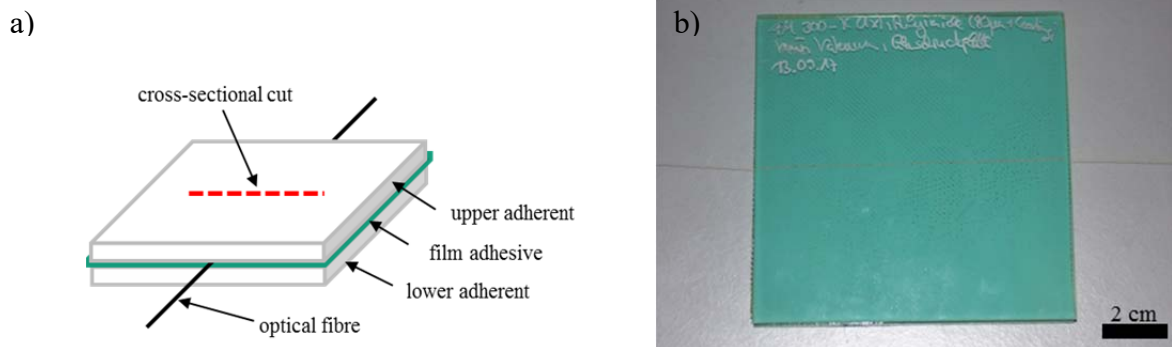


Fig. 2: a) Schematic sketch of the lay-up of a bonded joint specimen with an optical glass fibre embedded in the adhesive. The red dashed line indicates the position where the cross-sectional cuts in paragraph 2.5 are taken from; b) Photography (top view) of a bonded joint glass specimen manufactured as described in paragraph 2.4 with an embedded optical glass fibre. The glass slate adherents allow a visual evaluation of the bonded joint quality.

3. RESULTS

3.1. Glass slate adherents: visual inspection of the adhesive distribution, the number and size of air inclusions and the interface in samples with different embedded optical glass fibres

Photographs of the manufactured bonds between glass slates carrying the different glass fibre diameter and coating combinations are presented in Fig. 4. The FM[®] 300-2M specimens A1, A2 and A4 all show a good adhesive distribution with a small number of air inclusions despite different fibre diameters. The air inclusions are evenly distributed across the bondline. Only the specimens with the polyimide and acrylate and coated 125 µm glass fibres (specimen A3 and A5) show a slightly higher number of air inclusions (compare Fig. 4). On the contrary, in the FM[®] 300K specimens the number and size of air inclusions increase with increasing total optical glass fibre diameter. The FM[®] 300K specimens carrying the polyimide coated 50 µm and 80 µm fibres (B1 and B2) show a good adhesive distribution with a small amount of air inclusions and the air inclusions are evenly distributed across the bondline. In

the FM[®] 300K specimens carrying the polyimide coated 125 µm fibre (B3) and the acrylate coated 80 µm fibre (B4) the number of air inclusions increase in comparison to the specimens B1 and B2 and the distribution of the air inclusions across the bondline is more uneven (compare Fig. 3). A higher number of air inclusions is visible on one side of the embedded glass fibre and a higher number on its other side. This is especially pronounced in the B3 specimen where a higher number of more uneven distributed air inclusions than in B4 are visible and a small darker green patch is found in the lower right corner of the specimen. The described development is even more pronounced in the specimen carrying the acrylate coated 125 µm fibre (B5). This specimen shows a high amount of highly unevenly distributed air inclusions and large dark green patches.

3.2. CFRP slate bonds and cross-sectional cuts: microscopic investigation of the glass fibre position in the bondline and the influence of the glass fibre diameter on the bondline thickness

Photomicrographs of the cross-sectional cuts of the FM[®] 300-2M and FM[®] 300K specimens are presented in Fig. 5. In some of the photomicrographs (A1, A2, A4, A5, B0, B1, B4), fabric carrier fibres from the film adhesive are visible. The cross-sectional cuts (A1, A2, B1, B2) indicate that in both adhesives the polyimide coated 50 µm and 80 µm fibres are intact and enclosed by adhesive. The glass fibre is not positioned in the middle of the bondline but in the upper half of the bondline. The cross-sectional cut of the polyimide coated 125 µm glass fibre in the FM[®] 300K (B3) shows that the glass fibre completely fills the bondline. The polyimide coated 125 µm glass fibre in the FM[®] 300-2M (A3) nearly fills the entire bondline. The cross-sectional cuts of the specimens carrying the acrylate coated glass fibres (A4, A5, B4, B5) indicate that in both adhesives the acrylate coating completely separated from the glass fibre during curing and that the glass fibre itself is damaged. Hollow spaces are visible around the fibre. Fig. 3 pictures a photomicrograph of a larger detail of a FM[®] 300K cross-sectional cut with an embedded polyimide coated 50 µm fibre. The photomicrograph also shows fabric carrier fibres. It is visible that in this cross-sectional cut (as in A1, A2, A5, B1) the optical glass fibre is situated on top of a fabric carrier fibre. Furthermore it is visible that the air inclusions are not located close to one of the interfaces but fill the whole bondline.

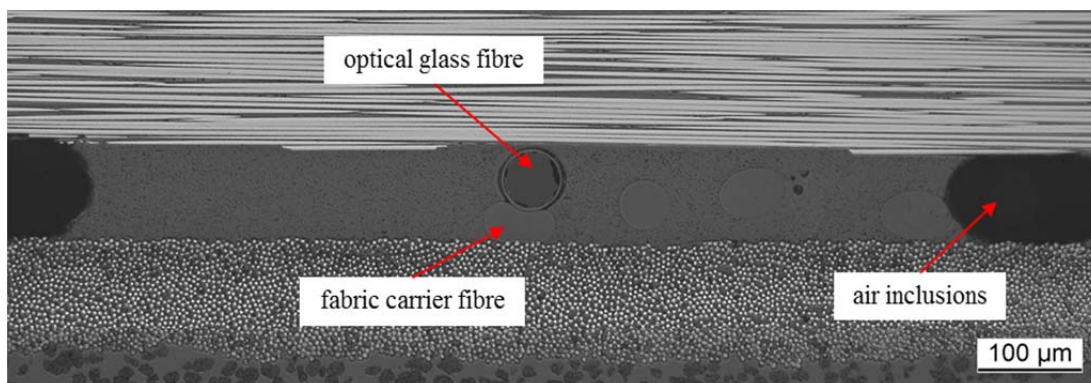


Fig. 3: Photomicrographs (100x) of a FM[®] 300K cross-sectional cut (compare Fig. 2a) with an embedded polyimide coated 50 µm fibre. Fabric carrier fibres and air inclusions are visible.

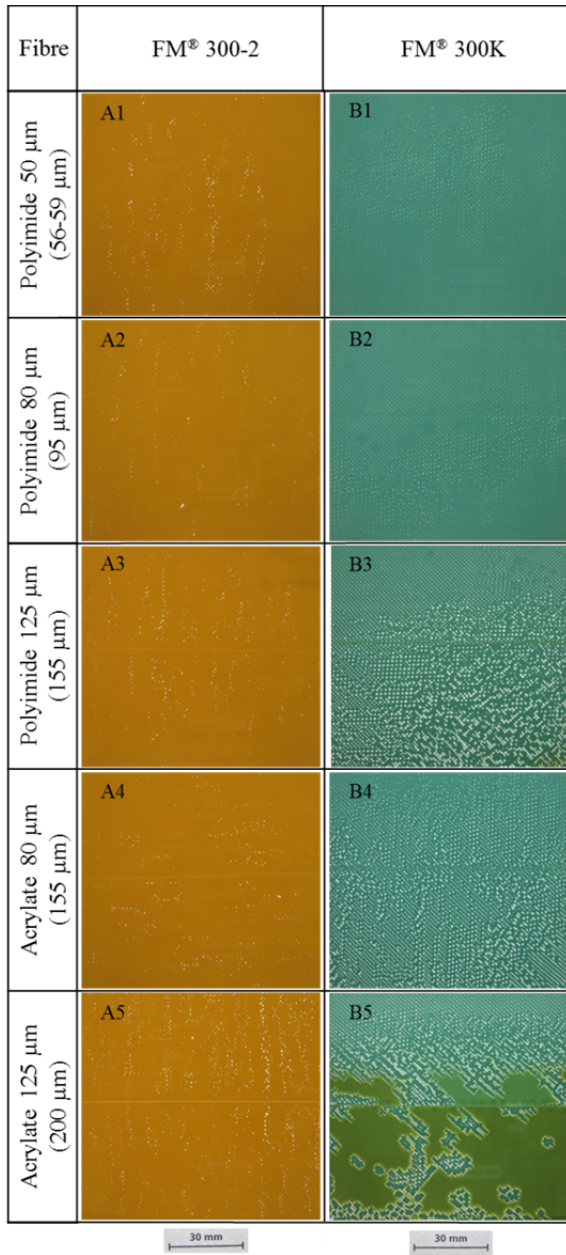


Fig. 4: Photographs (top view) of bonded glass slate joints with different embedded glass fibre types. Visual inspection of the bondline through the glass slate adherents allows the evaluation of the adhesive distribution, air inclusions and fibre position. The left column shows specimens manufactured with FM® 300-2M film adhesive and the right column specimens manufactured with FM® 300K film adhesive. The total fibre diameter increases from the top of to the bottom of both photo columns. Photographs are taken as shown in Fig. 2b.

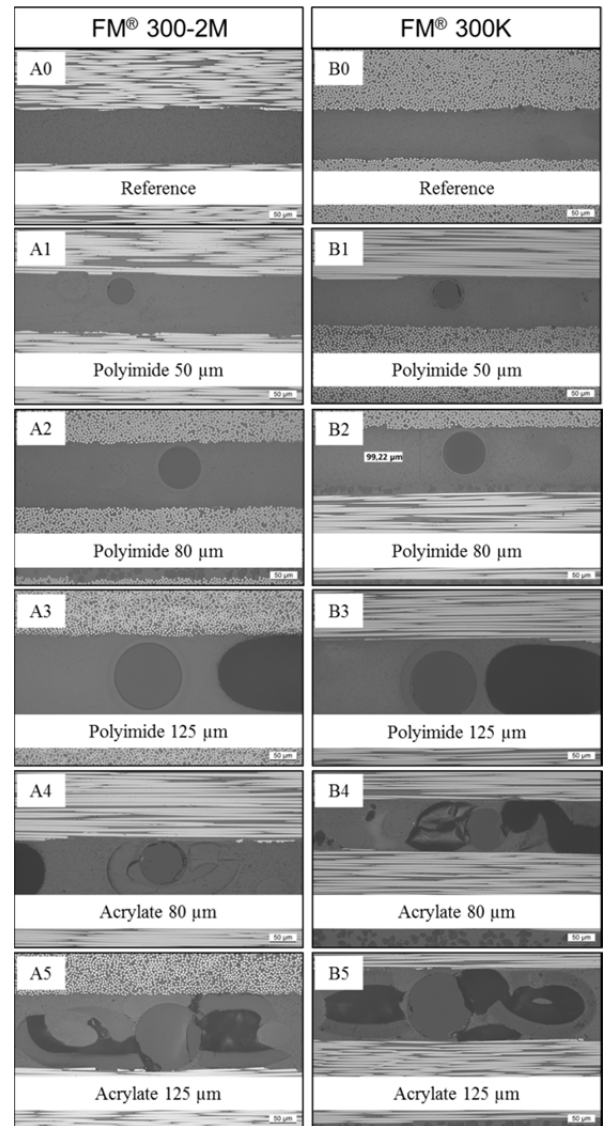


Fig. 5: Photomicrographs (200x) of cross-sectional cuts. The cuts are taken from the position indicated in Fig. 2a. Left column: samples of all fibre types embedded in FM® 300-2M adhesive bonds between CFRP adherents: Polyimide 50 µm (A1), Polyimide 80 µm (A2), Polyimide 125 µm (A3), Acrylate 80 µm (A4) and Acrylate 125 µm (A5). A0 is a reference sample without an embedded optical glass fibre. Right column: samples of all fibre types are embedded in FM® 300K adhesive bonds between CFRP adherents: Polyimide 50 µm (B1), Polyimide 80 µm (B2), Polyimide 125 µm (B3), Acrylate 80 µm (B4) and Acrylate 125 µm (B5). B0 is a reference sample without embedded optical glass fibre.

4. DISCUSSION

Tab. 3 summarizes the results from the visual inspection of the adhesive bondlines in the glass slate samples and the cross-sectional cuts. The evaluation of the results is indicated by the colouring of the table. Green colour indicates a good result. Yellow indicates an acceptable result: the result is not optimal but doesn't impede the employment of the respective fibre type in an SHM system for FM[®] 300-2M and FM[®] 300K film adhesives. Red indicates a not acceptable result: the result impedes the employment of the respective fibre type in an SHM system for the investigated adhesives.

Tab. 3: Results from the visual inspection of the adhesive bondlines in the glass slate samples and the cross-sectional cuts. The colouring of the fields indicates the results achieved in the different categories: green = good result; yellow = acceptable result; red = not acceptable result.

	Sample	Fibre type	Fully developed interface	Even adhesive distribution	Number of air inclusions	Fibre position	Full enclosure of fibre	Fibre damage
FM [®] 300-2M	A0	/						
	A1	P50						
	A2	P80						
	A3	P125						
	A4	A80						
	A5	A125						
FM [®] 300K	B0	/						
	B1	P50						
	B2	P80						
	B3	P125						
	B4	A80						
	B5	A125						

4.1. Polyimide coated 50 µm and 80 µm fibres (A1, A2, B1, B2); total diameter < 100 µm

In both adhesives the best results are achieved by the polyimide coated 50 µm and 80 µm optical glass fibres. Both optical glass fibres achieve in most categories a good result (green). Since the interface between the adherents is fully developed, the adhesive distribution is even and no visible increase in number and size of air inclusions is detected it is expected in accordance with Bascom and Cottingham [17] that the presence of the optical glass fibres doesn't affect the bond strength significantly. Therefore, these categories are evaluated green.

The fibre position is not centred and therefore evaluated yellow. The tendency of the embedded glass fibre to position itself closer to one side of the bond is likely to be caused by the specimen production process where the fibre is placed on top of the film adhesive. The presence of the fabric carrier is suspected to prevent the fibre from moving to the centre of the bondline (compare Fig. 3). It has to be investigated in future experiments how the sensor performance is influenced by the fibre position.

Since both fibres are fully enclosed with adhesive and the fibre remains undamaged after curing the two factors are expected to not affect the sensors functionality and therefore these categories are evaluated green.

4.2. Polyimide coated 125 µm fibres (A3, B3); total diameters ~ 145 µm

The polyimide coated 125 µm fibre achieves acceptable results in the FM[®] 300-2M adhesive bonds (A3). The interface is fully developed and the adhesive evenly distributed. Therefore both categories are rated green. Since a slight increase in air inclusions is visually detectable this category is evaluated yellow. According to Bascom and Cottingham [17] this might cause a reduction in bond strength. It will be investigated in a consecutive paper if a reduction in tensile shear strength is detectable in samples with an increased amount of air inclusions. The category fibre position is also rated yellow because the fibre completely fills the bondline. Big changes in adhesive layer thickness lead to changes in the stress distribution and might thus provoke changes in the crack growth and propagation as described by Lee et al. 2004 [21] for adhesives with included rubber particles. This might cause preliminary interlaminar failure. Therefore, the category fibre enclosure is rated yellow. Since the polyimide coated 125 µm fibre remains undamaged the category fibre damage is rated green.

For the FM[®] 300K adhesive bonds (B3) the results are evaluated as not acceptable. A not fully developed interface, an uneven adhesive distribution and a high increase of air inclusions are detected visually. According to Bascom and Cottingham [17] these factors are expected to reduce the bond strength and therefore the categories air inclusions and adhesive distribution are evaluated red and the category fully developed interface yellow. The categories fibre position and enclosure are evaluated yellow for the same reasons as for the FM[®] 300-2M adhesive bonds. Since the polyimide coated 125 µm fibre remains undamaged the category fibre damage is rated green.

4.3. Acrylate coated 80 µm and 125 µm fibres (A4, A5, B4, B5); total diameters 145 µm - 200 µm

The results for embedding the acrylate coated 80 µm and 125 µm fibres in both tested film adhesives are evaluated as not acceptable.

For the FM[®] 300-2M adhesive bonds, the A4 samples receive a green evaluation in the categories fully developed interface, adhesive distribution and air inclusions. No changes in comparison to the other samples are detected visually. The A5 samples receive a green evaluation in the categories fully developed interface and adhesive distribution and a yellow evaluation for the detected increase of air inclusions.

In the FM[®] 300K adhesive bonds the category fully developed interface is rated green for the acrylate coated 80 µm fibre samples (B4). The B5 samples are the only samples evaluated red in the category fully developed interface. The not fully developed interface is indicated by the dark green patches visible in B5. B4 and B5 show both an increased number of air inclusions and an uneven adhesive distribution. This leads to a yellow (B4) and red (B5) evaluation of the categories even adhesive distribution and number of air inclusions. The formation of the dark green patches and the uneven distribution of air entrapments between the areas left and right of the centrally placed glass fibre indicate that the embedded glass fibre acts as a wedge. Thus, air is entrapped in the interface between the film adhesive and the adherent on that side of the film adhesive where the glass fibre was placed. According to Bascom and Cottingham [17] the air entrapped between the film adhesive and the adherents during bonding is displaced into the resin during the heated curing process. This is confirmed by the findings in Fig. 3.

The embedding in both film adhesives damaged the acrylate coated fibres (acrylate coated 80 μm and 125 μm glass fibre) beyond functionality. In the specimens B4 and B5 (compare Fig. 5) the coating has completely separated from the fibre. It is concluded that the low thermal stability and the non-chemical bond to the glass fibre surface (compare Tab. 2) make the acrylate coating unsuited for embedding in FM[®] 300K and FM[®] 300-2M film adhesives. All fibre-related categories are evaluated red for the acrylate coated fibres. The separation of the acrylate coating might explain why specimen B4 (acrylate coated 80 μm fibre) has a slightly lower number of air inclusions than sample B3 (polyimide coated 125 μm fibre) and although both glass fibres have a similar total diameter of approximately 155 μm before curing. After the separation the acrylate coated 80 μm glass fibre does not have a total diameter of 155 μm anymore and the fibre most likely doesn't wedge open the bond as unevenly as the intact polyimide coated 125 μm fibre in specimen B3.

5. CONCLUSIONS

- 1) The cross-sectional cuts demonstrate that the tested film adhesives fully enclose the embedded glass fibre during the curing process as long as the embedded glass fibre diameter does not exceed a certain total diameter ($< 100 \mu\text{m}$). The not centred position of the optical glass fibre in the bondline leads to a thinner adhesive layer on one side of the optical glass fibre.
- 2) When the embedded optical glass fibre does not exceed a total diameter $< 100 \mu\text{m}$ no increase in air inclusions is detected visually. In FM[®] 300-2M adhesive bonds no increase in air inclusions are detected visually for embedded glass fibres not exceeding total diameters $< 145 \mu\text{m}$.
- 3) The results suggest that the standard telecommunication glass fibre (acrylate coating) with a total diameter of 200 μm is too thick for embedding in FM[®] 300 film adhesives. It causes a significant increase in air inclusions in both adhesives and leads to a not fully developed interface in FM[®] 300K adhesive bonds.
- 4) It is concluded that the acrylate coating is unsuited for embedding in FM[®] 300 film adhesive since it separates from the optical glass fibre during the curing procedure.

6. ACKNOWLEDGEMENTS

The research leading to the results was supported by the DAAD and Fraunhofer Talenta carrier program. We acknowledge RISE Acreo for the manufacturing and providing the optical glass fibres. Furthermore we acknowledge Kerstin Lunkwitz for preparing the cross-sectional cuts.

7. REFERENCES

- [1] Diamanti K, Soutis C (2010). Structural health monitoring techniques for aircraft composite structures; Progress in Aerospace Sciences, Volume 46, Issue 8, pp. 342-352
- [2] Löbel, T., Holzhüter, D., Sinapius, M., Hühne, C. (2016): A hybrid bondline concept for bonded composite joints; International Journal of Adhesion and Adhesives, Volume 68, pp. 229-238

- [3] Augustin, T., Karsten, J., Kötter, B., Fiedler, B. (2018): Health monitoring of scarfed CFRP joints under cyclic loading via electrical resistance measurements using carbon nanotube modified adhesive films; *Composites: Part A*, Volume 105, pp. 150–155
- [4] Jones, R., Galea, S. (2002): Health monitoring of composite repairs and joints using optical fibres; *Composite Structures*, Volume 58, pp. 397–403
- [5] Capell, T. F., Palaniappan, J., Ogin, S. L., Crocombe, A. D., Reed, G. T., Thorne, A. M., Mohanty, L., Tjin, S. C. (2007): The use of an embedded chirped fibre Bragg grating sensor to monitor disband initiation and growth in adhesively bonded composite/metal single lap joints; *Journal of Optics A: Pure and Applied Optics*, Volume 9, pp. 40–44
- [6] Palaniappan, J., Wang, H., Ogin, S. L., Thorne, A. M., Reed, G. T., Crocombe, A. D., Rech, Y., Tjin, S. C. (2007): Changes in the reflected spectra of embedded chirped fibre Bragg gratings used to monitor disbanding in bonded composite joints; *Composites Science and Technology*, Volume 67, pp. 2847–2853
- [7] Palaniappan, J., Ogin, S. L., Thorne, A. M., Reed, G. T., Crocombe, A. D., Capell, T. F., Tjin, S. C., Mohanty, L. (2008): Disbond growth detection in composite–composite single-lap joints using chirped FBG sensors; *Composites Science and Technology*, Volume 68, pp. 2410–2417
- [8] Bernasconi, A., Carboni, M., Comolli, L. (2011): Monitoring of fatigue crack growth in composite adhesively bonded joints using Fiber Bragg Gratings; *Procedia Engineering*, Volume 10, pp. 207–212
- [9] Webb, S., Shin, P., Peters, K., Zikry, M. A., Stan, N., Chadderdon, S., Selfridge, R., Schultz, S. (2014): Characterization of fatigue damage in adhesively bonded lap joints through dynamic, full-spectral interrogation of fiber Bragg grating sensors: 1. Experiments; *Smart Materials and Structures*, Volume 23, Issue 2, Article ID 025016, 14pp
- [10] Canal, L. P., Sarfaraz, R., Violakis, G., Botsis, J., Michaud, V., Limberger, H. G. (2014): Monitoring strain gradients in adhesive composite joints by embedded fiber Bragg grating sensors; *Composite Structures*, Volume 112, pp. 241–247
- [11] Da Silva, L. F. M., Moreira, P.M.G.P., Loureiro, A.L.D. (2014): Determination of the strain distribution in adhesive joints using Fiber Bragg Grating (FBG); *Journal of Adhesion Science and Technology*, Volume 28, P pp. 1480–1499
- [12] Li, H.-N., Zhou, G.-D., Ren, L., Li, D.-S. (2009): Strain Transfer Coefficient Analyses for Embedded Fibre Bragg Grating Sensors in Different Host Materials; *Journal of Engineering Mechanics*, Volume 135, No. 12, pp. 1343–1353
- [13] Strömberg, K., Borgenvall, S., Loukil, M., Noharet, B. (2015): Next Generation Manufacturing Fixtures: CFRP Structures Using “In Situ” Health Monitoring; *SAE Technical Paper 2015-01-2619*
- [14] Yang, N. (2010): Messungen mit Glasfasersensoren; In: *Fertigungs- & Maschinenautomation*, Heft S4/2010, pp. 2–7
- [15] Cytec Industries Inc: FM® 300 Epoxy Film Adhesive Technical Data Sheet; AEAD-00002, Rev. 02, 9 October 2013
- [16] Cytec Industries Inc: FM® 300-2M Epoxy Film Adhesive Technical Data Sheet; AEAD-00004, Rev. 02, 27 September 2011
- [17] Bascom, W. D., Cottingham, R. L. (1972): Air Entrapment in the Use of Structural Adhesive Films; *The Journal of Adhesion*, Volume 4, Issue 3, pp. 193–209

- [18] Betz, D. C., Staudigel, L., Trutzel, M. N., Kehlenbach, M. (2003): Structural monitoring using fiber-optic Bragg Grating sensors; Sage Publications, Volume 2, Issue 2, pp. 145–152
- [19] Huang, L., Dyer, R. S., Lago, R. J., Stolov, A. A., Li, J. (2016): Mechanical properties of polyimide coated optical fibers at elevated temperatures; Proceedings of the SPIE, SPIE BiOS (San Francisco/USA), Volume 9702, 8pp.
- [20] Haldeman, A. T., Shaughnessy, M., Berger, K., Morgan, B., Shetzline, J., DiMaio, J. R. (2018): Coatings for next-generation harsh environment system; Materials for Energy, Efficiency and Sustainability: TechConnect Briefs 2018, pp. 89-82
- [21] Lee, D.-B., Ikeda, T., Miyazaki, N., Choi, N.-K. (2004): Effect of Bond Thickness on the Fracture Toughness of Adhesive Joints; Journal of Engineering Materials and Technology, Volume 126, Issue 1, pp. 14-18

EXPERIMENTAL INVESTIGATIONS ON THE MECHANICAL DAMAGE BEHAVIOR OF MULTIFUNCTIONAL COMPOSITES WITH PRINTED ELECTRONICS

Max Linke*, Taha Genco* and Rolf Lammering*

* Institute of Mechanics

Helmut-Schmidt-University / University of the Federal Armed Forces Hamburg

Holstenhofweg 85, D-22043 Hamburg, Germany

e-mail: max.linke@hsu-hh.de, web page: <http://www.hsu-hh.de>

Key words: structural health monitoring, multifunctional composite, carbon fibre reinforced plastic, carbon nanotubes, interlaminar fracture toughness

Abstract. Multifunctional composites as means of structural health monitoring can parallelly carry structural loads and detect potential damage to the structure. The importance arises from enhanced lifetime and service interval estimations. Via inkjet printed and electrically conductive paths, as integral part of a carbon fibre reinforced plastic, damage assessment is possible by resistance measurements. A promising novel approach is to use carbon nanotubes as conductive elements in an epoxy-based matrix. In the current work, the effect of printed electronics from such materials on the mechanical damage behavior of the multifunctional composites is investigated. Conclusions are drawn from interlaminar fracture toughness values and failure mode distributions obtained from different loading modes applied to precracked specimens. The results create primal understandings of the damage behavior of such multifunctional composites and conclusion how to realize further improvements to this specific printed electronics material.

1 INTRODUCTION

Since most engineering structures, i.e. buildings, aircrafts and wind turbines, are designed to withstand loads over decades, they are subjected to an ageing process [1]. This leads to structural damage which limits the lifetime of the structures. In order to extend the operational life, damage tolerant designs are frequently used [1]. To prevent damage growth and catastrophic failure, visual inspections intervals for the structures are defined in parallel with the design [2]. A major drawback is the interruption of structure's operation.

To overcome this disadvantage, the damage state can be continuously observed by means of structural health monitoring (SHM). Via electronical sensors as integral part of the structure

and through-thickness electrical resistance measurements, information about existence, location and extent of damage are obtained during operation. Fundamental for this approach is the effect of the damage on the electrical properties. Recorded data are transferred via wired or wireless configurations to analysers which evaluate the criticality [3]. Since mass, space and costs are objectives during design, wireless conductive paths are more and more frequently applied to lightweight structures [3].

With respect to the location of the sensors, two different arrangements are possible. Heinrich has shown in [4], that electronics on the surface of a carbon fibre reinforced plastic (CFRP) stiffener can be used to determine a critical damage state. The positioning of the sensors in between the single layers of composite structures is another relevant approach [4]. This has a major effect on the structural damage behavior, since the conductive material becomes an integral part. It must be ensured, that it does not become the starting point for delaminations or other damage.

For both applications, an inkjet printing process is appropriate for additive manufacturing of sensor configurations. Wide ranges of materials are printable in arbitrary patterns on 3D surfaces combined with a small ink consumption [5]. Besides operational requirements like electrical conductivity and suitable mechanical properties, the printability of the ink is a main objective during ink composition.

Since CFRP structures are prone to develop internal non-visible damage, they are highly applicable to the SHM technology. Further, an ink based on carbon nanotubes (CNT) was found appropriate since Huang et. al. [6] proved their high electrical conductivity in epoxy resins. Hedia et. al. [7] found their reinforcing effect on the mechanical properties. Resulting multifunctional composites are appropriate for SHM of engineering structures.

In the current research the mechanical damage behavior of such multifunctional composites from CFRP laminates and printed CNT-based inks is tested. Results are obtained from two tests in a double cantilever beam (DCB) and an end notched flexure (ENF) configuration. Objectives for evaluation are the interlaminar fracture toughness and the failure mode distribution. Due to the novel character of the investigated multifunctional composites, first comparisons to the previous work of Heinrich [8], who used an ink based on silver nanoparticles, can be made. Furthermore, required modifications of the current ink composition can be derived.

2 MECHANICAL DAMAGE BEHAVIOR

As the printed electronics become part of the structure, they form a bonding interface with the CFRP substrates. It is characterized by cohesion forces of the single materials and by adhesion forces along the interface, which directly depend on the interaction between the joined materials [9]. In order to assess the quality of the interface, its peel strength and shear strength are main objectives. DCB and ENF specimens with intentionally precracked interfaces can be used for evaluation. The test procedures are representative for most common crack opening modes in structure operation. In the DCB test the crack is opened with a peeling mode I, see Figure 1 in accordance with Campbell [10]. The crack opening with shear mode II is tested with the ENF specimens. A tearing mode III is typically neglected in research since it is only relevant for thick laminates and torsional loads [11].

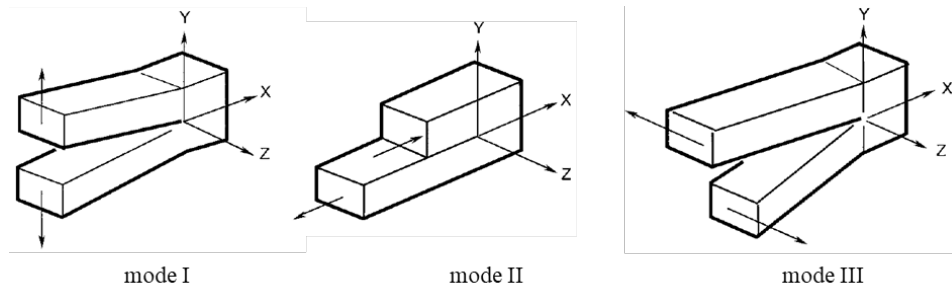


Figure 1: Modes of crack opening displacements according to [10]

As outlined in [12] and [13], both referenced tests base on the assumption of a linear elastic, cracked specimen. According to Sharpe [14], the total elastic energy of the quasi-static loaded system includes the work of external forces, the internal stored energy and the fracture energy per area of crack surface. In case of a constant crack length, the system is in equilibrium and the total elastic energy is extremal [14]. Thus, any crack propagation leads to a loss of the systems elastic energy. The critical loss of energy for an infinitesimal small crack propagation is defined as the interlaminar fracture toughness [12]. The higher this value the better is the multifunctional composites resistance to crack propagation. It can be calculated from the specimen geometry, the applied forces and recorded displacements in the DCB and ENF tests, see [12] and [13].

As the precracked interfaces are most likely the weak point, crack propagation is supposed along the adhesive bond. Depending on adhesion and cohesion forces, the crack propagates in areas with the smallest internal strength. Since both forces can vary along the interface due to inhomogeneities, the crack potentially alternate between the substrate surfaces (AF - adhesion failure) and the printed electronics material (CF - cohesion failure). In a subsequent fractography process, CF is characterised by the presence of ink on both fractured surfaces, whereas the ink is absent on one surface in case of AF [15]. The allocation as CF assumes an ideal dispersion of the components in the sintered ink. Since CNT tend to form agglomerations due to high van der Waals forces [16] when the ink is not fully cured, a decomposition potentially occurs during sintering and forms clusters of single ink components [17]. This results in varying cohesion forces and needs to be considered for failure mode identification. Thus, the CF is subdivided as follows: cohesive agglomeration failure (CAF) with CNT agglomerations on both fracture surfaces, cohesive interface failure (CIF) with CNT agglomerations on only one surface and cohesive resin failure (CRF) where no CNT are present on both surfaces. Additionally, unwetted areas (UA) must be recorded. The outlined failure modes are visualised in Figure 2.

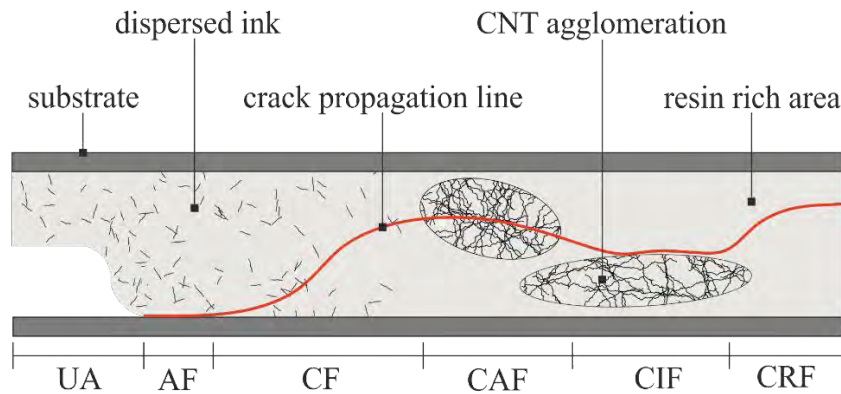


Figure 2: Potential failure modes for multifunctional composites from CNT ink

Any AF is not acceptable as the low corresponding fracture toughness increases the risk of in-service delamination which leads to a catastrophic failure of the multifunctional composite. It must be prevented by means of surface treatment. In contrast, the cohesion forces can be improved by use of a modified ink composition and application processes.

3 EXPERIMENTAL SETUP

The following experimental setup describes the methods which are used to prepare and execute the mechanical tests and to evaluate the obtained data.

3.1 Ink formulation

The used inks base on single-walled CNT with an outer diameter of 1.8 ± 0.4 nm and > 5 μm in length. Furthermore, ethyl cellulose (EC) as stabilizing polymer, N,N-dimethylacetamide (DMAc) with a purity of ≥ 99.8 % as dispersion medium and an epoxy resin with an associated hardener are added. An overview of the CNT content in the formulated ink is given in Table 1.

Table 1: Weight fractions of CNT in the formulated inks

ink label	CNT [wt.%]
RED01	0.000
CNT08	0.044
CNT02	0.087

The materials are introduced to each other in a three-step procedure. First, EC (~ 2.5 wt.%), resin and hardener (~ 10.0 wt.%) are fully diluted in DMAc. Second, CNT are added to the clear solution and then vigorously stirred for 10 minutes. Third, the mixture is homogenized in an ice bath using an ultrasonic probe *Sonopuls HD 2070* for 120 minutes at power amplitude of 32 % and cycle value of 8. The dispersed suspension is kept on stirrer plates. Before each printing session, the dispersion is ultrasonicated for 60 minutes under the same conditions.

After homogenization, the ink is filtered in a PTFE (polytetrafluorethylene) membrane with a pore size of 5 μm and then filled into the printing reservoir for inkjet printing.

3.2 Specimen preparation

CFRP laminates from *HexPly M21/35%/268/T800S* prepreg material are fabricated from *Hamburg University of Technology* in a $[0/90_2]_s$ configuration. The substrates are cured for two hours at 180 °C under 7 bar autoclave pressure and 750 mbar vacuum pressure. Following, the laminates are cut to the required geometry of 125 x 10 mm (see Figure 3) using a circular saw with a diamond blade.

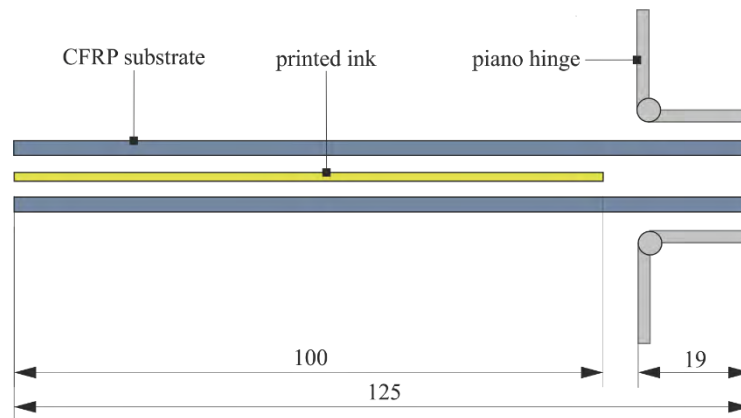


Figure 3: Exploded, schematic setup with the precrack on the right side for the DCB specimen in accordance with [12]. The ENF specimen in accordance with [13] is similar but without piano hinges. All measures are given in mm.

The formulated inks are deposited on the surface of CFRP specimens using a piezo-driven inkjet printhead *MD-K-140* from *Microdrop Technologies GmbH* with an inner nozzle diameter of 100 μm . Prior to application, the substrates are cleaned using isopropyl alcohol. Since two substrates are required per specimen, the ink is applied to both substrates to achieve better adhesion. Per substrate, 5 layers of the ink are printed with a drop spacing of 100 μm over an area of 98 x 8 mm which allows the ink to flow during the sinter process without leaking from the bonding gap. About 10 minutes after printing the final layers, the substrates are placed on top of each other so that the printed sides come together. A PTFE parting film of 30 μm thickness is used to assure the precrack. Subsequently, the specimens are placed in a custom-made PTFE fixture, which prevents the substrates from misalignments. A constant pressure is applied via 1 N weight elements. Following, the specimens are sintered for 4 h at 90 °C, 2 h at 110 °C and finally 4 h at 170 °C in a programmable oven.

After the sinter step, the preparation of ENF specimens is finished. For the DCB specimens, according to Figure 3, piano hinges need to be installed to the precracked side. The bonding surfaces are cleaned with isopropyl alcohol. A two-component epoxy glue is mixed and applied to the CFRP side using a paintbrush. The hinges are centrally aligned and the glue is cured at room temperature for 12 h. Additionally, polystyrene stripes are glued on the counterpart of the hinges to improve clamping properties during the test execution [4]. In the last step of the

experimental preparation, the width b of each specimen is measured at four equidistant distances. The mean value is used for further calculations.

3.3 Experimental procedure

For both experiments a tensile testing machine *TIRA TEST 2810* is used. The loads are applied via a moveable upper crosshead with a 100 N load transducer in DCB configuration and a 1 kN load transducer in ENF configuration.

For the DCB test, two clampings are installed to the test apparatus. The prepared specimen is mounted almost horizontally to the clampings using the piano hinges, see Figure 4. For test preparation, the upper crosshead is slowly moved upwards until the crack tip becomes visible with an optical microscope *Keyence VHX-5000*. The initial crack tip position a_0 is marked using a red fineliner and the current displacement δ_0 is recorded. Following, the displacement is set to 0 mm again and a cyclic boundary condition is programmed: The cyclic load is applied via a constant crosshead velocity of 1 mm/min until a first increment of $\delta_0 + 0.1$ mm is reached [8]. A potential new crack tip is marked using a blue fineliner and the displacement is set again to 0 mm. The cycle is repeated with increasing increments $\Delta\delta$ until a final fracture of the interface occurs. Since crack propagation is expected to slow down with progressive crack lengths, $\Delta\delta$ is 0.1 mm for the first 10 increments, 0.2 mm for the next 5 increments and finally 0.3 mm for higher increments. During the complete test, the applied force and the displacement are logged [12].

For the ENF test, setup and procedure are adopted from Heinrich [8]. The lower clamping is substituted by two rigid supports with a radius of 2 mm and 100 mm distance. A mandrel with a radius of 5 mm is installed to the moveable upper crosshead. The ENF specimen is mounted centered in a three-point bending configuration, see Figure 5. The initial crack tip and the bearing point on the precracked side are marked with a red fineliner. To force crack propagation, the specimen is loaded via a constant mandrel displacement. The velocity is set to a value of 1 mm/min. The end of the test is reached when the crack has propagated and then stagnated. The specimen is unloaded and the new clearly visible crack tip position a_f , identified using an optical microscope, is marked with a blue fineliner. Besides the initial fracture test, additional calibration measurements are required [13]. Therefore, five equidistant positions with approximately 5 mm distance are additionally marked with the blue fineliner on the cracked side of the specimen. They serve as new bearing points and thus change the effective crack length. All calibration measurements are carried out equivalently to the fracture test, but with a maximum load of 30 N. The velocity of the mandrel is 1 mm/min. For calculation of the $G_{II,C}$ value, the force and displacement values are logged during all measurements [13]. Since no complete failure of the printed interface occurs, both substrates are separated manually after the test, to observe the present fracture modes.



Figure 4: Mounted DCB specimen

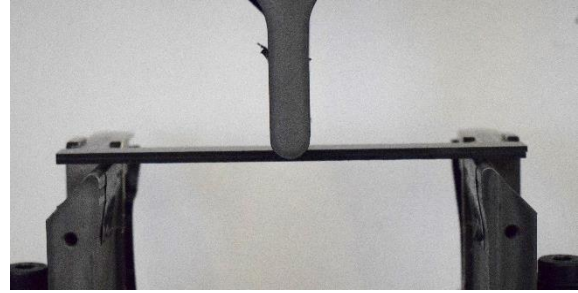


Figure 5: Mounted ENF specimen

3.4 Postprocessing

For the calculation of the interlaminar fracture toughness G_C , a data reduction method needs to be applied. Since only the compliance calibration method is available for both tests, it is used for further calculations [4].

In case of the DCB test in accordance with [12], a plot of the compliance $\log(\delta_i/P_i)$ over the initial crack length $\log(a_i)$ per increment i is created for every specimen. Therein, only increments are considered where the crack has propagated. Via the least-squares fit method a linear regression is obtained. The slope of the function is defined as parameter n . It is required to determine the mode I interlaminar fracture toughness using equation (1) from [12]. Since applied force P for advancing the crack, displacement δ and initial crack length a are recorded for each increment, multiple $G_{I,C}$ values for one specimen can be obtained resulting in a final median value [18].

$$G_{I,C} = \frac{nP\delta}{2ba} \quad (1)$$

In difference, for the ENF test analysis in accordance with [13] a plot of the compliance (δ_i/P_i) versus the cubed crack length $(a_i)^3$ is required including the results of the calibration measurements. A linear regression using a least-square fit leads to the slope m . With equation (2)¹ from [13], the fracture load P_{max} , the initial crack length a_0 and the specimen width b , it is used to calculate the interlaminar fracture toughness under a pure mode II loading. Only one $G_{II,C}$ value is obtainable per specimen.

$$G_{II,C} = \frac{3mP_{max}^2a_0^2}{2b} \quad (2)$$

Beside the calculation of fracture toughness values, a fracture mode analysis is executed. Therefore, microscopic images of both fracture surfaces are taken with a 20x magnification. Diverse appearing areas are allocated to the characteristic fracture modes. In this context, areas with agglomerations of CNT appear darker than adjacent areas, see Figure 6a) and b). They are located, recorded and surveyed via brightness evaluation of the microscope. By use of the image processing program *ImageJ*, such areas from related fracture surfaces can be converted to

¹ Designation of the force is changed compared to the referenced ASTM specification in order to achieve consistency with the DCB test.

binary images with only white and black pixel color values. An overlay of both images shows the overall agglomeration area in black (c). White areas in the overlay are CRF, provided that no UA and AF occurs. CAF areas, with agglomerations on both fracture surfaces, can be determined via multiplication of the binary images (d). Finally, CIF areas follow from subtracting the CAF color properties from the overlay image (e).

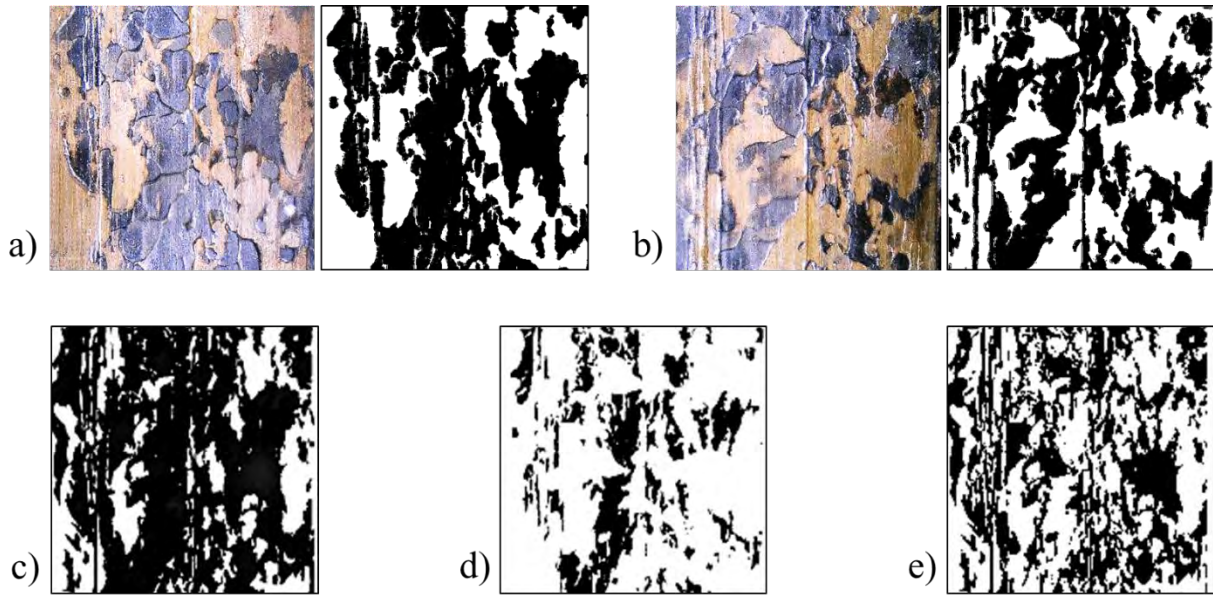


Figure 6: Representative evaluation of failure modes: a), b) conversion of fracture surfaces into binary images, c) overlay via addition of pixel color values, d) CAF via multiplication of pixel color values, e) CIF via difference of overlay and CAF

Since observed fracture of the ENF specimens is limited to the length between a_0 and a_f , evaluation of the fracture mode is restricted to this certain area. For the DCB specimens the fracture modes are evaluated for a representative length of 45 mm, which is the largest continuous observable dimension of the used microscope.

4 TEST RESULTS AND DISCUSSION

First test results are obtained from three DCB and ENF specimens fabricated from the inkjet printed CNT02 composition. The resulting interlaminar fracture toughness values are shown in Figure 7. As multiple results are obtainable from a single DCB specimen, $G_{I,C}$ values are displayed as boxplots outlining the median value, the total range and the interquartile range with 75 % of all values. For both tests, the majority of the median interlaminar fracture toughness is within a relatively low range from 2 to 6 N/m. On the other hand, values from a third specimen are significantly higher by a factor of 2 in case of DCB03, respectively factor 5 for ENF01. Allocated to their characteristic failure mode distribution, these specimens correlate with a higher portion of CRF.

Several conclusions are drawn from these results. First, a decomposition of the CNT enriched ink can be observed on the fracture surfaces. This results in clearly visible

agglomerations and in resin rich areas on 30 % to 50 % of the fracture zone. Therefore, the printed interface is found inhomogeneous with a wide range of interlaminar fracture toughness values. The larger the agglomerations, the smaller the CRF portion and the smaller both $G_{I,C}$ and $G_{II,C}$ values. Thus, a weakening effect of the agglomerated CNT is shown.

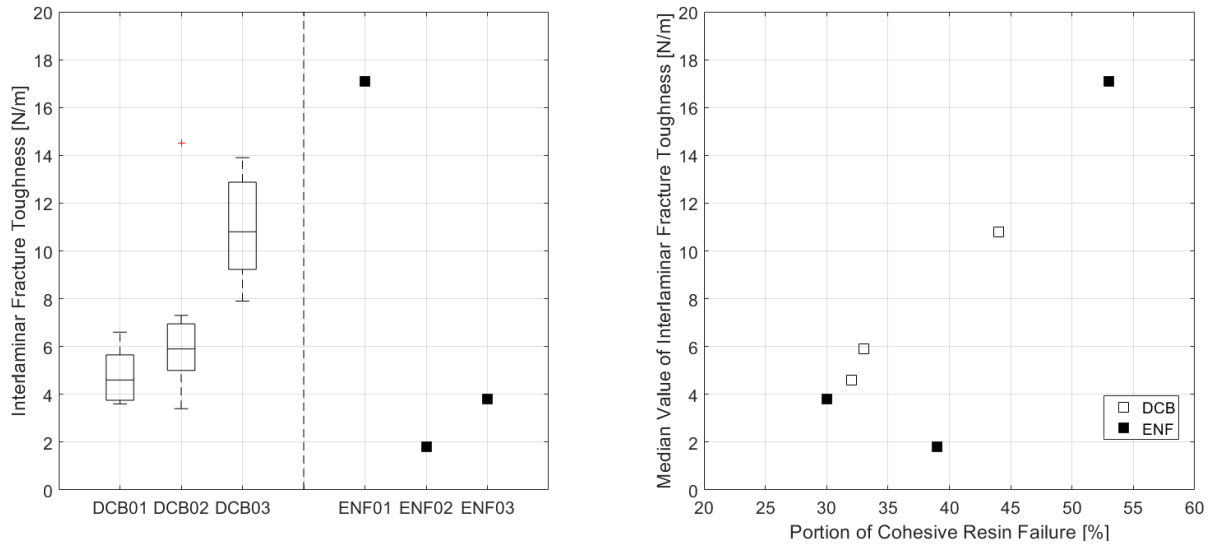


Figure 7: Interlaminar fracture toughness values and correlation with portion of CRF for valid DCB & ENF specimens for ink composition CNT02

This hypothesis is confirmed by results of two additional test series where the CNT are excluded (RED01) respectively reduced (CNT08). Without CNT the forming of agglomerations during the sinter process is precluded. A complete CRF of the printed interface can be observed, but with inhomogeneities with respect to the thickness distribution due to the DMAc evaporation. Results for each three valid DCB and ENF specimens of the RED01 series show significantly higher interlaminar fracture toughness values as in the previous tests. The median $G_{I,C}$ value is increased by 88 %, the corresponding value for a mode II load is increased by 271 % (see Figure 8).

Diverse results are obtained from the CNT08 series. The halving of the CNT content, compared to CNT02, does not lead to a reduction of the agglomeration area on the fracture surfaces. Contrary, the mean portion is found slightly increased from 62 % to 65 %. Therefore, the CNT fraction inside the agglomerations needs to be decreased and mitigate the local weakening effect. Due to this fact, the median $G_{II,C}$ value, obtained from only two valid specimens, is about 154 % higher than for the CNT02 series. The results from the DCB specimens show a different behavior. The change of the median value is negligible. Since the behavior of the agglomerations can be assumed to be transversal orthotropic with poor out-of-plane properties, the effect of the reduction of the CNT content vanishes for the corresponding mode I load.

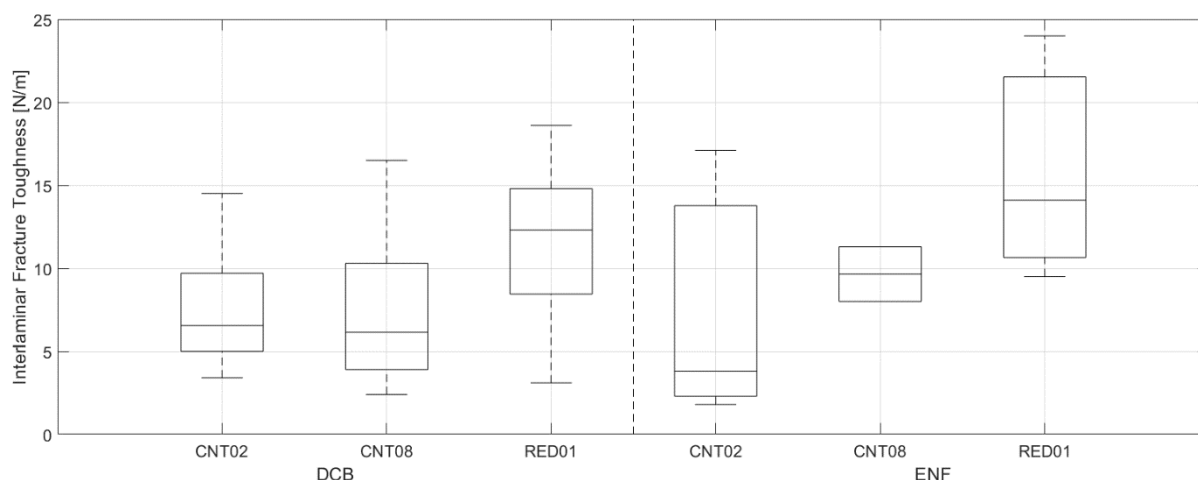


Figure 8: Interlaminar fracture toughness values of all ink compositions obtained from DCB specimens (left) and ENF specimens (right)

5 CONCLUSIONS

The CNT enriched inks were found to be prone to form agglomerations. The extent does not vary significantly with the added CNT content which causes several problems. First, the conductive path is very likely to be interrupted by resin rich areas. Further, the intended strengthening effect for the epoxy resin is inverted. Cohesion forces in agglomerations are smaller than in neat resin, which was confirmed with results from the RED01 series.

Furthermore, a negligible effect of the CNT content on the interlaminar fracture toughness value in DCB tests was shown. Since CNT are assumed to be mainly distributed in plane with the printed interface, transversal orthotropic properties are predominant. Thus, an effect was found for the in-plane shear mode II. A local reduction of CNT in the agglomerations improved the corresponding fracture toughness.

Nevertheless, the medians of the fracture toughness values were higher than the average values from Heinrich et. al. [8] investigating a silver particle-based ink, applicable to in-situ monitoring of damage [4]. Thus, the current results have shown the potential of CNT-based printed electronics regarding their enhanced damage behavior.

The objective for future works is the prevention of agglomerations by use of suitable chemical additives. This is fundamental for improved mechanical properties. The fracture toughness from the RED01 series shall be exceeded.

ACKNOWLEDGEMENT

Financial support by the *Deutsche Forschungsgemeinschaft* (DFG, project number 3933868053) is gratefully acknowledged. Sincere appreciation to *Hamburg University of Technology / Institute of Polymer Composites* for the provision of the CFRP substrates.

REFERENCES

- [1] C. Boller, “Structural Health Monitoring - Its Association and Use” in *New Trends in Structural Health Monitoring*, Vienna (AT): Springer-Verlag, 2013, pp. 1-79.
- [2] U.S. Department of Transportation Federal Aviation Administration, *Damage Tolerance Assessment Handbook*, Springfield, VA (US): National Technical Information Service, 1993.
- [3] V. Gattulli, “Implementation of Identification Methodologies on Large-Scale Structures” in *Identification Methods for Structural Health Monitoring*, Cham (CH): Springer International Publishing AG Switzerland, 2016, pp. 1-34.
- [4] F. Heinrich, *On the Mechanics of Printed Electronics: Experimental and Numerical Investigations Using Cohesive Zone Models*, Doctoral Thesis, Department of Mechanical Engineering of the Helmut-Schmidt-University / University of the Federal Armed Forces Hamburg, 2018.
- [5] A. Sridhar, T. Blaudeck and R. R. Baumann, “Inkjet printing as a key enabling technology for printed electronics” in *Material Matters - Volume 6, Number 1*, pp. 12-17, 2011.
- [6] Y. Huang, N. Li, Y. Ma, F. Du, F. Li, X. He, X. Lin, Gao, H. and Y. Chen, “The influence of single-walled carbon nanotube structure on the electromagnetic interference shielding efficiency of its epoxy composites” in *Carbon - Volume 45, Issue 8*, pp. 1614-1621, July 2007.
- [7] H. Hedia, S. Aldousari, A. Abdellatif and G. Abdel Hafeez, “Investigation of the mechanical properties of nanocomposite SWCNTS/EPOXY by micromechanics methods and experimental work” in *Journal of Naval Architecture and Marine Engineering*, pp. 103-114, December 2015.
- [8] F. Heinrich, H. H. Langner and R. Lammering, “On the identification of cohesive parameters for printed metal-polymer interfaces” in *Smart Materials and Structures - Volume 26, Number 5*, May 2017.
- [9] G. Habenicht, *Kleben - Grundlagen, Technologien, Anwendungen*, Berlin, Heidelberg (DE): Springer-Verlag, 2009.
- [10] F. C. Cambell, *Structural Composite Materials*, Materials Park, OH (US): ASM International, 2010.
- [11] E. Greenhalgh, *Failure analysis and fractography of polymer composites*, Cambridge (UK): Woodhead Publishing Limited, 2009.
- [12] ASTM International, *ASTM D 5528-01 (Reapproved 2007) - Standard Test Method for Mode I Interlaminar Fracture Toughness of Unidirectional Fiber-Reinforced Polymer Matrix Composites*, West Conshohocken, PA (US): 2007.

- [13] ASTM International, *ASTM D7905/D7905M-14 - Standard Test Method for Determination of the Mode II Interlaminar Fracture Toughness of Unidirectional Fiber-Reinforced Polymer Matrix Composites*, West Conshohocken, PA (US): 2014.
- [14] W. N. Sharpe Jr. (Ed.), *Springer Handbook of Experimental Solid Mechanics*, New York, NY (US): Springer Science + Business Media, LLC, 2008.
- [15] M. J. Davis and D. A. Bond, *The importance of failure mode identification in adhesive bonded aircraft structures and repairs*, Paris (FR): ICCM, 1999.
- [16] T. Wang, B. Song, K. Qiao, Y. Huang and L. Wang, “Effect of Dimensions and Agglomerations of Carbon Nanotubes on Synchronous Enhancement of Mechanical and Damping Properties of Epoxy Nanocomposites” in *Nanomaterials - Volume 8, Issue 12*, December 2018.
- [17] J. Pan and L. Bian, “Influence of agglomeration parameters on carbon nanotube composites” in *Acta Mechanica - Volume 230*, Vienna (AT): Springer, 2019, pp. 2207-2217.
- [18] S. Lee, P. C. Gaudert, R. C. Dainty and R. F. Scott, “Characterization of the Fracture Toughness Property (G_{Ic}) of Composite Laminates Using the Double Cantilever Beam Specimen” in *Polymer Composites Vol.10, No. 5*, Brookfield, CT (US): Society of Plastics Engineers, 1989, pp. 305-312.

A NOVEL CONCEPT OF A MODULAR SHAPE-ADAPTABLE SANDWICH PANEL ABLE TO ACHIEVE MULTIPLE SHAPES

OLEG TESTONI^{*}, SAMPADA BODKHE^{*}, ANDREA BERGAMINI[†] AND PAOLO
ERMANNI^{*}

^{*} Laboratory of Composite Materials and Adaptive Structures (CMASLab)
Eidgenössische Technische Hochschule Zürich
ETH Zurich, 8092, Zurich Switzerland
e-mail: testonio@ethz.ch, www.structures.ethz.ch

[†] Laboratory Acoustics / Noise Control
Eidgenössische Materialprüfungs- und Forschungsanstalt
Empa, 8600, Dübendorf, Switzerland
e-mail: Andrea.Bergamini@empa.ch, www.empa.ch

Key words: Shape-Adaptable Structures, Smart Structures, Shape-Memory-Alloy.

Abstract. Shape memory alloys (SMA) are well known for the high stress and the large strain that they can achieve simultaneously and, therefore, have been widely used as actuators in different shape-adaptable structures. While most of the adaptive structures found in the literature using SMAs as actuators have been designed to accomplish only a single type of deformation, we present in this work a novel structural concept able to achieve multiple shapes. The concept consists of a modular sandwich panel composed of rigid cells connected by active joints hosting SMA wires, which are used as actuators. Thanks to their geometry, the joints act both as stroke amplification systems and as bias springs, allowing for multiple actuations of one-way SMA wires. The active joints are placed in pairs both on the upper and on the lower face sheet of the panel and control the distance as well as the orientation of neighbouring panel cells. As a result, it is possible to deform the panel both in-plane and out-of-plane. In this paper, we present the working principle of the proposed concept and of its actuation system. The mechanical behaviour of the active joints is investigated both numerically and experimentally and the results obtained are implemented in a finite element model of the shape-adaptable sandwich panel. Four actuation strategies of the active joints are investigated and the achieved deformations returned by the corresponding simulations are compared with the experimental measurements carried out on a demonstrator.

1 INTRODUCTION

Sandwich panels are a type of construction widely used in lightweight structures due to the high specific stiffness and specific strength and the possibility to integrate additional functions such as thermal or acoustic insulation [1] or even liquid storage [2]. In this work, we want to make a step forward introducing the concept of shape-adaptable sandwich panels. This step is motivated by the growing interest in shape-adaptable lightweight structures by the aerospace

and the automotive industry, which see morphing structures as a possible way to realize reconfigurable lightweight systems or active aerodynamic surfaces able to improve performance and efficiency of the current technologies [3-6].

As underlined by Campanile et al. [7], the design of shape-adaptable lightweight structures tackles an inherent contradiction, since a certain compliance is required in order to accommodate for the changes in shape but, simultaneously, enough stiffness has to be provided to carry operational loads without undergoing excessive deformations and, at the same time, the weight constrain has to be met. In opposition to traditional technologies, which rely on rigid-body mechanisms to solve this problem, novel approaches take advantage of the combination of compliant structures and smart materials [8-12] or deploy a regular arrangement of unit cells and small, distributed actuators to create programmable structures capable of achieving complex changes in shape [13-14].

In this work, we merge these two principles to realize a shape-adaptable sandwich panel. The concept presented is based on the two dimensional arrangement of rigid cells connected with active compliant joints. Each joint hosts an actuation system based on shape memory alloys (SMA), which can be controlled independently. This fact allows us to selectively actuate only specific joints and to obtain multiple shapes from a single panel design.

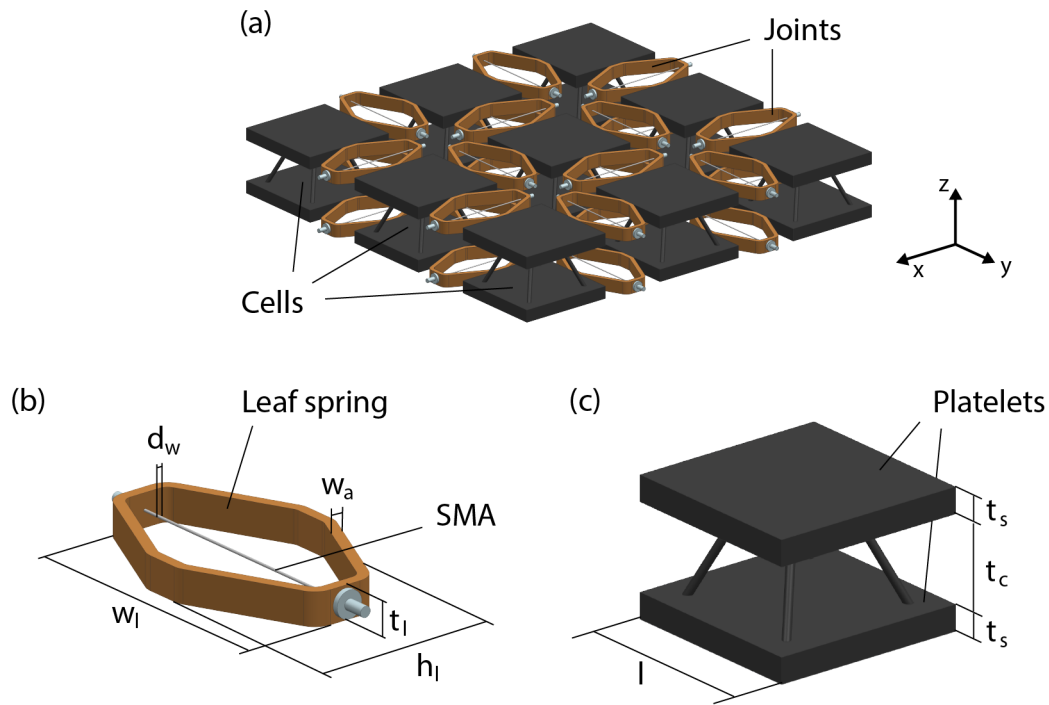


Figure 1: Geometry (a) of the shape-adaptable sandwich panel investigated, (b) of the active compliant joints and (c) of the stiff cells.

2 INVESTIGATED DESIGN CONCEPT

The shape-adaptable sandwich panel concept presented in this work is depicted in Fig. 1-a and consists of two deformable face sheets made of stiff square platelets connected through active compliant joints (Fig. 1-b). Corresponding platelets on opposite face sheets are connected by truss elements, which form the core of the panel, and, all together, form stiff cells (Fig. 1-c). In this arrangement, each cell is connected to its neighbours through two active compliant joints, which are placed, respectively, between the platelets of the upper and those of the lower face sheet (see Fig. 2-a). The joints consist of leaf springs hosting a pre-strained, one-way SMA wire, which acts as an actuator. When heated up, the SMA wire contracts, deforming the leaf spring, which in turn pushes the neighbouring platelets apart. This actuation principle is similar to the ‘Fish-mouth’ actuator presented by Campanile et al. [15] and relies on the leaf spring to pull back the SMA wire to its initial state, while the latter cools down, allowing us to obtain a result similar to a two-way shape memory effect with a one-way SMA wire.

The morphing capability of the presented concept is based on the placement of the active compliant joints between the platelets of the panel cells and on the possibility of their selective actuation. These two features allow for the control of the distance and of the angle α between neighbouring cells (see Fig. 2) and, therefore, they enable us to obtain both in-plane and out-of-plane deformations according to the actuation strategy of the SMA wires implemented. For example, if we consider two adjacent panel cells, we notice that, when both the upper and the lower active joint are actuated, the displacement between the upper and the lower cell platelets is equal and, therefore, the cells experience an in-plane translation (Fig. 2-a). On the other hand, if only the upper (Fig. 2-c) or the lower (Fig. 2-b) joint is actuated, the relative motion of the platelets is no longer equal and, consequently, the panel cells undergo an out-of-plane rotation. This effect, combined with the periodic arrangement of the panel cells in two dimensions, gives us the possibility to achieve complex 3D shapes, such as half pipes (Fig. 2-d), domes (Fig. 2-e), as well as shapes with multiple curvatures (Fig. 2-f).

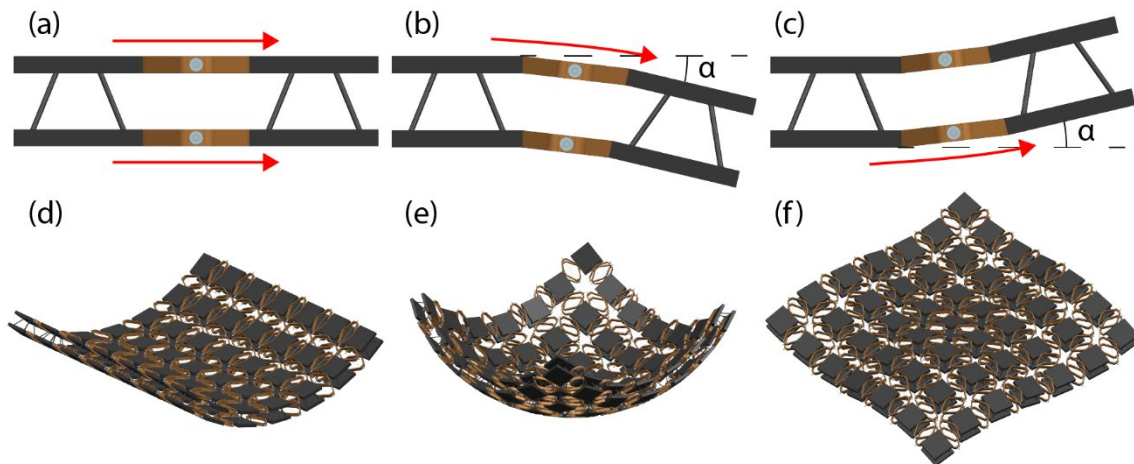


Figure 2: Behaviour of two neighbouring cells (a) when both active joints are actuated, (b) when only the upper joint is actuated and (c) when only the lower joint is actuated. Examples of possible shapes achievable by the shape-adaptable sandwich panel concept: (d) half pipe, (e) dome and (f) multi-curvature.

3 METHODS

In order to evaluate the capability of the presented concept to vary its shape, we considered a sandwich panel composed by 3x3 cells (Fig. 3-a). We first investigated the mechanical behaviour of the active compliant joints and we created a simplified numerical model that was later extended to the entire panel. This model was used to compute the deformations of the panel for different actuation strategies of the active joints under the assumption that no external load was acting on the panel. Finally, a demonstrator was manufactured and tested for four selected types of deformations to verify the numerical results.

We considered a design of the active compliant joints based on leaf springs of height $h_l = 32$ mm, width $w_l = 52$ mm, thickness $t_l = 6$ mm and arm thickness $w_a = 2$ mm. The leaf springs were 3D printed (Indimatec) in polyether ether ketone (PEEK) (Zyex, VICTREX PEEK 1.75 mm) with a single outer layer and a 60% rectangular infill. We opted for this material due to its high glass transition temperature, which lies above 140°C [16], in order to reduce the risk of thermal degradation and softening during the actuation of the SMA wires (SAES Group, SmartFlex05). The latter had a diameter $d_w = 0.5$ mm and were fixed to the outer side of the leaf springs using crimps (SAES Group, T Type Crimp) (see Fig. 3-b). Before the definitive fixation of the crimps, leaf springs were compressed of 5 %, so that their spring back could pre-strain the SMA wires and enable their actuation.

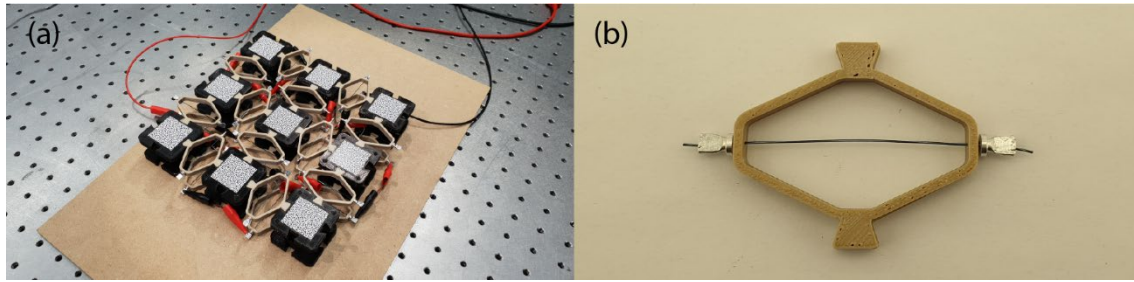


Figure 3: (a) Demonstrator of the shape-adaptable sandwich panel and (b) one of the compliant active joints tested.

Five identical active joints were tested in order to identify their average strain. The SMA wires were heated up with a current of 3 A applied with a DC power supply (Keysight, E3631A) for 30 s and then cooled down with a ventilator for 1 min. The contraction of the SMA wire was measured with a digital image correlation (DIC) system (Correlated Solutions, VIC-3D) and the difference between the maximum strain achieved by the SMA when heated up and the minimum strain achieved when cooled down was registered. Each actuation cycle was repeated six times but only the strains achieved in the last five cycles were considered for the calculation of the average strain. The average strain measured was used to estimate the force F generated by the SMA wires to be implemented in the numerical model. Five leaf springs were tested under compression in a universal testing machine (Zwick/Roell, Z005) and the force-strain diagram obtained was compared with the average deformation of the five actuators previously measured in order to estimate the value of F .

A linear FE model of the leaf spring was created in COMSOL Multiphysics® v. 5.4 assuming the material as isotropic and using solid 3D elements with a mesh of size of 1 mm.

The Young's modulus of the 3D printed PEEK was determined following the standard ASTM D790-10, while a Poisson's ratio value of 0.4 was chosen. This FE model was used to assess the force necessary to deform the leaf spring and to establish a comparison with the experimental results of the compression test. The model was then expanded to reproduce the entire panel. The panel cells were modelled as rigid bodies and the actuation of the panel was implemented by applying the previously estimated force F on the selected active joints at the fixation points of the SMA wires. Four different actuation strategies of the active joints were investigated (see Fig. 4). Each of them corresponds to a different type of deformation of the panel: a planar expansion (Fig. 4-a), an out-of-plane deformation with a single curvature (Fig. 4-b), an out-of-plane deformation with a double curvature (Fig. 4-c) and an out-of-plane deformation with both a positive and a negative curvature (Fig. 4-d).

The changes in shape obtained by the numerical model were compared with the measurements carried out on a demonstrator. 24 active compliant joints were printed and assembled to nine panel cells. For the sake of simplicity, the latter were 3D printed (Ultimaker, Ultimaker 2+) in polylactide (PLA) (Swiss 3D Tec, PLA filament, 3 mm) since in this work we did not apply any external load to the panel but only investigated the achievable shapes. The cell's platelets had an edge $l = 46$ mm and a thickness $t_s = 6$ mm. Moreover, they were endowed with four anchor points for the interlocking of the active joints, to which we added two dove tail elements (see Fig. 3-b). The truss core had a thickness $t_c = 20$ mm. Finally, the SMA wires of the active joints were connected in series according to the type of deformation investigated and a speckle pattern was applied on the upper surface of the cell platelets in order to track the deformation of the panel using a DIC system (Correlated Solutions, VIC-3D).

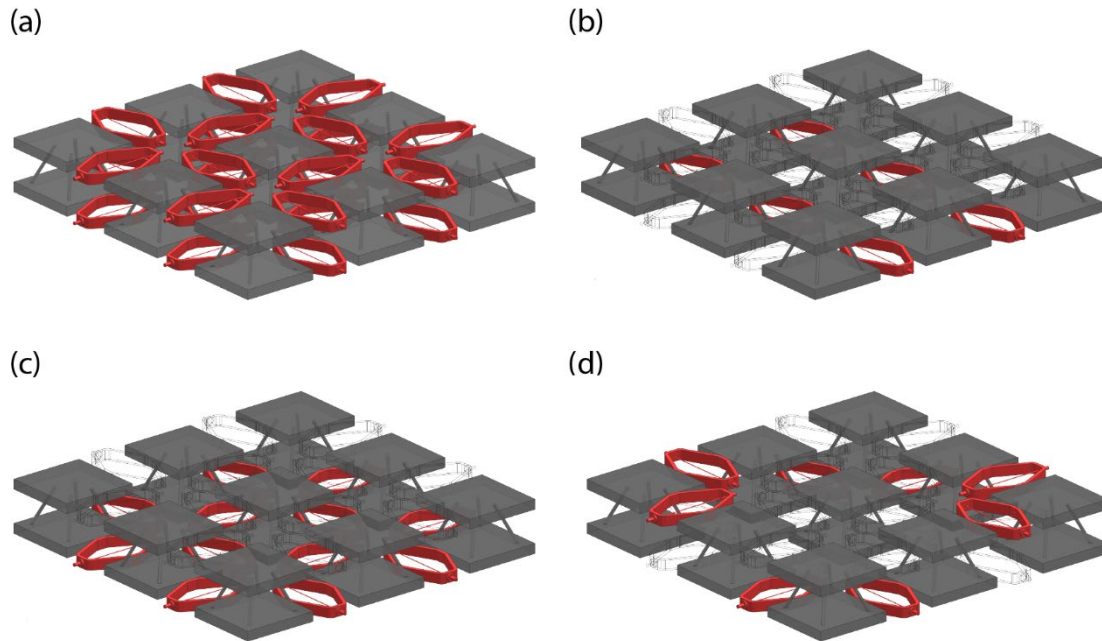


Figure 4: Actuation strategies of the active compliant joints for the four cases considered: (a) planar expansion, (b) single curvature, (c) double curvature and (d) positive and negative curvature (d). The joints actuated are marked in red.

4 RESULTS

The strains achieved by the SMA wires in the active joints tested are reported in Table 1. The average strain achieved was $(1.57 \pm 0.22)\%$, to which it corresponds a standard deviation of 14.01%. Fig. 5-a shows the results of the 3 points bending tests performed to characterize the 3D printed PEEK. The characterisation returned a Young's modulus of 2.859 GPa with a standard deviation of 19.55%. Fig. 5-b compares the results of the simulations of the compression behaviour of a single leaf spring with the results of the mechanical tests. By reading from this figure the values of the force corresponding to the previously determined average strain achieved by the SMA wires, an average force of 22.3 N generated by the SMA wires was estimated and used later in the simulations of the entire panel.

Table 1: Strain difference achieved by the active joints tested.

Sample	Cycle 1	Cycle 2	Cycle 3	Cycle 4	Cycle 5
1	1,47%	1,45%	1,43%	1,42%	1,41%
2	1,42%	1,40%	1,38%	1,37%	1,36%
3	2,01%	2,00%	1,97%	1,96%	1,96%
4	1,66%	1,66%	1,62%	1,61%	1,61%
5	1,44%	1,43%	1,41%	1,41%	1,40%
Average	$(1.57 \pm 0.22)\%$				

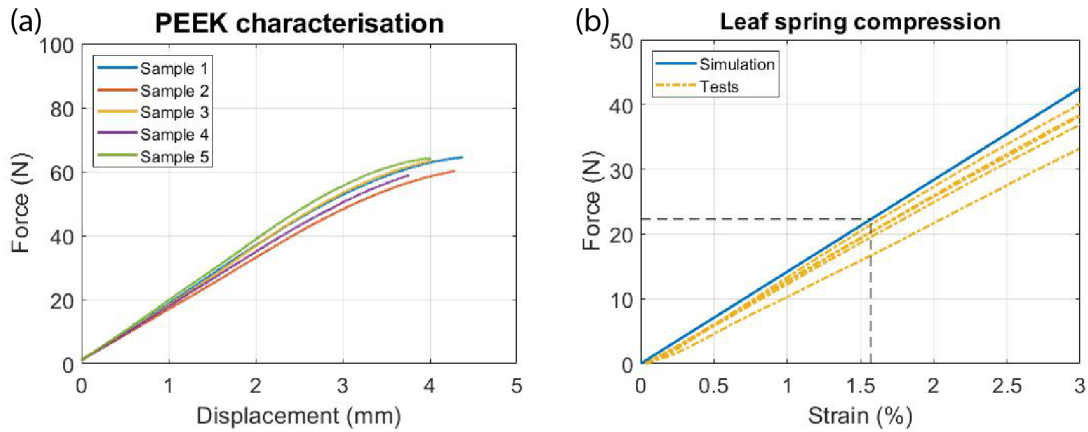


Figure 5: (a) Results of the 3 points bending tests performed on the 3D printed PEEK samples and (b) comparison of the simulated force necessary to compress the leaf spring with the experimental tests.

As far as the panel is concerned, Fig. 6 establishes a comparison between the numerical and the experimental results for the four cases considered. In the following subsections, each type of deformation investigated is treated separately and numerical and experimental results are presented.

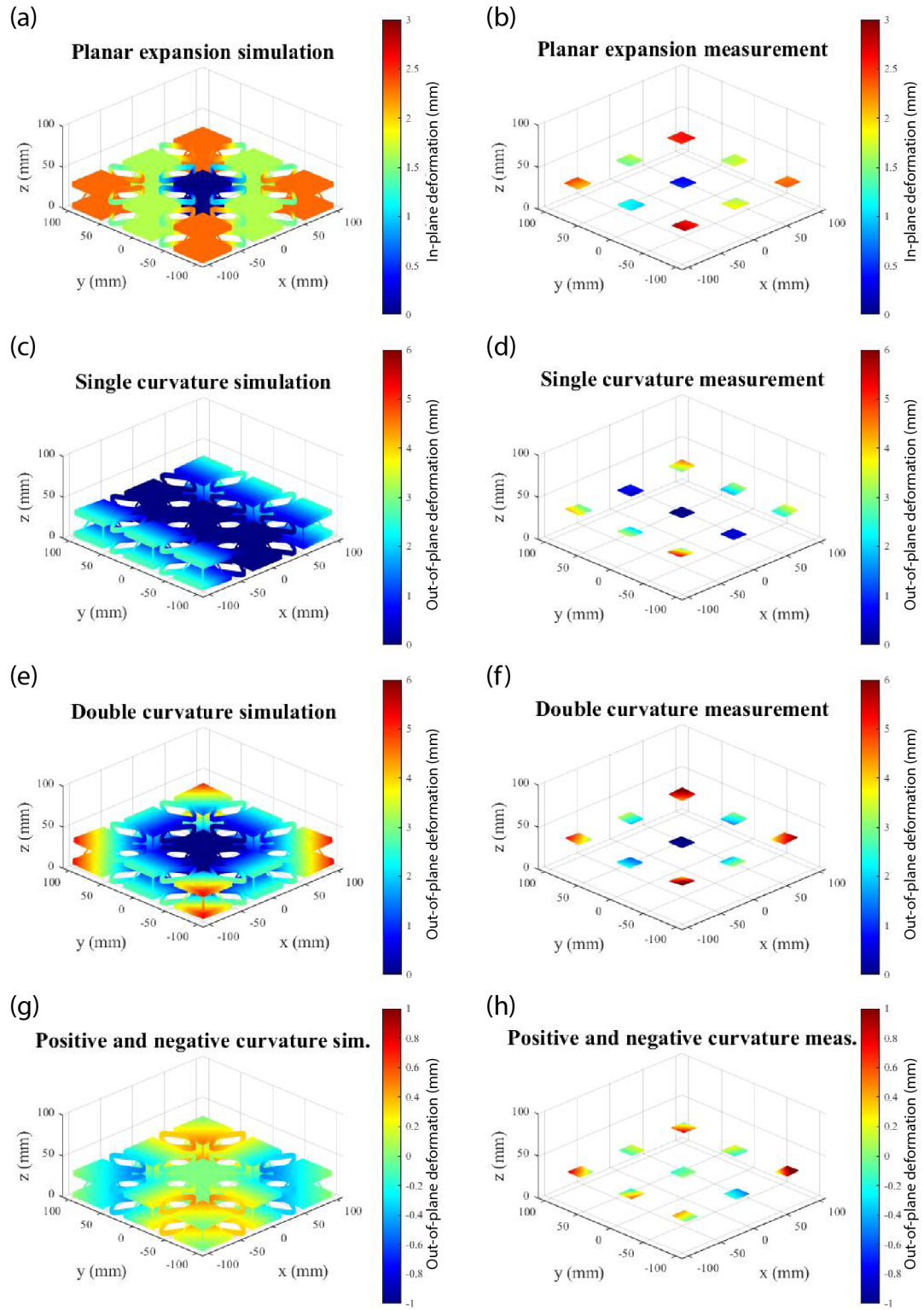


Figure 6: Comparison of the FE results (left) and the DIC measurements (right) for the four cases investigated: (a, b) planar expansion, (c, d) single curvature, (e, f) double curvature and (g, h) positive and negative curvature.

4.1 Planar expansion

The panel undergoes planar changes in shape when corresponding active joints on the upper and on the lower face sheets are actuated at the same time. As it is possible to notice in Fig. 6-a, no rotation of the panel cells occurs but only their planar translation. Moreover, the degree of this translation increases with the increasing distance of the cells from the centre of the panel. These effects can be seen as well in the DIC measurements (Fig. 6-b), which are in good agreement with the numerical results for most of the panel cells.

4.2 Single curvature

In order to obtain a single positive curvature of the panel, only the active joints on the lower face sheet aligned in the same direction were actuated. As a result, the lower face sheets expands in a single direction, introducing a moment in the panel cells, which rotate lifting the neighbouring cells. Both the simulation (Fig. 6-c) and the DIC measurements (Fig. 6-d) show how the central cells of the panel do not displace, while the external cells rotate slightly upwards giving a positive curvature to the panel.

4.3 Double curvature

When all active joints in the lower face sheets are actuated, the latter expands uniformly in both planar directions introducing two perpendicular moments into the structure. Fig. 6-e and Fig. 6-f show how this actuation strategy results in a double curvature of the panel both in the simulation as well as in the DIC measurements, respectively.

4.4 Positive and negative curvature

The results of the numerical calculations and of the DIC measures obtained for the last type of deformation investigated are plotted in Fig. 6-g and Fig. 6-h, respectively. If we consider the profile of the edges of the panel, we notice how the cells on the vertices of the panel rotate in pairs towards the centre or towards the outside of the panel, while the cells in the middle of the edges rotate in pairs around an axis parallel to the x or to the y-axis. As results, the edges of the panel assume a slight s-shape, which witnesses the presence of both a positive and a negative curvature.

5 DISCUSSION

The results of the tests conducted on the active joints demonstrate the proper working of the concept and the possibility to obtain multiple actuation cycles using one-way SMA wires like in [15] but with an easier manufacturing process. On the other side, the results also show that the strain achieved by each active joint tends to slight decrease with the increase in actuation cycles and that the deviation in the strain achieved by different joints tested is about 14%. This deviation might be justified considering the deviation in the Young's modulus of the 3D printed PEEK, which amounts to almost 20%. The difference in stiffness of the 3D printed PEEK can be also distinguished in the results of the compression tests carried out on the leaf springs. In Fig. 5-b, we can clearly notice the difference in the slope of the curves of the different leaf springs tested. Similar leaf springs, printed with the same 3D printer and with the same process parameters, were used to assemble the active joints tested. Therefore, we can expect that the

variation in the Young's modulus of the 3D printed PEEK has a major effect on the performance of the active joints, since the stiffness of the leaf springs affects both the maximum strain that the SMA wires can achieve and the capability of the leaf springs to act as a bias spring. On the other side, Fig. 5-b shows also that for the given geometry of the leaf spring and for the strains achieved by the SMA wires, we can assume a linear behaviour of the active joints and, therefore, the use of a linear model in the simulations of the entire panel is justified.

Considering the observed variance in strain achieved by the active joints, the simulations of the deformation of the entire panel and the DIC measurements carried out on the demonstrator were in good agreement. As is it possible to notice comparing the left and the right column of Fig. 6, some misalignments in the displacement of the panel cells are present and they make the final shape not always perfectly symmetric. Nevertheless, the deformations measured are always close to the numerical predictions and the targeted final shape is clearly distinguishable in all cases investigated. Only in the case of positive and negative curvature the difference between simulations and measurement is larger, but this fact might be attributed to the smaller displacements involved. Indeed, since the out-of-plane deformation shown in Fig. 6-g and Fig. 6-h is an order of magnitude lower than in the other cases and in the range of tenths of millimetre, this higher difference might be related also to small imperfections in the manual assembly of the panel.

6 CONCLUSIONS AND OUTLOOK

The results presented in this paper demonstrate the capability of the presented concept to achieve multiple changes in shape involving both in-plane and out-of-plane deformations with a single design. This versatility derives from the high number of degrees of freedom provided by the distributed actuation system and by the disposition of the active joints on both on the upper and on the lower face sheets of the panel. The results achieved suggest that this concept might find application in highly variable environments, where multiple shapes might be beneficial to optimize the structural performance at the different conditions. As possible applications, we envisage active surfaces for morphing wings or car body panels, or even reconfigurable modular structures for space antennas. When considering possible applications, further specific constraints, such as maximum weight or load carrying capability, have to be taken into account and their effect on the morphing capability of the proposed concept have to be evaluated. Moreover, a robust manufacturing process has to be selected, in order to reduce the variance on performance of the active joints and a suitable control system assuring the independent actuation of each joint has to be developed.

Further work will focus on the improvement of the manufacturing process and particularly on the optimisation of the mechanical properties of the 3D printed components. Moreover, the design of the leaf spring and of the active joints will be optimized selecting a specific application and taking into account the specific requirements. Finally, a proper control system able to actuate each active joint independently will be developed and integrated into the panel design.

ACKNOWLEDGMENTS

The authors would like to thank the ETH board for funding the project. The Digital Image Correlation (DIC) equipment was purchased through the Swiss National Science Foundation R'Equip grant 206021_150729.

REFERENCES

- [1] Zenkert, D. *An Introduction To Sandwich Constructions*. Warley Engineering Materials Advisory Services (1995).
- [2] Vinson, J. R. Sandwich structures. *Appl. Mech. Rev.* (2001) 54 201–214.
- [3] Barbarino S., Bilgen, O., Ajaj, R. M., Friswell, M. I. and Inman D. J. A review of morphing aircraft. *J. Intell. Mater. Syst. Struct.* (2011) 22 (9) 823–877.
- [4] Gomez, J. C. and Garcia, E. Morphing unmanned aerial vehicles. *Smart Mater. Struct.* (2011) 20(10):103001.
- [5] Lachenal, X., Daynes, S. and Weaver, P. M. Review of morphing concepts and materials for wind turbine blade applications. *Wind Energy* (2013) 16 (2) 283–307.
- [6] Daynes, S., and Weaver, P. M. Review of shape-morphing automobile structures: concepts and outlook. *Proc. IMechE* (2013) 227 (11) 1603–1622.
- [7] Campanile, L. F. *Adaptive Structures: Engineering Applications*. New York: Wiley (2007).
- [8] Sun, J., Guan, Q., Liu, Y. and Leng, J. Morphing aircraft based on smart materials and structures: A state-of-the-art review. *J. Intell. Mater. Syst. Struct.* (2016) 27 (17) 2289–2312.
- [9] Hartl, D. J., and Lagoudas, D. C. Aerospace applications of shape memory alloys. *Proc. IMechE* (2007) 221(4) 535–552.
- [10] Han, M. W., Rodrigue, H., Cho, S., Song, S. H., Wang, W., Chu, W. S. and Ahn, S. H. Woven type smart soft composite for soft morphing car spoiler. *Composites Part B* (2016) 86 285–298.
- [11] Furst, S. J., Peele, B. and Seelecke, S. Design and fabrication of an SMA actuated bat. *SMASIS2012*-8198, pp. 697–706.
- [12] Keihl, M. M., Bortolin, R. S., Sanders, B., Joshi, S. and Tidwell, Z., Mechanical properties of shape memory polymers for morphing aircraft applications. *Proc. SPIE 5762*, Smart Structures and Materials 2005: Industrial and Commercial Applications of Smart Structures Technologies, (5 May 2005).
- [13] Valdevit, L. and Bauer, J. *Fabrication of 3D micro-architected/nano-architected materials*. Elsevier BV (2016).
- [14] Shaw, L. A. and Hopkins, J. B. An Actively Controlled Shape-Morphing Compliant Microarchitected Material. *Journal of Mechanisms and Robotics* (2016) Vol. 8.
- [15] Campanile, L. F., Keimer, R. and Breitbach, E. J. The “Fish-mouth” Actuator: Design Issues and Test Results. *J. Intell. Mater. Syst. Struct.* (2004) Vol. 15.
- [16] Wu, W., Geng, P., Li, G., Zhao, D., Zhang, H. and Zhao, J. Influence of Layer Thickness and Raster Angle on the Mechanical Properties of 3D-Printed PEEK and a Comparative Mechanical Study between PEEK and ABS. *Materials* (2015) 8, 5834–5846.

ANALYSIS OF MULTIFUNCTIONAL SMA/PIEZOELECTRIC/COMPOSITE BEAM STRUCTURE FOR MORPHING AND ENERGY HARVESTING

NILANJAN MALLIK*

* Department of Mechanical Engineering
Indian Institute of Technology (BHU), Varanasi
Varanasi-221005, Uttar Pradesh, India

e-mail : nmallik.mec@iitbhu.ac.in, Web page : <https://www.iitbhu.ac.in/dept/mec/people/nmallikmec>

Key words: Multifunctional composites, Smart Structures, Morphing, Energy harvesting, SMA, Piezoelectric.

Abstract. This paper deals with morphing and energy harvesting analysis of new innovative multifunctional hybrid composite beam structure consisting of conventional fiber reinforced composite as substrate layer, a shape memory alloy fiber reinforced composite layer for the purpose of morphing actuation and a piezoelectric composite layer for the purpose of energy harvesting. One dimensional Tanaka type model using Reuss scheme with multi variant martensite is adopted to model SMA behavior and transformation model of SMA solved numerically as Young's modulus depends on martensite fraction. Multicell micromechanics approach is adopted to calculate effective properties of fiber reinforced composites. The objective of the present work is to analytically investigate the free and forced vibration of this newly proposed hybrid composite beams in pre/post-buckled domains and also to analytically estimate energy harvesting capability.

1 INTRODUCTION

Morphing is defined as the ability of certain wing to change its geometrical form during flight. Morphing concept is inspired from bird wings that are able to change wing shapes during flight at varied surrounding conditions. Such wing will enable the aircraft to accommodate multiple flight regimes and obtain better flight performance [1-3]. There can be several types of morphing possible viz. span, chord, sweep, chord-wise, span-wise and twist etc. Several mechanisms are also reported in literature to achieve particular type of morphing viz. tendon actuated compliant cellular truss, lattice based cellular structure, Parker variable camber wing, number of flap and slat mechanisms, variform wing, compliant mechanism, piezoelectric actuated wing, SMA actuated wing, reconfigurable wing and smart wing [4-13]. Of late multifunctional smart materials are being developed to achieve several functionalities simultaneously. Apart from multiple functionalities these materials can reduce weight of the structure thus enable fuel savings [14]. Shape memory alloy (SMA) and piezoelectric actuators are used for wing morphing in different flight regimes and are reported in literature [15-19].

Similarly, SMA strips and wires in laminated composites structures are also used for mechanism of morphing in aircraft wing structure [20]. In literature many researchers addressed the investigation of camber morphing mechanism [21]. The implementation of an actuator that enables smooth deformation is achieved through the use of SMAs. SMA components not only accommodate but actually induce the chord-wise axial strains in the skin needed for camber changes while preserving structural integrity and providing high stiffness. Many studies focus on analysis of pre/post buckling behaviour, bending behaviour and vibration behaviour of laminated composite structures embedded with SMA wires [22-32]. Modeling of SMA wire can be found in literature [33, 34]. Effective properties of piezoelectric fiber reinforced composites is investigated by Mallik and Ray [35] by strength of materials and method of cells approach. An elaborated demonstration of energy harvesting technologies including vibration based technologies can be found in book by Priya and Inman [36].

Investigation of laminated composite structure embedded with SMA wire for morphing capability and energy harvesting capability is scarce in literature. Hence, morphing and energy harvesting analysis of new innovative multifunctional hybrid composite beam structure consisting of conventional fiber reinforced composite as substrate layer, a shape memory alloy fiber reinforced composite later for the purpose of morphing actuation and a piezoelectric composite layer for the purpose of energy harvesting. One dimensional Tanaka type model using Reuss scheme with single variant martensite is adopted to model SMA behavior and transformation model of SMA solved numerically as Young's modulus depends on martensite fraction. Strength of materials approach is adopted to predict effective properties of piezoelectric composite. The objective of the present work is to analytically investigate the free and forced vibration of this newly proposed hybrid composite beams in pre/post-buckled domains and also to analytically estimate energy harvesting capability.

2 GENERAL SPECIFICATIONS

Present paper deals with morphing and energy harvesting analysis of new innovative multifunctional hybrid composite beam structure consisting of conventional fiber reinforced composite as substrate layer, a shape memory alloy fiber reinforced composite layer for the purpose of morphing actuation and a piezoelectric composite layer for the purpose of energy harvesting.

3 METHODOLOGY

One dimensional Tanaka type model using Reuss scheme with single variant martensite is adopted to model SMA behavior and transformation model of SMA solved numerically as Young's modulus depends on martensite fraction. Strength of materials approach is adopted to predict effective properties of piezoelectric composite. The objective of the present work is to analytically investigate the free and forced vibration of this newly proposed hybrid composite beams in pre/post-buckled domains and also to analytically estimate energy harvesting capability.

3.1 SMA constitutive model

One dimensional constitutive model proposed by Brinson is adopted in the presented study.

Based on this constitutive model quantities stress (σ), strain (ϵ) and temperature (T) are related through martensite fraction (ξ) as:

$$\sigma - \sigma_0 = E(\xi)(\epsilon - \epsilon_0) + \Omega(\xi)\xi_S - \Omega(\xi_0)\xi_{S0} + \theta(T - T_0) \quad (1)$$

Where, θ is thermoelastic modulus related to thermal expansion coefficient α ; Ω is phase transformation modulus; $E(\xi)$ is Young's modulus dependent on martensite fraction (ξ); subscript 0 denotes initial conditions. Young's modulus is predicted using Reuss scheme as

$$E(\xi) = \frac{E_A}{1 + (\frac{E_A}{E_M} - 1)\xi} \quad (2)$$

Where, E_A and E_M are Young's modulus of austenite and martensite phases, respectively. According to multiple variant model, martensite fraction (ξ) is represented as

$$\xi = \xi_S + \xi_T \quad (3)$$

Where, ξ_S and ξ_T are fraction of stress induced martensite or detwinned martensite and fraction of temperature induced martensite, respectively. The transformation modulus is related to Young's modulus as given below and can be determined experimentally by converting all austenite to detwinned martensite at a temperature less than austenite start temperature.

$$\Omega = -\epsilon_L E(\xi) \quad (4)$$

Where, ϵ_L is the maximum residual strain. As proposed by Brinson and Huang after simplification Tanaka type constitutive model can be obtained as

$$\sigma - \sigma_0 = E(\xi)(\epsilon - \epsilon_L \xi_S) + \Omega(\xi)\xi_S + \theta(T - T_0) \quad (5)$$

Based on Brinson model, in martensite to austenite conversion phase for $T > A_s$, $dT > \frac{d\sigma}{C_A}$ and $C_A(T - A_f) < \sigma < C_A(T - A_s)$, the resultant equation for thermally induced martensite fraction ($\xi_T = \xi_{T0} \frac{\xi}{\xi_0}$) and stress induced martensite fractions ($\xi_S = \xi_{S0} \frac{\xi}{\xi_0}$) can be written in terms of cosine function as

$$\xi = \frac{\xi_0}{2} \left[\cos \left\{ \frac{\pi}{A_f - A_s} \left(T - A_s - \frac{\sigma}{C_A} \right) \right\} + 1 \right] \quad (6)$$

Similarly, for austenite to martensite conversion phase for $T < M_s$, $dT < \frac{d\sigma}{C_M}$ and $C_M(T - M_s) < \sigma < C_M(T - M_f)$, the resultant equation for thermally induced martensite fraction ($\xi_T = \xi_{T0} \frac{\xi}{\xi_0}$) and stress induced martensite fractions ($\xi_S = \xi_{S0} \frac{\xi}{\xi_0}$) can be written in terms of cosine function as

$$\xi = \frac{1 - \xi_0}{2} \cos \left\{ \frac{\pi}{M_s - M_f} \left(T - M_f - \frac{\sigma}{C_M} \right) \right\} + \frac{1 + \xi_0}{2} \quad (7)$$

As Young's modulus is dependent on martensite fraction same is calculated numerically. The composite effective properties are calculated based on multicell micromechanics approach [1].

The effective properties of the composite are listed below:

$$E_{11} = E_{sf}(\xi)v_{sf} + E_{1m}v_m \quad (8)$$

$$E_{22} = E_{2m} \left[(1 - \sqrt{v_{sf}}) + \frac{\sqrt{v_{sf}}}{1 - \sqrt{v_{sf}} \left(1 - \frac{E_{2m}}{E_{sf}(\xi)} \right)} \right] \quad (9)$$

$$G_{13} = G_{12} = G_{12m} \left[(1 - \sqrt{v_{sf}}) + \frac{\sqrt{v_{sf}}}{1 - \sqrt{v_{sf}} \left(1 - \frac{G_{12m}}{G_{sf}(\xi)} \right)} \right] \quad (10)$$

$$\mu_{11} = \mu_{12sf}v_{sf} + \mu_{12m}v_m \quad (11)$$

$$\alpha_1 = \frac{v_{sf}\alpha_{sf}E_{sf}(\xi) + v_m\alpha_{1m}E_{1m}}{E_{11}} \quad (12)$$

$$\alpha_2 = \frac{E_{2m}}{E_{22}} \left[\alpha_{2m}(1 - \sqrt{v_{sf}}) + \frac{\alpha_{2m}\sqrt{v_{sf}} - v_{sf}(\alpha_{2m} - \alpha_{sf})}{1 - \sqrt{v_{sf}} \left(1 - \frac{E_{2m}}{E_{sf}(\xi)} \right)} \right] \quad (13)$$

$$G_{sf}(\xi) = \frac{E_{sf}(\xi)}{2(1 + \mu_{12sf})} \quad (14)$$

$$\rho = \rho_{sf}v_{sf} + \rho_mv_m \quad (15)$$

$$v_{sf} + v_m = 1 \quad (16)$$

3.2 Analysis of hybrid beam

Based on first order shear deformation theory, the displacement components of a material point within the domain of hybrid composite can be expressed as

$$u(x, z, t) = u_0(x, t) + z\varphi(x, t) \quad (17)$$

$$w(x, z, t) = w_0(x, t) \quad (18)$$

Where, u_0 and w_0 are midplane displacements and φ is the rotation of the mid-plane. Non-linear Green-Lagrange strain tensor is taken for analysis and represented as under

$$\epsilon_x = \frac{\partial u_0}{\partial x} + \frac{1}{2} \left(\frac{\partial w_0}{\partial x} \right)^2 + z \frac{\partial \varphi}{\partial x} \quad (19)$$

$$\gamma_{xz} = \varphi + \frac{\partial w_0}{\partial x} \quad (20)$$

The linear thermo-elastic constitutive relation for a general k^{th} layer of the hybrid beam with fiber orientation θ^k can be written as:

$$\sigma_x^k = \bar{Q}_{11}^k \epsilon_x^k - \bar{Q}_{11}^k \alpha_x^k \Delta T + \cos^2(\theta^k) v_{sf} \sigma_r^k \quad (21)$$

$$\tau_{xz}^k = \bar{Q}_{55}^k \gamma_{xz}^k \quad (22)$$

$$\alpha_x^k = \cos^2(\theta^k) \alpha_1 + \sin^2(\theta^k) \alpha_2 \quad (23)$$

Where, superscript k indicates layer number; \bar{Q}_{ij}^k are transformed reduced stiffness; α_i^k are the co-efficient of thermal expansion; ΔT is the temperature difference with respect to reference temperature where there is no thermal strain and σ_r is the recovery stress generated by the temperature induced reverse phase transformation of the pre-strained SMA fibers from detwinned martensite to austenite.

In order to derive the equation of motion of the hybrid beam the extended Hamilton's principle is applied given as:

$$\int_{t_1}^{t_2} (\delta K - \delta U - \delta W) dt = 0 \quad (24)$$

Where, δ represents the variational symbol; $[t_1, t_2]$ describes arbitrary time interval; K , U and W are respectively kinetic energy, strain energy and applied external work, defined as below:

$$\delta K = \int_A \int_{-h/2}^{h/2} \rho \{ \dot{w}_0 \delta \dot{w}_0 + (\dot{u}_0 + z \dot{\phi}) (\delta \dot{u}_0 + z \delta \dot{\phi}_0) \} dz dA \quad (25)$$

$$\delta U = \int_A \int_{-h/2}^{h/2} (\sigma_x \delta \epsilon_x + K_S \tau_{xz} \delta \gamma_{xz}) dz dA \quad (26)$$

$$\delta W = \int_A q \delta w_0 dA \quad (27)$$

Where, K_S is the shear correction factor to compensate for parabolic transverse shear stress; A is the surface area of the beam; $q = q(x, t)$ is the external load per unit area. By using equations (17 – 23) and (25 – 27) into extended Hamilton's principle and integrating over the beam thickness, equations of motion of the beam are obtained and given as under:

$$\frac{dN_x}{dx} = I_1 \ddot{u}_0 + I_2 \ddot{\phi}_0 \quad (28)$$

$$Q_{xz} - \frac{\partial M_x}{\partial x} = I_2 \ddot{u} + I_3 \ddot{\phi} \quad (29)$$

$$\frac{\partial}{\partial x} \left(N_x \frac{\partial w_0}{\partial x} \right) + \frac{\partial Q_{xz}}{\partial x} + q = I_1 \ddot{w}_0 \quad (30)$$

Where, $(N_x, M_x, Q_x) = \int_{-h/2}^{h/2} (\sigma_x, z \sigma_x, K_S \tau_{xz}) dz$ and $(I_1, I_2, I_3) = \int_{-h/2}^{h/2} \rho (1, z, z^2) dz$. The quantities are expressed as below:

$$N_x = A_{11} \left[\frac{\partial u_0}{\partial x} + \frac{1}{2} \left(\frac{\partial w_0}{\partial x} \right)^2 \right] + B_{11} \frac{\partial \phi}{\partial x} - N^T + N^r \quad (31)$$

$$M_x = B_{11} \left[\frac{\partial u_0}{\partial x} + \frac{1}{2} \left(\frac{\partial w_0}{\partial x} \right)^2 \right] + D_{11} \frac{\partial \phi}{\partial x} - M^T + M^r \quad (32)$$

$$Q_{xz} = K_S A_{55} \left(\phi + \frac{\partial w_0}{\partial x} \right) \quad (33)$$

Where,

$$(N^T, M^T) = \sum_{k=1}^n \int_{h_{k-1}}^{h_k} (\bar{Q}_{11}^k \alpha_x^k) \Delta T(1, z) dz, (N^r, M^r) = \sum_{k=1}^n \int_{h_{k-1}}^{h_k} \sigma_r^k v_{sf} \cos^2(\theta^k)(1, z) dz,$$

$$(A_{11}, B_{11}, D_{11}) = \sum_{k=1}^n \int_{h_{k-1}}^{h_k} \bar{Q}_{11}^k(1, z, z^2) dz, A_{55} = \sum_{k=1}^n \int_{h_{k-1}}^{h_k} \bar{Q}_{55}^k dz.$$

3.3 Buckling domain

The resultant force in pre and post buckling domains are expressed respectively as $N_x^* = -(N^{T*} - N^{r*})$ and $N_x^* = -\frac{\pi^2 P_1 P_2}{\pi^2 P_1 + P_2}$

Where,

$$N^{T*} = N^{r*} + \frac{\pi^2 P_1 P_2}{\pi^2 P_1 + P_2}, N^{T*} = \frac{N^T}{E_m^{ref} h}, N^{r*} = \frac{N^r}{E_m^{ref} h}, f_1 = \frac{A_{11}}{E_m^{ref} h}, f_2 = \frac{B_{11}}{E_m^{ref} h L}, f_3 = \frac{D_{11}}{E_m^{ref} h L^2},$$

$$g_1 = \frac{A_{55}}{E_m^{ref} h}, P_1 = \frac{f_3 f_1 - f_2^2}{f_1}, P_2 = g_1.$$

3.4 Vibration analysis

Vibration analysis is performed assuming harmonic solution and solving eigen value problem and non-trivial solution is obtained by setting determinant to zero.

3.5 Energy harvesting

Strain on the surface of the piezoelectric patch at a distance of y from the neutral axis can be obtained from following relation:

$$\epsilon(x) = -y \frac{\partial^2 w(x, t)}{\partial x^2} \quad (34)$$

Where, $w(x, t) = \varphi_1(x) \varphi_2(t)$ and the output voltage and power from the patch can be expressed as follows:

$$V\left(\frac{x}{L}\right) = g_{31} E_p \epsilon\left(\frac{x}{L}\right) L_p \quad (35)$$

$$P = \frac{V^2}{R_L} \quad (36)$$

4 RESULTS AND DISCUSSIONS

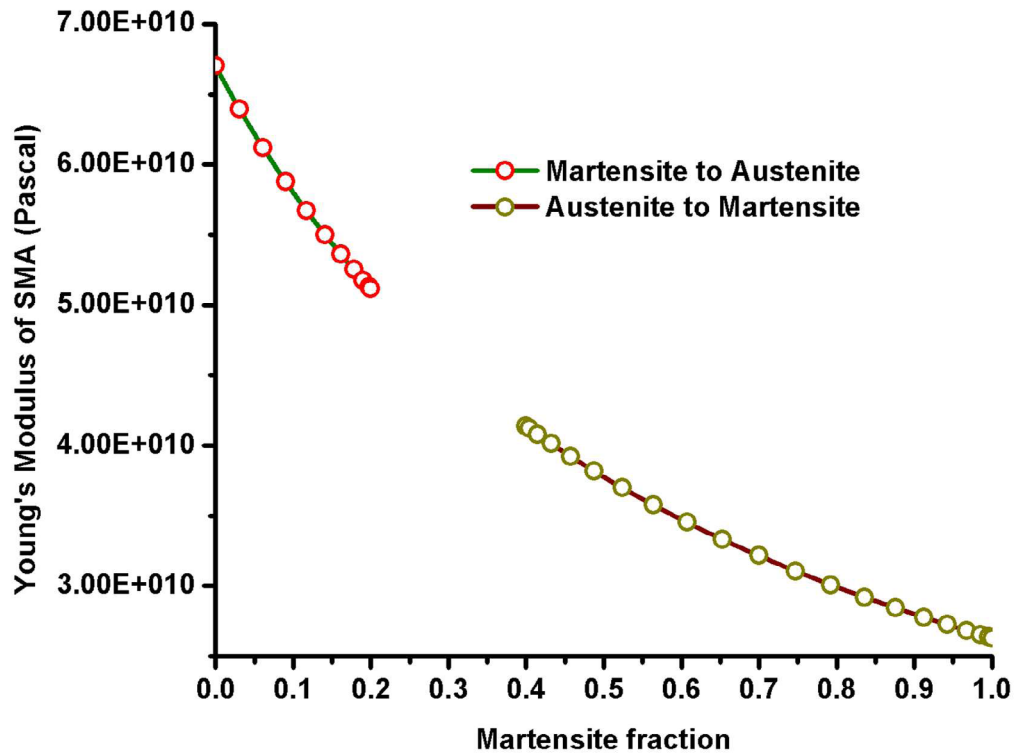


Figure 1: Variation of Young's modulus with respect to martensite fraction

5 CONCLUSIONS

Present paper demonstrates capability of hybrid sma/piezoelectric composite structure for morphing and energy harvesting.

REFERENCES

- [1] Barbarino, S., Bilgen, O., Ajaj, R.M., Friswell, M.I. and Inman, D.J. A review of morphing aircraft. *Journal of Intelligent Material Systems and Structures* (2011) **22**:823-877.
- [2] Rodriguez, A.R. Morphing aircraft technology survey. *45th AIAA Aerospace Sciences Meeting and Exhibit 8 to 11 January 2007 Reno Nevada* (2007) 1-16.
- [3] Sofla, A.Y.N., Meguid, S.A., Tan, K.T. and Yeo, W.K. Shape morphing of aircraft wing: status and challenges. *Journal Materials and Design* (2010) **31**:1284-1292.
- [4] Ramrakahyani, D.S., Lesieutre, G.A., Frecker, M. and Bharti, S. Aircraft structural

- p morphing using tendon actuated compliant cellular trusses.
- 45th AIAA/ASME/ASCE/AHS/ASC Structures, Structural Dynamics and Materials Conference 19 to 22 April 2004 Palm Springs California*
- (2004) 1-10.
- [5] Jenett, B., Calisch, S., CellucCi, D., Cramer, N., Gershenfeld, N., Swei, S. and Cheung, K.C. Digital morphing wing: Active wing shaping concept using composite lattice based cellular structures. *Soft Robotics* (2017) **4**(1):33-48.
 - [6] Kota, S. and Lu, K.J. Design of compliant mechanisms for morphing structural shapes. *Journal of Intelligent Materials Systems and Structures* (2003) **14**:371-391.
 - [7] Hua, Z., Weidong, L., Shengqiang, Z., Yalei, B., Yuan, W. and Chunsheng, Z. In-plane corrugated cosine honeycomb for 1D morphing skin and its application on variable camber wing. *Chinese Journal of Aeronautics* (2013) **26**(4):935-942.
 - [8] Kammegne, M.J.T., Grigori, L.T., Botez, R.M. and Koreanschi, A. Design and wind tunnel experimental validation of a controlled new rotary actuation system for a morphing wing application. *Proc IMechE Part G: J Aerospace Engineering* (2016) **230**(1):132-145.
 - [9] Qiu, J., Wang, C., Huang, C., Ji, H. and Xu, Z. Smart skin and actuators for morphing structures. *Procedia IUTAM 23rd International Congress of Theoretical and Applied Mechanics* (2014) **10**:427-441.
 - [10] Kumar, D., Ali, S.F. and Arockiarajan, A. Structural and aerodynamics studies on various wing configurations for morphing. *IFAC PapersOnLine* (2018) **51**(1):498-503.
 - [11] Thill, C., Etches, J.A., Bond, I.P., Potter, K.D. and Weaver, P.M. Composite corrugated structures for morphing wing skin applications. *Smart Mater. And Struct.* (2010) **19**:1-10.
 - [12] Stowers, A.K. and Lentink, D. Folding in and out: passive morphing in flapping wings. *Bioinspiration and Biomimetics* (2015) **10**:1-16.
 - [13] Min, Z., Kien, V.K. and Richard, L.J.Y. Aircraft morphing wing concepts with radical geometry change. *The IES Journal Part A: Civil & Structural Engineering* (2010) **3**:3:188-195.
 - [14] Ferreira, A.D.B.L., Novoa, P.R.O. and Marques, A.T. Multifunctional material systems: a state-of-the-art review. *Composite Structures* (2016) **151**:3-35.
 - [15] Brailovski, V., Terriault, P., Georges, T. and Coutu, D. SMA actuators for morphing wings. *Physics procedia; 3rd International Symposium on Shape Memory Materials for Smart Systems* (2010) **10**:197-203.
 - [16] Koreanschi, A., Gabor, O.S., Acotto, J., Brianchon, G., Portier, G., Botez, R.M., Mamou, M. and Mebarki, Y. Optimization and design of an aircraft's morphing wing-tip demonstrator for drag reduction at low speed, Part I – Aerodynamic optimization using genetic, bee colony and gradient decent algorithms. *Chinese Journal of Aeronautics* (2017) **30**(1):149-163.
 - [17] Changchuan, X., Ying, B., Chao, A., and Chao, Y. Gust load alleviation wind tunnel tests of a large-aspect-ratio flexible wing with piezoelectric control. *Chinese Journal of Aeronautics* (2017) **30**(1):292-309.
 - [18] Cho, M. and Kim, S. Structural morphing using two-way shape memory effect of SMA. *International Journal of Solids and Structures* (2005) **42**:1759-1776.
 - [19] Ronch, A.D., Xiang, J., Li, D., Zhao, S., Drofelnik, J., Li, Y., Zhang, L., Wu, Y., Kintscher, M., Monner, H.P., Rudenko, A., Guo, S., Yin, W., Kirn, J., Storm, S. and Breuker, R.D. A review of modeling and analysis of morphing wings. *Progress in aerospace sciences* (2018) **100**:46-62.

- [20] Han, M.W., Rodrigue, H., Kim, H.I., Song, S.H. and Ahn, S.H.. Shape memory alloy/glass fiber woven composite for soft morphing winglets of unmanned aerial vehicle. *Composite Structures* (2016) **140**:202-212.
- [21] Hartl, D.J., Leal, P.B.C. and Savi, M.A. Aero-structural optimization of shape memory alloy based wing morphing via a class/shape transformation approach. *Proc IMechE Part G: J Aerospace Engineering* (2018) **232(15)**:2745-2759.
- [22] Kuo, S.Y., Shiau, L.C. and Chen, K.H. Buckling analysis of shape memory alloy reinforced composite laminates. *Composite Structures* (2009) **90**:188-195.
- [23] Wang, B., Zhou, M., Fu, Y. and Al-Furjan, M.S.H. Vibration analysis of a longitudinal polarized piezoelectric tubular energy harvester. *Applied Acoustic* (2019) **146**:118-133.
- [24] Kiani, Y., Asadi, H., Shakeri, M. and Eslami, M.R. Exact solution for non-linear thermal stability of hybrid laminated composite Timoshenko beams reinforced with SMA fibers. *Composite Structures* (2014) **108**:811-822.
- [25] Lau, K. Vibration characteristics of SMA composite beams with different boundary conditions. *Materials and Design* (2002) **23**:741-749.
- [26] Bodaghi, M., Asadi, H., Shakeri, M. and Aghdam, M.M. On the free vibration of thermally pre/post-buckled shear deformable SMA hybrid composite beams. *Aerospace Science and Technology* (2013) **31**:73-86.
- [27] Yuvaraja, M. and Senthilkumar, M. Comparative study on vibration characteristics of a flexible GFRP composite beam using SMA and PZT actuators. *Procedia Engineering* (2013) **64**:571-581.
- [28] Sadighi, M., Samadpour, M., Shakeri, M. and Zamani, H.A. Vibration analysis of thermally buckled SMA hybrid composite sandwich plate. *Composite Structures* (2015) **119**:251-263.
- [29] Baghani, M., Fahimi, P., Eskandari, A.H. and Taheri, A. A semi-analytical solution for bending response of SMA composite beams considering SMA asymmetric behavior. *Composites Part B* (2019) **163**:622-633.
- [30] EkhteraeiToussi, H. and Bayat, Y. Exact solution of thermal buckling and post-buckling of composite and SMA hybrid composite beam by layerwise theory. *Aerospace Science and Technology* (2017) **67**:484-494.
- [31] Fortini, A., Suman, A., Merlin, M., and Garagnani, G.L. Morphing blades with embedded SMA strips: An experimental investigation. Two good friends. *Materials and Design* (2015) **85**:785-795.
- [32] Cassio, T.F., Marqui Jr., C.D., Inman, D.J., and Lopes Jr., V. Non-linear dynamic model and simulation of morphing wing profile actuated by shape memory alloys. *Chinese Chapter 2 of Topics in non-linear dynamics: Conference proceedings of the society for experimental mechanics series 28: D. Adams et. al. (Eds.)* (2012) **3**:21-28.
- [33] Lecce, L. and Concilio, A. *Shape Memory Alloy Engineering for Aerospace, Structural and Biomedical Engineering*. Butterworth-Heinemann, Elsevier, (2015).
- [34] Machado, L.G. and Lagoudas, D.C. Thermomechanical constitutive modeling of SMAs. *Chapter 3 in Shape Memory Alloys: Lagoudas D.C. (Ed.) Springer* (2008) 121-187.
- [35] Mallik, N. and Ray, M.C. Effective coefficients of piezoelectric fiber reinforced composites *AIAA Journal* (2003) **41(4)**:704-710.
- [36] Priya, S. and Inman, D.J. Energy harvesting technologies. *Springer* (2009).

INTEGRATION OF THE SPIRAL PULLEY NEGATIVE STIFFNESS MECHANISM INTO THE FISHBAC MORPHING WING

C. WANG*, J. ZHANG*, A.D. SHAW*, M. AMOOZGAR*, M.I. FRISWELL* AND
B.K.S. WOODS[†]

* College of Engineering, Swansea University, Swansea, SA1 8EN, UK
Email: chen.wang@swansea.ac.uk

[†] Department of Aerospace Engineering, University of Bristol, Bristol, BS8 1TR, UK

Key words: Morphing aircraft, Actuation system, Morphing wing, Negative stiffness, Energy balancing

Abstract.

The actuation system of morphing aircraft plays an important role in any promising morphing design. If the structure of the morphing wing needs to be deformed elastically, the actuation system will be required to provide an adequate actuation force while the weight and cost added to the morphing aircraft should be limited to the extent that the performance of the morphing aircraft will not be compromised.

The spiral pulley negative stiffness concept, which uses its stored elastic energy and a negative stiffness mechanism to passively balance the energy requirements of the morphing device, is a promising solution to design the actuation system. The negative stiffness is achieved by the spiral pulley with a spooling cable, which is connected to a pre-stretched spring. The rotation of the spiral pulley can release the energy stored in the spring, and generate the torque to deform the morphing structure. Due to the geometric configuration of the spiral pulley and the kinematic tailoring it provides, negative torque of increasing magnitude is generated as rotation increases, such that the mechanism shows a 'negative stiffness', which will balance the positive stiffness of the morphing structure. Geometry optimisation of the spiral pulley is used to achieve the cancellation. By adopting the negative stiffness mechanism, it is expected that the energy requirement will be balanced, which can significantly reduce the input of external energy and therefore the weight and cost of the actuation system.

In the current study, the spiral pulley negative stiffness mechanism is integrated into a morphing wing employing the Fish Bone Active Camber (FishBAC) morphing concept. The FishBAC wing is actuated by a torque to enable its elastic shape change. The torque requirement to deform the FishBAC wing is measured to identify the positive stiffness. The corresponding negative stiffness is then realised by the optimisation of the geometry configurations of the spiral pulleys, which shows the potential of saving energy of the actuation mechanism.

1 INTRODUCTION

Morphing aircraft have been an important research subject for the last few years. The overall performance of the aircraft can be enhanced by changing the aerodynamic shape actively according to the flight conditions [1-3] .

The idea of changing the aerodynamic shape is not new, indeed it can be traced back to the early period of the aviation age. For example, the wing-warping design was adopted by the Wright brothers' Flyer I for the lateral control [4]. The shape-changing can be achieved through the elastic deformation of the aircraft structure or making use of the novel properties of the smart materials [5, 6], such as the shape memory alloys [7-9] or the piezoelectric materials [10-12] . The wing-warping design is a typical instance of the elastic shape-changing, although it was replaced by the aileron due to the increased flight speeds and the requirement for stiffer structures to avoid aeroelastic failures. The requirement to keep the balance between the flexibility to change shape and the stiffness to carry loads is one of the key factors of a promising morphing aircraft, especially when the weight of the aircraft is also taken in account [13]. A promising morphing aircraft should be capable of changing shape when the aircraft is subject to the corresponding aerodynamic loads, and the morphing structure is usually designed to tailor its stiffness for this purpose.

The actuation system must provide high output force/torque for the minimal system weight, and a high energy efficiency, especially when the shape-changing is achieved by the elastic deformation of the morphing structure. A reduction in actuator mass can potentially be achieved by integrating a negative stiffness mechanism into the structure [14-17]. The negative stiffness mechanism can release the energy stored in a pre-stretched spring and drive the rotation of the spiral pulley, which will provide a negative torque of increasing magnitude against the rotation. The structural stiffness can be balanced by the negative stiffness of the spiral pulley mechanism, which will lead to the zero-stiffness mechanism of the overall system. Since the entire system is balanced and energy is stored in the pre-stretched spring, the energy consumption from external resources can be reduced significantly, which has the potential to reduce the weight of the actuation system and its associated power supply system.

While previous studies have demonstrated this principle in desktop demonstrators [16-18], it has not previously been demonstrated this principle in a true aerodynamic structure. In the current study, the negative stiffness mechanism is integrated into the Fish Bone Active Camber (FishBAC) morphing wing [19-21]. The FishBAC morphing wing is a camber morphing design, which can provide a smooth surface change, and has the potential to increase the lift-to-drag ratio [22, 23]. The shape-changing of FishBAC is generated through the elastic deformation of the bending spine, and servo motors have been adopted to drive the structure. Integration of the negative stiffness mechanism has the potential to improve the performance of the actuation system.

The integration is undertaken in the following steps:

- 1) Initial wing design: considering the installation of the spiral pulley mechanism;
- 2) Measurement of the FishBAC structure stiffness;
- 3) Optimisation of the spiral pulley geometry;
- 4) Static and wind tunnel test.

In this paper, Section 2 gives a brief discussion of the FishBAC design and the spiral pulley based negative stiffness mechanism. Section 3 discusses the experimental setup to measure the

structural stiffness of FishBAC wing, which is used in Section 4 to optimise the geometry of the spiral pulleys, and lays the foundation of the development of a demonstration model.

2 MODEL DEFINITION

Figure 1 shows the schematic of the FishBAC design, which was driven by servo motors [19, 24]. Two tendons are attached to the solid trailing edge section, and the torque generated by the servo motors is transferred onto the spine, which will cause the deformation of the spine. The design, analysis and manufacturing methods have been developed as introduced in the literature and the current study is focused on the integration of the negative stiffness mechanism rather than the FishBAC itself.

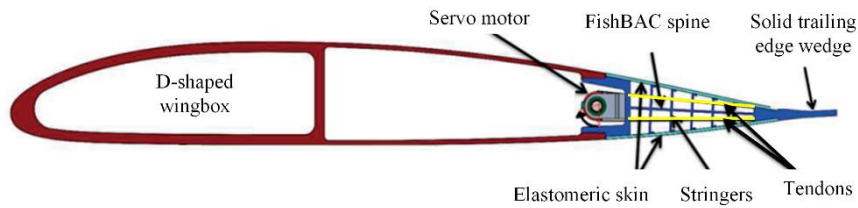


Figure 1: Schematic of FishBAC wing actuated by servo motors [21]

A NACA23012 aerofoil section is selected for the integration, and the chord and span are 270mm and 250mm respectively. One of the difficulties of the integration is the space available in the wing, which is very limited due to the low thickness of the aerofoil. The current approach uses the cable from the load pulley to drive the tendons on the FishBAC directly as shown in Figure 2, which simplifies the mechanism but can still demonstrate the potential of the spiral pulley.

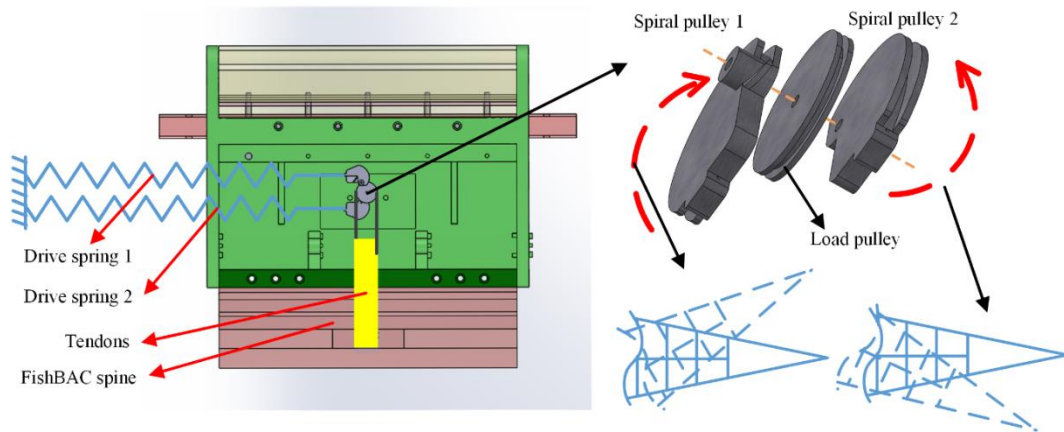


Figure 2: Concept of the integration

The negative stiffness concept used is the bidirectional concept described by Zhang et al. in [17, 18], to assist both positive and negative flap deflections. The drive spring connected to the spiral pulley is pre-stretched with the extension L_0 to store the energy before it is integrated into

the wing. If the stiffness rate of the drive spring is denoted as K , the entire energy stored in the drive spring is then $0.5KL_0^2$; this quantifies the maximum amount of available work that can be provided by the mechanism to assist actuation. Two spiral pulleys are mounted onto one centre shaft, and the bidirectional motion can be achieved through the rotation of the pulleys in the opposite directions.

The planar geometry of the spiral pulley is shown in Figure 3.

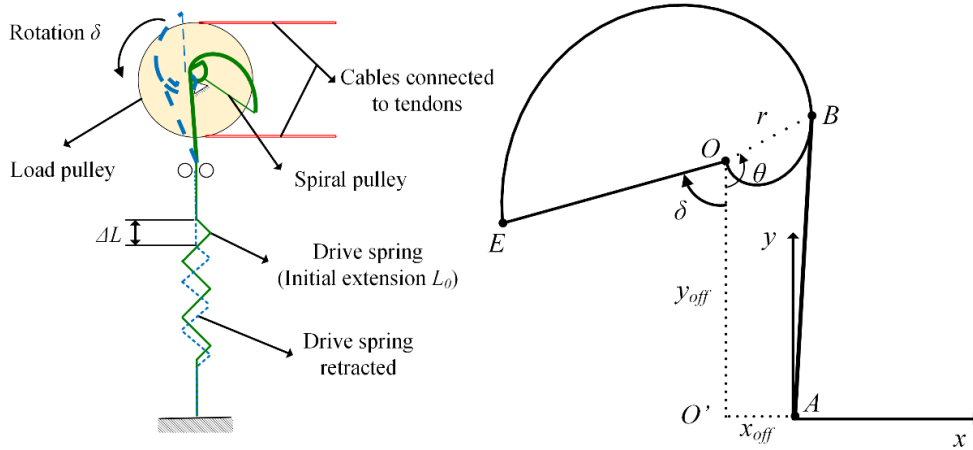


Figure 3: Geometry of the spiral pulley

The radius, r , about point O , which is the centre of the rotation shaft can be defined as an exponential function

$$r = r_0 + k_1 e^{k_2(\theta + \delta + \delta_0)} \quad (1)$$

where δ is the rotation angle of the spiral pulley and θ is an associated angle. The parameters k_1 , k_2 are the pre-exponent and exponent terms of the spiral pulley. And the coordinate components of point A , x_{off} , y_{off} , are also needed to fully define the pulley geometry, together with the initial pulley radius r_0 and the initial rotation angle δ_0 .

The drive torque output by the spiral pulley is given by

$$\begin{aligned} T_d &= F_d l_m \\ F_d &= f(\delta, K, L_0, r_0, \delta_0, k_1, k_2, x_{off}, y_{off}) \\ l_m &= g(\delta, r_0, \delta_0, k_1, k_2, x_{off}, y_{off}) \end{aligned} \quad (2)$$

The expression of the drive torque has been derived in [15, 17]. The force caused by the drive spring, F_d , is determined by the rotation angle, the parameters of the spiral pulley geometry and the drive spring. The moment arm, l_m , also varies with the rotation of the spiral pulley. It can be seen that the drive torque is influenced by the geometry parameters of the spiral pulley and the drive spring stiffness and the initial extension. A decreasing torque can be provided against the rotation of the pulley, which leads to the so-called negative stiffness. In the meantime, the load torque, T_l , is required to deform the structure. If the stiffness of the structure can be balanced by the negative stiffness of the spiral pulley mechanism, a zero-

stiffness system can be designed, which means the energy required to deform the structure is provided by the energy stored in the pre-stretched drive springs, and no external energy is needed to deform the structure.

3 STRUCTURE STIFFNESS MEASUREMENT

To design a zero-stiffness mechanism, the relationship between the load torque and the corresponding rotation angle needs to be obtained. The experimental setup is shown in Figure 4. As the focus is the integration of the negative stiffness mechanism, the structure components, including the FishBAC spine, are 3D printed. A baseline load pulley is installed, and the cables from the load pulley are bonded to the tendons of the FishBAC. The baseline load pulley is used to transfer the load torque onto the FishBAC structure in the measurement, and is installed at the same location of the spiral pulley to ensure the integration can be realised. By applying the torque directly onto the load pulley with a torque wrench, the FishBAC spine will be deformed under the specific torque, and the rotation angle is recorded using a protractor.

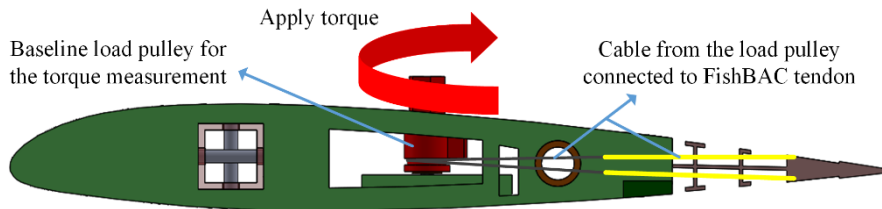


Figure 4: Schematic of the wing platform for the measurement of the FishBAC structure stiffness

As shown in Figure 5(a), both the upward and downward deflections of the FishBAC are achieved. An external load, which is in the opposite direction of the deflection, is applied to on the structure. The relationship between the measured load torque and the rotation angle is shown in Figure 5(b).

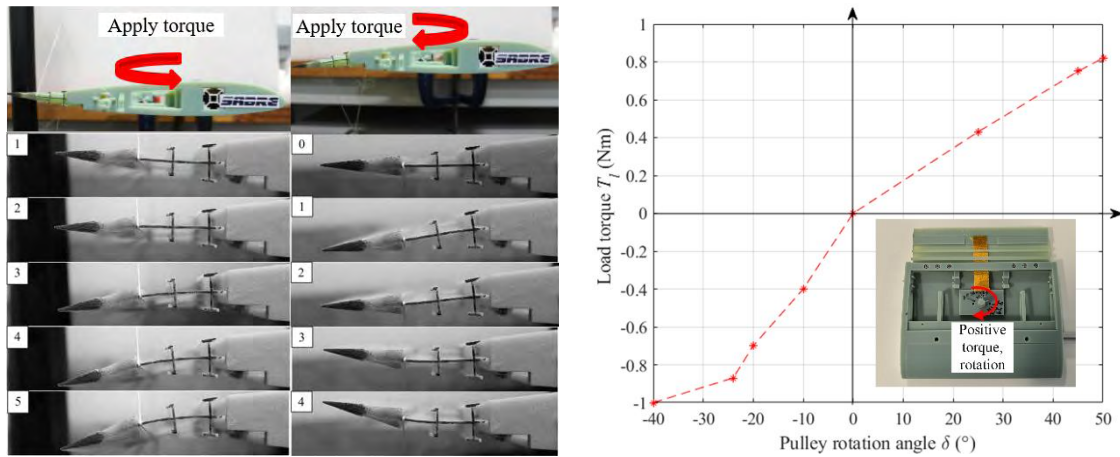


Figure 5: (a) Downward and upward deflection of the FishBAC subject to the load torque, (b) Measured load torque vs the rotation angle of the baseline pulley

The positive torque and rotation angle are defined when they correspond to the upward deflection of the FishBAC tip. It can be seen that the upward and downward deflection of the FishBAC have different stiffnesses, which could be caused by the direction the tendon is aligned, the offset due to the bonding of the tendon, etc. The measurement indicates an approximately linear relationship between the load torque and the rotation angle, although the first data point with the minimum rotation angle is neglected due to measurement errors.

4 OPTIMISATION OF THE SPIRAL PULLEY

To provide a zero-stiffness system, the geometry of the spiral pulley needs to provide the drive torque that can balance the load torque. The geometry parameters are optimised to find the maximum objective defined as

$$\max \eta_e = \frac{E_o}{E_r} \quad (3)$$

where the energy output by the spiral pulley system, E_o , and the energy required by the FishBAC structure, E_r , can be obtained as

$$\begin{aligned} E_o &= \int_0^{\delta} |T_d| d\delta \\ E_r &= \int_0^{\delta} |T_l| d\delta \end{aligned} \quad (4)$$

The ranges of the variables are given by

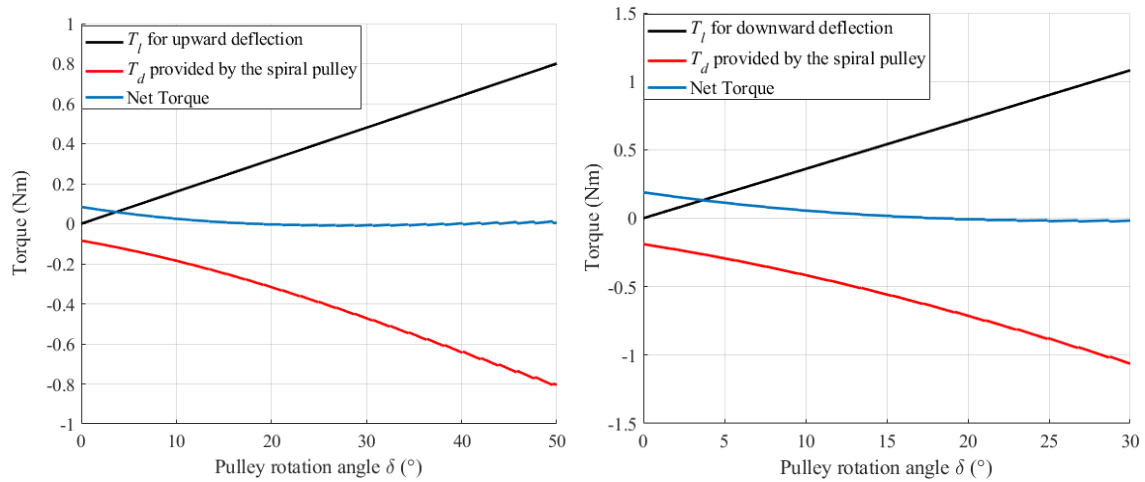
$$\left\{ \begin{array}{l} -30/1000 \leq r_0 \leq 10/1000 \text{ (m)} \\ -0.001 \leq k_1 \leq 0.02 \\ 0 \leq k_2 \leq 1 \\ -50\pi/180 \leq \delta_0 \leq 50\pi/180 \\ -0.05 \leq L_0 \leq 0.4 \text{ (m)} \\ 100 \leq K \leq 1400 \text{ (N/m)} \\ -0.1 \leq x_{off} \leq 0.1 \text{ (m)} \\ -0.05 \leq y_{off} \leq 0.1 \text{ (m)} \end{array} \right. \quad (5)$$

The Matlab nonlinear programming solver, '*fmincon*', is used to perform the optimisation [25]. Two optimisation cases are performed to find the optimal geometry of the two spiral pulleys for the upward and downward deflections separately, and the optimisation results are summarised in Table 1.

The influence of the spiral pulley on the stiffness is shown in Figure 6. It is found that in both spiral pulleys, the drive torque T_d , can balance the load torque T_l , and the net torque is close to zero, which indicates the zero-stiffness of the mechanism.

Table 1. Optimised parameters of the spiral pulley negative stiffness mechanism

Name of the variable	For the upward deflection	For the downward deflection	Unit
Initial pulley radius r_0	-0.029	-0.030	m
Pre-exponent term k_1	0.005	0.016	
Exponent term k_2	0.991	1.000	
Drive spring extension L_0	0.170	0.218	m
Drive spring rate K	567.153	910.891	N/m
Initial rotation angle of the spiral pulley δ_0	-0.814	-0.758	rad
x coordinate to define point A x_{off}	-0.019	-0.064	m
y coordinate to define point A y_{off}	0.069	0.012	m

**Figure 6:** Effect of the optimised spiral pulley on the torque (a) For the upward deflection, (b) For the downward deflection

The influence on the required energy is shown in Figure 7. Obviously, with the spiral pulley mechanism, the external energy, which is required to deform the structure, is reduced significantly, as the energy stored in the pre-stretched spring can drive the mechanism.

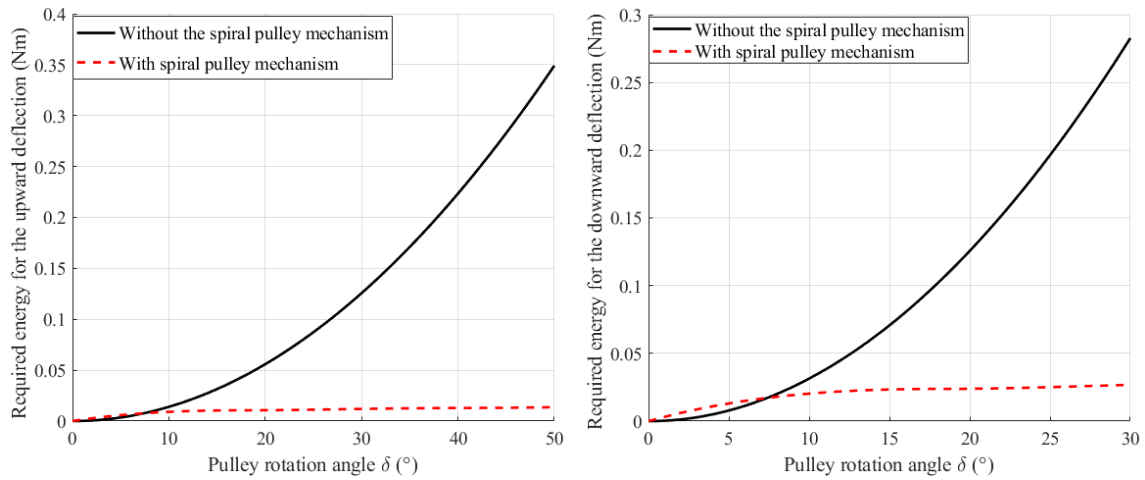


Figure 7: Effect of the optimised spiral pulley on the required energy (a) For the upward deflection, (b) For the downward deflection

5. CONCLUSION

In this paper, the negative stiffness mechanism based on the spiral pulley is integrated into the FishBAC morphing wing.

The load torque, which is required to deform the FishBAC morphing structure, is measured first to obtain the structure stiffness. The geometry parameters of the spiral pulley are then optimised to provide an energy balancing system. The optimisation results indicate that the spiral pulley mechanism is able to provide a negative stiffness against the structure stiffness, which induces a net zero-stiffness of the entire system.

Optimisation work has shown that the spiral pulley is able to provide a high energy efficiency for the morphing structure, and future work will demonstrate a functional model for the static and wind tunnel test.

ACKNOWLEDGEMENTS

The authors acknowledge the financial support provided by the EU H2020 project SABRE, grant agreement 723491.

REFERENCES

1. Barbarino, S., Bilgen, O., Ajaj, R.M., Friswell, M.I., and Inman, D.J., *A review of morphing aircraft*. Journal of Intelligent Material Systems and Structures, 2011. 22(9): p. 823-877.
2. Li, D., Zhao, S., Da Ronch, A., Xiang, J., Drobniak, J., Li, Y., Zhang, L., Wu, Y., Kintscher, M., Monner, H.P., Rudenko, A., Guo, S., Yin, W., Kirn, J., Storm, S., and Breuker, R.D., *A review of modelling and analysis of morphing wings*. Progress in Aerospace Sciences, 2018. 100: p. 46-62.

3. Weisshaar, T.A., *Morphing aircraft technology-new shapes for aircraft design*. Access number: ADA479821. <https://apps.dtic.mil/docs/citations/ADA479821>.
4. NASA. *Wing warping*. Available from: <https://www.grc.nasa.gov/WWW/Wright/airplane/warp.html>.
5. Sun, J., Guan, Q., Liu, Y., and Leng, J., *Morphing aircraft based on smart materials and structures: A state-of-the-art review*. Journal of Intelligent Material Systems and Structures, 2016. 27(17): p. 2289-2312.
6. Thill, C., Etches, J., Bond, I., Potter, K., and Weaver, P., *Morphing skins*. The Aeronautical Journal, 2008. 112(1129): p. 117-139.
7. Chen, S., Chen, Y., Zhang, Z., Liu, Y., and Leng, J., *Experiment and analysis of morphing skin embedded with shape memory polymer composite tube*. Journal of Intelligent Material Systems and Structures, 2014. 25(16): p. 2052-2059.
8. Hartl, D., Lagoudas, D., Calkins, F., and Mabe, J., *Use of a Ni60Ti shape memory alloy for active jet engine chevron application: I. Thermomechanical characterization*. Smart Materials and Structures, 2009. 19(1).
9. Hartl, D., Mooney, J., Lagoudas, D., Calkins, F., and Mabe, J., *Use of a Ni60Ti shape memory alloy for active jet engine chevron application: II. Experimentally validated numerical analysis*. Smart Materials and Structures, 2009. 19(1): p. 015021.
10. Bilgen, O., Kochersberger, K., Diggs, E., Kurdila, A., and Inman, D. *Morphing Wing Micro-Air-Vehicles via Macro-Fiber-Composite Actuators*. 48th AIAA/ASME/ASCE/AHS/ASC Structures, Structural Dynamics, and Materials Conference. April 23-26, 2007, Honolulu, Hawaii, USA.
11. Bilgen, O., Kochersberger, K.B., and Inman, D.J., *Macro-fiber composite actuators for a swept wing unmanned aircraft*. The Aeronautical Journal, 2009. 113(1144): p. 385-395.
12. Guha, T.K., Oates, W.S., and Kumar, R., *Characterization of piezoelectric macrofiber composite actuated winglets*. Smart Materials and Structures, 2015. 24(6): p. 065043.
13. Campanile, L.F., *Initial Thoughts on Weight Penalty Effects in Shape-adaptable Systems*. Journal of Intelligent Material Systems and Structures, 2005. 16(1): p. 47-56.
14. Woods, B.K.S., Friswell, M.I., and Wereley, N.M., *Advanced Kinematic Tailoring for Morphing Aircraft Actuation*. AIAA Journal, 2014. 52(4): p. 788-798.
15. Woods, B.K. and Friswell, M.I., *Spiral pulley negative stiffness mechanism for passive energy balancing*. Journal of Intelligent Material Systems and Structures, 2016. 27(12): p. 1673-1686.
16. Zhang, J., Shaw, A.D., Amoozgar, M., Friswell, M.I., and Woods, B.K.S., *Bidirectional torsional negative stiffness mechanism for energy balancing systems*. Mechanism and Machine Theory, 2019. 131: p. 261-277.
17. Zhang, J., Shaw, A.D., Mohammadreza, A., Friswell, M.I., and Woods, B.K.S. *Spiral Pulley Negative Stiffness Mechanism for Morphing Aircraft Actuation*. ASME 2018 International Design Engineering Technical Conferences and Computers and Information in Engineering Conference. August 26-29, 2018, Quebec City, Quebec, Canada.
18. Zhang, J., Shaw, A.D., Mohammadreza, A., Friswell, M.I., and Woods, B.K.S., *Bidirectional Spiral Pulley Negative Stiffness Mechanism for Passive Energy Balancing*. Journal of Mechanism and Robots, 2019: Accepted, in press.
19. Woods, B.K.S. and Friswell, M.I., *Preliminary Investigation of a Fishbone Active Camber Concept*. 2012(45103): p. 555-563.

20. Woods, B.K., Dayyani, I., and Friswell, M.I., *Fluid/structure-interaction analysis of the fish-bone-active-camber morphing concept*. Journal of Aircraft, 2014. 52(1): p. 307-319.
21. Rivero, A.E., Weaver, P.M., Cooper, J.E., and Woods, B.K.S., *Parametric structural modelling of fish bone active camber morphing aerofoils*. Journal of Intelligent Material Systems and Structures, 2018. 29(9): p. 2008-2026.
22. Woods, B.K., Bilgen, O., and Friswell, M.I., *Wind tunnel testing of the fish bone active camber morphing concept*. Journal of Intelligent Material Systems and Structures, 2014. 25(7): p. 772-785.
23. Woods, B.K.S., Parsons, L., Coles, A.B., Fincham, J.H.S., and Friswell, M.I., *Morphing elastically lofted transition for active camber control surfaces*. Aerospace Science and Technology, 2016. 55: p. 439-448.
24. Rivero, A.E., Fournier, S., Weaver, P.M., Cooper, J.E., and Woods, B.K. *Manufacturing and characterisation of a composite FishBAC morphing wind tunnel model*. ICAST2018: 29th International Conference on Adaptive Structures and Technologies. September 30th-October 4th, 2018, Seoul, Korea.
25. Mathworks. *MATLAB*. 2016; Available from: <https://uk.mathworks.com/products/global-optimization.html>.

SHAPE MEMORY ALLOY ACTUATION TECHNOLOGY FOR ADAPTIVE LOW BOOM SUPERSONIC TRANSPORTS

JAMES H. MABE^{*}, DIMITRIS C. LAGOUDAS,[†] AND DARREN J. HARTL[†]

^{*} The Boeing Company
6300 James S McDonnell Blvd
St Louis, MO, 63134, USA
Email: james.h.mabe@boeing.com

[†] Texas A&M University
Aerospace Engineering 3141
College Station, TX, 77843-3141, USA
Email: lagoudas@tamu.edu
Email: darren.hartl@tamu.edu

Key words: Smart Structures, Adaptive Structures, Shape Memory Alloys, Sonic Boom, Actuators, Low Boom.

Abstract. To enable the return to flight of civil supersonic transport (SST) aircraft, configurations must be developed that meet noise and efficiency requirements across a range of operating conditions. A team of researchers, led by Texas A&M University, is investigating real-time geometry changes, driven by compact and lightweight Shape Memory Alloy (SMA) actuators, to minimize boom signatures across all flight phases in response to changing aircraft configurations and environmental conditions. Since 2005 Boeing and Texas A&M, along with numerous industry, academic, and government partners have made significant advances in the area of SMA technology, including improved materials, design and modeling tools, and approved test methods. Many of these advances in SMA technology and tools are now being applied to the development of adaptive aircraft structures as part of NASA's University Leadership Initiative (ULI) led by Texas A&M University titled *Adaptive Aerostructures for Revolutionary Civil Supersonic Transportation*. In this paper the ULI program is described, including its goals and objectives. Strategies for integrated SMA design and design optimization are discussed. Examples of hardware demonstrations of morphing structures for shock wave control in supersonic wind tunnel tests and structural shape control are shown.

1. INTRODUCTION

For years the promise of Shape Memory Alloy (SMA) actuators as an enabling technology has seemed poised to revolutionize the design of adaptive structures and smart systems for aircraft. As far back as 2005 Boeing successfully integrated SMA actuators into the fan nozzle of a 777-300ER GE-115B engine to modify nozzle geometry in flight for community and cruise noise reduction [1-2]. Shape Memory Alloys were an ideal choice for the actuation mechanism for the Variable Geometry Chevron (VGC) flight test. Shape Memory Alloys are active materials that convert thermal energy into mechanical energy. Heating the material above its Austenitic transition temperature activates a crystalline structural phase change causing the material to revert to a previously "remembered" shape. When cooled below the transition temperature the SMA transforms into its more compliant (lower modulus) Martensitic form. It can be easily deformed when a load is applied during transition from Austenite to Martensite

or when in the final Martensite state. The concept for using an SMA to morph the shape of the VGC is shown in **Fig. 1**. The VGC was designed for two modes of operation. Autonomous operation utilizes changes in the ambient temperature from take-off to cruise to activate the chevron shape change. In powered mode internal heaters are used to individually control the VGC temperatures enabling variable immersions and the ability to test a variety of chevron configurations.

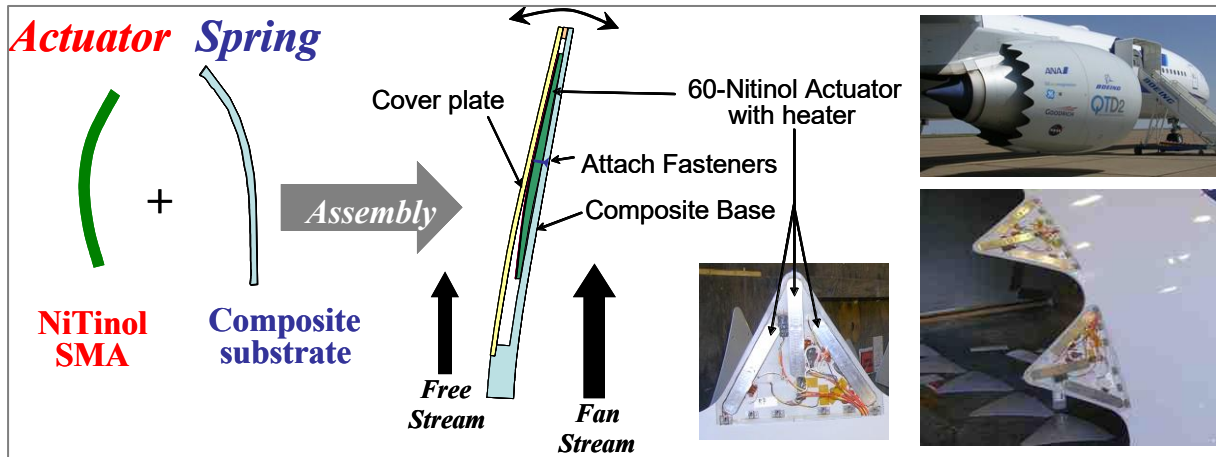


Figure 1: Variable Geometry Chevron Design Concept

2. TECHNOLOGY GAPS, DEVELOPMENT, AND DEMONSTRATIONS

While the Variable Geometry Chevron (VGC) flight tests clearly demonstrated that SMA technology can enable solutions for challenging aerospace applications, it also exposed critical technology gaps and needs that would be essential to advancing SMA technology. Identified needs included:

- Improved tools for modelling, simulation, and design optimization.
- Alloy compositions, processing, and fabrication to increase stability, fatigue, and work output.
- High temperature alloys for stable operation in worldwide thermal environments.
- Improved controller for precise and repeatable load displacement control.

A critical part of the technology development since the VGC program has been regular laboratory and flight demonstrations showing a high technology readiness level (TRL). Key applications and demonstrations are shown in **Fig. 2**.

2.1. The Adaptive Trailing Edge (ATE)

The ATE program was part of a Boeing and Federal Aviation Administration (FAA) collaboration [3]. The ATE program combined advances in SMA actuation and control with the aerodynamic understanding of transport aircraft wing design to demonstrate deployable and controllable trailing-edge elements that improve aircraft performance at all flight conditions. Small SMA actuated control surfaces (miniature flaps) were placed along the wing trailing edge of a 737-700 aircraft demonstrating a simple and effective way to improve aerodynamic performance at multiple configurations that vary with flight segments. Flaps could then be deployed for enhanced takeoff, cruise, or approach performance, and retracted when not needed. Closed loop control of the flap's position, using the SMA actuators, was demonstrated at multiple flight conditions during flight tests.

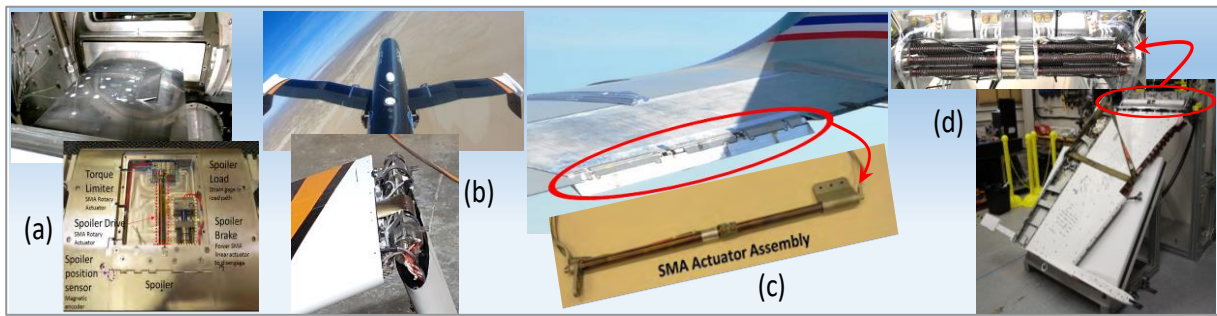


Figure 2: SMA Applications and Tests Demonstrating Boeing Tools for Design, Simulation, and Control. (a) Actuated Wind Tunnel Models (b) Spanwise Adaptive Wing UAV (c) FAA Adaptive Trailing Edge and (d) F-18 Wing Ground Fold.

2.2. The Spanwise Adaptive Wing (SAW) Flight Test

The SAW project included the development, integration, and test of a compact integrated SMA actuator system to fold the outboard wing sections of the PTERA UAV during flight. High temperature NiTi-20Hf SMA torsional components were processed by Boeing to produce stable actuation at loads up to 45 N*m (400 in-lbs) and 88° of angular range. The SMA components were incorporated into a hinge assembly that mechanically coupled the inboard wing and the outboard folding winglet. Instrumentation was installed to provide position, load, and temperature feedback. A compact on-board control system used angle, torque, and temperature readings to maintain a range of commanded wingtip angles over a wide range of flight and test conditions. An integrated simulation of the SMA actuators was developed to aid in the design of the actuator control system and for preflight performance predictions. The simulation was deployed using compact electronics and integrated into NASA's PTERA flight simulator. This complete actuator system was tested using a combination of bench and wind tunnel testing prior to integration into the PTERA vehicle and flight tests. The performance of the actuator control system, the SMA actuation, and the actuator simulation model were validated during flight tests. Preflight Simulations compared to flight data are shown in **Fig 3**.

2.3. The Spanwise Adaptive Wing (SAW) Ground Test

The SAW ground test demonstrated scale-up of SMA actuators to 2260 N*m (20,000 in*lbs). High temperature NiTi-20Hf SMAs, developed at NASA Glenn, was used for these actuators due to their high strength and high transition temperatures suitable for wing applications. Simply increasing the size of the SMA components may not be a viable solution for larger torques. The cost of manufacturing, limited existing design data, and increased heating and cooling rates can make large tubes impractical. Boeing has demonstrated an SMA actuator design that overcomes the limitations of very large SMA tubes by combining multiple smaller tubes into a single assembly. The design is modular and adaptable, trading output forces and displacements through a simple gearing mechanism. For the large multi-tube actuators material was produced in large scale (>120 lbs batches) and processed into rods from which torque tubes with outer diameters ranging from 0.75 to 1.5 inches were produced. These tubes were used to design and build integrated large scale actuation mechanisms for folding the outer wing section of an F/A-18 wing. The mechanism was tested on a F/A-18 surplus outer wing and was shown to operate at loads up to 2260 N*m (20,000 in*lbs) and angular displacements of up to 90 degrees.

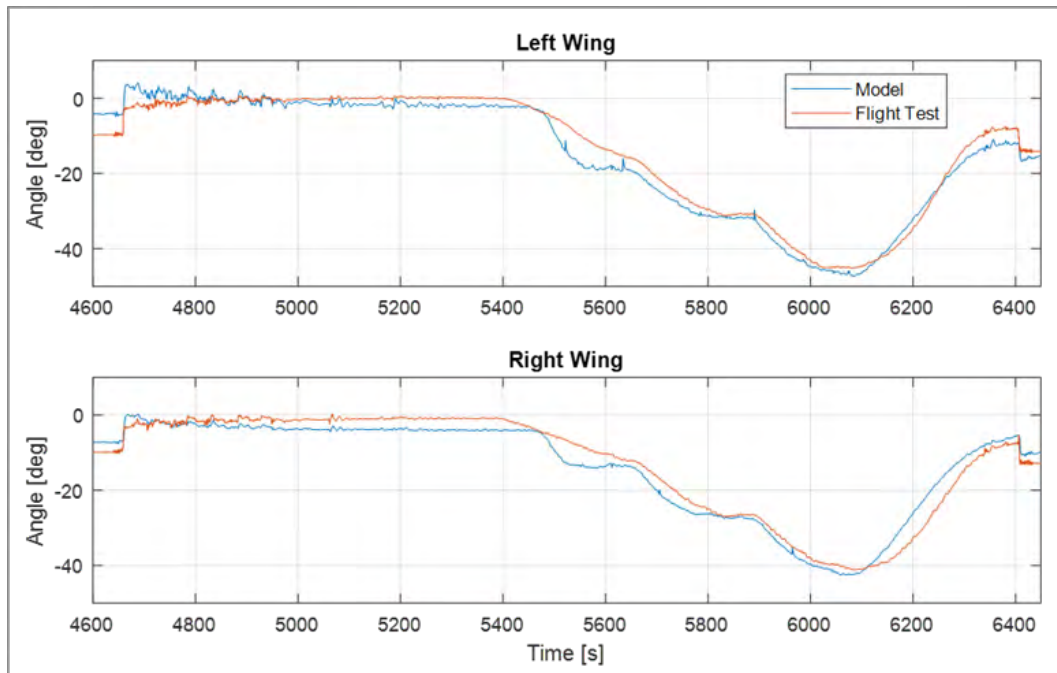


Figure 3: Spanwise Adaptive Wing Model and Flight Test Data Comparison.

2.4. SMA Actuated Wind Tunnel Models

SMA actuated wind tunnel models enable efficient test methods and improved data. Compact and precisely controller SMA actuators have been integrated into models used in high pressure cryogenic wind tunnels. Using traditional fixed parts is expensive due the high cost of tunnel shut down, parts swap, and tunnel restart. Remote actuation can greatly increase productivity and data quality while reducing cost. Shape Memory Alloy technology has been demonstrated as a simple actuator that enables efficient remote actuation of cryogenic wind tunnel models. Previous testing at the European Transonic Wind Tunnel and NASA transonic Cryogenic Tunnel demonstrated actuation under representative loads, precise control and repeatable control as shown in **Fig 4**. Collaboration with leading High Speed wind tunnels has been key to validating the technology and developing new operational methods that will greatly improve testing productivity.

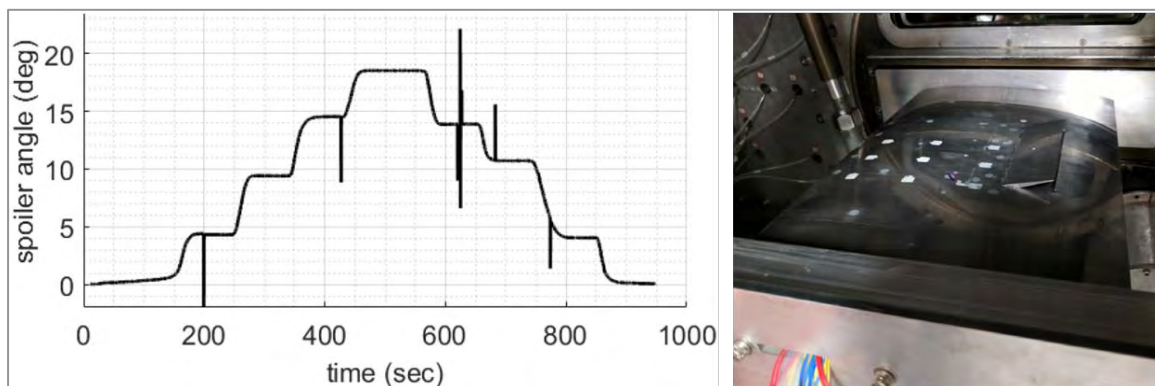


Figure 4: Angle Increment Control at -100°C, Mach 0.7, and 3.35 mega Pascal

3. University Leadership Initiative (ULI)

Renewed interest in sonic boom noise mitigation in recent years has brought attention to technology development for quiet supersonic aircraft. A multidisciplinary team headed by the Department of Aerospace Engineering at Texas A&M University and Boeing Research & Technology (BR&T) in St. Louis, Missouri, is investigating commercially viable civil supersonic transport aircraft that can modify their shape during flight under a range of conditions to meet noise and efficiency requirements for overland flight. This project is sponsored under NASA's University Leadership Initiative (ULI) program. [4]

Overland flight of supersonic aircraft is limited by the over-pressure on the ground caused by the propagation and coalescence of shock waves generated by the aircraft. The perceived loudness of the resultant sonic boom, depends on many factors including the shape of the aircraft, the aircraft's flight conditions such MACH, angle of attack, and altitude, and atmospheric conditions such as humidity.

The calculation of the sonic boom's perceived loudness (PLdB) is completed in a multi-step process. The various stages of sonic boom loudness calculation are shown in **Fig. 5**. First the pressure signature at a certain distance from the body of the aircraft in what is termed the near-field region is determined. The near-field pressure signature is determined by using a computational fluid dynamics (CFD) solver. The near-field pressure is then propagated through the atmosphere, accounting for relevant atmosphere conditions, to the ground. The ground pressure signature is further analyzed to determine the perceived loudness that results from the over-pressure.

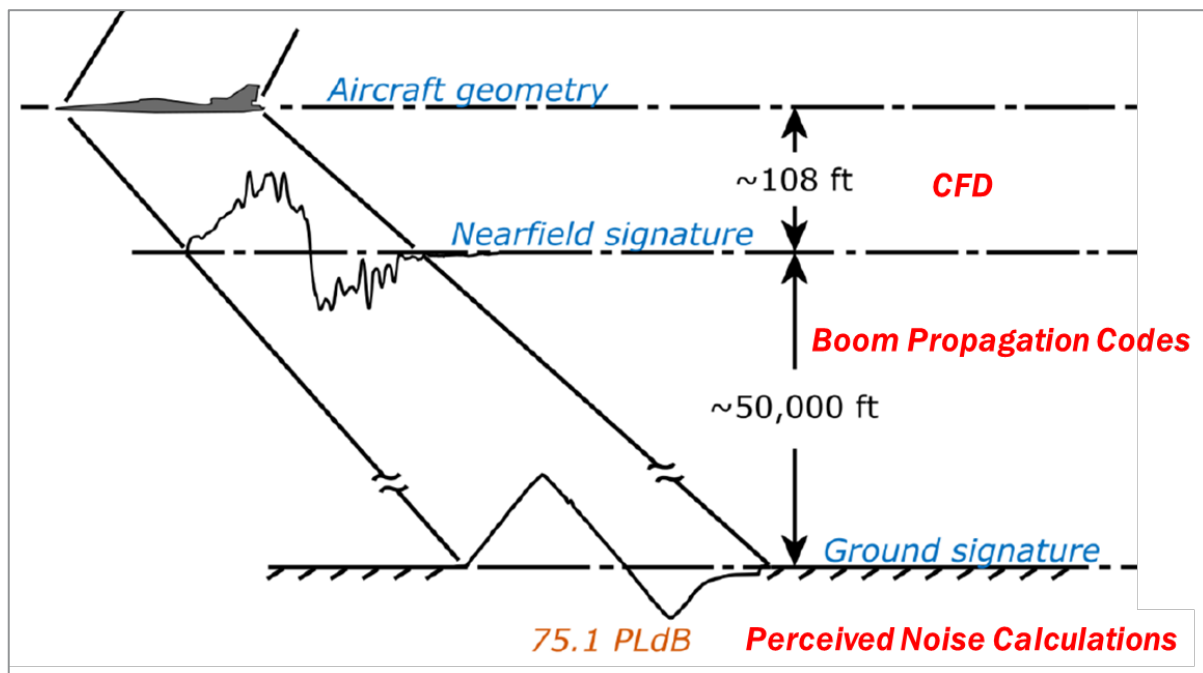


Figure 5: Strategy for Perceived Noise Calculation Based on Aircraft Geometry

Previous studies have shown that small changes in flight conditions, such as Mach or angle of attack, can have an adverse effect on the boom signature [5]. However, to be commercially viable, a supersonic transport must be able to meet low boom noise limits for

all flight conditions. This will require the ability for aircraft to adapt and reconfigure to changing flight conditions to maintain a low boom signature.

As an example, the same near-field pressure was propagated to the ground through two measured atmospheric conditions, one in a humid location, Jacksonville Florida, and one in a dry location, Las Vegas Nevada. The ground pressure signature and the resultant perceived noise is shown in **Fig 6**. A 6 PLdB difference is calculated for the identical aircraft configuration.

Embedded shape memory alloy (SMA) actuators can provide small real-time geometric reconfigurations to the outer mold line (OML) of the aircraft to impact the boom signatures and enable optimal low-boom and low-drag configurations across all environments and flight conditions. The Texas A&M ULI team is combining improved supersonic computational fluid dynamic (CFD) methods, SMA actuator design and optimization tools, and boom propagation models into a multidisciplinary design framework. Modeling and designs are initially being validated in small scale supersonic wind tunnel tests.

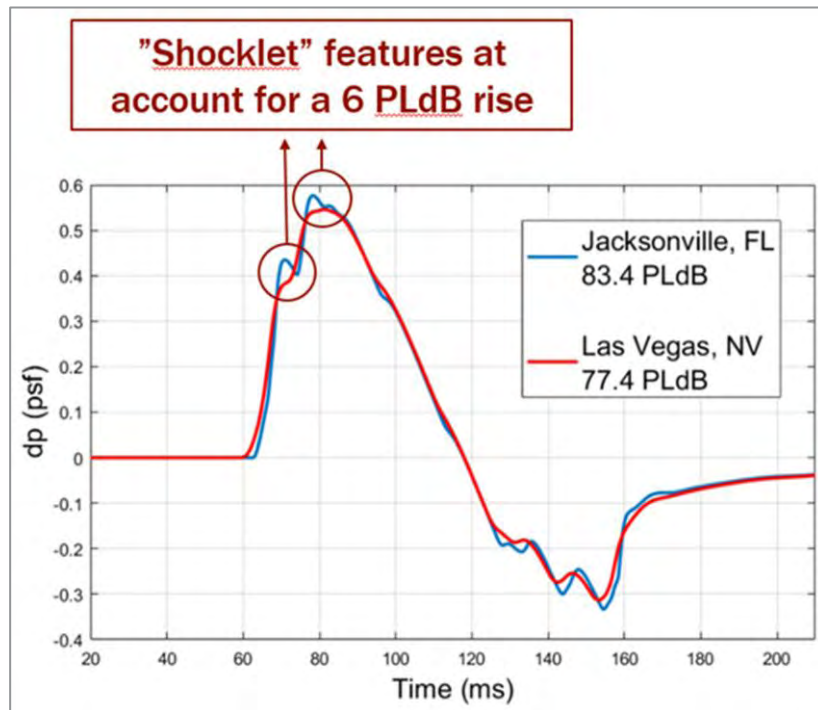


Figure 6: Perceived Noise increase due to propagation through high humidity

3.1. Low Boom Predictions and Off Design Flight Conditions.

Initial ULI studies of the off-design low-boom performance have focused on the NASA 25D configuration. A methodology for identifying potential surface morphing locations where SMA solutions can likely improve boom signature under adverse conditions is being developed. CFD studies have shown that Mach number and angle-of-attack can adversely impact perceived boom noise. Additionally atmospheric conditions, particularly humidity, can also adversely impact perceived sonic boom noise on the ground.

The resulting change in ground signature loudness for an initial set of Mach and angle of attack perturbations is shown in **Fig. 7**. It is evident that small perturbations in Mach and angle of attack degrade the designed boom loudness for the NASA 25D model. This implies that appropriate vehicle modifications should be studied to enable greater boom robustness when encountering off-design flight conditions. In this initial analysis the loudness sensitivity to ΔM is more severe than its sensitivity to $\Delta \alpha$. Mach number variations due to temperature gradients and angle of attack variations due to gusts at the design altitude were estimated to within the bounds of Fig. 7 perturbations [6].

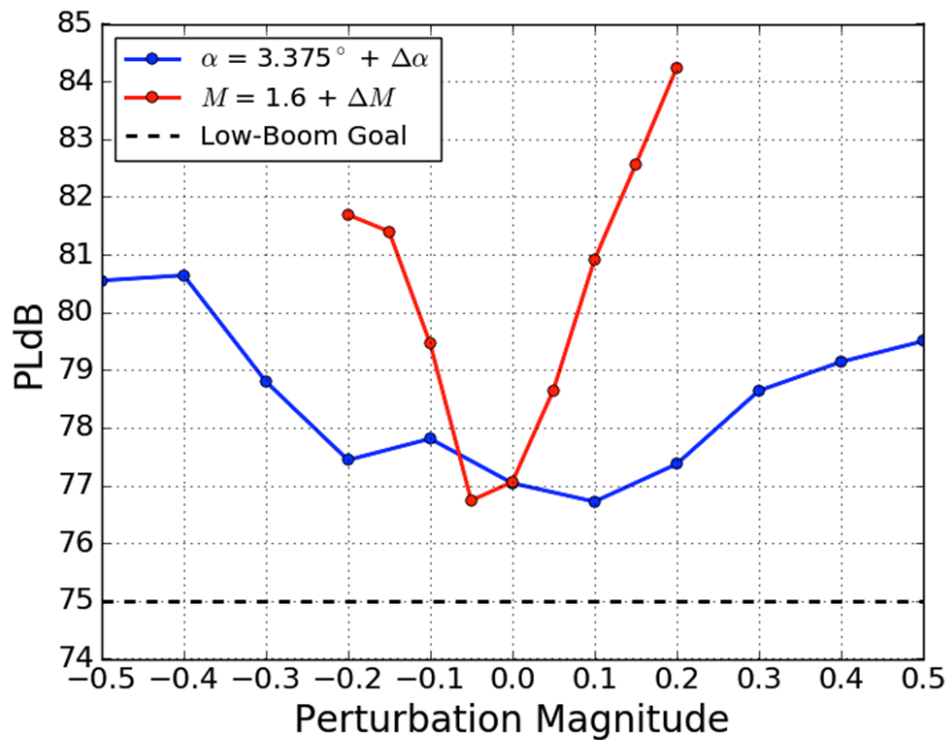


Figure 7: Perceived Noise Increase due to Mach and Angle of Attack Changes.

A full simulation including near-field CFD with Cart3D, followed by atmospheric wave propagation with sBOOM and noise assessment with LCASB, was utilized to create a model for PLdB off-design conditions including varying Mach and angle of attack. A surrogate was also created to model the location of maximum ground-signature sensitivity to near-field perturbations. Target regions and areas where surface morphing could improve boom signature in adverse conditions were identified. In particular, a region of the vehicle nose was found to be sensitive to Mach perturbations and an aft region was sensitive to angle of attack perturbations as shown in **Fig. 8**. These results provide insight into the appropriate allocation of SMA actuators for the NASA 25D model.

Both of these regions on the model are therefore candidate locations for SMA actuators to have the most impact on off-design signatures. Future work will explore what type of SMA deformation is best suited for these regions to accomplish robust boom performance.

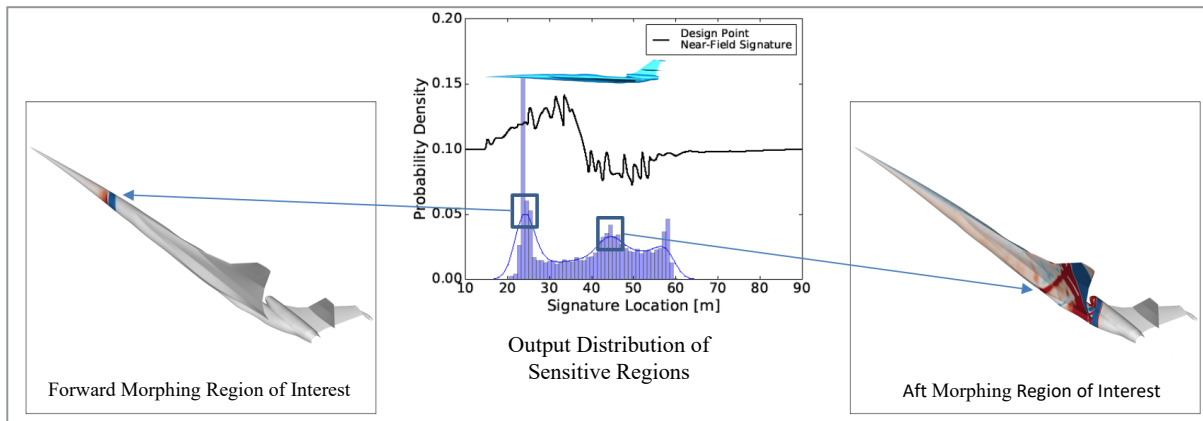


Figure 8: Identified Morphing Regions of Interest

3.2. Actuated Supersonic Wind Tunnel Model

To explore the feasibility of using SMA actuation to control shock wave characteristics in supersonic flow a SMA-actuated wind tunnel model was designed, built, and tested. The wind tunnel model hardware consists of two coupled panels mounted in the floor of a Mach 2.2 wind tunnel at Texas A&M's National Aerothermochemistry and Hypersonics Laboratory (NAL). SMA torque tubes were integrated into the hinge assemblies and were used to articulate each panel up into the flow. Shock wave formation, location, and characteristics were measured using a Schlieren image system [7].

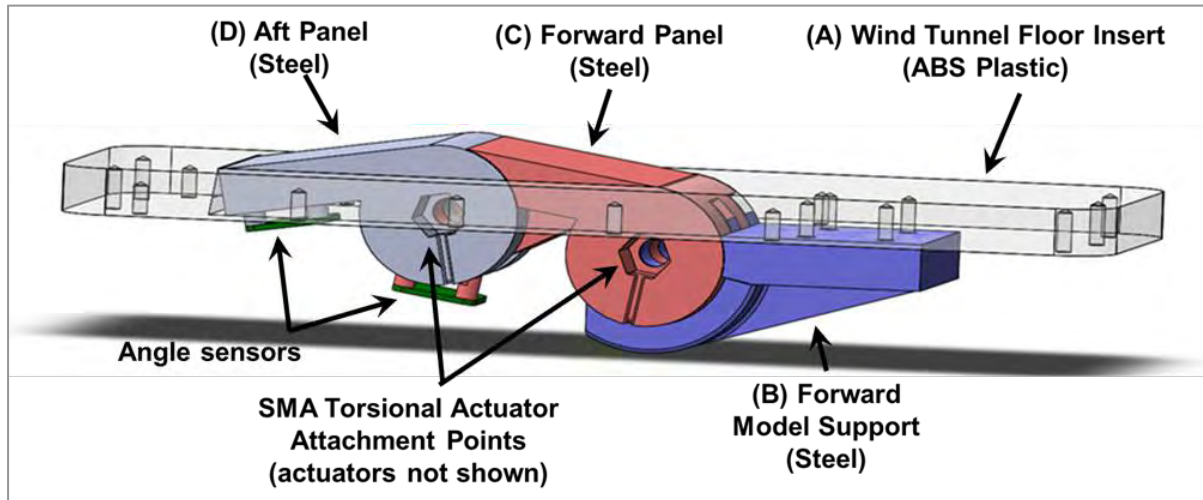


Figure 9: SMA-actuated wind tunnel model. Torsional actuators are integrated into the hinge between the forward model support and the forward panel and into the hinge between the forward panel and the aft panel.

The wind tunnel model was designed by a Texas A&M undergraduate team. A drawing of the model is shown in **Fig. 9**. The two actuated panels use SMA torsional tube actuators, each independently controlled. Cartridge heaters are used to heat the SMA, varying the actuator's temperature, tube twist, and the panel's angle. The SMA actuators act as hinge pins connecting the forward panel to the forward model support and the aft panel to the

forward panel. One end of each tube is attached to the element upstream of the tube, and the other is attached to the part downstream of the tube as shown in **Fig 10**. The forward panel's angle is directly correlated to the rotation of the forward SMA actuator. The aft panel is mechanically coupled to the forward panel and its angle is the sum of the forward panel angle and the aft SMA actuator's rotation.

The SMA torsional actuators are made from equi-atomic NiTi trained and stabilized to have approximately 5% two-way shear strain shape memory effect (SME). There are no restoring springs or other forces in this actuation design, relying on the two-way SME on cooling to reduce the panel angle.

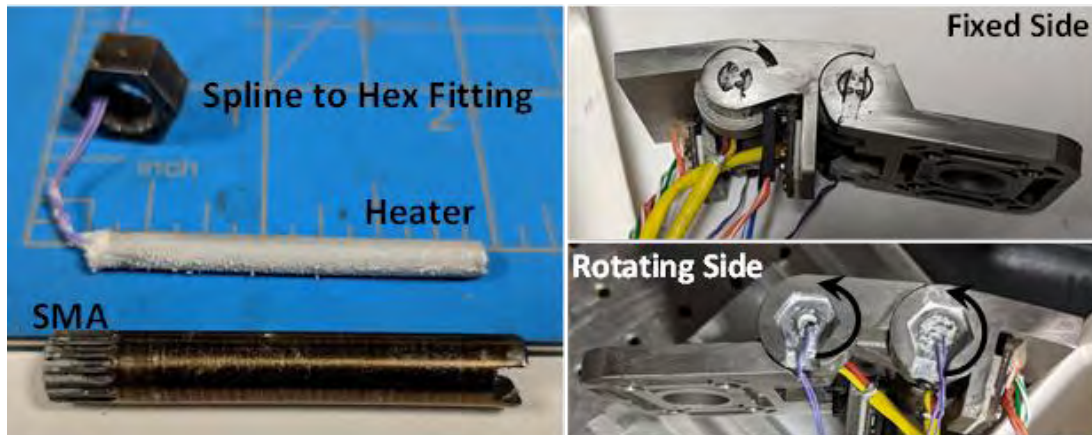


Figure 10: SMA torsional actuator and cartridge heater left. SMA tubes integrated into wind tunnel model

The model was mounted in the floor of the tunnel as shown in **Fig 11**. Closed loop control of angle was demonstrated on the bench, **Fig 12**, however angle sensor issues limited closed loop control under high Mach conditions, so open loop heating of the SMA was used to control the angle of each ramp. Schlieren images of the shock characteristic for a range of ramp angles is shown in **Fig 13**. Shocks are easily seen originating at the leading edge of each panel. The shock angles vary with ramp angles and the feasibility of controlled the shock waves was demonstrated.

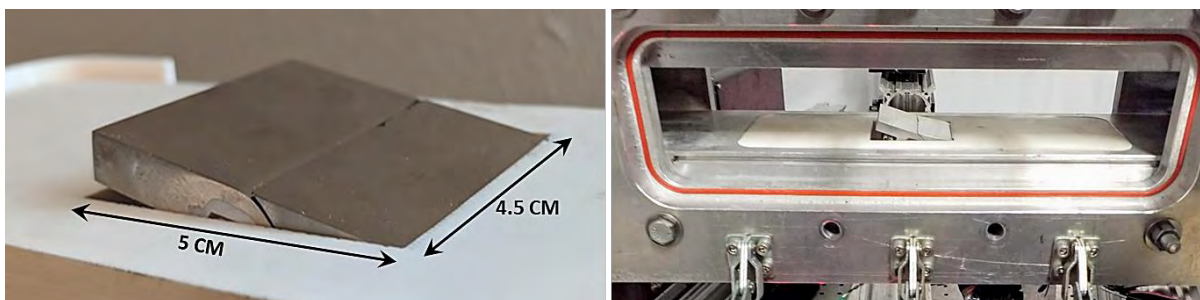


Figure 11: Dual Ramp SMA Actuated Wind Tunnel Model, flow is right to left.

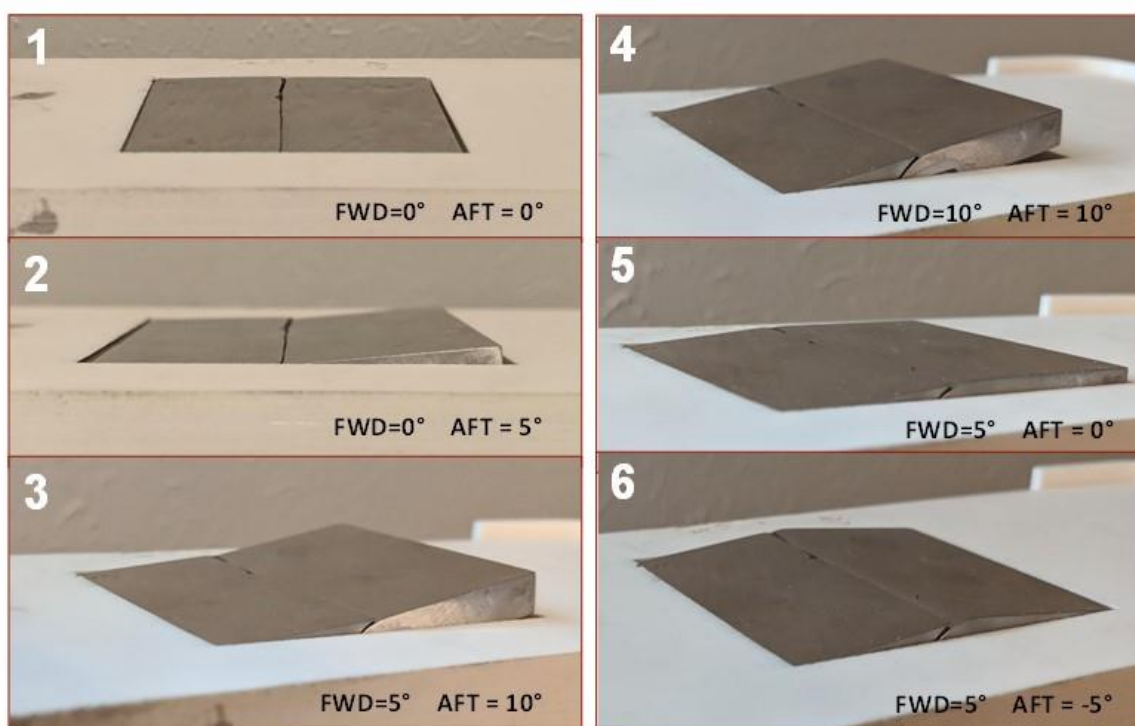


Figure 12: Closed loop angle control of the forward and aft panel during bench-top testing.

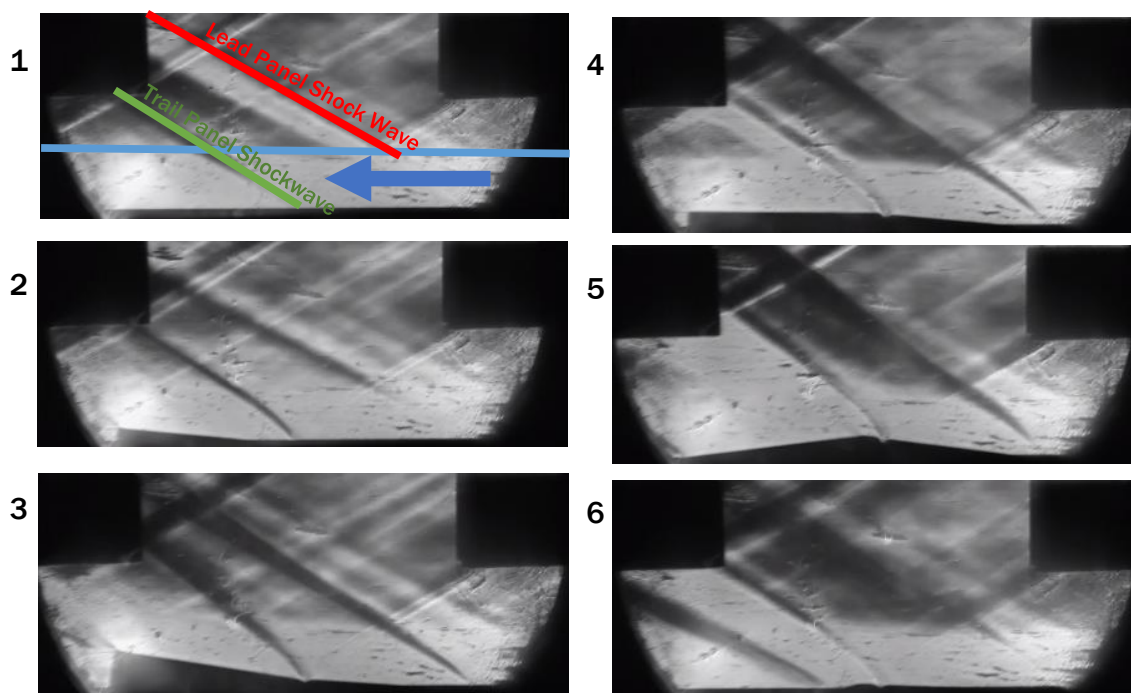


Figure 13: Schlieren images of the shock characteristic for a range of ramp angles

An improved wind tunnel model design is currently being fabricated and will be tested summer of 2019. Improvements include accurate angle sensing for closed loop control, measurement of SMA hinge loads, and pressure taps for validation of CFD models.

4. CONCLUSIONS

- Demonstrations of SMA actuator design tools, advanced materials, precise control methods, and aircraft integration have verified the high TRL of SMA actuation.
- The return of commercial supersonic overland flight can be enabled by lightweight SMA actuation to modify aircraft geometry in flight and minimize sonic boom noise in adverse conditions.
- SMA actuated surfaces have been tested in MACH 2.2 flow and the feasibility of controlling shock characteristics has been demonstrated.

Acknowledgments

This work is supported by the NASA *University Leadership Initiative* (ULI) program under federal award number NNX17AJ96A, titled *Adaptive Aerostructures for Revolutionary Civil Supersonic Transportation*.

REFERENCES

- [1] J.H. Mabe, F.T. Calkins, G.W. Butler, "Boeing's Variable Geometry Chevron: Morphing aerostructure for jet noise reduction" 47nd AIAA Adaptive Structures Conference, AIAA-2006-2142, Newport RI, May 2006.
- [2] Calkins, F., and Mabe, J., "Shape Memory Alloy Based Morphing Aerostructures," *Journal of Mechanical Design* 132, November 2010, 111012-1.
- [3] F.T. Calkins, J.H. Mabe, Flight Test of a Shape Memory Alloy Actuated Adaptive Trailing Edge Flap, Proceedings of the ASME 2016 Conference on Smart Materials, Adaptive Structures and Intelligent Systems SMASIS2016 September 28-30, 2016, Stowe, VT, USA
- [4] <https://engineering.tamu.edu/news/2017/06/researchers-working-to-create-a-quieter-transforming-supersonic-aircraft-for-commercial-use.html>
- [5] Ordaz, I., and Li, W., "Adaptive Aft Signature Shaping of a Low-Boom Supersonic Aircraft Using Off-Body Pressures," AIAA 2012-0020, 50th AIAA Aerospace Sciences Meeting, January 2013.
- [6] D. Lazzara, T. Magee, H. Shen† J. Mabe, Off-Design Sonic Boom Performance for Low-Boom Aircraft, AIAA Scitech 2019 Forum, San Diego, CA, 7-11 January 2019,
- [7] Mabe, James H., Darren J. Hartl, Nathan Tichenor, Murphy Zackery, Eric Blades, and Michael Nucci. "Fluid-Structure Interaction Modeling of a Shape-Memory Alloy Actuated Supersonic Wind Tunnel Model Alloy." AIAA Scitech 2019 Forum, San Diego, CA, 7-11 January 2019.

TAILORED NONLINEAR NEGATIVE STIFFNESS MECHANISMS FOR LINEAR MOTION

JIAYING ZHANG^{*}, ALEXANDER D. SHAW, CHEN WANG,
MOHAMMADREZA AMOOZGAR AND MICHAEL I. FRISWELL

Zienkiewicz Centre for Computational Engineering (ZCCE)

Swansea University

Swansea SA1 8EN, United Kingdom

^{*}e-mail: jiaying.zhang@swansea.ac.uk

Key words: Negative stiffness mechanism; Linear motion; Kinematics tailoring; Energy balancing; Actuator efficiency.

Abstract. Traditional ways to achieve the desired motion of mechanisms or deformation of morphing structures require external energy for actuation. Frequently the use of these actuators to drive the system can cost noteworthy energy for each cycle of operation and the spent energy cannot be recovered. This work investigates a passive energy balancing concept for linear motion systems by strategically using a negative stiffness mechanism. The energy balance concept is achieved by employing a negative stiffness system to couple with the positive stiffness mechanical system to create zero stiffness which can be driven with smaller actuators. The negative stiffness mechanism proposed here uses a pre-tensioned spring to produce a passive torque and therefore to transfer the passive torque through a crankshaft for linear motion. The kinematics of the negative stiffness mechanism is first developed to satisfy the required linear motion and its geometry is then optimised to achieve minimal energy requirements. The performance of the optimised negative stiffness mechanism is evaluated through the net force and the total required energy. Exploiting the negative stiffness mechanism has a significant benefit in the field of energy sensitive applications.

1 INTRODUCTION

Traditional mechanisms and smart structures are designed by using actuators or smart materials to overcome the internal (e.g. structure deformation) resistance and external (e.g. aerodynamic) loads to generate motion of the system. These integrated systems allow shape changes of the structure, and thus control its motion with acceptable precision. In particular, morphing requires deformation against the internal loads, and the frequent use the actuators to drive the system can cost noteworthy energy for each cycle of operation and the spent energy cannot be recovered. In other words, the work done to reach the target state requires the input of energy, while the subsequent dissipation of that energy to recover the initial state generates waste heat. Traditional actuators, such as electromechanical actuation, can be used as linear and rotary actuators, combined with mechanisms to provide a powerful tool for morphing [1]. Moreover, with the development of smart materials, many traditional actuation systems based

on electric motors, hydraulics, or pneumatics may be replaced by smart material systems. For example, piezoelectric materials have been used as actuators to control wing panels [2,3], spanwise deflection [4] and trailing-edge flaps [5,6]. Concepts have been proposed to reduce the required force or torque and therefore to allow smaller and lighter actuators, or even no actuator, to be employed to drive the system. For some typical cases, such as gravity equilibrators, a weight can be carried throughout its range of motion without any external energy by using spring mechanisms or counterweights [7–9]. Such static balancing is described as “zero stiffness” or “neutral stability”, as the system can be moved without operating energy. In general, many systems have force that is purely a function of displacement, as shown in Fig. 1(a), known as an elastic force response. In order to produce a static balancing for such systems with a zero stiffness property, negative stiffness is required to assist the imposed deformation. Figure 1(b) shows a representative nonlinear stiffness property, which has a completely nonlinear behaviour compared to the positive stiffness system and helps to construct an energy balancing system in a certain working range shown in Fig. 1(c). As the actuation is returned to zero, the elastic energy stored in the driven structure will force the negative stiffness system back to its original state, again at zero net actuation force. Therefore, Figure 1 shows that for a system assumed to be perfectly elastic, the negative stiffness can drive required actuation force to zero. Of course, many real systems include significant inelastic forces, which can be rate or history dependent, or due to external disturbances, and these cases represent a more complex problem that will be the subject of future work. In what follows, it is assumed that the driven structure has a purely elastic force displacement response.

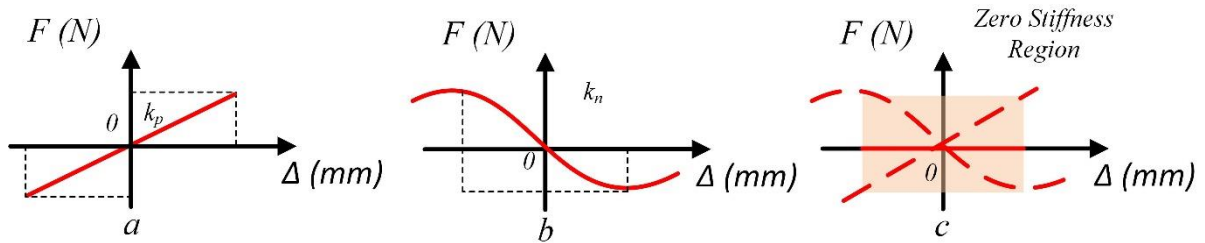


Figure 1. Schematic of the energy balancing system force curve. k_p is the stiffness of the load system and k_n is the negative stiffness system. (a) Increasing force system. (b) Nonlinear stiffness system. (c) Energy balancing system in a certain working range.

The negative stiffness mechanism can be coupled to the target positive stiffness system to produce an energy balancing system and the energy required to actuate the existing system can be balanced by the stored energy in the negative stiffness system. Figure 2 shows that a net zero stiffness device may be achieved by adding the negative stiffness system to a positive stiffness system, and the coupled system can therefore be considered as an energy balancing system. Figure 2(a) shows that a traditional way to actuate a system with internal stiffness k_p and the external load L , which requires a high power actuator. However, by coupling the negative stiffness mechanism, the total stiffness of the whole system becomes $k_p + k_n$ and a key benefit is that a small actuator can be used to determine the same output with regards to the same external load L , as shown in Fig. 2(b).

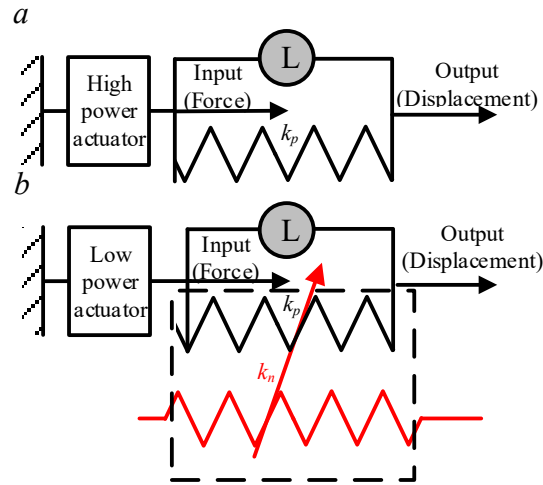


Figure 2. Minimalistic model of a negative stiffness mechanism for energy balancing. L denotes the external load, k_p is the internal stiffness of the load system and k_n is the negative stiffness system. (a) Traditional actuated system. (b) Energy balancing system by adding the negative stiffness mechanism.

It can be assumed that if the required input, such as force or torque, can be completely eliminated by the negative stiffness, then in principle no energy is required to move the system, other than to overcome dissipation. Therefore, the use of negative stiffness systems is likely to benefit energy constrained systems, such as those present in the aerospace and automotive industries.

Many applications have been proposed that use a negative stiffness for passive energy balancing. Clingman and Ruggeri [10] described a negative stiffness nonlinear over-centre linkage used on a tilt-rotor blade for active twist. This negative stiffness linkage mechanism uses the stored energy of a compressed spring to rotate the output shaft, resulting in an effectively softened blade that requires 70% reduction in torque for morphing. In addition, a pulley based balancer has been proposed with a varying radius pulley to preserve moment equilibrium between a constant load and a varying spring length [11,12]. By using such a spiral pulley negative stiffness mechanism, the required torque for the morphing actuation can be satisfactorily matched to create a nearly zero stiffness which requires minimal energy. A bidirectional torsional negative stiffness mechanism by using a series of pre-compressed springs has investigated for energy balancing systems [13]. This integrated BTNS mechanism was then verified to tailor the kinematics of the required torque driving the active camber and the results showed a similar torque-rotation profile can be generated. The proposed device provides actuation to change the state of the system, such as deforming a structure or lifting a mass; hence the energy provided by the actuator transforms into an increased potential energy in the system. Once the system returns to its original state, all of the energy provided by the actuator will be recovered, if the system is conservative. In other words, the work done to reach the target state require the input of energy, while the subsequent dissipation of that energy to recover the initial state generates waste heat.

In a previous work [14], an energy efficient concept for bidirectional morphing aircraft actuation was investigated by using a negative stiffness mechanism. The torsional negative

stiffness with an off centre spring (TNSOCS) mechanism was proposed that uses a pre-tensioned spring to convert the decreasing spring force available in the spring into an increasing output balanced torque. A significant contribution can be provided by the negative stiffness mechanism to balance the positive stiffness rotation motion system. This work extends [14] by applying the torsional negative stiffness mechanism to a linear motion actuation. This paper proceeds as follows. Firstly, a prototype of this energy balancing device is proposed and the kinematics of the bidirectional torque shaft, the linear motion mechanism and rotation angle are investigated. Then, the characteristics of the negative stiffness mechanism is proposed and a linear spring is chosen as the positive stiffness load system for investigation. Finally, the design parameters are optimised to exactly match the requirements of the linear motion requirement.

2 KINEMATIC ANALYSIS

The prototype of this energy balancing device is shown in Fig. 3 with the detailed geometry definition of two mechanisms. The torsional negative stiffness with an off centre spring (TNSOCS) mechanism [14] is developed to produce the actuating force and the slider-crank mechanism is designed to transfer the torque to linear motion actuation. The shaft is centred at O and θ is the shaft rotation angle. A pre-stretched spring is fixed on the shaft and point B is the off centre point for the spring. Then, the slider-crank mechanism is connected to the torsional negative stiffness mechanism and point E is the joint. Therefore, when the pulley rotates, the slider can move in the horizontal direction as denoted by q_m .

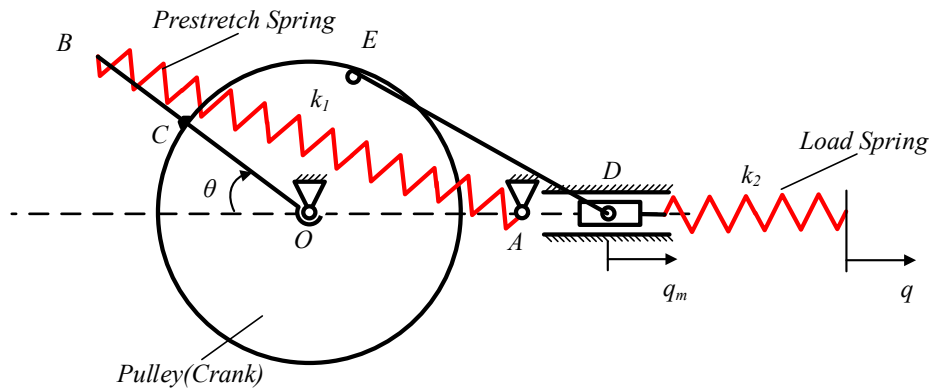


Figure 3. Schematic representation of a variable stiffness cam mechanism. In this mechanism k denotes the stiffness of the linear spring, q is the extra output position, θ is the input angle, while q_m denotes the motion of the slider.

In order to investigate the tailored nonlinear negative stiffness mechanism for linear motion, the kinematics of the system should be derived. Two springs are shown here, one is designed as an energy storage device for the negative stiffness system and the other represents the load system. Therefore, the potential energy function of this mechanism is given by:

$$V(\theta, q) = \frac{1}{2}k_1(l - l_0)^2 + \frac{1}{2}k_2(q_m - q)^2 \quad (1)$$

where l_0 is the initial length of the spring and l is the length of the spring at its current position. k_2 is the stiffness of the output system and can be considered as a linear system when k_2 is constant. Then, the additional required moment imposed by the negative stiffness modulating mechanism is

$$M_{in}(\theta, q) = \frac{\partial V}{\partial \theta} = k_1(l - l_0) \frac{\partial l}{\partial \theta} + k_2(q_m - q) \frac{\partial q_m}{\partial \theta} \quad (2)$$

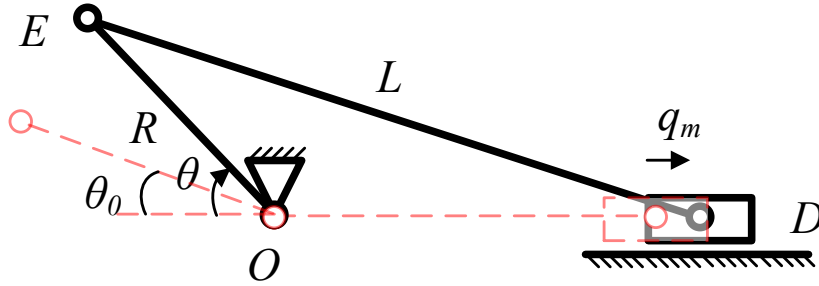


Figure 4. The slider-crank mechanism: displacement q_m of the slider for different λ and θ .

Moreover, the displacement q_m of the slider can be determined as

$$q_m = L \left(\left(\sqrt{1 - \lambda^2 \sin^2 \theta} - 1 \right) + \lambda(1 - \cos \theta) \right) \quad (3)$$

where $\lambda = R/L$ denotes the ratio of the radius of the crank shaft and the length of the connecting rod. Figure 5 shows the displacement of the slider for different λ when the crank shaft rotates. It can be seen that the larger the value of λ , the higher the displacement that can be achieved.

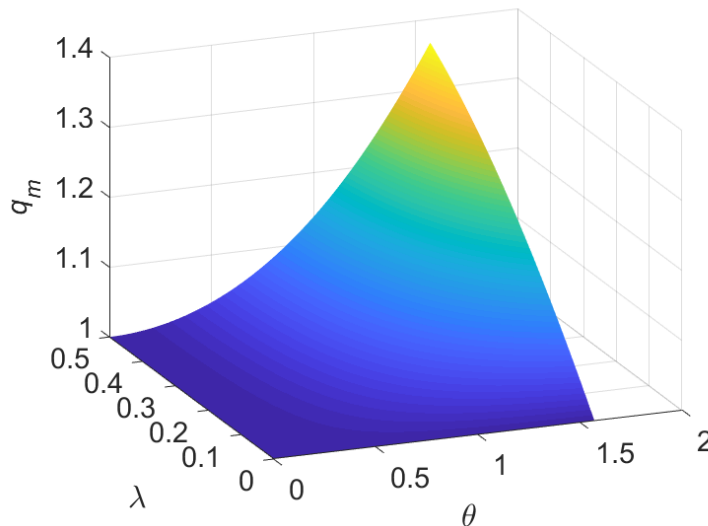


Figure 5. Displacement q_m for different λ and θ .

The kinematics of the torsional negative stiffness shaft is now investigated. Figure 6 shows that the cable is fixed on the shaft and point B is the off centre point for the spring. The Cartesian coordinates can then be defined with the origin at A and the coordinates of any point B' are then defined as

$$x_B = -l_{off} - b \cos \theta \quad (4)$$

$$y_B = b \sin \theta \quad (5)$$

where r is the length of the vector \overline{OB} and l_{off} is the length of the vector \overline{OA} .

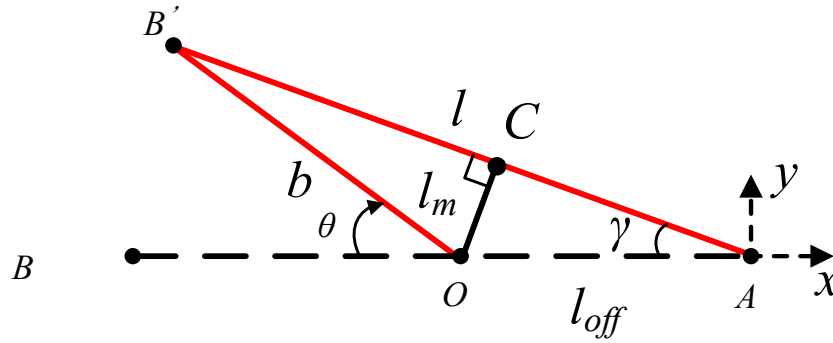


Figure 6. Torsional negative stiffness shaft geometry analysis with moment arm details.

Therefore, the length of the vector $\overline{AB'}$ is equal to

$$l = \sqrt{x_B^2 + y_B^2} = \sqrt{(b \sin \theta)^2 + (l_{off} + b \cos \theta)^2} \quad (6)$$

The change of the length l with the shaft rotation angle θ can be calculated as

$$\frac{\partial l}{\partial \theta} = -l_{off} b \sin \theta / \sqrt{(b \sin \theta)^2 + (l_{off} + b \cos \theta)^2} \quad (7)$$

The motion of the slider can also be calculated as

$$\frac{\partial q_m}{\partial \theta} = L \left(\lambda \sin \theta - \lambda^2 \sin \theta \cos \theta / (\sqrt{1 - \lambda^2 \sin^2 \theta}) \right) \quad (8)$$

Therefore, the additional required moment can be obtained by substituting Eqs. (7) and (8) into Eq. (2), to give

$$\begin{aligned} M_{in}(\theta, q) = \frac{\partial V}{\partial \theta} = & k_1 \left(\sqrt{(b \sin \theta)^2 + (l_{off} + b \cos \theta)^2} - l_0 \right) \\ & \times \left(-l_{off} b \sin \theta / \sqrt{(b \sin \theta)^2 + (l_{off} + b \cos \theta)^2} \right) \\ & + k_2 L^2 \left(\left(\sqrt{1 - \lambda^2 \sin^2 \theta} - 1 \right) + \lambda(1 - \cos \theta) - q \right) \\ & \times \left(\lambda \sin \theta - \lambda^2 \sin \theta \cos \theta / \sqrt{1 - \lambda^2 \sin^2 \theta} \right) \end{aligned} \quad (9)$$

In Eq.(9), for an ideal energy balancing system, we require $M_{in}(\theta, q) = 0$, where k_1 , b , l_{off} , L , l_0 , q , λ , k_2 are system constants. For a potential actuation system with known k_2 and q , the parameters can be optimised for passive energy balancing. Moreover, Eq. (9) can be modified by employing $k_1 = 0$ and $q = 0$ to obtain the ordinary required moment to actuate the system without the proposed negative stiffness mechanism as

$$M_r = k_2 L^2 \left(\left(\sqrt{1 - \lambda^2 \sin^2 \theta} - 1 \right) + \lambda(1 - \cos \theta) \right) \times \left(\lambda \sin \theta - \lambda^2 \sin \theta \cos \theta / \left(\sqrt{1 - \lambda^2 \sin^2 \theta} \right) \right) \quad (11)$$

Figure 7 shows the required moment and actuation force for the different input angle, and demonstrates that the required moment has a strong nonlinearity. Moreover, the system will be turned from positive stiffness to negative stiffness at a specific angle.

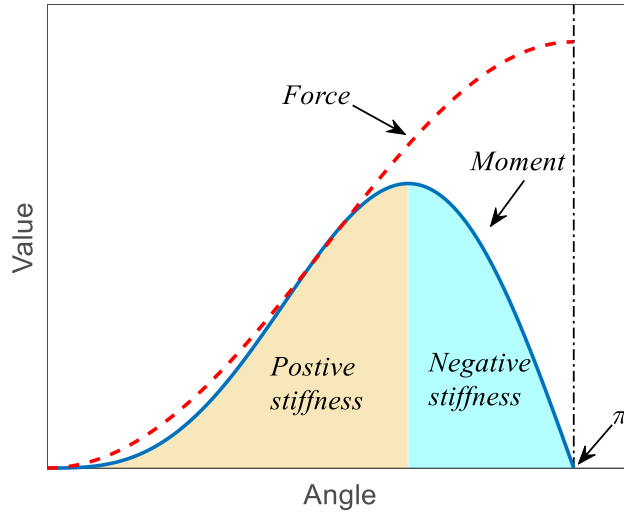


Figure 7. Required moment and actuation force as a function of input angle.

Therefore, in order to improve the performance of the total system, an initial established angle θ_0 of the bar mechanism is proposed as an additional parameter, as shown in Fig. 4. Then, the displacement q_m of the slider becomes

$$q_m = L \left(\left(\sqrt{1 - \lambda^2 \sin^2(\theta + \theta_0)} - 1 \right) + \lambda(1 - \cos(\theta + \theta_0)) \right) \quad (12)$$

Moreover, the turning point θ_t of the system can be obtained by solving

$$\frac{\partial M_r}{\partial \theta} = 0 \quad (13)$$

In order to evaluate the performance of the energy balancing system, it is useful to establish a force metric. As the system is continuous with limited constants, it is hard to construct a perfect energy balancing system using finite unknown constants. Therefore, an error metric is established to evaluate the performance of the energy balancing system. Figure 8 shows the schematic diagram of the actuation force error for different input angles. The error metric could theoretically integrate this actuation error from a zero angle to the current position and is written as

$$\eta_{err} = \int_0^{\theta} |M_{in}| d\theta \quad (14)$$

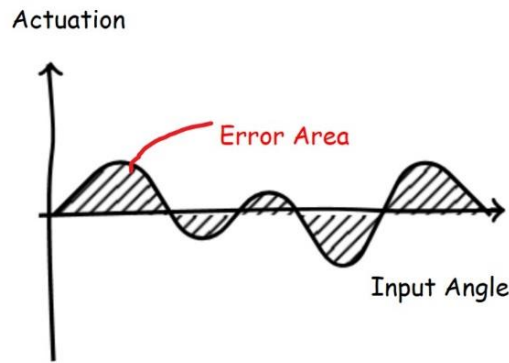


Figure 8. Schematic diagram of the actuation force error for the input angle.

This is a meaningful metric to evaluate the error for the passive energy balancing (PEB) system, as this implies the additional energy required during actuation. With this actuation force error metric, the performance of the energy balancing system can be obtained, and the geometric parameters of the system can be optimized using the *fmincon* function in Matlab. The energy conversion efficiency metric η_{err} is used as the objective function to make the torque available from the negative stiffness mechanism match as closely as possible the requirement to actuate the linear motion system over the entire prescribed rotation range.

3 DESIGN CASE

In order to investigate how to use this negative stiffness mechanism for linear motion actuation, a linear spring stiffness $k_2 = 69$ N/m is chosen as the drive load for study and the rotation input angle is between 0 and $\theta_t - \theta_0$. The resulting optimised parameters are shown in Table 1. All the components used here are ubiquitous and already manufactured over a very broad range of scales. The intention of this initial study is therefore to show the considerable energy storage achievable in a moderate size demonstrator.

Table 1. Design parameters for the NS mechanism for linear motion optimisation.

Parameter	Lower bound	Upper bound	Optimised value	Units
Drive spring rate, k_1	0.01	1	0.0238	N/mm
Drive spring length, l_0	10	500	146.186	mm
Off centre length, l_{off}	10	500	124.270	mm
Link bar length, L	10	500	100.000	mm
Shaft length, b	10	500	125.146	mm
Ratio R/L , λ	0.1	1	0.2709	-
Initial established angle, θ_0	0	90	78.9890	degree

With the optimised parameters shown in Table 1, the effectiveness of the optimal negative stiffness mechanism to construct an energy balancing system for the proposed target positive stiffness linear motion spring system can be investigated. Figure 9 shows the linear motion displacement along with the rotation angle provided by the negative stiffness mechanism. While there is a strong nonlinearity in the moment function, the output displacement presents a linear

relationship with respect to the rotation during the optimised operation interval, which can also be seen in Fig. 7. Hence this characteristic implies that the negative stiffness mechanism can provide a suitable linear motion output by careful design and optimisation.

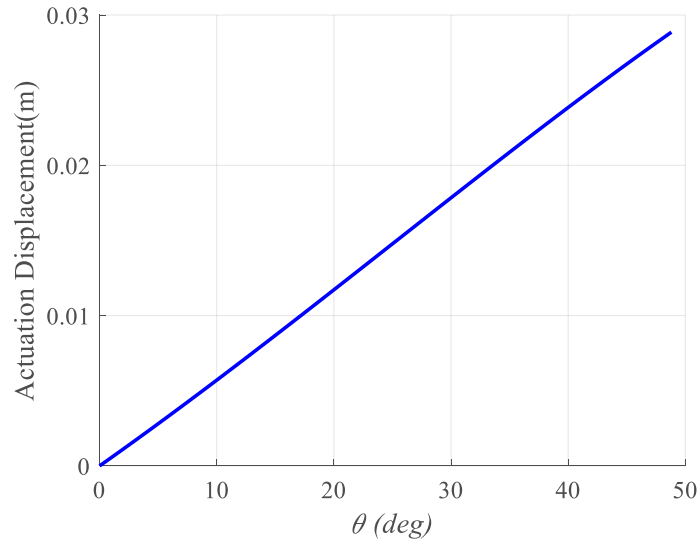


Figure 9. Predicted actuation displacement with rotation.

The performance predicted for the optimised torque shaft profile shows satisfactory matching of the linearised torque requirements. Figure 10 shows that the evolution of torque with rotation for the spring and the linear motion system and the net torque of the whole system. The torque provided by the negative mechanism matches the torque required closely to provide a linear motion, and the maximum torque required by the extra actuator is approximately zero.

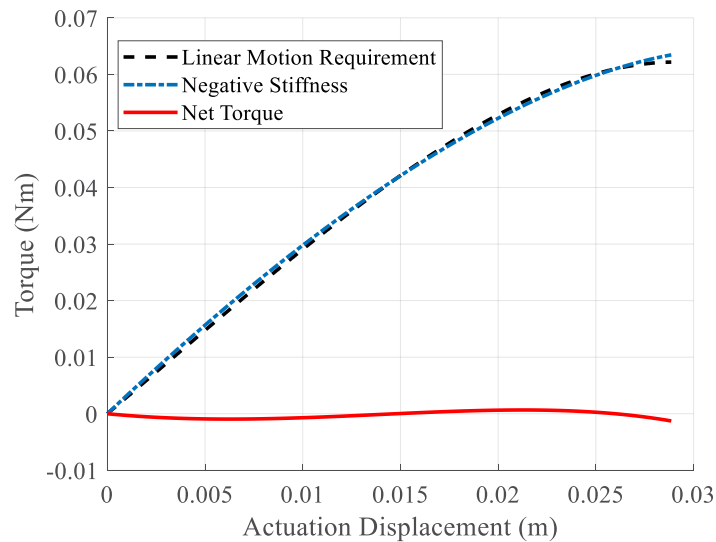


Figure 10. Predicted torque with optimised negative stiffness mechanism.

Integrating both the torque versus the rotation angle provides the mechanical energy required to actuate the target spring, and is shown in Fig. 11. By comparing the energy required with and without the negative stiffness mechanism, the negative stiffness mechanism shows a strong ability to passively balance the required torque. Figure 11 shows that the predicted energy reduction is almost 98%, with the energy required reduced from 0.032 J to 0.0005 J. This is the contribution of the energy stored in the extended spring in the initial position.

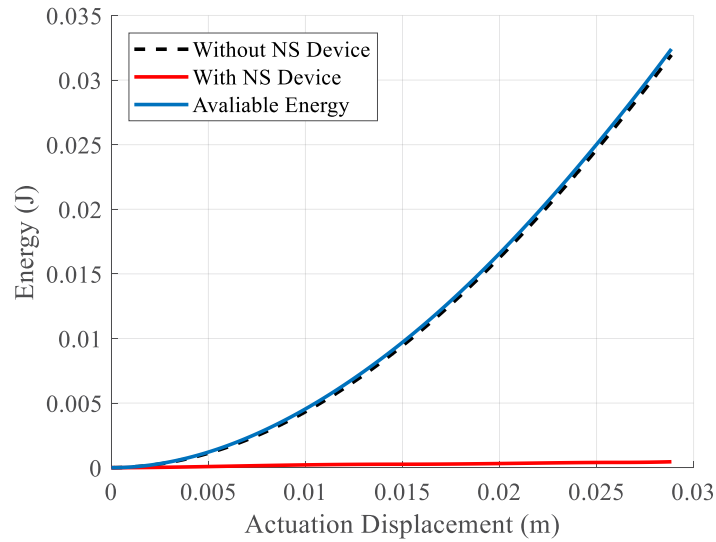


Figure 11. Comparison of the predicted energy required with and without the negative stiffness mechanism.

The objective error function plotted in Fig. 12 shows that the optimised configuration of the negative stiffness mechanism provides significant benefits in terms of energy efficiency.

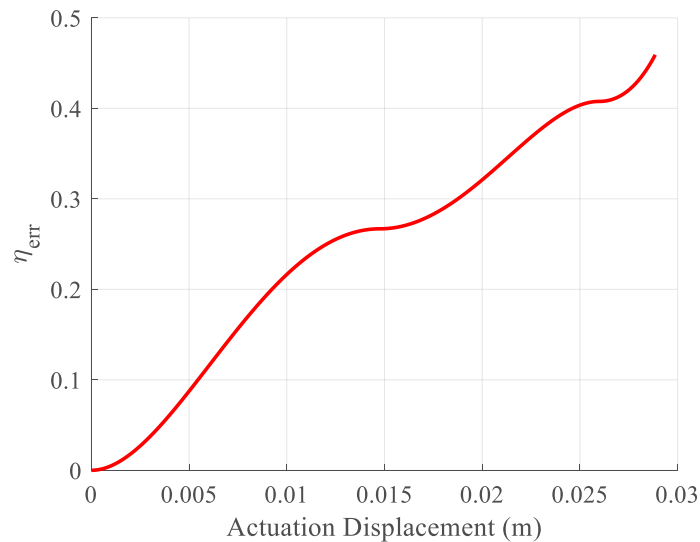


Figure 12. Evolution of efficiency with rotation.

Based on this study, it can be seen that the negative stiffness mechanism provides a significant contribution to balancing the positive stiffness system, and can provide a suitable linear motion output by careful design and optimisation. High energy conversion efficiency can be provided by the extension spring and a smaller actuator can be used in the system.

4 CONCLUSION

A new concept using a torsional negative stiffness with an off centre spring (TNSOCS) mechanism for linear motion actuation has been presented. The proposed negative stiffness device is designed to have the capability to passively balance the actuation requirement of systems displaying positive stiffness. The motivation for using such a mechanism was presented and the kinematics of the tailored nonlinear negative stiffness mechanism was introduced. An error metric function was introduced to provide a basis for evaluation and also act as the objective function to optimise the geometry of the tailored nonlinear negative stiffness mechanism. The optimised tailored nonlinear negative stiffness mechanism was shown to be able to generate a torque that matches the required force of a linear spring closely, which means a significant contribution can be provided by the tailored nonlinear negative stiffness mechanism to convert the torque to linear actuation and balance the positive stiffness system. The concept shown here can be extended to many potential actuation design applications which need frequent state switching to reduce the mean power consumption and waste heat dissipation. While the example used in this paper is relatively simple, it provides an insight into the low energy actuation design problem, both in the field of bidirectional morphing aircraft and other fields.

ACKNOWLEDGEMENT

This research leading to these results has received funding from the European Commission under the European Union's Horizon 2020 Framework Programme 'Shape Adaptive Blades for Rotorcraft Efficiency' grant agreement 723491.

REFERENCES

- [1] I. Dimino, G. Amendola, B. Di Giampaolo, G. Iannaccone, A. Lerro, Preliminary design of an actuation system for a morphing winglet, in: 2017 8th Int. Conf. Mech. Aerosp. Eng. ICMAE 2017, 2017: pp. 416–422. doi:10.1109/ICMAE.2017.8038683.
- [2] R. Vos, R. Barrett, R. De Breuker, P. Tiso, Post-buckled precompressed elements: A new class of control actuators for morphing wing UAVs, *Smart Mater. Struct.* 16 (2007) 919–926. doi:10.1088/0964-1726/16/3/042.
- [3] R. Vos, R. De Breuker, R.M. Barrett, P. Tiso, Morphing Wing Flight Control Via Postbuckled Precompressed Piezoelectric Actuators, *J. Aircr.* 44 (2007) 1060–1068. doi:10.2514/1.21292.
- [4] S.A. Tawfik, D. Stefan Dancila, E. Armanios, Unsymmetric composite laminates morphing via piezoelectric actuators, *Compos. Part A Appl. Sci. Manuf.* 42 (2011) 748–756. doi:10.1016/j.compositesa.2011.03.001.
- [5] T. Lee, I. Chopra, Design of piezostack-driven trailing-edge flap actuator for helicopter rotors, *Smart Mater. Struct.* 10 (2001) 15–24. doi:10.1088/0964-1726/10/1/302.
- [6] S.R. Hall, E.F. Prechtel, Development of a piezoelectric servoflap for helicopter rotor

- control, *Smart Mater. Struct.* 5 (1996) 26–34. doi:10.1088/0964-1726/5/1/004.
- [7] M.J. French, M.B. Widden, The spring-and-lever balancing mechanism, George Carwardine and the Anglepoise lamp, *Proc. Inst. Mech. Eng. Part C J. Mech. Eng. Sci.* 214 (2000) 501–508. doi:10.1243/0954406001523137.
 - [8] R. Barents, M. Schenk, W.D. van Dorsser, B.M. Wisse, J.L. Herder, Spring-to-Spring Balancing as Energy-Free Adjustment Method in Gravity Equilibrators, in: Vol. 7 33rd Mech. Robot. Conf. Parts A B, 2009: pp. 689–700. doi:10.1115/DETC2009-86770.
 - [9] Y.-L. Chu, C.-H. Kuo, A Single-Degree-of-Freedom Self-Regulated Gravity Balancer for Adjustable Payload ¹, *J. Mech. Robot.* 9 (2017) 021006. doi:10.1115/1.4035561.
 - [10] D.J. Clingman, R.T. Ruggeri, Mechanical strain energy shuttle for aircraft morphing via wing twist or structural deformation, in: E.H. Anderson (Ed.), *Proc. SPIE Smart Struct. Mater. 2004 Ind. Commer. Appl. Smart Struct. Technol.*, San Diego, CA, 2004: p. 288. doi:10.1117/12.538681.
 - [11] B.K.S. Woods, M.I. Friswell, Spiral pulley negative stiffness mechanism for passive energy balancing, *J. Intell. Mater. Syst. Struct.* 27 (2016) 1673–1686. doi:10.1177/1045389X15600904.
 - [12] J. Zhang, A.D. Shaw, A. Mohammadreza, M.I. Friswell, B.K.S. Woods, Spiral Pulley Negative Stiffness Mechanism for Morphing Aircraft Actuation, in: Vol. 5B 42nd Mech. Robot. Conf., ASME, 2018: p. V05BT07A003. doi:10.1115/DETC2018-85640.
 - [13] J. Zhang, A.D. Shaw, M. Amoozgar, M.I. Friswell, B.K.S. Woods, Bidirectional torsional negative stiffness mechanism for energy balancing systems, *Mech. Mach. Theory.* 131 261–277. doi:10.1016/j.mechmachtheory.2018.10.003.
 - [14] J. Zhang, A.D. Shaw, M. Amoozgar, M.I. Friswell, B.K.S. Woods, Torsional Negative Stiffness Mechanism for Bidirectional Morphing Aircraft Actuation, in: *Proc. 6th Aircr. Struct. Des. Conf.*, Bristol, 2018.

Adaptable ball-screw inerter for optimal impact absorption

R. Faraj*, C. Graczykowski, Ł. Jankowski and J. Holnicki-Szulc

Institute of Fundamental Technological Research Polish Academy of Sciences,
Pawinskiego 5B, 02-106 Warsaw, Poland

e-mail: rfaraj@ippt.pan.pl, web page: <http://www.ippt.pan.pl/staff/rfaraj>

Key words: ball-screw inerter, impact absorption, passive absorber, variable inertance, variable moment of inertia, inertial damping.

Abstract. For over two decades, inerter-based devices are a subject of research papers, patents and engineering reports. Since 2002, when the inerter was introduced as the missing element of mechanical networks, various applications of the inerter have been proposed. They include solutions for earthquake engineering, suspensions of vehicles, aircraft landing gears and even systems improving walking performance of humanoid robots. In contrast to majority of the inerter-based systems, which are mainly developed for vibration mitigation problems, this paper concerns the inerter as the shock-absorber protecting objects excited by the impact. In particular, adaptive performance of the ball-screw inerter with variable moment of the flywheel inertia is investigated. In order to ensure efficient adaptation of the inerter to various excitation conditions, the single reconfiguration technique, which was successfully applied for pneumatic absorber, is now adjusted and implemented in the proposed inertial system. The contribution consists of the concept introduction, discussion of the mathematical model of the system, theoretical as well as numerical analyses. Results of the presented study show that optimal impact absorption can be obtained in semi-passive manner. The properly adjusted geometry of the surface guides for the inertial elements ensure appropriate variability of the flywheel moment of inertia. Variable moment of the flywheel inertia provides optimal deceleration of the amortized object. The calculated moment of inertia depends on the mass of amortized object and friction but it is independent of the impact velocity.

1 INTRODUCTION

Although smart materials and advanced control systems are commonly known and even implemented in commercially produced systems, e.g., magnetorheological suspensions of cars [1], there are some applications for which passive solutions are still preferable, e.g., base isolations for earthquake protections of buildings [2]. As a result, the currently conducted research concerns both design of passive devices [3] and elaboration of control methods for active devices [4, 5]. In recent years the research of many scientists from all over the world was focused on the application of passive mechanical system, which is called the ‘inerter’ [6]. Typically the inerter is implemented in the tuned mass dampers (TMD) and used for mitigation of the forced vibrations amplitudes [7, 8]. Nevertheless, other practical applications of the inerter have been proposed and they include also suspensions of vehicles, aircraft landing gears and even systems improving walking performance of humanoid robots. Moreover, there appear contributions in which inerter-based devices are used for absorption of mechanical impacts [9].

Similarly, this paper relates to the problem of adaptive impact absorption and presents further development of the idea introduced in [10], where the ball-screw inerter is designed in such a way that the optimal deceleration of the amortized object is obtained.

Presented contribution reveals a conceptual solution which is based on two promising ideas: passive system with parameters dependent on the displacement of working element and single reconfiguration technique, which allows to obtain semi-passive, optimal performance of the system. Variable moment of the flywheel inertia is obtained by equipping the inerter flywheel with additional weights, whose position depends on the geometry of the surface mounted in the inerter housing. Shape of the surface varies with the displacement of the screw relative to housing and as a result the moment of the flywheel inertia changes also as a function of the screw displacement. In case the inerter is used for mitigation of impacts exciting objects of different masses the single reconfiguration technique is applied by reshaping of the guiding surface to the identified impact conditions.

2 BALL-SCREW INERTER AS THE SHOCK-ABSORBER

2.1 Problem formulation

Let us consider simple 1-DOF system described by classical equation of motion:

$$m\ddot{x} + F_{abs}(x(t)) = F_{ext}(t) \quad (1)$$

with initial conditions: $\dot{x}(0) = v_0$, $x(0) = 0$.

The first l.h.s. term of (1) is the inertia force of the decelerated object under impact conditions (Fig. 1), F_{abs} is the value of absorber reaction force, F_{ext} is the value of external force acting on the excited system.

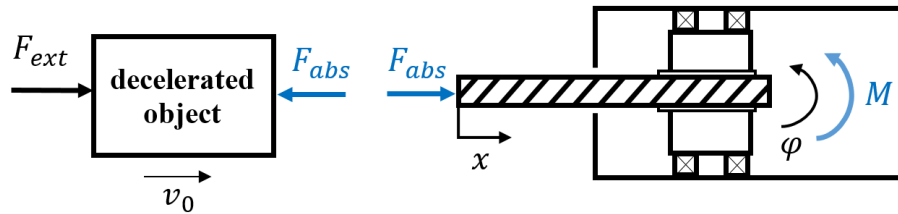


Figure 1: Free body diagram of the object decelerated with the use of the ball-screw inerter.

As shown in the free body diagram, in this paper the ball-screw inerter is analyzed and applied to the problem of optimal impact absorption, which can be formulated in general form:

$$\begin{cases} \max_{\mathbf{u}(x(t))} (F_{abs}(x(t)) - F_{ext}(t)) = \min \\ \int_d \mathbf{F}_{abs} d\mathbf{s} = E_{init} + \int_d \mathbf{F}_{ext} d\mathbf{s} \end{cases} \quad (2)$$

where \mathbf{u} is the control vector, d is the inerter stroke and E_{init} is the initial kinetic energy of the object amortized by the inerter. The inerter includes a screw with the thread lead P and a nut with a flywheel of the total moment of inertia I_b . We assume that the housing of the inerter is fixed so additional degrees of freedoms have not be introduced. In presented study the control

will be performed by variable moment of the flywheel inertia I_b which will be changed in passive manner and it will be the function of displacement x .

2.2 Reaction force and optimal change of the moment of the flywheel inertia

In order to obtain adaptive and optimal performance of the ball-screw inerter the problem (1) should be solved for every impact conditions. Nevertheless, it will be shown further that the optimal response of the system is independent from impact velocity and only adaptation to different values of amortized object mass has to be performed. In presented study it is assumed that the control of the moment of flywheel inertia is realized by autonomous mechanism, which utilizes several weights mounted on arms of variable length and guiding surface. Geometry of the surface results in specified change of the distance between weights and the axis of the screw. As a result, it provides change of the flywheel moment of inertia being a function of the screw displacement. The shape of guiding surface should be calculated for predicted or identified online impact conditions in order to ensure appropriate variability of the flywheel moment of inertia. If the guiding surface is appropriately reshaped just before or at the very beginning of the impact absorption process, the optimal response of the inerter will be obtained.

Now, let us derive the model of the ball-screw inerter with variable moment of inertia. Geometric constraints of the ball-screw connection result in kinematic relation between the velocity of impacting object \dot{x} and angular velocity of the flywheel $\dot{\phi}$:

$$\dot{\phi} = \frac{2\pi}{P} \dot{x} \quad (3)$$

The torque acting on the flywheel is equal to the time derivative of the flywheel's angular momentum:

$$M = \frac{d}{dt}(I_b(x)\dot{\phi}) = \frac{2\pi}{P} \left(I_b(x)\ddot{x} + \frac{dI_b}{dx} \dot{x}^2 \right) \quad (4)$$

Simultaneously, the torque is derived from the balance of forces acting on the ball-screw connection and it equals:

$$M = \frac{D \sin \beta - \mu \cos \beta}{2 \cos \beta + \mu \sin \beta} F_{abs} \quad (5)$$

where μ is the friction coefficient, D is the diameter of the ball-screw connection and β is the inclination angle described by simple relation:

$$\tan \beta = \frac{P}{\pi D} \quad (6)$$

The reaction force F_{abs} generated by the inerter with the variable moment of the flywheel inertia $I_b(x)$ is described by the following equation:

$$F_{abs}(x) = \frac{4\pi}{D} \frac{\pi D + \mu P}{P^2 - \pi \mu D P} \left(I_b(x)\ddot{x} + \frac{dI_b}{dx} \dot{x}^2 \right) \quad (7)$$

3 ADAPTATION TO THE IMPACT CONDITIONS

3.1 Adaptation technique

In Fig. 3. the general block diagram describing operation of the proposed ball-screw inerter with variable moment of the flywheel inertia is presented. The adaptation to actual impact conditions is performed according to the principles of Adaptive Impact Absorption (AIA) [11] and the inerter ensures so-called ‘adaptable’ performance [12], which is obtained by adaptation to the identified impact conditions and passive realization of the impact absorption process.

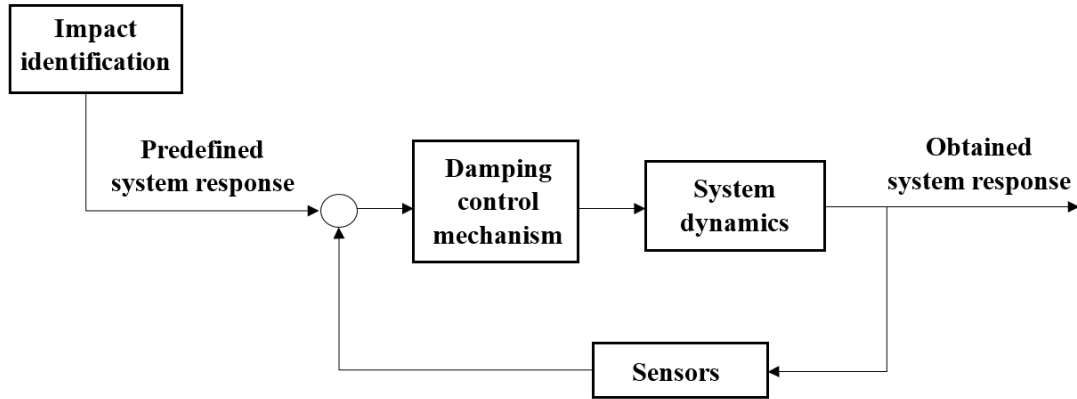


Figure 2: Block diagram of the adaptable system.

Inserting (7) into (1) and assuming that impact conditions are defined by initial velocity v_0 and any external force is not acting on the decelerated object, the particular form of the equation of motion is obtained:

$$\ddot{x} \left(\frac{m}{I_b(x)} + \frac{4\pi}{D} \frac{\pi D + \mu P}{P^2 - \pi \mu D P} \right) + \frac{4\pi}{D} \frac{\pi D + \mu P}{P^2 - \pi \mu D P} \frac{d}{dx} \ln I_b(x) \dot{x}^2 = 0 \quad (8)$$

Assuming that globally optimal response of the system is feasible, the constant value of the object deceleration $\ddot{x} = -\frac{v_0^2}{2d}$ is introduced to (8) and by its solving the optimal change of the flywheel moment of inertia is obtained in the closed-form:

$$I_b(x) = \sqrt{\frac{d}{d-x} \left(\frac{mDP(\pi \mu D - P)}{4\pi(\pi D + \mu P)} - I_{b_0} \right)} + \frac{mDP(\pi \mu D - P)}{4\pi(\pi D + \mu P)} \quad (9)$$

It should be pointed out that the obtained solution is independent from the impact velocity v_0 .

For calculated optimal changed of the flywheel moment of inertia $I_b(x)$ the shaped of guiding surface can be calculated. The particular formula depends on practical implementation of the systems so it will not be discussed in this contribution.

3.2 Numerical case study

In Tab. 1 parameters of the inerter, which were used for numerical simulations are presented.

Table 1: Parameters of the inerter assumed for numerical simulations.

inerter stroke	200	[mm]
diameter of the ball-screw connection	20	[mm]
initial flywheel moment of inertia	100	[kg·mm ²]

Fig. 3 and Fig. 4 present variability of the flywheel moment of inertia, which ensures optimal impact mitigation (minimal, constant deceleration of the object at the entire stroke), for different values of the object mass and dry friction coefficients, respectively.

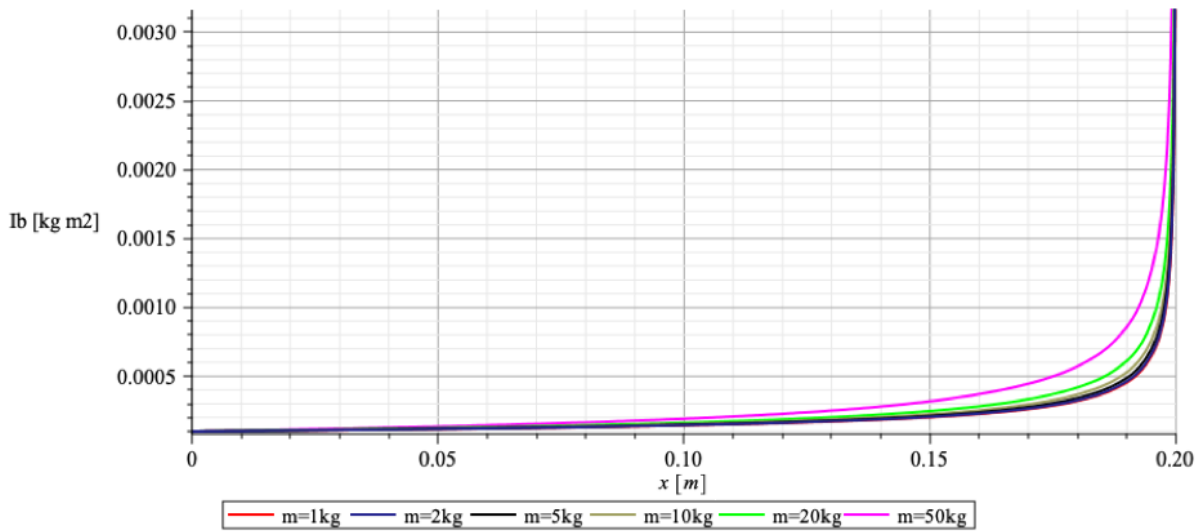


Figure 3: Moment of the flywheel inertia as a function of screw displacement for different values of the amortized object mass, dry friction coefficient $\mu = 0.01$.

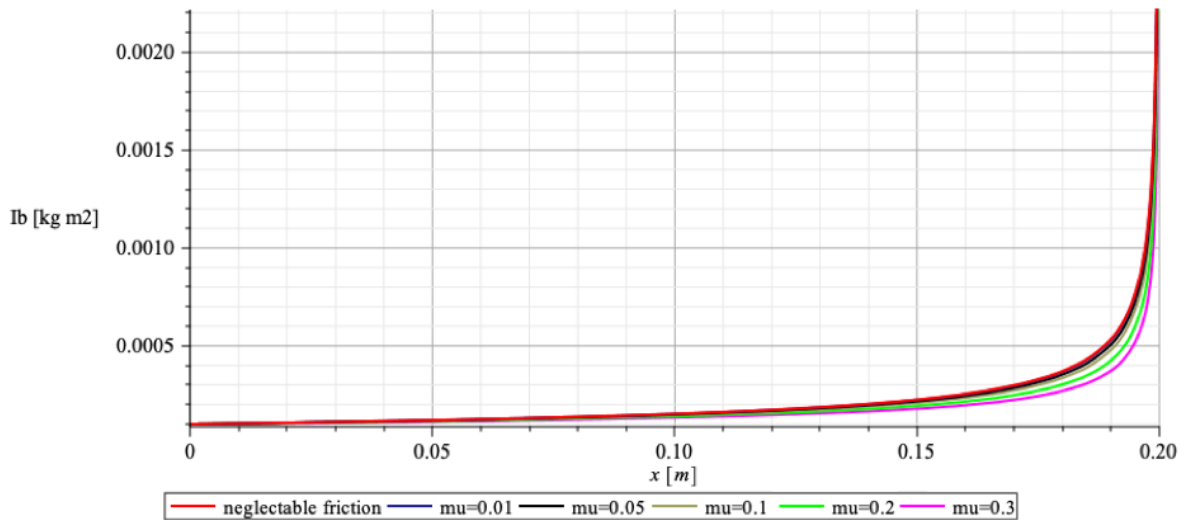


Figure 4: Moment of the flywheel inertia as a function of screw displacement for different values dry friction

coefficient, object mass $m = 10$ kg.

It can be easily noticed that for small values of impacting mass and small values of dry friction coefficient the variability of the flywheel moment of inertia does not change significantly. Nevertheless, for higher values of these parameters the optimal moment of the flywheel inertia becomes noticeably different.

4 CONCLUSIONS

The paper briefly discusses the concept of adaptable ball-screw inerter, which is designed for impact mitigation. Adaptation mechanism is based on the guiding surface, which regulates the distance of the weights mounted on the inerter flywheel and as a result controls the flywheel moment of inertia. Appropriate shaping of the guiding surface is based on the solution of the inverse dynamics problem, in which change of the flywheel moment of inertia is a function of displacement and it is calculated for different values of amortized object's mass. In case of various initial velocities of the impacting object, any additional action is not required because system response is independent from the impact velocity. Presented study is illustrated by numerical example revealing influence of the impacting object mass, as well as influence of the dry friction coefficient appearing at the ball-screw connection.

REFERENCES

- [1] Choi, S-B., Li, W., Yu, M., Du, H., Fu, J. and Do, P.X. State of the art of control schemes for smart systems featuring magneto-rheological materials. *Smart Mater. Struct.* (2016) **25**:043001.
- [2] Domenico, D.D., Ricciardi, G. Improving the dynamic performance of base-isolated structures via tuned mass damper and inerter devices: a comparative study. *Struct. Control Health Monitor.* (2018) **25**(10):2234.
- [3] Faraj, R., Graczykowski, C., Holnicki-Szulc, J. Adaptable pneumatic shock absorber. *J. Vib. Control* (2018) **25**(3):711–721.
- [4] Popławski, B., Mikułowski, G., Mróz, A. and Jankowski, Ł. Decentralized semi- active damping of free structural vibrations by means of structural nodes with an on/off ability to transmit moments. *Mech. Syst. Signal Pr.* (2018) **100**:926-939.
- [5] Pisarski, D. Decentralized stabilization of semi-active vibrating structures. *Mech. Syst. Signal Pr.* (2018) **100**(2018):694-705.
- [6] Smith, M. C. Synthesis of mechanical networks: the inerter. *IEEE Trans. Automat. Contr.* (2002) **47**:1648-1662.
- [7] Lazar, I. F., Neild, S. and Wagg, D. Using an inerter-based device for structural vibration suppression. *Earthq. Eng. Struct. D.* (2013) **43**:1129–1147.
- [8] Brzeski, P., Pavlovskaja, E., Kapitaniak, T. and Perlikowski, P. The application of inerter in tuned mass absorber. *Int. J. Nonlin. Mech.* (2015) **70**:20-29.
- [9] Faraj, R., Holnicki-Szulc, J., Knap, L. and Seńko J. Adaptive inertial shock-absorber. *Smart Mater. Struct.* (2016) **25**(3):035031.

- [10] Faraj, R., Jankowski, Ł., Graczykowski, C. and Holnicki-Szulc, J. Can the inerter be a successful shock-absorber? The case of a ball-screw inerter with a variable thread lead. *J. Franklin I.* (2019) <https://doi.org/10.1016/j.jfranklin.2019.04.012>.
- [11] Holnicki-Szulc, J. (Ed.) *Smart Technologies for Safety Engineering*. Willey (2008).
- [12] Faraj, R., Graczykowski, C. Hybrid Prediction Control for self-adaptive fluid-based shock-absorbers. *J. Sound Vib.* (2019) **449**:427-446.

ANALYSIS AND CONTROL OF DAMPED FLEXIBLE STRUCTURES

YORAM HALEVI

Faculty of Mechanical Engineering (CIMNE)
Technion – Israel Institute of Technology
Haifa 32000, Israel
e-mail: yoramh@technion.ac.il

Key words: Flexible Structures, Damping, Transfer Function, Control, Fractional Order.

Abstract. The paper considers the properties of damped flexible structures and dedicated methods of control. The main tool is an accurate, infinite dimension, transfer function (TF), from actuation to measurement. . In case of undamped systems, or systems with boundary damping, the TF consists of pure time delays and low order rational terms. The paper considers also two types of domain boundary and in those cases the TFs are fractional order in both the delays and the "rational parts". The time domain, e.g. delays and frequency domain, e.g. poles of the systems are investigated. Absolute vibration suppression (AVS) is a dedicated control method for flexible structures which is based on the TFs. The paper gives the resulting AVS controller for each case and discusses the differences between the cases.

1 INTRODUCTION

Spatially continuous flexible structures appear in diverse engineering applications, ranging from MEMS actuators and sensors on the small scale to cranes, air and space systems, robotic arms and even bridges and buildings on the large scale. The main advantage of flexible structures is their light weight. It should be kept in mind that flexible is a relative term, depending both on the excitation bandwidth and the accepted level of vibration. Higher performance (faster maneuvers, better accuracy) requires therefore acknowledging the flexibility in systems that could otherwise be considered as rigid.

The classical models of flexible structures are energy conservative, and this is the basic assumption of the comprehensive modal theory where the notions of natural frequencies and modeshapes are central to the analysis of the time domain behavior [1]. The same is true for the traveling wave approach [2]. However, in practice, the free vibration decays with time due to the presence of damping, both at the supports, and throughout the structure [3].

In a series of publications by the author, [4-8] a comprehensive modeling and control method for flexible structures was presented. The model for a system without domain damping is given in terms of infinite dimension transfer functions, consisting of delays and low order rational terms. Models that recognize domain damping include in their transfer functions elements that are not integer powers of "s" - the Laplace operator [7,8]. These elements represent fractional order differentiation and integration. It turns out that fractional calculus is known almost since the development of the integer order calculus (first credit is

assigned to Leibniz and L'Hospital, 1695). In recent years, fractional calculus has been applied to many fields of science, engineering and mathematics [9,10].

Feedback control has two important tasks in flexible structure design: adding "artificial rigidity" for tracking systems, and absorbing energy. A flexible, light weight, system with carefully designed controller can exhibit the same behavior as a rigid system with larger and heavier damping devices.

The paper uses the Absolute Vibration Suppression (AVS) controller [4,5,7] which belongs to the family of dedicated control approaches, e.g. [11, 12] that use the physical properties of flexible structures. In particular the control strategy can be related to the traveling wave approach [13]. This is in contrast with the approach of generic mathematical control laws that in theory can be applied to all dynamic systems, regardless of their physical origin. In mathematical terms the key point is the infinite dimension transfer functions. In previous publications these transfer functions, were used to design a dedicated control law with boundary actuation that stops the wave reflections, thus achieving absolute vibration suppression (AVS) in the system. Having fractional order models requires the extension of the AVS method and of standard dead time compensation algorithms to such cases.

2 THE MODEL

The case that is used in this proposal to demonstrate the modeling and control methodologies is the taut string shown in Fig. 1 where w is the traverse displacement and Ψ is the distributed load. Clearly the same model applies to a rod in tension or in torsion as well. It was also shown that it applies also each mode of a membrane after a modal decomposition in one dimension [7]. The damping shown in the figure is what we call external distributed domain, but in this paper we consider other configurations as well.

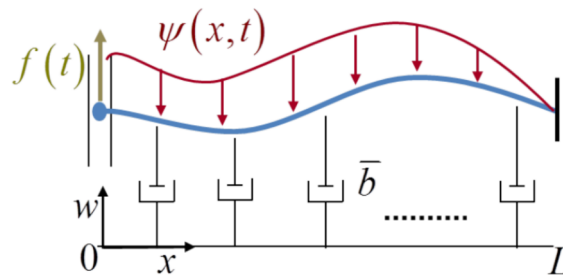


Figure 1: Model of a taut damped string.

The model that is used in the paper is as follows.

$$c^2 w_{xx}(x,t) - w_{tt}(x,t) + \mu \Psi(x,t) = \alpha w_t(x,t) + \beta w_{xt}(x,t) - \gamma c^2 w_{xxt}(x,t) \quad (1)$$

The left-hand side is the classical, undamped wave equation with $c=(T/\rho)^{1/2}$ where T is the tension and ρ is mass per unit length and $\mu=1/\rho$. The right hand side includes three times of (potentially) domain damping mechanisms. It can be shown obvious, based on energy considerations that such the mixed term $\beta w_{xt}(x,t)$ does not provide damping into the system (actually it represents a situation where the progressive and regressive waves have different speed). Therefore it will not be discussed in the sequel. The linear boundary conditions (BC)

consist of lumped inertia, spring and damper and an external point force (later on this will be identified as the control force) at each end.

$$\begin{aligned} -Tw_x(0,t) + (J_0 w_{tt}(0,t) + D_0 w_t(0,t) + K_0 w(0,t)) &= f_0(t) \\ Tw_x(L,t) + (J_L w_{tt}(L,t) + D_L w_t(L,t) + K_L w(L,t)) &= f_L(t) \end{aligned} \quad (2)$$

To show the essentials of the problem a simpler model is used in this paper. The disturbance is assumed to decompose into a product of spatial and time functions, i.e. $\Psi(x,t) = \psi(x)d(t)$. The BC, except for the case of boundary damping will be either free-free (Neumann BC) or free-fixed (mixed Neumann and Dirichlet BC).

2.1 The undamped wave equation with general boundary conditions

This case was treated in detail before in [4,6] and is given here in a concise manner as it forms the basis for the system with domain damping. To derive the transfer functions from the end force $f(t)$ and the domain load $d(t)$ we solve first an auxiliary problem where the only external excitation is a point force $p(t)$ acting at $x=\xi$.

$$c^2 w_{xx}(x,t) + \mu \delta(x-\xi) p(t) = w_{tt}(x,t) \quad (3)$$

Applying Laplace transform with respect to time to (3), assuming zero initial condition, as in the definition of a transfer function, gives

$$w_{xx}(x,s) = \left(\frac{s}{c}\right)^2 w(x,s) - \frac{\mu}{c^2} \delta(x-\xi) p(s) \quad (4)$$

This is an ODE in x and its general solution is

$$w(x,s) = -\frac{\mu p(s)}{4cs} \left(e^{\frac{s|x-x_0|}{c}} - e^{-\frac{s|x-x_0|}{c}} \right) + C_1(s) e^{\frac{sx}{c}} + C_2(s) e^{-\frac{sx}{c}} \quad (5)$$

Applying the (homogeneous!) boundary conditions (2) the coefficients $C_1(s)$, $C_2(s)$, which are linear in $p(s)$ are found. Rearranging, the transfer function from $p(s)$ to a displacement $w(x,s)$ is given by

$$G(x,\xi,s) = \frac{w(x,s)}{p(s)} = \frac{e^{-|\tau_x - \tau_\xi|s} + R_0(s)e^{-(\tau_x + \tau_\xi)s} + R_L(s)e^{-(2\tau - \tau_x - \tau_\xi)s} + R_0(s)R_L(s)e^{-(2\tau - |\tau_x - \tau_\xi|)s}}{2\phi s(1 - R_0(s)R_L(s)e^{-2\tau s})} \quad (6)$$

Where

$$\phi = c\rho, \quad \tau = L/c, \quad \tau_x = x/c, \quad \tau_\xi = \xi/c$$

And

$$R_i(s) = \frac{\phi s - (J_i s^2 + D_i s + K_i)}{\phi s + (J_i s^2 + D_i s + K_i)}, \quad i=0,L \quad (7)$$

Physically the exponents represent delays, resulting from the wave motion at velocity c . The transfer functions $R_i(s)$ can be thought of a dynamic reflection coefficients. It is easily

seen that for a free end $R_i = 1$, and for a fixed end, setting either one of the parameters to infinity, $R_i = -1$. By setting $\xi=0$ we obtain the transfer function from $f(s)$ and using (6) as a Green function the one from the load $d(t)$ is found. Hence

$$w(x, s) = G(x, 0, s)f(s) + G_d(x, s)d(s) \quad (8)$$

Where

$$G(x, 0, s) = \frac{(1 + R_0(s))(e^{-\tau_x s} + R_L(s)e^{-(2\tau - \tau_x)s})}{\phi s(1 - R_0(s)R_L(s)e^{-2\tau s})} \quad , \quad G_d(x, s) = \int_0^L G(x, \xi, s)\psi(\xi)d\xi \quad (9)$$

The transfer function leads to many observations regarding the system, as well as tools for analysis and design [4-8]. In this work we use the fact that the poles can be easily computed from

$$1 - R_0(s)R_L(s)e^{-2\tau s} = 0 \quad (10)$$

The pole at $s=0$ exists if there is a rigid body motion, otherwise it is cancelled out by a zero of the transfer function.

2.2 Boundary damping

This is a particular case of the general one in the previous sub-section. If the only element in the BC is a lumped damper, the reflection coefficients in this case become a constant

$$R_i(s) = \frac{\phi - D_i}{\phi + D_i} \quad , \quad i = 0, L \quad (11)$$

In terms of traveling waves that means that each time the wave hits the boundary it is reflected scaled by that value. Notice that R_i ranges between -1 (fixed) and +1 (free) and that in case the damper has the value ϕ then $R_i=0$, which means no reflection at all. This property, known as impedance matching is discussed in detail in [4,5] and is utilized in the design of the AVS controller.

The poles of the system are easily computed as

$$p_n = \begin{cases} \frac{1}{2\tau} \{ \ln(R_0 R_L) + 2n\pi i \} & R_0 R_L > 0 \\ \frac{1}{2\tau} \{ \ln(|R_0 R_L|) + (2n+1)\pi i \} & R_0 R_L < 0 \end{cases} \quad ; n = 0, \pm 1, \dots \quad (12)$$

They all share an identical real part and their imaginary parts are exactly the natural frequencies of a free-free or a fixed-free undamped system.

2.3 External domain damping

To concentrate of the effect of domain damping we assume in this sub-section that the BC, are either free-free (Neumann BC) or free-fixed (mixed Neumann and Dirichlet BC)

$$-Tw_x(0, t) = f(t) \quad , \quad Tw_x(L, t) = 0 \quad \text{or} \quad -Tw_x(0, t) = f(t) \quad , \quad w(L, t) = 0 \quad (13)$$

The three terms on the RHS of Eq. (1) have different effect and will be treated separately. We start with the “distributed skyhook damping” term $\alpha w_t(x,t)$. To derive the transfer functions in this case we set up an auxiliary problem similar to eq. (3).

$$c^2 w_{xx}(x,t) + \mu \delta(x-\xi) p(t) = w_{tt}(x,t) + \alpha w_t(x,t) \quad (14)$$

Applying Laplace transform gives

$$w_{xx}(x,s) = \left(\frac{\lambda(s)}{c} \right)^2 w(x,s) - \mu \delta(x-\xi) p(s) \quad (15)$$

Where

$$\lambda(s) = \sqrt{s^2 + bs} \quad (16)$$

The general solution of this ODE is

$$w(x,s) = -\frac{\mu p(s)}{4c\lambda(s)} \left(e^{\frac{\lambda(s)|x-x_0|}{c}} - e^{-\frac{\lambda(s)|x-x_0|}{c}} \right) + C_1(s) e^{\frac{\lambda(s)x}{c}} + C_2(s) e^{-\frac{\lambda(s)x}{c}} \quad (17)$$

Since the BC that are used in this sub-section do not include any expression containing explicitly the Laplace variable s , the situation is similar to the case with no domain damping with $\lambda(s)$ replacing ‘ s ’ everywhere.

$$G(x,\xi,s) = \frac{w(x,s)}{p(s)} = \frac{e^{-|\tau_x - \tau_\xi| \lambda(s)} + R_0 e^{-(\tau_x + \tau_\xi) \lambda(s)} + R_L e^{-(2\tau - \tau_x - \tau_\xi) \lambda(s)} + R_0(s) R_L(s) e^{-(2\tau - |\tau_x - \tau_\xi|) \lambda(s)}}{2\phi \lambda(s) (1 - R_0 R_L e^{-2\tau \lambda(s)})} \quad (18)$$

Where

$$\phi = 1/c\mu, \quad \tau = L/c, \quad \tau_x = x/c, \quad \tau_\xi = \xi/c, \quad R_0 = 1, \quad R_L = \pm 1$$

The transfer function from $f(s)$ is given now as (G_d is given by the same integral)

$$G(x,0,s) = \frac{e^{-\tau_x \lambda(s)} + R_L e^{-(2\tau - \tau_x) \lambda(s)}}{\phi \lambda(s) (1 - R_L e^{-2\tau \lambda(s)})} \quad (19)$$

In the undamped case $\lambda(s) = s$, the exponents become pure time delays, and the transfer function coincides with that given in Eq. (7). Most of the components, such as the time constants τ , τ_x and τ_ξ , the impedance ϕ , the reflection coefficients R_0 and R_L and the wave propagation velocity c are independent of the damping α . The components of $G(x,\xi,s)$ that depend on α are the exponents. For $\alpha > 0$ they become nonlinear in s , and the system is of fractional order. Since the exponents are no longer pure delays, they not only shift the input but also distort it.

The denominator roots of $G(x,0,s)$ are the roots of $\lambda(s)$, which are $s = 0$ and $s = -\alpha$, and those of

$$1 - R_0 R_L e^{-2\tau \lambda(s)} = 0 \quad (20)$$

In the free-fixed case the limit of $G(x,0,s)$ at the roots of $\lambda(s)$ is finite, hence $s = 0$ and $-\alpha$ are not open loop poles. In other words, they are cancelled by zeros in the numerator. The poles of $G(x,0,s)$ are therefore given by

$$p_m = \begin{cases} -\frac{1}{2}\alpha \pm j\frac{1}{2}\sqrt{\left(\frac{(2m+1)\pi}{\tau}\right)^2 - \alpha^2} & \text{free - fixed} \\ -\frac{1}{2}\alpha \pm j\frac{1}{2}\sqrt{\left(\frac{2m\pi}{\tau}\right)^2 - \alpha^2} & \text{free - free} \end{cases}, \quad m=0,1,\dots \quad (21)$$

In the free-free case $m=0$ yields two real poles, $p_{01}=0$ and $p_{02}=-\alpha$. All open loop poles of $G(x,0,s)$, except for the pole at the origin (rigid body dof), have a negative real part and are thus located in the open left half plane (OLHP). Most of the poles are complex valued with the same real part. In both settings, as m becomes larger (or for small α) the distance between the imaginary parts approaches π/τ , as for undamped systems. Comparing the real parts, which dictate the convergence rate, we have for a free-free configuration with one relatively small damper on the far side

$$-\frac{1}{2}\alpha = \frac{1}{2\tau} \ln(R_L) = \frac{1}{2\tau} \ln\left(\frac{\phi - D_{eq}}{\phi + D_{eq}}\right) \quad (22)$$

Which gives

$$\frac{D_{eq}}{\phi} = \frac{1 - e^{-\alpha\tau}}{1 + e^{-\alpha\tau}} \quad (23)$$

And for small damping

$$D_{eq} \cong \phi\alpha\tau \quad (24)$$

At high frequencies, where the influence of the damping on the imaginary part becomes negligible, the poles' matching is complete.

2.3 Internal domain damping

We consider now the internal damping (the term 'structural damping' is usually reserved to yet another model) term $\gamma c^2 w_{xx}(x,t)$. To derive the transfer functions in this case we set up an auxiliary problem similar to Eq. (14).

$$c^2 w_{xx}(x,t) + \mu\delta(x-\xi)p(t) = w_{tt}(x,t) - \gamma c^2 w_{xx}(x,t) \quad (25)$$

Applying Laplace transform gives

$$w_{xx}(x,s) = \left(\frac{\sigma(s)}{c}\right)^2 w(x,s) - \mu\delta(x-\xi)p(s) \quad (26)$$

Where

$$\sigma(s) = \frac{s}{\sqrt{1 + \gamma s}} \quad (27)$$

Though the physical nature and the resulting properties are very different than the internal case the derivation is the same with $\sigma(s)$ replacing $\lambda(s)$.

$$G(x,0,s) = \frac{e^{-\tau_x \sigma(s)} + R_L e^{-(2\tau - \tau_x)\sigma(s)}}{\phi \sigma(s) (1 - R_L e^{-2\tau \sigma(s)})} \quad (28)$$

While we kept the format identical with the previous case, due to the nature of $\sigma(s)$ the time constants τ , τ_x and τ_ξ , are no longer proportional to the delay, as will be shown in section 3. The first indication comes from the poles. The denominator roots of $G(x,0,s)$ are the root of $\sigma(s)$, which is $s = 0$ (same situation regarding free or fixed) and those of

$$1 - R_0 R_L e^{-2\tau \sigma(s)} = 0 \quad (29)$$

Straightforward calculation gives the poles for a free-free as

$$p_m = -\frac{m^2 \pi^2 \gamma}{2\tau^2} \pm \sqrt{\left(\frac{m^2 \pi^2 \gamma}{2\tau^2}\right)^2 - \frac{m^2 \pi^2}{\tau^2}} \quad , \quad m = 0, 1, \dots \quad (30)$$

For fixed-free m is replaced by $(m+1/2)$. Here too all open loop poles of $G(x,0,s)$, except for the pole at the origin (rigid body dof), are in the OLHP. However the situation is different from the previous cases. First, the system may have a finite number of complex poles at low frequencies (may not have them at all for a large enough γ) but from a certain index m on all the poles are real with one branch approaching $-\infty$ proportional to m^2 while the other approaches zero proportional to m^{-1} . Contrary to external domain damping, similarity to lumped damping is only at low frequencies but even then the real part is not constant.

3 RESPONSE PROPERTIES AND ANALYSIS

To illustrate the wave motion which is closely related to the structure of the transfer function we consider first a system which is free at the actuating side and has a lumped damper at the other. By long division the transfer function can be written as the infinite series

$$G(x,0,s) = \frac{1}{\phi s} \left\{ e^{-\tau_x s} + R_L e^{-(2\tau - \tau_x)s} + R_L e^{-(2\tau + \tau_x)s} + R_L^2 e^{-(4\tau - \tau_x)s} + \dots \right\} \quad (31)$$

Since $|R_L| < 1$, the series consists of repeated scaled down versions of the fundamental function which is the integral of the force. If the input is finite, with duration $T < 2(\tau - \tau_x)$ the waves do not coincide at point x and each wave can be seen clearly as in Fig. 2. Apart from timing, the response is identical at all points along the domain.

One can perform the same expansion for a system with external domain damping.

$$G(x,0,s) = \frac{1}{\phi \lambda(s)} \left\{ e^{-\tau_x \lambda(s)} + R_L e^{-(2\tau - \tau_x)\lambda(s)} + R_L e^{-(2\tau + \tau_x)s} + R_L^2 e^{-(2\tau - \tau_x)\lambda(s)} + \dots \right\} \quad (32)$$

Where R_L now is either 1 or -1. The question is whether the situation is the same, in other words is there a constant wave speed c and therefore real delays. except for the different. The inverse Laplace transform of each expression, with a general ‘delay’ θ is given by [14]

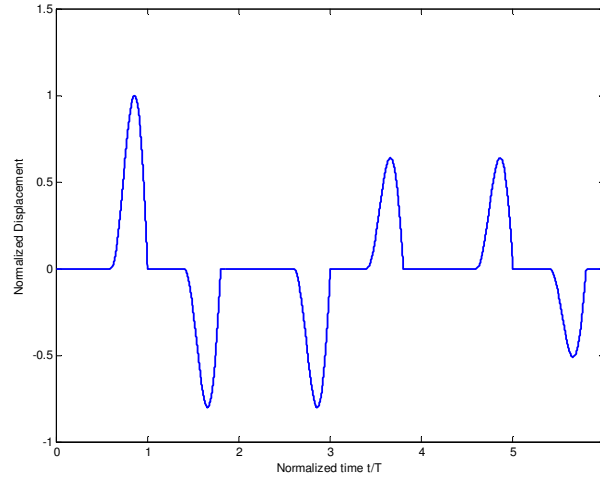


Figure 2: Response at $x=0.6L$ to finite duration force at $x=0$.

$$v(\theta, t) = L^{-1} \left\{ \frac{1}{\sqrt{s^2 + \alpha s}} e^{-\theta \sqrt{s^2 + \alpha s}} \right\} = e^{-\frac{1}{2}\alpha t} I_0 \left(\frac{1}{2} \alpha \sqrt{t^2 - \theta^2} \right) U(t - \theta) \quad (33)$$

U is the Heaviside function and it indicates that the response in (33) is indeed delayed by θ . I_0 is the zero order modified Bessel function of the first kind. $I_0(0) = 1$, which means that for $\alpha = 0$, the term reduces to pure delay. Detailed analysis leads to the conclusion that for $t \gg \theta$, $v(\theta, t) \approx 1 / \sqrt{\pi \alpha t}$. This means that each term is decaying at a rate inversely proportional to the square root of time. Figure 3 shows the wave reflection process through the velocity response of fixed end. For $\alpha = 0$ the input is simply shifted, but for $\alpha > 0$ it undergoes a distortion as well. The response is shown at four time instants, $t/\tau = 0.2, 0.7, 1.2$ and 1.7 . In the last two the response is after reflection from the fixed end and is therefore flipped.

Seemingly exactly the same procedure can be applied to a system with internal damping, with $\sigma(s)$ instead of $\lambda(s)$. While we do not present an explicit inverse Laplace transform in that case, simulations show that the wave phenomenon is practically destroyed with different parts of the input moving at different speed according to their frequency content.

4 ABSOLUTE VIBRATION SUPPRESSION (AVS) CONTROL

The AVS control law [4,7] is a dedicated control methodology for control of flexible structures. It is a collocated rate feedback at $x=0$ with a concentrated force actuation.

$$f(s) = Mr(s) - H(s)w(0; s) \quad (34)$$

The collocation is essential since non-collocated controllers destabilize the system (move the poles into the RHP) [4]. The actuation at an end enables the main feature of the AVS which is the elimination of a block with infinite number of poles, to be shown below. The controller transfer function is given by

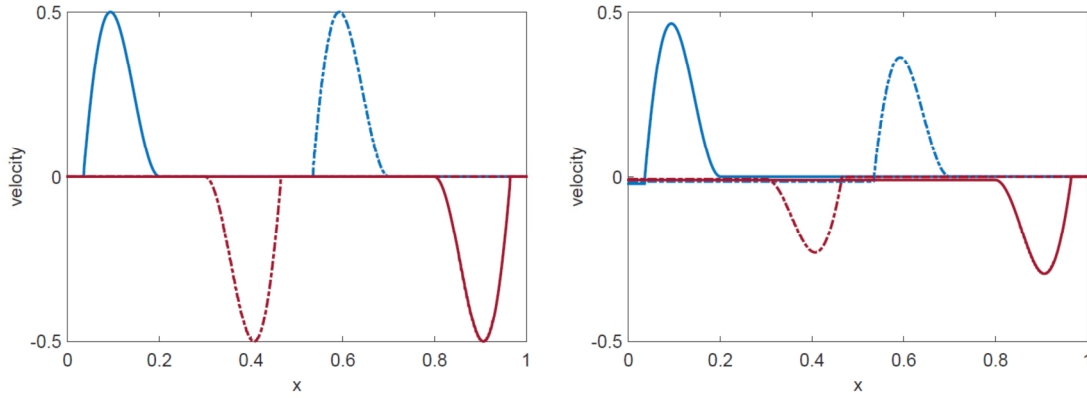


Figure 3: Wave motion in a free-fixed string with (left) and without (right) external domain damping.

$$H(s) = \begin{cases} \phi s & \text{Boundary damping} \\ \phi \lambda(s) & \text{External domain damping} \\ \phi \sigma(s) & \text{Internal domain damping} \end{cases} \quad (35)$$

The closed loop transfer function is then

$$\frac{w(x;s)}{r(s)} = \frac{MG(x;s)}{1 + H(s)G(0;s)} = \frac{M}{2\phi A(s)} \left(e^{-\tau_x A(s)} + R_L e^{-(2\tau - \tau_x)A(s)} \right) \quad (36)$$

$A(s)$ stands for s , $\lambda(s)$ or $\sigma(s)$ according to the case. Hence with the special form of $H(s)$, the AVS controller eliminates all the exponents (delays in the undamped case) from the characteristic equation and the closed loop system. Physically that means that there are no reflections from the left end. M is a scaling factor to guarantee unity gain. The physical interpretation of the action of the AVS controller is impedance matching. It creates, by means of the feedback, an equivalent BC that is identical with the impedance of the domain. Since there is no discontinuity the wave is not reflected and the actuating end becomes a sink.

While the derivation here focused on tracking, i.e. following a reference signal $r(t)$, it can be shown that the controller suppresses, in a similar way, the response to non-steady disturbances and non-zero initial conditions. An example is given in Fig. 4 which depicts the closed versus the open loop responses to a disturbance of finite time duration, for various values of external domain damping. The vibration is absolutely suppressed in closed loop, where for $\alpha = 0$ it happens in finite time.

The controller (35) can be looked at as a rate feedback and that solves the issue of properness. With boundary damping it reduces into a constant rate feedback with a very specific gain. The controller in the two other cases is non-rational which poses theoretical and practical difficulties. Table 1 gives the properties of the normalized rate controllers $\tilde{H}(s) = H(s)/\phi s$ and Figure 5 shows their bode plots. Practically, the controllers should be approximated by a rational transfer function.

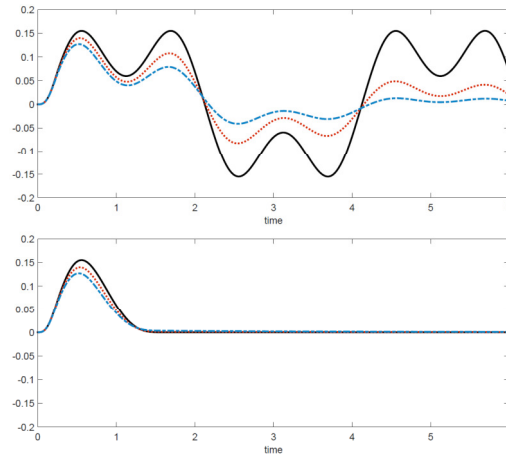


Figure 4: Open (top) and closed (bottom) loop responses to disturbance.

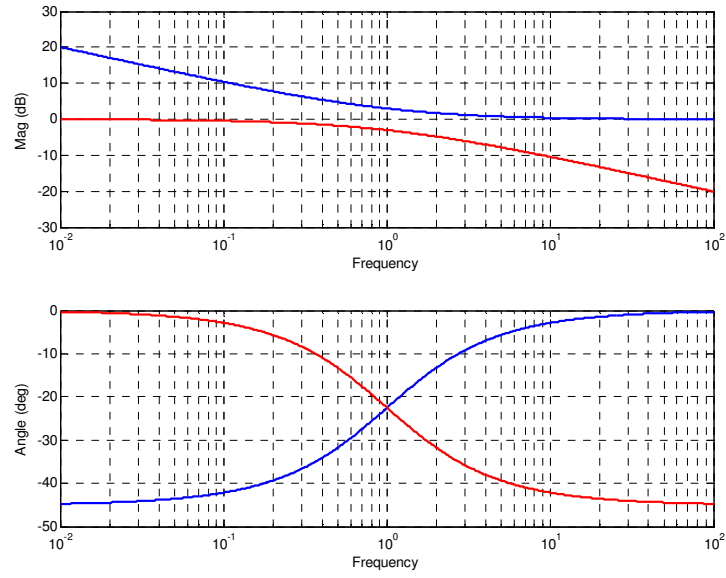


Figure 5: Bode plot of $\tilde{H}(s)$ for systems with external (blue) and internal (red) domain

Table 1: Example of the construction of one table

	TF	Magnitude		Angle		Approximation	
		$\omega \rightarrow 0$	$\omega \rightarrow \infty$	$\omega \rightarrow 0$	$\omega \rightarrow \infty$	Low freq.	High freq.
$\tilde{H}(s)$	1	1	1	0	0	1	1
$\tilde{H}_\lambda(s)$	$(1 + \frac{\alpha}{s})^{1/2}$	∞	1	-45	0	$\phi \alpha^{1/2} s^{-1/2}$	$1 + \frac{1}{2} \alpha s^{-1}$
$\tilde{H}_\sigma(s)$	$(1 + \gamma s)^{-1/2}$	1	0	0	-45	$(1 + \frac{1}{2} \gamma s)^{-1}$	$\gamma^{-1/2} s^{-1/2}$

5 CONCLUSIONS

The paper considered the problems of modeling and control of systems with damping. Three configurations were investigated, boundary damping and two mechanisms of domain damping. It was shown that for boundary damping the model is a transfer function that despite being infinite dimension is easy to implement and use since it involves only pure time delays and low order rational terms that act like reflection coefficients. In domain damping those elements become fractional order with irrational terms for both the delays and the coefficient. It is shown that with external domain damping the response and properties are somewhat similar to boundary damping. Internal domain damping on the other hand results in fundamentally different response. The absolute vibration suppression (AVS) controller, which is closely related to the model transfer function is affected by the damping in a similar manner. It is a constant rate feedback for boundary damping but assumes non-standard fractional order forms in the cases of domain damping.

REFERENCES

- [1] Inman, D.J., *Engineering Vibration*, Prentice – Hall, (1994).
- [2] Graff, K.F., *Wave Motion in Elastic Solids*, Clarendon Press, Oxford, (1975).
- [3] Fahroo, F., Optimizing the decay rate in the damped wave equation: a numerical study, *American Control Conference*, Denver, CO, (2003).
- [4] Halevi, Y., Control of flexible structures governed by the wave equation using infinite dimensional transfer functions”, *ASME Journal of Dynamic Systems, Measurement, and Control*, (2005) **127**: 579-588.
- [5] Peled, I., O'Connor, W., and Halevi, Y., On the relationship between wave based control, absolute vibration suppression and input shaping, *Mechanical Systems and Signal Processing*, (2013) **39**(1): 80–90.
- [6] Sirota, L. and Halevi, Y., The complete infinite series and traveling wave solution of systems governed by the second order wave equation with boundary damping, *Wave Motion*, (2014) **51**(1):114-214,.
- [7] Sirota, L. and Halevi, Y., Fractional order control of the two-dimensional wave equation, *Automatica*, (2015) **59**:152–163.
- [8] Sirota, L., Halevi, Y. and Krstic M., On the relationship between the absolute vibration suppression and back-stepping methods in control of the wave equation with possibly unstable boundary conditions, *American Control Conference*, Boston, MA ,(2016).
- [9] Podlubny, I., Fractional-order systems and $PI^{\lambda}D^{\mu}$ -controllers, *IEEE Transactions on Automatic Control*, (1999) **44**(1):208-21.
- [10] Kilbas, A.A., Srivastava, H.M. and Trujillo, J.J., *Theory and Applications of Fractional Differential Equations*, North-Holland Mathematical Studies, Vol. 204 (2006).
- [11] Balas, M.J., Direct velocity feedback control of large space structures, *J. of Guidance and Control*, (1979) **2**: 252-253.
- [12] Pao, L.Y. and Singhose, W.E., Robust minimum time control of flexible structures, *Automatica*, (1998) **34**: 229-236.
- [13] O'Connor, W.J., Wave-based analysis and control of lump-modeled flexible robots, *IEEE Transactions on Robotics*, (2007) **23**(2): 342-352.
- [14] Kreyszig, E., *Advanced engineering mathematics*, John Wiley & Sons, (2010).

BENDING WAVES FOCUSING IN ARBITRARY SHAPED PLATE-LIKE STRUCTURES: APPLICATION TO SPATIAL AUDIO

N. BENBARA*, M. REBILLAT* AND N. MECHBAL*

*Processes and Engineering in Mechanics and Materials laboratory (PIMM)

ENSAM, CNRS, CNAM, HESAM Université

151 Boulevard de l'Hôpital, 75013 Paris, France

e-mail: nassim.benbara@ensam.eu,

Key words: Spatial vibration Control, Piezoelectric actuators, Bending wave focusing, Multifunctional Materials, Advanced signal processing

Abstract. Advanced audio applications are more and more demanding with respect to the visual impact of loudspeakers while still requiring more channels for high quality spatial sound rendering. The use of arbitrary plate-like structures driven by electromagnetic actuators or by piezoelectric elements appears as a promising solution to tackle both issues. However, to meet spatial rendering audio constraints (omnidirectional piston-like sources), the generated bending waves must be focused to a certain extent within the host plate. Theoretically, this means being able to invert the spatio-temporal wave propagation operator for the generated bending waves to fit a given target shape. Several methods are here investigated to perform this task depending on the available knowledge of wave propagation in the plate (theoretical, partial spatial and full spatial knowledge) and using several projection bases (modal basis and eigenvalue basis). The various methods are presented in a unified theoretical framework and their performances are compared by means of two key performance indexes (focus localization error and spatial contrast).

1 INTRODUCTION

In the past decades, several studies were performed on the sound restitution using an array of loudspeakers. The main idea is to calibrate each loudspeaker of the array to reproduce with high fidelity the physics and the acoustics of the primary source [1]. Historically, spatial rendering methods such as stereophony (VBAP), binaural rendering or holophony (ambisonic or Wave Field Synthesis (WFS)) are used with electromagnetic loudspeakers. There are many constraints imposed by such methods for them to work properly: a flat and omnidirectional response for the speaker, and several piston-like actuators to avoid spatial aliasing and to cover the whole restitution area [2]. Distributed Mode Loudspeakers (DML) were introduced as a new kind of loudspeaker with a low visual profile [3]. The idea is to produce sound waves by exciting the bending waves of a thin stiff plate through an actuator. This technology was used to render spatial sound by the WFS Method [4, 5]. However, this technology suffers from some drawbacks because of the aliasing caused by joint panels and the modal behaviour at low frequency of the plate which causes distortions of the signal and does not meet spatial audio requirements. Therefore, a new technology using larger plates called MultiActuator Panels (MAP) or much larger called Large MultiActuator Panels (LaMAP) has been designed to overcome these limitations. The main idea is to excite the plate with several actuators driven by different signals to reproduce different sound sources [6].

This technology was successfully used in the context of the wave field synthesis to render spatial sound [7, 8, 9]. However, some drawbacks such as the modal behavior at low frequencies and the interferences between sources causing sound distortions and poor sound quality still exists with this technology.

Particularly in the automotive industry, using spatial sound rendering coupled with flat panel loudspeaker will be very interesting. Indeed, it will allow to alert the users from several dangers and provide high quality spatial sound. Moreover, this approach will decrease weight by replacing electrodynamical loudspeakers with piezoelectric actuators and improve design purposes and visual impact. However, the reconstitution zone is small, with a very limited number of canals and with very complex operational conditions. Considering the previous observations, the focusing of the bending waves on arbitrary plate-like interior parts of the car to create independent sound source appears as the best way to create an array for spatial sound rendering.

In the literature, there are various methods that allow to focus bending waves in a media. The first method called modal control (MC) is based on modal superposition [10]. Indeed, it allows to focus a monochromatic vibro-tactile peak on plates [11, 12], or an audio source on a rectangular plate by computing FIR filters of order 3 [13]. The method is based on a simple approach and is sensitive to modeling error. The second method available in the literature is based on the time reversal (TR) principle, initially described by Fink et al. in [14]. It allows to focus a wave at a specific point in the space by learning partially the waves received at the actuators positions and initiated at the focusing point. Besides, the same author shows that this method can be adapted for acoustic purposes to control precisely acoustic wave propagation in reverberating cavities or in waveguides [15]. Additionally, this method is also used in [16] to focus an audio impulse in a room. Finally, the ease of implementation of the time reversal encouraged many researchers to use it in haptic feedback applications [17]. The third method studied in this paper is the spatio-temporal inverse filtering (STIF), initially studied by [18] and [19] to find a solution to the lack of robustness of the time reversal method. Firstly, the method consists in learning the propagation of the waves in the whole media, then, an inverse filter is created and used as input for each actuator. Then, the method was extended to the time domain [20], and after experimentally applied in heterogeneous, absorbing and highly reverberating medias such as a human skull [21], or to focus acoustic waves in rooms [22]. Finally, another method based on the learning of the large band dynamic behavior of the structure, using the maximization of the contrast between the radiating zone and the whole media. It was initiated for room acoustics in [23], and applied on a plate structure in [24].

The objective of this study is to propose an approach enabling for the localization of bending waves in a defined area of a geometrically complex structure and with arbitrary boundary conditions to make it vibrate as a piston. First of all, this approach should be precise in terms of spatial focusing. Moreover, this method must operate in a wide frequency range and be suitable for the audio restitution. Besides, the method used should also be insensitive to noise and model error. Finally, the method should not rely on too much experimental measurements for practical reasons as the automotive is targeted as the applicative field. Several methods inspired by the previous analysis will be investigated in this study and adapted to perform the focusing task in the audio context. These methods will be presented in a unified formalism and compared numerically to highlight advantages and drawbacks of each method.

2 PROBLEM STATEMENT

Let S denote a plate-like structure of arbitrary shape and with arbitrary boundary conditions. Assuming that this structure lies in the (x, y) plane, the positions of the N piezoelectric actuators bonded on S are given by $\{(x_n, y_n)\}_{n \in [1, N]}$ and the out-of-plane displacement of the bending wave velocity field is denoted $u(x, y, t)$.

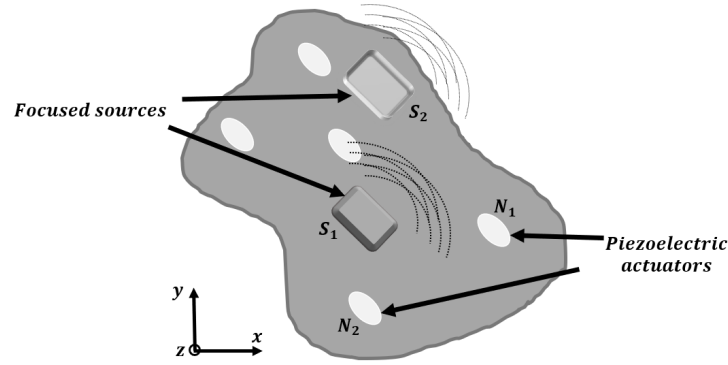


Figure 1: Arbitrary shaped-like structure with piezoelectric actuators and localized audio sources

The objective is now, for any input audio signal $a(t)$, to focus the bending wave field $u(x, y, t)$ to fit a given target shape $\phi(x, y)$ using the N actuators through N FIR filters $r_n(t)$ applied to the audio input. Mathematically, this means that we would like to achieve:

$$\forall t \ u(x, y, t) = \phi(x, y) a(t) \quad (1)$$

Or equivalently in the frequency domain, with $U(x, y, f)$ and $A(f)$ the Fourier transforms of the displacement and the audio signal respectively:

$$\forall f \ U(x, y, f) = \phi(x, y) A(f). \quad (2)$$

Assuming the system is globally linear, the contributions $u_n(x, y, t)$ of all the N actuators generating the field $u(x, y, t)$ sum up and can be written as:

$$\forall t \ u(x, y, t) = \sum_{n=1}^N u_n(x, y, t) = \sum_{n=1}^N h_n(x, y, t) * r_n(t) * a(t), \quad (3)$$

where “ $*$ ” stands for the convolution product and $h_n(x, y, t)$ is the spatiotemporal impulse response of the n^{th} actuator. Or equivalently in the frequency domain:

$$\forall f \ U(x, y, f) = \sum_{n=1}^N U_n(x, y, f) = \sum_{n=1}^N H_n(x, y, f) R_n(f) A(f). \quad (4)$$

By combining both expressions (2) and (4) of $U(x, y, f)$, the objective to achieve is then expressed in the frequency domain and independent of the audio input signal $a(t)$ as:

Find $\{R_n(f)\}_{n \in [1, N]}$ such that $\forall f, \phi(x, y) = \sum_{n=1}^N H_n(x, y, f) R_n(f)$.

(5)

This means that the spatiotemporal propagation operators $H_n(x, y, f)$ associated with the N actuators needs to be inverted to design the N FIR filters $R_n(f)$ able to focus the bending wave field on the target shape $\phi(x, y)$ whatever the frequency f .

3 BENDING WAVES FOCUSING METHODS UNIFIED THEORETICAL DESCRIPTION

In this section, several methods able to invert the spatiotemporal propagation operators $H_n(x, y, f)$ are presented. The methods differ depending on the available knowledge of wave propagation in the plate they rely on (theoretical, partial spatial and full spatial knowledge) and on the projection basis they use (modal basis and eigenvalue basis). They are all presented within a unified theoretical framework for comparison purpose.

3.1 Methods relying on a theoretical knowledge of $H_n(x, y, f)$

The first class of methods presented here assumes that a theoretical knowledge of wave propagation within the host structure is known. For bending wave, the out-of-plane displacement $u(x, y, t)$ of the host structure subject to the external point load $p(x, y, t)$ can be expressed as [33]:

$$D\nabla^4 u(x, y, t) + \rho h \ddot{u}(x, y, t) + c \dot{u}(x, y, t) = p(x, y, t) \quad \text{with} \quad D = \frac{Eh^3}{12(1-\nu^2)}. \quad (6)$$

In the above equations, E , ν , and ρ are the Young's modulus, Poisson's ratio, and density of the panel respectively. Additionally, c is the damping constant and h is the panel thickness.

Let $\theta_m(x, y)$ be the theoretical orthogonal modes associated with the structure under study which can be computed analytically or through FEM models. The displacement can be written as a decomposition in the mode shape basis:

$$u(x, y, t) = \sum_{m=1}^{\infty} u_m(t) \theta_m(x, y), \quad (7)$$

where the coefficients $u_m(t)$ denote the modal amplitudes. By reinjecting the displacement expression (7) in the movement equation (6), and by projecting the obtained equation on the M first modes, the orthogonality property allows to get the decoupled equation for each modal displacement $u_m(t)$:

$$\forall m \in [1, M], \quad \ddot{u}_m(t) + c \dot{u}_m(t) + (2\pi f_m)^2 u_m(t) = \frac{1}{S_m} p_m(x, y, t) \quad \text{with} \quad f_m = \frac{1}{2\pi} \sqrt{\frac{D}{\rho h}} k_m^2 \quad (8)$$

In the above equation, f_m is the eigen frequency corresponding to the m^{th} mode and k_m^2 the wave number depending on the geometry. Additionally, S_m is the projection term and $p_m(x, y, t)$ the modal force given by:

$$S_m = \iint_S \rho h \theta_m(x, y)^2 dx dy \quad \text{and} \quad p_m(x, y, t) = \iint_S p(x, y, t) \theta_m(x, y) dx dy. \quad (9)$$

We can then write in the frequency domain, and at the n^{th} actuator:

$$\forall m \in [1, M], \forall f, \quad U_{n,m}(f) = \frac{1}{S_m((2\pi f_m)^2 + (i2\pi f)c + (i2\pi f)^2)} P_{n,m}(x, y, f). \quad (10)$$

In case of piezoelectric actuation (where the area is denoted S_{PZT}), the modal force is given by :

$$P_{n,m}(x, y, f) = \left[\iint_{S_{PZT}} b_n(x, y) \theta_m(x, y) dx dy \right] R_n(f) A(f) = B_n R_n(f) A(f), \quad (11)$$

where $b_n(x, y)$ is a shape function characterizing the spatial distribution of each actuator.

Finally, by summing over all modes and actuators, one obtains:

$$\forall f, \quad U(x, y, f) = \sum_{n=1}^N \left[\sum_{m=1}^M \frac{B_n \theta_m(x, y)}{S_m((2\pi f_m)^2 + (i2\pi f)c + (i2\pi f)^2)} \right] R_n(f) A(f) = \sum_{n=1}^N H_n(x, y, f) R_n(f) A(f) \quad (12)$$

This constitutes a theoretical expression of the spatiotemporal bending wave propagation operator $H_n(x, y)$ that needs to be inverted.

Now, by decomposing the target $\phi(x, y)$ on the host structure mode shapes $\theta_m(x, y)$ as:

$$\phi(x, y) = \sum_m^M \phi_m \theta_m(x, y) \quad \text{with} \quad \phi_m = \iint_S \phi(x, y) \theta_m(x, y) dx dy. \quad (13)$$

We can write the following equation after projecting on each mode ϕ_m :

$$\forall f, \forall m \quad \phi_m = \sum_n^N \left[\frac{\iint_S B_n(x, y) \theta_m(x, y) dx dy}{S_m((2\pi f_m)^2 + (i2\pi f)c + (i2\pi f)^2)} \right] R_n(f). \quad (14)$$

with the number of modes M chosen equal to the number of actuators or superior (potential matrix conditioning problem during the inversion). Moreover, it can be shown [13] that such equation can be easily inverted and expressed in the discrete-time domain as follows:

$$R_n(z) = J_n + K_n z^{-1} + L_n z^{-2}. \quad (15)$$

Where J_n , K_n and L_n can be expressed using the modal parameters $(k_m, \theta_m(x_n, y_n))$ as well as the target shape parameters ϕ_m .

The method described above offers the advantage of not needing any prior experiments. Indeed, only the analytical knowledge of the model is needed. In addition, the computation cost is low because the FIR filter order is 3 and the method is not sensitive to noise, because no prior measures are done. Finally, the method allows to reproduce arbitrary target shapes. However, the advantages listed before are available only for very simple structures. Indeed, only simple structures as rectangular or circular plates with boundary conditions known analytically can be used. Additionally, for an audio purpose the frequency bandwidth is in general large and the number of modes to be addressed might be high. However, the theory assumes that the number of modes controlled is equal to or a bit higher than the number of actuators so that the matrix can be inverted, or pseudo-inverted and matrix conditioning issues can be avoided, but it will not be the case practically.

3.2 Methods relying on a partial spatial knowledge of $H_n(x, y, f)$

Let us now assume that a partial spatial knowledge of the propagation operator is available. More precisely, it is assumed here that the spatiotemporal operator is known for an excitation located at one spatial position (x_i, y_i) and measurements performed at actuator positions $\{(x_n, y_n)\}_{n \in [1, N]}$. Mathematically, what is known in the frequency domain is $\{\hat{H}(x_n, y_n, f)\}_{n \in [1: N]}$ such that:

$$\forall n \in [1, N] \quad \hat{H}(x_n, y_n, f) = \text{conj}[H_n(x_k, y_k, f)], \quad (16)$$

according to the spatial reciprocity principle [15]. Thus, by choosing:

$$R_n(f) = \text{conj}[\hat{H}(x_n, y_n, f)]. \quad (17)$$

One should be able to focus the bending waves in the neighborhood of the location (x_i, y_i) . Using previous notation, this means that the target shape to be reconstructed corresponds here to a Dirac function located at (x_i, y_i) , *i.e.*, $\phi(x, y) = \delta(x - x_i, y - y_i)$.

According to the theory, this method is based on the time invariance principle of partial derivative equations in a non-dispersive media. Moreover, this method is also based on the principle of spatial reciprocity of frequency response functions. Indeed, if a structure is excited at a point A and the wave measured at the point B, therefore the excitation at B and measurement at A gives the same response function. Those two invariances ensure the filter robustness. However, this method maximizes the amplitude at a point in the space, but it does not act on secondary lobes which are in general emphasized. One must extend the method to a wider target shape because for the moment there is no control of the width. Finally, the computation cost must be discussed. Theoretically, impulse responses must be measured between each focus point and actuator. Although it could cost many storage capacities. If the position of the focus area location is known, the number of initial measurements will be very low. The method may also be sensitive to the experimental noise.

3.3 Methods relying on a complete spatial knowledge of $H_n(x, y, f)$

Let us now assume that a complete spatial knowledge of the propagation operator is available. More precisely, it is assumed here that the spatiotemporal operator is known for any actuator $n \in [1, N]$ and that measurements are performed over a complete grid of K points on the structure for positions $\{(x_k, y_k)\}_{k \in [1, K]}$. Mathematically, what is known in the frequency domain is $\{H_n(x_k, y_k, f)\}_{n \in [1, N], k \in [1, K]}$.

The problem to be solved can then be rewritten on the measurement spatial grid as:

$$\phi(x_k, y_k) = \sum_{n=1}^N H_n(x_k, y_k, f) R_n(f). \quad (18)$$

Thus, in the matrix form:

$$\Phi = H(f)R(f). \quad (19)$$

The resulting matrix can first be directly pseudo-inversed in the frequency range of interest by keeping only large enough eigenvalues. This leads directly to the FIR filters $R_n(f)$:

$$R(f) = H(f)^+ \Phi, \quad (20)$$

where “+” denotes the pseudo-inversion operator.

It is important to note that the pseudo-inversion step is sensitive to noise. Hence, during the pseudo-inversion step, the lowest singular values are canceled to deal with those matrix conditioning issues. More details are available in [21].

This method offers several advantages in comparison with the others evoked previously. Firstly, the method is robust because it allows to acquire information about the wave propagation in the whole media. Additionally, the filters size is chosen by the user. Hence, the model takes into account the real structure and its complexity, with eventual losses, and the notion of modal density is not crucial. Finally, this method is very interesting for its ease of implementation. Nevertheless, the points evoked above are also sources of drawbacks. Indeed, it is necessary to realize several experiments between all the points of the structure and the actuators, this complicates numerically the method. Moreover, the model is sensitive to the noise, mainly during the pseudo-inversion step. Thus, it will need a regularization step which is numerically heavy.

4 NUMERICAL STUDY OF THE INVESTIGATED FOCUSING METHODS

4.1 Structures under study

In order to test the previous methods and to compare their performances, a simple and a ribbed clamped polypropylene plate are chosen, a material often used for car passenger garnishments. The dimensions of the plate are given in Figure 2a. Besides, ribs which length of 1 cm and thickness of 3 mm are added to approach as much as possible the surfaces used in the automotive industry. Indeed, the ribs are stiffening the plate, shifting the eigenmodes to higher frequencies and introducing localized modes around the ribs. The goal is to see which method deals best with this configuration.

The material used is polypropylene, with a Young modulus of $E = 1.1\text{GPa}$, a Poisson's ratio of $\nu = 0.33$ and a density of $\rho = 990\text{ Kg/m}^3$. Mode shapes of the structures with piezoelectric actuators glued on it are computed thanks to a finite element model implemented on the software SDT [25] and an experimental modal analysis was performed jointly to identify modal dampings, available in Table 1. The plate is modeled with shell elements. The control algorithms are developed and implemented in Matlab with SDT jointly. The meshes are available Figure 2b and Figure 2c.

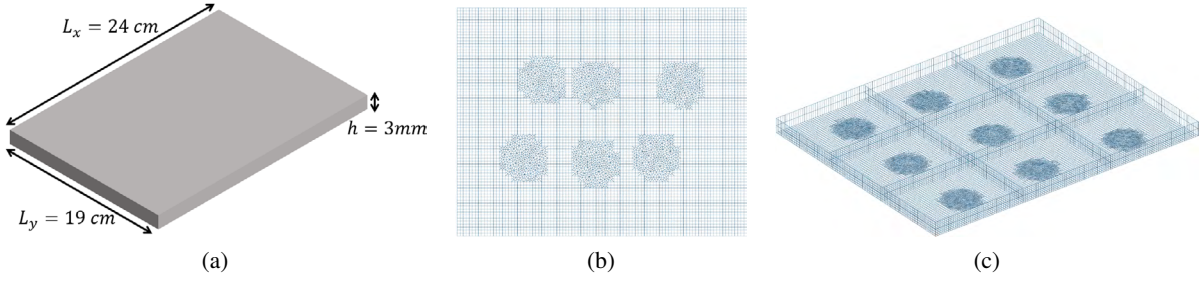


Figure 2: (a) Dimensions of the plate and (b) meshes of the studied plate and (c) ribbed plate.

The target shape consists of a rectangle measuring $(0, 15L_x; 0, 2L_y)$ and centered at $(0, 3L_x; 0, 55L_y)$. Moreover, the audio signal to be reconstructed is a sweep sine with a duration of 2 seconds, from 100 Hz to 800 Hz, sampled at 40 kHz. The chosen frequencies allow to excite the 6 first modes. In addition, a set of "NCE51" piezoelectric actuators developed by Noliac are used, with a diameter of 25 mm and a thickness of 1 mm. Indeed, there are 6 used for the simple plate and 9 between each rib for the second structure, placed quasi randomly, and equally spaced along y . One should notice that the number of actuators and their disposition change the final results. Here, an example with few actuators is studied, because in the real applications as in automotive industry, only a small number of actuators can be embedded for reasons of compactness.

Table 1: First eigen frequencies and damping coefficients of the plate

Index	Eigen frequency (Hz)	Damping (%)
Mode (1,1)	120	3,35
Mode (2,1)	212	2,19
Mode (1,2)	277	3,5
Mode (2,2)	350	4,59
Mode (3,1)	360	1,59
Mode (3,2)	476	2,25

4.2 Indicators for the parametric study

Let $u(x, y, t)$ be the out-of-plane displacement of the plate and $U(x, y, f)$ its Fourier transform. Two criterions will be used and described below:

Localization error: given a reconstructed target shape, the first criterion is the measurement between the center of the target shape and the maximum amplitude of the reconstructed shape. Thus, the lower the distance is, the more the shape is localized precisely from a spatial point of view.

Spatial contrast: the second criterion is the computation of the contrast between the energy in the reconstructed area (S_R) and energy of the total area ($S_T = L_x \times L_y$), so that:

$$C(f) = \frac{\int_{S_R} |U(x, y, f)|^2 dS}{\int_{S_T} |U(x, y, f)|^2 dS}. \quad (21)$$

If $C(f) = 1$, then all the energy is present in the target shape and nothing outside, and if $C(f) = 0$, then all the energy is outside the target shape.

5 NUMERICAL RESULTS

5.1 Results localization on a simple structure

The three methods described previously are applied numerically, and compared to a case where no control is imposed, with only the nearest actuator to the target shape actuated.

The spot error and the contrast in the frequency band [100 Hz;800 Hz] for each method are plotted in Figure 3. Firstly, we can observe that the STIF method allows to achieve a very high localization performance, in comparison with others. Indeed, it shows a very low spot error, which is around 12% of the total length in the [100 Hz;210 Hz] region, and lower than 10% above 210 Hz approximately until 540 Hz (Figure 3a). It is important to notice that this frequency corresponds to the limit where the modal density (number of modes/Hz) is very high. Thus, above this frequency the plate could not be described with a modal behavior anymore [7]. Moreover, the contrast drops drastically at modal frequencies, with a peak of the error at 208 Hz and a small around 360 Hz (Figure 3b). It corresponds to the eigenmodes which influences the target shape pattern. Therefore, the STIF method can achieve a precise localization from 100 Hz to 540 Hz, after the algorithm does not focus vibrations anymore. It is interesting to notice that there is the same behavior around 120 Hz and 208 Hz for the MC and for the case without control, also influenced by eigenmodes. Besides, according to the spot error and contrast curves, the MC method can only focus on a narrow bandwidth between 100 Hz and 350 Hz. The time reversal (TR) also operates in a narrow band, around 130 Hz to 300 Hz approximately, with a high influence of the first mode shape. Finally, it is also interesting to note that without any control strategy, the plate localizes vibrations around the actuator even at low frequency, given the material and properties of this example (high damping particularly).

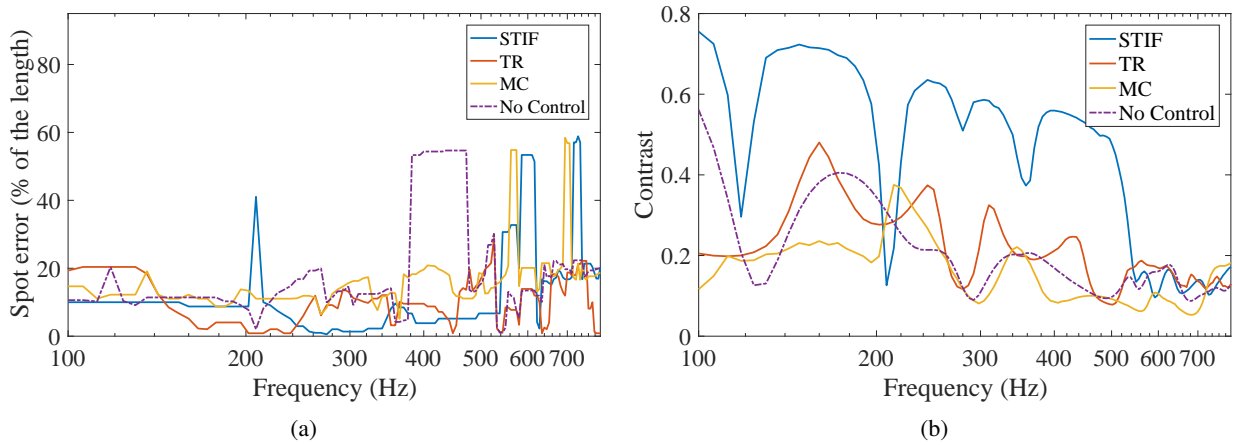


Figure 3: (a) Spot error and (b) contrast for the simple plate.

The results of localization obtained at the frequency band of interest are plotted in Figure 4. Thus, the normalized mean quadratic displacement amplitude of bending waves in the frequency range of interest, defined by:

$$\langle |U(x,y)|^2 \rangle = \frac{1}{f_{max} - f_{min}} \int_{f_{min}}^{f_{max}} |U(x,y,f)|^2 df, \quad (22)$$

is plotted. The MC induces several analytical steps to focus the target shape. However, the Figure 4c shows that it localizes very poorly the bending waves with this actuators configuration. Indeed, the

method is very sensitive to the mode shapes of the structure, and the deformation mode of the PZT. On the other side, the STIF is based on the learning of the propagation operators between each observation point and actuator. Hence, this method is easier to implement than the MC but requires much more computation time. This means that the STIF allows to focus far better bending waves in the frequency band of interest, as shown in Figure 4a. In contrast, the TR based on a partial knowledge requires less computation time than the STIF, but in this case is less performing and gives poorer localization precision (Figure 4b). Indeed, the TR needs to be used in a high reverberating media to catch the whole dynamics, here the plate is very damped. Finally, when there is no control, the energy stays around the actuator due to the high damping ratio (Figure 4d). It is very important to point out that the results depend on the number of actuators. With more actuators, the STIF can localize more effectively. This parameter must be taken into account to obtain the best compromise.

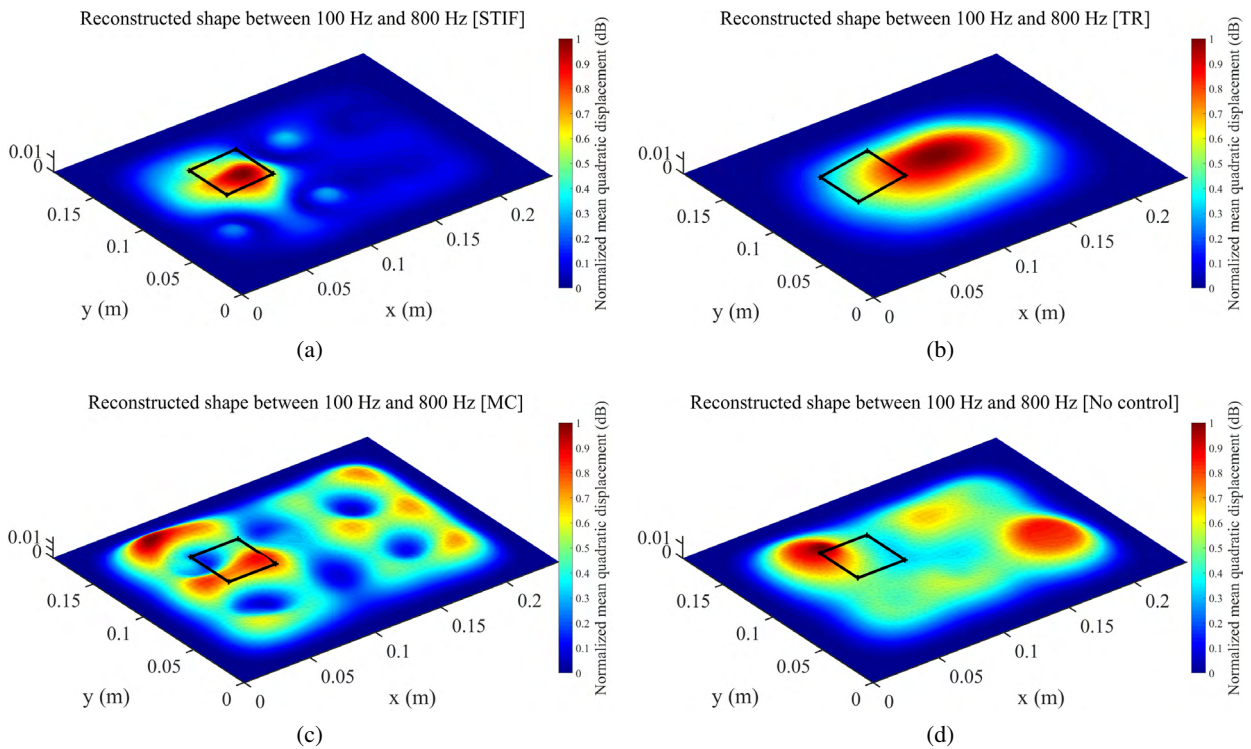


Figure 4: Reconstructed shapes with (a) STIF, (b) TR, (c) MC and (d) without control.

5.2 Results localization on a structure with ribs

The studied structure is now the plate as introduced above with ribs fixed on it. The main idea is to see which method will still work on a more complex structure. Moreover, the modal frequencies are higher than before, from 154 Hz to 590 Hz, and the modal amplitudes are localized between ribs.

The Figure 5 shows the spot error and the contrast. On the frequency band between 100 Hz and 800 Hz, the STIF localizes the energy on the target area, compared to the simple case with 6 actuators (Figure 6a). Additionally, the contrast drops at frequencies where modes appear. However, the higher values of the error between 270 and 380 Hz correspond to high amplitude vibrations on actuators around the target area but the shape is still reproduced with high contrast. In addition, the TR can focus the

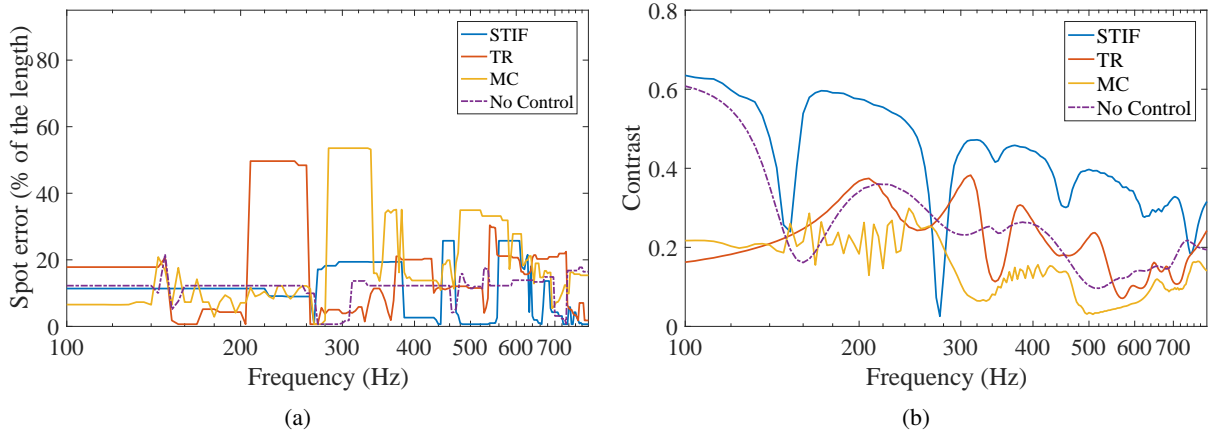


Figure 5: (a) Spot error and (b) contrast for the plate with ribs.

waves in the frequency band (Figure 6b), but it does not maintain the target shape for each frequency. Similarly, the MC localizes the energy alternatively next to the target shape and between ribs (Figure 6c), but does not work well since the mode shapes are not conventional flexural modes but a mixture of global and local modes. Finally, without control strategy, the energy is also confined between the ribs near the target shape and shows better precision than MC and TR (Figure 6d). The initial learning of the dynamic behavior allows to have better focusing precision by considering the local modes in the dynamics, in a wider frequency band. When the number of actuators is higher, it increases the localization capabilities.

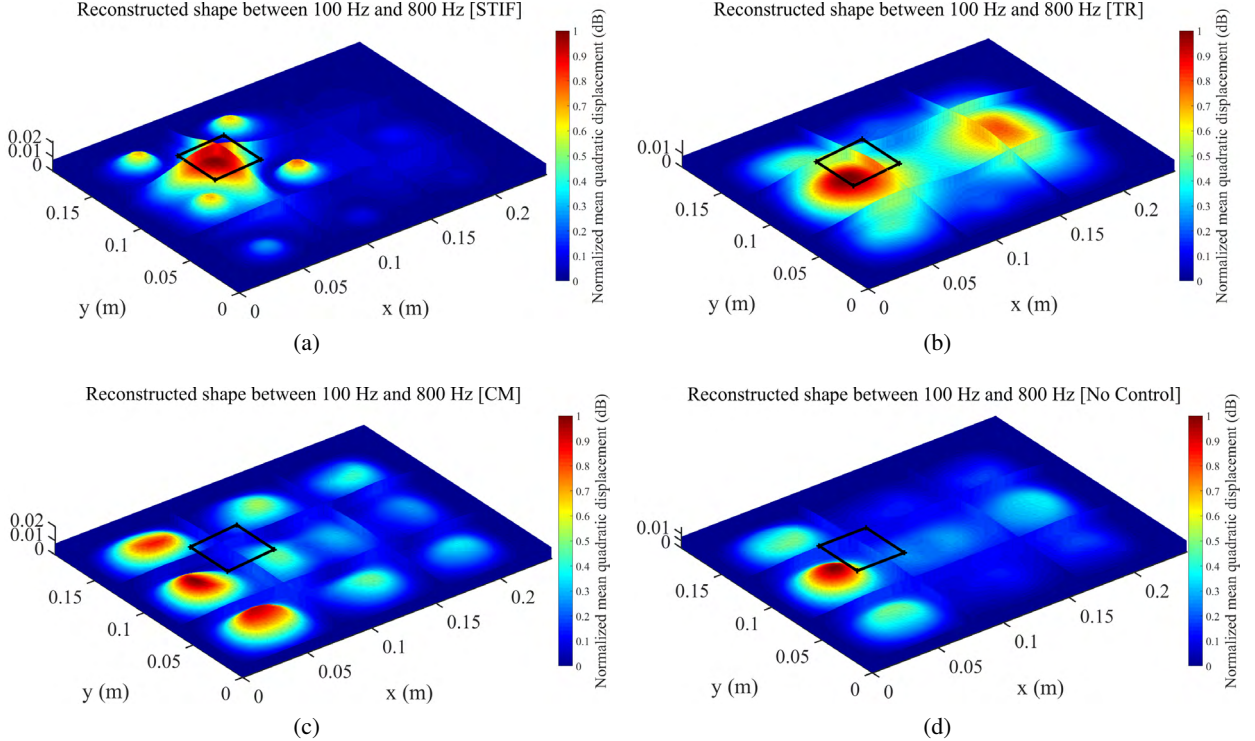


Figure 6: Reconstructed shapes with (a) STIF, (b) TR, (c) MC and (d) without control.

6 CONCLUSION

To conclude, three focusing wave methods were tested and adapted for bending wave in the case of sound reproduction. Within the context of automotive industry and spatial sound rendering, it is obvious that the spatio-temporal inverse filtering method is easier to implement and gives better results compared to others, even on a complexe structure. Indeed, the filters are computed without prior knowledge about boundaries or theoretical dynamic behavior. However, the computation cost is higher, because the structure dynamic must be learned before. Above a certain frequency where the methods focus poorly, only exciting the actuator located near the target shape would be enough. Mainly for higly damped structures and at high frequencies. Finally, several parameters as the number of actuators and the boundary conditions have been studied but not presented here, influence the localization results, and must be taken into account, regardless of the complexity of the structure.

ACKNOWLEDGEMENT

This work was financially supported by the French National Research Agency (ANR, contract ANR-17-CE33-0004).

REFERENCES

- [1] A. J. Berkhout, D. de Vries, and P. Vogel. Acoustic control by wave field synthesis. *The Journal of the Acoustical Society of America*, 93(5):2764–2778, 1993.
- [2] Rudolf Rabenstein and Sascha Spors. Spatial aliasing artifacts produced by linear and circular loudspeaker arrays used for wave field synthesis. In *Audio Engineering Society Convention 120*, May 2006.
- [3] Neil Harris and Malcolm J. Hawksford. The distributed-mode loudspeaker (dml) as a broad-band acoustic radiator. In *Audio Engineering Society Convention 103*, Sep 1997.
- [4] Marinus M. Boone and Werner P. J. de Bruijn. On the applicability of distributed mode loudspeaker panels for wave field synthesis-based sound reproduction. In *Audio Engineering Society Convention 108*, Feb 2000.
- [5] Ulrich Horbach, Diemer de Vries, and Etienne Corteel. Spatial audio reproduction using distributed mode loudspeaker arrays. In *Audio Engineering Society Conference: 21st International Conference: Architectural Acoustics and Sound Reinforcement*, Jun 2002.
- [6] Martin Kuster, Diemer De Vries, Daniel Beer, and Sandra Brix. Structural and acoustic analysis of multiactuator panels. *J. Audio Eng. Soc*, 54(11):1065–1076, 2006.
- [7] Marc Rébillat. *Vibrations of large multi-actuator panels for the creation of audio-visual virtual environments: acoustical, mechanical and perceptual approaches*. Theses, Ecole Polytechnique X, November 2011.
- [8] José Escolano, José J. López, Basilio Pueo, and German Ramos. On large multiactuator panels for wave field synthesis applications. In *Audio Engineering Society Convention 124*, May 2008.
- [9] Basilio Pueo, José J. López, José Escolano, and Lars Hörchens. Multiactuator panels for wave field synthesis: Evolution and present developments. *J. Audio Eng. Soc*, 58(12):1045–1063, 2011.

- [10] A. Preumont. *Vibration Control of Active Structures: An Introduction*. Solid Mechanics and Its Applications. Springer Netherlands, 2011.
- [11] E. Enferad, C. Giraud-Audine, F. Giraud, M. Amberg, and B. Lemaire-Semail. Differentiated haptic stimulation by modal synthesis of vibration field. In *2018 IEEE Haptics Symposium (HAPTICS)*, pages 216–221, March 2018.
- [12] Jung-Han Woo and Jeong-Guon Ih. Vibration rendering on a thin plate with actuator array at the periphery. *Journal of Sound and Vibration*, 349:150 – 162, 2015.
- [13] Michael C. Heilemann, David Anderson, and Mark F. Bocko. Sound-source localization on flat-panel loudspeakers. *J. Audio Eng. Soc.*, 65(3):168–177, 2017.
- [14] M. Fink. Time reversal of ultrasonic fields. i. basic principles. *IEEE Transactions on Ultrasonics, Ferroelectrics, and Frequency Control*, 39(5):555–566, Sept 1992.
- [15] Mathias Fink and Claire Prada. Acoustic time-reversal mirrors. *Inverse Problems*, 17(1):R1, 2001.
- [16] Sylvain Yon, Mickael Tanter, and Mathias Fink. Sound focusing in rooms: The time-reversal approach. *The Journal of the Acoustical Society of America*, 113(3):1533–1543, 2003.
- [17] C. Hudin, J. Lozada, and V. Hayward. Localized tactile feedback on a transparent surface through time-reversal wave focusing. *IEEE Transactions on Haptics*, 8(2):188–198, April 2015.
- [18] Yuvi Kahana, Philip A. Nelson, Ole Kirkeby, and Hareo Hamada. A multiple microphone recording technique for the generation of virtual acoustic images. *The Journal of the Acoustical Society of America*, 105(3):1503–1516, 1999.
- [19] Mickaël Tanter, Jean-Louis Thomas, and Mathias Fink. Time reversal and the inverse filter. *The Journal of the Acoustical Society of America*, 108(1):223–234, 2000.
- [20] M. Tanter, J.-F. Aubry, J. Gerber, J.-L. Thomas, and M. Fink. Optimal focusing by spatio-temporal inverse filter. i. basic principles. *The Journal of the Acoustical Society of America*, 110(1):37–47, 2001.
- [21] J.-F. Aubry, M. Tanter, J. Gerber, J.-L. Thomas, and M. Fink. Optimal focusing by spatio-temporal inverse filter. ii. experiments. application to focusing through absorbing and reverberating media. *The Journal of the Acoustical Society of America*, 110(1):48–58, 2001.
- [22] Sylvain Yon, Mickaël Tanter, and Mathias Fink. Sound focusing in rooms. ii. the spatio-temporal inverse filter. *The Journal of the Acoustical Society of America*, 114(6):3044–3052, 2003.
- [23] Joung-Woo Choi and Yang-Hann Kim. Generation of an acoustically bright zone with an illuminated region using multiple sources. *The Journal of the Acoustical Society of America*, 111(4):1695–1700, 2002.
- [24] Ziqing Li, Pingzhan Luo, Chengshi Zheng, and Xiaodong Li. Vibrational contrast control for local sound source rendering on flat panel loudspeakers. In *Audio Engineering Society Convention 145*, Oct 2018.
- [25] *Structural Dynamics Toolbox (for use with MATLAB)*. SDTools, Paris, France, <https://www.sdtools.com/>, Sep 1995-2019.

OPEN-LOOP TRANSIENT CONTROL OF MODES FOR THE GENERATION OF LOCALIZED TACTILE TUNABLE PATTERNS ON HAPTIC DEVICES

C. GIRAUD-AUDINE^{*,1}, E. ENFERAD², F. GIRAUD², M. AMBERG² and B. LEMAIRE-SEMAIL²

¹ Arts et Métiers Paris Tech, ² Université de Lille,
EA 2697 - L2EP - Laboratoire d'Electrotechnique et d'Electronique de Puissance,
F-59000 Lille, France
e-mail: christophe.giraud-audine@ensam.eu

Key words: Piezoelectric, Smart Structures, Focusing

Abstract. In the field of haptic, some researches focus on localized stimulations on screens. To that end, a velocity field is generated, where high velocities are produced within a chosen region at a given time. Time reversal or phased array have been studied on screens equipped with piezoelectric ceramics. However, these solutions can lack robustness or sharpness.

Closed loop (CL) control of the mode transients may address these issues. Therefore, we propose to use the modal basis to reproduce a specified velocity field with a predefined transient. In this paper, a preliminary proof of concept toward CL is presented. We propose a methodology to select the modes and practically synthesize the voltages to achieve an open-loop controlled focusing in a prescribed time. The experimental results show the versatility of the method and a good agreement with the theory. Both realization of the field distribution and localization are observed. Moreover, preliminary haptic tests shows a consistent detection thresholds for a simulated button click despite the open loop conditions.

1 INTRODUCTION

Tactile displays are now ubiquitous, e.g smartphones or tablets, but they also have a great potential to realize virtual control panel for such machine tools or automotive applications. At the moment though, the main feedback channel toward the user is visual, which can be incompatible with secure operations. So far, tactile or auditive feedback are crude, although it is commonly admitted and demonstrated that multiple sensory channels can enhance task performances and usability [1, 2]. Hence, part of the researches aim at reducing the cognitive overload induced by visual confirmation during human machine interaction by stimulating the fingertip [3].

For that purpose, elastic waves are interesting in the sense that they propagate, and thus, the actuators may not be colocated to the active region, which is an obvious constraint in the case of a screen. Moreover, if the actuators are glued piezoelectric patches, the modification to the whole design is minimal thanks to good factor form. Some applications already exploit standing or traveling waves to modulate friction on a screen [4, 5, 6], in such examples, the whole surface is active. In the case where localized stimuli are required, such as in virtual button or switches, several approaches using wave focusing have been proposed such as phased array [7, 8] or time-reversal[9, 10]. In these techniques however, the focus

pattern and its transient are not controlled, moreover external parameters can mitigate the effects [11]. In this paper, a truncated modal decomposition is used to design a specified velocity field. By defining, high low speed regions, an approached focusing is obtained which has been proven to generate stimuli [12]. First, we present the method to specify the time evolution to specify a given velocity field. The second part, voltages are optimized to avoid saturation of the power supply. In the third part, we demonstrate experimentally the validity and present evidences that a "click" effect can be produced. Finally, the last section is devoted to conclusion.

2 PRINCIPLES

2.1 Projection

The general set-up consists in an elastic media, on which piezoelectric patches are glued. Considering that low deformation are used, the approach relies on the well-known results of linear elasticity. In particular, noting T_{ij} the stress tensor components and \mathbf{u} the displacement vector, it is well known that the elastic vibration problem of an elastic body occupying volume Ω at rest given by [13]:

$$T_{ij,j} = \rho \ddot{u}_i \quad (1)$$

with specified kinematic conditions on some portions Γ_k on the boundary:

$$\mathbf{u} = 0 \quad (2)$$

and no load applied defines a Sturm-Liouville problem. Therefore it admits an infinity of so-called eigenfrequencies ω_k , each corresponding to a mode shape (the degenerate cases are not considered here). Denoting the later $\bar{\Phi}_k$ after mass normalization (the index $k \in \mathbb{N}^*$ denotes the k^{th} solution), the main result used here is the orthogonality of the modes, and the decomposition theorem [14] which states that any arbitrary shape that fulfils the kinematic constraints (2) can be given by the following infinite time varying linear combination:

$$\mathbf{u}(\mathbf{x}, t) = \sum_{k=1}^{\infty} \bar{\Phi}_k(\mathbf{x}) \eta_k(t) \quad (3)$$

This equation implies that the modal shapes $\bar{\Phi}_k$ form a basis. The $\eta_k(t)$ are referred to modal coordinates in the sequel, and the method described here aims at defining their evolution as a function of time. More precisely, we are interested in reaching a specified configuration at a given time t_f , that is:

$$\mathbf{u}(t_f) = \mathbf{u}^* \quad (4)$$

Since the modes shapes are orthogonal and normalized, they satisfy:

$$\int \rho \bar{\Phi}_j \cdot \bar{\Phi}_k d\Omega = \delta_{jk} \quad (5)$$

where δ_{jk} is the kronecker symbol. Hence, combining (3) and (5) one can obtain the modal coordinates of the target shape using the inner product:

$$\eta_k^* = \int_{\Omega} \rho \bar{\Phi}_k \mathbf{u}^* d\Omega \quad (6)$$

2.2 Time evolution and modal forces

In the case of a mechanical loading $\mathbf{p}(\mathbf{x}, t)$ on a subset of the boundary Γ_p , projecting the equation (1) on the modal basis results in eliminating the spatial dependence of the equation and the problem is transformed into an infinite set of dynamic ordinary differential equation of the second order [13]:

$$\ddot{\eta}_k + \omega_k^2 \eta_k = \psi_k(t) \quad (7)$$

with

$$\psi_k(t) = \int_{\Gamma_p} \mathbf{p}(\mathbf{x}, t) \cdot \bar{\boldsymbol{\Phi}}_k(\mathbf{x}) d\Gamma \quad (8)$$

the modal forces.

The deformed configuration being known, it remains to specify the time evolution of the modal coordinates. Since the objective is to simulate a "click", in other word, a fast transient leading from rest configuration to the specified one must be realized to suggest the behavior of a pressed button. It should be noted though that the objective here is not a realistic rendering. It is rather a metaphor that the user can accept as a mechanical confirmation at the tip of his finger when interacting via an interface (the tactile screen). It has been observed in previous works [12] that the velocity is more relevant for that purpose. So the choice here is to impose $\dot{\eta}_k(t)$. Since $\dot{\mathbf{u}} = \sum_{k=1}^{\infty} \bar{\boldsymbol{\Phi}}_k(\mathbf{x}) \dot{\eta}_k(t)$, the procedure discussed above remains valid.

Considering the eq. (7), and modifying to take into account the modal damping ξ_k , one gets:

$$\ddot{\eta}_k + 2\xi_k \omega_k \dot{\eta}_k + \omega_k^2 \eta_k = \psi_k(t) \quad (9)$$

Taking the Laplace transform of the equation:

$$\frac{(s + a_k)^2 + b_k^2}{s} \mathcal{L}[\dot{\eta}_k](s) = \mathcal{L}[\psi_k](s) \quad (10)$$

with $a_k = \xi_k \omega_k$ and $b_k = \sqrt{1 - \xi_k^2} \omega_k$. The core idea is to compute by "inverse filtering" in the modal basis by specifying $\mathcal{L}[\dot{\eta}_k](s)$. To compute a causal modal force, attention must be paid when specifying the modal velocities, namely $\deg \mathcal{D}(s) \geq \deg \mathcal{N}(s)$ where $\mathcal{D}(s)$ and $\mathcal{N}(s)$ denote respectively the denominator and numerator appearing on the left hand side of the previous equation. In this work, the modal velocity are defined as a modulated envelop, at the mode frequency ω_k :

$$\dot{\eta}_k(t) = f_k(t) \sin(\omega_k t) \quad (11)$$

The consideration behind this choice is that the energy supplied to the system is minimized since it is at resonance. By setting, for instance:

$$f_k(t) = A_k e^{\gamma_k a_k t}$$

where γ_k is a scaling factor introduced to tune the growth of the mode, and A_k , the amplitude, will be used later to realize the initial condition.

Using the Laplace transform, one can write:

$$\frac{(s + a_k)^2 + b_k^2}{s} \mathcal{L}[f_k(t) \sin(b_k t)] = \mathcal{L}[\psi_k(t)]$$

yielding:

$$\mathcal{L}[\psi_k(t)] = A_k \frac{(s + a_k)^2 + b_k^2}{(s - \gamma_k a_k)^2 + b_k^2}$$

So the modal force is:

$$\psi_k(t) = \Psi_k e^{a_k \xi_k \omega_k t} [C_k \sin(b_k t) + D_k \cos(b_k t)] + E_k \quad (12)$$

with :

$$\begin{aligned} \Psi_k &= A_k \frac{a_k (\gamma_k + 1)}{a_k^2 \gamma_k^2 + b_k^2} \\ C_k &= (a_k^2 \gamma_k (\gamma_k + 1) + 2b_k^2) \\ D_k &= a_k b_k (\gamma_k - 1) \\ E_k &= b_k \frac{a_k^2 + b_k^2}{a_k^2 \gamma_k^2 + b_k^2} \end{aligned}$$

To compute the various constants above, we finally set the transient duration. Defining $\Delta t_k = t_f - t_k$ where t_k is the time when the excitation for a given mode is started, we set $\omega_k \Delta t_k = \frac{\pi}{2} + 2\pi N_k$. This condition ensure that a focusing time t_f , all the modal forces are synchronized at their maximum. A_k is such that:

$$\dot{\eta}_k^* = A_k e^{\gamma_k \xi_k \omega_k \Delta t_k}$$

Similarly, the differential equation could also be directly used for more general envelop.

2.3 Practical considerations

The actual device is supposed to be an elastic structure with several piezoelectric patches glued on its surface. In such case, the modal forces are actually the superimposition of the contribution of each patch. Each contribution is proportional to the voltage applied to the ceramic considered. Hence, supposing that the devices features n_p patches, the modal force corresponding the k^{th} is given by:

$$\psi_k = \sum_{i=1}^{n_p} \alpha_{ik} U_i \quad (13)$$

The coefficient α_{ik} depend on the geometry and the material properties of the considered patch i but also on its location relatively to the mode shape k [15, 16]. It is thus theoretically possible to choose the various parameters to have a decoupling such that one voltage controls directly one mode. In practice however, it is a difficult task given the standard dimensions of patches available. So, the approach here is to take advantage of all the voltages. To do so, the voltages U_i are rewritten as a linear combination of the modal forces calculated by eq. 12, and assuming that n_m are used to realize a given vector field:

$$U_i(t) = \sum_{k=1}^{n_m} m_{ik} \psi_k(t)$$

where the weights m_{nk} are used to allocate the desired modal force among the ceramics. Thus, the modal dynamic equation is now:

$$\ddot{\eta}_k + \omega_k^2 \eta_k = \sum_{i=1}^{n_p} \alpha_{ki} \left(\sum_{k=1}^{n_m} m_{ik} \psi_k(t) \right) \quad (14)$$

Assuming that the modes can be excited separately owing to the frequency selectivity, we require the conditions:

$$\sum_{i=1}^{N_b} \alpha_{ki} m_{ik} = 1 \text{ for } k = \{1, \dots, n_m\} \quad (15)$$

to ensure that the necessary modal force is indeed applied. Then, the weight can be tuned to reduce the voltages U_i actually applied to the ceramics by stating the following optimization problem:

$$\begin{aligned}
 & \underset{m_{ik}}{\text{minimize}} && \| \mathbf{M} \boldsymbol{\Psi} \| \\
 & \text{subject to} && |U_i| \leq U_{\max}, i = 1, \dots, n_p. \\
 & \text{and to} && \sum_{i=1}^{n_p} \alpha_{ki} m_{ik} = 1 \text{ for } k = \{1, \dots, n_m\}
 \end{aligned} \tag{16}$$

where \mathbf{M} is the matrix of the weights (which coefficients are the m_{ik} , $\dim(\mathbf{M}) = n_p \times n_m$). $\boldsymbol{\Psi}$ is a matrix which k -th row vector is constituted by ordered samples of the modal forces $\psi_k(nT_s + t_0)$. The number of samples N_s and the sampling should be chosen such that $N_s T_s + t_0 = t_f$, and to cover a time interval where the modal forces ψ_k become large with respect to the voltages rating. In this work, the Frobenius norm was used.

3 EXPERIMENTAL RESULTS

3.1 Experimental set-up

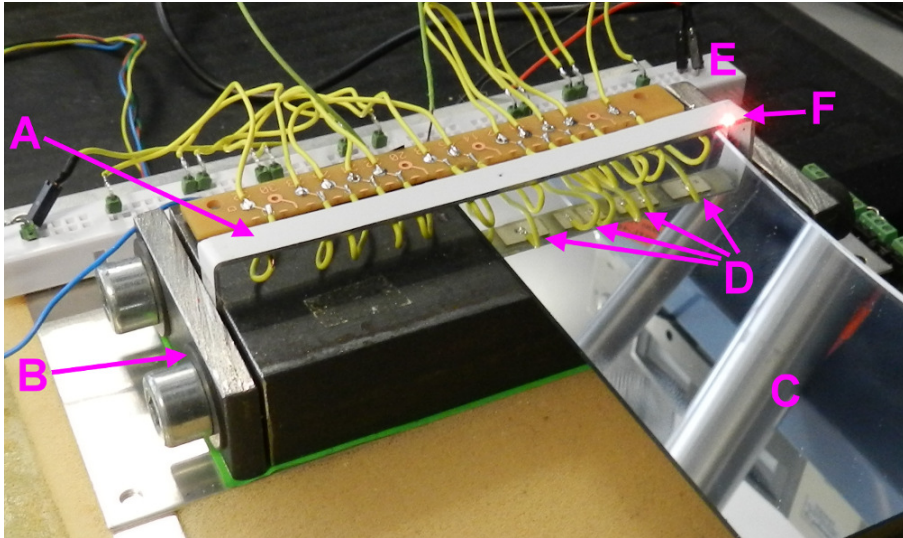


Figure 1: Picture of the experiment: **A)** Staple shaped aluminum beam, the velocity is controlled within a rectangular region on the upper part; **B)** Fixture of the beam to realize clamp-clamp boundary conditions; **C)** Mirror showing the ceramics; **D)** Reflection revealing some of the ceramics fixed beneath the beam. The second ceramic from the left is split as explained in the text; **E)** Electrical connections of transducers allowing the reconfiguration according to the set of ceramics used; **F)** Laser spot positioned at one of the corner of the studied region.

The demonstrator is a clamped staple-shaped aluminium beam equipped with piezoelectric patches Noliac NC51 with dimensions $(9 \times 5 \times 0.5) \text{ mm}^3$ as visible on the picture in fig. 1. This peculiar shape was chosen because i) it reduces the surface to be scanned hence the velocities cartography are considerably faster to realize; ii) it demonstrates that the method is usable even if actual solutions to the eigen problem are not known. As discussed above, the ability of a voltage U_i to excite the k -th mode depends on the α_{ik} coefficient eq (13) which depends on the geometry and location of the patches. To avoid to use several ceramics geometries, the electrodes were actually splitted (e.g second ceramic from the left).

By properly choosing these cuts, it is possible to evenly excite the modes.

The identification was realized using a white noise identification procedure. The surface of the staple is scanned by fixing the set-up on a x-y positioning table and measuring the velocities thanks to laser vibrometer (OFV 505 Polytec). The velocity vs input voltage frequency response function was recorded at points defined on a regular grid on the upper part of the beam. The mapped region was defined between the limits of the curved parts, with a step small enough with regard to the smallest spatial wavelength. During the process the end ceramics were used in conjunction (same voltages) or in opposition (opposite voltages), to excite the even and odd modes respectively, because they are able to excite all the bending modes in the 100 Hz-80 kHz band. During these measurements, the other ceramics are in short-circuit conditions. Modes were selected using the resonance peaks. Knowing the phase and amplitude at resonant frequencies at each measured point, the mode shapes were reconstructed. When the signal to noise ratio was too low, the mode shapes were more precisely mapped at resonance choosing ceramics with more effective participation coefficients.

The orthogonality of the measured modes, however, is only approximatively verified because the scanning cannot cover the whole structure, but only a rectangular area on the top. Indeed, finite element simulation shows that for low frequency modes (having large wavelength) the corners of the staple where acting as clamps, i.e. the modes are located on the top of the staple only. As the frequency increases, modes progressively tend to occupy the whole staple. To address this problem, the modes are re-orthogonalized using a Gram-Schmidt procedure to construct a truncated basis. The time synthesis of the voltages discussed previously requires a fair knowledge of the damping of a mode, which was done by measuring the -3 dB bandwidth. It was verified that the quality factor were high enough to validity the frequency selectivity of modes assumption. Finally, the participation coefficients were estimated from the measurement of the velocity at resonance obtained when supplying each ceramic individually (the other being short-circuited).

3.2 Validation of the voltages assignement

First, the effectiveness of the methodology to assign the voltages and excite the mode independently is illustrated. As explained, the voltages deduced from the prescribed modal forces given by eq. (12) can be "mixed" between the patches using a linear combination (15). Here, the scenario examined is to control modes 1 and 3 (with resonant frequencies $f = 364$, and 2240 Hz) simultaneously, and reach at a prescribed focusing time velocities of 20 mm s^{-1} for the modes φ_1 and φ_3 at the center of the experimental set-up (i.e a total velocity of 40 mm s^{-1} at focusing time). Moreover, a speed up of $\gamma_1 = 4$ and $\gamma_3 = 1$ over the natural decaying speed of modes φ_1 and φ_3 is imposed. Finally, φ_1 and φ_3 should achieve the focusing within $N_1 = 10$ and $N_3 = 25$ oscillations respectively. For the purpose of the demonstration, two set of patches were selected. The first one (denoted set 1 in the sequel) has a strong effect on φ_1 , but a very weak effect on the second, while the second set is more balanced with a prominent effect on φ_3 . This results in the voltages depicted in fig. 2 (bottom).

To assess the effect of "mixing" the voltages, a second run consisted in applying the optimisation procedure in order to conceal the voltages amplitude below 50 V as long as possible during the transient. The resulting voltages (named case 2), depicted in fig. 2 (middle graph), are indeed respecting the constraint as far as possible. Due to the poor ability of patch 1 to energize the second mode, the optimization procedure favors the use of the second patch to reduce the voltage amplitudes. This is clearly visible on the spectra of fig. 3. This figure also confirms that the bandwidth of the excitation signal is well controlled since the second, 4th and 5th modes (at $f = 963$, 3907 and 5719 Hz) are not excited. The transients are still very similar as expected, and the velocity at focusing time is still realized.

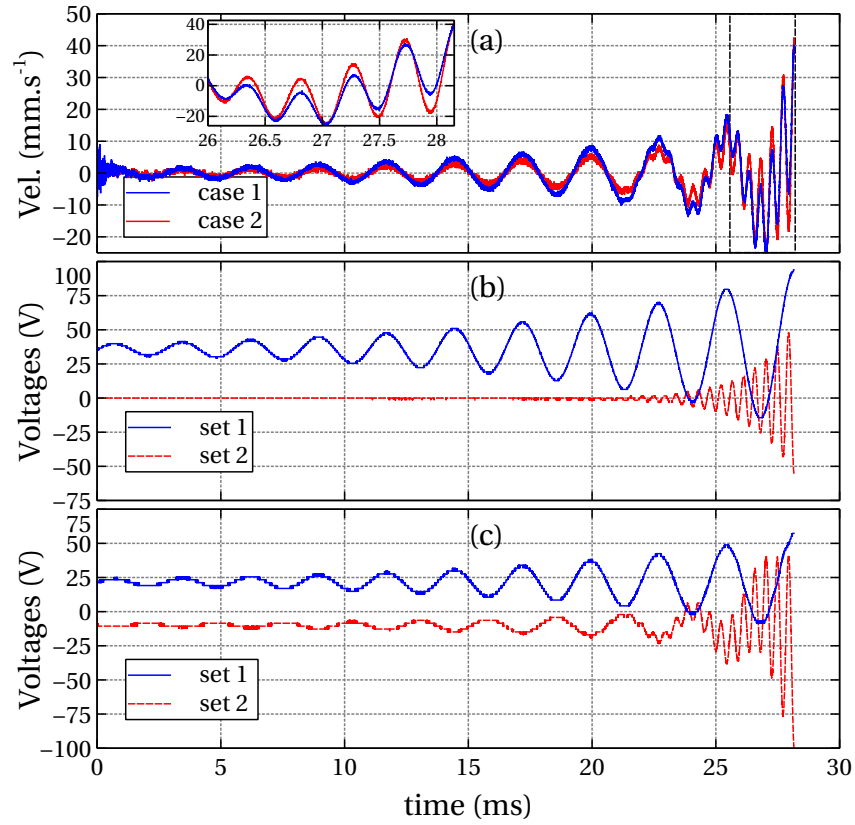


Figure 2: Validation of the voltages allocation strategy: (a) velocity measurement with "one mode one patch" strategy (case 1 black) and mixed voltages between patches (case 2 dark grey). The corresponding voltages applied to the patches set are depicted in the case 1 (b) and case 2 (c).

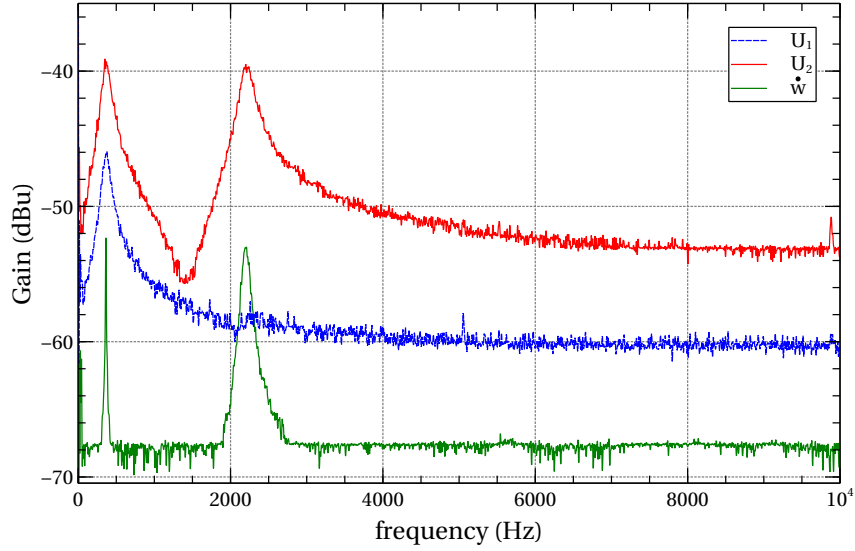


Figure 3: Spectra of the voltages and velocity at the center for case 2: since set 1 of ceramics is poorly coupled to the 3rd mode, the optimization requires that the set 2 is used also to excite mode 1, hence reducing the voltages as shown in fig. 2

3.3 Velocity field control

The main experiments presented here aimed at testing the viability of the approach to reproduce a specified shape on the top of the "staple". As an illustration, the velocity map for the out of plane component of the velocity is defined as follows:

$$\dot{w}(t_f) = \begin{cases} A \exp\left(-\frac{1}{1-\left(\frac{x-x_c}{a}\right)^2}\right) & \text{if } x \in (-a+x_c, a+x_c) \\ 0 & \text{otherwise} \end{cases} \quad (17)$$

known as the bump function and where A is a scaling factor, x_c the center coordinate, and a controls the width. This function has interesting continuity properties and its Fourier transform is rapidly decaying [17]. Intuitively, there exists an analogy between the Fourier transform and the modal projection, hence a limited number modes is expected. The reference field is windowed with a Kaiser window having a sharp transition to ensure a nil value at the boundary as required by the kinematic constraints at the end of the beam.

For practical reason, the modal projection must be truncated. To select the modes, a criterion is defined. Considering that twice the kinetic energy is given by:

$$\mathcal{K} = \int_{\Omega} \rho \dot{\mathbf{u}} \cdot \dot{\mathbf{u}} d\Omega = \int_{\Omega} \rho \bar{\Phi}^T \bar{\Phi} d\Omega \dot{\eta}_k^2 = \sum_{k=1}^{\infty} \dot{\eta}_k^2 \quad (18)$$

one can define the τ -score criterion for a truncation order N_m :

$$\tau = \left(1 - \sum_{k=1}^{N_m} \frac{\dot{\eta}_k^2}{\mathcal{K}^2}\right)^{\frac{1}{2}} \quad (19)$$

where \mathcal{K} can be determined directly from the specified velocity field \dot{w} . The τ -score is thus a measure of the residue resulting from the truncation.

For each test, the velocity field was measured, projected on the modal basis and compared to the specified modal coordinates resulting from the truncation. The criterion \mathfrak{v} -score, used to assess the "misalignment" of the obtained shape compared to the specified one, is defined as:

$$\mathfrak{v} = \frac{\text{cov}[\dot{\mathbf{w}}^*(x_m), \dot{\mathbf{w}}(x_m, t_f)]}{\sqrt{\text{var}[\dot{\mathbf{w}}^*(x_m)] \times \text{var}[\dot{\mathbf{w}}(x_m, t_f)]}} \quad (20)$$

where var and cov are the variance and the covariance respectively, x_m are the location where the velocities are sampled. $\dot{\mathbf{w}}^*$ and $\dot{\mathbf{w}}$ are considered as vectors of reference and measurement of the out of plane component in this case. The criterion is chosen to evaluate the discrepancies between the truncated modal projection and the experimental modal projection, regardless of the error on the amplitude which can be due to some miscalibration. In this way, one can appreciate whether the obtained shape is similar to the (truncated) reference up to a scaling factor.

Five different focusing locations, equidistantly distributed on the beam, were tested at $x_c = -46, -24, 0, 24$ and 46 mm of the high velocity zone (25 mm of width at mid-height of the active area) are presented in fig. 4. For each test, the specified, the approached and the measured velocities at focusing time along the center line in the y direction are presented (left column). The approached reference velocity field results from the truncation of the actual modal decomposition. The τ -score, which dictates the choice for the truncation, and the \mathfrak{v} scores, which validate the experimental focused velocity field, are summed up in Tab. 1. The results demonstrate the validity of method. Note that the poorer τ -scores on the outermost points are due to the trade-off on the number of modes used in the truncation.

Pulse center	P_1	P_2	P_3	P_4	P_5
τ -score	0.8285	0.9727	0.9544	0.9816	0.8717
\mathfrak{v} -score	0.9877	0.9953	0.9911	0.9609	0.9973

Table 1: Effect of the truncation (τ -score) and synthesis accuracy (\mathfrak{v} -score) for the various location studied.

3.4 Haptic evaluation

To mimic a "click, the previous set-up is fixed to a force sensor that measure the force applied in the vertical direction. The hypothesis tested in this experiment is that the user can be lured by triggering the focus at a consistent level of pressure. By doing so, it is expected that an unconscious association with the real-life experience "pressure implies movement of the button" can be suggested.

Data were collected from 15 healthy volunteers aged between 22 and 62 (4 females). Participants were wearing noise-cancelling headphones in order to prevent potential interference from auditory cues. All participants gave written informed consent. The investigation conformed to the principles of the Declaration of Helsinki and experiments were performed in accordance with relevant guidelines and regulations. The purpose of this experiment was 1) to assess the proposed idea 2) to evaluate the detection threshold. To do so, the participants were first asked to answer "yes" or "no" to the question "Do you feel a click when pressing on the surface of the device?" when they pressed at the center of the beam. As a preliminary tuning, different levels of the velocity field between 0 mm s^{-1} up to 240 mm s^{-1} using a dichotomy. The procedure was repeated 4 times to ensure the consistency of the results, and then confirmed by a one-down two-up procedure. In all cases, the threshold for each participant could be confirmed within 10 %. Based on these preliminary test, a set of samples was generated and presented randomly. During a test, 6 levels around the participant anticipated threshold were tested, as well as the extreme values, each level appearing five times. The test was repeated three times for a participant.

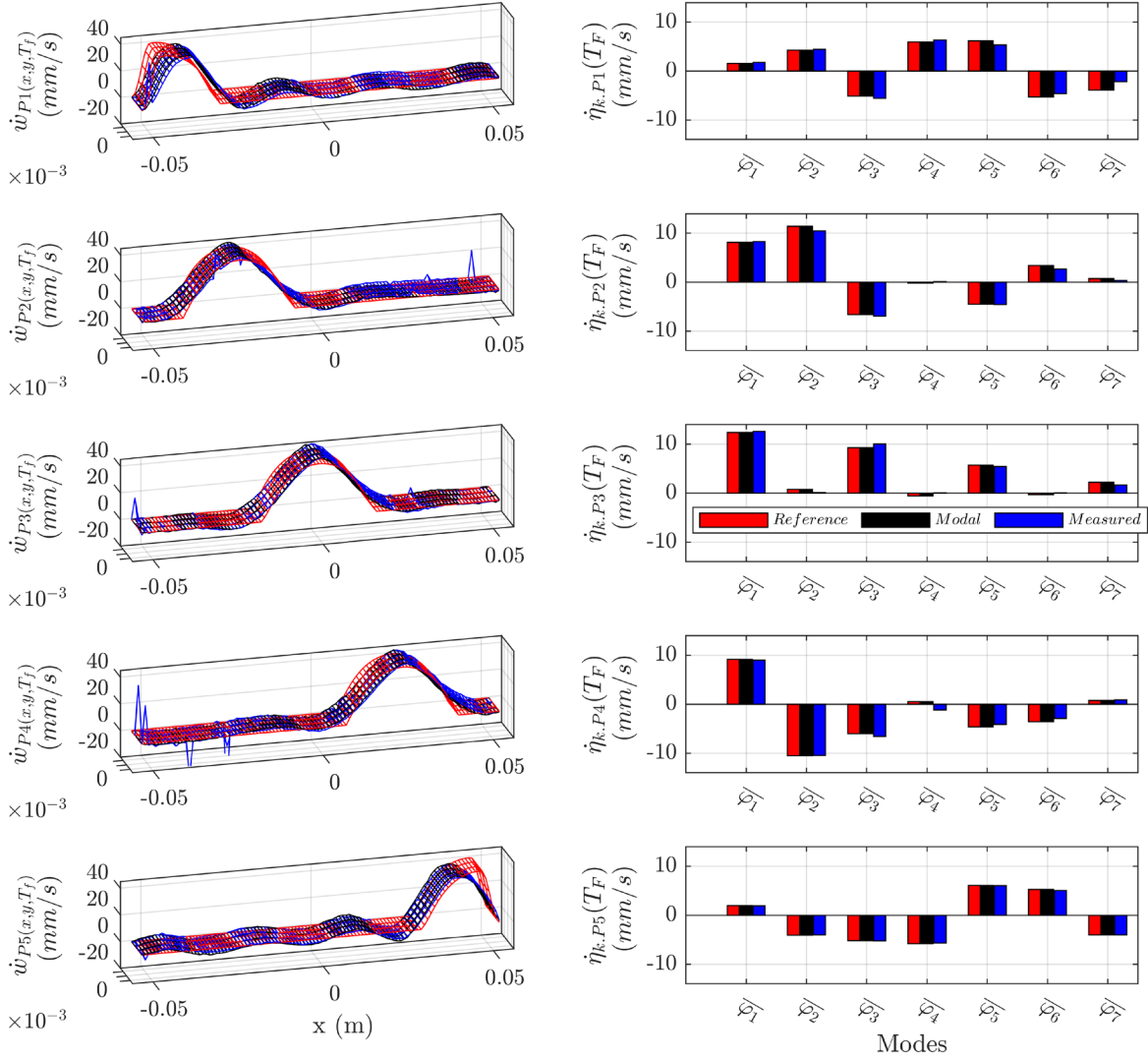


Figure 4: Test results of approximated bump velocity profiles at location points -46 , -24 , 0 , 24 and 46 mm, on the left velocity fields for the references, the approached ones and the measured velocities (resp. red, black and blue) and their respective modal projection (right). The truncation includes 7 modes, based on the distortion criteria.

For each level tested, the probability of detection is estimated supposing a binomial law. Then, a log normal cumulative probability density was fitted between the previously obtained probabilities to yield a "per-level" detection probability. The result of the procedure is depicted on the graph of fig 5 for seven of the participant (for clarity). The detection threshold is clear for every participant and generally lying between 10 mm s^{-1} and 50 mm s^{-1} . Only one outlier had a threshold of 140 mm s^{-1} . It should also be noted that all the participant were able to detect the "click".

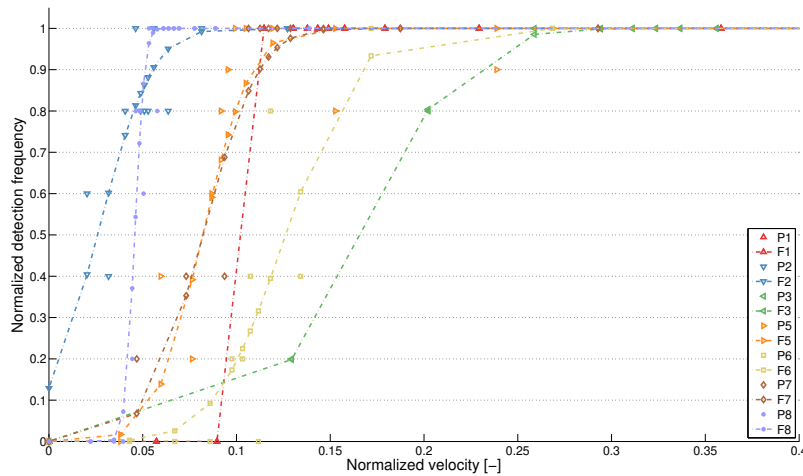


Figure 5: Estimation of the 50 % probability detection threshold.

4 CONCLUSIONS

A methodology to realize a reference velocity field in an elastic equipped with piezoelectric patches has been presented. Unlike previous methods, such as time reversal, the velocity field can be arbitrarily defined as long as it verifies the kinematic conditions. Since the study was in open loop, the voltages are computed, and an optimization procedure has been proposed to mix the voltages among the patches in order to respect the technological limitation (saturation).

Experimental were verified against newly defined criteria and the effectiveness of the methodology has been verified both for the ability to synthesize a given velocity field and to efficiently distribute the voltages.

Finally, a preliminary study to assess the "click" haptic rendering has showed that most participant do have a clear detection threshold within a consistent velocity interval. This latest result is surprising and promising since closed loop should improve repetability by mitigating the perturbation introduced by the participants finger.

REFERENCES

- [1] Seung-Chan Kim, Tae-Hon Yang, Byung-Kil Han, Dong-Soo Kwon, Interaction with a display panel - an evaluation of surface-transmitted haptic feedback, in: 2008 International Conference on Control, Automation and Systems, IEEE, 2008, pp. 278–283.
- [2] M. S. Prewett, L. R. Elliott, A. G. Walvoord, M. D. Covert, A Meta-Analysis of Vibrotactile

- and Visual Information Displays for Improving Task Performance, *IEEE Transactions on Systems, Man, and Cybernetics, Part C (Applications and Reviews)* 42 (1) (2012) 123–132.
- [3] J. Pasquero, V. Hayward, Tactile feedback can assist vision during mobile interactions, in: *Proceedings of the 2011 annual conference on Human factors in computing systems - CHI '11*, ACM Press, Vancouver, BC, Canada, 2011, pp. 3277–3280.
 - [4] T. Watanabe, S. Fukui, A method for controlling tactile sensation of surface roughness using ultrasonic vibration, in: *, 1995 IEEE International Conference on Robotics and Automation, 1995. Proceedings, Vol. 1, 1995*, pp. 1134–1139.
 - [5] M. Biet, F. Giraud, B. Lemaire-Semail, Squeeze film effect for the design of an ultrasonic tactile plate, *IEEE Transactions on Ultrasonics, Ferroelectrics, and Frequency Control* 54 (12) (2007) 2678–2688.
 - [6] s. Ghenna, E. Vezzoli, C. Giraud-Audine, F. Giraud, M. Amberg, B. Lemaire-Semail, Enhancing Variable Friction Tactile Display using an ultrasonic travelling wave, *IEEE Transactions on Haptics* (2016) 296–301.
 - [7] S.-Y. Kim, J.-O. Kim, K. Kim, Traveling vibrotactile wave - a new vibrotactile rendering method for mobile devices, *IEEE Transactions on Consumer Electronics* 55 (3) (2009) 1032–1038.
 - [8] J.-H. Woo, J.-G. Ih, Vibration rendering on a thin plate with actuator array at the periphery, *Journal of Sound and Vibration* 349 (2015) 150–162.
 - [9] M. R. Bai, Y. K. Tsai, Impact localization combined with haptic feedback for touch panel applications based on the time-reversal approach, *The Journal of the Acoustical Society of America* 129 (3) (2011) 1297–1305.
 - [10] C. Hudin, J. Lozada, V. Hayward, Localized tactile feedback on a transparent surface through time-reversal wave focusing, *IEEE Transactions on Haptics* 8 (2) (2015) 188–198.
 - [11] C. Hudin, J. Lozada, V. Hayward, Spatial, temporal, and thermal contributions to focusing contrast by time reversal in a cavity, *Journal of Sound and Vibration* 333 (6) (2014) 1818–1832.
 - [12] E. Enferad, C. Giraud-Audine, F. Giraud, M. Amberg, B. Lemaire-Semail, Differentiated haptic stimulation by modal synthesis of vibration field, in: *2018 IEEE Haptics Symposium (HAPTICS)*, IEEE, San Francisco, CA, 2018, pp. 216–221.
 - [13] M. Géradin, D. Rixen, *Mechanical vibrations: theory and application to structural dynamics*, third edition Edition, Wiley, Chichester, West Sussex, United Kingdom, 2015.
 - [14] L. Meirovitch, *Fundamentals of vibrations*, Waveland Press, Long Grove, Illinois, 2010.
 - [15] A. Preumont, *Vibration Control of Active Structures*, Vol. 246 of *Solid Mechanics and Its Applications*, Springer International Publishing, Cham, 2018. doi:10.1007/978-3-319-72296-2.
 - [16] A. Deraemaeker, G. Tondreau, F. Bourgeois, Equivalent loads for two-dimensional distributed anisotropic piezoelectric transducers with arbitrary shapes attached to thin plate structures, *The Journal of the Acoustical Society of America* 129 (2) (2011) 681–690.
 - [17] S. G. Johnson, Saddle-point integration of C_∞ “bump” functions, *ArXiv e-prints* arXiv:1508.04376.

PIEZOELECTRIC TRANSDUCER FOR LOW FREQUENCY SOUND GENERATION ON SURFACE LOUDSPEAKERS

CHRISTIAN BOLZMACHER^{*}, NASSIM BENBARA[†], MARC REBILLAT[†] AND
NAZIH MECHBAL[†]

^{*} CEA, LIST, Sensorial and Ambient Interfaces Laboratory, 91191 - Gif-sur-Yvette CEDEX, France.
e-mail: christian.bolzmacher@cea.fr, www-list.cea.fr

[†] Processes and Engineering in Mechanics and Materials Laboratory (CNRS, CNAM, ENSAM), 151,
Boulevard de l'Hôpital, Paris, F-75013, France.

Key words: Piezoelectric actuators, Surface loudspeaker, Bending wave loudspeaker.

Abstract. This paper describes the comparison of three different types of piezoelectric actuators for application in sound emitting panels so-called load-bearing surface loudspeaker. The first actuator is a piezoelectric ring glued directly to a polypropylene surface of dimension 300 x 200 x 3 mm³. The other two are mechanically amplified piezoelectric actuators of the flat and the cymbal flextensional-type tested in a reactive configuration on the same sized polypropylene panel. Those actuators are compared in terms of vibration response measured with a laser vibrometer and audio response measured with a microphone.

1 INTRODUCTION

In the foreseeable future, the adoption of multifunctional car structure (MCS) will offer the potential to radically upgrade the abilities of vehicles in terms of ecological requirements emerging from the social and legal environment. Integrating car structures with functional systems that monitor structural integrity and aging, change shape at local level, act as sound sources and tackle noise vibration harshness issues will eliminate many of the weight, volume, and signature penalties associated with the current approach of designing, manufacturing and maintaining vehicles and functional systems separately. One type of MCS that appears as very promising and which we propose to investigate in this paper is a Load-bearing Loudspeaker Structure (LLS). A LLS refers to structures that are equipped with active elements such as piezoelectric elements that allow for music reproduction and 3D sound spatialization. We consider the fact that the passenger cabin of cars consists of many large surrounding surfaces such as door panels, roof trim panel, trims and dashboards, which can act as membranes. The objective is thus to design surface loudspeaker able to efficiently reproduce sound in the low, medium and high frequency range depending on the sound panel size. Piezoelectric transducers chosen because of their small size, low weight and high force output are investigated in this paper. They are coupled to mechanical amplification units to increase displacement amplitudes to overcome the lack of low frequency sound production [1,2] and are compared to a piezoceramic ring. The goal is to efficiently excite the full audio spectrum.

2 PIEZOELECTRIC ACTUATORS

Piezoelectric materials used in this work are ceramic perovskite materials made from lead zirconate titanate (PZT) that expands or contracts when an electrical charge is applied, generating motion and force called the inverse piezoelectric effect. Piezoelectric actuators use this motion to provide very short high force strokes with high frequency and fast response times at small size giving them a significant power-to-size ratio. Bulk piezo ceramics with external electrodes provide deformations in the range of 300 ppm with fields of 600 kV/m requiring high driving voltages. Multi-layer piezoelectric ceramics have been developed with the aim to reduce the required voltage by reducing the PZT layers to 50 to 100 μm thickness placed between internal electrodes. Those materials can be driven with a maximum electric field up to 2 MV/m with a voltage of less than 200 V achieving a deformation of about 1000 ppm.

Depending on the application, piezoelectric ceramics can be glued directly to a surface or a structure introducing a bending-type deformation. Alternatively, the high output force can be transformed into an amplified deformation at the expense of the size of the actuator due to the required amplification unit. If the amplification unit is rigidly coupled to the piezoceramic, these actuators are called flextensional actuators. Three different actuator types are described in the next sections:

- Piezoelectric rings
- Flat flextensional piezoelectric actuators
- Cymbal-type flextensional piezoelectric actuators

3.1 Piezoelectric ring

The first prototype of a sound-emitting panel uses a piezoceramic ring of dimension OD50 mm, ID20 mm, and TH 0.5 mm. It is made of a hard Navy I-type material called Pz26 from Meggitt Ferroperm with good coupling factors, high Curie temperature, high mechanical quality factor, low dielectric loss and very good stability over time. Table 1 shows the material characteristics. This piezoceramic ring is glued centered to a 300 x 200 x 3 mm³ plate made of polypropylene, a material often used for car passenger garnishments. The plate is screwed via a spacer (thickness 6.7 mm) to another stiffer plate made of Delrin creating a closed housing. The final assembly is shown in Figure 1.

Table 1: Material parameters Meggitt Pz26.

Relative dielectric permittivity k33	-	1300
Curie temperature	°C	230
Piezoelectric charge coefficient d33	pC/N	300
Density	kg/m ³	7700

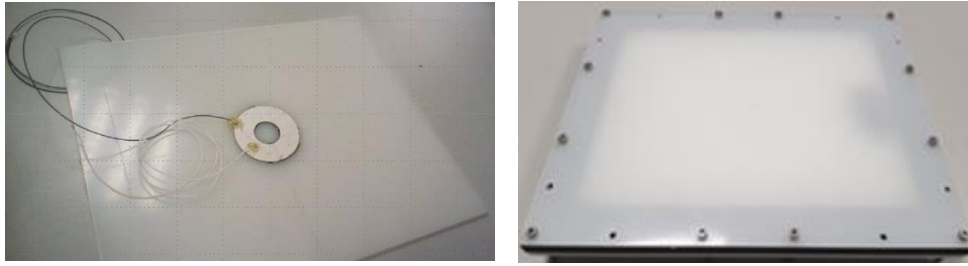


Figure 1: Polypropylene plate with centered piezoelectric ring (left) and prototype speaker with housing (right).

3.2 Flat flextensional piezoelectric actuator

Flat flextensional piezoelectric actuators transform the high output force of piezoelectric ceramics into an amplified displacement. The actuator used in this work is called “Amplified Piezoelectric Actuator” (APA) developed by Cedrat Technologies based on a low voltage piezoelectric ceramics stack. The mechanical amplification is obtained due to an external monolithic shell of elliptic shape made of stainless steel, which magnifies the stack deformation in normal direction. This elliptical frame preloads the piezoelectric ceramic stack and protects it from tensile force. This kind of mechanical amplifiers is especially well-suited for dynamic drive conditions and provide relatively high force and large displacement while being compact in size. The APA400MML model has been chosen because of its good compromise between force and displacement output. Characteristics are given in Table 2. For the experimental tests, the actuator has been screwed in a reactive configuration centered between two plates. The sound emitting membrane of size 300 x 200 x 3 mm³ is made of polypropylene and the back plate is made of Delrin (thickness 6.7 mm) as shown in Figure 2.

Table 2: Characteristics of an APA400MML from Cedrat Technologies.

Max. no load displacement	μm	295-434
Blocked force	N	171-231
Stiffness	N/μm	0.547
Resonance frequency (blocked-free)	Hz	634
Capacitance	μF	10
Drive voltage	V	0-120
Dimensions	HxLxW in mm	24x78x11.5
Mass	g	47.5

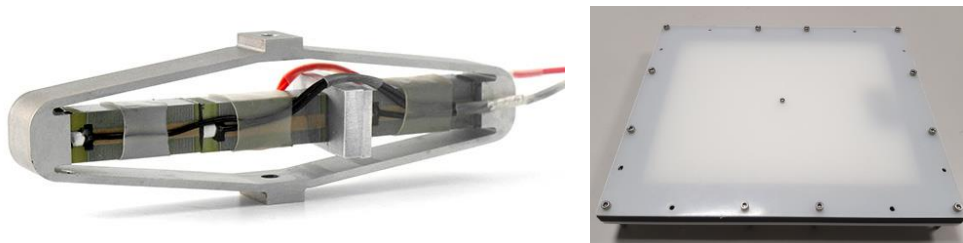


Figure 2: APA400MML from Cedrat Technologies (left) and surface speaker prototype with centered actuator (right).

3.3 Cymbal-type flextensional piezoelectric actuator

The cymbal transducer consists of a piezoelectric or ceramic disc (either in single layer or multilayer form) sandwiched between two metal endcaps, each having a truncated conical shape. These metal endcaps serve as a mechanical transformer for converting and amplifying the lateral displacement of the ceramic into an axial motion of the endcaps. Both the d_{33} and d_{31} piezoelectric coefficients contribute to the axial displacement of the composite. Displacement increases exponentially with increasing cavity diameter and increases linearly with increasing cavity depth. Displacement is inversely proportional to the endcap thickness. Displacement and generative force show a position dependent behavior.

TDK PowerHap™ piezoelectric actuators provide high performance in terms of acceleration, force, and response time. They are made of multilayer piezo plates with copper inner electrodes. This allows the actuators to be driven with relatively low operating voltages up to 120V. Once activated, the piezo plates only expand minimally in the z axis, but due to the constant volume of the piezo effect contract simultaneously in both the x and y axes. The actuators employ cymbals on both sides of the plate as levers to amplify the contraction by a factor of 15 in the z axis. The biggest actuator of the PowerHap™ series, the PowerHap™ 15G, is used in this paper with its characteristics given in Table 3. The actuator is also fixed in a reactive configuration between two plates of dimensions 300 x 200 mm³.

Table 3: Characteristics of the TDK PowerHap 15G actuator.

Max. no load displacement	μm	200
Blocked force	N	20
Stiffness	N/mm	100
Resonance frequency (blocked-free)	kHz	8
Drive voltage	V	0-120
Capacitance	μF	3.6
Dimensions	LxWxH in mm	26x26x2.4



Figure 3: TDK PowerHap piezoelectric actuators.

4 EXPERIMENTAL TEST SET-UPS

Dynamic displacement measurements have been carried out using a laser vibrometer to

investigate the dynamic behavior of the actuators. Figure 4 shows the experimental test set-up using a Polytec OFV-5000 laser vibrometer with an OFV-534 laser head mounted on a 3-axes cartesian robot. This experimental set-up allows to measure the dynamic displacement response of a single point on an actuator or a surface as well as the scanning of a complete surface to determine the mode shapes of the vibrating plate.

Acoustic characterizations are carried out in a semi-anechoic chamber (i.e. whose floor is not covered with foam) in order to not alter the acoustic signal recorded by the microphone (Figure 4). The prototype plate is on a stand, at the same height and a distance of 1 m from the microphone, itself on a tripod (1 m from the ground). An APEX220 microphone from Apex Electronics is used for the measurements connected via an XLR cable to a Focusrite Scarlet2 6i6 soundcard connected via USB to the computer. Each set of measurements begins with a "blank" measurement of the room, with a sound level meter, to determine the sound level (about 29 dB within the room in general). The amplified piezoelectric actuators in this paper are driven with a Piezomechanik LE 150/100 EBW amplifier. It generates voltages between 0 V and 150 V to be obtained with a preset offset voltage from a 0 V to 5 V input. The gain is x30 and its no load bandwidth extends up to 70 kHz. The amplifier can supply up to 350 mA continuously and 1200 mA peak. This leads to a rapid decrease in its bandwidth with increasing load. The piezoceramic ring is driven with an ELBATEC T-500 symmetrical high-voltage amplifier. It generates voltages of ± 200 V from a ± 10 V input. The maximum current is 400 mA and the no-load bandwidth extends up to 100 kHz.

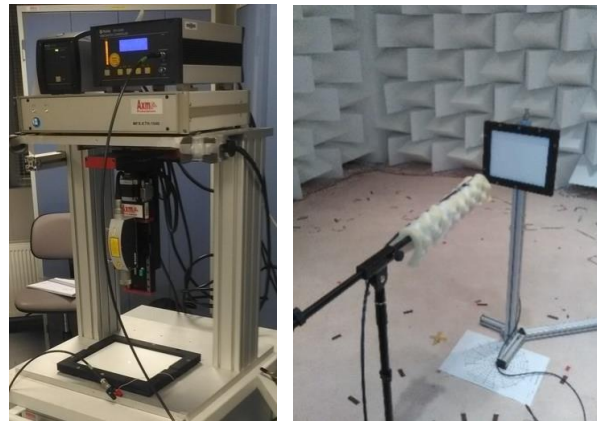


Figure 4: Set-up for displacement measurements with a laser vibrometer (left) and acoustic measurements in a semi-anechoic chamber (right).

5 MEASUREMENT RESULTS

5.1 Piezoelectric ring

First, the displacement behavior at the center of the plate is measured with the laser vibrometer. Therefore, a 400 Vpp sine sweep is applied to the piezoelectric ring element. The loudspeaker is screwed to the base of the scanning table as shown in Figure 4 to prevent any unintended movement. Figure 5 shows the result for an excitation frequency from 50 Hz to 20 kHz. It can be seen that the absolute displacements are in the low micrometer range from 0.3 μm to 25 μm decreasing towards higher frequencies.

Next, the sound pressure level of the piezoelectric ring speaker has been characterized from 100 Hz to 20 kHz for a driving voltage of 400 Vpp. The sound pressure level (SPL, the reference level corresponds to the threshold of hearing, 20 μ Pa) is shown in Figure 6 measured in the semi-anechoic chamber. A 1/12 octave filter has been applied to the SPL curve. Due to the low capacitance of the ring actuator, high frequencies with relatively low power consumption can be attained. However, the low frequency range is quite limited. Despite of a few acoustic holes an average SPL of 80 dB is emitted up to 20 kHz. The lower cut-off frequency with this polypropylene plate is around 400 Hz reaching a SPL of 75 dB.

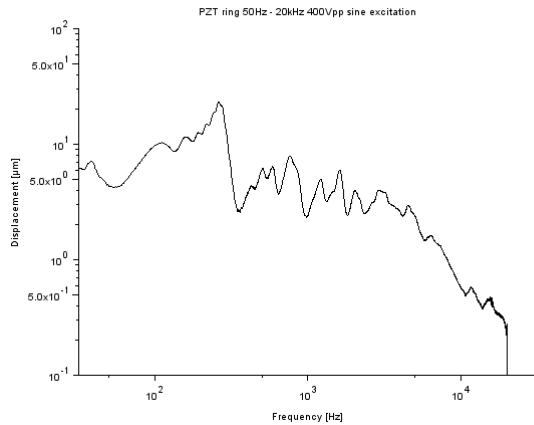


Figure 5: Displacement response of the PZT ring speaker measured at the center of the plate.

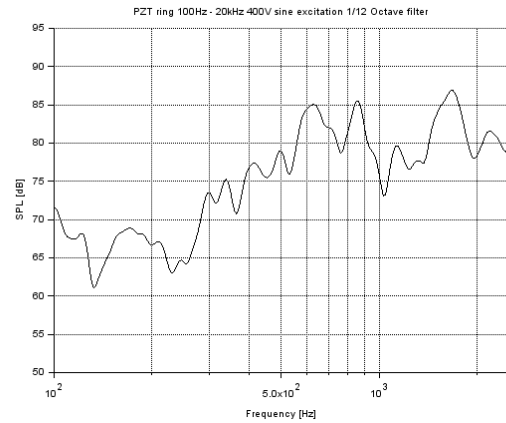


Figure 6: SPL of the PZT ring speaker measured at 1 m at 400 Vpp.

5.2 Flat flextensional piezoelectric actuator

As for the piezoelectric ring, laser vibrometer displacement measurements have been carried out for the APA400MML actuator. First, the frequency response has been measured for frequencies from 20 Hz to 20 kHz for the actuator only. A 7.5 Vpp sine sweep (offset 3.75 V) was applied to the piezoelectric actuator with a duration of 2 s. The result is shown in Figure 7. It can be seen that the APA400MML actuator has linear displacement behavior up to its first resonance frequency indicated at 634 Hz by the supplier. Figure 8 shows the displacement frequency response for a 150 Vpp (offset 75 V) sine sweep from 100 Hz to 500 Hz. This is the maximum driving voltage that can be applied to the actuator. At those driving voltages, the actuator cannot be actuated on its first resonance, which would cause failure to the ceramic due to excessive tensile stress. The supplier indicated a mean maximum peak to peak displacement amplitude of 368 μ m up to the first resonance frequency. It has to be noted that one of the three piezoelectric ceramics composing the APA400MML actuator was electrically damaged and has been electrically removed from the actuator. Driven with only two ceramics the measured peak displacement amplitude is around 150 μ m before the first resonance frequency but the voltage amplifier can now fully charge the actuator up to 500 Hz.

Next, the Cedrat Technologies APA400MML speaker has been characterized in the semi-anechoic chamber. A 7.5 Vpp sine sweep of 5 s has been applied to the actuator and measured with the microphone. In Figure 9, the 1/12 octave filtered sound pressure level from 100 Hz to 20 kHz is shown. It can be seen that even at very low driving voltages relatively high levels can

be attained in the range from 400 Hz to 2 kHz. For higher frequencies, the membrane material as well as the characteristics of the actuator induce damping lowering the maximum sound pressure level. Figure 10 shows the transfer function for a 150 Vpp (75 V offset) sine sweep excitation from 100 Hz to 500 Hz. As described earlier, this kind of actuator cannot be driven in resonance, which would lead to breakdown of the ceramics. It can be seen that SPLs exceeding 75 dB can be achieved from 1500 Hz to 600 Hz using this kind of actuators and the current surface size. It may be convenient to increase the size of the membrane to achieve higher levels at lower frequencies.

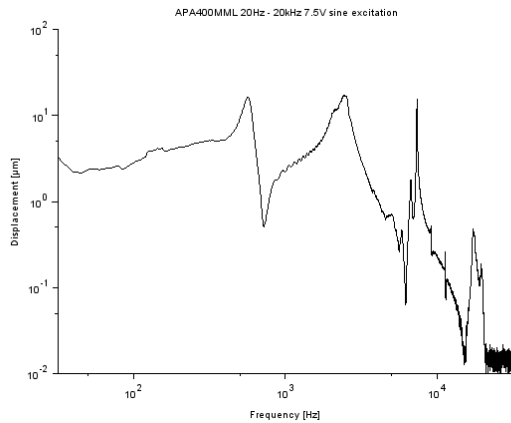


Figure 7: Displacement amplitude frequency response of the APA400MML actuator for a 7.5 Vpp driving voltage (2 s sine sweep) from 10 Hz to 20 kHz.

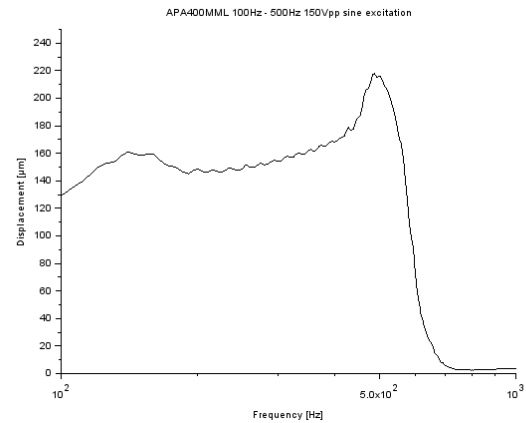


Figure 8: Displacement amplitude frequency response of the APA400MML actuator for a 150 Vpp driving voltage (2 s sine sweep) from 100 Hz to 500 Hz.

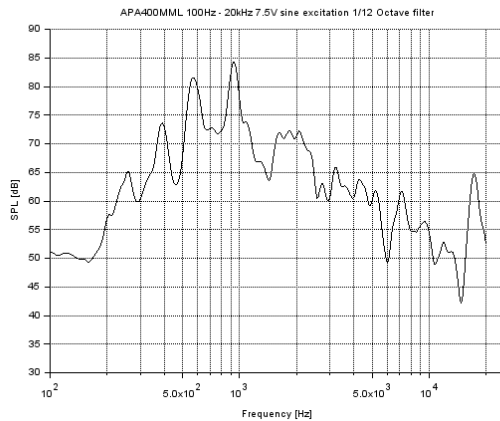


Figure 9: SPL from 100 Hz to 20 kHz of the APA400MML speaker at 7.5 Vpp.

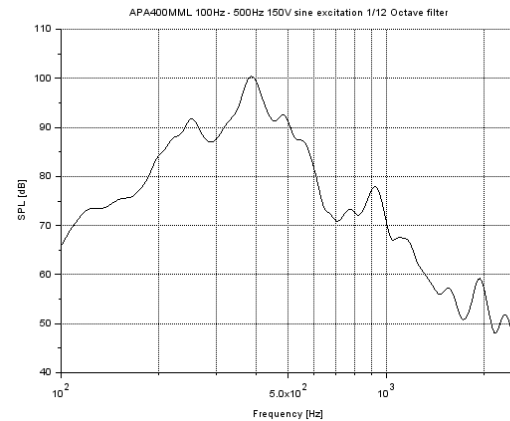


Figure 10: SPL from 100 Hz to 500 Hz of the APA400MML speaker at 150 Vpp.

4.3 Cymbal-type flexensional piezoelectric actuator

Finally, the displacement amplitude of the TDK PowerHap 15G actuator has been measured. Figure 11 shows the peak displacement amplitude from 100 Hz to 20 kHz with an almost linear

zone below the first resonance frequency around 8 kHz. The mean peak amplitude at 7.5 V is around 10 μm . Figure 12 shows the frequency response for a 2 s sine sweep from 100 Hz to 1 kHz at 120 Vpp with an offset of 60 V (maximum driving voltage). The almost horizontal plateau has a peak displacement amplitude of 80 μm . This actuator can be fully charged up to 1 kHz by the amplifier used in this paper.

The sound pressure level of the TDK PowerHap 15G speaker has been characterized in the semi-anechoic chamber. A 120 Vpp (offset 60 V) sine sweep of 5 s has been applied to the actuator and measured with the microphone. Figure 13 shows the sound pressure level from 100 Hz to 20 kHz. Relatively high SPLs are achieved between 500 Hz and 2.5 Hz. There is a small hole present in the transfer function from 1.2 kHz to 1.6 kHz due to the insufficient charging of the actuator by the amplifier (limited to 1 kHz for this actuator). Next to the APA actuators, this actuator is an interesting candidate to excite the car structures because of its compact geometry, relatively low power consumption and high displacement amplitude.

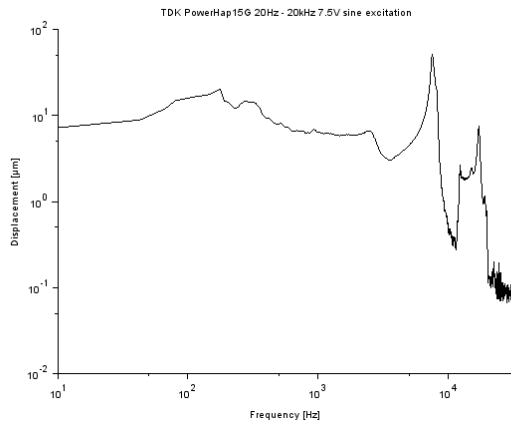


Figure 11: Displacement amplitude frequency response of the TDK PowerHap 15G actuator for a 7.5 Vpp driving voltage (2 s sine sweep) from 100 Hz to 20 kHz.

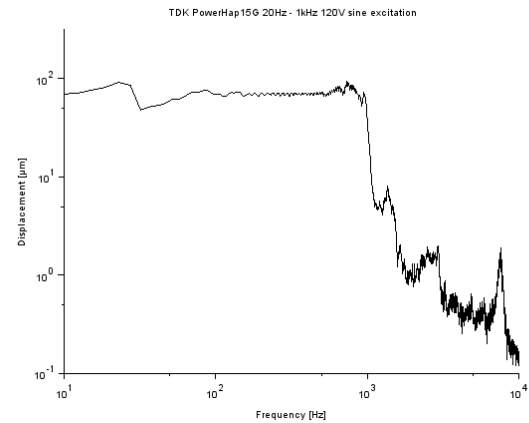


Figure 12: Displacement amplitude frequency response of the TDK PowerHap 15G actuator for a 120 Vpp driving voltage (2 s sine sweep) from 100 Hz to 1 kHz.

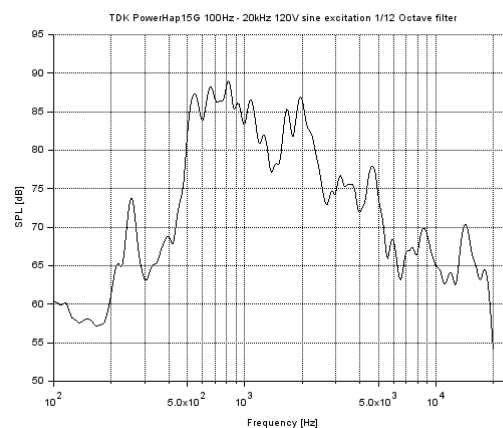


Figure 13: SPL of the TDK PowerHap 15G speaker at 120Vpp.

6 DISCUSSION

The study revealed that the piezoceramic ring can be used for exciting the medium to high frequency audio range. In practice, lower maximum voltages will be applied reducing the sound pressure level and thus affecting primarily the lower end of the excited frequencies. This will shift the addressable audio range to higher frequencies. This can be partially compensated by using multiple piezoceramic actuators. The advantage if these actuators is their minimal size requirement and surface conform integration.

The amplified piezoelectric actuators can address the medium low frequencies from 150 Hz to 2.5 kHz. The APA series can easily be adapted to a targeted audio range but may introduce actuators of bigger size. The PowerHap actuators stand out by their small size and relatively high output displacement. Output force may be an issue depending on the LLS stiffness. In both cases, the voltage amplifiers are the main limitation factor for speaker applications. Using different membrane materials with higher Young's modulus and lower damping than the polypropylene material used in this paper can increase the sound pressure level but may introduce coloration to the created sound. In general, to achieve a proper radiation efficiency and radiated sound power, the Young's modulus cannot be too low. A tradeoff between Young's modulus and the density needs to be found to design efficient LLS.

Compared to classical electrodynamic speaker, the piezoelectric actuators are not visible and can be applied to structures that have initially other functions than creating sound. After equalization, LLS performance could be similar to electrodynamic speaker, at least subjectively. The process of equalization basically cancels out the lack of certain frequency band, and thus, is no longer affecting the performance. The use of sophisticated control schemes applied by a digital signal processor when using multiple actuators could significantly improve sound quality even on complex structures. The implementation of piezoelectric actuators is then a good choice because they can be more easily controlled than electrodynamic exciter technology.

7 CONCLUSIONS

Three different actuators have been compared in this paper in terms of maximum displacement amplitude and maximum sound pressure level on 300 x 200 x 3 mm³ speaker surfaces. A flat piezoelectric ring glued to a surface is compared to amplified piezoelectric actuators. The ring actuator produces good sound pressure levels at frequencies higher than 400 Hz but excites confuse mode patterns due to the stiff ceramic glued to the surface making control schemes more challenging. The other two actuators have been tested in a reactive configuration (fixed between two plates) to overcome the diffuse mode patterns created by a piezoceramic disc or ring glued to a surface. Highest output displacements can be obtained with the APA400MML flextensional actuator from Cedrat Technologies, which is limited to a maximum frequency of around 500 Hz due to its first mechanical resonance. Due to the high capacitance, this actuator is relatively power consuming. Its maximum output force of 200 N is not necessary for the speaker surface used in this paper but gives much design space for applications with complex and stiff structures. A smaller piezoceramic stack could be used to reduce power consumption. The flat cymbal actuator from TDK named PowerHap 15G produces a force of 20 N, which is enough to displace the membrane. Good acoustic power is

produced between 500 Hz and 2.5 kHz. Power consumption is reduced by a factor of three compared to the APA400MML actuator because of the lower capacitance (3.6 μ F compared to 10 μ F). The very compact design (26 x 26 x 2.4 mm³) could make this actuator a good choice for medium frequencies in car applications. The limiting factor for high frequency sound generation using those amplified piezoelectric actuators is the availability of high-power electric amplifiers. In order to cover a large audio spectrum, the combination of simple piezoelectric ceramics with amplified piezoelectric actuators on the same loudspeaker panel can be advantageous to maintain low power consumption.

ACKNOWLEDGEMENTS

This work was financially supported by the French National Research Agency (ANR, contract ANR-17-CE33-0004).

REFERENCES

- [1] Bai, M.R. and Lu, Y. Optimal Implementation of Miniature Piezoelectric Panel Speakers Using the Taguchi Method and Genetic Algorithm. *J. Vib. Acoust* (2004) **126**(3):359-369.
- [2] Sugimoto, T., Ono, K., Ando, A., Kurozumi, K., Hara, A., Morita, Y. and Miura, A. PVDF-driven flexible and transparent loudspeaker. *Applied Acoustics* (2009) **70**(8):1021-1028.
- [3] APA400MML from Cedrat Technologies, <https://www.cedrat-technologies.com/en/products/actuators/amplified-piezo-actuators.html>.
- [4] PowerHap 15G from TDK Corporation, https://product.tdk.com/info/en/products/sw_piezo/haptic/powerhap/index.html.

ULTRA-LIGHT, SELF-DEPLOYABLE, ROD-CABLE STRUCTURES

ANDRZEJ ŚWIERCZ^{*}, JAN HOLNICKI-SZULC[†]

^{*} Institute of Fundamental Technological Research, Polish Academy of Sciences,
Pawińskiego 5B, 02-106 Warsaw, Poland
e-mail: aswiercz@ippt.pan.pl

[†] Institute of Fundamental Technological Research, Polish Academy of Sciences,
Pawińskiego 5B, 02-106 Warsaw, Poland
e-mail: holnicki@ippt.pan.pl

Key words: self-deployable structures, prestressed truss-like structures, rod-cable structures, joint connections, vibration reduction.

Abstract. This article is devoted to space truss-like structures commonly used for solar panel installations or telecommunication antennas. Such structures have obvious advantage of beneficial ratio of their stiffness to mass. One of challenges in satellite engineering is focused on special design of ultra-light structures, compacted during transportation to the orbit, able to deploy into large cantilever with e.g. photovoltaic panels (being on the orbit). This approach allows for better withstands the launch loads in compact configuration. The proposed smart topology (SMARTOP) of the structure enables for easy, zero-energetic transformation from the compact, two-dimensional form into the final, tree-dimensional configuration, making use of stored pre-stress energy, released with use of specially controlled clutches. Main innovations are in specially design topology and so-called smart clutches performing controlled release of stored strain energy in a proper timing. Numerical simulations of the SMARTOP structure functionalities are presented.

1 INTRODUCTION

The aim of this paper is to present specially designed, self-deployable rod-cable structure, applicable in satellite engineering, where the structure has to be launched into the orbit in a compact form (due to protection against high accelerations) and then, deployed into the very extended, flexible form (due to low gravitation and mass saving).

The structures on the orbit are subjected to thermal loads or can oscillate shortly after self-deploying. Therefore, an effective technique, in order to suppress the transient vibrations in low frequency range, is a very appealing solution. To this end, active (for example utilizing a force feedback control algorithm presented in [1]) and semi-active approaches (e.g. friction-based dampers [2-3]) have been developed by researchers. Mitigation of vibrations in the presented structure can be done utilizing by control of slacking and prestressing the cables embedded into the truss.

2 GENERAL CONCEPT OF THE DEPLOYABLE STRUCURE

The structural topology (Fig. 1a), according to the patent pending claim [4], allows switching from the stable, functional form (as a supporting isostatic truss structure) into the collapsed, compact form (Fig. 1d) ready for transportation with high overloading. Both configurations are switchable. The compact form of the structure can be fixed due to prestressed actuators and blocking devices, where release of them causes automatically structural development into the flexible truss form. Stability of this final form is guaranteed by strings located inside, along selected rod-tube elements (1 and 2) and by blocking of hinge devices (3).

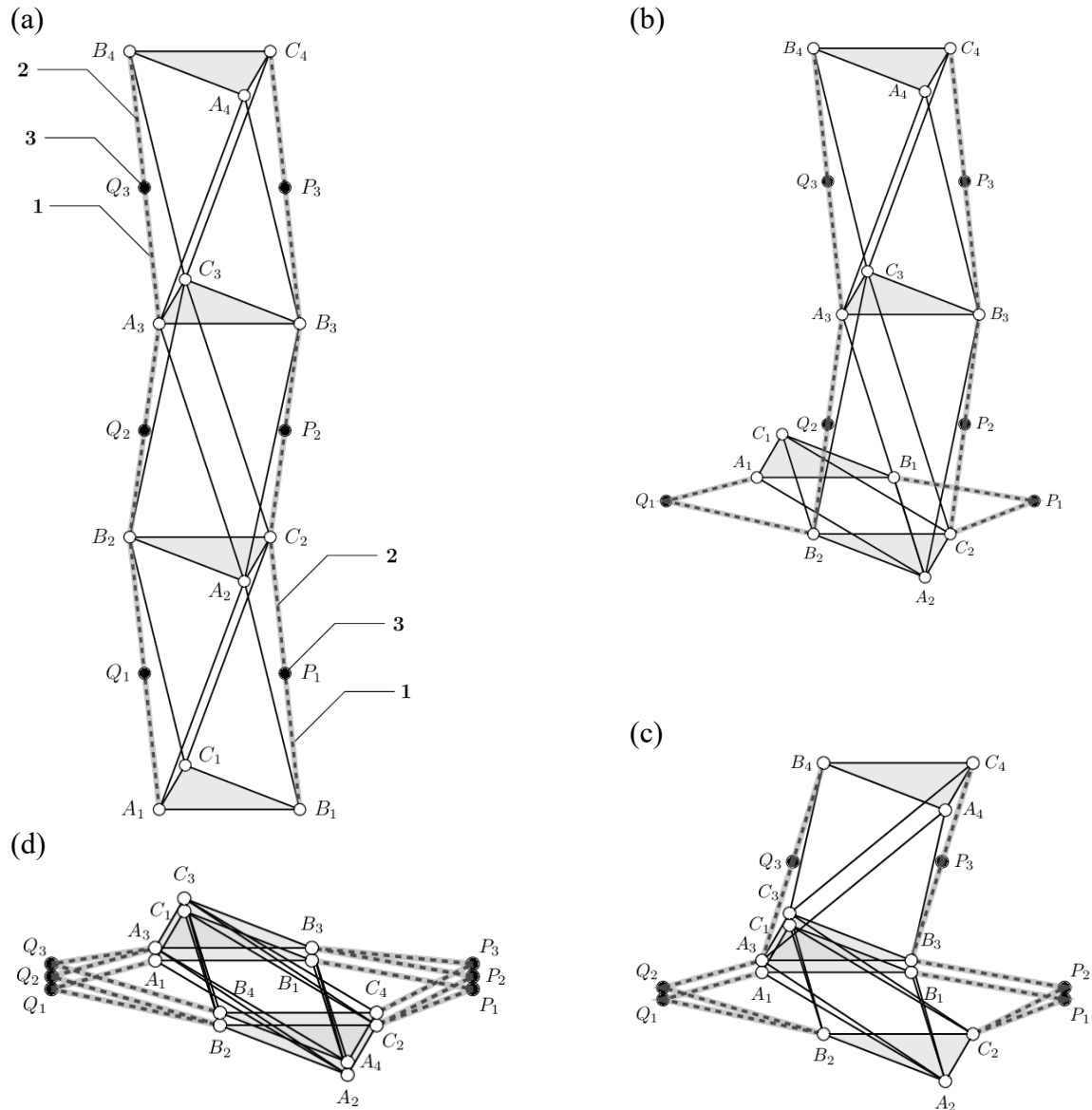


Figure 1: The SMARTOP configuration forms during sequential folding: (a) operational (initial) configuration; (b) configuration with folded the lower section; (c) configuration with folded the lower and middle sections; (d) fully folded configuration.

The truss topology (Fig. 1a) allows applying three pairs of rod-cable elements: $A_3B_4-B_3C_4$, $B_2A_3-C_2B_3$ and $A_1B_2-B_1C_2$ (one pair in each segment), realization of the planned modification of structural configuration. Rods (1) contain cable strings (2) inside and the controllable hinge mechanism (3) – blocked or released. When cables are pre-tensioned and hinge mechanism released, the sections collapse. After section collapsing, the hinge mechanism becomes blocked again. The structural configuration, after bottom section collapsing (deactivation of hinge mechanisms Q_1 and P_1 needed) is shown in Fig. 1b, while after bottom and middle section collapse (deactivation of hinge mechanisms Q_1-P_1 and Q_2-P_2 necessary) – on Fig. 1c. Finally, deactivation of all hinge mechanisms leads to the configuration shown on Fig. 1d. The sequence of collapsing sections to the 2D format can be arbitrary planned.

Simultaneous release of trigger springs initiating vertical movement up of all three levels of the structure together with deactivation of hinge mechanisms for pairs: Q_1-P_1 , Q_2-P_2 , and Q_3-P_3 , lead to rebuilding of the functional configuration of the structure. However, fixing of this configuration requires again initiation of cable pre-tensioning and hinge mechanisms reactivation.

Finally, three properly controlled smart devices: triggering springs, prestressing cables and blocking hinges allow automatic realization of two scenarios: controlled collapse and deployment of the structure.

3 BASIC DYNAMIC ANALYSIS

The vibrations of the structure were numerically tested. Firstly, the influence of the prestressing state in cables on modal parameters was investigated, and next the dynamic behaviour during unfolding was simulated. To this end, in both cases the following structural parameters were assumed:

- The truss structure composed with carbon fibers elements have pipe cross-sectional area with the wall thickness of 1mm and the outer diameter 10 mm. The applied elements have length: 0.60 m (horizontal element in the unfolded structure) and 0.85 m (remaining elements). The Young's modulus and density are equal to 60 GPa and 2100 kg/m^3 , respectively.
- The steel cable elements, placed inside selected truss elements (Fig 1a), with circular cross-section area with radius of 3 mm. The Young's modulus and density are equal to 200 GPa and 7850 kg/m^3 , respectively.
- Free-free structure only for modal analysis.

The numerical model and analyses were performed utilizing Abaqus software.

3.1 Eigenfrequencies and eigenmodes

Modal analysis was preceded by the computations of the statically loaded truss structure caused by the prestressed cables located as shown in Fig 2a (red lines). There were considered three prestressing states in the cables (out of structure): 20 kPa, 50 MPa and 200 MPa. The longitudinal stresses in the truss elements computed for the prestressed cables at level of 50 MPa are presented in Fig 2b. It is clearly visible, that the most loaded elements are co-located with the cables, whereas the remaining elements are slightly stressed. The displacement map of

the structure along the vertical axis (Z-axis) determined for this case is illustrated in Fig. 2c.

Next, taking into account the above mentioned prestressing levels, the modal analyses were performed. The obtained eigenfrequencies for the different prestressing states in the cables are shown in the Tab. 1. The first six modes corresponding to the rigid motions were omitted. For comparison, the results calculated for slackened cables were also included in the Tab. 1. The gathered results show the significant influence of the presence of prestressed state in the cables for the structural eigenfrequencies. On the other hand, the initial prestressing level is of secondary importance. Comparison of the overlapped corresponding mode shapes obtained for non-tensioned structure (black lines) and prestressed one (50 MPa, blue lines) are presented in Fig. 3.

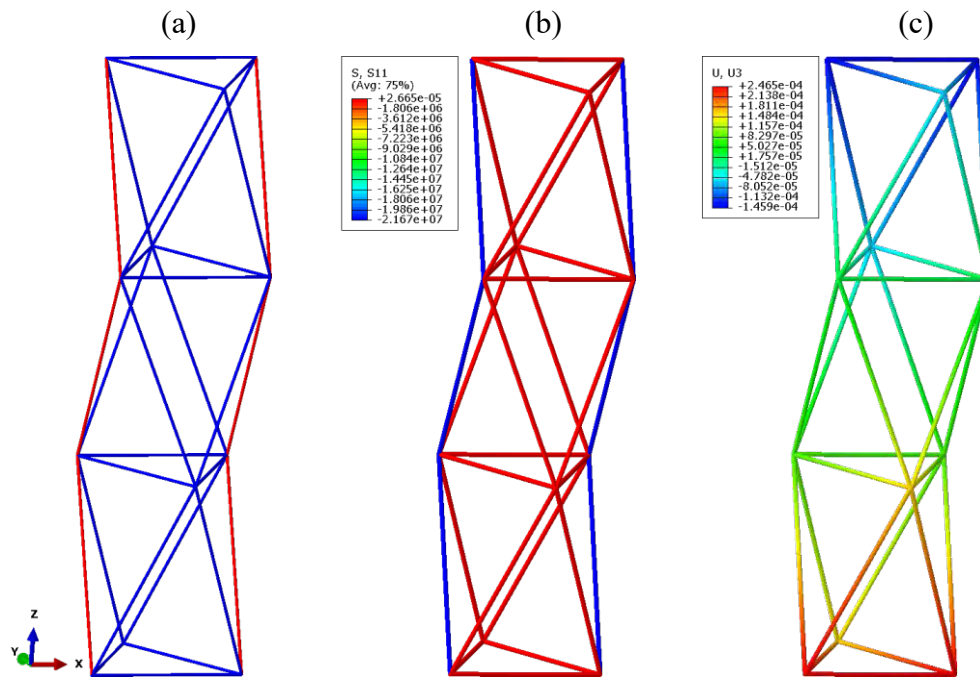


Figure 2: Statically prestressed structure (initial stress in the cable: 50 MPa): (a) tendon locations (red lines); (b) axial stress in the truss elements; (c) displacement map along Z-axis.

Table 1: List of the first six eigenfrequencies (corresponding to non-rigid mode shapes) obtained for non-tensioned and prestressed structures.

Mode number	Eigenfrequencies [Hz]			
	Non-tensioned	Prestressed 20 kPa	Prestressed 50 MPa	Prestressed 200 MPa
7	178.45	188.02	188.06	188.18
8	191.60	194.80	194.93	195.30
9	224.52	234.48	234.49	234.51
10	300.15	301.33	301.30	301.21
11	311.27	340.50	340.67	341.17
12	368.62	381.33	381.45	381.81

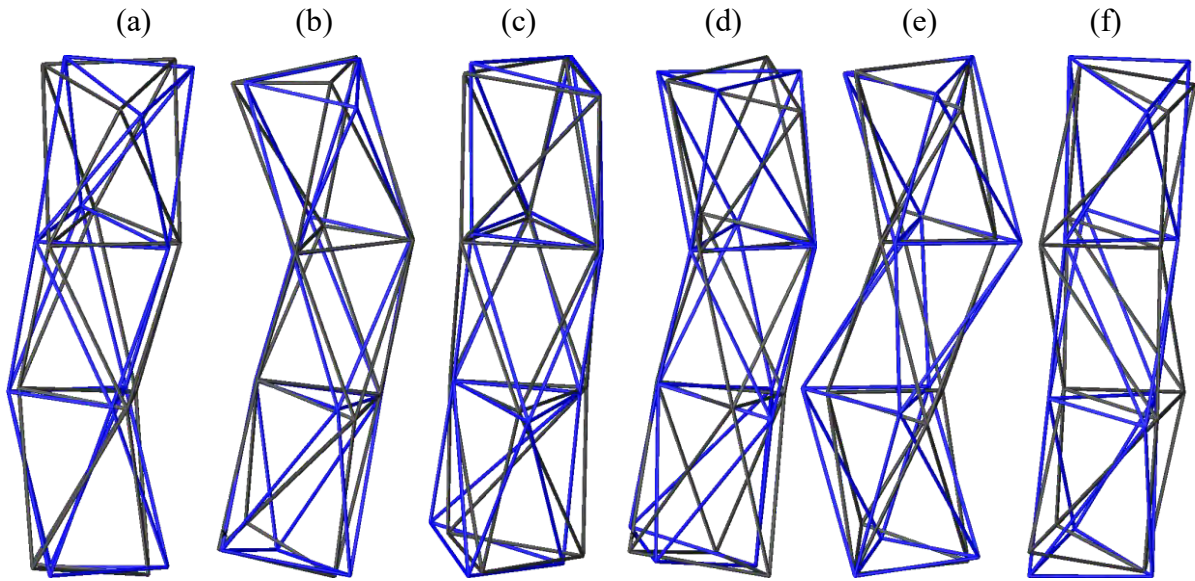


Figure 3: The eigenmodes (7-12) obtained for the non-tensioned and prestressed (50 MPa) structures.

3.2 Unfolding-induced vibrations

For testing purposes of the unfolding dynamics a single section of the structure was considered. Additionally, the structure was simply supported at the nodes (nos. 1, 2, 3) in the bottom section as shown in Fig. 4. Initially, the remaining nodes of the structure was clamped in the folded mode (Fig. 4a). Releasing the clamped nodes (nos. 4-8) and simultaneously imposing initial velocities at nodes of upper section (nos. 4-6) the structure is transformed into the operational form. The transformation requires a change of pin-joints (nos. 7, 8) into a rigid joints in a proper time. This approach generates excessive structural vibrations as well as bending moments and transversal forces in the elements adjacent to the switchable joints. Therefore, these elements have to be considered as beams during the transformation process.

For mitigation such effects an appropriate strategy during unfolding of the structure has to be applied. The further research work will be focused on:

- damping of unfolding-induced vibrations utilizing the switchable cable between the slackened and prestressed states,
- minimization of the bending moments and transversal forces in the structural elements caused by a status change of the switchable joints.

4 CONCLUSIONS

In this article a concept of a deployable truss structure was presented. The structure has a special designed topology allowing for easy transformation from folded mode (transportation mode) into operational mode as well as allowing for damping vibrations. The structural mode change is possible thanks to application of switchable joints blocked at the final stage of the

unfolding process. The second attribute – damping vibration – can be performed utilizing *on–off* switching the prestressed states in the cables. The presented numerical results show the significant modification of the modal parameters of the structure.

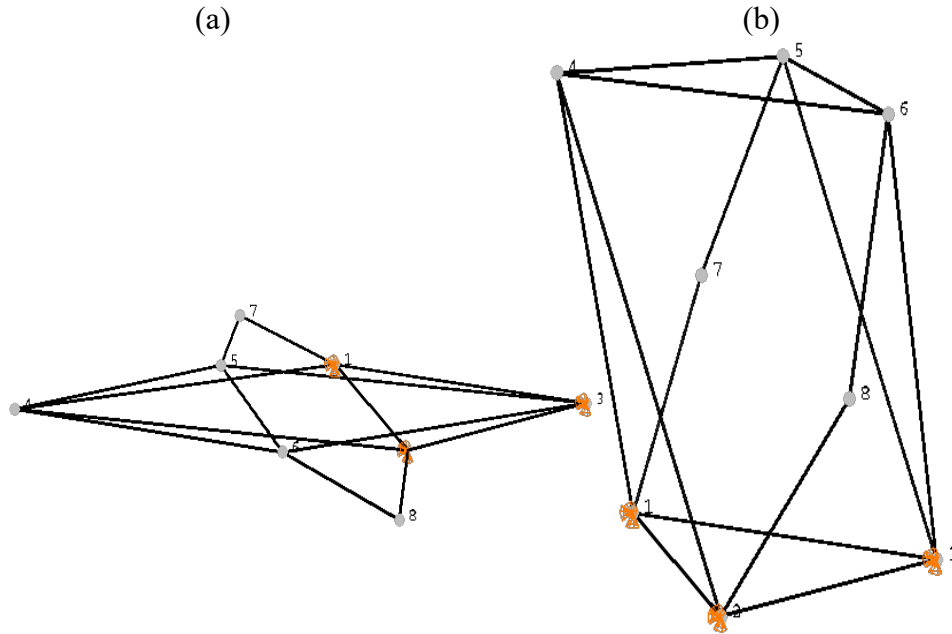


Figure 4: Two stages of the single section unfolding: (a) initial stage, (b) close to final stage.

ACKNOWLEDGEMENTS

The authors gratefully acknowledge the co-financing of the National Centre for Research and Development, Poland, granted in the framework of the TANGO programme (TANGO2/341494/NCBR/2017) and of the National Science Centre, Poland, granted through the project Re-Con (DEC-2017/25/B/ST8/01800).

REFERENCES

- [1] Guo, T., Liu, Z. and Cai, L. *An Improved Force Feedback Control Algorithm for Active Tendons*, Sensors, MDPI AG, Vol. 12(8), pp. 11360-11371, 2012.
- [2] Garrido, H., Curadelli, O. and Ambrosini, D. *Semi-active friction tendons for vibration control of space structures*, Journal of Sound and Vibration, Elsevier BV, Vol. 333(22), pp. 5657-5679, 2014.
- [3] Park, Y.-m. and Kim, K.-j. *Semi-active vibration control of space truss structures by friction damper for maximization of modal damping ratio*, Journal of Sound and Vibration, Elsevier BV, Vol. 332(20), pp. 4817-4828, 2013.
- [4] Holnicki-Szulc, J., Swiercz, A. and Knap L. *Self-deployable space truss-like structure*, Polish Patent Office, patent pending, 2019.

ACCURATE CHARACTERIZATION OF FLUIDIC ARTIFICIAL MUSCLE FORCE RESPONSE FOR IMPROVED MODEL FIDELITY

JONATHAN M. CHAMBERS AND NORMAN M. WERELEY

Department of Aerospace Engineering
University of Maryland
College Park, MD 20742, USA
web page: <https://aero.umd.edu/>

Key words: Fluidic Artificial Muscles, Pressure Control Circuits, Working Fluid Comparison

Abstract. There is currently an increased interest in extending the application of McKibben actuators for a range of working fluids. Extensive efforts have already established force response models for pneumatically driven McKibben actuators that are independent of working fluid material properties, however the model's independence to working fluid choice has yet to be validated with empirical evidence. This paper experimentally investigates the effect of working fluid choice on the quasi-static pressure dependent force-contraction response of McKibben actuators, and tests the hypothesis that FAM actuation force is dependent on inflation pressure while being independent of all other working fluid properties. Using air or water as the working fluid, characteristic isobaric force-contraction response curves are compared for a small scale McKibben actuator. To ensure truly isobaric force-contraction characterizations, hydraulic and pneumatic pressure systems were developed to provide precise and accurate control of pressure. Experimental testing showed that using air or water as a working fluid resulted in nearly identical isobaric force-contraction response curves, and demonstrated that the quasi-static force of McKibben actuators is independent of working fluid. This establishes that the previously developed force response models for pneumatic McKibben actuators can now be easily extended to use with other permissible liquid or gaseous fluids. With the conclusion of this research, McKibben actuators can be readily adapted to a wider range of uses with working fluid choice catered to application requirements independent of their force response.

1 INTRODUCTION

An increasingly diverse number of applications are utilizing McKibben actuators due to their many desirable characteristics. Previous work established McKibben actuators as an ideal form of actuator when compliant, high force-to-weight ratio actuation is desired [4, 5, 14]. McKibben actuators, known more generally as fluidic artificial muscles (FAMs), have often been operated using air (PAMs). Research efforts have also been focused on the accuracy and fidelity of modeling pneumatic FAMs for control purposes. Using empirical test data, semi-mechanistic models that achieve a high degree of accuracy have been developed for pneumatic FAMs.

Research efforts for FAMs have recently expanded to use with different working fluids as the FAM's source of internal pressure. Although FAMs have typically been operated pneumatically, applications of FAMs also include water [6, 15], and aerospace applications [2, 9] making it necessary to study working fluids that are best suited to these environments.

Few researchers have studied hydraulically powered FAM actuators [1, 6, 8, 10, 11, 12] while even fewer have directly compared FAM actuators pressurized with air or water [3, 7, 13]. Tiwari tested the assumption made in pneumatic FAM (PAM) models that indicate pneumatic and hydraulic powered FAMs should provide the same force response independent of the choice of working fluid in quasi-static operation. Tiwari used a 3.18 mm (1/8 in) FAM to conduct constant pressure tests with water and air, with results showing substantial discrepancies between their force response. The difference in the force response of the two working fluids was cited as likely being a result of inaccurate control of the fluid pressure.

This research describes the effect of working fluid selection on the quasi-static pressure dependent force-contraction response of FAMs. Testing either air or water as the working fluid, characteristic isobaric force-contraction response curves are compared for a small scale McKibben actuator. Improving upon the work done by Tiwari, where inaccurate pressure control resulted in an inconclusive comparison between pressurization using air or water, in this study hydraulic and pneumatic pressure systems were developed to provide precise and accurate control of pressure to ensure a dependable comparison between the two working fluids. Consecutive testing using water and then air is conducted to show the independence of working fluid choice on the quasi-static response of FAMs, and demonstrates that pressure is the independent variable.

Pneumatic FAM models have been developed and refined through the years to provide an accurate representation of their quasi-static force response. A semi-mechanistic model based on a force balance approach was recently updated to include empirically fit coefficients that represent the material properties of the elastomeric bladder [9]. This force response model is a function of the working fluid pressure, P , and the PAM actuator length, L , and is given as follows:

$$F(P, L) = \frac{P}{4\pi N^2} (3L^2 - B^2) + \sigma_z \left(\frac{V_b}{L} \right) - \sigma_c \left(\frac{tL^2}{2\pi RN^2} \right) \quad (1)$$

where the number of turns of a single braid fiber about the actuator's diameter, N , the length of that braid fiber, B , and the volume of the incompressible bladder, V_b , are set values that describe the geometry of the FAM actuator. The thickness of the bladder, t , radius of the actuator, R , and the longitudinal bladder stress, σ_z , and circumferential bladder stress, σ_c , are values that are functions of the instantaneous actuator length, L . Inspection of this model shows that actuation force is a function of only the PAM's geometry, materials, and working fluid pressure. With no reliance on fluid properties other than pressure, it is assumed that this model can be transferrable to use with FAMs for other working fluids besides air. This study was performed to validate the accuracy of this assumption, and to then extend the use of the force response models used for PAMs more generally to use with FAMs independent of the chosen working fluid.

2 EXPERIMENTAL TEST SETUP

The FAM was experimentally tested with either air or water as the working fluid. The routine of characterizing the actuator's isobaric force-contraction response was adopted from previous PAM characterization testing [4]. The FAM is slowly stroked at 5.1 mm/sec (0.2 in/sec) from its resting length to its zero force length at constant pressure. The FAMs were stroked at set pressures of 138-689 kPa (20-100 psi) in 138 kPa (20 psi) increments.

Testing for this study was conducted in a MTS material testing machine that strokes the FAM while recording inputs from a pressure transducer (Omega PC209-200G5V) and load cell (Honeywell Model 31 Mid). The FAM is tested with each working fluid consecutively to ensure retention of the FAMs reference length state and alignment. Fixtures to connect the FAM to the MTS machine were fabricated to be adaptable to the hardware necessary for either air or water testing without requiring removal of the FAM from the testing machine.

2.1 FAM Test Specimens

A small scale FAM (4.8 mm (3/16 in) diameter) was fabricated for comparison testing of air and water powered actuation to ensure size independence of observed phenomenon (Fig. 1). This FAM typically produces a maximum force in the blocked force condition of about 222 N (50 lbf), and can achieve a maximum/free contraction of 25-35%.

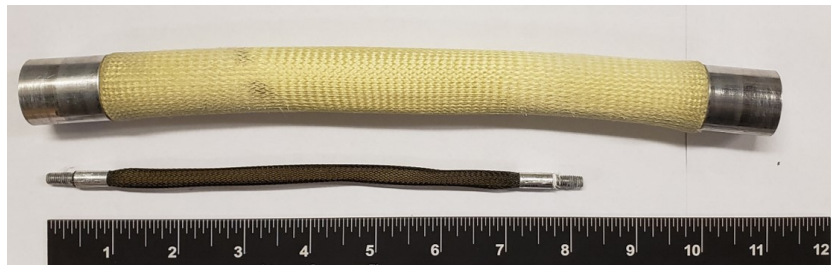


Figure 1: 22.2 mm FAM (top) versus the 4.8 mm FAM (bottom) used in this test

2.2 FAM Test Specimens

An accurate comparison between air and water working fluids requires precise and accurate control of the pressure supplied to the FAM to maintain a true isobar for each stroke cycle test of the FAM. Careful regulation of pressure is required to ensure that any difference between the FAM force response for each working fluid could be correctly attributed to the working fluid and not by any imprecision in feed pressure. This drove the decision to develop pressure control systems for water and air. The water pressure systems for each working fluid are detailed in the following sections.

2.2.1 Pneumatic Pressure System

The air pressure system for pneumatic FAM testing, shown in Fig. 2, is the same as what has been used for previous PAM testing with the addition of a proportional valve to more precisely

regulate airflow. An air compressor (DeWalt D55146) was used to store and provide pressurized air. A pressure regulator (Excelon R73G) was used to set a constant supply pressure of 793 kPa (115 psi), 103kPa (15 psi) above the maximum pressure to be tested. A proportional control valve (Enfield Technologies LS-V05s) was used to directly control FAM pressure. An Arduino was used as a controller to direct proportional valve actuation to control pressure. The Arduino received pressure state values for controller feedback through a pressure transducer (Omega PX209-200G5V) mounted to the fixture just above the air inlet of the FAM. A 4448 N (1000 lbf) load cell (Honeywell Model 31 Mid) was placed in line with the FAM to measure the contraction force of the FAM.

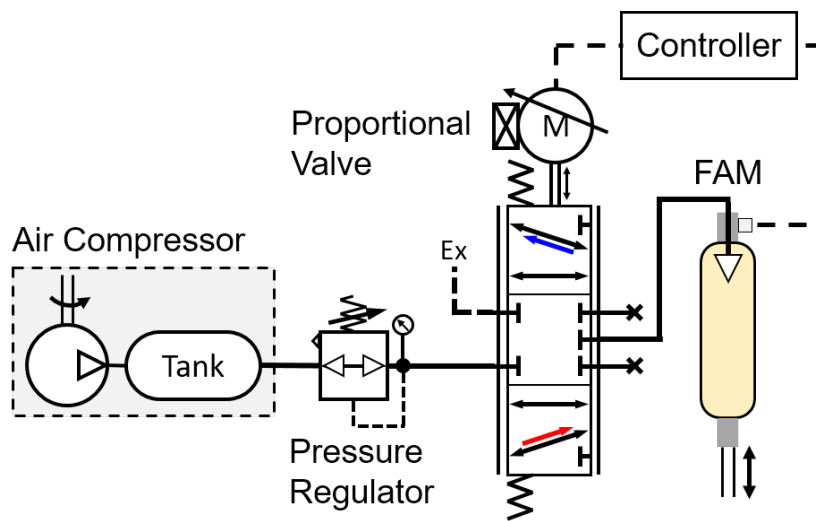


Figure 2: Pneumatic pressure system schematic

2.2.2 Hydraulic Pressure System

Testing the FAM with water required the development of a hydraulic pressure system (Fig. 3). The incompressibility of water, as well as the limited number of water compatible components, resulted in a hydraulic system that is very different in nature from the pneumatic system. The hydraulic system uses a continuously running, variable-speed pump. A fixed displacement gear pump (Fluid-o-Tech FG204) uses a fluid reservoir as the water source. To avoid damaging hydraulic hammer effects from requiring the motor to constantly switch directions about a pressure set point, the FAM was made open at each end to allow continuous flow of water in a single direction through the FAM. To buildup pressure in the system, flow is restricted downstream of the FAM using a needle valve. An adjustable relief valve (Watts LF 530-C STD) was positioned between the pump and FAM to relieve pressure if it exceeds 758 kPa (110 psi). Pump speed is controlled using an Arduino to achieve the desired isobaric pressure.

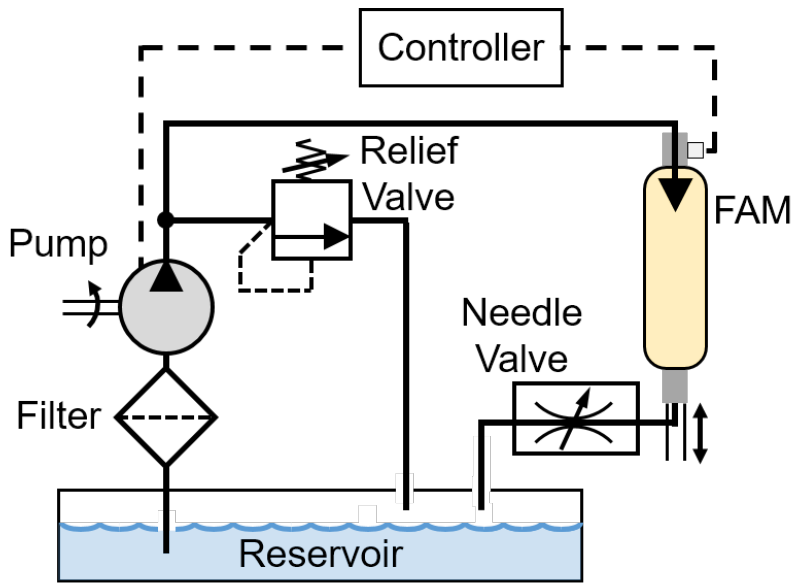


Figure 3: Hydraulic pressure system schematic

2.3 Pressure Control System

A proportional-integral (PI) closed-loop feedback controller was used to regulate each pressure system to the desired isobar. The controller input acts to minimize the error, $e(t)$ between the desired set pressure, P_{set} , and the actual pressure, P_{meas} . The controller receives a pressure sensor voltage as input, and outputs a control signal in the form of a 5V pulse width modulation (PWM) signal. The Arduino produces a command value of 0-255 as a digital representation of the PWM output that translates to a 0-100% duty cycle. This enables the digital based Arduino to output the 0-5V analog input values required for control of the proportional valve and pump. The controller was tuned for the pneumatic and hydraulic pressure circuits for the FAM resulting in two gains, the proportional gain, K_p and the integral gain, K_i , which were tuned through iterative testing.

3 TEST RESULTS

Accurate pressure control was achieved for both the hydraulic and pneumatic pressure systems, resulting in a high fidelity comparison of the response of the two tested working fluids. The results of the pressure control, as well as the characterization of the FAM response with air and water working fluids are detailed in the following sections.

3.1 Pressure Control Results

Results for the measured pressure during characterization testing are given in Table 1 below. Average pressure and standard deviation values are given for both air and water testing. Together, these values provide a depiction of how well the pressure systems provided a true isobar for each set pressure test to enable a good comparison between each working fluid. Although there is a slight offset in the set pressure versus the test pressures, the average pressures when

using air or water correlated very closely with one another with a minimum deviation from the set pressures.

Table 1: Average pressure and standard deviation for the force response characterization test at each test pressure

Commanded Set Pressure	138 kPa	276 kPa	414 kPa	552 kPa	689 kPa
Average Pressure, Air (kPa)	145.17	284.37	422.34	561.16	699.82
Average Pressure, Water (kPa)	145.13	284.17	422.13	560.55	699.18
Standard Deviation, Air (kPa)	1.58	1.24	1.42	1.77	1.99
Standard Deviation, Water (kPa)	1.04	1.02	1.52	1.97	1.41

3.2 Characterization Results

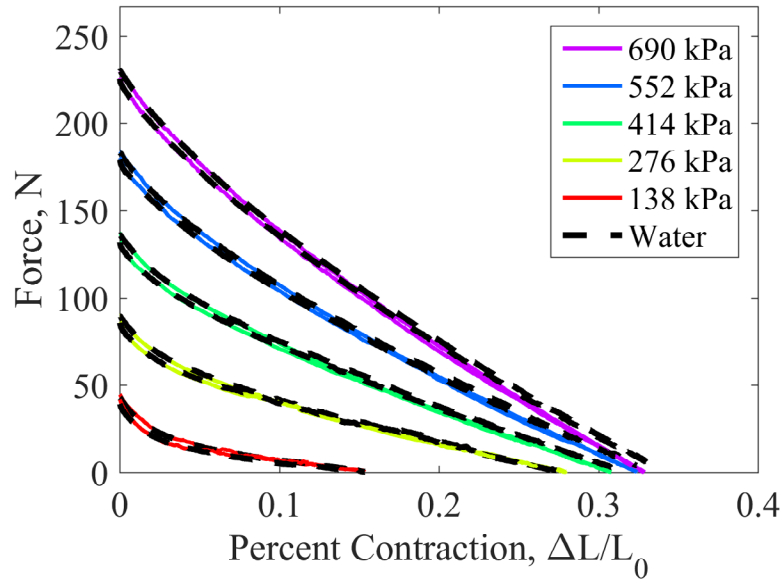


Figure 4: Results of each isobaric force-contraction characterization test for the 4.8 mm FAM

Characterization testing of the FAM with each working fluid showed nearly identical results when using either air or water for all tested pressures. Results from each characterization test are plotted in Fig. 4. To provide a quantitative comparison of the force response difference between the two working fluids, the root mean squared error (RMSE) between the two responses was calculated for each pressure. The root mean squared error was calculated using the following equation:

$$RMSE_{avg} = \sqrt{\frac{1}{N_i} \sum_i ((F_i)_{air} - (F_i)_{water})^2} \quad (2)$$

where F is the experimental force for each test, and N is the total number of data points of each test with i representing each respective measurement point from 1 to N . RMSE values for both working fluids at each pressure are given in Table 2.

Table 2: Root-mean-square error (RMSE) at each test pressure

	138 kPa	276 kPa	414 kPa	552 kPa	689 kPa	Overall Average
4.8 mm Dia. (N)	0.85	1.20	2.00	2.05	3.34	1.82

4 Conclusion

This study examined the effect of working fluid choice on the quasi-static force response of FAMs. Past studies showed that the working fluid can affect the dynamic behavior and efficiency of FAMs, but none conclusively demonstrated the assumption that the quasi-static force response is independent of the working fluid used to power it. To study this assumption, a small scale FAM was fabricated, and had its force response characterized using water and air as the working fluid. To ensure an accurate comparison between using air and water, control systems were developed to precisely control fluid pressure for each isobaric force-contraction characterization test. Testing of each working fluid resulted in nearly identical isobaric force-contraction response curves. This confirms that the FAM's quasi-static force response is independent of working fluid, allowing force response models previously developed for PAMs to be adopted for use with FAMs with any working fluid, and motivates the use of FAMs with an expanded range of application dependent working fluids.

REFERENCES

- [1] M. De Volder and D. Reynaerts. Pneumatic and hydraulic microactuators: a review. *Journal of Micromechanics and microengineering*, 20(4):043001, 2010.
- [2] S. A. DeLaHunt. *Variable Recruitment in Bundles of Miniature Pneumatic Artificial Muscles and Space Qualified Pneumatic Artificial Muscles*. PhD thesis, 2016.
- [3] M. Focchi, E. Guglielmino, C. Semini, A. Parmiggiani, N. Tsagarakis, B. Vanderborght, and D. G. Caldwell. Water/air performance analysis of a fluidic muscle. In *2010 IEEE/RSJ international conference on intelligent robots and systems*, pages 2194–2199. IEEE, 2010.
- [4] E. G. Hocking and N. M. Wereley. Analysis of nonlinear elastic behavior in miniature pneumatic artificial muscles. *Smart Materials and Structures*, 22(1):014016, 2012.
- [5] A. Huber, Fleck. The selection of mechanical actuators based on performance indices. *Proceedings of Royal Society of London. Series A: Mathematical, physical and engineering sciences*, 453(1):2185–2205, 1997.

- [6] K. K. Ku, R. Bradbeer, K. Lam, and L. Yeung. Exploration for novel uses of air muscles as hydraulic muscles for underwater actuator. In *OCEANS 2008-MTS/IEEE Kobe Techno-Ocean*, pages 1–6. IEEE, 2008.
- [7] M. A. Meller, M. Bryant, and E. Garcia. Reconsidering the mckibben muscle: Energetics, operating fluid, and bladder material. *Journal of Intelligent Material Systems and Structures*, 25(18):2276–2293, 2014.
- [8] M. Mori, K. Suzumori, S. Seita, M. Takahashi, T. Hosoya, and K. Kusumoto. Development of very high force hydraulic mckibben artificial muscle and its application to shape-adaptable power hand. In *Robotics and Biomimetics (ROBIO), 2009 IEEE International Conference on*, pages 1457–1462. IEEE, 2009.
- [9] T. E. Pillsbury, N. M. Wereley, D. L. Akin, et al. Pneumatically power assisted extra-vehicular activity glove. 45th International Conference on Environmental Systems, 2015.
- [10] D. Ryu, K.-W. Moon, H. Nam, Y. Lee, C. Chun, S. Kang, and J.-B. Song. Micro hydraulic system using slim artificial muscles for a wearable haptic glove. In *Intelligent Robots and Systems, 2008. IROS 2008. IEEE/RSJ International Conference on*, pages 3028–3033. IEEE, 2008.
- [11] D. Sangian, S. Naficy, G. M. Spinks, and B. Tondu. The effect of geometry and material properties on the performance of a small hydraulic mckibben muscle system. *Sensors and Actuators A: Physical*, 234:150–157, 2015.
- [12] B. Solano, J. Laloy, and C. Rotinat-Libersa. Compact and lightweight hydraulic actuation system for high performance millimeter scale robotic applications: modeling and experiments. In *ASME 2010 Conference on Smart Materials, Adaptive Structures and Intelligent Systems*, pages 405–411. American Society of Mechanical Engineers, 2010.
- [13] R. Tiwari, M. A. Meller, K. B. Wajcs, C. Moses, I. Reveles, and E. Garcia. Hydraulic artificial muscles. *Journal of Intelligent Material Systems and Structures*, 23(3):301–312, 2012.
- [14] B. K. Woods, M. F. Gentry, C. S. Kothera, and N. M. Wereley. Fatigue life testing of swaged pneumatic artificial muscles as actuators for aerospace applications. *Journal of intelligent material systems and structures*, 23(3):327–343, 2012.
- [15] H. Yoshinada, T. Yamazaki, T. Suwa, T. Naruse, and H. Ueda. Seawater hydraulic actuator for subsea manipulator. *Proceedings of the ISART*, pages 559–566, 1991.

ACELAN-COMPOS PACKAGE FOR FINITE ELEMENT SIMULATION OF ACTIVE COMPOSITE MATERIALS

ANDREY V. NASEDKIN

Institute of Mathematics, Mechanics and Computer Science
Southern Federal University
Miltchakova str., 8a., 344090 Rostov-on-Don, Russia
e-mail: nasedkin@math.sfedu.ru

Key words: Magnetoelectric Composite, Piezoelectricity, Effective Moduli, Nanomechanics, Surface Stress, Interphase Boundary, Finite Element Method, ACELAN-COMPOS

Abstract. This research deals with computer modelling in finite element software ACELAN-COMPOS of multiscale two-phase magnetoelectric (piezomagnetoelectric) bulk composites that consist of piezo-magnetic and/or piezoelectric fractions of irregular structures. The proposed technique is based on the models of micro- and nanoscale materials with interface or surface effects, the effective moduli method, the modelling of representative volumes, and the use of finite element technologies for solving the problems in the representative volumes.

1 INTRODUCTION

In the present paper, as active materials we will understand the materials in which sufficiently noticeable deformations can be caused by external nonmechanical influences. Such materials are piezoelectric, magnetoelectric, pyroelectric and other materials with coupling between mechanical fields and fields of a different nature: electric, magnetic or thermal. These materials are widely used in modern engineering as active elements of transducers, sensors, actuators and other devices. Recently, new materials with improved characteristics are being intensively developed to improve the efficiency of these devices. Especially important are the problems of developing active composite materials consisting of materials of different phases. Methods of mathematical and computer modelling help us to predict the effective properties of composite materials depending on the characteristics of the initial phases, their percentage ratio and the peculiarities of the internal structure.

The problems of determining effective properties, also called homogenization problems, can be solved on the basis of various approaches known in the mechanics of composite materials. For active materials whose behavior is described by a sufficiently complicated system of differential equations, it is convenient to use the method of effective moduli. For example, for piezoelectric composites according to this method, it is necessary to solve a set of boundary-value problems of piezoelectricity (electroelasticity) with special boundary conditions providing for homogeneous materials the exact solutions with constant field gradients (strains, stresses, electric field and electrical induction). In a non-uniform representative volume, these gradients, naturally, will not be constant, but their averaged integral characteristics will permit to determine the effective moduli of the composite material [14, 15].

For nanostructured composites, in which inclusions or pores have nanodimensions, the nanoscale effect can be taken into account in the framework of the theory of surface stresses ([4, 6, 22, 23], et al)

and its generalizations to the problems with coupling fields ([3, 5, 19, 24], et al). In the theory of surface stresses for the interfaces of materials with different phases, the special equations are written that relate stress jumps in volumes with fields for surface stresses. Finally, in recent years, the technologies have been proposed for creating the new materials composed of piezoelectric matrix and of inclusions from other materials or pores, on which interface boundaries the particles of third type materials are deposited [20].

To solve the homogenization problems for all active composites described in this paper, the specialized software was developed, which is based on the finite element solution of boundary problems in representative volumes and takes into account the main features of the internal structure of composites.

Namely, the program systems written in the APDL ANSYS language were created, which allow in the automated mode to solve in the ANSYS package the homogenization problems for active composites of various types and determining their effective moduli. To generate the structures of representative volumes in addition to the simple random ANSYS algorithm, external programs that implement various algorithms were created [14, 15, 16]: 3-x algorithm implemented by S.V. Bobrov, supporting the connectivity of finite elements of the first phase, up to 90 % of inclusions of the second phase; 3-0 algorithm with a regular structure of connectivity of the first phase in three axial directions and with a closed structure of the elements of the second phase; cluster algorithms implemented by V.V. Remizov (Witten-Sander method, cluster of the second phase method; method of "growth out of the plane"; method of initial concentration, etc.)

However, in the ANSYS package there were no basic means for solving the problems of magnetoelectricity and there were no piezoelectric and magnetoelectric shell finite elements. In this regard, at the Department of Mathematical Modelling of Southern Federal University, a specialized finite element package ACELAN-COMPOS was developed. The ACELAN-COMPOS package is focused on solving the homogenization problems with coupled mechanical and electromagnetic fields. In this package, implemented new algorithms 3-3 connectivity [9, 12], supporting the connectivity of the two phases; algorithm 3-0 connectivity, creating the granular structures [10, 12]; and algorithm 1-3 connectivity, creating the structures with rod elements in a matrix [11, 12].

For all these models of representative volumes, the algorithms have been developed for the automated search for finite elements located at the interphase boundaries and placing shell elements on them that simulate the presence of surface effects for nanoscale inclusions or pores. For transversely isotropic materials, an algorithm was additionally implemented for the plate surface elements, parallel to the coordinate axes, with the material properties that inherit the anisotropy structure of the neighboring volume elements.

The models of magnetoelectricity and the models of representative volume elements of the ACELAN-COMPOS package are briefly presented in this paper. Other means of ACELAN-COMPOS and a more detailed presentation of models, algorithms and results are presented in [8, 9, 10, 11, 12, 17], et al.

2 SETTING OF HOMOGENIZATION PROBLEMS

The technology of homogenization problem solving implemented in ACELAN-COMPOS is applicable for a fairly wide class of composite materials of various stochastic structures with coupling physico-mechanical fields. It is only important that linear stationary equations of divergent type should be considered. For example, let Ω be the representative volume of a piezomagnetoelectric (magnetoelectric) composite body consisting of two materials. We assume that this volume is filled with materials of two types (phases): $\Omega = \Omega^{(1)} \cup \Omega^{(2)}$. These phases can have various coupled fields. Thus, the phase $\Omega^{(1)}$ can have piezoelectric properties, while the phase $\Omega^{(2)}$ can be piezomagnetic. Another case is the active

materials with inclusions or pores. Then, the first phase of the main fills up the volume or set of volumes $\Omega^{(1)}$, and the second phase (inclusions or pores) fills the volume or set of volumes $\Omega^{(2)}$. Here, for a porous material, the phase $\Omega^{(1)}$ should be connected.

For modelling of nanoscale effects in the framework of the Gurtin–Murdoch theory and its generalizations, surface fields are set on the interfaces of the two phases $\Gamma^s = \partial\Omega^{(1)} \cap \partial\Omega^{(2)}$. The external boundary of the representative volume $\Gamma = \partial\Omega$ will be used to specify the boundary conditions in the homogenization problems.

In accordance with the effective moduli method, we will consider in the volume Ω the following boundary value problem of the static theory of magnetoelectroelasticity with respect to the displacement functions $\mathbf{u}(\mathbf{x})$, the electric potential $\varphi(\mathbf{x})$ and the magnetic potential $\phi(\mathbf{x})$:

$$\mathbf{L}^*(\nabla) \cdot \mathbf{T} = 0, \quad \nabla \cdot \mathbf{D} = 0, \quad \nabla \cdot \mathbf{B} = 0, \quad \mathbf{x} \in \Omega, \quad (1)$$

$$\mathbf{T} = \mathbf{c} \cdot \mathbf{S} - \mathbf{e}^* \cdot \mathbf{E} - \mathbf{h}^* \cdot \mathbf{H}, \quad \mathbf{D} = \mathbf{e} \cdot \mathbf{S} + \mathbf{\kappa} \cdot \mathbf{E} + \mathbf{\alpha} \cdot \mathbf{H}, \quad \mathbf{B} = \mathbf{h} \cdot \mathbf{S} + \mathbf{\alpha}^* \cdot \mathbf{E} + \mathbf{\mu} \cdot \mathbf{H}, \quad (2)$$

$$\mathbf{S} = \mathbf{L}(\nabla) \cdot \mathbf{u}, \quad \mathbf{E} = -\nabla\varphi, \quad \mathbf{H} = -\nabla\phi, \quad (3)$$

$$\mathbf{L}^*(\nabla) = \begin{bmatrix} \partial_1 & 0 & 0 & 0 & \partial_3 & \partial_2 \\ 0 & \partial_2 & 0 & \partial_3 & 0 & \partial_1 \\ 0 & 0 & \partial_3 & \partial_2 & \partial_1 & 0 \end{bmatrix}, \quad \nabla = \begin{Bmatrix} \partial_1 \\ \partial_2 \\ \partial_3 \end{Bmatrix}, \quad (4)$$

$$\mathbf{L}^*(\mathbf{n}) \cdot [\mathbf{T}] = \mathbf{L}^*(\nabla^s) \cdot \mathbf{T}^s, \quad \mathbf{n} \cdot [\mathbf{D}] = \nabla^s \cdot \mathbf{D}^s, \quad \mathbf{n} \cdot [\mathbf{B}] = \nabla^s \cdot \mathbf{B}^s, \quad \mathbf{x} \in \Gamma^s, \quad (5)$$

$$\mathbf{T}^s = \mathbf{c}^s \cdot \mathbf{S}^s - \mathbf{e}^{s*} \cdot \mathbf{E}^s - \mathbf{h}^{s*} \cdot \mathbf{H}^s, \quad \mathbf{D}^s = \mathbf{e}^s \cdot \mathbf{S}^s + \mathbf{\kappa}^s \cdot \mathbf{E}^s + \mathbf{\alpha}^s \cdot \mathbf{H}^s, \quad \mathbf{B}^s = \mathbf{h}^s \cdot \mathbf{S}^s + \mathbf{\alpha}^{s*} \cdot \mathbf{E}^s + \mathbf{\mu}^s \cdot \mathbf{H}^s, \quad (6)$$

$$\mathbf{S}^s = \mathbf{L}(\nabla^s) \cdot \mathbf{u}^s, \quad \mathbf{u}^s = \mathbf{A} \cdot \mathbf{u}, \quad \mathbf{A} = \mathbf{I} - \mathbf{n} \otimes \mathbf{n}, \quad \mathbf{E}^s = -\nabla^s \varphi, \quad \mathbf{H}^s = -\nabla^s \phi, \quad \nabla^s = \nabla - \mathbf{n}(\partial/\partial n), \quad (7)$$

$$\mathbf{u} = \mathbf{L}^*(\mathbf{x}) \cdot \mathbf{S}_0, \quad \varphi = -\mathbf{x} \cdot \mathbf{E}_0, \quad \phi = -\mathbf{x} \cdot \mathbf{H}_0, \quad \mathbf{x} \in \Gamma. \quad (8)$$

Here $\mathbf{T} = \{\sigma_{11}, \sigma_{22}, \sigma_{33}, \sigma_{23}, \sigma_{13}, \sigma_{12}\}$, $\mathbf{S} = \{\varepsilon_{11}, \varepsilon_{22}, \varepsilon_{33}, 2\varepsilon_{23}, 2\varepsilon_{13}, 2\varepsilon_{12}\}$ are the arrays of the stress components σ_{ij} and the strain components ε_{ij} ; \mathbf{D} and \mathbf{E} are the vectors of the electrical induction or the electric displacement and of the intensity electric field; \mathbf{B} and \mathbf{H} are the vectors of magnetic induction and of the intensity magnetic field, respectively; $\mathbf{c} = \mathbf{c}^{E,H}$ is the 6×6 matrix of stiffness moduli; $\mathbf{e} = \mathbf{e}^H$ is the 3×6 matrix of piezomoduli; $\mathbf{h} = \mathbf{h}^E$ is the 3×6 matrix of magnetostriction moduli or piezomagnetic moduli; $\mathbf{\kappa} = \mathbf{\kappa}^{S,H} = \mathbf{\varepsilon}^{S,H}$ is the 3×3 matrix of dielectric permittivity moduli (dielectric constants); $\mathbf{\alpha} = \mathbf{\alpha}^S$ is the 3×3 matrix of magnetoelectric coupling coefficients; $\mathbf{\mu} = \mathbf{\mu}^{S,E}$ is the 3×3 matrix of magnetic permeability moduli; \mathbf{S}_0 , \mathbf{E}_0 and \mathbf{H}_0 are constant six-dimensional array, and three-dimensional vectors, respectively; the superscripts of the moduli indicate for which constant fields they were calculated; $(\dots)^*$ is the transpose operation.

Interface relations (5)–(7) on the interphase surface Γ^s are used only for modelling of composites at the nano-level. In (5)–(7), the surface fields and moduli are marked with superscript s ; $[(\dots)] = (\dots)^{(1)} - (\dots)^{(2)}$ is the jump of the corresponding quantity across the interphase boundary; \mathbf{n} is the unit normal vector to Γ^s , external to the domain $\Omega^{(1)}$.

If the interface boundary conditions (5)–(7) are missing, then the problem (1)–(4), (8) is the homogenization problem for piezomagnetoelectric composite with usual phase sizes (inclusions or pores).

In the case of a composite of arbitrary anisotropy class to determine the full set of its effective moduli $c_{\beta\zeta}^{\text{eff}}$, $e_{i\zeta}^{\text{eff}}$, $e_{i\zeta}^{\text{eff}}$, κ_{ij}^{eff} , α_{ij}^{eff} , μ_i^{eff} , it is required to solve the twelve problems (1)–(8), differing in boundary conditions (8), in which only one of the components $S_{0\gamma}$, E_{0k} , H_{0k} ($\gamma = 1, \dots, 6$; $k = 1, 2, 3$) should be set not equal to zero:

— cases I – VI ($\zeta = 1, 2, \dots, 6$)

$$S_{0\gamma} = S_0 \delta_{\zeta\gamma}, \quad \mathbf{E}_0 = 0, \quad \mathbf{H}_0 = 0 \Rightarrow c_{\beta\zeta}^{\text{eff}} = \langle T_\beta \rangle / S_0, \quad e_{i\zeta}^{\text{eff}} = \langle D_i \rangle / S_0, \quad h_{i\zeta}^{\text{eff}} = \langle B_i \rangle / S_0, \quad (9)$$

cases VII – IX ($j = 1, 2, 3$)

$$\mathbf{S}_0 = 0, \quad E_{0j} = E_0 \delta_{jk}, \quad \mathbf{H}_0 = 0 \Rightarrow e_{j\beta}^{\text{eff}} = -\langle T_\beta \rangle / E_0, \quad \kappa_{ij}^{\text{eff}} = \langle D_i \rangle / E_0, \quad \alpha_{ji}^{\text{eff}} = \langle B_i \rangle / E_0, \quad (10)$$

cases X – XII ($j = 1, 2, 3$)

$$\mathbf{S}_0 = 0, \quad \mathbf{E}_0 = 0, \quad H_{0j} = H_0 \delta_{jk} \Rightarrow h_{j\beta}^{\text{eff}} = -\langle T_\beta \rangle / H_0, \quad \alpha_{ij}^{\text{eff}} = \langle D_i \rangle / H_0, \quad \mu_{ji}^{\text{eff}} = \langle B_i \rangle / H_0, \quad (11)$$

where $\beta = 1, 2, \dots, 6; i = 1, 2, 3$;

$$\langle (\dots) \rangle = \frac{1}{|\Omega|} \left(\int_{\Omega} (\dots) d\Omega + \int_{\Gamma^s} (\dots)^s d\Gamma \right). \quad (12)$$

As we can see from (9)–(12), taking into account the interface conditions leads to the necessity of calculation of the averaged field characteristics not only by the volume Ω , but also by the interface boundary Γ^s . Since the interface boundaries complicate the internal structure of the representative volume, it is possible to solve boundary-value homogenization problems only numerically, for example, by the finite element method described below.

3 FINITE ELEMENT APPROXIMATIONS

In order to solve the problems of magneto-electroelasticity I – XII for an inhomogeneous composite material in a representative volume Ω , one can proceed to their weak statements and use the classical technique of finite element approximations. Let Ω_h be the region occupied by a finite element mesh, $\Omega_h \subset \Omega$, $\Omega_h = \Omega_h^{(1)} \cup \Omega_h^{(2)}$, $\Omega_h^{(j)} \subset \Omega^{(j)}$, $\Omega_h^{(j)} = \cup_k \Omega_{ek}^{(j)}$, where $\Omega_{ek}^{(j)}$ is a separate finite element with the number k and with the material properties of the phase $j = 1, 2$. Let also Γ_h^s be a grid of the surface finite elements, conforming with the volume mesh Ω_h , $\Gamma_h^s = \partial\Omega_h^{(1)} \cap \partial\Omega_h^{(2)}$, $\Gamma_h^s = \cup_m \Gamma_{em}^s$, while Γ_{em}^s is a separate surface finite element with number m , which is a common face of the corresponding volume elements $\Omega_{ek}^{(j)}$ on the phase interface ($\Gamma_h^s \approx \Gamma^s$).

We will use Lagrangian or serendipity finite elements with degrees of freedom of nodal displacements, electrical potentials and magnetic potentials. It is important that, due to the structure of the surface fields (5)–(7), we can use membrane elements with degrees of freedom of nodal displacements, electrical potentials and magnetic potentials (without degrees of freedom of the rotation angles). Then approximate solutions of $\mathbf{u}_h \approx \mathbf{u}$, $\varphi_h \approx \varphi$, $\phi_h \approx \phi$ on the finite element mesh Ω_h can be searched in the form

$$\mathbf{u}_h = \mathbf{N}_u^* \cdot \mathbf{U}, \quad \varphi_h = \mathbf{N}_\varphi^* \cdot \Phi, \quad \phi_h = \mathbf{N}_\phi^* \cdot \Psi, \quad (13)$$

where \mathbf{N}_u^* is the matrix of basis or form functions for displacements; \mathbf{N}_φ^* , \mathbf{N}_ϕ^* are the row vector of basis functions for electric and magnetic potentials; \mathbf{U} , Φ , Ψ are the vectors of nodal displacements, electric potentials and magnetic potentials.

In accordance with the classical finite element technique, we approximate the continual weak formulation of the problems I – XII in the finite dimensional spaces associated with the basis functions from (13). Substituting (13) and similar representations of the projection functions \mathbf{u}_h , φ_h , θ_h into weak statements of magneto-electroelastic problem, we obtain the following finite element system

$$\mathbf{K} \cdot \mathbf{a} = \mathbf{F}, \quad (14)$$

$$\mathbf{K} = \begin{bmatrix} \mathbf{K}_{uu} & \mathbf{K}_{ub} \\ \mathbf{K}_{ub}^* & -\mathbf{K}_{bb} \end{bmatrix}, \quad \mathbf{a} = \begin{bmatrix} \mathbf{U} \\ \mathbf{b} \end{bmatrix}, \quad \mathbf{F} = \begin{bmatrix} \mathbf{F}_u \\ -\mathbf{F}_b \end{bmatrix}, \quad (15)$$

$$\mathbf{K}_{bb} = \begin{bmatrix} \mathbf{K}_{\varphi\varphi} & \mathbf{K}_{\varphi\phi} \\ \mathbf{K}_{\varphi\phi}^* & \mathbf{K}_{\phi\phi} \end{bmatrix}, \quad \mathbf{K}_{ub}^* = \begin{bmatrix} \mathbf{K}_{u\varphi}^* \\ \mathbf{K}_{u\phi}^* \end{bmatrix}, \quad \mathbf{b} = \begin{bmatrix} \Phi \\ \Psi \end{bmatrix}, \quad \mathbf{F}_b = \begin{bmatrix} \mathbf{F}_\varphi \\ \mathbf{F}_\phi \end{bmatrix}, \quad (16)$$

Vectors \mathbf{F}_u , \mathbf{F}_φ , \mathbf{F}_ϕ in (15), (16) appear when taking into account the essential boundary conditions (8), and they are differ for various boundary conditions from (9)–(11).

In (14)–(16) the matrices contain both usual for the problems of the magnetoelectroelasticity the matrices, calculated on the volumes of finite element mesh, and the additional matrices, calculated on the interface boundaries. For example, the stiffness matrix \mathbf{K}_{uu} has the following structure:

$$\mathbf{K}_{uu} = \mathbf{K}_{uu\Omega} + \mathbf{K}_{uu\Gamma}, \quad \mathbf{K}_{uu\Omega} = \int_{\Omega_h} \mathbf{B}_u^* \cdot \mathbf{c} \cdot \mathbf{B}_u d\Omega, \quad \mathbf{K}_{uu\Gamma} = \int_{\Gamma_h^s} \mathbf{B}_u^{s*} \cdot \mathbf{c}^s \cdot \mathbf{B}_u^s d\Gamma, \quad (17)$$

$$\mathbf{B}_u = \mathbf{L}^*(\nabla) \cdot \mathbf{N}_u^*, \quad \mathbf{B}_u^s = \mathbf{L}^*(\nabla^s) \cdot \mathbf{A} \cdot \mathbf{N}_u^*. \quad (18)$$

Note that the matrix \mathbf{K} of the system of linear algebraic equations (14) is symmetric. In addition, by virtue the properties of positive definiteness of the volume and surface energies, the matrix \mathbf{K}_{uu} and \mathbf{K}_{bb} will be at least non-negative definite. Therefore, the symmetric matrix \mathbf{K} in (14) will have the properties of a quasi-defined matrix, typical for the problems with a saddle point.

In this connection, in ACELAN-COMPOS package we use an effective algorithms for symmetric positive definite and quasi-definite matrices for solving the system of linear algebraic equations (14) [1, 2, 21]. All basic procedures that we need in finite element manipulations, such as the degree of freedom rotations, mechanical, electric and magnetic boundary condition settings, etc., we can also provide in a symmetric form.

4 MODELS OF REPRESENTATIVE VOLUMES AND SOME RESULTS

In ACELAN-COMPOS package the representative volume element (RVE) is simulated in the form of a cubic array of finite elements, where the elements also have cubic shapes. In accordance with the accepted structure of second phase, we assign the properties of the skeleton material of the first phase to some part of the finite elements, and assign the properties of the second phase to the remaining part of the elements.

In ACELAN-COMPOS there are the opportunities to create different types of representative volumes. Examples of representative volumes, created by different algorithms of the ACELAN-COMPOS package, are shown in Fig. 1–4. In all cases, the percentage of occurrence of the second phase was approximately the same (about 15 %), and the order of RVE is the same and equal $16 \times 16 \times 16$. Everywhere in Fig. 1–4, *a*) the whole RVE is shown, in Fig. 1–4, *b*) the elements of the first phase are shown, in Fig. 1–4, *c*) the elements of the second phase are shown, and in Fig. 1–4, *d*) the surface elements are shown.

In the first case, the finite elements of second phase are selected by a random number generator (Fig. 1). It is obvious that the model created by using a simple random number generator is easy to build. However, such model does not support the connectivity of the elements for the first phase and does not reflect the connectivity structure of the elements for the second phase.

Two other algorithms in ACELAN-COMPOS create the structures of the two-component materials with the connectivity for both phases (3–3 connectivity) [9, 11, 12]. In the case of porous composites, the 3–3 connectivity algorithms generate materials with open porosity. In these algorithms, the representative volumes consist of domains with $8 \times 8 \times 8$ finite elements. Number 8 for the domain size was chosen

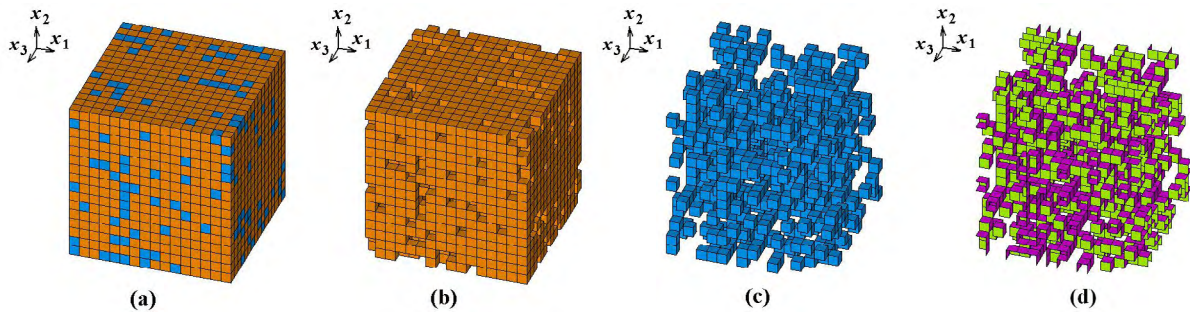


Figure 1: Example of RVE of with a random arrangement of the elements of the second phase

for the convenience of implementing numerical procedures to verify the phase connectivity and generate different data structures. In a direct version of the 3–3 algorithm, the process of the domain generation is implemented in such way that the connectivity of the elements of the first phase is maintained through the domain vertices, and the connectivity of the structure of the second phase is maintained through the elements located approximately in the midpoints of the domain edges. In the inverted version of this algorithm, the first phase and the second phase are interchanged.

Each domain is created by a partially random way, and the representative volumes of $8n \times 8n \times 8n$ order are formed as a result of generating the sequence of n domains along each of three coordinate axes. Thus, generally speaking, each resulting domain differs from the other. Nevertheless, it maintains the connectivity of both phases and the connectivity of the total volume structure, being formed either by a direct 3–3 algorithm or by an inverse 3–3 algorithm.

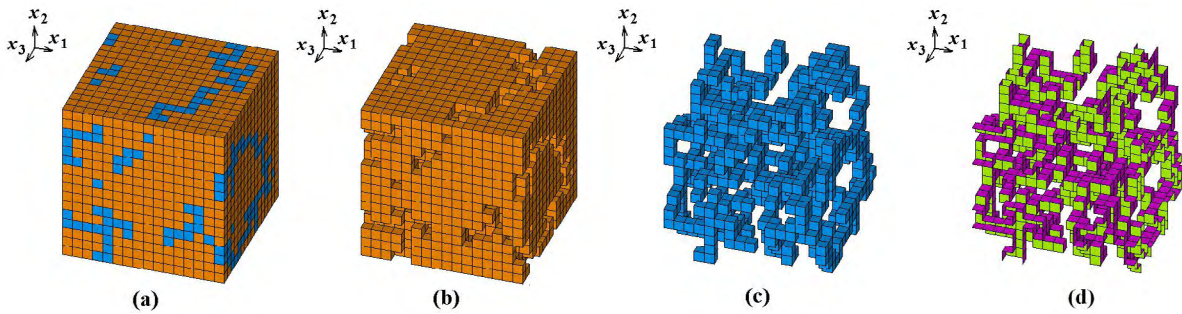


Figure 2: Example of RVE with 3–3 connectivity (direct algorithm)

A detailed description of these algorithms is given in [9, 12]. Some examples of the representative volumes with the porosity $p \approx 15\%$ for $n = 2$ (eight domains) are shown in Fig. 2 for direct algorithm and in Fig. 3 for inverse algorithm, respectively. As can be seen from Fig. 2, the direct algorithm distributes a significant amount of the framework elements (elements of the first phase) near the domain edges. On the contrary, the inverse algorithm gathers the most part of the framework elements (elements of the first phase) in the central part of the domain. For a larger number of domains ($n = 3$, $n = 4$, etc.), these effects are leveled, since some parts of the domain boundaries become located inside of the representative volume.

For simulate the element of second phase as granules, consisting of one or more structural elements not connected with other granules, in ACELAN-COMPOS package the 3–0 algorithm exists [10, 11, 12]. In the case of porous composites, the 3–0 connectivity algorithms generate materials with closed porosity.

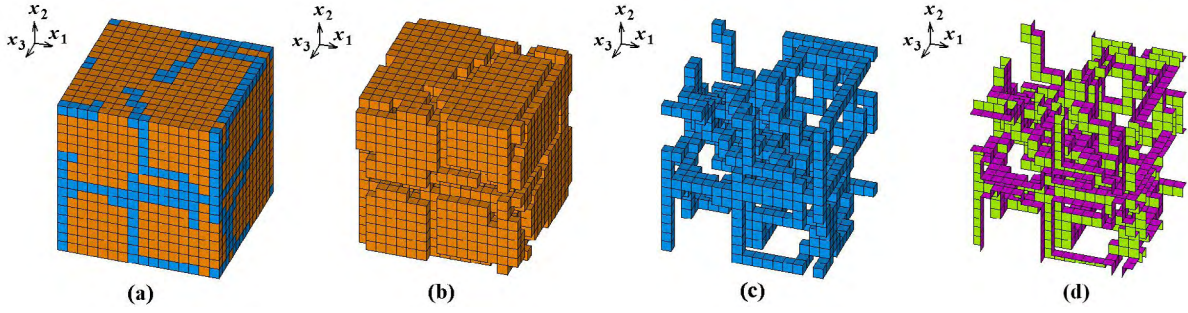


Figure 3: Example of RVE with 3–3 connectivity (inverse algorithm)

In this algorithm, the representative volumes also consist of domains with $8 \times 8 \times 8$ elements. The input user data are the granule size and the maximum quantum of inclusions. Random choice of the supporting elements for the granules ensures in the result the partially stochastic distribution of the elements of second phase in the RVE. The granule grows in the domain according to an algorithm that allows the granule to be shaped as possible close to the ball, while avoiding highly elongated elements.

As in 3–3 algorithms, each domain in 3–0 algorithm is created by a partially random way, and the representative volumes of $8n \times 8n \times 8n$ order are formed in the result of generating the sequence of domains along three coordinate axes. Thus, here each resulting domain differs from the other. Nevertheless, it maintains the connectivity of the elements of the main first phase. A detailed description of the 3–0 algorithm is contained in [10, 12]. One example of the RVE for $n = 2$ (eight domains), constructed by the 3–0 algorithm, is shown in Fig. 4.

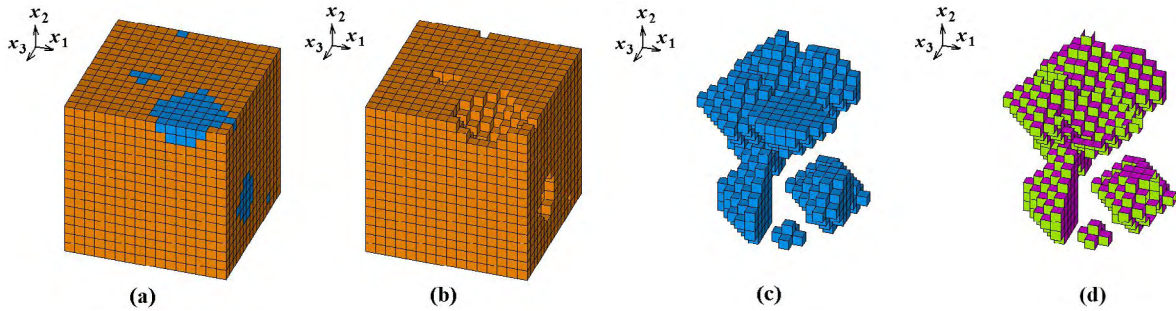


Figure 4: Example of RVE with 3–0 connectivity

In 1–3 (3–1) algorithm of the ACELAN-COMPOS package, the representative volume contains rods placed in the skeleton of the main material. This is a simple algorithm based on placing two-dimensional pattern on the bottom of the volume and extruding it through the body [8, 12].

For nanostructured composites, for all variants of representative volumes, it is possible to automatically find the interphase boundaries Γ^s and place on them the shell (membrane) finite elements that simulate the surface effects (Fig. 1–4, *d*). For the shell elements it is necessary to insure the anisotropy type, which corresponds to the anisotropy of the volume finite element. This correspondence was implemented only for transversely isotropic phases and for elements parallel to the Ox_1x_2 plane (painted in light green in Fig. 1–4, *d*) or x_3 axis (painted in crimson in Fig. 1–4, *d*).

For representative volumes shown in Fig. 1–4, we will present here as an example the calculation results of solving the homogenization problem for a porous piezoceramic material without taking into

account the surface effects (Table 1) and taking into account only uncoupled surface stresses according to the methodology presented in [7, 13] (Table 2). For RVE of this composite the domain $\Omega^{(1)}$ occupied by the dense piezoceramics and the domain $\Omega^{(2)}$ occupied by the pores: $c_{\alpha\beta} = c_{\alpha\beta}^{E(i)}$, $e_{j\beta} = e_{j\beta}^{(i)}$, $\kappa_{jj} = \epsilon_{jj}^{S(i)}$ for $\mathbf{x} \in \Omega^{(i)}$, $i = 1, 2$.

In Tables 1, 2 we give the relative values of the effective material moduli $r(c_{\alpha\beta}) = c_{\alpha\beta}^{\text{eff}}/c_{\alpha\beta}$, $r(e_{j\beta}) = e_{j\beta}^{\text{eff}}/e_{j\beta}$, $r(\kappa_{jj}) = \kappa_{jj}^{\text{eff}}/\kappa_{jj}$ and $r(d_{j\beta}) = d_{j\beta}^{\text{eff}}/d_{j\beta}$ for porous piezoceramics PZT-5. Here $c_{\alpha\beta} = c_{\alpha\beta}^{E(1)}$, $e_{j\beta} = e_{j\beta}^{(1)}$, $\kappa_{jj} = \epsilon_{jj}^{S(1)}$ and $d_{j\beta} = d_{j\beta}^{(1)}$ are the corresponding values for the dense piezoceramics, $\mathbf{d} = \mathbf{e} \cdot \mathbf{c}^{-1}$.

For dense piezoceramics PZT-5 we take the following mechanical, dielectric and piezoelectric constants: $c_{11}^{E(1)} = 12.1 \cdot 10^{10}$; $c_{12}^{E(1)} = 7.54 \cdot 10^{10}$; $c_{13}^{E(1)} = 7.52 \cdot 10^{10}$; $c_{33}^{E(1)} = 11.1 \cdot 10^{10}$; $c_{44}^{E(1)} = 2.11 \cdot 10^{10}$ (N/m²); $e_{33}^{(1)} = 15.8$; $e_{31}^{(1)} = -5.4$; $e_{15}^{(1)} = 12.3$ (C/m²); $\epsilon_{11}^{S(1)} = 916\epsilon_0$; $\epsilon_{33}^{S(1)} = 830\epsilon_0$; $\epsilon_0 = 8.85 \cdot 10^{-12}$ (F/m). For the pores, we set negligibly small elastic moduli $c_{\alpha\beta}^{E(2)} = \eta c_{\alpha\beta}^{E(1)}$, $\eta = 1 \cdot 10^{-10}$, piezomoduli $e_{j\beta}^{(2)} = \eta$ (x1 C/m²) and $\epsilon_{jj}^{S(2)} = \epsilon_0$. For the case of nanoporous piezoceramics with uncoupled surface stresses we accept the size of cube finite element $a = 10^{-10}$ (m), $c_{\alpha\beta}^s = a c_{\alpha\beta}^{E(1)}$, $e_{j\beta}^s = 0$, $\kappa_{jj}^s = 0$.

Table 1: Effective moduli of porous piezoceramics PZT-5 without surface stresses

Material moduli	SR, $p = 14.99$	3–3 (direct), $p = 14.84$	3–3 (inverse), $p = 15.21$	3–0, $p = 15.04$
$r(c_{11})$	0.76	0.71	0.69	0.66
$r(c_{12})$	0.72	0.65	0.62	0.61
$r(c_{13})$	0.71	0.64	0.61	0.58
$r(c_{33})$	0.75	0.69	0.68	0.64
$r(c_{44})$	0.81	0.79	0.78	0.77
$r(e_{31})$	0.73	0.66	0.64	0.56
$r(e_{33})$	0.84	0.83	0.83	0.81
$r(e_{15})$	0.80	0.77	0.77	0.74
$r(\kappa_{11})$	0.85	0.85	0.84	0.84
$r(\kappa_{33})$	0.84	0.83	0.83	0.83
$r(d_{31})$	0.95	0.92	0.92	0.88
$r(d_{33})$	0.99	0.98	0.99	0.98
$r(d_{15})$	0.98	0.98	0.98	0.96
$ \Gamma^s / \Gamma $	1.91	1.32	1.13	0.68

It can be noted that even with the same porosity for the simple random (SR) algorithm, the area of interface boundaries $|\Gamma^s|$ is larger than for the 3–3 connectivity direct algorithms, the area of interface boundaries for the 3–3 direct algorithms is larger than for the 3–3 inverse algorithms, and the area of interface boundaries for the 3–3 inverse algorithms is larger than for the 3–0 algorithms. So, as we can conclude from Tables 1, 2, for the representative volumes with SR distribution of inclusions and with 3–3 or 3–0 connectivity for various interphase areas we obtain different values of the effective moduli, moreover the SR model is slightly stiffer and more electromechanical active than the 3–3 models, and the 3–3 connectivity models are stiffer and more electromechanical active than the 3–1 model.

Accounting for surface stresses here is equivalent to the placement of elastic membrane elements on the interface boundaries. Therefore, when taking into account surface stresses, the size of the interface

Table 2: Effective moduli of porous piezoceramics PZT-5 with surface stresses

Material moduli	SR, $p = 14.99$	3–3 (direct), $p = 14.84$	3–3 (inverse), $p = 15.21$	3–0, $p = 15.04$
$r(c_{11})$	1.09	0.98	0.93	0.77
$r(c_{12})$	0.93	0.85	0.80	0.70
$r(c_{13})$	0.92	0.84	0.79	0.66
$r(c_{33})$	1.09	0.98	0.92	0.75
$r(c_{44})$	1.08	1.00	0.98	0.88
$r(e_{31})$	0.84	0.78	0.74	0.63
$r(e_{33})$	0.84	0.83	0.83	0.81
$r(e_{15})$	0.83	0.80	0.79	0.76
$r(\kappa_{11})$	0.84	0.83	0.83	0.83
$r(\kappa_{33})$	0.83	0.82	0.82	0.82
$r(d_{31})$	0.59	0.63	0.66	0.75
$r(d_{33})$	0.60	0.66	0.69	0.83
$r(d_{15})$	0.76	0.80	0.81	0.87
$ \Gamma^s / \Gamma $	1.91	1.32	1.13	0.68

area has a very significant effect on the effective stiffness moduli (Table 2). Thus, we can conclude that the internal structures of nanoporous composites can have a significant effect on the effective stiffness moduli values. Meanwhile, from a comparison of Tables 1 and 2, we can infer that the uncoupled surface stresses have much less effect on the effective piezomoduli $e_{j\beta}^{\text{eff}}$ and almost do not influence on the dielectric permittivities κ_{jj}^{eff} .

Note that using the described approaches in [7, 8, 9, 10, 14, 15] et al, the of homogenization problems were solved for different structures of representative volumes. Anisotropic elastic and piezoelectric composites were investigated, both on ordinary scale levels and on nanoscale. It was found that the types of connectivity and the internal structure of a composite can have a significant influence on effective moduli (see also Tables 1, 2), and taking into account surface or interface effects can even lead to a change in the decreasing properties of moduli on their growth and even lead to superiority of effective moduli compared to moduli of initial phases (Table 2).

An analysis of the advantages and disadvantages of various algorithms for the formation of representative volumes is given in [12]. Additionally, it can be noted that the piezoceramic finite elements of all types of representative volume structures can be automatically equipped with their elemental coordinate systems rotated relative to the initial Cartesian coordinate system in accordance with the direction of the non-uniform polarization fields [14, 15, 18], and for 3–0 connectivity models the algorithms for the account of electrode surfaces for metallized interfaces have been developed [17, 18].

Acknowledgments The author is grateful for the support of the Ministry of Science and Higher Education of the Russian Federation, project No. 9.1001.2017/4.6.

REFERENCES

- [1] Benzi, M., Golub, G.H., Liesen, J. Numerical solution of saddle point problems. *Acta Numerica*. (2005) **14**: 1–137.

- [2] Benzi, M. and Wathen, A.J. Some preconditioning techniques for saddle point problems. In: *Model Order Reduction: Theory, Research Aspects and Applications*. Eds. W.H.A. Schilders, H.A. van der Vorst and J. Rommes. *Mathematics in Industry*. (2008) **13**, 195–211.
- [3] Chen, T. Exact size-dependent connections between effective moduli of fibrous piezoelectric nanocomposites with interface effects. *Acta Mech.* (2008) **196**: 205–217.
- [4] Eremeyev, V.A. On effective properties of materials at the nano- and microscale considering surface effects. *Acta Mech.* (2016) **227**: 29–42.
- [5] Gu S.-T. and He Q.-C. Interfacial discontinuity relations for coupled multifield phenomena and their application to the modeling of thin interphases as imperfect interfaces. *J. Mech. Phys. Solids*. (2011) **59**: 1413–1426.
- [6] Hamilton, J.C. and Wolfer, W.G. Theories of surface elasticity for nanoscale objects. *Surface Science*. (2009) **603**: 1284–1291.
- [7] Iovane, G. and Nasedkin A.V. Numerical modelling of two-phase piezocomposites with interface mechanical anisotropic effects. In: *Dynamical Processes in Generalized Continua and Structures*. Ser. *Advanced Structured Materials*. Vol. 103. Eds. H. Altenbach, A. Belyaev, V. Eremeyev, A. Krivtsov, A. Porubov Springer, (2019), 293–304.
- [8] Kudimova, A.B., Mikhayluts, I.V., Nadolin, D.K., Nasedkin, A.V., Nasedkina, A.A., Oganessian, P.A., Soloviev, A.N. Computer design of porous and ceramic piezocomposites in the finite element package ACELAN. *Procedia Structural Integrity*. (2017) **6**: 301–308.
- [9] Kudimova, A.B., Nadolin, D.K., Nasedkin, A.V., Nasedkina, A.A., Oganessian, P.A., Soloviev, A.N. Models of porous piezocomposites with 3–3 connectivity type in ACELAN finite element package. *Mater. Phys. Mech.* (2018) **37**: 16–24.
- [10] Kudimova, A.B., Nadolin, D.K., Nasedkin, A.V., Oganessian, P.A., Soloviev, A.N. Finite element homogenization models of bulk mixed piezocomposites with granular elastic inclusions in ACELAN package. *Mater. Phys. Mech.* (2018) **37**: 25–33.
- [11] Kurbatova, N.V., Nadolin, D.K., Nasedkin, A.V., Nasedkina, A.A., Oganessian, P.A., Skaliukh, A.S., Soloviev, A.N. Models of active bulk composites and new opportunities of ACELAN finite element package. In: *Wave Dynamics and Composite Mechanics for Microstructured Materials and Metamaterials*. Ser. *Advanced Structured Materials*. Vol. 59, Ed. M.A. Sumbatyan. Springer, Singapore, (2017), 133–158.
- [12] Kurbatova, N.V., Nadolin, D.K., Nasedkin, A.V., Oganessian, P.A., Soloviev, A.N. Finite element approach for composite magneto-piezoelectric materials modeling in ACELAN-COMPOS package. In: *Analysis and Modelling of Advanced Structures and Smart Systems*. Ser. *Advanced Structured Materials*. Vol. 81, Eds. H. Altenbach, E. Carrera, G. Kulikov. Springer, Singapore, (2018), 69–88.
- [13] Nasedkin, A.V. Some homogenization models of nanosized piezoelectric composite materials of types ceramics – pores and ceramics – ceramics with surface effects. In: *VIII ECCOMAS Thematic Conf. on Smart Structures and Materials, VI Int. Conf. on Smart Materials and Nanotechnology in Engineering – SMART 2017, 5-8 June 2017, Madrid, Spain*. Eds. A. Guemes, A. Benjeddou, J. Rodellar and J. Leng. CIMNE, (2017), 1137–1147.

- [14] Nasedkin, A.V. and Shevtsova, M.S. Improved finite element approaches for modeling of porous piezocomposite materials with different connectivity. In: *Ferroelectrics and Superconductors: Properties and Applications*. Ed. I.A. Parinov. Nova Science Publ., (2011), 231–254.
- [15] Nasedkin, A.V. and Shevtsova, M.S. Multiscale computer simulation of piezoelectric devices with elements from porous piezoceramics. In: *Physics and mechanics of new materials and their applications*. Eds. I.A. Parinov and S.-H. Chang. Nova Science Publ., (2013), 185–202.
- [16] Nasedkin, A.V., Nasedkina, A.A., Remizov, V.V. Finite element modeling of porous thermoelastic composites with account for their microstructure. *Vychisl. mekh. splosh. sred - Computational Continuum Mechanics*. (2014) **7**(1): 100–109.
- [17] Nasedkin, A., Nasedkina, A., Rybyanets, A. Finite element simulation of effective properties of microporous piezoceramic material with metallized pore surfaces. *Ferroelectrics*. (2017) **508**: 100–107.
- [18] Nasedkin, A.V., Nasedkina, A.A., Rybyanets, A.N. Numerical analysis of effective properties of heterogeneously polarized porous piezoceramic materials with local alloying pore surfaces. *Mater. Phys. Mech.* (2018) **40**: 12–21.
- [19] Pan, X.H., Yu, S.W., Feng, X.Q. A continuum theory of surface piezoelectricity for nanodielectrics. *Science China: Physics, Mechanics & Astronomy*. (2011) **54**(4): 564–573.
- [20] Rybyanets, A.N. and Naumenko A.A. Nanoparticles transport in ceramic matrixes: a novel approach for ceramic matrix composites fabrication. *J. Modern Physics*. (2013) **4**(8): 1041–1049.
- [21] Vanderbei, R.J. Symmetric quasidefinite matrices. *SIAM J. Optim.* (1995) **5**: 100–113.
- [22] Wang, J., Huang, Z., Duan, H., Yu, S., Feng, X., Wang, G., Zhang, W., Wang, T. Surface stress effect in mechanics of nanostructured materials. *Acta Mechanica Solida Sinica*. (2011) **24**(1): 52–82.
- [23] Wang, K.F., Wang, B.L., Kitamura, T. A review on the application of modified continuum models in modeling and simulation of nanostructures. *Acta Mech. Sin.* (2016) **32**(1): 83–100.
- [24] Yan, Z. and Jiang, L. Modified continuum mechanics modeling on size-dependent properties of piezoelectric nanomaterials: A review. *Nanomaterials*. (2017) **7**: 27.

APPLICATION OF A DUAL PZT SPARSE ARRAY WITH LAMB WAVE MODE DECOMPOSITION FOR DAMAGE LOCALIZATION IN AN ALUMINUM AIRCRAFT WING

JACOB R. MCCULLUM^{*}, BYUNGSEOK YOO^{*}, DARRYLL J. PINES^{*}, AND
NORMAN M. WERELEY^{*}

^{*} Department of Aerospace Engineering
University of Maryland
College Park, MD, United States
e-mail: jmcc22@terpmail.umd.edu

Key words: Structural Health Monitoring, Lamb Waves, Aircraft, Piezoelectrics, Sparse Array

Abstract. Dual lead zirconate titanate (PZT) transducers have recently been developed for structural health monitoring (SHM) applications. These transducers have been shown to be a suitable option for decomposing a guided Lamb wave response that contains a mixture of the fundamental symmetric (S0) and antisymmetric (A0) modes. This ability to decompose the wave response, or more accurately, to highlight an individual mode, is applied in this experimental work for damage localization using a sparse transducer array. For this paper, studies were performed on a section of an aluminum alloy skin plate of a Piper Cherokee wing. The skin plate is supported by structural features common to most aircraft such as stringers, ribs, and rivets. Such features often pose a challenge to guided wave SHM over a large area due to scattering effects, mode conversion, and attenuation of the guided waves. Damage was simulated using magnets of various strengths and shapes placed on either side of the wing skin. Sparse array images were constructed using baseline-subtracted signals from all possible sensor actuator pairs using ellipse summation and correlation algorithms. This work shows that dual PZTs can potentially be used to improve sparse array imaging techniques due to the transducers' mode decomposition capability. Specifically, preliminary results suggest that the decomposed S0 mode can be used at certain frequencies and farther damage locations where neither the A0 or S0 mode are as effective with single element transducers. Also, this study provides a general comparison between the A0 and S0 modes and their damage localization capability with the given experimental setup. Furthermore, this work demonstrates that if a baseline is used, structural features such as stringers and ribs in the present configuration do not significantly affect the localization capabilities of the proposed sparse array method.

1 INTRODUCTION

Structural health monitoring (SHM) refers to the broad field regarding topics such as autonomous detection and characterization of damage in a system, usage monitoring, remaining life calculation, and autonomously prescribed maintenance. This work focuses on the autonomous detection and characterization of damage category of SHM and particularly emphasizes localization of damage. One class of damage detection and localization methods

makes use of Lamb waves, or in real structures, guided Lamb Waves (GLW). These elastic waves are a type of vibration in plates and have been well studied for their potential applications in SHM particularly for aircraft [1,2]. In order to excite and measure Lamb waves in a practical structure, in-situ transducer networks must be installed as part of the system. Use of lead zirconate titanate (PZT) transducers as the excitation and sensing devices are common due to their simplicity, efficiency, and relatively well-understood properties. Given an excitation voltage and a relatively low excitation frequency, for an isotropic material such as aluminum, a PZT bonded to the surface will excite both the fundamental symmetric (S_0) and antisymmetric (A_0) Lamb wave modes. However, for many GLW localization algorithms, a structural response consisting of one mode is ideal. One solution to this is to bond collocated transducers on either side of a plate in order to selectively excite or decompose a mode of interest [3]. But it is difficult to collocate transducers accurately, and this practice is impractical for aerospace applications where sensors interfering with an aircraft's outer mold line are not ideal. One could also take advantage of the PZT tuning curve to excite the guided waves at frequencies where one mode is dominant, but this cannot perfectly generate only one mode, and it limits the excitation frequencies which can be used significantly [4]. As an alternative to collocated PZTs, a dual PZT transducer concept was developed [5,6]. These transducers are constructed from a pair of concentric ring and disc PZT-5A elements and thus can be mounted on one side of a plate and allow for highlighting of the constitutive A_0 and S_0 modes in a GLW signal.

The sparse array GLW method makes use of a large, spatially distributed network of transducers and is ideal for monitoring a large surface area, such as the skin of an aircraft. This method usually requires a baseline or pristine condition dataset. Baseline-free methods have been developed due to the drawbacks of relying on a baseline such as varying temperature environments and other unknown operating conditions [7,8]. However, due to the complexity of as-built aircraft structures, methods employing a baseline provide better localization capability if environmental influences can be controlled. Lamb wave theory depends on infinite flat plates, so the introduction of structural features such as stringers, ribs, and rivets creates significant challenges. Riveted structures and plate edges cause a GLW scattering effect, and reflections from plate edges and other features make GLW signals in these structures complex [9,10].

In this study, a sparse array was constructed using dual PZT transducers and was installed on a section of a Piper Cherokee skin plate. Damage to this structure was simulated with magnets in various cases. The GLW signal S_0 and A_0 modes were highlighted using the dual PZT mode decomposition process, and signals were compared to a baseline set of data. Sparse array imaging techniques were employed, and the damage localization results are shown here. An analysis of the impacts of mode decomposition and complex structural features is also presented.

2 METHODOLOGY

2.1 Dual PZT Transducers and Mode Decomposition

The basis for using dual element PZT transducers for GLW SHM applications is rooted in the tuning curves of PZT wafers. Specifically, lamb wave amplitudes change at different rates for different sized PZT wafers. Manipulation of this property allows for Lamb wave mode decomposition without requiring collocated sensors on two sides of a plate. For this work an

array of five dual PZTs was constructed. The placement of this array is explained in further detail in the experimental setup section. In order to decompose the fundamental Lamb wave A0 and S0 modes for a given transducer pair and excitation frequency, two types of pitch-catch signals are needed. For the first signal, $RD_{ij}(t)$, the ring portion of the i^{th} transducer is excited and the inner disc section of the j^{th} transducer measures the GLW response. The other signal, $DD_{ij}(t)$, is formed when the inner disc portion of the i^{th} transducer is excited and the inner disc section of the j^{th} transducer measures the GLW response. Figure 1 shows the dimensions of the PZT-5A transducers used for this work as well as a diagram illustrating the signal nomenclature.

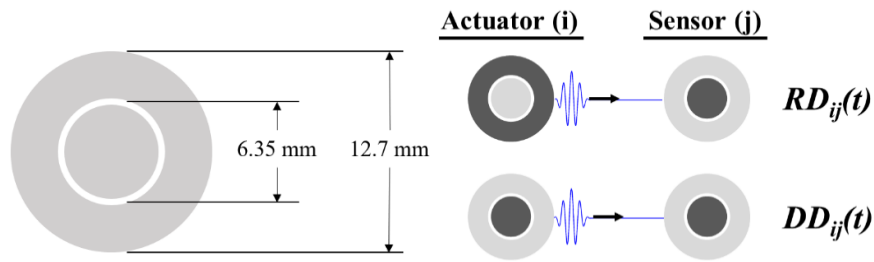


Figure 1 : Dual PZT dimensions and signal nomenclature (the active PZT elements are highlighted above).

For this work, only these two signals were necessary for adequate highlighting of the constitutive modes however a total of 9 signals can be collected if desired. In order to decompose the individual A0 and S0 modes, the ring and disc signals were combined and scaled according to equations 1 and 2.

$$A0_{ij}(t) = RD_{ij}(t) - C_{A0,ij}DD_{ij}(t) \quad (1)$$

$$S0_{ij}(t) = RD_{ij}(t) + C_{S0,ij}DD_{ij}(t) \quad (2)$$

The scaling factors, $C_{A0,ij}$ and $C_{S0,ij}$ were determined experimentally by comparing the magnitudes of particular modes in the ring and disc signals. For example, the scaling factor $C_{A0,ij}$ was determined by measuring the ratio of the magnitudes of the S0 mode first arrivals for $RD_{ij}(t)$ and $DD_{ij}(t)$. Thus, applying equation 1 with this scaling factor essentially removes the S0 mode from the signal, and the opposite is true applying equation 2. An example of this decomposition is shown in Fig. 2. Here the signal, $DD_{12}(t)$, is used as the reference undecomposed signal since it is essentially equivalent to a signal that would be found using more common single element PZT discs. The figure shows that the dual PZT processing method is at a minimum able to highlight the first arrival and edge reflections of a particular mode.

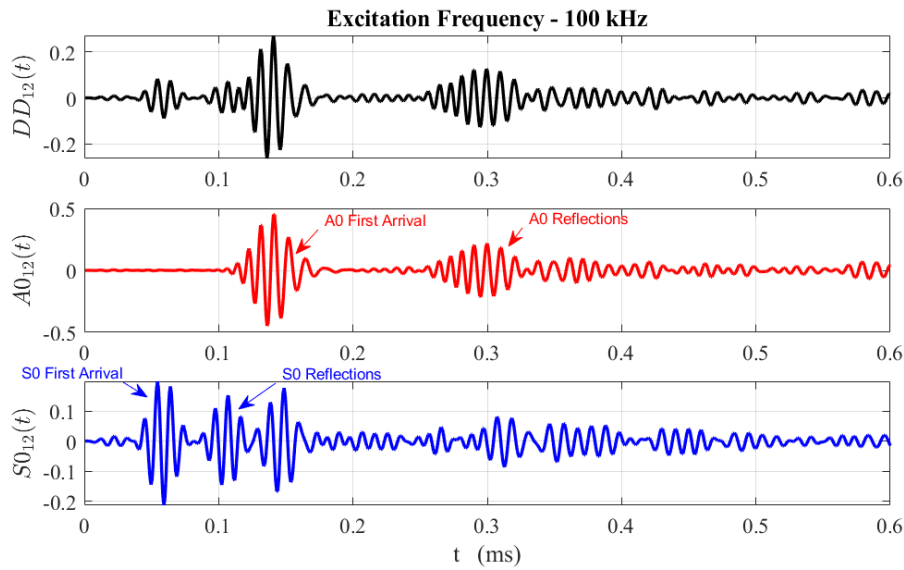


Figure 1 : Actuator-sensor pair 1-2 undecomposed (black) and decomposed A0 (red) and S0 (blue) mode signals with an excitation frequency of 100 kHz.

2.2 Sparse Array Technique

Damage maps were constructed using the sparse array technique. This method relies on an approximation of the group velocities for the item under test which can be obtained experimentally or analytically if the material properties are known *a priori*. This method is also dependent on baseline subtraction of damage signals due to the complexity of the aircraft structure. Baseline subtraction highlights the scattered portions of the signal from any damage introduced after the baseline was taken. These portions of the signal are then converted from the space domain to the time domain using the group velocity of a particular mode. The signal must be assumed to predominantly consist of only one mode for this conversion to be successful. In our case, the decomposed signals are used providing a potentially more accurate result. This space domain conversion is repeated for all points in time and all sensor-actuator pairs yielding a triangulation effect at points of damage.

For this work, two triangulation methods were used, these being summation and correlation algorithms. These algorithms are described in more detail in [11,12]. The correlation algorithm provides greater clarity by focusing more on ellipse intersections; however, it can be prone to false alarms and missed detections if faux intersections outweigh the intersection at an actual damage location or if there are multiple damage locations present in the inspection area. A higher number of transducers tends to produce a better result for both methods. For the localization algorithms, the experimentally determined group velocities shown in Fig. 3 were used. For the frequency range of interest (40-200 kHz), a PZT bonded to an aluminum plate will excite only the A0 and S0 modes.

2.3 Experimental Setup

Experimental work for this study used a Piper Cherokee wing section as the test specimen. The panel of interest was constructed from a 1-mm thick aluminum alloy skin plate and was

built up with various stringers, ribs, and a spar. These features were generally riveted to the skin plate, and no other bonding materials were used. The five-element transducer array was constructed in the shape of a spiral as a non-axisymmetric distribution was desired for optimal performance. The array was positioned on the bottom of the wing just aft of the leading edge as shown by Fig. 4. Damage was simulated to the wing skin using a strong pair of magnets placed on either side of the skin. This generates a localized force on the plate which is strong enough to produce GLW scattering similar to an actual crack.

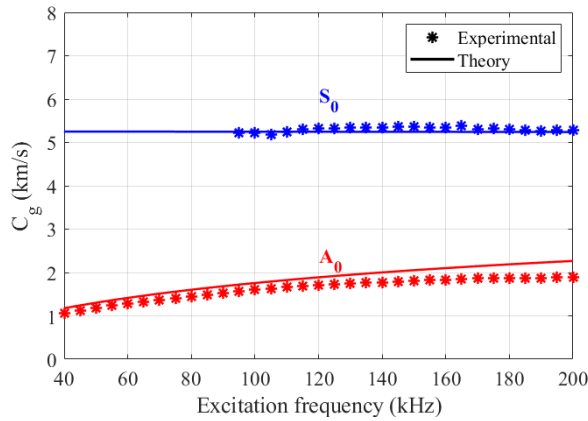


Figure 3 : Experimental and theoretical group velocities assuming typical properties for 1 mm Al 2024.



Figure 4: Bottom view of Piper Cherokee wing with a 5-element dual PZT array.

3 RESULTS AND DISCUSSION

A series of studies assessed the capabilities and limitations of the mode decomposition technique combined with the sparse array method. Three case studies are presented here, each testing different aspects to the present method including range, individual mode effectiveness, and the influence of complex structural features such as ribs, stringers, and lap joints.

3.1 Case Study 1 - Damage Distant from the Array

The first study examined the range of damage detection and potential influences of a rib mounted to the skin plate by placing simulated damage over 0.5 m from the center of the sparse array with a rib joint in the direct path to the damage. Due to the dispersion of the A0 mode and the relatively long distance of the damage from the array, this mode did not accurately locate damage as its reflections were likely too weak. Thus, the decomposed S0 mode summation and correlation images are shown in figure 5. Both algorithms show damage at the appropriate location using the experimentally determined S0 mode group velocity. This figure also highlights the difference between the two algorithms for a single damage location case. Henceforth, only the correlation algorithm images are shown since the summation algorithm images are typically similar but less clear. In general, this study demonstrates the advantage of using the S0 mode for maximum inspection range, and it shows that using the decomposed signal, reflections from damage are not too attenuated at over 0.5 m from the array.

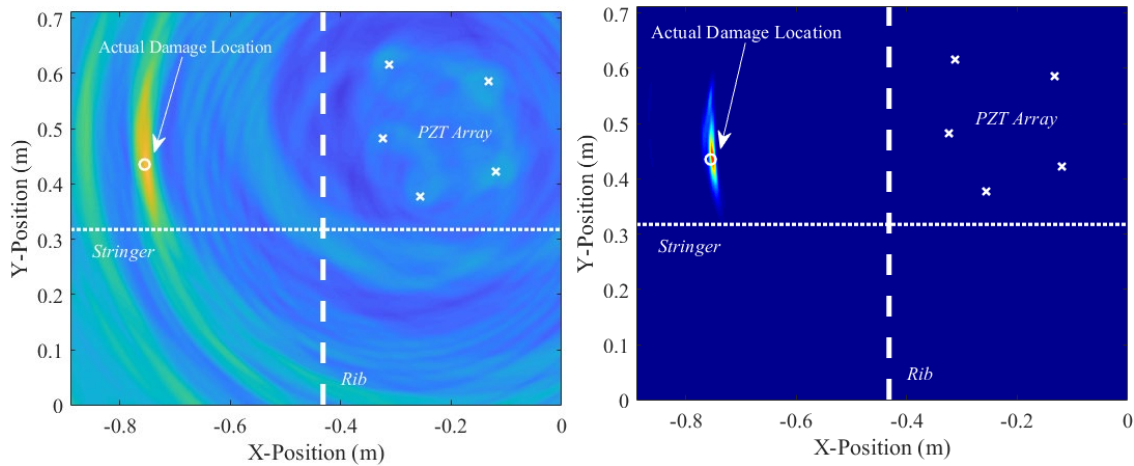


Figure 5: S0 Decomposed 140 kHz excitation summation algorithm image (left) and correlation algorithm image. The damage location is represented by a white circle.

3.2 Case Study 2 - Damage within the Array

For the next case study damage was placed near the center of the array, as this could pose potential problems with first arrival packet interference. Additionally, the proximity to the array implies that both the S0 and A0 reflections should be relatively strong, and an assumption that the signal is predominantly one mode may not provide ideal results in all frequency cases. Figure 6 demonstrates this by showing the damage maps for the undecomposed and decomposed S0 mode signals using the S0 mode group velocity. On the left, the undecomposed signal has dominant A0 mode reflections, so use of the faster S0 mode group velocity provides an inaccurate damage location. By using the decomposed S0 signal, the spurious A0 mode reflections are clearly removed, and use of the S0 group velocity yields a damage image that accurately locates damage. This case study demonstrates that the decomposed S0 mode signal can be used for damage detection close to the array where A0 reflections are typically dominant. Mode decomposition removes these spurious reflections if using the S0 group velocity.

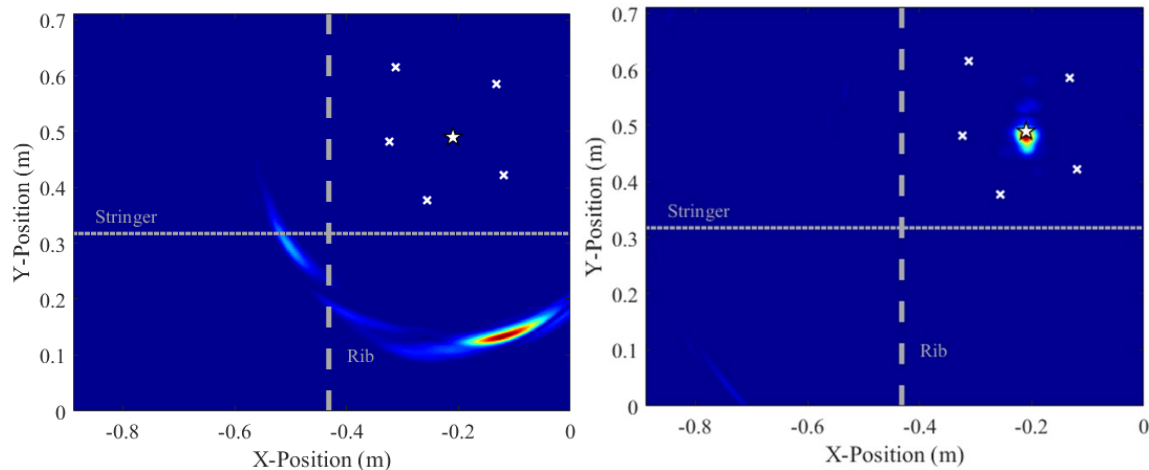


Figure 6: S0 undecomposed 120 kHz excitation correlation algorithm image (left) and S0 decomposed correlation algorithm image (right). The damage location is represented by a white star.

3.3 Case Study 3 - Damage Across Lap Joint

The third case study examines the influence of a lap joint on damage detection capabilities. This lap joint connects two skin plate sections with rivets, and this discontinuity is expected to reduce the amplitude of GLW reflections. To study this, simulated damage was placed just below the lap joint on a separate plate section from the array. Due to the distance from the array, the A0 mode decomposed signal was not effective in locating this damage, so figure 7 examines the effectiveness of S0 mode decomposition. In this figure, the solid line parallel to the dashed stringer line represents the lap joint, and the star represents the damage location. Without mode decomposition, the S0 mode reflections due to introduced damage are not strong enough to locate this damage. With mode decomposition, the image correctly shows damage at the damage location with a few spurious reflections. This case study suggests that the decomposed S0 mode signal can increase the damage detection sensitivity, and that mode decomposition makes damage detection across lap joints possible.

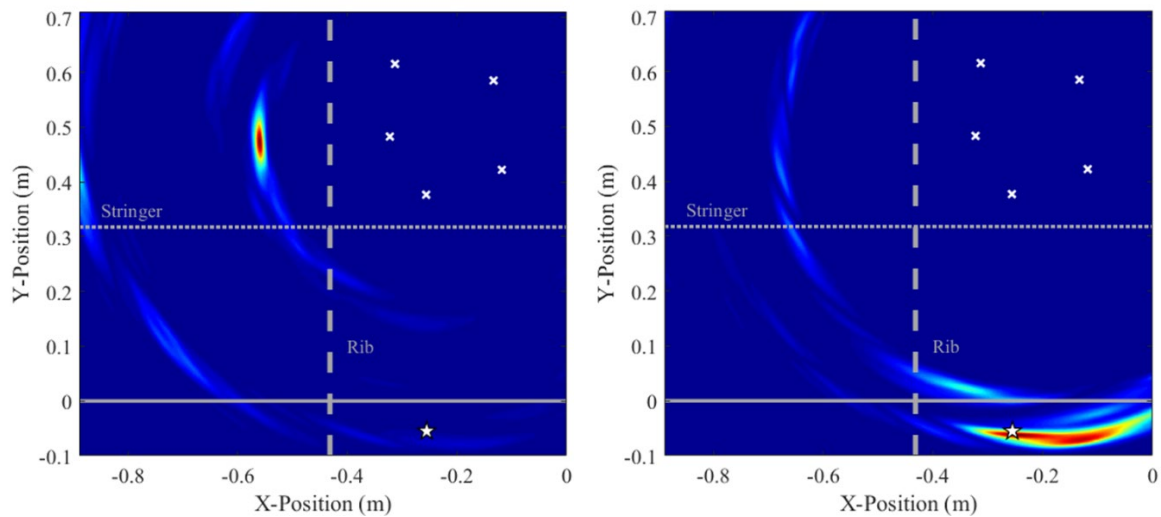


Figure 7: S0 undecomposed 120 kHz excitation correlation algorithm image (left) and S0 decomposed correlation algorithm image (right). The damage location is represented by a white star.

4 CONCLUSIONS

In this paper, a previously developed damage decomposition method using dual element PZT transducers [5,6] was applied to a sparse array GLW damage localization scheme. Experimental studies were performed with an aluminum Piper Cherokee wing since it imposes additional, realistic challenges that are not present when testing with an ideal simple plate. Several cases showed that the sparse array method using dual PZTs to decompose the GLW modes was effective at localizing simulated damage. It was shown that the S0 mode was more effective in localizing damage in cases farther away from the array (greater than 0.5 m) likely due to its lack of dispersion. Additionally, the results suggest that the decomposed S0 mode may be used in almost all cases, and this signal is more sensitive to damage at long distances when compared to the undecomposed signal. Finally, the results suggest that if a baseline data set is used and measurements are made in a consistent environment, structural features do not

significantly influence the damage localization results. The only significant influence is signal attenuation over longer distances and transmission through multiple lap joints. For the cases shown, no structural features prevented damage from being localized accurately. Thus, these results suggest that the presented method can be used to locate crack-like damage in a relatively large section of a wing, likely greater than 1 m². An array that is distributed over a larger area and not restricted to a featureless section of the plate as presented here may allow for damage detection over an even larger area.

5 ACKNOWLEDGEMENTS

Author Jacob McCullum thanks the SMART Scholarship Program for its support which is funded by USD/R&E (The Under Secretary of Defense-Research and Engineering), National Defense Education Program (NDEP) / BA-1, Basic Research.

REFERENCES

- [1] Dalton, R. P., Cawley, P., and Lowe, M. J. S., “The Potential of Guided Waves for Monitoring Large Areas of Metallic Aircraft Fuselage Structure,” *Journal of Nondestructive Evaluation*, vol. 20, Mar. 2001, pp. 29–46.
doi: 10.1023/A:1010601829968
- [2] Gao, H., Shi, Y., and Rose, J. L., “Guided Wave Tomography on an Aircraft Wing with Leave in Place Sensors,” *AIP Conference Proceedings*, vol. 760, Apr. 2005, pp. 1788–1794.
doi: 10.1063/1.1916887
- [3] GÓMEZ-ULLATE, Y., and Espinosa, F. M. de, “Selective Excitation of Lamb Wave Modes in Thin Aluminium Plates using Bonded Piezoceramics : FEM Modelling and Measurements.”
- [4] Sohn, H., and Lee, S. J., “Lamb Wave Tuning Curve Calibration for Surface-Bonded Piezoelectric Transducers,” *Smart Materials and Structures*, vol. 19, Nov. 2009, p. 015007.
- [5] Sohn, H., and Kim, S. B., “Development Of Dual PZT Transducers for Reference-Free Crack Detection in Thin Plate Structures,” *IEEE Transactions on Ultrasonics, Ferroelectrics, and Frequency Control*, vol. 57, Jan. 2010, pp. 229–240.
- [6] Yeum, C. M., Sohn, H., and Ihn, J. B., “Lamb Wave Mode Decomposition Using Concentric Ring and Circular Piezoelectric Transducers,” *Wave Motion*, vol. 48, Jun. 2011, pp. 358–370.
- [7] Qiang, W., and Shenfang, Y., “Baseline-free Imaging Method based on New PZT Sensor Arrangements,” *Journal of Intelligent Material Systems and Structures*, vol. 20, May 2009, pp. 1663–1673.
doi: 10.1177/1045389X09105232
- [8] Sohn, H., Park, H. W., Law, K. H., and Farrar, C. R., “Combination of a Time Reversal Process and a Consecutiv Outlier Analysis for Baseline-free Damage Diagnosis,” *Journal of Intelligent Material Systems and Structures*, vol. 18, Apr. 2007, pp. 335–346.
doi: 10.1177/1045389X0606629
- [9] Diligent, O., Grahn, T., Boström, A., Cawley, P., and Lowe, M. J. S., “The Low-Frequency Reflection and Scattering of the S0 Lamb Mode From a Circular Through-

- Thickness Hole in a Plate: Finite Element, Analytical and Experimental Studies,” *The Journal of the Acoustical Society of America*, vol. 112, Dec. 2002, pp. 2589–2601.
doi: 10.1121/1.1512292
- [10] Hinders, M. K., “Lamb Wave Scattering from Rivets,” *Review of Progress in Quantitative Nondestructive Evaluation: Volume 15A*, D.O. Thompson and D.E. Chimenti, eds., Boston, MA: Springer US, 1996, pp. 209–216.
doi: 10.1007/978-1-4613-0383-1_26
- [11] Ihn, J.-B., and Chang, F.-K., “Pitch-catch Active Sensing Methods in Structural Health Monitoring for Aircraft Structures,” *Structural Health Monitoring*, vol. 7, Mar. 2008, pp. 5–19.
doi: 10.1177/1475921707081979
- [12] Yu, L., Bottai-Santoni, G., and Giurgiutiu, V., “Shear Lag Solution for Tuning Ultrasonic Piezoelectric Wafer Active Sensors with Applications to Lamb Wave Array Imaging,” *International Journal of Engineering Science*, vol. 48, Oct. 2010, pp. 848–861.
doi: 10.1016/j.ijengsci.2010.05.007

BENDING SHAPE MEMORY PROCESS OF A FABRIC-REINFORCED SHAPE MEMORY POLYMER COMPOSITE PLATE: EXPERIMENTAL INVESTIGATION AND NUMERICAL SIMULATION

PENGXUAN FAN^{*}, WUJUN CHEN, JIFENG GAO, GUANGQIANG FANG[†], FUJUN
PENG[†] AND ZHENGLI CAO[†]

^{*} Space Structures Research Center (SSRC)
Shanghai Jiao Tong University
Minhang Campus, 200240 Shanghai, China
E-mail: cwj@sjtu.edu.cn, web page: <http://www.ssrc.cn>

[†] Aerospace System Engineering Shanghai (ASES)
Minhang District, 200118 Shanghai, China
E-mail: c767116442@126.com, web page: <http://www.sast.cn>

Key words: Fabric-reinforced shape memory polymer composite plate (FSMPCP), Shape memory constitutive model, Stiffness homogenization, Tension-compression asymmetry.

Abstract. Fabric-reinforced shape memory polymer composite plate (FSMPCP) with high levels of stiffness, strength and shape memory property are important stimuli-controlled smart materials which have significant potential to be applied in large size smart structures. Shape memory property and the corresponding mechanical constitutive model of FSMPCP are the essential issues to be addressed before utilizing the material. In this work, a long carbon-fiber reinforced FSMPCP was developed via vacuum infiltration molding process (VIMP) to investigate the shape memory process and further to establish the constitutive model. Mechanical experiments including tension and compression were carried out firstly, where the anisotropy and the tension-compression asymmetry were detected. Then, the thermal shape memory property in bending case was investigated through a typical four-step shape memory experiments. To establish an effective shape memory constitutive model of FSMPCP, a bi-phasic description was used where the stiffness was considered to be contributed by an active-phase and a frozen-phase. A homogenization process using representative volume element (RVE) was conducted to obtain the effective elastic properties. Besides, a linear two-modulus model was applied to depict the asymmetry of tension-compression. To validate the constitutive model, numerical simulation method was also developed based on the UMAT in ABAQUS. Finally, finite element simulations of bending shape memory experiments were carried out using the proposed constitutive model. The comparison between numerical and experimental results revealed that the constitutive model was effective to depict the anisotropy, the tension-compression asymmetry and the shape memory process of the FSMPCP.

1 INTRODUCTION

Fabric-reinforced shape memory polymer composite plates (FSMPCPs) have drawn a wide

range of interests due to its superior performance in stiffness, strength and the special shape memory ability. Compared with the shape memory ceramic composites, FSMPCPs behave better in larger deformation and could be easily fabricated. Compared with the shape memory alloy, FSMPCPs are more economical and have more design flexibility. In this case, FSMPCPs can be applied in composite hinges [1], morphing skins [2] and large space deployable structures [3, 4]. Before the utilization of FSMPCs, shape memory property and corresponding constitutive model are fundamental issues to be addressed.

There are usually two method to take the shape memory effect (SME) and heterogeneity of FSMPCPs into account when considering the constitutive model. The first method is directly numerical method, where the composite structure of FSMPCPs including the fabrics and matrix is directly built in finite element model, then the SME is introduced by assigning the matrix as shape memory viscoelastic polymer [5, 6]. The second method is homogenization method, where the heterogeneity is considered by a homogenization process, then the material is regarded as anisotropic material and the SME is introduced by regarding the homogenized material as viscoelastic material [7, 8]. The first method could depict the mechanical properties accurately but is very limited to be used in analysis of large scale structures since the number of element is too big to be processing in a normal finite element analysis program. The second method has reduced the size of global matrix by homogenization across scales, however, the FSMPCPs are not viscoelastic material but elastic material [9, 10]. Therefore, this work will utilize homogenization method to evaluate the heterogeneity of FSMPCPs. Then a bi-phasic description of the material constituent will be used to consider the SME effect in order to establish effective constitutive model for FSMPCPs which is nearly elasticity, where the stiffness was considered to be contributed by an active-phase and a frozen-phase.

The work was organised as follows, the material introduction and experiments were presented firstly, based on which the shape memory constitutive model was established and then validated through finite element simulation. At last, future works and conclusions were briefly listed.

2 MATERIAL AND EXPERIMENT

2.1 Specimen preparation

Carbon fiber FSMPCPs lamina with thickness of 0.8mm was manufactured by vacuum resin transfer molding (VTRM) process, where the mixture of epoxy monomer E44 and poly-bis-ether [11] were poured into the mold to infiltrate the T800-12 K carbon-fiber cloth with 3-up-1-down woven pattern. Then the air was evacuated through the exit of the mold and the infiltrated carbon fiber cloth was cured at 100°C. The woven patterns were plotted in Figure 1 (planform view) and Figure 2 (cross section view) while the geometrical parameters of the elliptic yarn were listed in Table 1. As the glass transformation point (T_g) was determined to be 56.5°C for warp direction and 56.2°C for weft direction, the mechanical experiments of tension and compression were chosen to be 25°C and 85°C, which were corresponded to glassy state and rubbery state of the material, respectively. The initial FSMPCPs was processed to be rectangle specimens using the milling machine with high smoothness processing level. Tension and compression experiments were carried out using UTM-4000 universal testing machine (Produced by Shenzhen SANSEI). Dimensions of specimen for tension experiment was

20mm × 200mm. When considering the compression experiment, the length-width ratio was reduced to avoid buckling effect during the test. Therefore, the dimension for compression experiment was 30mm × 70mm.

Table 1: Geometrical parameters of the elliptic yarn

Direction	2a/mm	2b/mm
Warp	1.72	0.36
Weft	1.71	0.33

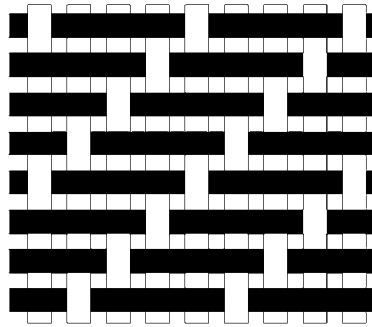


Figure 1: Graphical illustration of the woven pattern of the broken twill FSMPCs in planform view

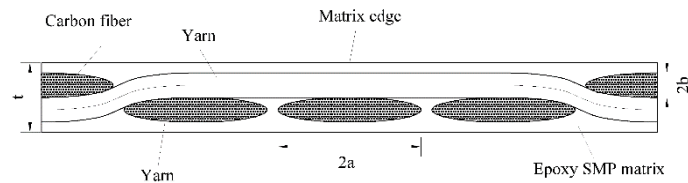


Figure 2: Yarn distribution of the broken twill FSMPCs in cross section view

2.2 Mechanical and shape memory experiments

(1) Tension experiments

In the uniaxial tensile experiments, the clamped length of specimens was 50mm in each side and the gauge length was 100mm. Specimen was firstly clamped on the fixtures and the tank temperature was set to be the expected value. Then the heat module was started and all the heating and loading devices were hold about 40 minutes to make the thermal field steady in the tank room. After which, the extension was applied to the specimen with constant rate of 1mm/min. Tensile displacement, force and time were recorded in the experiment. The stress-strain curves were plotted in Figure 3 using nominal strain and nominal stress. As presented in the stress-strain curves, the response was nearly linear elasticity in both glassy state and rubbery state. However, the tensile modulus in warp direction was always larger than that in weft direction. Meanwhile, the modulus in rubbery state was significantly smaller than that in glassy state. As a result, the average tensile-modulus in warp and weft directions were 16.5 GPa and 13.7 GPa at 25°C of glassy state. For the rubbery state, the average tensile modulus in warp and

weft directions were 4.9 GPa and 3.3 GPa at 85°C.

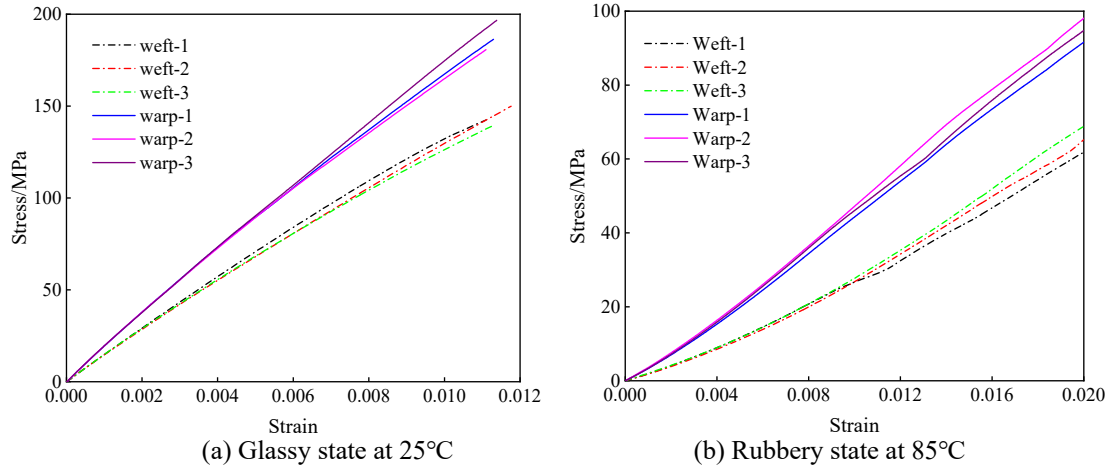


Figure 3: Stress-strain of uniaxial tension experiments in warp and weft directions

(2) Compression experiments

Uniaxial compression experiments were carried out using a dedicated compression test fixture for the local buckling effect using conventional ASTM test fixture. The compression test fixture was consisted by two housing blocks and two matched cover plates, used to prevent the thin woven composite from premature buckling. One could see the details of the fixture in our former work [12]. The temperature control steps were same to the tension experiments, where a thermal balance time of 40 minutes were adopted before loading and the compression rate was also 1mm/min. In this case, the average compression modulus in warp and weft directions were 5.6 GPa and 4.4 GPa at 25°C, while the values were 1.5 GPa and 1.1 GPa at 85°C. Overall, the compression modulus were about one third of tensile modulus for both warp and weft directions.

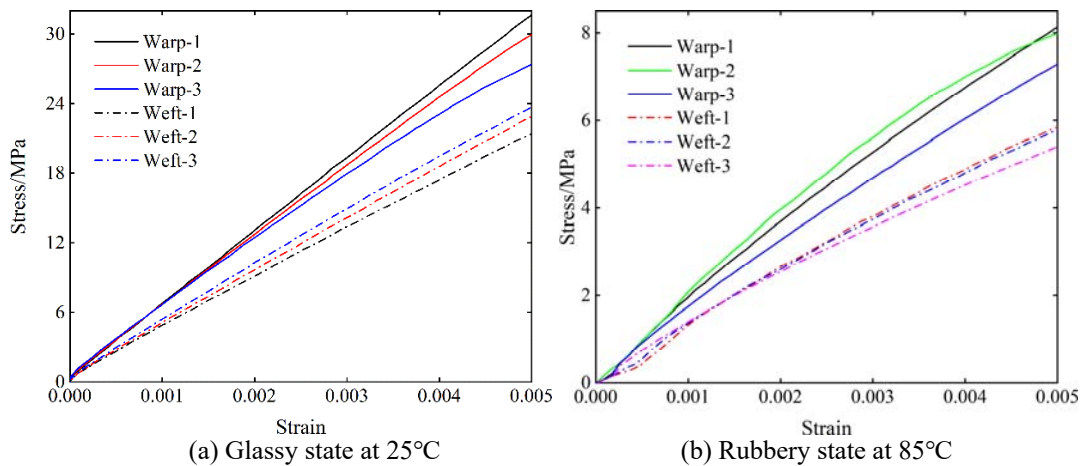


Figure 4: Stress-strain of uniaxial compression experiments in warp and weft directions

(3) Shape memory experiments

Shape memory experiments in three-point bending mode were carried out using DMA-Q800

equipment according to the typical four step shape memory process: i. Apply the deformation at temperature above T_g ; ii. Cool down the temperature with the displacement constraints; iii. Release the constraints at temperature below T_g and most of the deformation would retain except for the elastic bounce; iv. Heat the specimen and the shape would recovery to the original state. In the experiments, the heating and cooling rates were set to be $3^\circ\text{C}/\text{min}$. Dimension of specimens were $10\text{mm} \times 30\text{mm}$, where the span of the supporting in three-point bending was 20mm . Except for free recovery, the constraint recovery case was also measured, where the displacement freedom degree was constrained in the heating step. The experiment results were plotted in Figure 5, where the force value of unit width was plotted as Z axis.

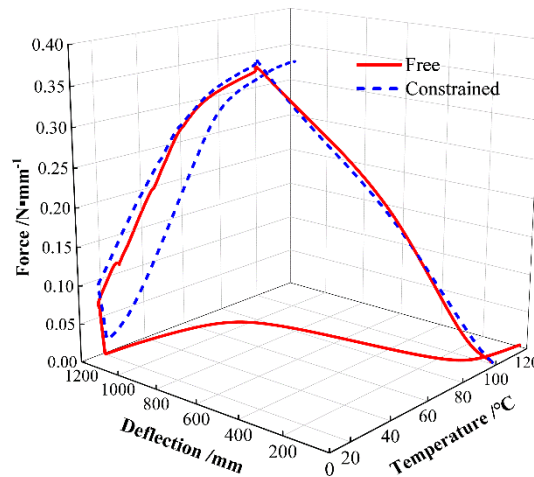


Figure 5: Deflection and loading force during the shape memory process

3 CONSTITUTIVE MODELLING

There are two issues in the shape memory modelling of FSMPCPs, the mechanical modelling which considering the composite properties and the thermal modelling which considering the memory process. Here the mechanical modelling was carried out by a homogenization process, where the inner-fabric-structure was considered. The thermal modelling was carried out by a phase-transition concept proposed by Liu et al. [13].

3.1 Homogenization and tension-compression asymmetry

Two scale linear elasticity homogenization analysis was firstly carried out to evaluate the anisotropic properties caused by the inner-composite-structure of FSMPCPs. Details of the homogenization process were referred to Fish [14], where the analysis was divided into two steps. Firstly, a unit cell problem with multiple right-hand sides was solved and the stress influence functions were obtained. Then the overall constitutive tensor components were evaluated by volume averaging. When conduct the homogenization process, properties of the yarn were firstly calculated and inputted as initial parameters with the properties of the polymer matrix, which were listed in Table 2. In this case, the matrix was considered to be isotropic material and yarns were assumed to be transversely isotropic homogenous material. The overall constitutive tensor components \mathbf{D} were obtained in Table 3. According to the stiffness matrix \mathbf{D} , the tensile modulus could be calculated to be 17.2GPa and 14.35GPa , with deviation of 3.8%

and 4.6% with the results in tensile experiments at 25°C.

Table 2: Material properties (25°C) used in homogenization analysis

Parameters	E_t /GPa	E_a /GPa	G_a /GPa	ν
Matrix	1.41		0.52	0.34
Fiber	294.0		113.1	0.30
Yarn	158.1	4.98	1.85	0.32

Table 3: Overall constitutive tensor components

Indices	1	2	3	4	5	6
1	18.37	2.53	1.95	0.00	0.00	0.01
2	2.53	15.47	1.93	0.00	0.00	0.00
3	1.95	1.92	3.78	0.00	0.00	0.00
4	0.00	0.00	0.00	1.18	0.00	0.00
5	0.00	0.00	0.00	0.00	1.06	0.00
6	0.02	0.00	0.00	0.00	0.00	1.05

Then it came to the tension-compression asymmetry, a linear two-modulus model as plotted in Figure 6 was utilized here, where the compression modulus was about 1/3 of the tensile modulus. In the calculations, material stiffness matrix was inputted as initial parameters and the stress state of the material point was firstly judged, if the point was in compression state, the corresponding characters in stiffness matrix would be reduced with a reduction coefficient of 1/3.

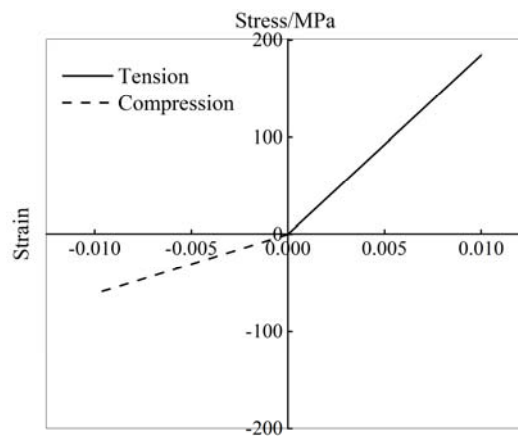


Figure 6: Linear two-modulus model for FSMPCPs

3.2 Shape memory effect

The concept of two-phase material model of Liu [13] was utilized here, where the material was regarded as anisotropic homogeneous material with frozen phase and active phase. When temperature was at high temperature ($\gg T_g$), the material would be made up by the frozen constituent. When temperature was at low temperature ($\ll T_g$), the material would be made up by the active constituent. In the phase transition process, both active and frozen constituents would coexist in the material and transfer to each other according to the thermal environment. In the shape memory process, total strain $\boldsymbol{\varepsilon}$ was divided into elastic strain $\boldsymbol{\varepsilon}_E$, storage strain $\boldsymbol{\varepsilon}_S$ and thermal strain $\boldsymbol{\varepsilon}_T$. The overall stress components can be calculated by equation (1). The storage strain which control the shape storage and recovery was related to the temperature by equation (3), where f_s was a volume ratio of the frozen constituent and a function of temperature. In order to make the model more flexibility and accurate to depict the shape memory process, the material stiffness tensor was also split into two part as equation (4), where the subscript "f" and "a" denoted the frozen and active constituents, respectively.

$$\boldsymbol{\sigma} = \mathbf{D} \cdot (\boldsymbol{\varepsilon} - \boldsymbol{\varepsilon}_S - \boldsymbol{\varepsilon}_T) \quad (1)$$

$$\boldsymbol{\varepsilon} = \boldsymbol{\varepsilon}_E + \boldsymbol{\varepsilon}_S + \boldsymbol{\varepsilon}_T \quad (2)$$

$$\boldsymbol{\varepsilon}_S = (\boldsymbol{\varepsilon} - \boldsymbol{\varepsilon}_T) \cdot f_s \quad (3)$$

$$\mathbf{D} = \mathbf{D}_f \cdot f_f + \mathbf{D}_a (1 - f_f) \quad (4)$$

Both f_s and f_f were temperature-dependent functions. In a typical four-step free recovery shape memory process, by inserting the constitutive model into the boundary and thermal conditions, the stress and strain evolution in shape memory process could be calculated [15]. Then f_s could be obtained from the strain evolution of the recovery step, while the f_f could be obtained from the stress evolution of the cooling step. In this work, the above constitutive model was coded into ABAQUS as a UMAT, based on which we can carry out the simulation of shape memory process.

4 FINITE ELEMENT SIMULATION

Shape memory experiments were simulated using the above constitutive model, where the specimen was meshed with 3D cubic element named as C3D8. All the thermal conditions and displacement boundaries were same to the experiments, where the temperature revolution inputted in the model was measured from the experiments. Both free and constrained recovery shape memory process were simulated. Results with derivation less than 10% were obtained as plotted in Figure 7. Due to the linear elastic assumption was utilized in modelling the mechanical response of FSMPCPs, the nonlinear response in loading step was not considered here. As indicated in the loading step, bending stiffness was appropriately considered using the tension-compression asymmetry model.

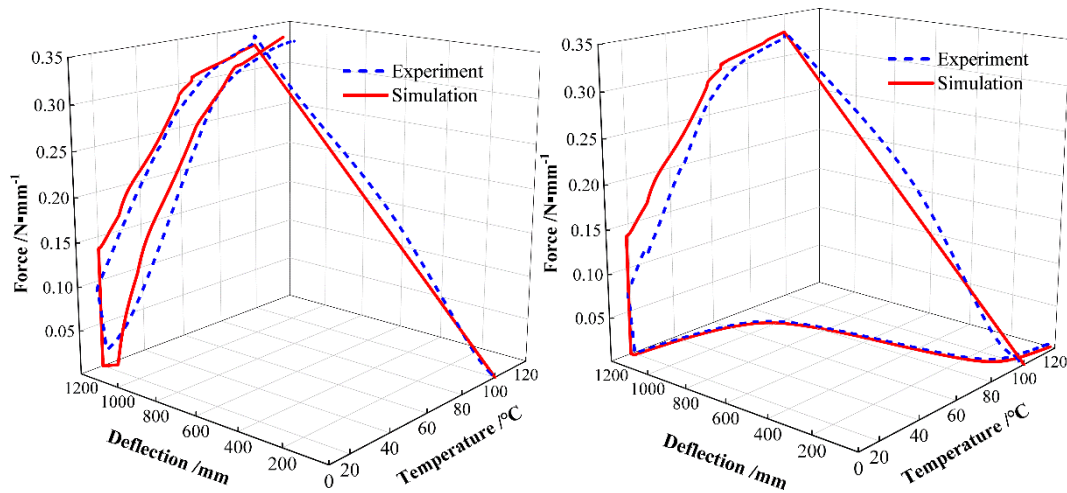


Figure 7: Simulation results using the constitutive model

5 CONCLUSIONS

FSMPCPs would behavior both heterogeneity and shape memory properties, of which the constitutive modelling could be divided into two steps, including the homogenization and the thermal modelling. As inducted in this research, the RVE homogenization analysis and phase-transition concepts could be successfully adopted to established the shape memory constitutive model of the FSMPCPs in elastic regime.

REFERENCES

- [1] Thanh, D.D., Ngoc, S.H., Goo, N.S., Yu, W. Design, fabrication, and bending test of shape memory polymer composite hinges for space deployable structures. *J Intel Mat Syst Str* (2018)**29**: 1560-1574.
- [2] Fan, X., Chung, J.Y., Lim, Y.X., Li, Z., Loh, X.J. Review of Adaptive Programmable Materials and Their Bioapplications. *Acs Appl Mater Inter* (2016)**8**: 33351-33370.
- [3] Zhang, R., Guo, X., Liu, Y., Leng, J. Theoretical analysis and experiments of a space deployable truss structure. *Compos Struct* (2014)**112**: 226-230.
- [4] Luo, H., Zhou, X., Xu, Y., Wang, H., Yao, Y., Yi, G., Hao, Z. Multi-stimuli triggered self-healing of the conductive shape memory polymer composites. (2018)**47**: 1-6.
- [5] Yarali, E., Baniassadi, M., Baghani, M. Numerical homogenization of coiled carbon nanotube reinforced shape memory polymer nanocomposites. *Smart Mater Struct* (2019)**28**: 35026.
- [6] Azzawi, W.A., Epaarachchi, J.A., Islam, M., Leng, J. Implementation of a finite element analysis procedure for structural analysis of shape memory behaviour of fibre reinforced shape memory polymer composites. *Smart Mater Struct* (2017)**26**: 125002.
- [7] Qiao, T., Liu, L., Li, F., Lan, X., Liu, Y., Leng, J. Strength property analysis for fiber-reinforced shape memory polymer composite laminate. *J Intel Mat Syst Str* (2016)**28**: 1627-1639.
- [8] Gu, J., Xie, Z., Wang, S., Sun, H., Zhang, X. Thermo-mechanical modeling of woven fabric reinforced shape memory polymer composites. *Mech Adv Mater Struc* (2018)**0**: 1-11.
- [9] Gao, J., Chen, W., Fan, P., Zhao, B., Hu, J., Zhang, D., Fang, G., Peng, F. Experimental

- determination of mechanical properties of a single-ply broken twill 1/3 weave reinforced shape memory polymer composite. *Polym Test* (2018)**69**: 100-106.
- [10] Zhang, W., Zhang, F., Lan, X., Leng, J., Wu, A.S., Bryson, T.M., Cotton, C., Gu, B., Sun, B., Chou, T. Shape memory behavior and recovery force of 4D printed textile functional composites. *Compos Sci Technol* (2018)**160**:224-230.
- [11] Zheng, N., Fang, G., Cao, Z., Zhao, Q., Xie, T. High strain epoxy shape memory polymer. *Polym Chem-Uk* (2015)**6**: 3046-3053.
- [12] Gao, J., Chen, W., Fan, P., Zhao, B., Hu, J., Zhang, D., Fang, G., Peng, F. Experimental determination of mechanical properties of a single-ply broken twill 1/3 weave reinforced shape memory polymer composite. *Polym Test* (2018)**69**: 100-106.
- [13] Liu, Y., Gall, K., Dunn, M.L., Greenberg, A.R., Diani, J. Thermomechanics of shape memory polymers: Uniaxial experiments and constitutive modeling. *Int J Plasticity* (2006)**22**: 279-313.
- [14] Fish, J. *Practical multiscaleing*. John Wiley & Sons, Ltd, Chichester, Vol. I, (2014).
- [15] Fan, P., Chen, W., Zhao, B., Hu, J., Gao, J., Fang, G., Peng, F. Formulation and numerical implementation of tensile shape memory process of shape memory polymers. *Polymer* (2018)**148**: 370-381.

DESIGN OF ELECTRO-VISCOELASTIC SANDWICH PANELS FOR NOISE REDUCTION

Francisco S. Vieira^{*}, Aurelio L. Araujo[†]

^{*}Instituto Superior Tecnico
Universidade de Lisboa

Av. Rovisco Pais, 1049-001 Lisboa, Portugal

e-mail: francisco.sousa.vieira@tecnico.ulisboa.pt - Web page: <http://tecnico.ulisboa.pt>

[†] IDMEC, Instituto Superior Tecnico
Universidade de Lisboa

Av. Rovisco Pais, 1049-001 Lisboa, Portugal

e-mail: aurelio.araujo@tecnico.ulisboa.pt - Web page: <http://www.idmec.ist.utl.pt/>

Key words: Sandwich, Piezoelectricity, Viscoelasticity, Shunted Damping, Multiobjective Optimization

Abstract. This paper addresses vibration and noise reduction in laminated sandwich plates using both viscoelastic and piezoelectric elements, using the capabilities of the commercial software programme ANSYS. In the low frequency range, noise and vibration damping is accomplished through piezoelectric patches bonded to the surfaces of the sandwich panels, using passive RL damping circuits. For higher frequency ranges, damping is obtained from viscoelastic materials that are used as the core of the sandwich panels. The sound transmission characteristics of the panels are evaluated by computing their radiated sound power, using the Rayleigh integral method. Optimization of thicknesses, fibre orientation of the composite layers and location of the piezoelectric patches is also conducted for minimization of weight and radiated sound power. Results are presented to illustrate the performance of the optimized sandwich panels in terms of weight and noise reduction efficiency.

1 INTRODUCTION

In the transportation industry, sandwich composite panels may represent an optimized solution for both sound radiation and structural vibration in most frequency ranges. Viscoelastic materials are an efficient way of reducing structural vibrations and providing noise attenuation, which allied to piezoelectric elements may lead to broader control capabilities regarding acoustic emissions. The use of commercial software programmes allows for an acceleration in the design cycles, but due to some limitations in these codes when dealing with material viscoelastic behaviour combined with piezoelectric elements, it is sometimes necessary to develop user codes that can overcome these limitations [1]. Recently, Iurlova et al. [2] developed an algorithm that solved the natural frequency problem of electro-viscoelastic structures with electric circuit through the extraction of global FE matrices from ANSYS. Control of vibrations and noise reduction have also been addressed recently by Larbi et al. ([3], [4]), with the use of RL shunt circuits.

In the present work thicknesses, fibre orientation of the composite layers and location of the piezoelectric patches are optimized in an electro-viscoelastic sandwich panel with the objective of noise reduction.

Commercial software ANSYS is used together with Matlab to achieve this purpose.

2 STRUCTURAL MODEL

2.1 Electro-viscoelastic sandwich panel

The addressed structure is a sandwich plate. The core is made of a viscoelastic material, and the top and bottom faces are made of carbon fibre composite laminates. Piezoelectric patches are bonded to the top of the plate, and a shunted RL circuit is connected to each patch. This forms the electro-viscoelastic sandwich panel as shown in Figure 1.

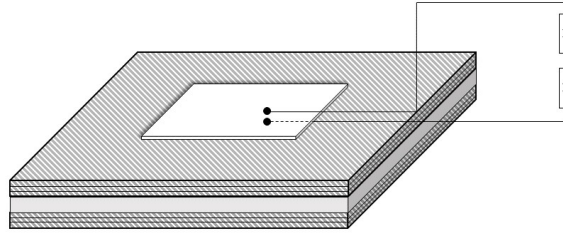


Figure 1: Electro-viscoelastic sandwich panel

2.2 Orthotropic elastic material

Each lamina of the composite laminated faces of the sandwich plate can be modelled as an orthotropic elastic material. The constitutive equation of an orthotropic material, in its principal material directions is

$$\begin{Bmatrix} \epsilon_1 \\ \epsilon_2 \\ \epsilon_3 \\ \epsilon_{23} \\ \epsilon_{13} \\ \epsilon_{12} \end{Bmatrix} = \begin{bmatrix} s_{11} & s_{12} & s_{13} & 0 & 0 & 0 \\ s_{12} & s_{11} & s_{13} & 0 & 0 & 0 \\ s_{13} & s_{13} & s_{33} & 0 & 0 & 0 \\ 0 & 0 & 0 & s_{44} & 0 & 0 \\ 0 & 0 & 0 & 0 & s_{44} & 0 \\ 0 & 0 & 0 & 0 & 0 & s_{66} \end{bmatrix} \begin{Bmatrix} \sigma_1 \\ \sigma_2 \\ \sigma_3 \\ \sigma_{23} \\ \sigma_{13} \\ \sigma_{12} \end{Bmatrix} = \begin{bmatrix} \frac{1}{E_1} & -\frac{\nu_{12}}{E_1} & -\frac{\nu_{13}}{E_1} & 0 & 0 & 0 \\ -\frac{\nu_{12}}{E_1} & \frac{1}{E_2} & -\frac{\nu_{32}}{E_3} & 0 & 0 & 0 \\ -\frac{\nu_{13}}{E_1} & -\frac{\nu_{32}}{E_3} & \frac{1}{E_3} & 0 & 0 & 0 \\ 0 & 0 & 0 & \frac{1}{G_{23}} & 0 & 0 \\ 0 & 0 & 0 & 0 & \frac{1}{G_{13}} & 0 \\ 0 & 0 & 0 & 0 & 0 & \frac{1}{G_{12}} \end{bmatrix} \begin{Bmatrix} \sigma_1 \\ \sigma_2 \\ \sigma_3 \\ \sigma_{23} \\ \sigma_{13} \\ \sigma_{12} \end{Bmatrix} \quad (1)$$

where ϵ_{ij} are the elastic strain components, σ_{ij} are the corresponding stress components in the principal material directions and s_{ij} are the components of the compliance matrix, also represented in terms of the usual engineering moduli E_i , G_{ij} and ν_{ij} .

2.3 Viscoelastic material

Using the elastic-viscoelastic equivalence principle, a problem with viscoelastic materials in the frequency domain can be solved as an elasticity problem [5], where the complex moduli are given by

$$E_i(j\omega) = E'_i(\omega) (1 + j\eta_{E_i}(\omega)) \quad (2a)$$

$$G_{ij}(j\omega) = G'_{ij}(\omega) (1 + j\eta_{G_{ij}}(\omega)) \quad (2b)$$

$$\nu_{ij}(j\omega) = \nu'_{ij}(\omega) (1 + j\eta_{\nu_{ij}}(\omega)) \quad (2c)$$

and where primed (') quantities denote storage moduli and η denotes the material loss factor. The product between the storage modulus and the loss factor is the loss modulus.

2.3.1 Fractional derivative models

Classical viscoelastic models deal only with spring and dashpot elements, meaning integer order time derivatives are involved, while fractional derivative models are a more powerful way to describe viscoelastic behaviour since they allow the use of non-integer derivatives. Therefore, more accurate behaviour of viscoelastic materials can be captured with the use of these models.

A model that describe well the overall behaviour of a viscoelastic material is the five parameter fractional model developed by Pritz [6]. According to this model, the frequency dependent shear modulus for a viscoelastic isotropic material becomes

$$G(j\omega) = G_0 + G_0(d-1) \frac{(j\omega\tau)^\alpha}{1 + (j\omega\tau)^\beta} \quad (3)$$

where $d = \frac{G_\infty}{G_0}$ is the ratio of high-frequency limit value of the dynamic shear modulus, G_∞ , to the static shear modulus, G_0 , the order of the derivatives of strain and stress are α and β , respectively, and τ is the relaxation time. For more details the reader is referred to reference [6].

2.4 Piezoelectric material

For a transversely isotropic piezoelectric material the constitutive equations are given by

$$\begin{Bmatrix} \sigma_x \\ \sigma_y \\ \sigma_z \\ \sigma_{yz} \\ \sigma_{xz} \\ \sigma_{xy} \end{Bmatrix} = \begin{bmatrix} c_{11} & c_{12} & c_{13} & 0 & 0 & 0 \\ c_{12} & c_{11} & c_{13} & 0 & 0 & 0 \\ c_{13} & c_{13} & c_{33} & 0 & 0 & 0 \\ 0 & 0 & 0 & c_{44} & 0 & 0 \\ 0 & 0 & 0 & 0 & c_{44} & 0 \\ 0 & 0 & 0 & 0 & 0 & c_{66} \end{bmatrix}^E \begin{Bmatrix} \epsilon_x \\ \epsilon_y \\ \epsilon_z \\ \epsilon_{yz} \\ \epsilon_{xz} \\ \epsilon_{xy} \end{Bmatrix} - \begin{bmatrix} 0 & 0 & 0 & 0 & e_{15} & 0 \\ 0 & 0 & 0 & e_{15} & 0 & 0 \\ e_{31} & e_{31} & e_{33} & 0 & 0 & 0 \end{bmatrix}^T \begin{Bmatrix} E_1 \\ E_2 \\ E_3 \end{Bmatrix} \quad (4a)$$

$$\begin{Bmatrix} D_1 \\ D_2 \\ D_3 \end{Bmatrix} = \begin{bmatrix} 0 & 0 & 0 & 0 & e_{15} & 0 \\ 0 & 0 & 0 & e_{15} & 0 & 0 \\ e_{31} & e_{31} & e_{33} & 0 & 0 & 0 \end{bmatrix} \begin{Bmatrix} \epsilon_x \\ \epsilon_y \\ \epsilon_z \\ \epsilon_{yz} \\ \epsilon_{xz} \\ \epsilon_{xy} \end{Bmatrix} + \begin{bmatrix} \epsilon_{11} & 0 & 0 \\ 0 & \epsilon_{11} & 0 \\ 0 & 0 & \epsilon_{33} \end{bmatrix}^S \begin{Bmatrix} E_1 \\ E_2 \\ E_3 \end{Bmatrix} \quad (4b)$$

in which σ_{ij} are the components of the stress vector, c_{ij}^E are the components of the elasticity matrix evaluated at constant electric field, e_{ij} are the components of the piezoelectric coefficient matrix (which couples the structural and electric fields), E_i denotes the components of the electric field vector, ϵ_{ij} are the components of the strain vector, D_i are the components of the electric displacement vector and ϵ_{ij}^S are the components of the dielectric matrix, evaluated at constant strain.

2.5 Shunted damping

Shunted damping is a type of structural damping that consists of an electrical circuit, with a resistance R and an inductor L , connected to the electrodes of a piezoelectric material. In this work an RL resonant

shunt is used, consisting of an RL circuit with the resistance and the inductor in series. This circuit is then connected to the piezoelectric patch, which acts as a capacitor, as depicted in Figure 1. This assembly forms the well known LRC circuit, that one can take advantage of by tuning its resonant electrical frequency to the mechanical resonant frequency of the system. Knowing the system natural frequency of interest ω_n , the inductor value L can be calculated by

$$\omega_n = \frac{1}{L_i C_{pi}^S} \Leftrightarrow L_i = \omega_n^2 C_{pi}^S \quad (5)$$

where C_{pi}^S is the capacitance of the piezoelectric patch. In [7], Hagood et al. derived an expression for the resistance to obtain the optimal system damping:

$$R_i = \frac{\sqrt{2K_{ij}^2}}{C_{pi}^S \omega_n (1 + K_{ij}^2)} \quad (6)$$

where K_{ij} is the generalized electromechanical coupling coefficient, which can be calculated easily through the short-circuit (SC) and open-circuit (OC) natural frequencies, using the following expression:

$$K_{ij}^2 = \frac{(\omega_n^{OC})^2 - (\omega_n^{SC})^2}{(\omega_n^{SC})^2} \quad (7)$$

2.6 Radiated sound power

When subjected to external excitation, the sound power that is radiated through an area S of the sandwich panel in a semi-infinite rigid baffle is given by:

$$\Pi = \frac{1}{2} \Re \left\{ \int_S p(G) v_n^H(G) dS \right\} \quad (8)$$

where S is the area of the radiating panel, G is a point on the plate surface, p is the sound pressure in the fluid and v_n^H is the complex conjugate of the normal velocity of the surface of the plate. While the velocity can be obtained almost automatically from the displacement (nodal solution) of the finite element model, if the fluid is not discretized one can use the Rayleigh integral to calculate the pressure [8]:

$$p(\omega, M) = \rho_0 \frac{i\omega}{2\pi} \int_S v_n(\omega, G) \frac{e^{-ikr}}{r} dS \quad (9)$$

where ρ_0 is the fluid density, k is the wave number given by $\frac{\omega}{c_0}$, c_0 is the sound speed in the fluid domain, M is a point inside the external acoustic domain and $v_n(\omega, G)$ is the normal velocity at point G . One way to calculate this integral is through the elementary radiators method. Using this technique, the plate is divided into elementary subdomains (as in the finite element method) and the velocities and pressures used in the calculations are the ones in the center of the elements. Equation (8) becomes:

$$\Pi = \frac{S_e}{2} \Re \{ \mathbf{v}_n^H \mathbf{p} \} \quad (10)$$

where S_e is the area of each elementary radiator. Expanding the pressure, the last equation becomes

$$\Pi = \mathbf{v}_n^H \mathbf{R} \mathbf{v}_n \quad (11)$$

where the radiation resistance matrix is given by:

$$\mathbf{R} = \frac{\omega^2 \rho_0 S_e^2}{4\pi c_0} \begin{bmatrix} 1 & \frac{\sin(kr_{12})}{kr_{12}} & \dots & \frac{\sin(kr_{1R})}{kr_{1R}} \\ \frac{\sin(kr_{21})}{kr_{21}} & 1 & \dots & \frac{\sin(kr_{2R})}{kr_{2R}} \\ \vdots & \vdots & \ddots & \vdots \\ \frac{\sin(kr_{R1})}{kr_{R1}} & \frac{\sin(kr_{R2})}{kr_{R2}} & \dots & 1 \end{bmatrix} \quad (12)$$

and r_{ij} is the distance between the centers of elements i and j .

2.7 ANSYS finite element model

The material used for the face layers of the sandwich is carbon fibre, with properties: $E_1 = 130.8$ GPa, $E_2 = 10.6$ GPa, $E_3 = 10.6$ GPa, $\nu_{12} = 0.36$, $\nu_{23} = 0.767$, $\nu_{13} = 0.36$, $G_{12} = 5.6$ GPa, $G_{23} = 3.0$ GPa, $G_{13} = 4.2$ GPa and $\rho = 1543$ kg/m³. Three layers are considered for each face of the sandwich, with symmetric layup.

The parameters for the viscoelastic core material are: $d = 570$, $\alpha = 0.566$, $\beta = 0.558$, $\tau = 7.23 \times 10^{-10}$, $G_0 = 0.8$ MPa, the Poisson's ratio is $\nu = 0.49$ and the mass density is $\rho = 1300$ kg/m³.

Regarding the piezoelectric material, its properties are: $c_{11} = 126$ GPa, $c_{22} = 126$ GPa, $c_{33} = 117$ GPa, $c_{13} = 84.1$ GPa, $c_{23} = 84.1$ GPa, $c_{12} = 79.5$ GPa, $c_{44} = 23$ GPa, $c_{55} = 23$ GPa, $c_{66} = 23.3$ GPa; $e_{15} = 17$ C/m², $e_{24} = 17$ C/m², $e_{33} = 23.3$ C/m², $e_{31} = -6.5$ C/m², $e_{32} = -6.5$ C/m²; $\epsilon_{11} = 150.3 \times 10^{-10}$ F/m, $\epsilon_{22} = 150.3 \times 10^{-10}$ F/m, $\epsilon_{33} = 130 \times 10^{-10}$ F/m; $\rho = 7500$ kg/m³.

The sandwich has fixed in-plane dimensions of 200×300 mm² and is modelled in ANSYS with a solid-shell element, SOLSH190, and the piezoelectric elements are modelled with SOLID5 elements. Both elements have 8 nodes. SOLSH190 has 3 degrees of freedom at each node (3 translations) and SOLID5 has 4 nodal degrees of freedom (3 translations and 1 electric potential). To model the electric circuit elements CIRC94 is used, which is a line element with 2 nodes and 1 degree of freedom at each node (electric potential). Different element options are used depending on the type of electric component (resistance or inductance).

The sandwich plate structure is simply supported, and has a pressure load of 200 Pa applied to the bottom face.

3 SANDWICH PANEL OPTIMIZATION

With the aim of reducing the levels of acoustic emission of the sandwich structure a first optimization will be conducted. With the objective of reducing the acoustic levels without the addition of any external elements (e.g. without piezoelectric patches), the radiated sound power (RSP) will be minimized in a given frequency range. This will be accomplished by choosing the objective function to minimize as the length of the radiated sound power curve in that frequency range. The design variables in this first optimization will be the thicknesses of the core and laminated carbon fibre layers and also the orientation angles of the layers of the carbon fibre plies.

Mathematically, the optimization problem can be formulated as

$$\begin{aligned} \min_{\mathbf{x} \in \Omega} \quad & f(\mathbf{x}) \\ \text{s.t.} \quad & 1.016 \text{ mm} \leq \mathbf{x}_{\text{CoreThickness}} \leq 10.030 \text{ mm}; \\ & 0.17 \text{ mm} \leq \mathbf{x}_{\text{PlyThickness}} \leq 1.02 \text{ mm}; \\ & -89^\circ \leq \mathbf{x}_{\text{Angle}} \leq 90^\circ; \end{aligned} \quad (13)$$

where f is the length of the RSP curve and the vector \mathbf{x} is the vector of design variables. The design variables include the three angles and three thicknesses corresponding to the three plies of carbon fibre in each face, plus the thickness of the viscoelastic core (see Figure 2). In total, 7 design variables are considered. Note that the number of plies of the carbon fibre is fixed to three and a symmetric stacking sequence is kept.

The constraints are the lower and upper limits of the angles: -89° and $+90^\circ$ respectively; the lower and upper limits of the thicknesses: 0.17 mm and 1.02 mm for the carbon fibre, and 1.016 mm and 10.03 mm for the viscoelastic core.

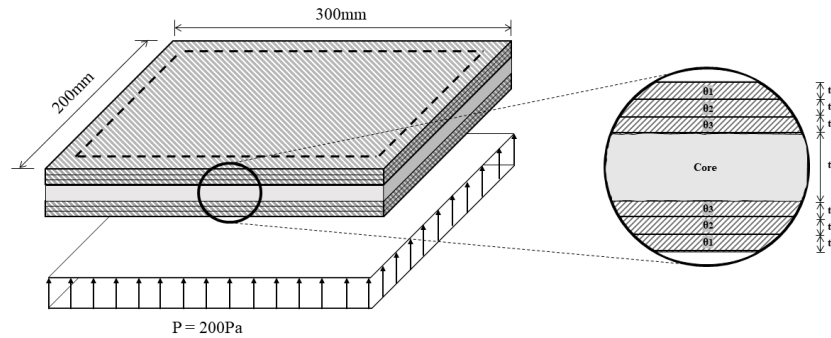


Figure 2: Sandwich structure to be optimized: geometry, boundary conditions and loads.

3.1 Implementation

A Matlab program was developed to control the optimization process through the `patternsearch` function. To use this function, it is necessary to provide the value of the length of the RSP curve, given the values of the design variables. Initial point and constraints are optional. At the end of the optimization, the `patternsearch` function outputs the optimum set of design variables and the respective value of the objective function.

Besides the lower and upper limits that were imposed to these variables, in order to reduce the computational time, the design variable space was transformed from continuous to discrete. Basically, the thickness of the core varies in multiples of 0.127 mm and the thickness of the carbon fibre in multiples of 0.170 mm. In the case of the angles, they are set to take integer values between -89° and 90° .

In using the pattern search algorithm, it is important to assure that all the variables are properly scaled. For instance, it would be inadequate to have the algorithm using angle values in degrees mixed with lengths in millimeters. Hence it was decided that each of the 7 design variables would be scaled to vary between 0 and 1.

To scale the objective function, the length of the RSP curve is multiplied by a large number (in the present work, 10^6). Then a residual number is subtracted, the length of the frequency range multiplied by 10^6 . For example, if the range of the curve is from 2 Hz to 500 Hz, the value to be subtracted is 498×10^6 .

Due to the different order of magnitudes of the sensitivities of the objective to the design variables, a three step optimization approach is taken. The first step is the optimization of only the angles. After this an optimization of the thicknesses is made, starting from the optimal angle values from the first step. Finally, starting with the optimum of the last optimization step, all 7 variables were considered simultaneously in the last optimization stage. The results and details can be observed in the next section. Regarding the finite element mesh, a 20×30 in-plane discretization is used with three elements through

the thickness, one for each different sandwich component (one for each face and one for the core).

3.2 Results

A summary of the optimization results can be found in Table 1. It can be seen that the design variable vector \mathbf{x} has a different number of entries depending on the optimization. In the last optimization it has 7 entries, with the first three being the angles and the last 4 the thickness multiplication factors, the first three corresponding to the thickness of the carbon fibre plies and the last one to the thickness of the core. Note that the thickness is obtained by multiplying the multiplication factors by 0.170 mm for the carbon fibre and by 0.127 mm for the core. For the initial point the objective function value is $f_{obj} = 1240.535$

Table 1: Sandwich optimization results

Optimization	Design Variables	Initial Point	Final Point	f_{obj}
1st Step	$[\theta_1, \theta_2, \theta_3]$	$[0^\circ, 90^\circ, 45^\circ]$	$[-85^\circ, 19^\circ, -1^\circ]$	461.213
2nd Step	$[t_1, t_2, t_3, t_c]$	$[3, 3, 3, 20]$	$[2, 2, 2, 79]$	10.134
3rd Step	$[\theta_1, \theta_2, \theta_3, t_1, t_2, t_3, t_c]$	$[-85^\circ, 19^\circ, -1^\circ, 2, 2, 2, 79]$	$[-86^\circ, 21^\circ, -1^\circ, 2, 2, 2, 79]$	10.132

The RSP curves resultant from each optimization stage can be found in Figure 3.

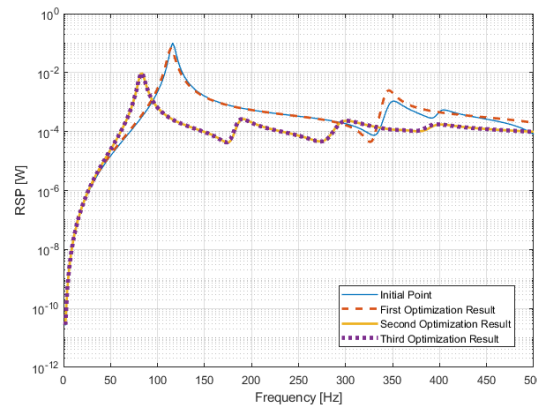


Figure 3: Comparison of the final points of each optimization.

Just by looking at the values in the table, one is able to see that the optimization is much more sensitive to changes in values of the thicknesses. The changes in fibre orientation introduced some improvement in the first optimization, but when compared with optimization of the thicknesses, the latter allowed a larger change in the shape of the curve. It is visible that the value of the thickness of the viscoelastic core reached its highest possible value in the first time that the thicknesses are optimized, which was expected due to the fact that this increase in the core thickness promotes the damping capabilities of the sandwich. In Figure 3 it can be seen that the change in the thicknesses had an effect of reducing the resonant frequencies as well as reducing its the amplitudes.

4 OPTIMIZATION OF THE PIEZOELECTRIC MATERIAL DISTRIBUTION

In this section the performance of the previously optimized sandwich plate with respect to attenuation of acoustic emissions will be further improved by using piezoelectric patches with RL shunt circuits

tuned to the first resonant frequency. The problem is formulated as determining the optimal distribution of the piezoelectric patches in order to reduce the length of the RSP curve, with all the RL circuits targeted for the first resonant frequency. This optimization problem is a binary problem in which, using a finite element mesh, each sandwich shell element can have a piezoelectric element above it (1) or not (0), depending on the optimizer output. Figure 4 illustrates this idea.

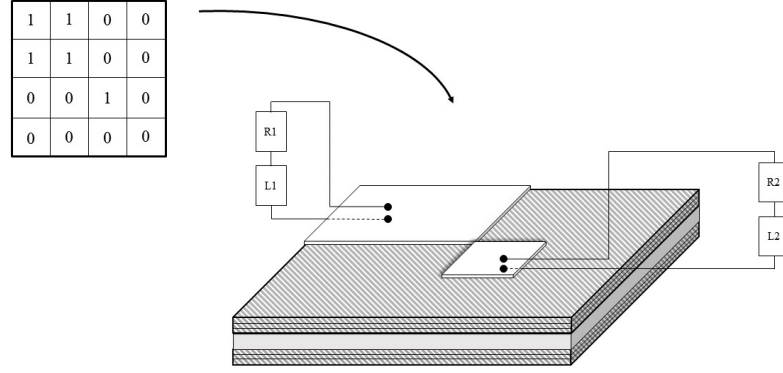


Figure 4: Correspondence between design variables matrix and the sandwich structure

While adding more piezoelectric material will decrease the radiated sound power response, the mass of the structure will increase. A compromise between mass and acoustic response can be achieved by using multiobjective optimization. The number of piezoelectric regions can also be taken into account and minimized, as each region represents one electroded patch with equipotential conditions imposed on the electrodes, having its own RL circuit. Hence, minimizing the number of regions or patches is the same as minimizing the number of RL circuits. This results in 3 objectives to minimize: the added mass of the piezoelectric patches, the acoustic response and the number of regions. This problem can be formulated as follows:

$$\begin{aligned} \min_{\mathbf{x} \in \Omega} \quad & F(\mathbf{x}) \equiv (f_1(\mathbf{x}); f_2(\mathbf{x}); f_3(\mathbf{x}))^T \\ \text{s.t.} \quad & x_i \in \{0, 1\} \end{aligned} \quad (14)$$

in which f_1 is the length of the RSP curve in a given frequency range, f_2 is the total mass of the structure, and f_3 is the number of different piezoelectric patch regions.

4.1 Implementation

Regarding the optimization of the piezoelectric patches, a Matlab program was developed to control the optimization process, in which the function `paretosearch` was used. Similarly to the single-objective optimization described before with the `patternsearch` function, the optimization is controlled by this function, with the user having to supply only the objective function values for each point in the design space and, if needed, initial points and some constraints. The dimension of the design variables vector is the number of elements of piezoelectric finite elements in the model. For instance, if the structure is discretized with a 10×10 mesh, the design variables vector will have dimensions 100×1 , in which each entry can take values between 0 and 1 (1 means there is a piezoelectric element and 0 its absence). The majority of the times, the values will not be integer, since the algorithm works with continuous variables. Therefore, if the value is below 0.5 it gets rounded to 0, and otherwise, it is rounded to 1. Figure 5 represents a flowchart describing the procedure used to calculate the objective function

values.

Due to the fact that a RL shunt circuit is implemented, the values of the resistance and inductance need to be known *a priori*. Using Equations (5) and (6), the optimal values of the resistance and inductance for a particular resonance can be obtained from the values of ω_n^{OC} , ω_n^{SC} and C_{pi} . Therefore, before conducting the harmonic analysis, two modal analysis have to be done (one with the piezoelectric patches in short-circuit and another in open-circuit) to get the natural frequencies, and a static analysis has to be done in order to get the capacitance. Note that due to the fact that in modal analysis viscoelastic materials are not allowed in ANSYS, a programming loop takes place to get the converged properties of the viscoelastic material at the natural frequency to be obtained, as can be observed in Figure 5.

The added mass is obtained simply by counting the number of piezoelectric elements and then multiplying this number by the volume of each element and the respective density. The calculation of the RSP curve length is conducted as before and the number of regions can be calculated by considering the elements that are adjacent to one another.

Some approaches were used in order to reduce the computational time. For instance, whenever the number of regions was equal or higher than 5, the value of the objective functions were increased several orders of magnitude above the normal values, penalizing these solutions. This avoids running ANSYS to evaluate these points. Another approach to decrease computational time was the reduction of the range of the harmonic analysis: it was decided that only the neighborhood of the targeted frequency would be analysed: $f_{oc} - 20 < f_{oc} < f_{oc} + 20$ Hz, where f_{oc} is the fundamental resonant frequency in open circuit, in Hz. Also, in this work, a mesh of 6×6 elements was used to generate a first approximation of the solution. The generated solutions were then used as initial points for an optimization using a 12×12 mesh. Then, the resultant points were used as initial points for the final optimization using the most refined 24×24 mesh discretization. This procedure allows the faster convergence of the solutions for larger patch regions. It was also taken advantage of the symmetry of the problem. In fact, by looking at the first mode of vibration of the sandwich, it can be seen that it is symmetric. Hence, the design variables were reduced to $\frac{1}{4}$ of the maximum number of piezoelectric elements.

4.2 Results

As a result of the multiobjective optimization, a set of non-dominated points was obtained, forming the Pareto front. Having 3 objective functions, resulted in a 3D Pareto surface. The evolution of the Pareto front with the different meshes is shown in Figure 6. It is clear that the Pareto front moves to improved solutions with the refinement of the mesh.

A more detailed analysis can be made by choosing 11 distinct Points of the Pareto front, as a better understanding of the behavior of the structure can be inferred in this way. In Figure 7(a) these points can be observed in the projection of the Pareto front in the plane formed by Objectives 1 and 2. Their RSP curves are displayed in Figure 7(b). These selected points and their design parameters are shown in Table 2. Looking at the results, it can be seen that for less mass the region that starts to be covered by the piezoelectric elements is the centre of the plate which was expected, given the high strain energy in that location for the first mode. It is also important to note that, generally, with more piezoelectric elements a tendency of the frequencies to increase is observed. This is explained by the fact that the stiffness effect introduced dominates the added mass effect. For the configurations with lower mass the R and L values presented are really high, even impracticable in the case of inductance. This changes when the added mass increases and the values become more feasible. Even though the first mode was the original target, the other modes get influenced by the added mass. In fact, for configurations 50, 52 and 29, the peak of the second resonant frequencies is almost as high as the magnitude of the first resonant frequency.

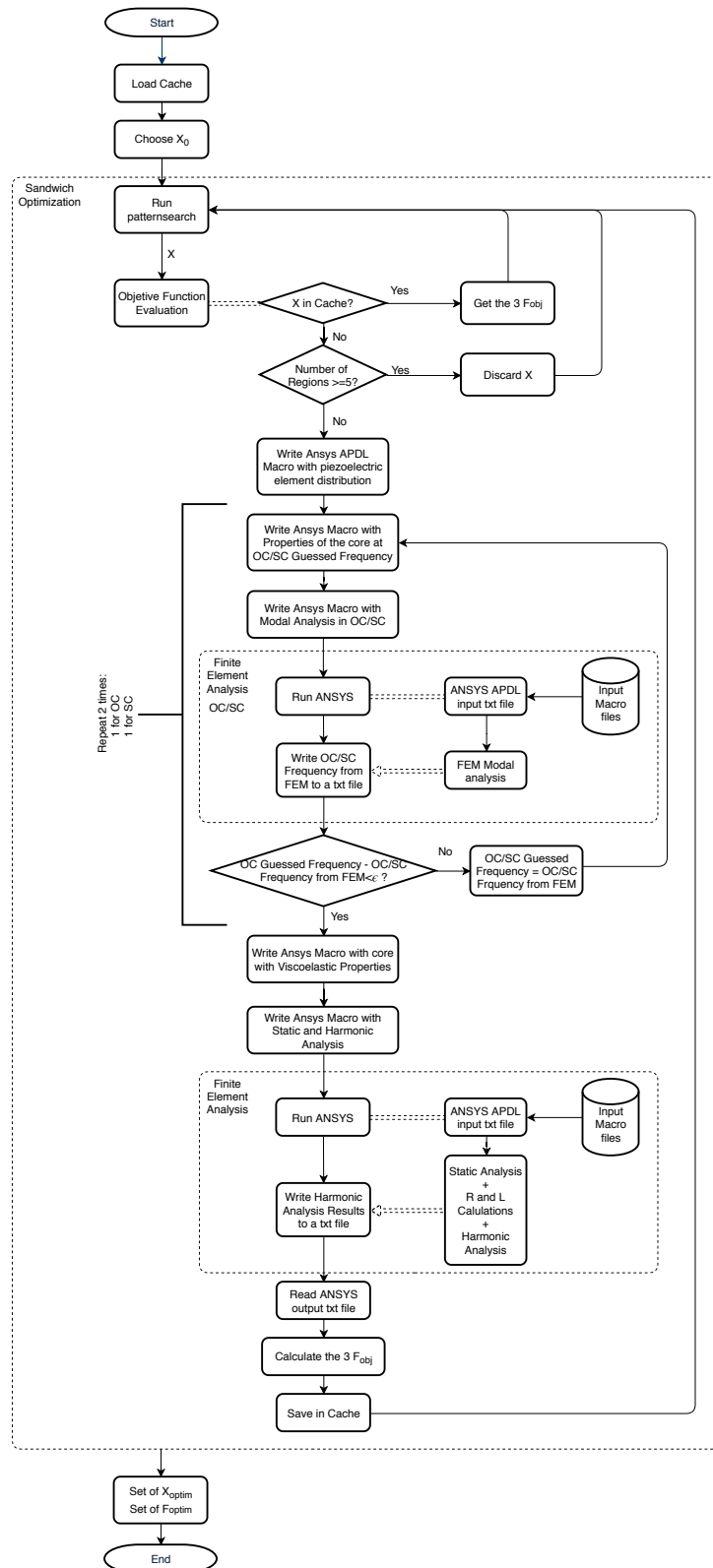
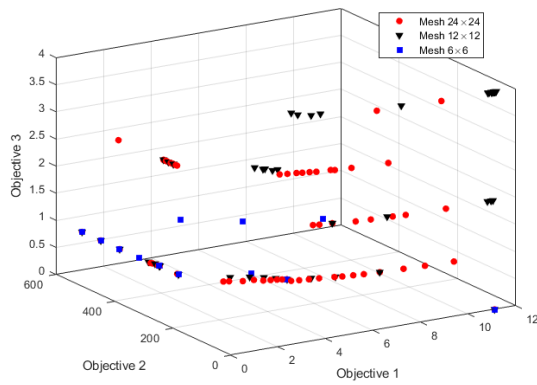
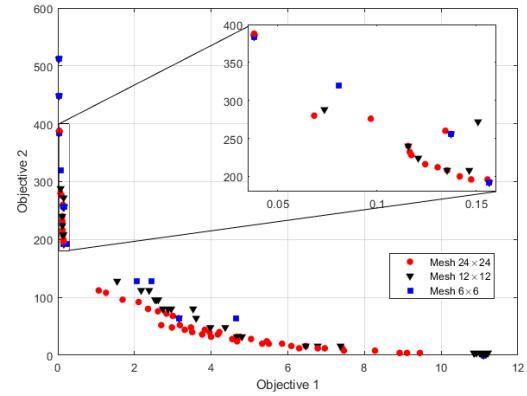


Figure 5: Flowchart of the multiobjective optimization of the piezoelectric patches.

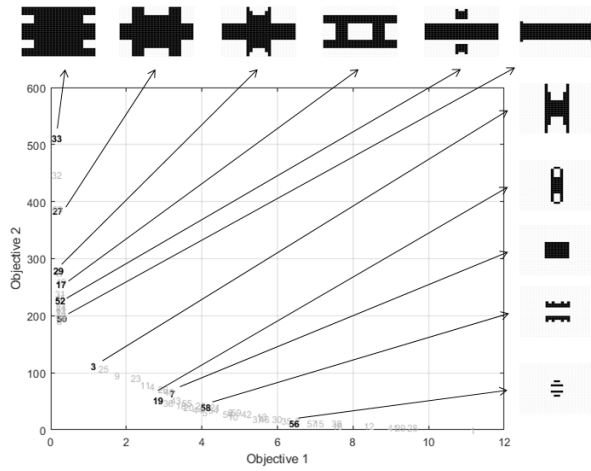


(a) Pareto front

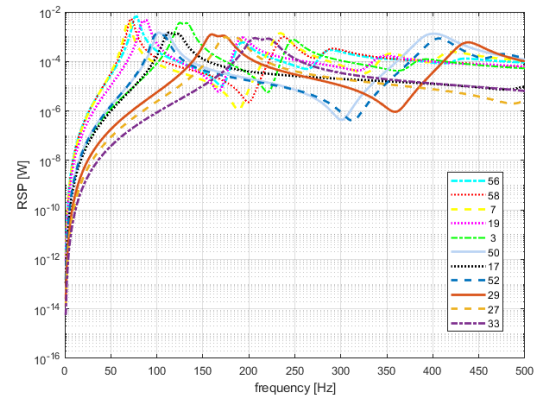


(b) Projection in Objective 1 and 2 plane

Figure 6: Evolution of the Pareto Front with the different meshes. (Objective 1 is the RSP curve length, Objective 2 is the added mass (number of piezoelectric elements) and Objective 3 is the number of regions)



(a) Selected points in the Objective 1 and Objective 2 plane.



(b) RSP vs frequency curves of the selected points

Figure 7: Selected solution points for analysis.

5 CONCLUSIONS

With the aim of reducing its acoustic response a sandwich structure was optimized with respect to the laminate fibre orientation and ply thicknesses, as well as to its viscoelastic core thickness. To further reduce the acoustic response, piezoelectric patches with resonant RL shunts were introduced in a multiobjective optimization. The location of the piezoelectric elements were the design variables and the objective functions were the mass, the acoustic response, and the number of shunt circuit regions. The implementation was described and the results were analysed, allowing us to conclude that the proposed methodologies and implementations are efficient and adequate to solve the problem.

Table 2: Chosen solutions from the multiobjective optimization

#	Mass	No.Regions	R [Ω]	L [H]	f_{sc} [Hz]	f_{oc} [Hz]
56	12	4	36603 18306	3521 1760	77.04	77.05
58	40	2	5827	408	71.92	71.93
7	64	1	1793	139	68.68	68.70
19	52	3	96971 4031	2815 214	86.43	86.51
3	112	1	1987	22.68	128.15	128.53
50	196	1	2027	18.96	105.18	105.86
17	256	1	1426	11.84	116.66	117.43
52	228	3	22535 2125	217.3 20.5	102.2	102.86
29	280	1	838.8	5.44	164.5	165.4
27	384	1	529.38	3.36	178.8	179.67
33	512	1	303.65	1.8	211.9	212.8

ACKNOWLEDGEMENTS

This work has been supported by National Funds through Fundação para a Ciência e Tecnologia (FCT), through IDMEC, under LAETA, project UID/EMS/50022/2019.

REFERENCES

- [1] Araujo, A.L., Carvalho, V.S., Mota Soares, C.M., Belinha, J. and Ferreira, A.J.M. Vibration analysis of laminated soft core sandwich plates with piezoelectric sensors and actuators. *Composite Structures*. (2016) **151**:91–98.
- [2] Iurlova, N., Sevodina, N., Oshmarin and D., Iurlov, M. Algorithm for solving problems related to the natural vibrations of electro-viscoelastic structures with shunt circuits using ANSYS data. *International Journal of Smart and Nano Materials*. (2019) **10**(2):156–176.
- [3] Larbi, W., J. F. Deu, and R. Ohayon. Finite element formulation of smart piezoelectric composite platescoupled with acoustic fluid. *Composite Structures*.(2012) **94**:501–509.
- [4] Larbi, W., J. F. Deu, and R. Ohayon. Vibroacoustic analysis of double-wall sandwich panels with viscoelastic core *Computers and Structures*. (2016) **174**:92–103.
- [5] Christensen R.M. *Theory of Viscoelasticity*. Academic Press, 2nd Edition (1982).
- [6] Pritz, T., Five-parameter fractional derivative model for polymeric damping materials. *Journal of Sound and Vibration* (2003) **265**:935–952.
- [7] Hagood, N. W. and von Flotow, A. Damping of structural vibrations with piezoelectric materials and passive electric networks. *Journal of Sound and Vibration* (1991) **146**(2):243–268.
- [8] Fahy, F. and P. Gardonio *Sound and Structural Vibration: Radiation, Transmission and Response*. Academic Press, 2nd Edition (2006).

ENVIRONMENTALLY-FRIENDLY PIEZOELECTRIC COMPOSITES FOR ADDITIVE MANUFACTURING: NONLOCAL AND NONLINEAR EFFECTS

JAGDISH A. KRISHNASWAMY^{*}, FEDERICO C. BURONI[†],
RODERICK MELNIK^{*}, LUIS RODRIGUEZ-TEMBLEQUE[§], ANDRES SAEZ[§]

^{*} MS2Discovery Interdisciplinary Research Institute
Wilfrid Laurier University
75 University Ave W, Waterloo, Ontario, Canada, N2L 3C5
e-mail: ajagdish@wlu.ca, rmelnik@wlu.ca, www.wlu.ca

[†] Department of Mechanical Engineering and Manufacturing
Universidad de Sevilla
Camino de los Descubrimientos s/n, Seville E-41092, Spain
email: fburoni@us.es, www.us.es

[§] Department of Continuum Mechanics and Structural Analysis
Universidad de Sevilla
Camino de los Descubrimientos s/n, Seville E-41092, Spain
email: luisroteso@us.es, andres@us.es, www.us.es

Key words: Lead-free composite, piezoelectric, flexoelectricity, nonlocal and nonlinear effects, electrostriction, finite element analysis

Abstract. Lead-free piezocomposites represent an environmentally friendly route for sensing mechanical stimuli and for interconversion of electrical and mechanical energy. Current lead-free composites lag state-of-the-art lead-based composites in terms of performance. A major approach to bridge this gap is to devise design strategies to enhance the piezo-response of lead-free composites. Fundamental to this is the understanding of the roles of various physical processes which are conventionally overlooked. From a modelling perspective, it is necessary to develop refined models which account for non-local and non-linear effects, which could have significant roles in deciding the response of the composite. This paper develops such refined electro-elastic models considering the flexoelectric and electrostrictive contributions to the piezo-response in addition to the linear piezoelectric response. The roles of these non-local and non-linear contributions are studied on a simple architecture consisting of a BaTiO₃ inclusion within a polymer matrix. Insights obtained through this model will be further used to develop efficient piezoelectric composites.

1 INTRODUCTION

Piezoelectric composites generally consist of piezoelectric crystalline inclusions embedded in a polymer matrix. This enables the optimal combination of electrical and elastic properties of both the matrix and the filler, resulting in a composite material that can be designed to suit specific application needs. For example, by embedding highly rigid piezoelectric crystalline inclusions, such as BaTiO_3 , PZT and so on, with polymer matrices, it is possible to make piezoelectric composites which are flexible [1]. The recent interest in such composite materials stems from the fact that there is a need to develop lead-free materials which can perform at par with the state-of-the-art lead-based composites [1]. The development of such materials is important from the point of view of sustainable green technology, with current materials posing long-term ecological threats [1, 2]. A second motivation to study such materials is the ease with which the associated devices can be fabricated using the emerging scalable methods such as 3D printing which offer detailed resolutions down to the micrometer scale in the material distribution [3]. The gap in the performance between these two classes of materials is due to the intrinsic properties of the piezoelectric inclusions and therefore most design strategies involve tuning the electro-elastic properties of the surrounding matrix to enhance the piezoelectric response. These approaches involve either hardening the matrix [4] to improve the coupling of mechanical stimuli to the embedded inclusions or improving the permittivity of the matrix [5] to allow easy flow of the generated electric flux to the electrodes enclosing the composite. Recent efforts in material design and modelling have explored these avenues to tune these electro-elastic properties of the matrix to improve the piezo-response. However, these models overlook some physical processes which could significantly control the piezoelectric response. Some of these processes include (a) flexoelectricity – non-local generation of electric flux by strain-gradients as opposed to linear piezoelectricity where a homogeneous strain generates electric flux and (b) electrostriction – non-linear coupling between the strain and the electric field. Flexoelectricity can occur even in non-centrosymmetric materials [6] and electrostriction is a common process in most dielectrics [7]. Although such effects might often be negligible at the macroscopic level, they can influence the overall design principles of composite materials, created on the basis of hierarchically architected microstructures, for 3D printing and subsequent applications. Moreover, possible defects and agglomerations of added nanoparticles in such composite materials under certain conditions may create an environment for flexoelectricity to play a more pronounced role. Both these aspects hint the possibility of even the matrix materials contributing to the piezoelectric response. Further, lead-free materials such as BaTiO_3 have flexoelectric coefficients which are relatively larger compared to other piezoelectric materials [8], thus offering a possible route to enhancing the performance of the composite. Therefore, our focus in this contribution is on the design and modelling issues of lead-free piezoelectric composites, amenable to 3D printing, in order to achieve their higher performance. Although the developed modelling framework is quite general and can be applied to other materials, as an example, our results are discussed in the context of barium titanate piezoelectric inclusions embedded into a polymeric matrix. In what follows, we will first provide the details of the electro-elastic model which includes these non-local and non-linear effects. Following this, we will discuss some preliminary results which can provide important insights relating to the contributions of these effects to the overall material performance.

2 ELECTRO-ELASTIC MODEL

In this section, we will provide the details of the mathematical framework that describes the electroelastic behavior of piezoelectric composites, accounting for flexoelectric (strain-gradient) and electrostrictive contributions. The constitutive relations are obtained from the electrical Gibbs free energy density defined as follows [6, 9, 10]:

$$G = \frac{1}{2}c_{ijkl}\varepsilon_{ij}\varepsilon_{kl} - \frac{1}{2}\epsilon_{ij}E_iE_j - e_{kij}E_k\varepsilon_{ij} - \frac{1}{2}B_{kl ij}E_kE_l\varepsilon_{ij} - \mu_{ijkl}E_i\varepsilon_{j,kl} \quad (1)$$

The terms on the right-hand side of (1) are contributions to the free energy density from the elastic, electric, linear piezoelectric, electrostrictive, and flexoelectric processes, respectively. Here, c_{ijkl} , ϵ_{ij} , e_{ijk} , B_{ijkl} , and μ_{ijkl} are the elastic, permittivity, piezoelectric, electrostrictive, and flexoelectric coefficients. Additionally, the field variables include the strain tensor components ε_{ij} , the electric field components E_i and the strain-gradient components $\varepsilon_{i,jk}$.

The constitutive relations describing electro-elastic behavior are obtained as follows:

$$\begin{aligned} \sigma_{ij} &= \frac{\partial G}{\partial \varepsilon_{ij}} = c_{ijkl}\varepsilon_{kl} - e_{kij}E_k - \frac{1}{2}B_{kl ij}E_kE_l, \\ \hat{\sigma}_{ijk} &= \frac{\partial G}{\partial \varepsilon_{ij,k}} = \mu_{lij k}E_l, \\ D_i &= -\frac{\partial G}{\partial E_i} = \epsilon_{ij}E_j + e_{ijk}\varepsilon_{jk} + B_{ijkl}E_j\varepsilon_{kl} + \mu_{ijkl}\varepsilon_{jk,l}. \end{aligned} \quad (2)$$

In (2), $\hat{\sigma}_{ijk}$ and D_i are the higher order stress components and electric flux density components, respectively. These constitutive relations are further subjected to the governing balance laws given by:

$$\begin{aligned} (\sigma_{ij} - \hat{\sigma}_{ijk,k})_{,j} + F_i &= 0, \\ D_{i,i} &= 0, \end{aligned} \quad (3)$$

where F_i represent the components of the body forces, which are assumed to vanish in our model. This model is applied to a simple architecture consisting of a BaTiO₃ inclusion within a PDMS polymeric flexible matrix, illustrated in Figure 1. The boundary conditions applied to the composite architecture are also schematically illustrated in the Figure 1. The model is reduced to two dimensions in the x_1 - x_3 plane [5, 11].

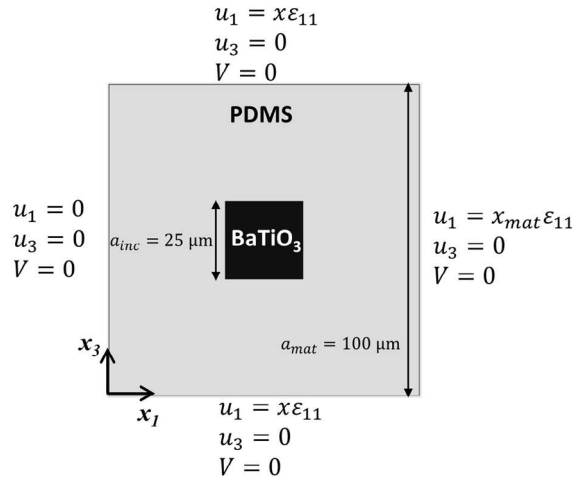


Figure 1 – The schematic of the RVE studied here along with the boundary conditions used.

The material properties adopted for this study are summarized in Table 1. It is to be noted that the electrostrictive coefficients entered in the table need to be transformed into a different form before using them in the constitutive equations. This transformation is given by $[B] = [C][M]$, where the matrix $[M]$ has the electric field-related electrostrictive coefficients [12]. Typically, experimental values of these coefficients are in terms of the polarization density, the conversion into the electric-field-related version of which requires the following transformation [13]:

$$M_{ijkl} = Q_{opkl} \eta_{oi} \eta_{pj}, \quad (4)$$

where Q_{opkl} represent the polarization-related electrostriction coefficients in the units of m^2C^{-4} , M_{ijkl} represent the electric-field-related electrostriction coefficients in the units of m^2V^{-2} , and the η_{oi} are the components of the dielectric susceptibility tensor of the material.

Table 1 – Electro-elastic material properties used in the simulations. Typical values of electrostrictive coefficients are considered for the polymer matrix ($M_{33} \approx 1 \times 10^{-17} \text{m}^2\text{V}^{-2}$ in conjunction with equation 4)

Material property	Values for BaTiO ₃	Values for PDMS matrix
Elastic coefficients (Moduli in Pa)		
c_{11}	275.1×10^9 [14]	$\lambda_m + 2\mu_m$
c_{13}	151.55×10^9	λ_m
c_{33}	164.8×10^9	$\lambda_m + 2\mu_m$
c_{44}	54.3×10^9	μ_m
Young's modulus, E_m	N.A.	2×10^6 [15]
Poisson's ratio, ν_m	N.A.	0.499 [15]
Relative permittivity		
ϵ_{11}/ϵ_0	1970 [14]	2.72 [15]
ϵ_{33}/ϵ_0	109	2.72
Piezoelectric coefficients (Cm ⁻²)		
e_{15}	21.3 [14]	Matrix is non-piezoelectric
e_{31}	-2.69	
e_{33}	3.65	
Flexoelectric coefficients (Cm ⁻¹)		
Longitudinal, μ_{11}	10×10^{-6} [8]	1×10^{-10} [6]
Transverse, μ_{12}	10×10^{-6}	1×10^{-10}
Shear, μ_{44}	0	0
Electrostrictive coefficients, b_{ijkl} (m ⁴ C ⁻²)		
Longitudinal, b_{11}	0.1 [16]	$1.7242e + 08$ [7]
Transverse, b_{12}	-0.034	0
Shear, b_{44}	0.029	0

3 RESULTS AND DISCUSSION

The current analysis in this paper centers around microscale inclusions in a polymer matrix. Under such conditions, the flexoelectric effect has negligible effect. The plots of the volume averaged electric flux density in the x_3 direction, shown in Figure 2(a), demonstrate this with the two curves obtained from the linear piezoelectric model alone and the model with

flexoelectric contributions almost coinciding. However, the contributions due to the non-linear effects are non-trivial. Although non-linear effects due to electrostriction have contributions to the generated electric flux which are negligible at small strains ($\varepsilon_{app} \approx 10^{-6}$) but show considerable increases at larger strains (for example at $\varepsilon_{app} = 10^{-2}$). This is illustrated in the volume averaged electric flux density plotted in the Figure 2(a), with and without the electrostrictive contributions. This shows that as the applied strain increases, while the linear piezoelectric model predicts a constant response, the presence of non-linear effects shows an increased volume averaged flux generation. This increase stems from the electrostrictive contributions in both the matrix and the inclusion, as seen from the increased flux density D_3 both in the inclusion and in the matrix (Figure 2(b) and (c)). These initial results clearly demonstrate the role of non-linear and non-local effects in deciding the electro-elastic response of lead-free piezoelectric composites.

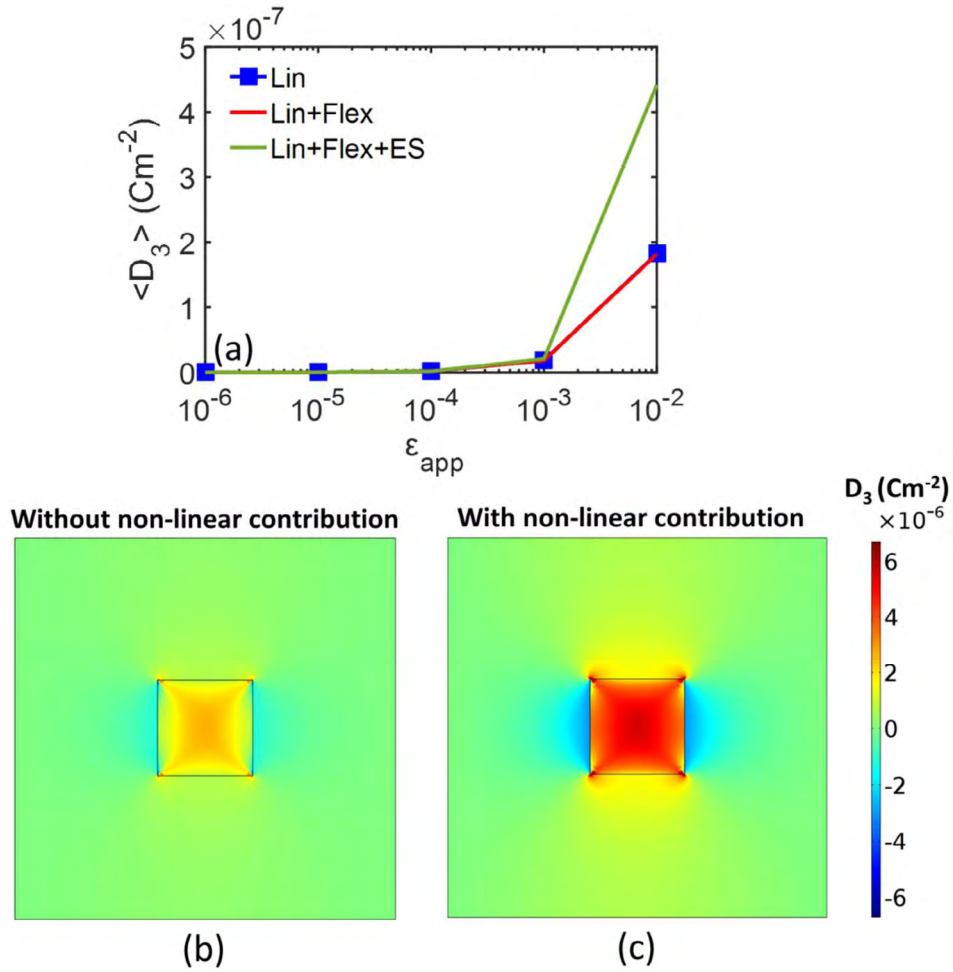


Figure 2 – (a) The volume averaged x_3 -component of the generated electric flux density with (i) linear piezoelectric model (Lin), (ii) linear model with flexoelectric contributions (Lin+Flex), (iii) Linear model with flexoelectric model and non-linear electrostrictive contributions (Lin+Flex+ES), (b) and (c) show the distribution of the D_3 flux density component with and without non-linear contributions, respectively.

4 CONCLUSIONS

We have developed a modeling framework for piezo-composites which accounts for the non-local flexoelectric effects and non-linear electrostrictive effects, with specific focus on lead-free BaTiO₃ based piezocomposites with polymer matrices, which are amenable to scalable 3D printing and additive manufacturing. On studying the implication of these effects in lead-free piezocomposites, we see that with microscale inclusions, while the flexoelectric effect has only negligible contributions, the non-linear electrostriction has considerable contributions which are more pronounced at higher operational strains. These findings clearly emphasize the need to consider these physical effects in the modelling-based design of high-performance environmentally friendly piezoelectric composite materials.

ACKNOWLEDGMENTS

This work was supported by the Ministerio de Economía y Competitividad of Spain and the European Regional Development Fund under projects DPI2014-53947-R and DPI2017-89162-R. RM and AKJ are also grateful to the NSERC and CRC program for their support.

REFERENCES

- [1] Maurya D, Peddigari M, Kang M-G, Geng L D, Sharpes N, Annapureddy V, Palneedi H, Sriramdas R, Yan Y and Song H-C 2018 Lead-free piezoelectric materials and composites for high power density energy harvesting *Journal of Materials Research* **33** 2235-63
- [2] Ibn-Mohammed T, Koh S, Reaney I, Sinclair D, Mustapha K, Acquaye A and Wang D 2017 Are lead-free piezoelectrics more environmentally friendly? *MRS Communications* **7** 1-7
- [3] Kim K, Zhu W, Qu X, Aaronson C, McCall W R, Chen S and Sirbully D J 2014 3D optical printing of piezoelectric nanoparticle-polymer composite materials *ACS nano* **8** 9799-806
- [4] Kim H, Torres F, Islam M T, Islam M D, Chavez L A, Garcia Rosales C A, Wilburn B R, Stewart C M, Noveron J C, Tseng T-L B and Lin Y 2017 Increased piezoelectric response in functional nanocomposites through multiwall carbon nanotube interface and fused-deposition modeling three-dimensional printing *MRS Communications* **7** 960-6
- [5] Jagdish A K, Buroni F C, Garcia-Sanchez F, Melnik R V N, Rodriguez-Tembleque L and Sáez A 2019 Improving the performance of lead-free piezoelectric composites by using polycrystalline inclusions and tuning the dielectric matrix environment (Submitted)
- [6] Sharma N, Landis C and Sharma P 2010 Piezoelectric thin-film superlattices without using piezoelectric materials *Journal of Applied Physics* **108** 024304
- [7] Luna A, Pruvost M, Yuan J, Zakri C c, Neri W, Monteux C c, Poulin P and Colin A 2017 Giant electrostrictive response and piezoresistivity of emulsion templated nanocomposites *Langmuir* **33** 4528-36
- [8] Ma W and Cross L E 2006 Flexoelectricity of barium titanate *Applied Physics Letters* **88** 232902

- [9] He B, Javvaji B and Zhuang X 2019 Characterizing Flexoelectricity in Composite Material Using the Element-Free Galerkin Method *Energies* **12** 271
- [10] Kuang Z-b 2009 Internal energy variational principles and governing equations in electroelastic analysis *International journal of solids and structures* **46** 902-11
- [11] Saputra A A, Sladek V, Sladek J and Song C 2018 Micromechanics determination of effective material coefficients of cement-based piezoelectric ceramic composites *Journal of Intelligent Material Systems and Structures* **29** 845-62
- [12] Joshi S P 1992 Non-linear constitutive relations for piezoceramic materials *Smart Materials and Structures* **1** 80
- [13] Budimir M 2006 Piezoelectric anisotropy and free energy instability in classic perovskites. EPFL)
- [14] Li J Y 2000 The effective electroelastic moduli of textured piezoelectric polycrystalline aggregates *Journal of the Mechanics and Physics of Solids* **48** 529-52
- [15] Johnston I, McCluskey D, Tan C and Tracey M 2014 Mechanical characterization of bulk Sylgard 184 for microfluidics and microengineering *Journal of Micromechanics and Microengineering* **24** 035017
- [16] Wang J, Meng F, Ma X, Xu M and Chen L 2010 Lattice, elastic, polarization, and electrostrictive properties of BaTiO₃ from first-principles *Journal of Applied Physics* **108** 034107

EXACT VIBRATION ANALYSIS OF LAMINATED PIEZOELECTRIC PLATES THROUGH STRONG SAS FORMULATION

G. M. KULIKOV, N. P. MERKUSHEVA AND S. V. PLOTNIKOVA

Laboratory of Intelligent Materials and Structures
Tambov State Technical University
Sovetskaya, 106, Tambov 392000, Russia
e-mail: gmkulikov@mail.ru

Key words: Piezoelectricity, 3D Vibration Analysis, Laminated Piezoelectric Plate, Sampling Surfaces Method.

Abstract. This paper focuses on implementation of the sampling surfaces (SaS) method for the 3D vibration analysis of laminated piezoelectric plates. The SaS formulation is based on choosing inside the layers the arbitrary number of SaS parallel to the middle surface to introduce the displacements and electric potentials of these surfaces as basic plate variables. Such choice of unknowns allows the presentation of the laminated piezoelectric plate formulation in a very compact form. The feature of the proposed approach is that all SaS are located inside the layers at Chebyshev polynomial nodes that improves the convergence of the SaS method significantly. The use of outer surfaces and interfaces is avoided that makes possible to minimize uniformly the error due to Lagrange interpolation. Therefore, the strong SaS formulation based on direct integration of the equations of motion and the charge equation can be applied efficiently to the obtaining of exact solutions for laminated piezoelectric plates, which asymptotically approach the 3D solutions of piezoelectricity as the number of SaS tends to infinity.

1 INTRODUCTION

The exact vibration analysis of laminated piezoelectric plates was first carried out by Heyliger and Brooks [1], and Heyliger and Saravanos [2] using the Pagano approach. The most popular state space approach was utilized for the free vibration of simply supported electroelastic plates in works [3-7]. Messina and Carrera [8] proposed to employ the transfer matrix method to solve the ordinary differential equations in terms of the displacements and electric potential derived from the system of partial differential equations through the separating variable procedure. The dynamic response of laminated piezoelectric plates by a Taylor series expansion through the thickness was studied in papers [9-11]. The SaS approach was also used for the free vibration analysis of piezolaminated plates [12].

The SaS method [13] has been applied effectively to the 3D stress analysis of laminated piezoelectric structures by Kulikov and Plotnikova [14-17]. According to this method, we choose the arbitrary number of SaS throughout the layers parallel to the middle surface and located at Chebyshev polynomial nodes in order to introduce the displacements and electric potentials of these surfaces as basic plate unknowns. Such choice of unknowns with the consequent use of Lagrange polynomials in the through-thickness distributions of displacements, strains, electric potential and electric field leads to a robust laminated

piezoelectric plate formulation. The above works are based on the variational SaS formulation, which requires including the interfaces into a set of SaS. However, it is important to take all SaS located at Chebyshev polynomial nodes due to the convergence criterion [18].

The present paper is intended to extend the variational SaS formulation for the free vibration of laminated piezoelectric plates [12] to the strong SaS formulation. The latter is based on the choice of all SaS inside the layers at Chebyshev polynomial nodes and direct integration of the equations of motion and the charge equation. The use of interfaces is avoided that allows one to minimize uniformly the error due to the higher-order Lagrange interpolation [19-22]. Thus, the strong SaS formulation can be applied efficiently to the 3D vibration analysis of piezolaminated plates.

2 BASIC ASSUMPTIONS

Consider a laminated piezoelectric plate of the thickness h . Let the middle surface Ω be described by Cartesian coordinates x_1 and x_2 . The coordinate x_3 is oriented in the thickness direction. According to the SaS concept, we choose inside the n th layer I_n SaS $\Omega^{(n)1}, \Omega^{(n)2}, \dots, \Omega^{(n)I_n}$ parallel to the middle surface (see Figure 1), where $n=1, 2, \dots, N$; N is the number of layers and $I_n \geq 3$. The transverse coordinates of SaS of the n th layer located at Chebyshev polynomial nodes (roots of the Chebyshev polynomial of order I_n) are written as

$$x_3^{(n)i_n} = \frac{1}{2}(x_3^{[n-1]} + x_3^{[n]}) - \frac{1}{2}h_n \cos\left(\pi \frac{2i_n - 1}{2I_n}\right), \quad (1)$$

where $x_3^{[0]} = -h/2$, $x_3^{[N]} = h/2$; $x_3^{[m]}$ are the transverse coordinates of interfaces $\Omega^{[m]}$; $h_n = x_3^{[n]} - x_3^{[n-1]}$ is the thickness of the n th layer; the index $m=1, 2, \dots, N-1$ identifies the belonging of any quantity to the interface; the indices $i_n, j_n = 1, 2, \dots, I_n$ identify the belonging of any quantity to the SaS of the n th layer.

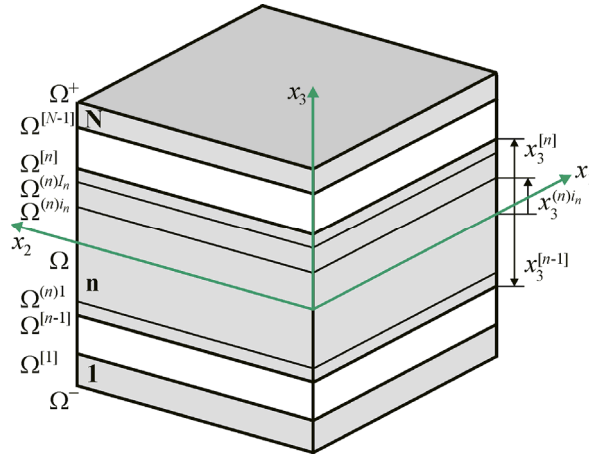


Figure 1: Geometry of the laminated piezoelectric plate

The through-thickness SaS approximations can be expressed as

$$[u_i^{(n)}, \varepsilon_{ij}^{(n)}, \sigma_{ij}^{(n)}, \varphi^{(n)}, E_i^{(n)}, D_i^{(n)}] = \sum_{i_n} L^{(n)i_n} [u_i^{(n)i_n}, \varepsilon_{ij}^{(n)i_n}, \sigma_{ij}^{(n)i_n}, \varphi^{(n)i_n}, E_i^{(n)i_n}, D_i^{(n)i_n}], \quad (2)$$

where $u_i^{(n)}, \varepsilon_{ij}^{(n)}, \sigma_{ij}^{(n)}, \varphi^{(n)}, E_i^{(n)}, D_i^{(n)}$ are the displacements, strains, stresses, electric potential, electric field and electric displacements of the n th layer; $u_i^{(n)i_n}, \varepsilon_{ij}^{(n)i_n}, \sigma_{ij}^{(n)i_n}, \varphi^{(n)i_n}, E_i^{(n)i_n}, D_i^{(n)i_n}$ are the displacements, strains, stresses, electric potential, electric field and electric displacements of SaS of the n th layer $\Omega^{(n)i_n}$; $L^{(n)i_n}(x_3)$ are the Lagrange basis polynomials of degree $I_n - 1$ corresponding to the n th layer:

$$L^{(n)i_n} = \prod_{j_n \neq i_n} \frac{x_3 - x_3^{(n)j_n}}{x_3^{(n)i_n} - x_3^{(n)j_n}}. \quad (3)$$

3 STRONG SAS FORMULATION

For simplicity, we consider the case of linear piezoelectric materials given by

$$\sigma_{ij}^{(n)} = C_{ijkl}^{(n)} \varepsilon_{kl}^{(n)} - e_{kij}^{(n)} E_k^{(n)}, \quad (4)$$

$$D_i^{(n)} = e_{ikl}^{(n)} \varepsilon_{kl}^{(n)} + \varepsilon_{ik}^{(n)} E_k^{(n)}, \quad (5)$$

where $C_{ijkl}^{(n)}, e_{kij}^{(n)}$ and $\varepsilon_{ik}^{(n)}$ are the elastic, piezoelectric and dielectric constants of the n th layer. Here, the summation on repeated Latin indices is implied.

The equations of motion and the charge equation of the laminated piezoelectric plate are written as

$$\sigma_{ij,j}^{(n)} = \rho_n \ddot{u}_i^{(n)}, \quad (6)$$

$$D_{i,i}^{(n)} = 0, \quad (7)$$

where ρ_n is the mass density of the n th layer; $\ddot{u}_i^{(n)}$ is the second order derivative of displacements with respect to time t ; the symbol $(\dots)_{,i}$ stands for the partial derivatives with respect to coordinates x_i .

The boundary conditions on bottom and top surfaces are defined as

$$u_i^{(1)}(-h/2) = w_i^- \text{ or } \sigma_{i3}^{(1)}(-h/2) = p_i^-, \quad \varphi^{(1)}(-h/2) = \phi^- \text{ or } D_3^{(1)}(-h/2) = Q^-, \quad (8)$$

$$u_i^{(N)}(h/2) = w_i^+ \text{ or } \sigma_{i3}^{(N)}(h/2) = p_i^+, \quad \varphi^{(N)}(h/2) = \phi^+ \text{ or } D_3^{(N)}(h/2) = Q^+, \quad (9)$$

where $w_i^-, p_i^-, \phi^-, Q^-$ and $w_i^+, p_i^+, \phi^+, Q^+$ are the prescribed displacements, surface tractions, electric potentials and electric charges at the bottom and top surfaces.

The continuity conditions at interfaces are

$$u_i^{(m)}(x_3^{[m]}) = u_i^{(m+1)}(x_3^{[m]}), \quad \sigma_{i3}^{(m)}(x_3^{[m]}) = \sigma_{i3}^{(m+1)}(x_3^{[m]}), \quad (10)$$

$$\varphi^{(m)}(x_3^{[m]}) = \varphi^{(m+1)}(x_3^{[m]}), \quad D_3^{(m)}(x_3^{[m]}) = D_3^{(m+1)}(x_3^{[m]}). \quad (11)$$

Satisfying equations of motion (6) and charge equation (7) at inner layer points $x_3^{(n)m_n}$ by using the SaS approximations (2), the following differential equations are obtained:

$$\sigma_{i1,1}^{(n)m_n} + \sigma_{i2,2}^{(n)m_n} + \sum_{i_n} M^{(n)i_n}(x_3^{(n)m_n}) \sigma_{i3}^{(n)i_n} = \rho_n \ddot{u}_i^{(n)m_n}, \quad (12)$$

$$D_{1,1}^{(n)m_n} + D_{2,2}^{(n)m_n} + \sum_{i_n} M^{(n)i_n}(x_3^{(n)m_n}) D_3^{(n)i_n} = 0, \quad (13)$$

where $M^{(n)i_n} = L_3^{(n)i_n}$ are the derivatives of the Lagrange basis polynomials whose values at SaS $\Omega^{(n)m_n}$ are presented in papers [14, 15]; $m_n = 2, 3, \dots, I_n - 1$.

Next, we satisfy the boundary conditions on bottom and top surfaces

$$\sum_{i_1} L^{(1)i_1}(-h/2) u_i^{(1)i_1} = w_i^- \text{ or } \sum_{i_1} L^{(1)i_1}(-h/2) \sigma_{i3}^{(1)i_1} = p_i^-, \quad (14)$$

$$\sum_{i_1} L^{(1)i_1}(-h/2) \varphi^{(1)i_1} = \phi^- \text{ or } \sum_{i_1} L^{(1)i_1}(-h/2) D_3^{(1)i_1} = Q^-,$$

$$\sum_{i_N} L^{(N)i_N}(h/2) u_i^{(N)i_N} = w_i^+ \text{ or } \sum_{i_N} L^{(N)i_N}(h/2) \sigma_{i3}^{(N)i_N} = p_i^+, \quad (15)$$

$$\sum_{i_N} L^{(N)i_N}(h/2) \varphi^{(N)i_N} = \phi^+ \text{ or } \sum_{i_N} L^{(N)i_N}(h/2) D_3^{(N)i_N} = Q^+,$$

and the continuity conditions at interfaces

$$\sum_{i_m} L^{(m)i_m}(x_3^{[m]}) u_i^{(m)i_m} = \sum_{i_{m+1}} L^{(m+1)i_{m+1}}(x_3^{[m]}) u_i^{(m+1)i_{m+1}}, \quad (16)$$

$$\sum_{i_m} L^{(m)i_m}(x_3^{[m]}) \sigma_{i3}^{(m)i_m} = \sum_{i_{m+1}} L^{(m+1)i_{m+1}}(x_3^{[m]}) \sigma_{i3}^{(m+1)i_{m+1}},$$

$$\sum_{i_m} L^{(m)i_m}(x_3^{[m]}) \varphi^{(m)i_m} = \sum_{i_{m+1}} L^{(m+1)i_{m+1}}(x_3^{[m]}) \varphi^{(m+1)i_{m+1}}, \quad (17)$$

$$\sum_{i_m} L^{(m)i_m}(x_3^{[m]}) D_3^{(m)i_m} = \sum_{i_{m+1}} L^{(m+1)i_{m+1}}(x_3^{[m]}) D_3^{(m+1)i_{m+1}}.$$

Thus, the proposed strong SaS formulation deals with $4N_{\text{SaS}}$ governing equations (12)-(17) for obtaining the same number of SaS displacements $u_i^{(n)i_n}$ and SaS electric potentials $\varphi^{(n)i_n}$, where $N_{\text{SaS}} = I_1 + I_2 + \dots + I_N$ is the total number of SaS. These differential and algebraic equations have to be solved to describe the dynamic response of the laminated piezoelectric plate.

4 FREE VIBRATION OF SIMPLY SUPPORTED PIEZOELECTRIC PLATE

In this section, we consider a laminated piezoelectric rectangular plate with simply supported edges. The boundary conditions on the edges are written as

$$\begin{aligned} \sigma_{11}^{(n)} = u_2^{(n)} = u_3^{(n)} = \varphi^{(n)} = 0 \text{ at } x_1 = 0 \text{ and } x_1 = a, \\ \sigma_{22}^{(n)} = u_1^{(n)} = u_3^{(n)} = \varphi^{(n)} = 0 \text{ at } x_2 = 0 \text{ and } x_2 = b, \end{aligned} \quad (18)$$

where a and b are the length and width of the plate.

To satisfy boundary conditions (18), we seek the analytical solution of the problem in the following form:

$$\begin{aligned} u_1^{(n)i_n} &= u_{1rs}^{(n)i_n} e^{i\omega_{rs}t} \cos \bar{r}x_1 \sin \bar{s}x_2, & u_2^{(n)i_n} &= u_{2rs}^{(n)i_n} e^{i\omega_{rs}t} \sin \bar{r}x_1 \cos \bar{s}x_2, \\ u_3^{(n)i_n} &= u_{3rs}^{(n)i_n} e^{i\omega_{rs}t} \sin \bar{r}x_1 \sin \bar{s}x_2, & \varphi^{(n)i_n} &= \varphi_{rs}^{(n)i_n} e^{i\omega_{rs}t} \sin \bar{r}x_1 \sin \bar{s}x_2, \end{aligned} \quad (19)$$

where $\bar{r} = r\pi/a$, $\bar{s} = s\pi/b$; r and s are the half-wave numbers in x_1 and x_2 directions; $u_{irs}^{(n)i_n}$ and $\varphi_{rs}^{(n)i_n}$ are the amplitudes of displacements and electric potentials of SaS; ω_{rs} is the circular frequency; $i = \sqrt{-1}$ is the imaginary unit.

Using (19) in relations between the SaS variables [12], one finds

$$\begin{aligned} (\varepsilon_{11}^{(n)i_n}, \varepsilon_{22}^{(n)i_n}, \varepsilon_{33}^{(n)i_n}, \sigma_{11}^{(n)i_n}, \sigma_{22}^{(n)i_n}, \sigma_{33}^{(n)i_n}) &= (\varepsilon_{11rs}^{(n)i_n}, \varepsilon_{22rs}^{(n)i_n}, \varepsilon_{33rs}^{(n)i_n}, \sigma_{11rs}^{(n)i_n}, \sigma_{22rs}^{(n)i_n}, \sigma_{33rs}^{(n)i_n}) e^{i\omega_{rs}t} \sin \bar{r}x_1 \sin \bar{s}x_2, \\ (E_3^{(n)i_n}, D_3^{(n)i_n}) &= (E_{3rs}^{(n)i_n}, D_{3rs}^{(n)i_n}) e^{i\omega_{rs}t} \sin \bar{r}x_1 \sin \bar{s}x_2, \\ (\varepsilon_{13}^{(n)i_n}, \sigma_{13}^{(n)i_n}, E_1^{(n)i_n}, D_1^{(n)i_n}) &= (\varepsilon_{13rs}^{(n)i_n}, \sigma_{13rs}^{(n)i_n}, E_{1rs}^{(n)i_n}, D_{1rs}^{(n)i_n}) e^{i\omega_{rs}t} \cos \bar{r}x_1 \sin \bar{s}x_2, \\ (\varepsilon_{23}^{(n)i_n}, \sigma_{23}^{(n)i_n}, E_2^{(n)i_n}, D_2^{(n)i_n}) &= (\varepsilon_{23rs}^{(n)i_n}, \sigma_{23rs}^{(n)i_n}, E_{2rs}^{(n)i_n}, D_{2rs}^{(n)i_n}) e^{i\omega_{rs}t} \sin \bar{r}x_1 \cos \bar{s}x_2, \\ (\varepsilon_{12}^{(n)i_n}, \sigma_{12}^{(n)i_n}) &= (\varepsilon_{12rs}^{(n)i_n}, \sigma_{12rs}^{(n)i_n}) e^{i\omega_{rs}t} \cos \bar{r}x_1 \cos \bar{s}x_2, \end{aligned} \quad (20)$$

where

$$\begin{aligned} \varepsilon_{11rs}^{(n)i_n} &= -\bar{r}u_{1rs}^{(n)i_n}, & \varepsilon_{22rs}^{(n)i_n} &= -\bar{s}u_{2rs}^{(n)i_n}, & 2\varepsilon_{12rs}^{(n)i_n} &= \bar{s}u_{1rs}^{(n)i_n} + \bar{r}u_{2rs}^{(n)i_n}, \\ 2\varepsilon_{13rs}^{(n)i_n} &= \bar{r}u_{3rs}^{(n)i_n} + \beta_{1rs}^{(n)i_n}, & 2\varepsilon_{23rs}^{(n)i_n} &= \bar{s}u_{3rs}^{(n)i_n} + \beta_{2rs}^{(n)i_n}, & \varepsilon_{33rs}^{(n)i_n} &= \beta_{3rs}^{(n)i_n}, \\ \beta_{irs}^{(n)i_n} &= \sum_{j_n} M^{(n)j_n} (x_3^{(n)i_n}) u_{irs}^{(n)j_n}, \\ E_{1rs}^{(n)i_n} &= -\bar{r}\varphi_{rs}^{(n)i_n}, & E_{2rs}^{(n)i_n} &= -\bar{s}\varphi_{rs}^{(n)i_n}, & E_{3rs}^{(n)i_n} &= -\sum_{j_n} M^{(n)j_n} (x_3^{(n)i_n}) \varphi_{rs}^{(n)j_n}. \end{aligned} \quad (21)$$

In the case of the piezoelectric material with $4mm$ symmetry, the constitutive equations (4) and (5) can be written in terms of SaS variables

$$\sigma_{ijrs}^{(n)i_n} = C_{ijkl}^{(n)} \varepsilon_{klrs}^{(n)i_n} - e_{kij}^{(n)} E_{krs}^{(n)i_n}, \quad (22)$$

$$D_{irs}^{(n)i_n} = e_{ikl}^{(n)} \varepsilon_{klrs}^{(n)i_n} + \epsilon_{ik}^{(n)} E_{krs}^{(n)i_n}. \quad (23)$$

For the vibration analysis of piezoelectric plates with stress-free and voltage-free external surfaces, the boundary conditions (14) and (15) are used with $p_i^\pm = 0$ and $\phi^\pm = 0$. Substituting (19)-(23) in governing equations (12)-(17), we arrive at the homogeneous system of linear equations

$$\left(\begin{bmatrix} \mathbf{K}_{rs}^{uu} & \mathbf{K}_{rs}^{u\varphi} \\ \mathbf{K}_{rs}^{\varphi u} & \mathbf{K}_{rs}^{\varphi\varphi} \end{bmatrix} - \omega_{rs}^2 \begin{bmatrix} \mathbf{M}_{rs} & \mathbf{0} \\ \mathbf{0} & \mathbf{0} \end{bmatrix} \right) \begin{bmatrix} \mathbf{U}_{rs} \\ \mathbf{\Phi}_{rs} \end{bmatrix} = \mathbf{0}, \quad (24)$$

where \mathbf{K}_{rs}^{uu} , $\mathbf{K}_{rs}^{u\varphi}$, $\mathbf{K}_{rs}^{\varphi u} = (\mathbf{K}_{rs}^{u\varphi})^T$ and $\mathbf{K}_{rs}^{\varphi\varphi}$ are the mechanical, piezoelectric and dielectric stiffness matrices; \mathbf{M}_{rs} is the mass matrix; \mathbf{U}_{rs} is the SaS displacement vector of order $3N_{\text{SaS}}$; $\mathbf{\Phi}_{rs}$ is the SaS electric potential vector of order N_{SaS} given by

$$\mathbf{U}_{rs} = [\mathbf{U}_{1rs}^T \mathbf{U}_{2rs}^T \mathbf{U}_{3rs}^T]^T, \quad (25)$$

$$\begin{aligned} \mathbf{U}_{irs} &= [u_{irs}^{(1)1} u_{irs}^{(1)2} \dots u_{irs}^{(1)I_1} u_{irs}^{(2)1} u_{irs}^{(2)2} \dots u_{irs}^{(2)I_2} \dots u_{irs}^{(N)1} u_{irs}^{(N)2} \dots u_{irs}^{(N)I_N}]^T, \\ \mathbf{\Phi}_{rs} &= [\varphi_{rs}^{(1)1} \varphi_{rs}^{(1)2} \dots \varphi_{rs}^{(1)I_1} \varphi_{rs}^{(2)1} \varphi_{rs}^{(2)2} \dots \varphi_{rs}^{(2)I_2} \dots \varphi_{rs}^{(N)1} \varphi_{rs}^{(N)2} \dots \varphi_{rs}^{(N)I_N}]^T. \end{aligned} \quad (26)$$

Eliminating the vector $\mathbf{\Phi}_{rs}$ from (24), one gets

$$\mathbf{\Phi}_{rs} = -(\mathbf{K}_{rs}^{\varphi\varphi})^{-1} \mathbf{K}_{rs}^{\varphi u} \mathbf{U}_{rs}. \quad (27)$$

Inserting (27) in the first row of (24), the following reduced homogeneous system is obtained

$$(\mathbf{K}_{rs} - \omega_{rs}^2 \mathbf{M}_{rs}) \mathbf{U}_{rs} = \mathbf{0}, \quad (28)$$

which has a non-trivial solution only if

$$\det(\mathbf{K}_{rs} - \omega_{rs}^2 \mathbf{M}_{rs}) = 0, \quad (29)$$

where $\mathbf{K}_{rs} = \mathbf{K}_{rs}^{uu} - \mathbf{K}_{rs}^{u\varphi} (\mathbf{K}_{rs}^{\varphi\varphi})^{-1} \mathbf{K}_{rs}^{\varphi u}$ is the stiffness matrix of order $3N_{\text{SaS}} \times 3N_{\text{SaS}}$.

The polynomial equation (29) has to be solved to obtain the circular frequencies $0 < \omega_{rs}^{(1)} < \omega_{rs}^{(2)} < \dots < \omega_{rs}^{(3N_{\text{SaS}}-6N)}$ arranged in an increasing order. The number of frequencies $\omega_{rs}^{(q)}$ for each set of SaS depends on the number of zero rows in a mass matrix \mathbf{M} , where the superscript $q = 1, 2, \dots, 3N_{\text{SaS}} - 6N$ stands for the number of through thickness modes. The eigenvectors $\mathbf{U}_{rs}^{(q)}$ associated with the corresponding eigenvalues $\lambda_{rs}^{(q)} = (\omega_{rs}^{(q)})^2$ can be evaluated by using the linear system (28).

5 FORCED VIBRATION OF SIMPLY SUPPORTED PIEZOELECTRIC PLATE

Here, we study forced vibrations of the simply supported laminated piezoelectric rectangular plate with boundary conditions on the bottom and top surfaces

$$\begin{aligned} \sigma_{13}^{(1)} = \sigma_{23}^{(1)} = \sigma_{33}^{(1)} = \varphi^{(1)} = 0 \text{ at } x_3 = -h/2, \\ \sigma_{13}^{(N)} = \sigma_{23}^{(N)} = 0, \quad \sigma_{33}^{(N)} = p_3^+, \quad \varphi^{(N)} = \phi^+ \text{ at } x_3 = h/2. \end{aligned} \quad (30)$$

Consider time-harmonic loading distributed on the top surface as follows:

$$\text{Problem A: } p_3^+ = p_0 e^{i\omega t} \sin \frac{\pi x_1}{a} \sin \frac{\pi x_2}{b}, \quad \phi^+ = 0; \quad (31)$$

$$\text{Problem B: } p_3^+ = 0, \quad \phi^+ = \phi_0 e^{i\omega t} \sin \frac{\pi x_1}{a} \sin \frac{\pi x_2}{b}, \quad (32)$$

where ω is the forcing frequency.

To satisfy boundary conditions (18), we seek the analytical solution of the problem in the following form:

$$\begin{aligned} u_1^{(n)i_n} &= u_{10}^{(n)i_n} e^{i\omega t} \cos \frac{\pi x_1}{a} \sin \frac{\pi x_2}{b}, \quad u_2^{(n)i_n} = u_{20}^{(n)i_n} e^{i\omega t} \sin \frac{\pi x_1}{a} \cos \frac{\pi x_2}{b}, \\ u_3^{(n)i_n} &= u_{30}^{(n)i_n} e^{i\omega t} \sin \frac{\pi x_1}{a} \sin \frac{\pi x_2}{b}, \quad \varphi^{(n)i_n} = \varphi_0^{(n)i_n} e^{i\omega t} \sin \frac{\pi x_1}{a} \sin \frac{\pi x_2}{b}, \end{aligned} \quad (33)$$

where $u_{i0}^{(n)i_n}$ and $\varphi_0^{(n)i_n}$ are the amplitudes of displacements and electric potentials of SaS of the n th layer.

The described algorithm was performed with the Symbolic Math Toolbox, which incorporates symbolic computations into the numeric environment of MATLAB. This makes possible to obtain the analytical solutions for free and forced vibrations of the simply supported laminated piezoelectric rectangular plate in the framework of the SaS formulation, which asymptotically approaches the 3D exact solutions of electroelasticity as the number of SaS goes to infinity.

As a numerical example, we consider a simply supported two-ply square plate [0/90] made of the graphite epoxy composite and covered with PZT-4 piezoelectric layers at the bottom and at the top. Therefore, we deal here with a hybrid four-layer plate [PZT/0/90/PZT] with ply thicknesses $[0.25h/0.25h/0.25h/0.25h]$. The material properties of the PZT-4 [12] polarized in the thickness direction are $E_1=E_2=81.3$ GPa, $E_3=64.5$ GPa, $G_{12}=30.6$ GPa, $G_{13}=G_{23}=25.6$ GPa, $\nu_{12}=0.329$, $\nu_{13}=\nu_{23}=0.432$, $e_{311}=e_{322}=-5.2$ C/m², $e_{333}=15.08$ C/m², $e_{113}=e_{223}=12.72$ C/m², $\epsilon_{11}=\epsilon_{22}=13.06$ nF/m, $\epsilon_{33}=11.51$ nF/m and $\rho=7600$ kg/m³. The material properties of the graphite epoxy [12] are $E_1=172.5$ GPa, $E_2=E_3=6.9$ GPa, $G_{12}=G_{13}=3.45$ GPa, $G_{23}=1.38$ GPa, $\nu_{12}=\nu_{13}=0.25$, $\nu_{23}=0.35$, $\epsilon_{11}=0.031$ nF/m, $\epsilon_{22}=\epsilon_{33}=0.027$ nF/m and $\rho=1800$ kg/m³.

To evaluate the results effectively, we introduce the dimensionless frequency [12]

$$\bar{\omega} = \omega a^2 \sqrt{\rho_0 / E_0} / h \quad (34)$$

and dimensionless basic variables at crucial points as functions of the thickness coordinate

$$\begin{aligned} \bar{u}_3 &= 10^9 u_3(a/2, a/2, z) / h, \quad \bar{\sigma}_{11} = \sigma_{11}(a/2, a/2, z) / p_0, \\ \bar{\sigma}_{13} &= \sigma_{13}(0, a/2, z) / p_0, \quad \bar{\sigma}_{33} = \sigma_{33}(a/2, a/2, z) / p_0, \\ \bar{\varphi} &= \varphi(a/2, a/2, z) / \phi_0, \quad \bar{D}_3 = 10^9 \phi_0 D_3(a/2, a/2, z) / ap_0, \quad z = x_3 / h, \end{aligned} \quad (35)$$

where $a=1$ m, $h=0.1$ m, $E_0=81.3$ GPa, $\rho_0=7600$ kg/m³, $p_0=1$ Pa and $\phi_0=1$ V.

Figures 2 and 3 display the distributions of displacements, stresses, electric potential and electric displacement (35) through the thickness of the plate for the forcing frequencies $\bar{\omega} = 0, 0.8\bar{\omega}_0, 0.95\bar{\omega}_0$ and $1.05\bar{\omega}_0$ using seven SaS inside each layer, where $\bar{\omega}_0 = 6.0932$ is the fundamental frequency in the case of stress-free and voltage-free external surfaces [12]. It is seen that the boundary conditions on bottom and top surfaces for the transverse stresses and the continuity conditions at interfaces for the transverse stresses and electric displacement are satisfied correctly. Note also that the displacements and stresses become larger as the forcing frequency approaches the fundamental frequency.

ACKNOWLEDGEMENTS

This work was supported by the Russian Science Foundation under Grant No. 18-19-00092.

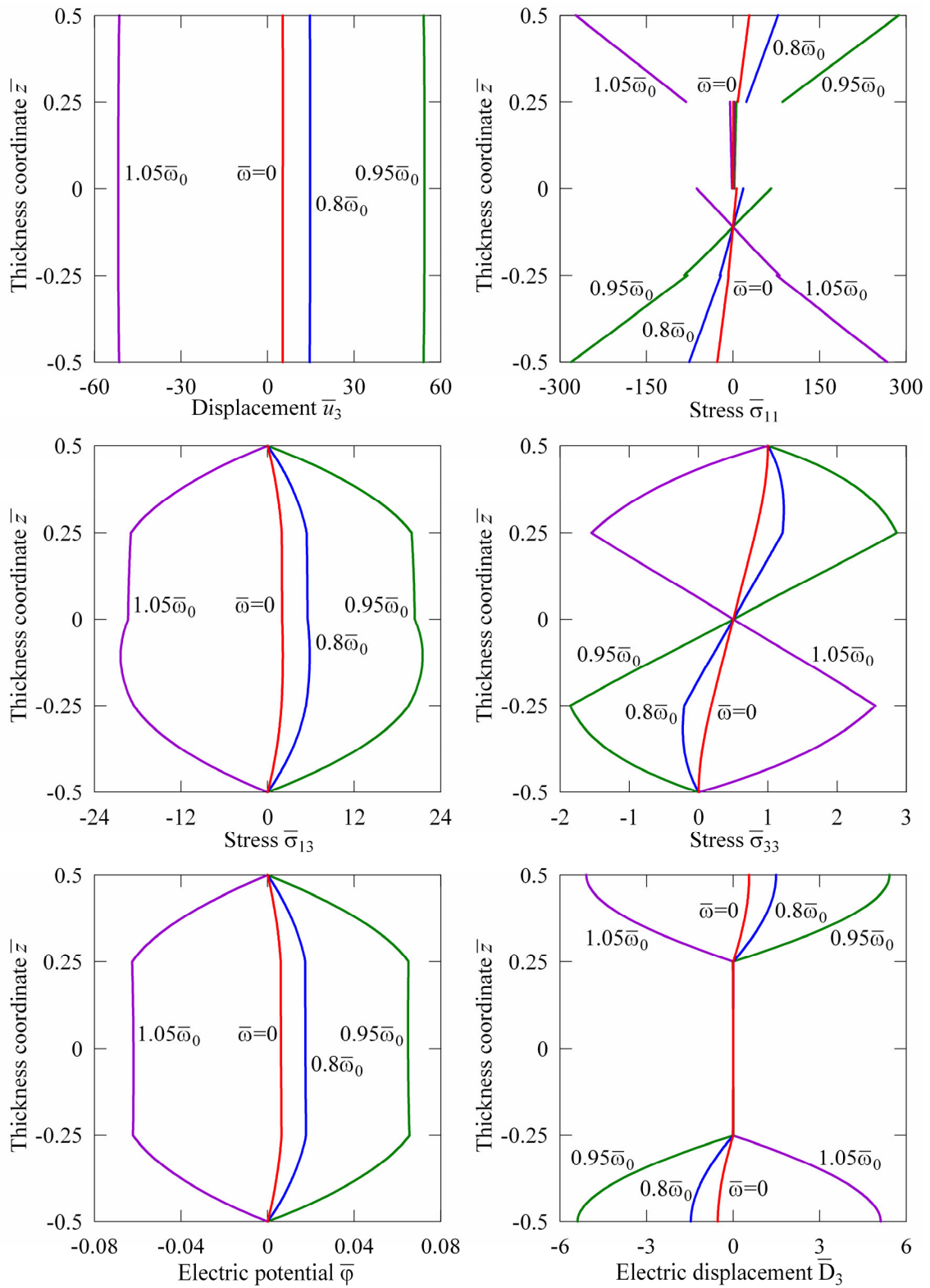


Figure 2: Through-thickness distributions of transverse displacement, stresses, electric potential and electric displacement for the four-layer plate subjected to mechanical loading (problem A)

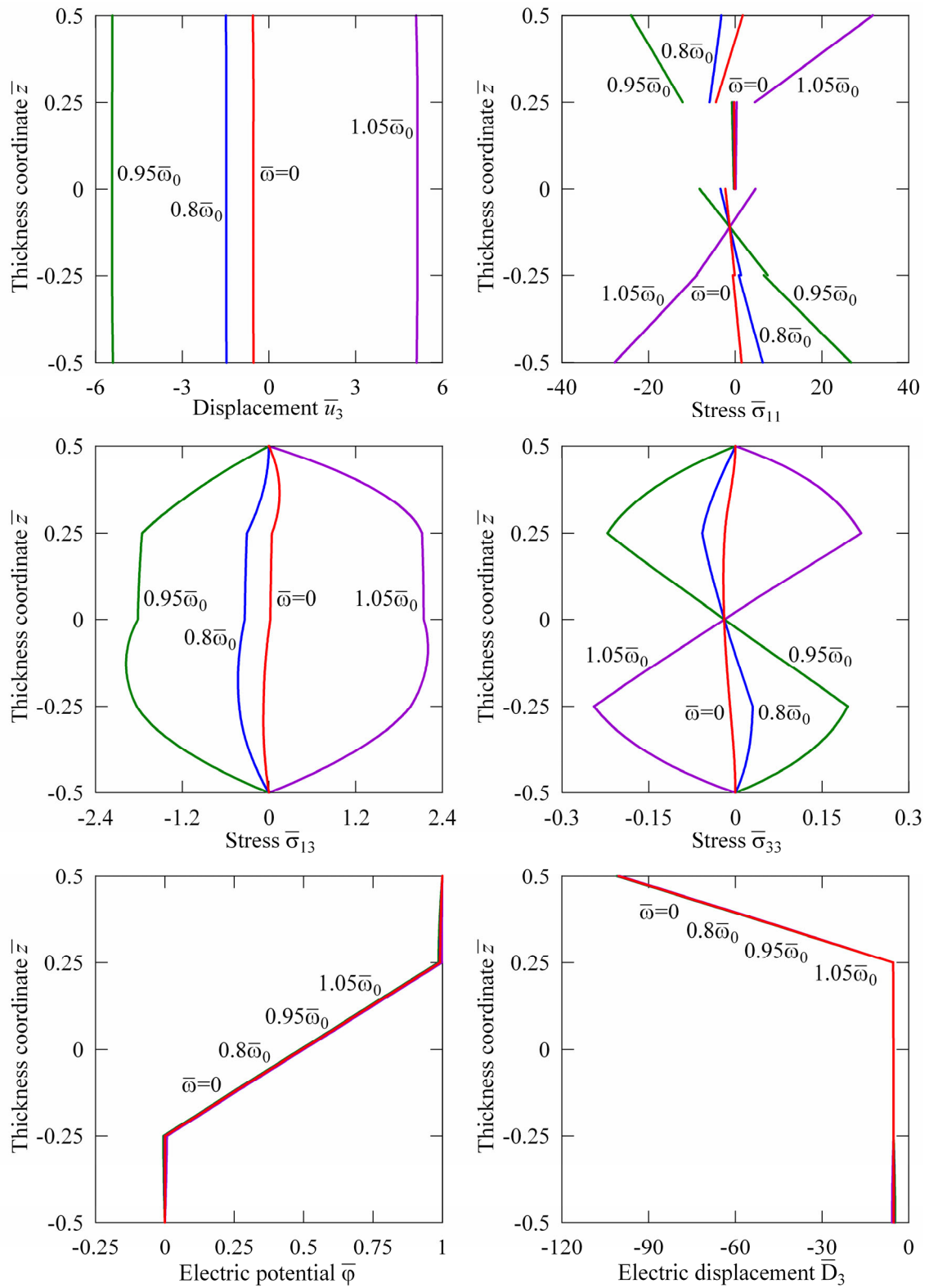


Figure 3: Through-thickness distributions of transverse displacement, stresses, electric potential and electric displacement for the four-layer plate subjected to electric loading (problem B)

REFERENCES

- [1] Heyliger, P. and Brooks, S. Free vibration of piezoelectric laminates in cylindrical bending. *Int. J. Solids Struct.* (1995) **32**:2945–2960.
- [2] Heyliger, P. and Saravanan, D.A. Exact free-vibration analysis of laminated plates with embedded piezoelectric layers. *J. Acoust. Soc. America* (1995) **98**:1547–1557.
- [3] Chen, W.Q., Xu, R.Q. and Ding, H.J. On free vibration of a piezoelectric composite rectangular plate. *J. Sound Vibr.* (1998) **218**:741–748.
- [4] Ding, H.J., Xu, R.Q., Chi, Y.W. and Chen, W.Q. Free axisymmetric vibration of transversely isotropic piezoelectric circular plates. *Int. J. Solids Struct.* (1999) **36**:4629–4652.
- [5] Chen, W.Q. and Ding, H.J. On free vibration of a functionally graded piezoelectric rectangular plate. *Acta Mech.* (2002) **153**:207–216.
- [6] Deü, J.F. and Benjeddou, A. Free-vibration analysis of laminated plates with embedded shear-mode piezoceramic layers. *Int. J. Solids Struct.* (2005) **42**:2059–2088.
- [7] Zhong, Z. and Yu, T. Vibration of a simply supported functionally graded piezoelectric rectangular plate. *Smart Mater. Struct.* (2006) **15**:1404–1412.
- [8] Messina, A. and Carrera, E. Three-dimensional free vibration of multi-layered piezoelectric plates through approximate and exact analyses. *J. Intel. Mater. Systems Struct.* (2015) **26**:489–504.
- [9] Gao, J.X., Shen, Y.P. and Wang, J. Three dimensional analysis for free vibration of rectangular composite laminates with piezoelectric layers. *J. Sound Vibr.* (1998) **213**:383–390.
- [10] Vel, S.S., Mewer, R.C. and Batra, R.C. Analytical solution for the cylindrical bending vibration of piezoelectric composite plates. *Int. J. Solids Struct.* (2004) **41**:1625–1643.
- [11] Baillargeon, B.P. and Vel, S.S. Exact solution for the vibration and active damping of composite plates with piezoelectric shear actuators. *J. Sound Vibr.* (2005) **282**:781–804.
- [12] Kulikov, G.M. and Plotnikova, S.V. Benchmark solutions for the free vibration of layered piezoelectric plates based on a variational formulation. *J. Intel. Mater. Systems Struct.* (2017) **28**:2688–2704.
- [13] Kulikov, G.M. and Plotnikova, S.V. On the use of a new concept of sampling surfaces in a shell theory. *Adv. Struct. Mater.* (2011) **15**:715–726.
- [14] Kulikov, G.M. and Plotnikova, S.V. Three-dimensional exact analysis of piezoelectric laminated plates via a sampling surfaces method. *Int. J. Solids Struct.* (2013) **50**:1916–1929.
- [15] Kulikov, G.M. and Plotnikova, S.V. A new approach to three-dimensional exact solutions for functionally graded piezoelectric laminated plates. *Compos. Struct.* (2013) **106**:33–46.
- [16] Kulikov, G.M. and Plotnikova, S.V. A sampling surfaces method and its application to three-dimensional exact solutions for piezoelectric laminated shells. *Int. J. Solids Struct.* (2013) **50**:1930–1943.
- [17] Kulikov, G.M., Plotnikova, S.V. Exact electroelastic analysis of functionally graded piezoelectric shells. *Int. J. Solids Struct.* (2014) **51**:13–25.
- [18] Bakhvalov, N.S. *Numerical methods: Analysis, algebra, ordinary differential equations*. MIR Publishers, Moscow, (1977).

- [19] Kulikov, G.M. and Plotnikova, S.V. Strong sampling surfaces formulation for laminated composite plates. *Compos. Struct.* (2017) **172**:73–82.
- [20] Kulikov, G.M. and Plotnikova, S.V. Strong sampling surfaces formulation for layered shells. *Int. J. Solids Struct.* (2017) **121**:75–85.
- [21] Kulikov, G.M. and Plotnikova, S.V. Strong SaS formulation for free and forced vibrations of laminated composite plates. *Compos. Struct.* (2017) **180**:286–297.
- [22] Kulikov, G.M. and Plotnikova, S.V. Three-dimensional vibration analysis of simply supported laminated cylindrical shells and panels by a strong SaS formulation. *ZAMM – J. Appl. Math. Mech.* (2019) **99**:1–17.

MULTI-DIMENSIONAL MODELS FOR THE GLOBAL-LOCAL ANALYSIS OF SMART LAYERED STRUCTURES

Enrico Zappino and Erasmo Carrera

* Mul² Team, Politecnico di Torino, Corso Duca degli Abruzzi 24, 10129 Torino, Italy.
e-mail: enrico.zappino@polito.it, erasmo.carrera@polito.it; web page: <http://www.mul2.com/>

Key words: Node-dependent kinematic, global-local, Carrera Unified Formulation

Abstract. The present paper presents a multidimensional model for the global-local analysis of smart layered structures. The use of the Carrera Unified Formulation has lead to a general framework for the development of one-, two- and three-dimensional models. The use of the node-dependent kinematic approach makes it possible to easily connect elements with incompatible kinematics, that is, refined kinematic elements can be connected with classical elements without the need of *ad hoc* connection strategies. The capabilities of this numerical model have been exploited to develop enhanced global-local models for smart layered structures where high-fidelity models are used only in those areas where complex phenomena appear, e.g. around a piezo-patch. The results show the accuracy and efficiency of the present approach and make it suitable for future applications in the design of smart structures.

1 INTRODUCTION

The design of smart structures requires numerical models able to deal with complex phenomena with reasonable computational cost. Smart structures, such as piezoelectric devices, are usually built by a classical structure, acting as a substrate, with a number of patches or layers locally applied to provide sensor/actuator capabilities. Finite element models are widely used for the design of such complex structures but the accuracy required to catch the behavior of the active material may lead to very expensive models. 3D brick elements for piezoelectric modeling were presented by [1], and [2]. Since solid elements are computational costly when used to model thin piezoelectric layers, various 2D and 1D models were proposed as alternative choices. As shown by Kim *et.al.* [11] the use of global-local approaches may lead to an efficient modeling approach that uses the refined models only in those areas where it is necessary, exploiting the efficiency of the classical finite elements approach elsewhere. This approach requires to couple elements with different kinematic fields such as beam or plate elements with three-dimensional elements. Different coupling approaches have been presented in literature. Surana [15, 16] proposed an approach to couple three and two-dimensional elements. The connection between solid and shell elements was also investigated in [12] and [7]. The work by Gmur [9] deals with the connection of solid isoparametric and super-parametric shell elements, while the connection between one- and three-dimensional elements was investigated in [10]. McCune *et.al.* [13] and Monaghan *et.al.* [14] introduced a mixed-dimensional coupling scheme, based on geometrical assumptions, while Garusi and tralli [8] used a transition element to develop solid-to-beam and plate-to-beam connections.

The present work aims to extend the use of the multi-dimensional modeling approach presented by the authors in [17, 4] to refine locally those models that could not provide an adequate accuracy level

for multi-field analyses. The structural models have been derived in the frameworks of the Carrera Unified Formulation [3] that allows the kinematic field to be refined in a unified and efficient fashion. The node-dependent kinematic approach presented in [5] and recently extended to the piezo-electric problem [6], will be exploited to switch between models with different kinematics without the need on any *ad hoc* formulation or compatibility equations. The results obtained from the solution of well known benchmarks show that the present approach may be used to reduce the computational costs without affecting the accuracy of the solution.

2 NODE-DEPENDENT KINEMATIC ELEMENTS

The development of refined one- and two- and three-dimensional finite element models requires to derive the stiffness/mass matrix for each kinematic approximation adopted. Moreover, the introduction of the node-dependent kinematics formulation would ask for an *ad-hoc* formulation of the matrices for each element. A general and unified approach for the derivation of the matrices for any kinematic model has been proposed by [3] and will be used to derive the NDK elements formulation.

The generic three-dimensional solution of the problem can be written as follows:

$$\mathbf{u} = \mathbf{u}(x, y, z). \quad (1)$$

where $\mathbf{u}(x, y, z)$ is a three-dimensional function solution of the problem. The vector \mathbf{u} contains the three displacement components when the mechanical problem is considered. The if piezo-mechanical problem is considered \mathbf{u} has four components, the three-displacements and the electric potential:

$$\mathbf{u}(x, y, z)^T = \{u_x, u_y, u_z, \phi\} \quad (2)$$

When all the three dimensions of the structure are comparable it is not possible to reduce the dimension of the problem, that is, a three-dimensional problem should be solved. When the structure has a dimension, z , which can be neglected with respect to the others, x and y , it is possible to introduce a plate/shell model, in this case the Equation 2 can be reduced to:

$$\mathbf{u} = \mathbf{u}_\tau(x, y)F_\tau^{1D}(z), \quad \tau = 1 \dots M, \quad (3)$$

where F_τ^{1D} represents a generic function expansion used to approximate the displacement field through the thickness, and M is the number of terms in the expansion. If two dimensions, x and z , are negligible with respect to the other, y , it is possible to reduce Equation (2) in the form:

$$\mathbf{u} = \mathbf{u}_\tau(y)F_\tau^{2D}(x, z), \quad \tau = 1 \dots M \quad (4)$$

where F_τ^{2D} represents the function expansion used to approximate the solution over the cross-section of the beam model, and M is the number of terms in the expansion. Whatever is the problem considered, one- or two-dimensional, the functions F_τ can be assumed *a priori*. The choice of F_τ depends on the structural model to be used in the analysis. The function u_τ is the unknown of the structural problem. The solution of the problem can be obtained introducing the FE model. Therefore the domain is discretized in a finite number of elements where the solution is approximated using the shape functions, N_i . The generic displacement field can be written as:

$$\mathbf{u} = \mathbf{u}_{i\tau}N_iF_\tau, \quad \tau = 1 \dots M; \quad i = 1 \dots N_n. \quad (5)$$

Where the index i comes from the FE model and the index τ comes from the kinematics used in the structural model approximation. N_n is the number of nodes in the finite element. $\mathbf{u}_{i\tau}$ is the coefficient of

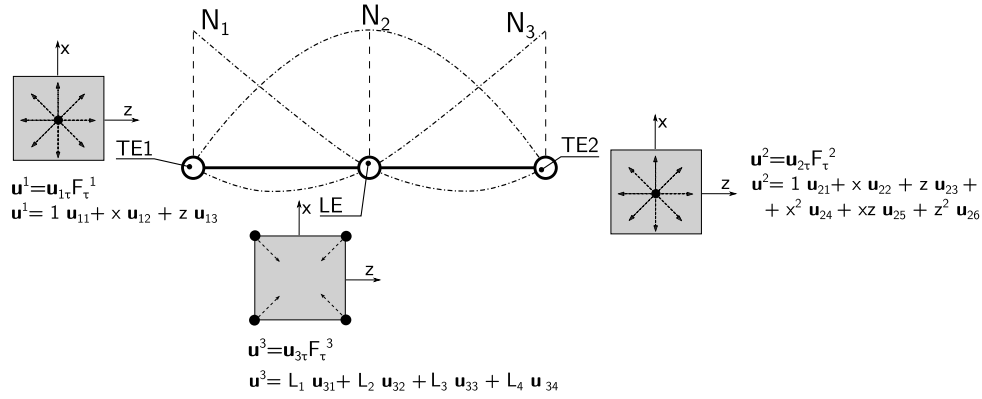


Figure 1: A three-node one-dimensional element with node-dependent kinematics.

the expansion and it is also the unknown of the problem. The indicial form showed in Equation (5) is common for all the structural models, the choice of N_i and F_τ makes the difference:

$$3D \longrightarrow \mathbf{u} = \mathbf{u}_i N_i^{3D}(x, y, z) \cdot 1 \quad (6)$$

$$2D \longrightarrow \mathbf{u} = \mathbf{u}_{i\tau} N_i^{2D}(x, y) F_\tau^{1D}(z) \quad (7)$$

$$1D \longrightarrow \mathbf{u} = \mathbf{u}_{i\tau} N_i^{1D}(y) F_\tau^{2D}(x, z) \quad (8)$$

Where N_i^{2D} and N_i^{1D} are the FEM shape functions of the two- and one-dimensional model respectively, while F_τ^{1D} and F_τ^{2D} are the expansion used thorough-the-thickness of the two-dimensional element or over the cross-section of the one dimensional model. The choice of F_τ depends on the structural model used. In the following sections are reported the kinematic assumptions used in the present paper for the one- and two-dimensional model while the three-dimensional model does not require any approximation other than the FEM. In the case of node-dependent kinematics models, NDK, each node of the FEM discretization can assume a different kinematic, see Figure 1.

The displacement field of an element with node-dependent kinematics can be written including two main novelties:

$$F_\tau(x, z) \longrightarrow F_\tau^i(x, z) \quad (9)$$

$$M \longrightarrow M^i \quad (10)$$

The first equation, Eq. 9, states that the function expansion is not a property of the element, but of the nodes, that is, the index i is included in the notation. Eq. 10 remarks that the number of terms in the expansion, M , can be different at each node, and the notation M^i is used to underline this aspect. The generic displacement field can be written as:

$$3D \longrightarrow \mathbf{u} = \mathbf{u}_i N_i^{3D}(x, y, z) \cdot 1, \quad i = 1 \dots N_n. \quad (11)$$

$$2D \longrightarrow \mathbf{u} = \mathbf{u}_{i\tau} N_i^{2D}(x, y) F_\tau^{i,1D}(z), \quad \tau = 1 \dots M^i; \quad i = 1 \dots N_n. \quad (12)$$

$$1D \longrightarrow \mathbf{u} = \mathbf{u}_{i\tau} N_i^{1D}(y) F_\tau^{i,2D}(x, z), \quad \tau = 1 \dots M^i; \quad i = 1 \dots N_n. \quad (13)$$

3 MULTI-DIMENSIONAL MODELS

The assembly of multidimensional models required to impose the displacement continuity at the interface. In this work the capabilities of Lagrange models have been exploited to easily connect models

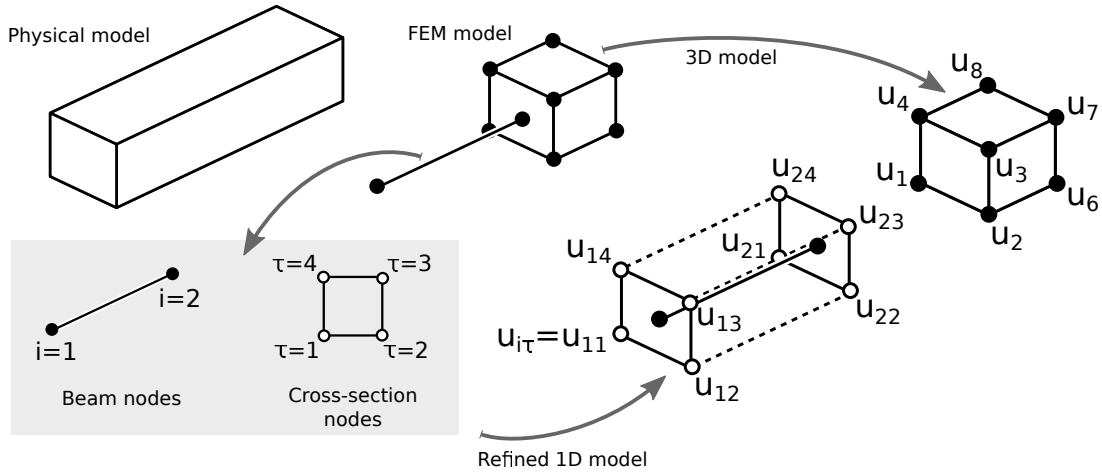


Figure 2: Example of a multi-dimensional model: connection between a beam and a solid elements.

with incompatible kinematics. When Lagrange models are used, does not matter if a one-, two- or three-dimensional model is considered, the unknown vector contains only pure displacements and the electric potential as unknown. This property make it possible to connect plate, beam and solid elements without any ad hoc technique.

3.1 The assembling procedure

To explain the assembling procedure, the simple configuration shown in Figure 2 is considered. A prismatic structure has to be modelled with a beam and a solid element. The beam uses a four node Lagrange element over the cross-section and a two node beam element along the axis. Figure 2 shows that the refined beam model has four node in each cross-section where the displacements are the unknown, u_{11} to u_{14} in the section on the first axial node and u_{21} to u_{24} in the second node. At the same time, the solid element has eight nodes in which the displacements have to be defined. Since both models have the same unknowns, the imposition of compatibility between the shared nodes is straightforward:

$$\mathbf{u}_{21} = \mathbf{u}_1, \quad \mathbf{u}_{22} = \mathbf{u}_2, \quad \mathbf{u}_{23} = \mathbf{u}_3, \quad \mathbf{u}_{24} = \mathbf{u}_4; \quad (14)$$

The conditions shown in Equation 14 can be used during the assembly procedure to identify the nodes that have to be connected. The matrices of the two elements can be used to build the global matrix of the whole structure simply summing the contributions of the shared nodes.

3.2 Governing Equations

The governing equations can be derived by applying the principle of virtual displacement (PVD). Consider the energy of the system:

$$\delta L_{int} = \int_V \delta \bar{\mathbf{\epsilon}}^T \bar{\boldsymbol{\sigma}} dV = \delta L_{ext} \quad (15)$$

where V is the volume of the integration domain, and δL_{int} is the internal energy and δL_{ext} is the external work. $\bar{\boldsymbol{\epsilon}}$ and $\bar{\boldsymbol{\sigma}}$ are the generalized strain and tress vectors that include both the mechanical and the electrical quantities. By considering the geometrical relations, constitutive equations, end the generic displacement field, the internal work can be written as:

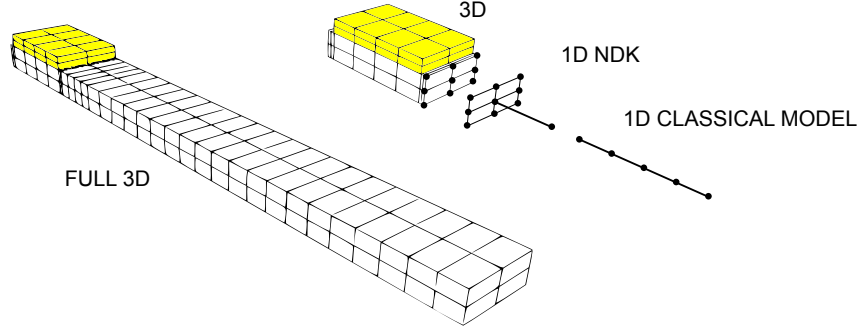


Figure 3: Example of a global-local modeling of a beam with a piezo-patch.

$$\delta L_{int} = \delta \mathbf{q}_{js} \int_V N_j F_s^j \mathbf{D}^T \tilde{\mathbf{H}} \mathbf{D} F_\tau^i N_i dV \mathbf{q}_{i\tau} \quad (16)$$

In a compact form, the above expression can be written as:

$$\delta L_{int} = \delta \mathbf{q}_{js}^T \mathbf{k}_{ij\tau s} \mathbf{q}_{i\tau} \quad (17)$$

where $\mathbf{k}_{ij\tau s}$ represents the electromechanical *fundamental nuclei* (FNs), which is a core unit of the generalized stiffness matrix:

$$\mathbf{k}_{ij\tau s} = \int_V N_j F_s^j \mathbf{D}^T \tilde{\mathbf{H}} \mathbf{D} F_\tau^i N_i dV \quad (18)$$

Actually, $\mathbf{k}_{ij\tau s}$ can be further written as:

$$\mathbf{k}_{ij\tau s} = \begin{bmatrix} \mathbf{k}^{uu} & \mathbf{k}^{u\phi} \\ \mathbf{k}^{\phi u} & \mathbf{k}^{\phi\phi} \end{bmatrix}_{ij\tau s} \quad (19)$$

in which the mechanical stiffness FN \mathbf{k}^{uu} is a 3×3 matrix, while the electromechanical coupling FNs $\mathbf{k}^{u\phi}$ and $\mathbf{k}^{\phi u}$ are 3×1 and 1×3 , respectively. The dimension of the pure electric part $\mathbf{k}^{\phi\phi}$ is 1×1 .

3.3 Global-local models for layered smart structures

The capability to build multidimensional models, as well as, the possibility to vary the kinematic within the same element make it possible to derive efficient global-local approaches. The present work proposes to use the NDK approach to refine the kinematic where required and to impose a compatible kinematic at the interface between elements with different dimensions. A cantilevered beam with a piezo-patch is considered as an example. Figure 3 shows two different modeling approach. The first uses a full three-dimensional model that ensure a high-fidelity solution but could require a large computational cost. The second approach aims to preserve the three-dimensional model accuracy in the patch area but, through the 1D NDK element, allows classical beam elements to be used for the substrate where the patch is not present.

4 NUMERICAL RESULTS

A simple beam clamped at both the ends has been considered to assess the present approach. The geometry is reported in Fig. 4. The substrate is built in aluminum while the piezoceramic material PZT-H5 has been used for the patch. Three different modeling approaches have been used. The first approach

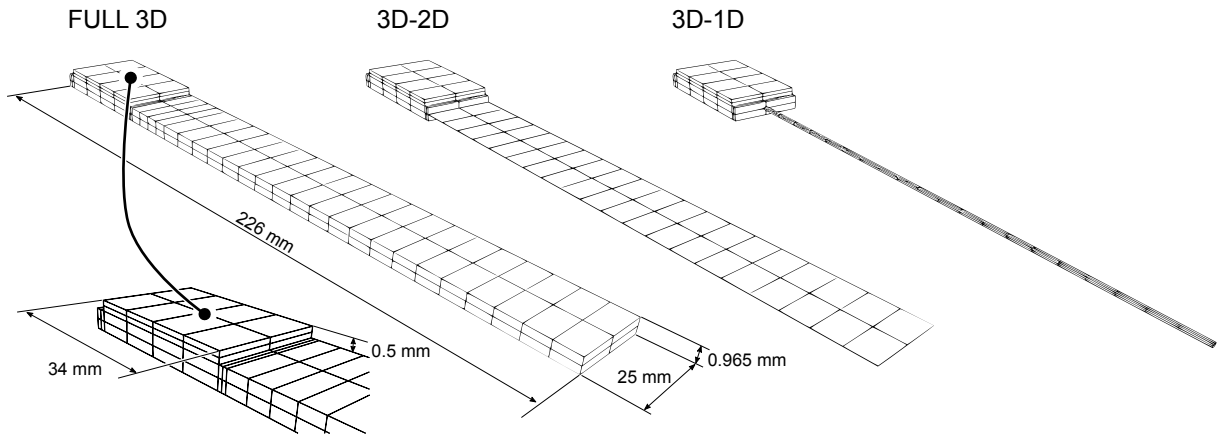


Figure 4: Geometry and models description.

Model	$u_z \times 10^{-6}$ [m]	DOFs	$\Delta u_z(\%)$
Full 3D	1.919	1026	-
3D-2D	1.923	858	0.21
3D-1D	1.923	618	0.21

Table 1: Vertical displacement at the beam mid-span.

considers a full three-dimensional model. The second approach uses a three-dimensional model in the patch area and a plate model elsewhere, a FSDT model has been considered. The third model beams, based on a Taylor expansion of the first order, instead plate elements in the area where the patch is not applied. The deflection due to a potential of 5V applied to the patch has been evaluated.

Table 1 reports the displacements at the mid-span of the beam. It can be seen that the models that used plate and beam elements are able to reproduce the three-dimensional solution. The use of a global-local approach leads to a reduction of the computational costs and, in the case of the $3D - 1D$ model, 618 DOFs are required instead 1026, that is a reduction of the 40% is guaranteed.

Figure 5 report the maps of the vertical displacement field for all the three models considered.

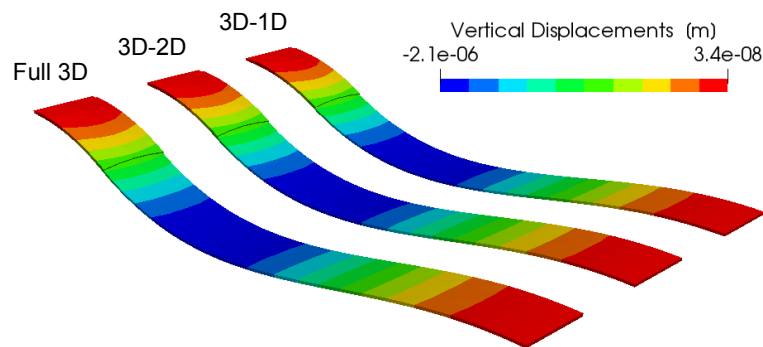


Figure 5: Vertical displacement evaluated with the three models.

5 CONCLUSIONS

The present paper presents an innovative approach in the global-local analysis of layered smart structures. The capabilities of the node-dependent kinematic models, developed in the framework of the Carrera Unified Formulation, have been successfully exploited to connect classical 1D and 2D structural models to 3D models. The approach has been assessed considering a beam under the action of a piezopatch. The results obtained with the present global-local approach can be considered as accurate as the full-three-dimensional solution but a significant reduction in the computational cost has been obtained. The use of the present approach does not require any ad hoc connection technique and ensures a continuous displacement field even in the transition zone. The present approach could find future applications in the design of smart devices such as energy harvester, sensors or MEMS.

REFERENCES

- [1] Henno Allik and Thomas JR Hughes. Finite element method for piezoelectric vibration. *International journal for numerical methods in engineering*, 2(2):151–157, 1970.
- [2] RC Batra and XQ Liang. Finite dynamic deformations of smart structures. *Computational mechanics*, 20(5):427–438, 1997.
- [3] E. Carrera, M. Cinefra, M. Petrolo, and E. Zappino. *Finite element analysis of structures through unified formulation*. John Wiley & Sons, 2014.
- [4] E. Carrera and E. Zappino. Carrera Unified Formulation for free-vibration analysis of aircraft structures. *AIAA Journal*, 54:280–292, 2016. doi: 10.2514/1.J054265.
- [5] E. Carrera and E. Zappino. One-dimensional finite element formulation with node-dependent kinematics. *Computers and Structures*, 192:114–125, 2017. doi: 10.1016/j.compstruc.2017.07.008.
- [6] E. Carrera, E. Zappino, and G. Li. Analysis of beams with piezo-patches by node-dependent kinematic finite element method models. *Journal of Intelligent Material Systems and Structures*, 29(7):1379–1393, 2018. doi: 10.1177/1045389X17733332.
- [7] W.F. Cofer and K.M. Will. A three-dimensional, shell-solid transition element for general nonlinear analysis. *Computers and Structures*, 38(4), 1991.
- [8] E. Garusi and A. Tralli. A hybrid stress-assumed transition element for solid-to-beam and plate-to-beam connections. *Computers and Structures*, 80(2):105–115, 2002.
- [9] T. C. Gmür and R. H. Kauten. Three-dimensional solid-to-beam transition elements for structural dynamics analysis. *International Journal for Numerical Methods in Engineering*, 36(9):1429–1444, may 1993.
- [10] T. C. Gmür and A. M. Schorderet. A set of three-dimensional solid to shell transition elements for structural dynamics. *Computers and Structures*, 46(4), 1993.
- [11] J. Kim, VV.V. Varadan, and V.K. Varadan. Finite element modelling of structures including piezoelectric active devices. 832(May 1995):817–832, 1997.
- [12] C. L. Liao, J. N. Reddy, and S. P. Engelstad. A solid-shell transition element for geometrically nonlinear analysis of laminated composite structures. *International Journal for Numerical Methods in Engineering*, 26(8):1843–1854, aug 1988.

- [13] R. W. McCune, C. G. Armstrong, and D. J. Robinson. Mixed-dimensional coupling in Finite element models. *International Journal for Numerical Methods in Engineering*, 49(6):725–750, 2000.
- [14] D. J. Monaghan, Ian W. Doherty, D. Mc Court, and C. G. Armstrong. Coupling 1D Beams to 3D Bodies. In *7th International Meshing Roundtable, Sandia National Laboratories*, pages 285–293, 1998.
- [15] K. S. Surana. Transition finite elements for threedimensional stress analysis. *International Journal for Numerical Methods in Engineering*, 15(7), 1980.
- [16] K. S. Surana. Geometrically non-linear formulation for the three dimensional solid-shell transition finite elements. *Computers and Structures*, 15(5), 1982.
- [17] E. Zappino and E. Carrera. Multidimensional model for the stress analysis of reinforced shell structures. *AIAA Journal*, 56(4):1647–1661, 2018. doi: 10.2514/1.J056384.

OPTIMIZATION OF PIEZOELECTRIC PATCHES WITH PASSIVE SHUNTED DAMPING FOR NOISE REDUCTION IN SANDWICH PANELS

Aurélio L. Araújo^{*}, José F.A. Madeira^{†*}

[†] IDMEC, Instituto Superior Técnico
Universidade de Lisboa

Av. Rovisco Pais, 1049-001 Lisboa, Portugal

e-mail: aurelio.araujo@tecnico.ulisboa.pt - Web page: <http://www.idmec.ist.utl.pt/>

^{*} ADM, ISEL

Instituto Politécnico de Lisboa

Rua Conselheiro Emídio Navarro 1, 1959-007 Lisboa, Portugal

e-mail: aguilmadeira@tecnico.ulisboa.pt - Web page: <http://www.isel.pt/>

Key words: Sandwich Panels, Piezoelectric Patches, Shunt damping, Viscoelasticity, Multiobjective Optimization

Abstract. This paper addresses the issue of vibration and noise reduction in laminated sandwich plates using piezoelectric patches with passive shunted damping. A finite element implementation of a laminated sandwich plate with viscoelastic core and surface bonded piezoelectric patches is used to obtain the frequency response of the panels. The sound transmission characteristics of the panels are evaluated by computing their radiated sound power using the Rayleigh integral method. RL (Resistor and Inductor) shunt damping circuits are used to add damping to the sandwich panels. The optimal location of the surface bonded piezoelectric patches is then obtained, along with the RL circuits resistance and inductance, using Direct MultiSearch (DMS) optimization to minimize added weight, number of patches and noise radiation. Trade-off Pareto optimal fronts and the respective optimal patch configurations are obtained.

1 INTRODUCTION

The generalized introduction of lightweight composites in the automotive and aerospace industries, while leading to significant weight reductions and associated fuel savings, pose a serious problem of low acoustic performance when these structures are subjected to mechanical or acoustic excitations. Passive damping technologies are nowadays frequently used to control sound and vibration levels through the use of viscoelastic materials, while active devices such as surface bonded piezoelectric patches can also be effectively used to control these undesired sound and vibration levels in lightweight composite structures. Sandwich composite panels may represent an optimized solution for both sound radiation and structural vibration for most frequency ranges. Viscoelastic materials are an efficient way of reducing structural vibrations and providing noise attenuation, which allied to piezoelectric elements may lead to broader damping capabilities regarding acoustic emissions.

The open literature regarding the subject of vibration and sound radiation from passive or active composite and sandwich structures is quite scarce. Regarding the vibration control using passive tech-

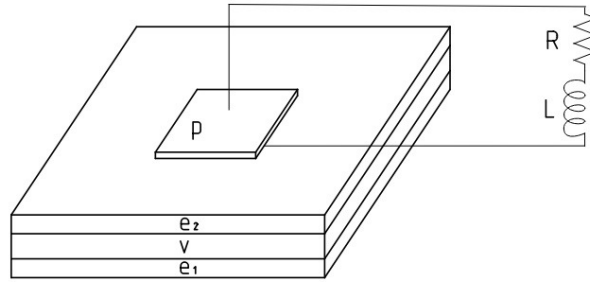


Figure 1: The sandwich plate with the piezoelectric patch and associated RL circuit

nologies, previous works have been presented for mechanical vibration suppression [1] and sound level attenuation [2–5]. The vibroacoustic problem has been recently addressed by Larbi et al. in smart piezoelectric composite and sandwich plates [6, 7] and also in double-wall sandwich panels [8].

In the present work we apply a layerwise sandwich finite element model, previously developed by the authors [9], with frequency dependent viscoelastic core, composite laminated skin layers and piezoelectric patches with associated RL circuits. The model is used to calculate the frequency response of sandwich panels and the structural results from the model are then used to calculate the radiated sound power of the panel.

In this paper we present a multiobjective approach for the optimal distribution of surface bonded piezoelectric patches in composite laminated panels. The objective is to obtain designs that simultaneously minimize weight and maximize damping using the minimum number of RL circuits. A topological optimization approach is used along with the DMS (Direct MultiSearch) solver. DMS [10] is a solver for multiobjective optimization problems which does not use any derivatives of the objective functions. It is based on a novel technique called direct multisearch, developed by extending direct search from single to multiobjective optimization. It was recently used to solve the problem of minimum weight and maximum damping of a viscoelastic sandwich plate [11], simultaneously minimizing weight and material cost and maximizing modal damping [12] and to find the optimal positioning of surface bonded piezoelectric sensors and actuators for active damping maximization in a given frequency range [13]. An application to a clamped rectangular sandwich panel is described and some Pareto front solutions are analyzed.

2 SANDWICH PLATE MODEL

The *layerwise* sandwich finite element model is briefly described here, to analyze sandwich laminated plates with a viscoelastic (v) core, two composite laminated face layers (e_1 , e_2) and piezoelectric patch or layer (p) bonded to the top outer surface of the plate (Figure 1).

The basic assumptions in the development of the sandwich plate model are: The origin of the z axis is the medium plane of the core layer; No slip occurs at the interfaces between layers; The displacement is C^0 along the interfaces; Elastic and piezoelectric layers are modeled with first order shear deformation theory (FSDT) and viscoelastic core with a higher order shear deformation theory (HSDT); All materials are linear, homogeneous and orthotropic and the elastic layers (e_1) and (e_2) are made of laminated com-

posite materials; For the viscoelastic core, material properties are complex and frequency dependent; The top piezoelectric layer has an RL circuit attached to its top and bottom electroded surfaces, consisting of a resistance and an inductor in series (Figure 1).

After enforcing displacement continuity at the layer interfaces we retain 17 mechanical unknowns. For more details on the model and its validation, the reader is directed to [9].

2.1 Constitutive relations

We consider that fibre-reinforced laminae in elastic multi-layers (e_1) and (e_2), viscoelastic core (v), and piezoelectric (p) layer are characterized as orthotropic. However, due to the different nature of the displacement fields in the face layers and in the core, the constitutive relations are going to be different.

For the laminas in the elastic laminated face layers or in the piezoelectric layer, constitutive equations for each lamina may be expressed in the principal material directions, assuming zero transverse normal stress as in [14].

For the viscoelastic core, a full 3D orthotropic stiffness matrix is used in the principal material directions [15] and the stiffness coefficients are complex quantities, since the complex modulus approach was used in this work, using the elastic-viscoelastic correspondence principle [16].

2.2 Finite element formulation

The equations of motion for the plate are obtained by applying the extended Hamilton's principle, the solution of which was obtained through the finite element method, using an eight node serendipity element with 17 mechanical degrees of freedom per node, and one electric potential degree of freedom per piezoelectric layer. The system equilibrium equations are obtained in the usual way through assembly of the element equations, yielding:

$$\begin{bmatrix} \mathbf{M}_{uu} & \mathbf{0} \\ \mathbf{0} & \mathbf{0} \end{bmatrix} \begin{bmatrix} \ddot{\mathbf{u}} \\ \ddot{\phi} \end{bmatrix} + \begin{bmatrix} \mathbf{K}_{uu} & \mathbf{K}_{u\phi} \\ \mathbf{K}_{u\phi}^T & \mathbf{K}_{\phi\phi} \end{bmatrix} \begin{bmatrix} \mathbf{u} \\ \phi \end{bmatrix} = \begin{bmatrix} \mathbf{F}_t \\ \mathbf{Q}_t \end{bmatrix} \quad (1)$$

where \mathbf{u} , $\ddot{\mathbf{u}}$, ϕ and $\ddot{\phi}$ are mechanical degrees of freedom and corresponding accelerations, electric potential and corresponding second time derivatives, respectively. \mathbf{M}_{uu} and \mathbf{K}_{uu} are the mass and complex stiffness matrices, respectively, corresponding to purely mechanical behavior, while $\mathbf{K}_{\phi\phi}$ is the dielectric stiffness matrix, $\mathbf{K}_{u\phi}$ is the stiffness matrix that corresponds to the coupling between the mechanical and the piezoelectric effects, \mathbf{F}_t is the externally applied mechanical load vector, and \mathbf{Q}_t is the electrical charge vector, both in the time domain.

The electric potential difference ϕ_i across the electrodes of the piezoelectric patch i can be related to the the resistance R_i and inductor L_i values as:

$$\phi_i = -R_i \dot{Q}_i - L_i \ddot{Q}_i \quad (2)$$

where \dot{Q}_i and \ddot{Q}_i are the first and second time derivatives of the surface charge Q_i of patch i , respectively. Assuming harmonic vibrations, this relation can be written for all the potential degrees of freedom of all np patches in vector form as:

$$\phi = -\mathbf{G}\mathbf{Q} \quad (3)$$

where \mathbf{Q} is the vector of charge amplitudes and G is a diagonal matrix:

$$\mathbf{G} = \begin{bmatrix} j\omega R_1 - \omega^2 L_1 & 0 & \cdots & 0 \\ 0 & j\omega R_2 - \omega^2 L_2 & \cdots & 0 \\ \vdots & \vdots & \ddots & \vdots \\ 0 & 0 & \cdots & j\omega R_{np} - \omega^2 L_{np} \end{bmatrix} \quad (4)$$

where j is the imaginary unit.

By condensing the degrees of freedom of electric potential in the system equilibrium equations (1) and using equation (3), the final equilibrium equation, assuming harmonic vibrations, can be written as:

$$[\mathbf{K}^*(\omega) - \omega^2 \mathbf{M}_{uu}] \mathbf{U} = \mathbf{F} \quad (5)$$

where the condensed stiffness matrix is given by:

$$\mathbf{K}^*(\omega) = \mathbf{K}_{uu}(\omega) - \mathbf{K}_{u\phi} \mathbf{G} [\mathbf{I} + \mathbf{K}_{\phi\phi} \mathbf{G}]^{-1} \mathbf{K}_{u\phi}^T \quad (6)$$

where $\mathbf{K}_{uu}(\omega)$ is a complex matrix, \mathbf{I} is the identity matrix, and \mathbf{U} and \mathbf{F} are the vectors of the amplitudes of displacement and applied mechanical force, respectively.

It is worthwhile noting that when electroded surfaces exist in a given patch or layer, equipotential conditions should be imposed before condensing the electric degrees of freedom.

The forced vibration problem is solved in the frequency domain, which implies the solution of the following linear system of equations for each frequency point:

$$[\mathbf{K}^*(\omega) - \omega^2 \mathbf{M}_{uu}] \mathbf{U}(\omega) = \mathbf{F}(\omega) \quad (7)$$

where $\mathbf{F}(\omega) = \mathcal{F}(\mathbf{F}_t(t))$ is the Fourier transform of the time domain force history $\mathbf{F}_t(t)$.

3 ACOUSTIC INDICATOR

When subjected to external excitation, the sandwich plate radiates noise into the surrounding acoustic medium. For a light fluid, the fluid mass may be neglected and both acoustic and structural problems can be solved independently, whereas for heavy fluids the problem is more complex owing to strong acoustic radiation damping and added mass effects which may significantly change the inertia of the coupled structure. In the present work we are concerned mainly with radiation involving light fluids such as air. Hence, the fluid loading is neglected in the present approach, and in order to evaluate the acoustic performance of the active sandwich panels, the radiated sound power (Π) is the acoustic indicator chosen in this work.

The sound power that is radiated through an area S of the panel is given by:

$$\Pi = \frac{1}{2} \Re \left(\int_S p(G) v_n^*(G) dS \right) \quad (8)$$

where G is a point on the plate surface, p is the sound pressure applied as an external loading and v_n is the normal velocity. The complex conjugate is denoted by $*$ and \Re denotes the real part of the integral.

For a flat plate embedded in an infinite rigid plane baffle and radiating in a semi infinite fluid, the pressure p can be obtained using the Rayleigh Integral [17]:

$$p(\omega, M) = \rho_0 \frac{i\omega}{2\pi} \int_S v_n(\omega, G) \frac{e^{-ikr}}{r} dS \quad (9)$$

where ρ_0 is the mass density of the external acoustic domain, $k = \omega/c_0$ is the wave number, where c_0 is the speed of sound in air, M is a point inside the external acoustic domain and $v_n(\omega, G)$ is the normal velocity at point G , which is easily obtained from the finite element formulation presented in the previous sections.

In this work, the finite element method is used to obtain the normal velocity distribution, assuming a sufficient number of discrete radiating elements, according to the smallest wavelength to be observed. The transverse vibration of the plate is specified in terms of the normal velocities at the center positions of each one of the rectangular finite elements in the mesh. We assume that the dimensions of these elements are small when compared to the structural and acoustic wavelengths, so that the total radiated sound power in Equation (8) can be expressed as the sum of the powers radiated by each element:

$$\Pi = \frac{S_e}{2} \Re(\mathbf{v}_n^H \mathbf{p}) \quad (10)$$

where the superscript H denotes the hermitian transpose, \mathbf{v}_n and \mathbf{p} are the vectors of complex amplitudes of the normal velocity and acoustic pressure in all elements, respectively, and S_e is the area of each element. The pressure on each element is generated by the vibrations of all elements of the panel. The vector of sound pressure can therefore be obtained using the impedance matrix:

$$\mathbf{p} = \mathbf{Z} \mathbf{v}_n \quad (11)$$

where \mathbf{Z} is the (symmetric) impedance matrix with components $Z_{ij} = (i\omega\rho_0 S_e / 2\pi r_{ij}) e^{-ikr_{ij}}$ and r_{ij} is the distance between the centers of elements i and j . Substituting Equation (11) in Equation (10), we obtain:

$$\Pi = \frac{S_e}{2} \Re(\mathbf{v}_n^H \mathbf{Z} \mathbf{v}_n) = \frac{S_e}{4} \Re(\mathbf{v}_n^H [\mathbf{Z} + \mathbf{Z}^H] \mathbf{v}_n) = \mathbf{v}_n^H \mathbf{R} \mathbf{v}_n \quad (12)$$

where \mathbf{R} is the radiation resistance matrix for the elementary radiators which is given by:

$$\mathbf{R} = \frac{\omega^2 \rho_0 S_e^2}{4\pi c_0} \begin{bmatrix} 1 & \frac{\sin(kr_{12})}{kr_{12}} & \dots & \frac{\sin(kr_{1R})}{kr_{1R}} \\ \frac{\sin(kr_{21})}{kr_{21}} & 1 & \dots & \frac{\sin(kr_{2R})}{kr_{2R}} \\ \vdots & \vdots & \ddots & \vdots \\ \frac{\sin(kr_{R1})}{kr_{R1}} & \frac{\sin(kr_{R2})}{kr_{R2}} & \dots & 1 \end{bmatrix} \quad (13)$$

This method can be applied to any plane surface in an infinite baffle, independently of the boundary conditions, as it only requires the knowledge of the surface geometry, the properties of the fluid and the normal velocity field distribution.

4 PROBLEM STATEMENT

A laminated hybrid sandwich plate is considered with a viscoelastic core described by a fractional derivative constitutive law. The plate is a 300 mm \times 200 mm laminated sandwich with all edges clamped and made of carbon fibre plies and a central isotropic viscoelastic damping material core. The stacking sequence for carbon fibre laminates is $[0^\circ/90^\circ/+45^\circ]$ for (e_1) and $[+45^\circ/90^\circ/0^\circ]$ for (e_2) . The thickness of each carbon fibre ply is 0.5 mm, and the viscoelastic core is 2.5 mm thick.

Material properties for the isotropic viscoelastic damping polymer are described by a five parameter fractional derivative constitutive model [18], where $\nu = 0.49$ and $\rho = 1300 \text{ kg/m}^3$, have been assumed here. The expression for the complex shear modulus is as follows:

$$G(j\omega) = G_0 + G_0(d-1) \frac{(j\omega\tau)^\alpha}{1 + (j\omega\tau)^\beta} \quad (14)$$

where $G_0 = 0.8$ MPa is the static shear modulus, $d = 1$, $\alpha = 0.566$, $\beta = 0.558$, and $\tau = 7.23 \times 10^{-10}$ s is the relaxation time.

For the carbon fiber plies, material properties are $E_1 = 130.8$ GPa, $E_2 = 10.6$ GPa, $G_{12} = 5.6$ GPa, $G_{13} = 4.2$ GPa, $G_{23} = 3.0$ GPa, $\nu_{12} = 0.36$, and $\rho = 1543$ kg/m³.

Surface electroded 0.9 mm thick piezoelectric patches are also bonded to the upper surface of the plate. Material properties for these piezoelectric patches are $E_1 = 50.9$ GPa, $E_2 = 46.1$ GPa, $G_{12} = 14.3$ GPa, $G_{13} = 8.0$ GPa, $G_{23} = 20.6$ GPa, $\nu_{12} = 0.29$, $\rho = 7800$ kg/m³, $e_{31}^* = -17.0$ N/Vm, $e_{32}^* = -12.2$ N/Vm, and $\epsilon_{33}^{*e} = 1.549 \times 10^{-8}$ F/m.

A 100 Pa incident pressure wave is applied at $t = 0$ to the bottom surface of the plate.

The optimization problem is defined in terms of five objectives. The first objective is to minimize the added mass of the patches $f_1 = \sum_i m_i$, where m_i is the mass associated to the patch of element i . The second objective is to minimize the number of equipotential zones f_2 at the surface of the plate. This allows for the minimization of the total number of individual RL circuits needed for each equipotential zone. In this work we also minimize simultaneously the amplitude of the response of the first three modes of vibration in the radiated sound power response curve. Thus, objectives f_3 , f_4 and f_5 correspond to the largest 3 peaks of the radiated sound power curve defined through Eq. (12).

$$\begin{aligned} \min \quad & F(x) \equiv (f_1(x), f_2(x), f_3(x), f_4(x), f_5(x))^T \\ \text{s. t.} \quad & x_i \in [x_i^l, x_i^u] \end{aligned} \quad (15)$$

Two types of design variables are defined: the patch position design variables and the design variables associated to the values of each resistance and inductor of the RL circuits. The position design variables take values of 0 or 1, where the zero value means that there is no patch and a one represents a patch at that particular element. Since DMS uses real valued design variables and our problem has discrete variables, we consider a vector of real variables in the interval $[0,1]$ with length equal to the number of elements in the mesh. If a design variable value is greater or equal to 0.5, we consider that the patch exists, otherwise the patch is not present at that particular element. Regarding the values of the resistances and inductors for each RL circuit, the resistance varies from zero to 1 M Ω in intervals of 100 Ω and the inductors vary between 0 and 1 H in intervals of 10 mH.

For the application described in this paper, symmetry conditions on the distribution of the piezoelectric patches is considered. The finite element mesh will be a 6×6 mesh with a total of 36 elements. Hence we are considering only 9 position design variables, corresponding to a quarter of symmetry.

The optimization problem is solved using Direct MultiSearch (DMS) [10] which is a solver for multiobjective optimization problems, without the use of derivatives and does not aggregate any components of the objective function. It essentially generalizes all direct-search methods of directional type from single to multiobjective optimization. DMS maintains a list of feasible non-dominated points (from which the new iterates or poll centers are chosen). The search step is optional and when included it aims at improving numerical performance. DMS tries, however, to capture the whole Pareto front from the polling procedure itself. At each iteration, the new feasible evaluated points are added to this list and the dominated ones are removed. Successful iterations correspond then to changes in the iterate list, meaning that a new feasible non-dominated point was found. Otherwise, the iteration is declared as unsuccessful.

When a point is infeasible, the components of the objective function F are not evaluated, and the values of F_Ω are set to $+\infty$. This approach allows to deal with black-box type constraints, where only

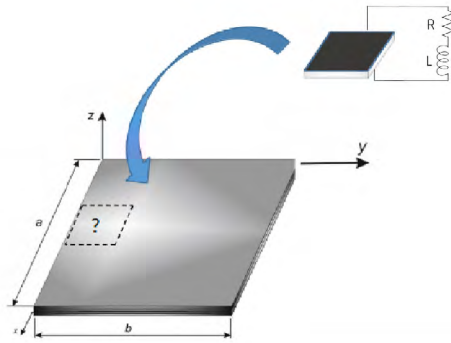


Figure 2: The problem of optimal distribution of piezoelectric patches on the sandwich laminated plate

a yes/no type of answer is returned. A number of details of the algorithm are omitted and the reader is referred to [10] for a complete description. The authors in [10] prove under the common assumptions used in direct search for single objective optimization that at least one limit point of the sequence of iterates generated by DMS lies in (a stationary form of) the Pareto front.

5 RESULTS

We present in this section some of the results obtained for the multiobjective optimization described in the previous section. There are a total of 155 nondominated solutions, from which we have retained solutions number 43, 34, 9 and 118, represented in Figure 3. Solutions 43, 34 and 9 correspond to the best possible values of objectives f_3 , f_4 and f_5 , respectively, and solution 118 is the best for the sum of f_3 , f_4 and f_5 . It should be noted that in Figure 3 the values of f_1 correspond to the number of added piezoelectric elements, which are directly proportional to the added mass and objectives f_3 to f_5 are scaled by a factor of 10^6 .

Figure 4 displays the radiated sound power curves for the three selected solutions, where the baseline curve corresponds to the sandwich plate with no added piezoelectric patches. The effect of the noise reduction can be clearly noticed from these response curves. The optimal values of the resistors and inductors for each solution can be found in Table 1.

It is worthwhile mentioning that these are preliminary results, in the sense that convergence has not yet been obtained. Further iterations of the optimization algorithm are necessary to guarantee that these solution in fact represent optimal configurations. Fully converged results will be presented at the conference.

6 CONCLUSIONS

A vibroacoustic optimization of laminated sandwich panels with surface bonded piezoelectric patches has been addressed in this paper. The radiated sound power has been calculated for a sandwich panel with a viscoelastic core and RL circuits have been used to implement the additional damping using the piezoelectric patches. The optimal location of the piezoelectric patches has been obtained for five objectives: minimum added mass, minimum number of RL circuits and minimum radiated sound power response amplitudes for the first three modes of vibration. This methodology proved to be efficient in maximizing damping over this frequency range.

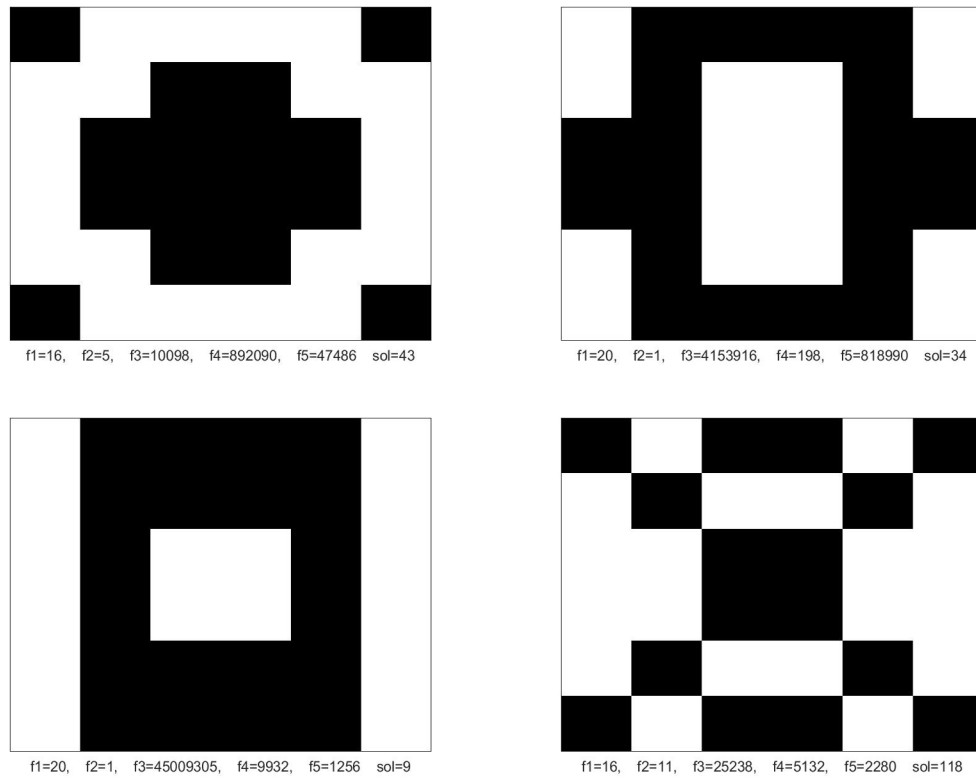


Figure 3: Nondominated solutions 43, 34, 9 and 70

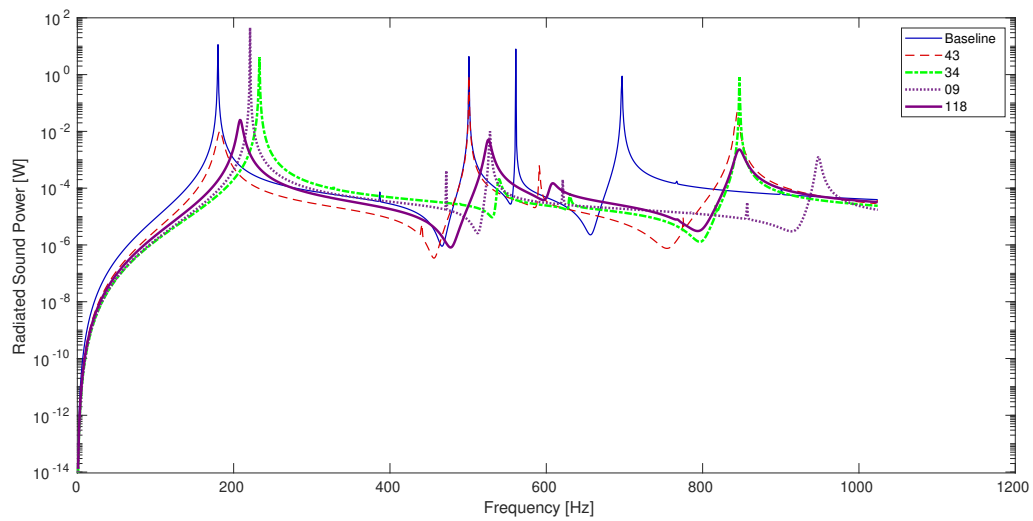


Figure 4: Radiated sound power curves for solutions number 43, 34, 9 and 118, along with the baseline solution

Table 1: Optimal values of resistance R and inductor L for each patch and for the different solutions

Solution	R [k�]	L [mH]
43	8.0	1
	8.0	1
	1.6	1
	8.0	1
	8.0	1
34	0.5	0
9	0.5	0
118	8.0	1
	8.0	1
	8.0	1
	8.0	1
	8.0	1
	8.0	1
	8.0	1
	8.0	1
	8.0	1
	8.0	1
	8.0	1

ACKNOWLEDGEMENTS

This work has been supported by National Funds through Funda  o para a Ci ncia e Tecnologia (FCT), through IDMEC, under LAETA, project UID/EMS/50022/2019.

REFERENCES

- [1] M. D. Rao. Recent applications of viscoelastic damping for noise control in automobiles and commercial airplanes. *Journal of Sound and Vibration*, 262(3):457–474, 2003.
- [2] O. Foin, J. Nicolas, and N. Atalla. An efficient tool for predicting the structural acoustic and vibration response of sandwich plates in light or heavy fluid. *Applied Acoustics*, 57(3):213–242, 1999.
- [3] S. Subramanian, R. Surampudi, K.R. Thomson, and S. Vallurupalli. Optimization of damping treatments for structure borne noise reduction. *Sound and Vibration*, 38(9):14–18, 2004.
- [4] S. Assaf, M. Guerich, and P. Cuvelier. Vibration and acoustic response of damped sandwich plates immersed in a light or heavy fluid. *Computers & Structures*, 88(13-14):870–878, 2010.
- [5] A. Lored, A. Plessy, A. El Hafidi, and N. Hamzaoui. Numerical vibroacoustic analysis of plates with constrained layer damping patches. *Journal of the Acoustical Society of America*, 129(4):1905–1918, 2011.
- [6] W. Larbi, J. F. Deu, and R. Ohayon. Finite element formulation of smart piezoelectric composite plates coupled with acoustic fluid. *Composite Structures*, 94:501–509, 2012.

- [7] W. Larbi, J. F. Deu, and R. Ohayon. Finite element reduced order model for noise and vibration reduction of double sandwich panels using shunted piezoelectric patches. *Applied Acoustics*, 108:40–49, 2016.
- [8] W. Larbi, J. F. Deu, and R. Ohayon. Vibroacoustic analysis of double-wall sandwich panels with viscoelastic core. *Computers & Structures*, 174:92–103, 2016.
- [9] A. L. Araujo, V. S. Carvalho, C. M. Mota Soares, J. Belinha, and A. J. M. Ferreira. Vibration analysis of laminated soft core sandwich plates with piezoelectric sensors and actuators. *Composite Structures*, 151:91–98, 2016.
- [10] A. L. Cust dio, J. F. A. Madeira, A. I. F. Vaz, and L. N. Vicente. Direct multisearch for multiobjective optimization. *SIAM Journal of Optimization*, 21:1109–1140, 2011.
- [11] J. F. A. Madeira, A. L. Ara jo, C. M. Mota Soares, and C. A. Mota Soares. Multiobjective optimization of viscoelastic laminated sandwich structures using the direct multisearch method. *Computers & Structures*, 147:229–235, 2015.
- [12] J. F. A. Madeira, A. L. Ara jo, C. M. Mota Soares, C.A. Mota Soares, and A. J. M. Ferreira. Multiobjective design of viscoelastic laminated composite sandwich panels. *Composites Part B*, 77:391–401, 2015.
- [13] A. L. Ara jo, J. F. A. Madeira, C. M. Mota Soares, and C. A. Mota Soares. Optimal design for active damping in sandwich structures using the direct multisearch method. *Composite Structures*, 105:29–34, 2013.
- [14] A. L. Ara jo, H. M. R. Lopes, M. A. P. Vaz, C. M. Mota Soares, J. Herskovits, and P. Pedersen. Parameter estimation in active plate structures. *Computers & Structures*, 84:1471–1479, 2006.
- [15] J. N. Reddy. *Mechanics of Laminated Composite Plates and Shells: Theory and Analysis*. CRC Press, Boca Raton, 2nd edition, 2004.
- [16] R. M. Christensen. *Theory of Viscoelasticity*. Academic Press, New York, 2nd edition, 1982.
- [17] F. Fahy and P. Gardonio. *Sound and Structural Vibration: Radiation, Transmission and Response*. Academic Press, 2nd edition, 2006.
- [18] T. Pritz. Five-parameter fractional derivative model for polymeric damping materials. *Journal of Sound and Vibration*, 265:935–952, 2003.

REAL-TIME MONITORING OF THE INFUSION PROCESS OF A POLYMER-MATRIX COMPOSITE WITH AN EMBEDDED PIEZOELECTRIC TRANSDUCER

CORENTIN TULOUP^{*}, WALID HARIZI^{*}, ZOHEIR ABOURA^{*} AND YANN MEYER^{*†}

^{*} Département Ingénierie Mécanique, Laboratoire Roberval FRE UTC-CNRS 2012

Sorbonne Universités – Université de Technologie de Compiègne

Centre de Recherches de Royallieu - CS 60319 – 60203 Compiègne Cedex FRANCE

e-mail: corentin.tuloup@utc.fr

[†] : Univ. Bourgogne Franche-Comté - UTBM

90010 Belfort Cedex FRANCE

e-mail: yann.meyer@utbm.fr

Key words: Polymer-Matrix Composite, Process Monitoring, In-situ Piezoelectric transducer, Liquid Resin Infusion, Smart Materials.

Abstract. This article investigates the Liquid Resin Infusion (LRI) manufacturing of glass fiber/polyester composite plates embedding a thin piezoelectric (PZT) disk. The real-time in-situ Process Monitoring (PM) of this technique is performed using the electrical capacitance signature of the embedded PZT transducer. To help with the understanding of capacitance variations, an internal/external multi-instrumentation (Infrared Thermography, thermocouples, Acoustic Emission, Z-displacement sensing, pressure sensing) was set on the infusion systems, so that it was possible to make couplings between the various obtained measurements and the PZT capacitance curves. Rheological tests were also performed on resin samples to find correlations between the matrix chemo-physical transitions during curing and PZT capacitance inflections during its final decrease. It was shown that the PZT capacitance is sensitive to several key moments of the infusion process, such as the end of preform impregnation, the isolation of the system at the end of resin injection, and the different resin curing stages such as gelation and vitrification. It is therefore a cheap and quite powerful in-situ Non-Destructive Testing device for the PM of the LRI manufacturing.

1 INTRODUCTION

In the Polymer-Matrix Composite (PMC) materials industry, the parameters of Liquid Composite Moulding (LCM) manufacturing processes such as mould filling rate, fiber impregnation quality, resin curing kinetics or internal temperature gradients are relatively difficult to evaluate, especially in real time. Knowledge of these parameters can be of great help in order to optimize these processes and thus obtain parts having better mechanical properties and good dimensional tolerances. Various research teams have already undertaken the study and control of these parameters, called “Process Monitoring” (PM), ([1] - [5]). However, there

is still little work on PM using Non Destructive Testing (NDT) techniques, the latter being mainly used for monitoring the life in service of composite structures already manufactured ([6] - [8]). Current contributions to the PM of PMC by NDT use a variety of techniques, both internal and external. External (or ex-situ) techniques, which are more common, may involve the use of pressure sensors [9], thermocouples [10], electrical measurements ([11] - [13]) or ultrasound ([14] - [17]). In-situ techniques, on the other hand, allow the measurement to take place at the heart of the part being manufactured, by inserting the NDT system inside the composite. It is thus possible to integrate them with optical fibers ([18], [19]), piezoresistive systems ([20], [21]) or also dielectric analysis sensors (DEA) ([18], [22]).

In the continuity of the works related to in-situ PM of PMC, this paper focuses on the insertion of a thin piezoceramic disk (PZT) inside a fiberglass / polyester matrix composite plate realized by infusion, with the objective of real-time follow-up of this process thanks to the PZT electrical capacitance information. To understand the evolution of this capacitance during manufacturing, a multi-instrumentation with both internal (2 thermocouples) and external (1 infrared camera, 4 acoustic emission sensors, 1 pressure sensor and 2 vertical displacement sensors) NDT systems is set around the infusion system, allowing to highlight the potential multi-physical couplings existing between these data and those provided by the PZT. The sensitivity of the PZT to the state transitions of the resin during its curing was also investigated using oscillatory rheology tests performed aside on the polyester resin alone. The details of the experiments are explained in the next section.

2 MATERIAL AND METHODS

PZT discs (Wealthland - China) of 25mm diameter and 0.135mm thickness were used for this study. Their static capacitance was measured and compared to the manufacturer's information before integration into the fibrous preform consisting of 6 fiberglass (twill weave 2/2) plies of dimensions 150 * 150mm², as shown in Figure 1. The wiring of the PZT is made using tinned copper wires with a diameter of 210µm.

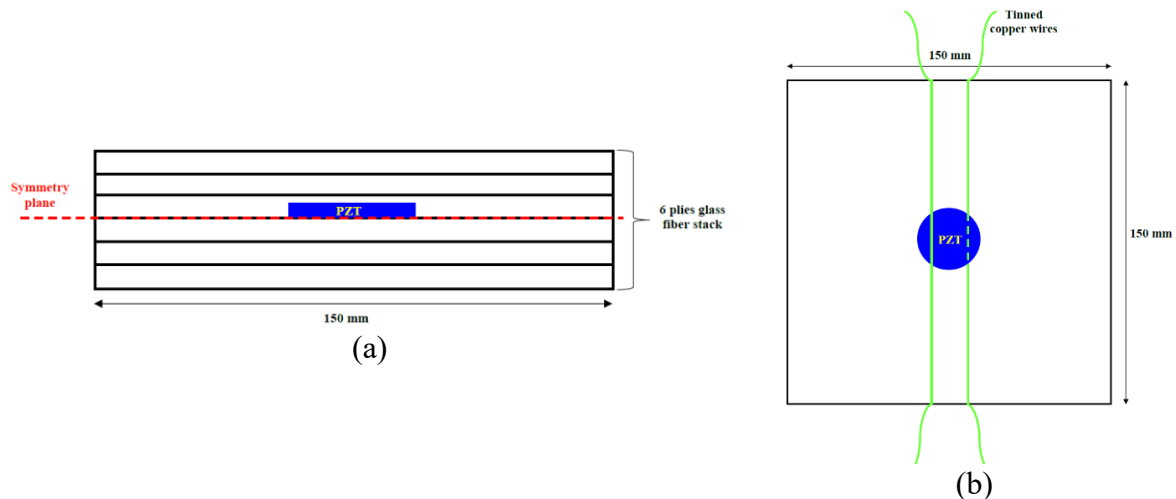


Figure 1: (a) PZT location inside the fiber stack, (b) Wiring of the PZT

The infusion is then performed at room temperature using an unsaturated polyester resin mixed at fixed concentration (1% wt) with a Methyl Ethyl Ketone Peroxide (MEKP) type hardener. During infusion, both internal and external multi-instrumentation is used to retrieve real-time information on the manufacturing process. This multi-instrumentation composed of 1 infrared thermography (IRT) camera, 4 acoustic emission (AE) sensors, 1 pressure sensor, 2 vertical displacement sensors (LVDT) and 2 thermocouples (1 at the heart of the preform, 1 on its surface) is shown schematically in Figure 2 a. A digital multimeter is used to measure the electrical capacitance of the in-situ PZT. The injection of the resin conditions the simultaneous triggering of all the instrumentations, to be able to work on the same time base. The stop of the acquisitions and the demolding of the plate are carried out 6 hours after the injection, to have the certainty of the quasi-complete curing of the resin. The complete experimental setup is presented in Figure 2 b. Three plates were made to ensure the repeatability of the experiment.

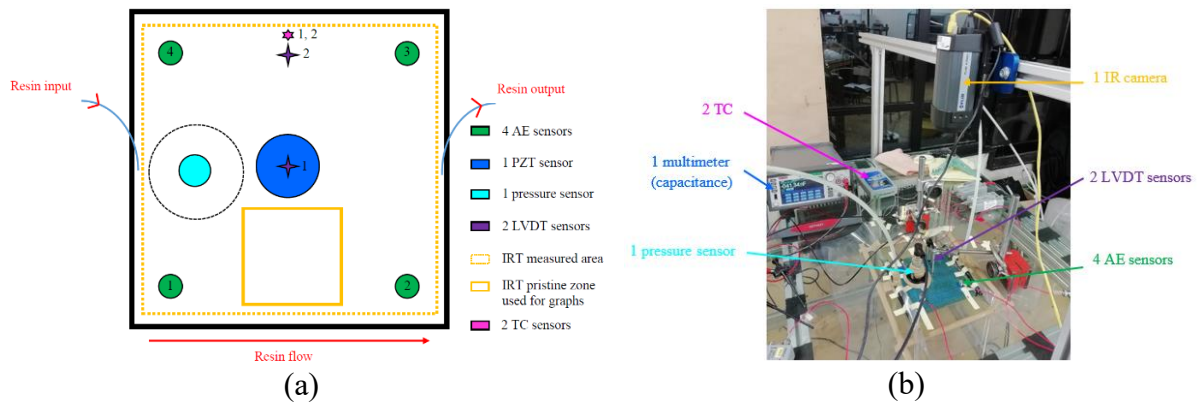


Figure 2: (a) Sketch of the multi-instrumentation system, (b) Complete setup before resin injection

The oscillatory rheology tests (3 repeatability) were carried out at room temperature on resin samples mixed with the same MEKP hardener with a concentration identical to the one used for the infused composite plates. The test consists of a dynamic shear of the mixture between two parallel planar plates held at a constant distance (1mm) from each other, at a constant shear strain $\gamma = 1\%$ and at a constant oscillation frequency $f = 1\text{Hz}$. The test is conducted until the complex viscosity modulus $|\eta^*|$ is stabilized. To be able to plot the rheology and infusion curves together and detect the potential couplings, a constant Δt was maintained between the resin + hardener mixing and the start of the test for both types of experiments.

3 RESULTS AND DISCUSSIONS

3.1 Multi-instrumented infusion: couplings between in and ex-situ signatures

Typical results obtained for the multi-instrumented infusion are shown in Figure 3 a.

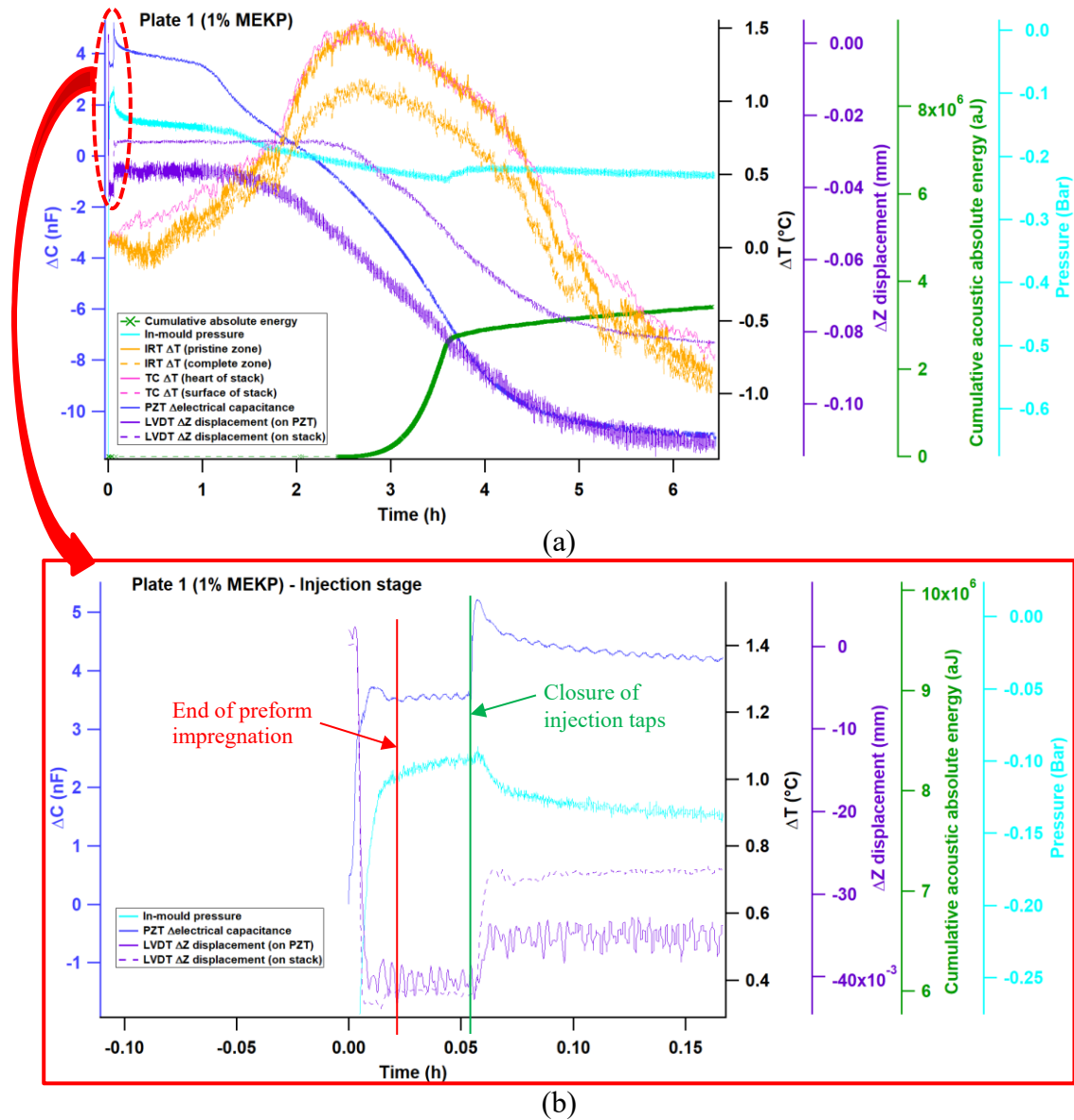


Figure 3: Results of the multi-instrumented infusion: (a) full experiment, (b) resin injection step (plate 1)

It is easy to see on Fig. 3. a) that the signatures of the TC placed at the heart of the preform and the IRT ones taken in the virgin zone of the plate are similar. It is therefore justified to trust IRT to measure thermal phenomena inside the plate, and this will be the case for the rest of this work. However, it is necessary to perform IRT measurements on a virgin zone (no instrumentation placed on it), not to disturb the camera with parasitic reflections and differences in thermal emissivity, which results in underestimated temperature measurement when it is taken on the full plate. Several couplings are observable between the various in and ex-situ signatures. The beginning of each curve appears chaotic, which corresponds to the step of resin injection into the infusion system. Figure 3 b allows highlighting the various phenomena occurring during this stage. The arrival of the resin in the preform causes a fall in the vacuum created by the vacuum pump, associated with an increase in the electrical capacitance (ΔC) of

the PZT and a descent of the LVDTs. The behavior of the capacity is explained by the progressive release of the pressure applied on the PZT by the vacuum during the impregnation of the preform [23], whereas the fall of the LVDT is due to their sliding in one of the cavities of the draining fabric positioned under the vacuum bag. A stabilization of these signatures is then observed, corresponding to the end of the impregnation of the fibrous stack (red demarcation on the Figure 3 b): a steady state begins then, during which the resin continues to flow through the preform to eliminate potential air bubbles as much as possible. The end of the injection is associated with the closing of the two resin inlet and outlet taps, which isolates the preform from the vacuum pump (green demarcation on the Figure 3 b). This results in an immediate response of the 3 signals, related to a gradual stabilization of the pressure in the isolated system: the PZT reacts to the closure (peak) and is then gradually compressed again, this reasoning going hand in hand with the reaction of the LVDTs. The rest of the manufacturing (Figure 3 a) shows new behaviors and couplings. The IRT (virgin zone) shows a progressive exothermal behavior associated with the curing of the resin, which decreases thereafter once the reaction on its end. After a plateau, the capacitance drops continuously until the end of the experiment. The beginning of this fall being associated with the rise in temperature, it is clear that the PZT is sensitive to the start of the curing of the polyester matrix. Indeed, the more a PZT is constrained in its environment (here the progressive contraction of the curing resin), the more its electrical capacitance drops [23]. The signature of the LVDTs provides information on the vertical displacement of the vacuum bag on which they are positioned: it is notable that when the resin contracts during curing, the associated shrinkage causes a negative Z-displacement of the plate, and therefore a reaction of LVDTs. However, it should be noted that LVDTs are less sensitive to the start of the crosslinking than the PZT, their fall occurring later in time than the one of ΔC . This is due to the fact that the PZT is directly surrounded by the resin, which makes its measurement much more local and sensitive than those of the LVDTs. The capacitance and LVDTs signatures appear to stabilize after the end of the exothermal peak, which means that the curing is not complete yet at the temperature peak. The AE signals are also rich in information: after some signals initially sensed corresponding to the passage of the resin front during the injection step, no signal is noticed until the exothermal peak, from which the acoustic activity reappears in the form of an increase in the cumulative absolute energy (CAE) of detected AE bursts. This behavior is associated with the variation of the physical properties of the resin during manufacturing: before the exothermal peak, the resin attenuates the acoustic signals too much so that they can be detected by the 4 AE sensors on the surface. It is necessary to wait for a sufficient degree of cure for the signals to be transmitted through the plate, which suggests that the exothermal peak / CAE rise coupling corresponds to a major state transition of the resin. The acoustic activity related to the rise of the CAE is mainly due to the vibration of the PZT, this being confirmed by the location of the corresponding AE bursts in the integration zone of the PZT (Figure 4). Two slopes are observable in the CAE curve, the transition from one to the other occurring at the beginning of the temperature decrease. Given the quasi-constancy of the second CAE regime, it is clear that at this stage the properties of the resin are stabilized, thus providing information on the end of the curing matrix curing.

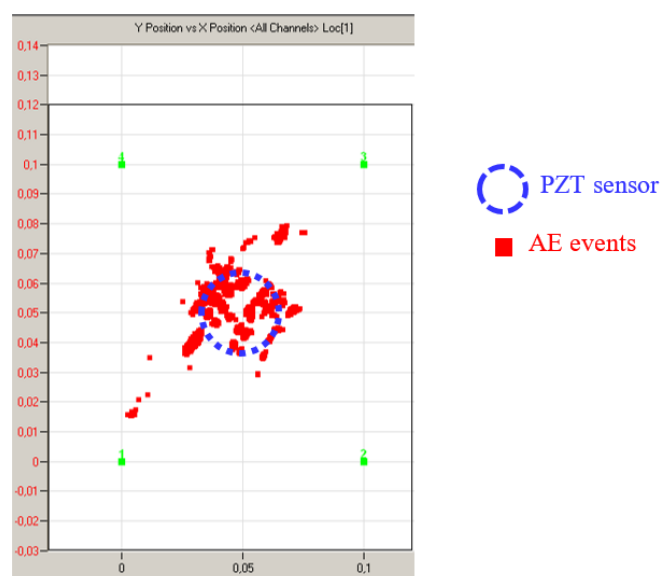


Figure 4: Location of AE events on a plate being cured (AEwin software)

The pressure variation can finally be combined with the other measurements: it follows the trend of the capacitance and LVDTs signals, thus linking the curing of the resin to a progressive depression in the infusion system. A point of interest corresponds to a not negligible increase in pressure at the end of the test, correlated with the previously described temperature drop and second EAC regime, thus confirming the existence at this stage of another transition in the resin curing.

The multi-instrumentation has shown the reaction of the PZT to the resin curing and the existence of state transitions inside it, the next part focuses on the sensitivity of the PZT to detect these transitions.

3.2 Sensitivity of the PZT to the state transitions of the curing resin

The capacitance decrease being related to the crosslinking of the polyester matrix, the study focused on the analysis of this decrease. The observation of Figure 5 reveals three regimes, separated by inflections (regime changes). The existence and the temporal appearance of these regimes and inflections being repeatable for each manufactured plate, the hypothesis was emitted that these inflections corresponded to state transitions of the resin during its curing, and that they therefore framed different chemo physical states (stable or unstable) of the resin.

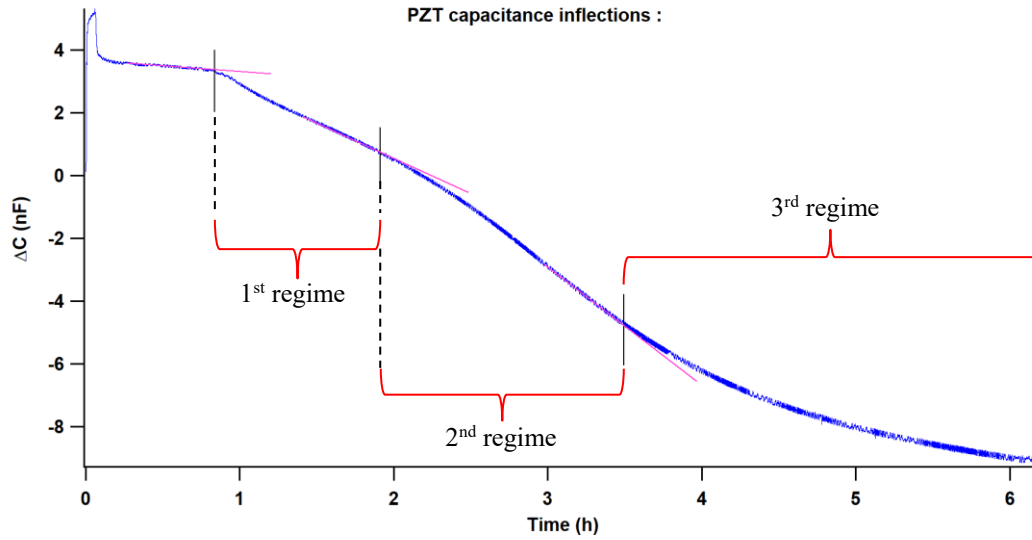


Figure 5: Methodology for the measurement of regime changes (inflections) of the PZT electrical capacitance

These inflections were subsequently correlated with the signatures coming from the multi-instrumentation for each of the manufactured plates. The first inflection had already been attributed to the start of resin curing in § 3.1. The second inflection appears just before the exothermal peak and the increase in the CAE, which confirms the hypothesis emitted earlier that a major state transition of the resin occurs at this time. The third capacity inflection occurs after the exothermal peak, following the start of the second (almost constant) growth regime of the CAE associated with the final pressure re-increase described above: it therefore corresponds to another transition state, this one leading to the near-final state of the resin (chemical reaction substantially completed). At this time, the resin is almost completely cured, which is also confirmed by the progressive stabilization of the plate retraction measured by the LVDTs.

Since strong hypotheses have been put forward on the sensitivity of the PZT to the resin curing and to the various transitions that compose it, it remains to characterize these transitions and to confirm their direct link with the inflections and regimes detected on the decay of PZT electrical capacitance. Consequently, chemo physical characterization tests of the resin alone by oscillatory rheology were undertaken. A thermoset such as the polyester resin passes through different states during its curing, the two main ones being gelation and vitrification [24]. Gelation allows the resin to change from a liquid state to a gel state, then this gel gradually hardens until it becomes a glass (vitrification stage). After the vitrification stage, the chemical reaction slows down (even stops), even if the system temperature is increased [24]. Other events, such as devitrification or phase separation may occur during curing, but these do not occur in this study. The objective is to characterize these two main states, to be able to correlate them with the signatures obtained during infusion. Since the chemo physical characterization of the infused plates is not possible in real time, several pure resin samples (with MEKP) were tested in oscillatory rheology as detailed in section 2. The tests were carried out under conditions as close as possible from those used during infusion manufacturing, namely at room temperature and shear and oscillations as low as possible to reproduce the stable state of the resin when it cures in the plate. These dynamic tests, highlighting the viscoelastic behavior of the resin, make it possible to reveal the gelation by the crossing of the storage modulus (G')

and loss modulus (G'') curves if the test is conducted at constant oscillation frequency ([25] - [27]); this crossing goes hand in hand with an increase in the viscosity complex modulus $|\eta^*|$. The vitrification is determined by the maximum of G'' [28], and each result is normalized with respect to its own mass. The tests are conducted until the appearance of a plateau of $|\eta^*|$, associated with a significant slowing of the curing reaction. This plateau is considered as the end of the vitrification, knowing that it is associated with a drop of G'' meaning that the resin (reticulated) no longer has viscous properties (elastic solid with a maximized G'). The obtained results being repeatable, only those of sample 1 are presented below. These results were then correlated with those obtained in infusion, as shown in Figure 6. Analysis of the latter makes it possible to associate the first inflection of electrical capacitance with the G' / G'' crossing, that is to say gelation. This confirms that when the resin goes from the liquid state to the gel state, it begins to compress the PZT transducer, effectively lowering its capacitance. In the gel state, the resin is a medium in which the acoustic waves are strongly attenuated (and thus not transmitted to the external AE sensors), which is why the CAE signal is flat during this period. The pressure is decreasing at the first inflection because the resin is gradually curing (increased exothermal behavior), consequently the depression of the infusion system is increased. At the beginning of the vitrification (maximum of G''), the second inflection of capacitance appears. This coupling is coherent because the vitrification makes the resin go from a gel state to a much more rigid glass state, which increases the compression seen by the PZT and thus induces a change in the decrease of its capacitance. This second inflection also sees the temperature coming close to its peak, while the CAE prepares to enter its first rise. These other couplings are also consistent: since the chemical curing reaction generates heat throughout its duration, the associated temperature will be close to its maximum when the appearance of the final state change (vitrification) of the resin will occur. Moreover, since the resin gradually transforms into a glass state, its physical properties become more and more similar to those of a sufficiently continuous propagation medium able to transmit the acoustic waves generated by the vibration of the PZT, explaining the rise of CAE to come. However, the resin still being cured at this stage, the depression continues its decline. The third capacitance inflection occurs more than three hours after the resin injection step: at this point, the G' has already converged to a final plateau, and the G'' has returned to zero. It should be noted, however, that this last inflection always happens at a time never reached in rheology, due to the risk of breakage of the rheometer when a very rigid sample is tested too long. The behavior of G' and G'' indicates that the resin is almost completely cured at this stage because as a purely vitreous solid, it has only an elastic behavior and no more viscous properties. This third inflection of electrical capacitance is associated with the change in slope of the CAE (previously mentioned) towards a quasi-linear behavior until the end of the infusion manufacturing, which confirms the hypothesis that at this stage the resin possesses its final properties and therefore always transmits acoustic waves in the same way. A correlation with the temperature drop following the exothermal peak as well as with the final rise in pressure is also observable. This means that since the resin is almost completely cured, the almost complete chemical reaction releases practically no more heat (hence the gradual decrease in temperature), and that the opening made in the vacuum bag to perform the pressure measurement has partially obstructed by the vitrified resin. An important point is the continuity of the decay (albeit much slower than before) of the electrical capacitance after this last inflection, a sign that the curing, although practically complete, is still active. There are still some residual percentages of resin to be cured at this stage.

It is henceforth possible to associate each of the three inflections of the in-situ PZT electrical capacitance with the start of a chemo physical transformation of the polyester resin in crosslinking: gelation, vitrification and finally the slow transformation of a small amount of residual resin still uncured after the end of vitrification.

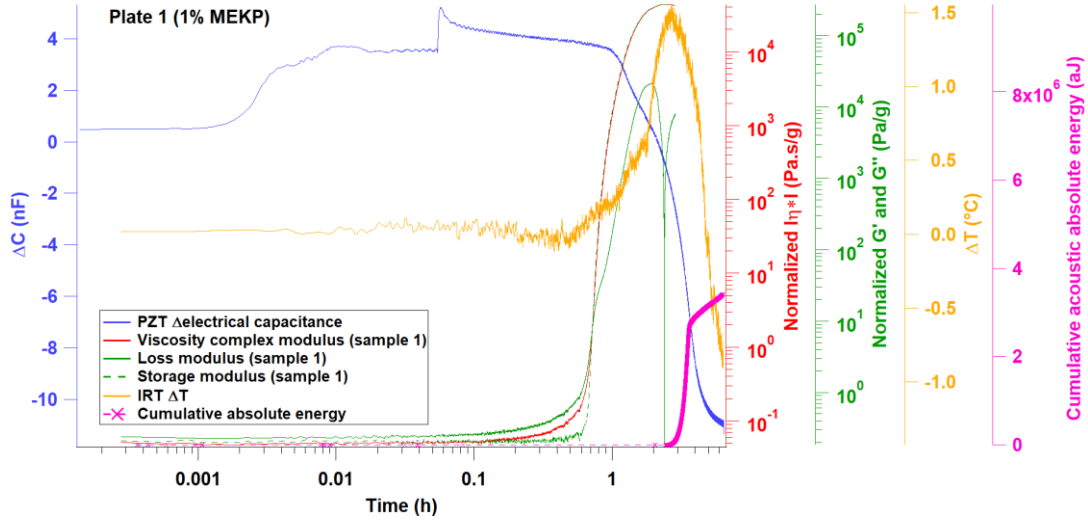


Figure 6: Comparison of the infusion and rheological measurements

4 CONCLUSION AND OUTLOOK

This article studies the interest of inserting a thin piezoelectric ceramic disc (PZT) inside a PMC preform in order to carry out an in-situ and real-time monitoring of its infusion manufacturing. Several in and ex-situ NDT instrumentations are used in addition to the PZT to obtain correlations between the different signatures. Multiple couplings are observed, providing information both on the impregnation of the preform during the injection stage and on the curing of the resin. The electrical capacitance signal of the PZT has three different inflections during its final decay phase, and these have been studied thanks to the multi-instrumentation data associated with oscillatory rheology measurements made on resin samples alone. These last tests made it possible to associate the first capacitance inflection with the beginning of gelation of the resin, the second with the beginning of its vitrification and the last with the curing of the last resin percentages still not transformed at the end of vitrification. The in-situ PZT giving repeatable and relatively accurate information about the various major transitions (chemo physical or not) occurring during the infusion process, its potential is obvious. The end of vitrification (third capacitance inflection) is particularly interesting because it can be used in industrially to determine when to unmold composite parts without risk of damaging them, and thus increase production rates. These information on transitions can also be very useful for processes using closed molds, such as Resin transfer Molding (RTM), where it is impossible to visualize the progress of manufacturing. This work has also demonstrated the interest of using a multi-instrumentation to monitor this process in real time, and in particular the use of the PZT (transducer) - AE (sensors) couple to detect the presence of the vitrification phase by the

acousto-ultrasonic method. The ultimate interest of this study lies in obtaining a "smart" composite material with an embedded and functional PZT transducer after manufacturing. The PZT can then be used for health monitoring applications of composite structures in use, when the latter are subjected to various physical loads. Finding thresholds to know when to stop the structure to control it more accurately or replace it completely, all without having to use the external and cumbersome NDT techniques available on the market, would be a major breakthrough in the composite materials industry.

REFERENCES

- [1] A. Hautefeuille, S. Comas-Cardona, and C. Binetruy, "Mechanical signature and full-field measurement of flow-induced large in-plane deformation of fibrous reinforcements in composite processing," *Compos. Part A Appl. Sci. Manuf.*, vol. 118, no. December 2018, pp. 213–222, 2019.
- [2] B. Gourichon, C. Binetruy, and P. Krawczak, "Experimental investigation of high fiber tow count fabric unsaturation during RTM," *Compos. Sci. Technol.*, vol. 66, no. 7–8, pp. 976–982, 2006.
- [3] D. May *et al.*, "In-Plane Permeability Characterization of Engineering Textiles Based On Radial Flow Experiments: A Benchmark Exercise," *Compos. Part A Appl. Sci. Manuf.*, vol. 121, no. March, pp. 100–114, 2019.
- [4] V. H. Nguyen, M. Deléglise-Lagardère, and C. H. Park, "Modeling of resin flow in natural fiber reinforcement for liquid composite molding processes," *Compos. Sci. Technol.*, vol. 113, pp. 38–45, 2015.
- [5] S. P. Bancora, C. Binetruy, S. G. Advani, E. Syerko, and S. Comas-Cardona, "Effective permeability averaging scheme to address in-plane anisotropy effects in multi-layered preforms," *Compos. Part A Appl. Sci. Manuf.*, vol. 113, no. July, pp. 359–369, 2018.
- [6] W. Harizi, S. Chaki, G. Bourse, and M. Ourak, "Mechanical damage characterization of glass fiber-reinforced polymer laminates by ultrasonic maps," *Compos. Part B Eng.*, vol. 70, pp. 131–137, 2015.
- [7] A. T. Martins, Z. Aboura, W. Harizi, A. Laksimi, and K. Khellil, "Structural health monitoring for GFRP composite by the piezoresistive response in the tufted reinforcements," *Compos. Struct.*, 2018.
- [8] K. Hamdi, Z. Aboura, W. Harizi, and K. Khellil, "Improvement of the electrical conductivity of carbon fiber reinforced polymer by incorporation of nanofillers and the resulting thermal and mechanical behavior," *J. Compos. Mater.*, p. 002199831772658, 2017.
- [9] S. Leonard-Williams, "The crossover from RTM to resin infusion," *Reinf. Plast.*, vol. 52, no. 10, pp. 28–29, Nov. 2008.
- [10] M. Deléglise, C. Binétruy, P. Castaing, and P. Krawczak, "Use of non local equilibrium theory to predict transient temperature during non-isothermal resin flow in a fibrous medium," *Int. J. Heat Mass Transf.*, vol. 50, no. 11–12, pp. 2317–2324, 2007.
- [11] K. Hoes *et al.*, "New set-up for measurement of permeability properties of fibrous reinforcements for RTM," *Compos. - Part A Appl. Sci. Manuf.*, vol. 33, no. 7, pp. 959–969, 2002.

- [12] R. Matsuzaki, S. Kobayashi, A. Todoroki, and Y. Mizutani, "Cross-sectional monitoring of resin impregnation using an area-sensor array in an RTM process," *Compos. Part A Appl. Sci. Manuf.*, vol. 43, no. 4, pp. 695–702, 2012.
- [13] S. Kobayashi, R. Matsuzaki, and A. Todoroki, "Multipoint cure monitoring of CFRP laminates using a flexible matrix sensor," *Compos. Sci. Technol.*, vol. 69, no. 3–4, pp. 378–384, 2009.
- [14] N. Ghodhbani, P. Marechal, and H. Duflo, "Ultrasonic broadband characterization of a viscous liquid: Methods and perturbation factors," *Ultrasonics*, vol. 56, pp. 308–317, 2015.
- [15] R. Kline, N. Parasnis, and R. Konanur, "Ultrasonic monitoring of the dynamic properties of composites during manufacture," *Ultrason. Symp.*, vol. 9, no. 6, pp. 0–87, 1992.
- [16] N. Samet, P. Maréchal, and H. Duflo, "Ultrasound monitoring of bubble size and velocity in a fluid model using phased array transducer," *NDT E Int.*, vol. 44, no. 7, pp. 621–627, 2011.
- [17] N. Samet, P. Marechal, and H. Duflo, "Monitoring of an ascending air bubble in a viscous fluid/fiber matrix medium using a phased array transducer," *Eur. J. Mech. B/Fluids*, vol. 54, pp. 45–52, 2015.
- [18] E. Marin, L. Robert, S. Triollet, and Y. Ouerdane, "Liquid Resin Infusion process monitoring with superimposed Fibre Bragg Grating sensor," *Polym. Test.*, vol. 31, no. 8, pp. 1045–1052, 2012.
- [19] L. P. Canal, M. Benavente, M. Hausmann, and V. Michaud, "Process-induced strains in RTM processing of polyurethane/carbon composites," *Compos. Part A Appl. Sci. Manuf.*, vol. 78, pp. 264–273, 2015.
- [20] M. A. Ali, R. Umer, K. A. Khan, Y. A. Samad, K. Liao, and W. Cantwell, "Graphene coated piezo-resistive fabrics for liquid composite molding process monitoring," *Compos. Sci. Technol.*, vol. 148, pp. 106–114, 2017.
- [21] J. M. Park, S. Il Lee, and J. H. Choi, "Cure monitoring and residual stress sensing of single-carbon fiber reinforced epoxy composites using electrical resistivity measurement," *Compos. Sci. Technol.*, vol. 65, no. 3–4, pp. 571–580, 2005.
- [22] U. Müller, C. Pretschuh, R. Mitter, and S. Knappe, "Dielectric analysis as a cure monitoring system for UF particle boards," *Int. J. Adhes. Adhes.*, vol. 73, pp. 45–50, 2017.
- [23] N. Elvin, A. Elvin, and B. Z. Senderos, "Capacitance changes in thin piezoelectric transducers embedded in isotropic host materials," *J. Intell. Mater. Syst. Struct.*, vol. 29, no. 5, pp. 816–829, Mar. 2018.
- [24] M. C. Kazilas, *Acquisition and Interpretation of Dielectric Data For Thermoset Cure Monitoring*. 2003.
- [25] H. H. Winter and F. Chambon, "Analysis of Linear Viscoelasticity of a Crosslinking Polymer at the Gel Point," *J. Rheol. (N. Y. N. Y.)*, vol. 30, no. 2, pp. 367–382, Apr. 1986.
- [26] M. Haider, P. Hubert, and L. Lessard, "Cure shrinkage characterization and modeling of a polyester resin containing low profile additives," vol. 38, pp. 994–1009, 2007.
- [27] S. Dev, P. N. Shah, Y. Zhang, D. Ryan, C. J. Hansen, and Y. Lee, "Synthesis and mechanical properties of flame retardant vinyl ester resin for structural composites,"

- Polymer (Guildf).*, vol. 133, pp. 20–29, 2017.
- [28] B. Van Mele, H. Rahier, G. Van Assche, and S. Swier, “The Application of Modulated Temperature Differential Scanning Calorimetry for the Characterisation of Curing Systems,” pp. 83–160, 2006.

THE DEVELOPMENT OF THE PROTOTYPE OF THE SYSTEM FOR MONITORING A STRESS-STRAIN STATE OF A OUTLET GUIDE VANE WITH THE HELP OF A FIBER OPTICAL SENSORS SYSTEM

ALEKSANDR N. ANOSHKIN, GLEB S. SHIPUNOV, ANDREY A. VORONKOV,
KONSTANTIN A. PELENEV, RUSTAM T. MURZAKAEV AND ALEKSANDRA A.
TIKHONOVA

Perm National Research Polytechnic University; PNRPU
29 Komsomolsky prospekt, Perm, Perm krai, Russia, 614990
e-mail: rector@pstu.ru, web page: [http://www. pstu.ru](http://www.pstu.ru)

Key words: Polymeric composite material, stress-strain state, fiber-optic sensor, numerical simulation, monitoring system.

Abstract. The paper presents a prototype of a system for monitoring the deformed state of a typical part of an aircraft engine – an outlet guide vane (OGV) made of composite materials. The system includes: fiber optic sensors (FOS) based on Bragg gratings, an ASTRO X327 interrogator, and software interrogating and recording data from the FOS. In addition, the system includes a module for calculating the stress-strain state and comparing the calculated strains with the readings of the FOS. The results of approbation of the system for the control of stress-strain state in laboratory tests of OGV are presented. The results of mathematical modeling of the mechanical behavior of the OGV in the software package ANSYS are given. A comparison of experimental data and numerical simulation results was made.

1 INTRODUCTION

Polymer composite materials (PCM) are increasingly used in the manufacture of elements of aircraft propulsion systems. Previously PCM were used for the manufacture of lightly loaded body parts, such as, fairings, casings, engine nacelle shells. Currently, PCM are used in the manufacture of power parts, working in conditions of complex stress state, for example, the outlet guide vanes and fan blades [1-4]. Periodic monitoring, evaluation of the performance and residual strength of such parts during long-term operation is an important task, which causes interest in developing systems for monitoring the state of such parts.

In the civilian sector, there are many examples of existing monitoring systems. The Austrian group of companies belonging to the association NBG Holding GmbH developed systems for monitoring the condition of various structures and infrastructure, such as bridges, tunnels, roads and railways [5]. The monitoring systems described in the literature include the long-term monitoring system of a historic building of the 16th century [6], the stinger condition monitoring system when laying deep-water pipes [7], the monitoring and assessing system for the condition of the wind generator, which makes it possible to make a decision on extending the service life or replacing blades. [eight].

A number of systems have been developed for monitoring composite structures. In [9, 10], the types of damage to composite structural elements arising from the operation of aircraft and the options for building monitoring systems for these structures are considered. In these monitoring systems, it is proposed to use various types of sensors: piezoelectric, acoustic emission, fiber-optic, as well as a non-contact method of monitoring the infrared field emitted by the object. The papers propose the use of these systems for monitoring the condition of airframe elements. The described systems make it possible to record deformations, accumulation of damage, or destruction of controlled elements during the entire life cycle.

Recently, fiber-optic sensors (FOS), which allow to measure temperature and deformation, are increasingly being used as sensitive elements of condition monitoring systems. FOS,

possessing dimensions of the order of 0.15 mm, are capable of withstanding deformations comparable to those of a composite, they are immune to electrical interference, are highly sensitive and can be installed on the surface of a controlled object or embedded in the structure of a composite material to control the structure during the entire life cycle [11,12]. Interrogators, which are part of such systems, depending on the maximum sampling frequency of the sensors, can be used to monitor the state of the object in the quasi-static or dynamic loading mode.

2 Conceptual diagram of the developed monitoring system prototype

Traditionally, systems for monitoring the state of aircraft engines estimate integral indicators such as temperature, pressure, exhaust gas velocity, turbine speed, etc. [13]. Modern systems are aimed at assessing structural damage to structural elements using various sensors. This approach is used along with traditional methods of non-destructive testing and allows you to quickly assess the state of integrity of composite structures. Early detection of defects increases safety and allows for less capital and costly repairs, and also minimizes the problem of human factors in the process of flaw detection [14].

Since 2006, for example, Sandia National Laboratories has been actively working in this direction in collaboration with the Structural Monitoring System, Sykorsky, Boeing, AEM, Acellent, and others [15]. The main line of research is related to automated data analysis for the detection of delaminations and cracks in composite structures using piezoelectric and vacuum sensors. The main task of the prototype system for monitoring structures made of PCM considered in this paper is to monitor the stress-strain state of aircraft engine parts during bench or flight tests. The various elements of such a monitoring system have their own requirements. In particular, sensitive elements placed on the surface or in the structure of the monitoring object should remain operable under complex dynamic and static loading. The sensors must withstand temperatures from -55 to +150 C, and in the case of sensors embedded in the structure of the composite material, and the maximum temperature of technological processing of the material, for example, +160 within 4 hours. The interrogator and information processing modules should be located on board the aircraft, therefore, mass and dimensional restrictions are imposed on them.

The composition of the monitoring system developed in this article includes: a monitoring facility, fiber-optic sensors, peripheral measuring equipment, a computer with software. Fiber-optic sensors can be located on the surface of the monitoring object or be embedded in its structure. The introduction of FOS into the structure of a controlled object is preferable, therefore, in previous studies [16], the technology of introducing FOS into the structure of PCM, obtained by hot pressing and autoclave molding, was developed. Figure 1 shows an outlet guide vane manufactured using autoclave molding technology and the corresponding layout of glued and embedded fiber-optic sensors. The layout of the FOS on the OGV surface (Figure 1, b) was chosen to test the operation of the prototype system based on the results of numerical simulation. Sensors S001-203 are located in areas of large deformations and deformation gradients, and sensors S301-302 are located in the zone of the most probable primary delamination of the OGV structure under quasistatic loading. In the case of placing FOS into the structure of the material (Figure 1, d), the scheme is more convenient from a technological point of view. This scheme allows you to embed 3 lines of four sensors FOS with the formation of 4 groups of FOS with different orientations ($0, \pm 45$) relative to the longitudinal axis, in order to calculate the total deformations based on the readings of these groups in different sections.

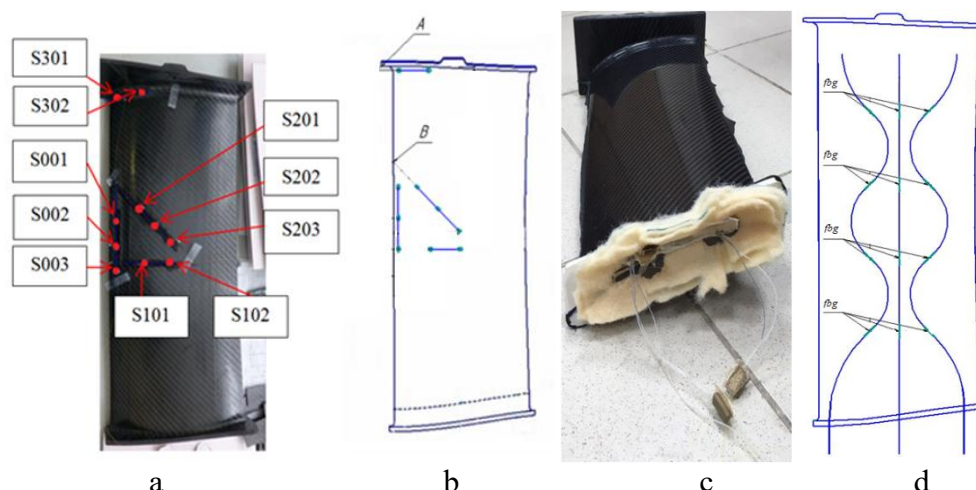


Figure 1. OGV with the FOS lines pasted on the surface (a) and embedded (c). Layout of FOS on the surface (b) and in the construction of the OGV (d).

The peripheral measuring equipment (interrogator) receives information about the resonant wavelengths of Bragg gratings and transmits it to the software module for further processing. The frequency of his work determines the dynamic range of effects that the system can measure.

The system contains two levels of software. The lower level software includes modules that perform primary data processing. In the case of the introduction of FOS into the structure of the PCM, technological factors cause the initial deformation of the fibers, which leads to the birefringence effect and the appearance of noise in the spectrum of the signal of FOS. The lower level software filters noise by a specially developed algorithm, calculates the deviation of the resonant wavelength from the base for each grating, calculates the deformations and transfers these values to the upper level software for further processing.

The upper level software consists of modules with mathematical models of controlled objects for calculating stress-strain state. These programs allow you to compare the deformations recorded by the sensors at specific points in the structure with the calculated values and, in case of compliance, determine stresses and deformations at all points of the object. Indirectly, the simulation results allow us to assess the nature and level of loads acting on the object. It is intended to develop an information analysis module for assessing the safety margin of a structure under a given stress-strain state and a module for detecting the occurrence of defects such as cracks, delaminations or break of layers in a structure during long-term operation or abnormal effects. In addition, it is planned to develop a wrapper program that provides output of various information to the operator interface. The block structure of the monitoring system being developed is shown in Figure 2.

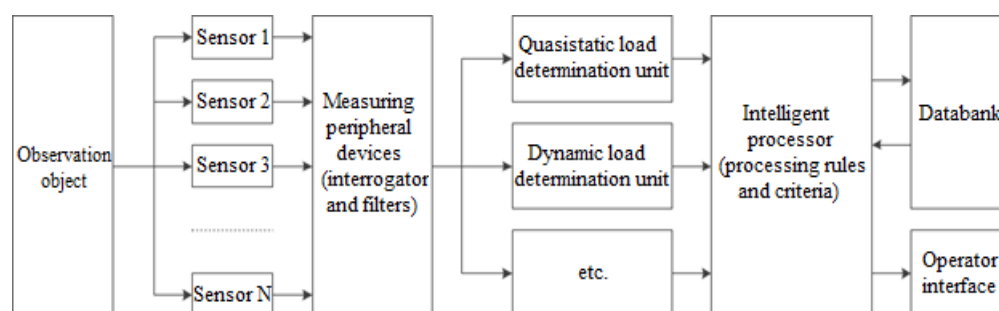


Figure 2. Block structure of the system for monitoring the state of structures

The use of the system implies monitoring both in real time of the structure operation (in flight) and in the post-analysis mode (on the ground) based on the data collected in flight. The

structure of the system implies the possible inclusion of other blocks, for example, by determining the stress-strain state at shock loads or artificial (post-flight) loads, to analyze its deformed state in order to search for possible defects.

3 PCM OGV monitoring system prototype

The object of control in the monitoring system being developed is the outlet guide vane (OGV) of an aircraft engine (Figure 1). The blade is made of carbon-fiber plastic according to pre-peg technology with autoclave molding at a temperature of 160 C. In the design of the blade, can be seen feather and shelves, by means of which the blade is fixed, both in the propulsion system and in the rigging equipment.

As sensitive elements of the monitoring system prototype, fiber-optic sensors with resonant wavelengths were used for:

S001=1565.069nm, S002=1535.032nm, S003=1505.020nm, S101=1564.929nm,
S102=1535.032nm, S201=1565.040nm, S202=1534.985nm, S203=1504.986nm,
S301=1534.990nm, S302=1505.043nm.

Below are considered the results of testing the OGV sample with sensors pasted on the surface (Fig. 1, b). The gluing scheme of the sensors is shown in figure 1, c, where A is the base of longitudinal dimensions, B is the point for the orientation of the inclined line.

The sensors were polled by the ASTRO X327 interrogator. The interrogator generates and transmits a broadband optical signal $\psi(\lambda)$ through an optical fiber (λ is the wavelength). On the Bragg grating part of this signal is reflected. The main part of the reflected optical signal occurs at the resonant wavelength λ , the value of which is directly proportional to the effective refractive index n and the Bragg grating period L . The polling of the sensors can determine the difference of the resonant wavelengths of the reflected spectrum $\Delta\lambda = \lambda - \lambda^*$ in the current λ and initial λ^* time. The relative difference of the resonance wavelength of the reflected spectrum $\Delta\lambda / \lambda$ will be proportional to the relative change in the period $\Delta L / L$ of the Bragg grating, which makes it possible to evaluate its relative mechanical deformations ε and temperature change ΔT [17]:

$$\Delta\lambda/\lambda = K_\varepsilon \varepsilon + K_T \Delta T, \quad (1)$$

where K_ε , K_T are the deformation and temperature coefficients, respectively. These coefficients depend on the optical and mechanical properties of the optical fiber and are known constants.

In the developed monitoring system, information on the change in the resonant wavelength was transmitted to the software module of the lower level. When placing the FOS on the surface of the monitoring object, changes in the spectrum were not observed in the FOS signal. This made it possible not to perform additional signal processing and filtering. The constant temperature during the tests allows not to take into account the influence of the second term of the formula (1) on the signal of the ESP. The software of the lower level received information about the resonant wavelengths of each WATER, carried out the calculation of the deviations of the wavelengths, the calculation of deformations for each sensor using the formula (1). In the upper level software, the monitoring object's stress-strain state was calculated under laboratory loads, the calculated and experimental deformations were compared, and under the condition of satisfactory agreement, the structure's safety margin was estimated from the calculated stress values.

4 Testing a monitoring system prototype

The tests of the developed system were intended to check the operation of all its components under quasi-static loading and to compare the deformations recorded by FOS with the results of the numerical calculation of the stress-strain state of the OGV under study. The OGV was loaded in a specially designed metal tooling through a rubber gasket 20 mm

thick onto the surface of the vane blade. The sensors were attached to another surface of the feather free of load. The tests were carried out on a Zwick Z100 servo-hydraulic machine with a cylinder of 90mm diameter (complex of equipment of the “Unique Scientific and Technological Complex of Automated Layout” PNRPU) at a constant temperature. During the tests, load monitoring and registration of fiber-optic sensors with a sampling frequency of 100 Hz were carried out. The general scheme of the tests is presented in figure 3.

To process the sensor signal and calculate the strain, the software described above was used. Tests have shown that the chosen technology of gluing sensors ensures their reliable fixation on the surface of the object, this, in turn, ensures the registration of the signal with minimal distortion.

Deformations obtained according to the indications of the FOS, depending on the applied load, are shown in figure 4. The analysis of these dependences shows the non-linear nature of the deformation, which is especially pronounced with the S201-S203 sensors oriented at an angle to the OGV axis. Further, the readings of the sensors are compared with the results of the OGV numerical simulation.

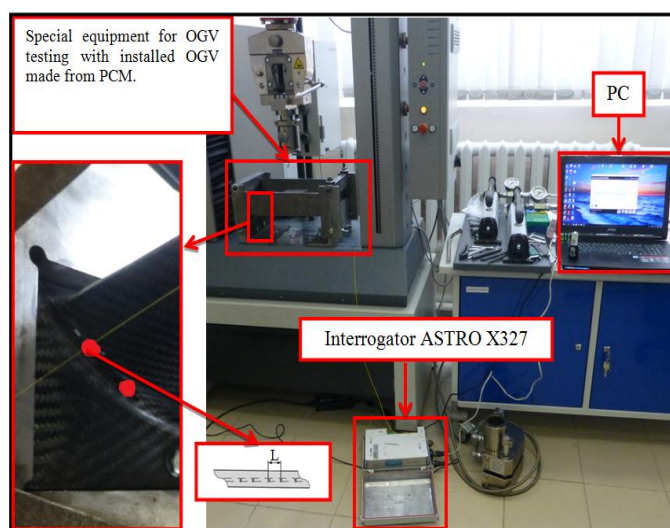


Figure 3. Test scheme of the OGV monitoring system.

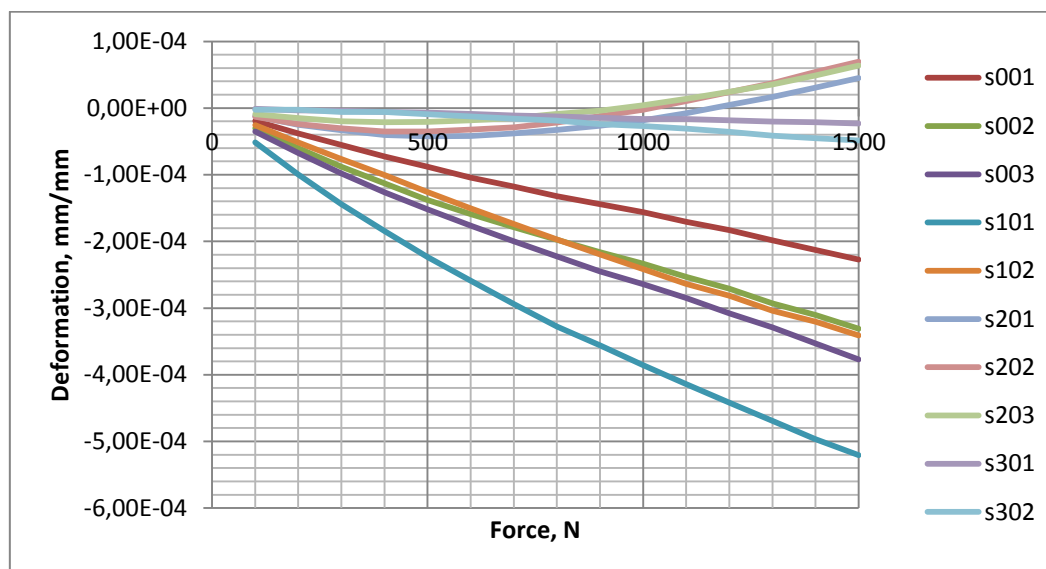


Figure 4. Dependence of the strain on the applied load, obtained from FOS, placed on the free surface of the OGV, the sensor numbers are shown in Figure 1a.

5 Numerical modeling and comparison of results

For the numerical simulation of mechanical deformation of the OGV, a three-dimensional computer model was developed. The model explicitly describes the vane reinforcement scheme in the form of a set of anisotropic CFRP layers with different geometries. The loading scheme corresponded to the laboratory test conditions. On the top shelf of the vane, rigid fastening was set on the bolt joint holes, on the bottom shelf the absence of movements in two directions UX, UY was set. A proportionally increasing distributed load was applied to the vane tip through the rubber plate (Figure 5). The rubber plate was deformed nonlinearly, the deformation of carbon fiber was considered linear, the elastic properties of the material of the layers in the coordinate system of the OX1X2X3 layer are given in (Table 1).

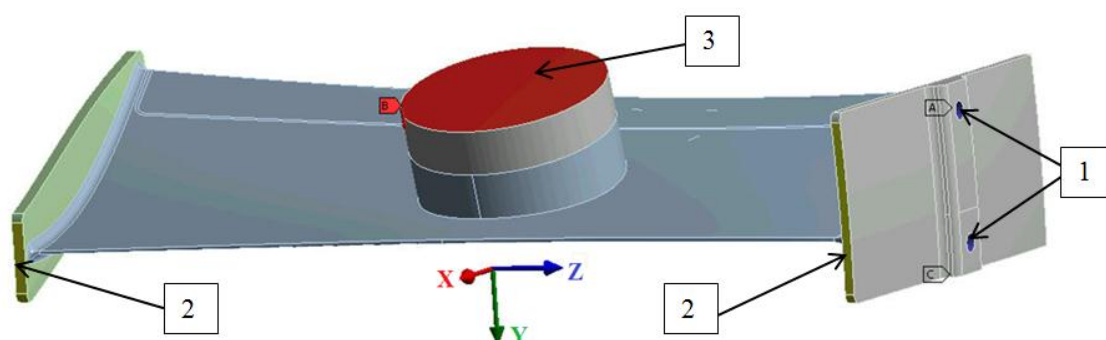


Figure 5. The design scheme of OGV 1 is rigid attachment, 2 is the prohibition of UX, UY movements, 3 is the load.

Table 1. Elastic properties of composite material.

Material	E11, GPa	E22, GPa	E33, GPa	G12, GPa	G13, GPa	G23, GPa	v21	v13	v32
Equal Strength Carbon Fiber	63,9	63,9	5,0	19,5	2,7	2,7	0,04	0,3	0,3

The solution of the nonlinear three-dimensional problem of mechanics of inhomogeneous media for the vane under consideration with an explicit description of the reinforcement scheme requires large computational resources. Therefore, in the present work, the simulation of mechanical deformation of a vane was carried out for a homogeneous anisotropic material with effective elastic properties of a layers package. The effective elastic properties of a layers package were calculated separately on the basis of the reinforcement scheme and the properties of the layers (Table 1). The problem was solved in the ANSYS Workbench software package using the spatial finite elements SOLID 86. The load was set from the initial total load of 100 N to the load of 1500 N with a step of 100 N.

Figure 6 shows deformation fields of the free of loading vane surface obtained as a result of the calculation for a load of 1500 N. It also shows the values of deformations in the vicinity of the location of the FOS in directions that coincide with the axis of sensitivity of the FOS. Calculations show that the deformation fields are non-uniform, and there are areas of compressive and tensile deformations on the surface of the blade. It should be noted that FOSs were installed in the most dangerous zones of compressive deformations.

Table 2 for load values of 500, 1000, and 1500 N presents a comparison of the deformations determined from the FOS readings and the calculated values of the deformations at the sensor locations.

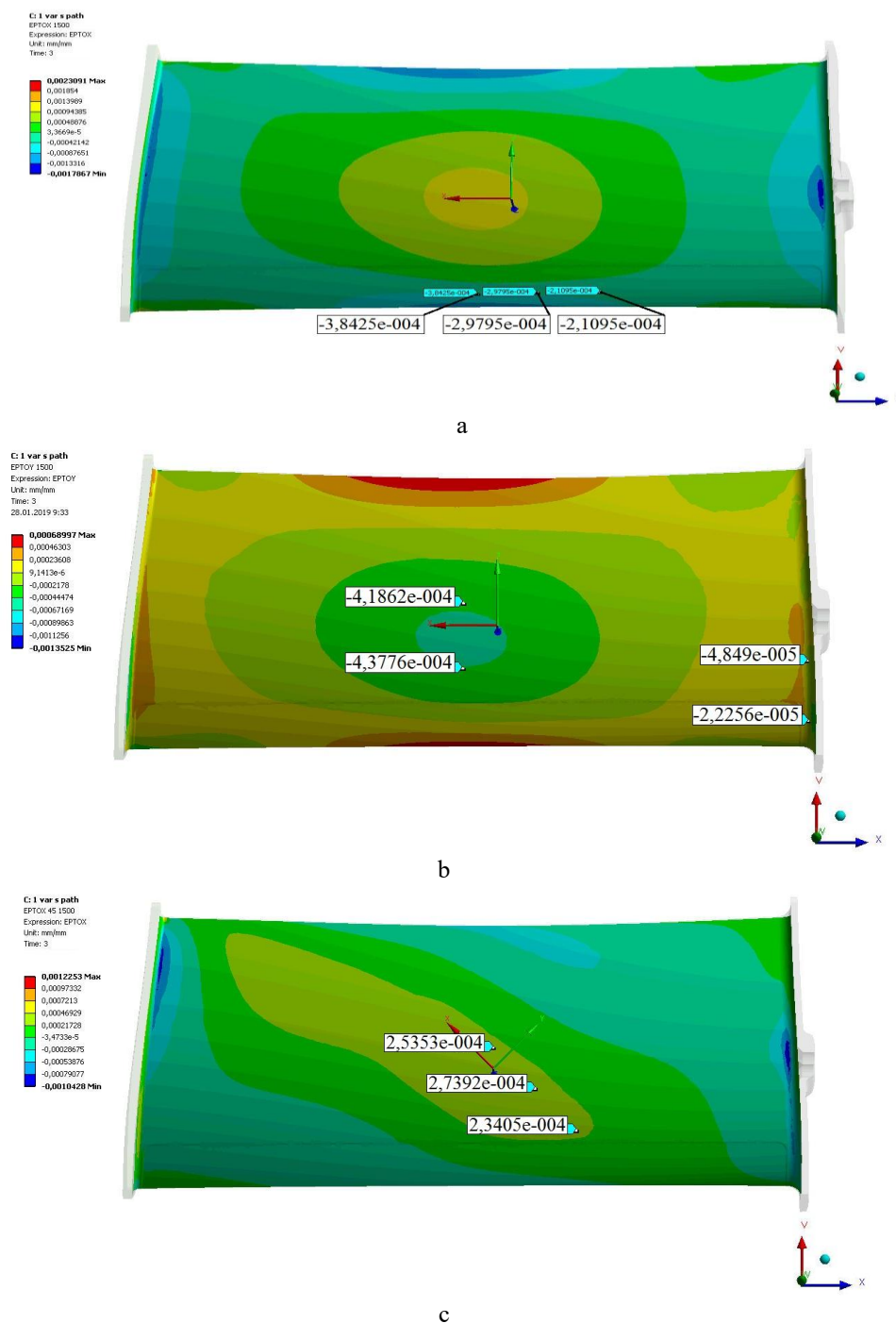


Figure 6. The field of axial deformations on the free surface of the OGV feather in the area of mounting the FOS at 1500H in the local layer coordinate system in the directions a) ϵ_x b) ϵ_y c) ϵ_{x45°

TABLE 2. Comparison of deformations determined by the FOS indications, and calculated values of deformations at the sensor locations under loads of 500, 1000 and 1500 N

Parameter		Longitudinal direction			Cross direction				At 45° angle		
	Load , N	S001	S002	S003	S101	S102	S301	S302	S201	S202	S203
Deformations FOS*, 10 ⁻⁴ .	500	-0,88	-1,38	-1,52	-2,23	-1,26	-0,07	-0,09	-0,42	-0,35	-0,21
	1000	-1,56	-2,34	-2,64	-3,85	-2,24	-0,16	-0,27	-0,18	-0,03	-0,04
	1500	-2,27	-3,31	-3,77	-5,21	-3,41	-0,23	-0,48	0,45	0,69	0,64
Calculated deformations · 10 ⁻⁴ .	500	-0,86	-1,10	-1,26	-1,13	-1,42	-0,08	-0,09	0,78	0,94	0,90
	1000	-1,51	-2,13	-2,41	-2,91	-2,76	-0,16	-0,22	1,55	1,85	1,73
	1500	-2,11	-2,98	-3,84	-4,19	-4,38	-0,22	-0,48	2,34	2,74	2,54
Deviation, %	500	2,12	25,04	20,30	98,55	11,66	9,22	8,77	154,6	137,3	123,0
	1000	3,63	9,53	9,80	32,55	12,58	5,74	21,27	111,8	101,3	97,65
	1500	7,69	11,18	1,94	24,41	22,13	4,89	-0,23	80,75	74,62	74,79
	$\bar{\Delta}$	4,48	15,25	9,39	51,83	15,46	0,47	9,94	115,7	104,4	98,51

$\bar{\Delta}$ Mean deviation

Table 2 data analysis shows that the deformations in the longitudinal and cross directions detected by the sensors S001, S002, S003, S102, S301, S302 are close to the calculated values. The difference in strain at a point is from 2 to 25%, the average difference in strain in the three measurement options (calculations) is from 4.5 to 15.5%.

The lateral deformations detected by the S101 sensor differ from the calculated deformations by 24.5-98.5%. Deformations at an angle of 45 °, recorded by the sensors S201, S 202, S203, differ from the calculated deformations by 74.6-154.6%. It should be noted that the sensors S201, S202, S203, S301 and S302 record the strain values that are included in the equipment error zone (0.5 10-4). In this case, the readings of the sensors S301 and S302 are in satisfactory agreement with the calculation, and the readings of the sensors S201, S202, S203, differ significantly.

The difference between the calculated and experimentally obtained values of deformations using FOS is apparently due to the error in the simulation of the deformation of the vane using the effective material properties and the error in determining the Poisson coefficients for the material layer.

In further studies, it is planned to obtain an updated solution to the problem of mechanical deformation of the vane with a complete description of its reinforcement scheme and an updated value of the Poisson's ratio of the layers material. After a satisfactory coincidence of the calculated and experimental values of deformations, it is planned to obtain a calculated estimate of the strength margin of the vane under laboratory load and to experimentally verify the accuracy of this estimate.

6 Conclusion

A technology has been developed for introducing and gluing fiber optic sensors into a composite material structure, manufactured using prepreg technology of hot pressing. A prototype of a system for monitoring the stress-strain state of outlet guide vane made of composite materials using fiber-optic sensors on Bragg gratings and a mathematical model of the structure has been developed. The prototype of the monitoring system was checked in laboratory tests of the vane. A satisfactory coincidence (calculated on average to 15.5%) was obtained for the calculated and experimental FOS registered deformation values at six control points of ten. The significant (over 100%) difference in deformations at four control points is explained by the error of calculations due to the use of a simplified mathematical model of the structure and the error in determining the Poisson's ratio of the layers material. In further

studies, it is planned to obtain an updated solution of the problem of mechanical deformation of the vane for a satisfactory agreement between the calculated and experimental values of the deformations at all control points. Next, it is planned to obtain a calculated estimate of the safety margin of the vane under laboratory load and to experimentally test the accuracy of this estimate. This will test the possibility of using a monitoring system prototype for assessing the safety margin of a structure during testing.

7 ACKNOWLEDGMENTS

The work was performed in the framework of the State Task No. 11.2391.2017 / 4.6.

REFERENCES

- [1] Technologies and tasks of the mechanics of composite materials for creating an outlet guide vane of an aircraft engine / A.N. Anoshkin, V.Yu. Zuyko, G.S. Shipunov, A.A. Tretyakov // Bulletin of the Perm National Research Polytechnic University. Mechanics. – 2014. – № 4. – P. 5–44. DOI:10.15593/perm.mech/2014.4.01
- [2] Composite vane mounting. Patent No.: US 8734101 B2. McDonald S.A. et al. General Electric Co., 2014.
- [3] Warwick G. Carbon redux // Aviation Week & Space Technology. – Vol. 175. – No. 24. – P. 27
- [4] C. Bellini, J. Carney. The GENx: Next generation aviation // University of Pittsburgh Swanson School of Engineering's 12th Annual Freshman Engineering Conference. – 2012.
- [5] Proposed monitoring systems by group NBG Holding GmbH URL : <https://www.nbg.tech/sensing-overview/> (date of the application: 20.05.2019)
- [6] Esequiel Mesquita António Arêde Nuno Pinto Paulo Antunes Humberto Varum «Long-term monitoring of a damaged historic structure using a wireless sensor network» // Engineering Structures Volume 161, 15 April 2018, Pages 108-117
- [7] Hongsheng Yan, Daxing Wei, Xiao-bo Wang, Yong-xin Chen, Xiang-wei Meng «Research of structural health monitoring system for stinger of large deep water pipe-laying ship» // Ocean Engineering Volume 171, 1 January 2019, Pages 361-376
- [8] T.Rubert, G.Zorzi, G.Fusiek, P.Niewczas, D.McMillan, J.McAlorum, M.Perry. «Wind turbine lifetime extension decision-making based on structural health monitoring» // Renewable Energy Volume 143, December 2019, Pages 611-621
- [9] Raffaella Di Sante “Fibre Optic Sensors for Structural Health Monitoring of Aircraft Composite Structures: Recent Advances and Applications” //Sensors 2015, 15, 18666-18713; doi:10.3390/s150818666
- [10] Verma Rahul, Shukla Alokita , Kandasamy Jayakrishna , V.R. Kar , M. Rajesh , S. Thirumalini , M. Manikandan «Structural health monitoring of aerospace composites» // Structural Health Monitoring of Biocomposites, Fibre-Reinforced Composites and Hybrid Composites Woodhead Publishing Series in Composites Science and Engineering 2019, Pages 33-52
- [11] RECENT DEVELOPMENT OF STRUCTURAL HEALTH MONITORING TECHNOLOGIES FOR AIRCRAFT COMPOSITE STRUCTURES IN JAPAN N. Takeda and S. Minakuchi Dept. Advanced Energy, Graduate School of Frontier Sciences The University of Tokyo
- [12] Mustagime Tülin Yildirim, Bülent Kurt Aircraft Gas Turbine Engine Health Monitoring System by Real Flight Data // International Journal of Aerospace Engineering Volume 2018, <https://doi.org/10.1155/2018/9570873>
- [13] A. J. Volponi, “Gas turbine engine health management: past,present, and future trends” // Journal of Engineering for Gas Turbines and Power, vol. 136, no. 5, article 051201, 2014.

- [14] Costa J. M., Black R. J., Moslehi B., Oblea L., Patel R., Sotoudeh V., Abouzeida E., Quinones V., Gawayed Y., Soobramaney P., Flowers G. Fiber-optically sensorized composite wing// Smart Sensor Phenomena, Technology, Networks, and Systems Integration 2014. V. 9062 <https://doi.org/10.1117/12.2057943>
- [15] Speckmann H, Henrich R. Structural health monitoring (SHM) - overview on technologies under development. In: Proceedings of the 16th world conference on NDT(WCNDT). Montreal, Canada, August 30-September 3; 2004.
- [16] Matveenko, V.P., Kosheleva, N.A., Shardakov, I.N., Voronkov, A.A. « Temperature and strain registration by fibre-optic strain sensor in the polymer composite materials manufacturing» // International Journal of Smart and Nano Materials 9(2), c. 99-110
- [17] E.N. Kablov "Application of optical fiber as a strain sensors in polymer composite materials" All materials. Encyclopedic Guide. 2010, №3. pp. 10-15.

A COMPLETE DIRECT APPROACH TO ELECTROSTRICTIVE POLYMER PLATES AND SHELLS

MICHAEL KROMMER*, ELISABETH HANSY-STAUDIGL* and
ALEXANDER HUMER†

* Institute of Mechanics and Mechatronics, TU Wien
Getreidemarkt 9, A-1060 Vienna, Austria
e-mail: {michael.krommer,elisabeth.hansy-staudigl}@tuwien.ac.at

† Institute of Technical Mechanics, JKU Linz
Altenberger Straße 69, A-4040 Linz, Austria
e-mail: alexander.humer@jku.at

Key words: Nonlinear plates and shells, Direct approach, Electrostrictive polymers

Abstract. In this paper we discuss modeling of electrostrictive polymer plates and shells as electro-elastic material surfaces. A complete direct approach is developed without the need to involve the three-dimensional formulation. Electrostatic forces as well as constitutive coupling by means of electrostriction are accounted for. We propose a rational formulation for the augmented free energy of electro-elastic material surfaces incorporating electrostriction by a multiplicative decomposition of the surface stretch tensor and an additive decomposition of the surface curvature tensor into elastic and electrical parts. Results computed within the framework of this complete direct approach are compared to results computed with a method that requires the numerical integration of the three-dimensional constitutive relations through the thickness of the plate or shell.

1 INTRODUCTION

Elastic dielectrics, such as piezoelectric materials and electro-active polymers, belong to the class of electro-active materials, which are materials with an inherent electromechanical coupling due to electrostatic forces as well as constitutive coupling resulting from e.g. ferroelectricity, piezoelectricity and electrostriction. Electro-active polymers are divided into two types, ionic and field-activated electro-active polymers, of which we are solely interested in field-activated electro-active polymers in this paper. The latter can further be sub-divided into dielectric elastomers, electrostrictive polymers and ferroelectric polymers; see Pelrine et.al. [1] or Bar-Cohen [2]. Dielectric elastomers are actuated through electrostatic and ponderomotive forces only, ferroelectric polymers exhibit an electrostrictive effect in a non-poled virgin state, but show piezoelectric behavior in the poled state, and electrostrictive polymers are actuated by both, electrostatic and ponderomotive forces as well as through a molecular alignment resulting into electrostriction; see e.g. Zäh and Miehe [3]. Constitutive modeling in field-activated electro-active polymers is based on a proper specification of the Helmholtz free energy, see Dorfmann and Ogden [4] and

Vu et.al. [5]. When it comes to ferroelectric polymers and electrostrictive polymers, coupling by means of electrostriction becomes involved. In such a case a multiplicative decomposition of the deformation gradient tensor for finite strains is typically applied, in which the electrostrictive and the piezoelectric part of the deformation is accounted for by means of a purely electric part of the deformation gradient tensor. In the context of electro-active polymers we refer to Skatulla [6] and Zäh and Miehe [3] and our own previous work, Staudigl et.al. [7], and for reversible piezoelectric materials see Humer and Krommer [8].

In many cases structures with integrated electro-active materials can be assumed as thin plates and shells, such that the theories of structural mechanics come into play. A common approach in nonlinear structural mechanics - often denoted as direct approach - is to consider these structures as two-dimensional material surfaces with specific mechanical degrees of freedom for each material point of the surface - typically translations and rotations. Dealing with plates and shells with integrated electro-active materials electrical degrees of freedom must be introduced for the material surface as well and the modeling must be completed by consistently incorporating electrostatic and ponderomotive forces as well as the appropriate two-dimensional form of the Helmholtz free energy on the structural level of the material surface. In contrast to the direct approach, various other approaches to the modeling and analysis for electro-elastic plates and shells are reported in the literature in the context of piezoelectric materials; see Vetyukov et.al. [9] and the literature cited there. Concerning electro-elastic plates and shells made of field-activated electro-active polymers the literature is by no means exhaustive. Typically, such plates and shells are either modeled based on the implementation of three-dimensional solid plate or shell elements (e.g. Klinkel et al. [10] and Bishara and Jabareen [11] for dielectric elastomer plates) or on the full three-dimensional formulation (e.g. Vu et.al. [5], Skatulla [6] and Zäh and Miehe [3]). So far, a direct approach to the modeling of the nonlinear behavior of electro-elastic plates and shells was applied to piezoelectric shells by Vetyukov et.al. [9] and to dielectric elastomer plates by Staudigl et.al. [12]. In this latter reference the direct approach was only concerned with the geometry of deformation and forces; yet, the specific form of the structural two-dimensional augmented free energy was not discussed, but rather the three-dimensional form was numerically integrated through the thickness by making a-priori assumptions on the thickness distribution of the deformation. A first account for a complete direct approach for dielectric elastomer plates was presented by Krommer and Staudigl in [13].

In the present paper we summarize the material independent equations for electro-elastic material surfaces. Then, we focus on proposing a rational formulation for the augmented free energy of such surfaces for the case the underlying plates and shells are made of an electrostrictive polymer. Electrostriction will be accounted for by a multiplicative decomposition of the surface stretch tensor and an additive decomposition of the surface curvature tensor into elastic and electrical parts. Finally, the proposed theory is validated.

2 ELECTRO-ELASTIC PLATES AS MATERIAL SURFACES

In this section we discuss the governing equations of thin plates modeled as a two-dimensional electro-elastic material surface with mechanical and electrical degrees of freedom. In particular, we consider the plate as a two-dimensional continuum with five mechanical degrees of freedom, three translations and two rotations. Concerning the electrical degrees of freedom, we use only the dominant one, i.e., the electric potential difference V .

2.1 Strain measures

The material surface is plane in the reference configuration, and it is denoted as reference surface. In the deformed or actual configuration the material surface is denoted as actual surface. The first metric tensor of the plane reference surface $\mathbf{A} = \mathbf{I}$ is the two-dimensional identity tensor and the second metric tensor is zero, $\mathbf{B} = \mathbf{0}$. For the actual surface the first and second metric tensors are \mathbf{a} and \mathbf{b} . The reference configuration and the actual configuration of the material surface are related to each other by means of a deformation gradient tensor $\mathbf{F} = (\nabla_0 \mathbf{r})^T$ with the differential operator ∇_0 of the reference surface and the position vector \mathbf{r} of points of the material surface in the actual configuration. Also note that the second metric tensor of the actual surface is $\mathbf{b} = \mathbf{b}^T = -\nabla \mathbf{n}$ with the unit normal vector \mathbf{n} of the actual surface, and $\mathbf{a} = \nabla \mathbf{r} = \mathbf{I}_3 - \mathbf{n}\mathbf{n}$ with the three-dimensional identity tensor \mathbf{I}_3 holds for the first metric tensor. The differential operators ∇_0 and ∇ with $\nabla_0 = \mathbf{F}^T \cdot \nabla$ refer to either the reference surface or the actual surface. We introduce two tensor valued Green strain measures for the material surface, which are defined as the difference between the two metric tensors in the two configurations, with the proper transformation by means of \mathbf{F} ,

$$\boldsymbol{\varepsilon} = \frac{1}{2} (\mathbf{F}^T \cdot \mathbf{F} - \mathbf{I}) , \quad \boldsymbol{\kappa} = -\mathbf{F}^T \cdot \mathbf{b} \cdot \mathbf{F}. \quad (1)$$

Both strain measures remain constant if and only if the motion of the material surface is a rigid body motion, see [14] for a discussion. A theory with these strain measures is denoted as Kirchhoff-Love theory.

2.2 Material independent equations

A variational principle is introduced for the electro-elastic material surface as

$$\int_{A_0} (\delta\Omega - (\mathbf{p} \cdot \delta\mathbf{r} - \mathbf{m} \times \mathbf{n} \cdot \delta\mathbf{n} + \sigma\delta V)) dA_0 - \delta A^{e,b} = 0, \quad (2)$$

with the area A_0 of the reference surface, the external electric charge σ per unit area of the reference surface and the voltage V . \mathbf{p} and \mathbf{m} are purely mechanical external forces and moments per unit area of the reference surface and Ω is the plate augmented free energy. External forces and moments acting at the boundary, which involve both, mechanical and electrical contributions, are accounted for by means of the virtual work $\delta A^{e,b}$. Due to the fact that external forces and moments \mathbf{p} and \mathbf{m} are assumed purely mechanical, ponderomotive forces must be accounted for by means of Ω . With ease one can show that the plate augmented free energy per unit reference area of the plate has the form $\Omega = \Omega(\boldsymbol{\varepsilon}, \boldsymbol{\kappa}, V)$. Formally computing the variation of this energy to

$$\delta\Omega = \frac{\partial\Omega}{\partial\boldsymbol{\varepsilon}} \cdot \cdot \delta\boldsymbol{\varepsilon} + \frac{\partial\Omega}{\partial\boldsymbol{\kappa}} \cdot \cdot \delta\boldsymbol{\kappa} + \frac{\partial\Omega}{\partial V} \delta V, \quad (3)$$

and noting the general relation $\delta\Omega = \boldsymbol{\tau} \cdot \cdot \delta\boldsymbol{\varepsilon} + \boldsymbol{\mu} \cdot \cdot \delta\boldsymbol{\kappa} - q\delta V$ finds the constitutive relations of the electro-elastic material surface to

$$\boldsymbol{\tau} = \frac{\partial\Omega}{\partial\boldsymbol{\varepsilon}} , \quad \boldsymbol{\mu} = \frac{\partial\Omega}{\partial\boldsymbol{\kappa}} , \quad q = -\frac{\partial\Omega}{\partial V}. \quad (4)$$

Here, $\boldsymbol{\tau}$ and $\boldsymbol{\mu}$ are two second Piola-Kirchhoff type stress tensors and q is the internal charge per unit area of the reference surface.

2.3 Constitutive modeling for isotropic dielectric elastomer plates

The present approach to modeling of plates as electro-elastic material surfaces involves two strain measures, $\boldsymbol{\varepsilon}$ and $\boldsymbol{\kappa}$. Talking about hyperelastic plates, we rather work with the right Cauchy-Green tensor \mathbf{C} than with $\boldsymbol{\varepsilon}$; hence, we recall the definitions

$$\mathbf{C} = \mathbf{F}^T \cdot \mathbf{F}, \quad \boldsymbol{\kappa} = -\mathbf{F}^T \cdot \mathbf{b} \cdot \mathbf{F}. \quad (5)$$

Next, we introduce the polar decomposition of the deformation gradient tensor as $\mathbf{F} = \mathbf{R} \cdot \mathbf{U}$, in which \mathbf{R} is an orthogonal tensor with $\mathbf{n} = \mathbf{R} \cdot \mathbf{N}$ and $\mathbf{U} = \mathbf{U}^T$ is the symmetric stretch tensor of the material surface. Then, the two strain measures may as well be written in the form

$$\mathbf{C} = \mathbf{U}^2, \quad \boldsymbol{\kappa} = -\mathbf{U} \cdot \mathbf{R}^T \cdot \mathbf{b} \cdot \mathbf{R} \cdot \mathbf{U}. \quad (6)$$

For the purpose of constitutive modeling, we involve the alternative second strain measure

$$\mathbf{K} = \mathbf{U}^{-1} \cdot \boldsymbol{\kappa} \cdot \mathbf{U}^{-1} = -\mathbf{R}^T \cdot \mathbf{b} \cdot \mathbf{R}, \quad (7)$$

which we denote as curvature tensor. Then, $\Omega = \Omega(\mathbf{C}, \mathbf{K}, V)$ holds.

2.3.1 Augmented free energy

The bottleneck in our formulation is the specific form of the augmented free energy $\Omega = \Omega(\mathbf{C}, \mathbf{K}, V)$; in particular, when it involves hyperelastic material laws. In this paper, we will only concern ourselves with thin plates with thickness h made of isotropic and incompressible hyperelastic materials, for which the material is assumed homogenous through the thickness and obeys a neo-Hookean law. In order to introduce the specific form of the plate augmented free energy we start with an additive decomposition of $\Omega = \Omega(\mathbf{C}, \mathbf{K}, V)$ into a mechanical part and a total electrical part,

$$\Omega = \eta_0 \Psi_{me}(\mathbf{C}, \mathbf{K}) + \eta_0 \Psi_{el,tot}(\mathbf{C}, \mathbf{K}, V). \quad (8)$$

Strain energy We start with a discussion of the mechanical part, i.e., the strain energy, for which the polar decomposition $\mathbf{F} = \mathbf{R} \cdot \mathbf{U}$ enables an additive decomposition into a membrane and a bending part, $\eta_0 \Psi_{me}(\mathbf{C}, \mathbf{K}) = W_m(\mathbf{C}) + W_b(\mathbf{C}, \mathbf{K})$. The membrane part is taken in analogy to a plane stress incompressible neo-Hookean strain energy as

$$W_m = \eta_0 w_m = \frac{1}{2} \frac{A}{4} (\text{tr} \mathbf{C} + (\det \mathbf{C})^{-1} - 3). \quad (9)$$

Here, $A = Yh(1 - \nu^2)^{-1}$ is the membrane stiffness well known from linear plate theory. With $\nu = 0.5$ we have Young's modulus as $Y = 3\mu$ and $A = 4\mu h$ holds. η_0 is the mass per unit reference area and w_m the membrane energy per unit mass. In order to introduce the bending energy, we recall the polar decomposition $\mathbf{F} = \mathbf{R} \cdot \mathbf{U}$, by means of which the deformation gradient tensor is multiplicatively decomposed into a plane part \mathbf{U} and an orthogonal part \mathbf{R} . As the first part does not contribute to the bending deformation, the bending energy must not directly depend on the stretch tensor \mathbf{U} , and the corresponding intermediate configuration must be free of bending stresses. Therefore, the bending energy should be formulated in terms of the curvature tensor only, and be referred to the mass η per unit area in the intermediate configuration with a plate

stiffness \tilde{D} accounting for the thickness of the plate in the intermediate configuration. Hence, we write the bending energy per unit area in the intermediate configuration in analogy to the one of an isotropic incompressible Kirchhoff plate as

$$\eta w_b = \frac{1}{2} \tilde{D} ((\text{tr} \mathbf{K})^2 - \det \mathbf{K}). \quad (10)$$

Here, we have taken the standpoint that the curvature tensor is of an order of smallness that justifies the use of an incompressible Saint-Venant Kirchhoff strain energy. With the area change from the reference configuration to the intermediate configuration $J = \det \mathbf{U} = \det \mathbf{F}$, $\eta = J^{-1} \eta_0$ holds; obviously, η also represents the mass per unit actual area. Noting in addition the three-dimensional incompressibility condition $J_3 = 1 = J F_{33}$ with the thickness stretch $U_{33} \equiv F_{33} = \lambda_3$, the plate stiffness in the intermediate configuration is $\tilde{D} = J^{-3} D$, in which $D = Y h^3 / 12 (1 - \nu^2)^{-1}$ is the classical plate stiffness, which is $D = \mu h^3 / 3$ for $\nu = 0.5$. Therefore, we have

$$W_b = \eta_0 w_b = \frac{1}{2} (\det \mathbf{C})^{-1} D ((\text{tr} \mathbf{K})^2 - \det \mathbf{K}). \quad (11)$$

Total electrical energy In a homogenous plate with a homogenous electric field through the thickness, the contribution from the total electrical free energy is written in analogy to a capacitor as $2\eta\psi_{el,tot} = -\tilde{c}V^2$, with the voltage V and the capacity \tilde{c} and mass η per unit actual area; the latter is identical to the mass per unit area in the intermediate configuration emerging by means of \mathbf{U} . \tilde{c} is related to the capacity per unit reference area c by $\tilde{c} = Jc$. Therefore, we have

$$\Omega_{el,tot} = \eta_0 \psi_{el,tot} = -\frac{1}{2} c V^2 (\det \mathbf{C}) \quad (12)$$

for the electrically homogenous case. In such a case, the total electrical free energy only contributes to the membrane part of the augmented free energy, which only depends on \mathbf{C} . In the more general scenario of a non-homogenous electric field through the thickness of the plate, the total electrical free energy must also contribute to the bending part of the augmented free energy; therefore, it must depend also on \mathbf{K} . In order to introduce this contribution, we propose the overall bending part of the augmented free energy in the form

$$\eta \omega_b = \frac{1}{2} \left(\tilde{D} ((\text{tr} \mathbf{K})^2 - \det \mathbf{K}) - 2\tilde{m}^* \text{tr} \mathbf{K} \right), \quad (13)$$

which formally constitutes the classical bending energy of an isotropic Kirchhoff plate with a so-called *Eigenspannungsquelle* \tilde{m}^* ; the second term represents the bending part of the total electrical free energy. Here, we have naturally extended our previous standpoint, that the curvature tensor is of an order of smallness that justifies the use of an incompressible Saint Venant–Kirchhoff strain energy to the electrical energy. Keeping in mind that \tilde{m}^* is an *Eigenspannungsquelle* per unit area in the intermediate configuration, it relates to the *Eigenspannungsquelle* per unit area in the reference configuration m^* by virtue of $\tilde{m}^* = Jm^*$. Therefore,

$$\eta_0 \omega_b = \frac{1}{2} ((\det \mathbf{C})^{-1} D ((\text{tr} \mathbf{K})^2 - \det \mathbf{K}) - 2(\det \mathbf{C}) m^* \text{tr} \mathbf{K}) \quad (14)$$

holds. The first part is the bending energy from above, whereas the second part can be combined with the electrical energy introduced for a homogenous electric field to

$$\Omega_{el,tot}(\mathbf{C}, \mathbf{K}, V) = \eta_0 \psi_{el,tot} = -\frac{1}{2}cV^2 \det \mathbf{C} - \frac{1}{2}2(\det \mathbf{C})m^* \text{tr} \mathbf{K}. \quad (15)$$

As m^* must be proportional to V^2 and the capacity per unit reference area c is a constant, we write $m^* = c\alpha V^2$ and obtain the final form of the total electrical contribution to the augmented free energy as

$$\Omega_{el,tot}(\mathbf{C}, \mathbf{K}, V) = \eta_0 \psi_{el,tot} = -\frac{1}{2}cV^2 \det \mathbf{C} (1 + 2\alpha \text{tr} \mathbf{K}), \quad (16)$$

in which α is a parameter characterizing the non-homogeneity of the electric field through the thickness.

Summarizing our result, the augmented free energy of an isotropic, elastically homogenous and incompressible hyperelastic neo-Hookean electro-elastic plate is proposed as

$$\begin{aligned} \Omega(\mathbf{C}, \mathbf{K}, V) &= \frac{1}{2} \frac{A}{4} (\text{tr} \mathbf{C} + (\det \mathbf{C})^{-1} - 3) + \frac{1}{2} (\det \mathbf{C})^{-1} D((\text{tr} \mathbf{K})^2 - \det \mathbf{K}) \\ &\quad - \frac{1}{2} cV^2 \det \mathbf{C} (1 + 2\alpha \text{tr} \mathbf{K}). \end{aligned} \quad (17)$$

Finally, we note that the relations $\text{tr} \mathbf{K} = \text{tr}(\mathbf{U}^{-1} \cdot \boldsymbol{\kappa} \cdot \mathbf{U}^{-1}) = \text{tr}(\mathbf{C}^{-1} \cdot \boldsymbol{\kappa})$, $\det \mathbf{K} = \det(\mathbf{U}^{-1} \cdot \boldsymbol{\kappa} \cdot \mathbf{U}^{-1}) = \det(\mathbf{C}^{-1} \cdot \boldsymbol{\kappa})$ and $\mathbf{C} = \mathbf{I} + 2\boldsymbol{\varepsilon}$ enable us to write the augmented free energy as $\Omega = \Omega(\boldsymbol{\varepsilon}, \boldsymbol{\kappa}, V)$, which closes the theory of electro-elastic material surfaces for the case of plates and in the absence of constitutive coupling by means of electrostriction.

2.3.2 Electrostrictive coupling

The augmented free energy as proposed in the previous section accounts for electrostatic forces, but not for constitutive coupling by means of electrostriction. A straightforward extension is obtained by replacing the strain measures \mathbf{C} and \mathbf{K} by their elastic counterparts \mathbf{C}_e and \mathbf{K}_e in the strain energy part of the augmented free energy. Hence, we write

$$\begin{aligned} \Omega(\mathbf{C}_e, \mathbf{K}_e, \mathbf{C}, \mathbf{K}, V) &= \frac{1}{2} \frac{A}{4} (\text{tr} \mathbf{C}_e + (\det \mathbf{C}_e)^{-1} - 3) + \frac{1}{2} (\det \mathbf{C}_e)^{-1} D((\text{tr} \mathbf{K}_e)^2 - \det \mathbf{K}_e) \\ &\quad - \frac{1}{2} cV^2 \det \mathbf{C} (1 + 2\alpha \text{tr} \mathbf{K}). \end{aligned} \quad (18)$$

It remains to define the elastic strain measures. For this sake we introduce a multiplicative decomposition of the total stretch tensor and an additive decomposition of the total curvature tensor in the following.

First, we use a multiplicative decomposition $\mathbf{U} = \mathbf{U}_e \cdot \mathbf{U}_{el}$ for the symmetric stretch tensor \mathbf{U} of the material surface into an electrical part $\mathbf{U}_{el} = \mathbf{U}_{el}(V)$ and an elastic part \mathbf{U}_e . Analogous multiplicative decompositions have been introduced by different authors for electro-active polymers but also piezoelectric materials in a three-dimensional framework, see [6], [3] and [8]. Introducing the multiplicative decomposition for the stretch tensor rather than for the deformation gradient tensor restricts the electrical part to be symmetric, which in the present paper is fully justified. Moreover, due to isotropy we consider the electrical part as spherical, $\mathbf{U}_{el} = \lambda_{el} \mathbf{I}$

with $\lambda_{el} = \lambda_{el}(V)$. With the decomposition at hand, the right Cauchy-Green tensor of the material surface is

$$\mathbf{C} = \mathbf{U}_{el} \cdot \mathbf{C}_e \cdot \mathbf{U}_{el} = \lambda_{el}^2 \mathbf{C}_e. \quad (19)$$

Here, $\mathbf{C}_e = \mathbf{U}_e^2$ is the elastic right Cauchy-Green tensor, which can also be written as

$$\mathbf{C}_e = \lambda_{el}^{-2} \mathbf{C}. \quad (20)$$

Concerning the curvature tensor we use an additive decomposition $\mathbf{K} = \mathbf{K}_e + \mathbf{K}_{el}$, from which the elastic curvature tensor follows to

$$\mathbf{K}_e = \mathbf{K} - \mathbf{K}_{el} = \mathbf{U}^{-1} \cdot (\boldsymbol{\kappa} - \boldsymbol{\kappa}_{el}(V)) \cdot \mathbf{U}^{-1}. \quad (21)$$

Eventually, $\lambda_{el}(V)$ and $\boldsymbol{\kappa}_{el}(V)$ must be properly specified. With \mathbf{C}_e and \mathbf{K}_e at hand, the augmented free energy is $\Omega = \Omega(\mathbf{C}_e, \mathbf{K}_e, \mathbf{C}, \mathbf{K}, V)$, in which $\mathbf{C}_e = \lambda_{el}^{-2}(V) \mathbf{C}$ and $\mathbf{K}_e = \mathbf{K} - \mathbf{K}_{el} = \mathbf{U}^{-1} \cdot (\boldsymbol{\kappa} - \boldsymbol{\kappa}_{el}(V)) \cdot \mathbf{U}^{-1} = \mathbf{U}^{-1} \cdot \boldsymbol{\kappa}_e \cdot \mathbf{U}^{-1}$ hold.

2.3.3 Electrical part of the stretch tensor and the curvature tensor

To complete the constitutive modeling for plates, we must introduce the electrical stretch tensor $\mathbf{U}_{el}(V)$ as well as the electrical part of the curvature tensor $\mathbf{K}_{el}(V)$. Concerning the latter we note the relation $\mathbf{K}_{el} = \mathbf{U}^{-1} \cdot \boldsymbol{\kappa}_{el} \cdot \mathbf{U}^{-1}$ and rather introduce $\boldsymbol{\kappa}_{el} = \boldsymbol{\kappa}_{el}(V)$. Due to the specific material structure, we have

$$\mathbf{U}_{el} = \lambda_{el} \mathbf{I}, \quad \boldsymbol{\kappa}_{el} = \kappa_{el} \mathbf{I}. \quad (22)$$

The electrical stretch and the material electrical curvature are taken as functions of the square of the voltage, $\lambda_{el} = \lambda_{el}(V^2)$ and $\kappa_{el} = \kappa_{el}(V^2)$. In general, one must identify these functions from experiments. In the present paper, we will discuss the specific form of λ_{el} and κ_{el} only for the example presented in the final section.

3 EXTENSION TO SHELLS

In contrast to plates the reference surface of a shell is not plane; hence, the two metric tensors of the reference surface are $\mathbf{A} = \mathbf{I}_3 - \mathbf{N}\mathbf{N}$ and $\mathbf{B} = \mathbf{B}^T = -\nabla_0 \mathbf{N}$. In this case the total strain measures become

$$\boldsymbol{\varepsilon} = \frac{1}{2} (\mathbf{F}^T \cdot \mathbf{F} - \mathbf{A}), \quad \boldsymbol{\kappa} = -(\mathbf{F}^T \cdot \mathbf{b} \cdot \mathbf{F} - \mathbf{B}). \quad (23)$$

As in the plate theory we introduce the curvature tensor \mathbf{K} as

$$\mathbf{K} = -(\mathbf{R}^T \cdot \mathbf{b} \cdot \mathbf{R} - \bar{\mathbf{B}}) \quad (24)$$

with $\bar{\mathbf{B}} = \mathbf{U}^{-1} \cdot \mathbf{B} \cdot \mathbf{U}^{-1}$. Using again the additive decomposition of the curvature tensor $\mathbf{K} = \mathbf{K}_e + \mathbf{K}_{el}$, we obtain the elastic part of the curvature tensor to

$$\mathbf{K}_e = -(\mathbf{R}^T \cdot \mathbf{b} \cdot \mathbf{R} - \bar{\mathbf{B}}) - \mathbf{K}_{el} = -(\mathbf{R}^T \cdot \mathbf{b} \cdot \mathbf{R} - \mathbf{B}_{el}), \quad (25)$$

in which we have introduced an effective second metric tensor \mathbf{B}_{el} of the intermediate configuration, which evolves through the total stretch tensor \mathbf{U} from the reference configuration; note

that \mathbf{B}_{el} is not an actual metric tensor, as it is not necessarily the negative gradient of some unit normal vector. This effective second metric tensor \mathbf{B}_{el} with

$$\mathbf{B}_{el} = \bar{\mathbf{B}} - \mathbf{K}_{el} = \mathbf{U}^{-1} \cdot (\mathbf{B} - \boldsymbol{\kappa}_{el}) \cdot \mathbf{U}^{-1} \quad (26)$$

takes the role of $\bar{\mathbf{B}}$, which is present in the total curvature tensor, in the definition of the elastic curvature tensor. Therefore, we can write the augmented free energy for a shell as

$$\begin{aligned} \Omega(\mathbf{C}_e, \mathbf{K}_e, \mathbf{C}, \mathbf{K}, V) = & \frac{1}{2} \frac{A}{4} (\text{tr} \mathbf{C}_e + (\det \mathbf{C}_e)^{-1} - 3) + \frac{1}{2} (\det \mathbf{C}_e)^{-1} D((\text{tr} \mathbf{K}_e)^2 - \det \mathbf{K}_e) \\ & - \frac{1}{2} c V^2 \det \mathbf{C} (1 + 2\alpha \text{tr} \mathbf{K}), \end{aligned} \quad (27)$$

with $\mathbf{C}_e = \lambda_{el}^{-2} \mathbf{C}$ and $\mathbf{K}_e = \mathbf{U}^{-1} \cdot (\boldsymbol{\kappa} - \kappa_{el} \mathbf{I}) \cdot \mathbf{U}^{-1}$, which is formally identical to the plate formulation, with the only difference being the presence of \mathbf{B} in the definition of the strain measure $\boldsymbol{\kappa}$.

4 VALIDATION

Having proposed a novel form for the augmented free energy of electro-elastic thin plates and shells made of incompressible isotropic electrostrictive polymers, we proceed with a first validation of the theory. We validate the theory against an alternative approach, for which numerical solution computed with Finite elements are available. This formulation is based on the three-dimensional augmented free energy for an incompressible neo-Hookean electro-elastic material, which is

$$\Omega_3 = \frac{\mu}{2} (\text{tr} \mathbf{C}_{3,e} - 3) - \frac{1}{2} \varepsilon \boldsymbol{\mathcal{E}} \cdot (\mathbf{C}_3^{-1} \cdot \boldsymbol{\mathcal{E}}). \quad (28)$$

The three-dimensional elastic right Cauchy-Green tensor

$$\mathbf{C}_{3,e} = \mathbf{F}_{el,3}^{-T} \cdot \mathbf{C}_3 \cdot \mathbf{F}_{el,3}^{-1} \quad (29)$$

follows from a multiplicative decomposition of the deformation gradient tensor at the three-dimensional level with $\mathbf{F}_3 = \mathbf{F}_{e,3} \cdot \mathbf{F}_{el,3}$; here $\mathbf{F}_{el,3}$ is the electrical part of the deformation gradient tensor, which already accounts for incompressibility. Hence, we write

$$\mathbf{F}_{el,3} = \lambda_{el,3} (\mathbf{I}_3 - \mathbf{M} \mathbf{M}) + \lambda_{el,3}^{-2} \mathbf{M} \mathbf{M}, \quad (30)$$

in which $\lambda_{el,3} = \lambda_{el,3}(\mathcal{E}^2)$ is the stretch in any direction perpendicular to the direction \mathbf{M} of the material electric field vector $\boldsymbol{\mathcal{E}} = \mathcal{E} \mathbf{M}$. Specific forms for $\lambda_{el,3}$ have been proposed in the literature as

$$\lambda_{el,3} = (1 + \frac{3k}{2} \mathcal{E}^2)^{1/3}, \quad \lambda_{el,3} = e^{\frac{k}{2} \mathcal{E}^2}, \quad (31)$$

in which the first law was suggested by Zäh and Miehe [3] and the second one by Skatulla et al. [6]. Identifying the direction of the electric field with the thickness direction, $\mathbf{M} = \mathbf{N}$, and assuming a plane stress condition for the total second Piola-Kirchhoff stress tensor together with the incompressibility condition $\det \mathbf{C}_3 = 1$, the plane stress augmented free energy becomes

$$\Omega_2 = \frac{\mu}{2} \left(\lambda_{el,3}^{-2} \text{tr} \mathbf{C}_2 + \lambda_{el,3}^4 (\det \mathbf{C}_2)^{-1} - 3 \right) - \frac{1}{2} \varepsilon \det \mathbf{C}_2 \mathcal{E}^2. \quad (32)$$

\mathbf{C}_2 is the plane part of \mathbf{C}_3 . Eventually, \mathbf{C}_2 is approximated with $\mathbf{C}_2 = 2(\boldsymbol{\varepsilon} + Z\boldsymbol{\kappa}) + \mathbf{I} = \mathbf{C} + Z\boldsymbol{\kappa}$. A numerical integration through the thickness then finds the plate augmented free energy, see e.g. [7] or [15]. For the case of problems without constitutive coupling by means of electrostriction, this type of modeling is already well tested against results from the literature in [12] using Finite Elements within the geometrically exact formulation.

4.1 Bi-morph bending actuator

As a numerical example, we study a bi-morph rectangular homogenous plate with dimensions $L \times b \times h = 100\text{mm} \times 50\text{mm} \times 1\text{mm}$ with two identical layers made of polyurethane with the material parameters $\varepsilon_r = 8.8$, $k = 6.86 \times 10^{-16} \text{m}^2 \text{V}^{-2}$ and $\mu = 1.2 \times 10^6 \text{Pa}$, which are taken from [16]. However, only the bottom layer is used for actuation and the top layer is short-circuited. Accordingly, a bending actuator is obtained. Before we proceed to the results, we must first discuss the electrical stretch λ_{el} and the electrical curvature κ_{el} , the capacity c and the geometry parameter α in the augmented free energy. As a starting point, we note that the material electric field $\mathcal{E} = V(h/2)^{-1}$ acts only in the bottom layer, such that the electric field is not homogenous through the thickness. Then, $\lambda_{el,3} = 1$ holds in the top layer, whereas

$$\lambda_{el,3} = e^{\frac{k}{2}\mathcal{E}^2} \quad (33)$$

is true in the bottom layer. We compute the plate electrical stretch as the mean value and the electrical curvature as the first moment of the stretch $\lambda_{el,3}$ to

$$\lambda_{el} = \frac{1}{h} \int_h \lambda_{el,3} dZ, \quad \kappa_{el} = \frac{12}{h^3} \int_h \lambda_{el,3} Z dZ. \quad (34)$$

The capacity per unit reference area of the bottom layer is $c = \varepsilon(h/2)^{-1}$ and the geometry parameter α is taken as $\alpha = h/4$, which is the thickness center of the bottom layer. The plate is clamped at $x = 0$ and free on the other three edges and a voltage V is applied between the electrodes of the bottom layer. In this problem, the augmented free energy of the plate is

$$\begin{aligned} \Omega = & \frac{1}{2} \frac{A}{4} (\lambda_{el}^{-2} \text{tr} \mathbf{C} + \lambda_{el}^4 (\det \mathbf{C})^{-1} - 3) \\ & + \frac{1}{2} \lambda_{el}^4 (\det \mathbf{C})^{-1} D ((\text{tr} (\mathbf{C}^{-1} \cdot (\boldsymbol{\kappa} - \kappa_{el} \mathbf{I})))^2 - \det (\mathbf{C}^{-1} \cdot (\boldsymbol{\kappa} - \kappa_{el} \mathbf{I}))) \\ & - \frac{1}{2} c V^2 \det \mathbf{C} (1 + 2\alpha \text{tr} (\mathbf{C}^{-1} \cdot \boldsymbol{\kappa})), \end{aligned} \quad (35)$$

because $\text{tr} \mathbf{K} = \text{tr} (\mathbf{C}^{-1} \cdot \boldsymbol{\kappa})$, $\text{tr} \mathbf{K}_e = \text{tr} (\mathbf{C}^{-1} \cdot \boldsymbol{\kappa}_e)$ and $\det \mathbf{K}_e = \det (\mathbf{C}^{-1} \cdot \boldsymbol{\kappa}_e)$ hold. Hence, with $\mathbf{C} = 2\boldsymbol{\varepsilon} + \mathbf{I}$ we have $\Omega = \Omega(\boldsymbol{\varepsilon}, \boldsymbol{\kappa}, V)$. In this conservative problem with a prescribed voltage, the principle of virtual work reduces to a stationarity principle,

$$\delta \Sigma = 0 \quad \text{with} \quad \Sigma = \int_{A_0} \Omega(\boldsymbol{\varepsilon}, \boldsymbol{\kappa}, V) dA. \quad (36)$$

As we are mainly interested in verifying the proposed form of the augmented free energy, we compute solutions with a simple Ritz approximation within the framework of the Novozhilov nonlinear plate theory (see Amabili [17]) rather than for the fully geometrically nonlinear theory. Therefore, the strain measures $\boldsymbol{\varepsilon}$ and $\boldsymbol{\kappa}$ are approximated as

$$\boldsymbol{\varepsilon} = \frac{1}{2} (\nabla_0 \mathbf{u}^S + (\nabla_0 u \nabla_0 u + \nabla_0 v \nabla_0 v + \nabla_0 w \nabla_0 w)) , \quad \boldsymbol{\kappa} = -\nabla_0 \nabla_0 w, \quad (37)$$

in which w is the deflection of the plate, $\mathbf{u} = [u \ v \ 0]^T$ is the in-plane displacement vector and $\nabla_0 \mathbf{u}^S$ denotes the symmetric part of the plane displacement gradient tensor. For the Ritz-Ansatz we set

$$u(x, y) = \sum_{i=1}^3 \sum_{j=0}^1 x^i y^{2j} u_{ij}, \quad v(x, y) = \sum_{i=1}^2 \sum_{j=0}^1 x^i y^{2j+1} v_{ij}, \quad w(x, y) = \sum_{i=1}^4 \sum_{j=0}^1 x^{i+1} y^{2j} w_{ij}. \quad (38)$$

We use this Ansatz and the Novozhilov kinematics for the present theory as well as the one based on the three-dimensional augmented free energy; results computed with the latter approach will be denoted with *Gauss* in the figures.

We increase the voltage in the bottom layer starting with $V = 0\text{V}$ up to $V = 2000\text{V}$ and show results for the non-dimensional end point deflection wh^{-1} and the non-dimensional end point axial position xh^{-1} in the center of the free end in Fig. 1. Clearly, our complete direct

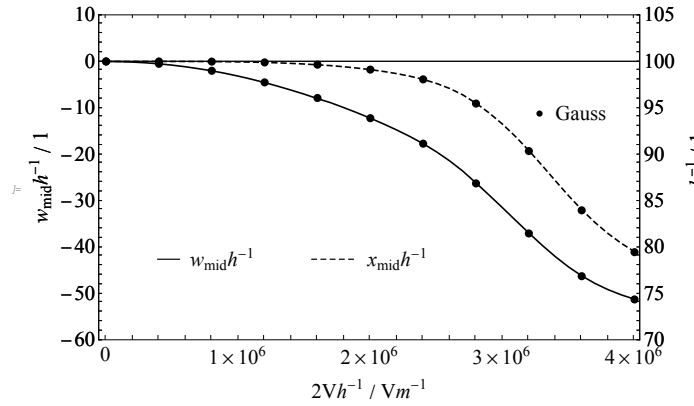


Figure 1: Non-dimensional end point deflection wh^{-1} and non-dimensional end point axial position xh^{-1} for the bending actuator.

approach results into a solution, which is hardly to be distinguished from the approach based on the three-dimensional augmented free energy.

Finally, we use the three-dimensional approach to compute numerical solutions of the fully geometrically nonlinear plate formulation using plate Finite elements. A comparison between the present theory and the Finite element solution for the non-dimensional end point deflection wh^{-1} and the non-dimensional end point axial position $xh^{-1}h$ in the center of the free end is shown Fig. 2. The solid line corresponds to the Finite elements and the circular markers to the present theory. A reasonable agreement is found up to the voltage $V = 2000\text{V}$. Finally the end point position is presented in Fig. 3.

5 Conclusions

In the present paper we have proposed a complete direct approach to modeling of thin plates and shells made of electrostrictive polymers. In particular, an electro-elastic Kirchhoff-Love theory as a special case of a Cosserat surface was developed, in which the augmented free energy was directly introduced for the material surface. Electrostriction was incorporated by means of a multiplicative decomposition of the surface stretch tensor and an additive decomposition of the surface curvature tensor. The resulting formulation was tested against a theory derived from the

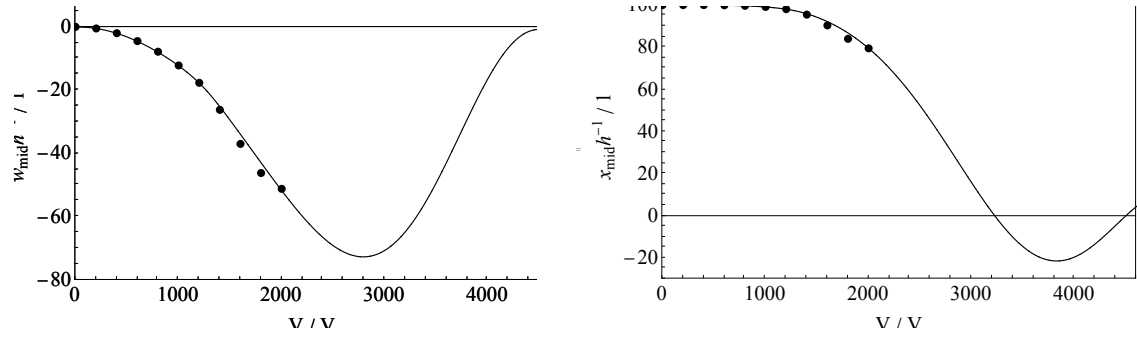


Figure 2: Non-dimensional end point deflection wh^{-1} (left) and non-dimensional end point axial position xh^{-1} (right) for the bending actuator: Finite Element solution (solid line) vs. Ritz approximation (circular markers).

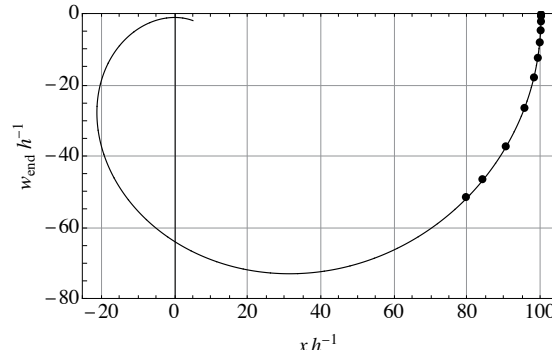


Figure 3: Non-dimensional end point position for the bending actuator: Finite Element solution (solid line) vs. Ritz approximation (circular markers).

three-dimensional formulation based on a plane stress assumption and an a-priori assumption concerning the distribution of the strain through the thickness. An excellent agreement was observed.

Acknowledgement A. Humer acknowledges the support by the COMET-K2 Center of the Linz Center of Mechatronics (LCM) funded by the Austrian federal government and the federal state of Upper Austria.

REFERENCES

- [1] Pelrine RE, Kornbluh RD and Joseph JP (1998) Electrostriction of polymer dielectrics with compliant electrodes as a means of actuation. *Sensors and Actuators A: Physical* **64**, 77–85.
- [2] Bar-Cohen Y (2004) *Electroactive Polymer (EAP) Actuators as Artificial Muscles: Reality, Potential, and Challenges*, SPIE, Bellingham, WA.
- [3] Zäh D and Miehe C (2015) Multiplicative electro-elasticity of electroactive polymers accounting for micromechanically-based network models, *Computational Methods in Applied Mechanics and Engineering* **286**, 394–421.

- [4] Dorfmann A and Ogden RW (2005) Nonlinear electroelasticity. *Acta Mechanica* **174**, 167–183.
- [5] Vu DK, Steinmann P and Possart G (2007) Numerical modelling of non-linear electroelasticity, *International Journal for Numerical Methods in Engineering* **70**, 685–704.
- [6] Skatulla S, Sansour C and Arockiarajan A (2012) A multiplicative approach for nonlinear electro-elasticity. *Computer Methods in Applied Mechanics and Engineering* **245–246**, 243–255.
- [7] Staudigl E, Krommer M and Humer A (2018) Modeling of Dielectric Elastomers Accounting for Electrostriction by Means of a Multiplicative Decomposition of the Deformation Gradient Tensor. In *Analysis and Modelling of Advanced Structures and Smart Systems*, Altenbach H, Carrera E and Kulikov G (eds.), Springer, Vienna, 2018.
- [8] Humer A and Krommer M (2015) Modeling of Piezoelectric Materials by Means of a Multiplicative Decomposition of the Deformation Gradient. *Mechanics of Advanced Materials and Structures* **22**, 125–135.
- [9] Vetyukov Y, Staudigl E and Krommer M (2018) Hybrid asymptotic-direct approach to finite deformations of electromechanically coupled piezoelectric shells. *Acta Mechanica* **229**(2), 953–974.
- [10] Klinkel S, Zwecker S and Mueller R (2013) A Solid Shell Finite Element Formulation for Dielectric Elastomers. *Journal of Applied Mechanics* **80**, 021026-1–021026-11.
- [11] Bishara D and Jabareen M (2017) An optimal solid-shell finite element for modeling dielectric elastomers. In *Proceedings of the 7th GACM Colloquium on Computational Mechanics for Young Scientists from Academia and Industry*, 6 pages.
- [12] Staudigl E, Krommer M and Vetyukov Y (2017) Finite deformations of thin plates made of dielectric elastomers: Modeling, Numerics and Stability. *Journal of Intelligent Material Systems and Structures*, published online October 2017, 19p.
- [13] Krommer M and Staudigl-Hansy E (2019) A complete direct approach to modeling of dielectric elastomer plates as material surfaces. In *Dynamics and Control of Advanced Structures and Machines: Contributions from the 3rd International Workshop, Perm, Russia*, Metveenkov V, Krommer M, Belyaev AK and Irschik H (eds.), SpringerNature.
- [14] Vetyukov Y (2014) *Nonlinear Mechanics of Thin-Walled Structures: Asymptotics, Direct Approach and Numerical Analysis*, SpringerViennaNewYork.
- [15] Breslavsky ID, Amabili M and Legrand M (2014) Nonlinear vibrations of thin hyperelastic plates, *Journal of Sound and Vibration* **333**(19), 4668–4681.
- [16] Diaconu I and Dorhoi DO (2005) Properties of polyurethane thin films, *Journal of Optoelectronics and Advanced Materials* **7**(2), 921–924.
- [17] Amabili M (2008) *Nonlinear Vibrations and Stability of Shells and Plates*, Cambridge University Press, New York.

DEVELOPMENT OF A SCALE-ADAPTIVE INDICATOR FOR THE SIMULATION OF THERMOMECHANICALLY LOADED SMA MATRIX COMPOSITES

M. Praster and S. Klinkel

Lehrstuhl für Baustatik und Baudynamik (LBB)

RWTH Aachen

Mies-van-der-Rohe-Str. 1, 52074 Aachen, Germany

e-mail: praster@lbb.rwth-aachen.de, web page: <http://www.lbb.rwth-aachen.de>

Key words: Shape Memory Alloy, Matrix Composite, Multiscale Analysis, Scale Adaptive Method

Abstract. Shape memory alloys (SMA) are used for smart devices due to their mechanical-thermal coupling properties. Because of the high costs, SMAs are currently employed only in special applications. One possibility is to use them in combination with a low-cost matrix material. From a numerical point of view, such composite materials require a considerable additional effort in the simulation. Especially with regard to the nonlinear behaviour of SMA, and with respect to thermal and mechanical coupling, the computational effort increases considerably. A multi-scale simulation offers a possibility to consider the deformation and thermal dependent material properties of SMA composites. The macroscopic material properties are determined with an accompanying homogenization on the micro level. Commonly, the accompanying homogenization is performed at each Gaussian point of the macroscale. In the frame of FE^2 method the accompanying homogenization results in an exponential growth of the equations depending on the macroscopic/microscopic discretization. This contribution is concerned with a method to reduce the computational cost of the nested homogenization within an FE^2 formulation. The SMA, however, shows constant material properties within a certain range of deformation, therefore the material properties of the macroscopic material parameters do not change. Here, an indicator on the macroscale is introduced, which indicates if an accompanying homogenization is necessary or not. The indicator is a function of the the strain and in addition of the temperature state of the material point. It detects whether the material behaves linearly on the microscale or not. In case the microstructure behaves linear, no accompanying homogenization is necessary. The computational savings are discussed in several numerical simulations of SMA composite structures.

1 INTRODUCTION

Shape memory alloys are materials which are able to restore the current permanent deformations to their original state when heated. These properties follow from the different crystal lattice structures at different temperatures, see e.g. [1]. This paper deals with Ni-Ti alloys and a large number of other alloys such as ceramics or polymers. The rearrangement of atoms are induced by variable temperature and electric fields. The structural phases of SMAs depend on the material temperature and are known as martensitic (low temperature) and austenitic (high temperature) phase. In addition to the shape memory effect, superelasticity is also a remarkable property of the material. SMA are expensive, hence there-

fore they are often embedded in a composite material. The result is a new material, from which the material properties can be determined either from cost-intensive experiments or alternatively with numerical methods such as homogenization. The micro-scale, which represents the heterogeneous material structure, is modeled by a representative volume element (RVE) to calculate the effective macroscopic material properties. The definition of the RVE is a crucial task, for further details the reader is referred to e.g. [2]. One possibility is to model the RVE by the finite element method, which leads to a numerical homogenization. Since the macro-structure is also modeled by finite elements, an accompanying nested finite element analysis is observed. The advantage of a nested finite element method is remarkable in the in situations of non-linear material behavior, where a homogenization is provided for the current deformation state and load step, respectively. The so-called FE^2 or multilevel finite element method is discussed in e.g. [3]. Since the iterations are nested, an extremely high computational capacity is needed. In the present contribution, an indicator for an adaptive FE^2 method is developed by considering a SMA-matrix composite, where the matrix material is assumed to be linear elastic. It is remarked that an accompanying homogenization is only necessary for non-linear material behavior. Hence, the indicator on the macroscopic scale needs to predict the non-linear behavior, which depends on the stress and temperature field on the microscopic scale. A limit strain state associated with the phase-transition stress of the SMA is employed. In case the indicator is reached, an accompanying numerical homogenization is performed.

2 Macro and Micro Boundary Value Problem

Let $\bar{\Omega}$ be an arbitrary macroscopic body with the two mechanical boundaries $\partial\Omega_{\sigma}$ for the tractions $\bar{\mathbf{t}}$ (Neumann) and the displacements $\partial\Omega_{\mathbf{u}}$ (Dirichlet) in the mechanical BVP, the whole boundary is defined as $\partial\Omega = \partial\Omega_{\sigma} \cup \partial\Omega_{\mathbf{u}}$, the thermal BVP is given with the two thermal boundaries $\partial\Omega_q$ for the heat flux $\bar{\mathbf{q}}$ and the temperature θ as the Dirichlet boundary condition $\partial\Omega_{\theta}$. The description of the kinematics is in the context of small strains and described by the gradient of the macroscopic displacement $\bar{\mathbf{u}}$, resulting in the macroscopic strain

$$\bar{\boldsymbol{\varepsilon}} = \bar{\nabla}^{sym} \bar{\mathbf{u}}(\bar{\mathbf{X}}), \quad (1)$$

where $\bar{\nabla}^{sym} = \frac{1}{2}(\bar{\nabla} + \bar{\nabla}^T)$.

The governing equations for the mechanical macro-problem are the balance of linear and angular momentum. The balance of linear momentum yields

$$\text{div } \bar{\boldsymbol{\sigma}} + \bar{\mathbf{b}} = \mathbf{0} \quad \text{in } \bar{\Omega}_0 \quad \text{and} \quad \mathbf{t}_0 = \bar{\boldsymbol{\sigma}} \mathbf{N}, \quad (2)$$

with $\bar{\mathbf{b}}$ denoting the body force density and $\bar{\boldsymbol{\sigma}}$ the macroscopic stress. The symmetry of the stress $\bar{\boldsymbol{\sigma}} = \bar{\boldsymbol{\sigma}}^T$ follows from the balance of angular momentum. The thermal field in the body $\bar{\Omega}$ can be defined as

$$\bar{\boldsymbol{\gamma}} = \nabla \bar{\theta}(\bar{\mathbf{X}}), \quad (3)$$

where $\bar{\nabla}$ denotes the gradient operator and $\bar{\theta}$ the temperature at point $\bar{\mathbf{X}}$. The governing balance law for the thermal sub-problem excluding heat sources appear with Fourier's law as

$$\bar{\rho} \bar{c}_V \dot{\bar{\theta}} + \text{div } \bar{\mathbf{q}} = 0, \quad (4)$$

where $\bar{\rho}$ is the macroscopic density and \bar{c}_V the volumetric heat capacity of the macroscopic body. For the microscopic body, due to the ansatz of scale separation the volume forces can be neglected and the linear balance of momentum on the micro-scale reads

$$\text{div } \boldsymbol{\sigma} = \mathbf{0} \quad \text{with} \quad \boldsymbol{\sigma} = \boldsymbol{\sigma}_M + \boldsymbol{\sigma}_F. \quad (5)$$

Hereby, the stress $\boldsymbol{\sigma}$ refers to the matrix or to the fiber, denoted as $\boldsymbol{\sigma}_M$ and $\boldsymbol{\sigma}_F$, respectively. Fourier's law in the microscopic body is given as

$$\rho c_V \dot{\theta} + \operatorname{div} \mathbf{q} = 0. \quad (6)$$

2.1 Boundary conditions of the micro-scale

When solving the BVP at the micro-scale, the definition of the boundary condition is needed. In the classical strain-driven-homogenization process, the conditions are a direct consequence of the Hill-Mandel condition [4]. To incorporate the thermal part, we introduce a generalized macro-homogeneity condition based on the work of [5] and [6] as

$$\begin{aligned} \bar{\Psi} &= \langle \Psi \rangle_{RVE}, \\ \bar{\boldsymbol{\sigma}} : \bar{\boldsymbol{\varepsilon}} - \bar{\mathbf{q}} \cdot \bar{\boldsymbol{\gamma}} &= \langle \boldsymbol{\sigma} : \boldsymbol{\varepsilon} \rangle_{RVE} - \langle \mathbf{q} \cdot \boldsymbol{\gamma} \rangle_{RVE}, \end{aligned} \quad (7)$$

where $\langle \bullet \rangle_{RVE} := \frac{1}{V} \int_V (\bullet) dV$ denotes the average over the RVE. The solution of the BVP on the lower scale must satisfy the generalized macro-homogeneity condition. The two parts, the mechanical and the thermal one, have to hold independently. Thus,

$$\underbrace{\bar{\boldsymbol{\sigma}} : \bar{\boldsymbol{\varepsilon}}}_{\bar{\Psi}_{mech}} = \underbrace{\langle \boldsymbol{\sigma} : \boldsymbol{\varepsilon} \rangle_{RVE}}_{\Psi_{mech}}, \quad \underbrace{\bar{\mathbf{q}} \cdot \bar{\boldsymbol{\gamma}}}_{\bar{\Psi}_{therm}} = \underbrace{\langle \mathbf{q} \cdot \boldsymbol{\gamma} \rangle_{RVE}}_{\Psi_{therm}}. \quad (8)$$

Hill's lemma transforms the right side in terms of a surface integral over the boundary of the RVE and leads to the following equations.

$$\bar{\boldsymbol{\sigma}} : \bar{\boldsymbol{\varepsilon}} - \langle \boldsymbol{\sigma} : \boldsymbol{\varepsilon} \rangle_{RVE} = \int_{\partial\Omega} [\mathbf{t} - \bar{\boldsymbol{\sigma}} \mathbf{n}] [\mathbf{u} - \bar{\boldsymbol{\varepsilon}} \mathbf{x}] da, \quad \bar{\mathbf{q}} \cdot \bar{\boldsymbol{\gamma}} - \langle \mathbf{q} \cdot \boldsymbol{\gamma} \rangle_{RVE} = \int_{\partial\Omega} [\boldsymbol{\theta} - \bar{\boldsymbol{\gamma}} \cdot \mathbf{x}] [Q - \bar{\mathbf{q}} \cdot \mathbf{n}] da. \quad (9)$$

In equation (9), the right-side should identically clear out to fulfill the Hill-Mandel condition. The following conditions satisfy the Hill-Mandel condition.

$$\begin{aligned} \mathbf{t} &= \bar{\boldsymbol{\sigma}} \cdot \mathbf{n}, & \mathbf{u} &= \bar{\boldsymbol{\varepsilon}} \cdot \mathbf{x}, \\ Q &= \bar{\mathbf{q}} \cdot \mathbf{n}, & \boldsymbol{\theta} &= \bar{\boldsymbol{\gamma}} \cdot \mathbf{x}, \end{aligned} \quad (10)$$

where Q is the thermal surface flux density. For the sake of completeness there is also the possibility of periodic Dirichlet boundary conditions and antiperiodic Neumann conditions for the RVE. Due to the considered random micro-structure, this approach cannot be used and it is not further discussed.

3 Material Model of the SMA

The model for the fiber is described as one-dimensional. For the assumption of small deformations the geometric field equation reduces to linear strains $\boldsymbol{\varepsilon} = \frac{\partial \mathbf{u}}{\partial \mathbf{x}} = \mathbf{u}'$. Due to the fact that for applications in civil engineering, e.g. shape memory fiber reinforced concrete, only small deformations occur small strains with an additive decomposition $\boldsymbol{\varepsilon} = \boldsymbol{\varepsilon}^e + \boldsymbol{\varepsilon}^i$, into an elastic and plastic part are assumed.

3.1 Free energy equation

The material model is derived on the basis of a free Helmholtz energy function. A certain form for this energy function

$$\Psi = z \cdot \Psi^M + (1 - z) \cdot \Psi^A \quad (11)$$

is proposed in [7]. Here, the overall free energy is additively decomposed in a free energy part for the martensitic and the austenitic fraction. The proportion of each phase is controlled via the martensite volume fraction z . Due to the balance of mass the latter one is of scalar type and takes values between zero and one ($0 \leq z \leq 1$). The martensitic ratio is spilt into $z = z_{//} + z_{\gg}$ whereby the oriented martensite $z_{//}$ is stress-induced and the twinned martensite z_{\gg} depends on the change of temperature. The martensitic and the austenitic energy part are given as

$$\begin{aligned} \psi^{A/M} = & \frac{1}{2} \epsilon^e E^{A/M} \epsilon^e + \frac{1}{2} \alpha K^{A/M} \alpha \\ & + c_d^{A/M} (\theta - \theta_0) + u_0^{A/M} - \theta \left[c_d^{A/M} \ln \frac{\theta}{\theta_0} + \eta_0^{A/M} \right] \end{aligned} \quad (12)$$

and have the same form. It consists of an elastic, a plastic and a calorian energy part. The last term can be interpreted as an additional term to classic plasticity models. Assuming the same material parameters for each phase and inserting equation (12) into equation (11) yields the simplified free energy function

$$\begin{aligned} \psi = & \frac{1}{2} \epsilon^e E \epsilon^e + \frac{1}{2} \alpha K \alpha + z_{//} \cdot (\Delta u_0 - \theta \Delta \eta_0) \\ & + z_{\gg} \cdot (\Delta u_0 - \theta \Delta \eta_0) - \theta \cdot \left[c_d \ln \frac{\theta}{\theta_0} + \eta_0^A - c_d \right] - c_d \theta_0 + u_0^A. \end{aligned} \quad (13)$$

In this equation the elastic energy part can be recognized by the use of Young's modulus E and the elastic strain ϵ^e . Further, the plastic energy part incorporates the hardening modulus K with the inelastic, inner variable α and the energy difference $(\Delta u_0 - \theta \Delta \eta_0)$ with the oriented martensite fraction $z_{//}$. The last term to be found in equation (13) is a calorian function. In addition to the martensite volume fraction z the temperature θ and the effective heat capacity c_d occur. The variable u_0 stands for the inner energy and η_0 for the entropy in unloaded conditions. Δ indicates the difference of the inner energy u and respectively the entropy η between the austenitic and the martensitic phase.

3.2 Constitutive equations

The constitutive equations are derived by taking the partial derivative of the free energy function with respect to the inner variables ϵ^e , α and $\Delta \psi$. The cauchy stress σ is defined as

$$\sigma = \frac{\partial \psi}{\partial \epsilon^e} = E \cdot \epsilon^e = E \cdot (\epsilon - \epsilon^i) . \quad (14)$$

In the same way, a quantity p is derived by

$$p = -\frac{\partial \psi}{\partial \alpha} = -K \cdot \alpha . \quad (15)$$

This quantity is also of stress type. In comparison to classical plasticity, p is similar to a "backstress", well known from the kinematic hardening rheological model. At least, the derivation with respect to the martensitic volume fraction z reads

$$\Delta \psi = \Delta \psi(\theta) = \frac{\partial \psi}{\partial z} = \Delta u_0 - \theta \Delta \eta_0 . \quad (16)$$

$\Delta \psi$ is very important for the phase transition of the presented model. In literature it is referred to as *driving force* or *thermodynamic force*.

3.3 Phase transition conditions

Classical plasticity theory uses one yield condition to differentiate between the elastic and plastic range. The elastic range defines the set of the admissible stresses. Shape memory alloys provide a more complex stress-strain-behavior due to the temperature dependency. The "yield condition" for the SMA arises from the phase transition condition. Here, only the loading case is regarded, which leads to the following phase transition condition, where the loading is bonded by

$$\vec{\Phi}(\sigma, p, \Delta\psi) = \left| \sigma - p - \frac{\langle \Delta\psi \rangle}{\beta} \cdot \text{sign}(\sigma - p) \right| - \sigma_y \leq 0. \quad (17)$$

The Macaulay-bracket $\langle \dots \rangle$ is defined as $\langle x \rangle = (|x| + x)/2$. The description of phase transitions in the case of loading necessitates a stress criterion which is given as

$$\sigma \stackrel{!}{\geq} \sigma_{\text{ctrl}} = |\sigma - p| - \frac{\langle \Delta\psi \rangle}{\beta}. \quad (18)$$

In comparison to classical plasticity the yield condition has the additional term $\Delta\psi$ which is like an offset, scaled by the material parameter of maximum hysteresis width β . It always refers to the center of each hysteresis. The driving force $\Delta\psi$ is the most important quantity for the transformation of the material from pseudoplasticity at low temperature to pseudoelasticity at the high temperature range, see Fig. 1.

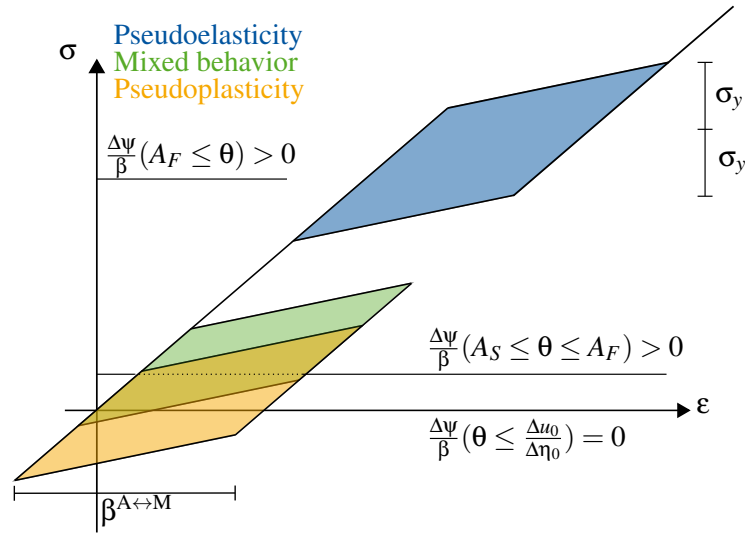


Figure 1: Off-set properties of $\Delta\psi$ and other material parameters

4 Adaptive FE² method

4.1 Nested mechanical finite element formulation

The nested finite element formulation is only needed for the mechanical part of the coupled problem. This results from the non-temperature-dependent thermal properties of the composite, which only requires initial homogenization, see section 4.3. A strain-driven homogenization is used for the accompanying homogenization, see e.g. [8], [9] and the references therein. In the strain-driven homogenization the Dirichlet boundary condition (DBC) results directly from the Hill-Condition. Here, every single

node on the surface of the RVE is constrained for both degrees of freedom. The displacements $\hat{\mathbf{u}}$ of the boundary nodes of the RVE are prescribed. They are defined via the macroscopic strain state as

$$\hat{\mathbf{u}} = \mathbf{D} \bar{\boldsymbol{\epsilon}}_i = \begin{bmatrix} \hat{u}_x \\ \hat{u}_y \end{bmatrix} = \begin{bmatrix} x & 0 & y \\ 0 & y & x \end{bmatrix} \begin{bmatrix} \epsilon_{11} \\ \epsilon_{22} \\ 2\epsilon_{12} \end{bmatrix}, \quad (19)$$

where x and y are the coordinates of the RVE boundary. Equation (19) transforms the macro-strain to the micro-deflection on the surface of the RVE. An explanation of the governing macro and microscopic equations is presented in Section 2.1 and 2.2. In the following, the static field equations for the global and local BVP are summarized with the neglect of volume forces for the sake of simplicity.

$$\text{Div } \bar{\boldsymbol{\sigma}} = 0 \quad \text{in } \bar{\Omega}, \quad (20)$$

$$\text{Div } \boldsymbol{\sigma}_m + \text{Div } \boldsymbol{\sigma}_{sf} - \text{Div } \boldsymbol{\sigma}_{mf} + \mathbf{b} = 0 \quad \text{in } \Omega_i. \quad (21)$$

For the sake of brevity, the derivation of the linear system is omitted. For further details, the reader is referred to e.g. [8], [10].

$$\mathbf{L}[g(\bar{\mathbf{v}}^h, \delta \bar{\mathbf{v}}^h), \Delta \bar{\mathbf{v}}^h] = \sum_{e=1}^{numel} \begin{bmatrix} \delta \bar{\mathbf{v}} & \delta \boldsymbol{\epsilon}_1 & \dots & \delta \boldsymbol{\epsilon}_i & \dots & \delta \boldsymbol{\epsilon}_{NGP} \end{bmatrix}_e \cdot \left\{ \begin{bmatrix} \bar{\mathbf{k}}(\bar{\mathbb{C}}_i) & \mathbf{0} & \vdots & \mathbf{0} & \vdots & \mathbf{0} \\ \mathbf{0} & \mathbb{C}_1 & \vdots & \mathbf{0} & \vdots & \mathbf{0} \\ \dots & \dots & \ddots & \mathbf{0} & \dots & \dots \\ \mathbf{0} & \mathbf{0} & \mathbf{0} & \mathbb{C}_i & \mathbf{0} & \mathbf{0} \\ \dots & \dots & \dots & \mathbf{0} & \ddots & \dots \\ \mathbf{0} & \mathbf{0} & \dots & \mathbf{0} & \dots & \mathbb{C}_{NGP} \end{bmatrix} \begin{bmatrix} \Delta \bar{\mathbf{v}} \\ \Delta \boldsymbol{\epsilon}_1 \\ \vdots \\ \Delta \boldsymbol{\epsilon}_i \\ \vdots \\ \Delta \boldsymbol{\epsilon}_{NGP} \end{bmatrix} + \begin{bmatrix} \bar{\mathbf{f}}(\bar{\boldsymbol{\sigma}}_i) \\ \boldsymbol{\sigma}_1 \\ \dots \\ \boldsymbol{\sigma}_i \\ \dots \\ \boldsymbol{\sigma}_{NGP} \end{bmatrix} \right\}_e \quad (22)$$

It turns out that the two scales are coupled in $\bar{\boldsymbol{\sigma}}_i$, $\bar{\mathbb{C}}_i$ and the strains $\boldsymbol{\epsilon}_i$. The non-linear system of equations is then solved with a Newton-Raphson-scheme simultaneously. Equilibrium in a load-step is achieved when each micro-problem in each Gauss point and the macro problem have attained equilibrium, see Fig. 2.

4.2 The adaptive FE² approach

The previous Section describes the standard FE² deformation-driven method. One of the main disadvantages is the high computational effort due to the accompanying homogenization in every Gauss-point on the macro scale. The adaptive approach arises from the idea, that a accompanying homogenization is only needed in the case of non-linear behavior on the lower scale. The macroscopic material answer remains linear-elastic until the first fiber reaches the phase-transition condition, see equation (17). Afterward, the homogenization of the micro-scale results in a different macro-stress $\bar{\boldsymbol{\sigma}}$ and material tangent $\bar{\mathbb{C}}$. The aim of the adaptive approach is to predict the non-linear material behavior of the fibers in the RVE. From [11] or [12] it is well known, that a traction boundary condition (Neumann) for the mechanical problem and a heat flux condition for the thermal one [6] (NBC) of the lower scale leads to a softer material stiffness prediction than the displacement or temperature boundary condition (Dirichlet). Considering the Voigt and the Reuss bound it follows, for the Eigenvalues of the different material tangents or the overall heat conductivity tensor,

$$\bar{\mathbb{C}}_{Neu.} \leq \bar{\mathbb{C}} \leq \bar{\mathbb{C}}_{Dir.} \quad \bar{\mathbf{H}}_{Neu.} \leq \bar{\mathbf{H}} \leq \bar{\mathbf{H}}_{Dir.}, \quad (23)$$

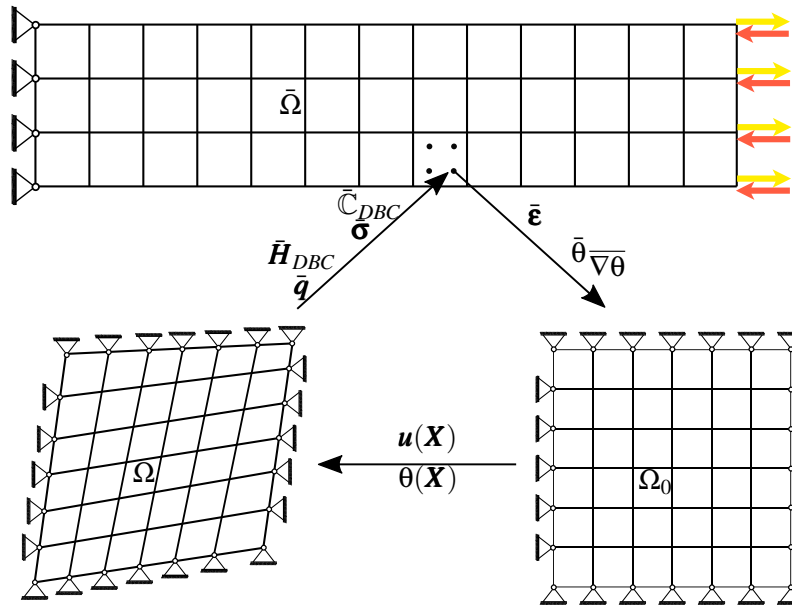


Figure 2: FE² scheme for strain driven RVEs. Every Gauss points of the macro-structure is associated to a RVE. The macroscopic strain $\bar{\mathbf{e}}_i$ is applied as the displacement boundary condition on the micro-scale BVP. Solving the BVP on the micro-scale leads to the macro-stress $\bar{\mathbf{\sigma}}$ and material tangent $\bar{\mathbb{C}}_i$

see e.g. [11]. This relation is used for the adaptive approach. Instead of the classic strain-driven formulation, the initial homogenization is realized by traction boundary conditions in a stress free reference configuration. The resulting material tangent \mathbb{C}_{Neu} underestimates the stiffness and is employed for the macroscopic constitutive equation of the macro problem,

$$\bar{\boldsymbol{\sigma}} = \bar{\mathbb{C}}_{New.} : \bar{\boldsymbol{\varepsilon}}. \quad (24)$$

The finite element analysis by Neumann boundary conditions leads to an overestimation of the displacement and thus the strain rate. The accompanying homogenization is not needed in the linear elastic regime. An indicator for an accompanying homogenization is introduced by utilizing the phase transition condition of the fiber model. The prediction of the nonlinear behavior is done via the reformulation of the phase transition condition, see equation (17) in the so called "phase transition strain" $\epsilon_{sf,pt}$

$$\epsilon_{sf,pt} = \frac{\sigma_{F,y} + \frac{\Delta\psi}{\beta}}{E_{sf}}. \quad (25)$$

Equation (25) shows the temperature dependence of the strain-based indicator for the macro-scale. The relation of the actual macroscopic strain $\bar{\epsilon}$ and the fiber strain in the RVE needs to be defined. Here a randomly distributed fiber contribution is given. In this case, the principal strains are calculated via the Eigenvalue problem,

$$(\bar{\mathbf{e}} - \lambda \mathbf{I}) \mathbf{n} = \mathbf{0}. \quad (26)$$

The principal strains are assumed to coincide with the direction of the fibers which will yield first. The indicator for the accompanying homogenization, in case of randomly distributed fibers, reads

$$\max(\epsilon_1, \epsilon_2) \geq \epsilon_{sf,pt}. \quad (27)$$

Accordingly, the algorithm frame for the adaptive FE² scheme can be described by the flowchart depicted in Fig.3.

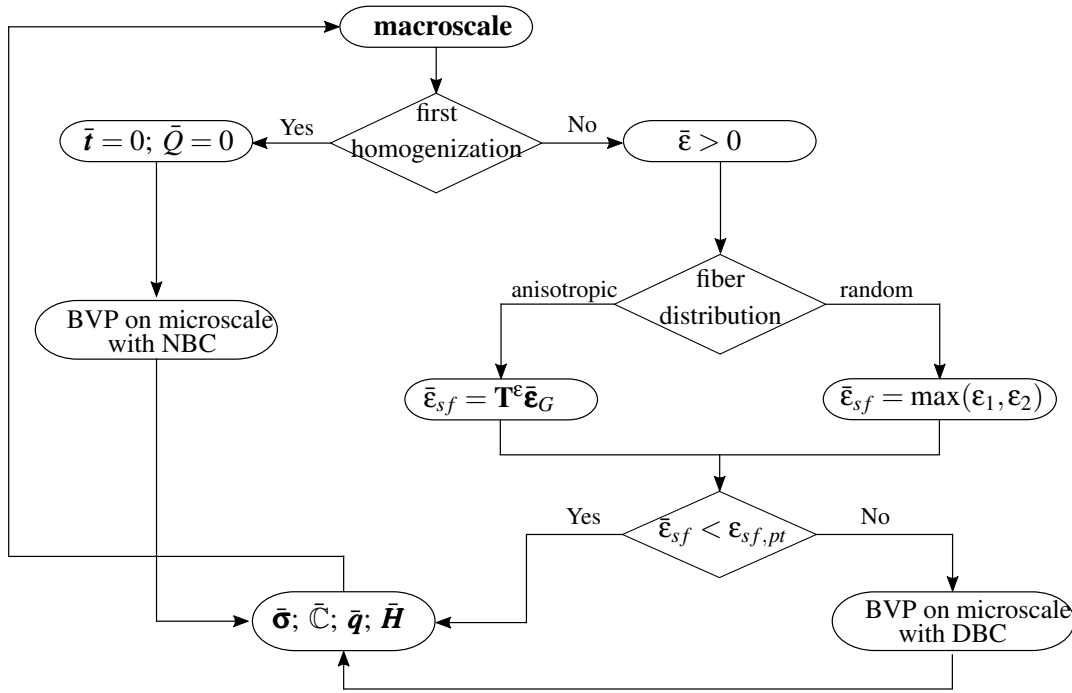


Figure 3: Flowchart of the adaptive FE² approach

4.3 Initial homogenization for the mechanical and thermal problem

As described in Section 4.2, the adaptive FE² needs an initial homogenization with Neumann boundary conditions for the mechanical and the thermal problem. Therefore the first homogenization is performed by the application of traction and heat flux boundary conditions, see e.g. [13], [14], [15]. The algorithm in the present approach is based on the variational formulation. The advantage of this method is given by the possibility to incorporate the macro-strains $\bar{\boldsymbol{\epsilon}}$ or rather of the macro temperature gradient $\bar{\boldsymbol{\gamma}}$ as the input quantity for the traction and heat flux boundary condition. The discretized boundary value problem needs the definition of the nodal area vector \mathbf{a}_i , see [12]. This nodal area vector is defined for the 2D case as

$$\mathbf{a}_i = \frac{1}{2} [\mathbf{x}_{i+1} - \mathbf{x}_{i-1}] \times \mathbf{e}_3. \quad (28)$$

The effective macroscopic material tangent and the heat conduction tensor are determined by eliminating the interior degrees of freedom by a static condensation as

$$\begin{aligned} \bar{\mathbf{C}}_{NBC} &= [\mathbf{\Xi} \tilde{\mathbf{K}}_{bb}^{-1} \mathbf{\Xi}^T]^{-1} \quad \text{with} \quad \tilde{\mathbf{K}}_{bb} = \mathbf{K}_{bb} - \mathbf{K}_{ba} \mathbf{K}_{aa}^{-1} \mathbf{K}_{ab}, \\ \bar{\mathbf{H}}_{NBC} &= [\mathbf{\Xi}_{th} (\tilde{\mathbf{K}}_{bb,th})^{-1} \mathbf{\Xi}_{th}^T]^{-1} \quad \text{with} \quad \tilde{\mathbf{K}}_{bb,th} = \mathbf{K}_{bb,th} - \mathbf{K}_{ba,th} \mathbf{K}_{aa,th}^{-1} \mathbf{K}_{ab,th}. \end{aligned} \quad (29)$$

In equation (29) $\bar{\mathbf{C}}_{NBC}$ denoting the overall material tangent with traction boundary conditions, $\mathbf{\Xi}$ is the assembled nodal vector components area matrix, $\tilde{\mathbf{K}}_{bb}$ is the static condensed stiffness matrix. The subscripts a stand for the inner nodes and b for the boundary nodes of the RVE. The resulting macroscopic heat conduction tensor with zero heat flux is $\bar{\mathbf{H}}_{NBC}$, in the equation the introduced subscript th denotes the thermal subproblem with the thermal assembled nodal vector components area matrix $\mathbf{\Xi}_{th}$ and stiffness matrix \mathbf{K}_{th} .

5 Numerical Example

In the following example the ability of the presented approach is demonstrated. The example employs a random fiber orientation on the microscale. On the macroscale a variation of different temperature load cases are considered. For the matrix and the fiber, the set of material parameters is given in Tab.1.

Table 1: material parameters for the SMA-Matrix composite

Material parameter	Notation	Unit	Value
Young's modulus (SMA)	E_{sf}	MPa	60000
Hardening modulus (SMA)	K_{sf}	MPa	2000
Half hysteresis height	σ_y	MPa	120
Max. hysteresis width	β		0.05
Diff. of inner energy	Δe_0	MPa	-204.00
Diff. of inner entropy	$\Delta \eta_0$	MPa/°K	-0.8
Martensite-finish	M_F	°K	241.25
Martensite-start	M_S	°K	247.50
Austenite-start	A_S	°K	256.25
Austenite-finish	A_F	°K	262.50
fiber proportion	ρ_f	%	10
fiber diameter	d_{sf}	m	10^{-3}
Young's modulus (matrix)	E_m	MPa	100
Poisson ratio (matrix)	ν_m		0.0

5.1 Cook's membrane with random fiber distribution

The Cook's membrane with an uniformly distributed load, with a magnitude of $F = 0.25 \cdot \lambda$ is analyzed, see Fig. 4. The thermal boundary conditions for the cook's membrane are given as follows. The bottom and upper side has a zero heat flux, while we distinguish between different Dirichlet boundary conditions on the left and right side, see Tab. 2. The micro-structure of the composite is defined by a

Table 2: Thermal boundary conditions for Cook's Membrane

Localisation	case I	case II	case III
Left side	255°K	270°K	255°K
Right side	255°K	270°K	270°K

unit cell with a length of 2. The RVE is generated by 1000 randomly distributed fibers under the constraint of an orientation distribution which approximates isotropic material behavior. The macro-domain is discretized by 400 elements and the RVE by 400 elements. To show the adaptivity for the random fiber distribution, the stationary temperature field in the membrane is given. A comparison between the standard and the adaptive FE² method is performed for the three cases. Within the standard FE² the accompanying homogenization is performed at each integration point. The deviation in the displacement response is displayed on the left side in Fig. 5. The maximum deviation of 5% for a very small load step is observed in all three cases. It occurs due to the different boundary conditions for the RVE. The standard FE² method employs Dirichlet boundary conditions whereas the adaptive FE² approach utilizes Neumann boundary conditions for the initial homogenization. The colored lines shows the deviation,

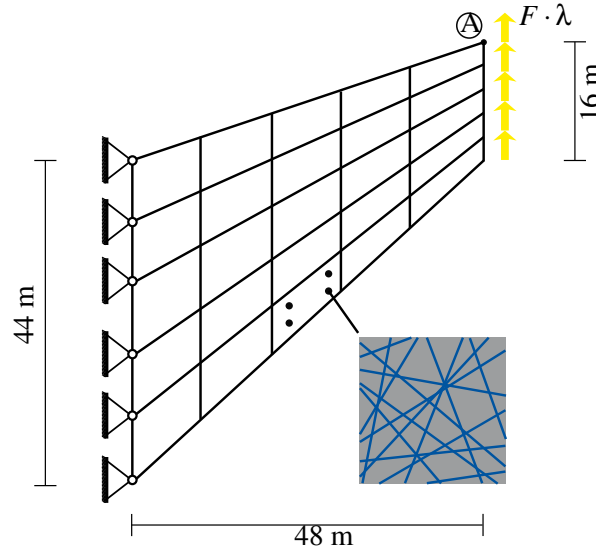


Figure 4: Cook's membrane with a uniform distributed load λ at the free end tip of the structure. The micro-structure consists of a random fiber distribution.

which is getting smaller with the increasing load factor. The decrease of the deviation is getting smaller due to the higher temperatures which arises from a longer simulation with the softer material tangent from the initial homogenization. The number of elements which reach the indicator and therefore re-

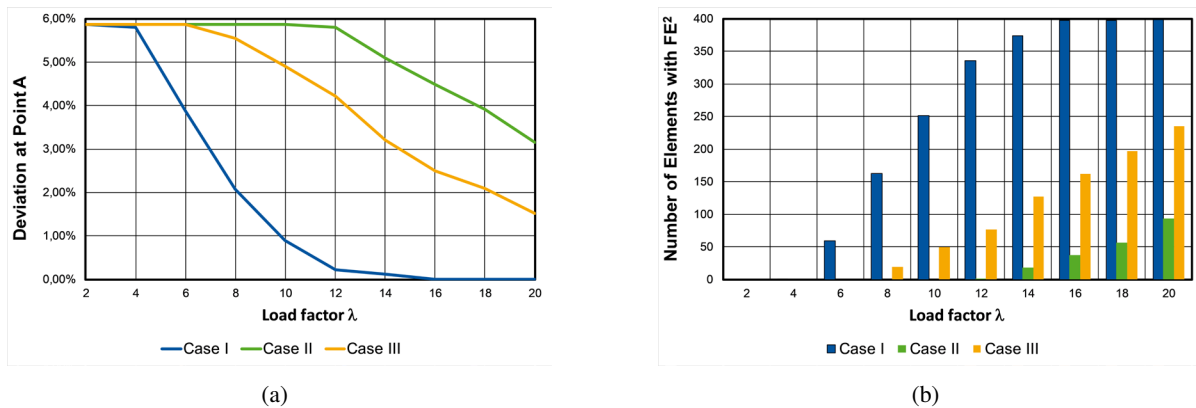


Figure 5: Left: The deviation of point A for the displacement in y-direction. Right: The representation of multiscale elements (green) which are triggered by the FE^2 indicator in dependency of the temperature boundary conditions and λ .

quire an accompanying homogenization are represented as columns in Fig. 5 on the right side. In order to compare the different cases with regard to the numerical effort and to demonstrate the development of the multiscale elements, Fig. 6 shows the multiscale elements for the load factors $\lambda = 10$ and $\lambda = 20$. The color of the tetragon indicates if the indicator for FE^2 is fulfilled and an accompanying homogenization is necessary. In case of an accompanying homogenization, the tetragons are denoted as multiscale elements and are marked with green color. Otherwise, the points are denoted as single scale element and marked with blue color. Like in the previous example, one can see the temperature dependency with respect to the number of multiscale elements. The computational saving at load factor $\lambda = 10$ for the adaptive

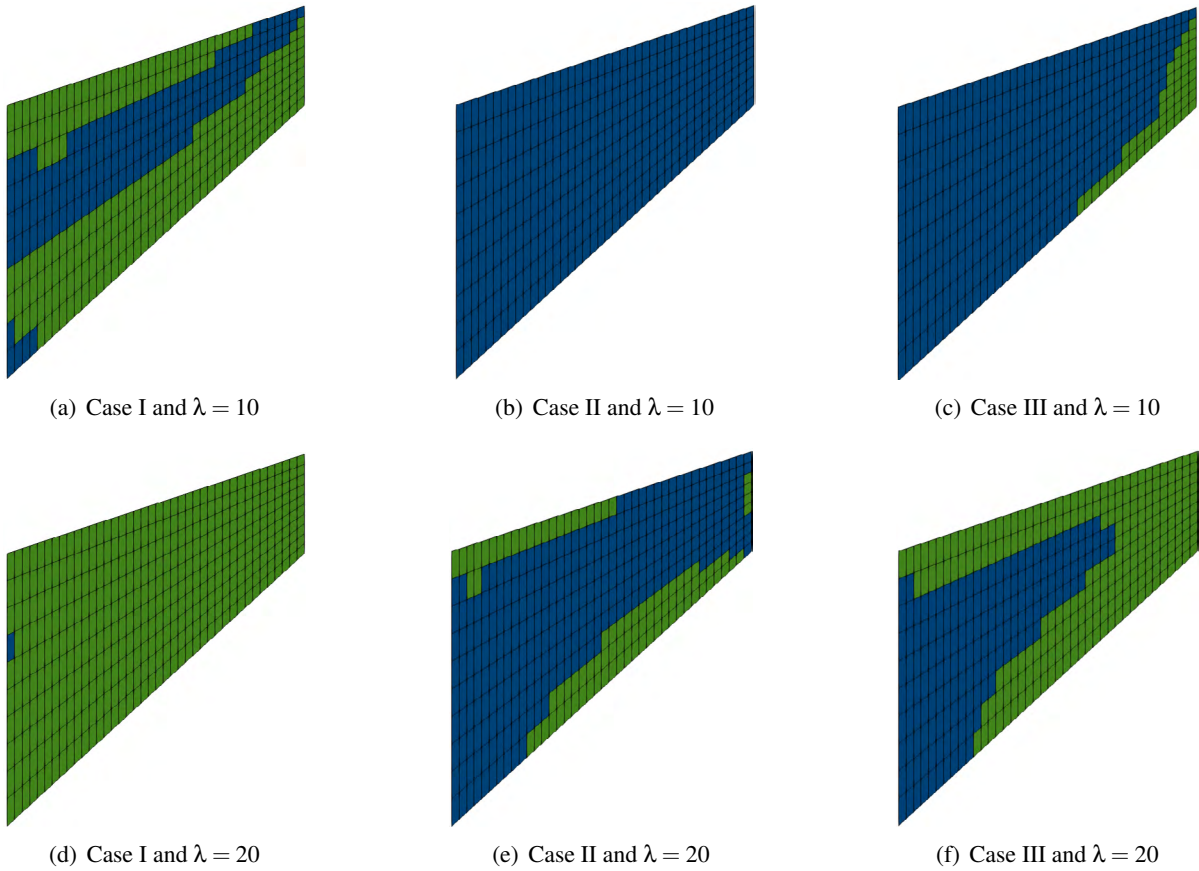


Figure 6: Representation of multi-scale elements (green) which are triggered by the FE^2 indicator in dependency of the fiber orientation and λ .

approach is hereby for case I: $cs_I = 36.96\%$, for case II: $cs_{II} = 99.89\%$ and for case III: $cs_{III} = 87.40\%$, respectively.

6 CONCLUSIONS

The adaptive approach shows a significant reduction of the computational effort without loss of accuracy with respect to the standard FE^2 approach and the method has the potential to be applied to many other applications in the context of heterogeneous micro-structures.

REFERENCES

- [1] Lecce, L. *Shape memory alloy engineering: for aerospace, structural and biomedical applications*. Elsevier (2004)
- [2] Gitman, I., Askes, H. and Sluys, L. *Representative volume: existence and size determination*. Engineering Fracture Mechanics (2007)
- [3] Feyel, F. and Chaboche, J. *FE 2 multiscale approach for modelling the elastoviscoplastic behaviour of long fibre SiC/Ti composite materials*. Computer Methods in Applied Mechanics and Engineering (2000)

- [4] Hill, R. *Elastic properties of reinforced solids: some theoretical principles* Journal of the Mechanics and Physics of Solids (1963)
- [5] Schröder, J., Labusch, M. and Keip, M.A. *Algorithmic two-scale transition for magneto-electro-mechanically coupled problems: FE2-scheme: localization and homogenization*. Computer Methods in Applied Mechanics and Engineering (2016)
- [6] Özdemir, I., Brekelmans, W. and Geers, M. *FE2 computational homogenization for the thermo-mechanical analysis of heterogeneous solids*. Computer Methods in Applied Mechanics and Engineering (2008)
- [7] Helm, D. and Haupt, P. *Shape memory behaviour: modelling within continuum thermomechanics*. International Journal of Solids and Structures(2003)
- [8] Gruttmann, F. and Wagner, W. *A coupled two-scale shell model with applications to layered structures*. International Journal for Numerical Methods in Engineering (2013)
- [9] Kohlhaas, B. and Klinkel, S. *An FE2 model for the analysis of shape memory alloy fiber-composites*. Computational Mechanics (2015)
- [10] Praster, M., Klassen, M. and Klinkel, S. *An adaptive FE2 approach for fiber–matrix composites*. Computational Mechanics (2018)
- [11] Huet, C. *Application of variational concepts to size effects in elastic heterogeneous bodies*. Journal of the Mechanics and Physics of Solids (1990)
- [12] Miehe, C. and Koch, A. *Computational micro-to-macro transitions of discretized microstructures undergoing small strains*. Archive of Applied Mechanics (2002)
- [13] Larsson, F. and Runesson, K. *RVE computations with error control and adaptivity: the power of duality*. Computational Mechanics (2007)
- [14] Fish, J. and Fan, R. *Mathematical homogenization of nonperiodic heterogeneous media subjected to large deformation transient loading*. International Journal for Numerical Methods in Engineering (2008)
- [15] Saeb, A., Saba, J., and Steinmann, P. *Aspects of Computational Homogenization at Finite Deformations: A Unifying Review From Reuss' to Voigt's Bound*. Applied Mechanics Reviews (2016)

ANALYSIS OF AN ENERGY-BASED MODEL OF THE POLARIZATION PROCESS IN FERROELECTRIC MATERIALS

ASTRID S. PECHSTEIN*, MARTIN MEINDLHUMER* AND ALEXANDER HUMER*

*Institute of Technical Mechanics

Johannes Kepler University Linz

Altenberger Str. 69, 4040 Linz, Austria

e-mail: astrid.pechstein@jku.at, martin.meindlhumer@jku.at, alexander.humer@jku.at

Key words: ferroelectricity, polarization, variational inequality, mixed finite elements

Abstract. We are concerned with the mathematical modeling of the polarization process in ferroelectric media. We assume that this dissipative process is governed by two constitutive functions, which are the free energy function and the dissipation function. The dissipation function, which is closely connected to the dissipated energy, is usually non-differentiable. Thus, a minimization condition for the overall energy includes the subdifferential of the dissipation function. This condition can also be formulated by way of a variational inequality in the unknown fields strain (or displacement), dielectric displacement, polarization and, for remanent straining models, remanent strain. We are concerned with analyzing the mathematical well-posedness of this problem, and try to give an existence result for a solution of the time-dependent incremental variational inequality. We propose to solve the update equation in a single Newton iteration for all unknowns at once. We propose to use mixed finite elements, where displacement, dielectric displacement and polarization are unknowns. Gauss' law of zero free charges is satisfied exactly. We present numerical examples gained in the open source software package Netgen/NGSolve.

1 INTRODUCTION

A thermodynamical framework for the description of ferroelectric materials based on the Helmholtz free energy was originally provided in the series of papers [1, 2, 3, 4] by Bassiouny, Ghaleb and Maugin. Their theory allows to describe multiaxial electromechanical loading procedures. The introduced notions are similar to elasto-plasticity, including internal variables, yield (or switching) criteria and hardening moduli. Explicit choices of energy and switching criteria were provided by Cocks and McMeeking [8] for the one-dimensional case. The multi-dimensional case follows in [14, 13]. In the former reference, the remanent polarization vector is the only internal unknown, and the polarization stress is linked directly to the remanent polarization. Contrarily, in the latter work remanent polarization and strain are independent of each other, but are determined by a common switching condition. With these theories, not only hysteresis loops can be tracked, but also butterfly hysteresis loops are predicted correctly. The models were validated against measurements provided by Huber and Fleck [10] for non-proportional loading procedures.

Miehe, Rosato and Kiefer [15] introduced an incremental variational principle for the even more general case of coupled electro-magneto-mechanics. They distinguish between *energy*-based and *enthalpy*-based models. For the latter, the independent unknowns are strain and electric field, whereas for

the former, strain and dielectric displacement are independent. While most finite element formulations use enthalpy-based models discretizing the electric potential, we provide theory for an energy-based setting with an independent dielectric displacement.

Semenov et al. [16] present an energy-based formulation using a vector potential for the dielectric displacement. Then, the dielectric displacement vector satisfies Gauss' law of zero divergence automatically. Contrarily, we propose to use $H(\text{div})$ conforming finite elements as can be found in the context of mixed methods [5]. Gauss' law is then introduced as a constraint enforced exactly by a Lagrangian multiplier. This way accuracy of the electric unknowns is improved, as no derivatives have to be taken. In some sense, the approach by Klinkel [12] may be seen as diametrically opposed, where an irreversible electric field is introduced instead of the remanent polarization vector.

In the current paper, we aim at proving existence and uniqueness of a solution to the problem of finding an update solution in the polarization process of ferroelectric media. To this end, we describe the polarization of ferroelectric media as a dissipative process in the mathematical framework of variational inequalities. We start from an energy-based model of the problem, from which we derive time-dependent variational equations and inequalities. The independent unknowns are then strain (or displacement), dielectric displacement, remanent polarization, and, if included in the model, remanent polarization strain. We provide an abstract mathematical framework for this problem. We see that, under the standard assumption of convexity of the free energy function, existence and uniqueness of a solution can be shown. These results fit well with the findings in [17, 6], where stability issues are discussed.

2 ENERGY-BASED CONSTITUTIVE MODELING

In the following, we present a variational inequality that describes the problem of polarization of ferroelectric media. We postpone mathematical exactness concerning solution spaces, (weak) differentiability and other issues to Section 3, in order not to complicate matter too much. Let $\Omega \subset \mathbb{R}^d$, $d = 2, 3$ denote the body of interest. Concerning the mechanical quantities, we use \mathbf{u} for the displacement field and \mathbf{T} for the total stress. We assume small deformations, thus we identify deformed and undeformed configuration, and use the linear strain $\mathbf{S} = \frac{1}{2}(\nabla \mathbf{u} + \nabla \mathbf{u}^T)$. Additionally, we assume to be in the quasistatic regime. The electric part of the problem is then characterized by the electric potential ϕ , while $\mathbf{E} = -\nabla \phi$ is the electric field. The dielectric displacement vector shall be denoted as \mathbf{D} . We are interested in finding the remanent polarization \mathbf{P}^i and the remanent strain \mathbf{S}^i .

We assume the material is characterized by a Helmholtz free energy function

$$\Psi = \Psi^r(\mathbf{D}, \mathbf{P}^i, \mathbf{S}, \mathbf{S}^i) + \Psi^i(\mathbf{P}^i, \mathbf{S}^i), \quad (1)$$

which consists of a *reversible* or *stored* part Ψ^r , and a part Ψ^i that is associated only to the internal variables of remanent polarization and strain. This part may tend to infinity as the polarization approaches saturation. For a similar characterization we refer to [13].

The independent reversible unknowns are strain and dielectric displacement, where the latter additionally has to satisfy Gauss' law, $\text{div } \mathbf{D} = 0$. Electric field and mechanic stress are dependent quantities, and defined as derivatives of the free energy with respect to dielectric displacement and strain,

$$\mathbf{E} = \frac{\partial \Psi}{\partial \mathbf{D}}, \quad \mathbf{T} = \frac{\partial \Psi}{\partial \mathbf{S}}. \quad (2)$$

As strain and dielectric displacement are not constrained, or constrained to the linear subspace of divergence-free functions in the latter case, there holds the following variational equality,

$$\mathbf{E} \cdot \delta \mathbf{D} + \mathbf{T} \cdot \delta \mathbf{S} = \delta W_{ext} \quad \text{for all } \delta \mathbf{D}, \text{div } \delta \mathbf{D} = 0 \text{ and } \delta \mathbf{S} = \mathbf{S}(\delta \mathbf{u}). \quad (3)$$

In (3), all virtual strains and divergence-free virtual dielectric displacements are considered, where $\delta \mathbf{D}$ and $\delta \mathbf{u}$ have to satisfy the respective boundary conditions. On the right hand side, all virtual work by external forces is summarized as δW_{ext} . This formula is well-known as *principle of virtual works*.

Polarization of ferroelectric materials is a dissipative process. The *dissipative driving forces* are

$$\hat{\mathbf{E}} = -\frac{\partial \Psi}{\partial \mathbf{P}^i}, \quad \hat{\mathbf{T}} = -\frac{\partial \Psi}{\partial \mathbf{S}^i}. \quad (4)$$

The dissipation is then given by the inner product of these driving forces and the *dissipative fluxes* $\dot{\mathbf{P}}^i$ and $\dot{\mathbf{S}}^i$,

$$\mathcal{D} = \hat{\mathbf{E}} \cdot \dot{\mathbf{P}}^i + \hat{\mathbf{T}} : \dot{\mathbf{S}}^i. \quad (5)$$

The dissipation function Φ relates the driving forces $\hat{\mathbf{E}}$, $\hat{\mathbf{T}}$ to the driving rates $\dot{\mathbf{P}}^i$, $\dot{\mathbf{S}}^i$. Typically, the dissipation function is not smooth, but weakly lower semicontinuous and allows for a *subdifferential*¹. The driving forces are contained in the respective subdifferentials, i.e.

$$\hat{\mathbf{E}} \in \partial_{\dot{\mathbf{P}}^i} \Phi(\dot{\mathbf{P}}^i, \dot{\mathbf{S}}^i) \quad \text{and} \quad \hat{\mathbf{T}} \in \partial_{\dot{\mathbf{S}}^i} \Phi(\dot{\mathbf{P}}^i, \dot{\mathbf{S}}^i). \quad (7)$$

By definition of the subdifferential, eq. (7) is equivalent to the variational inequality

$$-\hat{\mathbf{E}} \cdot (\tilde{\mathbf{P}}^i - \dot{\mathbf{P}}^i) - \hat{\mathbf{T}} : (\tilde{\mathbf{S}}^i - \dot{\mathbf{S}}^i) + \Phi(\tilde{\mathbf{P}}^i, \tilde{\mathbf{S}}^i) - \Phi(\dot{\mathbf{P}}^i, \dot{\mathbf{S}}^i) \geq 0 \quad \forall \tilde{\mathbf{P}}^i, \tilde{\mathbf{S}}^i. \quad (8)$$

To arrive at one single variational inequality, we add up (3) and (8). In (3), we use the admissible virtual dielectric displacement $\delta \mathbf{D} = \tilde{\mathbf{D}} - \dot{\mathbf{D}}$, where $\text{div } \tilde{\mathbf{D}} = \text{div } \dot{\mathbf{D}} = 0$. The virtual strain is defined from the admissible displacement update $\tilde{\mathbf{u}}$ and $\dot{\mathbf{u}}$ by $\delta \mathbf{S} = \mathbf{S}(\tilde{\mathbf{u}}) - \mathbf{S}(\dot{\mathbf{u}})$. With these choices, we deduce for all $\tilde{\mathbf{u}}$, $\tilde{\mathbf{D}}$, $\tilde{\mathbf{P}}^i$ and $\tilde{\mathbf{S}}^i$,

$$\mathbf{E} \cdot (\tilde{\mathbf{D}} - \dot{\mathbf{D}}) + \mathbf{T} : (\mathbf{S}(\tilde{\mathbf{u}}) - \dot{\mathbf{S}}) - \hat{\mathbf{E}} \cdot (\tilde{\mathbf{P}}^i - \dot{\mathbf{P}}^i) - \hat{\mathbf{T}} : (\tilde{\mathbf{S}}^i - \dot{\mathbf{S}}^i) + \Phi(\tilde{\mathbf{P}}^i, \tilde{\mathbf{S}}^i) - \Phi(\dot{\mathbf{P}}^i, \dot{\mathbf{S}}^i) \geq \delta W^{ext}. \quad (9)$$

3 A MATHEMATICAL FRAMEWORK

We define the variational inequality that describes the polarization process in a mathematical framework. Therefore, we introduce compact notation, which is compatible with the literature on variational inequalities, especially the monograph [9]. We use

$$\mathbf{w} = [\mathbf{S}(\mathbf{u}), \mathbf{D}, \mathbf{S}^i, \mathbf{P}^i]^T \quad \text{for the reactions} \quad (10)$$

$$\mathbf{z} = [\mathbf{S}(\tilde{\mathbf{u}}), \tilde{\mathbf{D}}, \tilde{\mathbf{S}}^i, \tilde{\mathbf{P}}^i]^T \quad \text{for admissible rates.} \quad (11)$$

A priori, we assume the different quantities to live in the following Sobolev spaces, and use compound spaces for compact notation,

$$\mathbf{u} \in \mathbb{U} := \{\mathbf{u} \in [H^1(\Omega)]^d : \mathbf{u} = 0 \text{ on } \Gamma_{fix}\}, \quad (12)$$

$$\mathbf{D} \in \mathbb{D}_0 := \{\mathbf{D} \in \mathbb{D} : \text{div } \mathbf{D} = 0\} \quad \text{with} \quad \mathbb{D} := \{\mathbf{D} \in H(\text{div}) : \mathbf{D} \cdot \mathbf{n} = 0 \text{ on } \Gamma_{ins}\}, \quad (13)$$

$$\mathbf{S}^i \in \mathbb{S} := [L^2(\Omega)]_{sym}^{d \times d}, \quad (14)$$

$$\mathbf{P}^i \in \mathbb{P} := [L^2(\Omega)]^d, \quad (15)$$

$$\mathbb{H} := \mathbb{U} \times \mathbb{D} \times \mathbb{S} \times \mathbb{P}, \quad \text{and} \quad \mathbb{H}_0 := \mathbb{U} \times \mathbb{D}_0 \times \mathbb{S} \times \mathbb{P}. \quad (16)$$

¹The subdifferential of some function j with respect to u is denoted by $\partial_u j$ and represents a set, namely

$$z \in \partial_u j(u) \quad \Longleftrightarrow \quad j(v) - j(u) \geq z \cdot (v - u) \quad \text{for all } v. \quad (6)$$

Depending on the definition of the irreversible energy Ψ^i , the free energy Ψ may tend to infinity as \mathbf{P}^i approaches saturation. We introduce the *effective domain* of Ψ by (cf. [9, p 73])

$$\mathbb{X} := \{\mathbf{z} \in \mathbb{H} : \Psi(\mathbf{z}) < \infty\}, \quad \mathbb{X}_0 := \mathbb{X} \cap \mathbb{H}_0. \quad (17)$$

We define the nonlinear operator $A : \mathbb{X} \rightarrow \mathbb{H}^*$ mapping reaction to forces,

$$\langle A(\mathbf{w}), \mathbf{z} \rangle := \left\langle \frac{\partial \Psi}{\partial \mathbf{w}}(\mathbf{w}), \mathbf{z} \right\rangle, \quad A(\mathbf{w}) = A(\mathbf{S}(\mathbf{u}), \mathbf{D}, \mathbf{S}^i, \mathbf{P}^i) = [\mathbf{S}(\mathbf{u}), \mathbf{D}, -\mathbf{S}^i, -\mathbf{P}^i]^T. \quad (18)$$

The work of external forces δW^{ext} shall be represented by the linear functional $\ell \in \mathbb{H}^*$. Note that, for the present choice of independent unknowns \mathbf{u} and \mathbf{D} , the external work also contains boundary conditions on the electric potential. In the exemplary case of a body under mechanical volume load \mathbf{f} , surface tractions \mathbf{t} on the boundary part Γ_{trac} , and a prescribed potential ϕ_0 on the electrodes Γ_{el} , this functional is defined as

$$\langle \ell, \mathbf{z} \rangle := \int_{\Omega} \mathbf{f} \cdot \tilde{\mathbf{u}} \, dx + \int_{\Gamma_{trac}} \mathbf{t} \cdot \tilde{\mathbf{u}} \, ds - \int_{\Gamma_{el}} \phi_0 \tilde{\mathbf{D}}_n \, ds. \quad (19)$$

Thus, the variational inequality (9) translates to the abstract variational inequality of the form: Find $\mathbf{w} : [0, T] \rightarrow \mathbb{X}_0$ such that

$$\langle A(\mathbf{w}), \mathbf{z} - \dot{\mathbf{w}} \rangle + \Phi(\mathbf{z}) - \Phi(\dot{\mathbf{w}}) \geq \langle \ell, \mathbf{z} - \dot{\mathbf{w}} \rangle \quad \text{for all } \mathbf{z} \in \mathbb{H}_0. \quad (20)$$

The variational inequality can be extended to hold for all $\mathbf{z} \in \mathbb{H}$, i.e. also for dielectric displacement updates with non-zero divergence. To this end, the dissipation function needs to be augmented by this restriction, see [9]. Indeed, the augmented dissipation maps all dielectric displacements with non-zero divergence to infinity. In the following, it shall be denoted by $j : \mathbb{H} \rightarrow \bar{\mathbb{R}}^+ := \mathbb{R} \cup \{+\infty\}$ and is defined as

$$j(\mathbf{z}) := \Phi(\mathbf{z}) + \sup_{\phi \in L^2(\Omega)} \int_{\Omega} \operatorname{div} \tilde{\mathbf{D}} \phi \, dx. \quad (21)$$

Note that, when restricted to \mathbb{H}_0 , $j(\cdot)$ and $\Phi(\cdot)$ are equivalent. Therefore, we will use $j(\cdot)$ in the following, and consider the variational inequality (equivalent to (20)),

$$\langle A(\mathbf{w}), \mathbf{z} - \dot{\mathbf{w}} \rangle + j(\mathbf{z}) - j(\dot{\mathbf{w}}) \geq \langle \ell, \mathbf{z} - \dot{\mathbf{w}} \rangle \quad \text{for all } \mathbf{z} \in \mathbb{H}. \quad (22)$$

3.1 Assumptions

We collect assumptions on the various functionals, that we need to proof existence and uniqueness of the update in a time-discrete scheme. In Section 4, we show whether these assumptions are satisfied for some standard material models. The following definitions are taken from Brezis [7].

Definition 1. Let E be a Hilbert space. A functional $\phi : E \rightarrow \bar{\mathbb{R}}^+$ is called *convex* iff for all $\rho \in [0, 1]$, $u_1, u_2 \in E$,

$$\phi(\rho u_1 + (1 - \rho)u_2) \leq \rho \phi(u_1) + (1 - \rho)\phi(u_2). \quad (23)$$

The functional ϕ is called *lower semicontinuous* iff for all $u \in E$, and all sequences $u_n \rightarrow u$,

$$\liminf \phi(u_n) \geq \phi(u). \quad (24)$$

It is weakly lower semicontinuous if (24) holds for all weakly convergent sequences $u_n \rightharpoonup u$.

An operator $A : X \rightarrow E$ is called *hemicontinuous* on a convex subset $X \subset E$ if for all $x, y \in X$ the mapping

$$[0, 1] \rightarrow \mathbb{R}, \quad t \mapsto \langle A((1-t)x + ty), x - y \rangle \quad (25)$$

is continuous.

As a minimal assumption on the Helmholtz free energy we demand it to be lower semicontinuous and convex. Its Frechet (or full) derivative shall exist and define the operator A ,

$$\Psi : \mathbb{X} \rightarrow \mathbb{R} \text{ is convex, lower semicontinuous and Frechet differentiable.} \quad (26)$$

To get convergence estimates and stability bounds, we need further that $A : \mathbb{X}_0 \rightarrow \mathbb{H}^*$ is strongly monotone, i.e. there exist $m > 0$ such that for all $\mathbf{w}_1, \mathbf{w}_2 \in \mathbb{X}_0$,

$$\langle A(\mathbf{w}_1) - A(\mathbf{w}_2), \mathbf{w}_1 - \mathbf{w}_2 \rangle \geq m \|\mathbf{w}_1 - \mathbf{w}_2\|_{\mathbb{H}}^2. \quad (27)$$

The dissipation function $\Phi : \mathbb{H} \rightarrow \mathbb{R}$ as well as its augmented counterpart $j : \mathbb{H} \rightarrow \overline{\mathbb{R}}^+$ need not be differentiable, but non-negative, proper, and positively homogeneous,

$$\begin{aligned} j(\mathbf{w}) &\geq 0 \text{ for all } \mathbf{w}, \mathbf{z} \in \mathbb{H}, \text{ and it exists at least one } \mathbf{w} \in \mathbb{H} \text{ with } j(\mathbf{w}) < \infty, \text{ and} \\ j(\alpha \mathbf{z}) &= \alpha j(\mathbf{z}) \text{ for all } \alpha > 0, \mathbf{z} \in \mathbb{H}. \end{aligned} \quad (28)$$

Additionally, we assume

$$j : \mathbb{H} \rightarrow \overline{\mathbb{R}}^+ \text{ is convex and lower semicontinuous.} \quad (29)$$

3.2 Time discrete update equation

We use a uniform partitioning of the time interval $[0, T]$ into N sub-intervals,

$$0 = t_0 < t_1 < \dots < t_{N-1} < t_N = T \quad \text{with} \quad t_n - t_{n-1} = \Delta T = T/N. \quad (30)$$

For N fixed, we will define a sequence $\{\mathbf{w}_n\}_{n=0}^N \in [\mathbb{H}_0]^{N+1}$ as consecutive solutions to (spatial but time-independent) variational inequalities. We use the backward difference $\Delta \mathbf{w}_n = \mathbf{w}_n - \mathbf{w}_{n-1}$ and $\ell_n = \ell(t_n)$. We show that this sequence is defined uniquely, and that stability estimates are satisfied. We use the following existence result by Brezis:

Theorem 1 (Corollaire 30 in [7]). *Let E be a reflexible Banach space, and let $X \subset E$ be closed and convex with $0 \in X$. Let $A : X \rightarrow E^*$ be weakly pseudo-monotone and $\phi : X \rightarrow]-\infty, +\infty]$ be convex lower semicontinuous with $\phi(0) < \infty$. If*

$$\lim_{\|x\| \rightarrow \infty} \frac{\langle A(x), x \rangle + \phi(x)}{\|x\|} = \infty, \quad (31)$$

then for $\ell \in E^*$ there exists a solution $u \in X$ to

$$\langle A(u), v - u \rangle + \phi(v) - \phi(u) \geq \langle \ell, v - u \rangle \quad \forall v \in X. \quad (32)$$

If A is additionally strongly monotone, the solution is unique.

The main result of this section is the following:

Theorem 2. *Let $\Psi : \mathbb{X} \rightarrow \mathbb{R}$ be convex, lower semicontinuous and Frechet differentiable as in (26), and let $A : \mathbb{X} \rightarrow \mathbb{H}^*$ be its derivative. Let $j : \mathbb{H} \rightarrow \overline{\mathbb{R}}^+$ be non-negative, proper, convex, positively homogeneous and lower semicontinuous as in (28) and (29). Let moreover $A : \mathbb{X}_0 \rightarrow \mathbb{H}^*$ be strongly monotone on \mathbb{X}_0 as in (27).*

Then, for N fixed and any given $\{\ell_n\}_{n=0}^N$ with $\ell_n \in \mathbb{H}^$ and $\ell_0 = 0$, there exists a unique sequence $\{\mathbf{w}_n\}_{n=0}^N$ such that $\mathbf{w}_n \in \mathbb{X}_0$ and $\Delta \mathbf{w}_n \in \mathbb{H}_0$ and*

$$\langle A(\mathbf{w}_n), \mathbf{z} - \Delta \mathbf{w}_n \rangle + j(\mathbf{z}) - j(\Delta \mathbf{w}_n) \geq \langle \ell_n, \mathbf{z} - \Delta \mathbf{w}_n \rangle \quad \forall \mathbf{z} \in \mathbb{H}. \quad (33)$$

The set of test functions can be equivalently restricted to $\mathbf{z} \in \mathbb{H}_0$. For m the constant of monotonicity in (27), the solution satisfies the stability estimate

$$\|\Delta \mathbf{w}_n\|_{\mathbb{H}} \leq 1/m \|\Delta \ell_n\|_{\mathbb{H}^*}. \quad (34)$$

Proof. We use Theorem 1 from convex analysis to show existence and uniqueness of the solutions. For the stability estimates, we progress along the lines of proof of [9] and see that some of their assumptions can be weakened. To show existence and uniqueness of the sequence $\{\mathbf{w}_n\}_{n=0}^N$, we proceed inductively from $\mathbf{w}_0 = \mathbf{0}$, assuming \mathbf{w}_{n-1} known. We rewrite the variational inequality (33) in terms of the unknown $\Delta \mathbf{w}_n$ and \mathbf{w}_{n-1} ,

$$\langle A(\Delta \mathbf{w}_n + \mathbf{w}_{n-1}), \mathbf{z} - \Delta \mathbf{w}_n \rangle + j(\mathbf{z}) - j(\Delta \mathbf{w}_n) \geq \langle \ell_n, \mathbf{z} - \Delta \mathbf{w}_n \rangle \quad \forall \mathbf{z} \in \mathbb{H}_0. \quad (35)$$

We show that we can apply Theorem 1 to obtain existence of a solution $\Delta \mathbf{w}_n$. As solution space we choose $E = \mathbb{H}_0$. We see that admissible updates are in the set $\mathbb{X}_{0, \mathbf{w}_{n-1}} := \mathbb{X}_0 - \mathbf{w}_{n-1} = \{\mathbf{z} : \mathbf{z} + \mathbf{w}_{n-1} \in \mathbb{X}_0\}$ where saturation is not reached. From [7, Proposition 1] we know that convexity of Ψ implies monotony and hemicontinuity of A on the open set $\mathbb{X}_{0, \mathbf{w}_{n-1}}$, which further implies pseudo-monotony of A . But still we cannot use $\mathbb{X}_{0, \mathbf{w}_{n-1}}$ directly for X in Theorem 1, as this set is not closed. Instead, we use the parameter-dependent closed sub-set

$$\mathbb{X}_{0, \mathbf{w}_{n-1}}(c) := \{\mathbf{z} \in \mathbb{X}_0 : \langle A(\mathbf{w}_{n-1} + \mathbf{z}), \mathbf{z} \rangle - \langle \ell, \mathbf{z} \rangle \leq c \|\mathbf{z}\|\}, \quad (36)$$

with the choice of $c > 0$ still to be determined. We show that this set is closed: Assume a sequence $\mathbf{z}_k \in \mathbb{X}_{0, \mathbf{w}_{n-1}}(c)$ that converges strongly to some $\mathbf{z} \in \mathbb{H}$. To show closedness of $\mathbb{X}_{0, \mathbf{w}_{n-1}}(c)$ we need to prove that $\mathbf{z} \in \mathbb{X}_{0, \mathbf{w}_{n-1}}(c)$. Starting from the defining condition of (36) applied for \mathbf{z}_k ,

$$\langle A(\mathbf{w}_{n-1} + \mathbf{z}_k), \mathbf{z}_k \rangle - \langle \ell, \mathbf{z}_k \rangle \leq c \|\mathbf{z}_k\|, \quad (37)$$

we apply $\liminf_{k \rightarrow \infty}$ on both sides. Proposition 6 in [7] and continuity of ℓ ensure that

$$\langle A(\mathbf{w}_{n-1} + \mathbf{z}), \mathbf{z} \rangle - \langle \ell, \mathbf{z} \rangle \stackrel{[7]}{\leq} \liminf_{k \rightarrow \infty} \langle A(\mathbf{w}_{n-1} + \mathbf{z}_k), \mathbf{z}_k \rangle - \langle \ell, \mathbf{z}_k \rangle \leq c \liminf_{k \rightarrow \infty} \|\mathbf{z}_k\| = c \|\mathbf{z}\|. \quad (38)$$

Thus we have shown $\mathbf{z} \in \mathbb{X}_{0, \mathbf{w}_{n-1}}(c)$ due to (36), and further that $\mathbb{X}_{0, \mathbf{w}_{n-1}}(c)$ is closed for any fixed $c > 0$.

The functional $\phi = j$ satisfies the conditions of Theorem 1. With all assumptions of Theorem 1 satisfied, there exists a solution $\Delta \mathbf{w}_n^c$ to the parameter-dependent variational inequality

$$\langle A(\Delta \mathbf{w}_n^c + \mathbf{w}_{n-1}), \mathbf{z} - \Delta \mathbf{w}_n^c \rangle + j(\mathbf{z}) - j(\Delta \mathbf{w}_n^c) \geq \langle \ell_n, \mathbf{z} - \Delta \mathbf{w}_n^c \rangle \quad \forall \mathbf{z} \in \mathbb{X}_{0, \mathbf{w}_{n-1}}(c). \quad (39)$$

The solution is unique if A is strongly monotone.

It remains to show that the variational inequality holds also for test functions $\mathbf{z} \in \mathbb{H}_0 \setminus \mathbb{X}_{0, \mathbf{w}_{n-1}}(c)$ provided c is larger than some fixed value not depending on the solution. Additionally we have to show that no $\mathbf{w} \in \mathbb{X}_0 \setminus \mathbb{X}_{0, \mathbf{w}_n}(c)$ can be an additional solution to preserve uniqueness.

For the first task, choose $c_{n-1} = c(\mathbf{w}_{n-1})$ depending on the previous iterate such that

$$\langle A(\mathbf{w}_{n-1}), \mathbf{z} \rangle - \langle \ell, \mathbf{z} \rangle \leq c_{n-1} \|\mathbf{z}\| \quad \forall \mathbf{z} \in \mathbb{H}_0. \quad (40)$$

This constant exists since for $\mathbf{w}_{n-1} \in \mathbb{X}_0$ fixed, the derivative $A(\mathbf{w}_{n-1})$ is a continuous linear operator. Now set $c = 2c_{n-1}$, and let $\mathbf{z} \in \mathbb{X}_0 \setminus \mathbb{X}_{0, \mathbf{w}_{n-1}}(2c_{n-1})$, i.e.

$$\langle A(\mathbf{w}_{n-1} + \mathbf{z}), \mathbf{z} \rangle - \langle \ell, \mathbf{z} \rangle > 2c_{n-1} \|\mathbf{z}\|. \quad (41)$$

From the hemicontinuity of A we deduce that there exists some $t_0 > 0$ such that for all $t \in [0, t_0]$

$$\langle A(\mathbf{w}_{n-1} + t\mathbf{z}), t\mathbf{z} \rangle - \langle \ell, t\mathbf{z} \rangle \leq 2c_{n-1} t \|\mathbf{z}\|, \quad (42)$$

i.e. $t\mathbf{z} \in \mathbb{X}_{0, \mathbf{w}_{n-1}}(2c_{n-1})$. But then the variational inequality (39) is satisfied for $t\mathbf{z}$, and due to linearity and positive homogeneity of j , it is thus satisfied also for test function $\mathbf{z} \in \mathbb{H}$.

On the other hand we have to show that there cannot exist any $\Delta \mathbf{w} \in \mathbb{X}_0 \setminus \mathbb{X}_{0, \mathbf{w}_{n-1}}(2c_{n-1})$ that is also solution to (35). But for such a $\Delta \mathbf{w}$ we know

$$-\langle A(\mathbf{w}_n + \Delta \mathbf{w}), \Delta \mathbf{w} \rangle + \langle \ell_n, \Delta \mathbf{w} \rangle < -2c_{n-1} \|\mathbf{w}\| < 0. \quad (43)$$

Together with the positivity of dissipation, one immediately obtains that the variational inequality (35) is not satisfied for $\mathbf{z} = 0$. Thus $\Delta \mathbf{w}_n$ is the only solution to (35).

We proceed to the stability estimates (34). We additionally assume strong monotonicity of A as in (27). Note that in this case, condition (31) is trivially satisfied. In (35), we set $\mathbf{z} = 0$ to obtain

$$\langle A(\Delta \mathbf{w}_n + \mathbf{w}_{n-1}), \Delta \mathbf{w}_n \rangle + j(\Delta \mathbf{w}_n) \leq \langle \ell_{n-1} + \Delta \ell_n, \Delta \mathbf{w}_n \rangle. \quad (44)$$

Next, in (33) at time step $n - 1$, we use $\mathbf{z} = \Delta \mathbf{w}_n + \Delta \mathbf{w}_{n-1} \in \mathbb{H}_0$. By algebraic manipulations, using convexity and positive homogeneity of $j(\cdot)$, we see

$$\langle A(\mathbf{w}_{n-1}), \Delta \mathbf{w}_n \rangle + \underbrace{j(\Delta \mathbf{w}_n + \Delta \mathbf{w}_{n-1}) - j(\Delta \mathbf{w}_{n-1})}_{\leq j(\Delta \mathbf{w}_n)} \geq \langle \ell_{n-1}, \Delta \mathbf{w}_n \rangle. \quad (45)$$

Subtracting (45) from (44) and applying strong monotonicity on the one and continuity of $\Delta \ell_n$ on the other hand we arrive at the desired result (34),

$$m \|\Delta \mathbf{w}_n\|_{\mathbb{H}}^2 \leq \langle A(\Delta \mathbf{w}_n + \mathbf{w}_{n-1}) - A(\mathbf{w}_{n-1}), \Delta \mathbf{w}_n \rangle \leq \langle \Delta \ell_n, \Delta \mathbf{w}_n \rangle \leq \|\Delta \ell_n\|_{\mathbb{H}^*} \|\Delta \mathbf{w}_n\|_{\mathbb{H}}. \quad (46)$$

□

4 APPLICATION TO SPECIAL FERROELECTRIC MATERIAL MODELS

The assumptions from the previous section are reasonable ones. We motivate this for the example of the ferroelectric material model for non-remnant straining as proposed by Landis [13]. We will see that all assumptions of the previous section are satisfied if material parameters are in common ranges. We derive the form of the dissipation function $\Phi(\dot{\mathbf{P}}^i)$ when given the switching surface depending on $\hat{\mathbf{E}}$.

We use the reversible part of the energy as proposed by [13],

$$\Psi^r := \frac{1}{2}(\mathbf{S} - \mathbf{S}^i) : \mathbf{c} : (\mathbf{S} - \mathbf{S}^i) - (\mathbf{S} - \mathbf{S}^i) : \mathbf{h} \cdot (\mathbf{D} - \mathbf{P}^i) + \frac{1}{2}(\mathbf{D} - \mathbf{P}^i) \cdot \boldsymbol{\beta} \cdot (\mathbf{D} - \mathbf{P}^i). \quad (47)$$

For non-remanent straining, one supposes $\mathbf{S}^i = 0$ and \mathbf{c} , \mathbf{h} and $\boldsymbol{\beta}$ depend on the remanent polarization. Quite similarly, one might introduce a kinematic assumption for the remanent strain $\mathbf{S}^i = \mathbf{S}^i(\mathbf{P}^i)$, as done in [14, 15]. For simplicity, we do not consider this case in the analytical deductions below, but in our numerical examples. The irreversible part of the energy is assumed as [13, Section 5]

$$\Psi^i = \frac{H_0 P_0^2}{(m-1)(m-2)} \left(1 - \frac{|\mathbf{P}^i|}{P_0} \right)^{2-m} - \frac{H_0 P_0}{m-1} |\mathbf{P}^i| \quad \text{if } m \neq 2 \text{ and} \quad (48)$$

$$\Psi^i = -H_0 P_0^2 \log \left(1 - \frac{|\mathbf{P}^i|}{P_0} \right) - H_0 P_0 |\mathbf{P}^i| \quad \text{if } m = 2. \quad (49)$$

In [13], it has been shown that the free energy is differentiable, and all differentiations are provided analytically. We assume that the material constants are such that the compound material tensor has positive eigenvalues bounded away from zero independently of \mathbf{P}^i . This issue has been treated in detail by Stark et al. [17], conditions on the material parameters are given there. Considering the special form of Ψ^r , then its derivative $A^r := \partial \Psi^r / \partial \mathbf{w}$ is strictly monotone in the sense that

$$\langle A^r(\mathbf{w}) - A^r(\mathbf{z}), \mathbf{w} - \mathbf{z} \rangle \geq c_1 (\|\mathbf{S} - \tilde{\mathbf{S}}\|_{L^2}^2 + \|\mathbf{D} - \mathbf{P}^i - \tilde{\mathbf{D}} + \tilde{\mathbf{P}}^i\|_{L^2}^2) \quad (50)$$

The irreversible and saturation part $A^i := \partial(\Psi^i + \Psi^s) / \partial \mathbf{w}$ are strictly monotone in the remanent polarization,

$$\langle A^i(\mathbf{w}) - A^i(\mathbf{z}), \mathbf{w} - \mathbf{z} \rangle \geq c_2 \|\mathbf{P}^i - \tilde{\mathbf{P}}^i\|_{L^2}^2. \quad (51)$$

Thus, for the sum $A = A^r + A^i$, one immediately deduces that

$$\langle A(\mathbf{w}) - A(\mathbf{z}), \mathbf{w} - \mathbf{z} \rangle \geq \frac{1}{2} \min(c_1, c_2) (\|\mathbf{S} - \tilde{\mathbf{S}}\|_{L^2}^2 + \|\mathbf{D} - \tilde{\mathbf{D}}\|_{L^2}^2 + \|\mathbf{P}^i - \tilde{\mathbf{P}}^i\|_{L^2}^2). \quad (52)$$

The last, essential ingredient to strict monotonicity is the fact that we restricted the full space of all dielectric displacements \mathbb{D} to those which are divergence-free, $\operatorname{div} \mathbf{D} = 0$, and that this space \mathbb{D}_0 is closed. In this case, the L^2 norm is equivalent to the full $H(\operatorname{div})$ norm on \mathbb{D}_0 , and (52) is sufficient for strict monotonicity of A on \mathbb{H}_0 .

As a second task, we show that the assumptions on the dissipation function are satisfied. To this end, we first characterize the dissipation function in detail. Usually, it is defined by a threshold or switching surface, i.e. a condition on the forces $\hat{\mathbf{E}}$ and $\hat{\mathbf{T}}$. We assume a condition of the form $\varphi(\hat{\mathbf{E}}) = |\hat{\mathbf{E}}|/E_0 - 1 \leq 0$. Then the dissipation function Φ is then given as

$$\Phi(\dot{\mathbf{P}}^i) = \sup \left\{ \int_{\Omega} \dot{\mathbf{P}} \cdot \hat{\mathbf{E}} \, dx : \varphi(\hat{\mathbf{E}}) \leq 0 \right\} = \int_{\Omega} E_0 |\dot{\mathbf{P}}^i| \, dx. \quad (53)$$

In [9] it is shown that dissipation functions of the above format satisfy all assumptions such as convexity, lower semicontinuity and positive homogeneity. Indeed, in case of elasto-plasticity the dissipation function is of the same abstract form, where the coercitive electric field E_0 resembles the yield stress.

5 FINITE ELEMENT IMPLEMENTATION

5.1 Finite element spaces

We propose to use conforming finite element spaces for the discretization of the variational inequality. For a simplicial finite element mesh $\mathcal{T} = \{T\}$, we use the nodal space for the displacements, the Raviart-Thomas space \mathcal{RT}_0 for the divergence-conforming dielectric displacement (see e.g. [5]), and piecewise constant remanent polarizations,

$$\mathbf{u} \in \mathbb{U}_h := \{\mathbf{u} \in [H^1(\Omega)]^d : \mathbf{u}|_T \in [P^1(T)]^d, \mathbf{u} = 0 \text{ on } \Gamma_{fix}\} \subset \mathbb{U}, \quad (54)$$

$$\mathbf{D} \in \mathbb{D}_h := \mathcal{RT}_0 \subset \mathbb{D}, \quad (55)$$

$$\mathbf{P}^i \in \mathbb{P} := \{\mathbf{P} \in [L^2(\Omega)]^d : \mathbf{P}|_T \in [P^0(T)]^d\} \subset \mathbb{P}. \quad (56)$$

Gauss' law of divergence free dielectric displacements is enforced by a Lagrangian multiplier in the sense of (21), which resembles the electric potential ϕ and is discretized also by piecewise constant functions,

$$\phi \in \mathbb{W}_h := \{\phi \in L^2(\Omega) : \phi|_T \in P^0(T)\}. \quad (57)$$

Note that it is essential to choose dielectric displacement and its Lagrangian multiplier in a stable combination of spaces, such that not only

$$\int_{\Omega} \operatorname{div} \mathbf{D} \phi \, dx = 0 \text{ for all } \phi \in \mathbb{W}_h \text{ implies } \operatorname{div} \mathbf{D} = 0, \quad (58)$$

but also the discrete inf-sup condition holds independently of the mesh size,

$$\inf_{\mathbf{D} \in \mathbb{D}_h} \sup_{\phi \in \mathbb{W}_h} \frac{\int_{\Omega} \operatorname{div} \mathbf{D} \phi \, dx}{\|\mathbf{D}\|_{H(\operatorname{div})} \|\phi\|_{L^2}} \geq c. \quad (59)$$

This condition is satisfied for the pair \mathcal{RT}_0 and piecewise constants. For a thorough theoretical background we refer the interested reader to the exhaustive monograph [5] on mixed problems.

5.2 Regularization of the dissipation function

For solving variational inequalities, different numerical algorithms are proposed in the literature. Well-known for dual variational inequalities is the *return-mapping algorithm* in different variants. There, after a predictor step, in the corrector step the generalized stress is projected back to the admissible set in a consistent way. Also for primal variational inequalities, as derived in this work, predictor/corrector iterations have been analyzed e.g. in the application of elasto-plasticity [9, Section 12.2].

In contrast, we propose to regularize the non-differentiable dissipation function, such that the problem can be solved “all at once” in a single Newton iteration. This *regularization technique* has been analyzed for convergence and accuracy in [9, Section 12.4]. Briefly, for some given parameter ε , the non-differentiable dissipation j is replaced by a smooth function j_ε , which differs from j only by ε (see Section 6 for a special choice). If the findings from [9] can be transferred to the ferroelectric polarization problem, one can expect that the solution \mathbf{w}_ε converges to \mathbf{w} in \mathbb{H} , and $\|\mathbf{w} - \mathbf{w}_\varepsilon\|_{\mathbb{H}} \leq c\sqrt{\varepsilon}$. However, we do not aim at proving these convergence estimates for the present problem. In the present manuscript, we used the following regularized version of the dissipation,

$$j_\varepsilon(\dot{\mathbf{P}}^i) := \int_{\Omega} E_0 |\dot{\mathbf{P}}^i|_\varepsilon \, dx \quad \text{with } |\dot{\mathbf{P}}^i|_\varepsilon := \begin{cases} |\dot{\mathbf{P}}^i| - \varepsilon/2 & \text{if } |\dot{\mathbf{P}}^i| \geq \varepsilon, \\ 1/(2\varepsilon) |\dot{\mathbf{P}}^i|^2 & \text{else.} \end{cases} \quad (60)$$

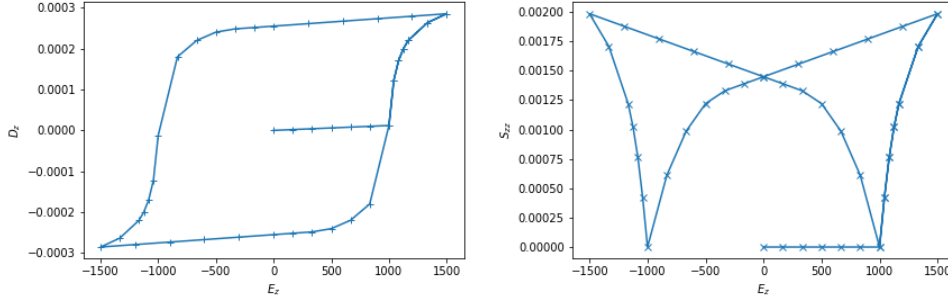


Figure 1: Loadcase electric polarization and depolarization: Hysteresis of dielectric displacement (left) and strain (right).

6 NUMERICAL RESULTS

We provide a patch test example, where we reproduce known hysteresis effects and mechanical depolarization on a ferroelectric cube. In the second example, a ferroelectric cantilever is polarized by an applied electric field, and partially depolarized in bending. In both examples, we use the energies Ψ^r and Ψ^i as described in (47), (48) and (49). We assumed the permittivity at constant strain $\beta = \epsilon^{-1}\mathbf{I}$ to be independent of \mathbf{P}^i . The piezoelectric tensor \mathbf{d} depends on \mathbf{P}^i in the standard way as given in [13, eq. (4.3)]. Then the coupling tensor \mathbf{h} and the stiffness at constant dielectric displacement can be computed algebraically by β , \mathbf{d} and the (assumed constant) stiffness at constant electric field, cmp. [13].

We use the open source all-purpose finite element code Netgen/NGSolve², where high-order hierarchical finite elements for all element types (segments, triangles, quadrilaterals, tetrahedra, hexahedra, prisms, ...) and many different spaces (continuous or discontinuous, curl or div conforming, ...) are implemented. Via a python interface, variational equations or even energies can be entered symbolically. In a nonlinear problem, the (symbolic) equations are differentiated automatically, and a Newton iteration can be realized in a straightforward manner, without need to implement tedious tangent stiffnesses etc. by hand for each formulation.

6.1 Patch test

Consider a cube of side length 2 mm whose normal displacement is fixed at the three coordinate planes. The cube is electroded on top and bottom, the other faces are electrically insulated. We use material constants derived from the dimensionless constants proposed by [14]. We set $E_0 = 1$ MV/m, $P_0 = 0.3$ C/m², $S_0 = 0.002$, $m = 2$, $\epsilon = 12$ nC/(V m), $E_Y = 30$ GPa, $\nu = 0.3$, $d_{31} = -2.1 \times 10^{-10}$ N/(V m), $d_{33} = 4.2 \times 10^{-10}$ N/(V m), $H_0 = \frac{1}{3}$ MV m/C. The regularization parameter from Section 5.2 is set to $\varepsilon = 10^{-6} P_0$.

We provide hysteresis curves for the standard load case of electric polarization and depolarization by an electric field of $1.5E_0$ in Figure 1. Moreover, Figure 2 shows the effect of mechanical depolarization by a compressive load of 200 N/mm² applied to the top surface of the cube.

6.2 Ferroelectric cantilever

The second example is that of a ferroelectric cantilever beam of length 10 mm and cross section 2×2 mm, which was proposed by [18]. The clamped end as well as the tip of the beam are electroded.

²available at <https://ngsolve.org>

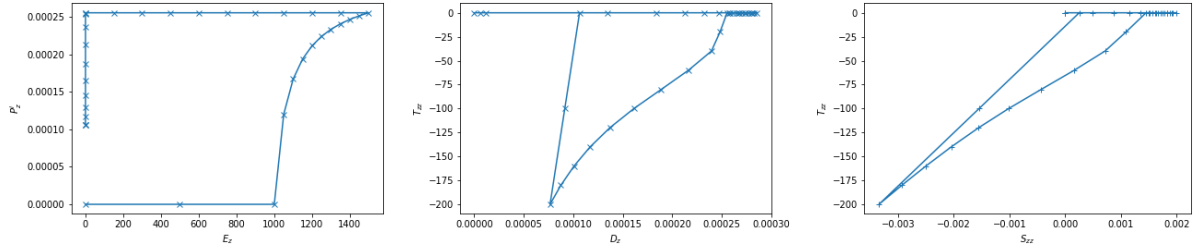


Figure 2: Loadcase mechanic depolarization: Remanent polarization as a function of the applied electric field (left), stress evolution over dielectric displacement (center) and over strain (right).

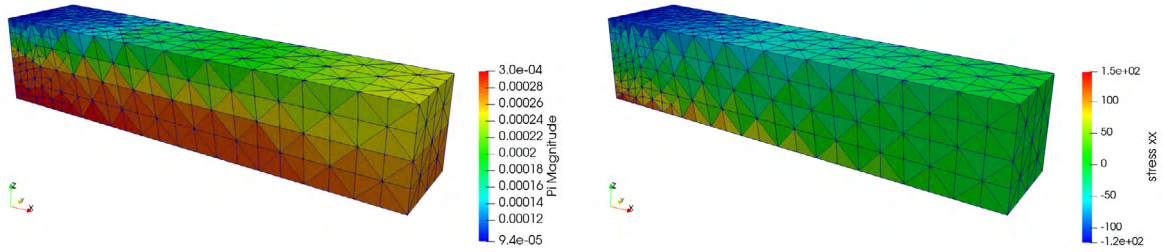


Figure 3: Mechanical depolarization of a polarized cantilever beam under a vertical tip force – absolute value of remanent polarization $|P_i|$ (left) and stress distribution T_{xx} .

First, the beam is polarized applying an electric potential to the beam tip while keeping the other electrode grounded. The electric field is raised in 12 load steps amounting to $3E_0$, then lowered back to zero. Afterwards, a vertical tip force of 16 N is applied to the tip surface. Due to the compression in the upper part of the beam, the material depolarizes mechanically in this section.

The obtained values cannot be compared directly to the original work of [18], as in this reference a different material model based on Kamlah's work [11] is used. We chose material constants close to their values, using $E_0 = 1 \text{ MV/m}$, $P_0 = 0.3 \text{ C/m}^2$, $S_0 = 0.002$, $m = 1.1$, $\epsilon = 15 \text{ nC/(V m)}$, $E_Y = 10 \text{ GPa}$, $\nu = 0.3$, $d_{31} = -2.74 \times 10^{-10} \text{ N/(V m)}$, $d_{33} = 5.93 \times 10^{-10} \text{ N/(V m)}$, $H_0 = 1 \text{ MV m/C}$. The d_{15} effect was neglected in the current implementation, the regularization parameter is $\varepsilon = 10^{-6} P_0$.

The absolute value of the remanent polarization $|P^i|$ after bending, and the corresponding stress distribution T_{xx} , are depicted in Figure 3. As observed in [18], the cantilever depolarizes in the region close to the clamped end where compressive stresses arise. This depolarization reduces the stress level there to a maximum of -123.771 N/mm^2 , which compares well to the values listed in the original reference. However, due to the different description of the ferroelectric material, the region of depolarization is much larger.

7 ACKNOWLEDGEMENTS

Astrid Pechstein and Alexander Humer acknowledge support by the Linz Center of Mechatronics (LCM) funded by the Austrian federal government and the federal state of Upper Austria. Martin Meindl-

humer acknowledges support of Johannes Kepler University Linz, Linz Institute of Technology (LIT).

REFERENCES

- [1] E. Bassiouny, A.F. Ghaleb, and G.A. Maugin. Thermodynamical formulation for coupled electromechanical hysteresis effects—I. Basic equations. *International Journal of Engineering Science*, 26(12):1279–1295, 1988.
- [2] E. Bassiouny, A.F. Ghaleb, and G.A. Maugin. Thermodynamical formulation for coupled electromechanical hysteresis effects—II. Poling of ceramics. *International Journal of Engineering Science*, 26(12):1297–1306, 1988.
- [3] E. Bassiouny and G.A. Maugin. Thermodynamical formulation for coupled electromechanical hysteresis effects—III. Parameter identification. *International Journal of Engineering Science*, 27(8):975–987, 1989.
- [4] E. Bassiouny and G.A. Maugin. Thermodynamical formulation for coupled electromechanical hysteresis effects—IV. Combined electromechanical loading. *International Journal of Engineering Science*, 27(8):989–1000, 1989.
- [5] D. Boffi, F. Brezzi, and M. Fortin. *Mixed finite element methods and applications*, volume 44 of *Springer Series in Computational Mathematics*. Springer, Heidelberg, 2013.
- [6] C.J. Bottero and M.I. Idiart. An evaluation of a class of phenomenological theories of ferroelectricity in polycrystalline ceramics. *Journal of Engineering Mathematics*, 113(1):13–22, 2018.
- [7] H. Brezis. Equations et inéquations non linéaires dans les espaces vectoriels en dualité. In *Annales de l’institut Fourier*, volume 18, pages 115–175, 1968.
- [8] A.C.F. Cocks and R.M. McMeeking. A phenomenological constitutive law for the behaviour of ferroelectric ceramics. *Ferroelectrics*, 228(1):219–228, 1999.
- [9] W. Han and B.D. Reddy. *Plasticity: Mathematical Theory and Numerical Analysis*, volume 9. Springer Science & Business Media, 1999.
- [10] J.E. Huber and N.A. Fleck. Multi-axial electrical switching of a ferroelectric: theory versus experiment. *Journal of the Mechanics and Physics of Solids*, 49(4):785–811, 2001.
- [11] M. Kamlah. Ferroelectric and ferroelastic piezoceramics—modeling of electromechanical hysteresis phenomena. *Continuum Mechanics and Thermodynamics*, 13(4):219–268, 2001.
- [12] S. Klinkel. A phenomenological constitutive model for ferroelastic and ferroelectric hysteresis effects in ferroelectric ceramics. *International Journal of Solids and Structures*, 43(22-23):7197–7222, 2006.
- [13] C.M. Landis. Fully coupled, multi-axial, symmetric constitutive laws for polycrystalline ferroelectric ceramics. *Journal of the Mechanics and Physics of Solids*, 50(1):127–152, 2002.
- [14] R.M. McMeeking and C.M. Landis. A phenomenological multi-axial constitutive law for switching in polycrystalline ferroelectric ceramics. *International Journal of Engineering Science*, 40(14):1553–1577, 2002.
- [15] C. Miehe, D. Rosato, and B. Kiefer. Variational principles in dissipative electro-magneto-mechanics: A framework for the macro-modeling of functional materials. *International Journal for Numerical Methods in Engineering*, 86(10):1225–1276, 2011.
- [16] A.S. Semenov, H. Kessler, A. Liskowsky, and H. Balke. On a vector potential formulation for 3d electromechanical finite element analysis. *Communications in Numerical Methods in Engineering*, 22(5):357–375, 2006.
- [17] S. Stark, P. Neumeister, and H. Balke. Some aspects of macroscopic phenomenological material models for ferroelectroelastic ceramics. *International Journal of Solids and Structures*, 80:359 – 367, 2016.
- [18] W. Zouari, T.B. Zineb, and A. Benjeddou. A ferroelectric and ferroelastic 3d hexahedral curvilinear finite element. *International Journal of Solids and Structures*, 48(1):87–109, 2011.

APPLICATION OF A MICROSTRUCTURAL MODEL TO SIMULATION OF A TINI BEAM BENDING PERFORMANCE AND CALCULATION OF THICKNESS STRESS DISTRIBUTIONS

ALEKSANDR E. VOLKOV^{*}, MARGARITA E. EVARD^{*}, NATALIA A. VOLKOVA^{*},
AND EGOR A. VUKOLOV^{*}

^{*} Saint Petersburg State University
Pr. Universitetskiiy, 28, 198504 Saint-Petersburg, Russia
e-mail: a.volkov@spbu.ru
.semni.org

Key words: Shape Memory Alloys, Bending, Boundary-Value Problem, Modeling.

Abstract. This work presents a numerical simulation of a TiNi shape memory alloy (SMA) beam performance in the mode of pure bending with the use of Bernoulli-Euler hypotheses. The beam is subjected to an action of a bending torque, an axial force and temperature variations. Thickness distributions of the stress and strain as well as the beam deflection for various stages of thermomechanical loading are obtained. The formulation of the boundary-value problem includes the equations describing the mechanical equilibrium and the constitutive behavior of an SMA representative volume, for which two models - a microstructural and a macroscopic ones are used. They account for the deformations due to elasticity, thermal expansion and phase transformation. It is noted that since the microstructural model automatically accounts for the tension-compression asymmetry of TiNi the use of this model for the description of the SMA behavior predicts that the neutral line of the bent beam does not pass through its center and the beam performance in the mode of bending differs from that in the mode of tension.

1 INTRODUCTION

In many applications shape memory alloy (SMA) parts are used as working bodies of actuators, force elements [1,2], medical staples [3], endovascular stents [4], etc., in which they experience strain accumulation and recovery in the mode of bending. This mode of deformation is distinguished by an inhomogeneous stress and strain fields. Moreover the tensile stress has different signs on the inner and outer surfaces of the bent beam. Keeping in mind that some SMA, such as the widely used TiNi-based alloys, demonstrate the tension-compression asymmetry [5, 6], one can conclude that the functional properties of a bent SMA beam cannot be the same as the properties of a rod, subjected only to tension or only to compression.

To find the dependences of the beam curvature and deflection under the action of the bending torque as well as the martensite phase and stress distributions over the beam cross-section one must solve a boundary-value problem. Such an attempt is made in this work.

2 CONSTITUTIVE RELATIONS: MICROSTRUCTURAL MODEL

Microstructural models have significant advantages, since they can account for the structure of SMA and the specific features of their mechanical behavior. Most well developed models are [7,8]. In this work an earlier developed microstructural model [9-11] was used to describe the deformation of the SMA. The equations are formulated for the physical processes, producing micro-strain in the micro-regions and the macroscopic strain of a representative volume is calculated by averaging of strains of micro-regions constituting this volume. The primary structural elements of martensite are considered to be Bain's variants (domains) originated from the parent phase in each grain by different but crystallographically equivalent variants of Bain's deformation. Therefore, the internal variables in this model are the volume fractions of the Bain's variants. Note that another choice of these elements used in [12] and leading to similar results is the martensitic plates bearing the martensitic shift on a habit plane.

The representative volume V of a SMA (fig.1) consists of a set of grains, each characterized by the orientation ω of its crystallographic axes.

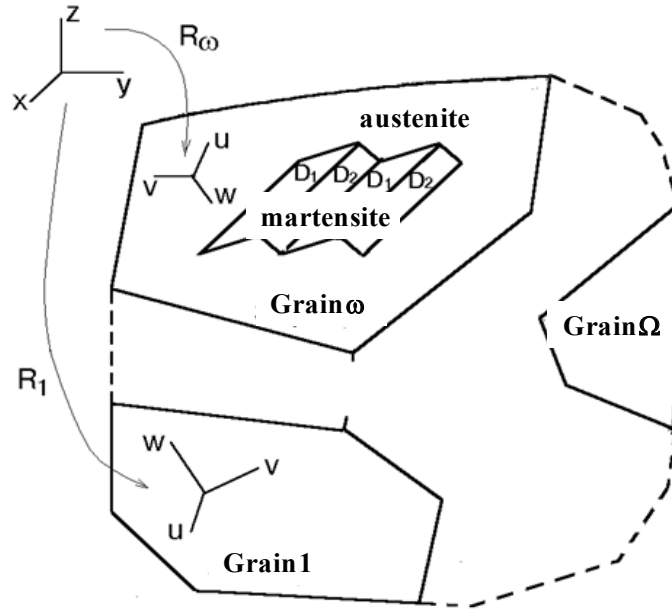


Fig.1. Scheme of the representative volume of SMA

The A. Reuss' hypothesis is accepted according to which the macroscopic strain can be calculated as the average of all micro-strains. In this model the spatial averaging of the micro-strains, is substituted by the orientation averaging, thus expressing the macroscopic strain ε and the volume fraction Φ^M of martensite by the formulae:

$$\varepsilon = \sum_{\omega} f(\omega) \varepsilon^{\text{gr}}(\omega), \quad \Phi_M = \sum_{\omega} f(\omega) \Phi^{\text{gr}}(\omega)$$

where the sum is taken over all grains, $f(\omega)$ is the volume fraction of the grains with orientation ω (a discrete analogue of the orientation distribution function), $\varepsilon^{\text{gr}}(\omega)$ and $\Phi^{\text{gr}}(\omega)$

are the strain tensor and the volume fraction of martensite in a grain with orientation ω (in this article small deformation tensors are used).

In each grain there exist N orientational variants of martensite obtained from austenite by different but crystallographically equivalent Bain's deformations D_n ($n = 1, \dots, N$). For the transformation of cubic phase into monoclinic one $N=12$ (shuffles are not considered since they do not change the homogeneous part of the Bain's strain). Thus, martensite is characterized by the internal variables Φ_n ($n = 1, \dots, N$), such that $(1/N)\Phi_n$ is the volume fraction of the domain occupied by the n -th orientational variant of martensite. For the phase deformation of this grain one has:

$$\varepsilon^{\text{gr}} = (1 - \Phi^{\text{gr}})\varepsilon^{\text{A}} + \frac{1}{N} \sum_{n=1}^N \Phi_n \varepsilon_n^{\text{M}}$$

The superscripts A and M denote austenite and martensite, ε^{A} and ε^{M} are the deformations of the austenitic and martensitic phases. In general, each of the strains ε^{A} and ε^{M} can be expressed as the sum of the elastic strain ε^{e} , thermal expansion strain ε^{T} , dislocation slip plastic strain ε^{P} , phase strain ε^{Ph} (strain due to the phase transformation) and the micro-plastic strain ε^{MP} , which is the strain occurring by the localized dislocation slip under the action of the inter-phase stresses. In the present work we consider the case when $\varepsilon^{\text{MP}} = \varepsilon^{\text{P}} = 0$. Elastic and thermal strains are calculated by commonly known formulae, which we do not write down here. Since the phase strain is the strain, which occurs as the result of the transformation of austenite to martensite we put that for the austenite $\varepsilon^{\text{PhA}} = 0$ and for the n -th variant of martensite $\varepsilon_n^{\text{PhM}} = D_n$. So, the total phase strain of a grain is

$$\varepsilon^{\text{Ph gr}} = \frac{1}{N} \sum_{n=1}^N \Phi_n D_n.$$

The evolution equations for Φ_n is formulated in terms of the generalized thermodynamic forces, which are derived from the Gibbs' potential. G . For a unit volume:

$$G = G^{\text{eig}} + G^{\text{mix}}, \quad G^{\text{eig}} = (1 - \Phi^{\text{gr}})G^{\text{A}} + \frac{1}{N} \sum_{n=1}^N \Phi_n G_n^{\text{M}}, \quad G_n^{\text{mix}} = \frac{\mu}{2} \sum_{m,n=1}^N A_{mn} \Phi_m \Phi_n$$

where G^{A} , G_n^{M} , G^{eig} are the potentials of non-interacting austenite and martensite and their average value; G^{mix} is the potential of the interaction equal to the elastic energy of the internal stresses. In the work [13] this potential is referred to as the "phase interaction energy function" (PIEF). The eigenpotentials G^{A} and G_n^{M} at temperature T and stress σ can be expressed by the formula:

$$G^{\text{a}} = G_0^{\text{a}} - S_0^{\text{a}}(T - T_0) - \frac{c_{\sigma}^{\text{a}}(T - T_0)^2}{2T_0} - \varepsilon^{\text{0a}}(T) : \sigma - \frac{1}{2} \sigma : Q^{\text{a}} : \sigma, \quad \text{a} = \text{A, M}$$

where T_0 is the temperature of the thermodynamic equilibrium of austenite and martensite at zero stress, G_0^{a} and S_0^{a} are the values of the Gibbs' potential and of the entropy at $T=T_0$ and $\sigma=0$, c_{σ}^{a} is the specific heat (per unit volume), $\varepsilon^{\text{0a}}(T)$ is the strain at $\sigma=0$, Q^{a} is the tensor of elastic compliances, symbol ":" denotes double scalar product of tensors.

Potential G^{mix} is estimated by a quadratic form of the internal parameters describing the phase deformation. The matrix A_{mn} of this quadratic form accounts for the interactions between the different variants of martensite. The matrix A_{mn} of this quadratic form accounts for the interactions between the different variants of martensite. In TiNi the transformation is from cubic B2 phase into monoclinic B19' phase. For this transformation there exists 12 different Bain's deformations. These variants group into pairs called the Corresponding Variants Pairs (CVP) [14-16]. This martensite structure allows lowering the elastic energy of the interphase stresses. The tendency of the Bain's variants for grouping is taken into account by the matrix A_{mn} . Enumerating the Bain's variants in a proper order the following structure of the matrix A_{mn} was suggested:

$$A = \begin{pmatrix} A_1 & 0 & 0 \\ 0 & A_1 & 0 \\ 0 & 0 & A_1 \end{pmatrix}, \quad A_1 = \begin{pmatrix} 1 & -\alpha & -\alpha & 0 \\ -\alpha & 1 & 0 & -\alpha \\ -\alpha & 0 & 1 & -\alpha \\ 0 & -\alpha & -\alpha & 1 \end{pmatrix}$$

where α is a material constant ($0 \leq \alpha < 1/2$) measuring the degree of the interaction between the Bain's variants forming one CVP.

The evolution equation for the internal variables is deduced from the condition of equilibrium of the thermodynamic forces, which are obtained as the derivatives of the Gibbs' potential.

$$F_n = -\frac{\partial G}{\partial \Phi_n} \approx \frac{q_0(T-T_0)}{T_0} + \sigma: D_n - \mu \sum_{m=1}^N A_{nm} \Phi_m,$$

Here q_0 is the latent heat of the transformation ($q_0 < 0$); T_0 is the phase equilibrium temperature, for which the approximation $T_0 = (M_s + A_f)/2$ suggested in [17] is used; μ is a material constant. The transformation does not occur at the equilibrium state, i.e. at $F_n = 0$, but rather at a state apart from equilibrium, when there is an excess of the driving force. So, the condition of the transformation can be formulated in the form:

$$F_n = \pm F^{\text{tr}},$$

Sign “+” must be taken for the direct and “-” for the reverse transformation; material constant F^{tr} determines the extent of the deviation from equilibrium and it is responsible for the temperature – phase hysteresis of the transformation.

To describe the reorientation (twinning) of martensite three hypotheses are accepted: (1) any variant of martensite can be transformed in any other variant; (2) reorientation occurs along the direction in the space Φ_1, \dots, Φ_N , which corresponds to the fastest decrease of the Gibbs' potential; (3) reorientation starts when the thermodynamic force reaches some critical

value. To find the direction of the reorientation we use vector $F_n = \left\{ -\frac{\partial G}{\partial \Phi_1}, \dots, -\frac{\partial G}{\partial \Phi_N} \right\}$ and

take its projection L onto plane $\Phi_1 + \dots + \Phi_N = \text{const}$. Then if for some n it holds that $\Phi_n = 0$ and $L_n < 0$ we substitute L for its projection L' onto intersection of planes $\Phi_n = 0$ and

$\Phi_1 + \dots + \Phi_N = \text{const}$, repeating this procedure for other components of L_n if necessary. Finally we obtain the direction l , which does not lead to a violation of conditions $\Phi_1 + \dots + \Phi_N < 1$, $\Phi_n > 0$, $n=1, \dots, N$. For this direction we postulate the condition of reorientation:

$$F^{\text{tw}}(l) = F^{\text{fr tw}},$$

where $F^{\text{tw}}(l) = -\frac{\partial G}{\partial l} = -\sum_{n=1}^N l_n \frac{\partial G}{\partial \Phi_n} = \sum_{n=1}^N l_n F_n$, $F^{\text{fr tw}}$ is a material constant, characterizing the critical driving force for reorientation. From hypotheses 1 and 2 it follows that the increments $d\Phi_n$ are proportional to l_n : $d\Phi_n = l_n d\phi$, where $d\phi$ is the proportionality factor.

There are rather few material constants in the model for the deformation of a SMA accounting only for the elastic thermal and phase deformation. The values for most of the constants are found from independent experiments: the Bain's strain is determined from the X-ray diffraction data and the scheme of the crystal lattice deformation; values for F^{fr} and μ are derived from the values of the characteristic temperatures M_f , M_s , A_s , A_f , and the latent heat q_0 (all of them can be measured on the differential scanning calorimeter). The adjustable parameters are $F^{\text{fr tw}}$ and α . The first of them is related to the phase yield limit of martensite and is easily found from the tensile test. The second controls the value of the reversible phase strain accumulated on cooling of the specimen under a constant stress: with the growth of α the tendency of the Bain's variants to form self-accommodated configurations becomes more pronounced and the macroscopic phase strain decreases. The number of grains N is the model parameter, which affects the anisotropy of a simulated SMA. For a single crystal ($N=1$) the material is anisotropic, becoming almost isotropic when N exceed 300. So, this parameter must correlate to the ratio of the grain diameter to the characteristic dimension of the specimen. For TiNi the values of the constants were determined in the previous works [9-11].

This microstructural approach proved to be efficient for simulating the deformation of a specimen in different states (martensitic, two-phase and austenitic) as well as strain accumulation on cooling and heating under a constant or varying load.

3 BOUNDARY-VALUE PROBLEM FOR BENDING OF AN SMA BEAM

Consider the boundary problem of bending of an SMA beam (fig.2). We assume that loading is made in isothermal conditions, which means that the rod is in contact with the thermostat over its entire surface and, besides, the cross-sectional shape is such that heat transfer processes occur fast, so that the temperature is distributed over the section uniformly.

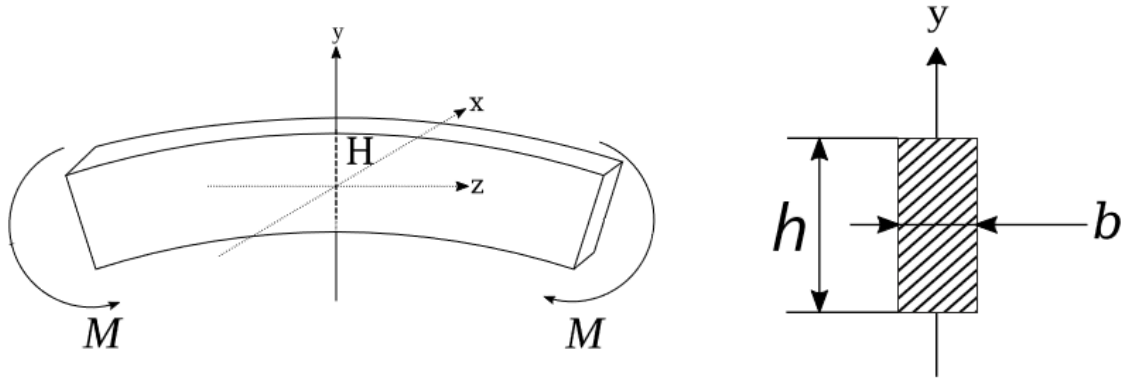


Fig.2. Scheme of pure bending.

For simplicity, we consider a beam with a rectangular cross-section with width b and a small thickness h , loaded by a bending torque M and thus, experiencing pure bending, in which the plane of the bending moment coincides with the plane of the curvature of the beam. For pure bending, the Bernoulli plane-sections hypothesis and the hypothesis of non-compression of layers are valid. In this case, the distribution of relative deformations over the cross section of the rod can be calculated by the formula

$$\varepsilon_{zz}(y) = \kappa y + \bar{\varepsilon}, \quad (1)$$

where κ is the curvature of the central layer of the beam and $\bar{\varepsilon}$ is the relative elongation of this layer. The only non-vanishing stress is σ_{zz} . Further, for simplicity notations ε and σ are used for ε_{zz} and σ_{zz} . The Hook's law gives:

$$\sigma = E(\varepsilon - \varepsilon^{ne}) \quad (2)$$

where E is the Young's modulus and ε^{ne} is the non-elastic strain.

For a given distribution $\sigma(z)$ the equilibrium conditions are valid:

$$\int_{-h/2}^{h/2} b\sigma(y)dy = 0, \quad \int_{-h/2}^{h/2} b\sigma(y)ydy = M. \quad (3)$$

In this work we do not consider thermal expansion, thus, the non-elastic strain consists only of the phase strain, the increment of which as well of the increments of the internal parameters as well as the increments of the internal variables are given by the microstructural model described in section 2, and which can be schematically expressed as

$$\Delta\varepsilon^{ne}(y) = F_1(\Delta T, \Delta\sigma(y), X(y)), \quad \Delta X(y) = F_2(\Delta T, \Delta\sigma(y), X(y)) \quad (4)$$

where the functions F_1 and F_2 are defined by microstructural model and by X is denoted the set of internal variables $\Phi_n(\omega)$, that is the volume fractions of martensite for each variant n in each grain ω .

To solve the problem specified by equations (1) – (4) we use the discrete scheme, dividing the interval $[-h/2, h/2]$ into K equal segments and search for the values $\sigma_j = \sigma(y_j)$, $\varepsilon_j = \varepsilon(y_j)$,

where $y_j = (jh/K), j = 0, \dots, K$.

Then we split the whole problem into two parts. The first problem is the problem of the mechanical equilibrium and it is to find the “vector” $\{\sigma_j\}$ for given torque M and “vector” $\{\varepsilon_j^{ne}\}$ using formulae (1) – (3). Denoting the operator solving this problem by Mech, we write

$$\{\sigma_j\} = \text{Mech}(M, \{\varepsilon_j^{ne}\}) \quad (5)$$

The second (“rheological”) problem is to find the increments of the non-elastic strains $\{\Delta\varepsilon_j^{ne}\}$ for known increments ΔT and $\{\Delta\sigma_j\}$ using the microstructural model (4). Denoting this operator by Rheo, we write:

$$\{\Delta\varepsilon_j^{ne}\} = \text{Rheo}(\Delta T, \{\Delta\sigma_j\}) \quad (6)$$

Now it is possible to formulate the scheme of passing from the “vector” $\{\varepsilon_j^{ne}(t)\}$ corresponding to the time instant t to the “vector” $\{\varepsilon_j^{ne}(t+\Delta t)\}$, where the time increment Δt corresponds to the increments ΔT and ΔM of the temperature and of the bending torque. This scheme is as follows.

1. Choose the 0-th approximation $\{\varepsilon_j^{ne}\}^{(0)} = 0$ for “vector” $\{\varepsilon_j^{ne}\}$.
2. Find $\{\sigma_j\}^{(1)} = \text{Mech}(M + \Delta M, \{\varepsilon_j^{ne}\}^{(0)})$.
3. Find the 1-st approximation $\{\varepsilon_j^{ne}\}^{(1)} = \lambda \{\varepsilon_j^{ne}\}^{(0)} + (1-\lambda) \text{Rheo}(\Delta T, \{\Delta\sigma_j\}^{(1)})$.
4. Repeat steps 1 – 3 until $\max_j (\{\varepsilon_j^{ne}\}^{(i+1)} - \{\varepsilon_j^{ne}\}^{(i)}) < e$,

where λ is the iteration parameter ($0 < \lambda \leq 1$) and e denotes the admissible error.

Thus, for given regime of the thermomechanical loading specified by the values of temperature T_i and bending torque M_i corresponding to time instants t_i , one can find the values $\{\varepsilon_j^{ne}(t_i)\}$ and $\{\sigma_j(t_i)\}$ as well as the values κ_i of the curvature.

4 SIMULATION RESULTS

For simulation the following beam dimensions were chosen: length $l = 50$ mm, width $b = 10$ mm, thickness $h = 2.8$ mm. The characteristic temperatures M_f , M_s , A_s , A_f , were 300, 315, 350 365 K, and the latent heat $q_0 = -150.0$ J/cm³. The diagram of bending is presented on Fig.3 (the deflection measured at the center of the bent arc) and the height distributions of the stress and phase are presented on fig.4.

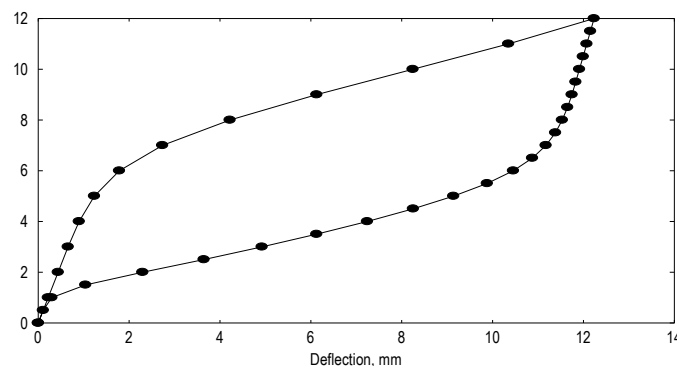


Fig.3. The dependence of the bending torque on the deflection of the beam during its deformation at 375 K.

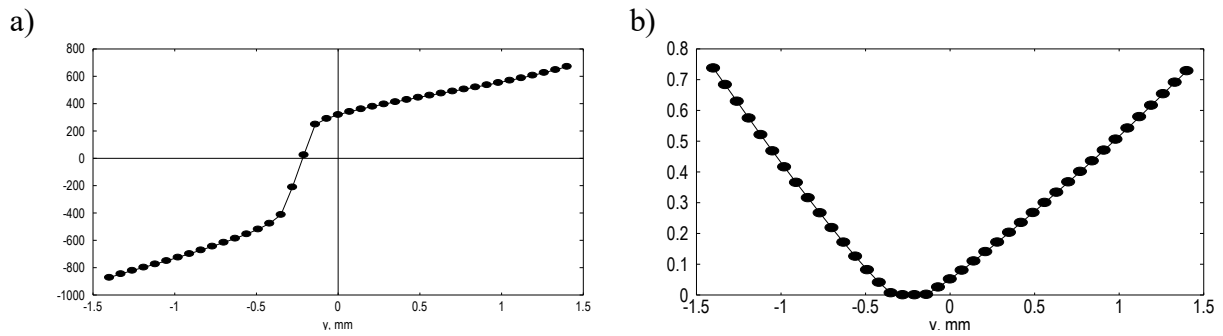


Fig.4. Distribution of the normal stress (a) and of the volume fraction of martensite (b) along the height of the pseudoelastic beam loaded at 375 K by a bending torque 12 N · m

Since the microstructural model automatically takes into account the asymmetry of TiNi properties with respect to tension – compression, the simulation using this model predicts that the neutral line of the bent beam does not pass through its center, but rather is shifted towards the compressed beam layers. The maximum absolute value of the compressive stress is bigger than the tensile stress. This circumstance should be taken into account when assessing the functional properties of the SMA tested in bending mode.

Analogous dependences of the maximum deflection on the bending moment are obtained during isothermal bending of the beam in the pseudoplastic (martensitic) state.

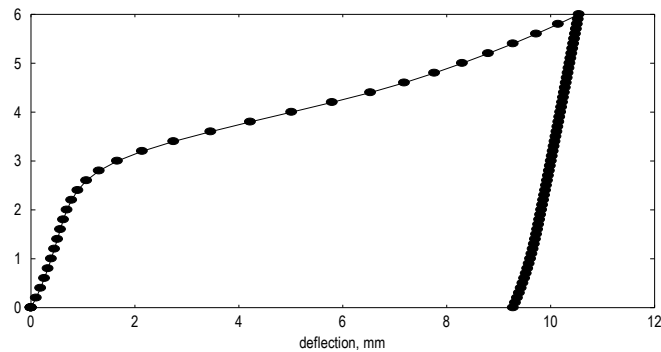


Fig.5. The dependence of the bending torque on the deflection of the beam during its deformation at 295 K

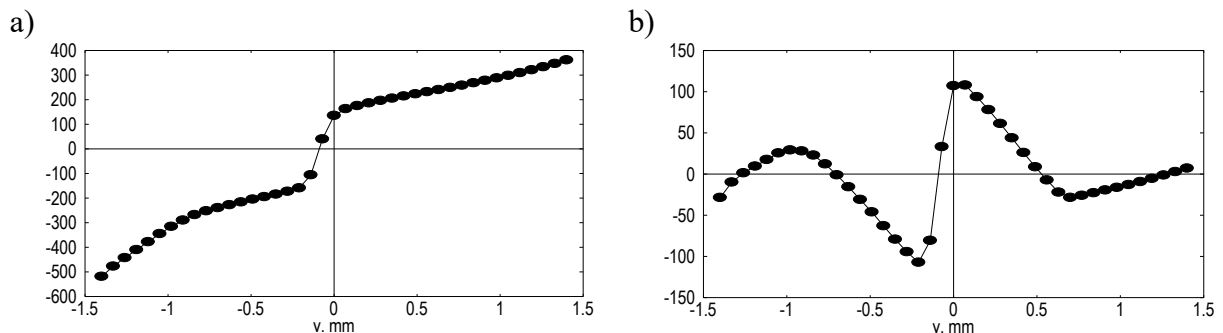


Fig.6. Distribution of the normal stress along the height of the beam loaded at 295 K by a bending torque 12 N · m (a) and after unloading (b).

Again one can see that distribution of the stress is not symmetric and the compressive stress is much higher than the tensile one. The asymmetry of the distribution of stress is present also after unloading of the beam.

11 CONCLUSIONS

- Microstructural modeling allows solving simple boundary-value problems for thermomechanical loading of SMA in the pure bending mode, revealing the inhomogeneity of the distributions of the stress.
- The tension – compression asymmetry of SMA leads to the asymmetric distribution of the stress, at which the compressed side of the bent beam is under a higher stress than the stretched side.

This work was supported by the Russian Foundation for Basic Research, grant number 18-01-00594.

REFERENCES

- [1] Duerig, T.W., Melton, K.N., Stöckel D. (eds.), *Engineering Aspects of Shape Memory Alloys*,: Butterworth-Heinemann (1990), 512 p.
- [2] Wanhill R.J.H., Ashok B. (2017) *Shape Memory Alloys (SMAs) for Aerospace Applications*. In: Prasad N., Wanhill R. (eds) *Aerospace Materials and Material Technologies*. Indian Institute of Metals Series. Springer, Singapore.
- [3] Wei Zhang, Yonggang Zhang, Guoquan Zheng, Ruyi Zhang, and Yan Wang, A Biomechanical Research of Growth Control of Spine by Shape Memory Alloy Staples, *BioMed Research International* (2013) **2013**, Article ID 384894, <http://dx.doi.org/10.1155/2013/384894>.
- [4] Petrini L., Bertini A. et al., Part H: J. of Engineering in Medicine (2017) **231**, 391-404.
- [5] Volkov A.E., Emelyanova E.V., Evard M.E., Volkova N.A., An explanation of phase deformation tension–compression asymmetry of TiNi by means of microstructural modeling, *Journal of Alloys and Compounds*, (2013) 577(S1), S127-S130.
- [6] Chatziathanasiou D., Chemisky Y., Meraghni F., Chatzigeorgiou G., Patoor, E., Phase Transformation of Anisotropic Shape Memory Alloys: Theory and Validation in Superelasticity, *Shape Memory and Superelasticity* (2015) **1**: 359-374.
- [7] Niclaeys C., Zineb T.B., Patoor E. (2004) Influence of Microstructural Parameters on Shape Memory Alloys Behavior. In: Ahzi S., Cherkaoui M., Khaleel M.A., Zbib H.M., Zikry M.A., Lamatina B. (eds) *IUTAM Symposium on Multiscale Modeling and Characterization of Elastic-Inelastic Behavior of Engineering Materials*. Solid Mechanics and Its Applications, vol 114. Springer, Dordrecht.
- [8] Yang, Z, Li, X., Brinson, L,C, Choudhary, A.N., Chen W., Agrawal, A. (2018). Microstructural Materials Design Via Deep Adversarial Learning Methodology. *Journal of Mechanical Design*. 140. 10.1115/1.4041371.
- [9] Evard, M.E., Volkov A.E., Modeling of the martensite accommodation effect on mechanical behavior of shape memory alloys, *J. Eng. Mater. and Technol.* (1999) **121**: 102-104.

- [10] Volkov A.E., Casciati F., Simulation of dislocation and transformation plasticity in shape memory alloy polycrystals, in: F.Auricchio, L.Faravelli, G.Magonette and V.Torra (Eds.) *Shape Memory Alloys. Advances in Modelling and Applications*, Barcelona, 2001, p.88-104.
- [11] Evard, M.E., Volkov A.E., Belyaev F.S., A Microstructural Model of SMA with Microplastic Deformation and Defects Accumulation: Application to Thermocyclic Loading, *Materials Today: Proceedings* (2015), **2**, Suppl. 3, S583-S587.
- [12] E. Patoor, A. Eberhardt, M. Berveiller, Micromechanical modelling of superelasticity in shape memory alloys, *J. de Physique IV, Coll. C1*. (1996) **6(1)**, 277-292.
- [13] Nae, F.A., Matsuzaki, Y., Ikeda, T., Micromechanical modeling of polycrystalline shape-memory alloys including thermo-mechanical coupling, *Smart Materials and Structures*, (2003) **12**, 6-17.
- [14] Nishida M., Nishiura T., Kawano H., Imamura T. Self-accommodation of B19' martensite in Ti-Ni shape memory alloys – Part I. Morphological and crystallographic studies of variant selection rule, *Philosophical. Magazine* (2012) **92**, 2215–2233.
- [15] Nishida M., Okunishi E., Nishiura T., Kawano H., Imamura T., Li S., Hara T. Self-accommodation of B19' martensite in Ti-Ni shape memory alloys – Part II. Characteristic interface structures between habit plane variants, *Philosophical. Magazine*, (2012) **92**, 2234–2246.
- [16] Imamura T., Nishiura T., Kawano H., Hosoda H., Nishida M. Self-accommodation of B19' martensite in Ti-Ni shape memory alloys – Part III. Analysis of habit plane variant clusters by the geometrically nonlinear theory, *Philosophical. Magazine*, (2012) **92**, 2247–2263.
- [17] Salzbrenner R.J., Cohen M. On the thermodynamics of thermoelastic martensitic transformations, *Acta Metallurgica*, (1979) **27**, N 5, 739–748.

ASSESSMENT OF SECOND PIOLA-KIRCHHOFF STRESS TENSOR IN LAMINATED PIEZOELECTRIC STRUCTURES THROUGH SAS SHELL FORMULATION

M. G. KULIKOV^{*}, S. V. PLOTNIKOVA[†], S. A. MAMONTOV[†] AND
G. M. KULIKOV[†]

^{*} Department of Applied Mathematics and Mechanics
Tambov State Technical University
Sovetskaya, 106, Tambov 392000, Russia
e-mail: adiosmsu@gmail.com

[†] Laboratory of Intelligent Materials and Structures
Tambov State Technical University
e-mail: plotnikovasvetlana62@gmail.com, gmkulikov@mail.ru

Key words: Laminated Piezoelectric Shell, Nonlinear Exact Geometry Solid-Shell Element, Hybrid-Mixed Method, Sampling Surfaces Formulation.

Abstract. The paper presents a robust nonlinear exact geometry or geometrically exact (GeX) laminated piezoelectric four-node solid-shell element using the method of sampling surfaces (SaS). The term GeX reflects the fact that the parametrization of the middle surface is known and, therefore, the coefficients of the first and second fundamental forms and Christoffel symbols are taken exactly at element nodes. The SaS method is based on choosing inside the n th layer I_n SaS parallel to the middle surface in order to introduce the displacements and electric potentials of these surfaces as basic shell unknowns. Such choice of unknowns with the consequent use of Lagrange polynomials of degree $I_n - 1$ in assumed approximations of displacements, strains, electric potential and electric field through the layer thickness yields the efficient higher-order piezoelectric shell formulation. The inner SaS are located inside each layer at Chebyshev polynomial nodes that makes it possible to minimize uniformly the error due to Lagrange interpolation. The nonlinear GeX solid-shell element formulation utilizes the Green-Lagrange strain tensor that exactly represents the arbitrarily large rigid-body motions of a shell in any curvilinear coordinate system. This permits one to calculate the transverse components of the second Piola-Kirchhoff stress tensor with a high accuracy. The developed solid-shell element is based on the hybrid-mixed method and allows the use of load steps, which are much larger than possible with existing displacement-based solid-shell elements. The tangent stiffness matrix is evaluated by efficient 3D analytical integration. As a result, the GeX/SaS solid-shell element exhibits a superior performance in the case of coarse meshes. It can be useful for the 3D stress analysis of thick and thin doubly-curved laminated piezoelectric shells undergoing finite rotations.

1 INTRODUCTION

In recent years, a considerable progress has been achieved on the development of continuum-based finite elements that can handle the geometrically nonlinear analysis of laminated piezoelectric shells satisfactorily [1-5]. These elements are typically defined by two layers of nodes on the bottom and top surfaces of the shell with three displacement degrees of freedom (DOFs) and one electric potential DOF per node and known as isoparametric 6-parameter piezoelectric solid-shell elements taking into account the number of only displacement DOFs. However, the 6-parameter piezoelectric solid-shell element formulation based on the complete constitutive equations of piezoelectricity is deficient because thickness locking occurs. This is due to the fact that the linear displacement field in the thickness direction results in a constant transverse normal strain, which in turn causes artificial stiffening of the shell element in the case of non-vanishing Poisson's ratios. It should be mentioned that the errors caused by thickness locking do not decrease with the mesh refinement because the reason of stiffening lies in the shell theory itself rather than the finite element discretization. To prevent thickness locking, the transverse normal strain is enriched in the thickness direction by a linear term [6].

In a more general 9-parameter piezoelectric solid-shell element formulation, three layers of nodes located on the bottom, middle and top surfaces with three displacement DOFs and one electric potential DOF per node are introduced [7, 8]. Such choice of sampling surfaces (SaS) with the use of Lagrange polynomials of the second degree in the through-thickness approximations of displacements, strains, electric potential and electric field leads to a very compact form of the 9-parameter piezoelectric solid-shell element formulation. Moreover, this model allows one to derive the Green-Lagrange strain tensor, which exactly represents arbitrarily large rigid-body motions of the shell in convected curvilinear coordinates. Considering that the displacement vectors of SaS are resolved in the middle surface basis, the higher-order shell formulation with nine displacement DOFs is very suitable to develop the exact geometry or geometrically exact (GeX) piezoelectric solid-shell elements. The term GeX means that the parametrization of the middle surface is known a priori and, therefore, the coefficients of the first and second fundamental forms and the Christoffel symbols are taken exactly at element nodes.

It should be noted that the 6- and 9-parameter solid-shell elements do not describe correctly the transverse components of the second Piola-Kirchhoff stress tensor and electric displacement vector in laminated piezoelectric shells. To evaluate them, the advanced computational techniques should be invoked. The present paper is intended to overcome this gap in the finite element literature and develop the four-node solid-shell element for calculating the second Piola-Kirchhoff stresses in laminated piezoelectric shells. For this purpose, the GeX nonlinear solid-shell element in the framework of the SaS formulation [9] is proposed. The SaS laminated shell formulation is based on choosing inside each layer I_n SaS parallel to the middle surface in order to introduce the displacements and electric potentials of these surfaces as fundamental shell unknowns. Such choice of unknowns with the consequent use of Lagrange polynomials of degree $I_n - 1$ in the through-thickness approximations of displacements, strains, electric potential and electric field of the n th layer yields a robust higher-order layerwise shell formulation, in which all basic variables including strains, stresses, electric field and electric displacement are related to SaS. Recently, the SaS

formulation has been employed to analyze analytically and numerically the electroelastic and thermoelectroelastic response of laminated and functionally graded piezoelectric shells [10–14]. However, the nonlinear solid-shell elements for the analysis of laminated piezoelectric shells through the SaS formulation have not been developed yet.

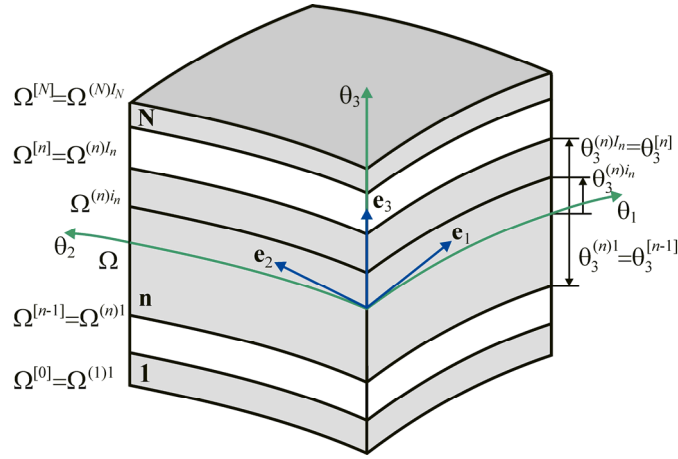


Figure 1: Geometry of the laminated piezoelectric shell

2 HU-WASHIZU VARIATIONAL SAS FORMULATION

Consider a laminated piezoelectric shell of the thickness h . Let the middle surface Ω be described by orthogonal curvilinear coordinates θ_1 and θ_2 , which are referred to the lines of principal curvatures of its surface. The coordinate θ_3 is oriented along the unit vector $\mathbf{e}_3(\theta_1, \theta_2)$ normal to the middle surface. Introduce the following notations: $\mathbf{e}_\alpha(\theta_1, \theta_2)$ are the orthonormal base vectors of the middle surface; $A_\alpha(\theta_1, \theta_2)$ are the coefficients of the first fundamental form; $k_\alpha(\theta_1, \theta_2)$ are the principal curvatures of the middle surface; $c_\alpha = 1 + k_\alpha \theta_3$ are the components of the shifter tensor; $c_\alpha^{(n)i_n}(\theta_1, \theta_2) = 1 + k_\alpha \theta_3^{(n)i_n}$ are the components of the shifter tensor at SaS; $\theta_3^{(n)i_n}$ are the transverse coordinates of SaS of the n th layer $\Omega^{(n)i_n}$ given by

$$\theta_3^{(n)1} = \theta_3^{[n-1]}, \quad \theta_3^{(n)I_n} = \theta_3^{[n]}, \quad (1)$$

$$\theta_3^{(n)m_n} = \frac{1}{2}(\theta_3^{[n-1]} + \theta_3^{[n]}) - \frac{1}{2}h_n \cos\left(\pi \frac{2m_n - 3}{2(I_n - 2)}\right), \quad (2)$$

where $h_n = \theta_3^{[n]} - \theta_3^{[n-1]}$ is the thickness of the n th layer; $\theta_3^{[m]}$ are the coordinates of interfaces $\Omega^{[m]}$ depicted in Figure 1; the index n identifies the belonging of any quantity to the n th layer and runs from 1 to N , whereas the index m identifies the belonging of any quantity to the interface and runs from 1 to $N-1$; N is the number of layers; the indices m_n running from 2 to $I_n - 1$ describe the inner SaS of the n th layer, whereas the indices i_n, j_n, k_n running from 1 to I_n describe all SaS of the n th layer; I_n is the total number of SaS of the n th layer; Latin indices i, j, k, l range from 1 to 3, whereas Greek indices α, β range from 1 to 2.

It is seen from equation (2) that the transverse coordinates of inner SaS $\theta_3^{(n)m_n}$ coincide with Chebyshev polynomial nodes (roots of the Chebyshev polynomial of degree $I_n - 2$). This fact has a great meaning for a convergence of the SaS method [9-12].

The SaS approximations through the thickness [9] can be written as

$$[u_i^{(n)} \ \varepsilon_{ij}^{(n)} \ S_{ij}^{(n)} \ \varphi^{(n)} \ E_i^{(n)}] = \sum_{i_n} L^{(n)i_n} [u_i^{(n)i_n} \ \varepsilon_{ij}^{(n)i_n} \ S_{ij}^{(n)i_n} \ \varphi^{(n)i_n} \ E_i^{(n)i_n}], \quad (3)$$

where $u_i^{(n)}, \varepsilon_{ij}^{(n)}, S_{ij}^{(n)}, \varphi^{(n)}, E_i^{(n)}$ are the displacements, Green-Lagrange strains, second Piola-Kirchhoff stresses, electric potential and electric field of the n th layer; $u_i^{(n)i_n}, \varepsilon_{ij}^{(n)i_n}, S_{ij}^{(n)i_n}, \varphi^{(n)i_n}, E_i^{(n)i_n}$ are the displacements, Green-Lagrange strains, second Piola-Kirchhoff stresses, electric potential and electric field of SaS of the n th layer; $L^{(n)i_n}(\theta_3)$ are the Lagrange basis polynomials of degree $I_n - 1$ related to the n th layer:

$$L^{(n)i_n} = \prod_{j_n \neq i_n} \frac{\theta_3 - \theta_3^{(n)j_n}}{\theta_3^{(n)i_n} - \theta_3^{(n)j_n}}. \quad (4)$$

In the orthonormal basis \mathbf{e}_i , the relations between strains and displacements of SaS of the n th layer are written as

$$\begin{aligned} 2\varepsilon_{\alpha\beta}^{(n)i_n} &= \frac{1}{c_{\beta}^{(n)i_n}} \lambda_{\alpha\beta}^{(n)i_n} + \frac{1}{c_{\alpha}^{(n)i_n}} \lambda_{\beta\alpha}^{(n)i_n} + \frac{1}{c_{\alpha}^{(n)i_n} c_{\beta}^{(n)i_n}} \lambda_{i\alpha}^{(n)i_n} \lambda_{i\beta}^{(n)i_n}, \\ 2\varepsilon_{\alpha 3}^{(n)i_n} &= \frac{1}{c_{\alpha}^{(n)i_n}} \lambda_{3\alpha}^{(n)i_n} + \beta_{\alpha}^{(n)i_n} + \frac{1}{c_{\alpha}^{(n)i_n}} \lambda_{i\alpha}^{(n)i_n} \beta_i^{(n)i_n}, \\ 2\varepsilon_{33}^{(n)i_n} &= 2\beta_3^{(n)i_n} + \beta_i^{(n)i_n} \beta_i^{(n)i_n}, \end{aligned} \quad (5)$$

where $\lambda_{i\alpha}^{(n)i_n}$ are the strain parameters of SaS of the n th layer; $\beta_i^{(n)i_n}$ are the values of the derivative of displacements with respect to thickness coordinate on SaS defined as

$$\begin{aligned} \lambda_{\alpha\alpha}^{(n)i_n} &= \frac{1}{A_{\alpha}} u_{\alpha,\alpha}^{(n)i_n} + B_{\alpha} u_{\beta}^{(n)i_n} + k_{\alpha} u_3^{(n)i_n}, \quad \lambda_{\beta\alpha}^{(n)i_n} = \frac{1}{A_{\alpha}} u_{\beta,\alpha}^{(n)i_n} - B_{\alpha} u_{\alpha}^{(n)i_n} \text{ for } \beta \neq \alpha, \\ \lambda_{3\alpha}^{(n)i_n} &= \frac{1}{A_{\alpha}} u_{3,\alpha}^{(n)i_n} - k_{\alpha} u_{\alpha}^{(n)i_n}, \quad B_{\alpha} = \frac{1}{A_{\alpha} A_{\beta}} A_{\alpha,\beta} \text{ for } \beta \neq \alpha, \\ \beta_i^{(n)i_n} &= \sum_{j_n} M^{(n)j_n}(\theta_3^{(n)i_n}) u_i^{(n)j_n}, \end{aligned} \quad (6)$$

where $M^{(n)j_n} = L_{,3}^{(n)j_n}$ are the polynomials of degree $I_n - 2$; their values on SaS are

$$\begin{aligned} M^{(n)j_n}(\theta_3^{(n)i_n}) &= \frac{1}{\theta_3^{(n)j_n} - \theta_3^{(n)i_n}} \prod_{k_n \neq i_n, j_n} \frac{\theta_3^{(n)i_n} - \theta_3^{(n)k_n}}{\theta_3^{(n)j_n} - \theta_3^{(n)k_n}} \text{ for } j_n \neq i_n, \\ M^{(n)i_n}(\theta_3^{(n)i_n}) &= - \sum_{j_n \neq i_n} M^{(n)j_n}(\theta_3^{(n)i_n}). \end{aligned} \quad (7)$$

In equation (5) and below, the summation on repeated Latin indices is implied.

In the orthonormal basis \mathbf{e}_i , the relations between the electric field and electric potentials of SaS of the n th layer [9] are expressed as

$$\begin{aligned} E_\alpha^{(n)i_n} &= -\frac{1}{A_\alpha c_\alpha^{(n)i_n}} \varphi_{,\alpha}^{(n)i_n}, \\ E_3^{(n)i_n} &= -\sum_{j_n} M^{(n)j_n} (\theta_3^{(n)i_n}) \varphi^{(n)j_n}. \end{aligned} \quad (8)$$

The proposed hybrid-mixed piezoelectric solid-shell element is based on the Hu-Washizu variational equation of electroelasticity in which displacements, strains, stresses and electric potential are utilized as independent variables [7, 8]:

$$\delta \iint \sum_n \int_{\theta_3^{[n-1]}}^{\theta_3^{[n]}} \left[\frac{1}{2} \eta_{ij}^{(n)} C_{ijkl}^{(n)} \eta_{kl}^{(n)} - E_k^{(n)} e_{kij}^{(n)} \eta_{ij}^{(n)} - \frac{1}{2} E_i^{(n)} \epsilon_{ij}^{(n)} E_j^{(n)} - \sigma_{ij}^{(n)} (\eta_{ij}^{(n)} - \epsilon_{ij}^{(n)}) \right] dV = \delta W, \quad (9)$$

where $\eta_{ij}^{(n)}$ are the displacement-independent strains of the n th layer; $C_{ijkl}^{(n)}$, $e_{kij}^{(n)}$ and $\epsilon_{ij}^{(n)}$ are the elastic, piezoelectric and dielectric constants of the n th layer; $dV = A_1 A_2 c_1 c_2 d\theta_1 d\theta_2 d\theta_3$ is the infinitesimal volume element; W is the work done by external electromechanical loads.

According to the SaS technique, we introduce the through-thickness approximation of displacement-independent strains choosing them similar to the displacement-dependent strain approximation (3):

$$\eta_{ij}^{(n)} = \sum_{i_n} L^{(n)i_n} \eta_{ij}^{(n)i_n}. \quad (10)$$

Substituting the through-thickness distributions (3) and (10) in variational equation (9) and introducing

$$\Lambda^{(n)i_n j_n} = \int_{\theta_3^{[n-1]}}^{\theta_3^{[n]}} L^{(n)i_n} L^{(n)j_n} c_1 c_2 d\theta_3, \quad (11)$$

one can write the Hu-Washizu variational equation in terms of only SaS variables as

$$\begin{aligned} \delta \iint \sum_n \sum_{i_n} \sum_{j_n} \Lambda^{(n)i_n j_n} \left[\frac{1}{2} (\boldsymbol{\eta}^{(n)i_n})^T \mathbf{C}^{(n)} \boldsymbol{\eta}^{(n)j_n} - (\mathbf{E}^{(n)i_n})^T \mathbf{e}^{(n)} \boldsymbol{\eta}^{(n)j_n} \right. \\ \left. - \frac{1}{2} (\mathbf{E}^{(n)i_n})^T \boldsymbol{\epsilon}^{(n)} \mathbf{E}^{(n)j_n} - (\mathbf{S}^{(n)i_n})^T (\boldsymbol{\eta}^{(n)j_n} - \boldsymbol{\epsilon}^{(n)j_n}) \right] A_1 A_2 d\theta_1 d\theta_2 = \delta W, \end{aligned} \quad (12)$$

where

$$\begin{aligned} \boldsymbol{\epsilon}^{(n)i_n} &= [\epsilon_{11}^{(n)i_n} \quad \epsilon_{22}^{(n)i_n} \quad \epsilon_{33}^{(n)i_n} \quad 2\epsilon_{12}^{(n)i_n} \quad 2\epsilon_{13}^{(n)i_n} \quad 2\epsilon_{23}^{(n)i_n}]^T, \\ \boldsymbol{\eta}^{(n)i_n} &= [\eta_{11}^{(n)i_n} \quad \eta_{22}^{(n)i_n} \quad \eta_{33}^{(n)i_n} \quad 2\eta_{12}^{(n)i_n} \quad 2\eta_{13}^{(n)i_n} \quad 2\eta_{23}^{(n)i_n}]^T, \\ \mathbf{S}^{(n)i_n} &= [S_{11}^{(n)i_n} \quad S_{22}^{(n)i_n} \quad S_{33}^{(n)i_n} \quad S_{12}^{(n)i_n} \quad S_{13}^{(n)i_n} \quad S_{23}^{(n)i_n}]^T, \\ \mathbf{E}^{(n)i_n} &= [E_1^{(n)i_n} \quad E_2^{(n)i_n} \quad E_3^{(n)i_n}]^T, \end{aligned} \quad (13)$$

$$\mathbf{C}^{(n)} = \begin{bmatrix} C_{1111}^{(n)} & C_{1122}^{(n)} & C_{1133}^{(n)} & C_{1112}^{(n)} & 0 & 0 \\ C_{2211}^{(n)} & C_{2222}^{(n)} & C_{2233}^{(n)} & C_{2212}^{(n)} & 0 & 0 \\ C_{3311}^{(n)} & C_{3322}^{(n)} & C_{3333}^{(n)} & C_{3312}^{(n)} & 0 & 0 \\ C_{1211}^{(n)} & C_{1222}^{(n)} & C_{1233}^{(n)} & C_{1212}^{(n)} & 0 & 0 \\ 0 & 0 & 0 & 0 & C_{1313}^{(n)} & C_{1323}^{(n)} \\ 0 & 0 & 0 & 0 & C_{2313}^{(n)} & C_{2323}^{(n)} \end{bmatrix}, \quad (14)$$

$$\mathbf{e}^{(n)} = \begin{bmatrix} 0 & 0 & 0 & 0 & e_{113}^{(n)} & e_{123}^{(n)} \\ 0 & 0 & 0 & 0 & e_{213}^{(n)} & e_{223}^{(n)} \\ e_{311}^{(n)} & e_{322}^{(n)} & e_{333}^{(n)} & e_{312}^{(n)} & 0 & 0 \end{bmatrix}, \quad \mathbf{\epsilon}^{(n)} = \begin{bmatrix} \epsilon_{11}^{(n)} & \epsilon_{12}^{(n)} & 0 \\ \epsilon_{21}^{(n)} & \epsilon_{22}^{(n)} & 0 \\ 0 & 0 & \epsilon_{33}^{(n)} \end{bmatrix}.$$

3 HYBRID-MIXED FOUR-NODE SOLID-SHELL ELEMENT FORMULATION

The finite element formulation is based on a simple interpolation of the shell via GeX four-node piezoelectric solid-shell elements

$$u_i^{(n)i_n} = \sum_r N_r u_{ir}^{(n)i_n}, \quad \varphi^{(n)i_n} = \sum_r N_r \varphi_r^{(n)i_n}, \quad (15)$$

where $N_r(\xi_1, \xi_2)$ are the bilinear shape functions of the element; $u_{ir}^{(n)i_n}$ and $\varphi_r^{(n)i_n}$ are the displacements and electric potentials of SaS of the n th layer at element nodes; ξ_1, ξ_2 are the normalized curvilinear coordinates θ_1, θ_2 (Figure 2); the nodal index r runs from 1 to 4.

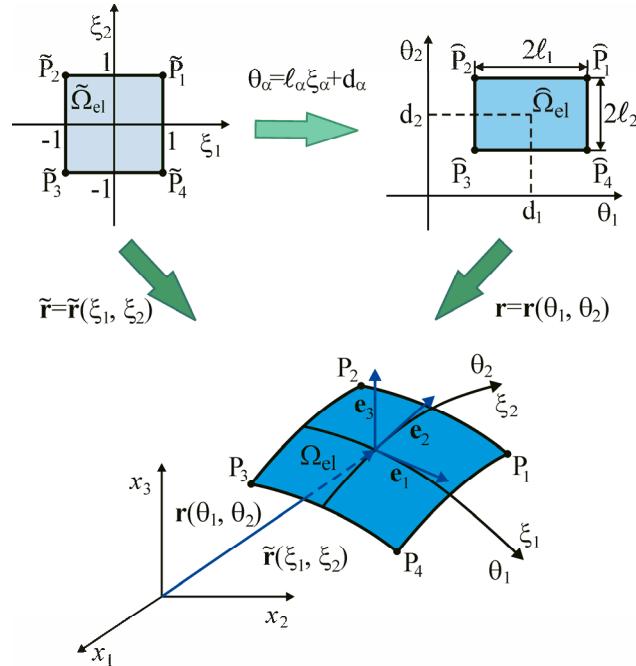


Figure 2: Biunit square in (ξ_1, ξ_2) -space mapped into the middle surface of the GeX piezoelectric solid-shell element in (x_1, x_2, x_3) -space

To implement the efficient analytical integration throughout the element, the extended ANS method is employed:

$$\varepsilon_{ij}^{(n)i_n} = \sum_r N_r \varepsilon_{ijr}^{(n)i_n}, \quad E_i^{(n)i_n} = \sum_r N_r E_{ir}^{(n)i_n}, \quad (16)$$

where $\varepsilon_{ijr}^{(n)i_n}$ and $E_{ir}^{(n)i_n}$ are the displacement-dependent strains and electric field of SaS of the n th layer at element nodes. The main idea of such approach can be traced back to the ANS method developed by many scientists [1-6] for the isoparametric solid-shell element formulation. In contrast with above formulation, we treat the term ANS in a broader sense. In the proposed GeX four-node solid-shell element formulation, all components of the displacement-dependent strain tensor and electric field vector are assumed to vary bilinearly throughout the biunit square in (ξ_1, ξ_2) -space.

Further, it is convenient to rewrite the ANS interpolation (16) in the following form:

$$\varepsilon^{(n)i_n} = \sum_{r_1, r_2} (\xi_1)^{r_1} (\xi_2)^{r_2} \varepsilon_{r_1 r_2}^{(n)i_n}, \quad \mathbf{E}^{(n)i_n} = \sum_{r_1, r_2} (\xi_1)^{r_1} (\xi_2)^{r_2} \mathbf{E}_{r_1 r_2}^{(n)i_n}, \quad (17)$$

$$\varepsilon_{r_1 r_2}^{(n)i_n} = [\varepsilon_{11r_1 r_2}^{(n)i_n} \quad \varepsilon_{22r_1 r_2}^{(n)i_n} \quad \varepsilon_{33r_1 r_2}^{(n)i_n} \quad 2\varepsilon_{12r_1 r_2}^{(n)i_n} \quad 2\varepsilon_{13r_1 r_2}^{(n)i_n} \quad 2\varepsilon_{23r_1 r_2}^{(n)i_n}]^T, \quad \mathbf{E}_{r_1 r_2}^{(n)i_n} = [E_{1r_1 r_2}^{(n)i_n} \quad E_{2r_1 r_2}^{(n)i_n} \quad E_{3r_1 r_2}^{(n)i_n}]^T, \quad (18)$$

where the indices r_1 and r_2 run from 0 to 1.

Using equations (5), (6), (8) and (18), one obtains

$$\varepsilon_{r_1 r_2}^{(n)i_n} = (\mathbf{B}_{r_1 r_2}^{(n)i_n} + \mathbf{A}_{r_1 r_2}^{(n)i_n}(\mathbf{q})) \mathbf{q}, \quad \mathbf{E}_{r_1 r_2}^{(n)i_n} = -\mathbf{B}_{\varphi r_1 r_2}^{(n)i_n} \Phi, \quad (19)$$

where $\mathbf{B}_{r_1 r_2}^{(n)i_n}$ and $\mathbf{A}_{r_1 r_2}^{(n)i_n}(\mathbf{q})$ are the nodal matrices [15] of order $6 \times 12N_{\text{SaS}}$ corresponding to linear and non-linear strain-displacement transformations; $\mathbf{B}_{\varphi r_1 r_2}^{(n)i_n}$ are the nodal piezoelectric matrices [13, 14] of order $3 \times 4N_{\text{SaS}}$; \mathbf{q} and Φ are the displacement and electric potential vectors of the shell element defined as

$$\mathbf{q} = [\mathbf{q}_1^T \quad \mathbf{q}_2^T \quad \mathbf{q}_3^T \quad \mathbf{q}_4^T]^T, \quad \Phi = [\Phi_1^T \quad \Phi_2^T \quad \Phi_3^T \quad \Phi_4^T]^T, \quad (20)$$

$$\mathbf{q}_r = \left[(\mathbf{u}_r^{[0]})^T (\mathbf{u}_r^{(1)2})^T \dots (\mathbf{u}_r^{(1)I_1-1})^T (\mathbf{u}_r^{[1]})^T (\mathbf{u}_r^{(2)2})^T \dots (\mathbf{u}_r^{(N-1)I_{N-1}-1})^T (\mathbf{u}_r^{[N-1]})^T (\mathbf{u}_r^{(N)2})^T \dots (\mathbf{u}_r^{(N)I_N-1})^T (\mathbf{u}_r^{[N]})^T \right]^T,$$

$$\mathbf{u}_r^{[m]} = [u_{1r}^{[m]} \quad u_{2r}^{[m]} \quad u_{3r}^{[m]}]^T, \quad \mathbf{u}_r^{(n)m_n} = [u_{1r}^{(n)m_n} \quad u_{2r}^{(n)m_n} \quad u_{3r}^{(n)m_n}]^T,$$

$$\Phi_r = \left[(\varphi_r^{[0]})^T (\varphi_r^{(1)2})^T \dots (\varphi_r^{(1)I_1-1})^T (\varphi_r^{[1]})^T (\varphi_r^{(2)2})^T \dots (\varphi_r^{(N-1)I_{N-1}-1})^T (\varphi_r^{[N-1]})^T (\varphi_r^{(N)2})^T \dots (\varphi_r^{(N)I_N-1})^T (\varphi_r^{[N]})^T \right]^T,$$

where $u_{ir}^{[0]}$ and $u_{ir}^{[N]}$ are the nodal displacements of bottom and top surfaces; $u_{ir}^{[m]}$ are the nodal displacements of interfaces $\Omega^{[m]}$; $N_{\text{SaS}} = \sum_n I_n - N + 1$ is the total number of SaS.

To circumvent shear and membrane locking and have no spurious zero energy modes, the robust stress interpolation [15] is utilized

$$\mathbf{S}^{(n)i_n} = \sum_{r_1+r_2 < 2} (\xi_1)^{r_1} (\xi_2)^{r_2} \mathbf{Q}_{r_1 r_2} \mathbf{S}_{r_1 r_2}^{(n)i_n}, \quad (21)$$

$$\mathbf{S}_{00}^{(n)i_n} = [\chi_1^{(n)i_n} \chi_2^{(n)i_n} \chi_3^{(n)i_n} \chi_4^{(n)i_n} \chi_5^{(n)i_n} \chi_6^{(n)i_n}]^T,$$

$$\mathbf{S}_{01}^{(n)i_n} = [\chi_7^{(n)i_n} \chi_9^{(n)i_n} \chi_{11}^{(n)i_n}]^T, \quad \mathbf{S}_{10}^{(n)i_n} = [\chi_8^{(n)i_n} \chi_{10}^{(n)i_n} \chi_{12}^{(n)i_n}]^T,$$

where $\mathbf{Q}_{r_1 r_2}$ are the projective matrices given by

$$\mathbf{Q}_{00} = \begin{bmatrix} 1 & 0 & 0 & 0 & 0 & 0 \\ 0 & 1 & 0 & 0 & 0 & 0 \\ 0 & 0 & 1 & 0 & 0 & 0 \\ 0 & 0 & 0 & 1 & 0 & 0 \\ 0 & 0 & 0 & 0 & 1 & 0 \\ 0 & 0 & 0 & 0 & 0 & 1 \end{bmatrix}, \quad \mathbf{Q}_{01} = \begin{bmatrix} 1 & 0 & 0 \\ 0 & 0 & 0 \\ 0 & 1 & 0 \\ 0 & 0 & 0 \\ 0 & 0 & 1 \\ 0 & 0 & 0 \end{bmatrix}, \quad \mathbf{Q}_{10} = \begin{bmatrix} 0 & 0 & 0 \\ 1 & 0 & 0 \\ 0 & 1 & 0 \\ 0 & 0 & 0 \\ 0 & 0 & 0 \\ 0 & 0 & 1 \end{bmatrix}. \quad (22)$$

The similar interpolation [15] can be used for the displacement-independent strains, that is,

$$\boldsymbol{\eta}^{(n)i_n} = \sum_{r_1+r_2 < 2} (\xi_1^{r_1} \xi_2^{r_2} \mathbf{Q}_{r_1 r_2} \boldsymbol{\eta}_{r_1 r_2}^{(n)i_n}), \quad (23)$$

$$\boldsymbol{\eta}_{00}^{(n)i_n} = [\psi_1^{(n)i_n} \psi_2^{(n)i_n} \psi_3^{(n)i_n} \psi_4^{(n)i_n} \psi_5^{(n)i_n} \psi_6^{(n)i_n}]^T,$$

$$\boldsymbol{\eta}_{01}^{(n)i_n} = [\psi_7^{(n)i_n} \psi_9^{(n)i_n} \psi_{11}^{(n)i_n}]^T, \quad \boldsymbol{\eta}_{10}^{(n)i_n} = [\psi_8^{(n)i_n} \psi_{10}^{(n)i_n} \psi_{12}^{(n)i_n}]^T.$$

Substituting finite element approximations (15), (17), (21) and (23) into the Hu-Washizu variational equation (12), one can integrate analytically throughout the finite element. As a result, the following equilibrium equations of the GeX hybrid-mixed solid-shell element are obtained:

$$\boldsymbol{\eta}_{r_1 r_2}^{(n)i_n} = \mathbf{Q}_{r_1 r_2}^T (\mathbf{B}_{r_1 r_2}^{(n)i_n} + \mathbf{A}_{r_1 r_2}^{(n)i_n}(\mathbf{q})) \mathbf{q} \quad \text{for } r_1 + r_2 < 2, \quad (24)$$

$$\mathbf{S}_{r_1 r_2}^{(n)i_n} = \mathbf{Q}_{r_1 r_2}^T (\mathbf{C}^{(n)} \mathbf{Q}_{r_1 r_2} \boldsymbol{\eta}_{r_1 r_2}^{(n)i_n} + (\mathbf{e}^{(n)})^T \mathbf{B}_{\varphi r_1 r_2}^{(n)i_n} \boldsymbol{\Phi}) \quad \text{for } r_1 + r_2 < 2, \quad (25)$$

$$\sum_n \sum_{i_n} \sum_{j_n} \Lambda^{(n)i_n j_n} \sum_{r_1+r_2 < 2} \frac{1}{3^{r_1+r_2}} (\mathbf{B}_{r_1 r_2}^{(n)i_n} + 2\mathbf{A}_{r_1 r_2}^{(n)i_n}(\mathbf{q}))^T \mathbf{Q}_{r_1 r_2} \mathbf{S}_{r_1 r_2}^{(n)j_n} = \mathbf{F}_u, \quad (26)$$

$$\sum_n \sum_{i_n} \sum_{j_n} \Lambda^{(n)i_n j_n} \sum_{r_1+r_2 < 2} \frac{1}{3^{r_1+r_2}} (\mathbf{B}_{\varphi r_1 r_2}^{(n)i_n})^T (\mathbf{e}^{(n)} \mathbf{Q}_{r_1 r_2} \boldsymbol{\eta}_{r_1 r_2}^{(n)j_n} - \mathbf{e}^{(n)} \mathbf{B}_{\varphi r_1 r_2}^{(n)j_n} \boldsymbol{\Phi}) = \mathbf{F}_\varphi, \quad (27)$$

where \mathbf{F}_u and \mathbf{F}_φ are the element-wise mechanical and electric surface vectors.

Because of equilibrium equations (24)-(26) are nonlinear, the Newton-Raphson method is employed to linearize them

$$\mathbf{q}^{[k+1]} = \mathbf{q}^{[k]} + \Delta \mathbf{q}^{[k]}, \quad \boldsymbol{\Phi}^{[k+1]} = \boldsymbol{\Phi}^{[k]} + \Delta \boldsymbol{\Phi}^{[k]},$$

$$\mathbf{S}_{r_1 r_2}^{(n)i_n[k+1]} = \mathbf{S}_{r_1 r_2}^{(n)i_n[k]} + \Delta \mathbf{S}_{r_1 r_2}^{(n)i_n[k]}, \quad \boldsymbol{\eta}_{r_1 r_2}^{(n)i_n[k+1]} = \boldsymbol{\eta}_{r_1 r_2}^{(n)i_n[k]} + \Delta \boldsymbol{\eta}_{r_1 r_2}^{(n)i_n[k]}, \quad (28)$$

where $k = 0, 1, \dots, \text{NIter}$; NIter is the total number of iterations.

By using a standard technique, we arrive at the linearized equilibrium equations. Eliminating then stresses $\Delta \mathbf{S}_{r_1 r_2}^{(n) i_n [k]}$ and displacement-dependent strains $\Delta \boldsymbol{\eta}_{r_1 r_2}^{(n) i_n [k]}$ on the element level, the following system of equations are obtained:

$$\begin{bmatrix} \mathbf{K}_{uu} & \mathbf{K}_{u\varphi} \\ \mathbf{K}_{\varphi u} & \mathbf{K}_{\varphi\varphi} \end{bmatrix} \begin{bmatrix} \Delta \mathbf{q}^{[k]} \\ \Delta \Phi^{[k]} \end{bmatrix} = \begin{bmatrix} \mathbf{F}_u^{[k]} \\ \mathbf{F}_\varphi^{[k]} \end{bmatrix}, \quad (29)$$

where \mathbf{K}_{uu} , $\mathbf{K}_{u\varphi}$, $\mathbf{K}_{\varphi u} = (\mathbf{K}_{u\varphi})^T$, $\mathbf{K}_{\varphi\varphi}$ are the displacement, piezoelectric and dielectric stiffness matrices of the element.

The equilibrium equations (29) for each element are assembled to form the global equilibrium equations. These equations should be performed until the required accuracy of the solution is reached employing the displacement-based convergence criteria as follows:

$$\|\Delta \mathbf{U}^{[k+1]} - \Delta \mathbf{U}^{[k]}\| < \varepsilon \|\Delta \mathbf{U}^{[k]}\|, \quad (30)$$

where $\|\cdot\|$ stands for the Euclidean norm; $\Delta \mathbf{U}$ is the global vector of nodal displacements and electric potentials; ε is the prescribed tolerance.

4 NUMERICAL EXAMPLE

The performance of the developed GeX/SaS laminated piezoelectric four-node solid-shell element, called the GeXSaS4 element, is evaluated with the help of the nonlinear isoparametric 5-parameter piezoelectric shell element [16] and 20-node SOLID226 element from the software package ANSYS [17].

Consider a cantilever square plate composed of the T300/976 graphite/epoxy composite with the PZT G1195 actuators attached to its bottom and the top surfaces. The direction of fibers coincides with the y -axis. The actuators are polarized in opposite directions parallel to the thickness direction and subjected to opposite electric potentials $-\hat{\varphi}$ and $\hat{\varphi}$, as shown in Figure 3, to induce the bending actuation. The electrodes on the interfaces are assumed to be grounded. The mechanical properties of materials are

$$\begin{aligned} \text{G1195 [1]: } E = 63 \text{ GPa, } G = 24.23 \text{ GPa, } \nu = 0.3, e_{311} = e_{322} = 44.37 \text{ C/m}^2, e_{333} = 50.18 \text{ C/m}^2, \\ e_{113} = e_{223} = 14.15 \text{ C/m}^2, \epsilon_{11} = \epsilon_{22} = 1.53 \cdot 10^{-8} \text{ F/m, } \epsilon_{33} = 1.5 \cdot 10^{-8} \text{ F/m;} \end{aligned} \quad (31)$$

$$\begin{aligned} \text{T300/976 [16]: } E_L = 150 \text{ GPa, } E_T = 9 \text{ GPa, } G_{LT} = 7.1 \text{ GPa, } G_{TT} = 2.5 \text{ GPa, } \nu_{LT} = \nu_{TT} = 0.3, \\ \epsilon_{11} = \epsilon_{22} = \epsilon_{33} = 2.7 \cdot 10^{-11} \text{ F/m.} \end{aligned} \quad (32)$$

To compare the results with the finite element solution [16], the geometrical parameters are taken to be $a = b = 40 \text{ mm}$, $h_1 = h_3 = 0.15 \text{ mm}$ and $h_2 = 0.2 \text{ mm}$.

Due to symmetry of the problem, only one half of the plate is modeled by regular meshes. Table 1 lists results of the convergence study via longitudinal and transverse displacements of the middle surface \bar{u}_1 and \bar{u}_3 at point A($a, 0$) choosing three and four SaS for each layer. A comparison with the SOLID226 element [17] is also given. It is seen that only one load step

and five Newton iterations are needed to find the converged solution with the chosen criterion and tolerance, where NStep denotes a number of load steps employed to equally divide the maximum load. Note that the GeXSaS4 element allows the use of coarse meshes.

Figure 4 shows the displacements of the middle surface at point A of the three-layer plate versus the applied voltage using three SaS for each layer compared to those obtained by the 5-parameter isoparametric piezoelectric shell element [16] and SOLID226 element [17]. As can be seen, all results agree closely but the developed GeXSaS4 element is less expensive due to 3D analytical integration that leads to the economical computation of its tangent stiffness matrix. Figure 5 presents the through-thickness distributions of second Piola-Kirchhoff stresses, electric potential and electric displacement at points B($a/2, b/2$) and C($a/2, b/4$) for the three-layer plate under applied voltage $\hat{\phi} = 2000 \text{ V}$ employing four SaS for layers and a fine 64×32 mesh compared to those obtained by the SOLID226 element [17] using $64 \times 32 \times 2$ mesh for each layer. One can see that the SOLID226 element leads to a worse prediction for the transverse stresses. It should be noted that it is impossible for this solid element to satisfy the boundary conditions on outer surfaces and the continuity conditions at interfaces choosing a more number of elements in the thickness direction.

ACKNOWLEDGEMENTS

This work was supported by the Russian Science Foundation under Grant No. 18-19-00092.

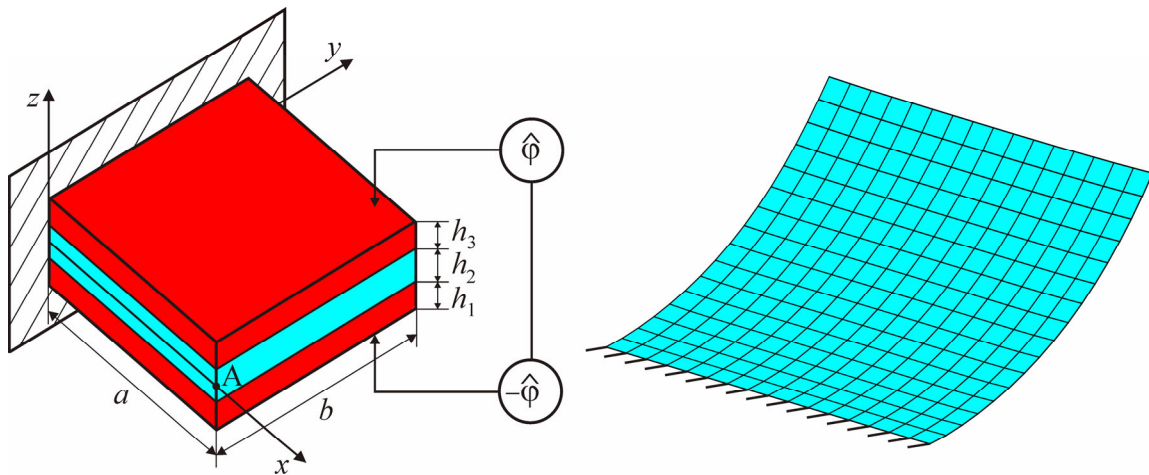
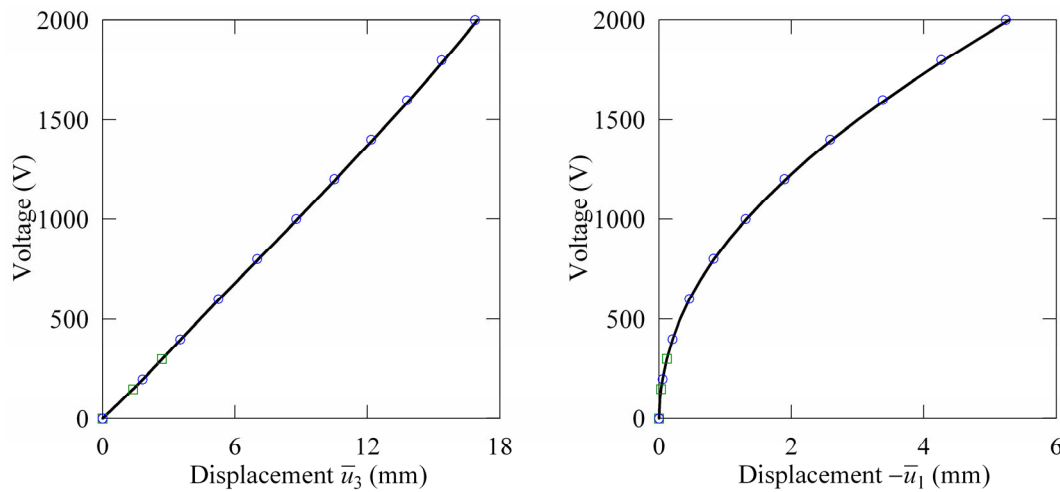


Figure 3: Cantilever three-layer square plate: geometry and deformed configuration corresponding to the applied voltage $\hat{\phi} = 2000 \text{ V}$ (modeled by three SaS inside each layer and 16×16 mesh)

Table 1: Convergence study for the three-layer square plate under applied voltage $\hat{\phi} = 2000$ V using the displacement-based criterion with $\varepsilon = 10^{-4}$

	$I_1 = I_2 = I_3 = 3$					$I_1 = I_2 = I_3 = 4$				
Mesh	8×4	16×8	32×16	64×32	SOLID226 $64 \times 32 \times 1$	8×4	16×8	32×16	64×32	SOLID226 $64 \times 32 \times 2$
$\bar{u}_3(A)$, mm	17.53	17.15	16.98	16.90	16.82	17.53	17.15	16.98	16.90	16.82
$-\bar{u}_1(A)$, mm	5.585	5.380	5.294	5.254	5.206	5.584	5.379	5.293	5.253	5.208
NStep	1	1	1	1	4	1	1	1	1	4
NIter	5	5	5	5	37	5	5	5	5	37

**Figure 4:** Voltage applied to the bottom and top surfaces versus displacements of the middle surface at point A(a, 0) for the three-layer plate: GeXSa4 element using three SaS inside each layer and 32×16 mesh (—), Marinkovic et al. [16] (\square) and SOLID226 element [17] using $64 \times 32 \times 1$ mesh for each layer (\circ) that corresponds to a chosen number of SaS

REFERENCES

- [1] Tan, X.G. and Vu-Quoc, L. Optimal solid shell element for large deformable composite structures with piezoelectric layers and active vibration control. *Int. J. Numer. Methods Eng.* (2005) **64**:1981–2013.
- [2] Klinkel, S. and Wagner, W. A geometrically non-linear piezoelectric solid shell element based on a mixed multi-field variational formulation. *Int. J. Numer. Methods Eng.* (2006) **65**:349–382.
- [3] Klinkel, S. and Wagner, W. A piezoelectric solid shell element based on a mixed variational formulation for geometrically linear and nonlinear applications. *Comput. Struct.* (2008) **86**:38–46.

- [4] Lentzen, S. *Nonlinearly coupled thermopiezoelectric modelling and FE-simulation of smart structures*. Fortschritt-Berichte VDI, Reihe 20, Nr. 419, Düsseldorf, VDI Verlag, (2009).
- [5] Schulz, K., Klinkel, S. and Wagner, W. A finite element formulation for piezoelectric shell structures considering geometrical and material non-linearities. *Int. J. Numer. Methods Eng.* (2011) **87**:491–520.
- [6] Buchter, N., Ramm, E. and Roehl, D. Three-dimensional extension of nonlinear shell formulation based on the enhanced assumed strain concept. *Int. J. Numer. Methods Eng.* (1994) **37**:2551–2568.
- [7] Kulikov, G.M. and Plotnikova, S.V. Finite rotation piezoelectric exact geometry solid-shell element with nine degrees of freedom per node. *Comp. Mater. Continua* (2011) **23**:233–264.
- [8] Kulikov, G.M. and Plotnikova, S.V. The use of 9-parameter shell theory for development of exact geometry 12-node quadrilateral piezoelectric laminated solid-shell elements. *Mech. Adv. Mater. Struct.* (2015) **22**:490–502.
- [9] Kulikov, G.M. and Plotnikova, S.V. A sampling surfaces method and its application to three-dimensional exact solutions for piezoelectric laminated shells. *Int. J. Solids Struct.* (2013) **50**:1930–1943.
- [10] Kulikov, G.M. and Plotnikova, S.V. Exact electroelastic analysis of functionally graded piezoelectric shells. *Int. J. Solids Struct.* (2014) **51**:13–25.
- [11] Kulikov, G.M., Mamontov, A.A. and Plotnikova, S.V. Coupled thermoelectroelastic stress analysis of piezoelectric shells. *Compos. Struct.* (2015) **124**:65–76.
- [12] Kulikov, G.M. and Plotnikova, S.V. Assessment of the sampling surfaces formulation for thermoelectroelastic analysis of layered and functionally graded piezoelectric shells. *Mech. Adv. Mater. Struct.* (2017) **24**:392–409.
- [13] Kulikov, G.M. and Plotnikova, S.V. Exact geometry SaS solid-shell element for 3D stress analysis of FGM piezoelectric structures. *Curved Layered Struct.* (2018) **5**:116–135.
- [14] Kulikov, G.M., Plotnikova, S.V. and Carrera, E. Hybrid-mixed solid-shell element for stress analysis of laminated piezoelectric shells through higher-order theories. *Adv. Struct. Mater.* (2018) **81**:45–68.
- [15] Kulikov, G.M. and Plotnikova, S.V. Finite rotation exact geometry solid-shell element for laminated composite structures through extended SaS formulation and 3D analytical integration. *Int. J. Numer. Methods Eng.* (2019) doi:10.1002/nme.6075.
- [16] Marinković, D., Köppe, H. and Gabbert, U. Degenerated shell element for geometrically nonlinear analysis of thin-walled piezoelectric active structures. *Smart Mater. Struct.* (2008) **17**:015030:1–10.
- [17] *ANSYS: Version 12.0*. Canonsburg, PA, ANSYS Inc, (2009).

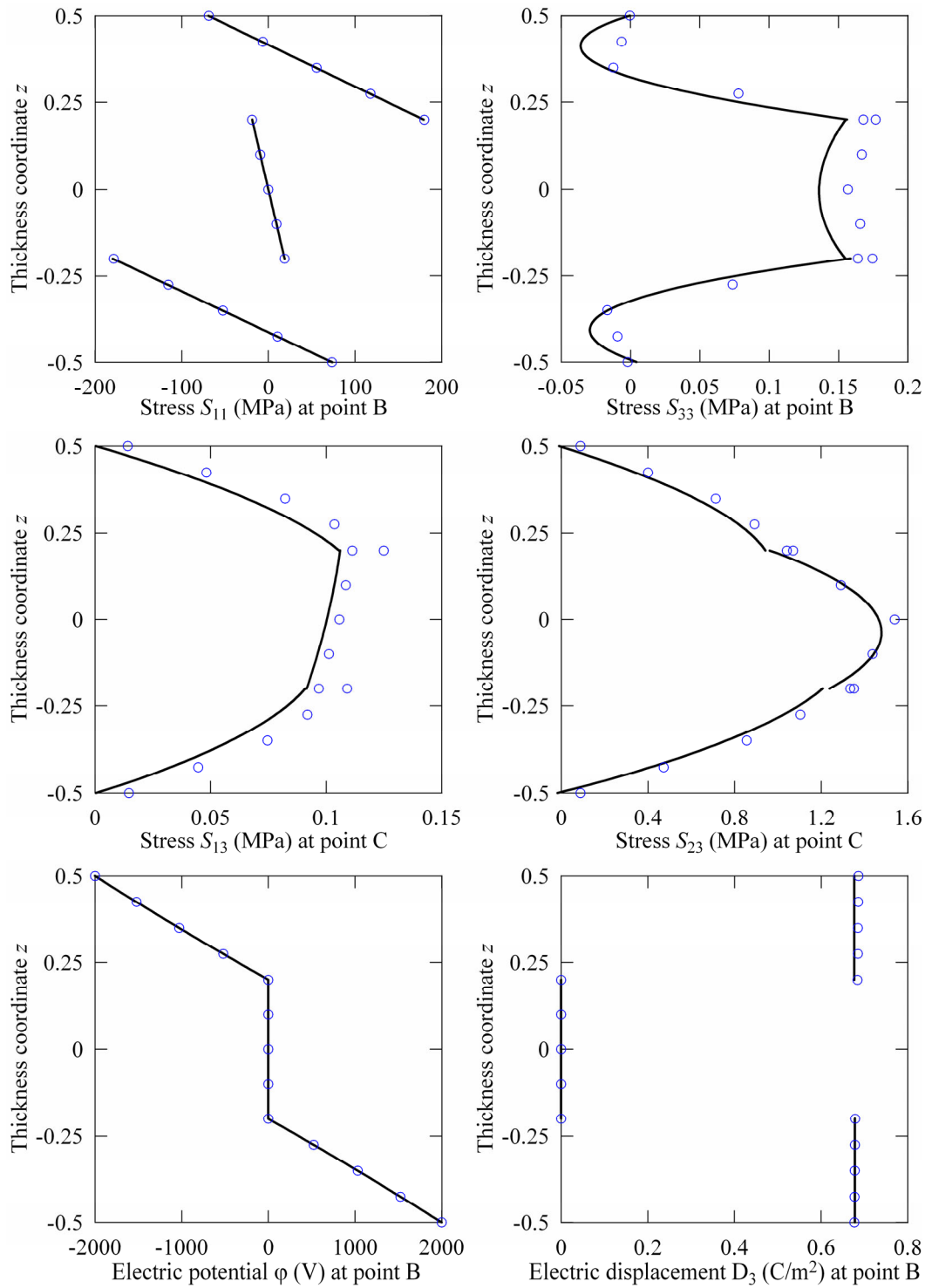


Figure 5: Through-thickness distributions of the second Piola-Kirrhoff stresses, electric potential and electric displacement at points $B(a/2, b/2)$ and $C(a/2, b/4)$ for the three-layer plate under applied voltages $\hat{\phi} = 2000 \text{ V}$: GeXSa4 element using four SaS inside the layers and 64×32 mesh (—) and SOLID226 element [17] using $64 \times 32 \times 2$ mesh for each layer (\circ)

FINITE ELEMENT REDUCED-ORDER MODELS TO PREDICT THE GEOMETRICALLY NONLINEAR DYNAMICS OF PIEZOELECTRIC LAMINATED STRUCTURES

ARTHUR GIVOIS^{*,†}, OLIVIER THOMAS^{*} AND JEAN-FRANÇOIS DEÜ[†]

^{*}Arts et Métiers ParisTech, Laboratoire d'Ingénierie des Systèmes Physiques et Numériques
(LISPEN EA 7515)
8 bd. Louis XIV 59046 Lille
e-mail: arthur.givois@ensam.eu, olivier.thomas@ensam.eu

[†] Laboratoire de Mécanique des structures et des systèmes couplés (LMSSC EA 3196),
Conservatoire National des Arts et Métiers
292 rue Saint-Martin, 75141, Paris Cedex 03, France
e-mail: jean-francois.deu@cnam.fr

Key words: Model Reduction, Finite Element Model, Geometrical Nonlinearities, Non-intrusive approach, Electromechanical coupling, Piezoelectric materials

Abstract. This study aims to predict the nonlinear dynamics of elastic structures equipped with piezoelectric devices, for application such as reduction vibration, energy harvesting or design of nonlinear resonant M/NEMS such as ultra-sensitive sensors. In this context, reduced-order model (ROM) based on a modal expansion are used to compute the response of the structures, including both geometrical nonlinearities and the electromechanical (EM) coupling. This approach results to a system of coupled oscillators, in which geometrically nonlinear and electromechanical terms appear separately, along with less classical terms stemming from both effects. This system is solved in the frequency domain with the Harmonic Balance Method associated with an Asymptotic Numerical Method. The parameters of the ROM are computed thanks to a non-intrusive method and a finite element commercial code. This study focuses first on the computation of these coefficients, which is separately performed in the EM and non-linear cases. The EM coefficients are validated by comparison with the effective and modal EM coupling factors (EEMCF, MEMCF). A validation of the procedure is proposed by studying the nonlinear dynamics of an elastic circular plate equipped with eight piezoelectric patches equally spaced and placed along an inner circumference. This configuration enables to excite and measure several vibration modes, either axisymmetric or asymmetric. Curved frequency responses are obtained, both in free nonlinear vibrations (backbone curves) and under voltage forcing. In the case of asymmetric modes, 1:1 internal resonances are obtained, showing the coupling between both companion modes. Experimental validations are also proposed.

1 INTRODUCTION

The prediction of the geometrically nonlinear mechanical behavior of electrically driven structures is an issue of great interest in the context of Micro- or Nano-ElectroMechanical Systems (M/NEMS) developments [1, 2, 3, 4] or energy harvesting [5]. The geometrical nonlinearities are due to the large

amplitude of the displacements of the structures. In this framework, the investigated structures present often complex geometries, such that multilayered thin systems, for which a finite element approach offer great flexibility in modelling. To solve the nonlinear dynamical system, the model must be reduced in size. The modal basis is used to identify the reduced-order models because of its efficiency to capture the relevant displacement components of the structures, particularly when the targeted application focuses on resonant phenomena. An original approach to estimate efficient reduced-order models (ROM) and validate them by comparison with experimental results is proposed in this study. The approach to identify the ROM parameters is based on non-intrusive methods, which suppose to compute the nonlinear components of the proposed problem without modifying the source of a finite element code. The present paper proposes first a generalization of the use of non-intrusive methods - initially devoted to study only geometrical nonlinearities of dynamical systems [6] - to electromechanical systems. Secondly, the article presents in detail an experimental procedure to identify the geometrically nonlinear parameters of a vibrating structure with an electric actuation and detection, by taking into account the electromechanical coupling.

2 MODEL REDUCTION

2.1 General formulation of the problem and modal expansion

Here is considered an elastic structure equipped with P piezoelectric patches denoted with indice (p) . The governing equations of the free, undamped, piezoelectric and nonlinear problem is written as :

$$\mathbf{M}_m \ddot{\mathbf{u}} + \mathbf{K}_m \mathbf{u} + \mathbf{f}_{nl} + \sum_{p=1}^P [\mathbf{f}_c^{(p)} + \mathbf{P}_c^{(p)} \mathbf{u}] V^{(p)} = \mathbf{0}, \quad (1a)$$

$$\mathbf{C}^{(p)} V^{(p)} - [\mathbf{f}_c^{(p)} + \frac{1}{2} \mathbf{P}_c^{(p)} \mathbf{u}]^T \mathbf{u} = \mathcal{Q}^{(p)}. \quad (1b)$$

where \mathbf{K}_m , \mathbf{M}_m , \mathbf{u} and \mathbf{f}_{nl} denote respectively the mechanical stiffness and mass matrices, and the mechanical displacements and the geometrically nonlinear internal force vectors. $V^{(p)}$, $\mathbf{C}^{(p)}$ and $\mathcal{Q}^{(p)}$ are the voltage, the electrical capacitance and the electrical charge contained in one of the electrodes of the p^{th} patch. Finally, $\mathbf{f}_c^{(p)}$ and $\mathbf{P}_c^{(p)}$ denote the electromechanical forcing vector and the electromechanical coupling matrix related to geometric nonlinearities.

The expansion basis consists of N_m mechanical linear eigenmodes Φ_k :

$$\mathbf{u}(t) = \sum_{k=1}^K \Phi_k q_k(t). \quad (2)$$

where $q_k(t)$ is the k -th. unknown modal coordinate. The eigenmodes are solutions of:

$$(\mathbf{K} - \omega_k^2 \mathbf{M}) \Phi_k = \mathbf{0}. \quad (3)$$

Multiplying Eq.(1) by a linear mode Φ_k^T yields the following system of coupled oscillators :

$$\ddot{q}_k(t) + \omega_k^2 q_k(t) + \sum_{i=1}^K \sum_{j=1}^K a_{ij}^k q_i q_j + \sum_{i=1}^K \sum_{j=1}^K \sum_{l=1}^K b_{ijl}^k q_i q_j q_l + \sum_{p=1}^P \chi_k^{(p)} V^{(p)} + \sum_{p=1}^P \sum_{i=1}^K \Theta_{ik}^{(p)} q_i V^{(p)} = 0, \quad (4a)$$

$$\mathbf{C}^{(p)} V^{(p)} - \sum_{k=1}^K \chi_k^{(p)} q_k + \sum_{i=1}^K \sum_{j=1}^K \frac{1}{2} \Theta_{ij}^{(p)} q_i q_j = \mathcal{Q}^{(p)}, \quad (4b)$$

The nonlinear stiffnesses a_{ij}^k , b_{ijl}^k , and electromechanical linear and nonlinear coupling coefficients $\chi_k^{(p)}$ and $\Theta_{ij}^{(p)}$ characterize the nonlinear system. In order to compute nonlinear responses with this reduced order model, these coefficients must be estimated at an initial stage. In the next paragraph, they constitute the unknowns of the problem.

2.2 Estimation of the ROM coefficients

2.2.1 Presentation of the non-intrusive approach

The system of equations (4) gives the possibility to study separately the purely mechanical geometrically nonlinear (NL) effects, the linear electromechanical (EM) coupling and finally the electromechanical nonlinear coupling (EM-NL).

Following this partition of the different effects, an original approach proposes to compute these coefficients in three successive steps :

(i) the identification of the nonlinear stiffness coefficients by solving a set of geometrically nonlinear problems. In this case, there is no electrical equation and the expanded system writes

$$\ddot{q}_k + \omega_k^2 q_k + \sum_{i=1}^K \sum_{j=i}^K a_{ij}^k q_i q_j + \sum_{i=1}^K \sum_{j=i}^K \sum_{l=j}^K b_{ijl}^k q_i q_j q_l = F_k. \quad (5)$$

A family of non-intrusive methods initially proposed in [7] enables to estimate the nonlinear coefficients a_{ij}^k and b_{ijl}^k by prescribing static displacement fields as linear combination of eigenmodes, and computing the resulting internal forces.

(ii) the estimation of the linear coefficients $\chi_k^{(p)}$. The new approach proposed here consists in imposing the static displacement fields with short-circuited piezoelectric patches, as combinations of eigenmodes, and computing the resulting electric charge on the electrodes of the piezoelectric patches. In the linear case, the linear terms of the electrical equation (6) are computed :

$$-\sum_{k=1}^K \chi_k^{(p)} q_k = Q^{(p)}. \quad (6)$$

This method allows to estimate the linear coefficients $\chi_k^{(p)}$ of all patches p of a given vibration mode k .

(iii) Finally, the previous procedure generalized to a geometrically nonlinear problem leads to :

$$-\sum_{k=1}^K \chi_k^{(p)} q_k + \sum_{i=1}^K \sum_{j=1}^K \frac{1}{2} \Theta_{ij}^{(p)} q_i q_j = Q^{(p)}. \quad (7)$$

Just as in the case of the coefficients a_{ij}^k and b_{ijl}^k , the coefficients $\Theta_{ij}^{(p)}$ can be computed by prescribing as many static loads than coefficients $\Theta_{ij}^{(p)}$ contained in the ROM.

When the ROM has been built, the resulting nonlinear system can be solved thanks to a asymptotic numerical method associated with a harmonic balance method, which allows to equally compute the forced as well as the free response of the plane structures [9]. The interested reader can refer to [8] for a detailed procedure and a validation of the computation of the mechanical nonlinear coefficients a_{ij}^k and b_{ijl}^k , which includes also the computations of the nonlinear free and forced response computed from

the ROMs of mechanical structures. Note that in order to estimate all the coefficients of the ROM with this non-intrusive approach, the finite element code used for the computations must possess for a same computation electromechanical and geometrically nonlinear abilities. In our case the 3D finite element formulation of Abaqus is used. The validation stage of only the electromechanical linear coefficients is presented in detail in this article. The validation stage of the computation of the EM-NL coefficients $\Theta_{ij}^{(p)}$ is still under progress at the present time.

2.2.2 Case study: estimation of the linear electro-mechanical coefficients $\chi_k^{(p)}$

The validation of the linear EM coefficients is performed on a bi-layered beam shown on the figure 1, and made on an elastic material and a piezoelectric material. The validation step founds on a comparison with an analytical model with an Euler-Bernoulli kinematics, presented in [10]. The dimensions and material properties used for the numerical model are presented in the Tab. 1: the isotropic elastic material is characterized with a Young Modulus Y_e and a Poisson's ratio ν_e , whereas the transversely isotropic piezoelectric material requires more coefficients, the values assigned here are deduced from a piezoelectric constitutive law and values of the provider PI Ceramic available in the public domain [11]. The finite element model consists of 30 elements in the length of the beam, 4 elements in the width, and 3 and 2 elements in the thicknesses, respectively of the elastic and piezoelectric layers. 20-noded cubic elements are used in this model.

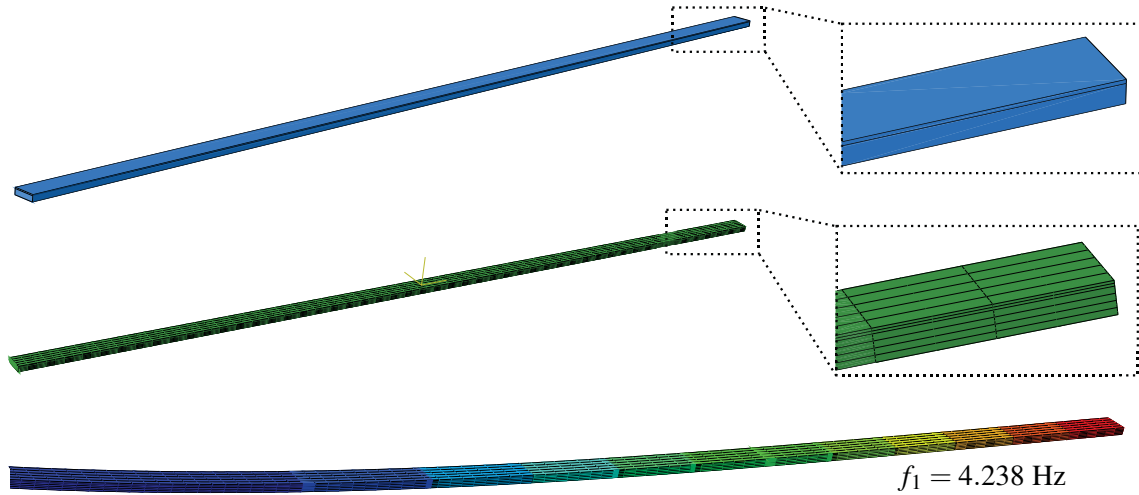


Figure 1: Presentation of the cantilever bi-layered test-case: geometry, mesh and shape of the first eigenmode

Y_e (GPa)	ν_e	$C_{11} = C_{22}$ (GPa)	C_{33}	C_{12}	$C_{13} = C_{23}$	$C_{44} = C_{55}$	C_{66}	ρ_e (kg.m ⁻³)	ρ_p
72.0	0.3	107.6	100.4	63.12	63.85	19.62	22.24	2700	7760

L (m)	b (m)	h_e (m)	h_p (m)	d_{31} (pm.V ⁻¹)	d_{33}	d_{15}	$\epsilon_{33}^e = \epsilon_{22}^e$ (nF.m ⁻¹)	ϵ_{33}^e
1	0.02	0.005	0.001	-214	423	600	9.83	7.54

Table 1: Set of the parameters of the beam test case. In order of appearance: elastic constants and densities of the elastic (e) and piezoelectric (p) layers, dimensions, piezoelectric and dielectric coefficients.

To validate the coefficients, the EM coupling factor is written on an dimensionless form defined by:

$$k_{\text{mod},k} = \frac{\chi_k}{\omega_{k,\text{sc}}\sqrt{C}}, \quad (8)$$

known as the Modal ElectroMechanical Coupling Factor (MEMCF) [12]. In this equation, $\omega_{k,\text{sc}}$ denotes the k^{th} eigenpulsation of the short-circuited system, and C refers to the capacitance of the patch. The physical interpretation of the MEMCF is that it measures the energy that can be exchanged between the coupled electrical circuit and the mechanical structure in a given modal motion. It is often considered as equal to Efficient ElectroMechanical Coupling Factor (EEMCF), which is computed from the following expression [12, 13]:

$$k_{\text{eff},k} = \sqrt{\frac{\omega_{k,\text{oc}}^2 - \omega_{k,\text{sc}}^2}{\omega_{k,\text{sc}}^2}} \quad (9)$$

where $\omega_{k,\text{oc}}^2$ is the eigenpulsation of the open-circuited system. The comparison between numerical and analytical values of the MEMCF and the computed values of the EEMCC obtained with the finite element modesl are plot in the Tab. 2. The values of the numerical MEMCF are validated by comparison with

Bending mode number	1	2	3	4	5	6
ω_k (numeric)	4.238	26.55	74.332	145.61	240.62	359.30
ω_k (analytic)	4.229	26.50	74.20	145.41	240.37	359.07
χ_k (numeric)	0.002837	-0.009698	0.01640	-0.02199	0.02996	-0.03418
$k_{\text{mod},k}$ (numeric)	-0.1926	0.1051	-0.06346	0.04346	-0.03582	0.02737
$k_{\text{mod},k}$ (analytic)	-0.1858	0.1030	-0.06038	0.04317	-0.03357	0.02747
$k_{\text{eff},k}$ (EEMCF)	0.2047	0.1123	0.06787	0.04689	0.03869	0.02890

Table 2: Comparison of the numerical and analytic computations of short-circuited pulsations and modal electro-mechanical coupling factor. The Effective EMCF is also presented.

analytical ones. The EEMCF slightly overestimates the coupling. It can be explained by the assumption of modal truncation, which is necessary to compute the EEMCF [12]. More details on the models and computations are needed to explain the small difference between analytical and numerical MEMCF: it can be due to the numerical approximation, or because of the assumptions on the kinematics or the electric field in the analytic model.

3 EXPERIMENTAL INVESTIGATION

An elastic circular plate made of brass and equipped with eight piezoelectric patches, has been considered for these experiments. The piezoelectric material is the PIC151, the patches are equally spaced and placed along an inner circonference, following the configuration presented on the figure 2. Three holes of small radius are equally spaced near the outer edge of the structure to hang up the plate with nylon threads and thus to set up experimental free boundary conditions. This plate has been built by gluing the piezoelectric patches to the elastic plate: preliminary capacitance measurements verified that the layer of glue is sufficiently thin in order that the electric potential at the lower electrode of all patches equals to the potential of the plate. Consequently, the voltage applied to the patches is imposed by connecting the electric ground to the lower electrode of only one patch, and imposing the potential at the upper electrodes of the other patches. An experimental continuation procedure detailed in [14] is performed, which

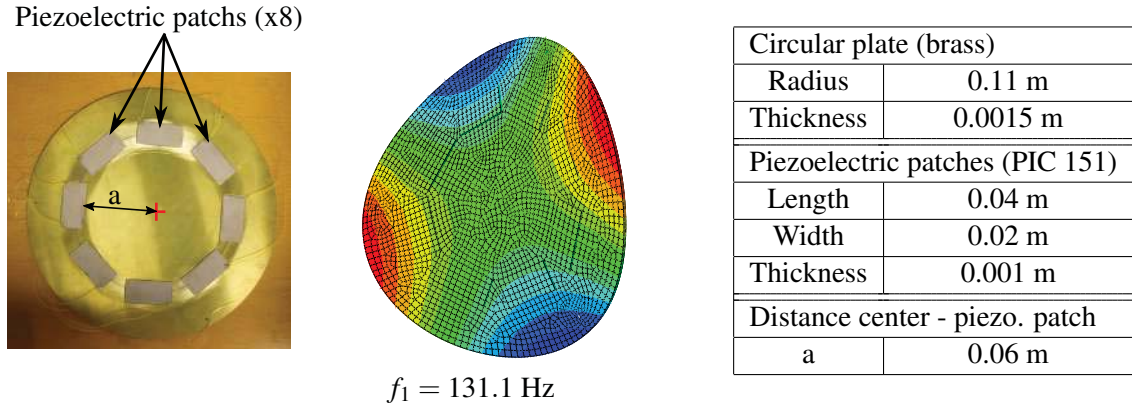


Figure 2: Characteristics of the piezoelectric circular plate: overview, shape of the first eigenmode computed from a finite element model and dimensions of the plate and piezoelectric patches.

enables to measure the equivalent of the free response as well as the forced responses of the system. The principle is founded on the adjustment of the excitation frequency of the forcing signal, in order to control the phase lag between the forcing and the output response, which can be controlled in real-time. This procedure consists of three blocks: first a phase detector estimates the phase lag between the forcing and the response signals thanks to a synchronous demodulation. Secondly, a controller corrects the frequency excitation compared with the initial one. Finally, the adjusted frequency is used as the input of a Voltage Control Oscillator which generates the excitation signal. These three main steps are computed in a Simulink scheme and performed in real-time via a MicroLabBox dSPACE, with a frequency step fixed at 50 kHz. High values of the integral and proportional gains are used for the experimental continuation, in order to avoid the instability regions of the control system in closed-loop case. It has been shown that for mechanical systems the equivalent of free undamped responses - called also *backbone curves* or nonlinear modes - can be measured by locking the phase at $\phi = \pi/2$ between the displacement and the excitation, and by increasing the forcing. Moreover the forced responses are measured by imposing a phase variation from $\phi = 0$ to $\phi = \pi$ between the excitation and the displacement signals, and by keeping the excitation amplitude constant.

3.1 Experimental set-up

The figure 3 shows the experimental set-up to investigate the dynamical and nonlinear behavior of the free circular plate with piezoelectric actuation and detection. The vibrating circular plate (a) and the PLL performed via the dSpace MicroLabBox (c) are the main blocks of the set-up. By electromechanical coupling, the piezoelectric patches can generate a voltage with potentially high amplitude values. Since the dSpace can not support input voltage bigger than 10 V, the input signals are attenuated thanks to two resistances connected in serie (b): in these experiments the values of the two resistances are chosen at $R_1 = 680 \text{ k}\Omega$ and $R_2 = 10 \text{ k}\Omega$, thus the input signals $V_m = \frac{R_2}{R_1 + R_2} V_{in}$ are attenuated with a gain close to 69. Since the dSpace changes the excitation signals V_{exc} with potential discontinuities in amplitude and frequency, a low-pass filter (d) is applied to these signals in output of the dSpace. This filter consists in a RC-circuit with a resistance value fixed at $R_{lp} = 750 \text{ }\Omega$ and a capacitor $C_{lp} = 69 \text{ nF}$, such that the cut-off frequency $f_{lp} = \frac{1}{2\pi R_{lp} C_{lp}} \approx 3 \text{ kHz}$ of the filter is larger than the frequency of interest.

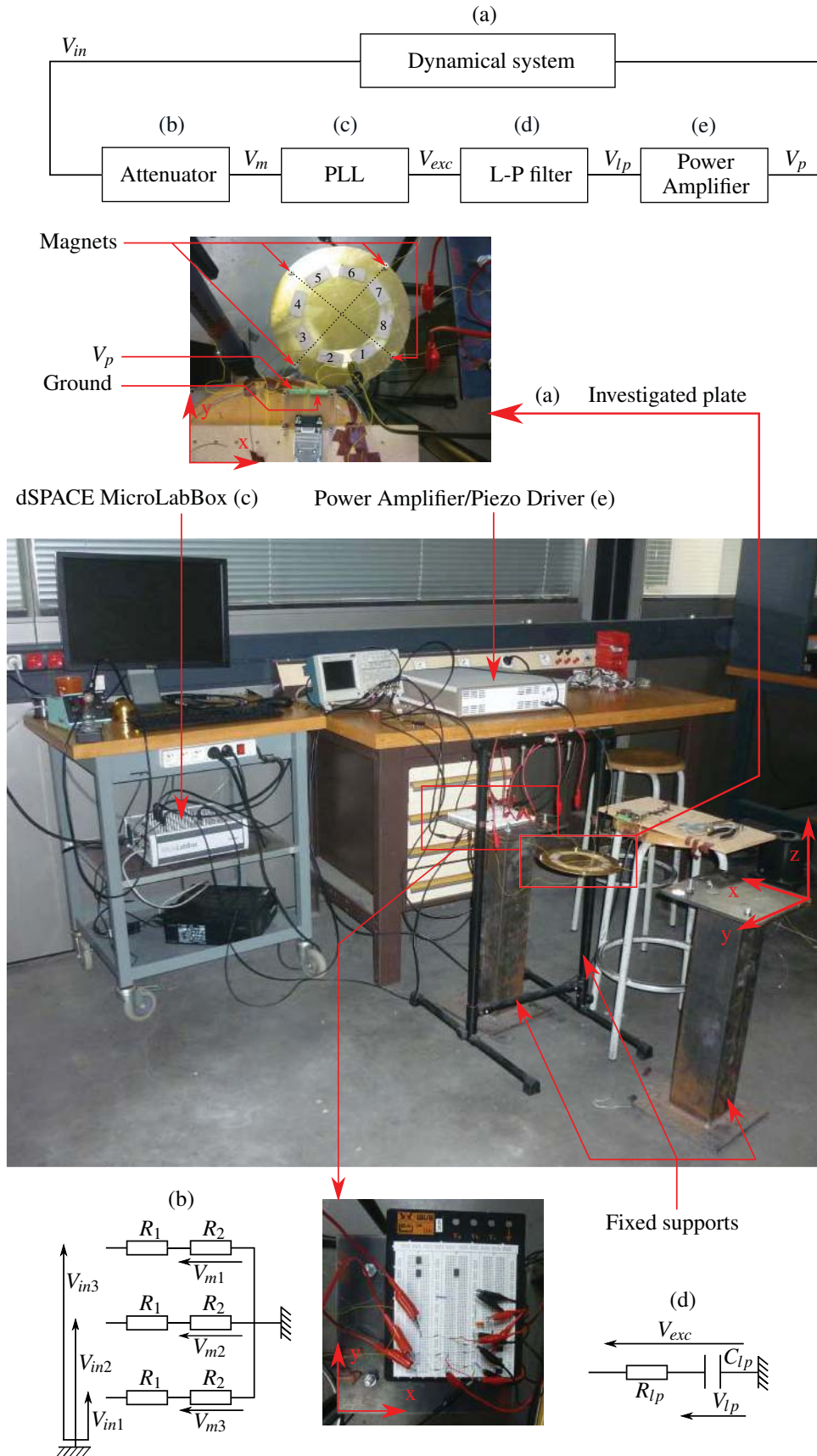


Figure 3: Experimental set-up: the upper part shows the main steps of the global loop, with (a) the circular plate, (b) the attenuators of input signals V_{in} measured at piezoelectric patches, (c) the Phase-Locking Loop (PLL), (d) the low-pass filter of the excitation signal V_{exc} and (e) the amplification.

Finally, a power amplifier (e) PZD700A-M/S dedicated to piezoelectric actuation enables to amplify the filtered excitation signal V_{lp} to inject in the piezoelectric patches a voltage V_p with a maximum amplitude value at 700 V. A preliminary modal analysis has been performed from velocity measurements measured and processed thanks to a scanning laser vibrometer and its software environment.

3.2 Case of an axisymmetric mode

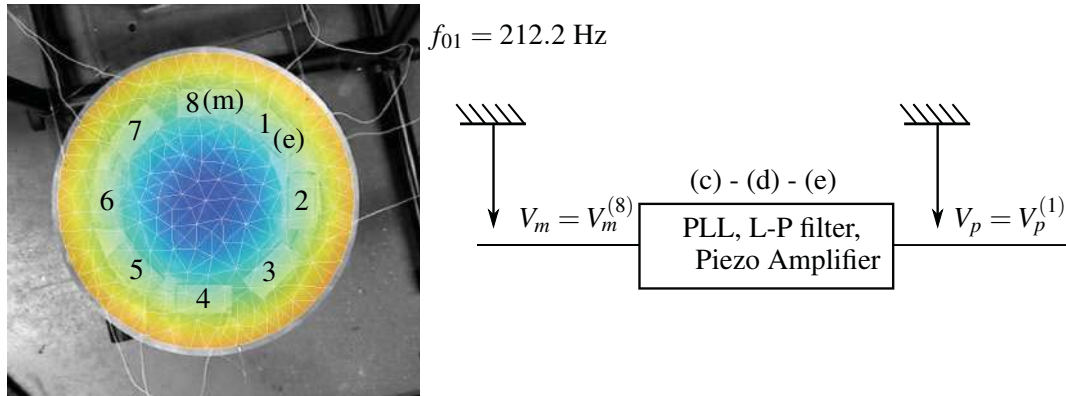


Figure 4: Operational shapes of the plate at frequencies of the (0,1) mode and connection of the patches for the excitation (e) and measurements (m).

The configuration around the first axisymmetric mode of the circular plate is studied: the modal analysis identified the frequency of this mode at $f_{01} = 212.2 \text{ Hz}$. The notation (01) means that the mode shape presents no nodal diameter and one nodal circle, as shown on the operational shape of the figure 4. The application of the procedure described in section verifies that the linear EM coupling coefficients of the eight patches are theoretically equal. Thus this configuration can equally be studied by forcing and measuring with any configuration of patches.

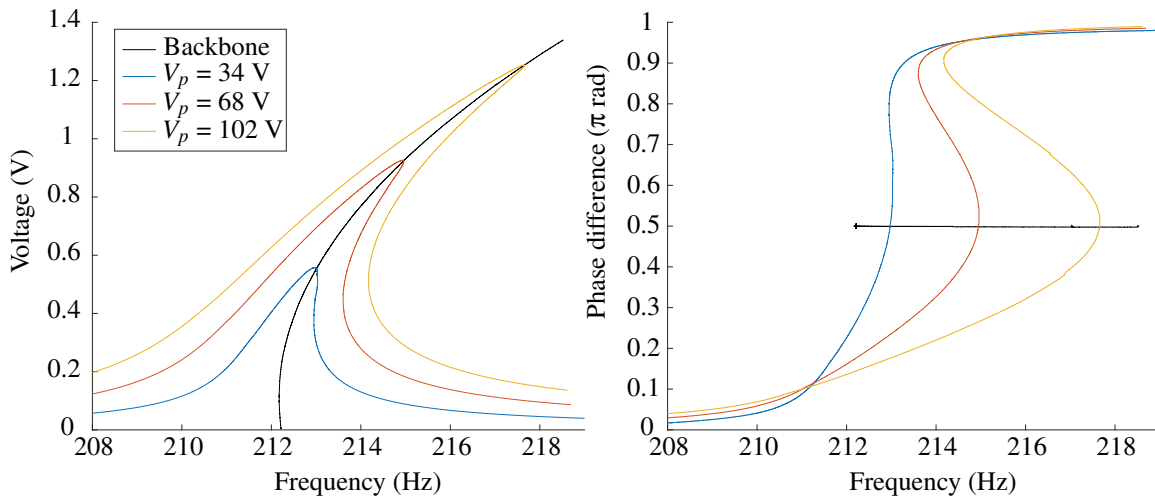


Figure 5: Amplitudes and phases of the measured voltage V_m during an amplitude sweep (Backbone) and phase sweeps (Forced) at different electric excitation levels V_p .

In the present case, the patch 1 is used for the excitation whereas patch 8 is connected for the measurements. The curves in amplitude (on the Fig. 4 - left) presented on the figure 5 show that the forced responses at different excitation levels lie around the backbone curve (undamped free response, in black), with a main hardening effect, indeed the frequency increases with the amplitude. A very slight softening effect is noticeable at the low amplitudes of the free response, which could be explained by the effects of material nonlinearities. The phase differences (on the Fig. 4 - right) are increasing from 0 to π , which is consistent with the command applied to the system.

3.3 Case of a pair of asymmetric modes: 1:1 internal resonance

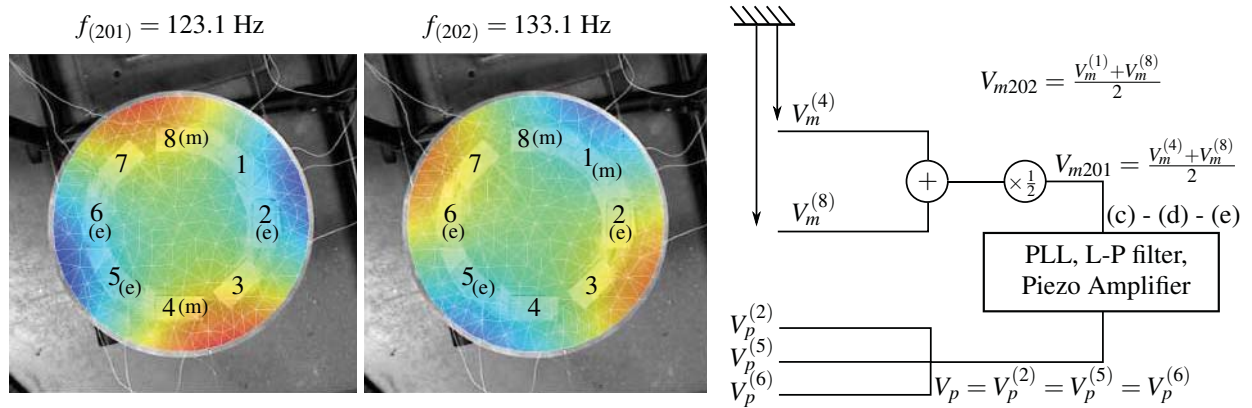


Figure 6: Operational shapes of the plate at frequencies of the (0,1) mode and connection of the patches for the excitation (e) and measurements (m).

The two first mode of the circular plate are companion modes of similar shapes: they have both two nodal diameters and no nodal circle. The two configurations present a spatial dephasing with their nodal diameters, in accordance with the Fig. 6 -. They theoretically have the same frequencies, which differ in experimental conditions because of unavoidable imperfections of the structure. They are referred to as (2,0,1) and (2,0,2) modes where the last indice denotes the lower (indice 1) and upper (indice 2) frequency. In order to observe energy exchange between two preferential configurations, magnets are placed as additional lests on the anti-nodes of the (2,0,2) mode to reduce its frequency and bring it nearer from the frequency of the (2,0,1) mode: in this case the frequency has been reduced from 133.1 Hz to $f_{202} = 125.9$ Hz. With the present disposition of the mode shapes, the nodal diameter are placed between the patch. Thus linear EM coupling coefficients are either quasi-equal, or quasi-opposed for each of the two companion modes. To capture the modal components of the two configurations, the averages between two pairs of patches are computed in real-time, one for each of the configuration: the voltage at patch 4 and 8 are added for the (2,0,1) mode, whereas the sum of the voltage at the patch 1 and 8 is computed for the (2,0,2) mode. The gains of the input voltage of the PLL are adjusted at low amplitudes such that the signals are perfectly either equal, or perfectly opposed. Three patches are connected in parallel for the excitation - at patches 2, 5 and 6 - to force effeciently the (2,0,1) configuration.

The figure 7 shows the amplitude responses of the average voltage V_{m201} : as for the (0,1) mode, the forced responses lie around the backbone curve, with a hardening behavior, and a slight softening behavior at low amplitudes which could be due to material nonlinearities. At the right hand side of the resonances, some forced responses make appear a discontinuity or a secondary resonance curve which could be explained by the influence of a possible interaction with the (2,0,2) mode.

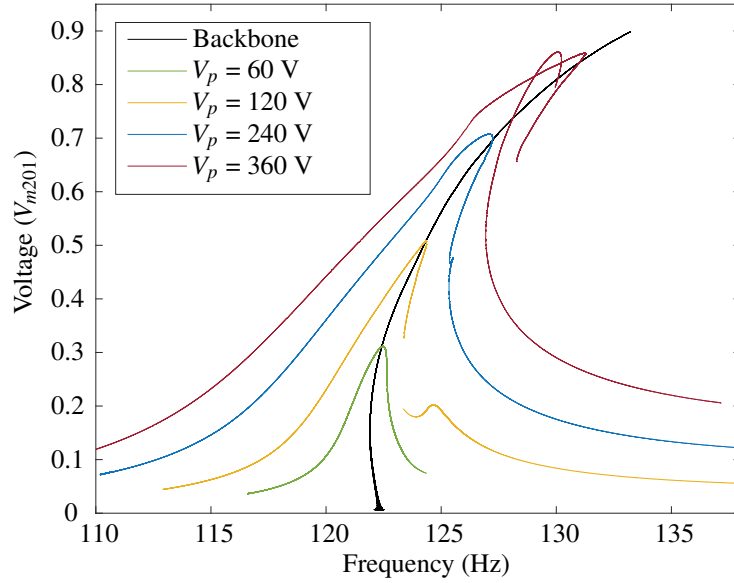


Figure 7: Amplitudes of the measured output voltage V_{m1} during an amplitude sweep (Backbone) and phase sweeps at different electric excitation levels V_p .

To ensure this point, the amplitude and phase of only one forced response at the V_{m201} and V_{m202} measurement signals are presented on the figure 8: the amplitude responses highlights the emergence of a second resonance in the V_{m202} which was not noticeable on the voltage V_{m201} . When the amplitude of this last one continues to increase, with a slight change of curvature when the resonance in the V_{m202} was activated. Moreover, this resonance curve lies around the free response measured at the V_{m202} signal. The activation of the second resonance is partially confirmed on the phase response curves (Fig. 8 - left),

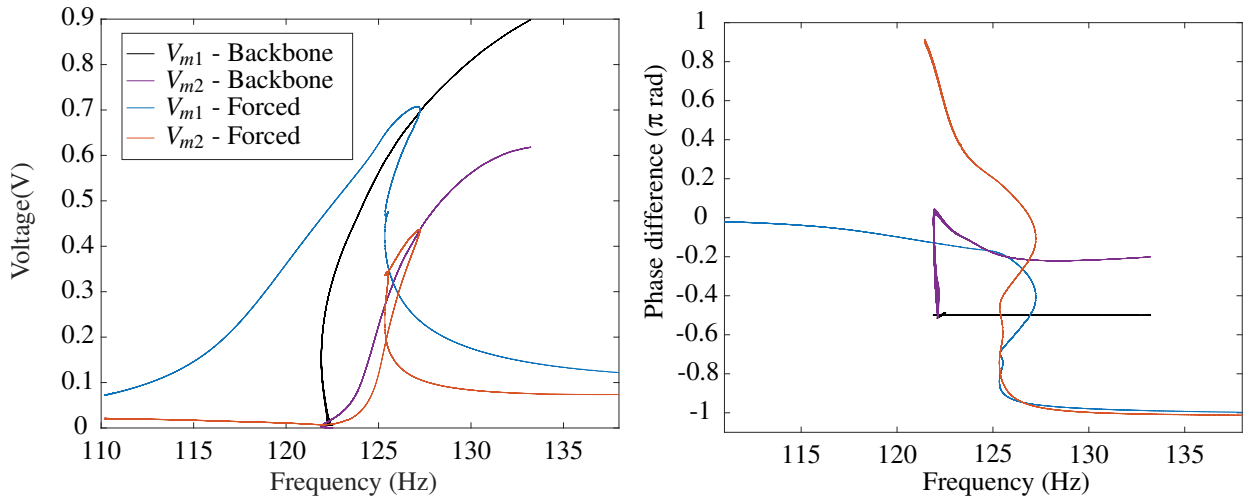


Figure 8: Amplitudes and phases of the measured voltage V_{m1} and V_{m2} corresponding to the modes $(2,0,1)$ and $(2,0,2)$ during an amplitude sweep (Backbone) and a phase sweep (Forced) at constant excitation level $V_p = 240$ V.

indeed the phase follows a path which decreases with a detuning with the phase of the V_{m201} signal, and reaches a maximum in frequency when the signal is in phase with the excitation.

4 CONCLUSIONS

This paper presented an original procedure to compute the nonlinear dynamical responses of systems with an electromechanical coupling and a piezoelectric device for the actuation and detection. Different approaches are proposed to validate the numerical computations : analytical models are used to validate the finite element ROMs at the coefficient's level, and an experimental procedure to measure the nonlinear free and forced responses on a laminated piezoelectric structure has been set up. To complete the validation process, the perspectives include the computation of the last family of coefficients of the ROM and the comparison of the computed responses with the experimental results. The approach could then be applied to a large range of application.

REFERENCES

- [1] Dezest, D. and Thomas, O. and Mathieu, F. and Mazenq, L. and Soyer, C. and Costecalde, J. and Remiens, D. and Deü, J.-F. and Nicu, L. Wafer-scale fabrication of self-actuated piezoelectric nano-electromechanical resonators based on lead zirconate titanate (PZT), *J. Micromech. and Microeng.* (2015) **25**(3):035002.
- [2] Nayfeh, A. and Younis, M. I. and Abdel-Rahman, E. M. Reduced-order models for MEMS applications, *Nonlinear dyn.* (2005), **41**(1):211–236.
- [3] Lazarus, A. and Thomas, O. and Deü, J.-F. Finite elements reduced order models for nonlinear vibrations of piezoelectric layered beams with applications to NEMS, *Finite Elem. Anal. Des.* (2012), **49**(1):35–51.
- [4] Thomas, O. and Mathieu, F. and Mansfield, W. and Huang, C. and Trolier-McKinstry, S. and Nicu., L. Efficient parametric amplification in MEMS with integrated piezoelectric actuation and sensing capabilities, *Appl. Phys. Lett.* (2013), **102**(16):163504.
- [5] Quinn, D.D. and Triplett, A.L. and Vakakis, A.F. and Bergman, L.A. Energy harvesting from impulsive loads using intentional essential nonlinearities, *J. Vib. Acous.* (2011) **133**(1):011004.
- [6] Mignolet, M. and Przekop, A. Rizzi, S.A. Spottswood, S.M. A review of indirect/non-intrusive reduced order modeling of nonlinear geometric structures, *J. Sound Vib.* (2013) **332**(10):2437–2460.
- [7] Muravyov, A. A. and Rizzi, S. A. Determination of nonlinear stiffness with application to random vibration of geometrically nonlinear structures. *Comput. Struc.*, **81**(15):1513–1523.
- [8] Givois, A. and Grolet, A. and Thomas, O. and Deü, J.-F. On the frequency response computation of geometrically nonlinear flat structures using reduced-order finite element models, *Nonlinear dyn.*, submitted.
- [9] Cochelin, B. and Damil, N. and Potier-Ferry, M. *Methode asymptotique numerique*, Hermes Lavoisier, (2007).
- [10] Ducarne, J. and Thomas, O. and Deü, J.-F. Placement and dimension optimization of shunted piezoelectric patches for vibration reduction, *J. Sound Vib.* (2012) **331**(14):3286–3303.

- [11] PI Ceramic, Open source on <http://fisica.cab.cnea.gov.ar/bt/images/d/d3/PICat.pdf> (Accessed: 24-09-2018.).
- [12] Thomas, O. and Ducarne, J. and Deü, J.-F. Vibrations of an elastic structure with shunted piezo-electric patches: efficient finite element formulation and electromechanical coupling coefficients, *Int. J. Numer. Meth. Eng.* (2009) **80**:235–268.
- [13] Trindade, M.A. and Benjeddou, A. Effective electromechanical coupling coefficients of piezo-electric adaptive structures: critical evaluation and optimization, *Mech. Adv. Mater. Struc.* (2009) **16**(3):210–223.
- [14] Denis, V. and Jossic, M. and Giraud-Audine, C. and Chomette, B. and Renault, A. and Thomas, O. Identification of nonlinear modes using phase-locked-loop: experimental continuation and normal form. *Mech. Syst. Signal Process.* (2018) **106**:430–452.

NON-LINEAR ELECTROMECHANICAL COUPLING: LARGE DEFORMATION AND HYSTERESIS

ALEXANDER HUMER^{*,†}, ASTRID S. PECHSTEIN[†], MARTIN MEINDLHUMER[†]
AND MICHAEL KROMMER[‡]

[†] Institute of Technical Mechanics
Johannes Kepler University Linz
Altenberger Str. 69, 4040 Linz, Austria
e-mail: {alexander.humer, astrid.pechstein, martin.meindlhumer}@jku.at

[‡] Institute of Mechanics and Mechatronics
Vienna University of Technology
Getreidemarkt 9/E325, 1060 Vienna, Austria
e-mail: michael.krommer@tuwien.ac.at

Key words: Ferroelectric Materials, Polarization, Finite Deformation, Smart Structures

Abstract. Smart materials respond to external stimuli as, e.g., electric fields, which enables their usage as actuators and, possibly, also as sensors. The electromechanical coupling of the direct and converse piezoelectric effects, for instance, is used for both actuation and sensing in diverse engineering applications. The response of ferroelectric materials depends on their state of remanent polarization and the presence of an external electric field. To extend the operational range of sensors and actuators, an accurate understanding of the evolution of the material's state of polarization is required, which requires both physical and geometrical non-linearities to be taken into account. Moreover, polymeric materials as PVDF allow significantly larger deformation as compared to conventional piezoelectric ceramics. The electro-mechanical coupling in piezoelectric materials manifests in ferroelectric and ferroelastic hystereses, which are related to both reversible and irreversible processes. Focusing on the latter, we transfer phenomenological models for domain switching in ferroelectric materials to the geometrically non-linear regime. For this purpose, we follow related concepts of geometrically non-linear elastoplasticity, where the concept of a multiplicative decomposition of the deformation gradient plays a key role. Accordingly, an additional deformation path that describes the evolution of the poled state from the unpoled referential configuration is introduced. The constitutive response of the material to mechanical and electrical loads is discussed and dissipative internal forces that drive the evolution of the remanent polarization are derived within a thermodynamical framework and the principle of maximum dissipation.

1 INTRODUCTION

Ferroelectric materials have been adopted as sensors and actuators in diverse fields of applications, which range from microelectromechanical systems (MEMS) for high-precision positioning to vibrational and structural noise control. Typically, ferroelectric ceramics as, e.g., PZT, are used due to their comparatively high coupling coefficients. These polycrystalline ceramics are characterized by a relatively

high brittleness, which is why they do not admit large strains. For this reason, their constitutive models are usually formulated within the range of small (linearized) strains, which gives Voigt's linearized theory of piezoelectricity for the reversible response, see, e.g., [1, 13]. The response of ferroelectric materials is intrinsically related to their state of remanent polarization, which is assumed to be constant for most applications. Electro-mechanical loadings beyond so-called coercive electric fields or coercive stresses, however, induce an irreversible re-orientation of dipoles in the material and therefore a change of the remanent polarization [3]. These mechanisms are referred to as "switching" and result in ferroelectric and ferroelastic hystereses. The mathematical modeling and the computational approximation of switching phenomena in ferroelectric materials shares many aspects with well-established approaches in elasto-plasticity, see, e.g., [4].

Unlike ceramic materials, ferroelectric polymers as, e.g., PVDF, can be subjected to comparatively large strains well beyond the linear range. Based on the modeling of the reversible electro-mechanically coupled response presented in [2], we propose a first attempt towards the continuum modeling of the ferroelectric hysteresis in the geometrically non-linear range of deformation. For this purpose, we repeatedly adopt the concept of a multiplicative decomposition of the deformation gradient, which has successfully been applied to the modeling of inelastic processes, see [6] for an overview. The idea of multiple multiplicative decompositions is discussed in [8]. In the present approach, the deformation gradient is decomposed into three parts: the irreversible part governs the evolution of a poled (intermediate) configuration from the unpoled reference configuration. The second part describes the reversible local response of a poled volume element subjected to an electric field, which deforms into a second intermediate configuration, which can be regarded as de-stressed, i.e., the current configuration is relieved from stresses. Third part accounts for the mechanical stress response of the material. The modeling of the dissipative response follows the concepts of finite strain elasto-plasticity [10, 11, 12], where ideas of damage modeling are included to incorporate changes of the material parameters due to poling [5]. The evolution equation for the dissipative internal forces follow as an associative flow rule from the constrained optimization problem that is obtained from the principle of maximum dissipation [10, 9]. In our first approach, we want to restrict ourselves to the ferroelectric hysteresis, i.e., the mechanisms of mechanical depolarization are not accounted for.

2 BALANCE EQUATIONS OF NON-LINEAR ELECTRO-MECHANICS

We start our considerations recalling fundamental ideas of reversible electro-mechanics, in which no changes of the state of remanent polarization takes place. In the quasi-static case, the local balance of linear momentum gives the spatial representation of the equilibrium relation as

$$\operatorname{div} \boldsymbol{\sigma} + \mathbf{f} + \mathbf{f}^E = \mathbf{0}, \quad \mathbf{f}^E = (\operatorname{grad} \mathbf{e}) \cdot \mathbf{p} = \operatorname{div} \boldsymbol{\sigma}^E. \quad (1)$$

The Cauchy stress tensor is denoted by $\boldsymbol{\sigma}$, and \mathbf{f} are mechanical body forces; \mathbf{e} and \mathbf{p} denote the electric field and the polarization vector, respectively. A dielectric material body that is subjected to an electric field experiences additional body forces \mathbf{f}^E , which can be represented by means of the divergence of the electrostatic stress tensor $\boldsymbol{\sigma}^E$. The balance of angular momentum yields the symmetry of the sum of the Cauchy stresses and the polarization stresses $\boldsymbol{\sigma}^P$

$$\boldsymbol{\sigma} + \boldsymbol{\sigma}^P = (\boldsymbol{\sigma} + \boldsymbol{\sigma}^P)^T, \quad \boldsymbol{\sigma}^P = \mathbf{e} \mathbf{p}. \quad (2)$$

We obtain the total (Cauchy) stress tensor as the sum of the (mechanical) Cauchy stress and the (non-symmetric) electrostatic stress tensor,

$$\boldsymbol{\sigma}^{\text{tot}} = \boldsymbol{\sigma} + \boldsymbol{\sigma}^E, \quad \boldsymbol{\sigma}^E = \mathbf{e} \mathbf{d} - \frac{1}{2} \epsilon_0 (\mathbf{e} \cdot \mathbf{e}) \mathbf{I}, \quad (3)$$

where \mathbf{d} denotes the dielectric displacement. The dielectric displacement is related to the electric field and the polarization \mathbf{p} through

$$\mathbf{d} = \epsilon_0 \mathbf{e} + \mathbf{p}. \quad (4)$$

We note that the (mechanical) Cauchy stress tensor is not symmetric due to electrostatic couples induced in a dielectric body. We further observe that the definition of the electrostatic stress tensor is not unique since any divergence-free tensor can be added without changing the electrostatic body forces \mathbf{f}^E . The electrostatic stress tensor, in turn, can be represented as the sum of polarization stress σ^P and the Maxwell stress tensor σ^M

$$\sigma^M = \sigma^E - \sigma^P = \mathbf{e}\mathbf{e} - \frac{1}{2} \epsilon_0 (\mathbf{e} \cdot \mathbf{e}) \mathbf{I}. \quad (5)$$

From Maxwell's equations, we have Gauss' law of conservation of charge, which reduces to

$$\operatorname{div} \mathbf{d} = 0, \quad (6)$$

for the case of dielectric materials, for which the free charge density vanishes. The quasi-static form of Faraday's law of induction yields

$$\operatorname{curl} \mathbf{e} = \mathbf{0} \quad \Leftrightarrow \quad \mathbf{e} = -\operatorname{grad} \phi, \quad (7)$$

where ϕ denotes the electric potential. The electro-mechanical power density (per unit volume in the current configuration) p is immediately related to the rate of the specific free energy ψ , for which the local form of the balance equation reads

$$p = \rho \dot{\psi} = \sigma : \operatorname{grad} \mathbf{v} - \mathbf{p} \cdot \dot{\mathbf{e}}. \quad (8)$$

The velocity field is denoted by \mathbf{v} ; ρ is the mass density per unit (current) volume. The spatial velocity gradient can be expressed in terms of the (material) deformation gradient tensor \mathbf{F} as $\operatorname{grad} \mathbf{v} = \dot{\mathbf{F}} \cdot \mathbf{F}^{-1}$.

Note that the current configuration is the natural configuration in problems of electrostatics, in which a deformation of the material is neglected. On the other hand, we often prefer to relate mechanical quantities to the known referential state of the body rather than the unknown current configuration which may significantly deviate from the referential state in general. Material quantities associated with the reference configuration and their spatial counterparts associated with the current configuration are related by push-back and pull-forward operations, see, e.g., [7]. We can introduce material fields corresponding to the electric quantities. The respective pull-back operations are defined by the nature of the global balance equations, see, e.g., [13], which preserves the structure of the local balance laws. The Piola transformation is used for the dielectric displacement and the polarization. The electric field is pulled back using the deformation gradient, which relates and material gradients. In what follows, we stick with the spatial formulation for the sake of brevity.

To determine the constitutive equations for the total stresses and the dielectric displacement, the free energy is augmented by the vacuum contribution

$$\psi^{\text{tot}} = \psi + \psi^{\text{aug}}, \quad \psi^{\text{aug}} = -\frac{\epsilon_0}{\rho} \mathbf{e} \cdot \mathbf{e}. \quad (9)$$

By direct computation, we can show that the total electro-mechanical power follows to

$$p^{\text{tot}} = \rho \dot{\psi}^{\text{aug}} = \sigma^{\text{tot}} : \mathbf{d} - \mathbf{d} \cdot \dot{\mathbf{e}}, \quad (10)$$

where \mathbf{d} denotes the symmetric part of the spatial velocity gradient, i.e., $\text{grad } \mathbf{v} = \mathbf{d} + \mathbf{w}$, with

$$\mathbf{d} = (\dot{\mathbf{F}} \cdot \mathbf{F}^{-1})_s = \frac{1}{2} \left(\dot{\mathbf{F}} \cdot \mathbf{F}^{-1} + \mathbf{F}^{-T} \cdot \dot{\mathbf{F}}^T \right), \quad \mathbf{w} = (\dot{\mathbf{F}} \cdot \mathbf{F}^{-1})_a = \frac{1}{2} \left(\dot{\mathbf{F}} \cdot \mathbf{F}^{-1} - \mathbf{F}^{-T} \cdot \dot{\mathbf{F}}^T \right). \quad (11)$$

Comparing the balance law (10) with the rate of the augmented free energy $\dot{\psi}^{\text{tot}} = \dot{\psi}^{\text{tot}}(\mathbf{F}, \mathbf{e})$,

$$\dot{\psi}^{\text{tot}} = \frac{\partial \psi^{\text{tot}}}{\partial \mathbf{F}} : \dot{\mathbf{F}} + \frac{\partial \psi^{\text{tot}}}{\partial \mathbf{e}} \cdot \dot{\mathbf{e}}, \quad (12)$$

we can identify the constitutive relations as

$$\boldsymbol{\sigma}^{\text{tot}} = \rho \frac{\partial \psi^{\text{tot}}}{\partial \mathbf{F}} \cdot \mathbf{F}^T, \quad \mathbf{d} = -\rho \frac{\partial \psi^{\text{tot}}}{\partial \mathbf{e}}. \quad (13)$$

Well aware of the abuse of notation, we omit all superscripts “tot” in what follows, since we only use total stresses and the dielectric displacement as primary dependent variables subsequently.

Next, we consider the constitutive equation for the case of a dissipative response that occurs once we admit the state of remanent polarization to change. We adopt the concept of internal variables to describe the dissipative response of the material. In the simplest case, the remanent polarization itself plays the role of an internal variable. We then assume the free energy to additionally depend on the remanent polarization, i.e.,

$$\psi = \psi(\mathbf{F}, \mathbf{e}, \mathbf{p}_i), \quad \dot{\psi} = \frac{\partial \psi}{\partial \mathbf{F}} : \dot{\mathbf{F}} + \frac{\partial \psi}{\partial \mathbf{e}} \cdot \dot{\mathbf{e}} + \frac{\partial \psi}{\partial \mathbf{p}_i} \cdot \dot{\mathbf{p}}_i. \quad (14)$$

The dissipation density d (per unit current volume) is introduced in (10),

$$p = \rho \dot{\psi} + d. \quad (15)$$

The second law of thermodynamics requires the energy that is dissipated into heat to be positive, i.e.,

$$d = p - \rho \dot{\psi} \geq 0. \quad (16)$$

For a given electro-mechanical power $p = \boldsymbol{\sigma} : \mathbf{d} - \mathbf{d} \cdot \dot{\mathbf{e}}$, we obtain the relation

$$d = \left(\boldsymbol{\sigma} - \rho \frac{\partial \psi}{\partial \mathbf{F}} \cdot \mathbf{F}^T \right) : \mathbf{d} - \left(\mathbf{d} - \rho \frac{\partial \psi}{\partial \mathbf{e}} \right) \cdot \dot{\mathbf{e}} - \rho \frac{\partial \psi}{\partial \mathbf{p}_i} \cdot \dot{\mathbf{p}}_i \geq 0. \quad (17)$$

With the stresses and the dielectric displacement being defined as in the reversible case (13), the dissipation follows to

$$d = \mathbf{f}_i \cdot \dot{\mathbf{p}}_i \geq 0, \quad \mathbf{f}_i = -\rho \frac{\partial \psi}{\partial \mathbf{p}_i}, \quad (18)$$

where \mathbf{f}_i denotes the internal forces conjugate to the remanent polarization \mathbf{p}_i , which can be regarded as dissipative driving forces.

3 MULTIPLICATIVE DECOMPOSITION

To begin with, we briefly recall the underlying physical processes and the phenomena observed when a ferroelectric material is irreversibly polarized. A polarizable material is characterized by the presence of microscopic structures (unit cells) that possess a spontaneous polarization, i.e., the centers of positive and negative charges do not coincide and an electric dipole is formed. The unit cells may form so-called domains in which the spontaneous polarization of the unit cells is oriented in the same direction. Due to

the random orientation of dipoles/unit cells, the net polarization on the macroscopic level vanishes in the unpoled state. Ferroelectric materials can be polarized by exposing them to a sufficiently strong electric field. Beyond the so-called coercive field, the dipoles of the unit cells re-orient (“switching”) themselves along the applied field and maintain that orientation once the field is removed again, i.e., the process is irreversible and a hysteretic behavior is observed (ferroelectric hysteresis). From a mechanical point of view, we note the following phenomena that need to be accounted for by appropriate phenomenological models:

- A change of remanent polarization is accompanied by (irreversible) deformation due to the rotation of the dipoles. The poling induced deformation is isochoric.
- Both the electrical and the mechanical response depend on the state of polarization. In fact, the piezoelectric effect is only present if a material is polarized. The poling process induces a principal direction along the poling direction in ferroelectric materials. Initially isotropic materials therefore exhibit a transversally isotropic behavior once they have been poled.
- A poled specimen can be irreversibly de-poled by sufficiently strong mechanical loadings that exceed the so-called coercive stress (ferroelastic hysteresis). In this case, the dipoles switch into the plane perpendicular to the applied force vector. Note that the mechanical de-polarization is not addressed in the present approach.

From a mechanical point of view, the polarization process bears a close resemblance to phenomenological models of elasto-plasticity, which is reflected in both the structure of the constitutive models and numerical methods used for the construction of approximate solutions. This observation is the starting point for our attempt to translate constitutive models from finite-strain plasticity to non-linear electro-elasticity.

If we leave the range of infinitesimal deformations, the conventional additive decomposition of stresses and strain measures into reversible and irreversible parts lacks a physical underpinning. For this purpose, we begin our considerations by multiplicatively splitting the deformation gradient \mathbf{F} into an irreversible part \mathbf{F}_i and a reversible part \mathbf{F}_r ,

$$\mathbf{F} = \mathbf{F}_r \cdot \mathbf{F}_i. \quad (19)$$

Such multiplicative decomposition introduces the notion of an intermediate configuration that enters the deformation path. The irreversible part of the deformation gradient \mathbf{F}_i describes the evolution of the poled intermediate configuration from the unpoled state of the material due to changes of the state of remanent polarization, whereas \mathbf{F}_r describes the response due to reversible processes induced by mechanical or electric loadings. Owing to the electro-mechanical coupling, the reversible response involves an inelastic electric part and an elastic mechanical part, for which we want to adopt a second multiplicative decomposition, i.e.,

$$\mathbf{F}_r = \mathbf{F}_{r,m} \cdot \mathbf{F}_{r,e}. \quad (20)$$

The electrical part \mathbf{F}_e governs the local response of a poled material due to the presence of an electric field. The current state of stress, in turn, is determined from the mechanical part \mathbf{F}_m . In the proposed model, the total deformation \mathbf{F} is consequently composed from three parts,

$$\mathbf{F} = \mathbf{F}_{r,m} \cdot \mathbf{F}_{r,e} \cdot \mathbf{F}_i, \quad (21)$$

hence, a second intermediate configuration is introduced into the deformation path.

In the constitutive modeling, we assume that the free energy is split into three parts that are associated with the individual paths related to three components of the deformation gradient:

$$\psi = \psi_e + \psi_{r,m} = \psi_i + \psi_r, \quad \psi_e = \psi_i + \psi_{r,e}, \quad \psi_r = \psi_{r,e} + \psi_{r,m}. \quad (22)$$

The stress response is governed by the (reversible) mechanical part of the free energy $\psi_{r,m}$, which is associated with the deformation path from the second intermediate configuration to current configuration. The (second) intermediate configuration can be regarded as a configuration that is obtained from the current configuration upon de-stressing at a constant electric field. Note that de-stressing does not imply that the total stresses vanish in the intermediate configuration, see [2] for a discussion.

We can choose any suitable strain energy function of non-linear elasticity, as, e.g., a Neo-Hookean material or the physically linearized St. Venant-Kirchhoff law, where the right Cauchy-Green strain in the (second) intermediate configuration serves as Lagrangian deformation measure. As the material properties generally change in the course of poling, we also need to include a dependence on the remanent polarization \mathbf{p}_i . Following concepts proposed for the modeling of damage in large-strain plasticity [5], we can adopt the notion of a second-order structural tensor $\mathbf{a}(\mathbf{p}_i)$ to describe anisotropy induced by the poling process. Relating the structural tensor to the remanent polarization in the current configuration, we may define it as

$$\mathbf{a} = \frac{\|\mathbf{p}_i\|}{p_{\text{sat}}} \mathbf{n} \mathbf{n}, \quad \mathbf{n} = \frac{\mathbf{p}_i}{\|\mathbf{p}_i\|}, \quad (23)$$

where p_{sat} denotes the saturation polarization. Transversal isotropy can be described by augmenting the integrity basis by invariants of the structural tensor and mixed invariants of the structural tensor and the respective strain measure. The free energy of the mechanical part of the deformation gradient therefore can be introduced as a function of the corresponding right Cauchy-Green tensor \mathbf{C}_m and the structural tensor $\bar{\mathbf{a}}$, which is pulled back from the current configuration,

$$\psi_{r,m} = \psi_{r,m}(\mathbf{C}_m, \bar{\mathbf{a}}), \quad \bar{\mathbf{a}} = J_m^2 \mathbf{F}_{r,m}^{-1} \cdot \mathbf{a} \cdot \mathbf{F}_{r,m}^{-T}, \quad J_m = \det \mathbf{F}_{r,m}. \quad (24)$$

The (total) Cauchy stresses are obtained from the derivative of the mechanical pure energy with respect to \mathbf{C}_m upon a push-forward to the current configuration,

$$\boldsymbol{\sigma} = \rho \mathbf{F}_{r,m} \cdot \frac{\partial \psi_{r,m}}{\partial \mathbf{C}_m} \cdot \mathbf{F}_{r,m}^T + \rho \frac{\partial \psi_e}{\partial \mathbf{F}} \cdot \mathbf{F}^T, \quad (25)$$

where the dependence of the electrical parts on the deformation gradient is also regarded. We have introduced double over-bars to distinguish quantities that are related to the second intermediate configuration. We will use a single bar if quantities are related to the first intermediate configuration.

The reversible part of the electric deformation gradient $\mathbf{F}_{r,e}$ describes the evolution of the poled (first) intermediate configuration into the de-stressed (second) intermediate configuration in the presence of an electric field. For this reason, it is constitutively defined as a function of the electric field in the poled intermediate configuration, $\bar{\mathbf{e}} = \mathbf{e} \cdot \mathbf{F}_r = \boldsymbol{\mathcal{E}} \cdot \mathbf{F}_i^{-1}$, e.g., a series expansion of the form

$$\mathbf{F}_{r,e}(\bar{\mathbf{e}}, \bar{\mathbf{a}}) = \mathbf{I} + \bar{\mathbf{e}} \cdot {}^3\bar{\mathbf{d}}(\bar{\mathbf{a}}) + \bar{\mathbf{e}}\bar{\mathbf{e}} : {}^4\bar{\mathbf{b}}(\bar{\mathbf{a}}) + \dots, \quad (26)$$

where ${}^3\bar{\mathbf{d}}$ and ${}^4\bar{\mathbf{b}}$ represent coefficients describing piezoelectric and electrostrictive coupling, respectively. The reversible part of the electric free energy is related to the permittivity, which includes the vacuum contribution (9) and a term governed by the susceptibility χ of the material. For the present

choice of dependent variables, we have an additional term that couples the electric field and the remanent polarization,

$$\psi_{r,e} = \psi_{r,e}(\mathbf{e}, \mathbf{a}) = -\frac{1}{2} \rho^{-1} \mathbf{e} \cdot (\chi(\mathbf{a}) + \epsilon_0 \mathbf{I}) \cdot \mathbf{e} - \rho^{-1} \mathbf{e} \cdot \mathbf{p}_i. \quad (27)$$

If the irreversible part of the electric free energy ψ_i depends on the remanent polarization \mathbf{p}_i only, the constitutive relation for (spatial) dielectric displacement follows as

$$\mathbf{d} = -\rho \frac{\partial \psi_{r,e}}{\partial \mathbf{e}} + \rho \frac{\partial \psi_{r,m}}{\partial \mathbf{F}_{r,e}} : \frac{\partial \mathbf{F}_{r,e}}{\partial \mathbf{e}}, \quad (28)$$

where the mechanical part of the free energy generally depends on the electric field through the (reversible) electric part of the deformation gradient $\mathbf{F}_{r,e}$.

The evolution of the poled state from the unpoled, undeformed reference configuration is governed by the irreversible part of the deformation gradient \mathbf{F}_i , for which we have to provide a constitutive definition. As the deformation induced by the poling is typically isochoric, we may use a stretching type deformation with a saturation strain S_{sat} as proposed in [14]:

$$\mathbf{F}_i(\mathbf{p}_i) = \left(1 - \frac{3}{2} S_{\text{sat}} \frac{\|\mathbf{p}_i\|}{p_{\text{sat}}}\right)^{-2/3} \left\{ \left(1 - \frac{3}{2} S_{\text{sat}} \frac{\|\mathbf{p}_i\|}{p_{\text{sat}}}\right) \mathbf{I} + \frac{3}{2} S_{\text{sat}} \frac{\|\mathbf{p}_i\|}{p_{\text{sat}}} \mathbf{N} \mathbf{N} \right\}, \quad \mathbf{N} = \frac{\mathcal{P}_i}{\|\mathcal{P}_i\|}. \quad (29)$$

where the material polarization is defined as

$$\mathcal{P}_i = J \mathbf{p}_i \cdot \mathbf{F}^{-T}, \quad J = \det \mathbf{F}. \quad (30)$$

The poled (first) intermediate configuration can be regarded as a configuration that is stress-free and in which no (external) electric field is present. Due to the deformation induced by the poling, the intermediate configuration is incompatible in general. The corresponding part of the free energy ψ_i related to the poling process can exemplarily be assumed as quadratic function in the remanent polarization,

$$\psi_i = \psi_i(\mathbf{p}_i) = \frac{1}{2} (\rho J)^{-1} c \mathbf{p}_i \cdot \mathbf{p}_i, \quad (31)$$

where c denotes a kinematic hardening parameter. By introducing the (constant) density in the reference configuration $\rho_0 = \rho J$, we avoid a dependence on the deformation gradient \mathbf{F} , i.e., $\partial \psi_i / \partial \mathbf{F} = \mathbf{0}$. The dissipative internal forces conjugate to the remanent polarization are obtained from the individual parts of the free energy as

$$\mathbf{f}_i = -\rho \frac{\partial \psi_i}{\partial \mathbf{p}_i} - \rho \frac{\partial \psi_{r,e}}{\partial \mathbf{p}_i} - \rho \frac{\partial \psi_{r,m}}{\partial \mathbf{p}_i}. \quad (32)$$

Analogously to a rate-independent elasto-plastic response, we use the principle of maximum dissipation to derive the evolution equations of the remanent polarization. We expect the dissipation to assume a maximum, i.e., the dissipative forces \mathbf{f}_i are determined such such that

$$d = \sup_{\mathbf{f}_i \in \mathbb{E}} \mathbf{f}_i \cdot \dot{\mathbf{p}}_i, \quad (33)$$

where \mathbb{E} denotes the reversible domain, which is defined by a threshold (switching) function f ,

$$\mathbb{E} = \{ \mathbf{f}_i \in \mathbb{R}^3 \mid f(\mathbf{f}_i) \leq 0 \}. \quad (34)$$

For example, if we require the norm of the dissipative forces to be constrained from above by a so-called coercive field e_c , we can use the threshold function

$$f = \|\mathbf{f}_i\| - e_c \leq 0. \quad (35)$$

The constrained maximization problem can be solved using a Lagrange multiplier λ , i.e.,

$$d = \sup_{\mathbf{f}_i, \lambda \geq 0} (\mathbf{f}_i \cdot \mathbf{p}_i + \lambda f(\mathbf{f}_i)), \quad (36)$$

from which we obtain an “associative flow rule” that governs the evolution of the remanent polarization as the necessary condition

$$\dot{\mathbf{p}}_i = \lambda \frac{\partial f(\mathbf{f}_i)}{\partial \mathbf{f}_i}, \quad (37)$$

as well as the classical Kuhn-Tucker conditions for loading/unloading:

$$\lambda \geq 0, \quad f \leq 0, \quad \lambda f = 0. \quad (38)$$

Unlike plasticity, in which plastic strains can accumulate until a material eventually breaks, the remanent polarization saturates as the reservoir of switchable dipoles/domains is finite. Saturation can be accounted for, e.g., by means of a hardening parameter that depends on the (norm of the) remanent polarization, i.e., $c = c(\|\mathbf{p}_i\|/p_{\text{sat}})$.

4 CONCLUSION

In the present paper, we have discussed a constitutive framework for the modeling of both the reversible and the irreversible response of ferroelectric materials in the geometrically non-linear domain. Our approach is based on the concept of the multiplicative decomposition of the deformation gradient into three parts that are associated with the irreversible poling, the (local) electric response and the elastic stress response. The individual parts of the free energy are related to the respective configuration in the deformation path. The constitutive equations for the stresses, the dielectric displacement and the dissipative forces follow from standard arguments of thermodynamics. The evolution equation for the remanent polarization is obtained from the principle of maximum dissipation.

5 ACKNOWLEDGEMENTS

Alexander Humer and Astrid Pechstein acknowledge the support by the COMET-K2 Center of the Linz Center of Mechatronics (LCM) funded by the Austrian federal government and the federal state of Upper Austria. Martin Meindlhumer acknowledges support of the Johannes Kepler University Linz, Linz Institute of Technology (LIT).

REFERENCES

- [1] A. C. Eringen and G. A. Maugin. *Electrodynamics of Continua I*. Springer New York, New York, NY, 1990.
- [2] A. Humer, E. Staudigl, and M. Krommer. Nonlinear electro-elasticity for piezoelectric materials and structures using a multiplicative decomposition of the deformation gradient. In A. Güemes, A. Benjeddou, J. Rodellar, and J. Leng, editors, *Proc. 8th ECCOMAS Themat. Conf. Smart Struct. Mater. SMART 2017*, pages 1316–1327, 2017.

- [3] M. Kamlah. Ferroelectric and ferroelastic piezoceramics – modeling of electromechanical hysteresis phenomena. *Contin. Mech. Thermodyn.*, 13(4):219–268, aug 2001.
- [4] S. Klinkel. A phenomenological constitutive model for ferroelastic and ferroelectric hysteresis effects in ferroelectric ceramics. *Int. J. Solids Struct.*, 43(22-23):7197–7222, 2006.
- [5] V. A. Lubarda. An analysis of large-strain damage elastoplasticity. *Int. J. Solids Struct.*, 31(21):2951–2964, 1994.
- [6] V. A. Lubarda. Constitutive theories based on the multiplicative decomposition of deformation gradient: Thermoelasticity, elastoplasticity, and biomechanics. *Appl. Mech. Rev.*, 57(2):95, 2004.
- [7] J. E. Marsden and T. J. R. Hughes. *Mathematical foundations of elasticity*. Dover Publications, 1994.
- [8] Á. Meggyes. Multiple decomposition in finite deformation theory. *Acta Mech.*, 146(3-4):169–182, 2001.
- [9] C. Miehe, D. Rosato, and B. Kiefer. Variational principles in dissipative electro-magneto-mechanics: A framework for the macro-modeling of functional materials. *Int. J. Numer. Methods Eng.*, 86(10):1225–1276, 2011.
- [10] J. C. Simo. A framework for finite strain elastoplasticity based on maximum plastic dissipation and the multiplicative decomposition: Part I. Continuum formulation. *Comput. Methods Appl. Mech. Eng.*, 66(2):199–219, 1988.
- [11] J. C. Simo. A framework for finite strain elastoplasticity based on maximum plastic dissipation and the multiplicative decomposition. Part II: Computational aspects. *Comput. Methods Appl. Mech. Eng.*, 68(1):1–31, 1988.
- [12] J. C. Simo and T. J. R. Hughes. *Computational Inelasticity*, volume 7 of *Interdisciplinary Applied Mathematics*. Springer-Verlag, New York, 1998.
- [13] J. Yang. *An Introduction to the Theory of Piezoelectricity*, volume 9 of *Advances in Mechanics and Mathematics*. Kluwer Academic Publishers, Boston, 2005.
- [14] D. Zäh and C. Miehe. Multiplicative electro-elasticity of electroactive polymers accounting for micromechanically-based network models. *Comput. Methods Appl. Mech. Eng.*, 286:394–421, 2015.

NONLINEAR ELECTROMECHANICAL CONVERSION OF MULTI-STABLE PIEZOELECTRIC SHALLOW SHELLS WITH PIEZOELECTRIC FILMS

DIMITRIS S. VARELIS^{*} AND DIMITRIS A. SARAVANOS[†]

^{*} Department of Aeronautical Sciences
Hellenic Air Force Academy (HAFA)
Dekelia Air Force Base, Dekelia-Attiki 13671, Greece
e-mail: dimitrios.varelis@hafa.haf.gr

[†] Department of Mechanical Engineering & Aeronautics (MEAD)
University of Patras
Patras 26500, Greece
email: dsaravanos@upatras.gr

Key words: Shells, Nonlinear, Snap Through Buckling, Piezoelectric, Electromechanical Energy, Finite Element.

Abstract. In this paper a theoretical and computational framework are presented for analyzing the nonlinear electromechanical response of shallow doubly curved laminated shells with attached piezopolymer film sensors, undergoing elastic snap through instability and eventually a transition between at least two stable equilibrium paths. The computational framework is based on nonlinear mechanics, incorporating full coupling between mechanical and electric fields and encompassing geometric nonlinearity effects due to large displacements and rotations. The governing equations are formulated explicitly in orthogonal curvilinear coordinates and are combined with the kinematic assumptions of a multi-field shear-layerwise shell laminate theory. A finite element methodology is adopted to yield the discrete coupled nonlinear equations which are linearized and iteratively solved, using the Cylindrical Arc Length Method in combination with the Newton-Raphson iterative technique. Numerical results demonstrate the capability of the method to predict the complex sensory electromechanical response of shallow cylindrical shells that transit between two stable equilibrium states. At the same time the generated sensory electric potential, electric charge and the stored electric energy in the piezoelectric films during the nonlinear bistable loading and unloading paths is predicted. The feasibility to detect and monitor the onset of snap-through instability, and to enhance the electromechanical energy conversion efficiency of the system for improved energy dissipation/harvesting systems, is also investigated. The influence of shell thickness, curvature and laminate configuration on the electromechanical conversion is finally investigated

1 INTRODUCTION

Shallow shell structures under external transverse loads (mechanical pressure, point load) exhibit a complex nonlinear multi-stable behavior, manifested as instantaneous snap through

instability, which transits the shell between two stable equilibrium configurations, via an unstable equilibrium state, that is associated with large deflections and shape changes. Various mostly experimental studies have explored the active multi-stability of shell for developing morphing structures [1-8]. On the other hand, it is highly desirable to detect the onset of snap through instability, through the sensor signals that describe the local response of piezoelectric sensor patch and eventually the global structural response. Additionally, the nonlinear electromechanical conversion of the attached piezoelectric elements prior and during to the snap through instability associated with electric charge generation and stored electric energy for improving energy harvesting/dissipation systems must be thoroughly modelled and understood. The current work represents an extension of the previous authors work [6] for analyzing the snap through buckling instability of smart shell structures, with emphasis on the equation of electric charge conservation and electromechanical coupling. Building upon the nonlinear multifield mechanics an eight-node shell finite element is developed to yield the coupled nonlinear equations of motion in discrete form, which are subsequently linearized and solved, using the Cylindrical Arc Length Method in combination with the Newton-Raphson iterative method. Numerical results illustrate the capability of the present model to predict the complex sensory electromechanical response (electric potential, electric charge, electric energy) of multi-stable cylindrical smart shells, during the bistable loading and unloading paths. The feasibility of smart shells to detect the onset of snap through instability, via the monitoring of sensory voltages, as well as to enhance the electromechanical energy conversion efficiency is also investigated. The influence of geometric parameters (thickness, curvature) on the electromechanical conversion efficiency is finally quantified.

2 PIEZOELECTRIC LAMINATED SHALLOW SHELL

All governing equations for doubly curved piezoelectric laminated shells are described and derived on an orthogonal curvilinear coordinate system $O\xi\eta\zeta$ with ξ, η axes lying on reference mid-surface A_o , while ζ axis remains straight and perpendicular on A_o . The material of each ply of the piezoelectric laminate is assumed to remain within the range of linear piezoelectricity:

$$\begin{aligned}\sigma_i &= C_{ij}^E S_j - e_{ik} E_k & i, j &= 1, \dots, 6 \\ D_l &= e_{lj} S_j + \varepsilon_{lk}^S E_k & k, l &= 1, \dots, 3\end{aligned}\tag{1}$$

σ_i, S_i are the mechanical stresses and Green's engineering strains in extended vectorial notation, C_{ij} is the elastic stiffness tensor in structural coordinates, e_{ik} is the piezoelectric tensor, E_k is the electric field vector, D_l is the electric displacement vector and ε_{lk} is the electric permittivity tensor of the material. Superscripts E and S indicate constant electric field and strain conditions, respectively.

The theory combines linear displacement field with a linear layer-wise electric potential field consisting of $N-1$ discrete segments, thus representing all state variables through the piezo-laminate thickness. According to the previous kinematic assumptions, the mechanical strain and generalized electric field approximations through the laminate thickness are given below:

$$\begin{aligned}
S_1^o &= \left[\frac{1}{g_{11}^o} (u_{,\xi}^o + \frac{g_{11,\eta}^o}{g_{22}^o} v^o) + \frac{w^o}{R_1} \right] + \frac{\zeta}{g_{11}^o} [\beta_{\xi,\xi}^o + \frac{g_{11,\eta}^o}{g_{22}^o} \beta_\eta^o] + \frac{1}{2} \left[\frac{w^{o^2}}{R_1^2} + \frac{u^{o^2}}{R_1^2} + \frac{w_{,\xi}^{o^2}}{g_{11}^o} - 2 \frac{u^o w_{,\xi}^o}{R_1 g_{11}^o} \right] \\
S_2^o &= \left[\frac{1}{g_{22}^o} (v_{,\eta}^o + \frac{g_{22,\xi}^o}{g_{11}^o} u^o) + \frac{w^o}{R_2} \right] + \frac{\zeta}{g_{22}^o} [\beta_{\eta,\eta}^o + \frac{g_{22,\xi}^o}{g_{11}^o} \beta_\xi^o] + \frac{1}{2} \left[\frac{w^{o^2}}{R_2^2} + \frac{v^{o^2}}{R_2^2} + \frac{w_{,\eta}^{o^2}}{g_{22}^o} - 2 \frac{v^o w_{,\eta}^o}{R_2 g_{22}^o} \right] \\
S_3^o &= 0 \\
S_6^o &= \left[\frac{1}{g_{11}^o} (v_{,\xi}^o - \frac{g_{11,\eta}^o}{g_{22}^o} u^o) + \frac{1}{g_{22}^o} (u_{,\eta}^o - \frac{g_{22,\xi}^o}{g_{11}^o} v^o) \right] + \\
&\quad \left[\frac{\zeta}{g_{11}^o} (\beta_{\eta,\xi}^o - \frac{g_{11,\eta}^o}{g_{22}^o} \beta_\xi^o) + \frac{\zeta}{g_{22}^o} (\beta_{\xi,\eta}^o - \frac{g_{22,\xi}^o}{g_{11}^o} \beta_\eta^o) \right] + \left[\frac{w_{,\xi}^o w_{,\eta}^o}{g_{11}^o g_{22}^o} + \frac{u^o v^o}{R_1 R_2} - \frac{u^o w_{,\eta}^o}{R_1 g_{22}^o} - \frac{v^o w_{,\xi}^o}{R_2 g_{11}^o} \right] \\
S_4^o &= \beta_\eta^o + \frac{w_{,\eta}^o}{g_{22}^o} - \frac{v^o}{R_2} \\
S_5^o &= \beta_\xi^o + \frac{w_{,\xi}^o}{g_{11}^o} - \frac{u^o}{R_1}
\end{aligned}$$

$$\begin{aligned}
E_1(\xi, \eta, \zeta, t) &= \sum_{m=1}^N -\frac{1}{g_{11}^o} (\Phi_{,\xi}^{m+1}(\xi, \eta) \Psi^{m+1}(\zeta) + \Phi_{,\xi}^m(\xi, \eta) \Psi^m(\zeta)) \\
E_2(\xi, \eta, \zeta, t) &= \sum_{m=1}^N -\frac{1}{g_{22}^o} (\Phi_{,\eta}^{m+1}(\xi, \eta) \Psi^{m+1}(\zeta) + \Phi_{,\eta}^m(\xi, \eta) \Psi^m(\zeta)) \\
E_3(\xi, \eta, \zeta, t) &= \sum_{m=1}^N -(\Phi^{m+1}(\xi, \eta) - \Phi^m(\xi, \eta)) / h_m
\end{aligned} \tag{2}$$

where in Eqs. (2) the in-plane strains consist of both linear and nonlinear strains while the out of plane strains consist only of linear terms; $h_m = \zeta_{m+1} - \zeta_m$ is the thickness of the layer within a piezoelectric layer, Φ^{m+1} and Φ^m denote the electric potentials at the corresponding thickness points, respectively. Using the divergence theorem, neglecting both the inertia effects and the free body charge density, and integrating through the piezolaminate thickness, the stress equilibrium and electric charge conservation can be obtained over the whole piezolaminated medium by the following variational form:

$$\begin{aligned}
\delta \mathbf{u}^T \Psi_u &= - \int_V \delta \mathbf{S}^T \boldsymbol{\sigma} dV + \int_V \delta \mathbf{u}^T \mathbf{b} dV + \int_{\Gamma_r} \delta \mathbf{u}^T \bar{\boldsymbol{\tau}} d\Gamma \quad \rightarrow = 0 \quad \text{at equilibrium} \\
\delta \boldsymbol{\phi}^T \Psi_e &= - \int_V \delta \mathbf{E}^T \mathbf{D} dV + \int_{\Gamma_q} \delta \boldsymbol{\phi}^T \bar{q} d\Gamma \quad \rightarrow = 0 \quad \text{at equilibrium}
\end{aligned} \tag{3}$$

The focus in this work is placed on the second equation of Eqs. (3), which describes the balance of electric charge in the piezoelectric elements. The vectors Ψ_u , Ψ_e represent generalized

imbalances between internal and external multifield forces and electric charges, respectively, which both vanish at equilibrium; $\bar{\tau}, \bar{q}$ are the applied surface tractions and electric charges on the bounding surfaces Γ_τ and Γ_q , respectively; b are the body forces over the volume V . Substituting Eqs. (1)-(2) into Eqs. (3) and making substantial calculations the individual electromechanical terms of the coupled system are derived [6].

3 COUPLED NONLINEAR SHELL FINITE ELEMENT

3.1 Discrete Generalized Equations of Motion

An eight-node coupled shell finite element, encompassing the previous generalized coupled mechanics was developed, in order to yield the discrete coupled nonlinear equations. The electromechanical state variables are approximated by the nodal values on the reference surface A_o with local interpolation functions:

$$\begin{aligned} \{u^o, v^o, w^o, \beta_\xi^o, \beta_\eta^o\}(\xi, \eta, t) &= \sum_{i=1}^W \{u^{oi}, v^{oi}, w^{oi}, \beta_\xi^{oi}, \beta_\eta^{oi}\}(t) P^i(\xi, \eta) \\ \{\varphi^m\}(\xi, \eta, t) &= \sum_{i=1}^W \{\varphi^{mi}\}(t) P^i(\xi, \eta), \quad m = 1, \dots, N \end{aligned} \quad (4)$$

where W is the number of element nodes; P denotes C_o continuous shape functions. Combining Eqs. (1)-(2) with Eq. (4) and substituting into Eqs. (3), after collecting the common elastic and electric nodal terms, the coupled system of nonlinear equations is finally derived:

$$\begin{aligned} \Psi_u(u, \varphi) &= [K_{uu}(u)]\mathbf{u} + [K_{ue}(u)]\boldsymbol{\varphi}^A + [K_{ue}(u)]\boldsymbol{\varphi}^S - \mathbf{F} \rightarrow = 0 \quad \text{at equilibrium} \\ \Psi_e(u, \varphi) &= [K_{eu}(u)]\mathbf{u} + [K_{ee}(u)]\boldsymbol{\varphi}^A + [K_{ee}(u)]\boldsymbol{\varphi}^S - \mathbf{Q} \rightarrow = 0 \quad \text{at equilibrium} \end{aligned} \quad (5)$$

where $\mathbf{u}(u, v, w, \beta_\xi, \beta_\eta)$ is the nodal displacement vector; $\boldsymbol{\varphi}^A$ is the applied nodal electric potential at actuators and $\boldsymbol{\varphi}^S$ is the free nodal electric potential at sensors. K_{uu} is the actual stiffness matrix including linear and nonlinear (dependence on \mathbf{u}) terms, K_{ue} , K_{eu} are the actual piezoelectric matrices including linear and nonlinear (dependence on \mathbf{u}) terms; K_{ee} is the actual electric permittivity matrix including only linear terms:

$$\begin{aligned} [K_{uu}(u)] &= [K_{uu}^o] + [K_{uu}^L] = [K_{uu}^o] + [P_1(u)]/2 + [P_2(u^2)]/3 \\ [K_{ue}(u)] &= [K_{ue}^o] + [K_{ue}^L] = [K_{ue}^o] + [P_3(u)] \\ [K_{eu}(u)] &= [K_{eu}^o] + [K_{eu}^L] = [K_{eu}^o] + [P_4(u)]/2 \\ [K_{ee}] &= [K_{ee}^o] \end{aligned} \quad (6)$$

In the first of Eqs. (5), the piezoelectric matrix $K_{ue}(u)$ multiplying by the electric potential vector $\boldsymbol{\varphi}^A$ represents the piezoelectric force (consisting of both linear and nonlinear terms) imposed on the laminate additionally to external mechanical forces \mathbf{F} ; in the second of Eqs. (5) the piezoelectric matrix $K_{eu}(u)$ multiplying by the displacement vector \mathbf{u} represents the electric

charge (consisting both of linear and nonlinear terms) generated at piezoelectric electrodes, additionally to external applied electric charge \mathbf{Q} , given by the following form:

$$\mathbf{Q}_{Gen} = [\mathbf{K}_{eu}] \mathbf{u} \quad (7)$$

Combining Eqs. (5)-(6), the following expressions for the elastic strain energy (ES), piezoelectric energy (PE), for both mechanical force equilibrium and electrical charge conservation, and stored electric energy (EE), over the whole volume of the piezoelectric laminate, are derived:

$$\begin{aligned} H_{ES} &= \frac{1}{2} \left\{ \mathbf{u}^T \right\} [\mathbf{K}_{uu}^o] \left\{ \mathbf{u} \right\} + \left(\frac{1}{2} \left\{ \mathbf{u}^T \right\} ([P_1(u)]/2 + [P_2(u^2)]/3) \left\{ \mathbf{u} \right\} \right) \\ H_{PE}^{mechanical_equilibrium} &= \frac{1}{2} \left\{ \mathbf{u}^T \right\} [\mathbf{K}_{ue}^o] \left\{ \boldsymbol{\varphi}^A \right\} + \frac{1}{2} \left\{ \mathbf{u}^T \right\} [P_3(u)] \left\{ \boldsymbol{\varphi}^A \right\} \\ H_{PE}^{electrical_equilibrium} &= \frac{1}{2} \left\{ \boldsymbol{\varphi}^{S^T} \right\} [\mathbf{K}_{eu}^o] \left\{ \mathbf{u} \right\} + \frac{1}{2} \left\{ \boldsymbol{\varphi}^{S^T} \right\} ([P_4(u)]/2) \left\{ \mathbf{u} \right\} \\ H_{EE} &= \frac{1}{2} \left\{ \boldsymbol{\varphi}^{S^T} \right\} [\mathbf{K}_{ee}^o] \left\{ \boldsymbol{\varphi}^S \right\} \end{aligned} \quad (8)$$

where in the above energy expressions the first and second RHS terms denote linear and nonlinear energy components, respectively. It must be also noticed that in case of open electric circuit conditions all the generated piezoelectric energy is converted and stored as electric energy into the piezoelectric sensor films.

3.2 Solution Scheme for Coupled Nonlinear Equations

In order to solve the coupled nonlinear Eqs. (5), the Cylindrical Arc Length method (CAL) is extended to enable the simultaneous solution for the mechanical force and electric charge imbalance equations, capturing eventually both the stable and unstable trajectory paths. The applied external loads may include combinations of mechanical loads (concentrated force or pressure) and applied electric potentials at actuators. The Newton-Raphson iterative technique is also adopted and combined with the CAL method such that the coupled nonlinear equations linearized and iteratively solved, until the electromechanical equilibrium $\boldsymbol{\Psi}_u = \boldsymbol{\Psi}_e = 0$. The coupled nonlinear system for the i^{th} iteration can be described more analytically below:

$$\begin{aligned} \boldsymbol{\Psi}_u^i(u^i, \boldsymbol{\varphi}^i, \lambda^i) &= [\mathbf{K}_{uu}(u^i)] \mathbf{u}^i + [\mathbf{K}_{ue}(u^i)] \boldsymbol{\varphi}^{S^i} + [\mathbf{K}_{ue}(u^i)] \boldsymbol{\varphi}^{A^i} - \lambda^i \mathbf{F}^i \\ \boldsymbol{\Psi}_e^i(u^i, \boldsymbol{\varphi}^i, \lambda^i) &= [\mathbf{K}_{eu}(u^i)] \mathbf{u}^i + [\mathbf{K}_{ee}] \boldsymbol{\varphi}^{S^i} - \mathbf{Q}^i \end{aligned} \quad (9)$$

where, λ is the mechanical (force or pressure) loading multiplier. In effort to achieve the convergent solution point ($\boldsymbol{\Psi}_u = \boldsymbol{\Psi}_e = 0$) the imbalance force and charge vectors are written for the next iteration ($i+1$) using the Taylor series expansion (considering only sensory voltage variation i.e $\delta \boldsymbol{\varphi} = \delta \boldsymbol{\varphi}^S$ and $\delta \boldsymbol{\varphi}^A = 0$ and keeping only the first derivative:

$$\begin{aligned}\Psi_u^{i+1}(u^{i+1}, \varphi^{i+1}, \lambda^{i+1}) &= \Psi_u^i(u^i, \varphi^i, \lambda^i) + \frac{\partial \Psi_u^i}{\partial u^i} \delta u^{i+1} + \frac{\partial \Psi_u^i}{\partial \varphi^{S^i}} \delta \varphi^{S^{i+1}} + \frac{\partial \Psi_u^i}{\partial \lambda^i} \delta \lambda^{i+1} = 0 \\ \Psi_e^{i+1}(u^{i+1}, \varphi^{i+1}, \lambda^{i+1}) &= \Psi_e^i(u^i, \varphi^i, \lambda^i) + \frac{\partial \Psi_e^i}{\partial u^i} \delta u^{i+1} + \frac{\partial \Psi_e^i}{\partial \varphi^{S^i}} \delta \varphi^{S^{i+1}} + \frac{\partial \Psi_e^i}{\partial \lambda^i} \delta \lambda^{i+1} = 0\end{aligned}\quad (10)$$

Substituting Eqs. (9) into Eqs. (10) and making the extended derivatives, substantial calculations and collecting the common elastic and electric nodal terms the coupled linearized system of equations is derived:

$$\begin{aligned}[\bar{K}_{uu}(u^i)]\delta u^{i+1} + [\bar{K}_{ue}(u^i)]\delta \varphi^{S^{i+1}} &= -\Psi_u(u^i, \varphi^i, \lambda^i) - \delta \lambda^{i+1} F \\ [\bar{K}_{eu}(u^i)]\delta u^{i+1} + [\bar{K}_{ee}] \delta \varphi^{S^{i+1}} &= -\Psi_e(u^i, \varphi^i, \lambda^i)\end{aligned}\quad (11)$$

where $\bar{K}_{uu}, \bar{K}_{ue}, \bar{K}_{eu}, \bar{K}_{ee}$ are the tangential stiffness, piezoelectric, piezoelectric and electric permittivity matrices respectively, associated directly with the actual matrices [6]. The Eqs. (11) includes three unknown variables $\delta u^{i+1}, \delta \varphi^{S^{i+1}}, \delta \lambda^{i+1}$ and are combined with a third additional equation known as *Cylindrical Arc-Length equation* described as:

$$\Delta u^{i+1T} \Delta u^{i+1} = \Delta u^{iT} \Delta u^i = \Delta l^2 \quad (12)$$

where the quantity Δu express incremental displacement vector; Δl is the radius of the specified norm, which is calculated from an initial incremental load value $\Delta \lambda^0$ [9]. The cumulative (u, λ) and incremental $(\Delta u, \Delta \lambda)$ quantities are updated at each iteration by the following expressions:

$$\begin{aligned}\lambda^{i+1} &= \lambda^i + \delta \lambda^{i+1} \quad , \quad \Delta \lambda^{i+1} = \Delta \lambda^i + \delta \lambda^{i+1} \\ u^{i+1} &= u^i + \delta u^{i+1} \quad , \quad \Delta u^{i+1} = \Delta u^i + \delta u^{i+1}\end{aligned}\quad (13)$$

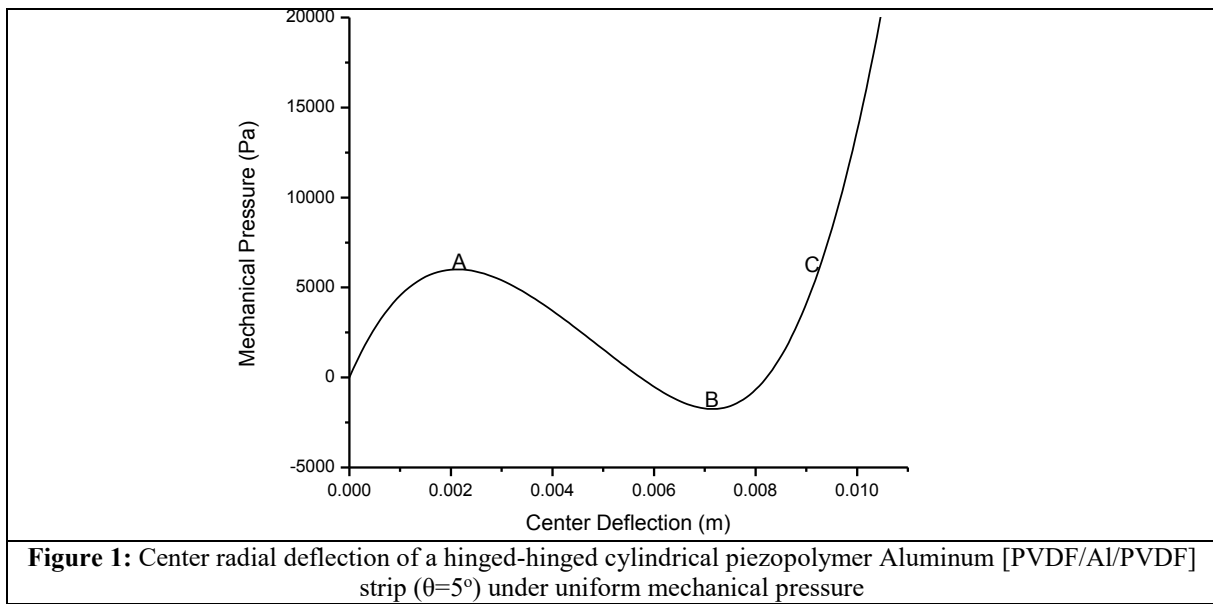
The sensory electric potential is updated at each iteration by the following form:

$$\varphi^{S^{i+1}} = \varphi^{S^i} + \delta \varphi^{S^{i+1}} \quad (14)$$

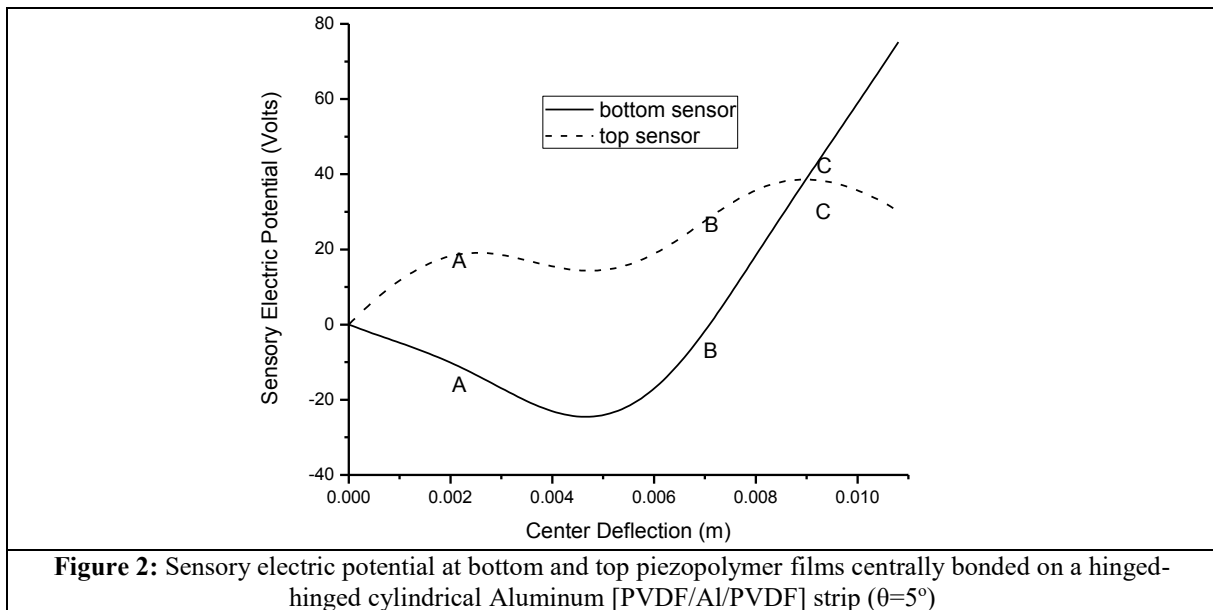
4 NUMERICAL RESULTS

4.1 Electromechanical Response of Low-Curvature Cylindrical Aluminum [p/Al/p] Strip

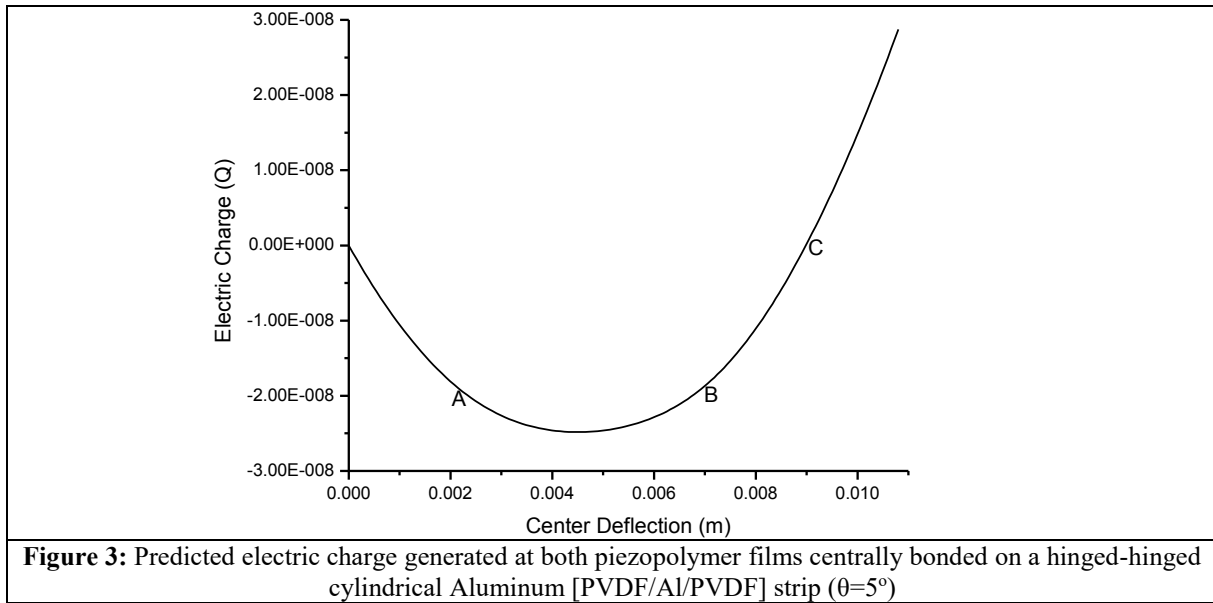
The nonlinear electromechanical response of a hinged-hinged cylindrical ($\theta=5^\circ$) Aluminum [PVDF/Al/PVDF] strip, centrally covered with a pair of piezopolymer film sensors, each attached on the upper and lower surface was analyzed. The hoop length of the core and the piezopolymer film were $L_\xi=400\text{mm}$ and $L_{p\xi}=50\text{mm}$ respectively, while the widths were equal to $L_\eta=L_{p\eta}=20\text{mm}$. The Aluminum and piezopolymer layer thicknesses were $h_{Al}=3\text{mm}$ and $h_p=0.1\text{mm}$, respectively. An increasing lateral uniform mechanical pressure was applied at the outer surface of the strip, with direction towards the center of curvature. The inner terminals of each film were assumed to be grounded while the outer remained free. Fig. 1 shows the predicted radial center deflection of the strip versus the applied pressure. Initially, mechanical



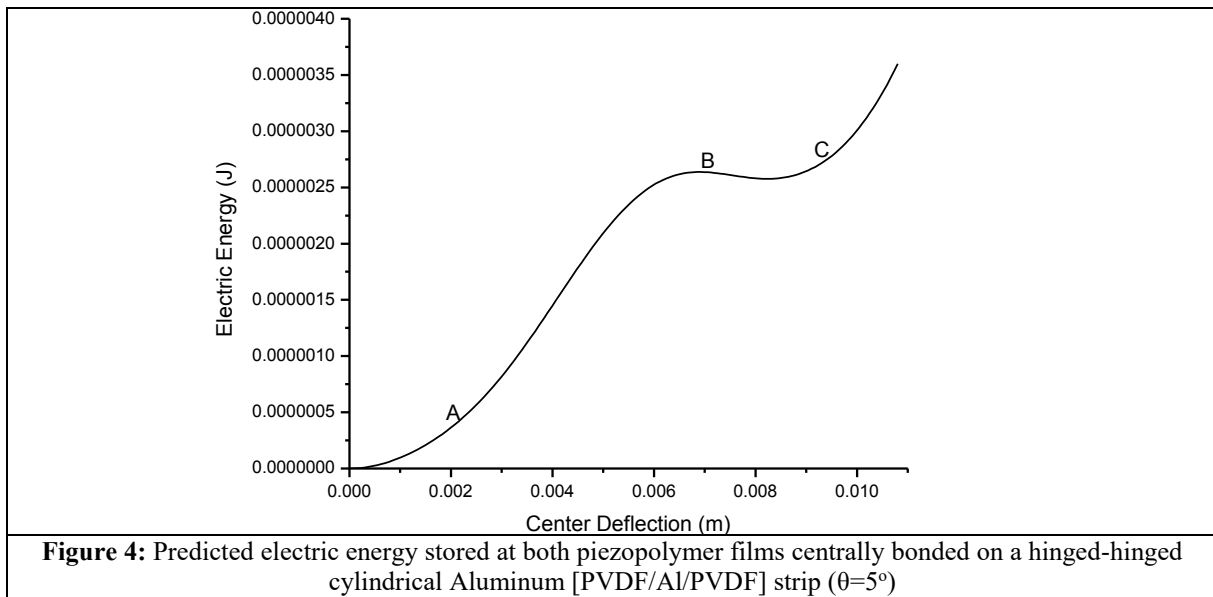
compressive membrane stresses are induced on the strip resulting in a reduction on the flexural stiffness, due to membrane- flexural stiffness coupling, until the limit point A is reached where the tangential stiffness vanishes. Beyond the point A the strip enters into an unstable path AB



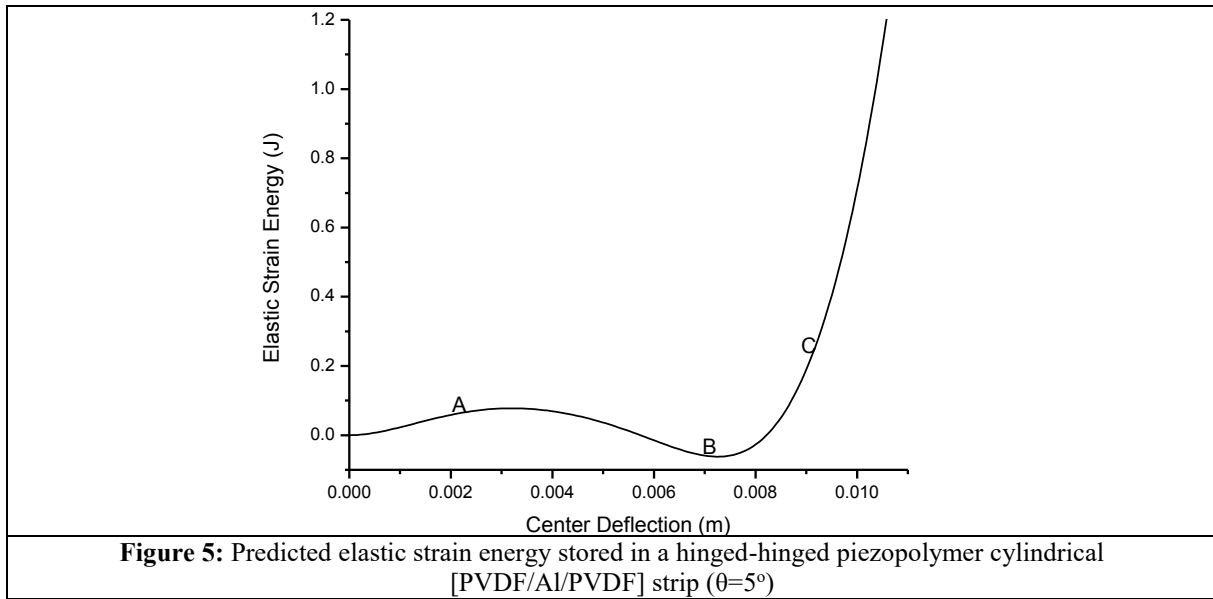
which is accompanied by a “negative” tangential stiffness, and finally reaches a second equilibrium stable state starting at inflection point B. After this point, the radial deflection has been increased enough such as to activate the membrane stiffening effects and transition of the shell to second stable path. Fig. 2 shows the predicted electric potential in the bottom and top piezofilms versus the center deflection. Initially, the two signals are increased until the point A receiving opposite polarity due to induced compressive membrane stresses, while beyond A the



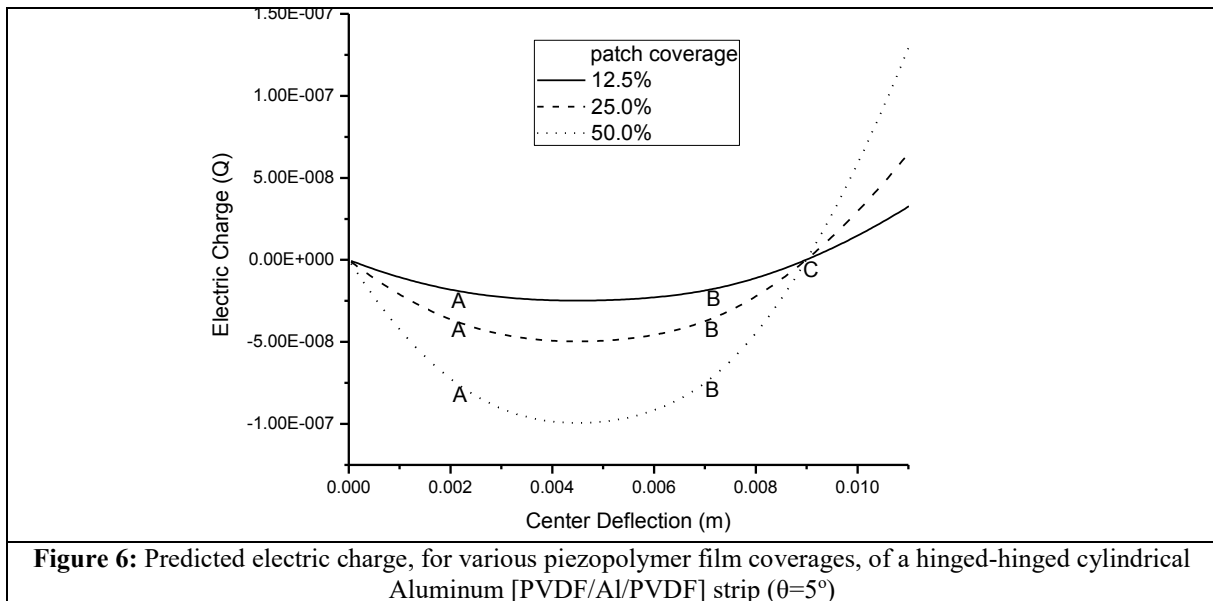
two signals behave highly nonlinearly and tend to converge in the same value due to dominant bending stresses as the strip enters into the new stable path BC. Finally, the two electric signals are distinguished again beyond the point C due to large membrane stiffening effects. Fig. 3 shows the predicted electric charge generated in both of films versus the deflection, which is initially increased until a maximum value and following an opposite path is reduced until point



C, where beyond that point is increased again accompanied by a conversion of polarity. The predicted electric energy stored in both of piezofilms is shown in Fig. 4, where is monotonically increased passing from an inflection point B, due to redistribution of stresses during the stable-unstable-stable trajectory paths. Fig.5 illustrates the elastic strain energy stored in the whole piezolaminated strip which follows a similar trajectory path with the pressure-deflection curve



The switching from positive to-negative and again to positive values is due both to the redistribution of stresses and the electromechanical energy conversion takes place during the snap through instability.



Effect of piezopolymer film coverage on electromechanical response. Figs. (6)-(7) show the predicted electric charge and energy, respectively, for various piezofilm coverages, where both of two electric quantities are increased for piezofilm coverage enhancement, due to higher electromechanical conversion of distributed mechanical strains to electric potential along the shell circumferential. Both the predicted electric charge and stored electric energy are efficiently increased with the higher electromechanical conversion rate occurred during the unstable path.

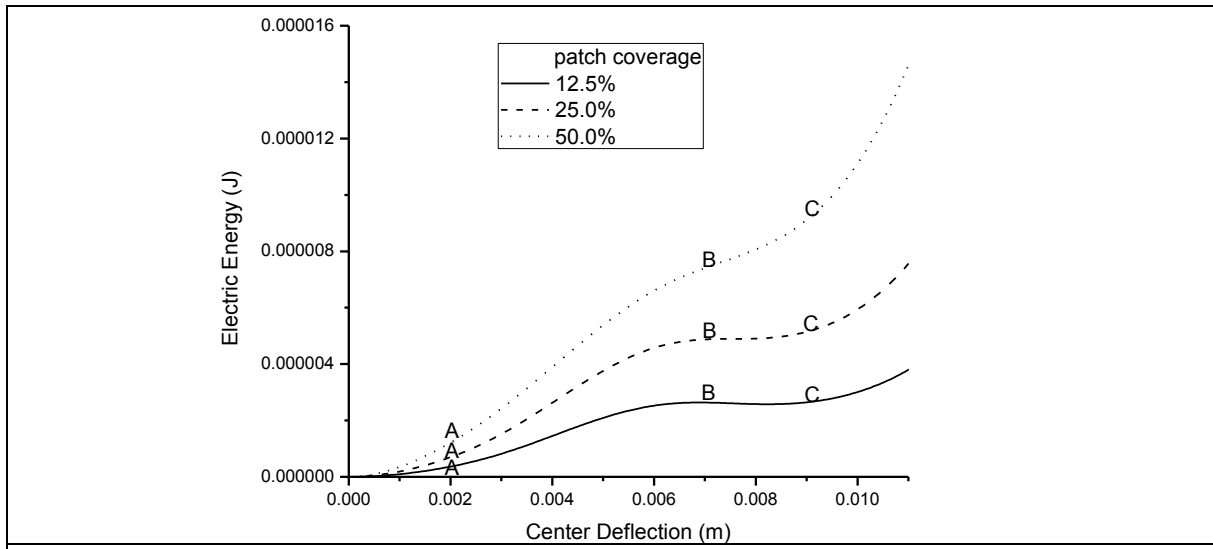


Figure 7: Predicted electric energy, for various piezopolymer film coverages, of a hinged-hinged cylindrical Aluminum [PVDF/Al/PVDF] strip ($\theta=5^\circ$)

Effect of core thickness on electromechanical response. Figs. (8)-(9) illustrate the predicted electric charge and energy, respectively, for various core thicknesses. The thicker shell snaps under higher pressure values (following the trajectory path ABC for both of two graphs) due to higher membrane-flexural stiffness coupling and eventually higher amount of potential energy

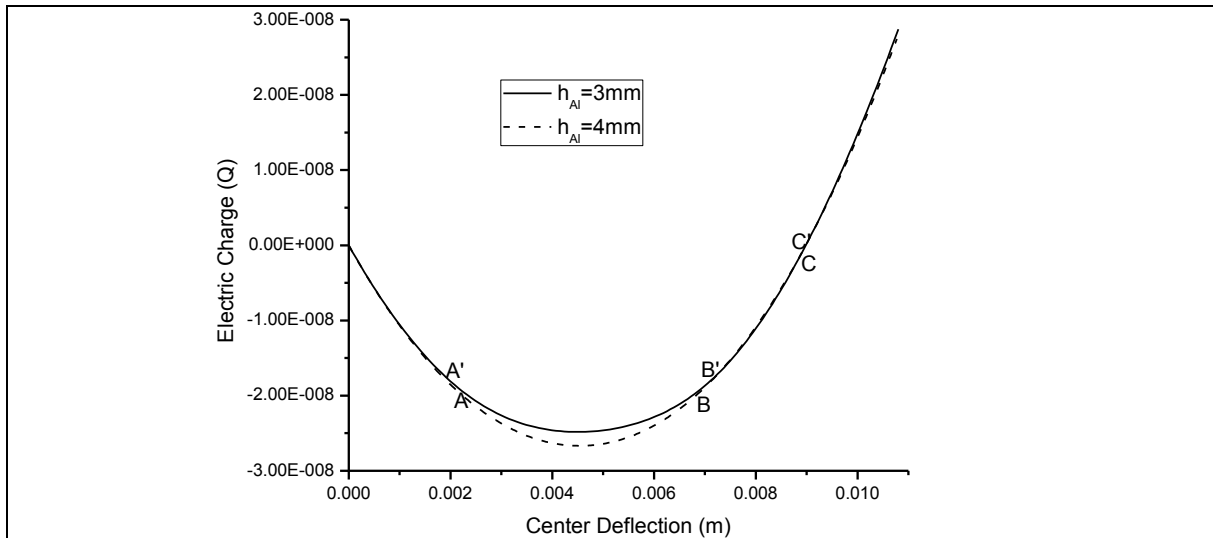
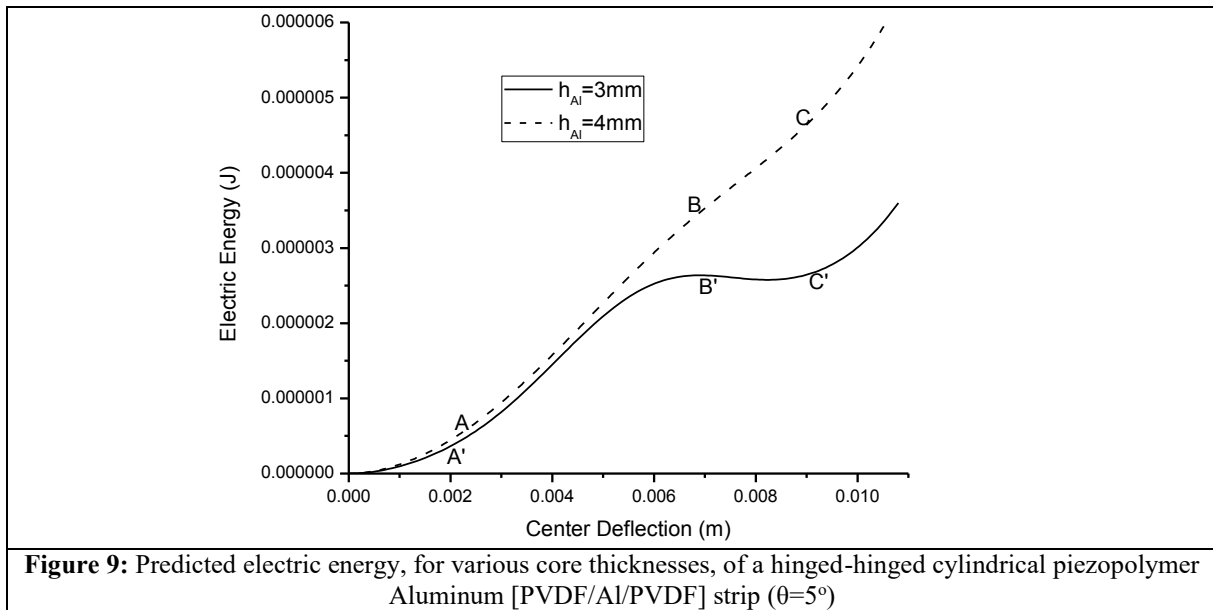


Figure 8: Predicted electric charge, for various core thicknesses, of a hinged-hinged cylindrical piezopolymer Aluminum [PVDF/Al/PVDF] strip ($\theta=5^\circ$)

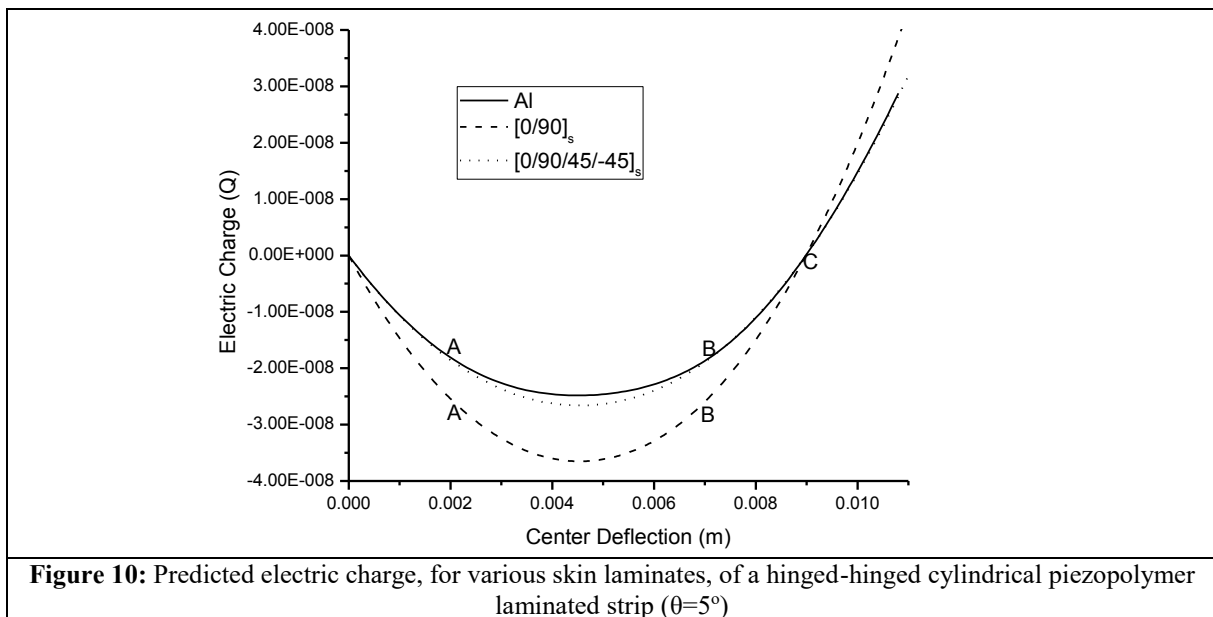
is converted both to stored electric and strain energy. Instead of the above, the electric charge is weakly depended on the thickness enhancement.

Effect of skin lamination on electromechanical response. The predicted electric charge and energy, for various skin laminates, are shown in Figs. (10)-(11), respectively. The higher

electromechanical conversion efficiency is corresponding to composite laminates due to their higher membrane-flexural stiffness coupling with the cross ply laminate being more proper, as



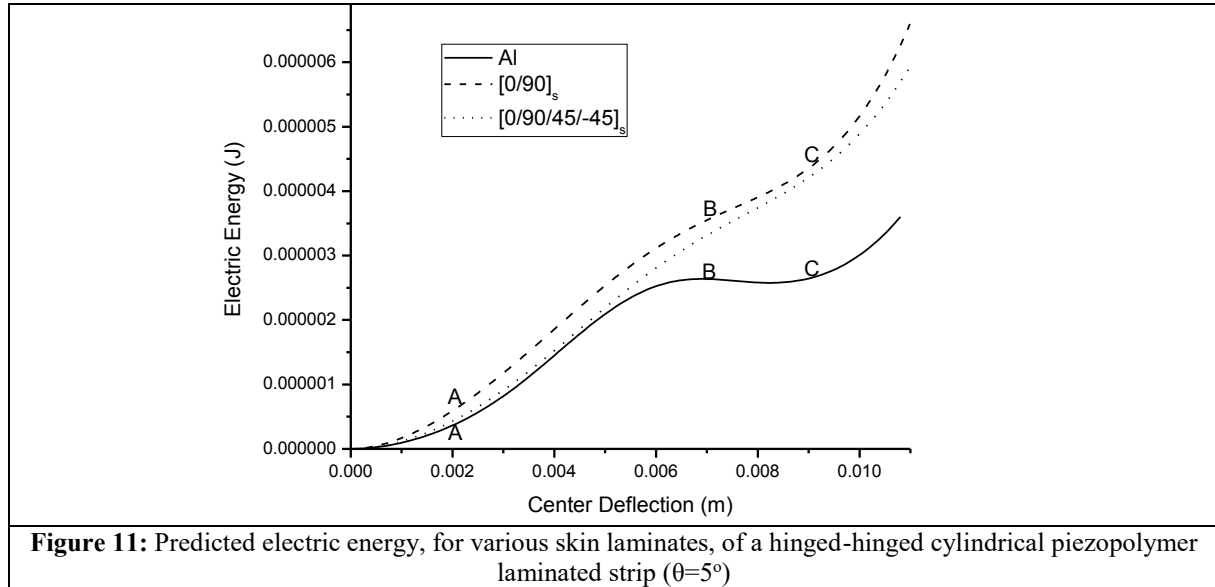
it snaps under larger pressure values. are converted to electric than elastic energy.



5 CONCLUSIONS

A computational framework based on coupled nonlinear mechanics was presented to predict the nonlinear electromechanical response of shallow cylindrical shells with attached piezopolymer films, undergoing to snap through instability under mechanical loads. The results illustrated the highly nonlinear sensor signal prediction in both of stable and unstable regions.

- The feasibility of smart shells to detect the onset of snap through instability, via the monitoring of sensory voltages is represented.
- The electromechanical energy conversion efficiency through the snap through buckling instability is quantified and the influence of thickness, laminate configuration and piezofilm coverage is finally investigated.



REFERENES

- [1] Schultz, M.R. and Hyer, M.W. Snap-through of unsymmetric cross ply laminates using piezoceramic actuators. *J. Intell. Mater. Syst. Struct* (2003) **14**:795-814.
- [2] Schultz, M.R., Hyer, M.W., Williams, R.B., Wilkie, W.K. and Inman, D.J. Snap-through of unsymmetric laminates using piezocomposite actuators. *Compos. Sci. Technol* (2006) **66**:2442-2448.
- [3] Arrieta, A.F., Bilgen, O., Friswell, M.I. and Hagedorn, P. Dynamic control for morphing of bi-stable composites. *J. Intell. Mater. Syst. Struct* (2013) **24**:266-273.
- [4] Varelis, D. and Saravanos, D.A. Coupled mechanics and finite element for nonlinear laminated piezoelectric shallow shells undergoing large displacements and rotations. *Int. J. Numer. Methods. Eng* (2006) **66**:1211-1233.
- [5] Oh, I.K. Piezoelectric suppression of thermoelastic snap-through in active piezolaminated curved shells. *Smart. Mater. Struct* (2006) **15**:1616-1626.
- [6] Varelis, D. and Saravanos, D.A. Nonlinear coupled multi-field mechanics and finite element for active multi-stable piezoelectric shells. *Int. J. Numer. Methods. Eng* (2008) **76**:84-107.
- [7] Kundu, C.K., Maiti, D.K. and Singha, P.K. Post buckling analysis of smart laminated doubly curved shells. *Comp. Struct* (2007) **81**:314-322.
- [8] Bisegna, P., Caruso, G., Caselli, F. and Nodargi, N. A corotational triangular facet shell element for geometrically nonlinear analysis of thin piezoactuated structures. *Comp. Struct* (2017) **172**:267-281.
- [9] Palazotto, A.N. and Dennis, S.T. *Nonlinear analysis of shell structures*. AIAA Education Series, (1992).

PARAMETER-FREE OPTIMIZATION OF MATERIAL ORIENTATION FOR HIGH PERFORMANCE COMPOSITE SHELL STRUCTURES

M. SHIMODA^{*} AND Y. MURAMATSU[†]

^{*} Department of Advanced Science and Technology
Toyota Technological Institute
2-12-1 Hisakata, Tenpaku-ku, Nagoya 468-8511, Japan
e-mail: shimoda@toyota-ti.ac.jp

[†] Graduate School of Engineering, Advanced Science and Technology
Toyota Technological Institute
2-12-1 Hisakata, Tenpaku-ku, Nagoya 468-8511, Japan

Key words: Fiber-reinforced Plastics, Composite Material, Material Orientation, Parameter-free Optimization, Shell Structures, Variational Method, H^1 Gradient Method.

Abstract. In this study, we present an approach for the optimum material-orientation design of a laminated composite shell structure using the parameter-free optimization method. It is assumed that the fiber in a structure consisting of orthotropic materials can be arbitrarily oriented layer by layer, and the each optimum free-orientation is determined. We introduce the square displacement error norm between the thermal displacements on specified points and their target values as an objective functional, and minimize it under the equilibrium equation constraint. This makes it possible to tailor the deformation of a composite shell. The optimum design problem is formulated as a distributed-parameter optimization problem, and the sensitivity function is derived based on the variational method. The optimum orientation variation is determined by the H^1 gradient method with Poisson's equation, a parameter-free optimization method. This approach makes it simultaneously possible both to reduce the objective functional and to maintain the smooth material orientation of this large scale optimization problem. The design example shows the effectiveness of the proposed approach for tailoring the deformation of a laminated composite shell structure, or for designing a high-performance laminated composite shell structure with the optimum material orientation.

1 INTRODUCTION

Laminated composite shell structures are used in a variety of industrial products, especially in vehicles for their lightweight design, where the usage of carbon-fiber-reinforced plastics (CFRP) in shell structures has been increasing, since they have higher specific mechanical performances compared to metals. Moreover, "Automated fiber placement (AFP)" has enabled the manufacture of curvilinear-distributed material orientation, which can pulled out their potential and improve the mechanical performances more sufficiently. Most of the proposed optimization methods for the curvilinear-distributed material orientation design consider maximizing the stiffness to an external force as their design objective. In the practical design of laminated shell structures, deformation tailoring, (or controlling the

displacements to the desired values) to external loading is needed to achieve high quality, and to maintain mechanical performances and functions required. We focus on thermal loading in this study, since most of the industrial products are exposed to severe temperature environments. Especially, laminated composite shell structures deform unusually due to the coupling and the cross-elasticity effects. It is extremely important for designers to avoid this problem, or to tailor the thermal deformation of the laminated composite shell structures.

The deformation tailoring was called “homology design” or “compliant mechanism design” in the previous papers. The concept of homology design was presented for the design of large radio telescopes by Hoerner [1], where the deformation of the structure was defined as homologous if a given geometrical relation holds for the deformation. Liu and Shimoda developed an optimization method to solve a shape identification problem of linear elastic free-form shells with the purpose of achieving a desired deformation under external forces [2]. However, studies on the homology design and the compliant mechanism are limited and not reported for laminated shell structures.

Focusing on material orientation optimization, many methods and their application techniques for plates or shells have been reported. The representative optimization methods are a sensitivity based gradient method [3], a direct material optimization method (DMO) [4], a normal distribution fiber optimization method (NDFO) [5] and genetic algorithm (GA) based methods [6]. The sensitivity based gradient approach has the advantage of solving large-scale structure optimization problems mechanically. However, it may cause multiple local minima including the unsmooth distributions, and it is highly dependent on the initial material orientation distribution. On the other hand, DMO and NDFO methods are ameliorations for simple-gradient methods, in which the element-based penalization coefficient is used to force the candidate orientations to only one candidate. These methods are categorized into a parametric method. The design variable parameterization is effective for reducing the design freedom, for reducing the risk of obtaining local minima and results in a lower computational cost; however, the obtained mechanical performance is limited since the optimal solution is highly dependent on the pre-defined parameters. GA is also expected to find some local minima and has the potential to provide the global minimum solution, where sensitivity analysis is unnecessary. On the other hand, the application of GA to practical structural problems is limited since Finite Element analyses of large-scale structures with a large number of design variables, especially with every element in every layer of a laminated shell results in a significant calculation cost problem. In addition, considering a parameter-free orientation design problem, or an enormous design degrees of freedom design problem, it is not easy to control their behaviours. Without a countermeasure, the ill-condition like the checkerboard problem of topology optimization or the jaggging problem of shape optimization may happen.

On the contrary, the authors proposed a parameter-free gradient-based material orientation optimization method, or the H^1 gradient method with Poisson’s equation, for compliance minimization problem [7], in which the optimal material distribution can be obtained without design variable parameterization such as the candidate material orientations or the polynomials to express the material distribution. In other words, the materials are varied freely over the entire region with enormous design degrees of freedom. The proposed method overcame the issues including the ill-condition risk aforementioned. The main advantages of the proposed method are that it can conventionally determine the smooth distribution of the

design variables and decrease the objective function simultaneously without design variable parameterization.

Under these backgrounds, we present an approach for the optimum material-orientation design using the H^1 gradient method with Poisson's equation for tailoring thermal displacements of laminated composite shell structures in this study. The approach is applied to a shell design example to confirm the effectiveness of the proposed approach.

2 FORMULATION OF MATERIAL ORIENTATION OPTIMIZATION PROBLEM

2.1 Governing equation for a laminated shell structure

As shown in Fig. 1, a laminated shell structure consists of N layers, and the i^{th} ply of a laminated shell structure has an initial design domain Ω_i , middle surface A_i with boundary ∂A_i , and thickness t_i . The bounded domain of each layer is composed of a set of infinitesimal flat surfaces dA_i . For simplicity, we assume that a laminated shell structure consists of N layers.

It is assumed that the mapping of the local coordinate system $(x_1, x_2, 0)$, which gives the position of the global mid-surface of the laminated shell structure, to the global coordinate system (X_1, X_2, X_3) is piecewise smooth. The Mindlin-Reissner plate theory is employed for plate bending. Using the sign convention on the small triangle domain $d\Omega_i (= dA_i \times t_i)$ in Fig. 1, the displacements of i^{th} ply expressed by the local coordinates $\mathbf{u}^{(i)} = \{u_k^{(i)}\}_{k=1,2,3}$ are considered by dividing them into the displacements in the in-plane direction $\{u_\alpha^{(i)}\}_{\alpha=1,2}$ and the displacements in the out-of-plane direction $u_3^{(i)}$, shown as

$$u_\alpha^{(i)}(x_1^{(i)}, x_2^{(i)}, x_3^{(i)}) \equiv u_{0\alpha}^{(i)}(x_1^{(i)}, x_2^{(i)}) - x_3^{(i)} \theta_\alpha^{(i)}(x_1^{(i)}, x_2^{(i)}), \quad (1)$$

$$u_3^{(i)}(x_1^{(i)}, x_2^{(i)}, x_3^{(i)}) \equiv w^{(i)}(x_1^{(i)}, x_2^{(i)}), \quad (2)$$

where $\{u_{0\alpha}^{(i)}\}_{\alpha=1,2}$, $w^{(i)}$ and $\{\theta_\alpha^{(i)}\}_{\alpha=1,2}$ express in-plane displacement, out-of-plane displacement and rotational angles of the mid-area of the i^{th} ply of the laminated shell structure,

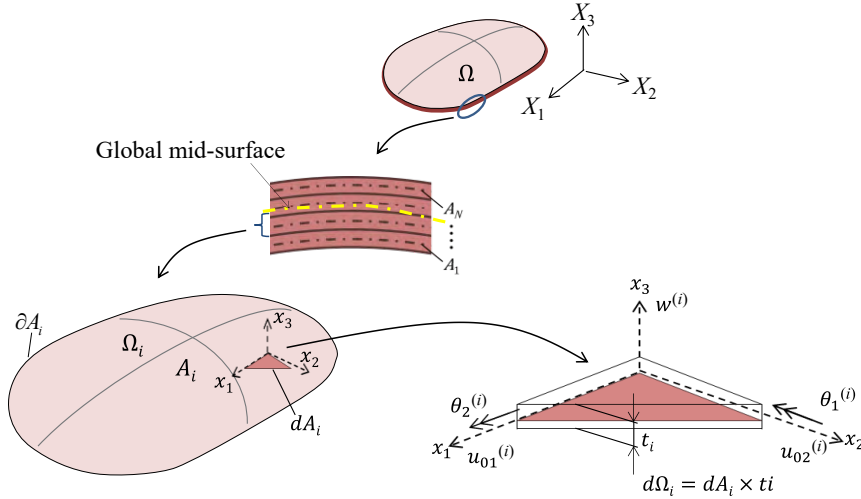


Figure 1: Laminated shell with N layers as a set of infinitesimal flat surfaces.

respectively. Then, the weak form state equation with respect to $\mathbf{u}^{(i)} = (\mathbf{u}_0^{(i)}, w^{(i)}, \boldsymbol{\theta}^{(i)})$, ($i = 1, \dots, N$) can be expressed as Eq. (3) by substituting Eq. (4) and (5) into the variational equation of the three-dimensional linear elastic body, considering $\sigma_{33}^{(i)} = 0$ and eliminating $\varepsilon_{33}^{(i)}$.

$$a\left((\mathbf{u}^{(1)}, \mathbf{u}^{(2)}, \dots, \mathbf{u}^{(N)}), (\bar{\mathbf{u}}^{(1)}, \bar{\mathbf{u}}^{(2)}, \dots, \bar{\mathbf{u}}^{(N)})\right) = l(\bar{\mathbf{u}}^{(1)}, \bar{\mathbf{u}}^{(2)}, \dots, \bar{\mathbf{u}}^{(N)}), \forall (\bar{\mathbf{u}}^{(1)}, \bar{\mathbf{u}}^{(2)}, \dots, \bar{\mathbf{u}}^{(N)}) \in \bar{U}, \quad (3)$$

$$\mathbf{u}^{(i)} = (\mathbf{u}_0^{(i)}, w^{(i)}, \boldsymbol{\theta}^{(i)}) \in U \quad (i = 1, \dots, N)$$

where $\mathbf{u}^{(i)} = [\mathbf{u}_0^{(i)}, w^{(i)}, \boldsymbol{\theta}^{(i)}]^T$, and $(\bar{\bullet})$ expresses a variation. In addition, the bilinear form $a(\cdot, \cdot)$ and linear form $l(\cdot)$ for the state variables $(\mathbf{u}_0, w, \boldsymbol{\theta})$ are respectively defined as

$$a\left((\mathbf{u}^{(1)}, \mathbf{u}^{(2)}, \dots, \mathbf{u}^{(N)}), (\bar{\mathbf{u}}^{(1)}, \bar{\mathbf{u}}^{(2)}, \dots, \bar{\mathbf{u}}^{(N)})\right) \quad (4)$$

$$\begin{aligned} &= \sum_{i=1}^N \int_{A_i} \left\{ \left\{ \boldsymbol{\kappa}^{(i)T}(\boldsymbol{\theta}) - \boldsymbol{\alpha}^T \frac{T_g^{(i)}}{t_i} \right\} \mathbf{E}^{B(i)} \bar{\boldsymbol{\kappa}}^{(i)}(\bar{\boldsymbol{\theta}}) + \left\{ \boldsymbol{\varepsilon}_0^{(i)T}(\mathbf{u}_0) - \boldsymbol{\alpha}^T T_m^{(i)} \right\} (\mathbf{u}_0) \mathbf{E}^{M(i)} \bar{\boldsymbol{\varepsilon}}_0^{(i)}(\bar{\mathbf{u}}_0) \right. \\ &\quad + \left\{ \boldsymbol{\kappa}^{(i)T}(\boldsymbol{\theta}) - \boldsymbol{\alpha}^T \frac{T_g^{(i)}}{t_i} \right\} \mathbf{E}^{C(i)} \bar{\boldsymbol{\varepsilon}}_0^{(i)}(\bar{\mathbf{u}}_0) + \bar{\boldsymbol{\kappa}}^{(i)T}(\bar{\boldsymbol{\theta}}) \mathbf{E}^{C(i)} \left\{ \boldsymbol{\varepsilon}_0^{(i)}(\mathbf{u}_0) - \boldsymbol{\alpha} T_m^{(i)} \right\} \\ &\quad + \left\{ \boldsymbol{\varepsilon}_0^{(i)T}(\mathbf{u}_0) - \boldsymbol{\alpha}^T T_m^{(i)} \right\} \mathbf{E}^{C(i)} \bar{\boldsymbol{\kappa}}^{(i)}(\bar{\boldsymbol{\theta}}) + \bar{\boldsymbol{\varepsilon}}_0^{(i)T}(\bar{\mathbf{u}}_0) \mathbf{E}^{C(i)} \left\{ \boldsymbol{\kappa}^{(i)}(\boldsymbol{\theta}) - \boldsymbol{\alpha} \frac{T_g^{(i)}}{t_i} \right\} \\ &\quad \left. + \boldsymbol{\gamma}^{(i)T}(w, \boldsymbol{\theta}) \mathbf{E}^{S(i)} \bar{\boldsymbol{\gamma}}^{(i)}(\bar{w}, \bar{\boldsymbol{\theta}}) \right\} dA_i, \end{aligned}$$

$$l(\bar{\mathbf{u}}^{(1)}, \bar{\mathbf{u}}^{(2)}, \dots, \bar{\mathbf{u}}^{(N)}) \quad (5)$$

$$= \sum_{i=1}^N \left[\int_{A_i} \left(\mathbf{f}^T \bar{\mathbf{u}}_0^{(i)} - \mathbf{m}^T \bar{\boldsymbol{\theta}}^{(i)} + q \bar{w}^{(i)} \right) dA_i + \int_{\partial A_i} \left(\mathbf{N}^T \bar{\mathbf{u}}_0^{(i)} - \mathbf{M}^T \bar{\boldsymbol{\theta}}^{(i)} + Q \bar{w}^{(i)} \right) ds_i \right].$$

The external loadings with respect to the local coordinate system $(x_1, x_2, 0)$ are defined as \mathbf{f} , \mathbf{m} , q , \mathbf{N} , \mathbf{M} , and Q , which denote in-plane load, out-of-plane moment, out-plane load on the global middle surface, in-plane load, bending moment, and shearing force on the global sub-boundaries, respectively. The notations $\mathbf{E}^{B(i)}$, $\mathbf{E}^{M(i)}$, $\mathbf{E}^{C(i)}$ and $\mathbf{E}^{S(i)}$ express the orthotropic elastic matrices with respect to bending, membrane, coupling and shear component of the i^{th} ply, respectively. $\boldsymbol{\alpha} = \{\delta_{ij} \alpha_{ij}\}_{i,j=1,2}$, $T_m^{(i)}$ and $T_g^{(i)} / t_i$ indicate coefficients of thermal expansion, mean temperature difference and temperature gradient, respectively. Additionally, $\boldsymbol{\varepsilon}^{(i)} = \{\varepsilon_{\alpha\beta}\}_{\alpha,\beta=1,2}^{(i)}$, $\boldsymbol{\kappa}^{(i)} = \{\kappa_{\alpha\beta}\}_{\alpha,\beta=1,2}^{(i)}$, $\boldsymbol{\varepsilon}_0^{(i)} = \{\varepsilon_{0\alpha\beta}\}_{\alpha,\beta=1,2}^{(i)}$ and $\boldsymbol{\gamma}^{(i)} = \{\gamma_{\alpha 3}\}_{\alpha=1,2}^{(i)}$ express strain tensor, curvature tensor, in-plane strain tensor and transverse shear strain vector on the middle surface of the i^{th} ply, respectively; and they are defined by the following equations:

$$\varepsilon_{\alpha\beta}^{(i)} \equiv \frac{1}{2} (u_{\alpha,\beta}^{(i)} + u_{\beta,\alpha}^{(i)}), \quad (6)$$

$$u_{\alpha,\beta}^{(i)} = u_{0\alpha,\beta}^{(i)} - x_3^{(i)} \theta_{\alpha,\beta}^{(i)}, \quad (7)$$

$$\gamma_{\alpha}^{(i)} \equiv w_{,\alpha}^{(i)} - \theta_{\alpha}^{(i)}, \quad (8)$$

$$\kappa_{\alpha\beta}^{(i)} \equiv \frac{1}{2}(\theta_{\alpha,\beta}^{(i)} + \theta_{\beta,\alpha}^{(i)}), \quad (9)$$

$$\varepsilon_{0\alpha\beta}^{(i)} \equiv \frac{1}{2}(u_{0\alpha,\beta}^{(i)} + u_{0\beta,\alpha}^{(i)}). \quad (10)$$

The displacement continuity and the Cauchy stress vector between each layer are satisfied as

$$\mathbf{u}^{(i)bottom} = \mathbf{u}^{(i-1)top}, \quad (11)$$

$$\mathbf{n}^{(i)bottom} = -\mathbf{n}^{(i-1)top}, \quad \boldsymbol{\sigma}^{T(i)bottom} \mathbf{n}^{(i)bottom} = -\boldsymbol{\sigma}^{T(i-1)top} \mathbf{n}^{(i-1)top}, \quad (12)$$

where $(\cdot)^{(i)bottom}$ and $(\cdot)^{(i-1)top}$ indicate the value on the bottom surface of the i^{th} ply and the top surface of the $(i-1)^{th}$ ply, respectively. In addition, \mathbf{n} and $\boldsymbol{\sigma}$ are the unit outward normal vector and the Cauchy stress tensor, respectively. Note that, in this paper, the subscripts of the Greek letters are expressed as $\alpha=1,2$ and the tensor subscript notation uses Einsteins summation convention and a partial differential notation with respect to the spatial coordinates $(\cdot)_{,j} = \partial(\cdot)/\partial x_j$.

It will be also noted that U and \bar{U} in Eq. (3) are the spaces of the kinematically admissible displacements given by the following equations:

$$U = \left\{ \left(u_{01}^{(i)}, u_{02}^{(i)}, w^{(i)}, \theta_1^{(i)}, \theta_2^{(i)} \right) \in \left(H^1(A) \right)^5 \left| \begin{array}{l} \text{satisfying the constraint conditon appropriately on the} \\ \text{Dirichlet boundary} \end{array} \right. \right\}, \quad (13)$$

$$\bar{U} = \left\{ \left(\bar{u}_{01}^{(i)}, \bar{u}_{02}^{(i)}, \bar{w}^{(i)}, \bar{\theta}_1^{(i)}, \bar{\theta}_2^{(i)} \right) \in \left(H^1(A_i) \right)^5, (i=1, \dots, N) \left| \begin{array}{l} \bar{u}_{01}^{(i)} = \bar{u}_{02}^{(i)} = \bar{w}^{(i)} = \bar{\theta}_1^{(i)} = \bar{\theta}_2^{(i)} = 0 \\ \text{on each Dirichlet subboundary} \end{array} \right. \right\}, \quad (14)$$

where $H^1(=W^{1,2})$ is the Sobolev space of square integrable and differentiable of order 1.

2.2 Formulation of controlling problem of thermal or static deformation

We aim at tailoring the thermal displacements of a laminated shell structure to desired target values by optimizing the material orientations of every layer. Using the state equation as the constraint condition, and square displacement error norm between the displacements and the target values as the objective function to be minimized, a distributed-parameter optimization problem for determining the optimal distribution of the material orientation is formulated as

$$\text{Find} \quad \delta\varphi^{(i)}(\mathbf{x}) \quad (15)$$

$$\text{that minimizes} \quad d(\mathbf{u}^{(M)} - \hat{\mathbf{u}}^{(M)}, \mathbf{u}^{(M)} - \hat{\mathbf{u}}^{(M)}) \quad (16)$$

$$\text{subject to} \quad \text{Eq. (3)} \quad (17)$$

where $\delta\varphi^{(i)}(\mathbf{x}), (\mathbf{x} \in A_i)$ is the variation of the material orientation from its original material orientation function $\varphi^{(i)}(\mathbf{x})$ of $E_1^{(i)}$ on the i^{th} ply, and the updated material orientation function $\varphi_s^{(i)}(\mathbf{x})$ is described as $\varphi_s^{(i)}(\mathbf{x}) = \varphi^{(i)}(\mathbf{x}) + \delta\varphi^{(i)}(\mathbf{x})$ (shown in Fig. 2). $\mathbf{u}^{(M)}$ and $\hat{\mathbf{u}}^{(M)}$ indicate the actual displacement and the target displacement at the global mid-surface of laminated shell

structure, respectively. Eq. (16) shows the square displacement error norm between $\mathbf{u}^{(M)}$ and $\hat{\mathbf{u}}^{(M)}$.

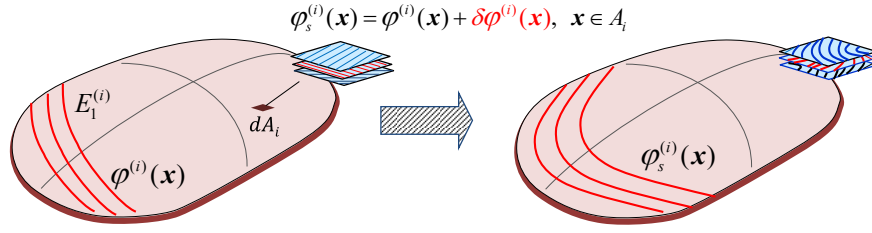


Figure 2: Variation of material orientation $E_1^{(i)}$ in orthotropic material of the i^{th} ply.

2.3 Derivation of sensitivity function

The Lagrange multiplier method is used to transform this constrained material orientation optimization problem to a non-constrained material orientation optimization problem. Letting $(\bar{\mathbf{u}}_0^{(i)}, \bar{\mathbf{w}}^{(i)}, \bar{\boldsymbol{\theta}}^{(i)})$ denote the Lagrange multiplier with respect to the strong-formed state equation, the Lagrange functional L associated with this problem is expressed as

$$L\left(\left(\mathbf{u}^{(1)}, \mathbf{u}^{(2)}, \dots, \mathbf{u}^{(N)}\right), \left(\bar{\mathbf{u}}^{(1)}, \bar{\mathbf{u}}^{(2)}, \dots, \bar{\mathbf{u}}^{(N)}\right)\right) = d(\mathbf{u}^{(M)} - \hat{\mathbf{u}}^{(M)}, \mathbf{u}^{(M)} - \hat{\mathbf{u}}^{(M)}) + l\left(\bar{\mathbf{u}}^{(1)}, \bar{\mathbf{u}}^{(2)}, \dots, \bar{\mathbf{u}}^{(N)}\right) - a\left(\left(\mathbf{u}^{(1)}, \mathbf{u}^{(2)}, \dots, \mathbf{u}^{(N)}\right), \left(\bar{\mathbf{u}}^{(1)}, \bar{\mathbf{u}}^{(2)}, \dots, \bar{\mathbf{u}}^{(N)}\right)\right). \quad (18)$$

Using the variation of $\varphi^{(i)}(\mathbf{x})$, i.e. the design variable field $\delta\varphi^{(i)}(\mathbf{x})$ to represent the amount of the material orientation variation, the first variation δL of the Lagrange functional L with respect to the material orientation variation can be expressed as

$$\delta L = l\left(\bar{\mathbf{u}}^{(1)}, \bar{\mathbf{u}}^{(2)}, \dots, \bar{\mathbf{u}}^{(N)}\right) - a\left(\left(\mathbf{u}^{(1)}, \mathbf{u}^{(2)}, \dots, \mathbf{u}^{(N)}\right), \left(\bar{\mathbf{u}}^{(1)}, \bar{\mathbf{u}}^{(2)}, \dots, \bar{\mathbf{u}}^{(N)}\right)\right) - a\left(\left(\mathbf{u}^{(1)}, \mathbf{u}^{(2)}, \dots, \mathbf{u}^{(N)}\right), \left(\bar{\mathbf{u}}^{(1)}, \bar{\mathbf{u}}^{(2)}, \dots, \bar{\mathbf{u}}^{(N)}\right)\right) + 2d\left(\mathbf{u}^{(M)} - \hat{\mathbf{u}}^{(M)}, \mathbf{u}^{(M)} - \hat{\mathbf{u}}^{(M)}\right) + \left\langle G_{\varphi}^{(i)}, \delta\varphi^{(i)} \right\rangle_{\varphi}, \quad (19)$$

$$\text{where, } \left\langle G_{\varphi}^{(i)}, \delta\varphi^{(i)} \right\rangle_{\varphi} = \sum_{i=1}^N \int_{A_i} G_{\varphi}^{(i)} \delta\varphi^{(i)} dA_i \quad (20)$$

$$\begin{aligned} &= \sum_{i=1}^N \int_{A_i} \left[\left\{ \boldsymbol{\kappa}^{(i)T}(\boldsymbol{\theta}) - \boldsymbol{\alpha}^T \frac{T_g^{(i)}}{t_i} \right\} \frac{\partial \mathbf{E}^{B(i)}}{\partial \varphi} \bar{\boldsymbol{\kappa}}^{(i)}(\bar{\boldsymbol{\theta}}) + \left\{ \boldsymbol{\varepsilon}_0^{(i)T}(\mathbf{u}_0) - \boldsymbol{\alpha}^T T_m^{(i)} \right\} \frac{\partial \mathbf{E}^{M(i)}}{\partial \varphi} \bar{\boldsymbol{\varepsilon}}_0^{(i)}(\bar{\mathbf{u}}_0) \right. \\ &\quad + \left\{ \boldsymbol{\kappa}^{(i)T}(\boldsymbol{\theta}) - \boldsymbol{\alpha}^T \frac{T_g^{(i)}}{t_i} \right\} \frac{\partial \mathbf{E}^{C(i)}}{\partial \varphi} \bar{\boldsymbol{\varepsilon}}_0^{(i)}(\bar{\mathbf{u}}_0) + \bar{\boldsymbol{\kappa}}^{(i)T}(\bar{\boldsymbol{\theta}}) \frac{\partial \mathbf{E}^{C(i)}}{\partial \varphi} \left\{ \boldsymbol{\varepsilon}_0^{(i)}(\mathbf{u}_0) - \boldsymbol{\alpha} T_m^{(i)} \right\} \\ &\quad + \left\{ \boldsymbol{\varepsilon}_0^{(i)T}(\mathbf{u}_0) - \boldsymbol{\alpha}^T T_m^{(i)} \right\} \frac{\partial \mathbf{E}^{C(i)}}{\partial \varphi} \bar{\boldsymbol{\kappa}}^{(i)}(\bar{\boldsymbol{\theta}}) + \bar{\boldsymbol{\varepsilon}}_0^{(i)T}(\bar{\mathbf{u}}_0) \frac{\partial \mathbf{E}^{C(i)}}{\partial \varphi} \left\{ \boldsymbol{\kappa}^{(i)}(\boldsymbol{\theta}) - \boldsymbol{\alpha} \frac{T_g^{(i)}}{t_i} \right\} \\ &\quad \left. + \boldsymbol{\gamma}^{(i)T}(\mathbf{w}, \boldsymbol{\theta}) \frac{\partial \mathbf{E}^{S(i)}}{\partial \varphi} \bar{\boldsymbol{\gamma}}^{(i)}(\bar{\mathbf{w}}, \bar{\boldsymbol{\theta}}) \right] \delta\varphi^{(i)} dA_i, \end{aligned}$$

and where $(\cdot)'$ indicates the first variation with respect to the design variable field $\delta\varphi^{(i)}(\mathbf{x})$.

When Eqs. (21) and (22) are satisfied,

$$a\left(\left(\mathbf{u}^{(1)}, \mathbf{u}^{(2)}, \dots, \mathbf{u}^{(N)}\right), \left(\bar{\mathbf{u}}^{(1)}, \bar{\mathbf{u}}^{(2)}, \dots, \bar{\mathbf{u}}^{(N)}\right)\right) = l\left(\bar{\mathbf{u}}^{(1)}, \bar{\mathbf{u}}^{(2)}, \dots, \bar{\mathbf{u}}^{(N)}\right), \quad (21)$$

$$\left(\mathbf{u}^{(1)}, \mathbf{u}^{(2)}, \dots, \mathbf{u}^{(N)}\right) \in U, \quad \forall \left(\bar{\mathbf{u}}^{(1)}, \bar{\mathbf{u}}^{(2)}, \dots, \bar{\mathbf{u}}^{(N)}\right) \in \bar{U},$$

$$a\left(\left(\mathbf{u}'^{(1)}, \mathbf{u}'^{(2)}, \dots, \mathbf{u}'^{(N)}\right), \left(\bar{\mathbf{u}}^{(1)}, \bar{\mathbf{u}}^{(2)}, \dots, \bar{\mathbf{u}}^{(N)}\right)\right) = 2d\left(\mathbf{u}^{(M)} - \hat{\mathbf{u}}^{(M)}, \mathbf{u}^{(M)'}\right), \quad (22)$$

$$\left(\bar{\mathbf{u}}^{(1)}, \bar{\mathbf{u}}^{(2)}, \dots, \bar{\mathbf{u}}^{(N)}\right) \in \bar{U}, \quad \forall \left(\mathbf{u}'^{(1)}, \mathbf{u}'^{(2)}, \dots, \mathbf{u}'^{(N)}\right) \in U,$$

then Eq. (19) becomes

$$\delta L = \left\langle G_{\varphi}^{(i)}, \delta\varphi^{(i)} \right\rangle_{\varphi}. \quad (23)$$

Eq. (21) is the governing equation for the state variable $\mathbf{u}^{(i)} = (\mathbf{u}_0^{(i)}, \mathbf{w}^{(i)}, \boldsymbol{\theta}^{(i)})$, ($i = 1, 2, 3, \dots, N$) and coincides with the state equation (Eq. (3)). Eq. (22) is the adjoint equation for the adjoint variable $\bar{\mathbf{u}}^{(i)} = (\bar{\mathbf{u}}_0^{(i)}, \bar{\mathbf{w}}^{(i)}, \bar{\boldsymbol{\theta}}^{(i)})$, ($i = 1, 2, 3, \dots, N$). Finally, the material orientation sensitivity function $G_{\varphi}^{(i)}$ of this problem is derived as

$$\begin{aligned} G_{\varphi}^{(i)} = & \left\{ \boldsymbol{\kappa}^{(i)T}(\boldsymbol{\theta}) - \boldsymbol{\alpha}^T \frac{T_g^{(i)}}{t_i} \right\} \frac{\partial \mathbf{E}^{B(i)}}{\partial \varphi} \bar{\boldsymbol{\kappa}}^{(i)}(\bar{\boldsymbol{\theta}}) + \left\{ \boldsymbol{\varepsilon}_0^{(i)T}(\mathbf{u}_0) - \boldsymbol{\alpha}^T T_m^{(i)} \right\} \frac{\partial \mathbf{E}^{M(i)}}{\partial \varphi} \bar{\boldsymbol{\varepsilon}}_0^{(i)}(\bar{\mathbf{u}}_0) \\ & + \left\{ \boldsymbol{\kappa}^{(i)T}(\boldsymbol{\theta}) - \boldsymbol{\alpha}^T \frac{T_g^{(i)}}{t_i} \right\} \frac{\partial \mathbf{E}^{C(i)}}{\partial \varphi} \bar{\boldsymbol{\varepsilon}}_0^{(i)}(\bar{\mathbf{u}}_0) + \bar{\boldsymbol{\kappa}}^{(i)T}(\bar{\boldsymbol{\theta}}) \frac{\partial \mathbf{E}^{C(i)}}{\partial \varphi} \left\{ \boldsymbol{\varepsilon}_0^{(i)}(\mathbf{u}_0) - \boldsymbol{\alpha} T_m^{(i)} \right\} \\ & + \left\{ \boldsymbol{\varepsilon}_0^{(i)T}(\mathbf{u}_0) - \boldsymbol{\alpha}^T T_m^{(i)} \right\} \frac{\partial \mathbf{E}^{C(i)}}{\partial \varphi} \bar{\boldsymbol{\kappa}}^{(i)}(\bar{\boldsymbol{\theta}}) + \bar{\boldsymbol{\varepsilon}}_0^{(i)T}(\bar{\mathbf{u}}_0) \frac{\partial \mathbf{E}^{C(i)}}{\partial \varphi} \left\{ \boldsymbol{\kappa}^{(i)}(\boldsymbol{\theta}) - \boldsymbol{\alpha} \frac{T_g^{(i)}}{t_i} \right\} \\ & + \boldsymbol{\gamma}^{(i)T}(\mathbf{w}, \boldsymbol{\theta}) \frac{\partial \mathbf{E}^{S(i)}}{\partial \varphi} \bar{\boldsymbol{\gamma}}^{(i)}(\bar{\mathbf{w}}, \bar{\boldsymbol{\theta}}). \end{aligned} \quad (24)$$

The each term in Eq. (24) is calculated by Eqs. (21) and (22), and the finite element method can be employed to solve those equations. The components of the elastic matrices on the right side of Eq. (24) is introduced in [7, 8]. Note that the material orientation sensitivity function for static deformation can be obtained by neglecting the thermal expansion terms of Eq. (24).

The derived material orientation sensitivity function $G_{\varphi}^{(i)}$ will be applied to the H^1 gradient method with Poisson's equation in Section 3.

3 H^1 GRADIENT METHOD WITH POISSON'S EQUATION FOR FREE-MATERIAL ORIENTATION OPTIMIZATION

The original H^1 gradient method called traction method at first was proposed for shape optimization of a linear elastic structure by Azegami and Wu [9]. and Shimoda and Liu extended it for free-form optimization of shells [10], which is a gradient method in the Hilbert space, and is theoretically possible to treat infinite design degrees of freedom. In these methods, the optimal distribution of the vector design variable can be determined via a linear elastic equation. In addition, the H^1 gradient method is further extended to size optimization

[11]. The extended H^1 gradient methods can determine the optimal distribution of the scalar design variable via Poisson's equation. The authors extended this method moreover for the material-orientation optimization problem [7]. The H^1 gradient method with Poisson's equation proposed for the optimal material-distribution is as follows:

When the state and the adjoint equations are satisfied, the perturbation expansion ΔL of Eq. (23) can be expressed as

$$\Delta L = \langle G_\varphi^{(i)}, \Delta s \delta \varphi^{(i)} \rangle. \quad (25)$$

where Δs is a sufficient small positive value.

In order to obtain the optimal material orientation variation field $\delta \varphi^{(i)}(\mathbf{x})$ of the i^{th} ply, the following weak-formed Poisson's equation for $\delta \varphi^{(i)}(\mathbf{x})$ is introduced.

$$\begin{aligned} b(\delta \varphi^{(1)}, v^{(1)}, \dots, \delta \varphi^{(N)}, v^{(N)}) + \beta_\varphi \langle \delta \varphi^{(i)}, v^{(i)} \rangle &= -\langle G_\varphi^{(i)}, v^{(i)} \rangle, \quad \forall v^{(i)} \in C_v, \delta \varphi^{(i)} \in C_\varphi, \\ b(\delta \varphi^{(1)}, v^{(1)}, \dots, \delta \varphi^{(N)}, v^{(N)}) &= \sum_{i=1}^N \int_{A_i} \delta \varphi_i^{(i)} k_{ij} v_j^{(i)} dA_i, \end{aligned} \quad (26)$$

where $\delta \varphi^{(i)}(\mathbf{x})$ denotes the material orientation field to be determined. The notations $\beta_\varphi (> 0)$ and k_{ij} are equivalent to the heat transfer coefficient and the thermal conductivity matrix in the heat transfer analysis, respectively. C_φ is the function space of the kinematically admissible temperatures that satisfy the Dirichlet conditions for material orientation variation $\delta \varphi^{(i)}(\mathbf{x})$, and C_v is the function space of the kinematically admissible temperatures defined as

$$C_v = \{v^{(i)} \in H^1 \mid v^{(i)} = 0 \text{ on the Dirichlet boundaries}\}. \quad (27)$$

The Dirichlet conditions can be arbitrarily defined by only considering the design requirement for the material orientations. Substituting Eq. (26) into Eq. (25) and considering the arbitrariness of $v^{(i)}$ in Eq. (26), we obtain

$$\Delta L = \langle G_\varphi^{(i)}, \Delta s \delta \varphi^{(i)} \rangle = -\Delta s \left(b(\delta \varphi^{(1)}, \delta \varphi^{(1)}, \dots, \delta \varphi^{(N)}, \delta \varphi^{(N)}) + \beta_\varphi \langle \delta \varphi^{(i)}, \delta \varphi^{(i)} \rangle \right). \quad (28)$$

Furthermore, considering the positive definitiveness of $\beta_\varphi \langle \delta \varphi^{(i)}, \delta \varphi^{(i)} \rangle > 0$ and $b(\delta \varphi^{(1)}, v^{(1)}, \dots, \delta \varphi^{(N)}, v^{(N)}) > 0$ in Eq. (28), we have $\Delta L < 0$. This relationship holds true in a piecewise convex design space. As above-mentioned, the sensitivity function is not applied directly to update the material orientation variation but it is once replaced by a fictitious internal heat generation and applied to the design domain. Then, the material orientation variation is determined as the temperature field obtained by the Poisson's equation. This makes it possible both to reduce the objective functional and to maintain the smoothness of the material orientation distribution, simultaneously. β_φ has a role of smoothing filter for controlling the influence range of the sensitivity function at a point. With larger β_φ , the influence area of the material orientation sensitivity function is smaller. With smaller β_φ , the influence area of the material orientation sensitivity function is larger, and then the material orientation distribution becomes smoother, or the curvature change of the material orientation flow becomes smaller. Generally, there is a trade-off relationship between them.

Fig. 3 shows the schematic flowchart with the concept illustrations of the optimization system developed in this study. The material orientation optimization process is summarized as: (1) Stiffness and adjoint analyses by Eqs. (21) and (22), and evaluation of objective function; (2) Calculation of material orientation sensitivity function by Eq. (24) using Eqs.

(21) and (22); (3) The negative material orientation sensitivity function $-G_\phi^{(i)}$ is applied layer by layer as a distributed internal heat generation to a fictitious elastic shell structure to the design surface of the i^{th} ply. The material orientation variation field $\delta\phi(x)$ is obtained as the temperature field solved by the Poisson's equation; (4) Updating of the material orientation by $\delta\phi(x)$. This process is repeated until the convergence or the given iteration number. A commercial FEM code is used for the processes in orange. The optimization system can be easily constructed in combination with a commercial FEA code because the proposed method does not need to manipulate the stiffness matrix in each process.

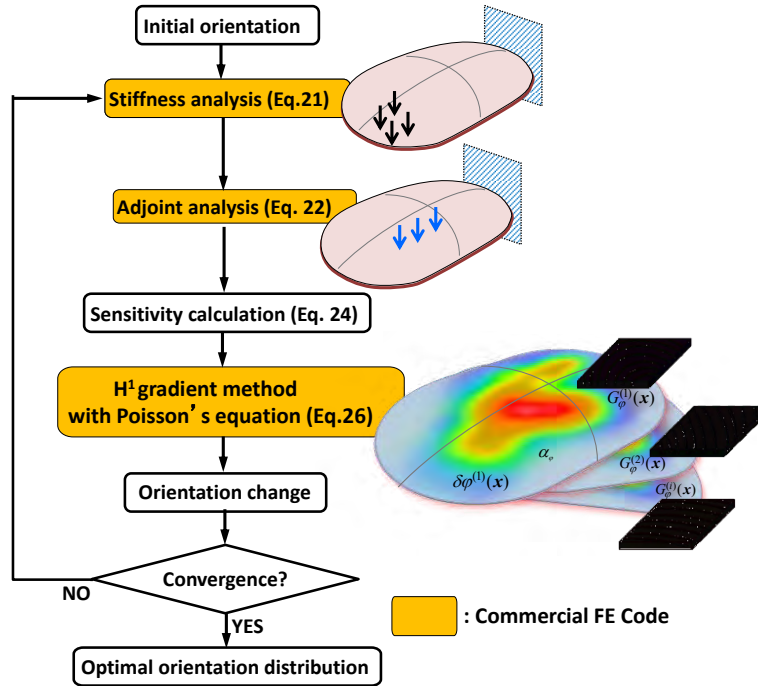


Figure 3: Schematic flowchart with concept illustration of optimization system.

4 NUMERICAL EXAMPLE

From a practical point of view, most of the industrial products are exposed in thermal environments, and it is important to maintain the required mechanical performances under thermal stress. Here, consider a 3-layer square shell illustrated in Fig. 4, which is loaded 60 K temperature difference between the top and bottom surfaces. The four corners are simply supported. The design domain, which has 200 mm length in each span and the unit thickness for each layer, has 1600 triangular elements. The initial material orientation of E_1 is parallel to x -axis. Young's moduli of each orthotropic element E_1 and E_2 are 210 GPa and 21 GPa, respectively. Transverse elasticity modulus is $G_{12} = 65$ GPa and Poisson ratio is $\nu_{12} = 0.3$. The thickness of each layer is set as 1 mm, and the ratio of each of coefficients of thermal expansion α_1 and α_2 is set as 1:7.

The objective of this problem is to reduce the overall thermal displacements to 1/10 of the initial displacement at each node. Fig. 5 shows the optimal material orientation of E_1 on each

layer, which has a different optimal material orientation while maintaining its smooth distribution. The iteration history of the square displacement error norm is shown in Fig. 6, and it is confirmed that it is monotonically decreased to 94 %. Fig. 7 shows the comparison of the thermal deformations between the initial and the optimized. It is confirmed that the thermal deformation is globally reduced by the optimization.

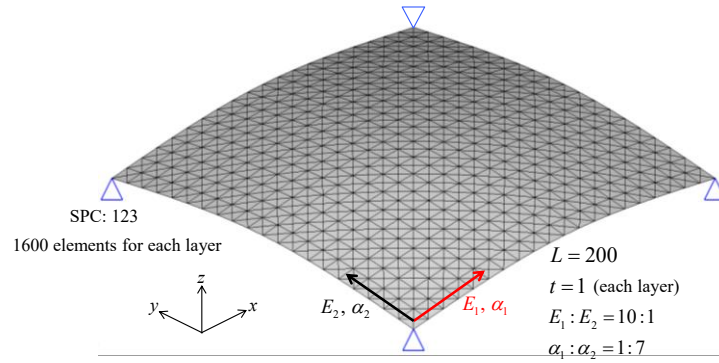


Figure 4: Boundary conditions of three-layer square shell.

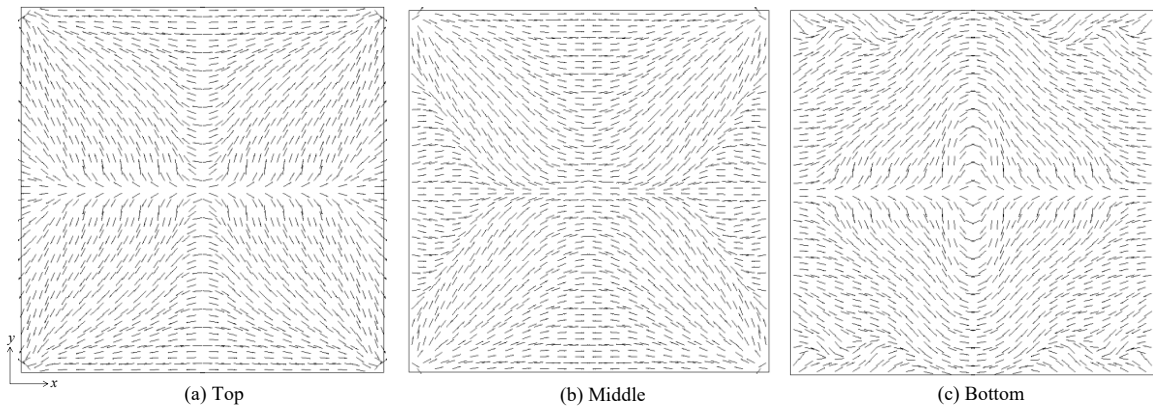


Figure 5: Optimal material orientation of E_1 on each layer.

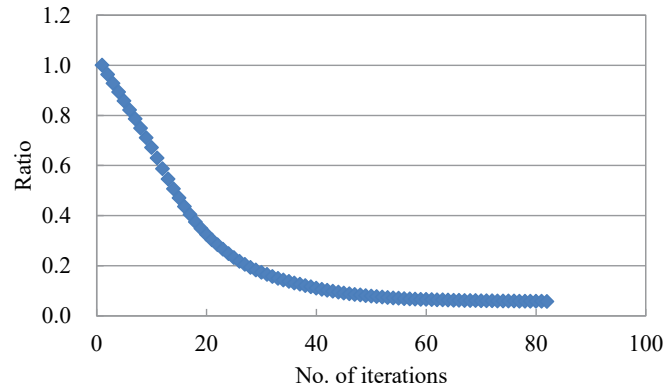


Figure 6: Iteration history of objective function normalized to the initial value.

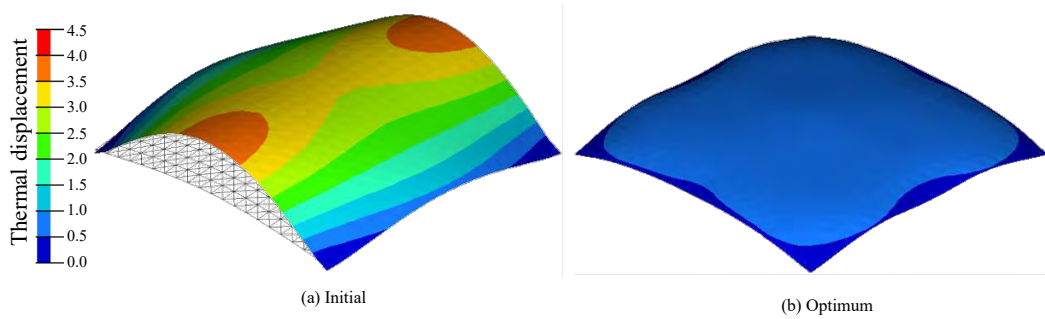


Figure 7: Comparison of thermal deformations (indicated by 10 times).

5 CONCLUSIONS

In this study, we presented an approach for the optimum material-orientation design of a laminated composite shell structure using the H^1 gradient method with Poisson's equation. It was assumed that the fiber in a structure consisting of orthotropic materials could be arbitrarily oriented layer by layer, and the each optimum free-orientation was determined for tailoring the thermal deformation to the desired values. The square displacements error norm was used as the objective function. The optimization problem was formulated and the sensitivity function for material orientation variation was theoretically derived using the Lagrange multiplier method and the adjoint variable method.

With the proposed approach, the arbitrary and smooth optimal distribution of the material orientation of a laminated anisotropic shell structure could be conventionally created for tailoring the thermal deformation. The proposed approach is especially effective for large-scale material orientation design problems of complicated-shape structures with multi-layer, and will become an effective tool for designing a high-performance laminated composite shell structure.

REFERENCES

- [1] Hoerner, S.V. Homologous deformations of tiltable telescopes. *Proc ASCE, J. Struct. Div.* 1967;93:461-85.
- [2] Liu, Y. and Shimoda, M. A non-parametric solution to shape identification problem of free-form shells for desired deformation mode. *Compos. Struct.* 2014;144:1-11.
- [3] Hyer, M. W. and Lee, H. H. The use of curvilinear fiber format to improve buckling resistance of composite plates with central circular holes. *Compos. Struct.* 1991;18(3):239-261.
- [4] Stegmann, J and Lund, E. Discrete material optimization of general composite shell structures. *Int. J. Numer. Methods Eng.* 2005;62 (14):2009–27.
- [5] Kiyono, C. Y, Silva, E.C.N. and Reddy, J. N. A novel fiber optimization method based on normal distribution function with continuously varying fiber path. *Compos. Struct.* 2017;160 (15):503-515.
- [6] Le, R. R and Haftka, R. T. Optimization of laminate stacking sequence for buckling load maximization by genetic algorithm. *AIAA Journal* 1993;31:951-956.
- [7] Muramatsu, Y. and Shimoda, M. Distributed-parametric optimization approach for free-orientation of laminated shell structures with anisotropic materials. *Struct. Multidiscip. Optim.*, 2018: doi 10.1007/s00158-018-2163-4).
- [8] Gürdal, Z., Haftka, R. T. and Hajela, P. *Design and optimization of laminated composite materials*. John Wiley & Sons 1999.
- [9] Azegami, H. and Wu, Z. C. Domain optimization analysis in linear elastic problems: approach using traction method. *Trans. JSME Ser. A* 1994;60(578): 2312–2318.
- [10] Shimoda, M. and Liu, Y. A non-parametric free-form optimization method for shell structures. *Struct. Multidiscip. Optim.* 2014;50:409–423.
- [11] Ikeya, K., Shimoda, M. and Shi, J. X. Multi-objective free-form optimization for shape for shape and thickness of shell structures. *Compos. Struct.* 2016;135:262–275.

RATE-DEPENDENT THERMOMECHANICAL MODELING OF ENTROPY CHANGES IN SUPERELASTIC SMA

A. KAUP, O. ALTAY AND S. KLINKEL

Department of Civil Engineering
RWTH Aachen University
Mies-van-der-Rohe-Str. 1, 52074 Aachen, Germany
e-mail: kaup@lbb.rwth-aachen.de, web page: <http://www.lbb.rwth-aachen.de>

Key words: Shape-memory alloy, Entropy, Smart material, Constitutive model, Strain-rate

Abstract. Superelastic shape-memory alloys (SMAs) are unique smart materials with a considerable energy dissipation potential for dynamic loadings with varying strain-rates. The energy dissipation arises from a hysteretic phase transformation of the polycrystalline atomic grid structure. In fact, the nucleation from austenite to martensite phase and vice versa exhibits a strong thermomechanical coupling. In particular, the hysteresis depends on the latent heat generated by the austenitic-martensitic transformation and the convection of that heat. High strain-rate interferes with the release of the latent heat to the environment and reduces the hysteresis surface. However, the degree of atomic disorder and accordingly the change in entropy influences the reverse phase transformation from martensite to austenite. In other words, the stability of the martensitic state affects the stress-level of the reverse transformation. Consequently, in phenomenological material models for SMAs, the effects of the rate-dependent entropy change must be considered to describe the energy dissipation behavior.

To incorporate the rate-dependent entropy change, we improved a one-dimensional numerical model by introducing an additional control variable in the free-energy formulation for solid-solid phase transformation in superelastic SMAs. In the present model, the observed effects of the strain-rate on the reverse transformation are taken into account by calculating the rate-dependent entropy change. A comparison of the numerical results with the experimental data shows that the model calculates the dynamic superelastic hysteresis of SMAs more accurate.

1 INTRODUCTION

The application field of polycrystalline shape-memory alloys (SMAs) with initial superelasticity covers aeronautic, automotive and civil engineering as well as biomechanics. Most SMA-based engineering applications experience strain-rate varied and cyclic loadings. Especially in civil engineering both seismic events and wind cause dynamic loading on structures. Hence, researchers have investigated numerous structural control strategies to mitigate structural vibrations. Commonly used damping systems, such as steel-hysteresis-dampers, dissipate structural vibration energy by inelastic deformations. However, inelastic damping devices cannot recover deformations and thus suffer loss of damping effects. This problem motivates research into SMA-damping devices. In fact, superelastic SMA-damping devices can reduce structural vibrations significantly without irreversible deformation due to unique hysteretic behavior. The superelastic hysteretic material behavior of NiTi-SMA is thermomechanically triggered and

includes both martensitic transformation and reverse transformation. The phase transformation depends on strain-rate and loading history. On the macroscopic level the nucleation from austenite to martensite is composed by the formation of martensitic transformation bands.

Knowledge of the strain-rate dependent evolution of macroscopic transformation bands is essential to consider strain-rate effects in constitutive modeling of superelastic SMAs. A primary investigation on the macroscopic formation of phase transformation fronts in NiTi was conducted by Shaw [1]. Another seminal study regarding both the macroscopic and microscopic behavior of NiTi under cyclic loading was operated by Otsuka [2]. Based on these investigations, Feng [3] used electromechanical-opting testing machines and high resolution optical recorders to capture images of the material surface during varying strain-rate loadings. Pieczyska [4], furthermore used differential scanning calorimetry (DSC) to record the thermal evolution of the macroscopic phase transition bands, while additionally using infrared cameras to obtain thermograms. Moreover, Xiao [5] investigated the strain field and the temperature field of NiTi specimen with 3D strain field cameras and infrared cameras. Thus, state-of-the art research offers numerous experimental and numerical investigations on the strain-rate dependency formation of transformation bands in NiTi.

The strain-rate dependent constitutive modeling of superelastic SMA for civil engineering applications is predominantly formulated as macroscopic material models. On the macroscopic level, Brinson [6] and Auricchio [7], among others, investigated fundamental macroscopic models. In the last decades, researchers developed several thermomechanical constitutive models for superelastic SMAs. One such example is Ozbulut's numerical model based on neural networks and fuzzy logic, that covers both the rate- and temperature dependent behavior of SMAs [8]. Moreover, numerically simpler macroscopic and thus computationally more efficient models were developed. Auricchio [9] developed a thermomechanical rate-dependent, one-dimensional model based on his primary research.

Superelastic hysteresis is thermomechanically coupled. Accordingly, the dynamic character of excitations strongly influences the thermal evolution and the hysteretic behavior. However, constitutive models developed so far do not explicitly consider the strain-rate dependent phase stability. In particular, the evolution of martensitic transformation bands is influenced by the strain-rate of the excitation. Simultaneously, martensitic phase stability modifies with the rate-dependent evolution of transition fronts.

This work proposes a one-dimensional numerical model that allows integrating changes in phase stability that depend on strain rate. More specifically, the change in phase stability is calculated with the rate-dependent entropy change in the superelastic SMA. In addition, experimental uniaxial tensile shaking-table tests on trained NiTi SMA wires validate the numerical model.

The following is subdivided into three sections. Section 2 includes both the experimental setup and the dynamic behavior of SMA. Subsequently, Section 3 presents a constitutive model for superelastic SMA. Finally, the validation of numerical calculations with the experimental results is presented in Section 4.

2 PRELIMINARY

2.1 Dynamic material properties

The superelastic behavior of NiTi is thermomechanically coupled. For superelastic NiTi, the austenite grid structure is energetically more effective. Thus, energy such as tensile stress has to be applied to initiate a phase transition. Auricchio [9] defines in detail, the stress-induced phase transformation as indicated by the critical martensitic transformation start and finish points R_s^{AM} and R_f^{AM} and inversely by R_s^{MA} and R_f^{MA} . Superscript AM indicates a transformation from austenite to martensite and MA vice versa. To incorporate the thermomechanical coupling, the critical transition point R depends on the stress level

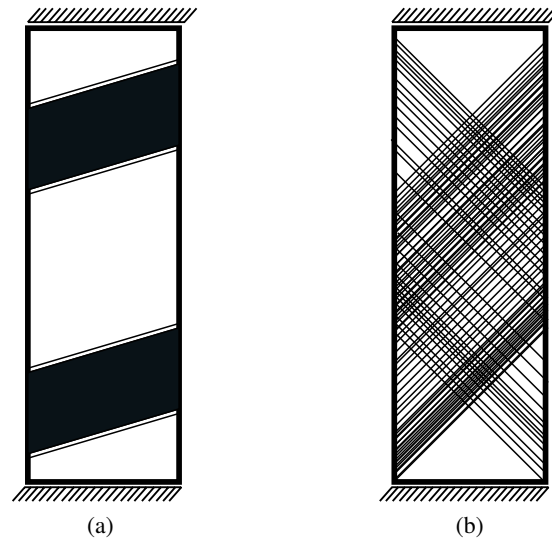


Figure 1: Schematic martensitic transformation induced band evolution for a quasi-static (a) and a dynamic (b) excitation. Martensite-fraction in the NiTi specimen illustrated as transformation bands.

σ and the thermal level T .

$$R = \sigma - T(\eta) \quad (1)$$

SMAs thermal evolution depends on the latent heat generation during the exothermic process when the atomic grid restructures from a austenitic cubic to a martensitic monoclinic grid. Indeed, both the latent heat generation and the convection of generated heat depend on the transformation-rate. As a result, especially the critical transformation points R_f^{AM} and R_s^{MA} shift upwards for a higher material temperature and consequently the slope of the hysteretic transformation area increases.

The strain-rate and transformation-rate dependent thermal evolution during phase transition has an essential influence on the hysteresis surface. However, the martensitic phase stability influences additionally the reverse transformation. For instance, Figure 1 illustrates the evolution of the martensitic transition fronts for both a quasi-static (a) and a dynamic excitation (b). In a quasi-static load-state, the growth of localized martensite bands determines the phase transition [5]. In general terms, for quasi-static excitation the stress field specifies the position of the transition fronts; hence they are located next to the fixture points [1]. Evolution of quasi-static martensite bands leads to wider bands and comparative phase-stable martensitic modes. In contrast, a higher strain-rate causes a homogeneous distribution of small transformation bands all over the specimen. An increase in the band quantity concurrently implies a decrease in the band width. The martensitic phase stability reduces as a result, even if the amount of martensite-volume in the specimen is comparable to the quasi-static case. In addition, the higher transformation-rate raises the degree of atomic disorder and hence the motion of atoms. Indeed, a more unstable atomic state is concomitant with increasing entropy in the material [10]. As a consequence, the reverse transformation process is initiated on a higher stress level, since the martensitic phase becomes too unstable and the material strives for the energetically more effective and more stable austenite grid structure.

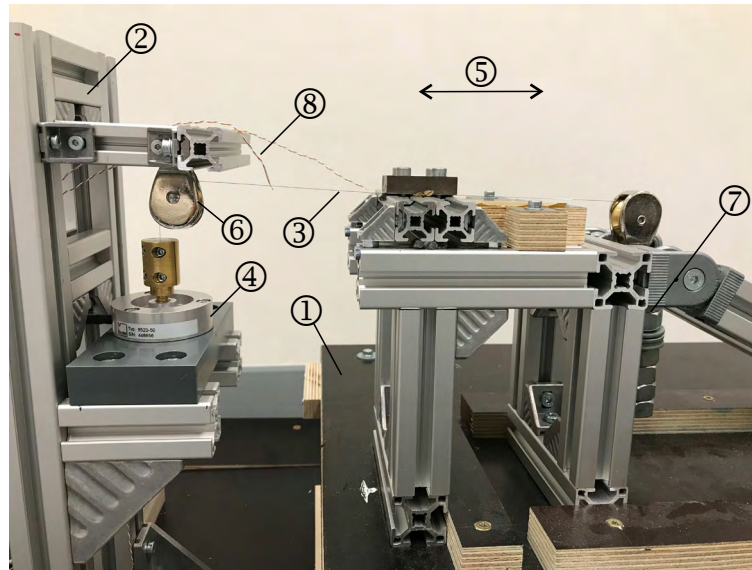


Figure 2: Utilized experimental setup, side-view. (1) shaking table, (2) test rig, (3) NiTi-wire, (4) load cell, (5), uniaxial strain direction, (6) pulley, (7) weights.

2.2 Experimental setup

Figure 2 shows the utilized shaking table for uniaxial cyclic-tensile tests. The uniaxial horizontal shaking table is 0.50 m x 0.50 m in size and can simulate both cyclic and stochastic loadings. The major constituents of the experimental setup are the shaking table (1) and a fixed test rig (2). For the tensile tests, NiTi wires (3) are attached to a vertically installed load cell (4) at the test rig. The distance from load cell to the right side fixture is 150 mm and thus sets the NiTi wire length for the experimental investigations. The uniaxial direction movement (5) causes tensile and pressure stress on the NiTi wire. Indeed, uniaxial tests are representative for SMA-braced structures, where only tensile loads excite the SMA-wires. To avoid buckling, which is owing to pressure, a pulley (6) redirects the SMA wire and ensure centric load application to the load cell. Additionally, weights (7) pre-stress the NiTi wire to induce martensitic transformation in a both faster and controlled manner. Moreover, two T-Type thermocouples (8) are installed 5 mm and 60 mm distanced from the right-side fixture. This position enables local temperature evolution measurement and the identification of local thermal differences. To control the table and to record the measurements data a MATLAB/Simulink environment is used. A CAN-hub connects the MATLAB/Simulink code with the shaking table and introduces the excitation signals. Finally, all sensors are connected with BNC-wires via a National Instruments 'NI USB-6210' A/D converter to a target PC.

3 RATE-DEPENDENT CONSTITUTIVE SMA MODEL

This section introduces briefly the rate-dependent constitutive model of Auricchio [9] and describes further advancements developed in this study. To cover the thermomechanical behavior of superelastic SMAs, the constitutive model is based on thermodynamic potential state laws. In general, the internal variable ξ , representing the martensitic volume fraction in the material, is expressed for martensitic

transformation in term of the following evolutionary equation

$$\dot{\xi} = \beta^{AM} \xi \frac{\dot{F}}{(F - R_f^{AM})^2}, \quad (2)$$

as a function of the external variables; the Temperature T and the uniaxial strain ϵ and can further be controlled with the speed-parameter β^{AM} . This cubic evolutionary depends moreover on the driving force F and the thermo-coupled limit stress level for martensitic transformation R_f^{AM} where both are depend on σ and T according to Auricchio [9]. To take into account the thermomechanical coupling, the constitutive model is based on a free energy for formulation ψ . In particular, the derivation of ψ originates from Raniecki and Bruhns thermo-elastic free energy formulation for single-phase materials [11] and reads

$$\psi = \psi_0(T) + \psi^e(\epsilon^e) - (T - T_0)\eta^e(\epsilon^e, T) + C \left[(T - T_0) - T \ln \frac{T}{T_0} \right]. \quad (3)$$

In this case, ψ_0 states the temperature-dependent free energy connection to the materials internal energy u and entropy η in the reference state and ψ^e states the free energy dependency on elastic strain. Moreover, C is the material heat capacity and T_0 the reference temperature. Based on Eq. 3, Auricchio and Sacco proposed a free energy formulation [7] for solid-solid phase transformation in superelastic SMAs as,

$$\psi = [(u_A - T\eta_A) - \xi(\Delta u - T\Delta\eta)] + C \left[(T - T_0) - T \log \frac{T}{T_0} \right] + \frac{1}{2}E\epsilon^e{}^2 - (T - T_0)\epsilon^e E\alpha, \quad (4)$$

where the subscript $-_A$ defines the austenite, Δ the difference between austenite and martensite values, α the thermal expansion and E the elastic modulus, which follows the Reuss-scheme. Accordingly, the stress σ and the temperature T are defined to the corresponding derivations of the free-energy formulation. Hence, we define the σ and T , which is based on the heat equation as

$$\sigma = \frac{\partial \psi}{\partial \epsilon^e} = E\epsilon^e - E\alpha(T - T_0) \quad (5)$$

and

$$C\dot{T} = T \frac{\partial^2 \psi}{\partial T \partial \epsilon^e} \dot{\epsilon} + T \frac{\partial^2 \psi}{\partial T \partial \xi} \dot{\xi} + \sigma \dot{\epsilon} - \frac{\partial \psi}{\partial \epsilon} \dot{\epsilon} - \frac{\partial \psi}{\partial \xi} \dot{\xi} - \gamma(T - T_{ext}). \quad (6)$$

To incorporate the rate-dependent entropy change, we rewrite the free-energy formulation by way of introducing the initial entropy difference $\Delta\eta_0$ to define ψ as

$$\psi = [(\Delta u_0 - T\Delta\eta_0) - \xi(\Delta\eta)] + C \left[(T - T_0) - T \ln \frac{T}{T_0} \right] + \frac{1}{2}E\epsilon^e{}^2 - (T - T_0)\epsilon^e E\alpha \quad (7)$$

Since we deal with thin wires, we neglect the thermal expansion factor α subsequently. Thus, we introduce

$$\eta = -\frac{\partial \psi}{\partial T} = \Delta\eta_0 + \xi(\Delta\eta) + C \ln \frac{T}{T_0} \quad (8)$$

as an additional control variable. Here, $\Delta\eta$ defines the difference between the current entropy level η and the initial entropy level $\Delta\eta_0$. The rate-dependent entropy change calculation enables to consider

observed strain-rate effects on the reverse transformation. The rate-dependency of the calculation arises directly from ξ , which depends on the phase transformation-rate, and from T . To consider the strain-rate effects both on the initial reverse transition stress level and on the martensitic-austenitic hysteresis slope, we reformulate the thermo-coupled initial stress level for reverse transformation and the speed parameter as

$$R_s^{MA} = \sigma_s^{MA} - T_R \frac{\eta}{\epsilon_L} \quad (9)$$

and

$$\beta^{MA} = \frac{\eta}{\Delta\eta_0} . \quad (10)$$

The thermal-coupled initial stress level R_s^{MA} determines the initial reverse transformation strain $\epsilon_s^{MA}(\eta)$ and thus also the linear-elastic part of the austenitic-martensitic phase transition. In brief, the free-energy reformulation enables a rate-dependent calculation of the entropy change and hence the introduction of both the entropy dependent speed parameter $\beta^{MA}(\eta)$ and the entropy dependent initial reverse transformation strain $\epsilon_s^{MA}(\eta)$.

4 RESULTS AND DISCUSSION

The experimental results in Figure 3 visualize the strain-rate effects during cyclic-tensile excitation with a strain amplitude of 4% on trained 0.2 mm Ni-55.8%-Ti-43.55%-SMA wires, produced by 'SAES Getters S.p.A.' (SAES). While comparing the whole hysteresis surface for frequencies of 0.05, 0.1, 0.5, 1.0 and 2.0 Hz, we also visualize both the linear-elastic and the transformation section of the reverse transition. In fact, we focus on the first loading cycle of each cyclic tensile test. Therefore, the decrease of linear-elastic reverse transformation for increasing strain-rates becomes evident, as marked in the plots. The decreasing linear-elastic section and the resulting reverse transformation on a higher stress level strongly influence the shape of the reverse transition hysteresis. This strain-rate dependent reverse transition shape is triggered by the decreasing martensitic phase-stability. However, state-of-the-art constitutive models do not consider these strain-rate dependent changes in reverse transformation. Subsequently, we present the effect of the entropy-change dependent calculation step by step, both of the initial reverse transformation strain $\epsilon_s^{MA}(\eta)$ and the adjusted speed parameter β^{MA} . More precisely, the results are presented in the following order: no rate-dependent entropy change, entropy change adjustment of $\epsilon_s^{MA}(\eta)$, entropy-change adjustment of $\epsilon_s^{MA}(\eta)$ and $\beta^{MA}(\eta)$.

We selected the material parameters, apart from the thermodynamic parameters, on the basis of quasi-static tensile tests taken both from the SAES data-sheet and self-conducted experimental results. The thermodynamic parameters were not determined experimentally. Accordingly, we chose the following thermodynamic parameters appropriately the behavior of the constitutive model and physically consistent, see Table 1. The material parameter ϵ_L is the maximum residual strain, γ is a heat convection coefficient and T_{ext} and T_R are the external and the reference temperatures, respectively. The chosen values for Δu and $\Delta\eta$ differentiate from Auricchio's parameter sets, but allow for the entropy calculation.

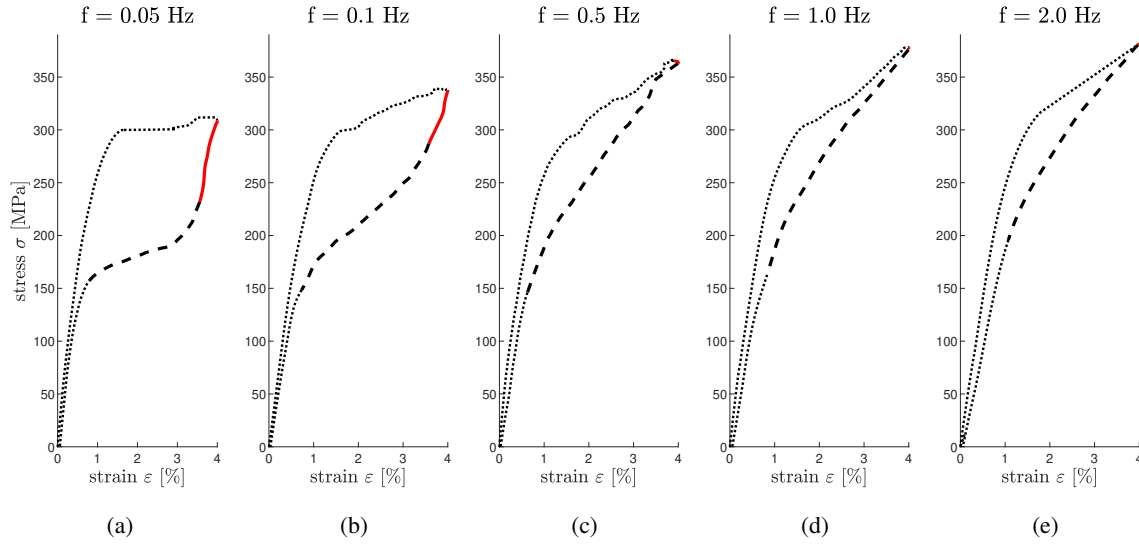


Figure 3: Cyclic-tensile-tests on Ni-55.8%-Ti-43.55%-SMA wires. Red-marked solid line: martensitic linear-elastic section. Dashed line: reverse transformation. Strain amplitude: $\varepsilon = 4\%$. Excitation frequency: $f = 0.05/0.1/0.5/1.0/2.0\text{ Hz}$. Wire length: $L = 150\text{ mm}$. Wire diameter: $\varnothing = 0.2\text{ mm}$. Pre-stress: $\sigma_0 = 432\text{ N/mm}^2$. Ambient temperature: $T = 22.5\text{ }^\circ\text{C}$

Table 1: Material parameter for constitutive model

Parameter	Value		Parameter	Value	
E_A	32350	MPa	Δu	1320	MPa
E_M	18550	MPa	$\Delta\eta_0 = \Delta\eta$	0.0093	MPaK ⁻¹
ε_L	3.34	%	γ	0.1	-
σ_s^{AM}	85	MPa	C	4.0	MPaK ⁻¹
σ_f^{AM}	305	MPa	T_u	573	K
σ_s^{MA}	225	MPa	$T_{ext} = T_0 = T_R$	293	K
σ_f^{MA}	200	MPa			

To show the influence of the rate-dependent entropy change on $\varepsilon_s^{MA}(\eta)$, we first compare the numerical results, excluding the entropy calculation, with the experimental results, see Figure 4. The linear-elastic part of the calculation is again separately marked. Indeed, the calculation of the martensitic-transformation is highly plausible for the three frequencies of 0.05, 0.1 and 0.5 Hz. Although the calculation of the rate-dependent thermal evolution is only qualitatively correct, the model can represent the thermomechanical coupling for austenitic-martensitic transition. However, the linear-elastic reverse-transformation section does not change and the reverse-transformation shape remains nearly the same. Figure 5, shows the included entropy-change effect on $\varepsilon_s^{MA}(\eta)$. To illustrate the effects of the entropy change on $\varepsilon_s^{MA}(\eta)$, we compare Figure 5 to Figure 4 to conclude that the linear-elastic section decreases for increasing strain-rate when entropy-change effects are included in the numerical model. Nevertheless, the reverse transformation shape remains uniform even though the phase transformation is introduced on a higher stress level. Accordingly, further entropy dependent adjustments are necessary for a more accu-

rate calculation of martensitic phase stability.

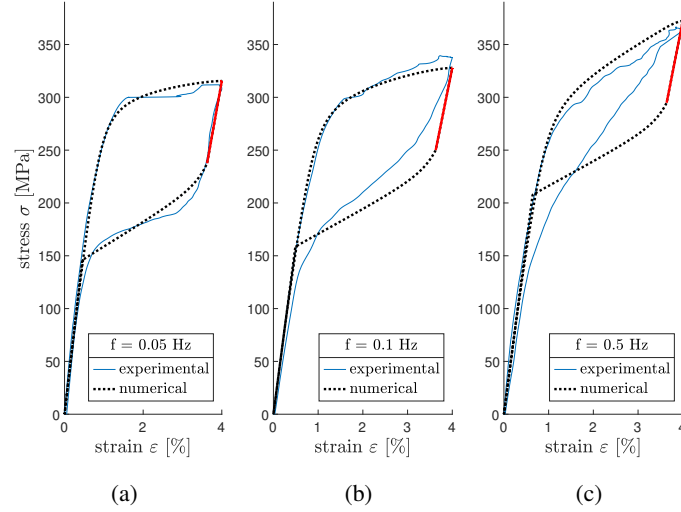


Figure 4: Comparison of experimental data with with numerical results excluding entropy-change effects. Red-marked solid line: martensitic linear-elastic section. $\epsilon = 4\%$. $f = 0.05/0.1/0.5\text{ Hz}$.

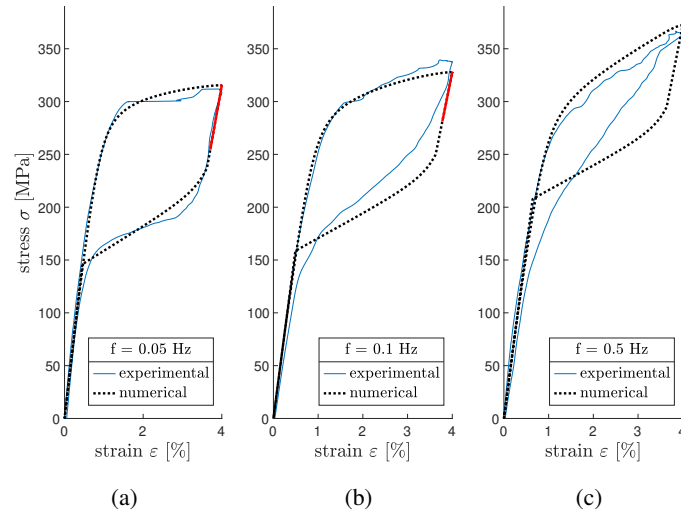


Figure 5: Comparison of experimental data with numerical results including entropy-change effects on $\epsilon_s^{MA}(\eta)$. Red-marked solid line: martensitic linear-elastic section. $\epsilon = 4\%$. $f = 0.05/0.1/0.5\text{ Hz}$.

To incorporate the change in reverse transformation curve, we introduce the rewritten speed parameter β^{MA} as a function of η . In fact, $\beta^{MA}(\eta)$ defines the shape of the cubic evolutionary equation for the reverse transformation and increases with increasing entropy, see Eq. 10. Figure 6 shows the numerical results both including and excluding entropy changes, and further compares the numerical with the exper-

imental results. The inclusion of the rate-dependent entropy change for the reverse transition improves the calculation accuracy. On the one hand, the austenite transformation changes for higher strain-rate from a convex to a slightly concave curve due to the entropy dependent calculation of $\beta^{MA}(\eta)$. On the other, the initial level for reverse transformation rises for increasing strain-rates. Consequently, the advancements on the one-dimensional material model cause – especially for high strain-rates – a more accurate calculation of the hysteresis surface without negative impact on the numerical efficiency of the algorithm.

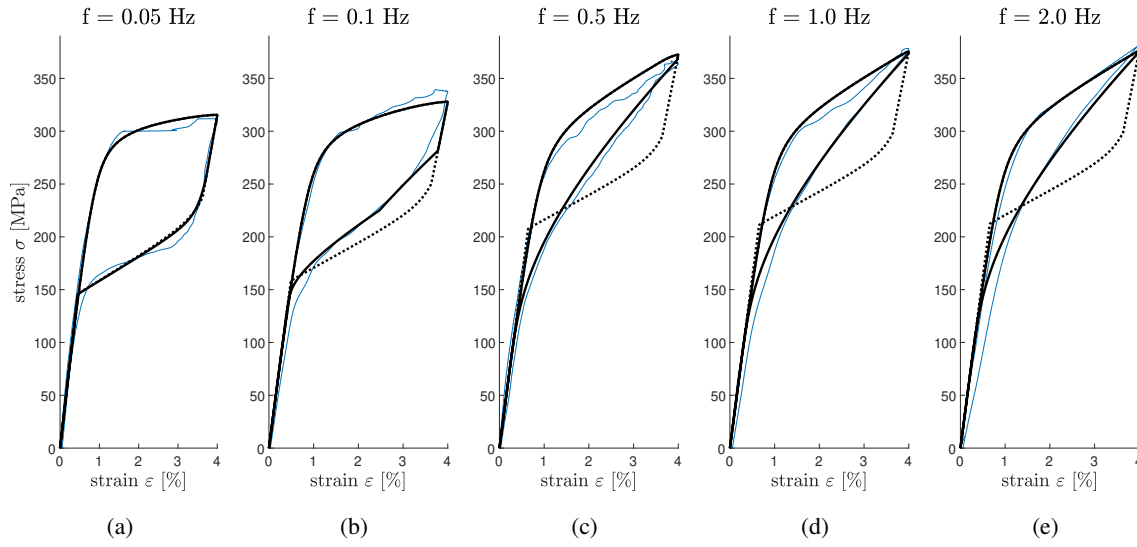


Figure 6: Comparison of experimental data with numerical results both excluding and including entropy change. Thin solid line (blue): experimental investigation. Width solid line (black): numerical results; including entropy change. Dotted line: numerical results; excluding entropy change. Entropy-change effects on $\epsilon_s^{MA}(\eta)$ and $\beta^{MA}(\eta)$. $\epsilon = 4\%$. $f = 0.05/0.1/0.5/1.0/2.0\text{ Hz}$.

5 CONCLUSION

In this paper, the influence of rate-dependent phase-stability during martensitic transformation of superelastic SMA-wires on the hysteresis surface is investigated. To consider rate-dependent phase-stability in a numerical model, we advanced a one-dimensional constitutive model by way of an adjusted free-energy formulation for phase transition in superelastic SMAs. The rewritten free-energy formulation Eq. 4 enables the rate-dependent entropy change calculation in the material to consider the decreasing martensitic phase-stability for increasing strain-rates. In brief, the entropy change calculation enables a strain-rate dependent calculation of the initial strain level for reverse transformation. The advancement further influences the reverse evolutionary equation and thus the shape of martensitic-austenitic transformation. Hence, the change from a convex to a concave reverse transition shape for increasing strain-rates can be calculated. The significant influence of strain-rate on the reverse transformation was observed by experimental investigations. In particular, we performed cyclic-tensile tests with varying strain-rates on NiTi-wires, using a uniaxial horizontal shaking table. In further process, the dynamic material was analyzed according to state-of-the-art research on the evolution of martensitic transformation bands. Thus, both the relationship between strain-rate and martensitic phase stability and the need for nu-

merical inclusion of this relationship have been noted. Furthermore, the experimental results validate the modified one-dimensional model. In conclusion, the rate-dependent thermomechanical modeling of entropy change in superelastic SMAs enables considering martensitic phase stability effects on the reverse transformation. Hence, we calculate the hysteresis surface more accurately with neither impairment of the numerical models simplicity nor the robustness of the solution algorithm.

ACKNOWLEDGMENT

The authors would like to express their sincere appreciation for the financial support from the German Research Foundation (Deutsche Forschungsgemeinschaft, DFG) with the grant number: KL 1345/12-1.

REFERENCES

- [1] Shaw, J. A. and Kyriakides, S. On the nucleation and propagation of phase transformation fronts in a NiTi alloy. *Acta Mater.* (1997) **45**:683-700
- [2] Miyazaki, S., Imai, T. and Otsuka, K. Effect of cyclic deformation on the pseudoelasticity characteristics of Ti-Ni alloys. *Int. J. Solids Struct.* (2001) **38**:6123-6145
- [3] Feng, P. and Sun, Q.P. Experimental investigation on macroscopic domain formation and evolution in polycrystalline NiTi microtubing under mechanical. *J. Mech. Phys. Solids* (2006) **54**:1568-1603
- [4] Pieczyska, E. A., Tobusji, H. and Kulasinski, K. Development of transformation bands in TiNi SMA for various stress and strain rates studied by a fast and sensitive infrared camera. *Smart Mater.* (2013) **22**:035007
- [5] Xiao, Y., Liu, Y. and Novak, V. On the origin of Lüders-like deformation of NiTi shape memory alloys. *J. Mater. Eng. Perf.* (2015) **24**:3755-3760
- [6] Brinson, L. C., One-dimensional constitutive behaviour of shape memory alloys: Thermomechanical derivation with non-constant material functions and redefined martensite internal variable. *J. Intell. Mater. Syst. Struct* (1993) **4**:229-242
- [7] Auricchio, F. and Sacco, E. A one-dimensional model for superelastic shape-memory alloys with different elastic properties between austenite and martensite. *Int. J. Non Linear Mech* (1996) **32**:1101-1114
- [8] Acar, E., Ozbulut, O. E. and Karaca, H. E. Experimental investigation and the modeling of the loading rate and temperature dependent superelastic response of a high-performance shape memory alloy. *Smart Mater. Struct.* (2015) **24**:075020
- [9] Auricchio, F. and Sacco, E. Thermo-mechanical modeling of a superelastic shape-memory wire under cyclic stretching-bending loadings. *Int. J. Solids Struct.* (2001) **38**:6123-6145
- [10] Tatar, C. and Yildirim, Z. Phase transformation kinetics and microstructure of NiTi shape memory alloy: Effect of hydrostatic pressure. *Bull. Mater. Sci.* (2017) **40**:799-803
- [11] Raniecki, B. and Bruhns, O. Thermodynamic reference model for elasto plastic solids undergoing phase transitions. *Arch. o. Mech.* (1991) **43**:343-376
- [12] Sittner, P., et.al. Experimental investigation on rate dependence of thermomechanical response in superelastic NiTi Shape memory alloy *J. Mech. Phys. Solids* (2005) **53**:1719-1746

Shear behaviour of magnetorheological elastomers: viscoelastic and magnetorheological properties

Alberto Bellelli¹, Andrea Spaggiari^{1*}

¹Department of Sciences and Methods for Engineering, University of Modena and Reggio Emilia, Italy

ABSTRACT

This paper presents the mechanical characterization of several specimens of magnetorheological elastomers (MRE), under shear stress, up to failure. The specimens were designed and manufactured with different ratio of ferromagnetic particles, curing conditions and applied magnetic field. The MRE elastomer is composed by two main ingredients: a base elastomer and carbonyl iron powder, which are mixed in the desired weight ratio, following a structured experiment plan. The PDMS elastomer, is polymerized by mixing the base material with a curing agent and the iron particles at the same time. We decide to characterize the shear behaviour of the bulk MRE in a condition quite close to a typical application such as an isolation mount. This requires the design of a special rig to apply both the load to the cylindrical specimens and the magnetic field at the same time. This method, compared to the use of a traditional rheometer as already present in technical literature, grants the possibility to test the specimen in large deformation and up to failure. The specimens were manufactured and tested according to a Design of Experiment method, in order to obtain a statistically significant influence of the variables considered: particles volume fraction, isotropicity and applied field. Moreover, the MRE was tested both at low shear rate, in order to avoid the viscoelastic effects as well as at high shear rates, in order to evaluate the dynamic effects. An analysis of variance performed on the test results is used to highlight which are the most important variables that affect the output responses and could be exploited to build a simplified phenomenological model of the MRE shear behaviour.

INTRODUCTION

The magnetorheological elastomers (MRE) are a class of smart materials which modifies their

mechanical properties due to an external stimulus, the magnetic field. These materials are gaining increasing popularity nowadays, since the possibility to have free shape MREs could lead to the design of smart components or sensors, which exhibits full integration with the structure. Therefore, the proper design of a MRE system first requires the knowledge of the magneto-mechanical properties of the MRE material. These materials have already gained the attention of the researcher, but still some open questions remain in technical literature. One of the first MRE ever produced was created due to the curiosity towards a toy, the Silly Putty (Cross, 2012; Marc Hartzman, 2013) a viscoelastic material which can be found also in a magnetic sensitive form (Golinelli et al., 2015). Silly Putty is extremely stiff when subjected to high deformation rates, while it is more than soft in case of quasi-static applied stress (Cross, 2012), reaching a quasi-fluid behaviour. This very strong viscoelastic behaviour makes Silly Putty unsuitable for engineering applications: it cannot keep a predefined shape it tends to collapse under its own weight, its behaviour changes dramatically according to the loading rate. More interesting performances are offered by the magnetorheological elastomers (MREs), which are similar to the Silly Putty, but consist of a non-magnetic elastomeric matrix with ferromagnetic micrometric particles in a non colloidal suspension (Davis, 1999; Guan et al., 2008; Ruddy et al., 2008) such that the elastomeric matrix maintains its shape and does not exhibit a fluid-like behaviour. The magnetic interaction between the particles in these composite materials depends on the spatial arrangement of the particle and their volume fraction and this feature leads to an interesting number of magneto-mechanical phenomena (de Vicente et al., 2011; Ginder et al., 2000; Kallio, 2005). The technical literature reports several studies in compressive behaviour, considering both dynamic and quasi static conditions, but scarce information are retrieved in shear and especially regarding the ultimate failure stress (Schubert and Harrison, 2015) since the shear test requires an ad hoc design of the gripper system.

The purpose of this work is to expand the applicability of MREs towards the more industrialized field of magnetorheological fluids (MRFs) which are based on the same concept but exploiting a fluid matrix which makes them suitable for vibration damping and shock absorbers (Carlson and Jolly, 2000; Chen et al., 2007; Shen et al., 2004; Spaggiari et al., 2016; Yang et al., 2015). Compared to MRFs, magnetorheological elastomers show an always solid behaviour, i.e. they do not pass from fluid to quasi-solid state, however their mechanical characteristics in terms of stiffness and damping are a function not

only of the external mechanical loads, but also of the applied external magnetic field. On the one hand the solid matrix prevents the ferromagnetic particles to move and therefore the MR effect is limited, on the other hand the very same solid matrix cancels the problem of confinement and compatibility with standard gaskets damage typical of MRF (Güth et al., 2013; Wiehe and Maas, 2012). Moreover, having the matrix lead to the possibility to make MREs both in isotropic and anisotropic configurations. This feature could be done during the manufacturing of the samples, by applying a magnetic field when the elastomer is still liquid. Figure 1a (Chen et al., 2007) show the or they can be forced to form chain-like column structures, as as shown in Figure 1b with higher magnification.

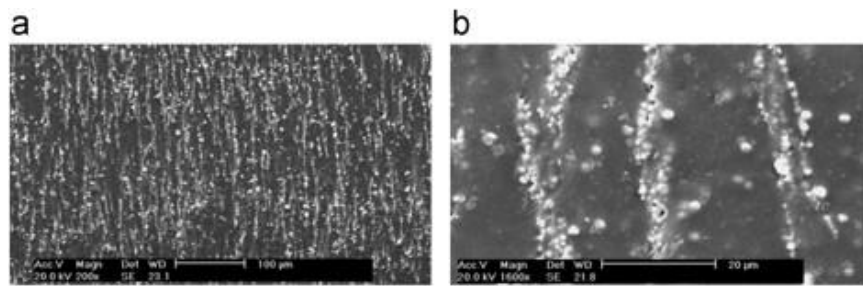


Figure 1. SEM image with 200 times magnification of MRE prepared in 800 mT (b) SEM image with 1600 times magnification of MRE prepared in 800 mT (Chen et al., 2007)

This paper investigates a custom MRE made by a PDMS elastomeric matrix, which can be cast in various shapes, it undergoes large deformations under shear tests and exhibits a interesting behaviour for a potential use as smart controllable mount.

1. MATERIALS AND METHODS

The manufacture of the specimens was carried out following a Design of Experiment procedure (Montgomery, 2004). We considered as design variables three different volume fractions of ferromagnetic particles, the isotropicity of the specimens and the application of an external magnetic field, which is provide with permanent supermagnets. For each configuration we manufactured 2 samples for a total of 14 specimens. Subsequently, the shear tests, with or without an external magnetic field with cyclic and monotonic loading up to failure are applied.

2.1 Experimental apparatus

The elastomeric matrix is a commercial two-component PDMS (Polydimethylsiloxane) base, Sylgard 184 (Dow Corning Sylgard 184 TDS | Krayden, 2013), which is a material which is widely used in electronic applications, especially for encapsulation of microelectronics circuits. This material shows very interesting properties as an electret (Kachroudi et al., 2017) and it was already described and studied in (Kachroudi et al., 2015), where its viscoelastic, thermal and dielectric properties can be found. Its behaviour as MRE Matrix was already tested in compression in a previous authors' work (Bellelli and Spaggiari, 2019). The aim of this paper is to study and discuss its magnetorheological properties when enriched by various volume fractions of ferromagnetic particles. The elastomeric base was mixed with carbonyl iron particles with an average size of $45\text{ }\mu\text{m}$ - Ferchim RI 63/3.2 by Pometon (Pometon, n.d.). The three ingredients (curing agent, silicone base and iron powder), after being weighted to obtain the desired volume fraction, were deposited and mixed in a 3d printer mold designed to obtain two desired specimens at one time. The mold was made out of nylon reinforced with microparticles of carbon and is shown in Figure 2. All the parts are kept in position and securely tightened through stainless steel screws, which do not disturb the magnetic field, when applied.

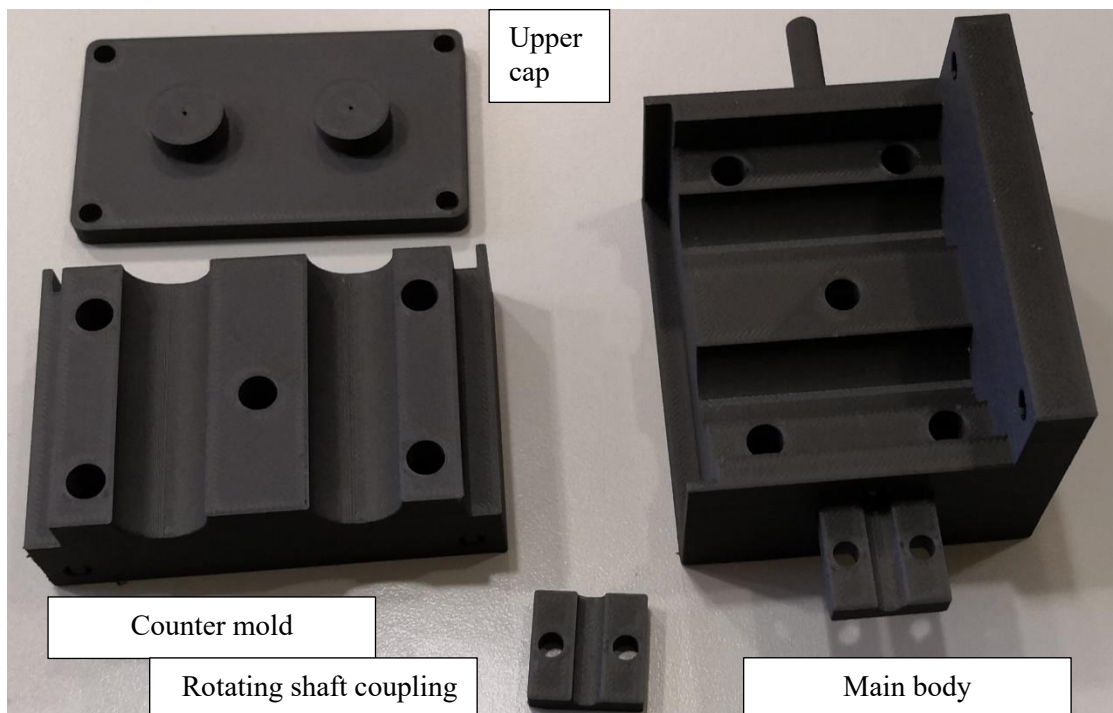


Figure 2. – 3d Printed mold.

The specimens are cylindrical with a diameter of 16mm and a height of 31mm. The mold was designed in order to facilitate the extraction of the specimen and to improve the degassing phase. This phase is mandatory to avoid air bubbles inside the specimen, since the manual mixing always introduces air inside the mold. The top cover was thus equipped with a set of holes which allowed gas extraction, obtained by using a vacuum chamber at -0.8 bar. The mold, containing the reagents still in the liquid phase, was left for 15 minutes in the vacuum chamber to ensure a proper elimination of air bubbles and then the curing step started. The mold was placed in rotation through a stepper motor in order to avoid the settling of the iron particles due to the gravity and it was kept for six hours in a climatic chamber at 45°C to ensure the complete polymerization of the elastomeric matrix. Without this procedure the specimens particles are going to settle and the volume fraction in the specimen changes, as shown in Figure 3a. The rotating system and the specimen filling operation need to be carefully done, otherwise inner formation of air bubbles could occur. This issue is particularly difficult to be spotted, since the centripetal acceleration on the air bubbles lead al the porosity to coalesce in one big cavity in the center of the specimens, which can be seen only by halving the specimen as show in Figure 3b.

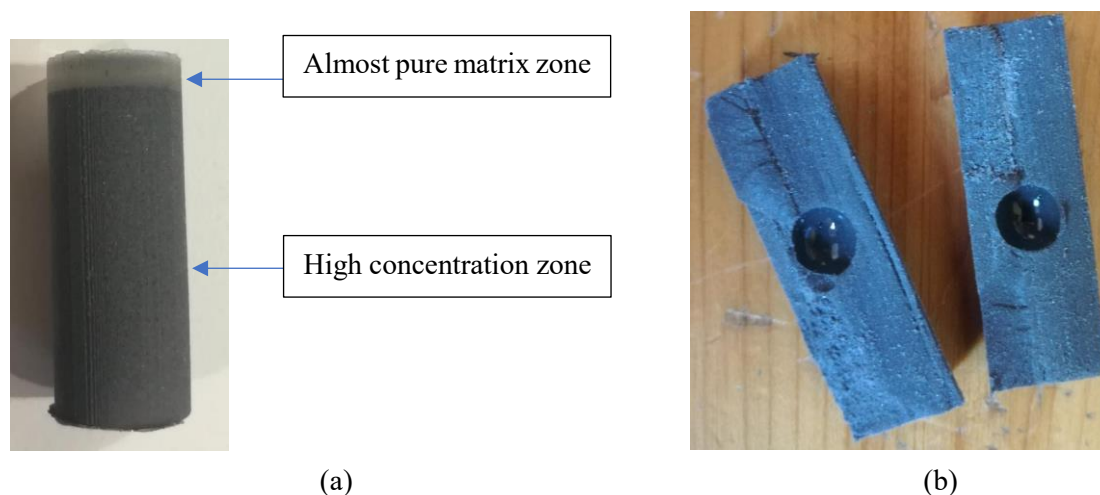


Figure 3. Specimen without the rotating system, effect of gravity (a), specimen with high rotation speed, effect of centripetal acceleration on air.

A total of 14 specimens were manufactured according to the previously described procedure. First, the isotropic specimens were obtained, with different percentages by weight of ferromagnetic material (60%

- 70% -80%), three samples for each volume fraction considered. In order to produce the other 8 anisotropic specimens, a couple of Nd-Fe-Br permanent magnets were placed around the mold when the system was still uncured. The mold was designed to kept the magnet in place while rotating, proving a constant magnetic field inside the specimens. The effect of the magnetic field led to the formation of an aligned arrangement of particles inside the specimens. The magnetic induction field provided by the magnets, measured experimentally through a Gaussmeter (in air), was around 200 mT, enough to obtain particle movement and chain formation. In the end, the last 2 control specimens of pure PDMS, with no ferromagnetic particles, were manufactured to estimate the base material properties under the same test conditions of the magnetorheological samples. The specimens were tested in shear, by means of a classical pin and fork rig, as shown in Figure 4. This configuration allows a quasi pure shear on the MRE without any need of other fixtures or adhesives. The shear stress in the cylinder can be easily determined, according to following equation and to the dimensions in the sketch reported in Figure 4a.

$$\tau = \frac{F}{2\pi d^2/4}$$

The shear strain is, using a small strain approach

$$\gamma = \frac{d}{h}$$

Being h the gap between the two rigid fixtures, which is equal to 0.2mm.

The complete system is reported in Figure 4b. The elastomeric matrix is very soft and the stiffness of the 3D printed system is nearly two times higher, so that the deformation measure is not disturbed by the test rig. The tensile test was not taken into consideration because the gripping of elastomers causes severe stress concentrations, which undermine the test results, and in addition the elastomers do not perform well under tensile stresses. The shear stress test procedure was divided in two parts. The first set of tests were non-destructive since we decided to limit the test to the elastic properties of the material and no plasticization is expected for a hyper elastic material. The desired test conditions were ensured by limiting the maximum force to 100 N and applying a cyclic displacement. This limit values were calibrated after a set of preliminary tests, in order to avoid possible damage of the specimen. The tests have the aim to register the loading/unloading curve in order to estimate the viscoelastic effect. The

experimental plan included the execution of the compression and the three-point bending tests on 18 specimens. Table 1 reports a synthetic representation of the variables considered.

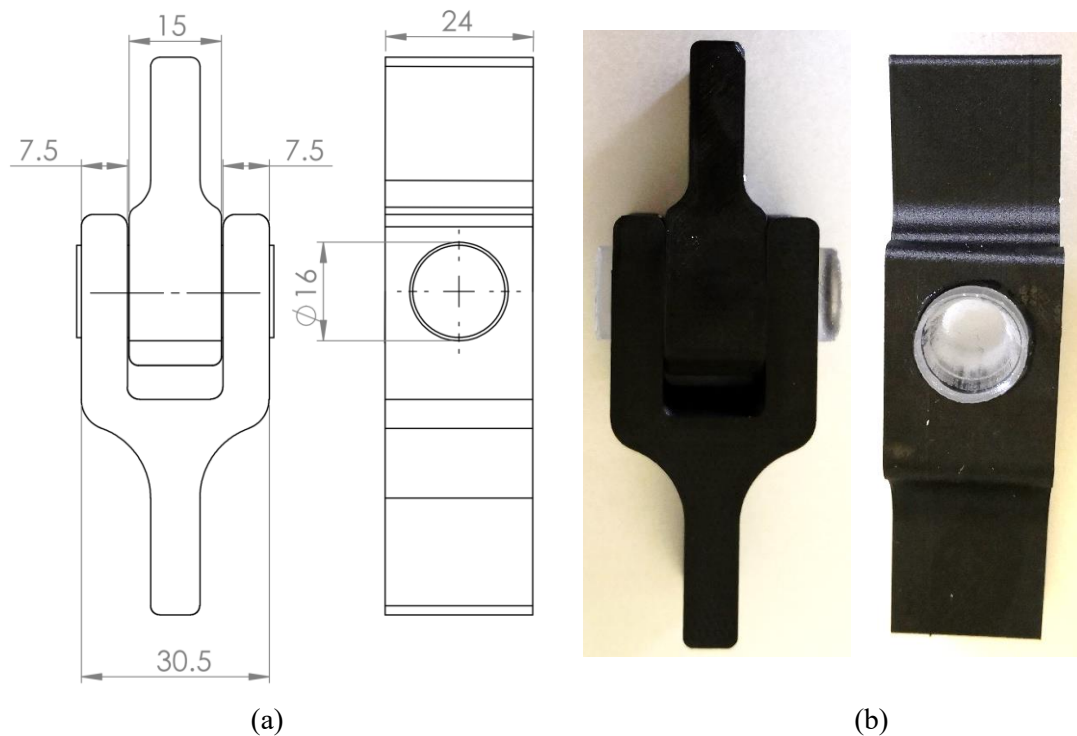


Figure 4. Schematic of the test rig with dimensions (not to scale) and 3d printed test rig with pure elastomeric specimen.

Table 1. Specimens considered in the design plan

Variable	Number of Levels							
% ferromagnetic material	3 levels	0	60		70		80	
Isotropy	Boolean	N/A	YES	NO	YES	NO	YES	NO
Replicates	2	2	2		2		2	
Total specimens	14	2	4		4		4	

The output responses to be computed on the basis of the experimental curves are:

- Tangential stiffness, as the slope of the first elastic part of the stress-strain curves (MPa)
- Specific dissipated energy (mJ/mm³)
- Maximum tangential stress at failure (MPa)
- Maximum tangential strain at failure (%)

2. PRELIMINARY RESULTS

Figure 5 shows the τ - γ curves for the isotropic specimens without the applied field (a) and with the field applied during the compression test (b). The curves in red represents the pure elastomer specimen, which is the same for both the charts, while the three brownish curves in Figure 5a represents the isotropic specimens while the three blue curves in Figure 5b show the anisotropic ones. The other destructive test are under analysis at the moment and will be added to the complete presentation of the results during the Ecomas – Smart Conference.

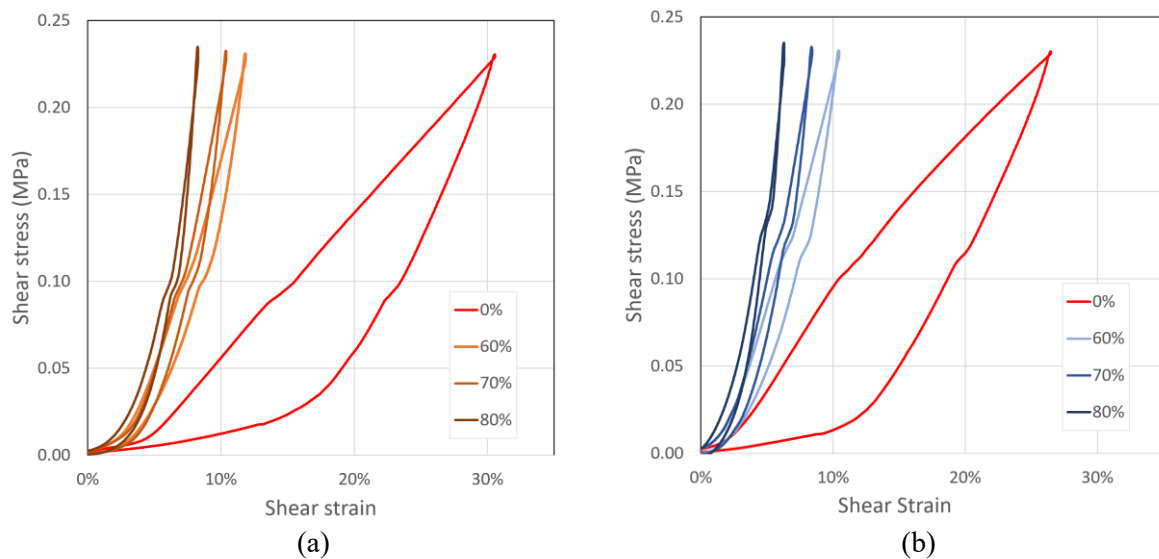


Figure 5. Shear test on isotropic specimens, without (a) and with the field applied (b).

3. DISCUSSION AND CONCLUSION

The discussion and the conclusion of the present work are undermined by several experimental issue occurred during the experimental tests, which drastically stopped the test campaign. The main cause of was an unexpected failure of the control board of the machine needed to carry out the cyclic test, which prevented the experimental campaign to be completed. The selected statistical analysis of the results make little sense with only partial results. The authors believe the test machine will be restored in time to present a proper discussion of the results during the conference.

REFERENCES

- Anderson MJ and Whitcomb PJ (2007) DOE Simplified: Practical Tools for Effective Experimentation, Second Edition. *DOE Simplified: Practical Tools for Effective Experimentation, Second Edition*. Productivity Press: Productivity Press; 2 edition.
- Bellelli A and Spaggiari A (2019) Magneto-mechanical characterization of magnetorheological elastomers. *Journal of Intelligent Material Systems and Structures*. SAGE PublicationsSage UK: London, England: 1045389X1982882. DOI: 10.1177/1045389X19828828.
- Carlson JD and Jolly MR (2000) MR fluid, foam and elastomer devices. *Mechatronics* 10(4–5): 555–569. DOI: 10.1016/S0957-4158(99)00064-1.
- Chen L, Gong XL and Li WH (2007) Microstructures and viscoelastic properties of anisotropic magnetorheological elastomers. *Smart Materials and Structures* 16(6): 2645–2650. DOI: 10.1088/0964-1726/16/6/069.
- Cross R (2012) Elastic and viscous properties of Silly Putty. *American Journal of Physics* 80(10). American Association of Physics Teachers: 870–875. DOI: 10.1119/1.4732086.
- Davis LC (1999) Model of magnetorheological elastomers. *Journal of Applied Physics* 85(6): 3348. DOI: 10.1063/1.369682.
- de Vicente J, Klingenberg DJ and Hidalgo-Alvarez R (2011) Magnetorheological fluids: a review. *Soft Matter* 7(8). The Royal Society of Chemistry: 3701. DOI: 10.1039/c0sm01221a.
- Dow Corning Sylgard 184 TDS | Krayden (2013). Available at: https://krayden.com/technical-data-sheet/dow_corning_184_technical_data_sheet/ (accessed 13 September 2018).
- Ginder JM, Nichols ME, Elie LD, et al. (2000) Controllable-stiffness components based on magnetorheological elastomers. *SPIE's 7th Annual International Symposium on Smart Structures and Materials* 3985: 418–425. DOI: 10.1117/12.388844.
- Golinelli N, Spaggiari A and Dragoni E (2015) Mechanical behaviour of magnetic Silly Putty: Viscoelastic and magnetorheological properties. *Journal of Intelligent Material Systems and Structures*: 1045389X15591655-epub ahead of print July, 8 2015. DOI: 10.1177/1045389X15591655.

- Guan X, Dong X and Ou J (2008) Magnetostrictive effect of magnetorheological elastomer. *Journal of Magnetism and Magnetic Materials* 320(3–4): 158–163. DOI: 10.1016/j.jmmm.2007.05.043.
- Güth D, Wiebe A, Maas J, et al. (2013) Design of shear gaps for high-speed and high-load MRF brakes and clutches. *Journal of Physics: Conference Series* 412(1). IOP Publishing: 012046. DOI: 10.1088/1742-6596/412/1/012046.
- Kachroudi A, Basrour S, Rufer L, et al. (2015) Piezoelectric cellular micro-structured PDMS material for micro-sensors and energy harvesting. *Journal of Physics: Conference Series* 660(1). IOP Publishing: 012040. DOI: 10.1088/1742-6596/660/1/012040.
- Kachroudi A, Basrour S and Sylvestre A (2017) Thermal Stability of Micro-Structured PDMS Piezo-Electrets under Various Polymeric Reticulation Ratios for Sensor Applications. *Proceedings* 1(4): 310. DOI: 10.3390/proceedings1040310.
- Kallio M (2005) *The elastic and damping properties of magnetorheological elastomers*, PhD Thesis. Vtt Publications. VTT Technical Research Centre of Finland.
- Marc Hartzman (2013) A Touch of Knowledge: The Very Serious History of Silly Putty | HuffPost. Available at: https://www.huffingtonpost.com/marc-hartzman/a-touch-of-knowledge-the-_2_b_1308405.html?guccounter=1 (accessed 13 September 2018).
- Mead R (1990) *The Design of Experiments: Statistical Principles for Practical Applications*. Cambridge University Press. Available at: <https://books.google.com/books?hl=it&lr=&id=CaFZPbCllrMC&pgis=1> (accessed 3 November 2015).
- Montgomery DC (2004) Design and Analysis of Experiments. *Design and Analysis of Experiments*. Wiley: John Wiley and Sons.
- Pometon (n.d.) Metal granules production iron powders supplier - POMETON POWDER. Available at: http://www.pometon.com/materialsScheda_eng.php/prodotto=selefer/id_prod=17/from=search (accessed 13 September 2018).
- R. Mead, S. G. Gilmour AM (2012) *Statistical Principles for the Design of Experiments: Applications to Real Experiments*. Available at: <http://www.amazon.com/Statistical-Principles-Design-Experiments-Probabilistic/dp/0521862140> (accessed 3 November 2015).

- Ruddy C, Ahearne E and Byrne G (2008) A REVIEW OF MAGNETORHEOLOGICAL ELASTOMERS: PROPERTIES AND APPLICATIONS. Available at: [http://www.ucd.ie/mecheng/ams/news_items/Cillian Ruddy.pdf](http://www.ucd.ie/mecheng/ams/news_items/Cillian_Ruddy.pdf) (accessed 8 March 2017).
- Schubert G and Harrison P (2015) Large-strain behaviour of Magneto-Rheological Elastomers tested under uniaxial compression and tension, and pure shear deformations. *Polymer Testing* 42. Elsevier Ltd: 122–134. DOI: 10.1016/j.polymertesting.2015.01.008.
- Shen Y, Golnaraghi MF and Heppler GR (2004) Experimental Research and Modeling of Magnetorheological Elastomers. *Journal of Intelligent Material Systems and Structures* 15(1): 27–35. DOI: 10.1177/1045389X04039264.
- Spaggiari A, Castagnetti D, Golinelli N, et al. (2016) Smart materials: Properties, design and mechatronic applications. *Proceedings of the Institution of Mechanical Engineers, Part L: Journal of Materials: Design and Applications* 0(0): 1–29. DOI: 10.1177/1464420716673671.
- Wiehe A and Maas J (2012) Large-scale test bench for the durability analysis of magnetorheological fluids. *Journal of Intelligent Material Systems and Structures* 24(12): 1433–1444. DOI: 10.1177/1045389X12453960.
- Yang C, Fu J, Yu M, et al. (2015) A new magnetorheological elastomer isolator in shear–compression mixed mode. *Journal of Intelligent Material Systems and Structures* 26(10). SAGE PublicationsSage UK: London, England: 1290–1300. DOI: 10.1177/1045389X14541492.

VARIATIONAL INEQUALITIES FOR FERROELECTRIC CONSTITUTIVE MODELING

MARTIN MEINDLHUMER*; ASTRID S. PECHSTEIN* AND
ALEXANDER HUMER*

*Institute of Technical Mechanics
Johannes Kepler University Linz
Altenberger Str. 69, 4040 Linz, Austria
e-mail: martin.meindlhumer@jku.at, astrid.pechstein@jku.at, alexander.humer@jku.at

Key words: ferroelectricity, polarization, variational inequality, mixed finite elements

Abstract. This paper is concerned with modeling the polarization process in ferroelectric media. We propose to use variational inequalities to describe electromechanical hysteresis phenomena as arise in piezoelectric materials. Thermodynamically consistent formulations are based on the free energy, phenomenological models usually comprise a set of switching and saturation conditions for the onset and saturation of the remanent polarization and strains. While thermodynamically consistent models naturally lead to variational formulations, we aim at combining the different phenomenological conditions into one variational inequality. In our formulation we use one Lagrange multiplier for each condition (the onset of domain switching and saturation), each satisfying Karush-Kuhn-Tucker conditions. An update for reversible and remanent quantities is then computed within one, in general nonlinear, iteration.

1 INTRODUCTION

In the current work we aim at describing the process of polarization in ferroelectric media. Polarization has been described as a dissipative process in a thermodynamically consistent framework based on the Helmholtz free energy in a series of papers by Bassiouny, Ghaleb and Maugin [1, 2, 3, 4]. The notions introduced there are close to the theory of elasto-plasticity, including internal variables, yield conditions and hardening moduli. The evolution of the internal variables is based on inequality constraints, such as the so-called switching condition. This condition defines the onset of remanent polarization in ferroelectric media.

McMecking and Landis [12] as well as Landis [11] developed their theory of multi-axial polarization based on those early works. The internal variables are the polarization vector in [12], and an independent polarization strain is added in [11]. They specified non-linear free energy functions that account also for the saturation phenomenon. Once reaching saturation, the polarization cannot grow any further, but may change direction or be reduced by (electric or mechanic) depolarization.

Kamlah and Tsakmakis [8] chose a different set of conditions to describe the polarization process, see also the overview given in [7]. They assume the reversible part of the free energy to be quadratic, and add separate switching and saturation conditions for remanent polarization and remanent polarization strain.

All of these frameworks have been implemented in finite element codes by various authors. Kamlah and Boehle [9] provided the increments for the evolution polarization and polarization strain for the material described in [8]. Klinkel [10] presented a return mapping algorithm realizing Landis-type material properties. Semenov et al. [20] provide such an algorithm for a finite element formulation including the vector (not scalar) potential of the dielectric displacement vector. Elhadrouz and co-workers [5] implemented a material model including different switching functions for polarization and polarization strain, similar as proposed by [8]. Zouari et al. [22] proposed a quadratic element realizing a Kamlah-type constitutive law.

We will follow Kamlah's approach, but formulate the theory in the framework of variational inequalities. These inequalities arise naturally from energy-based constitutive models with dissipation, see [14] for the application to Landis-type and also ferromagnetic materials. In our case, we add both switching and saturation condition for the remanent polarization. In the following derivations, we will see that, in the variational framework, these conditions are not independent as proposed in [7], but that the Lagrangian multiplier enforcing saturation becomes an additional term in the switching criterion. This way, both criteria can be satisfied at once.

Concerning the finite element implementation, we use mixed finite elements for the mechanical unknowns, adding independent stresses. We use non-standard TDNNS elements, where tangential displacements and the normal component of the normal stress are chosen as degrees of freedom [15, 18]. These elements were adapted to linear piezoelectricity in [17, 13].

2 A PHENOMENOLOGICAL MATERIAL LAW

In this section we briefly introduce the phenomenological material model in the spirit of Kamlah [7], before switching to an energy-based model in the next section. We consider a ferroelectric body in the domain $\Omega \in \mathbb{R}^3$ with the boundary $\partial\Omega$. We are concerned with isothermic, rate independent and quasi-static deformation and polarization processes. We are interested in finding the displacement field \mathbf{u} , the electric potential ϕ and the remanent polarization \mathbf{P}_I .

The electric field is introduced as the negative gradient of the electric potential $\mathbf{E} = -\nabla\phi$, whereas we use the linear strain tensor $\boldsymbol{\varepsilon} = \frac{1}{2}(\nabla\mathbf{u} + \nabla\mathbf{u}^T)$. The electrical and mechanical balance equations are

$$-\operatorname{div} \boldsymbol{\sigma} = \mathbf{f} \quad (1)$$

$$-\operatorname{div} \mathbf{D} = 0 \quad (2)$$

for the stress tensor $\boldsymbol{\sigma}$ and the dielectric displacement \mathbf{D} . The mechanical boundary conditions are

$$\mathbf{u} = \mathbf{u}_0 \text{ on } \Gamma_1 \quad \text{and} \quad \boldsymbol{\sigma} \cdot \mathbf{n} = \boldsymbol{\sigma}_0 \text{ on } \Gamma_2 = \partial\Omega \setminus \Gamma_1, \quad (3)$$

and the electrical boundary conditions

$$\phi = \phi_0 \text{ on } \Gamma_3 \quad \text{and} \quad \mathbf{D} \cdot \mathbf{n} = \rho_0 \text{ on } \Gamma_4 = \partial\Omega \setminus \Gamma_3. \quad (4)$$

The constitutive model relates stress $\boldsymbol{\sigma}$ and dielectric displacement \mathbf{D} to strain $\boldsymbol{\varepsilon}$ and electric field \mathbf{E} as well as to the remanent polarization \mathbf{P}_I . A basic assumption is the additive decomposition of dielectric displacement and elastic strain into a reversible and a remanent part. For the reversible parts, constitutive equations analogous to Voigt's linear theory are assumed

$$\boldsymbol{\varepsilon}_R = \boldsymbol{\varepsilon} - \boldsymbol{\varepsilon}_I = \mathbf{S}^E \cdot \boldsymbol{\sigma} + \mathbf{d}^T \cdot \mathbf{E} \quad (5)$$

$$\mathbf{D}_R = \mathbf{D} - \mathbf{P}_I = \mathbf{d} \cdot \boldsymbol{\sigma} + \boldsymbol{\epsilon}^\sigma \cdot \mathbf{E}. \quad (6)$$

The mechanical compliance tensor \mathbf{S}^E as well as the dielectric tensor ϵ^σ are assumed to be isotropic and constant. The components of the dielectric tensor depend on \mathbf{P}_I via

$$d_{kji}(\mathbf{P}_I) = \frac{\mathbf{P}_I}{P_{sat}} \left[d_p e_i^P e_j^P e_k^P + d_n (\delta_{ij} - e_i^P e_j^P) e_k^P + d_t \frac{1}{2} ((\delta_{ki} - e_k^P e_i^P) e_j^P + (\delta_{kj} - e_k^P e_j^P) e_i^P) \right] \quad (7)$$

with unit vector in direction of polarization

$$\mathbf{e}^P = \frac{\mathbf{P}_I}{|\mathbf{P}_I|}, \quad (8)$$

and the Kronecker delta

$$\delta_{ij} = \begin{cases} 1, & \text{if } i = j, \\ 0, & \text{if } i \neq j. \end{cases} \quad (9)$$

The unpolarized material does not show any piezoelectric coupling effects. The dielectric tensor grows (linearly) with the norm of \mathbf{P}_I . The constants d_p , d_n and d_t correspond to the standard parameters d_{33} , d_{31} and d_{15} , respectively, for the fully poled state with polarization in direction of \mathbf{e}_3 . As proposed by McMeeking and Landis [12], the remanent strain is volume-preserving and depends only on the polarization via

$$\epsilon_I = \frac{3}{2} \frac{S_{sat}}{P_{sat}^2} \left(\mathbf{P}_I \otimes \mathbf{P}_I - \frac{1}{3} \mathbf{I} |\mathbf{P}_I|^2 \right), \quad (10)$$

where S_{sat} characterizes the maximum possible remanent strain. The polarization strain ϵ_I is a deviatoric uni-axial strain and does not cause any further remanent strain.

The evolution of the remanent polarization \mathbf{P}_I is determined by switching and saturation conditions. Once the electric field is increased above the coercive field strength E_C , the material will be polarized irreversibly. The switching condition is a condition on the electric driving force $\hat{\mathbf{E}}$ which will be defined in Section 3. In the simplest case, the absolute value of $\hat{\mathbf{E}}$ may not exceed E_C ,

$$f_P = |\hat{\mathbf{E}}| - E_C \leq 0. \quad (11)$$

On the other hand, the saturation condition states that the remanent polarization must not exceed the saturation polarization, which resembles the fully polarized state. The condition reads

$$f_S(\mathbf{P}_I) = |\mathbf{P}_I| - P_{sat} \leq 0 \quad (12)$$

3 ENERGY/ENTHALPY-BASED FORMULATION

We provide energies matching the constitutive equations from the previous section as a basis for all further deductions. According to the literature [11, 7, 21], the free energy decomposes into two parts,

$$\Psi = \Psi^R + \Psi^I, \quad (13)$$

with the reversible or stored part Ψ^R and the (irreversible) additional contribution Ψ^I . The reversible part Ψ^R is given by

$$\Psi^R = \frac{1}{2} \mathbf{E} \cdot (\mathbf{d} : \boldsymbol{\sigma} + \epsilon \cdot \mathbf{E}) + \frac{1}{2} \boldsymbol{\sigma} : (\mathbf{S}^E : \boldsymbol{\sigma} + \mathbf{d} \cdot \mathbf{E}). \quad (14)$$

The additional contribution of the free energy is given by

$$\Psi^I = \frac{1}{2} c \mathbf{P}_I \cdot \mathbf{P}_I, \quad (15)$$

in the simplest case as used by Kamlah [7].

An additional term representing saturation is added in the following. The saturation condition $f_S \leq 0$ (cmp. (12)) is equivalent to an inequality involving the Lagrangian multiplier λ_S ,

$$\lambda_S f_S(\mathbf{P}_I) \leq 0 \quad \text{for all } \lambda_S \geq 0. \quad (16)$$

The updated energy function Ψ^S taking into account saturation is then given by

$$\Psi^S = \Psi^R + \Psi^I + \sup_{\lambda_S \geq 0} \lambda_S f_S(\mathbf{P}_I). \quad (17)$$

As long as $f_S \leq 0$, the supremum in (17) takes zero value, and Ψ^S is equal to the energy function Ψ in (13). If the saturation condition is violated ($f_S > 0$), $\sup_{\lambda_S \geq 0} \lambda_S f_S$ tends to infinity, and with it the energy function Ψ^S .

The enthalpy is introduced as a function of the electric field \mathbf{E} , the mechanical stress $\boldsymbol{\sigma}$, the irreversible polarization \mathbf{P}_I via

$$H = \Psi^R + \Psi^I + \sup_{\lambda_S \geq 0} f_S(\mathbf{P}_I) \lambda_S - \mathbf{E} \cdot \mathbf{D}(\mathbf{E}, \boldsymbol{\sigma}, \mathbf{P}_I) - \boldsymbol{\sigma} : \boldsymbol{\varepsilon}(\mathbf{E}, \boldsymbol{\sigma}, \mathbf{P}_I), \quad (18)$$

with $\mathbf{D}(\mathbf{E}, \boldsymbol{\sigma}, \mathbf{P}_I)$ and $\boldsymbol{\varepsilon}(\mathbf{E}, \boldsymbol{\sigma}, \mathbf{P}_I)$ according to (5) and (6), respectively. From the (total) enthalpy H the driving force $\hat{\mathbf{E}}$ mentioned in Section 2 can be derived. It is defined as the (negative) derivative of the enthalpy by the irreversible quantities, in our case by \mathbf{P}_I . In contrast to the original model by Kamlah, the driving force thus contains λ_S , which is non-zero in case of saturation,

$$\hat{\mathbf{E}} = -\frac{\partial H}{\partial \mathbf{P}_I} = \mathbf{E} + \boldsymbol{\sigma} : \left(\frac{d}{d\mathbf{P}_I} \mathbf{d} \right) \cdot \mathbf{E} + \boldsymbol{\sigma} : \left(\frac{d}{d\mathbf{P}_I} \boldsymbol{\varepsilon}_I \right) - c \mathbf{P}_I - \lambda_S \frac{df_S}{d\mathbf{P}_I} \quad (19)$$

The energy dissipation rate is given by [14]

$$\Phi = \hat{\mathbf{E}} \cdot \dot{\mathbf{P}}_I. \quad (20)$$

3.1 From an Incremental optimization principle to a variational inequality

The (total) free energy and the dissipation can be related to an incremental constitutive minimization principle, which can be found in detail in [14]. As the enthalpy is to be minimized and maximized with respect to different quantities we, in the sequel use the terminus optimization problem. The (total) enthalpy and dissipated energy are to be optimized under side constraints. These are the switching condition (10) and the balance equations (1) - (2).

$$H + \Phi \rightarrow \max_{\mathbf{E}} \max_{\boldsymbol{\sigma}} \min_{\mathbf{P}_I} \text{ subject to } \begin{cases} \operatorname{div} \boldsymbol{\sigma} = 0 \\ f_P(\hat{\mathbf{E}}) \leq 0 \end{cases} \quad (21)$$

Note that, here and in the remainder of Section 3, we neglect the work of external forces. Of course, in finite element implementations, external forces are added in the standard way to the right hand side of the variational equations or inequalities.

The treatment of equilibrium side condition is well known. For the mechanical balance equation the deformation \mathbf{u} can be interpreted as an Lagrangian multiplier, and therefore the product $-\operatorname{div} \boldsymbol{\sigma} \cdot \mathbf{u}$ is added.

In order to consider the inequality side condition for the polarization, another Lagrangian multiplier is introduced, such that the Karush-Kuhn-Tucker conditions (KKT-conditions) are fulfilled,

$$f_P \leq 0, \quad \lambda_P \geq 0, \quad \lambda_P f_P = 0 \quad (22)$$

The Lagrangian of the enthalpy is introduced below, where both λ_S and λ_P as well as \mathbf{u} are viewed as independent unknowns. For convenience, it also contains the dissipated energy,

$$\hat{H}(\mathbf{E}, \boldsymbol{\sigma}, \mathbf{P}_I, \mathbf{u}, \lambda_S, \lambda_P) = \Psi^R + \Psi^I + \Phi - \mathbf{E} \cdot \mathbf{D} - \boldsymbol{\sigma} : \boldsymbol{\varepsilon} + f_S(\mathbf{P}_I) \lambda_S + \lambda_P f_P(\hat{\mathbf{E}}) - \operatorname{div} \boldsymbol{\sigma} \cdot \mathbf{u}. \quad (23)$$

The optimization problem to be solved is now

$$\hat{H} \rightarrow \min_{\mathbf{u}} \max_{\mathbf{E}} \max_{\boldsymbol{\sigma}} \min_{\mathbf{P}_I} \max_{\lambda_P} \max_{\lambda_S} \quad (24)$$

As the Lagrangian multipliers λ_S and λ_P are constrained to be non-negative, the variation of \hat{H} leads to a variational inequality. Variation with respect to \mathbf{u} , \mathbf{E} , $\boldsymbol{\sigma}$ and \mathbf{P}_I can be done in the standard way, as any virtual values $\delta \boldsymbol{\sigma}$, $\delta \mathbf{u}$, $\delta \mathbf{E}$ and $\delta \mathbf{P}_I$ which fulfill the kinematic (Dirichlet) boundary conditions are admissible. A variational equation is obtained, where the right hand side has to be replaced by δW^{ext} when including external forces,

$$\frac{\partial \hat{H}}{\partial \mathbf{E}} \cdot \delta \mathbf{E} + \frac{\partial \hat{H}}{\partial \boldsymbol{\sigma}} : \delta \boldsymbol{\sigma} + \frac{\partial \hat{H}}{\partial \mathbf{P}_I} \cdot \delta \mathbf{P}_I + \frac{\partial \hat{H}}{\partial \mathbf{u}} \cdot \delta \mathbf{u} = 0. \quad (25)$$

The saturation and polarization condition, which are given as inequalities, cannot be treated in the standard way. As the set of admissible λ_P and λ_S is restricted $\delta \lambda_P$ and $\delta \lambda_S$ are not arbitrary. These conditions directly lead to variational inequalities, we refer to the monograph [6] for an introduction into variational inequalities in the framework of elasto-plasticity. For both, λ_P and λ_S a test function $\bar{\lambda}_P$ and $\bar{\lambda}_S$ is introduced. One directly deduces that \hat{H} is maximized with respect to λ_P if and only if for all other admissible choices $\bar{\lambda}_P \geq 0$ there holds

$$\bar{\lambda}_P f_P(\hat{\mathbf{E}}) \leq \lambda_P f_P(\hat{\mathbf{E}}) \quad \forall \bar{\lambda}_P \geq 0, \quad (26)$$

For λ_S , the situation is a bit more involved, as $\hat{\mathbf{E}}$ depends on λ_S . Writing $\tilde{\mathbf{E}}$ for $\hat{\mathbf{E}}(\bar{\lambda}_S)$ for some $\bar{\lambda}_S \geq 0$, one finds that \hat{H} is maximized with respect to $\bar{\lambda}_S$ if and only if

$$\tilde{\mathbf{E}} \cdot \dot{\mathbf{P}}_I + \bar{\lambda}_S f_S(\mathbf{P}_I) + \lambda_P f_P(\tilde{\mathbf{E}}) \leq \hat{\mathbf{E}} \cdot \dot{\mathbf{P}}_I + \lambda_S f_S(\mathbf{P}_I) + \lambda_P f_P(\hat{\mathbf{E}}) \quad \forall \bar{\lambda}_S \geq 0. \quad (27)$$

Inserting the definition of $\tilde{\mathbf{E}}$, which implies that $\tilde{\mathbf{E}} - \hat{\mathbf{E}} = -(\bar{\lambda}_S - \lambda_S) d\mathbf{f}_P / d\mathbf{P}_I$, the above inequality can be further reduced to

$$(\bar{\lambda}_S - \lambda_S) \left(-\frac{df_S}{d\mathbf{P}_I} \cdot \dot{\mathbf{P}}_I + f_S - \lambda_P \frac{df_P}{d\mathbf{E}} \frac{df_S}{d\mathbf{P}_I} \right) \leq 0 \quad \forall \bar{\lambda}_S \geq 0. \quad (28)$$

Summing up, the variational inequality to hold for all $\delta \mathbf{E}$, $\delta \boldsymbol{\sigma}$, $\delta \mathbf{P}_I$ and $\delta \mathbf{u}$ as well as $\bar{\lambda}_S \geq 0$ and $\bar{\lambda}_P \geq 0$ reads

$$\frac{\partial \hat{H}}{\partial \mathbf{E}} \cdot \delta \mathbf{E} + \frac{\partial \hat{H}}{\partial \boldsymbol{\sigma}} : \delta \boldsymbol{\sigma} + \frac{\partial \hat{H}}{\partial \mathbf{P}_I} \cdot \delta \mathbf{P}_I + \frac{\partial \hat{H}}{\partial \mathbf{u}} \cdot \delta \mathbf{u} + (\bar{\lambda}_P - \lambda_P) f_P + (\bar{\lambda}_S - \lambda_S) \left(f_S - \frac{df_S}{d\mathbf{P}_I} \cdot (\lambda_P \frac{df_P}{d\mathbf{E}} + \dot{\mathbf{P}}_I) \right) \leq 0. \quad (29)$$

3.2 Interpretation of the Lagrangian multipliers

For the uncoupled, purely electrical problem we briefly explain the meaning of the Lagrangian multipliers λ_P and λ_S . In this case, the driving force reduces to

$$\hat{\mathbf{E}} = \mathbf{E} - c\mathbf{P}_I - \lambda_S \frac{\mathbf{P}_I}{|\mathbf{P}_I|}. \quad (30)$$

The variational inequality (29) reads

$$\delta \left[-\frac{1}{2} \mathbf{E} \cdot \boldsymbol{\epsilon} \cdot \mathbf{E} - \mathbf{E} \cdot \mathbf{P}_I + \frac{c}{2} \mathbf{P}_I \cdot \mathbf{P}_I + \hat{\mathbf{E}} \cdot \dot{\mathbf{P}}_I \right] + \lambda_P \left(\frac{df_P}{d\hat{\mathbf{E}}} \frac{\partial \hat{\mathbf{E}}}{\partial \mathbf{E}} \delta \mathbf{E} + \frac{\partial f_P}{\partial \mathbf{P}_I} \delta \mathbf{P}_I \right) \quad (31)$$

$$+ (\bar{\lambda}_P - \lambda_P) f_P + (\bar{\lambda}_S - \lambda_S) \left(f_S - \frac{df_S}{d\mathbf{P}_I} \cdot (\lambda_P \frac{df_P}{d\hat{\mathbf{E}}} + \dot{\mathbf{P}}_I) \right) \leq 0 \quad (32)$$

We consider an update step with the (updated) solutions \mathbf{E} , \mathbf{P}_I , λ_P and λ_S . We introduce $\Delta \mathbf{P}_I$ as the update of the irreversible polarization between two calculation steps. As the considered process is rate independent and quasi-static the dissipation is given via $\hat{\mathbf{E}} \cdot \Delta \mathbf{P}_I$. Splitting up (31)-(32) into individual (in)equalities for the single variational quantities we get

$$\delta \mathbf{E} \left[\boldsymbol{\epsilon} \cdot \mathbf{E} - \mathbf{P}_I + \frac{\partial \hat{\mathbf{E}}}{\partial \mathbf{E}} \Delta \mathbf{P}_I + \lambda_P \frac{df_P}{d\hat{\mathbf{E}}} \frac{\partial \hat{\mathbf{E}}}{\partial \mathbf{E}} \right] = 0 \quad (33)$$

$$\delta \mathbf{P}_I \left[-\mathbf{E} + c\mathbf{P}_I + \hat{\mathbf{E}} + \frac{\partial \hat{\mathbf{E}}}{\partial \mathbf{P}_I} \Delta \mathbf{P}_I + \lambda_P \frac{df_P}{d\hat{\mathbf{E}}} \frac{\partial \hat{\mathbf{E}}}{\partial \mathbf{P}_I} + \lambda_S \frac{df_S}{d\mathbf{P}_I} \right] = 0 \quad (34)$$

$$(\bar{\lambda}_P - \lambda_P) f_P \leq 0 \quad (35)$$

$$(\bar{\lambda}_S - \lambda_S) \left(f_S - \frac{df_S}{d\mathbf{P}_I} \cdot (\lambda_P \frac{df_P}{d\hat{\mathbf{E}}} + \Delta \mathbf{P}_I) \right) \leq 0 \quad (36)$$

To get an interpretation of λ_P , consider a state, at which the polarization process has started, such that $f_P = 0$ and λ_P non-negative. From the variational equation (34), taking into account the definition (30) of $\hat{\mathbf{E}}$ and that $df_P/d\hat{\mathbf{E}} = \hat{\mathbf{E}}/|\hat{\mathbf{E}}|$, we get a relation between λ_P and $\Delta \mathbf{P}_I$

$$\frac{\partial \hat{\mathbf{E}}}{\partial \mathbf{P}_I} \left(\Delta \mathbf{P}_I + \lambda_P \frac{\hat{\mathbf{E}}}{|\hat{\mathbf{E}}|} \right). \quad (37)$$

From (37) one deduces that the polarization update $\Delta \mathbf{P}_I$ is in direction of $\hat{\mathbf{E}}$ with norm λ_P . On the other hand, if the coercive field is not reached and $f_P < 0$, (35) ensures that $\lambda_P = 0$ and further $\Delta \mathbf{P}_I = 0$.

Before we give an interpretation for λ_S , we first show that (36) really ensures the saturation condition. In case the coercive electric field is reached and $f_P = 0$, (37) holds, and thereby the last term in (36) reduces to zero, leaving KKT conditions for the saturation condition only. On the other hand, if the coercive field is not reached and $f_P < 0$, we have that $\lambda_P = 0$ and $\Delta \mathbf{P}_I = 0$, which again reduces the last term in (36) to zero. Thus the saturation condition has to be satisfied in any case.

For the interpretation of λ_S , we consider a fully poled state where the polarization condition is satisfied exactly. If one now takes a look at the polarization condition, which has to satisfy

$f_P = 0$ for this particular state, one observes

$$f_P = |\mathbf{E} - c\mathbf{P}_I - \lambda_S \frac{\mathbf{P}_I}{|\mathbf{P}_I|}| - E_C = 0. \quad (38)$$

If the electric field is reduced to a level below the coercive field, λ_S reduces to zero. A graphical interpretation of λ_P and λ_S can be found in Figure 1.

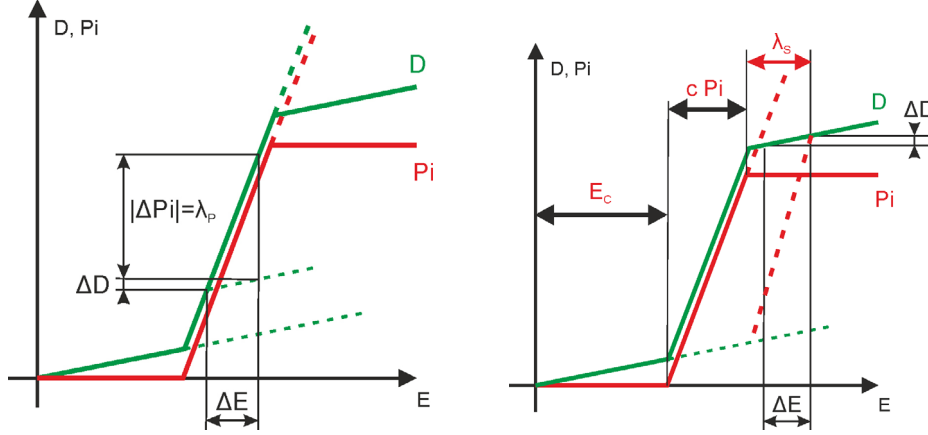


Figure 1: Graphical interpretation of Lagrange multipliers for polarization and saturation condition

4 FINITE ELEMENT METHOD

In this section, the proposed finite element discretization is described. For the electric potential continuous, nodal finite elements are used, while the polarization vector is approximated constant on each element. Also, the Lagrangian multipliers are realized taking one value per element. As already done in the derivations of Section 3, displacement and stress are considered independent unknowns. To do so, a mixed finite element scheme is used. The specific approach taken in this work uses tangential displacements and normal normal stresses as degrees of freedom, which motivate the abbreviation “TDNNS”. This method was originally developed for elastic solids [15, 16] and later extended for linear piezoelectric materials [17, 13] and for geometrically nonlinear electro-mechanically coupled problems [19].

This work is based on [17, 13] for linear piezoelectrics. Note that, for the mixed TDNNS method, the \mathbf{d} -tensor formulation can be used directly, and there is no need to transfer the electric permittivity at constant stress ϵ^σ to that at constant strain ϵ^ϵ algebraically, as is necessary in standard formulations. As the underlying mathematics of the TDNNS method are rather involved, we skip it here, and only mention that work pairs such as $\int_\Omega \boldsymbol{\sigma} : \boldsymbol{\epsilon}$ or $\int_\Omega \text{div } \boldsymbol{\sigma} \cdot \mathbf{u}$ need to be considered in distributional sense and involve additional integration on element boundaries.

To solve the variational inequality, an active-set strategy is proposed. This means, in each iterative step, two active sets are identified beforehand: the switching active set A_P where the switching condition shall be enforced as $f_P = 0$, and the saturation active set A_S where the polarization condition is enforced as $f_S = 0$. On the other hand, for all elements not in the active set, the Lagrangian multipliers λ_P and λ_S are set to zero, respectively. For these fixed active sets, the nonlinear equations are solved by Newton’s method, with λ_S and λ_P free in their

respective active sets. On convergence, the Kuhn-Tucker compatibility conditions are checked. All elements, where either saturation or switching condition are violated are added to the active set. On the other hand, all elements where a Lagrangian multiplier is found negative are removed from the respective active set. An according algorithm can be found in Algorithm 1

Data: values for $\mathbf{u}_0, \boldsymbol{\sigma}_0, \phi_0, \mathbf{P}_{I0}, \lambda_{S0}, \lambda_{P0}$ and active sets A_{S0}, A_{P0} from the last converged time step
Result: values for $\mathbf{u}, \boldsymbol{\sigma}, \phi, \mathbf{P}_I, \lambda_S, \lambda_P$, active sets A_S, A_P
initialize unknowns with initial data, active sets $A_S = A_{S0}, A_P = A_{P0}$;
while *the active sets change* **do**
 solve non-linear problem with $\lambda_S = 0$ in $\Omega \setminus A_S$, $\lambda_P = 0$ in $\Omega \setminus A_P$ and λ_S free in A_S ,
 λ_P free in A_P ;
 using starting values from last iteration;
 for *all elements* T **do**
 if $T \in A_P, T \notin A_S$ and $\lambda_P < 0$ **then**
 | remove T from A_P ;
 else if $T \notin A_P$ and $f_P > 0$ **then**
 | add T to A_P ;
 end
 if $T \notin A_S, T \in A_P$ and $f_S > 0$ **then**
 | add T to A_S ;
 else if $T \in A_S$ and $\lambda_S < 0$ **then**
 | remove T from A_S ;
 end
 end
end

Algorithm 1: Active set strategy for solving the variational inequality.

5 NUMERICAL RESULTS

In this section we show numerical results for two examples. First we show the standard hysteresis curves for the fully coupled homogeneous (uni-axial) problem. We show that the method allows mechanical depolarization. Our second example is mechanical depolarization of a fully polarized ferroelectric beam. This example was introduced as a ferroelastic benchmark by Zouari et. al [22].

5.1 Butterfly hysteresis

In our first example we show, that our implementation is capable of both, electrical polarization as well as electrical and mechanical depolarization. We consider an initially unpolarized unit square (1 mm by 1 mm) with electrodes on top and bottom. The material parameters are listed in Table 1. First the electrical polarization is shown. An electric field with a strength of two times the coercive field strength $2E_C$ is applied, is then reduced to $-2E_C$, and again increased up to $2E_C$. The resulting electric hysteresis, as well as the corresponding (mechanical) butterfly hysteresis are shown in Figure 2. The electric field is normalized by E_C , the polarization and the dielectric displacement by P_{Sat} and the (mechanical) strain by S_{sat} .

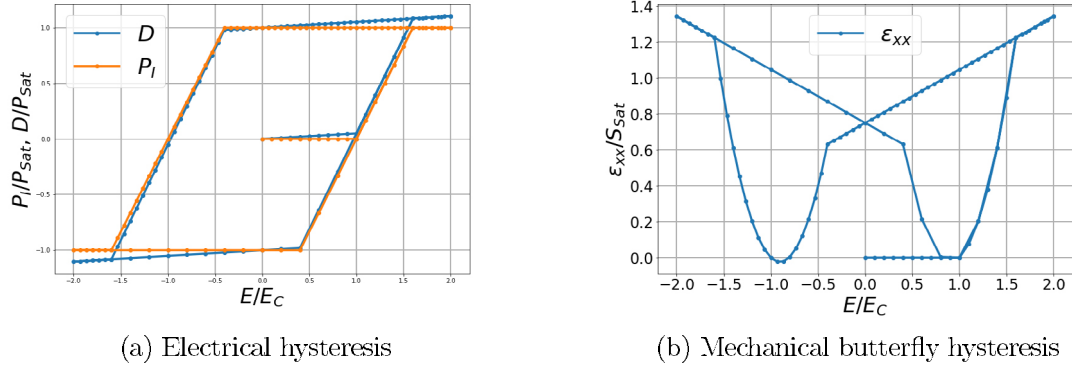


Figure 2: Electrical polarization of ferroelectric material

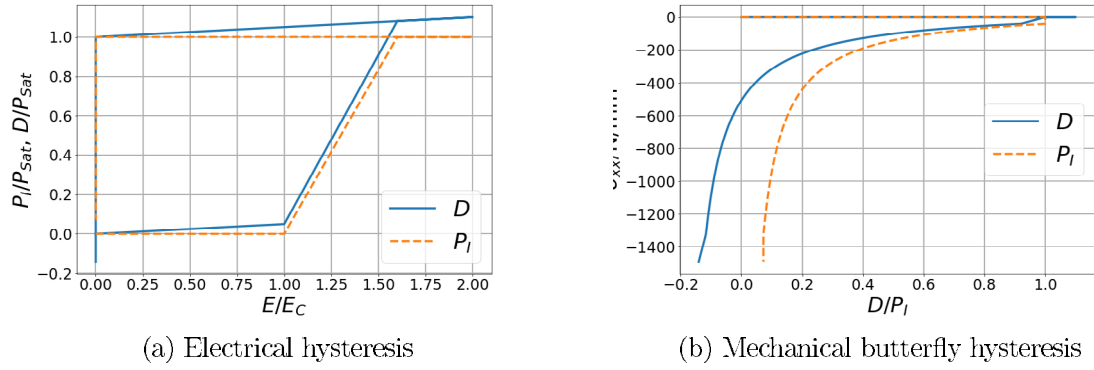


Figure 3: Electrical polarization of ferroelectric material

Next we show the effect of mechanical depolarization. The specimen is electrically polarized (field strength $2E_C$), then the electric field is reduced to 0. A mechanical compressive stress (aligned in polarization direction) is applied to the polarized material and mechanical depolarization can be observed. The mechanical depolarization curve is shown in Figure 3. Note, that the implemented constitutive material model leads to total mechanical depolarization ($\mathbf{P}_I = \mathbf{0}$) for sufficient high mechanical stress.

Table 1: Material parameter

Young's modulus	10^4 MPa	c	$2 \cdot 10^6$ Vm/C
Poisson's ratio	0.3	d_p	$5.93 \cdot 10^{-10}$ m/V
Coercive field	1 MV/m	d_n	$-2.74 \cdot 10^{-10}$ m/V
Saturation strain S_{sat}	0.002	d_t	$7.41 \cdot 10^{-10}$ m/V
Saturation polarization P_{sat}	0.3 C/m ²	ϵ	$1.5 \cdot 10^{-8}$ C/Vm

5.2 Depolarization of a ferroelectric beam

Our second example is a benchmark for ferroelastic media taken from the literature [23]. It is a cantilevered beam, fully polarized in its longitudinal direction and loaded with a tip force at its end. A sketch of the problem can be found in Figure 4. Grounded electrodes ($\phi = 0$) are located at the clamped and at the tip face (illustrated in red). The clamping is realized by restricting longitudinal displacement at the clamped face (blue dashed line) and transversal displacement in the middle of the beam (blue dot).

The tip force is realized as stress boundary condition, applying $\sigma_{xy} = 4 \text{ N/mm}^2$ at the tip face. Taking into account the dimensions this load equals the tip force in [23]. The bending of the beam leads to a compressive stress and therefore mechanical depolarization can be observed. The resulting polarization is shown in Figure 5. It decreases at the clamped face to 78% of the saturation polarization. The resulting stresses are shown in Figure 6. Due to the unsymmetrical remanent straining an unsymmetrical distribution of the bending stresses is to be observed. The results fit to [23]. Note that, in contrast to the reference, only ferroelectric but no ferroelastic effects are considered in the constitutive model.

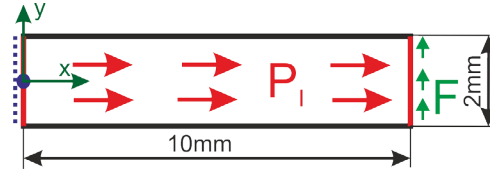


Figure 4: Sketch of fully polarized cantilever beam with tip load

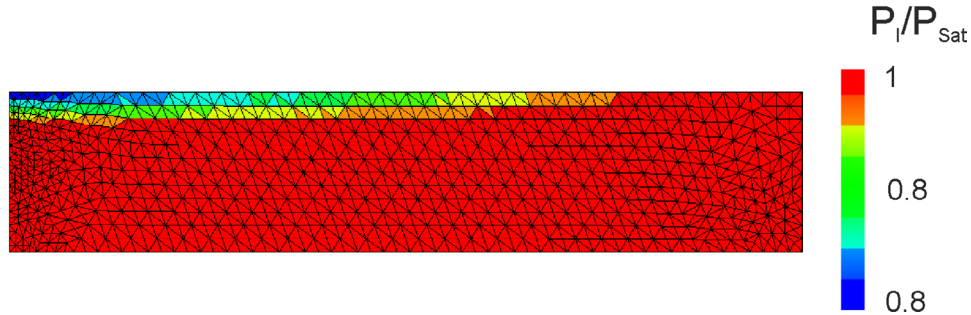


Figure 5: Polarization of the ferroelectric beam under tip load

6 ACKNOWLEDGEMENTS

Martin Meindlhumer acknowledges support of Johannes Kepler University Linz, Linz Institute of Technology (LIT).

REFERENCES

- [1] E. Bassiouny, A.F. Ghaleb, and G.A. Maugin. Thermodynamical formulation for coupled electromechanical hysteresis effects–I. Basic equations. *International Journal of Engineering Science*, 26(12):1279–1295, 1988.

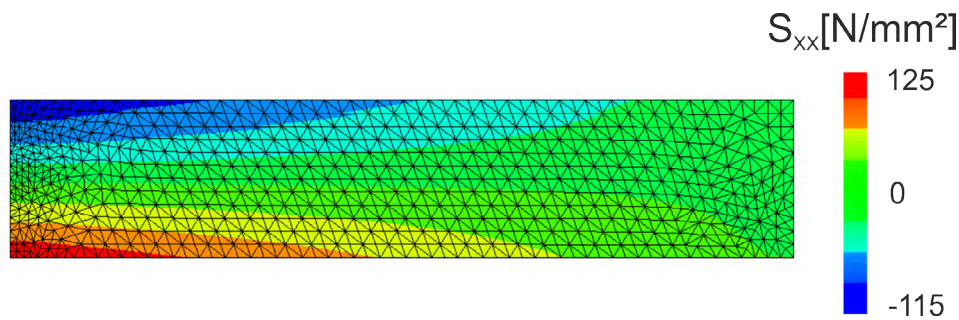


Figure 6: Stress σ_{xx} of the ferroelectric beam under tip load

- [2] E. Bassiouny, A.F. Ghaleb, and G.A. Maugin. Thermodynamical formulation for coupled electromechanical hysteresis effects–II. Poling of ceramics. *International Journal of Engineering Science*, 26(12):1297–1306, 1988.
- [3] E. Bassiouny and G.A. Maugin. Thermodynamical formulation for coupled electromechanical hysteresis effects–III. Parameter identification. *International Journal of Engineering Science*, 27(8):975–987, 1989.
- [4] E. Bassiouny and G.A. Maugin. Thermodynamical formulation for coupled electromechanical hysteresis effects–IV. Combined electromechanical loading. *International Journal of Engineering Science*, 27(8):989–1000, 1989.
- [5] Mourad Elhadrouz, Tarak Ben Zineb, and Etienne Patoor. Constitutive law for ferroelastic and ferroelectric piezoceramics. *Journal of intelligent material systems and structures*, 16(3):221–236, 2005.
- [6] W. Han and B.D. Reddy. *Plasticity: Mathematical Theory and Numerical Analysis*, volume 9. Springer Science & Business Media, 1999.
- [7] M. Kamlah. Ferroelectric and ferroelastic piezoceramics–modeling of electromechanical hysteresis phenomena. *Continuum Mechanics and Thermodynamics*, 13(4):219–268, 2001.
- [8] M. Kamlah and C. Tsakmakis. Phenomenological modeling of the non-linear electromechanical coupling in ferroelectricsfn2fn2dedicated to professor dr d. munz on the occasion of his 60th birthday. *International Journal of Solids and Structures*, 36(5):669 – 695, 1999.
- [9] Marc Kamlah and Ulrich Böhle. Finite element analysis of piezoceramic components taking into account ferroelectric hysteresis behavior. *International Journal of Solids and Structures*, 38(4):605–633, 2001.
- [10] S. Klinkel. A phenomenological constitutive model for ferroelastic and ferroelectric hysteresis effects in ferroelectric ceramics. *International Journal of Solids and Structures*, 43(22-23):7197–7222, 2006.
- [11] C.M. Landis. Fully coupled, multi-axial, symmetric constitutive laws for polycrystalline ferroelectric ceramics. *Journal of the Mechanics and Physics of Solids*, 50(1):127–152, 2002.

- [12] R.M. McMeeking and C.M. Landis. A phenomenological multi-axial constitutive law for switching in polycrystalline ferroelectric ceramics. *International Journal of Engineering Science*, 40(14):1553–1577, 2002.
- [13] Martin Meindlhumer and Astrid Pechstein. 3d mixed finite elements for curved, flat piezoelectric structures. *International Journal of Smart and Nano Materials*, 0(0):1–19, 2018.
- [14] C Miche, D Rosato, and B Kiefer. Variational principles in dissipative electro-magneto-mechanics: A framework for the macro-modeling of functional materials. *International Journal for Numerical Methods in Engineering*, 86(10):1225–1276, 2011.
- [15] A. Pechstein and J. Schöberl. Tangential-displacement and normal-normal-stress continuous mixed finite elements for elasticity. *Math. Models Methods Appl. Sci.*, 21(8):1761–1782, 2011.
- [16] A. Pechstein and J. Schöberl. Anisotropic mixed finite elements for elasticity. *Int. J. Numer. Methods Engrg.*, 90(2):196–217, 2012.
- [17] A.S. Pechstein, M. Meindlhumer, and A. Humer. New mixed finite elements for the discretization of piezoelectric structures or macro-fiber composites. *Journal of Intelligent Material Systems and Structures*, 2018. online first.
- [18] A.S. Pechstein and J. Schöberl. An analysis of the TDNNS method using natural norms. *Numerische Mathematik*, 139(1):93–120, 2018.
- [19] Astrid S Pechstein. Large deformation mixed finite elements for smart structures. *Mechanics of Advanced Materials and Structures*, pages 1–11, 2019.
- [20] A.S. Semenov, A.C. Liskowsky, and H. Balke. Return mapping algorithms and consistent tangent operators in ferroelectroelasticity. *International journal for numerical methods in engineering*, 81(10):1298–1340, 2010.
- [21] Jan Tichý, Jirí Erhart, Erwin Kittinger, and Jana Privratska. *Fundamentals of piezoelectric sensorics: mechanical, dielectric, and thermodynamical properties of piezoelectric materials*. Springer Science & Business Media, 2010.
- [22] W. Zouari, T.B. Zineb, and A. Benjeddou. A ferroelectric and ferroelastic 3d hexahedral curvilinear finite element. *International Journal of Solids and Structures*, 48(1):87–109, 2011.
- [23] Wajdi Zouari, Tarak Ben Zineb, and Ayech Benjeddou. A ferroelectric and ferroelastic 3d hexahedral curvilinear finite element. *International Journal of Solids and Structures*, 48(1):87 – 109, 2011.

A THERMOMECHANICALLY COUPLED FINITE-STRAIN CONSTITUTIVE MODEL FOR IRON-BASED SHAPE MEMORY ALLOYS ACCOUNTING FOR COUPLING BETWEEN PHASE TRANSFORMATION AND PLASTIC SLIDING

A. SALLAMI^{*}, W. KHALIL[§], T. BOURAOUI^{*} AND T. BEN ZINEB[⋄]

^{*} Laboratoire de Génie Mécanique (LGM)

École Nationale d'Ingénieurs de Monastir (ENIM)

Université de Monastir

Avenue Ibn El Jazzar, 5019 Monastir, Tunisie

e-mail: achref.sallami@enim.rnu.tn, tarak.bouraoui@enim.rnu.tn - Web page:

<http://hal.tn/PresentationSite.xhtml?labo=lgm>

[§] Institut Supérieur des Systèmes Industriels de Gabès (ISSIG)

Université de Gabès

Rue, Slaheddine El Ayoubi, 6032 Gabès, Tunisie

e-mail: walid4m@yahoo.fr - Web page: <http://www.issig.rnu.tn>

[⋄] Laboratoire d'Étude des Microstructures et de Mécanique des Matériaux (LEM3)

Université de Lorraine, CNRS, Arts et Métiers ParisTech

2 rue Jean Lamour, 54500 Vandœuvre lès Nancy, France

e-mail: tarak.ben-zineb@univ-lorraine.fr - Web page: <http://www.lem3.univ-lorraine.fr>

Key words: Fe-SMAs, Finite-strain behavior law, Phase transformation, Plastic sliding, MATLAB

Abstract. Iron-based Shape Memory Alloys (Fe-SMAs) present a specific behavior compared to NiTi and Cu-based SMAs related to a high coupling between plastic sliding and phase transformation inducing only a partial recovering of inelastic strain during heating. Few models in literature describe such specific behavior. However, they are formulated with the framework of small perturbations. Therefore, they cannot predict the effect of an applied high loading level inducing large deformations and rotations. Against this background, a new thermomechanical behavior law for Fe-SMAs, is developed with the framework of finite transformations. This law is an extension of Khalil et al. [1] small-strain model. Two important characteristic behaviors of the Fe-SMA, the phase transformation and the plastic sliding, are considered in the development of this model. Two internal variables, the martensite volume fraction and the accumulative plastic strain, have been defined to integrate those latter specific behaviors. This model considers the classical multiplication of the kinematic deformation gradient into elastic and inelastic parts. The inelastic part is also decomposed into phase transformation and plastic slip related ones. The corresponding constitutive equations are solved with the Newton-Raphson method combined with an implicit integration scheme. Further, an exponential map approach is carried out to integrate the evolution equations. In order to validate this model, the numerical results have been compared with experimental results of Khalil et al. [2]. Obtained results are in a good agreement with the experimental data and enhance the small-strain model [1] by enhancing the prediction of the nonlinear plastic hardening at

high strain levels. Additional simulations with higher loading levels, showed that the present model well predict the Fe-SMA thermomechanical behavior in finite-strain.

1 INTRODUCTION

Since their discovery [3, 4], Iron-based Shape Memory Alloys (Fe-SMAs) have drawn the attention for their good quality / price ratio. Their thermomechanical behavior is different, than NiTi and Cu-based SMAs, by a high coupling between phase transformation and plastic sliding. The Shape Memory Effect (SME) for Fe-SMAs comes from mechanically induced forward phase transformation, austenite phase to martensite phase, and from the reverse phase transformation activated after heating, martensite phase to austenite phase [5, 6]. Also, and unlike Cu-SMAs and Ni-Ti SMAs, the plasticity activates only in the scale of austenite [2, 7].

There are several nuances of Fe-SMAs, different in chemical composition : Fe-Mn-Si, Fe-Pt, Fe-Ni-Co-Ti, Fe-Mn-Si-Cr ... Manganese (Mn) and Silicon (Si) are the two most important elements because of their positive effects on the SME and the resistance to corrosion. According to the literature, manganese helps the austenite formation [5] and silicon increases the activation stress of plastic slip [2], improves resistance to corrosion [8], facilitates the reversible movement of dislocations [9] and improves the SME [7].

The phase transformation-plasticity diagram of yield stresses, giving an inelastic deformation, as a function of temperature [7] describes the Fe-SMAs behavior. Two domains, Phase transformation and plasticity, are differentiated by a temperature that will be noted T_0 (labeled M_s^σ in [7]). If the the material temperature is lower than T_0 , the phase transformation of the austenite to martensite has priority, if not, the activation of the plasticity in the austenite will take place preventing the nucleation of the martensite.

In order to predict an Fe-SMA behavior, tremendous researchers investigated the material behavior and formulated constitutive laws describing Fe-SMA response [10]. Jemal et al. [11] developed the first 3D behavior law for this material. They defined, two internal variables which are χ , for the martensite volume fraction, and γ , for the accumulative plastic strain, and two control variables which are the stress Σ and the temperature T . A Gibbs energy has been used to describe different Fe-SMA specific behaviors (Phase transformation, Plasticity and their interactions). Khalil et al. [1] model present an enhancement for the latter one. They kept the same internal and control variables but with some modification to be more faithful to the material behavior. They defined a new loading function for the reverse phase transformation and change the plasticity yield force to make it temperature dependent. Recently, Cissé et al. [12] developed a behavior law for Fe-SMAs inspired from Zaki and Moumni Ni-Ti Behavior law [13]. An expression of Helmholtz energy has been defined as the sum of energies in austenite, martensite and an interaction one. All these models are developed in the small strain hypothesis. But, Fe-SMA can reach high deformation levels due to their plastic hardening. For this, a small strain behavior law is not suitable to predict material large strain response. This was the main idea to develop a new finite strain behavior law for Fe-SMAs.

In this present work, a finite strain thermomechanical behavior law based on an extension of Khalil et al. small strain model has been proposed. In order to describes the phenomena of phase transformation and plasticity, a Helmholtz free energy Ψ has been used and driving and yield forces has been defined. This new thermomechanically behavior law is based on the multiplicative decomposition of the total deformation gradient \mathbf{F} into elastic, \mathbf{F}_{el} , and inelastic, \mathbf{F}_{ine} , deformation gradients. This latter is decomposed into phase transformation and plasticity gradients, \mathbf{F}_{tr} and \mathbf{F}_{pl} , respectively. This model constitutive equations have been implemented using MATLAB software. The constitutive equations are

solved with a Newton-Raphson method mixed with prediction correction method. This model parameters have been set with Khalil et al. experimental results [2]. The model present a good agreement with experimental results and it is able to predict plastic hardening better then Khalil et al. model [1]. After that, large strain simulations have been done to predict Fe-SMA response for higher loading levels. Obtained results show a concordance with the expected Fe-SMAs response in large strain loading.

The paper organized as follows: Section 2 details the constitutive model derivation. In section 3 a model validation with Khalil et al. experimental results [2] in order to validate it, and a large strain simulations have been taken into account to predict Fe-SMA response in finite strain. Finally, Section 4 draws the conclusion of this work and some prospects.

2 IRON-BASED SMAs LARGE STRAIN THERMOMECHANICAL BEHAVIOR LAW

2.1 Deformation gradient

Fe-SMAs present a high coupling between the phase transformation and the plasticity. For that, an assumption of a tripartite multiplicative decomposition of the deformation gradient into elastic, phase transformation, and plastic components as follow:

$$\mathbf{F} = \mathbf{F}_{el}\mathbf{F}_{ine} = \mathbf{F}_{el}\mathbf{F}_{tr}\mathbf{F}_{pl} \quad (1)$$

where \mathbf{F}_{el} is defined with respect to an intermediate configuration, \mathbf{F}_{tr} with respect to the reference configuration, and \mathbf{F}_{pl} with respect to a phase transformed configuration, if the temperature is less than M_s^σ . Else, \mathbf{F}_{pl} is defined with respect to the reference configuration, and \mathbf{F}_{tr} with respect to plasticized configuration.

2.2 Inelastic strain rate

Phase transformation and plasticity coupling occur whatever is the material temperature, and it is difficult to justify the procedure to separate phase transformation and plastic deformation gradients for a Representative Volume Elementary (RVE). In this case, additive decomposition of inelastic strain rate [14] into phase transformation and plastic components is more appropriate:

$$\mathbf{D}_{ine} = \mathbf{D}_{tr} + \mathbf{D}_{pl} \quad (2)$$

with

$$\mathbf{D}_{tr} = \dot{\chi} \bar{\epsilon}_{max}^{tr} \mathbf{N}^{tr} \quad (3)$$

$$\mathbf{D}_{pl} = (1 - \chi) \dot{\gamma} \mathbf{N}^{pl} \quad (4)$$

where $\bar{\epsilon}_{max}^{tr}$ is the equivalent maximal transformation strain, \mathbf{N}_{tr} and \mathbf{N}_{pl} are the transformation and plastic flow direction vectors.

2.3 Free energy function

The Helmholtz free energy Ψ is the sum of elastic Ψ_{el} , inelastic Ψ_{ine} and inner potential Ψ_{IC} energies. The Helmholtz free energy depends on the elastic right Cauchy-Green C_{el} , martensite volume fraction χ , accumulative plastic strain γ and the temperature T :

$$\Psi = \Psi_{el} + \Psi_{ine} + \Psi_{IC} \quad (5)$$

with

$$\Psi_{el} = \frac{\mu}{2} (I_{C_{el}} - 3) - \mu \ln J + \frac{\lambda}{2} (\ln J)^2 \quad (6)$$

$$\Psi_{ine} = c_v \left[(T - T_0) - T \ln \left(\frac{T}{T_0} \right) \right] + B(T - T_0)\chi + G_g(\mathbf{E}_{ine}) + [G_v(\chi) + (1 - \chi)G_s(\gamma) + G_{sv}(\gamma, \chi)] \quad (7)$$

$$\Psi_{IC} = -\ell_1\chi - \ell_2(1 - \chi) \quad (8)$$

where:

For the elastic energy, μ and λ are equivalent Lamé constants by assuming an isotropic elastic behavior with the same properties at the martensitic and austenitic states. $I_{C_{el}}$ is the first cauchy invariant of \mathbf{C}_{el} and $J = \det(\mathbf{F})$ is the deformation Jacobian (third invariant of \mathbf{F}).

For the inelastic energy, T is the current temperature, c_v , B and T_0 are the material parameters, $G_g(\mathbf{E}_{ine})$ is the intergranular interaction energy and G_v , G_s , G_{sv} are, respectively, the interaction functions between martensite variants, between plastic slip systems and between martensite variants and plastic slip systems. They are defined as follow:

$$G_g(\mathbf{E}_{ine}) = \frac{H_g}{(n_g + 1)} (\mathbf{E}_{ine} : \mathbf{E}_{ine})^{n_g + 1} \quad (9)$$

$$G_v(\chi) = \frac{H_v}{n_v + 1} \chi^{n_v + 1} \quad (10)$$

$$G_s(\gamma) = \frac{H_s}{n_s + 1} \gamma^{n_s + 1} \quad (11)$$

$$G_{sv}(\gamma, \chi) = \frac{H_{sv}}{n_{sv} + 1} (\gamma\chi)^{n_{sv} + 1} \quad (12)$$

with H_g is a material parameter characterizing intergranular interactions and n_g is a coefficient characterizing the interaction non linearity evolution. The coefficients n_v , n_s and n_{sv} reflect the nonlinearities of these interactions. The terms H_v , H_s and H_{sv} are respectively the interaction coefficients between the martensite variants, the slip systems, and the martensite variants and the slip systems.

For the inner potentiel ℓ_1 and ℓ_2 are a Lagrangian multipliers reflect the reality that the martensite volume fraction is always between 0 and 1. This two multipliers obey the Kuhn-Tucker conditions :

$$\begin{cases} \ell_1 \geq 0 \text{ and } \ell_1\chi = 0 \\ \ell_2 \geq 0 \text{ and } \ell_2(1 - \chi) = 0 \end{cases} \quad (13)$$

2.4 Constitutive equations

Substituting The Helmholtz free energy in the Clausius-Duhem inequality and taking into account mathematical processing:

$$\Lambda_{dr}^\chi \dot{\chi} + \Lambda_{dr}^\gamma \dot{\gamma} \geq 0 \quad (14)$$

with Λ_{dr}^χ and Λ_{dr}^γ are respectively the phase transformation and plasticity driving forces defined as follow:

$$\Lambda_{dr}^\chi = \bar{\epsilon}_{\max}^{tr} (\mathbf{M} + H_g (\mathbf{E}_{ine} : \mathbf{E}_{ine})^{n_g} \mathbf{F}_{ine} \mathbf{E}_{ine} \mathbf{F}_{ine}^T) : \mathbf{N}^{tr} - B(T - T_0) - H_v \chi^{n_v} + \frac{H_s}{(n_s + 1)} \gamma^{n_s + 1} - H_{sv} \gamma (\chi \gamma)^{n_{sv}} + \ell_1 - \ell_2 \quad (15)$$

$$\Lambda_{dr}^\gamma = (1 - \chi) (\mathbf{M} + H_g (\mathbf{E}_{ine} : \mathbf{E}_{ine})^{n_g} \mathbf{F}_{ine} \mathbf{E}_{ine} \mathbf{F}_{ine}^T) : \mathbf{N}^{pl} - (1 - \chi) H_s \gamma^{n_s} - H_{sv} \gamma (\chi \gamma)^{n_{sv}} \quad (16)$$

where \mathbf{M} present the Mandel stress, \mathbf{E}_{ine} is the inelastic Green-Lagrange tensor.

The yield forces for, forward and reverse phase transformation, and plastic slip are defined respectively as follow:

$$\Lambda_y^{tr,m} = \sigma_y^m \bar{\epsilon}_{tr}^{\max} + \zeta_m (T_0 - M_s) - H_\gamma \gamma^2 \quad (17)$$

$$\Lambda_y^{tr,a} = \sigma_y^a \bar{\epsilon}_{tr}^{\max} + \zeta_a (T_0 - A_s) - H_\chi \chi \quad (18)$$

$$\Lambda_y^{pl} = \sigma_y^\gamma - K_T T \quad (19)$$

with σ_y^m , σ_y^a and σ_y^γ are respectively the yield stress of, forward and reverse phase transformation and plasticity, ζ_a and ζ_m are control parameters, M_s is the start forward martensitic transformation temperature, A_s is the start reverse martensitic transformation and K_T represents the evolution slope of the yield plastic stress with the temperature.

In addition, we emphasize that the evolution equations satisfy the loading functions for the direct phase transformation, reverse phase transformation and plasticity.

$$\Upsilon_{tr}^m = \Lambda_{dr}^\chi - \Lambda_y^{tr,m} \quad (20)$$

$$\Upsilon_{tr}^a = -\Lambda_{dr}^\chi - \Lambda_y^{tr,a} \quad (21)$$

$$\Upsilon_{pl}^a = \Lambda_{dr}^\gamma - \Lambda_y^{pl} \quad (22)$$

The solving of equations (20) to (22) for a given loading increment allow to determine the kind of behavior and the evolution of the unknown variables.

3 RESULTS AND DISCUSSIONS

The model constitutive equations has been solved using, a Newton-Raphson method implicitly integrated throw MATLAB software, and, an elastic predictor inelastic corrector technique to manage nonlinear responses. The Fe-SMA loading function have been calculated in every increments iterations. Based on their values, the Fe-SMA behavior is distinguished. To test the model validity, a comparison with khalil et al.[2] experimental results have been done. Then, a presentation of large strain response is discussed.

3.1 Small Strain results

This subsection presents the numerical results for tensile loading-unloading at different constant temperature followed by a heating. These results are compared to experimental ones from [2] regarding the alloy Fe-Mn_{31.6}-Si_{6.45}-C_{0.018}(wt%). The adopted model parameters are calibrated from experimental results and their values are illustrated in table 1.

Table 1: Model parameters

Parameter	Value	Parameter	Value
σ_y^m (MPa)	137.7	A_s (°C)	96
σ_y^a (MPa)	125.2	T_0 (°C)	79.4
σ_y^v (MPa)	210	H_v (MPa)	27.2
ν	0.3	H_s (MPa)	632.5
μ (MPa)	65385	H_{sv} (MPa)	1000
λ (MPa)	98077	H_g (MPa)	627
$\bar{\epsilon}_{\max}^{tr}$	0.048	n_v	0.44
ζ_m (MPa/°C)	0.086	n_s	0.55
ζ_a (MPa/°C)	0.036	n_{sv}	0.45
B (MPa/°C)	0.104	n_g	3.07
K_T (MPa/°C)	0.45	H_χ (MPa)	-3
M_s (°C)	-25	H_γ (MPa)	500

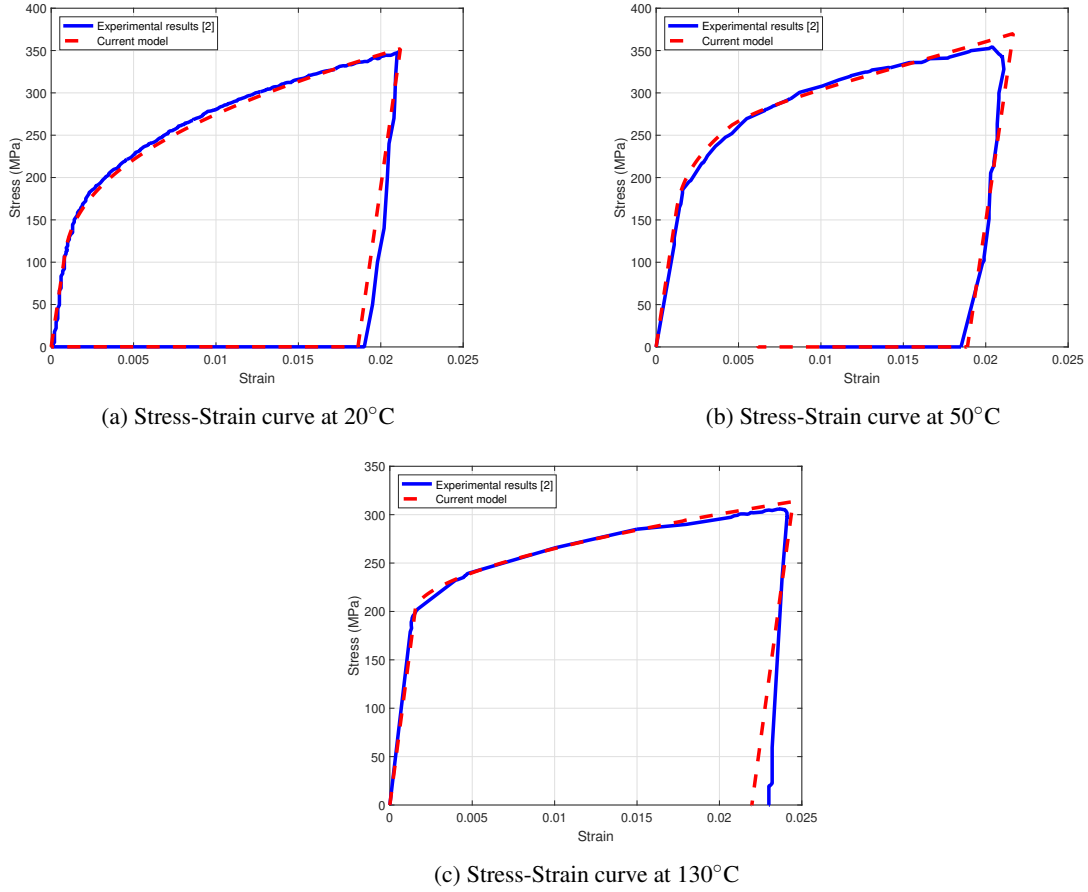


Figure 1: Comparison with Khalil et al. [2] experimental results

Figure 1 present comparisons, respectively for, 20°C, 50°C and 130°C. Figures show, as observed experimentally, that only phase transformation is occurring at 20°C, a coupled phase transformation and plasticity are observed at 50°C and only plasticity is activated at 130°C. The current model is able to predict different temperature behavior.

3.2 Finite Strain results

Large strain simulations have been carried out at different temperature to predict Fe-SMA tensile test response. Figure 2 presents loading-unloading-heating cycle for 20, 50 and 130°C, respectively, at 20% of strain. Results show that the plasticity dominates the Fe-SMA behavior for higher loading levels. These results are very faithful to experimental diagram seen in Bouraoui et al. work [7].

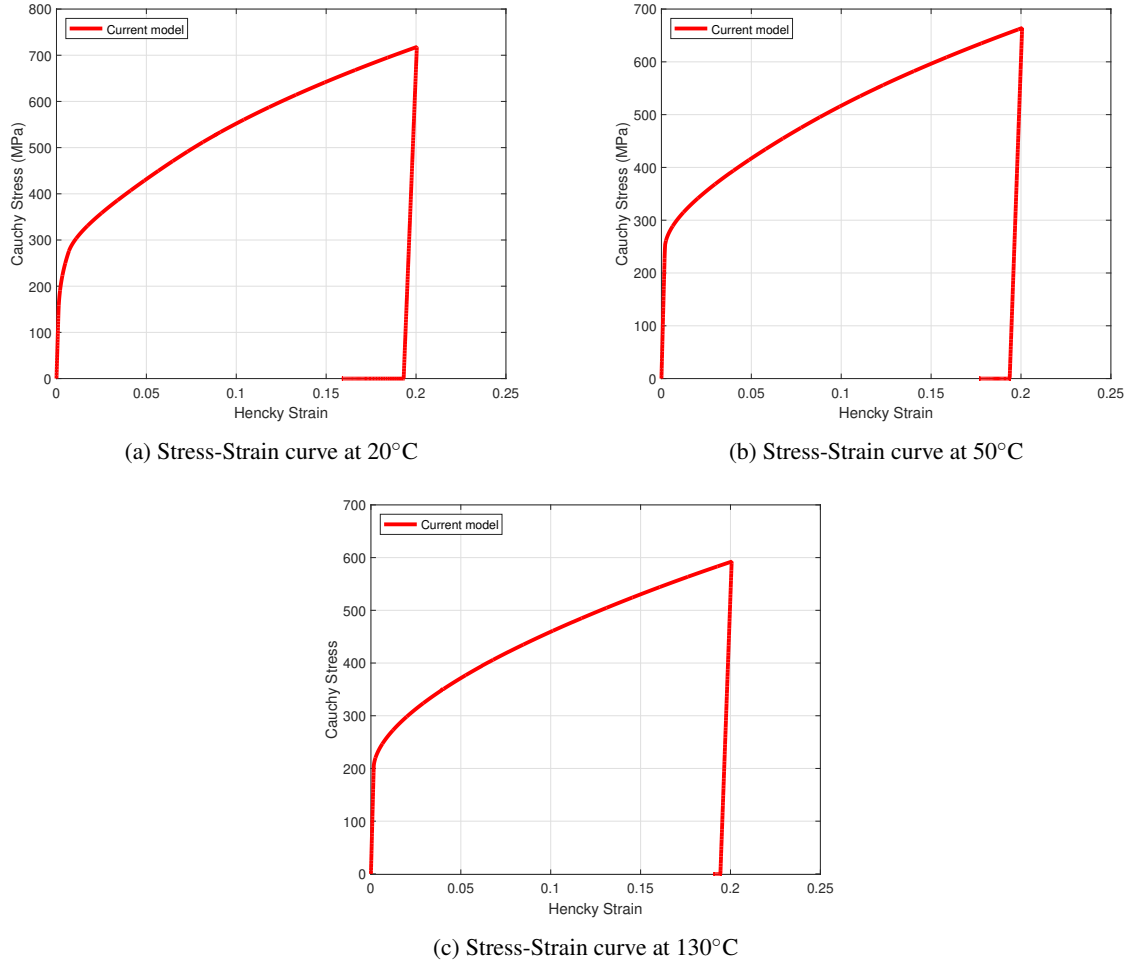


Figure 2: Stress-Strain curves for 20% of strain loading followed by unloading and heating

The evolution of the internal variables (χ and γ) shows that in 20°C (figure 3.a) the volume fraction of martensite begins to evolve first, then, the accumulative plastic strain activates. At this point, the martensite volume fraction slope evolution decreases until getting stabilized when it reaches 52%. At this range, the accumulative plastic strain slope evolution increases until the end of loading. Even at 50°C (figure 3.b), it is remarkable the same evolution of internal variables, but, at this range the martensite volume fraction stabilized at 26%. Figure 3.c shows the evolution of the internal variables with the strain at 130°C. At this temperature, the accumulative plastic strain starts first and only 5.5% of martensite has been created.

Fe-SMAs are a particular class of material, they are distinguished by a high coupling form between phase transformation and plasticity. High level strain simulations show that, going forward in loading favorite the plasticity and even the recovered strain due to the reverse phase transformation is so small in comparing with the plastic one. This model present good results and gives a prediction for an Fe-SMA high level loading response.

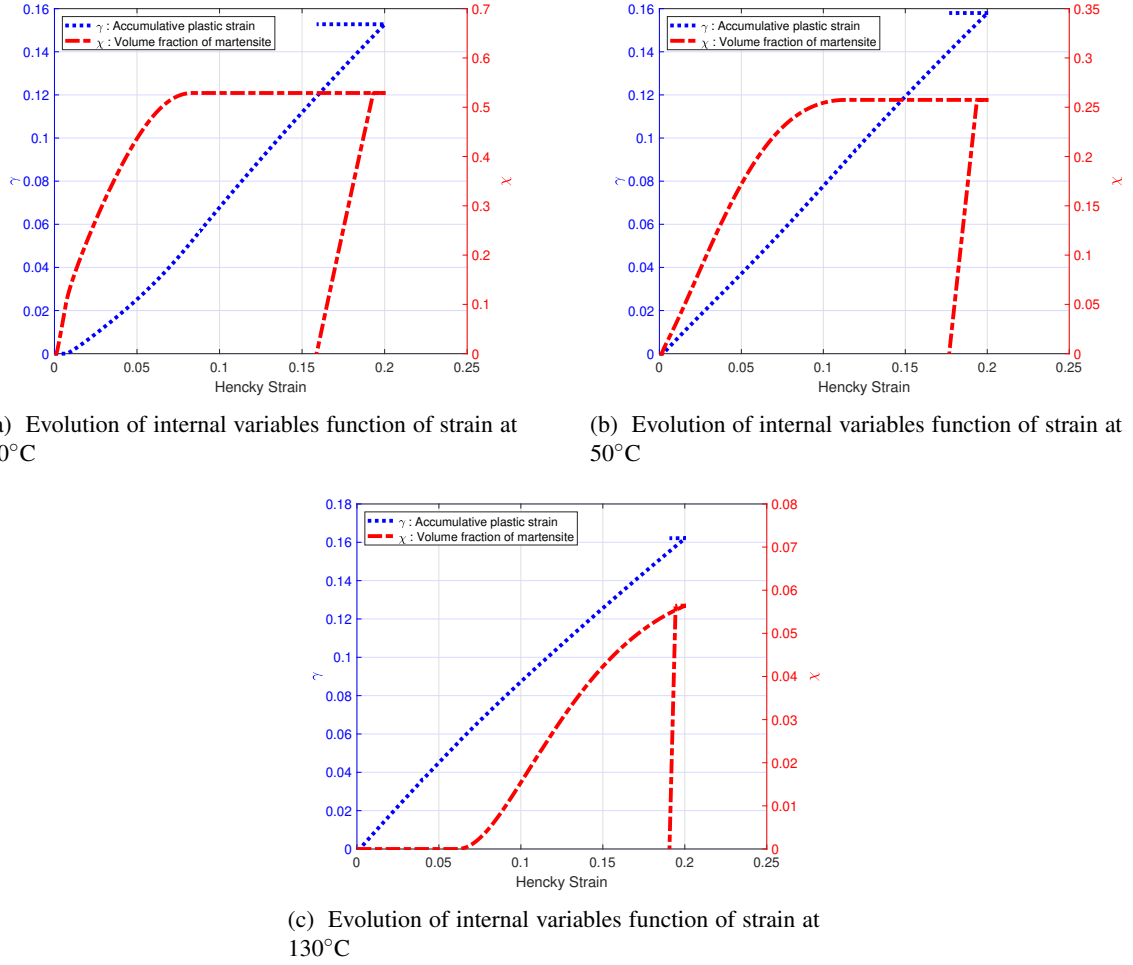


Figure 3: Evolution of the martensite volume fraction and the accumulative plastic strain function of strain

4 CONCLUSIONS

In this paper, a nonlinear finite strain model was proposed for Fe-SMAs. The model starts with a kinematic hypothesis that the deformation gradient is splitted in a multiplicative decomposition into, elastic, phase transformation and plastic sliding. The model constitutive equation was derived from the Helmholtz free energy. This latter, Helmholtz energy, is the sum of elastic, inelastic and inner potential energies. Using MATLAB software, time-discrete equations have been integrated implicitly.

This new model presents a good agreement with experimental results [2]. Also, it is able to predict finite strain response. The Large strain simulations show a consistent behavior of this type of materials.

As prospect, this model will be integrated in a finite element software via routine(UMAT). This UMAT will be used in order to predict complex configurations response in finite-strain.

REFERENCES

- [1] Khalil, W. and Mikolajczak, A. and Bouby, C. and Ben Zineb, T., A constitutive model for Fe-based shape memory alloy considering martensitic transformation and plastic sliding coupling : Applica-

- tion to a finite element structural analysis. *Journal of Intelligent Material Systems and Structures*. (2012) **23**:1143–1160.
- [2] Khalil, W. and Saint-Sulpice, L. and Arbab Chirani, S. and Bouby, C. and Mikolajczak, A. and Ben Zineb, T., Experimental analysis of Fe-based shape memory alloy behavior under thermomechanical cyclic loading. *Mechanics of Materials* (2013) **63**:1–11.
- [3] Koval, Y. N. and Kokorin, V. V. and Khandros, L. G., Shape memory effect in Fe-Ni-Co-Ti alloys. *Phys. Met. Metallogr.* (1979) **48**:162–164.
- [4] Sato, A. and Chishima, E. and Soma, K. and Mori, T., Shape memory effect in $\gamma \rightleftharpoons \varepsilon$ transformation in Fe-30Mn-1Si alloy single crystals. *Acta Metallurgica* (1982) **30**:1177–1183.
- [5] Gu, Q. and Humbeeck, J. V. and Delaey, L., A review on the martensitic transformation and shape memory effect in Fe-Mn-Si alloys. *Journal of physics IV* (1994) **4**:273–275.
- [6] Cissé, C. and Zaki, W. and Ben Zineb, T., A review of constitutive models and modeling techniques for shape memory alloys. *International Journal of Plasticity* (2016) **76**:244–284.
- [7] Bouraoui, T. and Jemal, F. and Ben Zineb, T., Tensile properties of a Fe-32Mn-6Si shape memory alloy. *Strength of Materials* (2008) **40**:203–211.
- [8] Charfi, A. and Bouraoui, T. and Feki, M. and Bradai, C. and Normand, B., Surface treatment and corrosion behaviour of Fe-32Mn-6Si shape memory alloy. *C. R. Chimie* (2009) **12**:270–275.
- [9] Iwamoto, T. and Cao, B., A review on experimental investigations of rate sensitivity of deformation behavior in Fe-Based Shape Memory Alloys. *Advanced structured Materials* (2017) **73**:31–42.
- [10] Cissé, C. and Zaki, W. and Ben Zineb, T., A review of modeling techniques for advanced effects in shape memory alloy behavior. *Smart Materials and Structures* (2016) **35**:1–36.
- [11] Jemal, F. and Bouraoui, T. and Ben Zineb, T. and Patoor, E. and Bradai, C., Modeling of martensitic transformation and plastic slip effects on the thermomechanical behaviour of Fe-based shape memory alloys. *Mechanics of Materials* (2009) **41**:849–856.
- [12] Cissé, C. and Zaki, W. and Gu, X. and Ben Zineb, T., A nonlinear 3D model for iron-based shape memory alloys considering different thermomechanical properties for austenite and martensite and coupling between transformation and plasticity. *Mechanics of Materials* (2017) **107**:1–21.
- [13] Zaki, W. and Moumni, Z., A three-dimensional model of the thermomechanical behavior of shape memory alloys. *Journal of the Mechanics and Physics of Solids* (2007) **55**:2455–2490.
- [14] Feng, B. and Levitas, I. V., Coupled elastoplasticity and plastic strain-induced phase transformation under high pressure and large strains: Formulation and application to BN sample compressed in a diamond anvil cell. *International Journal of Plasticity* (2017) **96**:156–181.

AMBIENT HEAT TRANSFER EFFECTS ON MAGNETIC SHAPE MEMORY ALLOY ACTUATORS

SHAOBIN ZHANG^{*,†}, GUOSHUN QIN[†], YONGJUN HE[†]

^{*} School of Mechanics, Civil Engineering and Architecture,
Northwestern Polytechnical University, Xi'an, China
e-mail: zhang.shaobin@nwpu.edu.cn

[†] IMSIA, UMR 8193 CNRS-EDF-CEA-ENSTA, Université Paris Saclay, Palaiseau, France
e-mail: yhe@ensta.fr, <https://cv.archives-ouvertes.fr/yongjun-he>

Key words: Magnetic Shape Memory Actuator, Heat Transfer Effect, Strain Oscillation, Amplitude Modulation, Thermo-magneto-mechanical Coupling

ABSTRACT. Magnetic Shape Memory Alloy (MSMA) is a promising candidate for high-frequency large-stroke actuators applications as it is able to provide a large recoverable deformation with high-frequency magnetic-field-induced martensite reorientation. Recent experiments revealed that thermo-magneto-mechanical coupling effect needs to be considered to obtain a reliable performance of MSMA actuators. Particularly, the heat generation from the energy dissipation of the high-frequency martensite twin-boundary motions causes a temperature rise in the material, which influences the temperature-dependent martensite reorientation process and/or triggers the temperature-induced martensite-austenite phase transformation so that the output strain can be influenced significantly. Therefore, besides the usual magneto-mechanical conditions (such as the magnetic field frequency, the applied mechanical stress and the system mechanical stiffness), the ambient heat-exchange efficiency between MSMA actuator and the ambient (which counteracts the temperature rise) is important in controlling the output strain amplitude under the high-frequency magnetic actuation. In this paper, we study the strain amplitude modulation of MSMA actuator by controlling the ambient heat transfer efficiency by applying an ambient airflow (the airflow velocity can be tuned via a compressed air source). The results are helpful not only for the optimization design of the large-stroke MSMA actuators, but also for the insight into the principles of the multi-physics coupling in similar smart materials.

1. Introduction

Magnetic Shape Memory Alloy (MSMA) is a kind of smart material with thermo-magneto-mechanical coupling, which has capability to output a high-frequency large recoverable strain (up to 10%) through magnetic-field-induced martensite reorientation [1–4]. This advantage makes MSMA a very promising candidate for high-frequency large-stroke actuators [5–8], where the large output strain amplitude is one of the most important performances. So far, various studies have been attracted to investigate the governing factors on the high-frequency

strain of MSMA, such as the applied magnetic-field frequency, the initial compressive stress, and the system stiffness [9–13]. Moreover, recent experiments revealed that thermo-magneto-mechanical coupling effect needs to be considered to obtain a reliable strain performance of MSMA actuators[4,14]. Particularly, the heat accumulation from the energy dissipation of the high-frequency frictional twin-boundary motions causes a temperature rise in the material, which influences the temperature-dependent martensite reorientation process and is likely to trigger the temperature-induced martensite-to-austenite phase transformation so that the output strain can be influenced significantly[4,14,15]. Therefore, besides the well-known magneto-mechanical conditions (such as the magnetic field frequency, the applied mechanical stress and the system mechanical stiffness) [9–13], the heat transfer efficiency between MSMA actuator and the ambient (which counteracts the temperature rise) should be an important factor in controlling the output strain amplitude under the high-frequency magnetic actuation.

In this work, during the magneto-mechanical actuation on MSMA, the ambient heat transfer efficiency is controlled by applying an ambient airflow (whose velocity can be tuned via a compressed air source) to study the heat transfer effects on the output strain amplitude of the MSMA actuator. The experimental results demonstrate that the strain amplitude of MSMA depend on the heat transfer efficiency non-monotonically due to two competing (opposite) aspects of the thermal effect. On the one hand, the temperature rise triggers the phase transformation from martensite to austenite in some parts of the specimen, reducing the output strain amplitude (as austenite has no reorientation and the specimen has less martensite reorientation); On the other hand, the temperature rise reduces the dissipative force (twinning stress) of martensite reorientation so that the dynamic strain oscillation can be increased, leading to larger output strain amplitude. Therefore, changing the ambient heat transfer to control the temperature rise (or the specimen working temperature) can modify these two competing aspects. At certain critical ambient heat transfer efficiency, the compromise between these two aspects leads to a maximum output strain amplitude. Based on this study, an actuator with strain amplitude modulated by the heat exchange efficiency can be designed.

2. Material properties and experiment process

A $\text{Ni}_{50}\text{Mn}_{28}\text{Ga}_{22}$ (at. %) single crystal MSMA specimen (from ETO Magnetic GmbH) was used in the experiments. The specimen was cut to a rectangular bar with dimensions in $10 \times 5 \times 2$ mm from an ingot, with all faces of the specimen parallel to the $\{100\}$ planes of the parent cubic austenite (with a lattice parameter of a_0). The specimen is in the state of 10M martensite phase at room temperature. Note that the martensite variants are slightly monoclinic in this material, but in this work it is assumed that they are tetragonal with two long axes “ a ” and one short axis “ c ” for the simplicity of the analysis. The material characteristic phase transformation temperatures M_s , M_f , A_s and A_f were obtained as 38.6 °C, 36.3 °C, 44.8 °C and 46.8 °C respectively from a DSC test (differential scanning calorimetry).

To experimentally investigate the MSMA actuator performances, a magneto-spring loading system is developed as shown in Fig. 1(a). Before each test, the martensite specimen is fully compressed along y -axis (by applying a large mechanical compression stress, > 10 MPa) to obtain a single variant state with the short-axis (c -axis) along y -direction (so-called stress-preferred variant, shown as M_1 in Fig. 1(b)), so that all the tests can take the same reference

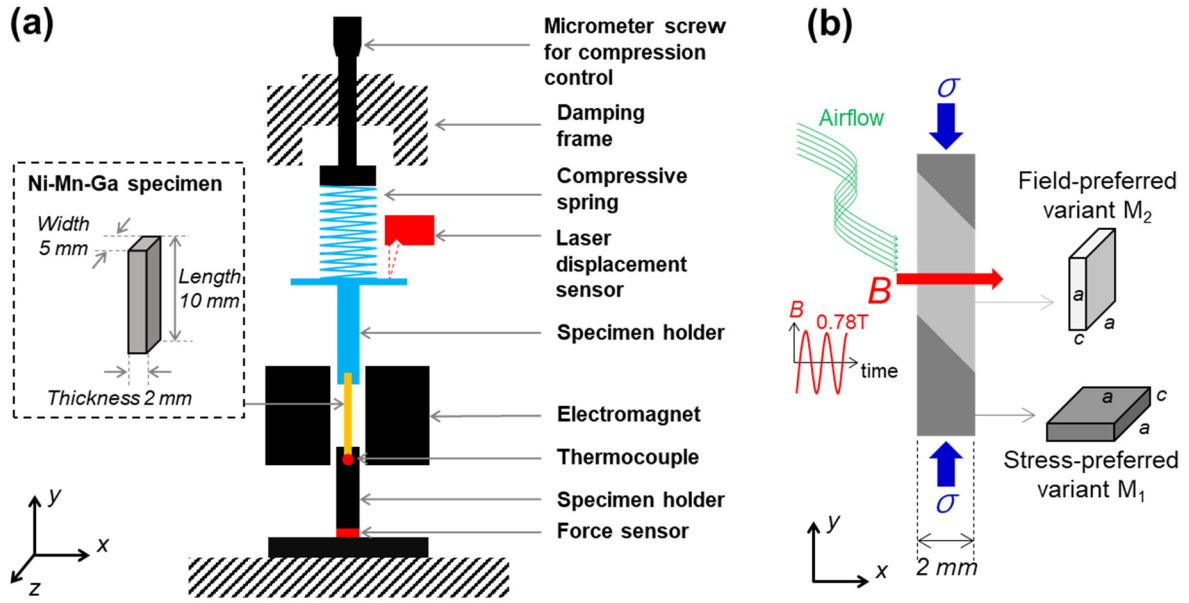


Figure 1. Experimental setup

state (i.e., zero strain) for calculations of the specimen deformation strain in this work. The specimen is installed between two magnetic poles with the long side along y -direction by two lightweight plexiglas holders. At the beginning of each test, an initial compressive stress σ_{ini} is applied on the specimen along y -direction by a compressed spring. Then a magnetic field (with magnetic flux density B cyclically varying between $[-0.78, 0.78]$ Tesla with a triangular waveform) of frequency f_{mag} is applied horizontally by the electro-magnet to drive the martensite reorientation from M_1 to M_2 (so-called magnetic field preferred variant with the short axis along x -direction and the long axis a along y -direction) as shown in Fig. 1(b). During this martensite reorientation process, the macroscopic specimen length L_y changes due to the microscopic difference between lattice parameters a (for M_2) and c (for M_1) along y -direction, which changes the spring length so that the spring compressive stress along y -direction changes at the same time. Thus, the interaction between the cyclic magnetic field (along x -direction) and the correspondingly evolving compressive stress (from the spring along y -direction) eventually leads to a cyclic deformation strain of MSMA (by cyclic martensite reorientation between the variants M_1 and M_2). In this experimental system, during the magneto-mechanical cyclic loading, the ambient heat transfer efficiency of the MSMA specimen can be controlled by forcing an ambient airflow of different velocities to pass through the specimen.

During the actuation, the deformation of the specimen along y -direction is measured by a laser displacement sensor (Keyence LK-H027) at the upper holder, and the average temperature of the specimen is monitored by a thermocouple (K-type, 0.5 mm sheath diameter) at bottom of the specimen. Because the specimen holders are made of plexiglas of low thermal conductivity to reduce the heat conduction from the specimen ends to the fixtures, it is assumed that the heat convection via the specimen surface is the most dominant path of the heat exchange rather than the heat conduction via the specimen ends. The heat transfer efficiency can be quantified by a characteristic heat transfer time t_h which depends on the ambient airflow velocities (this method has been employed in previous studies [4,16,17]). That means, a large

airflow velocity leads to a high heat transfer efficiency corresponding to a short characteristic heat transfer time t_h .

3. Experimental results and discussions

To investigate the heat transfer effect on the high-frequency strain amplitude of MSMA actuator, a magnetic actuation test is conducted under a stepwise increasing heat transfer efficiency (controlled by applying an airflow with increasing velocity step by step). The frequency of the applied field (f_{mag}) is 110 Hz, and the applied initial compressive stress (σ_{ini}) is 0.4 MPa. Under these loading conditions, the MSMA actuator is capable to achieve a large strain amplitude (with the strain oscillation frequency $f_{\text{strain}} = 2 f_{\text{mag}} = 220$ Hz). The strain and the temperature evolutions of the MSMA actuator are shown in Fig. 2(a) and the magnified strain curves for typical instants are shown in Fig. 2(b). It is seen that, at the beginning of the actuation (< 26 s) where the specimen is in the still air ambient, a large strain amplitude $\Delta\epsilon$ (the strain difference between the maximum and the minimum nominal strains) around 4.0% can be obtained. At the same time, the specimen temperature increases rapidly corresponding to the high-frequency large deformation, until a significant reduction in the strain amplitude at around $t \approx 27$ s (so-called strain drop phenomenon[4], marked by a red arrow in Fig. 2(a)), which is caused by the martensite-to-austenite phase transformation (non-active austenite phase appears in the specimen, as shown by the schematic of t_1 in Fig. 2(b)). After the strain drop, both the output strain amplitude $\Delta\epsilon$ and the specimen temperature T reach stable states with strain amplitude of 1.3% and temperature of 37.8 °C, see the evolutions of the strain and the temperature at $t_1 \approx 40$ s in Fig. 2.

Generally, the strain drop phenomenon is harmful for engineering applications as the output strain is significantly reduced. To overcome this drawback, during the test, the heat transfer time t_h is decreased stepwise by increasing the velocity of the ambient airflow passing through the specimen (note: for each step, the airflow changes rapidly in less than 1 second). It is seen that, when t_h decreases from 80.0 s to 14.9 s stepwise, the strain amplitude increases to 3.8% gradually, while the stable temperature only slightly decreases (see Fig. 2(a)). For example, at $t_2 \approx 100$ s where the t_h is 25.4 s, the strain amplitude increases to 2.6% and the stable temperature slightly decreases to 37.3 °C. When t_h is decreased to 14.9 s, the strain amplitude increases to 3.8% while the specimen temperature decreases to 36.7 °C (see the evolutions of the strain and the temperature at $t_3 \approx 180$ s); This recovered strain amplitude is close to that before the strain drop (4.0%). The temperature evolutions in these situations are within the material characteristic phase transformation temperatures, particularly $M_f < T_{\text{specimen}} < A_f$, which allows the coexistence of martensite and austenite. According to the ambient change (changing t_h), the MSMA specimen adjusts its volume fractions of the two phases so that the dissipative martensite reorientation (dissipative strain oscillation) generate a proper amount of heat that can be efficiently transformed to ambient without causing further temperature rise, see the schematics of the local phase evolution at the instants t_1 and t_2 in Fig. 2(b). In the case of $t_h = 14.9$ s, the specimen is almost fully occupied by martensite and the strain amplitude recovers to a large value (with large dissipation heat in the specimen).

However, when the heat transfer time t_h is further decreased, both the strain amplitude and the temperature decrease significantly as shown in Fig. 2(a). For example, when t_h decreases to 10.0 s, the strain amplitude and the specimen temperature decreases to 2.1% and 26.4 °C

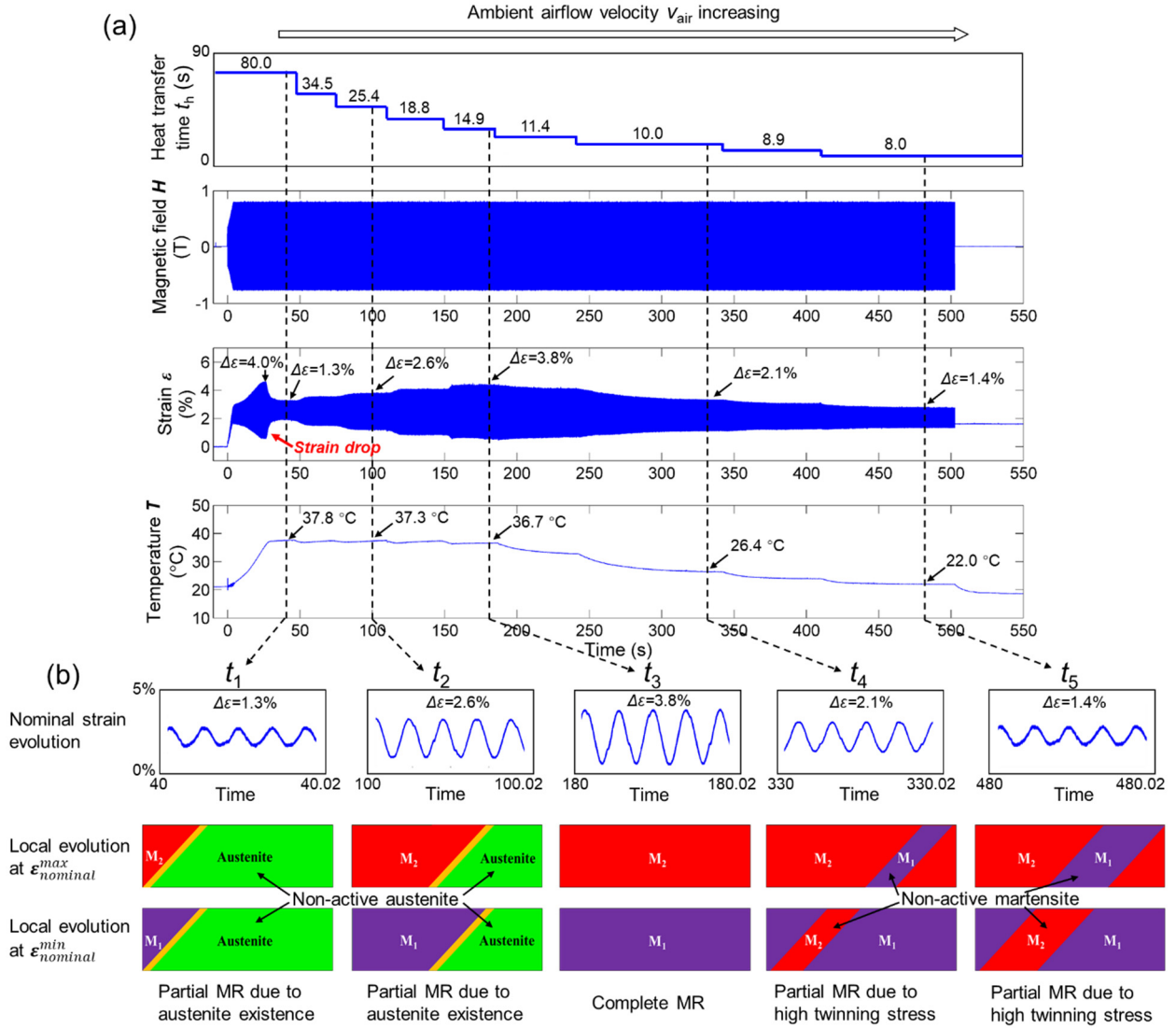


Figure 2. (a) The strain and temperature responses of MSMA under continuously increasing airflow velocities; (b) the nominal strain evolutions and sketches of the local phase/variant evolutions at 5 typical time instants ($t_1 \sim t_5$).

respectively (see the responses at $t_4 \approx 330$ s). When t_h is further decreased to 8.0 s, the strain amplitude and the stable temperature decrease to 1.4% and 22.0 °C respectively ($t_5 \approx 480$ s). The temperature evolutions in these situations are well below M_f , which means only martensite exists. But not all the martensite take reorientation to contribute to the strain oscillation as shown in the schematics of t_4 and t_5 of Fig.2(b) where there are some zones in the specimen with unchanged martensite states, fixed M_1 or M_2 (so-called non-active martensite zones). The volume fractions of the non-active zones change with the ambient condition (with the changing t_h). The reason for the existence of non-active martensite zone might be that, at strong ambient heat transfer making specimen temperature lower, the temperature-dependent dissipative force (twinning stress) increases [18,19], i.e. martensite reorientation becomes difficult; in other

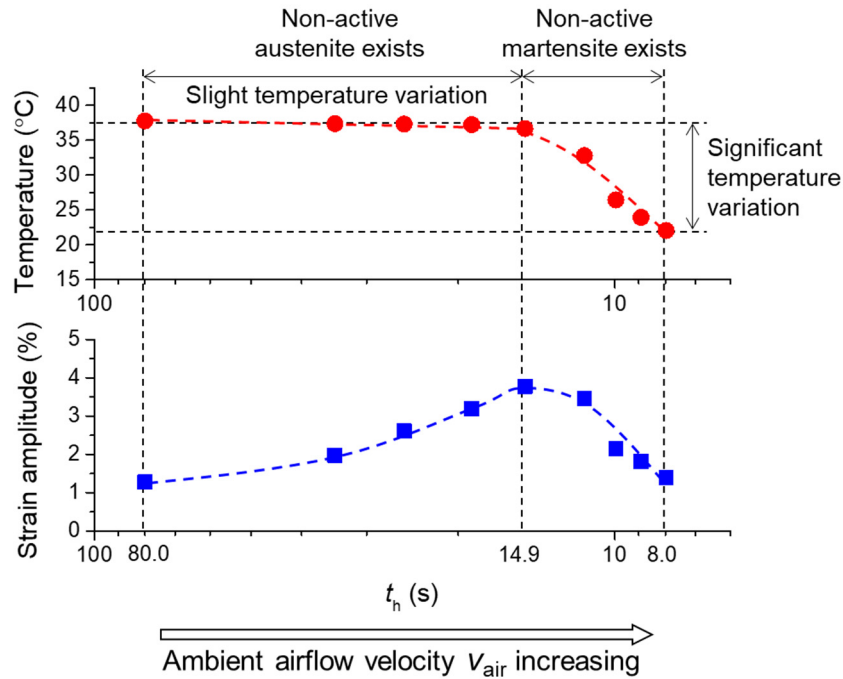


Figure 3. The stable strain amplitude and the stable temperature of MSMA under different heat transfer time t_h . The dashed lines are for guiding eyes.

words, higher damping in the dynamic oscillating system leads to lower output oscillation amplitude.

The stable temperature and the stable strain amplitude at all the steps of the heat transfer time t_h are summarized in Fig. 3 where the output strain amplitude $\Delta\varepsilon_{\text{stable}}$ changes non-monotonically while the stable temperature T_{stable} decreases monotonically. For the cases under weak ambient heat transfer condition ($t_h = 80.0 \text{ s} \sim 14.9 \text{ s}$), the strain amplitude increases with decreasing t_h while the temperature decreases slightly, keeping higher than M_f . In contrast, for the cases under strong heat transfer condition ($t_h = 14.9 \text{ s} \sim 8.0 \text{ s}$), the increasing heat transfer efficiency (i.e. decreasing t_h) significantly reduces the output strain amplitude and the temperature simultaneously. Therefore, to achieve the maximum output strain amplitude, a proper ambient heat transfer condition is needed (here $t_h < 14.9 \text{ s}$) to make the specimen working temperature is close to (but lower than) M_f so that all the specimen is occupied by martensite phase and the temperature dependent twinning stress is relatively low.

4. Summary and conclusions

In this work, the experiments of high-frequency magnetic field actuation of MSMA are performed under the stepwise increasing heat exchange efficiency. It is found that the heat exchange between the MSMA actuator and the ambient influences the actuator working temperature **monotonically** (i.e. stronger ambient heat transfer leads to lower stable working temperature), but changes the strain oscillation amplitude **non-monotonically** (i.e. there is an optimal thermal boundary condition to achieve the maximum output strain amplitude). This

study enables us to tune the strain amplitude of MSMA actuator by controlling the ambient heat transfer efficiency without changing the magneto-mechanical loading condition. More systematic experiments and the associated modelling are on-going to further understand the thermo-magneto-mechanical coupling behaviors of MSMA.

References

- [1] H. Karaca, I. Karaman, B. Basaran, Y. Chumlyakov, H. Maier, Magnetic field and stress induced martensite reorientation in NiMnGa ferromagnetic shape memory alloy single crystals, *Acta Mater.* 54 (2006) 233–245. doi:10.1016/j.actamat.2005.09.004.
- [2] S.J. Murray, M. Marioni, S.M. Allen, R.C. O’Handley, T.A. Lograsso, 6% magnetic-field-induced strain by twin-boundary motion in ferromagnetic Ni–Mn–Ga, *Appl. Phys. Lett.* 77 (2000) 886–888. doi:10.1063/1.1306635.
- [3] R.C. O’Handley, S.J. Murray, M. Marioni, H. Nembach, S.M. Allen, Phenomenology of giant magnetic-field-induced strain in ferromagnetic shape-memory materials (invited), *J. Appl. Phys.* 87 (2000) 4712–4717. doi:10.1063/1.373136.
- [4] S. Zhang, X. Chen, Z. Moumni, Y. He, Thermal effects on high-frequency magnetic-field-induced martensite reorientation in ferromagnetic shape memory alloys: An experimental and theoretical investigation, *Int. J. Plast.* 108 (2018) 1–20. doi:10.1016/j.ijplas.2018.04.008.
- [5] E. Pagounis, A. Laptev, J. Jungwirth, M. Laufenberg, M. Fonin, Magnetomechanical properties of a high-temperature Ni–Mn–Ga magnetic shape memory actuator material, *Scr. Mater.* 88 (2014) 17–20. doi:10.1016/j.scriptamat.2014.06.013.
- [6] R. Techapiesancharoenkij, J. Kostamo, J. Simon, D. Bono, S.M. Allen, R.C. O’Handley, Acoustic-assisted magnetic-field-induced strain and stress output of Ni–Mn–Ga single crystal, *Appl. Phys. Lett.* 92 (2008) 32506. doi:10.1063/1.2837195.
- [7] R. Techapiesancharoenkij, J. Kostamo, S.M. Allen, R.C. O’Handley, Frequency response of acoustic-assisted Ni–Mn–Ga ferromagnetic-shape-memory-alloy actuator, *J. Appl. Phys.* 105 (2009) 93923. doi:10.1063/1.3125307.
- [8] R. Yin, F. Wendler, B. Krevet, M. Kohl, A magnetic shape memory microactuator with intrinsic position sensing, *Sensors Actuators, A Phys.* 246 (2016) 48–57. doi:10.1016/j.sna.2016.05.013.
- [9] C.P. Henry, D. Bono, J. Feuchtwanger, S.M. Allen, R.C. O’Handley, ac field-induced actuation of single crystal Ni–Mn–Ga, *J. Appl. Phys.* 91 (2002) 7810. doi:10.1063/1.1449441.
- [10] Y.W. Lai, R. Schafer, L. Schultz, J. McCord, Direct observation of AC field-induced twin-boundary dynamics in bulk NiMnGa, *Acta Mater.* 56 (2008) 5130–5137. doi:10.1016/j.actamat.2008.06.030.
- [11] R. Techapiesancharoenkij, J. Simon, D. Bono, S.M. Allen, R.C. O’Handley, Acoustic-assist effect on magnetic threshold field and twinning-yield stress of Ni-Mn-Ga single crystals, *J. Appl. Phys.* 104 (2008) 33907. doi:10.1063/1.2961331.
- [12] R. Techapiesancharoenkij, The effect of magnetic stress and stiffness modulus on resonant characteristics of Ni–Mn–Ga ferromagnetic shape memory alloy actuators, *J. Magn. Magn. Mater.* 323 (2011) 3109–3116. doi:10.1016/j.jmmm.2011.06.066.

- [13] R. Techapiesancharoenkij, J. Kostamo, S.M. Allen, R.C. O’Handley, Frequency Response of Acoustic-Assisted Ni – Mn – Ga Ferromagnetic- Shape-Memory-Alloy Actuator Accessed, *J. Appl. Phys.* (2013).
- [14] O.Z. Pascan, Y.J. He, Z. Moumni, W.H. Zhang, Temperature rise of high-frequency martensite reorientation via Type II twin boundary motion in NiMnGa Ferromagnetic Shape Memory Alloy, *Scr. Mater.* 104 (2015) 71–74. doi:10.1016/j.scriptamat.2015.04.006.
- [15] S. Zhang, X. Chen, Z. Moumni, Y. He, Coexistence and compatibility of martensite reorientation and phase transformation in high-frequency magnetic-field-induced deformation of Ni-Mn-Ga single crystal, *Int. J. Plast.* 110 (2018) 110–122. doi:10.1016/j.ijplas.2018.06.010.
- [16] Y. He, H. Yin, R. Zhou, Q. Sun, Ambient effect on damping peak of NiTi shape memory alloy, *Mater. Lett.* 64 (2010) 1483–1486. doi:10.1016/j.matlet.2010.03.068.
- [17] Y.J. He, Q.P. Sun, Rate-dependent domain spacing in a stretched NiTi strip, *Int. J. Solids Struct.* 47 (2010) 2775–2783. doi:10.1016/j.ijsolstr.2010.06.006.
- [18] L. Straka, A. Soroka, H. Seiner, H. Hänninen, A. Sozinov, Temperature dependence of twinning stress of Type I and Type II twins in 10M modulated Ni-Mn-Ga martensite, *Scr. Mater.* 67 (2012) 25–28. doi:10.1016/j.scriptamat.2012.03.012.
- [19] A. Sozinov, A. Soroka, N. Lanska, M. Rameš, L. Straka, K. Ullakko, Temperature dependence of twinning and magnetic stresses in Ni₄₆Mn₂₄Ga₂₂Co₄Cu₄ alloy with giant 12% magnetic field-induced strain, *Scr. Mater.* 131 (2017) 33–36. doi:10.1016/j.scriptamat.2016.12.032.

BENDING MODEL FOR LAMINATED COMPOSITE CANTILEVER BEAMS WITH MULTIPLE EMBEDDED SHAPE MEMORY ALLOY LAYERS

W. ZAKI^{*}, V. NGUYEN^{*}

^{*} Department of Mechanical Engineering
Khalifa University of Science and Technology
P.O. box 127788, Abu Dhabi, UAE
e-mail: wael.zaki@ku.ac.ae, www.kustar.ac.ae

Key words: Shape Memory Alloys, Asymmetry, Composites, Analytical Methods.

Abstract. A new model is proposed for composite laminate beams comprising multiple alternating shape memory alloy (SMA) and elastic layers. The model fully considers asymmetry in SMA behavior, which is found to significantly influence the behavior of the laminates. Moreover, the equations governing the response of the SMA-reinforced beams are derived for a complete loading-unloading cycle considering a Timoshenko beam model combined with well-established constitutive relations for SMAs. The derivation procedure involves first identifying the solid phase structure of the beam for a given applied load, followed by integration of the stress and strain in a cross section to obtain moment and shear force equations.

1 INTRODUCTION

Because of their superelasticity and shape memory effect, shape memory alloys have been utilized for innovative applications in aerospace [1], automotive engineering [2], robotics [3] and in the biomedical field [4]. In particular, SMA-reinforced composite materials were successfully used for shape adaptation and control [5], enhancement of resistance to buckling [6], structural frequency tuning [7], damage repair [8], vibration control [9], and for reducing impact stress and energy [10, 11]. Research into smart SMA-reinforced composites, in particular, has been the focus of extensive theoretical and experimental research. From an experimental point of view, Lee et al. [12] investigated the use of SMA reinforcement to enable self-healing of cracked cement mortar beams; Alebrahim et al. [13] analyzed the behavior of a smart composite beam comprising SMA elements and subjected to quasi-static loading; Kim et al. [14] reported on the use of SMAs for improving resistance to low-velocity impact in composite plates; Han et al. [15] studied the response of SMA-glass fiber woven composites for shape morphing of UAV winglets; Thomson et al. [16] utilized SMA actuators to improve the post-buckling behavior of a composite panel; Wang et al. [17] showed improvement in average strain at failure and tensile and compressive strengths in laminates reinforced with SMA layers; etc. In conjunction with experimental work, a great deal of effort has been dedicated to modeling and simulating the response of SMA composites. In this regard, Hamada et al. [18] investigated the thermomechanical behavior of smart composites consisting of 6061 Al matrix reinforced with multiple SMA fibers; Viet and Zaki [19] introduced an analytical model for concrete beams comprising multiple SMA wires; Taya et al. [20] designed a

reversible bending actuator comprising an SMA core bonded to two shape memory polymer (SMP) layers; Park et al. [21] analytically and experimentally investigated the deflection of SMA-SMP laminates subjected to loading at the tip, etc. For the case of SMA-reinforced composite beams in particular, existing analytical and semi-analytical solutions present a number of limitations, including the assumption of uniform SMA layer thickness [18] and material properties of the matrix [21], the limitation of detailed analytical derivations to monotonic loading [22], the consideration of identical elastic stiffness for the austenite and martensite phases, and the assumption of symmetric SMA response in tension and compression [22,23]. These limitations are addressed in this work, in which a semi-analytical model is derived to describe the behavior of laminated composite cantilever beams with multiple embedded SMA layers. The proposed derivations are based on the ZM constitutive model [24] for SMAs and on Timoshenko beam theory. The model accounts for asymmetric behavior in tension and compression of the SMA elements and provides analytical and semi-analytical relations governing the behavior of the beam during a complete loading-unloading cycle.

2 MATHEMATICAL DERIVATIONS

The dimensions and boundary conditions of the beam are illustrated in Fig. 1 below.

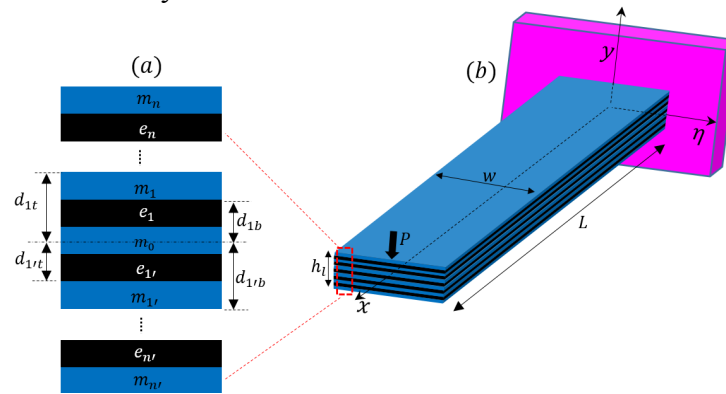


Fig. 1 Dimensions and boundary conditions of the laminated beam (a) layered structure; (b) 3D model.

As shown in the insert, the beam consists of alternating layers of SMA and elastic materials. The structures are such that the central, top and bottom layers are SMA. The total number of layers is therefore $n + n' + 1$ SMA and $n + n' - 1$ elastic. An elastic layer above (resp. below) the midplane is denoted e_h (resp. $e_{h'}$), where the index h is the layer number, starting from the midplane. The SMA layers are designated by m_h and $m_{h'}$. The distance from the midplane to the bottom (resp. top) of SMA layer m_h is denoted d_{hb} (resp. d_{ht}). The elastic stiffness of elastic layer e_h is E_{eh} .

2.1 Constitutive SMA relations

The behavior of the SMA is represented using constitutive equations from the ZM model [25], for which the evolution of the volume fraction z of martensite is governed by the following loading functions in the case of uniaxial tension/compression:

$$F_{j\pm} = \text{sign}(\times) \left[\left(\frac{El_{MA} + P_{MA}}{2} \right) \sigma_{j\pm}^2 + \sigma_{j\pm} \varepsilon_{0\pm} \right] + \left\{ a - b - \text{sign}(\times) \left(G + (\alpha - \beta) \left\{ k_h \left(\left(\frac{3}{4} \right)^{3/2} \varepsilon_{0\pm}^3 - c_h \frac{\varepsilon_{0\pm}^3}{3.8} \right) \right\}^{2/3} \right) \right\} z - \text{sign}(\times) \left(\frac{\beta}{2} \left\{ k_h \left(\left(\frac{3}{4} \right)^{3/2} \varepsilon_{0\pm}^3 - c_h \frac{\varepsilon_{0\pm}^3}{3.8} \right) \right\}^{2/3} + C(T) \right) - a \quad (1)$$

In Eq. (1), j is l during loading, in which case $\text{sign}(\times)$ is 1, or u during unloading, in which case $\text{sign}(\times)$ is -1 ; the sign \pm is $-$ for compression or $+$ for tension; P_{MA} , El_{MA} , ξ_T , a , b , α , β , and G are material parameters; $C(T)$ is an expression of temperature written $C(T) = \xi_T(T - A_f^0) + k_T$, where T is temperature, A_f^0 is the austenite finish temperature, and k_T is a material constant; k_h and c_h are parameters accounting for asymmetric hardening; ε_{0+} and ε_{0-} are the maximum transformation strains in tension and compression. The Young's moduli of austenite and martensite are denoted E_A and E_M respectively and both phases are considered to have the same Poisson ratio ν . A detailed introduction of the material parameters can be found in [25].

The uniaxial stress-strain relation for the SMA is written

$$\sigma_{j\pm} = \left[\frac{1}{E_A} + z_{j\pm} \left(\frac{1}{E_M} - \frac{1}{E_A} \right) \right]^{-1} [\varepsilon_{j\pm} - \varepsilon_{0\pm} z_{j\pm}] \quad (2)$$

which can be rearranged to get

$$z_{j\pm} = \frac{\varepsilon_{j\pm} - \sigma_{j\pm} / E_A}{(1/E_M - 1/E_A) \sigma_{j\pm} + \varepsilon_{0\pm}} \quad (3)$$

The stress-strain relation in the region of mixed austenite and martensite can be shown to obey [26, 27] the following equality:

$$\sigma_{j\pm}^3 + \Pi_{j1} \sigma_{j\pm}^2 + \Pi_{j2} \sigma_{j\pm} + \Pi_{j3} \varepsilon_{j\pm} + \Pi_{j4} = 0 \quad (4)$$

where

$$\Gamma_{\pm} = \left\{ k_h \left(\left(\frac{3}{4} \right)^{3/2} \varepsilon_{0\pm}^3 - c_h \frac{\varepsilon_{0\pm}^3}{3.8} \right) \right\}^{2/3}; \quad \Pi_{j1\pm} = \frac{2\varepsilon_{0\pm} \left(\frac{El_{MA} + P_{MA}}{2} + \frac{1}{E_M} - \frac{1}{E_A} \right)}{(El_{MA} + P_{MA})(1/E_M - 1/E_A)};$$

$$\Pi_{j2\pm} = 2 \frac{\varepsilon_{0\pm}^2 - \frac{\text{sign}(\times)[a - b - (\alpha - \beta)\Gamma_{\pm}] - G}{E_A} - \left(\frac{\beta}{2} \Gamma_{\pm} + C(T) + \text{sign}(\times)a \right) \left(\frac{1}{E_M} - \frac{1}{E_A} \right)}{(El_{MA} + P_{MA})(1/E_M - 1/E_A)};$$

$$\Pi_{j3\pm} = 2 \frac{\text{sign}(\times)(a - b) - G - (\alpha - \beta)\Gamma_{\pm}}{(El_{MA} + P_{MA})(1/E_M - 1/E_A)}; \quad \Pi_{j4\pm} = -2 \frac{\varepsilon_{0\pm} \left(\frac{\beta}{2} \Gamma_{\pm} + C(T) + \text{sign}(\times)a \right)}{(El_{MA} + P_{MA})(1/E_M - 1/E_A)};$$

Eq.(4) gives the explicit stress-strain relation

$$\sigma_{j\pm} = \Pi_{j1\pm}^* + \Pi_{j2\pm}^* \varepsilon_{j\pm} + \Pi_{j3\pm}^* \varepsilon_{j\pm}^2 + \Pi_{j4\pm}^* \varepsilon_{j\pm}^3 + \Pi_{j5\pm}^* \varepsilon_{j\pm}^4 \quad (5)$$

where the different coefficients are defined as follows:

$$Q_{j\pm} = \frac{3\Pi_{j2\pm} - \Pi_{j1\pm}^2}{9}, \quad \Omega_{1j\pm} = \frac{\pi}{2} - \frac{1}{\sqrt{-Q_{j\pm}}} \left(\frac{9\Pi_{1j\pm}\Pi_{2j\pm} - 2\Pi_{1j\pm}^3 - 27\Pi_{4j\pm}}{54} \right),$$

$$\Omega_{2j\pm} = \frac{\Pi_{3j\pm}}{2\sqrt{-Q_{j\pm}}},$$

$$\Pi_{j1+}^* = 2\sqrt{-Q_{j+}} \left(1 - \frac{\Omega_{1j+}^2}{18} + \frac{\Omega_{1j+}^4}{1944} \right) - \frac{\Pi_{j1+}}{3}; \Pi_{j2+}^* = 2\sqrt{-Q_{j+}} \left(\frac{4\Omega_{1j+}^2\Omega_{2j+}}{1944} - \frac{\Omega_{1j+}\Omega_{2j+}}{9} \right);$$

$$\Pi_{j3+}^* = 2\sqrt{-Q_{j+}} \left(\frac{6\Omega_{1j+}^2\Omega_{2j+}^2}{1944} - \frac{\Omega_{2j+}^3}{18} \right); \Pi_{j4+}^* = 2\sqrt{-Q_{j+}} \frac{4\Omega_{1j+}\Omega_{2j+}^3}{1944}; \Pi_{j5+}^* = 2\sqrt{-Q_{j+}} \frac{\Omega_{2j+}^4}{1944};$$

$$\Pi_{j1-}^* = 2\sqrt{-Q_{j-}} \left(1 - \frac{\Omega_{1j-}^2}{18} + \frac{\Omega_{1j-}^4}{1944} \right) \cos\left(\frac{2\pi}{3}\right) - 2\sqrt{-Q_{j-}} \sin\left(\frac{2\pi}{3}\right) \left(\frac{\Omega_{1j-}}{3} + \frac{\Omega_{1j-}^3}{162} \right) - \frac{\Pi_{j1-}}{3};$$

$$\Pi_{j2-}^* = 2\sqrt{-Q_{j-}} \left(\frac{4\Omega_{1j-}^2\Omega_{2j-}}{1944} - \frac{\Omega_{1j-}\Omega_{2j-}}{9} \right) \cos\left(\frac{2\pi}{3}\right) - 2\sqrt{-Q_{j-}} \sin\left(\frac{2\pi}{3}\right) \left(\frac{\Omega_{2j-}}{3} + \frac{3\Omega_{1j-}^2\Omega_{2j-}}{162} \right);$$

$$\Pi_{j3-}^* = 2\sqrt{-Q_{j-}} \left(\frac{6\Omega_{1j-}^2\Omega_{2j-}^2}{1944} - \frac{\Omega_{2j-}^3}{18} \right) \cos\left(\frac{2\pi}{3}\right) + 2\sqrt{-Q_{j-}} \sin\left(\frac{2\pi}{3}\right) \left(\frac{3\Omega_{1j-}\Omega_{2j-}^2}{162} \right);$$

$$\Pi_{j4-}^* = 2\sqrt{-Q_{j-}} \frac{4\Omega_{1j-}\Omega_{2j-}^3}{1944} \cos\left(\frac{2\pi}{3}\right) + 2\sqrt{-Q_{j-}} \sin\left(\frac{2\pi}{3}\right) \frac{\Omega_{2j-}^3}{162}; \Pi_{j5-}^* = 2\sqrt{-Q_{j-}} \frac{\Omega_{2j-}^4}{1944} \cos\left(\frac{2\pi}{3}\right).$$

Eq. (5) is used to plot the experimental curves used in characterizing the parameters of the SMA model in [25]. As shown in Fig. 2, the equation provides a good representation of the asymmetric behavior of the SMA.

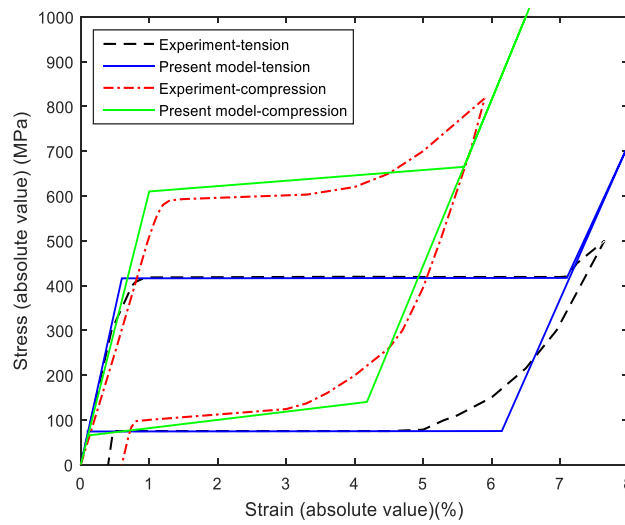


Fig. 2 Model versus experimental data considering tensile-compressive asymmetry.

2.2 Moment and shear force relations

The Timoshenko theory gives the following equations for the beam:

$$\begin{cases} \varepsilon_{tx} = Yd\theta/dx = Yk \\ d\omega/dx = \gamma - \theta \end{cases} \quad (6)$$

where θ is the slope, ω is the vertical displacement of the beam, γ is the shear strain, $k = d\theta/dx$ is the curvature and Y is the vertical coordinate measured from the neutral axis.

Eq. (1) gives the martensite start and finish stresses σ_{\pm}^{Ms} and σ_{\pm}^{Mf} during loading

$$\begin{cases} \sigma_{\pm}^{Ms} = \frac{-\varepsilon_{0\pm} \pm \sqrt{\varepsilon_{0\pm}^2 + 2(El_{MA} + P_{MA})(\beta\Gamma_{\pm}/2 + C(T) + a)}}{El_{MA} + P_{MA}} \\ \sigma_{\pm}^{Mf} = \frac{-\varepsilon_{0\pm} \pm \sqrt{\varepsilon_{0\pm}^2 - 2(El_{MA} + P_{MA})(a - G - b - (\alpha - 3\beta/2)\Gamma_{\pm} + C(T) + a)}}{El_{MA} + P_{MA}} \end{cases} \quad (7)$$

To enable the derivation of the equations governing the deformation of the beam throughout a monotonic loading case, it is important to distinguish the different solid phase structures that develop within the beam as the load varies [26]. Indeed, different distributions of solid phase regions are possible, corresponding to the situations in Fig. 3.

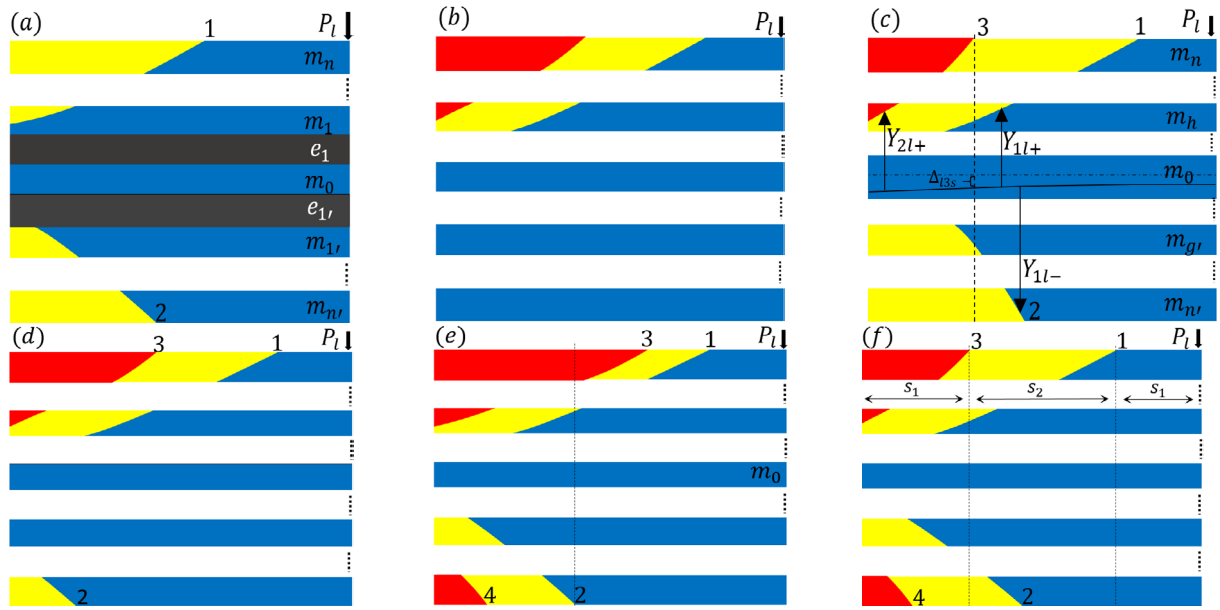


Fig. 3 Solid phase structure within the beam as the load is monotonically varied.

In the figure, austenite is shown in blue, martensite in red, and the regions of phase mixture are shown in yellow. Each longitudinal portion in which the number and order of solid phase structures in the vertical direction does not change is denoted s_i [26], where i is an index equal to one toward the free end and takes increasing integer values as one approaches the fixed end. For the problem addressed here, i can be anywhere between 1 and 4 (see figure). In each longitudinal section s_i , the moment, axial force, shear force, curvature, and deflection of the neutral axis are respectively denoted M_{ji} , F_{jxi} , Q_{ji} , k_{ji} and Δ_{ji} . Equivalent normalized properties are indicated with a hat symbol $\hat{\cdot}$, so that $\hat{M}_{ji} = M_{ji}/w$, $\hat{F}_{jxi} = F_{ji}/w$, and $\hat{Q}_{ji} = Q_{ji}/w$.

The vertical coordinate of the interface between adjoining solid phases in s_i (Fig.4) are given by the relations

$$\begin{cases} Y_{1l\pm} = \frac{\sigma_{\pm}^{Ms}}{k_{li}E_A} = \frac{\delta_{1\pm}}{k_{li}} \\ Y_{2l\pm} = \frac{\sigma_{\pm}^{Mf} + \varepsilon_{0\pm}E_M}{k_{li}E_M} = \frac{\delta_{2\pm}}{k_{li}} \end{cases} \quad (8)$$

in which $\delta_{1\pm} = \sigma_{\pm}^{Mf}/E_A$ and $\delta_{2\pm} = (\sigma_{\pm}^{Mf} + \varepsilon_{0\pm}E_M)/E_M$.

For the beam cross section containing boundary 3 (Fig. 3), the neutral surface is located using the following system of equalities:

$$\begin{cases}
 Y_{2l+} = \frac{\delta_{2+}}{k_{l3s}} = d_{nt} + \Delta_{l3s} \\
 \hat{F}_{lx3s} = \sum_{\lambda=1}^{n'} E_{e\lambda} \frac{k_{l3s} Y^2}{2} \Big|_{\Delta_{l3s}-d_{\lambda t}}^{\Delta_{l3s}-d_{(\lambda-1)b}} + \sum_{\lambda=1}^n E_{e\lambda} \frac{k_{l3s} Y^2}{2} \Big|_{d_{(\lambda-1)t}+\Delta_{l3s}}^{d_{\lambda b}+\Delta_{l3s}} + E_A \frac{k_{l3s} Y^2}{2} \Big|_{\Delta_{l3s}-d_{0b}}^{\Delta_{l3s}+d_{0t}} + \sum_{\lambda=1}^{h-1} E_A \frac{k_{l3s} Y^2}{2} \Big|_{\Delta_{l3s}+d_{\lambda b}}^{\Delta_{l3s}+d_{\lambda t}} \\
 + E_A \frac{k_{l3s} Y^2}{2} \Big|_{\Delta_{l3s}+d_{hb}}^{Y_{l+}} + E_A \frac{k_{l3s} Y^2}{2} \Big|_{Y_{l-}}^{\Delta_{l3s}-d_{g't}} + \sum_{\lambda=1}^{g'-1} E_A \frac{k_{l3s} Y^2}{2} \Big|_{\Delta_{l3s}-d_{\lambda b}}^{\Delta_{l3s}-d_{\lambda t}} \\
 + \sum_{\lambda=h+1}^n \left(\Pi_{l+}^* Y + \frac{\Pi_{l2+}^* k_{l3s} Y^2}{2} + \frac{\Pi_{l3+}^* k_{l3s}^2 Y^3}{3} + \frac{\Pi_{l4+}^* k_{l3s}^3 Y^4}{4} + \frac{\Pi_{l5+}^* k_{l3s}^4 Y^5}{5} \right) \Big|_{\Delta_{l3s}+d_{\lambda b}}^{\Delta_{l3s}+d_{\lambda t}} \\
 + \left(\Pi_{l+}^* Y + \frac{\Pi_{l2+}^* k_{l3s} Y^2}{2} + \frac{\Pi_{l3+}^* k_{l3s}^2 Y^3}{3} + \frac{\Pi_{l4+}^* k_{l3s}^3 Y^4}{4} + \frac{\Pi_{l5+}^* k_{l3s}^4 Y^5}{5} \right) \Big|_{Y_{l+}}^{\Delta_{l3s}+d_{ht}} \\
 + \sum_{\lambda=g'+1}^{n'} \left(\Pi_{l-}^* Y + \frac{\Pi_{l2-}^* k_{l3s} Y^2}{2} + \frac{\Pi_{l3-}^* k_{l3s}^2 Y^3}{3} + \frac{\Pi_{l4-}^* k_{l3s}^3 Y^4}{4} + \frac{\Pi_{l5-}^* k_{l3s}^4 Y^5}{5} \right) \Big|_{\Delta_{l3s}-d_{\lambda b}}^{\Delta_{l3s}-d_{\lambda t}} \\
 + \left(\Pi_{l-}^* Y + \frac{\Pi_{l2-}^* k_{l3s} Y^2}{2} + \frac{\Pi_{l3-}^* k_{l3s}^2 Y^3}{3} + \frac{\Pi_{l4-}^* k_{l3s}^3 Y^4}{4} + \frac{\Pi_{l5-}^* k_{l3s}^4 Y^5}{5} \right) \Big|_{\Delta_{l3s}-d_{g'b}}^{Y_{l-}} = 0
 \end{cases}
 \quad (9)$$

In the above system, Y_{2l+} is the Y coordinate of line 3, Δ_{l3s} is the deviation of the neutral axis, F_{lx3s} is the axial force, and k_{l3s} is the curvature. The following constraints must simultaneously be enforced:

$$\begin{cases}
 d_{hb} + \Delta_{l3s} < Y_{l+} = \frac{\delta_{1+}}{k_{l3s}} < d_{ht} + \Delta_{l3s} \\
 \Delta_{l3s} - d_{g'b} < Y_{l-} = \frac{\delta_{1-}}{k_{l3s}} < \Delta_{l3s} - d_{g't}
 \end{cases}
 \quad (10)$$

The bending moment M_{l3s} is then obtained by integration. It is worth noting that a correct solution requires proper determination of the correct sequence in which new solid phases form and evolve within the beam as the load is applied (Fig. 4).

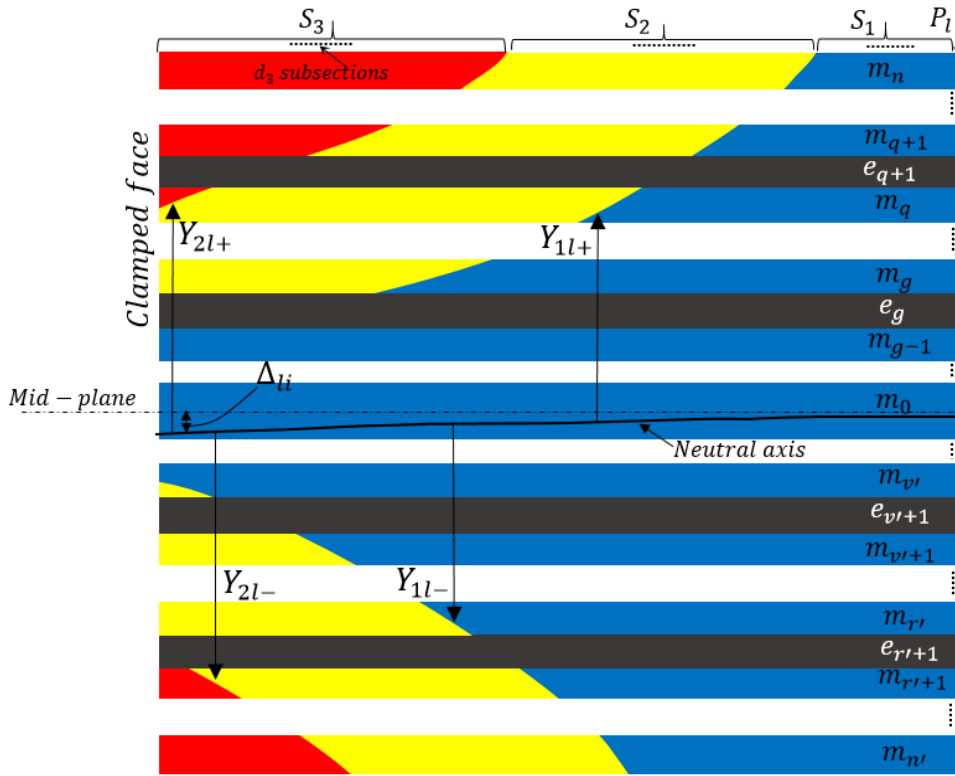


Fig.4 Solid phase distribution within the beam during stage 3 of loading.

The mathematical details of this procedure are not presented here in the interest of brevity. In Fig. 4, each of the sections s_1 , s_2 and s_3 requires separate mathematical treatment because of different solid phase structure resulting in different governing equations. In section s_3 , the conditions of force and moment equilibria are given by

$$\begin{cases} \hat{F}_{lx1} = \hat{F}_e + \hat{F}_{m-} + \hat{F}_{m+} + \hat{F}_a + \hat{F}_{t+} + \hat{F}_{t-} = 0 \\ \hat{M}_{l1} = \hat{M}_e + \hat{M}_{m-} + \hat{M}_{m+} + \hat{M}_a + \hat{M}_{t+} + \hat{M}_{t-} \end{cases} \quad (11)$$

where the indices e , a , m and t indicate elastic, austenite, martensite and active phase transformation regions, respectively. Moreover, the tensile region is denoted with a $+$ and the compressive region with a $-$ symbol. By integration, the total force and moment acting on the section are such that

$$\begin{aligned} \hat{F}_{lx1} = & \sum_{\lambda=1'}^{n'} E_{e\lambda} \frac{k_{l1} Y^2}{2} \Big|_{\Delta_{l1}-d_{\lambda t}}^{\Delta_{l1}-d_{(\lambda-1)b}} + \sum_{\lambda=1}^n E_{e\lambda} \frac{k_{l1} Y^2}{2} \Big|_{d_{(\lambda-1)t}+\Delta_{l1}}^{d_{\lambda b}+\Delta_{l1}} + \sum_{\lambda=r'+1}^{n'} E_M \left(\frac{k_{l1} Y^2}{2} - \varepsilon_{0-} Y \right) \Big|_{\Delta_{l1}-d_{\lambda b}}^{\Delta_{l1}-d_{\lambda t}} \\ & + \sum_{\lambda=q+1}^n E_M \left(\frac{k_{l1} Y^2}{2} - \varepsilon_{0+} Y \right) \Big|_{\Delta_{l1}+d_{\lambda b}}^{\Delta_{l1}+d_{\lambda t}} + E_A \frac{k_{l1} Y^2}{2} \Big|_{\Delta_{l1}-d_{0b}}^{\Delta_{l1}+d_{0t}} + \sum_{\lambda=1}^g E_A \frac{k_{l1} Y^2}{2} \Big|_{\Delta_{l1}+d_{\lambda b}}^{\Delta_{l1}+d_{\lambda t}} + E_A \frac{k_{l1} Y^2}{2} \Big|_{Y_{1l-}}^{\Delta_{l1}-d_{v't}} \\ & + \sum_{\lambda=1'}^{v'-1} E_A \frac{k_{l1} Y^2}{2} \Big|_{\Delta_{l1}-d_{\lambda b}}^{\Delta_{l1}-d_{\lambda t}} + \sum_{\lambda=g+1}^{q-1} \left(\Pi_{l1+}^* Y + \frac{\Pi_{l2+}^* k_{l1} Y^2}{2} + \frac{\Pi_{l3+}^* k_{l1}^2 Y^3}{3} + \frac{\Pi_{l4+}^* k_{l1}^3 Y^4}{4} + \frac{\Pi_{l5+}^* k_{l1}^4 Y^5}{5} \right) \Big|_{\Delta_{l1}+d_{\lambda b}}^{\Delta_{l1}+d_{\lambda t}} \end{aligned}$$

$$\begin{aligned}
 & + \left(\Pi_{l1+}^* Y + \frac{\Pi_{l2+}^* k_{l1} Y^2}{2} + \frac{\Pi_{l3+}^* k_{l1}^2 Y^3}{3} + \frac{\Pi_{l4+}^* k_{l1}^3 Y^4}{4} + \frac{\Pi_{l5+}^* k_{l1}^4 Y^5}{5} \right) \Big|_{\Delta_{l1} + d_{qb}}^{Y_{2l+}} \\
 & + \sum_{\lambda=v+1}^r \left(\Pi_{l1-}^* Y + \frac{\Pi_{l2-}^* k_{l1} Y^2}{2} + \frac{\Pi_{l3-}^* k_{l1}^2 Y^3}{3} + \frac{\Pi_{l4-}^* k_{l1}^3 Y^4}{4} + \frac{\Pi_{l5-}^* k_{l1}^4 Y^5}{5} \right) \Big|_{\Delta_{l1} - d_{\lambda b}}^{\Delta_{l1} - d_{\lambda t}} \\
 & + \left(\Pi_{l1-}^* Y + \frac{\Pi_{l2-}^* k_{l1} Y^2}{2} + \frac{\Pi_{l3-}^* k_{l1}^2 Y^3}{3} + \frac{\Pi_{l4-}^* k_{l1}^3 Y^4}{4} + \frac{\Pi_{l5-}^* k_{l1}^4 Y^5}{5} \right) \Big|_{\Delta_{l1} - d_{v'b}}^{Y_{l1-}} = 0 \\
 \hat{M}_{l1} & = \sum_{\lambda=1'}^{n'} E_{e\lambda} \frac{k_{l1} Y^3}{3} \Big|_{\Delta_{l1} - d_{\lambda t}}^{\Delta_{l1} - d_{(\lambda-1)b}} + \sum_{\lambda=1}^n E_{e\lambda} \frac{k_{l1} Y^3}{3} \Big|_{d_{(\lambda-1)t} + \Delta_{l1}}^{d_{\lambda b} + \Delta_{l1}} + \sum_{\lambda=r'+1}^{n'} E_M \left(\frac{k_{l1} Y^3}{3} - \frac{Y^2}{2} \varepsilon_{0-} \right) \Big|_{\Delta_{l1} - d_{\lambda b}}^{\Delta_{l1} - d_{\lambda t}} \\
 & + \sum_{\lambda=q+1}^n E_M \left(\frac{k_{l1} Y^3}{3} - \frac{Y^2}{2} \varepsilon_{0+} \right) \Big|_{\Delta_{l1} + d_{\lambda b}}^{\Delta_{l1} + d_{\lambda t}} + E_A \frac{k_{l1} Y^3}{3} \Big|_{\Delta_{l1} - d_{0b}}^{\Delta_{l1} + d_{0t}} + \sum_{\lambda=1}^g E_A \frac{k_{l1} Y^3}{3} \Big|_{\Delta_{l1} + d_{\lambda b}}^{\Delta_{l1} + d_{\lambda t}} + E_A \frac{k_{l1} Y^3}{3} \Big|_{Y_{l1-}}^{\Delta_{l1} - d_{v't}} \\
 & + \sum_{\lambda=1'}^{v'-1} E_A \frac{k_{l1} Y^3}{3} \Big|_{\Delta_{l1} - d_{\lambda b}}^{\Delta_{l1} - d_{\lambda t}} + \sum_{\lambda=g+1}^{q-1} \left(\frac{\Pi_{l1+}^* Y^2}{2} + \frac{\Pi_{l2+}^* k_{l1} Y^3}{3} + \frac{\Pi_{l3+}^* k_{l1}^2 Y^4}{4} + \frac{\Pi_{l4+}^* k_{l1}^3 Y^5}{5} + \frac{\Pi_{l5+}^* k_{l1}^4 Y^6}{6} \right) \Big|_{\Delta_{l1} + d_{\lambda b}}^{\Delta_{l1} + d_{\lambda t}} \\
 & + \left(\frac{\Pi_{l1+}^* Y^2}{2} + \frac{\Pi_{l2+}^* k_{l1} Y^3}{3} + \frac{\Pi_{l3+}^* k_{l1}^2 Y^4}{4} + \frac{\Pi_{l4+}^* k_{l1}^3 Y^5}{5} + \frac{\Pi_{l5+}^* k_{l1}^4 Y^6}{6} \right) \Big|_{\Delta_{l1} + d_{qb}}^{Y_{2l+}} \\
 & + \sum_{\lambda=v+1}^r \left(\frac{\Pi_{l1-}^* Y^2}{2} + \frac{\Pi_{l2-}^* k_{l1} Y^3}{3} + \frac{\Pi_{l3-}^* k_{l1}^2 Y^4}{4} + \frac{\Pi_{l4-}^* k_{l1}^3 Y^5}{5} + \frac{\Pi_{l5-}^* k_{l1}^4 Y^6}{6} \right) \Big|_{\Delta_{l1} - d_{\lambda b}}^{\Delta_{l1} - d_{\lambda t}} \\
 & + \left(\frac{\Pi_{l1-}^* Y^2}{2} + \frac{\Pi_{l2-}^* k_{l1} Y^3}{3} + \frac{\Pi_{l3-}^* k_{l1}^2 Y^4}{4} + \frac{\Pi_{l4-}^* k_{l1}^3 Y^5}{5} + \frac{\Pi_{l5-}^* k_{l1}^4 Y^6}{6} \right) \Big|_{\Delta_{l1} - d_{v'b}}^{Y_{l1-}}
 \end{aligned}$$

(12)

where the volume fraction of martensite is given by

$$z_{l1\pm} = \frac{k_{l1} Y}{\delta_{2\pm} - \delta_{1\pm}} - \frac{\delta_{1\pm}}{\delta_{2\pm} - \delta_{1\pm}} = a_{l1\pm} Y + b_{l1\pm} \quad (13)$$

In Eq. (15), $a_{l1\pm} = k_{l1} / (\delta_{2\pm} - \delta_{1\pm})$, $b_{l1\pm} = -\delta_{1\pm} / (\delta_{2\pm} - \delta_{1\pm})$ [26]. The total shear force is then written

$$\hat{Q}_{l1} = \hat{Q}_e + \hat{Q}_{m-} + \hat{Q}_{m+} + \hat{Q}_a + \hat{Q}_{t+} + \hat{Q}_{t-} \quad (14)$$

which can be fully developed into the following form:

$$\begin{aligned}
 \hat{Q}_{11} = & \sum_{\lambda=1}^{n'} K_s G_{e\lambda} \gamma_{11} Y \Big|_{\Delta_{11}-d_{1u}}^{\Delta_{11}-d_{(\lambda-1)b}} + \sum_{\lambda=1}^n K_s G_{e\lambda} \gamma_{11} Y \Big|_{d_{(\lambda-1)t}+\Delta_{11}}^{d_{\lambda b}+\Delta_{11}} + \sum_{\lambda=r'+1}^{n'} K_s G_M (\gamma_{11} - \gamma_{0-}) Y \Big|_{\Delta_{11}-d_{1b}}^{\Delta_{11}-d_{1u}} \\
 & + \sum_{\lambda=g+1}^n K_s G_M (\gamma_{11} - \gamma_{0+}) Y \Big|_{\Delta_{11}+d_{1b}}^{\Delta_{11}+d_{1u}} + K_s G_A \gamma_{11} Y \Big|_{\Delta_{11}-d_{0b}}^{\Delta_{11}+d_{0t}} + \sum_{\lambda=1}^g K_s G_A \gamma_{11} Y \Big|_{\Delta_{11}+d_{1b}}^{\Delta_{11}+d_{1u}} + K_s G_A \gamma_{11} Y \Big|_{Y_{1l-}}^{\Delta_{11}-d_{1t}} + \sum_{\lambda=1}^{v'-1} K_s G_A \gamma_{11} Y \Big|_{\Delta_{11}-d_{1b}}^{\Delta_{11}-d_{1u}} \\
 & + \sum_{\lambda=g+1}^{q-1} K_s G_M G_A \left[\frac{\ln\{G_M + b_{11+}(G_A - G_M)Y\}}{a_{11+}(G_A - G_M)} \gamma_{11} - \gamma_{0+} \frac{a_{11+}(G_A - G_M)Y - G_M \ln\{G_M(a_{11+}Y + b_{11+} - 1) - G_A(a_{11+}Y + b_{11+})\}}{a_{11+}(G_A - G_M)^2} \right] \Big|_{\Delta_{11}+d_{1b}}^{\Delta_{11}+d_{1u}} \\
 & + K_s G_M G_A \left[\frac{\ln\{G_M + b_{11+}(G_A - G_M)Y\}}{a_{11+}(G_A - G_M)} \gamma_{11} - \gamma_{0+} \frac{a_{11+}(G_A - G_M)Y - G_M \ln\{G_M(a_{11+}Y + b_{11+} - 1) - G_A(a_{11+}Y + b_{11+})\}}{a_{11+}(G_A - G_M)^2} \right] \Big|_{\Delta_{11}+d_{1b}}^{Y_{21+}} \\
 & + \sum_{\lambda=v'+1}^{r'} K_s G_M G_A \left[\frac{\ln\{G_M + b_{11-}(G_A - G_M)Y\}}{a_{11-}(G_A - G_M)} \gamma_{11} - \gamma_{0-} \frac{a_{11-}(G_A - G_M)Y - G_M \ln\{G_M(a_{11-}Y + b_{11-} - 1) - G_A(a_{11-}Y + b_{11-})\}}{a_{11-}(G_A - G_M)^2} \right] \Big|_{\Delta_{11}-d_{1b}}^{\Delta_{11}-d_{1u}} \\
 & + K_s G_M G_A \left[\frac{\ln\{G_M + b_{11-}(G_A - G_M)Y\}}{a_{11-}(G_A - G_M)} \gamma_{11} - \gamma_{0-} \frac{a_{11-}(G_A - G_M)Y - G_M \ln\{G_M(a_{11-}Y + b_{11-} - 1) - G_A(a_{11-}Y + b_{11-})\}}{a_{11-}(G_A - G_M)^2} \right] \Big|_{\Delta_{11}-d_{1b}}^{Y_{1l-}}
 \end{aligned}
 \tag{15}$$

where G_A , G_M and $G_{e\lambda}$ are the shear moduli of martensite, austenite, and the elastic layer, $\gamma_{0\pm} = \sqrt{3}\varepsilon_{0\pm}/2$ [26,27], $K_s = 5/6$ is a correction factor and γ_{11} is the shear strain. The shear stiffness G is such that [24]:

$$G = \frac{G_A G_M}{G_M + z(G_A - G_M)} \tag{16}$$

2.3 Solution during unloading

In the general case, unloading proceeds according to the following 4 stages, in sequence: elastic unloading, reverse transformation in part of the mixed region, reverse transformation in the entire mixed phase region until complete transformation to austenite, and elastic unloading of austenite. Because of space limitations, the corresponding derivations could not be reproduced here. The reader is referred to [26] for a complete discussion. The key complication in this case comes from the initial state of the beam, post-loading, which may comprise a non-homogeneous distribution of martensite.

3. CONCLUSION

A new analytical treatment of the problem of a multilayered elastic-SMA beam was proposed using a combination of the ZM constitutive relations for asymmetric SMAs and the Timoshenko theory. The procedure for deriving the governing equations of the beam was fully detailed for the case of monotonic loading and closed-form analytical formulations were pursued to the extent possible. A guide was also provided on the process to follow for solving the same problem during unloading. The model allows, in particular, the analytical determination of the bending moment, axial force and shear force in a cross section. It also allows finding the location of the neutral surface throughout the length of the beam as well as the beam deflection.

REFERENCES

- [1] Jani JM, Leary M, Subic A, Mark AM. Gibson. A review of shape memory alloy research, applications and opportunities. *Materials and Design* 2014; 56: 1078–1113.
- [2] Butera F, Coda A, Vergani G. Shape memory actuators for automotive applications. In: *Nanotec IT newsletter*. Roma: AIRI/nanotec IT 2007; 12–6.
- [3] Fujita H. Studies of micro actuators in Japan. In: *IEEE international conference on robotic automation*. Institute of Industrial Science, Tokyo University 1989; 1559–64.
- [4]. Machado LG, Savi MA. Medical applications of shape memory alloys. *Brazilian Journal of Medical and Biological Research* 2003; 36 : 683–91.
- [5] Otsuka K, Wayman CM. *Shape Memory Materials*. Cambridge University Press, Cambridge 1998.
- [6] Birman V. Theory and Comparison of the Effect of Composite and Shape Memory Alloy Stiffeners on Stability of Composite Shells and Plates. *International Journal of Mechanical Sciences* 1997; 39 (10) : 1139–1149.
- [7] Chen Q, Levy C. Vibration Analysis and Control of Flexible Beam by Using Smart Damping Structures. *Composites: Part B* 1999; 30(4) : 395–406.
- [9] Fuller CR, Elliott SJ, Nelson PA. *Active Control of Vibration*, Academic Press Ltd., London 1993.
- [10] Birman V, Chandrashekhara K, Sain S. An Approach to Optimization of Shape Memory Alloy Hybrid Composite Plates Subjected to Low-Velocity Impact. *Composites: Part B* 1996; 5: 439– 446.
- [11] Angioni SL, Meo M, Foreman A. Impact damage resistance and damage suppression properties of shape memory alloys in hybrid composites—a review. *Smart Materials and Structures* 2011; 20.
- [12] Lee KJ, Lee JH, Jung CY, Choi E. Crack-closing performance of NiTi and NiTiNb fibers in cement mortar beams using shape memory effects. *Composite Structures* 2018; 202, 15: 710-718.
- [13] Alebrahim R, Sharifishourabi G, Sharifi S, Alebrahim M, Ayob A. Thermo-mechanical behaviour of smart composite beam under quasi-static loading. *Composite Structures* 2018; 201: 21-28.
- [14] Kim EH, Lee I, Roh JH, Bae JS, Koo KN. Effects of shape memory alloys on low velocity impact characteristics of composite plate. *Composite Structures* 2011; 93: 2903-2909.
- [15] Han MW, Rodrigue H, Kim HI, Song SH, Ahn SH. Shape memory alloy/glass fiber woven composite for soft morphing winglets of unmanned aerial vehicles. *Composite Structures* 2016; 140: 202-212.
- [16] Thompson SP, Loughlan J. Enhancing the post-buckling response of a composite panel structure utilising shape memory alloy actuators – a smart structural concept. *Composite Structures* 2001; 51, 1: 21-36.
- [17] Wang E, Tian Y, Wang Z, Jiao F, Guo C, Jiang F. A study of shape memory alloy NiTi fiber/plate reinforced (SMAFR/SMAPR) Ti-Al laminated composites. *Journal of Alloys and Compounds* 2017; 696: 1059-1066.
- [18] Hamada K, Lee JH, Mizuuchi K, Taya M, Inoue K. Thermomechanical Behavior of TiNi Shape Memory Alloy Fiber Reinforced 6061 Aluminum Matrix Composite. *Metallurgical and Materials Transactions A* 1998; 29: 1127-1135.

- [19] Viet NV, Zaki W. Analytical investigation of the behavior of concrete beams reinforced with multiple circular superelastic shape memory alloy bars. *Composite Structures* 2019; 210: 958-970.
- [20] Taya M, Liang Y, Namli OC, Tamagawa H, Howie T. Design of two-way reversible bending actuator based on a shape memory alloy/shape memory polymer composite. *Smart Materials and Structures* 2013; 22, 105003 (12pp).
- [21] Park J, Headings ML, Dapino MJ, Baur JW, Tandon GP. Investigation of interfacial shear stresses, shape fixity, and actuation strain in composites incorporating shape memory polymers and shape memory alloys. *Frontier in Materials* 2015; 2.
- [22] Marfia S, Sacco E, Reddy JN. Superelastic and Shape Memory Effects in Laminated Shape-Memory-Alloy Beams. *AIAA JOURNAL* 2003; 41.
- [23] Solomou AG, Machairas TT, Saravanos DA, Hartl DJ, Lagoudas DC. A coupled layered thermomechanical shape memory alloy beam element with enhanced higher order temperature field approximations. *Journal of Intelligent Material Systems and Structures* 2016; 27 (17): 2359-2384.
- [24] Zaki W, Moumni Z. A three-dimensional model of the thermomechanical behavior of shape memory alloys. *Journal of the Mechanics and Physics of Solids* 2007; 55:2455–2490.
- [25] Zaki W, Moumni Z, Morin C. Modeling tensile-compressive asymmetry for superelastic shape memory alloys. *Mechanics of Advanced Materials and Structures* 2011; 18 (7): 559-564.
- [26] Viet NV, Zaki W, Umer R. Bending models for superelastic shape memory alloy laminated composite cantilever beams with elastic core layer. *Composites Part B* 2018; 147 (15) : 86-103.
- [27] Viet NV, Zaki W, Umer R. Analytical model of functionally graded material/shape memory alloy composite cantilever beam under bending. *Composite Structures* 2018; 203 : 764-776.

EFFECT OF COBALT PARTICLE MORPHOLOGY ON PROPERTIES OF MAGNETORHEOLOGICAL ELASTOMERS

XUFENG DONG^{*}, YU TONG^{*}, MIN QI^{*} AND NING MA[†]

^{*} School of Materials Science and Engineering

Dalian University of Technology

Dalian 116024, People's Republic of China

e-mail: dongxf@dlut.edu.cn, tongyu@mail.dlut.edu.cn, minqi@dlut.edu.cn, www.dlut.edu.cn

[†] School of Civil Engineering

Dalian University of Technology

Dalian 116024, People's Republic of China

e-mail: maning@dlut.edu.cn, www.dlut.edu.cn

Key words: Magnetorheological, Cobalt particles, Morphology, Smart Materials.

Abstract. The magnetorheological (MR) performance of MR elastomers mainly depends on the types of matrix and magnetic particles. Whether the MR effect of MR elastomers can be enhanced by using flower-like particles as the active phase was left unknown. In this study, flower-like cobalt particles and sphere cobalt particles with similar particle size were synthesized and used as the active phase to prepare MR elastomers. The experimental results indicated the MREs with flower-like cobalt particles present higher crosslink density and enhanced interfacial bond strength, which leads to their higher storage modulus and higher loss modulus with respect to the MREs with sphere cobalt particles. More meaningfully, the field-induced storage modulus tunable range was also improved by using flower-like cobalt particles as the dispersing phase.

1 INTRODUCTION

Magnetorheological (MR) elastomers are smart materials whose dynamic viscoelasticity can be tuned and modified reversibly within a few milliseconds by applying an external magnetic field.^[1-4] The magnetic field dependent dynamic viscoelasticity is defined as MR effect. Such unique effect makes MR elastomers have a wide range of engineering applications, such as suspension bushings, seismic protection, engine mounts, adaptively tuned vibration absorbers, stiffness tunable isolators and so on.^[5-10] Typical MR elastomers are composed of magnetizable particles and non-magnetic polymer matrix. The MR performance of MR elastomers mainly depends on the types of matrix and magnetic particles. In the past decades, most studies focused on matrix, and various kinds of polymer, such as silicone rubber, natural rubber, polyurethane, and polybutadiene rubber have been used to prepare MR elastomers with different properties.^[11-15] In contrast to plenty choices of matrix, limit kinds of particles can be used as the active phase; besides carbonyl iron particles, which were widely used due to their excellent soft magnetic properties and low cost, only cobalt particles and nickel particles^[16-17] have the potential to

be used to prepare MR elastomers.

In terms of composition, MR elastomers can be considered as a kind of particles filled polymer-based composites (PFPCs). Therefore, it can be expected that the interaction between particles and polymer matrix also has non-negligible effect on their MR effect as well as mechanical properties. Gong et al. used silane coupling agents to improve the interaction between the carbonyl iron particles (CIPs) and silicone rubber, and obtained an enhanced MR performance.^[19] Yu et al studied the effect of PANI-modified CIPs on improving the interfacial interactions of MR elastomer based on PU/EP IPNs matrix, which indicated that the strong interfacial interactions of PANI-MRE improved the MR effect and reduced the loss factor.^[13]

Although the influence of matrix, particles composition, and particle/matrix interface on MR properties of MR elastomers have been fully investigated, to the best of our knowledge, few studies analysed the effect of particles morphologies; in previous studies, sphere CI particles were the most widely used active phase of MR elastomers.^[20-22] By contrast, the influence of particles morphology on properties of MR gels and MR fluids, which are another two branches of MR materials, have been reported recently. Yang et.al synthesized a magnetorheological gel based on the conventional CIPs and flower-like CIPs. The experimental results indicate that, with flower-like CIPs, the maximum dynamic yield stress and magneto-induced shear yield stress of MR gel were 1.39 and 1.37 times of the MR gel with conventional sphere CIPs.^[23] We prepared a magnetorheological fluid with flower-like cobalt particles. Compared with the MR fluid with sphere cobalt particles, the flower-like cobalt particles based MR fluids showed higher yield stress and better sedimentation stability.^[24] However, whether the MR effect of MR elastomers can be enhanced by using flower-like particles as the active phase was left unknown. In this study, we designed experiments to find the detail influence of particles' flower-like morphology on MR effect of MR elastomers.

2 EXPERIMENTAL

The flower-like cobalt particles (FCPs) and the sphere cobalt particles (SCPs), which used to prepare different MR elastomers were prepared by a typical solvothermal reaction according to our previous report.^[24] The main reagents used were cobalt chloride hexahydrate ($\text{CoCl}_2 \cdot 6\text{H}_2\text{O}$), sodium hydroxide (NaOH), ethylene glycol, 1,3-propanediol. All reagents were of analytical grade and used without further purification. Silicon rubber RTV-2 and catalyst were obtained from Zhuhai COCA New Material Co., Ltd. Dimethyl silicon oil ($\eta=100 \text{ mPa}\cdot\text{s}$, 25°C) was bought from Beijing Hangping Silicon and Chemical Co., Ltd. To prepare MR elastomers, the silicon rubber and dimethyl silicon oil with equal weight were mixed at room temperature by using a stirrer bar. After 10 min, they were mixed with cobalt particles. All the ingredients were mixed at room temperature during 30 min by a stirrer bar. Subsequently, the homogeneous mixture was placed into a mold with a cylinder cavity of $\phi 20 \text{ mm} \times 1 \text{ mm}$. The curing process was performed in a 240 mT orientation magnetic field along the thickness of the sample for about 6 h.^[25] The orientation filed could make the particles align to form column-like structures, and obtain anisotropic MR elastomers. A number of studies have proved that anisotropic MR elastomers have more excellent MR response than isotropic composites with random distributed particles.^[26,27] The percentage of cobalt particles

were 10% in volume for all the samples. The samples with sphere cobalt particles and flower-like particles are named as SCP-MRE and FCP-MRE for short, respectively.

The brittle fraction sections of MR elastomers were cryogenically fractured in liquid nitrogen and the fracture surfaces of the MR elastomers after a swelling treatment were cut off by a knife. All the samples were coated with a thin layer of gold prior to SEM (ZEISS SUPRA 55) observation. Magnetic measurements were carried out using a vibrating sample magnetometer (JDM-13T).

The crosslink densities of the MREs were obtained from a swelling measurement. First, pre-weighted dry MRE samples were immersed in 80 mL of toluene at 30 °C for 72 h in a vacuum case. The toluene was replaced once at 36 h to make sure all the MREs achieved swelling equilibrium. The MRE samples were taken out after 72 h and the toluene on their surface was dried with filter paper. After recording the swollen mass of these MRE samples, they were transferred to a vacuum at 80 °C for 24 h, which was prepared for the SEM observation. For each type of MRE, three specimens were measured and the average values were calculated. According to the Flory–Rehner equations, the crosslink density of MREs can be estimated^[28, 29].

The dynamic viscoelasticity of MR elastomers under various conditions were measured by a Physica MCR301 rheometer (Anton Paar, Austria) fitted with a magneto-rheological module (MRD180), which can apply different magnetic fields on the parallel-plates system (PP20) by changing direct current. The test gap was 1 mm. The dynamic viscoelasticity of MR elastomers was tested by an oscillatory mode. In order to get the appropriate amplitude and frequency of shear strain, the changes of storage modulus and loss modulus with strain amplitude (0.001~100%) and frequency (0.1~50 Hz) under different magnetic flux density (0, 115, 234 and 456 mT) were tested. Thereafter, the influence of the magnetic flux density on dynamic viscoelasticity was measured by setting the measured appropriate constant strain amplitude and frequency. All measurements were performed at 25 °C.

3 RESULTS AND DISCUSSIONS

3.1 Characterization of cobalt particles

Figure 1 shows the crystal phase, magnetic properties and SEM images of the cobalt particles with different morphologies. It indicates that the two kinds of particles have similar crystal structures, similar magnetic properties, and similar diameters (2~5 μm).

3.2 Structures of MR elastomers

The section SEM microphotographs of the FCP-MRE and SCP-MRE samples used in the swelling measurements are shown in Figure 2. As shown in Figure 2a and Figure 2b, both sphere cobalt particles and flower-like cobalt particles form chain-like structures along the direction of the orientation magnetic field applied during the preparation process. As expected, the silicon oil in the matrix has not participated in the crosslinking reactions of the MR elastomers. The dissolving of silicon oil and the swelling of the silicon rubber proceeded in toluene, and the weak connections between the particles and the matrix was destroyed during this treatment. By contrast, as shown in Figure 2c and

Figure 2d, some bridging structures are observed between particles and rubber matrix, indicating strong connections between the particles and the rubber. Figure 3 shows the crosslink density of the MREs filled with the two kinds of cobalt particles. It indicates the crosslink density of the FCP-MRE is about 30% higher than that of the SCP-MRE.

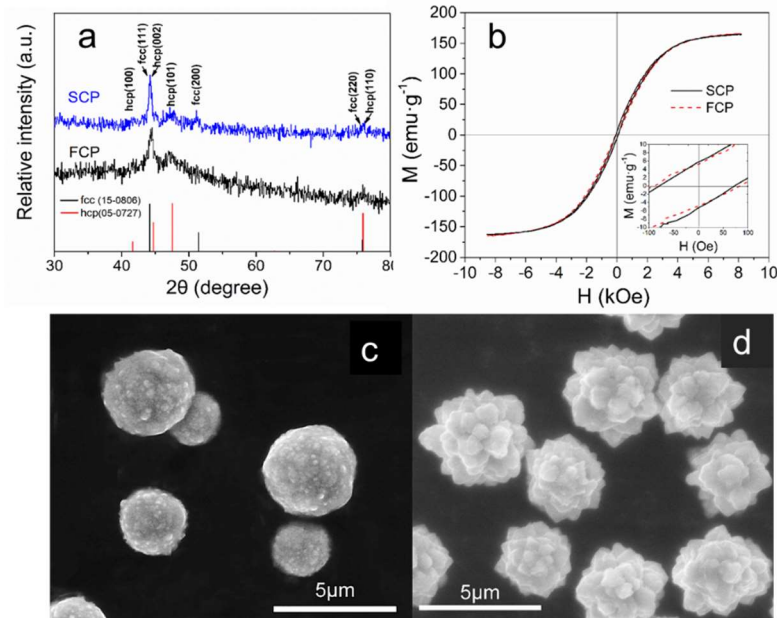


Figure 1: (a) Crystal phase, (b) magnetic properties and (c, d) SEM images of the sphere cobalt particles and flower-like cobalt particles

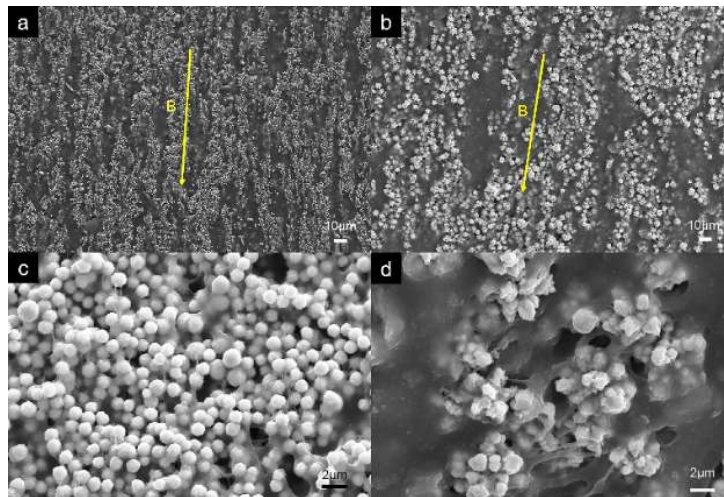


Figure 2: SEM microphotographs of (a) SCP-MRE and (b) FCP-MRE and (c, d) the magnification images of (a, b)

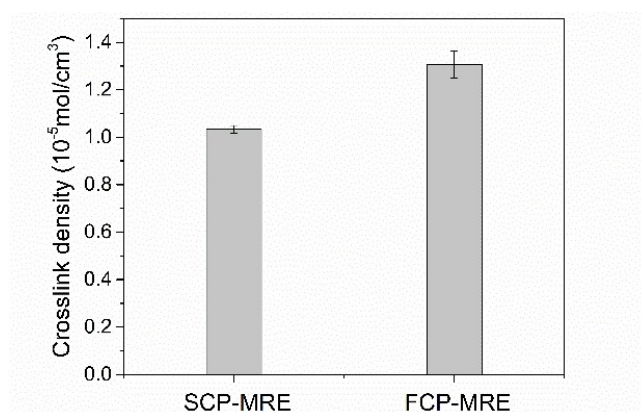


Figure 3: Crosslink densities of SCP-MRE and FCP-MRE

3.3 Dynamic viscoelasticity of MR elastomers

Figure 4 shows the storage modulus and loss modulus of the MRE samples as a function of applied strain amplitude under constant frequency (5 Hz) and different magnetic flux densities (0, 115, 234 and 456 mT). In absence or present of a magnetic field, as shown in Figure 4a, their storage modulus keeps unchanged at low strain amplitude and then decreases with increasing strain amplitude when it reaches a critical value ($\sim 0.1\%$). Below the critical strain amplitude, the MR elastomers are considered in their linear viscoelastic (LVE) region. As particles filled rubber-based composites, the particles form a microscopic network structure. At low strain amplitude, the structure is stable, while over the critical value, the structure is destroyed, which is the Payne effect. In addition, the low magnitude of the Payne effect factor can reflect the strong interaction in particle-particle and particle-matrix.^[30] From Figure 4a, the Payne effect factor in absence of magnetic field was calculated^[31]. The Payne effect factors are 77% for SCP-MRE and 72% for FCP-MRE, respectively. It indicates the particle-particle and particle-matrix interaction in FCP-MRE is stronger than that in SCP-MRE. When the shear amplitude exceeds the critical value, the network structure formed by the particles become unstable, it consumes more energy than when no magnetic field is applied. This corresponds to the larger loss modulus value shown in Figure 4b when the strain amplitude exceeds $\sim 0.1\%$ in different magnetic field strengths. Furthermore, the storage modulus and the loss modulus of the two samples increase with increasing magnetic field strength, which can be attributed to the stronger network structure at higher magnetic field. It indicates both SCP-MRE and FCP-MRE present significant magnetorheological effect.

Figure 5 shows the dependence of the storage modulus and loss modulus of the MR elastomers on magnetic flux density at a constant strain amplitude of 0.01% and constant frequency of 5 Hz. As the magnetic flux density rises, the storage modulus of the two MRE samples increases. It means both SCP-MRE and FCP-MRE present typical MR effect, which can be attributed to the increasing magnetic attractive interaction between the adjacent particles along the field direction. Besides, the storage modulus of the FCP-MRE is much higher than that of the SCP-MRE in absence and present of magnetic field,. The initial enhancement of the storage by using flower-like particles with respect to

sphere particles can be attributed to the higher crosslink density due to the larger specific surface area. Under an applying magnetic field, the attractive interaction between the neighboring flower-particles is stronger than that between the neighboring sphere particles due to the improved interface transferring properties. As a result, the storage modulus of FCP-MRE is higher than that of SCP-MRE. For the same reason, the loss modulus of FCP-MRE is higher than that of SCP-MRE. Interestingly, the loss modulus curve in Figure 6b first increases and then decreases. This can be explained by Chen's research.^[32] Loss modulus reflects the dissipation of material energy during deformation. The magnetic interaction (F_m) between particle and matrix is accordingly increased with the increase of the magnetic field. The larger F_m will lead to more energy dissipated on the interface slipping of the MR elastomers. In these conditions, the loss modulus increases with the increase of the magnetic field. On the other hand, the slip displacement is not a constant but a function of the F_m . It is easy to understand that if large normal force is applied, the slipping will become difficult, and the displacement of interfacial slipping will be reduced. As the increase of the magnetic field and the magnetic force, the slip displacement is reduced. Accordingly, the loss modulus declines. For those reason, the loss modulus initially increases at low field levels but decreases at high field levels.

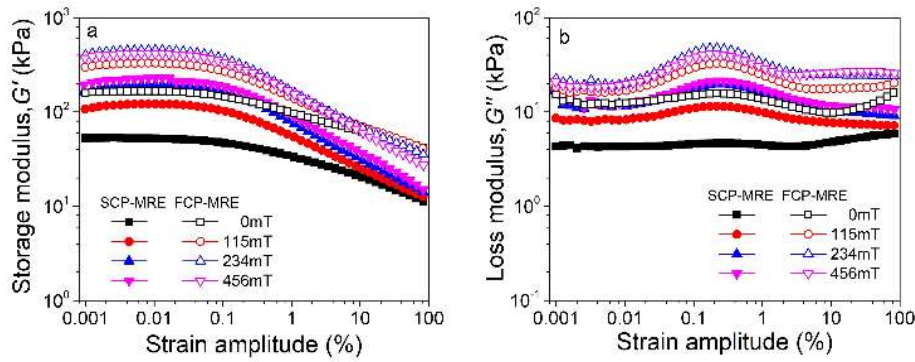


Figure 4: Storage modulus G' (a) and loss modulus G'' (b) of SCP-MRE and FCP-MRE under different magnetic flux densities as a function of strain amplitude

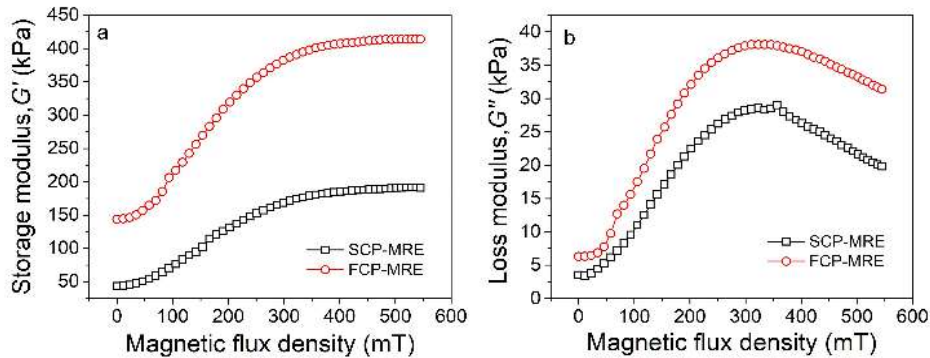


Figure 5: Storage modulus G' (a) and loss modulus G'' (b) of SCP-MRE and FCP-MRE at a constant strain amplitude and frequency as a function of magnetic flux density

The magnetic field-induced storage modulus $\Delta G'$ is an important indicator to evaluate the properties of MR elastomers, which is defined as the value of the storage modulus at each magnetic flux density G' minus zero-field storage modulus G_0' . Figure 6 shows the dependence of the magnetic field induced storage modulus of the two MR elastomers on magnetic flux density. As it is shown, the field-induced storage modulus tunable range was enlarged by using flower-like particles. In Figure 6, when the magnetic field exceeds 50 mT, both SCP-MRE and FCP-MRE present a sharply increasing $\Delta G'$ with rising magnetic field, hereafter, the increases in $\Delta G'$ of both samples tend to be gentle after the magnetic flux density reaches about 400 mT. Taking into account the similar magnetic properties of the two MRE samples, the difference between their $\Delta G'$ is mainly due to their different particle morphology. During the shear process, the particles in MREs tend to keep a linear structure along the magnetic field, while the rubber matrix easy to move along the shear direction. If the adhesion between rubber matrix and particles is weak, there will be gaps presenting at the interface between the particles and rubber matrix due to the debonding. This will cause the microstructure of MREs become unstable and reduce the storage modulus of MREs. Flower-like particles can increase cross-linking with the rubber matrix and the adhesion due to the undulating surface. This may be the reason that FCP-MRE shows higher magnetic field-induced storage modulus during the shear stress.

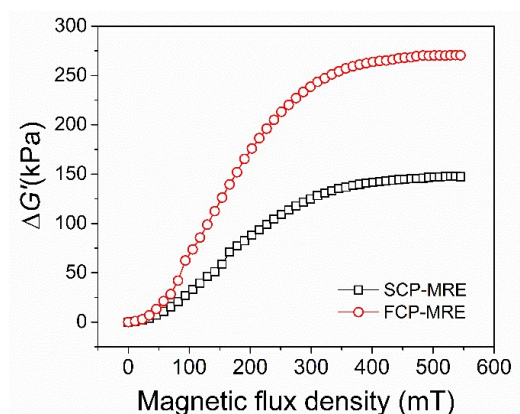


Figure 6: Magnetic field induced storage modulus of SCP-MRE and FCP-MRE as a function of magnetic flux density

4 CONCLUSIONS

Flower-like cobalt particles and sphere cobalt particles with similar particle size were used to prepare different MREs, whose dynamic viscoelasticity was tested and compared to verify the mechanism model. The experimental results indicated the flower-like cobalt particles based MREs presented enhanced storage modulus in absence and present of magnetic field with respect to sphere cobalt particles based ones. More meaningfully, the field-induced storage modulus tuneable range was also improved by using flower-like cobalt particles as the dispersing phase.

REFERENCES

- [1] Davis, L. C. Model of magnetorheological elastomers. *J. Appl. Phys.* (1999) 85: 3348-3351.
- [2] Carlson, J. D.; Jolly, M. R. MR fluid, foam and elastomer devices. *Mechatronics*. (2000) 10: 555-569.
- [3] Jolly, M. R.; Carlson, J. D.; Munoz, B. C. A model of the behaviour of magnetorheological materials. *Smart Mater. Struct.* (1996) 5: 607.
- [4] Sutrisno, J.; Purwanto, A.; Mazlan, S. A. Recent progress on magnetorheological solids: materials, fabrication, testing, and applications. *Adv Eng. Mater.* (2015) 17: 563-597.
- [5] Cantera, M. A.; Behrooz, M.; Gibson, R. F.; Gordaninejad, F. Modeling of magneto-mechanical response of magnetorheological elastomers (MRE) and MRE-based systems: a review. *Smart Mater. Struct.* (2017) 26:023001.
- [6] Li, Y.; Li, J.; Li, W.; Samali, B. Development and characterization of a magnetorheological elastomer based adaptive seismic isolator. *Smart Mater. Struct.* (2013) 22: 035005.
- [7] Du, H.; Li, W.; Zhang, N. Semi-active variable stiffness vibration control of vehicle seat suspension using an MR elastomer isolator. *Smart Mater. Struct.* (2011) 20: 105003.3
- [8] Deng, H. X.; Gong, X. L.; Wang, L. H. Development of an adaptive tuned vibration absorber with magnetorheological elastomer. *Smart Mater. Struct.* (2006) 15: N111.
- [9] Sun, S.; Yang, J.; Du, H.; Li, W. Overcoming the conflict requirement between high-speed stability and curving trafficability of the train using an innovative magnetorheological elastomer rubber joint. *J. Intel. Mater. Syst. Struct.* (2017) 1045389X17698591.
- [10] Liu, G.; Lu, K.; Zou, D.; Xie, Z.; Rao, Z.; Ta, N. Development of a semi-active dynamic vibration absorber for longitudinal vibration of propulsion shaft system based on magnetorheological elastomer. *Smart Mater. Struct.* (2017) 26: 075009.
- [11] Xu, Y. G.; Gong, X. L.; Zhang, S. H.; Xuan, W.; Fan, Y. C. A High-Performance Magnetorheological Material: Preparation, Characterization and Magnetic-Mechanic Coupling Properties. *Soft Matter*. (2011) 7: 5246-5254.
- [12] Chen, L.; Gong, X. L.; Jiang, W. Q.; Yao, J. J.; Deng, H. X.; Li, W. H. Investigation on magnetorheological elastomers based on natural rubber. *J. Mater. Sci.* (2007) 42: 5483-5489.
- [13] Yu, M.; Qi, S.; Fu, J.; Zhu, M.; Chen, D.. Understanding the reinforcing behaviors of polyaniline-modified carbonyl iron particles in magnetorheological elastomer based on polyurethane/epoxy resin IPNs matrix. *Compos. Sci Technol.* (2017) 139: 36-46.
- [14] Wang, Y.; Zhang, X.; Oh, J.; Chung, K. Fabrication and properties of magnetorheological elastomers based on CR/ENR self-crosslinking blends. *Smart Mater. Struct.* (2015) 24: 095006.
- [15] Bunoiu, M.; Bica, I. Magnetorheological elastomer based on silicone rubber, carbonyl iron and Rochelle salt: Effects of alternating electric and static magnetic fields intensities. *J. Industrl Eng Chem* (2016) 37: 312-318.
- [16] Padalka, O.; Song, H. J.; Wereley, N. M.; Filer II, J. A.; Bell, R. C. Stiffness and damping in Fe, Co, and Ni nanowire-based magnetorheological elastomeric composites. *IEEE Trans.Magn.* (2010) 46: 2275-2277.
- [17] Rodríguez-Arco, L.; López-López, M. T.; Kuzhir, P.; Bossis, G.; Durán, J. D. Optimizing the magnetic response of suspensions by tailoring the spatial distribution of the particle magnetic material. *ACS Appl. Mater. Interfaces.* (2013) 5:12143-12147.

- [18] Landa, R. A.; Soledad Antonel, P.; Ruiz, M. M.; Perez, O. E.; Butera, A.; Jorge, G.; Oliveira, C. L. P.; Negri, R. M. Magnetic and elastic anisotropy in magnetorheological elastomers using nickel-based nanoparticles and nanochains. *J. Appl. Phys.* (2013) 114: 213912.
- [19] Wang, Y.; Hu, Y.; Chen, L.; Gong, X.; Jiang, W.; Zhang, P.; Chen, Z. Effects of rubber/magnetic particle interactions on the performance of magnetorheological elastomers. *Polym. test.* (2006) 25: 262-267.
- [20] Fang, F. F.; Liu, Y. D.; Choi, H. J.; Seo, Y. Core-shell structured carbonyl iron microspheres prepared via dual-step functionality coatings and their magnetorheological response. *ACS Appl. Mater. Interfaces.* (2011) 3: 3487-3495.
- [21] Seo, J. S.; Kim, M. S.; Yang, K. M.; Lee, J. H.; Chung, K. H. Study of the Physical Properties of Carbonyl Iron Particles-Oriented Magneto-Rheological Elastomer. *Asian. J. Chem.* (2013) 25: 5171.
- [22] Perales-Martínez, I. A.; Palacios-Pineda, L. M.; Lozano-Sánchez, L. M.; Martínez-Romero, O.; Puente-Cordova, J. G.; Elías-Zúñiga, A. Enhancement of a magnetorheological PDMS elastomer with carbonyl iron particles. *Polym. Test.* (2017) 57: 78-86.
- [23] Yang, P.; Yu, M.; Luo, H.; Fu, J.; Qu, H.; Xie, Y. Improved rheological properties of dimorphic magnetorheological gels based on flower-like carbonyl iron particles. *Appl. Surf. Sci.* (2017) 416: 772-780.
- [24] Tong, Y.; Dong, X.; Qi, M. High performance magnetorheological fluids with flower-like cobalt particles. *Smart Mater. Struct.* (2017) 26: 025023.
- [25] Mietta, J. L.; Negri, R. M.; Tamborenea, P. I. Numerical simulations of stick percolation: application to the study of structured magnetorheological elastomers. *J. Phys. Chem. C.* (2014) 118: 20594-20604.
- [26] Sapouna, K.; Xiong, Y.P.; Shenoi, R. A. Dynamic mechanical properties of isotropic/anisotropic silicon magnetorheological elastomer composites. *Smart Mater. Struct.* (2017) 26: 115010.
- [27] Yunus, N. A.; Mazlan, S. A.; Choi, S. B.; Imaduddin, F.; Aziz, S. A. A.; Khairi, M. H. A. Rheological properties of isotropic magnetorheological elastomers featuring an epoxidized natural rubber. *Smart Mater. Struct.* (2016) 25: 107001.
- [28] Pickering, K. L.; Khimi, S. R.; Ilanko, S. The effect of silane coupling agent on iron sand for use in magnetorheological elastomers Part 1: Surface chemical modification and characterization. *Composites Part A.* (2015) 68: 377-386.
- [29] Flory, P. J.; Rehner Jr, J. Statistical mechanics of cross-linked polymer networks I. Rubberlike elasticity. *J. Chem. Phys.* (1943) 11: 512-520.
- [30] Mark, J. E. *Polymer Data Handbook*; Oxford University Press: New York, 1999: 415
- [31] Sorokin, V. V.; Ecker, E.; Stepanov, G. V.; Shamonin, M.; Monkman, G. J.; Kramarenko, E. Y.; Khokhlov, A. R. Experimental Study of the Magnetic Field Enhanced Payne Effect in Magnetorheological Elastomers. *Soft Matter.* (2014) 10: 8765-8776.
- [32] Chen, L.; Gong, X.; Li, W. Damping of magnetorheological elastomers. *Chin. J. Chem. Phys.* (2008) 21: 581.

FATIGUE ANALYSIS OF NITINOL STENT USED IN ENDOVASCULAR ANEURYSM REPAIR (EVAR) CONSIDERING ANISOTROPIC AORTIC WALLS

RAJA JAYENDIRAN*, BAKR NOUR[†] AND ANNIE RUIMI*

*Texas A&M University at Qatar

Doha (Qatar)

email: jayendiran.raja@qatar.tamu.edu; annie.ruimi@qatar.tamu.edu

[†] Weill Cornell Medicine-Qatar

Doha (Qatar)

Key words: Nitinol, superelasticity, stent, fatigue, Smith-Watson-Topper model

Abstract. In this work, a fatigue/failure analysis of Nitinol stents such as those employed in endovascular aneurysm repair (EVAR) is presented. The study is conducted for one billion hemodynamic cycles, that is more than 15 years of service life. The strain-stress curves are obtained using the fluid-structure interaction (FSI) analysis in Abaqus/Simulia and the high-cycle loading fatigue analysis is done on Ansys.

The stent we use for the study is a honeycomb closed-cell structure. It our own design. The geometry of the aorta is a cylindrical shell with three concentric layers. The aorta is modelled with the Holzapfel-Gasser-Ogden (HGO) hyperelastic equations which account for the anisotropy of the aorta. We use Nitinol superelastic property to study the stent structural fatigue. This is done with the Smith-Watson-Topper (SWT) model which takes into account the mean stress on the structure. The fatigue behaviour is obtained from fatigue life, fatigue damage, fatigue safety factor and a biaxiality indication contour plots.

Results indicate that the stent can withstand 10 years of pulsatile hemodynamic load, as recommended by the US Federal Food & Drug Administration (FDA). The fatigue safety factor (FSF) decreases as the number of cycle increases. Increasing the load by 25% decreases the stent life by approximately half (down to $5.61e8$ cycles) and doubling the load results in the stent failing. Areas of the stent struts subjected to pure uniaxial load are shown to be most prone to failure.

This study can give insights into the optimal design of self-expanding stents in addition to new directions to improve their functionality.

1 INTRODUCTION

Aortic aneurysm (AA) is characterized by an enlargement of the aorta to at least 1.5 times its initial size. It causes the walls to weaken and possibly rupture, resulting in over 10,000 people in the United States to die each year. Among possible surgical treatments, endovascular aneurysm repair (EVAR) using stents or stent-grafts require only minor incision. The patient can return to daily activities faster than with open-heart surgeries so EVAR procedures have become increasingly popular during the last fifteen years. Typically, arteries pulse at 72 times a minute, that is some 40 million times per year. This

causes significant stresses and strains on the stent, which can lead to fatigue and ultimately device failure [1, 2]. Thus, it is important to keep this in mind when designing stent, particularly that the US Food & Drug Administration (FDA) recommends that stents be able to withstand between ten and fifteen years of pulsatile loading cycles during testing before failure, that is between 400 to 600 million loading cycles [3, 4, 5, 6]. It is true that in comparison to blocked stent due to the body endothelial cells growth on the device (in-stent restenosis), stent fracture may not be the most common type of device failure but even so, the potential for the stent to fracture does not seem to be widely recognised and is largely underestimated [7].

Among stent materials, stainless steel is common and cheap but wires are thick which can prevent designing stents with complex geometries. In addition, the material is not completely biocompatible with human tissues. On the other hand, Nitinol (NiTi) is an alloy of Nickel and Titanium belonging to the family of smart material alloy (SMA). The material is expensive but with an excellent biocompatibility and a good resistance to fatigue and corrosion, it is widely used in the manufacturing of self-expanding endovascular stents and other medical devices [8].

Nitinol possesses a superelastic and a shape memory effect (SME) property. Superelasticity refers to the ability of the material to stretch extraordinarily, up to 10 times the original length and return to its original length when the loads are removed. SME involves the material crystallographic structure reacting to a temperature change and causing the material to return to its original shape when unloaded. However, these very same properties are also responsible for causing a complex fatigue behaviour, in contrast to conventional metals [8].

Typically for an healthy adult, the hemodynamic load can be described as oscillating between 80 mmHg and 120 mmHg. Such loading pattern generates a mean stress (average of maximum and minimum stress) and an alternating stress (difference between max and min stress/2) which need to be accounted for. The stress cycle is also not completely reversed because of the different max and min values of stress. Another thing to consider is that for Nitinol and other SMAs, the failure criterion is strain-based in contrast to most metals, where a particular combination of stresses serve as a criterion for failure [9, 10]. In [11], the authors show that the alternating strain plays a major role in predicting the life of Nitinol as opposed to the mean strain.

Generally speaking, structural fatigue can occur as a result of high cycle loadings (HCF between 10^4 to 10^8 cycles) or low cycle loadings (LCF) which is the term used when failure occurs for less than 10^4 cycles. In high-cycle loading, material fatigue is stress-based and is characterized by a stress-cycle (S-N) curve. In low-cycle loading, accounting for the stress is not as relevant but instead, the strain can provide more accurate information. Strain-based fatigue life can also be used when dealing with HCF and be used in determining if crack initiates in the structure [12].

Finally, Nitinol has a structural and a functional fatigue component. The structural fatigue refers to the physical failure of Nitinol stents while the term functional fatigue is used to describe some loss of superelasticity and shape memory properties during cyclic loading [13].

In this paper, numerical simulations are used to understand the structural fatigue of Nitinol and to predict the life of the stent subjected to ten years of blood flow. We do not evaluate the life of the aorta. Two commercial finite element packages Abaqus/Simulia (Version 6.13 [14]) and Ansys (Version 18.2 [12]) are used. That is because Abaqus/Simulia possesses a low-cycle fatigue but not a high-cycle fatigue analysis scheme. On the other hand, Ansys does not have in it library of materials, the constitutive equations for anisotropic materials which are needed to accurately describe the aorta. Abaqus/Simulia does.

The methodology is thus two-fold: we first conduct a fluid-structure interaction (FSI) analysis of a stented-aorta structure subjected to blood flow using the built-in capability in Abaqus/Simulia. We

generate stress-strain curves for three cardiac cycles. The stress-strain curves are then exported to Ansys and we proceed to a strain-based fatigue analysis of the material using mean and alternating strains.

The fatigue analysis is based on the Smith-Watson-Topper (SWT). This model takes into account the mean stress on the structure and the amount of strain it generates. With that strain vs. number of cycle (E-N) curves can be manipulated to predict the number of cycles at which the structure will fail.

Details of the methodology are included in Section 2. We present the results of the analysis in Section 3 before ending with some conclusive comments in Section 4.

2 METHODOLOGY

The first part of the analysis deals with the interaction of the fluid (blood) on the structure (stented-aorta) and generates stress-strain curves.

2.1 FSI

We use the built-in fluid-structure interaction (FSI) analysis in Abaqus/Simulia. The FSI analysis assumes that the walls are deformable, not rigid as in the elementary theory. This is indeed the case since during a cardiac cycle, the aortic walls can deform between 10% -15% [15]. The basis for FSI is to insert a fluid domain into the solid domain of the same dimensions provided conditions at the interface are enforced. FSI combines a finite element (FEM) solution for the solid to a computational a fluid dynamic (CFD) analysis for the fluid.



Figure 1: Aorta and stent model used in the numerical simulation

Table 1: Dimension and material properties of human aorta [16, 17]

	Material	Thickness t (mm)	Fiber orientation θ (deg)	μ (kPa)	k_1 (kPa)	k_2 (kPa)	Poisson's ratio
Human Aorta (3 layer, hy- perelastic, anisotropic)	Intima	0.33	18.8 ± 8.2	20.30	182.59	228.58	0.49
	Media	1.32	37.8 ± 20.6	2.31	8.45	12.84	0.49
	Adventitia	0.96	58.9 ± 14.8	6.16	32.89	167.31	0.49

The geometry of aorta is a cylindrical structure 6.2 cm long, 2.54 mm inner diameter and 2.61 mm thick with three layers representing the intima, media and adventitia aortic layers (Fig. 1). The aorta is meshed with 153849 modified quadratic tetrahedral hybrid elements (C3D10MH). The aorta is modeled with the Holzapfel-Gasser-Ogden (HGO) equations that were developed in year 2000 to describe human

tissues [18]. This is a powerful hyperelastic model which takes into account the anisotropic behaviour of the aorta due to the layers, each having its own stiffness.

The geometry of the stent is generated with the 2015 \times 64 Edition of Solidworks (Fig. 1). It is 6.2 cm long, 25 mm in inner diameter and 0.3 mm thick. The stent diameter is slightly below the diameter of the aorta. This in order to provide complete sealing upon expansion and prevent the stent from migrating. It is meshed with 38840 modified quadratic tetrahedral elements (C3D10M). We use the superelastic constitutive model developed by Auricchio and Taylor (1997) for Nitinol [19]. The material properties of the human aorta and Nitinol are shown in Table 1 and Table 2 respectively.

Table 2: Nitinol material's properties[14]

Properties	Symbol	Values
Density	ρ	6450 kg/m ³
Austenite elasticity	E_A	68 GPa
Austenite Poisson's	ν_A	0.33
Martensite elasticity	E_M	36 GPa
Martensite Poisson's	ν_M	0.33
Transformation strain	ε^L	0.041
$\delta\sigma/\delta T$ loading	$\left(\frac{\delta\sigma}{\delta T}\right)_L$	6.5
Start of transformation loading	σ_{tL}^S	520 MPa
End of transformation loading	σ_{tL}^E	635 MPa
Reference temperature	T_0	37°C
$\delta\sigma/\delta T$ unloading	$\left(\frac{\delta\sigma}{\delta T}\right)_U$	6.5
Start of transformation unloading	σ_{tU}^S	180 MPa
End of transformation unloading	σ_{tU}^E	26 MPa

Blood is assumed to be an incompressible, Newtonian and turbulent medium. These are chosen to represent physiological human conditions. In Abaqus/Simulia, the equations for such a flow can be solved with standard Navier-Stokes equations [20]. Blood flow has a time-dependent profile (Fig. 2). The blood dynamic viscosity is 0.003 Pa.s and its density is 1050 kg/m³. We use the Spalart-Allmaras (SA), one of the two turbulent models available in Abaqus/Simulia. This model is recommended when solving problems with pressure gradients. The blood is meshed with 29610 linear wedge elements of type FC3D6. There are three boundaries: inlet, outlet and a surface with outer normal in the positive Z direction (Fig. 3).

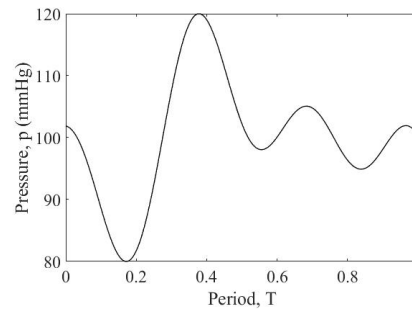


Figure 2: Blood physiological pressure profile

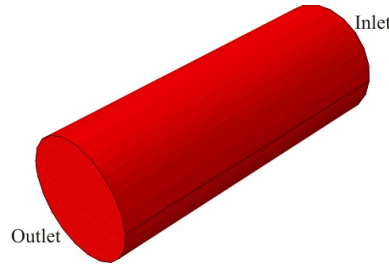


Figure 3: Blood model used in the numerical simulation

Contact is assumed between the aorta and the stent. It is implemented in Abaqus/Simulia via an algorithm that uses the inner wall of the aorta as the master surface and the stent outer diameter is the slave surface. A contact friction coefficient of 0.2 is also needed to guard against slipping between the surfaces and to prevent the stent from migrating. Displacement in the axial and the radial directions is allowed but it is constrained in the circumferential direction.

2.2 Fatigue analysis

With the stent being subjected to that many loading and unloading cycles, it is inevitable that material weakening will occur and alter the stent intended functions. In this work, the fatigue analysis is done on Ansys. It is based on a strain-life method as should be the case for Nitinol. In addition, cyclic loading fatigue tests often assume completely reversed loading with constant amplitude. This is not the case here. The cyclic hemodynamic load generates a mean stress on the stent, which is always tensile (positive difference in pressure). Smith-Watson-Topper (SWT) proposed an equation to account for the mean-stress in strain-life prediction. This model adequately predicts fatigue due to tensile stress.

SWT is expressed as,

$$\sigma_{max} \frac{\Delta \epsilon}{2} = \frac{(\sigma_f)^2}{E} (2N_f)^{2b} + \sigma_f \epsilon_f (2N_f)^{b+c} \quad (1)$$

where the various symbols are fatigue strength coefficient σ_f , number of reversals to failure $2N_f$, fatigue ductility coefficient ϵ_f , fatigue strength exponent b , fatigue ductility exponent c , modulus of elasticity E to measure the maximum stress σ_{max} and total strain amplitude $(\Delta \epsilon/2)$.

The strain-life fatigue properties of Nitinol are taken from reference [8] and have been generated experimentally. They are summarized in Table 3. It shows that the number of cycles to failure (N_f) of Nitinol is $1e9$.

Table 3: Strain-life fatigue properties of Nitinol[8]

Properties	Symbol	Values
Fatigue strength coefficient	σ_f	1335 MPa
Fatigue ductility coefficient	ϵ_f	2.11
Fatigue strength exponent	b	-0.085
Fatigue ductility exponent	c	-0.679
Fatigue strength factor	k_f	0.42
Loading ratio	R_e	$\epsilon_{min}/\epsilon_{max}$
Cycles		$1e9$
Ultimate stress	σ_u	1040 MPa

In Ansys, the fatigue analysis returns four contour plots: fatigue life, fatigue damage, fatigue safety

factor and biaxiality indication.

Fatigue life is an indicator of how long the structure will last before it fails. It is a measure of the number of loading cycles a structure can sustain before it fails. The material, structure, geometry and temperature are factors that influence the fatigue life of a component. The methodology for obtaining the fatigue life from SWT model can be summarised as follows: first, we input the coefficients from Table 3 in Eq. 1 and get the strain amplitude. The strain values obtained from the FSI simulations in Abaqus are exported to Ansys to serve as input to the fatigue analysis. We compare the strain values obtained from the fatigue analysis with the strain amplitude calculated from the SWT model (Eq. 1). If the numerical strain is less than the value calculated from Eq. 1, the stent will last 10e8 cycles (fatigue life).

Fatigue damage is expressed as the ratio of design-life to available life. Here the design-life of the stent is 10e8 cycles. The value of available life is obtained from the simulations. Damage is irreversible. A value greater than 1 indicates that the structure will fail before the design life is reached.

Fatigue safety factor (FSF) relates the maximum stress to the design stress (aka allowable stress or working stress). A FSF equal to 1 means the structure (stent) experiences the same amount of stress as the design stress. The structure cannot support any additional load. Any additional increase of the load on the structure will result in failure.

Biaxiality indication shows how accounting for a multi-state of stress, not just a uniaxial stress, affects the material fatigue. It is defined as the ratio of minimum principal stress to maximum principal stress. A 0 value of biaxiality indication corresponds to a uniaxial stress, a -1 value corresponds to pure shear, and a 1 value corresponds to a pure biaxial state of stress. Principal stresses close to zero are neglected.

3 RESULTS

3.1 FSI

We obtained the stress-strain response of the stented aorta for three cardiac cycles using the FSI analysis capability in Abaqus/Simulia. The blood pressure profile used in the simulations is shown in Fig. 2. One can recognise the 120 mmHg peak value and the 80 mmHg minimum value corresponding to the systole and diastole blood pressure. The principal stress contours on the stented aortic region obtained from the simulations are shown on Fig. 4 and the principal strain contours on Fig. 5. It shows that the maximum stress experienced by the stent is 145 MPa (red color) while it is approximately 0.7 MPa for the aorta (blue color). On the other hand, the stent undergoes about half the strains (0.6%) compared to the aorta (1.5%) (Fig. 5). Simulations have been conducted assuming a 37°C temperature for Nitinol was maintained.

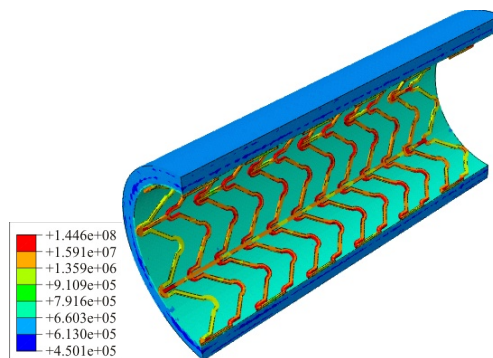


Figure 4: Principal stresses on the aorta and the stent. (Recorded at systolic pressure, Units are Pascals)

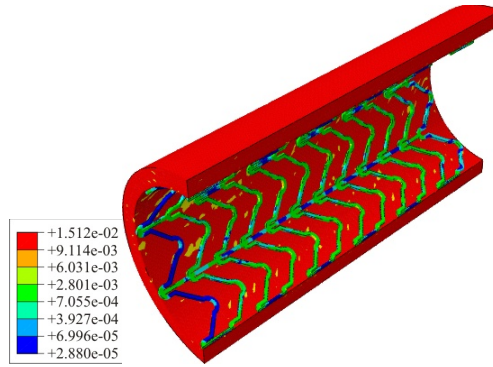


Figure 5: Principal strains on the aorta and the stent. (Recorded at systolic pressure)

Figure 6 shows the strain experienced by the stent during three cardiac cycles. It is clearly oscillating. Relevant computed quantities shown on the figure are: maximum strain ($\epsilon_{max} = 0.6\%$) and minimum strain ($\epsilon_{min} = 0.48\%$), from which the other quantities, mean strain (ϵ_m), alternating strain (ϵ_a) and a strain range (ϵ_r) can be calculated using

$$\epsilon_m = \frac{\epsilon_{max} + \epsilon_{min}}{2} \quad (2)$$

$$\epsilon_a = \frac{\epsilon_{max} - \epsilon_{min}}{2} \quad (3)$$

$$\epsilon_r = \epsilon_{max} - \epsilon_{min} \quad (4)$$

Figure 6 shows that the maximum strain (ϵ_{max}) occurs during the systole stage and the minimum (ϵ_{min}) strain, during the diastole. Here ϵ_{max} and ϵ_{min} are both tensile. Using these values, one can compute ϵ_m , ϵ_r and ϵ_a as 0.53%, 0.143% & 0.072% respectively. These values are used in the fatigue analysis.

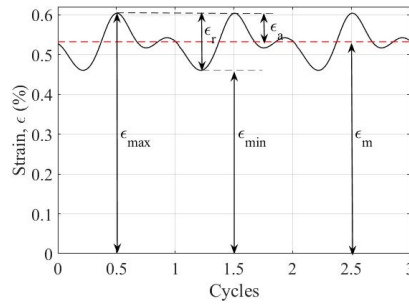


Figure 6: Principal strains experienced by the stent during three cardiac cycles

3.2 Fatigue

3.2.1 Fatigue life

Figure 7 shows the fatigue life contours on the stent obtained on Ansys. The red color indicates that the stent can withstand one billion (10^8) cycles without failure. There is no indication from the contours

obtained that some parts of the stent are more prone to failure than others. On the contrary, every part of the stent has the same life and it can sustain 400 million cycles, the equivalent amount of cycles for 10 year-operation.

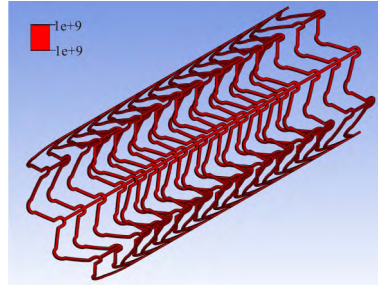


Figure 7: Stent fatigue life contour

Figure 8 shows the loading cycles vs. the loading history as described in Ansys. On the figure, the range for the horizontal axis is 0.5 to 2.5. These represent the % of the current load. For instance, 0.5 means that the load is 50% of the current load, 2.5 means that the load is 250% of the current load and 1 refers to the current loading (100%). The curves shows that increasing the load by 25% (i.e. 1.25) will result in the stent-life decaying rapidly until the stent is subjected to approximately twice the load (i.e. 2), value at which the stent will fail (zero).

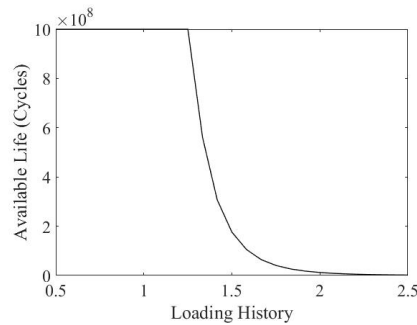


Figure 8: Stent available life vs. loading history

3.2.2 Fatigue Damage

Figure 9 shows the fatigue damage of the stent obtained for one billion ($10e8$) cycles, which is above the 400-600 million cycles threshold recommended by the FDA. The fatigue damage contour was generated using the design life ($10e8$ cycles) and the available life of the stent (also equal to $10e8$) obtained from Fig. 9. The blue contours on the stent are equal to one, which can be interpreted as meaning that the stent will not fail until the design life value is reached.

3.2.3 Fatigue Safety Factor

Figure 10 shows the fatigue safety factor (FSF) contours obtained from the FEM simulations. With sufficient zooming, one can see that the stent struts are orange, indicating a fatigue factor of safety above

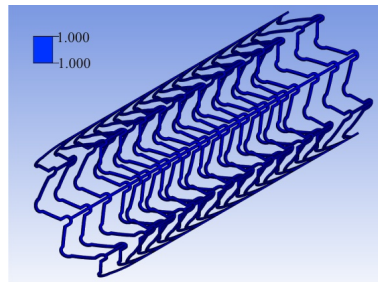


Figure 9: Stent fatigue damage contour

to one, even though these regions can fail first due to the curvatures. The other regions are either blue or green, which correspond to a very high factor of safety (10-15) or 5-10, respectively. There is no red-color contours, where FSF is less than one. Red color contour would mean failure of the stent before the time it has been designed to operate is reached. Thus, our stent as designed, can safely operate for 10 years.

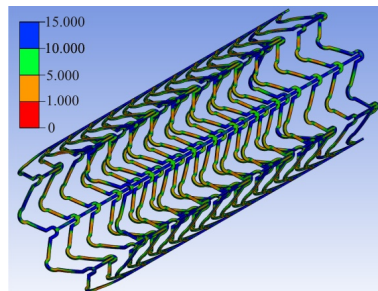


Figure 10: Stent fatigue safety factor contour

Figure 11 shows the FSF as a function of the loading history. The loads range from 0.5 to 2.5 which correspond to loading the sent at a 50% and 250% increase of the original load, respectively. The value 1 (i.e. 100%) represents the life of the stent at the current level of loading. The results indicate that when the original load is increased by 25% or more (i.e. 1.25 value), FSF drops below 1 and the stent cannot be deemed safe to operate.

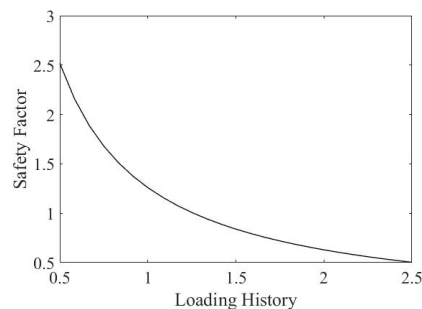


Figure 11: Stent fatigue safety factor vs. loading history

3.2.4 Biaxiality Indication

Figure 12 shows the biaxiality indication on the stent due to the hemodynamic load. The color coding is such that red, orange, yellow are positive values less than one and the others are negative values between zero and one. Green coding has some positive and some negative values close to zero, which means that most regions of the stent are in pure uniaxial stress, although not completely. Again, with enough image zooming, one can see that the struts curvatures experience some pure shear (blue color) and that the end cells are in a pure biaxial state of stress (red color). Combined with the fatigue safety factor contours, we can say that the most vulnerable regions of the stent are those experiencing pure uniaxial stresses. This indicates that uniaxial stress is the primary mode of failure for the stent.

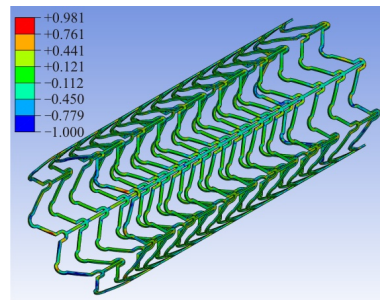


Figure 12: Stent biaxiality indication contour

4 CONCLUSIONS

In this work, we analysed the fatigue/failure behaviour of a Nitinol stent used in endovascular aneurysm repair (EVAR) procedures. The analysis assumed that the stent was subjected to one billion cycles (design life), representing more than twenty years of cycling hemodynamic loading.

The fluid-structure interaction (FSI) analysis in Abaqus/Simulia was first employed to generate the stress-strain curves of a stented aorta during three cardiac cycles. The aorta was modeled as an anisotropic material. The stress-strain curves were exported to Ansys for a strain-based high-cycle fatigue life analysis using the Smith-Watson-Topper (SWT). This model takes into account the mean stress on the structure.

Four contour plots were generated on Ansys: fatigue life, fatigue damage, fatigue safety factor and a biaxiality indication.

Results indicated that the stent was able to sustain $10e8$ cycles without failing. The fatigue factor of safety decreased exponentially as the number of cycles increased. Increasing the load by 25% decreased the stent life by approximately half ($5.61e8$ cycles) and doubling the load will result in the stent failing.

The biaxiality indication showed that the pulsatile hemodynamic load mostly caused the stent to experience a pure uniaxial state of stress. Area of the struts subjected to pure uniaxial loading were most prone to failure.

This fatigue analysis showed that our honeycomb stent design was capable of withstanding 10-15 years of pulsatile hemodynamic load, as recommended by the FDA.

This study can provide insights into optimal design of self-expanding stents as well as giving new directions to improve their functionality.

5 ACKNOWLEDGEMENT

This publication was made possible by the NPRP award # 7-032-2-016 from the Qatar National Research Fund (a member of Qatar Foundation). The statements made herein are solely the responsibility of the authors.

REFERENCES

- [1] M. J. Mahtabi, N. Shamsaei, and M. R. Mitchell. Fatigue of Nitinol: The state-of-the-art and ongoing challenges. *J. Mech. Behavior Bio. Mat.*, 50:228–254, 2015.
- [2] A. Kaladji, A. Daoudal, A. Dumenil, C. Goksu, A. Cardon, E. Clochard, A. Lucas, and F. Lalys. Predictive Models of Complications after Endovascular Aortic Aneurysm Repair. *Annals of Vasc. Surg.*, 40.
- [3] H. Santos, F. Auricchio, and M. Conti. Numerical fatigue life assessment of cardiovascular stents: A two-scale plasticity-damage model. *Journal of Physics:Conference Series*, 451.
- [4] US Food and Drug Administration: The guidance for industry and FDA staff: non-clinical tests and recommended labeling for intravascular stents and associated delivery systems pages. <https://www.fda.gov>.
- [5] S. W. Robertson, A. R. Pelton, and R. O. Ritchie. Mechanical fatigue and fracture of Nitinol. *Int. Mat. Rev.*, 57.
- [6] F. Auricchio, A. Constantinescu, M. Conti, and G. Scalet. Fatigue of Metallic Stents: From Clinical evidence to Computational Analysis. *Annals of Biomedical Engineering*, 44:287–301, 2016.
- [7] M. Mohsen, A. Alqahtani, and J. A. suwaidi. Stent Fracture: How Frequently Is It Recognized? *Heart Views*, 14:72–81, 2013.
- [8] M. J. Mahtabi and N. Shamsaei. A modified energy-based approach for fatigue life prediction of superelastic NiTi in presence of tensile mean strain and stress. *J. Mech. Behavior Bio. Mat.*, 117:321–333, 2016.
- [9] D. Tolomeo, S. Davidson, and M. Santinoranont. Cyclic properties of superelastic nitinol: design implications. In *In SMST-2000: Proceedings of the International Conference on Shape Memory and Superelastic Technologies, Pacific Grove, CA. Russell MS & Pelton AR (Eds)*, pages 471–476, 2000.
- [10] M. F. Urbano, A. Cadelli, F. Sczerzenie, P. Luccarelli, S. Beretta, and A. Coda. Inclusions Size-based Fatigue Life Prediction Model of NiTi Alloy for Biomedical Applications. *Shape Memory and Superelasticity*, 1(2):240–251, Jun 2015.
- [11] W. J. Harrison and Z. C. Lin. The study of nitinol bending fatigue. In *In SMST-2000: Proceedings of the International Conference on Shape Memory and Superelastic Technologies, Pacific Grove, CA. Russell MS & Pelton AR (Eds)*, pages 391–396, 2000.
- [12] ANSYS, INC 18.2. *Theory reference manual*. 2017.
- [13] G. kang and D. Song. Review on structural fatigue of niti shape memory alloys: Pure mechanical and thermo-mechanical ones. *Theor. Appl. Mech. Let.*, 5:245–254, 2015.

- [14] Abaqus version 6.13. *Analysis User's Manual*. Dassault Systems Simulia Corp, 2013.
- [15] F. R. Arko, E. H. Murphy, C. M. Davis, E. D. Johnson, S. T. Smith, and C. K. Zarins. Dynamic geometry and wall thickness of the aortic neck of abdominal aortic aneurysms with intravascular ultrasonography. *J. Vasc. Surg.*, 46:891–897, 2007.
- [16] G. A. Holzapfel. Determination of material models for arterial walls from uniaxial extension tests and histological structure. *Journal of Theoretical Biology*, 238:290–302, 2006.
- [17] E. Widman, E. Maksuti, C. A. Carrascal, M. W. Urban, and M. Larsson. Evaluating arterial and plaque elasticity with shear wave elastography in an ex vivo porcine model. In *2015 IEEE International Ultrasonics Symposium (IUS)*, pages 1–4, 2015.
- [18] G. A. Holzapfel, T. C. Gasser, and R. W. Ogden. A New Constitutive Framework for Arterial Wall Mechanics and a Comparative Study of Material Models. *Journal of Elasticity*, 61:1–48, 2000.
- [19] F. Auricchio, R. L. Taylor, and J. Lubliner. Shape memory alloys: macromodelling and numerical simulations of the superelastic behavior. *Comput. Methods Appl. Mech. Engrg.*, 146:281–312, 1997.
- [20] J. Donea and A. Huerta. *Finite Element Methods for Flow Problems*. John Wiley & Sons, 2003.

FATIGUE CRACK GROWTH RESISTANCE OF NITI SHAPE MEMORY ALLOY – SMART 2019

J. YAACOUB^{*}, H. SEHITOGLU^{*†}

^{*} Department of Mechanical Science and Engineering,
University of Illinois at Urbana-Champaign
1206 W. Green St., Urbana IL 61801, USA
Email: huseyin@illinois.edu

[†]Corresponding Author:

Email: huseyin@illinois.edu, phone number +1 217-333-4112, fax +1 217-244-6534

Key words: Fatigue Crack Growth, Shape Memory Alloys, Stress Intensity, Stress Induced Martensite, NiTi

Abstract

This paper discusses new findings on fatigue crack growth in an NiTi shape memory alloy. Despite the importance of the topic, there are very few papers that systematically studied fatigue crack growth with investigation of measurements of effective stress intensity at crack tips. It has become clear that one must account for the crack tip wake closure forces in modeling of crack tip stress intensity as they could produce net forces that are substantial. The tractions in the crack wake can reduce the driving forces but the calculation is rather complicated. Instead, we present stress intensity determination based on experimental displacement measurements at crack tips. We utilize digital image correlation to establish vertical and horizontal displacements in NiTi. We then compare the stress intensity determination based on regression of displacement results, which is termed the effective stress intensity range, with that of the stress intensity range based on LEFM. We find that the effective stress intensity range is lower than that based on classical LEFM solution, the difference being more significant at longer crack lengths.

1 INTRODUCTION

Since their discovery in the early 1960s, the NiTi shape memory alloys (SMA) have captivated the attention of the materials science community with potential for a multitude of applications ranging from biomedical stents to advanced instruments in space exploration. Two characteristic properties of SMAs are often exploited in applications: the shape memory effect, where large levels of deformation are recovered upon heating, or the superelastic effect, where again large levels of deformation are spontaneously recovered upon unloading. Despite significant advances in SMA research, knowledge gaps still persist particularly under fatigue loading conditions, motivating further research [1].

Various shape memory material compositions have been developed over the years in addition to NiTi, such as NiTiCu, CuZnAl, CuNiAl, NiFeGa, CoNiAl, CoNiGa, NiTiHf, FeNiCoTi and FeMnSi among others [1]. However, NiTi continues to be the most important SMA, partly because of its biocompatibility. It also exhibits large transformation strains and better functionality compared to other alloys especially in polycrystalline form. It is important to note that large number of fundamental studies have been undertaken on single crystals; however, it is important to report on polycrystalline properties as they are relevant to applications.

The most comprehensive previous work on fatigue crack growth in NiTi has been undertaken by Ritchie et al.[2-4]. More recently there has been efforts to report on NiTi single crystals. One must note that the compositional effects, texture effects, grain sizes and heat treatments are all expected to affect the results so direct comparison of results is difficult. In a recent study, effective stress intensity calculations accounting for closure forces were compared to stress intensities measured via regression of displacements with excellent agreement [5]. This provides a justification for the present approach of determining the stress intensity from the measured displacements. Extracting the effective stress intensity by measuring the normal and horizontal displacement fields at the crack tip and fitting them to the elasticity theory solutions resulted in 10- 30% reduction in maximum stress intensity in NiFeGa [5, 6]. Therefore, our current paper builds upon these novel experimental techniques outlined previously and applied them to investigate the NiTi fatigue crack growth behavior in the temperature regime where superelastic conditions prevail. We note that only preliminary findings are presented in this paper.

2 EXPERIMENTAL TECHNIQUES

The current investigation considers polycrystalline NiTi samples, of composition with an at. Ni of 50.8%. The material is the same NiTi that is reported in our early studies with an aging treatment of 450°C for 1.5 hours[7, 8]. The transformation temperatures were $A_s = 21^\circ\text{C}$; $A_f = 38^\circ\text{C}$; $M_s = 0^\circ\text{C}$; and $M_f = -20^\circ\text{C}$. The specimens were of the dog-bone geometry with a gauge section of 10 mm in length, 1.5mm thickness and 3mm in width. Edge notches 0.5 mm in length are introduced using EDM. Prior to testing, all specimens were polished using SiC paper, after which a fine speckle pattern was applied for full-field strain and displacement measurements using Digital Image Correlation (DIC).

Fatigue crack growth experiments were conducted with an R ratio of 0.05 and a 3 Hz frequency. The tests were run at a temperature of 45°C, at which the behavior was confirmed to be superelastic by uniaxial tension experiments. A constant stress amplitude of 142 MPa was employed. Optical images were collected during each loading cycle allowing for extraction of displacement fields, from which the stress intensity factor was calculated via regression which will be further explained in the next section.

3 EXTRACTION OF STRESS INTENSITY FACTOR FROM DISPLACEMENTS USING ANISOTROPIC ELASTICITY VIA REGRESSION

The displacement fields determined with Digital Image Correlation (DIC) are fitted to the crack tip displacement fields. These solutions are available by Sih *et. al* [6]. It is then possible to extract the stress intensity by regression fit to the following equations:

$$\begin{aligned} u^1 = & K_1 \sqrt{2r} \operatorname{Re} \left[\frac{1}{\mu_1 - \mu_2} (\mu_1 p_2 \sqrt{\cos \theta + \mu_2 \sin \theta} - \mu_2 p_1 \sqrt{\cos \theta + \mu_2 \sin \theta}) \right] \\ & + K_2 \sqrt{2r} \operatorname{Re} \left[\frac{1}{\mu_1 - \mu_2} (p_2 \sqrt{\cos \theta + \mu_2 \sin \theta} - p_1 \sqrt{\cos \theta + \mu_2 \sin \theta}) \right] + \\ & a_{11} Tr \cos \theta + Ar \sin \theta + B_u \end{aligned} \quad (1)$$

$$\begin{aligned} v^1 = & K_1 \sqrt{2r} \operatorname{Re} \left[\frac{1}{\mu_1 - \mu_2} (\mu_1 q_2 \sqrt{\cos \theta + \mu_2 \sin \theta} - \mu_2 q_1 \sqrt{\cos \theta + \mu_2 \sin \theta}) \right] \\ & + K_2 \sqrt{2r} \operatorname{Re} \left[\frac{1}{\mu_1 - \mu_2} (q_2 \sqrt{\cos \theta + \mu_2 \sin \theta} - q_1 \sqrt{\cos \theta + \mu_2 \sin \theta}) \right] + \\ & a_{12} Tr \cos \theta + Ar \sin \theta + B_v \end{aligned} \quad (2)$$

$$a_{11} \mu^4 - 2a_{16} \mu^3 + (2a_{12} + a_{66}) \mu^2 - 2a_{26} \mu + a_{22} = 0 \quad (3)$$

Where Re represents the real part of a complex number, T is the T-stress, A is the rigid body rotation, B_u and B_v are the rigid body translations in u^1 and v^1 directions, respectively. The terms a_{11} , a_{12} , a_{16} , a_{22} , a_{26} and a_{66} are the compliance components in the coordinate system of the crack, r and θ are the polar coordinates with their origin at the crack tip. μ_1 and μ_2 are the roots of equation (3). The p_i and q_j in equations (1) and (2) are the anisotropic terms defined as:

$$\begin{aligned} p_i &= a_{11} \mu_i^2 + a_{12} - a_{16} \mu_i \\ q_i &= a_{12} \mu_j + \frac{a_{22}}{\mu_j} - a_{26} \end{aligned} \quad (4)$$

The formulation above is general but for purposes of simplicity the fitting was conducted for isotropic case. In the above formulation we allow for provision of Mode II stress intensity levels as well. The details of the methodology have been published earlier [5, 9-11].

4 EXPERIMENTAL RESULTS

The regression-extracted stress intensity is plotted against that acquired with a classical handbook calculation for a single edge notch case. The results are seen in Figure 1. The results in the Paris regime can be described with the following equation

$$\frac{da}{dN} = 3.10^{-9} (\Delta K_{\text{eff}})^{1.73} \text{ where } \frac{da}{dN} \text{ is measured in m/cycle and } \Delta K_{\text{eff}} \text{ is measured MPa}\sqrt{\text{m}}.$$

It is evident that the material's effective stress intensity levels (red) are substantially lower compared to that determined from LEFM solution (black). The LEFM solution is the product of stress range and square root of crack length and the correction for an edge crack for finite width effects. The effective threshold stress intensity is reduced by about $2 \text{ MPa}\sqrt{\text{m}}$ compared to the LEFM value using the entire stress range. The threshold stress intensity based on LEFM is $9 \text{ MPa}\sqrt{\text{m}}$ while it is $7 \text{ MPa}\sqrt{\text{m}}$ upon fitting the experimental displacement fields. This difference increases substantially as evident from Figure 1. Many factors play a role in the reduction of the crack tip stress intensity compared to the external loading based levels. The residual stress induced transformation zone is verified in the crack wake and ahead of the crack tip based on comparing the strains from digital image correlation at different stages of crack growth. Additional closure effects associated with plastic flow in the form of slip further contribute to the reduction of stress intensity levels.

The regression window is outlined on the left of Figure 2 with a dashed red box. It is approximately centered at the crack tip. The crack tip is marked with a large dot and the displacements are measured with respect to the crack tip. Because the crack front is normal to the applied loading direction the zero displacement contours are horizontal along the crack line. Experimentally measured and regression determined displacement fields are superimposed on the same plot on the right of Figure 2. It is evident that experiment (blue) and theory (red) are in very good agreement increasing the confidence in the measurement of effective stress intensity. The regression-based results represent a more accurate measure of the crack tip driving forces as all possible crack tip phenomena such as plasticity and stress induced transformation are reflected in the results. Further analysis of the results is needed to confirm the evolution of the residual displacements and strains that are responsible for shielding effects. This is a topic that is far from resolved in shape memory alloys.

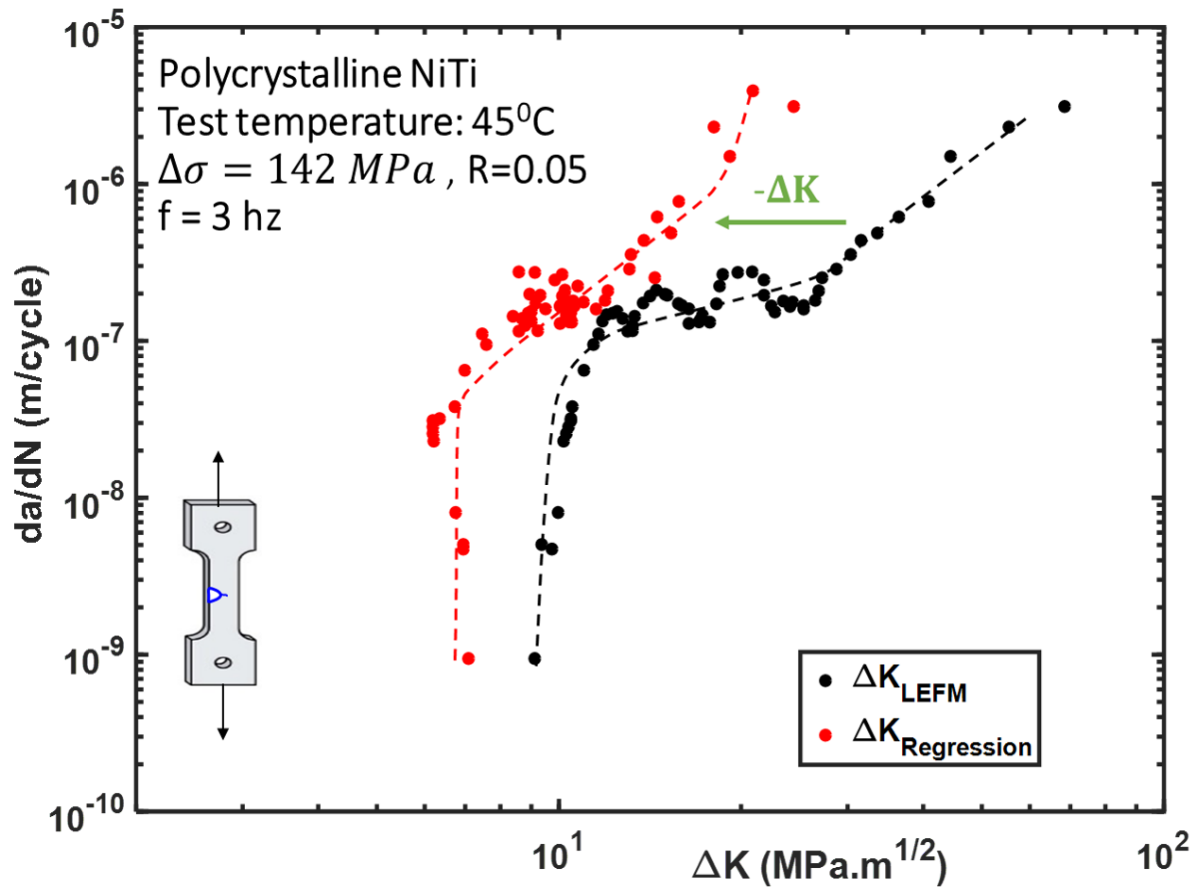


Figure 1 – $\frac{da}{dN}$ vs ΔK plot. The red data points are acquired via regression (also termed the effective stress intensity range), while the black points represent the classical handbook solution for the single edge notch case calculated using the full range of applied stress. The reduction in stress intensity due to shielding effects is indicated with an arrow and increases (the difference between the two curves) with increasing crack length.

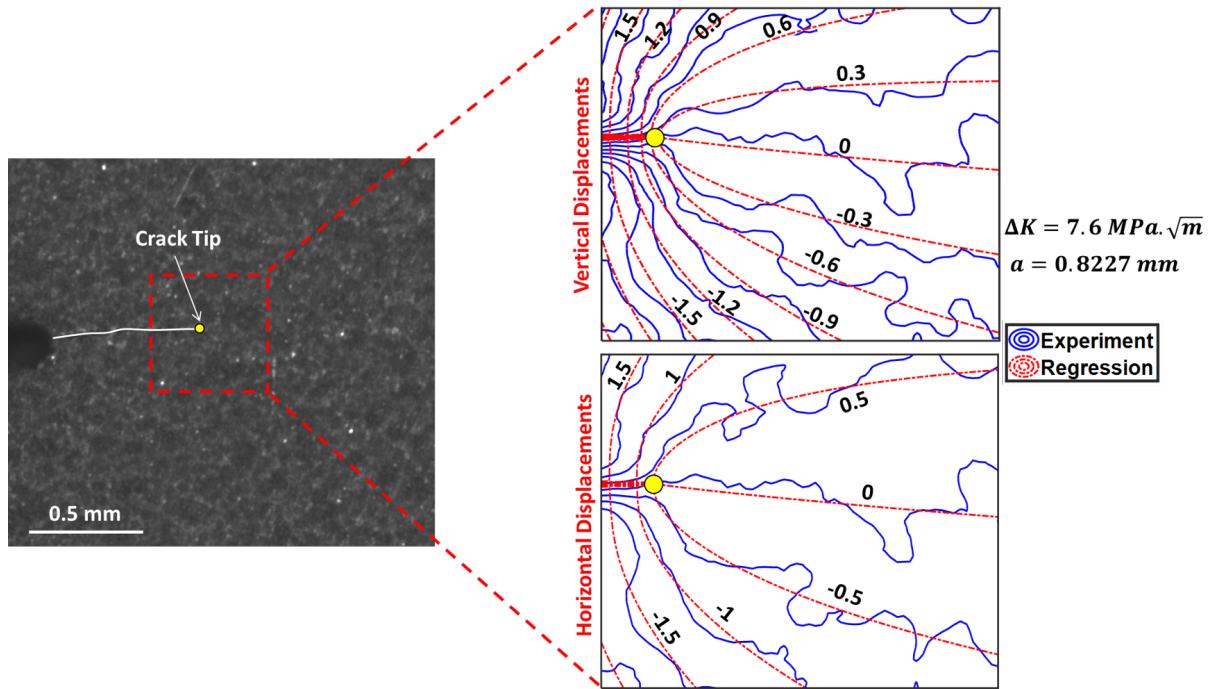


Figure 2 – Regression and experimental displacement contours overlay. The displacements are given in microns and the extracted stress intensity is $7.6 \text{ MPa}\sqrt{\text{m}}$ in this case.

5 CONCLUSIONS

The work supports the following conclusions:

- 1) The superelastic NiTi, undergoing reversible stress induced martensitic transformation, exhibits an effective threshold stress intensity level of $7 \text{ MPa}\sqrt{\text{m}}$ based on the present work. The experimentally determined effective stress intensity range is substantially lower than the stress intensity range calculated based on stress intensity handbook (LEFM) solutions particularly at longer crack lengths. Also, the experimental results produce a Paris exponent of 1.73, which is rather small and indicative of fatigue crack growth resistance. These results suggest potentially significant shielding effects, ie. reduction of crack tip stress intensity ranges.
- 2) The determination of effective stress intensity based on crack tip displacements encompasses the cumulative role of various shielding mechanisms that are rather complex. These effects include the role of transformation induced slip and residual transformation strains. In this study, an experimental determination of the effective stress intensity range based on regression of crack tip displacements during loading and unloading was undertaken which provides insight into the role of shielding effects on crack tip driving forces.

ACKNOWLEDGEMENTS

The work is supported by the National Science Foundation Grant NSF-DMR Grant No 1709515 which is gratefully acknowledged.

REFERENCES

- [1] K. Otsuka and C. M. Wayman, *Shape memory materials*. Cambridge university press, 1999.
- [2] A. L. McKelvey and R. O. Ritchie, "Fatigue-crack growth behavior in the superelastic and shape-memory alloy Nitinol," (in English), *Metallurgical and Materials Transactions a-Physical Metallurgy and Materials Science*, journal article vol. 32, no. 3a, pp. 731-743, Mar 2001.
- [3] A. L. McKelvey and R. O. Ritchie, "Fatigue-crack propagation in Nitinol, a shape-memory and superelastic endovascular stent material," (in eng), *J Biomed Mater Res*, vol. 47, no. 3, pp. 301-8, Dec 5 1999.
- [4] S. W. Robertson, A. Mehta, A. R. Pelton, and R. O. Ritchie, "Evolution of crack-tip transformation zones in superelastic Nitinol subjected to in situ fatigue: A fracture mechanics and synchrotron X-ray microdiffraction analysis," *Acta Materialia*, vol. 55, no. 18, pp. 6198-6207, 2007.
- [5] Y. Wu, A. Ojha, L. Patriarca, and H. Sehitoglu, "Fatigue Crack Growth Fundamentals in Shape Memory Alloys," (in English), *Shape Memory and Superelasticity*, vol. 1, no. 1, pp. 18-40, Mar 2015.
- [6] G. C. Sih, P. C. Paris, and G. R. J. I. J. o. F. M. Irwin, "On cracks in rectilinearly anisotropic bodies," journal article vol. 1, no. 3, pp. 189-203, September 01 1965.
- [7] K. Gall and H. Sehitoglu, "The role of texture in tension-compression asymmetry in polycrystalline NiTi," *International Journal of Plasticity*, vol. 15, no. 1, p. 69, 1999.
- [8] K. Gall, H. Sehitoglu, Y. I. Chumlyakov, I. V. Kireeva, and H. J. Maier, "The Influence of Aging on Critical Transformation Stress Levels and Martensite Start Temperatures in NiTi: Part I—Aged Microstructure and Micro-Mechanical Modeling," *Journal of Engineering Materials and Technology*, vol. 121, no. 1, pp. 19-27, 1999.
- [9] J. Carroll *et al.*, "Investigation of fatigue crack closure using multiscale image correlation experiments," *Engineering Fracture Mechanics*, vol. 76, no. 15, pp. 2384-2398, 2009.
- [10] G. J. Pataky, M. D. Sangid, H. Sehitoglu, R. F. Hamilton, H. J. Maier, and P. Sofronis, "Full field measurements of anisotropic stress intensity factor ranges in fatigue," *Engineering Fracture Mechanics*, vol. 94, pp. 13-28, 2012.
- [11] E. Sgambitterra, C. Maletta, F. Furguele, and H. Sehitoglu, "Fatigue crack propagation in [0 1 2] NiTi single crystal alloy," *International Journal of Fatigue*, vol. 112, pp. 9-20, 2018.

PHENOMENOLOGICAL MODELING OF POROUS SHAPE MEMORY ALLOYS

GÜLCAN ÖZERİM^{*†}, ZIAD MOUMNI^{*} AND GÜNAY ANLAŞ[†]

^{*} École Nationale Supérieure de Techniques Avancées (ENSTA ParisTech)

Chemin de la Hunière, 91120 Palaiseau, France

e-mail: ozerim.gulcan@ensta-paristech.fr

e-mail: ziad.moumni@ensta-paristech.fr

[†] Boğaziçi University

Bebek Mah., 34342, Beşiktaş/Istanbul, Turkey

e-mail: gulcan.ozerim@boun.edu.tr

e-mail: anlas@boun.edu.tr

Key words: Shape memory alloys, porous NiTi, phenomenological modeling

Abstract. Porous NiTi's mechanical behaviour is similar to the human bone's and it shows good biocompatibility which make it an attractive material for biomedical applications. In this study, the aim is to develop a macro-scale phenomenological model to describe the mechanical behavior of porous NiTi SMAs within the framework of generalized standard materials with internal constraints including the porosity as an additional internal variable. The model includes the effect of hydrostatic pressure due to the presence of porosity. The constitutive equation obtained is used to simulate the pseudoelastic compressive response of a porous NiTi. In addition to stress-strain behaviour, evolution of phase transformation and porosity are also calculated. Numerical results show a qualitative agreement with the experimental results in the literature.

1 INTRODUCTION

Similar to the bulk NiTi SMA, porous form of NiTi which possesses the shape memory effect, pseudoelasticity and good biocompatibility is an attractive material in many applications including energy absorption or light-weight actuators, and most commonly the biomedical applications [1]. In addition, porous NiTi has some additional benefits superior to classical metallic foams (e.g., Ti or stainless steel), such as low density, high specific surface area and high permeability [2, 3], and it shows a mechanical behavior similar to the human bone as a result of its unique pseudoelastic characteristic near ambient temperature [4]. Especially with the low density and elastic modulus, achieved by controlling the porosity, porous NiTi is one of the most widely used materials for hard-tissue implantation [4].

In the literature, there are some experimental studies to observe the mechanical behaviour of porous NiTi produced by different powder metallurgy techniques [5–11]. Since porous NiTi is mainly exposed to compressive loadings under operation, researchers focus on the mechanical behaviour under compression. Zhao et al. [7] presented the stress-strain diagrams of 13% and 25% porous NiTi produced by spark plasma sintering, under uniaxial compression. It is observed that the stress plateau shifts down and the slope of the elastic portion decreases significantly with increasing porosity. They also stated that the

phase transformation has decreased with increasing porosity due to the weak interconnection between NiTi powders. Namet et al. [8] showed the superelastic loop of 12% porous NiTi and observed 1% residual strain after unloading of the specimen which was loaded upto 6% global strain. Bram et al. [9] and Guo et al. [10] performed studies on the compressive behaviour of high porosity NiTi SMAs and showed that the amount of superelastic strain is lower under high porosity. More recently, Saedi et al. [11] tested the NiTi under compression with different porosity and observed the effect of porosity. From the experimental results in the literature, the effects of porosity on pseudoelastic compressive behaviour of NiTi can be summarized as the decrease in critical stresses for phase transformation, elastic modulus and the amount of transformation.

Due to the unusual behavior of SMAs such as pseudoelasticity, modeling of porous SMAs is not a simple procedure. Some researchers used the micromechanical averaging techniques or unit cell finite element method as reviewed by Yuan et al. [2]. Although these techniques can give estimates of the stress-strain curves, they are not sufficient to observe the evolution of phase transformation or porosity. In the literature, there are only a few studies where the porosity is introduced as a parameter into the analytical model. Since porous materials are pressure sensitive, Olsen and Zhang [12] proposed the Gurson [13] type yield function, which includes the hydrostatic part of the stress tensor, to calculate the transformation strain of porous SMAs. Similarly, Ashrafi et al. [14] introduced the effect of hydrostatic pressure by using a yield function which was originally proposed by Deshpande and Fleck [15] based on their experimental studies on metallic foams. It is seen that there is a limited number of studies on analytical modeling of the mechanical behaviour of the porous SMAs, thus the subject is open to further contributions.

In this study, a macro-scale phenomenological modeling to describe the mechanical behavior of porous SMAs is presented. The original ZM (Zaki-Moumni) model [16] for dense SMAs within the framework of generalized standard materials with internal constraints [17] is modified to include the porosity as an additional internal variable. The constitutive equation obtained is then used to simulate the 1D compressive behaviour of porous NiTi SMA in Matlab. In addition to the stress-strain curve, the phase transformation and the evolution of porosity are also observed. Numerical results have shown that the present model is capable of qualitatively representing the effect of porosity on the pseudoelastic behaviour of porous NiTi under compression.

2 ANALYTICAL MODELING

In the following, the analytical modeling of the porous SMAs which is a generalization of the phenomenological ZM model for SMAs is presented. More details regarding the original ZM model can be found in [16].

2.1 State variables and free energy formulation

The phenomenological ZM model [16] for dense SMAs is modified including the effect of porosity. The representative elementary volume (REV) is a combination of the solid SMA matrix and the porosity as shown in Figure 1, which is called the skeleton. In this study, the porous region is assumed to be connected and the occluded porosity which is usually small compared to the amount of connected porosity is neglected.

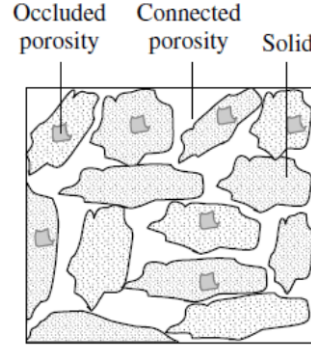


Figure 1: Skeleton particle [18]

The free energy density, ψ , of the REV is formulated as a function of the following variables:

$$\psi = \psi(\boldsymbol{\epsilon}', \theta, T, \boldsymbol{\epsilon}'_A, \boldsymbol{\epsilon}'_M, \boldsymbol{\epsilon}_{ori}, z, \phi) \quad (1)$$

where $\boldsymbol{\epsilon}'$ and θ are the deviatoric and hydrostatic parts of the strain tensor of the skeleton ($\boldsymbol{\epsilon} = \boldsymbol{\epsilon}' + \frac{\theta}{3}\mathbf{I}$), T is the temperature, $\boldsymbol{\epsilon}'_i$ is the local deviatoric strain tensor of the corresponding phase (A for austenite, M for martensite), $\boldsymbol{\epsilon}_{ori}$ is the orientation strain tensor of martensite, z is the volume fraction of martensite and ϕ is the porosity which is defined as the porous volume divided by the total volume of the REV. In short, the porosity is introduced into the ZM model as an additional internal variable.

In classical ZM model for bulk SMAs, the free energy density of a REV is constructed as follows;

$$\psi = (1 - z)\psi_A + z\psi_M + I_z \quad (2)$$

where ψ_i is the free energy density of the corresponding phase and I_z is the interaction energy between the phases or martensite variants. For the porous SMA, the free energy density of the skeleton particle is formulated as follows:

$$\psi = (1 - \phi)[(1 - z)\psi_A + z\psi_M + I_z] + \frac{1}{2}H\theta^2 \quad (3)$$

where H is a material parameter related to hardening and θ is the inelastic volumetric strain due to the change in porosity. It is assumed that the volume change of the matrix is negligible compared to the one of the porosity ($\theta_A = \theta_M = 0$).

The energy terms in Equation 3 are written as follows:

$$\psi_A = \mu_A(\boldsymbol{\epsilon}'_A : \boldsymbol{\epsilon}'_A) \quad (4)$$

$$\psi_M = \mu_M[(\boldsymbol{\epsilon}'_M - \boldsymbol{\epsilon}_{ori}) : (\boldsymbol{\epsilon}'_M - \boldsymbol{\epsilon}_{ori})] + C(T) \quad (5)$$

$$I_z = G\frac{z^2}{2} + \frac{z}{2}[\alpha z + \beta(1 - z)]\left[\frac{2}{3}\boldsymbol{\epsilon}_{ori} : \boldsymbol{\epsilon}_{ori}\right] \quad (6)$$

where μ_i is the shear modulus, $C(T)$ is the latent heat density due to phase transformation and G , α and β are material parameters.

2.2 Constraint equations and Lagrange potential

The state variables must obey some physical rules as stated below:

$$(1 - z)\boldsymbol{\epsilon}'_A + z\boldsymbol{\epsilon}'_M - \boldsymbol{\epsilon}' = 0 \quad (7)$$

$$z \geq 0; \quad (1 - z) \geq 0 \quad (8)$$

$$\epsilon_0 - \sqrt{\frac{2}{3} \epsilon_{ori} : \epsilon_{ori}} \geq 0 \quad (9)$$

$$\phi - \phi_0 - \theta = 0 \quad (10)$$

$$\phi \geq 0; \quad (1 - \phi) \geq 0 \quad (11)$$

where ϵ_0 is the limit for transformation strain and ϕ_0 is the initial porosity. Using the constraint equations above, a Lagrange potential is constructed as follows,

$$\begin{aligned} \psi_l = -\lambda : [(1 - z)\epsilon'_A + z\epsilon'_M - \epsilon'] - v_1 z - v_2(1 - z) - \mu[\epsilon_0 - \sqrt{\frac{2}{3} \epsilon_{ori} : \epsilon_{ori}}] \\ - \lambda_1[\phi - \phi_0 - \theta] - v_3 \phi - v_4(1 - \phi) \end{aligned} \quad (12)$$

where λ , μ , μ_1 and v_i are Lagrange multipliers. ψ and ψ_l together construct the Lagrangian $L = \psi + \psi_l$, which is then used to obtain the state equations:

$$\begin{aligned} L = (1 - \phi) \left[(1 - z) \left(\mu_A(\epsilon'_A : \epsilon'_A) \right) + z \left(\mu_M[(\epsilon'_M - \epsilon_{ori}) : (\epsilon'_M - \epsilon_{ori})] + C(T) \right) \right] + G \frac{z^2}{2} \\ + \frac{z}{2} [\alpha z + \beta(1 - z)] \left[\frac{2}{3} \epsilon_{ori} : \epsilon_{ori} \right] + \frac{1}{2} H \theta^2 - \lambda : [(1 - z)\epsilon'_A + z\epsilon'_M - \epsilon'] - v_1 z - v_2(1 - z) \\ - \mu[\epsilon_0 - \sqrt{\frac{2}{3} \epsilon_{ori} : \epsilon_{ori}}] - \lambda_1[\phi - \phi_0 - \theta] - v_3 \phi - v_4(1 - \phi) \end{aligned} \quad (13)$$

2.3 State equations

State equations below are obtained based on the Clausius-Duhem inequality for a solid medium:

$$s = \frac{\partial L}{\partial \epsilon'} = \lambda \quad (14)$$

$$\frac{tr(\sigma)}{3} = \frac{\partial L}{\partial \theta} = \lambda_1 + H \theta \quad (15)$$

$$0 = \frac{\partial L}{\partial \epsilon'_A} = (1 - z) [2\mu_A \epsilon'_A (1 - \phi) - \lambda] \quad (16)$$

$$0 = \frac{\partial L}{\partial \epsilon'_M} = z [2\mu_M (\epsilon'_M - \epsilon_{ori}) (1 - \phi) - \lambda] \quad (17)$$

$$\begin{aligned} -A_\phi = \frac{\partial L}{\partial \phi} = - \left[(1 - z) \mu_A(\epsilon'_A : \epsilon'_A) + z \left(\mu_M(\epsilon'_M - \epsilon_{ori}) : (\epsilon'_M - \epsilon_{ori}) + C(T) \right) \right] + G \frac{z^2}{2} \\ + \frac{z}{2} [\alpha z + \beta(1 - z)] \left[\frac{2}{3} \epsilon_{ori} : \epsilon_{ori} \right] - \lambda_1 \end{aligned} \quad (18)$$

$$\begin{aligned} -A_z = \frac{\partial L}{\partial z} = (1 - \phi) \left[-\mu_A(\epsilon'_A : \epsilon'_A) + \left(\mu_M[(\epsilon'_M - \epsilon_{ori}) : (\epsilon'_M - \epsilon_{ori})] + C(T) \right) \right] + G z + \\ [\alpha z + \beta(\frac{1}{2} - z)] \left[\frac{2}{3} \epsilon_{ori} : \epsilon_{ori} \right] - \lambda(\epsilon'_M - \epsilon'_A) \end{aligned} \quad (19)$$

$$-A_{ori} = \frac{\partial L}{\partial \epsilon_{ori}} = (1 - \phi) z \left[2\mu_M(\epsilon_{ori} - \epsilon'_M) + \frac{2}{3} \epsilon_{ori}(\alpha z + \beta(1 - z)) \right] + \frac{2}{3} \mu \left[\frac{\epsilon_{ori}}{\sqrt{\frac{2}{3} \epsilon_{ori} : \epsilon_{ori}}} \right] \quad (20)$$

where A_z , A_ϕ and \mathbf{A}_{ori} are the thermodynamic forces associated with phase transformation, volume change and orientation of martensite, respectively.

The constitutive relation between deviatoric stress and strain is obtained from the state equations as shown below:

$$\mathbf{s} = 2(1 - \phi)\mu_{eq}[\boldsymbol{\varepsilon}' - z\boldsymbol{\varepsilon}_{ori}] \quad (21)$$

where

$$\mu_{eq} = \left(\frac{1-z}{\mu_A} + \frac{z}{\mu_M} \right)^{-1} \quad (22)$$

The thermodynamic forces can be rewritten as follows:

$$A_z = \frac{1}{3}\sigma_{VM}^2 \frac{(1+\nu)}{(1-\phi)} \left(\frac{1}{E_M} - \frac{1}{E_A} \right) + \mathbf{s} : \boldsymbol{\varepsilon}_{ori} + (1-\phi)(-C(T) - Gz - [\alpha z + \beta(\frac{1}{2} - z)][\frac{2}{3}\boldsymbol{\varepsilon}_{ori} : \boldsymbol{\varepsilon}_{ori}]) \quad (23)$$

$$A_\phi = \frac{1}{3}\sigma_{VM}^2 \frac{(1+\nu)}{E_{eq}} + zC(T) + Gz^2 + \frac{z}{2}[\alpha z + \beta(1-z)][\frac{2}{3}\boldsymbol{\varepsilon}_{ori} : \boldsymbol{\varepsilon}_{ori}] + \frac{tr\boldsymbol{\sigma}}{3} - H(\phi - \phi_0) \quad (24)$$

$$\mathbf{A}_{ori} = z\mathbf{s} - \frac{2}{3}z(1-\phi)(\alpha z + \beta(1-z))\boldsymbol{\varepsilon}_{ori} - \frac{2}{3}\mu \left[\frac{\boldsymbol{\varepsilon}_{ori}}{\sqrt{\frac{2}{3}\boldsymbol{\varepsilon}_{ori} : \boldsymbol{\varepsilon}_{ori}}} \right] \quad (25)$$

where

$$E_{eq} = \left(\frac{1-z}{E_A} + \frac{z}{E_M} \right)^{-1} \quad (26)$$

2.4 Dissipation pseudo-potential and evolution of internal variables

In the framework of generalized standard materials, evolution of internal variables is obtained from a dissipation pseudo-potential which is a function of the rates of dissipative variables, $D(\dot{z}, \dot{\boldsymbol{\varepsilon}}_{ori}, \dot{\phi})$.

Assume;

$$D = (1-\phi)[a(1-z) + bz]|\dot{z}| + z^2 Y \sqrt{\frac{2}{3}\dot{\boldsymbol{\varepsilon}}_{ori} : \dot{\boldsymbol{\varepsilon}}_{ori}} + P(1-\phi)|\dot{\phi}| \quad (27)$$

where a , b , Y and P are positive materials constants. The dissipation pseudo-potential is related to thermodynamic forces as follows:

$$A_z \in \partial_{\dot{z}} D; \quad A_{ori} \in \partial_{\dot{\boldsymbol{\varepsilon}}_{ori}} D; \quad A_\phi \in \partial_{\dot{\phi}} D \quad (28)$$

which give the set of yield functions:

$$F_z^1 \leq 0, \quad F_z^2 \leq 0, \quad F_{tr} \leq 0, \quad F_\phi^1 \leq 0, \quad F_\phi^2 \leq 0 \quad (29)$$

associated to the forward martensitic transformation, reverse martensitic transformation, martensite orientation, increase in porosity and decrease in porosity, respectively. The yield functions are given below:

$$F_z^1 = \frac{1}{3}\sigma_{VM}^2 \frac{El_{MA}}{(1-\phi)} + \mathbf{s} : \boldsymbol{\varepsilon}_{ori} + (1-\phi) \left(-C(T) - Gz - [\alpha z + \beta(\frac{1}{2} - z)][\frac{2}{3}\boldsymbol{\varepsilon}_{ori} : \boldsymbol{\varepsilon}_{ori}] - [a(1-z) + bz] \right) \quad (30)$$

$$F_z^2 = -\frac{1}{3}\sigma_{VM}^2 \frac{El_{MA}}{(1-\phi)} - \mathbf{s} : \boldsymbol{\varepsilon}_{ori} - (1-\phi) \left(-C(T) - Gz - [\alpha z + \beta(\frac{1}{2} - z)][\frac{2}{3}\boldsymbol{\varepsilon}_{ori} : \boldsymbol{\varepsilon}_{ori}] \right)$$

$$- [a(1-z) + bz] \quad (31)$$

$$F_{ori} = \frac{F_{tr}}{z} = \left\| \mathbf{s} - \frac{2}{3}(1-\phi)(\alpha z + \beta(1-z))\boldsymbol{\epsilon}_{ori} - \frac{2\mu}{3z} \left[\frac{\boldsymbol{\epsilon}_{ori}}{\sqrt{\frac{2}{3}\boldsymbol{\epsilon}_{ori} : \boldsymbol{\epsilon}_{ori}}} \right] \right\|_{VM} - zY \quad (32)$$

$$F_{\phi}^1 = \frac{1}{3}\sigma_{VM}^2 \frac{(1+\nu)}{E_{eqt}} + zC(T) + Gz^2 + \frac{z}{2}[\alpha z + \beta(1-z)] \left[\frac{2}{3}\boldsymbol{\epsilon}_{ori} : \boldsymbol{\epsilon}_{ori} \right] + \frac{tr\boldsymbol{\sigma}}{3} - H(\phi - \phi_0) - P(1-\phi) \quad (33)$$

$$F_{\phi}^2 = -\frac{1}{3}\sigma_{VM}^2 \frac{(1+\nu)}{E_{eqt}} - zC(T) - Gz^2 - \frac{z}{2}[\alpha z + \beta(1-z)] \left[\frac{2}{3}\boldsymbol{\epsilon}_{ori} : \boldsymbol{\epsilon}_{ori} \right] - \frac{tr\boldsymbol{\sigma}}{3} + H(\phi - \phi_0) - P(1-\phi) \quad (34)$$

During evolution of the internal variables, the yield functions must satisfy the following conditions:

$$F = 0, \quad \dot{F} = 0 \quad (35)$$

where F is the corresponding yield function; \dot{z} , $\dot{\epsilon}_{ori}$ and $\dot{\phi}$ are calculated using Equation 35.

2.5 Parameter identification

The material parameters listed in Table 1, except for P and H , can be calculated from orientation and pseudoelastic uniaxial experiments performed on a dense SMA as explained in [16]. For now, transformation temperatures are assumed to be constant under different porosity.

P and H are the additional material parameters to be determined for a porous material. For now, P is chosen to be 10 MPa and H is assumed to depend on porosity as $H = H_0(1 - \phi_0)^2$ to observe the evolution of porosity in the simulations.

Table 1: Material parameters used in the simulations [16]

Parameter	Value	Parameter	Value
E_A	39100 MPa	a	28.94 MPa
E_M	18000 MPa	b	27.46 MPa
ν	0.33	ϵ_0	0.102
Y	265 MPa	G	37.3 MPa
α	539 MPa	β	3137 MPa
ζ	0.4775 MPa °C ⁻¹	κ	13.9 MPa
A_f^0	40 °C	T_0	50 °C
P	10 MPa	H_0	10000 MPa

3 NUMERICAL STUDY ON COMPRESSION OF POROUS NiTi

Since the experimental studies in the literature are devoted to compressive behaviour of the porous NiTi, the present model is simplified to simulate uniaxial compression.

3.1 Simplification of the model to uniaxial compression (1D)

The equations above are simplified to their 1D version in order to observe the pseudoelastic behavior of the porous SMAs under uniaxial compression; the stress-strain relation can be written as follows:

$$\sigma = 3(1 - \phi)\mu_{eqv}\left[\varepsilon - \frac{(\phi - \phi_0)}{3} - z\varepsilon_{ori}\right] \quad (36)$$

For the ease of simplicity, it is assumed that the martensite is completely transformed if the temperature is well above austenite finish temperature A_f^0 , and under this condition $\varepsilon_{ori} = \varepsilon_0$. In addition, the volume change is assumed to be totally irreversible, therefore there is no increase in volume during unloading.

For uniaxial compression, the yield functions are obtained as follows:

$$F_z^1 = \frac{3}{4} \frac{El_{MA}}{(1 - \phi)} s^2 + \frac{3}{2} s \varepsilon_0^2 + (1 - \phi) \left(-C(T) - Gz - \varepsilon_0^2 [\alpha z + \beta(\frac{1}{2} - z)] \right) - [a(1 - z) + bz] \quad (37)$$

$$F_z^2 = -\frac{3}{4} \frac{El_{MA}}{(1 - \phi)} s^2 - \frac{3}{2} s \varepsilon_0^2 - (1 - \phi) \left(-C(T) - Gz - \varepsilon_0^2 [\alpha z + \beta(\frac{1}{2} - z)] \right) - [a(1 - z) + bz] \quad (38)$$

$$F_\phi = -\frac{3}{4} \frac{(1 + \nu)}{E_{eq}} s^2 - zC(T) - Gz^2 - \frac{z}{2} [\alpha z + \beta(1 - z)] \varepsilon_0^2 - \frac{s}{2} + H(\phi - \phi_0) - P(1 - \phi) \quad (39)$$

3.2 Algorithm and numerical results

The phenomenological model for 1D compression test is programmed in Matlab following the algorithm below. Here, exponent test indicates an estimate for the step $i + 1$ by using the values of z and ϕ at step i .

Input: model parameters, ε , T , z^0 , ϕ^0

Output: z , ϕ

While $i < n$

divide the loading path into n intervals: $\varepsilon^{i+1} \leftarrow \varepsilon^i + \Delta\varepsilon$

- compute $\sigma^{(i+1),test}$ using ε^{i+1} , z^i , ϕ^i
- compute $F_z^{1,(i+1),test}$, $F_z^{2,(i+1),test}$, $F_\phi^{(i+1),test}$
- **if** $F_z^{1,(i)} > 0$ **and** $F_z^{1,(i+1),test} > F_z^{1,(i)}$ **and** $1 - z > 0$
forward phase transformation
- **if** $F_z^{2,(i)} > 0$ **and** $F_z^{2,(i+1),test} > F_z^{2,(i)}$ **and** $z > 0$
reverse phase transformation
- **if** $F_\phi^{(i)} > 0$ **and** $F_\phi^{(i+1),test} > F_\phi^{(i)}$ **and** $\phi > 0$
porosity change
- **if** no active transformation and porosity change
 $\Delta z = 0$, $\Delta\phi = 0$
- **if** forward phase transformation only
 $\dot{F}_z^1 = 0$ gives Δz , $\Delta\phi = 0$

- **if** reverse phase transformation only
 $\dot{F}_z^2 = 0$ gives $\Delta z, \Delta \phi = 0$
 - **if** porosity change
 $\dot{F}_\phi = 0$ gives $\Delta \phi, \Delta z = 0$
 - **if** forward phase transformation and porosity change
 $\dot{F}_z^1 = 0$, and $\dot{F}_\phi = 0$ give $\Delta z, \Delta \phi$
 - **if** reverse phase transformation and porosity change
 $\dot{F}_z^2 = 0$, and $\dot{F}_\phi = 0$ give $\Delta z, \Delta \phi$
- $z^{(i+1)} \leftarrow z^{(i)} + \Delta z, \phi^{(i+1)} \leftarrow \phi^{(i)} + \Delta \phi$, compute $\sigma^{(i+1)}$ with $z^{(i+1)}$ and $\phi^{(i+1)}$
 $i \leftarrow i + 1$, compute $F_z^{1,(i)}$
End while

Fig. 2 shows the comparison of the stress-strain curves of dense and 25% porous NiTi under uniaxial compression. Numerical results demonstrate that the porous NiTi shows a similar hysteresis loop with some differences when compared to the one of the dense NiTi. As expected, elastic modulus, critical stresses for forward and reverse phase transformation and hysteresis area decrease under porosity. It is also observed that there is a residual strain at the end of unloading due to the irreversible volumetric strain resulting from the evolution of porosity.

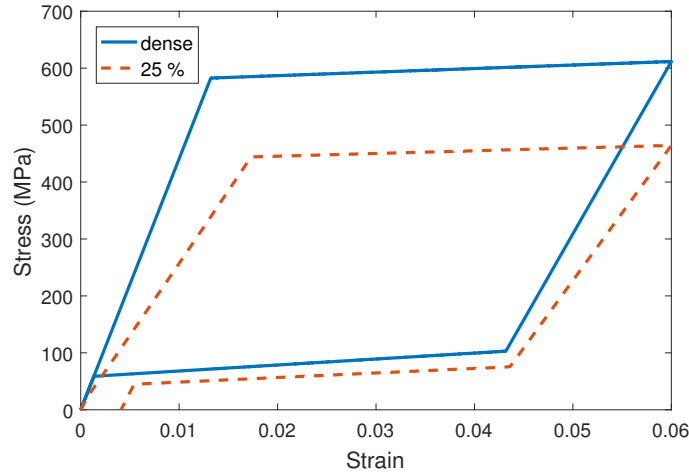


Figure 2: Numerical results of the stress-strain behaviour of dense and 25% porous NiTi under compression

The effects of porosity explained in the previous paragraph are more pronounced in Figures 3, 4a and 4b where the results are compared for different porosity levels. Fig. 3 shows that the amount of residual strain is increasing with increasing the porosity as observed by Saedi et al. [11]. The same result can also be seen by looking at Fig. 4a where the evolution of porosity is presented. Fig. 4b shows the evolution of martensitic phase transformation by following the volume fraction of martensite. It is

observed that the phase transformation is recovered back, but the amount of martensite phase produced decreases by increasing the porosity which is also stated by Zhao et al. [7] according to their experimental results. This result can also be related to the decrease in the hysteresis area which is a sign of martensitic transformation.

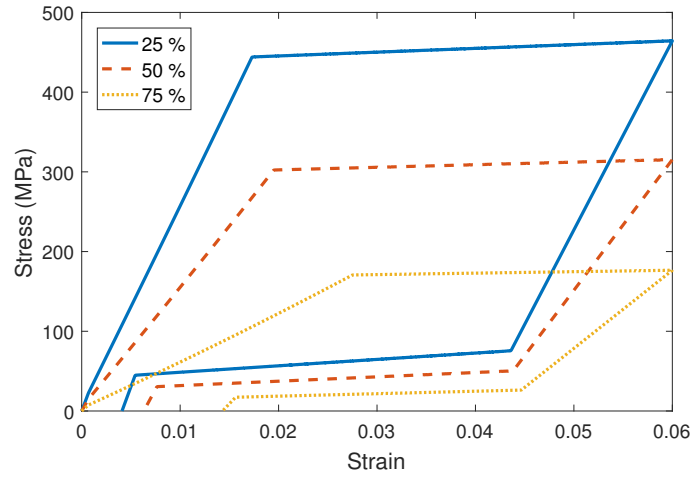


Figure 3: Numerical results of the stress-strain behaviour of 25%, 50% and 75% porous NiTi under compression

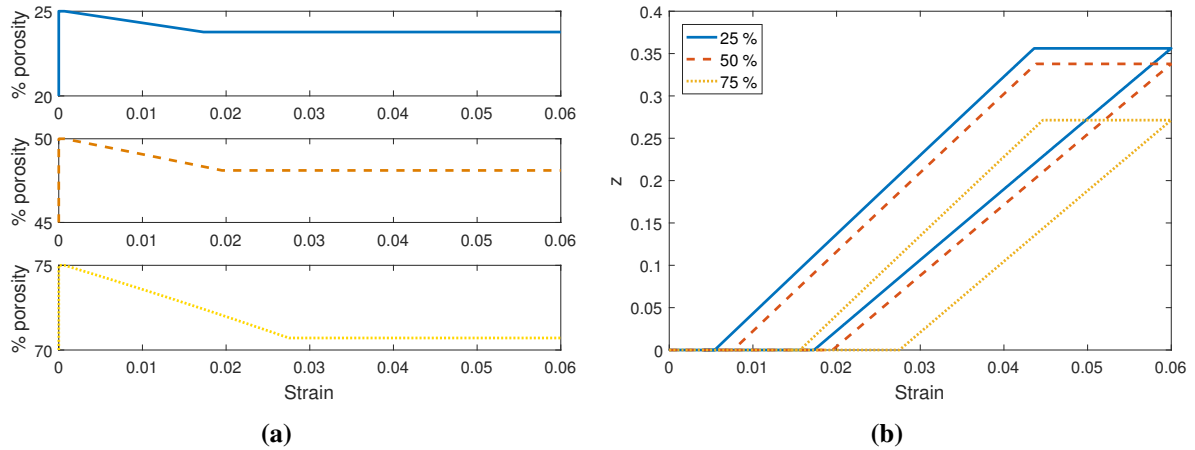


Figure 4: Numerical results of the evolution of (a) porosity and (b) martensitic volume fraction of 25%, 50% and 75% porous NiTi under compression

The numerical results show that the present phenomenological model is able to represent qualitatively the effect of porosity on the compression behaviour of NiTi SMA, and continuing research on the model holds a great promise. In order to achieve a quantitative agreement with experimental results, the material parameters in the model must be determined precisely. The dissipation potential will also be formulated more precisely after performing a few experiments on a porous NiTi.

4 SUMMARY

In this paper, a macro scale phenomenological model of porous SMAs is presented. The analytical model is a generalization of the ZM model which represents the mechanical behaviour of dense SMAs within the framework of generalized standard materials with internal constraints. The porosity is introduced into the ZM model as an additional internal variable and the effect of hydrostatic pressure is taken into account. The model is then simulated numerically using Matlab for uniaxial behaviour of a porous NiTi SMA under compression. The stress-strain behaviour of the NiTi SMA is presented and the evolution of martensitic phase transformation and porosity are calculated for different porosity levels. The numerical results have qualitative agreement with the experimental results available in the literature and it shows that the present model is able to represent the effect of porosity on the pseudoelastic uniaxial compression behaviour of a porous SMA. Experiments on porous NiTi are needed to characterize additional material parameters and to obtain a quantitative agreement between the analytical model and experiments.

REFERENCES

- [1] Mohammad H Elahinia, Mahdi Hashemi, Majid Tabesh, and Sarit B Bhaduri. Manufacturing and processing of niti implants: A review. *Progress in materials science*, 57(5):911–946, 2012.
- [2] Bin Yuan, Min Zhu, and Chi Chung. Biomedical porous shape memory alloys for hard-tissue replacement materials. *Materials*, 11(9):1716, 2018.
- [3] A Bansiddhi, TD Sargeant, SI Stupp, and DC Dunand. Porous niti for bone implants: a review. *Acta biomaterialia*, 4(4):773–782, 2008.
- [4] Boris M Silberstein and Victor Gunter. Shape-memory implants in spinal surgery: long-term results (experimental and clinical studies). In *Shape memory implants*, pages 147–152. Springer, 2000.
- [5] SL Zhu, XJ Yang, DH Fu, LY Zhang, CY Li, and ZD Cui. Stress–strain behavior of porous niti alloys prepared by powders sintering. *Materials Science and Engineering: A*, 408(1-2):264–268, 2005.
- [6] Ampika Bansiddhi and David C Dunand. Shape-memory niti foams produced by solid-state replication with naf. *Intermetallics*, 15(12):1612–1622, 2007.
- [7] Ying Zhao, Minoru Taya, Yansheng Kang, and Akira Kawasaki. Compression behavior of porous niti shape memory alloy. *Acta materialia*, 53(2):337–343, 2005.
- [8] Sia Nemat-Nasser, Yu Su, Wei-Guo Guo, and Jon Isaacs. Experimental characterization and micromechanical modeling of superelastic response of a porous niti shape-memory alloy. *Journal of the Mechanics and Physics of Solids*, 53(10):2320–2346, 2005.
- [9] Martin Bram, Manuel Köhl, Hans Peter Buchkremer, and Detlev Stöver. Mechanical properties of highly porous niti alloys. *Journal of materials engineering and performance*, 20(4-5):522–528, 2011.
- [10] Zhiqiang Guo, Huimin Xie, Fulong Dai, Haichang Qiang, Lijian Rong, Pengwan Chen, and Fenglei Huang. Compressive behavior of 64% porosity niti alloy: An experimental study. *Materials Science and Engineering: A*, 515(1-2):117–130, 2009.

- [11] Soheil Saedi, Sayed E Saghaian, Ahmadreza Jahadakbar, Narges Shayesteh Moghaddam, Mohsen Taheri Andani, Sayed M Saghaian, Y Charles Lu, Mohammad Elahinia, and Haluk E Karaca. Shape memory response of porous niti shape memory alloys fabricated by selective laser melting. *Journal of Materials Science: Materials in Medicine*, 29(4):40, 2018.
- [12] JS Olsen and ZL Zhang. Effect of spherical micro-voids in shape memory alloys subjected to uniaxial loading. *International Journal of Solids and Structures*, 49(14):1947–1960, 2012.
- [13] Arthur L Gurson. Continuum theory of ductile rupture by void nucleation and growth: Part i yield criteria and flow rules for porous ductile media. *Journal of engineering materials and technology*, 99(1):2–15, 1977.
- [14] MJ Ashrafi, J Arghavani, R Naghdabadi, and S Sohrabpour. A 3-d constitutive model for pressure-dependent phase transformation of porous shape memory alloys. *journal of the mechanical behavior of biomedical materials*, 42:292–310, 2015.
- [15] VS Deshpande and NA Fleck. Isotropic constitutive models for metallic foams. *Journal of the Mechanics and Physics of Solids*, 48(6-7):1253–1283, 2000.
- [16] Wael Zaki and Ziad Moumni. A three-dimensional model of the thermomechanical behavior of shape memory alloys. *Journal of the Mechanics and Physics of Solids*, 55(11):2455–2490, 2007.
- [17] Z Moumni and QS Nguyen. A model of material with phase change and applications. *Le Journal de Physique IV*, 6(C1):C1–335, 1996.
- [18] Olivier Coussy. *Poromechanics*. John Wiley & Sons, 2004.

SELF-HEATING AND FATIGUE OF SUPERELASTIC SHAPE MEMORY ALLOY STRUCTURES

L. Saint-Sulpice*, S. Arbab Chirani*, S. Calloch[†], C. Doudard[†] and V. Legrand*[†]

* ENI Brest, UMR CNRS 6027, IRDL, F-29200 Brest, France
Technopôle Brest-Iroise - CS 73862
29238 Brest cedex 3
e-mail: arbab@enib.fr, web page: <https://www.enib.fr>

[†] ENSTA Bretagne, UMR CNRS 6027, IRDL, F-29200 Brest, France
2, rue François Verny
29806 Brest cedex 9

Key words: Thermal signature, thermo-mechanical coupling, dissipation

Abstract. Several applications use superelastic shape memory alloys (SMA) parts in order to benefit from their large recoverable strain. These structures are generally subject to cyclic loadings, which can lead to fatigue rupture. Unfortunately, the fatigue of SMA has not been much studied and their fatigue is not taken into account in the dimensioning of SMA structures.

In this study, we begin to determine fatigue properties of the material by using a fast method based on self-heating measurements firstly proposed for steels.

A model describing the probabilistic apparition of superelastic inclusion in an elastic matrix is developed based on a macroscopic model of SMA behavior. It permits to reproduce self-heating results and then, by choosing an adapted fatigue criteria, is able to predict fatigue properties of the samples. These results have been validated using classic fatigue tests on the hourglass samples.

1 INTRODUCTION

The shape memory alloys (SMA) are materials able to recover a large elastic deformation under thermomechanical loading. These properties are due to a very particular aspect of the mechanical behavior: the superelasticity. When these materials are loaded at a temperature higher than the A_f temperature (Austenite Finish), an reversible strain occurred and can reach 6% to 10%. The strain mechanism at the origin of this phenomena is based on a solid-solid phase transformation [1]. The properties of these alloys make them interesting for innovative applications. For example they are used for biomedical applications or in transport. The thermomechanical behavior of these alloys has been studied since several years. Several models have been developed to describe the behavior. Unfortunately, the fatigue property of these alloys remains an unexplored area. Currently in the design phase of structures using SMA, fatigue is not considered. This is the reason for which we try to determine fatigue properties of nickel-titanium (NiTi) is studied in this study. However fatigue tests are time consuming, thus we proposed a fast method to determine fatigue properties of SMA. This study begins by conducting self-heating measurements on samples. They permit to empirically estimate the mean endurance limit of the material. Then a two-scale probabilistic model has been developed. It permits to simulate the temperature evolution in the material

during self-heating tests and to identify some fatigue related parameters of the material. Finally a fatigue criterion has been used in order to predict the fatigue curves associated to probability of failure. The results have been validated by comparison with classic fatigue tests on the same samples.

2 EXPERIMENTAL SELF-HEATING

In this section, the material and the geometry of specimens are presented. Then, the loading conditions of self-heating tests are explained and the resulting self-heating curves are shown and analyzed. Finally, an empirical analysis, allowing the prediction of the mean endurance limit corresponding to a failure probability of 50% at 2 million cycles, is applied.

2.1 Material and geometry of specimens

The shape memory alloy used in this study is an as-received medical graded NiTi (50.8 at.% – 49.2 at.%). The alloy is superelastic at room temperature.

The specimens are obtained from cold-drawn wires of 1 mm diameter. In order to avoid influence of limit conditions in the grips on fatigue life, to force localization of martensitic transformation in a specific spot and then to make the study of self-heating feasible, an hourglass shaped notch has been realized on the samples using same manufacturing process as the one used for the fabrication of endodontic files.

The mechanical behavior in traction of these samples have been determined using an extensometer with an initial length of 10 mm which covers more than the entire hourglass shape. The identified Young modulus, E , transformation yield stress, σ_0 , hysteresis size, δ , and slope of transformation plateau, C , are reported in table 1. The results on figure 1 show a classic NiTi shape memory alloy behavior with a transformation plateau. The transformation limit is high compared to the ones observed in other tests from literature which doesn't take precaution about localization of transformation in the jaws like we did by the use of the hourglass shape of the specimen.

Table 1: Behavior characteristics of the specimens.

E (GPa)	σ_0 (MPa)	δ (MPa)	C (MPa/%)
72	770	410	0.17

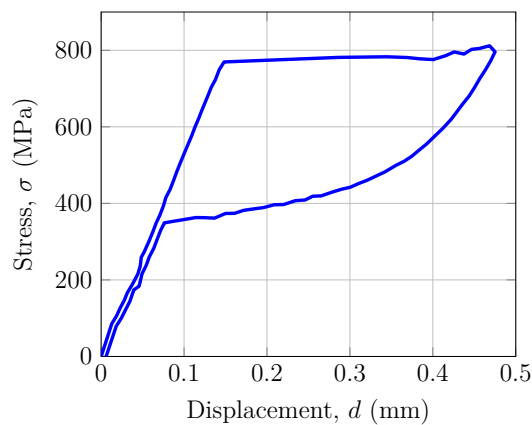


Figure 1: Stress-displacement behavior of NiTi hourglass specimens at 20 °C.

2.2 Loading and measurements conditions

Self-heating loadings consist of several steps with increasing maximum stress. During each step, a sinusoidal cyclic loading is applied between 10 MPa and given maximum stress for 100 seconds at 30 Hz, followed by a pause during another 100 seconds to let the specimen cool down to ambient temperature.

During a step, the temperature of each points of the central part of the specimen is registered using the infrared camera using a frequency of 100 Hz. The spatial mean temperature of the notched zone for each frame is calculated. To this temperature is subtracted the mean temperatures of the grips to obtained the mean temperature elevation. Then, a temporal mean temperature is determined from this one to give the mean cycle temperature elevation. Finally, the stabilized value of this temperature elevation during each cyclic loading step is extract to give the stabilized mean cycle temperature elevation, $\bar{\theta}_{cycle}^{0D}$.

The result of self-heating tests is the self-heating curve that represent for each step the stabilized mean cycle temperature elevation, $\bar{\theta}_{cycle}^{0D}$, versus the corresponding maximum stress (figure 2).

2.3 Empirical identification of the mean endurance limit

As it is proceeded for metallic materials like in [2], we performed an empirical identification of the mean endurance limit using the self-heating results, $\bar{\Sigma}_{\infty}^{sh}$. It consists of a linear regression on last points of the self-heating curve. Then the mean endurance limit correspond to the intersection of this line with the x-axis (see figure 2). The results are shown in table 2.

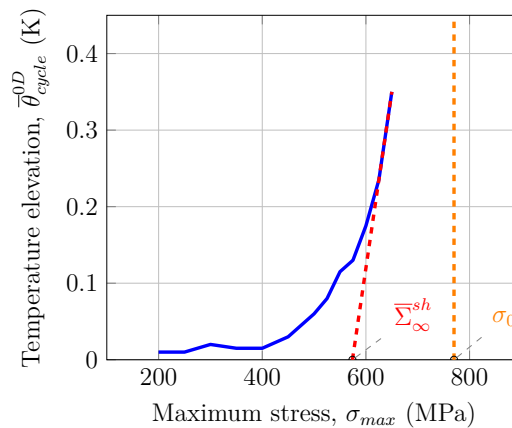


Figure 2: Temperature elevation versus maximum stress, with empirical determination of mean endurance limit.

If self-heating is related to fatigue behavior, then this value should correspond to the mean endurance limit determined by classic fatigue tests, $\bar{\Sigma}_{\infty}^{fat}$.

2.4 Experimental fatigue

In order to validate the self-heating results, classic fatigue tests have been realized using the same type of specimens, set-up and experimental conditions that were used for self-heating tests.

2.4.1 Whöler curves

The tests were carried up to two millions cycles if not rupture occurs. The obtained Whöler curves are shown on figure 3. The dashed green line represent the least squares power law fitting, and the dashed

red line, the corresponding mean endurance limit.

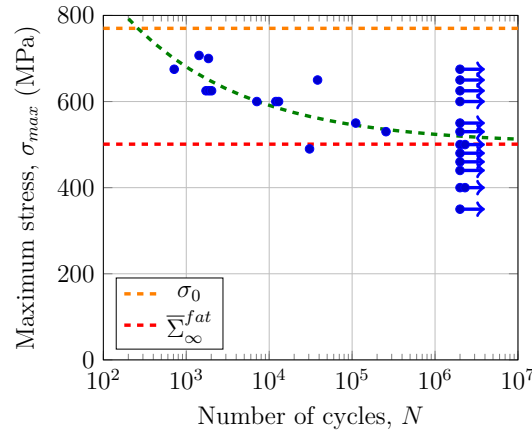


Figure 3: Maximum stress versus number of cycles to rupture.

We observe a large dispersion of the fatigue results, which is normal for high cycle fatigue tests.

2.4.2 Mean endurance limit comparison

The comparison of the mean endurance limit between classic fatigue tests and self-heating tests has been realized in table 2. It shows a good agreement between the mean endurance limits determined by the two methods.

Table 2: Comparison of mean endurance limits determined with classic fatigue tests and empirical determination using self-heating.

$\bar{\Sigma}_{\infty}^{fat}$ (MPa)	$\bar{\Sigma}_{\infty}^{sh}$ (MPa)	Δ (%)
501	574	14.5

This results show that the self-heating of SMA is probably related to the fatigue behavior. This first empiric approach permits to determine the mean endurance limit of an SMA from self-heating curve, but it only use a small part of the informations that self-heating curves contain. To extract this informations we need to develop a model permitting to simulate the self-heating during cyclic tests.

3 TWO-SCALE PROBABILISTIC MODEL

In order to simulate self-heating curves of SMA we need a two-scale probabilistic model. Indeed, firstly, the self-heating curves are realized in elastic part of the behavior of SMA as maximum stress is lower than transformation yield stress. So we assume that some phase transformation occurs at a lower scale and generate heat. Secondly, the shape of the self-heating curve suggest a probabilistic behavior since a deterministic one should leads to a two-slope curve of self-heating instead of a curved curve [3].

Then we consider a Representative Elementary Volume (REV) constitute of an elastic matrix containing inclusions presenting phase transformation at a lower stress than the apparent transformation yield stress of material (see figure 4). The probabilistic behavior is taken into account into the distribution of the transformation yield stress of inclusions.

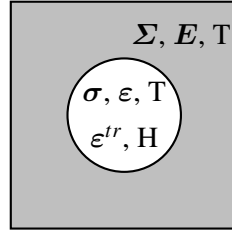


Figure 4: Representation of an inclusion in the matrix.

3.1 Behavior of an inclusion

In this part we present the behavior of an inclusion by describing the thermodynamic framework and calculate the induced dissipation.

As self heating tests consist of stress driven cyclic uniaxial loadings, we can write the evolution of the stress tensor in the matrix as

$$\boldsymbol{\sigma} = \tilde{f}(t)\mathbf{N} \quad (1)$$

with $\tilde{f}(t)$ a time periodic function that must observe $\tilde{f}(0) = 0$, and $\mathbf{N} = \begin{bmatrix} 1 & 0 & 0 \\ 0 & 0 & 0 \\ 0 & 0 & 0 \end{bmatrix}$.

3.1.1 Thermodynamic framework

An inclusion is considered to have a low transformation yield stress and then present phase transformation at studied stress amplitudes. We propose to take the following specific free energy for an inclusion

$$\rho\psi^i(\boldsymbol{\epsilon}, T, \boldsymbol{\epsilon}^{tr}, H) = \rho W_{\text{elast}}^i + \rho z W_{\text{chem}}^i + \rho W_{\text{int}}^i \quad (2)$$

with W_{elast}^i the elastic work in the inclusion

$$\rho W_{\text{elast}}^i = \frac{1}{2} \boldsymbol{\epsilon}^e : \underline{\underline{\mathbf{C}}} : \boldsymbol{\epsilon}^e + \rho C_\alpha \left(T - T_0 - T \ln \frac{T}{T_0} \right) \quad (3)$$

W_{chem}^i the chemical work in the inclusion due to transformation

$$\rho W_{\text{chem}}^i = \mu_0 (T - T_*) \boldsymbol{\epsilon}^{tr} : \mathbf{N}' \quad (4)$$

W_{int}^i the work induced by interactions between martensite variants

$$\rho W_{\text{int}}^i = \gamma H \quad (5)$$

$\boldsymbol{\epsilon}$ the total strain tensor in the inclusion, $\boldsymbol{\epsilon}^{tr}$ the transformation strain tensor, H an internal variable, z the martensite volume fraction, $\boldsymbol{\epsilon}^e$ the elastic strain tensor in the inclusion, μ_0 the slope of the evolution of forward transformation (austenite to martensite) yield stress versus temperature, T_* the reference temperature for forward transformation, \mathbf{N}' the deviatoric part of \mathbf{N} and γ the maximum transformation strain.

In the inclusion, we assume the strain decomposition into elastic strain, transformation strain and thermal strain

$$\boldsymbol{\epsilon} = \boldsymbol{\epsilon}^e + \boldsymbol{\epsilon}^{tr} + \lambda \theta \mathbf{I} \quad (6)$$

Thermodynamics forces are the stress tensor in inclusion, σ , associated to the total strain tensor in inclusion

$$\sigma = \rho \frac{\partial \Psi^i}{\partial \varepsilon} = \underline{\underline{C}} : (\varepsilon - \varepsilon^{tr} - \lambda \theta \mathbf{I}) \quad (7)$$

the entropy in inclusion, s , associated to temperature

$$s = -\frac{\partial \Psi^i}{\partial T} = \frac{E\lambda}{\rho(1-2\nu)} \text{tr}(\varepsilon - \varepsilon^{tr}) + C_\alpha \ln \frac{T}{T_0} - \frac{\mu_0}{\rho} \varepsilon^{tr} : \mathbf{N}' \quad (8)$$

a thermodynamic force tensor, π , associated to the transformation strain tensor

$$\pi = -\rho \frac{\partial \Psi^i}{\partial \varepsilon^{tr}} = \underline{\underline{C}} : (\varepsilon - \varepsilon^{tr} - \lambda \theta \mathbf{I}) - \mu_0 (T - T_*) \mathbf{N}' = \sigma - \mu_0 (T - T_*) \mathbf{N}' \quad (9)$$

and a thermodynamic force, P , associated to the internal variable H

$$P = -\rho \frac{\partial \Psi^i}{\partial H} = -\gamma \quad (10)$$

The thermoelastic coupling term is then

$$\rho T \frac{\partial^2 \Psi^i}{\partial T \partial \varepsilon} : \dot{\varepsilon} = -\frac{E\lambda T}{1-2\nu} \text{tr}(\dot{\varepsilon}) = -\lambda T \dot{f}(t) - \frac{3E\lambda^2 T}{1-2\nu} \dot{\theta} \quad (11)$$

The thermo-mechanical transformation coupling term is

$$\rho T \frac{\partial^2 \Psi^i}{\partial T \partial \varepsilon^{tr}} : \dot{\varepsilon}^{tr} = T \left(\frac{E\lambda}{1-2\nu} \mathbf{I} + \mu_0 \mathbf{N}' \right) : \dot{\varepsilon}^{tr} \quad (12)$$

As martensitic transformation in SMA is almost isochoric [4, 5], it is often assumed that transformation strain is deviatoric. Furthermore, normality rule implies that the direction of transformation strain is identical to elastic strain direction (in the deviatoric plan) for uniaxial loadings. And finally transformation strain is proportional to martensic volume fraction. The transformation strain can then be express as

$$\varepsilon^{tr} = \frac{3}{2} \gamma_z \mathbf{N}' \quad (13)$$

So

$$\rho T \frac{\partial^2 \Psi^i}{\partial T \partial \varepsilon^{tr}} : \dot{\varepsilon}^{tr} = \mu_0 T \gamma \dot{z} \quad (14)$$

The thermo-mechanical interaction coupling term is

$$\rho T \frac{\partial^2 \Psi^i}{\partial T \partial H} : \dot{H} = 0 \quad (15)$$

The transformation dissipation term is

$$\rho \frac{\partial \Psi^i}{\partial \varepsilon^{tr}} : \dot{\varepsilon}^{tr} = -\pi : \dot{\varepsilon}^{tr} = -(\tilde{f}(t) - \mu_0 (T - T^*)) \gamma \dot{z} \quad (16)$$

And the interaction dissipation term is

$$\rho \frac{\partial \Psi^i}{\partial H} : \dot{H} = \gamma \dot{H} \quad (17)$$

In order to include this terms in the heat equation and resolve it, we need to express \dot{z} and \dot{H} in terms of θ , $\dot{\theta}$ and t .

In order to express \dot{z} , we use a simplified version of the thermo-mechanical model developed in [6], which give

$$\dot{z} = \frac{\dot{f}(t) - \mu_0 \dot{\theta}}{\gamma C} \quad (18)$$

Using the assumption that the intrinsic dissipation is the same during loading and during unloading we then obtain

$$H(z) = \frac{\gamma C z - \delta}{2} z \quad (19)$$

and then

$$\dot{H}(z) = \left(\gamma C z - \frac{\delta}{2} \right) \dot{z} \quad (20)$$

3.1.2 Dissipation during cyclic loading

The purpose of this modeling is to determine the stabilized mean cycle temperature elevation, $\bar{\theta}_{cycle}^{0D}$ during cycling loading. We have then to calculate the mean dissipation of an inclusion during a stabilized cycle as a function of the transformation yield stress of the inclusion. The dissipation in an inclusion is defined as

$$\Delta_i = \sigma : \dot{\epsilon} - \rho (\dot{\psi}^i + s \dot{T}) \quad (21)$$

Then

$$\Delta_i = -\rho \frac{\partial \psi^i}{\partial \epsilon^{tr}} : \dot{\epsilon}^{tr} - \rho \frac{\partial \psi^i}{\partial H} \dot{H} = (\sigma - \mu_0(T - T_*)) : \dot{\epsilon}^{tr} - \gamma \left(\gamma C z - \frac{\delta}{2} \right) \dot{z} \quad (22)$$

Self-heating curves correspond to the stabilized temperature during a cyclic loading. We can then integrate the dissipation during a thermodynamical cycle to obtain the cyclic dissipated energy

$$D_i(\sigma_0) = \oint \Delta_i dt = \oint \sigma : \dot{\epsilon}^{tr} dt + \oint \mu_0(T - T_*) : \dot{\epsilon}^{tr} dt - \oint \left(\gamma C z - \frac{\delta}{2} \right) dz \quad (23)$$

Since we integrate on a thermodynamic cycle, the last two integrals are equal to zero

$$\oint \mu_0(T - T_*) : \dot{\epsilon}^{tr} dt = \oint \left(\gamma C z - \frac{\delta}{2} \right) dz = 0 \quad (24)$$

The expression of the first one and then of the cyclic dissipated energy depends on the value of the transformation yield stress, σ_0 , in the inclusion

$$D_i(\sigma_0) = \frac{\delta}{C} (\sigma_{max} - \sigma_0) \quad (25)$$

3.2 Activation and dissipation of inclusions

As said previously, the probabilistic behavior is taken into account into the distribution of the transformation yield stress of inclusions. For this, a Point Poisson Process (PPP) is used [7, 8]

$$N(\sigma_{max}) = \lambda V \quad (26)$$

with N the quantity of active inclusions (i.e., with a transformation yield stress σ_0 lower or equal to the maximum stress, σ_{max}) in the considered domain of volume V , and λ the mean density of active inclusions. The evolution of this mean density with maximum stress is assumed to be a power law

$$\lambda(\sigma_{max}) = \frac{1}{V_0} \left(\frac{\sigma_{max}}{S_0} \right)^m \quad (27)$$

with m and $V_0 S_0^m$ two material parameter or set of parameters.

Then, the quantity of inclusions with a transformation yield stress of σ_0 can be expressed as the derivation of the quantity of active inclusions for a maximum stress σ_{max} equal to the transformation yield stress

$$N'(\sigma_0) = \left. \frac{dN}{d\sigma_{max}} \right|_{\sigma_{max}=\sigma_0} \quad (28)$$

The density of inclusions with a transformation yield stress of σ_0 is then

$$\lambda'(\sigma_0) = \left. \frac{d\lambda}{d\sigma_{max}} \right|_{\sigma_{max}=\sigma_0} \quad (29)$$

In order to obtain the total dissipated energy, we have to integrate the dissipated energy of the total population of inclusions versus their transformation yield stress. The total dissipated energy for inclusions with a transformation yield stress of σ_0 is the dissipated energy for one inclusion with this transformation yield stress, $D_i(\sigma_0)$ (expressed in equation 25) multiplied by the quantity of inclusion with this transformation yield stress, $N'(\sigma_0)$

$$D = \int_{\sigma_0=0}^{\infty} D_i(\sigma_0) N'(\sigma_0) d\sigma_0 = \int_{\sigma_0=0}^{\infty} D_i(\sigma_0) \lambda'(\sigma_0) V d\sigma_0 \quad (30)$$

Using equation 25, we obtain

$$D = \frac{\delta V}{CV_0 S_0^m (m+1)} \left((\delta + \sigma_{min} - \gamma C)^{m+1} - (\delta + \sigma_{min})^{m+1} - (\sigma_{max} - \gamma C)^{m+1} + \sigma_{max}^{m+1} \right) \quad (31)$$

As γC (stress increase during the plateau) is very low for NiTi, this equation can be simplified using a Taylor decomposition as

$$D = \frac{\delta V \gamma}{V_0 S_0^m} (\sigma_{max}^m - (\delta + \sigma_{min})^m) \quad (32)$$

3.3 Description of self-heating curves

The heat conduction equation on a specimen is given by

$$\begin{aligned} \rho C_\alpha \left(\dot{\theta} + \frac{\theta}{\tau_{eq}} \right) = & -f_v \rho \frac{\partial \psi^i}{\partial \epsilon^{tr}} : \dot{\epsilon}^{tr} - f_v \rho \frac{\partial \psi^i}{\partial H} \dot{H} + f_v \rho T \frac{\partial^2 \psi^i}{\partial T \partial \epsilon^{tr}} : \dot{\epsilon}^{tr} \\ & + f_v \rho T \frac{\partial^2 \psi^i}{\partial T \partial H} \dot{H} + f_v \rho T \frac{\partial^2 \psi^i}{\partial T \partial \epsilon} : \dot{\epsilon} + (1 - f_v) \rho T \frac{\partial^2 \psi^m}{\partial T \partial E} : \dot{E} \end{aligned} \quad (33)$$

with τ_{eq} the characteristic time of the specimen and f_v the volume fraction of inclusions.

If we integrate this equation on a thermodynamic cycle, the temperature elevation, θ , becomes the mean cycle temperature elevation, θ_{cycle}^{0D} , the coupling terms become zero, and the dissipation terms become the cyclic dissipated energy D multiplied by the loading frequency, f_r

$$\rho C_\alpha \left(\dot{\theta}_{cycle}^{0D} + \frac{\theta_{cycle}^{0D}}{\tau_{eq}} \right) = f_v f_r D \quad (34)$$

And since self-heating tests represent the stabilized mean cycle temperature elevation, we can just consider the stabilized solution of this equation

$$\frac{\rho C_\alpha}{\tau_{eq}} \bar{\theta}_{cycle}^{0D} = f_v f_r D \quad (35)$$

And, using equation 32, as a function of the maximum stress, σ_{max}

$$\bar{\theta}_{cycle}^{0D} = \frac{f_v f_r \tau_{eq} \delta V \gamma}{\rho C_\alpha V_0 S_0^m} (\sigma_{max}^m - (\delta + \sigma_{min})^m) \quad (36)$$

Since δ has already been identified on macroscopic behavior curves (see table 1), and σ_{min} is constant, there is only two parameter or set of parameters to identify: m and $\frac{f_v f_r \tau_{eq} \delta V \gamma}{\rho C_\alpha V_0 S_0^m}$. Their values are presented in table 3.

Table 3: Identified parameters of the self-heating model.

$\frac{f_v f_r \tau_{eq} \delta V \gamma}{\rho C_\alpha V_0 S_0^m} (\text{K} \cdot \text{MPa}^{-m})$	$m (-)$
6.23×10^{-19}	6.31

The self-heating curve is compared to the experimental one on figure 5 with, in orange, the simulated self-heating curves plus or minus the precision error of the thermal measurements with the infrared camera (± 25 mK).

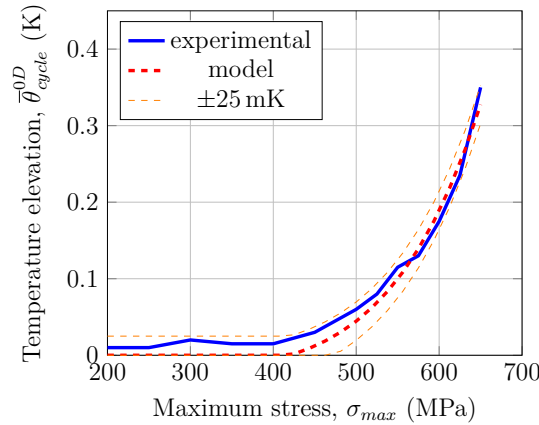


Figure 5: Temperature elevation versus maximum stress, with parameters identification.

3.4 Prediction of fatigue properties

Assuming that the inclusion activation governs the physical process of fatigue initiation, the developed self-heating model can then be used to predict the fatigue properties of the material.

In order to determine the fatigue life of the material from the model, a fatigue criterion is also needed. For our material, it is assumed that failure initiation occurs when a given critical energy, E_c is dissipated in an inclusion. As dissipated energy is constant between each stabilized cycles, the critical energy can be expressed in function of the number of cycles to failure, N , and the dissipation in the inclusion, D_i

$$E_c = N(\sigma_{max}, P_F) D_i(\Sigma_\infty(P_F)) f_v V \quad (37)$$

where the dissipation can be expressed as

$$D_i(\Sigma_\infty(P_F)) = \frac{\delta}{C} (\sigma_{max} - \Sigma_\infty(P_F)) \quad (38)$$

with $\Sigma_\infty(P_F)$ the fatigue limit for a given probability of failure

$$\frac{\ln(1 - P_F)}{\ln(1 - 1/2)} = \left(\frac{\Sigma_\infty(P_F)}{\Sigma_\infty(1/2)} \right)^m \quad (39)$$

and $\Sigma_\infty(1/2) = \bar{\Sigma}_\infty \frac{\ln(2)^{\frac{1}{m}}}{\Gamma(1 + \frac{1}{m})} \approx \bar{\Sigma}_\infty = \bar{\Sigma}_\infty^{sh}$.

The number of cycles to failure is then

$$N(\sigma_{max}, P_F) = \frac{E_c C}{f_v V \delta (\sigma_{max} - \Sigma_\infty(P_F))} \quad (40)$$

with parameter $\frac{E_c C}{f_v V \delta}$ identified using number of cycles to failure of highest maximum stress loading.

The corresponding curves are plot and compared to experiment results on figure 6. We can observe a very good agreement between classic fatigue tests results and probability curves determined with self-heating tests and modeling.

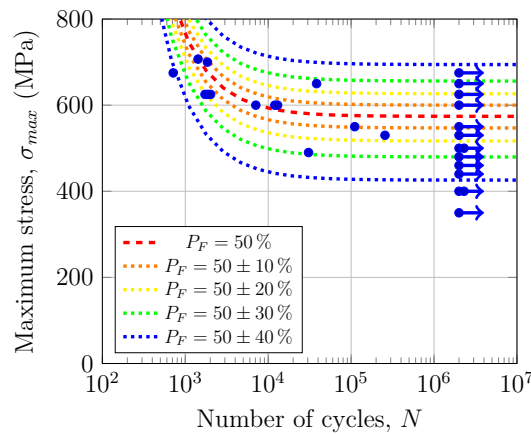


Figure 6: Expected maximum stress versus number of cycles to rupture curves with several probability of failure.

4 CONCLUSION

In this paper we describe a method that permits to determine the fatigue properties of NiTi shape memory alloys (mean endurance limit and SNP curves). The benefits of this method are that it only need one sample and results can be obtained in a few hours of tests and post-processing of data, when classic fatigue method would require at least a month of continuous testing. The method is based on a self-heating test and a dedicated modeling of self-heating that permits to identify material parameter m and to relate the number of cycles to failure to the loading maximum stress, the probability of failure and the critical energy.

A validation of the method has been realized by comparing its results from two types of NiTi SMA samples with results of classic fatigue tests.

REFERENCES

- [1] Patoor, E., Berveiller, M., Jun. 1994. Technologie des alliages à mémoire de forme. Traité des nouvelles technologies série matériaux. Hermes Science Publications.
- [2] Doudard, C., Calloch, S., Cugy, P., Galtier, A., Hild, F., Mar. 2005. A probabilistic two-scale model for high-cycle fatigue life predictions. *Fatigue & Fracture of Engineering Materials & Structures* 28 (3), 279–288.
- [3] Munier, R., Doudard, C., Calloch, S., Weber, B., Jun. 2014. Determination of high cycle fatigue properties of a wide range of steel sheet grades from self-heating measurements. *International Journal of Fatigue* 63, 46–61.
- [4] Gall, K., Sehitoglu, H., Chumlyakov, Y. I., Kireeva, I. V., Dec. 1998. Pseudoelastic cyclic stress-strain response of over-aged single crystal Ti-50.8at%Ni. *Scripta Materialia* 40 (1), 7–12.
- [5] Orgéas, L., Favier, D., Sep. 1998. Stress-induced martensitic transformation of a NiTi alloy in isothermal shear, tension and compression. *Acta Materialia* 46 (15), 5579–5591.
- [6] Saint-Sulpice, L., Arbab Chirani, S., Calloch, S., May 2012. Thermomechanical cyclic behavior modeling of Cu-Al-Be SMA materials and structures. *International Journal of Solids and Structures* 49 (9), 1088–1102.
- [7] Gulino, R., Phoenix, S. L., Jun. 1991. Weibull strength statistics for graphite fibres measured from the break progression in a model graphite/glass/epoxy microcomposite. *Journal of Materials Science* 26 (11), 3107–3118.
- [8] Jeulin, D., 1991. Modèles morphologiques de structures aléatoires et de changement d'échelle. Ph.D. thesis, Université de Caen.
- [9] Weibull, W., 1951. A Statistical Distribution Function of Wide Applicability. *Journal of Applied Mechanics* 18, 293–297.
- [10] Hild, F., Billardon, R., Marquis, D., 1992. Hétérogénéité des contraintes et rupture des matériaux fragiles. *Comptes rendus de l'Académie des sciences de Paris, série II* 315, 1293–1298.
- [11] Euler, L., 1738. On transcendental progressions, that is, those whose general terms cannot be given algebraically. *Commentarii academiae scientiarum Petropolitanae* 5 (1730/1), 36–57.

Sensors integrated inside metal castings verified to respond to force

Raul Carlsson^{□*}, Andreas Thore[□], Lennart Elmquist[□], Christer Johansson[†], Fredrik Ahrentorp[†], Vincent Schaller[†], Pontus Johannisson[†], Björn Israelsson^{*}, Magnus Törnvall^{*}, Patrik Zander[♦]

[□]RISE SWECAST

P.O. Box 2033, SE-550 02 Jönköping, Sweden

e-mail: raul.carlsson@ri.se*, andreas.thore@ri.se, lennart.elmquist@ri.se, www.ri.se

[†]RISE Acreo

P.O. Box 53071, SE-400 14 Göteborg, Sweden

e-mail: christer.johansson@ri.se, fredrik.ahrentorp@ri.se, vincent.schaller@ri.se,
pontus.johannisson@ri.se, www.ri.se

^{*}SKF Mekan AB

P.O. Box 89, 641 21 Katrineholm, Sweden

e-mail: bjorn.israelsson@skf.com, www.skf.com

[♦]Husqvarna AB

Drottninggatan 2, 561 31 Huskvarna, Sweden

e-mail: magnus.tornvall@husqvarnagroup.com, www.husqvarnagroup.com

Key words: sensors, material integrated, metal castings, extreme temperatures, static force, dynamic force

Abstract. We have developed a method to integrate sensor functionality into metal castings during the casting process. The method allows for cost efficient total integration into the foundry production process, for both iron and aluminium castings. The sensors are added to the casting mould before the molten metal is poured into the mould. Several sensor functionality tests have been performed on the resulting cast metal component. Tests verify that the signals from the integrated sensor have a clear relationship to static or dynamic forces applied to the castings. Tests also indicate that the integrated sensors do not have significant effects on the mechanical properties of the castings, though this need to be tested for each new application. It is expected that specific guidelines for integrated sensor may need to be developed. Our method has advantages compared to both after mounted sensors and more advanced sensors, particularly with regards to cost and robustness, but particularly since they allow for integration in high scale serial production. Hereby these integrated sensors enable any piece of cast metal to be equipped with sensors, which in practice establishes sensor equipped cast metal as an innovation platform for digital business innovation on and for metal components.

The development has been achieved as a spearhead innovation and development project (Smart castings, Dnr 2017-01973) between the RISE - Rise Research Institutes of Sweden, Husqvarna and SKF, with financial support from Vinnova - Sweden's innovation agency.

1 INTRODUCTION

This paper presents the verification of a uniquely new method to integrate sensor functionality into metal castings during the casting process. The verification and method is based on our previous reported work [1-3]. The method allows for cost efficient total integration of sensors into the casting during the foundry casting process while the metal is liquid, in both iron and aluminium castings.

The goal has been to achieve effective and robust digitally active cast metal components, that are low weight and cost efficient. The technology has many potentials, including effective contributions to several of the UN sustainability goals, as well as allows for a revolution of metal-based industry, and for entirely new and widespread applications for embedded robust and cost-efficient sensor systems in machinery, equipment and constructions.

The advantages of adding sensors during the casting, compared to both after mounted sensors and more advanced sensors, regards not only cost and robustness, but particularly because the technology allows for integration in high scale serial production. Hereby these integrated sensors enable any piece of cast metal to be equipped with sensors. In practice this establishes sensor equipped cast metal as an innovation platform for digital business innovation on and for metal components, and not only an innovation in itself.

Technically a full sensor system consists of several subsystem including both the sensor itself as well as signal amplification, filtering and signal analysis in order to obtain the total output signal (see figure 1). The sensor element (sensor material) reacts on an external stimulus (e.g. force) that can be measured using an appropriate sensor method. In order to obtain the total output signal the raw sensor signal generally needs to be amplified and filtered, as well as be processed by some signal analysis (e.g. calibration).

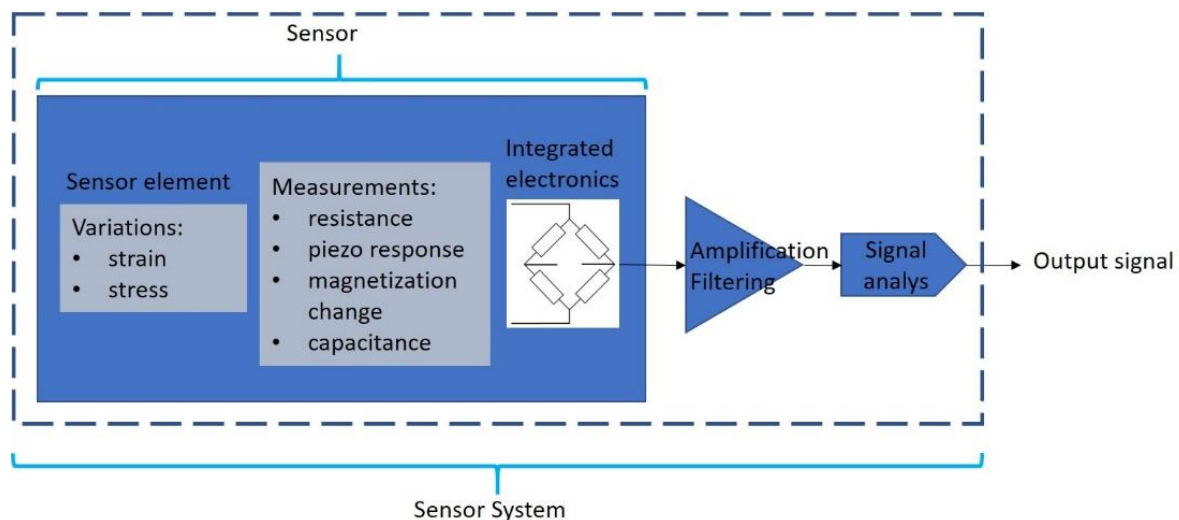


Figure 1: Schematic picture of full sensor system showing the sensor element (including the sensor element and integrated electronics in case of active sensors) and amplification, filtering and signal analysis in order to obtain the total sensor output signal.

In order to measure mechanical properties such as force and strain in metal systems several sensor methods can be used, such as strain gauges, fiber-optics, magnetoelastic and piezoelectric sensors.

Commercial products and previous studies have shown integrated sensors in metal parts after production of the metal parts, for instance of measuring tension in bolts using commercial strain gauge sensors [4] and using piezo-sensors in rock-bolts [5]. Some sensors have been implemented in production processes in ultrasonic 3D printing of the metal parts and, in this case, using fiber-optics [6] for monitoring force and strain. Of course there are sensor methods to monitor the mechanical state by measuring from outside the metal to inside of the metal using no integrated metal parts in the cast metal, i.e. non-destructive evaluation methods (NDE), for instance using eddy-currents [7], or acoustic resonance spectroscopy (ARS) [8] or acoustic emission (AE) [9], but in these cases it is hard to exactly know from where the signal originates from the metal part, as compared to integrated sensor elements at a specific positions and orientations.

To succeed with actually integrating a sensor system in a casting metal during the high temperature casting process (ca 650 C° for aluminium and ca 1500 C° for iron) it is only the sensor element (i.e. sensor material) that can be integrated in the casting metal. The electronics and signal analysis are instead placed outside the cast metal, after the casting and its post-processing is completed. This is the key to this innovative technology. In this paper we present how we have verified that this innovative technology also works in practice, by summarizing how we have developed and verified it.

The work has been achieved as a spearhead innovation and development project between the RISE - Rise Research Institutes of Sweden, and the companies Husqvarna and SKF, with financial support from Vinnova - Sweden's innovation agency.

2 PRINCIPLE

Figure 2 presents a schematic picture of the prototype system together with the integrated thread and its dimensions.

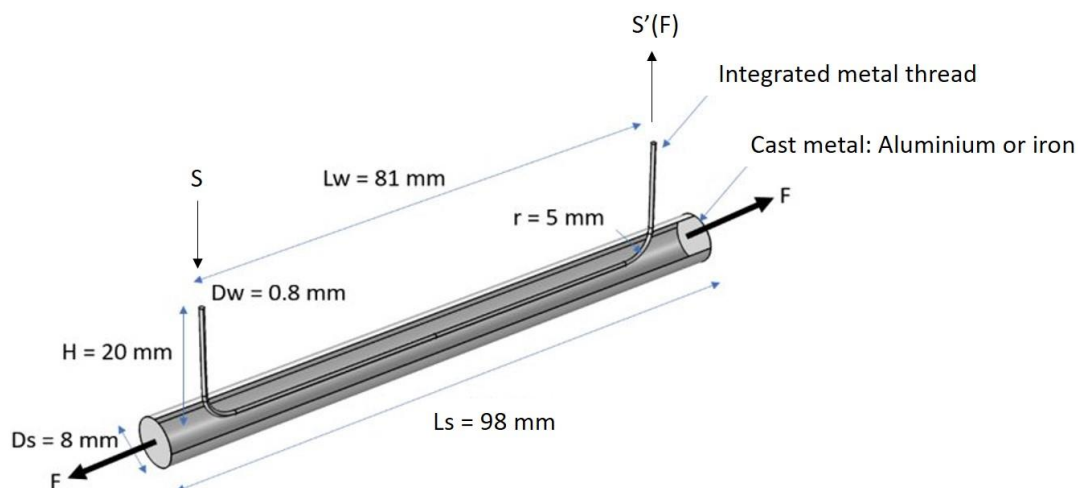


Figure 2: Schematic picture of the integrated metal thread in the aluminium or iron cast metal. The dimensions of the circular part of the prototype and the metal thread are also shown in the figure. The prototypes were

mounted in a tensile testing system that creates a force (F) on the prototype. In the end and start of the above shown cylindrical part of the prototype, mounting parts to the tensile testing system was also constructed (part in the casting process). The signal S is actuated into the metal thread and the resulting force dependent signal $S'(F)$ is measured.

The general approach is to create internal solidified structures for both sensing and traversing sensor signals. Such structures may be introduced as threads of gradually deviating material integrated during the casting process, or as identifiable boundaries between differently solidified areas that are either induced or that naturally arise during the casting process within the cast metal structure. The signal S is any physically induced signal appropriate for the combination of choices of cast metal and thread material and of the application. It is not necessary that S and $S'(F)$ are at opposite ends of the thread. $S'(F)$ may as well be the reflected signal. In this paper we show how we have verified that this simple approach has a technologically large potential. This will enable cast metal components to provide data about e.g. the component's elongation, shear, temperature and vibrations, with purpose to monitor and control systems based on one or several of these components.

3 METHODS

3.1 Metal casting and sensor integration

The sensors are added to the casting mould before the molten metal is poured into the mould. Metallurgical and mechanical tests indicate that the integrated sensors do not have significant effects on the properties of the castings, though this need to be tested for each new application. It is expected that specific guidelines for integrated sensor may need to be developed.

Metal threads are integrated in the casting prototypes during the casting process. The choice of integrated metals was chosen from the melting temperature of the casting material relative to the metal threads. Further, the metal threads were placed in the centre of the prototype and the thread was sticking out a few cm from the cast metal on each side of the integrated thread to be used for actuation and oscillation detection of the threads. Figure 3 shows a set of 12 aluminium prototypes while still in the 3D-printed sand mould, all equipped with different threads of different materials and different casting/thread properties to be tested.



Figure 3: Photo of a set 12 prototype castings with different integrated threads, not yet taken out of the 3D-printed sand mould and rinsed from excessive material.

3.2 Actuation and measurement system

From one side of the integrated metal thread (S in Figure 2) the thread was actuated with mechanical sinusoidal oscillations within a specific frequency range that creates elastic oscillations in the mechanically coupled cast and metal thread system. On the other outer part of the thread from the cast metal (S'(F) in Figure 2) we detected the amplitude of oscillations by a dedicated detection unit that was specially developed in the project. The signals from the detection unit was measured with a lock-in amplifier (LIA) that used the actuating oscillation frequency as a reference signal (see figure 4). The prototypes were mounted in a tensile testing system, so it was possible to subject the casting metal/integrated metal thread system with different forces (F). At sequentially applied force steps the amplitude distribution over a frequency spectrum around the actuation frequency were detected by the Detection unit and the frequency at the peak amplitude was logged.

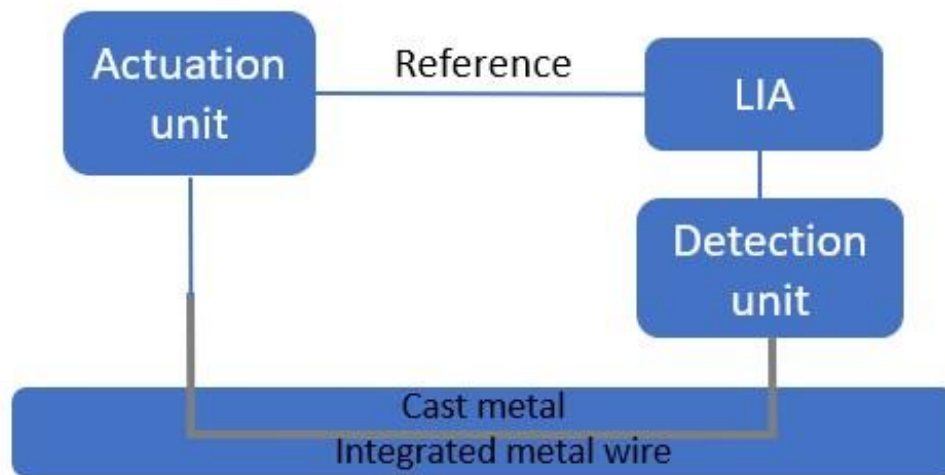


Figure 4: The different parts in the measurement unit to actuate and sense the oscillations of the cast metal and integrated metal thread. The actuation unit and the lock-in-amplifier (LIA) are all controlled by a computer (Labview program).

Furthermore, the developed measurement system was correlated with a laser doppler vibrometer (LDV) system and we found similar result when comparing with the measurement system.

4 RESULT AND DISCUSSION

In Figure 5 oscillation amplitude versus frequency of the aluminium and iron cast metal can be seen at different applied forces to the cast metal system.

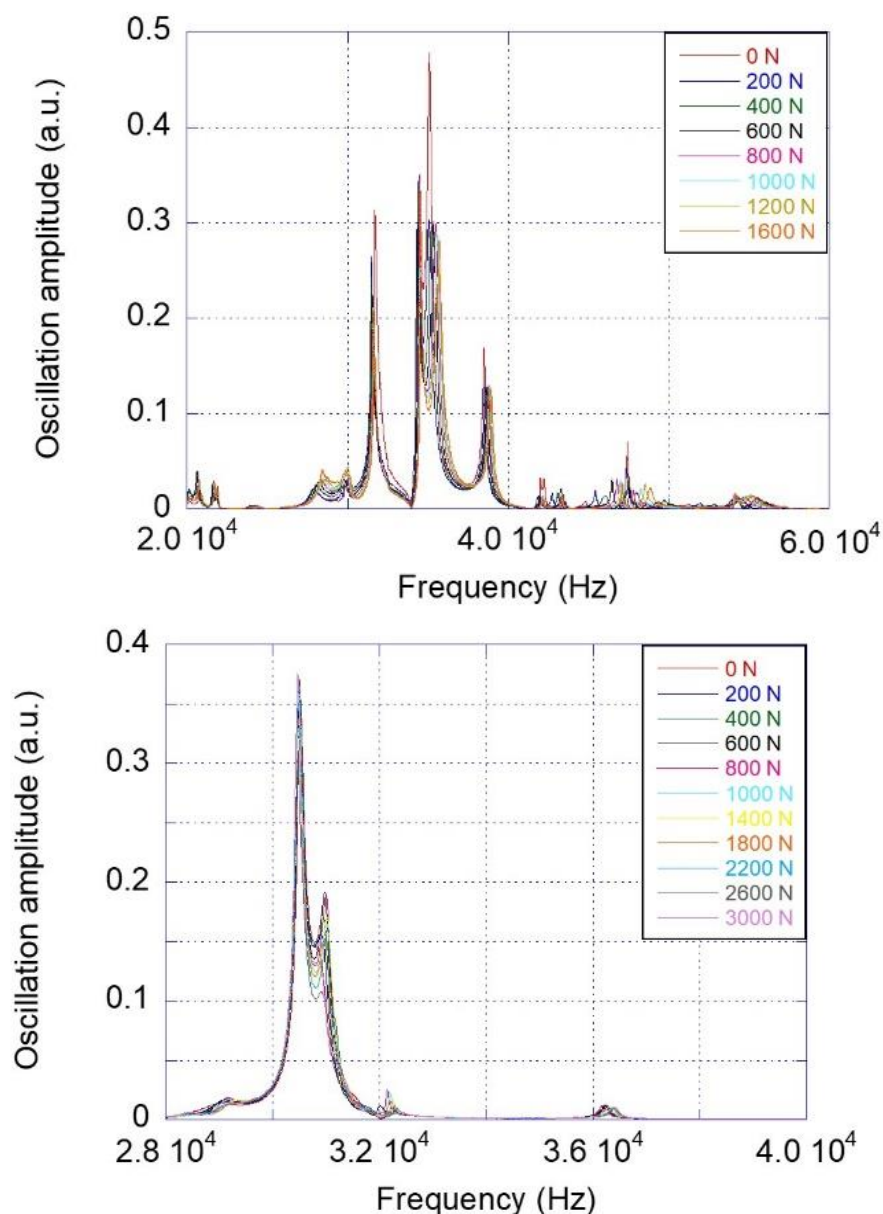


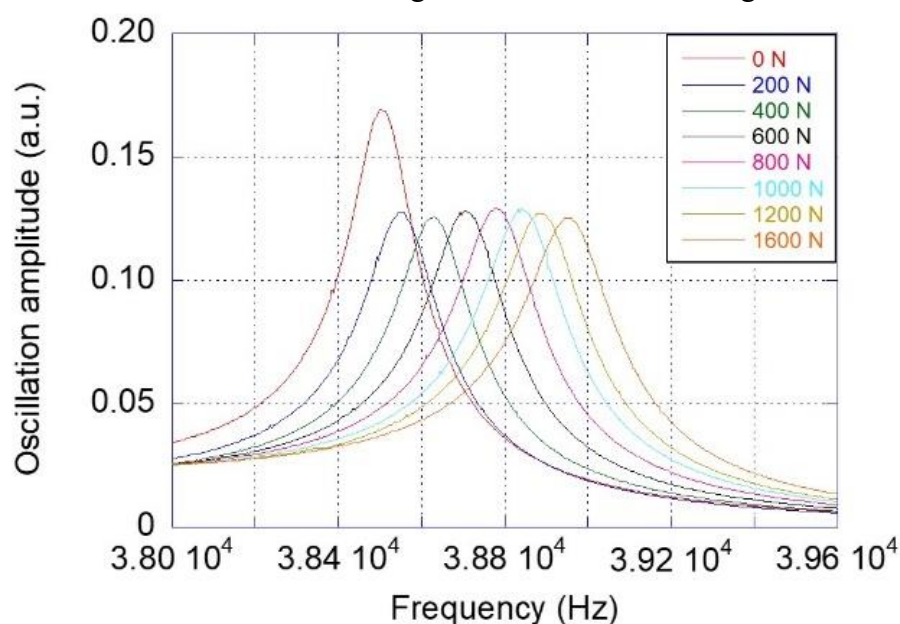
Figure 5: Oscillation amplitude versus excitation frequency for aluminium casting (top) and the iron cast metal (below) at different applied forces to the prototypes (as listed in the legends). The figure shows the spectra were all of the resonance peaks are located in the frequency plane. At lower and higher frequencies compared to the frequencies shown in the figures, no resonance peaks could be found for both aluminium and iron cast metal.

As can be seen in figure 5 at specific frequencies there is an increase in the oscillation amplitudes that is due to mechanical resonances and also that the coupled system cast metal and integrated metal thread, shows a very complex shaped mechanical resonance spectrum. The obtained resonance frequencies at zero applied force correspond somewhat to the frequencies of standing waves in the prototype, using the sound velocities of the cast metal (longitudinal and transversal sound velocities) and wavelengths that corresponds to multiples of the length of the prototype. However, as seen in Figure 3 the resonance frequencies are not evenly spread

in the frequency plane that have been expected if it was an ordinary standing wave phenomenon in the prototype systems.

We noted the similarities between these resonance frequency spectrums and the resonance frequency spectrums of Acoustic Resonance Spectrums (ARS) [8]. We therefore performed experimental tests with discontinual threads (i.e. the thread is cut off inside of the casting, disconnecting the two ends of the integrated thread from each other by a gap that contains only the cast metal) not traversing complete through the cast metal. These results showed that the resonance spectrums were damped in oscillation amplitude as well as constituted by a very different resonance spectrum indicating that the integrated metal thread enhance the resonances and probably that the induced elastic waves is somewhat concentrated to the integrated metal thread. These verifications are not presented in this paper.

When we zoom in on the resonance spectra around 38.4 kHz for the aluminium cast metal and around 36.2 kHz for the iron metal casting the result is shown in Figure 6 and Figure 7.



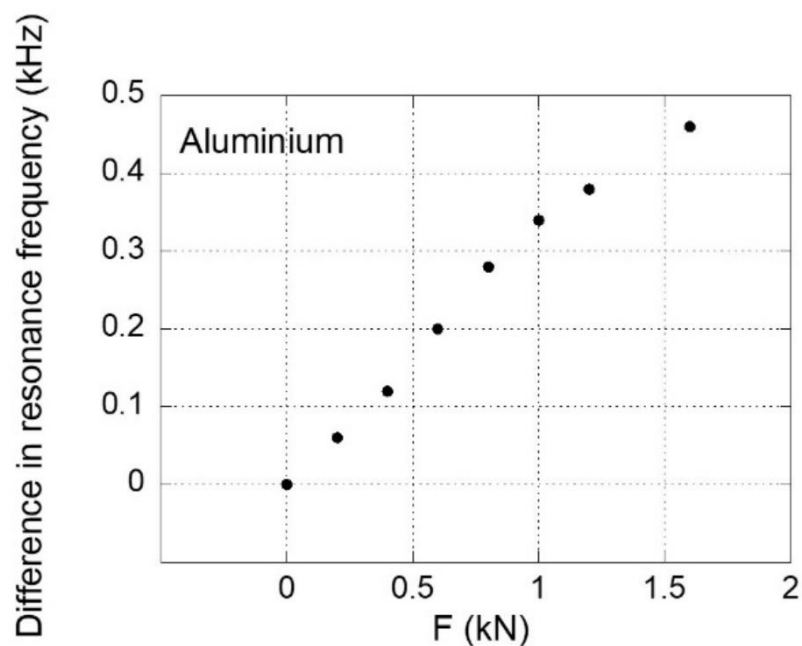
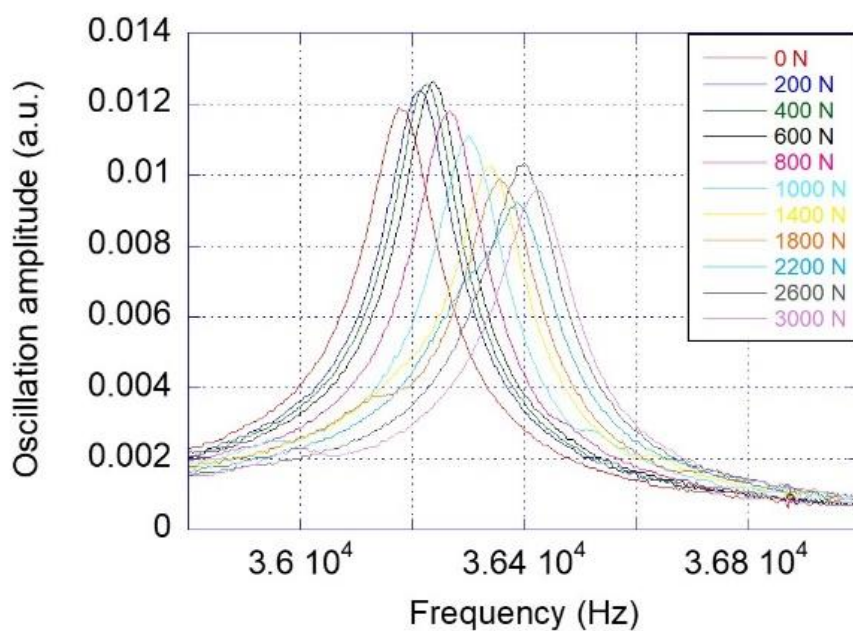


Figure 6: Oscillation amplitude versus excitation frequency for the aluminium casting (top) around frequencies of 38.4 kHz and the difference in resonance frequencies relative to the resonance frequency at zero force (below) at different applied forces (listed in the legend). The resonance frequency is defined as the frequency where the oscillation amplitude peaks.



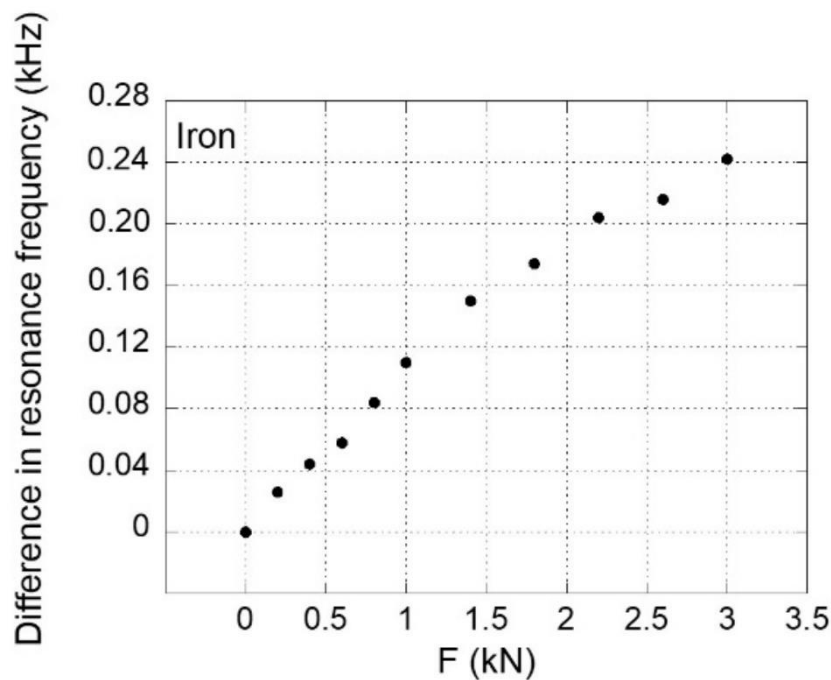


Figure 7: Oscillation amplitude versus excitation frequency for the iron casting (top) around frequencies of 36.2 kHz and the difference in resonance frequencies (relative to the resonance frequency at zero force) (below) at different applied forces (listed in the legend). The resonance frequency is defined as the frequency where the oscillation amplitude peaks.

As can be seen in Figure 6 and Figure 7 the resonance frequency increases with applied force for both aluminium and iron cast metal, in a linear behaviour at low forces and a slight non-linear behaviour at higher forces. The resonance frequency change for a specific force change in the linear range is larger for aluminium than compared to iron casting (0.34 kHz/kN for aluminium and 0.1 kHz/kN for iron), which scales almost to the inverse of the elastic modulus for respective cast material (60 GPa for aluminium and 200 GPa for iron). Further, the onset of the non-linearities occurs at lower forces for aluminium than compared to the iron cast metal. In fact, the non-linearities starts at lower forces when comparing to the onset of the non-linearities in the stress-strain curves for respective prototype system. The large amount of increase in resonance frequency when the force is increased cannot be explained by just studying the relative length change of the prototype (i.e. the obtained strain from the applied stress divided with the elastic modulus) and also that the resonance frequency increases for increasing applied forces. From modelling of the prototype (force applied to a cylinder performing transversal oscillations) and Finite-Element (FE) analysis of the prototype we have obtained a linear increase in resonance frequency when increasing the applied force but the change in resonance frequency per applied force is much lower than compared to the experimental obtained values. This can probably be explained by that the change in resonance frequency when the force is applied, is enhanced by the integrated metal thread and that several resonance modes take part in the total resonance process.

At the moment of writing this we are working with decreasing the measurement time using optimal pulsed actuation, continuing the FE analysis in order to understand the resonance

phenomena in more detail and also how to develop the sensing system in more complex casting structures. In this spirit we have implemented the sensing system in an aluminium prototype cast component of a Husqvarna AB product, see Figure 8. Measurements on this cast metal component is in progress.

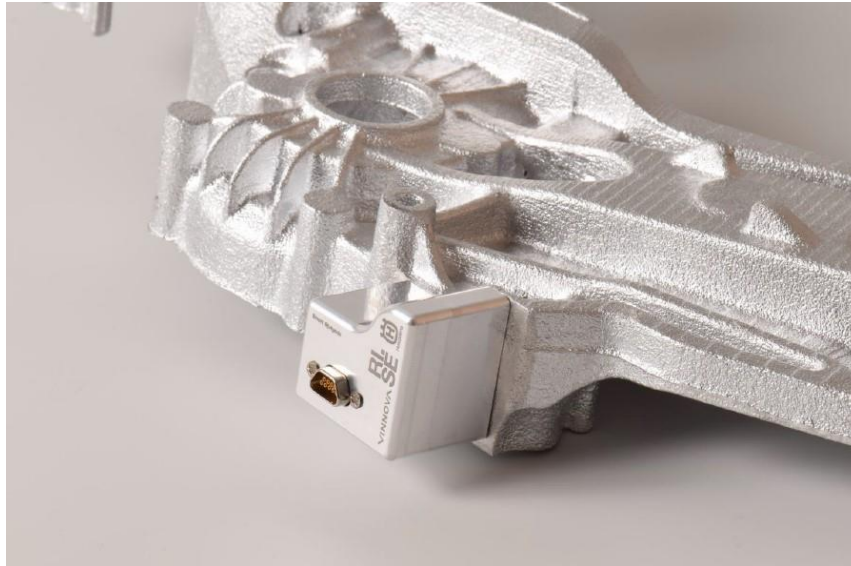


Figure 8: Implementation of the sensing system where the actuation and detection unit are integrated in the chassis that is connected to the cast metal product.

5 CONCLUSIONS

We have shown that it is possible to integrate metal threads during the cast metal process that together with the host cast metal can be used in a sensing system for measuring mechanical forces in cast metal systems. From the experimentally obtained resonance spectra we have seen that in some parts of the spectrum the change in resonance frequency correlates well with the applied force and can be used to monitor the force in the prototype. Analyzing all measurements presented in figures 5 to 7, the theoretical modelling and the measurements made with a discontinual thread, we believe that we have verified that the large shift in resonance frequency to the applied force shown in figures 5 to 7 is likely to result from the integrated metal thread.

REFERENCES

- [1] Carlsson, R., Elmquist, L., Johansson, C., Cast metal with intelligence – from passive to intelligent cast components, Conference: *VIII ECCOMAS Thematic Conference on Smart Structures and Materials SMART 2017*, Madrid, Spain, June 2017
- [2] Elmquist, L., Carlsson, R., Johansson, C., Cast Iron Components with Intelligence, Conference Proceedings of *11th International Symposium on the Science and Processing of Cast Iron (SPCI-XI)*

- [3] Carlsson, R., Elmquist, L., Thore, A., Ahrentorp, F., Johansson, C., Israelsson, B., Connecting sensors inside smart castings *7th edition of the International Symposium on Air/Craft Materials (ACMA)*, 24-26 April, 2018, Compiègne, France
- [4] For instance see <https://www.hbm.com/tw/7452/lb11-strain-gauge-for-measuring-within-screws-and-bolts/>.
- [5] Huo L., Wang B., Chen D. and Song G., Monitoring of Pre-Load on Rock Bolt Using Piezoceramic-Transducer Enabled Time Reversal Method. *Sensors* 2017, 17, 2467.
- [6] Hehr A. Norfolk M., Wenning J, Sheridan J., Leser P., Leser P., Newman J.A., Integrating Fiber Optic Strain Sensors into Metal Using Ultrasonic Additive Manufacturing. *JOM*, Vol. 70, No. 3, 2018.
- [7] Dahia A., Eric Berthelot E., Bihan Y.L. and Daniel L., A model-based method for the characterisation of stress in magnetic materials using eddy current non-destructive evaluation, *J. Phys. D: Appl. Phys.* 48 (2015) 195002.
- [8] Sinha D.N., Acoustic resonance spectroscopy (ARS), *IEEE Potentials*, Volume: 11, Issue: 2, April 1992.
- [9] Tonolini F., Sala A., Villa G., General review of developments in Acoustic Emission methods, *International Journal of Pressure Vessels and Piping* Volume 28, Issues 1–5, 1987, Pages 179-201.

STUDY OF THE PSEUDOELASTIC DAMPING BEHAVIOUR OF THE FE-30MN-6SI-5CR SHAPE MEMORY ALLOY

M. MEGDICHE^{†*}, A. SALLAMI[†], F. THIEBAUD[†], T. BOURAOUT[†], T. BEN ZINEB[†]
AND S. A. CHIRANI[×]

[†]Laboratoire de Génie Mécanique (LGM)

Université de Monastir

Avenue Ibn El Jazzar, 5000 Monastir, Tunisie

e-mail: malekmegdiche@gmail.com-achref.sallami@enim.rnu.tn - tarak.bouraoui@enim.rnu

Web page: <http://hal.tn/PresentationSite.xhtml?labo=lgm>

[†]Laboratoire d'Étude des Microstructures et de Mécanique des Matériaux (LEM3)

Université de Lorraine, CNRS, Arts et Métiers Paris Tech 2 rue Jean Lamour, 54500, Vandœuvre lès
Nancy, France

e-mail: frederic.thiebaud@gmail.com - tarak.ben-zineb@univ-lorraine.fr

Web page: <http://www.lem3.univ-lorraine.fr>

[×]Institut de Recherche Dupuy de Lôme (IRDL)

UMR CNRS 6027

ENIB - Technopôle Brest-Iroise, CS 73862, 29238 Brest Cedex 3 –France

e-mail : arbab@enib.fr

Key words: Iron based Shape Memory Alloys (Fe-SMA), Pseudoelasticity, Dynamic Mechanical Analyzer (DMA), Heat Treatment.

Abstract. Since their discovery, Iron based Shape Memory Alloys (Fe-SMA) have attracted much attention of researchers and industrials thanks to their low cost and excellent workability combined to smart properties such as SME (Shape Memory Effect) and damping capacity [13] due to pseudoelasticity [7]. In this paper, the damping capacity of the Fe-30Mn-6Si-5Cr is investigated through pseudoelasticity characterization by cyclic tensile tests using a tensile machine and a Dynamic Mechanical Analyzer (DMA). Specimens underwent a specific heat treatment in order to improve their properties. At ambient temperature, the studied alloy can be found at different microstructures. In order to define the best alloy initial conditions guaranteeing maximum damping capacity, different types of the alloy microstructures were investigated: purely austenitic state and biphased states (austenite + stress induced and/or thermal martensite). Specimens were studied under different parameters such as vibration frequencies (0.1 Hz, 0.5 Hz, 1 Hz and 5 Hz), pre strain amount (4%, 8% and 14%) and stress amplitudes at different temperatures.

1 INTRODUCTION

High performance and low cost Fe-Mn-Si based alloys are known to be a prospective candidate in civil applications. When deformed, iron based Shape Memory Alloys (SMA) can recover their initial shape by simple heating until a strain amount of 2-4%. This behaviour, called the Shape Memory Effect (SME) [1] or the one way SME, is due to a martensitic transformation stress induced from parent phase austenite FCC (Face Centred Cubic) to

martensite HCP (Hexagonal Close Packed) that can be reversed by heating. In addition, this class of materials has been found to exhibit internal friction and thus have a noticeable damping capacity. These excellent properties combined to good mechanical properties, low cost and excellent workability [2] and weldability[3] made of iron based SMA a good alternative in civil applications.

Authors, with slight differences, have agreed that damping capacity in iron based SMA, arising from internal friction, is associated to $\varepsilon \rightarrow \gamma$ reverse transformation [4] and precisely to the reversible motion of ε/γ interfaces attributed to ε martensite and stacking faults in common [5] which is accomplished by the reversible movement of Shockley partial movement at the tip of the martensite variant[6]. It was also found that pseudoelasticity also called partial super-elasticity is attributed to the reversibility of the γ/ε transformations [7] by the reversible motion of Shockley partial dislocation [8-9]. Besides, some authors attributed it to the existence and formation of stacking faults and the reversible movement of their associated partial dislocations [10]. Thus, damping capacity for iron based SMA can be linked and resulting from pseudoelastic behavior of the material.

The present work aims to assess the damping behaviour arising from the alloy pseudoelasticity. Tensile sinusoidal loading unloading cycles were realised using an electro dynamic testing machine. Hysteretic loops area resulting were measured to characterize the damping behaviour of the studied alloy under different conditions.

The contribution targeted in this study is an optimization establishment of the Fe-30Mn-6Si-5Cr damping behaviour for civil purposes. In this context, and in order to define conditions guaranteeing good damping capacity at service conditions, test were realised under several parameters: Temperature (from ambient to 70 °C), frequency (0.2 Hz to 5 Hz), static pre-strain (4%, 8% and 12%) and stress amplitude.

In this paper, the material, experimental equipment and tests conditions will be described first. Then results and interpretation will be detailed.

2 MATERIAL AND METHODS

The studied alloy is the Fe-30Mn-6Si-5Cr an iron based shape memory alloy obtained from Awaji Company¹. Its precise chemical composition given in table 1 has been determined by an EDS (Energy Dispersive spectroscopy) analysis whose spectrum is illustrated in figure 1.

In order to guaranty a homogeneous austenite structure, the conventional heat treatment that iron based shape memory alloys are subjected to is a 1 hour annealing for 1 hour at 600°C followed by water quenching. When applied to the as received alloy, shape memory effect was not so good. Besides, its martensite start transformation temperature point is a bit low. In order to ameliorate these deficiencies, the alloy has been subjected to a 1 hour annealing at 1050°C followed by water quenching then a second annealing at 600°C for 30 min followed by an air quenching.

¹ AWAJI MATERIA CO., LTD.: a Japanese company with a capital of 80 million yen and specialized in shape memory alloys products manufacturing

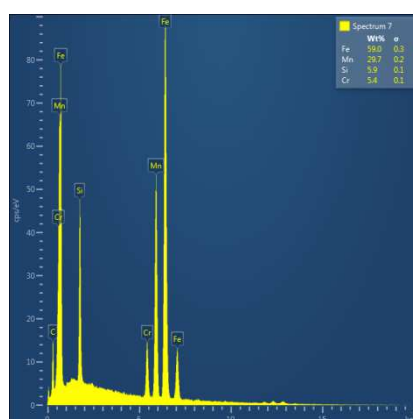


Figure 1.EDS spectrum of the alloy studied

Table 1. Chemical composition of the studied SMA iron based in weight percent

Element	Fe	Mn	Si	Cr
Wt (%)	59	29.7	5.9	5.4

Specimens of 1 mm thickness were cut by wire EDM (Electrical Discharge Machining). Their dimensions are as schematised in figure 2. They were subsequently heated for 30min at 600°C to eliminate any possible microstructure modification due to machining.

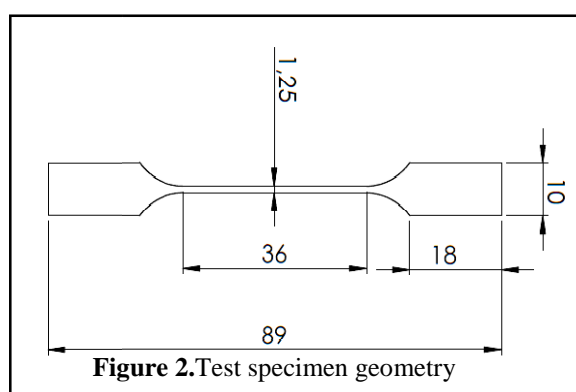


Figure 2.Test specimen geometry

Tests were realised using a Zwick/Roell LTM1 (1kN) electro dynamic testing machine equipped with a heating cell. As illustrated in figure 3, first phase is a tension loading until a strain percentage of 4, 8 or 12 at a strain rate of $10^{-4}.s^{-1}$. The second consists in 3 sets of 20 sinusoidal cycles of loading unloading between σ_{max} and 0MPa at a given frequency (0.2 Hz, 0.5Hz, 1Hz and 5Hz). In each set, σ_{max} is 100 MPa less than previous one. For example, for a tension loading rate of 4%: $\sigma_{max1} = 350MPa$, $\sigma_{max2}=250 MPa$ and $\sigma_{max3}=150 MPa$.In order to study the damping behaviour at service conditions, tests were done in a variety of temperature from ambient to 60 °C (20, 30, 40, 50 and 70°C).

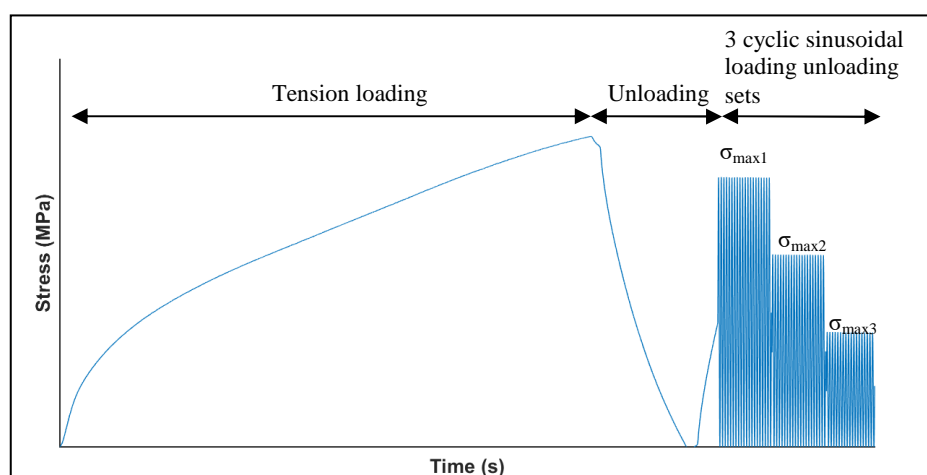


Figure 3. Test phases diagram

3 ANALYSIS CONCEPT

Among several metric characterization methods of damping capacity in literature, in this paper, the energy loss during loading unloading cycles [11] that is in our case revealed by hysteretic loops areas has been adopted. Therefore, we used this method in order to characterize the damping capacity of the studied alloy at different parameters. The loops area resulted during loading unloading cycles have been measured at each cycle in all tests. In fact, it represents the energy dissipated during loading unloading due to the alloy pseudoelasticity.

4 RESULTS AND DISCUSSION

4.1. EFFECT OF FREQUENCY

As illustrated in figures (4, 5 and 6), loops area decrease while cycling progressing up to a stable average of 75% of first loop area (frequency 0.2Hz and 0.5Hz in figure 4).

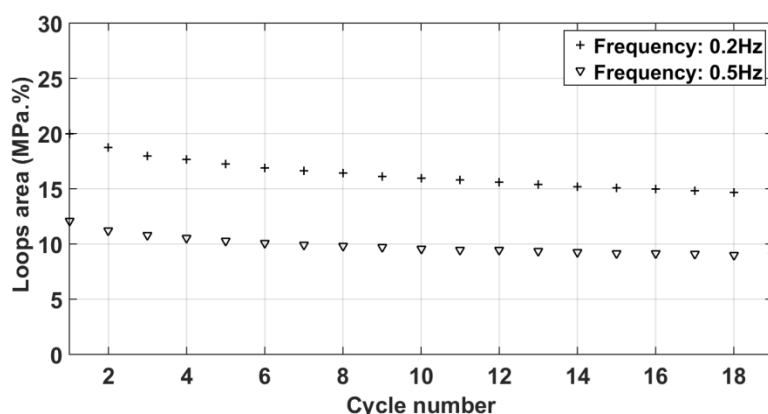


Figure 4. Loops area measures during 19 sinusoidal tension loading unloading (400 MPa) cycles at ambient temperature for 0.2 Hz and 0.5 Hz test frequency on 4% pre strained specimen

Cycling tests of tension loading unloading ($\sigma_{\max}=320$ MPa) performed on a 4% tensile pre strained specimen at ambient temperature with different frequencies: 0.2 Hz and 0.5 Hz showed respectively stabilised loops area values of 14.6 (MPa.%) and 9 (MPa.%). Hence, the frequency affects noticeably the damping behaviour of the alloy. It decreases with frequency increase.

4.2. EFFECT OF STRESS AMPLITUDE

Tests performed at 4% tensile pre strained specimen at ambient temperature and 0.5 Hz cycling frequency showed that loops area increase with stress amplitude increase. Tests with different stress amplitudes (350 MPa, 250 MPa, and 150 MPa) realised on the same specimen revealed that the loops area stabilised value is respectively 19, 4.3, and 0.5 (MPa.%) (see figure 5). Likewise, tests done separately with same frequency, pre strain and temperatures values with different stress amplitude showed that loops area value increases with stress amplitude: 19 and 21.5 (MPa.%) for respectively 400 MPa and 350 MPa (see figure 6).

In fact, when stress is above a critical value, the damping capacity of iron based shape memory alloys is coming from the breaking away of Shockley partial dislocations. Therefore, with the stress increasing, the amount of Shockley partial dislocations that possibly can break away from pinning points increases quickly, thus the alloy internal friction increases sharply [12]. Consequently, the damping behaviour is enhanced by stress amplitude increase as shown in figure 5 and 6.

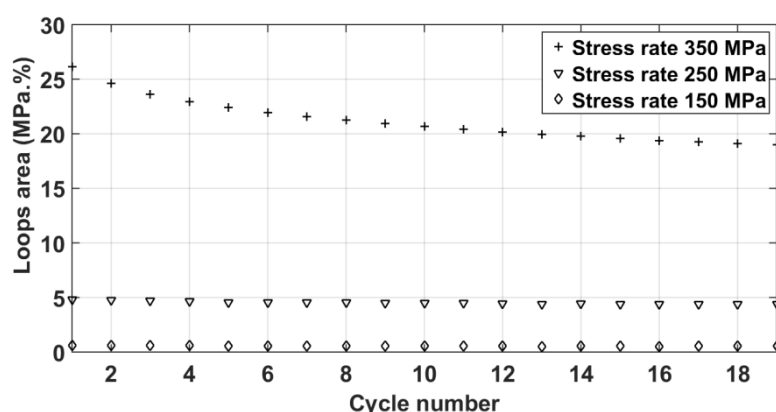


Figure 5. Loops area measures during 19 sinusoidal tension loading unloading cycles at ambient temperature for 0.5 Hz test frequency on 4% pre strained specimen with 3 stress amplitudes: 350 MPa, 250 MPa and 150 MPa during the same test (internal loops).

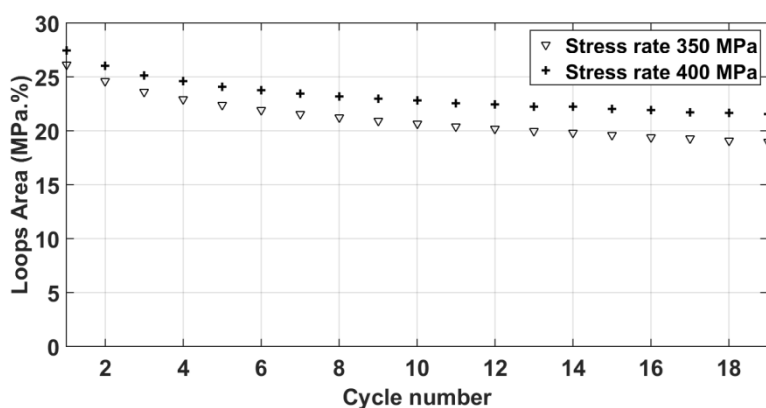


Figure 6. Loops area measures during 19 sinusoidal tension loading unloading cycles at ambient temperature for 0.2 Hz test frequency on separate specimens 4% pre strained at 2 stress amplitudes: 400 MPa and 350 MPa.

5 CONCLUDING REMARKS:

From this preliminary study, it was found that the pseudoelastic damping behaviour of the Fe-30Mn-6Si-5Cr assessed from loops area tensile cycles during dynamic test decreases until stabilizing at 75% of its first cycle value.

Furthermore, it increases considerably with cycles stress amplitude increase.

Moreover, it was clearly observed that frequency has a determinate impact on the damping behaviour of the studied alloy, it decrease obviously with frequency increase.

This preliminary study is been actually continuing experimentally with more details: frequencies higher, various microstructures and temperature influence and will be joined very soon. This study will allow setting an optimization of the pseudoelastic damping behaviour of the studied alloy.

5 REFERENCES

- [1] G. F. Lee, B. Hartmann, *Specific damping capacity for arbitrary loss angle*, Journal of Sound and Vibration 211(2), 265–272, U.S.A.(1998).
- [2] A. Baruj, G. Bertolino H.E. Troiani, *Temperature dependence of critical stress and pseudoelasticity in a Fe–Mn–Si–Cr pre-rolled alloy*, Journal of Alloys and Compounds 502 54–5 (2010).
- [3] A.Sato, E.Chishima, K.Soma,T. Mori, *Shape memory effect in γ/ϵ transformation in Fe–30Mn–1Si alloy single crystals*,Acta Metall;30:1177–83.(1982)
- [4] Kajiwar S., *Characteristic features of shape memory effect and related transformation behavior in Fe-based alloys*, Mater SciEngA 273–275:67–88.(1999)
- [5] H. Otsuka, *Fe–Mn–Si based shape memory alloys*, Mat Res Soc Symp Proc;246:309–(1992).

- [6] T. Sawaguchi, T. Kikuchi, F. Yin, S.Kajiware , *Internal friction of an Fe–28Mn–6Si–5Cr–0.5NbC shape memory alloy*, Materials Science and Engineering A 438–440 796–799, Japan(2006).
- [7] O. Matsumura, T.Sumii, N. Tamura, K. Sakao, T. Furukaw, H.Otsuka, *Pseudoelasticity in an Fe–28Mn–6Si–5Cr shape memory* Materials Science and Engineering A279 201–206(2000).
- [8] W.J. Lee, B. Weber, G. Feltrin, C. Czaderski, M. Motavalli, C. Leinenbach, *Phase transformation behavior under uniaxial deformation of an Fe-Mn-Si-Cr-Ni-VC shape memory alloy*, (2013).
- [9] C. Leinenbach, A. Arabi-Hashemi, W.J. Lee, A. Lis, H. Van Swygenhoven, *Characterization of the deformation and phase transformation behavior of VC-free and VC-containing FeMnSi-based shape memory alloys by in situ neutron diffraction*, (2017).
- [10] S.K. Huang, N. Lia, Y.H. Wen, J. Teng, S. Ding, Y.G. Xu, *Effect of Si and Cr on stacking fault probability and damping capacity of Fe–Mn alloy*, Materials Science and Engineering A 479 223–228, (2008).
- [11] A. Sato, Kozo Ozaki, Y. Watanabet and T. MORI, *Internal friction due to $\epsilon \rightarrow \gamma$ reverse transformation in an Fe-Mn-Si-Cr shape memory alloy*, Materials Science and Engineering A, 101, 25-30 25,(1988).
- [12] K.K. Jee, W.Y. Jang, S.H. Baik, M.C. Shin and C.S. Choi, *Damping capacity in Fe-Mn based alloys*, (1997)
- [13] Z. C. Zhou, C. E. Wen, H. Yang, and Y. J. Yan, *Low frequency damping capacity in a strained Fe–Mn–Si alloy*, Phys. Status Solidi., A 207, Vol. 2, pp. 338–343, (2010).

A ROBUST CALIBRATION PROCEDURE FOR MULTIPLE ELECTROMECHANICAL SHUNT ABSORBERS ON A FLEXIBLE STRUCTURE

JAN HØGSBERG

Department of Mechanical Engineering, Technical University of Denmark
DK-2800 Kongens Lyngby, Denmark, e-mail: jhg@mek.dtu.dk

Key words: Vibration damping, Electromagnetic and piezoelectric shunt damping, Smart Structures

Abstract. Electromagnetic (series) RC and piezoelectric (parallel) RL shunt damping can both be represented by an equivalent mechanical vibration absorber with a spring, dashpot and inerter in series. A common calibration procedure for these electromechanical shunt dampers is therefore obtained from this mechanical equivalence. It includes the influence from residual vibration modes of the flexible structure via an augmented modal representation of the absorber motion with two additional correction terms that are explicitly calibrated from the natural frequencies associated with fully locked absorber dashpots. Furthermore, the mechanical equivalence between the two shunt dampers implies that the electromagnetic shunt can be directly calibrated from principles derived for a piezoelectric shunt, and vice versa. The theory is expanded to multiple vibration absorbers targeting a single resonant vibration mode and the numerical examples demonstrate that accurate absorber calibration is obtained.

1 INTRODUCTION

Electromechanical transducers may be installed in vibrating structures to mitigate excessive dynamic response due to for example resonant loading by dissipation in supplemental shunts. For piezoelectric transducers, the concept of *RL* shunt damping was propelled by [1] and [2], analyzing and calibrating series and parallel *RL* shunts, respectively. Various calibration strategies for both series and parallel *RL* shunts have been derived based on different optimization criteria [3, 4, 5]. The electromechanical coupling effect is also available in electromagnetic transducers, for which calibration of a series *RC* shunt has been a recent research problem [6, 7, 8].

In several cases the calibration of electromagnetic series *RC* shunts has been based on the calibration principles by [1] for piezoelectric series *RL* shunts. However, as demonstrated in the present paper, a mechanical analogy instead exists between the electromagnetic series *RC* and the parallel *RL* shunt for piezoelectric transducers. And therefore a common calibration procedure for these two electromechanical systems is provided. Initially, the governing equations for electromagnetic and piezoelectric shunt damping are summarized and a common vibration absorber is proposed, with a spring, dashpot and inerter placed in series. Both electromechanical shunt dampers can therefore be consistently calibrated based on the tuning principles for the equivalent mechanical vibration absorber. The influence from the residual vibration modes of the flexible structure is represented by an augmented modal representation adopted from [9, 10], where the correction terms can be adjusted using the natural frequencies of the structure for infinite absorber damping. These limiting frequencies can be determined numerically or

even experimentally, and as demonstrated the correction procedure is accurate for multiple vibration absorbers acting on a flexible structure.

2 ELECTROMECHANICAL SYSTEMS

The mechanical properties of electromechanical transducers are in the following described with respect to a physical displacement (elongation) x across the apparent transducer terminals. For an electromagnetic transducer the displacement x directly represents the relative motion of the coil, with a force $f = K_m I$ proportional to the current I in the wire by the electromechanical coupling coefficient (motor constant) K_m . For a piezoelectric transducer, x represents the apparent deformation obtained by the integration of the corresponding strain over the effective transducer length and the force $f = K_p V$ is instead proportional to the voltage with K_p representing the effective coupling coefficient. In the following harmonic motion is assumed, with a temporal dependence represented by the factor $\exp(i\omega t)$, where i is the imaginary unit, ω is the angular frequency and t is time.

2.1 Electromechanical shunt damping

The aim of the shunt damping concept is to formulate a common resonant absorber format for electromagnetic and piezoelectric transducers. The transducer models contain intrinsic damping, represented by an equivalent resistor, whereby the resulting absorber damping is comprised of intrinsic and shunt contributions. The equivalent mechanical absorber model is shown in Fig. 1(a), with a spring k , viscous dashpot c and inerter m placed in series, whereby its mechanical flexibility relation can be written as

$$x = \left(\frac{1}{k} + \frac{1}{i\omega c} - \frac{1}{\omega^2 m} \right) f \quad (1)$$

As demonstrated in the following, the stiffness k and damping c are composed of contributions from both the transducer and the supplemental shunt, while the absorber inertance $m = m_s$ is entirely realized by the shunt. It is demonstrated that resonant shunts can be formulated for both electromagnetic and piezoelectric transducers that in theory retain the series absorber model in Fig. 1(a).

2.1.1 Electromagnetic transducer

The electrical load applied by the moving coil inside an electromagnetic transducer is represented by an alternating voltage source $V_m = i\omega K_m x$, proportional the velocity amplitude $i\omega x$ of the transducer

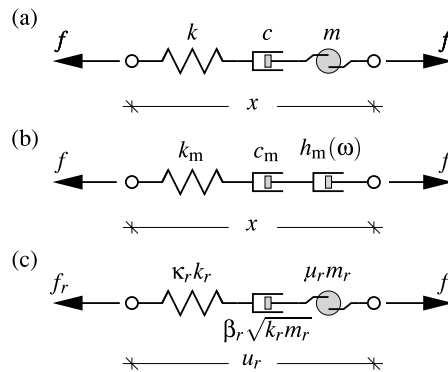


Figure 1: (a) Desired mechanical absorber, (b) electromagnetic shunt absorber and (c) effective modal absorber.

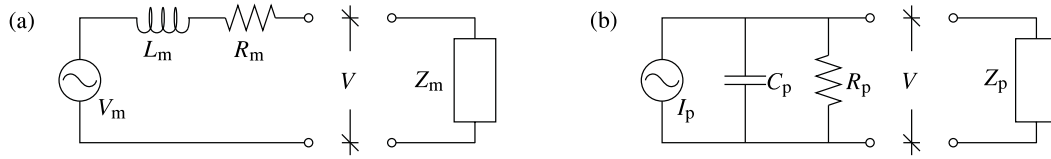


Figure 2: Electric network for (a) electromagnetic and (b) piezoelectric transducer with shunt $Z(\omega)$.

deformation. When the transducer terminals are shorted, the current I in the coil is governed entirely by its inherent electrical impedance, which can be represented by an inductance L_m and a resistance R_m , as illustrated in Fig. 2(a). The desired damping is introduced by a supplemental shunt with impedance $Z_m(\omega)$, defined by $V = Z_m(\omega)I$, where V is the voltage across the terminals. The amplitude of the voltage source V_m can now expressed both in terms of the structural motion and the electrical network,

$$V_m = i\omega K_m x = (R_m + i\omega L_m + Z_m(\omega))I \quad (2)$$

The latter relation then determines an apparent mechanical flexibility relation

$$x = \left(\frac{L_m}{K_m^2} + \frac{R_m}{i\omega K_m^2} + \frac{Z_m(\omega)}{i\omega K_m^2} \right) f = \left(\frac{1}{k_m} + \frac{1}{i\omega c_m} + \frac{1}{i\omega h_m(\omega)} \right) f \quad (3)$$

defining an apparent spring stiffness, viscous coefficient and frequency dependent damping coefficient,

$$k_m = \frac{K_m^2}{L_m}, \quad c_m = \frac{K_m^2}{R_m}, \quad h_m(\omega) = \frac{K_m^2}{Z_m(\omega)} \quad (4)$$

as shown in Fig. 1(b). Thus, the impedance $Z(\omega)$ must be constructed so that the frequency dependent viscous parameter $h_m(\omega)$ provides the necessary inertance m to recover the series absorber in Fig. 1(a).

2.1.2 Piezoelectric transducer

For the piezoelectric transducer the induced electrical loading from local straining velocity amplitude $i\omega x$ is described by the current source $I_p = i\omega K_p x$, as shown in Fig. 2(b). The piezoelectric material is dielectric and when covered by electrodes it exhibits a substantial capacitance C_p placed in parallel with the current source I_p . Furthermore, an intrinsic loss of energy from hysteresis may be represented by an equivalent resistance R_p , whereby the resulting transducer model is governed by the network in Fig. 2(b). The current I is now expressed by the impedance relation $V = Z_p(\omega)I$ for the shunt in Fig. 2(b) with impedance function $Z_p(\omega)$. The current source I_p can be expressed in terms of either the mechanical straining or the transducer network model in Fig. 2(b), whereby

$$I_p = i\omega K_p x = \left(i\omega C_p + \frac{1}{R_p} + \frac{1}{Z_p(\omega)} \right) V \quad (5)$$

As for the electromagnetic transducer, the latter equality determines an equivalent mechanical model

$$x = \left(\frac{1}{K_p^2 C_p^{-1}} + \frac{1}{i\omega K_p^2 R_p} + \frac{1}{i\omega K_p^2 Z_p(\omega)} \right) f = \left(\frac{1}{k_p} + \frac{1}{i\omega c_p} + \frac{1}{i\omega h_p(\omega)} \right) f \quad (6)$$

defining the stiffness, viscous damping and shunt damping function as

$$k_p = K_p^2 C_p^{-1}, \quad c_p = K_p^2 R_p, \quad h_p(\omega) = K_p^2 Z_p(\omega) \quad (7)$$

This model corresponds to that in Fig. 1(b) for the electromagnetic transducer, when replacing subscript m by p .

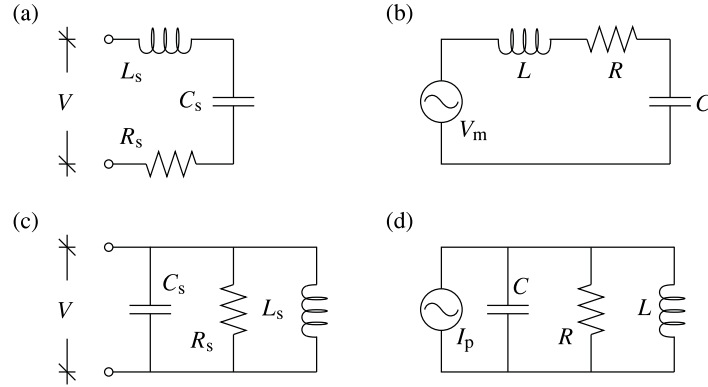


Figure 3: Shunts (a,c) and resulting circuits (c,d) for electromagnetic (a,c) and piezoelectric (b,d) transducers.

2.2 Resonant vibration absorber

The viscous transfer functions $h_m(\omega)$ and $h_p(\omega)$ are constructed to recover the desired series absorber in Fig. 1(a). For both transducers, the supplemental shunt must therefore provide the supplemental inertance m , while the introduction of additive stiffness and damping elements yields a more flexible absorber design, as for example negative shunt components have become more recognized [11].

2.2.1 Electromagnetic shunt

An equivalence between the series shunt absorbers in Fig. 1(a) and (b) is obtained by the shunt in Fig. 3(a), with shunt inductance L_s , resistance R_s and capacitance C_s connected in series. When introducing this shunt impedance $Z_m(\omega)$ into the network in Fig. 2(a), the resulting circuit for the shunt electromagnetic transducer is shown in Fig. 2(b), with resulting components

$$L = L_m + L_s, \quad R = R_m + R_s, \quad C^{-1} = C_s^{-1} \quad (8)$$

The equivalent mechanical components k , c and m of the series vibration absorber in Fig. 1(a) are subsequently obtained as summarized in Table 1.

Table 1: Mechanical vibration absorber parameters.

Absorber	Electromagnetic	Piezoelectric
k	$\frac{K_m^2}{L_m + L_s}$	$K_p^2 \frac{C_p^{-1} C_s^{-1}}{C_p^{-1} + C_s^{-1}}$
c	$\frac{K_m^2}{R_m + R_s}$	$K_p^2 \frac{R_p R_s}{R_p + R_s}$
m	$\frac{K_m^2}{C_s^{-1}}$	$K_p^2 L_s$

2.2.2 Piezoelectric shunt

For piezoelectric shunt damping the desired equivalence with the mechanical vibration absorber is obtained by the shunt in Fig. 3(c), with shunt components L_s , R_s and C_s placed in parallel. The resulting circuit model for the shunted piezoelectric transducer is therefore as shown in Fig. 2(d), with

$$\frac{1}{C^{-1}} = \frac{1}{C_p^{-1}} + \frac{1}{C_s^{-1}} \quad , \quad \frac{1}{R} = \frac{1}{R_p} + \frac{1}{R_s} \quad , \quad L = L_s \quad (9)$$

and equivalent mechanical components given in the last column of Table 1. It is found that increasing values of C_s^{-1} , R_s and L_s result in increasing mechanical parameters k , c and m , respectively. For piezoelectric transducers the inverse of the inherent capacitance C_p^{-1} is notoriously small for low-frequency vibrations and the required shunt inductance L_s must therefore be realized synthetically.

3 STRUCTURAL DYNAMICS

A mechanical vibration absorber may be calibrated based on a suitable compromise between maximum damping in the targeted vibration mode and minimum response amplitude when the structure is excited near the corresponding resonance frequency [1, 12]. However, for absorbers placed locally on a flexible structure, the interaction with non-resonant or residual vibration modes may be taken into account [9]. In the following, an augmented modal representation of the absorber displacement contains additional terms that represent the additional contributions from the residual modes.

3.1 Dynamic equations

In a frequency domain formulation, the equations of motion for a flexible structure can be written as

$$(-\omega^2 \mathbf{M} + \mathbf{K})\mathbf{u} + \mathbf{W}\mathbf{f} = \mathbf{f}_e \quad (10)$$

where \mathbf{u} contains the complex response amplitude, \mathbf{f}_e represent the external loading, whereas \mathbf{M} and \mathbf{K} are mass and stiffness matrices, respectively (omitting structural damping). The vector \mathbf{f} represents the transducer forces, at individual locations on the structure determined by the columns in the participation array \mathbf{W} . Figure 4 shows a classic 10-storey shear frame with absorbers in storeys 1, 2 and 6, whereby the participation array \mathbf{W} contains three columns, as further demonstrated in the numerical example.

It is assumed that all (three) absorbers are governed by the flexibility relation (1) associated with the same mechanical model in Fig. 1(a). The deformation across the series vibration absorbers is contained

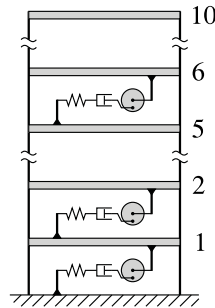


Figure 4: Shear frame structure with three vibration absorbers at storeys 1, 2 and 6, respectively.

in the vector $\mathbf{x} = \mathbf{W}^T \mathbf{u}$, whereby the mechanical relation for multiple absorbers can be written as

$$\mathbf{x} = \mathbf{W}^T \mathbf{u} = \left(\frac{1}{k} + \frac{1}{i\omega c} - \frac{1}{\omega^2 m} \right) \mathbf{f} \quad (11)$$

Hereby all transducers simultaneously target the same structural resonance. The closed-loop equations (10) to (11) can now be written in block matrix format as

$$\left(-\omega^2 \begin{bmatrix} \mathbf{M} & \mathbf{0} \\ -m\mathbf{W}^T & m\mathbf{I} \end{bmatrix} + i\omega \begin{bmatrix} \mathbf{0} & \mathbf{0} \\ \mathbf{0}^T & \frac{km}{c}\mathbf{I} \end{bmatrix} + \begin{bmatrix} \mathbf{K} & k\mathbf{W} \\ \mathbf{0}^T & k\mathbf{I} \end{bmatrix} \right) \begin{bmatrix} \mathbf{u} \\ \mathbf{f}/k \end{bmatrix} = \begin{bmatrix} \mathbf{f}_e \\ \mathbf{0} \end{bmatrix} \quad (12)$$

The homogeneous form is used in the subsequent numerical example to obtain complex root trajectories.

3.2 Modal properties

The modal characteristics of the flexible structure are determined from the homogeneous form of (10) without absorbers ($\mathbf{f} = \mathbf{0}$),

$$(-\omega_j^2 \mathbf{M} + \mathbf{K}) \mathbf{u}_j = \mathbf{0} \quad (13)$$

governing the real-valued natural frequency ω_j and mode shape vector \mathbf{u}_j . This eigenvalue problem therefore corresponds to the open-circuit limit ($I = 0$) for the electromagnetic transducer, while for the piezoelectric transducer it oppositely corresponds to shorted electrodes ($V = 0$). The vibration amplitude is represented by an expansion in the mode shape vectors,

$$\mathbf{u} = \sum_j \frac{\mathbf{u}_j}{v_j} u_j \quad , \quad v_j^2 = \mathbf{u}_j^T \mathbf{W} \mathbf{W}^T \mathbf{u}_j \quad (14)$$

where the individual vibration modes are conveniently normalized by the square root of the corresponding modal strain energy factor v_j^2 .

In the following the vibration absorbers are calibrated with respect to a single resonant vibration mode $j = r$, with modal equation obtained by substitution of (14) into (10) followed by pre-multiplication with \mathbf{u}_r^T / v_r ,

$$(-\omega^2 m_r + k_r) u_r + f_r = f_r^e \quad (15)$$

The modal mass, stiffness, load and modal absorber force are given as

$$m_r = \frac{1}{v_r^2} \mathbf{u}_r^T \mathbf{M} \mathbf{u}_r \quad , \quad k_r = \frac{1}{v_r^2} \mathbf{u}_r^T \mathbf{K} \mathbf{u}_r \quad , \quad f_r^e = \frac{1}{v_r} \mathbf{u}_r^T \mathbf{f}_e \quad , \quad f_r = \frac{1}{v_r} \mathbf{u}_r^T \mathbf{W} \mathbf{f} \quad (16)$$

where f_r comprises modal contributions from each individual absorber targeting mode $j = r$.

3.3 Augmented modal representation

As demonstrated in [9] the interaction with residual modes can be accurately represented by the augmented representation of the modal displacement

$$\mathbf{x}_r = v_r^{-1} \mathbf{W}^T \mathbf{u}_r u_r = \mathbf{x} + \left(\frac{1}{\kappa_r' k_r} - \frac{1}{\mu_r' m_r \omega^2} \right) \mathbf{f} \quad (17)$$

where $\mathbf{x}_r = v_r^{-1} \mathbf{W}^T \mathbf{u}_r u_r$ is the absorber deformation from the resonant mode $j = r$. The terms in the parenthesis represent modal flexibility and inertia from non-resonant residual modes, constituting the

discrepancy between \mathbf{x} and \mathbf{x}_r . First the absorber displacement \mathbf{x} is eliminated by (11), while the equation is subsequently pre-multiplied by $\mathbf{v}_r^{-1} \mathbf{u}_r^T \mathbf{W}$. Hereby, the last equality in (17) can be written as

$$u_r = \left(\frac{1}{\kappa_r k_r} + \frac{1}{i\omega \beta_r \sqrt{k_r m_r}} - \frac{1}{\mu_r m_r \omega^2} \right) f_r \quad (18)$$

introducing the modal stiffness ratio κ_r , mass ratio μ_r and damper ratio as

$$\frac{1}{\kappa_r} = \frac{k_r}{k} + \frac{1}{\kappa'_r}, \quad \frac{1}{\mu_r} = \frac{m_r}{m} + \frac{1}{\mu'_r}, \quad \beta_r = \frac{c}{\sqrt{k_r m_r}} \quad (19)$$

Thus, the correction parameters κ'_r and μ'_r represent changes to the actual single mode stiffness and mass ratios, respectively. The mechanical model associated with the modal deflection u_r is shown in Fig. 1, while the corresponding scalar equations (15) and (18) now govern the vibrations of mode $j = r$.

4 Residual mode parameters and design procedure

The modal correction coefficients κ'_r and μ'_r are determined to secure the correct modal properties of the full flexible structure with rigid absorber dashpots associated with $c \rightarrow \infty$ for all absorbers. The coupled equations (12) are in this limit reduced to

$$\left(\begin{bmatrix} \mathbf{K} & \tilde{k}\mathbf{W} \\ \mathbf{0}^T & \tilde{k}\mathbf{I} \end{bmatrix} - \omega^2 \begin{bmatrix} \mathbf{M} & \mathbf{0} \\ -\tilde{m}\mathbf{W}^T & \tilde{m}\mathbf{I} \end{bmatrix} \right) \begin{bmatrix} \mathbf{u} \\ \mathbf{f}/\tilde{k} \end{bmatrix} = \begin{bmatrix} \mathbf{0} \\ \mathbf{0} \end{bmatrix} \quad (20)$$

where $(\tilde{\cdot})$ refers to representative estimates of the absorber parameters.

Assume that N_a absorbers are placed on the flexible structure and initially calibrated independently with respect to the targeted vibration mode $j = r$. When the $(\tilde{\cdot})$ -parameters are chosen sufficiently accurate, it is possible from the above eigenvalue problem (20) to identify $N_a + 1$ natural frequencies associated with the targeted mode $j = r$. The present procedure relies on the fact that two of these frequencies are associated with coupled absorber-structure vibrations, while the remaining $N_a - 1$ frequencies represent redundant absorber modes with significant damping. For the 10-storey shear frame building in Fig. 4, with three absorbers attached, the root locus diagram is shown in Fig. 5, where the two trajectories from ω_A and ω_B govern the dynamics of the flexible structure, while the remaining two poles approach the imaginary axis along a central backbone locus from ω_C . The residual mode parameters κ'_r and μ'_r may thus be calibrated to recover ω_A and ω_B in the limit $c \rightarrow \infty$ (for all absorbers).

The free vibration characteristics of the targeted vibration mode are governed by the roots of the characteristic equation, represented by the denominator of the modal frequency response function $u_r k_r / f_r^e$ obtained by eliminating f_r between (15) and (18). For vanishing damping by $\beta_r \rightarrow \infty$, the characteristic equation reduces to

$$\tilde{\mu}_r \left(\frac{\omega}{\omega_r} \right)^4 - \left[(1 + \tilde{\kappa}_r) \tilde{\mu}_r + \tilde{\kappa}_r \right] \left(\frac{\omega}{\omega_r} \right)^2 + \tilde{\kappa}_r = 0 \quad (21)$$

The two roots $\omega^2 = \omega_A^2$ and ω_B^2 to this quadratic equation are obtained from the eigenvalue problem (20) with absorber stiffness $k = \tilde{k}$ and inertance $m = \tilde{m}$. The stiffness ratio $\tilde{\kappa}_r$ and mass ratio $\tilde{\mu}_r$ can therefore be determined from (21). The sum and product of the two roots can be written as

$$\left(\frac{\omega}{\omega_r} \right)_A^2 + \left(\frac{\omega}{\omega_r} \right)_B^2 = 1 + \tilde{\kappa}_r + \frac{\tilde{\kappa}_r}{\tilde{\mu}_r}, \quad \left(\frac{\omega}{\omega_r} \right)_A^2 \left(\frac{\omega}{\omega_r} \right)_B^2 = \frac{\tilde{\kappa}_r}{\tilde{\mu}_r} \quad (22)$$

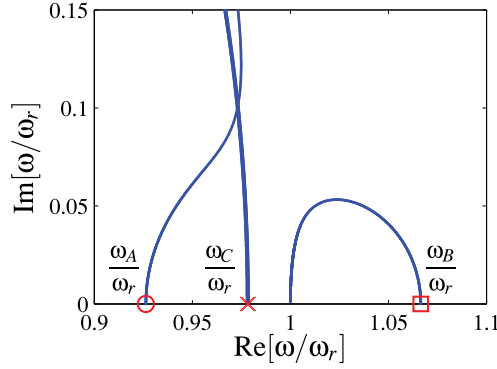


Figure 5: Trajectories for resonant mode $r = 1$ of shear frame in Fig. 4 with three identical absorbers.

Elimination of the ratio $\tilde{\kappa}_r/\tilde{\mu}_r$ determines the apparent stiffness ratio $\tilde{\kappa}_r$, while the mass ratio is then obtained from the latter equation. The two parameter ratios are obtained as

$$\tilde{\kappa}_r = \left[1 - \left(\frac{\omega}{\omega_r} \right)_A^2 \right] \left[\left(\frac{\omega}{\omega_r} \right)_B^2 - 1 \right] \quad , \quad \tilde{\mu}_r = \left[1 - \left(\frac{\omega_r}{\omega} \right)_B^2 \right] \left[\left(\frac{\omega_r}{\omega} \right)_A^2 - 1 \right] \quad (23)$$

The correction coefficients κ'_r and μ'_r can finally be determined from the definitions in (19) as

$$\frac{1}{\kappa'_r} = \frac{1}{\tilde{\kappa}_r} - \frac{k_r}{\tilde{k}} \quad , \quad \frac{1}{\mu'_r} = \frac{1}{\tilde{\mu}_r} - \frac{m_r}{\tilde{m}} \quad (24)$$

The parameters \tilde{m} and \tilde{k} are conveniently obtained by simply applying the classic tuning without residual mode correction.

Some of the most common calibration formulae are summarized in Table 2, whereby the estimates $m = \tilde{m}$ and $k = \tilde{k}$ follow directly from (19) when $\kappa'_r = 0$ and $\mu'_r = 0$. In the present case, the bottom expressions with a ‘balanced calibration’ and equal modal damping is applied, whereby a desired supplemental damping ratio ζ_{des} is a suitable design parameter [13]. It follows from [5] that the corresponding modal stiffness ratio is $\kappa_r = 8\zeta_{\text{des}}^2$, whereby the mass and damper ratio are subsequently obtained by

$$\mu_r = \kappa_r \quad , \quad \beta_r = \sqrt{\frac{1}{2}\kappa_r} \quad (25)$$

Table 2: Calibration formulae for vibration absorber.

Principle	μ_r	β_r
Minimum amplitude [2]	$\frac{\kappa_r}{1 - \frac{1}{2}\kappa_r}$	$\sqrt{\frac{1}{2}\kappa_r}$
Fixed point [4]	$\frac{\kappa_r}{1 - \frac{1}{2}\kappa_r}$	$\sqrt{\frac{2}{3}\kappa_r}$
Maximum damping [3]	κ_r	$\sqrt{\frac{1}{4}\kappa_r}$
Balanced calibration [5]	κ_r	$\sqrt{\frac{1}{2}\kappa_r}$

Table 3: Design procedure for shunt damping.

1)	Determine κ_r
2)	Determine μ_r and β_r from Table 2
3)	Determined \tilde{k} and \tilde{m} from (26)
4)	Determine $(\omega/\omega_r)_{A,B}$ by solving (20)
5)	Determine $\tilde{\kappa}$ and $\tilde{\mu}$ from (23)
6)	Determine κ'_r and μ'_r from (24)
7)	Determine k , m and c from (19)
8)	Determine L_s , R_s and C_s from Table 1

Next the preliminary absorber parameters are determined as

$$\tilde{k} = \kappa_r k_r, \quad \tilde{m} = \mu_r m_r \quad (26)$$

without influence from the, yet to be determined, correction ratios κ'_r and μ'_r . Now the frequency ratios $(\omega/\omega_r)_A$ and $(\omega/\omega_r)_B$ are determined from (20) or from measurements on the actual structure, whereby $\tilde{\kappa}_r$ and $\tilde{\mu}_r$ are obtained by (23). Thus, the residual mode coefficients μ'_r and κ'_r can finally be obtained by the expressions in (24). The design procedure is summarized in Table 3.

5 Damping of shear frame

The shear frame structure in Fig. 4 is used to demonstrated the design procedure. Figure 6 shows the first three vibration modes of the shear frame with absorber locations represented by the red inter-storey crosses. At each storey the figure provides the local modal mass ratio m_s/m_j^* , where m_s is the total translational mass of the structure, while m_j^* represents the modal mass determined by (16a) for a single absorber placed within the specific storey. Absorbers are optimally placed where this mass ratio is large, resulting in the absorber locations inside storeys 1, 2 and 6, as indicated in the figure. For identical sizing

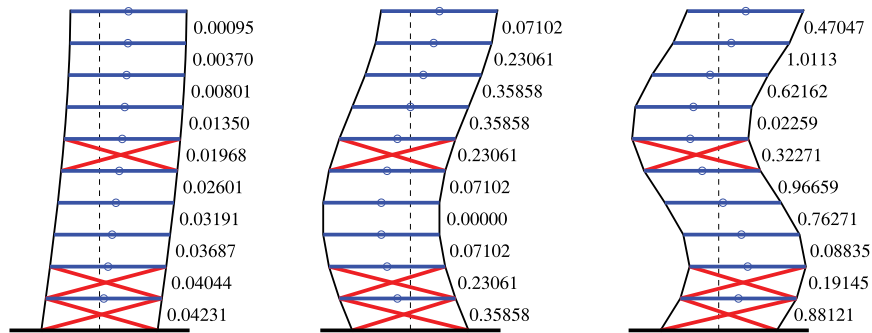


Figure 6: Modes $j = 1$ to 3 with mass ratio m_s/m_j^* obtained for a single absorber placed at the particular storey.

Table 4: Absorber parameters for shear frame modes $r = 1$ to 3, with $\mu_r = \kappa_r = 0.02$ and $c/\sqrt{k_r m_r} = 0.10$.

r	κ'_r	μ'_r	k/k_r	m/m_r
1	0.7792	19.616	0.0205	0.0200
2	0.5632	3.3588	0.0207	0.0201
3	3.0608	16.171	0.0201	0.0200

of the absorbers, the participation array becomes

$$\mathbf{W}^T = \begin{bmatrix} 1 & 0 & 0 & 0 & 0 & 0 & 0 & 0 & 0 & 0 \\ -1 & 1 & 0 & 0 & 0 & 0 & 0 & 0 & 0 & 0 \\ 0 & 0 & 0 & 0 & -1 & 1 & 0 & 0 & 0 & 0 \end{bmatrix}$$

The modal mass ratio m_s/m_r , with m_r in (16a) obtained for this participation array, is determined for the first three vibration modes as $m_s/m_1 = 0.1024$, $m_s/m_2 = 0.8198$ and $m_s/m_3 = 1.3954$, which corresponds to the sum of the individual mass ratios in Fig. 6.

Three calibration cases are considered, in which the three vibration absorbers are jointly calibrated with respect to target modes $r = 1, 2$ and 3 , respectively. In all three cases the desired damping ratio is $\zeta_{\text{des}} = 0.05$, whereby the modal stiffness ratio $\kappa_r = 8\zeta_{\text{des}}^2 = 0.02$, whereas $\mu_r = \kappa_r = 0.02$ follows from the bottom row of in Table 2. The residual mode parameters for the three cases are given in Table 4, from which it is seen that the residual mode flexibility κ'_r has the greater impact on the absorber calibration. It is seen that the residual mode correction implies a 3.5% increase of k for damping of mode $r = 2$.

Table 5 presents the six damping ratios associated with the first three vibration forms of the shear frame when the targeted mode is $r = 1, 2$ and 3 , respectively. The first three columns represent the damping ratios obtained with the proposed calibration procedure, while the last three columns are obtained without residual mode correction ($\kappa'_r = 0$ and $\mu'_r = 0$). Because $N_a = 3$, four of the six modes in each column of the table are associated with the resonant vibration form $j = r$, while the remaining two damping ratios represent the damping introduced to the two other (non-targeted) vibration forms ($j \neq r$). The damping ratios are ordered with respect to ascending frequency and the values for the targeted mode are highlighted in boldface. The first and last damping ratios for the specific target mode are associated with structural vibrations, while the two intermediate damping ratios represent the redundant absorber modes. For the calibration with residual mode correction (first three columns), the damping ratios of the two structural modes are almost exactly equal to the desired value $\zeta_{\text{des}} = 0.05$, while the pure absorber modes are highly damped with damping ratios that are approximately twice the desired value. The two non-targeted modes are virtually unaffected by the presence of the absorbers. Without residual mode correction (last three columns), the two structural modes are not equally damped and for the three cases

Table 5: Damping ratios for first three modes, with and without residual mode correction.

j	with correction			without correction		
	$r = 1$	$r = 2$	$r = 3$	$r = 1$	$r = 2$	$r = 3$
1	0.0499	0.0001	0.0000	0.0552	0.0001	0.0000
2	0.0988	0.0499	0.0017	0.0976	0.0559	0.0017
3	0.0991	0.0989	0.0494	0.0978	0.0969	0.0506
4	0.0499	0.0990	0.0916	0.0434	0.0971	0.0913
5	0.0007	0.0499	0.0925	0.0007	0.0420	0.0922
6	0.0003	0.0019	0.0498	0.0002	0.0018	0.0483

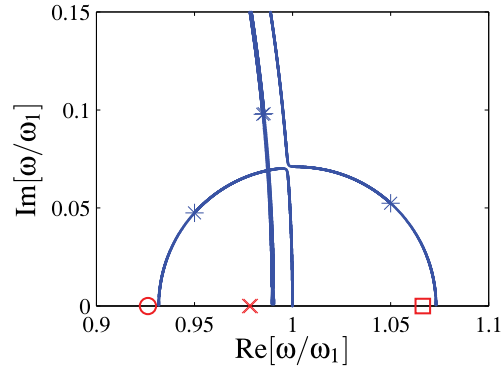


Figure 7: Complex root trajectories for resonant mode $r = 1$ of shear frame structure with three identical vibration absorbers. Balanced calibration with residual mode correction.

the reduction in damping ratio is 13.2%, 16.0% and 3.4%, respectively.

Figure 7 shows the complex trajectories of the four modes associated with the first vibration form ($r = 1$). The (red) markers indicate the real-valued frequencies ω_A (○), ω_B (□) and ω_C (×) introduced in connection with Fig. 5, which are all slightly lower than the corresponding frequencies in Fig. 7 for the optimally calibrated set of vibration absorbers. Furthermore, the two outer trajectories in Fig. 7 meet at the bifurcation point, indicating that an optimal balance is found between the two modes [5]. The asterisks (*) represent the complex poles associated with the optimal damper calibration $\beta_r = 0.1$, based on $\mu_r = \kappa_r = 0.02$. For the outer trajectories associated with structural vibrations, the two complex roots (*) are located with sufficient separation from the bifurcation point, to avoid undesirable vibration amplification at resonance, while the two (almost coinciding) redundant poles on the backbone curve appear well above the bifurcation point.

6 CONCLUSION

The mechanical equivalence between parallel RL shunt damping with piezoelectric transducers and series RC shunt damping by electromagnetic transducers is used to formulate a common vibration absorber format that contains a spring, dashpot and inerter placed in series. Thus, optimal calibration is obtained simultaneously for both transducer types when determining the desired properties of this representative vibration absorber. Furthermore, the equivalence implies that tuning results derived for piezoelectric (parallel) RL shunt damping can be directly used for electromagnetic (series) RC shunt damping. The theory is subsequently extended to multiple vibration absorbers acting on a flexible structure with multiple vibration modes, although only targeting a single dominant vibration form. For transducers acting locally on the flexible structure, the absorber calibration is often distorted by the interaction with residual vibration modes not targeted by the set of shunt dampers. A simple correction principle is however devised, in which the natural frequencies of the structure with fully locked absorber dashpots are used to determine two correction coefficients, which represent the interaction with the residual modes. For piezoelectric shunt damping these limiting frequencies are associated with infinite (shunt) resistance, while in the case of electromagnetic shunt damping they are determined for vanishing resistance. The frequencies are readily obtained numerically from a mathematical model of the structure, while in experimental analysis the presence of intrinsic damping (represented by R_m or R_p) might slightly deteriorate the determination of the correction coefficients. The accuracy and robustness of the shunt calibration procedure is verified by a numerical example.

References

- [1] Hagood NW and von Flotow A (1991) Damping of structural vibrations with piezoelectric materials and passive electrical networks. *Journal of Sound and Vibration* 146: 243–268.
- [2] Wu SY (1996) Piezoelectric shunts with a parallel R-L circuit for structural damping and vibration control. *Proceedings of the Society of Photo-Optical Instrumentation Engineers (SPIE)* 2720, San Diego, California, 259–269.
- [3] Caruso G (2001) A critical analysis of electric shunt circuits employed in piezoelectric passive vibration damping. *Smart Materials and Structures* 10: 1059–1068.
- [4] Yamada K, Matsuhisa H, Utsuno H and Sawada K (2010) Optimum tuning of series and parallel LR circuits for passive vibration suppression using piezoelectric elements. *Journal of Sound and Vibration* 329: 5036–5057.
- [5] Høgsberg J and Krenk S (2012) Balanced calibration of resonant shunt circuits for piezoelectric vibration control. *Journal of Intelligent Material Systems and Structures* 23: 1937–1948.
- [6] Inoue T, Ishida Y and Sumi M (2008) Vibration suppression using electromagnetic resonant shunt damper. *Journal of Vibration and Acoustics* 130: 041003 (8pp).
- [7] Zhu SY, Shen WA and Qian X (2013) Dynamic analogy between an electromagnetic shunt damper and a tuned mass damper. *Smart Materials and Structures* 22: 115018 (11pp).
- [8] Tang XD, Liu YL, Cui W and Zuo L (2016) Analytical solutions to H-2 and H-infinity optimizations of resonant shunted electromagnetic tuned mass damper and vibration energy harvester. *Journal of Vibration and Acoustics* 138: 011018 (8pp).
- [9] Krenk S and Høgsberg J (2016) Tuned resonant mass or inerter-based absorbers: unified calibration with quasi-dynamic flexibility and inertia correction. *Proceedings of the Royal Society A - Mathematical, Physical and Engineering Sciences* 472: 20150718 (23pp). DOI: 10.1098/rspa.2015.0718.
- [10] Høgsberg J and Krenk S (2017) Calibration of piezoelectric RL shunts with explicit residual mode correction. *Journal of Sound and Vibration* 386: 65–81.
- [11] Berardengo M, Thomas O, Giraud-Audine C and Manzoni S (2016) Improved resistive shunt by means of negative capacitance: new circuit, performances and multi-mode control. *Smart Materials and Structures* 25: 075033 (23pp).
- [12] Krenk S (2005) Frequency analysis of the tuned mass damper. *Journal of Applied Mechanics* 72: 936–942.
- [13] Krenk S and Høgsberg J (2013) Equal modal damping design for a family of resonant vibration control formats. *Journal of Vibration and Control* 19: 1294–1315.

BROADBAND VIBRATION DAMPING OF A NON-PERIODIC PLATE BY PIEZOELECTRIC COUPLING TO ITS ELECTRICAL ANALOGUE

R. DARLEUX*, B. LOSSOUARN[†] AND J.-F. DEÜ[†]

* [†] Laboratoire de Mécanique des Structures et des Systèmes Couplés (LMSSC)

Conservatoire national des arts et métiers (Cnam)

292 rue Saint-Martin, 75003 Paris, France

e-mail: robin.darleux@lecnam.net, web page: <http://www.lmssc.cnam.fr>

Key words: Vibration control, Multimodal damping, Piezoelectric coupling, Direct electromechanical analogy, Finite Element model

Abstract. Several solutions for multimodal vibration damping of thin mechanical structures based on piezoelectric coupling have been developed over the years. Among them, piezoelectric network damping consists in using piezoelectric transducers to couple a structure to an electrical network, where the transferred electrical energy can be dissipated. In particular, the effectiveness of coupling rods, beams and plates to networks which are their electrical analogues has been proven. This work is the first step going towards more complex structures. After defining and experimentally validating a new electrical analogue of a simply-supported plate, the study is extended to the damping of a non-periodic plate. Experiments show that in this case, a broadband damping is achieved once the piezoelectric transducers are coupled to an adequate analogous network. A finite element model of the structure coupled to its analogous network is concurrently developed and validated.

1 INTRODUCTION

Single mode damping of mechanical vibrations using the piezoelectric coupling goes back to the 1990s, when the resonant shunt was described by Hagood and Von Flotow [1]. The concept of piezoelectric damping has then been extended to multimodal damping. Some passive solutions consider connecting a multi-branch shunt to a piezoelectric transducer [2, 3]. While adding only one piezoelectric transducer to the structure is barely intrusive, its position and dimensions cannot simultaneously maximize the electromechanical coupling for all modes [4]. For these reasons, the damping performance might be limited. Other solutions include several independent piezoelectric transducers, each one being shunted in order to damp one mode of the structure. However, the resulting electromechanical coupling coefficients are inferior to the ones that would be induced by interconnecting all piezoelectric transducers.

In the early 2000s, the idea of interconnecting piezoelectric transducers with electrical components emerged. The concept of achieving broadband damping by coupling a structure to an electrical network was first proposed by Vidoli and dell'Isola [5]. Meanwhile, the electrical analogues of mechanical structures, as defined by MacNeal and Bescoter [6, 7] in the early 1950s, have been revived for multimodal vibration attenuation purposes [8]. As a consequence, piezoelectric network damping of plates has been studied [9, 10], and implemented recently [11, 12]. The next objective is to study the multimodal damping of complex structures coupled to their electrical analogues. To study the case of a non-periodic plate is considered as the first step towards this goal.

Moreover, a predictive model of the dynamics of the coupled system would be helpful to investigate the limits of the analogy between the structure and its electrical analogue. It could also be used to find the resistive components to add to the network to get an optimized damping performance. To develop such a model, the work of Thomas et al. [13] concerning a structure covered by thin piezoelectric patches is taken as the starting point.

Section 2 explains how to define a plate electrical analogue. It is applied to a practical setup of a simply-supported plate, and validated by comparing mechanical and electrical measurements. In section 3, we develop a finite element model of the plate coupled to its electrical analogue. The model is validated by comparing simulated and experimental results. Finally, the case of a non-periodic plate is addressed in section 4. A mass is added on the plate to break its symmetry. The designed electrical analogue is experimentally validated and passive broadband damping is still achieved.

2 PLATE ELECTRICAL ANALOGUE

In this first section, the direct electromechanical analogy is applied to a finite difference model of a square plate. The resulting set of equations can be represented by an electrical circuit with lumped elements. The electrical analogue of a square plate is then assembled to produce a plate electrical analogue, which is implemented and validated. The validation is conducted by comparing the operational shapes of the plate and of its electrical analogue.

2.1 Finite difference model of a square plate

The motion of a plate of thickness h , mass density ρ and bending stiffness D is described by the Kirchhoff-Love plate theory, so that

$$-D \left(\frac{\partial^4 w}{\partial x^4} + 2 \frac{\partial^4 w}{\partial x^2 \partial y^2} + \frac{\partial^4 w}{\partial y^4} \right) = \rho h \ddot{w}. \quad (1)$$

In harmonic motion at angular frequency Ω , Eq. (1) is equivalent to

$$\begin{cases} \frac{\partial Q_x}{\partial x} + \frac{\partial Q_y}{\partial y} = -\frac{m}{a} \Omega^2 w \\ M = aD \left(\frac{\partial \theta_x}{\partial x} + \frac{\partial \theta_y}{\partial y} \right) \end{cases} \quad \text{where} \quad Q_x = -\frac{\partial M}{\partial x}, \quad Q_y = -\frac{\partial M}{\partial y}, \quad \theta_x = \frac{\partial w}{\partial x}, \quad \theta_y = \frac{\partial w}{\partial y}. \quad (2)$$

With these notations, w is the displacement in the direction normal to the plate, a is the side of the square plate, $m = \rho h a^2$ is its mass, Q_x and Q_y are the shear forces in the plate, θ_x and θ_y are the angles along the principal directions, and M is a linear combination of the bending moments along the x and y directions defined by Timoshenko in [14]. A finite difference pattern, as represented in Figure 1, is then applied to the plate model. The resulting system of equations obtained from Eqs. (2) is expressed by

$$\begin{cases} Q_T - Q_B + Q_R - Q_L = -m\Omega^2 w_I \\ M_I = D(\theta_T - \theta_B + \theta_R - \theta_L) \end{cases}, \quad \frac{a}{2} \begin{pmatrix} -Q_B \\ -Q_L \\ Q_R \\ Q_T \end{pmatrix} = \begin{pmatrix} M_I - M_B \\ M_I - M_L \\ M_I - M_R \\ M_I - M_T \end{pmatrix}, \quad \frac{a}{2} \begin{pmatrix} \theta_B \\ \theta_L \\ -\theta_R \\ -\theta_T \end{pmatrix} = \begin{pmatrix} w_I - w_B \\ w_I - w_L \\ w_I - w_R \\ w_I - w_T \end{pmatrix} \quad (3)$$

2.2 Design of the plate electrical analogue

The direct electromechanical analogy, such as presented by Bloch in [15], allows the representation of mechanical structures with passive electrical components. In the case here studied, this means that the electrical analogue of a square plate is defined by replacing mechanical quantities in Eqs. (3) by electrical quantities, according to the analogy in Table 1. The first two equations in the system of Eqs. (3) can

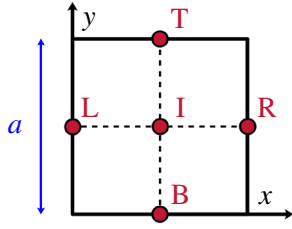


Figure 1: Discretization grid, where I, B, L, R, T refer to the central, bottom, left, right and top positions, respectively

Mechanical quantities

Force Q
 Moment M
 Linear velocity \dot{w}
 Angular velocity $\dot{\theta}$
 Compliance $1/D$
 Mass m
 Lever arm $a/2$

\iff

Electrical quantities

Voltage V_w
 Voltage V_θ
 Electrical current \dot{q}_w
 Electrical current \dot{q}_θ
 Capacitance C
 Inductance L
 Transformer ratio $\hat{a}/2$

Table 1: Direct electromechanical analogy

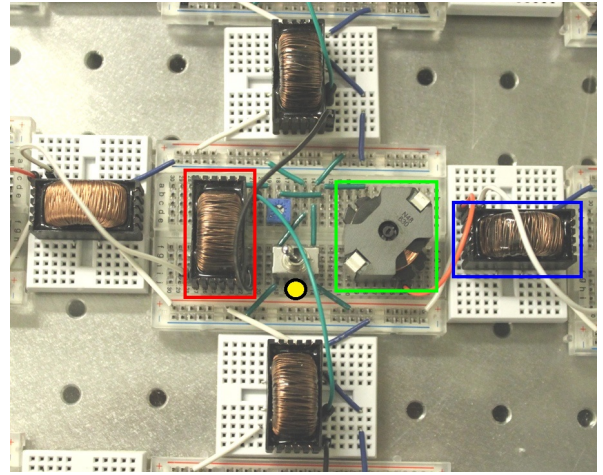
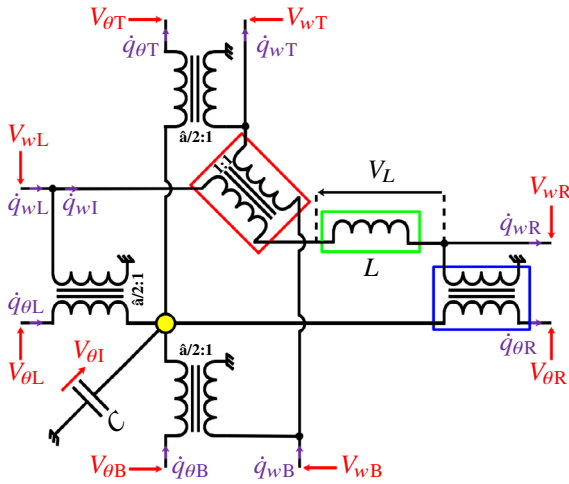


Figure 2: Scheme and picture of the electrical analogue of a square plate, which highlight the central transformer in red, a side transformer in blue, the inductance in green, and the capacitance connection in yellow

be understood as constitutive equations of an ideal inductor of inductance m and an ideal capacitor of capacitance $1/D$. The remaining equations can be interpreted as constitutive equations of transformers of ratio $a/2$. Hence, the Figure 2 represents the unit cell of the plate electrical analogue. The electrical analogue of a rectangle plate can then be defined by assembling this unit cell along the x and y directions.

Moreover, the boundary conditions of the plate should be reproduced in the electrical network. In particular, the simply-supported and clamped edges have direct equivalent electrical connections. Indeed, if for example the left edge of the unit cell is a boundary, then the simply-supported condition is equivalent to command that $V_{\theta L} = 0$ and $\dot{q}_{wL} = 0$, while the clamped condition is equivalent to command $\dot{q}_{\theta L} = 0$ and $\dot{q}_{wL} = 0$ [12].

Finally, the electrical components should be tuned so that the natural frequencies of the network are equal to the natural frequencies of the plate [11]. This ensures identical bending wave propagation properties in the two media. In this case, the modal coupling condition is

$$\frac{1}{a^2} \frac{D}{m} = \frac{1}{\hat{a}^2} \frac{1}{LC}. \quad (4)$$

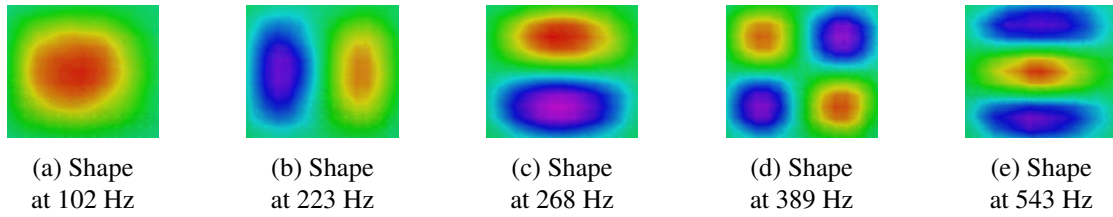


Figure 3: Measurement of five operational deflection shapes of the plate

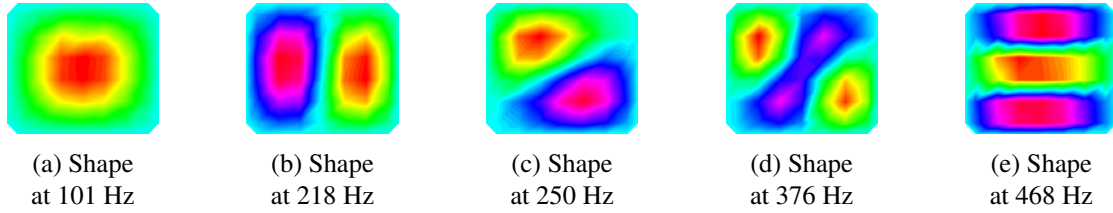


Figure 4: Measurement of five operational electrical current shapes in the network

2.3 Validation of the plate electrical analogue

The considered setup is a simply-supported aluminium plate of dimensions $420 \times 360 \times 3 \text{ mm}^3$. It is periodically covered with 42 square piezoelectric patches of dimensions $50 \times 50 \times 0.5 \text{ mm}^3$. The objective is to develop the electrical analogue of this structure. Hence, a network made of 42 identical unit cells has been assembled. The structure and its analogous network are shown in Figure 7, while one unit cell is shown in Figure 2. A way to validate the plate electrical analogue is to compare its operational electrical current shapes to the deflection shapes of the plate.

Since the network should be tested alone for validation, the piezoelectric patches are replaced by ceramic capacitors which have a nominal capacitance of 145 nF. Then, following the method described in [16], the inductors are made by winding conductive wire around a RM10 core of N48 ferrite material from Epcos TDK. The nominal inductance and series resistance of the produced inductors are $L = 244 \text{ mH}$ and $R_{sL} = 13.7 \Omega$. Finally, the ratio of the transformers is $\hat{a} = 4$, and their nominal series resistance is 16.8Ω when used with a 1:1 ratio. An inductor and several transformers are pictured in Figure 2.

By analogy with an exciting external force, an external voltage is applied between two unit cells of the network. The voltage V_{ex} is applied through an isolation transformer of ratio k , such as represented in Figure 5. At the same time, the voltage drop V_L across each inductor of the network is measured. Dividing V_L by the impedance $R_{sL} + jL\Omega$ leads to the electrical current \dot{q}_{wI} flowing through each inductor. As a consequence, plotting the shapes of $\dot{q}_{wI}/kV_{\text{ex}}$ is equivalent to plotting the operational deflection shapes of a plate excited by a point load. Several operational deflection shapes of the plate have been measured using a laser vibrometer and are represented in Figure 3. These can be compared to the operational current shapes in Figure 4. Plotted shapes look alike, even though some shapes are slightly different, such as in Figure 3c and Figure 4c. This can be explained by the heavy damping due to resistive components in the electrical network. Hence, operational electrical current shapes may spill over onto each other. It is the case in Figure 4c, where the measured current distribution looks like a combination of modes (1,2) and (2,1). For this reason, further investigations could include the experimental modal analysis to separate the contributions of modes. Anyway, comparing operational shapes offers a first validation of the plate electrical analogue.

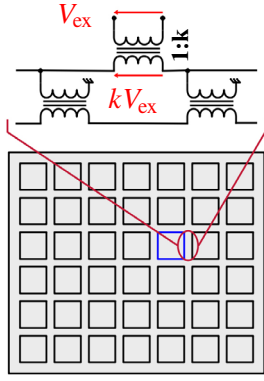


Figure 5: Schematic representation of the excitation setup for the measurement of network modes

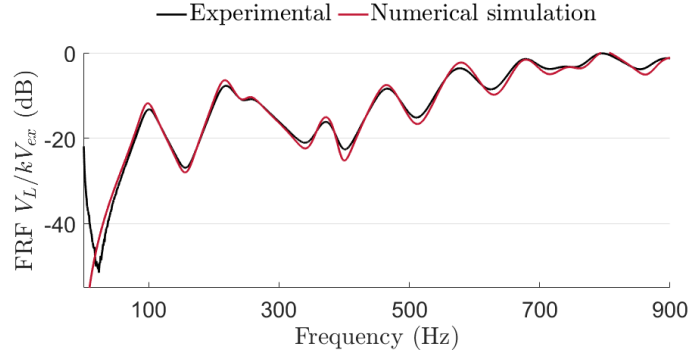


Figure 6: Experimental and simulated FRFs, with V_L measured across the inductor of the unit cell highlighted in blue in Figure 5

Furthermore, we developed a lumped model of the entire network. The unit cells, as schematised in Figure 2, are put together following an assembly process. The boundary conditions are then set such as described in section 2.2. The numerical Frequency Response Functions (FRFs) V_L/kV_{ex} can thus be compared to measurements. As an example, a comparison is plotted in Figure 6 for V_L measured in the unit cell highlighted in blue in Figure 5. The simulated FRFs fit with the the measured ones. The remaining differences can be reduced by taking other parasitic elements of the transformers into account, such as the magnetizing branch and the winding capacitance. These kinds of refined models are not presented for the sake of conciseness, and because the correlation between the proposed model and experiments is considered good enough to validate the concept of the plate electrical analogue.

3 FINITE ELEMENT MODEL OF A STRUCTURE COUPLED TO ITS ELECTRICAL ANALOGUE

The main steps to model the dynamics of a mechanical structure covered by piezoelectric patches are recalled. Then, the effect of the interconnections between patches via an electrical network is accounted for. The simulated results are finally compared to experiments in order to validate the approach.

3.1 Finite element formulation

To model the vibrations of a continuous medium covered with piezoelectric patches, we follow the method described by Thomas et al. in [13]. Though all equations are not detailed in this paper, the main steps to develop a finite element model of the structure are recalled.

The electric field is denoted \mathbf{E} . The electric displacement is denoted \mathbf{D} . Using the Voigt notation, the linearized stress and strain vectors are respectively denoted $\boldsymbol{\sigma}$ and $\boldsymbol{\varepsilon}$. The electro-mechanical constitutive equations linking these quantities are

$$\begin{aligned}\boldsymbol{\sigma} &= \mathbf{C}^E \boldsymbol{\varepsilon} - \mathbf{e}^T \mathbf{E}, \\ \mathbf{D} &= \mathbf{e} \boldsymbol{\varepsilon} + \boldsymbol{\epsilon}^E \mathbf{E},\end{aligned}\tag{5}$$

where \mathbf{C}^E is the matrix of elastic coefficients at constant electric field, \mathbf{e} is the matrix of piezoelectric coefficients, and $\boldsymbol{\epsilon}^E$ is the matrix of dielectric permittivities at constant strain. The structure is modelled as an isotropic homogeneous linear elastic medium in which $\mathbf{e} = \mathbf{0}$. Furthermore, the piezoelectric transducers exhibit transverse isotropic properties and are polarized in their transverse directions $\mathbf{n}^{(i)}$. The

patches thickness's, denoted $h^{(j)}$, are considered small when compared to their longitudinal dimensions. Hence, the electrical field $\mathbf{E}^{(j)}$ in the j -th piezoelectric patch is supposed uniform and normal to the electrodes. It can be expressed as a function of the potential difference $V^{(j)}$ between electrodes of each patch:

$$\mathbf{E}^{(j)} = -\frac{V^{(j)}}{h^{(j)}} \mathbf{n}^{(j)}. \quad (6)$$

To derive the mechanical equation of the variational formulation, the elastodynamic equation, in which prescribed body forces are neglected, is considered. To derive the electrical equation, it is Gauss's law involving no free charges which is considered. These equations are then multiplied by test functions and integrated over the entire volume of the structure. The prescribed surface forces and free charge densities are taken into account as boundary conditions. Then, the constitutive equations of the medium are applied to get the variational formulation in terms of displacement \mathbf{u} and electric potential $V^{(j)}$.

The equations of the variational formulation are then discretized. Following an assembly process, we obtain a finite element formulation of the coupled problem:

$$\begin{pmatrix} \mathbf{M}_m & \mathbf{0} \\ \mathbf{0} & \mathbf{0} \end{pmatrix} \begin{pmatrix} \ddot{\mathbf{U}} \\ \ddot{\mathbf{V}} \end{pmatrix} + \begin{pmatrix} \mathbf{K}_m & \mathbf{K}_c \\ -\mathbf{K}_c^T & \mathbf{K}_e^{-1} \end{pmatrix} \begin{pmatrix} \mathbf{U} \\ \mathbf{V} \end{pmatrix} = \begin{pmatrix} \mathbf{F} \\ \mathbf{Q} \end{pmatrix}, \quad (7)$$

where \mathbf{U} contains the nodal values of the displacement field \mathbf{u} and \mathbf{V} contains the voltage values $(V^{(1)}, \dots, V^{(P)})$ on the upper electrodes of the piezoelectric patches. \mathbf{F} represents the external mechanical forces applied to the structure, while \mathbf{Q} are the electrical charges on the upper electrodes of the piezoelectric patches. \mathbf{K}_c is the coupling matrix, and \mathbf{M}_m and \mathbf{K}_m are the mass and mechanical stiffness matrices. \mathbf{K}_e is a diagonal matrix in which the j -th term is the inverse of the blocked piezoelectric capacitance $C^{(j)}$ of the j -th patch, which is

$$C^{(j)} = \frac{\epsilon_{33}^{\mathcal{E}} S^{(j)}}{h^{(j)}}, \quad (8)$$

where $S^{(j)}$ is the j -th patch surface and $\epsilon_{33}^{\mathcal{E}}$ is the transverse permittivity of a piezoelectric medium with no strain. In the case of plate bending, this quantity can be estimated with materials constants. More details are available in [11].

3.2 Coupling of a structure to its electrical analogue

The piezoelectric patches bound to the structure are interconnected via the plate electrical analogue. Hence, using the notations in Figure 2, \mathbf{V} contains in fact the voltage values $(V_{\theta I}^{(1)}, \dots, V_{\theta I}^{(P)})$, while the j -th element of \mathbf{Q} is equal to the charge $q_{\theta B}^{(j)} - q_{\theta T}^{(j)} + q_{\theta L}^{(j)} - q_{\theta R}^{(j)}$ flowing through the capacitance $C^{(j)}$. As a consequence, the network is a passive electrical controller that commands a relationship between \mathbf{V} and \mathbf{Q} . We choose to express these vectors in terms of the 42 electrical charges q_{wI} flowing through the inductors of the network, whose values are contained in the vector \mathbf{Q}_w . Using a symbolic solver, we obtained these relations:

$$\begin{aligned} \mathbf{V} &= -(\mathbf{M}_e \ddot{\mathbf{Q}}_w + \mathbf{D}_e \dot{\mathbf{Q}}_w), \\ \mathbf{Q} &= \mathbf{P} \mathbf{Q}_w, \end{aligned} \quad (9)$$

which leads to the finite element formulation of the mechanical structure coupled to its electrical analogue:

$$\begin{pmatrix} \mathbf{M}_m & \mathbf{0} \\ \mathbf{0} & \mathbf{M}_e \end{pmatrix} \begin{pmatrix} \ddot{\mathbf{U}} \\ \ddot{\mathbf{Q}}_w \end{pmatrix} + \begin{pmatrix} \mathbf{0} & \mathbf{0} \\ \mathbf{0} & \mathbf{D}_e \end{pmatrix} \begin{pmatrix} \dot{\mathbf{U}} \\ \dot{\mathbf{Q}}_w \end{pmatrix} + \begin{pmatrix} \mathbf{K}_m + \mathbf{K}_c \mathbf{K}_e \mathbf{K}_c^T & \mathbf{K}_c \mathbf{K}_e \mathbf{P} \\ \mathbf{K}_e \mathbf{K}_c^T & \mathbf{K}_e \mathbf{P} \end{pmatrix} \begin{pmatrix} \mathbf{U} \\ \mathbf{Q}_w \end{pmatrix} = \begin{pmatrix} \mathbf{F} \\ \mathbf{0} \end{pmatrix}. \quad (10)$$

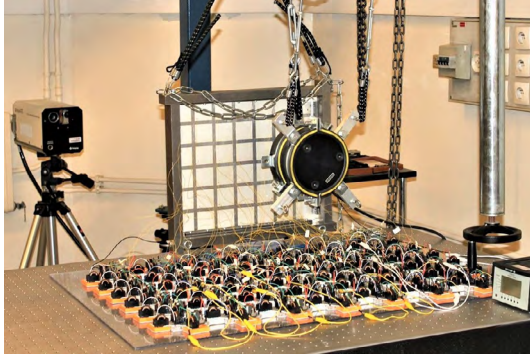


Figure 7: Setup including the plate covered with piezoelectric transducers, a shaker, a laser vibrometer and the plate electrical analogue

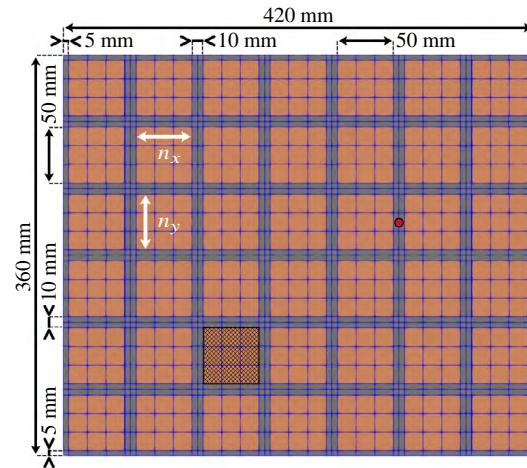


Figure 8: Meshing of the mechanical structure and location (in red) of both the excitation and the velocity measurement

The expressions of the electrical "mass" matrix \mathbf{M}_e , the electrical damping matrix \mathbf{D}_e , and the transfer matrix \mathbf{P} are not detailed in this work for the sake of conciseness. We just precise these three matrices depend on the transformer ratio \hat{a} . Moreover, \mathbf{M}_e is a function of the inductance value L , while \mathbf{D}_e is a function of the series resistance of the inductors R_{sL} and the series resistance of the transformers.

3.3 Validation of the finite element model

Numerical simulations are compared to practical measurements to validate the finite element model developed in the previous sections. The experimental setup is presented in Figure 7. The simply-supported plate periodically covered with piezoelectric patches is suspended. A shaker applies a point load and a force transducer measures it. A laser vibrometer measures the velocity on the other side of the plate. The red marker in Figure 8 represents the location of both the excitation and the velocity measurement. Moreover, the upper electrodes of the patches are either connected to the ground or to the network thanks to switches, which can be spotted in Figure 2.

The structure is modelled with 20-node hexahedral elements. Both the plate and the piezoelectric patches are meshed with one element in depth. In the other directions, the piezoelectric patches as well as the plate beneath them are meshed with $n_x \times n_y$ elements. Taking $n_x = n_y = 3$ leads to converged values for natural frequencies of the undamped structure up to 1 kHz. As a consequence, the Figure 8 represents the mesh used to obtain all the following numerical results.

The plate is made of duralumin. Its Poisson's ratio and density are respectively set at 0.346 and 2800 kg/m³. Its Young's modulus is set at 68.8 GPa to adjust the eleventh natural frequency of the plate calculated with short-circuited piezoelectric patches to the corresponding resonances in the experimental measurement. This corresponds to the last peak before 900 Hz as plotted in Figure 9. The piezoelectric patches are made of the PIC 153 PZT material. The coefficients of matrices in Eq. (5) are either taken from manufacturer's data when available, or extrapolated from datasheets of other PZT materials.

The case of short-circuited patches is simulated by imposing all voltage values in \mathbf{V} to ground potential in Eq. (7). The plotted results in Figure 9 show that the numerical simulation forecasts the dynamics of the structure up to 900 Hz rather well. Moreover, the remaining differences between numerical and experimental results could be reduced. First of all, the plate is linked to a rigid frame via thin supports.

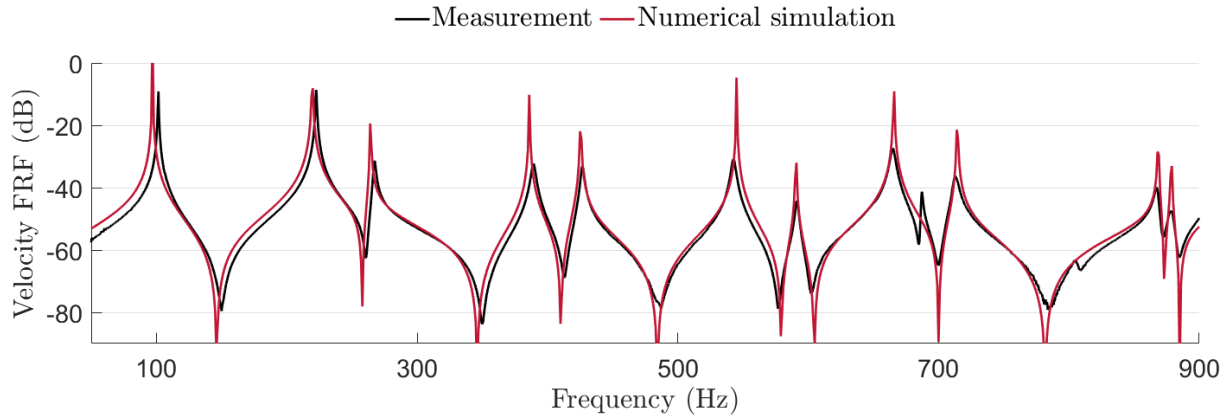


Figure 9: Experimental and simulated FRFs with short-circuited piezoelectric patches

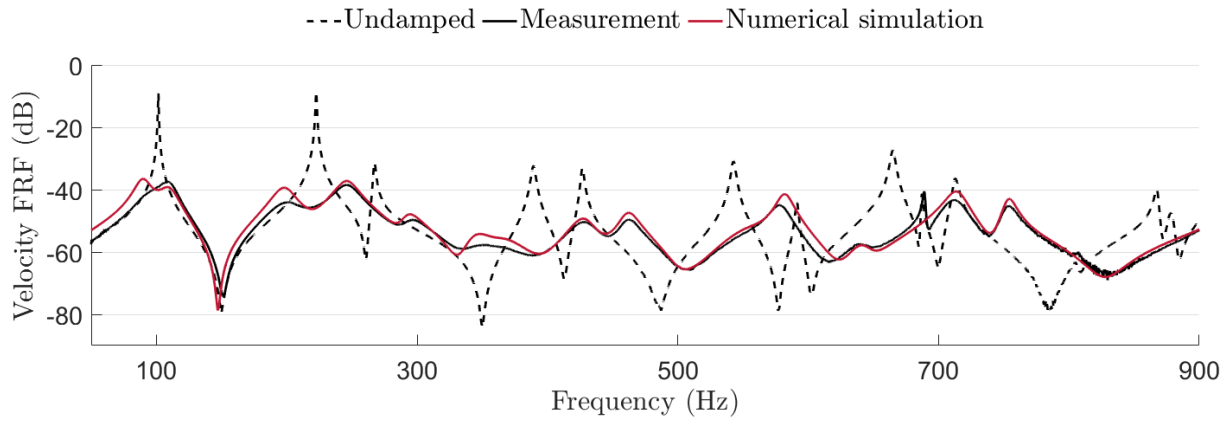


Figure 10: Experimental and simulated FRFs when the plate is coupled to its electrical analogue

The plate is the only part of the assembly that is modelled. Since the peak at 687 Hz is a frame mode, it can not be predicted. Furthermore, the gaps between the first simulated and measured peaks can be attributed to the non-ideal experimental boundary conditions. This has been explained by Robin et al., who designed a first version of the setup in [17]. Finally, the structural damping has been neglected, which explains the amplitude differences at resonances.

The case of the structure being coupled to its passive electrical analogue is then considered. As seen in Figure 10, a broadband vibration damping is achieved. Meanwhile, the frame mode at 687 Hz is barely affected by the connection to the network, which was expected. Besides, the model in Eq. (10) is able to predict the dynamics of the structure coupled to its electrical analogue. The modelling limits highlighted in Figure 9 remain true in this case. Hence, this model could be used to find the optimal resistive components to be added to the network in order to optimize the damping performance.

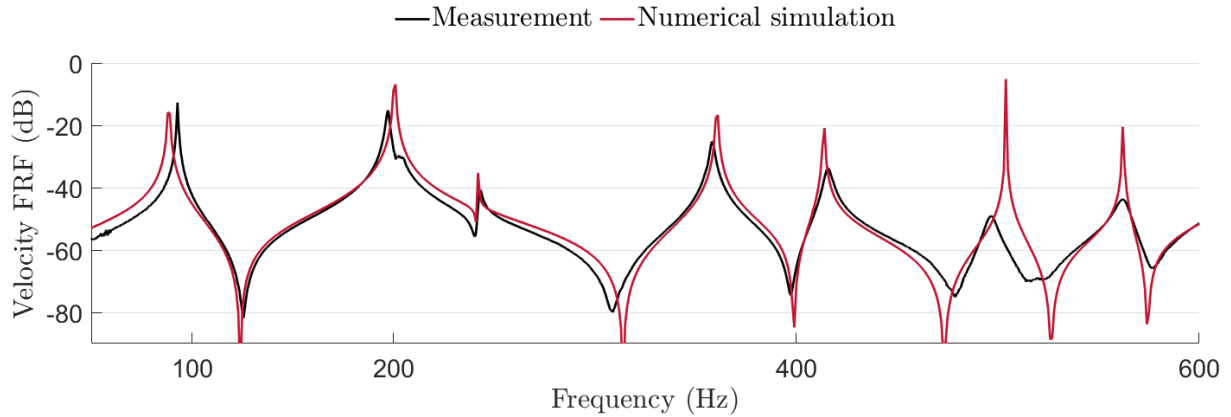


Figure 11: Experimental and simulated FRFs with short-circuited piezoelectric patches and an added mass

4 BROADBAND VIBRATION DAMPING OF A NON-PERIODIC PLATE

In this section, the broadband damping achieved by coupling a structure to its electrical analogue is extended to the case of a non-periodic plate. A mass is locally added on the plate, and its influence on the dynamics of the system is modelled. We then define the non-periodic plate electrical analogue and verify that the first few modes of the structure are significantly damped.

4.1 Non-periodic plate electrical analogue and validation

Designing the electrical analogue of a non-periodic plate is the first step towards more complex structures. As a consequence, we decided to add a mass which is a 22 mm thick, 40 mm diameter cylindrical rod of 207 g. This mass is added on the side of the plate which is not covered by piezoelectric patches, on the hatched position in Figure 8.

The mass is added in the finite element model as well, in the form of a 22 mm thick patch covering the same surface as a piezoelectric patch. Its Young modulus is set at 325 MPa. This way, the seventh simulated natural frequency of the plate with short-circuited patches is adjusted to the seventh peak on the measured FRF. The correlation between numerical and experimental results in this case is shown in Figure 11. When compared to the results in Figure 9, one can notice that the natural frequencies of the plate have been lowered, that the contact with the added mass induces damping in the measured FRF, and that a frame mode at 203 Hz is now excited. Since the structural damping and the frame are not taken into account, their effects are not foreseen by our model. The simulated FRF fits quite well with the measured one nonetheless.

The non-periodic plate here considered is obtained by locally adding some mass and some stiffness to the structure. To get its electrical analogue, the first natural frequency of the electrical network should be adjusted to the first natural frequency of the non-periodic plate. The first simulated resonance in Figure 11 is used as a reference value for the structure. In other words, Eq. (4) should remain true, while a and \hat{a} have set values and D and m are locally modified. Thus, one should modify the product of the capacitance C by the inductance L of the corresponding unit cell of the network. Not to deteriorate the electromechanical coupling [18], only L is modified to adjust the first natural frequency of the electrical network. The calculations, which are not detailed here, show in this case that the initial inductance of

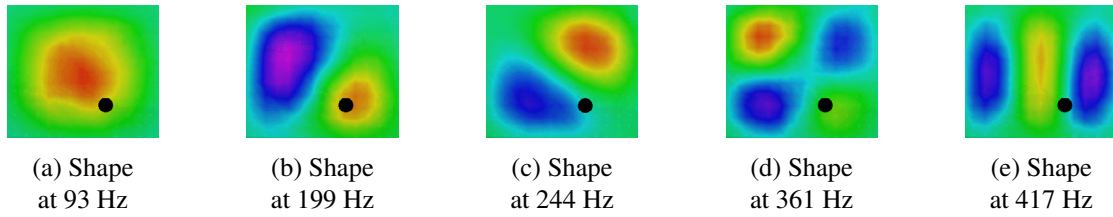


Figure 12: Measurement of five operational deflection shapes of the plate when a 207 g mass (in black) is added

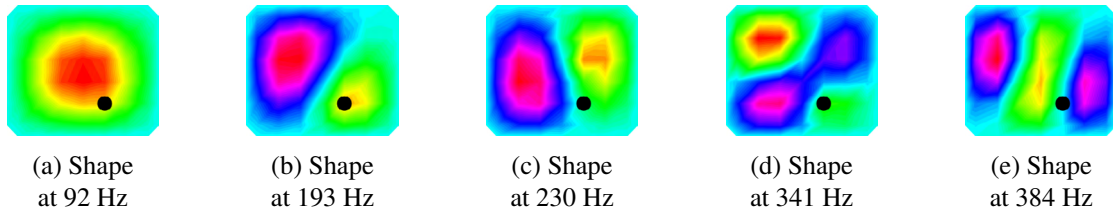


Figure 13: Measurement of five operational electrical current shapes in the network when a 1.34 H inductance (in black) replaces a 244 mH inductance of the network

244 mH should be replaced by an inductance of 1.34 H.

As previously explained in section 2.3, one way to validate the non-periodic plate electrical analogue is to compare the mechanical and electrical operational shapes. The measurements are still made with the setups presented in Figures 7 and 5. The results are shown in Figures 12 and 13. Since the plotted shapes look alike, we consider that the non-periodic network is the electrical analogue of the modified structure.

4.2 Multimodal vibration damping

The non-periodic plate is now coupled to its passive electrical analogue. The FRF measurement is made with the same setup as described in section 3.3. As seen in Figure 10, broadband damping is achieved in this case as well. This result validates the approach of coupling a non-periodic structure to its fully passive electrical analogue for multimodal damping purposes.

Moreover, the simulated results fit rather well with the measured ones. The remaining differences are due to the differences already spotted in Figure 11, and hence could be reduced by modelling the structural damping. As it is, it seems that the finite element model developed in this work can be used to predict the dynamics of a complex structure coupled to its electrical analogue. It could also be used to forecast where resistive components could be added in the network to improve the damping performance.

5 CONCLUSION

The first objective of this work is to develop a finite element model of a structure coupled to an electrical network interconnecting piezoelectric transducers. A structure covered with thin piezoelectric patches is considered. The electrical network is viewed as a passive controller that commands a relationship between the voltages and the charges on the upper electrodes of the piezoelectric transducers. The numerical results show a good agreement with measurements, even though the model could be improved. In the case here studied, the possible improvements include taking into account the structural damping

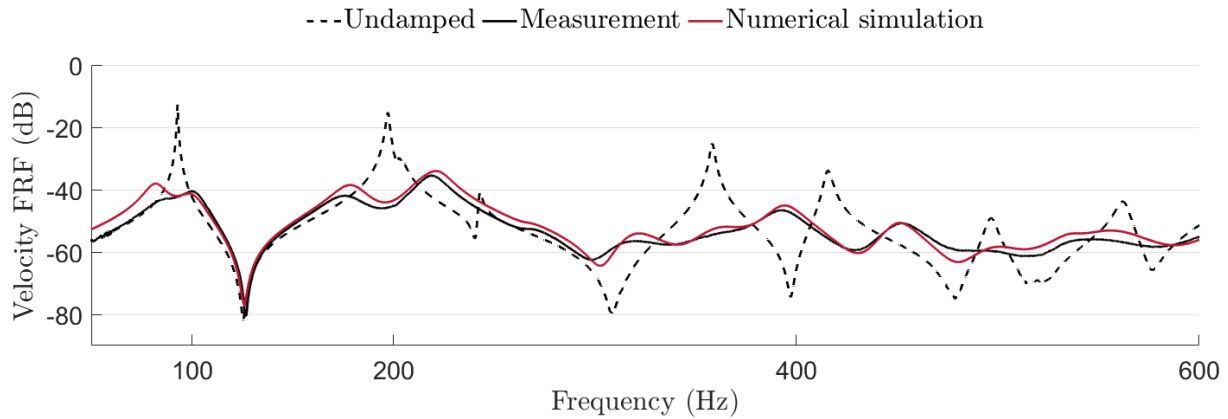


Figure 14: Experimental and simulated FRFs when the non-periodic plate is coupled to its electrical analogue

of the plate and the non-ideal boundary conditions of the setup. Anyway, the actual model can predict the dynamics of the coupled system. It could also be used to validate the analogy between a mechanical structure and its electrical analogue.

The other objective of this work is to extend to non-periodic structures the concept of coupling to an electrical analogue for passive multimodal damping purposes. To do that, the electrical analogue of a simply-supported plate is designed and its dynamics is experimentally validated. Finally, we measure the damping performance that is attainable by connecting the plate electrical analogue to the structure. These steps are repeated in the case of a plate on which a mass has been added in order to make it non-periodic. The final measurements highlight the achievable damping performance with a fully passive electrical network connected to the non-periodic structure. It is a first step towards trying to couple a complex structure to its electrical analogue for multimodal damping purposes.

REFERENCES

- [1] N. W. Hagood, A. Von Flotow, Damping of structural vibrations with piezoelectric materials and passive electrical networks, *Journal of Sound and Vibration* 146 (2) (1991) 243–268. doi: 10.1016/0022-460x(91)90762-9.
- [2] S. Behrens, S. O. R. Moheimani, A. J. Fleming, Multiple mode current flowing passive piezoelectric shunt controller, *Journal of Sound and Vibration* 266 (5) (2003) 929–942. doi: 10.1016/s0022-460x(02)01380-9.
- [3] M. Berardengo, S. Manzoni, A. M. Conti, Multi-mode passive piezoelectric shunt damping by means of matrix inequalities, *Journal of Sound and Vibration* 405 (2017) 287–305. doi: 10.1016/j.jsv.2017.06.002.
- [4] J. Ducarne, O. Thomas, J.-F. Deü, Placement and dimension optimization of shunted piezoelectric patches for vibration reduction, *Journal of Sound and Vibration* 331 (14) (2012) 3286–3303. doi: 10.1016/j.jsv.2012.03.002.
- [5] S. Vidoli, F. dell’Isola, Modal coupling in one-dimensional electromechanical structured continua, *Acta Mechanica* 141 (1-2) (2000) 37–50. doi: 10.1007/bf01176806.

- [6] R. H. MacNeal, The solution of partial differential equations by means of electrical networks, Ph.D. thesis, California Institute of Technology (1949).
- [7] S. U. Benscoter, R. H. MacNeal, Equivalent-plate theory for a straight multicell wing, NACA Technical Note 2786.
- [8] S. Alessandroni, F. dell'Isola, M. Porfiri, A revival of electric analogs for vibrating mechanical systems aimed to their efficient control by PZT actuators, *International Journal of Solids and Structures* 39 (20) (2002) 5295–5324. doi:10.1016/s0020-7683(02)00402-x.
- [9] S. Alessandroni, U. Andreaus, F. dell'Isola, M. Porfiri, Piezo-ElectroMechanical (PEM) kirchhoff-love plates, *European Journal of Mechanics - A/Solids* 23 (4) (2004) 689–702. doi:10.1016/j.euromechsol.2004.03.003.
- [10] S. Alessandroni, U. Andreaus, F. dell'Isola, M. Porfiri, A passive electric controller for multimodal vibrations of thin plates, *Computers & Structures* 83 (15-16) (2005) 1236–1250. doi:10.1016/j.compstruc.2004.08.028.
- [11] B. Lossouarn, J.-F. Deü, M. Aucejo, K. A. Cunefare, Multimodal vibration damping of a plate by piezoelectric coupling to its analogous electrical network, *Smart Materials and Structures* 25 (11) (2016) 115042. doi:10.1088/0964-1726/25/11/115042.
- [12] B. Lossouarn, M. Aucejo, J.-F. Deü, K. A. Cunefare, Design of a passive electrical analogue for piezoelectric damping of a plate, *Journal of Intelligent Material Systems and Structures* (2017) 1045389X1773123doi:10.1177/1045389x17731232.
- [13] O. Thomas, J.-F. Deü, J. Ducarne, Vibrations of an elastic structure with shunted piezo-electric patches: efficient finite element formulation and electromechanical coupling coefficients, *International Journal for Numerical Methods in Engineering* 80 (2) (2009) 235–268. doi:10.1002/nme.2632.
- [14] S. P. Timoshenko, S. Woinowsky-Krieger, *Theory of plates and shells*, McGraw-Hill, 1959.
- [15] A. Bloch, Electromechanical analogies and their use for the analysis of mechanical and electromechanical systems, *Journal of the Institution of Electrical Engineers - Part I: General* 92 (52) (1945) 157–169. doi:10.1049/ji-1.1945.0039.
- [16] B. Lossouarn, M. Aucejo, J.-F. Deü, B. Multon, Design of inductors with high inductance values for resonant piezoelectric damping, *Sensors and Actuators A: Physical* 259 (2017) 68–76. doi:10.1016/j.sna.2017.03.030.
- [17] O. Robin, J.-D. Chazot, R. Boulandet, M. Michau, A. Berry, N. Atalla, A plane and thin panel with representative simply supported boundary conditions for laboratory vibroacoustic tests, *Acta Acustica united with Acustica* 102 (1) (2016) 170–182. doi:10.3813/aaa.918934.
- [18] A. J. Fleming, S. Behrens, S. O. R. Moheimani, Reducing the inductance requirements of piezoelectric shunt damping systems, *Smart Materials and Structures* 12 (1) (2003) 57–64. doi:10.1088/0964-1726/12/1/307.

ENHANCEMENT OF A DYNAMIC VIBRATION ABSORBER BY MEANS OF AN ELECTROMAGNETIC SHUNT DAMPER

Michel A. Auleley^{*,†}, Olivier Thomas^{*}, Christophe Giraud-Audine[#] and Hervé Mahé[†]

^{*} Laboratoire d'Ingénierie des Systèmes Physiques et Numériques (LISPEN) EA 7515
Arts et Métiers ParisTech
8 bd. Louis XIV, 59046 Lille, France
e-mail: michel.auleley@ensam.eu, olivier.thomas@ensam.eu

[†] Centre d'Etude des Produits Nouveaux Espace Industriel Nord, Valeo Transmissions
Route de Poulainville, 80009 Amiens Cedex 1, France
e-mail: herve.mahe@valeo.com

[#] Laboratoire d'électrotechnique et d'électronique de Puissance de Lille (L2EP) EA 2697
Arts et Métiers ParisTech
8 bd. Louis XIV, 59046 Lille, France
e-mail: christophe.giraud-audine@ensam.eu

Keywords: Vibration control, Electromagnetic Shunt Damper, Electromechanical Coupling Factor, Tuning and Optimization

Summary: *In this study, we address the topic of the reduction of structural vibrations by means of an electromagnetic shunt damper (EMSD) made up of a voice coil actuator (VCA) with an electronic circuit. The classical resistive and resonant shunt solutions are studied. The main goal of this paper is to estimate the damping performance of shunts combined with a tuned mass damper (TMD), in the case of forced vibrations, for an arbitrary resonant elastic host structure. Two architectures, that differs with the placement of the EMSD with respect to the TMD, are tested. It is shown that the EMSD enhances the vibration control for a specific combination of TMD and EMSD. If the TMD parameters cannot be changed, the performance of vibration reduction is affected by one free parameter: the Electromechanical Coupling Factor (EMCF). This factor conditions the optimal mitigation of a mechanical vibration mode. Experiments are proposed and a good agreement with the theoretical model is obtained, validating it. For these experiments, a digital signal processor (DSP) generates the EMSD (the tuning parameters depend on the VCA and the DSP itself as well). A cantilever beam with a mass clamped at its free end serves as the TMD, whose tuning parameters include the bending stiffness and the clamped mass.*

1 INTRODUCTION

The conception and the optimisation of an electromagnetic shunt damper (EMSD) are studied. The EMSD is used to obtain a dissipation of mechanical energy by converting mechanical

vibrations into electrical energy through a magnetic interaction realised by a voice coil actuator (VCA). This transducer is composed of a coil, connected to the shunt circuit, which oscillates in a magnetic field created by a permanent magnet. Like piezoelectric materials, VCA has a fundamental electromechanical reversibility. So, the EMSD can be compared to a mechanical damper [1], e.g. the traditional Frahm damper, also called the tuned mass damper (TMD) [2], or the traditional piezoelectric shunt [3, 4]. Optimum tuning parameters have been defined for classic passive dampers by Den Hartog [5] on the one hand and for equivalent shunt systems [3, 6] on the other hand.

In comparison to a piezoelectric transducer, the VCA can be advantageously oversized in order to increase the Electromechanical Coupling Factor (EMCF). Actually, the effective EMCF, as a function of the actuator mass for both electromagnetic transducers and piezoelectric transducers, has allowed to show that, for an equivalent actuator mass, piezoelectric transducers depend only on the material properties and do not depend on transducer size in first approximation, while the coupling factor of the VCA increases with its mass [7]. Some studies have used the combination of piezoelectric shunt damper and the EMSD in order to reduce the vibrations and/or to harvest it in electrical energy [8, 9, 10, 11, 12].

The objective of this paper is to apply an EMSD in order to enhance the vibration control of a TMD in the case of forced vibrations, for an arbitrary resonant elastic host structure. Two architectures, that differ with the placement of the EMSD with respect to the TMD [13, 14], are tested in the conservative case. In the first section of this paper, we present the global system made up of a combination of the primary system, the TMD and the EMSD for the two kinds of combinations only for conservative system. In the following section, we discuss and comment the experiments and their results. Finally, the last section leads to the conclusion that experiments give a good agreement with the theory.

2 MODELS

We consider a primary system like a single degree of freedom (SDOF) coupled with a TMD and with an EMSD with two architectures possible seen in Figure 1. m_1 , c_1 , k_1 are the mass, the viscous damping coefficient and the stiffness coefficient of the primary system, respectively. An external force F sets in motion this system, which its displacement is x_1 . The natural frequency of the primary system is $\omega_1 = \sqrt{\frac{k_1}{m_1}}$ and the damping ratio is $\xi_1 = \frac{c_1}{2\sqrt{k_1 m_1}}$. The TMD [2] is designed by a mass m_2 , a viscous damping coefficient c_2 and a stiffness coefficient k_2 . The displacement of m_2 is x_2 . However, we prefer to use x_d , the relative displacement x_2 in relation to x_1 ($x_d = x_2 - x_1$). The natural frequency of the TMD is $\omega_2 = \sqrt{\frac{k_2}{m_2}}$ and the damping ratio is $\xi_2 = \frac{c_2}{2\sqrt{k_2 m_2}}$. The mass ratio between the TMD and the primary system $\mu = \frac{m_2}{m_1}$ is the coupling factor of both systems. We consider the EMSD also like a resonant conservative system composed by an electrical circuit with the inductance of the VCA L and an impedance in serial connection made up by a capacitance C and a resistance R . This system is named the RC-shunt [4]. An electric charge Q flowed through the shunt. The natural frequency of the RC-shunt is

$\omega_e = \frac{1}{\sqrt{LC}}$ and the damping ratio is $\xi_e = \frac{R}{2} \sqrt{\frac{C}{L}}$. The EMSD is coupled with the primary system by the means of the VCA that induced a Lorentz force $\Phi \dot{Q}$ on the primary system and an electromotive force $\Phi \dot{x}_1$ on the shunt circuit, such as Φ is the force factor of the VCA [15] and $(\dot{})$ the derivate with respect to time. The force factor is the coupling factor between the primary system and the EMSD. It depends on the coil displacement, the coil geometry and the magnetic flux density generated through the air gap of the VCA, but it could be considered as a constant [16].

The dampers can be designed as conservative ($\xi_e = \xi_2 = 0$) or dissipative. The optimum criteria from these two systems are different. For the conservative resonant dampers, we want to design an antiresonance at the resonance of the primary system and also take away the two news resonances from the antiresonance designed. These two optimisation criteria are gathered by the knowledge of the frequency distance $\Delta\omega$. It corresponds to the difference between the resonant frequency of the primary system alone with the new resonant frequency generated by the coupling of both systems: the primary system and the damper. This optimisation is suited to mono-frequency excitation. For the dissipative system, we want to reduce the spectrum magnitude of the primary system. This method is called H_∞ optimisation [1]. We loose the antiresonance with this method but we benet from a weak resonant magnitude. This optimisation is suited to a large frequency range.

Den Hartog has dened the resonance frequencies in the case of two Degrees Of Freedom (2DOF) conservative mechanical system composed by a primary system and a TMD [5] as :

$$\omega_{r1} = \omega_2 \sqrt{1 + \frac{\mu}{2} - \sqrt{\mu + \frac{\mu^2}{4}}}, \quad \omega_{r2} = \omega_2 \sqrt{1 + \frac{\mu}{2} + \sqrt{\mu + \frac{\mu^2}{4}}}, \quad (1)$$

If ω_2 is tuned on ω_1 , we obtain an antiresonance frequency at ω_1 and the frequency distance is, in the case of a TMD, for $\mu \ll 1$:

$$\forall \mu \ll 1, \quad \Delta\omega_{TMD} \simeq \omega_1 \frac{\sqrt{\mu}}{2}. \quad (2)$$

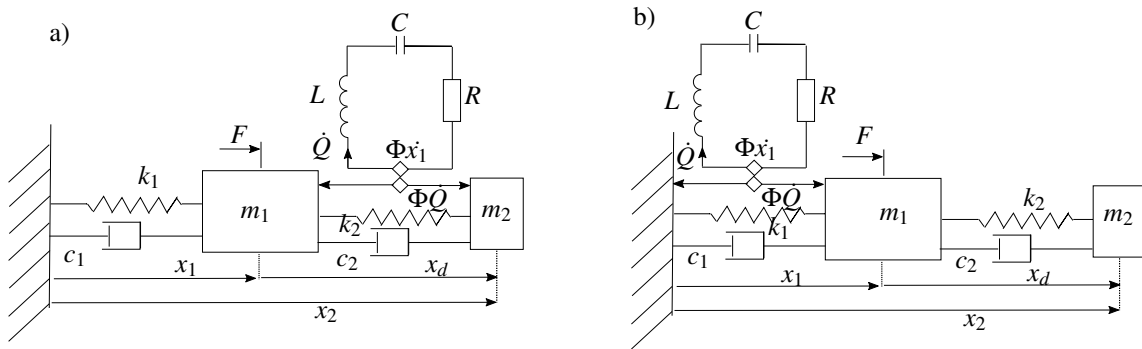


Figure 1: Schematic of primary system coupled with a TMD and an EMSD : a) Architecture I : EMSD placed between the primary system and the TMD (on the left), b) Architecture II : EMSD placed between the primary system and its building (on the right).

In regards to equation (2), we see the mass ratio μ is the parameter which defines the frequency distance.

2.1 EMSD between the primary system and the TMD

The governing equations of this first architecture (Arch. I) shown in Figure 1.a is made up of the mechanical equation of motion and the Kirchhoff's voltage law :

$$(1 + \mu)\ddot{x}_1 + \mu\ddot{x}_d + 2\xi_1\omega_1\dot{x}_1 + \omega_1^2x_1 = \frac{F_1}{m_1}, \quad (3)$$

$$\ddot{x}_d + \ddot{x}_1 + 2\xi_2\omega_2\dot{x}_d + \omega_2^2x_d + \kappa_2\omega_2\dot{\bar{Q}} = 0, \quad (4)$$

$$\ddot{\bar{Q}} + 2\xi_e\omega_e\dot{\bar{Q}} + \omega_e^2\bar{Q} - \kappa_2\omega_2\dot{x}_d = 0, \quad (5)$$

with \bar{Q} the equivalent electrical charge and κ_2 the EMCF of Arch. I :

$$\bar{Q} = \sqrt{\frac{L}{m_2}}Q, \quad \kappa_2 = \frac{\Phi}{\omega_2\sqrt{m_2L}}. \quad (6)$$

The Frequency Response Functions (FRFs) associated to equations (3) (4) (5) for conservative systems ($\xi_1 = \xi_2 = \xi_e = 0$) are :

$$\hat{x}_1 = \frac{F_1}{m_1} \frac{(-\Omega^2 + \omega_e^2)(-\Omega^2 + \omega_2^2) - \kappa_2\omega_2^2\Omega^2}{D_2(\Omega)}, \quad (7)$$

$$\hat{x}_d = \frac{F_1}{m_1} \frac{-\Omega^2(-\Omega^2 + \omega_e^2)}{D_2(\Omega)}, \quad (8)$$

$$\hat{\bar{Q}} = \frac{F_1}{m_1} \frac{j\kappa_2\omega_2\Omega^3}{D_2(\Omega)}, \quad (9)$$

with :

$$D_2(\Omega) = -\Omega^6 + [\omega_1^2 + (1 + \mu)(1 + \kappa_2^2)\omega_2^2 + \omega_e^2]\Omega^4 - [(1 + \kappa_2^2)\omega_1^2\omega_2^2 + \omega_1^2\omega_e^2 + (1 + \mu)\omega_2^2\omega_e^2]\Omega^2 + \omega_1^2\omega_2^2\omega_e^2, \quad (10)$$

with \hat{x}_1 , \hat{x}_d , $\hat{\bar{Q}}$ the complex amplitude of x_1 , x_d , \bar{Q} respectively defined by $x_1(t) = \Re(\hat{x}_1 e^{j\Omega t})$ and in the same way for x_d , \bar{Q} , and Ω the frequency of external force. The complex amplitude of the electrical current \hat{I} that flows through the shunt circuit is thus $\hat{I} = j\Omega\hat{\bar{Q}}$. In the case of conservative systems, we want to generate an antiresonance instead of the resonance frequency of the primary system ω_1 . Therefore, we need to determinate the antiresonance frequencies of \hat{x}_1 from equation (7), as follows :

$$\omega_{ar,I-} = \frac{1}{\sqrt{2}} \left[(1 + \kappa_2^2)\omega_2^2 + \omega_e^2 - \sqrt{[(1 + \kappa_2^2)\omega_2^2 + \omega_e^2]^2 - 4\omega_2^2\omega_e^2} \right]^{\frac{1}{2}}, \quad (11)$$

$$\omega_{ar,I+} = \frac{1}{\sqrt{2}} \left[(1 + \kappa_2^2)\omega_2^2 + \omega_e^2 + \sqrt{[(1 + \kappa_2^2)\omega_2^2 + \omega_e^2]^2 - 4\omega_2^2\omega_e^2} \right]^{\frac{1}{2}}. \quad (12)$$

So, we impose $\omega_{ar,I-}$ and $\omega_{ar,I+}$ equal to ω_1 . It allowed for the determining of the tuning terms of ω_e , and the following solutions are obtained :

$$\omega_e = \sqrt{\frac{\omega_1^4 - (1 + \kappa_2^2)\omega_1^2\omega_2^2}{\omega_1^2 - \omega_2^2}}, \quad (13)$$

$$\text{if } \omega_2 < \omega_1, \text{ for } \kappa_2 \leq \sqrt{\frac{\omega_1^2 - \omega_2^2}{\omega_2^2}}, \quad (14)$$

$$\text{else-if } \omega_2 > \omega_1, \forall \kappa_2. \quad (15)$$

However, the tuning frequency in equation (13) prevents the tuning of the TMD with the primary system $\omega_2 = \omega_1$, because it requires in practice the de-tuning of the TMD.

To check the efficiency of Arch. I, we use the FRFs corresponding to the primary system coupled with the TMD like references in relation with several FRFs related to these architecture. When looking at Figure 2, the criteria described in equations (13), (14) and (15) enable

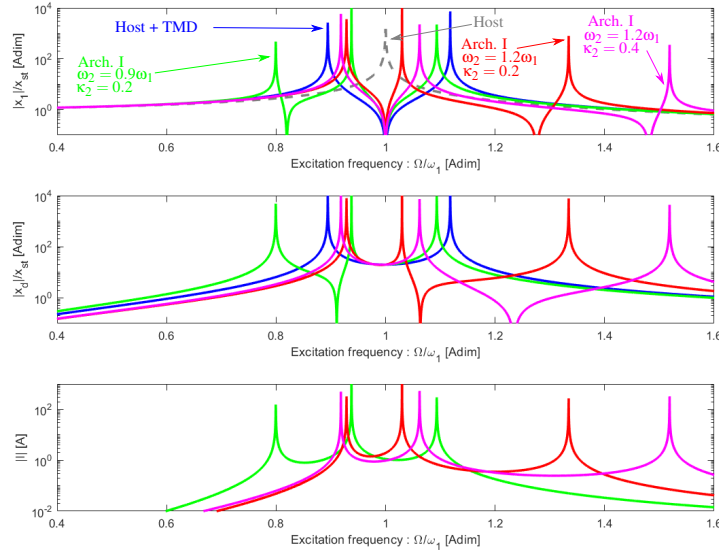


Figure 2: Frequency response functions of the architecture I (Arch. I) for some values of both natural frequencies of the TMD ω_2 and the EMSD ω_e , and the EMCF κ_2 . The mass ratio is $\mu = 0.05$.

to generate an antiresonance at ω_1 . However, the nearest resonance of this antiresonance is systematically observed in return compared to the reference case with the coupled system of both primary system and the TMD, the reference case seen in Figure 2. The dynamics of this architecture is governed by three resonances and it is difficult to take them away from the antiresonance frequency. In the conservative case, Arch. I seems unsuitable to reduce largely the

vibration of the primary system owing to the EMSD placement, which is between the primary system and the TMD. This is a wrong option when considering to enhance the performance of a TMD in conservative case. However, this kind of architecture is seen in the study of energy harvesting systems because of it can improves the harvesting power can be improved when used in relation to a traditional SDOF energy harvester (i.e. shunt damper) [13, 17].

2.2 EMSD between the primary system and its support

The governing equations of this second architecture (Arch. II) shown in Figure 1.b is made up of the mechanical equation of motion and the Kirchhoff's voltage law :

$$(1 + \mu)\ddot{x}_1 + \mu\ddot{x}_d + 2\xi_1\omega_1\dot{x}_1 + \omega_1^2x_1 + \kappa_1\omega_1\dot{\bar{Q}} = \frac{F_1}{m_1}, \quad (16)$$

$$\ddot{x}_d + \ddot{x}_1 + 2\xi_2\omega_2\dot{x}_d + \omega_2^2x_d = 0, \quad (17)$$

$$\ddot{\bar{Q}} + 2\xi_e\omega_e\dot{\bar{Q}} + \omega_e^2\bar{Q} - \kappa_1\omega_1\dot{x}_1 = 0, \quad (18)$$

with \bar{Q} the equivalent electrical charge and κ_1 the EMCF of Arch. II :

$$\bar{Q} = \sqrt{\frac{L}{m_1}}Q, \quad \kappa_1 = \frac{\Phi}{\omega_1\sqrt{m_1L}}. \quad (19)$$

So, the FRFs of the equations (16)-(17)-(18) for conservative systems ($\xi_1 = \xi_2 = \xi_e = 0$) are :

$$\hat{x}_1 = \frac{F_1}{m_1} \frac{(-\Omega^2 + \omega_e^2)(-\Omega^2 + \omega_2^2)}{D_1(\Omega)}, \quad (20)$$

$$\hat{x}_d = \frac{F_1}{m_1} \frac{\Omega^2(-\Omega^2 + \omega_e^2)}{D_1(\Omega)}, \quad (21)$$

$$\hat{\bar{Q}} = \frac{F_1}{m_1} \frac{j\kappa_1\omega_1\Omega(-\Omega^2 + \omega_2^2)}{D_1(\Omega)}, \quad (22)$$

with :

$$D_1(\Omega) = -\omega^6 + [(1 + \kappa_1^2)\omega_1^2 + (1 + \mu)\omega_2^2 + \omega_e^2] \Omega^4 - [(1 + \kappa_1^2)\omega_1^2\omega_2^2 + \omega_1^2\omega_e^2 + (1 + \mu)\omega_2^2\omega_e^2] \Omega^2 + \omega_1^2\omega_2^2\omega_e^2. \quad (23)$$

In order to generate an antiresonance at ω_1 , we need to determine the antiresonance frequencies of \hat{x}_1 from equation (20), as follows :

$$\omega_{ar,II-} = \omega_2, \quad \omega_{ar,II+} = \omega_e, \quad (24)$$

When looking at the equation (7), the condition to generate an antiresonance at ω_1 is possible by the tuning of $\omega_e = \omega_1$ and $\omega_2 = \omega_1$, and creates a double antiresonance. In regards to the

application of this double antiresonance tuning, the expression of the resonance frequencies, obtainable by equation (23), is in ascending order :

$$\omega_{p-} = \omega_1 \sqrt{\frac{2 + \mu + \kappa_1^2 - \sqrt{(2 + \mu + \kappa_1^2)^2 - 4}}{2}}, \quad (25)$$

$$\omega_{p0} = \omega_1, \quad (26)$$

$$\omega_{p+} = \omega_1 \sqrt{\frac{2 + \mu + \kappa_1^2 + \sqrt{(2 + \mu + \kappa_1^2)^2 - 4}}{2}}, \quad (27)$$

In this case, we note ω_1 is at the same time an antiresonance frequency and an eigenfrequency, implying that the associated eigenmode has a motionless primary system. To check the efficiency of Arch. II, we use the FRF corresponding to the primary system coupled with the TMD like references in relation with several FRFs related to these architecture. In Figure 3, we notice

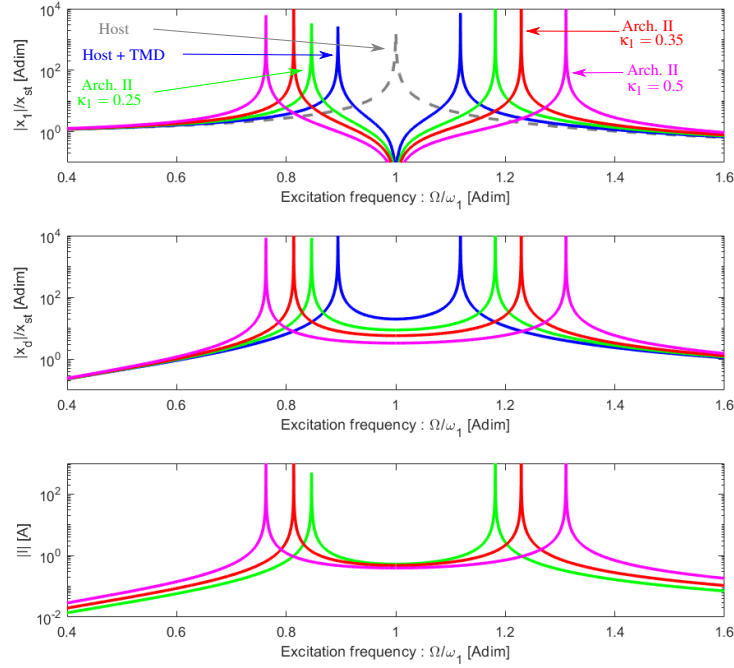


Figure 3: Frequency response function of the architecture II (Arch. II) for some values of both natural frequencies of the TMD ω_2 and the EMSD ω_e , and the EMCF κ_1 . The mass ratio is $\mu = 0.05$.

that the EMSD adds efficiency to the TMD. For Arch. II, we see that the increase of the EMCF κ_1 upgrades the frequency distance of this architecture II. Besides the mathematical expression of

the resonance frequencies (25) (27) in comparison to the resonance frequencies with a conservative TMD see in [5], in tuning the dampers on ω_1 , the role of μ and κ_1^2 are similar, so that we can define a coupling factor as the sum of both factors for this system. In regards to equations (25) and (27), the frequency distance following for $\mu, \kappa_1 \ll 1$ is :

$$\forall \mu, \kappa_1 \ll 1, \quad \Delta_{\omega, II} \simeq \omega_1 \frac{\sqrt{\mu + \kappa_1^2}}{2}. \quad (28)$$

Therefore, tuning $\omega_{ar, II-}$ and $\omega_{ar, II+}$ on ω_1 produces a larger frequency distance compared to the frequency distance for the primary system plus TMD tunes on ω_1 in equation (2). Moreover the graphic of \hat{x}_d shows more the EMCF increases more \hat{x}_d at the vicinity of ω_1 decreases. The dynamics of this architecture is ruled by three resonances, including one that can be avoided.

Another possible option with this architecture is to create an antiresonance at any frequency Ω by the tuning of the EMSD eigenfrequency at this Ω . Indeed if the antiresonance frequency $\omega_{ar, II-} = \omega_1$, then $\omega_{ar, II+}$ could be equal to any other frequency. That is possible because the EMSD tuning is uncoupled with the TMD tuning in this architecture. However, a third resonance will appear because there is no more degenerated eigenmode.

In the following section, the experimental setup of Arch. II is described then the results with this architecture are commented.

3 EXPERIMENTS

3.1 Experimental setup

We design a host structure made up of two equals aluminium plates sustained by four equals aluminium beams. Through geometric and mechanical properties, the two first eigenmodes of this structure are configured as the two first bending eigenmodes B_{x1} and B_{x2} in the direction called \vec{e}_x . Figure 4 shows the studied model and its equivalent model considered with m the

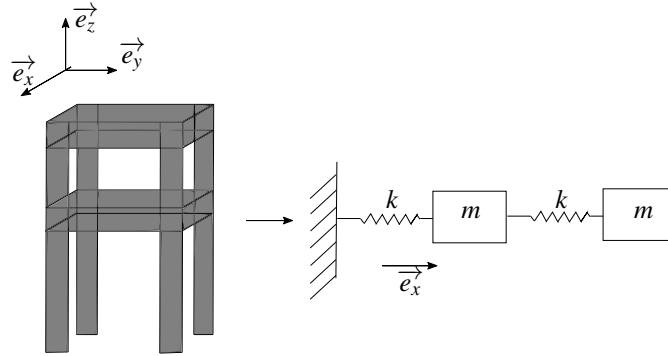


Figure 4: Schematic of the studied model equivalent at a Two Degrees Of Freedom (2DOF).

mass of a plate and k the bending stiffness of four parallel cantilever beams in the direction \vec{e}_x .

We obtain the eigenfrequencies :

$$\omega_{B_{x1}} = \sqrt{\frac{k}{m} \left(\frac{3 - \sqrt{5}}{2} \right)}, \quad \omega_{B_{x2}} = \sqrt{\frac{k}{m} \left(\frac{3 + \sqrt{5}}{2} \right)}. \quad (29)$$

The dimension of the host structure is chosen thanks to the equations (29), and a Finite Element Method (FEM) through a CAD software (Catia, Dassault Systèmes, France) in order to determine the two first torsional mode of this structure T_1 and T_2 . The established setup for the host structure are plates of 240mm long, 200mm wide, 12mm thick, and beams of 200mm long, 40mm wide and 5mm thick.

A laser Doppler vibrometer (PSV-400, Polytec, Germany) with its acquisition computer or an accelerometer (352C65, PCB Piezotronics, USA) with acquisition cards (NI 9234, National Instruments, USA) are used for measuring the FRFs. A function generator, from the vibrometer equipment, is used in order to emit an excitation chirp signal amplified by a power amplifier (Amplifier type 2719, Brüel and Kjaer, Denmark) and transmitted to a magnetic exciter. This exciter made up of a coil and a neodymium cylindrical magnet, small enough to ignore its mass, put in movement the host structure. The exciter magnet is set on the larger face of one upper beam, near to the upper plate. The exciter coil is radially centring near to the magnet, and the half of the magnet is set at the interior of the coil. The signal emitted to the coil is controlled in current and the interaction between the magnetic ux density of the magnet and this current generate a stress on the host structure. As the magnetic exciter is placed in order to create a force excitation in the direction of the bending modes B_{x1} and B_{x2} (\vec{e}_x), the bending modes corresponding to the two others direction are not excited. Only the bending mode like B_{x1} , B_{x2} , and the torsional modes like T_1 , T_2 , are sensed (shown in Figure 5). The FRF in Figure (5) is obtained with the laser Doppler vibrometer. The eigenfrequencies and the damping ratio associated to one eigenmode are the B_{x1} mode with a frequency of 34.9Hz and a damping ratio of 0.0096, the B_{x2} mode with a frequency of 85.0Hz and a damping ratio of 0.0014, the T_1 mode with a frequency of 118.8Hz and a damping ratio of 0.0029 and the T_2 mode with a frequency of 460.3Hz and a damping ratio of 0.0011. These eigenmodes are weakly damped (less 1%). So we can used a TMD made by aluminium in order to design an experimental TMD with a weak damping ratio. This TMD is a cantilever beam with a mass clamped at its free end as seen in Figure 6. This TMD is tuned thanks to the beam length L_a in using the eigenmode reliant on the mass clamped m_a and the bending beam deflection v_a in the case of a concentrated load at the free end F_a which defined the stiffness coefficient associated k_a . The tunable resonance frequency is :

$$\omega_a = \sqrt{\frac{3Eb_a h_a^3}{12m_a L_a^3}}, \quad (30)$$

with E the Young's modulus, L_a the beam length, b_a the beam width and h_a the beam thickness. The tuning is mainly done with the beam length adjustment.

The EMSD consists of a VCA (AE30-01-01, Pack' Aero, France) without guidance made up of

a magnetic field assembly attached to an aluminium hollow structural section clamped to the host structure frame and a coil placed at the bottom of the upper plate of the host structure. Naturally, this VCA is placed in order to work in the direction \vec{e}_x such the coil go through the air gap of the magnetic field assembly. We determine the force factor at $2.98N/A$, which is an important constant for the vibration reduction, the coil inductance of $664\mu H$ and the coil internal resistance of 3.4Ω . In order to produce a conservative EMSD, we need a total resistance circuit of 0Ω . However, in this case we get a short circuit that we cannot generate. So we need to reduce this resistance as closely as possible to zero. Then, this shunt is resonant in adding a capacitor to the circuit. The tuning of ω_e (24) on bending eigenmodes of the primary structure requires a capacitance of :

$$C = \frac{1}{L\omega_1^2}, \quad (31)$$

such as ω_1 is one bending eigenfrequency. As we consider the B_{x1} mode, its eigenfrequency is $34.9Hz$ and the determined capacitance is $31.3mF$. This capacitance value is high for a standard capacitor. It is why a digital signal processor (MicroLabBox DS1202, dSPACE, Germany) is used so as to synthesize the RC-shunt. The DSP works on a sampling frequency of $30kHz$ that is enough for the measuring and the application in the range frequency $[0 - 400]Hz$. An interface circuit connect the VCA to the DSP, made of two operational amplifiers (Op-Amp). The first (OPA 445, Texas Instruments, USA) is used for measuring the current I by an inverting amplifier

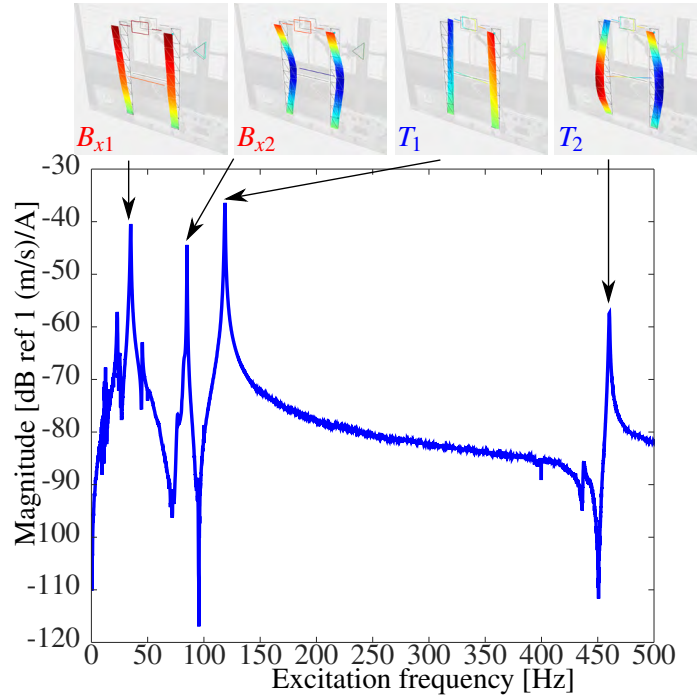


Figure 5: Frequency response function of the host structure on a top left measurement point.

with a gain $G_{inv} = -1$ and a measuring resistance $R_m = 28.4\Omega$. So the current measured is $I_m = \frac{1}{R_m} \left(\frac{1}{G_{inv}} V_{in} \right)$ with V_{ADC} the ADC input voltage. The second (OPA 547T, Texas Instruments, Etats-Unis) is used for a voltage follower with a gain $G_{fol} = 1$. The two Op-Amp are supplied by a DC power supply (FI 1333, Française d'Instrumentation, France). The DSP is designed to be equivalent to an impedance Z_{sh} in order to generate a resonant shunt :

$$Z_{sh}(\Omega) = R_{sh} + \frac{1}{j\Omega C_{sh}}, \quad (32)$$

with the shunt resistance and capacitance, R_{sh} and C_{sh} respectively. The shunt resistance is in fact chosen negative to cancel the internal coil resistance r_L , in order to obtain a fully conservative resonant shunt and an antiresonance as perfect as possible.

3.2 Host structure coupled with a tuned mass damper and a digital resonant shunt

Now the TMD and the EMSD are used and tuned on the B_{x1} eigenmode of the host structure alternately then simultaneously like seen in Figure 6. The accelerometer measures the FRFs

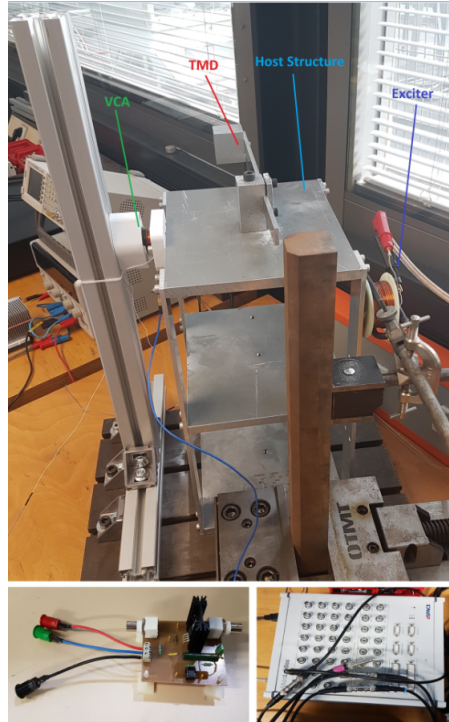


Figure 6: Photograph of the host structure, the TMD (on the top). For the EMSD : the VCA (on the top), the interface circuit (on the left bottom) and the DSP (on the right bottom).

of the host structure dynamics. For the purpose of tuning the TMD, we use a beam of 300mm long, 20mm wide and 3mm thick with a mass clamped of 0.15kg and we tuned $L_a = 160mm$,

which is considered as the distance between the clamped mass m_a and the TMD support. The tuning of the RC-shunt is realised by the application of the numerical values $R_{sh} = -3.35\Omega$ et $C_{sh} = 31.3mF$. We note the EMCF of the B_{x1} mode $\kappa_{B_{x1}}$. By the correlation between models and experimentals measured, we can determine the mass ratio μ and the the EMCF $\kappa_{B_{x1}}$ for the combination of the host structure with the TMD and the EMSD respectively. Then the model for the host structure coupled with the TMD and the RC-shunt is used with the previous values determined of μ and $\kappa_{B_{x1}}$. Finally, Figure 7 shows the FRFs of experimental measurements and numerical modelling for the host structure alone, coupled with the TMD, coupled with the EMSD and coupled with the both damping systems. In Figure 7, experiments gives $\xi_{B_{x1}} =$

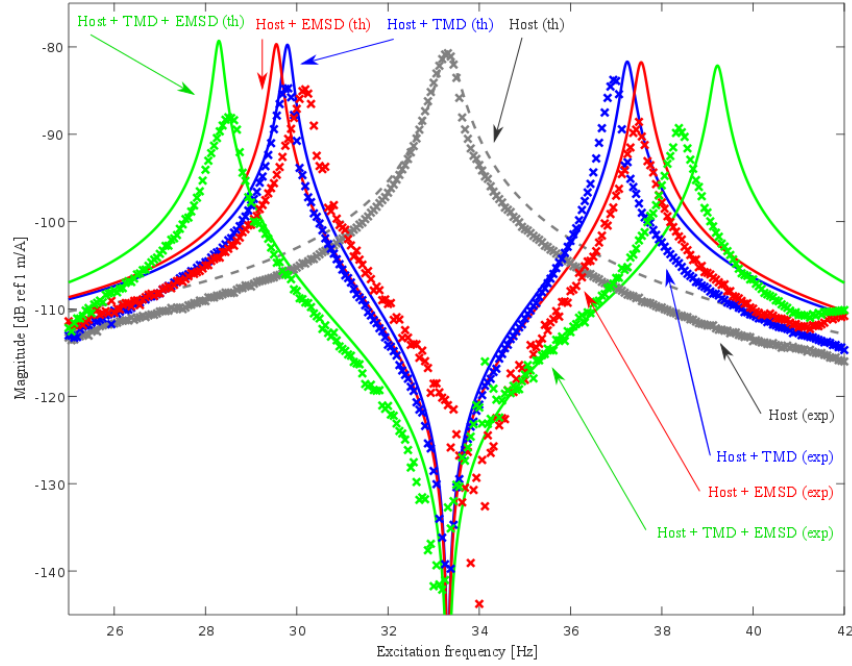


Figure 7: Magnitude of the frequency responses functions in the vicinity of the B_{x1} eigenmode

0.00728, $\mu = 0.05$ and $\kappa_{B_{x1}} = 0.24$. The theoretical models are computed ((th) in Figure 7) and present a good agreement with the experiments ((exp) in Figure 7). The superposition effect of the EMSD on the TMD are clearly made an enhancement on the vibration reduction of the host structure, even if these systems are weakly damped. In fact, the frequency distance is approximately gone from $3Hz$ to $5Hz$. So, these experimental results validate the theory on the enhancement of the vibration reduction in the conservative case. However, limitations on these experiments are the fact we need EMSD and TMD weakly damped in order to apply efficiency this method. This is why using a DSP as a digital shunt enables the reducing of the resistance in the RC-shunt, especially the coil resistance.

4 CONCLUSION

In this paper, an elastic host structure, a TMD and a shunt circuit which composed two kinds of architectures, Arch. I and Arch. II, are studied. The goal was to enhance the vibration reduction induced by the TMD in using the EMSD. We determined optimum parameters of the TMD and the EMSD systems in these architectures for a SDOF system, which corresponds to an eigenmode of the elastic host structure. It demonstrated Arch. II is more pertinent in comparison of host structure and TMD combination for conservatives dampers.

The vibration reduction is obtained by means of the TMD and/or the EMSD and conclusions attest of the correlation between theoretical models and experimental tests. For conservative systems, we observe that the application of these two damping systems is optimum when we apply the both same tuning parameters for the TMD and for the EMSD, when each is coupled with the host structure.

We have made a RC-shunt using a DSP in order to make a synthetic shunt. On the contrary of an analog shunt, the digital shunt has an advantage of tuning the RC-shunt by numerical inputs. The DSP generate a negative resistance aiming at reducing the total resistance induced by resistors and the VCA coil, and generate a capacitance aiming at create a resonant EMSD.

REFERENCES

- [1] Zhu, S. et al. Dynamic analogy between an electromagnetic shunt damper and a tuned mass damper. *Smart Materials and Structures* (2013) **22**:115018.
- [2] Frahm, H. *Device for damping vibrations of bodies*. U.S. Patent, (1911) No. 989958, Apr.
- [3] Hagood, N.W. and von Flotow, A. Damping of structural vibrations with piezoelectric materials and passive electrical networks. *Journal of Sound and Vibration* (1991) **146**:243-268.
- [4] Thomas, O. et al. Performance of piezoelectric shunts for vibration reduction. *Smart Materials and Structures* (2012) **21**:015008.
- [5] Den Hartog, J.P. *Mechanical Vibrations*. McGraw-Hill, Vol. 4, (1956).
- [6] Behrens, S. et al. Electromagnetic Shunt Damping. *Proceedings of the IEEE/ASME International Conference on Advanced Intelligent Mechatronics* (2003) 1145-1150.
- [7] Elliott, S.J. et al. Scaling of electromagnetic transducers for shunt damping and power harvesting. *Proceedings of International Conference on Noise and Vibration Engineering including International Conference on Uncertainty in Structure Dynamics* (2012).
- [8] Yan, B. et al. Shunt damping vibration control technology : a review. *Applied Sciences* (2017) **7**.
- [9] Arroyo, E. and Badel, A. Electromagnetic vibration energy harvesting device optimization by synchronous energy extraction. *Sensors and Actuators A* (2011) **171**:266-273.

- [10] Wang, H.-Y. et al. A 2DOF hybrid energy harvester based on combined piezoelectric and electromagnetic conversion mechanisms. *Journal of Zhejiang University-SCIENCE A (Applied Physics and Engineering)* (2014) **15(9)**:711-722.
- [11] Xu, Z. et al. A novel tunable multi-frequency hybrid vibration energy harvester using piezoelectric and electromagnetic conversion mechanisms. *Applied Sciences* (2016).
- [12] Xia H. et al. Analysis of piezoelectric–electromagnetic hybrid vibration energy harvester under different electrical boundary conditions. *Sensors and Actuators A : Physical* (2015) **234**:87-98.
- [13] Zuo, L. and Cui, W. Dual-functional energy-harvesting and vibration control : electromagnetic resonant shunt series tuned mass Dampers. *Journal of Vibration and Acoustics* (2013) **135**.
- [14] Wang, H.-Y and Tang, L. Modeling and experiment of bistable two-degree-of-freedom energy harvester with magnetic coupling. *Mechanical Systems and Signal Processing* (2017) **86**:29-39.
- [15] Black, B. et al. Basics of Voice Coil Actuators. *PCIM Power Electronics Systems* (1993) 44-46.
- [16] Multon, B. et al. Actionneur électromagnétique à bobine mobile. *La Revue 3E.I* (1997) **10**.
- [17] Tang, X. and Zuo, L. Enhanced vibration energy harvesting using dual-mass systems. *Journal of Sound and Vibration* (2011) **330**:5199–5209.

HIGH VOLTAGE SYNTHETIC INDUCTOR IN PIEZOELECTRIC SHUNT TO DAMP FLEXIBLE VIBRATING STRUCTURES

KEVIN DEKEMELE*, PATRICK VAN TORRE[†] AND MIA LOCCUFIER*

*Department of Electrical energy, Metals, Mechanical Constructions and Systems
Ghent University, Technology park 125, 9052 Ghent, Belgium
e-mail: kevin.dekemele@ugent.be

[†] Department of Information Technology
Ghent University, Technology park 126, 9052 Ghent, Belgium

Key words: Piezoelectric Shunt, Synthetic Inductor, High Voltage

Abstract. The use of resonant piezoelectric shunts is a well-established solution to mitigate vibrations in flexible mechanical structures. However, very large inductance values are required in the shunt. These values are difficult to obtain for passive inductors and therefore, inductance values are often synthesized with operational amplifiers (OpAmp). The downside is that standard OpAmps can only handle up to 30V peak-to-peak and the state of the art amplifiers up to 100Vpp. Piezoelectric materials typically generate high voltages even for low vibration levels. With the increasing push towards lighter and more slender mechanical structures, the increased vibration levels result in even higher voltage levels such that even the most advanced OpAmps fall short. In this research, a synthetic inductor is proposed and built by combining the bridge amplifier configuration and the output voltage boost configuration, effectively quadrupling the range of the synthetic inductor to 400Vpp. The synthetic inductor is then employed to shunt a piezoelectric patch bonded on a cantilever beam.

1 INTRODUCTION

Excessive vibrations in mechanical structures are typically reduced by adding another mechanical oscillator on the structure, called a tuned mass damper (TMD) [1]. With addition of a well-designed TMD, the vibrations are relocated from the original structure to this oscillator where they are dissipated, significantly decreasing vibrations in the mechanical structure. Piezoelectric (PE) materials can convert mechanical into electrical energy and vice versa. Therefore, bonding PE material to a vibrating structure and shunting it with a resonant electrical circuit will have the same effect as a TMD [2]. However, very large inductance values are required in the shunt such that resonance in the electrical shunt matches one of the mechanical vibration frequencies. It is impractical to design a wirewound inductor coil with such a very large inductance and a low resistance at the same time. Therefore, this large inductance is often realized as a synthetic inductor, i.e., an active electronic circuit which mimics the electrical impedance of an inductor. A synthetic inductor consists of one or more operational amplifiers (OpAmps) and a number of passive resistors and capacitors. Another advantage of this approach is that the inductance can easily be made modified.

A well-known feature of piezoelectric material is its typically high-voltage and low-current operation. As OpAmps are limited in the voltage which they receive on their inputs, researchers have employed

“high voltage” OpAmps. The state-of-the-art high voltage OpAmps are the OPA445 (90V peak-to-peak) [3], used in many shunts which synthesize an inductor [4, 5], or more advanced, a negative capacitance [6] and more recently digital impedance [7]. The OPA454 (100Vpp) is another high-voltage OpAmp with better specifications and an exposed metal pad for cooling the chip [8].

As mechanical structures nowadays tend to be more light and slender, the magnitude of vibration during resonance can reach levels that induce much higher voltages than 100Vpp in a PE patch. Similar concerns were raised in [9], where it was claimed a shunt was built which could handle 350 Vpp. However, the design of the circuit was not disclosed.

In the field of analogue electronics, several techniques are known to boost the output voltage range of an amplifier. The most straightforward technique is the “bridge amplifier configuration”, where two similar amplifiers are driven anti-phase. The load is connected between the two amplifier outputs, effectively doubling the output voltage range.

Another, less common technique is the “output voltage boost configuration”, where the positive and negative power supply voltages of the main amplifier are delivered by supply boost amplifiers. By selecting the proper boost amplifier supplies and gain factors it is possible to create a set of power supply voltages for the main amplifier, of which the average tracks the desired output signal, effectively doubling the output voltage range in an alternative way.

Employing a combination of both techniques, it is possible to quadruple the output voltage range. A new circuit has been designed and built, employing 6 high-voltage operational amplifiers, successfully synthesizing an inductor for a voltage range up to 400V. The circuit is tested experimentally as a shunt to mitigate the vibrations of a small flexible cantilever beam. The measured deflection of the beam under resonance with and without shunt confirms the expected mitigation even when the shunt is subjected to higher voltage levels than 100Vpp.

2 HIGH VOLTAGE SYNTHETIC INDUCTOR

2.1 High-voltage gyrator

The high-voltage synthetic inductor is built around a high-voltage gyrator of which the circuit diagram is shown in Fig. 1. This gyrator employs an OPA454 OpAmp, produced by Texas Instruments, which is to our knowledge the OpAmp with the highest voltage of operation commercially available. The OPA454 is specified at 100V (or +50V and -50V) supply voltage, with an absolute maximum rating of 120V.

The simulated input impedance is given by Ohm’s law as

$$Z_{in} = \frac{V_{in}}{I_{in}}$$

The OpAmp is configured as a voltage buffer, delivering an output voltage

$$V_{out} = V_{in} \cdot \frac{R}{R + \frac{1}{j\omega C}} = V_{in} \cdot \frac{j\omega RC}{1 + j\omega RC}$$

Hence the voltage drop across R_L is equal to the difference between the input voltage and the OpAmp’s output voltage. Therefore the current through R_L can be found from Ohm’s law. As the components are chosen in order to make $R_L \ll R$, the input current is approximately equal to the current through R_L :

$$I_{in} \approx \frac{V_{in} - V_{out}}{R_L} = \frac{V_{in} - V_{in} \cdot \frac{j\omega RC}{1 + j\omega RC}}{R_L} = \frac{V_{in}}{R_L (1 + j\omega RC)}$$

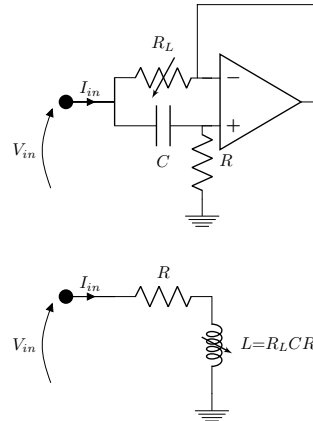


Figure 1: High-voltage gyrator with OPA454 OpAmp

The resulting simulated impedance is

$$Z_{in} = \frac{V_{in}}{I_{in}} \approx j\omega RC \cdot R_L + R_L$$

This means the gyrator simulates an inductor with a value of $C \cdot R \cdot R_L$ Henry, in series with a small resistor R_L .

If the gyrator circuit is employed as a shunt to attenuating mechanical vibrations with piezo transducers, a series resistor larger than R_L often required so the presence of R_L does not compromise the performance of the vibration damping. Therefore it is not necessary to employ gyrator circuits without series resistance but with a higher OpAmp component cost, such as the standard Antoniou circuit, used in many resonant shunts [4, 5, 10].

2.2 Power supply boost configuration

It is possible to extend the voltage range of an amplifier by dynamically modifying the power supply voltages depending on the desired output voltage. The power supplies V_{pos} and V_{neg} of the central amplifier, used for the gyrator circuit, are now delivered by two similar OPA454 OpAmps, one supplied with a positive voltage and one with a negative voltage, referred to ground. By means of an equal-resistor voltage divider between the OpAmp's output and the positive or negative power supply voltage, followed by a voltage buffer, the supply boost OpAmps deliver

$$V_{pos} = \frac{V_{out} + 100V}{2}$$

$$V_{neg} = \frac{V_{out} - 100V}{2}$$

The principle is schematically drawn on Figure 2, where both left and right a gyrator is supplied this way.

Therefore the central amplifier's output voltage range is now extended to $200V_{pp}$ as the power supply voltages track the output voltage when referring to ground level, whereas the total supply voltage across the central OpAmp always remains equal to

$$V_{supply} = V_{pos} - V_{neg} = 100V$$

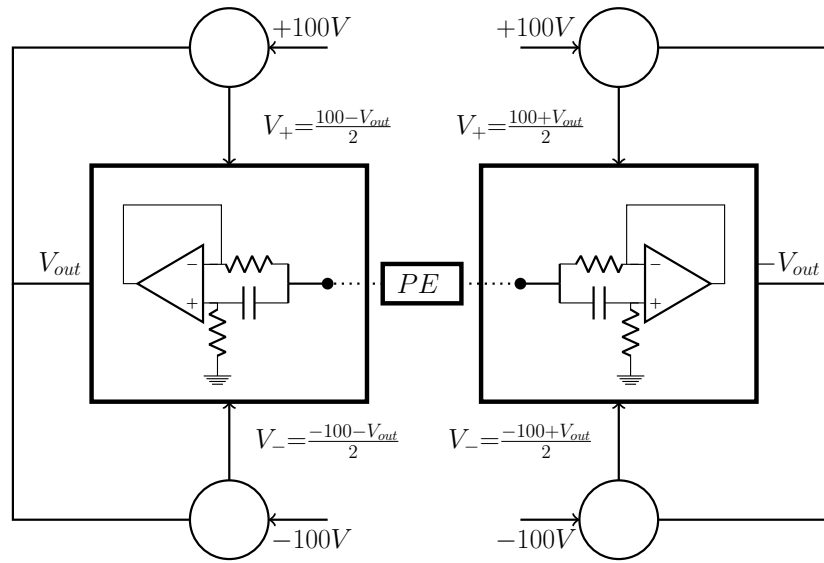


Figure 2: Extending the voltage range of a synthetic inductor with Power Supply Boost and Bridge configuration. Voltages determined based on antisymmetric excitation by the central piezo element PE.

The principle of operation is illustrated by means of the waveforms in Fig. 3. In this graph the power supply boosted gyrator is driven to its full output voltage range on a $\pm 100\text{V}$ symmetric power supply.

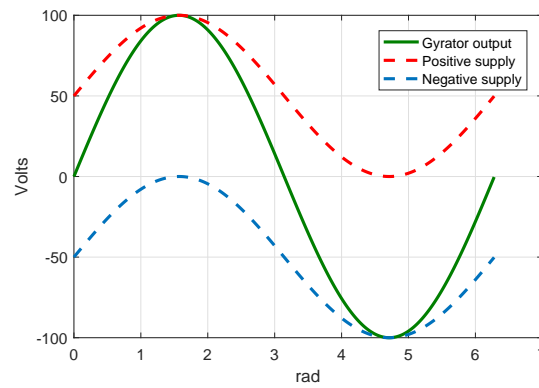


Figure 3: Power supply boost operation

2.3 Bridge configuration

The Bridge Tied Load (BTL) configuration is well-known in the field of amplifier design to be able to deliver an output amplitude which is twice the voltage range of an individual amplifier. To achieve this range extension, two amplifiers are driven antiphase and the load is connected between the two outputs. On Figure 2, the left and right gyrators are indeed driven antiphase, with the piezo element PE functioning as a source in between the two outputs, sourcing current in one terminal and sinking the same current from the other terminal.

This approach is used to provide a second doubling of the voltage range of the gyrator. Basically two simulated inductors with voltage boost configuration are employed in series, effectively quadrupling the output voltage range to $400V_{pp}$. Because the piezo transducer is connected between two gyrator outputs, the gyrators appear in series with respect to the piezo transducer, doubling also the simulated impedance. Using similar component values in both gyrator circuits, the resulting impedance is equal to

$$Z = 2j\omega C \cdot R \cdot R_L + 2R_L$$

Practical component values are $C = 1\mu F$, $R = 1M\Omega$ and $R_L = 100\Omega$, resulting in an inductance of 200H in series with a 200 Ω resistor. In the implementation R is determined by a 1M Ω potentiometer, allowing the inductor to be adjusted from 0 to 200H. On Figure 5a and Figure 5b show the experimentally constructed circuit.

3 ELECTROMECHANICAL SYSTEM

3.1 Theoretical model and tuning

The vibrating mechanical structure of the experiment is a cantilever beam, bonded with 2 PE patches near its fixed end, as shown on Figure 4. The first PE patch will be used to excite the beam, while the other patch on the opposite side will be shunted by the RL shunt, synthesized by the circuit presented in the previous section.

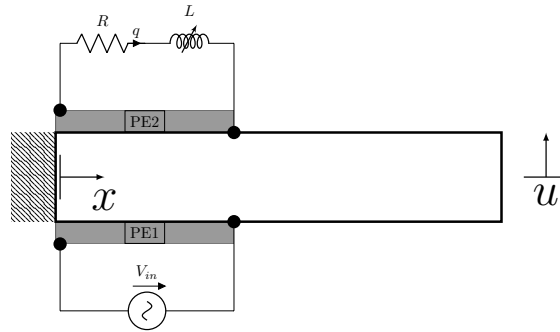


Figure 4: The considered dynamical system, a cantilever beam with PE1 used as an actuator and PE2 shunted with a RL shunt

By decomposing the dynamic deflection of the beam in a mode shape and a modal time coordinate $u(x,t) = \phi(x)r(t)$, the dynamical equation of the full system can be written as [11]

$$\begin{cases} \ddot{r} + 2\zeta\omega_n\dot{r} + \omega_n^2 r - \theta_2 V_2 = \theta_1 V_{in} \\ C_{p,2} V_2 + \theta_2 r = q \end{cases} \quad (1)$$

with ω_n the short circuit natural frequency, ζ the modal damping, θ_1 and θ_2 the modal coupling coefficient of each PE patch and C_p the capacitance of the second PE patch. The equation (1) can be seen as a mechanical oscillator excited by the first piezo and an electrical interaction with the second piezo, depending on shunt circuit. When shunted by an RL shunt, $V_2 = -R\dot{q} - L\ddot{q}$, the R and L can be optimized in such a way that the vibrations at the resonance conditions of the mechanical oscillator are minimized, while also avoiding to create other significant resonances. In this research, the optimizing

procedure is based on how mechanical TMD's are optimized [1], applied to resonant shunts [10]. The optimal electrical parameters are :

$$\omega_e = \omega_n \sqrt{1 + k^2} \quad \zeta_e = \sqrt{\frac{3}{8}} k$$

with $\omega_e = \frac{1}{\sqrt{LC_{p,2}}}$ the electrical natural frequency, $\zeta_e = \frac{RC_{p,2}\omega_e}{2}$ the electrical damping and $k = \sqrt{\frac{\omega_n^2 - \omega_{n,CC}^2}{\omega_{n,CC}^2}}$ the effective coupling coefficient with $\omega_{n,SC}^2$ the resonance frequency of the mechanical oscillator when $V_2 = 0$, meaning when the second patch is shorted over its terminals.

3.2 Experiment

The optimization described above is very practical as only the open and closed-circuit resonances are needed, two parameters which are easily found experimentally.

A 166 mm long, 35 mm wide and 0.2 mm thick aluminum beam was fitted with two PIC255 piezoelectric patches which are 30 mm wide, 50 mm long and 0.2 mm thick and have a C_p of 103 nF. Further material constants are found on [12]. To identify the closed and open circuit resonances, a sine sweep with amplitude 100 V was applied to the actuating PE-patch with the other patch first in closed circuit, then open circuit, and finally with the optimized circuit. The deflection of the beam at the free end is measured with a laser vibrometer and both the applied voltage and measured deflection are used to construct an experimental frequency response function as shown on Figure 6a. The experimental open-circuit resonance frequency is 67.68 Hz and the closed 67.33 Hz. The generalized coupling coefficient is $k = 0.1021$ resulting in an optimal $R = 2.9k\Omega$ and $L = 54$ H. As expected, the FRF when using the shunting PE patch, seen on Figure 6a, shows a significant, almost 10-fold decrease of the vibrations near the resonance of the mechanical oscillator.

To verify the high voltage over the RL shunt during vibration damping, the open circuit resonance frequency is applied to PE1 as a 200Vpp sine wave, while the voltage over PE is measured, once in open circuit and once when the RL shunt is applied, Figure 6b. The synthetic inductor can easily handle the measured voltage over the shunt (178Vpp), which would not be possible with conventional OpAmps, or with a single high-voltage OpAmp. Note that the applied voltage, 100V, corresponds to only 7 mm amplitude at the tip of the beam, Figure 6a when PE2 is in open or closed circuit.

4 CONCLUSIONS

This research presented a high-voltage synthetic inductor consisting of 6 operational amplifiers, with an increased range from 100Vpp up to 400Vpp. This way, resonant shunts used to mitigate vibration of mechanical structures are able to deal with the increasingly high vibration levels which induce high voltages in these shunts. By supplying a single gyrator circuit by output voltage boost configuration, where the supply of operational amplifiers depend on their output, the voltage range of the gyrator was doubled. Another doubling was achieved by then supplying two of these gyrators in an anti-phase manner. The circuit was designed and used as a shunt for a piezoelectric patch bonded to a cantilever beam. The vibration in the beam induced voltages up to 178Vpp in the shunt, a voltage level where previous implementations of synthetic inductors are not able to deal with.

References

- [1] Jacob Pieter Den Hartog. *Mechanical vibrations*. Courier Corporation, 1934.

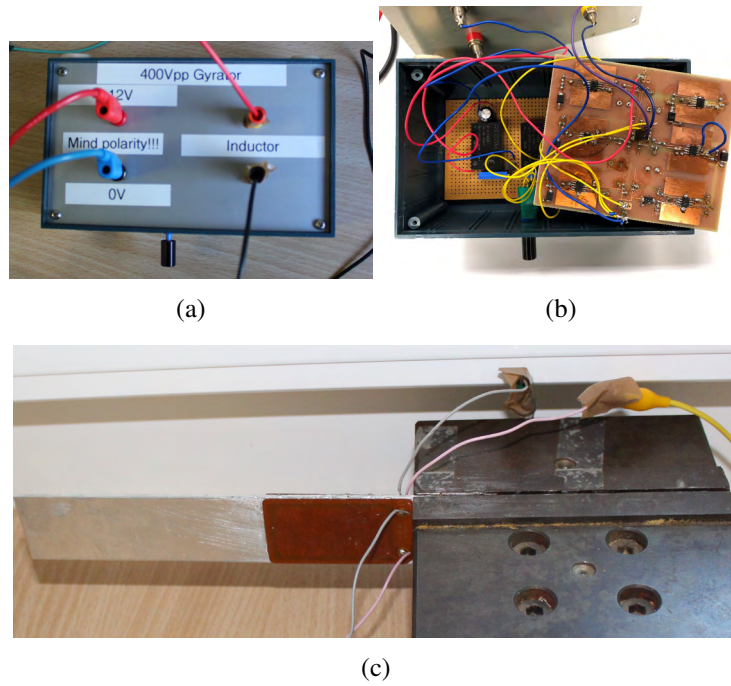


Figure 5: The case of the 400Vpp synthetic inductor, closed (a) and open (b). The variable resistor is seen at the bottom center. The beam with PE patch bonded (c) on both sides.

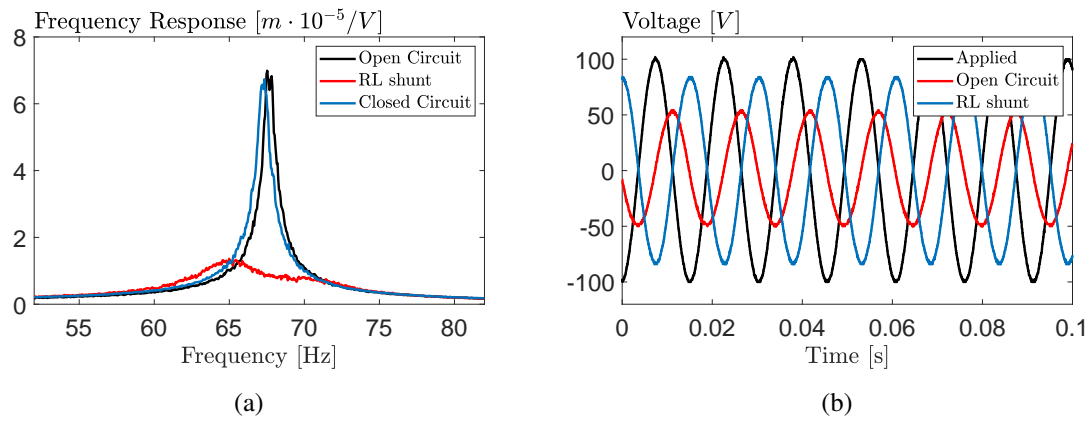


Figure 6: Frequency response function with PE2 open, closed circuit and shunted (a) and resonant voltage applied to PE1 and generated by PE2 (b).

- [2] Nesbitt W Hagood and Andreas von Flotow. Damping of structural vibrations with piezoelectric materials and passive electrical networks. *Journal of Sound and Vibration*, 146(2):243–268, 1991.
- [3] Texas Instruments. *High Voltage FET-Input OPERATIONAL AMPLIFIER*, 4 2008.
- [4] Francesco dell’Isola, Corrado Maurini, and Maurizio Porfiri. Passive damping of beam vibrations through distributed electric networks and piezoelectric transducers: prototype design and experimental validation. *Smart Materials and Structures*, 13(2):299, 2004.
- [5] Marta Berardengo, Stefano Manzoni, Olivier Thomas, and Marcello Vanali. Piezoelectric resonant shunt enhancement by negative capacitances: Optimisation, performance and resonance cancellation. *Journal of Intelligent Material Systems and Structures*, 29(12):2581–2606, 2018.
- [6] Marcus Neubauer, Robert Oleskiewicz, Karl Popp, and Tomasz Krzyzynski. Optimization of damping and absorbing performance of shunted piezo elements utilizing negative capacitance. *Journal of sound and vibration*, 298(1-2):84–107, 2006.
- [7] J Nečásek, J Vaclavik, and P Marton. Digital synthetic impedance for application in vibration damping. *Review of Scientific Instruments*, 87(2):024704, 2016.
- [8] Gang Wang, Jianqing Cheng, Jingwei Chen, and Yunze He. Multi-resonant piezoelectric shunting induced by digital controllers for subwavelength elastic wave attenuation in smart metamaterial. *Smart Materials and Structures*, 26(2):025031, 2017.
- [9] Oliver Heuss, Rogério Salloum, Dirk Mayer, and Tobias Melz. Tuning of a vibration absorber with shunted piezoelectric transducers. *Archive of Applied Mechanics*, 86(10):1715–1732, 2016.
- [10] Olivier Thomas, Julien Ducarne, and Jean-François Deü. Performance of piezoelectric shunts for vibration reduction. *Smart Materials and Structures*, 21(1):015008, 2011.
- [11] Donald J Leo. *Engineering analysis of smart material systems*. Wiley Online Library, 2007.
- [12] PI ceramics. *Piezoceramic Materials*, 4 2008. <http://fisica.cab.cnea.gov.ar/bt/images/d/d3/PICat.pdf>.

HYBRIDIZATION OF ACTIVE CONTROL AND PASSIVE RESONANT SHUNT

Ahmad Paknejad^{*}, Ghislain Raze[†], Guoying Zhao^{*}, Michel Osée^{*}, Arnaud Deraemaeker[‡], Frédéric Robert^{*}, Gaëtan Kerschen[†] AND Christophe Collette^{*†}

^{*}Université Libre de Bruxelles, BEAMS Department, 50 F.D.Roosevelt Av, B-1050 Brussels, Belgium

[†]Université de Liège, Department of Aerospace and Mechanical Engineering, Allée de la Découverte 9, 4000 Liège, Belgium

[‡]Université Libre de Bruxelles, BATir Department, 50 F.D.Roosevelt Av, B-1050, Brussels, Belgium

Key words: Vibration damping, Hybridization, Smart Structures, Electromagnetic transducer

Abstract. Resonant shunt circuit applied on a transducer such as a piezoelectric element or a voice coil is widely used as a passive control technique to damp a specific vibration mode. While very simple and robust, the damping capability is proportional to the electromechanical coupling of the transducer. On the other hand, one of the major difficulties that arises in practical implementation of purely active vibration control is the power consumption required for conditioners and control units. The idea of using a hybrid control system is proposed in this study to combine the passive shunt device with an active control in order to improve the performance with low power consumption. Both active voltage source and active current source are proposed and compared. The method of maximum damping, i.e. maximizing the exponential time-decay rate of the response subjected to the external impulse forcing function, is used to optimize the parameters of the passive and hybrid control systems. The advantage of using an hybrid control configuration in comparison with purely active control system is also investigated in terms of power consumption.

1 INTRODUCTION

Recently, the electromagnetic shunt damper has been proposed as a very simple and effective passive control technique. The key idea of this technique is to connect a capacitor of capacitance C and a resistor of resistance R to the electromagnetic transducer of inductance (L) to form a resonant R-L-C circuit. The absorber dissipates the vibrational energy by the resistor when the resonance of the circuit is tuned close to the resonance of the primary system thanks to the tuned capacitor [1]. Many optimization methods have been proposed to optimize the parameters R and C . de Marneffe [2] optimized the parameters through the root-locus analysis and H_∞ minimization when the system is under base excitation. He has also compared the resonant R-L-C shunt with a resistive shunt. Inoue et al. [3] derived the optimal parameters by using the fixed point theory for the mechanical vibration absorber proposed by Den Hartog [4]. In [5], the optimal parameters have been obtained analytically using both the H_2 and H_∞ optimization methods which consist in minimizing the root-mean-square (RMS) vibration under random excitation and the peak amplitude in the frequency domain, respectively. Moreover, Zhu et al.

[6] studied the analogy between the electromagnetic shunt damper and a tuned mass damper (TMD). Then, the optimal parameters of an electromagnetic shunt have been adapted from the optimal parameters of the TMD (obtained by Ormondroyd and Den Hartog [7]) by using an equivalent mass, stiffness and damping coefficient for the electromagnetic shunt damper. The main shortcoming of this method is that the optimal parameters can be used only when the equivalent mass ratio is small enough because a full dynamic analogy does not exist.

The hybrid control system may be an effective control configuration by combining the advantages of both active and passive control systems [8]. In other words, the active part of a hybrid system requires much less power than a similar purely active system, while providing better vibration suppression than the passive system alone. Despite this interest, no one to the best of our knowledge has studied the hybridization of the passive electromagnetic shunt damper with an active control system for the purpose of vibration damping improvement.

In the literature, there are a number of studies on active-passive hybrid piezoelectric network (APPN). In 1994, Agnes [9] proposed the concept of APPN and Tsai et al [10] presented more insight and fundamental understandings to the APPN configuration. Basically, the APPN integrates piezoelectric shunt damping with an active voltage or charge source to improve the control performance of the structure [11]. Morgan et al. [12] used active coupling feedback to enhance the electromechanical coupling of the transducer. In most studies about the APPN, a collocated piezoelectric sensor has been used to generate the feedback signal. However, MingMing et al. [13] employed a velocity feedback control for the application of the APPN by using a displacement sensor. The optimal values of the resistance and inductance could be quite different from those of the purely passive system in the case of APPN. Therefore, Tsai et al. [14] proposed a methodology to determine the optimal values of the resistor and inductor simultaneously with the control law.

In the present study, the active-passive hybrid electromagnetic shunt damper is proposed. This paper is organized as follows. First, a purely passive electromagnetic shunt damper is studied and the parameters of the R and C are optimized according to the method of maximum damping in Section 2. Then in Section 3, the hybrid configuration is modeled by combining either active voltage source in series and current source in parallel with the designed RC circuit. The power which flows between the structure and the transducer thanks to the application of an active control system with an hybrid configuration is discussed in Section 4. The conclusions are drawn in Section 5.

2 PASSIVE CONTROL SYSTEM

Figure 1 shows the system under consideration. It is an undamped single-degree-of-freedom (SDOF) oscillator with a mass m , spring k and an electromagnetic device connected to a resistor of resistance R and a capacitor of capacitance C . The system is excited by a disturbance force f_d ; in particular, and the impulse response of the SDOF system is of interest. The electromagnetic device which is made of a permanent magnet and a coil has the following parameters: coupling constant T , coil inductance L and coil resistance R_{coil} . It can generate a force f_a which is proportional to the current i flowing inside the coil. In addition, the voltage across the transducer V is proportional to the velocity of the mass. The governing equations of motion are written as:

$$m\ddot{x} + kx = f_d + f_a \quad (1a)$$

$$f_a = -Ti = -T\dot{q} \quad (1b)$$

$$V = L\ddot{q} + R\dot{q} + \frac{1}{C}q = T\dot{x} \quad (1c)$$

where q is the charge flowing inside the coil. For the sake of simplicity, R is considered as the total resistance of the circuit (Figure 1b). The above equations are normalized with respect to the dimensionless time $\tau = \omega_0 t$ where $\omega_0 = \sqrt{k/m}$ as below:

$$x_1'' + x_1 = f - \beta_1 \omega_0 x_2' \quad (2a)$$

$$x_2'' + 2\xi \alpha x_2' + \alpha^2 x_2 = \beta_2 / \omega_0 x_1' \quad (2b)$$

where the normalized parameters are:

$$\begin{aligned} \tau = \omega_0 t, \quad x_1(\tau) = x(t), \quad x_2(\tau) = q(t), \quad \Omega = \omega / \omega_0, \quad f = \frac{1}{k} f_d, \quad \beta_1 = \frac{T}{k} \\ \beta_2 = \frac{T}{L}, \quad \beta = \beta_1 \beta_2, \quad \omega_f = \frac{1}{\sqrt{LC}}, \quad \alpha = \frac{\omega_f}{\omega_0}, \quad \xi = \frac{R}{2} \sqrt{\frac{C}{L}} \end{aligned} \quad (3)$$

The transfer function of the system from the normalized external force f to the normalized displacement of the mass x_1 is then given by:

$$\frac{x_1}{f} = \frac{s^2 + 2\xi \alpha s + \alpha^2}{(s^2 + 1)(s^2 + 2\xi \alpha s + \alpha^2) + \beta s^2} \quad (4)$$

where $s = j\Omega$ is the Laplace variable. According to Eq. (4), the passive control system adds another DOF to the system which makes the closed-loop response having two complex poles. In order to obtain the optimal parameters, the method of maximum damping, i.e. minimizing the settling time of the transient response of the system to the impulse disturbance, is used. This can be achieved by realizing equal damping ratio and tuning the frequency of both poles of the closed-loop response. In other words, two

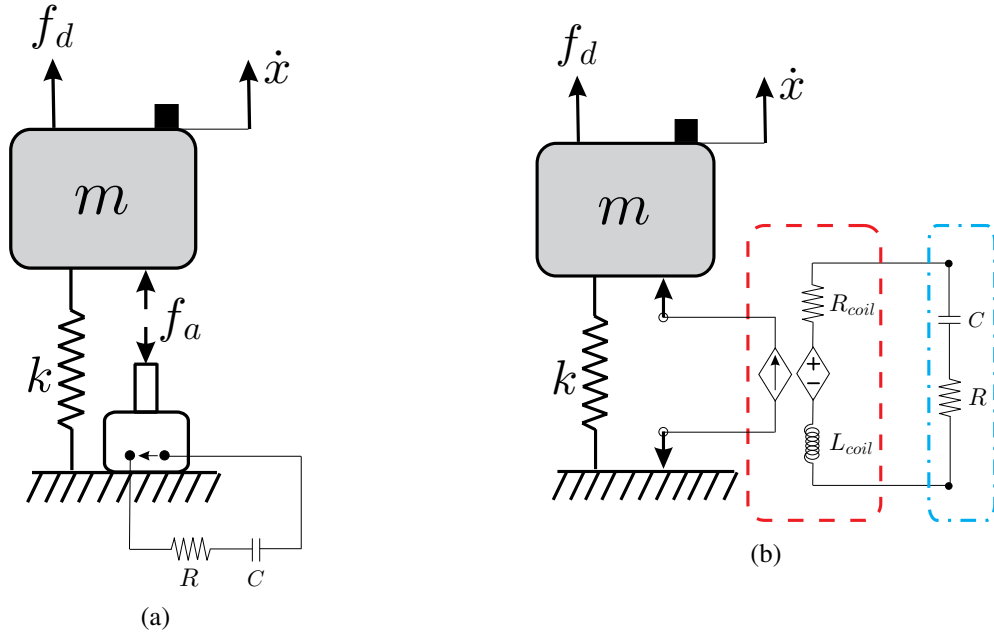


Figure 1: Single-degree-of-freedom (SDOF) oscillator combined with the electromagnetic shunt damper. (a) Mechanical model and (b) Electrical equivalent model of the transducer

poles are merged together. In this case, the normalized transfer function can be simplified as:

$$\frac{x_1}{f} = \frac{s^2 + 2\xi\alpha s + \alpha^2}{(s^2 + 2\eta\gamma s + \gamma^2)^2} \quad (5)$$

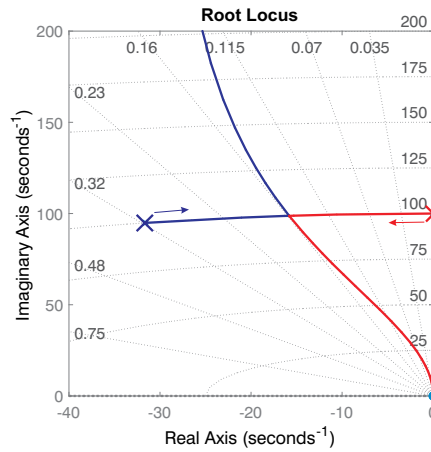
where η is the damping ratio, ω_c , and $\gamma = \omega_c/\omega_0$ are the resonance frequency and the normalized resonance frequency of the closed-loop response function, respectively. By matching the polynomial coefficients of the denominators of Eq. 4 and Eq. 5, the set of equations can be obtained as below:

$$4\eta\gamma = 2\xi\alpha \quad (6a)$$

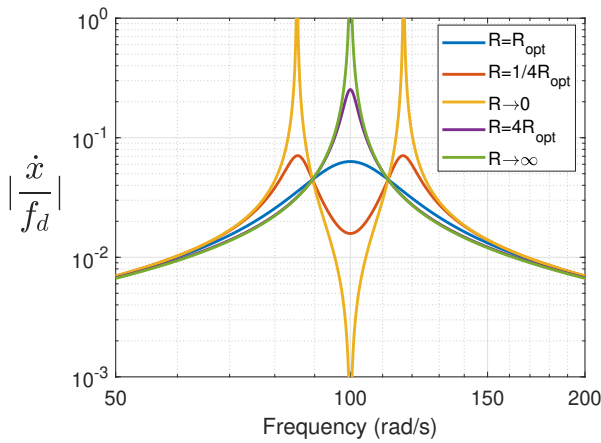
$$4\eta^2\gamma^2 + 2\gamma^2 = \alpha^2 + \beta + 1 \quad (6b)$$

$$4\eta\gamma^3 = 2\xi\alpha \quad (6c)$$

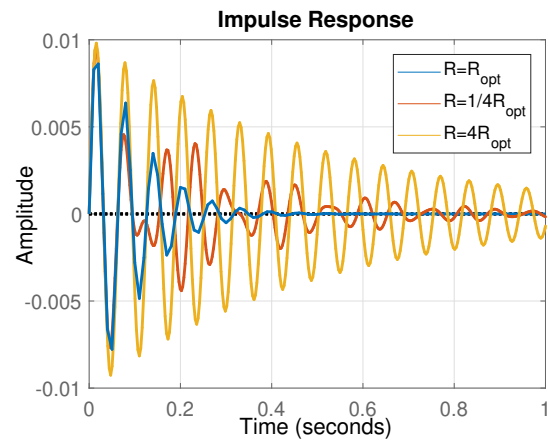
$$\gamma^4 = \alpha^2 \quad (6d)$$



(a)



(b)



(c)

Figure 2: For the attached passive RC circuit, (a) root-locus of the system for a specific value of the resistance R and capacitance C , (b) frequency response as well as (c) the impulse response for different values of R

From Eqs. (6a), (6c) and (6d), it can be concluded that

$$\gamma_{opt} = \alpha_{opt} = 1 \quad (7)$$

which means that the optimal frequency of the circuit and the closed-loop resonance frequency of the system are equal to the resonance frequency of the primary system. Considering the above equation and Eq. (6b) yields:

$$\xi_{opt} = \sqrt{\beta} \quad (8)$$

As a consequence, the optimal parameters of resistance and capacitance can be obtained as:

$$C_{opt} = \frac{1}{L\omega_0^2} \quad (9a)$$

$$R_{opt} = \frac{2T}{\sqrt{kC_{opt}}} \quad (9b)$$

In the remaining of the paper, the following numerical values are used: $m=1\text{kg}$, $k=10^4\text{N/m}$, $T=1\text{N/Amp}$, $L=L_{coil}=10^{-3}\text{H}$, and $R_{coil}=0\Omega$ (the resistance of the coil is included in R). The root-locus of the system with an attached passive RC shunt circuit is shown in Figure 2a. The locus consists of two loops (red and blue) starting from the pole of the primary system (red pole) and the pole of the resonant shunt (blue pole), respectively. One of the loop goes to the origin and the other one goes to infinity. Both loops are intersecting at one point when using the optimal values of resistance R_{opt} and capacitance C_{opt} . Figure 2b shows the frequency response for five different values of the resistance R . All the curves are intersecting at two points which are called fixed-points. For $R < R_{opt}$, two resonances with equal peaks appear in the vicinity of the resonance frequency of the primary system. The controller is no longer effective in the terms of amplitude reduction when $R \rightarrow 0$. In addition, the performance degradation can also be observed when $R > R_{opt}$. Especially when $R \rightarrow \infty$, the controlled system acts like a primary system with no additional damping. The impulse response in the time domain is also shown in Figure 2c for three different values of R . As it can be seen, the minimum settling time can be achieved by considering the designed optimal value of R obtained in Eq. (9b)

3 HYBRID CONTROL SYSTEM

From Eqs. (6)-(8) and (3), it can be concluded that the optimal closed-loop damping is $\eta_{opt} = T/(2\sqrt{kL})$. This shows that the stiffness of the structure as well as the coupling constant and the inductance of the transducer limit the maximum achievable damping obtained by the passive control system. The potential of using active control to improve the control performance of the system in terms of magnitude of the response is investigated.

In the present study, two different configurations for the hybridization of the passive resonant shunt with an active control are considered (Figure 3). In the first configuration shown in Figure 3a, the electromagnetic transducer is connected in series with RC elements and an active voltage source. The active voltage source is proportional to the velocity of the structure. The total voltage across the transducer (V) is then obtained by the summation of the active input voltage (V_{in}) and the voltage across the RC shunt circuit (V_{shunt}). Furthermore in the second configuration shown in Figure 3b, the electromagnetic transducer is connected in series with the RC circuit, and the active current source is in parallel with the shunting elements. Considering this configuration, the total current flowing in the transducer (i) is given by the summation of the input active current (i_{in}) and the current flowing inside the RC shunt circuit ($i_{shunt} = \dot{q}_{shunt}$).

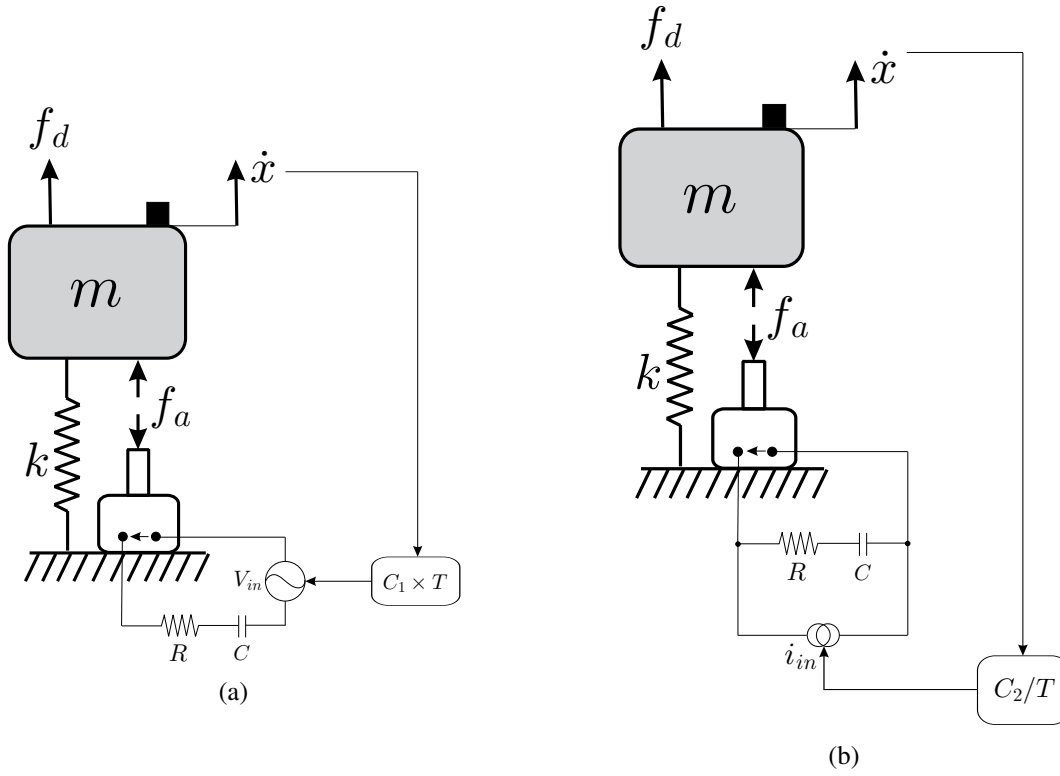


Figure 3: Schematic of a SDOF oscillator attached to an hybrid control system consisting of an electromagnetic transducer connected to the passive RC shunt (a) in series with an active voltage source and (b) in parallel with an active current source

3.1 Hybridization with an active voltage source

Considering the active voltage source, the equations of motion are modified as:

$$m\ddot{x} + x = f_d + f_a \quad (10a)$$

$$f_a = -T^* \dot{q} \quad (10b)$$

$$L\ddot{q} + R\dot{q} + \frac{1}{C}q + V_{in} = T\dot{x} \quad (10c)$$

$$V_{in} = -C_1 T \dot{x} \quad (10d)$$

By substituting Eq. (10d) into Eq. (10c), it can be seen that the active voltage source directly affects the effective coupling constant of the transducer. It is assumed that the transducer is ideal and there is a perfect balance between the electrical energy and the mechanical energy which means that there is no energy to be stored in the transducer [15]. According to the concept of energy conservation principle [16], the variation of the stored energy is the sum of the external power input and the internal power generation. This concept can be written for the electromagnetic transducer in the presence of the active voltage source when there is no shunt as:

$$dW = V dq + f_a dx = T(1 + C_1) \frac{dx}{dt} idt + T^* idx \quad (11)$$

where d and W are the derivative operator and the stored energy, respectively. By equating the above equation to zero, T^* can be obtained as:

$$T^* = T(1 + C_1) \quad (12)$$

Figure 4a shows the root locus of the system, shunted with a RC circuit and the active voltage source in series, for the variation of feedback gain C_1 . One sees that the system is stable because the poles are always placed in the left half plane of the locus for all values of the feedback gain C_1 . The locus has two complex poles and two zeros at the origin. By increasing the value of the feedback gain C_1 , one pole goes toward the origin and the other one goes to infinity. It makes the system having two different resonances in the vicinity of the primary ones with the lower values of the damping than the damping of the passive control system. According to the Eq. (9b), the optimal values of the resistance R is proportional to the coupling constant of the transducer. Considering the new constant of the transducer (Eq. (12)), the optimal value of the resistance can be modified as:

$$R_{opt}^* = \frac{2T}{\sqrt{kc}}(1 + C_1) \quad (13)$$

Figure 5a compares the frequency response of the system with the passive control system combined with the active voltage source for two different values of the feedback gain C_1 . For each value of C_1 , the result is shown with and without correction of the resistance R according to Eq. (13) and Eq. (9b), respectively. By updating the value of the resistance in this case, more energy can be dissipated in the resistor which leads to increase the damping of the system. A larger value of resistance is required by the application of the active voltage source than the purely passive system. In order to have a fail-safe and optimum design, the value of resistance should be changed to the lower one when the active control is turned off. For a specific value of the feedback gain C_1 , the impulse response is shown in Figure 5b when the value of the resistance R is modified based on Eq. (13). It can be seen that the exponential time-decay rate is maximized by updating the value of the resistance.

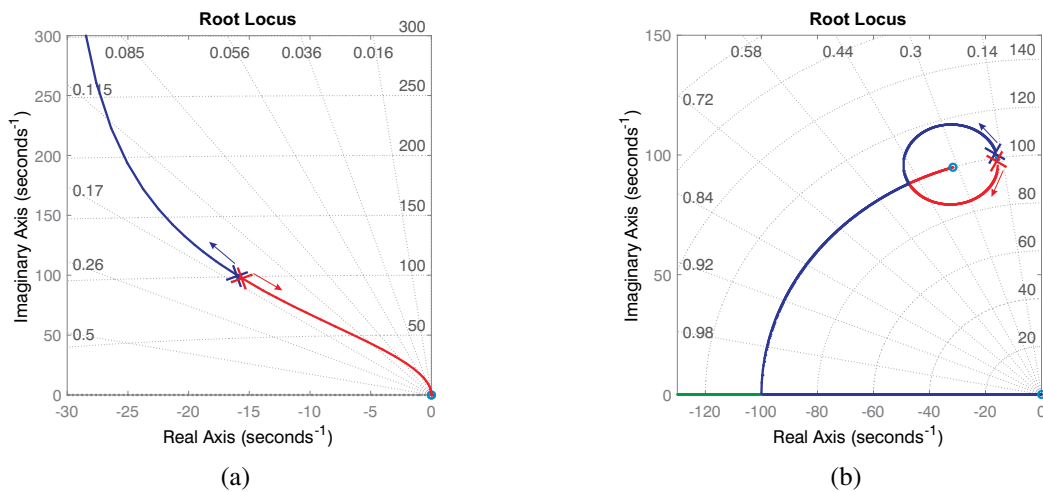


Figure 4: Root-locus of the system shunted with RC circuit combined with (a) active voltage source under and (b) active current source

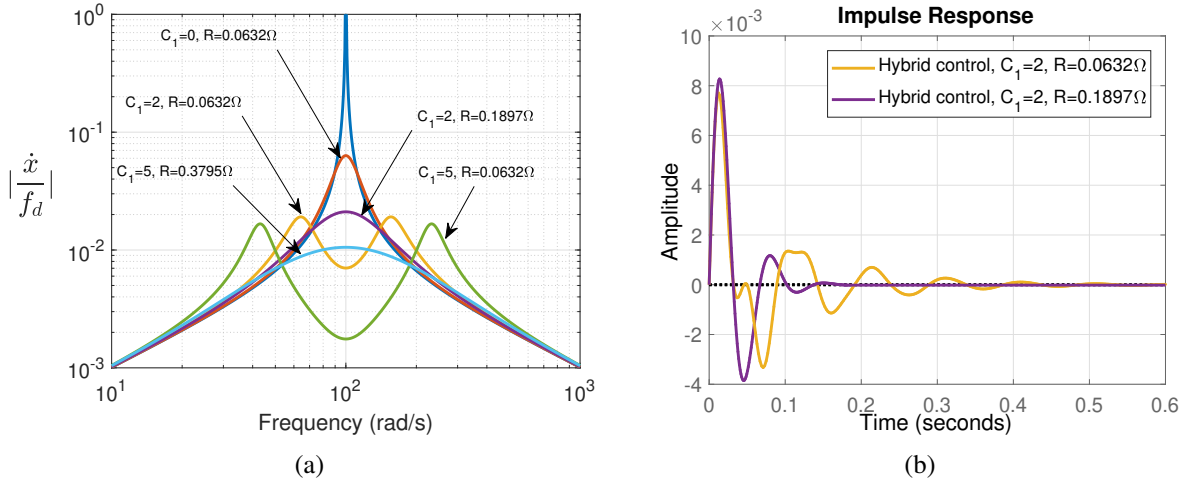


Figure 5: With the application of the passive control system combined with the active voltage source, (a) the frequency response of the system for different values of the feedback gain C_1 as well as the resistance R and (b) the impulse response with and without the correction of the resistance R

3.2 Hybridization with an active current source

The equations of motion with the application of the active current source read:

$$m\ddot{x} + kx = f_d + f_a \quad (14a)$$

$$f_a = -T(\dot{q} + i_{in}) \quad (14b)$$

$$i_{in} = \frac{C_2}{T}\dot{x} \quad (14c)$$

$$L\ddot{q} + R\dot{q} + \frac{1}{C}q = T\dot{x} \quad (14d)$$

The corresponding root locus of the system is shown in Figure 4b for the variation of feedback gain C_2 . The system is always stable by the application of the active current source because the closed-loop poles are always in the left half plane. Two poles are moving on the blue and red branches. The optimal feedback gain C_2 can be obtained when the two loops are intersecting at one point. Considering $\lambda = C_2\omega_0/k$ and Eqs. (3), (7), as well as (8), the normalized equations of motion are written as:

$$x_1'' + x_1 = f - \beta_1\omega_0x_2' - \lambda x_1' \quad (15a)$$

$$x_2'' + 2\sqrt{\beta}x_2' + x_2 = \beta_2/\omega_0x_1' \quad (15b)$$

The closed-loop transfer function from the normalized disturbance force f to the normalized displacement x_1 is obtained as:

$$\frac{x_1}{f} = \frac{s^2 + 2\sqrt{\beta}s + 1}{(s^2 + \lambda s + 1)(s^2 + 2\sqrt{\beta}s + 1) + \beta s^2} \quad (16)$$

When the two poles of the system have the same damping μ and normalized resonance frequency δ , the closed-loop transfer function can be re-written as:

$$\frac{x_1}{f} = \frac{s^2 + 2\sqrt{\beta}s + 1}{(s^2 + 2\mu\delta s + \delta^2)^2} \quad (17)$$

The following equations are obtained by equating the polynomial coefficients of the denominator of the fraction on the right hand side of Eqs. (16) and (17):

$$4\mu\delta = 2\sqrt{\beta} + \lambda \quad (18a)$$

$$4\mu^2\delta^2 + 2\delta^2 = 2\sqrt{\beta}\lambda + \beta + 2 \quad (18b)$$

$$4\mu\delta^3 = 2\sqrt{\beta} + \lambda \quad (18c)$$

$$\delta^4 = 1 \quad (18d)$$

The optimal value of the normalized tuning frequency δ is obtained from Eq. (18d) as:

$$\delta_{opt} = 1 \quad (19)$$

which shows that the closed-loop system has the same resonance frequency as the resonance frequency of the primary one. The optimal value of the normalized feedback gain can be realized by substituting the damping ratio μ obtained from Eq. (18a) and Eq. (19) into Eq. (18b):

$$\lambda_{opt} = 4\sqrt{\beta} \quad (20)$$

which yields:

$$C_2^{opt} = 4 \frac{T}{\omega_0} \sqrt{\frac{k}{L}} \quad (21)$$

It should be mentioned that the parameters of the passive RC circuit do not change. Figure 6a compares the frequency response of the passive control system combined with the active current source for two different values of the feedback gain C_2 . The optimal value is first used for the feedback gain $C_2 = 126.49$ and then it is increased to $C_2 = 200$ when a closed-loop pole touches the real axis and the other one merges with the zero. In this case, the zero cancels one of the poles and the other one adds damping to the system. This gain ($C_2 = 200$) can be defined as the second optimal value due to the fact that it

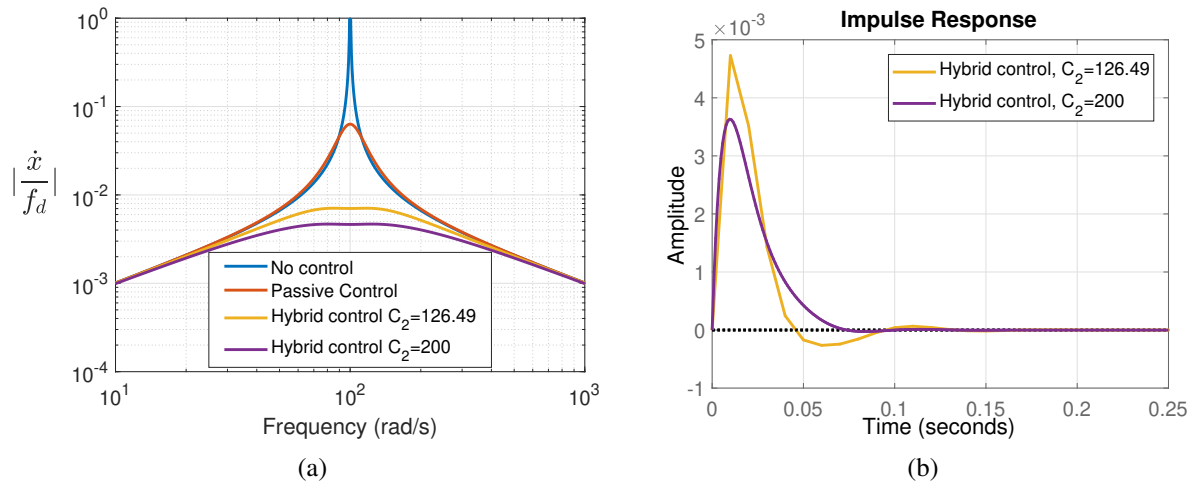


Figure 6: With the application of the passive control system combined with the active current source, (a) the frequency response and (b) the impulse response of the system for two different values of the feedback gain C_2

has almost the same settling time (Figure 6b) as the one corresponding to the first optimal value. For more than this value of the gain, the settling time is no longer minimized although it might realize lower magnitude of response than the magnitude of response obtained with the optimal values of the feedback gain. It should be mentioned that by the application of the active current source, the hybrid control system is fail-safe because it will continue to behave as the passive electromagnetic shunt damper described in Section 2 when the controller is turned off. The controller behaves like a direct-velocity-feedback (DVF) which is able to damp several modes as well. This topic is proposed for future studies

4 POWERFLOW ANALYSIS

In the previous section, it was shown that the hybrid control system can improve the control performance of the system in terms of the amplitude of response at the resonance frequency. A question may arise here is what is the main advantage of using a hybrid control system compared to a purely active control system. To answer this question, it is proposed to analyze the powerflow between the device and the primary structure due to the fact that an active control system requires an external power source for its operation. The less external power required, the better. The power which flows at the interface of the structure and the actuator device can be written as:

$$P(s) = F_{aa}(s) \times \dot{x}^*(s) \quad (22)$$

where P , F_{aa} and \dot{x} are the power, the control force applied by the active control system, and the velocity of the mass, respectively. The superscripts "*" represents the complex conjugate transpose. Considering $s = j\omega$, the real part of P is called the active power which corresponds to the dissipative behavior and the imaginary part is named the reactive power which corresponds to the energy exchanging between the device and the structure [17]. The average active power P_{ac} and the reactive power P_{re} can be written as:

$$P_{ac} = 1/2\Re(P(s)) = \frac{f_d^2}{2}\Re(G_f(s) \times G_{CL}(s) \times G_{CL}^*(s)) \quad (23a)$$

$$P_{re} = 1/2\Im(P(s)) = \frac{f_d^2}{2}\Im(G_f(s) \times G_{CL}(s) \times G_{CL}^*(s)) \quad (23b)$$

where $G_f(s)$ and $G_{CL}(s)$ are the transfer function from the velocity of the structure to the control force and the transfer function from the input force disturbance to the velocity.

For a unit forcing amplitude, Figure 7a compares the active and reactive power at a specific value of the closed-loop damping for purely active control system and the hybrid control system using active voltage source and current source, separately. DVF is used for the purely active control system. One can observe that the active power for all configurations is always positive through the entire frequency range. This means that the device does not deliver energy in the system and it is *hyperstable*. The reactive power for the hybrid control system when active voltage source is applied is positive before the resonance frequency and negative after that. This shows the amount of energy exchanged between the structure and the transducer. The total positive and negative reactive power is almost zero.

Figure 7b compares the H_2 norm of the active power as a function of the closed-loop damping ratio. One sees that the active power is zero for 16% damping ratio and below. This is because the passive control system is doing the job. While there is no external power required to realize 16% damping ratio by the passive control system, a similar purely active control system requires a large amount of external power. In addition, the active power for the hybrid control systems is always less than purely active control system. However, for high values of the closed-loop damping, the active power for the hybrid configurations is close to the active power for the purely active control system. This is because most of the work is done by the active portion of the hybrid systems.

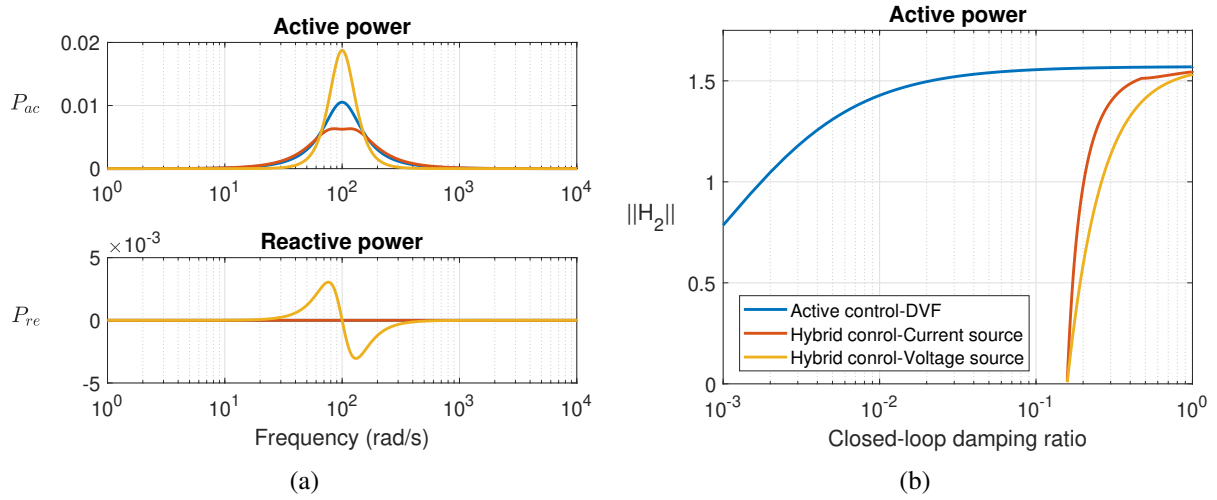


Figure 7: Comparison between the purely active control system (DVF) and Hybrid control systems using active voltage source and current source separately. (a) active and reactive power for a specific closed-loop damping ratio, (b) the H_2 norm of the active power

5 CONCLUSIONS

The hybridization of the passive electromagnetic shunt damper with the active control systems has been proposed and analyzed in details. The RC shunt has been used in series with an electromagnetic transducer as the passive control system and its parameters have been optimized based on the method of maximum damping. Both the active voltage source in series with RC elements and the active current source in parallel with it have been proposed for the hybrid configurations. It was shown that the system "electromagnetic device + active voltage source" can be seen as an equivalent transducer with an enhanced coupling constant T ; equivalence formulae have been presented. In this case, it was shown that the optimal value of the resistance R is modified to a larger value as a function of the feedback gain C_1 in order to improve the damping of the system. In addition, it was shown that the active current source behaves like a DVF. In this case, the feedback gain C_2 has been optimized based on the method of maximum damping while there is no need to change the parameters of the passive RC circuit. The fact that R does not need to be changed in this configuration is a major advantage compared to the implementation of the active voltage source, as it is much easier to implement a fail-safe system. Moreover, the power consumption was highlighted to compare the hybrid control systems and purely active control system (using DVF). As a consequence, it has been demonstrated that both hybrid control systems can improve the control performance of the purely passive system while it has less power consumption in comparison with the purely active control system.

Acknowledgment

The authors are grateful to the financial support of MAVERIC (Wal'innov project 1610122).

REFERENCES

- [1] Behrens, Sam, Andrew J. Fleming, and SO Reza Moheimani. "Passive vibration control via electromagnetic shunt damping." *IEEE/ASME transactions on mechatronics* 10, no. 1 (2005): 118-122.

- [2] De Marneffe, Bruno. "Active and passive vibration isolation and damping via shunted transducers." These, Faculté des Sciences Appliquées, Université Libre de Bruxelles (2007).
- [3] Inoue, Tsuyoshi, Yukio Ishida, and Masaki Sumi. "Vibration suppression using electromagnetic resonance shunt damper." *Journal of Vibration and Acoustics* 130, no. 4 (2008): 041003.
- [4] Den Hartog, Jacob Pieter. *Mechanical vibrations*. Courier Corporation, 1985.
- [5] Tang, Xiudong, Yilun Liu, Wen Cui, and Lei Zuo. "Analytical solutions to H_2 and H_∞ optimizations of resonance shunted electromagnetic tuned mass damper and vibration energy harvester." *Journal of Vibration and Acoustics* 138, no. 1 (2016): 011018.
- [6] Zhu, Songye, Wenai Shen, and Xin Qian. "Dynamic analogy between an electromagnetic shunt damper and a tuned mass damper." *Smart materials and structures* 22, no. 11 (2013): 115018.
- [7] Ormondroyd J and Den Hartog J P 1928 "The theory of the dynamic vibration absorber" *ASME J. Appl. Mech.* 50 13.
- [8] Collette, Christophe, and Simon Chesne. "Robust hybrid mass damper." *Journal of Sound and Vibration* 375 (2016): 19-27.
- [9] Agnes, Gregory S. "Active/passive piezoelectric vibration suppression." In *Smart Structures and Materials 1994: Passive Damping*, vol. 2193, pp. 24-35. International Society for Optics and Photonics, 1994.
- [10] Tsai, M. S., and K. W. Wang. "On the structural damping characteristics of active piezoelectric actuators with passive shunt." *Journal of Sound and Vibration* 221, no. 1 (1999): 1-22.
- [11] Tang, J., and K. W. Wang. "Active-passive hybrid piezoelectric networks for vibration control: comparisons and improvement." *Smart Materials and Structures* 10, no. 4 (2001): 794.
- [12] Morgan, R. A., and K. W. Wang. "An active-passive piezoelectric absorber for structural vibration control under harmonic excitations with time-varying frequency, part 1: algorithm development and analysis." *Journal of vibration and acoustics* 124, no. 1 (2002): 77-83.
- [13] Li, MingMing, Bo Fang, DengQing Cao, and WenHu Huang. "Modeling and analysis of cantilever beam with active-passive hybrid piezoelectric network." *Science China Technological Sciences* 56, no. 9 (2013): 2326-2335.
- [14] Tsai, M. S., and K. W. Wang. "A coupled robust control/optimization approach for active-passive hybrid piezoelectric networks." *Smart materials and structures* 11, no. 3 (2002): 389.
- [15] Preumont, André, and Bilal Mokrani. "Electromagnetic and Piezoelectric Transducers." In *Active and Passive Vibration Control of Structures*, pp. 213-248. Springer, Vienna, 2014.
- [16] Slotine, Jean-Jacques E., and Weiping Li. *Applied nonlinear control*. Vol. 199, no. 1. Englewood Cliffs, NJ: Prentice hall, 1991.
- [17] Chesne, S., K. Billon, C. Collette, and G. Zhao. "Power Flow Analysis for Hybrid Mass Damper Design." In *ASME 2018 International Design Engineering Technical Conferences and Computers and Information in Engineering Conference*, 2018.

INTEGRATION OF PIEZOSTACKS AS FREQUENCY DEPENDENT STIFFNESS ELEMENTS IN LOAD BEARING STRUCTURES

Jascha Schmied*, Andrea Bergamini†

* CMASLab, ETH Zurich, Leonhardstrasse 21, CH 8092 Zurich, Switzerland
e-mail: jschmied@ethz.ch

† Acoustics / Noise Control, Empa, Überlandstrasse 129, CH 8600 Dübendorf, Switzerland
e-mail: andrea.bergamini@empa.ch

Key words: piezodamping, local resonators, coupled resonators, piezostack

Abstract. In previous work we have described the use of piezoelectric elements as means to obtain variable connectivity between the elements of a phononic crystal by exploiting the frequency dependent stiffness of resonantly shunted piezoelectric elements. There, piezoelectric disks were intercalated between an aluminum plate and aluminum stubs and were used to effectively disconnect the stubs creating a phononic structure from the substrate. Given the function of the investigated object, no special structural requirements were set to the piezoelectric disks. Here, we present work related to the structural integration of piezoelectric elements in a load bearing structure. The goal of the integration is to exploit frequency dependent stiffness properties of resonantly shunted piezos to modify the stiffness matrix of a simple truss structure. In order to demonstrate the proposed approach, a ring-shaped piezo-stack is axially mounted into the diagonal strut of a square frame. In order to guarantee the function of the piezoelectric element under the expected load conditions, axial pre-compression needs to be applied. This contribution describes the design, implementation and initial investigation of the dynamic response of a variable connectivity truss structure.

1 INTRODUCTION

The use of shunted piezoelectric elements for vibration damping purposes has now been demonstrated [1] for four decades, further developed and divulged in innumerable contributions [2, 3, 4, 5] and represents in some ways the golden standard in integrated multi-field vibration mitigation treatments. However, the implementation of this type of treatments implies the ability to correctly tailor the position and frequency response of the piezoelectric device and is subject to detuning or incorrect placement of the shunted piezoelectric element due to varying operational conditions, deterioration of the integrity of the structure or environmental effects. As such, in spite of their undoubted efficacy, their practical application is still limited to very specific cases. Recent research indicates that under certain conditions, the implementation of distributed elements for the mitigation of mechanical vibrations can offer substantial advantages in terms of robustness of the system. In this sense, with the understanding that structural vibrations are nothing else than the expression of the interaction of low frequency waves propagating through a structure and interacting with its boundaries and the imposed conditions, the focus of research is shifted to avenues for the manipulation of the propagation of mechanical waves. Here, the

groundbreaking work of Liu [6] has successfully demonstrated the wavenumber-independent attenuation of mechanical waves at a specific frequency using sub-wavelength features, employing local mechanical resonators and providing for robustness against the misplacement of the energy absorbers within the structure. Inspired by these findings, elegant implementations of local resonators based on electromechanical systems were devised, such as the ones presented by Spadoni [7], and Casadei [8], among others. This approach to wave propagation control offers the undoubted advantages of wavenumber independent attenuation of waves and orthogonality to structural properties [9] originating from the local nature of the resonators, however at the cost of a very narrow band effect. Wu [10] has demonstrated the realization of complete Bragg bandgaps in macroscopic systems, echoing the seminal work of Brillouin [11] on the propagation of waves in periodic media. Here it has been shown that in periodic arrangements of mass and spring elements the propagation of waves in certain ranges is suppressed by scattering phenomena. This effect can cover wide frequency ranges [12, 13, 14]. As long as the modulus, density, unit cell size of the phononic crystal allow for it, the position of the bandgaps can be positioned at arbitrarily low frequencies. However, it should be noticed that there are limits to what can be achieved in these terms [15]. In previous work we have shown a possible use of electromechanical resonators as variable stiffness elements to modify the connectivity in phononic crystals [16]. There, we introduced resonantly shunted piezoelectric disks between the stubs and the plate of a stubbed plate as described in [10]. If the resonance frequency of the piezoelectric element was positioned within the Bragg type bandgap created by the lattice created by the periodically arranged stubs, we could observe the appearance of a passband. We interpreted this observation as due to the effective modification of the connectivity of the stubs and the plate, due to the frequency dependence of the effective modulus of the piezoelectric disk around the electric resonance of the LC shunt. In this contribution we explore the implementation of frequency dependent stiffness elements (embodied by resonantly shunted piezoelectric elements) in lattice-type phononic crystals, as a way to adaptively modify the connectivity of the lattice, with the expectation that some useful property would emerge from this. The baseline expectation is that, the adaptive connectivity of the lattice can be used to strongly affect its response to dynamic loads. Here we present a numerical investigation of dynamic properties of a lattice structure with adaptive connectivity trusses and of the unit cell it is made of. Finally, we show the state of advancement of our effort to experimentally verify the behavior predicted by our models.

2 STRUCTURES WITH FREQUENCY-DEPENDENT STIFFNESS ELEMENTS

The implementation of active elements in truss structures has been presented in [17], where the effectiveness of discrete piezoelectric elements in an active vibration suppression scheme is outstandingly demonstrated. Here, we will discuss a passive approach, in which piezoelectric elements are implemented as frequency dependent stiffness elements. First, we will investigate the frequency response of the base element of the two-dimensional structure, that we will consider as the unit cell of a periodic structure and assess the frequency dependent stiffness of the unit cell (see fig. 1). Then we will show the effect of distributed frequency dependent elements in a periodic structure (see fig. 2) on its frequency response. The frequency dependent stiffness elements are represented by bulk piezoelectric elements in the numerical models presented in the following sections, for the sake of simplicity. Accordingly, the inductance values selected to obtain the electrical resonance of shunts at the frequencies of interest are very high. In the practical implementation, briefly discussed at the end of this work, piezostacks are chosen, over piezoelectric patches as a more effective way to exploit the electromechanical coupling in a load carrying structure. The simplification made in the numerical models does not affect the validity of the general findings they provide.

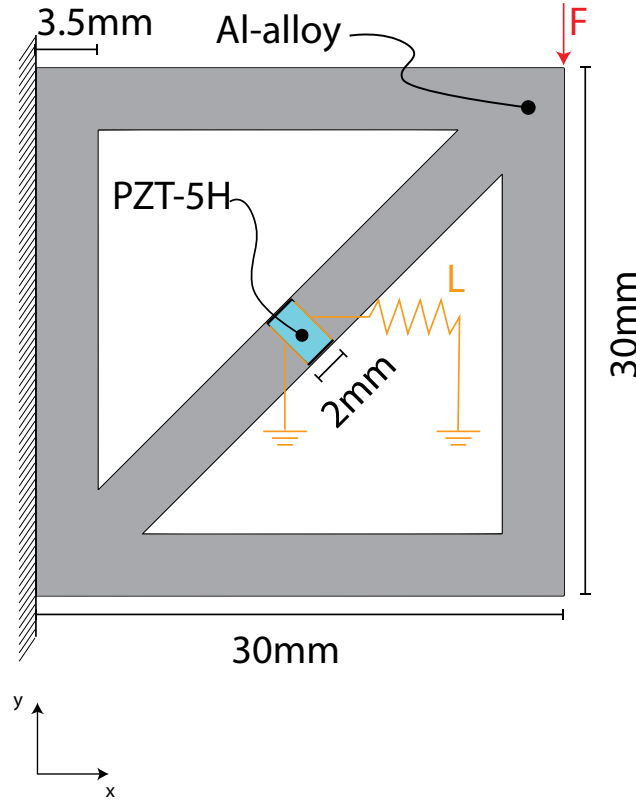


Figure 1: Base unit of the truss structure with frequency dependent stiffness elements, consisting of a diagonal brace, in which a piezoelectric element shunted over an inductor L is integrated, horizontal beams, and vertical beams to close the frame. In the model, the unit cell is fixed along its left edge.

2.1 Unit Cell

In two dimensions, a square frame with a diagonal shear stiffening element represents a very simple component from which a larger structure can be created by simple symmetry operations such as translation, rotation, and mirroring. The properties of such a structure are known to carry the imprint of its constituting components [18]. So, we are interested in understanding the effect of the electrical resonance in the shunted piezo on the dynamic properties of the unit cell. Assuming that the shunted piezoelectric element provides the frequency dependent stiffness postulated in [16], we can expect the shear stiffness of the truss to strongly vary as a function of frequency, around the resonant frequency of the piezoelectric resonator. The host structure is modeled in COMSOL Multiphysics as a two-dimensional object, assuming plain strain conditions, with an assigned thickness (z -direction) of 3.3mm. The host structure (grey) is modeled as an aluminum alloy, the piezoelectric element representing a piezoelectric stack is taken to have the properties of PZT-5H. The dimensions and the mechanical boundary conditions are shown in figure 1. A point force in $-y$ direction is applied to top right corner of the unit cell.

2.2 Structure

The structure we consider is inspired by the unit cell discussed above. The diagonal braces with the integrated piezoelectric element are identical with the one implemented in the unit cell. The horizontal

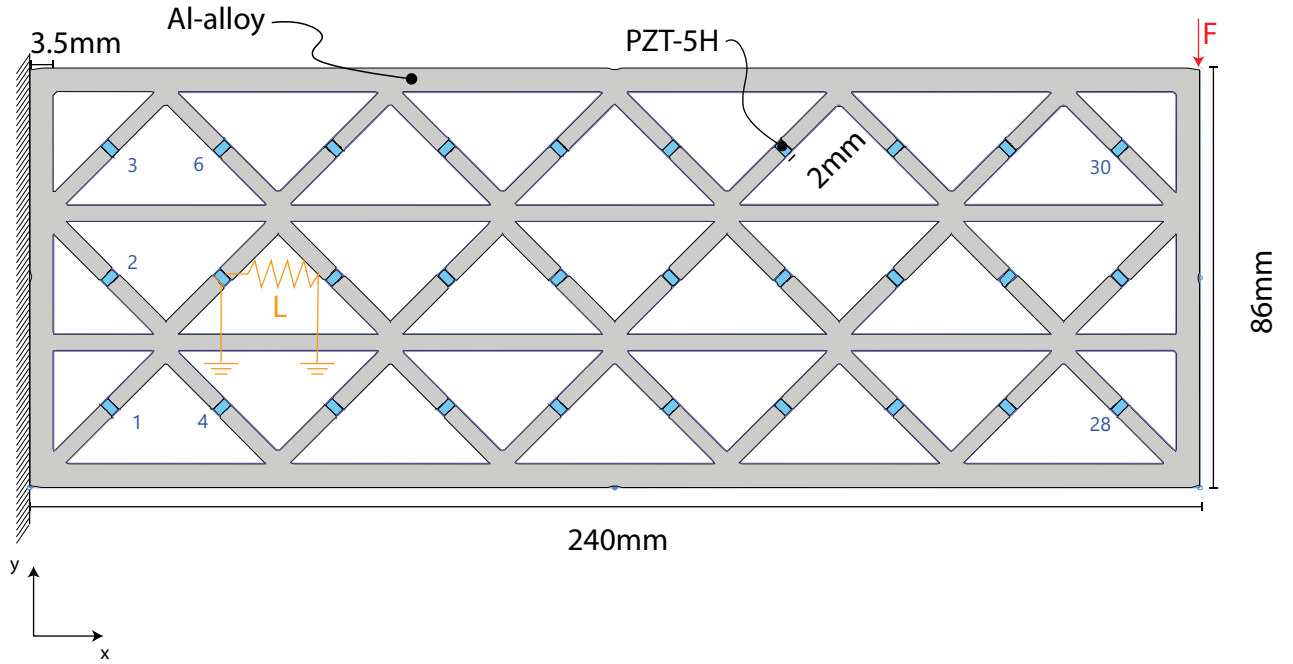


Figure 2: Structure that includes diagonal braces as discussed in the previous section. Additionally some horizontal beams are added to maintain the free length of the braces. The width of the outer frame is the same as in figure 1. The figure shows only one electric shunt (inductor $L=210.5H$), implying that each piezoelectric element is shunted individually over identical circuits. The numbers in blue color, next to the piezos, indicate the numbering scheme for the piezoelectric elements.

trusses have the same width as the quadratic frame of the unit cell, while the frame of the structure is slightly wider. In order to be able to include periodic arrays of braces with the same length as in figure 1, horizontal elements were included. The resulting structure is presented in figure 2. As in the model presented in the previous section, the left edge of the structure is fixed both in x - and in y -direction. The materials considered in the 2-dimensional model of the structure are the same as for the unit cell. The model also assumes plain strain conditions and has an assigned thickness of 3.3mm. A point force in y -direction is applied to top right corner of the unit cell.

The frequency response of the two structures described in the sections above, represented as the displacement amplitude for a unit force applied to the structure and the time average of the electric energy density within the piezoelectric elements will give us information about the effect of the the integrated variable stiffness elements on the dynamic response of the two structures.

3 RESULTS and DISCUSSION

In the following we report the displacement-amplitude recorded at the position where the point force is applied as a function of frequency for three different electrical boundary conditions applied to the piezoelectric elements: open circuit, where no current can flow in the shunt, short circuit, where the potential between the electrodes is zero and where the impedance of the shunt is determined by an ideal inductor with $L = 210.5H$. The reported quantity represents the compliance of the structure, with the units [mm/N]. For the same boundary conditions, we report also the time averaged electrical energy density in the piezoelectric elements, as a measure of the energy exchanged by the structure with the

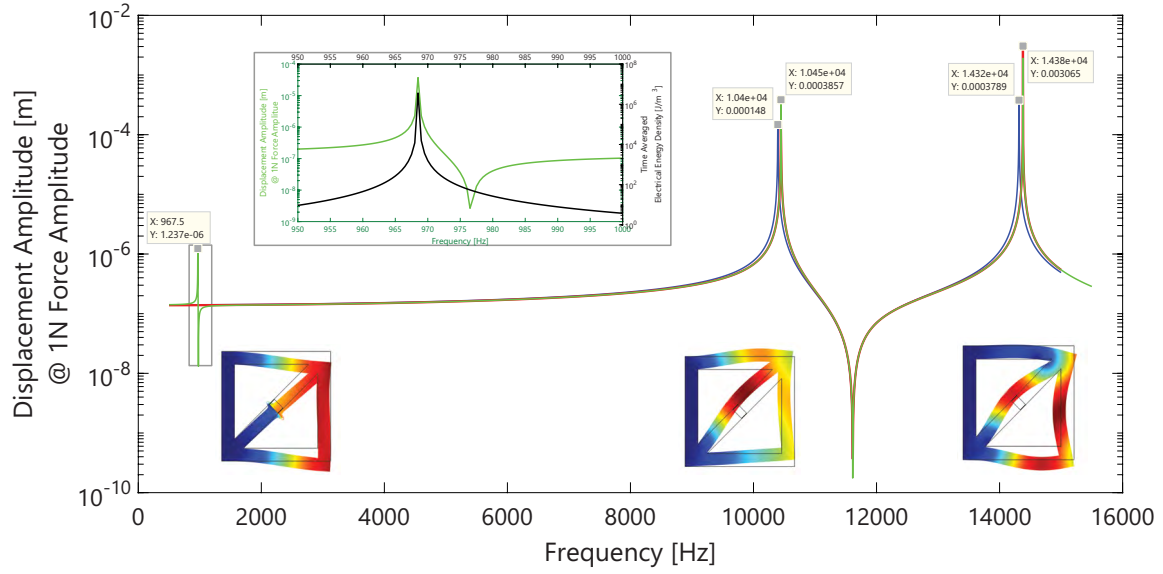


Figure 3: Overview of the frequency response (green, displacement amplitude) of the unit cell under open circuit, short circuit and inductively shunted ($L = 210.5H$) conditions, the color figures show the modal shapes for the corresponding eigenfrequencies, the insert shows a detail of displacement and electrical energy density (black) in proximity of the eigenfrequency of the LC resonator (shunted piezo).

shunted piezos.

3.1 Unit Cell

The frequency response of the unit cell, expressed as its compliance, well agrees in its essence with the results reported in [16]: The stiffness of the piezoelectric element is known to drop at frequencies immediately below the resonance frequency of the LC shunt and to increase again as the frequency exceeds it, accordingly the compliance of the structure increases and decreases again to values similar to the ones far away from resonance. Also the comparison between open and short-circuit boundary conditions confirms what we know: It is reasonable to state that -unsurprisingly- also in the configuration presented in this work, piezoelectric elements can be regarded as elements that can change their effective stiffness as a consequence of the electric boundary conditions.

3.2 Structure

The integration of shunted piezoelectric elements in a larger, periodically arranged structure is expected to carry in itself to a large extent the footprint of its constitutive elements. If in the piezoelectric elements a variation of the stiffness of the components occurs at a specific frequency, the effect of this variation can be expected to affect also the behavior of the larger structure. Now, since under the ideal conditions offered by a numerical model, we were able to tune all LC circuits composed of the piezoelectric element and the inductor to the same frequency (approximately $484Hz$ for the given piezos and an inductance value of $L = 842H$), the expectation would be to see an increase in compliance, i.e. of displacement amplitude in correspondence to the electric resonance, similar to what we see for the unit cell comprised of one piezoelectric element. This corresponds also to the observation made for local

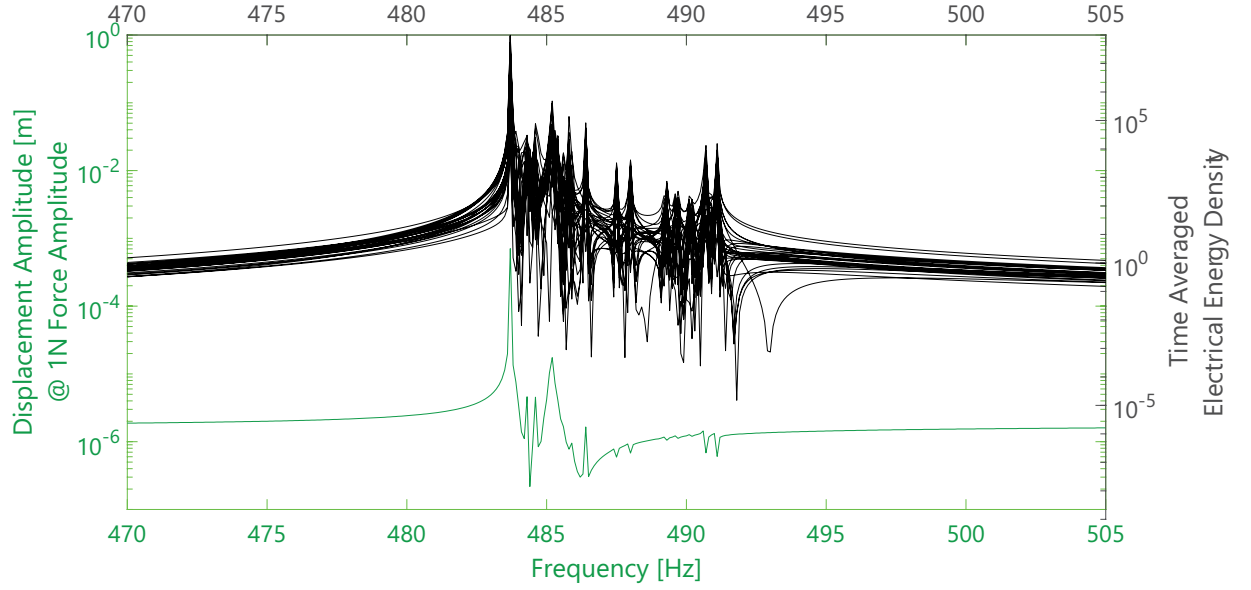


Figure 4: Frequency response (displacement amplitude, black, and time-averaged electric energy density in the piezoelectric elements, colors) of the unit cell under inductively shunted ($L = 842H$) conditions at frequencies below the first global, structural eigenfrequency ($968.5Hz$).

piezoelectric resonators, as discussed in [8, 7], where a dip in the transmissibility of waves through the structure. Here, however, we observe phenomena that qualitatively and quantitatively deviate from the response of a single or of an array of *local* resonators: instead of a single peak and subsequent dip in compliance, the frequency response of the structure at hand shows a much richer behavior, spanning over a fairly wide range of frequencies, and characterized by a series of local displacement amplitude peaks and valleys. Interestingly, the electric energy density in the piezoelectric elements shows a rich frequency dependent behavior around the electric resonance, whereas, farther below and above it, this quantity only slightly differs among different piezos, and has a smooth behavior, as a function of frequency.

The plots of figures 5 and 6 show how the structure behaves, when the nominal resonance frequency of the shunted piezoelectric resonators is tuned to a structural eigenfrequency. Also here, if the array of tuned piezoelectric resonators were to act as local resonators, or if there were only one piezoelectric element coupled to the structure, the expected response would be the one of a two degrees of freedom (2DOF) system with two resonance peaks and one antiresonance, as shown in [1, 2]. However, the complexity that we have seen emerge from the presence of multiple resonators, tuned at the same nominal frequency, is visible also here. Globally, two resonance peaks at the edge of the frequency range in which the multi-resonator behavior is observed, are given (fig 5).

4 CONCLUSIONS and OUTLOOK

The numerical investigations of a structure comprised of multiple, tuned, piezoelectric resonators presented in this work, point to the emergence of phenomena originating from the interaction between mechanically coupled piezoelectric resonators: It appears that in spite of all being electrically identical, the shunted piezoelectric elements display inhomogeneous frequency responses among them, as clearly indicated by plots of the electrical energy density for the individual elements. An interpretation for this

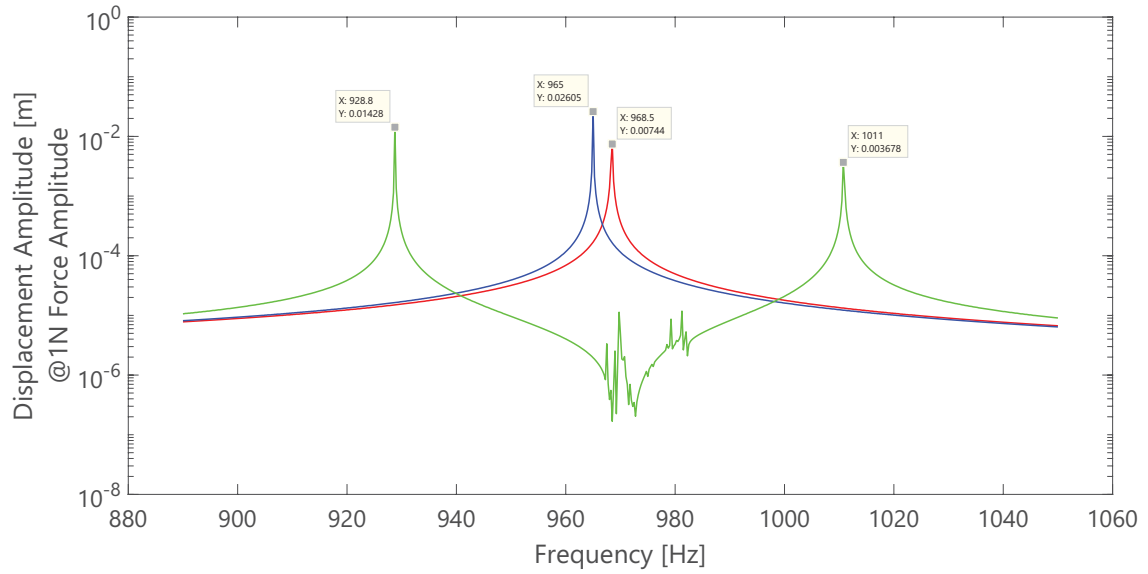


Figure 5: Overview of the frequency response (displacement amplitude) of the truss structure under open circuit (red), short circuit (blue) and inductively shunted (green, $L = 210.5H$) conditions, around its first mechanical resonance.

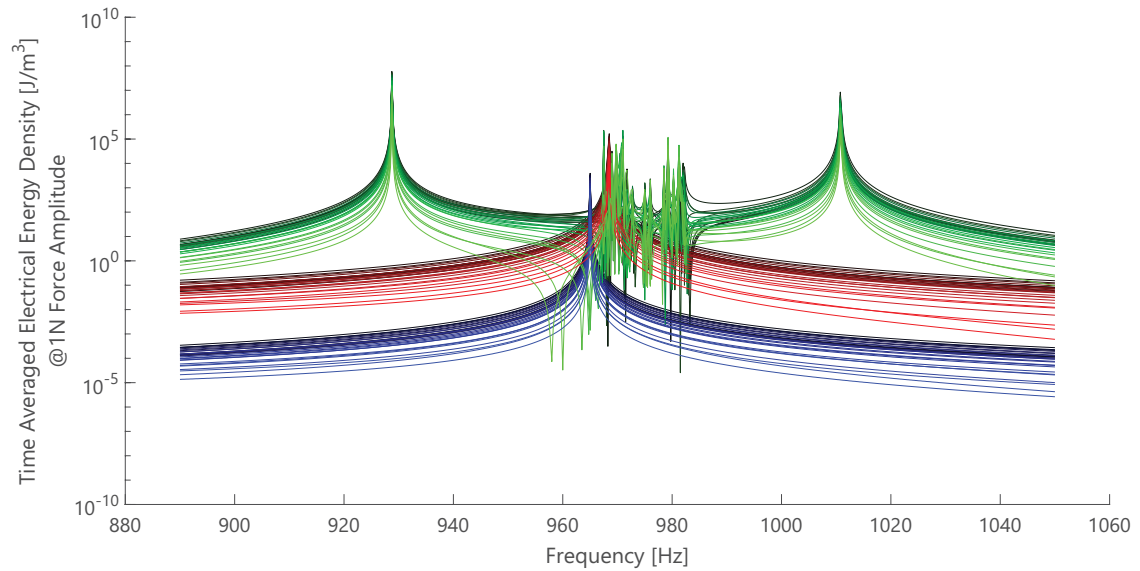


Figure 6: Frequency response (time-averaged electrical energy density in the piezo. for each piezo) of the truss structure under open circuit (red), short circuit (blue) and inductively shunted (green, $L = 210.5H$) conditions, around its first mechanical resonance. The shade of the respective color indicates the piezo number the line refers to: black \rightarrow 1, color \rightarrow , see figure 2 for the piezo numbering scheme

observation can be found in the fact that not only do the mechanical properties of piezoelectric materials depend on the electric boundary conditions, but also the dielectric properties of the material depend on the mechanical boundary conditions. Out of this coupling arise complex interactions between the piezoelectric elements, mediated by the structure that lead to the rich response of the array of mechanically coupled resonators. Thanks to these emergent phenomena, distributed, coupled variable stiffness elements realized via shunted piezos, appear to qualitatively distinguish themselves from discrete piezoelectric treatments. The mechanisms that lead to the interesting dynamic behavior of the described structure will need further investigation.

4.1 Experimental verification and challenges

The next challenge of this work will be the experimental verification of these findings. For this purpose a way to properly integrate piezoelectric elements has to be devised. Unlike in the numerical model, the integration in a real setting presents a few practical challenges:

- Piezoelectric elements come in discrete sizes and designs, the structure needs to be designed around the best suitable candidate for the purpose
- To guarantee proper function, thick piezoelectric transducers need to be pre-compressed
- First investigations based on the numerical model appear to indicate that the system is sensitive to material damping and that the described phenomena are most easily observed in a weakly damped system. For this reason the use of conventional polymer based adhesives does not seem to be ideal.

The challenges listed above have lead us to design a 'dry mounted' system in which load transfer relies on clamping a ring stack actuator within the diagonal brace. This should allow to meet the requirements we have recognized as relevant so far. However, the realization of a clamped, pre-stressed structure, as the one shown in figure 7, requires high precision components and careful assembly. First experimental results to confirm the findings of the numerical model of the unit cell are expected soon. The preparation of a multi-resonator structure will be tackled once the technique for the preparation of the unit cell will have been refined.

5 Acknowledgements

This work was supported by the Air Force Office of Scientific Research grant FA9550-15-1-0397 "Integrated multi-field resonant metamaterials for extreme, low frequency damping."

References

- [1] Forward RL (1979) Electronic damping of vibrations in optical structures. *Applied optics* 18(5):690–697
- [2] Hagood NW, von Flotow A (1991) Damping of structural vibrations with piezoelectric materials and passive electrical networks. *Journal of Sound and Vibration* 146(2):243–268
- [3] Guyomar D, Badel A (2006) Nonlinear semi-passive multimodal vibration damping: An efficient probabilistic approach. *Journal of Sound and Vibration* 294(1-2):249–268
- [4] Delpero T, Bergamini AE, Ermanni P (2013) Identification of electromechanical parameters in piezoelectric shunt damping and loss factor prediction. *Journal of intelligent material systems and structures* 24(3):287–298

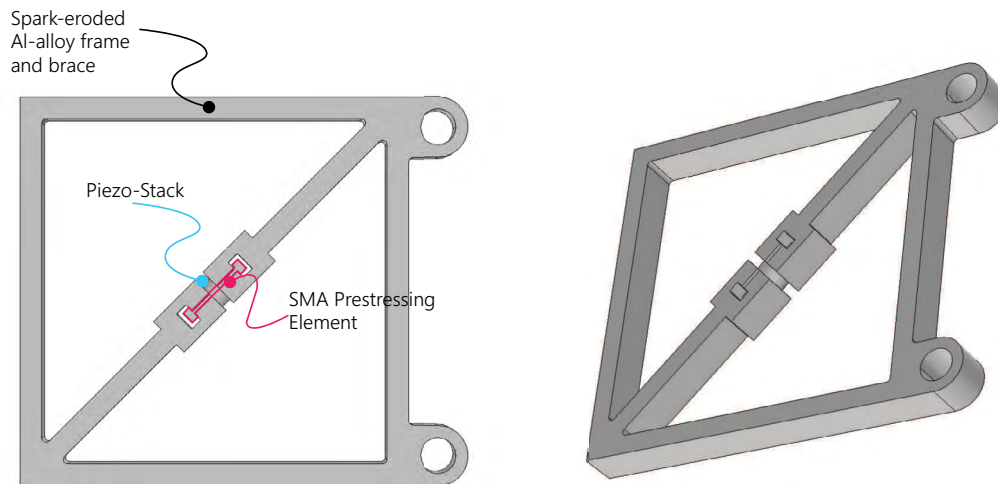


Figure 7: Frequency response (time-averaged electrical energy density in the piezo) of the truss structure under open circuit, short circuit and inductively shunted ($L = 210.5H$) conditions, below its first mechanical resonance.

- [5] Suzuki S, Yamaguchi T (2019) Panel vibration suppression by using piezoelectric damping system. In: Active and Passive Smart Structures and Integrated Systems XII, International Society for Optics and Photonics, vol 10967, p 1096705
- [6] Liu Z, Zhang X, Mao Y, Zhu Y, Yang Z, Chan C, Sheng P (2000) Locally Resonant Sonic Materials. *Science* 289(5485):1734–1736, DOI 10.1126/science.289.5485.1734, URL <http://www.sciencemag.org/cgi/doi/10.1126/science.289.5485.1734>
- [7] Spadoni A, Ruzzene M, Cunefare K (2009) Vibration and wave propagation control of plates with periodic arrays of shunted piezoelectric patches. *Journal of Intelligent Material Systems and Structures* 20(8):979–990
- [8] Casadei F, Delpero T, Bergamini A, Ermanni P, Ruzzene M (2012) Piezoelectric resonator arrays for tunable acoustic waveguides and metamaterials. *Journal of Applied Physics* 112:064,902
- [9] Krödel S, Delpero T, Bergamini A, Ermanni P, Kochmann DM (2014) 3 d auxetic microlattices with independently controllable acoustic band gaps and quasi-static elastic moduli. *Advanced Engineering Materials* 16(4):357–363
- [10] Wu TT, Huang ZG, Tsai TC, Wu TC (2008) Evidence of complete band gap and resonances in a plate with periodic stubbed surface. *Applied Physics Letters* 93(11):111,902, DOI 10.1063/1.2970992, URL <http://scitation.aip.org/content/aip/journal/apl/93/11/10.1063/1.2970992>
- [11] Brillouin L (1946) *Wave Propagation in Periodic Structures*. McGraw-Hill Book Company, Inc.
- [12] D’Alessandro L, Belloni E, Ardito R, Corigliano A, Braghin F (2016) Modeling and experimental verification of an ultra-wide bandgap in 3d phononic crystal. *Applied Physics Letters* 109(22):221,907
- [13] Bilal OR, Hussein MI (2011) Ultrawide phononic band gap for combined in-plane and out-of-plane waves. *Physical Review E* 84(6):065,701

- [14] Coffy E, Lavergne T, Addouche M, Euphrasie S, Vairac P, Khelif A (2015) Ultra-wide acoustic band gaps in pillar-based phononic crystal strips. *Journal of Applied Physics* 118(21):214,902
- [15] Bergamini A, Miniaci M, Delpero T, Hannema G, Leibacher I, Zemp A (2019) Shapely atoms. *arXiv preprint arXiv:190208763*
- [16] Bergamini A, Delpero T, Simoni LD, Lillo LD, Ruzzene M, Ermanni P (2014) Phononic crystal with adaptive connectivity. *Advanced Materials* 26(9):1343–1347
- [17] Preumont A, De Marneffe B, Deraemaeker A, Bossens F (2008) The damping of a truss structure with a piezoelectric transducer. *Computers & structures* 86(3-5):227–239
- [18] Jensen JS (2003) Phononic band gaps and vibrations in one- and two-dimensional mass-spring structures. *Journal of Sound and Vibration* 266:1053–1078, DOI 10.1016/S0022-460X(02)01629-2

PASSIVE VIBRATION DAMPING OF HYDROFOILS USING RESONANT PIEZOELECTRIC SHUNT

L. PERNOD^{*†}, B. LOSSOUARN^{*}, J.-A. ASTOLFI[†] AND J.-F. DEÜ^{*}

^{*} Laboratoire de Mécanique des Structures et des Systèmes Couplés (LMSSC),
Conservatoire national des arts et métiers (Cnam),
292 rue Saint-Martin, 75 003 Paris, France
email: laetitia.pernod@lecnam.net,
boris.lossouarn@lecnam.net
jean-francois.deu@cnam.fr,
www.lmssc.cnam.fr/en

[†] Institut de Recherche de l'Ecole Navale (IRENav)
EA 3634, Ecole Navale, 29 240, Brest, France
email: jacques-andré.astolfi@ecole-navale.fr,
www.ecole-navale.fr/en/The-Naval-Academy-Research%2C1804

Key words: Flow-induced vibrations, Resonant piezoelectric shunt, Passive vibration damping.

Abstract. Marine lifting surfaces undergo flow-induced vibrations leading to shorter life cycles due to structural fatigue and reduced acoustic performances. As such, accurate understanding of the fluid-structure response of marine structures, as well as vibrations control and damping, are critical to many maritime applications. In particular, this work investigates the potential of the electromechanical coupling inherent to piezoelectric materials for passive vibration damping of hydrofoils under hydrodynamic flows. An aluminium flat plate equipped with piezoelectric patches connected to a resonant shunt is considered. The structure is first tested under hydrodynamic flows for various Reynolds numbers to investigate its flow-induced vibrations. This allows to determine the natural frequency of interest to test the control solution. Second, an experimental modal analysis is carried out to determine the open and short circuit natural frequencies in order to compute the piezoelectric coupling factor. Indeed, the latter is related to the expected performance of the passive vibration damping strategy. Third, the values for the resistive and inductive components of the RL-shunt are inferred from the coupling factor and the natural frequencies. Last, the control solution is tested in still air and water in open and short circuits configurations. Comparisons of these two configurations are realised and the resonant shunt performance for vibration reduction of hydrofoils is estimated.

1 INTRODUCTION

Applications for high-speed ships fitted with hydrofoils, such as fast passenger-ferries and racing sailing boats, are progressively expanding and gaining economic importance. This leads to a renewed interest in the physical understanding of flow-induced vibrations of light flexible structures subjected to strong fluid-structure interactions. There is also a growing demand for

vibration control and damping solutions. Indeed, flow-induced vibrations may trigger a sharp increase in the vibration amplitude when there is a coincidence between a natural frequency of the structure and a hydrodynamic excitation frequency. The consequences of such high-amplitude vibrations are reduced acoustic performances (*e.g.* hydrofoil singing), and shorter life cycles [1,2]. As such, it is of prime importance to develop methods for vibration damping.

Several researches have been completed on the high potential of piezoelectricity for vibration control and damping. In particular, Lossouarn et al. [3] and Thomas et al. in 2012 [4] in 2017 successfully demonstrated the ability of passive piezoelectric shunts to reduce the amplitude of the vibrations of structures in air. Academic research is now turning to the application of this solution to the maritime domain [5]. The purpose of this work is to provide a first experimental prototype for the application of vibration damping using a resonant piezoelectric shunt in water. The methodology used to assess the performance of the solution and design the electrical components of the resonant shunt (inductance and resonance) from the natural frequencies in open circuit and closed circuit is first described. We then present a case of application on a flat aluminium plate.

2 VIBRATION DAMPING USING A RESONANT PIEZOELECTRIC SHUNT

Vibration damping using piezoelectricity consists in converting part of the vibratory mechanical energy into electrical energy, which is then dissipated through a resistor R . Moreover, it is possible to create an electric resonance with the addition of an inductance L to the electrical circuit. When this electric resonance matches one of the natural frequencies of the structure the energy transfer is increased. As a consequence, a passive resonant piezoelectric shunt behaves similarly to a tuned mass-damper [3]. Figure 1 represents a model for a mass-spring system (mass m and stiffness K) coupled to a resonant piezoelectric shunt and subjected to a force F . U represents the displacement of the mass, q represents the electric charge displacement, C the capacitance of the piezoelectric patch, and e is the piezoelectric constant, R and L respectively being the resistance and the inductor of the shunt.

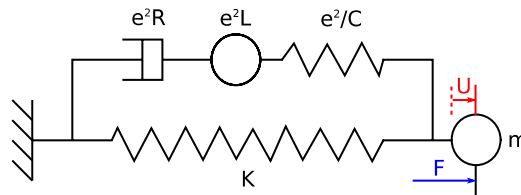


Figure 1: Purely mechanical model of a structure coupled to a resonant piezoelectric shunt

Important electrical conditions and their corresponding natural frequencies are the “short circuit” and “open circuit” conditions. The former corresponds to zero voltage across the piezoelectric patch and a natural frequency ω_{sc} , while the latter corresponds to zero electric charge displacement ($q = 0$) and to a natural frequency ω_{oc} . The performances of the vibration damping solution are only dependant on the coupling factor k_c defined by the short circuit and open circuit natural frequencies:

$$k_c = \sqrt{\frac{\omega_{oc}^2 - \omega_{sc}^2}{\omega_{sc}^2}} \quad (1)$$

Once the coupling factor is known, the electrical inductor and resistor of the resonant shunt have to be designed according to:

$$L = \frac{I}{C\omega_{oc}^2} \quad (2)$$

$$R = \sqrt{\frac{3}{2}} \frac{1}{C\omega_{oc}^2} \quad (3)$$

These conditions correspond to the optimal values of L and R in order to set the electrical resonance on the mechanical resonance of interest [5]. Passive inductors are then produced according to these specifications using copper wire and appropriate magnetic circuits.

3 EXPERIMENTAL SETUP AND TECHNIQUES

3.1 Experimental Facility and Sensors

Experiments were carried out in the hydrodynamic tunnel at the Institut de Recherche de l'Ecole Navale (IRENav) in Brest, France, illustrated on Figure 2. The tunnel test section is 1 m long with a 192 mm square section. Available operational velocities in the test section range from 0 m/s to 12 m/s and available pressures range from 0.1 bar to 3 bar. Both are set up using a regulation system. Moreover, a honeycomb grid upstream of the test section allows for a 2% free stream turbulent intensity at the mid-section. Vibration measurements are realised using a scanning Doppler laser vibrometer located above the structure and a single point Doppler laser vibrometer located below the structure. For more information about the hydrodynamic tunnel and the experimental techniques, the interested reader may refer to [1,6].

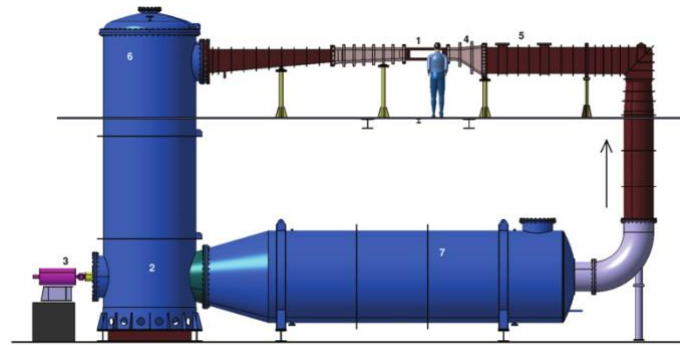


Figure 2: Hydrodynamic tunnel at IRENav, [6]

3.2 Geometry and Materials

The structure considered in this work is a flat plate made of aluminium 5083 and equipped with four piezoelectric patches (two patches on each side of the plate). Base dimensions of the plate are 191 mm x 100 mm x 6 mm, with a 80 mm x 31 mm x 10 mm extension at its base, as

illustrated on Figure 3. This extension is used to clamp the structure to the tunnel wall. Furthermore, the piezoelectric patches are embedded in the structure *via* two pockets machined on both sides of the plate (Figure 3 and Figure 4). Indeed, embedding the patches in the structure avoids creating local roughness, which may cause added turbulence or flow detachment if the roughness size is in the order of the boundary layer thickness. The piezoelectric patches are vacuum-glued in the pockets using epoxy, then a layer of paraffin is added to fill the residual depth of the pocket. Pathways are also machined in the plate and the extension to allow the passage of cables from the electrodes (two on each patch) to the components of the electrical control circuit.

Figure 5 presents the geometry and dimensions of the piezoelectric transducers, in which a PIC 255 piezoelectric ceramic (black rectangle) is encapsulated. The dimensions of the patch are 61 mm long, 35 mm wide and 0.8 mm thick, for a piezoelectric part 50 mm long, 30 mm wide and 0.5 mm thick.

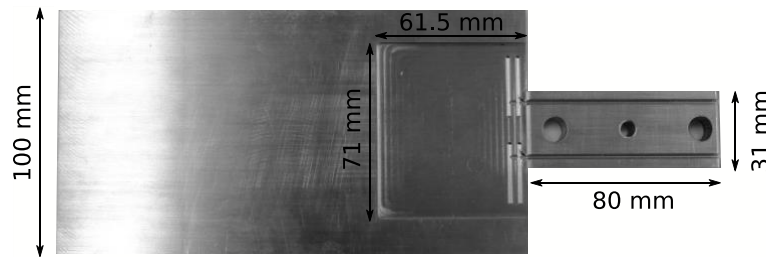


Figure 3: Geometry and dimensions of the structure

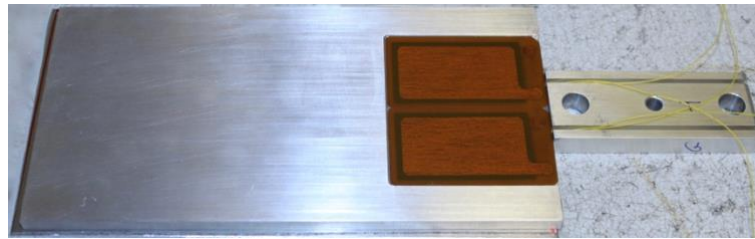


Figure 4: Flat plated equipped with the piezoelectric patches

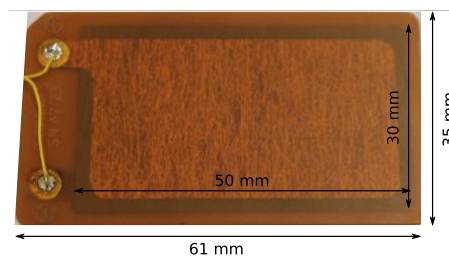


Figure 5: Geometry and dimensions of the piezoelectric patches

4 RESULTS

4.1 Test Cases Under Hydrodynamic Flows

Experiments are first carried out with the plate placed in water at an incidence of 0° , and incident flow velocities ranging from 1 m/s to 10.5 m/s, *i.e.* moderate Reynolds numbers from 10^5 to 1.05×10^6 . The objective is to investigate the flow-induced vibrations of the structure in order to determine the natural frequency of interest to test the control solution. Indeed, as detailed in Section 2, one has to know the value of the frequency to be controlled to guide the design choices of the electrical circuit (inductor and resistor). Therefore, piezoelectric patches are inactive in this first series of tests. Figure 6 shows the vibration spectra of the plate for the range of incident velocities considered. The first three natural frequencies are visible for respective values of 26.4 Hz, 174.1 Hz and 265.6 Hz. The spectra also exhibit additional components with a strong dependence to the Reynolds number: the local maximum close to 50 Hz for a Reynolds number of 1.5×10^5 is progressively shifted towards the high frequencies when increasing the Reynolds number. This phenomenon is characteristic of a vortex shedding process associated to Von Kármán alleyways [1,2,7,8]: The boundary layer is developing on both sides of the plate but meets with a singularity at the trailing edge. The boundary layer then starts to shed alternatively from both sides of the plate, leading to the formation of a vortex street in the turbulent wake. This alternate shedding causes a periodic fluctuation of the hydrodynamic loads applied on the plate and is thus a source of excitation associated to a shedding frequency f_{shed} . In the present case, we can observe a strong fluid-structure interaction between the second mode of the structure (corresponding to the first torsion mode) and the shedding frequencies when their respective values coincide (around 174 Hz). This strong fluid-structure interaction is characterised by a sharp increase of the vibration amplitude.

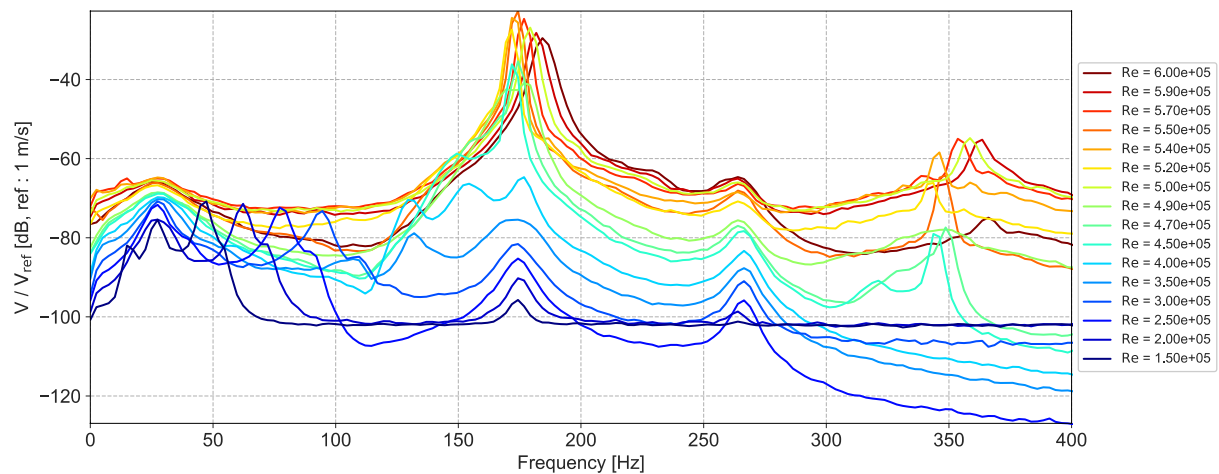


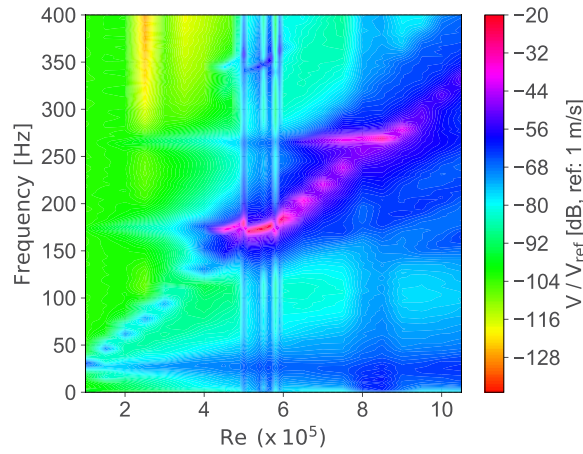
Figure 6: Vibration spectra under hydrodynamic flow for different incident velocities

Figure 7a presents the corresponding Reynolds-frequency diagram, which clearly highlights the linear evolution of the hydrodynamic excitation frequency with the Reynolds number, and therefore the velocity of the incident flow. This linear evolution is given by (4), with a constant Strouhal number close to 0.2 when vortex shedding occurs (d is the thickness of the plate and

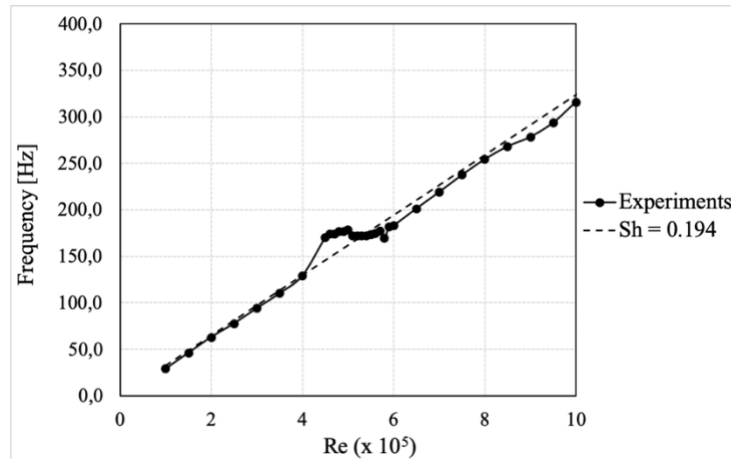
U_0 the incident velocity) [7,8].

$$Sh = \frac{f_{shed} d}{U_0} \quad (4)$$

The linear evolution of the shedding frequencies with the Reynolds number according to Strouhal's law is also highlighted on Figure 7b, where the experimental data points correspond to the local maxima of the spectra presented on Figure 6. One can see that in the present case the Strouhal number is constant to 0.194, confirming the existence of vortex shedding. However, for some Reynolds numbers between 4×10^5 and 6×10^5 the shedding frequencies no longer follow Strouhal's law, but instead keep a constant value of 174 Hz, despite the increase in the number of Reynolds. This is the phenomenon of frequency lock-in around the first mode of torsion: Von Kármán's turbulent wake no longer evolves with its own dynamics (4) but is organized around the natural frequency of the structure [8,9]. As a consequence, the strong fluid-structure interaction previously mentioned corresponds to this lock-in phenomenon.



(a)



(b)

Figure 7: (a) Reynolds-frequency diagram and (b) shedding frequency vs Reynolds number and lock-in

4.2 Test Cases in Still Air and Water

The first series of tests highlighted the existence of a strong fluid-structure interaction between the first torsion mode and the hydrodynamic excitation frequencies due to Von Kármán vortex shedding, resulting in a large increase in the vibration amplitude. As a consequence, this structure is an interesting test case for the application of the vibration damping solution (described in Section 2) to the first torsion mode. The objective is to reduce the amplitude of the vibrations thanks to a passive resonant piezoelectric shunt adjusted on the natural frequency of the structure where the strong fluid-structure interaction occurs. As a first attempt for vibration damping in water using a piezoelectric shunt, this solution is indeed easier to setup than a Reynolds-dependent shunt that would follow the frequency shift of the hydrodynamic excitation.

For this purpose, a second series of tests is carried out both in air and then in still water in order to determine the open and short circuit natural frequencies and evaluate the performances of the control solution in a simplified case. Since the flow no longer provides the excitation of the structure, an alternative source of excitation is used: an electrical voltage is imposed on one of the patches (using a function generator) which then generates a vibratory excitation on the structure through the inverse piezoelectric effect. The other three patches are for the moment kept inactive. The main advantage of this method lies in its ability to provide the frequency responses functions (FRF) of the structure as both the input (voltage imposed on the patch) and output (velocity measured by the vibrometer) are known. On the contrary, when the excitation is generated by the hydrodynamic flow, the input is unknown. Here, a sinus excitation swept across the entire frequency band between 1 Hz and 100 Hz is applied on one of the patches. The temporal signal of this excitation is shown on Figure 8a and the corresponding temporal signal of the in-air and in-water responses are shown on Figure 8b.

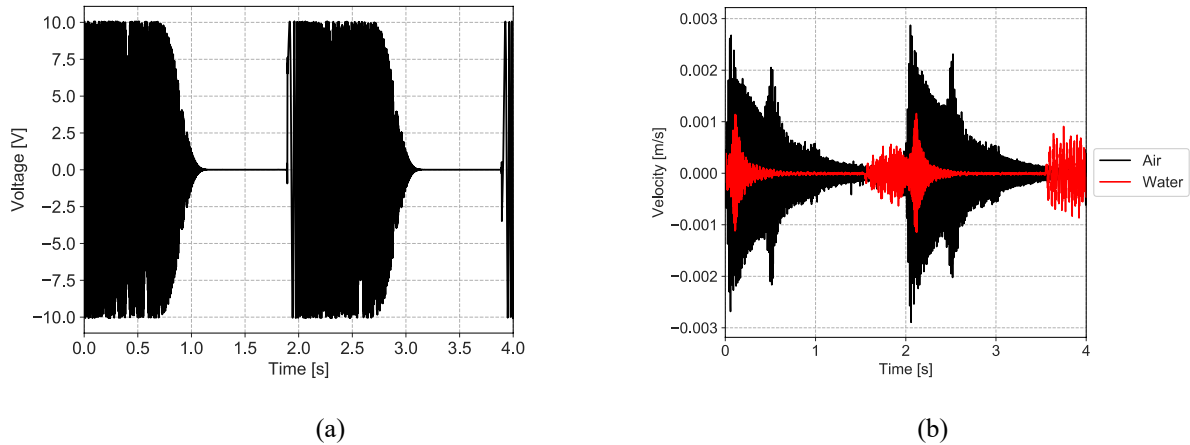


Figure 8: Temporal signals associated to (a) the excitation by sweep and (b) the in-air and in-water vibrations of the structure

The frequency responses derived from the temporal signals are presented on Figure 9, where the first two modes of the structure are visible in air and the first three modes are visible in

water. Corresponding values are reported in Table 1: the comparison of the natural frequencies in air and in water shows significant added mass effects, with a reduction of the in-air natural frequencies up to 58.8%.

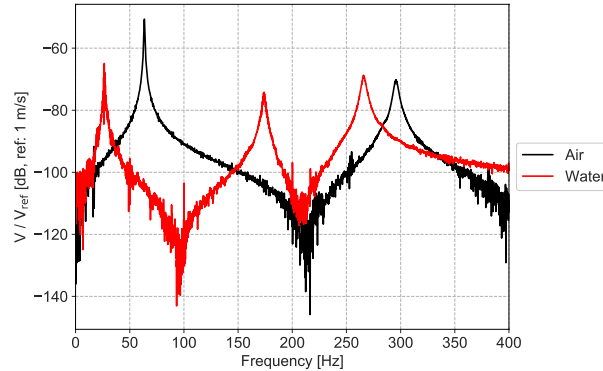


Figure 9: In-air and in-water frequency responses (without flow)

Table 1: Comparison of the in-air and in-water natural frequencies and added mass effects

	f_1	f_2	f_3
f_{air} [Hz]	63.3	295.9	-
f_{water} [Hz]	26.4	174.1	265.6
$\% f_{air}$	58.3	41.2	-

Last, a third series of tests was performed to evaluate the performances of the coupling solution with one of the patches providing the excitation, and the other patches activated for vibration damping. However, the coupling factors obtained (of the order of 3% for the first torsion mode) did not allow to observe a significant reduction of the amplitude of vibration. Such low coupling factors may be explained, on the one hand, by a problem of water sealing on the cables, and on the other hand by a poor placement of the patches to control the first torsion mode. To tackle this issue, two solutions may be considered. First, smaller patches could be used. This way, the location of the patches would be better suited for the control of the first torsion mode. Another solution is to control the first bending mode instead of the first torsion mode, as the coupling factors are more favourable for the bending. However, in order to get an electrical signal that is strong enough for clear measurements, it is preferable to increase the frequency of the first bending mode, for instance by decreasing the length of the plate from 191 mm to 100 mm. This second solution is currently under investigation.

5 CONCLUSIONS

This work presents the testing in water of an aluminium flat plate equipped with four piezoelectric patches. It constitutes a first experimental assessment of vibration damping in water using a resonant piezoelectric shunt. The dynamic response of the structure under hydrodynamic flow was first studied for various incident velocities, then the performances of the control solution were estimated. Prior characterization of the dynamic response of the

structure is indeed needed to determine the short and open circuit natural frequencies in order to compute the coupling factors and the optimal values for the inductance and resistance components of the piezoelectric shunt.

Results showed a strong fluid-structure interaction phenomenon between the natural frequencies of the structure and the hydrodynamic excitation frequencies due to Von Kármán vortex shedding in the turbulent wake. In particular, the hydrodynamic excitation frequencies present a linear dependence to the Reynolds number, with a constant Strouhal of 0.194, with the exception of a frequency lock-in around the first torsion mode (around 174 Hz). An original method for obtaining the frequency responses of the structure (FRF) in still water has also been implemented using one of the patches to provide the excitation of the structure, which allow non-contact excitation and measurement. However, the coupling factors obtained during these first tests to control the first torsion mode were too low to observe a significant reduction of the vibration amplitude, in particular due to a non-optimal placement of the piezoelectric patches. New tests are currently underway with a modified structure to ensure a better placement of the piezoelectric patches. A numerical analysis is also being carried out in order to numerically estimate the coupling factors before testing in water.

REFERENCES

- [1] Lelong, A., Guiffant, P. and Astolfi, J.-A. An Experimental Analysis of the Structural Response of Flexible Lightweight Hydrofoils in Cavitating Flow. *J. Fluids Eng.* (2018) **2**:021116.
- [2] Reese, M.C. Vibration and Damping of Hydrofoils in Uniform Flow. Ph.D. The Pennsylvania University (2010).
- [3] Lossouarn, B., Aucejo, M., Deü J.-F. and Multon, B. Sensors and Actuators A: Physical Design of inductors with high inductance values for resonant piezoelectric damping *Sensors Actuators A. Phys.* (2017) **259**:68–76.
- [4] Thomas, O., Ducarne, J. and Deü, J.-F. Performance of piezoelectric shunts for vibration reduction *Smart Mater. Struct.* (2012) **21**.
- [5] Li, C., Chae, E.J., Young, Y.L., Wang, X. and Alben, S. Passive Vibration Control of Flexible Hydrofoils Using Piezoelectric Material. *Fourth International Symposium on Marine Propulsors*. (2015) Austin, Texas, USA.
- [6] Gaugain, F. *Analyse expérimentale et simulations numériques de l'interaction fluide-structure d'un hydrofoil élastique en écoulements subcavitant et cavitant*, Ph.D. Ecole Nationale Supérieure d'Arts et Métiers (2013).
- [7] Blake, W.K. Excitation of Plates and Hydrofoils by Trailing Edge Flows *J. Vib. Acoust. Stress. Reliab. Des.* (1984) **106**:351–63.
- [8] Naudascher, E. and Rockwell, D. *Flow-Induced Vibrations: An Engineering Guide*. Dover Publications Inc. (2005).
- [9] Zobeiri, A. *Effect of Hydrofoil Trailing Edge Geometry on the Wake Dynamics*. Ph.D. Ecole Polytechnique Fédérale de Lausanne (2012).

RESONANT PIEZOELECTRIC SHUNT TUNING BASED ON THE ELECTRIC CURRENT AND VOLTAGE RESPONSE TO PSEUDO-RANDOM VIBRATION EXCITATION

JOHAN FREDERIK TOFTEKÆR* AND JAN HØGSBERG*

*Department of Mechanical Engineering, Technical University of Denmark
Nils Koppels Allé, Building 404, DK-2800 Kgs. Lyngby, Denmark
e-mail: jotof@mek.dtu.dk, jhg@mek.dtu.dk

Key words: *RL* shunts, Piezoelectric damping, Structural dynamics, Experimental analysis, ANSYS®

Abstract. A tuning procedure for resonant piezoelectric shunt damping based on measurable experimental data is proposed. The procedure is derived from a proposed resonant shunt tuning method designed for the implementation in commercial finite element (FE) software, including the contribution from non-resonant vibration modes. It has been found that this procedure is robust and effective for vibration mitigation in both beam and plate structures. In the present procedure a pseudo-random excitation signal is imposed on a structure with attached piezoceramic patches, while the piezoelectric electrodes are respectively in short- or open circuit. In both cases a time record of respectively the electric current and voltage is measured with a high quality multimeter. A Fast-Fourier-Transform is then used on these time records in order to determine the electric current and voltage frequency response functions. Finally, the optimum resonant shunt inductances and resistances are determined from the corresponding modal properties, which are extracted from the two frequency response functions. The method is demonstrated for a free beam with two pairs of piezoceramic patches, one pair used for the vibration excitation and the other for vibration mitigation. The experimental results are found to be in good agreement with the results from a corresponding numerical model build up in the commercial FE-software ANSYS®.

1 INTRODUCTION

The concepts of resonant piezoelectric shunt damping origin from the work by Forward [1], in which the mechanical equivalence to an electric capacitance, resistance and inductance are presented. It is then suggested that the shunt inductance (L) is tuned in order to neutralize the inherent capacitance of the piezoelectric material, whereby the damping introduced by the shunt resistance (R) is maximized. A concrete procedure for the optimum tuning of the resonant LR -shunt circuit was subsequently proposed by Hagood and von Flotow [2]. The method assumes the structural response around a target resonant frequency to be sufficiently represented by the corresponding modal properties. The tuning formulas are thus derived from a representative two degrees of freedom coupled electromechanical system. In [2] the series shunt circuit is considered, while the parallel shunt circuit was suggested later by Wu [3]. Alternative methods for the precise series and parallel shunt tuning have been suggested subsequently [4, 5], all based on the modal approximation. In recent years several authors have discussed the influence from the non-resonant vibration modes on the structural response, which alternate the optimum piezoelectric shunt tuning [6, 7, 8]. In [9] the influence from the non-resonant modes was described by a flexibility and

an inertia correction terms and the influence on the optimum tuning of tuned mass and inerter-based absorbers was demonstrated. In [8] the equivalence to resonant piezoelectric shunt damping was presented and in [10] an alternative formulation suitable for implementation in commercial software was suggested. In the present work, it is the aim to demonstrate the latter method through experiments carried out on a free beam employed with two pairs of piezoceramic patches.

The experimental design with a free beam is chosen in order to achieve high correlation between the experimental and numerical results. Disparancies between numerical and experimental results have been encountered in numerous contributions [2, 3, 4], where one of the common uncertainties is associated with an inaccurate numerical or theoretical approximation of the actual boundary conditions of the experimental setup. This can be dealt with by updating the finite element (FE) model according to the experimental results as proposed in [11]. However, such a procedure can be rather cumbersome, hence the free beam is chosen in the present case.

2 NUMERICAL SHUNT TUNING

In the present section the optimum shunt tuning procedure presented in [10] is summarized and an alternative way of determining the effective electromechanical coupling coefficient (EMCC) presented, where the latter becomes useful when reformulating the tuning formulas for subsequent experimental implementation. Optimum tuning of one shunt circuit is considered, which however may be connected to a network of several piezoceramic patches glued on to a mechanical structure. The coupled vibration problem of a mechanical structure with interconnected and shunted piezoceramic patches may be written according to [10], as

$$\left(\begin{bmatrix} K^E & k_{me}^E \\ (k_{me}^E)^t & -\tilde{C}_p^{\epsilon^S} \end{bmatrix} - \omega^2 \begin{bmatrix} M & 0 \\ 0 & 0 \end{bmatrix} \right) \begin{Bmatrix} U \\ V \end{Bmatrix} = \begin{Bmatrix} 0 \\ -Q \end{Bmatrix} \quad (1)$$

where $[K^E]$ is the elastic stiffness matrix of the structure with short circuit (SC) piezoceramic patch(es), $[M]$ is the mass matrix, $\{k_{me}^E\}$ the electromechanical coupling vector and $\tilde{C}_p^{\epsilon^S}$ the resulting modified capacitance of the piezoceramic patch(es).

The vibration problem Eq. (1) is limited by two eigenvalue problems associated with, respectively, SC and open circuit (OC) piezoceramic patch electrodes. When having SC electrodes the voltage vanishes $V = 0$ and the associated eigenvalue problem can be written as

$$([K^E] - \omega_j^2[M]) \{U\}_j = \{0\} \quad (2)$$

for a particular vibration mode j with circular frequency ω_j . The second equation in Eq. (1) further provides the (sensed) modal charge

$$\tilde{Q}_j = -\{k_{me}^E\}^t \{U\}_j \quad (3)$$

When no current can flow between the interface electrodes, the piezoceramic patch(es) is(are) said to be in OC. Vanishing current implies that the charge is zero, whereby the corresponding eigenvalue problem follows from Eq. (1), with $Q = 0$, as

$$\left([K^E] + \frac{1}{\tilde{C}_p^{\epsilon^S}} \{k_{me}^E\} \{k_{me}^E\}^t - \omega_j^2[M] \right) \{\hat{U}\}_j = \{0\} \quad (4)$$

while the second equation of Eq. (1) provides an OC modal voltage given as

$$\tilde{V}_j = \frac{1}{\tilde{C}_p^{\epsilon^S}} \{k_{me}^E\}^t \{\hat{U}\}_j \quad (5)$$

Table 1: Numerical parallel and series shunt tuning to target vibration mode r .

Parallel (p)	Series (s)
$L_p = \frac{\kappa_r^2}{Q_r^2} \quad , \quad R_p = \frac{\kappa_r^2 \omega_r}{Q_r^2} \sqrt{\frac{1}{2\kappa_r^2}}$	$L_s = \frac{\kappa_r^2}{Q_r^2(1 + \kappa_r^2)^2} \quad , \quad R_s = \frac{\kappa_r^2 \omega_r}{Q_r^2} \sqrt{\frac{2\kappa_r^2}{(1 + \kappa_r^2)^3}}$

The authority of the piezoceramic patch(es) on a given vibration mode of the electromechanical structure is associated with the relative difference between the SC and OC modal strain energies and defined by the effective EMCC. The effective EMCC is for resonant vibration mode $j = r$, given as

$$\kappa_r^2 = \frac{\hat{\omega}_r^2 - \omega_r^2}{\omega_r^2} \quad (6)$$

Pre-multiplying Eq. (2) with $\{\hat{U}\}_r^t$ and Eq. (4) with $\{U\}_r^t$, the terms involving $[K^E]$ may be eliminated such that the effective EMCC alternatively can be expressed as

$$\kappa_r^2 = \frac{\{U\}_r^t \{k_{me}^E\} \{k_{me}^E\}^t \{\hat{U}\}_r}{\omega_r^2 \bar{C}_p^{\epsilon^S} \{U\}_r^t [M] \{\hat{U}\}_r} \quad (7)$$

Introducing the SC modal charge Eq. (3) and OC voltage Eq. (5), the effective EMCC Eq. (7) can be written as

$$\kappa_r^2 = \frac{\tilde{Q}_r \tilde{V}_r}{\omega_r^2 \{U\}_r^t [M] \{\hat{U}\}_r} = \frac{Q_r V_r}{\omega_r^2} \quad (8)$$

The latter expression in Eq. (8) follows by normalizing the modal charge and voltage from Eqs. (3) and (5) by the intermediate modal mass $\tilde{m}_r = \{U\}_r^t [M] \{\hat{U}\}_r$ in the denominator of Eq. (8) as

$$Q_r = \frac{\tilde{Q}_r}{\sqrt{\tilde{m}_r}} \quad , \quad V_r = \frac{\tilde{V}_r}{\sqrt{\tilde{m}_r}} \quad (9)$$

In regard to experiments, the intermediate modal mass \tilde{m}_r may beneficially be determined from Eq. (8),

$$\tilde{m}_r = \frac{\tilde{Q}_r \tilde{V}_r}{\omega_r^2 \kappa_r^2} \quad (10)$$

In reality the intermediate modal mass \tilde{m}_r would be close to both the modal mass of the SC or OC electromechanical structure, since the corresponding mode shapes are almost identical and the mass distribution remains virtually unchanged.

In [10], a reduced order model was introduced in order to determine the optimum parallel and series resonant RL shunt tuning. The tuning formulas are provided in Table 1 for clarity, while the reader is referred to [10] for the extensive derivations. It is noted that the inertia effect from the non-resonant vibration modes on the shunt tuning is neglected according to [10].

The tuning formulas provided in Table 1 are favorable in terms of FE-analysis since the mode shapes and modal charge can be normalized in order to obtain unit modal masses as described in [10]. In terms of tuning based on experimental data it become beneficial to reformulate these tuning formulas as demonstrated subsequently in section 3.

3 EXPERIMENTAL SHUNT TUNING

In this section the resonant shunt tuning procedure in section 2 is reformulated to be dependent on measurable experimental data. The experimental procedure is very simple and consists of two steps. First, the electromechanical structure is excited by a pseudo-random excitation signal with a given frequency bandwidth and intensity, while the piezoceramic patch(es) are in SC condition. The SC condition is realized by connecting the interface electrodes of the piezoceramic patch(es) to a multimeter measuring the time record of the corresponding electric current $I(t)$. In the second step, a random excitation signal with the same frequency bandwidth and intensity is applied to the electromechanical structure with the piezoceramic patches in OC condition. The OC condition is realized by adjusting the multimeter to measure electric voltage $V(t)$, whereby an infinitely large resistance is imposed between the interface electrodes. From the measured current and voltage time records two frequency response functions (FRF) can be determined using a fast Fourier transform (FFT), from which the SC and OC frequencies and modal current and voltage amplitudes are read for each vibration mode in the analyzed frequency band.

The modal voltage is found directly as the resonant peaks $\tilde{V}_j = \tilde{V}(\hat{\omega}_j)$ in the generated frequency response, while the measured electric current time response $I(t)$ is used to determine the corresponding charge $\tilde{Q}(t)$. The electric current is given as the time derivative ($\dot{(\cdot)} = d/dt$) of the electric charge

$$I(t) = \dot{Q}(t) \quad (11)$$

Assuming harmonic solutions, the electric current and charge time functions may be expressed as

$$I(t) = \tilde{I}e^{i\omega t}, \quad Q(t) = \tilde{Q}e^{i\omega t} \quad (12)$$

with the complex amplitudes \tilde{I} and \tilde{Q} . Inserting (12) into (11) the relationship between the complex amplitudes of the current and charge may be written as

$$\tilde{I} = i\omega\tilde{Q} \quad (13)$$

Finally the modal charge are found as the resonant peaks $\tilde{Q}_j = \tilde{Q}(\omega_j)$ of the corresponding FRF.

The shunt tuning then follows by determining the effective EMCC Eq. (6) and the intermediate modal mass from Eq. (10), while the shunt tuning formulas in Table 1 can be reformulated by inserting κ_r^2 from Eq. (8) in the tuning formulas. For the parallel inductance tuning this gives

$$L_p = \frac{|V_r|}{|Q_r|\omega_r^2} = \frac{|\tilde{V}_r|}{|\tilde{Q}_r|\omega_r^2} \quad (14)$$

which is seen to be independent of any normalization of the modal charge and voltage and also does not require determination of the OC frequency and effective EMCC. The series inductance tuning and tuning of the optimum resistances follow similarly from inserting the effective EMCC κ_r^2 (Eq. (8)) into the tuning formulas provided in Table 1. The reformulated tuning formulas for the experimental RL shunt design are provided in Table 2 for both the parallel and series shunt circuits.

4 SYNTHETIC INDUCTOR

In the subsequent experimental verification of the tuning procedure presented in section 3, a so-called synthetic inductor is used to emulate the required shunt inductance. It consists of an Antoniou circuit [12] with the modification proposed in [13]. The circuit diagram of the modified Antoniou circuit and the prototype of the synthetic inductor used in the experiment can be seen in Figure 1.

Table 2: Experimental parallel and series shunt tuning to target vibration mode r .

Parallel (p)	Series (s)
$L_p = \frac{ \tilde{V}_r }{ \tilde{Q}_r \omega_r^2}$, $R_p = \frac{ \tilde{V}_r }{ \tilde{Q}_r \omega_r} \sqrt{\frac{1}{2\kappa_r^2}}$	$L_s = \frac{ \tilde{V}_r }{ \tilde{Q}_r \hat{\omega}_r^2 \hat{\omega}_r^2}$, $R_s = \frac{ \tilde{V}_r }{ \tilde{Q}_r \hat{\omega}_r} \frac{\omega_r^2}{\hat{\omega}_r^2} \sqrt{2\kappa_r^2}$

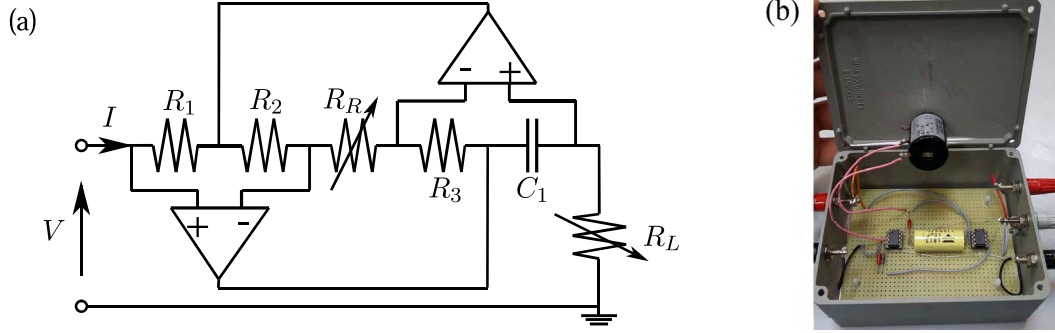


Figure 1: Synthetic inductor, circuit diagram (a) and prototype (b).

Details about the original Antoniou circuit can be found in [14], while the modification is given by the addition of the variable resistance R_R , see Figure 1(a). The latter permits the addition of negative resistance to the circuit impedance, added in order to compensate for eventual parasitic losses. The original Antoniou circuit was designed in order to emulate the effect of an inductance by keeping a constant current to voltage relationship at the circuit terminal defined as

$$V(t) = L\dot{I}(t) \quad (15)$$

Assuming harmonic solutions, the electric current may be expressed as in Eq. (12a) with a similar representation for the voltage,

$$V(t) = \tilde{V}e^{i\omega t} \quad (16)$$

Inserting Eqs. (12a) and (16) into Eq. (15) the emulated inductance can be defined as

$$L = \frac{|\tilde{V}|}{\omega|\tilde{I}|} \quad (17)$$

Analyzing the circuit diagram Figure 1(a), it may thus be found that the emulated inductance is given as

$$L = \frac{C_1 R_1 R_3}{R_2} R_L \quad (18)$$

The full effective impedance of the modified Anoniou circuit can further be determined as

$$Z = i\omega \frac{C_1 R_1 R_3}{R_2} R_L - \frac{R_1}{R_2} R_R \quad (19)$$

which is seen to correspond to the impedance of an inductance connected in series with a negative resistance. The properties of the constant electronic components are given by $R_1 = 2\text{k}\Omega$, $R_2 = 1\text{k}\Omega$,

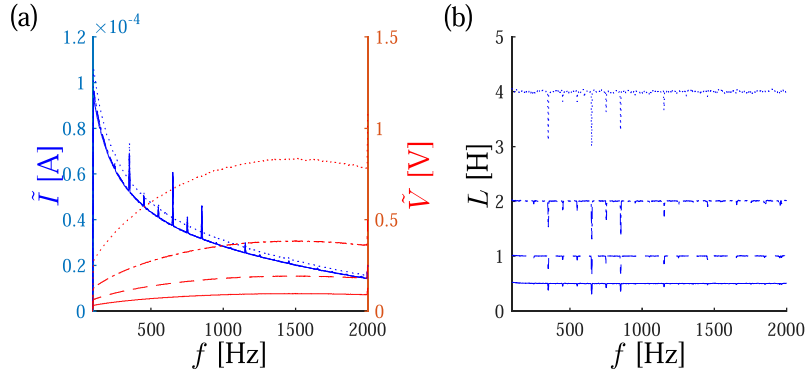


Figure 2: Verification of synthetic inductor (a) FRF for the current and voltage and (b) the corresponding emulated inductance value, for $R_L = 25\Omega$ (—), 50Ω (---), 100Ω (-.-.), 200Ω (.....).

$R_3 = 1\text{k}\Omega$ and $C_1 = 10\mu\text{F}$, whereby the inductance and negative resistance can be determined by constant factors multiplied by respectively the variable resistances R_L and R_R ($0 - 1\text{k}\Omega$), as

$$L = (0.02\text{H}/\Omega)R_L \quad , \quad R = -2R_R \quad (20)$$

In order to verify the analytic expression Eq. (20a) for the emulated inductance, the terminal of the synthetic inductor is excited by a pseudo-random voltage signal for different R_L values, while the resistance R_R is kept constant to zero. The corresponding electric current time record is then measured with a high quality multimeter connected in series with the synthetic inductor. Finally, an FFT is used on the voltage and current time records in order to obtain the corresponding FRFs. In Figure 2(a) the FRFs corresponding to R_L values of 25Ω , 50Ω , 100Ω and 200Ω are provided, while the corresponding emulated inductance values determined from Eq. (17) are shown in Figure 2(b). It is seen that the input voltage signal is increased for the tests with larger R_L -values, in order to minimize the effect of the electric hums that are clearly visible in the FRF of the electric current. Disregarding these electric hums, it is seen from Figure 2(b) that the emulated inductance values agree well with the values predicted from Eq. (20a) and are almost constant in the analyzed frequency band.

The synthetic inductor is further tested at higher R_L values of 400Ω , 800Ω , 1600Ω and 3200Ω for which the FRFs of the current and voltage and corresponding emulated inductance can be seen in Figure 3. Again, the electric hums are clearly apparent in the FRF of the current and corresponding emulated inductance. Again, disregarding this noise, constant emulated inductance values predicted by Eq. (20a) are observed in the considered frequency band, except for the case of $R_L = 3200\Omega$ where a slight decrease in the emulated inductance is noted at higher frequencies. This may indicate that the emulated inductance becomes slightly non-linear for large R_L values at high frequencies. However, larger R_L and corresponding inductance is only relevant for piezoelectric shunt tuning to low frequent vibrations, since the optimum inductance tuning is inversely proportional to the target resonant frequency, see Table 2. It is thus verified that Eq. (20a) precisely predicts the emulated inductance of the synthetic inductor.

5 EXPERIMENTAL VERIFICATION

In this section, the optimum piezoelectric shunt tuning to a free beam with two pairs of piezoceramic patches is determined according to the tuning procedure presented in section 3. The free beam and the position of the two piezoceramic patch pairs can be seen in Figure 4, while the exact dimensions and

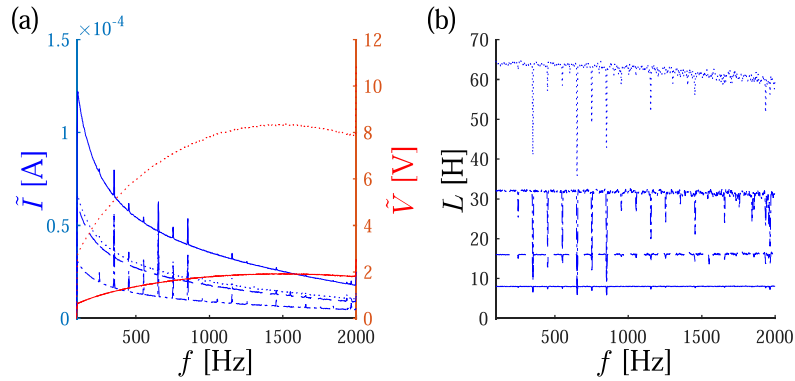


Figure 3: Verification of synthetic inductor (a) FRF for the current and voltage and (b) the corresponding emulated inductance value, for $R_L = 400\Omega$ (—), 800Ω (---), 1600Ω (-.-), 3200Ω (.....).

Table 3: Dimensions and material properties for free beam and piezoceramic patches.

	Beam		Piezoceramic patches NCE51 (CTS)		
Length (mm)	l	260	l_p	30	Center patch to center beam (mm)
Width (mm)	w	30	w_p	30	
Thickness (mm)	t	2	t_p	1	x_p 22
Density (kg/m ³)	ρ	2710	ρ_p	7850	Stress piezoelectric coefficient (10 ⁻¹² m/V)
Young's Modulus (GPa)	E	71	Stiffness Components (GPa)		
Poisson's ratio (-)	ν	0.33	C_{11}^E, C_{22}^E	134	e_{31}, e_{32} -6.06
			C_{12}^E	88.9	e_{33} 17.2
			C_{13}^E, C_{23}^E	90.9	e_{24}, e_{15} 13.7
			C_{33}^E	121	Relative permittivity*
			C_{44}^E, C_{55}^E	20.5	$\epsilon_{11}^p, \epsilon_{22}^p$ 906 ϵ_0
			C_{66}^E	22.4	ϵ_{33}^p 823 ϵ_0

*Reference vacuum permittivity $\epsilon_0 = 8.854 \times 10^{-12}$ F/m

material properties of the beam and piezoceramic patches are provided in Table 3. It is noted that the piezoceramic patches of each patch pair are oppositely poled and connected in series. As indicated in Figure 4 the left piezoceramic patch pair is used for vibration excitation, while the right patch pair mitigates vibrations by connecting it to an optimally tuned resonant shunt.

The experimental setup can also be seen in Figure 4, where the left piezoceramic patch pair is connected to a power amplifier, while the right patch pair is connected to a multimeter. Both power amplifier and multimeter are connected to a PC used for data acquisition. A Laser Doppler Vibrometer is used to measure the dynamic response of the free beam.

Following the steps presented in section 3 a pseudo-random voltage excitation signal is imposed between the interface electrodes of the left piezoceramic patch pair, while the right patch pair is connected to a multimeter set to measure respectively current, whereby the right patch pair is in its SC condition, and voltage corresponding to the OC condition. The bandwidth of the pseudo-random excitation signal is set to 2kHz and the sample rate of the multimeter to 250 μ s. The tip velocity is further measured by the

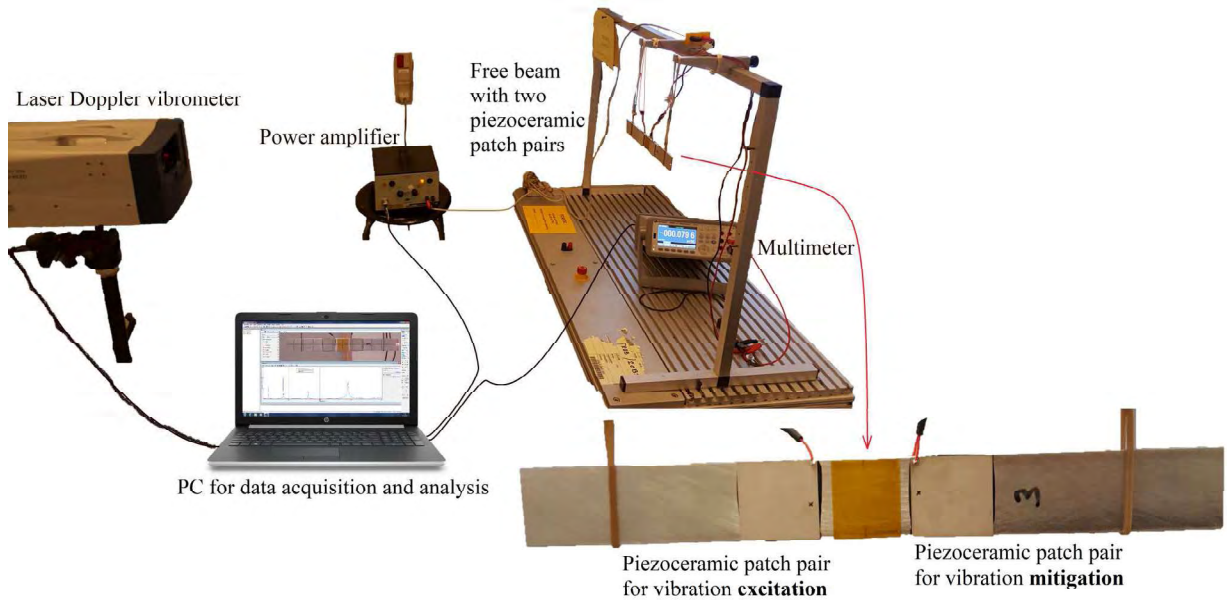


Figure 4: Free beam with two pairs of piezoceramic patches, experimental setup.

Laser Doppler Vibrometer in order to compare the mechanical response of the free beam and the electric response of the right piezoceramic patch pair. An FFT is performed on both mechanical and electrical time records, whereby the FRFs for, respectively, the tip displacements (determined from the tip velocity) in SC and OC condition and the electric current and voltage are obtained and shown in Figure 5.

It can be seen from Figure 5 that the mechanical and electrical responses correspond very well and that four resonant vibration modes appear in the investigated frequency band. In order to determine the optimum piezoelectric shunt tuning, only the FRFs for the electric charge and voltage in Figure 5(b) are considered, from which the SC and OC natural frequencies and modal charge and voltage are determined and provided in Table 4. The optimum shunt tuning then follows by the tuning formulas provided in Table 2 giving the optimum parallel and series shunt tuning listed in Table 4. For comparison, the free beam with the two piezoceramic patch pairs has been modeled in ANSYS®, where the SC and OC eigenvalue problems have been evaluated in order to determine the SC and OC frequencies and modal charge and voltage, which are also provided in Table 4. The FE-model used in ANSYS® consist of $225 \times 8 \times 4$ SOLID186 3D elements discretizing the beam and $100 \times 8 \times 2$ SOLID226 3D electromechanical elements discretizing each of the four piezoceramic patches. Finally, the equipotential condition is enforced for each piezoelectric electrode by applying a coupling constraint to the concerned electrical dofs, while the opposite polarization is obtained by using opposite signs for the stress piezoelectric coefficients in each piezoceramic patch pair.

It can be seen from Table 4 that there is a good correlation between the experimental and numerical SC and OC frequencies, except for the fourth torsional vibration mode predicted by the ANSYS® model, which can not be excited by the driving force from the left piezoceramic patch pair. The use of the left piezoceramic patch pair as the driving force for the vibrations means that only the flexural vibration modes are easily activated. Furthermore, the position of the patch pairs also influences how well each vibration mode may be sounded and damped. The mode shapes corresponding to the four flexural resonant frequencies in Table 4 and based on the measurement with the Laser Doppler Vibrometer can be

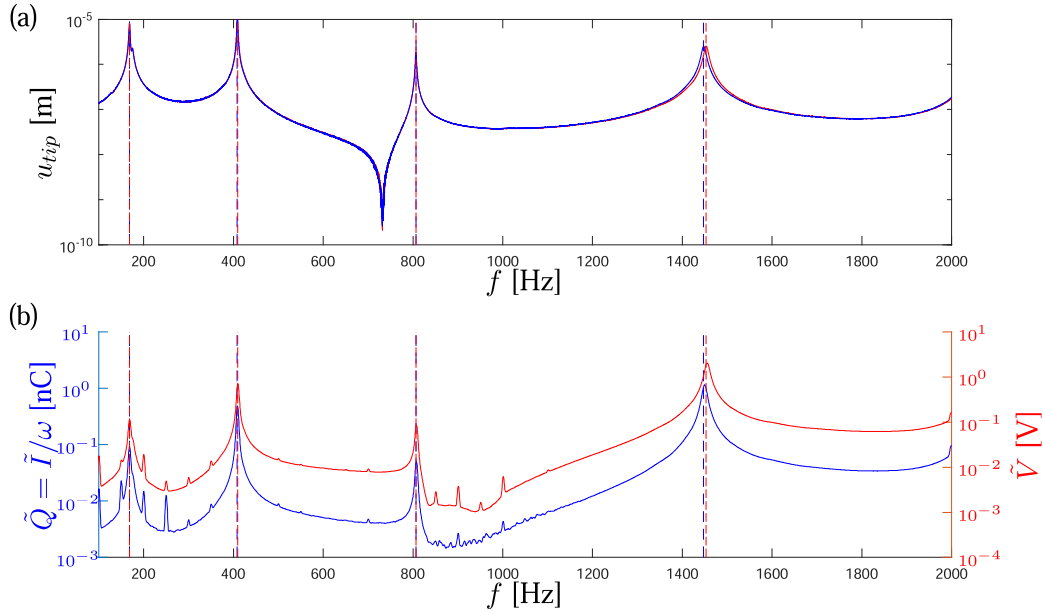


Figure 5: FRF for (a) the tip displacement and (b) the electric charge and voltage with respectively SC (blue line) and OC (red line) piezoceramic patch electrodes.

Table 4: Frequencies, effective EMCC, modal charge and voltage and optimum shunt tuning to the resonant vibration modes between 0 – 2kHz

Mode	Model	f [Hz]	\hat{f} [Hz]	κ_r^2 [%]	Q_r [mC]	V_r [MV]	L_p [H]	R_p [k Ω]	L_s [H]	R_s [k Ω]
1 Flex	ANS	170.9	171.4	0.52	6.618	0.907	118.9	1251	117.6	12.93
	Exp	168.5	169.0	0.58	7.242	0.899	110.7	1088	109.4	12.52
2 Flex	ANS	409.1	410.1	0.50	15.52	2.141	20.88	535.2	20.67	5.341
	Exp	409.3	409.8	0.24	10.38	1.522	22.18	825.3	22.07	3.928
3 Flex	ANS	813.5	813.7	0.03	7.224	0.992	5.256	1147	5.253	0.629
	Exp	807.8	807.8	0.02*	5.506	0.936	6.598	1674	6.532	0.670
4 Tors	ANS	958.6	958.6	0.00	-	-	-	-	-	-
	Exp	-	-	-	-	-	-	-	-	-
5 Flex	ANS	1446.6	1454.4	1.07	80.05	11.08	1.675	103.9	1.640	2.195
	Exp	1449.6	1455.4	0.81	61.70	10.89	2.129	152.3	2.095	2.438

* Effective EMCC based on frequencies determined from the FRF for the tip displacements, see Figure 5(a).

seen in Figure 6. The location of the piezoceramic patches are here indicated by the red arrows, and it can thus be seen that the third vibration mode is both hardly excited and damped since the two patch pairs are located close to a nodal point of the corresponding mode shape in Figure 6(c). This is also apparent by the corresponding effective EMCC in Table 4, which is close to zero. Oppositely, the largest effective EMCC is obtained for the fourth flexural vibration mode, for which it can be seen that the piezoceramic patches are located near a position of maximum curvature (Figure 6(d)) and therefore have good authority on the corresponding vibrations. The position of the piezoceramic patches with respect to the first and second vibration modes in Figure 6(a,b) are seen to be moderately good, also indicated

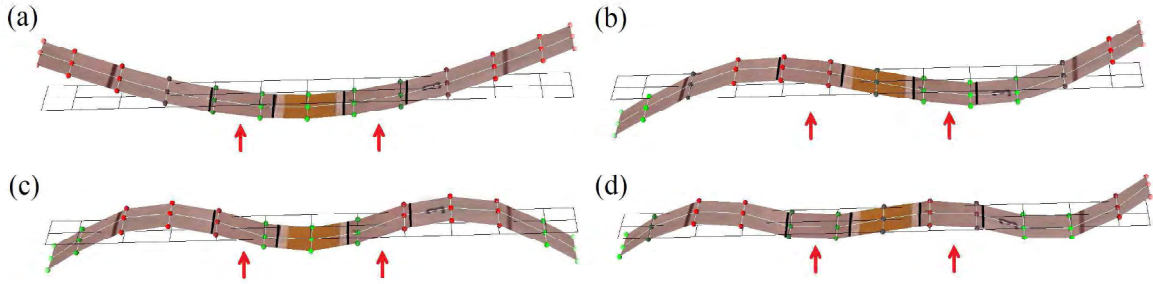


Figure 6: First four flexural mode shapes (a)-(d) of the free beam with two piezoceramic patch pairs located as indicated by the red arrows.

by the effective EMCCs in Table 4. Common for all the effective EMCCs is that there is a significant relative deviation between the numerical and experimental results. This may be explained by several uncertainties associated with the experimental setup, for instance the gluing of the piezoceramic patches to the beam, the actual electromechanical properties and eventual hysteretic behavior of the piezoceramic material, which is not considered in the tuning and numerical FE-model. Finally, it can be seen from Table 4 that there is good correlation between the numerical and experimental modal charge and voltage and the corresponding optimum parallel and series shunt tuning. The normalized modal charge and voltage are for the experiment determined from the measured modal charge and voltage amplitudes with Eq. (9), in which the intermediate modal mass is equated with Eq. (10).

It is now analyzed how well the optimum piezoelectric shunt tuning performs, when each individual shunt circuit for the four flexural vibration modes are wired in series to the right piezoceramic patch pair. The optimum inductance is emulated by the synthetic inductor described in section 4, which is further connected in series with a variable resistor. It is found that the optimum inductance values must be slightly altered in order to obtain the most optimum damping properties. The optimum inductance values are $L_1 = 128\text{H}$, $L_2 = 24.2\text{H}$, $L_3 = 6.6\text{H}$ and $L_5 = 2.0\text{H}$. The deviation between these values and the series tuning provided in Table 4 may be due to the neglect of structural damping in the tuning formulas and the fact that the forcing from the left piezoceramic patch pair does not act as an ideal modal load. However, the deviations are relatively small, in particular for the fourth flexural vibration mode with the largest effective EMCC. Regarding the resistance tuning to the first three flexural vibration modes, it is found that the parasitic loss in the synthetic inductor seems to exceed the optimum resistance tuning, even when negative resistance is added to the system through R_R . For the shunt circuit tuned to the fourth flexural vibration mode, the variable resistance is set to $R_4 = 2.4\text{k}\Omega$, approximately equal to the optimum series tuning in Table 4. With the respective implementation of these four shunt circuits the corresponding FRFs for both the tip displacements and electric voltages are determined using the FFT on the corresponding time records to a pseudo-random vibration excitation with the same frequency bandwidth and intensity as used previously. The FRFs can be seen in Figure 7.

It can be seen from Figure 7(a)-(d) that considerable amplitude reduction is obtained around each of the four flexural resonant frequencies when implementing the respective resonant shunt circuits. In particular, flexural vibration mode 4 in Figure 7(d) is seen to be highly damped and an almost flat plateau around the corresponding resonant frequency is obtained. The lowest vibration reduction is found for mode 3 in Figure 7(c), as expected due to the corresponding insignificant electromechanical coupling. Looking at the voltage responses in Figure 7(e)-(h), it can be seen that the damper response is increased around the resonant frequencies when implementing the resonant shunt circuits. This may be interpreted

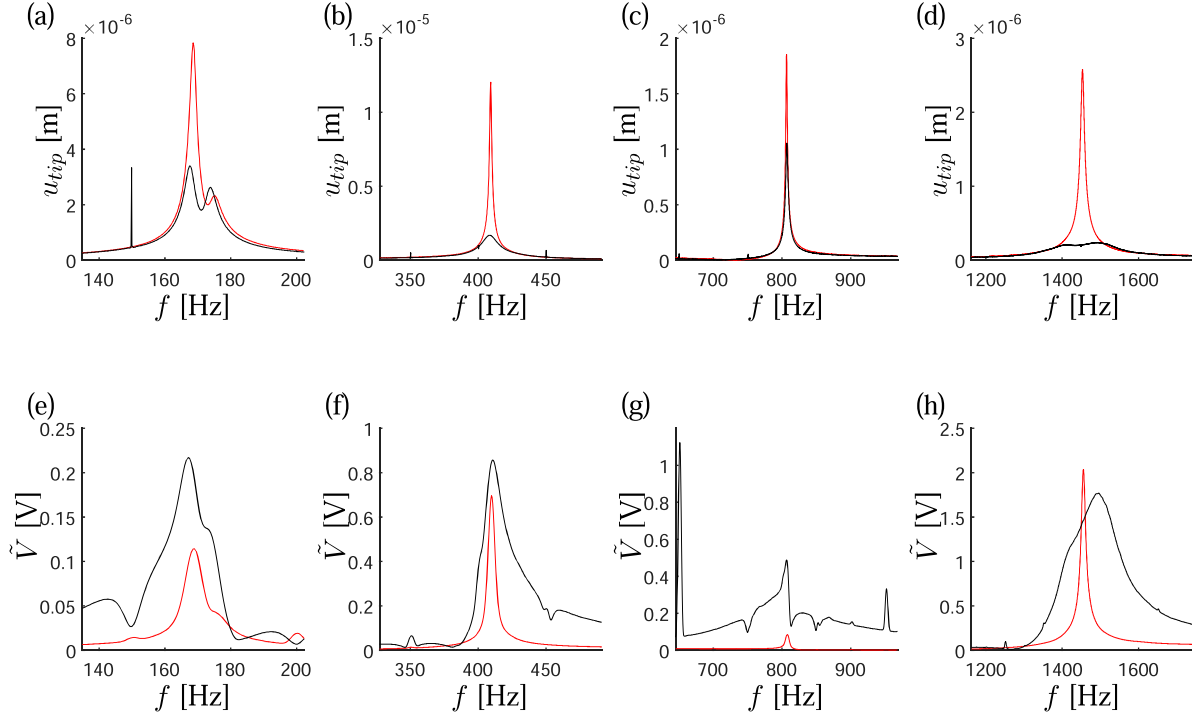


Figure 7: FRF for (a)-(d) the tip displacements and (e)-(f) shunt voltage, for OC (—) and optimally shunted to respectively flexural mode 1-4 (—) piezoceramic patches.

as an increase in the amount of energy dissipated by the shunt resistance. For the fourth flexural vibration mode in Figure 7(h) an almost flat plateau around the resonant frequency for the voltage is obtained, which agrees well with the theoretical damper response of the tuned piezoelectric shunt damper [10].

Although small deviations between the optimum and implemented shunt tuning has been encountered, the experimental shunt tuning method presented in section 3 has proven to be accurate and easy to implement, as the optimum shunt tuning to any resonant vibration mode in a given frequency band may be determined from only current and voltage responses to a pseudo-random vibration excitation.

6 CONCLUSIONS

A piezoelectric shunt tuning method based on measurable experimental data has been proposed. The procedure consists in imposing pseudo-random vibrations to a mechanical structure while the electric current and voltage responses are measured between the electrodes of an attached piezoelectric domain. A FFT is then used on the electric time records to obtain the FRF for the corresponding charge and voltage. The SC and OC natural frequencies and modal charge and voltage may finally be determined for each vibration mode in the analyzed frequency band, and the corresponding shunt circuit components optimally tuned. The method is verified by the analysis of a free beam with two pairs of piezoceramic patches, one pair used to excite the structure, while the second pair is connected to a shunt circuit optimally tuned to a target resonant vibration mode. The FRF for the electric charge and voltage have

been determined and the optimum shunt tuning evaluated for the first four flexural vibration modes of the free beam. Finally, it is found that the obtained optimum shunt tuning values are very close to the shunt tuning, which delivers the most substantial damping to the structure around the target resonant frequencies. The proposed method is beneficial as the necessary tuning parameters are determined from two FRF obtained by imposing pseudo-random vibrations to the investigated structure. Furthermore, the inductance tuning is independent of the relative difference between the SC and OC frequencies, which may be hard to determine. Instead, it relies on the ratio between the modal voltage and charge.

REFERENCES

- [1] Forward, R.L. Electronic damping of vibrations in optical structures. *Appl. Opt.* **18**(1979) 690-697.
- [2] Hagood, N.W. and von Flotow, A. Damping of structural vibrations with piezoelectric materials and passive electrical networks. *J. Sound Vib.* **146**(1991) 243-268.
- [3] Wu, S.Y. Piezoelectric shunts with a parallel R-L circuit for structural damping and vibration control. *In Proc. SPIE* **2720**(1996) 259-269.
- [4] Thomas, O., Ducarne, J. and Deü, J.-F. Performance of piezoelectric shunts for vibration reduction. *Smart Mater. Struct.* **21**(2012) 015008.
- [5] Soltani, P., Kerschen, G., Tondreau, G. and Deraemaeker, A. A Piezoelectric vibration damping using resonant shunt circuits: an exact solution. *Smart Mater. Struct.*, **23**(2014) 125014.
- [6] Berardengo, M., Thomas, O., Giraud-Audine C., Manzoni S., Improved resistive shunt by means of negative capacitance: new circuit, performances and multi-mode control. *Smart Mater. Struct.* **25**(2016) 075033.
- [7] Gardonio, P. and Casagrande, D. Shunted piezoelectric patch vibration absorber on two-dimensional thin structure: tuning considerations. *J. Sound Vib.* **395**(2017) 2647.
- [8] Høgsberg, J. and Krenk, S. Calibration of piezoelectric RL shunts with explicit residual mode correction. *J. Sound Vib.*, **386**(2017) 65-81
- [9] Krenk, S. and Høgsberg, J. Tuned resonant mass or inerter-based absorbers: Unified calibration with quasi-dynamic flexibility and inertia correction. *Proc. R. Soc. A*, **472**(2016) 20150718.
- [10] Toftekær, J.F., Benjeddou, A. and Høgsberg, J. General numerical implementation of a new piezoelectric shunt tuning method based on the effective electromechanical coupling coefficient. *Mech. Adv. Mater. Struc.* (2019).
- [11] Hamdi, M., Ghanmi, S., Benjeddou, A. and Nasri, R., Robust electromechanical finite element updating for piezoelectric structures effective coupling prediction, *J. Intell. Mater. Syst. Struct.* **25**(2014) 137-154.
- [12] Antoniou, A. Realization of Gyration Using Operational Amplifiers, and their Use in RC-Active-Network Synthesis. *In Proc. of IEEE* **116**(1969) 1838-1850
- [13] Von Wangeheim, L. Modification of the classical GIC structure and its application to RC-oscillators. *Electron. Lett.* **32**(1)(1996) 6-8
- [14] Sedra, A.S. and Smith, K.C. *Microelectronic Circuits*, 5th Edition, Oxford University Press (2007).

SEMI-ACTIVE PIEZOELECTRIC TUNED MASS DAMPER FOR MITIGATION OF AERODYNAMIC VIBRATIONS IN AIRCRAFT STRUCTURES

KONSTANTINOS I. GEORGOPOULOS-BOSINAS^a, NIKOLAOS A.
CHRYSOCHOIDIS^a, CHRISTOFOROS REKATSINAS^a AND DIMITRIS A.
SARAVANOS^{a*}

^a Department of Mechanical Engineering and Aeronautics,
University of Patras, Rion - Patras, Greece

Key words: Vibration control, Semi-active, Piezoelectric shunt, Tuned mass damper

Abstract. The analytical framework of a semi active tuned mass damper (SATMD) is developed for the reduction of low-frequency aerodynamic vibrations in aeronautics structures. The SATMD entails a shunted piezoelectric connected in series to an RL electric circuit. Initially, the theoretical model of the SATMD is presented, including the equivalent electrical RL circuit, applied on a simplified system consisting of two structural modes. Subsequently, the SATMD concept is evaluated experimentally on a scaled-down simplified aircraft prototype constructed for this purpose. Finally, the simulated model is correlated with experimental measurements. In summary, both experimental and numerical results, illustrate that by choosing an appropriate auxiliary mass for the SATMD a specific mode can be targeted and can be substantially damped using a properly tuned shunt resistor. Subsequently the inductance can retune the system to another mode of interest. The obtained results indicate capabilities to reduce the structural acceleration of the main structure up to 20dB.

1 INTRODUCTION

Excessive vibrations may lead to material fatigue and structural failure. In addition, regarding their repercussions on aeronautic structures may cause discomfort both to the passengers and the pilots. A well-established method of passive vibration absorption is the inclusion of a device to reduce vibration levels of the main structure [1],[2]. Such devices are called dynamic vibrations absorbers (DVA) or tuned mass dampers (TMD). The classic TMD consists of a mass-spring-damper system tuned on a specific frequency of interest in the manner that the kinetic energy of the main mass is transferred to the auxiliary mass of the TMD and subsequently dissipated through the dashpot. However, a passive TMD is hindered by a phenomenon called ‘detuning’ caused by deterioration of the mechanical properties of the structure for example mass change due to fuel consumption. In such cases a passive TMD ceases to be effective until it is retuned. Another method to enhance the damping of the structure [3] has been proposed by Hagood and Von Flotow in 1991 [4], where a piezoelectric patch is attached on a beam connected with a resistive and inductive shunts [5]-[7]. Part of the

mechanical energy due to the piezoelectric effect is transformed to electric energy which causes charge to flow through the electric circuit and is dissipated by the resistor. This circuit is equivalent to adding a spring-mass-damper, with the inductor adding virtual mass, the resistor being the damper and the material capacitance being the spring. Optimal tuning of the RL values can be obtained using the Den Hartog method [9].

Taking into consideration the aforementioned crucial drawback of a passive TMD, a semi active tuned mass damper [10],[11] (consisted of an auxiliary mass and a piezoelectric stack connected in series with an RL electric circuit) is proposed. The SATMD offers tuning flexibility while retaining the robustness of the passive system. That is to say, the baseline vibration reduction of the SATMD at a single frequency is provided by the tuned auxiliary mass, while the introduction of electromechanical inertia by the inductor provides additional vibration reduction by dissipation of the electric energy through a resistor.

The rest of the paper is organized as follows: Initially, in Section 2 the equations of motion for the baseline structure modeled by two structural modes whose modal characteristics are predicted by modal analysis of a detailed Abaqus FEA model. Then the theoretical framework of the coupled electromechanical system (the structure with the SATMD attached and the RL network) is presented. Subsequently on Section 3 the SAMTD concept is evaluated on a scaled-down simplified aircraft prototype manufactured for this purpose. Furthermore, the experimental validation with the numerical predictions are presented in Section 4. Finally, in Section 5 are entailed the concluding remarks of the proposed work along with suggestions for future work.

2 FORMULATION

2.1 Baseline structure model

Considering the fact that the simplified structure is modelled by two structural modes, as shown in Figure 1, the modal displacements can be derived by the following second order differential equation,

$$\begin{aligned} [\Phi]^T \cdot [m] \cdot [\Phi] \cdot \ddot{\underline{q}}(t) + [\Phi]^T \cdot [c] \cdot [\Phi] \cdot \dot{\underline{q}}(t) + [\Phi]^T \cdot [k] \cdot [\Phi] \cdot \underline{q}(t) &= \underline{\Phi}^T \cdot \underline{F}(t) \\ [M] \cdot \ddot{\underline{q}}(t) + [C] \cdot \dot{\underline{q}}(t) + [K] \cdot \underline{q}(t) &= \underline{P}(t) \end{aligned} \quad (1)$$

where $\underline{q}(t) = \{q_1(t), q_2(t)\}^T$ is the vector of modal displacements, $[\Phi]$ is the 2×2 modal matrix of the eigenvectors, $[m]$, $[c]$ and $[k]$ are the mass, damping and stiffness matrices respectively, while $\underline{F}(t)$ is the applied force., $[M]$, $[C]$ and $[K]$ are the 2×2 modal mass, modal damping and modal stiffness matrices respectively and $\underline{P}(t)$ is the modal force vector. Finally, the transformation back to physical coordinates can be performed as follows

$$\underline{x}(t) = [\Phi] \cdot \underline{q}(t) \quad (2)$$

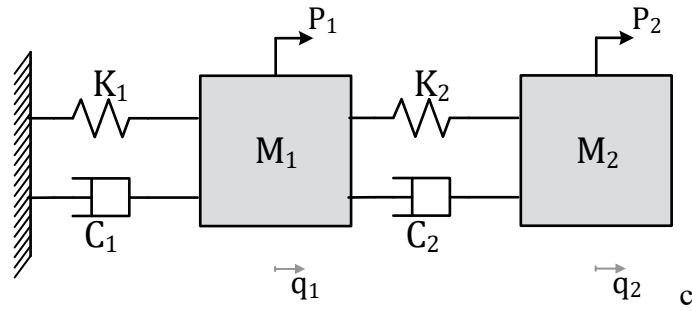


Figure 1: Baseline Structure Modal Representation

The baseline model parameters $[M], [\omega^n], [\zeta]$ are shown in Table 1, which were extracted from a detailed Abaqus FEA model of the Lab scale prototype presented in Section 3.

Table 1: Modal Data

	$i = 1$	$i = 2$	
M^i	4.09	4.38	$[kg]$
ω_i^n	48.8	65.3	$[Hz]$
ζ^i	0.1	0.1	$[\%]$

2.2 Structure with SATMD attached model

Assuming that the auxiliary mass and the piezostack stiffness are too small to change the mode shapes of the baseline structure, the new system (as shown on Figure 2) equations can be formulated.

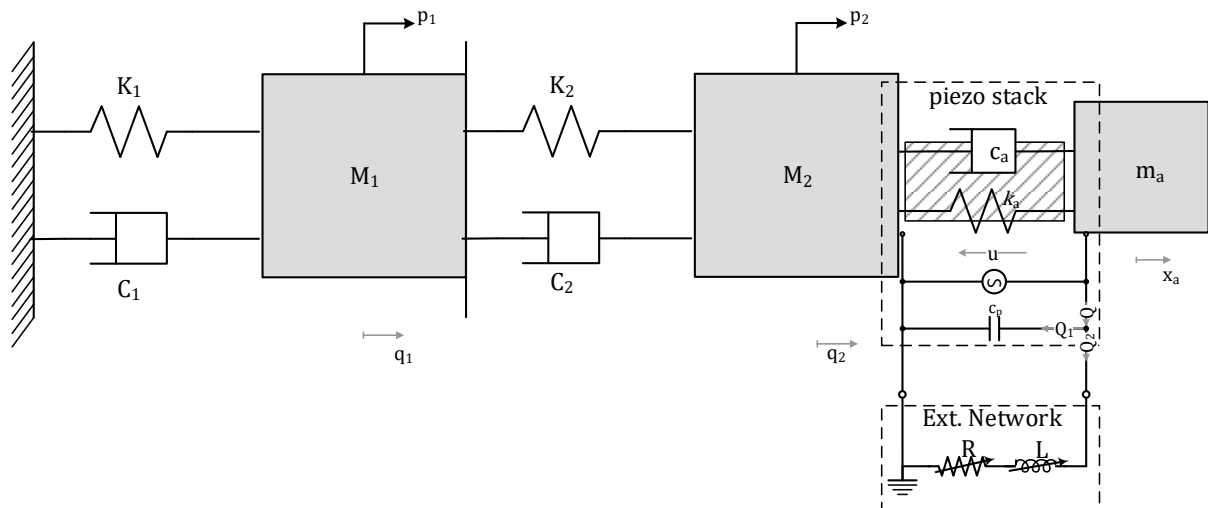


Figure 2: Structure with SATMD attached Representation

Therefore, one more degree of freedom is added as the displacement of the auxiliary mass, as well as one more degree of freedom for the electrical charge that flows from the external network. Hence, the electromechanical system can be described by the following second order differential equation:

$$\begin{bmatrix} M & 0 & -e \cdot L \cdot \varphi_n^T \\ 0 & m_a & e \cdot L \\ 0 & 0 & L \end{bmatrix} \begin{Bmatrix} \ddot{q} \\ \ddot{x}_a \\ \ddot{Q}_2 \end{Bmatrix} + \begin{bmatrix} C + c_a \cdot \varphi_n^T \cdot \varphi_n & c_a \cdot \varphi_n^T & -e \cdot R \cdot \varphi_n^T \\ c_a \cdot \varphi_n & c_a & e \cdot R \\ 0 & 0 & R \end{bmatrix} \begin{Bmatrix} \dot{q} \\ \dot{x}_a \\ \dot{Q}_2 \end{Bmatrix} + \begin{bmatrix} K + k_a \cdot \varphi_n^T \cdot \varphi_n & k_a \cdot \varphi_n^T & 0 \\ k_a \cdot \varphi_n & k_a & 0 \\ e/C_p \cdot \varphi_n & -e/C_p & 1/C_p \end{bmatrix} \begin{Bmatrix} q \\ x_a \\ Q_2 \end{Bmatrix} = \begin{Bmatrix} P \\ 0 \\ 0 \end{Bmatrix} \quad (3)$$

Where x_a is the physical displacement of the auxiliary mass, m_a, c_a and k_a is the auxiliary mass, actuator damping and stiffness respectively, e is the piezoelectric coefficient and C_p is the stack capacitance.

Table 2: SATMD Properties

k_a	87	$[kN / m]$
m_a	574	$[g]$
ζ_a	1.4	$[\%]$
e	0.73	$[N / V]$
C_p	40	$[\mu F]$

The SATMD properties shown in Table 2 were experimentally identified by a series of tests on the device solely.

3 EXPERIMENTS

3.1 Experimental Setup

The manufactured scaled-down simplified aircraft weights approximately 112 kg and consists of the following components:

- a 3m steel tubular beam representing the fuselage of the aircraft
- two aluminum plate-strips for the wings and the horizontal tail and
- Three plastic connectors made of ACETAL, for the mounting of the wings, the horizontal tail and the SATMD of the horizontal tube. All the aforementioned components are illustrated in Figure 3.

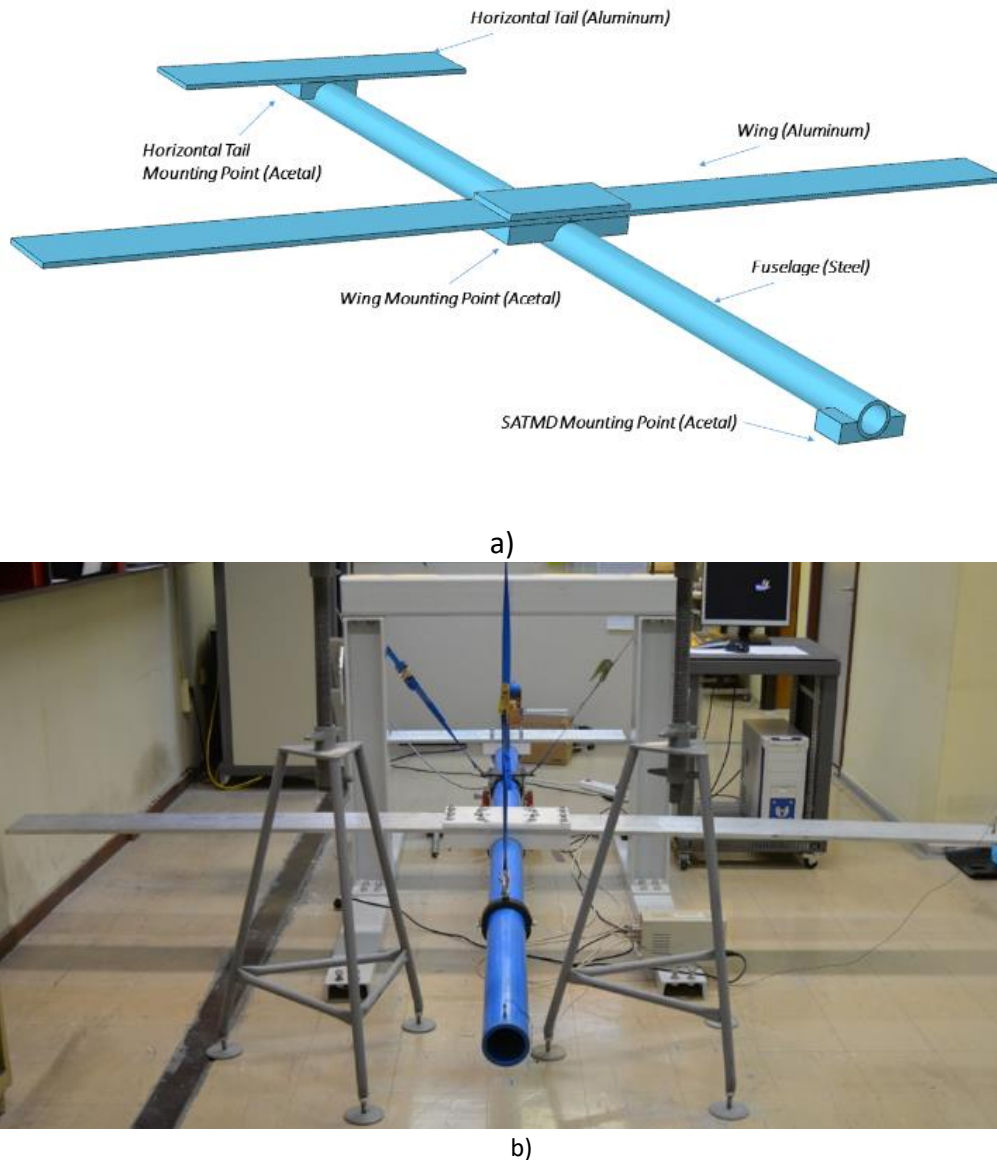


Figure 3: Design of Lab scale Aircraft Prototype; a) FEM model; b) Actual prototype

3.2 Experimental procedure

In order to simulate realistic testing flight conditions, the model was suspended with elastic belts from the modal points of the first bending modal frequency ($L/4$ and $3L/4$). The SATMD anti-vibration setup is placed on the Lab Prototype tip with the mechanism facing downwards. An electromechanical shaker was mounted at the middle of the rear horizontal tail, under the fuselage to excite the structure. The shaker was equipped with a load cell to measure the applied force on the prototype. A pair of accelerometers were used to measure the response located. One on the tip on the top of the tubular beam, while the second was located at the tip and the middle of the horizontal aluminium beam simulating the aircraft wing. The applied actuation

signal was a swept sine within the range of 1 to 200 Hz. The generated acceleration at the measuring locations as well as the applied force were collected via a National Instruments DAQ board, digitized and the corresponding frequency response functions were prepared.

This procedure was repeated with and without the SATMD attached to compare the system performance. Figure 4 presents the critical modal frequencies for the performed experimental analysis of the baseline, which are the 1st bending wing mode at 36Hz, the 1st bending modal frequency across the length of the fuselage at 48Hz and the 2nd bending modal frequency across the length of the fuselage at 65Hz.

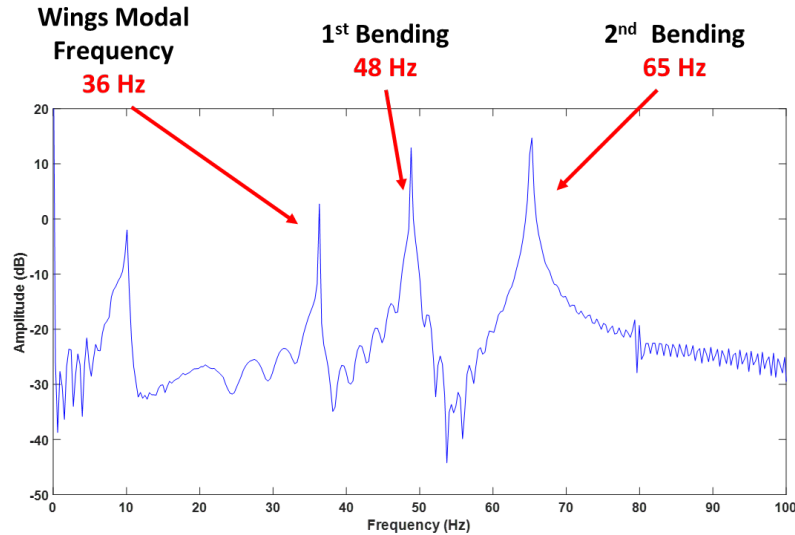


Figure 4: Baseline Prototype Acceleration Response

4 EXPERIMENTAL RESULTS

4.1 Mass Tuning at the 1st Bending Frequency (48 Hz)

Initially, an auxiliary mass of 1027 g was used to tune the SATMD at the first bending frequency of the structure (48Hz), in order to study its performance for various resistance levels connected to the SATMD terminals. Initially, the response of the structure was measured without the presence of the SATMD as baseline, then the resistance was gradually increased and finally the case of the open circuit was examined (passive operation). Figure 5 shows the experimental results while in Figure 6 the formulated model is presented which appears to be in good agreement with the experimental measurements. In both cases the optimal resistance was found to be at 50Ω . Increasing the resistance beyond that value the response of the structure starts to increase again.

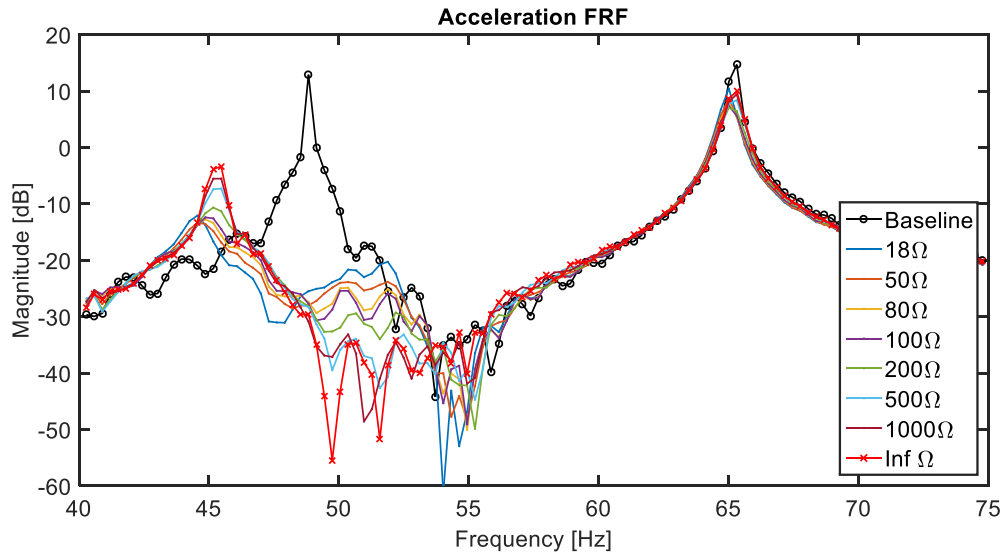


Figure 5: Measured Response for Variable Resistance levels Tuned at 48Hz

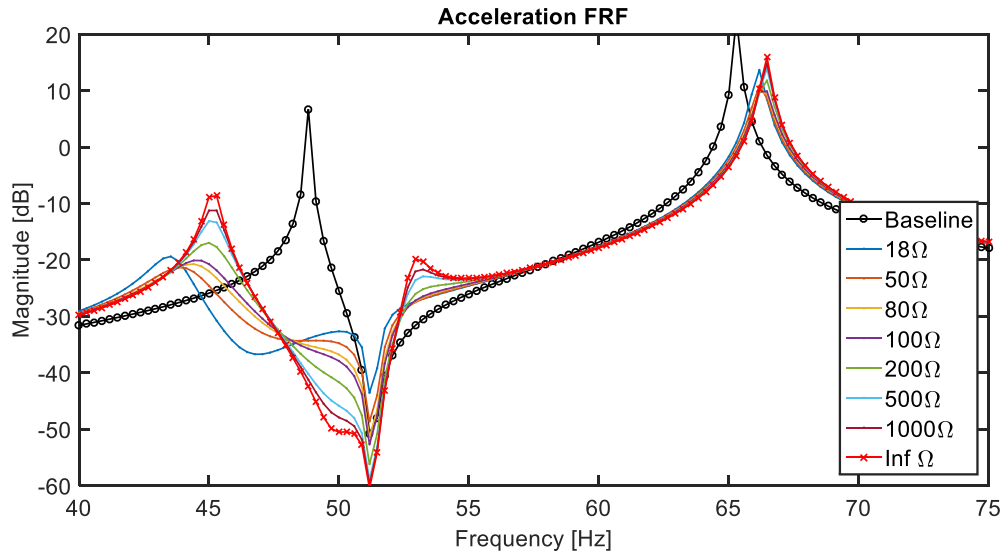


Figure 6: Simulated Response for Variable Resistance levels Tuned at 48Hz

Figure 7, presents a more complete picture of the reduction in dB of the acceleration compared to the baseline system achieved by various resistance levels in the neighbour of 40 to 50 Hz.

Both the experiment and the simulation present the same trends with the optimal value being at 50Ω . However the analytical model predicts a reduction of 28dB in comparison to the measured reduction of 26dB from the baseline at the experiment. This difference is negligible considering that in both cases the remaining oscillation is

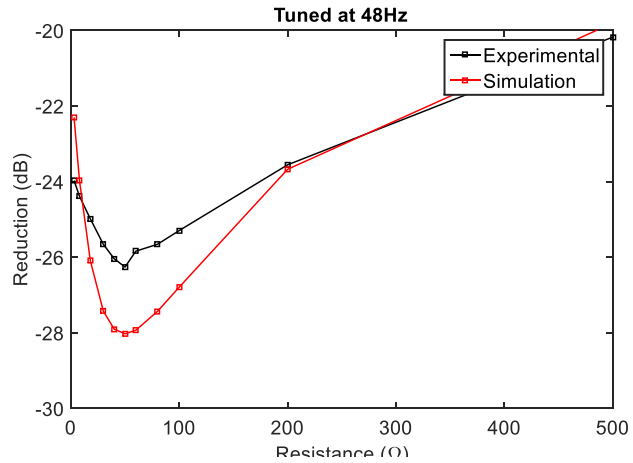


Figure 7: Effect of Resistance at the neighbour of 48 Hz

4.2 Mass Tuning at the 2nd Bending Frequency (65 Hz)

For the case of the 2nd bending mode, the SATMD was tuned by using a mass 574 g. Consequently, a shunt resistor was connected on the SATMD terminals while multiple resistance levels were examined up to the case of an open circuit (passive operation). A maximum reduction of 23 dB was achieved at the optimum resistance level of 91Ω as shown on Figure 8. Simultaneously, a 9 dB reduction on the first mode was observed. In Figure 9, the predictions of the analytical model are presented, whose results are in line with the experimental measurements.

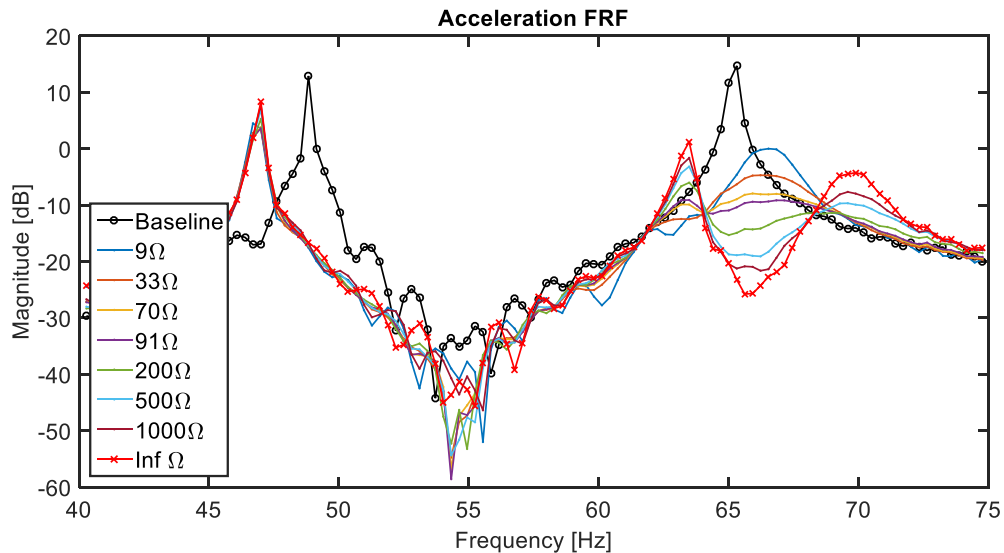


Figure 8: Measured Response for Variable Resistance levels Tuned at 65Hz

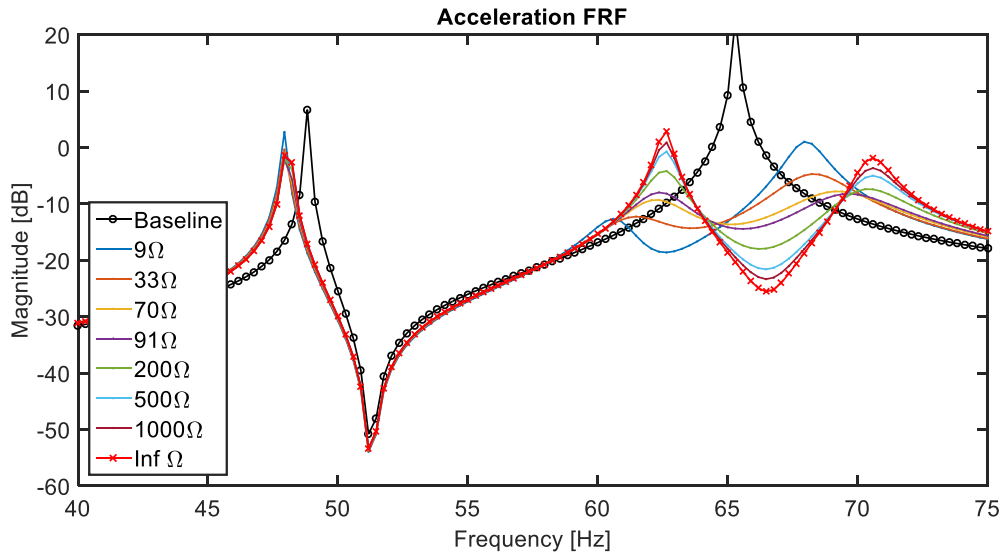


Figure 9: Simulated Response for Variable Resistance levels Tuned at 65Hz

Figure 10 presents the reduction of acceleration in dB compared to the baseline system in the neighbour of 60 to 75 Hz for various resistance levels.

Both the experiment and the simulation illustrate the same trends with the optimal value being at. However there is a discrepancy since the simulation predicts a reduction of 30dB in comparison to the measured reduction of 24dB from the baseline at the experiment.

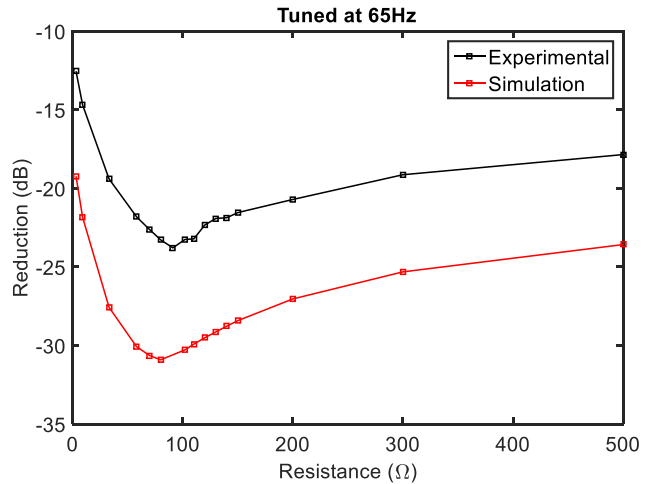


Figure 10: Effect of Resistance at the neighbour of 65 Hz

4.2.1 Operation under variable inductive loads.

Furthermore, the effect of inductance to the system performance was examined, aiming to retune the SATMD from the 1st bending frequency to the 2nd. Thus, we mounted on the tip of the fuselage the SATMD with 574 gr auxiliary mass providing tuning of the mechanism at 65Hz. The performance of the lab prototype was measured with various inductance-resistance levels connected on the terminals of the SATMD. The mentioned resistance was the one measured at the terminals of the actuator when the inductor was connected. Figure 11 presents the measured FRFs at the neighbour of the tuning frequency (65Hz), while Figure 12 illustrates the FRFs of the response at the neighbour of the 1st bending modal frequency at 48Hz. Significant reduction is achieved simultaneously at both modal frequencies as the inductive load increases.

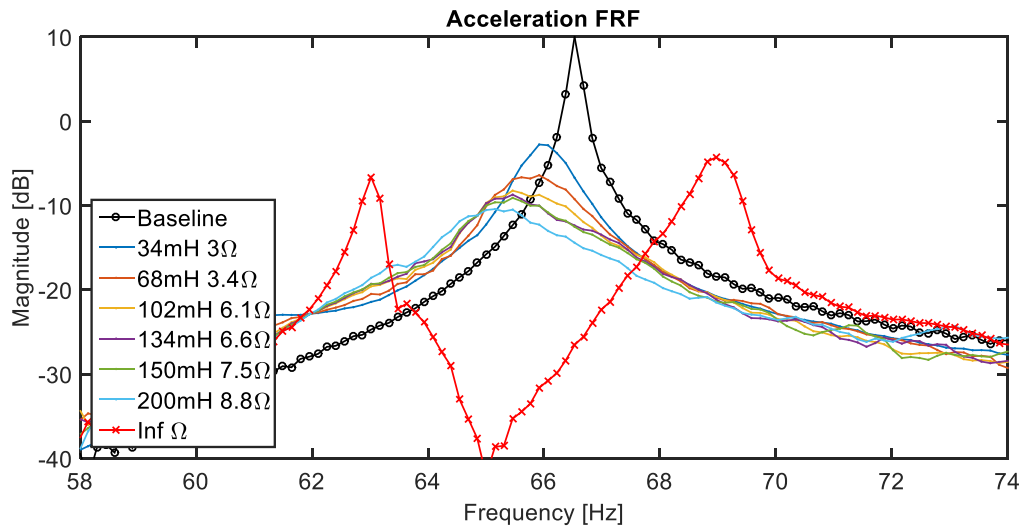


Figure 11: Measured Response for Variable Inductance levels in the neighbour of 65Hz

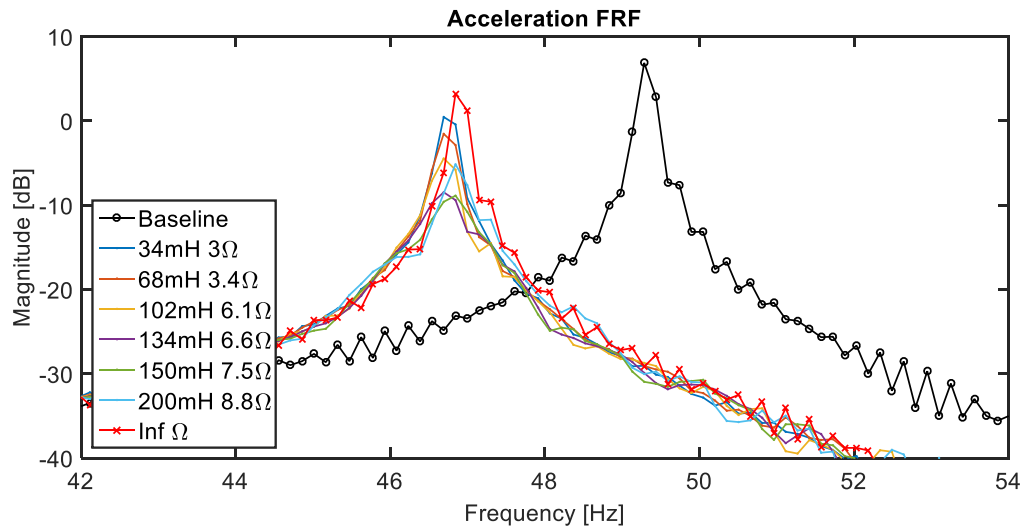


Figure 12: Measured Response for Variable Inductance levels in the neighbour of 48Hz

The overall performance of the anti-vibration setup with various inductive loads is illustrated in Figure 13. The achieved reduction on the 1st modal frequency as the inductance increases, while the mechanism is mechanically tuned at the 2nd modal frequency at 65Hz. The measured performance illustrates a reduction up to the level of 16dB for inductance values of 150mH

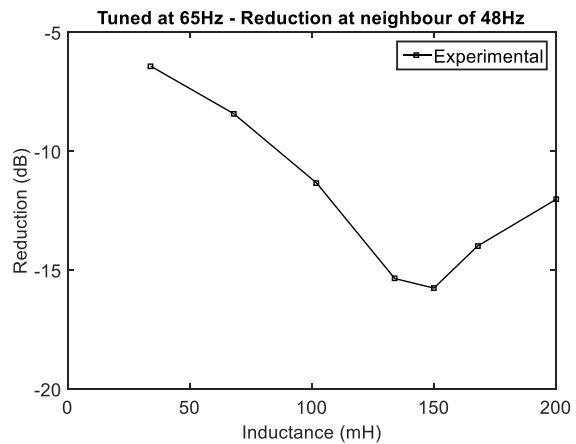


Figure 13: Effect of Inductance at the neighbour of 48 Hz

5 CONCLUSIONS

The scope of the present work was to develop an antivibration setup capable to tune at different frequencies. The proposed solution, the Semi-Active Tuned Mass Damper (SATMD) based on the support of the auxiliary TMD mass on a piezoceramic stack actuator, while a resistance and an inductor are connected parallel to the actuator. The presence of the resistance on the system adds damping via dissipation of the oscillation energy as the form of heat to the resistance terminals. Additionally, the dynamic characteristics of the inductor add virtual inertia on the oscillated mechanical system providing the flexibility to the SATMD to be tuned at various modal frequencies. Multiple tuning cases were examined and compared to the performance of the baseline system. Initially, the performance of a system while having solely adaptive resistance and concluding with the application of a R-L external network.

The manufactured lab-test prototype confirmed the analytical assumptions and the predicted dynamic characteristics were measured and validated. Two critical modal frequencies were identified, the 1st bending frequency at 48Hz and the 2nd bending at 65Hz.

Consequently, the assembled SATMD was attached on the prototype and tested under external mechanical excitation. The system was tested under various resistances, elucidating an optimal resistance of maximum performance of 91Ω with $23dB$ reduction at the tuned frequency, while at the same time the other resonance peak introduced a reduction of $9dB$.

Furthermore, by keeping the resistance constant, various values of inductance were applied. The outcome of this specific test was, that while changing the inductance the performance of the system could be tuned to a different frequency, resulting at an optimum value of $150mH$ with $16dB$ maximum reduction.

Finally, analytical simulations using the developed reduced-order mode superposition model were performed and correlated to the experimental measurements in order to validate the model. The correlations indicate that the analytical model is able to replicate very well the measured results concerning the effect of resistance. Regarding the effect of inductance discrepancies were observed, this specific issue seems to be quite complex and requires further investigation possibly due to nonlinearities of the piezoelectric stack thus requiring further investigation.

To sum up, the measured semi-active vibration reductions on the tested prototype has successfully demonstrated the feasibility of the proposed concept. The developed modelling tools produced reasonably good predictions of the measured prototype response.

REFERENCES

- [1] J.Q. Sun, M.R. Jolly, M.A. Norris, Passive, adaptive and active tuned vibration absorbers: a survey, ASME J. Mech. Des. 117 (1995) 234–242
- [2] C. Du, L. Xie, Modeling and Control of Vibration in Mechanical Systems, Taylor & Francis Group, LLC, 2010.
- [3] G.A. Lesieutre, Vibration damping and control using shunted piezoelectric materials, Shock and Vibration Digest 30 (1998) 187–195
- [4] Hagood, N.W. and Von Flotow, A. Damping of structural vibrations with piezoelectric materials and passive electrical networks. Journal of Sound and Vibration (1991) 146:243-268

- [5] Moheimani, S. O. R., 2003. "A survey of recent innovations in vibration damping and control using shunted piezoelectric transducers". *IEEE Transactions on Control Systems Technology*, 11(4), pp. 482–494
- [6] C. Davis, G. Lesieutre, An actively tuned solid-state vibration absorber using capacitive shunting of piezoelectric stiffness, *Journal of Sound Vibration* 232 (2000) 601–617
- [7] Plagianakos TS and Saravanos DA (2003) Hybrid multidamped composite plates with viscoelastic composite plies and shunted piezoelectric layers. *Journal of Intelligent Material Systems and Structures* 14(1): 57–66.
- [8] C.L. Davis, G.A. Lesieutre, A modal strain energy approach to the prediction of resistively–shunted piezoceramic damping, *Journal of Sound and Vibration* 184 (1995) 129–139.
- [9] Neubauer, M., Oleskiewicz, R., Popp, K. and Kryzyski, T. Optimization of damping and absorbing performance of shunted piezo elements utilizing negative capacitance. *Journal of Sound and Vibration* (2006) 298:84-107
- [10] N. Jalili, A comparative study and analysis of semi-active vibration-control systems, *J. Vib. Acoust.* 124 (2002) 593–605
- [11] Hrovat D, Barak P, Rabins M. Semi-active versus passive or active tuned mass dampers for structural control. *J Eng Mech.*1983;109(3):691-705.

STICK-SLIP OSCILLATIONS IN AN ELECTROMECHANICAL SYSTEM

R. Lima* and R. Sampaio*

* Departamento de Engenharia Mecânica

Pontifícia Universidade Católica do Rio de Janeiro

Rua Marquês de São Vicente, 225, 22451-900, Gávea, Rio de Janeiro, RJ, Brazil

e-mail: robertalima@puc-rio.br, rsampaio@puc-rio.br

Key words: Coupled system, Dry-friction, Stick-slip oscillations, Stick-duration.

Abstract. This work analyzes the nonlinear dynamics of a coupled system with dry-friction. The system has a mechanical part and an electromagnetic part. It is composed of a cart, whose motion is excited by a DC motor. The coupling between the motor and the cart is made by a mechanism called scotch yoke, so that the motor rotational motion is transformed in horizontal cart motion in a rail. It is considered the existence of dry-friction between the cart and the rail. The friction is modeled as Coulomb friction. The resulting motion of the motor can be characterized by two qualitatively different and alternate modes, the stick- and slip-modes, with a non-smooth transition between them. The focus of the work is to find the stick- and slip-mode parts of the trajectory for different values of the system parameters. This analysis could help in the development of control techniques to mitigate the occurrence of stick when this mode is not desirable in the system response.

1 INTRODUCTION

The analysis of electromechanical systems is not a new subject. The interest of analyzing their dynamic behavior is reflected by the increasing amount of research in this area. Electromechanical systems present an interesting behavior characterized by the mutual influence between the electrical and mechanical parts of the system, that is, the dynamics of the motor is heavily influenced by the mechanical system and the dynamics of the mechanical system depends on the dynamics of the motor [1, 2, 3, 4] Each part of the system affects the behavior of the other, i.e., they interact. The coupling varies with the coupling conditions, it is not a functional relation and depends on the initial conditions [5, 6] The dynamics of the coupled system is given by an initial value problem comprising a set of coupled differential equations [7, 8], in which the coupling torque appears as a parametric excitation, i.e., a time variation of the system parameters. The problem becomes even more interesting if it is considered the existence of dry-friction between bodies in the mechanical part of the system. The dry-friction can induce stick-slip oscillations [9, 10, 11]. The response of the mechanical part has a non-smooth behavior with two qualitatively different modes, the stick- and slip-modes. We call stick when the relative velocity between the bodies in contact is null in a time-interval and we call slip if the relative velocity is non-zero, or zero in isolated points. As these two modes have a non-smooth transition between them, stick-slip systems belong to the class of non-smooth systems, such as systems with stops, impacts, and hysteresis.

Depending on the values of the system parameters, the response of the mechanical part of the system can be composed of a sequence alternating stick and slip-modes. It is possible also to be composed of

just stick or just slip. The main motivation of this paper is to better understand what are the parameters that control the stick duration in an electromechanical system. We believe that the theoretical knowledge on the role of these parameters can provide improvements in the design of electromechanical systems and can help in the development of control techniques to mitigate the stick duration. These techniques could be implemented in many mechanical systems in which undesirable stick appears. Study of oscillatory conditions in dry-friction systems has practical significance for providing protection against vibrations, seismic isolation, reduction of noise, and friction-induced vibration, etc [12, 13]. Dry-friction could be the source of dynamic instability, noise, and reduction of performance.

Despite the great number of papers in the area of dry-friction, few of them address the problem in an electromechanical system. The majority of the references that characterizes dynamics with dry-friction only make it for a pure mechanical system.

2 DYNAMICS OF THE ELECTROMECHANICAL SYSTEM WITH DRY-FRICTION

The system analyzed in this paper is composed of a cart whose motion is driven by a DC motor. The motor is coupled to the cart through a pin that slides into a slot machined on a plexiglas plate that is part of the cart, as shown in Fig. 1. The pin hole is drilled off-center on a disk fixed in the axis of the motor, so that the motor rotational motion is transformed into horizontal cart motion over a rail. The dynamics

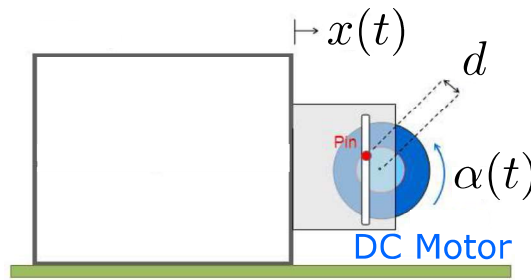


Figure 1: Electromechanical system with dry-friction between the cart and the rail.

of a DC motor is given by the following initial value problem (IVP). Given a source voltage v , find (α, c) such that, for all $t > 0$,

$$L\dot{c}(t) + r c(t) + k_e \dot{\alpha}(t) = v(t) , \quad (1)$$

$$j_m \ddot{\alpha}(t) + b_m \dot{\alpha}(t) - k_e c(t) = -\tau(t) , \quad (2)$$

with the initial conditions

$$\dot{\alpha}(0) = \dot{\alpha}_0 \quad , \quad \alpha(0) = \alpha_0 \quad , \quad c(0) = c_0 , \quad (3)$$

where t is the time, c is the electric current, $\dot{\alpha}$ is the angular speed of the motor, L is the electric inductance, j_m is the motor moment of inertia, b_m is the damping ratio in the transmission of the torque generated by the motor to drive the coupled mechanical system, k_e is the motor electromagnetic force constant and r is the electrical resistance. The magnitude of the available torque to the coupled mechanical system is τ . The source voltage is considered to be

$$v(t) = v_0 + v_1 \sin(\omega_v t) . \quad (4)$$

i.e., the source voltage oscillates around the level v_0 with amplitude v_1 and with frequency ω_v . The mass of the mechanical system is m and the horizontal cart displacement is represented by x . It is considered that the cart is not allowed to move in the vertical direction. Due to the problem geometry, and denoting $\|d\| = d$, the horizontal motion of the cart and the angular displacement α of the motor are related by the constraint

$$x(t) = d \cos(\alpha(t)). \quad (5)$$

In the model of the coupling between the motor and the mechanical system, it is assumed that the motor shaft is rigid. Thus, the available torque to the coupled mechanical system, τ , can be written as

$$\tau(t) = d(t) \times f(t), \quad (6)$$

where d is the eccentricity of the pin of the motor and f is the coupling force between the DC motor and the cart. The component of d , which is perpendicular to the plane of the cart movement, is always zero and, the others horizontal and vertical components can be calculated from the angular displacement α of the motor. Assuming that there is no friction between the pin and the slot machined on an acrylic plate, the vector f only has a horizontal component, called f , which is the horizontal force that the DC motor exerts on the cart. Thus, the magnitude of $\tau(t)$ is

$$\tau(t) = -f(t) d \sin \alpha(t). \quad (7)$$

Since the cart is modeled as a particle, its movement in the horizontal direction satisfies the equation:

$$m \ddot{x}(t) = f(t) + f_r(t), \quad (8)$$

where f_r is the dry-friction force between the cart and the rail. The initial value problem for the coupled motor-cart system with dry-friction is: given v , find (α, c) satisfying

$$I \dot{c}(t) + r c(t) + k_e \dot{\alpha}(t) = v_0 + v_1 \sin(\omega_v t), \quad (9)$$

$$\begin{aligned} \ddot{\alpha}(t) [j_m + m d^2 (\sin(\alpha(t)))^2] + \dot{\alpha}(t) [b_m + m d^2 \sin(\alpha(t)) \cos(\alpha(t))] \\ - k_e c(t) = -f_r(t) d \sin(\alpha(t)), \end{aligned} \quad (10)$$

for given initial conditions of electric current, angular speed and position of the motor.

3 DRY-FRICTION MODEL

The friction is modeled as Coulomb, which is a simple model, shown in Fig. 2.

The non-smooth behavior of the dry-friction force can induce stick-slip oscillations in the system. Depending on the values of the system parameters, the response of the system can be composed of a sequence of alternating stick and slip-modes.

During the stick-mode, the cart does not move, so the angle of disc is constant. The frictional force and the current can vary. Stick means no motion, the motor continues to change its state until it has enough power to move the car. The stick mode occurs when $\dot{\alpha} = 0$ in an interval and when the frictional force, which satisfies

$$k_e c(t) = f_r(t) d \sin(\alpha(t)), \quad (11)$$

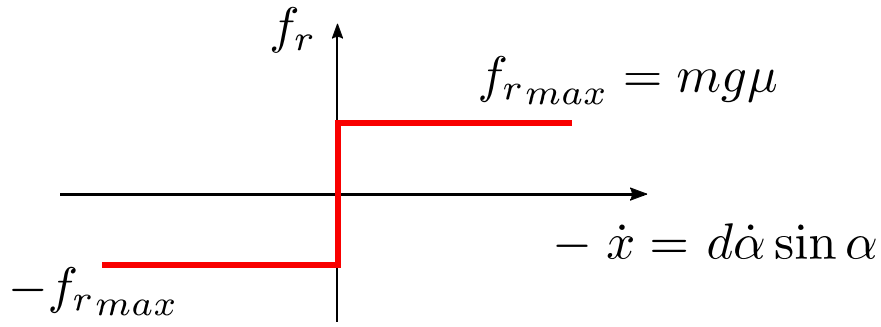


Figure 2: Coulomb dry-friction.

is in the interval $-f_{max} \leq f_r \leq f_{max}$, where $f_{max} = \mu mg$, g is the gravitational acceleration and μ is the friction coefficient between the cart and the rail. Equation (11) is obtained considering $\dot{\alpha} = 0$ and $\ddot{\alpha} = 0$ in Eq. (10). Remark that during the stick-mode, the frictional force varies and depends on the angular position of the motor. There is a functional relation between these two variables. Besides this, the initial value problem that describes the dynamics of the coupled motor-cart system with dry-friction is reduced to just one differential equation, given by

$$l\dot{c} + rc = v_0 + v_1 \sin(\omega_v t), \quad (12)$$

where the initial condition of the current is its value in the beginning of the stick-mode. Observe that during the stick-mode, the sum of the forces that act over the cart is zero (it does not move). The horizontal coupling force between the DC motor and the cart, f , is balanced by the dry-friction force, f_r . This balance lasts until the frictional force, given in Eq. (11), reaches its maximum value, f_{max} . During the stick-mode, the dynamics of the system is governed only by the dynamics of the electrical circuit of the motor. Electrical and mechanical systems do not interact: the system is decoupled. During the slip-mode, the dry-friction force is

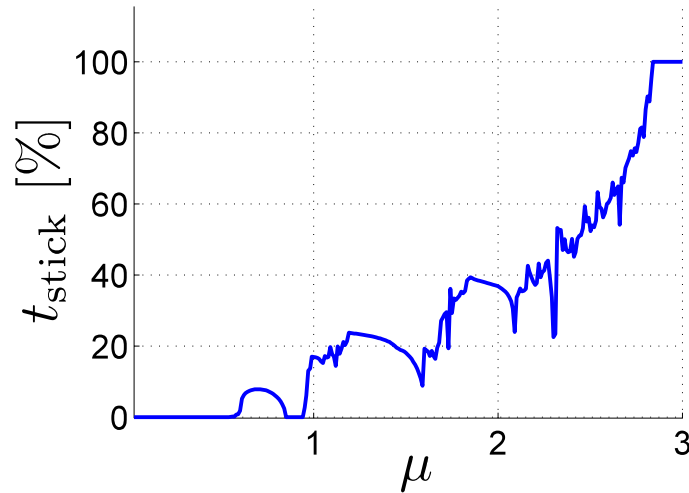
$$f_r(t) = -mg\mu \operatorname{sgn}(\dot{x}(t)) = -mg\mu \operatorname{sgn}(-\dot{\alpha}(t) d \sin(\alpha(t))). \quad (13)$$

4 NUMERICAL RESULTS

Once defined a time interval for analysis t_a , one of the variables of great interest in the analysis of systems with dry-friction is the total time of stick as function of the friction coefficient. For the electromechanical system analyzed in this work, this variable presents an interesting behavior, as shown in Fig. 3. When μ is lower than 0.57, there is no stick; when μ is greater than 2.84 the only mode is stick. For values of μ between 0.57 and 2.84, both can exist. For computation, duration t_a was chosen as 30 seconds. For the integration, it was used the function *ode45* of the *Matlab* software, which applies the Runge-Kutta 4th/5th-order method as time-integration scheme with a varying time-step algorithm. The maximal step size is equal to 10^{-4} seconds, and the relative and absolute tolerances are equal to 10^{-4} . The values of the parameters used in all simulations were $m = 5.0$ kg, $d = 0.01$ m, $v_0 = 4.0$ V, $v_1 = 4.0$ V and $\omega_v = 30$ rad/s. The motor parameters are given in Table 1 and the initial conditions of the system are $\alpha(0) = \pi/2$ rad, $\dot{\alpha}(0) = 0$ rad/s and $c(0) = v_0/r$ Amp.

Table 1: Values of the motor parameters used in simulations.

Parameter	Value
I	1.880×10^{-4} H
j_m	1.210×10^{-4} Kg m ²
b_m	1.545×10^{-4} Nm/(rad/s)
r	0.307 Ω
k_e	5.330×10^{-2} V/(rad/s)

**Figure 3:** Total time of stick as function of the friction coefficient.

5 CONCLUSIONS

In this article, it is analyzed the dynamics of an electromechanical system composed by a cart and a DC motor. The coupling between the motor and the cart is made by a mechanism called scotch yoke, so that the motor rotational motion is transformed into horizontal cart motion on a rail. It is considered the existence of dry-friction between the cart and the rail. The resulting motion of the motor can be characterized by stick- and slip-modes, with a non-smooth transition between them. A parametric analysis was performed numerically. It was analyzed the influence of the friction coefficient in the total time of stick. The results show that an increase of the friction coefficient does not assure an increase in the total time of stick.

ACKNOWLEDGMENTS

The authors acknowledge the support given by FAPERJ, CNPq and CAPES.

REFERENCES

- [1] Dantas, M.J.H., Sampaio, R. and Lima, R. Asymptotically stable periodic orbits of a coupled electromechanical system. *Nonlinear Dynamics*. (2014) **78**:29–35.

- [2] Dantas, M.J.H., Sampaio, R. and Lima, R. Existence and asymptotic stability of periodic orbits for a class of electromechanical systems: a perturbation theory approach. *Zeitschrift für angewandte Mathematik und Physik*. (2016) **67**:2.
- [3] Clerkin, E. and Sampaio, R. A bifurcation and symmetry discussion of the Sommerfeld effect. *Proceedings of 14th International Conference in Dynamical Systems Theory and Applications (Dynamical Systems Theory and Applications)*, (2017), Vol.1, Łódź, Poland.
- [4] Manhães, W., Sampaio, R., Lima, R., Hagedorn, P. and Deü, J-F. Lagrangians for Electromechanical Systems, *Mecánica Computacional*. (2018) vol. XXXVI, **42**:1911–1934.
- [5] Lima, R. and Sampaio, R. Two parametric excited nonlinear systems due to electromechanical coupling. *Journal of the Brazilian Society of Mechanical Sciences and Engineering*. (2016) **38**:931–943.
- [6] Lima, R. and Sampaio, R. Stochastic analysis of an electromechanical coupled system with embarked mass. *Mecánica Computacional*. (2012) vol. XXXI, **14**:2783–2800.
- [7] Lima, R., Sampaio, R. and Hagedorn, P. One alone makes no coupling. *Mecánica Computacional*. (2018) vol. XXXVI, **20**:931–944.
- [8] Lima, R. and Sampaio, R. Pitfalls in the dynamics of coupled electromechanical systems. *Proceeding Series of the Brazilian Society of Computational and Applied Mathematics (CNMAC 2018)*. (2018) Campinas, Brazil.
- [9] Lima, R. and Sampaio, R. Construction of a statistical model for the dynamics of a base-driven stick-slip oscillator. *Mechanical Systems and Signal Processing*. (2017) **91**:157–166.
- [10] Lima, R. and Sampaio, R. Parametric analysis of the statistical model of the stick-slip process. *Journal of Sound and Vibration*. (2017) **397**:141–151.
- [11] Lima, R. and Sampaio, R. Some remarks about stick-slip oscillators. *Mecánica Computacional*. (2013), vol. XXXII, **8**:647–668.
- [12] Feeny, B., Guran, A., Hinrichs, N. and Popp, K. A historical review on dry friction and stick-slip phenomena. *Applied Mechanics Reviews*. (1998) **51** (5):321–341.
- [13] Berger, E. Friction modeling for dynamic system simulation. *Applied Mechanics Reviews*. (2002) **52** (6):355–577.

SUPPRESSION OF DELAY-INDUCED INSTABILITIES OF DIGITAL PIEZOELECTRIC VIBRATION ABSORBERS

G. RAZE*, A. PAKNEJAD[†], G. ZHAO[†], V. BROUN[‡], C. COLLETTE[†] AND G. KERSCHEN*

*Space Structures and Systems Laboratory
University of Liège
Allée de la Découverte 9, 4000 Liège, Belgium

[†] Precision Mechatronics Laboratory
Université libre de Bruxelles
Avenue F.D.Roosevelt 50, 1050 Brussels, Belgium

[‡]Département ingénieur industriel
Haute École de la Province de Liège
Quai Gloesener 6, 4020 Liège, Belgium

Key words: Piezoelectric Absorber, Digital Vibration Absorber, Delayed System, Stability

Abstract. Digital piezoelectric vibration absorbers synthesizing passive shunt circuits may be subject to instabilities. This work investigates the cause for these instabilities, and highlights the role of sampling delays in their onset. If for practical reasons the sampling frequency cannot be increased, a stabilization procedure which anticipates the sampling delays is proposed. The theoretical developments in this work are experimentally validated on a piezoelectric beam.

1 INTRODUCTION

Engineering structures from various disciplines tend to be lighter or more slender. This trend usually goes along with smaller structural damping and increased susceptibility to vibrations. This in turn may shorten their lifespan, lower their performance or undermine their safety. Piezoelectric shunt damping is often considered as one potential solution to this issue. It was originally proposed by Forward [1], and formalized by Hagood and von Flotow [2]. The working principle of piezoelectric shunt damping is based on the transduction capability of piezoelectric materials: a piezoelectric transducer is able to convert a part of its mechanical energy into electrical energy. The latter can be dissipated by connecting a so-called shunt circuit to the electrodes of the transducer. A common type of shunt circuit is a resonant one, composed of a resistor and an inductor, arranged either in series or in parallel. The realization of this circuit may be challenging for several reasons. The first one is that the required inductance may be impractically large. A common workaround is to use virtual inductors or girators made up of analog electronics. Designing inductors with high inductances is not impossible though, as demonstrated by Lossouarn et al [3]. However, such components are not widely available and require some expertise to be built. The second reason is that the performance of the piezoelectric shunt is highly sensitive to the values

of the electrical components. Any misvaluation or time-variation of the system characteristics will result in sub-optimal performance, rectified by time-consuming modifications of the electrical parameters.

Fleming et al [4] introduced the concept of synthetic impedance as an alternative solution. The combination of a digital signal processor with a current source makes it possible to realize an arbitrary impedance. The synthetic impedance is an attractive option to realize shunt damping circuits owing to its flexibility. This nonetheless comes at the expense of the need for powering the digital unit and its associated electronics.

It was noted by the authors that instabilities of a system composed of a structure controlled by a synthetic impedance may arise. This work discusses the cause of these instabilities, namely, sampling delays, and proposes a stabilizing methodology. This paper is organized as follows. First, a digital vibration absorber is presented in Section 2. A simplified model is developed in Section 3, and the onset of instabilities is studied. Section 4 proposes a simple stabilization method to suppress these instabilities. The method is experimentally validated on a cantilever piezoelectric beam in Section 5. Finally, conclusions are drawn.

2 DIGITAL PIEZOELECTRIC VIBRATION ABSORBER

Connecting an electrical circuit to the electrodes of a piezoelectric transducer is equivalent to imposing a prescribed relation between the voltage across the electrodes and the current flowing through this transducer. This relation may be described by the impedance (voltage over current) or its inverse, the admittance. From the point of view of the transducer, any circuit which is able to impose this relation is equivalent to the original circuit.

The goal of the digital vibration absorber used in this work is to mimic a piezoelectric shunt circuit by measuring the voltage of a piezoelectric transducer and inject the desired current back into it. The voltage-to-current relation, i.e. the admittance, is programmed into a digital processing unit (DPU). The circuit layout of the digital vibration absorber used in this work is given in Figure 1, which is the same as that used by Matten et al [5].

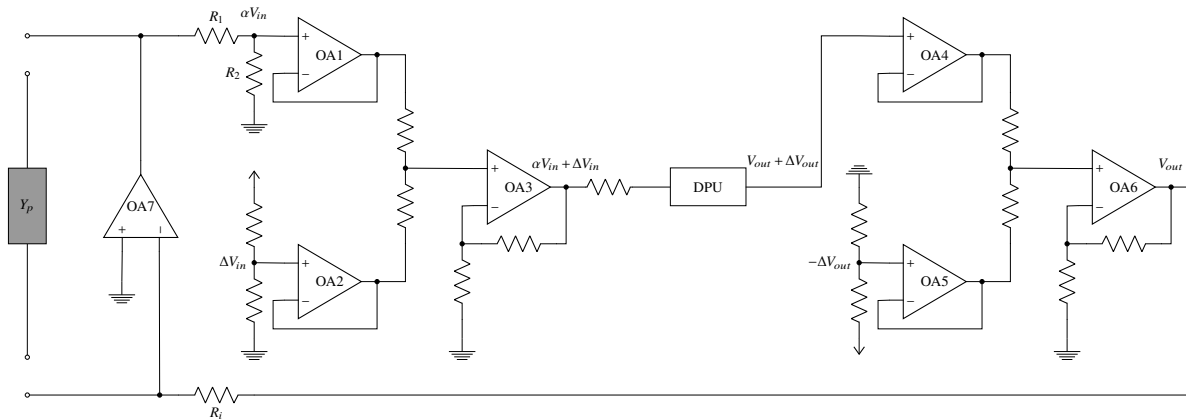


Figure 1: Layout of the digital absorber; the gray box represents a piezoelectric transducer.

The voltage divider composed of R_1 and R_2 is connected to the follower operational amplifier (Op-Amp) OA1, whose output is a scaled-down version of the piezoelectric voltage V_{in} by a factor $\alpha = R_2/(R_1 + R_2)$. OA2 follows a constant offset voltage ΔV_{in} which is added to the input by the summing amplifier OA3 before being fed to the analog to digital converter of the DPU. The DPU computes the

desired input-output relation and outputs via its digital to analog converter a voltage signal $V_{out} + \Delta V_{out}$, which is followed by OA4. A constant negative offset $-\Delta V_{out}$ followed by OA5 is added to the output by the summing amplifier OA6. This signal is applied to one pole of the resistor R_i , while the other is maintained to a virtual ground by OA7. Given the very high input impedance of OA7, the current injected into the piezoelectric transducer is thus V_{out}/R_i .

The input and output offset voltages are generated because the DPU used in this work can only work with positive input and output voltages. They are internally compensated for in the DPU software. An internal gain g is also applied to the transfer function programmed into the DPU for consistency. Indeed, if the desired relation between the piezoelectric voltage V_p and the current I_p is given by H_d , the digital absorber links these two quantities in the following way (assuming that the offsets are perfectly compensated)

$$I_p(s) = \frac{V_{out}(s)}{R_i} = \frac{g}{R_i} H_d(s) V_{in}(s) = \frac{\alpha g}{R_i} H_d(s) V_p(s) \quad (1)$$

where s is the Laplace variable. Assuming for now that the DPU is able to synthesize $H_d(s)$ exactly, a consistency relation is then derived

$$\frac{\alpha g}{R_i} = 1. \quad (2)$$

Typically, g can be computed from the measured values of α and R_i .

3 MODEL OF THE SYSTEM

3.1 Hardware model

The diagram shown in Figure 1 may be simplified while retaining the essential dynamical features of the digital absorber. Because of their large bandwidth (of the order of MHz), the followers and summing amplifiers (OA1 to OA6) are considered as ideal Op-Amps [6]. OA7 is modelled as a differential amplifier with one pole. This leads to the simplified circuit layout shown in Figure 2(a), which can be modelled according to Figure 2(b).

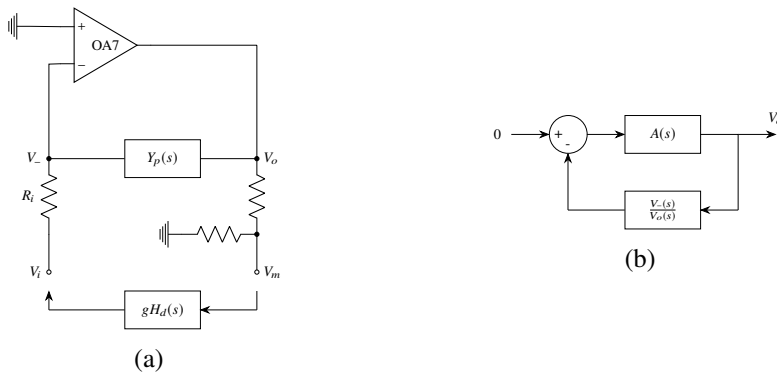


Figure 2: Feedback model of the voltage controlled current injector: simplified circuit layout (a) and equivalent block diagram (b).

From Figure 2(b), the following open-loop transfer function is derived

$$Y(s) = A(s) \frac{V_-(s)}{V_o(s)} = \frac{A_{OL}}{\frac{s}{2\pi f_0} + 1} \frac{V_-(s)}{V_o(s)}, \quad (3)$$

where A_{OL} is the Op-Amp open-loop gain, f_0 is its open-loop bandwidth, V_- is the voltage applied to its inverting input and V_o is its output voltage. Using Kirchhoff's voltage and current laws, the following relation can be derived

$$\frac{V_-(s)}{V_o(s)} = \frac{H_d(s) + Y_p(s)}{\frac{1}{R_i} + Y_p(s)} \quad (4)$$

where H_d is the transfer function synthesized by the DPU and Y_p is the admittance of the piezoelectric transducer, derived in the next subsection.

3.2 Piezoelectric admittance

The system composed of a structure coupled to a piezoelectric transducer may be modelled with the following set of equations

$$\begin{cases} \mathbf{H}_{sc}(s)\mathbf{x}(s) + \gamma\mathbf{B}V_p(s) = \mathbf{f}(s) \\ C_p^\varepsilon V_p(s) - \gamma\mathbf{B}^T \mathbf{x}(s) = q_p(s) \end{cases}, \quad (5)$$

where \mathbf{x} is the vector of generalized degrees of freedom, \mathbf{f} is the vector of conjugated generalized forces, \mathbf{H}_{sc} is the structural dynamic stiffness matrix when the piezoelectric transducer is short-circuited, C_p^ε is the piezoelectric capacitance at constant strain, $q_p = I_p/s$ is the electric charge flowing through the transducer and $\gamma\mathbf{B}$ is an electromechanical coupling vector [7]. The piezoelectric admittance is then found as

$$Y_p(s) = \left. \frac{s q_p(s)}{V_p(s)} \right|_{\mathbf{f}=0} = s C_p^\varepsilon + s \gamma^2 \mathbf{B}^T \mathbf{H}_{sc}^{-1}(s) \mathbf{B}. \quad (6)$$

The dynamic stiffness matrix may be expanded as

$$\mathbf{H}_{sc}^{-1}(s) = \Phi_{sc} \left(s^2 \mathbf{I} + s \mathbf{Z} \Omega_{sc} + \Omega_{sc}^2 \right)^{-1} \Phi_{sc}^T \quad (7)$$

where Φ_{sc} is the matrix of mass-normalized mode shapes when the piezoelectric transducer is short-circuited, \mathbf{I} is an identity matrix, \mathbf{Z} is a diagonal modal damping matrix and Ω_{sc} is a diagonal matrix containing the short-circuit resonance frequencies $\omega_{sc,i}$. The vector of modal strains in the piezoelectric transducer is given by

$$\mathbf{B}^T \Phi_{sc} = [\phi_1, \dots, \phi_N]. \quad (8)$$

Equations (6)–(8) give the following modal expansion

$$Y_p(s) = s C_p^\varepsilon \left(1 + \frac{\gamma^2}{C_p^\varepsilon} \sum_{i=1}^N \frac{\phi_i^2}{s^2 + 2\zeta_i \omega_{sc,i} s + \omega_{sc,i}^2} \right). \quad (9)$$

It is not straightforward to obtain the modal strains featured in Equation (9) experimentally. Further simplifying assumptions may be made to facilitate the experimental identification of the piezoelectric admittance. From Equation (5), the dynamic stiffness matrix when the piezoelectric transducer is open-circuited can be found to be

$$\mathbf{H}_{oc}(s) = \mathbf{H}_{sc}(s) + \frac{\gamma^2}{C_p^\varepsilon} \mathbf{B} \mathbf{B}^T \quad (10)$$

Equation (10) indicates that \mathbf{H}_{oc} and \mathbf{H}_{sc} only differ by a matrix independent of s . Assuming that this matrix is also diagonalized by the congruence transformation with Φ_{sc} ,

$$\Phi_{sc}^T (\mathbf{H}_{oc}(s) - \mathbf{H}_{sc}(s)) \Phi_{sc} = \frac{\gamma^2}{C_p^\varepsilon} \Phi_{sc}^T \mathbf{B} \mathbf{B}^T \Phi_{sc} \approx \Omega_{oc}^2 - \Omega_{sc}^2 \quad (11)$$

where $\mathbf{\Omega}_{oc}$ is a diagonal matrix containing the open-circuit resonance frequencies $\omega_{oc,i}$. Equating the diagonal entries in Equation (11) leads to the following relation

$$\frac{\gamma^2}{C_p^\varepsilon} \phi_i^2 \approx \omega_{sc,i}^2 K_{c,i}^2 \quad (12)$$

where

$$K_{c,i}^2 = \frac{\omega_{oc,i}^2 - \omega_{sc,i}^2}{\omega_{sc,i}^2} \quad (13)$$

is the square of the effective electromechanical coupling factor (EEMCF) [8]. Inserting Equation (12) into Equation (9), one gets the approximate piezoelectric admittance

$$Y_p(s) \approx sC_p^\varepsilon \left(1 + \sum_{i=1}^N \frac{\omega_{sc,i}^2 K_{c,i}^2}{s^2 + 2\zeta_i \omega_{sc,i} s + \omega_{sc,i}^2} \right) \quad (14)$$

Near the resonance frequency of a structural mode, the contribution from non-resonant modes may be neglected provided that the natural frequencies are well-separated. In this case, the piezoelectric admittance may be approximated as

$$Y_p(s)|_{s \approx j\omega_{sc,i}} \approx sC_p^\varepsilon \left(1 + \frac{K_{c,i}^2 \omega_{sc,i}^2}{s^2 + 2\zeta_i \omega_{sc,i} s + \omega_{sc,i}^2} \right) \quad (15)$$

3.3 Sampling delays model

The use of a DPU incurs delays associated with the sampling of input and output signals, as well as the clock frequency of the processor. The former (associated with frequencies of the order of kHz) being usually much slower than the latter (associated with frequencies of the order of MHz), only the delays induced by the sampling procedure are taken into account. They are simply modelled by a zero-order-hold operator [9]:

$$H_d(s) = \frac{1 - e^{-sT_s}}{sT_s} H(s), \quad (16)$$

where T_s is the sampling time and $H(s)$ is the synthesized transfer function. This model assumes that the DPU is able to compute the output instantaneously from the input, and keeps this output constant for one sampling period.

Now that all the terms involved in the open-loop transfer function (Equation (4)) are known, it is possible to assess the effect of these delays on the performance of the closed-loop system.

3.4 Delay-induced instabilities

As can be seen in Equations (3) and (4), the sampling delays only affect the zeros of the open-loop transfer function. As is well-known in feedback control theory [9], the zeros of the open-loop transfer function are asymptotic positions for the poles of the closed-loop transfer function as the open-loop gain tends to infinity. Hence, knowing their position is of paramount importance to assess the stability of the closed-loop system.

As an illustrative example, Figure 3 compares the poles and zeros of an ideal (i.e. without delays) transfer function and a delayed one. These transfer functions are computed from the characteristics of the experimental system described in Section 5, for which a shunt circuit is synthesized to mitigate the first then the second structural mode.

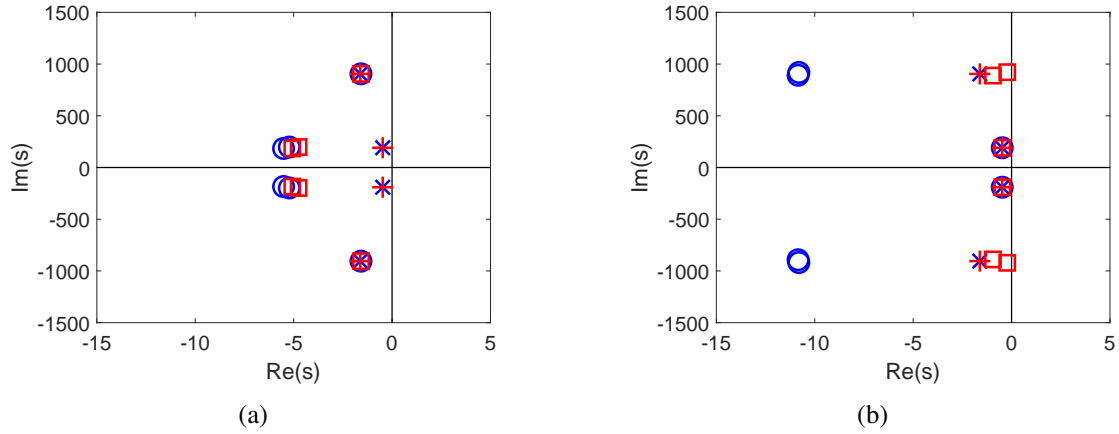


Figure 3: Poles (×) and zeros (○) of an ideal open-loop transfer function, and poles (+) and zeros (□) of a delayed open-loop transfer function: mode 1 (a) and mode 2 (b).

Figure 3(a) indicates that the delays effect is quite low for the first mode, although a small effect is visible on the zeros. In contrast, as seen in Figure 3(b), the delays cause a large shift of the zeros associated with mode 2 toward the right-half of the complex plane. The zeros almost become non-minimum phase, which signifies that the closed-loop system could be conditionally stable. As will be shown in Section 5, this estimate of the zeros is somewhat optimistic, and the closed-loop system is actually unstable.

3.5 Discussion

As the previous Subsection highlighted, the delays induced by the sampling procedure may lead to a destabilization of the vibration absorber, defeating completely its purpose. This destabilization is somewhat counter-intuitive, given that the DPU should synthesize a fully passive circuit, and that the sampling frequency is two orders of magnitude greater than the frequencies of interest. It should however be emphasized that this issue is solely hardware-related. A simple solution to this problem would be to increase the sampling frequency to a high enough value, but this is not always desirable for two reasons.

The first reason is linked to the power consumption of the DPU. The dynamic power consumption of an embedded system can be estimated by [10]

$$P = \beta C_L V_{cc}^2 f_{CPU} \quad (17)$$

where γ is the activity factor, C_L is the load capacitance, V_{cc} is the supply voltage and f_{CPU} is the clock frequency at which the DPU is operating. Increasing the sampling frequency will increase β and/or f_{CPU} , leading to a higher power consumption. Moreover, if f_{CPU} is increased, V_{cc} will also have to be increased, which leads to an actual power consumption proportional to f_{CPU}^3 [10].

The second reason is that the DPU sampling frequency may only be increased up to the hardware limits, which may be quickly reached. There could be the possibility to buy more powerful hardware, but the financial cost of such equipment could become prohibitive.

For these reasons, a stabilization method working for a given sampling frequency is proposed in the next section.

4 STABILIZATION PROCEDURE

The model developed in the previous section highlighted the role of sampling delays in the onset of instabilities. In this section, an anticipative method is proposed to cure the instability by placing the zeros of the delayed open-loop transfer function near or at the same location as those of the open-loop transfer function without delays.

The ideal transfer function of a hypothetical DPU without delays may be expressed as a rational transfer function

$$H(s) = \frac{\sum_{n=0}^N b_n s^n}{\sum_{m=0}^M a_m s^m} \quad (18)$$

and the zeros of the open-loop transfer function without delays satisfy

$$H(z_k) + Y_p(z_k) = 0, \quad \forall k \in [1, \dots, K] \quad (19)$$

The stabilization procedure consists in finding the modifications Δa_m and Δb_n to the coefficients a_m and b_n , respectively, such that the modified transfer function given as

$$\tilde{H}(s) = \frac{\sum_{n=0}^N (b_n + \Delta b_n) s^n}{\sum_{m=0}^M (a_m + \Delta a_m) s^m} \quad (20)$$

synthesized in the DPU give the same zeros as the idealized open-loop transfer function. In other words, the modifications should be such that the following equations are satisfied

$$H_d(z_k) + Y_p(z_k) = e^{z_k \beta T_s} \tilde{H}(z_k) + Y_p(z_k) = H(z_k) + Y_p(z_k) = 0, \quad \forall k \in [1, \dots, K]. \quad (21)$$

Using Equations (18) and (20), this equation becomes

$$e^{z_k \beta T_s} \frac{\sum_{n=0}^N (b_n + \Delta b_n) z_k^n}{\sum_{m=0}^M (a_m + \Delta a_m) z_k^m} = \frac{\sum_{n=0}^N b_n z_k^n}{\sum_{m=0}^M a_m z_k^m}, \quad \forall k \in [1, \dots, K]. \quad (22)$$

Carrying simple algebraic manipulations, Equation (22) can be recast into a linear system

$$\mathbf{M} \mathbf{\Delta} = \mathbf{r} \quad (23)$$

in which the unknowns are gathered in one vector

$$\mathbf{\Delta} = [\Delta a_0, \dots, \Delta a_M, \Delta b_0, \dots, \Delta b_N]^T \quad (24)$$

and \mathbf{M} and \mathbf{r} are deduced from Equation (22). Usually, $K \neq m + n + 2$ and the system is not square. A simple way of solving Equation (23) is to take its optimal solution in the least-squares sense

$$\mathbf{\Delta}^* = \left(\mathbf{M}^T \mathbf{M} \right)^{-1} \mathbf{M}^T \mathbf{r}. \quad (25)$$

The coefficients of a transfer function defined as in Equation (18) can all be multiplied by an arbitrary constant and still represent the same transfer function. This lack of unicity can lead to numerical issues. This can be fixed by setting one of the components of the vector $\mathbf{\Delta}$ to an arbitrary value. A simple choice is to choose one of the coefficients to be zero, which amounts to suppressing the corresponding column in the matrix \mathbf{M} .

5 EXPERIMENTAL VALIDATION

An experimental validation of the proposed approach is described in this section. A picture of the experimental setup is given in Figure 4. The structure is a cantilever beam with a thin, clamped lamina attached to its free end. The beam is covered with ten pairs of piezoelectric patches along its length. It is excited at midspan by an electrodynamic shaker (TIRA TV 51075) to which is also attached an impedance head (DYTRAN 5860B). An acquisition system (LMS SCADAS MOBILE) is used to record the signals. A more detailed description of the experimental setup can be found in Lossouarn et al [11].

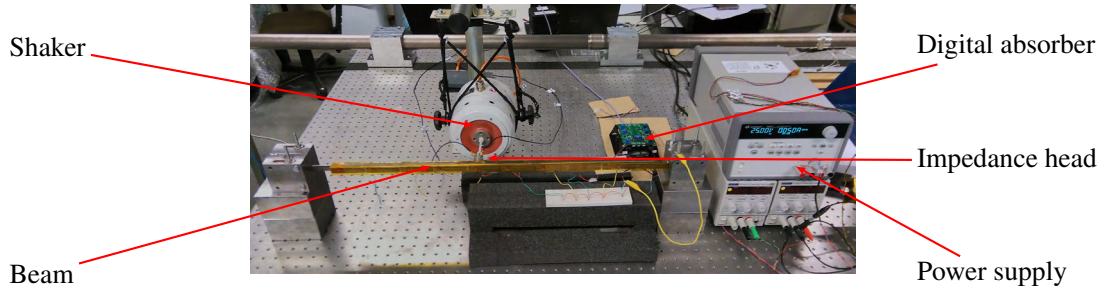


Figure 4: Picture of the experimental setup.

Five of the ten pairs of patches are connected in parallel to the digital absorber. The two first bending mode of the beam are sequentially targeted for shunt damping. To identify the system, the frequency response functions (FRFs) when the patches are short-circuited and when they are open-circuited are measured. These FRFs, noted x/f , are obtained with a low-level broadband excitation and are displayed in Figure 5.

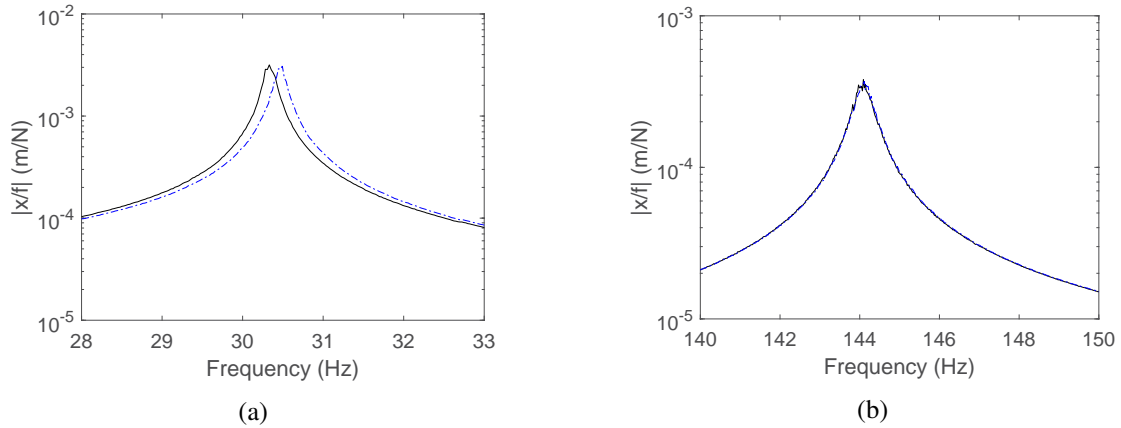


Figure 5: Experimental FRF of the beam when the piezoelectric patch are short-circuited (—) and open-circuited (---): close-up on mode 1 (a) and close-up on mode 2 (b).

The short-circuit and open-circuit resonance frequencies as well as the damping ratios are estimated by fitting the FRFs in Figure 5. The piezoelectric capacitance is measured with a multimeter (FLUKE 177). The parameters of the shunt circuit are then computed according to Soltani et al [12]. All these parameters are gathered in Table 1.

The DPU used in the digital absorber is an Arduino Due. The division ratio is given by $\alpha = 0.033$

Table 1: Identified and computed parameters.

Mode	f_{sc} (Hz)	f_{oc} (Hz)	ζ (-)	C_p^ε (nF)	L (H)	R (Ω)
1	30.35	30.47	0.24%	257	109.15	2,241.4
2	144.01	144.10	0.17%	257	4.8791	195.97

and the resistance of the current source is measured as $R_i = 265\Omega$. The series RL shunt circuit transfer function, theoretically given by

$$H(s) = \frac{1}{Ls + R} \quad (26)$$

is programmed into the DPU after discretizing it with Tustin's method, with a sampling frequency of $f_s = 10\text{kHz}$. The stabilizing method is used assuming that the approximation given in Equation (15) holds since the two modes are well-separated in frequency. The FRFs are compared when the transfer function is unmodified and when it is modified, with the coefficient of the numerator unchanged (i.e., $\Delta b_0 = 0$ is fixed). The open-loop transfer functions and experimentally obtained FRFs of the controlled structure are given in Figure 6, and the modified shunt circuit parameters are given in Table 2. Compared to the values given in Table 1, the synthesized inductances were empirically increased by 2% and 1% for mode 1 and 2, respectively, to obtain FRFs that exhibit equal peaks.

Table 2: Modified shunt circuit parameters.

Mode	\tilde{L} (H)	\tilde{R} (Ω)
1	109.09	2,440.1
2	4.868	395.49

As can be observed with the first mode in Figure 6(a), synthesizing the unmodified transfer function results in an already stable system which behaves as expected. The stabilization procedure brings negligible changes, as can also be observed in Figure 6(c). In contrast, a digitally synthesized shunt circuit for the second mode results in an unstable system, which is cured by the proposed procedure. The instability is confirmed by looking at the structural response in Figure 7: even when the structure is unforced, a significant acceleration is recorded. The system is thus self-excited, and its response is solely bounded thanks to the saturation of OA7. Figure 6(d) and Table 2 indicate that the physical action of the stabilization procedure is to increase the resistance in the shunt circuit, so as to bring the unstable poles back into the left-half complex plane.

6 CONCLUSIONS

Digital piezoelectric vibration absorbers are subject to instabilities caused by sampling delays. In the event of impossibility to increase the sampling frequency, a stabilization procedure was proposed. This method was experimentally validated on a piezoelectric beam. Future works may extend this method to discrete Laplace transform in order to work directly on the discretized transfer function.

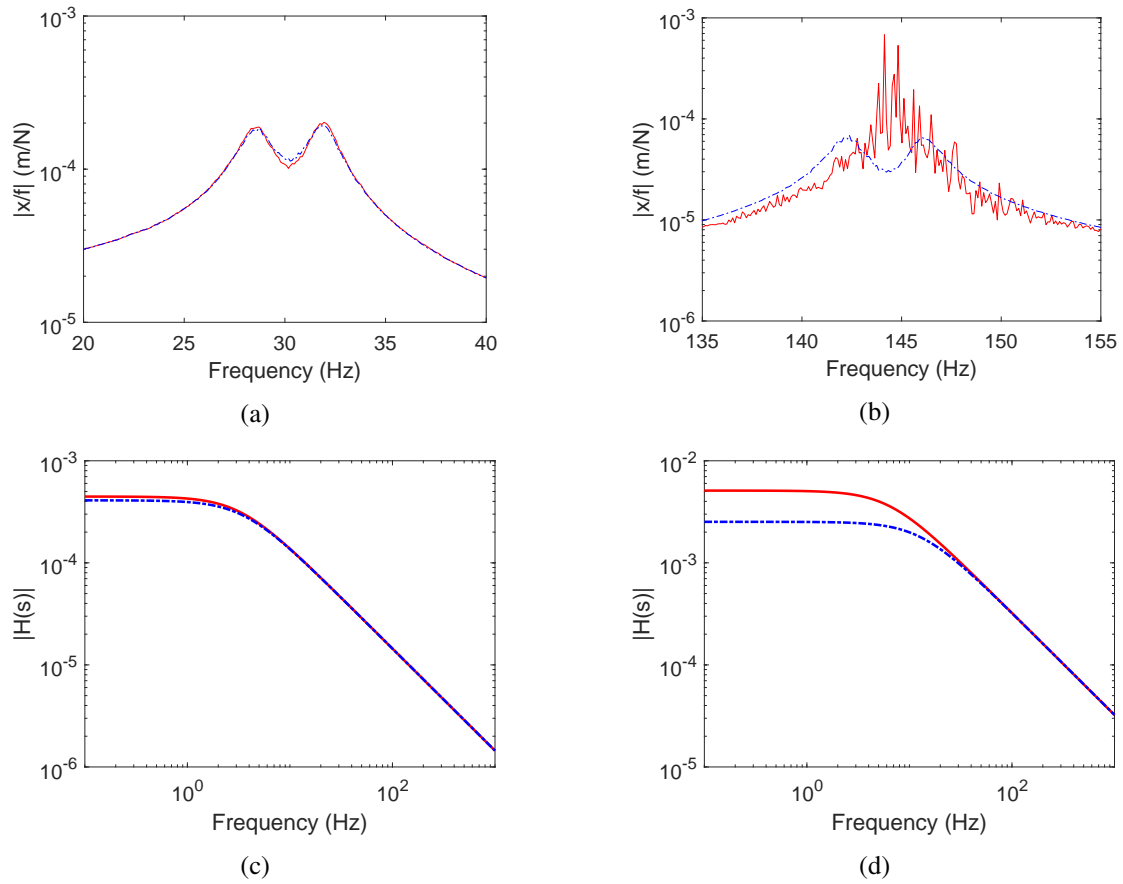


Figure 6: Experimental FRF for mode 1 (a) and mode 2 (b), and synthesized transfer function for mode 1 (c) and mode 2 (d): unmodified transfer function (—) and modified transfer function (---).

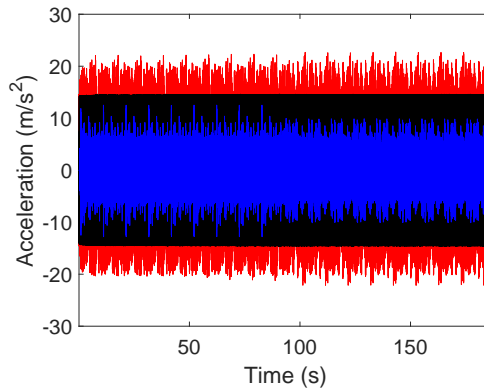


Figure 7: Recorded accelerations with a digital shunt circuit targeting mode 2: unmodified transfer function (—), unmodified transfer function and unforced structure (—) and modified transfer function (—).

7 ACKNOWLEDGEMENTS

The authors would like to acknowledge the financial support of the SPW (WALInnov grant 1610122).

REFERENCES

- [1] R. L. Forward, “Electronic damping of vibrations in optical structures,” *Applied Optics*, vol. 18, no. 5, p. 690, 1979.
- [2] N. W. Hagood and A. von Flotow, “Damping of Structural Vibrations with Piezoelectric Materials and Passive Electrical Networks,” *Journal of Sound and Vibration*, vol. 146, no. 2, pp. 243–268, 1991.
- [3] B. Lossouarn, M. Aucejo, J. F. Deü, and B. Multon, “Design of inductors with high inductance values for resonant piezoelectric damping,” *Sensors and Actuators, A: Physical*, vol. 259, pp. 68–76, 2017.
- [4] A. J. Fleming, S. Behrens, and S. O. R. Moheimani, “Synthetic impedance for implementation of piezoelectric shunt-damping circuits,” *Electronic Letters*, vol. 36, no. 18, pp. 1525–1526, 2000.
- [5] G. Matten, M. Collet, S. Cogan, and E. Sadoulet-Reboul, “Synthetic Impedance for Adaptive Piezoelectric Metacomposite,” *Procedia Technology*, vol. 15, pp. 84–89, 2014.
- [6] P. Horowitz and W. Hill, *The Art of Electronics*. Cambridge University Press, 3 ed., 2015.
- [7] N. W. Hagood, W. H. Chung, and A. V. Flotow, “Modelling of Piezoelectric Actuator Dynamics for Active Structural Control,” *Journal of Intelligent Material Systems and Structures*, vol. 1, no. 3, pp. 327–354, 1990.
- [8] O. Thomas, J.-F. Deü, and J. Ducarne, “Vibrations of an elastic structure with shunted piezoelectric patches: efficient finite element formulation and electromechanical coupling coefficients,” *International Journal for Numerical Methods in Engineering*, vol. 80, pp. 235–268, 2009.
- [9] G. F. Franklin, J. D. Powell, and M. L. Workman, *Digital Control of Dynamic Systems*. Addison-Wesley, 1998.
- [10] J. M. P. Cardoso, J. G. F. Coutinho, and P. C. Diniz, *Embedded Computing for High Performance: Efficient Mapping of Computations Using Customization, Code Transformations and Compilation*. Morgan Kaufmann, 2017.
- [11] B. Lossouarn, J.-F. Deü, and G. Kerschen, “A fully passive nonlinear piezoelectric vibration absorber,” *Philosophical Transactions of the Royal Society A: Mathematical, Physical and Engineering Sciences*, vol. 376, p. 20170142, 2018.
- [12] P. Soltani, G. Kerschen, G. Tondreau, and A. Deraemaeker, “Piezoelectric vibration damping using resonant shunt circuits: An exact solution,” *Smart Materials and Structures*, vol. 23, no. 12, 2014.

THE DEVELOPMENT OF THE MODEL OF ELECTRIC ANALOG FOR ELECTROMECHANICAL SYSTEMS TAKING INTO ACCOUNT MECHANICAL LOSSES

DMITRII A. OSHMARIN, MAKSIM A. IURLOV, NATALIYA V. SEVODINA,
NATALIIA A. IURLOVA

Department of complex problems of deformable solids mechanics
Institute of Continuous Media Mechanics of the Ural Branch of RAS (ICMM UB RAS)
Acad. Korolev str., 1, 613013 Perm, Russian Federation
e-mail: oshmarin@icmm.ru, www.icmm.ru

Key words: Electro-viscoelastic structure, Piezoelectric element, Electric circuit, Electric analogue, Natural vibrations, Complex eigenfrequencies.

Abstract. This paper is devoted to the construction of an electric analog for electromechanical systems, which contain elements made of viscoelastic energy dissipating materials and elastic piezoelectric elements. Two options of an electric analog in the form of an electric circuit are considered: a circuit made of elements with real-valued parameters of resistance inductance and capacitance and a circuit made of elements with complex-valued parameters. With these electric analogs it is possible to take into account the energy losses in an electromechanical system. The constructed electric analogs are used to find complex natural vibration frequencies, which are the dynamic characteristics of electro-viscoelastic systems. In this study the emphasis is placed on determining the values of such parameters as resistance, inductance and capacitance of the elements comprising the electric circuits.

1 INTRODUCTION

The analysis of the dynamic behavior of different engineering structures is associated with the evaluation of their dynamic characteristics, which can be determined by solving a number of relevant problems, such as the problem of steady-state vibrations, the problem of natural vibrations and the dynamic problem with initial conditions (transient analysis). The statement that the problem of natural vibrations is the most convenient and informative one from the viewpoint of the effectiveness of modeling the dynamic properties of a structure and optimisation of its dissipative characteristics has been considered and substantiated in [1]. Complex eigenvalues obtained by solving this problem define the frequencies of natural vibrations and their damping indices characterizing the damping rate of vibrations. The efficiency of the problem under consideration for optimization of the dynamic behavior of the structure can be judged by the independence of the obtained dynamic properties on the loading conditions.

Due to some peculiarities of the mathematical statement of the problem on natural vibrations of electro-viscoelastic bodies (viscoelastic structure with piezoelectric element), the numerical implementation of the algorithm for its solution using the finite element method is

a nontrivial task [2], and the search for the problem solution is a time-consuming process due to a large dimension of the resolving system of equations. At the same time, the mathematical equations, describing vibrations in the mechanical systems and current oscillations in the electric circuits demonstrate certain similarity. By this is meant that inductance is the analog of mass, resistance is the analogue of viscosity and capacitance is the analogue of stiffness. The coincidence of the mathematical descriptions suggests that in some cases we can use the electrical system instead of the mechanical one by substituting the equations for current oscillations in the equivalent electric circuit for the mechanical equations of motion [3-6]. In electrodynamics, there are also a number of well-defined approaches, for example, such as presented in [7-10], which are used to model the behavior of piezoelectric devices with the aid of their electric analogs in the form of equivalent electric circuits. However, in order to simulate the behavior of piezoelectric element attached to the structure, it is necessary to use a model, which can describe all resonant frequencies within a wide frequency range. This certainly generates the need for creating another model of electric circuit (equivalent circuit).

Representation of an electromechanical system in the form of discrete analog composed of the elements with lumped parameters allows us to significantly simplify the procedure of determining its dynamic properties. Nowadays, an approach, in which the structure is replaced by its electric analog in the form of equivalent electric circuit, is widely used especially in such applications, in which the understanding of the system performance determined by the interaction of its electrical and mechanical components is a question of utmost importance [11-12].

In the literature, there is a large number of options of electric analogs in the form of electric circuits, which are used for describing the electromechanical systems. In such systems, the parameters of the elements of electric circuits are represented both by the real (capacitance, inductance, resistance) and complex (complex inductance and capacitance) quantities [9].

The main problem is how to determine the values of the parameters for the elements of the electric circuit corresponding to the electric analog of the examined electro-viscoelastic system. The parameters of the elements comprising the examined electric circuit can be evaluated on the following basis: from the additional theoretical conditions and assumptions [5], from the data obtained from special experiments on the measurement of electric impedance of the system under consideration [3], or using the properties of the material, which are taken into account in designing an electric analog of the piezoelectric element with complex parameters [8].

It should be noted that the variety of existing approaches is explained by the complexity of the stated problem, the diversity of requirements specified for the electric analog being created, the necessity of an adequate description of the processes occurring in the system as well as the conformity to its dynamic characteristics

In this paper, we consider a method for constructing an electric analog for the examined electro-viscoelastic system and propose an approach for determining the parameters of the elements of electric circuit corresponding to the electric analog being created. The proposed techniques are based on the complex natural vibration frequencies, which are obtained from the experiment or by solving the natural vibration problem in a complete mathematical formulation.

2 MATHEMATICAL STATEMENT OF THE PROBLEM

The problem of natural vibrations for piecewise-homogeneous electro-viscoelastic bodies in the complete coupled mathematical formulation is considered in papers [13-14]. This problem is described by the following variational equation:

$$\int_{V_1} (\sigma_{ij} \delta \varepsilon_{ij} + \rho \ddot{u}_i \delta u_i) dV + \int_{V_2} (\sigma_{ij} \delta \varepsilon_{ij} - D_i \delta E_i + \rho \ddot{u}_i \delta u_i) dV = 0 \quad (1)$$

Here, the volume V_1 is related to a viscoelastic part of the structure; the volume V_2 is related to a piezoelectric part; D_i, E_i are the components of the vectors of electric flux density and electric field intensity, respectively; σ_{ij} are the components of the symmetric Cauchy stress tensor; ε_{ij} are the components of the linear strain tensor; u_i are the components of the displacement vector. The constitutive relations for the piezoelectric part of volume V_2 are written as follows:

$$\left. \begin{aligned} \sigma_{ij} &= C_{ijkl} \varepsilon_{kl} - \beta_{ijk} E_k \\ D_k &= \beta_{ijk} \varepsilon_{ij} + \varepsilon_{ki} E_i \end{aligned} \right\} \quad (2)$$

where C_{ijkl} are the components of the tensor of elastic constants; β_{ijk} and ε_{kl} are the components of the tensors of piezoelectric coefficients and dielectric coefficients, respectively ($i, j, k, l = 1, 2, 3$). Within the framework of this paper, we use the assumption that the behavior of viscoelastic material is described in terms of the complex dynamic moduli, as it was made in [14]. The dissipative mechanisms operating in the body of volume V_1 are described based on the model of linear hereditary viscoelasticity. The constitutive relations of this model can be written as

$$\begin{aligned} \sigma_{ij} - \sigma \delta_{ij} &= 2\tilde{G} \left(\varepsilon_{ij} - \frac{1}{3} \mathcal{G} \delta_{ij} \right) = 2(G_{\text{Re}} + iG_{\text{Im}}) \left(\varepsilon_{ij} - \frac{1}{3} \mathcal{G} \delta_{ij} \right), \\ \sigma &= \tilde{B} \mathcal{G} = (B_{\text{Re}} + iB_{\text{Im}}) \mathcal{G} \end{aligned} \quad (3)$$

where $\tilde{G} = G_{\text{Re}} + iG_{\text{Im}} = G_{\text{Re}} \left(1 - i \frac{G_{\text{Im}}}{G_{\text{Re}}} \right) = G_{\text{Re}} (1 - i\delta_g)$, $\tilde{B} = B_{\text{Re}} + iB_{\text{Im}} = B_{\text{Re}} \left(1 - i \frac{B_{\text{Im}}}{B_{\text{Re}}} \right) = B_{\text{Re}} (1 - i\delta_b)$ are the complex dynamic shear and bulk moduli; σ is the mean stress; \mathcal{G} is the volumetric strain; δ_g, δ_b are the mechanical loss tangents for the shear and bulk moduli, respectively; s_{ij}, e_{ij} are the components of deviatoric parts of the stress and strain tensors.

Let us consider the case, in which damping characteristics of the structure specified by the viscoelastic properties of the material it is made of are independent on the frequency, i.e. the shear and bulk moduli $G_{\text{Re}}, B_{\text{Re}}$ and the mechanical loss tangents δ_g, δ_b are constants. The solution to the problem of natural vibrations is sought in the form of $u(x, t) = u(x) e^{j\omega t}$, where $u(x) = \{u_1(x_1, x_2, x_3), u_2(x_1, x_2, x_3), u_3(x_1, x_2, x_3), \varphi(x_1, x_2, x_3)\}$ is the generalized state vector containing the components of mechanical displacements u_1, u_2, u_3 and electric potential φ ; $\omega = \omega_{\text{Re}} \pm i\omega_{\text{Im}}$ is the complex natural vibration frequency where ω_{Re} denotes the

angular natural frequency of vibrations and ω_{im} is the damping index characterizing the damping rate of vibrations.

The numerical implementation of the formulated problem is based on the finite element method (FEM). The application of the standard FEM procedures allows us to reduce the variational problem of natural vibrations described by equations (1-3) to the following matrix equation:

$$([K] - \omega^2 [M])\{\delta\} = \{0\} \quad (4)$$

where the stiffness matrix $[K]$ contains complex-valued coefficients [14].

The equivalent electric models including the elements with lumped parameters, such as the van Dyke model [4], are widely used for describing the dynamic behavior of piezoelectric element as an object with distributed parameters. The van Dyke model is represented by a series-connected elements of capacitance C , inductance L and resistance R and also the capacitance of the piezoelectric element C_0 connected in parallel to them (fig.1). This electric analog has a single resonance frequency of vibrations, which corresponds to the resonance frequency of mechanical vibrations of the piezoelectric element.

Let us consider each element of this model in detail. Here $C_0 + C$ is the inherent capacitance of piezoelectric element. The series-connected inductance element L and capacitance element C describe the resonant character of the process. The resistance element R describes losses, which occur due to the flow of electric current through the conducting elements [4].

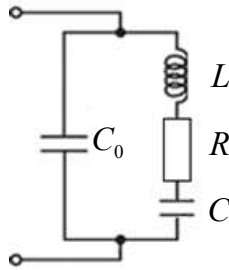


Figure 1: Equivalent circuit of the quartz resonator proposed by van Dyke [4].

In paper [13], the van Dyke model was expanded to an elastic structure with a piezoelectric element attached to its surface (fig.2a). Here, the method proposed in [13] for constructing an electric analog for the electroelastic system makes it possible to take into account several natural vibration frequencies of the structure. However, in this case the energy losses which may occur in real structures made of viscoelastic materials are ignored.

To take into account the energy losses caused by vibrations of viscoelastic structures, the equivalent circuit represented in fig.2a is modified by introducing the resistance R_i in each resonant branch C_i, L_i (see fig.2b). This additional resistance is responsible for the energy dissipation in the vicinity of resonance. Here also C_{0n}, R_{0n} are the capacitance and the resistance in the non-resonant branch.

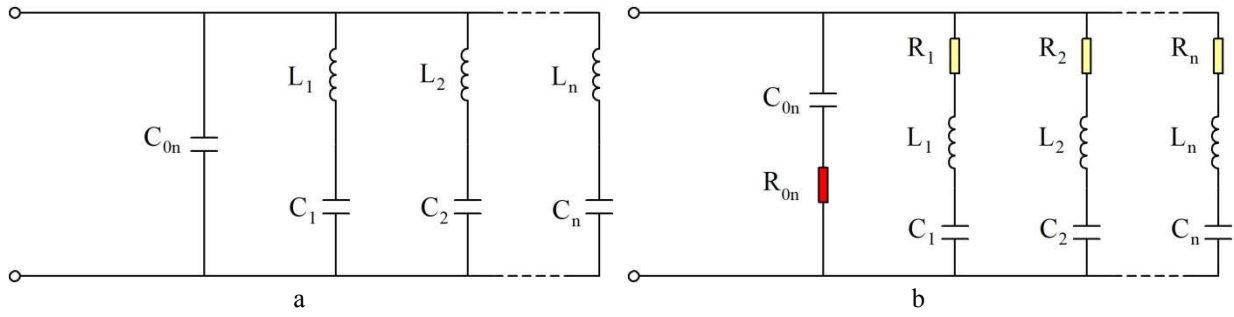


Figure 2: Equivalent circuits for electric analog of an electromechanical system without dissipation (a) and with dissipation (b)

According to the Kirghoff second law, the mathematical statement of the problem for the circuit represented in fig.2b is described by the following system of differential equations [13]:

$$L_i \frac{d^2 q_i}{dt^2} + R_i \frac{dq_i}{dt} + \frac{q_i}{C_i} + R_{0n} \sum_{k=1}^n \frac{dq_k}{dt} + \frac{1}{C_{0n}} \sum_{k=1}^n q_k = 0, \quad i = \overline{1, n} \quad (5)$$

Here n is the number of elementary closed electric circuits formed by the branch C_{0n}, R_{0n} and each of the resonant branches $R_i L_i C_i$; $n-1$ is the total number of parallel branches in the circuit. Representing the solution to the problem as $q_i = q_{0i} e^{j\lambda t}$, where $j^2 = -1$ is the imaginary unity, we reduce the system of differential equations (5) to the following form

$$-\lambda^2 L_i q_{0i} + j\lambda R_i q_{0i} + \frac{q_{0i}}{C_i} + j\lambda R_{0n} \sum_{k=1}^n q_{0k} + \frac{1}{C_{0n}} \sum_{k=1}^n q_{0k} = 0, \quad i = \overline{1, n} \quad (6)$$

Further, we construct the characteristic equation with respect to the unknown complex natural vibration frequency λ . The solution of this characteristic equation gives the spectrum of n complex natural vibration frequencies of the structure operating in the open circuit (o/c) mode. The spectrum of n complex natural vibration frequencies of the structure operating in the short circuit (s/c) mode can be obtained provided that each parallel branch of the circuit represented in fig.2 is short-circuited. In this case, each parallel branch is a closed oscillatory circuit. As a result, the terms containing multipliers $1/C_{0n}$ and R_{0n} are excluded from the systems of equations (5-6). Taking into account that the solution is represented as $q_i = q_{0i} e^{j\lambda t}$, the system of equations for determining the complex natural vibration frequencies of the structure operating in the short circuit mode can be written as:

$$-\lambda^2 L_i q_{0i} + j\lambda R_i q_{0i} + \frac{q_{0i}}{C_i} = 0, \quad i = \overline{1, n} \quad (7)$$

The problem of determining the parameters $R_i, R_{0n}, L_i, C_i, C_{0n}$ entering into the systems of equations (6-7) is discussed in Section 3. In the following, the values of complex natural vibration frequencies obtained on the basis of the complete mathematical formulation (1-4)

are denoted as ω . The values of complex natural vibration frequencies determined with the aid of the equivalent electric model (5-7) are denoted as λ .

3 THE CONSTRUCTION OF AN ELECTRIC ANALOG FOR ELECTRO-VISCOELASTIC SYSTEM

3.1 The circuit of an electric analog with real-valued coefficients

In order to determine the values of parameters $R_i, L_i, C_i, C_{0n}, R_{0n}$ (fig.3) for the electric analog of electro-viscoelastic system, we consider the part of the circuit, which corresponds to the vibration frequencies in the vicinity of the i -th resonance. In this case, in the short circuit mode at the i -th frequency, the electric current flows only through the R_i, L_i, C_i branch, whereas in the open circuit mode at the i -th frequency the current flows both through the branches R_i, L_i, C_i and R_{0i}, C_{0i} , which in this case are connected in series.

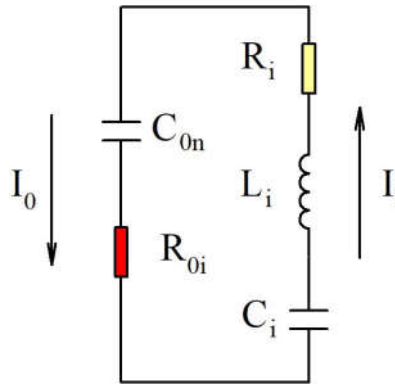


Figure 3: A part of the electric circuit corresponding to the system vibrations in the vicinity of the i -th natural vibration frequency.

By analogy with [13], the equations of balance of voltages are constructed according to the Kirghoff laws [15]. Here, the total capacitance of the electric circuit is assumed constant and equal to C_s :

$$C_s = \sum_{i=1}^n C_i + C_{0i} \quad (8)$$

$$L_i \frac{d^2 q_i}{dt^2} + R_s \frac{dq_i}{dt} + \frac{1}{C_i} q_i = 0 \quad \text{-- short circuit mode} \quad (9)$$

$$L_i \frac{d^2 q_0}{dt^2} + (R_i^s + R_{0i}^s) \frac{dq_0}{dt} + \frac{1}{C_i} q_0 + \frac{1}{C_s - C_i} q_0 = 0 \quad \text{-- open circuit mode} \quad (10)$$

where q_i is the variable charge in the i -th branch of the electric circuit.

The analysis of the solution of the natural vibration problem for electro-viscoelastic bodies obtained in the framework of a complete mathematical formulation (1-4) shows that when viscoelastic properties of the material are independent of frequency, the values of damping

indices are linearly dependent on the frequency of vibrations. Consequently, the damping coefficients $\xi_i = \omega_{Im}^i / \omega_{Re}^i$ have the same value for all frequencies. It means that the resistance of the electric circuit should be a variable quantity, i.e. should take different values at different frequencies of vibrations. Let this quantity be defined as $R_i^S = R_i / \lambda_i$, $R_{0n}^S = R_{0n} / \lambda_i$.

From condition (10) the following relation is obtained:

$$C_{0i} = C_s - C_i \quad (11)$$

The solution to equations (9-10) is sought in the form of $q_i = q_{0i} e^{j\lambda t}$, where $j^2 = -1$ is the imaginary unity. In view of equation (11), the equations (9) and (10) take the following form:

$$\left(-\lambda^2 L_i + j R_i + \frac{1}{C_i} \right) q_{0i} = 0 \quad (12)$$

$$\left(-\lambda^2 L_i + j(R_{0i} + R_i) + \frac{1}{C_i} + \frac{1}{C_s - C_i} \right) q_{0i} = 0 \quad (13)$$

In this case, the solution we are searching for are the eigenvalues $(\lambda)_k = (\lambda_{Re})_k + j(\lambda_{Im})_k$, which have positive imaginary parts $(\lambda_{Im})_k \geq 0$.

The values of complex natural vibration frequencies of unloaded electro-viscoelastic structure (in the case when the external circuit is absent) operating in the short circuit $(\omega_{s/c})_i = (\omega_{Re}^s)_i + j(\omega_{Im}^s)_i$ and open circuit $(\omega_{o/c})_i = (\omega_{Re}^o)_i + j(\omega_{Im}^o)_i$ modes are assumed to be known, since they can be obtained from the solution to the problem on natural vibrations of electro-viscoelastic system in the framework of a complete mathematical formulation of solid mechanics (1-4) [2]. Accordingly, the results of solution of equations (12) and (13) are expected to be the natural vibration frequencies $\lambda_i = (\omega_{s/c})_i$ and $\lambda_i = (\omega_{o/c})_i$.

It is necessary to determine four parameters: R_i , L_i and R_{0i} , C_i , which could be done with reference to condition (8). Equations (12) and (13) are the equations with complex-valued coefficients. Equality of the complex number to zero means that real and imaginary parts of this number must be equal to zero. Thus, we have four equations for four unknowns.

Let us consider equation (12), describing the short circuit mode at the i -th frequency. With regard to the relations for the known complex natural vibration frequencies, we can differentiate between the real and imaginary parts of the equation:

$$\begin{cases} -((\omega_{Re}^s)_i^2 - (\omega_{Im}^s)_i^2) L_i + \frac{1}{C_i} = 0 \\ -2(\omega_{Re}^s)_i (\omega_{Im}^s)_i L_i + R_i = 0 \end{cases} \quad (14)$$

From this it follows that:

$$R_i = 2(\omega_{Re}^s)_i (\omega_{Im}^s)_i L_i \quad L_i = \frac{1}{C_i ((\omega_{Re}^s)_i^2 - (\omega_{Im}^s)_i^2)} \quad (15)$$

By analogy, for the open circuit mode at the i -th frequency, after distinguishing the real and imaginary parts in the equation (13) we get:

$$\begin{cases} -\left((\omega_{\text{Re}}^o)_i^2 - (\omega_{\text{Im}}^o)_i^2\right)L_i + \frac{1}{C_i} + \frac{1}{C_s - C_i} = 0 \\ -2(\omega_{\text{Re}}^o)_i (\omega_{\text{Im}}^o)_i L_i + (R_i + R_{0i}) = 0 \end{cases} \quad (16)$$

Substituting in (16) the relations for R_i, L_i from (15) we obtain the relations for R_{0i} and C_i

$$R_{0i} = 2\left((\omega_{\text{Re}}^o)_i (\omega_{\text{Im}}^o)_i - (\omega_{\text{Re}}^s)_i (\omega_{\text{Im}}^s)_i\right)L_i \quad C_i = C_s \left[1 - \frac{\left((\omega_{\text{Re}}^s)_i^2 - (\omega_{\text{Im}}^s)_i^2\right)}{\left((\omega_{\text{Re}}^o)_i^2 - (\omega_{\text{Im}}^o)_i^2\right)} \right] \quad (17)$$

Thus, in the case when n resonant branches are retained in the numerical modeling, all parameters of the elements of the equivalent electric circuit can be evaluated using the relations (15) and (17). Here, the above parameters are determined in terms of the components of complex natural vibration frequencies, which are defined by the electric boundary conditions for the piezoelectric element of the system operating in the short circuit and open circuit modes.

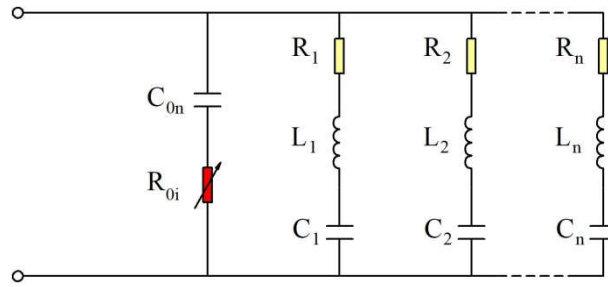


Figure 4: Equivalent electric circuit of the electro-viscoelastic system containing an element with variable resistance

However, it remains to be seen how the elements with additional resistance should be fit into the electric circuit, to make sure that the latter could be described by the equations in the form of (17). Obviously, the resistive elements with lumped parameters are not suitable for this purpose, since they cannot describe the dependence of resistance on frequency. In order to provide the equivalent circuit with the resistance required for realization of the open circuit mode, it was decided to use the option, at which the resistive element has a variable resistance [15]. As the result, the diagram of the equivalent electric circuit with real-valued coefficients is of the form shown in figure 4. This electric circuit corresponds to an electric analog of the electro-viscoelastic system. The element with variable resistance is colored red.

3.2 The circuit of an electric analog with complex-valued parameters

Let us consider the second option of constructing an electric analog for the electro-viscoelastic system, in which the external circuit is absent. In this option, the parameters of the elements comprising the electric circuit (capacitance and inductance) take complex values. In this case, the electric circuit is of the form represented in fig.1a, which corresponds to the

examined electroelastic structure. The parameters of the elements included into this circuitry are determined by analogy with the technique described above:

$$\tilde{C}_i = C_s \frac{(\omega_{o/c})_i^2 - (\omega_{s/c})_i^2}{(\omega_{o/c})_i^2}, \quad \tilde{L}_i = \frac{1}{\tilde{C}_i (\omega_{s/c})_i^2}, \quad C_s = \sum_{i=1}^n \tilde{C}_i + \tilde{C}_{0n} \quad (18)$$

The difference is in fact that the frequencies of vibrations $(\omega_{o/c})_i$, $(\omega_{s/c})_i$ and the values of parameters of the elements \tilde{C}_i , \tilde{L}_i , \tilde{C}_{0i} included into the equivalent circuit, describing an electric analog for the examined electro-viscoelastic system without the external electric circuits, are the complex numbers, except for the total capacitance of the piezoelectric element C_s . Note however, that all parameters of the electric elements \tilde{C}_i , \tilde{L}_i , \tilde{C}_{0i} are determined on the basis of the complex natural vibration frequencies of the electro-viscoelastic system, which operates in the open circuit and short circuit modes and is not connected to any external electric circuit.

The systems of equations, which describe oscillations of the charge in the electric circuit, corresponding to the electric analog of the electro-viscoelastic system with the attached piezoelectric element, which is not connected to an external circuit, take the same form as for the case of electroelastic system:

$$\begin{aligned} \frac{d^2 q_i}{dt^2} \tilde{L}_i + \frac{q_i}{\tilde{C}_i} &= 0, \quad i = 1, n \text{ - open circuit mode;} \\ \frac{d^2 q_i}{dt^2} \tilde{L}_i + \frac{q_i}{\tilde{C}_i} + \sum_{j=1}^n \frac{q_j}{\tilde{C}_{0n}} &= 0, \quad i = 1, n \text{ - short circuit mode} \end{aligned} \quad (19)$$

4 DETERMINATION OF NATURAL VIBRATION FREQUENCIES OF ELECTRO-VISCOELASTIC STRUCTURE USING ITS ELECTRIC ANALOG

In this section, the efficiency and reliability of both options of the electric analogs (with real parameters and with complex parameters) will be demonstrated by solving the problem of determining complex natural vibration frequencies of the cantilever viscoelastic plate with the attached elastic piezoelectric element, which operates in the open circuit and short circuit modes (figure 5). The cantilevered plate has the following dimensions: $l_1 = 210$ mm, $b_1 = 26$ mm, $h_1 = 0.5$ mm. The material of the plate has the following viscoelastic properties: instantaneous moduli are $G_{Re} = 1.5385 \cdot 10^{11}$ Pa, $B_{Re} = 1.6667 \cdot 10^{11}$ Pa; tangents of mechanical losses are $\delta_g = 0.01$, $\delta_b = 0$; mass density is $\rho = 7800$ kg/m³.

The piezoelectric element has a rectangular form with the following dimensions: $l_p = 50$ mm, $b_p = 20$ mm, $h_p = 0.36$ mm. It is located symmetrically about the longitudinal axis at a distance of 12 mm from the rigidly clamped end. The piezoelectric element is made of piezoceramics PZT-4 polarized along the z-axis, which has the standard physical and mechanical properties similar to those presented in [2]. The upper and lower surfaces of the piezoelectric element are covered with electrodes and the lower surface is grounded.

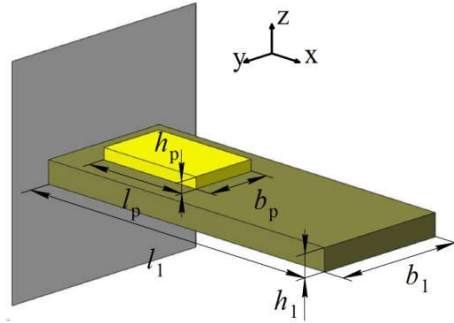


Figure 5: Computational model of the cantilever plate with attached piezoelectric element

Now let us calculate the complex natural vibration frequencies of the system under consideration for two limiting cases of boundary conditions specified for the piezoelectric element - the short circuit operating mode (s/c, zero-valued electric potential on both electrode surfaces) and open circuit operating mode (o/c, zero-valued electric potential on the lower electrode surface and the upper one is free of loads). Table 1 represents the values of complex natural vibration frequencies of the structure for the s/c and o/c modes obtained on the basis of the finite element solution of the coupled problem on natural vibrations of electro-viscoelastic bodies, on the basis of the electric analogue with real-valued parameters and on the basis of the electric analogue with complex-valued parameters.

The following notations are used in the table : $f^o = \omega_{o/c} / 2\pi$, $f^s = \omega_{s/c} / 2\pi$. In table 1, from all possible natural vibration frequencies we present only those frequencies, at which the electric potential is generated on the electrodes of piezoelectric element (coupled frequencies). These frequencies of vibrations are numbered in the ascending order of magnitude. For the calculations made on the basis of the electric analogs the number of retained branches n is equal to 10. This number corresponds to the frequencies of the examined system ranging from 0 up to 3100 Hz. However, only the first five frequencies of the frequency range from 0 to 700 Hz are presented. All eigenvalues, which have positive imaginary parts $(\omega_{lm})_i \geq 0$, $i = 1, n$ are the sought solutions of the problem.

The analysis of the obtained results allows us to conclude that the electric circuits with real and complex parameters, which correspond to the electric analog of the examined electro-viscoelastic system without the external electric circuit, are quite reliable from the viewpoint of obtaining values of natural vibration frequencies. What is also important, one of the advantages of the proposed option of the electric circuit with complex parameters is that there is no need to supplement the circuit of the electric analog with additional resistance.

Table 1: Complex natural vibration frequencies of the structure under study for the s/c and o/c modes obtained on the basis of the solution to the coupled problem of continuous media mechanics; using the electric analog with real-valued parameters or using the electric analog with complex-valued parameters.

Number of frequency	f_{Re}^s	f_{Im}^s	f_{Re}^o	f_{Im}^o
The coupled problem of continuous media mechanics				
1	13.5753	0.0467	13.8618	0.0491

2	72.1492	0.2895	72.3338	0.2903
3	197.8998	0.7906	198.3253	0.7949
4	399.7958	1.5119	404.1591	1.5420
5	665.4567	2.4731	674.9684	2.5090
The electric analogue with real-valued parameters				
1	13.5753	0.0467	13.8617	0.0487
2	72.1492	0.2895	72.3417	0.2902
3	197.8999	0.7906	198.3415	0.7945
4	399.7958	1.5119	404.3084	1.5389
5	665.4567	2.4730	675.7152	2.5067
The electric analogue with complex-valued parameters				
1	13.5753	0.0467	13.8617	0.0490
2	72.1492	0.2895	72.3416	0.2904
3	197.8990	0.7906	198.3415	0.7951
4	399.7958	1.5119	404.3084	1.5404
5	665.4567	2.4730	675.7152	2.5159

Moreover, the proposed model allows for such peculiarities of viscoelastic material of the structure as the dependence of material properties on frequency in the case when the external electric circuit is absent. However the question as to the advantages of using the electric circuit with complex parameters in the system connected to an external shunting electric circuit is still open to further investigation and discussion.

5 CONCLUSIONS

In this paper, we consider two options of constructing an electric analog in the form of electric circuits with real and complex-valued parameters for electro-viscoelastic systems. The both options of electric analogs allow describing the vibrations of electro-viscoelastic systems in the open circuit and short circuit operating modes. It is proposed that the element of an electric circuit with variable resistance should be used to describe the mechanism of energy dissipation in the framework of the model of linear hereditary viscoelasticity with complex dynamic moduli. This element allows taking into account the dissipative properties of the system, operating in the open circuit and short circuit modes. The results of numerical calculations showed the efficiency and reliability of the proposed method for determining the values of complex natural vibration frequencies of an electromechanical system including the elements of energy dissipation based on the construction of the electric analogs in the form of equivalent electric circuits.

ACKNOWLEDGEMENTS

The work is supported by RFBR, project №17-41-590152_r-a.

REFERENCES

- [1] Kligman, E.P. and Matveenko, V.P. Natural vibration problem of viscoelastic solids as

- applied to optimization of dissipative properties of constructions. *Int. J. Vibration and Control*. (1997) **3**(1): 87-102.
- [2] Matveenko, V.P., Oshmarin, D.A., Sevodina, N.V. and Iurlova, N.A. Natural vibration problem for electroviscoelastic body with external electric circuits and finite-element relations for its numerical implementation. *Computational Continuum Mechanics* (2016) **9**(4): 476-485.
- [3] Mason, W.P. Electrical and Mechanical Analogies. *The Journal of the Acoustical Society of America* (1942) **14**: 128-129.
- [4] Van Dyke, K.S. The Piezo-Electric Resonator and Its Equivalent Network. *Proc. Inst. Radio Eng.* (1928) **16**(6): 742-764.
- [5] Firestone, F.A. The mobility method of computing the vibration of linear mechanical and acoustical systems: Mechanical Electrical Analogies. *J. Appl. Phys.* (1938) **9**: 373-387.
- [6] Miles, J. Applications and Limitations of Mechanical-Electrical Analogies. New and Old. *The Journal of the Acoustical Society of America* (1943) **14**: 183-192.
- [7] Guan, M. and Liao, W.-H. Studies on the circuit models of piezoelectric ceramics. *Proc. International Conference on Information Acquisition. Hefei, China* (2004) 26-31.
- [8] Sherit, S., Wiederick, H.D., Mukherjee, B.K. and Sayer M. An accurate equivalent circuit for the unloaded piezoelectric vibrator in the thickness mode. *J. of Phys. D: Appl. Phys.* (1997) **30**(16): 2354-2363.
- [9] Park, C.H. On the circuit model of piezoceramics. *J. of Intelligent Material Systems and Structures* (2001) **12**(7): 515-522.
- [10] Mason, W.P. *Piezoelectric Crystals and Their Application to Ultrasonics*. New York: Van Nostrand Mason (1950).
- [11] Pang, S., Li, W. and Kan J. Optimization analysis of interface circuits in piezoelectric energy harvesting systems. *Journal of Power Technologies* (2016) **96**(1): 1-7.
- [12] Chen, Y.-Y. and Vasic D. Electrical interfacing circuit discussion of galloping-based piezoelectric energy harvester. *Physics Procedia* (2015) **70**: 1017-1021.
- [13] Matveenko, V., Iurlov, M., Oshmarin, D., Sevodina, N., and Iurlova N. Modelling of vibrational processes in systems with piezoelements and external electric circuits on the basis of their electrical analogue. *J. Intell. Material Syst. Struct.* (2018) **29**(16): 3254-3265.
- [14] Iurlova, N., Sevodina, N., Oshmarin, D. and Iurlov M. Algorithm for solving problems related to the natural vibrations of electro-viscoelastic structures with shunt circuits using ANSYS data. *Int. J. Smart Nano Mat.* (2018) **10**:156-176.
- [15] Charles, K.A. and Sadiku, M.N.O. *Fundamentals of electric circuits, 4th ed.* McGraw Hill (2009).

THE USE OF NEGATIVE CAPACITANCES TO IMPROVE THE VIBRATION ATTENUATION OF PIEZOELECTRIC RESONANT SHUNT

M. Berardengo*, S. Manzoni⁺, O. Thomas[†] and M. Vanali*

*Department of Engineering and Architecture

Università degli Studi di Parma

Parco Area delle Scienze 181/A, 43124 Parma, Italy

e-mail: marta.berardengo@unipr.it - marcello.vanali@unipr.it

⁺Department of Mechanical Engineering

Politecnico di Milano

Via La Masa 34, 20156 Milan, Italy

e-mail: stefano.manzoni@polimi.it

[†] Arts et Métiers ParisTech, LSIS UMR CNRS 7296

8 bd. Louis XIV 59046 Lille, France

e-mail: Olivier.THOMAS@ensam.eu

Key words: piezoelectric shunt, negative capacitance, resonant shunt, vibration control

Abstract. This paper addresses the use of piezoelectric shunt for suppressing vibrations. The focus of the work is on the coupling between the classical resonant shunt and negative capacitances. General formulations are provided for the tuning of the elements composing the shunt impedance and the consequent vibration attenuation performances are investigated. Moreover, the paper explains which issues could be encountered in practical applications and how to overcome them. The theoretical results are validated by means of an experimental campaign.

1 INTRODUCTION

This paper addresses the use of negative capacitances (NC) for improving the vibration attenuation provided by the piezoelectric resonant shunt. Piezoelectric resonant shunt is a way of attenuating vibrations of the structures based on the shunt of a piezoelectric actuator, bonded to the structure, with an electrical impedance Z_{sh} made from a resistance R and an inductance L connected in either parallel or series (see Fig. 1a) [1, 2, 3, 4, 5, 6, 7, 8].

The attenuation performance provided by the shunt of piezoelectric actuators can be improved by adding in the shunt circuit one [9, 10, 11, 12, 13] or two [14, 15] NCs. NCs do not exist in nature but they can be built synthetically by means of operational amplifiers (OP-AMP) [16, 17]. Different works in the literature treat the coupling between NCs and resistive shunt impedances (e.g. [11, 18]), while few address the coupling with resonant impedances (e.g. [19]).

The purpose of this paper is to show how to optimise the values of L and R when NCs are added in the shunt circuit, giving general formulations. Furthermore, the consequent attenuation performance is

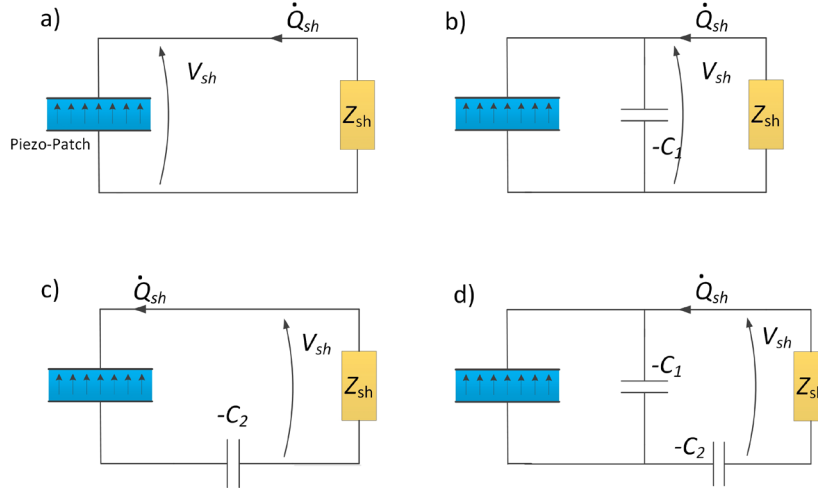


Figure 1: Piezoelectric shunt without NCs (a), with an NC ($-C_1$) connected in parallel (b), with an NC ($-C_2$) connected in series (c), with two NCs ($-C_1$ and $-C_2$) connected in series+parallel (SP) (d)

quantificated and analysed.

The second part of the paper then discusses the effect of the practical implementation of NCs on the stability of the whole system and hints are given to overcome possible problems. Therefore, the structure of the paper is as follows: Section 2 briefly describes the model employed in this paper to describe the electro-mechanical system. Then, Section 3 shows how to optimise the shunt circuit and provides estimates of the attenuations achievable with this type of vibration control strategy. Section 4 discusses practical issues related to the coupling between resonant shunt and NCs and explains how to solve them. Finally, Section 5 discusses an experimental campaign performed to validate the theoretical results.

2 MODEL OF THE ELECTRO-MECHANICAL STRUCTURE

The model used in this paper to describe the behaviour of the electro-mechanical system was developed in the works of Thomas et al. [20, 21] and Ducarne et al. [22] and then refined in the work of Berardengo et al. [18], where a detailed description of the dynamics of the electrical part of the system improves the accuracy of the whole model. These referenced works show that the dynamics of the electro-mechanical system in presence of NCs in the shunt circuit and in case of low modal density is described by the following equations at $\Omega \simeq \omega_i$ (where Ω is the angular frequency and ω_i is the i -th eigenfrequency of the system with the piezoelectric actuator short-circuited):

$$\ddot{q}_i + 2\xi_i \omega_i \dot{q}_i + (\omega_i^{\text{oc}})^2 q_i - \omega_i \tilde{k}_i \bar{Q}_{\text{sh}} = F_i \quad (1)$$

$$\bar{V}_{\text{sh}} - \bar{Q}_{\text{sh}} + \omega_i \tilde{k}_i q_i = 0 \quad (2)$$

Equation (1) describes the motion of the system, while Eq. (2) describes the dynamics of the electrical part of the system. Here, ξ_i is the non-dimensional damping ratio associated to ω_i and F_i is the modal forcing. ω_i^{sc} and ω_i^{oc} are the eigenfrequencies of the structure coupled to NCs when Z_{sh} is zero (SC) or $+\infty$ (OC), respectively; they can be written as functions of ω_i , $-C_1$, $-C_2$ (i.e. the NCs, see Fig. 1) and the capacitance of the piezoelectric patch (see [18]). Furthermore, q_i is the modal displacement. \bar{Q}_{sh} and \bar{V}_{sh} are the normalised charge and voltage seen by the impedance Z_{sh} ($\bar{Q}_{\text{sh}} = Q_{\text{sh}} / \sqrt{C_{\text{eq}}}$ and $\bar{V}_{\text{sh}} = V_{\text{sh}} \sqrt{C_{\text{eq}}}$),

respectively (see Fig. 1). Since the capacitance of the piezoelectric patch depends on the frequency, a particular capacitance value appears naturally in the equations: C_{pi} , which is the blocked capacitance corrected by a static term accounting for the higher modes (see [18]). C_{eq} is C_{pi} modified by the NCs. The expressions of C_{eq} , which are dependent on the type of connection of the NCs (see Fig. 1), can be found in [18]. \tilde{k}_i is the enhanced modal electro-mechanical coupling factor and it can be estimated as [18]:

$$|\tilde{k}_i| \simeq \sqrt{\frac{(\omega_i^{oc})^2 - (\omega_i^{sc})^2}{\omega_i^2}} \quad (3)$$

It is important to mention that, considering the elastic structure coupled to the NCs, the enhanced modal electro-mechanical coupling factor \tilde{k}_i appears naturally in the dynamical equations of the coupled system. \tilde{k}_i is the classical modal electro-mechanical coupling factor k_i increased by the effect of the NCs [9, 18]). This similarity enables to write the same model than for a classical shunt (see Eqs. (1) and (2)), with the effect of the NCs taken into account by \tilde{k}_i , ω_i^{sc} and ω_i^{oc} .

If the proper link between \bar{V}_{sh} and \bar{Q}_{sh} is derived, according to the type of connection between L and R (either parallel or series, see [5]), the frequency response function (FRF) of the system can be derived starting from Eqs. (1) and (2). The FRF in case of parallel connection between L and R is:

$$H_i^{par}(\Omega) = \frac{q_i}{F_i} = (-\Omega^2 + \omega_e^2 + 2j\xi_e\omega_e\Omega) \cdot [\Omega^4 - \Omega^2(\omega_e^2 + 4\xi_i\xi_e\omega_i\omega_e + (\omega_i^{oc})^2) + (\omega_i^{sc})^2\omega_e^2 + j\Omega[2\xi_e\omega_e((\omega_i^{sc})^2 - \Omega^2) + 2\xi_i\omega_i(\omega_e^2 - \Omega^2)]]^{-1} \quad (4)$$

while, for the series link, it is:

$$H_i^{ser}(\Omega) = \frac{q_i}{F_i} = (-\Omega^2 + \omega_e^2 + 2j\xi_e\omega_e\Omega) \cdot [\Omega^4 - \Omega^2(\omega_e^2 + 4\xi_i\xi_e\omega_i\omega_e + (\omega_i^{oc})^2) + (\omega_i^{sc})^2\omega_e^2 + j\Omega[2\xi_e\omega_e((\omega_i^{oc})^2 - \Omega^2) + 2\xi_i\omega_i(\omega_e^2 - \Omega^2)]]^{-1} \quad (5)$$

ω_e and ξ_e are the eigenfrequency and the non-dimensional damping ratio of the electrical circuit, respectively. They can be expressed as functions of L and R . The relationships, in case of parallel connection, are:

$$\omega_e = \frac{1}{\sqrt{LC_{eq}}}, \quad \xi_e = \frac{1}{2R} \sqrt{\frac{L}{C_{eq}}} \quad (6)$$

while, in case of a series link, they are:

$$\omega_e = \frac{1}{\sqrt{LC_{eq}}}, \quad \xi_e = \frac{R}{2} \sqrt{\frac{C_{eq}}{L}} \quad (7)$$

These FRFs are valid for all the types of NC connections, provided to use the proper formulation of the terms ω_i^{sc} and ω_i^{oc} , which are functions of the type of NC connection. The expressions of these two parameters for all the three NC links (parallel, series, and series+parallel (SP), see Fig. 1) can be found in [18, 19].

3 OPTIMISATION OF THE SHUNT AND ATTENUATION PERFORMANCES

To optimise the control system, the shunt network parameters (L , R and the NC) must be set. According to [18, 19], the value of the NC (in absolute value) must be set as close as possible to C_{pi} . However, a perfect equality between the NC (in absolute value) and C_{pi} is not possible because there are stability limits on the values of the NC. These stability limits are provided in [19]. It is noticed that the closer the value of the NC (in absolute value) is to the value of C_{pi} , the higher the value of $|\tilde{k}_i|$ is and, thus, the higher the attenuation performance is. High values of $|\tilde{k}_i|$ can be achieved thanks to the fact that the presence of NCs in the shunt circuit make the short- and open-circuit farther and farther (see Eq. (3), and refer to [18] for more details).

Relying on the FRFs of Eqs. (4) and (5), it is possible to optimise the values of L and R . The method used here is, indeed, a well-established approach already employed for optimising tuned mass dampers and passive (i.e. without NCs) piezoelectric shunts (e.g. [7, 21, 23, 24]), based on considerations on the shape of the transfer function of the controlled system. The value of L is set noticing that there exist two points of the FRF amplitudes, at ω_{F-} and ω_{F+} , respectively, at which all the curves obtained changing the ξ_e value, for a given value of ω_e , cross. Imposing the equality of the FRF amplitudes at ω_{F-} and ω_{F+} , the optimal value of ω_e (named here ω_e^{opt}) is derived, as well as that of L .

Then, the optimal value of ξ_e (named here ξ_e^{opt}), and thus that of R , can be found by imposing that the FRF amplitudes have a maximum first at ω_{F-} and, then, at ω_{F+} . The first condition allows to find a value of ξ_e named ξ_e^- , while the second condition allows to find a value of ξ_e , named ξ_e^+ . Then, the value of ξ_e^{opt} is derived as:

$$\xi_e^{\text{opt}} = \sqrt{\frac{(\xi_e^+)^2 + (\xi_e^-)^2}{2}} \quad (8)$$

The expressions of ω_e^{opt} and ξ_e^{opt} are provided in Table 1. Thanks to the general formulation used to model the system, these expressions are valid for all the NC configurations.

Table 1: Expressions of ω_e^{opt} and ξ_e^{opt}

parameter	L and R connected in parallel	L and R connected in series
$\omega_e^{\text{opt}} =$	$\sqrt{\frac{3(\omega_i^{\text{sc}})^2 - (\omega_i^{\text{oc}})^2}{2}}$	ω_i^{oc}
$\xi_e^{\text{opt}} =$	$\frac{\sqrt{3}}{2} \sqrt{\frac{(\omega_i^{\text{oc}})^2 - (\omega_i^{\text{sc}})^2}{3(\omega_i^{\text{sc}})^2 - (\omega_i^{\text{oc}})^2}}$	$\frac{\sqrt{3}}{2} \sqrt{\frac{(\omega_i^{\text{oc}})^2 - (\omega_i^{\text{sc}})^2}{(\omega_i^{\text{oc}})^2 + (\omega_i^{\text{sc}})^2}}$

The attenuation performance achievable by the optimised shunt can be measured by means of an index named A_{dB} and expressed in decibel, defined as:

$$A_{\text{dB}} = 20 \log_{10} \frac{H_{\text{sc}}}{H_{\text{shunt}}} \quad (9)$$

where H_{sc} is the maximum FRF amplitude value of the uncontrolled system (i.e. when the piezoelectric actuator is short-circuited without any NCs), while H_{shunt} is the FRF amplitude at ω_{F-} (this index is used because of the flat shape of the FRF amplitude around ω_i with the optimised shunt, see [21]).

Figure 2 shows the trend of A_{dB} as a function of the value of $|\tilde{k}_i|$ for an NC in either parallel or series. As for the SP configuration, the trends are not reported here because they are always between those of

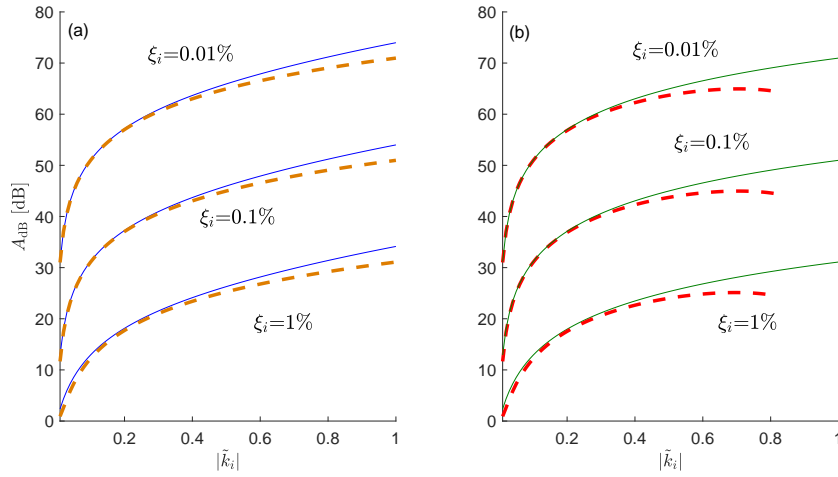


Figure 2: Trend of A_{dB} as a function of $|\tilde{k}_i|$ for an NC in parallel (a) and an NC in series (b) for different values of ξ_i . $k_i = 0.01$. Solid lines for R and L connected in series and dashed lines for R and L connected in parallel.

the parallel and the series. They slightly change according to the value set for the ratio C_{pi}/C_1 (where C_1 is the absolute value of the NC in parallel in the SP configuration, see Fig. 1).

The attenuation curves are close each other for all the NC layouts and the types of connection between L and R when the value of \tilde{k}_i is low. Conversely, when it increases, some differences become evident:

- the series connection between L and R offers higher attenuation levels compared to the parallel one;
- the NC in parallel offers slightly higher attenuations compared to the series NC. However, it is noticed that the parallel NC is usually used to attenuate high-order modes, while the series NC is employed for low-order modes. Thus, they must not be directly compared. Conversely, the SP configuration is suitable for all the modes;
- the curve of the NCs in series (and SP), when L and R are connected in parallel are stopped at $\tilde{k}_i \simeq 0.8$ because, over this threshold, the value of $[3(\omega_i^{sc})^2 - (\omega_i^{oc})^2]$ (see Tab. 1) becomes negative and ω_e^{opt} becomes imaginary;
- the A_{dB} values depend mainly on the values of $|\tilde{k}_i|$ and ξ_i and show a very small dependence on the ratio between the NCs and C_{pi} .

4 PRACTICAL ISSUES

This section analyses two different aspects related to possible issues which can arise in practical applications where piezoelectric shunt damping with NCs is employed. The two following subsections analyse them one by one.

4.1 The static gain for NCs in series and SP

When the value of $|\tilde{k}_i|$ is increased over about 0.8 using NCs in either series or SP, the curves shown in Fig. 2 can become non-accurate in describing the value of the actual attenuation provided by the shunt. Indeed, in these cases, the static gain of the FRF amplitude can become high, and even higher than the resonance peak (see, as an example, Fig. 3). Nevertheless, the curves of Fig. 2 are still able to properly

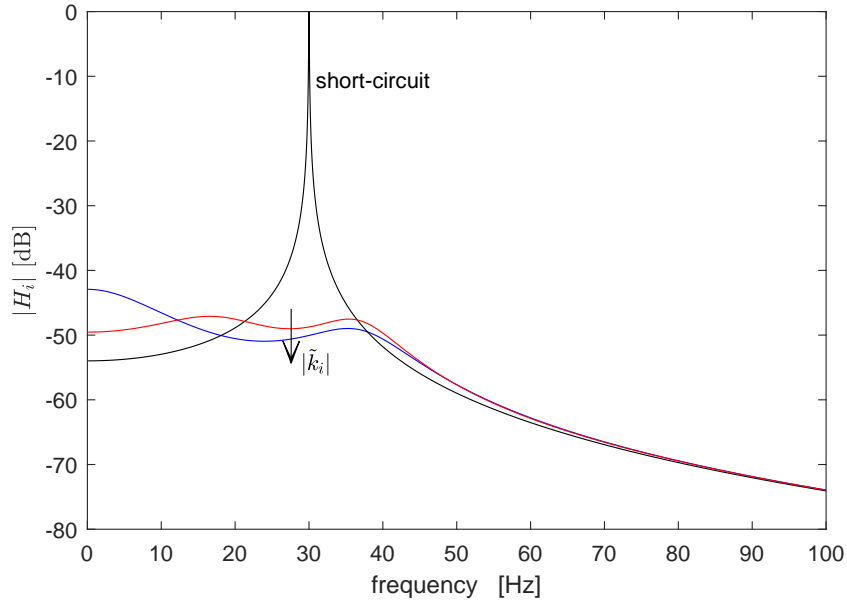


Figure 3: $|H_i|$ for $|\tilde{k}_i|$ equal to 0.7 and 0.9. $k_i=0.3$, $\omega_i/(2\pi)=30$ Hz and $\xi_i=0.1\%$

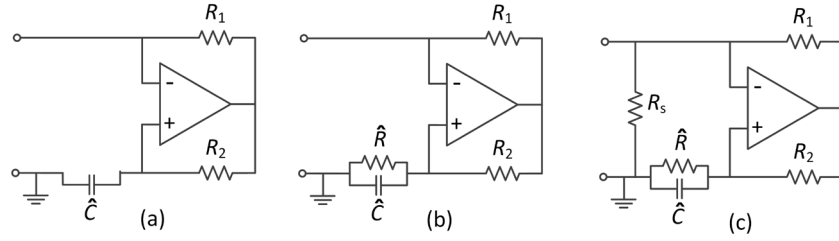


Figure 4: The electrical scheme for implementing a pure NC in series (a), the scheme with addition of \hat{R} , and the use of the compensation resistance R_s (c).

describe the attenuation if the interest is in the behaviour of the system at frequency values around ω_i . However, since the peak of the FRF amplitude is no more there, the A_{dB} curve is no more related to the maximum attenuation (which is worse). However, it must be highlighted that in many practical cases, like those discussed in this paper, the static gain is not so important and, thus, often this issue can be neglected.

Figure 3 also allows to evidence an important aspect: the use of NCs coupled to resonant shunt is potentially able to completely cancel a resonance peak. As an example, the curve related to $\tilde{k}_i = 0.7$ is almost flat up to about 40 Hz. This point will be addressed again in Section 5, where it will be shown that resonance cancellation is actually possible in practical applications.

4.2 The stability of NCs in series and SP

When NCs in either series or SP are used, sometimes the circuit used to build pure NCs (see, as an example, Fig. 4a) cannot be used because of electrical problems like bias currents. This requires the addition in the series NC, and in the NC in series in the SP configuration, of an additional resistance \hat{R} (see Fig. 4b). This additional component in the impedance makes it behave like the parallel of an NC

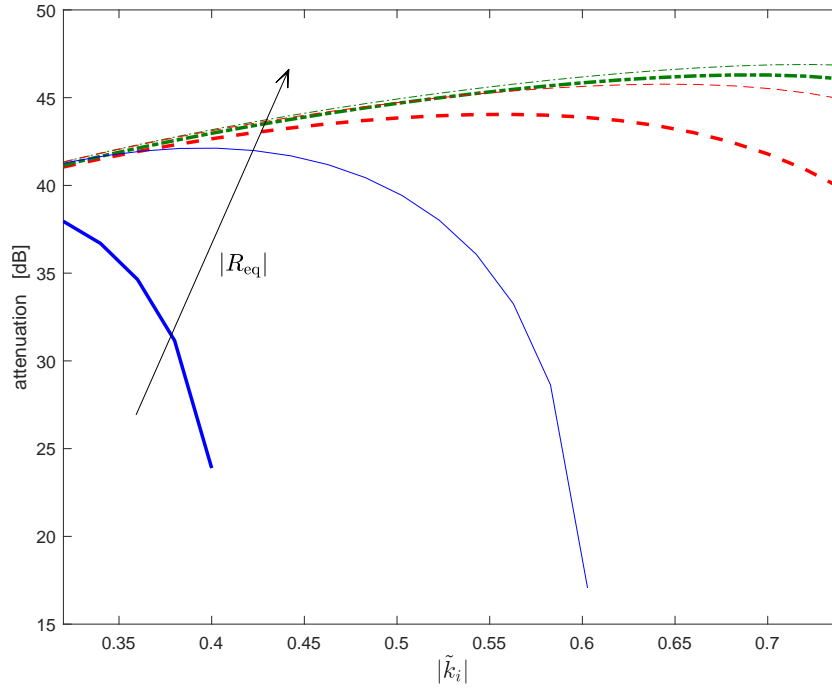


Figure 5: Trend of the attenuation as a function of $|\tilde{k}_i|$ for a system with $\omega_i/(2\pi)=30.5$ Hz, $\xi_i=0.1\%$, $k_i=0.2$ and different values of R_{eq} : -1 M Ω (solid curves), -10 M Ω (dashed curves) and -75 M Ω (dash-dotted curves). Thick lines for a series NC and thin lines for NCs in SP (with $C_1/C_{p_i}=0.5$). The trends of the theoretical A_{dB} curves are not reported because they have negligible differences compared to the curves with $R_{eq}=-75$ M Ω .

and a negative resistance [18]. This negative resistance has an influence on the attenuation performance at low frequency (e.g. below 20 Hz), thus changing the behaviour of the curves in Fig. 2b. However, the major problem caused by this layout is related to the fact that it has destabilising effects on the system [25]. Therefore, the theoretical stability limits do not hold anymore and the value of the NC must be moved away from that of C_{p_i} to guarantee system stability. This implies a worsening of the attenuation performance, even in case the vibration control is performed at high frequency.

There are two ways to prevent such a problem. The main one is the use of a compensation resistance R_s in parallel to the negative resistance (see Fig. 4c). If the values of R_s is chosen so that the total equivalent resistance becomes negative and with a high absolute value (e.g. -75 M Ω), then the problems related to the worsening of the attenuation performance at low frequency and the additional possibility of having system instability tend to disappear. This is because, with such a value of the total equivalent resistance, the electric circuit of Fig. 4c tends to behave like a pure NC.

The other way to overcome the mentioned problems is the use of the SP NC in place of the series NC. Indeed, with the same value of \tilde{k}_i and the same value of the equivalent resistance, the SP shows to be farther from instability than the series NC [19] and the achievable attenuation performance is higher (see Fig. 5, as an example).

5 EXPERIMENTS

This section aims at validating the previous theoretical outcomes by means of an experimental campaign. The set-up was made from a stainless steel cantilever beam (length 18 cm and thickness 1.1 mm) with two piezoelectric patches bonded at the clamped end (on opposite sides of the beam) and electri-

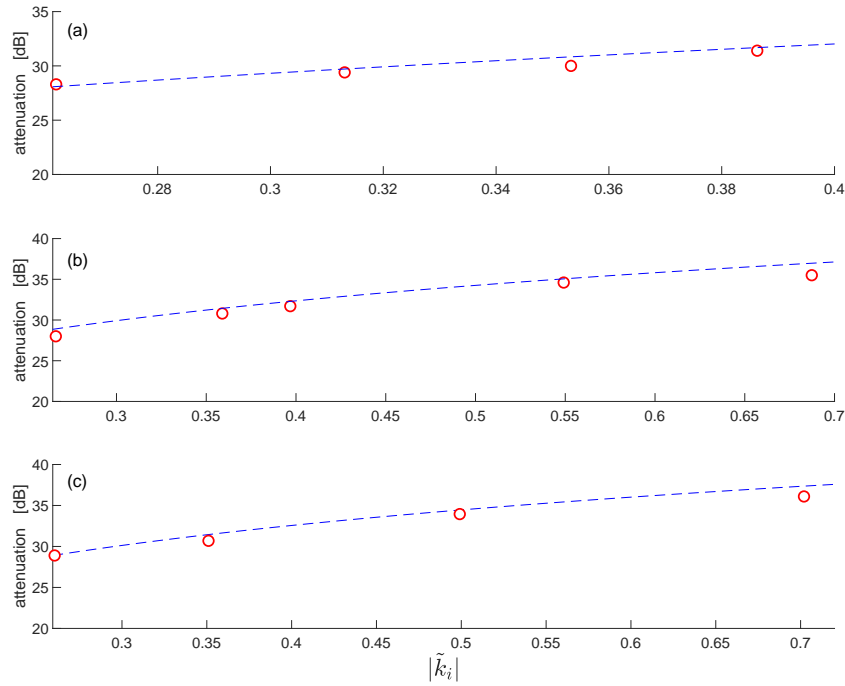


Figure 6: Numerical (dashed curves) and experimental (circles) for an NCs in parallel (a), series (b) and SP (c).

cally connected in series. The excitation to the structure was provided by a contactless electro-magnetic actuator [26] and the structural response was measured by means of a laser velocimeter. The NCs were built with OPA445 OP-AMPs, always supplied with a voltage of $\pm 30V$, as well as the inductance of the shunt due to its high values [27]. The layout used to build the inductance was the Antoniou's circuit [19, 21, 28].

The eigenmode chosen to carry out the tests was the first. Its modal parameters were estimated by means of an experimental modal analysis and their values for all the tests carried out are gathered in Tab. 2.

Table 2: Modal parameters identified experimentally

parameter	Test A	Test B	Test C
$\omega_i/(2\pi)$ [Hz]	34.42	34.45	34.50
ξ_i [%]	0.39	0.36	0.36
k_i	0.2618	0.2662	0.2603

Figure 6 shows the values of the A_{dB} index for NCs in parallel (plot a, test A), series (plot b, test B) and SP (plot c, test C) as a function of the value of $|\tilde{k}_i|$. The highest values of $|\tilde{k}_i|$ tested for the NCs in series and SP were much higher than in the case of the NC in parallel. This is due to the fact that, as mentioned, the parallel NC is used to control high order modes, while here the first mode is accounted for. This implies that it is not possible to achieve high values of $|\tilde{k}_i|$ with an NC in parallel due to stability limits, as demonstrated in [18, 19].

The plots of Fig. 6 show good agreement between theoretical expectations and experimental results.

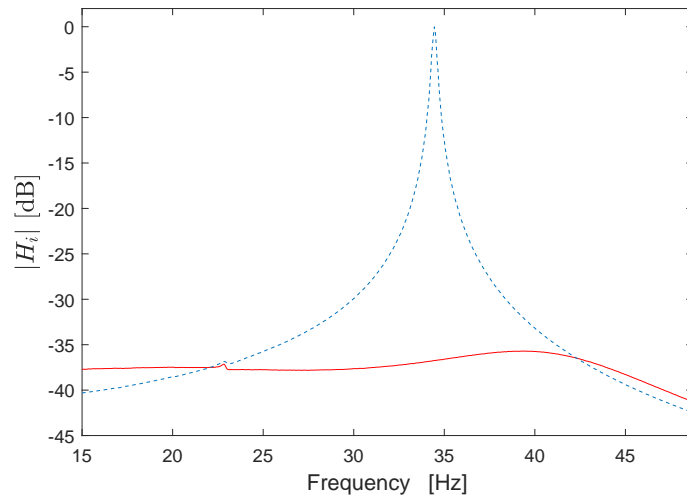


Figure 7: Experimental FRFs for test B: piezoelectric patch in SC without any NCs (dashed line) and shunted (solid line, NC in series, $\tilde{k}_i = 0.69$)

This demonstrates the reliability and the accuracy of the model used. Furthermore, the same plots show that the attenuation achievable by coupling NCs to the classical resonant shunt is very high. More details about the test campaign can be found in [19].

Finally, Fig. 7 shows some experimental FRFs in the case of test B. The main outcome of this figure is that it is actually possible to achieve resonance cancellation, as already mentioned in Section 4.2. Indeed, the curve in the figure related to $\tilde{k}_i=0.69$ is almost flat up to about 40 Hz. This demonstrates the great potentiality of the coupling between resonant shunt and NCs in practical application, because it allows to achieve very high attenuation levels, even allowing for resonance cancellation.

6 CONCLUSIONS

This paper has addressed the use of piezoelectric shunt for attenuating mechanical vibrations. Particularly, the shunt impedance treated in the paper is made from the classical resonant shunt impedance (an inductance and a resistance connected in either series or parallel) coupled to one or two NCs.

Optimisation formulas are provided for all the possible layouts of the shunt impedance. This allows to have general formulations for the tuning of the values of the inductance and the resistance. With these optimisation formulae, it is shown that the attenuation achievable by using this type of suppression approach can be very high. Basically, the attenuation for the optimised shunt is function of the values of the enhanced electro-mechanical coupling coefficient and of the mechanical non-dimensional damping ratio.

Furthermore, the paper shows which practical problems could occur in real applications and provides methods for overcoming them.

The theoretical results have been validated by carrying out experimental tests on a cantilever beam provided of two piezoelectric actuators electrically connected in series. One of the main outcomes of the experiments is that the coupling between resonant shunt and NCs is able to achieve resonance cancellation in real applications, thanks to the very high achievable attenuation levels.

REFERENCES

- [1] R. Darleux, B. Lossouarn, and J.-F. Deü. Passive self-tuning inductor for piezoelectric shunt damping considering temperature variations. *Journal of Sound and Vibration*, 432:105–118, 2018.
- [2] M. Berardengo, S. Manzoni, and A.M. Conti. Multi-mode passive piezoelectric shunt damping by means of matrix inequalities. *Journal of Sound and Vibration*, 405:287–305, 2017.
- [3] J. Høgsberg and S. Krenk. Calibration of piezoelectric shunts with explicit residual mode correction. *Journal of Sound and Vibration*, 386:65–81, 2017.
- [4] P. Soltani, G. Kerschen, G. Tondreau, and A. Deraemaeker. Tuning of a piezoelectric vibration absorber attached to a damped structure. *Journal of Intelligent Material Systems and Structures*, 28(9):1115–1129, 2017.
- [5] K. Yamada, H. Matsuhisa, H. Utsuno, and K. Sawada. Optimum tuning of series and parallel LC circuits for passive vibration suppression using piezoelectric elements. *Journal of Sound and Vibration*, 329(24):5036–5057, 2010.
- [6] G. Caruso. A critical analysis of electric shunt circuits employed in piezoelectric passive vibration damping. *Smart Materials and Structures*, 10(5):1059–1068, 2001.
- [7] N. Hagood and A. von Flotow. Damping of structural vibrations with piezoelectric materials and passive electrical networks. *Journal of Sound and Vibration*, 146:243–268, 1991.
- [8] P. Gardonio and D. Casagrande. Shunted piezoelectric patch vibration absorber on two-dimensional thin structure: tuning considerations. *Journal of Sound and Vibration*, 395:26–47, 2017.
- [9] B. de Marneffe and A. Preumont. Vibration damping with negative capacitance shunts: theory and experiment. *Smart Materials And Structures*, 17(3), 2008. Article ID 035015.
- [10] C. Bricault, C. Pézerat, M. Collet, A. Pyskir, P. Perrard, G. Matten, and V. Romero-Garcia. Multimodal reduction of acoustic radiation of thin plates by using a single piezoelectric patch with a negative capacitance shunt. *Applied Acoustics*, 145:320–327, 2019.
- [11] M. Neubauer, R. Oleskiewicz, K. Popp, and T. Krzyzynski. Optimization of damping and absorbing performance of shunted piezo elements utilizing negative capacitance. *Journal of Sound and Vibration*, 298(1-2):84–107, 2006.
- [12] S. Behrens, A. J. Fleming, and S. O. R. Moheimani. A broadband controller for shunt piezoelectric damping of structural vibration. *Smart Materials and Structures*, 12(1):18–28, 2003.
- [13] C. H. Park and A. Baz. Vibration control of beams with negative capacitive shunting of interdigital electrode piezoceramics. *Journal of Vibration and Control*, 11(3):331–346, 2005.
- [14] M. Berardengo, S. Manzoni, O. Thomas, and C. Giraud-Audine. A new electrical circuit with negative capacitances to enhance resistive shunt damping. In *Proceedings of the ASME 2015 Conference on Smart Materials, Adaptive Structures and Intelligent Systems - SMASIS 2015 - September 21-23, 2015 - Colorado Springs (CO, USA)*, 2015.

- [15] M. Berardengo, O. Thomas, C. Giraud-Audine, and S. Manzoni. Improved shunt damping with two negative capacitances: an efficient alternative to resonant shunt. *Journal of Intelligent Material Systems and Structures*, 28(16):2222–2238, 2017.
- [16] P. Horowitz and W. Hill. *The art of electronics*. Cambridge university press, 2nd. edition, 1989.
- [17] B.S. Beck, K.A. Cunefare, and M. Collet. The power output and efficiency of a negative capacitance shunt for vibration control of a flexural system. *Smart Materials and Structures*, 22, 2013. Article ID 065009.
- [18] M. Berardengo, O. Thomas, C. Giraud-Audine, and S. Manzoni. Improved resistive shunt by means of negative capacitance: new circuit, performances and multi mode control. *Smart Materials and Structures*, 25, 2016. Article ID 075033.
- [19] M. Berardengo, S. Manzoni, O. Thomas, and M. Vanali. Piezoelectric resonant shunt enhancement by negative capacitances: optimisation, performance and resonance cancellation. *Journal of Intelligent Material Systems and Structures*, 29(12):2581–2606, 2018.
- [20] O. Thomas, J.-F. Deü, and J. Ducarne. Vibration of an elastic structure with shunted piezoelectric patches: efficient finite-element formulation and electromechanical coupling coefficients. *International Journal of Numerical Methods in Engineering*, 80(2):235–268, 2009.
- [21] O. Thomas, J. Ducarne, and J.F. Deü. Performance of piezoelectric shunts for vibration reduction. *Smart Materials and Structures*, 21(1), 2012. Article ID 015008.
- [22] J. Ducarne, O. Thomas, and J.F. Deü. Placement and dimension optimization of shunted piezoelectric patches for vibration reduction. *Journal of Sound and Vibration*, 331(14):3286–3303, 2012.
- [23] J.P. den Hartog. *Mechanical Vibrations*. McGraw Hill, 1956.
- [24] K. Liu and J. Liu. The damped dynamic vibration absorbers: revisited and new result. *Journal of Sound and Vibration*, 284:1181–1189, 2005.
- [25] S. Manzoni, S. Moschini, M. Redaelli, and M. Vanali. Vibration attenuation by means of piezoelectric transducer shunted to synthetic negative capacitance. *Journal of Sound and Vibration*, 331:4644–4657, 2012.
- [26] O. Thomas, C. Touzé, and A. Chaigne. Asymmetric non-linear forced vibrations of free-edge circular plates. part ii: experiments. *Journal of Sound and Vibration*, 265(5):1075–1101, 2003.
- [27] C.H. Park and D.J. Inman. Enhanced piezoelectric shunt design. *Shock and Vibration*, 10(2):127–133, 2003.
- [28] L. von Wangeheim. Modification of the classical gic structure and its application to rc-oscillators. *Electronics Letters*, 32(1):6–8, 1996.

THEORETICAL AND EXPERIMENTAL STUDY OF PIEZOELECTRIC NON LINEAR RESONATORS FOR ENERGY HARVESTING AND VIBRATIONS CONTROL

VINCIANE GUILLOT*, ARTHUR GIVOIS[†], MATHIEU COLIN[†], OLIVIER THOMAS[†], ALIREZA TURE SAVADKOOHI* AND CLAUDE-HENRI LAMARQUE*

*Laboratoire de Tribologie et Dynamique des Systèmes (LTDS) UMR CNRS 5513
Université de Lyon, École Nationale des Travaux Publics,
3 rue Maurice Audin 69518 cedex Vaulx-en-Velin, France
e-mail: vinciane.guillot@entpe.fr, alireza.turesavadkoochi@entpe.fr, lamarque@entpe.fr

[†] Laboratoire d'Ingénierie des Systèmes Physiques et Numériques (LISPEN EA 7515)
Arts et Métiers Paristech,
8 boulevard Louis XIV 59000 Lille, France
e-mail: arthur.givois@ensam.eu, mathieu.r.colin@gmail.com, olivier.thomas@ensam.eu

Key words: Piezoelectric materials, Nonlinear Dynamics, Internal Resonance

Abstract. Theoretical and experimental results tracing non linear behaviors of an electro-mechanic beam are presented. Two configurations for the beam are studied: a homogeneous beam with a single piezoelectric patch (the unilateral configuration (1)) and a homogeneous beam with two piezoelectric materials patched symmetrically on each side of the beam (the bilateral configuration (2)). It is shown that by changing the position of the piezoelectric materials, internal resonances 1 : 2 and 1 : 3 between two modes can be achieved for both configurations. Tracing the mode shapes of the composite beams demonstrate their modification due to the presence of the piezoelectric patches. The configurations are supposed to present quadratic and cubic non linearities, when the configuration (1) posses more quadratic non linear terms than configuration (2). This conclusion is made through the theoretical part and experimental results traced for the direct excitation of one mode. Experimental results when the configuration (2) is set in its 1 : 3 internal resonance and excited on its lower mode are presented and an energy transfer toward the upper mode is exhibited.

1 INTRODUCTION

Piezoelectric materials can be used for the aim of control [1] and energy harvesting [2]. Several studies showed the interest of using non linear circuit with those materials to enhance the efficiency of control process by the piezoelectric materials [3, 4, 5, 6].

On the contrary of linear systems, nonlinear systems can present mode coupling(s) and energy exchange(s) between different modes due to internal resonances. This phenomenon can be used for passive control and/or energy harvesting [7]. The creation of internal resonances in non linear systems is influenced by the degree of nonlinearity of the considered system: in systems which present cubic nonlinearities, the internal resonance can happen if we have: $\omega_q \simeq \omega_r$, $\omega_q = 3\omega_r$, $\omega_k \simeq |\pm 2\omega_q \pm \omega_r|$, where

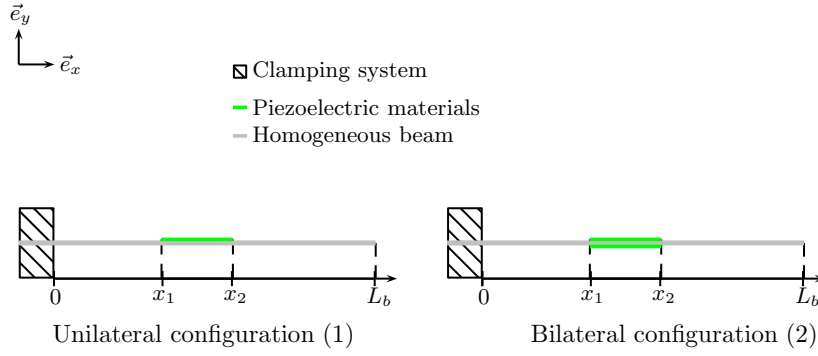


Figure 1: Schemes of the unilateral configuration (1), composed of one piezoelectric material patched on an homogeneous beam, and the bilateral configuration (2) consisting in two piezoelectric materials patched symmetrically on an homogeneous beam. The beam is supposed clamped-free of length L_b , and the piezoelectric materials are patched between the positions $x = x_1$ and $x = x_2$.

ω_i is the i^{th} natural frequency of the system. In systems with quadratic non linearity, besides the above conditions, the internal resonance can emerge if $\omega_q \simeq 2\omega_r$ and $\omega_k \simeq \omega_q \pm \omega_r, \dots$ [8, 9]. When an internal resonance is reached, a strong energy exchange between the modes can happen depending on the non-linear coefficients of the system.

The aim of this work is to use the energy exchanges between modes of a multi-physics system (an homogeneous beam and piezoelectric materials), due to internal resonances, for control and/or energy harvesting. For our study two configurations of beam with piezoelectric materials are studied: a configuration with only one piezoelectric material patch on an homogeneous beam, called as the unilateral configuration (1), the other one is named the bilateral configuration (2), it consists of two piezoelectric materials placed symmetrically on each side of the beam, as seen in Fig.1. While both configurations present cubic and quadratic non linearities, the effect of quadratic terms in configuration (1) is more evident compare to the configuration (2). From the theoretical developments it is deduced that the position of the piezoelectric patches on the beam can be used to create internal resonances between modes[10]. For example, internal resonances 1 : 2 and 1 : 3 can be achieved as: $\omega_3 \simeq 3\omega_2$ and $\omega_3 \simeq 2\omega_4$. The focus of this paper is studying the 1 : 3 internal resonance happening between the second and the third mode. The paper is structured as it follows: theoretical developments are presented in Section 2. In detail, after presenting governing system equations, spatio-temporal variables of the system are separated leading to detection of frequency and mode shapes of the composite beams. Then governing system equations are projected on: (i) one mode when the system doesn't have any internal resonances and (ii) two modes presenting an internal resonance 1 : 3, and are treated via a multiple scale method. In Section 3 experimental results are provided: First, natural frequencies and mode shapes are detected and compared with the theoretical results. Then results of two cases are presented and commented, (i) a single mode excitation traced via a Phase-Locked-Loop (PLL) [11] method and (ii) we set the bilateral configuration in its 1 : 3 internal resonance, and we detect the equilibrium points through a synchronous detection method.

2 THEORETICAL DEVELOPMENTS FOR THE DIFFERENT CONFIGURATIONS

Let us denote by $v(x, t)$ the displacement in the \vec{e}_y direction as seen in Fig.1. The piezoelectric materials (PIC151) are supposed to be polarized in the \vec{e}_y direction and they are positioned between $x = x_1$ and $x = x_2$. Then their free electrical enthalpy $H(\epsilon, E)$, with ϵ_{xx} and E_y the strain and the electrical

field in the direction \vec{e}_x and \vec{e}_y respectively, is expanded until the order 3 [10, 12] in its variables as:

$$H(\epsilon_{xx}, E_y) = \frac{s_{11}}{2}\epsilon_{xx} + d_{31}\epsilon_{xx}E_y + \xi_{33}\frac{E_y^2}{2} + r_{331}\epsilon_{xx}E_y^2 + d_{311}\epsilon_{xx}^2E_y + \xi_{333}\frac{E_y^3}{3} + \frac{s_{111}}{3}\epsilon_{xx}^3 \quad (1)$$

where s_{11} , d_{31} , ... are some constants coming from the piezoelectric materials non linear behavior. Then, the electro-mechanical equations of the 2-dimensional multi-physics system can be written as [10]:

$$\begin{aligned} \mu(x)\ddot{v} + c_v\dot{v} - Q_v = EI(x)[-v^{(iv)} - (v'(v'v''))'] + [v' \int_x^{L_b} (-\mu(x)/2) [\int_x^0 v'^2 dx] dx]' \quad (2) \\ + \int_{\frac{h_b}{2}}^{\frac{h_b}{2}+h_p} \int_{-\frac{b_p}{2}}^{\frac{b_p}{2}} \left[\left((\mathcal{H}(x_1) - \mathcal{H}(x_2))v''^2 + 2(\delta(x_1) - \delta(x_2))2v''v''' + (\delta'(x_1) - \delta'(x_2))v''^2 \right) y^3 s_{111} \right. \\ \left. + \left((\mathcal{H}(x_1) - \mathcal{H}(x_2))v^{(iv)} + 2(\delta(x_1) - \delta(x_2))v''' + (\delta'(x_1) - \delta'(x_2))v'' \right) \frac{2d_{311}}{h_p} y^2 V + \right. \\ \left. + (\delta'(x_1) - \delta'(x_2)) \left(\frac{-d_{31}}{h_p} yV + \frac{r_{331}}{h_p^2} yV^2 \right) \right] dydz \\ Q = \int_{x_1}^{x_2} \int_{-\frac{b_p}{2}}^{\frac{b_p}{2}} (d_{31}yv'' - \xi_{33}E_y + 2r_{331}yE_y - 2d_{311}y^3v''^2 - \xi_{333}E_y^2) dx dz \end{aligned}$$

when \cdot and $'$ stand for time and space derivations of a variable respectively, and c_v is the damping of the system, \mathcal{H} and δ are the Heaviside and Dirac functions and s_{111} is a nonlinear piezoelectric coefficients [12, 13], taking into account a nonlinear stiffness behavior of the piezoelectric materials, and:

$$\mu(x) = \begin{cases} \mu_1(x) = \mu_b & x \in [0, x_1[U, x_2, L_b] \\ \mu_2(x) = \mu_b + \chi \mu_p & x \in [x_1, x_2] \end{cases} \quad (3)$$

where μ_b and μ_p are the mass densities of the beam and the piezoelectric materials respectively, and $\chi = 1$ or 2 depending if the unilateral or bilateral configuration is considered, and:

$$EI(x) = \begin{cases} EI_1(x) = E_b \frac{b_b h_b^3}{12} & x \in [0, x_1[U, x_2, L_b] \\ EI_2(x) = E_b \frac{b_b h_b^3}{12} + \chi E_p \frac{b_p h_p^3}{12} & x \in [x_1, x_2] \end{cases} \quad (4)$$

E_b , b_b , h_b and E_p , b_p , h_p are the Young modulus, the width and the thickness of the beam and the piezoelectric materials respectively.

2.1 Treatment of spatial system equations

A separation of the spatio-temporal variables of the displacement $v(x, t)$ is done, as it follows:

$$v(x, t) = \phi(x)r(t) \quad (5)$$

To detect the natural frequencies of the system, the linear part in time of Eq. (2) is taken:

$$\mu(x)\ddot{r}(t)\phi(x) = EI(x)r(t)\phi^{(iv)}(x) \quad (6)$$

$\mu(x)$ and $EI(x)$ are defined by parts as seen in Eqs.(3) and (4), because of the position of the piezoelectric materials, this is why the mode functions $\phi(x)$ are written as:

$$\phi(x) = (1 - \mathcal{H}(x_1))\phi_1(x) + (\mathcal{H}(x_1) - \mathcal{H}(x_2))\phi_2(x) + \mathcal{H}(x_2)\phi_3(x) \quad (7)$$

Then the following differential equations arise:

$$\begin{aligned} \mu_1(x)\phi_1(x) &= EI_1(x)\phi_1^{(iv)}(x) \quad \text{with } x \in [0, x_1[\\ \mu_2(x)\phi_2(x) &= EI_2(x)\phi_2^{(iv)}(x) \quad \text{with } x \in [x_1, x_2] \\ \mu_1(x)\phi_3(x) &= EI_1(x)\phi_3^{(iv)}(x) \quad \text{with } x \in]x_2, L_b] \end{aligned} \quad (8)$$

where:

$$\phi_j(x) = A_j \cos(K_j x) + B_j \sin(K_j x) + C_j \cosh(K_j x) + D_j \sinh(K_j x) \quad (9)$$

with $j = 1, 2$ and 3 .

The beam is supposed to be clamped-free, as seen in Fig. 1. Moreover, since piezoelectric materials are fully patched on the beam, one should impose continuity conditions on the system modes at $x = x_1$ and $x = x_2$.

Those conditions allow us to access a critical equation to find the natural frequencies and the mode functions of both configurations of the multi-physics system [14, 5, 10].

2.2 Treatments of temporal system equations

From the section 2.1, the mode functions of the system are found. To solve the problem in time, Eq. (2) is projected on the mode(s) of interest(s), and the following equations in time are solved with a Multiple Scale method [9]. Two different cases are considered: (i) we suppose that only one mode is excited by the external excitation, (ii) we suppose that two modes are in a 1 : 3 internal resonance and the lower one is directly excited by the external excitation.

2.2.1 Case (i): a single mode excitation

For the case (i), let us suppose the d^{th} mode is directly excited, this way $v(x, t)$ is expanded as:

$$v(x, t) = \phi_d(x)r_d(t) \quad (10)$$

Eq.(2) projected on the mode d^{th} can be written as:

$$\begin{aligned} 0 &= T_0 \ddot{r}_d + T_1 \dot{r}_d + T_2 \Omega^2 \cos(\Omega t) + T_3 r_d + T_4 r_d^3 + T_5 r_d \overbrace{r_d^2}^{..} + T_6 r_d^2 + T_7 r_d V + T_8 V + T_9 V^2 \\ 0 &= S_1 r_d + S_2 V + S_3 r_d V + S_4 r_d^2 + S_5 V^2 \end{aligned} \quad (11)$$

$T_0, T_1, \dots, T_9, S_1, \dots$ and S_5 are some constants coming from the projection on the d^{th} mode and Ω is the frequency of the external excitation. It should be noted that for the configuration (2), $T_6 = T_9 = 0$, removing most of the quadratic non linear terms for this configuration.

The Multiple Scale hypothesis are written as follow:

$$\begin{aligned} T_1 &= T_2 = T_4 = T_5 = T_6 = T_7 = T_8 = T_9 = O(\epsilon) \\ r_d &= r_{d0} + r_{d1}\epsilon + r_{d2}\epsilon^2 \\ V &= V_0 + V_1\epsilon + V_2\epsilon^2 n \\ \Omega &= \omega_d + \epsilon\sigma \\ \frac{\partial}{\partial t} &= D_0 + \epsilon D_1 + \epsilon^2 D_2 \end{aligned} \quad (12)$$

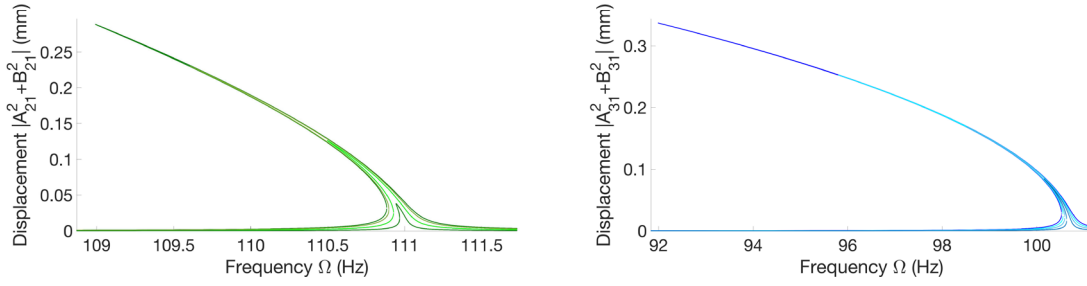


Figure 2: Theoretical curves for the second mode of $|A_{21}^2 + B_{21}^2|$ from the Cardano equation for both configurations: unilateral (1) (in green, on the left) and bilateral (2) (in blue, on the right). Nonlinear piezoelectric coefficients are taken from [15].

with σ a detuning parameter and ω_d the d^{th} frequency of the multi-physics system.

We then suppose that r_{d0} is expanded as:

$$r_{d0} = A_d + A_{d1} \cos(\Omega t) + B_{d1} \sin(\Omega t) \quad (13)$$

Studying system equations until $O(\varepsilon)$, a Cardano equation in $A_{d1}^2 + B_{d1}^2$ is obtained that can be solved and shows a Duffing behavior, and the quadratic nonlinear terms only allow to go from softening to hardening behavior [10] if those are high enough. Theoretical curves for both configurations are traced for the second mode in Fig. 2, nonlinear piezoelectric coefficients are taken arbitrarily from [15]. For the configuration (1), the effects of the quadratic non linear terms are not activated yet, but, [16, 17] show that the quadratic terms can be responsible for a change of curvature.

2.2.2 Case (ii): two modes in a 1 : 3 internal resonance with the lower one directly excited

For this problem, we suppose the n^{th} and the m^{th} modes to be in a 1 : 3 internal resonance ($\omega_m = 3\omega_n$), thus we suppose $v(x, t)$ expanded as:

$$v(x, t) = \phi_n(x)r_n(t) + \phi_m(x)r_m(t) \quad (14)$$

Projecting Eq. (2) on the n^{th} and the m^{th} modes, the following equations are found:

$$\begin{aligned} 0 = & N_0 \ddot{r}_n + N_1 \dot{r}_n + N_2 \Omega_2^2 \cos(\Omega_2 t) + N_3 r_n + N_4 r_n^3 + N_5 r_n^2 r_m + N_6 r_n r_m^2 + N_7 r_m^3 + N_8 r_n \overbrace{r_n^2}^{..} \\ & + N_9 r_n \overbrace{r_m^2}^{..} + N_{10} r_n \overbrace{r_n r_m}^{..} + N_{11} r_m \overbrace{r_n^2}^{..} + N_{12} r_m \overbrace{r_m^2}^{..} + N_{13} r_m \overbrace{r_n r_m}^{..} + N_{14} r_n^2 + N_{15} r_n r_m + N_{16} r_m^2 \\ & + N_{17} r_n V + N_{18} r_m V + N_{19} V + N_{20} V^2 \\ 0 = & M_0 \ddot{r}_m + M_1 \dot{r}_m + M_2 \Omega_2^2 \cos(\Omega_2 t) + M_3 r_m + M_4 r_n^3 + M_5 r_n^2 r_m + M_6 r_n r_m^2 + M_7 r_m^3 + M_8 r_n \overbrace{r_n^2}^{..} \\ & + M_9 r_n \overbrace{r_m^2}^{..} + M_{10} r_n \overbrace{r_n r_m}^{..} + M_{11} r_m \overbrace{r_n^2}^{..} + M_{12} r_m \overbrace{r_m^2}^{..} + M_{13} r_m \overbrace{r_n r_m}^{..} + M_{14} r_n^2 + M_{15} r_n r_m + M_{16} r_m^2 \\ & + M_{17} r_n V + M_{18} r_m V + M_{19} V + M_{20} V^2 \\ 0 = & L_1 V + L_2 r_n + L_3 r_m + L_4 V^2 + L_5 r_n^2 + L_6 r_m^2 + L_7 r_n r_m + L_8 r_n V + L_9 r_m V \end{aligned} \quad (15)$$

where $N_0, N_1, \dots, N_{16}, M_0, M_1, \dots, M_{16}$ and L_1, \dots, L_9 constants from the projection on the n^{th} and m^{th} modes respectively and Ω_2 is the frequency of the external excitation.

The hypothesis made for the Multiple Scale method are as follow:

$$N_1 = \varepsilon^2 N_{1p} \quad (16)$$

$$N_2 = \varepsilon^3 N_{2p}$$

$$M_1 = \varepsilon^2 M_{1p}$$

$$M_2 = \varepsilon^3 M_{2p}$$

$$N_{19} = \varepsilon N_{19p}$$

$$M_{19} = \varepsilon M_{19p}$$

$$r_n = r_{n1}\varepsilon + r_{n2}\varepsilon^2 + r_{n3}\varepsilon^3$$

$$r_m = r_{m1}\varepsilon + r_{m2}\varepsilon^2 + r_{m3}\varepsilon^3$$

$$\Omega_2 = \omega_n + \varepsilon^2 \sigma_2$$

$$\omega_m = 3\omega_n + \varepsilon^2 \sigma_3$$

$$\frac{\partial}{\partial t} = D_0 + \varepsilon D_1 + \varepsilon^2 D_2 \quad (17)$$

where σ_2 and σ_3 are detuning parameters.

We suppose r_{n1} and r_{m1} are expanded as:

$$r_{n1} = A_{n1} \cos(\Omega_2 t) + B_{n1} \sin(\Omega_2 t) \quad (18)$$

$$r_{m1} = A_{m3} \cos(3\Omega_2 t) + B_{m3} \sin(3\Omega_2 t) \quad (19)$$

At $O(\varepsilon^3)$, the solvability condition gives the following system of coupled equations:

$$0 = F_1(A_{n1}, B_{n1}, A_{m3}, B_{m3}) \quad (20)$$

$$0 = F_2(A_{n1}, B_{n1}, A_{m3}, B_{m3})$$

$$0 = F_3(A_{n1}, B_{n1}, A_{m3}, B_{m3})$$

$$0 = F_4(A_{n1}, B_{n1}, A_{m3}, B_{m3}) \quad (21)$$

This way, the amplitudes of r_{n1} and r_{m1} are coupled, meaning that although the n^{th} mode is directly excited, the m^{th} mode respond as well due to the mode coupling. From [10], supposing the piezoelectric materials linked to a resistor and an internal resonance 1 : 3 between the second and the third mode, we have Fig. 3, it shows that the first harmonic of the second mode and the third harmonic of the third mode are the ones responding as expected from the hypothesis Eq. (19). We can see that $|A_{21}^2 + B_{21}^2| \simeq 10|A_{33}^2 + B_{33}^2|$, showing that the nonlinear coefficients are not large enough to have a real exchange of energy between the modes.

3 EXPERIMENTAL RESULTS FOR BOTH CONFIGURATIONS

For the experimental set up, the multi-physics beams are fixed through a clamping system that is screwed on a shaker. The shaker is excited via an amplifier. An accelerometer is glued on the clamping system allowing us to monitor the input excitation given to the structure. Then, the velocity of a given

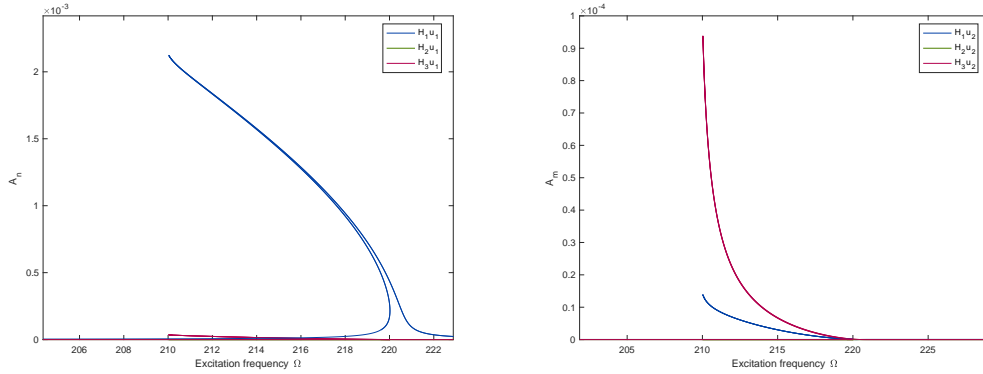


Figure 3: Theoretical curve for a problem with coupled modes and a electrical circuit solved with Manlab for r_n and r_m with three harmonics.

point of the structure is detected by a laser vibrometer. The software used allows us to find the different natural frequencies of the configuration and also to trace the modal deformations. A Phase-Locked-Loop (PLL) method [11] is also used, exciting one mode of the structure. Finally, a synchronous detection is performed on configuration (2) when set to present a 1 : 3 internal resonance between its second and third natural frequencies.

3.1 Experimentally results detected: frequencies and modal deformations

First, the Young Modulus E_b of the homogeneous beam is fixed thanks to a scaling between its theoretical and experimental frequencies. On both considered configurations, the piezoelectric materials are patched at a fixed position from the free end of the beam as $\Delta = L_b - x_2$ and their length is $x_2 - x_1 = 0.05 \text{ m}$. For the unilateral configuration (1), Δ is set equal to 0.06 m , as for the bilateral configuration (2), we have $\Delta = 0.07 \text{ m}$.

From the mechanical properties of the homogeneous beam and the piezoelectric materials (PIC151), detailed in Table 1 and 2, and knowing x_1 and x_2 for both configurations, theoretically and experimentally obtained frequencies of the fourth mode are compared in Fig. 4, for different length of the beam L_b . In Figs. 4 and 5, it is seen that experimental results are in a reasonable agreements with the theoretical ones.

Table 1: Mechanical properties of the homogeneous beam

$\mu_b \text{ (kg.m}^{-3}\text{)}$	$E_b \text{ (Pa)}$	$h_b \text{ (m)}$	$b_b \text{ (m)}$
7.8104×10^3	1.78881×10^{11}	0.5×10^{-3}	13×10^{-3}

Furthermore, the experiments showed that a 1 : 2 and 1 : 3 internal resonances can be created between the third and fourth modes and the second and third modes respectively, for a special length of the beam L_b . Figure 5 shows that mechanical (stiffness and mass addition) of the piezoelectric materials have an effect on the modal deformation, it also confirms that the function is different from the one of the beam only.

As a summary, the hypothesis that the modal deformation are modified by the presence of the piezoelec-

Table 2: Mechanical properties of the piezoelectric materials PIC151

$\mu_p \text{ (kg.m}^{-3}\text{)}$	$E_p \text{ (Pa)}$	$h_p \text{ (m)}$	$b_p \text{ (m)}$
8.5×10^3	66.7×10^9	0.5×10^{-3}	10×10^{-3}

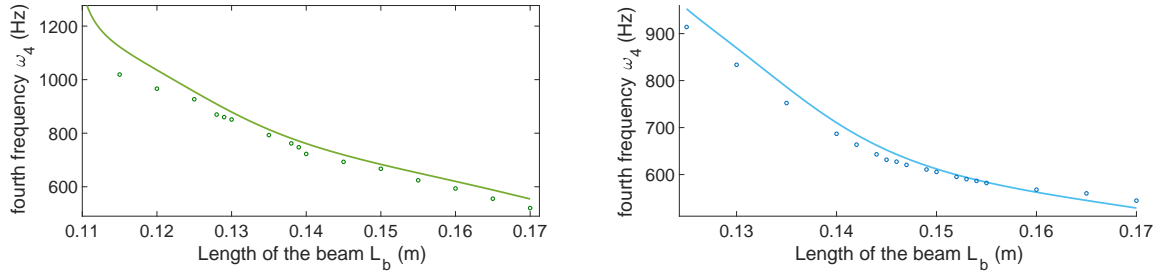


Figure 4: Theoretical (continuous line) and experimental (o) points where obtained for the fourth natural frequency of the unilateral configuration (1) (in green, on the left) and the bilateral configuration (2) (in blue, on the right) respectively, for different values of the length of the beam L_b .

tric patches and should be written by parts accordingly, is confirmed experimentally. Moreover, it is seen that the piezoelectric materials positions can help the creation of internal resonances.

3.2 Experimentally detected forced responses of the system

Two methods are used to study the behavior of the system excited around some of its natural frequencies by the shaker.

The first method is the PLL method [11]. For this method, the phase between the excitation and the vibration of the system is set to stay constant equal to 0 or $-\Pi$, depending on where the vibrometer laser is pointed on the structure. Then, starting around one of the natural frequency of the system, the forcing is gradually increased while the system keeps the difference of phase at 0 or $-\Pi$.

As for the synchronous detection, a loop is made to control the intensity given at the shaker in order to have the same excitation while a sweep in frequency is performed around a natural frequency of the system. For this excitation, the configuration (2) is set at a disposition where a 1 : 3 internal resonance is created between the second and third mode.

3.2.1 Single mode excitation, the Phase-Locked-Loop method

The PLL method is used to have the results for both configurations, at $L_b = 0.17$, assuring the configuration's natural frequencies are not in any internal resonances disposition.

It can be seen from Fig. 6, that for the unilateral configuration, there is a change of curvature that is not seen for the bilateral configuration. This can be explained by the presence of quadratic nonlinear terms in the unilateral configuration, that are less important for the bilateral configuration [16, 18], as it is supposed in the theoretical model, since $T_6 = T_9 = 0$ for the bilateral configuration in Eq. (12) removing most of the quadratic non linear terms.

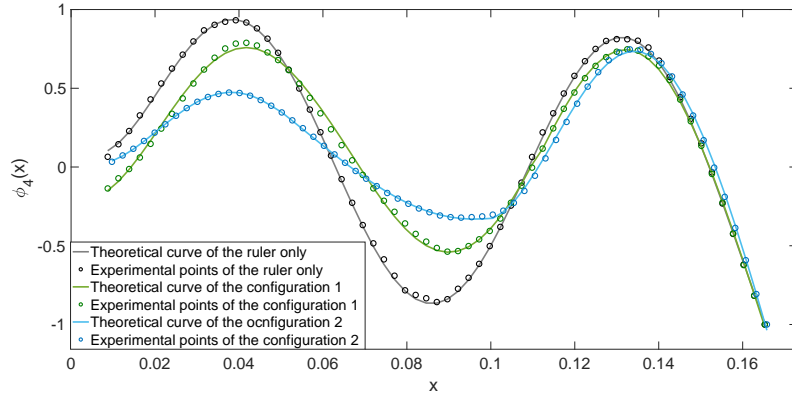


Figure 5: Experimental points (o) and theoretical curves (-) of the modal deformations of the fourth mode are presented for different configurations at $L_b = 0.17$. In black is the modal deformation of the homogenous beam, in green the one of the unilateral configuration (1) and in blue the one of the bilateral configuration (2).

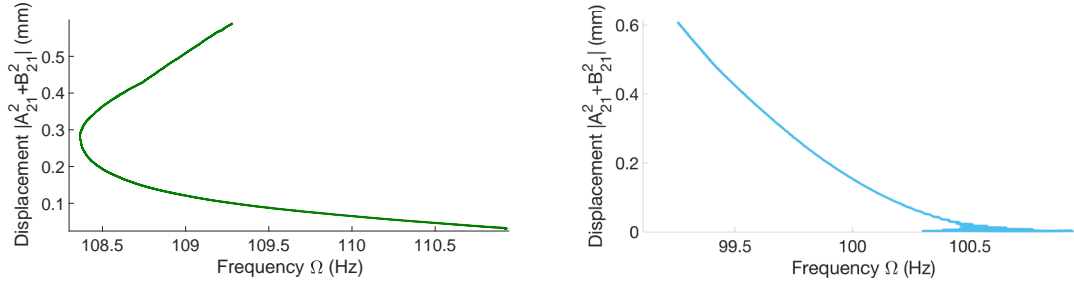


Figure 6: Forced response curves obtained via the PLL started around the second natural frequency of each configuration, the unilateral (in green, on the left) and the bilateral (in blue, on the right), respectively.

3.2.2 The 1 : 3 internal resonance with the lower mode excited, using a synchronous detection method

Here the second and the third mode are supposed to be in a 1 : 3 internal resonance, thus, from Eq. (17), $v(x, t)$ is expanded as:

$$v(x, t) = \phi_2(x)r_2(t) + \phi_3(x)r_3(t) \quad (22)$$

$$(23)$$

We develop $r_2(t)$ and $r_3(t)$ in Fourier Series of Ω_2 the frequency of excitation, as:

$$r_2(t) = \sum_{s=1}^{\infty} (A_{2s} \cos(s\Omega_2 t) + B_{2s} \sin(s\Omega_2 t)) \quad (24)$$

$$r_3(t) = \sum_{s=1}^{\infty} (A_{3s} \cos(s\Omega_2 t) + B_{3s} \sin(s\Omega_2 t))$$

Experimentally, we set the configuration (2) at a length $L_b = 0.12$ m allowing a resonance 1 : 3 between the second and the third mode. To compare the results of the experiment with what was expected from

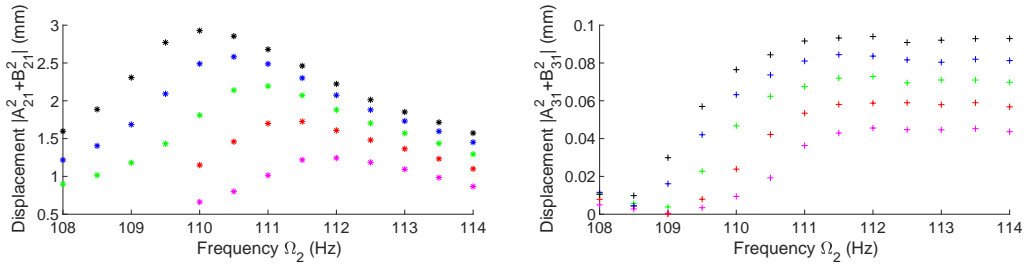


Figure 7: Experimental points of the synchronous detection method around the second natural frequency of the bilateral configuration at $L_b = 0.12\text{ m}$, allowing a $1 : 3$ internal resonance between the second and the third mode. The experimental points (*) of the first harmonic of the second mode at $x = x_{f3}$, are traced for different amplitude of excitation of the system, on the left. The experimental points (+) of the first harmonic of the third mode (at $x = x_{f2}$), are traced for the same different amplitude of excitation of the system, on the right.

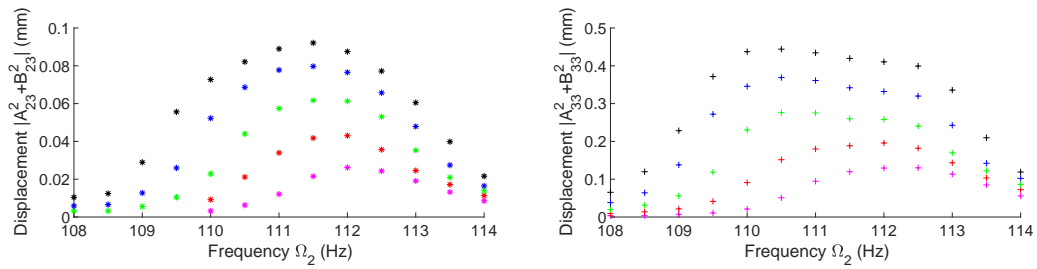


Figure 8: Experimental points of the synchronous detection method around the second natural frequency of the bilateral configuration at $L_b = 0.12\text{ m}$, allowing a $1 : 3$ internal resonance between the second and the third mode. The experimental points (*) of the third harmonic of the second mode (at $x = x_{f3}$), are traced for different amplitude of excitation of the system, on the left. The experimental points (+) of the third harmonic of the third mode (at $x = x_{f2}$), are traced for the same different amplitude of excitation of the system, on the right.

the Multiple Scale Method, the experiments are conducted at two different points on the system: $x = x_{f2}$ a node of the second mode and $x = x_{f3}$ a node of the third mode. This way, it can be written:

$$\text{At } x = x_{f2} \quad v(x = x_{f2}, t) \simeq \sum_{s=1}^{\infty} (A_{3s} \cos(s\Omega_2 t) + B_{3s} \sin(s\Omega_2 t)) \quad (25)$$

$$\text{At } x = x_{f3} \quad v(x = x_{f3}, t) \simeq \sum_{s=1}^{\infty} (A_{2s} \cos(s\Omega_2 t) + B_{2s} \sin(s\Omega_2 t)) \quad (26)$$

Thus, at $x = x_{f2}$ we trace the third harmonic of the response which correspond to $|A_{33}^2 + B_{33}^2|$ from the Multiple Scale comparison, and at $x = x_{f3}$ the first harmonic of the response which relates to $|A_{21}^2 + B_{21}^2|$. In Fig. 7, we trace the first harmonic of the second (at $x = x_{f3}$) and third mode (at $x = x_{f2}$) and in Fig. 8, we trace the third harmonic of the second (at $x = x_{f3}$) and third mode (at $x = x_{f2}$), respectively for the bilateral configuration. Figures 7 and 8 shows that $|A_{33}^2 + B_{33}^2| > |A_{31}^2 + B_{31}^2|$ and $|A_{21}^2 + B_{21}^2| > |A_{23}^2 + B_{23}^2|$ confirming the hypothesis from Eq. (17) that the first harmonic of the second mode and the third harmonic of the third mode are the one that are mainly responding. We also have $|A_{21}^2 + B_{21}^2| \simeq 6 \times |A_{33}^2 + B_{33}^2|$, this confirms the behavior from Fig. 3. Thus, we confirmed that the $1 : 3$ internal resonance is activated but there is no extreme exchange of energy between the modes. This assumption could be verified by trying to see which of the theoretical equations found from the Multiple

Scale method, with one mode excited or two modes in a 1 : 3 internal resonance is the best fit with the experimental results.

4 CONCLUSIONS

Experimental and theoretical results of dynamics and modal interactions of a multi-physics system, an homogeneous beam with piezoelectric materials, are presented. Two configurations are considered: the configuration (1) consists of an homogeneous beam with a single piezoelectric patch, and the configuration (2) has two piezoelectric materials patched symmetrically on the beam.

After separation of spatio-temporal variables of governing system equations, the equations in space provided natural frequencies and mode shapes of the system showing possibilities of 1 : 2 and 1 : 3 internal resonances, corresponding to $\omega_4 \simeq 2\omega_3$ and $\omega_3 \simeq 3\omega_2$ for both configurations ((1) and (2)) as investigated in experimental tests. As for the modal deformations, experimental results confirmed that the presence of the piezoelectric materials changes the mode shapes, and that the theoretical formulation of the functions expressed by parts for each segment of the beam, coupled to each other via continuity conditions are relevant.

As for the effects of the coefficients of the piezoelectric material, it is shown that non linear coefficients are responsible of the quadratic terms in the unilateral configuration, that decreased for the bilateral configuration, from the theoretical part. Tracing the responses of both configurations excited on one of their mode, a change of curvature in the frequency response curve is observed for the unilateral configuration, due to the quadratic non linear terms confirming their presence for configuration (1) and their almost absence for configuration (2).

Investigating the internal resonance 1 : 3, the bilateral configuration set on its resonance showed that although the lower mode is excited, the higher mode is also responding. Thus, the non linear coupling of those modes exist and is expressed.

To conclude, this paper highlighted that the presence of the piezoelectric materials on the beam play an important role on the creation of internal resonances and energy exchanges between modes. Meanwhile, in our experimental studies, the non linear coefficients of the piezoelectric material weren't sufficient to create visible energy exchanges between the modes. Thus, the experiments will be used to re-scale the theoretical model. Then, the model will be studied to enhance the non linear terms and design the exchange of energy between the modes.

REFERENCES

- [1] Soltani, P. and Kerschen, G. The Nonlinear Piezoelectric Tuned Vibration Absorber. *Journal of Smart Materials and Structures*. (2015) **24**(7).
- [2] Mam, K., Peigney, M. and Siegert, D. Finite strain effects in piezoelectric energy harvesters under direct and parametric excitations. *Journal of Sound and Vibration*. (2017) **389**:411–437.
- [3] Silva, T.M., Clementino, M.A., De Marqui, C. and Erturk, A. An experimentally validated piezoelectric nonlinear energy sink for wideband vibration attenuation. *Journal of Sound and Vibration*. (2018) **437**:68–78.
- [4] Lallart, M. Nonlinear technique and self-powered circuit for efficient piezoelectric energy harvesting under unloaded cases. *Energy Conversion and Management*. (2017) **133**:444–457.
- [5] Ducarne, J., Thomas, O. and Deü, J.-F. Placement and dimension optimization of shunted piezoelectric patches for vibration reduction. *Journal of Sound and Vibration*. (2012) **221**:3286–3303.

- [6] Badel, A., Sebald, G., Guyomar, D., Lallart, M., Lefeuvre, E., Richard, C. and Qiu, J. Piezoelectric Vibration Control by Synchronized Switching on Adaptive Voltage Sources: Towards Wide Band Semi-Active Damping. *The Journal of the Acoustical Society of America*. (2006) **119**:2815–2825.
- [7] Mook, D.T., Plaut, R.H. and HaQuang N. The influence of an internal resonance on non-linear structural vibrations under subharmonic resonance conditions. *Journal of Sound and Vibrations*. (1985) **102**:473–492.
- [8] Nayfeh, A.H. and Balachandran, B. Modal Interactions in dynamical and structural systems. *Applied Mechanics Review*. (1989) **42**:175–201.
- [9] Nayfeh, A.H. and Mook, D.T. *Nonlinear Oscillations*. Wiley-VCH (1995).
- [10] Guillot, V., Ture Savadkoohi, A. and Lamarque, C.-H. Analysis of a reduced order nonlinear model of a multi-physics beam. *Nonlinear Dynamics*. Submitted (2019).
- [11] Denis, V., Jossic, M., Giraud-Audine, C., Chomette, B., Renault, A. and Thomas, O. Identification of nonlinear modes phase-locked-loop experimental continuation and normal form. *Mechanical Systems and Signal Processing*. (2018) **106**:430–452.
- [12] Abdelkefi, A., Nayfeh, A.H. and Hajj, M.R. Global nonlinear distributed-parameter model of parametrically excited piezoelectric energy harvesters. *Nonlinear Dynamics*. (2012) **67**:1147–1160.
- [13] Samal, M.K., Seshu, P., Parashar, S.K., Von Wagner, U., Hagedorn, P., Dutta, B.K. and Kyshwaha, H.S. Nonlinear behaviour of piezoceramics under weak electric fields. Part-II: Numerical results and validation with experiments. (2006) **43**:1437–1458.
- [14] Maurini, C., Porfiri, M. and Pouget, J. Numerical methods for modal analysis of stepped piezoelectric beams. *Journal of Sound and Vibration*. (2006) **298**:918–933.
- [15] Abdelkefi, A. Global nonlinear analysis of piezoelectric energy harvesting from ambient and aeroelastic vibrations. Blacksburg, Virginia. (2012).
- [16] Kovacic, I. and Brennan, M. J. *The Duffing Equation: Nonlinear Oscillators and their behaviour*. John Wiley and Sons (2011).
- [17] Alamo Vargas, V., Gourdon, E. and Ture Savadkoohi, A. Nonlinear softening and hardening behavior in Helmholtz resonators for nonlinear regimes. *Nonlinear Dynamics*. (2018) **91**:217–231.
- [18] Shivashankar, P. and Kandagal, S.B. Characterization of elastic and electromechanical nonlinearities in piezoceramic plate actuators from vibrations of a piezoelectric-beam. *Mechanical Systems and Signal Processing*. (2019) **116**:624–640.

VIBRATION CONTROL OF SMART COMPOSITE PLATES USING SHUNTED PIEZOELECTRIC ELEMENTS

GEORGIOS K. TAIRIDIS^{*}, KONSTANTINOS MARAKAKIS^{*}, PANAGIOTIS KOUTSIANITIS^{*}, GEORGIA FOUTSITZI[†], JEAN-FRANÇOIS DEÜ[‡], GEORGIOS E. STAVROULAKIS^{*} AND ROGER OHAYON[‡]

^{*} Computational Mechanics and Optimization (CoMecO)
School of Production Engineering and Management
Technical University of Crete

University Campus, GR-73100 Chania, Greece

e-mail: tairidis@gmail.com, gestavr@dpem.tuc.gr, web page: <http://www.comeco.tuc.gr>

[†] Department of Informatics & Telecommunications
University of Ioannina
Kostakioi, GR-47100, Arta, Greece
e-mail: gfouts@uoi.gr

[‡] Structural Mechanics and Coupled System Laboratory (LMSSC)
Conservatoire National des Arts et Métiers,
2 Rue Conté, FR-75003 Paris, France

e-mail: jean-francois.deu@cnam.fr, roger.ohayon@cnam.fr, web page: <http://www.lmsc.cnam.fr>

Key words: Vibrations, Smart Structures, Piezoelectrics, Shunt Circuits.

Abstract. Smart structures, in general, have the ability to respond and reduce vibrations which are caused by external forces. The self-monitoring capability of smart structures is due to the properties of the involved materials, such as piezoelectric sensors or actuators. Passive damping of vibrations using shunted piezoelectric elements is quite common for structures such as beams, plates, smart panels, etc. In fact, shunted piezoelectric circuits can consume the kinetic energy of the controlled system by transferring it to a suitably defined electric impedance. The present investigation focuses on the control of the oscillations of a smart composite plate equipped with shunted piezoelectric transducers. Namely, resonant shunt circuits, i.e. circuits with a resistor and an inductor, which can deteriorate the vibrations near the resonant frequencies, are considered. The structural model of the plate is discretized by using the finite element method yielding to a smart laminate composite model with elastic and piezoelectric layers. For a laminate composite plate, a parametric analysis was performed to evaluate optimal locations along the plate plane (xy) that maximize the effective modal electromechanical coupling coefficient. Then, the particle swarm optimization (PSO) method was used to find the optimum values of resistance and inductance of each circuit for a network of optimally located shunted piezoelectric patches bonded to the plate. Numerical examples validate and demonstrate the potential of the proposed approach for the design of piezoelectric shunt devices. A vibration amplitude reduction for the first four vibration modes was observed.

1 INTRODUCTION

As piezoelectric effect is called the phenomenon where electrical voltage is produced under the application of mechanical stress or pressure. Etymologically, the term piezoelectricity is of Greek origin and namely, it is derived from words piezo ($\pi\acute{\epsilon}\zeta\omega$), which means to press, and electron ($\acute{\eta}\lambda\epsilon\kappa\tau\rho\nu$), which stands for amber. This phenomenon was discovered in Paris at August the 2nd 1880 by Pierre and Jaques Curie [1] and it mainly appears on certain crystal-like materials and ceramics, which, in turn, are called piezoelectric and piezoceramic materials respectively. Among others, the Quartz crystal (SiO_2), the Rochelle salt (Potassium Sodium Tartrate), the Ammonium Dihydrogen Phosphate ($\text{NH}_4\text{H}_2\text{PO}_4$), the Lithium Sulphate (Li_2SO_4), the Tourmaline, the Polyvinylidene Difluoride polymer $(\text{CH}_2\text{CF}_2)_n$ and the ceramic Lead Zirconate Titanate (PZT) are known materials which present piezoelectric properties. The piezoelectric effect can be explained by the transfer of free electric charge to the edges of the crystalline grid. The reverse phenomenon also exists, and it is realized with the appearance of deformation of the material when it is subjected to an electric voltage.

Shunt piezoelectric damping is a vibration suppression method, suitable for the control of smart flexible structures. The method is mainly characterized by the connection of an electric impedance (e.g. an electric resistance, an inductance or a capacitance) to a piezoelectric transducer. Thus, the concept behind these systems lies to the construction of an electric network, which can reduce mechanical vibrations on smart structures, such as beams [2,3], plates [4], smart panels [5], etc. An advantage of this method is that it does not need external sensing, and, if designed properly, it can guarantee the stability of the whole system [6].

The simplest shunt circuits -however, of low efficiency- are the so-called resistive shunts, which consist of an electric circuit of one or more resistors in series or in parallel. On the other hand, resonant shunts, i.e. circuits of one or more resistors and inductors in various combinations, are very powerful in terms of vibration suppression near resonant frequencies. These two techniques were introduced by Hagood and Von Flotow, in a pioneering work [7]. Of course, there are several more complicated systems, capable of multi-mode damping. In this case, the shunt circuits consist of combinations of resistors, capacitors and inductors, either in series or in parallel. These systems include, among others, online tuned systems, current block circuits and Holkamp current flow circuits [8]. A detailed literature review on the several types of shunt circuits is available in [9].

The performance of shunt circuits, designed for vibration suppression, is discussed in [10]. Namely, A reduced-order model is considered, and both resistive and resonant shunt circuits were tested. Numerical, along with experimental results, showed that both circuits are efficient, especially for low structural damping cases, which means that, as the damping increases, the performance of such circuits deteriorates. In a recent work which is described in [11], the optimization of the parameters of absorbers, which consist of shunted piezoelectric circuits is presented. A hybrid system, which is based on piezoelectric shunts in combination with conventional tuned-mass dampers is proposed in [12].

In this work the finite element model of laminate composite plates with bonded piezoelectric patches or layers that are connected to passive resonant shunt circuits is presented. The model is based on an equivalent single layer theory combined with FSDT. For a Graphite-Epoxy laminate composite plate, a parametric analysis is performed to evaluate optimal locations along the plate plane (xy) that maximize the effective modal electromechanical coupling coefficient.

Next, the optimum values of resistance and inductance are obtained for maximum reduction of vibration level at the first four target excitation frequencies using particle swarm optimization.

2 THE PLATE MODEL

The host structure consists of a smart composite plate based on the first-order shear deformation theory for laminated composite plates (FSDT), simply known as Mindlin theory. The elastic core of the plate is made of T300/976 graphite-epoxy composite material, which stacking sequence is antisymmetric angle-ply $([-45^\circ/45^\circ/-45^\circ/45^\circ])$ as seen in Figure 1. The structure is discretized by using the finite element method. The plate is of square shape and the length of each side is 0.2 m. The model is also equipped with piezoelectric elements, which are made by PZT G1195N material and they can be placed on one or more finite elements at a time.

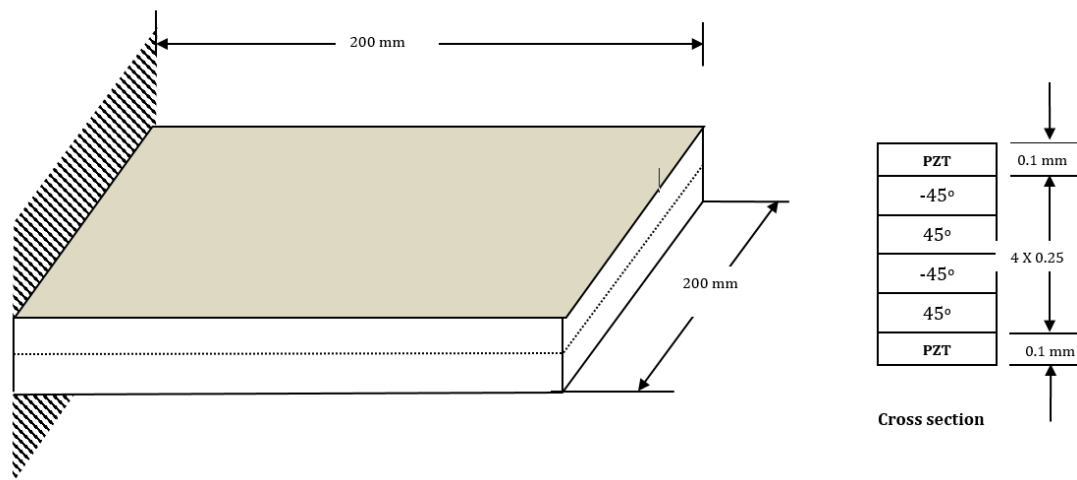


Figure 1: The plate model

The detailed material properties are given in Table 1. More information about this model can be found in [13,14].

Table 1: Material properties

Property	T300/976	PZT
Young's moduli (GPa)		
E_1	150	63
$E_2 = E_3$	9.0	63
Shear moduli (GPa):		
$G_{12} = G_{13}$	7.1	24.2
G_{23}	2.5	24.2
Poisson's ratio: $\nu_{12} = \nu_{13} = \nu_{23}$	0.3	0.3
Density: ρ (kg/m ³)	1600	7600
Piezoelectric constants (m/V): $d_{13} = d_{32}$	-	$254 \cdot 10^{-12}$
Electrical permittivity (F/m):		
$\xi_{11} = \xi_{22}$	-	$15.3 \cdot 10^{-9}$
ξ_{33}	-	$15.0 \cdot 10^{-9}$
Ply thickness (mm)	0.25	0.1

By using a set of practical assumptions (see ref. [3]) we can obtain an original variation formulation and then an efficient finite element formulation of the electromechanical problem:

$$\begin{bmatrix} M & 0 \\ 0 & 0 \end{bmatrix} \begin{Bmatrix} \dot{w} \\ \ddot{\phi} \end{Bmatrix} + \begin{bmatrix} K_{uu} & K_{u\phi} \\ -K_{u\phi}^T & K_{\phi\phi} \end{bmatrix} \begin{Bmatrix} w \\ \phi \end{Bmatrix} = \begin{Bmatrix} F_m \\ q \end{Bmatrix} \quad (1)$$

where $\{w\}$ is the column vector of nodal values of mechanical displacement of length N (N is the number of mechanical degrees of freedom); $[M]$ and $[K_{uu}]$ are the global mass and mechanical stiffness of the system of size $N \times N$ and $\{F_m\}$ is the column vector of mechanical force of length N . Moreover, $\{q\} = [q^{(1)}, q^{(2)}, \dots, q^{(P)}]^T$ and $\{\phi\} = [\phi^{(1)}, \phi^{(2)}, \dots, \phi^{(P)}]^T$ are the column vectors of electric charges (contained in the upper electrode) and potential differences in each patch; $[K_{u\phi}]$ is the electromechanical coupling matrix of size $N \times P$; and $[K_{\phi\phi}] = \text{diag}(C^{(1)}, C^{(2)}, \dots, C^{(P)})$ is a diagonal matrix filled with the P capacitances of the piezoelectric patches where $C^{(p)} = \xi_{33} S^{(p)} / h^{(p)}$, ξ_{33} being the piezoelectric permittivity in the direction normal to the electrodes and $S^{(p)}$ the area of the patch electrodes surfaces.

The above discretized formulation (1) can be used to the case where the piezoelectric patches are ‘shunted’, that is to stay connected to a passive electrical network. In this case, neither $\{\phi\}$ nor $\{q\}$ is prescribed by the electrical network but the latter imposes only a relation between them [7], where for the case of a resonant shunt composed of a resistor R and an inductor L in series, connected to the p th patch, can be written as

$$\phi^{(p)} - L\ddot{q}^{(p)} - R\dot{q}^{(p)} = 0 \quad (2)$$

Combining equations (1) and (2) and considering a mechanical viscous damping in the system, we finally obtain the general FE formulation of the electromechanical spectral problem when the piezoelectric patches are shunted

$$\begin{bmatrix} M & 0 \\ 0 & L_e \end{bmatrix} \begin{Bmatrix} \ddot{w} \\ \ddot{q} \end{Bmatrix} + \begin{bmatrix} 0 & 0 \\ 0 & R_e \end{bmatrix} \begin{Bmatrix} \dot{w} \\ \dot{q} \end{Bmatrix} + \begin{bmatrix} K_{uu} + K_{u\phi} K_{\phi\phi}^{-1} K_{\phi u} & K_{u\phi} K_{\phi\phi}^{-1} \\ K_{\phi\phi}^{-1} K_{\phi u} & K_{\phi\phi}^{-1} \end{bmatrix} \begin{Bmatrix} w \\ q \end{Bmatrix} = \begin{Bmatrix} F_m \\ 0 \end{Bmatrix} \quad (3)$$

where $[R_e]$ and $[L_e]$ are the diagonal matrices filled with the electrical resistances R and the electrical inductances L of the shunt circuits.

There exist two possible configurations for the piezoelectric patches, namely the short-circuit ($\{\phi\} = \{0\}$) and open-circuit ($\{q\} = \{0\}$) configurations. The electromechanical coupling coefficient (EMCC) of the piezoelectric patches is defined as:

$$K_j^2 = \frac{f_{oc}^{j^2} - f_{sc}^{j^2}}{f_{oc}^{j^2}} \quad (4)$$

where f_{oc}^j and f_{sc}^j is j -th eigen-frequency of the plate in open- and short-circuit respectively. The EMCC is used here as a metric to perform the positioning of four symmetric pairs of

patches throughout the plate, via parametric analysis, such that each patch maximizes the EMCC of one of the first four vibration modes of the laminate plate.

3 PARTICLE SWARM OPTIMIZATION

For the optimization of the parameters of the resonant shunt circuit, i.e. for the values of the resistance R and the inductance L , the particle swarm optimization (PSO) method was considered. More specifically, this nature-inspired algorithm imitates the movement of particles, i.e. birds or fish, towards the search of food, i.e. the optimal solution. PSO is a very powerful optimization method and it has been used in vibration suppression of smart structures [15]. The optimum is reached through an iterative process, until a criterion of performance is met. Several variations of the classical PSO method have been proposed. One of the most efficient is called inertia PSO and it was introduced by Shi and Eberhart in [16]. The main feature of this method is that it includes an inertial weight, influencing this way the convergence of the algorithm.

Inertia particle swarm optimization algorithm can be modeled considering the position and the velocity of the particles. The position is given by:

$$x_{ij}(t+1) = x_{ij}(t) + u_{ij}(t+1) \quad (5)$$

The velocity of the particles, in the case of inertia PSO is given by:

$$u_{ij}(t+1) = w u_{ij}(t) + c_1 r_1 (p_{best\ ij} - x_{ij}(t)) + c_2 r_2 (g_{best\ j} - x_{ij}(t)) \quad (6)$$

where r_1 and r_2 are random values in the interval $[0, 1]$ and c_1 and c_2 are the so-called cognitive and social parameters respectively. The values of these parameters can be calculated through modal analysis. The inertia w reads:

$$w = w_{max} - \frac{w_{max} - w_{min}}{max_iteration} t \quad (7)$$

where typical values of w_{max} and w_{min} are 0.99 and 0.01 respectively.

The personal best of each particle and the global best of the whole swarm are also kept:

$$p_{best\ ij} = \begin{cases} x_{ij}(t+1), & \text{if } f(x_{ij}(t+1)) < f(x_{ij}(t)) \\ p_{best\ ij}, & \text{elsewhere} \end{cases} \quad (8)$$

$$g_{best\ j} = \min\{f(p_{best\ 1j}), f(p_{best\ 2j}), \dots, f(p_{best\ nj})\}$$

where with n is denoted the total number of the iterations of the algorithm.

4 NUMERICAL RESULTS

As mention above, the optimal position of the piezoelectric patches is found taking into account the value of the EMCC [4]. Namely, a parametric investigation is carried out in order to find the positions where the coupling coefficient is maximized for each eigen-frequency. The optimal positions for the piezoelectric patches and the system response for the first four eigen-frequencies are given schematically in Figure 2 and 3 respectively.

The parameters of a resonant shunt circuit, i.e. the values of resistance R and inductance L are optimized using the inertia variation of the particle swarm optimization algorithm. The objective is the maximization of the attenuation, due to the electric circuit. The results for the optimal R, L values, along with the best position for the PZT patches is given in Table 2.

Mesh Discretization					
31	32	33	34	35	36
25	26	27	28	29	30
19	20	21	22	23	24
13	14	15	16	17	18
7	8	9	10	11	12
1	2	3	4	5	6

Figure 2: Optimal positions of piezoelectric patches

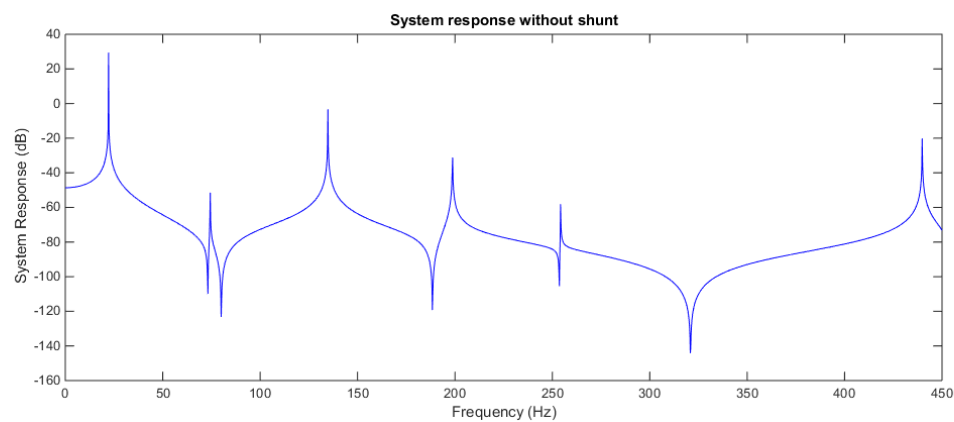


Figure 3: Frequency response of the system prior to the connection with the shunt circuit

Table 2: Position of PZT and optimized values for shunt parameters R , L using inertia PSO method

Eigen-freq.	PZT position	Frequency range (Hz)	R (Ω)	L (H)
1 st	19 th element	0-50	18707	595
2 nd	31 st element	100-150	1999.28	15.32
3 rd	25 th element	150-250	642.09	7.22
4 th	22 nd element	350-450	535.02	1.272

The design parameters for optimization are the values of the resistance R with bounds $[0\Omega, 100k\Omega]$ and the inductance L with bounds $[0H, 1000H]$. The parameters of the PSO algorithm are given in Table 3.

Table 3: Parameters of the PSO algorithm

Parameters of PSO	Numerical values	
Number of iterations	100	
Population	25	
Inertia	1	
Inertia weight damping	0.99	
Acceleration factors	$c_1=1.5$	$c_2=2$

The results of the application of each of the four optimized resonant shunt circuits on the frequency response of the system for the first four eigen-frequencies, along with the convergence of the particle swarm optimization algorithm are depicted in Figures 4-7.

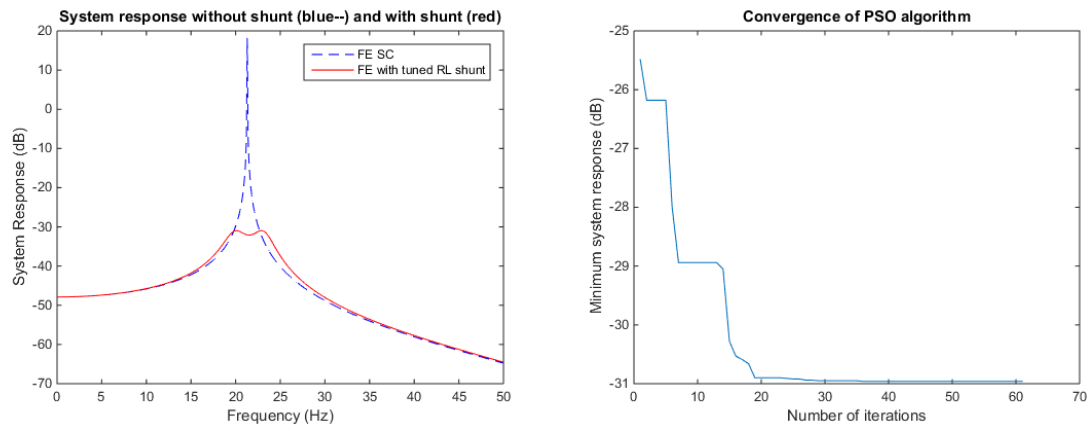


Figure 4: (a) Response of the system for the first eigen-frequency and (b) convergence of PSO algorithm

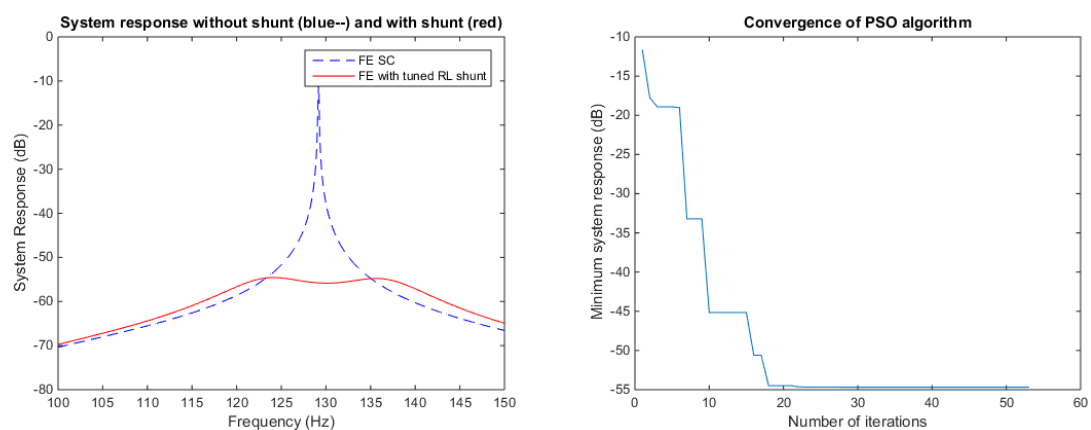


Figure 5: (a) Response of the system for the second eigen-frequency and (b) convergence of PSO algorithm

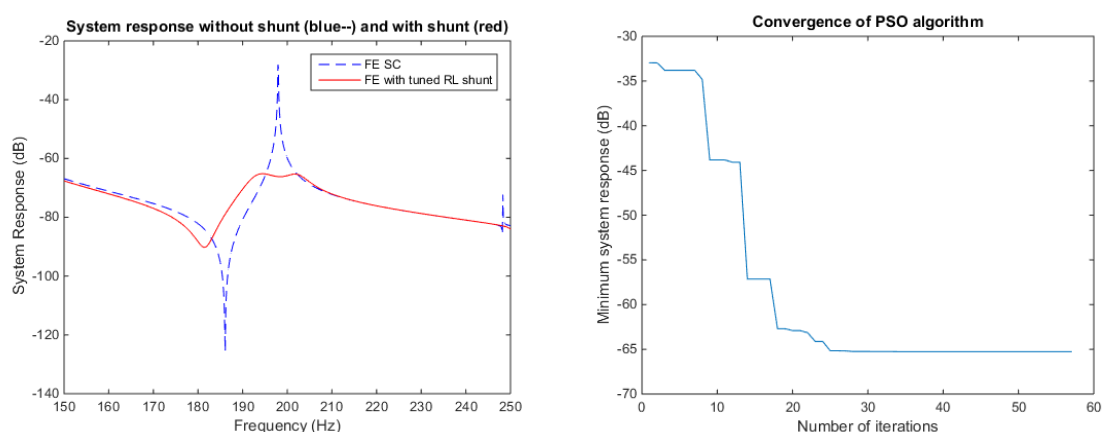


Figure 6: (a) Response of the system for the third eigen-frequency and (b) convergence of PSO algorithm

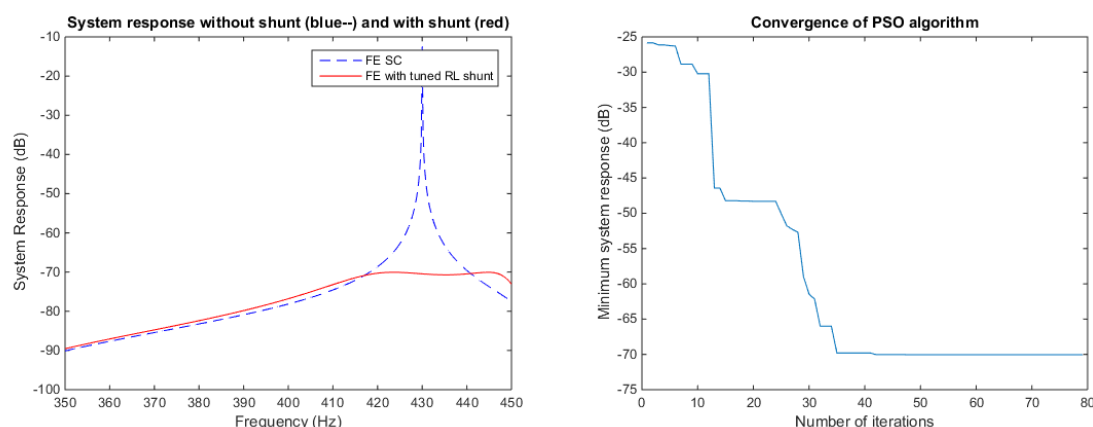


Figure 7: (a) Response of the system for the fourth eigen-frequency and (b) convergence of PSO algorithm

5 CONCLUSIONS

Resonant shunt circuits are proved to be very efficient in vibrational control of smart composite plates with piezoelectric elements. However, the calculation and fine-tuning of the values of the electrical parameters, i.e. the resistance and the inductance, is not always an easy task to perform.

From the numerical results of the present investigation, it is clearly shown that the inertia particle swarm optimization method is very powerful in terms of estimating the optimal values of the electric parameters of the resonant shunt circuit. More specifically, the occurrence of a second peak near each eigenfrequency, due to the presence of an extra electrical equation, along with the maximization of the attenuation, validate the feasibility and the effectiveness of the method. In most cases, the inertia PSO algorithm converged quite fast, i.e. before 20 iterations, except of the fourth case, where nearly 40 generations were required. It is possible to achieve faster convergence with modification of optimization parameters or by using other variations of the PSO algorithm. The selection of the positions of the PZT patches was also efficient, however, it could be further optimized in future investigations, by its inclusion as an extra design variable in the optimization scheme.

ACKNOWLEDGMENTS

Georgios Tairidis gratefully acknowledges the French Embassy in Greece and the French Government for the funding of his visit to the Structural Mechanics and Coupled Systems Laboratory of the institute Conservatoire National des Arts et Métiers, through the program “Sejours scientifiques de haut niveau” for new researchers. He also wants to acknowledge LMSSC laboratory of leCnam and its director, Prof. Jean-François Deü for covering the cost of participation to 9th ECCOMAS Thematic Conference on Smart Structures and Materials, SMART 2019.



The research work of Panagiotis Koutsianitis was supported by the Hellenic Foundation for Research and Innovation (HFRI) and the General Secretariat for Research and Technology (GSRT), under the HFRI PhD Fellowship grant (GA. no. 34254).

REFERENCES

- [1] Curie, J. and Curie, P. Développement par compression de l'électricité polaire dans les cristaux hémihédres à faces inclinées (Development, via compression, of electric polarization in hemihedral crystals with inclined faces). *Bulletin de la Société minérologique de France* (1880) **3**, 90-93.
- [2] Tairidis, G.K., Vibration control of smart composite structures using shunted piezoelectric systems and neuro-fuzzy techniques. *J Vib Control* (2018) JVC-18-0405.R1 (in press).
- [3] Thomas, O., Deü, J.-F. and Ducarne, J. Vibrations of an elastic structure with shunted piezoelectric patches: efficient finite element formulation and electromechanical coupling coefficients. *Int J Numer Methods Eng* (2009) **80**, 235-268.
- [4] Godoy, T.C. and Trindade, M.A. Modelling and analysis of laminate composite plates with embedded active-passive piezoelectric networks. *J Sound Vib* (2011) **330**, 194-216.
- [5] Larbi, W., Deu, J.-F. and Ohayon, R. Finite element reduced order model for noise and vibration reduction of double sandwich panels using shunted piezoelectric patches. *Applied Acoustics* (2016) **108**, 40-49.
- [6] Moheimani, R. S. and Fleming, A. J. *Piezoelectric Transducers for Vibration Control and Damping*, Springer-Verlag, (2006).
- [7] Hagood, N.W. and Von Flotow, A. Damping of structural vibrations with piezoelectric materials and passive electrical networks. *J Sound Vib* (1991) **146**, 243-68
- [8] Hollkamp, J.J. and Starchville, T.J.F. A Self-Tuning Piezoelectric Vibration Absorber. *J Intell Material Syst Struct* (1994) **5**, 559-566.
- [9] Marakakis, K., Tairidis, G.K., Koutsianitis P. and Stavroulakis G.E. Shunt piezoelectric systems for noise and vibration control: A review. *Front Built Environ* (2019) doi: 10.3389/fbuil.2019.00064
- [10] Thomas, O., Ducarne, J. and Deü, J.-F., Performance of piezoelectric shunts for vibration reduction. *Smart Mater Struct* (2012) **21**, 015088.
- [11] Gardonio, P. and Casagrande, D. Shunted piezoelectric patch vibration absorber on two-dimensional thin structures: Tuning considerations. *J Sound Vib* (2017) **17**, 26-47.
- [12] Heuss, O., Salloum, R., Mayer, D. and Melz, T. Tuning of a vibration absorber with shunted piezoelectric transducers. *Arch Appl Mech* (2016) **86**, 1715-1732.
- [13] Tairidis, G. *Optimal design of smart structures with intelligent control*, PhD dissertation, Technical University of Crete, (2016).
- [14] Lam, K.Y., Peng, X.Q., Liu, G.R. and Reddy, J.N. A finite-element model for piezoelectric composite laminates. *Smart Mater Struct* (1997) **6**, 583-591.
- [15] Marinaki, M., Marinakis, Y. and Stavroulakis, G.E. Vibration control of beams with piezoelectric sensors and actuators using particle swarm optimization. *Expert Syst Appl*, (2011) **38**, 6872-6883.
- [16] Shi, Y. and Eberhart, R. *A Modified Particle Swarm Optimizer*. Evolutionary Computation Proceedings, (1998) 69-73 DOI: 10.1109/ICEC.1998.699146.

VIBRATION MITIGATION OF MULTIPLE NONLINEAR RESONANCES THROUGH AN ANALOGOUS PIEZOELECTRIC NETWORK

B. LOSSOUARN^{*}, G. KERSCHEN[†] AND J.-F. DEÜ^{*}

^{*} Laboratoire de Mécanique des Structures et des Systèmes Couplés (LMSSC)
Conservatoire national des arts et métiers (Cnam),
292 Rue Saint-Martin, 75003 Paris, France
e-mail: boris.lssouarn@cnam.fr, web page: <http://www.lmssc.cnam.fr/>

[†] Department of Aerospace and Mechanical Engineering, University of Liège
Allée de la Découverte, 9, B-4000 Liège, Belgium

Key words: Vibration damping, Piezoelectric coupling, Broadband control, Nonlinear resonances

Abstract. The objective of this work is to investigate the interest of analogous piezoelectric networks for vibration mitigation of multiple nonlinear resonances. An electrical network providing a similar dynamics as the considered structure is first designed according to linear considerations. Then, a nonlinear electrical component is added to the network to ensure both a spatial analogy and a principle of similarity regarding the mathematical form of the mechanical nonlinearity. Once the electrical network and the mechanical structure are coupled through an array of piezoelectric elements, it is shown that such an analogous coupling offers strong benefits for vibration mitigation over a broad frequency range and a broad range of excitation amplitudes.

1 INTRODUCTION

Tuned vibration absorbers [1, 2] usually provide effective solutions for passive vibration mitigation. However, mechanical nonlinearities generate a detuning that seriously affects damping performance. A solution to this issue consists in the introduction of an additional nonlinearity in the absorber [3]. The interest of nonlinear piezoelectric shunts has already been proven for vibration mitigation of single nonlinear resonances [4, 5]. The concept was then extended to the design of a nonlinear and multi-branch piezoelectric shunt [6]. The present work addresses the development of a multimodal and fully passive piezoelectric analogous network that mitigates several resonances of a nonlinear structure.

An electrical network can be assembled to reproduce the dynamics of a cantilever beam in the linear regime of motion. In this case, several electrical resonances are simultaneously tuned to the mechanical resonances, thus providing the equivalent of a multimodal vibration absorber from electromechanical coupling through an array of piezoelectric patches [7, 8]. This allows broadband vibration mitigation at low forcing amplitudes. Yet, higher amplitudes still lead to a serious detuning of the absorber when considering nonlinear structures.

By extending a principle of similarity to spatial considerations, a nonlinear component is placed in the electrical network in order to mimic the dynamics of the mechanical structure. The electromechanical

analogy is thus ensured beyond the linear regime. In this work, the use of a nonlinear capacitor generates an autonomous adjustment of the electrical resonances for a wide range of excitation amplitudes. The interest of this method is investigated numerically and experimentally by focusing on structural vibrations over a broad frequency range that covers the first three modes of a beam with localized cubic nonlinearity.

2 SINGLE MODE DAMPING WITH A PIEZOELECTRIC TUNED VIBRATION ABSORBER

2.1 For linear and nonlinear resonances

The resonant piezoelectric shunt, also called piezoelectric tuned vibration absorber, is commonly used to reduce the vibration amplitude of a single linear resonance. It is made of a piezoelectric transducer of capacitance C at zero strain connected to an inductor and a resistor whose values are typically obtained from

$$L = \frac{1}{C\omega_0^2} \quad \text{and} \quad R = \sqrt{\frac{3}{2}} \frac{k_c}{C\omega_0}, \quad \text{where} \quad k_c = \sqrt{\frac{\omega_0^2 - \omega_s^2}{\omega_s^2}}. \quad (1)$$

The angular frequencies ω_s and ω_0 corresponds to the resonances in short- and open-circuit, respectively. This formulation highlights a coupling factor k_c , which is usually considered for the positioning of the piezoelectric elements. Indeed, since k_c is directly related to damping performance [9], maximizing the coupling factor implies minimizing vibration amplitude for an adequate tuning of the electrical circuit. As seen in Eq. (1), part of the tuning procedure is to ensure that the electrical resonance at angular frequency $1/\sqrt{LC}$ matches the open-circuit natural frequency. As a consequence, it is clear that a mechanical nonlinearity altering the angular frequency ω_0 would deteriorate the tuning of the piezoelectric shunt and thus the damping performance.

A solution to overcome the influence of mechanical nonlinearities on piezoelectric tuned vibration absorbers is to introduce nonlinearities in the electric shunt itself. Following a principle of similarity, the added nonlinearity should possess the same mathematical form as the one in the mechanical system. For example, if a nonlinear force is modeled by a cubic function of the displacement u ,

$$f_{NL} = K_{NL}u^3, \quad (2)$$

it has been shown that the required additional voltage in the shunt is also a cubic function of the electric charge q [4, 5]:

$$v_{NL} = \frac{1}{C_{NL}}q^3 \quad \text{with} \quad \frac{1}{C_{NL}} = 2 \left(\frac{L}{m} \right)^2 K_{NL}, \quad (3)$$

where m corresponds to the modal mass of the mechanical structure. This theoretical nonlinear capacitance in series with the inductor would ensure an adequate tuning of the resonant shunt by maintaining an equal-peak condition over a broader range of excitation amplitudes [4]. While the nonlinear voltage in Eq. (3) could be synthesized with a numerical controller, find a passive electrical component able to satisfy this purely nonlinear condition is not obvious [10]. In order to circumvent this limitation, it has been proposed to rather introduce the nonlinearity in the inductor [5]. Indeed, a one-term harmonic balance approximation shows that Eq. (3) is close to

$$v_{NL} = L(1 - \alpha \dot{q}^2) \ddot{q} \quad \text{with} \quad \alpha = 6 \frac{LK^{NL}}{m^2\omega_0^4}. \quad (4)$$

While no passive inductors seems to be able to precisely satisfy this nonlinear relation, the next experimental section still shows that it is possible to benefit from saturation of magnetic circuits to approximate the required nonlinearity.

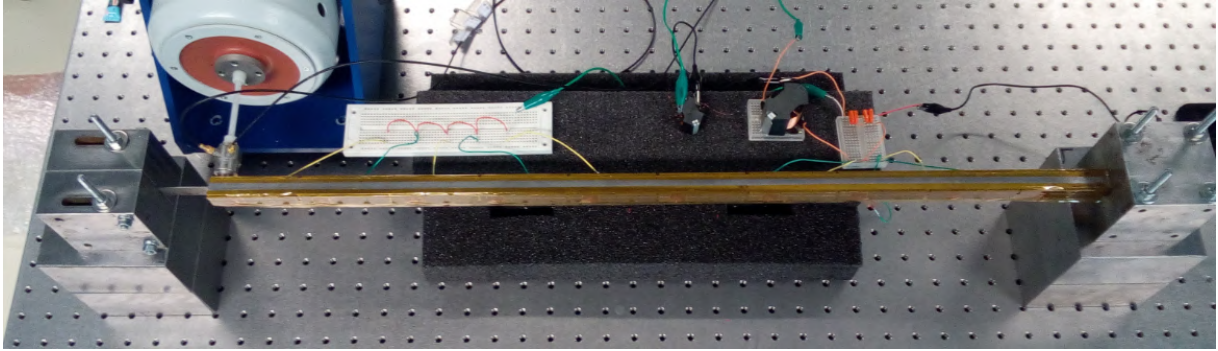
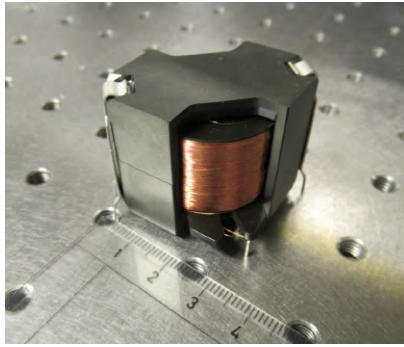
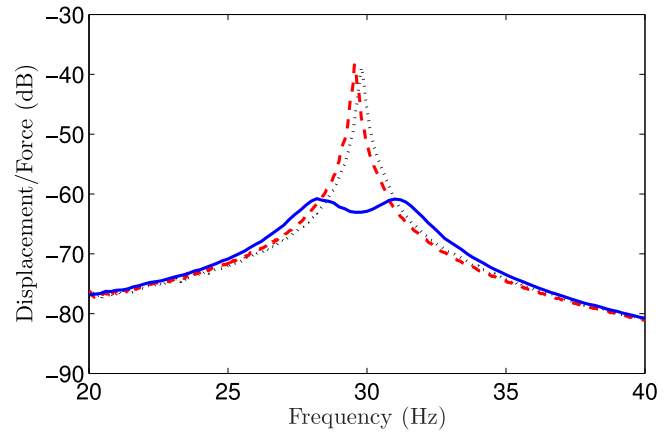


Figure 1: Beam covered with an array of piezoelectric patches; half of the patches are connected to a single resonant shunt for vibration damping of the first mode [5].



(a)



(b)

Figure 2: Piezoelectric tuned vibration absorber – (a) physical inductor, (a) experimental frequency response function around the first mechanical resonance, with short circuit (\cdots), with open circuit (\cdots) or with an optimal linear shunt (—).

2.2 Experimental validation of the principle of similarity

The experimental setup is based on a cantilever beam involving a cubic nonlinearity. As shown in Fig. 1, a thin lamina is clamped at the left end of the beam, which generates the hardening nonlinearity. The structure is covered with an array of piezoelectric patches in order to mitigate vibration with a piezoelectric tuned vibration absorber. The passive inductor in Fig. 2(a) is realized by winding copper wire around a magnetic circuit in ferrite material. When connected to the piezoelectric patches, Fig. 2(b) demonstrates that the passive inductor allows a strong reduction of the vibration amplitude at low excitation levels. However, Fig. 3(a) shows that an increasing forcing amplitude leads to a complete detuning of the resonant shunt because of the mechanical nonlinearity.

As mentioned previously, a solution to overcome this effect is to introduce in the absorber a nonlinearity similar to that of the primary structure. Here, the electrical circuit is made of an inductor whose inductance value depends on the current flowing through it. An approximation of the nonlinear relation in Eq. (4) is obtained by choosing a magnetic circuit that provides an adequate magnetic saturation.

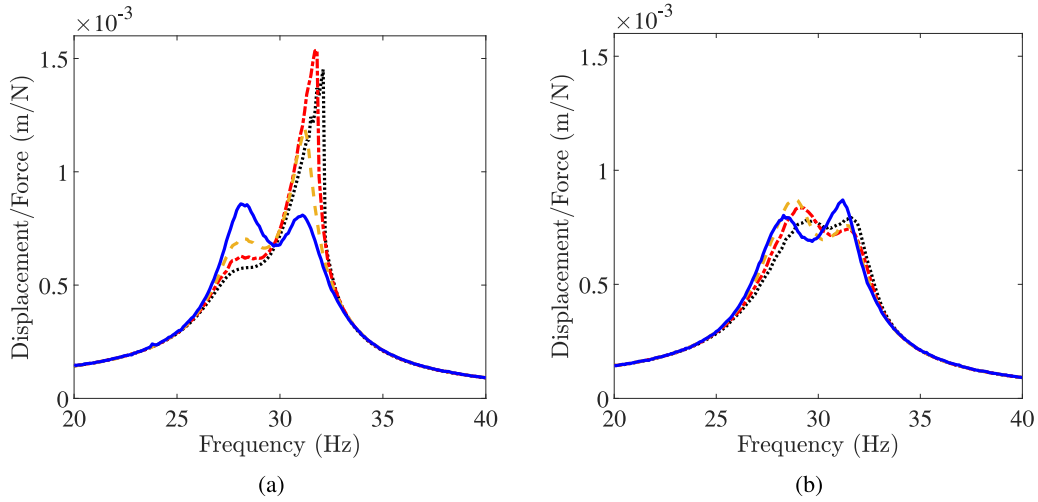


Figure 3: Experimental frequency response functions for various forcing amplitudes, $F = 0.2$ N (—), $F = 0.4$ N (— · —), $F = 0.6$ N (— · · —) and $F = 0.8$ N (···) – (a) linear shunt, (b) nonlinear piezoelectric tuned vibration absorber [5].

Restraining the analysis to the first harmonic, a decrease of the equivalent inductance value leads to an increasing electrical resonance frequency that follows the increase of the mechanical natural frequency due to the cubic stiffness. As shown in Fig. 3(b) this solution is able to maintain vibration mitigation performance compared to a case involving a linear shunt.

3 MULTIMODAL DAMPING WITH AN ANALOGOUS PIEZOELECTRIC NETWORK

3.1 Broadband damping in the linear regime

The extension of resonant piezoelectric shunts to multimodal structures consists in designing a multi-resonant circuit whose electrical natural frequencies are sufficiently close to the mechanical resonances to be controlled. With a single piezoelectric transducer, the most direct approach is the so-called multi-branch shunt [11, 12] made of inductors and capacitors organized with just as many branches as the target mechanical resonances. The main limitation is that this solution does not optimize the coupling factor k_c for all the considered modes. The first reason concerns the addition of external capacitors in the shunt which decreases electromechanical coupling [13]. The second reason is related to the positioning of the single piezoelectric patch that is generally not optimal for different mode shapes.

Another solution for multimodal damping is based on analogous piezoelectric coupling. This requires several piezoelectric transducers that are interconnected with electrical components so as to build a multi-resonant network with modal properties similar to that of the considered structure. The analogy is no more restrained to the natural frequencies as with the multi-branch shunts because similar mode shapes are also ensured. The design of the electrical analogue of a beam has been fully described in Ref. [8]. The first step consists in discretizing the bending wave differential equation from a finite difference approximation. Then, a direct electromechanical analogy is applied to find the unit cell of the electrical network. The complete network is built by reproducing this unit cell along one direction, taking into account that the number of unit cells per wavelength has to be sufficiently large to approximate the continuous mechanical medium. For the case of a beam, the electrical unit cell is made of an inductance L^* representing the analogue of a point mass, a capacitance C^* that represents the inverse of a bending

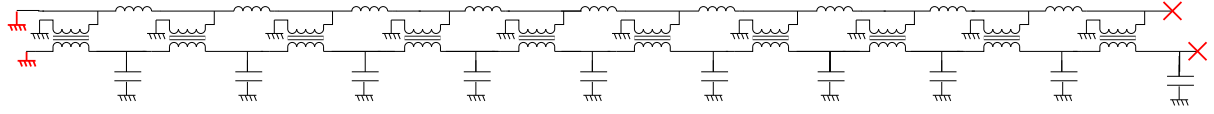


Figure 4: Electrical analogue of a cantilever beam.

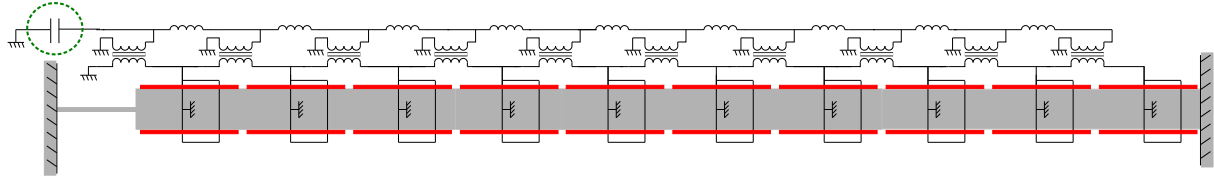


Figure 5: Beam coupled to its electrical analogue through an array of piezoelectric patches.

stiffness and a transformer of ratio \hat{a} that is analogous to a mechanical lever of length a .

A beam electrical analogue involving 10 unit cells is represented in Fig. 4. In order to approximate the mode shapes of a cantilever beam, we need to ensure analogous boundary conditions. This is realized by short-circuiting one end of the network (equivalent to zero force and moment), while leaving open the other end (equivalent to zero displacement and angle). Another critical condition is the tuning of the dispersion relation in the electrical waveguide. From the discrete model, it can be shown that the electrical parameters need to satisfy

$$\frac{1}{\hat{a}^2} \frac{1}{L^* C^*} = \frac{1}{a^2} \frac{K_\theta^*}{m^*}, \quad (5)$$

where K_θ^* is the bending stiffness of the mechanical unit cell, m^* is its mass and a its length [8].

Considering the practical example described in the last section, one wants to couple a clamped beam to its analogous electrical network with an array of piezoelectric patches. Thanks to the inherent capacitance C^* of the piezoelectric patches, there is no need for external capacitors for the analogue of the bending stiffness. Only transformers and inductors satisfying Eq. (5) are required for the analogue of a clamped beam. In the present case, however, one has to take into account the clamping through the thin lamina. In the linear regime, the lamina can be modeled by a linear spring of stiffness K^{end} . So, its analogue is a capacitor to be placed at the end of the electrical network, as shown in Fig. 5. Considering the nondimensionalized equations in the two domains when no coupling occurs, one can find a relation between the end capacitance and its analogous linear stiffness:

$$C^{\text{end}} = \frac{K_\theta^*}{K^{\text{end}}} \frac{\hat{a}^2}{a^2} C^*. \quad (6)$$

A last step consists in introducing appropriate damping in the electrical network. Coming back to Eq. (1), remark that the optimal electrical quality factor at ω_0 is $Q = L\omega_0/R = \sqrt{2/3}/k_c$. A similar damping ratio can be obtained with a resistance R_{L^*} in series with the inductance L^* or a resistance R_{C^*} in series with the capacitance C^* when

$$R_{L^*} = \sqrt{\frac{3}{2}} k_c \omega_0 L^* \quad \text{or} \quad R_{C^*} = \sqrt{\frac{3}{2}} \frac{k_c}{\omega_0 C^*}. \quad (7)$$

The dependence on ω_0 in those equations shows that using a resistance R_{L^*} that is optimal for the first mode of the structure would be too low for the next modes leading to an underdamped case. On the other hand an optimal resistance R_{C^*} for the first mode would lead to overdamped highest modes. In the present

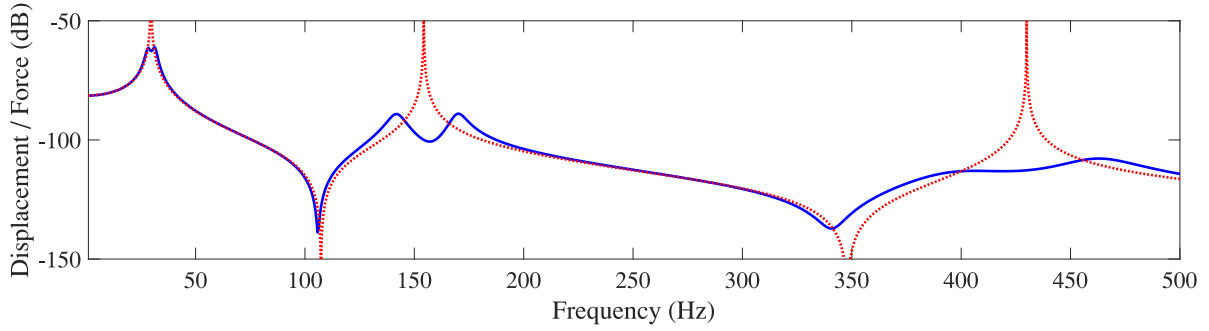


Figure 6: Simulated frequency response function of the beam with short-circuited patches (\cdots) and with the analogous electrical network ($—$).

case focusing on the first three modes of the beam which are fully separated, it is decided to benefit from both damping configurations by tuning R_{L^*} for the first mode and R_{C^*} for the third mode. This requires the computation of individual coupling factors for each modes by comparing natural frequencies when $L^* = 0$ and when this inductance tends to infinity. In the end, both resistances are reduced by 10% to be closer to the optimal damping because R_{C^*} still has a slight influence on the damping of the first mode. The resulting linear frequency response functions of the beam are represented in Fig. 6 with and without coupling. One can see the simultaneous vibration mitigation of the first three modes of the beam through the equivalent of a multimodal tuned mass damper. Note that damping of the second mode is not optimized (underdamped) because the considered tuning of two electrical quality factors on L^* and C^* only allows optimal damping at two specific frequencies around the first and third modes. A last remark concerns the third mode which does not ensure an equal peak condition. This is directly due to the fact that the discrete network only involve 10 unit cells inducing a slight mismatch between the mechanical and electrical resonances.

3.2 Damping of multiple nonlinear resonances

Although analogous piezoelectric coupling provides broadband damping in the linear regime, higher vibration amplitudes still lead to the undesired behavior illustrated in Fig. 3(a) if only linear electrical components are considered. The next objective is thus to find the adequate nonlinearity to be introduced in the electrical network. Here, contrary to the previous experimental validation involving a nonlinear inductor [5], a nonlinear capacitor is incorporated at the end of the electrical network to ensure a strict analogy with the nonlinear stiffness at the end of the beam. This actually combines the principle of similarity used for nonlinear control [3] and the spatial analogy used for multimodal damping [8].

Still, it remains the question of the numerical value for the nonlinear capacitance. Focusing on Eq. (3), it can be remarked that the nonlinear capacitance depends on the ratio of the inductance L over the modal mass m , which can be seen as a mass ratio between the absorber and the main structure. Using a single mode piezoelectric shunt $L/m = 1/CK$ where K is the open-circuited modal stiffness, which depends on the considered mode. However, considering two modal systems with similar mode shapes, all modal mass ratio L/m becomes equal to the same local mass ratio L^*/m^* , which does not depend on the mode of interest anymore. This is a critical point because Eq. (3) then leads to a tuning of the capacitance nonlinearity at the end of the network that does not depend on frequency:

$$\frac{1}{C_{NL}} = 2 \left(\frac{L^*}{m^*} \right)^2 K_{NL}. \quad (8)$$

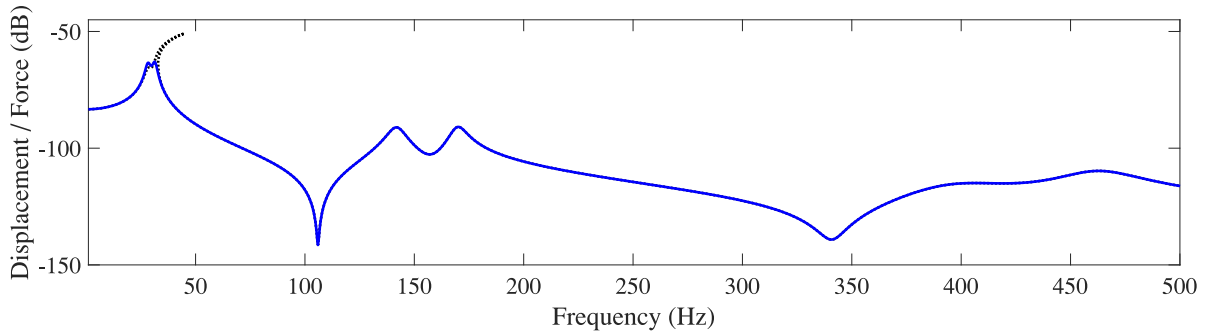


Figure 7: Simulated frequency response function of the nonlinear beam for $F = 0.8$ N without nonlinear capacitance (\cdots) and with nonlinear capacitance ($—$).

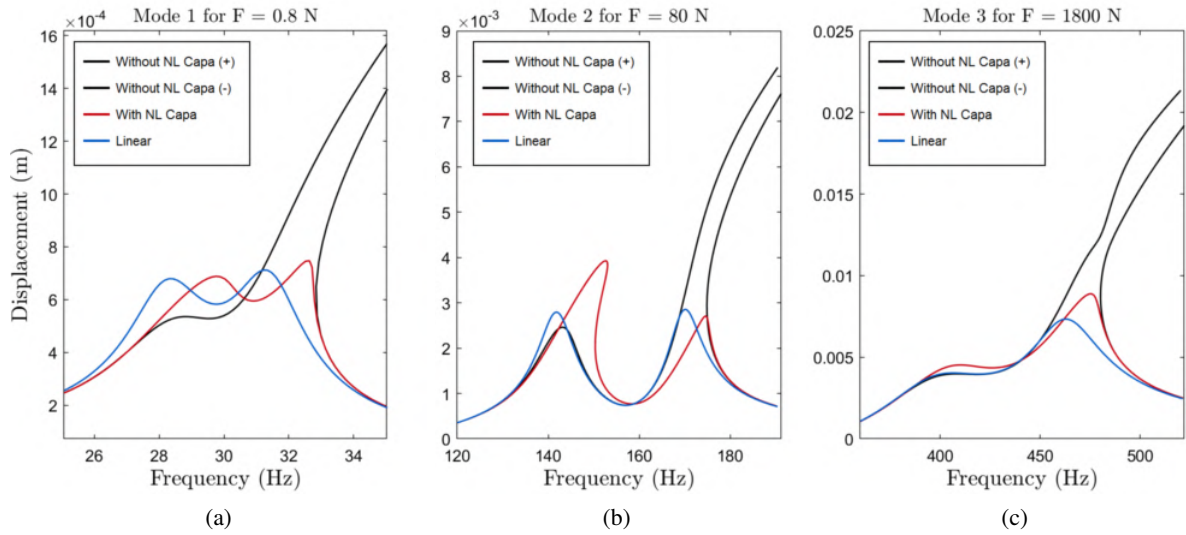


Figure 8: Simulated frequency responses for the first three modes – (a) mode 1 for $F = 0.8$ N, (b) mode 2 for $F = 80$ N, (c) mode 3 for $F = 1800$ N.

With the proposed nonlinear capacitor, the analogy is not only valid in the linear regime but also in the nonlinear regime. Damping performance is thus maintained over an extended range of forcing amplitudes. This is first observed in Fig. 7 which compares frequency responses with and without nonlinear capacitance. The results are obtained from a harmonic balance with three harmonics and a forcing amplitude equal to 0.8 N. This level of excitation does not induce a significant nonlinearity for the second and third modes but the first mode is seriously affected. In Fig. 8, the excitation amplitude is set independently for all three modes so as to provoke the merging of the right local maximum with a detached resonance curve when no nonlinearity is introduced in the electrical network. The addition of the nonlinear capacitance in Eq. (8) significantly reduces the vibration amplitude of all the considered modes. While we are close to an equal peak condition for mode 1, the responses for modes 2 and 3 are further from the linear case. Those differences are definitely due to the lack of damping for mode 2 and to the imprecise linear tuning for mode 3.

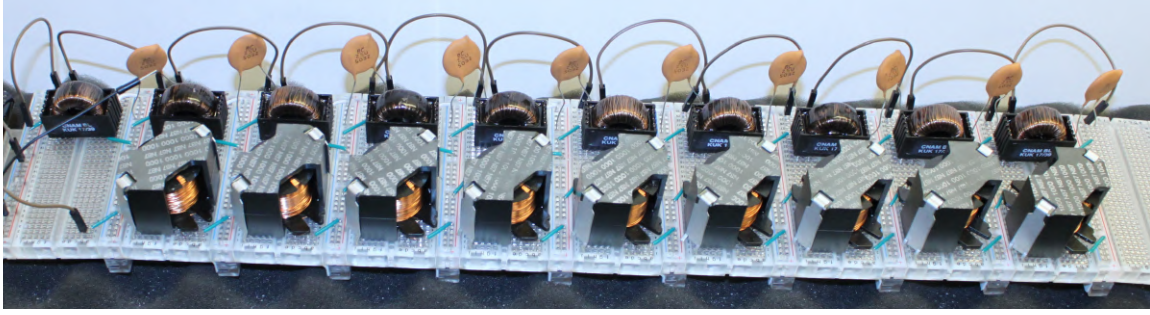


Figure 9: Electrical analogue of the cantilever beam with passive inductors, transformers and capacitors.

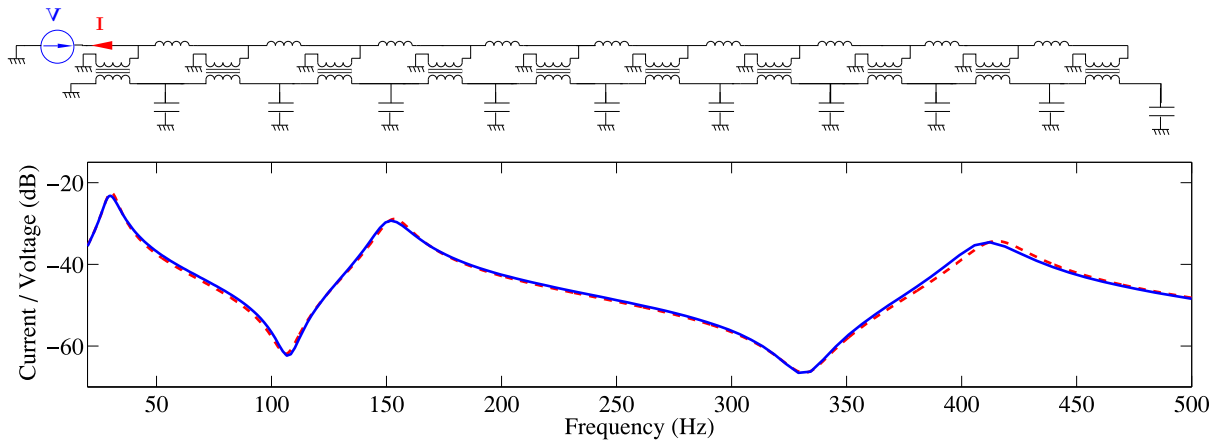


Figure 10: Experimental (—) and simulated (---) frequency response functions of the electrical network.

3.3 Development of the multi-resonant network

Starting with the linear case, assembling the previously described electrical network requires 9 inductors, 10 transformers and one capacitor as shown in Fig. 5. The magnetic components are specifically designed for this application. In order to first validate the electrical dynamics alone, the piezoelectric patches are replaced by ceramic capacitors. Then, an impedance meter is placed at the end of the network in order to measure the frequency response function of the current over the voltage that actually corresponds to the end admittance of the circuit.

Figure 10 shows the good agreement between the experimental results and the numerical simulations computed from the discrete set of equations that describe the electrical circuit. Note that the resistance of copper wire in the inductors and transformers has been added to the model because of its strong influence on the electrical quality factor. Even so, one can easily detect the three resonances corresponding to the first three modes of the electrical network. The distributions of the electrical current are then plotted at frequencies corresponding to those three maxima of admittance. As represented in Fig. 11, the electrical distributions are similar to mode shapes of a clamped beam which definitely validate the topology of the analogous network.

While those results validate the analogue of a beam that is clamped at one end, one has to remember that we also need to take into account the weak clamping through the thin lamina at the other end. As it can be modeled by a capacitor in the electrical domain, the influence of such a passive component at

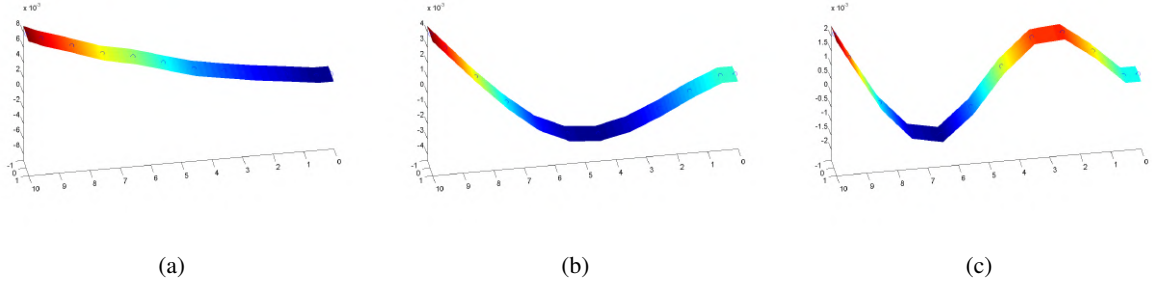


Figure 11: Experimental distributions of the electrical current – (a) mode 1 , (b) mode 2, (c) mode 3.

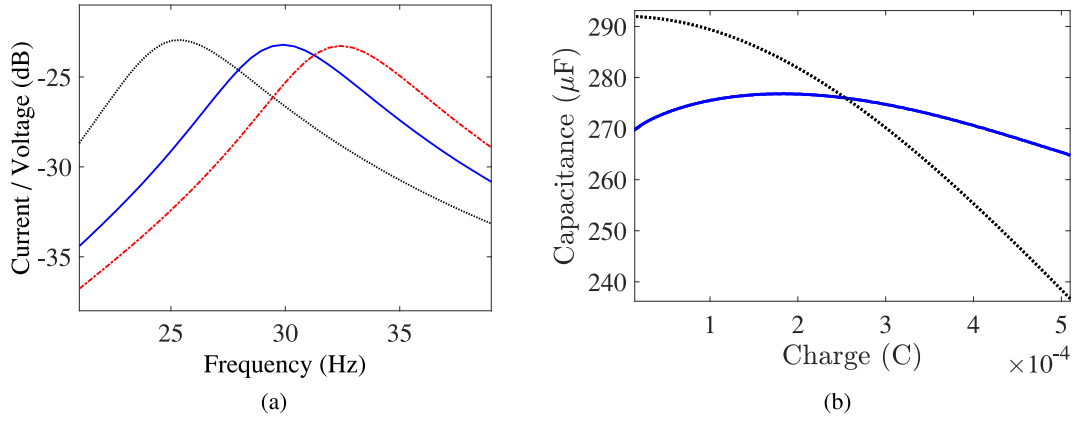


Figure 12: Choice of the capacitor at the end of the electrical network – (a) experimental frequency response function of the electrical network for various end-capacitors: 166 μF ($-\cdot-$), 266 μF ($—$) and infinite capacitance (\cdots), (b) objective for the nonlinear capacitor (\cdots) and measurement on a physical capacitor ($—$).

the end of the electrical network is investigated. The experimental admittance around the first resonance is plotted in Fig. 12(a) for various end capacitors. We note that a capacitance equal to 266 μF places the electrical resonance around the first natural frequency of the beam, which is consistent with Eq. (6).

While the considered end capacitor ensures modal coupling at low excitation level, it should also offer a nonlinear contribution in order to ensure a similarity with the nonlinear lamina. This contribution has to satisfy Eq. (3) whose first-harmonic approximation is $V_{\text{NL}} = \frac{3}{4C_{\text{NL}}}Q^3$, where V_{NL} is the amplitude of the nonlinear voltage contribution and Q is the amplitude of the electric charge. Supposing that the component that provides this nonlinear voltage is in series with a linear capacitor C^{end} , the equivalent variable capacitance is defined as

$$C_{\text{NL}}^{\text{end}}(Q) = \frac{1}{\frac{1}{C^{\text{end}}} + \frac{3Q^2}{4C_{\text{NL}}}}. \quad (9)$$

The variation of this capacitance as a function of the electrical charge is plotted in Fig. 12(b). This

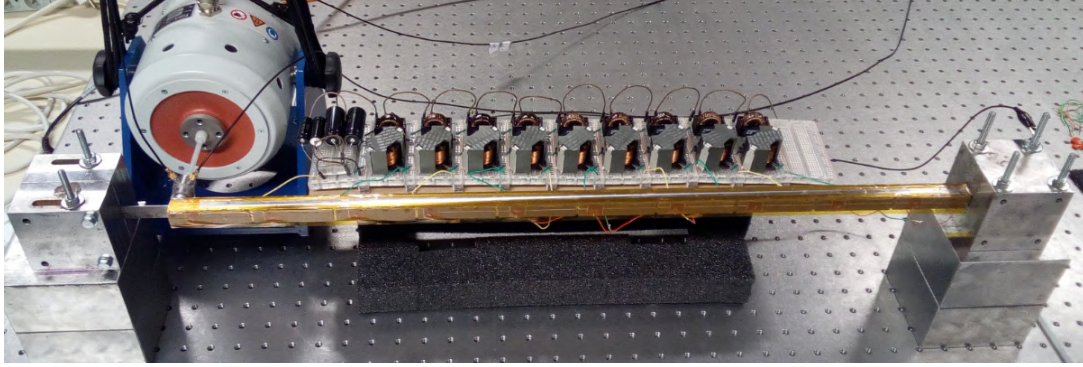


Figure 13: Experimental setup involving the beam coupled to its analogous electrical network.

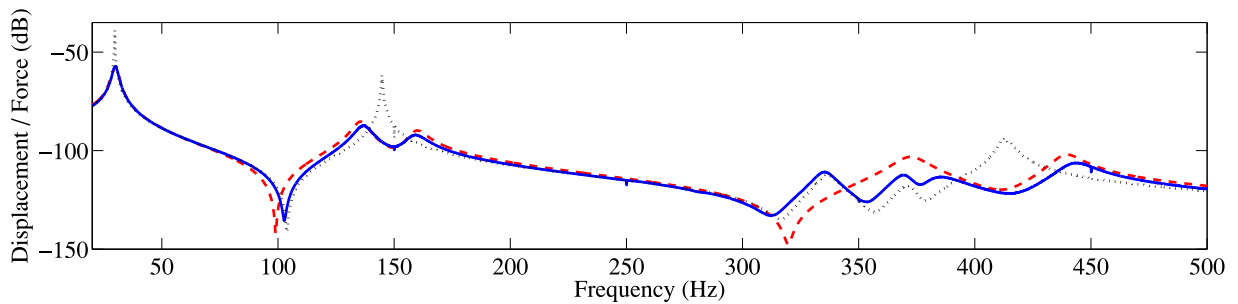


Figure 14: Frequency response functions at low excitation levels with short-circuited patches (\cdots) and with coupling to the analogous electrical network: model ($---$), experiment ($—$).

provides the objective function when looking for an appropriate nonlinear capacitor. Some multilayered ceramic capacitors offer saturation at relatively low voltage levels leading to a decrease of the equivalent capacitance. Unfortunately, up to now, no passive component has been found to correctly approximate the prescribed nonlinear function. Investigations are in progress to define if a non-passive numerical impedance is required or if a fully passive component can still be found.

3.4 First experimental results on multimodal damping of the nonlinear beam

The electrical network in Fig. 9 is coupled with the nonlinear beam through the array of piezoelectric patches. The full setup is seen in Fig. 13 that also shows the electromechanical shaker and the impedance head used for drive-point measurement at the end of the beam. The experimental and numerical frequency response functions appear in Fig. 14. First, the experimental response with short-circuited patches clearly shows the first and second modes of the beam but the third mode comes after two unpredicted resonances. Those extra resonances are finally related to the mounting system and this point will be corrected in the next version of the setup. In any case, multimodal damping is clear for the first three modes of the beam, which also validates the numerical model.

Concerning the tuning of the electrical network, note that it is slightly underdamped for modes 2 and 3 but it is overdamped for the first mode. This excessive damping is clearly observed on the first response in Fig. 15 that does not offer the local minimum normally observed with optimized tuned vibration absorbers. This shows a limit of the present analogous network whose copper losses in the magnetic components are not optimal for a broad frequency range. A new design of the electrical circuit will

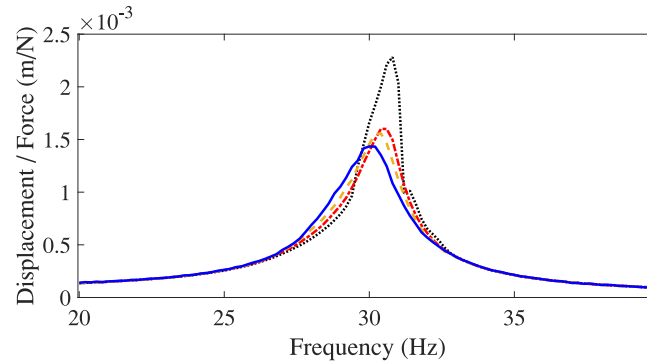


Figure 15: Experimental frequency response functions around the first mode for various forcing amplitudes, $F = 0.05$ N (—), $F = 0.1$ N (---), $F = 0.2$ N (- · -) and $F = 0.4$ N (···).

address this issue by providing optimal damping for the first mode and external resistors will be used to slightly lower the electrical quality factor at higher frequencies.

Another limitation of the present network is the lack of an adequate nonlinear capacitor. Consequently, the effect of the mechanical nonlinearity on the tuning of the piezoelectric vibration absorber is observed in Fig. 15. Increasing the forcing amplitude moves the mechanical resonance to higher frequency without similar adjustment of the corresponding electrical resonance. This results in an increase of the vibration amplitude similar to what has been observed in Fig. 3(a) for single mode control with optimized damping. The next step thus consists in finding an adequate nonlinear capacitor and place it in an optimally damped electrical network so as to retrieve similar results as in Fig. 3(b).

4 CONCLUSIONS

This work aims to show that the principle of nonlinear similarity can be extended to multimodal damping with piezoelectric networks. To this end, an analogous electrical circuit is proposed in order to reproduce the dynamics of the considered structure. A multimodal coupling offers vibration mitigation over a wide frequency range. For higher forcing amplitudes, however, a mechanical nonlinearity leads to a serious increase of the vibration amplitude. A nonlinear capacitor is thus placed in the electrical network at an analogous position. Numerical results show that using an electrical nonlinearity similar to the mechanical one can lead to a substantial gain in terms of damping performance around several modes of the mechanical structure. This definitely proves that broadband damping of a nonlinear structure can be achieved with a fully passive vibration absorber. Experiments will be conducted to obtain further results with an improved analogous electrical network.

REFERENCES

- [1] Den Hartog, J.P. *Mechanical Vibrations* McGraw-Hill (1940).
- [2] Hagood, N.W. and von Flotow, A. Damping of structural vibrations with piezoelectric materials and passive electrical networks. *J. Sound Vib.* (1991) **146**:243–268.
- [3] Habib, G. and Kerschen, G. A principle of similarity for nonlinear vibration absorbers. *Physica D* (2016) **332**:1–8.
- [4] Soltani, P. and Kerschen, G., The nonlinear piezoelectric tuned vibration absorber, *Smart. Mater. Struct.* (2015) **24**:075015.

- [5] Lossouarn, B., Deü, J.-F. and Kerschen, G. A fully passive nonlinear piezoelectric vibration absorber. *Phil. Trans. R. Soc. A* (2018) **376**:20170142.
- [6] Raze, G., Lossouarn, B., Paknejad, A., Zhao, G., Deü, J.-F., Collette, C. and Kerschen, G. A multimodal nonlinear piezoelectric vibration absorber. *In Proc. ISMA2018* (2018) 63-77.
- [7] Andreaus, U., dell’Isola, F. and Porfiri, M. Piezoelectric passive distributed controllers for beam flexural vibrations. *J. Vib. Control* (2004) **10**:625–659.
- [8] Lossouarn, B., Deü, J.-F. and Aucejo, M. Multimodal vibration damping of a beam with a periodic array of piezoelectric patches connected to a passive electrical network. *Smart Mater. Struct.* (2015) **24**:115037.
- [9] Thomas, O., Ducarne, J., Deü, J.-F. Performance of piezoelectric shunts for vibration reduction. *Smart. Mater. Struct.* (2012) **21**:015008.
- [10] Gluskin, E. The use of non-linear capacitors. *Int. J. Electron.* (1985) **58**:63–81.
- [11] Raze, G., Jadoul, A., Broun, V. and Kerschen, G. A Simplified Current Blocking Piezoelectric Shunt Circuit for Multimodal Vibration Mitigation. *In Proc. IMAC XXXVII* (2019).
- [12] Wu, S.Y. Method for multiple mode piezoelectric shunting with single PZT transducer for vibration control. *J. Intel. Mater. Syst. Struct.* (1998) **9**:991-998.
- [13] Fleming, A.J., Behrens, S. and Moheimani, S.O.R. Reducing the inductance requirements of piezoelectric shunt damping systems. *Smart Mater. Struct.* (2003) **12**:57.

A MULTI-SCALE REINFORCED SANDWICH PANEL FOR VIBROACOUSTIC APPLICATIONS: SHEAR TRANSITION EFFECTS

R. PALUMBO^{*,†}, D. IVANOV^{*}, C. DROZ[†], F. SCARPA^{*}, O. BAREILLE[†] AND M.N. ICHCHOU[†]

^{*} Bristol Composites Institute (ACCIS)

University of Bristol

Queen's Building, University Walk, BS8 1TR Bristol, United Kingdom

e-mail: work-with-accis@bristol.ac.uk - Web page:

<http://www.bristol.ac.uk/research/institutes/composites/>

[†] Vibroacoustics Complex Media Research Group (LTDS - CNRS UMR 5513)

Ecole Centrale de Lyon

69130, Ecully, France

e-mail: sandrine.bec@ec-lyon.fr - Web page: <http://ltds.ec-lyon.fr>

Key words: Sandwich panels, renewable materials, nanocomposites, shear core transition, vibroacoustics

Abstract. Sandwich panels exhibit outstanding mechanical performances due to their high bending-stiffness-to-weight ratio. However, a high specific rigidity has usually negative impact on vibroacoustic performances. In the current industrial scenario, acoustic comfort is a fundamental quality criterion and it is vital to start to include vibroacoustic design rules at early stages of products development. The aim of this work is the design of a sandwich panel with enhanced vibroacoustic performances in the low-to-mid frequency range. Novel materials and manufacturing techniques are adopted to develop the sandwich panel: flax fibers in poly furfuryl alcohol for the square-cell core and the skins; carbon-nanotube reinforced resin as viscoelastic inserts. The results of material characterization tests are presented in this work, as well as the application of a design procedure for the viscoelastic inclusions.

1 INTRODUCTION

Object of this work is the design of a sandwich panel with enhanced vibroacoustics characteristics. More in detail, the main target is to delay the panel's bending-shear transition frequency, ω_T , towards higher values by embedding viscoelastic depositions within the core, with the main limitation of keeping the added mass to low percentages. The bending-shear transition identifies the shift from the low frequencies range, where sandwich panels dynamic behaviour is governed by the whole section bending stiffness, to higher frequencies, where core shear effects become dominant [1]. The latter regime is usually associated with a lower transmission loss, leading to unsuitable acoustic comfort. Shifting ω_T towards higher frequencies mirrors an improvement in the sound transmission loss through the panel in the mid frequencies range [2] and allows an easier control of the acoustic transmission e.g. by adopting porous inclusions. This is why ω_T is becoming a vibroacoustic indicator of great interest [3] [4]. Figure 1 shows typical dispersion curves of sandwich panels, highlighting the above-mentioned transition.

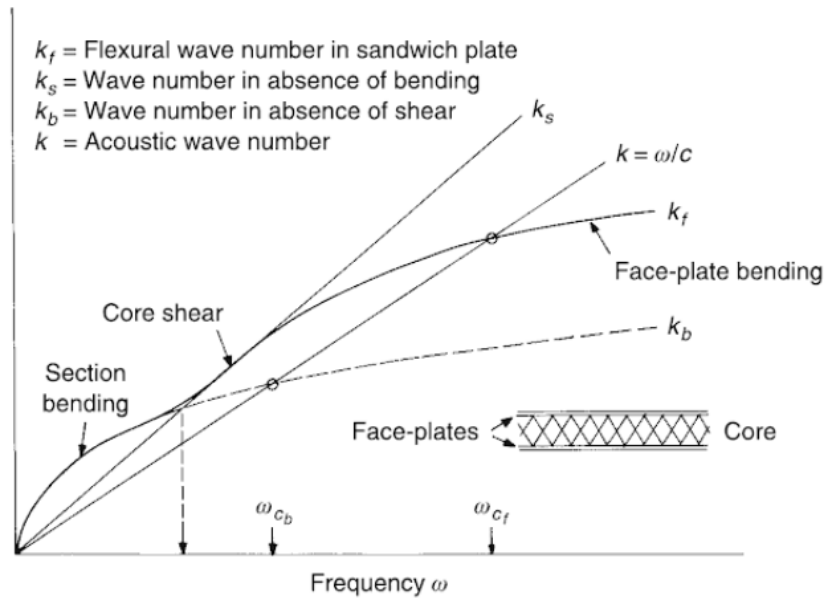


Figure 1: Typical sandwich panels dispersion curve [1]

Novel materials and manufacturing techniques are adopted to develop a multi-scale reinforced sandwich panel: flax fibers in poly furfuryl alcohol (PFA) resin for core walls and skins; carbon-nanotube (CNT) reinforced bio-resin for the viscoelastic depositions. Natural fibers provide lower environmental impact, higher vibration damping and lower density than traditionally used materials, i.e. polymers, aluminium. PFA is an eco-friendly, 100% bio-derived resin. Finally, viscoelastic inserts are deposited at the square-cell core walls junctions by means of a Liquid Resin Printing (LRP) technique. Other than offering core strengthening and vibration damping, their main purpose is increasing the out-of-plane shear stiffness of the sandwich panel, which has a direct impact on ω_t . Figure 2 shows the Finite Element model of a quarter of unit cell with no skins and the resin deposition at the corner [5].

This paper is structured in two main sections: firstly, the results of materials mechanical characterization tests are shown; then, the design procedure of viscoelastic inclusions described in [5] is applied to our case, taking into account the actual measured properties of core, skins and inserts' materials.

2 MATERIALS MECHANICAL CHARACTERIZATION

2.1 Core and skins: Biotex Flax

As introduced in the previous paragraph, the material chosen for the core walls and skins of the sandwich panels consists of natural fibers in a bio-derived epoxy resin. More in detail, the composite is a prepreg provided by Composites Evolution Ltd, Biotex Flax 400 g/m² 2x2 twill pre-impregnated in PFA resin. Flax fibers provide good performance, together with a combination of sustainability and processability. Moreover, they offer reduced weight, lower environmental impact, higher vibration damping and safer handling compared to traditionally used fibers, such as glass. On the other hand, PFA is a thermosetting bioresin derived from crop waste. It resembles phenolic resins, but with lower volatile organic compounds (VOC) emissions. Indeed, PFA presents fire retardant properties equivalent to phenolics, other than very good temperature and chemical resistance.

Laminates consisting of four layers of prepreg were cured in autoclave at a temperature of 140°

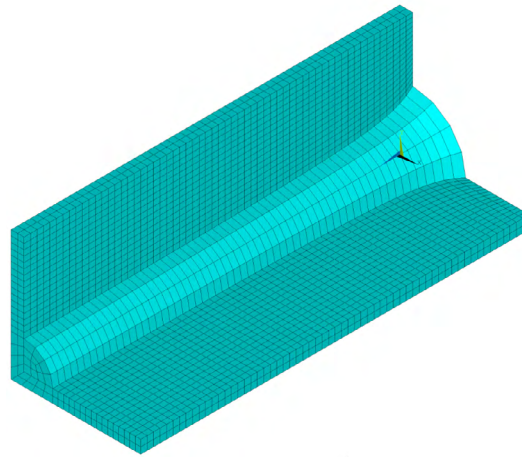


Figure 2: FE model of one-quarter unit cell in case of hyperbolic insert profile [5] - ANSYS® Mechanical APDL

degrees and a pressure of 100 psi. Two fibers orientations were considered: one with the twill at 0/90 degrees, the other at 45 degrees. Tensile tests specimens were cut from the final 2.2-mm-thick laminates according to the ASTM D3039 standards. Tensile tests were performed by means of a Shimadzu testing machine with 10 kN load cell. Emery cloth was used for the gripping of the samples, once checked that it was a valid and more practical substitute to end tabs. Finally, a video gauge was adopted for the measurements of longitudinal and transverse strains.

Data were post-processed in Matlab. Linear regression curves were calculated from the video gauge data in the material's elastic range and were used to evaluate the Poisson's ratio. The in-plane shear modulus was found by post-processing the data of tensile tests on specimens with fibers orientation at 45 degrees (ASTM D3518). All data underwent the Chauvenet criterion, in order to define the outliers to be discarded in the evaluation of the batches' statistic properties.

Figures 3 and 4 show the curves of tensile tests on the 0/90 degree and 45 degree fiber orientation samples.

Table 2.1 reports a summary of the Biotex Flax average in-plane mechanical properties, together with the statistic characteristics of data.

Table 1: Summary of in-plane elastic properties of autoclave-cured Biotex Flax laminates

	Mean Value	Standard deviation	Coefficient of variation
Elastic Modulus 0/90 deg	4.03 GPa	0.121 GPa	3.01%
Poisson's ratio	0.336	0.114	33.9%
Shear Modulus	0.957 GPa	0.0656 GPa	6.86%
Elastic Modulus 45 deg	2.93 GPa	0.100 GPa	3.42%

2.2 Viscoelastic inserts: CNT-reinforced resin

As mentioned in the first paragraph, viscoelastic inclusions will be injected at the junction corners of the sandwich core's walls. Their main purpose is increasing the bending-shear transition frequency, by increasing the shear stiffness of the core itself. However, they also contribute to strengthen the panel and

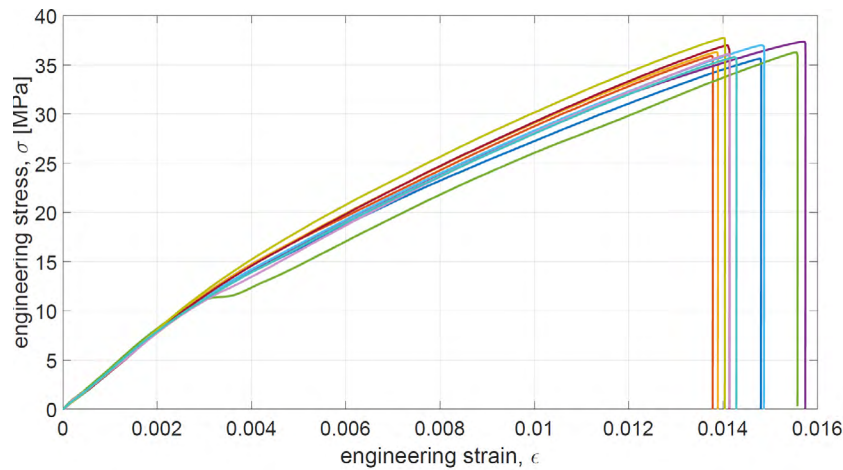


Figure 3: Tensile tests on flax fibers and PFA resin composite. Twill fabric, fibers orientation 0/90 degrees.

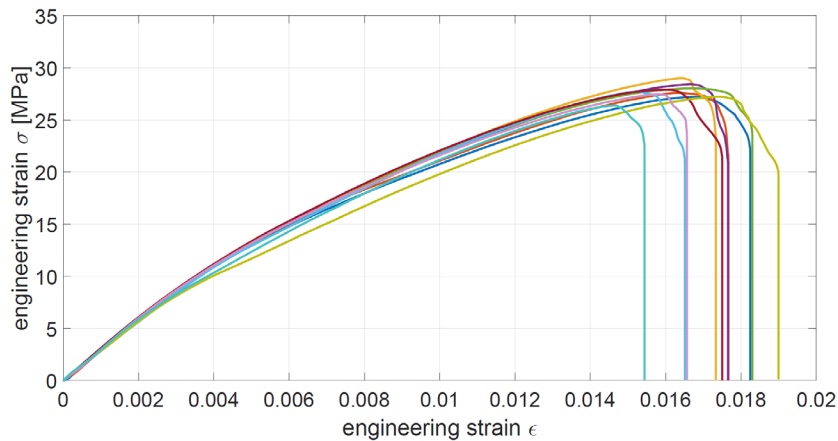


Figure 4: Tensile tests on flax fibers and PFA resin composite. Twill fabric, fibers orientation 45 degrees.

to the vibration damping and energy absorption.

The resin adopted for the inserts is SuperSap (SS) CLV, a special formulation of the highly regarded SuperSap resin system from Entropy Resins. SS CLV is a bio-derived epoxy resin, combining good mechanical properties with high levels of UV stability, clarity and a low viscosity. The low viscosity made it ideal for our purposes. Indeed, the inserts will be injected at the corners by means of a specifically designed injection mould applied to a medical syringe, and the narrow channels through which the resin flows made low viscosity a requirement. On the other hand, as the resin itself is reinforced with Carbon Nanotubes, it is also enough viscous so that once applied to the corners it does not flow too much under the effect of gravity. The resin was mixed to EPOCYL 128-06, a multi-walled-carbon-nanotube (MWCNT) Bis-A epoxy resin concentrate for high mechanical performances provided by Nanocyl SA, by means of a high shear rotor/stator laboratory mixer at 50 rpm. The heat generated in the stirring process helped to obtain a more homogeneous resin. The CNT weight percentage in the final resin is 0.477 wt%.

Specimens of the CNT-reinforced resin for tensile characterization were cured in a silicone mould for dumbbell-shaped specimens according to ASTM D638-14. Once again, tensile tests were performed

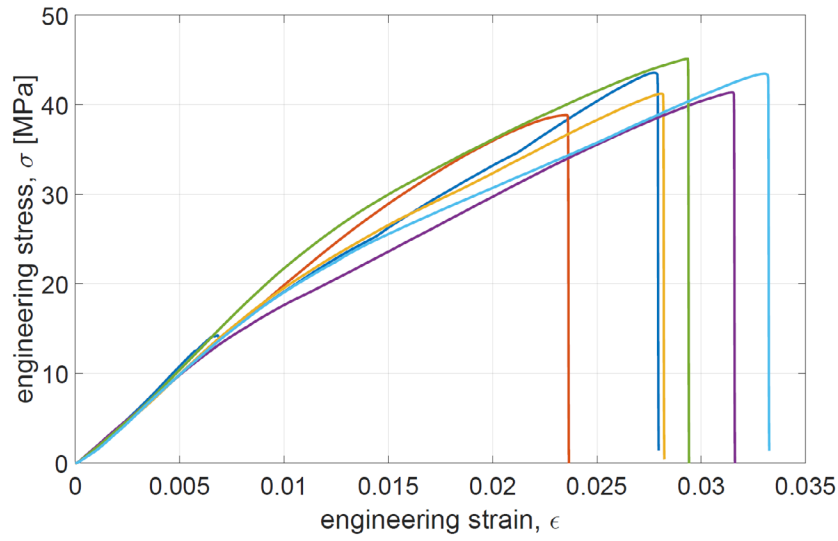


Figure 5: Tensile tests on CLV SS resin reinforced with MWNTs.

using a Shimadzu testing machine with 10 kN load cell and all data underwent the Chauvenet criterion, in order to define the outliers. The results of the tensile tests show a Young Modulus of 1.99 GPa, with a good statistic relevance (0.0655 GPa standard deviation and 3.29% coefficient of variation) - Figure 5.

The same tests were performed on pristine resin samples and in this case the results show a Young Modulus of 1.82 GPa.

In Figure 6, the experimental results are compared to the analytic prediction according to Halpin-Tsai formulation [6] with Thostenson correction [7]. For the resin of interest (Young Modulus of pristine resin of 1.82 GPa and 0.477 wt% - 0.0027 Volume fraction) the formulation predicts a Young Modulus of the resulting composite resin of 1.92 GPa, showing in fact a small error with respect to the measured value.

3 SANDWICH PANEL DESIGN PROCEDURE

The design steps of the viscoelastic inclusions follow the procedure developed in [5]. However, while in [5] the materials properties were assigned from literature values, the analytic and numerical models were here updated with the actual properties measured experimentally, so that the final curves of added mass and transition frequency in function of the inserts dimension are different from those presented in [5] - Figures 7 and 8. Furthermore, the transition analytic expression that was used in this work is the one derived in [8], where the transition phenomenon's definition results from the conversion of the flexural waves in the sandwich panel waveguide. Thus, the transition frequency formulation used here is:

$$\omega_T = \frac{2S}{\sqrt{3\mu D}} \quad (1)$$

where

$$S = h_c G_c \left(1 + \frac{h_s}{h_c} \right)^2 \quad (2)$$

and

$$D = E_s h_s \left(\frac{h_c^2}{2} + h_c h_s + \frac{2h_s^2}{3} \right) \quad (3)$$

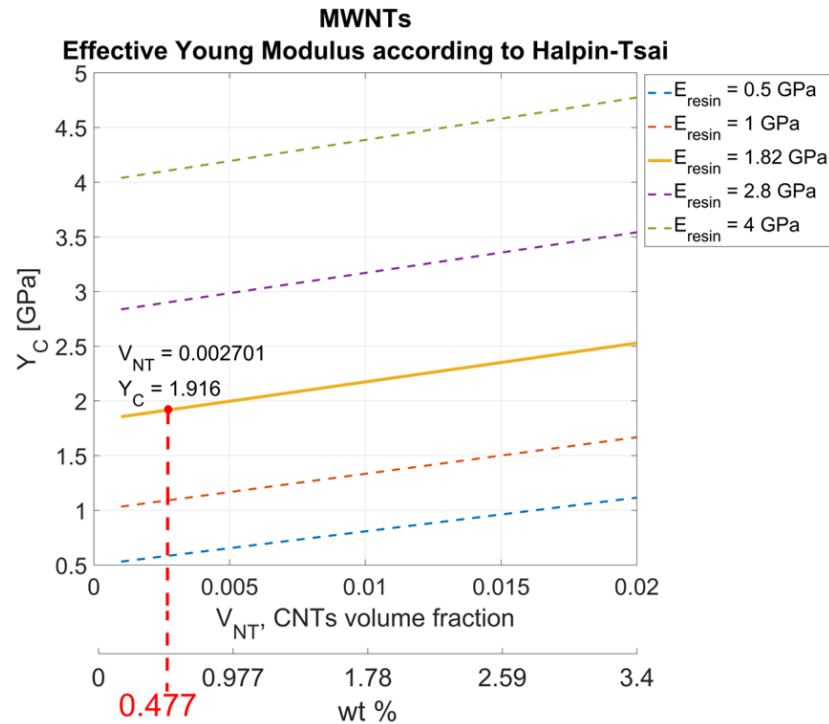


Figure 6: Halpin-Tsai prediction of the composite material's Young Modulus, Y_C , in function of the MWCNTs Volume fraction, V_{NT} , and the pristine resin's Young Modulus, E_{resin} .

are the transverse shear rigidity of the plate and its bending stiffness, respectively, and μ its mass per unit area. On the other hand, in [5] Guillaumie formulation was adopted [9], where the transition frequency is defined from the geometric intersection of the asymptotic bending and shear wavenumbers. This results in a further difference of the graphs presented here from those presented in [5].

Following, a summary of the sandwich panel design steps:

1. The insert's thickness is set to 1.4 mm by defining a limit on the desired added mass to 5% and by considering a cylindrical shape for the insert itself - Figure 7;
2. The inserts resin Young Modulus is a result from the Young Modulus of the pristine resin and the percentage of CNTs dispersed in it - about 2 GPa (3.9% error with the analytic prediction) - Figures 5 and 6;
3. Following the first two steps, the transition frequency is estimated according to [8], with the value of G_c evaluated numerically. Figure 8 shows the ratio between the transition frequency of the reinforced panel and the one of the bare panel. For our configuration, it is expected to be 1.07 (increment of 6.58% with respect to the base configuration).

4 CONCLUSIONS AND FUTURE WORK

This work presented the design of CNT-reinforced inserts of a sandwich panel for vibroacoustic purposes, following its constituent materials mechanical characterization. The design steps developed in a previous work were here updated according to the measured core, skins and inserts' materials properties. The design procedure aims to increase the sandwich panel's transition frequency by means of the

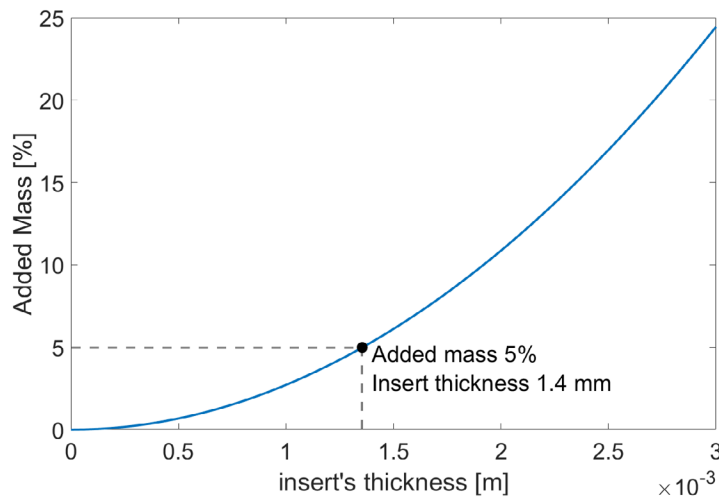


Figure 7: Estimated percentage of added mass in function of the insert dimensions.

viscoelastic inclusions, but at the same time setting limits to the added mass. Indeed, the final inserts thickness is set to 1.4 mm by taking into account a limit of 5% on the added mass to the panel, and an increment of about 7% to the transition frequency is estimated from the numerical/analytic models.

Future work will include the manufacturing of two large-scale sandwich panels of $700 \times 700 \text{ mm}^2$ - one with the viscoelastic inserts and one control panel without - and vibroacoustic numerical investigation and testing. Finally, samples for out-of-plane flatwise compression tests will be manufactured in order to define the inserts contribution to the strength of the panel.

5 Acknowledgements

This work is part of a project that has received funding from the European Unions Horizon 2020 research and innovation programme under the Marie Skłodowska-Curie grant agreement No 675441.

REFERENCES

- [1] Fahy, F. and Gardonio, P. *Sound and Structural Vibration: Radiation, Transmission and Response*. Academic Press, second edition, (2007).
- [2] Zergoune, Z., Ichchou, M. N., Bareille, O., Harras, B., Benamar, R. and Troclet, B. Assessments of shear core effects on sound transmission loss through sandwich panels using a two-scale approach. *Computers Structures* (2017) **182**:227-237.
- [3] Baho, O., Zergoune, Z., Ichchou, M. N., Harras, B., Benamar, R., Troclet, B., Bareille, O. On global bending-shear core transition effects for the vibroacoustics of sandwich structures: Analytical and numerical investigations. *Composite Structures* (2016) **154**:453-463.
- [4] Droz, C., Zergoune, Z., Boukadia, R., Bareille, O., Ichchou, M.N. Vibro-acoustic optimization of sandwich panels using the wave/finite element method. *Composite Structures* (2016) **156**:108-114.
- [5] Palumbo, R., Ivanov, D., Droz, C., Bareille, O., Ichchou, M. and Scarpa, F. Design of a multi-scale reinforced sandwich panel with enhanced vibroacoustics performances. *ISMA2018-USD2018 Proceedings*.

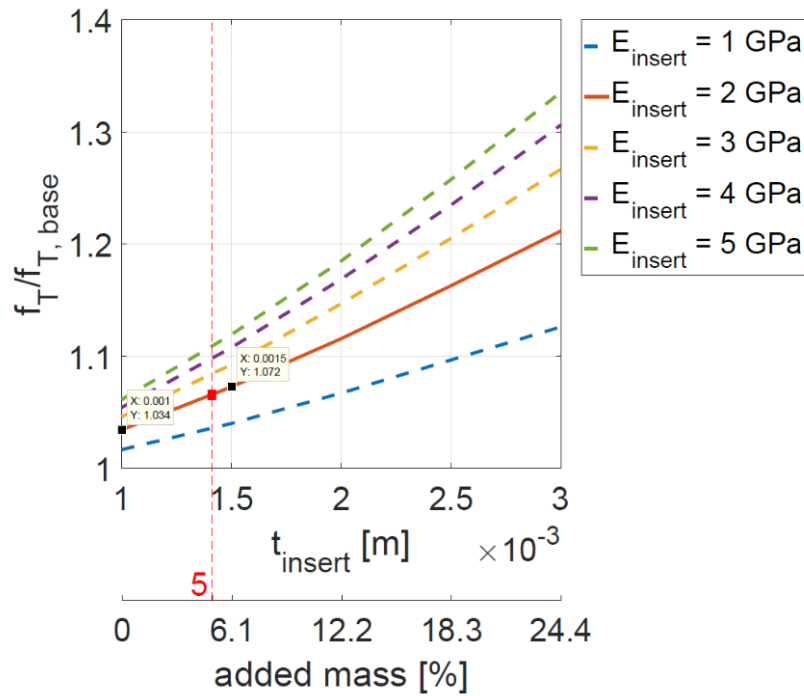


Figure 8: Predicted transition frequency ratio in function of the inserts resin stiffness and dimension.

- [6] Halpin, J. C., Tsai, S. W., Environmental factors in composite material design. *US Air Force Materials Laboratory Report* (1969), AFML-TR 67 - 423.
- [7] Thostenson, E. T., Chou, T. On the elastic properties of carbon nanotube-based composites: modelling and characterization. *Journal of Physics D: Applied Physics* (2003) **36**:573-582.
- [8] Droz, C., Bareille, O. and Ichchou, M. A new procedure for the determination of structural characteristics of sandwich plates in medium frequencies. *Composites Part B* (2017) **112**:103-111.
- [9] Guillaumie, L. Vibroacoustic flexural properties of symmetric honeycomb sandwich panels with composite faces. *Journal of Sound and Vibration* (2015) **343**:71-103.

A WAVE-BASED METHODOLOGY FOR THE OPTIMIZATION OF FINITE 1D METAMATERIALS

R. F. BOUKADIA^{1,2,3}, E. DECKERS^{1,2}, C. CLAEYS^{1,2}, M. ICHCHOU³,
W. DESMET^{1,2}

¹ Departement of Mechanical Engineering, PMA Section, Noise And Vibration Research Group
KU Leuven
Celestijnenlaan 300 - box 2420 3001 Leuven, Belgium
e-mail : regis.boukadia@kuleuven.be, elke.deckers@kuleuven.be, claus.claeys@kuleuven.be,
wim.desmet@kuleuven.be

² DMMS lab, Flanders Make

³ Vibroacoustics & Complex Media Research Group, LTDS – CNRS UMR 5513,
Ecole Centrale de Lyon, France
36 Avenue Guy de Colongue Bat. E6, 69134 Écully, France
e-mail: mohamed.ichchou@ec-lyon.fr

Key words: Optimization, WFEM, Source Effect, Boundary Conditions, Computing Methods.

Abstract. Metamaterials are artificial, engineered materials with properties that are not found in nature. They are typically formed by an assembly of reoccurring patterns whose scale is (generally) smaller than the phenomena they influence. In the vibro-acoustic community metamaterials are mostly known for their stopband behavior that can be used to reduce noise and vibrations beyond what is dictated by the mass law. This behavior can be predicted during the design stage using unit cell modeling techniques such as the Wave Finite Element Method (WFEM) and the Shift Cell Operator Method to compute the propagation constants of the relevant waves. As a consequence, most design optimization schemes have focused solely on maximizing the spatial attenuation of targeted waves. However, dispersion characteristics alone cannot predict the performance of metamaterial solutions once deployed because they neglect their operating environments, finiteness and boundary conditions applied. For instance, the presence of edge modes may result in increased and localized vibration energy, deteriorating the effect of the treatment. This paper presents a second order optimization scheme based on the 1D WFEM framework enabling the optimization of the response of finite metamaterial solutions. The proposed methodology is validated on a simple model updating case and subsequently applied to the design of a resonant metamaterial.

1 INTRODUCTION

As constraints on the weight and volume of vibro-acoustic packages become more important, the interest in metamaterial based solutions increase. This interest is mostly driven by the stopband behavior exhibited by some periodic structures enabling attenuation properties that

go beyond the mass law. So far, the Wave Finite Element Method and the Shift Cell Operator Method have been the most popular tools to study and engineer smart structures based on this concept because they allow the computation of the dispersion characteristics of a periodic medium by the discretization of a single unit cell (UC). Studies based on the analysis of dispersion curves and band diagrams have become standard and designs including perforations or resonant add-ons have been used to open bandgaps around targeted frequencies [1]–[3]. More recently, numerical methods have been used to obtain bandgaps with maximal width and attenuation properties in phononic crystals [4], [5] or specific anisotropic behavior in meta-structures [6]. However, most of the studies in the literature stop their analysis at the stop band level without investigating the impact of boundary conditions, operating environment, load characteristics and finite size effects on the performance of metamaterial solutions. While research targeted those topics from a theoretical or qualitative point of view [7]–[10], not many studies deal with those topics applying detailed numerical modeling [11]. This paper presents a second order optimization scheme based on the 1D WFEM framework that accounts for load characteristic, boundary conditions and finiteness of metamaterial solutions.

2 FORCED RESPONSE OF A 1D WAVEGUIDE USING THE WFEM

Given the unit cell of a 1D periodic structure, its mass, damping and stiffness matrices, K , M and C are considered. A partition of its degrees of freedom (dofs) U is also established following the spatial structure of the UC:

$$U = \begin{bmatrix} U_L \\ U_I \\ U_R \end{bmatrix} \quad (1)$$

The subscripts R , L and I are used for variables associated with the right, left and internal dofs of the UC. Additionally, the subscript B will be used for quantities associated to all interface dofs.

The first step in the direct WFEM scheme is to form the dynamic stiffness matrix G for a given circular frequency ω :

$$G = K + i \omega C - \omega^2 M \quad (2)$$

The internal dofs of the UC are then condensed in order to form D the condensed dynamic stiffness matrix:

$$D = G_{BB} - G_{BI} G_{II}^{-1} G_{IB} \quad (3)$$

Applying the Floquet-Bloch boundary conditions leads to an eigenvalue problem with propagations constants and waveshapes as solutions:

$$\left(\lambda D_{LR} + (D_{LL} + D_{RR}) + \frac{1}{\lambda} D_{RL} \right) \Psi = 0 \quad (4)$$

The eigenvalue problem of equation (4) yields the wave shapes Ψ_k and propagation constants λ_k of free waves in the periodic medium at the circular frequency ω . It should be noted that the propagation constants come in pairs $(\lambda_k, \frac{1}{\lambda_k})$ with eigenvectors (Ψ_k^+, Ψ_k^-) that correspond to waves traveling in the positive and negative direction. Using this information, it is possible to compute the forced response of a finite waveguide comprised of N UCs by relating the wave amplitudes to the excitations and boundary conditions. In case of a Clamped-Free waveguide, the following equations are given:

$$\begin{pmatrix} \Psi^+ & \Psi^- \Lambda^N \\ D_{RL} \Psi^+ \Lambda^{N-1} + D_{RR} \Psi^+ \Lambda^N & D_{RL} \Psi^- \Lambda + D_{RR} \Psi^- \end{pmatrix} \begin{bmatrix} q^+ \\ q^- \end{bmatrix} = \begin{bmatrix} U_L \\ F_R \end{bmatrix} \quad (5)$$

The displacement at the i^{th} section of the waveguide being given by:

$$V_i = \Psi^+ \Lambda^i q^+ + \Psi^- \Lambda^{N-i} q^- \quad (6)$$

3 SECOND ORDER NON-LINEAR OPTIMIZATION

This Section describes the second order optimization strategy used in the examples presented in Section 4. The strategy is developed to account for two characteristics of the WFEM. Firstly, obtaining accurate derivatives by numerical differentiation is very hard because of the low numerical accuracy of the WFEM as compared to usual FEM modeling [12]. Secondly, computing the response of a waveguide is relatively cheap because all computations are done on a single UC. It follows that semi-analytical gradients and Hessians of C^2 objective functions can be computed at an acceptable cost. Making use of the available second order information, an algorithm that combine both line search and trust region methods is proposed.

Let's note f an objective function and $p \in \mathbb{R}^n$ the vector of optimization variables. The variables may be subject to a set of n_e convex equality constraints $\forall i \in \llbracket 1, n_e \rrbracket E_i(p) = 0$ and n_c convex inequality constraints $\forall j, \llbracket 1, n_c \rrbracket C_j(p) \leq 0$. For a starting point p_0 , the function value $f(p_0)$, the gradient $\nabla f(p_0)$ and the Hessian $\nabla^2 f(p_0)$ are computed. A surrogate function \tilde{f} that approximates f around p_0 is then used.

$$f(p) \approx \tilde{f}(p) = f(p_0) + \nabla f(p_0)(p - p_0) + \frac{1}{2}(p - p_0)^T \nabla^2 f(p_0)(p - p_0) \quad (7)$$

If the Hessian is positive definite. A line search method is used:

$$v = \operatorname{argmin}\{\tilde{f}(p_0 + v), E_i(p_0 + v) = 0, C_j(p_0 + v) \leq 0\} \quad (8)$$

Equation (8) can be solved using the interior point method [13] or analytically when there are no constraints. Once the search direction v is obtained. f is minimized in the v direction:

$$\alpha_m = \operatorname{argmin}\{f(p_0 + \alpha v), \alpha \in [0; 1]\} \quad (9)$$

Defining the next iteration:

$$p_1 = p_0 + \alpha_m v \quad (10)$$

When the Hessian is not positive definite, a trust region method [13]–[16] is used. The first step is to define $|\nabla^2 f(p_0)|$. This matrix is obtained by keeping the eigenvectors of $\nabla^2 f(p_0)$ and taking the absolute value of all its eigenvalues. A supplementary constraint is then introduced:

$$T(p) = (p - p_0)^T |\nabla^2 f(p_0)| (p - p_0) - R_0^2 \leq 0 \quad (11)$$

The trust region's radius R_0 is updated at each iteration to make sure that the surrogate function can be trusted. In practice it is adjusted so that decreases or increases in the objective function are correctly predicted by the surrogate model:

$$\forall p \in \mathbb{R}^n, \quad T(p) \leq 0, \quad \frac{f(p) - f(p_0)}{\tilde{f}(p) - f(p_0)} > \frac{1}{4} \quad (12)$$

Guidelines and algorithms about how to update the trust region radius R_i at each iteration can be found in [13]. Summarized, the optimization algorithm consists of the following steps:

1. Select an initial point p_0 .
2. Compute $f(p_0)$, $\nabla f(p_0)$ and $\nabla^2 f(p_0)$
3. Assume: $f(p) \approx \tilde{f}(p) = f(p_0) + \nabla f(p_0)^T (p - p_0) + \frac{1}{2} (p - p_0)^T \nabla^2 f(p_0) (p - p_0)$
- 4.a If $\nabla^2 f(p_0) > 0$ use line search with Newton direction v .
Find an approximate the minimizer α_m of : $\{f(p_0 + \alpha v), \quad \alpha \in [0 ; 1]\}$
Define $p_1 = p_0 + \alpha_m v$
- 4.b Else a trust-region method is used to take the step:
Define $p_1 = \operatorname{argmin}\{\tilde{f}(p), T(p) \leq 0, E_i(p) = 0, C_j(p) \leq 0\}$
5. Iterate steps 2 to 4 until convergence.

4 NUMERICAL EXAMPLES

4.1 Application to parameter identification

In this subsection the method is used in a parameter identification scheme as mean of validation. A 1m meter long beam with a 1cm by 3cm rectangular cross-section and unknown material properties is considered. Assuming a Poisson's ratio of 0.3, the cross section of a beam with unitary density ρ and unitary Young's modulus E is modeled using ANYS APDL 17.0 to serve as the basis for a parametric model. The corresponding UC is shown in Figure 1. The mass matrix M_0 and stiffness matrix K_0 are then used in a model for which the density, the real part and the imaginary part of the Young's modulus are the parameters as specified in equation (13).

$$\begin{cases} K(p) = (E_r + iE_i)K_0 \\ M(p) = \rho M_0 \\ p = \begin{bmatrix} E_r \\ E_i \\ \rho \end{bmatrix} \end{cases} \quad (13)$$



Figure 1: Unit cell for the cross-section of the beam (1cm by 3cm by 0.556mm)

Clamped-Free boundary conditions are used and a unit force of 1N is applied at the free end of the beam. The direct forced response is computed on the 10Hz-1000Hz frequency range for material parameters values corresponding to those of aluminum:

- Real part of the Young modulus $E_r^0 = 69.10^9 Pa$
- Hysteretic damping $\eta_0 = 0.3\%$
- Imaginary part of the young modulus: $E_i^0 = E_r^0 \eta_0 = 2,07.10^9 Pa$
- Density $\rho^0 = 2700$
- Poisson's ratio $\nu = 0.3$

This response, $X_0(\omega)$, is used to build an error function f that evaluates the difference between the reference and a response obtained using a material property vector p .

$$f(p) = \frac{1}{\omega^+ - \omega^-} \int_{\omega^-}^{\omega^+} \|\log(|X_0(\omega)|) - \log(|X(\omega, p)|)\|^2 d\omega \quad (14)$$

In equation (14) the logarithm ensures that the objective function is sensitive to the information available on the full frequency range. Without this precaution, modal frequencies

would dominate the error evaluation because this is where most of the signal's energy is located.

The optimization process is started with material properties $\rho = 1300 \text{ kg.m}^{-3}$, $E_r = 90.10^9 \text{ Pa}$ and $E_i = 1,08.10^9 \text{ Pa}$. The optimization path of each variable is given in Figure 2.

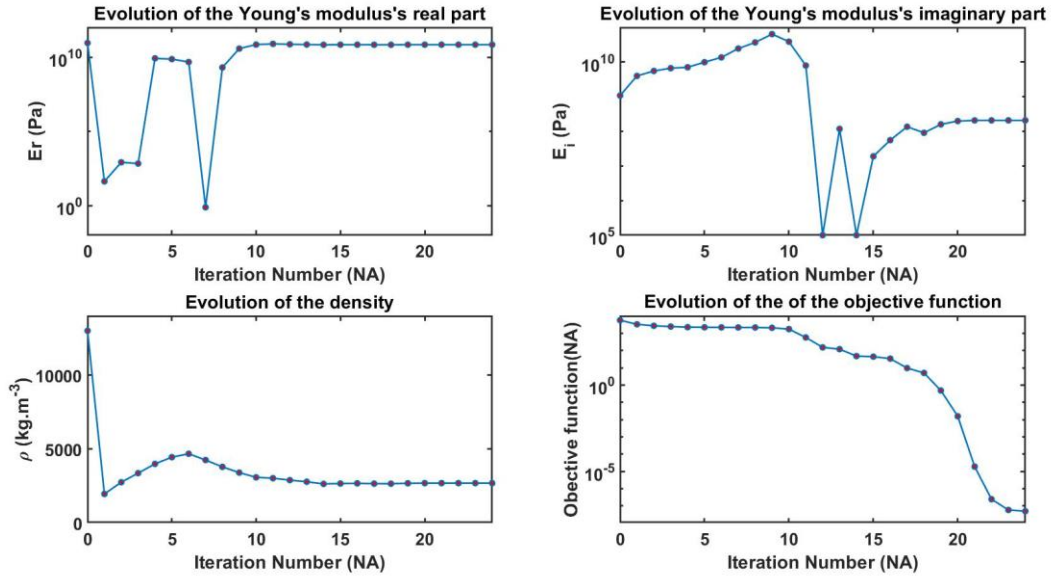


Figure 2: Evolution of the material properties and the objective function

Convergence to the original material properties is reached in 24 iterations validating the method and its implementation.

4.2 Optimization of a metamaterial design

In this subsection, the wave-based methodology is applied to the optimization of the mean square velocity of a 1 m long steel beam with a square section of side length 1cm and Clamped-Free boundary conditions, subjected to a 1N force applied on its free side. The optimization variables are the mass, stiffness and damping parameters of the periodic resonant add-ons used to treat the host structure. The length of the UC is decided beforehand and fixed to 5cm, hence the beam contains 20 UCs.

The variables of the problem are:

- The added mass to the UC (cannot be negative and shall not exceed 20% of the host structure).
- The stiffness of the spring (cannot be negative)
- The damping of the spring (cannot be negative and shall not exceed 10%)
- The position of the resonator in the UC (should be between 5mm and 4.5cm). The corresponding optimization variable is normalized to be in the $[0, 1]$ interval.

The objective function takes the form:

$$f(p) = \frac{1}{\omega^+ - \omega^-} \int_{\omega^-}^{\omega^+} \frac{1}{N} \sum_i \omega^2 |X_i(p, \omega)|^2 d\omega$$

Where $X_i(p, \omega)$ is the frequency forced response of the i^{th} section of the waveguide for a unitary load on the free side and N is the number of UCs.

The derivatives of the resonator's position are computed by taking advantage of the fact that length appears explicitly in the formula for Euler-Bernoulli elements. However, elements size do not change at each iteration. Instead, re-meshing occurs when different parameter values are used. For the optimization, the 5th mode of the bare structure around 712Hz is targeted. The frequency band of optimization, 648Hz-919Hz, is defined by the two anti-resonances surrounding the 5th mode in the direct forced response of the bare structure. The second order optimization methodology described in Section 2 is applied for a random starting p_0 in the design space and the results obtained are presented in Figure 3 and Figure 4.

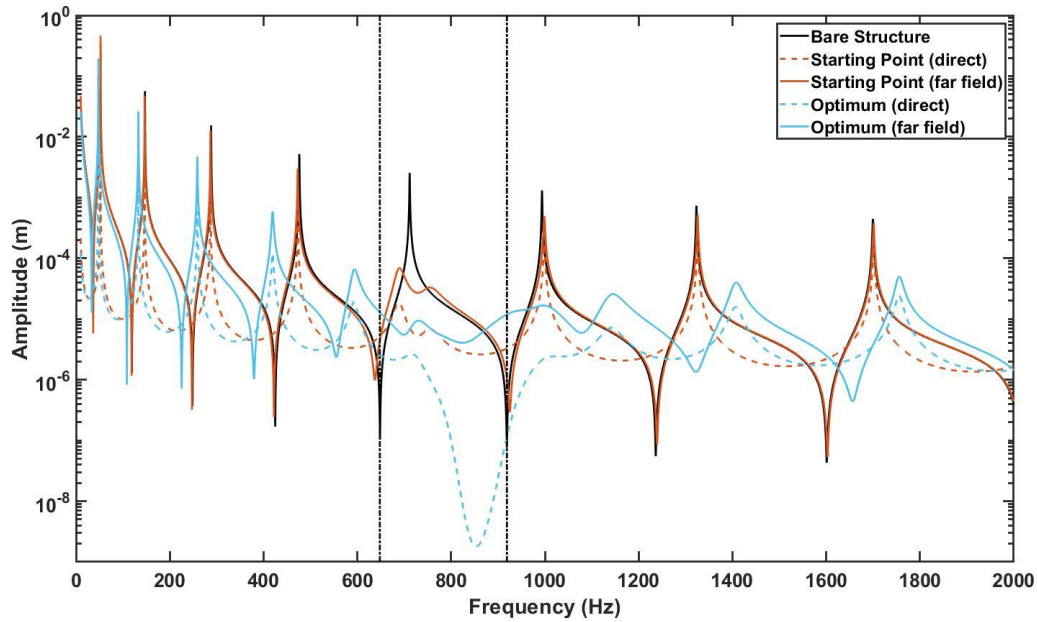


Figure 3: Response of the bare structure (direct), starting point (direct and far field) and optimum (direct and far field). The vertical dashed lines indicate the frequency band of optimization

In Figure 3 the direct forced response for the bare structure, the starting point of the optimization, and the optimum are shown. Additionally, the response at section 1 (near the clamped side) is presented for the starting point and the optimum so that the stopband behavior can be evaluated in both cases. The value of the optimization variables at each iteration can be observed in Figure 4.

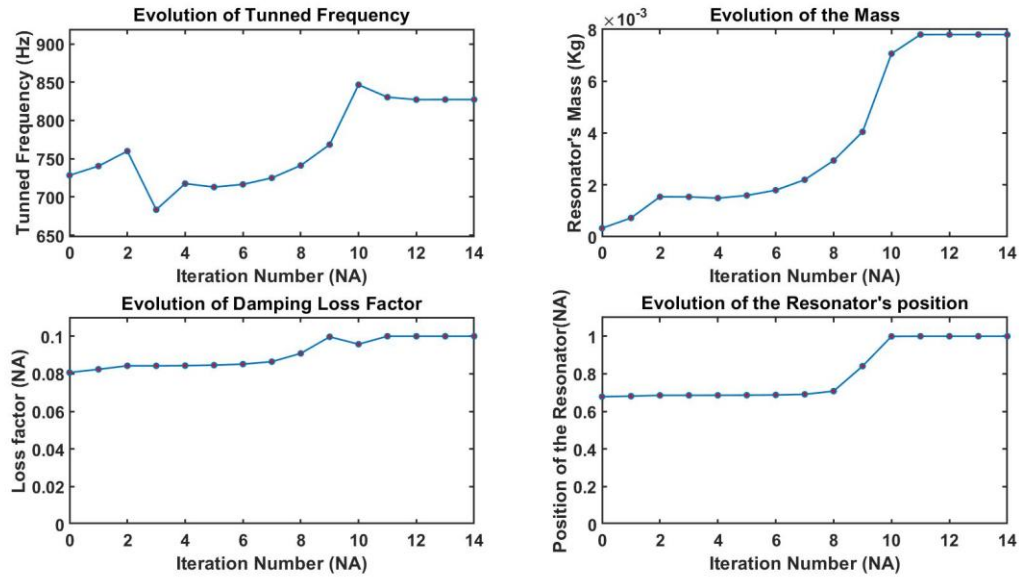


Figure 4: Optimization path in the design space

Unsurprisingly, maximizing the added mass and loss factor results in optimal performances. However, having the tuned resonance frequency on the targeted mode or at the center of the targeted frequency band does not. Similarly, the resonator's position in the UC is not a neutral parameter. These observations cannot be predicted from simple dispersion analysis and highlight the need to account for boundary conditions, finiteness and source location properties during the design phase.

5 CONCLUSIONS

A second order optimization scheme for 1D WFEM analysis was presented. The scheme accounts for both strong and weak points of the WFEM namely the decoupling of the computation cost from the size of the waveguide and the lower accuracy of the WFEM as compared to FEM. The method is versatile and can be used in a range of applications including parameter identification, homogenization, model updating and design optimization.

ACKNOWLEDGEMENTS

The research of R. F. Boukadia is funded by an Early Stage Researcher grant within the European Project VIPER Marie Curie Initial Training Network (GA 675441). The research of E. Deckers is funded by a grant from the Research Foundation – Flanders (FWO). This research is partially supported by Flanders Make, the strategic research centre for the manufacturing industry.

REFERENCES

- [1] A. Nateghi, L. Van Belle, C. Claeys, E. Deckers, B. Pluymers, and W. Desmet, “Wave propagation in locally resonant cylindrically curved metamaterial panels,” *Int. J. Mech. Sci.*, vol. 127, no. January 2016, pp. 73–90, 2017.
- [2] A. O. Krushynska, M. Miniaci, F. Bosia, and N. M. Pugno, “Coupling local resonance with Bragg band gaps in single-phase mechanical metamaterials,” *Extrem. Mech. Lett.*, vol. 12, pp. 30–36, 2017.
- [3] C. Claeys, N. G. Rocha de Melo Filho, L. Van Belle, E. Deckers, and W. Desmet, “Design and validation of metamaterials for multiple structural stop bands in waveguides,” *Extrem. Mech. Lett.*, vol. 12, pp. 7–22, 2017.
- [4] S. Hedayatrasa, K. Abhary, M. Uddin, and C. T. Ng, “Optimum design of phononic crystal perforated plate structures for widest bandgap of fundamental guided wave modes and maximized in-plane stiffness,” *J. Mech. Phys. Solids*, vol. 89, pp. 31–58, 2016.
- [5] S. Hedayatrasa, M. Kersemans, K. Abhary, M. Uddin, J. K. Guest, and W. Van Paeppegem, “Maximizing bandgap width and in-plane stiffness of porous phononic plates for tailoring flexural guided waves: Topology optimization and experimental validation,” *Mech. Mater.*, vol. 105, pp. 188–203, 2017.
- [6] E. Andreassen, H. R. Chang, M. Ruzzene, and J. S. Jensen, “Optimization of directional elastic energy propagation,” *J. Sound Vib.*, vol. 379, pp. 53–70, 2016.
- [7] M. Xiao, Z. Q. Zhang, and C. T. Chan, “Surface impedance and bulk band geometric phases in one-dimensional systems,” *Phys. Rev. X*, vol. 4, no. 2, pp. 1–12, 2014.
- [8] R. Süssstrunk and S. D. Huber, “Observation of phononic helical edge states in a mechanical topological insulator,” *Science*, vol. 349, no. 6243, pp. 47–50, Jul. 2015.
- [9] R. K. Pal, M. Schaeffer, and M. Ruzzene, “Helical edge states and topological phase transitions in phononic systems using bi-layered lattices,” *J. Appl. Phys.*, vol. 119, no. 8, 2016.
- [10] J. Zak, “Berrys phase for energy bands in solids,” *Phys. Rev. Lett.*, vol. 62, no. 23, pp. 2747–2750, 1989.
- [11] L. Sangiuliano, E. Deckers, and C. Claeys, “Control of edge modes in finite vibro-acoustic resonant metamaterials,” in *Proceedings of ISMA2018-USD2018*, 2018.
- [12] Y. Waki, B. R. Mace, and M. J. Brennan, “Numerical issues concerning the wave and finite element method for free and forced vibrations of waveguides,” *J. Sound Vib.*, vol. 327, no. 1–2, pp. 92–108, 2009.
- [13] J. Nocedal and S. Wright, *Numerical optimization, series in operations research and financial engineering*. 2006.
- [14] Y. Dauphin, R. Pascanu, C. Gulcehre, K. Cho, S. Ganguli, and Y. Bengio, “Identifying and attacking the saddle point problem in high-dimensional non-convex optimization,” pp. 1–9, 2014.
- [15] R. Pascanu, Y. N. Dauphin, S. Ganguli, and Y. Bengio, “On the saddle point problem for non-convex optimization,” May 2014.
- [16] T. Lefebvre, F. De Belie, and G. Crevecoeur, “A Radial Basis Function based Optimization Algorithm with Regular Simplex set geometry in Ellipsoidal Trust-

Regions,” May 2018.

ABSORPTION ENHANCEMENT IN PORO-ELASTIC MATERIALS BY MASS INCLUSION, EXPLOITING THE MASS-SPRING EFFECT

SEPID E AHSANI^{1,2}, ELKE DECKERS^{1,2}, TOMASZ G. ZIELIŃSKI³, LUKASZ JANKOWSKI³, CLAU S CLAEYS^{1,2}, AND WIM DESMET^{1,2}

¹ Department of Mechanical Engineering, Division PMA
KU Leuven
Celestijnenlaan 300-box 2420, 3001 Heverlee, Belgium
e-mail: sepide.ahsani@kuleuven.be

²DMMS lab, Flanders Make
3001 Heverlee , Belgium

³ Institute of Fundamental Technological Research
Polish Academy of Sciences
ul. Swietokrzyska 21, 00-049Warszawa, Poland

Key words: Meta-porous material, Biot-Allard poroelastic model, Mass-spring effect

Abstract. In this paper the possibility of enhancing the absorption coefficient of a poro-elastic material using small, elastic mass inclusions in frequencies lower than the quarter-wavelength resonance of the porous material is discussed. We show that absorption peaks can be achieved not only by what is known in literature as the trapped mode effect, but also by the resonance of small elastic inclusions at low frequencies, which can be interpreted as a mass-spring effect. In this work, the inclusion and the porous skeleton is considered elastic and fully coupled to each other, therefore accounting for all types of energy dissipation i.e. viscous, thermal, and structural losses and energy dissipated due to the relative motion of the fluid phase and the frame excited by the resonating inclusion. Additionally, the inclusions are also modeled as motionless and rigid to distinguish between the trapped mode and/or the modified frame mode effect and the mass-spring effect. Moreover, the distinction between these two effects are explained in more detail by comparing the dissipated energy by each mechanism (viscous, thermal and structural effect).

1 INTRODUCTION

Porous materials are proved to be efficient absorbers in the mid- and high-frequencies, where their thickness is equal/higher than quarter wavelength in the medium. On the other hand, they suffer from lack of efficiency in low-frequencies. A common solution to this problem is to use multi-layered structures, which is, however, limited by the allowable thickness [1]. In the past years, many researchers have been seeking to find alternative solutions to improve the absorption of poro-elastic materials at low-frequencies. One example is using periodic rigid inclusions with the size in the same order of the acoustic wavelength Groby et al. [2] proved that by trapping the energy between the motionless inclusion and the rigid backing, perfect absorption can be achieved under the quarter-wavelength limit. Another

alternative solution was suggested by Lagarrigue et al. [3], who used periodic array of rigid split-ring resonator inclusions to create a meta-porous system to increase the absorption coefficient of the foam with motionless frame significantly near the resonant frequency of the inclusions.

Complementary to the works mentioned above, Zieliński [4] showed that the absorption coefficient of the porous materials can also be improved by small periodic mass inclusions. Inspired by [4], in this paper we investigate the absorption enhancement of poro-elastic materials with small mass inclusions due to the mass-spring effect. Moreover, it is shown that at the resonant frequency of the inclusions, the elastic frame of foam is excited leading to an increase in the phase difference of the solid and fluid part, which results in viscous loss increase at low-frequency. The mass-spring effect is demonstrated by decomposing the absorption coefficient into the three different energy dissipation mechanisms [5] (the viscous, thermal, and structural loss). It is worth mentioning that this effect can be captured, when the targeted frequency lies in the viscous region, and therefore is only applicable to the foams with high value of flow resistivity and/or very small characteristic viscous length.

This paper is structured in four sections. In the second section, the modeling technique used for the porous material and the inclusion is explained. The third section is focused on describing the mass-spring effect by introducing the inclusion in the foam and comparing the acoustic behavior of the homogeneous porous foam layer to the foam layer with inclusion. At last, the paper is concluded in the forth section.

2 Modeling technique

This section consists of two parts. The first part explains the modeling technique used for the poro-elastic material, while the second part describes the models used for the inclusion.

2.1 Poro-elastic material modeling

As mentioned in the previous section, the mass-spring effect can be captured in foams with high viscous loss at low-frequencies, which translate to high value of flow resistivity. Therefore, the effect appears under the decoupling frequency, which requires using the theory of Biot [6] to model the porous material. In this paper the classical $u - p$ formulation [6] of the Biot theory, where the field variables are the displacements of the elastic frame (\mathbf{u}) and the pressure in the pores (p), is used. The Biot poro-elasticity equations in terms of $u - p$ variables are given in the equations below:

$$\nabla \cdot \boldsymbol{\sigma} + \omega^2 (\tilde{\rho}_{11} - \frac{\tilde{\rho}_{12}^2}{\tilde{\rho}_{22}}) \mathbf{u} + \tilde{\gamma} \nabla p = \mathbf{0}, \quad (1)$$

$$\nabla^2 p + \omega^2 \frac{\tilde{\rho}_{22}}{\tilde{R}} p - \omega^2 \tilde{\gamma} \frac{\tilde{\rho}_{22}}{\phi^2} \nabla \cdot \mathbf{u} = 0, \quad (2)$$

with

$$\tilde{\gamma} = \phi (\frac{\tilde{\rho}_{12}}{\tilde{\rho}_{22}} - \frac{\tilde{Q}}{\tilde{R}}). \quad (3)$$

The total inertial and viscous energy dissipation due to relative motion of the two phases is described by $\tilde{\rho}_{11}$, $\tilde{\rho}_{12}$, and $\tilde{\rho}_{22}$, see [6]. Moreover, $\boldsymbol{\sigma}$ is the stress tensor of the solid phase for the frame in vacuum; therefore, it is independent on the displacement (nor rather volumetric strain) in the fluid phase and related purely to the strain of the solid phase:

$$\boldsymbol{\sigma} = (A - \frac{\tilde{Q}^2}{\tilde{R}}) \text{tr}(\boldsymbol{\epsilon}) \mathbf{I} + 2N\boldsymbol{\epsilon}, \quad (4)$$

where $\boldsymbol{\epsilon}$ is the solid phase strain tensor, N is the second Lamé coefficient (the shear modulus of the material of visco-elastic frame), and \mathbf{I} is the second-order identity tensor. Additionally, the fluid stress dependency on the solid displacement and respectively the opposite is accounted for with the dilatational coupling factor i.e. \tilde{Q} . Moreover, \tilde{R} can be described as the fluid phase bulk stiffness at zero frame dilatation. The detail description of A , \tilde{Q} , and \tilde{R} can be found in [6].

2.2 Inclusion modeling

In this paper the inclusion is modeled in three different ways to differentiate between the different effects which may play a role, being the mass-spring effect and the trapped mode effect and/or modified mode of the frame. In the first approach the inclusion is considered as point mass, therefore accounting only for the effect caused by the concentrated mass (m_0) addition to the frame. As a result, it is modeled by adding an inertial weak contribution to the variational formulation of the poro-elastic material:

$$\mathcal{W}_{\mathcal{F}_p} + \int_{\Omega_p} \omega^2 m_0 \delta(\mathbf{x} - \mathbf{x}_0) \mathbf{u} \cdot \mathbf{w} = 0. \quad (5)$$

$\mathcal{W}_{\mathcal{F}_p}$ is the weak form for a poro-elastic material in the domain Ω_p , m_0 is the point mass of inclusion at the point \mathbf{x}_0 , δ is the Dirac delta function, and \mathbf{w} is the test function for \mathbf{u} .

In the second approach, the inclusion is considered as rigid and motionless, however, now it has a finite (small) volume, and the interface between the rigid motionless inclusion and the poroelastic domain Ω_p is denoted by Γ_{p-r} . The presence of such inclusion is modeled simply by applying the fixed-frame boundary conditions on this interface, i.e.:

$$\mathbf{u} = \mathbf{0} \quad \text{on} \quad \partial\Gamma_{p-r}. \quad (6)$$

Considering the inclusion as motionless results in capturing the trapped mode effect and/or modified mode of the frame with rigid backing.

In the third approach, which is the most complete one of all, the inclusion is considered to be elastic and it is fully coupled to the poro-elastic material accounting for the inertial, trapped mode effect, and modified mode of the frame all together. Therefore, the inclusion is modeled as an isotropic elastic medium and its displacement is fully coupled to the frame's displacement at the interface Γ_{p-e} between the both media, namely,

$$\mathbf{u} - \mathbf{u}^e = \mathbf{0} \quad \text{on} \quad \partial\Gamma_{p-e}. \quad (7)$$

3 Results and discussion

In this section the absorption enhancement of a poroelastic foam layer due to the mass-spring effect is illustrated by investigating three cases: the foam without inclusion and the foam with inclusion at two different positions. For each case, the three modeling approaches mentioned in previous section are applied. In the first and second part of this section the partial absorption coefficient due to each dissipation mechanism is shown for the three cases. The third part elaborates more on the dynamic behavior of the meta-porous system and its connection with the increase in sound absorption. In the third part, the average phase difference between the fluid and solid phases is calculated over the frequency range of interest and the results discussed.

3.1 Sound absorption for the foam without inclusion

A polyurethane foam with poro-elastic parameters given in Table 1 is used in these investigation. Firstly, a 24 mm layer of the foam (case 0) is considered, which is shown in Figure 1, as a reference in order to compare to the cases of the foam with inclusion.

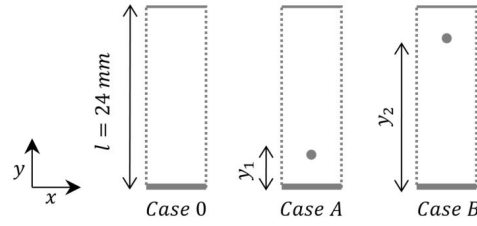


Figure 1: Schematic view of the cases considered in this paper.

$E[kPa]$	η	ν	$\rho[kg/m^3]$	ϕ	α_∞	$\Lambda[\mu m]$	$\Lambda'[\mu m]$	$\sigma[Pa.s/m^4]$
143	0.055	0.3	31	0.97	2.52	37	119	87000

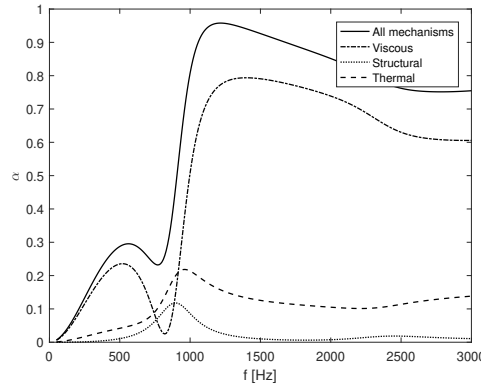
 Table 1: The Biot parameters of the foam. E , η - the Young modulus and loss factor of the material of frame, ν - the bulk Poisson ratio, ρ - the bulk density, ϕ - the porosity, α_∞ - the tortuosity, Λ , Λ' - the viscous and thermal characteristic lengths, σ - the airflow resistivity.


Figure 2: Partial absorption coefficient for different dissipation mechanisms for the foam without inclusion.

A 2D model of the foam is considered and it is clamped at the base in the y direction, and is excited by a plane wave at the other end in the normal direction. The foam is assumed periodic in the x direction, which is modeled as sliding boundary condition due to symmetry. The partial acoustic absorption coefficient of the foam due to three different energy dissipation mechanism (viscous, structural, and thermal) are calculated according to the expressions given in [5], and are shown in Figure 2.

To better understand Figure 2, the resonance frequency of the frame with rigid backing [6] is calculated, i.e. $f_r = \frac{1}{4l} \sqrt{\frac{Re(K_c)}{\rho_1}} \approx 820$ Hz, where l is the layer thickness (see Figure 2, $K_c = \frac{2(1-\nu)N}{(1-2\nu)}$, and ρ_1 is the bulk density of the solid phase. Figure 2 shows that at the resonance frequency of the frame there is a dip in the viscous loss, and simultaneously there is a peak in the structural loss. The mentioned behavior is due the fact that the viscous loss depends on the out-of-phase movement of the fluid and solid phase, while the structural loss depends on the solid phase strain. At the resonance frequency of the frame, the frame is excited and moving in-phase with the fluid part, therefore there is a decrease in phase difference of the solid and fluid part. Additionally, the dip is followed by a peak in viscous loss, which is due to the

out-of-phase displacement of the frame and the fluid part above the resonance of the frame.

3.2 Sound absorption for the foam with inclusions

Next, two cases of a foam with steel rod inclusions of diameter of 0.8 mm periodic in the x direction with the periodicity length of 8 mm are studied. In the first case (case A) the inclusion is located at $y_1 = 4 \text{ mm}$ from the rigid backing, while in the second case (case B) the inclusion is located at $y_2 = 20 \text{ mm}$ from the rigid backing, see Figure 1. The partial absorption coefficient for each case is calculated using the three different models for the inclusion i.e. elastic, rigid, and point mass, see Figure 3.

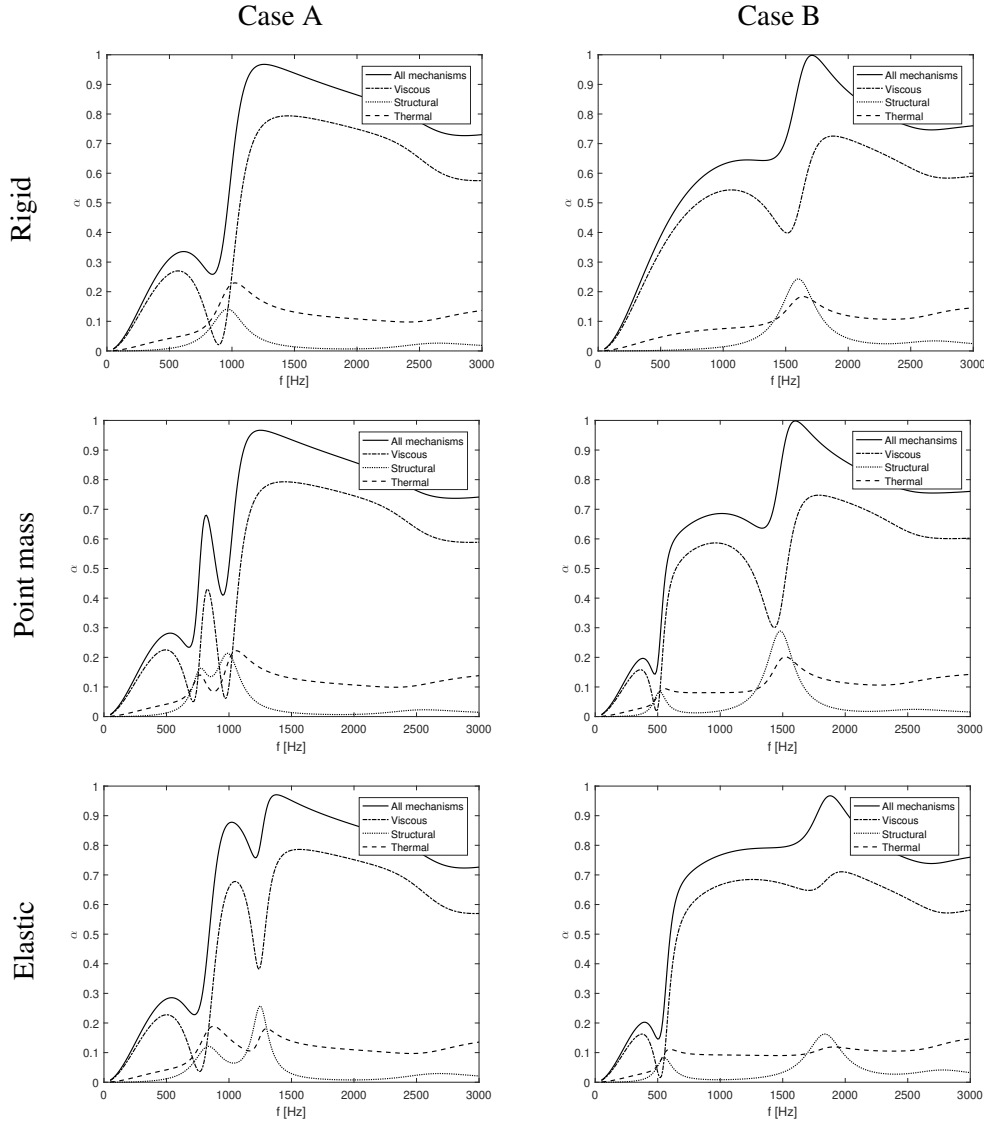


Figure 3: Partial absorption coefficients for different mechanism for case A(left) and case B(right), considering the inclusion as rigid(top), point mass(middle), and elastic(bottom).

Several conclusions can be drawn based on Figure 3. Firstly, different models of case A are compared to each other. It is clear that the rigid inclusion model misses the effect of inclusion, when it is close to

rigid backing. The only difference between the absorption coefficient of the rigid inclusion compared to the foam without inclusion (cf. Figure 3 (top) to Figure 2) is that the foam is slightly stiffened and the resonance frequency of the frame shifted to higher frequency (from 820 Hz to 910 Hz). Comparing the point mass inclusion model to the elastic inclusion model, it is observed that the effect is more localized, and is less pronounced, which is due to the fact that in the elastic inclusion model the effect of the inclusion size is also considered. Another remark is that the modified mode of the frame due to elastic inclusion is higher in frequency as compared to the point mass inclusion (from 1000 Hz for point mass inclusion to 1250 Hz for elastic inclusion) because the elastic inclusion model accounts for the stiffness of the inclusion, which leads to stiffening of the frame.

Secondly, different models of case B are compared to each other. In this case, the larger distance of inclusion and rigid backing leads to a shift of the frame mode to higher frequencies (from 820 Hz to 1600 Hz). The rigid inclusion model shows an absorption improvement, which is also noticeable in the point mass and elastic inclusion models (at 1500 Hz for point mass inclusion, and at 1850 Hz for the elastic inclusion). Moreover, in this case absorption enhancement is achieved over a broader frequency range because the two effects (the mass-spring effect and the modified mode of frame) are located further apart in frequency, creating a combined effect. On the other hand, since the modified mode of the frame is shifted to higher frequencies, the frequency at which the perfect absorption is reached is also moved to higher frequencies, creating a zone (from 980 Hz to 1750 Hz) with absorption reduction of maximum 17%. This behavior is the trade off between enhancing the absorption coefficient at lower frequencies and creating a zone of absorption reduction at higher frequencies.

Thirdly, when case B is compared to case A, we can see that the resonance frequency of the inclusion (the first peak of in the structural loss for the two cases) is shifted down, since the elastic foam between the inclusion and the rigid backing wall acts as the spring in the so-called mass-spring system. Therefore, by increasing the length of the foam below the inclusion, the stiffness of the spring is decreased, and consequently the resonance frequency is decreased.

At last, to show that the absorption improvement at higher frequencies for both cases, A and B, is due to the modified mode of the frame and not the trapped mode effect, we draw readers' attention to the peak appearing in structural loss at those frequencies (around 1000 Hz to 1250 Hz for case A, and around 1500 Hz to 1850 Hz for case B). A peak in structural loss relates to a resonance of the frame, while the trapped mode effect corresponds to trapping of the energy between the rigid backing and the inclusion, which is also apparent under the motionless frame assumption when the equivalent-fluid model is used instead of the poro-elastic one.. To further illustrate this reasoning, the absorption curve of the two cases are calculated using the equivalent fluid model with the same transport parameters ($\phi, \alpha_\infty, \Lambda, \Lambda^{prime}$, and σ) from Table 1 and representing the inclusion with rigid boundary conditions. As expected, the equivalent fluid model doesn't capture the mass-spring effect of the inclusion, and the shift in the frame resonance frequency due to the inclusion.

3.3 Phase difference of the fluid and solid part

The phase difference between the motion of the solid and fluid phase is calculated as follows:

$$phase(\mathbf{U}^f - \mathbf{u}) = \text{imag}(\log(\frac{\frac{\phi}{\bar{\rho}_{22}\omega^2} \nabla p - \frac{\bar{\rho}_{12}}{\bar{\rho}_{22}} \mathbf{u}}{\mathbf{u}})), \quad (8)$$

in order to demonstrate the increase in viscous loss due to the presence of inclusions. In the equation above $\frac{\phi}{\bar{\rho}_{22}\omega^2} \nabla p - \frac{\bar{\rho}_{12}}{\bar{\rho}_{22}} \mathbf{u}$ is the fluid displacement. For the sake of completeness, also the amplitude difference of the fluid and solid phase motion i.e. $\int_{\Omega_p} |\mathbf{U}^f - \mathbf{u}|$ is shown in Figure 6.

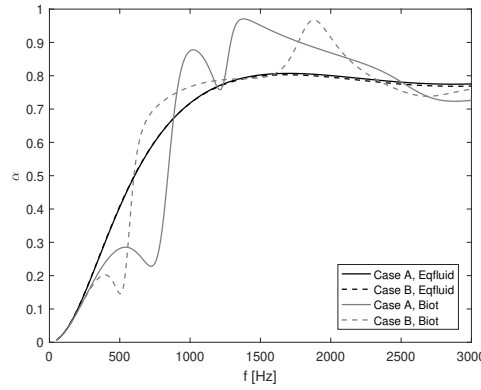


Figure 4: Absorption coefficient (for cases A and B) computed using the equivalent fluid model and the Biot-Allard model with elastic inclusions.

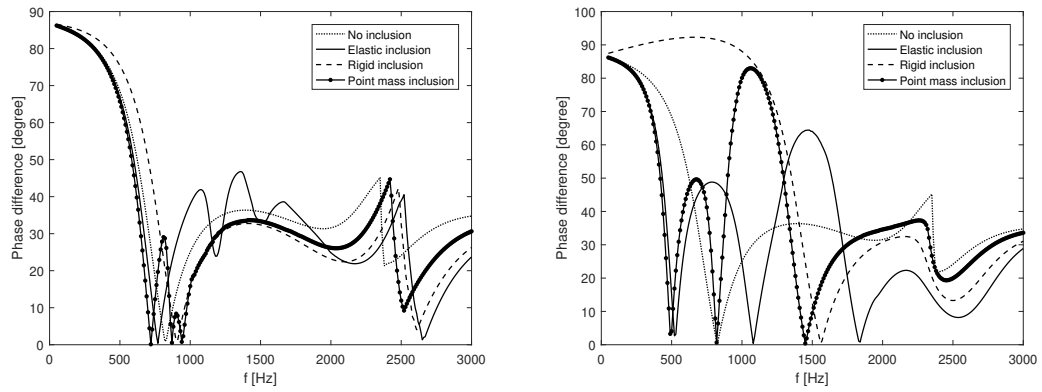


Figure 5: Average phase difference between the fluid and solid part for the case A(left) and B(right).

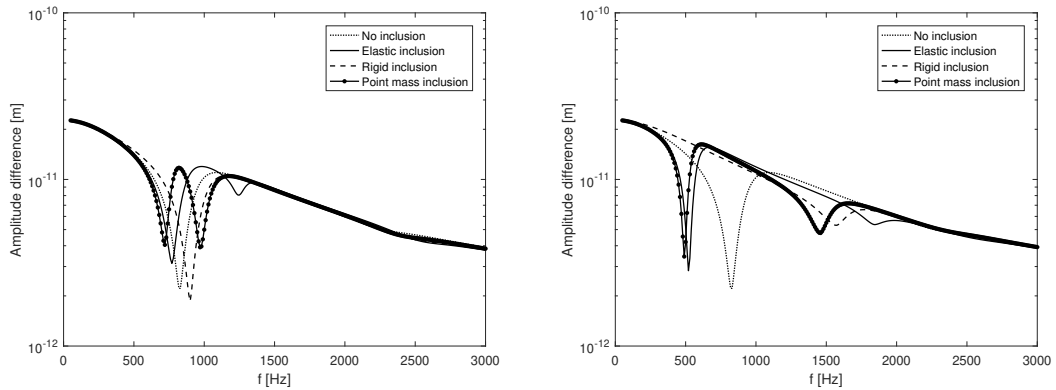


Figure 6: Amplitude difference between the fluid and solid phase motion for the case A(left) and B(right).

Considering the phase difference and the amplitude difference in case A and case B, it is clear that the peaks in Figure 5 and 6 corresponds to the peaks appearing in the partial absorption coefficient due to the viscous loss. Moreover, there is an additional peak for the point mass and elastic inclusion model

as compared to the rigid-motionless inclusion model for both cases, which is induced by the resonating inclusion, which creates an additional mode in the frame, therefore increasing the out-of-phase movement of the frame with fluid part.

4 Conclusion

In this paper, the absorption enhancement of poro-elastic material with small rod inclusions is studied. It is shown that the absorption coefficient can be improved under the quarter-wavelength frequency exploiting a mass-spring effect of the inclusions, when the porous medium is considered viscoelastic and fully coupled to the inclusion. By decomposing the absorption coefficient into energy dissipated by three mechanisms (viscous, structural, and thermal), it is illustrated that the resonating mass excites the frame and increases the out-of-phase movement of the frame and fluid, and consequently leads to an increase in viscous loss. Moreover, the inclusions were modeled using three different assumptions i.e. elastic, rigid, and point mass to differentiate between the mass-spring effect and what is known in literature as the modified mode of the frame. As it was expected, while the rigid model was able to illustrate the modified mode of frame effect, it came short in showing the mass-spring effect. Moreover, it was shown that by changing the location of the inclusion, which translates to changing the spring stiffness, the resonance frequency of the inclusion is changed, and therefore the absorption peak is shifted in frequency. This behavior shows that such meta-porous systems can be tuned to improve absorption coefficient at targeted frequencies below the quarter wavelength frequency, which can be also effectively used in active sound absorbing meta-porous treatments [7].

Acknowledgments

The European Commission is gratefully acknowledged for their support of the VIPER research project (GA 675441). The Research Fund KU Leuven is gratefully acknowledged for its support. The research of E. Deckers is funded by a grant from the Research Foundation – Flanders (FWO). This research was partially supported by Flanders Make, the strategic research centre for the manufacturing industry. T. G. Zielinski and L. Jankowski would like to acknowledge the financial support of the Project "Relations between the microgeometry and sound propagation and absorption in porous and poroelastic media", No. 2015/19/B/ST8/03979, financed by the Polish National Science Centre (NCN).

REFERENCES

- [1] L. Brekhovskikh, *Waves in layered media*, vol. 16. Elsevier, 2012.
- [2] J.-P. Groby, O. Dazel, A. Duclos, L. Boeckx, and L. Kelders, "Enhancing the absorption coefficient of a backed rigid frame porous layer by embedding circular periodic inclusions," *J. Acoust. Soc. Am.*, vol. 130, no. 6, pp. 3771–3780, 2011.
- [3] C. Lagarrigue, J. P. Groby, V. Tournat, O. Dazel, and O. Umnova, "Absorption of sound by porous layers with embedded periodic arrays of resonant inclusions," *J. Acoust. Soc. Am.*, vol. 134, no. 6, pp. 4670–4680, 2013.
- [4] T. G. Zieliński, "MODELLING OF POROELASTIC LAYERS WITH MASS IMPLANTS IMPROVING ACOUSTIC ABSORPTION- 19 th INTERNATIONAL CONGRESS ON ACOUSTICS MADRID , 2-7 SEPTEMBER 2007," No. September, pp. 2–7, 2007.

- [5] O. Dazel, F. Sgard, F.-X. Becot, and N. Atalla, “Expressions of dissipated powers and stored energies in poroelastic media modeled by $\{u, U\}$ and $\{u, P\}$ formulations,” *J. Acoust. Soc. Am.*, vol. 123, no. 4, pp. 2054–2063, 2008.
- [6] J. F. Allard, *Propagation of Sound in Porous Media*. Elsevier, 2011.
- [7] T. Zielinski, M. Galland, and E. Deckers, “Influencing the wave-attenuating coupling of solid and fluid phases in a poroelastic layer using piezoelectric inclusions and locally added masses,” *Proceedings of ISMA2018*, pp. 1195–1207, 2013.

BAND DIAGRAM AND FORCED RESPONSE ANALYSIS OF PERIODIC AND QUASI-PERIODIC PANELS

S. Timorian^{1,2}, M. Ouisse², N. Bouhaddi², S. De Rosa¹ and F. Franco¹

¹ Laboratory for Promoting experience in Aeronautics Structures,
Department of Industrial Engineering —Aerospace Section, University of Naples Federico II, Napoli,
via Claudio 21, 80125, Italy.
e-mail: safiullah.timorian@unina.it,
web page: <http://www.pastalab.unina.it/home.html>

² Femto-ST Institute, Department of Applied Mechanics,
Univ Bourgogne Franche-Comté, Besancon, 25000, France
e-mail: safiullah.timorian@femto-st.fr
Web page: <https://www.femto-st.fr/fr>

Key words: Quasi-periodic structures, band diagram, frequency stop-band, forced response, metamaterials

Abstract. The vast majority of structures introduce symmetry in one or two dimensions, which can be a periodicity in the case of constructing several identical unit cells. Periodic structures have found a big interest in engineering applications because they introduce frequency band effects, due to the impedance mismatch generated by periodic discontinuity in the geometry, which can improve the vibroacoustic performances. However, the presence of imperfections i.e. (defects, irregularity) in the structure, leads to a partial loss of regular periodicity (called quasi-periodic structure) that can have a noticeable impact on the vibrational and/or acoustic behaviour of the elastic system. The tailored irregularity, which is a designed loss of periodicity, can be used, therefore, to improve the dynamic behaviour of structures. In the present paper numerical studies on the vibrational analysis of two-dimensional non-planar periodic and quasi-periodic structures have been performed. The content deals with finite and infinite systems. The finite element models of solid structures focused on the band diagram analysis of the infinite systems and the forced responses of the finite structures. The quasi-periodicity is defined by invoking the Thue-Morse sequence for building the assigned variations (geometry) along the domain of finite element model. The wave characteristics in quasi-periodic panels, present some elements of novelty and could be considered for designing structural filters and controlling the properties of elastic waves.

1 INTRODUCTION

Periodic metamaterials are one of the central topics in vibration and acoustics domain. A degree of regular periodicity in arrays of engineered metamaterials, always leads to design and create frequency stop bands (i.e. waves cannot freely propagate in these frequency ranges). One of the main features associated with the periodic distribution of mechanical devices is the ability of the system to block the propagation of waves in specific frequency ranges [1]. Such structures behave as filtering systems, since in some ranges of frequencies waves propagate without attenuation (if damping is neglected), while in

others decay exponentially [2, 3]. They are also very well known metamaterials and phononic materials for exhibiting frequency band gaps, that can improve the vibroacoustic response of structures [4, 5]. Recent studies show interesting topics on architected material like phononic crystals, metamaterials, and auxetic sandwich cores [6] to control the propagation of elastic waves. These architected material rely on two mechanisms for forming band gaps. Phononic crystals can form Bragg type band gaps, but are limited in the low-frequency regimes because their unit cell size scales with wavelength. In contrary metamaterials overcome this size, because they rely on resonances, but the resulting band gaps are narrow [7, 8].

Numerical analyses lead to the design of nominally perfect periodic structures. However, the presence of imperfections i.e. defects or irregularities in post-manufacturing are highly likely to be occurred in regular periodic designs. Recent studies show that there are effects on random variability due to the additive manufacturing process on the performance of the elastic band gap behaviour in creating a stop band effect in the forced response of the waveguide [9]. On the contrary, the present work is focused on tailored irregularities, which is called (quasi-periodicity), which are considered to have impacts on dynamical behaviour of the structures. The first challenge is how to predict the frequency band gap in infinite quasi-periodic systems. In fact, the design of periodic configurations is usually based on the use of Floquet-Bloch (FB) theorem which considers a single cell with adequate boundary conditions [10, 11].

To design an enhanced quasi-periodic structure and analyse the impact of this design in terms of dynamics response, two methods are under investigation. A forced response of the finite quasi-periodic structure and a periodic panel which has commonality in terms of in-plane dimensions. In the second method in order to predict the frequency stop band zones a dispersion analysis of the infinite periodic structure is designed. In this design two meso-scale unit cells, which represent the dispersion analysis of the infinite periodic structures are considered. The predicted dispersion curves can be directly compared with its finite periodic counter parts for frequency band gaps prediction. In the forced response, those two meso-scale cells are combined using Thue-Morse morphism series in order to tailor a quasi-periodic panel. The FRFs of the quasi-periodic panel show effective results compared to strictly periodic panels in terms of band gaps width enlargement and level of attenuation.

2 MODEL AND LEXICON

2.1 Infinite structure

The model consists of a metamaterial waveguide. Metamaterials in the present investigation are an engineered sets of multiple elements to show some filtering properties. The waveguide consists of two different unit cells in meso-scale. The unit cells are made of polymers materials and the mechanical properties are given in Tab.1.

The unit cell is made of two sub-parts, on-board panel, and a resonator. The dimension of the meso-scale wave-guide is detailed in the Fig.1. The information of the control volume of the both unit cells are taken into account for modelling a lightweight, easy-to-manufacture metamaterial [12]. The on-board panel has a thickness of $2mm$ with an area of $35 \times 35 mm^2$. The resonator shape has a height of $17.5mm$ and a lateral and horizontal span of $30mm$. Cell A and cell B have two different shapes with approximated equal control volumes. The wall thickness of the cell A is $4.8mm$ and the circular hole in cell B has a radius of $8mm$.

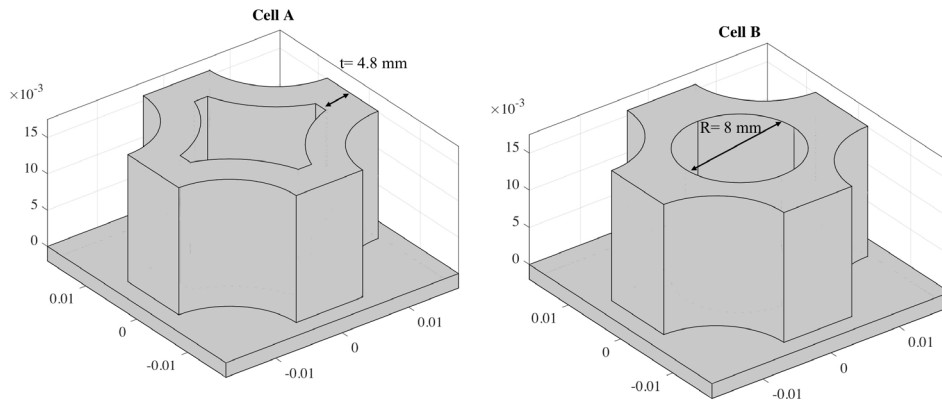


Figure 1: Meso-scale unit cells of infinite periodic panels

Table 1: Material properties of the metamaterial

Material	Polymer
Modulus of elasticity(Pa)	2.32×10^9
Density ($\text{kg} \cdot \text{m}^{-3}$)	1050
Poisson's ratio	0.34

2.2 Finite structure

In the finite panel two perfectly periodic and two quasi-periodic structure are considered. In the last two models specific Thue-Morse sequences are used to generate impedance mismatches in the view of desired degree of quasi-periodicity. The degree of quasi-periodicity might be controlled with mathematical rules that are introduced in the next section.

2.2.1 Thue-Morse sequence

A Thue-Morse sequence is binary sequence (an infinite sequence of 0s and 1s). The sequence starts with 0 then 01, 0110, 01101001, and so on, [13]. For the simplicity, let us define the Thue-Morse morphism to be the function s from the set of binary sequences to itself by replicating every 0 in a sequence with 01 and every 1 with 10 [14]:

$$s(x, y) = s(x)s(y) \quad (1)$$

Eq.1 defines a map s for all strings x, y . Defining the Thue-Morse morphism $s(0) = 01, s(1) = 10$ leads to the relations for increasing the quasi-periodicity pattern in two directions:

$$\begin{aligned} s(0) &= 01 = AB \\ s^2(0) &= s(s(0)) = 0110 = ABBA \end{aligned}$$

$$s^3(0) = s(s(s(0))) = 01101001 = ABBABAAB$$

Each 0 and 1 represents cell A and cell B respectively. In the present finite element model only 8 combined unit cells are used, it means that the Thue-Morse morphism map stops at s^3 .

Two types of quasi-periodic finite panels are considered. The first one is a pure quasi-periodic panel (8×8 unit cells) and the second quasi-periodic panel is designed similar to the first one with an addition of two bare panels without resonators in the right and left sides of the quasi-periodic one. These two bare panels are used as an input zone in the left and output zone in the right side of filtering domain shown in Fig.2.

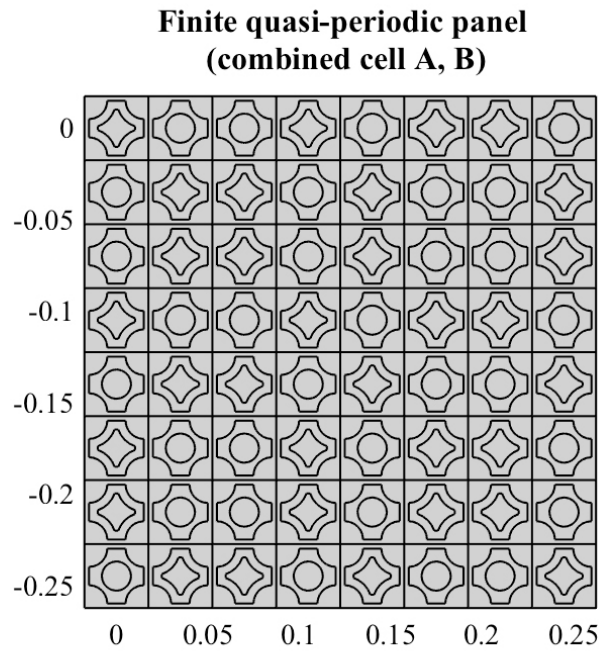


Figure 2: Quasi-periodic panel with the combination of cell A and B

2.2.2 Periodic sequence

The two periodic panels have a repetition of single cell A for first panel, and single cell B for second panel respectively with the dimensions of 8×8 shown in Fig.3. According to the Fig.3, the panel has a thickness of 2 mm, and the hollow resonator has a wall thickness of 4.8 mm.

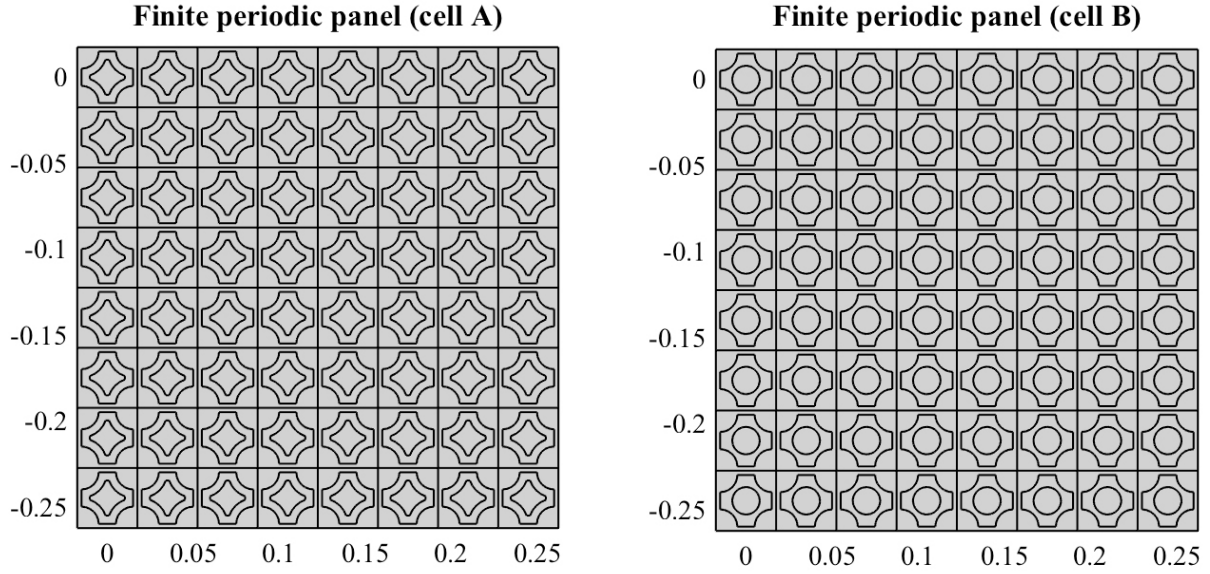


Figure 3: Two strictly periodic panels, left with cell A periodicity and right with cell B

3 STRUCTURAL DYNAMICS

3.1 Dispersion analysis

Classical FB method is used for the band diagram analysis of the strictly periodic infinite panel. The Floquet-periodicity is defined in the four side boundaries of the unit cell. The unit cell represents a bi-directional spatial periodicity in the given infinite structure. The band diagram is computed along the three symmetry directions of the first Brillouin zone shown in Fig. 4. Classical (FB) Floquet-Bloch theory is used as a periodic boundary condition using COMSOL Multiphysics for the analysis of dispersion curves. The periodicity boundary conditions in four sides of the lattice are

$$\mu_R = e^{-jk_x L} \mu_L \quad (2)$$

$$\mu_U = e^{-jk_y L} \mu_B \quad (3)$$

where, μ_R and μ_L are the displacement in the right and left side of the x axis and μ_U and μ_B are the displacement in the upper and bottom of the y axis. L is the length of reciprocal element, k_x and k_y are the wavenumbers in the x and y directions. Band diagrams are analysed by setting up eigensolver analysis as a parametric sweep using one parameter, k , which varies from 0 to π . The range of the k parameter spans three wave vectors starting from (A to R to S and back to A), covering the edges of the first irreducible Brillouin zone Fig. 4.

Two different unit cells are considered for the dispersion analysis. First cell A and second cell B. Both cells have commonalities in terms of mass, volume fraction, material and structural properties in order to be useful periodic tool to be compared with the quasi-periodic counter part. The results predicted by these two cells could lead to design a quasi-periodic lattice, which is a finite panel with a tailored irregularity that is invoked by Thue-Morse morphism deterministic approach. The results of the band diagram is plotted in Fig. 5 There are two complete frequency band gaps in each sub-figure. The first band gaps with small $\Delta\omega = 570$ Hz that represents the (resonance band gaps) following the larger Bragg

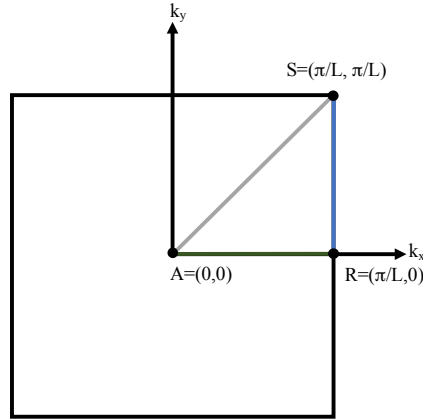


Figure 4: Diagram of the first irreducible Brillouin zone for a square lattice

band gaps $\Delta\omega = 2.9$ kHz around 11 kHz is predicted for the cell A. Cell B in the right hand side of the Fig.5 shows almost similar dispersion behaviour but with a wider resonance band gaps $\Delta\omega = 754$ Hz around 4 kHz and a slight wider Bragg band gaps 3.1kHz compared to cell A. According to a sensitivity analysis on both cells, the compromised wall thickness of the cell A = 4.8 mm and radius of the resonator shape cell B = 8 mm is selected to isolate the maximum vibration level.

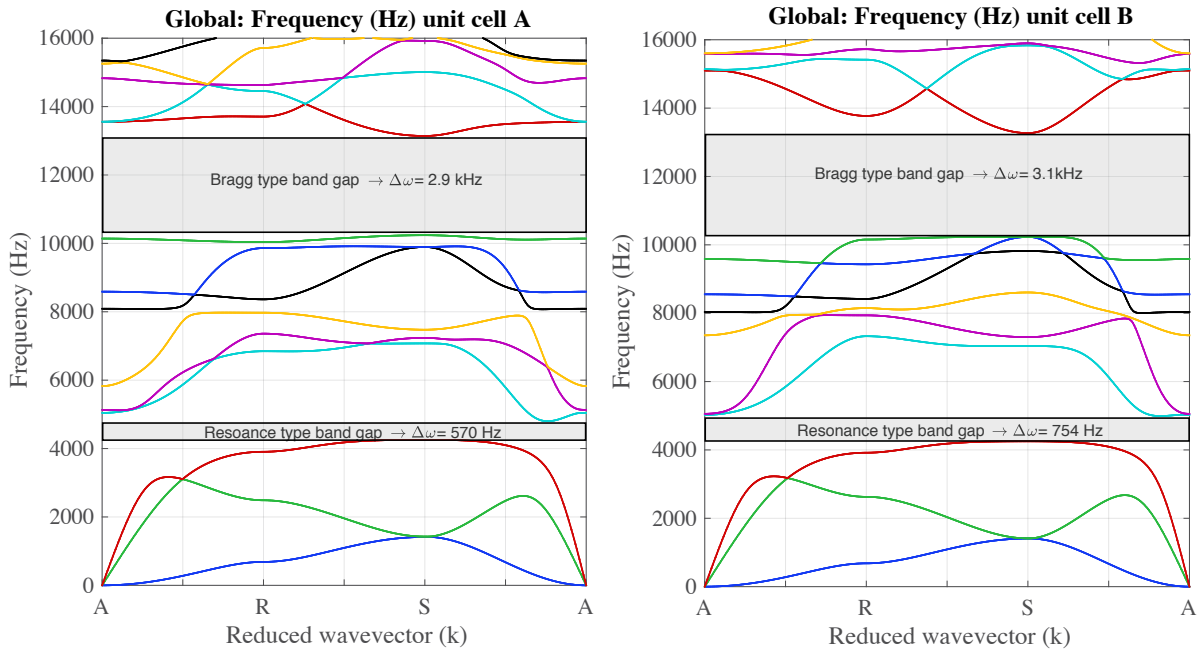


Figure 5: Band diagram of infinite panels with a representative, left cell A and right cell B

3.2 Finite element analysis

In this part, four types of investigations, on periodic and quasi-periodic panels; specifically, the aim is to apply on a finite structure the results obtained with a infinite periodic sequence.

Fig. 6 show three curves; by focusing on the Bragg type band gaps zone, the blue curve with dash lines corresponds to the cell B. It has thinner stop band wide compared to the other curves and there is also a slight shift in the stop bands towards the higher frequencies compared to the two cell A and combined (A, B). Despite of that cell A has a shift of the same band gaps zone towards the lower frequency ranges. Paying attention to the dark green solid curve that corresponds to the combined cell A and cell B, it has wider band gaps compared to both blue dash curve and dotted orange curve almost around 10.5 – 14.2 kHz. Also it should be mentioned that in the velocity amplitude response it has the lowest pick in comparison of two other curves. The highest picks could be seen at around 8.25 kHz, and the orange has the highest pick with the amplitude of 20dB.

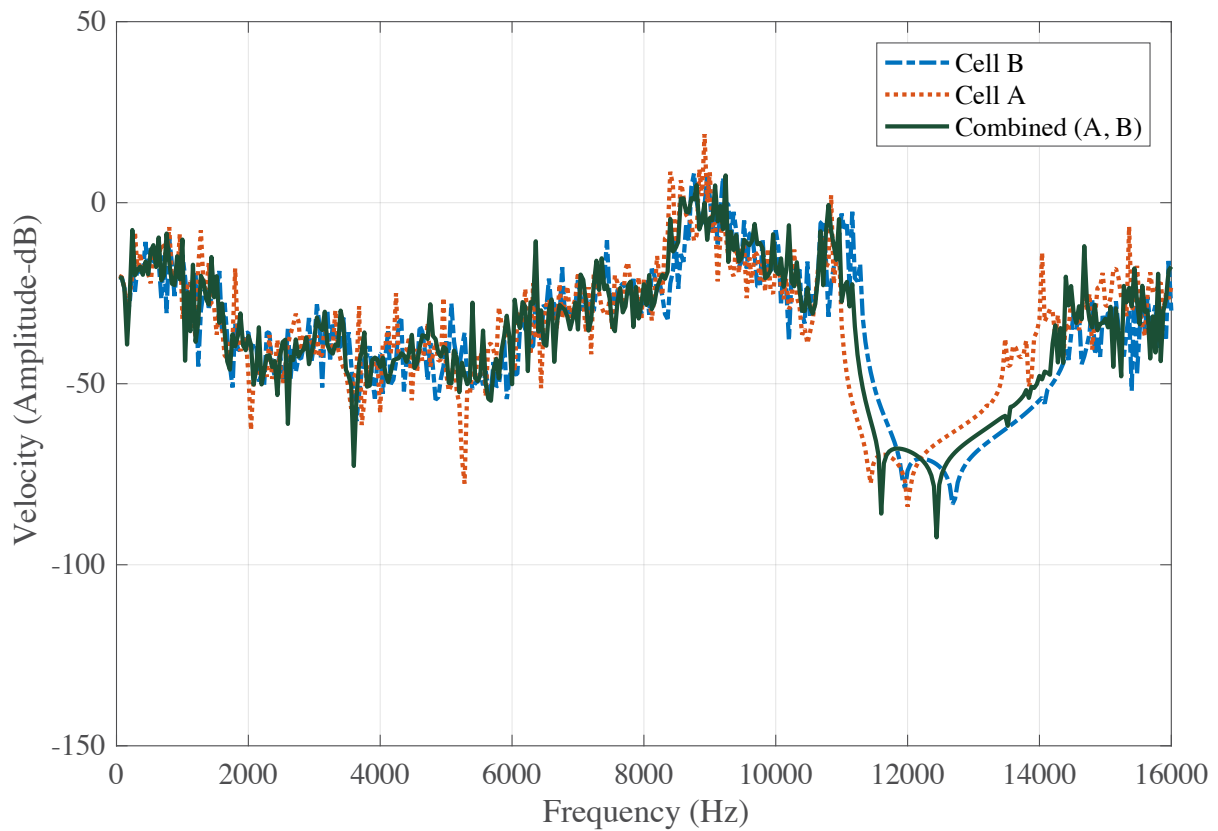


Figure 6: FRFs of three finite structures in terms of velocity amplitude in dB response

In conclusion of the first part, it could be predicted that the combination of two unit cells in finite quasi-periodic panel (8×8 unit cells) is a compromise model and it has impacts on the dynamic behaviour of panel compared to the two other strictly single periodic panels in terms of wide of band gaps and lower attenuation level.

In the second part of the finite element analysis, an FRF of the quasi-periodic structure with ($840 \times 280 \times 2 \text{ mm}^3$) is taken into account. This meta-structure shown in Fig.7 is made of three sub-parts. The middle part is a quasi-periodic panel of combined cell A and cell B and the two other parts in the left and right hand side bare panels with no resonators on it.

The panel has a cantilever constraint (fixed boundary condition) marked blue in Fig.7. A unit white spectrum force is applied to the input zone right left hand side bare panel (marked with red arrow) and the response is observed in terms of Root Mean Square (RMS) with the average node points in the input and output zones.

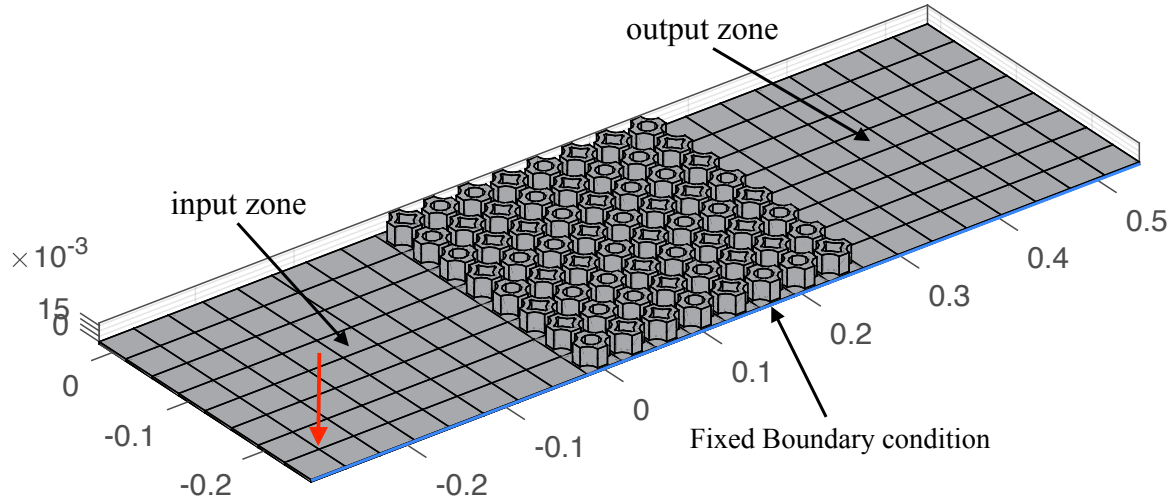


Figure 7: Geometry of meta-structure (filter)

Fig.8 shows FRF response in terms of velocity amplitude in dB. Practically, this type of panel is used as a junction filter between two bare panels. The induced vibration energy transfers through this junction, and it acts as a meta-material filtering property to the elastic waves due to the impedance mismatch in the shape of resonators embedded in the bare panels.

The FRF shows two types of curves, the blue one corresponds to the the average of the 64 nodes in the input zone, where all the elastic waves are confined in the zone and there is no sign of frequency stop bands. The orange curve corresponds to the response of the output zone. The frequency stop bands starts from 10.36 kHz and continues to 13.6 kHz. There are some picks around 12 kHz inside the band gap in shaded area. Three frequencies are chosen inside the shaded area and their operative modes or forced deflections are plotted in Fig. 9.

A similar procedure for the numerical modelling of filtering effects has been done in the paper of Billon et al [10]. They basically selected 4 points in the FRFs. Two points are located in the inside the predicted band gap and two outside the band gap. One point inside the band gap does not really reflects good response despite of being in the predicted band gaps. In fact, in the present FRFs only three points are considered, two of them are on the lower and upper bound of the band gaps and the third one is taken in the middle of the attenuation zone.

As it can be seen from the results in the paper of Billon et al [10], the average squared amplitude velocity around 43.3 kHz which is inside the predicted band gap zone, has visible deformed shapes over $-20dB$. In contrary, although there are some picks in the middle of band gap in the present result but they are bellow $-25dB$ with less deflections.

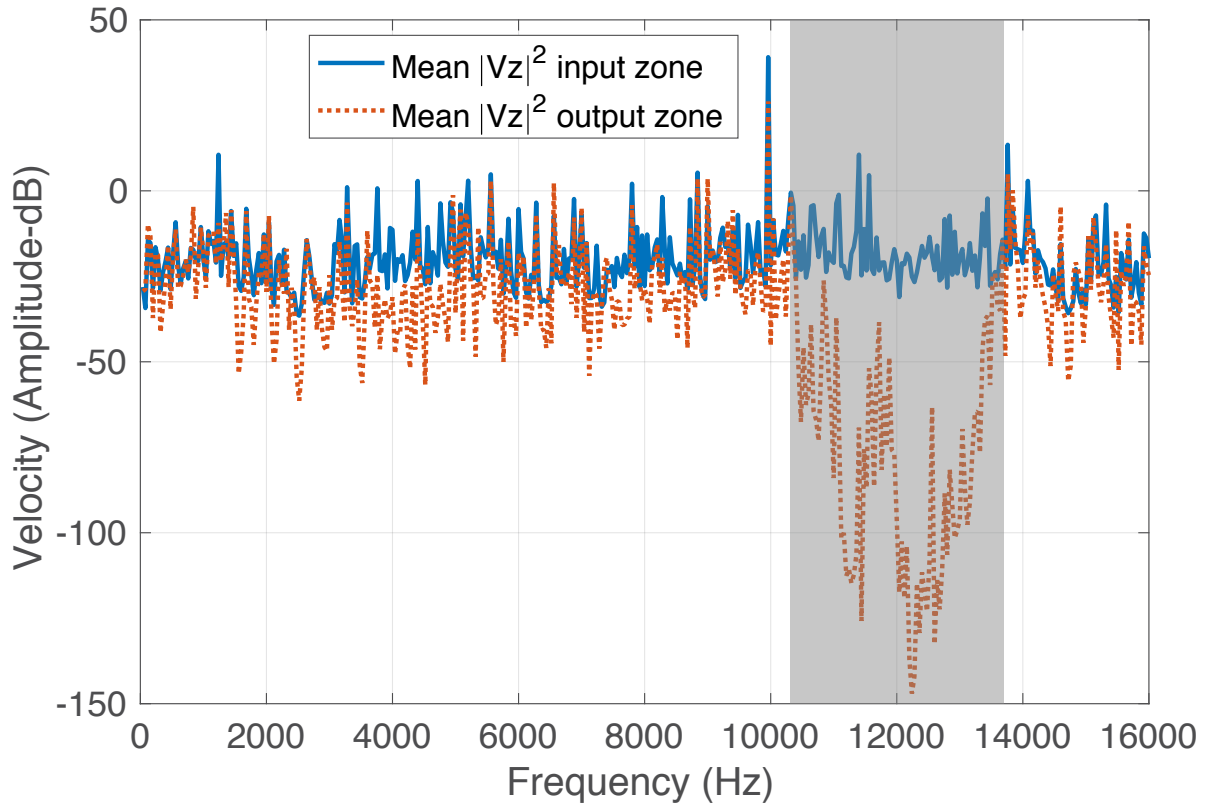


Figure 8: FRFs of the meta-structure in terms of RMS of velocity amplitude in dB

The operative modes in Fig.9 shows the deformation of the panel in 10.36 kHz, the start point of band gaps, 11.36 kHz middle of the band gaps, and 13.12 kHz almost at the finishing point of the band gaps. It can be seen that the panel has an efficient filtering effects by using quasi-periodic pattern.

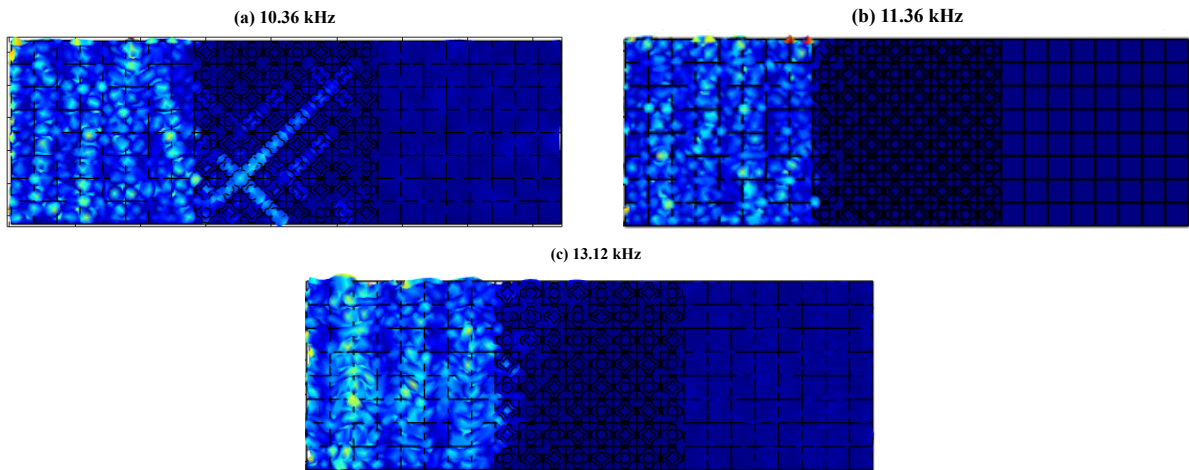


Figure 9: Operative modes of the meta-structure with three selected frequencies in the upper, lower and middle position of the attenuation level

4 CONCLUSIONS

The first aspect is formulating fundamental procedures to design a quasi-periodic meta-structure using Thue-Morse morphism sequence. The second aspect is dedicated to analysis of the impact of this design in terms of dynamical behaviour. The results of FRFs and dispersion analysis shows that quasi-periodic pattern have impact on dynamic behaviour of panels, especially in terms of isolating unwanted vibrational behaviour all over the metamaterial part of the span, specifically inside the attenuation level.

In this analysis, the presented tailored irregularity, which in higher extent is a designed loss of periodicity in finite structure has influential access to extend the attenuation level to lower velocity amplitude-dB and slightly increase the wide of the band gaps. These impact came due to the impedance mismatch of the combined (resonators) embedded on the bare panel. There are some points to be highlighted in the below:

The quasi-periodicity (Thue-Morse morphism) in two directions shows lower frequency band gaps compared to the one direction ones like Fibonacci sequences. Quasi-periodic panel in the present article has an efficient impacts on the vibrational analysis compared to the single periodic panels. In general quasi-periodic pattern is capable of confining the energy in some modes, and in higher extends there are possibilities to shift those localised modes in desired frequency bands.

ACKNOWLEDGEMENTS

This research was supported by the framework of the VIPER project (Vibroacoustic of PERiodic media). This project has received funding from European Union's Horizon 2020 research and innovation program under Marie Curie grant agreement No 675441 and EUR EIPHI (ANR 17-EURE-0002) project. Thanks to our colleagues who provided contributions with insights and expertise in this research.

REFERENCES

- [1] Collet, M., Ouisse, M., Ruzzene, M. and Ichchou, M.N., 2011. Floquet–Bloch decomposition for the computation of dispersion of two-dimensional periodic, damped mechanical systems. *International Journal of Solids and Structures*, 48(20), pp.2837-2848.
- [2] G., Movchan, A.B., Argani, L.P. and Bursi, O.S., 2016. Quasi-periodicity and multi-scale resonators for the reduction of seismic vibrations in fluid-solid systems. *International Journal of Engineering Science*, 109, pp.216-239.
- [3] Carta, G., Brun, M., Movchan, A.B. and Boiko, T., 2016. Transmission and localisation in ordered and randomly-perturbed structured flexural systems. *International Journal of Engineering Science*, 98, pp.126-152.
- [4] Kook, J., 2016, August. Investigation of Bandgap Structure in Coupled Acoustic-Mechanical System. In *INTER-NOISE and NOISE-CON Congress and Conference Proceedings* (Vol. 253, No. 6, pp. 2608-2615). Institute of Noise Control Engineering.
- [5] Hussein, M.I., Leamy, M.J. and Ruzzene, M., 2014. Dynamics of phononic materials and structures: Historical origins, recent progress, and future outlook. *Applied Mechanics Reviews*, 66(4), p.040802.
- [6] Qing-Tian, D. and Zhi-Chun, Y., 2010. Wave propagation in sandwich panel with auxetic core. *J Solid Mech*, 2(4), pp.393-402.

- [7] Matlack, K.H., Bauhofer, A., Krodel, S., Palermo, A. and Daraio, C., 2016. Composite 3D-printed metastructures for low-frequency and broadband vibration absorption. *Proceedings of the National Academy of Sciences*, 113(30), pp.8386-8390.
- [8] Krushynska, A.O., Miniaci, M., Bosia, F. and Pugno, N.M., 2017. Coupling local resonance with Bragg band gaps in single-phase mechanical metamaterials. *Extreme Mechanics Letters*, 12, pp.30-36.
- [9] Fabro, A.T., Beli, D., Arruda, J.R.F., Ferguson, N. and Mace, B., 2016. Uncertainty analysis of band gaps for beams with periodically distributed resonators produced by additive manufacturing.
- [10] Billon, K., Ouisse, M., Collet, M. and Sadoulet-Reboul, E., 2018, March. Design of smart metamaterials for vibration control: extension of Bloch approach to handle finite system boundary conditions. In *Health Monitoring of Structural and Biological Systems XII* (Vol. 10600, p. 106001J). International Society for Optics and Photonics.
- [11] Hakoda, C., Rose, J., Shokouhi, P. and Lissenden, C., 2018, April. Using Floquet periodicity to easily calculate dispersion curves and wave structures of homogeneous waveguides. In *AIP Conference Proceedings* (Vol. 1949, No. 1, p. 020016). AIP Publishing.
- [12] Miniaci, M., Mazzotti, M., Radzienski, M., Kherraz, N., Kudela, P., Ostachowicz, W., Morvan, B., Bosia, F. and Pugno, N.M., 2018. Experimental observation of a large low-frequency band gap in a polymer waveguide. *Frontiers in Materials*, 5, p.8.
- [13] Allouche, J.P. and Shallit, J., 1999. The ubiquitous prouhet-thue-morse sequence. In *Sequences and their applications* (pp. 1-16). Springer, London.
- [14] Berstel, J., 2009. Combinatorics on words: Christoffel words and repetitions in words (Vol. 27). American Mathematical Soc..

DECOUPLING OF ENERGY TRANSMISSION BETWEEN SUBSYSTEMS OF A COMPLEX STRUCTURE

G. MAZZEO ^{*1,2}, M. ICHCHOU¹, G. PETRONE², O. BAREILLE¹, F. FRANCO², S.
DE ROSA²

¹ Vibroacoustic and Complex Media Research Group, LTDS

École Centrale de Lyon

36 Avenue Guy de Collongue, 69134, Écully, France

E-mail : {giulia.mazzeo} {mohamed.ichchou} {olivier.bareille} @ec-lyon.r

² Pasta-Lab, Department of Industrial Engineering – Aerospace Section

University of Naples Federico II, via Claudio 21, 80125 Naples, Italy

E-mail : {giuseppe.petrone} {francesco.franco} {sergio.derosa} @unina.it

Key words: statistical energy analysis, structural design, wind tunnel, vibration, materials.

Abstract. Experimental vibroacoustic measurements are very common for the study of emitted noise reduction and vibration energy isolation of structures. The most important case is when structures are subjected to an aerodynamic excitation as Turbulent Boundary Layer (TBL). In this paper, a preliminary study is performed on the energy transmission between subsystems of a structure subjected to TBL. A numerical test is developed on a three-plates-in-row system at high frequencies, through the application of Statistical Energy Analysis (SEA). Parameters such as surface dimensions, thickness and damping loss factor are evaluated in different configurations for a first design of a testbench used for vibroacoustic measurements in a wind tunnel.

1 INTRODUCTION

In the aerospace engineering field, the study of vibroacoustic behaviour of complex structures is very popular as academic research, as well as for industrial purposes.

In fact, main topics are the emitted noise and the structural vibration of systems which are subjected to an aerodynamic excitation (i.e. Turbulent Boundary Layer, TBL), with the aim of guarantee a good comfort in terms of reduced emitted noise and isolation of structural vibration. Focusing the attention on the effect of a TBL at high flow speeds, it is important to have a relevant testbench, mounted in the wind tunnel that, for this specific excitation, can guarantee the quality and robustness of the measured experimental data. In other words, it is required that ideally no contamination effects, related to the impedance breaks between testbench and sample panel, affect the measurements.

For this reason, the decoupling of energy transmission between subsystems of a structure is the main topic of this paper. A similar work is done by Finnveden in [1,2]. The wind tunnel, at KTH laboratories, consists in a suspended flow duct in which an air flow is blown; the test panel is mounted on the wall of the above-mentioned duct. The validation of the wind tunnel,

which Finnveden [1,2] proposed through the application of the Statistical Energy Analysis (SEA), assumed that it is possible to consider the vibration of the test panel decoupled by the vibration of the flow duct.

In the present paper, a verification of the prior assumption is made, followed by a numerical procedure based only on SEA. The procedure uses the description of an aerodynamic excitation, such as TBL, as an equivalent “rain on the roof” excitation in the mid-high frequencies [3,4].

The following sections are organized in this order: first, the presentation of the adopted SEA method, second, the presentation of the Equivalent TBL model, and finally the presentation of results per categories: influence of surface, thickness and damping, respectively

2 STATISTICAL ENERGY ANALYSIS

Statistical Energy Analysis is based on the principle of energy balance between subsystems which are assumed to be linearly coupled. This energetic method has been studied and theorized by Lyon [5]. Among the assumptions thus theorized, it is considered the one for which the excitation spectrum is broadband, and the excitation forces are statistically independent: there are no pure tones in the input spectra.

The energy balance between two subsystems i and j can be expressed as

$$P_{in,j,i} = P_{diss,i} + (P_{ij} - P_{ji}) \quad (1)$$

$$P_{in,j,i} = \omega \eta_i E_i + \sum_{j=1}^2 \omega \eta_{ij} n_i \left(\frac{E_i}{n_i} - \frac{E_j}{n_j} \right) \quad (2)$$

where η_{ij} is the coupling loss factor (CLF), n_i is the modal density, E_i and E_j are the uncoupled total subsystem energies (Fig. 1).

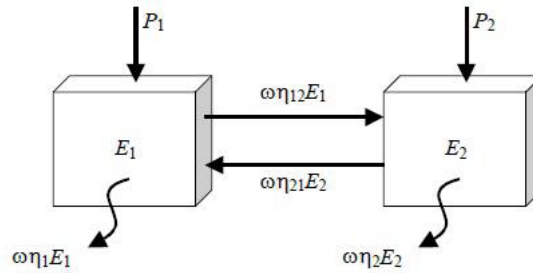


Figure 1: Simple SEA system.

SEA affirms that power always flows from the subsystem which has a higher energy to the one having lower energy

$$P_{ij} = \omega (\eta_{ij} E_i - \eta_{ji} E_j) = \omega \eta_{ij} n_i \left(\frac{E_i}{n_i} - \frac{E_j}{n_j} \right) \quad (3)$$

$$\eta_{ij} n_i = \eta_{ji} n_j \quad (4)$$

For a complex structure, the relation between the injected powers and the modal energies can be written as follows

$$\begin{Bmatrix} P_{inj,1} \\ \vdots \\ P_{inj,s} \end{Bmatrix} = \omega \begin{bmatrix} \eta_1 n_1 + \sum_{j=1}^s \omega \eta_{1j} n_1 & \cdots & -\eta_{1s} n_1 \\ \vdots & \ddots & \vdots \\ -\eta_{s1} n_s & \cdots & \eta_s n_s + \sum_{j=1}^{s-1} \omega \eta_{sj} n_s \end{bmatrix} \begin{Bmatrix} E_{m,1} \\ \vdots \\ E_{m,s} \end{Bmatrix} \quad (5)$$

$$\{P_{inj}\} = \omega[L]\{E_m\} \quad (6)$$

The energy distribution inside the subsystems of a complex structure is the result of a simple algebraic matrixial equation in which it is needed to know only three parameters, which are the injected powers in terms of Power Spectral Densities (PSD), the modal densities and the CLFs.

However, SEA presents some limitations of applicability, defined by Mace in [6,7]. It is here mentioned the modal overlap factor

$$m(\omega) = \eta \omega n(\omega) \quad (7)$$

as instrument for SEA validity. If $m \gg 1$ for all subsystems of the structure, in fact, it can be said that it is possible to use SEA. The frequency for which the modal overlap factor is equal to unity, is the limit frequency for SEA validity.

3 EQUIVALENT TBL EXCITATION

With the aim of designing a testbench for vibroacoustic measurements in wind tunnel, it is necessary to describe the effect of an aerodynamic load as a TBL excitation. But, as mentioned in the previous section, the type of excitation applied to a structure in SEA method should be a broadband statistically independent excitation, such as ‘rain on the roof’ excitation (ROF). For this reason, the Equivalent TBL presented by Ichchou in [3] is considered.

Referring to the Corcos model described as

$$C(x - x', y - y'; \omega) = e^{-\delta_x |x - x'|} \cos(\gamma_x (x - x')) e^{-\delta_y |y - y'|} \quad (8.a)$$

$$\begin{cases} \gamma_x = \omega / U_c \\ \delta_{x,y} = a_{x,y} \gamma_x \end{cases} \quad (8.b)$$

where U_c is the convective speed and $a_{x,y}$ are empirical coefficients, it is possible to define the Equivalent TBL auto-spectrum (Eq. 10) in function of an equivalent correlation function $C^{eq}(\omega)$ (Eq. 9) and ROF auto-spectrum

$$C^{eq}(\omega) = \int_{-\infty}^{+\infty} \int_{-\infty}^{+\infty} e^{-\delta_x |\zeta|} \cos(\gamma_x \zeta) e^{-\delta_y |\chi|} d\zeta d\chi = \frac{4\delta_x}{\delta_y (\delta_x^2 + \gamma_x^2)} \quad (9)$$

$$S_{pp}^{ETBL}(\omega) = C^{eq}(\omega) S_{pp}^{ROF}(\omega) = \frac{4\delta_x}{\delta_y (\delta_x^2 + \gamma_x^2)} S_{pp}^{ROF}(\omega) \quad (10)$$

In this way, it is possible to describe at high frequencies, the effect of an aerodynamic load on a structure as vibration levels, thanks to the application of Equivalent TBL (ETBL) excitation in a SEA approach.

4 NUMERICAL APPLICATIONS OF EQUIVALENT TBL (ETBL)

4.1 Generalities

Ref. [2] shows how to evaluate the modal density of a flow duct. Particularly at high frequencies, it has been observed that the dispersion curves of the flow duct follow the analytical thin-plate theory. At high frequencies, this means that it is possible to approximate a complex structure as an ensemble of thin plates.

According with this assumption, the energy transmission between a flow duct and a test panel can be described as an energy transmission among simple plates: the energy transmission between a testbench and a test panel can be also simplified as said before. Therefore, the preliminary study of energy transmission between three plate in a row (Fig. 3) is carried out.

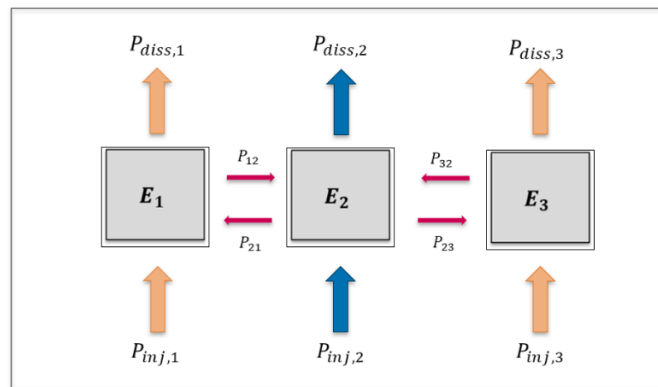


Figure 2: Equivalent SEA model.

Three is the lowest number of plates that can be chosen for the first study of energy flow direction among subsystems: the energy transmission referred to a test panel would be analyzed between more than one interface.

The plates of equivalent SEA system (Fig. 2) have the characteristics described in Table 1.

Table 1: Geometry and physical properties of the plate.

Geometry: Plate	Material: Aluminium
$L_x = 1.5m$	$E = 7.1e10 Pa$
$L_y = 0.9m$	$\nu = 0.33$
$h = 5mm$	$\rho = 2500 kg/m^3$
	$\eta = 0.005 (0.5\%)$

The energy transmission analysis of the equivalent SEA system is organized as follows.

A first solution has been evaluated keeping all three plates with the same identical properties; the other solutions calculated for different configurations would be compared with this as reference case ('case 0'). The SEA frequency limit for this configuration is 2500Hz. The first comparison is in function of difference of surface: the middle plate – which represents the test

panel – would have a reduced length $L_x = 0.5m$, having a consequential reduction of surface of 33% respect to the side plates surfaces.

The second comparison is in function of difference of thickness: the middle plate would have a reduced thickness $h = 1mm$, 1/5 of the side plates thickness.

The third and last comparison is in function of the damping loss factor: the side plates would present an increase of damping from 0.5% to 7%.

All the cases described above will be compared with ‘case 0’ in terms of: (i) Vibration velocity levels S_{VV} , in order to obtain a velocity gap between middle plate and side plates of at least 20 dB; (ii) Powers levels which act on subsystem ‘plate 2’, in order to understand how the energy spreads inside the system. The power levels are not presented as absolute values, but as ratio with the injected power on ‘plate 2’.

4.2 SEA Test-Cases

4.2.1 Surfaces

As first case, the length of middle plate is reduced from the initial value $L_x = 1.5m$ to $L_x = 0.5m$, as mentioned above. The reduction of surface applied at the middle plate changes its modal overlap factor and, consequently, increases the value of SEA frequency to ≈ 7000 Hz. The velocity gap obtained for a surface reduction of 33% is only of 6 dB (Fig. 3), which is too low for an energy isolation of the middle plate in terms of vibration velocity.

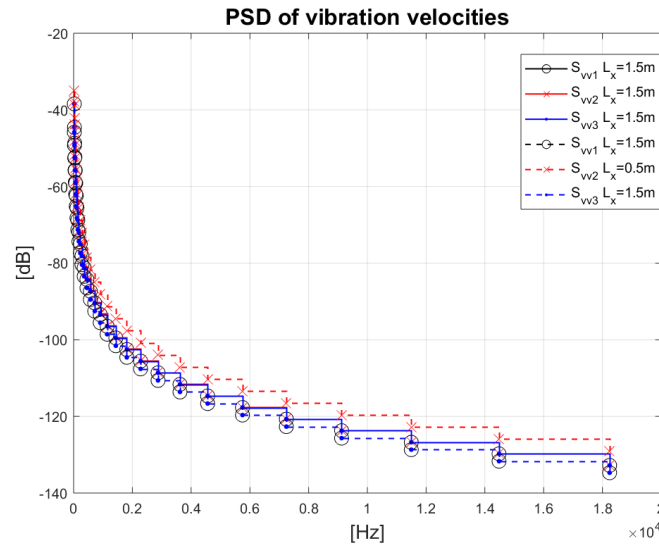


Figure 3: Vibration velocities of three plate in row subjected to an Equivalent TBL: same properties (-), subsystem ‘plate 2’ with $L_x = 0.5m$ (--).

The consequences of surface reduction of the middle plate can be seen in Fig. 4: the dissipated power, $P_{diss,2} = \omega \eta_2 E_2 = f[\langle v_2 \rangle^2]$, of ‘plate 2’ has reduced, while the transmitted energy of side plates has increased. This is not an acceptable configuration, because the aim is the reduction of the transmitted power from the other subsystems to the test panel, not the

opposite.

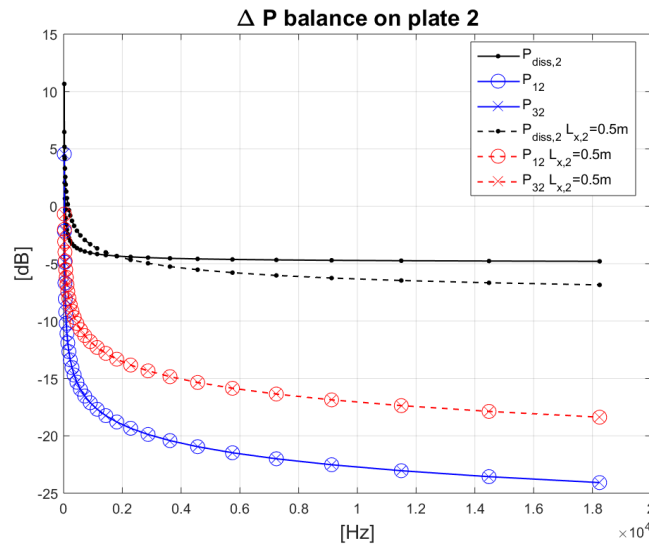


Figure 4: Difference of powers calculated in function of injected power acting on the subsystem 'plate 2': same properties (-), subsystem 'plate 2' with $L_x = 0.5m$ (--).

4.2.2 Thicknesses

In this second configuration, the middle panel had a reduction of thickness from $h = 5mm$ to $h = 1mm$. With this change of thickness, the modal overlap factor of the middle plate leads to a wider frequency range in which the SEA method is valid. But, because it must be considered the modal overlap factors of all the subsystems, the SEA frequency limit still remains over 2500Hz. The reduction of thickness leads also to a velocity gap between the middle plate and the side plates of 20 dB and more (Fig. 5), which can ensure an energy isolation of the middle plate from the side plates.

Observing Fig. 6, it is possible to notice that the dissipated power of 'plate 2' reaches almost the same value of the injected power; this could mean that the energy flows inside the middle plate and then it is directly dissipated without almost any transmission to the near subsystems. Moreover, the values of the transmitted energy by side plates is consistently reduced, which could mean that the velocity response of the middle plate it is a direct effect of the TBL.

Hence, it can be said that a change of thickness can ensure the energy isolation of a test panel from its testbench.

4.2.3 Damping loss factors

The last comparison refers to a change of damping loss factor; this has been increased in side plates, to see the effect of energy transmission between a high damped subsystem with a low damped subsystem. The increase of damping loss factor in a subsystem has a direct effect on the modal overlap factor, which even this time ensures a wider frequency range of SEA validity. But, because the modal overlap factor of the middle plate must be considered too, the SEA frequency limit still remains 2500 Hz.

In Fig. 7, a velocity gap of nearly 4 dB is shown. While the vibration velocity of the middle plate remains the same, the side plates present a reduction of vibration velocity. Considering the case of the testbench, it means that a damped frame system does not ensure a huge difference of vibration velocities between itself and the test panel. On the other hand, it is shown in Fig. 8 that an increase of damping loss factor in the side plates ensures a reduction of transmitted energy from them to the middle plate. As expected, the dissipated power of ‘plate 2’ seems not changed.

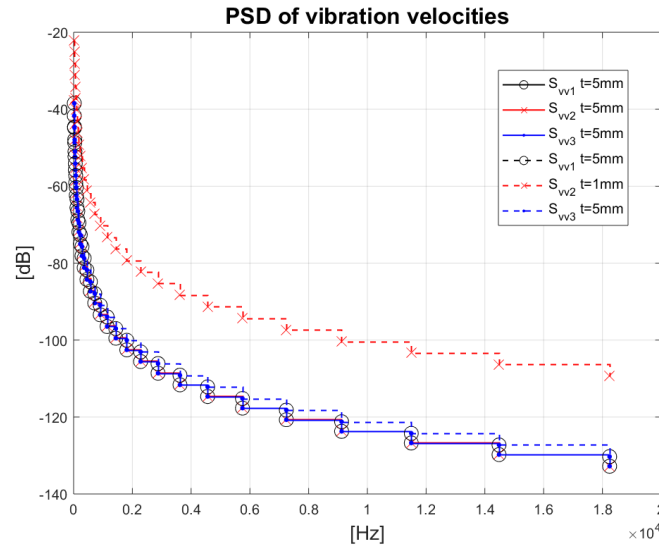


Figure 5: Vibration velocities of three plate in row subjected to an Equivalent TBL: same properties (-), subsystem ‘plate 2’ with $h = 1mm$ (--).

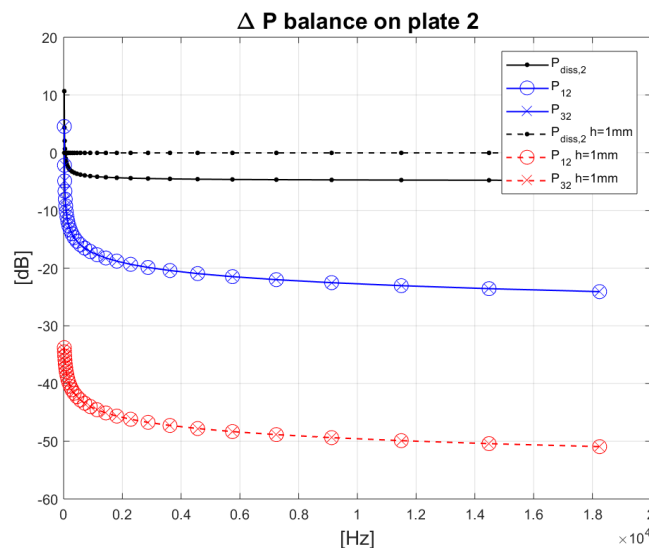


Figure 6: Difference of powers calculated in function of injected power acting on the subsystem ‘plate 2’: same properties (-), subsystem ‘plate 2’ with $t = 2.5mm$ (--).

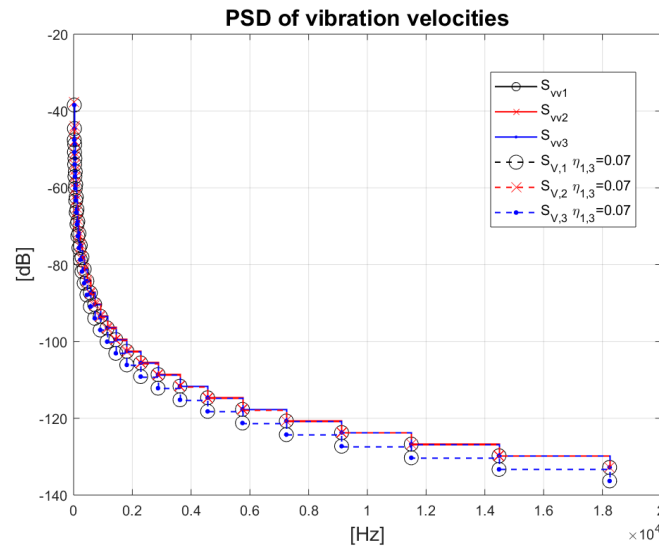


Figure 7: Vibration velocities of three plate in row subjected to an Equivalent TBL: same properties (-), subsystems 'plate 1' and 'plate 3' with $\eta = 0.07$ (7%) (--).

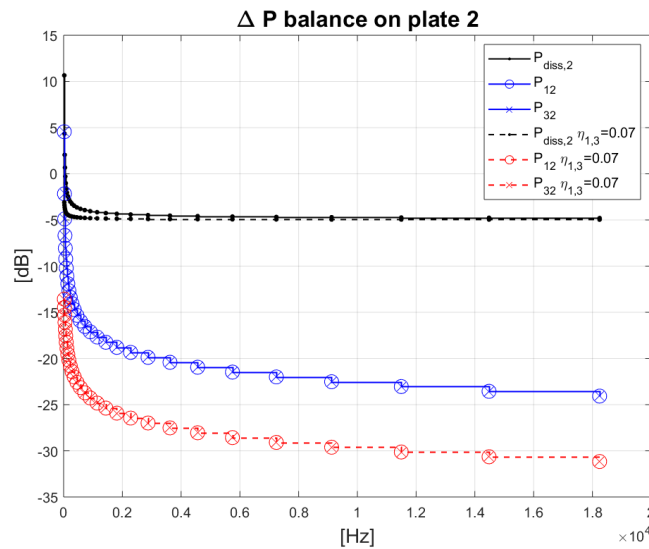


Figure 8: Difference of powers calculated in function of injected power acting on the subsystem 'plate 2': same properties (-), subsystems 'plate 1' and 'plate 3' with $\eta = 0.07$ (7%) (--).

5 CONCLUSIONS

From the above numerical tests based on SEA, it can be seen that there are different ways of changing the energy transmission between subsystems of a structure. Reducing the surface of the middle plate does not ensure its energetic isolation, but it implies only an increase of the energy transmission from the side plates to the middle one. On the other hand, the reduction of thickness is the best solution for a large velocity gap between the subsystems; in fact, the change

of thickness influences directly the impedance values of the subsystems, which consequently alters the way the energy is transmitted. Finally, modifying the damping loss factor only leads to a reduction of the transmitted energy; it could be taken in consideration as final option for the optimization of the structure in terms of energy isolation of the test panel.

This is only a preliminary study which can be conducted for a first design of a testbench. As following step, it is necessary to consider the indirect energy transmission between subsystems which are not physically connected each other. This second test can be carried on through the utilization of SEA-like method, which not only is able to estimate the indirect CLF, but it can also extend the study of energy transmission in the middle frequency range.

ACKNOWLEDGEMENTS

This work did receive a FERED/FSE Rhône-Alpes funding under the frame of the collaborative project IJES.

Authors warmly acknowledge the institutional support for this research.

REFERENCES

- [1] Finnveden S. et alii, “A model of wall pressure correlation for prediction of turbulence-induced vibration.”, *J. of Sound and Vibration*, Vol. **20**, pp. 1127-1143, (2005).
- [2] Finnveden S., “Evaluation of modal density and group velocity by a finite element method”, *J. of Sound and Vibration*, Vol. **273**, pp. 51-75, (2004).
- [3] M. N. Ichchou and B. Hiverniau, “Equivalent ‘rain on the roof’ loads for random spatially correlated excitations in the mid-high frequency range”, *J. of Sound and Vibration*, Vol. **322**, pp. 926-940, (2009).
- [4] F. Franco, S. De Rosa and E. Ciappi, “Numerical approximations on the predictive responses of plates under stochastic and convective loads”, *J. of Fluids and Structures*, Vol. **42**, 296-312, (2013).
- [5] R. H. Lyon, **Statistical Energy Analysis of Dynamical Systems: Theory and Applications**, MIT Press, (1975).
- [6] E. C. N. Wester and B. R. Mace, “Statistical Energy Analysis of two edge-coupled rectangular plates: ensemble averages”, *J. of Sound and Vibration*, Vol. **193**(4), pp. 793-822, (1996).
- [7] B. Mace, “Statistical Energy Analysis, energy distribution models and system modes”, *J. of Sound and Vibration*, Vol. **264**, pp. 391-409, (2003).

ELASTIC ENERGY TRANSPORT LEVERAGING TUNABLE TOPOLOGICAL STRUCTURES

DAVIDE E. QUADRELLI, EMANUELE RIVA, GABRIELE CAZZULANI AND
FRANCESCO BRAGHIN

Department of Mechanical Engineering (DMecc)

Politecnico di Milano

Campus Bovisa, Via La Masa 1, 20156 Milan, Italy

e-mail: gabriele.cazzulani@polimi.it, web page: <http://www.mecc.polimi.it/>

Key words: Topological phase, Negative capacitance, Tunable waveguides

Abstract. *The exploitation of non-trivial topological properties of band structures in Phononic Crystals has recently proved to be a proficient way to obtain robust waveguides showing immunity to backscattering at defects and capability to overcome sharp bends without reflections. This manuscript shows how it is possible to design an elastic waveguide that exploits the promising features of topological protection and at the same time achieves reconfigurability in the path followed by the carried signal. This is accomplished by integration in the structure of piezoelectric smart devices with negative capacitance shunting circuits. Moreover, the design of a mechanism to switch between different edge channels to convey at need elastic energy to distinct points of the structure is presented.*

1 INTRODUCTION

The design of engineered periodic lattices has become of great interest during the past decades as a means to obtain wave propagation control in elastic structures [1]. The exploitation of Bragg scattering at periodic discontinuities or the use of patterns of resonators are now established ways to shape phononic dispersion branches. In this context, the opportunity to observe and take advantage of topological phases in elastic systems has recently driven a growing interest to the subject. Such topological properties were firstly introduced in quantum systems of condensed matter [2, 3, 4] and have quickly spread to other fields of studies such as optics [5] and acoustics [6, 7] for the new promising ways of wave manipulation they offer. Indeed, the systematic study of the geometrical properties of band structures is now a powerful tool to predict the occurrence of efficient energy transport showing certain degree of immunity to backscattering. As a matter of fact, each topological phase can be indexed by a topological invariant. Moreover, the bulk-edge correspondence principle ensures that at the shared edge between two distinct phases a number of topologically protected states equal to the difference of their topological invariants will occur. In particular, in the following we will consider periodic mechanical structures establishing analogy with the quantum valley Hall effect (QVHE). This phenomenon can be obtained exploiting the valley degree of freedom as a pseudospin, given that inter-valley scattering is suppressed. Valley Hall phases have been successfully observed both in discrete mechanical lattices [8, 9, 10], and in continuum periodic structures [11, 12, 13]. A profitable way to obtain such Valley edge states is to lift the Dirac degeneracy occurring in Kagome lattices by break of spatial inversion symmetry (SIS). Exploiting

this design procedure, the aim of this paper is to show how it is possible to combine the unique features of topologically protected edge waves with adaptivity, achieved introducing piezoelectric inserts in the unit cell. Indeed, such patches are adopted to locally alter the stiffness of the unitary elements, using series negative capacitance shunting circuits [14, 15, 16]. In this way, the designed elastic structure is capable to route elastic energy along different paths, in addition to showing all the interesting features of topological protection. The manuscript is organized as follows: in the second section the design of the unit cell of the proposed structure is discussed. The occurrence of a topological phase transition when the elastic properties of the unit cell are smoothly changed by use of the shunting circuits is also underlined. In section 3 an analysis of the edge states occurring at interfaces created between topologically distinct lattices is performed. The design of a quantum point-like device capable of redirecting elastic energy in different directions is also added. Conclusions are drawn in the last section.

2 UNIT CELL ANALYSIS

A sketch of the Kagome geometry is provided in Figure 1(a) along with the selected unit cell of direct lattice and a drawing of its Brillouin zone. In its discrete version it can be obtained joining lumped masses with linear springs. By lowering the symmetries of the lattice it is known that the Dirac degeneracy occurring at K/K' points can be lifted and a topological bandgap opened [8]. This can be done by alternating soft and stiff springs as highlighted with different colors in Figure 1(a). This consideration provides the guidelines for the design of the unit cell that is employed in the following to realize the tunable waveguide.

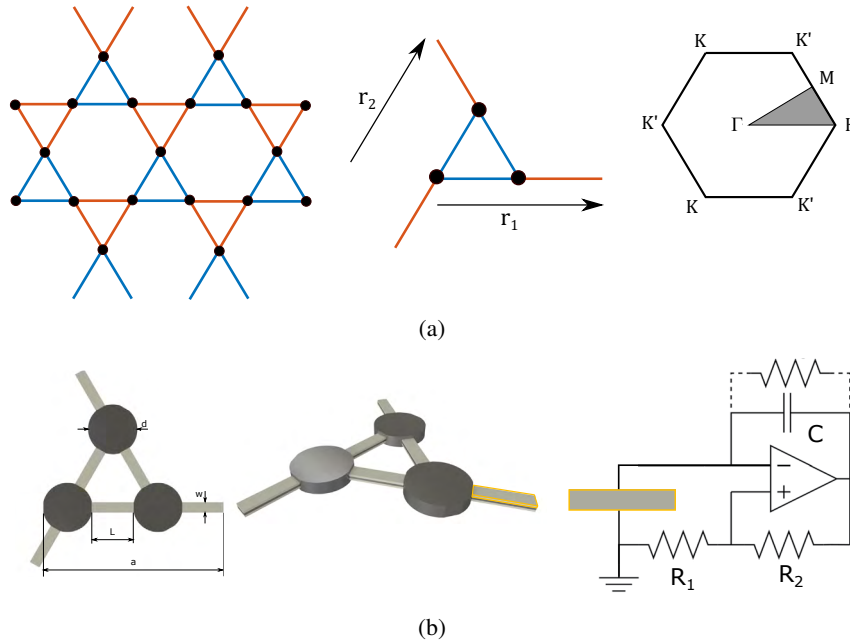
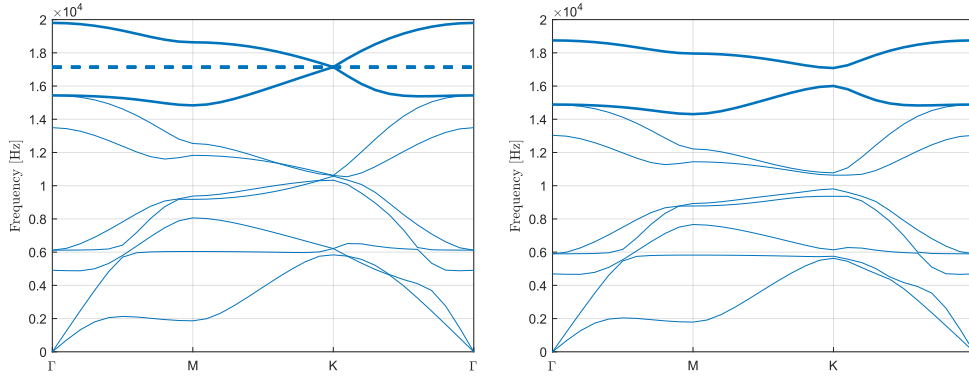


Figure 1: 1(a): Spring-mass discrete Kagome lattice, unit cell and Brillouin Zone. 1(b): Sketch of the continuum implementation of the tunable unit cell. Scheme of synthetic negative capacitance shunting circuit.

A schematic of such unit cell is shown in Figure 1(b): it is made by an Aluminum substrate and comprises three circular mass-elements connected by beam-elements acting as springs. Piezoelectric

Physical prop.	Substrate	PZT-5A	Geometrical prop.	
E	70 MPa	61.9 MPa	d	27.5 mm
ν	0.33	0.33	L	23 mm
ρ	2700 kg/m ³	7750 kg/m ³	$w = t$	6 mm
k_{31}		0.34	a	100 mm
ϵ_{33}^s		$13.3 \cdot 10^{-9}$ F/m	$h_s = h_p$	1 mm

Table 1: Unit cell physical and geometrical properties.


 Figure 2: Dispersion diagram for Kagome lattice: $\beta = 0$ (Left), $\beta = \pm 0.14$ (right).

patches are attached on both sides of the connecting elements, resulting in a bimorph configuration: h_s and h_p are the substrate and piezo thickness respectively (see Table 1 for all physical and geometric properties). Each patch is connected to a series negative capacitance shunting circuit. The resulting effective elastic modulus reads as [15, 16]:

$$E_p^{E*} = E_p^E \left(\frac{C_N - C_p^T}{C_N - C_p^S} \right) \quad (1)$$

considering E_p^E as the Young's Modulus at constant electric field and C_n the *negative capacitance* (NC) value. $C_p^{T,S}$ are the equivalent capacitance under free and blocked conditions, respectively:

$$C_p^T = \epsilon_{33}^T \frac{A}{h_p} \quad C_p^S = \epsilon_{33}^S \frac{A}{h_p} \quad (2)$$

being A the surface of the piezo patch and h_p its thickness. The piezoelectric coupling coefficient k_{31} relates ϵ_{33}^T and ϵ_{33}^S :

$$\epsilon_{33}^T = \frac{\epsilon_{33}^S}{(1 - k_{31}^2)} \quad (3)$$

The equivalent properties of the sandwich are obtained by the nominal ones of its sub-elements:

$$E_{eq} = \delta E_p^{E*} + (1 - \delta)E \quad \rho_{eq} = \delta \rho_p + (1 - \delta)\rho \quad (4)$$

with $\delta = \frac{2h_p}{h_s} = \frac{2}{3}$. Positive and negative modulation of the equivalent stiffness of the beam elements are

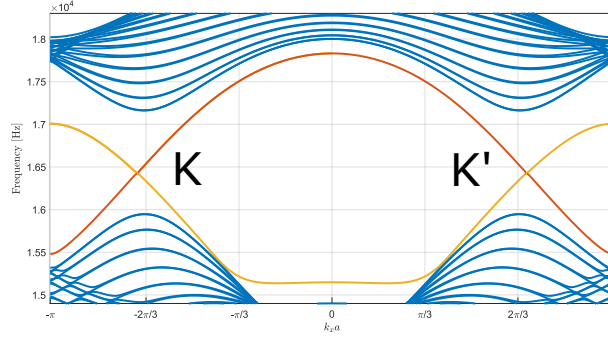


Figure 3: Band structure evaluated for the super cell depicted in Figure 4. Gap-less states are highlighted with different colors: red one appears at a Hard (H) interface, yellow ones a Soft (S) interface

achieved upon the application of a negative capacitance such as:

$$\frac{C_N}{C_P^T} = 1.25(1 \pm \beta) \quad (5)$$

where the constant 1.25 is required for stability reasons [15]. The value of β is tailored to obtain alternate soft and stiff spring elements, in analogy with the discrete case [8]. In particular, $+\beta$ is used for the three internal beams, and $-\beta$ for the remaining three. Figure 2 shows the dispersion diagram of the unit cell along the irreducible Brillouin zone, for $\beta = 0$. When no bias in the stiffness of the connecting elements is introduced, a degeneracy can be observed between the eighth and ninth branches at the high symmetry point K. Switching from $\beta = 0$ to $\beta = \pm 0.14$, a bandgap is opened between approximately 16 and 17 KHz, as a consequence of SIS break. In particular, the same stop band is obtained for $\beta = \pm 0.14$: despite representing two different unit cells (one has three internal soft springs, the other has three internal stiff springs) when repeated in infinite patterns the two lattices cannot be distinguished. Nevertheless, the band structures for $\beta > 0$ and $\beta < 0$ show different topological invariants: lattices with positive value of β cannot be smoothly deformed in ones with negative β without band-gap closing and reopening at $\beta = 0$. This witnesses the occurrence of a topological phase transition [8, 9]. That is, adjusting the value of the negative capacitance by switching from $\beta > 0$ to $\beta < 0$ causes the topological order of the structure to be changed.

3 TUNABLE TOPOLOGICALLY PROTECTED WAVEGUIDE

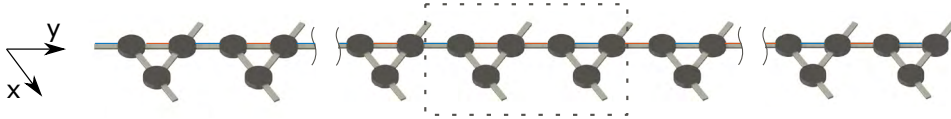


Figure 4: Finite strip made of 15 unit cell of type A followed by 15 B type elements. A so called Hard (H) interface is created in the middle: two hard connectors (highlighted in red) are facing at the discontinuity.

According to the bulk-edge correspondence principle, localized edge states are expected to occur at the interface between topologically distinct lattices having $\beta = \pm 0.14$. To observe their occurrence, a ribbon is made by $N_1 = 15$ unit cells with $\beta = 0.14$ (type A) and $N_2 = 15$ ones characterized by $\beta = -0.14$ (type B). This means that two halves built with different topological phases are joined together. If A-type unit cells are followed in the strip by B ones, a domain wall (DW) is created comprising two subsequent

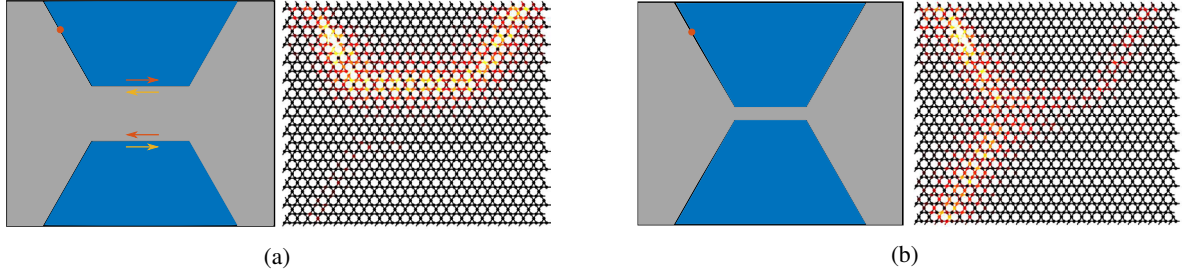


Figure 5: Figure 5(a): Frequency response function evaluated when two edge channels are kept apart. Seven rows of A type unit cells constitute the slice. Loading point is indicated with a red dot. K and K' -polarized modes are indicated with arrows. Figure 5(b): Energy is transferred between upper and lower edge channels if the number of rows in the slice is reduced.

stiff elements (Figure 4). A second kind of DW can be created reversing the order of the unit cells in the ribbon. This latter will be called S interface, consisting of two consequent soft connectors, while the former type will be indicated as H (hard) interface. The dispersion analysis of the super-cell is conducted letting the wave-vector vary between $\kappa_x \in [0, \pi/a]$. The resulting band structure is depicted in Figure 3. S-interface state is represented by the continuous yellow curve, while the red one describes the H-interface mode. In accordance with the bulk-edge correspondence principle, only one mode is obtained at each valley for each type of DW, being each phase indexed by a Valley Chern number $C_v = \pm 1/2$ [8]. Moreover, as long as inter-valley scattering is forbidden, forward and backward propagating modes cannot couple. This makes the topological waves protected against backscattering. As a consequence, the interface created facing two distinct phases constitutes an ideally perfect waveguide. It is worth noticing that the shape of such waveguide only depends on the spatial arrangement of A and B-type of unit cells inside the structure. Adaptivity is thus achieved considering that a topological phase transition from A cells to B ones and vice-versa can be induced manipulating the shunting circuits, upon variation of the parameter β which defines the value of the negative capacitance [16].

An interesting way to exploit such adaptivity is to design switch mechanisms in analogy with the quantum point-like devices developed in the context of QSHE [17]. Indeed, the coupling between topological states at different DWs can be exploited to switch edge channel. Consider a narrow bar made by A units surrounded at both sides by B elements: an H interface is obtained above such slice, while an S one is produced below (Figure 5(a)). On the former interface, the K polarized state is characterized by positive group velocity (forward propagation), while it exhibits negative group velocity on the other edge channel (backward propagation, see red arrows in Figure 5(a)). Upon tuning of the NC value inside the narrow slice, its width can be reduced or increased by inducing a phase transition of rows of unit cells. Until the width of the point contact is sufficiently opened, the two edge channels cannot couple, thus if excitation is applied to the H domain wall the forward propagating wave can reach the other end of the structure (Figure 5(a)). On contrast, a reduction of the width of the slice induces the forward state propagating on a DW to couple with the one which possesses the same valley index on the other, and the elastic signal is stirred back to the same side of the device (Figure 5(b)). In this way a switch is obtained between two possible paths, involving a reduced number of unit cells which need to be adjusted.

4 CONCLUSIONS

In this manuscript the design of a tunable topological waveguide was discussed. Adopting piezo-electric inserts it was possible to obtain semi-active control on the stiffness properties of the unit cell of the Kagome lattice, thus giving the opportunity to switch a topological phase into another at need. This allows to re-shape the interface constituting the waveguide itself. An example of switch mechanism between edge channels that exploits valley coupling was also shown, in analogy with quantum point-like structures.

REFERENCES

- [1] Hussein, M. I. and Leamy, M. J. and Ruzzene, M. *Dynamics of phononic materials and structures: Historical origins, recent progress, and future outlook*. Applied Mechanics Reviews, Vol. 66, n.4 (2014).
- [2] Thouless, David J., et al. *Quantized Hall conductance in a two-dimensional periodic potential*. Physical Review Letters 49.6 (1982): 405.
- [3] Haldane, F. Duncan M. *Model for a quantum Hall effect without Landau levels: Condensed-matter realization of the "parity anomaly"*. Physical Review Letters 61.18 (1988): 2015.
- [4] Klitzing, K. V., Gerhard Dorda, and Michael Pepper. *New method for high-accuracy determination of the fine-structure constant based on quantized Hall resistance*. Physical Review Letters 45.6 (1980): 494.
- [5] Lu, Ling, John D. Joannopoulos, and Marin Soljai. *Topological photonics*. Nature Photonics 8.11 (2014): 821.
- [6] Khanikaev, Alexander B., et al. *Topologically robust sound propagation in an angular-momentum-biased graphene-like resonator lattice*. Nature communications 6 (2015): 8260.
- [7] Ni, Xiang, et al. *Topological edge states in acoustic Kagome lattices*. New Journal of Physics 19.5 (2017): 055002.
- [8] Chen, H., H. Nassar, and G. L. Huang. *A study of topological effects in 1D and 2D mechanical lattices*. Journal of the Mechanics and Physics of Solids 117 (2018): 22-36.
- [9] Pal, Raj Kumar, and Massimo Ruzzene. *Edge waves in plates with resonators: an elastic analogue of the quantum valley Hall effect*. New Journal of Physics 19.2 (2017): 025001.
- [10] Chen, Yi, Xiaoning Liu, and Gengkai Hu. *Topological phase transition in mechanical honeycomb lattice*. Journal of the Mechanics and Physics of Solids 122 (2019): 54-68.
- [11] Liu, Ting-Wei, and Fabio Semperlotti. *Tunable acoustic ValleyHall edge states in reconfigurable phononic elastic waveguides*. Physical Review Applied 9.1 (2018): 014001.
- [12] Vila, Javier, Raj Kumar Pal, and Massimo Ruzzene. *Observation of topological valley modes in an elastic hexagonal lattice*. Physical Review B 96.13 (2017): 134307.
- [13] Torrent, Daniel, Didier Mayou, and Jos Snchez-Dehesa. *Elastic analog of graphene: Dirac cones and edge states for flexural waves in thin plates*. Physical Review B 87.11 (2013): 115143.

- [14] Zhu, R., et al. *Experimental study of an adaptive elastic metamaterial controlled by electric circuits*. Applied Physics Letters 108.1 (2016): 011905.
- [15] De Marneffe, Bruno, and Andr Preumont. *Vibration damping with negative capacitance shunts: theory and experiment*. Smart Materials and Structures 17.3 (2008): 035015.
- [16] Trainiti, Giuseppe, et al. *Time-Periodic Stiffness Modulation in Elastic Metamaterials for Selective Wave Filtering: Theory and Experiment*. Physical Review Letters 122.12 (2019): 124301.
- [17] Zhang, L. B., et al. *Electrical switching of the edge channel transport in HgTe quantum wells with an inverted band structure*. Physical Review B 83.8 (2011): 081402.

INVESTIGATIONS ABOUT THE MODELLING OF ACOUSTIC PROPERTIES OF PERIODIC POROUS MATERIALS WITH THE SHIFT CELL APPROACH

D. MAGLIACANO^{*†}, M. OUISSE^{*}, S. DE ROSA[†], F. FRANCO[†] AND A. KHELIF^{*}

^{*}Univ. Bourgogne Franche-Comté // FEMTO-ST Institute // CNRS/UFC/ENSM/UTBM
Department of Applied Mechanics // 25000 Besançon, FRANCE

[†]⌘ PASTA-Lab (Laboratory for Promoting experiences in Aeronautical Structures and Acoustics)
Department of Industrial Engineering - Aerospace Section
Università degli Studi di Napoli "Federico II"
Via Claudio 21, Edificio 11, 80125 Napoli, ITALY

Key words: vibroacoustics, periodic structure, shift cell, foam, inclusion

Abstract: The main advantage of designing sound packages with periodic arrangements is that they can provide a combination of absorption effects, resonance effects and wave interferences effects. This offers different applications in transportation (aeronautics, space, automotive, railway), energy and civil engineering sectors, where both weight and space, as well as vibroacoustic quality of performance and comfort, still remain as critical issues. The application of shift cell technique is presented and discussed for periodic porous media described with equivalent fluid models: it consists in a reformulation of classical Floquet-Bloch (F-B) conditions, whose major advantage stands in allowing the introduction of any frequency dependence of porous material behavior, through the resolution a quadratic eigenvalue problem, providing an efficient way to compute the dispersion curves of a porous material modelled as an equivalent fluid. The central part of this work shows the results, in terms of absorption coefficient and transmission loss curves, obtained through a numerical test campaign involving different melamine and polyurethane foams. The 48 test cases involve a cubic unit cell of porous material with a cylindrical inclusion. Furthermore, some absorption coefficient and transmission loss comparisons are shown, between a homogeneous unit cell and a unit cell with a perfectly rigid inclusion; the comparisons are carried out at fixed dimensions, then at fixed mass and then at fixed performance in the periodicity peak range. The results clearly point out the advantage of designing foam layer with periodic inclusion patterns in order to improve the performances in a specific range of frequencies, allowing a save both in terms of thickness and, most of all, mass, respect to a classical homogeneous foam layer.

1 INTRODUCTION

The inclusion of vibroacoustic treatments at early stage of product development, through the use of porous media with periodic inclusions, is a powerful strategy for the achievement of lightweight sound packages and represents a convenient solution for manufacturing aspects.

Indeed, although porous materials are commonly used for vibroacoustic applications, they suffer from a lack of absorption at low frequencies compared to their efficiency at higher ones; this difficulty is usually overcome by multi-layering [1]. However, while reducing the

impedance mismatch at the air-material interface, the efficiency of such devices relies on the allowable thickness [2].

A more efficient way to enhance the low frequency performances of sound packages consists in embedding periodic inclusions in a porous layer [3] in order to create wave interferences or resonance effects that may play a positive role in the dynamics of the system.

The classical approach, known as Floquet-Bloch (F-B) theory, provides a strategy to analyze the behavior of systems with a periodic structure.

In layered systems, due to the heterogeneity of the relevant elastic properties or to particular geometric features, or to both, only certain wave modes can physically propagate inside the structure. Each of these modes can be identified by a determined (generally nonlinear) function relating the time frequency and the spatial frequency (or wave number). These relationships are called dispersion curves and they summarize all the dynamic behavior of the system [4]. Therefore, dispersion curves offer a better perspective to explain the wave field behavior inside bodies.

For instance, the Helmholtz equation is a known example of equation describing the spatial behavior: there, the physical periodic structure of the studied object translates into spatial periodicity of its coefficients. Therefore, the F-B theory can be applied to obtain the dispersive properties of different mechanical periodic systems, reducing the problem to the calculations performed in the so-called unit cell under to certain specific boundary conditions derived from the F-B theory itself [5].

In order to develop efficient numerical techniques to handle the problem, the shift cell operator technique is presented. It allows the description of the propagation of all existing waves from the description of the unit cell through the resolution of a quadratic eigenvalue problem, in which the phase shift of the boundary conditions related to wave propagation is integrated into the partial derivative operator; consequently, the periodicity is included in the overall behavior of the structure, while continuity conditions are imposed at the edges of the unit cell. This is done through a $k(\omega)$ (wave number as a function of the angular frequency) method, which allows computing dispersion curves for frequency-dependent problems; instead of using the classical $\omega(k)$ (angular frequency as a function of wave number) that leads to non-linear eigenvalue problems.

Similar techniques, which use a modified F-B approach in order to handle a $k(\omega)$ problem, can be found in literature ([6]–[8]). The main reason why the shift cell method differs from them is that it consists in a reformulation of classical F-B conditions, in which the phase shift of the boundary conditions related to wave propagation is integrated into the partial derivative operator; consequently, the periodicity is included in the overall behavior of the structure, while continuity conditions are imposed at the edges of the unit cell. This technique has been successfully applied for describing the mechanical behavior of periodic structures embedding visco-elastic materials ([9], [10]) or piezoelectric materials [11]. Here it is proposed an extension to equivalent fluid models: this makes possible to overcome the limits of existing approaches by a more specific design of the system, through a process of optimization and testing of different inclusions, in order to obtain a device whose frequency efficiency outperforms existing designs.

The behavior of the porous materials is described by Johnson-Champoux-Allard (JCA) model ([12], [13]) in the following sections, but one can identically use any other equivalent fluid model ([14]–[16]).

2 SHIFT CELL OPERATOR TECHNIQUE

In this paper, a periodic arrangement of porous materials is considered. For a more detailed discussion, one can refer to [17]. The behavior of each material is described by an equivalent fluid model in the frequency domain, i.e.:

$$\rho \frac{\omega^2}{K} p + \Delta p = 0, \quad (1)$$

where $p = p(\mathbf{x}, \omega)$ is the acoustic pressure, $\mathbf{x} = (x, y, z)$ is the coordinate vector, ω is the angular frequency, $\rho = \rho(\mathbf{x}, \omega)$ is the equivalent fluid density and $K = K(\mathbf{x}, \omega)$ is the bulk modulus [18]. The periodicity is described by $\rho(\mathbf{x} + \mathbf{r}\mathbf{n}) = \rho(\mathbf{x})$ and $K(\mathbf{x} + \mathbf{r}\mathbf{n}) = K(\mathbf{x})$, $\forall \mathbf{x} \in \Omega$, where \mathbf{n} is a vector of integers normal to the face considered, $\mathbf{r} = (\mathbf{r}_1, \mathbf{r}_2, \mathbf{r}_3)$ is a matrix containing the three vectors defining the cell periodicity directions and lengths, and Ω is the domain of interest.

For the purpose of the shift cell technique development, considering Eq. 1 and applying the Bloch theorem such as $p(\mathbf{x}, \omega) = p(\mathbf{x})e^{j\mathbf{k}\mathbf{x}}$, where \mathbf{k} , for a 3D application, is

$$\mathbf{k} = k \begin{pmatrix} \cos\theta\cos\phi \\ \cos\theta\sin\phi \\ \sin\theta \end{pmatrix} \quad (2)$$

one can obtain

$$\rho \frac{\omega^2}{K} p + (\nabla + j\mathbf{k})^T (\nabla + j\mathbf{k}) p = 0. \quad (3)$$

$p(\mathbf{x})$ being periodic, the Dirichlet boundary conditions imply $p(L) = p(0)$.

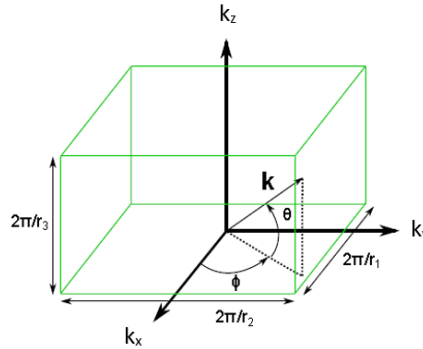


Figure 1: Reciprocal lattice vector in a 3D unitary cell.

2.1. Weak formulation

The aim of this section is the development of the weak formulation of the problem, in order to obtain a matrix equation that fully describes what happens inside a periodic unit cell of equivalent fluid. A weak formulation of Eq. (3) consists in finding p such that $\forall \tilde{p}$, which obeys to the periodic boundary conditions, one has:

$$\begin{aligned} \omega^2 \int_{\Omega} \frac{1}{K} \tilde{p} p \, d\Omega + \int_{\Omega} \frac{1}{\rho} \tilde{p} \nabla^T \nabla p \, d\Omega + j\mathbf{k} \int_{\Omega} \frac{1}{\rho} \tilde{p} \nabla^T p \, d\Omega + \\ + j\mathbf{k}^T \int_{\Omega} \frac{1}{\rho} \tilde{p} \nabla p \, d\Omega - k^T \mathbf{k} \int_{\Omega} \frac{1}{\rho} \tilde{p} p \, d\Omega = 0. \end{aligned} \quad (4)$$

After several passages, considering that $\boldsymbol{\varphi}$ is the eigenvector, the equation can be written in its matrix form

$$(\mathbf{K} + j\mathbf{k}\mathbf{L} + k^2\mathbf{H} - \omega^2\mathbf{M})\boldsymbol{\varphi} = \mathbf{0} \quad (5)$$

with the following matrices:

- $\mathbf{K} \propto \int_{\Omega} \frac{1}{\rho} \nabla \tilde{p} \nabla p \, d\Omega;$
- $\mathbf{L} \propto \int_{\Omega} \frac{1}{\rho} (\nabla \tilde{p} p - \tilde{p} \nabla p) \, d\Omega;$
- $\mathbf{H} \propto \int_{\Omega} \frac{1}{\rho} \tilde{p} p \, d\Omega;$
- $\mathbf{M} \propto \int_{\Omega} \frac{1}{K} \tilde{p} p \, d\Omega.$

Here, \mathbf{M} and \mathbf{K} are respectively the standard symmetric definite mass and symmetric semi-definite stiffness matrices, \mathbf{L} is a skew-symmetric matrix and \mathbf{H} is a symmetric semi-definite positive matrix. In this formulation, all matrices are frequency dependent.

3 NON-RIGID INCLUSIONS NUMERICAL TEST CAMPAIGN

Herein, all results are related to a 3D unit cell constituted by a cube with side equal to 2 cm (homogeneous case) and with a 0.5 cm radius cylindrical inclusion (cases with inclusion).

The analyses are carried out in the frequency range 0–17000 Hz. It is well known that the parameters of the equivalent fluid models can have a strong impact on the performances of the acoustic device [19], hence they should be determined in a confident way.

In the current case, the characteristics of the materials called “Melamine” and “Black PU” are experimentally determined, while those of the materials called “P1” and “M10” are taken from the work performed by Doutres et al. [20] and those related to “Melamine 173” and “P60” from a paper by Deckers et al. [21]. Except for the “Melamine” and “Melamine 173” materials, all the others are polyurethane foams. While dispersion curves are computed for an infinite repetition of unit cells, absorption coefficient and transmission loss are calculated for a finite repetition of five unit cells, using the same domain and boundary conditions of the infinite periodic system. This, in a first approximation, allows comparing the dispersion relations and the acoustical characteristics of the equivalent finite medium. Indeed, it has been noted that a further increasing in the number of repeated cells would lead to a change in the mean value of absorption coefficient and transmission loss respectively below 2% and 20% compared to the usage of a repetition of five unit cells.

The general definition of the sound absorption coefficient is the fraction of incident energy propagating into a sample material versus the energy propagating out. A part of the incident energy will be absorbed into the sample material, or rather dissipated inside it. The absorption coefficient α can be computed starting from the reflection coefficient R as

$$\alpha = 1 - |R|^2, \quad (16)$$

where R depends on the surface impedance Z_s . The surface impedance of the material is often presented in real and imaginary terms respectively; the real part describes the energy losses whereas the imaginary part describes the phase changes caused by the material [22]:

$$Z_s = \frac{p(L)}{v(L)} = Z_0 \frac{1+R}{1-R}. \quad (6)$$

This technique is only valid for plane waves impinging upon homogeneous media, and just at low frequencies for non-homogeneous ones. In a more general way, that is always correct, the absorption coefficient can be computed as [23]

$$\alpha = \frac{\Pi_{dissipated}}{\Pi_{incident}} \quad (7)$$

where

$$\Pi_{dissipated} = \Pi_{thermal} + \Pi_{viscous} \quad (8)$$

The terms can be expressed as [23]

$$\Pi_{incident} = \frac{S|p_{inc}|^2}{2\rho_0 c_0}, \quad (9)$$

$$\Pi_{thermal} = \frac{1}{2} \Im \left(-\omega \int_{\Omega_p} \frac{\phi^2}{K} p p^* d\Omega \right), \quad (10)$$

$$\Pi_{viscous} = \frac{1}{2} \Im \left(\int_{\Omega_p} \frac{\phi^2}{\omega \bar{\rho}_{22}} \underline{\nabla} p \cdot \underline{\nabla} p^* d\Omega \right), \quad (11)$$

where

- S = surface interested by incident pressure;
- p_{inc} = amplitude of the excitation mode (incident pressure);
- ρ_0 = density of the interstitial fluid (air);
- c_0 = sound speed in the interstitial fluid (air);
- Ω = poro-elastic volume;
- $p^* = conj(p)$;
- $\underline{\nabla}$ operator = gradient.

The transmission loss is numerically computed as

$$TL = 10 \log_{10} \frac{\Pi_{incident}}{\Pi_{transmitted}} \quad (12)$$

where $\Pi_{incident}$ and $\Pi_{transmitted}$ represent the incident and transmitted power, respectively.

Table 1: Non-acoustic parameters of the foams used for the numerical test campaign.

	Porosity	Tortuosity	Resistivity [Pa*s/m ²]	Viscous characteristic length [mm]	Thermal characteristic length [mm]
Melamine	0.99	1.02	8430	0.138	0.154
P1	0.956	1.06	3490	0.187	0.250
Black PU	0.96	1.075	5815	0.102	0.269
M10	0.982	1.25	3670	0.240	0.310
Mel. 173	0.98	1.01	9500	0.166	0.249
P60	0.98	1.17	3750	0.110	0.742

These values are obtained using an implementation of the plane wave forced response of the periodic cell accounting for fluid loading [24]. For a plane wave configuration, the value computed through Eq. (12) for homogeneous flat configurations is equivalent to the one obtained with the Transfer Matrix Method [1]:

$$TL = 10 \log \left(\frac{1}{4} \left| T_{11} + \frac{T_{12}}{\rho_0 c_0} + \rho_0 c_0 T_{21} + T_{22} \right|^2 \right), \quad (13)$$

$$\text{with } \begin{bmatrix} T_{11} & T_{12} \\ T_{21} & T_{22} \end{bmatrix} = \begin{bmatrix} \cos(kd) & j \sin(kd) Z_0 \\ \frac{j \sin(kd)}{Z_0} & \cos(kd) \end{bmatrix}. \quad (14)$$

3.1. Results

The JCA-modeled 3D unit cell that is described in the previous sections can be tested with some perfectly rigid and non-rigid inclusions. In particular, 48 setups are discussed here (Table 2), whose fundamental parameters are reported in Table 1.

Table 2: Combinations of foams and inclusions used for the numerical test campaign.

Configuration	Foam	Inclusion	Configuration	Foam	Inclusion
1	Melamine	none	25	M10	none
2		rigid	26		rigid
3		air	27		air
4		PU 1	28		PU 1
5		PU black	29		Melamine
6		M10	30		PU black
7		Mel. 173	31		Mel. 173
8		PU 60	32		PU 60
9	P1	none	33	Melamine 173	none
10		rigid	34		rigid
11		air	35		air
12		Melamine	36		PU 1
13		PU black	37		Melamine
14		M10	38		PU black
15		Mel. 173	39		M10
16		PU 60	40		PU 60
17	PU black	none	41	P60	none
18		rigid	42		rigid
19		air	43		air
20		PU 1	44		PU 1
21		Melamine	45		Melamine
22		M10	46		PU black
23		Mel. 173	47		M10
24		PU 60	48		Mel. 173

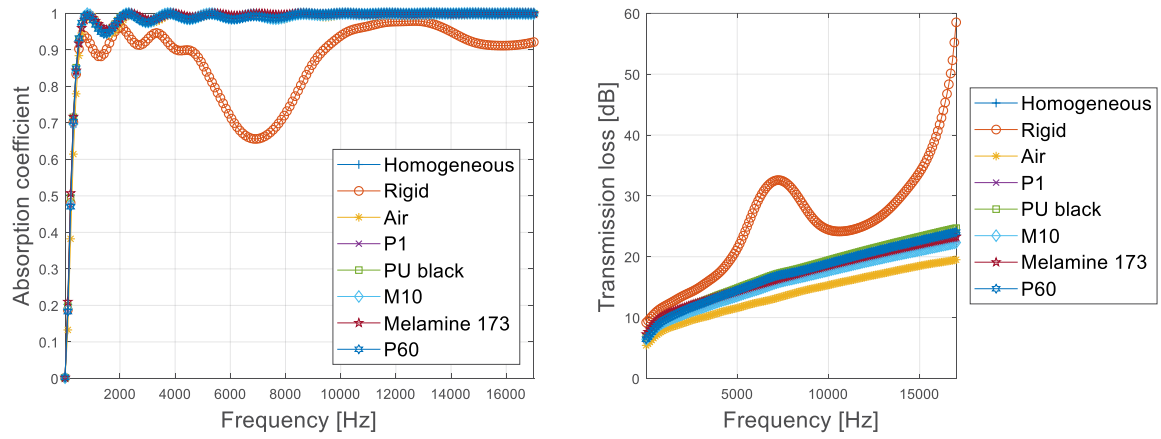


Figure 2: Comparison between absorption coefficient (on the left) and TL (on the right) curves for cases 1-8.

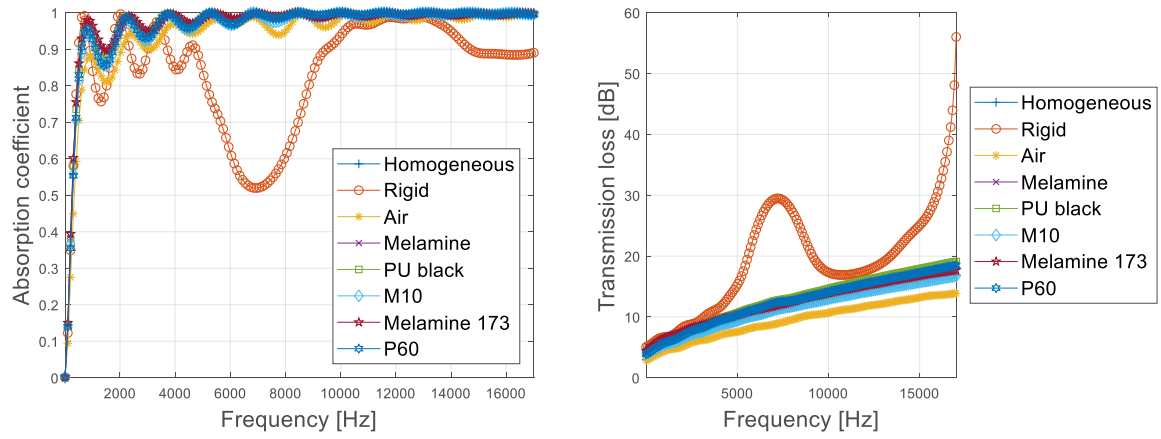


Figure 3: Comparison between absorption coefficient (on the left) and TL (on the right) curves for cases 9-16.

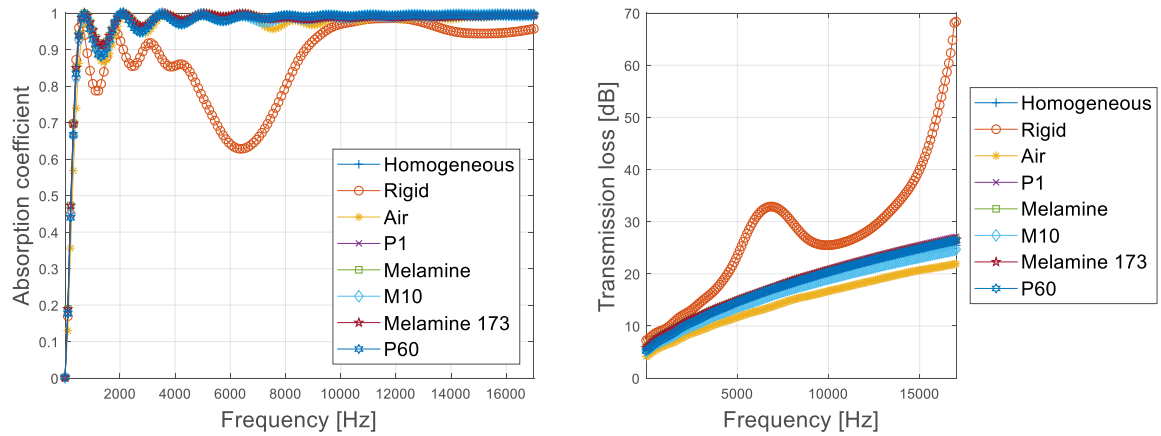


Figure 4: Comparison between absorption coefficient (on the left) and TL (on the right) curves for cases 17-24.

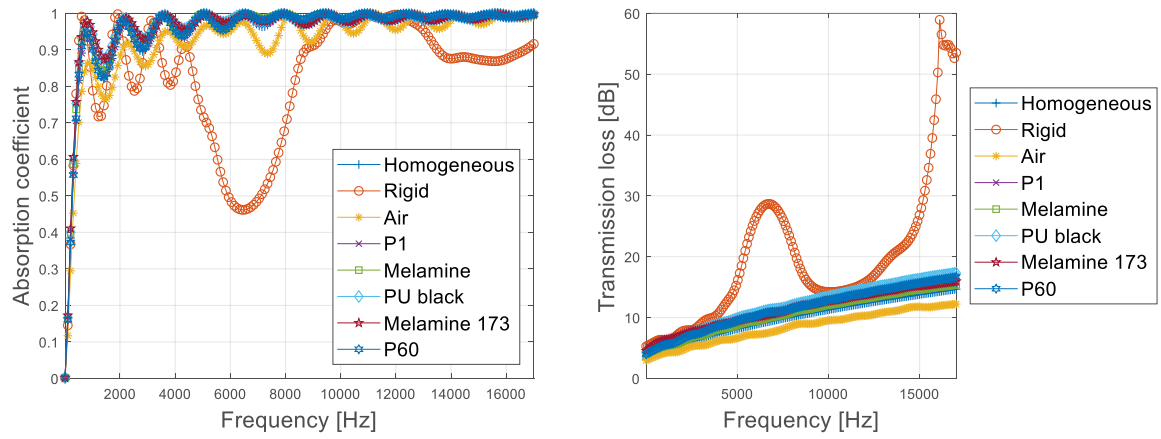


Figure 5: Comparison between absorption coefficient (on the left) and TL (on the right) curves for cases 25-32.

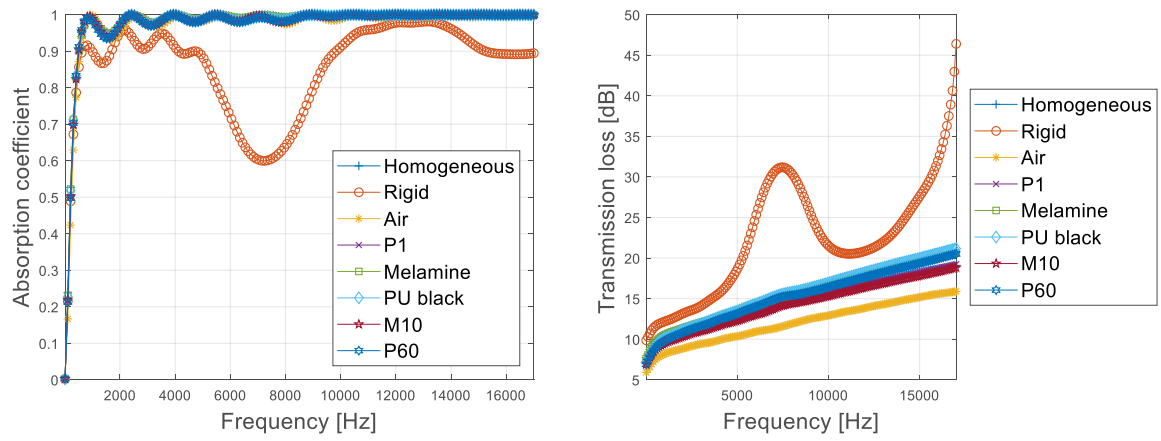


Figure 6: Comparison between absorption coefficient (on the left) and TL (on the right) curves for cases 33-40.

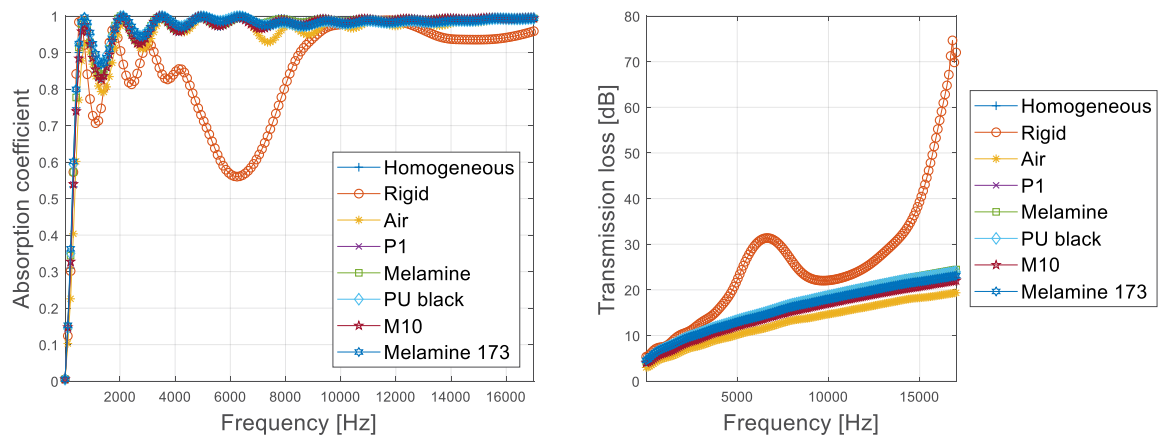


Figure 7: Comparison between absorption coefficient (on the left) and TL (on the right) curves for cases 41-48.

In Figures 2-7, some comparative absorption coefficient and transmission loss plots are shown for each of the 48 cases of study: in particular, each of the six foams is tested using eight different inclusions, according to the combinations reported in Table 2.

It can be noticed that, for what concerns the transmission loss, the effect of the inclusion is not particularly advantageous in these situations: in the case of the air, indeed, there is a drop of performances at all frequencies while, in the case of a foam inclusion, only a slight change of the values can be seen, as well as a very small effect of the periodicity when this is equal to half of the wavelength (around 7000 Hz).

Anyway, some different cases, that may be more interesting from the practical point of view, can be studied by modelling the foam unit cell through the use of the Biot model [25], instead that as an equivalent fluid; doing so, indeed, allows to take into account the elasticity of the skeleton and the entire problem formulation depends not anymore only on the pressure, but on the skeleton displacements too: this means that it should be possible to properly write the coupling conditions between the foam and an eventual (non-perfectly rigid) solid inclusion.

4 COMPARISON OF ACOUSTIC PERFORMANCES BETWEEN A HOMOGENEOUS UNIT CELL AND AN UNIT CELL WITH INCLUSION WITH FIXED MASS

In the previous sections, all the comparisons between homogeneous cases and cases with inclusions are made considering unit cells with the same dimensions; in other words, it means that the performances of a layer with periodic inclusions are estimated assuming that it has the same thickness of the related homogeneous one.

One may want also to compare absorption coefficient and transmission loss plots for the case in which the unit cell with inclusion has the same mass (and therefore different dimensions) respect to the homogeneous one. For example, considering an unit cell made of Melamine and with a perfectly rigid inclusion (Configuration 2 of Table 2), when comparing it to the homogeneous case with fixed dimensions, it obviously has a lower mass (75.56% of the homogeneous unit cell value); therefore, in order to perform a comparison with fixed mass respect to the homogeneous case, one should increase each dimension of the unit cell with inclusion of a certain quantity that, for the specific case, is equal to the 7.56%.

At this point, making some considerations based on the results shown in Figures 8 and 9, one may notice that the curve with fixed mass, respect to the one with fixed dimensions, has a performance peak caused by periodicity effect that is shifted at lower frequencies (this is due to the different dimensions between the two cases with inclusion) and also of different amplitude (due to the different mass of the compared unit cells).

Furthermore, in order to obtain the same transmission loss performances in the periodicity peak range (between 6000 and 8000 Hz, for the specific cases considered) by the use of a simple homogeneous layer made of the same foam, one should use a thickness that is around twice the one required for the cases with inclusion, therefore leading to an increment of the mass of about 100%. This clearly points out the advantage of designing foam layer with periodic inclusion patterns in order to improve the performances in a specific range of frequencies, allowing a save both in terms of thickness and, most of all, mass, respect to a classical homogeneous foam layer.

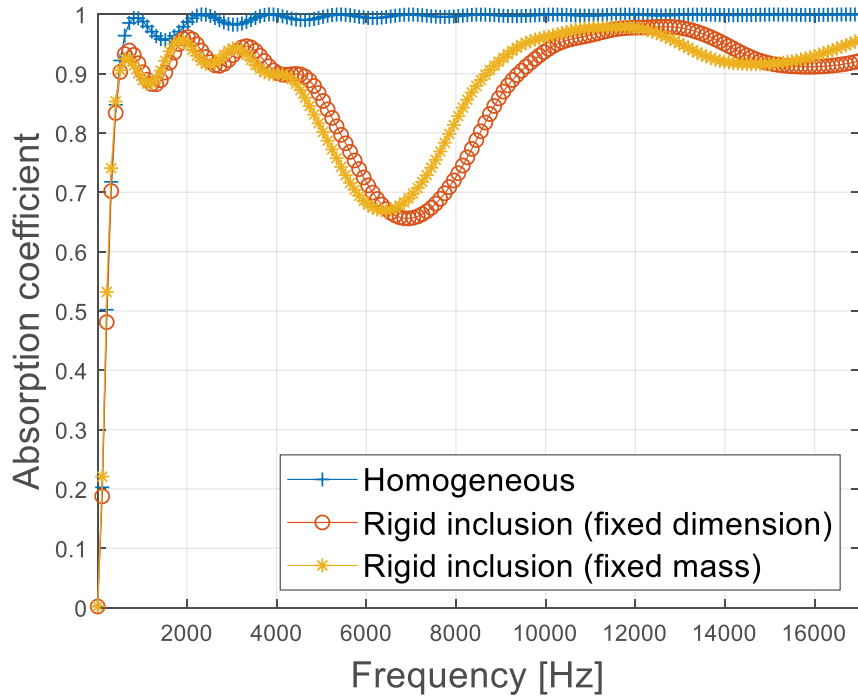


Figure 8: Comparison of absorption coefficient curves between the homogeneous case, the case with inclusion with fixed dimensions and the case with inclusion with fixed mass.

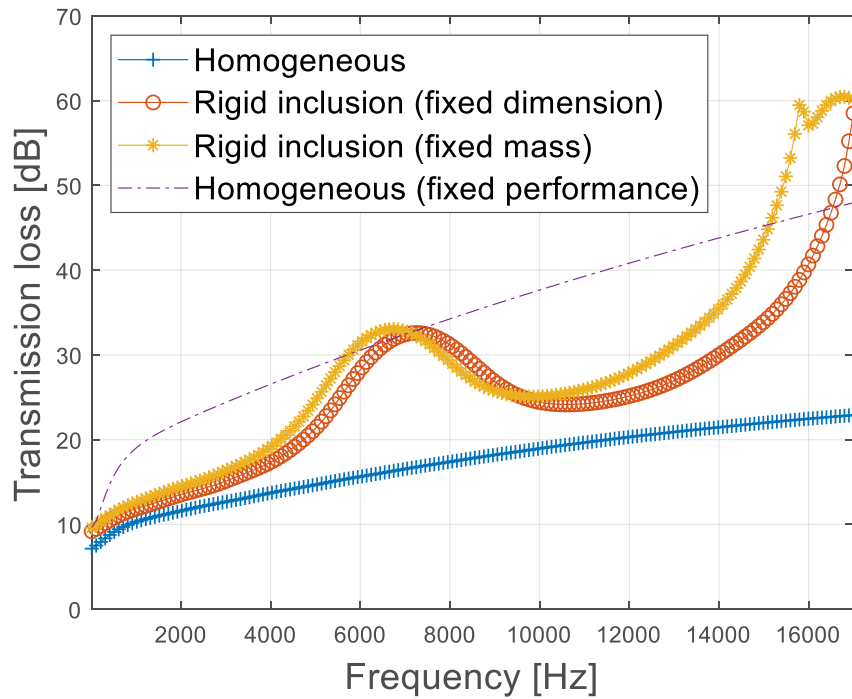


Figure 9: Comparison of transmission loss curves between the homogeneous case, the case with inclusion with fixed dimensions, the case with inclusion with fixed mass and the homogeneous case with fixed performance in the 6000-8000 Hz frequency range.

5 CONCLUSIONS

The shift cell technique has been presented, providing details on its numerical formulation.

Numerical results have been shown, in terms of absorption coefficient and transmission loss curves obtained through a test campaign involving 48 different JCA-modelled melamine and polyurethane foam unit cell configurations.

Furthermore, it has been shown the comparison between absorption coefficient and transmission loss plots for the case in which the unit cell with inclusion has the same mass (and therefore different dimensions) respect to the homogeneous one.

Further developments of the work will include the implementation of the shift cell technique using Biot model, for both 2D and 3D geometries, as well as the design and experimental tests of a specific unit cell configuration, chosen accordingly to an optimization process that will involve geometry, foam and inclusion material.

ACKNOWLEDGEMENTS

This project has received funding from the European Union's Horizon 2020 research and innovation program under the Marie Skłodowska-Curie grant agreement No. 675441.

REFERENCES

- [1] J. F. Allard and N. Atalla, *Propagation of Sound in Porous Media: Modelling Sound Absorbing Materials*, 2nd ed. Wiley, 2009.
- [2] T. Weisser *et al.*, "Acoustic behavior of a rigidly backed poroelastic layer with periodic resonant inclusions by a multiple scattering approach," *J. Acoust. Soc. Am.*, vol. 139, no. 2, pp. 617–629, 2016.
- [3] J.-P. Groby, a Wirgin, L. De Ryck, W. Lauriks, R. P. Gilbert, and Y. S. Xu, "Acoustic response of a rigid-frame porous medium plate with a periodic set of inclusions.," *J. Acoust. Soc. Am.*, vol. 126, no. 2, pp. 685–693, 2009.
- [4] Floquet and Gaston, "Sur les équations différentielles linéaires à coefficients périodiques," *Ann. Sci. l'École Norm. Supérieure*, vol. 12, no. Série 2, pp. 47–88, 1883.
- [5] P. G. García and J.-P. Fernández-Álvarez, "Floquet-Bloch Theory and Its Application to the Dispersion Curves of Nonperiodic Layered Systems," *Math. Probl. Eng. Math. Probl. Eng.*, vol. 2015, 2015.
- [6] M. A. Lewińska, J. A. W. van Dommelen, V. G. Kouznetsova, and M. G. D. Geers, "Towards acoustic metafoams: the enhanced performance of a poroelastic material with local resonators," *J. Mech. Phys. Solids*, 2018.
- [7] A. O. Krushynska, V. G. Kouznetsova, and M. G. D. D. Geers, "Visco-elastic effects on wave dispersion in three-phase acoustic metamaterials," *J. Mech. Phys. Solids*, vol. 96, pp. 29–47, 2016.
- [8] Y. F. Wang, Y. S. Wang, and V. Laude, "Wave propagation in two-dimensional viscoelastic metamaterials," *Phys. Rev. B - Condens. Matter Mater. Phys.*, vol. 92, no. 10, pp. 1–14, 2015.
- [9] M. Collet, M. Ouisse, M. Ruzzene, and M. N. Ichchou, "Floquet-Bloch decomposition for the computation of dispersion of two-dimensional periodic, damped mechanical systems," *Int. J. Solids Struct.*, vol. 48, no. 20, pp. 2837–2848, 2011.
- [10] K. Billon *et al.*, "Design and experimental validation of a temperature-driven adaptive

- phononic crystal slab,” *Smart Mater. Struct.*, vol. 28, no. 3, pp. 1–23, 2019.
- [11] M. Collet, M. Ouisse, and F. Tateo, “Adaptive metacomposites for vibroacoustic control applications,” *IEEE Sens. J.*, vol. 14, no. 7, pp. 2145–2152, 2014.
 - [12] D. L. Johnson, J. Koplik, and R. Dashen, “Theory of dynamic permeability and tortuosity in fluid-saturated porous media,” *J. Fluid Mech.*, vol. 176, no. 1, p. 379, 1987.
 - [13] Y. Champoux and J. F. Allard, “Dynamic tortuosity and bulk modulus in air-saturated porous media,” *J. Appl. Phys.*, vol. 70, no. 4, pp. 1975–1979, 1991.
 - [14] M. E. Delany and E. N. Bazley, “Acoustical properties of fibrous absorbent materials,” *Appl. Acoust.*, no. 3, 1969.
 - [15] Y. Miki, “Acoustical properties of porous materials-Modifications of Delany-Bazley models,” *J. Acoust. Soc. Jpn.(E)*, vol. 11, no. 1, pp. 19–24, 1990.
 - [16] D. Lafarge, P. Lemarinier, J. F. Allard, and V. Tarnow, “Dynamic compressibility of air in porous structures at audible frequencies,” *J. Acoust. Soc. Am.*, vol. 102, no. 4, pp. 1995–2006, 1997.
 - [17] D. Magliacano *et al.*, “Computation of dispersion diagrams for periodic porous materials modeled as equivalent fluids,” *J. Sound Vib.*, 2018.
 - [18] A. Bensoussan, J. L. Lions, and G. Papanicolaou, “Asymptotic Analysis of Periodic Structures,” *Stud. Math. its Appl.*, vol. 5, no. Elsevier, 1978.
 - [19] M. Ouisse, M. Ichchou, S. Chedly, and M. Collet, “On the sensitivity analysis of porous material models,” *J. Sound Vib.*, vol. 331, no. 24, pp. 5292–5308, 2012.
 - [20] O. Doutres, M. Ouisse, N. Atalla, and M. Ichchou, “Impact of the irregular microgeometry of polyurethane foam on the macroscopic acoustic behavior predicted by a unit-cell model,” *J. Acoust. Soc. Am.*, vol. 136, no. 4, pp. 1666–1681, 2014.
 - [21] E. Deckers, S. Jonckheere, and D. Vandepitte, “Modelling Techniques for Vibro-Acoustic Dynamics of Poroelastic Materials,” pp. 183–236, 2015.
 - [22] M. Wolkesson, “Evaluation of impedance tube methods - A two microphone in-situ method for road surfaces and the three microphone transfer function method for porous materials,” p. 69, 2013.
 - [23] F. Sgard, F. Castel, and N. Atalla, “Use of a hybrid adaptive finite element/modal approach to assess the sound absorption of porous materials with meso-heterogeneities,” *Appl. Acoust.*, vol. 72, no. 4, pp. 157–168, 2011.
 - [24] N. Atalla, *NOVAFEM User’s guide*. Sherbrooke (QC, Canada): Université de Sherbrooke, 2017.
 - [25] M. a Biot, “Mechanics of Deformation,” *J. Appl. Physics*, vol. 33, no. 4, pp. 1482–1498, 1962.

ON THE EFFECT OF DISTRIBUTED EMBEDDED RESONATORS IN CURVED SANDWICH PANELS LOADED BY TURBULENT BOUNDARY LAYER

F. ERRICO^{*,†}, M. ICHCHOU^{*}, S. DE ROSA[†], F. FRANCO[†] AND O. BAREILLE^{*}

^{*}VIAME - Laboratoire de Tribologie et Dynamique des Systems, Ecole Centrale de Lyon
36 Avenue Guy de Collongue, 69134, Ecully, France
e-mail: fabrizio.errico@ec-lyon.fr; mohamed.ichchou@ec-lyon.fr; olivier.bareille@ec-lyon.fr

[†] Department of Industrial Engineering, University of Naples Federico II
Via Claudio 21, 80125, Napoli, Italy
e-mail: fabrizio.errico@unina.it; sergio.derosa@unina.it; francesco.franco@unina.it

Key words: Periodic Structures, Metamaterials, Curved Panels, Turbulent Boundary Layer

Abstract. The effects of embedded resonators on the sound transmission loss of sandwich curved structures is investigated. The simulated loading is aerodynamic (turbulent boundary layer excitation), to simulate in-flight operational conditions for fuselages and nacelle fairings. The study is conducted numerically on double wall panels and auxetic-cored sandwiches, with periodic embedded resonant elements. A two-dimensional wave finite element method is used to model the metamaterial with a single periodic cell. The resonant elements are analysed in different tuning combination to investigate the effect on the aerodynamic coincidences and the ring frequency of the shell. The advantages regarding the sound transmission and the cost associated to the added-masses of the periodic resonators, are also discussed.

1 INTRODUCTION

While it is hard to renounce to the lightness of sandwich panels, proper counter-measures must be adopted to avoid high vibrational and noise levels which characterise this type of structures.

Many authors in the literature tried to optimize pre-existent sandwich panels' designs for acoustic purposes. For example, the shear-core effects on the larger acoustic radiation of sandwich panels, has been investigated by describing the panel using an equivalent shear core.¹⁻⁵ Palumbo et al.⁶ and Grosveld et al.,⁷ for example, experimentally studied honeycomb-cored sandwich plates with periodic voids in the core original geometry. Even though this creates a localised reduced bending stiffness, a strong benefit is observed in the sound transmission loss.

On the other hand, with the rise of modern numerical techniques as the Wave Finite Element Method (WFEM), detailed investigations on shear-core transitions and the acoustic radiation of sandwich structures, have been conducted easily by working with single elementary cells.⁸⁻¹⁰ In this context, the core geometry effects on the shear-core transition and sound transmission loss of honeycomb sandwich plates, were investigated in.¹¹ Zergoune et al.¹¹ showed the transmission loss sensitivity to most of the classic topological parameters of honeycomb cored sandwich panels, such as angles between walls, thickness and deformation of hexagonal core cells.

Alternative approaches, are connected to the use of periodically distributed resonant elements on a host plate.^{12–15} Even though, in this case, the addition of mass can not be avoided, some difficulties persist in targeting broadband enhancements of the acoustic performance of the panels. Particularly interesting is the work from Liu et al.¹⁴ which focuses on tuning spring-mass elements (the resonators) around the first coincidence region of the original panel to avoid the transmission loss drop typical in that regions. However, the work is mainly conducted, as for other works in the literature, for simplified excitation models or single acoustic plane-waves. Differently, the resonators are also used to target the ring frequency of shells, which is typically a tonal problem.¹⁵

In this work, some simple models of mechanical resonators embedded in curved sandwich/double-wall host plates are analysed under a turbulent boundary layer excitation. The idea is to approach more realistic operation conditions for curved sandwich plates commonly used in aerospace and in automotive industry. Simplified studies are also presented to understand how to set the first resonator's resonance frequency depending on the excitation model assumed.

The paper is structured as follows: Section 2 describes the numerical approach followed; Section 3 discusses about the use of embedded resonant elements to target acoustic and convective coincidences, as well as ring resonances and shows the different resonators designs used here; Section 4 shows the results in terms of dispersion curves and sound transmission loss.

2 NUMERICAL APPROACH

A 2D periodic structure is composed by an assembly, along arbitrary, even curved, directions, of identical elementary cells. The procedure used here is WFE-based and makes use of periodic links among degrees of freedom of finite element models of elementary cells. The mass and stiffness matrices of the cell, modelled with meshing convergence considerations for appropriate wavelengths description, can be extracted and post-processed. With reference to Fig. 1, the dynamic stiffness equation of the segment can be written as

$$[\mathbf{K} - \omega^2 \mathbf{M}] \mathbf{q} = \mathbf{D} \mathbf{q} = \mathbf{f} + \mathbf{e} \quad (1)$$

where \mathbf{q} , \mathbf{f} and \mathbf{e} are respectively the nodal vectors of degrees of freedom (DoFs), internal and external forces; \mathbf{K} , \mathbf{M} and \mathbf{D} are the stiffness, mass and dynamic stiffness matrices. The vectors and matrices are ordered as in Fig. 1. The wave motion through a periodic media can be analysed by imposing the Bloch-Floquet conditions^{8,9} to the finite element (FE) of a periodic cell, assuming time and space harmonic excitation. The periodicity conditions are translated in a magnitude and phase link among each point belonging to the periodic pattern, using a complex propagation constant for each wave type. Displacements and forces at any point of the cell can be connected, as follows (see Fig. 1):

$$\mathbf{q}_A = \mathbf{I} \lambda_Y \mathbf{q}_F; \quad \mathbf{q}_R = \mathbf{I} \lambda_X \mathbf{q}_L; \quad \mathbf{q}_2 = \mathbf{I} \lambda_X \mathbf{q}_1; \quad \mathbf{q}_3 = \mathbf{I} \lambda_Y \mathbf{q}_1; \quad \mathbf{q}_4 = \mathbf{I} \lambda_X \lambda_Y \mathbf{q}_1; \quad (2)$$

with

$$\lambda_{X,j} = e^{-ik_{X,j} L_X} \quad \lambda_{Y,j} = e^{-ik_{Y,j} L_Y} \quad (3)$$

where $k_{X,j}$ and $k_{Y,j}$ are wavenumbers of the propagating wave-type j in the periodicity directions X and Y , while L_X and L_Y represent the cell lengths along the same directions; \mathbf{I} is the identity matrix. In general a periodicity matrix Λ (see Eq. 2) can be built to link the whole set of degrees of freedom to a specific subset; i.e. the ones in one corner. Pre-multiplying Eq.1 by Λ^H , where H stands for the hermitian operator, the dynamic stiffness matrix of the reduced model is given by Eq. 4.

$$\mathbf{D}_S = \Lambda^H [\mathbf{K} - \omega^2 \mathbf{M}] \Lambda \quad (4)$$

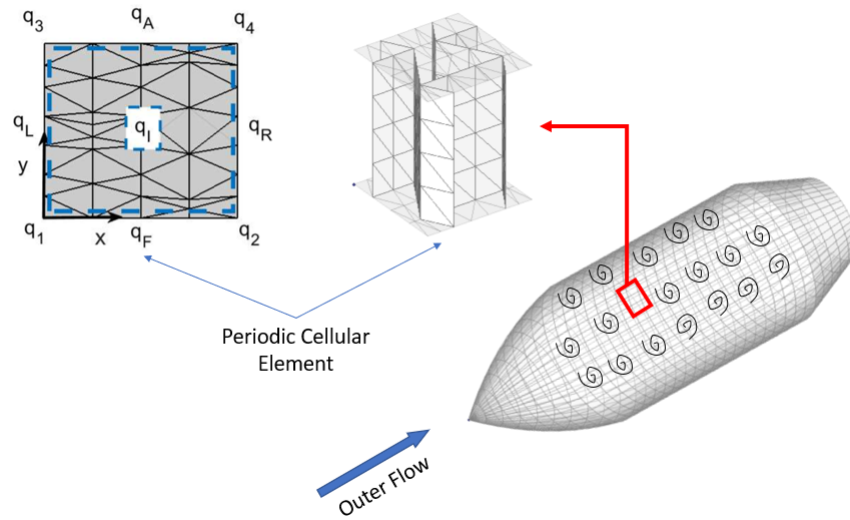


Figure 1: Example of a FE cell model with periodicity along the X-Y directions. a) Isometric view; b) Top view with nodes' subsets.

For the equilibrium of the internal forces between neighbouring cells, only external forces are considered (\mathbf{e} in Eq. 1). At this stage, different eigenvalue problems can be solved, if the target is the estimation of the dispersion curves of the periodic structure.¹⁰

2.1 Curvature Simulation

Being interested here in curved structures, with reference to Fig. 2, the idea is to rotate the local reference for each node belonging to the cell finite element model. This way, imposing the periodicity conditions, as shown in Eq. 3 and 4, the wave propagation is automatically analysed along the imposed curved path. Each translational DoF is rotated depending on its distance from the axis of rotation. In order to achieve the model of the curved cell, a rotational matrix \mathbf{r} is defined and assembled in a block

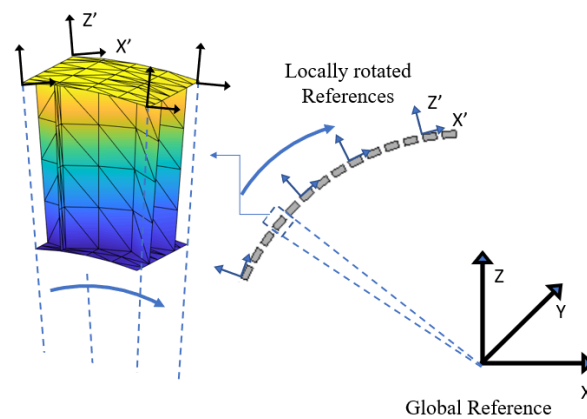


Figure 2: Rotation of the local system of reference for each node of the periodic cell FE model

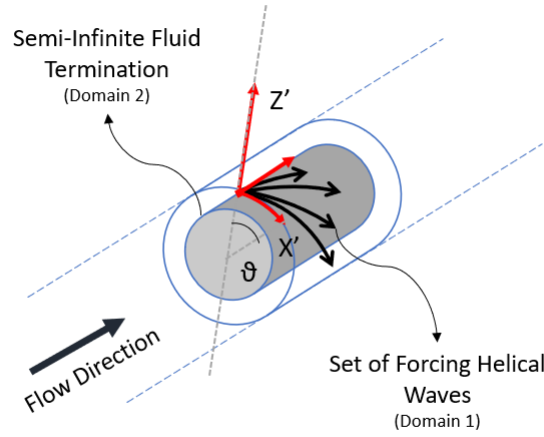


Figure 3: Scheme of the acoustic field and load approximations used within the numerical method described in section 2

diagonal matrix, **Rot**. The mass and stiffness matrices of the curved waveguide are obtained as:

$$\begin{aligned} \mathbf{M}_c &= \mathbf{Rot}^T \mathbf{M}_f \mathbf{Rot} \\ \mathbf{K}_c &= \mathbf{Rot}^T \mathbf{K}_f \mathbf{Rot}. \end{aligned} \quad (5)$$

where **Rot** is the rotation matrix, while the subscript *fl* refers to the FE matrices of the periodic cell being modelled as flat and the subscript *c* to the ones calculated simulating the curvature of the system. Forcing wavenumbers, imposed after Eq. 5, represent, in general, helical waves exciting the semi-infinite cylinder (see Fig. 3).

2.2 Fluid-Structure Coupling

Let us assume a forcing wave impinging on one face of the structure, with an amplitude p_I . The structure, as a result, transmits and reflects waves in the fluid adjacent to the top and bottom surfaces. On the excited side (subscript 1), the sound field is the superposition of the incident and reflected acoustic sound waves, while, in the receiver side (subscript 2), it is given by the transmitted waves assuming a semi-infinite fluid termination (see Fig. 3). Here, in the case of curved surfaces, as described also in subsection 2.1, the assumed plane wave is approximated through its projection components on the locally curved surface (Fig. 3):

$$HW = p_I e^{-i(k_{X'}X' + k_Y Y - k_{Z'}Z')} \approx p_I e^{-i(k_\theta \theta + k_Y Y - k_R Z')}, \quad (6)$$

where $k_{X'}$, k_Y and $k_{Z'}$ are the wavenumber components in the new locally rotated reference (see Fig. 2) and are directly proportional to the circumferential, axial and radial wavenumber components, respectively. It is worth to emphasize that a typical decomposition in cylindrical waves, implying the use of Bessel functions, is not necessary when using a locally rotated reference system as the one in Fig. 3: Eq. 6 depicts helical waves in cylindrical coordinates and the equivalent plane waves in Cartesian coordinates, respectively.^{10, 16–18} When non-homogenised periodic cells are considered, multiple harmonics are added to the k_X and k_Y terms;¹⁹ these are numerically accounted in the structural response of the radiating side

(subscript 2). In fact, when applying the WFE, discrete periodic conditions are applied for the forcing wavenumbers couple k_X and k_Y (Eq. 6) and a semi-infinite fluid termination is assumed to the domain 2 (see Fig. 3)

To express the nodal forces on the periodic cell as a function of the pressure amplitudes in the forcing and radiating side of the structure, the dynamic stiffness of the fluids can be used. From continuity of the normal particle velocity on the excited and radiating surfaces:

$$\begin{bmatrix} \mathbf{e}_T^{red} \\ \mathbf{e}_I^{red} \\ \mathbf{e}_B^{red} \end{bmatrix} = \begin{bmatrix} \mathbf{S} \cdot (\mathbf{p}_I + \mathbf{p}_R) \\ \mathbf{0} \\ \mathbf{S} \cdot \mathbf{p}_T \end{bmatrix} = \begin{bmatrix} \mathbf{S} \cdot (2\mathbf{p}_I - \mathbf{D}_{f,1}\mathbf{q}_{inc}) \\ \mathbf{0} \\ -\mathbf{S} \cdot \mathbf{D}_{f,2}\mathbf{q}_{rad} \end{bmatrix} \quad (7)$$

where:

$$D_{f,1} = \frac{-i\rho_1\omega^2}{k_{Z,1}}; \quad D_{f,2} = \frac{-i\rho_2\omega^2}{k_{Z,2}}, \quad (8)$$

where \mathbf{S} is vector of the free nodal surface of each excited node and \mathbf{p}_I , \mathbf{p}_R and \mathbf{p}_T are the nodal pressure vectors, ρ_1 and ρ_2 are the fluid densities, $D_{f,1}$ and $D_{f,2}$ the dynamic stiffness of the fluid in the incident and radiating domains; q_{in} and q_{rad} are the out-of-plane displacements, respectively of the incident and radiating surfaces.²⁰ The lumped-on-nodes forces act on the degrees of freedom of out-of-plane displacements, identified with the subscript T (top) and B (bottom), while all other degrees of freedom (not excited) are identified by I (internal).

The dynamic stiffness matrix and the reduced displacement vector can be rearranged in the same way as in Eq. 7, condensing all the non-excited (internal) nodes.²¹ Including the relations of Eqs. 4, 7 and 8, in the initial dynamic stiffness equation, the problem can be solved in \mathbf{p}_R and \mathbf{p}_T obtaining the power transmission coefficient τ associated with the couple of forcing wavenumbers k_X and k_Y .

$$\tau(k_X, k_Y) = \frac{(k_{Z,2}/\rho_2)\mathbf{S}|\mathbf{p}_T|^2}{(k_{Z,1}/\rho_1)\mathbf{S}|\mathbf{p}_I|^2}. \quad (9)$$

Finite size effects, can be included through correction factors, in order to increase the accuracy at low frequencies.^{22,23} The sound transmission to plane wave excitation, as discussed in Sec. 2, is not sufficient for many applications. A wavenumber-space load approximation to take into account a general type of excitation is proposed in²⁰ and is used here. The final sound transmission coefficient will be given by a weighted integration scheme:²⁰

$$\tau_{TOT}(\omega) = \frac{\int \int \tau(k_X, k_Y) \times W_A(k_X, k_Y, \omega) dk_X dk_Y}{\int \int W_A(k_X, k_Y, \omega) dk_X dk_Y} \quad (10)$$

where W_A is the matrix of the normalized amplitude function, of the wall surface waves, for all the wavenumber couples involved in the integration process.²⁰

3 STRUCTURAL DESIGNS ANALYSED

3.1 Resonators' Efficiency for Different Excitation Models

Depending on the excitation model assumed, the sound transmission loss of a panel changes. Similarly, the exotic nature of some excitation models might reduce the efficiency of the use of resonators. With reference to Eq. 10, each couple of forcing wavenumbers k_X and k_Y , contributes to the final transmission coefficient as a function of the weighting factors $W_A(k_X, k_Y, \omega)$. For a diffuse acoustic field, the integration scheme is equivalent to integrating all plane-wave inclinations.²¹ In Fig. 4a, some acoustic plane-wave trace wavenumbers versus frequency are plotted with the flexural ones of a 2mm-thick

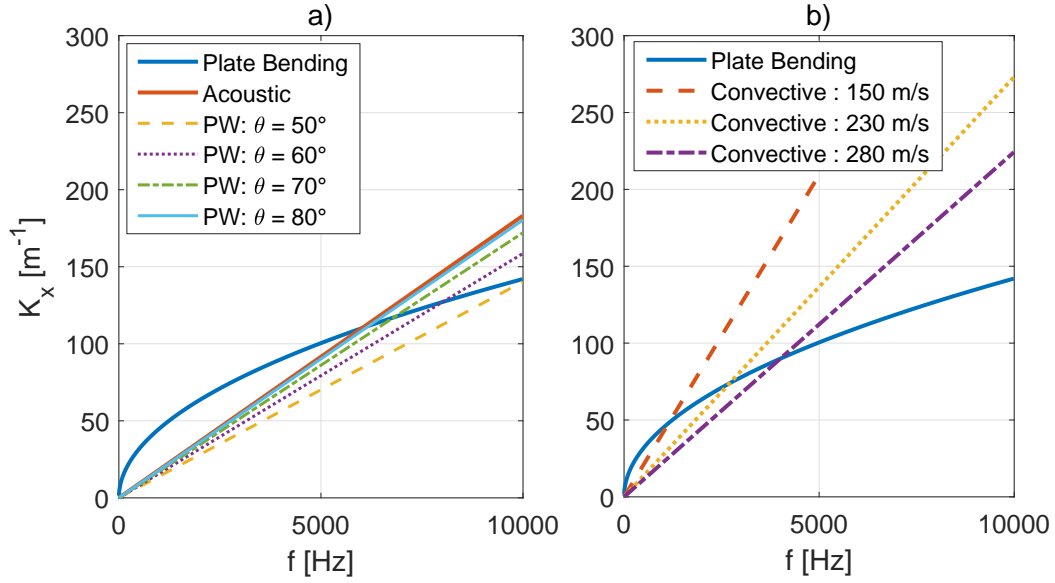


Figure 4: Dispersion Curves - The bending wavenumbers of a flat isotropic plate with: a) acoustic wavenumbers for different plane wave angles. b) convective wavenumbers for different flow speeds

aluminium plate; the coincidences shift depending on the inclination angle and the final coincidence we would obtain from integrating on every angle (Eq. 10), thus simulating a diffuse acoustic field, is the one give by assuming the acoustic wavenumber ω/c_0 , where c_0 is the speed of sound in the media analysed.

This means that tuning a single resonator on a specific coincidence/inclination, even if the global one, means, then, averaging its increased sound transmission losses over a large number of cases where the resonator is "mis-tuned" and thus induces a lower transmission loss, as shown in.¹⁴ The global advantages in using the resonant elements are attenuated (cancelled, in the worst cases), by the diffusiveness of the loading model.

Differently, for a turbulent boundary layer model, the aerodynamic coincidence (or critical frequency; see Fig. 4b) is stream-wise filtered by the physical nature of the load itself. Similarly, the structural-induced acoustic drops, as for the ring frequency of shells/curved panels, are not dependent on any inclination. For these reasons, the use of simple resonant elements (as beams) to contrast these frequency-fixed issues, can be a valid approach; the resonators "mis-tuning" effects are somewhat damped with respect to the ones integrated for a diffuse acoustic field.

3.2 Metamaterial Designs Analysed

The original panel designs analysed in this work are a double-wall with mechanical link (see Fig. 5a) and an auxetic-cored sandwich (see Fig. 6a). In both cases resonant laminas/beams are attached to the core walls (see Figs. 5b and 6b,c) and case-by-case tuned considering the first cantilever-beam-like mode. Both the models are made with skins in aluminium. The double-wall panels have a core in aluminium too and both skins and core walls are 0.6mm-thick, while the global thickness is 15mm. The auxetic core of the sandwich plates, which have a total thickness is 14mm, is instead made of an isotropic material with the following properties: $E = 1.45 \text{ GPa}$, $\nu = 0.27$, $\rho = 1100 \text{ Kg/m}^3$. In this case, the skins are 1mm-thick and the core walls are 0.5mm-thick.

Depending on the tuning and the number of the resonant elements, different configurations are stud-

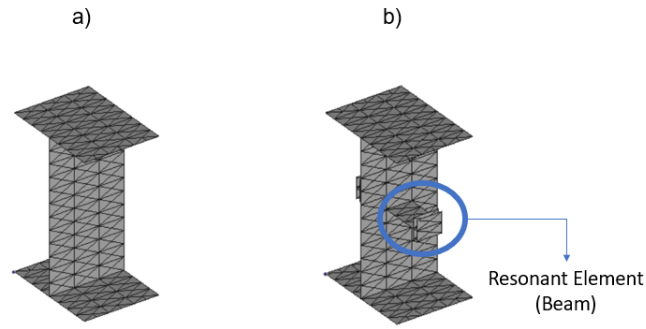


Figure 5: The periodic cell extracted from the double-wall panel with mechanical links. a) Standard design; b) Designs with Resonant Elements.

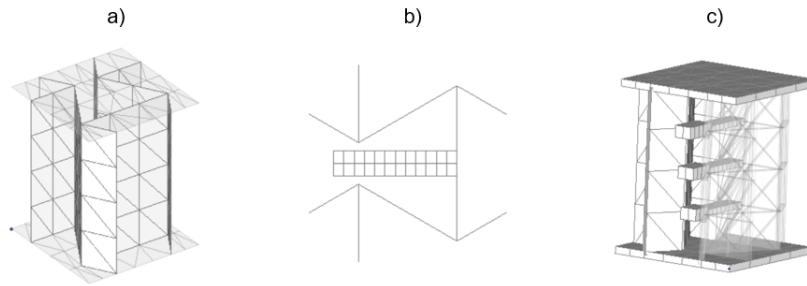


Figure 6: The periodic cell extracted from the Auxetic-Cored Sandwich Plate. a) Standard design; b) Designs with single Resonant Elements; c) Designs with triple Resonant Elements.

ied: for the double-wall plate three configurations are analysed and reported in Table 1; for the auxetic-cored sandwich panel four configurations are analysed instead and are reported in Table 2.

Considering the mass ratio influence, as discussed in,¹⁴ the effects of the resonant elements should be strongly visible for the double-wall panels, where the added masses are largely superior to the ones added in the auxetic-core configurations (see Tables 1 and 2)

4 RESULTS

The approach described in Sec. 2 is applied to simulate the sound transmission loss of the panel designs described in Sec. 3 under a turbulent boundary layer excitation (TBL). The Corcos model^{24,25} is used in these cases; the flow data are: $\delta = 0.027$ m, $\alpha = 0.125$ and $\beta = 0.83$.

Table 1: Double-Wall plate with mechanical links: Configurations Info

ID	Number of Resonant Elements	Added Mass [%]	Target Coincidence	Curvature [m]
Standard	0	0	N/A	1.6
Resonant (Ring) - D1	1	6	Ring Mode	1.6
Resonant (Aero)- D2	1	15	Aerodynamic	1.6
Doubly-Resonant (Aero)- D3	2	18	Aerodynamic	1.6

Table 2: Auxetic-Cored Sandwich Plate: Configurations Info

ID	Number of Resonant Elements	Added Mass [%]	Target Coincidence	Curvature [m]
Standard	0	0	N/A	1.0
Resonant (C1)	1	0.78	Ring Mode	1.0
Resonant (C2)	3	2.36	Ring Mode	1.0
Resonant (C3)	2	1.49	Ring Mode	1.0
Resonant (C4)	1	0.52	Aerodynamic	1.0

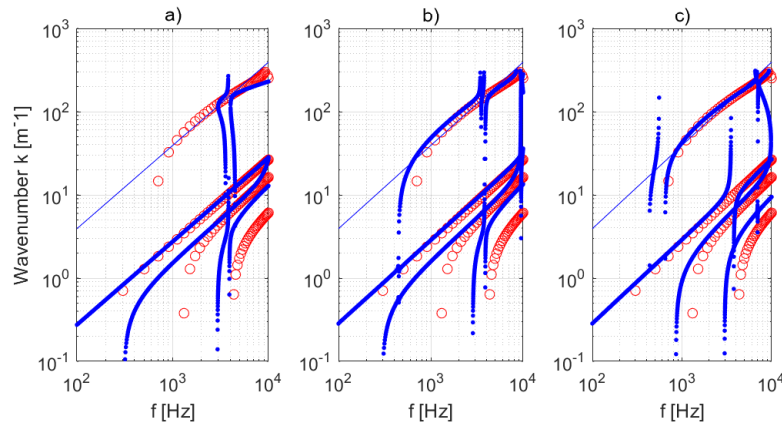


Figure 7: Dispersion curves for the double-wall panel with a 1.6m curvature. With reference to Table 1: a) D2; b) D3; c) D1. Legend: Or) Standard Configuration; .b) Resonant Configurations; -) Convective Wavenumbers for $U_c = 160$ m/s.

4.1 Dispersion Curves

First, the dispersion curves of the panel designs described in Sec. 3 are plotted in Figs. 7 and 8. In Fig. 7, the double-wall panel with mechanical links is analysed imposing a 1.6m curvature; due to the typical low core-shear stiffness of these types of structures, the presence of the resonant beam (see Fig. 5) seems to strongly influence even the ring frequency zone and, as shown later for the transmission loss, this will cause a shift of the ring frequency to lower values. For the resonant configurations targeting the aerodynamic coincidence (see Table 1 and Figs. 7a,b), resonance-induced band-gaps appear around the critical frequency.

Differently, in Fig. 8, the dispersion curves of three configurations presented in Table 2 for the auxetic-cored sandwich plate with a 1.0m curvature, are compared to the standard circumferential waves. In these cases, the presence of the resonant beams embedded in the auxetic core, does not influence the wave propagation in the original structure in frequency regions outside the resonance modes of the beams, as happens for the double-wall panel. This effect is connected to the reduced mass addition of this test-cases (see Table 2).

4.2 Sound Transmission Loss

Here, the sound transmission loss is finally calculated and compared, for all the configurations analysed, using the approach of Section 2. Infinite shells made with the elementary cells of Figs. 5 and 6 are simulated under an axial turbulent boundary layer flow. As a rule of thumb, the lower the mass addition

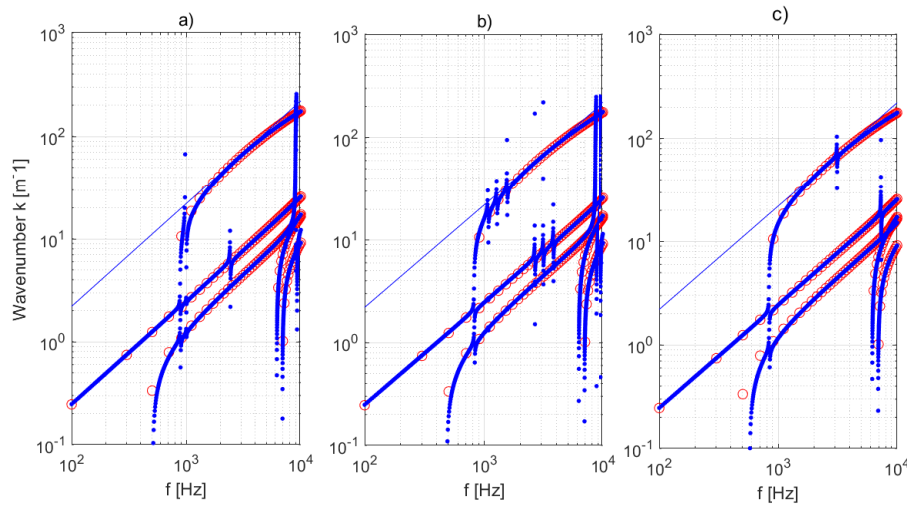


Figure 8: Dispersion curves for the Auxetic-cored sandwich panel with a 1.0 m curvature. With reference to Table 2: a) C1; b) C2; c) C4. Legend: Or) Standard Configuration; .b) Resonant Configurations; -) Convective Wavenumbers for $U_c = 285$ m/s.

the lower should be the advantages of the resonant elements around their frequency of resonance, in terms of sound transmission loss; with reference to Table 1 and 2 the addition of mass is between 6-18% for the double wall panel and between 0.5-2.4% for the auxetic-cored sandwich panel.

In Fig. 9 the sound transmission loss for the double-wall panel under a 160 m/s flow is presented. As evidenced also in the dispersion curves, the presence of the resonators shifts the ring frequency of the modified configurations and, thus, a mis-tuning of the resonance frequency of the embedded beams appears when targeting the original ring frequency of the shell. Differently, for the other configurations targeting the aerodynamic coincidence, a strong increase of the sound transmission loss is observed; a narrower band is targeted when using a single resonant beam, while a larger one, with a reduced peak of STL, is targeted when using two beams with a slightly different natural frequency. It is worth notice that the bands of increase of the sound transmission loss, when targeting the aerodynamic coincidence, are larger than expected by looking at the free wave propagation of the dispersion curves. This effect is attributable to the flow-induced increase of damping around the critical frequency (typical of TBL;^{20,26}), usually larger than the one observed for the acoustic coincidences.

On the other hand, in Fig. 10 the sound transmission loss for the sandwich panel with auxetic core, under a 285 m/s flow, is presented. Differently from the previous case, the increases of the STL are reduced because of the minimum addition of mass. Still, the configurations C1, C2 and C3 (see Table 2) induce a non-negligible increase of performance around the ring frequency region, as observed in Fig. 10. The use of three resonant elements with slightly shifted first natural frequencies (see C2 in Table 2 and Fig. 6c) helps in enlarging the coverage in frequency of the resonance-induced band-gaps and, thus, also the region of STL increase. Differently, the resonant configuration targeting the aerodynamic frequency (see C4 in Table 2) gives a relatively good increase of sound transmission loss even being single-element based and adding less than 1% of mass to the system.

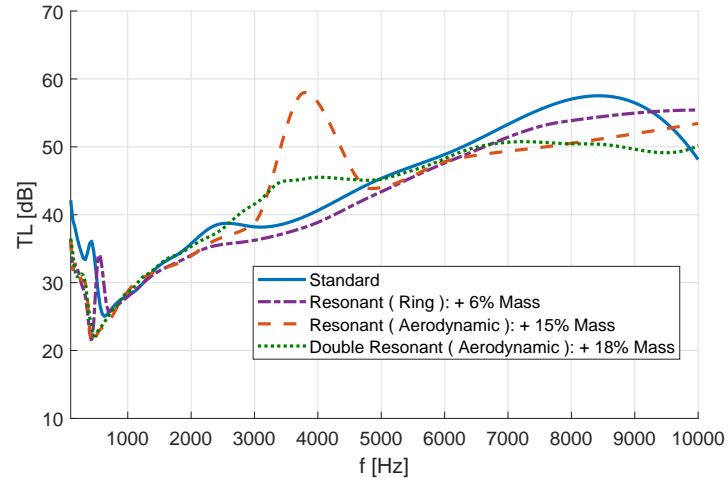


Figure 9: The sound transmission loss of the panel design in Fig. 5, with a 1.6 m curvature, under a TBL excitation at $U_c = 160$ m/s. Comparison between design configurations in Table 1.

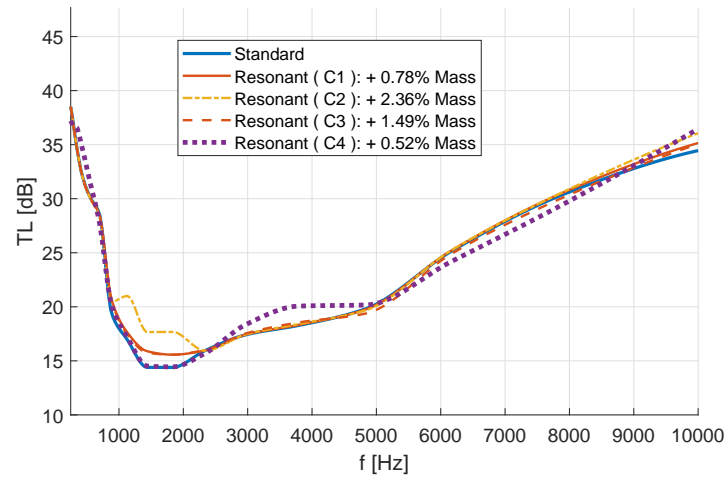


Figure 10: The sound transmission loss of the panel design in Fig. 6, with a 1.0 m curvature, under a TBL excitation at $U_c = 285$ m/s. Comparison between design configurations in Table 2.

5 CONCLUDING REMARKS

The effects of embedded resonators on the sound transmission loss of two types of sandwich cylindrical structures is numerically investigated under a turbulent boundary layer excitation. A two-dimensional wave finite element method is used to model the metamaterial with a single periodic cell, including the configurations with embedded resonant elements. The curvature of the models is simulated rotating the translations degrees of freedoms of the finite element model of the cells. A set of helical waves is used instead to simulate the random external pressure fluctuations and relate them to the periodic structural scale.

The resonant elements are analysed in different resonance tuning combination to investigate the effect on the aerodynamic coincidences and the ring frequency of the shell. A discussion on the use of such devices to target specific coincidences or resonances is also given. The effects of the resonant structural configurations with respect to the wave propagation, sound transmission and added-masses are observed and discussed.

ACKNOWLEDGEMENTS

This project has received funding from the European Unions Horizon 2020 research and innovation programme under the Marie Skłodowska-Curie grant agreement No. 675441.

REFERENCES

- ¹ F. J. Fahy, P. Gardonio, *Sound and structural vibration: radiation, transmission and response*, Elsevier, 2007.
- ² B. Clarkson, M. Ranky, Modal density of honeycomb plates, *Journal of Sound and Vibration* 91 (1) (1983) 103 – 118. doi:[https://doi.org/10.1016/0022-460X\(83\)90454-6](https://doi.org/10.1016/0022-460X(83)90454-6).
URL <http://www.sciencedirect.com/science/article/pii/0022460X83904546>
- ³ J. Han, K. Yu, X. Li, R. Zhao, Modal density of sandwich panels based on an improved ordinary sandwich panel theory, *Composite Structures* 131 (2015) 927 – 938. doi:<https://doi.org/10.1016/j.compstruct.2015.06.039>.
URL <http://www.sciencedirect.com/science/article/pii/S0263822315005036>
- ⁴ K. Renji, P. Nair, S. Narayanan, Modal density of composite honeycomb sandwich panels, *Journal of Sound and Vibration* 195 (5) (1996) 687 – 699. doi:<https://doi.org/10.1006/jsvi.1996.0456>.
URL <http://www.sciencedirect.com/science/article/pii/S0022460X96904563>
- ⁵ F. Franco, S. D. Rosa, T. Polito, Finite element investigations on the vibroacoustic performance of plane plates with random stiffness, *Mechanics of Advanced Materials and Structures* 18 (7) (2011) 484–497. doi:[10.1080/15376494.2011.604602](https://doi.org/10.1080/15376494.2011.604602).
URL <https://doi.org/10.1080/15376494.2011.604602>
- ⁶ D. L. Palumbo, J. Klos, *Development of quiet honeycomb panels*, Virginia, Langley Research Center; NASA/TM-2009-215954 (2009).
- ⁷ F. W. Grosveld, D. L. Palumbo, J. Klos, W. D. Castle, Finite element development of honeycomb panel configurations with improved transmission loss, *INTER-NOISE 2006 - 35th International Congress and Exposition on Noise Control Engineering*; 3-6 Dec. 2006; Honolulu, HI; United States (2006).
- ⁸ L. Brillouin, *Wave propagation in periodic structures: Electric filters and crystal lattices*, 2nd edition Dover Publications (Mineola, New York). doi:[10.1016/S0031-8914\(53\)80099-6](https://doi.org/10.1016/S0031-8914(53)80099-6).
- ⁹ D. Mead, Wave propagation in continuous periodic structures: research contributions from southampton, *Journal of Sound and Vibration* 190 (3) (1996) 495–524. doi:[10.1006/jsvi.1996.0076](https://doi.org/10.1006/jsvi.1996.0076).
- ¹⁰ E. Manconi, B. R. Mace, Modelling wave propagation in two dimensional structures using finite element analysis, *Journal of Sound and Vibration* 318(45) (2008) 884–902. doi:[10.1016/j.jsv.2008.04.039](https://doi.org/10.1016/j.jsv.2008.04.039).

- ¹¹ Z. Zergoune, M. Ichchou, O. Bareille, B. Harras, R. Benamar, B. Troclet, Assessments of shear core effects on sound transmission loss through sandwich panels using a two-scale approach, *Computers & Structures* 182 (2017) 227 – 237. doi:<https://doi.org/10.1016/j.compstruc.2016.11.017>.
URL <http://www.sciencedirect.com/science/article/pii/S0045794916304217>
- ¹² C. Claeys, P. Sas, W. Desmet, On the acoustic radiation efficiency of local resonance based stop band materials, *Journal of Sound and Vibration* 333 (14) (2014) 3203 – 3213. doi:<https://doi.org/10.1016/j.jsv.2014.03.019>.
URL <http://www.sciencedirect.com/science/article/pii/S0022460X14001990>
- ¹³ C. Claeys, K. Vergote, P. Sas, W. Desmet, On the potential of tuned resonators to obtain low-frequency vibrational stop bands in periodic panels, *Journal of Sound and Vibration* 332 (6) (2013) 1418 – 1436. doi:<https://doi.org/10.1016/j.jsv.2012.09.047>.
URL <http://www.sciencedirect.com/science/article/pii/S0022460X1200853X>
- ¹⁴ Z. Liu, R. Rumpler, L. Feng, Broadband locally resonant metamaterial sandwich plate for improved noise insulation in the coincidence region, *Composite Structures* 200 (2018) 165 – 172. doi:<https://doi.org/10.1016/j.compstruct.2018.05.033>.
URL <http://www.sciencedirect.com/science/article/pii/S0263822318303520>
- ¹⁵ Z. Liu, R. Rumpler, L. Feng, Investigation of the sound transmission through a locally resonant metamaterial cylindrical shell in the ring frequency region, *Journal of Applied Physics* 125 (11) (2019) 115105. doi:[10.1063/1.5081134](https://doi.org/10.1063/1.5081134).
- ¹⁶ E. Manconi, B. R. Mace, Wave characterization of cylindrical and curved panels using a finite element method, *The Journal of the Acoustical Society of America* 125 (1) (2009) 154–163. doi:[10.1121/1.3021418](https://doi.org/10.1121/1.3021418).
- ¹⁷ E. Manconi, B. R. Mace, R. Garziera, The loss-factor of pre-stressed laminated curved panels and cylinders using a wave and finite element method, *Journal of Sound and Vibration* 332 (7) (2013) 1704 – 1711. doi:[10.1016/j.jsv.2012.09.039](https://doi.org/10.1016/j.jsv.2012.09.039).
- ¹⁸ E. Manconi, B. R. Mace, Estimation of the loss factor of viscoelastic laminated panels from finite element analysis, *Journal of Sound and Vibration* 329 (19) (2010) 3928 – 3939. doi:[10.1016/j.jsv.2010.04.014](https://doi.org/10.1016/j.jsv.2010.04.014).
- ¹⁹ B. Mace, Sound radiation from fluid loaded orthogonally stiffened plates, *Journal of Sound and Vibration* 79 (3) (1981) 439–452. doi:[https://doi.org/10.1016/0022-460X\(81\)90321-7](https://doi.org/10.1016/0022-460X(81)90321-7).
- ²⁰ F. Errico, M. Ichchou, S. De Rosa, O. Bareille, F. Franco, A load approximation for the vibroacoustic analysis of periodic structures to fluid excitation, in: *ISMA 2018 Proceedings*, Leuven, Belgium, 2018.
- ²¹ A. Parrinello, G. Ghiringhelli, Transfer matrix representation for periodic planar media, *Journal of Sound and Vibration* 371 (2016) 196–209. doi:[10.1016/j.jsv.2016.02.005](https://doi.org/10.1016/j.jsv.2016.02.005).
- ²² F. Leppington, E. Broadbent, K. Heron, The acoustic radiation efficiency from rectangular plates, *Proc. R. Soc.* 382 (1982) 245–271. doi:[10.1098/rspa.1982.0100](https://doi.org/10.1098/rspa.1982.0100).
- ²³ M. Villot, C. Guigou, L. Gagliardini, Predicting the acoustical radiation of finite size multi-layered structures by applying spatial windowing on infinite structures, *Journal of Sound and Vibration* 245 (3) (2001) 433–455. doi:[10.1006/jsvi.2001.3592](https://doi.org/10.1006/jsvi.2001.3592).
- ²⁴ G. Corcos, Resolution of pressure in turbulence, *Journal of the Acoustical Society of America* 35 (1963) 192–199. doi:[10.1121/1.1918431](https://doi.org/10.1121/1.1918431).
- ²⁵ W. Graham, A comparison of models for the wavenumber-frequency spectrum of turbulent boundary layer pressures, *Journal of Sound and Vibration* 206(4) (1997) 541–565. doi:[10.1006/jsvi.1997.1114](https://doi.org/10.1006/jsvi.1997.1114).
- ²⁶ P. Gardonio, *Boundary layer noise – part 2: Interior noise radiation and control*, Springer Vienna (2013) 379–448doi:[10.1007/978-3-7091-1458-2_7](https://doi.org/10.1007/978-3-7091-1458-2_7).

ON THE STRUCTURAL CHARACTERIZATION THROUGH K-SPACE METHODS: ASSESSMENTS AND VALIDATIONS

G. TUFANO^{*,1,2}, C. DROZ¹, M. ICHCHOU¹, O. BAREILLE¹, A.-M. ZINE³, W. DESMET^{2,4} AND B. PLUYMERS^{2,4}

¹ Vibroacoustics and Complex Media Research Group, LTDS

École Centrale de Lyon

36 Avenue Guy de Collongue, 69134, Écully, France

e-mail: {giovanni.tufano}{christophe.droz}{mohamed.ichchou}{olivier.bareille}@ec-lyon.fr

² Noise and Vibration Research Group, PMA

KU Leuven

Celestijnenlaan 300 B, B-3001, Heverlee, Belgium

e-mail: {giovanni.tufano}{wim.desmet}{bert.pluymers}@kuleuven.be

³ Institut Camille Jordan, Département de Maths-Info

École Centrale de Lyon

36 Avenue Guy de Collongue, 69134, Écully, France

e-mail: abdel-malek.zine@ec-lyon.fr

⁴ DMMS core lab, Flanders Make, Belgium

Key words: Periodic structure, wavenumber, damping loss factor, dispersion curves

Abstract. The physical characteristics of periodic structures are employed to analyze the vibro-acoustic response of several complex structures in the wavenumber domain. This work is focused on the analysis of elastic periodic structures, designed in order to obtain a wave attenuation in certain frequency bands, generating the so-called band-gaps (mainly related to the Bragg's effect), and on the identification of the material properties of complex structures. In this context, an inverse wavenumber correlation method is developed to obtain the dispersion characteristics and the damping information of complex periodic structures. The wavenumbers and the damping loss factor are identified exciting the structure by a unit harmonic force and using the complete vibrational field as primary input.

1 INTRODUCTION

In literature, the complex wavenumber recovery of a vibrating structure is an open issue. Several methods are available to correctly extract the real part of the wavenumber, but the estimation of the related damping information is still an open challenge. In the domain of punctual harmonic excited structures, McDaniel et al.^{1,2} developed a semi-analytical approach based on damped plane wave propagation (1D guided waves), using an expression of the plane wave

of type $e^{\pm ikx}$, where i is the imaginary unit, k is the complex wavenumber and x is the spatial coordinate. Different methods based on Prony series have been developed over the past years; Grosh et al.³ applied their method on cylindrical shells subjected to point harmonic excitation, obtaining a good estimation of the dispersion relation. Using a similar approach presented by Grosh et al.,³ another method, called *Inhomogeneous Wave Correlation* (IWC) method has been developed by Berthaut et al.;⁴ the proposed approach estimates the flexural wavenumber and the dispersion relation of a vibrating plate under punctual harmonic excitation, correlating the complete displacement field and a damped traveling plane wave, of the type $e^{\pm ik(x\cos\theta+y\sin\theta)}$, where θ is the propagation angle of the inhomogeneous wave. An interesting application of the IWC method is presented in Ichchou et al.,⁵ obtaining the complete θ -dependent dispersion relation of a ribbed plate. The presented approaches based on plane waves propagation suffered of a disadvantage related to plane wave hypothesis: the vibrational field should be acquired in a steady state condition, trying to avoid the excitation region where the plane wave assumption is not valid. One of the main advantage of the IWC method is the estimation of the complex wavenumber, with the related damping information; Cherif et al.⁶ applied the IWC method to an aluminum panel and to a two different laminated composite panels with honeycomb core, correlating the measured vibrational field and the damped inhomogeneous wave; the flexural wavenumber and the damping loss factor are both successful estimated. Van Damme et al.^{7,8} obtained the dispersion relation and the complex wavenumber for complex 1D structures, showing a good description of the Bragg's band gaps, adopting a 1D formulation of the IWC method. An enriched formulation of the IWC method is shown in Van Belle et al.,⁹ where they obtained the dispersion relation of a metamaterial plate with periodic resonators; this formulation takes in account the location of the force to have a better estimation of the wave attenuation. An IWC formulation for curved and axial-symmetric structures is shown in Tufano et al.,¹⁰ obtaining a good description of the k -space domain.

To describe the vibrational field of a structure subjected to punctual harmonic excitation, the Green's functions and the related image source method are widely used in literature. An application of the method of images is shown in Gunda et al.¹¹; the authors used this approach to describe the harmonic response of beams and rectangular plates. Based on the method of the images, Cuenca et al.¹² described the vibrational field of a finite plate with simply supported boundary conditions by the reconstruction of the Green's function of a point excited plate. The same method has been applied by Cuenca et al.¹³ to estimate the equivalent material properties of a plate covered by a viscoelastic layer. Recently, Roozen et al.¹⁴ used the Green's function of a point excited plate, by using a set of Hankel's functions, into a complex wavenumber fit procedure, making a comparison between the acquired vibrational field and the Green's function; the procedure here described allows to retrieve the complex wavenumber and the equivalent material properties.

All the methods based on plane wave assumption are affected by some limitations due to the nature of the plane wave itself. The vibrational field should be acquired in a steady-state condition, sufficiently far from the excitation location (this is a singularity point where the plane wave hypothesis is not valid) and trying to distinguish between the direct, reflected and evanescent fields. In this paper, a method is proposed to combine advantages of the IWC method and of the image source method, which uses a set of Hankel's functions to obtain the vibrational

field of a point excited structure. The main advantage of this approach is the possibility to be close the excitation region, avoiding the problems related to the plane wave assumption. The proposed approach estimates the complex wavenumber and the dispersion relation of several complex structures, showing a good description of the periodicity effect (Bragg's band gaps); the damping loss factor is also well estimated.

2 METHODOLOGY

The complex dispersion relation of different structures is here estimated by a wave correlation method. The presented approach estimates, at each frequency f_0 , the complex wavenumber as the point of best agreement between the acquired vibrational field and the Green's function of the point excited structure. The Green's function is derived by the classical Kirchhoff's thin plate theory¹⁵; according to this theory, for an isotropic, homogeneous plate and of a constant thickness h , the flexural vibration, in terms of transverse displacement w , is expressed as follows

$$D\nabla^4 w(\vec{x}, t) + \rho h \frac{\partial^2 w(\vec{x}, t)}{\partial t^2} = P(\vec{x}_0, t) \quad (1)$$

where $D = \frac{Eh^3}{12(1-\nu^2)}$ is the bending stiffness, E is the Young's modulus, ν is the Poisson's coefficient, ρ is the mass density, ∇^4 is the biharmonic operator, t is the time variable, P is the force per unit area and \vec{x} , \vec{x}_0 are the position vectors of the acquisition and excitation points, respectively. Assuming an harmonic point excitation, the expression of the force becomes $P(\vec{x}_0, t) = F(\vec{x}_0)e^{i\omega t}$, being ω the angular frequency; consequently, the steady state response of the transversal vibrational field is $w(\vec{x}, t) = u(\vec{x})e^{i\omega t}$. Substituting these two expressions in Eq. 1, the governing equation assumes the following form

$$D\nabla^4 u(\vec{x}) - k^4 u(\vec{x}) = F(\vec{x}_0) \quad (2)$$

where $k^4 = \rho h \omega^2 / D$ is the flexural wavenumber.

For a plate of infinite lateral dimensions, the solution of Eq. 2 is given by

$$G_\infty(x, y) = \frac{1}{8k^2 D} \left[H_0^1(kr) - H_0^1(ikr) \right] \quad (3)$$

with G_∞ the Green's function of the infinite plate, H_0^1 the Hankel's function of first kind and order 0 and $r = \|x - x_0, y - y_0\|$ is the distance between the acquisition (x, y) and excitation (x_0, y_0) points.

At each frequency f_0 , the complex flexural wavenumber is found as the point of best agreement between the measured vibrational field and the Green's function expressed in the Eq. 3. Considering an acquisition region of area S in the plane (x, y) , indicating with \tilde{w} and w the measured vibrational field and the one described by Eq. 3, respectively, the normalized correlation function has the following expression

$$\mathcal{F}(k_{\mathbb{R}}, k_{\mathbb{I}}) = \frac{\left| \iint_S \tilde{w} \cdot w(k_{\mathbb{R}}, k_{\mathbb{I}})^* dx dy \right|}{\sqrt{\iint_S |\tilde{w}|^2 dx dy \cdot \iint_S |w(k_{\mathbb{R}}, k_{\mathbb{I}})|^2 dx dy}} \quad (4)$$

where $*$ denotes the complex conjugate. For discrete points measurement, the integrals in Eq. 4 are replaced by summations over the entire domain. The complex wavenumber is identified as the location of the maximum of the correlation function. From the estimated wavenumber amplitude, an estimation of the damping loss factor can be obtained, at each frequency, by the following relationship²

$$\eta = \left| \frac{\Im(k^4)}{\Re(k^4)} \right| \quad (5)$$

By choosing a proper direction of propagation, Eq. 3 can be applied to a narrow beam subjected to punctual harmonic excitation. Keeping the same notation and indicating with L the length of the acquisition region, the correlation function showed in Eq. 4 becomes

$$\mathcal{F}(k_{\mathbb{R}}, k_{\mathbb{I}}) = \frac{\left| \int_L \tilde{w} \cdot w(k_{\mathbb{R}}, k_{\mathbb{I}})^* dx \right|}{\sqrt{\int_L |\tilde{w}|^2 dx \cdot \int_L |w(k_{\mathbb{R}}, k_{\mathbb{I}})|^2 dx}} \quad (6)$$

The dispersion curves of the different structures have been validated using the Wave Finite Element Method (WFEM)^{16–18} ; this method is not here described.

3 NUMERICAL RESULTS AND VALIDATIONS

The proposed approach is applied on different structures. Firstly, two different beams are taken in account: isotropic and periodic (with varying material and cross-section along the length). Then, application cases on two different plates are shown, taking in account an isotropic and homogeneous plate and a composite one, made of three different layers in the thickness direction.

3.1 Isotropic and periodic narrow plates

The first application of the proposed approach has been conducted on a simple isotropic beam. The total length of the beam is 1.0 m and the cross-section has dimensions 10 x 1 mm²; the finite element model of the beam is shown in Fig. 1a. The employed material is a general thermoplastic polymer (ABS) with Young's modulus $E = 1.0 \text{ GPa}$, density $\rho = 980.0 \text{ kg m}^{-3}$ and Poisson's coefficient $\nu = 0.35$; two constant values of structural damping η are assumed: 2% and 4%. An analytical expression of the dispersion relation can be derived using Timoshenko's model for vibrating beams, resulting in

$$EIk^4 - \rho A \omega^2 - \left(\rho I + \frac{EI\rho}{KG} \right) k^2 \omega^2 + \frac{\rho^2 I}{KG} \omega^4 = 0 \quad (7)$$

where G is the shear modulus, $I = bh^3/12$ is the second moment of area, A is the beam's cross-section area and $K = 5/6$ is a constant to take in account the shear force variation.

A periodic beam is also investigated, to prove the feasibility of the proposed approach in describing the band-gaps due to the geometric periodicity of the structure. The finite element model of the unit cell of the considered structure is shown in Fig. 1b. The unit cell has total length of 0.04 m and it's characterized by a double periodicity: material and cross-section. The

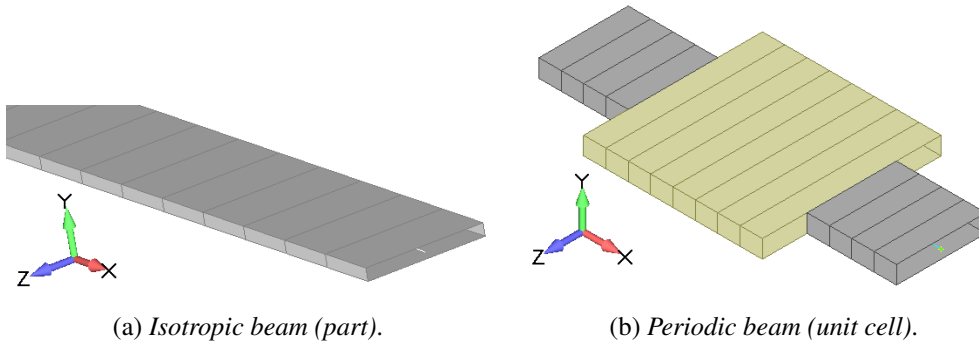


Figure 1: Finite element models of the isotropic and periodic beams

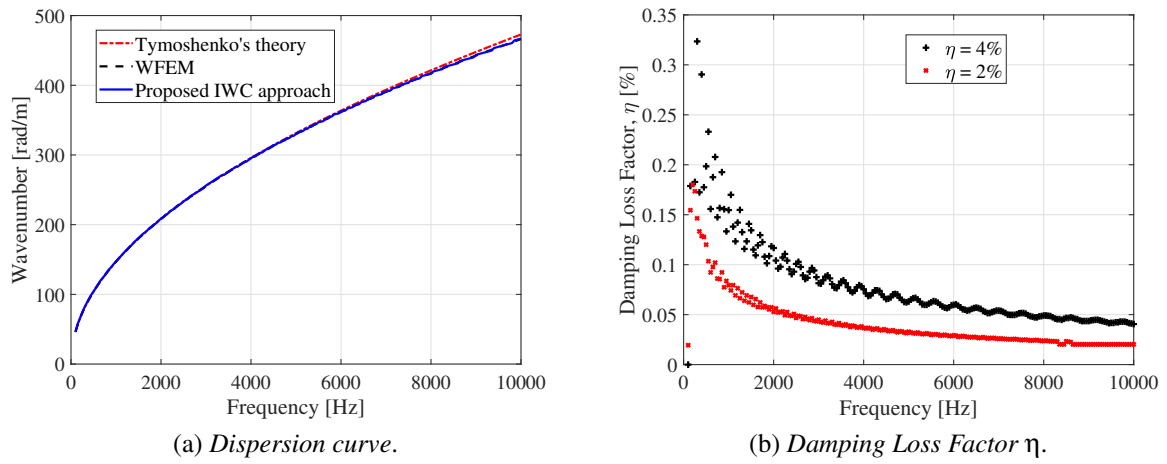


Figure 2: Dispersion curve and Damping Loss Factor estimation for the isotropic beam

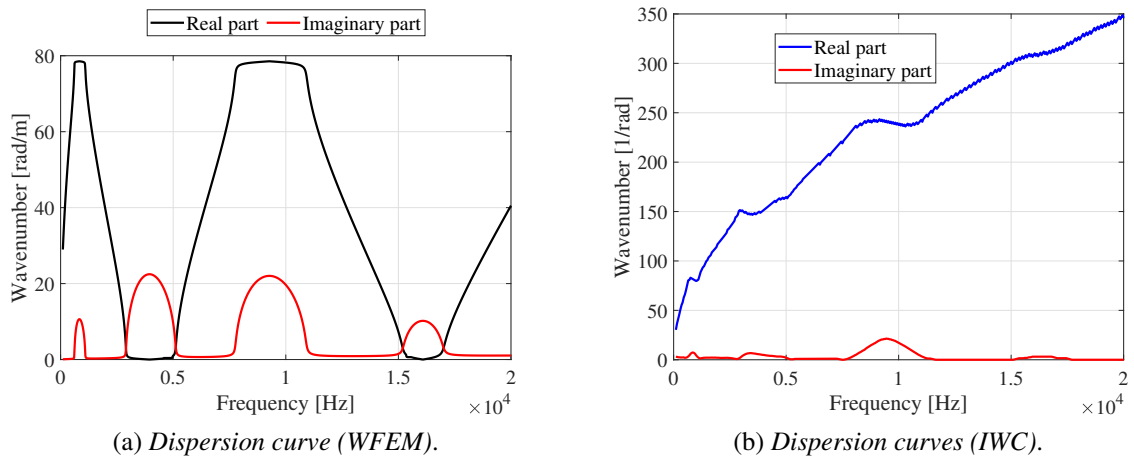


Figure 3: Real and imaginary dispersion curves of the periodic beam

employed materials are a standard aluminum alloy, with Young's modulus $E = 70.0 \text{ GPa}$, density $\rho = 2700.0 \text{ kg m}^{-3}$ and Poisson's coefficient $\nu = 0.33$, and the ABS previously described. The aluminum part has a cross-section of dimensions $10 \times 2 \text{ mm}^2$; the ABS part has dimensions $20 \times 2 \text{ mm}^2$. The propagative part of the dispersion curve for the isotropic beam is shown in Fig. 2a; the proposed IWC approach exhibits a very good agreement with the analytical model (cfr. Eq. 7) and the WFE method. In Fig. 2b is shown the damping loss factor estimation; in both cases, the identified complex wavenumbers give a reasonable estimation of the structural damping previously introduced.

The dispersion curve of the periodic beam are shown in Fig. 3; the dispersion curve calculated with the WFE method are limited to the first Brillouin zone, where the wavelengths are longer than one period of the structure (Fig. 3a). The real part of the wavenumber has periodicity π/Δ , with Δ the length of the unit cell, showing multiples band-gaps, but always with $k_{\Re} \in [0, \pi/\Delta]$. The dispersion curve estimation with the proposed approach is shown in Fig. 3b, being in good agreement with the one calculated with the WFE method, identifying the same wide band-gaps zone. The proposed IWC approach takes in account the whole structure, avoiding the periodicity issue previously described in the wavenumbers estimation.

3.2 Isotropic and laminated plates

The proposed approach has been extended to 2D structures, an isotropic plate, made of ABS, and a composite one, constituted of three layers: aluminum-ABS-aluminum, of thickness 1 - 8 - 1 mm, respectively; both plates have geometrical dimensions $1.0 \times 0.6 \times 0.01 \text{ m}^3$. The finite element models of the two unit cells are shown in Fig. 4; both unit cells are used in the WFE method to validate the results obtained with the proposed IWC approach. For both test cases, two different constant values of structural damping η are assumed: 2% and 5%.

For what concern the isotropic plate, an analytical expression of the dispersion relation can be derived by Kirchhoff's thin plate theory, obtaining the following expression for the flexural wavenumber

$$k = \sqrt{\omega} \left(\frac{\rho h}{D} \right)^{1/4} \quad (8)$$

The propagative part of the dispersion curve is shown in Fig. 5a; the proposed approach is in good agreement with the analytical formulation of Eq. 8 and the WFE method, showing a low overestimation in the high-frequency region. In Fig. 5b, the damping loss factor estimations are shown; the relation of Eq. 5 is used, based on the estimated complex wavenumbers.

The propagative part of the dispersion curve for the composite plate is shown in Fig. 6a; a good agreement between the proposed approach and the WFE method is obtained in the whole frequency band of investigation. A very good identification of the damping loss factor is performed, and shown in Fig. 6b. Using an inverse approach based on the estimated wavenumber, the equivalent bending stiffness and the equivalent Young's modulus of the structure have been calculated by the following formulas, directly derived from Eq. 2

$$D_{eq} = \frac{\omega^2 \rho h}{k^4} \quad \text{and} \quad E_{eq} = \frac{D_{eq} 12(1 - \nu^2)}{h^3} \quad (9)$$

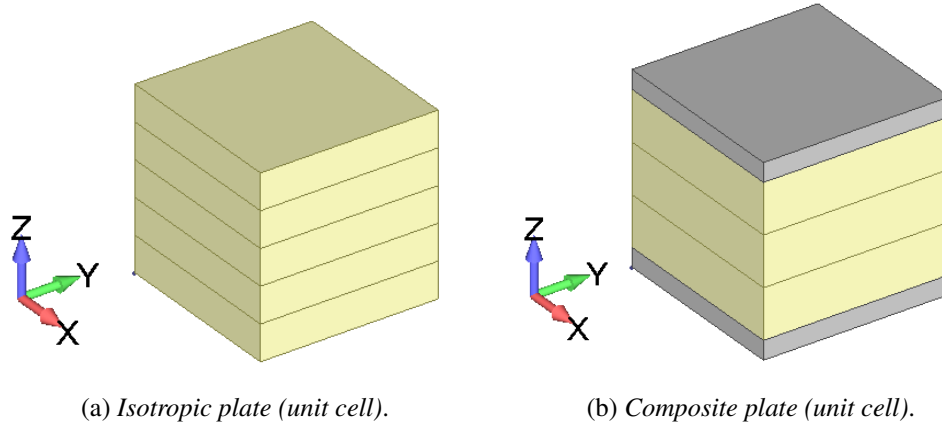


Figure 4: Finite element models of the isotropic and composite plates

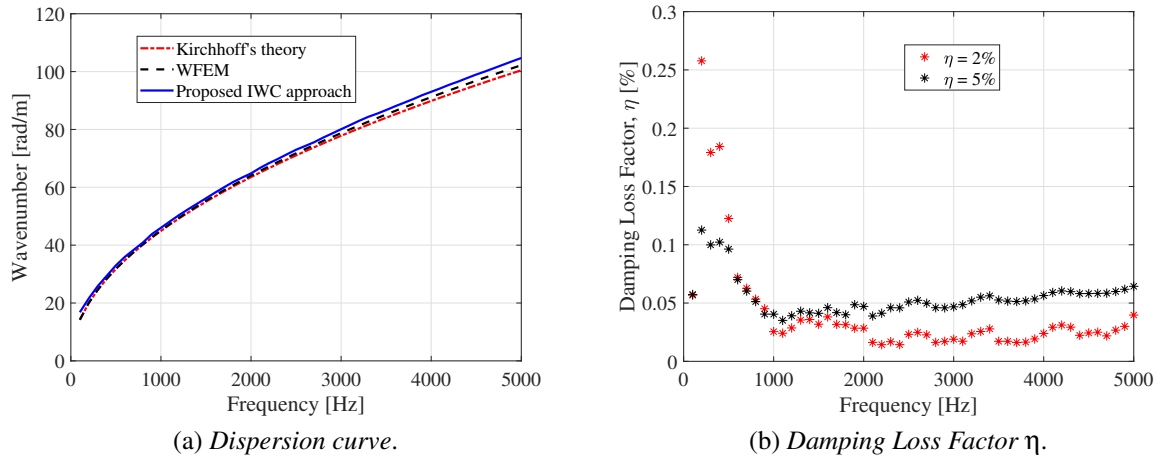


Figure 5: Dispersion curve and Damping Loss Factor estimation for the isotropic plate

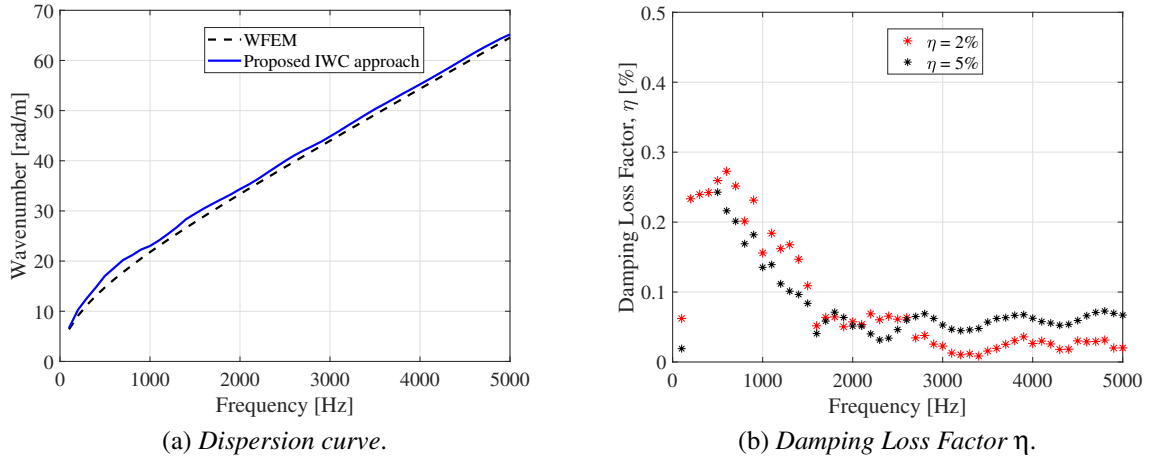


Figure 6: Dispersion curve and Damping Loss Factor estimation for the composite plate

The equivalent plate properties are shown in Fig. 7.

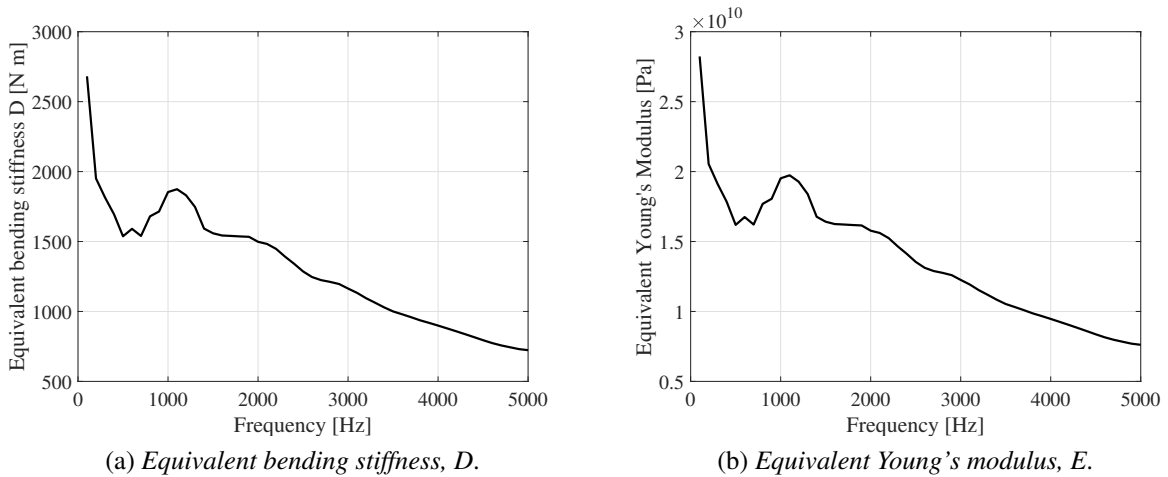


Figure 7: Dispersion curve and Damping Loss Factor estimation for the composite plate

4 CONCLUDING REMARKS

In this work, different ideas are successfully implemented in this extended IWC approach, showing a very good prediction of the complex dispersion relation of periodic narrow plates and laminated structures. An estimation of the damping loss factor is obtained; the calculated values of η fast converge to the structural damping introduced. The feasibility of this method in estimating the wave attenuation in a structure is successfully demonstrated.

The proposed approach allows to identify the resonance zones (stop-bands) due to the geometrical periodicity of the structure, showing a good agreement with the WFE method, based on

the unit cell theory, avoiding some limitations related to the latter method.

The proposed approach can be used in an inverse way to estimate the frequency dependent equivalent material properties of complex structures, when analytical models are not available or difficult to obtain.

ACKNOWLEDGMENT

This project has received funding from the European Union's Horizon 2020 research and innovation program under the Marie Skłodowska-Curie grant agreement No. 675441.

REFERENCES

- [1] J. G. McDaniel, W. S. Shepard-Jr., Estimation of structural wave numbers from spatially sparse response measurements, *The Journal of the Acoustical Society of America* 108 (2000) 1674. doi:10.1121/1.1310668.
- [2] J. McDaniel, P. Dupont, L. Savino, A wave approach to estimating frequency-dependent damping under transient loading, *Journal of Sound and Vibration* 231 (2000) 433–449. doi:10.1006/jsvi.1999.2723.
- [3] K. Grosh, E. J. Williams, Complex wave-number decomposition of structural vibrations, *The Journal of the Acoustical Society of America* 93 (1993) 836–848. doi:10.1121/1.405445.
- [4] J. Berthaut, M. N. Ichchou, L. Jezequel, *K*-space identification of apparent structural behavior, *Journal of Sound and Vibration* 280 (2005) 1125–1131. doi:10.1016/j.jsv.2004.02.044.
- [5] M. N. Ichchou, J. Berthaut, M. Collet, Multi-mode wave propagation in ribbed plates: Part I, wavenumber-space characteristics, *International Journal of Solids and Structures* 45 (2008) 1179–1195. doi:10.1016/j.ijsolstr.2007.09.032.
- [6] R. Cherif, J.-D. Chazot, N. Atalla, Damping loss factor estimation of two-dimensional orthotropic structures from a displacement field measurement, *Journal of Sound and Vibration* 356 (2015) 61–71. doi:10.1016/j.jsv.2015.06.042.
- [7] B. Van Damme, A. Zemp, Measuring Dispersion Curve for Bending Waves in Beams: A Comparison of Spatial Fourier Transform and Inhomogeneous Wave Correlation, *Acta Acustica United with Acustica* 104 (2018) 228–234. doi:10.3813/AAA.919164.
- [8] B. Van Damme, A. Zemp, Energy Distribution and Exchange Between Spatial Harmonics in Bending Wave Phononic Crystals, *Physical Review Applied* 10 (2018) 014001. doi:10.1103/PhysRevApplied.10.014001.
- [9] L. Van Belle, C. Claeys, E. Deckers, W. Desmet, On the impact of damping on the dispersion curves of a locally resonant metamaterial: Modeling and experimental validation, *Journal of Sound and Vibration* 409 (2017) 1–23. doi:10.1016/j.jsv.2017.07.045.

- [10] G. Tufano, C. Droz, O. Bareille, A.-M. Zine, B. Pluymers, W. Desmet, M. Ichchou, Wavenumber identification technique for axial-symmetric structures, *Proceeding of ISMA* 2018.
- [11] R. Gunda, S. M. Vijayakar, R. Singh, Method of images for the harmonic response of beams and rectangular plates, *Journal of Sound and Vibration* 185 (1995) 791–808. doi:10.1006/jsvi.1995.0418.
- [12] J. Cuenca, F. Gautier, L. Simon, The image source method for calculating the vibrations of simply supported convex polygonal plates, *Journal of Sound and Vibration* 322 (2009) 1048–1069. doi:10.1016/j.jsv.2008.11.018.
- [13] J. Cuenca, F. Gautier, L. Simon, Measurement of the complex bending stiffness of a flat panel covered with a viscoelastic layer using the image source method, *Proceeding of EURONOISE* 2009.
- [14] N. B. Roozen, Q. Leclère, K. Ege, Y. Gerges, Estimation of plate material properties by means of a complex wavenumber fit using Hankel's functions and the image source method, *Journal of Sound and Vibration* 390 (2017) 257–271. doi:10.1016/j.jsv.2016.11.037.
- [15] A. W. Leissa, *Vibration of plates*, Acoustical Society of America, 1993.
- [16] L. Brillouin, *Wave Propagation in Periodic Structures: Electric Filters and Crystal Lattices*, Dover Publications, 1953.
- [17] B. R. Mace, D. Duhamel, M. J. Brennan, L. Hinke, Finite element prediction of wave motion in structural waveguides, *Journal of the Acoustical Society of America* 117 (2005) 2835–2843. doi:10.1121/1.1887126.
- [18] E. Manconi, B. R. Mace, Modelling wave propagation in two dimensional structures using finite element analysis, *Journal of Sound and Vibration* 318 (2008) 884–902. doi:10.1016/j.jsv.2008.04.039.

ON THE VIBRATION ATTENUATION PROPERTIES OF FINITE PERIODIC LATTICES OF IMPACT DAMPERS

VASILIS K. DERTIMANIS*, SAMI F. MASRI[†] AND ELENI N. CHATZI*

*Institute of Structural Engineering
ETH Zurich

Stefano-Franscini-Platz 5, 8093 Zurich, Switzerland

e-mail: {v.derti,chatzi}@ibk.baug.ethz.ch, web page: <http://www.chatzi.ibk.ethz.ch/>

[†] Viterbi School of Engineering
University of Southern California
University Park, Los Angeles, CA 90089, USA
e-mail: masri@usc.edu

Key words: metamaterials, impact damper, nonlinear vibration

Abstract. The emergence of metamaterials as an alternative concept for the mitigation of structural vibration is increasingly attracting the interest of scientists and engineers. Recent studies confirm that the development of periodic structures assembled on the basis of unit cells of favourable properties, results in a filtering effect, preventing the propagation of vibration lying within a specific frequency band. The, so called, meta-structures are thus characterized by a frequency bandgap. For the purposes of structural vibration attenuation, two main interrelated challenges are currently associated with the conceptual design of such structures: the first corresponds to the feasibility of reducing the lower threshold of the band gap within a practical setting, while the second pertains to increasing the breadth of the bandgap. One approach to addressing these challenges lies in the use of the so-called “rainbow traps”, i.e., meta-structures consisting of unit cells with different properties. An alternative strategy pertains to use of nonlinear unit cells. Both schemes are so far little unexplored in terms of applicability for structural vibration mitigation. This study attempts to contribute to this research path, by exploring the nonlinear approach, by assessing the properties of finite lattices with unit cells composed of impact dampers. These devices have already demonstrated their attenuation potential, yet, their investigation has been mostly limited to systems of single, or two-degrees-of freedom. To this end, a one-dimensional finite lattice is herein considered, and the analysis is conducted over critical structural parameters, including the number and the individual stiffness properties of unit cells, the mass ratios, etc. The preliminary results demonstrate the potential of meta-structures composed of properly-designed impact dampers for vibration attenuation.

1 INTRODUCTION

Engineering vibration has traditionally comprised a very active research area, motivated by the abundance of associated technological applications. In this domain, the safety margins associated with the protection of humans, machines and structures, from undesired/uncontrolled motions of diverse frequency characteristics dictate design.

The attenuation of engineering vibration has been mostly treated using a mix of linear, passive, active and even semi-active methods. Passive vibration control typically dominates its active counterpart, for being simple, mature and of sufficiently lower lifecycle costs. Since structures are usually characterized by light damping (0.5% to 7%), the majority of actions for passive vibration control aims at integrating additional damping mechanisms that increase damping capacity up to 30%-40%. These include viscous and hysteretic energy dissipaters [1, 2, 3], friction dissipaters [4], oil dampers [5], visco-elastic dampers [6, 7, 8, 9], as well as tuned-mass and tuned-liquid dampers [10, 11, 12, 13, 14]. An inherent disadvantage, however, of passive devices is their inability to adapt, or at least to perform on par in wide frequency ranges; their properties remain fixed to their initial design and implementation. Tuned-mass dampers are a notable example of such a limited performance. To address this issue, semi-active and hybrid methods have been introduced, with promising results [15, 16, 17]. The effectiveness of active control is considerably improved with respect to its passive counterpart, as it can be adapted to an arbitrary set of specifications. However, they are significantly more expensive, they require continuous maintenance, and they are amenable to own faults, while the introduction of external energy to the structure raises stability issues. To cope with this, among available alternatives, devices relying on semi-active control schemes, such as magnetorheological dampers, are drawing increasing attention in real-time vibration mitigation and structural control [18, 19, 20, 21, 22, 23]. The increasing adoption of such systems may be attributed to the fact that semi-active control devices seem to gather the best features of both passive and active control systems and seem able to match adaptability of the active class without the associated large power requirements.

As an alternative to active control, a new concept for passive vibration mitigation has emerged by the exploration of metamaterials [24, 25]. The latter comprise a special class of periodic structures, characterized by fascinating filtering effects: when the frequency of the incoming excitation falls into their blind zone, the propagation of motion is arrested in any direction, thus forming a “band-gap”. An associated challenge, however, lies in the size of the band-gap, as well as in the arbitrary selection of the low-frequency threshold, which is critical in many engineering applications [26, 27, 28, 29, 30, 31]. In general, low wave speeds are required for obtaining a low-frequency band-gap, which may be succeeded via heavy inclusions in a soft medium and/or a large lattice constant [32, 33]. Weight, low stiffness and large size are unfavorable for lattices that are to be used for practical purposes.

In addressing this challenge, this study introduces strong nonlinearities to the finite lattice. In more detail and relying on the local resonator approach, a novel nonlinear neutralizer is thus proposed herein for passive vibration control. The envisaged periodic structure comprises an impact damper [34, 35, 36] as the unit cell. Impact dampers are studied since many years and their favorable properties have been already demonstrated [37, 38, 39, 40]. Still, their behavior in periodic configurations remains largely unexplored. To this end, a one-dimensional finite lattice is herein considered as a mean for the vibration attenuation of a linear oscillator that is amenable to harmonic excitation.

2 THE META-IMPACTOR

2.1 The impact damper

Figure 1 displays a schematic layout of an impact damper. It consists of an external mass, henceforth referred to as the container, which is attached to linear elastic and dissipative elements, of equivalent stiffness k and viscous damping c , respectively. Within the container, an auxiliary mass μ , herein corresponding to a frictionless solid particle, is constrained to oscillate with clearance D . The total length of the impact damper is L .

The nonlinearity of the impact damper stems from the successive impacts between the auxiliary mass

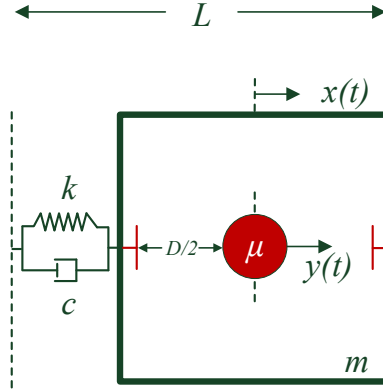


Figure 1: The impact damper (top view).

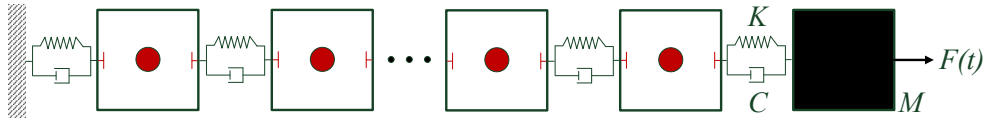


Figure 2: A periodic finite lattice of impact dampers attached to a linear oscillator (top view).

and the container, every time the former reaches the clearance limits of the latter. Under the assumption that the impulse duration is sufficiently smaller, compared to the natural frequency of the system, it can be deduced that the displacements of the container and the auxiliary mass right before and after the impact remain the same, while their velocities are discontinuously changed (see below). It is noted that, under the harmonic excitation that is considered in the current study, no prior assumption on the number of impacts per cycle at the steady state is adopted.

2.2 A finite lattice of impact damper unit cells

Consider now a structure that can be effectively described by a single degree of freedom linear oscillator of mass M , stiffness K and damping C , excited by a harmonic input force $F(t) = A \sin(2\pi ft)$. In reducing the effects of the external excitation, a periodic, finite lattice of N identical impact dampers is integrated as illustrated in Figure 2.

The equations of motion for the first (e.g. far left) unit cell of the lattice are

$$m\ddot{x}_1(t) = -kx_1(t) - c\dot{x}_1(t) - k[x_1(t) - x_2(t)] - c[\dot{x}_1(t) - \dot{x}_2(t)] \quad (1a)$$

$$\mu\ddot{y}_1(t) = 0, \quad |x_1 - y_1| < D/2 \quad (1b)$$

Similarly, the equations of motion for the i -th unit cell, $i = 2, \dots, N-1$, read

$$m\ddot{x}_i(t) = k[x_{i-1}(t) - x_i(t)] + c[\dot{x}_{i-1}(t) - \dot{x}_i(t)] - k[x_i(t) - x_{i+1}(t)] - c[\dot{x}_i(t) - \dot{x}_{i+1}(t)] \quad (2a)$$

$$\mu\ddot{y}_i(t) = 0, \quad |x_i - y_i| < D/2 \quad (2b)$$

while the ones for the last (N -th) unit cell of the meta-impactor and the linear oscillator are

$$m\ddot{x}_N(t) = k[x_{N-1}(t) - x_N(t)] + c[\dot{x}_{N-1}(t) - \dot{x}_N(t)] - K[x_N(t) - X(t)] - C[\dot{x}_N(t) - \dot{X}(t)] \quad (3a)$$

$$\mu\ddot{y}_N(t) = 0, \quad |x_N - y_N| < D/2 \quad (3b)$$

and

$$M\ddot{X}(t) = K[x_N(t) - X(t)] + C[\dot{x}_N(t) - \dot{X}(t)] + f(t) \quad (4)$$

respectively.

Under the assumptions adopted in Sec. 2.1, the states of the i -th unit cell, $i = 1, \dots, N$, immediately after the impact are calculated as

$$x_i^+ = x_i^-, \quad y_i^+ = y_i^- \quad (5a)$$

$$\dot{x}_i^+ - \dot{y}_i^+ = -r[\dot{x}_i^- - \dot{y}_i^-] \quad (5b)$$

where the superscripts \pm refer to time immediately after and before the impact, respectively, and r is the coefficient of restitution. Moreover, the conservation of momentum implies

$$m\dot{x}_i^+ + \mu\dot{y}_i^+ = m\dot{x}_i^- + \mu\dot{y}_i^- \quad (6)$$

From Eqs. 5b, 6, it follows that the velocity states of the i -th unit cell are computed from the following system of linear equations

$$\begin{bmatrix} m & \mu \\ 1 & -1 \end{bmatrix} \begin{bmatrix} \dot{x}_i^+ \\ \dot{y}_i^+ \end{bmatrix} = \begin{bmatrix} m\dot{x}_i^- + \mu\dot{y}_i^- \\ -r\dot{x}_i^- + r\dot{y}_i^- \end{bmatrix} \quad (7)$$

2.3 Simulation

For the parametric analysis that is carried out in the next section the system is brought into the form $\dot{\xi}(t) = g(\xi(t), f(t))$, where $\xi(t)$ is the state vector defined as (temporal variable is temporarily omitted for clarity)

$$\xi = \left[x_1, \dot{x}_1, y_1, \dot{y}_1 \mid \dots \mid x_N, \dot{x}_N, y_N, \dot{y}_N \mid X, \dot{X} \right]^T \quad [4N + 2 \times 1] \quad (8)$$

Based on Eq. 8, the equations of motion are now transformed as

$$\dot{\xi}_1(t) = \xi_2(t) \quad (9a)$$

$$\dot{\xi}_2(t) = -\frac{k}{m}\xi_1(t) - \frac{c}{m}\xi_2(t) - \frac{k}{m}[\xi_1(t) - \xi_5(t)] - \frac{c}{m}[\xi_2(t) - \xi_6(t)] \quad (9b)$$

$$\dot{\xi}_3(t) = \xi_4(t) \quad (9c)$$

$$\dot{\xi}_4(t) = 0, \quad |\xi_1 - \xi_3| < D/2 \quad (9d)$$

for the first unit cell, as

$$\dot{\xi}_{4(i-1)+1}(t) = \xi_{4(i-1)+2}(t) \quad (10a)$$

$$\begin{aligned} \dot{\xi}_{4(i-1)+2}(t) = & \frac{k}{m}[\xi_{4(i-2)+1}(t) - \xi_{4(i-1)+1}(t)] + \frac{c}{m}[\xi_{4(i-2)+2}(t) - \xi_{4(i-1)+2}(t)] \\ & - \frac{k}{m}[x_{4(i-1)+1}(t) - \xi_{4i+1}(t)] - \frac{c}{m}[\xi_{4(i-1)+2}(t) - \xi_{4i+2}(t)] \end{aligned} \quad (10b)$$

$$\dot{\xi}_{4(i-1)+3}(t) = \xi_{4(i-1)+4}(t) \quad (10c)$$

$$\dot{\xi}_{4(i-1)+4}(t) = 0, \quad |\xi_{4(i-1)+1} - \xi_{4(i-1)+3}| < D/2 \quad (10d)$$

for the i -th unit cell, $i = 2, \dots, N-1$, and as

$$\dot{\xi}_{4N-3}(t) = \xi_{4N-2}(t) \quad (11a)$$

$$\begin{aligned} \dot{\xi}_{4N-2}(t) = & \frac{k}{m}[\xi_{4N+1}(t) - \xi_{4N-3}(t)] + \frac{c}{m}[\xi_{4N+2} - \xi_{4N-2}(t)] \\ & - \frac{K}{m}[\xi_{4N-3}(t) - \xi_{4N+1}(t)] - \frac{C}{m}[\xi_{4N-2}(t) - \xi_{4N+2}(t)] \end{aligned} \quad (11b)$$

$$\dot{\xi}_{4N-1}(t) = \xi_{4N}(t) \quad (11c)$$

$$\dot{\xi}_{4N}(t) = 0, \quad |\xi_{4N-3} - \xi_{4N-1}| < D/2 \quad (11d)$$

and

$$\dot{\xi}_{4N+1}(t) = \xi_{4N+2}(t) \quad (12a)$$

$$\dot{\xi}_{4N+2}(t) = \frac{K}{M}[\xi_{4N-3}(t) - \xi_{4N+1}(t)] + \frac{C}{M}[\xi_{4N-2}(t) - \xi_{4N+2}(t)] + \frac{1}{M}f(t) \quad (12b)$$

for the last (N -th) unit cell of the meta-impactor and the linear oscillator, respectively. The post-impact velocity states of the i -th unit cell are computed by

$$\begin{bmatrix} m & \mu \\ 1 & -1 \end{bmatrix} \begin{bmatrix} \xi_{4(i-1)+1}^+ \\ \xi_{4(i-1)+2}^+ \end{bmatrix} = \begin{bmatrix} m\xi_{4(i-1)+1}^- + \mu\xi_{4(i-1)+2}^- \\ -r\xi_{4(i-1)+1}^- + r\xi_{4(i-1)+2}^- \end{bmatrix} \quad (13)$$

3 PARAMETRIC ANALYSIS

The behaviour of the meta-impactor is studied in the MATLAB[®] environment using the ode45 function (AbsTol=eps, RelTol=eps^(2/3), Refine=4 and MaxStep=0.01/sqrt(K/M), with eps corresponding to the *machine epsilon*). Impacts are being detected by an appropriate multiple event function. For each such impact, the simulation halts, the post-impact velocity states of the corresponding unit cell are calculated and the simulation continues from the same time instant by keeping all other states unaltered. A linear oscillator with $M = 1$ kg, $f_n = 1$ Hz and $\zeta_n = 2\%$ is chosen, subject to a harmonic excitation of unit amplitude ($A = 1$ N). For all the individual investigations the meta-impactor damping is selected to be zero ($c = 0$ Ns/m), while the coefficient of restitution remains constant ($r = 0.6$). Unless otherwise specified, the clearance is set at $D = 0.1$ m.

Following the findings of Dertimanis *et al.* [31], regarding the significance of the mass and stiffness ratios in the vibration attenuation performance of a linear, periodic, mass-in-mass lattice, a first insight is gained by varying these quantities of the meta-impactor. In specific, the ratios μ/m and K/k are varied within $[0.1, 1.0]$ and $[10, 100]$, respectively, at three fixed m/M ratios (namely, 1%, 50% and 100%) and for $N = 1, 2, 5$ and 10. For each realization, the maximum absolute vibration displacement response of the linear oscillator is recorded for a 10 s simulation time and an excitation frequency $f = f_n = 1$ Hz.

The results are expanded over Figs. 3– 6 and show that when $m/M = 0.01$ (e.g. far left plots in Figs. 3– 6), the performance of the meta-impactor is mainly dominated by the stiffness ratio. This is confirmed by the distinct vertical zones of the corresponding surf plots, inside which the variation of the vibration response due to different μ/m ratios is negligible. The addition of unit cells increases the vibration displacement response amplitude, as can be observed by the relative colobars on the right of each plot. This is attributed to the introduction of additional degrees of freedom, which most likely lead to higher transient response times (recall that the simulation is only 10 s). Yet, regardless the unit cell number, the vibration displacement response reaches its lowest levels (below 0.1 m) when $m/M = 1$ and for low μ/m and K/k ratios.

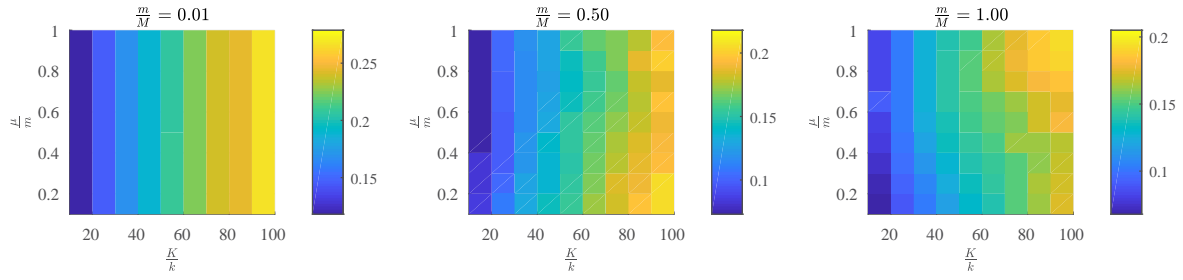


Figure 3: Maximum absolute displacement at 1 Hz for $N = 1$ and varying masses/stiffness ratios.

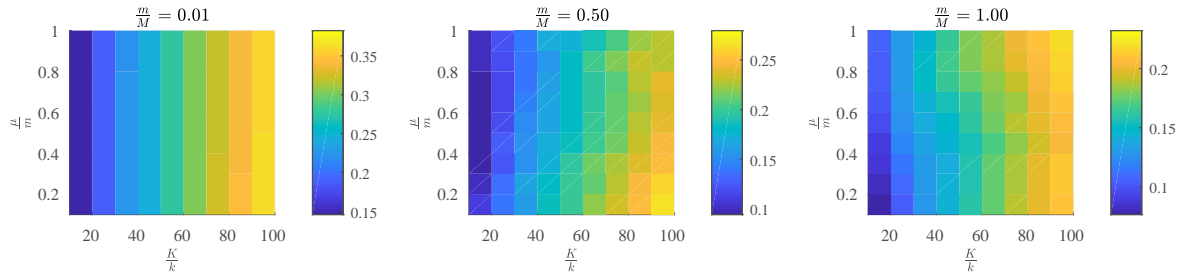


Figure 4: Maximum absolute displacement at 1 Hz for $N = 2$ and varying masses/stiffness ratios.

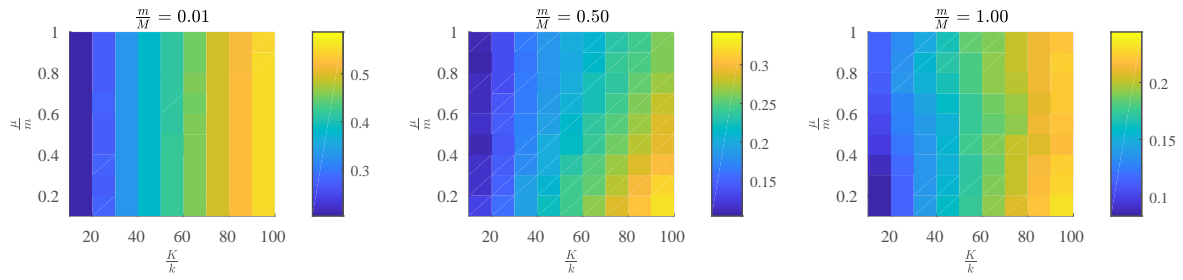


Figure 5: Maximum absolute displacement at 1 Hz for $N = 5$ and varying masses/stiffness ratios.

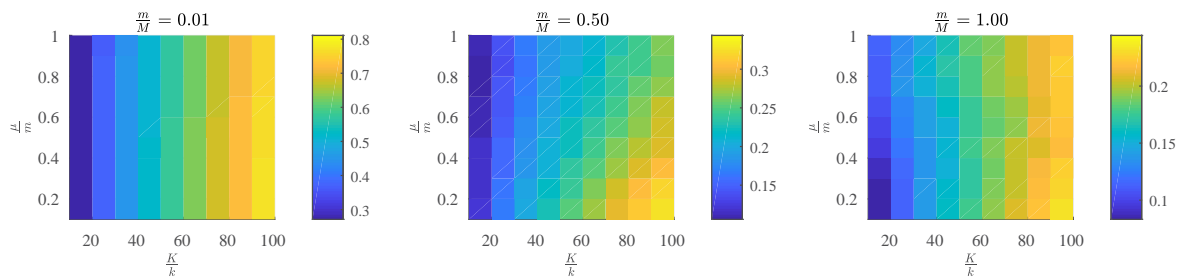


Figure 6: Maximum absolute displacement at 1 Hz for $N = 10$ and varying masses/stiffness ratios.

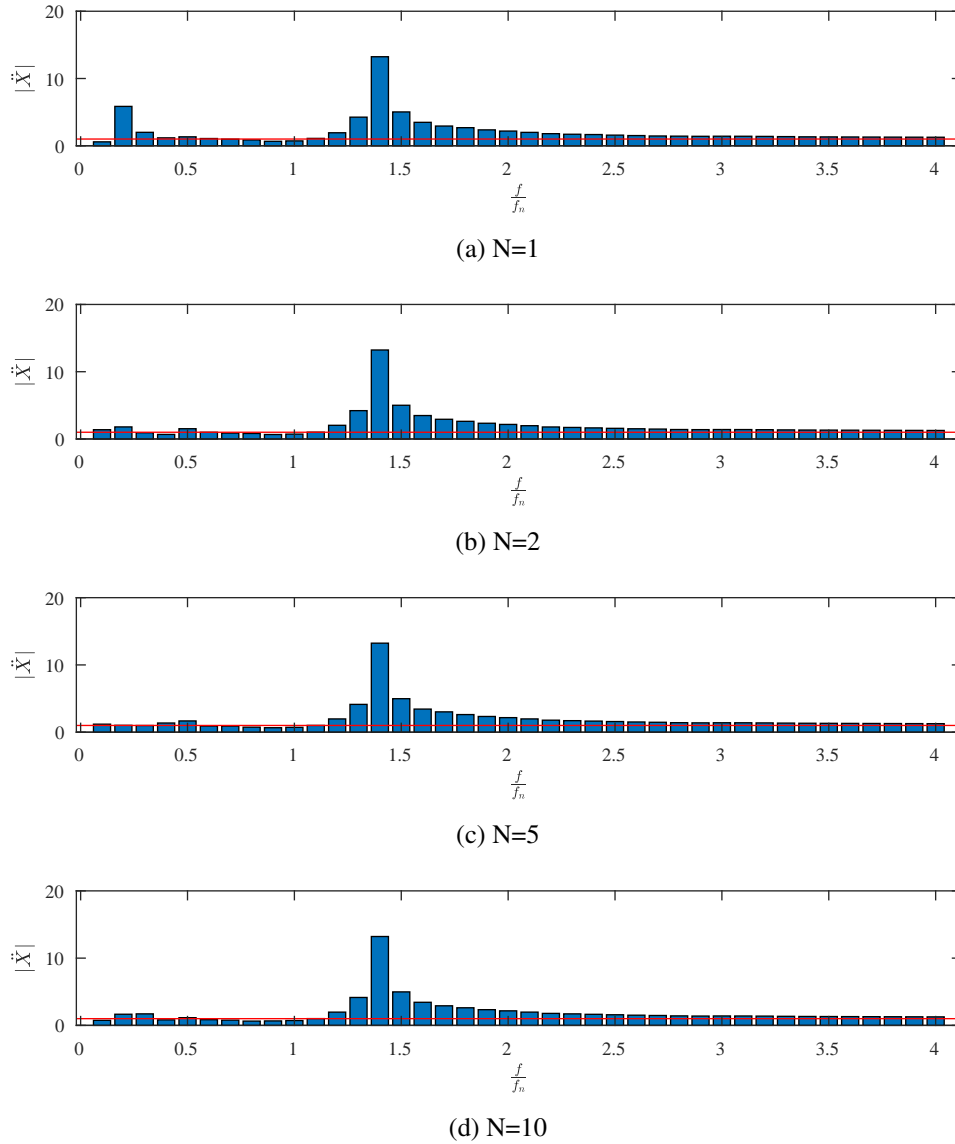
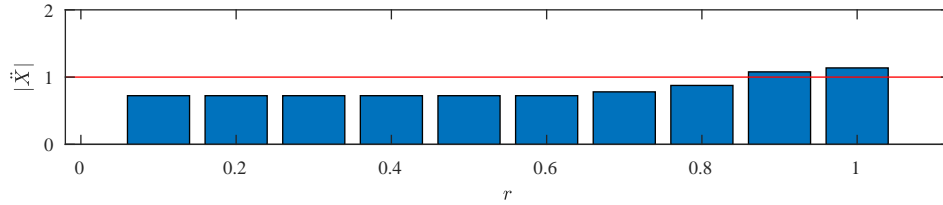


Figure 7: Maximum absolute acceleration of the linear oscillator for various unit cells of the meta-impactor, as a function of the frequency ratio. The red lines correspond to $|\ddot{X}| = 1$.

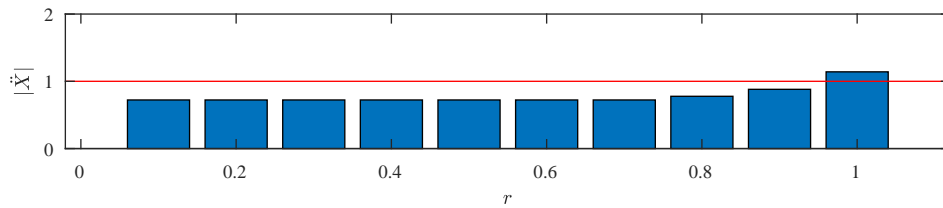
Based on these findings, a subsequent series of simulations is carried out for $m/M = 1$, $\mu/m = 0.1$, $K/k = 10$ and for the same number of unit cells as before. The simulation time is now increased to 50 s and the vibration acceleration response (maximum absolute value) of the linear oscillator is calculated for a frequency ratio f/f_n that varies in $[0.1, 4.0]$. As Fig. 7 indicates, there's a certain suppression of the response up to around 1.2 Hz (recall that the damping of the meta-impactor is zero). Increasing the number of unit cells does not significantly alters the suppression properties of the meta-impactor, yet, it is shown that when $N = 1$ there's a distinctive peak at 0.2 Hz, which does not appear in higher unit cell numbers.

A final investigation pertains to the coefficient of restitution. Figure 8 illustrates the maximum absolute vibration acceleration response of the linear oscillator for an excitation frequency $f = 1$ Hz, as a

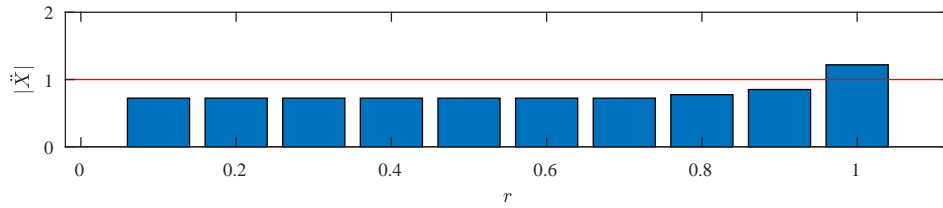
function of r ranging from 0.1 (almost plastic collision) to 1 (perfectly elastic). It can be observed that the response is not much sensitive to low values of the coefficient of restitution, yet it is getting larger when the collision goes close to the perfectly elastic range, while at the limit it is even amplified, compared to the excitation amplitude.



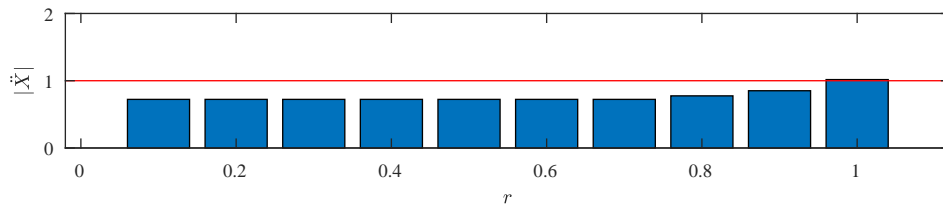
(a) $N=1$



(b) $N=2$



(c) $N=5$



(d) $N=10$

Figure 8: Maximum absolute acceleration of the linear oscillator for various unit cells of the meta-impactor, as a function of the coefficient of restitution. The red lines correspond to $|\ddot{X}| = 1$.

4 CONCLUSIONS

This study investigated a nonlinear device for vibration attenuation, the meta-impactor, consisting of impact dampers as unit cells. Critical parameters of the structure, including mass and stiffness ratios, as well as the coefficient of restitution and the number of unit cells were explored. The results indicate

a certain degree of effectiveness, yet, they have also shown that proper tuning of the meta-impactor is a highly non trivial problem. The authors are currently performing research on this direction, trying to gain more insight on the theoretical and design aspects of this nonlinear device, yet also to establish a series of experiments for assessing more thoroughly its actual behaviour.

REFERENCES

- [1] M.J.N. Priestley and D.N. Grant. Viscous damping in seismic design and analysis. *Journal of Earthquake Engineering*, 9(2):229–255, 2005.
- [2] S.H. Crandall. The Hysteretic Damping Model in Vibration Theory. *Proceedings of the Institution of Mechanical Engineers, Part C: Journal of Mechanical Engineering Science*, 205(1):23–28, 1991.
- [3] Z. Liang, G.C. Lee, G.F. Dargush, and J. Song. *Structural damping: Applications in Seismic Response Modification*. CRC Press, Boca Raton, FL, USA, 2012.
- [4] F. López-Almansa, S.T. de la Cruz, and C. Taylor. Experimental study of friction dissipators for seismic protection of building structures. *Earthquake Engineering and Engineering Vibration*, 10(4):475–486, 2011.
- [5] Y.L. Xu and Z. Yu. Mitigation of three-dimensional vibration of inclined sag cable using discrete oil dampers - II. Application. *Journal of Sound and Vibration*, 214(4):675–693, 1998.
- [6] R. Lewandowski and Lasecka-Plura. M. Design sensitivity analysis of structures with viscoelastic dampers. *Computers and Structures*, 164:95–107, 2016.
- [7] R. Lewandowski, A. Bartkowiak, and H. Maciejewski. Dynamic analysis of frames with viscoelastic dampers: A comparison of damper models. *Structural Engineering and Mechanics*, 41(1):113–137, 2012.
- [8] K. Fujita, A. Moustafa, and I. Takewaki. Optimal placement of viscoelastic dampers and supporting members under variable critical excitations. *Earthquake and Structures*, 1(1):43–67, 2010.
- [9] H.P. Zhu, D.D. Ge, and X. Huang. Optimum connecting dampers to reduce the seismic responses of parallel structures. *Journal of Sound and Vibration*, 330(9):1931–1949, 2011.
- [10] R. Rana and T.T. Soong. Parametric study and simplified design of tuned mass dampers. *Engineering Structures*, 20(3):193–204, 1998.
- [11] F. Sadek, B. Mohraz, A.W. Taylor, and R.M. Chung. A method of estimating the parameters of tuned mass dampers for seismic applications. *Earthquake Engineering and Structural Dynamics*, 26(6):617–635, 1997.
- [12] J. Salvi and E. Rizzi. Optimum tuning of tuned mass dampers for frame structures under earthquake excitation. *Structural Control and Health Monitoring*, 22(4):707–725, 2015.
- [13] S. Elias and V. Matsagar. Research developments in vibration control of structures using passive tuned mass dampers. *Annual Reviews in Control*, 44:129–156, 2017.
- [14] R.O. Ruiz, D. Lopez-Garcia, and A.A. Taflanidis. Modeling and experimental validation of a new type of tuned liquid damper. *Acta Mechanica*, 227(11):3275–3294, 2016.

- [15] L. Venanzi. A Review on Adaptive Methods for Structural Control. *The Open Civil Engineering Journal*, 10:653–667, 2016.
- [16] W. Yu and S. Thenozhi. *Active Structural Control with Stable Fuzzy PID Techniques*. Springer International Publishing, Switzerland, 2016.
- [17] H. Kurino, J. Tagami, K. Shimizu, and T. Kobori. Switching oil damper with built-in controller for structural control. *Journal of Structural Engineering*, 129(7):895–904, 2003.
- [18] M.S. Miah, E.N. Chatzi, V.K. Dertimanis, and F. Weber. Realtime experimental validation of a novel semiactive control scheme for vibration mitigation. *Structural Control and Health Monitoring*, 24(3):# e1878, 2017.
- [19] S.J. Dyke, B.F. Spencer Jr., M.K. Sain, and J.D. Carlson. Modeling and control of magnetorheological dampers for seismic response reduction. *Smart Materials and Structures*, 5(5):565–575, 1996.
- [20] F. Weber and C. Boston. Clipped viscous damping with negative stiffness for semi-active cable damping. *Smart Materials and Structures*, 20:# 045007, 2011.
- [21] F. Weber. Robust force tracking control scheme for MR dampers. *Structural Control and Health Monitoring*, 22(12):1373–1395, 2015.
- [22] L. Jansen and S. Dyke. Semiactive control strategies for MR dampers: comparative study. *Journal of Engineering Mechanics*, 126(8):795–803, 2000.
- [23] M.S. Miah, E.N. Chatzi, V.K. Dertimanis, and F. Weber. Nonlinear modeling of a rotational MR damper via an enhanced BoucWen model. *Smart Materials and Structures*, 24(10):# 105020, 2015.
- [24] M. Sigalas and E. Economou. Band structure of elastic waves in two dimensional systems. *Solid State Communications*, 86(3):141–143, 1993.
- [25] M.S. Kushwaha, P. Halevi, G. Martínez, L. Dobrzynski, and B. Djafari-Rouhani. Theory of acoustic band structure of periodic elastic composites. *Physical Review B*, 49(4):2313–2322, 1994.
- [26] P.-R. Wagner, V.K. Dertimanis, I.A. Antoniadis, and E.N. Chatzi. On the feasibility of structural metamaterials for seismic-induced vibration mitigation. *International Journal of Earthquake and Impact Engineering*, 1(1/2):20–56, 2016.
- [27] Z. Shi and J. Huang. Feasibility of reducing three-dimensional wave energy by introducing periodic foundations. *Soil Dynamics and Earthquake Engineering*, 50:204–212, 2013.
- [28] O. Casablanca, G. Ventura, F. Garescì, B. Azzerboni, B. Chiaia, M. Chiappini, and G. Finocchio. Seismic isolation of buildings using composite foundations based on metamaterials. *Journal of Applied Physics*, 123(17), 2018.
- [29] Z.B. Cheng and Z.F. Shi. Composite periodic foundation and its application for seismic isolation. *Earthquake Engineering and Structural Dynamics*, 47(4):925–944, 2018.
- [30] F. Basone, M. Wenzel, O.S. Bursi, and M. Fossetti. Finite locally resonant Metafoundations for the seismic protection of fuel storage tanks. *Earthquake Engineering and Structural Dynamics*, 48(2):232–252, 2018.

- [31] V.K. Dertimanis, I.A. Antoniadis, and E.N. Chatzi. Feasibility Analysis on the Attenuation of Strong Ground Motions Using Finite Periodic Lattices of Mass in Mass Barriers. *Journal of Engineering Mechanics*, 142(9):# 04016060, 2016.
- [32] A. Palermo, S. Krödel, K.H. Matlack, R. Zaccherini, V.K. Dertimanis, E.N. Chatzi, A. Marzani, and C. Daraio. Hybridization of Guided Surface Acoustic Modes in Unconsolidated Granular Media by a Resonant Metasurface. *Physical Review Applied*, 9(5):# 54026, 2018.
- [33] R. Zaccherini, V.K. Dertimanis, A. Palermo, S. Krödel, A. Marzani, C. Daraio, and E.N. Chatzi. Resonant Metabarriers as Seismic Attenuators in Granular Media. In *Proceedings of the ISMA2018 conference on Noise and Vibration Engineering*, Leuven, Belgium, 2018.
- [34] S.F. Masri. General Motion of Impact Dampers. *The Journal of the Acoustical Society of America*, 47:229–237, 1970.
- [35] S.F. Masri and T.K. Caughey. On the Stability of the Impact Damper. *Journal of Applied Mechanics*, 33(3):586–592, 1967.
- [36] S.F. Masri and A.M. Ibrahim. Response of the Impact Damper to Random Excitation. *The Journal of the Acoustical Society of America*, 53(1):200–211, 1973.
- [37] M.F. Dimentberg and D.V. Iourtchenko. Random Vibrations With Impacts: A Review. *Nonlinear Dynamics*, 36(2–4):229–254, 1973.
- [38] M.R. Duncan, C.R. Wassgren, and C.M. Krousgrill. The damping performance of a single particle impact damper. *Journal of Sound and Vibration*, 286(1–2):123–144, 2005.
- [39] O.V. Gendelman. Analytic treatment of a system with a vibro-impact nonlinear energy sink. *Journal of Sound and Vibration*, 331:4599–4608, 2012.
- [40] V.N. Philipchuk. Impact modes in discrete vibrating systems with rigid barriers. *International Journal of Non-Linear Mechanics*, 36(6):999–1012, 2001.

PARAMETRIC ANALYSIS OF A TRIPLE CORE PERIODIC UNIT CELL INCLUDING A MIDDLE RANDOM CORE – SMART 2019

N. GUENFOUD^{**†}, C. DROZ^{*}, M. ICHCHOU^{*}, O. BAREILLE^{*}, E. DECKERS[†], W.
DESMET[†]

^{*} Vibroacoustics & Complex Media Research Group (VIAME – LTDS)
Ecole Centrale de Lyon
36 Avenue Guy de Collongue, 69134 Écully
e-mail : nassardin.guenfoud@ec-lyon.fr

[†] Noise and Vibration Research Group, PMA
KU Leuven
Celestijnenlaan 300 B, B-3001, Heverlee, Belgium

Keywords: multi-layer core, sandwich panels, transmission loss, periodic structures.

Abstract. In the last decades, the main issue concerning structures is related to weight constraint. Many solutions are available as composites or sandwich panels. Nevertheless, it seems that metamaterials such periodic structures focus a specific attention nowadays. In this field, honeycomb structures remain wide used solutions especially in the aerospace industry, but they exhibit a high stiffness-to-weight ratio leading to poor acoustic properties. Consequently, some new designs are created to obtain better acoustic indicators. In this context, this paper proposes to study a new kind of periodic structures using multi-layer core topology systems consisting on stacking layers made of different geometry of cores (auxetic, hexagonal, rectangular...). Several new parameters should be considered to fully understand the dynamic and acoustic behaviour. In this paper we will limit the study to rectangular core combined with a random core located in between. Consequently, we will stack 3 kind of cores: Rect-Random-Rect. The main objective of this study is to analyse the results of the parametric survey. All configurations are constraint to have the same surface density. The chosen acoustic indicator is the Sound Transmission Loss (STL). The transition frequency will be also investigated as well as the compression and shear modulus and the bending waves. Modelling these structures is possible using either Wave Finite Element Method (WFEM) only or combining WFEM and the Transfer Matrix Method (TMM). We assume an infinite panel, real wavenumbers and that the structure is excited by plane waves with the angles of incidence and reflection equal. The model is implemented using MATLAB and ANSYS apdl. Because such structures are made using a 3D printer, the ABS is used as the material for the study. From the parametric study, it turned out that multi-layer core systems correspond to relevant solutions to highly improve the STL. Moreover, it is possible to find out an optimized design giving the best STL. However, as it will be shown, it goes along with less efficiency in terms of mechanical properties and thus should be relevant for some specific applications.

1 INTRODUCTION

Lightweight structures including composite panels, sandwich panels or porous media are still widely used in the industry due their low mass. Besides, sandwich panels made of periodic cores exhibit a great interest having a low stiffness to weight ratio but leading to unsatisfactory acoustical properties. Many researches are carried out to provide them better mechanical and acoustical performances according to the industrial application. Proposed designs in the literature begin from simple cases as composite panels, studying the stacking sequences between layers to improve their mechanical efficiency [1,2], up to more complex structures using more exotic shapes and/or adding add-ons [3,4,5,6], especially within the periodic media field. More recently, multi-layer core topology systems have been developed by stacking different layers of cores (auxetic, hexagonal, rectangular, random geometry) to operate with new parameters. A double-layer honeycomb panel has been studied in [7] to drastically reduce the effect of the critical frequency of the Sound Transmission Loss (STL). Besides, corrugated and truss cores are stacked for building applications [8,9,10] trying to reach a more desirable impact resistance. Most of time, authors add damping layers separating the cores. These last designs are mainly considered for their capacity to absorb energy for specific mechanical applications but not employed as concerns acoustics. It is then clearly expected that more complex structures will continue to be investigated in the future to obtain improved properties. Consequently, this paper intends to analyze multi-layer core topology systems within the framework of periodic structures and to perform a parametric survey with the involvement of new parameters. Such approaches have been already completed for vibroacoustic properties in standard cases using honeycomb cores [11,12] or by changing gradually the core from a honeycomb to an auxetic unit cell [13, 14]. They have shown up the influence of geometrical parameters on vibroacoustic indicators (transition frequency, the modal density, the group velocity) and the STL. All these indicators reveal a better comprehension of the phenomenon leading to the improvement of the acoustical performances. In this paper, the parametric survey will be characterized by a study of the geometrical parameters of one layer over three opening new configurations and new perspectives not limited as one-core unit cell structures and leading to a high improvement of the STL.

2 MULTI-LAYER CORE TOPOLOGY SYSTEMS

2.1 Description

Multi-layer core topology systems are made of several layers of periodic structures (hexagonal, auxetic, rectangular, ...), Fig. 1.

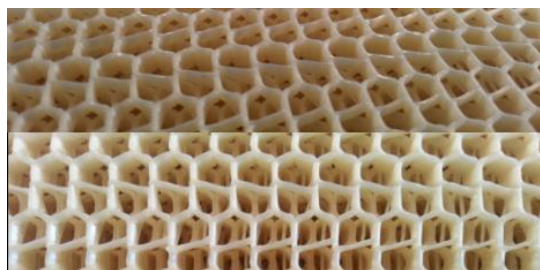


Figure 1 : Multi-layer core topology systems

Such structures involve new parameters to be considered to figure out the dynamic and the acoustic behavior. These parameters are listed as following:

1. The phase shift between layers
2. The rotation between layers
3. The interaction between geometrical parameters of each layer giving the possibility to modify the shape of the unit cell for each layer.
4. The size of the unit cell for each layer.
5. The periodicity of each layer.

The phase shift and the rotation make occur lower rigid contacts between layers leading to new phenomena which tend to affect the transition frequency and decrease the compression modulus of the structure. Nevertheless, their impact on the STL still need to be verified. The phase shift is possible along the direction x and y . In addition, the rotation between layers produces a non-periodic structure. The existing methods using the Wave Finite Element Method (WFEM) for the calculation of vibroacoustic indicators are not applicable. Finally, they offer a great added value by keeping the mass constant.

Changing the geometrical parameters for each layer turns out the possibility to have different shape for each layer, and then, combining a hexagonal core with an auxetic or a rectangular core, or more generally random cores and increasing the number of possibilities and the complexity of the unit cell.

Ultimately, the size of the unit cell and the periodicity for each layer are linked. Indeed, the only way to extract a unit cell in this configuration comes out when each layer has a unit cell size multiple to each other and without rotation.

Resulting from these parameters, it is then not always possible to extract the unit cell through the depth of the structure. The entire sandwich panel must be modeled and a high computational is expected. Therefore, some listed parameters will be constrained to have the opportunity to use the WFEM and to apply the model allowing to obtain the STL.

2.2 Parametric model

The illustrated parametric model (Fig. 2) will be used for the study. Each layer has the same unit cell size and no rotation is considered. The main purpose in this study is to identify the geometrical influence of the shape of the core. The thickness of the core and the skins as well as the height of each layer will be not altered since it is shown in [4] that they have a strong influence on the mechanical and acoustical properties. Thereby, by keeping the mass constant, only parameters defined in the parametric model influence the STL. An algorithm, developed in the lab, gives the possibility to obtain all configurations having the same surface density for a given size of unit cell. Since the size of the unit cell is maintained and the depth of each layer are equal and the parameter n is set to $1/2$, only 5 parameters are modified: a_1 , a_2 , a_3 , α and β . However, to represent correctly the result coming from the parametric survey it is necessary to reduce the number of parameters. Consequently, it is decided that $a_1 = a_2$.

The size of the unit cell is fixed to $L_x = 15$ mm and $L_y = 15$ mm. A sandwich panel with 3 layers is considered. The top and bottom layers correspond to a rectangular core while the middle core is a random core defined by the set of parameters. The depth of each layer is 5 mm. The thickness of the skins and the core is 0,6 mm. The sandwich panel is made of ABS since the 3D

printing technic is commonly used to manufacture these structures, with $E = 1,8 \times 10^9$ Pa, $\rho = 985$ kg/m³ and $\nu = 0,33$. The damping η is evaluated at 2 %. These values were acquired using a DMA test. From the algorithm, the number of configurations is obtained (Fig. 3) given a certain range of surface density with $a_3 = L_x/4$. They will be compared to a standard periodic structure with a rectangular core whose surface density is equal to 0,57 kg/m². Thereby, 216 configurations are possible. The parameter a_3 is then used to be shifted in the along x with 6 different values between 0 and L_x . Consequently, 1296 configurations in total will be computed. For each configuration the STL is calculated. A wise choice for the model must be done to avoid high computational cost.

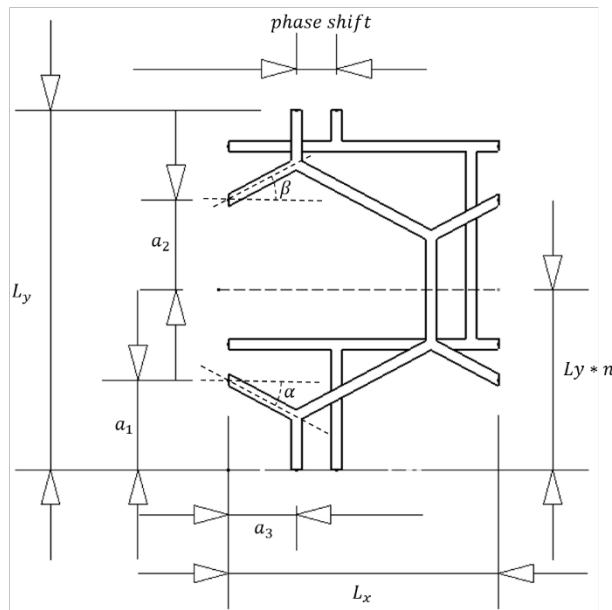


Figure 2 : Parametric model

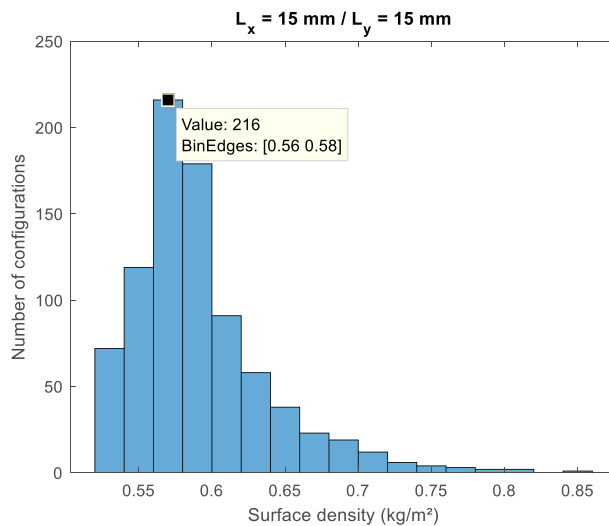


Figure 3 : Number of configurations with $L_x = 15$ mm and $L_y = 15$ mm and $a_3 = L_x/4$.

By taking this range of surface density and having all the possibilities for each parameter, it is possible to plot each parameter as a function of others. It occurs that the angle α and β are linked by a logarithmic function as shown in Fig. 4. Consequently, the set of parameters could be reduced to a_1 , a_3 and α since $\alpha = f(\beta)$.

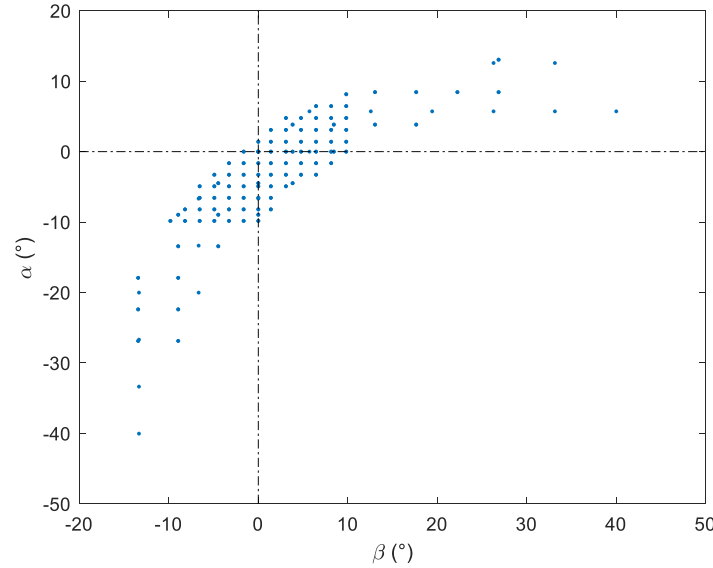


Figure 4 : $\alpha = f(\beta)$

3 MODELLING

During the last decade many models were developed to calculate vibroacoustic indicators. This paper is mainly focused on the STL as the acoustic indicator. Considering an incident plane wave impinging a structure with a specific angle, this will create 3 other waves corresponding to a reflected, transmitted and absorbed wave as illustrated in Fig 5. The STL is defined with the ratio $\tau = |W_t / W_i|$ which is the ratio between the acoustic power of the transmitted and incident wave and could be obtained for specific angles (Eq. 1).

$$STL(\theta, \phi, \omega) = -10 \log_{10} \frac{W_t}{W_i} \quad (1)$$

The STL is also calculated for a diffuse field by the integration over all angles $\theta \in [0^\circ, 90^\circ]$ and $\phi \in [0^\circ, 360^\circ]$ and yield to Eq. 2.

$$STL_d(\omega) = \frac{\int_0^{2\pi} \int_0^{\theta_{max}} \tau(\omega, \theta, \phi) \sin(\theta) \cos(\theta) d\theta d\phi}{\int_0^{2\pi} \int_0^{\theta_{max}} \sin(\theta) \cos(\theta) d\theta d\phi} \quad (2)$$

In 2016, two methods released [15, 16] using the nodal surfaces and the Transfer Matrix Method (TMM) concept combined with the WFEM respectively. They allow to model complex

structures without homogenization. More recently, [17] added their contribution by developing a hybrid wave-based method with finite element to add more complexity to the structure as resonators. It is possible to model other type of fluid on both sides of the structure such as strong fluid-structure interaction. In this paper, the method developed in [16] will be used. Indeed, the computational cost is drastically reduced since the skins are modeled using the analytical formulation for simple plate. The core is modeled with Ansys apdl using SHELL elements and MATLAB for post processing. It is assumed an infinite panel, real wavenumbers and that the structure is excited by plane waves with the angles of incidence and reflection equal. The principle of this method is illustrated in Fig. 6.

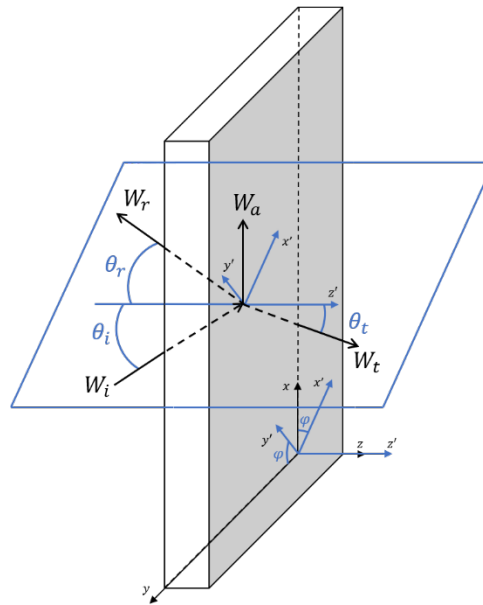


Figure 5 : Plane wave incidence, reflection, transmission and absorbed at the interface of a sandwich panel.

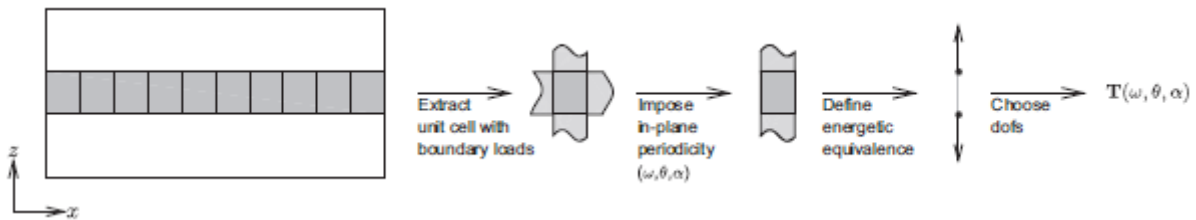


Figure 6 : Procedure for applying the method developed in [16]

Finally, to perform the parametric analysis two options are chosen for simplification. Firstly, due to the orthotropy of the structure resulting from the honeycomb core, it is not necessary to calculate the diffuse field. From the dispersion curves of the standard case corresponding to the rectangular core, bending waves reveals the direction x as critical to determine the acoustic efficiency of the structure. It is shown that the intersection with the acoustic wavenumber and bending waves occurs in the direction x . Thus, the STL will be calculated for an angle $\varphi = 0^\circ$ and $\theta = 45^\circ$ exciting the structure in its x -direction only. In addition, the target indicator is

defined as the integration of the STL over the frequencies as it is done in [18]. The more the value is high the more the structure is considered acoustically efficient.

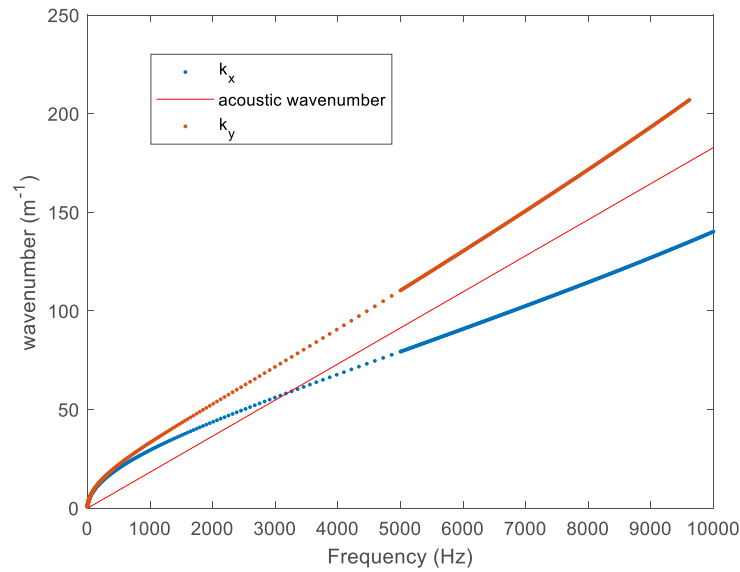


Figure 7 : Bending waves of the standard case (rectangular core)

3 PARAMETRIC SURVEY

The first result was obtained having all configurations with different values of a_3 . It is shown in Fig. 8 that a quasi-symmetry occurred related to the chosen parametric model. As it can be noticed, the parameter a_3 has a strong influence on the STL and the highest values of STL is obtained when $a_3 = Lx/4$. The next steps of the parametric analysis are carried out with $a_3 = Lx/4$.

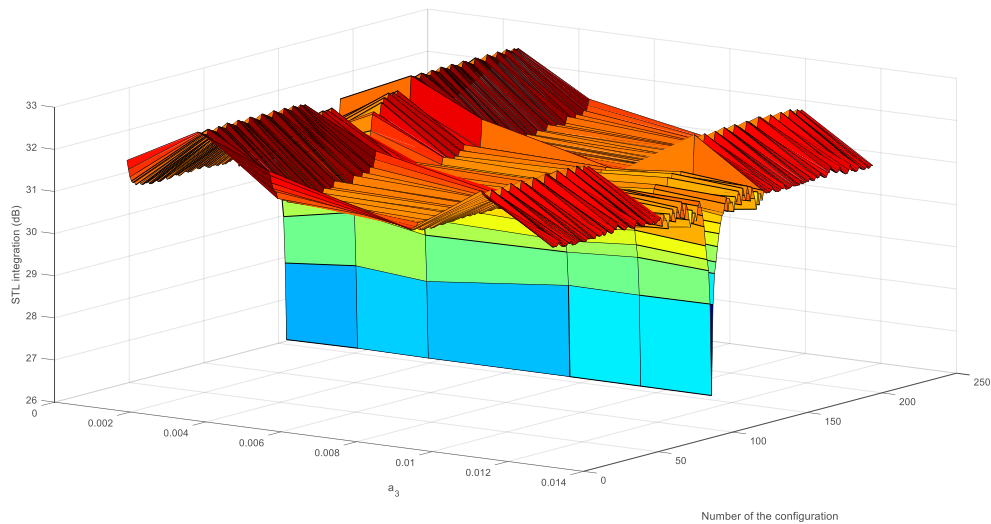


Figure 8 : Effect of the parameter a_3 on all configurations

Fig. 9 shows the effect on the STL of the angles α and β for different values of a_1 . The influence of the angles is highly dependent on the value of the parameter a_1 . The angles α and β become critical parameters when $a_1 = Ly/4$. Consequently, for such configuration it is necessary to make a wise choice on the angles. The highest values of the STL are obtained with $a_1 = 1,25$ mm and $a_1 = 6,25$ mm.

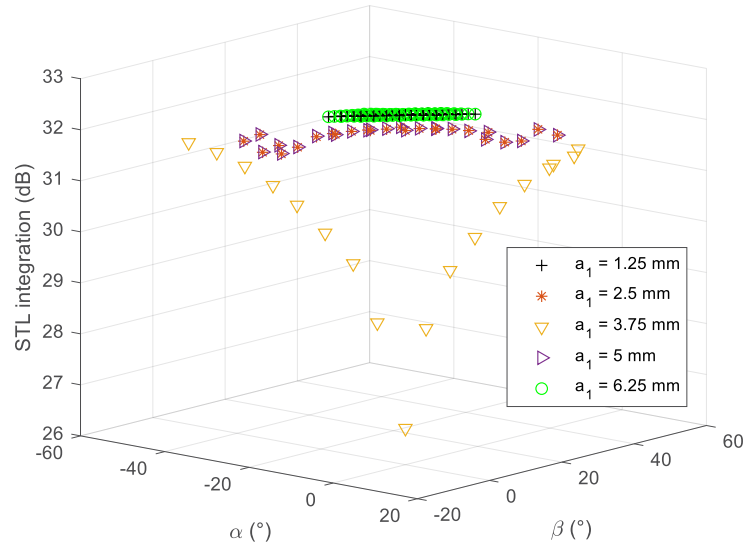


Figure 9 : Effect of the angles of the core α and β with specific values of the parameter a_1 .

Finally, the effect of the pair (α, β) is illustrated in Fig. 10. It is shown that depending on the value of the STL, the pairs (α, β) correspond to a linear function in which the value of the intercept has a critical influence. The highest value of STL occurs when the intercept is the lowest and the pairs (α, β) are highlighted in Fig. 10.

From this parametric study the optimized configuration can be listed in the following Tab. 1. with a_1 and a_2 equal to 1,25 mm or 6,25 mm and $a_3 = Lx/4$. Since the unit cell size is 15 mm by 15 mm, the angles are almost neglectable and could be considered as 0° . Nevertheless, the optimized unit cell with the highest STL value correspond to $(1,4^\circ, 0^\circ)$.

Table 1: Pairs of (α, β) for the optimized unit cell.

α (°)	-4,9	-3,3	-1,6	0	1,4	3	4,8
β (°)	-6,5	-4,9	-3,2	-1,6	0	1,4	3

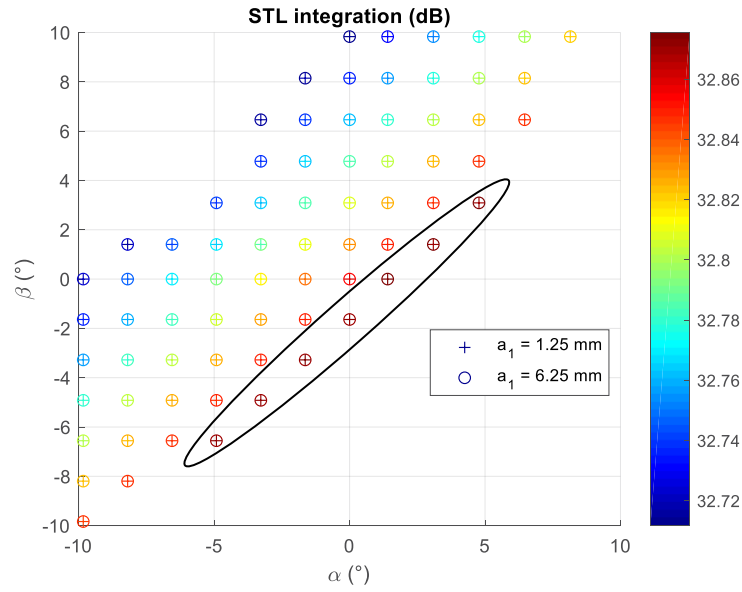


Figure 10 : Influence of the pair (α, β) given with $a_1 = 1,25$ mm and $a_1 = 6,25$ mm.

4 OPTIMIZED VS STANDARD STRUCTURE

Thanks to the parametric survey, it is then possible to compare the optimized structure with the standard rectangular core. The Fig. 11. shows the great improvement obtained with the multi-layer core system in all the frequency range. The coincident frequency is shifted to higher frequencies.

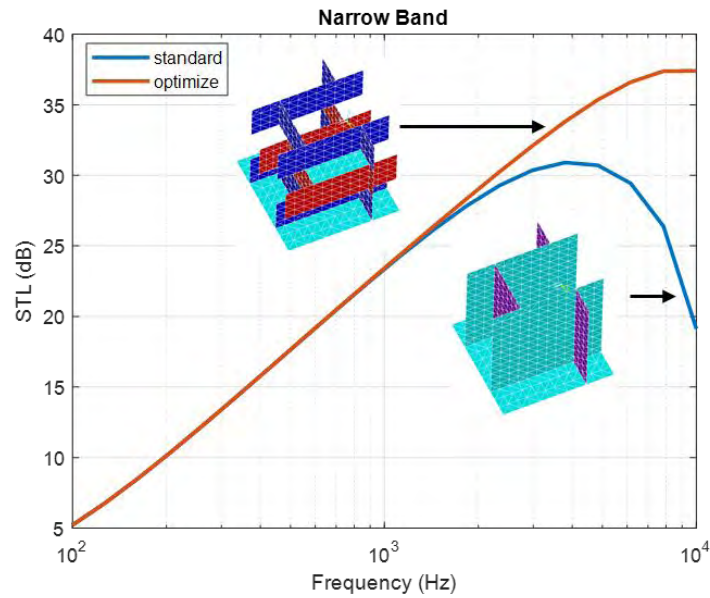


Figure 11 : Comparison of the STL ($\theta = 45^\circ$ and $\varphi = 0^\circ$) of the optimized structure with the standard case.

This result is confirmed with the comparison of bending waves in Fig. 12. The multi-layer core has lower equivalent mechanical properties in both direction x and y and lead to an intersection with the acoustic wavenumber to a higher frequency. The acoustic wavenumber is calculated for a diffuse field and the intersection correspond to the critical frequency. Consequently, the optimized structure should be still acoustically efficient in a diffuse field.

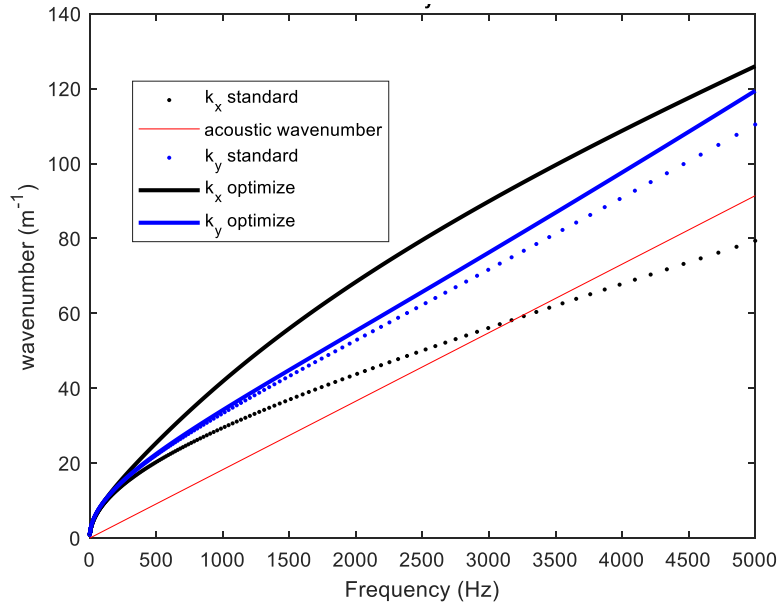


Figure 12 : Bending waves comparison of the optimized and standard structure.

Finally, the mechanical and acoustical properties for both structures are summarized in the following table (Tab. 2).

Table 2: Mechanical and acoustical properties.

	standard	optimized
Compression modulus (MPa)	227	92
Transition Frequency (Hz) (ftx, fty)	(2910, 1694)	(1388, 251)
STL integration (dB)	26,71	32,88

The compression modulus is calculated along z-axis. As it is noticed, the improvement of the STL goes along with a reduction of the compression modulus and the transition frequency in both directions. Multi-layer core systems show a great interest in terms of acoustic properties while mechanical properties seem to be lower than a standard one core unit cell. These results were obtained without altering the mass which is a critical parameter especially in the aerospace industry.

5 CONCLUSIONS

This paper has been focused on the study of multi-layer core topology systems made of 3 layers with a top and bottom rectangular core and a random middle core. It has been shown that this new kind of structure involves new geometrical parameters to be considered. A parametric survey has been suggested to study the influence of this geometrical parameters on the random core. The parameter a_1 and a_2 were considered equal. The STL has been chosen as the target acoustic indicator and a WFEM combined with the TMM method has been used to model the unit cell.

It occurs through the analysis that all parameters seem to have an interaction with the other and could become critical in some configurations. The parameter a_3 have a strong effect on the STL and is maximum when $a_3 = Lx/4$. In addition, the pair (α, β) have an impact on the STL when $a_1 = a_2 = Ly/4$ and their influence decrease when a_1 get close to 0 or $Ly/2$. Moreover, after fixing $a_1 = 1,25 \text{ mm}$ or $6,25 \text{ mm}$, it was shown that the pair (α, β) turned out a linear relationship according to the value of STL. Thereby, the optimized pair (α, β) corresponded to the equation with the lowest intercept. Consequently, an optimized structure with the same surface density of the standard rectangular core was obtained as well as the comprehension of the influence of each parameter of the parametric model.

Ultimately, the parametric analysis may introduce new target indicators as mechanical and vibroacoustic indicators. In addition, this parametric model proposes some tools to verify the influence of each parameter and could be applied to other standard structure as hexagonal and auxetic core widely spread in the industry. Finally, some vibroacoustic indicators as the transition frequency seems to be strongly influenced by the geometry of the multi-layer core and should be studied.

ACKNOWLEDGEMENT

This project has received funding from the European Union Horizon 2020 research and innovation program under the Marie Skłodowska-Curie grant agreement No. 675441. The author would like to acknowledge all the Institutions and Partners involved in the VIPER project. The research work of Elke Deckers is financed by a post-doctoral grant of the Research Foundation-Flanders (FWO)

REFERENCES

- [1] Roque, C. and Martins, P. Maximization of fundamental frequency of layered composites using differential evolution optimization. *Composite Structures* (2018) 183:77–83.
- [2] Reddy, J.N. *Mechanics of laminated composite plates and shells: theory and analysis*. CRC press; (2004).
- [3] Droz, C. Zergoune, Z. Boukadia, R. Bareille, O. and Ichchou, M. Vibro-acoustic optimisation of sandwich panels using the wave/finite element method. *Composite Structures* (2016) 156:108–114.
- [4] Han, B. Wang, W. Zhang, Z. Zhang, Q. Jin, F. and Lu, T. Performance enhancement of sandwich panels with honeycomb–corrugation hybrid core. *Theoretical and Applied Mechanics Letters* (2016) 6(1):54–59.
- [5] Mazloomi, M.S. Ranjbar, M. Boldrin, L. Scarpa, F. Patsias, S. and Ozada, N. Vibroacoustics of 2d gradient auxetic hexagonal honeycomb sandwich panels. *Composite Structures* (2018)

- 187:593–603.
- [6] de Melo Filho, N. Van Belle, L. Claeys, C. Deckers, E. and W. Desmet. Dynamic mass-based sound transmission loss prediction of vibro-acoustic metamaterial double panels applied to the mass-air-mass resonance. *Journal of Sound and Vibration* (2018).
 - [7] Wen-chao, H. and Chung-fai, N. Sound insulation improvement using honeycomb sandwich panels. *Applied Acoustics* (1998) 53(1-3):163–177.
 - [8] Hou, S. Shu, C. Zhao, S. Liu, T. Han, X. and Li, Q. Experimental and numerical studies on multi-layered corrugated sandwich panels under crushing loading. *Composite Structures* (2015) 126:371–385.
 - [9] Magnucka-Blandzi, E. Walczak, Z. Wittenbeck, L. and Rodak, M. Strength of a metal seven-layer rectangular plate with trapezoidal corrugated cores. *Journal of Theoretical and Applied Mechanics* (2017) 55(2):433–446.
 - [10] Xiong, J. Vaziri, A. Ma, L. Papadopoulos, J. and Wu, L. Compression and impact testing of two-layer composite pyramidal-core sandwich panels. *Composite Structures* (2012) 94(2):793–801.
 - [11] Baho, O. Zergoune, Z. Ichchou, M. Harras, B. Benamar, R. and Troclet, B. On global bending–shear core transition effects for the vibroacoustic of sandwich structures: Analytical and numerical investigations. *Composite Structures* (2016) 154:453–463.
 - [12] Zergoune, Z. Ichchou, M. Bareille, O. Harras, B. Benamar, R. and Troclet, B. Assessments of shear core effects on sound transmission loss through sandwich panels using a two-scale approach. *Computers & Structures* (2017) 182:227–237.
 - [13] Griese, D. Summers, J.D. and Thompson, L. The effect of honeycomb core geometry on the sound transmission performance of sandwich panels. *Journal of Vibration and Acoustics* (2014).
 - [14] Galgalikar, R. and Thompson, L.L. Design optimization of honeycomb core sandwich panels for maximum sound transmission loss. *Journal of Vibration and Acoustics* (2016) 138(5):051005.
 - [15] Christen, J.L. Ichchou, M. Zine, A. and Troclet, B. Wave finite element formulation of the acoustic transmission through complex infinite plates. *Acta Acustica united with Acustica* (2016) 102(6):984–991.
 - [16] Parrinello, A. and Ghiringhelli, G. Transfer matrix representation for periodic planar media. *Journal of Sound and Vibration* (2016) 371:196–209.
 - [17] Deckers, E. Jonckheere, S. Van Belle, L. Claeys, C. and Desmet, W. Prediction of transmission, reflection and absorption coefficients of periodic structures using a hybrid wave based–finite element unit cell method. *Journal of Computational Physics* (2018) 356:282–302.
 - [18] Galgalikar, R. Design automation and optimization of honeycomb structures for maximum sound transmission loss, (2012).

Uncertainties in wave characteristic of one-dimensional periodic media using the fuzzy wave finite element method

R. P. SINGH^{*1,2}, M. ICHCHOU², O. BAREILLE², F. FRANCO¹, S. DE ROSA¹

¹ Laboratory for promoting experiences in aeronautical structures and acoustics
Department of Industrial Engineering, University of Naples “Federico II”
Via Claudio 21, 80125 Napoli, Italy
E-mail: {ravipratap.singh} {sergio.derosa} {francesco.franco} @unina.it,

² Vibroacoustic and Complex Media Research Group, LTDS,
Ecole Centrale de Lyon,
36 Avenue Guy de Collongue, 69134 Ecully, France,
Email: {olivier.bareille} {mohamed.Ichchou} @ec-lyon.fr

ABSTRACT

To predict the wave characteristics of the periodic media in the presence of fuzzy uncertainties, the wave finite element method in conjunction with fuzzy logic and algebra has been applied. For one-dimensional wave propagation, firstly, the most significant input parameters such as Young's modulus and mass density are identified and then *fuzzified* using the membership functions. Then, the fuzzy variable is propagated through the numerical model of interval analysis. The dispersion curves for flexural and longitudinal waves with fuzzy parameters have been used to illustrate the generality of the proposed approach also looking at the possibility to have frequency region in which those waves cannot propagate (frequency band gaps). The triangular membership functions have been used in the numerical examples and the obtained results are compared against the classical Monte Carlo simulations (MCS). The approach was presented for very simplified test-cases but it is found to be more efficient when compared with the conventional MCS approach in terms of computational cost.

Key words: WFEM, uncertainty modeling, periodic media, bandgap, fuzzy analysis.

1 INTRODUCTION

In recent years the propagation of elastic waves in periodic media with periodic material and geometrical properties has been extensively studied. These periodic media offer property known as band gaps where the propagation of the elastic wave is restricted in all the directions. Such properties are demanded for the vibroacoustic performance and dynamics of the structure and especially sought in aeronautics, transport, energy and space for vibration reduction, acoustic blocking, acoustic channeling and acoustic cloaking [1].

Three different frequency ranges identified: at the low-frequency range, because of the low order modes and low sensitivity to variability generally, the finite element approaches are applicable; and high frequency, energy-based methods (e.g. Statistical Energy Analysis (SEA))

are well suited because of the involvement of many high order modes; finally the mid-frequency range affected by the variability of the model parameter and wave-based approaches has been developed by increasing computational efficiency [2].

The design of periodic media is generally based on deterministic models without considering the effect of intrinsic uncertainties existing in these media. In general, the design is aimed at controlling as much as possible the mechanical waves; however, inherent uncertainty may affect their characteristics. Periodic media are diffused in all the transportation engineering and demand a high level of robustness, which can be ensured with the careful consideration of the presence of uncertainty in the numerical models. The uncertainties, in terms of material properties and geometrical parameters, are mostly exhibited in both the manufacturing and assembly processes. To address this unavoidable actuality, the effects of uncertainties need to be considered when analyzing band structures (pass and stop bands). Generally, the stochastic characteristics of the periodic media can be determined by studying the design parameter uncertainties which are often modeled by random variables with consideration for spatial variability of the material and geometrical properties.

Manohar et al. studied the randomness in the wave propagation in waveguides using spectral element analysis [3]. Ichchou et al. proposed a numerical approach using the Wave Finite Element Method (WFEM) considering spatially homogeneous variability in waveguides using a first and second order perturbations are proposed [4][5]. Recently Rayleigh quotient method introduced to investigate the symplectic eigenvalue problem of random symplectic matrix [6]. The material or geometrical uncertainty often displays spatial correlation, in layered structures. There, random fields theory can be used to model spatially distributed variability with probability measure [7]. Also, this would be an approximate representation for the spatially varying system [8].

The probabilistic models to account for these uncertainties employ probabilistic methods which require a wealth of data on probabilistic parameters. The exact sources of uncertainty are rarely found since their identification represents a difficult task. Furthermore, even small inaccuracies in the data can lead to large errors in the computed probability of response [9].

When faced with incomplete information such as, “*Young’s modulus of the material lies between 70 GPa to 72.4 GPa,*” “*mass ration is about 4%,*” and “*lenght of side slightly larger than 1.2m,*” cannot be accomdated by deterministic model[10]. In fact, statements as “*the mean are approximately equal to..*” and “*the variance lies in the range..*” are typical when handling real mechanical data and by virtue of their subjective nature they deal with fuzzy uncertainties[11]; the adoption of the probabilistic approach can result in very challenging evaluations. In this scenario, the fuzzy set theory offers a way to approximating the uncertainty distribution in the form of the confidence interval through fuzzy membership functions. These are equivalent representations for the characterization of the linguistic, vague and missing data uncertainties.

The work reported so far in the literature with the best of the author's knowledge, is limited to wave propagation in elastic media and random media with probability method. In this work, a possibilistic method developed for the fuzzy uncertainty modeling and propagation in conjunction with WFEM and named as FWFEM (fuzzy wave finite element method). The approach was presented for a very simplified test-case 1D periodic bar and beam model with

fuzzy uncertainty. It is modeled using triangular membership function and uncertainty bound are computed with fuzzy arithmetic steps and α -cut method. The results of FWFEM formulation are compared to those obtained from MCS.

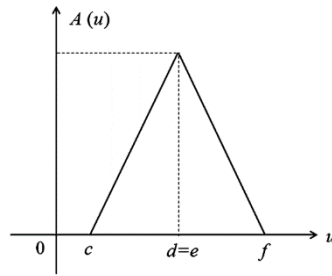
2 FORMULATION OF FWFEM

Firstly the definition of the fuzzy membership function is revisited [12]. Let U is a classical set of objects, it is called the universe. The generic elements of U are denoted u . Then the membership in a classical subset A of U can be viewed as a characteristic function μ_A from U to $\{0, 1\}$ such that

$$\mu_A(u) = \begin{cases} 1, & \text{if } u \in A \\ 0, & \text{if } u \notin A \end{cases} \quad (1)$$

The set $\{0, 1\}$ is called a valuation set. A set A is called a fuzzy set if the valuation set is allowed to be the real interval $[0, 1]$. The fuzzy set A is characterized by the set of pairs

$$A = \{[u, \mu_A(u)], u \in U\}$$



where $\mu_A(u)$ is called the grade of the membership function.

Figure 1: Triangular membership function

α - Cuts: When an element $u \in U$. The α -cut A_α of A , which is a fuzzy set of crisp values U and is the original set of membership values greater than some threshold $\alpha \in [0, 1]$.

If triangular fuzzy set A shown in Fig.1 is denoted by $A = \langle a, b, d \rangle$ then the α -cuts of the A can be shown as:

$$[a + \alpha(b - c), d - \alpha(d - b)], \quad \alpha \in [0, 1] \quad (2)$$

To propagate the fuzzy uncertainty in the dynamic model, the α -cut method is adopted. In this method, fuzzy membership function is discretized to different interval using α -cut level concept. For each α -cut, the interval analysis is performed with Sobol sequence to get the maximum and minimum bound of the response.

One dimensional periodic media obtained by formulating the unit cell and then repeating in the propagation direction. Then, the study of this media can be converted into a study of unit cell based on the Floquet-Bloch theorem [13]. The schematic representation is shown in Fig. 2.

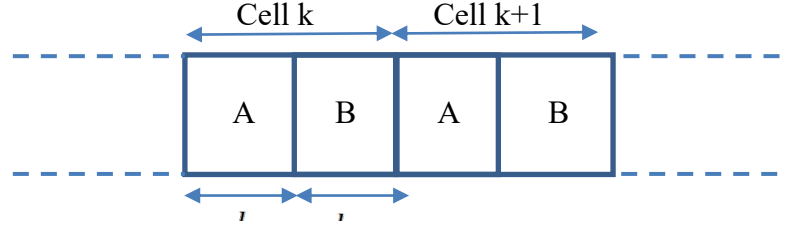


Figure 2: Schematic representation of periodic structure

The WFEM is used to study the behavior of periodic media. This is extended to apply the WFEM for the fuzzy uncertainty modeling. This starts with consideration of the fuzzy membership function as a supplementary dimension through the fuzzy arithmetic using fuzzy set theory. Which start from the discretization of one sub-element of length (d). This discretization leads to fuzzy dynamic equilibrium of any substructure. The imprecise or vague variables are modeled using the triangular membership function, such that the dynamical equilibrium is expressed as:

$$[-\omega^2 M(+)K(1+i\eta)](\cdot) \begin{pmatrix} q_L \\ q_R \end{pmatrix} = \begin{pmatrix} F_L \\ F_R \end{pmatrix} \quad (3)$$

The (\cdot) symbol denotes the fuzzy arithmetic.

The dynamic stiffness matrix is condensed into the left and right side denoted by L and R respectively.

$$\begin{pmatrix} D_{LL} & D_{LR} \\ D_{RL} & D_{RR} \end{pmatrix}(\cdot) \begin{pmatrix} q_L \\ q_R \end{pmatrix} = \begin{pmatrix} F_L \\ F_R \end{pmatrix} \quad (4)$$

By defining two state vectors in the left and right side of each element and are related by symplectic matrix S as:

$$u_R = S(\cdot)u_L \quad (5)$$

Where

$$S = \begin{pmatrix} -D_{LR}^{-1}(\cdot)D_{LL} & D_{LR}^{-1} \\ D_{RL} - D_{RR}(\cdot)D_{LR}^{-1}(\cdot)D_{LL} & -D_{RR}(\cdot)D_{LR}^{-1} \end{pmatrix}$$

Then using the periodicity and Bloch's theorem, spectral eigenvalue problem is expressed as

$$S(\cdot)\Phi_i = \mu_i(\cdot)\Phi_i \quad |S - \mu_i(\cdot)I_{2n}| = 0 \quad (6)$$

The solution of the above equation leads to identify the propagation constant and mode shapes. The considered structure is dissipative and the wave classified as incident ($|\mu_i^{inc}| < 1$) and reflected ones ($|\mu_i^{ref}| > 1$). Considering the above classification the wave basis Φ composed by eigenvectors in following form:

$$\Phi = \begin{pmatrix} \Phi_q^{inc} & \Phi_q^{ref} \\ \Phi_F^{inc} & \Phi_F^{ref} \end{pmatrix} \quad (7)$$

Where q and F are the displacement and force component of eigenvectors with $\Phi_q^{inc}, \Phi_F^{inc}, \Phi_q^{ref}, \Phi_F^{ref}$ of the size of $n \times n$ matrices.

To obtain the harmonic response, The amplitude of wave at the first element obtained using

$$\begin{pmatrix} Q^{inc(1)} \\ Q^{ref(1)} \end{pmatrix} = \begin{pmatrix} I_n & 0 \\ 0 & \mu^N \end{pmatrix} (.) \begin{pmatrix} \Phi_F^{inc} & \Phi_F^{ref} \mu^N \\ \Phi_q^{inc} \mu^N & \Phi_q^{ref} \end{pmatrix}^{-1} (.) \begin{pmatrix} -F \\ q \end{pmatrix}$$

Projection of kinematic variable on wave basis and compute the displacement at the m^{th} element by relation

$$(Q)^m = \begin{pmatrix} \mu^{inc} & 0 \\ 0 & \mu^{ref} \end{pmatrix}^{(m-1)} (.) \begin{pmatrix} Q^{inc(1)} \\ Q^{ref(1)} \end{pmatrix} \quad (8)$$

3 RESULTS

This section shows the validation of FWFEM formulation presented in the previous section. The analysis is performed for the periodic rod and beam. Periodic rod and beam consist of section A of length l_1 and section B of length l_2 with different materials as depicted in the Fig. 3. Firstly, the longitudinal wave studied for the band gap and frequency response function (FRF) then flexural wave in the beam is studied.

3.1 Periodic rod with fuzzy uncertainty

In this subsection, the FWFEM is used to study the effect of fuzzy parametric uncertainty on the band diagram and FRF of a longitudinal wave in the periodic rod. The section of periodic

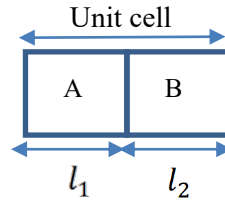


Figure 3: Symmetric unit cell

rod namely A and B made of aluminum and steel respectively. The length of section A is l_1 and section B is l_2 with 1m each with circular cross section of radius of 0.0644m.

To validate FWFEM results, a comparison made between the result from the proposed method and upper and lower bound obtained from MCS.

The uncertainty effect is studied considering fuzzy uncertain material properties modeled with triangular fuzzy membership function with lower and upper variation fixed at ± 10 percent of the nominal value. The considered frequency range for the numerical experiment from 1 Hz up to 5500 Hz. This frequency range considered to get the four complete band gap. The MCS

with 10000 samples is used to get the reference wave characteristics lower and upper bound of wave number.

In FWFEM formulation, stiffness and mass matrix of the two-node rod elements are considered.

The global stiffness and mass matrices formed with 100 elements in the unit cell of periodic rod in the MATLAB environment. The input material and geometric properties are shown in Table 1. It is to be mentioned that the material properties are chosen arbitrary for the test case.

Table 1: Geometric parameters and material properties of periodic rod

Geometrical and Material property	Nominal value
Rod length (A)	1 m
Rod length (B)	1 m
Radius of rod	0.0644 m
Young's modulus (A)	210 Gpa
Young's modulus (B)	70 Gpa
Mass density (A)	7800 kg/m ³
Mass density (B)	2700 kg/m ³
Loss factor (A) and (B)	0.001

The variation of fuzzy Young's modulus of section A (material 1) and section B (material 2) is considered as furnished in Fig.4.

FWFEM result at α -cut=0 (largest interval) in terms of upper and lower bounds of the wave number is compared with sampling upper and lower bound with 5000 samples. The comparison is shown in Fig.5. The results are in good agreement. The band gap envelopes for each value of the fuzzy elasticity in every α -cut can be extracted shown in Fig.6. It is visible that the effect of uncertainty (at the fixed level of uncertainty) on band gap bound is increasing with increasing frequency. The variation bound of the wave number at α -cut=0 is shown in Fig.7 and it can be inferred that the response membership function is not always symmetric about mean/crisp value. The upper bound of wave number is more sensitive to the uncertain elasticity.

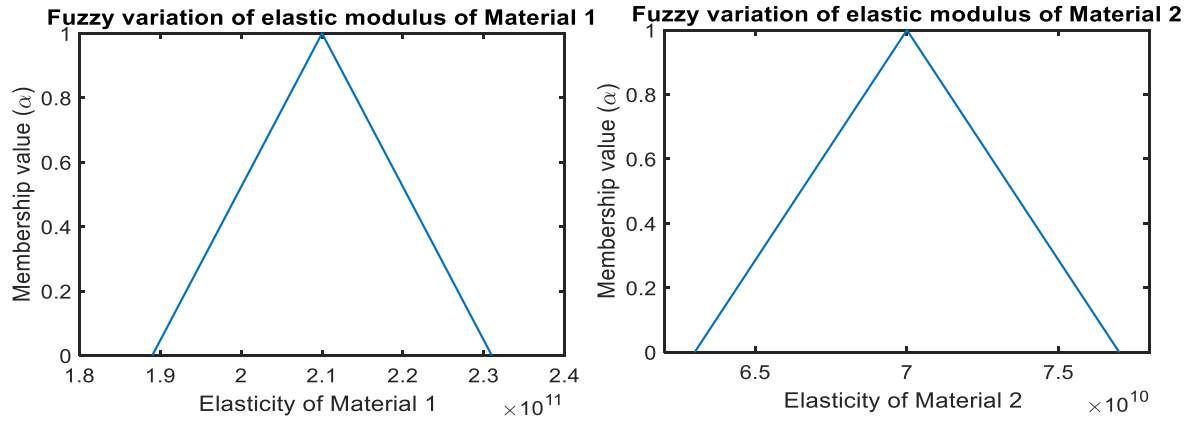


Figure 4: Membership function for the fuzzy parameter

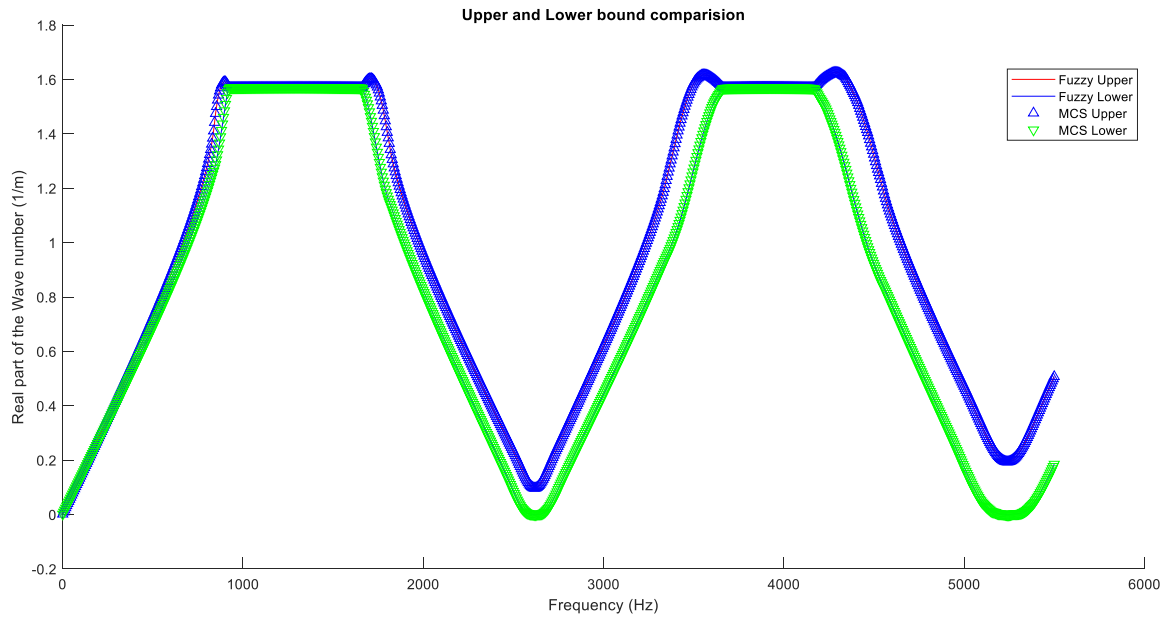


Figure 5: Upper and lower bound comparison

The FRF of a periodic rod of the finite extent of 20 m excited by unit force on the left end is furnished in Fig. 8 indicating the upper and lower bounds comparison at α -cut=0 (maximum bound). In Fig. 9 fuzzy bound of the FRF for the different value of α -cut is plotted. It can be seen that as the value of α -cut increase the fuzzy bound of FRF also decreases and finally at $\alpha=1$, without any simulation bound as expected, $\alpha=1$ represent the deterministic value.

3.2 Periodic beam with fuzzy uncertainty

In this subsection, the study of the fuzzy uncertainty effect on the flexural wave in the periodic beam is performed. For numerical simulation, Euler-Bernoulli beam theory is considered. The input material and geometrical properties are listed in Table 2.

For the fuzzy uncertainty propagation, the elasticity of material 1 and material 2 is fuzzified using triangular membership function and shown in Fig.4.

A two-node beam element with two degrees of freedom per node is considered. The global matrices (stiffness and mass) formed with 20 elements in the unit cell of the periodic beam in the MATLAB environment with input material and geometric properties given in Table 2.

FWFEM result at α -cut=0 is computed and compared with upper and lower bound obtained with MCS sampling (10000 samples) of the WFEM result and shown in Fig. 10. The frequency range of computation is 1-2000 Hz. The results are in good agreement. The variation bound of the wave number at a different frequency for the 11 α -cut levels is shown in Fig.11. it showed that at the same level of the α -cut upper bound of wave number is more sensitive to the uncertain elasticity.

Table 2: Geometric parameters and material properties of the periodic beam

Geometry/Property	Value
Beam length	0.5m
Height of beam	0.003m
Width of beam	0.003m
Young's modulus (A)	210 Gpa
Young's modulus (B)	70 Gpa
Mass density (A)	7800 kg/m ³
Mass density (B)	2700 kg/m ³
Loss factor (A) and (B)	0.01

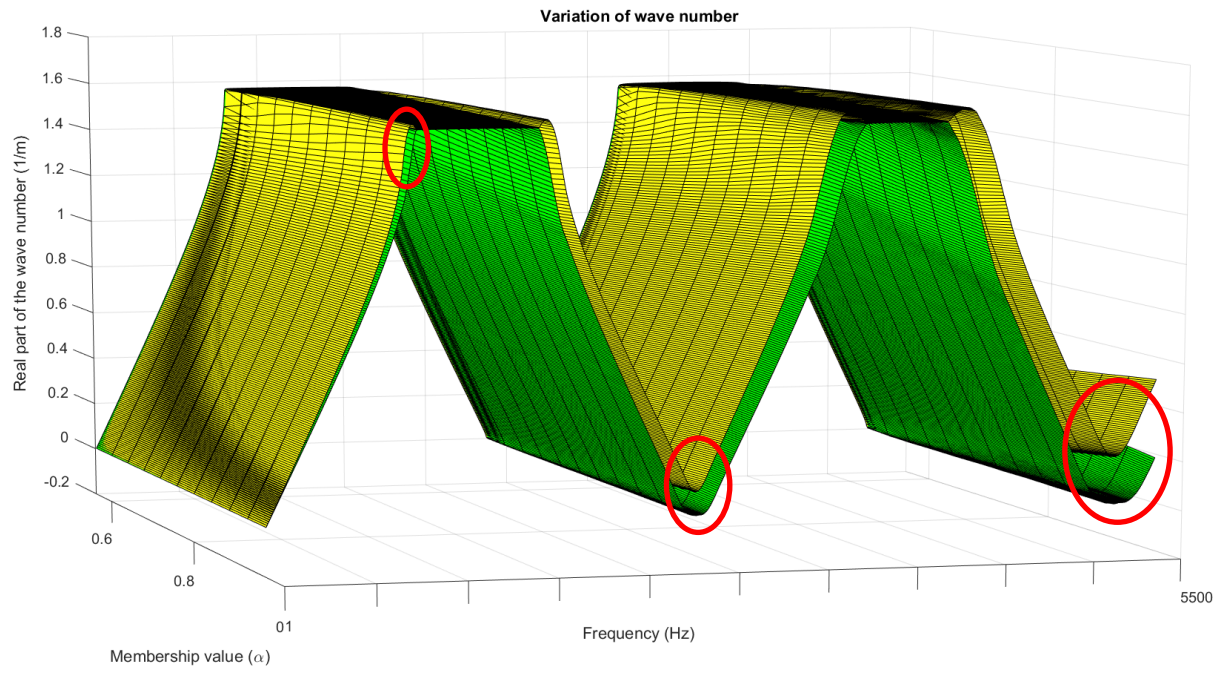


Figure 6: Band gap bound

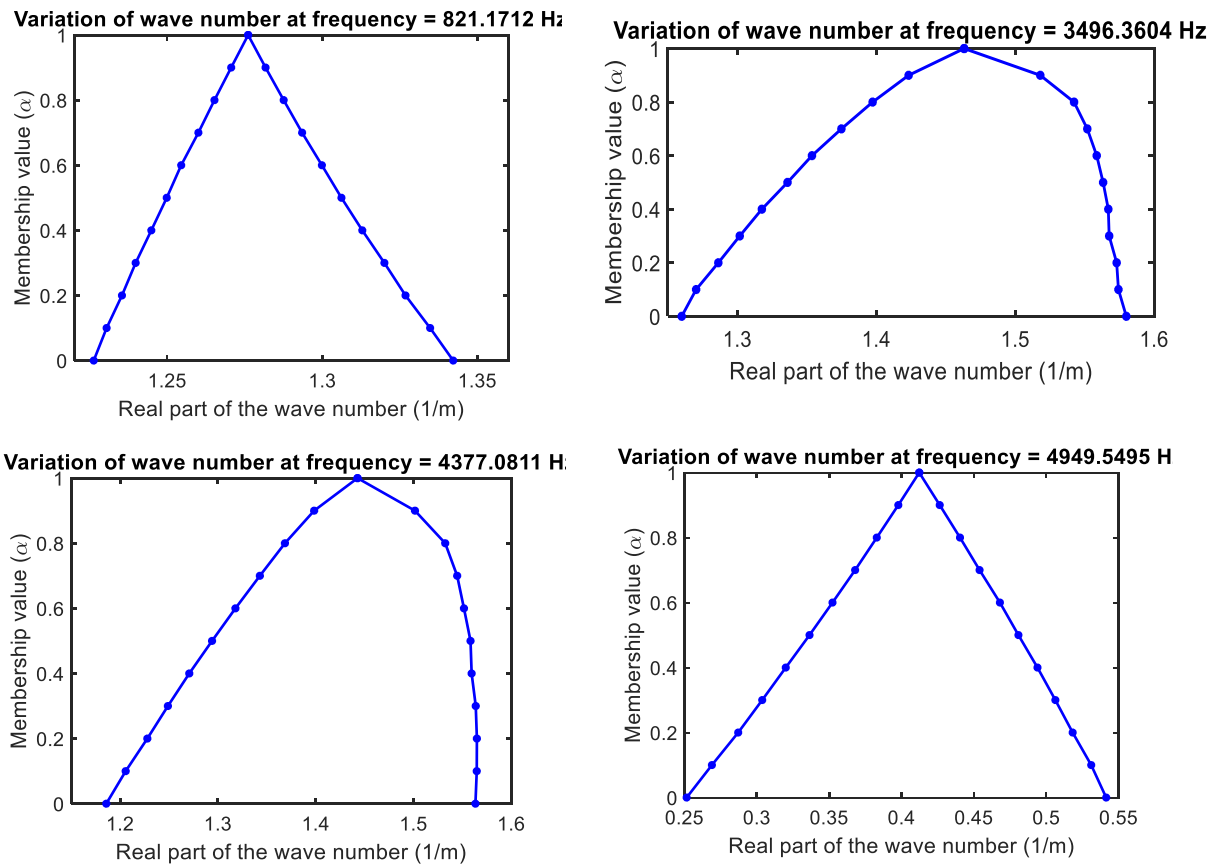


Figure 7: Variation bound of wave number at 11 α -cut level

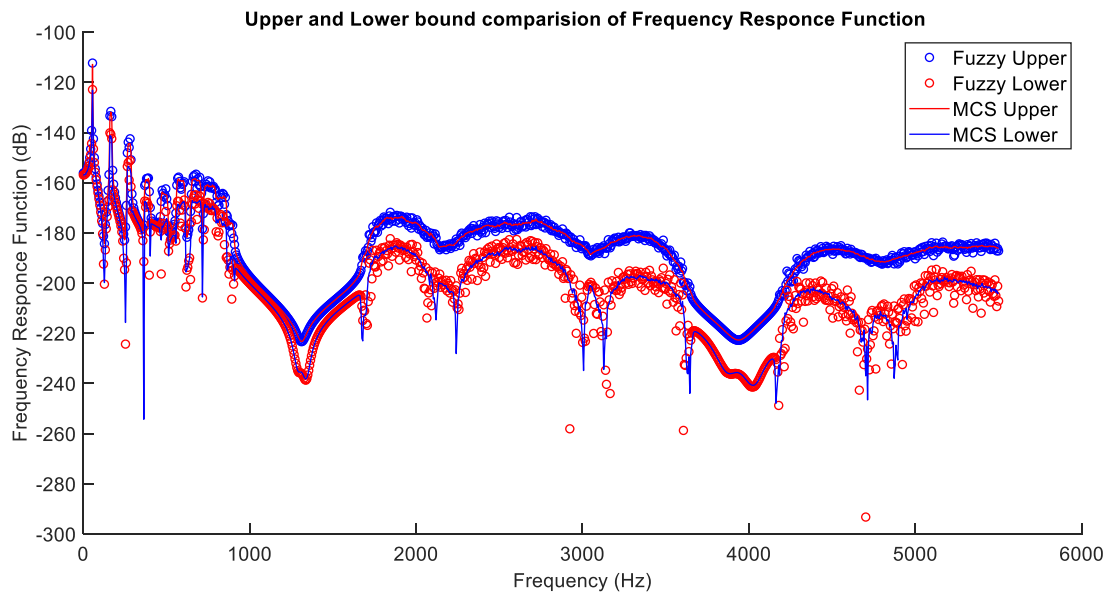


Figure 8: Upper and lower bound comparison of FRF

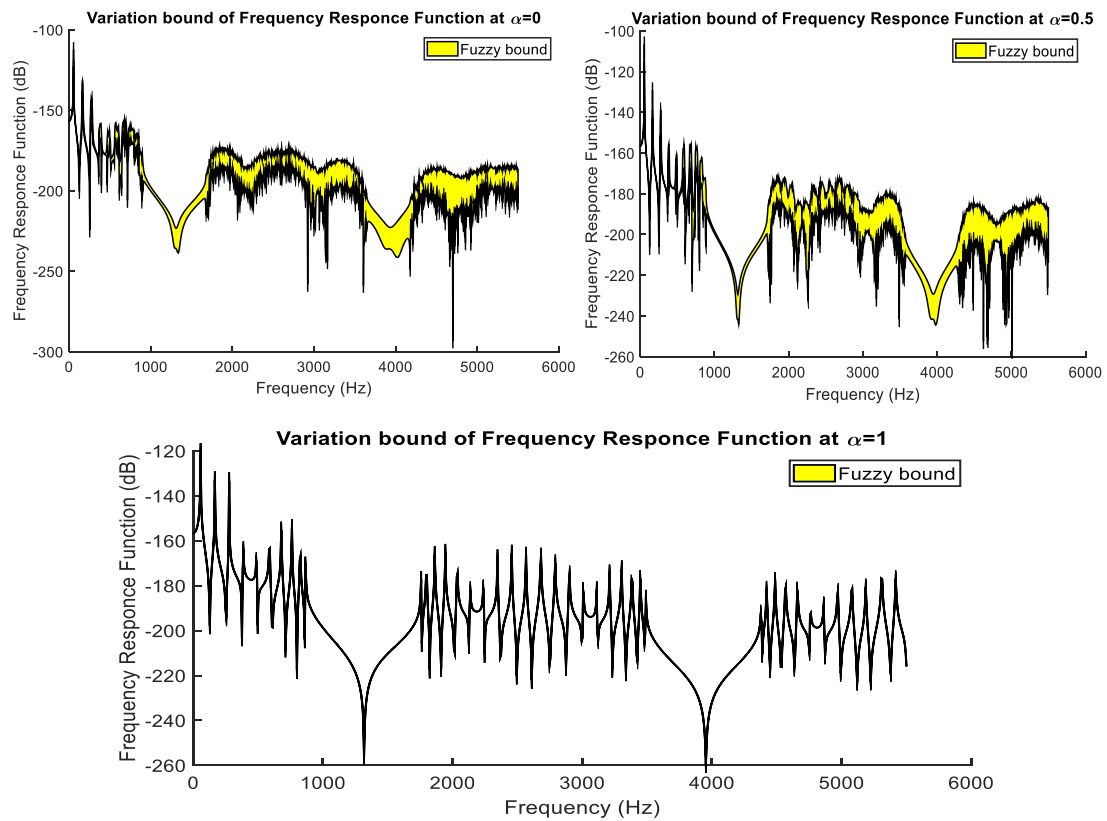


Figure 9: Fuzzy bound of FRF for the different value of α -cut

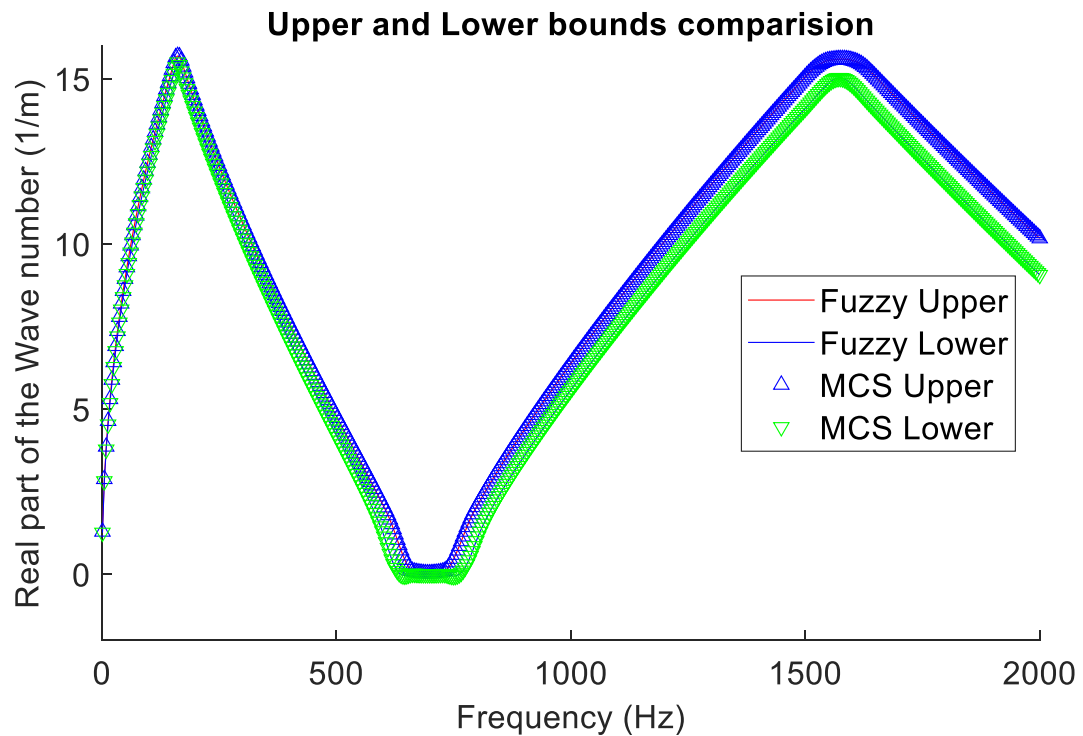


Figure 10: Upper and lower bound comparison

The FRF bound is shown in Fig. 12 representatives the bound at the different α -cut level. As α -cut value increase the fuzzy bound of FRF is expected to decrease. same can be seen from Fig. 13 as the value of membership increase the fuzzy bound is decreasing and lowest at $\alpha=0.9$.

For the computation cost comparison, elapsed time for the MCS and FWFEM obtained using homemade WFEM code which exploits the resources of the workstation with following characteristics, Intel® Core™i7 7820 HQ CPU@2.90GHz with 32 GB RAM and data storage using solid state drive. The comparison is presented in Table 3.

Table 3: Elapsed time comparison

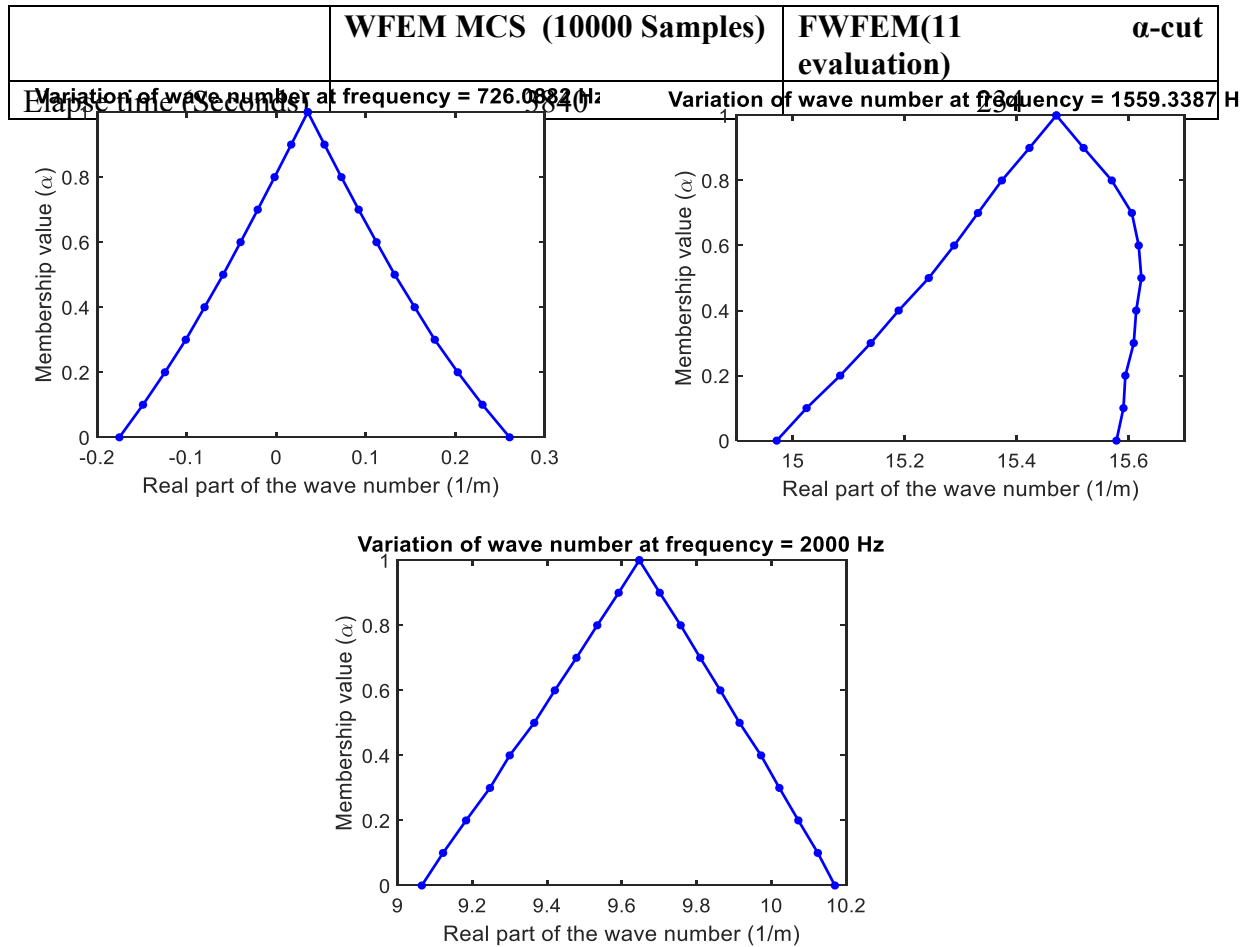


Figure 11: Variation bound of wave number at 11 α -cut level

CONCLUSION

This paper provides a computationally inexpensive possibilistic numerical method for uncertainty propagation in 1D periodic media in conjunction with WFEM. This study proposes a new approach to predict uncertainty bounds of the band gap and FRF of periodic

rod and beam with fuzzy variations. The uncertainty quantification of wave number and frequency response function with fuzzy variables are derived using WFEM.

The approach was presented for very simplified test-cases, but it is found to be more efficient when compared with the conventional MCS approach in terms of computational cost. The present study can be extended for the future investigation for the complex unit cell and a large number of fuzzy variables.

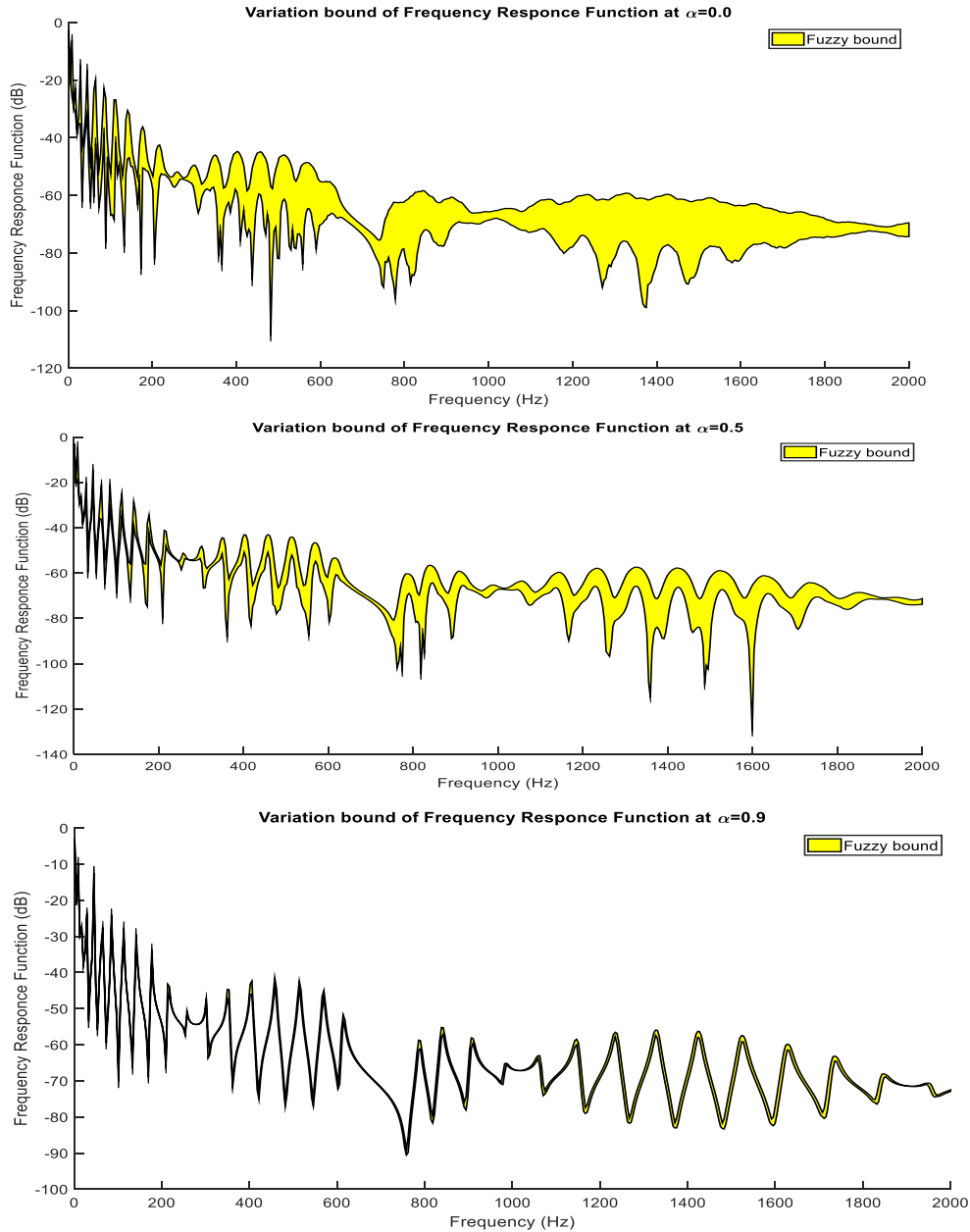


Figure 12: Fuzzy bound of FRF for the different value of alpha-cut

ACKNOWLEDGMENTS

The research of R.P. Singh was funded by an Early Stage Researcher grant within the European Project VIPER Marie Curie European Joint Doctorates (GA 675441).

REFERENCES

- [1] R. P. Singh, C. Droz, S. De Rosa, F. Franco, O. Bareille, and M. N. Ichchou, “A study of structured uncertainties in wave characteristic of one-dimensional periodic structures,” in *International Conference on Noise and Vibration Engineering*, 2018.
- [2] R. P. Singh, S. De Rosa, F. Franco, M. Ichchou, and O. Bareille, “A Literature Review for the Analysis of Structured and Unstructured Uncertainty Effects on Vibroacoustic,” in *MEDYNA 2017: 2nd Euro-Mediterranean Conference on Structural Dynamics and Vibroacoustics*, 2017.
- [3] C. S. Manohar and A. J. Keane, “Axial vibration of a stochastic rod,” *J. Sound Vib.*, (1993) vol. 165, no. 2, pp. 341–359.
- [4] M. N. Ichchou, F. Bouchoucha, M. A. Ben Souf, O. Dessombz, and M. Haddar, “Stochastic wave finite element for random periodic media through first-order perturbation,” *Comput. Methods Appl. Mech. Eng.*, (2011) vol. 200, no. 41–44, pp. 2805–2813.
- [5] F. Bouchoucha, M. N. Ichchou, and M. Haddar, “Stochastic wave finite element method in uncertain elastic media through the second order perturbation,” *J. Appl. Mech. Tech. Phys.*, (2017) vol. 58, no. 2, pp. 362–370.
- [6] Y. Zhao and Y. Zhang, “Symplectic Approach on the Wave Propagation Problem for periodic structures with uncertainty,” *Acta Mech. Solida Sin.*, 2019.
- [7] A. T. Fabro, N. S. Ferguson, T. Jain, R. Halkyard, and B. R. Mace, “Wave propagation in one-dimensional waveguides with slowly varying random spatially correlated variability,” *J. Sound Vib.*, (2015) vol. 343, pp. 20–48.
- [8] A. T. Fabro, N. S. Ferguson, and B. R. Mace, “Wave propagation in slowly varying waveguides using a finite element approach,” *J. Sound Vib.*, (2019) vol. 442, pp. 308–329.
- [9] A. Sarkar and R. Ghanem, “Mid-frequency structural dynamics with parameter uncertainty,” *Comput. Methods Appl. Mech. Eng.*, (2002) vol. 191, no. 47–48, pp. 5499–5513.
- [10] Q. Liu and S. S. Rao, “Fuzzy Finite Element Approach for Analysis of Fiber-Reinforced Laminated Composite Beams,” *AIAA J.*, (2005) vol. 43, no. 3, pp. 651–661.
- [11] G. Quaranta, “Finite element analysis with uncertain probabilities,” *Comput. Methods Appl. Mech. Eng.*, (2011) vol. 200, no. 1–4, pp. 114–129.
- [12] R. P. Singh, “Vibration and Bending Behavior of Laminated Composite Plate With Uncertain Material Properties Using Fuzzy Finite Element Method,” National Institute of Technology Rourkela, India, 2015.
- [13] J. M. Mencik and M. N. Ichchou, “Multi-mode propagation and diffusion in structures through finite elements,” *Eur. J. Mech. A/Solids*, (2005) vol. 24, no. 5, pp. 877–898.

WAVE-DIODE EFFECT EXPLOITING DISCRETELY MODULATED PHONONIC WAVEGUIDES

E. Riva*, G. Cazzulani, J. Marconi, F. Braghin

Department of Mechanical Engineering

Politecnico di Milano

Via La Masa, 1, 20156, Italy

e-mail: emanuele.riva@polimi.it, gabriele.cazzulani@polimi.it

Key words: Acoustic diode, Nonreciprocal wave propagation, Time-varying metamaterials, Bandgap, Plane Wave Expansion Method

Abstract. Space-time varying phononic materials have drawn great interest in the research community, due to their ability to break time reversal symmetry, therefore achieving one-way wave propagation in elastic structures. In analogy with their electric counterparts, these new devices are generally referred as acoustic wave diodes. In this manuscript we study discretely modulated beams, whose spatiotemporal unitary cells are made of sub-cells with time-varying elastic modulus. This new class of materials is able to break the mirror symmetry in the momentum space, which is necessary to achieve the acoustic wave-diode effect. Non-reciprocal Bloch diagram is computed using a generalization of the Plane Wave Expansion Method (PWEM) which can be applied to any modulation that can be written in a space-time Fourier basis. In this context, we show that the frequency spectrum is characterized by full and directional bandgaps, that are linked with the harmonic content of the spatiotemporal unit cell.

1 INTRODUCTION

Phononic crystals (PnCs) and acoustic metamaterials have been widely studied during the past years [1]. The growing interest in this field is motivated by the possibility to manipulate wave propagation in elastic media. That is, PnCs are characterized by spatial periodicity able to generate frequency bands - or bandgaps - in which waves cannot propagate. This feature can be exploited to design acoustic insulators [2], waveguides [3] and super-lenses [4], to name a few.

All these examples comply with the reciprocity principle, which means that waves propagate in the same manner from a point A to B and vice-versa. One possibility to achieve one-way wave propagation is to combine space and time varying material properties, mimicking the propagation of a wave [5, 6, 7, 8]. This new modulation concept is able to break the mirror symmetry in the momentum space, therefore generating bandgaps at different frequencies for left and right traveling waves. Although several works explain how time-space modulated waveguides support one-way wave propagation, there is no efficient and generally accepted method for the computation of the band diagram. Two valid alternatives are finite element Bloch-based method [9] and the *Plane Wave Expansion Method* (PWEM) [10]. If on the one hand the former, based on FEM, can be applied to a wide class of modulations (but to the expenses of computational resources and times), on the other hand the latter, based on PDEs, is faster but limited to plane wave modulations of material properties.

The first goal of this paper is to extend the formulation of the PWEM in order to make it applicable to a more general class of spatiotemporal materials, involving all the possible modulations in space and time. Once this new analysis tool is available, the second target of the work is to exploit the generalized PWEM for the analysis of discretely modulated periodic structures. In this context, we demonstrate that this new class of materials is characterized by full (reciprocal) and directional (non-reciprocal) bandgaps [11]. Specifically, linking the harmonic content of the unit cell to the symmetric and asymmetric parts in the frequency-momentum space.

2 Analytical procedure for band diagram computation

Consider an Euler-Bernoulli beam whose elastic and physical properties are spatially and temporally periodic, such that:

$$\begin{aligned} E(x, t) &= E(x + \lambda_m, t + T_m) \\ \rho(x, t) &= \rho(x + \lambda_m, t + T_m) \end{aligned} \quad (1)$$

where λ_m and T_m are spatial and temporal periods respectively. The governing equation describing longitudinal and transversal wave propagation writes:

$$\begin{aligned} \frac{\partial}{\partial x} \left\{ E(x, t) \frac{\partial u(x, t)}{\partial x} \right\} &= \frac{\partial}{\partial t} \left\{ \rho(x, t) \frac{\partial u(x, t)}{\partial t} \right\} \\ R_g \frac{\partial^2}{\partial x^2} \left\{ E(x, t) \frac{\partial^2 w(x, t)}{\partial x^2} \right\} &= - \frac{\partial}{\partial t} \left\{ \rho(x, t) \frac{\partial w(x, t)}{\partial t} \right\} \end{aligned} \quad (2)$$

being $R_g = J/A$ the radius of gyration and $u(x, t)$, $w(x, t)$ longitudinal and transversal displacement fields. The wave propagation characteristics of the medium can be computed exploiting a generalization of the PWEM. That is, material properties are written in terms of exponential functions:

$$\begin{aligned} E(x, t) &= \sum_{m=-M}^M \sum_{n=-N}^N \hat{E}_{m,n} e^{-j(m\kappa_m x - n\omega_m t)} \\ \rho(x, t) &= \sum_{m=-M}^M \sum_{n=-N}^N \hat{\rho}_{m,n} e^{-j(m\kappa_m x - n\omega_m t)} \end{aligned} \quad (3)$$

where the Fourier coefficients are computed performing a double integration in the time $[-\frac{T_m}{2}, \frac{T_m}{2}]$ and space $[-\frac{\lambda_m}{2}, \frac{\lambda_m}{2}]$ domains:

$$\begin{aligned} \hat{E}_{m,n} &= \frac{1}{T_m} \frac{1}{\lambda_m} \int_{-\frac{\lambda_m}{2}}^{\frac{\lambda_m}{2}} \int_{-\frac{T_m}{2}}^{\frac{T_m}{2}} E(x, t) e^{j(m\kappa_m x - n\omega_m t)} dx dt \\ \hat{\rho}_{m,n} &= \frac{1}{T_m} \frac{1}{\lambda_m} \int_{-\frac{\lambda_m}{2}}^{\frac{\lambda_m}{2}} \int_{-\frac{T_m}{2}}^{\frac{T_m}{2}} \rho(x, t) e^{j(m\kappa_m x - n\omega_m t)} dx dt \end{aligned} \quad (4)$$

The wave solution is therefore sought with the same associated periodicity, thus:

$$\begin{aligned} u(x, t) &= \sum_{p=-P}^P \sum_{q=-Q}^Q \hat{U}_{p,q} e^{j(p\kappa_m x - q\omega_m t)} e^{j(\kappa x - \omega t)} \\ w(x, t) &= \sum_{p=-P}^P \sum_{q=-Q}^Q \hat{W}_{p,q} e^{j(p\kappa_m x - q\omega_m t)} e^{j(\kappa x - \omega t)} \end{aligned} \quad (5)$$

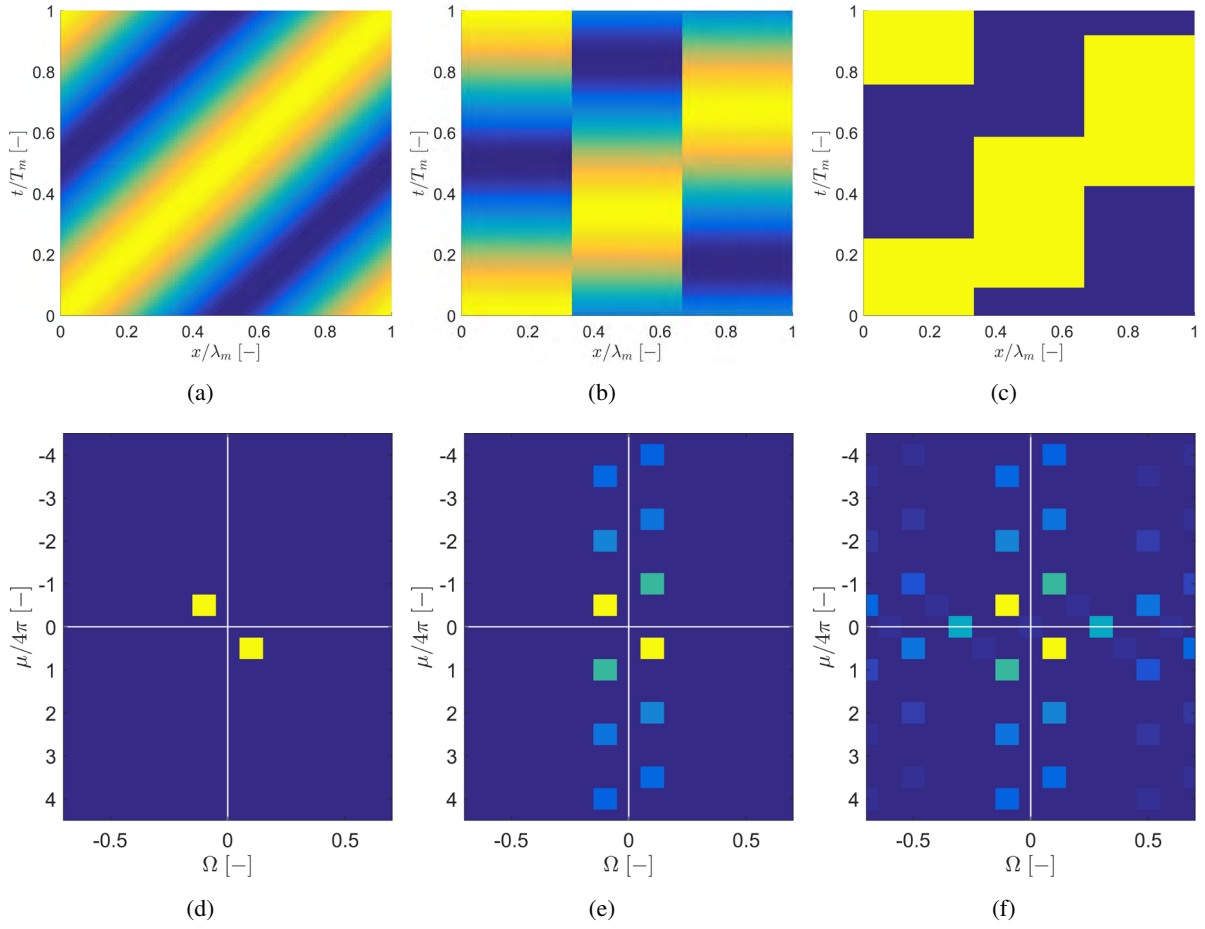


Figure 1: Plane Wave modulation 1(a) and corresponding 2D Fourier transform 1(d) in the wavenumber-frequency $\mu - \Omega$ plane. Here $\mu = \kappa\lambda_m$ and $\Omega = f\lambda_m/c_0$ are dimensionless quantities. Spatially discrete and temporally continuous unit cell 1(b) and associated spectral content 1(e), which includes more wavenumber components compared to plane wave modulation. Fully discrete space-time modulation 1(c) and 1(f). The spectral content is characterized by multiple wave components, which propagate along different directions.

Merging Eqs. 2-5 and enforcing orthogonality of exponential functions, the dispersion relation $\omega = \omega(\kappa)$ yields:

$$\begin{aligned} (\tilde{\mathcal{L}}_0^u(\kappa) + \tilde{\mathcal{L}}_1(\kappa)\omega + \tilde{\mathcal{L}}_2(\kappa)\omega^2) \tilde{\mathbf{u}} &= 0 \\ (\tilde{\mathcal{L}}_0^w(\kappa) + \tilde{\mathcal{L}}_1(\kappa)\omega + \tilde{\mathcal{L}}_2(\kappa)\omega^2) \tilde{\mathbf{w}} &= 0 \end{aligned} \quad (6)$$

which is a Quadratic Eigenvalue Problem (QEP) of size $\gamma = (2P + 1)(2Q + 1)$ being P, Q the Fourier series truncation orders.

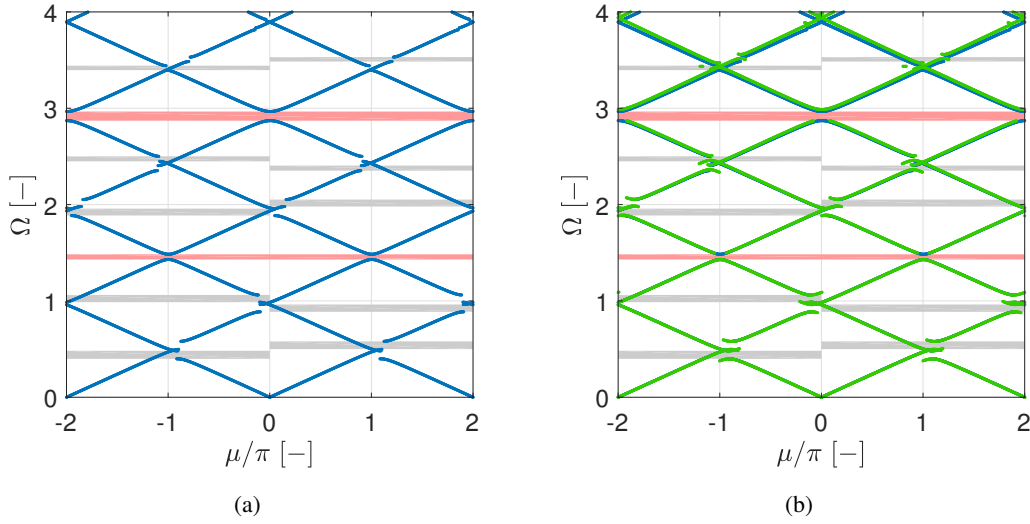


Figure 2: Bloch diagram for spatially discrete and temporally continuous unit cell 2(a) and comparison between generalized PWEM (blue line) and FE Bloch procedure (green line) 2(b). $\mu = \kappa\lambda_m$ and $\Omega = \omega\lambda_m/2\pi c_0$ are the dimensionless wavenumber and frequency respectively. Directional and full gaps are highlighted with colored bands.

3 Wave propagation in discretely modulated beams

Consider the longitudinal wave propagation problem in a discretely modulated beam, whose elasticity comply the following law:

$$E(x, t) = E_0 \left\{ 1 + \alpha_m \cos \left[-\omega_m t + (k(x) - 1) \frac{2\pi}{R_s} \right] \right\} \quad k(x) = \begin{cases} 1 & \text{if } 0 \leq x < \frac{\lambda_m}{R_s} \\ 2 & \text{if } \frac{\lambda_m}{R_s} \leq x < \frac{2\lambda_m}{R_s} \\ \dots & \\ R_s & \text{if } \frac{(R_s - 1)\lambda_m}{R_s} \leq x < \lambda_m \end{cases} \quad (7)$$

that is, spatially discrete and temporally continuous function. E_0 is the mean Young's Modulus value, α_m is the dimensionless modulation amplitude, R_s is the number of sub-elements constituting the spatio-temporal unit cell ($\alpha_m = 0.4$ and $R_s = 3$ in the remainder of this section). $v = \omega_m t / (\kappa_m c_0)$ is the dimensionless modulation speed which is set to 0.1 and $c_0 = \sqrt{E_0/\rho}$. The elasticity profile is represented in Figure 1 and compared with plane wave and fully discrete modulations, in terms of time-space and frequency-wavenumber domains. It is worth mentioning that discrete modulation is characterized by more spectral components having different propagation speed and direction. Specifically, one space-time harmonic for plane wave modulations and more components for discrete profiles.

The corresponding filtered ¹ dispersion relation (blue line) is represented in Fig. 2 which shows good agreement with the FE-based method (green line) described in Ref. [9]. Interestingly, the frequency spectrum is characterized by many directional gaps as the number of spatiotemporal harmonics owned by the unit cell Fourier decomposition in Fig. 1(e). Indeed, directional bandgap and unit cell spectral content share same periodicity, suggesting a direct relationship between them. The interaction between

¹i.e. only the leading component of the dispersion branches is plotted

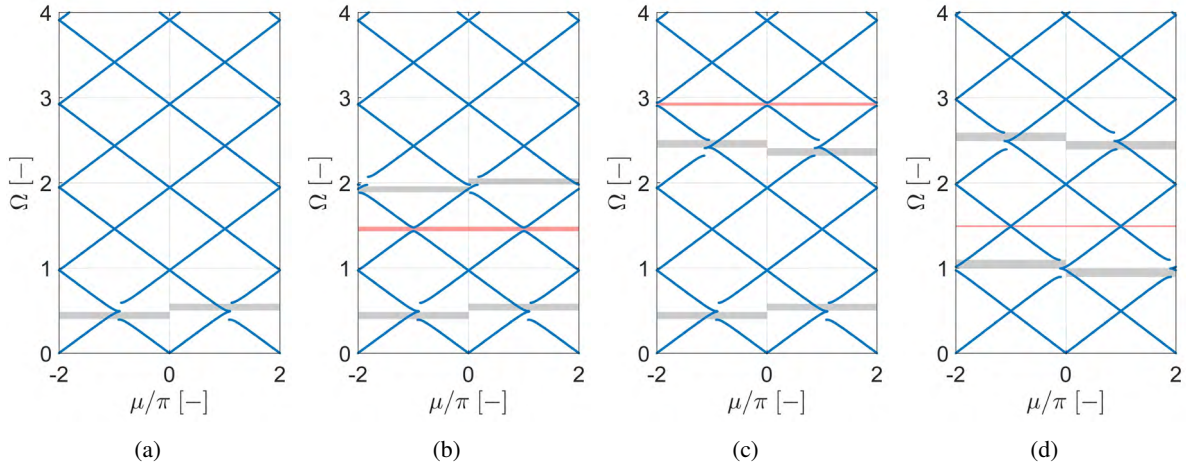


Figure 3: Filtered Bloch diagram for a plane wave modulation (1st harmonic only) 3(a). As a result, only a pair of directional gaps is supported by the media. Bloch diagram for a modulation given by the superposition of 1st and 4th unit cell spectral components 3(b). In addition to the first bandgap pair, full and directional gaps are present in the frequency domain. 1st and 5th 3(c). 2st and 5th 3(d).

spectral components - instead - generates full gaps at given frequencies. This is confirmed upon evaluation of the band diagram associated with a unit cell characterized by two plane wave components picked up from Fig 1(e). The result is shown in Fig. 3. When the unit cell is characterized by the first and fourth harmonics (both negative traveling pump waves), one gets two directional gaps at $\Omega = 0.5$ and $\Omega = 2$, plus one full gap centered at $\Omega = 1.5$, as shown in Fig. 3(b). Similar behavior is observed for the remaining pairs: first and fifth harmonics (which have negative and positive velocity sign respectively) generate first and fifth gaps, which are flipped to each others, see Fig 3(c) and one full gap for $\Omega = 3$.

4 Conclusion

In this work we presented a generalization of the PWEM which allows to study a wider class of spatiotemporal material. This new analysis tool has been exploited to study wave propagation in discretely modulated waveguides, demonstrating that this class of materials support one-way wave propagation at bandgap frequencies. Moreover, we demonstrated that the unit cell spectral content can be decomposed in plane waves, responsible for the generation of directional gaps. Their interaction instead lead to the formation of full bandgaps.

REFERENCES

- [1] Hussein, M. I., Leamy, M. J., Ruzzene, M. (2014). *Dynamics of phononic materials and structures: Historical origins, recent progress, and future outlook*. Applied Mechanics Reviews, **66**(4), 040802.
- [2] D'Alessandro, L., Zega, V., Ardito, R., Corigliano, A. (2018). *3D auxetic single material periodic structure with ultra-wide tunable bandgap*. Scientific reports, **8**(1), 2262.
- [3] Riva, E., Quadrelli, D. E., Cazzulani, G., Braghin, F. (2018). *Tunable in-plane topologically protected edge waves in continuum Kagome lattices*. Journal of Applied Physics, **124**(16), 164903.
- [4] Tol, S., Degertekin, F. L., Erturk, A. (2016). *Gradient-index phononic crystal lens-based enhancement of elastic wave energy harvesting*. Applied Physics Letters, **109**(6), 063902.

- [5] N. Chamanara, S. Taravati, Z.-L. Deck-Leger, C. Caloz, *Optical isolation based on space-time engineered asymmetric photonic band gaps*. Physical Review B **96** (10) (2017) 104110.
- [6] Nassar, H., Chen, H., Norris, A. N., Haberman, M. R., Huang, G. L., *Non-reciprocal wave propagation in modulated elastic metamaterials*. Proc. R. Soc. A **473**(2202), 20170188.
- [7] K. Yi, M. Collet, S. Karkar, *Frequency conversion induced by time-space modulated media*. Physical review B **96** (10) (2017) 104110.
- [8] M. Attarzadeh, M. Nouh, *Non-reciprocal elastic wave propagation in 2d phononic membranes with spatiotemporally varying material properties*. Journal of Sound and Vibration **422** (2018) 264-277.
- [9] J. Vila, R. K. Pal, M. Ruzzene, G. Trainiti, *A bloch-based procedure for dispersion analysis of lattices with periodic time-varying properties*. Journal of Sound and Vibration **406** (2017) 363-377.
- [10] G. Trainiti, M. Ruzzene, *Non-reciprocal elastic wave propagation in spatiotemporal periodic structures*. New Journal of Physics **18** (8) (2016) 083047.
- [11] Marconi, J., Cazzulani, G., Riva, E., Braghin, F. (2018). *Observations on the behavior of discretely modulated spatiotemporal periodic structures*. In Active and Passive Smart Structures and Integrated Systems XII (Vol. 10595, p. 105952N). International Society for Optics and Photonics.

COMPOSITE PLATE AUTOMATIC DAMAGE ISOLATION BASED ON SUPPORT VECTOR MACHINE CLASSIFICATION OF LAMB WAVE SIGNALS

Renan B. M. Santos^{*}, Pablo R. Souza[†], Nilson R. Inocente-Junior^{*} and Euripedes G. O. Nobrega^{*}

^{*}State University of Campinas (Unicamp)
Faculty of Mechanical Engineering, Computational Mechanics Department, Campinas, Sao Paulo,
Brazil
e-mail: eng.santosrenan@gmail.com and egon@fem.unicamp.br

[†] Federal Institute of Sao Paulo (IFSP)
Campus Piracicaba, Piracicaba, Sao Paulo, Brazil
e-mail: pablo@ifsp.edu.br

^{*} Federal Institute of Sao Paulo (IFSP)
Campus Salto, Salto, Sao Paulo, Brazil
e-mail: inocente@ifsp.edu.br

Key words: Artificial Intelligence, Machine Learning, Structural Health Monitoring, Support Vector Machine, Support Vector Classifier

Abstract. Artificial intelligence methods have been successfully used to solve complex problems in a wide variety of engineering fields. Support Vector Machine (SVM) is recognized as a reliable and efficient tool among current machine learning techniques, and is here adopted to automatize a Structural Health Monitoring (SHM) method aiming to detect and isolate the onset of damage. In a supervised learning approach, an experimental dataset is used to train the SVM algorithm so it would be able to predict the structural integrity of a target by means of new input data obtained during the inspection phase. A Lamb wave based effective monitoring uses the pitch-catch approach to generate the signals, and the SVM algorithm assesses the structures' integrity. The inspection is performed by means of an arrangement of piezoelectric transducers forming a circular array of eight sensors with a centered actuator, dividing the monitored area into eight regions. Damage presence causes waves scattering, which influences the amplitude of the measured signals, which differs from its respective regular behaviour. Discrete wavelet and Hilbert transform are applied to the raw signals in order to minimize noise and dispersion effects, and to propitiate clear damage indicators. Processed peak amplitudes from each of the eight signals are used as attribute axis for an eight-dimension SVM algorithm based on a Gaussian Radial Basis Function (RBF) kernel. Using a punctual mass placed on different positions inside the plate regions to simulate damage, a set of labeled measurements is obtained in order to train and test the SVM algorithm. Posterior experimental application of the classifier shows its effectiveness to automatically isolate the respective a damaged region.

1 INTRODUCTION

SHM systems aim at the continuous monitoring of structure areas prone to damage in order to detect, isolate and assess the severity of the damaged region. In this way, it is possible to repair or replace parts of the structure before any type of fault occurs. One has applied composite materials in a wide range of engineering systems, such as aircraft, automobiles and trains, due to their durability, strength and low density. This type of material may have defects inherent to their manufacturing process, such as delamination and voids, or damage like chemical corrosion and cracks that may arise during its use. Thus, many research has been conducted to develop reliable SHM systems to assess the integrity of structural parts made of composite material. Non-destructive evaluating (NDE) techniques are a key part in SHM systems. One of the most used approaches to assess the integrity of structures is through the Lamb waves propagation. These waves can be generated and received using piezoelectric transducers, which may be installed temporarily or permanently in the structure to be monitored. The information about the presence of damage, its location and its severity can be obtained by analyzing the parameters of the reflected and transmitted waves resulting from the interaction between the incident wave and the damage. Wang et al.[1] investigated the behavior of a glass fiber reinforced epoxy composite laminate plate subjected to damage like chemical corrosion, impact hole and crack, using Lamb waves to inspect and Gaussian Mixture Model to classify such kinds of damages. Huang et al.[2] used the time reversal method to detect impact damage on CFRP plate. An image of the plate showing the damage location was built using damage indexes based on the deviation between the reconstructed and the excitation signals.

Lamb waves propagation in composites exhibit a complex behavior, due to anisotropic properties and inhomogeneous composition of these materials. In order to properly evaluate structural integrity, some type of intelligence is necessary to analyze the extracted parameters of the signals obtained from the NDE technique applied. Recently, a new approach has been developed, with the use of artificial intelligence to automate the diagnosis of the structure. There are various artificial intelligence techniques, such as neural networks, fuzzy logic, deep learning, pattern recognition, machine learning. Among data driven techniques, machine learning has shown great potential to increase efficiency of SHM systems. This AI branch deals with the design of algorithms that can learn about the structural behavior from data and make predictions from learned data[3]. In the supervised learning approach, the model is built using samples that represent classes, and future inputs will be classified in one of them. Otherwise, in an unsupervised learning model, the objective is to cluster samples from the dataset that exhibits a high level of proximity. There is no labels for samples from the dataset. SVM is a suitable supervised machine learning technique to classify data. Gangsar and Tiwari[4] developed a methodology to classify ten different fault conditions of induction motors using SVM.

This paper proposes an effective methodology based on Lamb waves and support vector machine algorithm to assess the integrity of a composite plate. The inspection is performed by means of an arrangement of piezoelectric transducers forming a circular array of eight sensors with a centered actuator, dividing the monitored area into eight regions. Discrete wavelet and Hilbert transform are applied to the raw signals in order to minimize noise and dispersion effects as well as to improve the peak amplitude estimation. Damage indexes obtained from the acquired data are used as input to an eight-dimension SVM algorithm based on a grid search function to determine the best kernel and optimum kernel's parameters.

2 STRUCTURAL ASSESSMENT

Lamb waves have been widely used on non-destructive evaluation techniques to assess the structural integrity on SHM systems [5]. Piezoelectric transducers attached to the structure under inspection, generate and measure these waves. Information about the presence of damage, its location and its severity

are obtained by analysing the parameters of the reflected and transmitted waves resulting from the interaction between the incident wave and the damage. There are two methods for using Lamb waves to detect damage, known as pitch-catch and pulse-echo [6]. The simplest pitch-catch approach uses at least two transducers to inspect the region between them, as illustrated in Figure 1. It is seen in this figure an actuator and a sensor, both piezoelectric patch, where the actuator generates a burst signal captured by the sensor, which incorporates the medium characteristics. Damage onset on this region causes scattering of the waves, which modifies some measured signal parameters. Comparison between a known signature of the healthy structure and an recently measured signal may conduct to detection and identification of damage. Figure 2 shows how the signal may be affected by damage localized between the sensor and actuator. In this case, signal amplitudes measured by the sensor decreases due to attenuation of incoming wave on the damage. A different change of parameters may also occur if the damage is not in the direct line between the transducers.

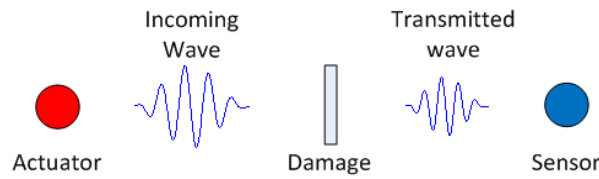


Figure 1: Positioning of transducers to the pitch-catch approach

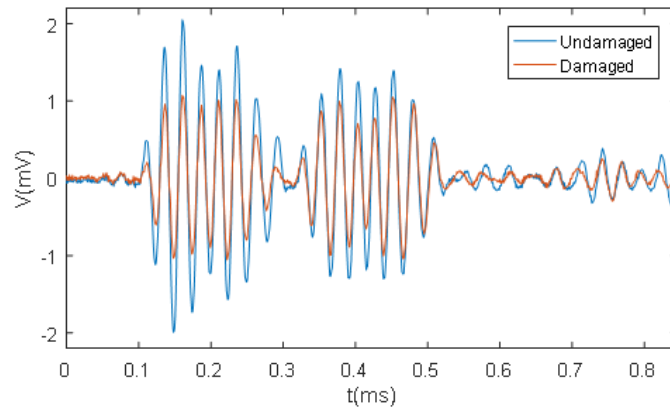


Figure 2: Acquired signals using the pitch-catch approach for damage and undamaged cases

Signals from the measuring system need to be processed by specific algorithms to separate information from noise, regular reflections and other interferences in the system. The wavelet transform is a signal processing technique used to represent signal features in time and frequency domains simultaneously. It has the ability to detect aperiodic short-time events, unlike the Fourier transform which is particularly useful for the analysis of periodic signals. These transient events are detected through the similarity between its shape in time domain and a waveform known as mother wavelet. This approach fits well to analyze non-stationary signals, because its spectral components vary along time. The propagation of Lamb waves is an example of signal with punctual occurrences. Mallat [7] presented an efficient method to implement the wavelet transform in discrete time, through multi-resolution analysis and digital

filter banks. This theory relates the Discrete Wavelet Transform (DWT) with a filter bank composed by high and low pass quadrature mirrored filters, through which the signal is decomposed into details and approximations. The approximation is obtained as the output of the low pass filter and is related to the smoothed signal. The output of the high pass filter provides the details of the signal, related to transient events contained in the signal. Figure 3(a) shows the layout of the filter bank, composed by high pass filter (H1) and low pass filter (H0), for two levels of resolution.

The symbol $\downarrow 2$ represents a down-sampling or decimation of the filtered signal. Each decomposition level separates the spectral components at frequency bands, which depends of the sampling frequency (f_s) of the signal acquired. Figure 3(b) shows the frequency response of high and low pass ideal filters for two level decomposition DWT.

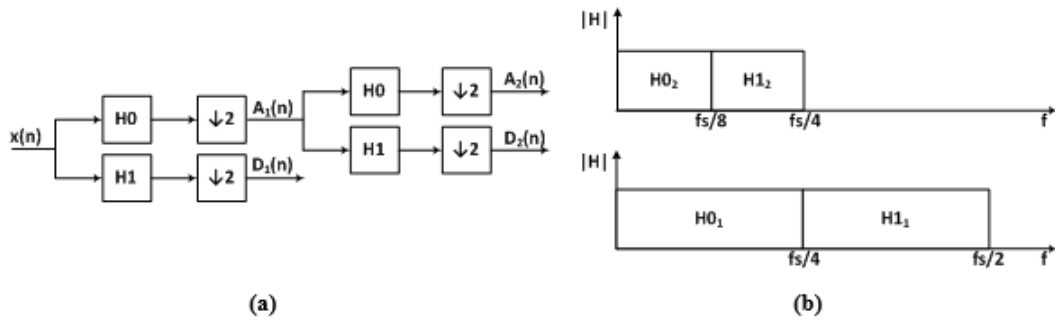


Figure 3: Two level analysis filter bank for DWT and frequency range of high and low pass filters

Higher frequency signal components are located at lower level details. Analysing the decomposed signal into several details provides information that could be hidden in the original signal, probably masked by noise from the measurement system. Considering a tone burst containing five cycles of a 40 kHz sine wave multiplied by a Hanning window applied to the actuator to excite Lamb waves at structure, the main component of the signal measured by sensors with a sample rate of 1,21MHz corresponds to the fourth level detail coefficients of DWT.

Hilbert transform can be used to highlight some specific points of the processed signal, for example, the amplitude and the instants that peaks occurs. This signal processing technique creates an analytical signal from a real signal[8]. The absolute value of the analytical signal corresponds to signal envelop.

In order to illustrate the effect of applying these signal processing techniques, Figure 4 shows the raw signal measured by a sensor, the detail coefficients of fourth level of its DWT with the mother wavelet Daubechies 40 and its envelop. It clearly minimizes the noise and eliminates the continuous voltage level present in the measurement system, enhancing the desired signal attributes. The peak amplitude and the instant they occur are much more evident on the signal envelop. These parameters can be used to monitor the integrity of the structure.

As shown in Figure 5, the onset of damage changes envelop peak amplitudes of signal measured by the sensor. Thus, a damage index (DI) could be defined by the percentage difference between peak amplitudes of the processed signals obtained from the healthy structure (A_h) and the damaged structure (A_d), given by:

$$DI\% = \frac{A_h - A_d}{A_h} * 100 \quad (1)$$

According to Equation (1), a decrease on the signal amplitude results in a positive DI. On the other hand, a negative DI indicates an increase on the signal amplitude.

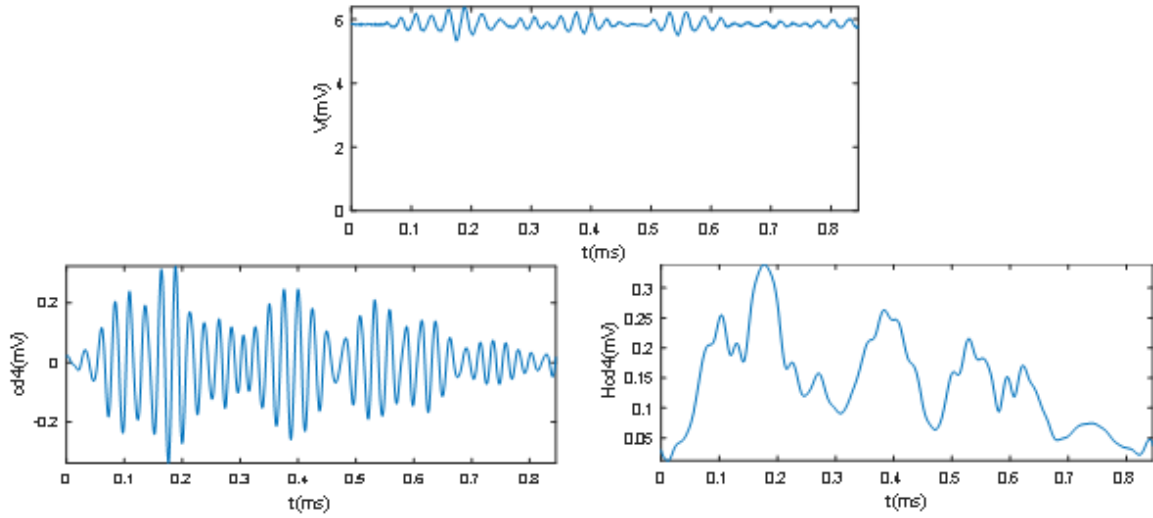


Figure 4: Raw signal measured by a sensor, DWT detail coefficients (cd4) and Hilbert transform (Hcd4)

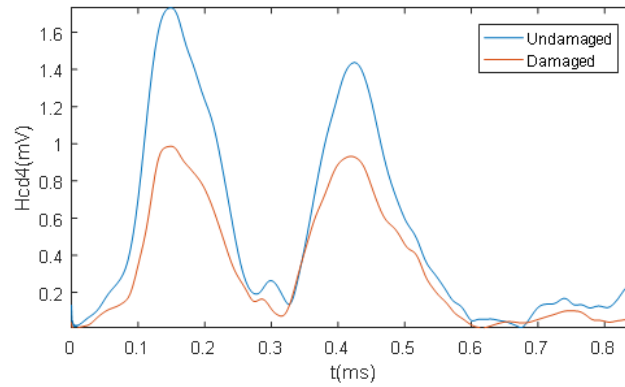


Figure 5: DWTs envelops coefficients of measured signals for an undamaged and a damaged structure

3 SUPPORT VECTOR MACHINE

3.1 The optimal hyperplane (linear SVM)

This section describes basic SVM concepts that can be found in [9], [10] and [11].

Having in hands a training set of instance-label pairs $(x_i, y_i), i = 1, 2, \dots, m$ where $x_i \in R^n$ and $y_i = +1, -1$, for the linearly separable case, a correct data points classification is given by:

$$\langle w \cdot x_i \rangle + b \geq +1 \quad \text{for } y_i = +1 \quad (2)$$

$$\langle w \cdot x_i \rangle + b \leq -1 \quad \text{for } y_i = -1 \quad (3)$$

One set of inequalities can be achieved combining Equations (2) and (3) .

$$y_i(\langle w \cdot x_i \rangle + b) \geq 1 \quad \forall i = 1, \dots, m \quad (4)$$

Solving the following optimization problem leads to the hyperplane with the maximum margin:

$$\text{Min}_{(w, b)} \frac{1}{2} w^T w \quad \text{subject to : } y_i(\langle w \cdot x_i \rangle + b) \geq 1 \quad (5)$$

To solve this problem one must find the saddle point of the Lagrange function:

$$L_p(w, b, a) = \frac{1}{2}w^T \cdot - \sum_{i=1}^m (\alpha_i y_i (\langle w, x_i \rangle + b) - 1) \quad (6)$$

On Equation (6) α_i represents the Lagrange multipliers, hence $\alpha_i \geq 0$. An optimal saddle point is needed because the L_p must be minimized with respect to the primal variables w and b and maximized with respect to the non-negative dual variable α_i . By differentiating L_p with respect to w and b :

$$\frac{\partial}{\partial b} = 0, w = \sum_{i=1}^m \alpha_i y_i \quad (7)$$

$$\frac{\partial}{\partial b} = 0, \sum_{i=1}^m \alpha_i y_i = 0 \quad (8)$$

The Karush KuhnTucker (KKT) conditions for the optimum constrained function are necessary and sufficient for a maximum of Equation (6). The corresponding KKT complementarity conditions are:

$$\alpha_i [y_i (\langle w, x_i \rangle + b) - 1] = 0 \quad \forall i \quad (9)$$

Substituting Equations (7) and (8) into (6), then L_p is transformed to the dual Lagrangian $L_D(\alpha)$:

$$\text{Min}_{\alpha} L_D(\alpha) = \sum_{i=1}^m (\alpha_i \alpha_j y_i y_j \langle x_i, x_j \rangle) \text{ Subject to : } \alpha_i \geq 0 \quad i = 1, \dots, m \text{ and } \sum_{i=1}^m (\alpha_i y_i) \quad (10)$$

The $L_D(\alpha)$ must be maximized with respect to non-negative α_i to find the optimal hyperplane. In order to determinate the dual optimization problem parameters w^* and b^* of the optimal hyperplane, one must find the solution α_i . Finally, we obtain an optimal decision hyperplane $f(x, \alpha^*, b^*)$ Equation (11) and an indicator decision function $\text{sign} [f(x, \alpha^*, b^*)]$.

$$f(x, \alpha^*, b^*) = \sum_{i=1}^m [(\alpha_i^* y_i (\langle x_i, x \rangle + b^*)) = \sum_{(i \in sv)}^m \alpha_i^* y_i (\langle x_i, x \rangle + b^*) \quad (11)$$

Only small subsets of the Lagrange multipliers α_i usually tend to be greater than zero in a typical classification task. These vectors are the closest to the optimal hyperplane, regarding geometrically aspects. The support vectors are the respective training vectors having nonzero α_i , given that the optimal decision hyperplane $f(x, \alpha^*, b^*)$ depends on them exclusively.

3.2 Non-linear SVM

For a higher dimensional problem, the nonlinear SVM maps the training samples via a mapping function, which are also called kernel function. In the dual Lagrange (Equation (10)), the kernel function (Equation (12)) replaces the inner products, and the non-linear SVM dual Lagrangian $L_D(\alpha)$ (Equation (13)) is similar with that in the linear generalized case.

$$(\Phi(x_i) \cdot \Phi(x_j)) = k(x_i, x_j) \quad (12)$$

$$L_D(\alpha) = \sum_{i=1}^m \alpha_i - \frac{1}{2} \sum_{i=1}^m \alpha_i \alpha_j y_i y_j (x_i, x_j) \quad (13)$$

Subject to: $0 \leq \alpha_i \leq C$, $i = 1, \dots, m$ and $\sum_{i=1}^m \alpha_i y_i = 0$

Using the method for solving the optimization in the separable case, one can solve this optimization model. Thus, the optimal hyperplane takes the form Equation (15). Including the bias term within the kernel function, the nonlinear SV classifier can be shown as Equation (16).

$$f(x, \alpha^*, b^*) = \sum_{i=1}^m y_i \alpha_i^* \langle \Phi(x_i), \Phi(x) \rangle + b^* \quad (14)$$

$$f(x, \alpha^*, b^*) = \sum_{i=1}^m y_i \alpha_i^* k(x_i, x) + b^* \quad (15)$$

$$f(x, \alpha^*, b^*) = \sum_{i=1}^m y_i \alpha_i^* \langle \Phi(x_i), \Phi(x) \rangle = \sum_{i=1}^m y_i \alpha_i^* k(x_i, x) \quad (16)$$

Some kernel functions include polynomial, radial basis function (RBF) and sigmoid kernel [12], which are represented by the functions Equations (17), (18), and (19). In order to improve the accuracy of the classification, these kernel parameters in the kernel functions should be properly set.

$$\text{Polynomial kernel: } k(x_i, x_j) = (1 + x_i \cdot x_j)^d \text{ where: } d = \text{polynomial degree} \quad (17)$$

$$\text{Radial Basis Function (RBF): } k(x_i, x_j) = \exp(-\gamma \|x_i - x_j\|^2) \quad (18)$$

$$\text{Sigmoid function: } k(x_i, x_j) = \tanh(k \cdot x_i \cdot x_j - \delta) \quad (19)$$

4 EXPERIMENTAL PROCEDURE

The experiments were conducted on a carbon fiber square plate of 300 mm x 300 mm x 1 mm to experimentally assess structural integrity. The experimental setup, shown in Figure 6 consists of nine circular buzzers of 20 mm diameter forming a circular arrangement with a centered actuator with 100mm radius. A Labview[®] instrumentation system were developed to apply a tone burst containing five cycles of a 40 kHz sine wave, multiplied by a Hanning window, to the central actuator. This system was also used to acquire the signals measured by the eight sensors, with a sample frequency of 1.2 MHz. Raw data were processed and analyzed using MatLab[®]. Mother wavelet Daubechies 10 was adopted in the DWT for all signals and the detail coefficients of fourth level corresponds to the Lamb wave propagation. A pair of magnetic cubes with 5x5x5 mm were used to obtain a punctual mass change on the plate, which may represent damage. This artificial damage was placed randomly within a monitored region to demonstrate the ability to isolate the damaged region inside the circular area, with each region tested separately.

Damage indexes extracted from the processed signals were used as input for a nine-dimension SVM algorithm implemented in Python using *sklearn* package [13]. The algorithm parameters were chosen using a technique called grid search. It tests the algorithm implementation with different values for the function parameters. The parameters tested were:

- Kernel Trick: RBF, Polynomial and Sigmoid;
- C-Parameter: a range from 1e-3 to 1e3;
- Gamma-Parameter: a range from 1e-7 to 1e3.

In this set up, several experiments were made using different combinations of parameters and, with every test made, the closer it was getting from the optimum combination.

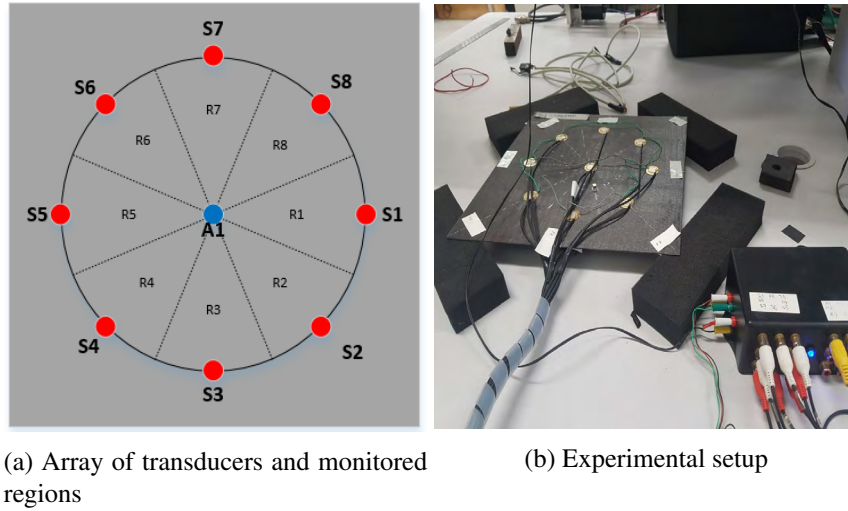


Figure 6: Plate's disposition of transducers and experimental setup

To reduce the variance problem, it was also used the K fold cross validation technique, with K equal to 5. In this technique, the data is divided in K-folds. Out of K folds, K-1 sets are used for training while the last set is used for testing. The algorithm is trained and tested K times and, with every loop, a new set is used as testing set while the others are used as training. The results obtained by the K fold cross validation technique is the average of the results obtained by each set.

For better understanding, Figure 7 shows a block diagram that visually explains the technique.

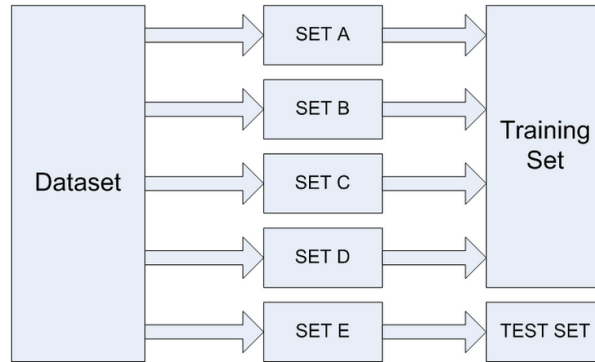


Figure 7: First instance of the 5-fold cross validation technique

The dataset was divided into 5 sets. The algorithm is trained and tested 5 times. In the first instance, SET A to SET D were used as training sets and SET E was used as testing set. The second instance used SET A as testing set while the remaining sets were used as training. The process continues until every set is used as testing set and as training set at least once.

Finally, the best results were optimized utilizing the RBF kernel, C-parameter value of 127 and gamma-parameter value of $3e-3$.

The experimentally gathered dataset was compounded by 900 measurements divided equally by all the 9 SVM algorithm classes, being R1 to R8 for damaged regions and R0 for the healthy structure

class. The test-train split was made utilizing 80% of the total data for training and the remaining 20% for testing.

5 RESULTS AND DISCUSSION

The algorithm had an accuracy of 70.5% , and its confusion matrix is shown in Table 1. Also, the bar chart presented on Figure 8 shows, in percentage, the accuracy of the classifier per class. Observing Table 1, one can see that, regarding the presence or absence of damage, out of 180 tests, the algorithm had a performance of no false positives and 0.3% (6 cases) of false negatives.

Table 1: SVM algorithm's confusion matrix

	R0	R1	R2	R3	R4	R5	R6	R7	R8
R0	20	0	0	0	0	0	0	0	0
R1	0	12	2	0	3	1	0	0	2
R2	0	1	16	1	2	0	0	0	0
R3	2	0	2	11	2	1	0	0	2
R4	1	0	0	0	18	0	0	0	1
R5	0	0	1	1	3	12	2	1	0
R6	1	0	0	0	1	1	13	4	0
R7	1	0	0	0	0	0	3	12	4
R8	1	3	0	1	0	0	1	1	13

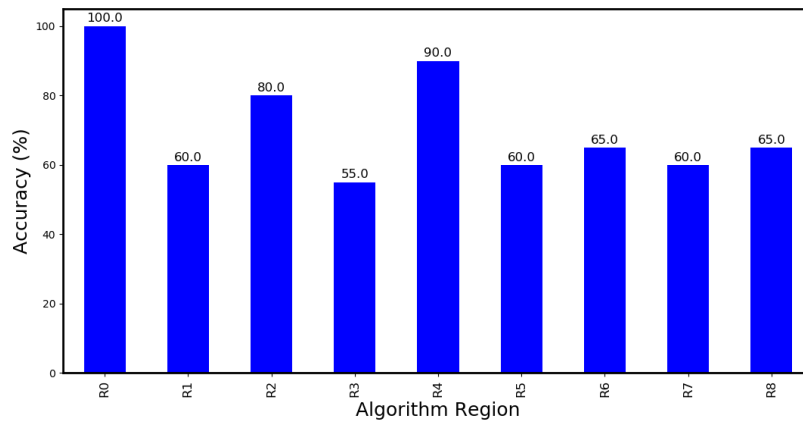


Figure 8: Algorithm's accuracy per class

A visual analysis of the classifiers behaviour can be a challenge as the algorithm works with an eight-dimension input. Even though one cannot clearly see the hyperplane that divides all the SVM classes, some patterns can still be identified observing the set of polar plots presented on Figure 9.

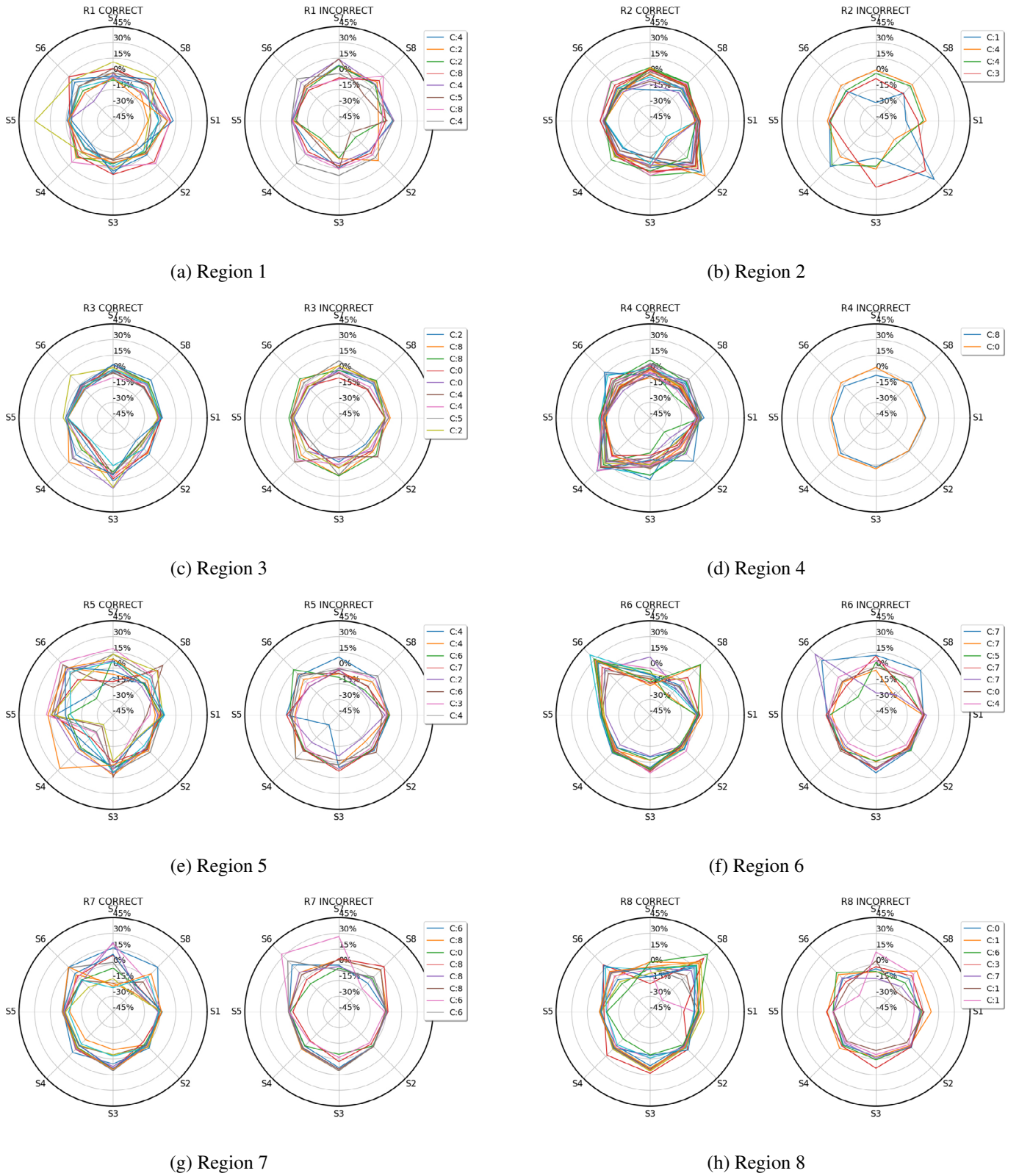


Figure 9: Damage indexes for correct and incorrect test predictions

The plots show the behaviour of the tests regarding the damage indexes (Equation (1)) of all the eight sensors, which were the input of the classifier. The radial axis corresponds to the DI while angular coordinates to its respective sensor. For an easier comprehension, the angular coordinate of each sensor were placed according with its real disposition on the plate, already showed on Figure 6.

The polar graphics to the left of each damaged region shows the behaviour presented by the correctly classified tests while the graphs to the right shows the incorrectly ones. The legend box next to the incorrect cases lists the true damaged region in each test.

It is worth mentioning that in most of the incorrect prediction cases, the classifier predicted damage in the neighbour region. For instance, for the eight wrong predictions of region 7, three indicated damage in region 6 and four indicated damage in region 8. Thus, despite giving a wrong classification, in a real situation it would at least give the user informations of damage presence and a direction of in which region it might be.

Another important aspect that can be mentioned is that, even though the DI of most regions present an expected behaviour, like the ones observed by Souza and Nobrega[14], they differ from the expected outcome in some regions, forming patterns that have not been yet identified. These changes in the expected behaviour could be attributed to the materials anisotropy. Despite these unexpected behaviours, the classifier still works its ways to automatically identify a pattern and predict the plates damaged region in most cases.

6 CONCLUSION

In this paper, the use of statistical indicators and machine learning methods were used as a strategy to detect structural changes in a composite material plate. The proposed approach used a SVM algorithm to identify the presence of damage and, if damage indeed exists, classify it in 8 pre defined regions.

In general, the method obtained good results even with the additional difficulty generated by the material's anisotropy, achieving a classification rate greater than 70%.

In practice, the main advantage of the proposed approach is to develop an continuous monitoring system that automatically identify and locates damage.

Even though statistical parameters do not show meaningful visual variation in some cases, they are still able to point out subtle differences among the vibration signals. These differences allow artificial intelligence methods to detect structural alterations caused by the presence of damage.

The good results achieved by the classifier emphasizes the effectiveness of the presented approach and motivates the continuous work on the development of the computer aided statistical analysis for SHM. In spite of the good results, the method using SVM, as in all methods based on supervised learning, has some limitations such as the large amount of data to train the models and the need of prior knowledge of the structural behaviour.

Future work will keep on investigating and developing supervised and unsupervised learning approaches as means to continuously increase their effectiveness and introduce new attributes such as automatically identify new target regions that were not pre defined.

REFERENCES

- [1] Wang, Q., Ma, S., and Yue, D. Identification Of Damage In Composite Structures Using Gaussian Mixture Model- Processed Lamb Waves. *Smart Mater. Struct.* (2018) 27:1-11.
- [2] Huang, L.; Zeng, L.; Lin, J. and Luo, Z. An improved time reversal method for diagnostics of composite plates using Lamb waves. *Composite Structures.* (2018) 190: 10-19.

- [3] H. Salehi and R. Burgueno, Emerging artificial intelligence methods in structural engineering, *Engineering Structures*, Vol. 171, pp. 170189, (2018)
- [4] Gangsar, P. and Tiwari, R. A support vector machine based fault diagnostics of induction motors for practical situation of multi-sensor limited data case. *Measurements*. (2019) 135: 694-711.
- [5] Dsouza, R., Sequeira, A., Jose, M. and Golani, G. Damage Inspection and Online Monitoring using Lamb Waves: A Comparative Study on Aluminium and Composite Plate Structures *IOP Conf. Ser.: Mater. Sci. Eng.*. (2018) 422:1-10.
- [6] Su, Z. and Ye, L. Identification of Damage Using Lamb Waves: From Fundamentals to Applications. *Springer*, (2009).
- [7] Mallat, S. G., 1989. A theory for multiresolution signal decomposition: The wavelet representation *IEEE Trans. Pattern. Anal. Machine Intell.*, , Vol. 2, pp. 674693.
- [8] Feldman M. (2011). Hilbert transform in vibration analysis. *Mechanical Systems and Signal Processing*, 25, 735-802.
- [9] B. Scholkopf, A.J. Smola. Statistical learning and kernel methods. *MIT Press*, Cambridge, MA (2000).
- [10] N. Cristianini, J. Shawe-Taylor. An introduction to support vector machines. *Cambridge University Press*, Cambridge (2000).
- [11] V. Kecman. Learning and soft computing *The MIT Press*, Cambridge, MA (2001)
- [12] C. Burges. 'A tutorial on support vector machines for pattern recognition' *Data Mining and Knowledge Discovery*, 2 (2) (1998), pp. 121-167
- [13] Pedregosa, F.; Varoquaux, G.; Gramfort, A.; Michel, V.; Thirion, B.; Grisel, O.; Blondel, M.; Prettenhofer, P.; Weiss, R.; Dubourg, V.; et al. 2011. Scikit-learn: Machine learning in python. *The Journal of Machine Learning Research* 12:28252830.
- [14] P. R. Souza and E. G. O. Nobrega. An effective structural health monitoring methodology for damage isolation based on multisensor arrangements *J Braz. Soc. Mech. Sci. Eng.*, Vol. 39, pp. 1351-1363, (2017)

DAMAGE SIZE QUANTIFICATION IN AERONAUTIC COMPOSITE STRUCTURES BASED ON IMAGING RESULTS POST-PROCESSING

William BRIAND*, Marc REBILLAT*, Mikhail GUSKOV* AND Nazih MECHBAL*

*PIMM Laboratory
ENSAM-CNAM-CNRS-HESAM
75013 Paris, France

Key words: Structural Health Monitoring, Damage imaging, Damage quantification, Aeronautic composite structures, Ultrasonic Lamb waves

Abstract. Thanks to their high strength to mass ratio, composite materials are now widespread in the aerospace industry. Nevertheless, this type of material is subject to various internal damages and it is mandatory to monitor in real time their structural integrity. Structural Health Monitoring (SHM) is a process based on embedded sensors whose aim is to detect, locate, classify and quantify potential damages appearing in a structure in order to avoid structures catastrophic failures and to estimate their residual life. The most widely used technique to perform SHM of aeronautical structures made up of composite materials is based on the use of ultrasonic Lamb waves. However, even if robust and precise SHM algorithms exist for damage detection and localization, there is still a huge need for reliable algorithms for damage quantification. In this paper, a damage quantification strategy based on a post-processing step of the results of damage imaging method is presented. Such a method allows for damage size assessment of a delaminated area by post-processing the images produced by damage localization algorithms. Localization methods take raw signals from sensor as input and return a map of index representing the likelihood of presence of a damage over the surface of the structure under study. From this spatial probability map, region of high localization index can be identified around the estimated damage location and the area this region can be computed. A data-driven model representing the mathematical relationship between the computed area and the actual size of the damage is then inferred. The proposed method is successfully validated on numerical simulation data carried out on CFRP plate samples equipped with a stiffener and of a piezoelectric sensor-actuator network with several configurations of damage size.

1 INTRODUCTION

Maintenance is a great cost for airlines since structure checks require to ground an aircraft for several days [1]. These inspections are fixed-interval with a rate provided by the constructor. Nevertheless, as the current state of the structure is unknown, this rate is not condition-based. That is why real time monitoring of structures is of high interest in the industry and in particular in aeronautics. This research field is known as Structural Health Monitoring or SHM.

Various techniques are used to monitor possible damage apparition in a structure. The most used is the emission and reception of ultrasonic Lamb waves [2, 3]. Such waves are easy to generate at high frequencies using ultrasonic transducers (such as piezoelectric elements called PZT) making them able to interact even with small damages [4]. Moreover, Lamb waves can propagate in large structures with

low dissipation thanks to their small attenuation ratio. Structures are usually equipped with a network of PZT components acting both as actuators and sensors [5]. A classical SHM process can be decomposed in four distinctive steps [6]:

- **Detection:** evaluation of presence of a damage in the structure under study;
- **Localization:** estimation of the position of damage;
- **Classification:** identification of the damage type (crack, delamination, etc.);
- **Quantification:** assessment of the damage's size.

However, even if robust and precise SHM algorithms exist for damage detection and localization, there is still a huge need for reliable algorithms for damage quantification. Several methods dedicated to this issue have already been proposed in the literature. One method consists in computing a relevant damage index that varies with the size of the damage [7]. Another approach is to train an Artificial Neural Network (ANN) on simulated data. The size of a damage is then estimated using experimental data as an input of this ANN [8]. Statistical methods have also been investigated. Bayesian updating techniques have been applied to crack size assessment [9] and delamination [10]. Multi-class classification for damage quantification with a support vector machine have been successfully validated on a beam [11]. These methods are interesting but do not take into account spatial information available at the end of the localization step of the SHM process that may be relevant also for quantification purposes.

Localization methods are on the basis of the damage quantification approach proposed here. These methods have been extensively studied in the literature. Time-of-arrival (TOA) [12] method is a triangulation algorithm used for localization. The idea is to compute the time of flight of the wave between the actuator and the sensor and to compare this time to the one taken by the wave scattered by the damage. It gives a locus of possible positions of the damage under the form of an ellipse. This process is used with at least 3 PZTs in order to get a unique damage localization estimate. Difference time-of-arrival (DTOA) [12] are based on the same principle. In this approach difference of time of arrival of the wave scattered by the damage are computed at two sensors. This gives a hyperbola of possible positions. As in the TOA algorithm, 3 PZTs or more are necessary to assess a unique position of the estimated damage location. In the delay-and-sum method (DAS) [13] for each point of the structure under interest and each actuator-sensor path, time of arrival of the Lamb wave are computed as if there was a damage at this position. Then, the residual of the signal is computed (*i.e.* the difference of magnitude between the reference signal and the one that is tested). For each tested point, the resulting damage index map is averaged over each actuator-sensor path. This method showed great results on an aluminum plate [14] and on a composite plate [15, 16]. RAPID (Reconstruction Algorithm for the Probabilistic Inspection of Damage) [17] algorithm consists in computing the probability of a defect occurrence using the relative amplitude of the signal change on each actuator-sensor path. This probability is computed using the signal difference coefficient and a ratio representing how far is the point from the direct path. The defect distribution probability within the sensor network is then expressed as a linear summation of all the signal change effects of every pair. For each point the signal is averaged between all path. This method has been successfully tested on aluminum plates [15].

Some attempts to post-process the results of the damage imaging methods mentioned above for damage size quantification purposes have already been tried in the literature. TOA algorithm has been used to quantify the size of an impact damage on a composite panel [18, 19]. This method has been validated on experimental and numerical data. Damage imaging methods results have also been applied to assess the position of crack tips. The size of the crack is then estimated from the area computed between the

tips position [20, 21]. However, none of these methods addressed the case of a delamination type damage which is crucial in composite structures.

In this paper, an alternate damage quantification strategy based on a post-processing step of the results of damage imaging method and focusing on delamination-type damage is presented. Such a method allows for damage size assessment of a delaminated area by post-processing the images produced by damage localization algorithms. Localization methods take raw signals from sensor as input and return a map of index representing the likelihood of presence of a damage over the surface of the structure under study. From this spatial probability map, region of high localization index is identified around the estimated damage location and the area of this region is computed. A data-driven model representing the mathematical relationship between the computed area and the actual size of the damage is then inferred. As more and more aeronautic structures are made of composite [22], SHM processes have to be tested on this type of material. That is why the proposed method is validated on numerical simulation data carried out on CFRP plate samples. These samples are equipped with a stiffener and of a piezoelectric sensor-actuator network with several configurations of damage size. The proposed method is detailed in Sec. 2 and validated on numerical data coming from simulation of a composite plate equipped with a stiffener described in Sec. 3. Results are shown and discussed in Sec. 4.

2 METHOD

The workflow of the damage size quantification algorithm based on the post processing of damage imaging algorithms is divided in two steps. The first one is the learning step. It consists in building a data-based model from numerical or experimental data. These data are raw signals from actuator and sensor placed on the structure under study for multiple sizes of damages. In the second step, the size of an unknown damage is predicted with the model previously built. The overview of the method is depicted in Figure 1. N_{sens} stands for the number of sensors, N_{rep} corresponds to the number of repetitions of the measure, N_{dam} represents the number of damage cases and N_{conf} stand for the number of PZTs configurations. A PZTs configuration is a subset of all the transducers glued to the structure. For example in a case where a sample is equipped with 3 PZTs, measures can be done with 4 different PZTs configurations: [1,2], [2,3], [1,3] and [1,2,3].

2.1 LEARNING STEP

For any localization algorithm, raw signals are first denoised, filtered and time-aligned for each damage case (*i.e.* for each different size of damage available in the data base used for learning). The group velocity of the ultrasonic Lamb waves is then computed to be used in the localization method picked by the user: TOA, DTOA, RAPID or DAS. Once the localization process is done, a damage localization index (DLI) map is obtained for each damage case. Next, the resulting DLI maps are post-processed for all damage cases. A threshold function is applied to the image to extract a binary map. Then an image segmentation algorithm is used to partition the binary DLI map in several regions of interest and to select the one surrounding the estimated damage position. This region is called “*high DLI region*” and its area is computed. At this point, the area of the “*high DLI region*” has been computed for multiple sizes of damage. The idea is now to learn the mathematical relationship existing between the “*high DLI region*” areas and the actual damage sizes. A regression is then performed on these data in order to infer the damage size quantification model.

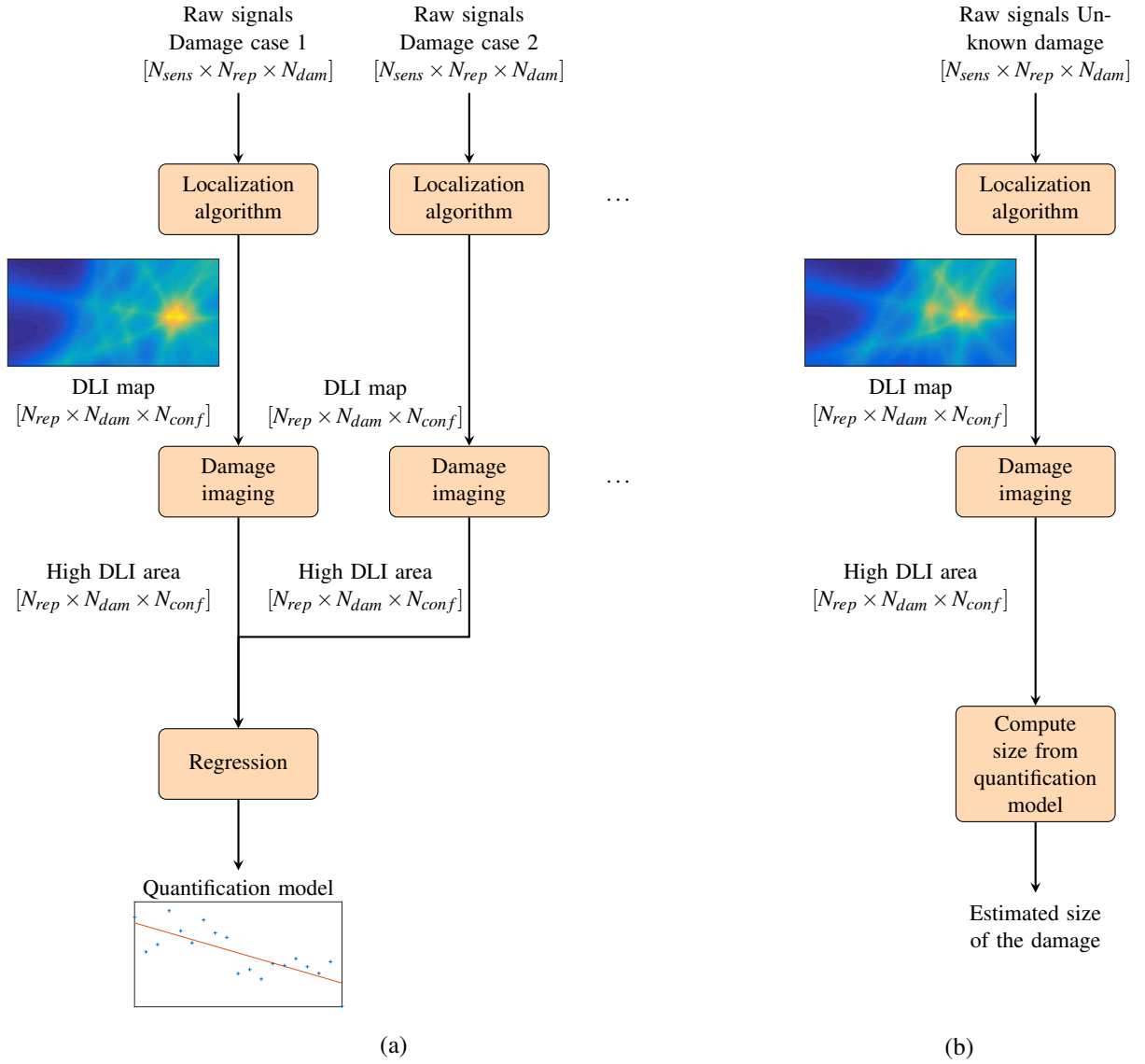


Figure 1: Overview of the damage size quantification algorithm based on the post processing of damage imaging algorithms. Description of the learning step (a) and the prediction step (b).

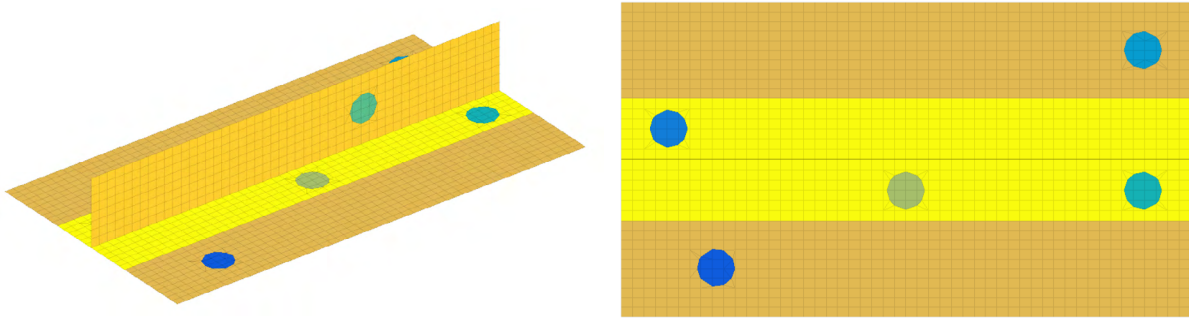


Figure 2: FEM model of the stiffened panel used for simulation

2.2 PREDICTION STEP

Now that a quantification model has been built, it can be used to estimate the size of an unknown damage. In this prediction process, raw signals coming from the structure in an unknown damaged state are denoised, filtered and time-aligned. Then the same localization algorithm and damage imaging process used for the learning step are applied. Finally the estimated size of the unknown damage is computed from the quantification model using the high DLI area computed.

3 STRUCTURE UNDER STUDY

The method described in this paper is validated using numerical data. The structure under consideration is a stiffened composite panel. The structure is made of graphite-epoxy plies with the stacking sequence $[45^\circ/0^\circ/45^\circ/90^\circ/-45^\circ/0^\circ]$ in the skin. The properties of one ply are given in Table 1.

Table 1: Material properties

	Density [g/cm^3]	$E(0^\circ)$ [GPa]	$E(90^\circ)$ [GPa]
Unidirectional	1.57	163	10
Woven	1.56	85	79

The structure is equipped with five PZTs components that can be used both as sensor and actuator. The FEM model with the PZT and damage position is shown in Figure 2. Coordinates of these piezoelectric elements and of the simulated damage can be found in Table 2.

Table 2: Coordinates of PZT elements and damage center

	PZT1	PZT2	PZT3	PZT4	PZT5	Damage
x(mm)	50	25	275	275	200	150
y(mm)	25	98.8	140	66.3	82.5	66.25

Damages have circular shape with a radius varying between 1mm and 10mm by step of 0.5mm leading to 19 damage cases. The damage is represented by a decrease of the Young modulus of 90% in the

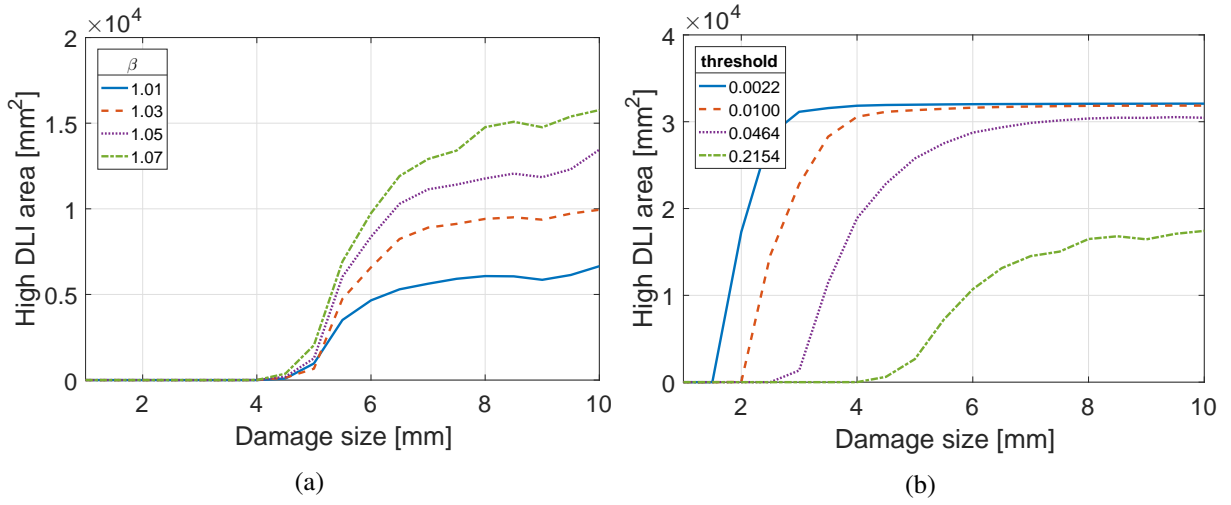


Figure 3: Sensitivity of the RAPID method to β parameter (a) and threshold (b).

damaged area. A healthy case *i.e.* without damage is used as reference for comparing the signals. Simulation have been conducted using the *Matlab* toolbox SDTools [23]. Signal used is a 5-cycles tone burst of 160 kHz central frequency with random noise in order to introduce variability in the data. The signal to noise ratio, as defined in Eq. (1), is 70dB.

$$SNR = 10 \log_{10} \left(\frac{P_{signal}}{P_{noise}} \right) \quad (1)$$

where P_{signal} and P_{noise} are signal and noise power respectively. For each damage case 10 repetitions have been performed. The sampling frequency is 2 MHz. Localization algorithm can be performed in two running mode. The first one is called “*test*”. It means that only the first repetition of the healthy state and the first repetition of the damage case will be compared. In the other mode called “*full*” each repetition is compared of the healthy state is compared with each repetition of the damage case in order to take the take the variability of the measure into account.

4 RESULTS AND DISCUSSION

4.1 PARAMETERS

The damage quantification method proposed in this paper has been tested with several localization algorithms: TOA, DTOA, RAPID and DAS. Each of these algorithms depend on a parameter. In the TOA and DTOA algorithms, a decay rate of an exponential windowed function applied is introduced to reduce secondary reflections [12]. DAS depends on the number of samples over which time integration is performed [13]. In the RAPID approach the user can set a parameter called β corresponding to the the spread of the ellipses around each path [15]. Moreover, the damage quantification method itself also has one parameter which is the threshold level. To show the influence of the parameters tuning, sensitivity of the RAPID algorithm to β parameter and threshold is depicted Figure 3.

Thus, for each localization method the best set of parameters has to be found in order to get the damage size regression with the minimum error. Computations were performed for a range of parameters in order to find the best set of parameters in this range. These computations were run in “*test*” mode. Table 3 provides the best sets of parameters that have been found. One can notice that the best threshold

value hardly varies between each method. For TOA and DTOA the ellipse or hyperbola shape of the high DLI region implies changeability of the high DLI area computed, leading to irregular variation of the goodness of fit over the decay parameter. Thus, finding a value of this parameter that minimize the error of the regression for any threshold value cannot be achieved efficiently. On the opposite, DAS method shows no influence of its specific parameter in the regression. RAPID algorithm gave better regression results with a β parameter slightly greater than 1 as noticed in [15].

Table 3: Parameters and best set of parameters for each localization method

	Localization parameter	Best localization parameter	Best threshold value
TOA	Decay rate of an exponential windowed function applied to reduce secondary reflections.	$6.0 \cdot 10^{-6}$	0.22
DTOA	Decay rate of an exponential windowed function applied to reduce secondary reflections.	$7.0 \cdot 10^{-6}$	0.22
DAS	Number of samples over which time integration is performed.	11	0.46
RAPID	Parameter set to adjust the spread of the ellipses around each path.	1.125	0.22

Once these best parameters have been selected, results are shown in Fig. 4. It appears that DAS and RAPID show a clear correlation between high DLI area computed and the actual size of the damage. However, results obtained with TOA and DTOA demonstrated poor regression quality.

Once these parameters have been found, the method was run in *full* mode. The quantification model was inferred using the first 14 damage cases *i.e.* from 1mm to 7.5mm. Next, the size of the damage for greater sizes are estimated as depicted in the Figure 1a. In an industrial context it corresponds to building a model from small size of a damage and use this model to estimate future size of the damage.

The estimated sizes are compared with the actual size of the damages in the Table 4. From this table it appears that quantification model built with DAS or RAPID methods give accurate results whereas model inferred with TOA or DTOA show poor precision when the size of the testing damage move away from the learning range. It could be explained by the difference between these two types of method. In one hand, TOA and DTOA only deal with time of arrival of the signal which is not influenced by the size of the damage. On the other hand, DAS and RAPID take amplitude of the signals into account which make the results more influenced by the size of the damage. Another reason of this difference could also be the shape of the high DLI region which has great influence on the quality of the regression. In the TOA and DTOA, high DLI region is made up of ellipse or hyperbola which area does not clearly vary with the damage size as discussed in the previous subsection. On the contrary high DLI region in the DAS and RAPID methods is circular and the high DLI variation is monotonic over the size of the damage which lead to a more accurate model. Another point is that in DAS and RAPID method high DLI computed is equal to zero for damage size under 4mm. It means that can only be build with damage greater than this value. Nevertheless this limitation is not an issue since in aeronautical applications only damages of 20mm of radius or more are sought. Finally, DAS method results is constant for each predicted damage size.

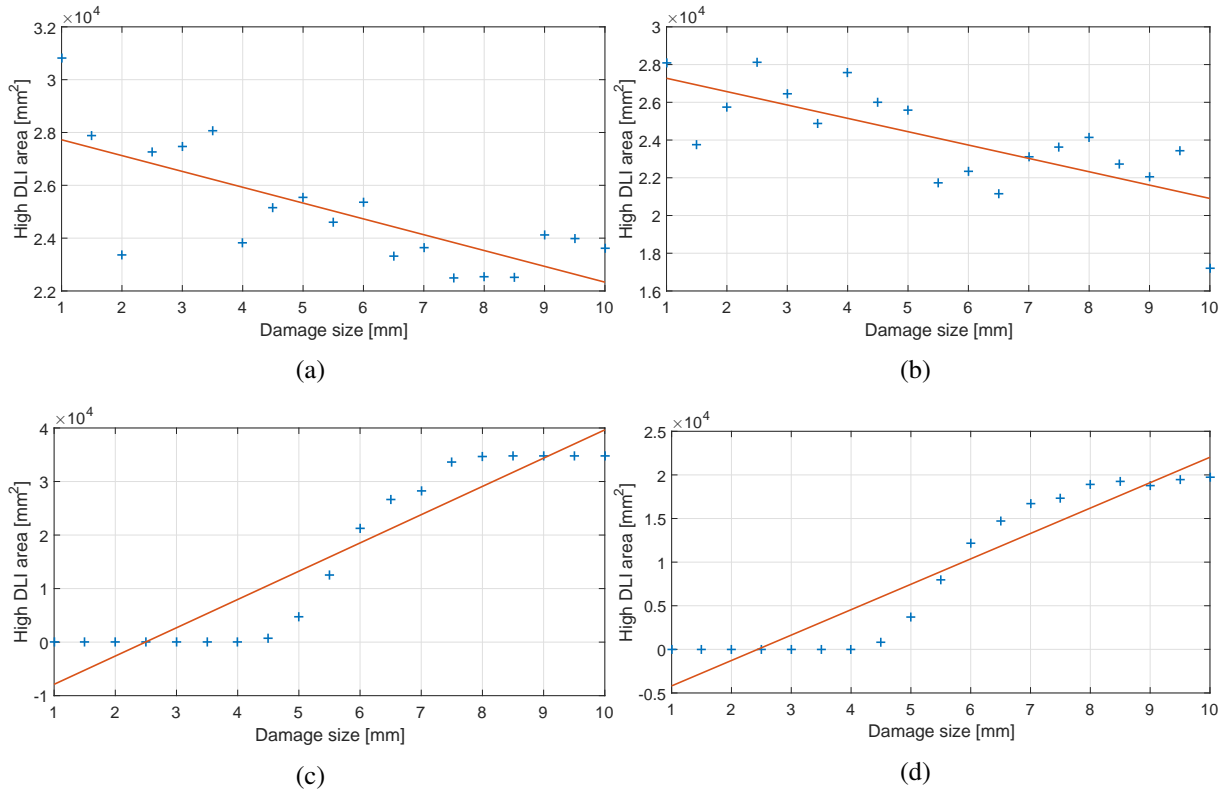


Figure 4: Results with best set of parameters for TOA (a), DTOA (b), DAS (c) and RAPID (d) methods. The line is the linear regression relation between high DLI area and damage size.

5 CONCLUSION

In this paper, a damage quantification strategy based on a post-processing step of the results of damage imaging method has been presented. Such a method allows for damage size assessment of a delaminated area by post-processing the images produced by damage localization algorithms such as TOA, DTOA, DAS and RAPID. From these images, region of high localization index can be identified around the estimated damage location and the area of this region can be computed. A data-driven model representing the mathematical relationship between the computed area and the actual size of the damage is then inferred. The proposed method has been successfully validated on numerical simulation data carried out on CFRP plate samples equipped with a stiffener and of a piezoelectric sensor-actuator network with several configurations of damage size. Results using RAPID method showed particularly promising results.

Future work will be focus on the validation of this method using experimental data.

6 ACKNOWLEDGMENT

This work has received funding from the European Union's Horizon 2020 research and innovation program under the REMAP project (grant agreement number 769288)

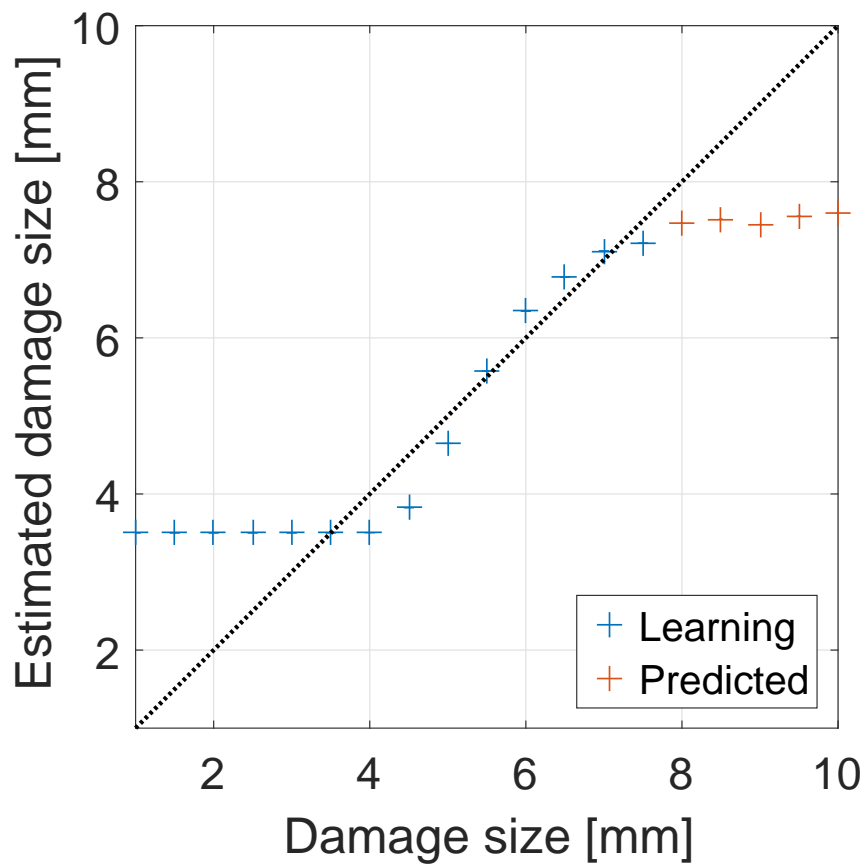


Figure 5: Estimated damage size computed with the data-driven model built using RAPID algorithm versus the actual size of the damage. The dotted line corresponds to an exact prediction.

Table 4: Error between the size estimated with the quantification model and the actual size of the damage in *full* mode.

Localization method	Actual damage size [mm]	Predicted damage size [mm]	Mean relative error (in%)	Standard deviation error (in %)
TOA	8.00	7.44	7	$4.15 \cdot 10^{-2}$
	9.00	6.83	24	$6.19 \cdot 10^{-2}$
	10.00	7.01	30	$4.83 \cdot 10^{-2}$
DTOA	8.00	6.92	13	$7.03 \cdot 10^{-2}$
	9.00	3.69	59	$5.40 \cdot 10^{-1}$
	10.00	11.83	18	$1.90 \cdot 10^{-2}$
DAS	8.00	7.37	8	$9.76 \cdot 10^{-15}$
	9.00	7.37	18	$2.79 \cdot 10^{-15}$
	10.00	7.37	26	$4.46 \cdot 10^{-15}$
RAPID	8.00	7.47	7	$1.52 \cdot 10^{-3}$
	9.00	7.45	17	$1.67 \cdot 10^{-3}$
	10.00	7.60	24	$3.25 \cdot 10^{-3}$

REFERENCES

- [1] S. P. Ackert, “Basics of Aircraft Maintenance Programs for Financiers,” Oct. 2010.
- [2] Z. Su and L. Ye, *Identification of damage using Lamb waves: from fundamentals to applications*. No. v. 48 in Lecture notes in applied and computational mechanics, Berlin: Springer-Verlag, 2009. OCLC: ocn428028202.
- [3] V. Giurgiutiu, *Structural Health Monitoring with Piezoelectric Wafer Active Sensors*. Elsevier, 2007.
- [4] K. Worden, C. R. Farrar, G. Manson, and G. Park, “The fundamental axioms of structural health monitoring,” *Proceedings of the Royal Society A: Mathematical, Physical and Engineering Sciences*, vol. 463, pp. 1639–1664, June 2007.
- [5] V. Giurgiutiu, “Tuned Lamb Wave Excitation and Detection with Piezoelectric Wafer Active Sensors for Structural Health Monitoring,” *Journal of Intelligent Material Systems and Structures*, vol. 16, pp. 291–305, Apr. 2005.
- [6] A. Rytter, *Vibrational based inspection of civil engineering structures*. PhD thesis, Aalborg University, 1993.
- [7] Y. Liu, M. Y. Fard, A. Chattopadhyay, and D. Doyle, “Damage assessment of CFRP composites using a time–frequency approach,” *Journal of Intelligent Material Systems and Structures*, vol. 23, pp. 397–413, Mar. 2012.
- [8] Z. Su and L. Ye, “Lamb Wave Propagation-based Damage Identification for Quasi-isotropic CF/EP Composite Laminates Using Artificial Neural Algorithm: Part II - Implementation and Validation,” *Journal of Intelligent Material Systems and Structures*, vol. 16, pp. 113–125, Feb. 2005.
- [9] J. Yang, J. He, X. Guan, D. Wang, H. Chen, W. Zhang, and Y. Liu, “A probabilistic crack size quantification method using in-situ Lamb wave test and Bayesian updating,” *Mechanical Systems and Signal Processing*, vol. 78, pp. 118–133, Oct. 2016.
- [10] T. Peng, A. Saxena, K. Goebel, Y. Xiang, S. Sankararaman, and Y. Liu, “A novel Bayesian imaging method for probabilistic delamination detection of composite materials,” *Smart Materials and Structures*, vol. 22, no. 12, p. 125019, 2013.
- [11] M. Ghrib, M. Rébillat, G. Vermot des Roches, and N. Mechbal, “Automatic damage type classification and severity quantification using signal based and nonlinear model based damage sensitive features,” *Journal of Process Control*, Oct. 2018.
- [12] C. Fendzi, N. Mechbal, M. Rebillat, M. Guskov, and G. Coffignal, “A General Bayesian Framework for Ellipse-based and Hyperbola-based Damage Localisation in Anisotropic Composite Plates,” p. 34, 2016.
- [13] J. E. Michaels, “Detection, localization and characterization of damage in plates with an in situ array of spatially distributed ultrasonic sensors,” *Smart Materials and Structures*, vol. 17, p. 035035, May 2008.
- [14] J. E. Michaels and T. E. Michaels, “Guided wave signal processing and image fusion for in situ damage localization in plates,” *Wave Motion*, vol. 44, pp. 482–492, June 2007.

- [15] Z. Sharif-Khodaei and M. H. Aliabadi, "Assessment of delay-and-sum algorithms for damage detection in aluminium and composite plates," *Smart Materials and Structures*, vol. 23, p. 075007, May 2014.
- [16] L. Qiu, M. Liu, X. Qing, and S. Yuan, "A quantitative multidamage monitoring method for large-scale complex composite," *Structural Health Monitoring: An International Journal*, vol. 12, pp. 183–196, May 2013.
- [17] X. Zhao, H. Gao, G. Zhang, B. Ayhan, F. Yan, C. Kwan, and J. L. Rose, "Active health monitoring of an aircraft wing with embedded piezoelectric sensor/actuator network: I. Defect detection, localization and growth monitoring," *Smart Materials and Structures*, vol. 16, pp. 1208–1217, June 2007.
- [18] A. Sorrentino, A. De Fenza, F. Romano, and U. Mercurio, "Experimental application of Lamb wave based SHM system at complex composite material structures," in *9th Workshop on Structural Health Monitoring, Manchester, UK*, 2018.
- [19] A. Sorrentino and A. De Fenza, "Damage Detection in Complex Composite Material Structures by using Elliptical Triangulation Method," in *Structural Health Monitoring 2017*, DEStech Publications, Inc., Sept. 2017.
- [20] A. Migot, Y. Bhuiyan, and V. Giurgiutiu, "Numerical and experimental investigation of damage severity estimation using Lamb wave-based imaging methods," *Journal of Intelligent Material Systems and Structures*, vol. 30, pp. 618–635, Mar. 2019.
- [21] J.-B. Ihn and F.-K. Chang, "Pitch-catch active sensing methods in structural health monitoring for aircraft structures," *Structural Health Monitoring*, vol. 7, no. 1, pp. 5–19, 2008.
- [22] "Hexcel ready to fly on the A350 XWB," *Reinforced Plastics*, vol. 57, pp. 25–26, May 2013.
- [23] E. Balmes, J.-P. Bianchi, and J.-M. Leclère, "Structural dynamics toolbox," *Users Guide, Version*, vol. 6, 2009.

DATA-DRIVEN AUTOREGRESSIVE MODEL IDENTIFICATION FOR STRUCTURAL HEALTH MONITORING IN ANISOTROPIC COMPOSITE PLATES

SAMUEL DA SILVA^{*,*}, JESSÉ PAIXÃO^{*}, MARC RÉBILLAT[†] AND NAZIH MECHBAL[†]

^{*,*}Departamento de Engenharia Mecânica, Universidade Estadual Paulista - UNESP
Av. Brasil 56, 15385-000, Ilha Solteira, SP, Brasil
e-mail: samuel.silva13@unesp.br, jesseag.paixao@gmail.com,
Web page: <http://www.dem.feis.unesp.br/>

[†] PIMM Laboratory, ENSAM/CNRS/CNAM
151 Boulevard de l'Hôpital, 75013 Paris, France
e-mail: marc.rebillat@ensam.eu, nazih.mechbal@ensam.eu,
Web page: <https://pimm.artsetmetiers.fr/>

Key words: AR Models, Multiple Models, Extrapolated Model, Quantification, Prognosis

Abstract. A simple data-driven AutoRegressive (AR) model may be used to assess a model to describe and to predict the time-series outputs of the PZT sensors receiving Lamb waves for different operating conditions in composite structures. Thus, this paper presents the potentiality of the use of a set of AR models to detect, locate, and, mainly, to extrapolate a damage sensitive index based on changes in one-step-ahead prediction errors. To illustrate this proposal, an aeronautical composite panel with bonded piezoelectric elements, that act both as sensors and actuators, is used to study the relationship between the variation of the parameters of the identified model and the presence of various simulated damage. A damage progression evaluation by extrapolating the AR parameters is also suggested and examined based on cubic spline functions to verify the future state and to observe how the damage could evolve, based on some simplified assumptions. This step could help to make a decision about a possible required repair without adopting a complicated and costly physical model.

1 INTRODUCTION

The structural health monitoring (SHM) approaches seem to be in a mature stage in the steps of detecting and localization of possible damages in structures with several powerful methods proposed and validated in the last decades. One way to address this issue may be using data-driven model identification based on guided wave propagation or random inputs. For example, Nardi et al. [1] using an autoregressive (AR) model were able to detect delamination in a carbon-fiber-reinforced-plastic laminate plate excited by random input using a couple of piezoelectric patches as actuator and sensors. Kim et al. [2] also showed a possible data-driven system identification through a state-space model to capture the wave motion in metallic structures. da Silva [3] applied autoregressive with exogenous input (ARX) model to perform predictions and a waveform generator in a 10 layers carbon-epoxy plate excited by

guided waves assuming different central frequencies and environmental conditions¹ and noted some benefits and disadvantages of the possible performance of this strategy for SHM.

However, to reach a high level in an SHM's hierarchy² numerous drawbacks need to be overcome yet. One of them is that it is essential to have an adequate mathematical model if the user wants to predict a future state based on previous past data to interrogate about the existence and evolution of damage propagation. So, these models demand to incorporate information about the damage behavior in its dynamics to gain a comprehensive physical insight of the monitored structure; consequently, this model should be most physical possible. However, to construct numerical models, for example, using finite element models with damages in an initial stage, require much time and may have a high cost for a real-time monitoring system in the industrial field, even modeling in its healthy state. Another limitation is that the behavior of damage evolution usually is much complicated to be modeled in a real-world application because complex types of damage can appear coincidentally with several confounding effects, like noise, uncertainties, temperature changes, operational variability, etc..

An identified data-driven model, as suggested by Nardi et al. [1] or da Silva [3], could be attractive to be adopted to extrapolate or to quantify a damage progression as a surrogate model to reach a subsequent application of higher forms of SHM's hierarchy. Thus, this paper is a first effort of the authors in this direction seeking to extrapolate AR polynomials through spline functions to extend how damage-sensitive index could evolve based on simplified assumptions. The proposed procedure has two steps to be implemented. First, damage detection and location using an index extracted by predictions errors filtered with a reference AR model is performed. To classify the structural states an analysis of variance is utilized [4]. Next, when damage is detected a new set of models, named by *initial damaged models*, is captured to extrapolate a projected state. A carbon-epoxy laminated plate with controlled progressive structural change similar to a real damage is used to exemplify the method. Next sections describe these steps and final remarks.

2 DAMAGE DETECTION USING PREDICTION ERRORS

Assuming a discrete time-series $y(k)$ measured by a PZT sensor in a healthy state, a normalization is conducted to remove offset and have mean 0 and scaled to have standard deviation 1:

$$\hat{y}(k) = \frac{y - \bar{y}}{\sigma(y)} \quad (1)$$

where $\hat{y}(k)$ is the normalized signal, \bar{y} is the mean and $\sigma(y)$ is the standard deviation. For simplicity, hereafter y is used to denote \hat{y} . Now, a simple AR model can be described by a compact difference equation [5]:

$$A(q)y(k) = e_{ref}(k) \quad (2)$$

where $e_{ref}(k)$ is the one-step-ahead error prediction in a healthy condition assumed to be a white noise and $A(q) = \sum_{i=0}^{n_a} a_i q^{-i}$ is the healthy AR polynomial³ with the coefficients a_i with a lag-order n_a , e. g., $y(k)a_i q^{-i} = a_i y(k-i)$, where q^{-i} is a lag operator and k is the time sample. The order can be estimated using Akaike information criterion (AIC) and the polynomial $A(q)$ may be identified through a least squares or Yule-Walker approach, fully available in Matlab or Octave software. When a new normalized

¹temperatures changes.

²for example, quantification and prognosis.

³Usually the coefficients a_i are normalized such that $a_0 = 1$.

data, $x(k)$, in an unknown state is measured, one can try to predict using the corresponding reference model:

$$A(q)x(k) = e_{unk}(k) \quad (3)$$

where $e_{unk}(k)$ is the unknown error prediction to be classified in a healthy or damaged state. Various papers have been using a simple damage-sensitive index \mathcal{DI} based on a comparison of the variance $\sigma^2(\cdot)$ of prediction errors [6]:

$$\mathcal{DI} = \frac{\sigma^2(e_{unk})}{\sigma^2(e_{ref})} \quad (4)$$

If \mathcal{DI} belongs a \mathcal{F} -distribution⁴ there is no damage and the unknown condition is associated to healthy state (null hypothesis \mathcal{H}_0 is true). On another hand, if the structure presents a damaged state, the probability distribution of the unknown error changes and the alternative hypothesis \mathcal{H}_1 is true [7, 6].

To classify the cluster of damages states, a one-way analysis of variance (ANOVA) can be also used to test the hypothesis that the samples in the running tests \mathcal{DI} belong to a population with the same means (null hypothesis \mathcal{H}_0), i.e., the systems is classified as healthy state, against the alternative hypothesis \mathcal{H}_1 that the population means are not all the same, i. e., damaged state [8, 4]. A Tukey's multiple comparison test to decide whether the results of ANOVA are statistically significant is also performed to enable us visible to distinguish the clusters correlated with different damages.

3 EXTRAPOLATION OF AR COEFFICIENTS

After clustering using ANOVA⁵, a new set of AR models for each initial damage recognized is estimated since the reference model given by Eq. (2) is not anymore accurate. This initial damaged model is described to predict the current state output $x_j(k)$ by:

$$\mathcal{A}_j(q)x_j(k) = e_{d_j}(k) \quad (5)$$

where $\mathcal{A}_j(q) = \sum_{i=0}^{n_a} \mathcal{A}_{ji}q^{-i}$ is the AR polynomial with coefficients \mathcal{A}_{ji} and $e_{d_j}(k)$ is the prediction error (white noise) in the damaged state $j = 1, \dots, n_d$ classified by ANOVA, where n_d is the number of initial damaged states. An important simplifying assumption is considered here: *this classified initial damage is an early state and do not change abruptly comparing with reference (healthy state)*. Consequently, the same regressive order n_a and framework (AR model) may be employed and the change is smooth between the coefficients, i.e., $A(q) \approx \mathcal{A}_j(q)$, once $|a_i - \mathcal{A}_{ji}| < \delta$ for all i and δ is a small value. It is essential to observe that the damage index given by eq. 4 is sensitive to the changes to detect damage, but the specific changes in the coefficients are in general smooths when this structural variation is in the initial states.

Rearranging the coefficients of reference model $A(q)$ and damaged $\mathcal{A}_j(q)$ as:

$$\mathbf{A} = \begin{bmatrix} a_0 & a_1 & \cdots & a_{n_a} \\ \mathcal{A}_{10} & \mathcal{A}_{11} & \cdots & \mathcal{A}_{1n_a} \\ \mathcal{A}_{20} & \mathcal{A}_{21} & \cdots & \mathcal{A}_{2n_a} \\ \vdots & \vdots & \ddots & \vdots \\ \mathcal{A}_{n_d0} & \mathcal{A}_{n_d1} & \cdots & \mathcal{A}_{n_dn_a} \end{bmatrix} \quad (6)$$

⁴i.e., e_{unk} and e_{ref} have a normal distribution

⁵Different classifiers can provide adequate results; the requirement here is to have the initial damage well classified to estimate a model for extrapolating.

where the first line of the matrix $\mathbf{A} \in \mathbb{R}^{n_d+1 \times n_a}$ is formed by the reference coefficients and the next one by the initial damage states. To enable to perform adequate extrapolations of the AR coefficients in the reference and damaged conditions, the number of states needs to be $n_d \geq 3$; otherwise, only linear extrapolation is plausible. So, it was assumed $n_d = 3$ structural states in damage clusters to permit to use cubic splines. This piecewise polynomials can be used to extend each polynomial coefficient λ_i associated to a future state through [9]:

$$\lambda_i(z) = f_i(z) + \xi_i, \quad i = 0, 1, \dots, n_a \quad (7)$$

where $z_0 < \dots < z_{n_a}$ are defined intervals associated with the order n_a , $f_i(z)$ a smoothing spline estimate by some minimizer of a penalized criterion, and ξ_i is an independent random error. More details to find the spline f_i can be seen in [10].

The important issue here is to recognize that now it is possible to have a future model to predict the data $x_j(k)$, when $j = n_d + 1$ represents a future state. This model is given by:

$$\Lambda(q)x_j(k) = \varepsilon_j(k) \quad (8)$$

where $\Lambda(q) = \sum_{i=0}^{n_a} \lambda_i q^{-i}$ is the extrapolated AR model in a future damage condition. The basic premise is that the damage progression occurs as previously captured by evolution in the lines of matrix \mathbf{A} . Thus, a new index and hypothesis tests can also be estimated to evaluate the progression and the changes of distribution of the extrapolated prediction error $\varepsilon_j(k)$ and in the damage index \mathcal{DI} .

4 EXPERIMENTAL EXAMPLE

Figure 1 shows a carbon-epoxy laminated with layup containing 10 plies unidirectionally oriented along 0° with four PZTs SMART Layers from Accelent Technologies, with 6.35 mm in diameter and 0.25 mm in thickness with a free-free boundary condition. PZT 1 is used as an actuator with a five-cycle tone burst input signal applied with 35 V of amplitude and center frequency of 250 kHz. The outputs are collected in PZT 2, PZT 3 and PZT 4 with a sampling rate of 5 MHz and timespan of 200 μ s. Data acquisition was controlled by Labview using a NI USB 6353 from National Instrument (NIDaq) and an oscilloscope DSO7034B Keysight assuming a controlled temperature of 30°C with all tests conducted inside a thermal chamber.

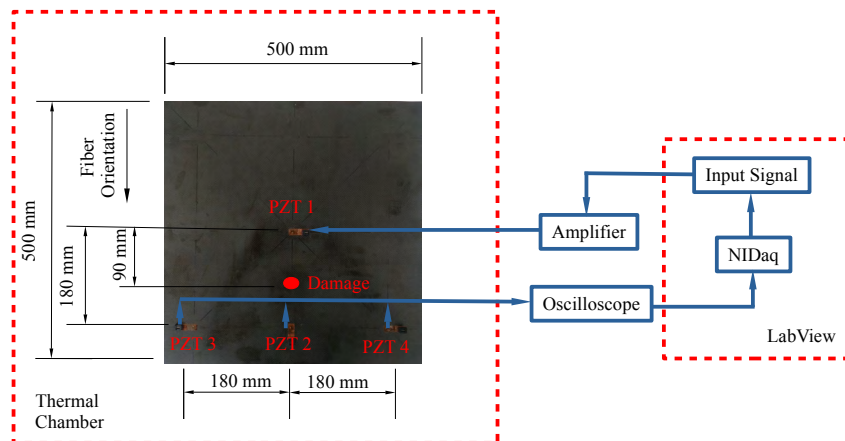


Figure 1: Illustration of the experimental setup with details about the geometry and instrumentation utilized.

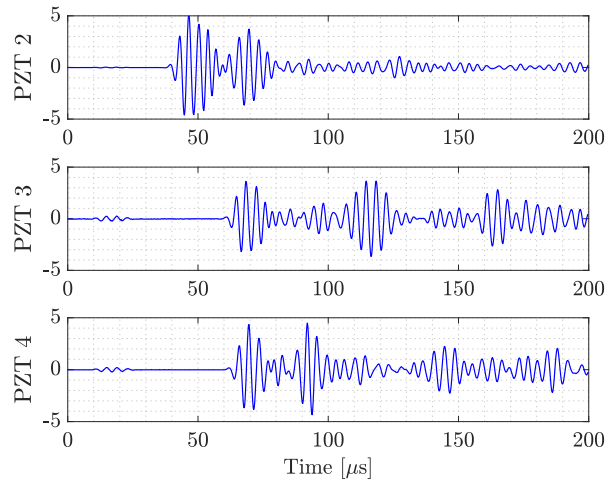


Figure 2: Healthy output time-series when PZT 1 acts as an actuator with a central frequency of 250 kHz.

Figure 2 illustrates the output time-series measured by PZTs in a healthy state normalized by Eq. 1. An industrial adhesive putty was glued on the plate surface to simulate gradual damage by an additional mass increasing progressively the coverage area in the path between PZT 1 and PZT 2. This change modifies local material properties with a similar effect to the real damages in composites structures as performed by Lee et al. [11]. In each structural state, 100 tests were repeated for an adequate statistical characterization of the proposed damage detection.

4.1 AR model identification

The AIC order selection with a focus of prediction indicates that order of $n_a = 40$ is sufficient to give an adequate validation for all paths of propagation, as seen in fig. 3. A raffle is performed to sort within 100 realizations randomly the signals in the PZT 2, PZT 3 and PZT 4 to be used as a reference and a specific healthy model $A(q)$ is identified in each path using the least square method. This is executed to reduce computational processing time. Other realizations were filtered using this reference model by Eq. 2 to estimate the prediction error in the healthy state.

Figure 4(a) shows the comparison between the measured versus predicted assuming one validation data. The analysis of the autocorrelation function of residuals also indicates that the prediction errors are white noises, i. e., the model has identified adequately, as observed in the fig. 4(b).

4.2 Damage detection

Once a reference model, named by H , is correctly identified, it is used to detect some possible structural change. Only half of the data in the healthy state is utilized, and the next 50 is applied to evaluate the presence of false positive using the hypothesis test. A set of blind tests using three different structural states associated with damage is performed, named by D1, D2 and D3 with progressive damage severity associated with area covered given by 490 mm^2 (0.19%), 707 mm^2 (0.28%) and, 962 mm^2 (0.38%), respectively. Each structural condition was also measured by 100 realizations in each path. It is worth noting that the algorithm admits that all these data are assumed in unknown condition to be classified initially in two groups: healthy or damage. The prediction errors of these unknown conditions are computed using Eq. 3 and then the damage index \mathcal{DI} is estimated by each test using the Eq. 4. The Lilliefors test is used to warranty that the variance of the prediction errors $\sigma^2(\cdot)$ in healthy states have normal

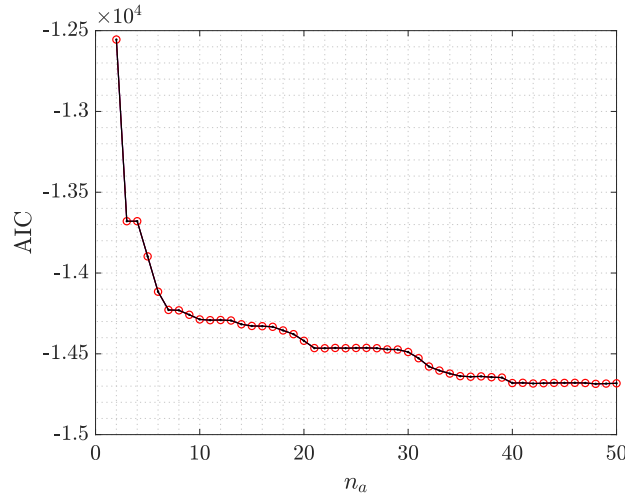


Figure 3: AIC order selection with focus in prediction.

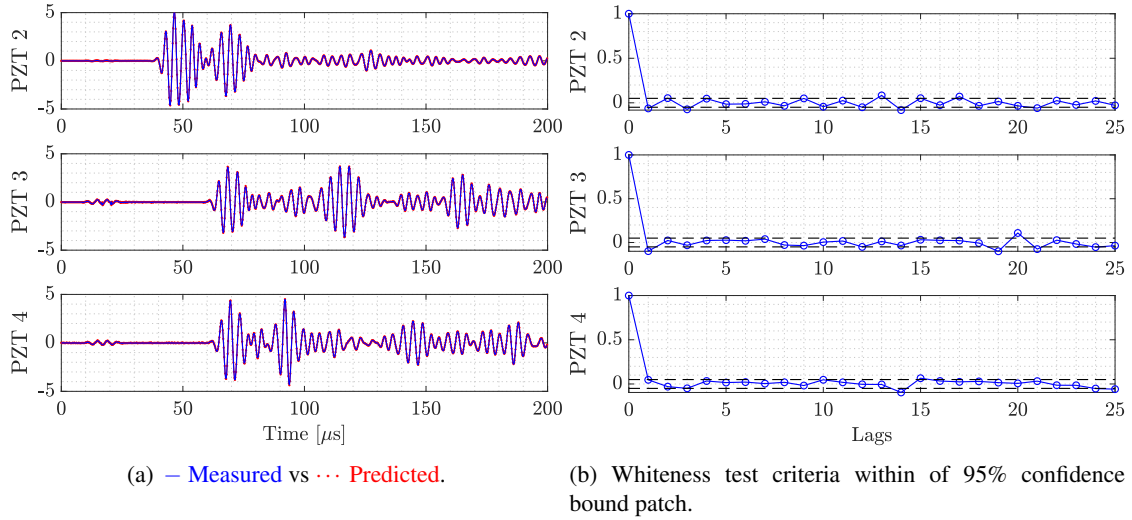


Figure 4: Healthy output predicted by healthy model AR(40).

distributions, i. e., the \mathcal{DI} trends to have a \mathcal{F} – distribution in the reference condition [6].

Figure 5(a) illustrates the index \mathcal{DI} , where is possible to observe, as presumed, that the sensor PZT 2 is sensible to the presence of damage while other PZTs the distinction between the different situations is not possible. Figure 5(b) displays the evolution of the indices with the increase of the damage using a box-and-whisker plot assuming known each damage state. A superposition in the upper quartile of the indices computed in the healthy state and the lowest quartile (even the median value) of damage states are also observed in PZT 3 and PZT 4.

Figure 6 illustrates the receiver operating characteristics (ROC) curve to detect damage against reference condition considering all PZTs sensors. The line (0,1) designates the correct classification that is achieved by PZT 2, that is the path where the damage is located. Additionally, the ANOVA procedure is computed to classify if the means are different or not, combined with a Tukey multiple comparisons to see whereby statistically significant the clusters are.

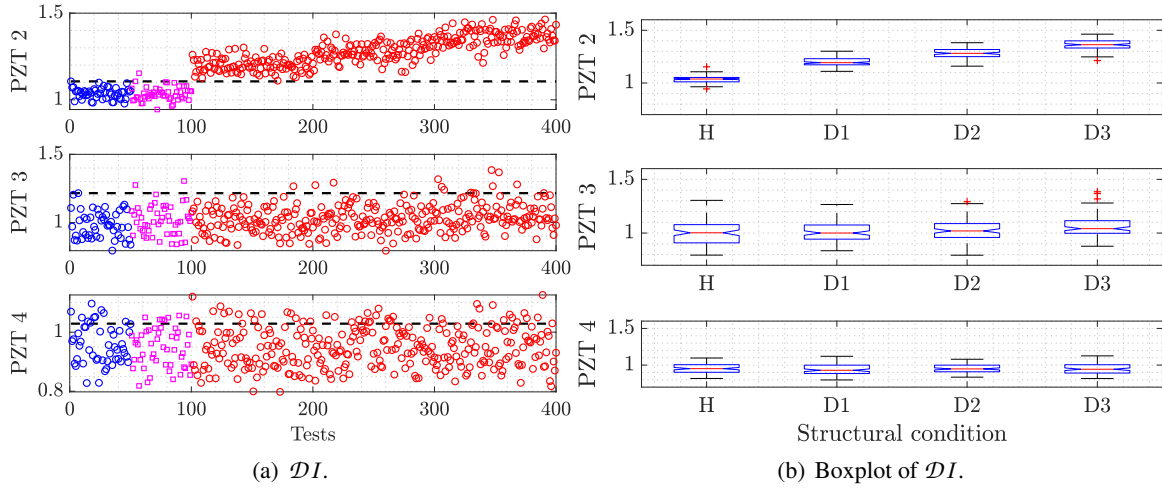


Figure 5: Damage index DI . (a) Damage index DI : Healthy - training data (o), Healthy - test data (□) and Damaged (o). — is the threshold line assuming a significance level of 5%. (b) Box plots to observe the median, quartiles and outliers in the index distribution.

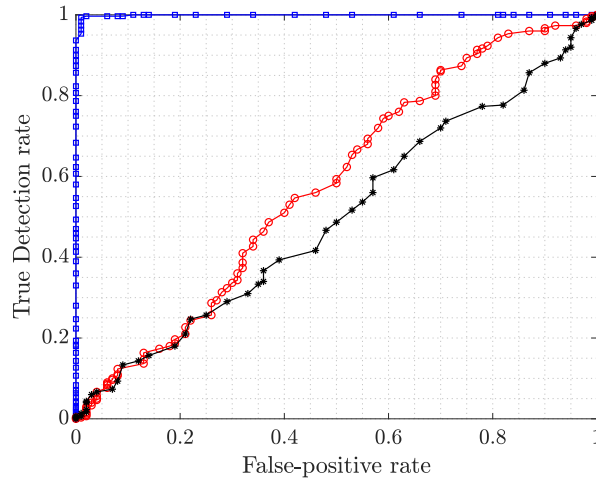


Figure 6: Receiver Operating Characteristics (ROC) curve: □ PZT 2, o PZT 3, and * is PZT 4.

Figure 7 presents this plot for PZT 2, where the circle is the mean value of the cluster with a 95% confidence interval. Three groups, $n_d = 3$, are distinctly separated and correlated with three possible structural states. After clustering, a new set of AR models in each damage group for PZT 2 is identified for monitoring the structural state and to implement the extrapolation explained in the next section. Other PZTs are not used here to identify new models because none variations are observed permitting the identification of a new polynomial $\mathcal{A}_j(q)$ in Eq. 5.

4.3 Prevision of future AR damaged model

Three damaged models are estimated using one of the conditions presents in the clusters in fig. 7 after detecting and clustering. Combined with the reference model, a matrix given by Eq. 6 is formed with $n_d = 3$ and $n_a = 20$ to help the extrapolation. A cubic spline polynomial created with the data in matrix

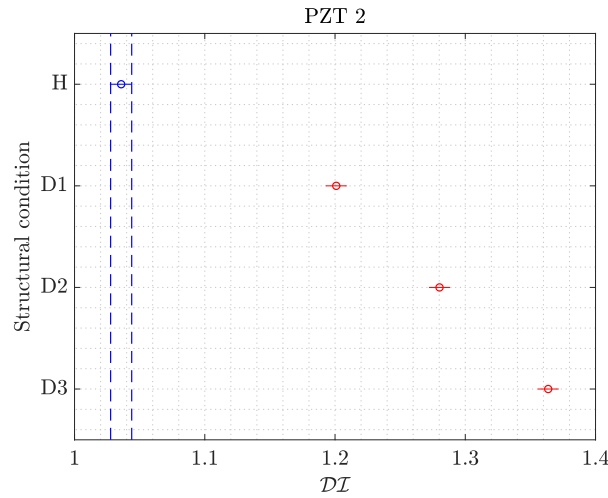


Figure 7: Classification of the clusters of different damage states using ANOVA of DI . 3 groups (in red) have means significantly different from healthy H .

\mathbf{A} permits to estimate an extrapolated model $\Lambda(q)$ to use Eq. 8 to predict future states.

More eight future damage conditions are simulated by increasing the covered area to prove the benefits of the extrapolated model. First, a damage $D4$ with a surface area covered of 0.5% is used to predict the future state. Figure 8(a) presents the comparison between the measured and predicted by the extrapolated model in damage condition $D4$. Figure 8(b) shows the residual analysis by the autocorrelation function to confirm an adequate prediction.

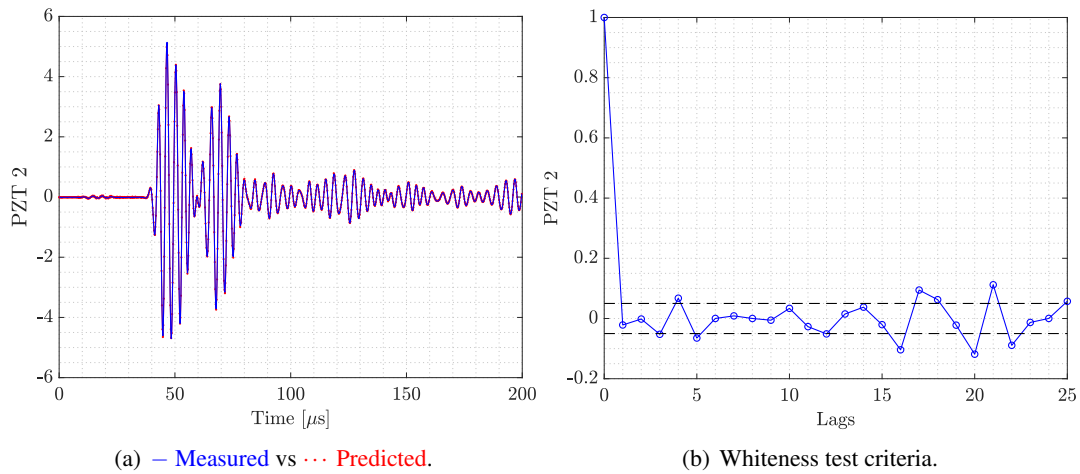


Figure 8: Output predicted by the extrapolated model AR(40) for damage condition $D4$.

When the damage condition is measured a model can be identified, and one can compare the DI obtained by model identified by extrapolation and when the damage happens, now assuming the new reference as $D4$. The box-plot is also presented in fig. 9(a) for the other damage conditions to observe its similarity comparing the real data measured and extrapolated. It is possible to observe a similarity, where the DI using the prediction errors filtered by extrapolated model presents a more significant dispersion. Figure 9(b) illustrates the predictions obtained by the filtered model using the real data (measured) and

extrapolated model. It is found a more significant dispersion to a broad horizon when the damage (surface area covered by the adhesive) is supposed severe and the model is not validated for this situation. This choice here of the validated horizon of prediction is correlated with the level of severity of the damage, once the extrapolation is done considering does not modify the framework and order of the AR model. Additionally, it is fundamental to observe that usually when damage is alerted in a monitored system, a repair or visual inspection can be performed to evaluate the structural safety. Thus, assuming a short horizon with initial damage, this extrapolated model has a nice feature almost equal to a real model identified when the damage increases and is helpful to make decisions.

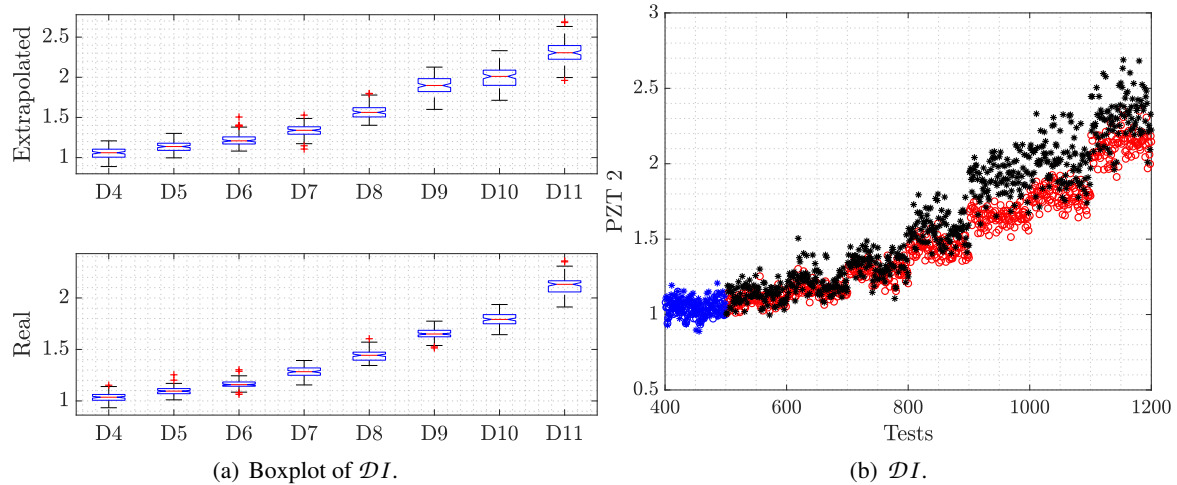


Figure 9: Damage index DI for PZT 2: (a) Box plots of the damage index DI in extrapolated condition D4 to observe the median, quartiles and outliers in the index distribution assuming the extrapolated model and damaged model. (b) \circ real damage D4 represents the new reference, $*$ extrapolated damaged D4 (extrapolated new reference), $*$ extrapolated damage, and \circ real Damaged (red) is the future damaged condition.

Figure 10 shows the ROC curve comparing the similar performance between the extrapolated and the real model to detect all future damage conditions. The extrapolated model in structural state D4 also allows dividing the clusters associated with the other damages using ANOVA, as seen in fig.11.

5 CONCLUSIONS

This paper demonstrated that multiple AR identified models in the healthy and in the initial damaged conditions could be helpful to perform an extrapolation to a future state if the damages progress in a similar way. This kind of technique combined with a Bayesian approach for extrapolating, seeking to reach high levels of SHM's hierarchy, may provide a significant physical insight if we compare with the trend curves computed by damage-sensitive index with some machine learning approach. First, a model is identified associated with parameters that can predict future states or conditions before the occurrence. Of course, the basic premise is that the evolution of the initial damage is not abrupt and does not happen in different points. Investigations regarding these issues are necessary because in a real-world scenario the behavior of a damage evolution is complex.

To identify with other input signals, for example, random input, and with different temperatures and operational conditions is required to be able to conduct tests with a focus in a simulation and not the only prediction. Other models can also be employed, in particular, Gaussian Process (GP) combined with AutoRegressive models because of the ability of these models to predict with band confidence and admit

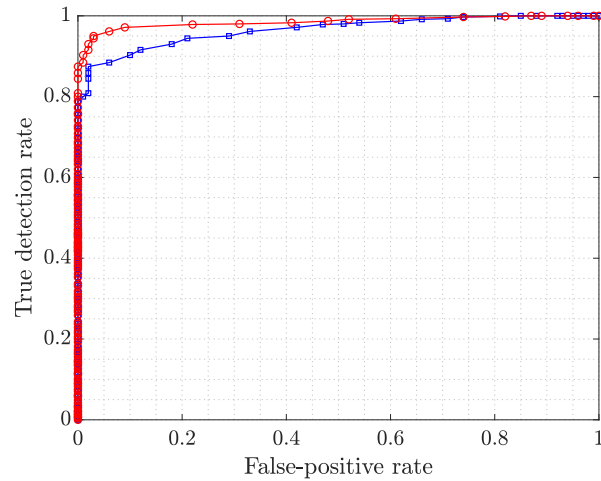


Figure 10: Receiver Operating Characteristics (ROC) curve: □ Extrapolated, and ○ Real.

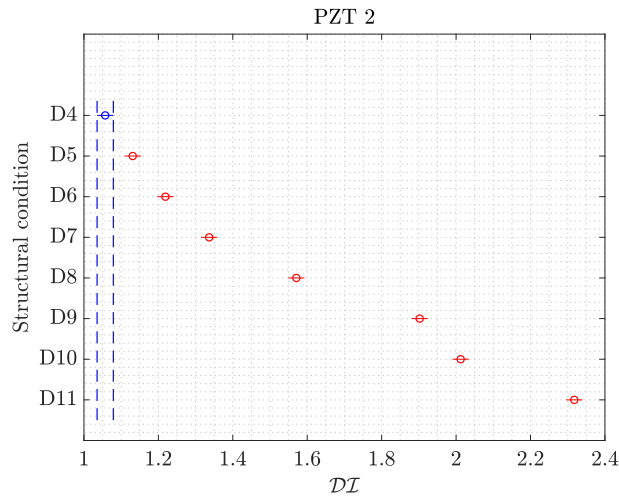


Figure 11: Classification of the clusters of different damage' states using ANOVA of DI assuming extrapolated model. 3 groups (in red) have means significantly different from healthy H .

a priori probability identified to extrapolate a future state. Numerical simulation using finite element models are further beneficial to correlate more intense and complicated damage progression with an extrapolated data-driven model, and some studies are started in this direction.

ACKNOWLEDGEMENTS

The first and second authors are thankful for the financial support provided from São Paulo Research Foundation (FAPESP) grants 2017/15512-8 and 2018/15671-1 and the Brazilian National Council for Scientific and Technological Development (CNPq) grant number 307520/2016-1.

REFERENCES

- [1] Nardi, D., Lampani, L., Pasquali, M., Gaudenzi, P. Detection of low-velocity impact-induced delaminations in composite laminates using Auto-Regressive models. *Comp. Struct.* (2016) **151**: 108-

113. <https://doi.org/10.1016/j.compstruct.2016.02.005>
- [2] Kim J., Kim, K. and Sohn, H. Subspace model identification of guided wave propagation in metallic plates. *Smart Mater. Struct.* (2014) **23**(3):035. <https://doi.org/10.1088/0964-1726/23/3/035006>
- [3] da Silva, S. Data-driven model identification of guided wave propagation in composite structures. *J. Braz. Soc. Mech. Sci. Eng.* (2018) **40**:543. <https://doi.org/10.1007/s40430-018-1462-4>
- [4] Gonzalez, C. G., da Silva, S., Brennan, M. J., Lopes Jr, V. Structural damage detection in an aeronautical panel using analysis of variance. *Mech. Syst. Signal Process.* (2015) **52-53**:206-216. <https://doi.org/10.1016/j.ymssp.2014.04.015>
- [5] Ljung, L., *System Identification*, 2nd edn. Prentice-Hall PTR, Upper Saddle River, (1998).
- [6] Shiki, S. B., da Silva, S., Todd, M. D. On the application of discrete-time Volterra series for the damage detection problem in initially nonlinear systems. *Struct. Health Monitor.* (2017) **16**(1): 62-78. <https://doi.org/10.1177/1475921716662142>
- [7] Kopsaftopoulos, F., Fassois, S. Vibration based health monitoring for a lightweight truss structure: Experimental assessment of several statistical time series methods. *Mech. Syst. Signal Process.* (2010) **24**:1977-1997. <https://doi.org/10.1016/j.ymssp.2010.05.013>
- [8] Hogg, R. V., Ledolter, J. *Engineering Statistics*, Mac Millan Publishing Company, University of Michigan, (1987), ISBN:9780023557903.
- [9] Wolberg, G., Alf, I. An energy-minimization framework for monotonic cubic spline interpolation. *Journ. of Comp. and Applied Math.* (2002) **143**:145-188. <https://www.sciencedirect.com/science/article/pii/S0377042701005064?via%3Dihub>.
- [10] Brien, C. M. Smoothing splines: Methods and applications by Yuedong Wang. *Intern. Statistical Rev.* (2012) **80**(3):475-476.
- [11] Lee, J. S., Park, G., Kim, C. G., Farrar, C. R. Use of relative baseline features of guided waves for in situ structural health monitoring. *Journal of Int. Mater. Syst. and Struct.* (2011) **22**(2):175-189. <https://doi.org/10.1177/1045389X10395643>.

INVESTIGATION OF NONLINEAR LAMB WAVE/DAMAGE INTERACTION: NUMERICAL AND EXPERIMENTAL APPROACHES

XIXI LI, ERIC MONTEIRO, MARC REBILLAT, MIKHAIL GUSKOV, NAZIH
MECHBAL

Process and Engineering in Mechanics and Materials laboratory (PIMM)
Ecole nationale supérieure d'arts et métiers
151 Boulevard de l'Hôpital, 75013 Paris, France

Abstract: One of the most important issues in engineering is the monitoring and the early detection of structural damages to prevent catastrophic failures. This process is referred to as Structural Health Monitoring and is expected to provide considerable improvements with respect to safety and maintenance costs. More particularly, the focus is here put on composite structure representative of aeronautic applications and the damages to be monitored are of “delamination” type. Nonlinear features generated by Lamb wave/damage interaction were employed for the detection of the delamination damage. Experiments are conducted on composite plates made of carbon fiber reinforced polymer equipped with two piezoelectric transducers. One plate is calibrated with a delamination damage at the center using laser shock wave technique. Nonlinear features of Lamb waves are observed in the experimental results. Finite element method is here used for investigating the nonlinear wave properties as well as the wave/damage interaction. Two damage models are studied and implemented at delamination area: a spring model and a contact model. An undamaged plate is also presented as reference in both finite element simulations and experiments. Results show that higher harmonics can be used as identification of the existence of delamination damage in a composite structure. A contact interaction model can represent the mechanical behavior of delamination damage and can be used for a real delamination modelling.

Key words: Structural Health Monitoring (SHM), Lamb wave, delamination, Finite Element method

1. INTRODUCTION

One of the most important issues in engineering is the monitoring and the early detection of structural damages to prevent catastrophic failures. This process is referred to as Structural Health Monitoring (SHM) and is expected to provide considerable improvements with respect to safety and maintenance costs [1]. In SHM, the first stage and the most important part is damage detection.

In the past decades, various techniques for damage detection have been investigated. Among them the wave propagation-based method has become the most commonly used method for its

convenience and low costs. Specifically, Lamb waves are widely used in beam- and plate-like structures due to the high sensitivity to multiple defects with high precision of identification, the ability to cover entire cross-sectional area, convenience for usage, cost-effectiveness and low energy consumption [2], [3]. With a high susceptibility to interference on a propagation path, e.g. damage or a boundary, Lamb waves can travel over a long distance even in materials with a high attenuation ratio, such as carbon fiber-reinforced composites, and thus a broad area can be quickly examined [4].

So far, most of the existing Lamb wave damage detection methods are based on linear wave propagation properties, such as time of flight, reflected waves, transmitted waves and mode conversion information at the excitation frequency [5]–[8]. However, these methods are only sensitive to large defects such as an open crack, but for tiny damages nonlinear techniques are required [9]. Compared to linear techniques, nonlinear Lamb waves are more sensitive to smaller, even barely visible damages such as delaminations in composite structures or cracks. Generally, the nonlinear phenomena are induced mainly due to two types of physical mechanisms. One mechanism is related to the nonlinear relationship between strain and stress of materials in structures and components [10], [11]. The other mechanism is the so-called non-classical nonlinearity, which is often due to other mechanisms such as, for example, a contact acoustic nonlinearity (CAN) [10]. Here in this paper, a delamination type damage is focused, where nonlinearities are induced due to the second mechanism, that is, the contact between the interfaces of the delamination in composite structures.

Generally, when the incident wave passes through the damage, the damage interfaces tend to move towards each other under compressive pressure, and opposite each other under tensile pressure [10]. This may lead to the interaction between damage interfaces. In this case, when Lamb wave interacts with contact-type of damage, such as delamination damage, higher harmonics can be generated due to the contact between damage interfaces [11]–[13].

Several studies focused on the higher harmonics generated by CAN in plate-like structures. Finite element (FE) simulations and experiments were conducted to investigate the nonlinear Lamb wave/damage interaction as well as the wave propagation. Yang *et al* [11] carried out a three-dimensional (3D) simulation and also experiments on an aluminum plate to investigate the second harmonic generation due to a fatigue crack. The investigations were conducted using S0 and A0 Lamb waves generated by eight piezoceramic discs. Delrue *et al* [14] built a 3D model for a composite rectangular plate containing a circular delamination for the investigation of its nonlinear behavior. The excitation was applied by out-of-plane nodal displacement. Ramadas *et al* [15] the mode conversion of Lamb waves due to the presence of delamination. The delamination was modelled by de-merging the nodes at delamination region. The excitation was modelled by giving out-of-plane displacements on the surface of the composite plate. Hong *et al* [16] developed a solid model for simulating the generation of the nonlinearities when ultrasonic waves traverse a fatigued medium. The excitation was applied by piezoelectric wafers on an aluminum plate. Soleimanpour *et al* [12] studied the potential of a baseline-free structural health monitoring techniques based on higher harmonics resulting from the interaction of guided wave with a delamination. They employed a 3D FE model to simulate the delamination damage behavior in a composite beam, with a displacement excitation.

From the above stated studies, it can be observed that in FE simulation study, a common way to generate Lamb waves is to apply an out-of-plane displacement excitation on plate structures. This is only a simplification of the excitation by piezoelectric transducers, which are

commonly used in experiments. However, the electro-mechanical behavior of piezoelectric transducer excitations and directly displacement excitations can be quite different, and thus the wave/damage interaction may be also different from experiments. Some scholars used piezoelectric wafers to induce Lamb waves in simulation, but mostly on aluminum plates. In this study, piezoelectric elements are employed to generate Lamb waves in composite plates.

In order to test and verify the nonlinear Lamb wave/damage interaction theories and the proposed finite element models, experimental investigations are necessary, and particularly, physical supports are firstly needed. Generally, Teflon inserts [12], [17], [18], attaching industrial putties [19] and convention impacts [20][21] are the major existing techniques used for delamination generation. The main weakness with these techniques is that they do not allow for an effective control of the induced damage. For example, the calibration of delamination using impacts may induce other types of damage. As for Teflon insert technique, the problem is that it remains far from a realistic delamination damage.

As an alternative to conventional damage generation techniques, a new method named Laser Shock Wave Technique (LSWT) [22] is used to calibrate delamination damages in composites. In this paper, studies are conducted using the composite specimens with delaminations generated by laser shock. Two damage models are presented to investigate the interaction between Lamb wave and a well-controlled real delamination damage. An undamaged model is used as baseline.

This paper is organized as follows. First, the experimental configuration and results are presented in section 2. Then the FE model of a composite plate and the delamination region as well as the simulation results are illustrated in section 3. In section 3, the comparison between FE simulation and experiments are also presented. Finally, the paper is concluded in section 4.

2. EXPERIMENTAL STUDY

In this section, experiments are performed for the detection of delamination damage in composite plates.

2.1 Experimental system

The experiments are conducted using a SHM system developed by author's team. The experimental setup is shown in Figure 1(a). The specimen is suspended to the workbench in nearly free boundary conditions in order to prevent the specimen from interacting with other supports (e.g. test bench). Two composite plates made of carbon-fiber reinforced polymer (CFRP) are employed for testing: a damaged plate and an undamaged plate. The plates are in the size of $315 \times 100 \times 2.24 \text{ mm}^3$, constituting of 16 plies with a stacking sequence of $[0^\circ/90^\circ]_8$. The material properties of this plate are listed in Table 1.

Each composite plate is equipped with two PZT disks (diameter 25 mm, thickness 0.5 mm) produced by Noliac, as shown in Figure 1(b). One PZT is used as transmitter for signal generation and the other is used as signal receiver. The excitation signals are transmitted from the signal generator through the amplifier to PZT1 to generate elastic waves inside the plate. The waves propagate inside the plate and arrive at PZT2. Then PZT2 transforms the elastic waves to electrical signals, and the signals are collected by the data acquisition system. The input signal is a sine wave signal at the frequency of 109kHz with its amplitude of 10V after amplification. The sampling frequency of data acquisition is 10^6 Hz .

The damaged plate contains a circular delamination damage at the center. Damage was introduced into samples in a calibrated way using laser shock wave technique. The specimen was subjected to a symmetrical laser impact of two laser beams. This resulted in a 7 mm diameter nearly circular delamination at midplane of the composite plate [23].

2.2 Experimental results

Figure 2 shows the experimental signals received by the PZT2 from both healthy and damaged plates. The results in Figure 2(a) are calculated by converting the time signal into the frequency domain using a fast Fourier transform (FFT) which includes the incident waves and the reflected waves from the plate edges and the delamination. From the signal amplitudes obtained from the undamaged plate, only one peak can be observed at 109kHz, which corresponds to the fundamental frequency. In contrast, the signal amplitudes obtained from the delaminated plate show the existence of second and third order harmonics in frequency domain. In addition, the subharmonics at 0.5 and 1.5 times of the fundamental frequency also appear. Figure 2(b) shows the short time Fourier transform of the received signal from the damaged plate. In this diagram, the subharmonics and superharmonics are also apparent. This is evidence that a delamination damage generated by laser shock induces nonlinear features of Lamb waves, and this phenomenon can be used as identification for real delamination damages in composite structures.

Table 1: Materials properties used in FE model (1 ply)

Density(kg/m ³)	E ₁₁ (GPa)	E ₂₂ (GPa)	G ₁₃ =G ₁₂ (GPa)	ν_{12}
1594	140	9	4.5	0.3

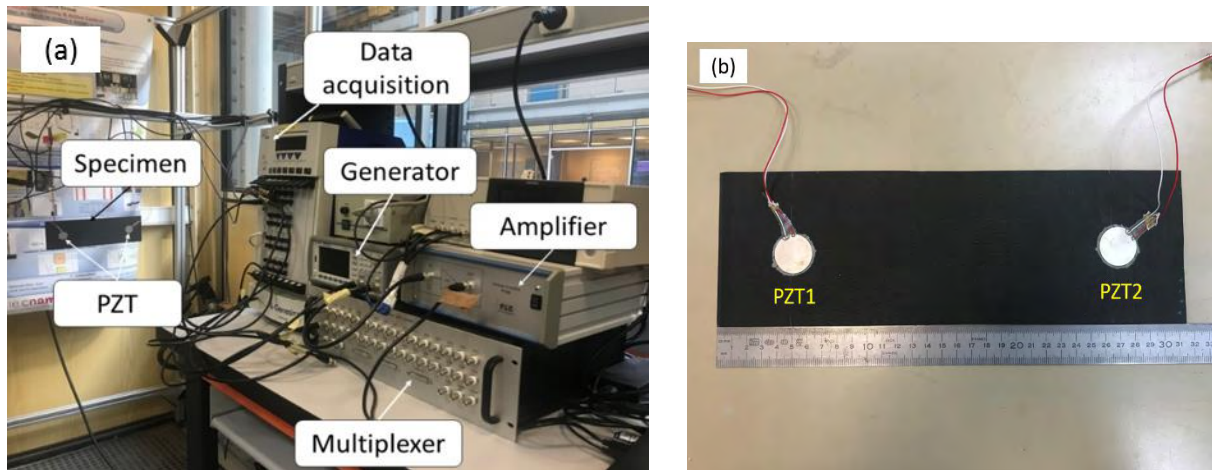


Figure 1: (a) Experimental system; (b) Specimen: composite plate equipped with two PZTs

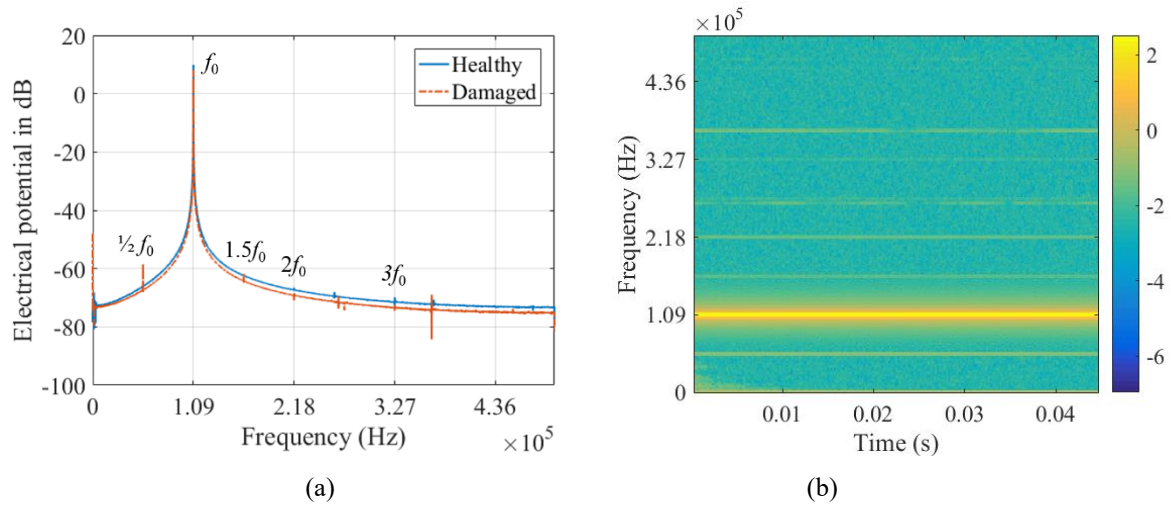


Figure 2: Experimental results: (a) comparison of the responses in frequency domain for the undamaged plate and the damaged plate. f_0 is the fundamental frequency. (b) Time-frequency distribution of the experimental signal received from the damaged plate

3. FINITE ELEMENT SIMULATION

In order to investigate the nonlinear phenomena appearing in the experiments, FE simulations are conducted. Two damage models are employed and compared, representing different interaction mechanisms between delamination interfaces.

3.1 Model of composite plate

In this section, the FE method is used to simulate the propagation of Lamb waves in a cross-ply laminated composite plate. Figure 3 shows the FE model built in the commercial software ABAQUS. In this model, the composite plate is modeled by bonding two shell layers using “tie” interaction except the delamination region. Each layer contains 8 plies. Eight-node shell elements (S8R) are used to avoid a high aspect ratio between length in the in-plane direction and thickness in through-thickness direction of the solid elements.

Two piezoelectric transducers (PZT) are bonded to the surface of the plate for transmitting and receiving electrical signals. The PZTs are modelled using quadratic solid piezoelectric elements (C3D20E). The meshes at the contact surfaces of piezoelectric elements and the plate are identical, which assures the coupling between PZT and the plate. The electrical potential of the bottom surfaces of the PZT elements are set to be 0. The input signal is exerted on the top surface of PZT1, and the electrical potential on the top surface of PZT2 is measured. A sinusoidal wave at the frequency of 109kHz is used as the excitation signal.

3.2 Element size and time step

It was shown previously [24] that in simulation of wave propagation temporal and spatial resolution should be small enough to satisfy the convergence requirements. In general, the time increment required for a dynamic analysis is

$$\Delta t < \frac{1}{10f_{max}}$$

where Δt is the time increment in the analysis procedure, and f_{max} is the highest frequency of interest. In this study, the higher harmonics in the received signals are of interest, which reflect the existence of delamination damage. Therefore, the highest frequency to be detected is the frequency of the third harmonics, i.e. $3 \times 109\text{kHz} = 327\text{kHz}$. Then the time increment can be expressed as $\Delta t < 3 \times 10^{-7}\text{s}$. In order to achieve better accuracy, the time step is set as $0.2\mu\text{s}$.

In a wave propagation study, the element size is usually associated with the investigated minimum wave length λ_{min} . It is generally recommended that more than 10 nodes per wave length should be used, and this criterion can be expressed as [24]

$$l_e < \frac{\lambda_{min}}{10}$$

where l_e is the element length.

Since the number of nodes in a single wavelength can influence the accuracy of wave propagation simulation, a convergence study for element size is conducted. The model used here is the same plate model illustrated previously but with a smaller size ($300\text{mm} \times 30\text{mm}$). The excitation is a 5-circle tone-burst displacement excitation applied as a boundary condition to the left edge of the plate. Two types of excitation are considered here: the out-of-plane displacement excitation for approximation of A0 wave and the in-plane displacement excitation for approximation of S0 wave [25]. Five cases of different element sizes are studied: 5mm, 2.5mm, 2mm, 1mm and 0.5mm. The time of flight (ToF) of the amplitude is measured in the convergence study.

The effects of element sizes on ToF for both in-plane displacement excitation and out-of-plane displacement excitation are depicted in Figure 4. A straight line parallel to x-axis is shown in Figure 4(a), indicating that the ToF curve may converge at element size larger than 5mm. Thus, 5mm is accurate enough for simulating S0 wave. Meanwhile, Figure 4(b) shows a monotonic increase in ToF by decreasing the element size. The ToF first increases drastically when element size decreases from 5mm to 2.5mm, and then it shows a slight increase with element size decreasing from 2.5mm to 0.5mm. The ToF converges to 0.1803ms at element size of 1mm. However, the ToF at 2mm is 0.1801ms, showing only 0.1% difference with respect to the convergent value. Therefore, in this study, the global element size is set to be 2mm along the in-plane direction to achieve a trade-off between the simulation accuracy and computational costs. In the delamination region the local element size is set to be 0.4mm.

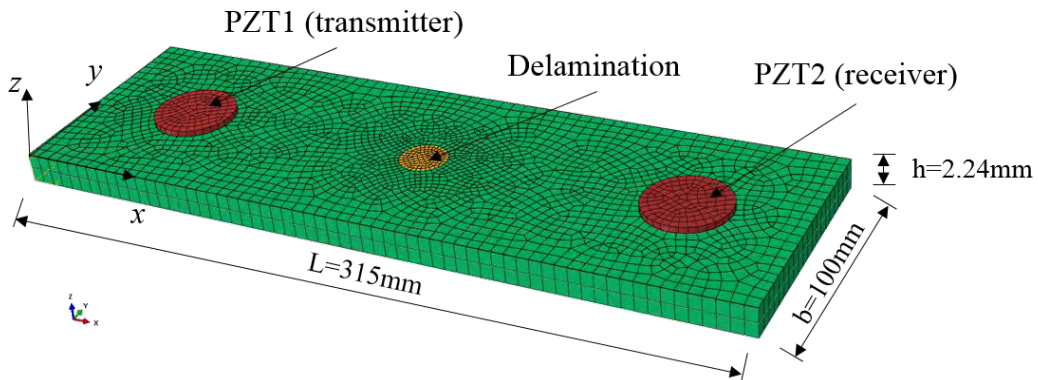


Figure 3. FE model of the composite plate using quadratic shell elements

3.3 Damage model

In this section, two damage models are presented: the spring model and the contact model. In the spring model, delamination is modelled by adding a set of linear spring elements. These spring elements connect the nodes distributed on the delamination interfaces, as shown in Figure 5. The relative movement between delamination interfaces are controlled by the spring stiffness, which is defined along the axial direction of the spring elements, that is, the through thickness direction of the plate.

In reality, no penetration will happen between contact surfaces; however, in finite element analysis, hypothetical penetration is possible. If the spring stiffness is too small, penetration may happen between the delamination interfaces, while with a spring stiffness far too large, there won't be any interaction between the interfaces. Therefore, an appropriate spring stiffness is needed. A sensitive analysis of spring stiffness was conducted. Several spring stiffnesses were investigated, and results show that the sensitive zone happens between $10^3 \text{N/m} \sim 10^6 \text{N/m}$, as shown in Figure 6. Therefore, in this study, the spring stiffness is $5 \times 10^4 \text{N/m}$.

The contact damage model is implemented by applying a surface-to-surface contact to the delaminated region. Figure 7 shows two types of relationship between contact pressure and overclosure (interpenetration) between the surfaces: "hard" contact interaction and the free boundary condition at contact surfaces. When the contact interfaces are separated, no pressure is exerted onto the surfaces, and if contact interfaces are in contact, the penetration is 0. This avoids the hypothetical penetration in FE simulation, at the cost of longer computational time.

The delamination is a circular area located in the mid-plane of the plate, i.e. between the 8th and 9th ply. The diameter of the delamination region is 7mm. The centroid of the delamination is located at the center of the plate. An undamaged plate is also investigated for reference.

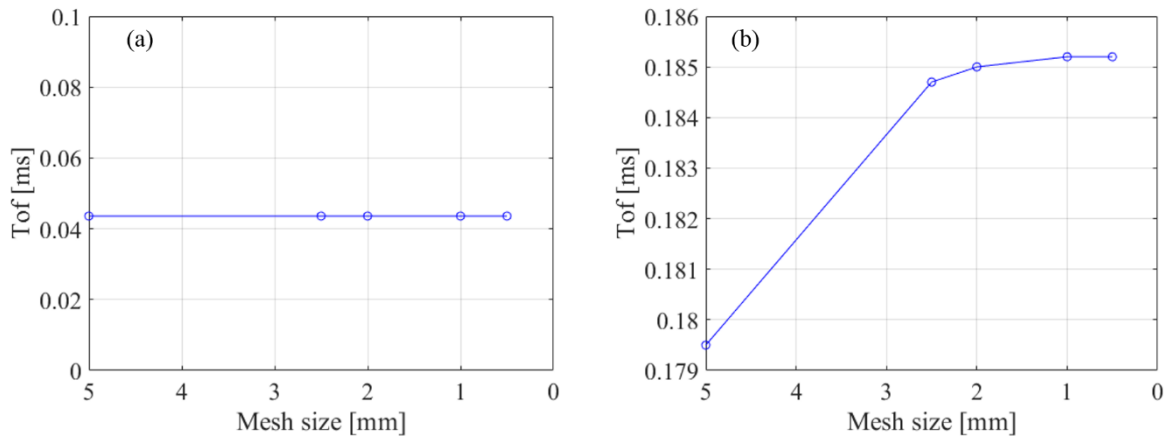


Figure 4: Effect of element size on ToF when the FE model subject to a displacement excitation at the left edge: (a) in-plane displacement excitation, (b) out-of-plane displacement excitation.

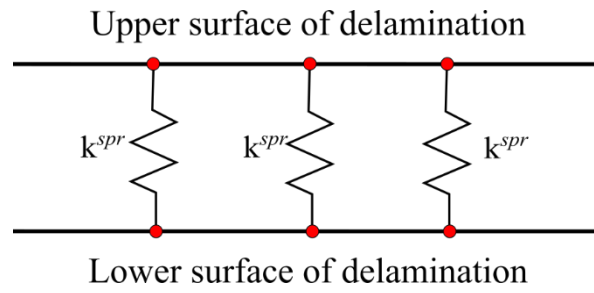


Figure 5: Schematic of the spring model at delamination region. The spring elements connect the nodes distributed on the delamination interfaces. k^{spr} is the spring stiffness.

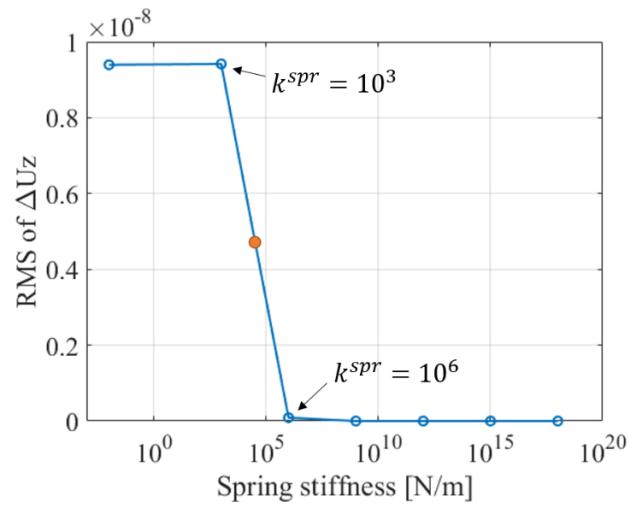


Figure 6: Sensitivity analysis of spring stiffness in the spring damage model. ΔU_z indicates relative out-of-plane displacements between delamination interfaces. k^{spr} is the spring stiffness.

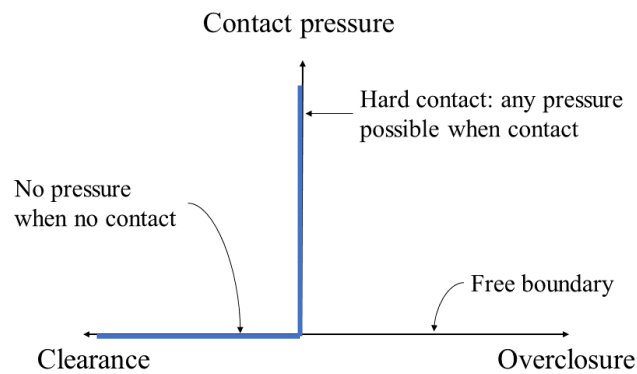


Figure 7: Schematic of the contact pressure-overclosure relationship in the surface-to-surface contact model at delamination region [26]

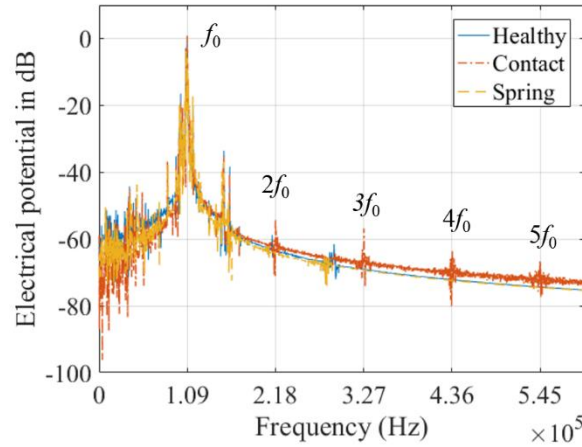


Figure 8: Simulation results: comparison of the models' responses in frequency domain for the undamaged plate model (healthy), damaged plate model with contact interaction (contact) and damaged plate model with spring elements (spring) at delamination region. f_0 is the fundamental frequency.

3.4 Simulation results

A comparison of the amplitudes of the received signals in frequency domain is shown in Figure 8 for the undamaged model, the spring model and contact model respectively. The signals are obtained by measuring the electrical potential at the receiving PZT and transforming into frequency domain. As shown in Figure 8, besides the fundamental frequency, the higher harmonics can be observed clearly from the contact model, including second, third, fourth and fifth order harmonics. However, in the healthy model and spring model, the peak amplitudes only appear at fundamental frequency. It can be concluded that a contact interaction model can be used to characterize the nonlinear features of Lamb wave/damage interaction, while a linear spring model is not appropriate for the representation.

3.5 Comparison between finite element simulation and experiments

Comparisons of the amplitudes of the received signals in frequency domain from experiments and FE simulations are shown in Figure 9. The results are obtained after baseline subtraction, i.e. subtract the signals from the healthy plate. Significant difference is observed in Figure 9(a), between experimental results and FE results from the spring model. From the FE results, no super-harmonics or subharmonics can be observed in the signal amplitudes, leading to a disagreement between experiments and FE results.

In contrast, it is possible to observe from Figure 9(b) that results from contact model show good agreement with the experimental results. Both show the second and third harmonics in the amplitudes. However, in case of FE simulation data many higher harmonics are observed. On the other hand, in case of experimental data second and third harmonics as well as subharmonic at half of the fundamental frequency are distinctly alongside the other harmonics. This discrepancy between FE simulation and experimental observations may be due to the effect of the experimental system and the presence of environmental noise. From the above discussion, it can be concluded that results from the contact model shows better agreement with those from experiments, compared to the linear spring model.

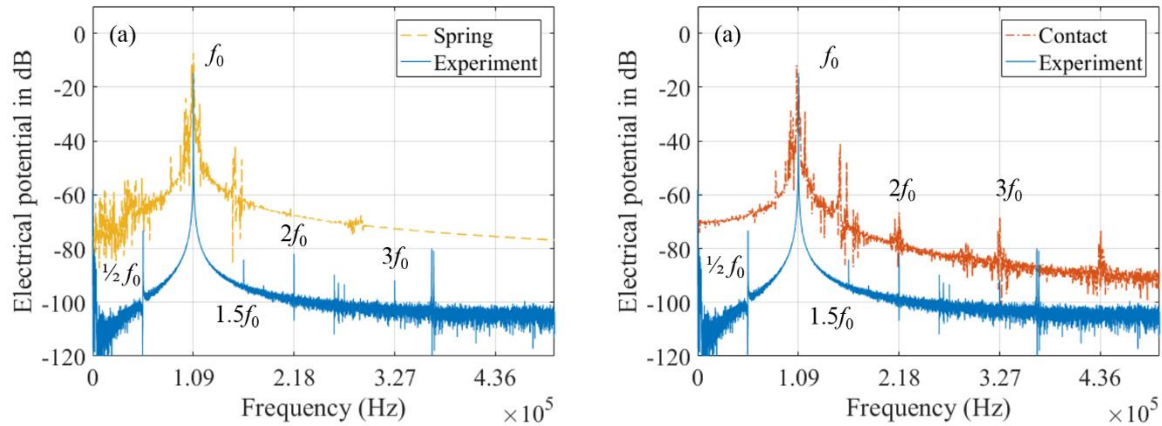


Figure 9: Comparison of amplitudes of receiving signals from experiments and FE simulations in frequency domain after baseline subtraction: (a) experiments and nonlinear damaged model (with contact interaction), (b) experiments and linear damaged model (with linear spring elements). f_0 is the fundamental frequency.

4. CONCLUSION

Nonlinear phenomena induced by delamination damage in composite structures are investigated in this paper. Experiments are conducted on a healthy plate and a plate with delamination damage generated by the laser shock technique. Fourier transform is used to transform the time signals into frequency domain. Experimental results from the damaged plate show superharmonics and subharmonics, while only fundamental frequency component appears in the healthy case. An analysis of the interaction between Lamb waves and delamination damage is performed using FE simulation method. Two damage models, the spring model and the contact model, are employed and calculated. The simulation results show that super-harmonics can be observed from the contact model, while only fundamental frequency exists in the spring model and healthy model. A comparison was conducted between experiments and FE simulations, showing that results from the contact model achieved good agreement with experimental results. It can be concluded that a contact interaction model is appropriate for characterizing the interaction between Lamb wave and a real delamination damage, and that it can be used to simulate nonlinear interaction between delamination interfaces.

REFERENCES

- [1] V. Giurgiutiu, *Structural health monitoring of aerospace composites*. 2015.
- [2] C. R. Farrar and K. Worden, "An introduction to structural health monitoring," *Philos. Trans. R. Soc. A Math. Phys. Eng. Sci.*, vol. 365, no. 1851, pp. 303–315, 2007.
- [3] J. L. Rose, "A Vision of Ultrasonic Guided Wave Inspection Potential," in *JProceedings of the 7th ASME NDE Tropical Conference - 2001*, 2001, pp. 1–22.
- [4] Z. Su and M. Hong, "13 - Nonlinear ultrasonics for health monitoring of aerospace structures using active sparse sensor networks," in *Structural Health Monitoring (SHM) in Aerospace Structures*, F.-G. Yuan, Ed. Woodhead Publishing, 2016, pp. 353–392.

- [5] P. Rajagopal and M. J. S. Lowe, "Scattering of the fundamental shear horizontal guided wave by a part-thickness crack in an isotropic plate," *J. Acoust. Soc. Am.*, vol. 124, no. 5, pp. 2895–2904, Nov. 2008.
- [6] C. M. Yeum, H. Sohn, H. J. Lim, and J. B. Ihn, "Reference-free delamination detection using Lamb waves," *Struct. Control Heal. Monit.*, vol. 21, no. 5, p. n/a-n/a, Aug. 2013.
- [7] C. T. Ng, "On Accuracy of Analytical Modeling of Lamb Wave Scattering at Delaminations in Multilayered Isotropic Plates," *Int. J. Struct. Stab. Dyn.*, vol. 15, no. 08, p. 1540010, Dec. 2015.
- [8] S. Shoja, V. Berbyuk, and A. Boström, "Delamination detection in composite laminates using low frequency guided waves: Numerical simulations," *Compos. Struct.*, vol. 203, no. May, pp. 826–834, 2018.
- [9] N. P. Yelve, M. Mitra, and P. M. Mujumdar, "Spectral damage index for estimation of breathing crack depth in an aluminum plate using nonlinear Lamb wave," *Struct. Control Heal. Monit.*, vol. 21, no. 5, p. n/a-n/a, Sep. 2013.
- [10] D. Broda, W. J. Staszewski, A. Martowicz, T. Uhl, and V. V. Silberschmidt, "Modelling of nonlinear crack-wave interactions for damage detection based on ultrasound - A review," *J. Sound Vib.*, vol. 333, no. 4, pp. 1097–1118, 2014.
- [11] Y. Yang, C. T. Ng, A. Kotousov, H. Sohn, and H. J. Lim, "Second harmonic generation at fatigue cracks by low-frequency Lamb waves: Experimental and numerical studies," *Mech. Syst. Signal Process.*, vol. 99, pp. 760–773, 2018.
- [12] R. Soleimanpour, C.-T. Ng, and C. H. Wang, "Higher harmonic generation of guided waves at delaminations in laminated composite beams," *Struct. Heal. Monit. An Int. J.*, vol. 16, no. 4, pp. 400–417, 2017.
- [13] S. He and C. T. Ng, "Modelling and analysis of nonlinear guided waves interaction at a breathing crack using time-domain spectral finite element method," *Smart Mater. Struct.*, vol. 26, no. 8, p. 85002, 2017.
- [14] S. Delrue and K. Van Den Abeele, "Three-dimensional finite element simulation of closed delaminations in composite materials," *Ultrasonics*, vol. 52, no. 2, pp. 315–324, 2012.
- [15] C. Ramadas, K. Balasubramaniam, M. Joshi, and C. V. Krishnamurthy, "Interaction of guided Lamb waves with an asymmetrically located delamination in a laminated composite plate," *Smart Mater. Struct.*, vol. 19, no. 6, 2010.
- [16] M. Hong, Z. Su, Q. Wang, L. Cheng, and X. Qing, "Modeling nonlinearities of ultrasonic waves for fatigue damage characterization: Theory, simulation, and experimental validation," *Ultrasonics*, vol. 54, no. 3, pp. 770–778, 2014.
- [17] C. A. C. Leckey, K. R. Wheeler, V. N. Hafiychuk, H. Hafiychuk, and D. A. Timuçin, "Simulation of guided-wave ultrasound propagation in composite laminates: Benchmark comparisons of numerical codes and experiment," *Ultrasonics*, vol. 84, pp. 187–200, Mar. 2018.
- [18] N. Quaegebeur, P. Micheau, P. Masson, and A. Maslouhi, "Structural health monitoring strategy for detection of interlaminar delamination in composite plates," *Smart Mater. Struct.*, vol. 19, no. 8, p. 85005, 2010.
- [19] H. Sohn, G. Park, J. R. Wait, N. P. Limback, and C. R. Farrar, "Wavelet-based active sensing for delamination detection in composite structures," *Smart Mater. Struct.*, vol. 13, no. 1, pp. 153–160, 2004.

- [20] A. Klepka, L. Pieczonka, W. J. Staszewski, and F. Aymerich, “Impact damage detection in laminated composites by non-linear vibro-acoustic wave modulations,” *Compos. Part B Eng.*, vol. 65, pp. 99–108, 2014.
- [21] H. Sohn *et al.*, “Delamination detection in composites through guided wave field image processing,” *Compos. Sci. Technol.*, vol. 71, no. 9, pp. 1250–1256, 2011.
- [22] M. Ghrib *et al.*, “Generation of controlled delaminations in composites using symmetrical laser shock configuration,” *Compos. Struct.*, vol. 171, pp. 286–297, 2017.
- [23] M. Ghrib, “Structural Health Monitoring of composite structures: LASER shock delamination generation and machine learning-based quantification,” L’École Nationale Supérieure d’Arts et Métiers, 2017.
- [24] F. Moser, L. J. Jacobs, and J. Qu, “Modeling elastic wave propagation in waveguides with the finite element method,” *NDT E Int.*, vol. 32, no. 4, pp. 225–234, Jun. 1999.
- [25] Y. Shen, “Structural health monitoring using linear and nonlinear ultrasonic guided waves,” *PhD Diss.*, p. 224, 2014.
- [26] *ABAQUS Documentation user’s guide for v6.14-5.* .

SPATIAL ATTENUATION PREDICTION OF LAMB WAVES IN COMPOSITE MATERIALS

SHUANGLIN GUO^{*}, MARC REBILLAT^{*} AND NAZIH MECHBAL^{*}

^{*} Procédés et Ingénierie en Mécanique et Matériaux (PIMM)
ENSAM-CNAM-CNRS-HESAM
e-mail: shuanglin.guo@ensam.eu

Key words: Structural health monitoring, Lamb wave, attenuation prediction, composite materials, viscoelastic damping.

Abstract. The inspection and detection of damage in composite materials using Lamb waves are particularly effective because Lamb wave can propagate over relatively large distance and hence can cover a large area with few testing time and equipment. However, comparing to the dispersion features that have been investigated systematically in the literature, predicting simply and reliably the spatial attenuation, which is the decrease of the amplitude of the propagating wave with distance, is still a challenge especially for structures large enough to industrial scale. In this paper, a simple model able to predict Lamb wave attenuation for different frequencies, which takes three damping models, Hysteretic, Kelvin-Voigt and Biot models into account, is derived directly from dispersion equations. Experiments on a practical aeronautical component, a Fan Cowl Structure, are carried out to validate the developed model. The merits of the proposed method lie in the fact that it is derived directly from dispersion equations instead of relying on complex finite element models and are thus simple to compute. Despite its simplicity, it is still effective when predicting attenuation coefficient for geometrically complex structures such as the Fan Cowl Structure.

1 INTRODUCTION

One of the most important issues in engineering concerns the monitoring and the early detection and localization of structural damages in order to prevent catastrophic failures. This process is referred to as Structural Health Monitoring (SHM) and is expected to provide considerable improvements with respect to safety and maintenance costs. Over half a century, modern SHM techniques have attained maturity in engineering practice, playing a significant role in evaluating the integrity and durability of engineered structures and assets [1]. With efficient, continuous and automated SHM techniques it is possible to identify structural damage at an early stage so as to prevent further failure occurring, producing huge economic and human benefit [2]. A SHM system generally focuses on three aspects: i) identifying the existence, location and classification of damage, ii) evaluating the severity of damage and iii) predicting the residual service life of structure.

Monitoring the health and integrity of complex aeronautical structures at the operation condition is mandatory. Among all kinds of SHM techniques, ultrasonic wave strategy based on Lamb waves is particularly effective in accomplishing this task because Lamb waves are able to propagate over relatively large distances and thus can cover a large with short testing time and few sensors. This benefit results in reduced labor and time to perform a test, and

makes long range inspection possible [3].

The dispersion and attenuation property of Lamb wave are two essential factors that need to be considered carefully when inspecting a structure by means of Lamb waves. Contrasting with dispersion which is the velocity change with frequency and that has already received sound exploration over the past decades, understanding and modeling the attenuation of Lamb wave in composite materials is still an open challenge. Existing efforts are limited to simulation and small-scale experiments. Recently, the damping effect on dispersion curves in plates was investigated theoretically [4]. The theoretical model to calculate the attenuation coefficient in viscoelastic anisotropic lamina was established based on linear 3D elasticity [5]. Two alternatives for this purpose were achieved via semi-analytical finite element method [6] and spectral collocation method [7]. The Rayleigh damping model was adopted to investigate the attenuated Lamb wave propagation in composite structures [8,9]. This model was also adopted to investigate damage detection of composite structures [10].

However, the investigation of Lamb wave attenuation in practical aeronautical structures caused by viscoelastic damping has been scarcely studied after the authors made an overall literature survey. This is owing to the complicated service conditions of aeronautical structures, including complex geometry and boundary of the structure itself, varying environment temperature and noise contamination etc. However, knowledge of in situ attenuation of Lamb waves for these structures is very desirable to deploy SHM strategies to monitor them. To solve this issue, this paper establishes a predictive model of Lamb wave attenuation for practical aeronautical structures and the experiment on a large-scale structure has been conducted to validate the model. Being able to predict spatial attenuation in such complex aeronautic structures paves the way for potential applications such as transducer network design optimization and amplitude-based damage localization algorithms development.

2 PREDICTIVE MODEL OF LAMB WAVE ATTENUATION

2.1 Attenuation representation of Lamb wave

When a Lamb wave mode is excited and propagates in a thin plate with infinite width, the displacement formula of the plate along the propagation direction can be expressed as follows [1].

$$u_x(x, t) = Ae^{j(kx - \omega t)} \quad (1)$$

where, A is the amplitude of wave at the origin point in temporal and spatial domain; k and ω are wavenumber and circular frequency respectively; x and t are the sensing distance and wave propagation time respectively; $j = \sqrt{-1}$.

It is supposed that as long as damping is considered the wavenumber is complex-valued,

$$k^* = k_r + jk_i \quad (2)$$

where, both k_r and k_i are real positive number. The superscript “*” denotes that the term correlated belongs to complex numbers space in this paper.

Substituting Eq. (2) into Eq. (1) can result in the following formula.

$$u_x(x, t) = Ae^{-k_i x} e^{j(k_r x - \omega t)} \quad (3)$$

Comparing Eq. (3) to Eq. (1), if the wavenumber is a complex number, the magnitude decays exponentially over the propagation distance, and this phenomenon is the so called

attenuation behavior of Lamb wave. Thus, k_i is defined as the attenuation coefficient in unit Np/m. Lamb wave attenuation is mainly caused by viscoelastic damping [6]. Hence, the damping models should be expounded firstly.

2.2 Damping effects on Lamb wave attenuation

There are generally two classical damping models to describe the viscoelasticity: Hysteretic (HR) model and Kelvin-Voigt (KV) model [11]. For both models, the Young modulus becomes a complex number E^* presented in Eqs. (4) and (5) respectively, in which the real part is defined as the storage modulus E representing the storage of energy and the imaginary part reflects the loss of energy. Besides the two models, a less common damping model named Biot (BT) model is used to investigate the damping effect on Lamb wave attenuation as presented in Eq. (6). This model is mainly applied to highly damped aerospace structures [12].

$$E^* = E(1 - j\gamma_{HR}) \quad \text{for Hysteretic model} \quad (4)$$

$$E^* = E \left(1 - j\gamma_{KV} \frac{f}{f_0} \right) \quad \text{for Kelvin - Voigt model} \quad (5)$$

$$E^* = E \left[1 + \frac{2}{\pi} \gamma_{BT} \ln \sqrt{1 + \left(\frac{2\pi f}{\epsilon} \right)^2} - j \frac{2}{\pi} \gamma_{BT} \arctan \left(\frac{2\pi f}{\epsilon} \right) \right] \quad \text{for Biot model} \quad (6)$$

where, γ_{HR} , γ_{KV} and γ_{BT} are the damping ratio for HR, KV and BT model respectively; ϵ is the scaling factor for BT model; f_0 is the reference frequency of KV model and it is set arbitrarily to be 250kHz in this paper. As this parameter is just a normalization parameter, setting arbitrarily its value is not an issue. If $\gamma_{KV} = \gamma_{HR}$ and $f = f_0$, KV model is equivalent to HR model at the frequency f_0 [11].

In light of the complex Young modulus, no matter which damping model being used, the classical dispersion equations become complex equations:

$$\begin{cases} \frac{\tan(\alpha_T^* h)}{\tan(\alpha_L^* h)} = -\frac{4k^2 \alpha_L^* \alpha_T^*}{(\alpha_T^{*2} - k^2)^2} & \text{for symmetric modes} \\ \frac{\tan(\alpha_T^* h)}{\tan(\alpha_L^* h)} = -\frac{(\alpha_T^{*2} - k^2)^2}{4k^2 \alpha_L^* \alpha_T^*} & \text{for anti - symmetric modes} \end{cases} \quad (7)$$

where, h is the half thickness of plate. $\alpha_L^* = \sqrt{\frac{\omega^2}{c_L^{*2}} - k^2}$ and $\alpha_T^* = \sqrt{\frac{\omega^2}{c_T^{*2}} - k^2}$; $c_L^* = \sqrt{\frac{\lambda^* + 2\mu^*}{\rho}}$

and $c_T^* = \sqrt{\frac{\mu^*}{\rho}}$ are the velocity of longitudinal and transverse mode respectively. $\lambda^* = \frac{E^* \nu}{(1+\nu)(1-2\nu)}$ and $\mu^* = \frac{E^*}{2(1+\nu)}$ are the Lamé constants. ν and ρ are the Poisson ratio and density respectively.

The phase velocity c_p is the quotient between circular frequency and real wavenumber. The group velocity c_g is the partial derivative of circular frequency to real wavenumber.

$$c_p = \frac{\omega}{k_r} \quad (8)$$

$$c_g = \frac{\partial \omega}{\partial k_r} = \frac{c_p^2}{c_p - \omega \frac{dc_p}{d\omega}} \quad (9)$$

2.3 Numerical algorithm of predicting Lamb wave attenuation

The solution of the real-valued dispersion equation forms the dispersion curve, which is usually expressed as two pairs (ω, c_p) and (ω, k) . However, the task of solving the complex dispersion equation is more complicated in the damped case because for the solution pair (ω, k^*) there are actually three real variables (ω, k_r, k_i) given that $k^* = k_r + jk_i$.

In order to overcome this issue, a two-step approach is proposed to work out the solution of the complex dispersion equation. In step 1, the solution pair (ω, k) for the real-valued equation $f(\omega, k) = 0$ is obtained, which can be easily achieved via many mature algorithms [13]. In step 2, the first three points of (ω, k^*) are acquired by directly solving the complex-valued equation $f^*(\omega, k^*) = 0$, during which the first three points of (ω, k) are taken as the initial guess because the real and complex solutions in (ω, k_r) plane mutually overlap at the initial stage of the dispersion curve. This is true since the effect of damping is relative low, such that $|k_i| \ll |k_r|$ and the strategy of searching the solutions of complex case in the neighborhood of the real case is working. For subsequent solutions, a curve tracing technique should be used in order to avoid branch crossing of different modes and thus guarantee a stable solution [13]. Specifically, the initial guess for the current solution is quadratically extrapolated from the previous three accurate solutions firstly, and then the current solution is obtained by directly solving the complex-valued dispersion equation. The presented two-step procedures form the numerical algorithm of predicting attenuation coefficient as summarized in Figure 1.

It should be noted that a strong complex equation solver is necessary for this algorithm. The authors hence employ the Levenberg–Marquardt based approach which is generally more efficient than Gauss-Newton method for solving a highly nonlinear equation to iteratively find the root of a complex equation from an initial guess [14].

3 DATA-DRIVEN BASED STRUCTURAL PARAMETERS ESTIMATION METHOD

It is evident from Figure 1 that in order to run the algorithm, the nine parameters should be provided in the first place. Normally, the thickness d , density ρ and reference frequency f_0 can be obtained easily. The other six parameters should be estimated from the collected Lamb wave signals, by which the group velocity and attenuation coefficient can be identified easily. Thus, the approach to identify the two parameters is described firstly.

3.1 Linear regression to identify group velocity and attenuation coefficient

3.1.1 Identification of group velocity

Under a specified frequency, a certain Lamb wave mode propagates in an isotropic plate or in an anisotropic plate but along a fixed direction with constant group velocity. Thus, the time-of-arrival (ToA) of Lamb wave is proportional to the sensing distance.

$$t_a = \frac{x}{c_g} + t_0 \quad (10)$$

where, t_a is the ToA; t_0 is the initial time of wave excited from actuator; x is the sensing distance; c_g is the group velocity for the propagating mode.

A series of t_a versus propagation distance x can be extracted from collected signals by indicating the time moment at the peak of the specified wave packet. If the scatter diagram

$(x_i, t_{a,i})$ is plotted, these scatter points should align with a straight line. Thus, linearly regressing these scatter points can be used to identify group velocity that is the inverse of the slope of the regressed line according to Eq. (10).

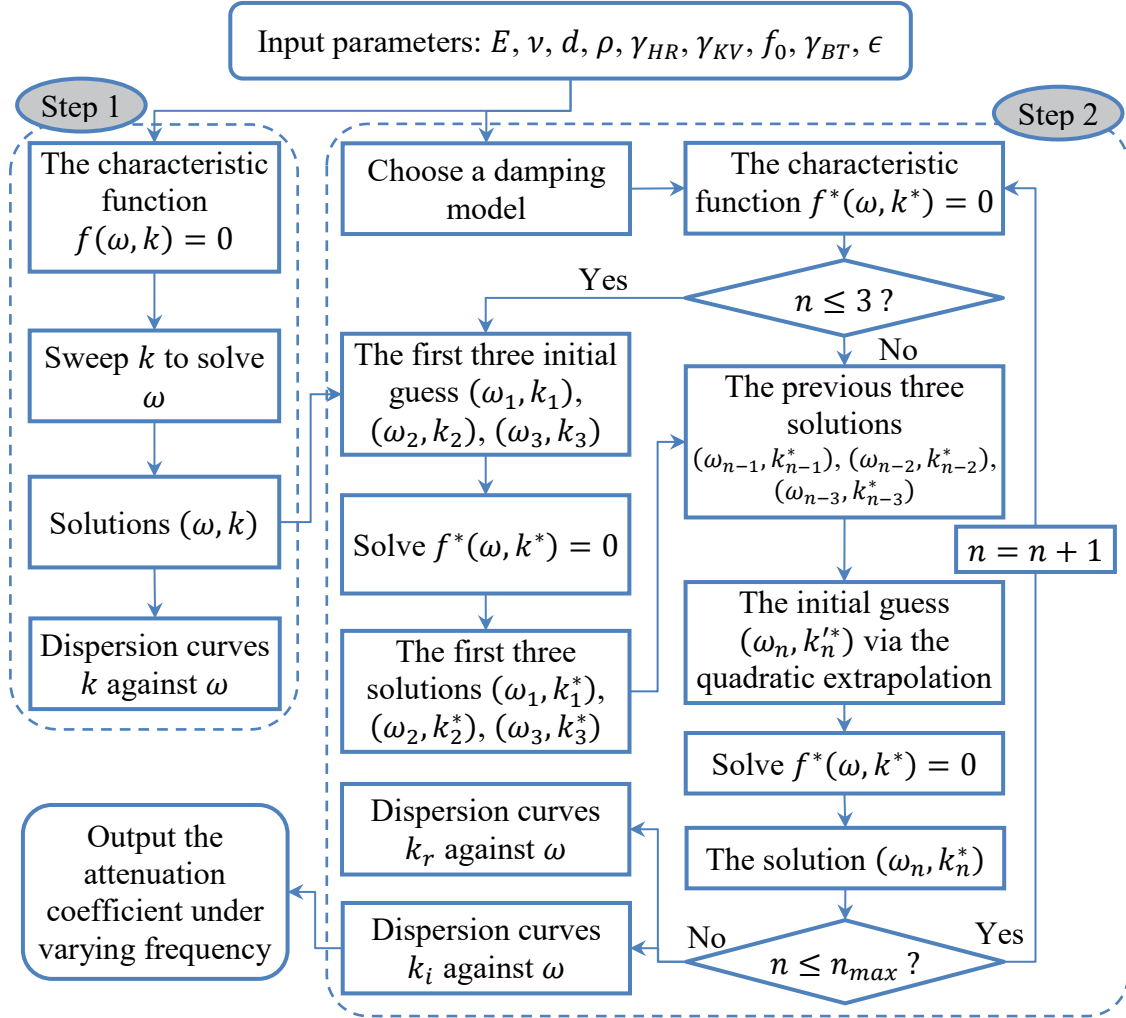


Figure 1: The flowchart of the numerical algorithm for predicting the attenuation coefficient

3.1.2 Identification of attenuation coefficient

Based on Eq. (3), the amplitude of wave exponentially decreasing over propagation distance is stated as following.

$$u_m = Ae^{-k_i x} \quad (11)$$

Making logarithm operation at two sides of Eq. (11) results in the linear formulation.

$$\ln u_m = -k_i x + \ln A \quad (12)$$

This equation manifests that the attenuation coefficient k_i can be identified from recorded signal by linearly regressing logarithmic amplitude of wave versus propagation distance, in which the attenuation coefficient is the negative of the slope of the regressed line.

3.2 The least square formulation for estimating material properties

The identified group velocity and attenuation coefficient can be used to estimate structural material properties.

3.2.1 Estimation of storage modulus and Poisson ratio

The theoretical group velocity that can be calculated from classical dispersion equations is expressed as the function with respect to storage modulus E and Poisson ratio ν if the frequency f is given.

$$c_g = G(E, \nu; f) \quad (13)$$

Once a series of group velocities under various frequencies are obtained from experiment, denoted as $(f_l, \tilde{c}_{g,l})$ ($l = 1, 2, \dots, m$), the least square formulation can be used to estimate storage modulus and Poisson ratio.

$$\arg \min_{E, \nu} \sum_{l=1}^m [G(E, \nu; f_l) - \tilde{c}_{g,l}]^2 \quad (14)$$

where the symbol “ \sim ” means that the variable it applies is extracted from experimental data. m is the number of excitation frequency during experiment.

3.2.2 Estimation of damping parameters

The theoretical attenuation coefficient k_i is expressed as the function with respect to a general damping parameter γ if the frequency f is given.

$$k_i = K(\gamma; f) \quad (15)$$

where, γ is γ_{HR} , γ_{KV} and γ_{BT} , ϵ for HR, KV and BT model respectively.

Therefore, if a series of attenuation coefficients under diverse frequencies are available from experiment, denoted as $(f_l, \tilde{k}_{i,l})$ ($l = 1, 2, \dots, m$), the least square method can be also used to estimate the damping parameter respectively for the three damping models.

$$\arg \min_{\gamma} \sum_{l=1}^m [K(\gamma; f_l) - \tilde{k}_{i,l}]^2 \quad (16)$$

It should be noted that during performing the least square model of estimating damping parameters, the storage modulus and Poisson ratio estimated through Eq. (14) should be used. When all the required parameters are available, they can be inputted into the algorithm stated in Figure 1 to predict attenuation coefficient.

4 EXPERIMENTAL INVESTIGATION FOR A PRACTICAL AND GEOMETRICALLY COMPLEX AERONAUTICAL STRUCTURE

4.1 Experimental setup and signal presentation

A practical aeronautical structure, namely a fan cowl structure (FCS), is employed to validate the proposed Lamb wave attenuation coefficient prediction algorithm. The structure is made up of composite materials. Its thickness and density are 2.24mm and 1554kg/m³ respectively. The geometry and transducers layout are shown in Figure 2. There are in total 13 piezoelectric lead zirconate titanate (PZT) transducers surface installed on the plate, among which PZT 1-6 and PZT 7-13 respectively align with an approximated straight line and are thus denoted as Group 2 and Group 3. Naturally, Group 1 includes all the PZTs. Since this

structure is large enough and a typical structure in aeronautical engineering, it is suitable for study the Lamb wave attenuation in composite plates.

During testing, input signal is chosen as a five-cycle sinusoid burst signal modulated by Hanning window. The central frequency varies from 50kHz to 250kHz with 5kHz increment. The signal from the function generator is passed through an amplifier for enlarging the voltage in order to produce Lamb wave signals powerful enough. In this experiment, the peak value of the excitation signal is $\pm 50V$. The actuator yields diverse Lamb wave modes and other sensors receive the signal. The data acquisition system (DAS) is adopted to collect signal and then stored in laptop for latter usage.

The sampling frequency is set to be 1MHz given that this value is the maximum capability of the DAS. In order to reduce noise, 10 repetition measurements are performed for each actuator excitation and then the 10 signals are processed with time averaging and wavelet denoising techniques. Figure 3 shows the typical Lamb wave signal in Group 2 in which PZT 1 serves as the actuator and its signal is normalized to the same magnitude of order than the receivers. It is evident that the signal amplitude decreases with the increasing of propagation distance.

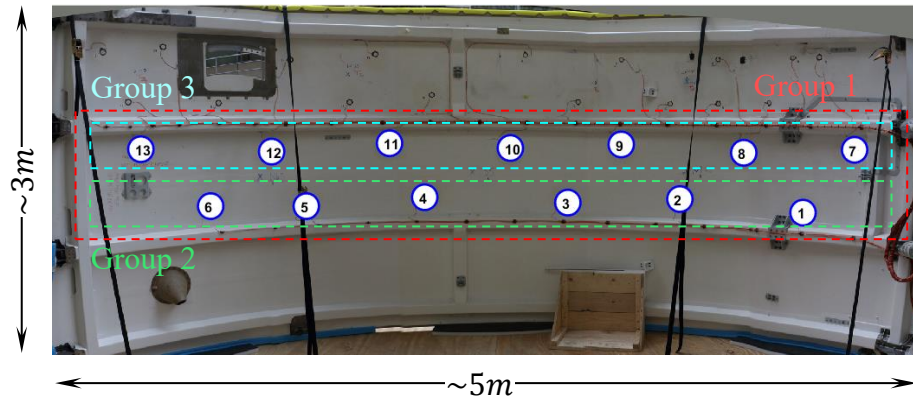


Figure 2: The FCS structure

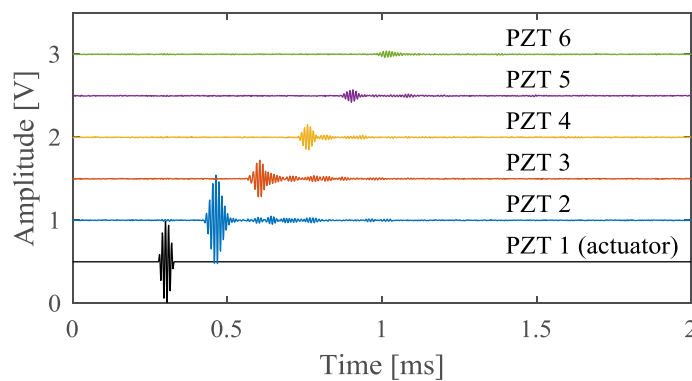


Figure 3: Typical Lamb wave signal (100kHz)

4.2 Dispersion curve identification for group velocity and attenuation coefficient

4.2.1 Group velocity and attenuation coefficient identification

The linear regression model described in section 3.1.1 is used to identify the group velocity at a given frequency. Taking the S0 mode of 100kHz as example, the experimentally measured scatter points between ToA and sensing distance are presented in Figure 4(a). The regressed lines for the three groups are also plotted based on these scatter points, for which the parameter $\alpha = 0.05$ is given to provide the confidence level (95%). In Table 1, the results including group velocity, the lower and upper bound of group velocity and the correlation coefficient of the three groups extracted from regression are listed. Combining Figure 4(a) and Table 1, it can be seen that the three kinds of sensor configuration produce pretty close group velocity identification result and meanwhile keep a very high correlation coefficient 0.99.

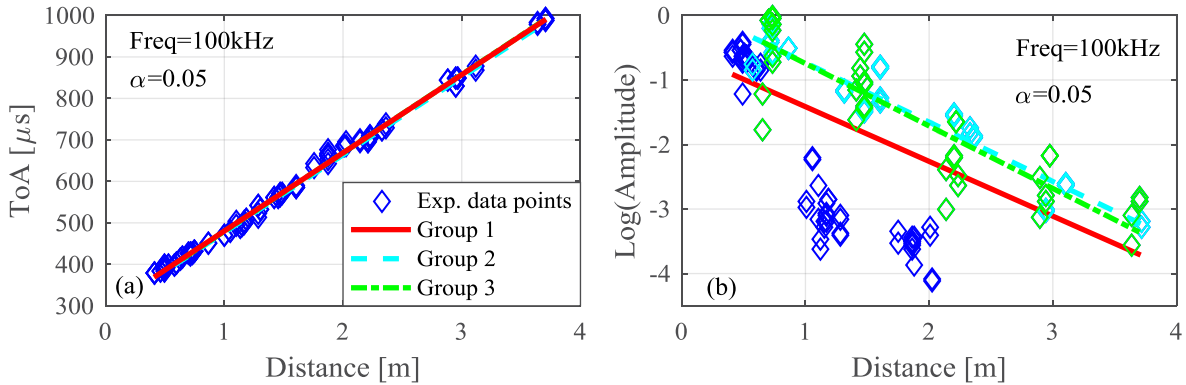


Figure 4: Example of (a) group velocity identification and (b) attenuation coefficient identification via linear regression method. In this figure, α is used to give the confidence level with $100(1 - \alpha)\%$.

The same strategy is designed to identify attenuation coefficient in section 3.1.2. Like Figure 4(a), the linear regression process is illustrated in Figure 4(b) under the same frequency 100kHz. The results extracted from Figure 4(b) are presented in Table 2, from which the dispersed scatter points can be observed. This is due to the difficulty to exactly extract the peak value of S0 mode wave packet given the low sampling frequency (1MHz) and noise contamination. Moreover, the lower correlation coefficient of Group 1 (smaller than 0.6) manifests that the anisotropy of composite materials has an essential impact on attenuation since all propagation directions in Group 1 are mixed together whereas in Group 2 and 3, there exists only one main direction. Thus, Group 2 and 3 are employed to identify the attenuation coefficient dispersion curves in subsequent section.

Table 1: Regression results for group velocity identification (corresponding to Figure 4(a))

Group 1			Group 2			Group 3		
c_g (m/s)	c_g bound (m/s)	R^2	c_g (m/s)	c_g bound (m/s)	R^2	c_g (m/s)	c_g bound (m/s)	R^2
5308	[5258,5359]	0.99	5340	[5279,5402]	0.99	5291	[5257,5325]	0.99

Table 2: The regression results for attenuation coefficient identification (corresponding to Figure 4(b))

Group 1			Group 2			Group 3		
k_i (Np/m)	k_i bound (Np/m)	R^2	k_i (Np/m)	k_i bound (Np/m)	R^2	k_i (Np/m)	k_i bound (Np/m)	R^2
0.85	[0.66,1.04]	0.39	0.92	[0.81,1.03]	0.92	0.97	[0.80,1.13]	0.79

4.2.2 Identified dispersion curves of group velocity and attenuation coefficient

The group velocity and attenuation coefficient at each frequency can be identified by using the method shown in Figure 4(a) and (b) respectively. After that, the group velocity dispersion curves can be formed as shown in Figure 5(a), in which only the result of Group 1 is presented given that the three groups generate pretty close group velocity dispersion curves, and the attenuation coefficient dispersion curves are shown in Figure 5(b). Additionally, Figure 5(c) presents the respective correlation coefficients for group velocity and attenuation. There is no doubt that for group velocity identification all correlation coefficients are greater than 0.95. Hence the identified S0 mode group velocity dispersion curve is reliable.

From the attenuation coefficient dispersion curves (Figure 5(b)) and its corresponding correlation coefficients (Figure 5(c)), the following findings are observed. Firstly, both groups' curves present the same trend, i.e., attenuation increasing with frequency firstly and then decreasing. Secondly, the correlation coefficients of both groups at the initial several points (50-60kHz) are smaller than 0.6. This may be explained by tuning effect of Lamb wave, for which at the lower frequency range, the amplitude of S0 mode is too small to be easily extracted from experimental signals [15]. Finally, the correlation coefficient starts to diminish after 150kHz for both groups, which could be explained by the low sampling frequency and high frequency noise contamination. In later damping parameters estimation, only the identified attenuation coefficients of Group 3 in frequency range from 70kHz to 150kHz are used to be the training data when implementing Eq. (16).

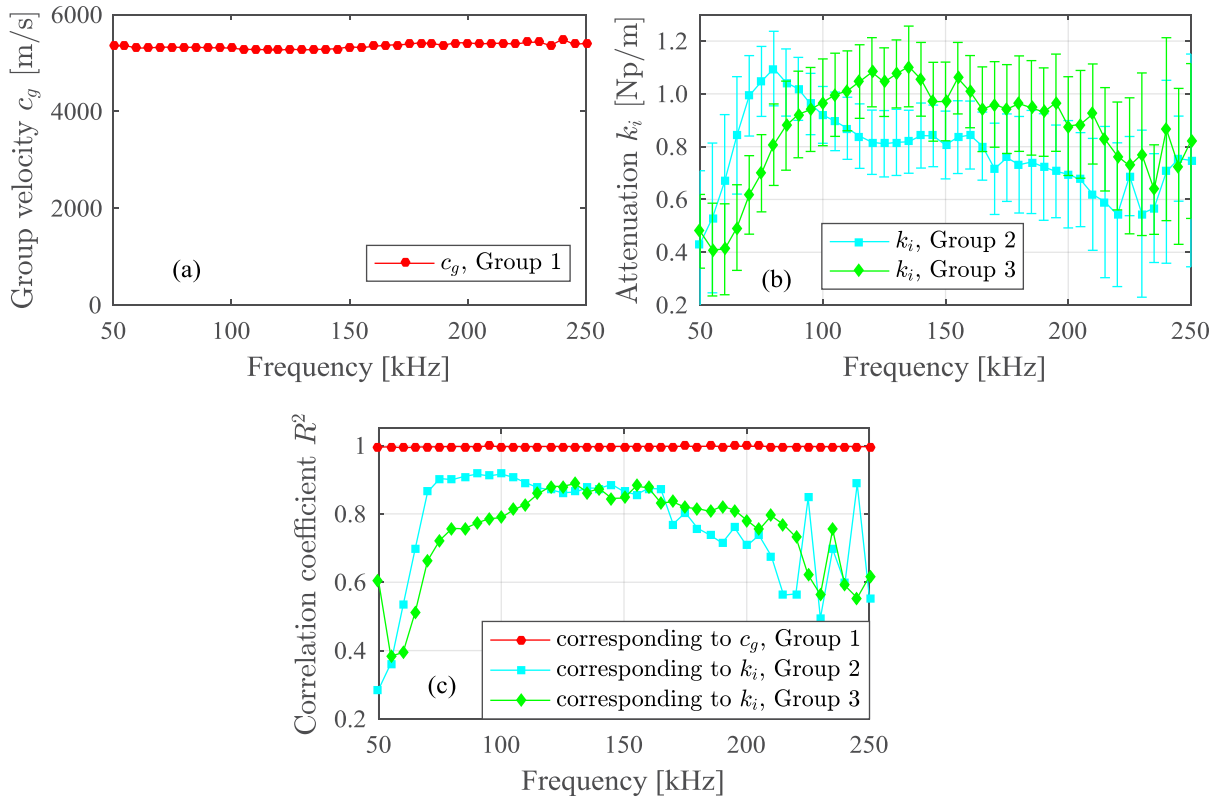


Figure 5: (a) the group velocity dispersion curve, (b) the attenuation coefficient dispersion curve and (c) correlation coefficient

4.3 Estimation of material properties

The experimentally identified dispersion curves of group velocity and attenuation coefficient are further employed to estimate the material properties via the least square method presented in section 3.2. Thus, the group velocity dispersion curve shown in Figure 5(a) is firstly adopted to estimate the storage modulus and Poisson ratio. The initial and optimal values of both parameters are listed in Table 3.

The calculated group velocity dispersion curves for S0 and A0 mode using the optimal value and the experimentally identified data points are depicted in Figure 6. It can be seen that the calculated S0 mode group velocity dispersion curve agrees well with the experiment. Besides, the calculated S0 mode phase velocity dispersion curve is provided as well in this figure which totally overlaps with the calculated group velocity dispersion curve in the frequency range. Comparing the calculated S0 and A0 mode group velocity dispersion curves, it is easy to infer that A0 mode Lamb wave propagates at approximately the half speed of S0 mode in the evaluated frequency range. Thus there is no any A0 mode group velocity can be identified from the experiment because of the abundant S0 mode wave reflections.

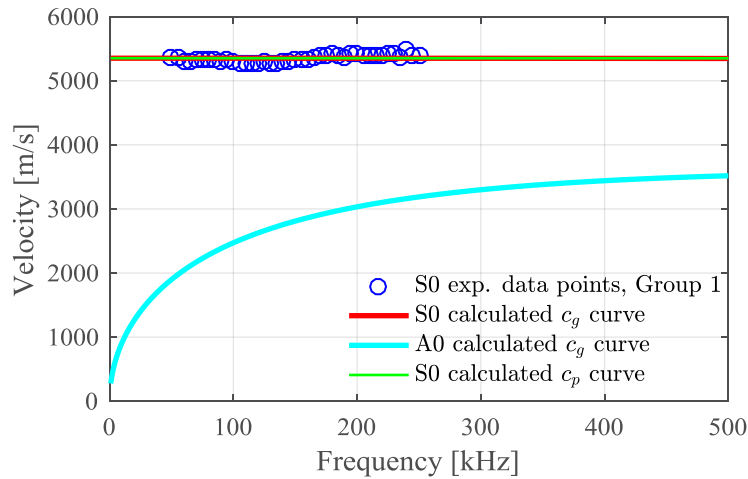


Figure 6: Comparison between the calculated and identified dispersion curve of group velocity

The experimentally identified attenuation coefficients are subsequently employed to estimate the damping parameters of the three damping models based on Eq. (16). The initial and optimal values are listed in Table 3, in which the optimal term γ_{KV} and ϵ do not change from its initial value, which is caused by accident.

Table 3: The estimated parameters of FCS

	E	ν	γ_{HR}	γ_{KV}	γ_{BT}	ϵ
Initial value	50GPa	0.2	0.03	0.03	0.03	10
Optimal value	44.4GPa	0.05	0.014	0.03	0.017	10

4.4 Attenuation coefficient prediction for a wide frequency range

All the required parameters are provided as inputs to the developed algorithm presented in Figure 1 and the attenuation coefficient for a wide frequency range is predicted as shown in Figure 7(a). The experimentally identified attenuation coefficient of Group 2 and 3 in the frequency range from 70kHz to 150kHz is provided as well for comparison. It can be seen that the predicted curves for HR and BT model agree well with the experimentally identified points with strictly linear trend. However, the curve of KV model presents the concave trend. Thanks to this reason, it is only suitable for predicting attenuation coefficient in a narrow frequency band for the current composite structure.

The developed numerical algorithm in Figure 1 is further used to predict the wavenumber which is extracted from the real part k_r of the complex solution as depicted in Figure 7(b). The identified wavenumber calculated via $k = \frac{\omega}{c_p}$ is also provided for comparison, in which c_p is replaced by c_g given that the approximated relation ($c_p \approx c_g$) from Figure 6. It can be seen that the theoretically calculated wavenumber dispersion curves for HR and KV model are consistent with the experimentally identified data points. But BT model predicts a minor smaller wavenumber in the evaluated frequency range than HR and KV model. The high coincidence between the predicted and identified wavenumber or group velocity reveals that the group velocity, phase velocity and wavenumber can be obtained more reliable from experiment or theoretical prediction than the attenuation coefficient.

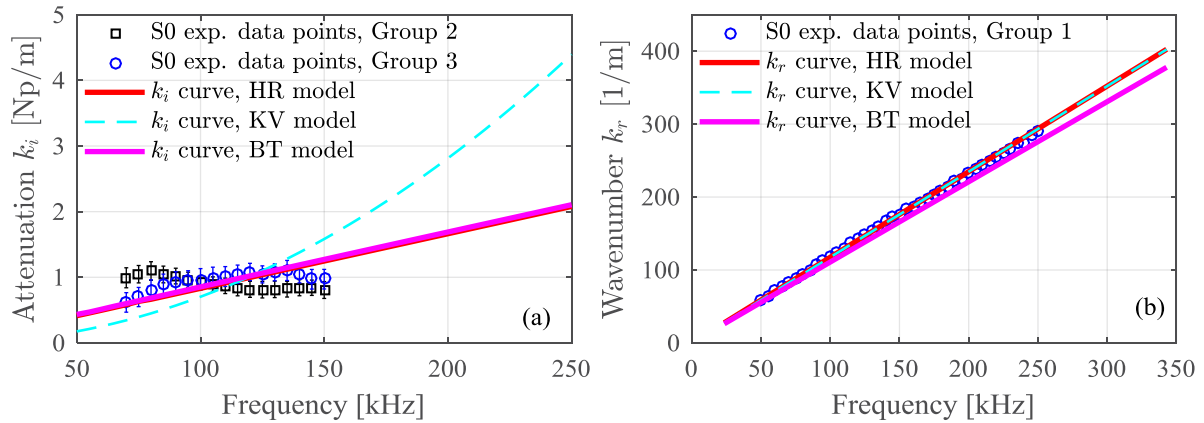


Figure 7: Prediction of (a) attenuation coefficient and (b) wavenumber at a wide frequency range

5 CONCLUSIONS

- In this article, a numerical algorithm to predict Lamb wave attenuation coefficient is proposed firstly. This algorithm is derived directly from dispersion equations by considering three damping models, HR, KV and BT model. The curve tracing technique is adopted to enhance the reliability of solving the complex equation.
- The linear regression method is used to identify group velocity and attenuation coefficient from experimentally measured Lamb wave signals. The least square formulation is designed for estimating the storage modulus and Poisson ratio of material as well as damping parameters of the three damping models.
- A comprehensive case study on a practical aeronautical structure validated that the

proposed attenuation coefficient prediction algorithm is feasible and effective. Comparing to group velocity, accurately identifying and predicting attenuation of Lamb wave in complex composite structures is more difficult and urgent. The presented outcomes in this article are an useful attempt.

REFERENCES

- [1] Su Z and Ye L. Identification of Damage Using Lamb Waves. *Springer* (2009).
- [2] Sohn, H., Farrar, C.R., Hemez, F.M., Shunk, D.D., Stinemates, D.W. and Nadler, B.R. A review of structural health monitoring literature: 1996–2001. *Los Alamos National Laboratory report* (2002).
- [3] Wilcox, P., Lowe, M., and Cawley, P. The effect of dispersion on long-range inspection using ultrasonic guided waves. *NDT&E International* (2001) **34**:1-9.
- [4] Manconi, E. and Sorokin, S. On the effect of damping on dispersion curves in plates. *International Journal of Solids and Structures* (2013) **50**:1966–1973.
- [5] Neau, G. Lamb waves in anisotropic viscoelastic plates: study of the wave fronts and attenuation. PhD Thesis, University of Bordeaux I, France, 2003.
- [6] Mei, H. and Giurgiutiu, V. Guided wave excitation and propagation in damped composite plates. *Structural Health Monitoring* (2018) **18**:690–714.
- [7] Quintanilla, F.H., Fan, Z., Lowe, M.J.S. and Craster, R.V. Guided waves' dispersion curves in anisotropic viscoelastic single- and multi-layered media. *Proc. R. Soc. A* 471 (2183), 20150268.
- [8] Ramadas, C., Balasubramaniam, K., Hood, A., Joshi, M. and Krishnamurthy, C.V. Modelling of attenuation of Lamb waves using Rayleigh damping: Numerical and experimental studies. *Composite Structures* (2011) **93**:2020–2025.
- [9] Gresil, M. and Giurgiutiu, V. Prediction of attenuated guided waves propagation in carbon fiber composites using Rayleigh damping model. *Journal of Intelligent Material Systems and Structures* (2015) **26**:2151–2169.
- [10] Wandowski, T., Kudela, P., Malinowski, P. and Ostachowicz, W. Guided wave attenuation in composite materials. *Proc. SPIE 10170, Health Monitoring of Structural and Biological Systems* (2017) 101701D.
- [11] Rose, J.L. Ultrasonic Guided Waves in Solid Media. *Cambridge University Press* (2014).
- [12] Mastroddi, F., Martarelli, F., Eugeni, M. and Riso, C. Time- and frequency-domain linear viscoelastic modeling of highly damped aerospace structures. *Mechanical Systems and Signal Processing* (2019) **122**:42–55.
- [13] Lowe, M.J.S. Matrix Techniques for Modeling Ultrasonic Waves in Multilayered Media. *IEEE Transactions on Ultrasonics, Ferroelectrics, and Frequency Control* (1995) **42**:525-542.
- [14] Lourakis, M.I. A Brief Description of the Levenberg-Marquardt Algorithm Implemented by levmar. (2005).
- [15] Mei, H. and Giurgiutiu, V. Effect of structural damping on the tuning between piezoelectric wafer active sensors and Lamb waves. *Journal of Intelligent Material Systems and Structures* (2018) **29**:2177-2191.

STRAIN-BASED DAMAGE ASSESSMENT OF STIFFENED COMPOSITE PANELS FOR STRUCTURAL HEALTH MONITORING PURPOSES

DIMITRIOS P. MILANOSKI AND THEODOROS H. LOUTAS

Laboratory of Applied Mechanics and Vibrations
Dept. of Mechanical Engineering and Aeronautics, University of Patras
Patras University Campus, GR-26504, Rio-Patras, Greece
e-mail: d.milanoski@g.upatras.gr; thloutas@upatras.gr

Key words: Parametric finite element model, Composite stiffened panel, Structural health monitoring, Fiber Bragg gratings, Non-linear buckling analysis.

Abstract. A common defect of composite stiffened panel structures is the disbond at the interface between the two constituents (skin/stringer), as a result of inefficient manufacturing process or foreign object impacts in service. Generally, discontinuities within the volume of an elastic solid media subjected to mechanical load, cause anomalies on the strain field in the near vicinity of the discontinuity. Utilizing this observation, the current work investigates the effect of artificially induced disbonds between skin/stiffener at a co-cured CFRP/epoxy single-stiffener generic element. A structural health monitoring methodology is developed, leveraging on numerically simulated strains along the stringer foot which aims to assess the health state of the sensorized structure as compared with a pristine baseline. The study is implemented with a parametric finite element model generating various disbonded cases. Longitudinal strain values are acquired at the exact points where in reality actual Fiber Bragg Grating sensors will be located.

1 INTRODUCTION

Primary airframe structures made of composites tend to increasingly replace more conventional materials. Their advantages correlate to the high specific mechanical properties over metallic materials. Nevertheless, these materials suffer from hidden damages, such as delaminations/disbonds which arise major concerns if not identified at an early stage. In this direction, researchers utilize Structural Health Monitoring technologies to identify and assess damage. Fiber optic sensors (FOS) technology has gained increasing popularity as an alternative method of real-time strain measurements during structural service with minimum additive weight. A popular category of FOS are fiber Bragg grating sensors (FBGs) [1]. Quite a few researchers developed health monitoring methodologies like Li et al. [2], who proposed an automated algorithm based on static strain FBG readings on naval composite T-joints. A baseline of the pristine specimen was developed through which disbond cases were qualitatively

detected. A new method to identify strain modification along disbonds, exploiting Artificial Neural Networks (ANNs), was proposed by Kesavan and co-authors on the aforementioned specimens [3]. Takeda et al. [4] investigated interlaminar damage occurred by low-velocity impacts on CFRP stiffened panels. They used embedded FBGs to monitor the reflection spectra using the central wavelength of the sensors. A framework utilizing FBG strain readings was proposed by Airolidi et al. [5]. The authors developed an integrated Health and Usage Monitoring System (HUMS) of composite spars belong to wing-box, aiming to monitor both load and damage. A study based on static strains obtained by closely placed optical fibers with FBGs, was implemented in [6]. In this case, the differential strain of closely attached sensors placed away from damage, maintained a linear relation with respect to a reference strain, while sensors closest to damage showed a non-linear behavior. Sbarufatti et al. [7] followed a model-based methodology leveraging on a global-local finite element model of a helicopter tail boom in order to evaluate real fatigue crack propagation events. Damage detection was enabled by utilizing the Mahalanobis distance, considering a damage index calculated at each sensor. The methodology was validated experimentally using permanently placed FBGs to record strain data. Finally, a parametric numerical model was created by Zarouchas and Alderliesten [8] to evaluate the damage tolerance capabilities of aluminum stiffened panels. A non-linear buckling analysis was applied, and critical stability aspects of the panel regarding the disbond characteristics, i.e. position and size were highlighted.

The objective of the present paper is to study the effect of disbonds in the strain-field developed on the feet of single-stiffener panels (SSPs) and propose strain-based Health Indicators (HIs) capable of identifying and monitoring structural damage and specifically skin/stringer disbonding. Parametric numerical modeling is implemented to this direction.

2 NUMERICAL ANALYSIS

The numerical modeling procedure is presented in the following. First, the SSP specimen is introduced and its geometrical characteristics are detailed. The test article is consisting of two individual parts, a thin composite flat plate, the skin, and a composite T-section stiffening beam, called i.e. the stringer. The present study investigates the distribution of longitudinal static strains on the outer surface of each stringer foot in health and defected scenarios. The main objective of this work is to utilize the baseline and the strain alterations caused by skin/stiffener disbond and propose suitable HIs to assess/monitor the health state of the structure. The interrogation points are selected in a manner to simulate permanently installed optical fiber sensors, with Bragg gratings in pre-selected locations. Initially, strains from the pristine (healthy) SSP are obtained. Then, a parametric finite element model is created, simulating several disbond cases, in order to assist the objective of this study. Further details regarding the parameterized way of modeling are given below.

2.1 Single-Stiffener Panel configuration

The geometrical dimensions of the SSP, expressed in *mm* are provided in Figure 1, accompanied by the stacking sequences of each member. The material used in this study is an IM7/8552 carbon/epoxy unidirectional continuum fiber-reinforced prepreg, with nominal cured

ply thickness 0.131 mm [9] and mechanical properties [10] as detailed in Table 1. From a numerical analysis point of view, the final geometry of the two members is modelled considering a co-bonding manufacturing technique, without adhesive film in the interfacial region.

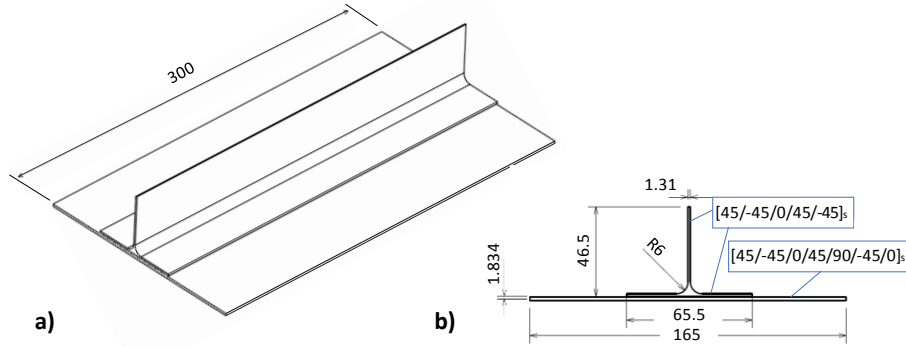


Figure 1: Dimensions of SSP specimen, a) perspective and b) cross-sectional view

Table 1: Engineering and interlaminar properties of IM7/8552 [10]

E_{11} (GPa)	E_{22} (GPa)	G_{12} (GPa)	ν_{12}	G_{Ic} (N/mm)	G_{IIc} (N/mm)	η (-)
150	9.08	5.29	0.32	0.277	0.788	1.6

2.2 Finite Element Model

The numerical model created, simulates the quasi-static compression of the pre-defined SSP. The SSP is loaded under displacement control, in an attempt to simulate the real test procedure. Cast-tab pots are used as load/support members to uniformly transmit the load to the specimen. Hence, two 30 mm exterior regions on the longitudinal direction bind to the pots. A schematic illustration of the test article is showed in Figure 2, indicating also the two SMARTapes[®] accommodating the optical fibers with FBGs (provided by SMARTEC-Switzerland) and the respective sensor spacing. These tapes are made of GFRP/epoxy and protect the accommodating optical fibers from harsh environmental conditions. The global coordinate system (XYZ) of the model is located at the symmetry plane of the top loading tab. Also, a local system (xyz) is defined at the start of each SMARTape[®] (one illustrated in Figure 2). Results regarding disbonds underneath this region will be expressed at the local coordinate system, as shown in Chapter 3.

The numerical study was implemented using the commercial finite element code Abaqus/Standard[®] [11]. Both members are modelled as one discrete layer of 4-node quadrilateral shell elements with reduced integration (S4R) and three integration points along the thickness. Every layer of composite laminates was modelled as a transverse isotropic material, according to the properties presented at Table 1, with thickness equal to the cured ply thickness the material provider suggests i.e. 0.131 mm. Earlier experimental works highlighted that degradation of the material properties is negligible in the early post-buckling region [12]. Thus, for the numerical modeling tasks associated with the present study, progressive

introduced in the imminent non-linear analysis, following the pattern of the considering buckling modes

- A constant, low amplitude force acting along the buckling direction

The second method can alter the strain field in the adjacent region of the actuation point, while the second represents a more sensible way to model the buckling behavior. In the present study, the first way of introducing imperfections is chosen, especially due to the need to obtain as much as possible reliable strain estimations. These imperfections in general are defined by superimposing multiple eigenmodes, and have the following amplitude form with respect to the global coordinate system:

$$\Delta x_i = \sum_{i=1}^n w_i \varphi_i \quad (1)$$

where w_i is the scale factor correlated with the i -th mode shape φ_i . Only the 1st buckling mode was introduced as the lowest modes are frequently more critical, and a scale factor equal to 10% of the stiffener thickness was used. A static Newton-Raphson (N-R) solver, incorporating non-linear geometry formulation was utilized to solve the equilibrium of the non-linear problem. A maximum displacement equal to 0.25 mm was set for loading BC, as deep post-buckling analysis was not relevant with the current study. Due to such excitation, buckling occurred and characterized by the non-linear relation between the reaction force and displacement of the panel. Also, the maximum lateral deflection of skin midplane reached 4.7 mm. So, as buckling load considered the limit load where the linear load-displacement relation is maintained. A mesh convergence study was implemented, regarding the buckling load as this was obtained from both linear and non-linear analysis.

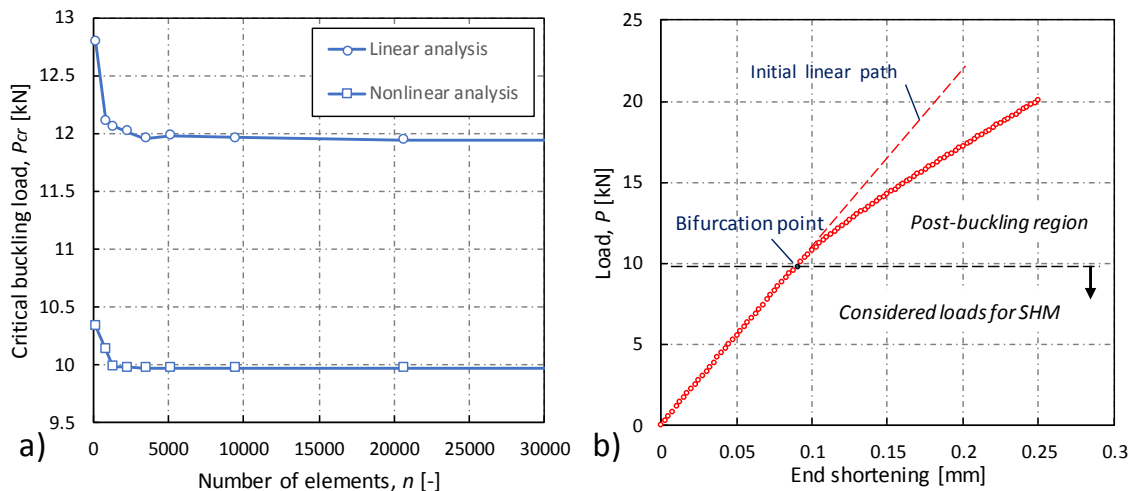


Figure 3: a) Mesh convergence and b) load-displacement curve for considered mesh density

The relevant results are depicted in Figure 3 and the load-displacement curve of the chosen mesh density is illustrated in Figure 3. Convergence was achieved in much lower number of elements, but in order to increase the fidelity of the model, an approximate element size of 2.00

mm was selected producing a total discretization of 20550 elements, as shown in Figure 4. Implementation of the Virtual Crack Closure Technique (VCCT) [13] also requires refined (global) mesh configurations or local refinement.

2.3 Parametric Analysis

The next task deals with the development of a parametric finite element model of the SSP with an artificially induced skin/stiffener, rectangle disbond. The parameterization concerns the position and the size of the disbond assuming a constant width along the right foot, as shown in Figure 4. In order to generate repetitive disbond scenarios at the skin/stiffener interface, a script written in Python® [14] was elaborated. The advantage of this method was the easy applicability, while the script was executed directly via the interface of Abaqus®. Most importantly, all manual tasks regarding the modeling using Graphical User Interface (GUI) of Abaqus® could be expressed in Python® language using proper libraries of the program. So, the script was created on the basis of iteratively generate the geometry, including the parametric position and size of the disbond, while it entailed all of the rest of the model attributes, as these have been previously described (material properties, mesh, BCs, etc.).

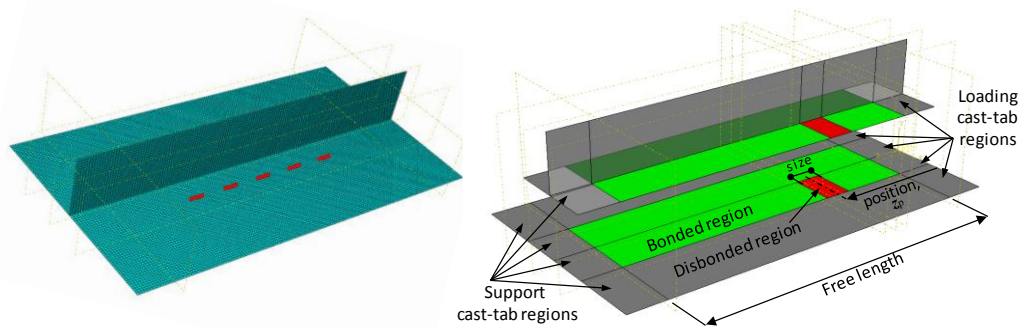


Figure 4: a) Discretized SSP, highlighting the right-foot FBG set, b) partitions of SSP

As we described previously, tie constraints were introduced at the interface region between the skin and the stiffener. Modeling the disbond was achieved by erasing that interaction and allow each of the individual regions of the disbond to freely move, without any kinematic constraint imposed by the other. The specimen was divided in partitions, in a manner of ensuring that coincident nodes at the interface of the two parts were generated. This approach prevented excessive distortion of the elements at the interface while it also allowed the correct implementation of the VCCT, in interfacial disbond propagation case studies. In current analysis, the VCCT was also used in order to assess if the disbonded regions do propagate under the defined loading condition. The interlaminar fracture properties of the IM7/8552 were used according to Table 1. Note that the VCCT is implemented by replacing the tie constraints with a contact interaction. This technique numerically calculates in every step the strain energy-release rate in a pre-defined crack/disbond front. For given critical strain energy-release rates of the material, the B-K criterion [15] controls the fracture initiation and allows the front

elements to separate if the criterion is satisfied. Also, the VCCT implementation requires to explicitly determine the unbonded region nodes in order to evaluate the strain energy release rate along the formed disbond fronts. This was also taken into consideration in the written script, so we can indicate the node sets that were created per iteration as:

- one node set, representing the bonded region, unique for every pair of disbond position and size
- ten node sets, representing the FBGs along each foot, unique for all pairs of disbond position and size

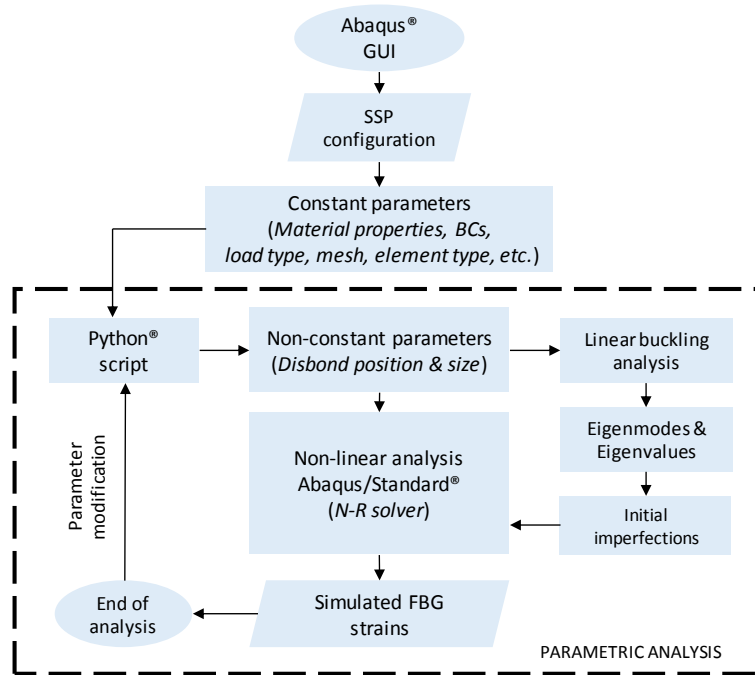


Figure 5: Explanation flow chart of the parametric analysis

None of the considered analyses showed propagation of the associated disbond. Generally, if it is ensured that fracture procedures are not involved, simple tie constraints can be utilized at the bonded region of the two members over the VCCT. A detailed flow chart describing the parametric implementation of the present work, is shown in Figure 5. After completion of every iteration, the disbond characteristics were updated, regarding either the position or the size.

3. DAMAGE ASSESSMENT OF SKIN-TO-STIFFENER DISBOND

In the current section, the effectiveness of two Health Indicators (HIs) on the detection of numerically simulated skin/stiffener disbonds will be investigated. The strain data obtained from the pristine specimen are considered as the baseline. Next, a SHM methodology based on the results obtained by the parametric analyses of skin-to-stiffener disbonds was evaluated. As mentioned before, the parametric analysis generates models with disbond in the interface of skin/stiffener, beneath the right foot. The assessment of disbond cases, within the assumed sensor topology, initiated by introducing a health indicator to estimate the sensitivity of the

FBGs to the disbond position. Finally, the behavior of a second health indicator was investigated versus the disbond size.

3.1 Baseline SHM Methodology

The static strains obtained from the pristine specimen after the non-linear analysis, establish the healthy-baseline which is utilized to reveal the presence of disbonds. Only strains prior to buckling, that belong to the linear portion of load-displacement curve are considered. Furthermore, regarding the disbond cases, similar data are gathered and stored, for each individual disbond scenario. The strains of every FBG are simulated for several load values as different displacements are imposed. Small discrepancies between the strains at the two feet are observed, mainly for the two FBGs closest to the loading tab. The presence of an interfacial disbond region, affects the strain distribution along the foot. An arbitrary case of disbond at position $z_p = 60 \text{ mm}$, and three different sizes, is depicted in Figure 6, under a constant static compressive load of 6.0 kN. The strain perturbation induced by the disbond can be clearly noticed in the vicinity of its edges. The gradient in those regions abruptly increases and the deviation from the pristine (dashed line) distribution is highlighted. The left (fully-bonded) foot shows no deviation from the baseline. Also, the marked points that illustrate FBG readings are highlighted along the curves. Generally, the difference between the strain reading of each FBG for disbonded case and the baseline i.e. the differential strain, shows an increasing trend proportional to the load. The most affected FBG shows higher discrepancies and is linearly increasing up to buckling load, as shown in Figure 6. Hence, a notable remark is extracted as the rest of the FBGs show almost negligible deviation from the baseline up to the buckling load. As the disbond changes position along the foot, a similar pattern of the strain discrepancy was obtained following the disbond position (not shown here). Moreover, the gradient and the amplitude of the discontinuity is not maintained constant and exhibits dependency both on position and load.

In order to estimate the impact of the disbond position to strain modification, a Health Indicator (HI) will be utilized based on the relative strain differences of each FBG in an arbitrary condition with the baseline. The HI is a metric of the strain change, under the same load amplitudes and is calculated as shown in eq. (2).

$$HI_i^1 = \left(\frac{|\varepsilon_{11}^{pristine} - \varepsilon_{11}^{disb}|}{\varepsilon_{11}^{pristine}} \right)_i, i = 1, 2, \dots, 10 \quad (2)$$

where i corresponds to the FBG number. To see the effect of changing external load, an average value of the HI with changing load can be simply calculated, considering n total load cases:

$$\overline{HI} = \frac{1}{n} \sum_{i=1}^n HI_i^1, i = 1, 2, \dots, 10 \quad (3)$$

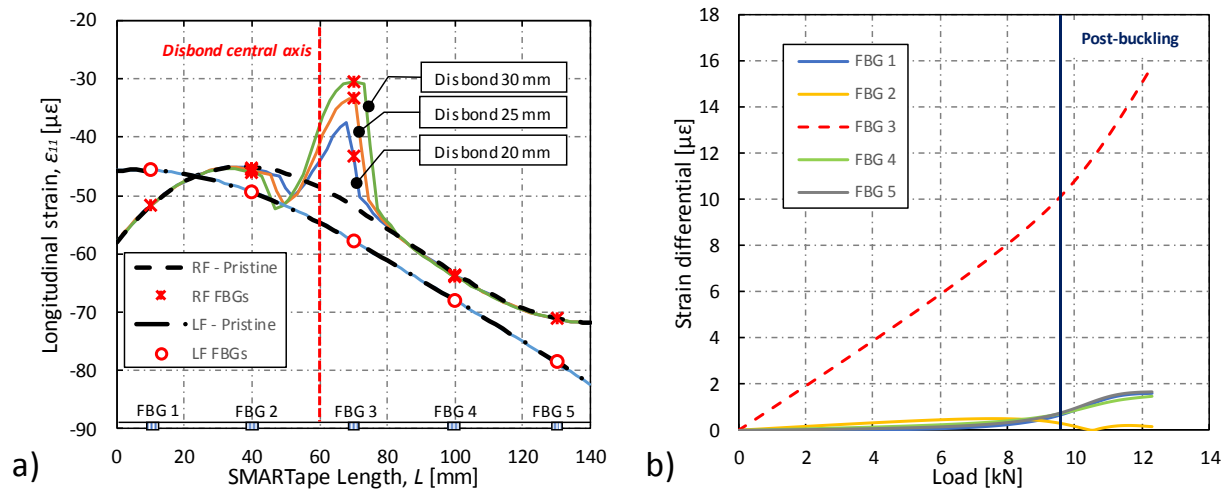


Figure 6: a) Simulated strain distributions along left (LF) and right (RF) foot, associated with disbond cases and b) differential strain over load on RF for 20mm disbond case

Assuming a constant disbond size of 20 mm, the HI indices of the FBGs located at the right foot ($i = 1, 2, 3, 4, 5$) are calculated. Through the parametric numerical model, disbands in several positions in a range 10-130 mm regarding the local coordinate system (xyz) are created. The disbond position is incrementally increasing by 5 mm. The average HI is calculated for every FBG, and the results versus the disbond position are depicted in Figure 7. HI values above 2% are obtained by the current sensor topology, to almost every position of the disbond along the foot. It can be noticed that lower discrepancies occur when a sensor is placed at central position along the disbond against the cases that a sensor is above the disbond front. This estimation can be evaluated by noticing the strain discontinuity profile as it is shown in Figure 6.

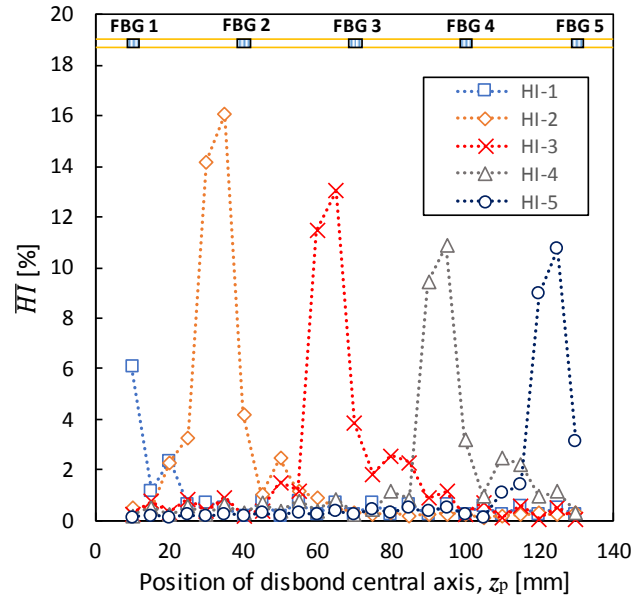


Figure 7: Health indicator predicted by each FBG versus the disbond position along RF

Next, we introduce a second HI fit for Structural Health Monitoring, while the disbond is increasing. This HI combines the strain readings from all sensors. In fact, it represents the percentage each FBG sensor holds of the cumulative strain among the five FBG sensors, and is defined as:

$$HI_i^2 = \varepsilon_i^N = \frac{\varepsilon_{11}^i}{\sum_i \varepsilon_{11}^i}, \text{ for RF: } i = 1, \dots, 5 \text{ and for LF: } i = 6, \dots, 10 \quad (4)$$

where again i corresponds to FBG numbering. This HI is inspired by the observation that the strain of the unaffected sensors shows minor deviation from the healthy condition. In Figure 8a the average values of the HI for every FBG are presented, indicating first the pristine values accompanied by several disbond size cases. The central axis of the growing disbond is at $z_p = 60 \text{ mm}$, as mentioned before and the disbond is assumed to grow by the same length from each side. Finally, in Figure 8b the HI is presented for every FBG under increasing size of disbond. The 3rd sensor on the RF is the most affected by the disbond front and this fact is illustrated with a monotonical drop on its index of about 8% regarding the intact specimen value. The rest FBG sensors show a slight increase of their HI values, no more than 2%. Only the 2nd sensor shows an increase higher than 2% in the case of 50 mm disbond as the disbond front reaches this sensor too.

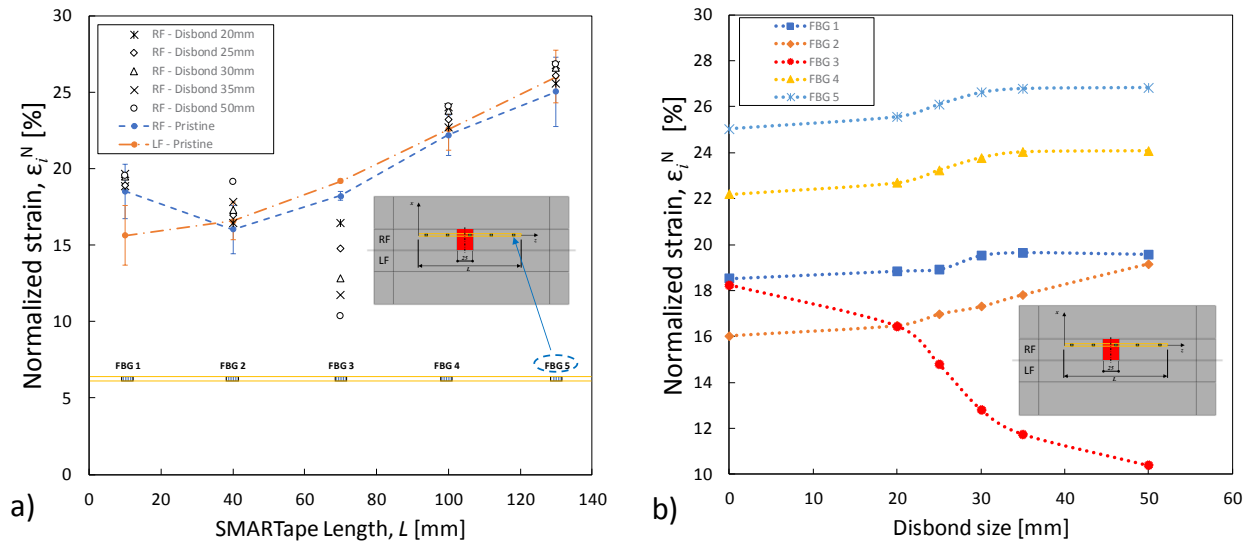


Figure 8: a) Normalized strain indices of FBGs on pristine and various disbonded specimens and b) gradual change of indices versus an increasing disbond size

4 CONCLUSIONS

In the current study, a model-based methodology for damage assessment on generic single-stiffener composite panels was approached. Towards that end, a finite element analysis was conducted in order to simulate the composite panel subjected to uniaxial compressive

loading. Longitudinal strains were computed at predefined regions where permanent FBG sensors will be attached. Initially, a non-linear buckling analysis was executed deriving the investigated strains on pristine (healthy) structure. Furthermore, numerous skin-to-stiffener disbonds were introduced via a parametric numerical model using Python[®] scripting.

First, by a strain differential methodology, the impact of the disbond positioning to the strain distribution was evaluated. For that purpose, a health indicator was used comparing longitudinal strains of the pristine baseline with the disbonded cases. Then, another indicator representing a strain normalization scheme of every sensor was calculated. The aforementioned index was illustrated for several disbond sizes and indicated a monotonic drop on the sensor that was more affected by the disbond. Conclusively, the first health indicator utilizes strains from the pristine baseline and those out of disbonded cases. It can be characterized as baseline-dependent. A drawback of this indicator lies on its load dependency, whilst a very interesting outcome is the small scatter that the indicator showed in the whole load range they were examined. On the other hand, the second indicator does not rely on baseline data. From that perspective and from the monotonic behavior it exhibits for increasing disbond size, it constitutes a promising choice for SHM.

ACKNOWLEDGEMENTS

The work presented in this paper was financially supported by the European Union's Horizon 2020 research and innovation programme ReMAP (Grant Agreement Number:769288). The support is appreciated by the authors.

REFERENCES

- [1] Güemes, A., Fernández-López, A. and Soller, B. Optical Fiber Distributed Sensing - Physical Principles and Applications. *Structural Health Monitoring* (2010) 9(3):233-245.
- [2] Li, H.C.H., Herszberg, I. and Mouritz, A.P. Automated Characterization of Structural Disbonds by Statistical Examination of Bond-line Strain Distribution. *Structural Health Monitoring* (2006) 5(1):83-94.
- [3] Kesavan, A., Sabu, J. and Herszberg, I. Strain-based Structural Health Monitoring of Complex Composite Structures. *Structural Health Monitoring* (2008) 7(3):203-213.
- [4] Takeda, S.-i., Aoki, Y. and Nagao, Y. Damage monitoring of CFRP stiffened panels under compressive load using FBG sensors. *Composite Structures* (2012) 94(3):813-819.
- [5] Airolidi, A., Bettini, P., Loutas, T., Koimtzoglou, C. and Sala, G. Design of health and usage monitoring systems based on optical fibers for composite wing spars. (2015) *28th ICAF Symposium*, Helsinki.

- [6] Fernández-López, A., Menendez, J.M. and Güemes, A. Damage Detection in a Stiffened Curved Plate by Measuring Differential Strains. (2007) *16th International Conference on Composite Materials*.
- [7] Sbarufatti, C., Corbetta, M., San Millan, J., Frovel, M., Stefaniuk, M. and Giglio, M. Model-assisted performance qualification of a distributed SHM system for fatigue crack detection on a helicopter tail boom. (2016) *8th European Workshop On Structural Health Monitoring (EWSHM)*, Bilbao, Spain.
- [8] Zarouchas, D.S. and Alderliesten, R.C. The effect of disbonds on stability aspects of adhesively bonded aluminum panels during compression loading. *Thin-Walled Structures* (2015) 96:372-382.
- [9] Hexcel Corporation, HexPly® 8552 Product Datasheet. (2016).
- [10] Bisagni, C., Vescovini, R. and Dávila, C.G. Assessment of the Damage Tolerance if Post-Buckled Hat-Stiffened Panels using Single Stringer Specimens. (2010) *51st AIAA/ASME/ASCE/AHS/ASC Structures, Structural Dynamics, and Materials Conference*.
- [11] Dassault Systèmes Simulia Corp, Abaqus Analysis User's Manual Guide. (2014) Providence, RI.
- [12] Dávila, C.G. and Bisagni, C. Fatigue life and damage tolerance of postbuckled composite stiffened structures with initial delamination. *Composite Structures* (2017) 161(1):73-84.
- [13] Krueger, R. Virtual crack closure technique: History, approach, and applications. *Appl. Mech. Rev* (2004) 57(2):109-143.
- [14] Python, Python Software Foundation (PSF), Python 3.7.0. (2018), *Wolfeboro Falls, NH 03896-0037, PO Box 37*.
- [15] Kenane, M. and Benzeggagh, M.L. Mixed-mode delamination fracture toughness of unidirectional glass/epoxy composites under fatigue loading. *Composites Science and Technology* (1997) 57(5):597-605.

STRUCTURAL STATE AWARENESS OF COMPOSITE STRUCTURES BY BLENDING PASSIVE AND ACTIVE ACOUSTIC-BASED HEALTH MONITORING METHODS

DIMITRIOS ZAROUCHAS, MILAD SAEEDIFAR

Structural Integrity & Composites Group
Aerospace Engineering Faculty, Delft University of Technology
Kluyverweg 1, 2629 HS, Delft, the Netherlands
e-mail: d.zarouchas@tudelft.nl, www.tudelft.nl

Key words: structural state awareness, acoustic emission, lamb waves

Abstract. This study aims to demonstrate the effectiveness of blending passive and active acoustic-based health monitoring methods to impact damage diagnostics of composite structures. The structural state awareness is introduced as a term to characterize the health condition that a structure is and how this condition can be quantified by blending health monitoring techniques. To this aim, a Carbon Fiber Reinforced Polymer (CFRP) composite plate was fabricated and subjected to a simulated low-velocity impact by performing repeated quasi-static indentation tests where a loading-unloading-reloading test profile was adopted. Two Acoustic Emission (AE) broadband sensors and a network of eight piezoelectric (PZT) sensors were attached on the composite plate surface. AE (passive method) was employed during the loading and reloading phases of the indentation tests to in-situ monitor the damage initiation and progression, while scanning of the plate with Lamb waves (active method) was done to localize the damage when the structure was unloaded. The obtained results showed that the proposed blended passive and active acoustic-based method has the potential to provide useful information about the impact-induced damage in composite structures.

1 INTRODUCTION

Structural state awareness implies that existence, location, type and size of damage should be known at any given time of a structure's life, enabling the engineering team to assess the structural integrity and make proper decisions about the structure's maintenance and repair plan. Sensing equipment should be embedded or permanently attached at the structure in order to provide in real time and continuously health monitoring data. It is well known that one technique cannot solely perform all the measurements required to describe the state awareness of a composite structure and a combination and synergy of at least two techniques is needed. Among several techniques, i.e. ultrasonic C-scan [1,2], active thermography [3,4] vibration and modal analyses [5,6], acoustic based methods such as Lamb waves and Acoustic Emission (AE) [7-12] have a great potential to be employed as Structural Health Monitoring

(SHM) techniques where they can be permanently installed at the structure and monitor its health state during operation.

This study aims to demonstrate the effectiveness of blending passive and active acoustic-based health monitoring methods. A composite plate was subjected to a low velocity impact by performing quasi-static indentation tests where a loading-unloading-reloading test profile was adopted. AE (passive method) was used to determine if damage occurred and its type, while lamb waves (active method) were used to locate the damage. Two acoustic emission broadband sensors and a network of 8 PZT sensors each were attached at the surface of the plate. AE was employed during the loading and reloading phases of the indentation tests while scanning of the plate with the lamb waves took place when the structure was unloaded. Multiple actuator-receiver paths were selected and each PZT emitted a five-cycle hanning window signal of several frequencies.

Results showed that AE successfully provided information, whether and at which load damage occurred, indicating its severity. It was found that results about location, provided by lamb waves, were sensitive on the selected excitation frequency. Section 2 presents the material and the equipment used as well it introduces the experimental campaign and the experimental set-up. Section 3 provides details about the damage image reconstruction algorithm (DIRMA) and the principal equations to calculate the damage index (DI). Section 4 presents the experimental results, analyses the observations and discusses the effectiveness of the blended process towards the establishment of the structural state awareness. Finally, in section 5, conclusions are drawn.

2 MATERIAL AND EXPERIMENTAL CAMPAIGN

One composite panel with dimensions of 500 mm×500 mm×2 mm were manufactured using CFRP prepregs with a layup [(0/90)/45/90/-45/0]_s and cured according to the manufacturer recommended cure cycle.

Selecting the optimal PZT sensor is not straightforward and besides the features of the PZT sensor, it depends on parameters such as the geometry of the structure, its material, the sensors network and the experiment type. In order to generate uniform guided waves in all directions, circular disk PZT sensors supplied by PI Ceramic GmbH were used. The specifications of the PZT disks are reported in Table 1.

Table 1. The specifications of the PZT sensors

Specifications	Value	Unit
Commercial Name	PI Ceramic 000053020 with silver wrap-around electrodes	-
Material	PIC255	-

Shape	Circular disk	-
Diameter	6.50	[mm]
Thickness	0.25	[mm]
Resonance frequency	308	[kHz]

An AMSY-6 Vallen, 8-channel AE system with 4 parametric input channels and maximum sampling rate of 10 MHz was used to perform the AE measurements. In order to record the AE activity during the out-of-plane loading of the composite plates, two broadband, resonant-type, and single-crystal piezoelectric transducers from Vallen Systeme GmbH, AE1045S-VS900M with operating frequency of [100-900 kHz], with two external 34 dB pre-amplifiers were utilized. The recording threshold and sampling rate were set 40 dB and 2 MHz, respectively. Sonotech Ultrasonic Couplant was applied between the sensor and specimen surfaces to get an appropriate acoustical coupling. The functionality of the AE sensors and the data acquisition system was checked by proceeding a pencil lead break test according to ASTM E976 standard [13].

The utilized equipment for baseline test is shown in Figure 1. The function generator Agilent 33500B Series was employed to generate Hanning-windowed sinusoidal tone burst excitation signals with a sampling frequency of 250 MHz and a 10V peak-to-peak amplitude. In addition, the effect of excitation frequency on the DIMRA results was investigated by repeating the baseline tests for four different excited signals with the central frequencies ranging from 150 to 450 kHz in steps of 100 kHz. In order to eliminate the effect of clamping fixture on the wave measurement, both of baseline and current state measurements were done on the clamped panels Fig. 1.b.

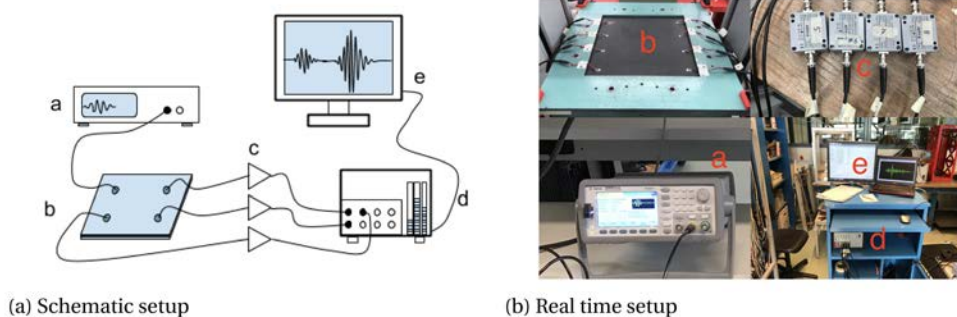


Figure 1. a) The schematic, and b) the real view of the experimental setup for baseline tests (test apparatus description: (a) Agilent 33500B Series waveform generator, (b) panel with attached sensors, (c) preamplifiers with a gain of 34 dB, (d) Vallen AMSY-6 acoustic signal processor, and (e) Laptop with Vallen Acquisition and Vallen Visual TM software).

The initiation and evolution of Barely Visible Impact Damage (BVID) in the scoping panel were studied using five designed sequential indentation tests where a step-by-step increasing load (saw tooth shape) was applied to the specimens. The indentation load was applied to the

specimen by pushing a semi-spherical indenter with diameter of 37 mm by a Zwick 20 kN tensile/compression machine. The indentation load was applied under displacement control condition with the loading rate of 2 mm/min at the position of X= 28 mm and Y= 32 mm from the upper right specimen's corner. The AE system was utilized to monitor the damage state during the loading stage and active PZT sensors were employed to explore the BVID location when the panel was unloaded (between two consecutive load cycles). In the loading and reloading stages, the panel was loaded up to the moment that a load drop in the force-displacement curve occurred. Then, the panel was unloaded. The maximum displacement and load for these five load cycles are presented in Table 3.

Table 2. Maximum displacement and load for different load cycles.

Load cycle	Maximum displacement [mm]	Maximum load [kN]
LC1	8.4	2.31
LC2	9.1	2.86
LC3	9.7	3.36
LC4	12.3	5.67
LC5	13.4	6.99

3 DAMAGE IMAGE RECONSTRUCTION ALGORITHM

The proposed DIMRA localizes BVID zone in the impacted panel by calculating the similarity of the recorded Lamb waves for the current state with the baseline state. DIMRA consists of the following four steps:

1. Each PZT functions as an actuator while all other PZTs act as the receiver. This process is iterated for all network PZT disks in the baseline and current states.
2. DI is calculated based on the similarity between the Lamb waves of the current state and baseline.
3. The Pixel Influence Weight (PIW) is calculated for each actuator-receiver pair.
4. The obtained results for different actuator-receiver pairs are combined to create a damage probability contour over the inspected area.

3.1 Damage Index

DI is based on Pearson Correlation Coefficient (PCC) and it is defined for each path of the PZTs network and shows the effect of damage on the desired path. The PCC shows the linear similarity between two signals by a real value between -1 and +1, which PCC of -1 shows completely opposite behavior of two signals and PCC of +1 illustrates that two signals have completely the same trend and finally PCC of 0 shows that there is no correlation between two signals. PCC (ρ) is calculated by Equation (1) [14]:

$$\rho = \frac{C_{BD}}{\sigma_B \sigma_D} \quad (1)$$

$$C_{BD} = \sum_{l=1}^L (X_B(l) - \mu_B)^2 \cdot (X_D(l) - \mu_D)^2$$

$$\sigma_B = \sqrt{\sum_{l=1}^L (X_B(l) - \mu_B)^2}$$

$$\sigma_D = \sqrt{\sum_{l=1}^L (X_D(l) - \mu_D)^2}$$

where subscripts B and D denote baseline and damaged states (current state), respectively. C_{BD} is the covariance between two the signals, σ is the standard deviation of signal, μ is the signal mean value, X is the signal samples, and L is samples number. The DI based on PCC is calculated as follows:

$$DI_{pearson} = 1 - |\rho| \quad (2)$$

$DI_{pearson}$ is varying from 0 to 1, which 0 indicates no damage state and 1 shows the highest damage probability.

3.2 Pixel influence weight

The PIW assumes that the probability of the damage for a specific path decreases with increasing the distance from the path. In order to apply this assumption a probability ellipse is created, by creating a mesh over the area of interest for inspection. Then, the probability distribution forms an ellipse that the two PZT sensors act as the focal points. The effect of the damage located outside the ellipse's boundaries on the sensing path is considered zero. To create the probability distribution inside the ellipse, a shape factor, β , is defined so that on a straight line between the sensors, the PIW is maximum, 1, and it linearly decreases to 0 on the ellipse's boundaries.

The probability ellipse is calculated using Equation (3). For every pixel on the grid, first the R value is created. R indicates the ratio of the length of the major axis, a , over the distance between the two focal points, $|AR|$. (X_A, Y_A) and (X_R, Y_R) are the coordinates of the actuator and receiver, while (x, y) indicates the location of the pixel and $S(x, y)$ represents the PIW [14, 15].

$$R(x, y) = \frac{\sqrt{(X_A - x)^2 + (Y_A - y)^2} + \sqrt{(X_R - x)^2 + (Y_R - y)^2}}{\sqrt{(X_R - X_A)^2 + (Y_R - Y_A)^2}} \quad (3)$$

$$S(x, y) = \frac{\beta - R(x, y)}{\beta - 1} ; \text{ for } \beta > R(x, y)$$

$$S(x, y) = 0; \text{ for } \beta \leq R(x, y)$$

The boundaries of the ellipse are controlled by shape factor β (Equation (4)), which is usually considered a value between 1.02 and 1.6 [16, 17]. The shape factor of 1.05 is considered for the present study.

$$a = \beta \cdot |AR|; \text{ Major axis} \quad (4)$$

$$b = |AR| \cdot \sqrt{\beta^2 - 1}; \text{ Minor axis}$$

3.3 Data fusion

For all the paths, the corresponding DI_{a-r} value is first multiplied to the corresponding $PIW_{a-r}(x, y)$ for all the pixels and then the pixel intensity ($P_{int}(x, y)$) is determined by taking the sum over all paths [15]. Figure 6 shows the data fusion for two paths.

$$P_{int}(x, y) = \sum_{a=1}^m \sum_{r=1}^n PIW_{a-r}(x, y) \cdot DI_{a-r} \quad (6)$$

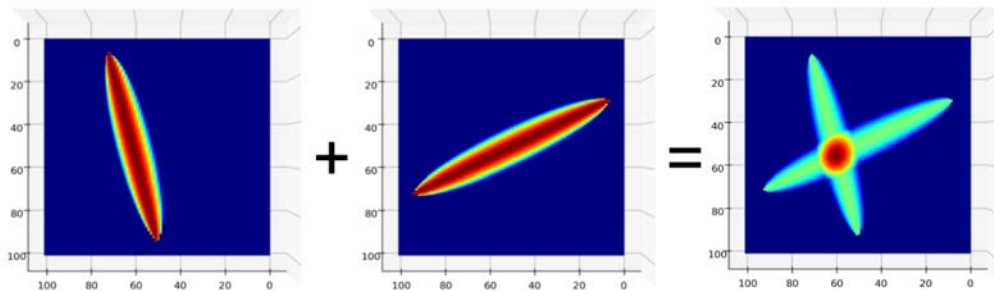


Figure 2. The data fusion of two paths in DIMRA.

4 RESULTS

4.1 Damage severity analysis using AE

The specimens were subjected to the five sequential indentation loads according to section and AE was used for in-situ monitoring of the induced damages in the specimens during the loading stage and Lamb wave technique was employed to localize the damaged zone in the specimen when it was unloaded between two consecutive load cycles. Figure 3 shows AE counts, AE energy, and load versus time curves for the five load cycles. The maximum load of the each loading cycle and the corresponded time are illustrated on the vertical and horizontal axes. The AE activities of load cycles LC1 and LC2 are initiated at the high load levels while some AE activities with the low values of energy and count are seen from the initial stage of loading at load cycles LC3 and LC4 which are probably related to matrix

cracks. The high energy and count AE activities in load cycles LC3 and LC4 are initiated after the maximum load level of the previous loading cycles that shows there is not a critical damage in the structure yet. However, during the loading cycle LC 5, initiation of high energy and count AE activities at a load level lower than the maximum load of the previous loading cycle in load cycle (LC4) illustrates the presence of critical damage with an unstable growth behavior in the structure.

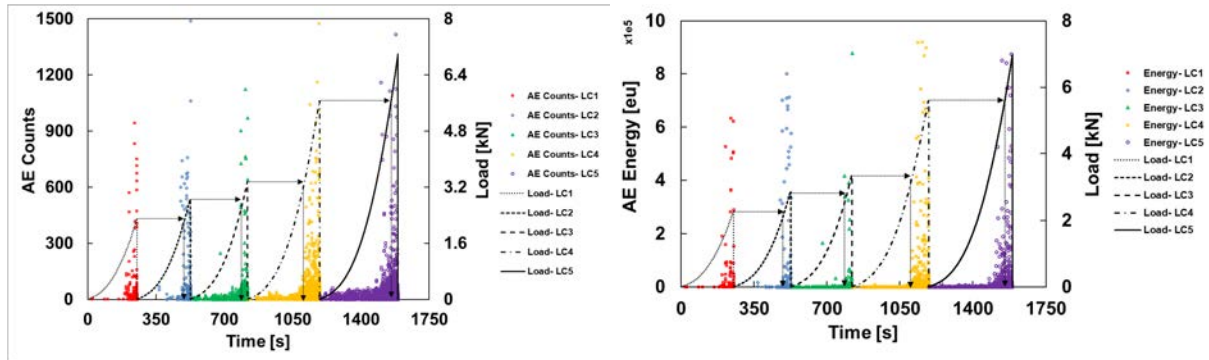


Figure 3. a) AE counts and load versus time, and b) AE energy and load versus time curves for the 5 load cycles.

In order to accurately detect the critical damage and also specify the severity of damage, Kaiser and Felicity effects are employed. Kaiser effect states that the considerable AE activities during the reloading cycle for an intact structure should initiate in the proximity of the maximum load of the previous loading cycle. While Felicity effect states that observing the considerable AE activities at the load level less than the maximum load of the previous load cycle is a sign of the presence of the critical damage in the structure [18]. In order to quantify damage severity, Felicity Ratio (FR) index is defined as follows:

$$FR = \frac{P_{AE}}{P_{max}} \quad (7)$$

where P_{AE} is the corresponding load to the initiation of the considerable AE activities in the current load cycle and P_{max} is the maximum load of the previous load cycle. FR values equal or greater than 1 showcase the Kaiser effect and FR values less than 1 proves the Felicity effect. Figure 4a, shows the cumulative AE energy versus load curve for the five load cycles. Kaiser effect can be easily seen for load cycles LC2 to LC4, while Felicity effect is obviously seen for load cycle LC5. The FR indices for load cycles LC2 to LC5 are presented in Figure 4b. As can be seen, the FR indices of load cycles LC2 to LC4 are larger than 1, validating the Kaiser effect and confirm that the damage induced to the structure is not critical while FR index of load cycle LC5 is considerably less than 1 that illustrates Felicity effect and that the structure is severely damaged.

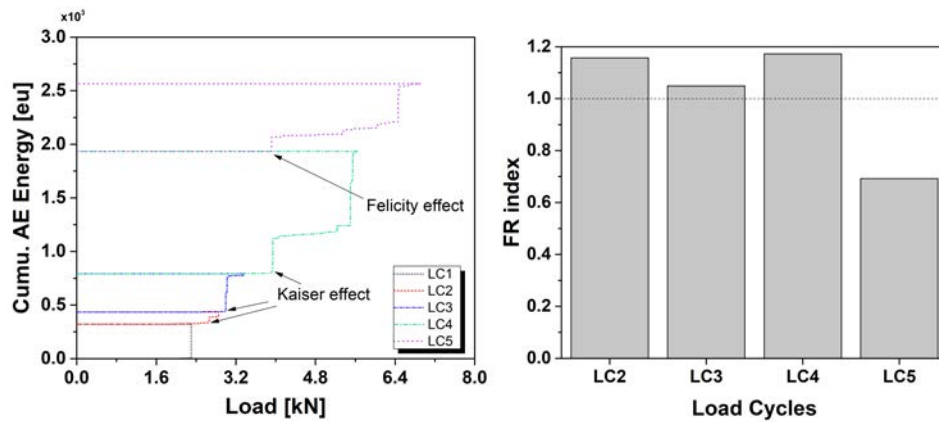


Figure 4. Cumulative AE energy versus load curve for the five load cycles.

4.2 Damage Localization using Lamb wave technique

Lamb wave technique was employed between each two consecutive load cycles to localize the damaged zone in the composite plate. In order to accurately localize the damaged zone, the best excitation frequency of the PZT actuator should be selected. To this aim, the PZT actuator was excited by four different frequencies. Figure 5 shows the predicted damage location by the IMRA for these excitation frequencies at load cycle LC4. The real location of the impact event is shown by a circle on the images. The pixel with the highest intensity shows the predicted location of damage in each image. As can be seen, by increasing the excitation frequency the localization error is increased. This is due to the fact that the increase of the excitation frequency decreases the Lamb wave's wavelength which causes the wave to become more sensitive to smaller damage types such as intralaminar matrix cracks that subsequently leads to higher values of DI. Moreover, due to the bias induced by the algorithm during data fusion, an increase in DI leads to relatively higher pixel intensities at the center of the sensors network where the most paths will overlap. Therefore, the excitation frequency of 150 kHz was finally selected for the damage localization in load cycles LC1 to LC5.

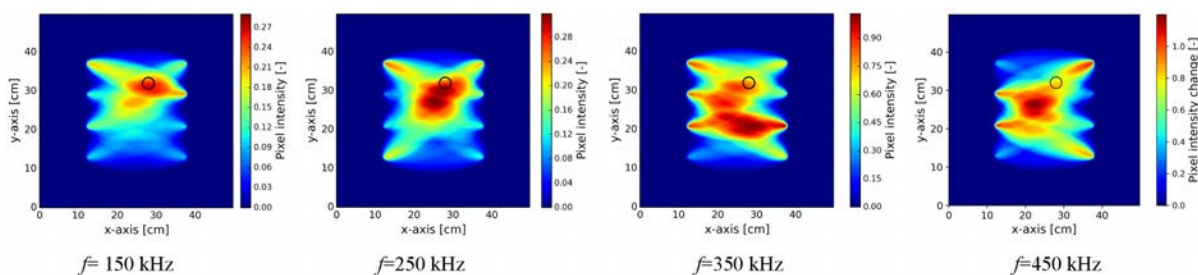


Figure 5. Image reconstruction at load cycle LC4 for different excitation frequencies.

The damage localization results for load cycles LC1 to LC5 are shown in Figure 6. As can be seen, by increasing the applied load from load cycle LC1 to load cycle LC5, the pixel intensity rises considerably that shows the severity of damage in the structure is continuously

increasing. The DI_{Pearson} using an excitation frequency of 150 kHz manages to localize the critical damage at load cycle LC5 with an error of 0.9 cm.

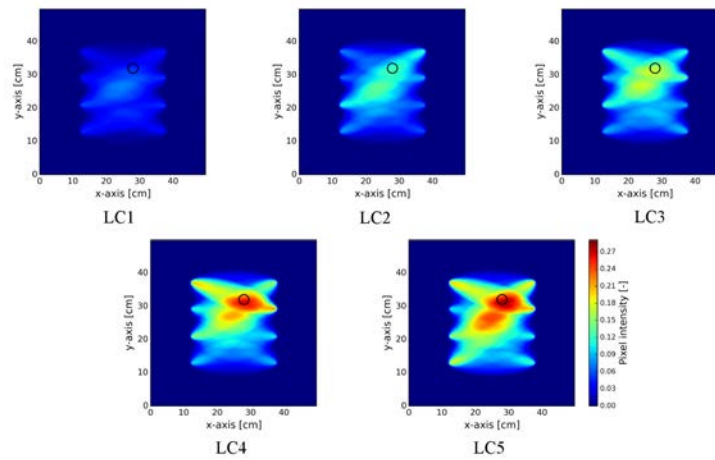


Figure 6. Image reconstruction for the five load cycles

5. CONCLUSIONS

This study proposed a blended passive and active acoustic-based health monitoring method for impact damage diagnostic in composite structures. A CFRP composite plate was fabricated and subjected to a sequential increasing indentation load. AE was used to in-situ detect the critical damage in the specimen during the loading stage. To this aim, FR index was utilized to identify the critical damage level. Due to the occurring of non-critical matrix cracks from the start of reloading stage, using the number of AE events to create FR index, leads to very conservative results while using the parameters of AE energy to calculate FR index could correctly detect the critical damage state which is corresponded to unstable delamination growth in the structure. Lamb wave technique was then employed to localize the damaged zone in the composite plate when the plate was unloaded between two consecutive load cycles. The proposed DIMRA located the damaged zone by comparing the current state Lamb wave with the baseline Lamb wave and introducing one damage index, DI_{Pearson} . The results illustrated that DI performance depends on the selected frequency of the Lamb wave signals; a high excitation frequency, i.e. 450 kHz, misleads the localization with an error up to 11cm, due to the sensitivity of short wavelengths towards interlaminar matrix cracks. In contrast, a Lamb wave with excitation frequency of 150 kHz is more sensitive to larger damage areas, such as delamination, which are present at loading case 5 and where the error between the actual and predicted damage location drops significantly to 0.9 cm.

REFERENCES

- [1] Růžek R, Lohonka R and Jironč J. Ultrasonic C-Scan and shearography NDI techniques evaluation of impact defects identification. *NDT&E Int* 2006; 39(2): 132-14.

- [2] Wronkiewicz A, Dragan K and Lis K. Assessment of uncertainty in damage evaluation by ultrasonic testing of composite structures. *Compos Struct* 2018; 203: 71-84.
- [3] Usamentiaga R, Venegas P, Guerediaga J, et al. Automatic detection of impact damage in carbon fiber composites using active thermography. *Infrared Phys Technol* 2013; 58: 36-46.
- [4] Chrysafi AP, Athanasopoulos N and Siakavellas NJ. Damage detection on composite materials with active thermography and digital image processing. *Int J Therm Sci* 2017; 116: 242-253.
- [5] Katunin A. Stone impact damage identification in composite plates using modal data and quincunx wavelet analysis. *Arch Civil Mech Eng* 2015; 15(1): 251-261.
- [6] Zhang Z, He M, Liu A, et al. Vibration-based assessment of delaminations in FRP composite plates. *Composites Part B* 2018; 144: 254-266.
- [7] Diamanti K, Hodgkinson JM and Soutis C. Detection of Low-velocity Impact Damage in Composite Plates using Lamb Waves. *Struct Health Monit* 2004; 3(1): 33-41.
- [8] Kaczmarek J. Lamb Wave Interaction with Impact-induced Damage in Aircraft Composite: Use of the A0 Mode Excited by Air-coupled Transducer. *J Compos Mater* 2003; 37(3): 217-232.
- [9] Poddar B, Bijudas CR, Mitra M, et al. Damage detection in a woven-fabric composite laminate using time-reversed Lamb wave. *Struct Health Monit* 2012; 11(5): 602-612.
- [10] Saeedifar M, Ahmadi Najafabadi M, Zarouchas D, et al. Barely visible impact damage assessment in laminated composites using acoustic emission. *Composites Part B* 2018; 152: 180-192.
- [11] Saeedifar M, Ahmadi Najafabadi M, Zarouchas D, et al. Clustering of interlaminar and intralaminar damages in laminated composites under indentation loading using Acoustic Emission. *Composites Part B* 2018; 144: 206-219.
- [12] Loutas T, Eleftheroglou N, Zarouchas D. A data-driven probabilistic framework towards the in-situ monitoring of fatigue of composites based on acoustic emission data. *Composite Structures* 2017; 161: 522-529.
- [13] ASTM E976–10. Standard guide for determining the reproducibility of acoustic emission sensor response. ASTM International, West Conshohocken, PA, 2010.
- [14] Zhao X, Gao H, Zhang G, et al. Active health monitoring of an aircraft wing with embedded piezoelectric sensor/actuator network: I. Defect detection, localization and growth monitoring. *Smart Mater Struct* 2007; 16: 1208-1217.
- [15] Memmolo V, Ricci F, Boffa ND, et al. Structural health monitoring in composites based on probabilistic reconstruction techniques. *Procedia Eng* 2016; 167: 48-55.
- [16] De Fenza A, Petrone G, Pecora R, et al. Post-impact damage detection on a winglet structure realized in composite material. *Compos Struct* 2017; 169: 129–137.
- [17] Wang D, Ye L, Lu Y, et al. Probability of the presence of damage estimated from an active sensor network in a composite panel of multiple stiffeners. *Compos Sci Technol* 2009; 69: 2054–2063.
- [18] Lovejoy SC. Acoustic emission testing of beams to simulate SHM of vintage reinforced concrete deck girder highway bridges. *Struct Health Monit* 2008; 7(4): 329-346.

EXPERIMENTAL STUDY ON VIBRATION CONTROL OF A VEHICLE SEMI-ACTIVE SUSPENSION WITH MAGNETO-RHEOLOGICAL DAMPER TRAVERSING SPEED BUMP

MIAO YU*, XIUMEI DU*, JIE FU*, CHAOQUN HUANG*

*Key Lab for Optoelectronic Technology and Systems, Ministry of Education, College of
Optoelectronic Engineering, Chongqing University, Chongqing 400044, China
E-mail: yumiao@cqu.edu.cn

Keywords: magneto-rheological damper; skyhook controller with GAG; speed bump, time-frequency analysis method.

Abstract. Speed bumps are widely used in roads to reduce the traffic accidents. However, the transient impact caused by the speed bumps may increase the health risk of drivers and passengers and damage of vehicle. In this paper, the traditional skyhook controller and skyhook controller with adaptive genetic algorithm (GAG) is designed to attenuate the unwanted vibration. For verifying the effectiveness of the skyhook controller with GAG, the road test of the B segment car installed with four MR dampers is undertaken. The time domain and time-frequency methods are both used to analysis the vibration, and the results demonstrate that the reduction of peak value of vertical acceleration of skyhook controller with GAG is better than that of skyhook controller, comparing with the uncontrolled system.

1. Introduction

In recent years, vehicle is widely used in people's life, meanwhile the number of traffic accidents were increasing. The excessive speed is often thought to be a major cause of traffic accident, hence speed limits will reduce the mean speed of traffic by at least one quarter [1]. In order to reduce the number and severity of traffic accidents and improve the local environment for people who live, work or visit any area, the speed bumps are widely mounted in all sorts of avenues and roads. Hence, many researchers studied the relation between the number, dimension, geometry and position of the speed bumps and the ride and handling of vehicle [2-7]. Several tests have been done with different speed bumps by D. Garcia-Pozuelo [6-7]. To keep comfort loss to a minimum, the speed limit of 30km/h would be adequate for the speed bump 5x60 [6]. Meanwhile, the vertical acceleration in the center of gravity is increasing with the width of speed bump but not increasing with vehicle speed [7]. Back pain is a disease that often appears on the bus driver, due to repeated exposure of mechanical shocks when frequently riding over traffic speed bumps [8], and the health risk increases with increased number of bumps per day. J. Sandover [9] shown clearly that transient vibrations with multiple shocks are more hazardous than stationary vibration. Z. Michaelvan [10] studied the impact damage to fruit during the passage of a truck over a speed bump, and the

largest amount of damage generally occurs at a driving speed close to 30 km/h. Hence, it is necessary to reduce the vibration of the vehicle body when it passing through the speed bumps at low velocities.

The vehicle suspension is used to absorb and buffer the vibration and impact of which from road to vehicle body. Generally, the suspension is divided into three types: passive, semi-active and active. Compared to the others, the semi-active suspension, this has characteristics of reliable, flexible, low-power, and fast response, is usually used to reduce the vibration of vehicle, especially the semi-active suspension with MR damper. The control of semi-active suspension with MR damper is always designed to reduce the vibration of vehicle body in various random roads [11-14]. X.M. Dong and M. Yu et al [9] applied the five representative control algorithms including the skyhook control, the hybrid controller, the LQG controller, the sliding mode controller and the fuzzy logic controller to the mini passenger car. The random road and various speeds (40 km/h, 60 km/h and 80 km/h) are chosen for the test, the results indicated the control performance of skyhook and sliding mode controllers are better than the others. The research is beneficial to select the control strategy in real-time vehicle suspension system control. T. R. M. Rao et al [15] studied the performance of an omnibus passing over a speed bump. The three-degree-of freedom quarter car semi-active suspension system is modelled, and to overcome the problem of integral of acceleration in the skyhook control, the semi-active constraints is modified by the product of the derivative of sprung mass acceleration and the relative velocity of between the sprung and unsprung mass. The simulation results shown the sprung mass acceleration can be reduced by 32%, when the car velocity is 40 km/h. S.B. Choi et al [16] studied performance characteristics of a real semi-active ER (electro-rheological) suspension system, and the result of bump test shown ride comfort of vehicle can be improved by employing four independent skyhook controllers. So far, the skyhook controller has approved to be effective in suspension control. Traditional skyhook controller will take a lot of time to adjust the four skyhook gains by using trial-and-error method, due to the complexity and nonlinearity of vehicle. To improve the control performance and efficiency, the adaptive genetic algorithm (AGA) was adopted in this study to optimize the four independent skyhook gains.

In this paper, the traditional skyhook controller and skyhook controller with GAG are adopted to control the vibration of a vehicle semi-active suspension with MR damper passing through speed bump with different velocities, respectively. In section 2, the traditional skyhook control and skyhook control with GAG are designed for the semi-active suspension system with MR damper. In section 3, the experimental apparatus was established and the results are analyzed. At last, some concluding remarks are given in Section 4.

2. Skyhook control with adaptive genetic algorithm design

2.1 Skyhook controller

The skyhook control, which is proposed by D. Karnopp [17], is widely used in the vehicle semi-active suspension system [18-20]. As a state feedback control with the vertical velocity of the sprung mass, the skyhook control aims to reduce the vertical acceleration of the sprung mass, by inserting a virtual damper between the sprung mass and an imaginary sky. However, it is impossible to implement in the real vehicle suspension system due to the limited space of the suspension. In the practice suspension system, the controlled damper (MR damper) is amounted between the sprung mass (frame) and unsprung mass (wheel). The controlled

damping force was generated to follow the virtual damper, and then the semi-active skyhook control law is expressed by,

$$f_i = \begin{cases} f_{i\max} & \dot{x}_{si}(\dot{x}_{si} - \dot{x}_{ui}) \geq 0, \text{ and } |-c_{si}\dot{x}_{si}| > |f_{i\max}| \\ -c_{si}\dot{x}_{si} & \dot{x}_{si}(\dot{x}_{si} - \dot{x}_{ui}) \geq 0, \text{ and } |-c_{si}\dot{x}_{si}| \leq |f_{i\max}| \\ f_{i\min} & \text{else} \end{cases} \quad (1)$$

Where $i=1,2,3,4$ represent four suspension units, f_i is the actual MR damping force, $f_{i\min}$ is the MR damping force in the absence of magnetic field, $f_{i\max}$ is the maximum of the MR damping force, and c_{si} is the skyhook gain.

The four independent semi-active skyhook controllers are adopted in the whole vibration control of a vehicle passing through speed bump, and the four skyhook gains are determined by using trial-and-error method.

2.2 Skyhook controller with Adaptive Genetic Algorithm

Genetic algorithms (GA) are the most promising optimization algorithm with powerful global search ability based on natural evolution rule. The traditional GA has the drawback of premature, low efficiency and local optimum. To overcome the drawback, the adaptive genetic algorithm (AGA) was used to obtain optimal skyhook gain coefficient. The schematic diagram of the AGA is shown in Figure 1.

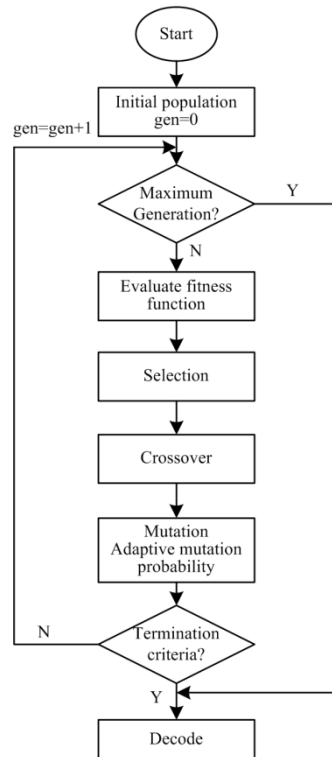


Figure 1. Schematic diagram of the AGA.

It is a key issue to encode the optimal parameters before AGA. There are three encode

algorithms are usually used, bit string encode, gray encode, real number encode. The bit string encode is adopted in this study because of its simplicity. The solution spaces (Γ_i) of four skyhook gains are given and the dimension of gene will be determined by equation (2). As a result, a chromosome will contain 4 genes, and its dimension is 56.

$$\left\{ \Gamma_i \mid \Gamma_i \in [0, 10000] \right\} \quad i = 1, 2, 3, 4 \quad (2)$$

$$2^{13} < (10000 - 0) < 2^{14}$$

Initial population. The initial population is generated randomly in the solution space. To improve the algorithm efficiency, the uniform random was used to ensure the individuals is uniform distributed in the solution space.

Fitness function. In this study, the goal is to improve the ride comfort of the driver when vehicle passing through speed bump. In other words, the object is to minimize the VDV's of vertical acceleration at driver's position. Therefore, the fitness function is given as follows,

$$f_i = \frac{1}{\left[\int_0^T a_d^4(t) dt \right]^{\frac{1}{4}}} \quad i = 1, 2, \dots, m \quad (3)$$

Where m is the size of population and $a_d(t)$ is the weighted acceleration of the driver.

Selection. The selection operator is based on pattern theory, since it will ensure the optimal solution of GA can increased exponentially. The individual will be chosen as parent population, if the individual's fitness higher than the population average fitness.

Crossover. The one-point crossover operator is used. Set a uniform random number between 0 and 1, if the random number less than the crossover probability P_c , then the adjacent individuals will cross, otherwise it will not.

Mutation. The simple mutation operator is used. Set a uniform random number between 0 and 1, if the random number less than the mutation probability P_m , then bit inverse the mutation point. In order to avoid destroying the good individual, the dynamic mutation probability is adopted. The mutation probability is big when the fitness of individual is small, and vice versa.

$$P_{mi} = 0.01 - \text{Index}_i \frac{0.01}{m} \quad i = 1, 2, \dots, m \quad (4)$$

Where Index_i is the index value of the i th individual.

Decode. The bit strings are always used in GA processing. To obtain the optimal skyhook gains, the optimal chromosome should be decoded. The decode equation as follows,

$$c_{si} = (\text{bitstring})_{dec} \frac{10000}{2^{14} - 1} \quad (5)$$

In this study, the crossover probability, maximum mutation probability, population size and maximal generation number are 0.8, 0.01, 50 and 50, respectively.

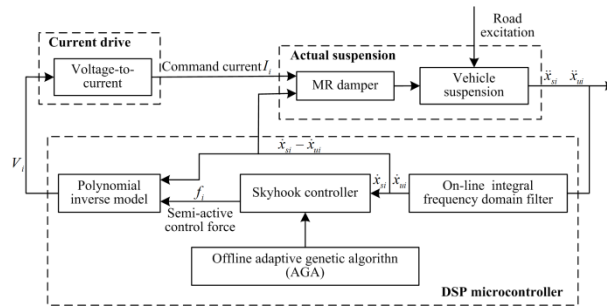
3. Road test and Result analysis

In order to experimentally validate the designed controller, a segment B vehicle has been

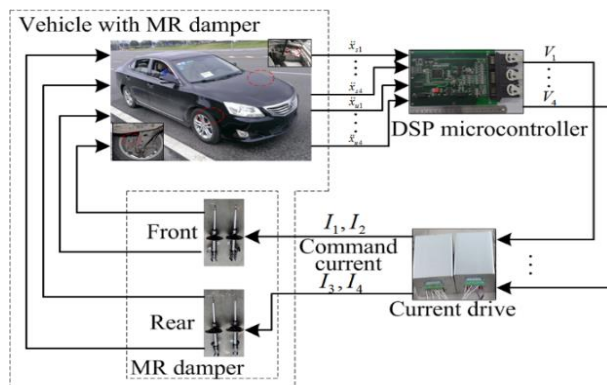
used, which is shown in Figure 2. The schematic of MR damper-based semi-active suspension system with controller is shown in Figure 3. In Figure 3, four acceleration sensors (Model ADXL335, ADI) are used to measure sprung acceleration of the front left suspension, front right suspension, rear left suspension and rear right suspension, respectively. And the another four acceleration sensors (Model MMA7361, Freescale) are used to measure unsprung acceleration of four corners of suspension, respectively. The eight acceleration signals are collected by DSP microcontroller (TMS320F28335, TI), and then the applied voltages are calculated by the DSP microcontroller with the control algorithm. Subsequently, the current drive converts the voltages to current which input to the dampers. The vibration of driver, as the evaluation index of ride comfort, is measured by acceleration (Model 356B40, PCB), which acquired by using Moveable Data Recorder (MDR05, Beijing AREODATA CO.LTD). The test road is asphalt road, and the rubber speed bump of 50mm height and 380mm width, which approximate trapezoidal shape, is shown in Figure 2.



Figure 2. Test vehicle



(a)



(b)
Figure 3. MR damper-based semi-active suspension system with controller (a) Schematic diagram
(b) photograph

The vehicle speeds are chosen as 10km/h, 20km/h and 30km/h, and the road test have been done on the basis of the method of running test-Automotive ride comfort (ISO 2631-1:1997(E)). The skyhook and skyhook with GAG algorithms (skyhook-GAG) are programming to the DSP microcontroller, respectively. The vertical acceleration responses at driver's position under different control strategies and vehicle speeds are shown in Figure 4, Figure 5 and Figure 6. It becomes obvious that the performance of the skyhook-GAG controller is better than the other two. Not only the bump response peak but also the random response had a great attenuation. Hence, this is directly indicates the improvement of the ride comfort of the skyhook-GAG controller. The peak values of acceleration response which the front wheel and rear wheel pass through the bump are shown in Table 1, Table 2 and Table 3. The peak values of vertical acceleration increased with the increase of vehicle speed, and the peak values of vertical acceleration with skyhook-GAG controller are less than that of vertical acceleration with passive and skyhook controllers. Compared to the passive controller, the peak values of vertical acceleration with skyhook-GAG controller for different vehicle speeds can be reduced by 26.23%, 31.59% and 15.34%, respectively. While the reduction of peak values of vertical acceleration with skyhook algorithm for different vehicle speeds are 15.94%, 9.96% and 10.04%, respectively. The VDVs for passive, skyhook controller and skyhook-GAG controller under different vehicle speeds are shown in Table 4. The VDVs of skyhook-GAG controller are less than the other two, which is in accordance with the peak values of vertical acceleration response. The experimental results presented evidently verify the effectiveness of the skyhook-GAG control scheme in terms of improved ride comfort, when vehicle pass through speed bump.

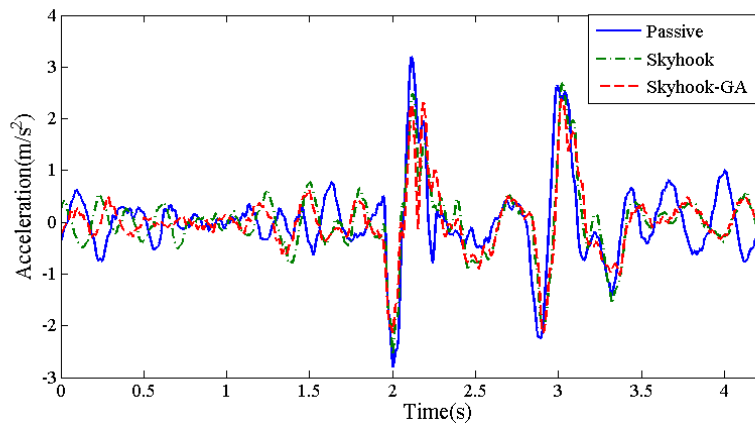


Figure 4. Acceleration of the driver at 10 km/h vehicle velocity

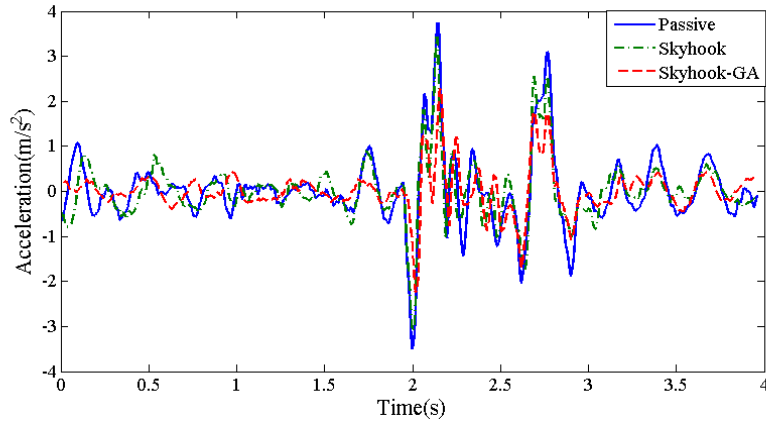


Figure 5. Acceleration of the driver at 20 km/h vehicle velocity

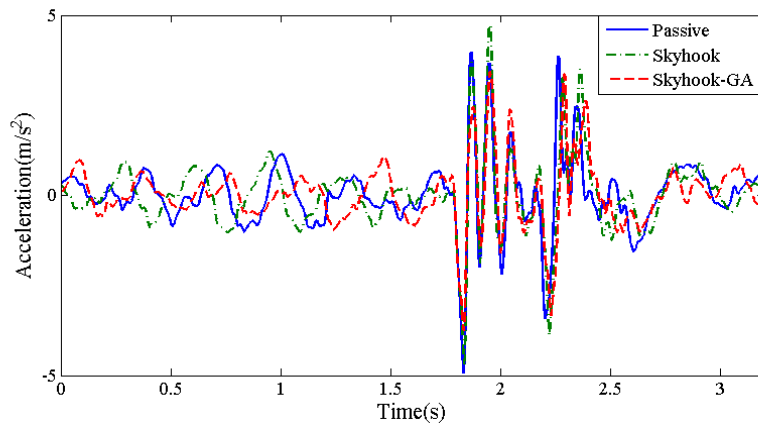


Figure 6. Acceleration of the driver at 30 km/h vehicle velocity

Table 1 Peak-to-peak values of vertical acceleration response at 10 km/h vehicle velocity

	Passive	Skyhook		Skyhook-AGA	
	(m/s^2)	(m/s^2)	Reduction(%)	(m/s^2)	Reduction(%)
Front	6.096	5.124	15.94	4.497	26.23
Rear	4.981	4.766	4.32	4.668	6.28

Table 2 Peak-to-peak values of vertical acceleration response at 20 km/h vehicle velocity

	Passive	Skyhook		Skyhook-AGA	
	(m/s^2)	(m/s^2)	Reduction(%)	(m/s^2)	Reduction(%)
Front	7.487	6.741	9.96	5.122	31.59
Rear	5.228	4.367	16.47	3.857	26.22

Table 3 Peak-to-peak values of vertical acceleration response at 30 km/h vehicle velocity

	Passive	Skyhook	Skyhook-AGA
	(m/s^2)	(m/s^2)	(m/s^2)
Front	8.865	7.975	7.5048
Rear	8.025	7.288	7.1568

Table 4 VDV for different vehicle velocities and controllers

Speed	Uncontrolled ($m/s^{1.75}$)	Skyhook ($m/s^{1.75}$)	Skyhook-AGA ($m/s^{1.75}$)
10km/h	9.568	7.874	6.482
20km/h	11.241	10.662	9.722
30km/h	13.435	12.643	11.998

In addition, joint time-frequency analysis method is also used to analysis the human's vibration, since the vibration of bump is actually a time variable nonstationary signal. As shown in Figure 7 to 9, the vibration energy with skyhook-AGA controller is lower than that with passive and skyhook controller. Meanwhile, the vertical acceleration response frequency at driver's position increases with the increase of speed. when the speed is equal to 30km/h, the main response frequency of vertical acceleration at driver's position is 10 to 15 Hz, which is close to the second resonance peak. Hence, once the speed is greater than 30km/h, the skyhook control algorithm is no longer suitable for the control of body vibration, since the skyhook will reduce the first resonance peak while increase the second resonance peak.

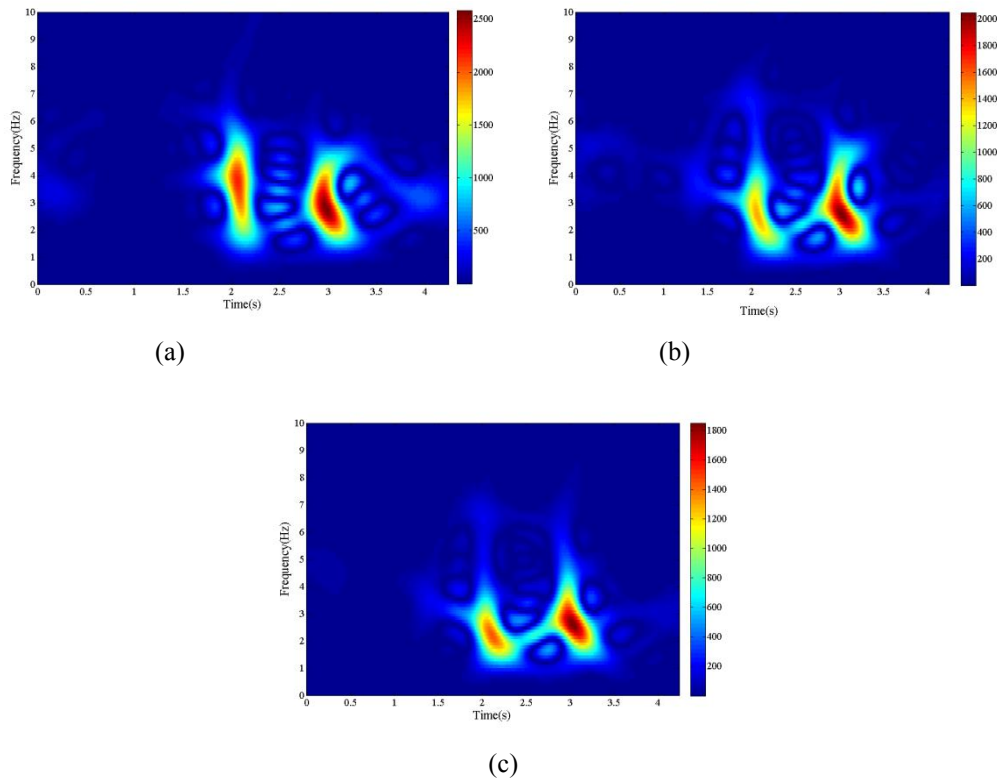


Figure 7. Time-frequency maps of acceleration of driver for different controllers at 10 km/h vehicle velocity: (a)

Passive (b) Skyhook (c) Skyhook-AGA

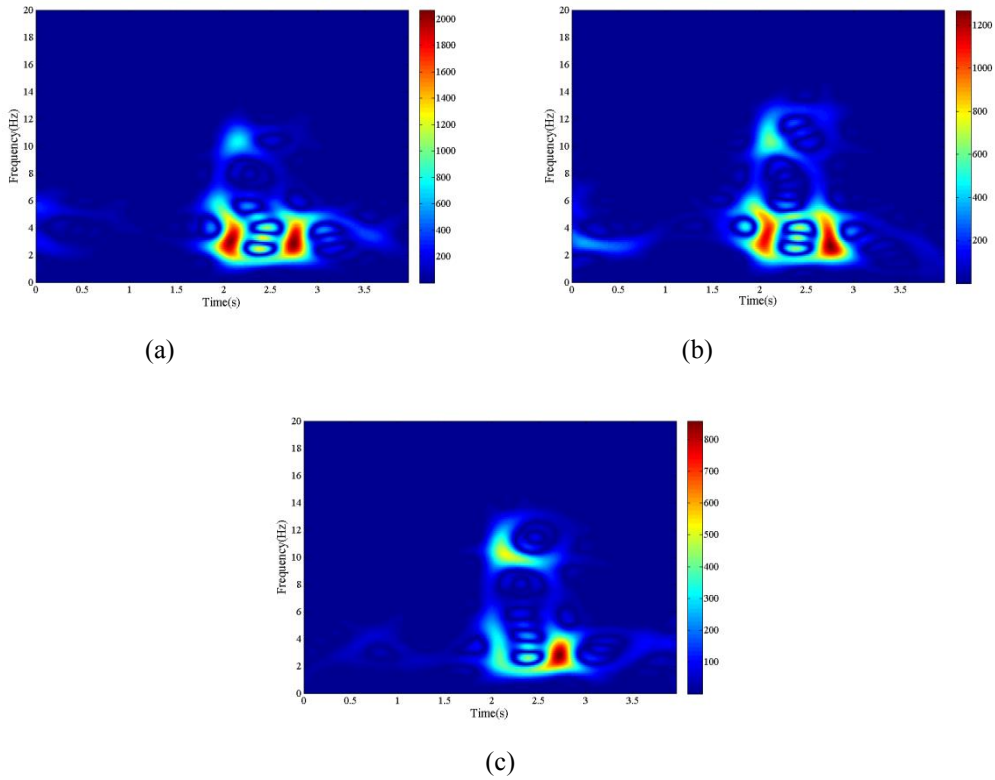
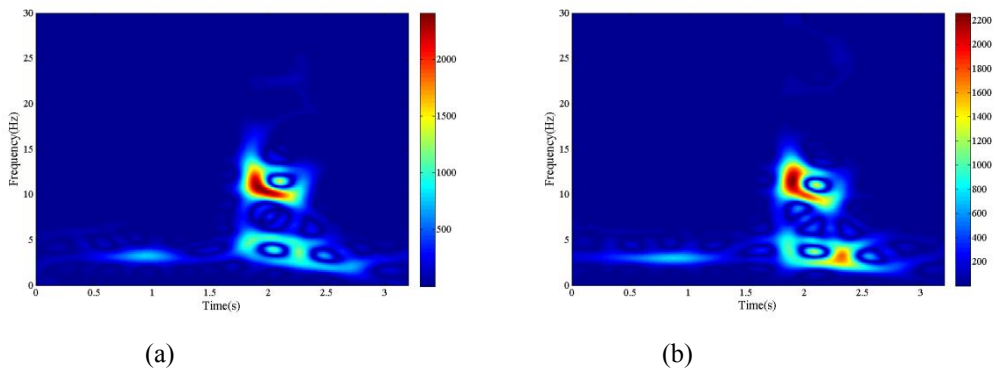
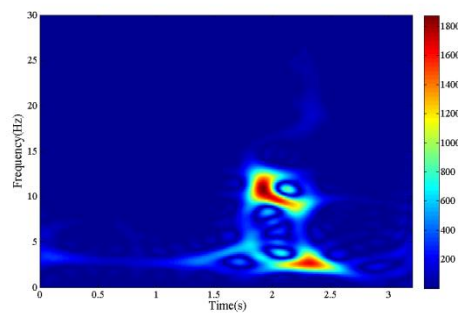


Figure 8. Time-frequency maps of acceleration of driver for different controllers at 20 km/h vehicle velocity: (a) Passive (b) Skyhook (c) Skyhook-AGA





(c)

Figure 9. Time-frequency maps of acceleration of driver for different controllers at 30 km/h vehicle velocity: (a) Passive (b) Skyhook (c) Skyhook-AGA

4. Conclusion

In this study, the vibration control of a vehicle semi-active suspension with MR damper passing through speed bump under low velocity is investigated. The traditional skyhook controller and skyhook controller with GAG (skyhook-GAG) was designed to reduce the vibration from the road surface to the driver. Meanwhile, in order to verify the effectiveness of the designed control, a road test of the B segment car installed with four MR dampers is undertaken. The traditional skyhook and skyhook-GAG controller are programmed to the DSP microcontroller, respectively. The results indicated that compared to the uncontrolled system, the performance of skyhook-GAG controller is better than that of skyhook controller, and the reduction of peak value of vertical acceleration with skyhook-GAG controller can up to 31.59%. Meanwhile, the result with time-frequency analysis method shown that the vertical acceleration response frequency at driver's position increases with the increase of speed, and the skyhook control algorithm is no longer suitable for the control of body vibration when the speed is greater than 30km/h.

Acknowledgements

This research is supported by the China National Science-Technology Support Plan (Grant No.2012BAF06B04). The authors wish to thank Changan Automotive Engineering Institute for providing test vehicle and thank Chongqing Materials Research Institute for providing test site.

References:

- [1] A.A. Aljanahi, A.H. Rhodes and A.V. Metcalfe. Speed, speed limits and road traffic accidents under free flow conditions, *Accident Analysis & Prevention*, 31(1999)161-168.
- [2] E. Khorshid, F. Alkalby, H. Kamal. Measurement of whole-body vibration exposure from speed control humps, *Journal of Sound and Vibration*, 304 (2007) 640–659.
- [3] V. Barone, D.W.E. Mongelli, and A. Tassitani. Vibrational Comfort on Board the Vehicle: Influence of Speed Bumps and Comparison between Different Categories of Vehicle. *Advances in Acoustics and Vibration*, 2016, (13):1-6.
- [4] M. Azman, P. D. King, and H. Rahnejat. Combined bounce, pitch, and roll dynamics of vehicles negotiating single speed bump events. *Proceedings of the Institution of Mechanical*

Engineers. Part K: Journal of Multi-body Dynamics, 2007,221(1):33-40.

[5] O. Kropá, P. Múcka. Effect of obstacles on roads with different waviness values on the vehicle response. *Vehicle System Dynamics*, 2008, 46(3): 155-178.

[6] D. García-Pozuelo, E. Olmeda, A. Gauchía and V. Díaz. Influence of speed bumps design on vehicle safety. *Proceedings of the ASME International Mechanical Engineering Congress & Exposition*, 2011, 9:127-136.

[7] D. Garcia-Pozuelo, A. Gauchia, E. Olmeda and V. Diaz. Bump Modeling and Vehicle Vertical Dynamics Prediction, *Adv Mech Eng*, 2014, 736576.

[8] J. Granlund, A. Brandt. Bus drivers' exposure to mechanical shocks due to speed bumps, *IMAC XXVI Conference & Exhibition on Structural Dynamics*, 10 pages, 2008.

[9] J. Sandover. High acceleration events: an introduction and review of expert opinion, *Journal of Sound & Vibration*, 215(1998)927-945.

[10] Z. Michaelvan, L. Geert, D. Edward, R. Herman, D. Geert, T. Engelbert. The simulation of the impact damage to fruit during the passage of a truck over a speed bump by means of the discrete element method, *Biosyst Eng*,101(2008)58-68.

[11] M. Yu, X.M. Dong, S.B. Choi, C.R. Liao. Human simulated intelligent control of vehicle suspension system with MR dampers, *Journal of Sound & Vibration*, 319(2009)753-767.

[12] S. Choi, H. Lee, Y. Park. Control performance of a full-vehicle suspension featuring magnetorheological dampers, *Vehicle System Dynamic*, 38(2002)341-360.

[13] X.M. Dong, M. Yu, C.R. Liao, W.M. Chen. Comparative research on semi-active control strategies for magneto-rheological suspension, *Nonlinear Dynam*,59(2010)433-453.

[14] G.Z. Yao, F.F. Yap, G. Chen, W.H. Li, S.H. Yeo. MR damper and its application for semi-active control of vehicle suspension system,*Mechatronics*,12(2002)963-973.

[15] T.R.M. Rao, G.V. Rao, K.S. Rao. A. Purushottam. Analysis of passive and semi active controlled suspension systems for ride comfort in an omnibus passing over a speed bump, *International Journal of Research & Reviews in Applied Sciences*,5(2010).

[16] S.B. Choi, H.K. Lee, E.G. Chang. Field test results of a semi-active ER suspension system associated with skyhook controller,*Mechatronics*,11 (2001)345-353.

[17] D.C. Karnopp, M.J. Croby, R.A. Harwood. Vibration control using semi-active force generators, *Journal of Engineering for Industry*, 96(1974)619-626.

[18] C. Chen, H. Li, H. Gao. Study on self-optimizing integrated skyhook control algorithm of semi-active suspension system. 2006.

[19] B.W. Bi, F. Xiao. The implementation of skyhook control for semi-active suspension based on Vi-Car Real Time, *Applied Mechanics & Materials*,713-715(2015)748-751.

[20] G. Priyandoko, M. Musa, H. Jamaluddin. Practical implementation of skyhook and adaptive active force control to an automotive suspension system, *J Virol*, 81(2007)11690-11702.

FUZZY-NEURAL NETWORK CONTROL FOR A MAGNETORHEOLOGICAL ELASTOMER VIBRATION CONTROL SYSTEM WITH SINUSOIDAL EXCITATIONS

Jie Fu*, Junfeng Bai*, Zening Yang*, Zhenyu Dai*, Jing Liu* and Miao Yu*

* Key Lab for Optoelectronic Technology and Systems, Ministry of Education, College of
Optoelectronic Engineering, Chongqing University, Chongqing 400044, China
e-mail: fujie@cqu.edu.cn, web page: <http://www.ssclab.cn/fujie/>

Key words: MRE isolator, FC, FNNC, Sinusoidal excitation.

Abstract. This paper presents the design method of a fuzzy-neural network controller (FNNC) for a MRE vibration control system with sinusoidal excitations to improve the vibration attenuation. A semi-active FC is designed to obtain the controlled force based on the feedback signals of the relative displacement and absolute displacement of the isolation structure, then the BP neural network with good learning capability is employed to emulate the dynamic behaviours of output force of fuzzy controller (FC), excitation displacement, velocity and controlled current applied to the coil in MRE isolator. The acceleration responses of the system with FNNC are evaluated by physical experiments, the results indicate that the FNNC could maintain satisfying control effect in the presence sinusoidal excitations and is also more optimal than conventional FC, the reason is that the neural network controller can approximate the nonlinear function relationship among the controlled force, excitation displacement, velocity and controlled current, but the function relationship is only considered as the linear function in conventional FC.

1 INTRODUCTION

Recently, magnetorheological elastomer (MRE) vibration control method, with the advantages of low power consumption, good stability and adjusting parameters under the applied magnetic fields, has attracted more and more attention in engineering fields [1-4], such as civil structures, precision manufacturing and vehicle suspension. Control strategies play an important role in MRE vibration control system with fixed system structure [2-5]. There are ON-OFF control, a clipped-optimal control, Lyapunov-based control, sub-optimal H_∞ control and fuzzy control. Due to the independence of system model and strong robust, fuzzy control has been paid more concern. However, FC designed in MRE vibration control system usually estimated the relationship of the feedback signals and controlled force, and was not describe the nonlinear function of controlled force and coil current (the inverse model of MRE isolator) accurately in real time control system, which made the limited vibration attenuation.

The inverse model of MRE isolator is critical element for real time control application. In general, there are two approaches to obtain the inverse models of systems. One is inverting the derived forward model. Some papers on the forward MRE isolator modelling are reported in [6-8] which are all focused on parametric models. Due to the highly nonlinearity of MRE isolator, there are too parameters to be identified. Moreover, if the inverse models are to be derived from these forward parametric models, the invertibility and zero dynamics of these models must be investigated first. Therefore, it is difficult to obtain the corresponding inverse dynamic model by inverting the derived forward parameters model. The other named non-parameter model is directly identifying the inverse model from the input and output data set without relying on a precise mathematical model.

Neural network is a kind of non-parametric modelling method to approximate any nonlinear mapping relationship between input and output, which is not able to be solved by a mathematical model. BP neural network has the simple structure and less computation, which is suitable to establish the inverse model of MRE isolator online [9]. The genetic algorithm (GA) [10-13] is a kind of optimization algorithm based on the mechanism of natural selection and evolution. It encodes the parameters to be solved and do some basic genetic operations on these codes, such as reproduction, crossover and mutation. Since the ability of GA to make a robust search for a global optimum in complex space, it has been applied in many applications. It has been shown that GA is quite well in identifying the BP network model for a wide class of non-linear systems [14, 15]. Therefore, GA is employed in this paper to optimize the structure of BP network for MRE isolation system.

The main contribution of this work is to propose a FNNC for sinusoidal excitations excitation to improve attenuation of the acceleration. The control force associated with the FC is generated by adopting the MRE isolator, and the BP neural network is employed to approximate the nonlinear function between controlled force, excitation displacement and velocity and controlled current. FNNC, consists of fuzzy controller, BP neural network based MRE isolator inverse model, is designed in Section 2. In section 3, control experiments are carried out to verify the effectiveness of the proposed FNNC. Finally, the conclusions are summarized in Section 4.

2. FNNC DESIGN

2.1 The dynamic model of MRE isolation system

The MRE vibration isolation system is shown in Figure 1. Base on the Newton's motion law, the dynamic equation of the isolation system are derived as

$$m\ddot{x}_2(t) = k_0(x_1(t) - x_2(t)) + c_0(\dot{x}_1(t) - \dot{x}_2(t)) + \Delta k(x_1(t) - x_2(t)) + \Delta c(\dot{x}_1(t) - \dot{x}_2(t)). \quad (2)$$

The output force generated by MRE isolator $F_{MRE}(t)$ is described by

$$F_{MRE}(t) = \Delta k(x_1(t) - x_2(t)) + \Delta c(\dot{x}_1(t) - \dot{x}_2(t)). \quad (3)$$

Where m represents the mass of the isolation structure. k_0 and Δk are the isolator stiffness without magnetic field application and the increment stiffness under the

electromagnetic field, respectively. c_0 and Δc are the damping coefficient with zero magnetic field and increased damping coefficient under the electromagnetic field. $x_1(t)$ and $x_2(t)$ are the displacement of the base and isolation structure, respectively.

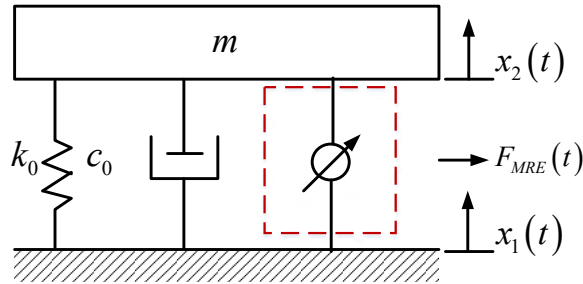


Figure 1. Dynamic model of MRE isolation system

The semi-active control law is described as [4]

$$F_{MRE}(t) = \begin{cases} F_{\max} & x_2(t)x_r(t) \geq 0, F_c(t) \geq F_{\max} \\ F_c(t) & x_2(t)x_r(t) \geq 0, F_c(t) < F_{\max} \\ 0 & x_2(t)x_r(t) < 0 \end{cases} \quad (4)$$

where F_{\max} is the maximum output force of the MRE isolator, $F_c(t)$ is the desired force computed by the designed FC in the following section, and $x_r(t) = x_2(t) - x_1(t)$ is the relative displacement between the isolation structure and base.

The scheme of MRE vibration isolation control system with FNNC is shown in Figure 2. The control system consists of MRE isolator, isolation structure, sensors and FNNC(FC and BP neural network controller). The FC and BP neural network controller will be designed in the following section.

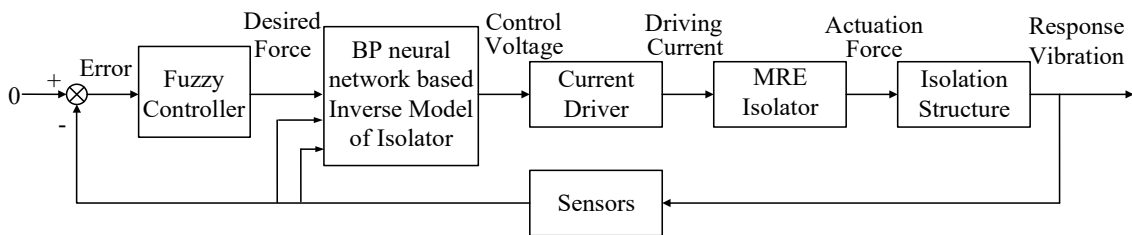


Figure 2 The scheme of MRE vibration isolation control system with FNNC

2.2 Fuzzy controller design

The input variables of the developed FC are selected as relative displacement $x_r(t)$ between the isolation structure and base, and the isolation structure displacement $x_2(t)$, while

the output is chosen as the force $F_{MRE}(t)$ generated by MRE isolator. There are seven input and output linguistic variables, such as negative big (NB), negative medium (NM), negative small (NS), zero (ZO), positive small (PS), positive medium (PM), and positive big (PB). The discourse domain of the variables is $[-7, 7]$. D , RD and U are the isolation structure's displacement, the relative displacement and the output force in the fuzzy set, respectively. The fuzzy rules, membership function and fuzzy inference are complete same with that in [4].

2.2 BP neural network based inverse model of MRE isolator

The BP neural network is employed to describe the functional relationship between applied current, displacement, velocity and output force in the paper. The network with the structure of input layer, output layer and hidden layer is shown in Figure 3.

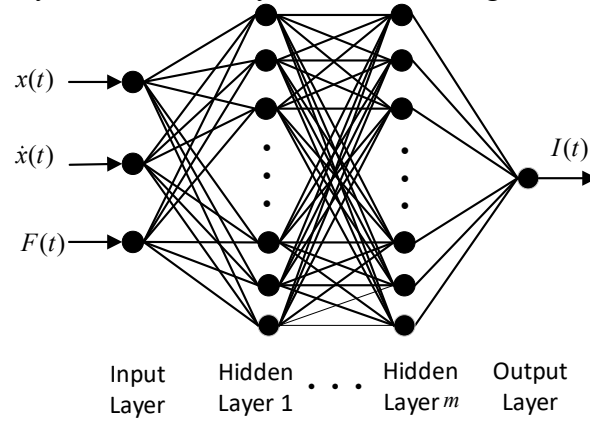


Figure 3 The structure of BP neural network for MRE isolator inverse model

How to determine the optimal structure of BP neural network is the first thing to be done. In this paper, the GA is used to optimize the structural parameters of BP neural network. Genetic algorithm is a global optimization algorithm based on natural selection and evolution mechanism, which is suitable for dealing with complex nonlinear problems that are difficult to solve by traditional search methods.

Let the number of neurons in each hidden layer be the same. The real number coding method is used to encode the number of hidden layers m and hidden layer neurons n in the BP network. Considering the complexity of the network structure, the values of the parameters to be optimized in the genetic algorithm are respectively set to: $m \in [1, 3]$, $n \in [1, 30]$ are positive integers. The network is trained by the weights generated by random initialization, and the mean square error value of the training samples under each network structure is calculated. The reciprocal of the mean square error value is used as the fitness function of the genetic algorithm. The optimization indicators and constraints are as follows:

$$\begin{aligned} \max \quad & F_{in} = 1 / \text{MSE}(e) \\ \text{s.t.} \quad & \begin{cases} m \in [1, 3] \\ n \in [1, 30] \end{cases} \end{aligned}$$

where e is the mean square error between the experimental current value and predicted current values with BP neural network.

The GA is used to optimize the above problems, and the individuals with the greatest fitness are selected to inherit to the next generation, and the evolutionary groups are genetically manipulated through crossover and mutation to generate a new generation of populations. The initial values of each parameter selected in the genetic algorithm are shown in Table 1. The BP network structure parameters obtained by real-coded genetic algorithm are shown in Table 2. The network is a four-layer structure network consisting of three input neurons, two hidden layers and one output layer, in each hidden layer. The number of neurons is 15. Therefore, the optimal structure of BP neural network is 7-15-15-1.

Table 1 Initiation and update of GA parameters

Initialization parametrs	Value
Maximum number of iterations	30
Number of populations	40
Mutation probability	0.01
Crossover probability	0.8

Table 2 Optimized values of BP neural network

Parameter to be optimized	Value
Implicit number of layers	2
Number of neurons in the hidden layer	15

According to the structure of BP neural network optimized by GA, the BP neural network based inverse model of MRE isolator is built. The input of the network is relative displacement, relative velocity, current force, and output variable is current. The experimental data obtained by the test is divided into a training data set and a test data set for training a BP network whose structure is determined by a genetic algorithm. Taking the same frequency sinusoidal excitation with excitation displacement amplitudes of 0.045mm, 0.09mm, 0.135mm, frequency of 40Hz, 60Hz, 80Hz and current of 0-1.5A, the mean square error (MSE) between predicted current and actual current is 0.0025. The experimental current and predicted current are shown in Figure 3(a). The error distribution is shown in Figure 3 (b), the range is small [-0.5046, 0.9854], and the regression coefficient shown in Figure 3(c) is 0.99427.

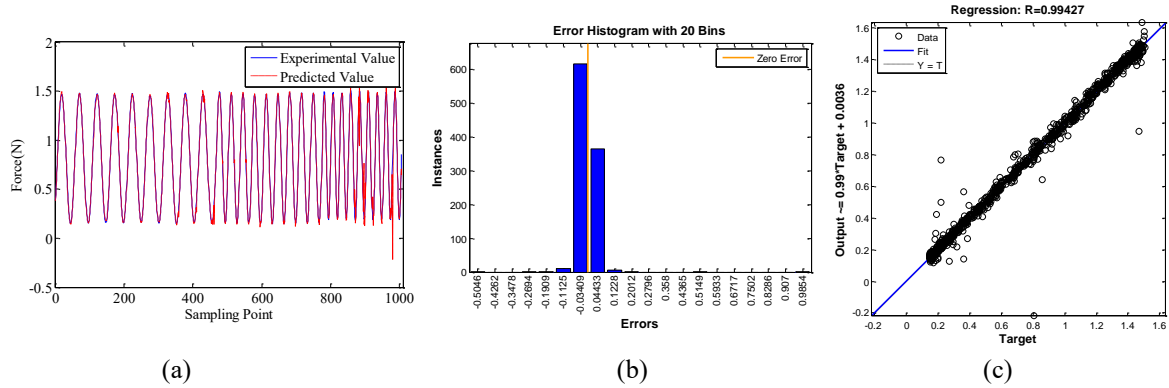


Figure 4 The training results with BP neural network for MRE isolator inverse model (a) force (b) error distribution (c) regression

The generalization ability of the BP neural network is verified by the test data set different from the training data set. The generalization result is shown in Figure 5, and the mean square error is 0.004. The error distribution range is $[-0.2594, 0.7572]$, the error is mainly concentrated near the zero value. The regression coefficient is 0.99059.

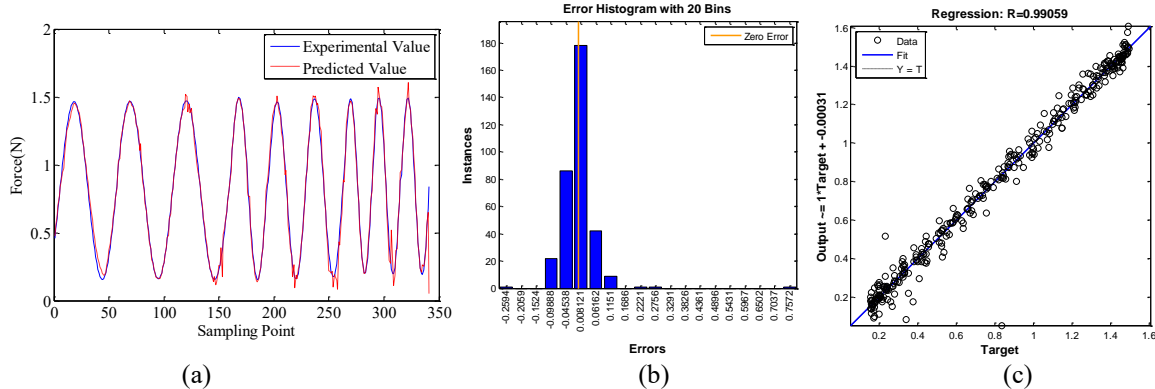


Figure 5 The generalization results with BP neural network for MRE isolator inverse model (a) force (b)error distribution (c) regression

From the inverse model generalization results, we can see that MSE value of BP network is 0.004 and the regression coefficient is 0.99059, which is close to 1. Therefore, the BP neural network performs a better estimated capacity for the inverse model of MRE isolator.

3. EXPERIMENTAL VERIFICATION AND ANALYSIS

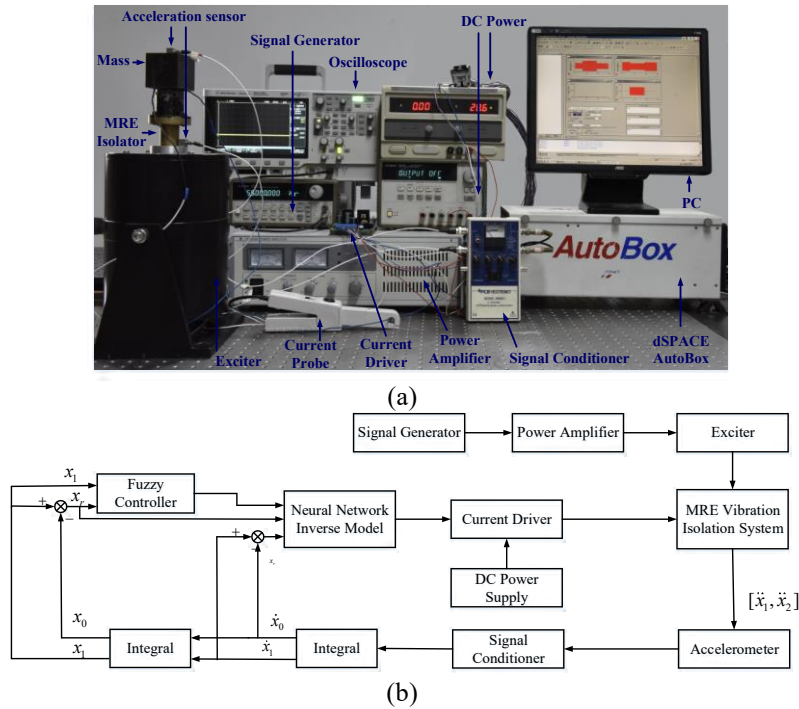


Figure 6 MRE vibration isolation Fuzzy-Neural Network control experimental system: (a) physical map; (b) system structure

The fuzzy-neural control experimental system for MRE vibration isolation system is shown in Figure 6. The MRE isolator is mounted on the surface of an electromagnetic exciter (JZK-50, Lianneng Electronics, China), and the load is connected to the top of the isolator by a screw. The sinusoidal excitation signal is generated by a signal generator (Model 33120A, Agilent, USA), which is amplified by a power amplifier (YE5874 type, Nerneng Electronics, China) to drive the exciter to generate vibration. Two piezoelectric accelerometers (Model 333B52, Piezotronics, USA) are mounted on the exciter table and the load to measure the base excitation acceleration signal and the load response acceleration signal, respectively. The signal measured by the sensor is a charge signal, which is converted into a voltage signal by a signal conditioner (Model 480B211, Piezotronics, USA), then acquired by dSPACE Autobox (DS1005, dSPACE, Germany), and fuzzy-neural network controller in Matlab/Simulink is downloaded to the dSPACE Autobox hardware-in-the-loop simulation system. The control current output from the controller is applied to the MRE isolators through the current driver. Two DC power supplies (model E3631A, Agilent, USA) supply the current driver.

3.1 Experimental results and analysis

The sinusoidal excitation is applied to MRE isolator with an amplitude of 0.2 g at a frequency of 30 Hz to 60 Hz and a step size of 10 Hz. The variation of the response acceleration amplitude of the FNNC and the traditional FC is shown in Figure 7-10. The

attenuation at different frequencies and the response RMS of the passive and controlled conditions of the controlled object are shown in Table 3. The attenuation ratio of the FNNC and the traditional FC is shown in Figure 11. It can be seen from figures and table that the acceleration RMS attenuation rate with FNNC is always more than that with FC, and the maximum value with former method reaches 42.12%, but the latter is only 34.26% when the excitation frequency is 50Hz.

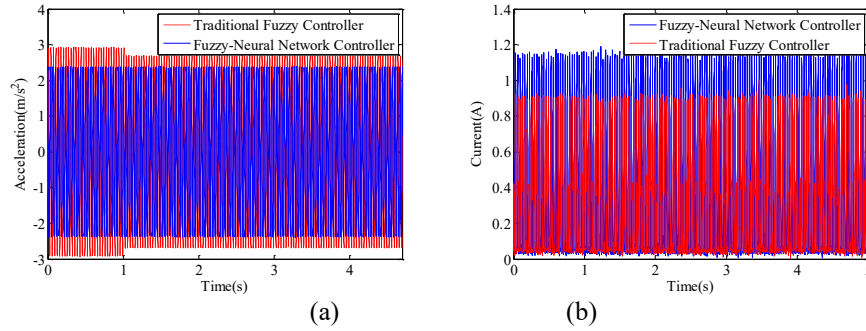


Figure 7 Results of FNNC and traditional FC with excitation amplitude of 0.2g and frequency of 30Hz (a) acceleration (b) Control current

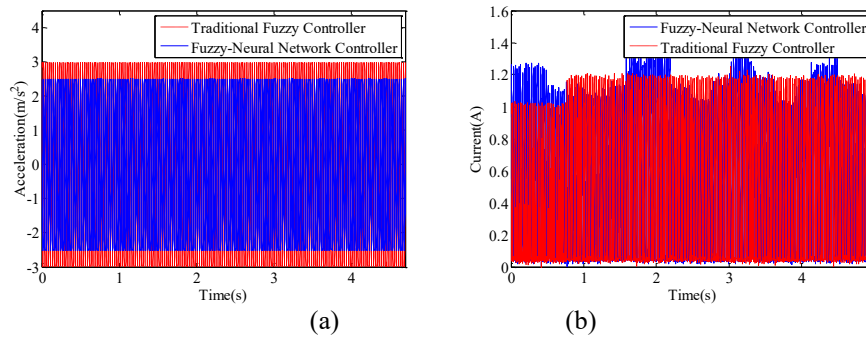


Figure 8 Results of FNNC and traditional FC with excitation amplitude of 0.2g and frequency of 40Hz (a) acceleration (b) control current

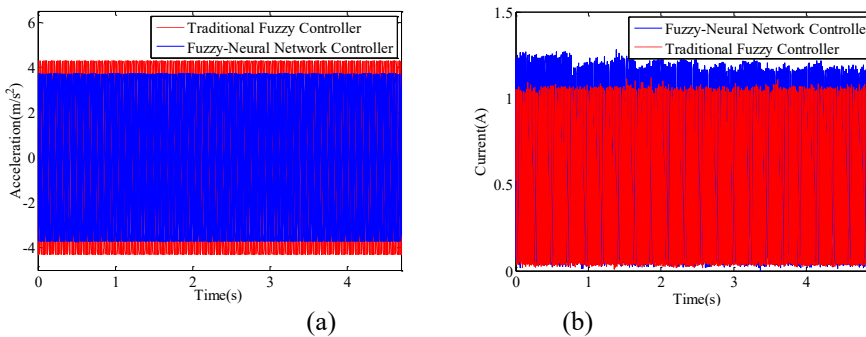


Figure 9 Results of FNNC and traditional FC with excitation amplitude of 0.2g and frequency of 50Hz (a) acceleration (b) control current

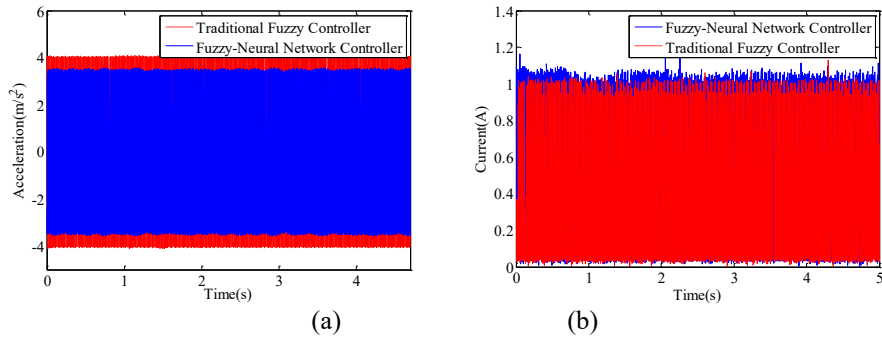


Figure 10 Results of FNNC and traditional FC with excitation amplitude of 0.2g and frequency of 60Hz (a) acceleration (b) control current

Table 3 The attenuation rate of the response of the different controllers to the controlled object under the condition that the excitation amplitude is 0.2g

Frequency	Acceleration response RMS with passive (m/s ²)	Acceleration response RMS with FC (m/s ²)	Attenuation rate (%)	Acceleration response RMS with FNNC (m/s ²)	Attenuation rate (%)
30	2.0701	1.8994	8.25	1.6822	17.06
40	3.0632	2.1099	31.12	1.7763	41.99
50	4.6103	3.0307	34.26	2.7135	42.12
60	2.9592	2.8757	2.82	2.4847	17.16

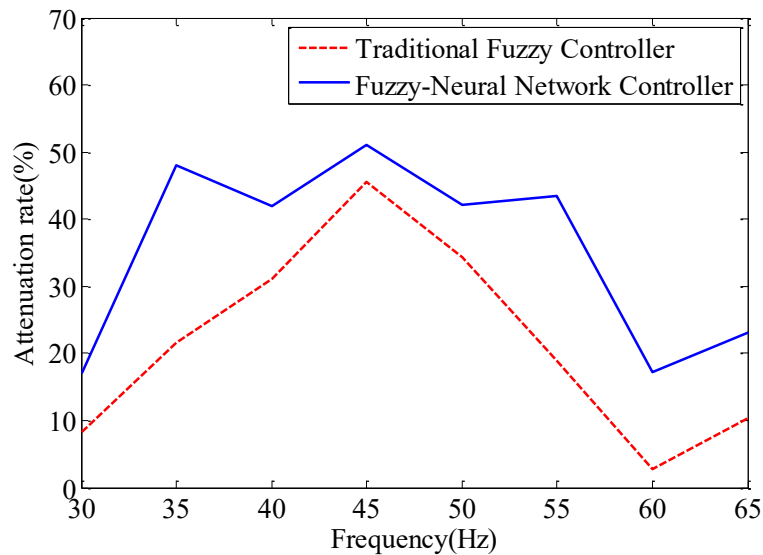


Figure 11 Comparison of attenuation rates of different controllers with different excitation amplitudes of 0.2g

4 CONCLUSIONS

This paper studies the FNNC design for a MRE vibration isolation system with sinusoidal excitations. The MRE isolation system's passive model is obtained from acceleration sweep experiment. An AFC is devised based on the working principle of the MRE isolator and fuzzy theory, the adaptive mechanism (factor adjustment) of which is constructed on passive system model and peak observer, which is implication of excitation frequency. Experimental results show that the decrease of the isolation structure acceleration under the FNNC is 42.12% higher at most than the one of the conventional FC. And the FC could maintain consistent performance in the presence of varying excitation parameters (amplitude from 2.0 m/s² frequency from 30Hz to 60 Hz).

REFERENCES

- [1] Li Y C, Li J C, Li W H, et al 2013 Development and characterization of a magnetorheological elastomer based adaptive seismic isolator *Smart Materials & Structures* **22** 035005
- [2] Behrooz M, Wang X J, Gordaninejad F 2014 Performance of a new magnetorheological elastomer isolation system *Smart Materials & Structures* **23** 045014
- [3] Du H P, Li W H, Zhang N 2011 Semi-active variable stiffness vibration control of vehicle seat suspension using an MR elastomer isolator *Smart Materials & Structures* **20** 105003
- [4] Fu J, Li P D, Wang Y, et al. 2016 Model-free fuzzy control of Magnetorheological elastomer vibration isolation system: analysis and experimental evaluation *Smart Materials & Structures* **25** 035030.
- [5] Opie S, YIM W 2011 Design and Control of a Real-Time Variable Modulus Vibration Isolator *Journal of Intelligent Material Systems and Structures* **22** 113-125
- [6] Yang J, Du H P, et al 2013 Experimental study and modeling of a novel magnetorheological elastomer isolator. *Smart Materials & Structures* **22** 117001
- [7] Behrooz M, Wang X J, Gordaninejad F 2014 Modeling of a new semi-active/passive magnetorheological elastomer isolator. *Smart Material and Structure* **23** 045013
- [8] Li Y C, Li J C 2015 A highly adjustable base isolator utilizing magnetorheological elastomer: experimental testing and modelling. *Journal of Vibration and Acoustics* **137** 011009
- [9] Yu Y, Li, Y C, Li J C 2015 Nonparametric modeling of magnetorheological elastomer base isolator based on artificial neural network optimized by ant colony algorithm. *Journal of Intelligent Material Systems and Structures* **26** 1789-98
- [10] Goldberg D E 1989 Genetic Algorithms in Search, Optimization, and Machine Learning. Addison-Wesley, Reading, Massachusetts.
- [11] Holland J H 1993 Adaptation in Natural and Artificial Systems: An Introductory Analysis with Application to Biology, Control, and Artificial Intelligence. MIT Press, Cambridge, Massachusetts.
- [12] Gen M, Cheng R 1997 Genetic Algorithms and Engineering Design. John Wiley, New York.
- [13] Man K F, Tang K S, Kwong S 1999 Genetic Algorithms, Concepts and Designs. Springer-Verlag, London.
- [14] Luh G C, Wu C Y 1999 Non-linear system identification using genetic algorithms. Proc. Instn Mech. Engrs, Part I, *Journal of Systems and Control Engineering* **213** 105-117
- [15] Li C J, Jeon Y C 1993 Genetic algorithm in identifying nonlinear auto regressive with exogenous input models for nonlinear systems. In Proceedings of the American Control Conference, San Francisco, California, **2-4** 2305-2309

INTERACTION BETWEEN CARRIER LIQUID AND IRON PARTICLES IN MR-BASED SEALINGS

CHRISTIAN HEGGER and JÜRGEN MAAS

Technische Universität Berlin

Mechatronic Systems Lab

Hardenbergstraße 36, 10623 Berlin, Germany

e-mail: christian.hegger@emk.tu-berlin.de, web page: <http://www.emk.tu-berlin.de>

Key words: Magnetorheological Fluids, smart MR-based sealing, capillary pressure

Abstract. In previous contributions an MR-sealing was developed to increase the energy-efficiency in idle-mode in combination with the MR-fluid movement control. While the maximum capable pressure of the sealing is based on the yield stress depending on the magnetic characteristics of the particle chain structure in this contribution the interaction between the carrier liquid and the particle structure will be in the focus of interest. The proposed investigation is based on a theoretical analysis considering the capillary pressure and the maximum intruding length. Along with the determination of significant material parameters an experimental study is performed on a novel test-setup to determine the mentioned interaction between the chain structure and the carrier liquid.

1 INTRODUCTION

Sealing approaches based on ferrofluids are already well investigated and applied in many different applications for example in hard drive discs, X-ray tubes, hermetic robots or loud speakers [1]. A low intrinsic friction in the absence of wear is the key feature of ferrofluids. Furthermore, the tightness can be maintained even at high eccentricities [2]. Unlike ferrofluids (FF), magnetorheological fluids (MRF) consist of iron particles with the diameter in a range of 4 to 12 μm , fairly normal distributed. The bigger particle size results in a significant higher magnetic moment \mathbf{m} as given in Eq.1.:

$$\mathbf{m}_{ma} = \int_V \mathbf{M} dV, \quad (1)$$

where \mathbf{M} is the magnetization of a object with the volume V . Consequently, higher magnetically induced forces can be observed resulting in higher yield stress. Thus, the field of application of MRF takes advantage of the higher yield stress which are utilized for the realization of dampers, brakes and clutches [3]. MR-based sealings offer higher pressure loads compared to FF, but suffering from the drag torque in rotating applications [4, 5].

The particles of the MRF form a chain structure under the impact of a magnetic field, therefore, increasing the yield stress significantly, while the carrier liquid remains within the space between the particles. The FF approach is classified as a stable dispersion due to the small particle size. However, Brownian motion superimposes all external effects and a separation into two individual phases (particles and carrier liquid) is not possible. This study deals with a detailed investigation of the interacting forces between

the iron particles and the carrier liquid of magnetorheological fluids for a better understanding for the design of MR-based sealings. The first MR-based sealing for the utilization in a MRF-based actuator was designed and successfully applied in [6] resisting a pressure load of about 2350 Pa. Lately, we presented an optimized design, which shows a significant increase in the compactness and energy-efficiency [7]. Both designs were developed by considering the maximum pressure load which can be compensated by the yield stress of the MRF due to the particle chains formed by the magnetic field. In this study a second effect is observed on the tightness of MR-based sealing, which is most likely related to the carrier liquid within the void between the chain structures. Thus, the pressure load is acting simultaneously on the particle structure and the carrier liquid. Thereby, the counter force of the liquid is based on the interaction between the particles and the liquid.

In the first section an overview of the developed MR-based sealing for MRF-actuators is presented. In the second section a theoretical analysis, based on a capillary pressure to describe and understand the phenomena is given. Along with the last section an experimental study is introduced to determine and prove the interaction between the particle chain structure and the carrier liquid.

2 APPLICATION OF MR-FLUID SEALINGS

In this section the application of MR-fluid sealings in energy-efficient MRF-based coupling elements is presented. Usually, for the separation of rotating parts in MRF-based coupling elements radial shaft sealings are required. But on the effective radius of the shear gap a conventional dynamic sealing needs huge space on the one hand. On the other hand it will occur friction-based losses. Thus a MRF-based coupling element was equipped with the smart MR-sealing in combination with the MR-fluid movement control [7]. The design is depicted in figure 1 a) showing also the distribution of the MRF for characteristic states of operation of the conditional stable MR-fluid movement control. The according distribution of the magnetic flux density is illustrated in figure 1 b). Each upper shear gap shows the loss-less idle mode. This state is achieved by the impact of radial accelerations due to rotational speed resulting in a separation of the two rotors. By this, drag torques caused by viscous friction can be completely prevented

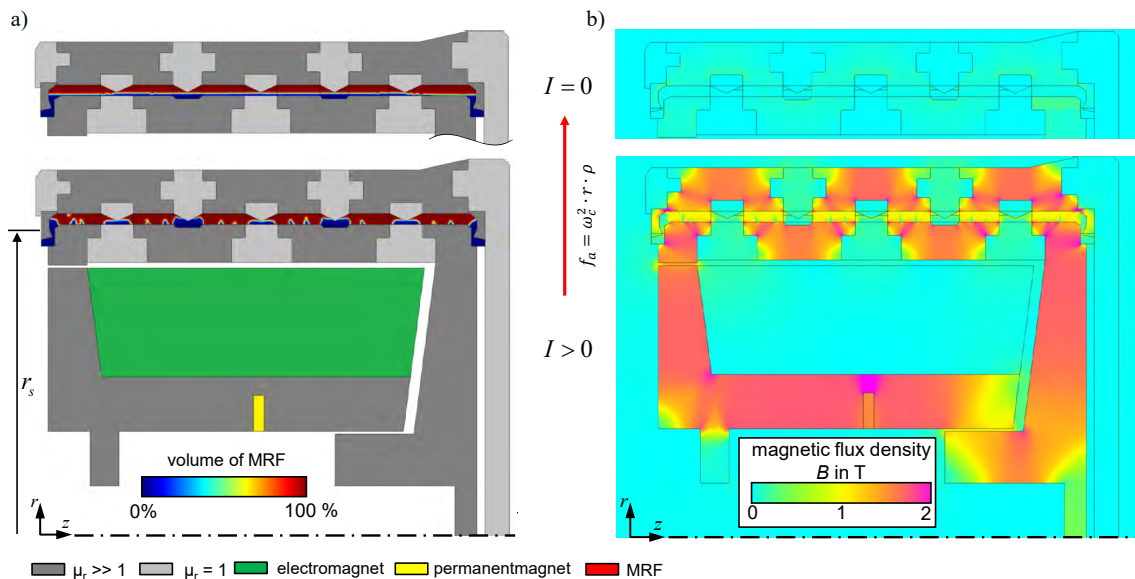


Figure 1: Magnetic circuit of an MRF-based coupling element with partially filled shear gaps operating with the conditional stable MR-fluid movement control a) and the according distribution of the magnetic flux density b).

above certain rotational speeds n . In the fully illustrated magnetic circuit the torque transmission mode is depicted. By the magnetic field of the electromagnet the MRF is moved by magnetically induced volume force densities, resp. Kelvin forces, to engage both rotors and transmit torque by the MR-effect. The movement of the MRF is simulated with the software Comsol Multiphysics. The more detailed design of the applied MR-fluid sealing for the MRF-based clutch equipped with a conditional stable MR-fluid movement control, as proposed in figure 1, is shown in figure 2 a-c). In figure 2 a) the clutch is shown in standstill and the MRF moves towards the smart sealing due to the impact of gravity. Due to the magnetic field of the permanent magnet (PM), positioned within the inner magnetic circuit below the center of the electromagnet (compare figure 1), the yield stress of the MRF is slightly increased in the area of the radial sealing gap and in the shear gap. Therefore, leakage at the sealing and sedimentation in the shear gap is avoided. Under the impact of higher rotational speeds (figure 2 b)), the MRF will be moved out of the sealing gap and placed at the outer rotor by radial acceleration f_a . Similar to the conditional MR-fluid movement control drag torque can be completely eliminated [7]. Activating the electromagnet (EM) in figure 2 c)) results in a movement of the MRF from the outer rotor towards the inner rotor to engage the clutch according to the MR-fluid movement control. Consequently, the MRF is utilized to transmit torque on the one hand and to realize a sealing on the other hand ensuring an energy-efficient operation. In figure 2 d) a novel measurements are shown focusing on the impact of certain degrees

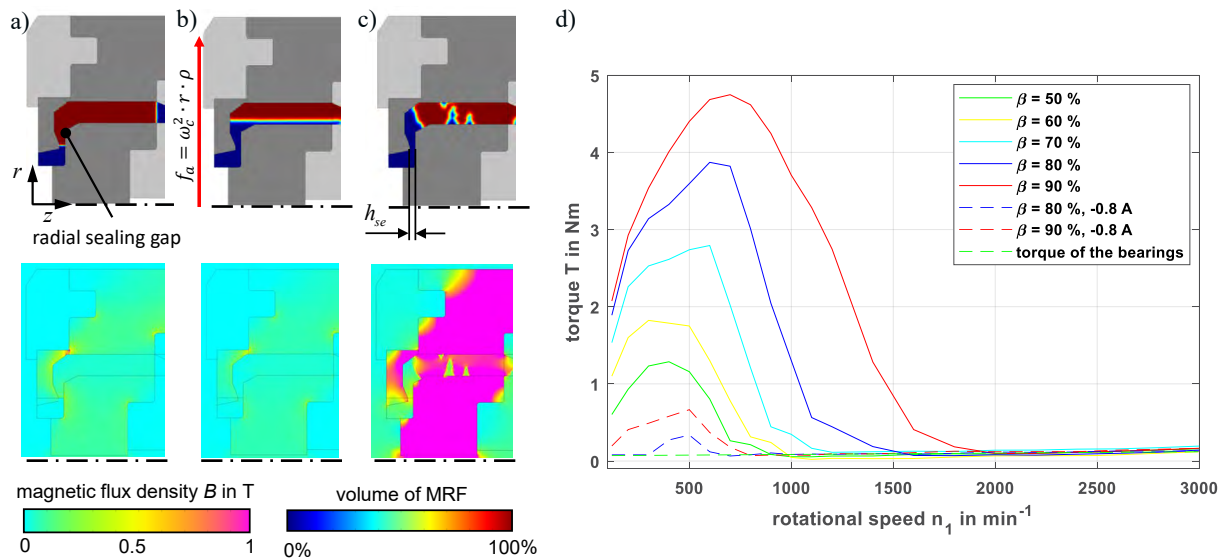


Figure 2: Schematically design of the smart MR-based sealing and distribution of the MRF during standstill (a), at rotational speed (b) and during torque transmission (c). Experimentally measured behavior of the idle torque at a rising rotational speed n_1 and a constant rotational speed of the inner rotor $n_2 = 100 \text{ min}^{-1}$ for certain degrees of filling β d).

of filling β on the critical rotational speed ω_c of the outer rotor. The degree of filling has a significant impact on the torque capacity of MR-actuators. A higher degree of filling results in a much higher torque capacity on the one hand. But, with rising volume of MRF in the shear gap it becomes also harder to separate the shear surfaces on the other hand. The changed drag torque behavior can be comprehended by figure 2. An increasing degree of filling β results in a much higher magnitude of the drag torque and also in an enhanced critical rotational speed ω_c . For example, a degree of filling of $\beta = 90\%$ results in the critical rotational speed of $\omega_c = 2000 \text{ min}^{-1}$. However, the compensation of the magnetic field of

the permanent magnet in the shear gap by the electromagnet can be used to significantly reduce the drag torque and the critical rotational speed ω_c during the operation. Due to the compensation the drag torque can be completely eliminated in the range of $n_1 > 750 \text{ min}^{-1}$ except the drag of the bearings for the maximum degree of filling of $\beta = 90\%$. The required electrical power for the compensating current I is $P_{el} < 1 \text{ W}$. Thus, an energy efficient operation can be provided also at high degrees of filling.

A separation of the particle and carrier liquid was not investigated so far. In literature no contribution is known dealing with the interaction between the carrier liquid and the particle chain structure of the MRF. Consequently, a first investigation of this interaction behavior will be presented in the next sections.

3 EXPECTED INTERACTION FORCES

As mentioned before, the arrangement of particles fixed by a magnetic field is assumed as particle chains. The structure can be also compared to porous media as illustrated in figure 3 a). Considering the carrier liquid within the chain structure the interaction between this porous media and the laminar homogeneous flow of the liquid is usually described by Darcy's law [8]. Darcys law is based on a special solution of the Navier-Stokes-Equation considering the permeability of the porous material and the friction of the liquid by the dynamic viscosity η as flow resistance. However, in a defined volume of MRF exposed to a magnetic field no flow of the carrier liquid was detected and therefore the Darcy's law is not applicable. At zero or very small velocities the impact of the surface tension become more important instead [9]. Hence, a model based approach focusing on the capillary pressure is applied in this section.

3.1 Analytical approach

The capillary pressure of fluids causes a rising behavior of fluids within the porous media. The model representation is based on capillary tubes, which capillary radius r_c correlates with the investigation of the proposed material. The time-dependent behavior of a liquid in a capillary can be described by the Hagen-Poiseuille-Equation [10]:

$$\frac{dh}{dt} = \frac{r^2 \cdot \Delta p}{8\eta \cdot h(t)}. \quad (2)$$

Therein, h represents the height of the capillary tube, η the dynamic viscosity and the pressure difference Δp . Especially the pressure difference determines the achievable rising height h which is ascribed to the hydrodynamic pressure p_p and the capillary pressure p_c expressed by the Young-Laplace-Equation:

$$\Delta p = p_c - p_p = \frac{2\lambda \cos \theta}{r_c} - \rho \cdot g \cdot h. \quad (3)$$

The Young-Laplace-Equation [11] describes the relationship between the surface tension λ and the curvature of the fluid surface resulting in the inner pressure. Since, no transient behavior is expected (respectively leakage would have been observed in previous works) the finite height h_{fin} can be used to describe the interaction forces. Therefore, Eq.3 is inserted in Eq. 2, also known as Washburn-Equation [12]. At steady state dh/dt vanishes by which the final length h_{fin} is calculated by:

$$h_{fin} = \frac{2\lambda \cdot \cos \theta}{r_c \cdot g \cdot \rho}. \quad (4)$$

The utilized parameters can be comprehend by figure 3 b). Hence, the capillaries in the porous medium are not comparable to the assumed tube geometry different approaches were developed to consider irregular capillaries. For example in [13] the porous media is assumed as an array out of particles resulting

in a periodical sinusoidally capillary size. Under consideration of the periodical contour only the average maximum radius $r_{c,max}$ of the capillary is required for the calculation of the stationary maximum height h_{fin} . The average maximum radius $r_{c,max}$ of the capillaries within the MRF particle chain structure can be calculated with respect to the particle volume fraction of $c_v = 0.47$ and the assumption of an homogeneous particle distribution, compare figure 3 c):

$$V_Q \cdot c_v = V_P \Rightarrow x_Q^2 \cdot 2r \cdot c_v = \frac{8}{3}\pi r^3. \quad (5)$$

Therein, x_Q is the edge length of the representative cuboid volume and r is the mean radius of an iron particle.

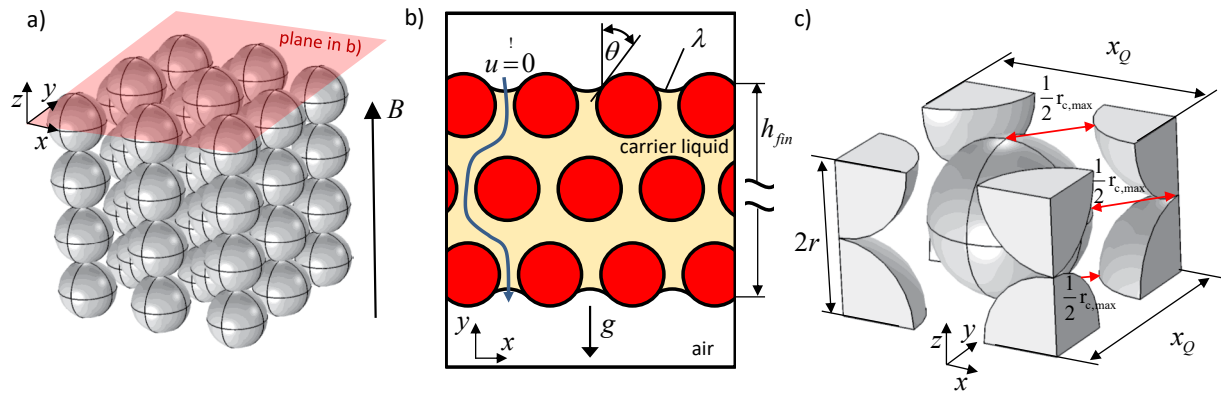


Figure 3: MRF-particles fixed by a magnetic field B a) showing the plane for the illustration of important modeling parameters in b). Representative cubit volume for the calculation of the capillary radius $r_{c,max}$. in c)

3.2 Determination of material parameters

The remaining surface tension λ and the angle of the surface curvature θ have to be determined by experimental investigation. Therefore, a setup based on two different capillary tubes was used [14]. Due to the capillary pressure the carrier liquid rises in the capillaries and by the height difference of Δh the surface tension can be determined, as illustrated in figure 4 a):

$$\lambda = \frac{\Delta h \cdot r_2 \cdot r_1 \cdot \rho \cdot g}{2 \cdot \cos(\theta) \cdot (r_2 - r_1)}. \quad (6)$$

The angle of the surface curvature on a glas surface was determined as $\theta = 8^\circ$, see figure 4 b). The measurement on the pure particle material was not applicable due to the absorption of the carrier liquid. However, the small surface curvature, which can be expected for oil, results in an almost neglectable impact in this approach. Applying Eq. 6 under consideration of the density of $\rho = 754 \text{ kg/m}^3$ the surface tension of the carrier liquid can be determined as $\lambda = 24.9 \text{ mJ/m}^2$. Thus, the final height of the carrier liquid within the particle structure can be calculated with equation 4 to $h_{fin} = 2.89 \text{ m}$ resulting in a capillary pressure of $p_p = 21.44 \text{ kPa}$. Hence, a test-setup with a length of 2.89 meter MRF exposed to a magnetic field is not feasible and not appropriate for the representation of the MRF in the shear or sealing gap a smaller gap is chosen for the test-setup in the next section. The remaining height h_{fin} is considered by an additional pressure load.

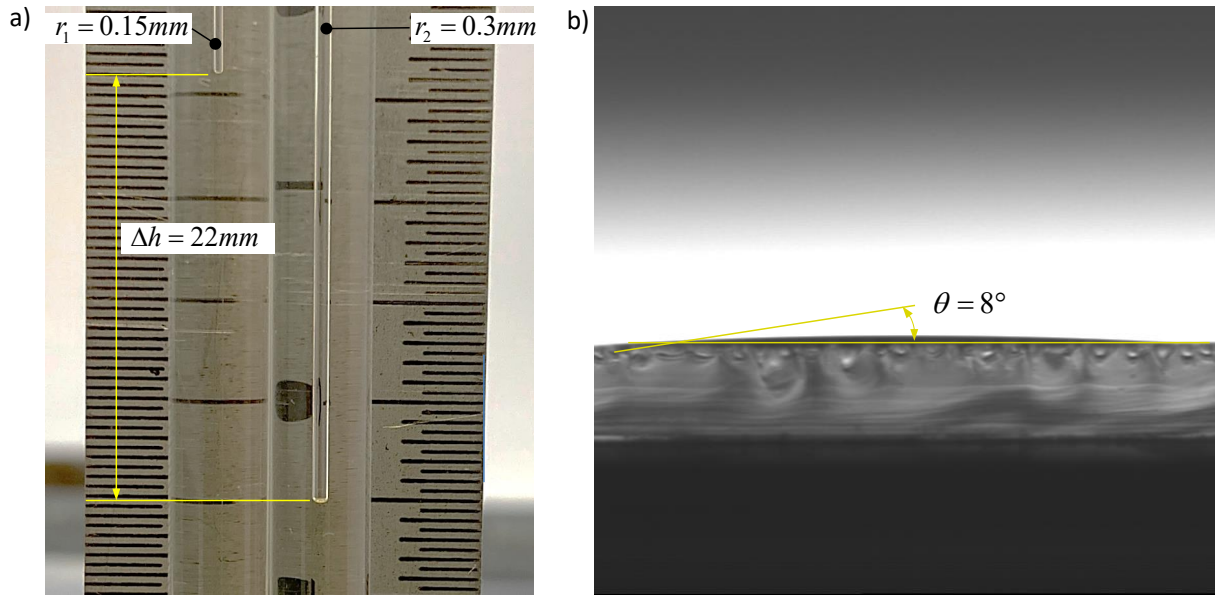


Figure 4: Experimental investigation of the surface tension λ with the double capillary method a) and determination of the angle of the surface curvature θ b).

4 EXPERIMENTAL INVESTIGATION OF THE CAPILLARY PRESSURE

As mentioned before the capillary pressure of the carrier liquid within the particle structure is in the focus of this investigation. The objective is the determination of the equilibrium between the capillary pressure and a defined pressure load.

4.1 Setup

Based on a magnetic circuit the MRF is exposed to a magnetic field in a small gap with the height h_g and the length l_g . An enclosing pressure chamber provides a well defined impact of the pressure load p_1 on the shear gap in z-direction. The whole test-setup is exposed to the ambient pressure p_0 as illustrated in figure 5 a). The pressure load p_1 will be controlled by the shown U-tube pressure gauge partially filled with water and air. Since the height of the gap is very small the impact of the hydrodynamic pressure of the carrier liquid in the probe is neglected. Hence, only the interaction force between the particle chain structure and the carrier liquid is in the focus of interest the yield stress of the MRF will be adjusted to resist at least a 5 times higher pressure load than the calculated capillary pressure. Thus a stable and homogeneous particle chain structure can be sustained. The required yield stress can be simply estimated by [3]:

$$\tau(|B|) = \Delta p \cdot \frac{h_g}{l_g \cdot 3}. \quad (7)$$

Therein describes $\tau(|B|)$ the yield stress depending on the magnetic flux density B . According to the characteristics of the utilized MRF Basonetic 5030 a magnetic flux density of approx. $B = 0.52\text{ T}$ is sufficient. Based on this requirements the magnetic circuit, illustrated in figure 5 b), was designed to affect on the MRF as proposed.

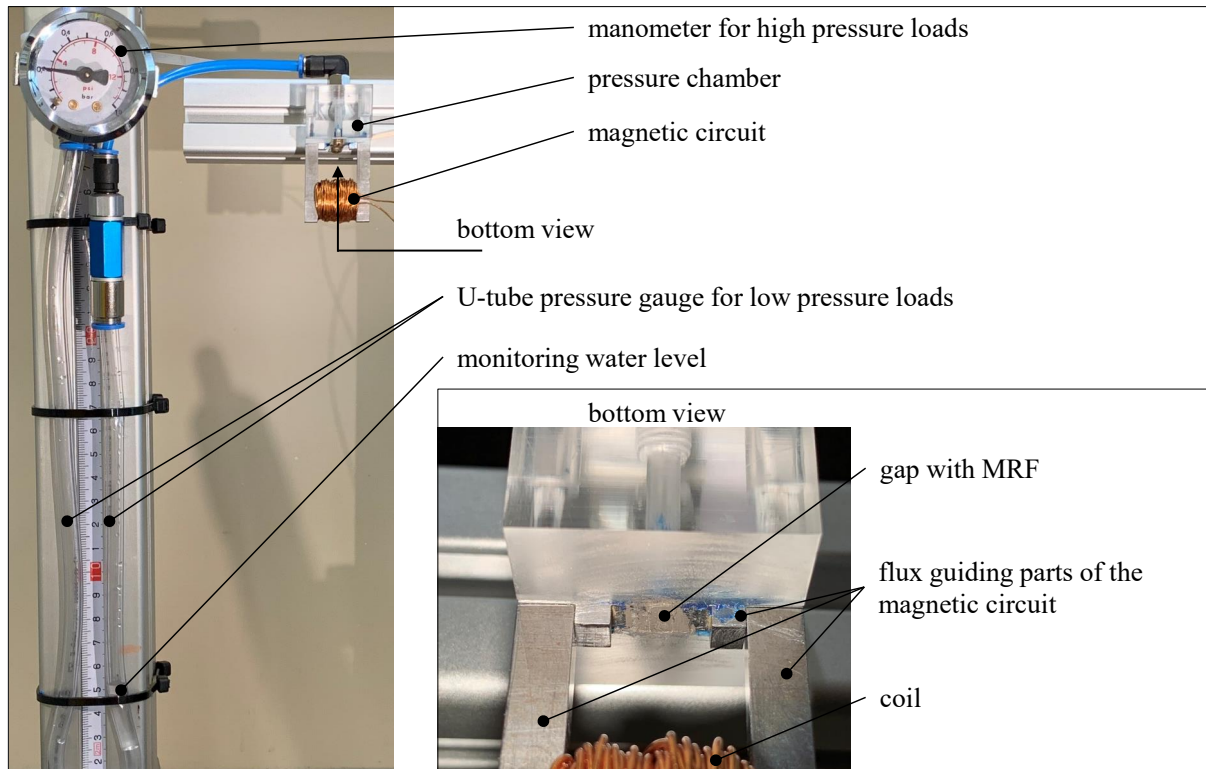


Figure 6: Photography of the test-setup for the experimental investigation showing the measurement at a pressure load of approx. $p_1 = 215$ kPa.

interaction between the particle structure and the carrier liquid. Consequently, a separation during the off-state in the sealing or shear gap due to gravity effects can be excluded. Moreover, it was observed that MR-fluid sealings are not feasible for a 100% leakage proof against gas at certain pressure loads. Compared to FF the void within the particle structure is the limiting factor of the MR-based sealing if a hermetic seal is required. In case of the sealing applied in energy-efficient MRF-based coupling elements with partially filled shear gaps this restraint is not relevant, since no significant pressure load occurs during operation.

5 CONCLUSIONS

Within this contribution the interaction between the particle chain structure and the carrier liquid of MRF are investigated to gain more information about the feasibility of MR-based sealings and the MR-fluid movement control. In an analytical approach based on the capillary pressure sufficient binding forces are determined, which are generally proved by an experimental investigation. Consequently, the interaction within a relevant continuum of MRF exposed to a magnetic field withstand the impact of gravity. The investigation revealed a very slight leakage flow of air (gas) through the voids of the particle structure, which demonstrates a disadvantage compared to sealings based on ferrofluids. Nevertheless, the proof of applicability in MRF-based coupling elements in combination with the MR-fluid movement control was found.

REFERENCES

- [1] Raj, K., Moskowitz, R., Commercial applications of ferrofluids *Journal of Magnetism and Magnetic Materials* (1990) **Vol. 85, No. 3**, p. 233-245.
- [2] Moskowitz, R., Dynamic Sealing with Magnetic Fluids *A S L E Transactions* (1975) **Vol. 18, No. 2**, p. 135-143.
- [3] Carlson, J.D., *Magnetorheological fluid actuators*, in [Adaptronics and Smart Structures - Basics, Materials, Design and Applications], Janocha, H., 2 ed., 2007, Springer, Berlin Heidelberg, p. 184-204.
- [4] Zhang, Y. and et.al., A Comparative Study of Ferrofluid Seal and Magnetorheological Fluid Seal *IEEE Transactions on magnetics* (2018) **Vol. 54, No. 12**.
- [5] Kordonski, W.I., Gorodkin, S.R., Magnetorheological Fluid-Based Seal, *Journal of Intelligent Material Systems and Structures* (1996) **Vol. 7, No. 5**.
- [6] Lampe, D., Thess, A., MRF- Clutch - Design Considerations and Performance *Proc. of Actuator 1998, 6th International Conference on New Actuators*, pp. 449-452.
- [7] Hegger, C., Maas, J., Smart sealing for magnetorheological fluid actuators *Journal of Intelligent Material Systems and Structures* (2019) **Vol. 30, No. 5**.
- [8] Scheidegger, A.E., *The physics of flow through porous media*, University of Toronto Press, Vol. I., (1957), Vol. II., (1960).
- [9] Miller, R.J. and Low, P.F., Threshold Gradient for Water Flow in Clay Systems. *Soil science society of America* (1963) **Vol. 27, No. 6** p. 605-609.
- [10] Suter, S.P., Skalak, R., The History of Poiseuille's Law, *Annual Review of Fluid Mechanics*, (1993), **Vol. 25**, p. 1-19.
- [11] Finn, R., *Equilibrium Capillary Surfaces*, SpringerVerlag New York Berlin Heidelberg Tokyo, Vol. I., (1986).
- [12] Washburn, E.W., The Dynamics of Capillary Flow, *Physical Review*, (1921), **Vol. 17, No. 3**, p. 273-283.
- [13] Staples, T.L., Shaffer, D.G. An experiment on surface tension using a double capillary method, *American Journal of Physics*, (2002), **Vol. 52**, p. 239-250.
- [14] Agrawal, D.C. and Menon, V.J. Wicking flow in irregular capillaries, *Colloids and Surfaces A: Physicochemical and Engineering Aspects*, (1984), **Vol. 52**, p. 472.

MULTI-AXIS MAGNETORHEOLOGICAL AIRCRAFT SEAT SUSPENSION

YOUNG T. CHOI^{*}, NORMAN M. WERELEY^{*} AND GREGORY HIEMENZ[†]

^{*} Department of Aerospace Engineer
University of Maryland
College Park, MD 20742 USA
e-mail: nicechoi@umd.edu, wereley@umd.edu, aero.umd.edu

[†] InnoVital Systems Inc.
Calverton, MD 20705 USA
email: ghiemenz@innovitalsystems.com, www.innovitalsystems.com

Key words: Multi-Axis, Vibration Isolation, Magnetorheological, Seat Suspension.

Abstract. This study presents the multi-axis vibration isolation performance of a full-scale magnetorheological (MR) fluid-based seat suspension for both individual and simultaneous three-axis directional inputs via experiment. To this end, a semi-active MR seat damper was designed and fabricated to cope with all three-axis directional excitation. The damping capability of the multi-axis MR seat damper was experimentally evaluated for both axial and lateral directions in terms of dynamic stiffness and loss factor by an servo-hydraulic testing machine. Before building a full-scale MR seat suspension, we constructed a 1/3rd scale MR seat suspension to check if the fabricated MR seat damper is capable of sufficiently reducing the seat vibration under practical excitation input levels. In addition, to efficiently suppress the seat vibration, a narrow-band frequency shaped semi-active control (NFSSC) algorithm was formulated. Finally, we constructed a full-scale MR seat suspension with a 50th percentile male dummy and conducted the three-axis vibration isolation testing by using a hydraulic multi-axis simulation table (MAST) for both individual (in this case, excitation input was swept over wider frequency range up to 200 Hz) and simultaneous three-axis directional inputs. The feasibility of the full-scale MR seat suspension effective for the seat vibration reduction was experimentally evaluated.

1 INTRODUCTION

Excessive vibration of aerial vehicles affects occupants with short-term effects such as discomfort, loss of situational awareness and fatigue. Occupants exposed to long-term whole-body vibration have chronic health issues such as back pain, cervical and spine injuries. Vibration spectra ranging up to 80 Hz effect various human body parts, e.g., the resonant frequency of the cervical and lumbar regions is from 2.5 to 5.5 Hz, and head and shoulder regions is from 20 to 30 Hz. Thus, prolonged vibration produces chronic musculoskeletal stress and may cause permanent damage. For these reasons, seat suspensions are a key vibration mitigation strategy for aerospace vehicles.

Most published research on MR seat suspensions has focused on vibration suppression in only the vertical direction because this vibration is dominant for most cases and most MR seat dampers can only produce a single-axis controllable damper force. But, in practical situations, occupants will be exposed to three-axis excitation inputs. In addition, the testing of vibration isolation performance in MR seat suspensions has been conducted primarily for a relatively low frequency range below 30 Hz, because most experimental setup have been constructed as a single degree-of-freedom (DOF) seat suspension system having one relatively low resonant frequency below 10 Hz. Moreover, most researches has been conducted to measure vibration attenuation on scaled-down MR seat suspensions. Therefore, a key research goal of this study was to test and evaluate multi-axis vibration isolation performance of a full-scale MR seat suspension for both individual (in this case, excitation input was swept over wider frequency range up to 200 Hz) and simultaneous three-axis directional inputs.

2 MULTI-AXIS MR SEAT DAMPERS FOR SEAT SUSPENSIONS

Figure 1 presents the schematic diagram of the multi-axis MR fluid-based seat damper. The electromagnetic coil is configured around the bobbin and the outer cylinder acts as the magnetic flux return. The bobbin is attached to the top elastomer through a connecting screw. When current is applied to the electromagnetic coil, the magnetic densities are concentrated on the bottom and radial sides of the bobbin. As a result, this MR seat damper can produce the resisting MR yield forces in both axial (i.e., vertical) and lateral (i.e., radial) directions. More detailed working principles of this MR seat damper can be found in reference [1].

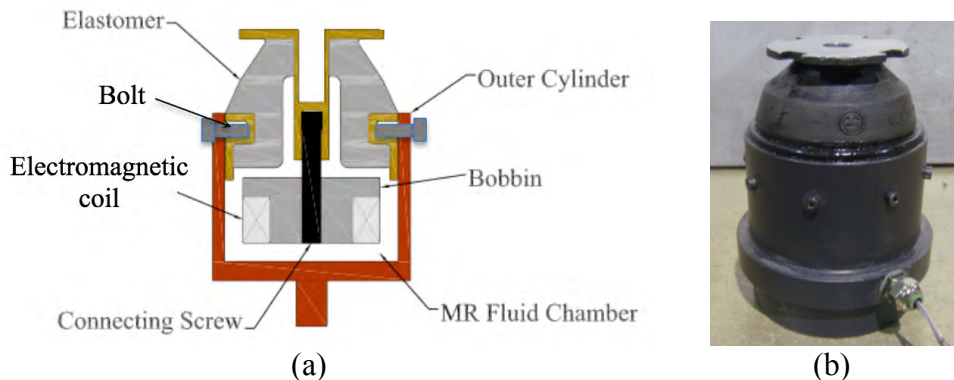


Figure 1: The multi-axis magnetorheological (MR) fluid-based seat damper. (a) schematic diagram. (b) fabricated seat damper.

Figure 2 presents the axial dynamic stiffness and loss angle of the multi-axis MR seat damper. In these tests, the MR seat damper was initially compressed in axial direction by 2 mm for emulating the static deflection due to the occupant's mass. As seen in this figure, the dynamic stiffness and loss angle increased as the frequency increased. But, in response to the applied current input, both the dynamic stiffness and loss angle significantly increased. Compared to zero-field (i.e., 0 A) input case, 3 A current input case shows about 4 times greater dynamic stiffness and loss angle. This implies that when current is applied, the stiffness of the MR seat damper becomes much greater and its damping also increases. Generally speaking, higher stiffness and high damping are good for the vibration reduction of

a system at an axial resonant frequency. On the other hand, similar to the axial excitation case, the lateral dynamic stiffness and loss angle also increased (see Figure 3), as the frequency increased. But, compared to the axial excitation case, the increments of the lateral dynamic stiffness and loss angle for the applied current input were smaller. But, the MR seat damper still shows at least 2 times larger dynamic stiffness and loss angle than zero-field input case for lateral direction.

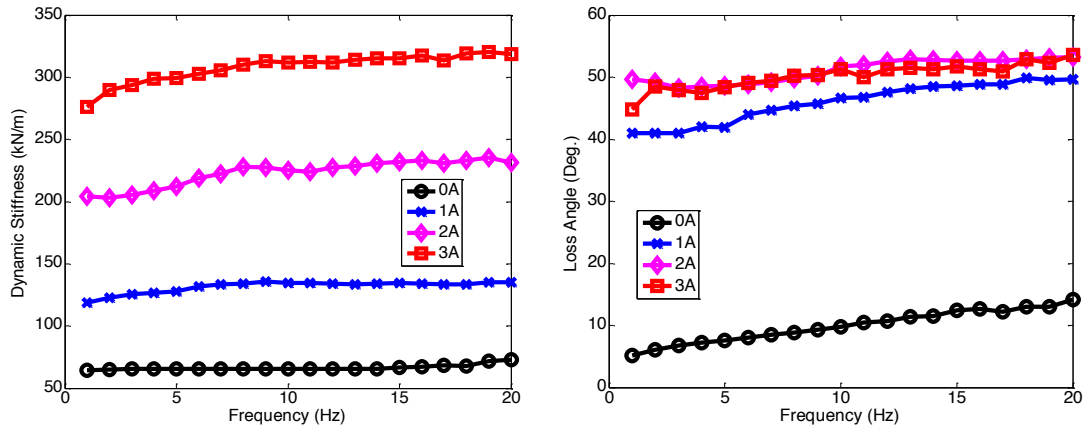


Figure 2: Axial dynamic stiffness and loss angle of the multi-axis MR seat damper under ± 1.0 mm excitation displacement.

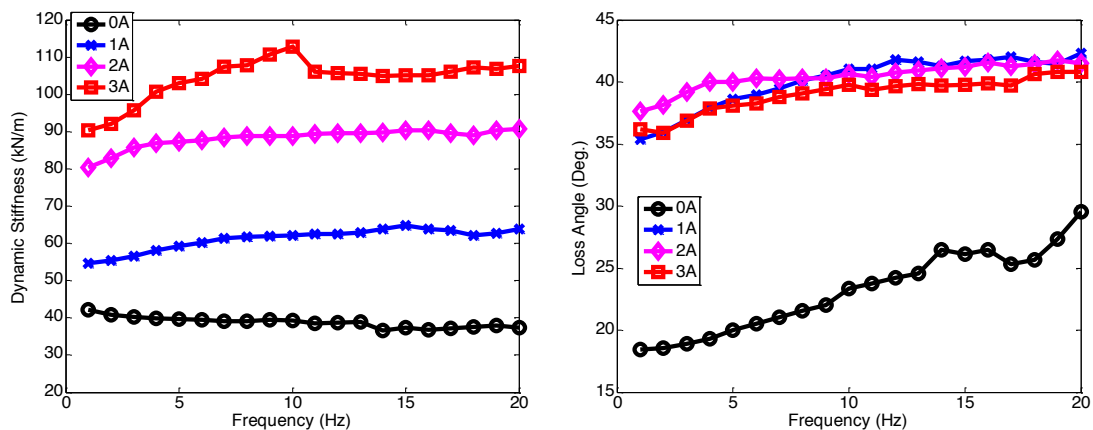


Figure 3: Lateral dynamic stiffness and loss angle of the multi-axis MR seat damper under ± 1.0 mm excitation displacement.

3 SCALED-DOWN SEAT SUSPENSION USING AN MR SEAT DAMPER

3.1 Testing setup

Figure 4 presents the photograph of the single DOF testing stand for the $1/3^{\text{rd}}$ scale-down MR seat suspension for the axial direction. The MR seat damper is placed between the mass and the hydraulic excitation actuator and the mass linearly moves along with the guiding rails. The mass is chosen to be equal to $1/3^{\text{rd}}$ of the full-scale system mass because the full-scale MR seat suspension has three MR seat dampers. In this study, two different masses of 65 and 95 lbs were chosen for the vibration isolation testing. The hydraulic excitation actuator

provides the excitation input displacement or acceleration. For applying a control current input to the MR seat damper, an in-house controller box was used. The in-house controller box has a digital signal processor (DSP) chip to program and has own computing power to execute a vibration control algorithm without any other laptop. In addition, the controller box has three-axis acceleration measurement capability and can be operated by a 28 V battery for portable purpose. Thus, without using other sensors and current amplifiers, the in-house controller box can determine a control current input from the acceleration measured by its own accelerometer.

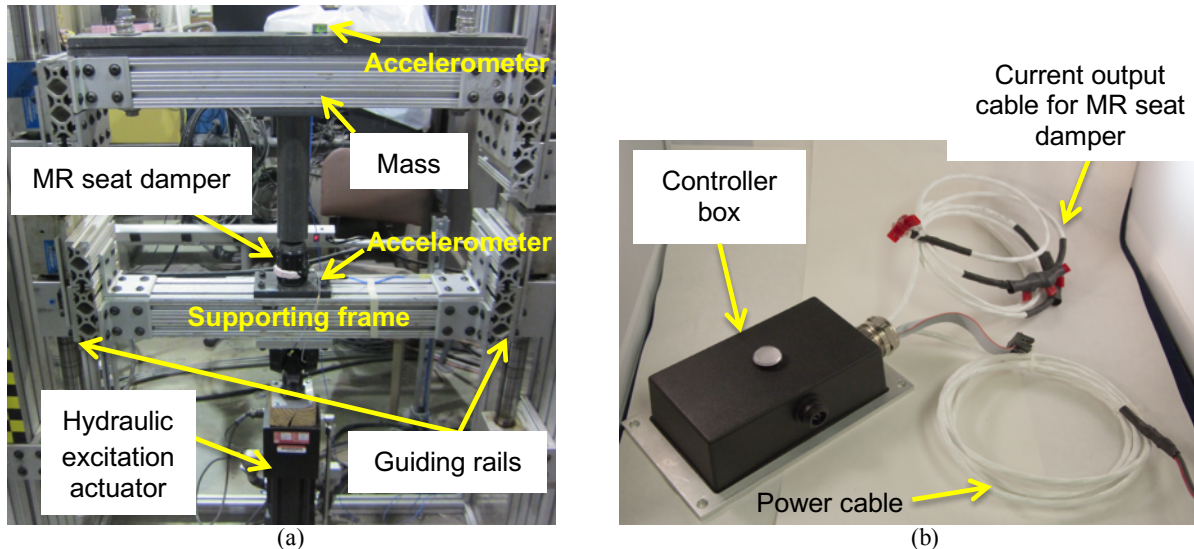


Figure 4: Photograph of the single degree-of-freedom (DOF) testing stand for the 1/3rd scale-down MR seat suspension for the axial (i.e., vertical) direction. (a) testing stand. (b) controller box.

3.2 Vibration control algorithm

In order to efficiently reduce the vibration of the MR seat suspension, we used the narrow-band frequency shaped semi-active control (NFSSC) algorithm [2]. Different from classical semi-active control algorithms, this NFSSC algorithm can be designed without resorting to an active vibration control algorithm superposed by the energy dissipation constraint (called “clipping control”). In addition, the NFSSC algorithm requires neither an accurate damper model nor system identification of damper model parameters. Thus, the NFSSC algorithm can be simply implemented by using fewer sensors.

The NFSSC algorithm will apply a larger current input to the MR seat damper when the dominant frequency of the excitation input is close to the resonant frequency of the MR seat suspension for achieving high damping. But, in frequencies other than the resonant frequency area, a minimized current input will be applied. The desired frequency shaping of the control input can be exactly matched to the frequency response behavior of the dynamics of a single DOF vibration isolation system as follows:

$$\left| \frac{z_{nout}(\omega)}{z(\omega)} \right| = \sqrt{\frac{1 + 4\zeta_{na}^2 \frac{\omega^2}{\omega_{na}^2}}{\left[\left(1 - \frac{\omega^2}{\omega_{na}^2}\right)^2 + 4\zeta_{na}^2 \frac{\omega^2}{\omega_{na}^2} \right]}} \quad (1)$$

Here, ω_{na} and ζ_{na} are the resonant frequency and damping ratio of the single DOF vibration isolation system, respectively. Also, z_{nout} is the output displacement of the single DOF vibration isolation system under the excitation displacement input, z . Note that the resonant frequency, ω_{na} of the single DOF vibration isolation system will be intentionally set to be close to the resonant frequency, ω_n of the MR seat suspension. Corresponding governing equation of the single DOF vibration isolation system given in Eq. (1) is obtained as follows:

$$\ddot{z}_{nout}(t) = -\omega_{na}^2 [z_{nout}(t) - z(t)] - 2\zeta_{na} \omega_{na} [\dot{z}_{nout}(t) - \dot{z}(t)] \quad (2)$$

The output displacement, z_{nout} , will increase around the resonant frequency, ω_n of the MR seat suspension. If the control current input is determined to be proportional to the amplitude given in Eq. (1), a larger current input will be obtained only in narrow-band frequency range where it corresponds to the resonant frequency area of the single DOF vibration isolation system given in Eq. (1). Finally, the control current input of the NFSSC algorithm is

$$i = \begin{cases} k_n \left| \frac{\ddot{z}_{nout}(t)}{\ddot{z}(t)} \right| & \text{if } i \leq i_{\max} \\ i_{\max} & \text{if } i > i_{\max} \end{cases} \quad (3)$$

Here, k_n is the control gain of the NFSSC algorithm. Note that the control current input given in Eq. (3) can be also implemented by using the ratio of the output displacement to the excitation displacement input. But, in this study, the acceleration was used in Eq. (3) because the acceleration could be measured more easily than the displacements for this MR seat suspension application.

To calculate the control input given in Eq. (3) in real-time, we need to solve Eq. (2) in real-time. For a simple implementation, Eq. (3) was discretized using the Euler method as follows:

$$\begin{aligned} z_{nout}(n) = & [2 - 2\zeta_{na} \omega_{na} h] z_{nout}(n-1) + [-1 - \omega_{na}^2 h^2 + 2\zeta_{na} \omega_{na} h] z_{nout}(n-2) \\ & + 2\zeta_{na} \omega_{na} h z(n-1) + [\omega_{na}^2 h^2 - 2\zeta_{na} \omega_{na} h] z(n-2) \end{aligned} \quad (4)$$

Here, n is the sampling number and h is the time step of the calculation. In this study, the time step was chosen to be $h=0.5$ ms. Using Eq. (4), the final control current input, $i(n)$ of the NFSSC is given by

$$i(n) = \begin{cases} k_n \left| \frac{z_{nout}(n) - 2z_{nout}(n-1) + z_{nout}(n-2)}{z(n) + \alpha} \right| & \text{if } i \leq i_{\max} \\ i_{\max} & \text{if } i > i_{\max} \end{cases} \quad (5)$$

Here, α is a constant used to prevent the denominator of Eq. (5) from becoming zero when $z(n)$ is zero.

3.3 Experimental testing results

Figure 5 presents the transmissibility of the 1/3rd scale-down MR seat suspension for the axial direction. In this case, the sinusoidal excitation input was swept from 1 to 30 Hz with the constant acceleration levels of ± 0.05 g and ± 0.1 g. Note that these vibration acceleration levels were chosen because these acceleration input values are practically available for seat suspensions in military propeller aircraft [3]. The maximum control current input was limited to 2 A by the consideration of the current output capability of the in-house controller box because three MR seat dampers will be used for a full-scale MR seat suspension and they should be activated by one controller box (maximum current output capability was 6 A). In order to improve the vibration isolation performance in the high frequency range, the measured acceleration input fed into Eq. (5) was filtered by a low-pass filter with the cutoff frequency of 15 Hz, and then, the current input below 0.3 A was made to be zero. In this figure, the thin solid line stands for no control case (i.e., 0 A case) and the thick solid line implies the results controlled by the NFSSC algorithm. The MR seat damper using the NFSSC algorithm can effectively reduce the vibration of the MR seat suspension under

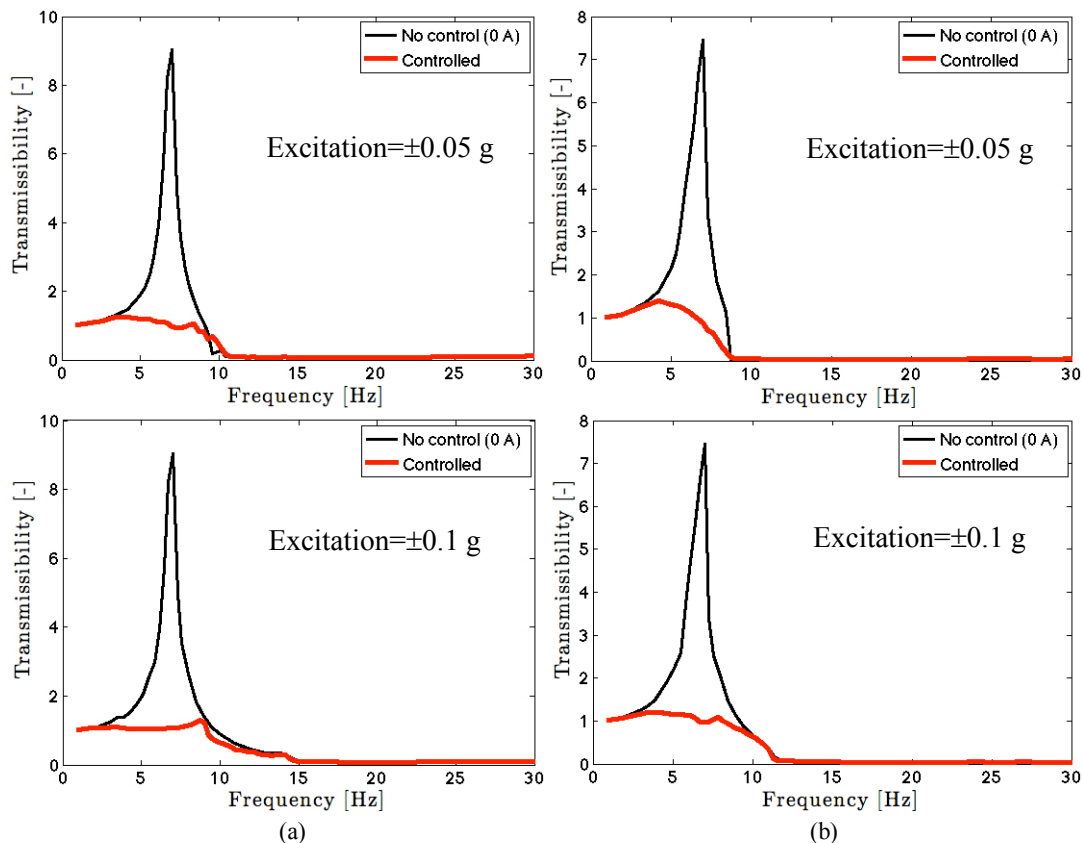


Figure 5: Transmissibility of the 1/3rd scale-down MR seat suspension for the axial direction. (a) 95 lbs of the mass. (b) 65 lbs of the mass.

practical excitation vibration input levels. In addition, for the variations of the masses and the excitation input levels, the MR seat damper under the NFSSC algorithm can still show good seat vibration suppress performances.

4 FULL-SCALE SEAT SUSPENSION USING MULTI-AXIS MR SEAT DAMPERS

Figure 6 presents the experimental testing configuration of a full-scale MR seat suspension. The seat base was rigidly attached to the floor. The dummy was installed upon the top part of the seat, and was tightly fasten by the seat belt to minimize unwanted dynamic impacts between the dummy and the seat. The seat pad (i.e., the cushion on the seat pan) was placed between the dummy and the seat pan to emulate practical seat condition. In this case, 50th percentile male dummy was chosen and its total mass including the backpack and the top part of the seat was 215 lbs. Three MR seat dampers were configured below the seat pan. These three MR seat dampers were electronically connected to the single controller box in serial. The seat can accommodate three (X, Y, Z axes) translational motions. Here, X-axis (i.e., fore-and-aft direction) is set by the normal direction to the face of the dummy pointing outward.

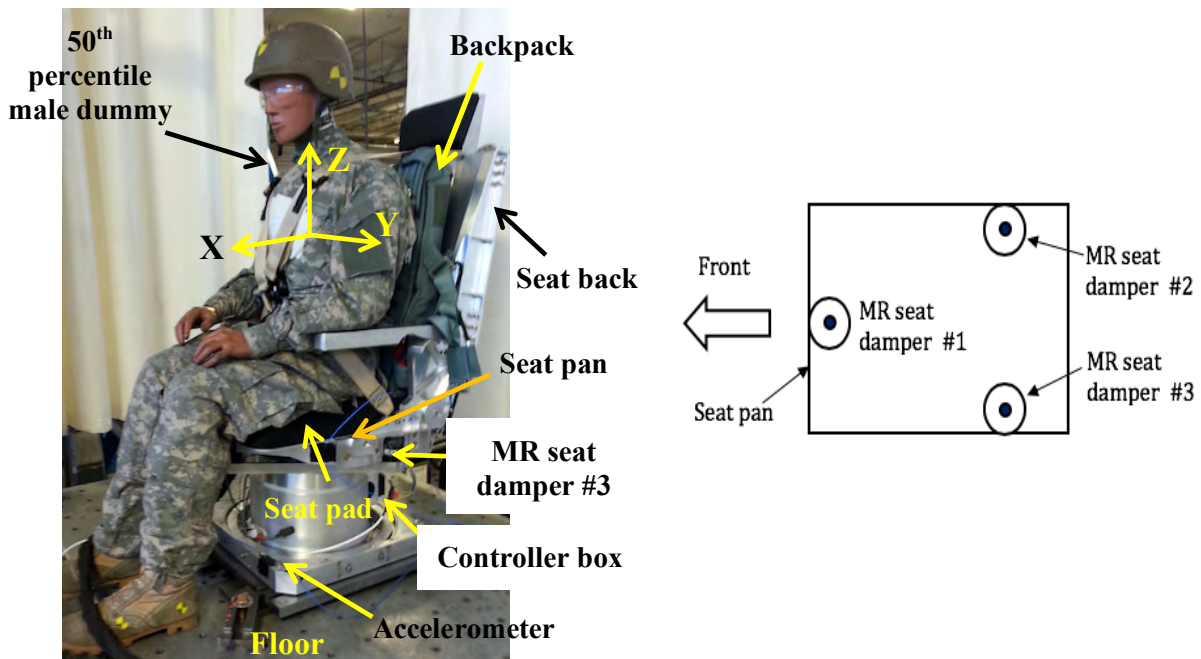


Figure. 6: Experimental testing configuration of a full-scale MR seat suspension on the hydraulic multi-axis simulation table (MAST).

Here, the Y-axis is the lateral direction and Z-axis is the vertical direction. For three-axis acceleration measurements, three-axis accelerometers were mounted on the floor, the seat pan, the seat pad, and the seat back. Note that these acceleration measurements were used only for the vibration isolation evaluation purpose, not for the vibration control purpose. For vibration isolation testing, the MR seat suspension was mounted on a hydraulic MAST and the floor was vibrated in three-axis direction either individually or simultaneously. In this study, two different excitation inputs were used: first is the sinusoidal input with a constant

acceleration level of ± 0.1 g and second is representative seat transient input. The controller box was installed at the backside of the seat base and determined a control current input based on the three-axis excitation inputs measured by its own three-axis accelerometer.

The control current inputs (i_x , i_y , and i_z) in each direction are given as follows:

$$i_d(n) = \begin{cases} k_{n,d} \left| \frac{y_{out,d}(n) - 2y_{out,d}(n-1) + y_{out,d}(n-2)}{y_d(n) + \alpha_d} \right| & \text{if } i_d \leq i_{max} \\ 0 & \text{if } i_d \leq 0.3A \\ i_{max} & \text{if } i_d \leq i_{max} \end{cases} \quad (6)$$

Here, the subscript, d is the indication of the axis direction like $d = x, y$ and z . Finally, the control input of the NFSSC algorithm for the vibration control of the three-axis full-scale MR seat suspension was given as follows:

$$i(n) = i_x(n) + i_y(n) + i_z(n) \quad (7)$$

4.1 Testing results under sinusoidal excitation input

Figure 7 presents three-axis transmissibility at the seat pan of the full-scale MR seat suspension under the NFSSC algorithm for each directional excitation input. In this figure, the solid line stands for the controlled MR damper case and the dashed line stands for rigid damper case. Note that, in the rigid damper case, three MR seat dampers were replaced by three rigid aluminum blocks. In this study, the rigid damper case was used as baseline performance because such rigid structured seat suspension with a seat pad has been used in military propeller aircraft. On the other hand, the subscript of “ o ” implies the output and the subscript of “ i ” implies the excitation input. In this testing, single excitation acceleration input for three-axis direction was individually applied to the full-scale MR seat suspension and the transmissibility was determined by using the input and output accelerations. Even though the excitation input was a single harmonic, the output is a three-axis acceleration. Thus, different from the SDOF testing case shown in Fig. 5, a total of nine different transmissibilities were obtained for the full-scale testing case. As seen in Fig. 7, when the excitation input’s direction is the same as the output accelerations’ direction (for example, $|\ddot{x}_o / \ddot{x}_i|$, $|\ddot{y}_o / \ddot{y}_i|$, and $|\ddot{z}_o / \ddot{z}_i|$), the transmissibility values at lower frequency range (i.e., below 20 Hz) become relatively larger. On the other hand, the rigid damper case shows low transmissibility value in lower frequency range, but much higher transmissibility values in higher frequency range (i.e., after 30 Hz). Such high transmissibility (greater than 1) in higher frequency range may come from high frequency resonant modes of the dummy and the seat. The controlled MR seat damper shows fairly low transmissibility value at relative lower frequency range that is close to the performance of the rigid damper case. In addition, in higher frequency range, the controlled MR seat damper achieved significant vibration isolation performance compared to the rigid damper case. Such a good vibration isolation performance of the full-scale MR seat suspension implies that the NFSSC algorithm could provide high damping (i.e., high current input) at only the low frequency resonant frequency area of the seat suspension as explained earlier.

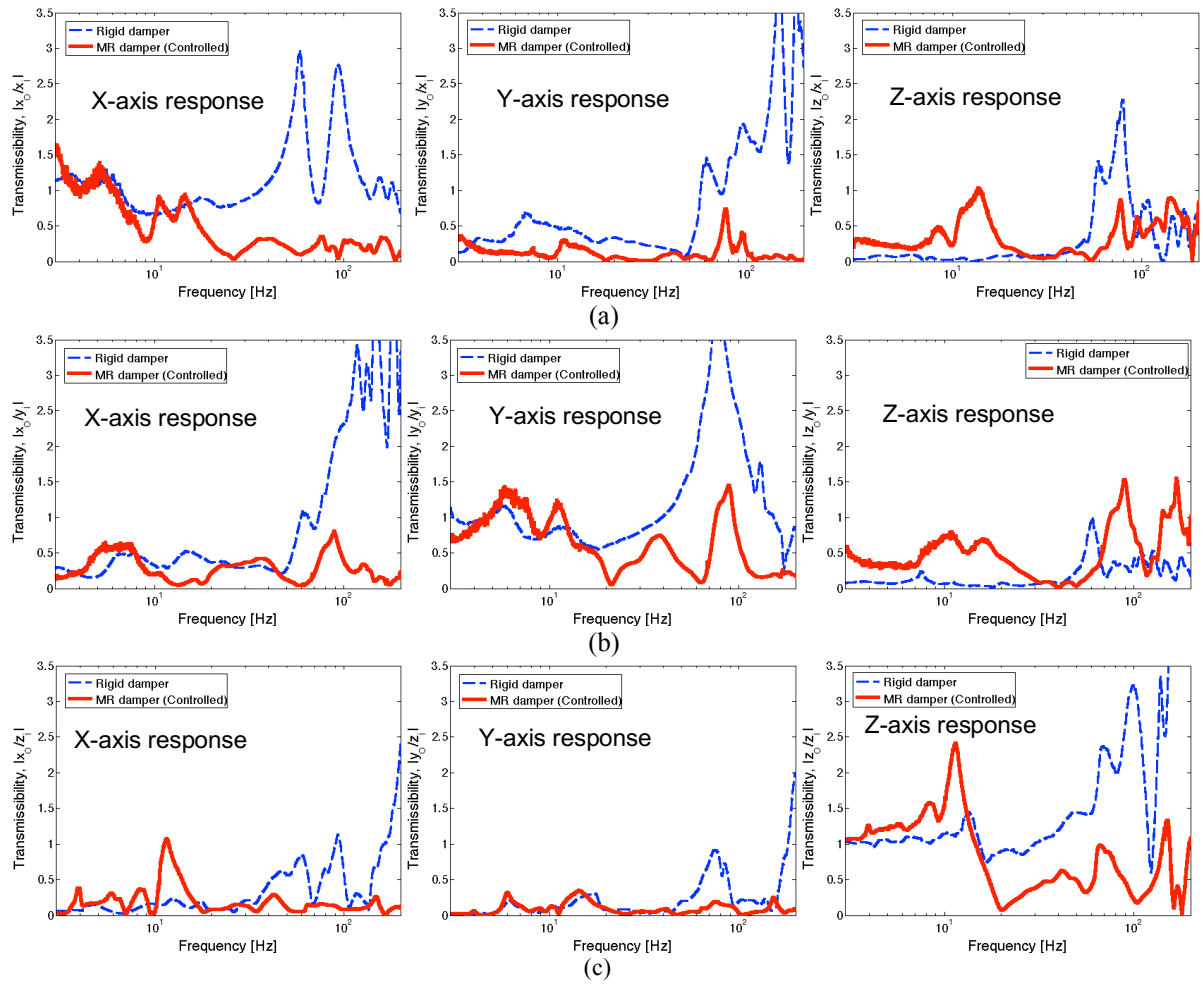


Figure 7: Three-axis transmissibility at the seat pan of the full-scale MR seat suspension under the NFSSC algorithm for each directional excitation input (excitation level: ± 0.1 g). (a) for X-axis excitation input. (b) for Y-axis excitation input. (c) for Z-axis excitation input.

For quantitative comparison on the transmissibility, we used the root mean square (RMS) transmissibility, T_{rms} , defined by

$$T_{rms} = \sqrt{\frac{1}{\omega_2 - \omega_1} \int_{\omega_1}^{\omega_2} T(\omega)^2 d\omega} \quad (8)$$

Here, $T(\omega)$ is the transmissibility in the frequency domain, ω_1 is the starting frequency, and ω_2 is the ending frequency. Smaller RMS transmissibility value implies better vibration isolation performance over the calculated frequency range. Figure 8 presents the RMS transmissibility of the full-scale MR seat suspension under the NFSSC algorithm for each directional excitation input. In the figure, the circle symbol stands for the rigid damper case and the rectangle symbol stands for the controlled MR seat damper case. In addition, the direction of “yx” in this figure implies Y-axis output to X-axis excitation input. The same notational rule can be applied to the other directional symbols like “zx”, “xy”, and “yz”, etc.

In this case, we divided the frequency domain into two regions: one is the relatively low frequency range of 3-20 Hz and the other is the higher frequency range of 20-200 Hz. As seen in this figure, for the relatively low frequency range, the controlled MR seat damper case shows good vibration isolation performance at the seat pan almost similar to the rigid damper case. Similar vibration isolation performance was also observed at the positions of the seat pad and the seat back. But, for the higher frequency range, the controlled MR seat damper case shows much better vibration isolation performance than the rigid damper case for most of different directional inputs. On the other hand, at the positions of the seat pan and the seat pad, the largest RMS transmissibility occurs in the direction of “zz”. But, at the position of the seat back, the largest RMS transmissibility occurs in the direction of “xx”. The reason is that the X-axis output at the seat back contains the front-and-back rocking motion also. Another interesting observation is that the seat pad could not effectively reduce the relatively low frequency dominant vibrations, but showed a little bit improved vibration isolation performance for the high frequency dominant vibrations. In addition, for the controlled MR seat damper case, the effect of the seat pad on the vibration suppression performance is insignificant.

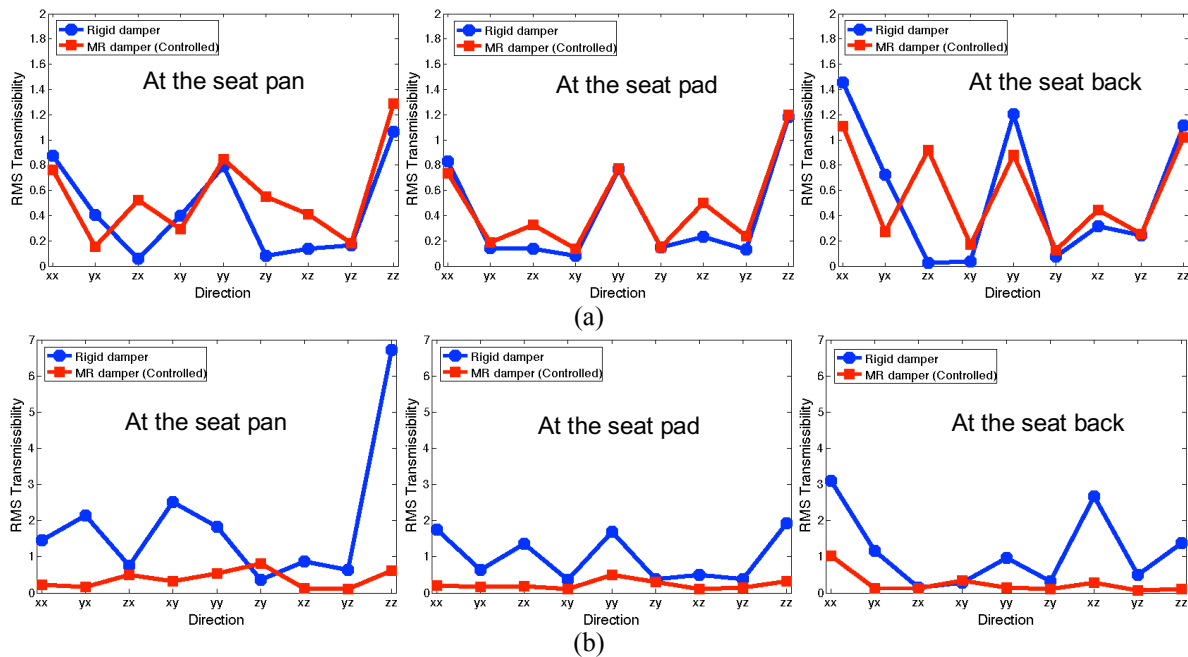


Figure 8: RMS transmissibility of the full-scale MR seat suspension under the NFSSC algorithm for each directional excitation input. (a) for the relative low frequency range (3-20 Hz). (b) for the higher frequency range (20-200 Hz).

4.2 Testing results representative seat transient inputs

Figure 9 presents the measured time responses at the seat pan of the full-scale MR seat suspension under the NFSSC algorithm for each directional representative transient excitation input [3]. In this figure, the dashed line stands for the rigid damper case and the solid line stands for the controlled MR seat damper case. As seen in this figure, X-axis excitation input case shows most severe transient acceleration outputs than other axes excitation input cases.

In addition, for X-axis transient input case, Z-axis acceleration output is larger than X-axis acceleration output. As seen in this figure, the controlled MR seat damper case shows much better vibration isolation performance than the rigid damper case for each directional representative transient input.

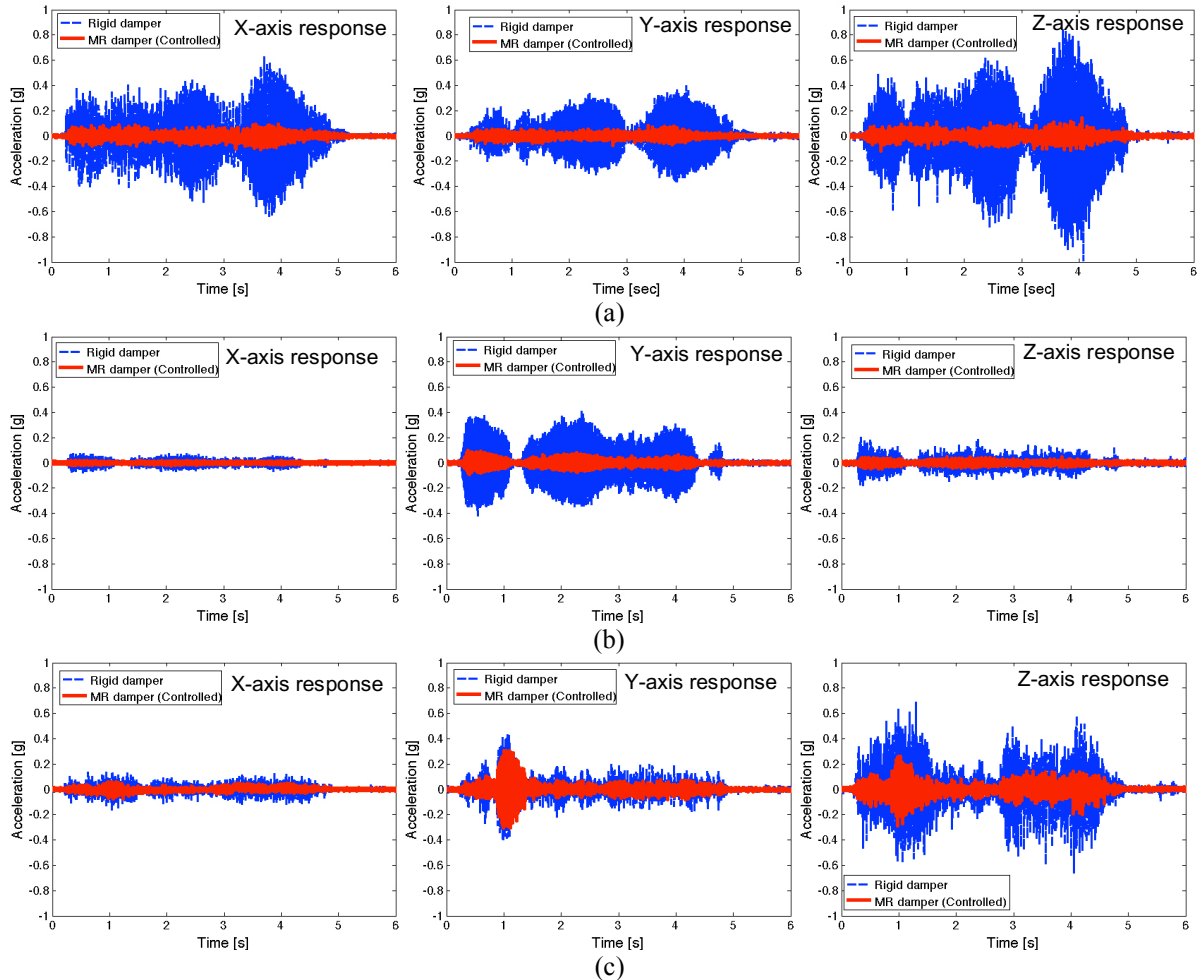


Figure 9: Measured time responses at the seat pan for the full-scale MR seat suspension under the NFSSC algorithm for each directional representative transient excitation input. (a) for X-axis excitation input. (b) for Y-axis excitation input. (c) for Z-axis excitation input.

Figure 10 presents the RMS accelerations of the full-scale MR seat suspension under the NFSSC algorithm. In Fig. 10a, the directional symbols like “xx”, “yx”, and “zx”, etc can be interpreted similar to the symbols in Fig. 8. As seen in Fig. 10a, the controlled MR seat damper case shows good vibration isolation performance at all measured positions for each directional excitation input. For observing the vibration isolation performance under simultaneous three-axis (i.e., X-, Y-, and Z-axis) excitation inputs, Fig. 10b was presented. Because of simultaneous three-axis excitation inputs, the output RMS acceleration levels in Fig. 10b were increased than the individual input case shown in Fig. 10a. But, for the controlled MR seat damper case, the increment of the RMS acceleration levels is much less than the rigid damper case. As observed in Fig. 10b, the controlled MR damper case still

showed good vibration isolation performance at the seat pan, seat pad, and seat back for simultaneous three-axis excitation inputs.

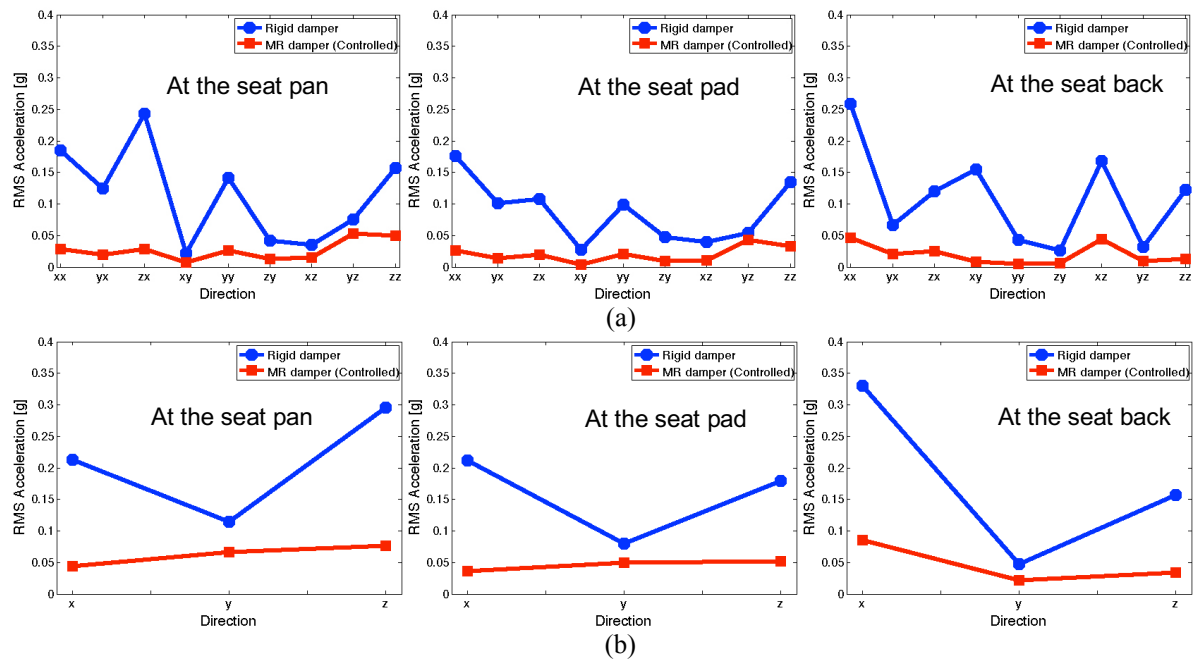


Figure 10: RMS accelerations of the full-scale MR seat suspension under the NFSSC algorithm. (a) for each directional transient excitation input. (b) for simultaneous three-axis transient excitation inputs.

5 CONCLUSIONS

In this study, the multi-axis vibration isolation performance of a full-scale magnetorheological (MR) seat suspension under a narrow-band frequency domain semi-active (NFSSC) algorithm was experimentally investigated for both individual (in this case, excitation input was swept over wider frequency range up to 200 Hz) and simultaneous three-axis directional inputs. From the results presented in this study, it was experimentally confirmed that the NFSSC algorithm could effectively suppress the multi-axis seat vibrations by using fewer sensors.

REFERENCES

- [1] Brigley, M., Choi, Y.-T., and Wereley, N.M., "Experimental and Theoretical Development of Multiple Fluid Mode Magnetorheological Isolators," *Journal of Guidance, Control, and Dynamics*, Vol. 31, No. 3, 2008, pp. 449-459.
- [2] Choi, Y.-T., Wereley, N.M., and Hiemenz, G.J., "Frequency Shaped Semi-active Control for Magnetorheological Fluid-based Vibration Control Systems," *ASME 2013 Conference on Smart Materials, Adaptive Structures and Intelligent Systems*, September 16-18, Snowbird, Utah, USA, 2013.
- [3] Smith, S.D., Jurcsisn, J.G., Walker, A.Y., Smith, J.A., and Bowden, D.R., 2007, *Dynamic Characteristics and Human Perception of Vibration Aboard a Military Propeller Aircraft*, Report, AFRL-HE-WP-TR-2007-0114, Air Force Research Laboratory.

THE EFFECT OF MESOCARBON MICROBEADS ON THE BEHAVIOR OF MAGNETORHEOLOGICAL FLUID

REBECCA M. PIERCE*, YOUNG-TAI CHOI* AND NORMAN M. WERELEY*

*Department of Aerospace Engineering

University of Maryland

Glenn L. Martin Hall, 20742 College Park, MD U.S.A.

e-mail: rmpierce@umd.edu, web page: <http://www.aero.umd.edu>

Key words: magnetorheological fluid, mesocarbon microbeads, MR effect, yield force, yield stress, rheology

Abstract. Magnetorheological (MR) fluids are composed of magnetizable particles, usually carbonyl iron particles (CIPs), suspended in a carrier fluid and change their viscosity with the application of a magnetic field. In the current study we investigate the effect of mesocarbon microbeads (MCMBs) with graphitization as an alternative particle substitute to increase the yield force of MR fluids. The MCMBs are defined as passive in response to a magnetic field when compared to the CIPs. This study presents the results of three different MR fluid compositions tested in a rheometer and in an MR damper with a 1 Hz sinusoidal displacement input. The yield stresses and yield forces are determined for a sweep of currents using the Bingham plastic model. Finally, the durability of each fluid is tested by cycling the MR damper at 2 Hz for 25,000 cycles.

1 INTRODUCTION

Magnetorheological (MR) fluids have variable viscosity and are composed, in their most basic form, of magnetizable particles, usually carbonyl iron particles (CIPs), suspended in a carrier fluid (e.g. hydrocarbon oil). The viscosity of an MR fluid changes with the introduction of a magnetic field. This is particularly useful for applications in hydraulic devices where a variable yield force is desirable. For example, MR fluids have seen applications in the aerospace [1-2] and biomedical [3] industries.

Although the observed MR effect is primarily due to the CIPs, several research studies have investigated the introduction of other particles to enhance the effect. In particular, several studies have characterized MR fluids employing nonmagnetizable particles [4-7]. An increase in either yield stress or yield force in these MR fluids has been shown in both experimental studies [4-5,7] and simulations [4,6-7]. The majority of studies investigating the effect of nonmagnetizable particles on MR fluids have focused on hollow glass spheres [4-5,7] with one study showing an increase in yield stress at magnetic saturation [4] and another study revealing a doubling of the yield force [5]. However, in the study including endurance testing, the yield force dropped back down to baseline levels as the glass beads were crushed during prolonged damper cycling at higher frequencies [5]. This study employs mesocarbon microbeads (MCMBs) in an effort to achieve yield force enhancement without the observed degradation over thousands of cycles. The MCMBs were chosen as the passive particles, in relation to the CIPs, because they are solid and are thus expected to be more durable than the hollow glass beads used in previous studies.

The increase in yield stress due to the substitution of nonmagnetizable particles in MR fluids has been attributed to a particle jamming-like mechanism [6]. In simulations, repulsive-force clusters form and increase the yield stress when nongmagnetizable particles of the same average diameter as the magnetizable particles are used in an MR fluid. Based on our previous study [5] and the study by Wilson et al. [6], the combination of the MCMBs and CIPs, will result in a fluid synergistically combining the magnetorheological effect and particle jamming.

2 METHODOLOGY

2.1 Fluid Formulation

This study utilizes MIL-PRF-83282D (AeroShell Fluid 31; Shell), a synthetic hydrocarbon hydraulic fluid with a kinematic viscosity of 14.0 mm²/s at 40 °C. MIL-PRF-83282D is commonly used for aircraft applications and is thus a viable carrier fluid with practical applications. A 35 volume percent (vol%) bidisperse mixture of carbonyl iron particles (1:1 ratio of 1.8-2.3 μm average diameter and 7-9.5 μm average diameter; BASF) and the appropriate vol% of MCMBs after graphitization (10-13 μm average diameter; Bonding Chemical) were mixed into the carrier fluid. The fluid compositions tested are listed in Table 1.

Table 1: MR Fluid Compositions

Sample Name	MIL-PRF-83282D, vol%	CIPs, vol%	MCMBs, vol%
MR-Fe35-C0	65	35	0
MR-Fe35-C5	60	35	5
MR-Fe35-C10	55	35	10

2.2 Rheometer Testing

All fluids were tested in an Anton Paar MCR 300 parallel plate rheometer with the shear rate ranging from 0.1 – 1000 Hz. Tests were conducted with the current ranging from 0-5 A.

2.3 Damper Testing

The MR fluids were also tested in flow mode with a LORD RD-8041-1 long stroke MR damper (LORD Corporation). The damper was pressurized to 2000 kPa and tested using a Material Test System (MTS) 810 machine (Figure 1). Each test applied a ± 12.7 mm sinusoidal displacement excitation to the damper's piston which was pre-compressed by 19.05 mm. The resulting force vs. displacement data was obtained for applied currents of 0-1 A with 0.2 A increments.

2.4 Endurance Testing

For one fluid composition, MR-Fe35-C10, the damper was cycled at 2 Hz and data was collected periodically using the procedure in § 2.3.

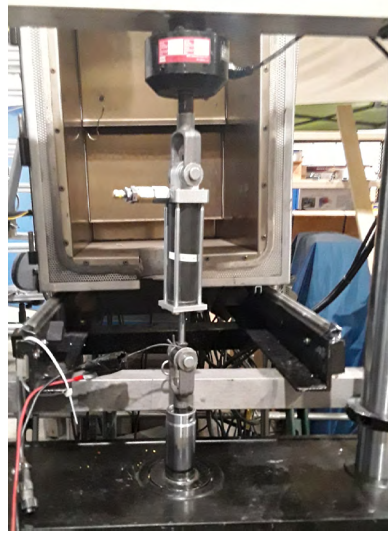


Figure 1: MR damper mounted on MTS machine

3 RESULTS

The effect of the MCMBs is characterized for Fe particle volume fraction, $\phi_{Fe} = 0.35$, and increasing MCMB volume fraction, ϕ_{MCMB} .

3.1 Rheometer Testing

The field off rheometer tests show an increase in viscosity (μ , defined as the slope of the shear stress, τ , vs. shear rate, $\dot{\gamma}$, curves) with increasing particle content (Figure 2a). The Bingham plastic model for shear stress is fit to the shear stress vs. shear rate data from $\dot{\gamma} = 300 - 1000 \text{ s}^{-1}$ to obtain the yield stress, τ_y :

$$\tau = \tau_y + \mu\dot{\gamma} \quad (1)$$

where τ_y is the intercept with the shear stress axis. Yield stress as a function of current is shown for each fluid in Figure 2b. The result of increasing ϕ_{MCMB} is inconclusive with respect to yield stress.

3.2 Damper Testing

The inconclusive rheometer tests necessitate the MR damper tests, thereby switching from shear mode to flow mode. An example force vs. displacement plot for MR-Fe35-C5 is shown in Figure 3a. This data is replotted as force vs. velocity (Figure 3b) and fitted with the Bingham plastic model to obtain the yield force, f_y :

$$F(t) = f_y \text{sgn}(\dot{x}) + C_{po}\dot{x} \quad (2)$$

where \dot{x} is the velocity, C_{po} is the post-yield damping, and f_y is the intercept with the force axis.

Yield force as a function of current is shown for each fluid in Figure 4. f_y increases as ϕ_{MCMB} increases. The increase is higher when ϕ_{MCMB} is increased from 0.05 to 0.10 than when it is increased from 0 to 0.05, indicating that the MCMBs have a nonlinear effect on the yield force when $\phi_{Fe} = 0.35$.

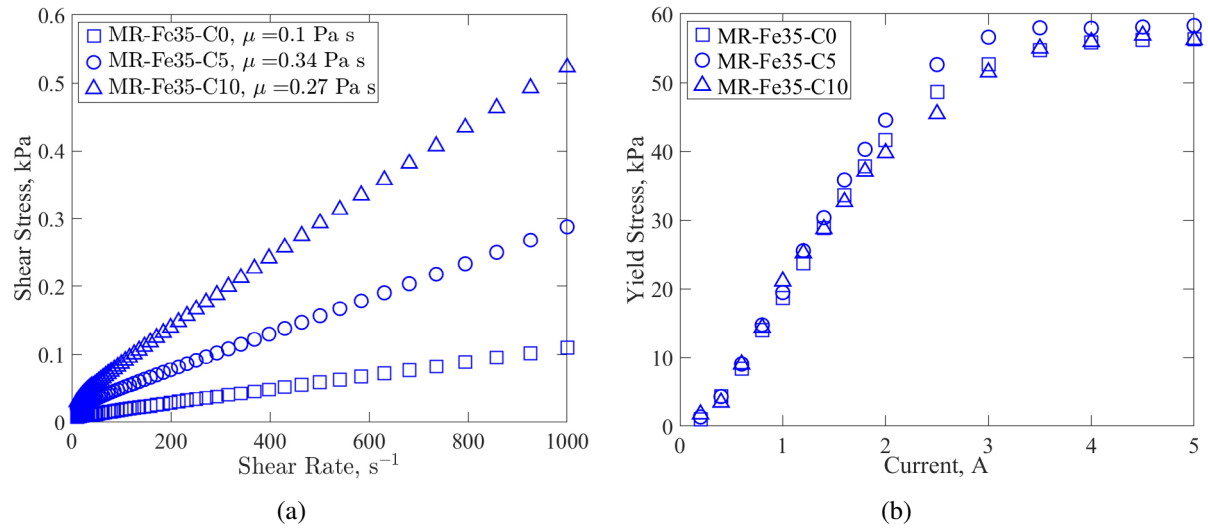


Figure 2: (a) Shear stress (τ) as a function of shear rate ($\dot{\gamma}$) with the field off for each fluid (b) Yield stress as a function of current for each fluid

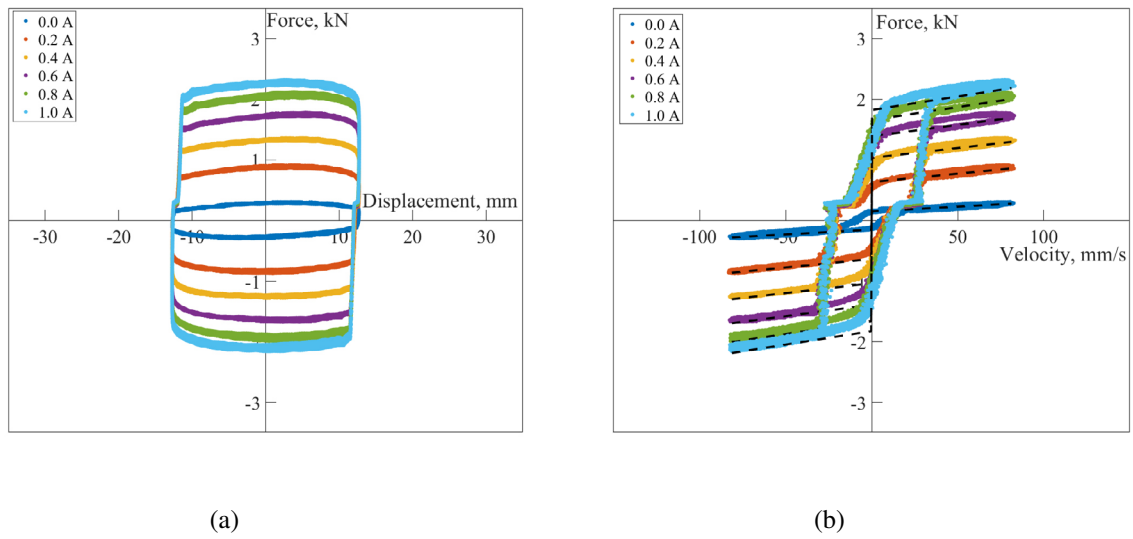


Figure 3: Representative plots of an MR damper filled with MR-Fe35-C5 (a) force vs. displacement data (b) force vs. velocity data fitted with the Bingham plastic model

4 Endurance Testing

The results of the endurance tests are shown in Figure 5. There is no clear reduction in yield force over 25,000 cycles.

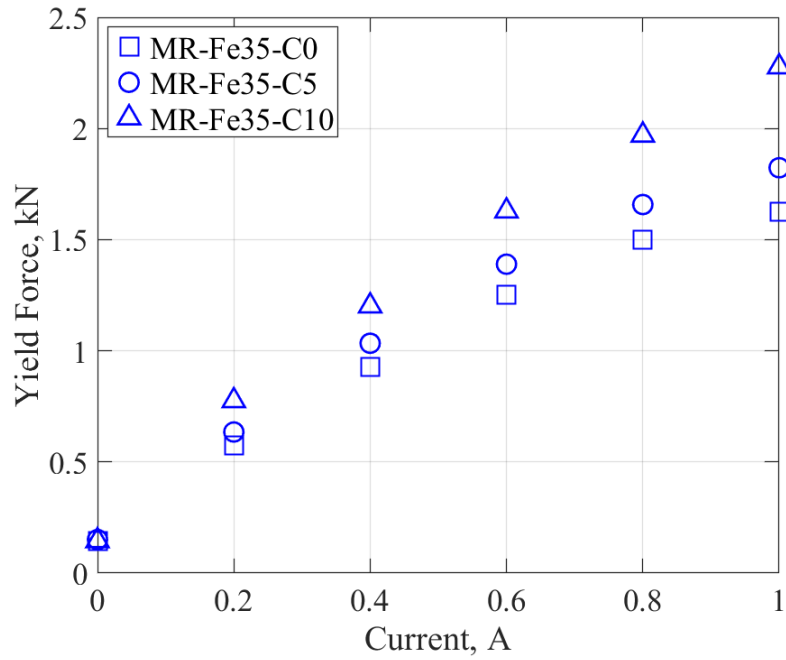


Figure 4: Yield force for MR fluids with $\phi_{Fe} = 0.35$ and $\phi_{MCMC} = 0, 0.05$, and 0.10

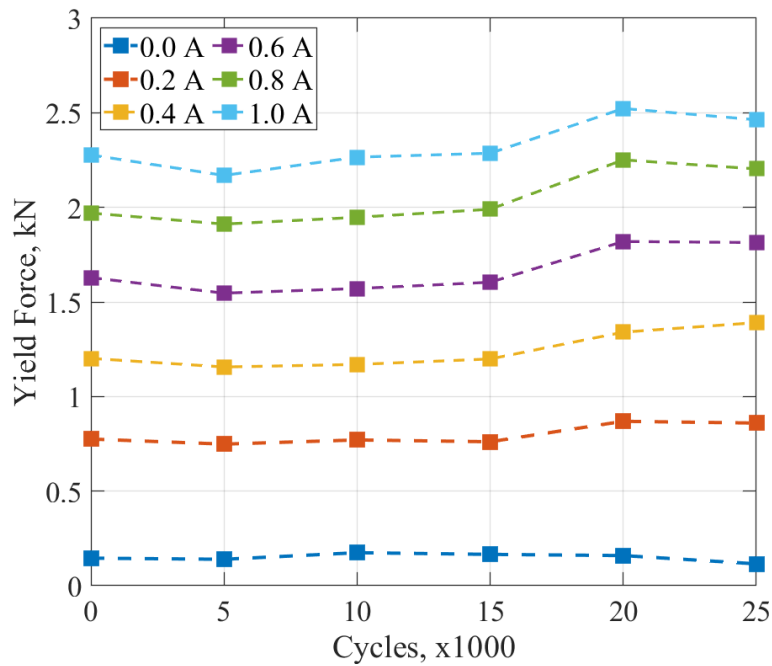


Figure 5: Endurance testing for Fe-35-C10 over 25,000 cycles

5 DISCUSSION

The field off rheometer tests exhibited darker circles of fluid in the middle of the sample post-testing while the field on tests exhibited darker circles surrounding the spindle plate post-testing. This suggests

a migration of carbon particles, which are darker in color than the Fe particles, due to centripetal acceleration. The migration of the particles off the platen during field on tests potentially contributes to the inconclusiveness of those reported results. However, because MR fluids are generally used in flow mode devices such as dampers and shock absorbers [1-3], it is the damper results that are of the greatest interest. The MR damper was cycled prior to each set of dynamic tests to promote fluid uniformity. The small volume of fluid expelled during the sealing of the damper may have resulted in slightly higher solids loading due to separation of the fluid from the particles near the top of the fluid reservoir. This can lead to a slight increase in the reported MCMB and Fe concentrations. Finally, the simulations run by Wilson et. al were done for magnetic and passive particles of the same average diameter [6], while the average diameter of the MCMBs in this study was slightly larger than that of the iron particles. The particle jamming-like effects observed in this study may thus follow a slightly different trend than those simulated by Wilson et al. [6].

6 CONCLUSIONS

Shear mode tests conducted with the rheometer yielded inconclusive results with respect to increasing carbon particle content in MR fluids with $\phi_{Fe} = 0.35$. However, flow mode tests using an MR damper revealed a nonlinear increase in yield force with increasing ϕ_C . Higher total particle content leads to greater enhancement of the yield force. If this effect is due to the particle jamming-like mechanism described in [6], the results suggest increased total particle content amplifies the effects of the mechanism. Furthermore, the yield force did not decrease over 25,000 cycles at 2 Hz. Future work would include endurance testing of a fluid with MCMBs over a greater number of cycles, to better characterize durability.

7 ACKNOWLEDGMENTS

This research was supported under the UMD Vertical Lift Research Center of Excellence (VLRCE), Army-Aviation Applied Technology Directorate, under award number W911S1720004. The first author thanks the Graduate School at the University of Maryland for travel support via the Jacob K. Goldhaber Travel Award and the International Conference Student Support Award (ICSSA).

REFERENCES

- [1] Hiemenz, G.J. Hu, W., and Wereley, N.M. Semi-active magnetorheological helicopter crew seat suspension for vibration isolation. *Journal of Aircraft*. (2008) **45.3**: 945-953.
- [2] Choi, Y.-T. and Wereley, N.M. Vibration control of a landing gear system featuring electrorheological/magnetorheological fluids. *Journal of Aircraft* (2003) **45.3**: 432-439.
- [3] Gao, F., Liu, Y.-N., and Liao, W.-H. Optimal design of a magnetorheological damper used in smart prosthetic knees. (2017) **26**: 035034.
- [4] Ulicny, J.C., Snaveley, K.S., Golden, M.A., and Klingenberg, D.J. Enhancing magnetorheology with nonmagnetizable particles. *Applied Physics Letters*. (2010) **96.23**: 231903.
- [5] Powell, L.A., Wereley, N.M., and Ulicny, J. Magnetorheological fluids employing substitution of nonmagnetic for magnetic particles to magnetorheological suspensions. *IEEE Transactions on Magnetics*. (2012) **48.11**: 3764-3767.

- [6] Wilson, B.T. and Klingenberg, D.J. A jamming-like mechanism of yield-stress increase caused by addition of nonmagnetizable particles to magnetorheological suspensions. *Journal of Rheology* (2017) **61.4**: 601-611.
- [7] Klingenberg D.J. and Ulicny, J.C. Enhancing Magnetorheology. *World Scientific*. (2011) 422-428.

ACOUSTIC ENERGY FOCUSING AND BAND GAP STRUCTURE OF ROBOCAST CERAMIC SCAFFOLDS

**Martin Koller^{1,*}, Tomáš Grabec¹, Petr Sedlák¹, Alena Kruisová¹,
Benito Román-Manso², Manuel Belmonte³, Pilar Miranzo³ and Hanuš Seiner¹**

¹ Institute of Thermomechanics of the Czech Academy of Sciences

Dolejšková 1402/5, 182 00 Praha 8, Czech Republic

*e-mail: koller@it.cas.cz, web page: <http://www.it.cas.cz/en/>

² School of Engineering and Applied Sciences, Harvard University

52 Oxford Str, 02318 Cambridge MA, USA

³ Institute of Ceramics and Glass (ICV-CSIC)

Kelsen 5, 28049 Madrid, Spain

Key words: Robocasting, Acoustic energy focusing, Frequency band gaps

Abstract. In this contribution, acoustic phenomena taking place in MHz frequency range in robocast ceramic scaffolds are presented. The acoustic properties of several scaffold geometries were studied both experimentally and numerically. The elastic responses were calculated by finite element method (FEM) where computational unit cells were designed to represent the periodic geometry of the sintered scaffolds. It is shown that tetragonal scaffolds, where the rods in the neighboring layers are perpendicular, focus acoustic energy along the principal directions of the ceramic rods. On the other hands, a hexagonal structure, which has the periodicity of 3 layers with the orientation angle of 60° between the neighboring rods, is in-plane isotropic in the low-frequency limit. The FEM study was also performed up to higher frequencies and it was found there are several frequency band gaps for the longitudinal waves.

1 INTRODUCTION

With the rise of additive manufacturing (AM) methods, various structures with complex geometries can be easily produced [1]. Therefore, the AM methods can be utilized for manufacturing of phononic crystals with periodic arrangements with the dimensions of several millimeters, where such structures can experience frequency band gaps in kHz to MHz ranges [2, 3, 4, 5]. Robocasting is an AM direct-ink writing method for the fabrication of scaffolds consisting of a layered structure of thin ceramic rods [6, 7]. At first, a ceramic powder is mixed with deionized water and organic additives to form a colloidal suspension with highly shear-thinning behavior. This suspension is subsequently extruded through a thin nozzle following a layer-by-layer 3D printing route to produce a ceramic green body. The organic additives are then burnt out, and the scaffolds are consolidated by spark plasma sintering. Usually, each layer consists of mutually parallel thin rods and the neighboring layers are oriented at a different angle. As the rods in the neighboring layers partially intersect and the scaffolds are typically made of tens of layers, the scaffolds have a periodic structure with phononic-crystal behavior [8].

2 MATERIALS AND METHODS

Elastic and acoustic properties of several types of scaffolds were studied by finite element method (FEM) using COMSOL Multiphysics software. These properties are strongly affected by the scaffolds geometry which lead to different types of macroscopic symmetry; in this work, the scaffolds with tetragonal, orthorhombic or hexagonal symmetry are studied.

For the tetragonal scaffolds, the rods of neighboring layers are mutually perpendicular with the constant in-plane spacing between the rods in the same layer, as shown in Figs. 1 and 2. These two tetragonal scaffolds differ mainly in the in-plane spacing of the rods l , which is equal to $650\text{ }\mu\text{m}$ for the LT sample (LT means "*large tetragonal*" due to the larger spacing between the rods) vs. $308\text{ }\mu\text{m}$ for the ST ("*small tetragonal*") sample, while the rods diameters d ($210\text{ }\mu\text{m}$ vs. $218\text{ }\mu\text{m}$) and the out-of-plane spacing h between the layers of the same rods orientation ($275\text{ }\mu\text{m}$ vs. $261\text{ }\mu\text{m}$) are almost identical. Also, due to the much higher in-plane spacing, the LT scaffold occupy relative space of 36.3% with the effective density of $1.212\text{ g}\cdot\text{cm}^{-3}$, and the ST scaffold occupy relative space of 76.5% with the effective density of $2.555\text{ g}\cdot\text{cm}^{-3}$.

In addition, another scaffold with the perpendicular orientation of the rods in the neighboring layers was studied; this scaffold, entitled RO as "*rectangular orthorhombic*", has two different in-plane spacings, $309\text{ }\mu\text{m}$ between the rods oriented in the x_1 axis and $591\text{ }\mu\text{m}$ between the rods in the x_2 direction, as shown in Fig. 3, and thus it exhibits orthorhombic symmetry. The rods have diameters of $238\text{ }\mu\text{m}$ and the out-of-plane spacing is $297\text{ }\mu\text{m}$, which gives an effective density of $2.165\text{ g}\cdot\text{cm}^{-3}$, when occupying a relative space of 64.8% .

Another scaffold with different geometry, named AO as "*angular orthorhombic*", also exhibit orthorhombic symmetry. This scaffold, shown in Fig. 4, consists of rods with diameter of $186\text{ }\mu\text{m}$ and in-plane spacing of $462\text{ }\mu\text{m}$, and the angle between the direction of rods in the neighboring layers is 46° . The scaffold has the periodicity of 2 layers and the out-of-plane spacing between the rods of same orientation is $250\text{ }\mu\text{m}$, with an effective density of $1.458\text{ g}\cdot\text{cm}^{-3}$.

Finally, elastic coefficients of a hexagonal scaffold, shown in Fig. 5, were determined. In this scaffold, the neighboring layers are rotated at 60° angle such that the scaffold geometry is periodical after 3 layers. The out-of-plane spacing between these 3 layers is $385\text{ }\mu\text{m}$, the rods have diameter of $215\text{ }\mu\text{m}$ and the in-plane spacing of the rods is $l = 576\text{ }\mu\text{m}$, where the distance between crossing points along the single rod is $a = 2l/\sqrt{3} = 665\text{ }\mu\text{m}$. Thus, the scaffold occupies the relative space of 44.4% with the effective density of $1.483\text{ g}\cdot\text{cm}^{-3}$.

The geometrical parameters of the additive-manufactured robocast scaffolds were used as templates for designing computational unit cells and the material parameters of SiC were utilized (density of $3.34\text{ g}\cdot\text{cm}^{-3}$, Young's modulus of 305 GPa and Poisson ratio of 0.19). Elastic coefficients C_{ijkl} of the studied scaffolds were obtained by the FEM calculation by applying tensile or shear straining modes. From the calculated elastic tensors C_{ijkl} , distributions of Young's moduli and group velocity were then plotted to illustrate the anisotropic properties of the scaffolds [10, 11]. In this paper, the resulting group velocity data is plotted as discrete points in order to show the acoustic energy focusing in the scaffolds; each point corresponds to the different direction of propagation, where the initial angles are equidistantly distributed within the studied plane. Therefore, when the density of the plotted points is higher in a certain direction, the acoustic energy is focused along such directions.

In addition, longitudinal frequency band gaps of the LT scaffold and the hexagonal scaffold were also obtained by the FEM analysis. The computational unit cells were utilized to calculate dispersion curves along the principal directions of the rods by Bloch wave solution, as described in [8]. The resulting

eigenmodes were then analyzed in order to find out at which frequency ranges there is no eigenmode with dominant longitudinal displacements, which thus correspond to longitudinal frequency band gaps.

3 RESULTS AND DISCUSSION

The elastic coefficients of the LT scaffold calculated by the FEM are:

$$c_{ij(LT)} = \begin{pmatrix} 63.62 & 3.01 & 5.15 & 0 & 0 & 0 \\ 3.01 & 63.62 & 5.15 & 0 & 0 & 0 \\ 5.15 & 5.15 & 33.58 & 0 & 0 & 0 \\ 0 & 0 & 0 & 5.78 & 0 & 0 \\ 0 & 0 & 0 & 0 & 5.78 & 0 \\ 0 & 0 & 0 & 0 & 0 & 2.64 \end{pmatrix} \text{ GPa.} \quad (1)$$

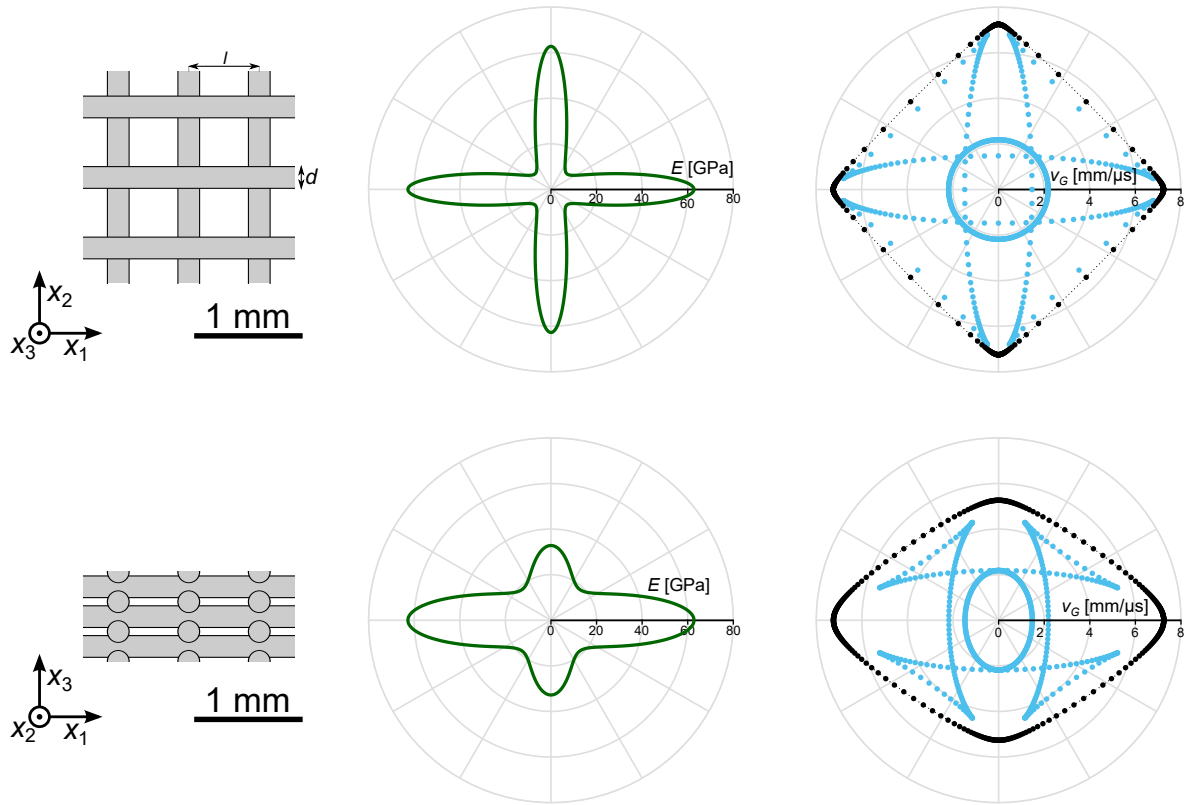


Figure 1: Young's modulus E and group velocity v_G distributions in the principal planes of the LT scaffold

The elastic coefficients of the LT scaffold suggest that this scaffold is strongly anisotropic, which is also clearly evident in the Young's modulus plots in Fig. 1. In the x_1x_2 plane, the Young's modulus in the direction of the rods is $E_1 = E_2 = 62.75$ GPa, while the minimum value in the direction between the rods is $E_{min,45^\circ} = 9.77$ GPa, i.e. more than 6 times lower than the maximum $E_1 = E_2$ value. This anisotropy is given by the scaffold geometry, as the perpendicular rods of neighboring layers intersect in very low overall area compared to the dimensions of the scaffolds. Therefore, the elastic coefficients of

c_{12} and c_{66} corresponding to the shearing modes in the x_1x_2 plane are significantly lower than the other c_{ij} coefficients, which results in the highly anisotropic Young's moduli distribution given in Fig. 1.

This anisotropy, given by the LT scaffold geometry, has also a strong effect on the group velocity properties, as shown in the right-hand section of Fig. 1. For the quasi-longitudinal waves (outer black-colored points in the group velocity plots) in the LT scaffold, the maximum value of $v_{G1} = v_{G2} = 7245 \text{ m}\cdot\text{s}^{-1}$ correspond to the wave propagation in the direction of the rods in the scaffold structure, and the minimum value in the x_1x_2 plane, $v_{G,min,45^\circ} = 5445 \text{ m}\cdot\text{s}^{-1}$, lies in the diagonal direction between the rods, similarly to the Young's modulus distribution in this plane. Moreover, the $v_{G,min,45^\circ}$ value is only slightly higher than the $v_{G1}/\sqrt{2}$ value ($5123 \text{ m}\cdot\text{s}^{-1}$) which suggests that the quasi-longitudinal waves propagates almost independently in the perpendicular ceramic rods. As a result, the acoustic energy of quasi-longitudinal waves propagating through the scaffold becomes strongly focused along the principal direction of the rods in the scaffold structure. Similar behavior of the acoustic focusing along the rods is also observed for one the quasi-transverse waves (blue-colored in the group velocity plot) with the polarization within the x_1x_2 , while the other quasi-transverse waves with the polarization vector lying close to the x_3 propagate with much smaller, but directionally independent velocity.

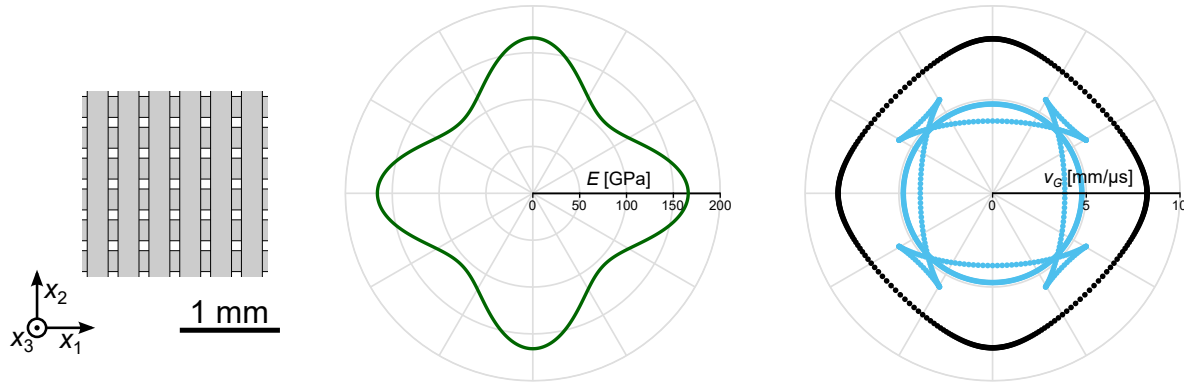


Figure 2: Young's modulus E and group velocity v_G distributions in the x_1x_2 plane of the ST scaffold

The elastic coefficients of the ST scaffold are:

$$c_{ij(ST)} = \begin{pmatrix} 173.56 & 23.80 & 32.43 & 0 & 0 & 0 \\ 23.80 & 173.56 & 32.43 & 0 & 0 & 0 \\ 32.43 & 32.43 & 181.65 & 0 & 0 & 0 \\ 0 & 0 & 0 & 57.94 & 0 & 0 \\ 0 & 0 & 0 & 0 & 57.94 & 0 \\ 0 & 0 & 0 & 0 & 0 & 37.99 \end{pmatrix} \text{ GPa}, \quad (2)$$

and the Young's modulus and group velocity distribution in the x_1x_2 plane are given in Fig. 2. This scaffold also exhibit elastic and acoustic anisotropy; nevertheless, due to much higher in-plane spacing between the rods and thus much higher relative density, the elastic anisotropy is significantly weaker than for the LT scaffold. The maximum values of the Young's modulus in the x_1x_2 plane are $E_1 = E_2 = 165.83 \text{ GPa}$, while the minimum value lies in the diagonal direction $E_{min,45^\circ} = 107.85 \text{ GPa}$. Similarly, the maximum value of the group velocity in the x_1x_2 plane is $v_{G1} = v_{G2} = 8242 \text{ m}\cdot\text{s}^{-1}$ and the minimum value is $v_{G,min,45^\circ} = 7314 \text{ m}\cdot\text{s}^{-1}$, which is much lower difference than for the LT scaffold.

The results for the tetragonal LT and ST scaffolds show that only by changing the scaffold geometry, the level of elastic anisotropy and the acoustic energy focusing can be significantly changed. In these

tetragonal scaffolds, the direction x_1 and x_2 are macroscopically equivalent as the in-plane spacing are the same through the whole scaffold, unlike for the RO scaffold, which has two different in-plane spacings in the x_1 vs. x_2 direction. The obtained elastic coefficients for this RO scaffold are:

$$c_{ij(RO)} = \begin{pmatrix} 163.78 & 11.84 & 17.86 & 0 & 0 & 0 \\ 11.84 & 93.63 & 17.69 & 0 & 0 & 0 \\ 17.86 & 17.69 & 105.87 & 0 & 0 & 0 \\ 0 & 0 & 0 & 33.56 & 0 & 0 \\ 0 & 0 & 0 & 0 & 23.26 & 0 \\ 0 & 0 & 0 & 0 & 0 & 15.43 \end{pmatrix} \text{ GPa.} \quad (3)$$

As expected, the highest Young's modulus and group velocity values, $E_1 = 159.90$ GPa and $v_{G1} = 8698 \text{ m}\cdot\text{s}^{-1}$, lie along the direction of more dense rods arrangement in the x_1 direction when compared to the x_2 direction, $E_2 = 90.19$ GPa and $v_{G2} = 6576 \text{ m}\cdot\text{s}^{-1}$. The minimum value of the Young's modulus in the x_1x_2 plane, $E_{min,48^\circ} = 49.19$ GPa, lies in the direction with 48° angle to the x_1 axis, i.e. slightly closer to the direction of less dense arrangement of the rods.

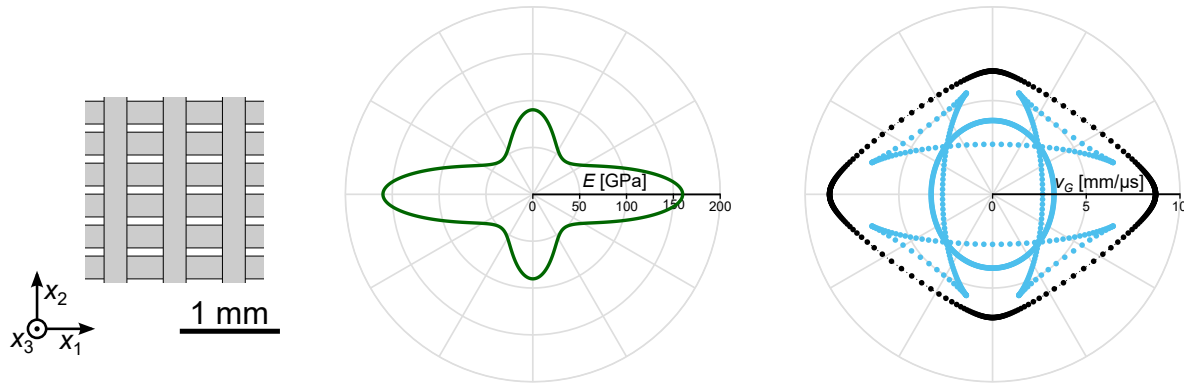


Figure 3: Young's modulus E and group velocity v_G distributions in the x_1x_2 plane of the RO scaffold

The elastic coefficients of the AO scaffold are:

$$c_{ij(AO)} = \begin{pmatrix} 107.12 & 40.22 & 10.30 & 0 & 0 & 0 \\ 40.22 & 51.07 & 24.84 & 0 & 0 & 0 \\ 10.30 & 24.84 & 49.68 & 0 & 0 & 0 \\ 0 & 0 & 0 & 2.93 & 0 & 0 \\ 0 & 0 & 0 & 0 & 14.77 & 0 \\ 0 & 0 & 0 & 0 & 0 & 22.42 \end{pmatrix} \text{ GPa.} \quad (4)$$

As shown in Fig. 4, the axes of x_1 and x_2 are chosen such that they intersect the angles between the rods in halves and thus they correspond to the symmetry axes within the x_1x_2 plane. The minimum value of the Young's modulus in this plane is $E_2 = 26.93$ GPa, and the maximum value $E_{max,21^\circ} = 75.70$ GPa lies close to the direction of the rods and it is slightly higher than the Young's modulus in the x_1 direction, $E_1 = 73.17$ GPa. For the group velocity, the minimum value in the x_1x_2 plane lies along the x_2 axis, $v_{G2} = 5918 \text{ m}\cdot\text{s}^{-1}$, while the maximum value lies along the x_1 axis, $v_{G1} = 8572 \text{ m}\cdot\text{s}^{-1}$. Moreover, in Fig. 4, it can be clearly seen that the density of the plotted group velocity data is much higher near the x_1 direction than near the x_2 direction, suggesting that in this type of scaffold geometry, the acoustic energy

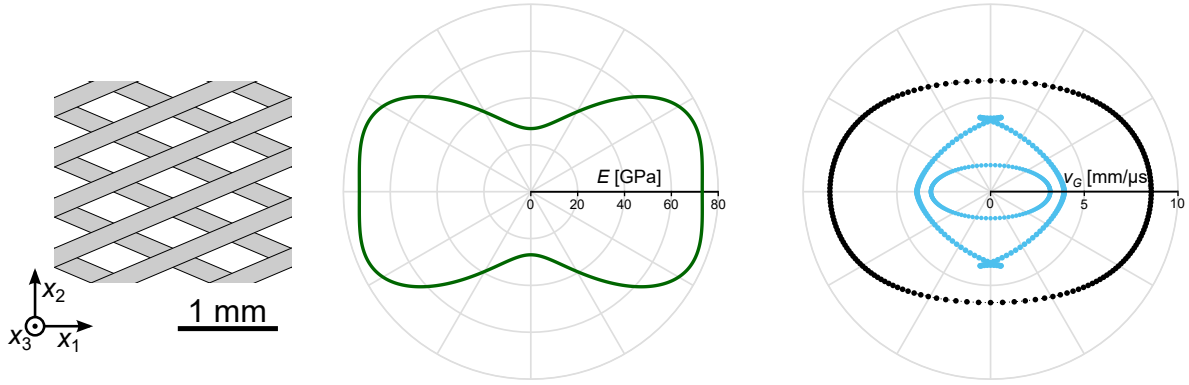


Figure 4: Young's modulus E and group velocity v_G distributions in the x_1x_2 plane of the AO scaffold

is focused not only along the rods but also along the directions which lie between the lower angle of 46° between the rods when compared to the perpendicular x_2 axis.

For the hexagonal scaffold, the computed elastic coefficients are:

$$c_{ij} = \begin{pmatrix} 66.05 & 19.45 & 8.80 & 0 & 0 & 0 \\ 12.96 & 66.05 & 8.80 & 0 & 0 & 0 \\ 8.80 & 8.80 & 44.32 & 0 & 0 & 0 \\ 0 & 0 & 0 & 9.30 & 0 & 0 \\ 0 & 0 & 0 & 0 & 9.30 & 0 \\ 0 & 0 & 0 & 0 & 0 & 23.30 \end{pmatrix} \text{ GPa.} \quad (5)$$

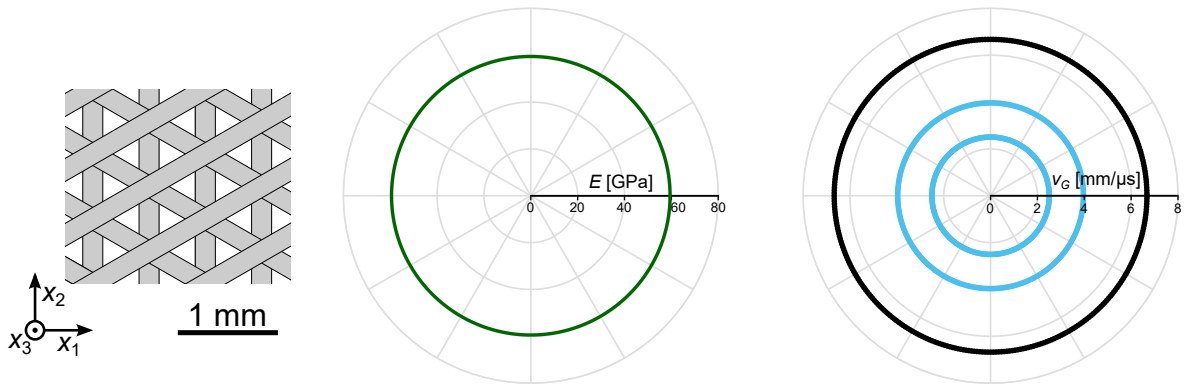


Figure 5: Young's modulus E and group velocity v_G distributions in the x_1x_2 plane of the LH scaffold

As this scaffold exhibit hexagonal symmetry, all the directions within the x_1x_2 plane are macroscopically equivalent and thus, Young's modulus of $E_1 = E_2 = 59.43$ GPa, and group velocities of qL waves, $v_{G1} = v_{G2} = 6674 \text{ m}\cdot\text{s}^{-1}$, and also qT waves are constant in this plane, as shown in Fig. 5. Nevertheless, all these calculations correspond to the quasi-static loading of tensile/shear straining modes, but when the dynamic loading is assumed, where the frequency of the acoustic waves is such high that the wavelengths become comparable to the in-plane spacing between the rods in one layer, acoustic energy can be focused along the principal directions of the rods even in the hexagonal scaffolds [9].

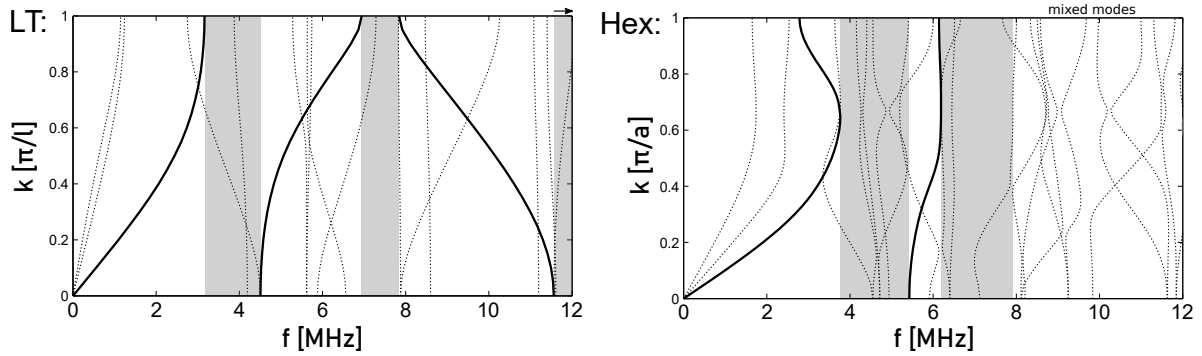


Figure 6: Calculated longitudinal band gaps (shaded areas) of tetragonal and hexagonal scaffolds up to 12 MHz, where the thick lines correspond to dispersion curves with dominant longitudinal displacements. The arrow above the 3rd band gap for the LT scaffold denotes that this band gap also continues up to higher frequencies.

The calculated longitudinal frequency band gaps up to 12 MHz for the LT scaffold and for the hexagonal scaffold are shown in Fig. 6, where the thick lines correspond to dispersion curves with dominant longitudinal displacement component. For the LT scaffold, there are three distinct dispersion curves with longitudinal character, which lead to frequency band gaps at ~ 3.2 – 4.5 MHz, ~ 6.9 – 7.8 MHz and another band gap beginning at ~ 11.6 MHz which continues up to higher frequencies above 12 MHz. For the hexagonal scaffold, there are two band gaps at ~ 3.8 – 5.4 MHz and ~ 6.2 – 7.8 MHz. Above 7.8 MHz, there are few dispersion curves which do not have strictly longitudinal or shear character, and thus some acoustic energy at these frequencies can be absorbed while another fraction of acoustic energy can still be transferred through the hexagonal scaffold when the longitudinal waves propagate along the direction of the rods.

Moreover, as the dispersion curves in Fig. 6 are linear in the low-frequency limit for both scaffolds, corresponding phase and group velocities are equal when the wavelengths are significantly higher than the in-plane spacings between the rods, i.e. when the wave number k is close to zero. Also, in Fig. 6, it can be seen that the velocity of qL waves in the LT scaffold is much higher than the velocities of qT waves, which is consistent with the group velocity values along the x_1 axis shown in Fig. 1. Similarly for the hexagonal scaffolds, dispersion curves for the qT waves have different slopes near $k = 0$ which correspond to different velocities for the qT waves, as shown in Fig. 5.

4 CONCLUSIONS

Elastic and acoustic properties of several types of scaffold structures were studied by FEM analysis. It is shown that these scaffolds can be strongly anisotropic depending on their geometry. For the scaffolds of perpendicular orientation of the rods in the neighboring layers, Young's moduli are higher in the principal direction along the rods than in the direction between the rods, which results in acoustic energy focusing along the rods directions. The level of elastic anisotropy and the acoustic energy focusing also depends on the in-plane spacings between the rods in each layer; the scaffolds with higher in-plane spacing have generally lower Young's moduli, but also the acoustic energy is much strongly focused along the rods in such structures. On the other hand, the scaffold with macroscopic hexagonal symmetry is in-plane isotropic at least in the low-frequency limit. The FEM analysis was also utilized for the determining longitudinal frequency band gaps. It is shown that one of the tetragonal scaffolds and the hexagonal scaffolds both experience several frequency band gaps with the first longitudinal band gap at ~ 4 MHz.

ACKNOWLEDGEMENT

This work was supported by the Czech Science Foundation grant no. GA17-01618S.

REFERENCES

- [1] Thompson, M.K. et al. Design for Additive Manufacturing: Trends, opportunities, considerations, and constraints. *CIRP Annals - Manufacturing Technology* (2016) **65**:737–760.
- [2] Lucklum, F. et al. Rapid Prototyping of 3D Phononic Crystals using High-resolution Stereolithography Fabrication. *Procedia Engineering* (2015) **120**:1095–1098.
- [3] Matlack, K.H. et al. Composite 3D-printed metastructures for low-frequency and broadband vibration absorption. *Proceedings of National Academy of Sciences* (2016) **113**:8386–8390.
- [4] Wormser, M. et al. Design and Additive Manufacturing of 3D Phononic Band Gap Structures Based on Gradient Based Optimization. *Materials* (2017) **10**:1125–1139.
- [5] D'Alessandro, L. et al. 3D auxetic single material periodic structure with ultra-wide tunable bandgap. *Scientific Reports* (2018) **8**:2262.
- [6] J.A. Lewis. Direct Ink Writing of 3D Functional Materials. *Advanced Functional Materials* (2006) **16**:21932204.
- [7] K. Cai et al. Geometrically Complex Silicon Carbide Structures Fabricated by Robocasting. *Journal of the American Ceramic Society* (2012) **95**:2660–2666.
- [8] Kruisová, A. et al. Ultrasonic bandgaps in 3D-printed periodic ceramic microlattices. *Ultrasonics* (2018) **82**:91–100.
- [9] Koller, M. et al. Anisotropic Elasticity of Ceramic Micro-Scaffolds Fabricated by Robocasting. *Acta Physica Polonica A* (2018) **134**:799–803.
- [10] Kruisová, A. et al. Acoustic metamaterial behavior of three-dimensional periodic architectures assembled by robocasting. *Applied Physics Letters* (2014) **105**:211904.
- [11] Koller, M. et al. Ceramic phononic crystals with MHz-range frequency band gaps. *Proceedings of Meetings on Acoustics* (2018) **32**:045005.

FINITE ELEMENT REDUCED ORDER MODELING OF PIEZOELECTRIC ENERGY HARVESTERS

R. ALOUI^{*,×}, W. LARBI^{*} AND M. CHOUCANE[×]

^{*}Conservatoire National des Arts et Métiers (CNAM)
Laboratoire de Mécanique des Structures et des Systèmes Couplés (LMSSC)
292, rue Saint-Martin, 75141 Paris Cedex 03, France
e-mail: rabie.aloui@enim.rnu.tn and walid.larbi@cnam.fr

[×]Université de Monastir, Ecole Nationale d'Ingénieurs de Monastir (ENIM)
Laboratoire de Génie Mécanique, LA-MA-05 (LGM)
5000, rue Ibn El Jazzar, 5035 Monastir, Tunisie
e-mail: mnaouar.chouchane@enim.rnu.tn

Key words: Vibration Energy Harvesting, Piezoelectric Materials, Finite Element Method

Abstract. In the last few years, piezoelectric materials have been widely used for vibration energy harvesting due to its efficiency for converting mechanical energy into electrical one. In the literature, various approaches have been devoted for modeling the piezoelectric harvesters in order to predict its electromechanical coupling responses. In this paper, we present a finite element modeling of a bimorph piezoelectric harvester as typical cantilever beam which is composed of an elastic substrate covered by two piezoceramic layers. The generated electricity is due to the vibration of the host structure. The main purpose of this work is to develop a reduced order model able to predict the responses of the harvester and to improve simulation efficiency with a low computation cost. In order to reach this goal, the electromechanical problem is projected on a truncated eigenvectors basis with short-circuited boundary conditions. Furthermore, a numerical example of a bimorph harvester as case study is presented and analyzed. Through this example, the effect of the basis truncation on the electromechanical outputs is discussed in term of computation error and time. Results show that for an optimal truncated basis, the reduced order model gives good results in comparison to the direct methods with lower cost of calculation.

1 INTRODUCTION

Piezoelectric has received a considerable attention for vibration energy scavenging over the last years. This material has been extensively used in vast engineering areas due to its specific characteristics. In fact, piezoelectric material enables the transformation of mechanical strain into electricity and vice-versa. These two conversion ways allow direct connection to electronic components and yield well to two applications: (1) the sensing using the direct effect piezoelectric (e.g. vibration energy harvesting) and (2) the actuating using the inverse effect piezoelectric (e.g. structural vibration reduction). This work focus on the energy harvesting using piezoelectric elements attached to an elastic structure and excited by the base motion.

Recently, various techniques have been appeared in the literature to investigate the electromechanical coupling of a composite cantilevered beam with piezoelectric elements, which is used often as a vibration energy harvester. An analytical solution based on a single degree of freedom model, considers that the composite cantilever beam is similar to a mass-spring-damper system. In this approach, the piezoelectric composite beam is modeled by a second order differential equation of the tip displacement of the harvester as variable [1]. Lately, Erturk and Inman [1, 2, 3] introduced an analytical distributed parameter solutions for bimorph and unimorph piezoelectric energy harvesters with closed-form expressions and showed that for sinusoidal base excitation, the model might yield highly agreement with physical experiments. Whereas, several studies used the finite element method as an alternative sophisticated technique to solve approximately the most complicated electromechanical problem. Bendary [4] developed a finite element model for sensors and actuators based on the classical laminate theory. Results show that as expected for thin plates, the classical theory gives acceptable accuracy with minimal computational effort. De Marqui [5] investigated an electromechanical coupled finite element plate to estimate the electrical output responses of unimorph and bimorph piezoelectric plate harvester devices. This model was derived based on the classic Kirchhoff plate theory, which neglects shear deformation. Amini [6] presented a finite element modeling for functionally graded piezoelectric harvesters based-on the Euler Bernoulli beam theory. The model is validated by comparison to the analytical solution of a similar bimorph piezoelectric energy harvester.

Reduced order modeling of mechatronic systems has become an interesting issue for improving simulation efficiency. For instance, many optimization algorithms require a high number of model evaluations which cause a high computational cost, hence the necessity for such reduced order model. In recent published research, H.-J. Xiang [7] introduced a reduced order model of piezoelectric energy harvesters using a Krylov subspace-based scheme. An implementation of this model with nonlinear energy harvesting circuits is made in a system level. This approach is validated with various harmonic response and transient response analysis. M. Kudryavtsev et al. [8] introduced a novel reduced order model techniques for a large-scale multiport model of a micro electromechanical system based piezoelectric energy harvester. Results show an excellent concordance between the full-scale and the reduced order models of the harvester for harmonic simulation.

This paper proposed an efficient finite element reduced order model of piezoelectric energy harvester able to predict its electrical outputs recovered in an efficient way. A bimorph cantilever beam is chosen as an energy harvester case study due to its widespread usage. A gait is proposed to determinate the reduced order model: (1) an electromechanical finite element formulation for the dynamic analysis of a general piezoelectric structure is first proposed, (2) the development of an appropriate reduced order model of the coupled electromechanical problem is then presented. The proposed methodology based on a normal mode expansion which requires the computation of the eigenmodes of the structure in short circuit condition. Despite its reduced size, this model is proven to be very efficient for simulations of harmonic vibration analyses of the harvester. In the last part of this research, a numerical example of a piezoelectric bimorph cantilever beam, is presented and analyzed.

2 FINITE ELEMENT REDUCED ORDER MODEL OF ELECTROMECHANICAL PROBLEM

The finite element formulation of elastic structure with piezoelectric elements proposed in [9, 10] is used. This formulation uses a standard discretization of the mechanical degrees of freedom and provides less restrictive assumptions for the electrical state which is fully described by very few global discrete unknowns: (i) the electric charge contained in the electrodes and (ii) the voltage between the electrodes. It is well adapted to practical applications since realistic electrical boundary conditions, such that equipotentiality on the electrodes and prescribed global electric charges, naturally appear [12]. Therefore, the governing undamped electromechanical problem of piezoelectric structure is thus obtained:

$$\mathbf{M}_m \ddot{\mathbf{U}}(t) + \mathbf{K}_m \mathbf{U}(t) + \mathbf{K}_c \mathbf{V}(t) = \mathbf{F}(t) \quad (1)$$

$$\mathbf{K}_e \mathbf{V}(t) + \mathbf{Q}(t) - \mathbf{K}_c^T \mathbf{U}(t) = \mathbf{0} \quad (2)$$

where \mathbf{M}_m is the global $(N \times N)$ mass matrix, \mathbf{K}_m is the global $(N \times N)$ stiffness matrix and \mathbf{K}_c is the global $(N \times P)$ electromechanical coupling matrix, \mathbf{K}_e is the diagonal global $(P \times P)$ capacitance matrix, $\mathbf{F}(t)$ is the global $(N \times 1)$ vector of mechanical forces, $\mathbf{Q}(t)$ is the global $(P \times 1)$ vector of electric charge outputs, $\mathbf{U}(t)$ is the global $(N \times 1)$ vector of mechanical coordinates and $\mathbf{V}(t)$ is the global $(P \times 1)$ vector of output voltages across the piezoelectric elements. Here, N and P respectively, are the number of mechanical degrees of freedom and the number of piezoelectric elements.

The Equation (1) corresponds to the mechanical equation of motion including the force induced by electromechanical coupling. Whereas, the Equation (2) corresponds to the electrical circuit equation with mechanical coupling.

The global mechanical damping matrix \mathbf{C}_m is often taken to be a linear combination of the mass and stiffness matrices as follow (Rayleigh damping):

$$\mathbf{C}_m = \alpha \mathbf{M}_m + \beta \mathbf{K}_m \quad (3)$$

where α and β are the constant of proportionality which are determined in physical experiments.

The charge-voltage global variables are also intrinsically adapted to include any external electrical circuit into the electromechanical problem. For the purpose to simulate the piezoelectric energy harvesting, the structure is dissipated through a resistive load. Using Ohm's law, we obtains the following additional equations:

$$\mathbf{V}(t) = R \dot{\mathbf{Q}}(t) \quad (4)$$

2.1 Normal modes of short-circuit condition

The system short-circuit normal modes present the solutions of Equation (1) with $\mathbf{V} = \mathbf{0}$ and $\mathbf{F} = \mathbf{0}$. In addition, these modes depend only on the mechanical properties of the system, thus:

$$[\mathbf{M}_m - \omega_i^2 \mathbf{K}_m] \Phi_i = \mathbf{0} \quad (5)$$

where ω_i is the natural frequency and Φ_i is the $(N \times 1)$ mode shape vector.

For orthogonality properties, these modes verify the following conditions:

$$\Phi_i^T \mathbf{M}_m \Phi_j = \delta_{ij} \quad \text{and} \quad \Phi_i^T \mathbf{K}_m \Phi_j = \omega_i^2 \delta_{ij} \quad (6)$$

where δ_{ij} is the Kronecker symbol.

2.2 Projection on the short-circuited basis

Equations (1) and (2) describe the electromechanical behavior of the piezoelectric structure with the dimension of matrices are usually very large, which requires a considerable computational effort. The aim of this section is to construct a reduced system with much smaller dimension [7] by introducing the modal matrix $\Phi = [\Phi_1, \Phi_2, \dots, \Phi_N]$ of size $(N \times N)$, N is the total number of degrees of freedom in the finite elements model associated to the structure. In fact, the displacement vector is sought as [11]:

$$\mathbf{U}(t) = \Phi \mathbf{q}(t) \quad (7)$$

where the vector $\mathbf{q} = [q_1 \ q_2 \ \dots \ q_N]^T$ is the unknown modal amplitudes.

By applying the Ritz-Galerkin projection method, which consists in inserting the above equation in Equations (1) and (2) including the damping term, and multiplying the first obtained equation by Φ^T and using the orthogonality properties of Equations (6), the problem writes including the damping term, for all $i \in \{1, \dots, N\}$ and $p \in \{1, \dots, P\}$ is:

$$\ddot{q}_i(t) + 2\zeta_i \omega_i \dot{q}_i(t) + \omega_i^2 q_i(t) + \sum_{p=1}^P \chi_i^{(p)} V^{(p)}(t) = F_i(t) \quad (8)$$

$$C^{(p)} V^{(p)}(t) + Q^{(p)}(t) - \sum_{k=1}^N \chi_k^{(p)} q_k(t) = 0 \quad (9)$$

where ζ_i is the modal damping coefficient defined as follows:

$$\zeta_i = \frac{\alpha}{2\omega_i} + \frac{\beta\omega_i}{2} \quad (10)$$

$\chi_i^{(p)}$ is the modal coupling coefficient of the p^{th} piezoelectric element, which is defined for all $i \in \{1, \dots, N\}$ by:

$$\chi_i = \Phi_i^T \mathbf{K}_c = (\chi_i^{(1)} \chi_i^{(2)} \dots \chi_i^{(p)}) \quad (11)$$

and $F_i(t) = \Phi_i^T \mathbf{F}(t)$ is the forcing term of the i^{th} mode.

For harmonic responses in the frequency domain and taking into account the connected resistive load introduced in Equation (4), the voltage of the p^{th} piezoelectric element is written as follows:

$$V^{(p)} = \frac{j\omega \sum_{i=1}^N \chi_i^{(p)} q_i}{\left(\frac{1}{R} + j\omega C^{(p)}\right)} \quad (12)$$

Substituting the expression of the voltage in Equation (12), N mechanical oscillators are given as follows:

$$-\omega^2 q_i + 2j\omega \zeta_i \omega_i q_i + \omega_i^2 q_i + j\omega \sum_{p=1}^P \frac{\left(\chi_i^{(p)}\right)^2}{\left(\frac{1}{R} + j\omega C^{(p)}\right)} q_i + j\omega \sum_{p=1}^P \sum_{\substack{k=1 \\ k \neq i}}^N \frac{\chi_i^{(p)} \chi_k^{(p)} q_k}{\left(\frac{1}{R} + j\omega C^{(p)}\right)} = F_i \quad (13)$$

The idea behind the reduced order modeling is the projection of the general electromechanical problem on a truncated short-circuited basis $\Phi^{trun} = [\Phi_1, \Phi_2, \dots, \Phi_{N_s}]$; where $N_s \in \{1, \dots, N\}$ is

the number of the projection modes and $N_s \ll N$. Consequently, the matrix system represents a reduced-order model using the short-circuited basis. If only few modes are kept for the projection, the size of this reduced-order model is $(N_s + P)$ which is much smaller than the full system $(N + P)$.

The major interest of choosing the short-circuit eigenmodes as the expansion basis is that its can be computed with a classical elastic mechanical problem. This operation can thus be done by any standard finite elements code.

3 APPLICATION TO A BIMORPH PIEZOELECTRIC ENERGY HARVESTER

In this section, the previous formulation is used for a bimorph piezoelectric vibration energy harvester excited by a harmonic base motion. The harvester consists in an Euler Bernoulli beam composed of two layers of piezoceramic and an elastic substrate which are assumed to be perfectly bonded to each other as shown in Figure 1. Thus, the total number of layers is equal to 3 and the number of piezoelectric elements is equal to 2 ($P = 2$). The piezoceramic layers (which are poled in the thickness direction) are covered by continuous electrodes (which are assumed to be perfectly conductive) of negligible thickness. A resistive electrical load is mounted in series with the two piezoceramic layers. The electrical voltage and the mechanical vibration of the harvester are presented by its Frequency Response Functions (FRFs) which are defined here as the response outputs of the harvester per base acceleration $a_b(t)$ (in terms of the gravitational acceleration $g = 9.81m.s^{-2}$) given in [5, 13].

The geometrical and physical parameters (adapted by Erturk and Inman [2]) used in this study are given in Table 1. The ratio of the overhang length to the total thickness is about 85.7, which makes it reasonable to neglect the shear deformation and the rotary inertia effects of the harvester for the first few vibration modes. For the purpose of simulation, one takes $\xi_1 = 0.010$ and $\xi_2 = 0.012$ as the mechanical damping ratios of the first two modes. The discretization provides $N = 90$ mechanical degrees of freedom using linear elements.

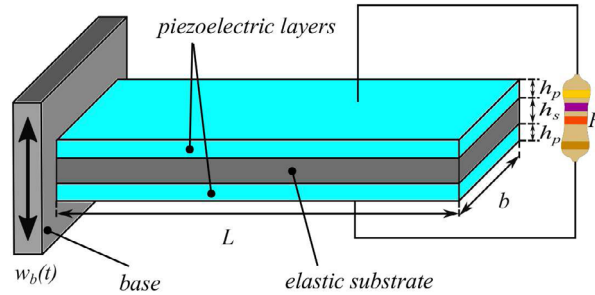


Figure 1: A Clamped free bimorph piezoelectric energy harvester under base excitation with a load resistance mounted in series

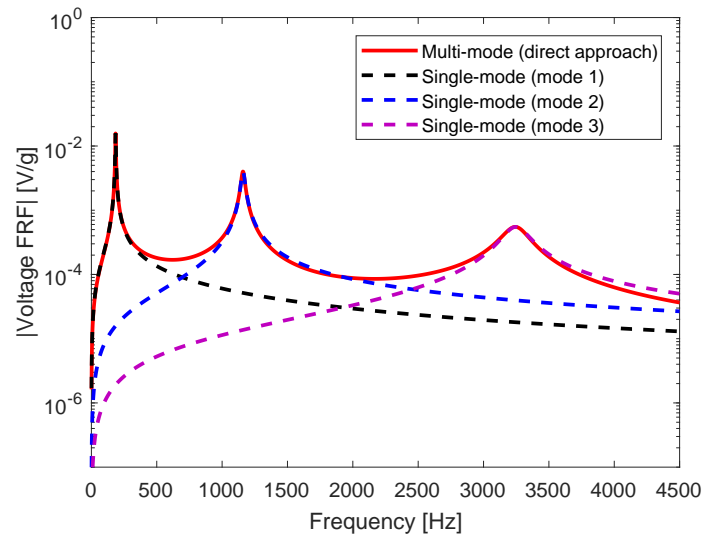
The analysis given here considers the frequency range from $f_s = 1 \text{ Hz}$ to $f_f = 4500 \text{ Hz}$. In this range three natural frequencies are appeared. The multi-mode and the single-mode of tip displacement and voltage FRFs are normalized with respect to the base acceleration g , and are computed from Equations (12) and (13). They are plotted in modulus (appointed H_D and H_V respectively for the modulus of the tip displacement FRF and the modulus of the voltage FRF)

Table 1: Material and electromechanical properties of the harvester shown in Fig.2

Parameters	Descriptions	Units	PZT-5A	Aluminum
L	Beam length	mm	30	30
b	Beam width	mm	5	5
h_p, h_s	Layers thickness	mm	0.15	0.05
E_p, E_s	Young's modulus	GPa	61	70
ρ_p, ρ_s	Mass density	kg/m^3	7750	2700
e_{31}	Piezoelectric constant	C/m^2	-10.4	—
ϵ_{33}	Permittivity constant	nF/m	13.3	—

for a set of resistance load.

In the following, the simulations of these single-mode expressions are compared to those of the multi-mode (obtained by direct method) for the first three vibration modes with a load resistance mounted in series with piezoelectric layers. Figure 2 shows the single-mode of voltage FRFs for $i = 1$, $i = 2$, and $i = 3$ along with the multi-mode for a load resistance equal to $R = 100 \Omega$. As can be seen in this figure, the single-mode solutions agree with the multi-mode solution only at the vicinity of the resonance frequency of the respective mode of interest.

**Figure 2:** Comparison of the multi-mode (direct approach) and the single-mode (modal projection) of voltage FRFs with $R = 100 \Omega$

The frequency response predictions of the single-mode tip displacement FRFs for $i = 1$, $i = 2$, and $i = 3$ are shown in Figure 3 along with the multi-mode tip displacement FRFs. Again, the single-mode FRFs exhibit agreement with the multi-mode FRFs around the modes of interest. The slight overestimation of the resonance frequencies due to ignoring the neighboring vibration modes is the case here too, and the error in the single-mode resonance frequencies is less than 0.1% for these vibration modes (compared to the resonance frequencies of the multi-mode) for excitations at the fundamental short- and open-circuit resonance frequencies. Note that the

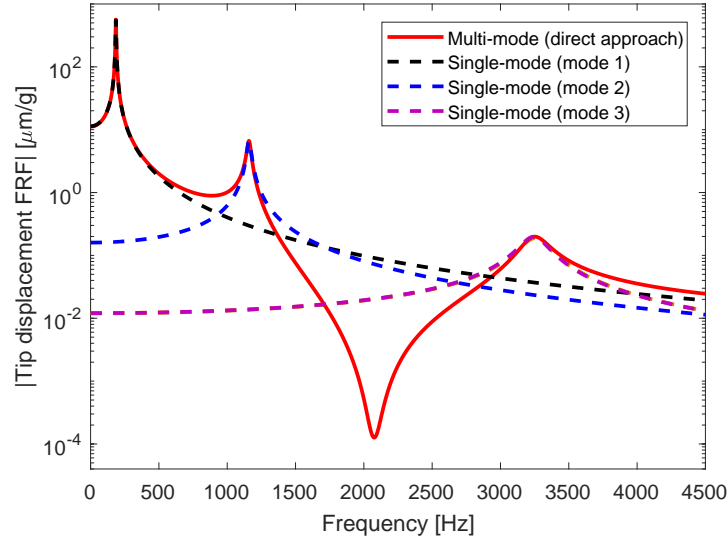


Figure 3: Comparison of the multi-mode (direct approach) and the single-mode (modal projection) of Tip displacement FRF $R = 100 \Omega$

slightly overestimated open-circuit resonance frequency is used in the single-mode simulations. The predictions of the single-mode FRFs for this most important vibration mode are very accurate. Therefore, it can comfortably be used as a first approximation in the modeling of a piezoelectric energy harvester beam for modal excitations.

To study the reduced order harvester model efficiency, we choose truncated basis contain a number of eignmodes which is a multiple of the number of the natural frequencies in the studied frequency range ($N_s = \{3, 6, 9, 69\}$) comparing with the full system projection ($N_s = N$).

Figures 4 and 5 show that the FRFs of the harvester are agree at the vicinity of the resonance frequencies for all basis of projection with the finite element direct method resolution but is not the case for the other excitation frequencies.

Two criteria are opted in this study: (1) the sum of the least square between the projected responses on the truncated basis and the direct method given in the following Equations (14) and (15) respectively for the tip displacement FRF and voltage FRF, which can give information about the accuracy of the reduced model simulation.

$$Obj^D = \sum_{f=f_s}^{f_f} \left(H_D^D(f) - H_D^{N_s}(f) \right)^2 \quad (14)$$

$$Obj^V = \sum_{f=f_s}^{f_f} \left(H_V^D(f) - H_V^{N_s}(f) \right)^2 \quad (15)$$

where H_D^D and H_V^D are respectively the modulus of tip displacement and voltage FRFs computed by the direct method and $H_D^{N_s}$ and $H_V^{N_s}$ are respectively the modulus of the tip displacement and voltage FRFs calculated by modal projection on a short-circuit truncated basis. (2) the second criteria is the time required for only one simulation.

Table 2 lists the two criteria for the harvester responses. Figure 6 shows the two criteria of

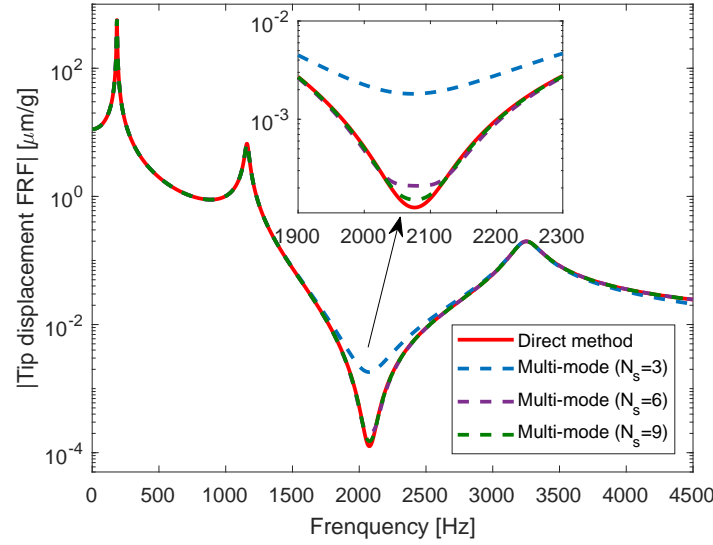


Figure 4: Comparison of the multi-mode Tip displacement FRF for different basis size with direct method, $R = 10^2 \Omega$

Table 2: Criteria of comparison of tip displacement and voltage FRFs for the short-circuit basis size

N_s	Tip displacement		Voltage	
	$Obj^D (\mu m/g)^2$	Time (s)	$Obj^V (\mu m/g)^2$	Time (s)
3	2.00 E-02	38.248	2.51 E-07	38.949
6	2.77 E-05	39.638	1.20 E-09	39.944
9	2.48 E-06	41.031	2.35 E-10	41.199
69	9.10 E-11	81.409	7.73 E-13	81.685
N	5.32 E-11	94.852	5.15 E-13	95.302

comparison for the harvester responses ((a) tip displacement FRF and (b) voltage FRF) versus the short-circuit basis size. Results show that for a small basis size, reduced order model simulation give responses with low precision (high Obj value) in a short computation time. Furthermore, the accuracy of the responses increase monotonically (Obj decreases) with the increase of the projection basis size, whereas the time of computation increase also. Indeed, high accuracy of simulation causes high numerical computation cost. For our case study, $N_s = 6$ is recommended for this frequency range.

4 CONCLUSIONS

In this research, the general finite element governing equations of the general electromechanical problem is firstly presented. Model reduction technique has been developed which consists in a modal projection of the system equations on a truncated basis of eigenvectors in order to reduce its matrices size. This basis is obtained with short circuit boundary conditions. The main goal is to predict the output responses of the harvester with high accuracy and low computational cost. Although an example of a bimorph piezoelectric energy harvesting, results show that the computational cost and the responses accuracy of the full-scale model have been reduced

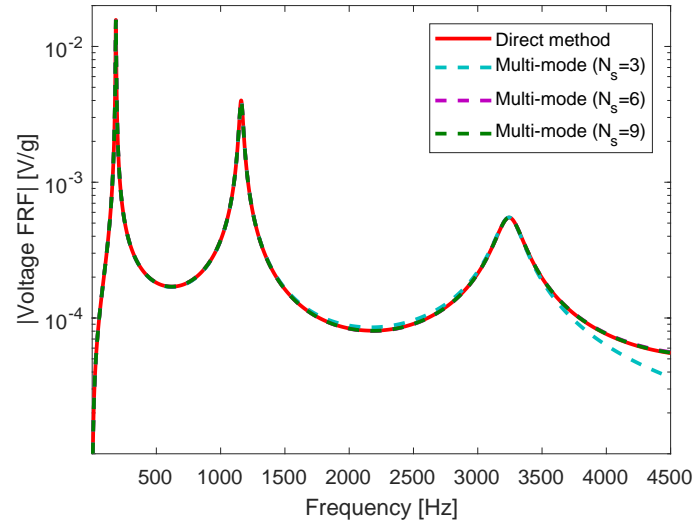


Figure 5: Comparison of the multi-mode voltage FRF for different basis size with direct method, $R = 10^2 \Omega$

monotonically with the reduction of the model scale. Moreover, the responses accuracy of the reduced order model is affected by errors introduced by the process of mode truncation that can be controlled or minimized by a modal truncation augmentation method [14]. In this method, the effects of the truncated modes are considered by their static effect only.

REFERENCES

- [1] A. Erturk and D. J. Inman, A Distributed Parameter Electromechanical Model for Cantilevered Piezoelectric Energy Harvesters, *J. Vib. Acoust.*, vol. 130, no. 4, p. 041002, 2008.
- [2] A. Erturk and D. J. Inman, *Piezoelectric energy harvesting*. Chichester: Wiley, 2011.
- [3] A. Erturk and D. J. Inman, Issues in mathematical modeling of piezoelectric energy harvesters, *Smart Mater. Struct.*, vol. 17, no. 6, p. 065016, Dec. 2008.
- [4] I. M. Bendary, M. A. Elshafei, and A. M. Riad, Finite Element Model of Smart Beams with Distributed Piezoelectric Actuators, *J. Intell. Mater. Syst. Struct.*, vol. 21, no. 7, pp. 747-758, May 2010.
- [5] C. De Marqui Junior, A. Erturk, and D. J. Inman, An electromechanical finite element model for piezoelectric energy harvester plates, *J. Sound Vib.*, vol. 327, no. 1-2, pp. 9-25, Oct. 2009.
- [6] Y. Amini, H. Emdad, and M. Farid, Finite element modeling of functionally graded piezoelectric harvesters, *Compos. Struct.*, vol. 129, pp. 165-176, Oct. 2015.
- [7] H.-J. Xiang, Z.-W. Zhang, Z.-F. Shi, and H. Li, Reduced-order modeling of piezoelectric energy harvesters with nonlinear circuits under complex conditions, *Smart Mater. Struct.*, vol. 27, no. 4, p. 045004, Apr. 2018.

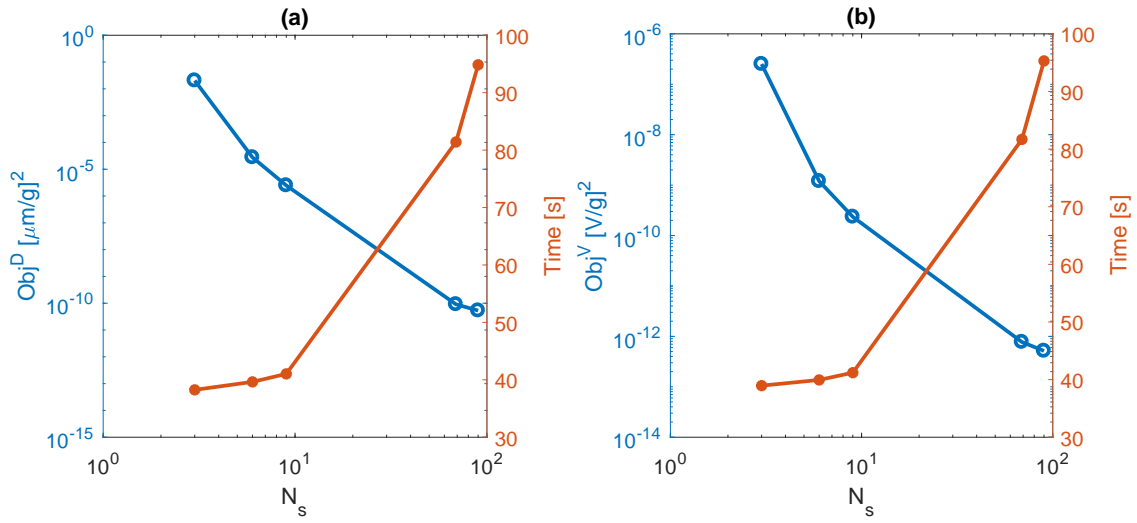


Figure 6: (a) Co-plot of criteria versus the basis size for the tip displacement FRF (b) Co-plot of criteria versus the basis size for the voltage FRF

- [8] M. Kudryavtsev, E. B. Rudnyi, J. G. Korvink, D. Hohlfeld and T. Bechtold, Computationally efficient and stable order reduction methods for a large-scale model of MEMS piezoelectric energy harvester, *Microelectronics Reliability*, 55(5SI), 747-757, 2015.
- [9] O. Thomas, J.-F. Deü, and J. Ducarne, Vibrations of an elastic structure with shunted piezoelectric patches: efficient finite element formulation and electromechanical coupling coefficients, *Int. J. Numer. Methods Eng.*, vol. 80, no. 2, pp. 235-268, Oct. 2009.
- [10] J. Ducarne, O. Thomas, and J.-F. Deü, Structural Vibration Reduction by Switch Shunting of Piezoelectric Elements: Modeling and Optimization, *J. Intell. Mater. Syst. Struct.*, vol. 21, no. 8, pp. 797-816, May 2010.
- [11] W. Larbi and J.-F. Deü, Reduced order finite element formulations for vibration reduction using piezoelectric shunt damping, *Appl. Acoust.*, Oct. 2018.
- [12] W. Larbi, J.-F. Deü, M. Ciminello, and R. Ohayon, Structural-Acoustic Vibration Reduction Using Switched Shunt Piezoelectric Patches: A Finite Element Analysis, *J. Vib. Acoust.*, vol. 132, no. 5, p. 051006, 2010.
- [13] R. Aloui, W. Larbi, and M. Chouchane, Sensitivity Analysis of Frequency Response Functions for Load Resistance of Piezoelectric Energy Harvesters, in *Advances in Acoustics and Vibration II*, pp. 136-148, 2019.
- [14] W. Larbi, J. F. Deü, and R. Ohayon, Vibroacoustic analysis of double-wall sandwich panels with viscoelastic core, *Civ.-COMP*, vol. 174, pp. 92-103, Oct. 2016.

THE INFLUENCE OF VISCOELASTIC ELEMENTS ON THE DISSIPATIVE PROPERTIES OF ELECTRO-VISCOELASTIC STRUCTURES

NATALIIA A. IURLOVA, NATALIYA V. SEVODINA,
DMITRII A. OSHMARIN, MAKSIM A. IURLOV

Department of complex problems of deformable solids mechanics
Institute of Continuous Media Mechanics of the Ural Branch of RAS (ICMM UB RAS)
Acad. Korolev str., 1, 613013 Perm, Russian Federation
Email: yurlova@icmm.ru - Web page: <http://www.icmm.ru>

Key words: Electro-viscoelastic structure, Piezoelectric element, Natural vibrations, Complex eigenfrequencies, Viscoelastic materials, Complex dynamic moduli.

Abstract. This paper presents the fragment of investigation related to modification of the original elastic structure in order to provide damping of the specified vibration modes in a structure with the imposed constraints on its mass and dimensions. It is proposed to supplement the initial structure with viscoelastic layer and attach a piezoelectric element, which is shunted by external electric circuit. Studies related to the selection of mechanical and geometric properties of viscoelastic layer, mutual disposition of viscoelastic and piezoelectric elements are presented. The investigation was carried out in the framework of the problem of natural vibrations for piecewise-homogeneous electro-viscoelastic bodies. The method was illustrated numerically by solving the natural vibration problem for a cantilevered plate.

1 INTRODUCTION

The processes of the design and operation of structures may give rise to situations, which require their modification associated with a change of their dynamic properties, for example, dissipative ones. Conventionally, the improvement of structure characteristics is based on the techniques, in which the original structure is fitted with the elements made of viscoelastic materials.

However, this approach has restrictions associated with the acceptable thickness of viscoelastic layer (the mass added to the original object), with the characteristics of the used material and with the possible area of coverage of the surface of a structure. Due to the development of smart-technologies, an increasing interest of researchers is focused by another approach, which is based on fitting viscoelastic structures with the elements made of piezoelectric materials connected to the external electric circuits. The presence of such elements provides additional energy dissipation, increasing thereby the dissipative properties of structures in a wide frequency range. Herewith the different mechanisms of energy dissipation complement each other in some frequency ranges and perform main work in other frequency ranges [1, 2]. In this regard, the approach based on the use of smart-technologies with piezoelectric materials connected to external electric circuits can offer considerable

promise for providing additional damping of vibrations when there are strict constraints on mass and dimensional parameters of structures, which are relevant for products in airspace, aircraft and automotive industries. In the literature, this approach depending on the strategy of structural dynamic behavior control is named either active constrained layer damping (ACLD) or passive constrained layer damping (PCLD).

The paper [3] should be mentioned as one of the first papers where such an approach is considered. The great interest of researchers in this method and the state of the art in this field demonstrated in the review papers [1, 2]. Despite the abundance of papers devoted to the problem there are still unsolved questions due to the complexity and versatility of the problem. Thus, the investigation of the possibility of using the piezoelectric and viscoelastic elements simultaneously to provide robust and efficient damping of structural vibrations at specified frequencies is rather relevant, especially with regard to existing structural restrictions.

The application of this technique bring up the following questions: what material should be used for viscoelastic layer, which area of a structure should be covered with it, what will be a response from the damping factors, how the system with the viscoelastic coating will respond to the attachment the piezoelectric element, how piezoelectric element should be located on a the structure and with respect to viscoelastic element, what values should take the parameters of external electric circuit for damping the specified modes of vibrations of the modified electro-viscoelastic structure, etc.

The present paper is a part of a series of studies devoted to estimation of viscoelastic and piezoelectric elements embedded into the original elastic structure on damping factors. These investigations were carried out on the basis of the solution to the problem of natural vibrations of electro-viscoelastic structures.

2 MATHEMATICAL STATEMENT OF THE PROBLEM

The problem of natural vibrations for piecewise-homogeneous electro-viscoelastic bodies in the complete coupled mathematical formulation is considered in paper [4]. This problem is described by the following variational equation:

$$\int_{V_1} (\sigma_{ij} \delta \varepsilon_{ij} + \rho \ddot{u}_i \delta u_i) dV + \int_{V_2} (\sigma_{ij} \delta \varepsilon_{ij} - D_i \delta E_i + \rho \ddot{u}_i \delta u_i) dV = 0 \quad (1)$$

Here, the volume V_1 is related to a viscoelastic part of the structure; the volume V_2 is related to a piezoelectric part; D_i, E_i are the components of the vectors of electric flux density and electric field intensity, respectively; σ_{ij} are the components of the symmetric Cauchy stress tensor; ε_{ij} are the components of the linear strain tensor; u_i are the components of the displacement vector. The constitutive relations for the piezoelectric part of volume V_2 are written as follows:

$$\left. \begin{aligned} \sigma_{ij} &= C_{ijkl} \varepsilon_{kl} - \beta_{ijk} E_k \\ D_k &= \beta_{ijk} \varepsilon_{ij} + \varepsilon_{ki} E_i \end{aligned} \right\} \quad (2)$$

where C_{ijkl} are the components of the tensor of elastic constants; β_{ijk} and ε_{ki} are the components of the tensors of piezoelectric coefficients and dielectric coefficients, respectively

($i, j, k, l = 1, 2, 3$). Within the framework of this paper, we use the assumption that the behavior of viscoelastic material is described in terms of the complex dynamic moduli, as it was made in [5]. The model of linear hereditary viscoelasticity describes the dissipative mechanisms operating in the body of volume V_1 . The constitutive relations of this model can be written as

$$\begin{aligned}\sigma_{ij} - \sigma\delta_{ij} &= 2\tilde{G}\left(\varepsilon_{ij} - \frac{1}{3}\vartheta\delta_{ij}\right) = 2(G_{\text{Re}} + iG_{\text{Im}})\left(\varepsilon_{ij} - \frac{1}{3}\vartheta\delta_{ij}\right), \\ \sigma &= \tilde{B}\vartheta = (B_{\text{Re}} + iB_{\text{Im}})\vartheta\end{aligned}\quad (3)$$

where $\tilde{G} = G_{\text{Re}} + iG_{\text{Im}} = G_{\text{Re}}\left(1 - i\frac{G_{\text{Im}}}{G_{\text{Re}}}\right) = G_{\text{Re}}(1 - i\delta_g)$, $\tilde{B} = B_{\text{Re}} + iB_{\text{Im}} = B_{\text{Re}}\left(1 - i\frac{B_{\text{Im}}}{B_{\text{Re}}}\right) = B_{\text{Re}}(1 - i\delta_b)$ are the complex dynamic shear and bulk moduli; σ is the mean stress; ϑ is the volumetric strain;; δ_g, δ_b are the mechanical loss tangents for the shear and bulk moduli, respectively; s_{ij}, e_{ij} are the components of deviatoric parts of the stress and strain tensors.

Let us consider the case, in which damping characteristics of the structure specified by the viscoelastic properties of the material it is made of are independent on the frequency, i.e. the shear and bulk moduli $G_{\text{Re}}, B_{\text{Re}}$ and the mechanical loss tangents δ_g, δ_b are constants. The solution to the problem of natural vibrations is sought in the form of $u(x, t) = u(x)e^{j\omega t}$, where $u(x) = \{u_1(x_1, x_2, x_3), u_2(x_1, x_2, x_3), u_3(x_1, x_2, x_3), \varphi(x_1, x_2, x_3)\}$ is the generalized state vector containing the components of mechanical displacements u_1, u_2, u_3 and electric potential φ ; $\omega = \omega_{\text{Re}} \pm i\omega_{\text{Im}}$ is the complex natural vibration frequency where ω_{Re} denotes the angular natural frequency of vibrations and ω_{Im} is the damping index characterizing the damping rate of vibrations. Damping factors of a vibrating structure (viscoelastic or electro-viscoelastic) ξ are defined using the following formula [6]:

$$\xi_j = (\omega_{\text{Im}})_j / (\omega_{\text{Re}})_j \quad (4)$$

Here ω_{Im} is the imaginary part of complex natural vibration frequency (damping index), ω_{Re} is the angular natural frequency of vibrations of an original elastic structure, $j = 1, \dots, M$ and M is the number of natural vibration frequencies being considered. The solution to the formulated problem of natural vibrations of electro-viscoelastic structures is sought using the method presented in [7].

3 FORMATION OF THE VISCOELASTIC STRUCTURE

Consider a cantilever plate made of isotropic material (figure 1) fully or partially covered with viscoelastic layer. The objective is to increase the level of damping of the first two flexural vibration modes of this plate. Let us specify some restrictions (for example, on the added mass and layer thickness) in compliance with the requirements for operation characteristics of the structure. The added mass should be less than 5% of the mass of the plate, and the thickness of the viscoelastic layer t should not exceed the thickness of the plate t_p , i.e. $t \leq t_p$. Changes in the dynamic properties of the structure induced by attaching the viscoelastic layer should be minimal. These limitations are of demonstrative and arbitrary nature. All further calculations is carried out based on these set of restrictions.

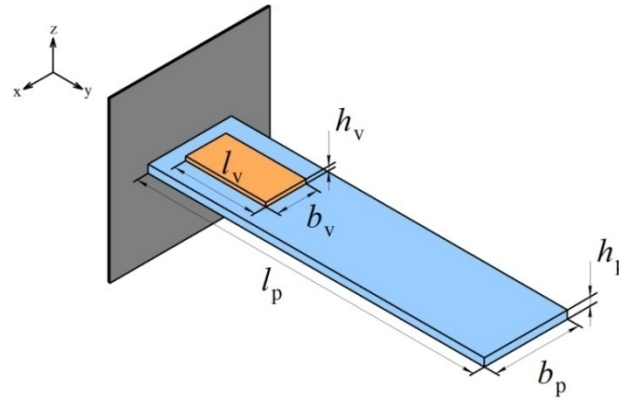


Figure 1: Computational scheme for the plate with viscoelastic layer.

The plate (fig.1) has the following dimensions $l_p = 210$ mm, $b_p = 26$ mm, $h_p = 0.6$ mm and made of elastic material with the following properties: Young's modulus $E = 2 \cdot 10^{11}$ Pa, Poisson's ratio $\nu = 0.49$, mass density $\rho = 7800$ kg/m³. The first two natural vibration frequencies are equal to 11.24 Hz and 70.39 Hz respectively.

Now, it is necessary to determine with account of the above mentioned operational restrictions what characteristics the viscoelastic material should have in order that the damping coefficient should reach the maximal values for the first two vibration modes. For this purpose physical and mechanical properties of viscoelastic materials are changed in the following ranges: Young's modulus $E = 2 \cdot 10^5 \div 2 \cdot 10^9$ Pa, Poisson's ratio $\nu = 0.3 \div 0.49$, mass density $\rho = 1000 \div 2000$ kg/m³, tangents of mechanical losses $\delta_g = 10^{-5} \div 0.2$, $\delta_b = 10^{-5} \div 0.2$. These properties correspond to different kinds of rubber, silicone and polyurethane [5]. The ranges of changing the shear modulus and bulk modulus are $G_{Re} = 7.4 \cdot 10^4 \div 7.5 \cdot 10^8$ Pa, $B_{Re} = 1.96 \cdot 10^5 \div 3.33 \cdot 10^{10}$ Pa, which are defined by relations (5)

$$G_{Re} = E / [2(1 + \nu)], \quad B_{Re} = E / [3(1 - 2\nu)] \quad (5)$$

When studying the influence of geometric factors (thickness and coverage area of the plate surface with viscoelastic layer) on the damping coefficients, the following characteristics were considered: shear modulus $G_{Re} = 0.177$ MPa, bulk modulus $B_{Re} = 8.8$ MPa, mechanical loss tangents $\delta_g = \delta_b = 0.2$, mass density $\rho = 1200$ kg/m³, that correspond to the class of viscoelastic materials under study.

Here, we restrict our consideration to the frequency-independent properties of the viscoelastic material such as shear modulus G_{Re} , bulk modulus B_{Re} and mechanical loss tangents δ_g, δ_b .

3.1. Determination of the viscoelastic layer thickness

First let's consider the worst option from the viewpoint of changes introduced into original structure: we assume that the surface area of the viscoelastic layer is equal to the surface area of the plate $l_v = l_p$, $b_v = b_p$, $h_v = h_p$.

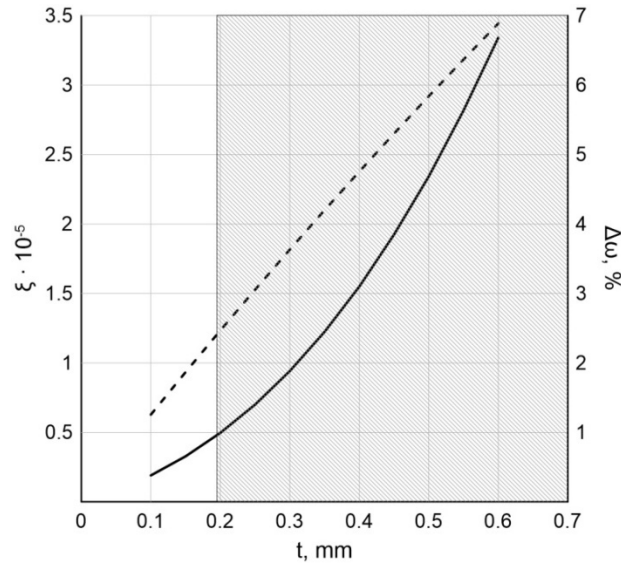


Figure 2: The vibration damping factors (solid line) and changes in the natural vibration frequencies (dashed line) versus the thickness of viscoelastic layer.

Figure 2 shows the plots of the coincident damping factors $\xi_1 = \xi_2 = \xi$ and the corresponding changes of natural vibration frequencies $\Delta\omega$ as a function of the thickness t of the viscoelastic layer. The shaded area corresponds to the constraint put on the mass of the structure after adding a viscoelastic layer (should not exceed 5%). This constraint leads to the maximal acceptable thickness is equal to 0.2 mm. Herewith the change in natural vibration frequencies values does not exceed 2%. For the further calculations, the thickness of the viscoelastic layer is set equal to 0.2 mm.

3.2. Determination of the coverage area of a structure with the viscoelastic layer

We impose that the dimensions of piezoelectric element limit minimal size of the viscoelastic layer because piezoelectric element will be attached in future to the structure, i.e. $l_v = 50$ mm, $b_v = 20$ mm, $h_v = 0.36$ mm. Next the dimensions of the viscoelastic layer are uniformly increased up to full coverage of the surface area of the structure $l_v = l_p$, $b_v = b_p$, $h_v = h_p$. First, using the approach presented in [8], we determine the location of piezoelectric element on the original plate, such that will allow damping of the vibrations at the first vibration mode. Then, we do the same for the second mode of vibrations.

In the first case the coordinates of the center of piezoelectric element mass should be $x = 37$ mm, $y = 0$ mm (the first option), and for the second case the coordinates are $x = 105$ mm, $y = 0$ mm (the second option). A viscoelastic layer of the size equal to the dimensions of the piezoelectric element is arranged correspondingly: at first, its arrangement corresponds to the first option and then - to the second option.

Figure 3 represents the plots of the damping factors for the first (ξ_1) and the second (ξ_2) vibration modes and changes of natural vibration frequencies $\Delta\omega_i$ ($i = 1, 2$) versus the covered

area of the palte surface S at the initial location of the viscoelastic layer according to the first option (fig.3a) and to the second option (fig.3b).

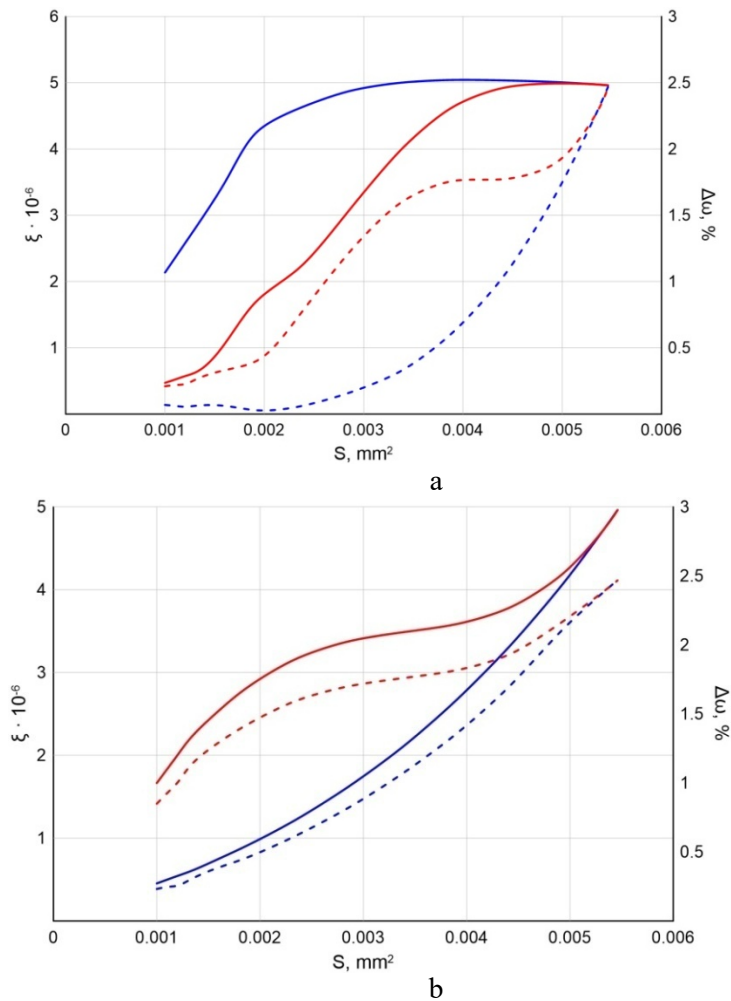


Figure 3: Relations of damping factors for damping the first (ξ_1 , blue solid line) and the second (ξ_2 , red solid line) vibration modes and changes of natural vibration frequencies (blue dashed line for the first one and red dashed line for the second one) depending on the area of the viscoelastic layer arranged according to the first (a) and the second (b) options.

The obtained results show that in order to reach the highest possible damping factor $\xi_1^{(1)}$ it is sufficient to cover 60% of the structure surface area, provided that the viscoelastic element is located according to the first option. Herewith the change in the value of the first natural vibration frequency is 0.3% and corresponding change for the second natural vibration frequency is 1.6%. In order to reach maximal achievable damping factor for the second frequency it is necessary to cover at least 80% of the structure surface area. In this case, the values of the corresponding natural vibration frequencies change by less than 2%.

If the viscoelastic layer covers, 80% of the plate surface area and is arranged on the plate surface according to the second option (in the middle), we obtain the following result:

$\xi_1^{(2)} / \xi_1^{(1)} = 53.6 \%$, $\xi_1^{(2)} / \xi_1^{(1)} = 72.2 \%$. If a viscoelastic layer, c extending length-wise from the clamped end of the plate, covers the same 80% of the plate surface, then the damping factors for both vibration modes are equal and maximal, herewith the change limitations in the structure are not violated.

3.3. Determination of the viscoelastic layer mechanical properties

First, we define the values of tangents of mechanical losses of complex shear and bulk moduli, which provide the highest values of coefficients of vibration damping with mentioned above limitations on modifying the structure. Earlier it was showed that for reaching the maximal damping of vibration modes in the considered frequency range from 0 to 100 Hz it is sufficient to cover with viscoelastic layer 80% of the plate length starting from the rigid clamp. Consider this coverage area with a margin and let the plate be covered by the viscoelastic layer by 90% starting from the clamp and across the full width. This made in order to expand the influence of the viscoelastic layer on other modes of vibrations.

The investigations results of influence of mechanical losses tangents values for shear modulus δ_g (for this case, $\delta_b = 0$) and bulk modulus δ_b (for this case, $\delta_g = 0.2$) on coefficients of vibration damping are presented in figure 4. Here $\xi_1 = \xi_2 = \xi$. This plot shows that quantities of δ_b and δ_g do not affect the damping factors until reaching some certain value. However, damping factors start dramatically increasing when δ_g reaches this certain value. For the further studies we set that $\delta_g = 0.2$ and $\delta_b = 0$.

Further, let us determine the magnitudes of instantaneous shear and bulk moduli that provide the highest values of coefficients of vibration damping for the specified conditions. For obtaining that the value of the one modulus (shear modulus, for example) was fixed and the values of the other modulus (bulk modulus) were varied, and vice versa. The obtained results depending on the values of Poisson's ratio are presented in figure 5. This figure also represents the plots of changing shear modulus and bulk modulus. The results presented in figure 5 shows that shear modulus substantially influence the magnitude of the vibration damping factor. Herewith bulk modulus has almost no influence on values of damping factor.

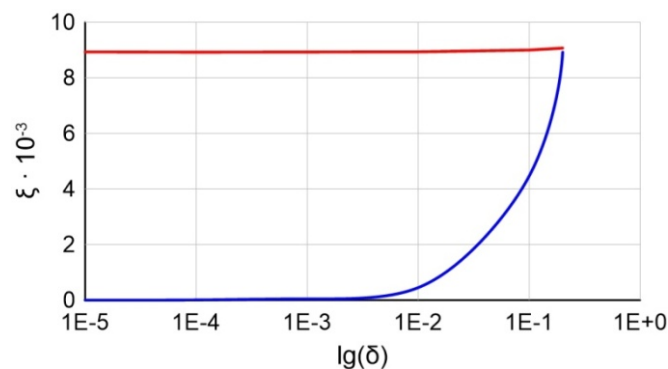


Figure 4: Damping factors $\xi_1 = \xi_2 = \xi$ depending on values of loss tangents of shear modulus (blue line) and bulk modulus (red line).

Investigations related to determination of properties of the viscoelastic coating of the original structure allow to conclude that the number of parameters have a significant impact on damping factor of the system. These parameters are: all geometrical parameters of viscoelastic layer (thickness, area); the layout of the viscoelastic layer, especially if the possibility of damping of several vibration modes within some specified frequency range is considered; shear modulus and tangent of mechanical losses corresponding to it. These factors must be taken into account when modifying the structure with viscoelastic layer.

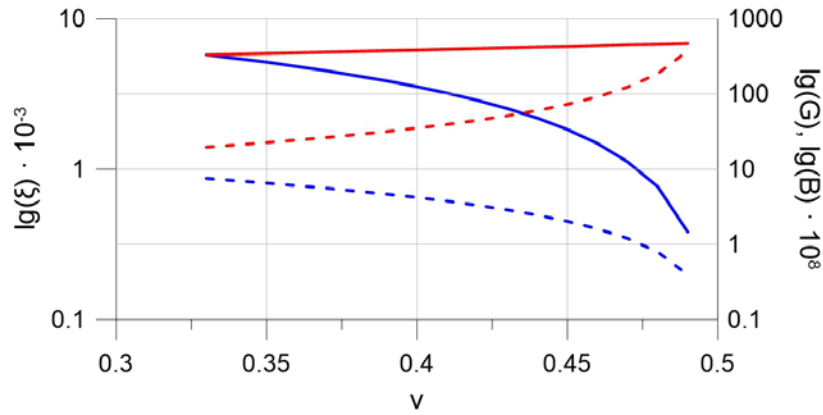


Figure 5: Damping factors depending on G_{Re} when $B_{Re} = const$ (blue solid line); depending on B_{Re} when $G_0 = const$ (red solid line); instantaneous shear modulus G_{Re} (blue dashed line) and bulk modulus B_{Re} (red dashed line) depending on values of Poisson's ratio.

Based on the performed investigations we can state that for reaching maximal damping factors for the first two vibration modes of the structure under limitations of acceptable changes in the properties of a structure it is necessary to cover by the viscoelastic layer the 80% of structure surface, starting from the clamp with 0.2 mm thickness. The most suitable for this purpose material should have the following physical and mechanical properties: Young's modulus $E = 2 \cdot 10^3$ MPa, Poisson's ratio $\nu = 0.49$ ($G_{Re} = 750$ MPa, $B_{Re} = 3.33 \cdot 10^4$ MPa), mass density $\rho = 1200$ kg/m³ and tangents of mechanical losses $\delta_g = 0.2$, $\delta_b = 0$. These properties correspond to the reinforced polyurethane of the Elastollan [5].

4 FORMATION OF THE ELECTRO-VISCOELASTIC STRUCTURE

Consider a cantilever piecewise-homogeneous isotropic viscoelastic plate (figure 1) which is formed by coating the original elastic structure with viscoelastic layer. In the section 3 of the present article it was showed that by appropriate choice of viscoelastic material the highest value of damping factor can be provided for two vibration modes in frequency range from 0 up to 100 Hz, $\xi = 0.012$.

In paper [9] it was demonstrated that coefficient of vibration damping of the initial structure can be increased by attaching piezoelectric element shunted with external electric circuit. Let us study how damping factors for the first two vibration modes changes if piezoelectric element with the dimensions 50x20x0.36 mm is attached to the piecewise-homogeneous viscoelastic structure.

Physical and mechanical properties of the plate: Young's modulus $E = 2 \cdot 10^{11}$ Pa, Poisson's ratio $\nu = 0.49$, mass density $\rho = 7800$ kg/m³. Those ones of viscoelastic layer: Young's modulus $E = 2 \cdot 10^9$ Pa, Poisson's ratio $\nu = 0.49$ ($G_{Re} = 750$ MPa, $B_{Re} = 3.33 \cdot 10^4$ MPa), mass density $\rho = 1200$ kg/m³, mechanical loss tangents $\delta_g = 0.2$, $\delta_b = 0$. Piezoelectric element is made of PZT-4 piezoceramics and has the following characteristics: $C_{11} = C_{22} = 13.9 \cdot 10^{10}$ N/m², $C_{12} = 7.78 \cdot 10^{10}$ N/m², $C_{13} = C_{23} = 7.43 \cdot 10^{10}$ N/m², $C_{33} = 11.5 \cdot 10^{10}$ N/m², $C_{44} = 3.06 \cdot 10^{10}$ N/m², $C_{55} = C_{66} = 2.56 \cdot 10^{10}$ N/m², $\beta_{31} = \beta_{32} = -5.2$ C/m², $\beta_{33} = 15.1$ C/m², $\beta_{32} = \beta_{61} = 12.7$ C/m², $e_{11} = e_{22} = 6.45 \cdot 10^{-9}$ F/m, $e_{33} = 5.62 \cdot 10^{-9}$ F/m, $\rho = 7500$ kg/m³.

In order to compare the efficiency of damping of the first two vibration modes between viscoelastic and electro-viscoelastic plates we consider that length and width of viscoelastic layer are equal to length and width of piezoelectric element. Herewith we set that maximal possible thickness of viscoelastic layer is equal to the thickness of the plate $t = 6$ mm. This thickness do not contravene the limitations put on its thickness and changes the mass of the system in less than 2.8%.

It is a well-known fact that the efficiency of application of piezoelectric element is substantially dependent on its layout on the surface. In this case, the location of piezoelectric element for damping each of the vibration modes under consideration is determined according to the approach proposed in paper [8] without viscoelastic layer on the surface of the structure. Center of masses of piezoelectric element should be located at 37 mm distance from the clamp (its coordinates are equal to $x = 37$ mm, $y = 0$ mm) (option 1) for damping the first vibration mode. Center of masses of piezoelectric element should be located at 105 mm distance from the clamp (its coordinates are equal to $x = 105$ mm, $y = 0$ mm) (option 2) for damping the second vibration mode.

Consider a four typical options of possible mutual disposition of viscoelastic layer and piezoelectric element on the surface of the structure (figure 6). Let us study how natural vibration frequencies of the structure affected by adding viscoelastic and piezoelectric elements. At the first stage, we assume that viscoelastic element is made from material with same properties as viscoelastic layer with no mechanical losses ($\delta_g = 0$; $\delta_b = 0$).

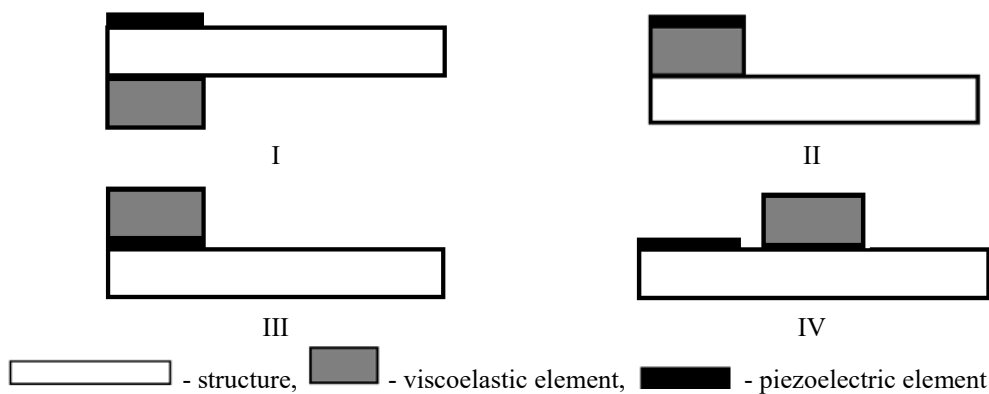


Figure 6: Options of possible mutual disposition of viscoelastic and piezoelectric elements.

Table 1 represents the first two natural vibration frequencies of the original plate for two location options of the center of masses of added viscoelastic layer and piezoelectric element for cases when either one of them, or both, of them are present depending on the four options of their mutual disposition, according to the figure 6.

Table 1: The influence of added elastic and piezoelectric structural elements on natural vibration frequencies of the plate.

Option of a structure				
Original: the plate	ω_1	11.24	ω_2	70.39
Location of the center of masses				
Option 1		Option 2		
	ω_1	ω_2	ω_1	ω_2
The plate with the added elastic layer	11.52	70.42	11.22	70.09
The plate with piezoelectric element	13.86	72.33	11.33	77.11
Options of mutual disposition of viscoelastic layer and piezoelectric element				
I	13.96	72.14	11.29	76.66
II	15.28	73.51	11.42	83.54
III	14.02	72.22	11.30	76.91
IV	13.53	71.70	11.17	77.44

Table 1 shows that natural vibration frequencies substantially depend on mutual disposition of piezoelectric element and added viscoelastic layer despite the fact that total mass of the system (the plate with additional elastic layer and piezoelectric element) remains the same.

Table 2: The influence of added viscoelastic and piezoelectric structural elements on natural vibration frequencies of the plate.

Option of a structure			
Location of the center of masses			
Option 1		Option 2	
$\omega_1 = \omega_{Re1} + i \omega_{Im1}$	ξ_1	$\omega_1 = \omega_{Re1} + i \omega_{Im1}$	ξ_1
$\omega_2 = \omega_{Re2} + i \omega_{Im2}$	ξ_2	$\omega_2 = \omega_{Re2} + i \omega_{Im2}$	ξ_2
The plate with viscoelastic layer			
11.52 + i 0.054	0.005	11.22 + i 0.011	0.001
70.42 + i 0.071	0.001	70.10 + i 0.265	/0.004
Options of mutual disposition of viscoelastic layer and piezoelectric element			
I	13.97 + i 0.020	0.002	11.29 + i 0.002
	72.14 + i 0.028	0.001	76.66 + i 0.101
II	15.29 + i 0.047	0.004	11.42 + i 0.005
	73.52 + i 0.098	0.002	83.57 + i 0.205
III	14.02 + i 0.029	0.003	11.30 + i 0.004
	72.22 + i 0.042	0.001	76.91 + i 0.146
IV	13.53 + i 0.019	0.002	11.68 + i 0.060
	71.71 + i 0.255	0.004	77.44 + i 0.072

The obtained results allows to note that the piezoelectric element plays main role in changes of spectrum of natural vibration frequencies. The elastic layer influences on the spectrum much less. The biggest change (36% for the first natural vibratrion frequency, 18.6 % for the second natural vibratrion frequency) occurs when piezoelectric element located above the viscoelastic layer.

Consider the same layout options of an electro-viscoelastic structure but with replacement of the elastic layer by viscoelastic one. The results of calculations are presented in table 2.

The comparison of the data represented in tables 1 and 2 leads to the conclusion that the substitution of viscoelastic material by eleastic one with the same properties has almost no influence on spectrum of natural vibrationfrequencies of the system.

This fact can be usefull for studying the dynamic behavior of electro-viscoelastic structures. Furthermore, the analysis of the results represented in table 2 leads to the following conclusion: in the most common case the attaching of piezoelectric element to viscoelastic structure decreases its damping properties. But this decrease depends on mutual disposition of viscoelastic layer and piezoelectric element. The least influence of piezoelectric element is observed in case when it is located above the viscoelastic layer (option II). When piezoelectric element located nearby of the viscoelastic layer (option IV) the damping properties of electro-viscoelastic structure do not decrease in compare to the purely viscoelastic one.

5 CONCLUSIONS

This paper presents the part of research related to modification of the original elastic structure in order to ensure the damping of specified vibration modes with applied mass and dimensional characteristics limitations. The modification is made by supplementing structure with a viscoelastic layer and connecting a piezoelectric element shunted by an electric circuit.

During this research, the first two vibration modes were taken into account.

The estimation of influence of viscoelastic and piezoelectric elements was demonstrated in order to get the comprehension of contribution of different energy dissipation mechanisms to total loss. The maximal achievable rate of vibration damping and corresponding parameters of viscoelstic layer are determined depending on the number of factors (mechanical properties, area of coverage, location and thickness). This study allowed us to determine physical and mechanical properties of material (from the perliminarly proposed) that can provide the highest values of damping factors with existing limitations on characteristis of a structure. The influence on the results of adding a viscoelastic layer, attaching piezoelectric element and its location relative to the viscoelastic layer are estimated.

Numerically demonstrated the well-known fact that adding piezoelectric elements substantially influence the dynamical properties of a structure only when connected to external electric circuits of arbitrary configuration [9].

ACKNOWLEDGEMENTS

The work is supported by RFBR, project № 19-01-00158_a.

REFERENCES

- [1] Trindade, M.A. and Benjeddou, A. Hybrid Active-Passive Damping Treatments Using Viscoelastic and Piezoelectric Materials: Review and Assessment. *J. Vibration and*

- Control* (2002) **8**:699-745.
- [2] Stanway, R., Rongong, J.A. and Sims, N.D. Active constrained-layer damping: A state-of-the-art review. *Proc. Instn. Mech. Engrs Part I: J. Systems and Control Engineering* (2003) **217**:437-456.
 - [3] Mead, D.J. *Passive vibration control*. John Wiley, Chichester, Sussex (1999).
 - [4] Matveenکو, V.P., Oshmarin, D.A., Sevodina, N.V. and Iurlova, N.A. Natural vibration problem for electroviscoelastic body with external electric circuits and finite-element relations for its numerical implementation. *Computational Continuum Mechanics* (2016) **9**(4): 476-485.
 - [5] Adamov, A.A., Matveyenko, V.P., Trufanov, N.A. and Shardakov, I.N. *Metody prikladnoy vyazkouprugosti. UrB RAS* (2003).
 - [6] Weaver Jr., W., Timoshenko, S.P. and Young, D.H. *Vibration problems in engineering, 5th edition*. Wiley (1990).
 - [7] Kligman, E.P., Matveenکو, V.P. and Sevodina, N.V. Determination of natural vibrations of piecewise homogeneous viscoelastic bodies using the ANSYS software package. *Computational Continuum Mechanics*. (2010) **3**(2):46-54.
 - [8] Iurlova, N.A., Matveenکو, V.P., Oshmarin, D.A., Sevodina, N.V. and Yurlov, M.A. Layout optimization of piezoelectric elements with external electric circuits in smart constructions based on solution of the natural vibrations problem. *ECCOMAS Congress 2016 VII European Congress on Computational Methods in Applied Sciences and Engineering Proceedings, (Crete Island, Greece, 5–10 June 2016)* (2016) **1**:1920-1929.
 - [9] Hagood, N. and Von Flotow, A. Damping of structural vibrations with piezoelectric materials and passive electrical networks. *J. Sound and Vibration*. (1991) **146**(2):243-268.

ON DYNAMICAL HIERARCHICAL TWO-DIMENSIONAL MODELS OF MULTILAYER THERMOELASTIC PIEZOELECTRIC SHELLS

GIA AVALISHVILI^{*} AND MARIAM AVALISHVILI[†]

^{*} Faculty of Exact and Natural Sciences
I. Javakhishvili Tbilisi State University
3 I. Tchavtchavadze Ave., 0179 Tbilisi, Georgia
e-mail: gavalish@yahoo.com

[†] School of Science and Technology
University of Georgia, Tbilisi
77a M. Kostava Str., 0175 Tbilisi, Georgia
email: m.avalishvili@ug.edu.ge

Key words: Thermo-electro-magnetoelasticity, Shells, Two-dimensional Models, Initial-boundary Value Problems, Modelling Error Estimate.

Abstract. In this paper, linear dynamical three-dimensional model of thermoelastic piezo-electric shell with variable thickness, which may vanish on a part of the lateral boundary, consisting of several inhomogeneous anisotropic layers with regard to magnetic field is considered. In order to construct dynamical two-dimensional models variational formulation in curvilinear coordinates of the initial-boundary problem corresponding to the three-dimensional model of the shell is obtained. Applying spectral approximation method a sequence of subspaces with special structure of the spaces corresponding to the original three-dimensional problem is constructed and on these subspaces a hierarchy of dynamical two-dimensional models is obtained. The constructed two-dimensional initial-boundary value problems are investigated in suitable spaces of vector-valued distributions with respect to the time variable with values in corresponding weighted Sobolev spaces and the existence and uniqueness of solutions are proved. Moreover, it is proved that the sequence of vector-functions of three space variables restored from the solutions of the two-dimensional problems converges in the corresponding function spaces to the exact solution of the three-dimensional initial-boundary value problem and under additional conditions the rate of convergence is estimated.

1 INTRODUCTION

Piezoelectric materials are widely used to build engineering smart structures, because of the ease of controlling by voltage, low weight and low power requirements. Inhomogeneous and, in particular, functionally graded materials are used to increase the durability and efficiency of engineering constructions undergoing high mechanical and thermal loads. Various parts of smart devices consisting of piezoelectric materials are often plate or shell like structures, and, therefore, construction and investigation of mathematical models of inhomogeneous thermoelastic piezoelectric plates and shells are important from both theoretical and practical

viewpoints. Mathematical models of interaction between elastic, electric and thermal fields in piezoelectric body were developed by W. Voigt [1] and further various models of piezoelectric solids were constructed and investigated by various authors (see [2] and the references given therein).

In order to construct two-dimensional models of thermoelastic piezoelectric shells we use spectral approximation method, which is a generalization of the method of constructing two-dimensional models for plates with variable thickness in the classical theory of elasticity suggested by I. Vekua in [3]. Various two-dimensional models constructed by Vekua were collected in his monograph [4]. The estimates of the order of approximation of static three-dimensional problem by two-dimensional ones constructed in [3] first were obtained in the spaces of classical regular functions in the paper [5], and the reduced two-dimensional models for thin shallow shells constructed in [4] were investigated in Sobolev spaces in [6]. Later on, dimensional reduction methods suggested by I. Vekua in [3, 4] and there generalizations were studied in the papers [7-11].

2 THREE-DIMENSIONAL MODEL

Throughout this paper we denote by $W^{r,2}(D) = H^r(D)$ and $H^r(\hat{\Gamma})$, $r \in \mathbf{R}$, the Sobolev spaces of order r based on the spaces $H^0(D) = L^2(D)$ and $H^0(\hat{\Gamma}) = L^2(\hat{\Gamma})$ of square-integrable functions, respectively, where $D \subset \mathbf{R}^p$, $p \in \mathbf{N}$, is a bounded Lipschitz domain [12] and $\hat{\Gamma} \subset \partial D$ is a Lipschitz surface. We denote by $\mathbf{H}^r(D) = [H^r(D)]^3$, $\mathbf{H}^r(\hat{\Gamma}) = [H^r(\hat{\Gamma})]^3$, $\mathbf{L}^2(D) = [L^2(D)]^3$, $\mathbf{L}^s(\hat{\Gamma}) = [L^s(\hat{\Gamma})]^3$, $s \geq 1$, $r, s \in \mathbf{R}$, the spaces of vector-valued functions. The trace operators we denote by $tr_{\hat{\Gamma}} : H^1(D) \rightarrow H^{1/2}(\hat{\Gamma})$ and $\mathbf{tr}_{\hat{\Gamma}} : \mathbf{H}^1(D) \rightarrow \mathbf{H}^{1/2}(\hat{\Gamma})$. For Banach space X , $C([0, T]; X)$ denotes the space of continuous functions on $[0, T]$ with values in X , $L^q(0, T; X)$, $1 \leq q \leq \infty$, is the space of such functions $g : (0, T) \rightarrow X$ that $\|g(t)\|_X \in L^q(0, T)$. We denote by $g' = dg/dt$ the generalized derivative of function $g \in L^q(0, T; X)$ [13].

Let us consider multilayer thermoelastic piezoelectric shell with initial configuration $\overline{\Omega}^* = \xi(\overline{\Omega})$, where $\overline{\Omega}$ is of the following form $\overline{\Omega} = \bigcup_{k=1}^K \overline{\Omega}_k$,

$$\Omega_k = \{(x_1, x_2, x_3) \in \mathbf{R}^3; h_k^-(x_1, x_2) < x_3 < h_k^+(x_1, x_2), (x_1, x_2) \in \omega \subset \mathbf{R}^2\},$$

where ξ is a C^2 diffeomorphism of $\overline{\Omega}$ onto $\overline{\Omega}^*$, so that the vectors $\mathbf{G}_i(x) = \partial_i \xi(x)$ are linearly independent at all points of $\overline{\Omega}$, ∂_i denotes the partial derivative with respect to x_i ($i = 1, 2, 3$). Since ξ is an injective mapping each point $x^* \in \overline{\Omega}^*$ in Cartesian coordinates $x^* = (x_1^*, x_2^*, x_3^*)$ can be unambiguously written as $x^* = \xi(x)$, $x \in \overline{\Omega}$, and the coordinates x_i of x are the curvilinear coordinates of x^* . The triplets $\{\mathbf{G}_i(x)\}$ and $\{\mathbf{G}^i(x)\}$ form the covariant and contravariant bases at the point $x^* = \xi(x)$, respectively, where $\mathbf{G}_i(x) \cdot \mathbf{G}^j(x) = \delta_{ij}$, δ_{ij} is the Kronecker delta. The mapping ξ defines metric tensor of $\overline{\Omega}^*$ with contravariant components

$G^{ij} = \mathbf{G}^i \cdot \mathbf{G}^j$ and Christoffel symbols $\Gamma_{ij}^p = \mathbf{G}^p \cdot \partial_i \mathbf{G}_j$, $i, j, p = \overline{1, 3}$. $\Omega \subset \mathbf{R}^3$ and $\omega \subset \mathbf{R}^2$ are bounded Lipschitz domains with boundaries $\partial\Omega$ and $\partial\omega$, respectively, $h_k^\pm \in C^0(\bar{\omega}) \cap C_{loc}^{1,1}(\omega)$, $k = 1, \dots, K$, are continuous on $\bar{\omega}$ and Lipschitz continuous in ω , $h_k^+(x_1, x_2) > h_k^-(x_1, x_2)$, for $(x_1, x_2) \in \omega \cup \tilde{\gamma}$, $\tilde{\gamma} \subset \partial\omega$ is a Lipschitz curve, $h_k^+(x_1, x_2) = h_k^-(x_1, x_2)$, for $(x_1, x_2) \in \partial\omega \setminus \tilde{\gamma}$, $h_k^+(x_1, x_2) = h_{k+1}^-(x_1, x_2)$, $k = 1, \dots, K-1$, for $(x_1, x_2) \in \bar{\omega}$. The upper and the lower face surfaces of the layer Ω_k defined by the equations $x_3 = h_k^+(x_1, x_2)$ and $x_3 = h_k^-(x_1, x_2)$, $(x_1, x_2) \in \omega$, we denote by Γ_k^+ and Γ_k^- , respectively, and the lateral surface of the layer Ω_k , where the thickness of Ω_k is positive, we denote by $\tilde{\Gamma}_k = \{(x_1, x_2, x_3) \in \mathbf{R}^3; h_k^-(x_1, x_2) < x_3 < h_k^+(x_1, x_2), (x_1, x_2) \in \tilde{\gamma}\}$.

We assume that each layer $\Omega_k^* = \theta(\Omega_k)$, $k = 1, \dots, K$, of the thermoelastic piezoelectric shell Ω^* consists of inhomogeneous anisotropic material with the mass density $\rho^{k*}(x^*)$ in the initial configuration, the elasticity tensor $(c_{ijpq}^{k*}(x^*))_{i,j,p,q=1}^3$, the piezoelectric $(\varepsilon_{pij}^{k*}(x^*))_{i,j,p=1}^3$ and piezomagnetic $(b_{pij}^{k*}(x^*))_{i,j,p=1}^3$ coefficients, the stress-temperature tensor $(\lambda_{ij}^{k*}(x^*))_{i,j=1}^3$, the permittivity $(d_{ij}^{k*}(x^*))_{i,j=1}^3$ and permeability $(\zeta_{ij}^{k*}(x^*))_{i,j=1}^3$ tensors, the coupling coefficients connecting electric and magnetic fields $(a_{ij}^{k*}(x^*))_{i,j=1}^3$, the thermal conductivity tensor $(\eta_{ij}^{k*}(x^*))_{i,j=1}^3$ and the thermal capacity $\chi^{k*}(x^*)$. We neglect the influence of thermal field on electric and magnetic fields and assume that pyroelectric and pyromagnetic coefficients vanish. The applied body force density we denote by $\mathbf{f}^{k*} = (f_i^{k*})_{i=1}^3 : \Omega_k^* \times (0, T) \rightarrow \mathbf{R}^3$, the density of electric charges we denote by $f^{\varphi, k*} : \Omega_k^* \times (0, T) \rightarrow \mathbf{R}$, and the density of heat sources we denote by $f^{\theta, k*} : \Omega_k^* \times (0, T) \rightarrow \mathbf{R}$. The temperature $\theta^* : \Omega^* \times (0, T) \rightarrow \mathbf{R}$ of the shell vanishes along the boundary $\Gamma^* = \partial\Omega^*$ of the domain Ω^* . The shell is clamped along a part $\tilde{\Gamma}_0^* = \xi(\tilde{\Gamma}_0)$, $\tilde{\Gamma}_0 = \bigcup_{k=1}^K \tilde{\Gamma}_{0,k}$, $\tilde{\Gamma}_{0,k} = \{(x_1, x_2, x_3) \in \tilde{\Gamma}_k; (x_1, x_2) \in \tilde{\gamma}_{0,k}\}$, $\tilde{\gamma}_{0,k} \subset \tilde{\gamma}$, of the lateral surface $\tilde{\Gamma}^* = \xi(\tilde{\Gamma})$, $\tilde{\Gamma} = \{(x_1, x_2, x_3) \in \Gamma = \partial\Omega; (x_1, x_2) \in \tilde{\gamma}\}$, and on the remaining part $\Gamma_1^* = \xi(\Gamma_1)$, $\Gamma_1 = \Gamma \setminus \tilde{\Gamma}_0$, of the boundary surface force with density $\mathbf{g}^* = (g_i^*) : \Gamma_1^* \times (0, T) \rightarrow \mathbf{R}^3$ is given. The electric field \mathbf{E}^* is potential $\mathbf{E}^* = -(\partial\varphi^* / \partial x_i^*)_{i=1}^3$ and electric potential $\varphi^* : \Omega^* \times (0, T) \rightarrow \mathbf{R}$ vanishes along a part $\tilde{\Gamma}_0^{\varphi*} = \xi(\tilde{\Gamma}_0^{\varphi})$, $\tilde{\Gamma}_0^{\varphi} = \bigcup_{k=1}^K \tilde{\Gamma}_{0,k}^{\varphi}$, $\tilde{\Gamma}_{0,k}^{\varphi} = \{(x_1, x_2, x_3) \in \tilde{\Gamma}_k; (x_1, x_2) \in \tilde{\gamma}_{0,k}^{\varphi}\}$, $\tilde{\gamma}_{0,k}^{\varphi} \subset \tilde{\gamma}$, of the lateral surface $\tilde{\Gamma}^*$ of the shell and on the remaining part $\Gamma_1^{\varphi*} = \xi(\Gamma_1^{\varphi})$, $\Gamma_1^{\varphi} = \Gamma \setminus \tilde{\Gamma}_0^{\varphi}$, of the boundary the normal component of the electric displacement with density $\mathbf{g}^{\varphi*} : \Gamma_1^{\varphi*} \times (0, T) \rightarrow \mathbf{R}$ is given. The magnetic field \mathbf{H}^* is potential $\mathbf{H}^* = -(\partial\psi^* / \partial x_i^*)_{i=1}^3$ and magnetic potential $\psi^* : \Omega^* \times (0, T) \rightarrow \mathbf{R}$ vanishes along $\tilde{\Gamma}_0^{\psi*} = \xi(\tilde{\Gamma}_0^{\psi})$, $\tilde{\Gamma}_0^{\psi} = \bigcup_{k=1}^K \tilde{\Gamma}_{0,k}^{\psi}$, $\tilde{\Gamma}_{0,k}^{\psi} = \{(x_1, x_2, x_3) \in \tilde{\Gamma}_k; (x_1, x_2) \in \tilde{\gamma}_{0,k}^{\psi}\}$, $\tilde{\gamma}_{0,k}^{\psi} \subset \tilde{\gamma}$, of the lateral surface $\tilde{\Gamma}^*$ and on the remaining part $\Gamma_1^{\psi*} = \xi(\Gamma_1^{\psi})$,

$\Gamma_1^\psi = \Gamma \setminus \overline{\tilde{\Gamma}_0^\psi}$, of the boundary the normal component of the magnetic induction with density $g^{\psi*} : \Gamma_1^{\psi*} \times (0, T) \rightarrow \mathbf{R}$ is given.

The linear dynamical three-dimensional model of the thermoelastic piezoelectric multilayer shell $\overline{\Omega^*}$ in differential form with quasi-static equations for electro-magnetic fields, where the rate of change of magnetic field is small, i.e. electric field is curl free, and there is no electric current, i.e. magnetic field is curl free, in Cartesian coordinates is given by the following system of partial differential equations [2]:

$$\rho^{k*} \frac{\partial^2 u_i^{k*}}{\partial t^2} - \sum_{j=1}^3 \frac{\partial \sigma_{ij}^{k*}}{\partial x_j^*} = f_i^{k*} \quad \text{in } \Omega_k^* \times (0, T), \quad i = 1, 2, 3, \quad (1)$$

$$\sum_{j=1}^3 \frac{\partial D_j^{k*}}{\partial x_j} = f^{\varphi, k*} \quad \text{in } \Omega_k^* \times (0, T), \quad (2)$$

$$\sum_{j=1}^3 \frac{\partial B_j^k}{\partial x_j} = 0 \quad \text{in } \Omega_k^* \times (0, T), \quad (3)$$

$$\chi^{k*} \frac{\partial \theta^{k*}}{\partial t} - \sum_{i,j=1}^3 \frac{\partial}{\partial x_i^*} \left(\eta_{ij}^{k*} \frac{\partial \theta^{k*}}{\partial x_j^*} \right) + \Theta_0 \frac{\partial}{\partial t} \sum_{i,j=1}^3 \lambda_{ij}^{k*} e_{ij}^*(\mathbf{u}^{k*}) = f^{\theta, k*} \quad \text{in } \Omega_k^* \times (0, T), \quad (4)$$

with mixed boundary conditions

$$\mathbf{u}^* = \mathbf{0} \quad \text{on } \tilde{\Gamma}_0^* \times (0, T), \quad \sum_{j=1}^3 \sigma_{ij}^* n_j^* = g_i^* \quad \text{on } \Gamma_1^* \times (0, T), \quad (5)$$

$$\varphi^* = 0 \quad \text{on } \tilde{\Gamma}_0^{\varphi*} \times (0, T), \quad \sum_{i=1}^3 D_i^* n_i^* = g^{\varphi*} \quad \text{on } \Gamma_1^{\varphi*} \times (0, T), \quad (6)$$

$$\psi^* = 0 \quad \text{on } \tilde{\Gamma}_0^{\psi*} \times (0, T), \quad \sum_{i=1}^3 B_i^* n_i^* = g^{\psi*} \quad \text{on } \Gamma_1^{\psi*} \times (0, T), \quad (7)$$

$$\theta^* = 0 \quad \text{on } \Gamma^* \times (0, T), \quad (8)$$

rigid contact conditions along the interfaces $\Gamma_k^{+*} = \theta(\Gamma_k^+)$, $k = 1, \dots, K-1$,

$$\mathbf{u}^{k*} = \mathbf{u}^{k+1*}, \quad \sum_{j=1}^3 \sigma_{ij}^{k*} n_j^* = \sum_{j=1}^3 \sigma_{ij}^{k+1*} n_j^* \quad \text{on } \Gamma_k^{+*}, \quad (9)$$

$$\varphi^{k*} = \varphi^{k+1*}, \quad \sum_{i=1}^3 D_i^{k*} n_i^* = \sum_{i=1}^3 D_i^{k+1*} n_i^* \quad \text{on } \Gamma_k^{+*}, \quad (10)$$

$$\psi^{k*} = \psi^{k+1*}, \quad \sum_{i=1}^3 B_i^{k*} n_i^* = \sum_{i=1}^3 B_i^{k+1*} n_i^* \quad \text{on } \Gamma_k^{+*}, \quad (11)$$

$$\theta^{k*} = \theta^{k+1*}, \quad \sum_{i,j=1}^3 \eta_{ij}^{k*} \frac{\partial \theta^{k*}}{\partial x_j^*} n_i^* = \sum_{i,j=1}^3 \eta_{ij}^{k+1*} \frac{\partial \theta^{k+1*}}{\partial x_j^*} n_i^* \quad \text{on } \Gamma_k^{+*}, \quad (12)$$

and initial conditions

$$u_i^*(x^*, 0) = u_{0i}^*(x^*), \quad \frac{\partial u_i^*}{\partial t}(x^*, 0) = \dot{u}_{0i}^*(x^*), \quad \theta^*(x^*, 0) = \theta_0^*(x^*) \quad \text{in } \Omega^*, \quad i = 1, 2, 3, \quad (13)$$

where $\mathbf{n}^* = (n_i^*)_{i=1}^3$ is the unit outward normal vector to the corresponding surface, $\mathbf{u}^* = (u_i^*)_{i=1}^3 : \Omega^* \times (0, T) \rightarrow \mathbf{R}^3$ is the mechanical displacement vector-function, $\mathbf{u}^{k*} = \mathbf{u}^*$, $\varphi^{k*} = \varphi^*$, $\psi^{k*} = \psi^*$, $\theta^{k*} = \theta^*$ in Ω_k^* , $\Theta_0 > 0$ is the temperature of thermoelastic piezoelectric body in natural state in the absence of deformation and electromagnetic fields, which is considered as a reference temperature, $\mathbf{u}_0^* = (u_{0i}^*)_{i=1}^3$ and $\mathbf{u}_1^* = (u_{1i}^*)_{i=1}^3$ are the initial displacement and velocity vector-functions, θ_0^* is the initial distribution of temperature, $e_{ij}^*(\mathbf{v}^*) = 1/2(\partial v_i^* / \partial x_j^* + \partial v_j^* / \partial x_i^*)$, $i, j = 1, 2, 3$, $\mathbf{v}^* = (v_i^*)_{i=1}^3$, is the strain tensor, $(\sigma_{ij}^{k*})_{i,j=1}^3$ is the mechanical stress tensor, $\mathbf{D}^{k*} = (D_j^{k*})_{j=1}^3$ is the electric displacement vector and $\mathbf{B}^{k*} = (B_j^{k*})_{j=1}^3$ is the magnetic induction vector in the layer Ω_k^* , which are given by the following constitutive equations:

$$\begin{aligned}\sigma_{ij}^{k*} &= \sum_{p,q=1}^3 c_{ijpq}^{k*} e_{pq}^*(\mathbf{u}^{k*}) + \sum_{p=1}^3 \varepsilon_{pij}^{k*} \frac{\partial \varphi^{k*}}{\partial x_p^*} + \sum_{p=1}^3 b_{pij}^{k*} \frac{\partial \psi^{k*}}{\partial x_p^*} - \lambda_{ij}^{k*} \theta^{k*}, \quad i, j = 1, 2, 3, \\ D_i^{k*} &= \sum_{p,q=1}^3 \varepsilon_{ipq}^{k*} e_{pq}^*(\mathbf{u}^{k*}) - \sum_{j=1}^3 d_{ij}^{k*} \frac{\partial \varphi^{k*}}{\partial x_j^*} - \sum_{j=1}^3 a_{ij}^{k*} \frac{\partial \psi^{k*}}{\partial x_j^*}, \quad j = 1, 2, 3, \\ B_i^{k*} &= \sum_{p,q=1}^3 b_{ipq}^{k*} e_{pq}^*(\mathbf{u}^{k*}) - \sum_{j=1}^3 a_{ij}^{k*} \frac{\partial \varphi^{k*}}{\partial x_j^*} - \sum_{j=1}^3 \zeta_{ij}^{k*} \frac{\partial \psi^{k*}}{\partial x_j^*}, \quad j = 1, 2, 3.\end{aligned}$$

We assume that the coefficients characterizing elastic, thermal, electric and magnetic properties satisfy the following symmetry conditions

$$\begin{aligned}c_{ijpq}^{k*} &= c_{ijqp}^{k*} = c_{jipq}^{k*}, \quad \varepsilon_{pij}^{k*} = \varepsilon_{pji}^{k*}, \quad b_{pij}^{k*} = b_{pji}^{k*}, \\ d_{ij}^{k*} &= d_{ji}^{k*}, \quad a_{ij}^{k*} = a_{ji}^{k*}, \quad \zeta_{ij}^{k*} = \zeta_{ji}^{k*}, \quad \lambda_{ij}^{k*} = \lambda_{ji}^{k*}, \quad i, j, p, q = 1, 2, 3, \quad k = 1, \dots, K.\end{aligned}\tag{14}$$

Let us consider variational formulation of initial-boundary value problem (1)-(13) in curvilinear coordinates, which is equivalent to the differential formulation in the space of smooth enough functions: Find the unknown vector-function $\mathbf{u} \in C([0, T]; \mathbf{V}(\Omega))$, $\mathbf{u}' \in C([0, T]; \mathbf{L}^2(\Omega))$, and functions $\varphi \in C([0, T]; V^\varphi(\Omega))$, $\psi \in C([0, T]; V^\psi(\Omega))$, $\theta \in L^2(0, T; H_0^1(\Omega))$, $\theta' \in L^2(0, T; H^{-1}(\Omega))$, which satisfy the following equations in the sense of distributions on $(0, T)$,

$$\frac{d}{dt}(\mathbf{P}^G \mathbf{u}', \mathbf{v})_{\mathbf{L}^2(\Omega)} + c(\mathbf{u}, \mathbf{v}) + \varepsilon(\varphi, \mathbf{v}) + b(\psi, \mathbf{v}) - \lambda(\theta, \mathbf{v}) = L^u(\mathbf{v}), \quad \forall \mathbf{v} \in \mathbf{V}(\Omega),\tag{15}$$

$$-\varepsilon(\bar{\varphi}, \mathbf{u}) + d(\varphi, \bar{\varphi}) + a(\psi, \bar{\varphi}) = L^\varphi(\bar{\varphi}), \quad \forall \bar{\varphi} \in V^\varphi(\Omega),\tag{16}$$

$$-b(\bar{\psi}, \mathbf{u}) + a(\varphi, \bar{\psi}) + \zeta(\psi, \bar{\psi}) = L^\psi(\bar{\psi}), \quad \forall \bar{\psi} \in V^\psi(\Omega),\tag{17}$$

$$\frac{d}{dt}(\chi^G \theta, \bar{\theta})_{L^2(\Omega)} + \eta(\theta, \bar{\theta}) + \Theta_0 \lambda(\bar{\theta}, \mathbf{u}') = L^\theta(\bar{\theta}), \quad \forall \bar{\theta} \in H_0^1(\Omega),\tag{18}$$

together with the initial conditions

$$\mathbf{u}(0) = \mathbf{u}_0, \quad \mathbf{u}'(0) = \mathbf{u}_1, \quad \theta(0) = \theta_0,\tag{19}$$

where $\mathbf{V}(\Omega) = \{\mathbf{v} \in \mathbf{H}^1(\Omega); \mathbf{tr}_\Gamma(\mathbf{v}) = \mathbf{0} \text{ on } \tilde{\Gamma}_0\}$, $V^\varphi(\Omega) = \{\bar{\varphi} \in H^1(\Omega); tr_\Gamma(\bar{\varphi}) = 0 \text{ on } \tilde{\Gamma}_0^\varphi\}$, $V^\psi(\Omega) = \{\bar{\psi} \in H^1(\Omega); tr_\Gamma(\bar{\psi}) = 0 \text{ on } \tilde{\Gamma}_0^\psi\}$, $H_0^1(\Omega) = \{\bar{\theta} \in H^1(\Omega); tr_\Gamma(\bar{\theta}) = 0 \text{ on } \Gamma\}$,

$$\begin{aligned} c(\mathbf{u}, \mathbf{v}) &= \int \sum_{\Omega^i, j, p, q=1}^3 c_{ijpq}^G e_{p||q}(\mathbf{u}) e_{i||j}(\mathbf{v}) dx, \quad \varepsilon(\varphi, \mathbf{v}) = \int \sum_{\Omega^i, j, p=1}^3 \varepsilon_{pij}^G \frac{\partial \varphi}{\partial x_p} e_{i||j}(\mathbf{v}) dx, \\ b(\psi, \mathbf{v}) &= \int \sum_{\Omega^i, j, p=1}^3 b_{pij}^G \frac{\partial \psi}{\partial x_p} e_{i||j}(\mathbf{v}) dx, \quad \lambda(\theta, \mathbf{v}) = - \int \sum_{\Omega^i, j, p, q=1}^3 v_p \frac{\partial}{\partial x_q} (\lambda_{ij} \theta) (\mathbf{G}^p)_i (\mathbf{G}^q)_j \sqrt{G} dx, \\ d(\varphi, \bar{\varphi}) &= \int \sum_{\Omega^i, j=1}^3 d_{ij}^G \frac{\partial \varphi}{\partial x_j} \frac{\partial \bar{\varphi}}{\partial x_i} dx, \quad a(\psi, \bar{\varphi}) = \int \sum_{\Omega^i, j=1}^3 a_{ij}^G \frac{\partial \psi}{\partial x_j} \frac{\partial \bar{\varphi}}{\partial x_i} dx, \quad \zeta(\psi, \bar{\psi}) = \int \sum_{\Omega^i, j=1}^3 \zeta_{ij}^G \frac{\partial \psi}{\partial x_j} \frac{\partial \bar{\psi}}{\partial x_i} dx, \\ \eta(\theta, \bar{\theta}) &= \int \sum_{\Omega^i, j=1}^3 \eta_{ij}^G \frac{\partial \theta}{\partial x_j} \frac{\partial \bar{\theta}}{\partial x_i} dx, \quad L^{\mathbf{u}}(\mathbf{v}) = \int \sum_{\Omega} f^i v_i \sqrt{G} dx + \int \sum_{\Gamma_1} g^i tr_{\Gamma_1}(v_i) \sqrt{G} d\Gamma, \\ L^\varphi(\bar{\varphi}) &= \int_\Omega f^\varphi \bar{\varphi} \sqrt{G} dx - \int_{\Gamma_1^\varphi} g^\varphi tr_{\Gamma_1^\varphi}(\bar{\varphi}) \sqrt{G} d\Gamma, \quad L^\psi(\bar{\psi}) = - \int_{\Gamma_1^\psi} g^\psi tr_{\Gamma_1^\psi}(\bar{\psi}) \sqrt{G} d\Gamma, \quad L^\theta(\bar{\theta}) = \int_\Omega f^\theta \bar{\theta} \sqrt{G} dx, \\ (\cdot, \cdot)_{\mathbf{L}^2(\Omega)} \text{ and } (\cdot, \cdot)_{L^2(\Omega)} &\text{ are the scalar products in the spaces } \mathbf{L}^2(\Omega) \text{ and } L^2(\Omega), \text{ respectively,} \\ u_i (i=1, 2, 3) &\text{ are the covariant component of the displacement vector field, } \theta(x, t) = \theta^*(x^*, t), \\ (x^*, t) \in \Omega^* \times (0, T), f^i \text{ and } g^i (i=1, 2, 3) &\text{ are the contravariant components of the applied body} \\ \text{force } \mathbf{f}^* \text{ and surface force } \mathbf{g}^* \text{ densities, } \mathbf{f}^* = \mathbf{f}^{k*} \text{ in } \Omega_k^*, k=1, \dots, K, \\ e_{p||q}(\mathbf{v}) &= 1/2(\partial_p v_q + \partial_q v_p) - \sum_{i=1}^3 \Gamma_{pq}^i v_i \text{ are the covariant components of the strain tensor,} \\ G = \det(G_{ij}), c_{ijpq}^G &= \sum_{k, l, r, s=1}^3 c_{klrs}(\mathbf{G}^i)_k (\mathbf{G}^j)_l (\mathbf{G}^p)_r (\mathbf{G}^q)_s \sqrt{G}, \quad \varepsilon_{pij}^G = \sum_{r, s, k=1}^3 \varepsilon_{rsk}(\mathbf{G}^p)_r (\mathbf{G}^i)_s (\mathbf{G}^j)_k \sqrt{G}, \\ b_{pij}^G &= \sum_{r, s, k=1}^3 b_{rsk}(\mathbf{G}^p)_r (\mathbf{G}^i)_s (\mathbf{G}^j)_k \sqrt{G}, \quad d_{ij}^G = \sum_{r, s=1}^3 d_{rs}(\mathbf{G}^i)_r (\mathbf{G}^j)_s \sqrt{G}, \quad a_{ij}^G = \sum_{r, s=1}^3 a_{rs}(\mathbf{G}^i)_r (\mathbf{G}^j)_s \sqrt{G}, \\ \zeta_{ij}^G &= \sum_{r, s=1}^3 \zeta_{rs}(\mathbf{G}^i)_r (\mathbf{G}^j)_s \sqrt{G}, \quad \eta_{ij}^G = \sum_{r, s=1}^3 \eta_{rs}(\mathbf{G}^i)_r (\mathbf{G}^j)_s \sqrt{G}, \quad \mathbf{P}^G = (\mathbf{P}_{ij}^G) \text{ is } 3 \times 3 \text{ matrix with elements} \\ \mathbf{P}_{ij}^G &= \rho g^{ij} \sqrt{G} \quad (i, j=1, 2, 3), \quad \chi^G = \chi \sqrt{G}, \quad \rho(x) = \rho^{k*}(x^*), \quad \chi(x) = \chi^{k*}(x^*), \quad c_{ijpq}(x) = c_{ijpq}^{k*}(x^*), \\ \varepsilon_{pij}(x) &= \varepsilon_{pij}^{k*}(x^*), \quad b_{pij}(x) = b_{pij}^{k*}(x^*), \quad \lambda_{ij}(x) = \lambda_{ij}^{k*}(x^*), \quad d_{ij}(x) = d_{ij}^{k*}(x^*), \quad a_{ij}(x) = a_{ij}^{k*}(x^*), \\ \zeta_{ij}(x) &= \zeta_{ij}^{k*}(x^*), \quad \eta_{ij}(x) = \eta_{ij}^{k*}(x^*), \quad i, j, p, q = 1, 2, 3, \quad f^\varphi(x) = f^{\varphi, k*}(x^*), \quad f^\theta(x) = f^{\theta, k*}(x^*), \\ x^* \in \Omega_k^*, g^\varphi(x) &= g^{\varphi*}(x^*), \quad x^* \in \Gamma_1^{\varphi*}, \quad g^\psi(x) = g^{\psi*}(x^*), \quad x^* \in \Gamma_1^{\psi*}, \quad k=1, \dots, K. \end{aligned}$$

3 TWO-DIMENSIONAL MODELS

In order to construct the hierarchy of two-dimensional models let us consider the subspaces $\mathbf{V}_N(\Omega)$ and $\mathbf{H}_N(\Omega)$ of $\mathbf{V}(\Omega)$ and $\mathbf{L}^2(\Omega)$, respectively, $\mathbf{N} = (N_1^1, N_2^1, N_3^1, \dots, N_1^K, N_2^K, N_3^K)$, consisting of vector-functions \mathbf{v}_N with components v_{N_i} ($i=1, 2, 3$), which are polynomials with respect to the variable x_3 in each layer Ω_k ,

$$v_{Ni} = v_{Ni}^k = \sum_{r_i^k=0}^{N_i^k} \frac{1}{h_k} \left(r_i^k + \frac{1}{2} \right) v_{Ni}^{r_i^k} P_{r_i^k}(z^k) \quad \text{in } \Omega_k, \quad v_{Ni}^{r_i^k} \in L^2(\omega), \quad 0 \leq r_i^k \leq N_i^k, \quad N_i^k \in \mathbb{N} \cup \{0\}, \quad i=1,2,3,$$

where $z^k = \frac{x_3 - \bar{h}_k}{h_k}$, $h_k = \frac{h_k^+ - h_k^-}{2}$, $\bar{h}_k = \frac{h_k^+ + h_k^-}{2}$, $k=1, \dots, K$, and P_r denotes the Legendre polynomial of order $r \in \mathbb{N} \cup \{0\}$. We also consider the subspaces $V_{N_\varphi}^\varphi(\Omega)$, $N_\varphi = (N_\varphi^1, N_\varphi^2, \dots, N_\varphi^K)$, and $V_{N_\psi}^\psi(\Omega)$, $N_\psi = (N_\psi^1, N_\psi^2, \dots, N_\psi^K)$, of $V^\varphi(\Omega)$ and $V^\psi(\Omega)$, respectively, which consist of the following functions

$$\bar{\varphi}_{N_\varphi} = \bar{\varphi}_{N_\varphi}^k = \sum_{r_\varphi^k=0}^{N_\varphi^k} \frac{1}{h_k} \left(r_\varphi^k + \frac{1}{2} \right) \bar{\varphi}_{N_\varphi}^{r_\varphi^k} P_{r_\varphi^k}(z^k) \quad \text{in } \Omega_k, \quad \bar{\varphi}_{N_\varphi}^{r_\varphi^k} \in L^2(\omega), \quad 0 \leq r_\varphi^k \leq N_\varphi^k, \quad N_\varphi^k \in \mathbb{N} \cup \{0\},$$

$$\bar{\psi}_{N_\psi} = \bar{\psi}_{N_\psi}^k = \sum_{r_\psi^k=0}^{N_\psi^k} \frac{1}{h_k} \left(r_\psi^k + \frac{1}{2} \right) \bar{\psi}_{N_\psi}^{r_\psi^k} P_{r_\psi^k}(z^k) \quad \text{in } \Omega_k, \quad \bar{\psi}_{N_\psi}^{r_\psi^k} \in L^2(\omega), \quad 0 \leq r_\psi^k \leq N_\psi^k, \quad N_\psi^k \in \mathbb{N} \cup \{0\},$$

and subspaces $V_{N_\theta}^\theta(\Omega)$ and $H_{N_\theta}^\theta(\Omega)$ of $H_0^1(\Omega)$ and $L^2(\Omega)$, consisting of the functions

$$\bar{\theta}_{N_\theta} = \bar{\theta}_{N_\theta}^k = \sum_{r_\theta^k=0}^{N_\theta^k} \frac{1}{h_k} \left(r_\theta^k + \frac{1}{2} \right) \bar{\theta}_{N_\theta}^{r_\theta^k} P_{r_\theta^k}(z^k) \quad \text{in } \Omega_k, \quad \bar{\theta}_{N_\theta}^{r_\theta^k} \in L^2(\omega), \quad 0 \leq r_\theta^k \leq N_\theta^k,$$

where $N_\theta^k \in \mathbb{N} \cup \{0\}$, $k=2, \dots, K-1$, $N_\theta^1 \geq 1$, $N_\theta^K \geq 1$, for $K \geq 2$, and $N_\theta^1 \in \mathbb{N}$, $N_\theta^1 \geq 2$, for $K=1$.

Since the functions h_k^+ and h_k^- are Lipschitz continuous in ω from Rademacher's theorem [14] we have that h_k^+ and h_k^- are differentiable almost everywhere in ω and $\partial_\alpha h_k^\pm \in L^\infty(\omega^*)$ for all subdomains ω^* , $\overline{\omega^*} \subset \omega$, $\alpha=1,2$. Therefore, the positiveness of h_k in ω implies that for

any vector-function $\mathbf{v}_N = (v_{Ni})_{i=1}^3 \in \mathbf{V}_N(\Omega)$ the corresponding functions $v_{Ni}^{r_i^k} \in H^1(\omega^*)$, for all ω^* , $\overline{\omega^*} \subset \omega$, i.e. $v_{Ni}^{r_i^k} \in H_{loc}^1(\omega)$, $0 \leq r_i^k \leq N_i^k$, $i=1,2,3$, $k=1, \dots, K$. Similarly, for all functions

$\bar{\varphi}_{N_\varphi} \in V_{N_\varphi}^\varphi(\Omega)$, $\bar{\psi}_{N_\psi} \in V_{N_\psi}^\psi(\Omega)$, $\bar{\theta}_{N_\theta} \in V_{N_\theta}^\theta(\Omega)$, the functions $\bar{\varphi}_{N_\varphi}^{r_\varphi^k}$, $\bar{\psi}_{N_\psi}^{r_\psi^k}$, $\bar{\theta}_{N_\theta}^{r_\theta^k}$ of two space

variables in the expressions of $\bar{\varphi}_{N_\varphi}$, $\bar{\psi}_{N_\psi}$, $\bar{\theta}_{N_\theta}$ belong to $H^1(\omega^*)$, $\overline{\omega^*} \subset \omega$, i.e. $\bar{\varphi}_{N_\varphi}^{r_\varphi^k}$, $\bar{\psi}_{N_\psi}^{r_\psi^k}$,

$\bar{\theta}_{N_\theta}^{r_\theta^k} \in H_{loc}^1(\omega)$, $r_\varphi^k = 0, \dots, N_\varphi^k$, $r_\psi^k = 0, \dots, N_\psi^k$, $r_\theta^k = 0, \dots, N_\theta^k$. Moreover, the norms $\|\cdot\|_{\mathbf{H}^1(\Omega)}$ and $\|\cdot\|_{H^1(\Omega)}$ in the spaces $\mathbf{H}^1(\Omega)$ and $H^1(\Omega)$ define weighted norms $\|\cdot\|_*$ and $\|\cdot\|_{\varphi^*}$, $\|\cdot\|_{\psi^*}$, $\|\cdot\|_{\theta^*}$

of vector-functions $\vec{v}_N = (v_{Ni}^{r_i^k}) \in [H_{loc}^1(\omega)]^{N_{1,2,3}^K}$, $N_{1,2,3}^K = \sum_{k=1}^K (N_1^k + N_2^k + N_3^k + 3)$, and $\vec{\bar{\varphi}}_{N_\varphi} = (\bar{\varphi}_{N_\varphi}^{r_\varphi^k}) \in$

$[H_{loc}^1(\omega)]^{\tilde{N}_\varphi^K}$, $\tilde{N}_\varphi^K = \sum_{k=1}^K (N_\varphi^k + 1)$, $\vec{\bar{\psi}}_{N_\psi} = (\bar{\psi}_{N_\psi}^{r_\psi^k}) \in [H_{loc}^1(\omega)]^{\tilde{N}_\psi^K}$, $\tilde{N}_\psi^K = \sum_{k=1}^K (N_\psi^k + 1)$, $\vec{\bar{\theta}}_{N_\theta} = (\bar{\theta}_{N_\theta}^{r_\theta^k}) \in$

$[H^1_{loc}(\omega)]^{\tilde{N}^k_\theta}$, $\tilde{N}^K_\theta = \sum_{k=1}^K (N^k_\theta + 1)$, such that $\|\vec{v}_N\|_* = \|\mathbf{v}_N\|_{\mathbf{H}^1(\Omega)}$ and $\|\vec{\bar{\varphi}}_{N_\varphi}\|_{\varphi^*} = \|\bar{\varphi}_{N_\varphi}\|_{H^1(\Omega)}$, $\|\vec{\bar{\psi}}_{N_\psi}\|_{\psi^*} = \|\bar{\psi}_{N_\psi}\|_{H^1(\Omega)}$, $\|\vec{\bar{\theta}}_{N_\theta}\|_{\theta^*} = \|\bar{\theta}_{N_\theta}\|_{H^1(\Omega)}$. Using the properties of the Legendre polynomials we can obtain explicit expressions of the norms $\|\cdot\|_*$ and $\|\cdot\|_{\varphi^*}$, $\|\cdot\|_{\psi^*}$, $\|\cdot\|_{\theta^*}$. In particular, $\|\cdot\|_*$ is given by the following expression:

$$\begin{aligned}
 \|\vec{v}_N\|_*^2 = & \sum_{k=1}^K \sum_{i=1}^3 \sum_{r_i^k=0}^{N_i^k} \left(r_i^k + \frac{1}{2} \right) \left[\left\| \sum_{s_i^k=r_i^k}^{N_i^k} \left(s_i^k + \frac{1}{2} \right) (1 - (-1)^{r_i^k+s_i^k}) h_k^{-3/2} v_{Ni}^k \right\|_{L^2(\omega)}^2 + \left\| h_k^{-1/2} v_{Ni}^k \right\|_{L^2(\omega)}^2 + \right. \\
 & \left. \sum_{\alpha=1}^2 \left\| \sum_{s_i^k=r_i^k+1}^{N_i^k} \left(s_i^k + \frac{1}{2} \right) (\partial_\alpha h_k^+ - (-1)^{r_i^k+s_i^k} \partial_\alpha h_k^-) h_k^{-3/2} v_{Ni}^k - h_k^{-1/2} \partial_\alpha v_{Ni}^k + (r_i^k + 1) h_k^{-3/2} \partial_\alpha h_k v_{Ni}^k \right\|_{L^2(\omega)}^2 \right].
 \end{aligned}$$

For components v_{Ni}^k and $\bar{\varphi}_{N_\varphi}^k$, $\bar{\psi}_{N_\psi}^k$, $\bar{\theta}_{N_\theta}^k$ of \vec{v}_N and $\vec{\bar{\varphi}}_{N_\varphi}$, $\vec{\bar{\psi}}_{N_\psi}$, $\vec{\bar{\theta}}_{N_\theta}$, which possess the properties $\|\vec{v}_N\|_* < \infty$ and $\|\vec{\bar{\varphi}}_{N_\varphi}\|_{\varphi^*} < \infty$, $\|\vec{\bar{\psi}}_{N_\psi}\|_{\psi^*} < \infty$, $\|\vec{\bar{\theta}}_{N_\theta}\|_{\theta^*} < \infty$ we can define the traces on $\tilde{\gamma}$. Indeed, the corresponding vector-function of three space variables $\mathbf{v}_N = (v_{Ni})_{i=1}^3$ and functions $\bar{\varphi}_{N_\varphi}$, $\bar{\psi}_{N_\psi}$, $\bar{\theta}_{N_\theta}$ belong to the spaces $\mathbf{V}_N(\Omega) \subset \mathbf{H}^1(\Omega)$ and $V_{N_\varphi}^\varphi(\Omega)$, $V_{N_\psi}^\psi(\Omega)$, $V_{N_\theta}^\theta(\Omega) \subset H^1(\Omega)$, respectively, and using the trace operator $tr_{\tilde{\Gamma}_k}^*$ we define the traces of v_{Ni}^k and $\bar{\varphi}_{N_\varphi}^k$, $\bar{\psi}_{N_\psi}^k$, $\bar{\theta}_{N_\theta}^k$ on $\tilde{\gamma}$, in particular,

$$tr_{\tilde{\gamma}}^*(v_{Ni}^k) = \int_{h^-}^{h^+} tr_{\tilde{\Gamma}_k}^*(v_{Ni}^k) P_{r_i^k}(z^k) dx_3, \quad r_i^k = 0, \dots, N_i^k, \quad i = 1, 2, 3, \quad k = 1, \dots, K.$$

Since the vector-functions \mathbf{v}_N from the subspaces $\mathbf{V}_N(\Omega)$ and $\mathbf{H}_N(\Omega)$, and the functions $\bar{\varphi}_{N_\varphi} \in V_{N_\varphi}^\varphi(\Omega)$, $\bar{\psi}_{N_\psi} \in V_{N_\psi}^\psi(\Omega)$, and $\bar{\theta}_{N_\theta}$ from $V_{N_\theta}^\theta(\Omega)$ and $H_{N_\theta}^\theta(\Omega)$ are uniquely defined by the functions v_{Ni}^k , $\bar{\varphi}_{N_\varphi}^k$, $\bar{\psi}_{N_\psi}^k$, $\bar{\theta}_{N_\theta}^k$ of two space variables, hence considering the original three-dimensional problem (15)-(19) on these subspaces, we obtain the following hierarchy of two-dimensional initial-boundary value problems: Find $\vec{u}_N \in C([0, T]; \vec{V}_N(\omega))$, $\vec{u}'_N \in C([0, T]; \vec{H}_N(\omega))$, $\vec{\varphi}_{N_\varphi} \in C([0, T]; \vec{V}_{N_\varphi}^\varphi(\omega))$, $\vec{\psi}_{N_\psi} \in C([0, T]; \vec{V}_{N_\psi}^\psi(\omega))$, $\vec{\theta}_{N_\theta} \in L^2(0, T; \vec{V}_{N_\theta}^\theta(\omega))$, $\vec{\theta}'_{N_\theta} \in L^2(0, T; (\vec{V}_{N_\theta}^\theta(\omega))')$, which satisfy the following equations in the sense of distributions on $(0, T)$,

$$\frac{d}{dt} R_N(\vec{u}'_N, \vec{v}_N) + c_N(\vec{u}_N, \vec{v}_N) + \varepsilon_{N_\varphi N}(\vec{\varphi}_{N_\varphi}, \vec{v}_N) + b_{N_\psi N}(\vec{\psi}_{N_\psi}, \vec{v}_N) - \lambda_{N_\theta N}(\vec{\theta}_{N_\theta}, \vec{v}_N) = L_N^u(\vec{v}_N), \quad (20)$$

$$-\varepsilon_{N_\varphi N}(\vec{\bar{\varphi}}_{N_\varphi}, \vec{u}_N) + d_{N_\varphi}(\vec{\varphi}_{N_\varphi}, \vec{\bar{\varphi}}_{N_\varphi}) + a_{N_\varphi N_\psi}(\vec{\psi}_{N_\psi}, \vec{\bar{\varphi}}_{N_\varphi}) = L_{N_\varphi}^\varphi(\vec{\bar{\varphi}}_{N_\varphi}), \quad (21)$$

$$-b_{N_\psi N}(\vec{\bar{\psi}}_{N_\psi}, \vec{u}_N) + a_{N_\varphi N_\psi}(\vec{\varphi}_{N_\varphi}, \vec{\bar{\psi}}_{N_\psi}) + \zeta_{N_\psi}(\vec{\psi}_{N_\psi}, \vec{\bar{\psi}}_{N_\psi}) = L_{N_\psi}^\psi(\vec{\bar{\psi}}_{N_\psi}), \quad (22)$$

$$\frac{d}{dt} R_{N_\theta}^\theta(\vec{\theta}_{N_\theta}, \vec{\theta}_{N_\theta}) + \eta_{N_\theta}(\vec{\theta}_{N_\theta}, \vec{\theta}_{N_\theta}) + \Theta_0 \lambda_{N_\theta N}(\vec{\theta}_{N_\theta}, \vec{u}'_N) = L_{N_\theta}^\theta(\vec{\theta}_{N_\theta}), \quad (23)$$

for all $\vec{v}_N \in \vec{V}_N(\omega)$, $\vec{\varphi}_{N_\varphi} \in \vec{V}_{N_\varphi}^\varphi(\omega)$, $\vec{\psi}_{N_\psi} \in \vec{V}_{N_\psi}^\psi(\omega)$, $\vec{\theta}_{N_\theta} \in \vec{V}_{N_\theta}^\theta(\omega)$, and the initial conditions

$$\vec{u}_N(0) = \vec{u}_{N_0}, \quad \vec{u}'_N(0) = \vec{u}_{N_1}, \quad \vec{\theta}_{N_\theta}(0) = \vec{\theta}_{N_\theta 0}, \quad (24)$$

where $\vec{V}_N(\omega) = \{\vec{v}_N = (v_{N_i}^k) \in [H_{loc}^1(\omega)]^{N_{1,2,3}^K}; \|\vec{v}_N\|_* < \infty, tr_{\tilde{\gamma}}(v_{N_i}^k) = 0 \text{ on } \tilde{\gamma}_{0,k}, r_i^k = 0, \dots, N_i^k, i = 1, 2, 3,$

$k = 1, \dots, K, \mathbf{tr}_{\Gamma_k^+}(\mathbf{v}_N^{\tilde{k}}) = \mathbf{tr}_{\Gamma_k^+}(\mathbf{v}_N^{\tilde{k}+1}), \tilde{k} = 1, \dots, K-1\}$, $\vec{H}_N(\omega) = \{\vec{v}_N \in [L^2(\omega)]^{N_{1,2,3}^K}; \|\vec{v}_N\|_{\vec{H}_N(\omega)}^2 =$

$\sum_{k=1}^K \sum_{i=1}^3 \sum_{r_i^k=0}^{N_i^k} \left\| h_k^{-1/2} v_{N_i}^{r_i^k} \right\|_{L^2(\omega)}^2 < \infty\}$, $\vec{V}_{N_\varphi}^\varphi(\omega) = \{\vec{\varphi}_{N_\varphi} = (\varphi_{N_\varphi}^{r_\varphi^k}) \in [H_{loc}^1(\omega)]^{N_\varphi^K}; \|\vec{\varphi}_{N_\varphi}\|_{\varphi^*} < \infty, tr_{\tilde{\gamma}}(\varphi_{N_\varphi}^{r_\varphi^k}) = 0$

on $\tilde{\gamma}_{0,k}^\varphi, r_\varphi^k = 0, \dots, N_\varphi^k, k = 1, \dots, K, tr_{\Gamma_k^+}(\varphi_{N_\varphi}^{\tilde{k}}) = tr_{\Gamma_k^+}(\varphi_{N_\varphi}^{\tilde{k}+1}), \tilde{k} = 1, \dots, K-1\}$, $\vec{V}_{N_\psi}^\psi(\omega) = \{\vec{\psi}_{N_\psi} = (\psi_{N_\psi}^{r_\psi^k}) \in$

$[H_{loc}^1(\omega)]^{N_\psi^K}; \|\vec{\psi}_{N_\psi}\|_{\psi^*} < \infty, tr_{\tilde{\gamma}}(\psi_{N_\psi}^{r_\psi^k}) = 0 \text{ on } \tilde{\gamma}_{0,k}^\psi, r_\psi^k = 0, \dots, N_\psi^k, k = 1, \dots, K, tr_{\Gamma_k^+}(\psi_{N_\psi}^{\tilde{k}}) = tr_{\Gamma_k^+}(\psi_{N_\psi}^{\tilde{k}+1}),$

$\tilde{k} = 1, \dots, K-1\}$, $\vec{V}_{N_\theta}^\theta(\omega) = \{\vec{\theta}_{N_\theta} = (\theta_{N_\theta}^{r_\theta^k}) \in [H_{loc}^1(\omega)]^{N_\theta^K}; \|\vec{\theta}_{N_\theta}\|_{\theta^*} < \infty, tr_{\tilde{\gamma}}(\theta_{N_\theta}^{r_\theta^k}) = 0 \text{ on } \tilde{\gamma}, r_\theta^k = 0, \dots, N_\theta^k,$
 $k = 1, \dots, K, \bar{\theta}_{N_\theta}^1 = 0 \text{ on } \Gamma_1^-, \bar{\theta}_{N_\theta}^K = 0 \text{ on } \Gamma_K^+, tr_{\Gamma_k^+}(\bar{\theta}_{N_\theta}^{\tilde{k}}) = tr_{\Gamma_k^+}(\bar{\theta}_{N_\theta}^{\tilde{k}+1}), \tilde{k} = 1, \dots, K-1\}$, $\vec{H}_{N_\theta}^\theta(\omega) = \{\vec{\theta}_{N_\theta} \in$

$[L^2(\omega)]^{N_\theta^K}; \|\vec{\theta}_{N_\theta}\|_{\vec{H}_{N_\theta}^\theta(\omega)}^2 = \sum_{k=1}^K \sum_{r_\theta^k=0}^{N_\theta^k} \left\| h_k^{-1/2} \theta_{N_\theta}^{r_\theta^k} \right\|_{L^2(\omega)}^2 < \infty\}$, the bilinear forms $R_N, c_N, \varepsilon_{N_\varphi N}, b_{N_\psi N}, \lambda_{N_\theta N},$

$d_{N_\varphi}, a_{N_\varphi N_\psi}, \zeta_{N_\psi}, R_{N_\theta}^\theta, \eta_{N_\theta}$ are defined as follows $R_N(\vec{v}_N, \vec{v}_N) = (\mathbf{P}^G \tilde{\mathbf{v}}_N, \mathbf{v}_N)_{L^2(\Omega)},$

$c_N(\vec{v}_N, \vec{v}_N) = c(\tilde{\mathbf{v}}_N, \mathbf{v}_N), \varepsilon_{N_\varphi N}(\vec{\varphi}_{N_\varphi}, \vec{v}_N) = \varepsilon(\bar{\varphi}_{N_\varphi}, \mathbf{v}_N), b_{N_\psi N}(\vec{\psi}_{N_\psi}, \vec{v}_N) = b(\bar{\psi}_{N_\psi}, \mathbf{v}_N), \lambda_{N_\theta N}(\vec{\theta}_{N_\theta}, \vec{v}_N) =$

$\lambda(\bar{\theta}_{N_\theta}, \mathbf{v}_N), \lambda_{N_\theta N}(\vec{\theta}_{N_\theta}, \vec{v}_N) = \lambda(\bar{\theta}_{N_\theta}, \mathbf{v}_N), d_{N_\varphi}(\vec{\varphi}_{N_\varphi}, \vec{\varphi}_{N_\varphi}) = d(\tilde{\varphi}_{N_\varphi}, \bar{\varphi}_{N_\varphi}), a_{N_\varphi N_\psi}(\vec{\varphi}_{N_\varphi}, \vec{\psi}_{N_\psi}) =$

$a(\bar{\varphi}_{N_\varphi}, \bar{\psi}_{N_\psi}), \zeta_{N_\psi}(\vec{\psi}_{N_\psi}, \vec{\psi}_{N_\psi}) = \zeta(\tilde{\psi}_{N_\psi}, \bar{\psi}_{N_\psi}), R_{N_\theta}^\theta(\vec{\theta}_{N_\theta}, \vec{\theta}_{N_\theta}) = (\chi^G \tilde{\theta}_{N_\theta}, \bar{\theta}_{N_\theta})_{L^2(\Omega)}, \eta_{N_\theta}(\vec{\theta}_{N_\theta}, \vec{\theta}_{N_\theta}) =$

$\eta(\tilde{\theta}_{N_\theta}, \bar{\theta}_{N_\theta}),$ for all vector-functions $\vec{v}_N, \vec{v}_N \in \vec{V}_N(\omega), \vec{\varphi}_{N_\varphi}, \vec{\varphi}_{N_\varphi} \in \vec{V}_{N_\varphi}^\varphi(\omega), \vec{\psi}_{N_\psi}, \vec{\psi}_{N_\psi} \in \vec{V}_{N_\psi}^\psi(\omega),$

$\vec{\theta}_{N_\theta}, \vec{\theta}_{N_\theta} \in \vec{V}_{N_\theta}^\theta(\omega),$ corresponding to $\tilde{\mathbf{v}}_N, \mathbf{v}_N \in \mathbf{V}_N(\Omega), \tilde{\varphi}_{N_\varphi}, \bar{\varphi}_{N_\varphi} \in V_{N_\varphi}^\varphi(\Omega), \tilde{\psi}_{N_\psi}, \bar{\psi}_{N_\psi} \in V_{N_\psi}^\psi(\Omega),$

$\tilde{\theta}_{N_\theta}, \bar{\theta}_{N_\theta} \in V_{N_\theta}^\theta(\Omega),$ respectively. The linear forms $L_N^u, L_{N_\varphi}^\varphi, L_{N_\psi}^\psi$ and $L_{N_\theta}^\theta$ are given by the

following expressions:

$$L_N^u(\vec{v}_N) = \sum_{k=1}^K \sum_{i=1}^3 \sum_{r_i^k=0}^{N_i^k} \left(r_i^k + \frac{1}{2} \right) \left[\int_\omega \frac{1}{h_k} v_{N_i}^{r_i^k} \left(f_i^{k,G} + g_i^{k,G,+} \lambda_{k,+} + g_i^{k,G,-} \lambda_{k,-} (-1)^{r_i^k} \right) d\omega + \int_{\gamma_{1,k}} \frac{1}{h_k} tr_{\tilde{\gamma}_k} (v_{N_i}^{r_i^k}) g_i^{k,G} d\gamma_{1,k} \right],$$

$$L_{N_\varphi}^\varphi(\vec{\varphi}_{N_\varphi}) = \sum_{k=1}^K \sum_{r_\varphi^k=0}^{N_\varphi^k} \left(r_\varphi^k + \frac{1}{2} \right) \left[\int_\omega \frac{1}{h_k} \varphi_{N_\varphi}^{r_\varphi^k} \left(f^{\varphi,k,G} - g^{\varphi,k,G,+} \lambda_{k,+} - g^{\varphi,k,G,-} \lambda_{k,-} (-1)^{r_\varphi^k} \right) d\omega - \int_{\gamma_{1,k}^\varphi} \frac{1}{h_k} tr_{\tilde{\gamma}_k} (\varphi_{N_\varphi}^{r_\varphi^k}) g^{\varphi,k,G} d\gamma_{1,k}^\varphi \right],$$

$$L_{N_\psi}^\psi(\vec{\bar{\psi}}_{N_\psi}) = - \sum_{k=1}^K \sum_{r_\psi^k=0}^{N_\psi^k} \left(r_\psi^k + \frac{1}{2} \right) \left[\int_{\omega} \frac{1}{h_k} \vec{\bar{\psi}}_{N_\psi} \left(g^{\psi,k,G,+} \lambda_{k,+} + g^{\psi,k,G,-} \lambda_{k,-} (-1)^{r_\psi^k} \right) d\omega + \int_{\gamma_{1,k}^\psi} \frac{1}{h_k} tr_{\tilde{\gamma}_k}^{r_\psi^k}(\vec{\bar{\psi}}_{N_\psi}) g^{\psi,k,G} d\gamma_{1,k}^\psi \right],$$

$$L_{N_\theta}^\theta(\vec{\bar{\theta}}_{N_\theta}) = \sum_{k=1}^K \sum_{r_\theta^k=0}^{N_\theta^k} \left(r_\theta^k + \frac{1}{2} \right) \int_{\omega} \frac{1}{h_k} \vec{\bar{\theta}}_{N_\theta}^{r_\theta^k} f^{\theta,k,G} d\omega,$$

where $f_i^{k,G} = f^i \sqrt{G}$, $f^{\varphi,k,G} = f^\varphi \sqrt{G}$, $f^{\theta,k,G} = f^\theta \sqrt{G}$ in Ω_k , $g_i^{k,G} = g^i \sqrt{G}$ on $\Gamma_1 \cap \partial\Omega_k$, $g^{\varphi,k,G} = g^\varphi \sqrt{G}$ on $\Gamma_1^\varphi \cap \partial\Omega_k$, $g^{\psi,k,G} = g^\psi \sqrt{G}$ on $\Gamma_1^\psi \cap \partial\Omega_k$, $g_i^{k,G,\pm}(x_1, x_2) = g^i(x_1, x_2, x_3) \sqrt{G}$, for $(x_1, x_2, x_3) \in \Gamma^{k,\pm} \cap \Gamma_1$, $g^{\varphi,k,G,\pm}(x_1, x_2) = g^\varphi(x_1, x_2, x_3) \sqrt{G}$, for $(x_1, x_2, x_3) \in \Gamma^{k,\pm} \cap \Gamma_1^\varphi$, $g^{\psi,k,G,\pm}(x_1, x_2) = g^\psi(x_1, x_2, x_3) \sqrt{G}$, for $(x_1, x_2, x_3) \in \Gamma^{k,\pm} \cap \Gamma_1^\psi$, and otherwise $g_i^{k,G,\pm} \equiv g^{\varphi,k,G,\pm} \equiv g^{\psi,k,G,\pm} \equiv 0$, $\gamma_{1,k} = \tilde{\gamma}_k \setminus \tilde{\gamma}_{0,k}^+$, $\gamma_{1,k}^\varphi = \tilde{\gamma}_k \setminus \tilde{\gamma}_{0,k}^\varphi$, $\gamma_{1,k}^\psi = \tilde{\gamma}_k \setminus \tilde{\gamma}_{0,k}^\psi$, $\lambda_{k,\pm} = \sqrt{1 + (\partial_1 h_k^\pm)^2 + (\partial_2 h_k^\pm)^2}$, $k=1, \dots, K$, $v^k = \int_{h_k^-}^{h_k^+} v^k P_r(z_k) dx_3$, for all functions $v^k \in L^2(\Omega_k)$, $r \in \mathbf{N} \cup \{0\}$.

For the constructed two-dimensional initial-boundary value problem (20)-(24) for thermoelastic piezoelectric shell the following existence and uniqueness theorem is proved.

Theorem 1. Suppose that $\Omega \subset \mathbf{R}^3$ is a bounded Lipschitz domain, $\tilde{\gamma}_0^\varphi \neq \emptyset$, $\tilde{\gamma}_0^\psi \neq \emptyset$, $\rho, \chi \in L^\infty(\Omega)$, $\rho(x) > \alpha_\rho = \text{const} > 0$, $\chi(x) > \alpha_\chi = \text{const} > 0$, for almost all $x \in \Omega$, c_{ijpq} , ε_{pij} , b_{pij} , d_{ij} , ζ_{ij} , a_{ij} , η_{ij} , $\lambda_{ij} \in L^\infty(\Omega)$, $\partial \lambda_{ij} / \partial x_q \in L^3(\Omega)$, $i, j, p, q = 1, 2, 3$, and conditions (14) and

$$\sum_{i,j,p,q=1}^3 c_{ijpq} \xi_{ij} \xi_{pq} \geq \alpha_c \sum_{i,j=1}^3 (\xi_{ij})^2, \quad \forall \xi_{ij} \in \mathbf{R}, \xi_{ij} = \xi_{ji}, \quad \sum_{i,j=1}^3 \eta_{ij} \xi_i \xi_j \geq \alpha_\eta \sum_{i=1}^3 (\xi_i)^2, \quad \forall \xi_i \in \mathbf{R},$$

$$\sum_{i,j=1}^3 d_{ij} \xi_j \xi_i + 2 \sum_{i,j=1}^3 a_{ij} \bar{\xi}_j \xi_i + \sum_{i,j=1}^3 \zeta_{ij} \bar{\xi}_j \bar{\xi}_i \geq \alpha \sum_{i=1}^3 ((\xi_i)^2 + (\bar{\xi}_i)^2), \quad \forall \xi_i, \bar{\xi}_i \in \mathbf{R},$$

are fulfilled. If the given functions satisfy the following conditions

$$h_k^{-1/2} f_i^k \in L^2(0, T; L^2(\omega)), \quad \lambda_{k,\pm}^{3/4} \frac{d^\alpha g_i^{k,G,\pm}}{dt^\alpha} \in L^2(0, T; L^{4/3}(\omega)), \quad h_k^{-1/4} \frac{d^\alpha g_i^{k,G}}{dt^\alpha} \in L^2(0, T; L^{4/3}(\gamma_{1,k})),$$

$$h_k^{-1/6} \frac{d^\alpha f^{\varphi,k}}{dt^\alpha} \in L^2(0, T; L^{6/5}(\omega)), \quad \lambda_{k,\pm}^{3/4} \frac{d^\alpha g^{\varphi,k,G,\pm}}{dt^\alpha} \in L^2(0, T; L^{4/3}(\omega)), \quad h_k^{-1/4} \frac{d^\alpha g^{\varphi,k,G}}{dt^\alpha} \in L^2(0, T; L^{4/3}(\gamma_{1,k}^\varphi)),$$

$$\lambda_{k,\pm}^{3/4} \frac{d^\alpha g^{\psi,k,G,\pm}}{dt^\alpha} \in L^2(0, T; L^{4/3}(\omega)), \quad h_k^{-1/4} \frac{d^\alpha g^{\psi,k,G}}{dt^\alpha} \in L^2(0, T; L^{4/3}(\gamma_{1,k}^\psi)), \quad h_k^{-1/6} \frac{d^\alpha f^{\theta,k,G}}{dt^\alpha} \in L^2(0, T; L^{6/5}(\omega)),$$

where $\alpha = 0, 1$, $r_i^k = 0, \dots, N_i^k$, $i = 1, 2, 3$, $r_\varphi^k = 0, \dots, N_\varphi^k$, $r_\psi^k = 0, \dots, N_\psi^k$, $r_\theta^k = 0, \dots, N_\theta^k$, $k = 1, \dots, K$, and $\vec{u}_{N_0} \in \vec{V}_N(\omega)$, $\vec{u}_{N_1} \in \vec{H}_N(\omega)$, $\vec{\theta}_{N_\theta} \in \vec{H}_{N_\theta}^\theta(\omega)$, then initial-boundary value problem (20)-(24) possesses a unique solution.

In the following theorem we present the results on the relationship between the obtained two-dimensional and original three-dimensional initial-boundary value problems, where we use the following Hilbert spaces

$$H_{h_{1,K}^{\pm}}^{1,1,s}(\Omega) = \{v; \partial_3^{r-1} v \in H^1(\Omega), \partial_\alpha h_k^{\pm} \partial_3^r v \in L^2(\Omega_k), 1 \leq k \leq K, \alpha = 1, 2, r = 1, \dots, s\}, \quad s \in \mathbf{N}.$$

Theorem 2. If $\Omega \subset \mathbf{R}^3$ is a bounded Lipschitz domain, $\tilde{\Gamma}_0^\varphi \neq \emptyset$, $\tilde{\Gamma}_0^\psi \neq \emptyset$, $\mathbf{u}_0 \in \mathbf{V}(\Omega)$, $\mathbf{u}_1 \in \mathbf{L}^2(\Omega)$, $\theta_0 \in L^2(\Omega)$, $\mathbf{f} = (f^i)_{i=1}^3 \in L^2(0, T; \mathbf{L}^2(\Omega))$, $\mathbf{g} = (g^i)_{i=1}^3, \mathbf{g}' \in L^2(0, T; \mathbf{L}^{4/3}(\Gamma_1))$, $f^\varphi, (f^\varphi)' \in L^2(0, T; L^{6/5}(\Omega))$, $g^\varphi, (g^\varphi)' \in L^2(0, T; L^{4/3}(\Gamma_1^\varphi))$, $g^\psi, (g^\psi)' \in L^2(0, T; L^{4/3}(\Gamma_1^\psi))$, $f^\theta \in L^2(0, T; L^{6/5}(\Omega))$, $\rho, \chi \in L^\infty(\Omega)$, $\rho(x) > \alpha_\rho = \text{const} > 0$, $\chi(x) > \alpha_\chi = \text{const} > 0$, for almost all $x \in \Omega$, $c_{ijpq}, \varepsilon_{pji}, b_{pji}, d_{ij}, \zeta_{ij}, a_{ij}, \eta_{ij}, \lambda_{ij} \in L^\infty(\Omega)$, $\partial \lambda_{ij} / \partial x_q \in L^3(\Omega)$, $i, j, p, q = 1, 2, 3$, conditions (14), (25) are fulfilled, and the functions $\mathbf{u}_{N_0} \in \mathbf{V}_N(\Omega)$, $\mathbf{u}_{N_1} \in \mathbf{H}_N(\Omega)$, $\theta_{N_{\theta 0}} \in H_{N_{\theta}}^\theta(\Omega)$, corresponding to the initial conditions $\bar{u}_{N_0} \in \bar{V}_N(\omega)$, $\bar{u}_{N_1} \in \bar{H}_N(\omega)$, $\bar{\theta}_{N_{\theta 0}} \in \bar{H}_{N_{\theta}}^\theta(\omega)$ of the two-dimensional problems, tend to $\mathbf{u}_0, \mathbf{u}_1$ and θ_0 in the spaces $\mathbf{H}^1(\Omega)$, $\mathbf{L}^2(\Omega)$ and $L^2(\Omega)$, respectively, as $N_{\min} = \min_{1 \leq k \leq K, 1 \leq i \leq 3} \{N_i^k, N_\varphi^k, N_\psi^k, N_\theta^k\} \rightarrow \infty$, then three-dimensional problem (15)-(19) possesses a unique solution and functions $\mathbf{u}_N(t)$, $\varphi_{N_\varphi}(t)$, $\psi_{N_\psi}(t)$, $\theta_{N_\theta}(t)$ restored from the solutions \bar{u}_N , $\bar{\varphi}_{N_\varphi}$, $\bar{\psi}_{N_\psi}$, $\bar{\theta}_{N_\theta}$ of two-dimensional problem (20)-(24), possess the following properties

$$\begin{aligned} \mathbf{u}_N(t) &\rightarrow \mathbf{u}(t) && \text{in } \mathbf{H}^1(\Omega), \\ \mathbf{u}'_N(t) &\rightarrow \mathbf{u}'(t) && \text{in } \mathbf{L}^2(\Omega), \\ \theta_{N_\theta}(t) &\rightarrow \theta(t) && \text{in } L^2(\Omega), \end{aligned} \quad \begin{aligned} \varphi_{N_\varphi}(t) &\rightarrow \varphi(t) && \text{in } H^1(\Omega), \\ \psi_{N_\psi}(t) &\rightarrow \psi(t) && \text{in } H^1(\Omega), \end{aligned} \quad \text{for all } t \in [0, T], \text{ as } N_{\min} \rightarrow \infty.$$

In addition, if $\|d^r \mathbf{u} / dt^r\|_{L^2(0, T; (H_{h_{1,K}^{\pm}}^{1,1,s_r}(\Omega))^3)} \leq c$, $s_r \in \mathbf{N}$, $r = 0, 1, 2$, $s_0 \geq s_1 \geq s_2 \geq 1$, $s_1 \geq 2$,

$$\|\varphi'\|_{L^2(0, T; H_{h_{1,K}^{\pm}}^{1,1,s_1^\varphi}(\Omega))} \leq c, \|\psi'\|_{L^2(0, T; H_{h_{1,K}^{\pm}}^{1,1,s_1^\psi}(\Omega))} \leq c, s_1^\varphi, s_1^\psi \in \mathbf{N}, s_1^\varphi \geq 2, s_1^\psi \geq 2, \|d^{\bar{r}} \theta / dt^{\bar{r}}\|_{L^2(0, T; H_{h_{1,K}^{\pm}}^{1,1,s_{\bar{r}}^\theta}(\Omega))} \leq c,$$

$c = \text{const} > 0$ is independent of h_k^\pm , $s_{\bar{r}}^\theta \in \mathbf{N}$, $\bar{r} = 0, 1$, $s_0^\theta \geq s_1^\theta \geq 1$, $s_0^\theta \geq 2$, then for suitable initial data \bar{u}_{N_0} , \bar{u}_{N_1} and $\bar{\theta}_{N_{\theta 0}}$ the following estimate is valid

$$\begin{aligned} &\|\mathbf{u} - \mathbf{u}_N\|_{C([0, T]; \mathbf{H}^1(\Omega))} + \|\mathbf{u}' - \mathbf{u}'_N\|_{C([0, T]; \mathbf{L}^2(\Omega))} + \|\varphi - \varphi_{N_\varphi}\|_{C([0, T]; H^1(\Omega))} + \|\psi - \psi_{N_\psi}\|_{C([0, T]; H^1(\Omega))} \\ &+ \|\theta - \theta_{N_\theta}\|_{C([0, T]; L^2(\Omega))} + \|\theta - \theta_{N_\theta}\|_{L^2(0, T; H^1(\Omega))} \leq \frac{(h_{\max})^s}{(N_{\min})^s} o(T, \mathbf{N}, \mathbf{N}_\varphi, \mathbf{N}_\psi, \mathbf{N}_\theta), \end{aligned}$$

where $s = \min\{s_2, s_1 - 1, s_1^\varphi - 1, s_1^\psi - 1, s_1^\theta, s_0^\theta - 1\}$, $h_{\max} = \max_{(x_1, x_2) \in \omega} \{h_k(x_1, x_2); k = 1, \dots, K\}$,

$o(T, \mathbf{N}, \mathbf{N}_\varphi, \mathbf{N}_\psi, \mathbf{N}_\theta) \rightarrow 0$, as $N_{\min} \rightarrow \infty$.

4 CONCLUSIONS

In this paper, we investigated initial-boundary value problem with mixed boundary

conditions for displacement, electric and magnetic potentials corresponding to linear three-dimensional model for multilayer inhomogeneous anisotropic thermoelastic piezoelectric shell with regard to magnetic field. We obtained a variational formulation of the three-dimensional problem in curvilinear coordinates in corresponding spaces of vector-valued distributions and proved existence and uniqueness of solution. We constructed a hierarchy of two-dimensional models for multilayer thermoelastic piezoelectric shell and studied the existence and uniqueness of solutions of the corresponding initial-boundary value problems. Moreover, we investigated the relationship between the obtained two-dimensional and original three-dimensional models.

5 ACKNOWLEDGEMENT

This work was supported by Shota Rustaveli National Science Foundation (SRNSF) [Grant number 217596, Construction and investigation of hierarchical models for thermoelastic piezoelectric structures].

REFERENCES

- [1] Voigt, W. Piëzo- und Pyroelectricität, diëlectrische Influenz und Electrostriction bei Krystallen ohne Symmetriecentrum. *Abh. der Könighchen Gesellschaft der Wissenschaft zu Göttingen* (1894) **40**:343-372.
- [2] Natroshvili, D. *Mathematical problems of thermo-electro-magneto-elasticity*. Lecture Notes of TICMI, **12**, Tbilisi State University Press, (2011).
- [3] Vekua, I.N. On a way of calculating of prismatic shells. *Proc. of A. Razmadze Inst. Math. of the Georgian Academy of Sciences* (1955) **21**:191-259 (Russian).
- [4] Vekua, I.N. *Shell Theory: General Methods of Construction*. Pitman Advanced Publishing Program, (1985).
- [5] Gordeziani, D.G. To the exactness of one variant of the theory of thin shells. *Dokl. Akad. Nauk SSSR* (1974) **216**, 4:751–754 (in Russian).
- [6] Gordeziani, D.G. On the solvability of some boundary value problems for a variant of the theory of thin shells. *Dokl. Akad. Nauk SSSR* (1974) **215**, 6:1289–1292 (in Russian).
- [7] Jaiani, G.V. On a mathematical model of bars with variable rectangular cross-sections. *Z. Angew. Math. Mech.* (2001) **81**, 3:147-173.
- [8] Dauge, M., Faou, E. and Yosibash, Z. Plates and shells: asymptotic expansions and hierarchical models. *Encyclopedia of Computational Mechanics* (2004) **1**:199-236.
- [9] Avalishvili, G. and Avalishvili, M. On dynamical hierarchical models of multistructures. *Bull. Georgian Natl. Acad. Sci.* (2007) **175**, 2:31-34.
- [10] Avalishvili, G. and Avalishvili, M. On the investigation of one-dimensional models for thermoelastic beams. *Bull. Georgian Natl. Acad. Sci.* (2009) **3**, 3:25-32.
- [11] Avalishvili, G. and Avalishvili, M. On hierarchical models of prismatic shells within the framework of the Chandrasekharaiah-Tzou nonclassical theory of thermoelasticity. *Bull. Georgian Natl. Acad. Sci.* (2013) **7**, 2:33-44.
- [12] McLean, W. *Strongly elliptic systems and boundary integral equations*. Cambridge University Press, (2000).
- [13] Dautray, R. and Lions, J.-L. *Mathematical analysis and numerical methods for science and technology. Vol. 5: Evolution problems I*. Springer-Verlag, (2000).
- [14] Whitney, H. *Geometric integration theory*. Princeton University Press, (1957).

PLATE/SHELL FINITE ELEMENT FOR PIEZOELECTRIC PATCH MODELLING

O. Polit, M. D'Ottavio and P. Vidal

LEME - UPL - Univ. Paris Nanterre

50 rue de Sèvres

92410 Ville d'Avray - France

e-mail: olivier.polit@parisnanterre.fr

Key words: Composite structures, finite element, high-order model, Zig-Zag function, piezoelectric patch analysis

Abstract. This paper presents a C^0 8-node quadrilateral finite element (FE) for geometrically linear piezoelectric plates/shells. It is based on a high-order kinematics proposed in [1] for the mechanical part. The approximation of the electric potential must be able to model piezoelectric patches, and a constant value is considered on each elementary domain while a cubic variation in each layer is used, based on the polynomial expansion given in [2]. Furthermore, Murakami's ZigZag functions [3] is superimposed for the three displacement components for improving the accuracy for multilayered modeling. A plate/shell FE is obtained with nine degrees of freedom (dof) per node for the mechanical part, twelve dofs if the ZigZag functions are included, [4].

This FE is evaluated on some standard piezo-electric plate/shell tests including sensor and actuator configurations. Tests concerning bimorph piezoelectric beam/plate/shell are presented in order to assess the high-order kinematics and the ZigZag effect. The role of electrode segmentation, i.e. the size of equipotential surfaces, on the electro-mechanical response has been also considered.

1 INTRODUCTION

Research and development concerning high-performance structures are very intense since some decades. Structural health monitoring, active vibration damping, and energy harvesting are some examples of possible applications of a multifunctional structural component. Piezoelectric materials permit to convert mechanical and electrical energy at frequency ranges that are most interesting for technical applications such as vibration damping and rapid shape adaptation [5]. Development of theoretical and numerical models for this kind of structures is very important and active. For this purpose and in the framework of two-dimensional plate/shell models, different choices can be made for the mechanical approximation and the following classification is classically admitted for the variation in the thickness direction: (i) Equivalent Single Layer (ESL) models, in which the number of unknowns is independent of the layer number; (ii) Layer-Wise (LW) descriptions, for which the number of unknowns and, thus, the computational cost increases with the number of layers. While most developments employ an ESL description for the mechanical behavior, and particularly the First order Shear Deformation Theory (FSDT), a Layer-Wise description is necessary for the piezoelectric approximation to impose electric boundary conditions at each piezoelectric layer interfaces, i.e., the electrodes, within the stack. Inside each piezoelectric layer, the electric potential can be linear, quadratic or higher and a comparison has been proposed in [6].

A review of different approaches is available in [7, 8] and in the framework of the Carrera Unified Formulation (CUF) in [9]. For the FE approximations, a recent review limited to shell models is also given in [10].

The limitation of the FSDT model is related to the constant transverse displacement hypothesis, inducing no thickness change and the use of the reduced 2D constitutive law. The use of the full 3D constitutive law is an important feature for a consistent representation of complex physical interactions like multi-field coupling. Furthermore, accurate modeling of thick structures needs the transverse normal stress and the 3D constitutive law.

Therefore, a high-order model is chosen with sinus function for the in-plane displacements and quadratic assumption along the thickness of the transverse deflection. Thus, the 3D constitutive law is retained and a parabolic distribution of the transverse shear strains and a non linear variation of the transverse normal strain are recovered. In order to introduce transverse strain discontinuities required to fulfill the interlaminar equilibrium, Murakami's Zig-Zag function (MZZF) [3] is superimposed to the high-order ESL kinematics for the 3 displacement components. Note that MZZF does not depend on the constitutive coefficients and is, hence, attractively simple in conjunction with three-dimensional constitutive laws including multi-field coupling. Based on this kinematics, an 8-node plate Finite Element (FE) is proposed, free of numerical illness such as transverse shear and Poisson lockings, oscillation and spurious mechanics [1]. The approximation of the electric potential must be able to model piezoelectric patches, and a constant value is considered on each elementary domain while a cubic variation in each layer is used, based on the polynomial expansion given in [2, 11].

The paper is organized as follows: Section 2 describes the plate problem, the approximations for the displacement and the electric potential and the system to be solved. The resulting FE are evaluated in Section 3 for a composite plate, in order to talk about the electrode segmentation modelling.

2 Description of the plate problem

2.1 Governing equations

Let us consider a plate occupying the domain $\mathcal{V} = \Omega \times [-\frac{e}{2} \leq z \leq \frac{e}{2}]$ in a Cartesian coordinate system $(x_1, x_2, x_3 = z)$. The plate is defined by an arbitrary surface Ω in the (x_1, x_2) plane, located at the midplane for $z = 0$, and by a constant thickness e .

The displacement is denoted $\vec{u}(x_1, x_2, z)$ and the electric potential is $\phi(x_1, x_2, z)$. $\epsilon_{ij}(x_1, x_2, z)$ and $\vec{E}(x_1, x_2, z)$ are the strain tensor components and the electric field vector, respectively, deduced from primal variables by the geometric relations. Furthermore, $\sigma_{ij}(x_1, x_2, z)$ and $\vec{D}(x_1, x_2, z)$ are the conjugated fluxes (stress tensor components and dielectric displacement vector, respectively) obtained from the constitutive equations given in the next subsection.

2.1.1 Constitutive relation

The 3D constitutive equation for a linear piezoelectric material is given by the following set of coupled equations [12] for a layer (k) :

$$[\sigma^{(k)}] = [C^{(k)}] [\epsilon^{(k)}] - [e^{(k)}]^T [E^{(k)}] \quad (1a)$$

$$[D^{(k)}] = [e^{(k)}] [\epsilon^{(k)}] + [\epsilon^{(k)}] [E^{(k)}] \quad (1b)$$

where we denote by $[C]$ the matrix of elastic stiffness coefficients taken at constant electric field, by $[e]$ the matrix of piezoelectric stress coefficients and by $[\epsilon]$ the matrix of electric permittivity coefficients taken

at constant strain. The explicit form of these matrices can be found in [10] for an orthotropic piezoelectric layer polarized along the thickness direction z . Eq. (1a) expresses the piezoelectric *converse* effect for actuator applications, whereas Eq. (1b) represents the piezoelectric *direct* effect which is exploited in sensor applications. Note that the constitutive law is expressed in the local reference frame associated to each layer.

2.1.2 The weak form of the boundary value problem

The classical piezoelectric variational formulation of [13] is employed in which the primary field variables are the “generalized displacements”, i.e. the displacement field, and the electrostatic potential. Using a matrix notation and for admissible virtual displacements \bar{u}^* and electric potential ϕ^* (virtual quantities are denoted by an asterisk), the variational principle is given by:

$$\begin{aligned} \int_{\mathcal{V}} \rho [u^*]^T [\ddot{u}] d\mathcal{V} = & - \int_{\mathcal{V}} [\epsilon(u^*)]^T [\sigma(u, \phi)] d\mathcal{V} + \int_{\mathcal{V}} [u^*]^T [f] d\mathcal{V} + \int_{\partial\mathcal{V}_F} [u^*]^T [F] d\partial\mathcal{V} \\ & + \int_{\mathcal{V}} [E(\phi^*)]^T [D(u, \phi)] d\mathcal{V} - \int_{\mathcal{V}} q \phi^* d\mathcal{V} - \int_{\partial\mathcal{V}_Q} Q \phi^* d\partial\mathcal{V} \end{aligned} \quad (2)$$

where $[f]$ is the body force vector, $[F]$ the surface force vector applied on $\partial\mathcal{V}_F$, q the volume charge density, Q the surface charge density supplied on $\partial\mathcal{V}_Q$ and ρ is the mass density. Finally, $\epsilon(u^*)$ and $E(\phi^*)$ are the virtual strain and virtual electric field that satisfy the compatibility gradient equations. In the remainder of this article we will refer only to static problems, for which the left-hand side term is set to zero. Furthermore, body forces and volume charge densities will be discarded ($[f] = [0]$; $q = 0$).

2.2 The mechanical part

2.2.1 The displacement field

Based on the sinus model, see [14], a new plate model which takes into account the transverse normal stress is presented in this section. This extension is based on following developments

- various models for beams, plates and shells based on the refined sinus theory, see [14, 15, 16, 17, 18, 19];
- our previous paper on a 7 parameter model for thermo-mechanical analysis [1].

In the framework of ESL approach, the kinematics of our model is assumed to have the following particular form

$$\begin{cases} U_1(x_\alpha, z) = u^0_1(x_\alpha) + z u^1_1(x_\alpha) + f(z) u^f_1(x_\alpha) \\ U_2(x_\alpha, z) = u^0_2(x_\alpha) + z u^1_2(x_\alpha) + f(z) u^f_2(x_\alpha) \\ U_3(x_\alpha, z) = u^0_3(x_\alpha) + z u^1_3(x_\alpha) + z^2 u^2_3(x_\alpha) \end{cases} \quad (3)$$

where $\alpha \in \{1, 2\}$ and $i \in \{1, 2, 3\}$. In Eq. (3), the superscript is associated to the expansion order in z while the subscript is related to the component of the displacement. Thus, u^0_i are the displacements of a point of the reference surface while (u^1_α, u^f_α) are measures for rotations of the normal transverse fiber about the axis $(0, x_\alpha)$. The functions u^{α}_3 permit to have a non-constant deflection for the transverse fiber and allow to have non zero transverse normal stretch. Furthermore, the quadratic assumption for the transverse displacement avoids the occurrence of Poisson (or thickness) locking, see [1].

In the context of the sinus model, we have

$$f(z) = \frac{e}{\pi} \sin \frac{\pi z}{e} \quad (4)$$

It must be noticed that the classical homogeneous sinus model [14] can be recovered from Eq. (3) assuming $u^1_\alpha = -u^0_{3,\alpha}$, and neglecting the unknown functions u^α_3 .

2.2.2 The Murakami's Zig-Zag terms

In order to evaluate the influence of Zig-Zag terms [3] in a high-order ESL model, the following displacement per layer (k) are added to Eq. (3):

$$\begin{cases} U_1^{(k)}(x_\alpha, z) = Z^{(k)}(z) u^{z_1}(x_\alpha) \\ U_2^{(k)}(x_\alpha, z) = Z^{(k)}(z) u^{z_2}(x_\alpha) \\ U_3^{(k)}(x_\alpha, z) = Z^{(k)}(z) u^{z_3}(x_\alpha) \end{cases} \quad (5)$$

with

$$Z^{(k)}(z) = (-1)^k \zeta_k(z) \quad \text{and} \quad \zeta_k(z) = \frac{2}{e_k} \left(z - \frac{1}{2}(z_k + z_{k+1}) \right) \quad (6)$$

where e_k is the thickness of the k^{th} layer while (z_k, z_{k+1}) are the bottom and top coordinates of this layer. It is obvious that $Z^{(k)}(z)$ is a piecewise linear function with bi-unit amplitude for all the layers as we have $\zeta_k(z) \in [-1, 1]$. Note that, despite the $Z^{(k)}(z)$ function depends on the layer index inside the stack, the amplitudes u^{z_i} are unique for the whole laminate, i.e., the ESL framework is still preserved.

2.3 The electric part

On each elementary domain Ω_e , the electric potential is assumed to be constant. Therefore, no variation with respect to x_α is considered. A cubic layerwise (LW) description is used across the thickness, according to the approximation introduced in [2] and used in [11]: In each layer (k), the electric potential distribution is described by the normal electric field components at the bottom and top surfaces, denoted E_{3b} and E_{3t} , respectively, and the potential difference $\Delta\phi$ between top and bottom surface. Using these dofs, the approximation of the electric potential can be written as:

$$[\phi^{(k)}] = [F_\phi] [Cst_\phi^{(k)}] [q_\phi^{e(k)}] \quad (7)$$

where the following definitions have been introduced:

$$[F_\phi] = [1 \quad z \quad z^2 \quad z^3]; \quad [q_\phi^{e(k)}]^T = [E_{3b}^{(k)} \quad \Delta\phi^{(k)} \quad E_{3t}^{(k)}] \quad (8)$$

and $[Cst_\phi^{(k)}]$ is a (4×3) matrix containing constant coefficients. The electric field vector in each layer $[E^{(k)}]$ is then obtained as:

$$[E^{(k)}] = \begin{bmatrix} 0 \\ 0 \\ -\phi_{,3}^{(k)} \end{bmatrix} = [F_E] [Cst_E^{(k)}] [q_\phi^{e(k)}] \quad \text{with} \quad [F_E] = [1 \quad z \quad z^2] \quad (9)$$

where $[Cst_E^{(k)}]$ is a (3×3) matrix. So, the adopted approximation yields a quadratic transverse electric field across the thickness of each layer.

2.4 The system to be solved

The FE approximations are not detailed here for the sake of brevity and can be found elsewhere [10, 1]. The eight-node quadrilateral finite element is used and classical FE approximation is used for the geometry. A special treatment is used to control the transverse shear locking by using a dedicated interpolation for $\gamma_{\alpha 3}^0$ according to the methodology presented in [1]. Note that since the electric potential is assumed to be constant on each elementary domain, there is no need to introduce any FE approximation for this field.

The elementary matrices are then deduced considering the bi-dimensional weak form obtained from Eq. (2). Assembling each elementary contribution in the global reference frame, the following discrete form of the coupled piezoelectric system is obtained:

$$\begin{bmatrix} [K_{uu}] & [K_{u\phi}] \\ [K_{u\phi}]^T & [K_{\phi\phi}] \end{bmatrix} \begin{bmatrix} [q_u] \\ [q_\phi] \end{bmatrix} = \begin{bmatrix} [L_u] \\ [L_\phi] \end{bmatrix} \quad (10)$$

where $[K_{uu}]$, $[K_{\phi\phi}]$ and $[K_{u\phi}]$ are the global stiffness, dielectric and piezoelectric matrices of the plate, respectively. The mechanical dofs are in the vector $[q_u]$, while the electrical dofs are in the vector $[q_\phi]$ and we have at the elementary level

$$\begin{aligned} [q_u^e] &= \left[(u^0_1 \ u^0_2 \ u^0_3 \mid u^1_1 \ u^1_2 \ u^1_3 \mid u^f_1 \ u^f_2 \ u^2_3 \mid u^z_1 \ u^z_2 \ u^z_3)_{i=1,8} \right] \\ [q_\phi^e] &= \left[(E_{3b}^{(k)} \ \Delta\phi^{(k)} \ E_{3t}^{(k)})_{k=1,Nl} \right] \end{aligned} \quad (11)$$

with Nl the number of layers. From the mechanical point of view, the Zig-Zag dofs can be activated or not and comparisons will be presented in the next section dedicated to numerical evaluations using no Zig-Zag dof (P9), using only in-plane Zig-Zag dof u^z_α (P9Z) and with all the Zig-Zag dof u^z_i (P9ZZ). Finally, the three models use 9, 11 or 12 kinematical unknown functions and the associated FE has 72, 88, 96 mechanical dofs per element, respectively.

Since the electric potential is assumed constant on each FE, the assembly involves only the approximation along the thickness. A piezoelectric patch comprising several FEs can be defined through the imposition of the equipotential condition between electrodes: the same $\Delta\phi$ is imposed on the piezoelectric layer for all elements belonging to the same patch. From the numerical point of view, this is accomplished through linear homogeneous and non-homogeneous Multi-Point Constraints (MPC) using penalty function method.

In Eq. (10), the load vectors $[L_u]$ and $[L_\phi]$ represent the external loading from applied forces and prescribed charges, respectively. Essential boundary conditions (i.e., prescribed displacements and electric potentials) are imposed numerically by a penalty technique. The coupled system is then solved by the classical static condensation procedure for the electrical dof:

$$[q_\phi] = [K_{\phi\phi}]^{-1}([L_\phi] - [K_{u\phi}]^T [q_u]) \quad (12a)$$

which yields the following purely mechanical system with a modified equivalent stiffness matrix:

$$\left[[K_{uu}] - [K_{u\phi}][K_{\phi\phi}]^{-1}[K_{u\phi}]^T \right] [q_u] = [L_u] - [K_{u\phi}][K_{\phi\phi}]^{-1}[L_\phi] \quad (12b)$$

In the remainder of the paper, $[L_\phi] = [0]$ will be considered.

3 Numerical results: clamped composite plate

This test is interesting to evaluate the segmentation of a piezoelectric layer using different number of patches. It considers the sensory response of a cantilever, rectangular, hybrid sandwich plate with one edge clamped and other edges free subjected to a uniform pressure load according to the following data [20]:

geometry rectangular plate $a \times b$ with $a = 10 \text{ mm}$, $a/b = 2$ and total thickness $e = 1 \text{ mm}$ (length-to-thickness ratio $S = 10$)

materials seven-layers plate $(pz, 0^\circ, 90^\circ, core, 90^\circ, 0^\circ, pz)$; the outer piezoelectric layers of thickness $0.1 e$ are made out of PZT-5A material; each layer constituting the laminated skins has a thickness $0.04 e$ and the core thickness equals $0.64 e$. The material properties for PZT-5A, skin layers and core are given in Tab. 1

boundary conditions clamped at $x_1 = 0$; uniform pressure load p_0 ; piezoelectric layers can be in open circuit ($\Delta\phi$ let free) or in closed circuit ($\Delta\phi = 0$)

mesh three regular meshes 5×2 , 10×4 and 20×8 are used

results and locations transverse displacement at the tip and piezoelectric potential in the element close to the clamped edge. They are made non-dimensional according to

$$\bar{u}_3 = u_3 (10^2 E_2^{(core)}) / (e S^4 p_0) \quad \bar{\phi} = \phi (10^4 E_2^{(core)} d_0) / (e S^2 p_0) \quad \text{with } d_0 = 374 \cdot 10^{-12} \text{ CN}^{-1}$$

Prop.	PZT-5A	skin	core	Prop.	PZT-5A	skin	core
E_1 [GPa]	61.0	172.5	0.276	e_{15} [C/m ²]	12.3	0	0
E_2 [GPa]	61.0	6.9	0.276	e_{24} [C/m ²]	12.3	0	0
E_3 [GPa]	53.2	6.9	3.45	e_{31} [C/m ²]	-7.2	0	0
ν_{23}	0.38	0.25	0.02	e_{32} [C/m ²]	-7.2	0	0
ν_{13}	0.38	0.25	0.02	e_{33} [C/m ²]	15.1	0	0
ν_{12}	0.35	0.25	0.25	ϵ_{11} [nF]	15.3	ϵ_0	ϵ_0
G_{23} [GPa]	21.1	1.38	.414	ϵ_{22} [nF]	15.3	ϵ_0	ϵ_0
G_{13} [GPa]	21.1	3.45	.414	ϵ_{33} [nF]	15.	ϵ_0	ϵ_0
G_{12} [GPa]	22.6	3.45	0.1104				

Table 1: Material properties employed in the considered problems.

This test can be used to compare the effect of the electrode segmentation: using the proposed FE meshes, the electrode sensor surface is subdivided in 1, 10, 40, 160 patches through the imposition of equipotential conditions.

Tab. 2 presents the convergence properties of the P9 FE when only one patch is used for each piezoelectric layer. In the open circuit configuration, the equipotential condition enforces $\Delta\phi$ in each layer to be the same for all elements. In the closed circuit condition, $\Delta\phi = 0$ for all elements (equipotential condition) and the maximum electric potential value inside the piezoelectric layers is reported. Note that the cubic approximation for ϕ allows to recover the electric potential induced by the local bending of the piezoelectric layers.

elec BC	mesh	5×2	10×4	20×8
OC	\bar{u}_3	22.649 (-1.9)	22.967 (-0.5)	23.089
	$\Delta\phi_{bottom}$	-23.003 (-2.7)	-23.408 (-1.0)	-23.649
	$\Delta\phi_{top}$	24.473 (-2.6)	24.886 (-1.0)	25.129
CC	\bar{u}_3	23.370 (-1.9)	23.698 (-0.3)	23.833
	$\bar{\phi}_{Max}$	-3.307	-5.212	-7.295

Table 2: Clamped composite plate with only one electric patch: convergence results for open circuit (OC) and closed circuit (CC).

The maximum displacement is located at the center of the tip edge $(a, b/2)$ while the maximum induced electric potential (ϕ_{max} for closed circuit) is in the FE close to the clamped edge. For the open circuit, the convergence is very fast for both displacement and electric potential difference – the percentage of error with respect to the 20×8 mesh results is indicated in parentheses. For the closed circuit, an asymptotic value is recovered for the displacement whereas ϕ_{max} still increases with mesh refinement; this is due to the decreasing size of the FE at the clamp, which increasingly localizes the bending deformation of the piezoelectric layers.

The distribution of the electric potential across the thickness is illustrated for the two electric boundary conditions in Fig. 1. The non-linear variation across the bottom and top piezoelectric layers is visible on both graphs and increases with mesh refinement. Due to the equipotential condition, it has no influence on the $\Delta\phi_{max}$ for the open circuit (left) but it is directly related to the Φ_{max} for the closed circuit (right). This non-linear effect measures the local bending deformation of the piezoelectric layers and is accordingly larger at the clamped edge than at the free tip of the plate.

Finally, the effect of electrode segmentation is discussed in Tab. 3 for the open circuit boundary condition. The corresponding distribution along the length of the plate of the electric potential difference is illustrated in Fig. 2 for all considered meshes and electrode segmentations. The induced potential difference $\Delta\phi$ reported in Tab. 3 is taken at the electrode next to the clamped edge, i.e., where it has its maximum value. Comparing the results for 10 patches obtained with two different meshes allows to appreciate the role of the mesh refinement: a finer mesh increases the tip displacement and enhances the sensed voltage. The same mesh with 10×4 elements is then used with two different number of electric patches, i.e., with different sizes of the equipotential surfaces: a very small influence on the tip deflection can be seen, with \bar{u}_3 slightly larger when the equipotential surfaces are larger; on the contrary, the electric potential induced at the clamped edge is clearly higher the smaller the electrode. Finally, considering the 20×8 with 160 patches (i.e., one electrode per FE), the tip displacement is slightly higher due to the refined mesh and the sensed voltage is further increased due to both, the larger deflection and the reduced electrode's size at the clamp.

4 Conclusion

This paper has presented a new family of FE for piezoelectric composite plates. A high-order ESL kinematic model is considered that includes the sinus function for the in-plane displacements, a quadratic polynomial expansion for the transverse displacement and Zig-Zag functions for introducing slope discontinuities at layers' interfaces for both, the in-plane and the transverse displacements. A LW cubic approximation is used for the electric potential in order to capture its non-linear distribution induced by the local bending of the piezoelectric layer; the elementary domain is considered as an equipotential surface (constant electric potential).

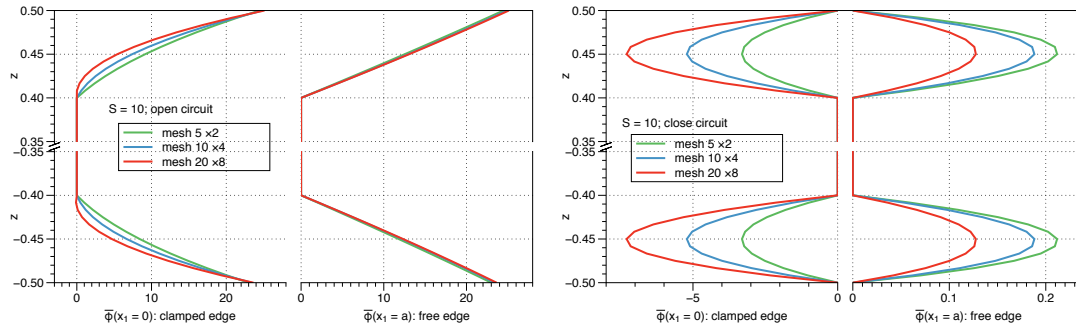


Figure 1: Clamped composite plate: electric potential distribution across the thickness for the OC (left) and CC (right) electric boundary conditions.

patch Nb	10	40	160
mesh	5×2	10×4	20×8
\bar{u}_3	22.230	22.533	22.510
$\Delta\Phi_{bottom}$	-62.776	-63.503	-80.004
$\Delta\Phi_{top}$	64.071	64.827	81.147

Table 3: Clamped composite plate in OC configuration: evaluations for different FE meshes and equipotential surface sizes.

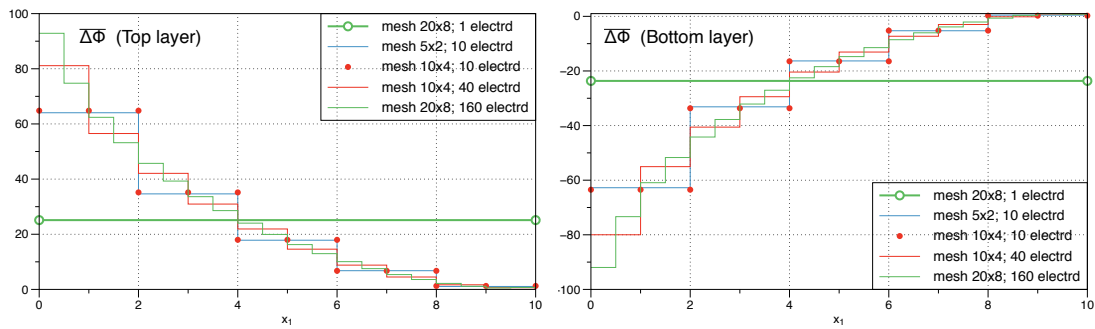


Figure 2: Clamped composite plate in OC configuration: distribution along the length of the sensed voltage at the top (left) and bottom (right) piezoelectric layer for different meshes and electrode segmentation.

The element has been validated through linear static case studies for both sensor and actuator configurations as well as homogeneous and laminated plates. The role of electrode segmentation, i.e., the size of equipotential surfaces, on the electro-mechanical response has been also evaluated. The results are in good agreement for actuator and sensor configurations for thin to very thick cases. The proposed P9ZZ FE, using only 12 mechanical dof per node, is very accurate, simple to use, without any numerical problem and could be used for a large range of plate problems involving piezoelectric patches or layers. Future works are pointed towards the extension of this model to piezoelectric shell structures.

REFERENCES

- [1] O. Polit, P. Vidal, M. D'Ottavio, Robust c^0 high-order plate finite element for thin to very thick structures: mechanical and thermo-mechanical analysis, *International Journal for Numerical Methods in Engineering* 90 (4) (2012) 429–451, doi: 10.1002/nme.3328.
- [2] J. Jiang, D. Li, A new finite element model for piezothermoelastic composite beam, *J. Sound Vibr.* 306 (2007) 849–864.
- [3] H. Murakami, Laminated composite plate theory with improved in-plane response, *J. App. Mech.* 53 (1986) 661–666.
- [4] O. Polit, M. D'Ottavio, P. Vidal, High-order plate finite elements for smart structure analysis, *Composite Structures* 151 (2016) 81–90.
- [5] I. Chopra, Review of state of art of smart structures and integrated systems, *AIAA Journal* 40 (2002) 2145–2187.
- [6] O. Polit, I. Bruant, Electric potential approximations for an eight node plate finite element, *Computers and Structures* 84 (22-23) (2006) 1480–1493.
- [7] S. Gopinathan, V. Varadan, V. Varadan, A review and critique of theories for piezoelectric laminates, *Smart Materials and Structures* 9 (1) (2000) 24–48.
- [8] R. Gibson, A review of recent research on mechanics of multifunctional composite materials and structures, *Compos. Struct.* 92 (2010) 2793–2810.
- [9] E. Carrera, M. Boscolo, A. Robaldo, Hierarchic multilayered plate elements for coupled multifield problems of piezo- electric adaptive structures: formulation and numerical assessment, *Archives of Computational Methods in Engineering* 14 (4) (2007) 383–430.
- [10] P. Vidal, M. D'Ottavio, M. Ben Thaïer, O. Polit, An efficient shell finite element for the static response of piezoelectric laminates, *Journal of Intelligent Material Systems and Structures* 22 (7) (2011) 671–690.
- [11] S. B. Beheshti-Aval, M. Lezgy-Nazargah, P. Vidal, O. Polit, A refined sinus finite element model for the analysis of piezoelectric-laminated beams, *Journal of Intelligent Material Systems and Structures* 22 (3) (2011) 203–219.
- [12] A. S. 176, IEEE Standard on Piezoelectricity, American National Standard Institute, 1987.
- [13] H. Tiersen, *Linear Piezoelectric Plate Vibrations*, Plenum, New-York, 1969.

- [14] M. Touratier, An efficient standard plate theory, *Int. J. Eng. Sci.* 29 (1991) 901–916.
- [15] M. Ganapathi, B. P. Patel, P. Boisse, O. Polit, Flexural loss factors of sandwich and laminated composite beams using linear and nonlinear dynamic analysis, *Composites Part B: Engineering* 30 (3) (1999) 245–256.
- [16] O. Polit, M. Touratier, A multilayered/sandwich triangular finite element applied to linear and non-linear analyses, *Composite Structures* 58 (1) (2002) 121–128.
- [17] F. Dau, O. Polit, M. Touratier, C1 plate and shell finite elements for geometrically nonlinear analysis of multilayered structures, *Computers and Structures* 84 (19-20) (2006) 1264–1274.
- [18] P. Vidal, O. Polit, A thermomechanical finite element for the analysis of rectangular laminated beams, *Finite Elements in Analysis and Design* 42 (10) (2006) 868–883.
- [19] P. Vidal, O. Polit, A family of sinus finite elements for the analysis of rectangular laminated beams, *Composite Structures* 84 (1) (2008) 56–72.
- [20] S. Kapuria, S. Kulkarni, Static electromechanical response of smart composite/sandwich plates using an efficient finite element with physical and electric nodes, *Int. J. of Mech. Sci.* 51 (2009) 1–20.

TOWARDS A NEW GENERATION OF SOFT ACTUATORS USING PHASE TRANSITION: APPLICATION TO MORPHABLE-TEXTURE SKINS AND SOFT GRIPPERS

Gilles Lubineau, Ragesh Chellatoan, Natanael Bolson and Arief Yudhanto

King Abdullah University of Science and Technology (KAUST)
Physical Sciences and Engineering Division, COHMAS Laboratory,
Thuwal 23955-6900, Saudi Arabia

e-mail: gilles.lubineau@kaust.edu.sa, web page: <http://www.cohmas.kaust.edu.sa>

Key words: Soft actuators, soft robots, smart skin, morphable texture, phase transition

Abstract. Soft robotics is an expanding and promising field that deeply transforms the way we design actuators and sensors. Despite recent progress, there is still a need for electrically driven actuators being capable of providing large motions under low voltage. We explore here the concept of phase transition-driven actuators, in which the actuation only results from the large expansion taking place during a liquid to a gas phase transition. We demonstrate that such a concept can be used for creating original applications, including a morphable skin with controllable texture and a soft gripper. It would be very challenging, if not impossible, to design such actuators with other actuation technologies while preserving the same compactness.

1 INTRODUCTION

Soft robotics emerged a few years ago as a new trend in the design of artificial robotics system. By leveraging the unique properties of highly deformable materials and systems, new functions can be imagined, including improved interaction between the robotic system and the user, complex mode of deformations bringing more flexibility compared to classical rigid-part based robots, integral processing through 3D printing. As in any robotic system, the success of such technology heavily relies on the availability of high-performance sensors and actuators.

Soft actuators are usually based on externally provided pressurized fluid (pneumatic and hydraulic systems) [1], shape memory polymer, electroactive polymers such as conductive soft polymers (PEDOT/PSS for example [7]), or piezoceramic fibers. These systems all suffer limitations that prevent today to explore the full potential of soft robotics. These limitations vary from one technology to another: high voltage, limited actuation (strain), need for bulky and expensive power sources. So there is still a need for an actuation principle that can provide large actuation, ideally based on electrical energy at relatively low voltage.

We propose here to explore the concept of Joule heating induced phase transition to the design of new families of actuators. In this concept, the transition from liquid to gas of well-chosen liquid based on electrically induced heating is leveraged. Such systems raise many challenges including the design of efficient heating element and microstructure.

We demonstrate this concept on two application.

The first example is an all-polymer base polymorph skin with controllable surface texture [2]. We present here an e-skin for which we control the surface morphology based on an electrical stimulus. Such skin is fully polymer-based, based on the concept of phase transition, and will find interesting applications in any process where the morphology of the surface plays an important role in controlling the interaction between the system and its environment such as drag control in pipe or gripping.

The second application is about the development of soft grippers that can experience large deformation and where the internal actuating pressure is only provided by phase transition [3]. We show here how a well-designed electrode and a predesigned cavity with sufficient liquid can result in a high performing system.

2 Experimental section

The proposed family of actuators relies on a very simple observation: liquid to gas phase-transition is one of the physical process coming with the largest dimensional expansion. On the other hand, phase-transition is a thermally activated process that can be easily controlled by providing heat energy to the system. Finally, heat energy is easily provided in-the-volume of any conductive material by making appropriate use of the Joule effect.

Then, the objective becomes to use at best the electrical-thermal-mechanical coupling. First, a heating element is designed to provide an adequate amount of heat when subjected to an electrical current. Second, a functional material should exhibit phase-transition when subjected to this additional heat. Finally, this expanding functional material should be properly mechanically constrained to force the system to deform in the way desired for the actuation.

This process is obviously not new as it is very similar to the one used in conductive polymer-based actuators such as PEDOT/PSS. PEDOT:PSS features a strong coupling between its chemical, mechanical and electrical behaviors which has resulted in many applications in the field of electro-mechanical actuators [6]. The mechanism of actuation comes from the hygroscopic nature of PSS that very easily absorbs water from the environment. Water molecules can actually exist in very different configurations. As shown by [5] based on the observation of isosteric heat of sorption, water molecules will mainly be adsorbed on hydrophilic sulfonic acid groups at low sorption degree. At higher sorption degree, the active sites are totally saturated and the water is in a free-water configuration. Absorbed water molecules increase the distance between PEDOT:PSS grains, causing a volume increase. When an electric current is applied, the Joule effect results in the generation of in-the-volume heat, consequently changing the temperature. It results in releasing the previously absorbed water molecules, which translates into geometrical shrinking at the macroscale. PEDOT:PSS based actuators can be operated under low voltages (0-10V) that makes them particularly appealing for wearable electronics applications [4].

However, this phase transition is relatively inefficient in PEDOT/PSS that only exhibits a few percent strain when actuated. This is due to the microstructural disorganization of the phase-changing domain, and to the very limited fluid content. Our objective is to design from scratch the microstructure so it actually features very high actuating properties.

2.1 Example 1: a morphable skin based on phase-transition

In this first example, we create an e-skin with a controllable texture. An elementary module is presented figure 1(a,b). E-skin can then be created by using periodical arrays of such elementary modules. As detailed above, this component requires a heating element, a functional material expanding under a thermal stimulus, and a constraining material to force the motion.

The heating element is here made of PEDOT/PSS by mixing an aqueous dispersion of PEDOT:PSS

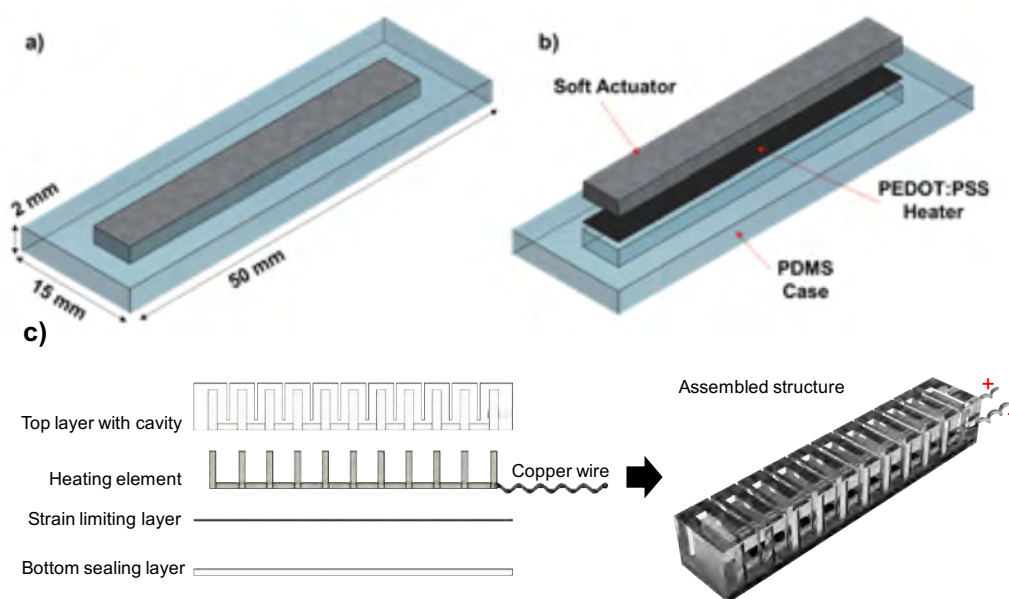


Figure 1: (a,b) The structure of the morphable skin based on phase-transition, (c) components of the phase-transition based soft gripper (left), assembled structure of soft gripper (right).

Clevios PH1000 (HC Starck) with 3% mass ratio of Ethylene glycol (EG) (Sigma-Aldrich). This blend is then magnetically stirred at 500 RPM for 6 hours so an homogeneous solution is obtained. The solution was later on drop-casted on a petri dish base coated with a Teflon sheet and subsequently cured inside a fume hood, at room temperature, for 48 hours, in order to obtain a 50 μm - thick film. To precisely cut the solution-casted PEDOT:PSS film, a CO₂ laser cutter PLS 6.75 (Universal Laser Systems) was used, with the following optimized parameters: power 3%, speed 5%, pulse per inch 1000, and focus distance of Z-axis of 4 mm.

The soft actuator itself (the functional material expanding when exposed to temperature increase) is here created by encapsulating liquid-phase containing bubbles inside an expandable silicone rubber (here, Ecoflex 00-50). The technology is then similar to the one proposed by [3]. One of the advantages is the simplicity of the fabrication. However, the main drawback is that the microstructure can not be very well controlled and then actuation properties can not be optimized. We are using as phase-transition liquid ethanol at 96% (VWR Chemicals) based on an optimization process for the fluid that was detailed in [2] where we compared different fluids. The preparation was optimized by mixing a 20% mass ratio of ethanol with Ecoflex. The silicone elastomer of Ecoflex (part A) and ethanol were first mixed for 2 min, the silicone crosslinker of Ecoflex (part B) was then added and mixed for another 2 min, at the recommended 1:1 mass ratio of part A and part B. The mixture was subsequently poured into a 3D-printed acrylonitrile butadiene styrene (ABS) mold and cured for 3 hours, at room temperature.

Then comes the assembly with the constraining material. To assemble the device, the Ecoflex based soft actuator was placed on a customized 3D-printed ABS mold. It was then covered with the PEDOT:PSS film to build the heating element. Contact electrodes were assembled on the PEDOT:PSS film, using copper wires fixed with colloidal silver liquid (Electron Microscopy Sciences). For the casing, PDMS was prepared using a silicon-based elastomer and curing agent Sylgard 184 (Dow Corning), with a 10:1 mass ratio. This PDMS is much stiffer than the soft actuator so it has an in-plane constraining

effect: the soft actuator can not expand in-plane and has to expand out-of-plane, resulting in the creation of the macroscopic texture. The mixture was degassed under vacuum for 30 min to remove air bubbles. Finally, PDMS was poured into the mold and cured at room temperature, for 48 hours, to package all the components.

This e-skin is here obtained by casting due to limitations in the available equipment. However, we should note that it is fully polymer based. It is fully printable and compatible with major printing technologies that makes it very easy to upscale.

2.2 Example 2: a soft gripper based on phase-transition

The soft actuator has four main components: a top layer with eleven cavities made of silicon rubber (Ecoflex-50), a heating element passing through all the cavities, a strain limiting layer and a flat bottom layer made of silicon rubber (Ecoflex-50); see Figure 1(c). We adopted a casting process using two different 3D-printed molds to fabricate the top and bottom layers, respectively. We poured Ecoflex-50 into the mold for the top layer and cured the material at 50 °C for at least 3 h. We then poured Ecoflex-50 into another mold for the bottom layer, inserted a thin cotton fabric (strain limiting layer that was already wetted with Ecoflex-50) into the mold, and cured the material (the mold was only filled halfway). Heating element made by twisting stainless steel micro-fibers was connected to copper wires for electrical connection and inserted into the cavities of the top layer. A valve for pouring actuation liquid was made in one of the cavities of the top layer. To make final assembly, we poured Ecoflex-50 to fully fill the remaining half of the mold of the bottom layer, and laid the top layer (with heating element and valve) over the mold of bottom layer. Once the Ecoflex was all cured, the liquid (ethanol) was pumped into the cavities through the valve, and the valve was fully patched with Ecoflex-50 to avoid leakage.

3 Results and discussion

3.1 Example 1: a morphable skin based on phase-transition

We can observe in figure 2(a) the progressive change in the shape of one module when subjected to a 6 V (0.7 A) electrical loading. The actuation of the device was monitored using a drop shape analyzer (Kruss), where an in-situ video was captured (as supplementary content), and image post-processing was carried out using ImageJ (an open source computer software). We can see that a substantial change in shape can be obtained using the phase-transition technology. Such a change in change would be difficult to achieve with classical actuators.

Using this module as a building block, we have shown that complete morphable skins can be fabricated and used in various applications including smart piping and active drag reduction at the fluid/pipe interface [2].

The main problem in this first technology is the limited durability of the heating element that is here made of PEDOT/PSS. To verify the lifetime and reliability of our device, we performed a cyclic test. Each cycle was composed of two periods: a heating period of 7 min in which the power was on, and a cooling period of 5 min with the power off. The voltage supplied during the heating period was 7 V, and a microscope (Leica S6D MC 190 HD) was used to capture images at the end of the 7 min period, to obtain the maximal actuation; image post-processing was once again carried out using ImageJ. We can observe that the actuation capabilities of the device are decreasing with the number of cycle (figure 2(b)). That is a consequence of the progressive degradation of the PEDOT/PSS electrodes, that results both in progressive increase in actuation power and decrease in actuation amplitude. This issue has been solved in the next generation where metallic porous electrodes are used as demonstrated in the next subsection.

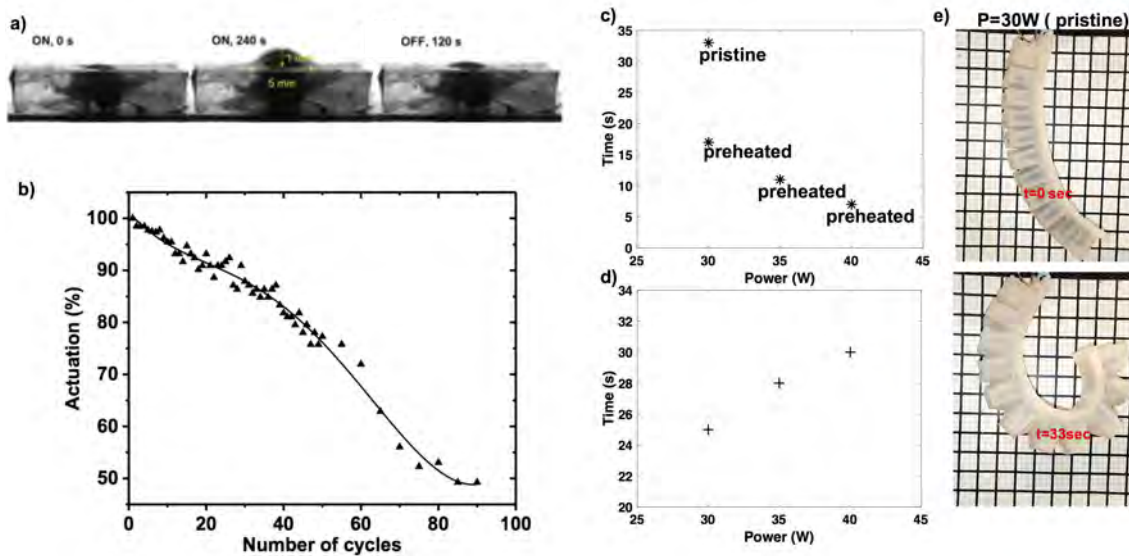


Figure 2: Example 1 (morphable skin): (a) progressive change in cross section of a single module of the morphable-skin, (b) the evolution of actuation amplitude with time. Example 2 (soft gripper): (c) time response of forward actuation, (d) time response of reverse actuation, (e) initial and actuated state of soft gripper at $P = 30$ W.

3.2 Example 2: a soft gripper based on phase-transition

Figure 2(c-d) shows the relationship between input power and the time required to actuate the soft gripper forward and reverse, respectively. Figure 2(c) shows that during forward actuation without pre-heating the gripper took 33 s to move from initial (resting) position to the full actuation. The heating element made of twisted steel micro-fibers was able to introduce a relatively uniform and quick heat flow to the fluid (ethanol). The liquid-to-vapor transition provided a sufficient pressure in the cavities, and due to the asymmetry (stiffness and geometry), a bending motion was created. The time requires was reduced by almost 80% when the gripper was pre-heated, while the power input was increased from 30 to 40 W. Pre-heating increases the internal heat energy that helps reduce the actuation time. Figure 2(d) shows that the reverse actuation took 25 s at 30 W power input; the time required to reverse was naturally longer when the input power was increased. Figure 2(e) shows the undeformed (pristine) and deformed state of the soft gripper. Nevertheless, reverse actuation time of 30 s at 40 W to restore from deformed to undeformed state is still considered fast for this passive cooling method. Furthermore, an appreciable bending configuration more than 180° could be achieved using relatively lower input voltage (25-40 V) in comparison to dielectric electro active polymers that require very high voltage source (kV) for large actuation strain.

Some remarks can be made with respect to our soft gripper. The corrugated design of the top layer with 11 cavities provides a significant increase of surface area with moderate increase in dead volume in comparison to a classical rectangular cavity. The increase of surface area improves the rate of convection heat transfer ($Q = hA\Delta T$) and enables a faster reverse motion. It should be noted that an active cooling system, e.g., peltier-based, water-based or air-based cooling, may improve the time required for reversibility, but this would increase the size and the energy consumption of our system. Our fast response, low voltage, large actuation soft gripper is considered promising for portable humanoid hand that deals with delicate objects and fast picking pace.

4 CONCLUSIONS

We demonstrate here that using phase-transition concepts for practical actuators is a viable alternative for soft robotics. The key-to-success is the ability to provide proper electrodes capable of ensuring simultaneously the electrical conduction, Joule effect-based heat generation, the heat transfer to the fluid and good durability. Here, we proposed two actuators: one based on conductive polymer, and another one based on porous metallic electrodes.

REFERENCES

- [1] B. Mosadegh et al. Pneumatic Networks for Soft Robotics that Actuate Rapidly. *Advanced Functional Materials*, (24):2163–2170, 2014.
- [2] N. Bolson, D. Singh, V. Lube, and G. Lubineau. All-Polymer Based Polymorph Skin with Controllable Surface Texture. *Smart Materials and Structures*, 2019, in press, <https://doi.org/10.1088/1361-665X/ab1c01>.
- [3] Miriyev, A. and Stack, K. and Lipson, H.I. Soft material for soft actuators. *Nature communications*, (8):596, 2017.
- [4] H. Okuzaki. Humidity-Sensitive Conducting Polymer Actuators. In Kinji Asaka and Hidenori Okuzaki, editors, *Soft Actuators: Materials, Modeling, Applications, and Future Perspectives*, chapter 8, pages 111–126. Springer, 2014.
- [5] H Okuzaki, K. Hosaka, H. Suzuki, and T. Ito. Effect of temperature on humido-sensitive conducting polymer actuators. *Sensors and Actuators A*, 157:96–99, 2010.
- [6] H Okuzaki, H Suzuki, and T Ito. Electrically driven PEDOT/PSS actuators. *Synthetic Metals*, 159(21-22):2233–2236, 2009.
- [7] J. Zhou, M. Mulle, Y. Zhang, X. Xu, E.Q. Li, F. Han, S.T. Thoroddsen, and G. Lubineau. Effect of temperature on humido-sensitive conducting polymer actuators. *Journal of Material Chemistry C*, 6(4):1238–1249, 2016.

CARBON NANOTUBES MODELED AS SIZE-DEPENDENT NANOBEAMS FOR MASS SENSING APPLICATIONS

S. CEBALLES^{*}, S. S. GHAFARI^{*}, B. SAUNDERS^{*}, AND A. ABDELKEFI^{*}

^{*}Department of Mechanical and Aerospace Engineering
New Mexico State University
Las Cruces, NM 88003, USA
E-mail: abdu@nmsu.edu

Key words: Carbon nanotubes, Eringen's nonlocal elasticity, mass sensor, external forcing, beam theory, boundary conditions

Abstract. In this effort, we investigate the necessary considerations for the modeling of carbon nanotubes (CNTs) acting as nano-scale mechanical resonators for the detection and mass identification of nanoparticles deposited on or within the CNT. Thus, we provide an overview of several studies that were conducted in this research group in the last several years related to this topic. Each of these studies help us to achieve the end goal of this research in order to develop reduced-order models of CNT-based mass sensors that are able to reflect the physical system, reliably predict phenomena occurring at the nano-scale, and can both qualitatively and quantitatively match and predict the response based on existing and future experimental trials for the proposed systems. In general, we study the CNT-based systems from a mechanics, dynamics, and vibrations point of view. Therefore, we consider theories in non-classical continuum mechanics to model the size-dependent phenomena, utilize Hamilton's principle to derive the nonlinear governing equations of the mass sensor, and account for various other system parameters. We have found that there are many factors that have a profound effect the system's static / dynamic response, stability, and sensitivity. These include, but are not limited to, the CNT length and diameter, the location and geometry of the deposited particle, the number of deposited particles, the size-dependent parameter, and external forces and excitations.

1 INTRODUCTION

Following the initial discovery of carbon nanotubes (CNTs) in the early 1990s by Iijima and his colleagues [1, 2], they have been studied, researched, and utilized in numerous applications for their unique properties. Some of the most notable properties of CNTs, which can be classified as allotropes of carbon with a cylindrical structure, include their high strength, high Young's modulus, high surface area-to-volume ratio, and impressive thermal and electrical properties. Due to these unique properties, several applications of the nanostructures have been reported in the literature, such as CNTs acting as targeted drug delivery devices, energy devices, nano-scale biomedical sensors, energy storage devices, or sensors for the detection and mass identification of single or grouped deposited atoms or molecules [3-6]. As such, there have been significant efforts in this research group that have focused on the development of reduced-order

models of CNT-based mass sensors.

It should be noted that when considering nano-scale mass sensors, the main operating principle of the system rely on measuring an induced shift in the natural frequency or amplitude of the CNT. This shift is between the states before and after a particle or particles have been deposited on or within the CNT in order to detect and identify their mass and thereby determine the detection sensitivity of the device [6]. Further, because certain pristine CNTs can possess ultra-high-quality factors, some studies have shown that the mass detection system is able to obtain a zeptogram ($1 \text{ zg} = 10^{-21} \text{ g}$) and yoctogram ($1 \text{ yg} = 10^{-24} \text{ g}$) resolution [7]. Additionally, the resolution of the CNT, *i.e.*, the smallest mass that can be detected for a specified frequency shift is dependent on a number of factors, such as temperature changes, exposure to a magnetic field, harmonic, or parametric excitations. For example, the mechanical behavior of nanostructures is highly dependent on different types of temperature changes in severe environments. Thus, it is required to include thermal effects to investigate the static and vibrational characteristics, which has been the subject of several research efforts in recent years [8-10]. Besides, any external forcing may alter the behavior and response of the system. This leads to an investigation on the nonlinear dynamics of forced single-walled carbon nanotube-based bio-mass sensors under uniform and non-uniform temperature distributions.

Other factors that can affect the system are different types of phenomena that occur at the nanoscale. Utilizing theories in classical continuum mechanics, which represent particles as a point mass subject only to translation, have been shown to fail at the nano-scale. Rather, at the nano-scale, particles should be represented as nano-volumes subjected to translation, rotation, and/or deformation. Depending on the crystallographic structure and size of the material, an appropriate theory in non-classical continuum mechanics should be selected. Of the available theories, Eringen's nonlocal theory has most notably been used to study the static and dynamic responses of CNTs. This theory represents particles as point masses subject to translation [11]. However, the stress at one point is influenced by the strain of all other points in the surrounding medium. In this work, a differential version of this theory is applied to include the residual stress. Additionally, while utilizing a nonclassical or nonlocal theory to account for the change in the behavior and response of a system at the nanoscale, it is also important to utilize an appropriate theory depending on the geometry of the CNT [9]. For example, for high aspect ratio CNTs, some researchers have shown the Euler-Bernoulli beam theory is appropriate, while Timoshenko beam theory is better suited for low aspect ratio, short, and stout structures.

After considering possible parameters and system modifications depending on the CNT size and environment, a set of nonlinear governing equations of motion, boundary conditions, and continuity conditions can be derived. In this case, the authors present the reduced-order model for a case in which the CNT-based mass sensor has one attached particle and is subject to uniform, linear, and nonlinear temperature rises and undergoes harmonic excitations. Then, the mathematical model is solved using the Method of Multiple Scales [12], while the proposed analytical solution satisfying clamped boundary conditions is employed to solve the nonlinear equations. Then, CNT-based mass sensors under uniform [13] and nonuniform temperature profiles through the thickness of the carbon nanotube and under a harmonic excitation force are studied, along with the effects of the nonlocal parameter, particle mass and location, surface temperature difference, and CNT dimensions.

2 DEVELOPMENT OF NONLOCAL NONLINEAR REDUCED-ORDER MODELS

To model a system at the nano-scale, it is important to first study the system from a physical or experimental point of view to understand what is happening physically. When that is understood, reasonable assumptions can be made on the accuracy, qualitative, and quantitative predictions. Some of these considerations are shown in Figure 1. One of the first things to consider is what theory is used to represent the displacement and strain field of the CNT depending on its dimensions. For example, Euler-Bernoulli beam theory is appropriate for high aspect ratio CNTs, while low aspect ratio CNTs should be modeled with Timoshenko beam theory to include the effects of shear deformation and rotary inertia. The most inclusive model is a shell model that may need to be used for thin-walled CNTs. However, this model is considerably more complicated. So, for the sake of simplicity, noting that the authors have not exceeded the limits of applicability of the beam models, they are used more often. Another consideration in the model is how to represent the deposited particles. For example, the authors must decide whether to model the mass as a point mass or a nano-volume. Additionally, it should be noted that the location and number of masses also affect the dynamic response of the structure. Lastly, it is important to include external factors, such as thermal or magnetic loadings or harmonic or parametric excitations.

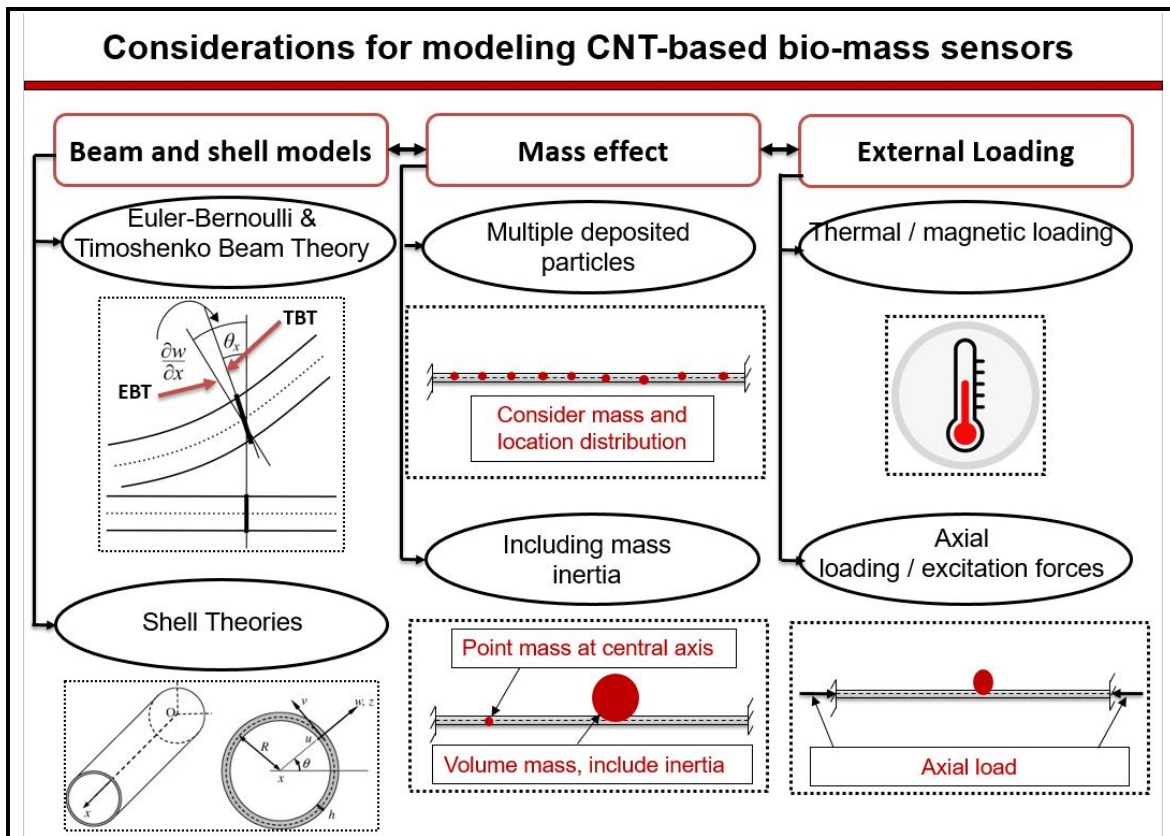


Figure 1. Considerations in the development of reduced-order models for CNT-based mass sensors.

At this point, several studies can be performed by neglecting or including different levels of assumptions and parameters. In this study, a focus is placed on two studies, namely, comparisons between Euler-Bernoulli beam theory and Timoshenko beam theory for different aspect ratio and CNTs and the dynamic response of CNT-based mass sensors under uniform, linear, and nonlinear temperature rise and harmonic excitation.

2.1 Eringen's nonlocal elasticity and the consideration of size-dependent phenomena

To model a system at the nano-scale, it is important to include size-dependent phenomena and/or to include the material structure. This is because at the nano-scale, the size of the structure is on the same order of magnitude as the internal lengths. Due to the material structure and properties of CNTs, Eringen's nonlocal theory is used to account for the size dependent phenomena in the structure. Using Eringen's nonlocal elasticity theory, the stress at one point in the medium is influenced by the strain of all other surrounding points. Thus, the nonlocal stress field, σ_{ij} is given as [12]:

$$\sigma_{ij}(x) = \int_{\Omega} \alpha(|x' - x|, e) t_{ij}(x) d\Omega(x') \quad (1)$$

where t_{ij} represents the local stress field, α is regarded as an attenuation function, and $e = e_0 a / l$ is the nonlocal parameter depending on the internal characteristic length, a , the external characteristic length, l , and material parameter, e_0 , that is determined by matching the longitudinal and transverse acoustic dispersions using approximations from atomic lattice dynamics or experiments. Because the integro-differential equations in Eringen's nonlocal elasticity are difficult to solve, the simplified differential form is used, yielding:

$$(1 - (e_0 a)^2 \nabla^2) \sigma_{ij} = c_{ijkl} \varepsilon_{kl} \quad (2)$$

2.2 Representation of uniform, linear, and nonlinear thermal loading

After introducing Eringen's nonlocal elasticity theory, the considered system and different thermal configurations are introduced and shown in Fig. 2. It should be noted that the CNT is of length L , a particle of mass m is deposited at location x_m , and that the harmonic excitation forces are denoted by F_1 and F_2 . Additionally, the three temperature rise expressions are provided in equations (3-5). UTR, LTR, and NLTR denote uniform temperature rise, linear temperature rise, and nonlinear temperature rise, respectively. These different representations of the temperature are expressed as:

$$\Delta T_{UTR} = T_{UTD} - T_{ref} \quad (3)$$

$$\Delta T_{LTR}(r) = \left(\frac{T_o - T_i}{r_o - r_i} \right) (r - r_o) + T_o - T_{ref} \quad (4)$$

$$\Delta T_{NLTR} = \frac{(T_o - T_i)}{\ln(r_o/r_i)} \ln(r) + \frac{(T_o + T_i)}{2} - \frac{(T_o - T_i)}{2 \ln(r_o/r_i)} \ln(r_i r_o) - T_{ref} \quad (5)$$

where T_{ref} represents the convenient ambient temperature, T_{UTD} denotes a uniform temperature distribution, T_o and T_i are the outer and inner surface temperature, respectively. The outer and inner radius of the CNT are given by r_o and r_i , as shown in Fig. 2.

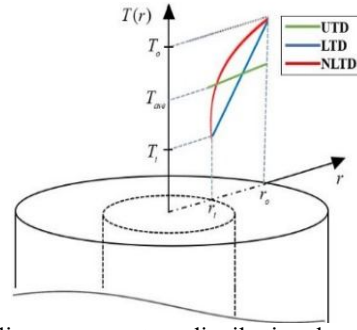


Figure 2. Uniform, linear, and nonlinear temperature distribution through the radial component of the CNT.

2.3 Von Kármán geometric nonlinearity and beam theories

In this study, only clamped-clamped CNTs are considered. Thus, it is important to include the effects of the mid-plane stretching of end-constrained beams. This is done through a modification of the strain tensor, shown in equation (6) as:

$$\varepsilon_{ij} = \frac{1}{2} \left(\frac{\partial u_i}{\partial x_j} + \frac{\partial u_j}{\partial x_i} \right) + \frac{1}{2} \left(\frac{\partial u_k}{\partial x_i} \frac{\partial u_k}{\partial x_j} \right) \quad (6)$$

Equation 6 is defined as the von Kármán strain tensor. Then, a comparison can be made between Euler-Bernoulli beam theory and Timoshenko beam theory, in which the shear deformation and rotary inertia are included. Thus, the strain field for both theories are shown in equations (7-9).

$$\varepsilon_{xx,TBT} = \frac{\partial u}{\partial x} + z \frac{\partial \phi}{\partial x} + \frac{1}{2} \left(\frac{\partial w}{\partial x} \right)^2 \quad (7)$$

$$\gamma_{xz,TBT} = 2\varepsilon_{xz} = \frac{\partial w}{\partial x} + \phi \quad (8)$$

$$\varepsilon_{xx,EBT} = \frac{\partial u}{\partial x} - z \frac{\partial^2 w}{\partial x^2} + \frac{1}{2} \left(\frac{\partial w}{\partial x} \right)^2 \quad (9)$$

In the remaining development of the governing equations, Euler-Bernoulli beam theory is used, while the derivation with the Timoshenko beam theory is omitted for brevity. However, it should be noted that the comparisons between the two models are discussed in later sections.

2.4 Governing equations of motion for a CNT-based mass sensor under thermal loading and external harmonic excitation

As earlier discussed, the authors present the governing equations of motion of the CNT under different types of thermal loads and harmonic excitation considering Euler-Bernoulli beam theory and the von Kármán strain tensor to include the effects of the geometric nonlinearity. The system is shown in Fig. 3.

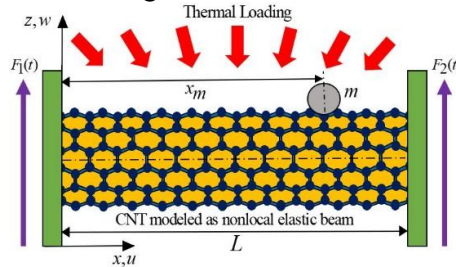


Figure 3. A bridged CNT-based nanoscale mass sensor subjected to external harmonic excitation and thermal loadings.

Then, using the extended Hamilton's principle, which is presented as:

$$\delta H = \int_{t_1}^{t_2} (\delta T_b + \delta T_m - \delta \Pi + \delta V) dt = 0 \quad (10)$$

where the authors include the first variation of the CNT, the deposited particle, the strain energy, and the work done by external forces, the normalized form of equations of motion for the carbon nanotube-based mass sensor exposed to a harmonic excitation force and three types of thermal loadings can be expressed as [13]:

$$\begin{aligned} W_{1,2}^{(4)} + \ddot{W}_{1,2} - \left(\frac{1}{2} \int_0^\eta (W'_{1,2})^2 d\chi + \frac{1}{2} \int_\eta^1 (W'_{2,2})^2 d\chi - T_n H \right) W''_{1,2} + 2\bar{\xi} \dot{W}_{1,2} \\ - e^2 \left[\ddot{W}''_{1,2} - \left(\frac{1}{2} \int_0^\eta (W'_{1,2})^2 d\chi + \frac{1}{2} \int_\eta^1 (W'_{2,2})^2 d\chi \right) W_{1,2}^{(4)} + 2\bar{\xi} \dot{W}''_{1,2} \right] - e^2 H T_n W_{1,2}^{(4)} \\ = \bar{F}_{1,2} \cos(\Omega \tau) \end{aligned} \quad (11)$$

and the corresponding dimensionless boundary conditions and continuity equations can be derived as follows [13]:

$$W_1(0) = W'_1(0) = W_2(1) = W'_2(1) = 0 \quad (12)$$

$$\begin{aligned} W_1(\eta) = W_2(\eta); \quad W'_1(\eta) = W'_2(\eta); \quad W''_1(\eta) = W''_2(\eta); \\ W'''_1(\eta) - W'''_2(\eta) + e^2 \left[\left(\frac{1}{2} \int_0^\eta (W'_1)^2 d\chi + \frac{1}{2} \int_\eta^1 (W'_2)^2 d\chi \right) - H T_n \right] \\ (W'''_1(\eta) - W'''_2(\eta)) - \ddot{W}_1 \mu(\eta) = 0 \end{aligned} \quad (13)$$

where details on the dimensionless variables and derivation procedure can be found in [13]. It should be noted that W_1 and W_2 refer to the transverse displacements of the first and the second portions of the mechanical resonator, e denotes the dimensionless nonlocal parameter, and μ is the mass ratio. Furthermore, the damping ratio and forcing terms have been included. Additionally, information can also be found on details for the linear analysis, Method of Multiple Scales formulation, and the static pre-/post-buckling configurations of the proposed CNT systems in [3] and [13].

3 RESULTS AND DISCUSSION

3.1 Euler-Bernoulli beam theory vs. Timoshenko beam theory

In this section, the authors compared the linear dynamic response of CNTs modeled as Euler Bernoulli beams (EBT) versus Timoshenko beams (TBT). The results are shown in Table 1 for fixed diameter, varying length, and varying nonlocal parameters. In this case, a single-walled carbon nanotube (SWCNT) is considered with a diameter of 0.8 nm, wall thickness of 0.34 nm, and a Young's modulus of 1 TPa [14]. In this table, there are a few interesting trends to be discussed. The first is that as the length of the CNT increases, so does the aspect ratio since the diameter remains constant. In this case, the discrepancy between EBT and TBT diminishes, which is expected. However, because the TBT model includes the effects of shear deformation and rotary inertia, it will always predict a lower natural frequency and higher deflection than EBT. Further, the discrepancy between the theories is pronounced for stout beams, particularly in the second and third natural frequencies. The next interesting result to study is the effect of

the nonlocal parameter of the system. In this case, clamped-clamped boundary conditions were considered. Thus, it is expected that increasing Eringen's nonlocal parameter will decrease the stiffness and thereby the linear natural frequency. However, it is shown that as the length of the CNT increases, the overall effect of the nonlocal parameter becomes negligible. This set of results is important for CNT-based mass sensors because it is imperative to ensure that the most appropriate beam or shell theory is utilized depending on the geometry of the CNT, with emphasis on its aspect ratio.

Table 1. Comparison of the first three natural frequencies of nonlocal CNT nanobeams modeled as Euler-Bernoulli beams vs. Timoshenko beams for different CNT lengths and nonlocal parameters.

CNT Length (nm)	Natural frequencies (GHz)	Nonlocal parameter (nm)					
		$e_0a = 0$		$e_0a = 1$		$e_0a = 2$	
		EBT	TBT	EBT	TBT	EBT	TBT
$L = 10$	ω_1	1433.73	1229.05	1352.71	1014.09	1172.03	803.37
	ω_2	3952.13	2506.21	3267.11	1866.33	2334.12	1389.08
	ω_3	7747.75	3737.18	5492.89	2680.91	3494.01	1950.68
$L = 50$	ω_1	57.35	56.81	57.21	55.45	56.79	52.30
	ω_2	158.09	149.05	156.65	133.92	152.56	113.66
	ω_3	309.91	263.42	303.95	217.67	287.95	173.96
$L = 100$	ω_1	14.33	14.30	14.32	14.21	14.30	13.95
	ω_2	39.52	38.87	39.43	37.33	39.16	34.26
	ω_3	77.48	73.27	77.10	66.12	75.99	56.42
$L = 200$	ω_1	3.58	3.58	3.58	3.58	3.58	3.56
	ω_2	9.88	9.84	9.87	9.72	9.86	9.42
	ω_3	19.37	19.07	19.35	18.35	19.27	16.90

3.2 Uniform, linear, and nonlinear temperature distributions

In order to perform a crucial study to explain how the surface temperature difference ($T_o - T_i$) and various types of temperature rise could affect the dynamic characteristics of the carbon nanotube-based mass detector, the first natural frequency shift considering the deposited Neon atom with the mass of 33.51 yg for three distinct levels of the surface temperature difference, as presented in Fig. 4. These results are given with assuming no forcing in the model. A close scrutiny of the obtained results reveals that in the pre-buckling region, the assumption of uniform and linear temperature gradients across the radius of the CNT estimates higher frequency shifts compared to the nonlinear temperature distribution. On the contrary, considering the non-linear thermal gradient yields the largest values of the frequency shift and hence the highest mass detection sensitivities of the CNT-based mass sensor in the post-buckling configuration. In addition, by improving the surface temperature difference, the discrepancy among the results under UTD, LTD, and NLTD in both the natural frequency and the frequency shift would rise drastically.

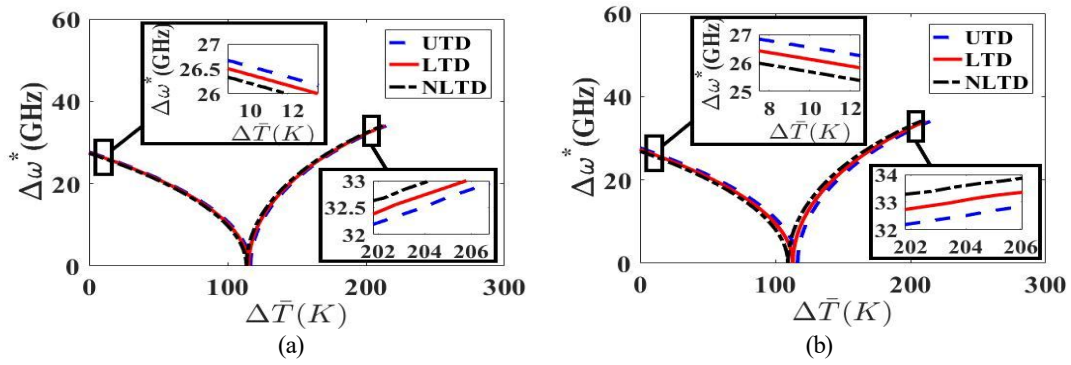


Fig. 4. The first natural frequency shift of the CNT subjected to UTD, LTD, and NLTD, considering $m_g=33.51$ yg, $L = 40$ nm, $D=0.8$ nm, $e_0a = 0.032$ nm, no forcing, and the surface temperature difference of (a) 20 K, (b) 50 K.

In Fig. 5 and Table 2, a comparison between the linear and nonlinear frequency shifts is presented, where the CNT-based mass detector is subjected to uniform, linear, and nonlinear thermal loadings. In the following discussion, the considered Q-factor and excitation force amplitude for the nonlinear dynamic response of the system are set equal to 10 and 1, respectively. Notably, the maps of the linear and nonlinear frequency shifts versus the location of the deposited mass are perfectly similar for the CNT under the first and the second mode vibrations. It is clearly seen that for both linear and nonlinear oscillation regimes, the maximum shifts induced in the first and the second frequencies are obtained for an atomic-scale particle placed at $\eta=0.5$ and $\eta \approx 0.3$ or $\eta \approx 0.7$, respectively. Moreover, it can be deduced that in all three thermal load conditions the assumption of the linear dynamic behavior of the CNT estimates larger values for the frequency shift and hence higher mass detection sensitivities compared to the nonlinear forced oscillation regime.

It is worth noting that the values of the percentage deviation of the nonlinear resonance frequency shift from the linear frequency shift in the first mode are higher than those in the second mode for the CNT under the aforementioned three thermal loading conditions. Moreover, it can be concluded that the assumption of the nonlinear temperature distribution through the thickness of the nanobeam yields the largest values of the percentage deviation of the nonlinear resonance frequency shifts. This is attributed to the fact that the softening effect of NLTD is more significant compared to the weakening effects of LTD and UTD on the structure of the CNT-based resonator. Consequently, the lowest values of the frequency shift and hence the highest percent deviations of the resonance frequency shifts are obtained in the case of NLTD.

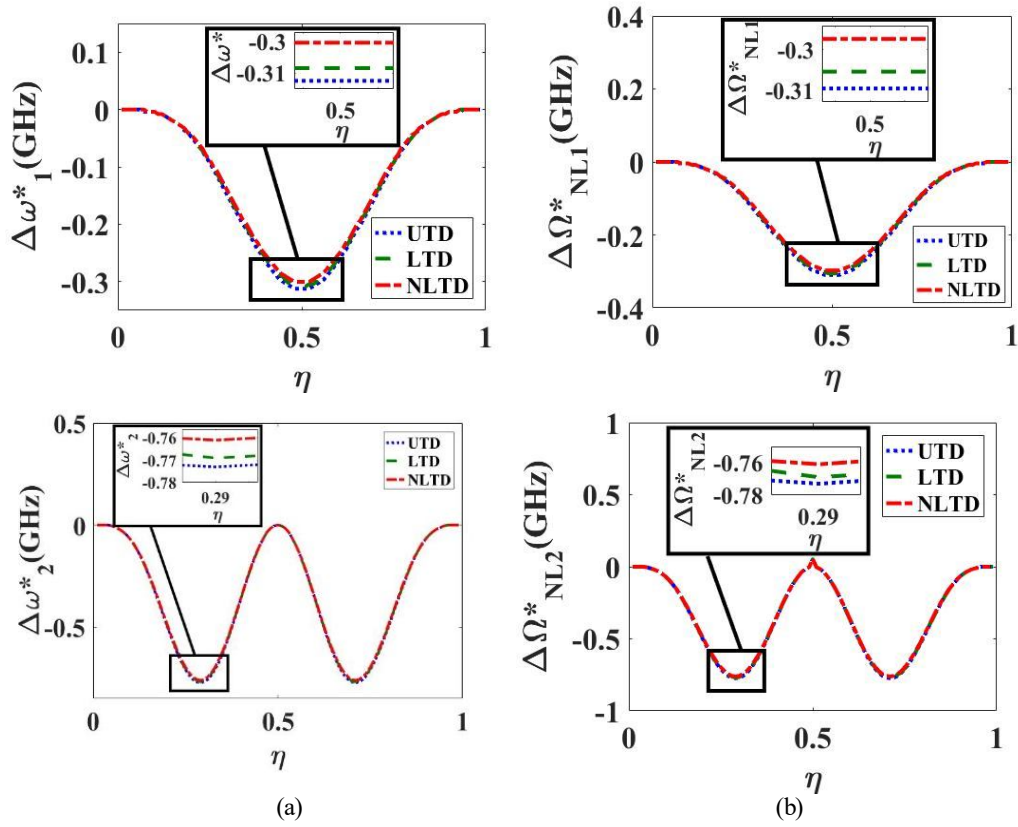


Fig. 5. The first and second frequency shift versus the location of the deposited atomic-scale mass with $Q=10$, $L=40$ nm, $m=0.218$ yg, $D=0.8$ nm, $\Delta T=0$ K, $e_0a=0.032$ nm, $(To-Ti)_{LTD}=(To-Ti)_{NLTD}=60$ K, for the two different values of the dimensionless excitation force amplitude (a) (linear natural frequency), (b) (nonlinear resonance frequency).

In what follows, the nonlinear response of the forced CNT-based resonator under external harmonic excitation is examined. In Figs. 6(a) and 6(b), the frequency-response functions near the first natural frequency (ω_1^*) of the nanobeam are plotted for different values of the excitation force amplitude and Q-factor. By inspecting the plots in Fig. 6, it can be found that Q-factor has remarkable impact on the large amplitude vibrations and nonlinear dynamic responses of the nanoscale structure. In fact, by augmenting Q-factor the nonlinear resonance frequency of the system increases dramatically. Further, it can be seen that the increase of the excitation force amplitude results in higher amplitude responses of the CNT. This is predicted because the nonlinear maximum displacement of the CNT-based resonator is proportional to the excitation force amplitude. These curves are especially important for mass sensing applications of CNTs, where detecting the induced shift in the resonance behavior of the nanostructure plays an important role in mass measurement.

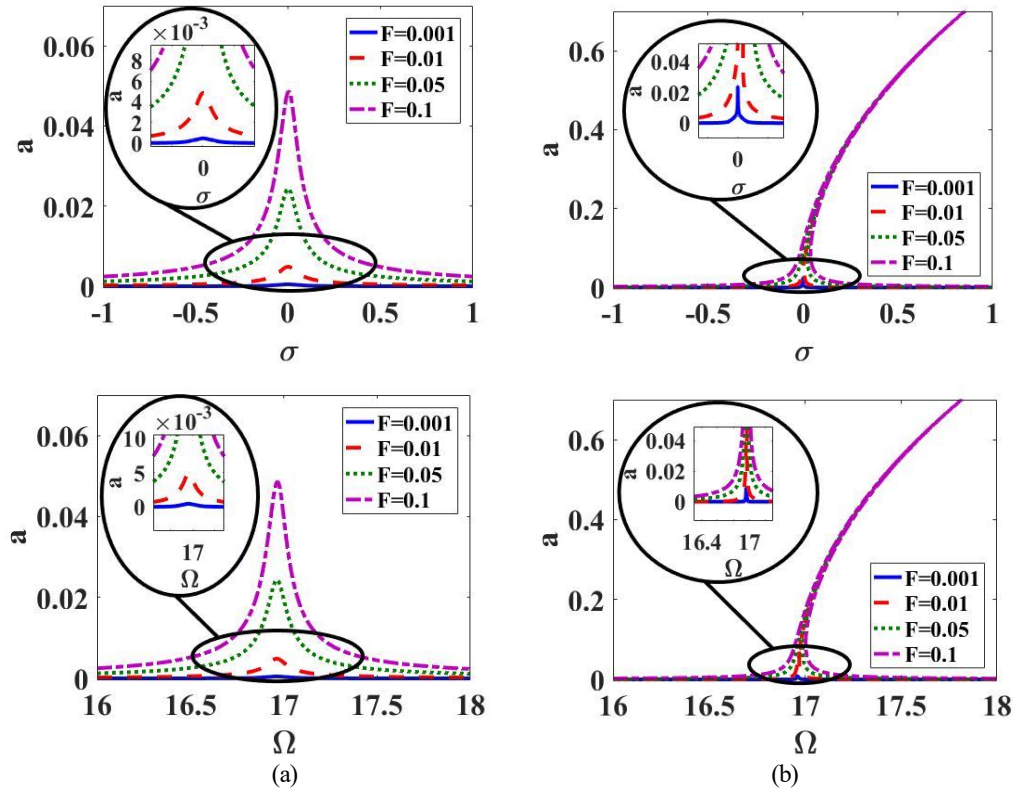


Fig. 6. The effects of the normalized excitation force amplitude on the variations of the nonlinear dimensionless real amplitude versus the detuning parameter and the nonlinear dimensionless excitation frequency considering $\Delta T=50$ K, $\eta=0.5$, $m=0.218$ yg, $L=40$ nm, $D=0.8$ nm, $e_0 a=0$ nm, and two different values of Q-factor of: (a) $Q=10$ and (b) $Q=100000$.

4 CONCLUSIONS

This study focused on several research works conducted by this research group and collaborators on CNT-based mass sensors. Several investigations on the behavior, response, and limits of applicability of the systems were presented. The authors worked to develop reduced-order models capable of detecting and identifying the mass of attached nanoparticles. In order to do so, a nonlocal continuum-based approach to account for phenomena occurring at the nanoscale, namely, Eringen's nonlocal elasticity. Additionally, many other possible considerations were discussed in the development of the models. These include selecting the appropriate beam or shell theory, such as Euler-Bernoulli beam theory or Timoshenko beam theory, and including the von Kármán geometric nonlinearity due to mid-plane stretching for end-constrained systems. Other factors that should be considered are the geometry of the particle, its geometry, its location with respect to the central axis of the CNT, and inclusion of multiple continuity conditions if multiple masses are attached. Finally, external factors were discussed, including possible axial uniform or nonuniform thermal or magnetic loads and harmonic or parametric excitations. Taking into account several of the discussed considerations, Hamilton's principle is used to derive the nonlocal nonlinear equations of motion for the system

and nondimensionalized for the case of a CNT-based mass sensor subject to thermal loading and harmonic excitations. Finally, both a linear and nonlinear analysis were performed in selected studies to determine the effects of each parameter on the system's sensitivity. These variables include the CNT length to diameter ratio, shear factor, nonlocal parameter, and landing location and effective geometry of the nanoscale object along the longitudinal axis of the CNT. Our preliminary studies show that shear deformation and rotary inertia effects will be significant for short, stout beams and at relatively high frequencies of vibration. Further, the results demonstrate the significance of the impacts of various temperature distributions, *i.e.*, UTD, LTD, and NLTD on the dynamic responses of CNT-based mass detectors in both the pre- and post-buckling configurations. From the obtained results, it is concluded that the vibration frequencies and frequency shifts of the CNT-based resonator are strongly dependent on the type of the temperature distribution and the surface temperature difference, leading to varying system sensitivity and resolution. Our derived model and analysis can be utilized by other researchers in this field who are conducting experiments at nano-scale. Our obtained results can be used as a good reference and can hopefully help to reduce the need to computationally expensive high-fidelity models at nano-scale, or costly experiments that are difficult to conduct.

5 ACKNOWLEDGEMENTS

The author S. Ceballes would like to acknowledge and thank the National Science Foundation Graduate Research Fellowship Program for funding support.

REFERENCES

- [1] Iijima, S. *Helical microtubules of graphitic carbon*. Nature. 353(6348), 56 (1991).
- [2] Iijima, S. and Ichihashi, T. *Single-shell carbon nanotubes of 1-nm diameter*. Nature. 363(6430), 603-605 (1993).
- [3] Ali-Akbari, H.R., Ceballes, S., Abdelkefi, A. *Nonlinear performance analysis of forced carbon nanotube-based bio-mass sensors*. International Journal of Mechanics and Materials in Design. 1-25 (2018).
- [4] Jensen, K., Kim, K., Zettl, A. *An atomic-resolution nanomechanical mass sensor*. Nature Nanotechnology. 3(9), 533-537 (2008).
- [5] Shaat, M., Abdelkefi, A. *Reporting the sensitivities and resolutions of CNT-based resonators for mass sensing*. Materials & Design. 114, 591-598 (2017).
- [6] Ali-Akbari, H.R., Shaat, M., Abdelkefi, A. *Bridged single-walled carbon nanotube-based atomic-scale mass sensors*. Applied Physics A. 122(8), 762 (2016).
- [7] Tao, Y., Boss, J.M., Moores, B.A., Degen, C.L. *Single-crystal diamond nanomechanical resonators with quality factors exceeding one million*. Nature Communications. 5, 3638 (2014).
- [8] Jiang, H., Liu, B., Huang, Y., Hwang, K.C. *Thermal expansion of single wall carbon nanotubes*. Journal of Engineering Materials and Technology, 126(3) 265-270 (2004).
- [9] Pradhan, S.C. Mandal, U. *Finite element analysis of CNTs based on nonlocal elasticity and Timoshenko beam theory including thermal effect*. Physica E: Low-Dimensional Systems and Nanostructures. 53, 223-232 (2013).
- [10] Ansari, R., Hemmatnezhad, M., Rezapour, J. *The thermal effect on nonlinear oscillations of carbon nanotubes with arbitrary boundary conditions*. Current Applied Physics, 11(3),

- 692-697 (2011).
- [11] Eringen, A.C., Edelen, D.G.B. *On nonlocal elasticity*. International Journal of Engineering Science, 10(3), 233-248 (1972).
 - [12] Nayfeh, A.H. *Introduction to Perturbation Techniques*. Wiley, New York, 2011.
 - [13] Ghaffari, S.S., Ceballes, S.C., Abdelkefi, A. *Role and significance of thermal loading on the performance of carbon nanotube-based mass sensors*. Materials & Design, 160, 229-250 (2018).
 - [14] Natsuki, T., Matsuyama, N., Shi, J., Ni, Q. *Vibration analysis of nanomechanical mass sensor using carbon nanotubes under axial tensile loads*. Appl. Phys. A 116, 1001–1007 (2014)

ENHANCING DAMPING FOR COMPOSITES AEROSPACE STRUCTURES WITH PIEZOELECTRIC AND CARBON NANOPARTICLES

**LUIS QUIROGA CORTES¹, LEONARDO SANCHES², LUDOVIC BARRIERE¹,
CAMILLE BESSAGUET¹, ERIC DANTRAS³, GUILHEM MICHON²,
MATHIEU CHEVALIER¹**

¹ Institut de Recherche Technologique (IRT) Saint Exupéry

Bât. B612 – 3 rue Tarfaya – 31405 Toulouse, France

luis.quiroga@irt-saintexupery.com, web page : <http://www.irt-saintexupery.com>

² Université de Toulouse, ICA, CNRS, ISAE-Supaéro,

3 rue Caroline Aigle, 31400 Toulouse, France

leonardo.sanches@isae-supero.fr

³ Université de Toulouse, Physique des Polymères, Institut Carnot CIRIMAT

Bât 3R1 B2 - 118 Route de Narbonne 31400 Toulouse, France

eric.dantras@univ-tlse3.fr

Key words: Composites, nanocomposites, vibration, piezoelectric fillers, damping

Abstract.

This paper describes the promising ability for dissipating mechanical energy of composite structures thanks to a passive damping concept based on the local transduction-dissipation phenomenon. This concept involves nanocomposites layers filled with unleaded piezoelectric and electrically conductive particles. Here nanocomposites were processed by extrusion and damping layers were obtained by hot press. Engineering Polyamide (PA) and high performance poly ether ketone ketone (PEKK) were used as host matrices. After the process step, damping layers were embedded in composite sandwich beams and honeycomb composites panels with different payloads configurations. The macroscopic piezoelectric behaviour of nanocomposites was achieved after poling step. The dynamic response of nanocomposites has been characterized by dynamic mechanical analysis and vibration tests before and after the polarization. The analysis of stress-strain hysteresis loops and the frequency response function (FRF) of composites structures showed non-linear effects, high dissipated energy up to 40 % and high vibration mitigations up to 50 % for the different structures. Results bring promising dissipative behaviour for aerospace applications.

1 INTRODUCTION

With the growing interest of carbon fibre composites, bringing new functionalities has become a main challenge of the last years [1]. High performance composites brought many advantages like weight reduction and advantageous stiffness/weight ratio plus the ability to manufacture complex shaped structures. However, the reduced amount of fasteners decrease the damping capacity and increase the vibration levels: Enhancing the dynamical and vibroacoustic responses of composites structures is a topic of great interest in the aerospace industry.

The current counter strategies consist in ensuring structures reliability by active control [2], design modifications, add-on extrinsic macroscopic elements [3], in order to adapt the dynamic response. However these solutions could increase the overall mass of targeted structures. For real weight and cost reductions, it is proposed to bring this functionality at material's scale integrated in polymers and organic matrix composites (Figure 1).

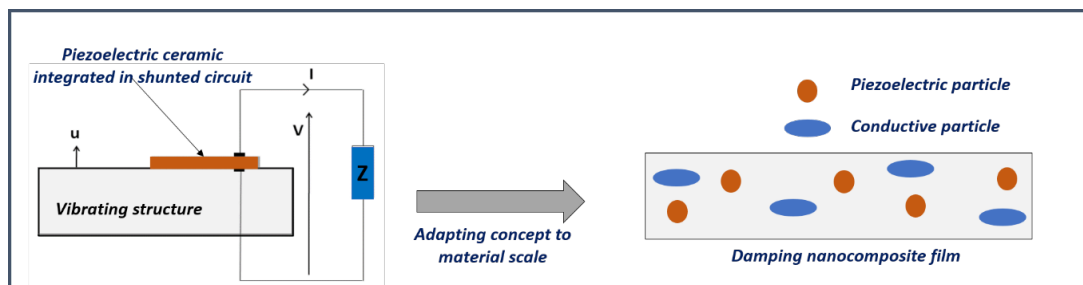


Figure 1. Passive control based on piezoelectric material: integrating functionality at material scale

The concept studied in this paper consists in dispersing piezoelectric and electrically dissipative particles in a polymer (Figure 1) in order to add a new contribution - the local transduction-dissipation [4] - to overall damping generally obtained thanks to structural, stick-slip and viscous contributions [5]. While piezoelectric particles ensure the mechano-electrical transduction the conductive particles locally dissipate the created charges in the polymer matrix by the Joule effect. This concept was recently studied by Carponcin et al. [6] with large damping efficiency by the synergy of PZT and CNT particles. Some works have pointed out the importance of the poling step conditions to improve piezoelectric [7-9] and damping behavior in nanocomposites [10].

Here the elaboration of a nanocomposite for vibration reduction is proposed based on thermoplastic polymer. The dynamic behaviour of composites structures containing the damping nanocomposite was followed by dynamic mechanical analysis and vibration tests in order to bring proofs about efficiency of the local transduction-dissipation phenomenon.

2 EXPERIMENTAL PROCEDURES

- Materials

Polyamide (PA) and Poly Ether ketone Ketone (PEKK) were provided by Arkema in powder or pellets shape. Both thermoplastic polymers were chosen as host matrices for its high mechanical properties, low moisture absorption and elevated thermal degradation. Micrometer sized BaTiO_3 (Sigma Aldrich) or NaNbO_3 (CIRIMAT Toulouse) ceramic particles were used as piezoelectric fillers while carbon black (CB – Sigma Aldrich) or carbon nanotubes (CNT – Arkema) were used as conductive fillers.

- Nanocomposites and composites processing

Fillers were dispersed by twin screw extruder in the thermoplastic matrix. The volume fraction of piezoelectric fillers is ranged between 10% and 30%. Homogenous dispersion is mandatory in order to avoid electrical breakdown during polarization and to maintain the mechanical properties of the polymer matrix. Moreover nanocomposites must be necessary insulator to achieve polarization. The volume fraction of conductive particles is directed linked to their aspect ratio (length over diameter) and their electrical percolation threshold when dispersed in a polymer matrix. A three phase nanocomposite film PA/ BaTiO_3 /NTC is shown in figure 2a).

Once the film was processed, it was embedded in the composite structure. Two different structures were studied: Sandwich beams (100 mm x 20 mm) where the damping nanocomposite is constrained between carbon fiber reinforced polymer plies (CFRP) as shown in Figures 2b) and 2c), and carbon-fiber aluminum-honeycomb sandwich panels (500 mm x 500 mm) where the damping film was integrated as a patch in the surface (figure 2d). For this last structure different payloads were fixed to the structure in order to explore larger energy and frequency ranges.

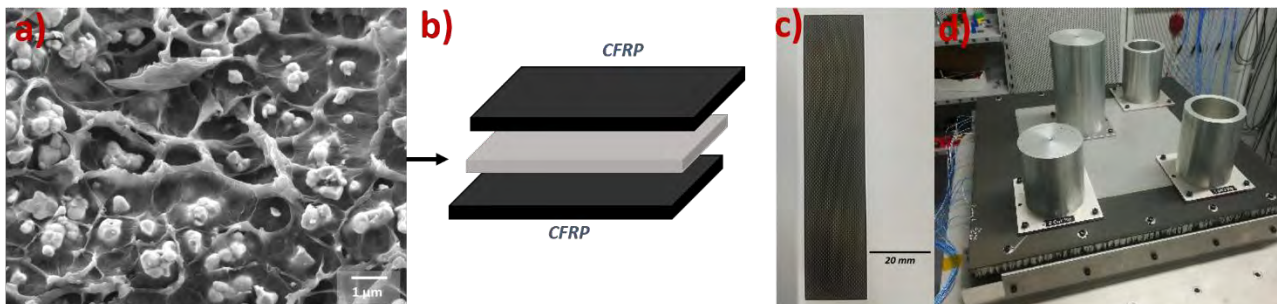


Figure 2. a) SEM image of a three-phase PA/ BaTiO_3 /NTC nanocomposite where BaTiO_3 particles appears in white while NTC are almost impossible to observe, b) Schematic representation of a constrained damping-layer between composites plies, c) sandwich beam sample for vibrations test, d) carbon-fiber aluminum-honeycomb sandwich panel containing the damping-film in the surface.

After consolidation, composites structures were poled under high electric field above glass transition temperature of the polymer matrix and for 1 min long. Polarization leads to the orientation of electric dipoles of ferroelectric particles and promotes piezoelectricity.

Shear stress-strain hysteresis loops were obtained by an ARES strain control rheometer in the rectangular shear mode before and after the poling step. Tests were performed at room temperature. When shear stress $\sigma(\omega)$ is plotted as a function of the shear strain $\gamma(\omega)$, $\sigma(\omega)$ describe a loop where its area represents the dissipated energy during one period. According to Piollet et al. [11], the stress-strain loops were mathematically modified by subtracting the linear part following $\sigma' = \sigma - P\gamma$, where P is the hysteresis slope measured at 0.1 % of deformation.

Vibration tests were performed with an electrodynamic shaker LDS V830-335 SPA16K 10KN from BRÜEL & KJÆR. A sinusoidal load of constant amplitude was applied for the different composites structures. Test were carried on at different load amplitudes (0,25g to 4g) in a large frequency range (0 to 2kHz) in order to observe the effects of poling on the overall structure behavior. The dynamic response as a function of excitation frequency was followed through a frequency response function (FRF) where resonance frequencies, as well as the damping levels were studied.

3 RESULTS AND DISCUSSIONS

Stress-strain hysteresis loops obtained for a PA/BaTiO₃/NTC damping nanocomposites at 25 °C were analyzed before and after polarization. Figure 3a) shows hysteresis loops for the non-poled samples at different strain rate.

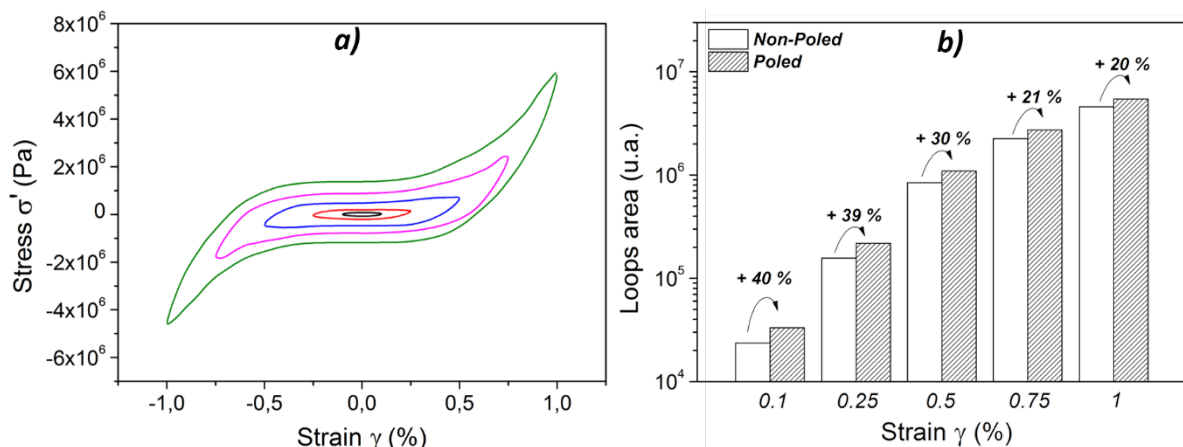


Fig. 3. a) Measured hysteresis loops at different strain rate at 25 °C of a damping film after the subtraction of the linear part, b) Hysteresis loops area at 25 °C as a function of strain, before and after polarization

The shape of the loops is complex and vary strongly with amplitude. Since the ellipsoid shape is characteristic of a linear behavior, here results highlight high nonlinear effects. The area of the loops is reported on Figure 3b) before and after polarization for different amplitudes. The hysteresis loops areas are significantly increased from 20 to 40 % after polarization: The local transduction-dissipation phenomenon leads to an important increase of dissipated energy.

Figure 4 presents the evolution of the frequency response function FRF of a damping nanocomposite in the sandwich beam configuration (Figures 2b and 2c) in the vicinity of the second bending vibration mode. The peak amplitude at resonance decreases when the imposed acceleration increases. This behavior is related to nonlinearities. After polarization, a small shift of the resonance peak to the low frequencies (softening effect). This phenomenon was already reported [6], however is not clear yet how polarization could lead to this shift. Polarization also is responsible for an amplitude decrease: While for an excitation level of 0,25g, the amplitude drop represents 54 % of initial amplitude. When excitation level attained 1g, the amplitude decrease represents 40% of initial amplitude. In average, the resonance amplitude decrease ratio is near to 45 %. These results show how the synergy between piezoelectric and conductive particles improves the damping of composite sandwich beams. Piezoelectric particles convert the energy of the mechanical vibrations into electrical charges and CNTs allow the evacuation of these charges by local conduction.

The damping nanocomposite was surface bonded in a representative aerospace structure. The system “Damping film + Composite” structure (Figure 2d) was manufactured following industrial processes. Vibration tests were later performed by fixing the panel horizontally over vibration shaker’s head. The evaluation of the nonlinear effects brought by the polarization and amplitude load on the resonance frequencies and dissipative energy are very complex: Plus, the modal properties varies significantly between two different payload configurations. In order to simplify our understanding, only the first and second bending vibration modes were analyzed before and after polarization at 0,25g (Figure 5).

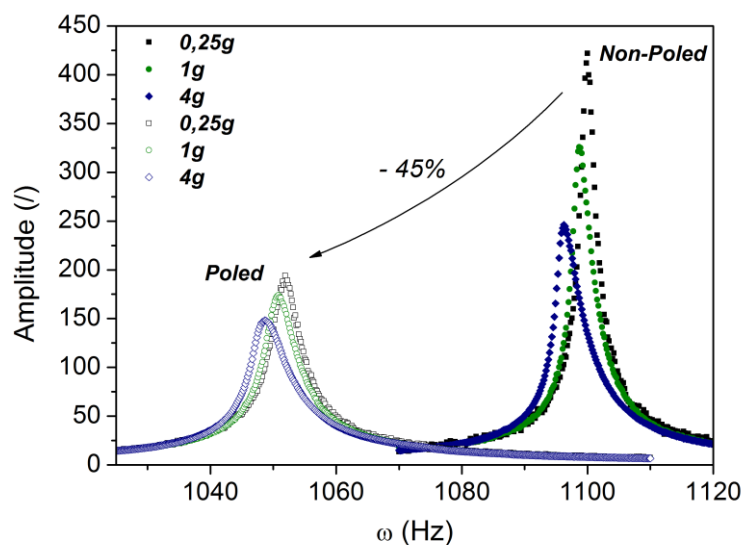


Figure. 4. FRF of the 2nd bending vibration mode of a composite sandwich beam containing the damping film before and after polarization

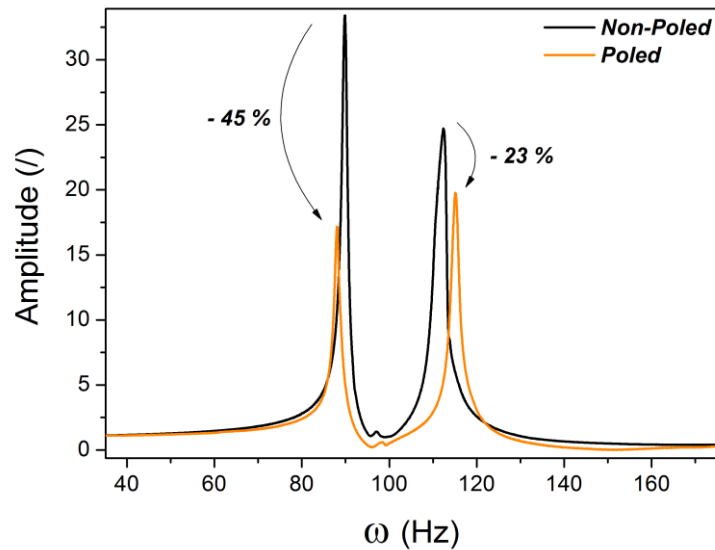


Figure. 5. FRF of the 1st and 2nd bending vibration modes of carbon-fiber aluminum-honeycomb sandwich panel containing the damping film before and after polarization

As it was observed for composites sandwich beams, polarization causes an amplitude decrease of 45 % and 23 % for the first and the second modes respectively. Equivalent damping performances were observed in both structures. Despite of the complexity of the structure, the transduction-dissipation phenomenon was proved by enhancing vibration mitigation to composite structures.

4 CONCLUSIONS

- A promising passive damping concept based on local transduction-dissipation phenomenon for aerospace composites structures was studied. The damping material is based on nanocomposite, where micrometer ceramic and carbon particles are homogeneously dispersed in a thermoplastic polymer.
- Processed nanocomposites films were embedded in composites sandwich-beams and carbon-fiber aluminum-honeycomb sandwich panels with different payloads configurations. The structures were poled after consolidation in order to promote piezoelectricity.
- Experimental shear tests on sandwich-beams highlighted strong non-linear effects, frequency and amplitude dependency by following stress-strain hysteresis loops. Moreover, an increase of the loops area and so the dissipated energy from 20 to 40 % was reported after polarization.

- Experimental vibration tests were performed on sandwich-beams. The resulting FRF showed strong non-linear behavior and amplitude decrease of the second bending mode up to 45% in average for different load amplitudes.
- Finally, experimental behavior performed in carbon-fiber aluminum-honeycomb sandwich panels containing the damping nanocomposite in the surface was followed. At low frequencies, results showed important decrease of amplitude up to 45 % for the first mode and 25 % for the second mode. The performance of the concept was proved in a representative aerospace structure.
- Further investigation containing multiscale physics and modeling of the material contribution to damping performances will be devoted.

Acknowledgements

These results were obtained under the research projects COMPINNOVTP and COMPINNOVTD at the IRT Saint Exupéry. We thank the industrial and academic members of the IRT who supported this project through their contributions, both financial and in terms of specific knowledge: AIRBUS OPERATIONS, ARIANE GROUP, AIRBUS GROUP, THALES ALENIA SPACE, STELIA, CIRIMAT, CNRS, ICA, IMRCP, ISAE and UPS. We also thank the Commissariat Général aux Investissements and the Agence Nationale de la Recherche for their financial support in the Programme d'Investissement d'Avenir (PIA).

REFERENCES

- [1] R.F. Gibson, A review of recent research on mechanics of multifunctional composite, *Compos. Struct*, vol. 92, pp. 2793–2810, 2010.
- [2] Y. K. Kang, H. C. Park, J. K. U, and S. Choi, “Interaction of active and passive vibration control of laminated composite beams with piezoceramic sensors/actuators,” *Mater. Des.*, vol. 23, pp. 277–286, 2002.
- [3] N. W. Hagoog and A. Von Flotow, “Damping in structural vibrations with piezoelectric materials and passive electrical networks,” *J. Sound Vib.*, vol. 146, no. 2, pp. 243–268, 1991.
- [4] Hori, T. Aoki, Y. Ohira, and S. Yano, “New type of mechanical damping composites composed of piezoelectric ceramics, carbon black and epoxy resin”, *Compos. Part A*, vol. 32, pp. 287-290, 2001
- [5] C. Barbier, R. Dendievel, and D. Rodney, “Role of friction in the mechanics of nonbonded fibrous materials,” *Phys. Rev. E*, vol. 80, pp. 1–5, 2009.
- [6] D. Carponcin, E. Dantras, G. Michon, J. Dandurand, G. Aridon, F. Levallois, L. Cadiergues, and C. Lacabanne, “New hybrid polymer nanocomposites for passive vibration damping by incorporation of carbon nanotubes and lead zirconate titanate particles”, *J. Non. Cryst. Solids*, vol. 409, pp. 20-26, 2015.
- [7] M. Alexandre, C. Bessaguet, C. David, E. Dantras and C. Lacabanne, “Piezoelectric

- properties of polymer/lead-free ceramic composites”, *Phase Transitions*, vol.89, pp.708-716, 2016.
- [8] D. Carponcin, E. Dantras, L. Laffont, J. Dandurand, G. Aridon, F. Levallois, L.Cadiergues, and C. Lacabanne, “Integrated piezoelectric function in a high thermostable thermoplastic PZT/PEEK composite”, *J. Non. Cryst. Solids*, vol. 388, pp. 32-36, 2014.
- [9] C. Bessaguet, E. Dantras, C. Lacabanne, M. Chevalier, and G. Michon, “Piezoelectric and mechanical behavior of NaNbO₃/PEKK lead-free nanocomposites”, *J. Non. Cryst. Solids*, vol. 459, pp. 83–87, 2017.
- [10] C. Bessaguet, Composite hybride à matrice polymère PEKK - Niobate de sodium - graphène ou noir de carbone, pour un amortissement vibratoire passif par transduction-dissipation locale, à finalité aéronautique et spatiale, Thèse de l’Université de Toulouse
- [11] E. Piollet, D. Poquillon, and G. Michon, “Dynamic hysteresis modelling of entangled cross linked fibres in shear,” *J. Sound Vib.*, vol. 383, pp. 248–264, 2016.
- [12] F. Al-Bender, W. Symens, J. Swevers, and H. Van Brussel, “Theoretical analysis of the dynamic behavior of hysteresis elements in mechanical systems,” *Int. J. Non. Linear. Mech.*, vol. 39, pp. 1721–1735, 2004.

INVESTIGATIONS ON THE DYNAMICS AND VIBRATIONS OF CARBON NANOTUBES WITH MULTIPLE DEPOSITED NANOPARTICLES

S. CEBALLES^{*}, D. FURTH^{*}, AND A. ABDELKEFI^{*}

^{*}Department of Mechanical and Aerospace Engineering
New Mexico State University
Las Cruces, NM 88003, USA
E-mail: abdu@nmsu.edu

Key words: Carbon nanotube, Eringen's nonlocal elasticity, mass sensor, nanoparticles, detection sensitivity, frequency shift.

Abstract. This study focuses on the free vibrations of carbon nanotubes (CNTs) with clamped-clamped boundary conditions and multiple deposited nanoparticles. The purpose of this work is to extend the limits of applicability for the theoretical modeling of nanoscale CNT-based mass sensors. Previous studies focused on determining the induced frequency shift or amplitude shifts that arise due to the deposition of a single nanoparticle on or within the CNT. In this effort, the reduced-order model is extended to include an arbitrary number of masses deposited on the CNT. This is a more realistic representation of experiments at the nanoscale. To perform a free vibration analysis, the governing equations are first derived by virtue of Hamilton's principle, considering Euler-Bernoulli beam theory. To account for the effects of mid-plane stretching for end constrained beams, the von Kármán geometric nonlinearity is included and effectively modifies the strain field. Eringen's nonlocal elasticity theory is employed to account for size dependent phenomena. Each deposited particle breaks up the displacement field, leading to continuity equations for the deflection, slope, moment, and shear. After all the governing equations, boundary conditions, and continuity conditions are obtained, a parametric study is performed to determine the impacts of increasing the number of nanoparticles that are deposited onto the CNT on the sensitivity of the carbon-nanotube based sensor. Results show that, even when keeping the total deposited mass constant, the number of particles and their location can significantly shift the natural frequencies and the mode shapes of the nano-sensor.

1 INTRODUCTION

Nowadays many researchers are aware of the potential to use carbon nanotubes (CNTs) in a variety of nanoscale applications. Since their initial discovery in the early 1990s [1, 2], CNTs have been widely studied for their unique mechanical, optical, thermal, and electrical properties. To clarify, CNTs are essentially rolled sheets of graphene with cylindrical structure that can have diameters on the order of several nanometers and lengths varying from several nanometers to a few microns in length. Further, the CNTs exist either as single-walled or multi-walled structures. In this research group, studies are primarily conducted from a theoretical, mechanics,

dynamics, and vibrations points of view through the development of reduced-order models. In the development of these models, there are several factors that must be considered. For example, in modelling structures at the nanoscale, it is important to consider the limits of applicability of classical continuum mechanics. At this scale, the size of the considered structure can approach the internal lengths in the structure and classical continuum mechanics assumptions can fail. In that case, particles in a continuum should no longer be treated simply as point masses subject only to translation, but rather as nano-volumes that can rotate, deform, and translate [3]. One of the most widely used theories is Eringen's nonlocal elasticity theory [4, 5]. This theory accounts for the effects of neighboring particles in a medium through an attenuation function. When the model is simplified to its differential form, it can be applied in a variety of models that need to take size-dependent effects into account [5-8].

After noting that CNTs can be used in a variety of applications, we narrow it down to considering CNTs to act as a nano-scale mechanical resonator or sensor that aims at detecting and identifying the mass of particles that are distributed on or within the CNT. The reason that they are considered in this application is that CNTs have a very high Young's modulus and therefore vibrate at a very high natural frequency. So, depositing even the smallest mass onto the CNT can cause a measurable shift in the frequency that can be converted back to an equivalent deposited mass. As such, there have been many efforts that focus on developing reduced-order models for CNT-based mass sensors [9-14].

So, for this work, we aim to extend the limits of applicability of CNT-based mass sensor by accounting for an arbitrary number of particles. The displacement field is defined by the Euler-Bernoulli beam theory. To account for mid-plane stretching of end-constrained beams, the von Kármán geometric nonlinearity is included. For size-dependent effects, we modify the stress field using Eringen's nonlocal theory. Then, to determine the governing equations of motion, boundary conditions, and continuity conditions, we utilize the Hamilton's principle. Finally, a free vibration analysis is performed to determine the shifts in the natural frequency for different numbers of deposited particles and varying centers of mass.

2 SIZE-DEPENDENT NONLINEAR GOVERNING EQUATIONS OF MOTION

In this section, the derivation for the governing equations of motion, boundary conditions, and continuity conditions are presented for the CNT-based mass sensor with multiple deposited nanoparticles. Consider a single-walled CNT of length L , diameter D , and wall thickness h , as shown in Figure 1. The total number of deposited nanoparticles is denoted by N . The location and individual mass of each particle are denoted by x_{mi} and m_i , respectively, where $i = 1, 2, 3, \dots, N$.

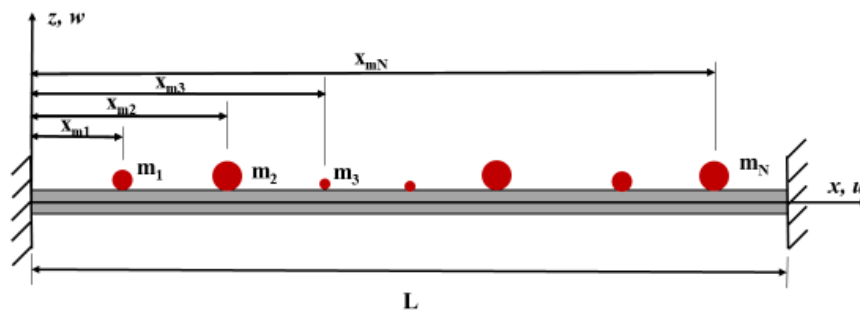


Figure 1. Schematic of CNT-based mass sensor with N deposited nanoparticles.

The total mass of the deposited particles can be represented by:

$$M = \sum_{i=1}^N m_i \quad (1)$$

In this study, the displacement field is defined according to Euler-Bernoulli beam theory, as shown in equation. (2). The von Kármán strain tensor, shown in equation (3), is used to determine the CNT's strain field, shown in equation (4).

$$u_x(x, z) = u(x) - z \frac{\partial w}{\partial x}; \quad u_y(x, z) = 0; \quad u_z(x, z) = w(x) \quad (2)$$

$$\varepsilon_{ij} = \frac{1}{2} \left(\frac{\partial u_i}{\partial x_j} + \frac{\partial u_j}{\partial x_i} \right) + \frac{1}{2} \left(\frac{\partial u_k}{\partial x_i} \frac{\partial u_k}{\partial x_j} \right) \quad (3)$$

$$\varepsilon_{xx} = \frac{\partial u}{\partial x} - z \frac{\partial^2 w}{\partial x^2} + \frac{1}{2} \left(\frac{\partial w}{\partial x} \right)^2 \quad (4)$$

Then, to account for each deposited mass, the displacement field is broken up as:

$$u(x, t) = \begin{cases} u_1(x, t), & 0 \leq x \leq x_{m1} \\ u_2(x, t), & x_{m1} < x \leq x_{m2} \\ \vdots & \\ u_{N+1}(x, t), & x_{mN} < x < L \end{cases}, \quad w(x, t) = \begin{cases} w_1(x, t), & 0 \leq x \leq x_{m1} \\ w_2(x, t), & x_{m1} < x \leq x_{m2} \\ \vdots & \\ w_{N+1}(x, t), & x_{mN} < x < L \end{cases} \quad (5)$$

where $u(x, t)$ and $w(x, t)$ represent the longitudinal and transverse displacement of the CNT, respectively. In breaking up the displacement field, continuity conditions are introduced at the location of each deposited mass. Before finalizing the derivations for the governing equations, it is important to note that Eringen's nonlocal theory is used in this study to account for the behavior and response of the structure at the nanoscale. The reason that it is important to include this theory into the derived model is that when the size of the considered structure is comparable to the internal lengths of the structure, size dependent behaviors appear. Because of the material structure of the CNT, it has been shown that Eringen's nonlocal elasticity theory is appropriate for CNTs. In this theory, each particle is modeled as a point mass, as in classical continuum mechanics. However, the stress at one reference point is influenced by the strain of all other points in the medium. Therefore, the nonlocal stress field σ_{ij} is represented as [3, 4]:

$$\sigma_{ij}(x) = \int_{\Omega} \alpha(|x' - x|, e) t_{ij}(x) d\Omega(x') \quad (6)$$

In this case, the local stress field is denoted by t_{ij} , α is an attenuation function that captures the effects of the neighboring particles. The nonlocal parameter is given as $e = e_0 a / l$. This parameter depends on the several other parameters including the internal and external characteristic lengths, represented by a and l , respectively. Additionally, the material parameter, e_0 , that is determined from the longitudinal and transverse acoustic dispersions can be found from molecular dynamics simulations or experiments. Noting that the integral formulation leads to equations that are difficult to solve analytically, the simplified differential form is used, yielding:

$$(1 - (e_0 a)^2 \nabla^2) \sigma_{ij} = c_{ijkl} \varepsilon_{kl} \quad (7)$$

Considering the displacement field, strain field, and size-dependency through Eringen's nonlocal elasticity, the governing equations of motion can be determined using the Hamilton's principle, given as:

$$\delta H = \int_{t_1}^{t_2} (\delta T_b + \sum_{i=1}^N \delta T_{mi} - \delta \Pi) dt = 0 \quad (8)$$

It should be noted that δT_b , δT_{mi} , and $\delta \Pi$ represent the first variation of the kinetic energy of the CNT, the first variation of the kinetic energy of each deposited particle, and the first variation of the potential energy, respectively. The full expressions for each term are omitted for brevity, but more details on these terms can be found in [9]. After determining the variations of the energy and substituting them into Hamilton's principle, the final nondimensional equations of motion are derived as:

$$\begin{aligned} & W_i^{(4)} + \ddot{W}_i - \left(\frac{1}{N+1} \int_0^{\eta_1} (W'_{1})^2 d\chi + \sum_{j=2}^N \frac{1}{N+1} \int_{\eta_j}^{\eta_{j+1}} (W'_j)^2 d\chi + \frac{1}{N+1} \int_{\eta_N}^{\eta_{N+1}} (W'_{N+1})^2 d\chi \right) W''_i \\ & - e^2 \left[\ddot{W}''_i - \left(\frac{1}{N+1} \int_0^{\eta_1} (W'_{1})^2 d\chi + \sum_{j=2}^N \frac{1}{N+1} \int_{\eta_j}^{\eta_{j+1}} (W'_j)^2 d\chi + \frac{1}{N+1} \int_{\eta_N}^{\eta_{N+1}} (W'_{N+1})^2 d\chi \right) W_i^{(4)} \right] \\ & = 0 \end{aligned} \quad (9)$$

where $i = 1, 2, 3, \dots, N$. Then, the boundary and continuity conditions are:

$$W_1(0) = W'_1(0) = W_{N+1}(1) = W'_{N+1}(1) = 0 \quad (10)$$

$$\begin{aligned} & W_i(\eta_i) = W_{i+1}(\eta_i); \\ & W'_i(\eta_i) = W'_{i+1}(\eta_i); \\ & W''_i(\eta_i) = W''_{i+1}(\eta_i); \\ & W'''_i(\eta_i) - W'''_{i+1}(\eta_i) \\ & + e^2 \left[\left(\frac{1}{N+1} \int_0^{\eta_1} (W'_{1})^2 d\chi + \sum_{j=2}^N \frac{1}{N+1} \int_{\eta_j}^{\eta_{j+1}} (W'_j)^2 d\chi + \frac{1}{N+1} \int_{\eta_N}^{\eta_{N+1}} (W'_{N+1})^2 d\chi \right) \right] \\ & (W'''_i(\eta_i) - W'''_{i+1}(\eta_i)) - \ddot{W}_i \mu_i(\eta_i) = 0 \end{aligned} \quad (11)$$

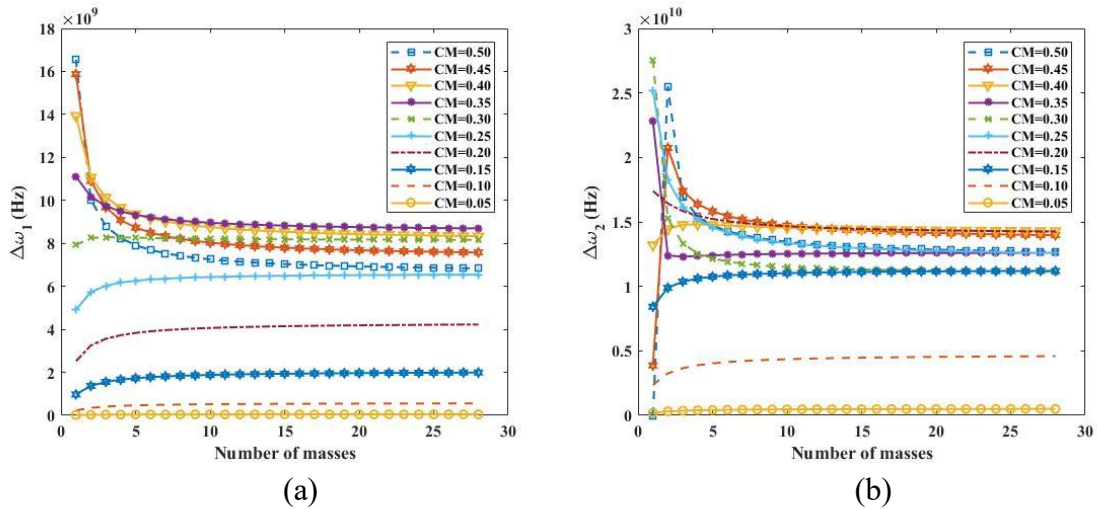
In this case, W denotes the nondimensional transverse displacement. The nondimensional mass of each particle is denoted by μ_i , the nondimensional location of each particle is represented by η_i . Finally, e represents the nondimensional nonlocal parameter and N represents the total number of deposited particles. Further details on these nondimensional parameters and derivation details can be found in [9]. After obtaining the full set of governing equations, the system is linearized for an eigenvalue problem analysis. In doing so, the shifts in the natural frequencies and the changes in the mode shapes due to each deposited particle can be determined. Results for varying the location and number of masses are presented in the next section.

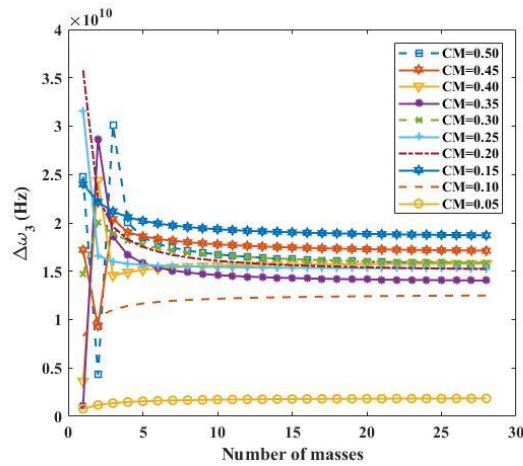
3 RESULTS AND DISCUSSION

The novelty of this work lies in investigating and discussing the importance in the differences between attaching a single nanoparticle on or within a CNT versus attaching multiple particles. One might predict that if the *total* mass that is deposited on the surface remains constant, denoted by M , that the shift in the natural frequencies before and after the particles have been deposited will also be constant. However, this is not the case. To demonstrate this phenomenon, we vary the number of deposited particles and the center of mass while keeping the total mass deposited on the surface constant.

3.1 Variations in the frequency shift by varying the number of deposited particles and center of mass

In Figure (2), the first, second, and third natural frequency shifts as a function of the number of deposited particles for varying centers of mass are presented. In all cases, the total mass M , remains constant. Furthermore, when more than one particle is considered, each particle has the same mass of $m_i = M/N$. This was done to study the effects of the location and effective center while maintaining the total mass. It is also possible to keep the mass of *each* particle constant and increase the total number of particles. In that case, the shift in the frequency would keep increasing as the number of particles increases. However, the purpose of Figure (2) is to show that if that total mass remains constant, the number of masses and their center of mass can significantly alter the frequency shift. To further explain, we consider specific configurations. The case where $CM = 0.5$ implies that particles are uniformly distributed across the entire length of the CNT. The case where $CM = 0.45$ implies that the particles are uniformly distributed along the first 90% of the beam. This trend continues until the particles are only uniformly distributed along the first 10% of the CNT, leading to $CM = 0.05$.





(c)

Figure 2. Shifts in the first, second, and third natural frequencies for a constant total deposited mass as a function of the number of masses and their center of mass.

In discussing the meaning of Figure 2, it should be mentioned that when only one particle is deposited, the maximum first natural frequency shift is obtained when the particle is deposited at the center, which makes sense physically. However, in keeping the center of mass a constant, increasing the number of particles that are uniformly distributed decreases the shift in the first natural frequency until reaching a nearly constant value at approximately 10 masses. This trend continues until reaching a critical value in the first mode in which increasing the number of masses increases the shift in the frequency. This can be seen in the bottom half of Figure 2(a). In addition, it can be seen in Figure 2(a), that there are different scenarios that lead to the same shift in the first natural frequency. In order to differentiate between the cases, we study the second and third shifts in the natural frequencies to eliminate the possibility of multiple scenarios leading to the exact same dynamic response. If the shifts in the natural frequencies are not enough to determine the scenario, it is possible to then look at the difference in the mode shapes. In studying Figures 2(b) and 2(c), it is shown that the behavior is not as uniform for the second and third shifts in the frequencies as they are for the first natural frequency shift. This is explained by the fact that in the first natural frequency, there is only one *optimal* location to deposit a single mass – the center of the CNT. Additionally, in the first mode, there are only two locations that lead to a complete inability to detect a shift in the frequency, and that is at the two ends of the beam. This is simpler than the cases of the second and third natural frequencies shifts. In these cases, even when only one deposited particle is considered, there are more than one *optimal* location to deposit a single mass and more than one location in which the shift in the second and third natural frequency is minimal or completely zero. Thus, it is shown that even by keeping the total mass deposited on the system constant, the dynamic response is still significantly affected by the number of particles and their center of mass.

3.2 Effects of the center of mass for a fixed number of deposited particles

After determining that the number of masses can significantly change the dynamic response of the CNT, the impact of the center of mass is further investigated. Because the total mass remains constant, there is a critical value for the number of masses that no longer leads to greater

shifts in the frequency. To be on the safe side, we investigate the case where 20 masses have been deposited. Then, by varying the center of mass, as shown in Figure 3, it is demonstrated that the *location* of the particles, even when there is a high number of them will change the shift in the natural. So, if one can determine the total number of masses that have been deposited on the surface, it is also possible to determine the optimal distribution in which the maximum frequency shift can be obtained. What is interesting is that these optimal locations vary as a function of the number of deposited particles and that the predicted locations are not as straightforward as they are for the case of a single deposited particle.

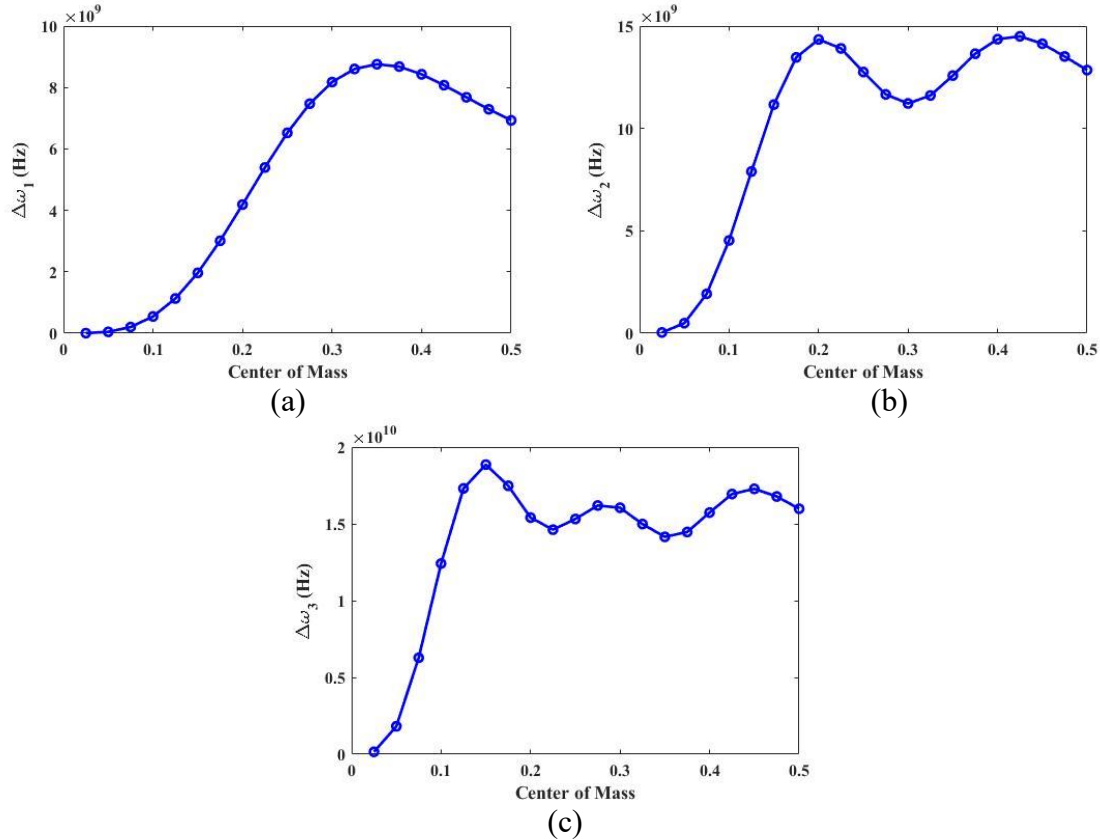


Figure 2. Shifts in the first, second, and third natural frequencies for a constant total deposited mass for 20 deposited particles as a function of the center of mass.

4 CONCLUSIONS

This study focused on determining the differences between the frequency shifts and mode shapes of CNT-based mass sensors, in which the total deposited mass remains constant, but the location and number of deposited particles varies. One might have predicted that in keeping the total mass, M , constant, that the obtained shift in the frequency would also be constant. This was not the case. It was shown that by varying the center of mass of the deposited particles, the shift in the frequency can be dramatically different. Further, even in keeping a constant center of mass and a constant total deposited mass, the number of masses alters the response of the system. This occurs until reaching a critical number of masses in which the shift in the frequency no longer varies as a function of the number of particles. This result is useful in that one can obtain the critical number of masses that are needed to approach a fixed behavior

of the system, which can be useful in reducing time and complications in both experiments and high-fidelity simulations. Additionally, it was shown that for a fixed number of deposited particles, the center of mass significantly changes the shift in the first, second, and third natural frequencies. Compared to a single deposited particle, the response differs. Overall, this study aides in extending the limits of applicability and robustness of reduced-order models for CNT-based mass sensors.

5 ACKNOWLEDGEMENTS

The authors S. Ceballes and A. Abdelkefi would like to acknowledge and thank the National Science Foundation Graduate Research Fellowship Program for funding support.

REFERENCES

- [1] Iijima, S. *Helical microtubules of graphitic carbon*. Nature. 353(6348), 56 (1991).
- [2] Iijima, S. and Ichihashi, T. *Single-shell carbon nanotubes of 1-nm diameter*. Nature. 363(6430), 603-605 (1993).
- [3] Shaat, M. and Abdelkefi, A. *On a second-order rotation gradient theory for linear elastic continua*. International Journal of Engineering Science, 100, 74-98 (2016).
- [4] Eringen, A.C., Edelen, D.G.B. *On nonlocal elasticity*. International Journal of Engineering Science, 10(3), 233-248 (1972).
- [5] Eringen, A.C. *On differential equations of nonlocal elasticity and solutions of screw dislocation and surface waves*. Journal of Applied Physics 54, 4703 (1983).
- [6] Dai, H.L., Wang, L., and Abdelkefi, A. *On nonlinear behavior and buckling of fluid-transporting nanotubes*. International Journal of Engineering Science. 87, (2014).
- [7] Pradhan, S.C. Mandal, U. *Finite element analysis of CNTs based on nonlocal elasticity and Timoshenko beam theory including thermal effect*. Physica E: Low-Dimensional Systems and Nanostructures. 53, 223-232 (2013).
- [8] Natsuki, T., Matsuyama, N., Shi, J., Ni, Q. *Vibration analysis of nanomechanical mass sensor using carbon nanotubes under axial tensile loads*. Appl. Phys. A 116, 1001–1007 (2014).
- [9] Ali-Akbari, H.R., Shaat, M., Abdelkefi, A. *Bridged single-walled carbon nanotube-based atomic-scale mass sensors*. Applied Physics A. 122(8), 762 (2016).
- [10] Ali-Akbari, H.R., Ceballes, S., Abdelkefi, A. *Nonlinear performance analysis of forced carbon nanotube-based bio-mass sensors*. International Journal of Mechanics and Materials in Design. 1-25 (2018).
- [11] Jensen, K., Kim, K., Zettl, A. *An atomic-resolution nanomechanical mass sensor*. Nature Nanotechnology. 3(9), 533-537 (2008).
- [12] Shaat, M., Abdelkefi, A. *Reporting the sensitivities and resolutions of CNT-based resonators for mass sensing*. Materials & Design. 114, 591-598 (2017).
- [13] Tao, Y., Boss, J.M., Moores, B.A., Degen, C.L. *Single-crystal diamond nanomechanical resonators with quality factors exceeding one million*. Nature Communications. 5, 3638 (2014).
- [14] Natsuki, T., Matsuyama, N., Shi, J., Ni, Q. *Vibration analysis of nanomechanical mass sensor using carbon nanotubes under axial tensile loads*. Appl. Phys. A 116, 1001–1007 (2014).

LARGE STRAIN MEASUREMENT METHOD BASED ON DYNAMIC REFERENCE IN DISTRIBUTED OPTICAL FIBER

LIUJIA SUO, ZHANJUN WU^{*}

^{*} State Key Laboratory of Structural Analysis for Industrial Equipment, Dalian University
of Technology, Dalian, China
E-mail: wuzhj@dlut.edu.cn

Key words: OFDR, distributed optical fiber, large strain, Rayleigh backscattering spectrum, Dynamic.

Abstract: Distributed optical fiber systems based on optical frequency domain reflectometry (OFDR) have received extensive attention in the field of structural health monitoring. By calculating the spectral offset by cross-correlation analysis of the reference Rayleigh backscattering spectrum (RBS) and the measured RBS, it is converted into the strain of the structural. The system based on OFDR has high spatial resolution and strain measurement accuracy. However, when the fiber is subjected to large strain (more than $5000\mu\epsilon$), the amplitude of the RBS signal will be sharply attenuated. Further, the cross-correlation analysis failed and the strain could not be demodulated. In this paper, a large-strain demodulation method for OFDR distributed fiber is proposed. The dynamic reference RBS of sub-region is used to replace the traditional fixed reference RBS to break the limitation of large strain measurement. The large strain measurement of the tensile test of composite laminates shows that the fiber strain demodulation method proposed in this paper can measure the large strain above $10000\mu\epsilon$ stably and reliably.

1 INTRODUCTION

Distributed optical fiber measurement technology based on OFDR which has high spatial resolution, high sensitivity and large dynamic measurement range, is used in the field of health monitoring [1]. Since M.Froggatt and Moore [2] applied OFDR technology to distributed fiber strain measurement in 1998, significant progress has been made in fiber strain demodulation methods [3]. RBS in the fiber is caused by the refractive index profile along the length of the fiber, which can be seen as weak fiber Bragg gratings with periodic variations [4]. Changes in strain or temperature cause spectral shifts in the local RBS of the fiber, and the offset is proportional to the amount of temperature or strain change [2]. Therefore, strain or temperature information can be obtained by measuring the spectral shift in the RBS.

Usually, a cross-correlation function is used to compare the RBS of the two sets of fibers in the initial state and the deformed state, and the maximum correlation coefficient is used to determine the offset of the corresponding RBS [5]. For example,

Boyd et al. [6] and Du et al. [7] used this method to measure small temperature changes in a low temperature environment from the RBS offset. However, the above-mentioned traditional strain demodulation method is only suitable for the case where the RBS offset is small, and cannot be applied to the large-scale offset of the RBS [8]. In particular, when the strain is large, the RBS signal of the fiber is abruptly attenuated, resulting in an uncorrelated measurement of the RBS and the reference RBS [9]. Therefore, the development of large strain demodulation methods for distributed optical fibers is a research topic worthy of attention.

Based on the strain demodulation principle of fiber RBS, a large strain partitioning strategy is applied. This paper proposes a method of sub-region dynamic reference RBS method to replace the original fixed reference RBS. The measured RBS of the sub-region is used as the reference RBS of the current sub-region, and the cross-correlation analysis is performed with the measured RBS of the current sub-region to determine the relative strain value of the current sub-region, and the final absolute strain is accumulated value. Finally, a composite strained plate tensile test with large strain (above $10000\mu\epsilon$) was performed to verify the effectiveness of the proposed large strain demodulation method.

2 PRINCIPLE

2.1 Distributed optical fiber strain measurement system based on OFDR

As shown in Fig.1, the OFDR system consists of a tunable linear swept laser, five couplers, two photodetectors, and an A/D digital capture card. The laser output from the tunable linear swept laser is divided into two optical paths through the coupler 1, that is, the auxiliary interferometer optical path and the main interferometer optical path.

In the auxiliary interferometer, the laser is split into two beams by the coupler 2, one of which passes through the delay fiber and merges with the other light in the coupler 3, which is a typical Mach-Zehnder interference beam path. Finally, the synthesized light passes through the photodetector and acts as an external clock to trigger the A/D digital acquisition card to work, converting the electrical signal into a digital signal that can be used for signal processing. The auxiliary interference optical path is used as an external clock for triggering the measurement interferometer, and a sinusoidal signal period is used as a clock signal for the purpose of compensating for the frequency scanning nonlinearity of the light source.

In the measuring interferometer, the laser is split into two beams by the coupler 4, one of which passes through the circulator and merges with the other light in the coupler 5 for collecting RBS data in the fiber under test. Finally, after the synthesized light passes through the balanced photodetector, the RBS data is triggered by the auxiliary interference optical path.

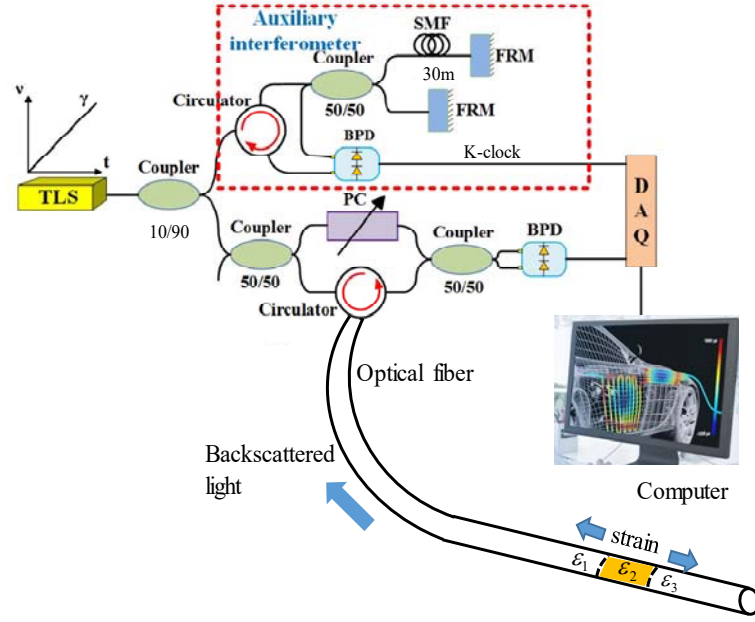


Figure 1: OFDR system

M. Forrgatt et al. [2] first proposed a distributed strain measurement method based on RBS in 1998. It was found that the RBS in the fiber shifts under strain or temperature change without changing the shape. By recording the RBS of the fiber before deformation (defined as the reference RBS) and the deformed RBS (defined as measuring the RBS), the spectral offset can be obtained by cross-correlation analysis. Convert to the corresponding strain information.

It is assumed that the i -th subset of the reference RBS is represented as $Ri(m)$, referred to as the reference subset, where m is the subset length, as shown in Figure 2(a). The i -th subset of the measured RBS can be expressed as $Mi(m)$, referred to as the measurement RBS subset, which is characterized by the fact that the intensity is constant but a wavelength offset $\Delta\lambda$ occurs. Since the strain causes the fiber to produce an elastic effect [10], the wavelength shift $\Delta\lambda$ can be describe as

$$\Delta\lambda = \lambda_0 \left\{ 1 - \frac{n_{eff}}{2} [p_{12} - (p_{11} - p_{12})]v \right\} \varepsilon = k\varepsilon, \quad (1)$$

where λ_0 is the center wavelength, p_{11} and p_{12} are the elastic coefficients of the fiber material, n_{eff} is the effective refractive index of the fiber, v is the Poisson's ratio of the fiber material, k is the strain sensitivity coefficient of the fiber relative to the wavelength shift, and ε is the fiber strain.

Assume that the fiber is a pure quartz material, then $p_{11} = 0.112$, $p_{12} = 0.270$, $v = 0.17$, and $n_{eff} = 0.456$. When the center wavelength of the light source is 1550 nm, the strain sensitivity coefficient $k = 1.2 \text{ pm}/\mu\varepsilon$ can be obtained.

It can be seen that when $\Delta\lambda$ is negative, it means that the measured RBS moves toward the low wavenumber direction (called blue shift), and the fiber is subjected to tensile strain ($\varepsilon > 0$). Conversely, when $\Delta\lambda$ is positive, it means that the measured RBS moves toward the high wavenumber direction (called red shift), and the fiber is subjected to compressive strain ($\varepsilon < 0$). The above is the basic principle of measuring

the strain using the fiber RBS.

2.2 Dynamic reference RBS

To control the difference between the reference RBS and the measured RBS, it means to adjust the measurable strain range. The large strain is divided into n intervals, as shown in FIG. 3, and the relative strain $\Delta\epsilon_i$ in the i -th sub-region satisfies the fault tolerance range of the cross-correlation analysis. Taking the measured RBS of the $(i-1)$ -th sub-region as the reference RBS of the i -th sub-region, the relative offset of the sub-region can be obtained by cross-correlation analysis with the scattering spectrum of the i -th sub-region. $\Delta\lambda_i$. Thus, the relative offsets in all intervals are accumulated as the absolute offset corresponding to the large strain.

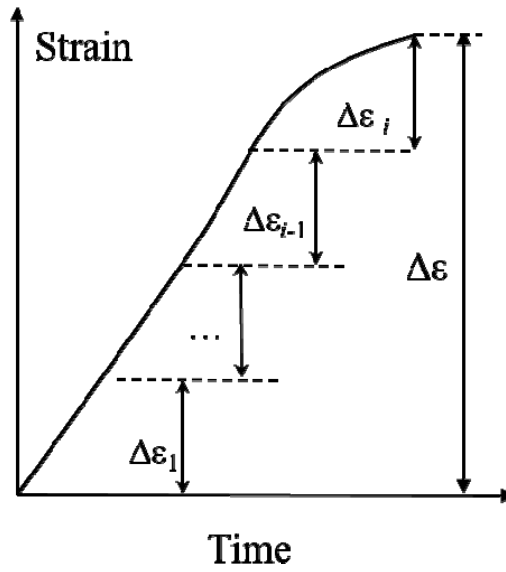


Figure 2: Principle of large strain partition measurement based on dynamic reference Rayleigh backscattering spectrum

Different from the traditional method, the initial state is different as the fixed reference RBS. The core of the above-mentioned large-strain partition demodulation principle is to measure the RBS signal M_{i-1} of the $(i-1)$ -th sub-region as the i -th sub-element. The reference RBS R_i of the region is called the dynamic reference RBS because the reference RBS is continuously updated as $F_i = G_{i-1}$.

Then, cross-correlation analysis is performed on the measured RBS signal M_i , thereby obtaining the relative wavelength shift amount $\Delta\lambda_i$, and summing with the previous $i-1$ times to obtain the final absolute offset

$$\Delta\lambda = \sum_{i=1}^i \Delta\lambda_i, \quad (2)$$

where i is the number of partitions with large strain. The final absolute strain $\epsilon = k\Delta\lambda$ is converted using the strain sensitivity coefficient k .

3 EXPERIMENT

The fiber used in the experiment was a standard single-mode fiber (SMF-28), and a precision displacement stretching device was used to calibrate the strain sensitivity coefficient of the fiber. In the axial tensile calibration experiment of the optical fiber, a given tensile displacement is applied to the optical fiber with a displacement step of 0.5 mm and a displacement range of [0, 5] mm. In the calibration experiment, the OFDR system was used to acquire the RBS of the fiber, and the ZNCC correlation function was used to determine the spectral offset. The tunable linear scan laser used in the calibration experiment was an Agilent 81680A with a spectral scan range of 1520 to 1540 nm and a scan rate of 40 nm/s.

The glass fiber reinforced composite laminate tensile test was used to verify the effectiveness of large strain measurement method. As shown in Fig. 6(a), an optical fiber was pasted on the surface of the sample and cured for 24 hours. For comparison, four positions A, B, C, and D were selected to paste the one-way strain gauge.

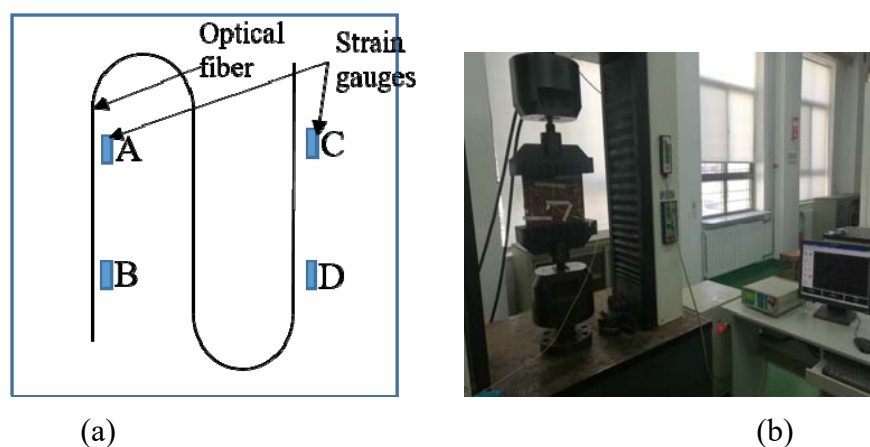


Figure 3: (a) Optical fiber and strain gauge attached composite laminate (b) tensile setup

The composite laminate was fixed in a stretching device with a self-designed fixture as shown in Fig. 6(b). The test machine (CSS-50T) was used for stretching, and the force control mode was used for grading loading. The loading step was 20kN, and the total loading was 200 KN with 10 steps. 11 sets of the RBS data was collected after force loading. The first set of the RBS data was recorded from the fiber with the initial state, and other 10 sets of the RBS data was recorded after different loads.

4. RESULTS AND DISCUSSION

4.1 Rayleigh backscattering spectrum in optical fiber

The RBS signal in spectral domain are transformed into the distance domain using FFT, and the amplitude of the RBS signal in the distance direction of the optical fiber can be obtained. As shown in FIG. 8, the RBS signal is transformed into the distance domain with force of 0kN, 80kN, 100kN, 200kN, where the gray shaded area is the fiber segment pasted on the composite board. It can be seen from Fig. 8 that as the external load increases, the RBS intensity measured by the optical fiber is

continuously attenuated. For example, when the load is 80kN, the signal strength is attenuated by about 9dB; when the load is raised to 200kN, the signal attenuation is more than 15dB, which is only about 5dB away from the intensity of the noise. In contrast, fibers that are not attached to a composite panel (unstressed) have a constant signal strength. The above experimental results show that as the fiber load increases, the RBS intensity in the fiber will decrease with the attenuation. When the fiber deformation reaches a certain level, the RBS signal will be submerged in the noise, thus the traditional strain demodulation method have failed.

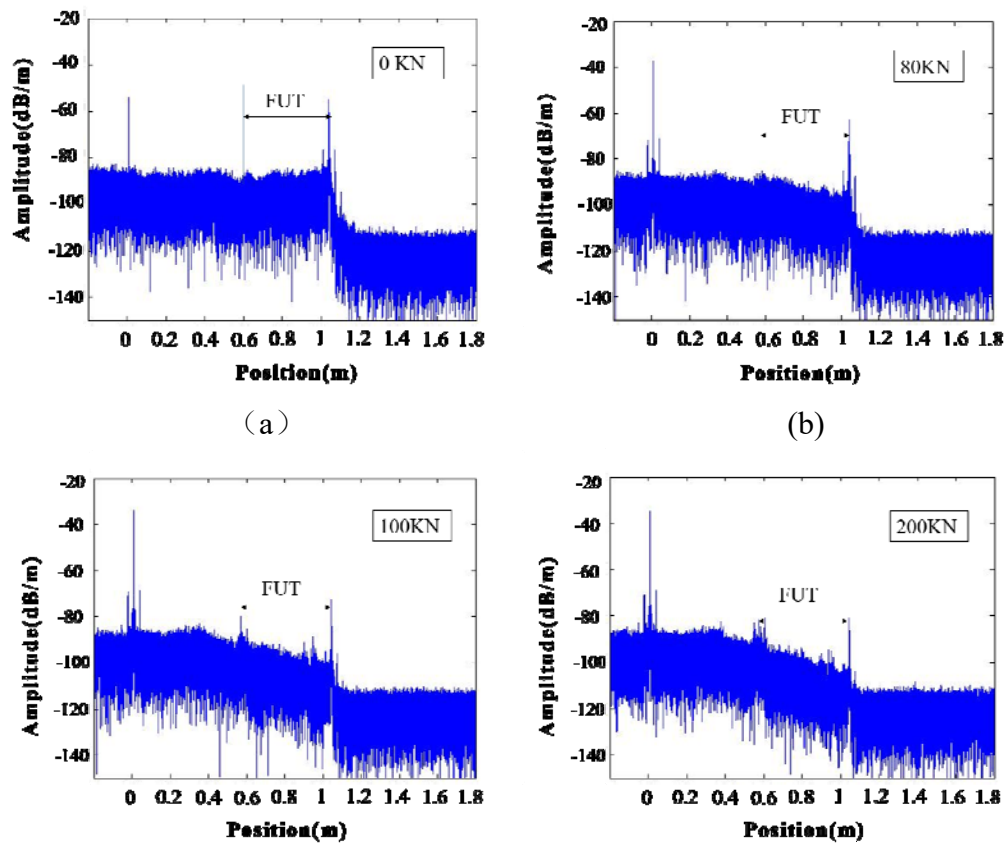


Figure 4: Rayleigh backscattering spectral distribution along fiber length under different loads of (a) 0kN, (b) 80kN, (c) 100kN and (d) 200kN

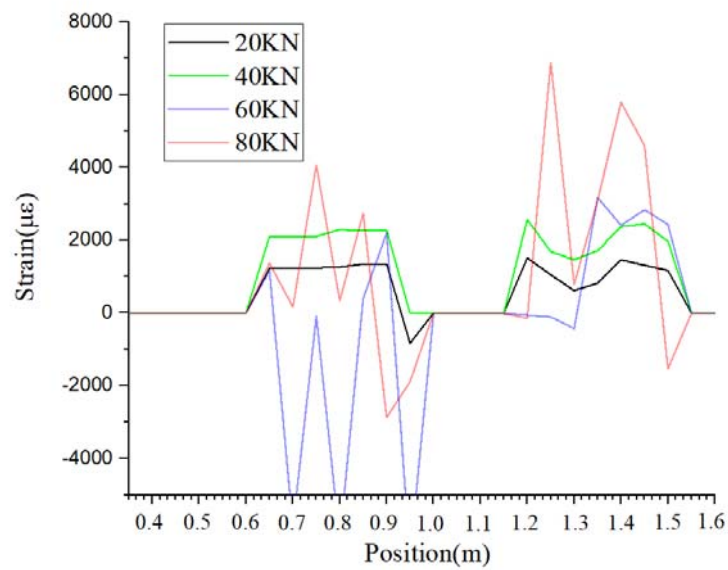
4.2 Strain demodulation

Fig. 10(a)(b) is a structural strain value of 11 sets of RBS data obtained by using the conventional demodulation method and the improved strain demodulation method proposed by the present invention.

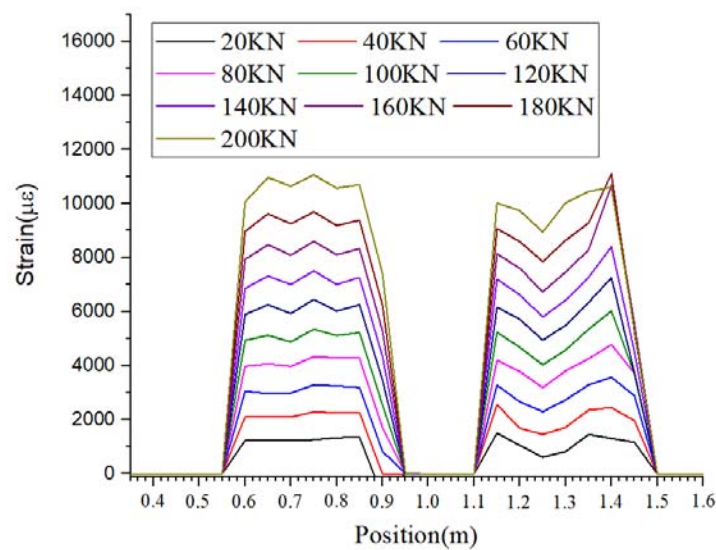
When the strain is solved by the traditional demodulation method (Fig. 10a), the strain value generated under the first two-stage test force (0~40kN) can be demodulated more stably and accurately, and the result is compared with the proposed improved strain demodulation method. Consistent. When loaded to the third level (40kN~80kN), a wide range of noise-like erroneous results begin to appear.

In contrast, the strain obtained by the large strain measurement method proposed in this paper increases linearly and stably after the end of each stage of loading, and

there is no erroneous result of the mutation, and the strain value collected with the adjacent strain gauge is very good. The anastomosis, as shown by position A in Fig. 8(b), the strain values measured by the strain gauges under the loading of each stage are [1335, 2247, 3224, 4264, 5031, 5998, 6983, 7989, 10368] $\mu\epsilon$. The strain values measured by the optical fiber in the adjacent position A are [1343, 2260, 3250, 4291, 5114, 6020, 7010, 8104, 9187, 10572] $\mu\epsilon$, and it can be seen that when the strain exceeds 10000 $\mu\epsilon$, the accuracy of the measurement result can be Up to 1.97%. At position B, the results measured by the strain gauges are [1039, 1641, 2613, 3713, 4598, 5612, 6515, 7498, 8481, 9597] $\mu\epsilon$, and the strain values measured by the fiber are [1052, 1687, 2666, 3791, 4687, 5718, 6625, 7604, 8593, 9739] $\mu\epsilon$, when the strain exceeds 10000 $\mu\epsilon$, the precision can reach 1.5%.



(a)



(b)

Figure 5: Strain demodulation results obtained by (a) the conventional demodulation method and (b)

It can be seen from Fig. 10 that the improved demodulation method proposed by the present invention can decompose larger strain information stably and accurately because of the demodulation strategy of the dynamic reference RBS. The reason why this method has obvious advantages in demodulating large strains is that it has a certain fault tolerance when using cross-correlation function for correlation analysis, that is, the cross-correlation function can distinguish between the reference RBS and the measured RBS. Changes, but such changes beyond a certain range can also lead to errors in cross-correlation analysis. The conventional demodulation method uses the fixed reference RBS as the RBS signal acquired by the fiber in the initial state, compared to the measured RBS signal amplitude acquired after the first and second stages of loading. The change is small, so that it can be demodulated more stably and accurately. As the amplitude of the measured RBS signal acquired after the third stage loading is larger and larger, the difference between the amplitude of the reference RBS signal and the measured RBS signal is also larger and larger, resulting in cross correlation. The analysis failed, resulting in a noise-like meaningless demodulation result. The demodulation method proposed in this paper adopts the dynamic reference RBS. Since the reference RBS is replaced with the recently acquired RBS signal before each demodulation, the RBS and the measured Rayleigh spectrum will be referenced. The difference in the scatter spectrum is controlled to a minimum, which improves the reliability and accuracy of the cross-correlation analysis to some extent.

4. CONCLUSION

OFDR-based distributed fiber strain measurement is a method that is easy to acquire structural strain information in a large area. However, large strains tend to cause the micro-bending of the fiber to cause amplitude attenuation of the Rayleigh scatter signal, and the correct strain information cannot be obtained using conventional demodulation methods. Based on the demodulation principle of the traditional demodulation method, this paper proposes a dynamic reference Rayleigh scattering spectrum method to improve the accuracy and reliability of strain information measurement. The experimental results show that the large strain measurement method proposed in this paper is used for distributed optical fiber measurement with large strain ($10000\mu\epsilon$) up to 1.9% measurement accuracy.

REFERENCES

- [1] X.Fan, Y. Koshikiya, and F. Ito, "2-cm spatial resolution over 40 km realized by bandwidth-division phase-noise-compensated OFDR," *Optical Fiber Communication Conference*, (2011), OMF3.
- [2] M. Froggatt and J. Moore, "High-spatial-resolution distributed strain measurement in optical fiber with Rayleigh scatter," *Applied Optics* (1998) 37,:1735-1740.

- [3] E. H. Templeton, M. A. Davis, J. R. Pedrazzani, and O. Ohanian, "Distributed high temperature measurement for monitoring bleed air lines and other aircraft structures," in *AIAA Information Systems-AIAA Infotech@ Aerospace* (2017), p. 0646.
- [4] B. J. Soller, D. K. Gifford, M. S. Wolfe, and M. E. Froggatt, "High resolution optical frequency domain reflectometry for characterization of components and assemblies," *Optics Express* (2005) 13: 666-674.
- [5] Z. Ding, X. S. Yao, T. Liu, Y. Du, K. Liu, Q. Han, Z. Meng, and H. Chen, "Long-range vibration sensor based on correlation analysis of optical frequency-domain reflectometry signals," *Optics express* (2012) 20:28319-28329.
- [6] C. D. Boyd, B. D. Dickerson, and B. K. Fitzpatrick, "Monitoring distributed temperatures along superconducting degaussing cables via Rayleigh backscattering in optical fibers," in *Proceedings of the Intelligent Ships Symposium IX*, 2011), 25-26.
- [7] Y. Du, T. Liu, Z. Ding, Q. Han, K. Liu, J. Jiang, Q. Chen, and B. Feng, "Cryogenic temperature measurement using Rayleigh backscattering spectra shift by OFDR," *IEEE Photonics Technology Letters* (2014) 26:1150-1153.
- [8] Suo L, Lei Z, Takezawa A, et al. Reliability-guided Rayleigh backscattering spectrum correlation method for distributed strain measurements in optical fibres[J]. *Journal of Modern Optics* (2019) 66(5): 512-520.
- [9] Heinze S, Echtermeyer A. A Running Reference Analysis Method to Greatly Improve Optical Backscatter Reflectometry Strain Data from the Inside of Hardening and Shrinking Materials[J]. *Applied Sciences* (2018) 8(7): 1137.
- [10] Başokur A T. Definitions of apparent resistivity for the presentation of magnetotelluric sounding data[J]. *Geophysical Prospecting*(1994) 42(2): 141-149.

MAGNETOSTRICTIVE COMPOSITES FOR WIRELESS STRESS SENSING APPLICATIONS

ALEX YOFFE AND DORON SHILO

Department of Mechanical Engineering
Technion

Haifa 3200003, Israel

e-mail: shilo@technion.ac.il, <https://meeng.technion.ac.il/members/doron-shilo/>

Key words: Magnetostrictive materials, Terfenol-D, Smart composites, Stress sensing.

Abstract. This article presents a theoretical and experimental study of the relationships between the stress, strain, and magnetic field emitted from epoxy-based Terfenol-D composite materials that are intended for stress sensing applications. The experimental results were analyzed and simulated by a new model that accounts for the inherent hysteretic and non-linear mechanical behavior of the epoxy. The results reveal a critical strain above which the perfect bonding between the Terfenol-D and the epoxy does not valid. This critical strain is very close to the transition strain, at which non-180° domain switching is finished and the magnetization rotation becomes the dominant process in the Terfenol-D. Comparisons between simulations and experimental results, obtained at strains smaller than the critical strain, revealed that most of the hysteresis in the magnetic field versus stress curves is derived from the inherent hysteresis in the stress-strain behavior of the epoxy. These results encourage the search for a more suitable epoxy that provides better bonding with Terfenol-D and smaller hysteresis. Despite the drawbacks of the currently used epoxy, both measured and simulated curves showed that for strain amplitudes smaller than the critical strain, the magnetic field vs. stress curve is approximately linear and has a minor amount of hysteresis, making the sensor suitable for stress-sensing applications.

1 INTRODUCTION

Magnetostrictive materials, such as Terfenol-D [1, 2], demonstrate stress induced magnetic field changes that can be utilized in force and stress sensing applications [3]. In particular, magnetostrictive composites, in which TD particles are incorporated into an epoxy matrix, enable overcoming the brittleness of TD and forming sensors with complicated shapes, such as thin washer shaped sensors for measuring compressive forces in bolted joints [4].

Stress-induced magnetic field changes in magnetostrictive composites have been studied in several previous works (e.g.[4–10]). In particular, Ref.[6] presented a model for the magneto-mechanical behavior of magnetostrictive composites that was based on an assumed sequence of micro-scale physical processes that occur during the material preparation and testing. The model provides a one-to-one relation between the applied stress and the magnetic field induced by the sample. Recently, it was demonstrated that the sequence of physical processes is reversed

upon unloading, and nearly reversible behavior is observed [4,5]. Nevertheless, a certain amount of hysteresis, which has not been accounted for in the previous model [6], has been observed experimentally [4,5]. The hysteresis induces measurement errors in sensing applications; therefore, its study is of significant importance.

The source for the hysteresis, e.g., whether due to the energy barrier for non-180° domain switching or due to the inherent viscoelastic behavior of the epoxy, is still unclear. Specifically, the relative contributions of the epoxy, the TD and the interface (bonding) between them to the hysteresis and irreversibility are unknown. In addition, the effect of the strain amplitude on the hysteresis and irreversibility has not yet been explored. One possible effect, which may occur at large strains, is a change in the strain compatibility at the interface between the epoxy and the TD, i.e., it is possible that at high strains there are no longer perfect bonding conditions, as has been assumed in the previous model [6].

In this study, we identified the effect of the inherent hysteretic and non-linear mechanical behavior of the epoxy on the magneto-mechanical response of the composite material. To this end, we introduced an expansion of the previous model presented in Ref. [6]. Specifically, we replaced the previously assumed linear stress vs. strain response of the epoxy material with real stress vs. strain curves measured using a monolithic epoxy sample. In addition, we introduced and applied a procedure for determining if the perfect bonding condition is valid under large strains.

The paper also presents a much more comprehensive comparison between model simulations and experimental results. Specifically, we compared both the magnetic field vs stress curves (as has been done previously [5,6]) and stress vs. strain curves (which have not been compared before) for the same tests. These comparisons demonstrate that the same values of the input parameters provided a good fit between the model simulations and measurements of all three variables (stress, strain, and magnetic field) in different tests (e.g., different strain amplitudes) and in samples with different volume fractions of TD. This result provides a significant validation of the model.

2 EXPANDED MODEL

In this section, we first (section 2.1) briefly survey the sequence of magneto-mechanical processes that occur during all stages of sample preparation and testing and emphasize important aspects relevant to this study. In section 2.2, we present the main assumptions of the model. In particular, we point on one assumption that has to be verified (Eq. (1)) and one assumption that constitutes an oversimplification, which requires revision (Eq. (4)). Then, in section 2.3, we present methods for expanding the model and testing the validity of its assumption.

2.1 Sequence of magneto-mechanical processes that occur during material preparation and testing

In the sample preparation stage, during the curing of the epoxy, the mixture of TD particles and liquid epoxy is subjected to an external magnetic field with an aim of poling the TD magnetization along the magnetic field direction. The sequence of magneto-mechanical processes that occur during this stage and the critical (hardest) process that eventually determines the efficiency of the poling process have been explored in Ref. [4]. Microscopy

observations showed that due to this poling process, TD particles are arranged in chains along the direction of the external magnetic field, which is denoted by the z -axis [6,10]. Each chain contains many particles closely packed together, and the chains are separated from each other by relatively large distances [6,10]. In light of these observations, Yoffe et al. [6] modeled the composite material as long cylindrical fibers of TD embedded in an epoxy matrix.

When the epoxy matrix is fully cured, the external magnetic field is turned off. At this stage, the average magnetization of the composite material tends to decrease due to the demagnetization energy related to the magnetic field induced by the sample. However, strain compatibility between the epoxy and the TD prevents magnetic processes that are associated with strain changes. Recently, we showed that in a significant portion of the TD volume, the magnetization passes 180° domain switching that is not accompanied by strain changes [5]. It was shown that this process results in a decrease of the initial magnetic field B_0 , which is induced by the sample before the compression test, by more than an order of magnitude.

Under uniaxial compression, the TD first undergoes non- 180° domain switching (DS). During this stage, the ratio B/B_0 (where B is the temporal magnetic field induced by the sample) is determined by the volume fraction x of the material, in which non- 180° DS occurred. The model calculations showed that during this stage, the slope of the magnetic field versus stress curve, which is a measure of the force-sensing sensitivity, is constant and maximal [6]. There is a critical load at which the stress-induced DS process is completed and $x = 1$.

Above that critical load, magnetization rotation (MR) off the easy axes can occur. Throughout this stage, B/B_0 is determined by the direction cosines α_i between the local magnetization and the z -axis. This process requires considerably higher energy and in accordance a considerably higher load. As a result, during the MR stage, the slope of the magnetic field versus stress curve decreases and the magnetic field tends towards zero at high stress values [6].

2.2 The model's assumptions

The simulation procedure begins with expressing all variables of the magneto-mechanical problem as a function of the degrees of freedom, i.e., x in the non- 180° DS regime and α_i in the MR stage. Then, the values of the x and α_i are calculated by expressing and minimizing the overall energy of the system. It was shown that during loading, the mechanical energy of the system is larger than the demagnetization energy by orders of magnitude [6]. In addition, it was shown that if the composite material is not constrained in the transverse plane, the contribution of the strains and stresses in the transverse plane to the total energy is negligible compared to other energy terms that are related to the axial strain and stress. Therefore, to a very good approximation, x and α_i are determined only by the axial stresses and strains. Therefore, in this paper, we use an abbreviated (scalar) notation of the stresses and strains that considers only the axial stresses and strains along the z -axis.

One of the basic assumptions of the model was perfect bonding between the TD cylinders and the epoxy matrix [6], which imposes that

$$\varepsilon_{TD} = \varepsilon_{EP} = \varepsilon \quad (1).$$

Here, ε_{TD} and ε_{EP} are the strains in the TD and epoxy, respectively, and ε is the strain imposed by the loading machine on the composite sample. Based on Eq. (1) and on the transverse isotropy of the TD cylinders, it was shown [6] that the axial stresses in the TD σ_{TD} and the epoxy σ_{EP} are uniform and satisfy the equation

$$\sigma = \sigma_{TD}\nu + \sigma_{EP}(1-\nu) \quad (2),$$

where σ is the average stress (traction) imposed by the loading machine and ν is the TD volume fraction. Equations (1) and (2) constitute the simple rule of mixture for the axial stresses and strains along the z -axis.

The overall strain in the TD is expressed by

$$\varepsilon_{TD} = \frac{\sigma_{TD}}{E_{TD}} + \Delta\varepsilon^{MS} \quad (3).$$

Here, the first term represents the elastic strain, where E_{TD} is the Young's modulus of TD, and the second term represents the strain change due to magnetization changes, which is determined by changes in x and α_i (see Ref. [6] for the expressions of $\Delta\varepsilon^{MS}$). In previous studies [5,6], a linear Hooke's law of the form

$$\sigma_{EP} = E_{EP}\varepsilon_{EP} \quad (4),$$

was assumed to describe the relation between the axial stress σ_{EP} and strain ε_{EP} in the epoxy, where E_{EP} is the epoxy's Young's modulus. This assumption is a significant oversimplification, which ignores the inherent hysteretic and non-linear mechanical behavior of the epoxy.

Previous comparisons of measured and calculated magnetic field vs stress curves implied that part of the TD particles do not undergo magnetization switching. These "impaired" particles behave as a stiff elastic material that increases the effective Young's modulus of the matrix [5,6]. Several possible reasons for the existence of impaired particles have been discussed in Ref. [5]. Nevertheless, the assumed existence of impaired particles has yet to be validated.

2.3 Methods for expanding the model and testing the validity of its assumptions

To account for the hysteretic and non-linear mechanical behavior of the epoxy, we replace Eq. (4) with the equation

$$\sigma_{EP} = \begin{cases} f^{load}(\varepsilon_{EP}) & \frac{\partial \sigma_{EP}}{\partial t} > 0 \\ f^{unload}(\varepsilon_{EP}) & \frac{\partial \sigma_{EP}}{\partial t} < 0 \end{cases} \quad (5),$$

where $f^{load}(\varepsilon_{EP})$ and $f^{unload}(\varepsilon_{EP})$ are stress vs. strain curves measured using a monolithic epoxy sample. The curves $f^{load}(\varepsilon_{EP})$ and $f^{unload}(\varepsilon_{EP})$ depend on the strain amplitude, i.e., the maximal strain in the experiment. Therefore, the strain amplitudes in the tests of the monolithic epoxy sample should be the same as the strain amplitudes in the tests of the composite samples.

The validity of the perfect bonding condition (Eq. (1)) can be investigated based on measurements of the stress vs. strain curves of a monolithic epoxy sample $\sigma_{EP}(\varepsilon)$ and the composite sample $\sigma(\varepsilon)$. Note that $\sigma_{EP}(\varepsilon)$ and $\sigma(\varepsilon)$ depend on the strain amplitude, and therefore, stress vs. strain curves with the same strain amplitude should be compared. By rephrasing Eq. (2), we can calculate the stress in the TD as a function of the strain as follows:

$$\sigma_{TD}(\varepsilon) = \frac{\sigma(\varepsilon) - (1-\nu)\sigma_{EP}(\varepsilon)}{\nu} \quad (6),$$

where $\sigma_{EP}(\varepsilon)$ and $\sigma(\varepsilon)$ are the measured functions. The substitution of Eq. (6) into Eq. (3) provides

$$\varepsilon_{TD}(\varepsilon) = \frac{\sigma(\varepsilon) - (1-\nu)\sigma_{EP}(\varepsilon)}{\nu E_{TD}} + \Delta\varepsilon^{MS} \quad (7).$$

The value of $\Delta\varepsilon^{MS}$ in Eq. (7) is bounded to be less than $\frac{3}{2}\lambda_{111} = 0.25\%$ [5,6]. Moreover, when the non-180° domain switching process ends, at a transition strain of approximately $\varepsilon_t = \frac{8}{3}\lambda_{111} = 0.43\%$ [5,6], the value of $\Delta\varepsilon^{MS}$ is already $\frac{4}{3}\lambda_{111} = 0.22\%$. This means that at $\varepsilon > \varepsilon_t$, $\Delta\varepsilon^{MS}$ is practically constant and Eq. (7) can be further simplified to

$$\varepsilon_{TD}(\varepsilon) \cong \frac{\sigma(\varepsilon) - (1-\nu)\sigma_{EP}(\varepsilon)}{\nu E_{TD}} + 0.25\% \quad (8).$$

Eqns. (7) and (8) can be used for evaluating the validity of Eq. (1), according to which $\varepsilon_{TD} = \varepsilon$.

To test the assumed existence of impaired particles and their effect on the magneto-mechanical behavior, we compare measured and calculated results of both magnetic field vs stress curves and stress vs. strain curves, for the same test. Such a comparison, performed on different samples, can provide much stronger conclusions regarding the existence of the impaired particles.

3 EXPERIMENTAL SETUP AND METHODOLOGY

The samples and their preparation procedure were the same as detailed in Refs. [5,6]. The TD particles were manufactured by Etrema Products, USA and were sieved for particle sizes smaller than $38\ \mu m$. The epoxy was prepared by mixing Hexion Epon 8280 resin with Hexion Epikure 3140 curing agent, in a ratio of 2:1. The sealed mold with the liquid composite material was placed for curing under an external magnetic field of $170\ kA/m$ for 7 days. Cylindrical samples with TD volume fraction of 18.4% and 10.8% were prepared and tested. The samples had a diameter of 6.35 mm and a length of 12.7 mm, in agreement with the compressive testing standard, ASTM D-695.

The magneto-mechanical test setup was the same as detailed in Ref. [5]. An MTS hydraulic mechanical testing machine, equipped with Sensotec 31/1432-08 load cell, was used for performing compression tests under a constant displacement rate. The average strain was measured by an EIR LE-05 laser extensometer system, using two light reflecting strips that were taped 1 mm from the sample ends. The magnetic field induced by the sample was

measured by Honeywell HMC1021S sensor that was mounted at the height of the center of the sample and at a radial distance of 10 mm from the sample.

4 EXPERIMENTAL RESULTS

4.1 Mechanical response of monolithic epoxy

Figure 1 presents stress vs. strain curves of a monolithic epoxy sample. The measurements were performed at a constant strain rate of $6.6 \times 10^{-5} \text{ s}^{-1}$ and up to different strain amplitudes, as indicated in the figure's legend. As shown, no distinguishable residual strain, which indicates plasticity, occurred except for minor non-repeatable behavior at small strains, which is likely related to changes in the contact region, as explained in Refs. [4,5].

The stress vs. strain curves presented in Fig. 1 demonstrate noticeable hysteresis that increases with the strain amplitude. In addition, the stress vs. strain relation is non-linear, especially at small strains. For instance, the slope of the curve changes from 0.7 GPa at small strains to 1.85 GPa at large strains. The hysteresis and non-linearity are typical of epoxy materials and are in agreement with the results reported in previous studies on other epoxy materials [12,13].

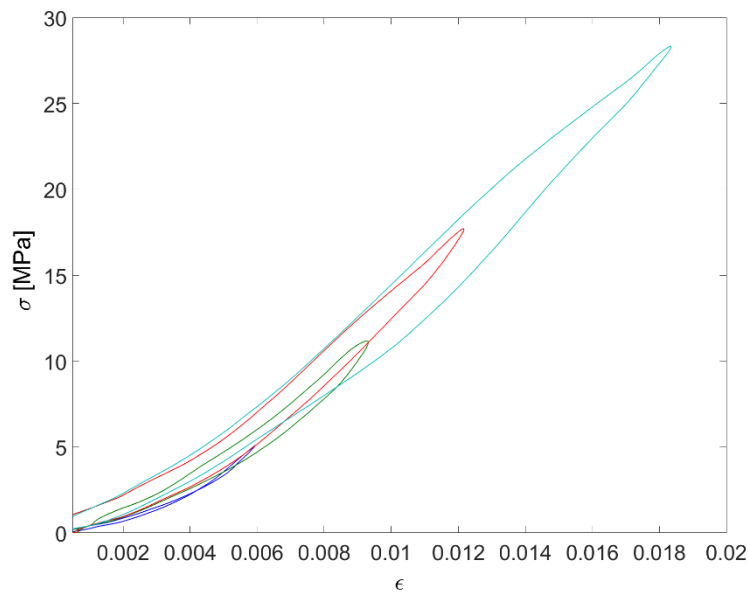


Figure 1: Stress vs. strain curves of the monolithic epoxy sample measured under different strain amplitudes.

4.2 Magneto-mechanical behavior of magnetostrictive composites

Figure 2 presents magneto-mechanical measurements obtained from a composite sample with 18.4% vol. TD particles. The measurements were taken at a constant strain rate of $6.6 \times 10^{-5} \text{ s}^{-1}$ and up to different strain amplitudes. A comparison of the stress vs. strain curves of the composite sample (Fig. 2(a)) and the monolithic sample (Fig. 1) reveals two observations. First, both curves have the same shape and demonstrate a similar mechanical behavior. Second, the

composite sample is stiffer, as expected due to the much larger Young's modulus of TD [14] compared with the modulus of the epoxy.

The stress vs. strain curves shown in Fig. 2(a) demonstrate no distinguishable residual strain that could indicate on an irreversible process. High levels of reversibility are also observed in Figs. 2(b) and 2(c), which present the magnetic field vs. the strain and the stress. In particular, upon unloading, the magnetic field reverts approximately to the same value at zero stress. This observation indicates that the sequence of magneto-mechanical processes is reversible, as demonstrated in Refs. [4,5].

Figure 2(c) demonstrates the transition from non-180° DS to MR, as explained in section 2.1. Non-180° DS occurs at small stresses, up to approximately 17 MPa. In this range, the magnetic field vs. stress curve is approximately linear. At higher stresses, the MR process is dominant and the magnetic field vs. stress curve is non-linear and approaches to zero at high stress values.

The most interesting result demonstrated by Fig. 2 is that the hysteresis is strongly dependent on the strain amplitude; a similar trend as demonstrated by the monolithic epoxy sample in Fig. 1. However, the hysteresis is mainly prominent in the stress vs. strain and magnetic field vs. strain curves. In fact, the hysteresis in the magnetic field versus stress curves (Fig. 2(c)) remains small, even at large strain amplitudes. In particular, at a strain amplitude of 0.5%, which is related to a stress of 17 MPa, the magnetic field vs. stress curve is approximately linear and has a minor amount of hysteresis (less than 4% of the full-scale output). This observation indicates the suitability of using magnetostrictive composites in force-sensing applications over this range of stress values.

5 COMPARISON OF SIMULATED AND MEASURED CURVES

Figures 3 and 4 compare measured and simulated curves for composite samples with 18% (Fig. 3) and 10.4% (Fig. 4) TD. For each sample, both the magnetic field vs. strain and stress vs. strain curves are shown for two different strain amplitudes. In part of the simulated curves, there is an artificial jump at the point of maximal strain due to the switching between $f^{load}(\varepsilon_{EP})$ and $f^{unload}(\varepsilon_{EP})$. This jump occurs because, in order to assure that the data of $f^{load}(\varepsilon_{EP})$ and $f^{unload}(\varepsilon_{EP})$ cover the entire strain range used in tests of the composite samples, we chose the strain amplitudes in the tests of the monolithic epoxy sample to be slightly larger (by less than 10%) than the strain amplitudes in the composite sample tests. In a portion of the measured curves, the response at very low stress values (below 3 MPa) was omitted because the curves measured over this range were non-repeatable due to changes in the contact region, as explained in section 4.1.

Table 1. Input parameters used in the simulations.

Property	Value	Reference
Magnetostriction coefficient λ_{111}	$1.64 \cdot 10^{-3}$	[2]
Young's modulus E_{TD} of TD	30 GPa	[14]
Magnetocrystalline anisotropy coefficient K_1	$-0.6 \cdot 10^5 \text{ J/m}^3$	[2]
Fraction of impaired TD particles	0% (green curve) 50% (blue curve)	

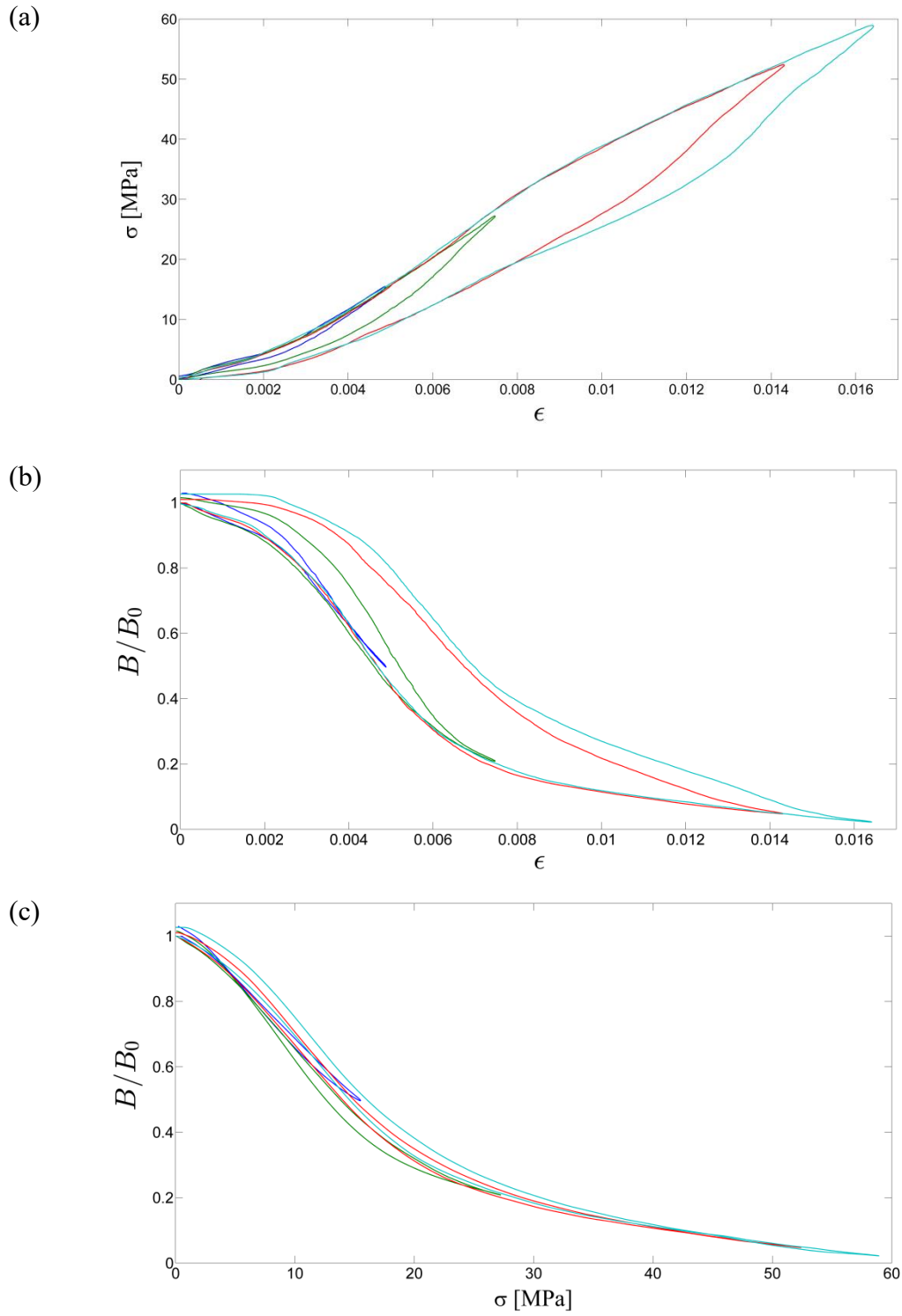


Figure 2: Stress vs. strain (a), magnetic field vs. strain (b) and magnetic field vs. stress (c) curves measured under different strain amplitudes.

The input parameters used in the calculated curves are listed in Table 1. It is important to emphasize that all input parameters were taken from the literature, except for the volume fraction of impaired TD particles. All sub-figures in Figs. 3 and 4 present two different simulated curves: one with no impaired particles (dashed green curves) and one in which 50% of the TD volume is occupied by impaired particles (dashed blue curves). The figures show that simulations with no impaired particles do not fit the measured results. On the other hand, simulations with 50% impaired particles demonstrate reasonable agreement with all measured curves presented in Figs. 3 and 4. This result provides significant evidence for the existence of impaired TD particles, particularly because the same values of the input parameters and the same portion of impaired TD particles were used in all simulations that fit all measured curves presented in Figs. 3 and 4.

Simulations of the magnetic field vs. stress curves presented in Figs. 3 and 4 reproduce the hysteresis in the measured curves well. This observation indicates that the inherent hysteresis in the mechanical response of the epoxy accounts for most of the hysteresis in the magnetic field versus stress response of the composite material. On the other hand, the amount of hysteresis in the simulated stress vs. strain curves is smaller than that in the measured curves. This observation implies that there is an additional mechanism that increases the hysteresis in the stress vs. strain curves of the composite material. It is likely that this mechanism is not related to the magneto-mechanical response of the TD, because it has no effect on the magnetic field vs stress curves.

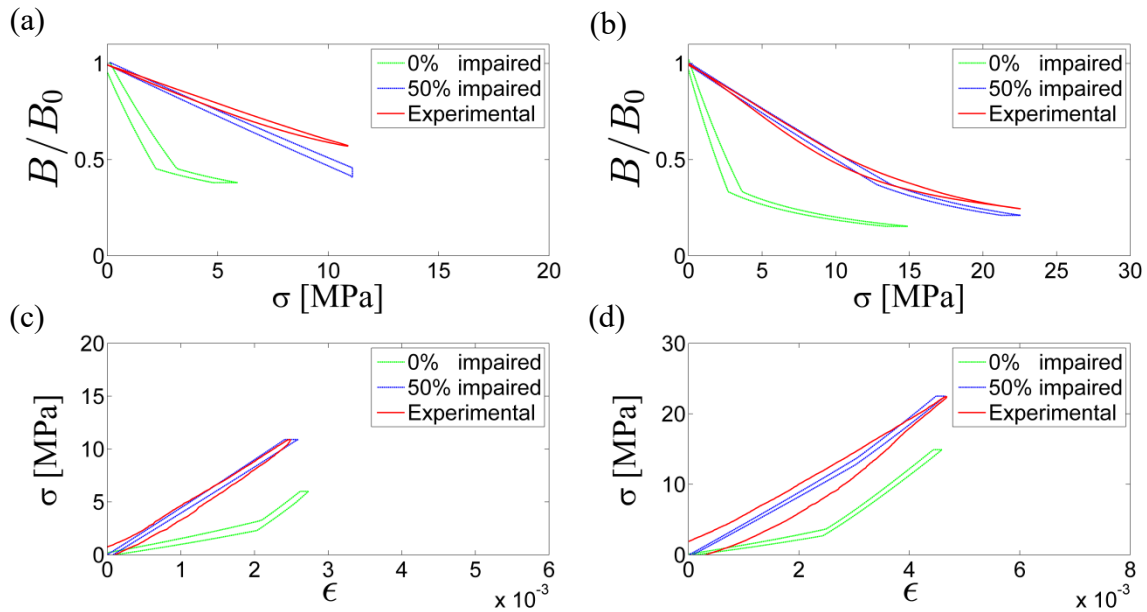


Figure 3: Comparison of the simulated and measured results for the 18% TD volume fraction sample: (a) magnetic field vs stress, strain amplitude 0.28%, (b) magnetic field vs stress, strain amplitude 0.45%, (c) stress vs stain, strain amplitude 0.28%, and (d) stress vs strain, strain amplitude 0.45%.

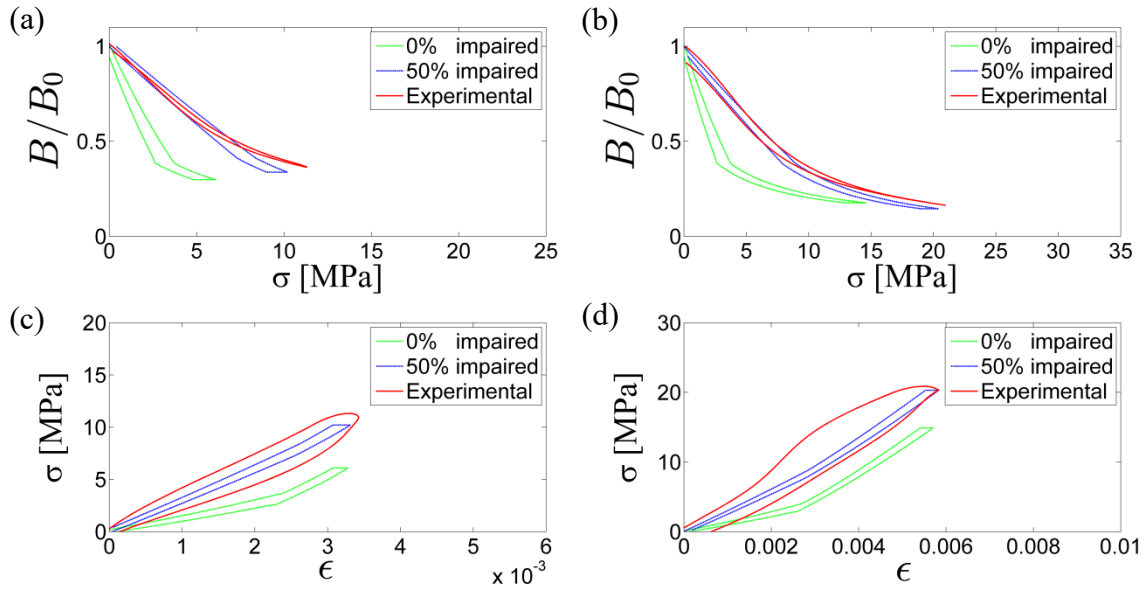


Figure 4: Comparison of the simulated and measured results the 10.4% TD volume fraction sample: (a) magnetic field vs stress, strain amplitude 0.35%, (b) magnetic field vs stress, strain amplitude 0.6%, (c) stress vs strain, strain amplitude 0.35%, and (d) stress vs strain, strain amplitude 0.6%.

All curves shown in Figs. 3 and 4 have strain amplitudes smaller than 0.6%. For larger strain amplitudes, comparisons of the simulated and measured curves revealed a significant discrepancy. In the following, we use the procedure discussed in section 2.3 and show that this discrepancy occurs because at larger strains, the perfect bonding assumption, as is formulated in Eq. (1), is no longer valid.

Figure 5 shows a plot of ϵ_{TD} vs. ϵ . The blue curve represents the perfect bonding assumption, according to which $\epsilon_{TD} = \epsilon$ (Eq. (1)). The green curve was calculated by substituting the measured $\sigma_{EP}(\epsilon)$ and $\sigma(\epsilon)$ curves into Eq. (7). Eq. (7) also has a contribution from $\Delta\epsilon^{MS}(\epsilon)$, which was taken from the simulations. It is observed that up to a critical strain of approximately $\epsilon_c = 0.4\%$, ϵ_{TD} is approximately equal to ϵ , i.e., in agreement with Eq. (1). This result is in accordance with the agreement between the simulations and measurements, as presented in Figs. 3 and 4 for small strains up to $\epsilon = 0.6\%$. On the other hand, above $\epsilon_c = 0.4\%$, ϵ_{TD} deviates from ϵ and becomes significantly smaller than ϵ at large strains.

The observed critical value of $\epsilon_c = 0.4\%$ is very close to the transition strain $\epsilon_t = 0.43\%$, at which the non-180° DS is expected to be finished according to the model [5,6]. At $\epsilon > \epsilon_t$, Eq. (8) can be used for calculating $\epsilon_{TD}(\epsilon)$ directly from the measured $\sigma_{EP}(\epsilon)$ and $\sigma(\epsilon)$ curves, without relying on the simulations. This calculation fully overlaps with the green curve presented in Fig. (5). This means that the difference between ϵ_{TD} and ϵ does not stem from the simulation of $\Delta\epsilon^{MS}(\epsilon)$. Thus, Fig. 5 provides direct evidence that at large strains, Eqns. (1) and (2) are not fulfilled. The observation that at large strains (and in accordance large stresses)

ϵ_{TD} becomes smaller than ϵ indicates that above a certain stress level, there is not perfect bonding between the TD cylinders and the epoxy matrix.

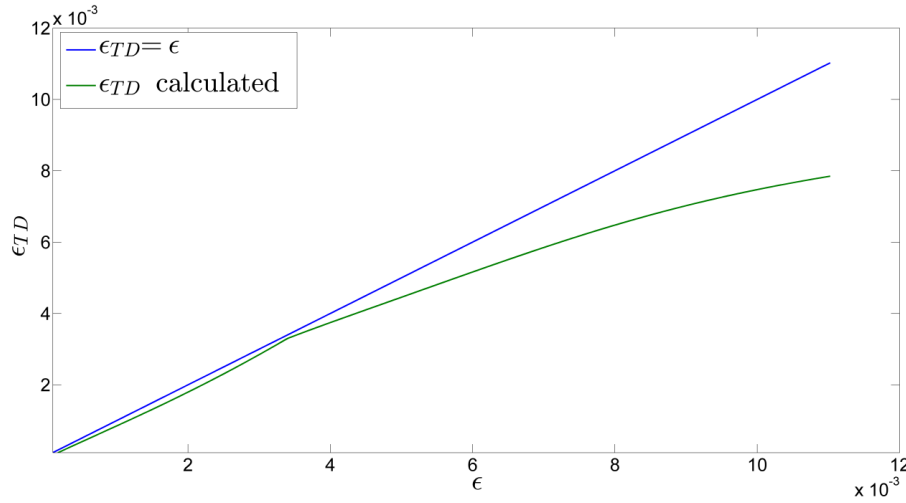


Figure 5: ϵ vs. ϵ_{TD} . The blue curve represents the basic model's assumption of perfect bonding ($\epsilon_{TD} = \epsilon$). The green curve was calculated based on Eqns. (7) and (8).

5 CONCLUSIONS

In this paper, we present a combination of experimental and theoretical studies of the magneto-mechanical response of epoxy-based TD composite materials for stress-sensing applications. We introduced an expanded model that accounts for the hysteretic and non-linear mechanical behavior of the epoxy by replacing the previously assumed linear stress vs. strain relations [6] with real stress vs. strain curves measured using a monolithic epoxy sample.

A direct evaluation of the strain in the TD, based on measured stress vs. strain curves in a monolithic epoxy and in composite samples, allowed us to test the validity of a basic model assumption, which is the perfect bonding between the TD and the matrix. This analysis (see Fig. 5) revealed a critical strain of approximately $\epsilon_c = 0.4\%$. Below this value, the strain in the TD is approximately equal to the strain in the matrix and the average strain applied to the sample, i.e., the perfect bonding assumption is fulfilled. Above this value, the strain in the TD becomes smaller than the applied strain. Under strains larger than 0.6%, this difference becomes significant and Eqns. (1) and (2), which constitute a basic assumption of the model, are not fulfilled. The observed critical strain ϵ_c is very close to the transition strain $\epsilon_t = 0.43\%$, at which the non-180° DS is expected to be finished according to the model [5,6].

Comparisons of measured and calculated curves demonstrated the necessity of the assumption regarding the presence impaired particles. Simulations with 50% impaired particles demonstrated reasonable agreement with all results of measurements performed at strains below 0.6%. It should be noted that the same values of input parameters and the same concentration of impaired particles were used in all simulations and provided a good fit with all measurement results. Specifically, the same simulations fit the measurements of all three variables (stress, strain, and magnetic field) in tests performed with different strain amplitudes and in samples

with different volume fractions of TD. This result largely validates the model and provides significant evidence for the existence of impaired TD particles and their effect on the magneto-mechanical behavior of the composite material.

Our experimental results (Fig. 2) showed that the amount of hysteresis is strongly dependent on the strain amplitude. Simulations of magnetic field vs stress curves reproduced the hysteresis well in the measured curves and indicated that most of the hysteresis is derived from the inherent hysteretic behavior of the epoxy. Simulations of stress vs. strain curves demonstrated that there is an additional source of hysteresis that affects only the mechanical behavior and is probably not related to the response of the TD.

This study provided several valuable insights for the development of stress sensing applications. In particular, it revealed the significant effect of the epoxy on the studied system, which determines the amount of hysteresis and the critical strain above which the perfect bonding between TD and epoxy is not fulfilled. Our results motivate the search for a more suitable epoxy that provides better performance in these two important respects. Despite the drawbacks of the currently used epoxy, both measured and simulated curves showed that for strain amplitudes smaller than 0.5%, the magnetic field vs. stress curve is approximately linear and has a minor amount of hysteresis. This observation indicates the suitability of using magnetostrictive composite materials in force-sensing applications over this range of applied strains.

6 REFERENCES

- [1] Clark A E 1993 High Power Rare Earth Magnetostrictive Materials *J. Intell. Mater. Syst. Struct.* **4** 70–5
- [2] Jiles D C and Thoelke J B 1994 Theoretical modelling of the effects of anisotropy and stress on the magnetization and magnetostriction of Tb_{0.3}Dy_{0.7}Fe₂ *J. Magn. Magn. Mater.* **134** 143–60
- [3] Kleinke D K and Uras H M 1994 A magnetostrictive force sensor *Rev. Sci. Instrum.* **65** 1699–710
- [4] Adelsberg N, Weber Y, Yoffe A and Shilo D Wireless Thin Layer Force Sensor Based on a Magnetostrictive Composite Material *Smart Materials Struct.* **26** 65013
- [5] Yoffe A and Shilo D The magneto-mechanical response of magnetostrictive composites for stress sensing applications *Smart Materials Struct.* **26** 65007
- [6] Yoffe A, Weber Y and Shilo D 2015 A physically based model for stress sensing using magnetostrictive composites *J. Mech. Phys. Solids* **85** 203–18
- [7] Yoffe A, Kaniel H and Shilo D The temperature effect on the magneto-mechanical response of magnetostrictive composites for stress sensing applications *Funct. Mater. Lett.* **10**, 1750060 (2017).
- [8] Quattrone R F, Berman J B, Trovillion J C, Feickert C A and Kamphaus J M 2000 *Investigation of Terfenol-D for Magnetostrictive Tagging of Fiber-Reinforced Polymer Composites*
- [9] Kubicka M, Mahrholz T, Kühn A, Wierach P and Sinapius M 2013 Magnetostrictive properties of epoxy resins modified with Terfenol-D particles for detection of internal stress in CFRP. Part 2: evaluation of stress detection *J. Mater. Sci.* **48** 6578–84

- [10] Or S W and Carman G P 2005 Dynamic magnetoelastic properties of epoxy-bonded terfenol-D particulate composite with a preferred [112] crystallographic orientation *IEEE Trans. Magn.* **41** 2790–2
- [11] Zhai C, Gan Y, Hanaor D, Proust G and Retraint D 2016 The Role of Surface Structure in Normal Contact Stiffness *Exp. Mech.* **56** 359–68
- [12] Shen X, Xia Z and Ellyin F 2004 Cyclic deformation behavior of an epoxy polymer. Part I: Experimental investigation *Polym. Eng. Sci.* **44** 2240–6
- [13] Littell J D, Ruggeri C R, Goldberg R K, Roberts G D, Arnold W A and Binienda W K 1061 Measurement of Epoxy Resin Tension, Compression, and Shear Stress–Strain Curves over a Wide Range of Strain Rates Using Small Test Specimens *J. Aerosp. Eng.* **21**
- [14] Terfenol-D Data sheet WWW.MATWEB.COM, last visited: 6/7/2017

ON THE MEASUREMENT OF GIANT MAGNETOSTRICTIVE MATERIAL PROPERTIES UNDER MECHANICAL LOADING

M. DOMENJOUR^{*}, E. BERTHELOT^{*} AND L. DANIEL^{*}

^{*} GeePs | Group of electrical engineering - Paris,
CNRS, CentraleSupélec, Univ. Paris-Sud, Université Paris-Saclay, Sorbonne Université
3 & 11 rue Joliot-Curie, Plateau de Moulon 91192 Gif-sur-Yvette Cedex, France.
e-mail: mathieu.domenjoud@centralesupelec.fr

Key words: compression stress, control of boundary conditions, magneto-elastic behavior, magnetic and piezomagnetic properties, Terfenol-D.

Abstract. Recently, an experimental setup dedicated to the characterization of GMM magneto-mechanical behavior under constant stress has been designed. This setup is able to reduce the dynamic stress variations induced by magnetic excitation variations below 0.1 MPa. The present work focuses on the effect of loading boundary conditions on the measurement of material properties of Terfenol-D under stress levels from 0 to 90 MPa. Comparison of measurement results obtained under controlled and uncontrolled stress conditions show that uncontrolled boundary conditions can be responsible for errors of several percent on the measurement of the maximum and remnant magnetic induction. The measurement of strain is even more sensitive to the boundary conditions, with errors up to 40% and 30% on the longitudinal and transverse strain, respectively. In addition, evolutions in the measurement of susceptibility and (longitudinal and transverse) piezomagnetic properties reach +30%, +125% and +300% respectively. This work highlights the utmost importance to precisely control the boundary conditions for an accurate characterization of GMM properties under mechanical loading.

1 INTRODUCTION

Giant Magnetostrictive Materials (GMM), such as Terfenol-D and Galfenol, are used to design actuators and sensors converting a magnetic input into a mechanical response, or conversely, a mechanical input into a magnetic signal. The design of magneto-mechanical systems is optimized based on a good knowledge of the material properties. Under standard operating conditions, these materials are subjected to stress. However, the behavior of these materials is highly nonlinear and very sensitive to mechanical loading [1, 2]. It is therefore important to characterize their properties under mechanical loading.

Various experimental setups have been used for the experimental characterization of GMM under mechanical stress. In the case of Galfenol and Terfenol-D, material properties obtained under mechanical loading with these setups show great variability [3, 4, 5, 6, 7, 8, 9]. These differences are due to different compositions of the materials tested, but also to imperfect control of loading boundary conditions.

This work deals with the role of loading boundary conditions on the material properties measurement of Terfenol-D under stress. In a first part, the characterization setup is described. In a second part, the experimental setup is used to characterize the effect of loading boundary conditions on the magneto-mechanical behavior as well as on magnetic and piezomagnetic properties of this GMM under stress.

2 EXPERIMENTAL SETUP

2.1 Magneto-mechanical characterization rig

The characterization setup is designed to measure magnetization and strain in a ferromagnetic specimen subjected simultaneously to magnetic field and uniaxial stress applied in the direction parallel to the magnetic field. A tension-compression machine is used for the application of stress, and a magnetic circuit has been designed for the application of the magnetic field (figure 1).

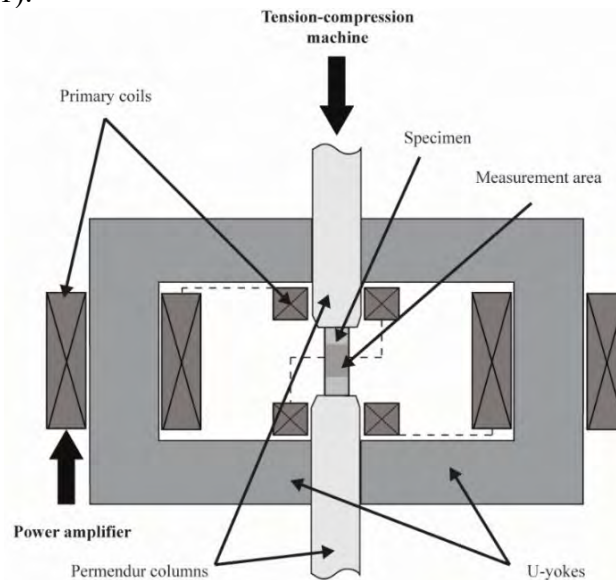


Figure 1: Magneto-mechanical characterization rig.

The electromagnetic device is constituted of two U-shaped ferrite yokes ensuring the closure of the magnetic flux. Associated to a power amplifier, a series circuit of four primary coils (one wound around each yoke – 600 turns each – and two around the specimen – 265 turns each) produces the magnetic field. Two coaxial magnetic columns (Permendur 49) connect the specimen to the apparatus and close the magnetic path.

The samples characterized in this study are cylindrical Terfenol-D rods with 3 cm height and 5 mm radius manufactured by TdVib LLC. This setup has been optimized to ensure the homogeneity of magnetic field and stress in a 15 mm height measurement area [10]. Measurements are performed at room temperature.

2.2 Characterization setup

The acquisition of measurement signals and the control of magnetic field and stress are performed by a DS 1006 dSPACE processor board, connected to a computer. Control of applied stress and position of the crosshead are ensured by the internal servo-controller of the compression machine. All the elements connected to the dSPACE acting during experiments are shown in figure 2. The magnetic field (H), the magnetic induction (B) and the strain components (S), are evaluated in the measurement area (figure 1).

The force (F) applied by the tension-compression machine (Zwick/Roell Z030) is measured using a 10 kN load cell. A Kepco 72-14MG amplifier is used to produce current (I) in the four primary coils (figure 1). This current is measured and used in a Proportional-Integral-Derivative (PID) control loop feedback. The magnetic field (H) is measured using a GM08 Gaussmeter and a transverse Hall probe. The variation of magnetic induction (δB) in the sample is calculated in real time through the integration of the induced voltage of a B-coil (65 turns) wound around the sample. The reference state for the evaluation of B is the demagnetized state [11].

The strain is measured through two rosette strain gauges glued face to face on the surface of the sample. Using a 4 channels strain gauge conditioner, two values on longitudinal direction (S_L) and one value on the transverse direction (S_T) are evaluated. In addition, shear strain (S_S) is calculated using gauge value in the 45° direction, S_L and S_T . A ball-and-socket joint (B&S joint) is placed between the load cell and the piezo stack actuator to minimize misalignment between the longitudinal direction of the sample and the column.

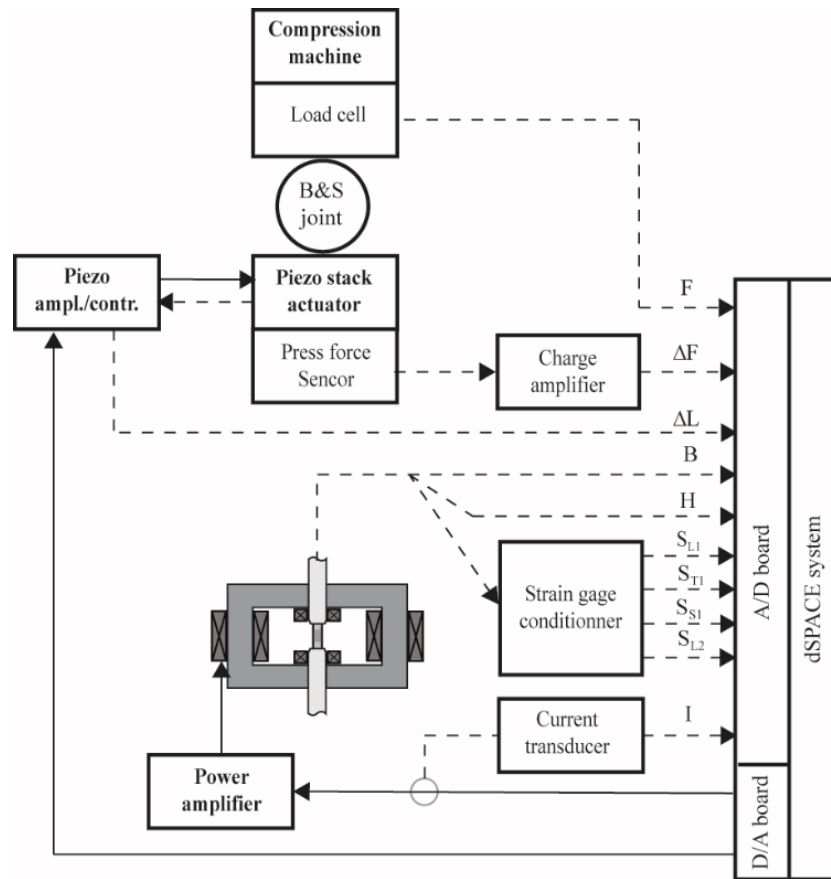


Figure 2: Measurement setup synoptic. Elements in bold are mechanical or electrical sources of the system.

The control of the dynamic force (ΔF) induced by the magnetic excitation is ensured by the combination of a piezoelectric force sensor, a piezo stack actuator and a PID control loop feedback. The piezoelectric press force sensor, associated to a charge amplifier, provides the dynamic component of the force. The actuator is a preloaded high load actuator, equipped with a positioning system to provide position information (ΔL) to the piezo amplifier/controller. The piezo amplifier/controller is a High-Performance Piezo amplifier. The system then ensures the cancellation of the dynamic force through the displacement provided by the actuator, controlled on the loop.

More details on the experimental setup are available in [11].

3 EFFECT OF LOADING BOUNDARY CONDITION ON THE MEASUREMENT OF TERFENOL-D PROPERTIES UNDER MECHANICAL LOADING

The magneto-mechanical behavior of Terfenol-D under various compression stress levels has been characterized using this experimental setup. Compression stresses will be considered positive. The lower level of stress is obtained by positioning the Permendur column alone on the top of the sample. This configuration is considered as the “stress-free condition” When connecting the top Permendur column to the compression machine, pre-stress levels (σ_0) of 125, 400, 700 kPa and 1, 2, 4, 8, 12, 16, 20, 25, 30, 35, 40, 45, 50, 55, 60, 70, 80, 90 MPa have been applied to the samples. For each level of stress, samples are submitted to a half periodic

sinusoidal magnetic loading, reaching 100 kA/m (H_{max}), at 1 Hz frequency. Tests are done under controlled stress conditions (CSC) and no-controlled stress conditions (noCSC). The reference state is the demagnetized state under pre-stress. Data presented in this work are raw data.

3.1 Measurement of magnetization and magnetostriction curves under controlled and no-controlled stress conditions

Figures 3 and 4 show the measured magnetization and magnetostriction (longitudinal and transverse) curves under compression stress levels in the two stress control conditions.

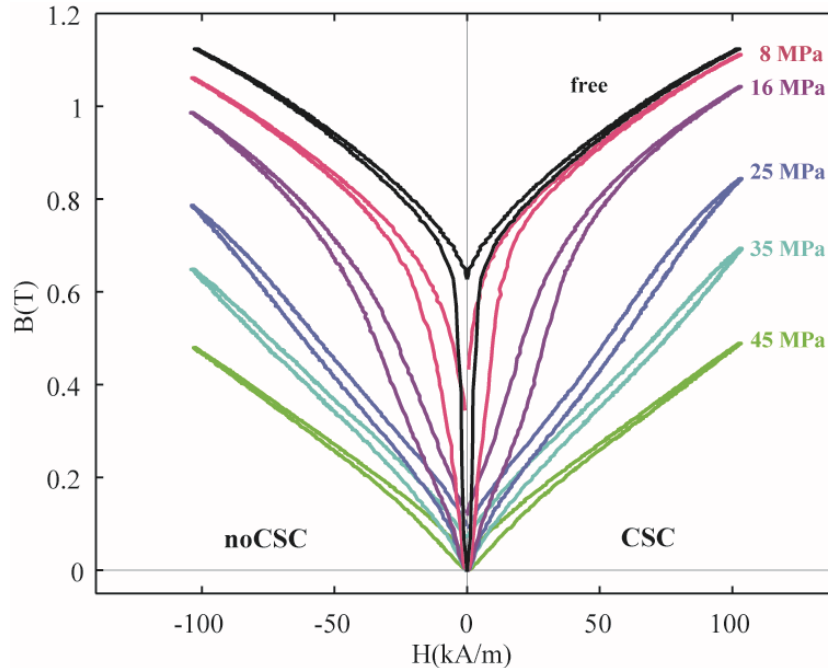


Figure 3: Magnetic behavior of Terfenol-D specimen for various uniaxial applied compressive stress under controlled stress conditions (CSC) and uncontrolled stress conditions (noCSC).

Magnetization curves are very sensitive to pre-stress levels. The decrease of induction with applied stress – for a given magnetic field – is very significant. The pre-stress significantly decreases the values of remnant and maximum magnetic induction (at 100 kA/m), B_r and B_{max} respectively. The values obtained under CSC can be up to 20% higher for B_r and up to 10% higher for B_{max} compared to the values obtained under noCSC.

Figure 4 shows that the magnetostrictive behavior is much more affected by stress than the magnetic behavior. The effect of stress on magnetostriction is non monotonic: the magnetostriction level first increases with stress, and then decreases. The maximum variations of magnetostriction with respect to magnetic field are observed at 16 MPa. At this stress level, the longitudinal and transverse strain measured under CSC can be up to 41% and 28% higher, respectively, than under noCSC.

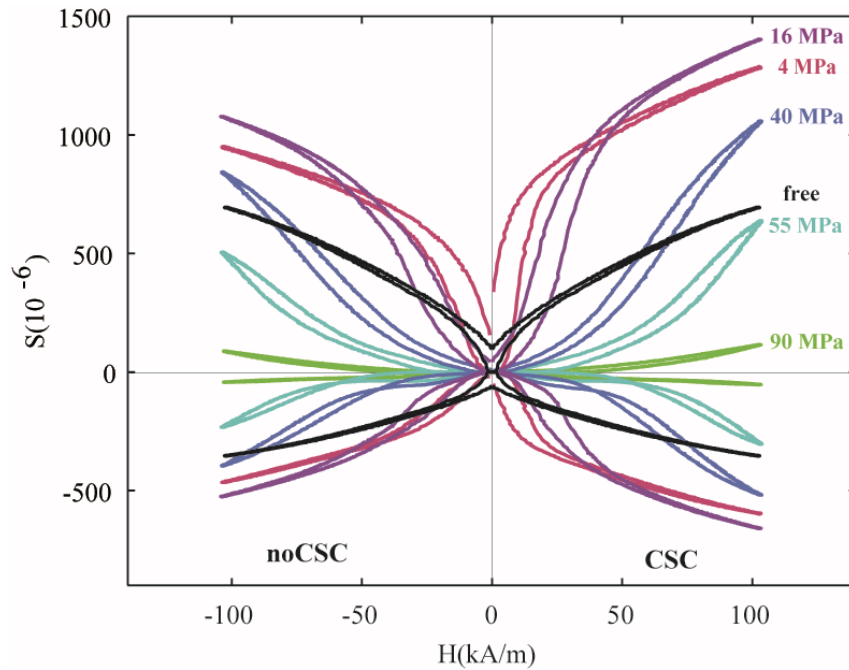


Figure 4: Longitudinal and transverse magnetostrictive behavior of Terfenol-D specimen for various uniaxial applied compressive stress under controlled stress conditions (CSC) and uncontrolled stress conditions (noCSC).

Whatever the level of pre-stress applied, the fluctuations of stress under CSC do not exceed 0.1 MPa. In contrast, the cancellation of this control system results in very significant fluctuations of stress. Table 1 presents the maximum stress variation levels ($\Delta^b \sigma_\theta$) observed under noCSC.

Table 1: Maximum stress variations during magnetic excitation under uncontrolled stress conditions.

σ_θ (MPa)	4	16	40	55	90
$\Delta^b \sigma_\theta \text{ max}$ (MPa)	8.6	10.6	7.2	5.2	2.5

These fluctuations are the direct image of longitudinal magnetostriction (figure 4) since the setup elastically responds to the deformation of the sample. Their levels are clearly unacceptable for an accurate characterization of the material properties.

3.2 Measurement of magnetic and piezomagnetic properties of Terfenol-D under controlled and no-controlled stress conditions

In this part, evolutions of magnetic susceptibility as well as longitudinal and transverse piezomagnetic properties of Terfenol-D sample are studied in function of the applied stress levels under the two stress conditions. These properties are calculated from a linear extrapolation of the magnetic and magnetostrictive curves, at the end of the cycle (near $H = 0$). These properties are presented on figure 5, under CSC and noCSC.

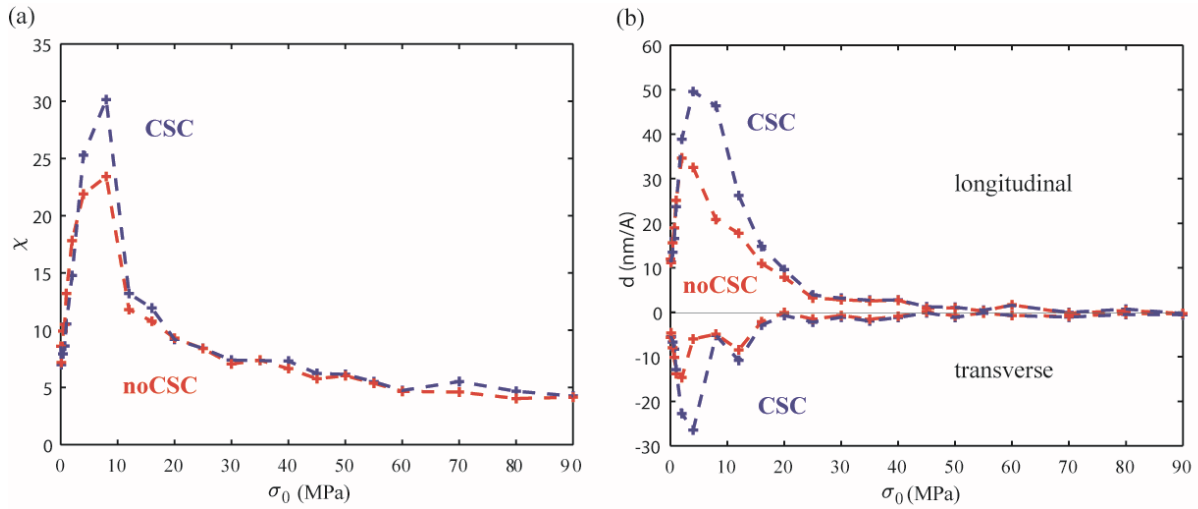


Figure 5: Magnetic susceptibility (a) and longitudinal and transverse piezomagnetic properties (b) of Terfenol-D specimen for various uniaxial applied compressive stress under controlled stress conditions (CSC) and no-controlled stress conditions (noCSC).

As expected, evaluation of material properties are very sensitive to the pre-stress levels. Maximum evolution of +30%, +125% and +300% are observed between magnetic susceptibility and longitudinal and transverse piezomagnetic values measured under CSC and noCSC. These plots clearly show the great importance to control the loading boundary condition when characterizing the properties of GMM under stress.

4 CONCLUSIONS

In this work, an experimental setup dedicated to the characterization of GMM properties under constant pre-stress has been described. Measurements have been performed on a Terfenol-D sample to show the dependence of magneto-mechanical behavior to compressive pre-stress levels from 0 to 90 MPa. Measurements obtained under control stress conditions (CSC) have been compared to those obtained without using the stress control (noCSC).

Under CSC, the setup can control the stress induced by the magnetic excitation and reduce it to levels below 0.1 MPa. Under noCSC, dynamic stress is very significant, and reaches 10.6 MPa at 16 MPa pre-stress level. The magnetization curves are sensitive to the stress control conditions. The values obtained under CSC can be up to 20% higher for the remnant magnetic induction and up to 10% higher for the maximum magnetic induction (at 100 kA/m) compared to the values obtained under noCSC. Longitudinal and transverse magnetostrictive behaviors have shown greater sensitivity to the control stress condition, with maximum differences about 40% and 30% respectively. Similarly, measured magnetic susceptibility and longitudinal and transverse piezomagnetic properties present maximum evolutions of +30%, +125% and +300% respectively, in function of the stress control condition.

This work emphasizes the great importance to accurately control the boundary conditions when characterizing the material properties of GMM, such as Terfenol-D, under stress.

REFERENCES

- [1] G. Engdahl, Handbook of Giant Magnetostrictive Materials, A. Press, Éd., 2000.
- [2] Z. Deng and M. J. Dapino, "Review of magnetostrictive materials for structural vibration control," *Smart Mater. Struct.*, vol. 27, p. 113001, 2018.
- [3] L. Kvarnsjö and G. Engdahl, "A set-up for dynamic measurements of magnetic and mechanical behavior of magnetostrictive materials," *IEEE Trans. Magn.*, vol. 25, pp. 4195-4197, 1989.
- [4] Y. Pei and D. Fang, "Magnetomechanical hydraulic-servo apparatus for investigation of magnetomechanical coupling properties of magnetic materials," *Rev. Sci. Instrum.*, vol. 77, p. 086101, 2006.
- [5] J. Atulasimha, A. B. Flatau and A. A. Kellog, "Sensing Behavior of Varied Stoichiometry Single Crystal Fe-Ga," *J. Intell. Mater. Syst. Struct.*, vol. 17, pp. 97-105, 2006.
- [6] M. Wun-Fogle, J. B. Restorff and A. E. Clark, "Soft and hard elastic moduli of Galfenol transduction elements (invited)," *J. Appl. Phys.*, vol. 105, p. 07A923, 2009.
- [7] Z. Deng, J. J. Scheidler, V. M. Asnani and M. J. Dapino, "Quasi-static major and minor strain-stress loops in textured polycrystalline Fe_{81.6}Ga_{18.4} Galfenol," *J. Appl. Phys.*, vol. 120, p. 243901, 2016.
- [8] L. Sandlund, M. Fahlander, T. Cedell, A. E. Clark, J. B. Restorff and M. Wun-Fogle, "Magnetostriction, elastic moduli, and coupling factors of composite Terfenol-D," *J. Appl. Phys.*, vol. 75, pp. 5656-5658, 1994.
- [9] A. E. Clark, M. Wun-Fogle, J. B. Restorff and T. A. Lograsso, "Magnetostrictive Properties of Galfenol Alloys Under Compressive Stress," *Mater. Trans.*, vol. 43, pp. 881-886, 2002.
- [10] N. Galopin, L. Daniel, F. Bouillault and M. Besbes, "Numerical analysis for the design of a magneto-elastic characterisation device," *Przegląd Elektrotechniczny*, vol. 83, pp. 44-47, 2007.
- [11] M. Domenjoud, E. Berthelot, N. Galopin, R. Corcolle, Y. Bernard and L. Daniel, "Characterization of Giant Magnetostrictive Materials under static stress: influence of loading boundary conditions," *to be published in Smart Mater. Struct.*, 2019.

ELECTROSTRICTIVE MULTILAYER POLYMER ACTUATOR DIMENSIONING AND MODELLING FOR CONTINUUM SNAKE LIKE ROBOT APPLICATION — SMART 2019

**Q.JACQUEMIN¹, D.THUAU², E.MONTEIRO¹, S.TENCE-GIRAULT^{1,3} and
N.MECHBAL¹**

¹PIMM, Arts et Metiers ParisTech, CNRS, Cnam, HESAM Université, 151 Bd de l'Hôpital, 75013 Paris, France

²Laboratoire de l'Intégration du Matériau au Système (IMS, UMR 5218) 351 Cours de la Libération, 33400 Talence, Cedex France.

³Arkema, CERDATO, Route du Rilsan, 27470 Serquigny, France

Key words: Smart system, soft actuator, electroactive polymer, electrostriction, Finite Element Modelling, continuum robot

Abstract. Electro-active polymers (EAP) are a kind of smart structures that undergo dimensional change in response to an applied electrical field. Due to their biocompatibility, conformability, low Young's modulus, high strain capabilities and relative low cost, EAPs are promising materials for the next generation of micro-scaled robotic devices. This paper describes the first result of the study of the terpolymer P(VDF-ter-TrFE-ter-CTFE), a relaxor ferroelectric characterized by its large electromechanical coupling, as the building block of a surgical micro-robot actuator. In order to deal with the large number of parameters involved in this active material (number of layers, material composition, substrate materials, etc), we develop a finite element model to support the experimental development.

INTRODUCTION

Different approaches have been studied to develop the automation of endoscopic surgical operations in order to assist surgeons in terms of efficiency and precision. From endoscopic capsules [1], [2] to traditional wire actuated poly-articulated snake like robot (figure 1) [3], [4] the research field is full of innovative perspectives.

Recently, smart materials have emerged as a key element for the conception of endoscopic surgical robot thanks to their compact design, dexterity and low cost. Among them, Nitinol, a shape memory alloy has been reported (figure 2) for a magnetic resonance imaging concentric tube robot actuator [5].

EAPs are another emerging family of promising materials for surgical automated actuator where biocompatibility, high strains and conformity to soft materials are desired features. EAPs can be classified into two categories: ionic EAPs and electronic EAPs [6]. The electrical activation of ionic EAPs is due to the migration of ions or electrically charged molecules. Whereas, electronic EAPs are activated by applied electric fields and Coulomb forces. Polypyrrole a CP Ionic Polymer has been used for an endoscopic medical robot [7]. Although Polypyrrole requires low voltage actuation compared to electronic

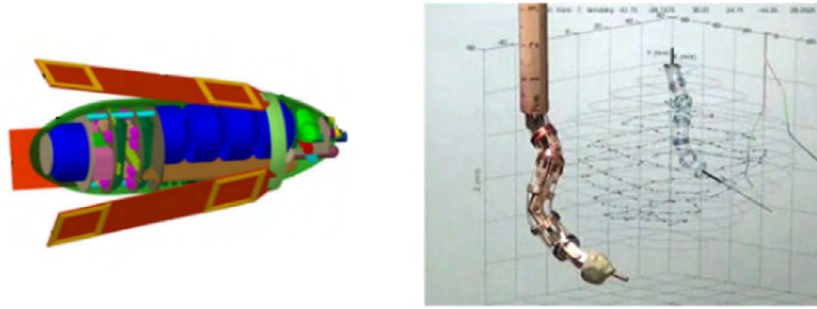


Figure 1: Endoscopic capsule robot [1] (left) and wire actuated snake like robot [4] (right)

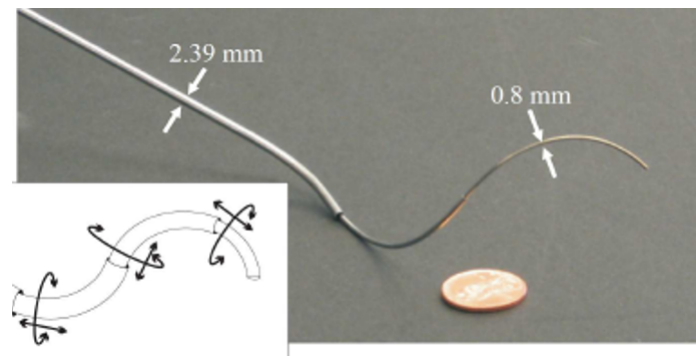


Figure 2: Nitinol actuator robot [5]

EAP and can hold strain under applied voltage which is essential in the case of a robot actuator, it exhibits a slow response time and induce a low actuation torque. On the contrary, electrostrictive polymers present a rapid response and the ability to generate large actuation force. Despite their high strain and energy density, electrostrictive materials require high actuation voltages which represents a major drawback that limited their implementation into real-life applications. To counter these issues, a multilayered concept is proposed. Due to the complexity of soft polymeric microstructures, analytical modeling will be performed to guide experimental design and fabrication of these electrostrictive based surgical actuators. In order to achieve large and controlled deformation a number of parameter (thickness, polymer formulation and passive materials composition) have been studied to lead the actuator design to reach the optimal performances. Concretely, Finite Element Model (FEM) results have enable to identify the curvature behaviour of the actuator to settle the control theory. In the context of surgical endoscopic robot, EAP smart material integration have raised others challenge in terms of control. Indeed, traditional discreet joints actuators and rigid links robots description is no more available for continuum soft robots. Smart materials actuators are part of the robot shape. Soft robots can reach an infinite number of degrees of freedom. A single EAP continuum actuator is equivalent with three discreet joints with the Denavit- Hartenberge (DH) modelling strategy [8],[9] (cf figure 3).

All three joints are related to the smart material curvature k as shown in figure 1. The DH parameters are linked to the soft robot parameters by a matrix integrated in the kinematic model.

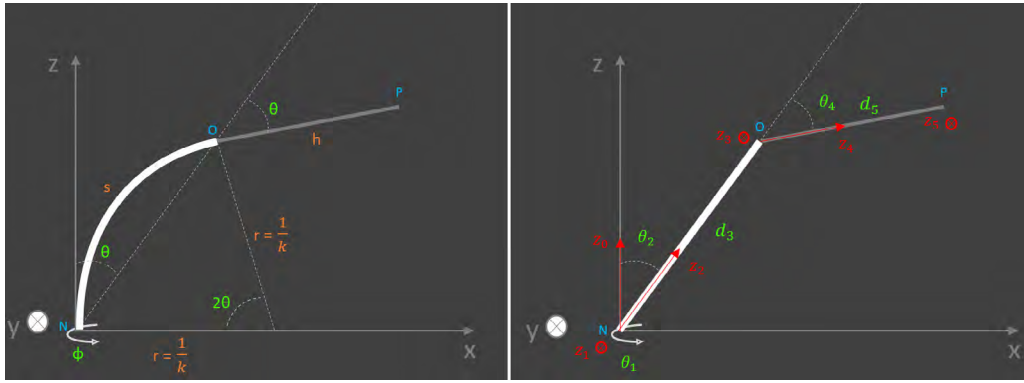


Figure 3: Parameters for one roll ϕ and one curvature (left). D-H modified equivalent structure (right).

Virtual joints	θ	d	a	α
1	$\theta_1 = \phi$	0	0	0
2	$\theta_2 = \frac{\pi}{2} - \frac{k_1 s_1}{2}$	0	0	$\frac{\pi}{2}$
3	$\theta_3 = 0$	$d_3 = \frac{2}{k_1} \sin(\frac{k_1 s_1}{2})$	0	0
4	$\theta_4 = \frac{k_1 s_1}{2}$	0	0	π

Table 1: DH modified virtual table

This paper is organized as follow. In the first section the electrostriction formulation and mechanism will be briefly presented. Then in section two the electro-mechanical behaviour of the EAP and the structure will be introduced to present the experimental model. This will lead to section three with the development of a finite element model (FEM) of a multilayer composite actuator designed to validate the feasibility in terms of maximum bending under electric field, materials characteristics, and number of layers. Finally, the results of the precedent section will induce the future expectation of this smart material and open the way to further integrated in a surgical robot structure.

1 Electrostriction

While electrostriction was long considered a higher-order nonlinear effect requiring stronger electric fields than typically used for piezoelectrics, the emergence of a new class of highly electrostrictive materials, known as relaxor ferroelectrics, has opened the path to the use of electrostriction as an alternative to the piezoelectricity for the large-strain actuation applications. In addition to the large strain capabilities, a major advantage of the electrostriction over the ferroelectric mechanism is that it enables a reproducible, non-hysteretic response. Various relaxor ferroelectric PVDF-based polymers have been reported to date such as electron-beam irradiated P(VDF-co-TrFE) copolymer or defect-modified P(VDF-co-TrFE) with added bulky CFE or CTFE monomers. In the case of P(VDF-ter-TrFE-ter-CTFE) it is the introduction of the third bulky monomer (CTFE) that disrupts the conformations ordering of the chains into the crystal and create ferroelectric nano-domains transforming it from a ferroelectric to a relaxor ferroelectric polymer [10], [11]. P(VDF-ter-TrFE-ter-CTFE) present a high dielectric constant (50), high electrostrictive strain (4%), good elastic energy densities with a reversible response time in the milliseconds range. These features make it extremely promising materials for smart actuators. [12],[13]. In particular, considering that single use tools are preferred in surgical robotic to reduce the sterilization cost and the risk of infection, the repeatability expectation of such a device would be reduced. The control processors and

voltage generator would not be embedded.

2 Experimental model

The mechanical behaviour of the relaxor ferroelectric is presented in [14] showing a quadratic evolution of the strain under electric field (figure 4). The curvature can be written as a function of E^2 with E

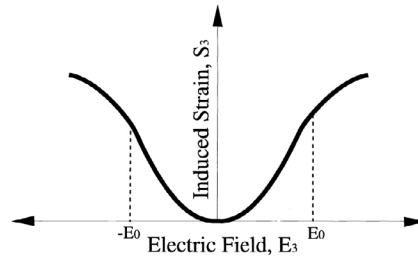


Figure 4: Electrostrictive response (strain) for a relaxor ferroelectric [14]

the electric field in V/m . When fixed at one side to a passive material, the strain is constraint to generate a bending in one direction. This assembly enables to use the EAP as a robot arm (figure 5) .

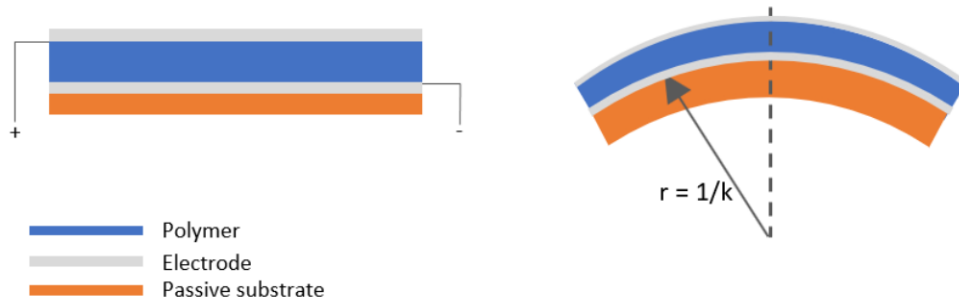


Figure 5: Structure of an EAP bending actuator

We have developed an experimental model to quantify the strain of the terpolymer P(VDF-ter-TrFE-ter-CTFE) provided by Piezotech S.A.S (Arkema group, France) with a ratio of 8% mol CTFE and an electrostrictive coefficient of $3.10^{18} m^2/V^2$. The polymer has been metalized with two aluminium electrodes and one passive substrate as in figure 6.

Materials and results

The EAP material fixed in the passive substrate has shown a reversible and repeatable bending under electric field with a maximum at $100 V/\mu m$ (figure 7). Nevertheless, such limited bending was mainly due to the fact that the applied electric field was kept significantly lower than the electric field breakdown of the terpolymers inducing low strain. In order to tackle these issues and to achieve high

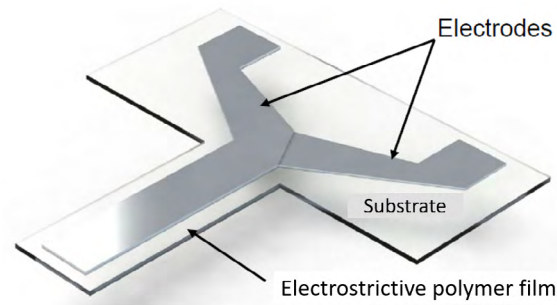


Figure 6: Schematic design of the experimental actuator

Component	Material	Young Modulus	Thickness	Electrostrictive coefficient
Passive substrate	PEN	5 GPa	50 μm	0
EAP	P(VDF-TrFE-CTFE)-8% CTFE	0.2 GPa	7 μm	$3.10^{-18} \text{m}^2/\text{V}^2$
Electrode	Al	70 GPa	300 nm	0

Table 2: Material characteristics for the FEM

deformation, two approaches have been investigated. First, the metal electrodes have been substituted by a low Young's modulus conductive polymer, (PEDOT:PSS) to increase the actuator bending at the same electric field conditions. Secondly, a multilayered/stacked approach has been developed to enhance the electro-mechanically induced force and displacement while keeping the applied voltage to an acceptable limit (500 V). In the multilayered configuration, electroded EAP films are layered on top of each other. The films are alternatively connected with high voltage and ground potential similar to a parallel capacitor connection. The conception of multilayered EAP actuators is a challenging task that should provide valuable insights on the influence of numerous geometrical and physical parameters on the device performance. Thanks to the quadratic behaviour of the strain, the voltage can be alternatively disposed without

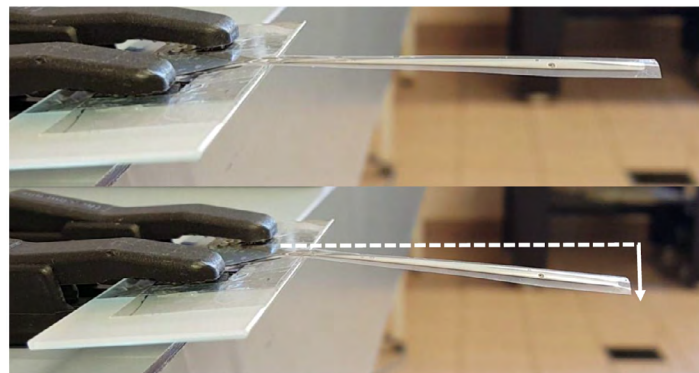


Figure 7: Monolayer 7 μm thin EAP actuator with Aluminium electrodes at 100V/ μm (left) and breakdown voltage result at 150V/ μm (right)

changing the bending side. So, for N layers of EAP material we need N + 1 layers of electrode (figure

8).

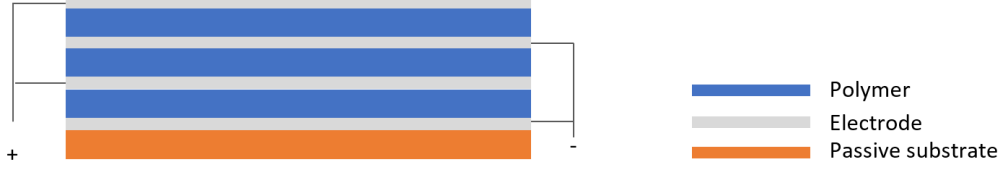


Figure 8: Multilayer beam actuator spatial convention

3 Finite element modelling

A model has been developed on abaqus, based on mechanical theory. The gap between global actuator dimension and polymer layer thickness (300 nm and 2 μm respectively) drove us to the design of a composite shell model with (SI millimetre analogy). Since the electrostrictive quadratic behaviour is not implemented on the software, we have made a thermal behaviour analogy by using a Fortran user subroutine. In order for our model to be used into a surgical robot actuator, the following boundary conditions have to be considered: the composite EAP must be able to bend itself by almost 100 degrees. The electric field has to be kept lower than the terpolymer breakdown electric field and thus considering the actuator dimensions, the maximum voltage should be kept at 500 V. Consequently, the presented FEM drives us finding the optimal actuator configuration in terms of layer's number, material characteristics and composite elements thickness (figure 11).

3.0.1 Composite materials behaviour

Terpolymer P(VDF-TrFE-CTFE) is an elastic isotrope material [13]. Its temperature dependency has not been taken into account in this study. The horizontal strain (X and Z axis) is expressed as follow in equation 2 and shown in figure 9. ϵ_0 is the strain at $y = 0$, ρ is the radius of curvature and $k = \frac{1}{\rho}$. e_p , e_e and e_s are respectively the terpolymer, electrode and substrate layers thickness [12].

$$\epsilon^x(y) = \epsilon_0^x + \frac{y}{\rho} = \epsilon_0^x + yk_x; \quad -e_s \leq y \leq n(e_e + e_p) \quad (1)$$

$$\epsilon^z(y) = \epsilon_0^z + \frac{y}{\rho} = \epsilon_0^z + yk_z; \quad -e_s \leq y \leq n(e_e + e_p) \quad (2)$$

For the polymer and electrode layers, $\epsilon_{elastic} = \epsilon_{total} - \epsilon_{electrostrictive}$ with $\epsilon_{electrostrictive} = M_i E^2$ with M_i the electrostrictive coefficient matrix and E the electric field in V/m.

$$\epsilon_x^{el}(y) = \epsilon_0^x + yk_x - M_x^i E^2; \quad -e_s \leq y \leq n(e_e + e_p) \quad (3)$$

$$\epsilon_z^{el}(y) = \epsilon_0^z + yk_z - M_z^i E^2; \quad -e_s \leq y \leq n(e_e + e_p) \quad (4)$$

$M_i = M_p$ for the terpolymer and $M_i = 0$ for the electrode and the substrate materials. The horizontal plane stress can be written as in equation 5.

$$\begin{pmatrix} \sigma_x \\ \sigma_z \\ \tau_{xz} \end{pmatrix}_i = \begin{pmatrix} Q_{11} & Q_{12} & Q_{16} \\ Q_{12} & Q_{22} & Q_{26} \\ Q_{16} & Q_{26} & Q_{66} \end{pmatrix}_i \begin{pmatrix} \epsilon_x^{el} \\ \epsilon_z^{el} \\ \gamma_{xz} \end{pmatrix}_i \quad (5)$$

Q_{ij} 's are the plane stress reduced elastic constants in the plate axes of the i^{th} layer. We can then introduce the resultant stress as:

$$\begin{pmatrix} N_x \\ N_z \\ N_{xz} \end{pmatrix} = \sum_{i=0}^{n+1} \begin{pmatrix} Q_{11} & Q_{12} & Q_{16} \\ Q_{12} & Q_{22} & Q_{26} \\ Q_{16} & Q_{26} & Q_{66} \end{pmatrix}_i \int_{h(i)} \begin{pmatrix} \epsilon_{xx} \\ \epsilon_{zz} \\ \gamma_{xz} \end{pmatrix}_i \quad (6)$$

With $h(i)$ the layer thickness depending on the material i .

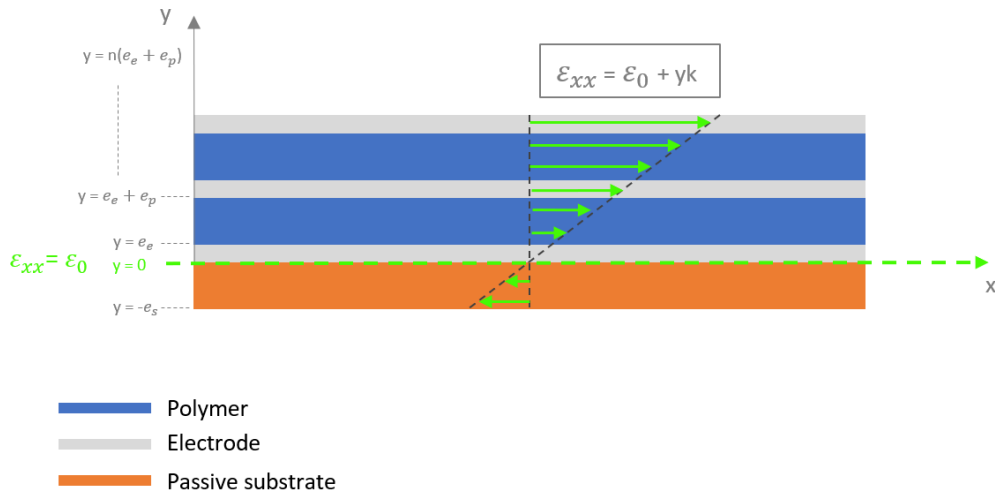


Figure 9: Multilayer beam convention with $\epsilon(0) = \epsilon_0$

3.0.2 Materials and results

In the figure 10 left, we have studied the influence of the number of layers. In this model, the total EAP thickness is fixed to $10 \mu\text{m}$ and divided into the number of layers. The voltage is also stuck at 500 V so that increasing the number of layers increases the electric field. The graphic shows the elements final position alongside the actuator length. For a five layer EAP of $2 \mu\text{m}$ each, the electric field is $250 \text{ V}/\mu\text{m}$. Studying the influence of the number of layers has highlighted the capability of reaching the expected bending performance as shown in figure 10 left. The electrode's Young Modulus of 0.02 GPa is no longer increasing the stiffness of the composite material. We have been looking for the best substrate material for this configuration (figure 10 right) and Pebax (0.3 GPa) (provided by Arkema) would suit. The figure 11 shows the bending performances of the composite actuator with characteristics from table

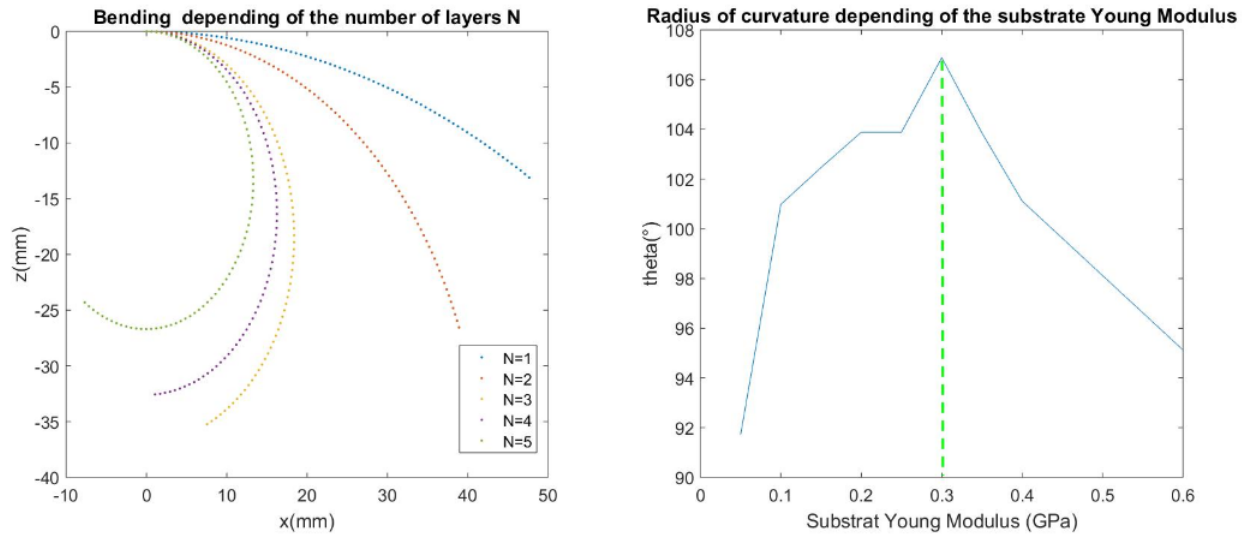


Figure 10: Spatial representation of the actuator behaviour depending of the number of layers N (left) and radius of curvature depending on the substrate Young Modulus (right)

3. This configuration enables a maximum bending of 110 degrees for a $50 \times 2 \text{ mm}$ EAP actuator at 500V as defined. The displacement induced force is also under study. However for the experimental device the number of layer is restricted by the design feasibility in the laboratory conditions.

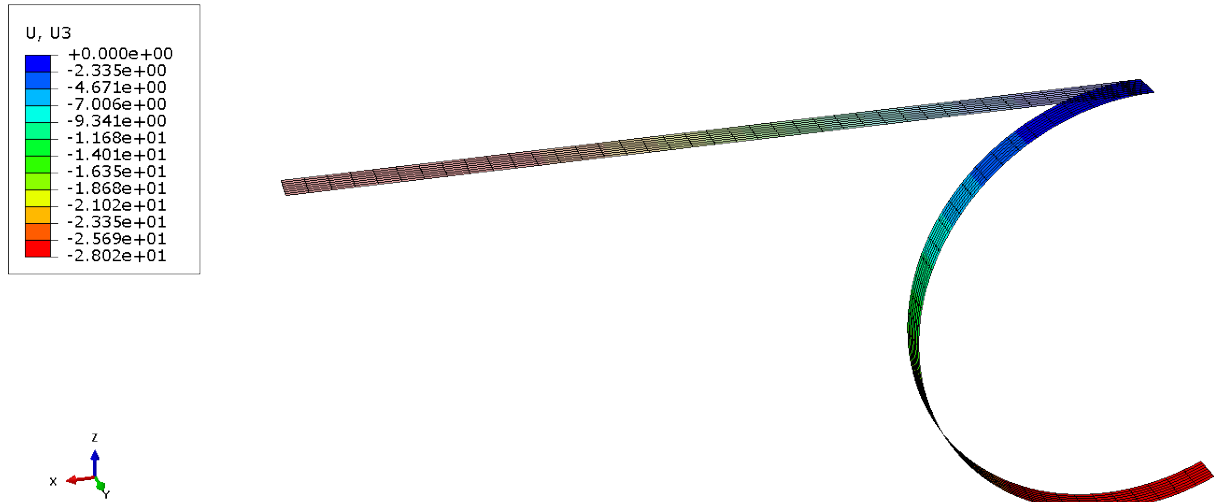


Figure 11: Five ($2 \mu\text{m}$ thin) layers actuator with polymer electrodes under $50 \text{ V}/\mu\text{m}$

Component	Material	Layers	Young Modulus	Thickness	Electrostrictive coefficient
Passive substrate	Pebax	1	0.2 GPa	10 μm	0
EAP	P(VDF-TrFE-CTFE)	5	0.3 GPa	2 μm	$3 \cdot 10^{-18}$ m/V
Electrode	Polymer	6	0.02 GPa	300 nm	0

Table 3: Material characteristics for the FEM

Conclusion

This paper has presented EAP actuators in the context of endoscopic robots in the medical area. Among other smart materials studied for this application, EAP and more specifically electrostrictive polymers has been selected for their large electromechanical strain. Those smart materials can be integrated into a robot structure to perform self-bending. A composite beam, made of a passive substrate, has been experimentally evaluated and has highlighted the high voltage requirement to achieved large bending. Although, To decrease the electric field and improve the bending, a multilayer composites smart material has been designed on abaqus. This model has demonstrated the efficiency of this formulation in terms of bending, and a five layers actuator of 2 μm each was found to be the optimized configuration to achieved the expected performances. Finally, an experimental multilayer device will be made from this results to confirm the achievement and readjust the theoretical parameters. The FEM will also evaluate the displacement induced force at the distal tip of the actuator to deal with external perturbations. Finally, to validate this smart material as an effective robotic actuator, the next step will be to focus on the repeatability of the actuation and the control accuracy. Indeed, as a robotic structure, the control of the smart material by an external power source has to be accurate and robust. An EAP actuated robot could be designed with serial actuators as in figure 12 to increase the degrees of freedom.

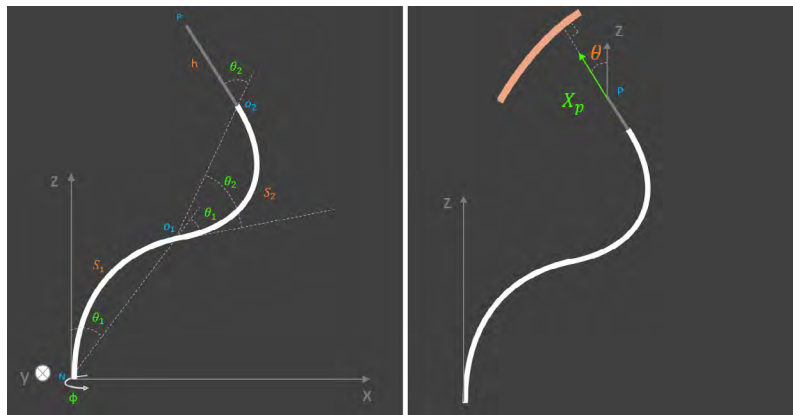


Figure 12: Structure and parameters of the two EAP actuator robot structure (left). Description of the control of the orientation between the distal tip and the target (left).

REFERENCES

- [1] Gábor Kósa, Péter Jakab, Gábor Székely, and Nobuhiko Hata. MRI driven magnetic microswimmers. *Biomedical Microdevices*, 14(1):165–178, February 2012.
- [2] Isabel N. Figueiredo, Carlos Leal, Luís Pinto, Pedro N. Figueiredo, and Richard Tsai. Hybrid multiscale affine and elastic image registration approach towards wireless capsule endoscope localization. *Biomedical Signal Processing and Control*, 39:486–502, January 2018.
- [3] Tingyu Qu, Jie Chen, Shen Shen, Zhen Xiao, Zhe Yue, and Henry YK Lau. Motion control of a bio-inspired wire-driven multi-backbone continuum minimally invasive surgical manipulator. In *Robotics and Biomimetics (ROBIO), 2016 IEEE International Conference on*, pages 1989–1995. IEEE, 2016.
- [4] T. D. Soper, M. P. Porter, and E. J. Seibel. Surface Mosaics of the Bladder Reconstructed From Endoscopic Video for Automated Surveillance. *IEEE Transactions on Biomedical Engineering*, 59(6):1670–1680, June 2012.
- [5] Hao Su, Weijian Shang, Gregory Cole, Gang Li, Kevin Harrington, Alexander Camilo, Junichi Tokuda, Clare M. Tempny, Nobuhiko Hata, and Gregory S. Fischer. Piezoelectrically Actuated Robotic System for MRI-Guided Prostate Percutaneous Therapy. *IEEE/ASME Transactions on Mechatronics*, 20(4):1920–1932, August 2015.
- [6] Y. Bar-Cohen. Electroactive polymers (EAP) as actuators for potential future planetary mechanisms. In *Proceedings. 2004 NASA/DoD Conference on Evolvable Hardware, 2004.*, pages 309–317, Seattle, WA, USA, 2004. IEEE.
- [7] Mohamed Taha Chikhaoui, Kanty Rabenorosoa, and Nicolas Andreff. Kinematics and performance analysis of a novel concentric tube robotic structure with embedded soft micro-actuation. *Mechanism and Machine Theory*, 104:234–254, October 2016.
- [8] Robert J. Webster and Bryan A. Jones. Design and Kinematic Modeling of Constant Curvature Continuum Robots: A Review. *The International Journal of Robotics Research*, 29(13):1661–1683, November 2010.
- [9] M. Hannan and I. Walker. Vision based shape estimation for continuum robots. In *2003 IEEE International Conference on Robotics and Automation (Cat. No.03CH37422)*, volume 3, pages 3449–3454, Taipei, Taiwan, 2003. IEEE.
- [10] François Bargain, Damien Thuau, Pierre Panine, Georges Hadziioannou, Fabrice Domingues Dos Santos, and Sylvie Tencé-Girault. Thermal behavior of poly(VDF-ter-TrFE-ter-CTFE) copolymers: Influence of CTFE termonomer on the crystal-crystal transitions. *Polymer*, 161:64–77, January 2019.
- [11] Lianyun Yang, Brady A. Tyburski, Fabrice Domingues Dos Santos, Maya K. Endoh, Tadanori Koga, Daniel Huang, Yijun Wang, and Lei Zhu. Relaxor Ferroelectric Behavior from Strong Physical Pinning in a Poly(vinylidene fluoride- *co* -trifluoroethylene- *co* -chlorotrifluoroethylene) Random Terpolymer. *Macromolecules*, 47(22):8119–8125, November 2014.
- [12] Saad Ahmed, Zoubaida Ounaies, and Erika Ann F. Arrojado. Electric field-induced bending and folding of polymer sheets. *Sensors and Actuators A: Physical*, 260:68–80, June 2017.

- [13] Mary I Frecker and William M Aguilera. Analytical modeling of a segmented unimorph actuator using electrostrictive P(VDF-TrFE) copolymer. *Smart Materials and Structures*, 13(1):82–91, February 2004.
- [14] J. C. Debus, B. Dubus, Michele D. McCollum, and S. Black. Finite-element modeling of PMN electrostrictive materials. page 913, Lyon, France, April 1996.

ENERGY HARVESTING USING A PIEZOELECTRIC-FLEXOELECTRIC NANOBEAM

Fehmi Najar*, Sourour Baroudi* and Hatem Samaali*

*Applied Mechanics and Systems Research Laboratory (LR03ES06), Tunisia Polytechnic School
University of Carthage, BP 743, Al Marsa 2078, Tunis, Tunisia.
e-mail: fehmi.najar@ept.rnu.tn, web page: <http://www.ept.rnu.tn>

Key words: Flexoelectricity, nanobeam, energy harvesting, strain gradient theory

Abstract. Flexoelectricity can be defined as an electromechanical coupling between polarization and strain gradient. In contrast with piezoelectricity, flexoelectricity is largely dominant at the nanoscale. Using a developed electromechanical model of a BaTiO_3 nanobeam, we simulate the dynamic behavior of the device when it is subject to a base harmonic excitation representing mechanical vibrations from the environment. The coupled electromechanical model is first derived using the Hamilton's principle and accounting for the von Karman strain for relatively large displacements and takes into account an initial static displacement due to residual stresses. The Galerkin approximation is used to discretize the space domain for the transverse displacement and the electric potential. The nonlinear dynamic response of the nanobeam and the generated electrical voltage are solved for limit-cycle solutions. The results depicted higher power density generation when the aspect ratio of the nanobeam is varied. It is found that the initial deflection can mitigate the expected performance of the device.

1 INTRODUCTION

Flexoelectric effect is an electromechanical coupling that can be used to enhance electrical response from mechanical stimuli for nanoscale structures [1, 2]. For nanobeams, taking into account interactions between electric polarization strain and strain gradient should be accompanied by other interactions of the same order of approximation. Elastic strain gradient theory can be used in this case to fulfill this requirement.

The flexoelectric effect was observed in centrosymmetric as well as noncentrosymmetric dielectric materials [3]. It was used as a transduction mechanism for actuators, sensors and energy harvesting applications [4, 5, 2].

Because relatively large displacements are easily obtained at the nanoscale, several researchers proposed the introduction of geometric nonlinearity in the modeling of nanobeams [6]. For energy harvesting applications accounting for large displacements only few attempts are found in the literature. Wang et al. [7] investigated the nonlinear response of a cantilever nanobeam for energy harvesting applications and concluded that the flexoelectric effect can extremely improve the harvested power (five times). Kumar et al. [8] proposed a bistable mechanism by using a pair of magnet placed at the tip of cantilever beam. They reported very large bandwidth response of the energy harvester when compared to a linear design. Rojas et al. [9] simulated the frequency-response of clamped-clamped and clamped-hinged nanobeam energy harvesters by taking into accounts the von Karman nonlinear strain. They reported that

size dependent model should be used to model flexoelectric nanobeam and reported large bandwidth only for the clamped-hinged nanobeam since their model was not able to capture the generated polarization for the clamped-clamped case.

In the proposed work, a piezoelectric flexoelectric clamped-clamped nanobeam is proposed as energy harvester. The analytical model takes into account a bidirectional electric field and strain gradient in the longitudinal and transverse directions to calculate the harvested voltage when base excitation is applied.

2 Nonlinear model of a Piezoelectric flexoelectric Nanobeam

A prismatic nanobeam, shown in Figure 1, is considered with length L along the x -axis, thickness h and width b . The nanobeam is made of BaTiO₃ material with density ρ . Two conductive electrodes cover its upper and lower faces. The Euler-Bernoulli beam theory is used to model the nanobeam when

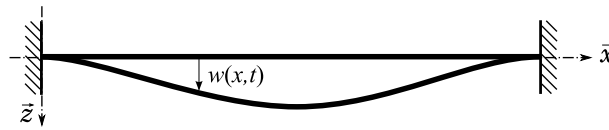


Figure 1: Clamped-clamped nanobeam made of BaTiO₃ material.

it undergoes relatively large displacements. The associated geometric nonlinearities are modeled using the von Karman strain. With low electric fields and non significant stress-strain hysteresis effects, one can consider a linear material behavior. We use the following enthalpy density of the nanobeam material [10]

$$H = W^L(\mathbf{S}, \nabla \mathbf{S}, \mathbf{P}) - \frac{1}{2} \epsilon \phi_{,i}^2 + P_i \phi_{,i} \quad i = x, y, z$$

where W^L is the internal energy density, \mathbf{S} is the Cauchy strain tensor, $\nabla \mathbf{S}$ is the strain gradient tensor, \mathbf{P} is the polarization vector, $\phi(x, z, t)$ is the potential of the electric field and ϵ is the permittivity of the media.

The internal energy density W^L can be expressed as [6]

$$W^L = \frac{1}{2} a_{11} P_x^2 + \frac{1}{2} a_{33} P_z^2 + \frac{1}{2} c_{11} \epsilon_{xx}^2 + d_{11} \epsilon_{xx} P_x + d_{31} \epsilon_{xx} P_z + f_{11} \epsilon_{xx,x} P_x + f_{14} \epsilon_{xx,z} P_z + \frac{1}{2} g_{11} \epsilon_{xx,x}^2 + \frac{1}{2} g_{11} \epsilon_{xx,z}^2 \quad (1)$$

where \mathbf{a} is the dielectric susceptibility tensor, \mathbf{c} is the elastic constant tensor, \mathbf{d} is the piezoelectric constant tensor, \mathbf{f} is the flexoelectricity tensor and \mathbf{g} is the strain gradient coefficients.

The axial strain component can be expressed by [11]

$$\epsilon_{xx} = u' + \frac{1}{2} w'^2 - z w'' \quad (2)$$

where $u(x, t)$ is axial displacement and $w(x, t)$ is the transverse displacement, prime corresponds to derivative with respect to x .

We use the Hamilton's principle to derive the governing electroelastic equations and the associated boundary conditions, it is given by

$$\int_{t_1}^{t_2} \left(\delta K - \int_V \delta H dV \right) dt = 0 \quad (3)$$

where K is the kinetic energy given by

$$\delta K = - \int_0^L m (\ddot{w} \delta w + \ddot{u} \delta u) dx \quad (4)$$

where $m = \rho b h$ is the mass per unit length, F is an external excitation.

Therefore, Equation (3), yields the governing equations

$$m\ddot{u} - N' = 0 \quad (5)$$

$$m\ddot{w} - M'' - (Nw')' = F \quad (6)$$

$$P_{x,x} + P_{z,z} - \epsilon \phi_{,xx} - \epsilon \phi_{,zz} = 0 \quad (7)$$

$$\phi_{,x} - E_1 = 0 \quad (8)$$

$$\phi_{,z} - E_3 = 0 \quad (9)$$

and the associated boundary conditions

$$u = 0, u' = 0, w = 0, \quad (10)$$

$$M + \tilde{N} w' = 0, \tilde{M} = 0, \text{ and } \phi' = 0$$

where

$$M = \int_A (z T_{11} + \tilde{T}_{113} - z \tilde{T}'_{111}) dA \quad (11)$$

$$\tilde{M} = \int_A (z \tilde{T}_{111}) dA \quad (12)$$

$$N = \int_A (T_{11} - \tilde{T}'_{111}) dA \quad (13)$$

$$\tilde{N} = \int_A \tilde{T}_{111} dA \quad (14)$$

and

$$T_{11} = c_{11} \epsilon_{xx} + d_{11} P_x + d_{31} P_z \quad (15)$$

$$\tilde{T}_{111} = f_{11} P_x + g_{11} \epsilon_{xx,x} \quad (16)$$

$$\tilde{T}_{113} = f_{14} P_z + g_{11} \epsilon_{xx,z} \quad (17)$$

$$-E_1 = a_{11} P_x + d_{11} \epsilon_{xx} + f_{11} \epsilon_{xx,x} \quad (18)$$

$$-E_3 = a_{33} P_z + d_{31} \epsilon_{xx} + f_{14} \epsilon_{xx,z} \quad (19)$$

A simplification is proposed in this case where the axial displacement is eliminated in the equations by assuming that the axial stress component N is constant along the nanobeam when the axial inertial is neglected [11, 6]. As a result, the polarization vector is expressed as

$$P_x = -\frac{1}{a_{11}} \left(\phi_{,x} - \left(z + \frac{d_{31} f_{14}}{\bar{E} a_{33}} \right) (d_{11} w'' + f_{11} w''') + \frac{d_{11}}{2L} \int_0^L w'^2 dx \right) \quad (20)$$

$$P_z = -\frac{1}{a_{33}} \left(\phi_{,z} - \left(z d_{31} + f_{14} + \frac{d_{31}^2 f_{14}}{\bar{E} a_{33}} \right) w'' + \frac{d_{31}}{2L} \int_0^L w'^2 dx \right) \quad (21)$$

When energy harvesting or sensing applications are sought, the voltage accross the electrodes $V(t)$ follows the Gauss's law given by [2]

$$\frac{V}{R} = \frac{1}{h} \frac{d}{dt} \int (P_z - \epsilon \phi_{,z}) dx dy dz \quad (22)$$

where R is the external electrical resistance load.

As a result, one can deduce the equation governing the voltage variation as follows:

$$\frac{bL}{h} \left(\epsilon + \frac{1}{a_{33}} \right) \dot{V} + \frac{V}{R} = \frac{b}{a_{33}} \left(f_{14} + \frac{d_{31}^2 f_{14}}{\bar{E} a_{33}} \right) \int_0^L \dot{w}'' dx - \frac{b d_{31}}{a_{33}} \int_0^L \dot{w}' w' dx \quad (23)$$

On the other hand, we assume that the electrical potential ϕ can be approximated by [2, 6]

$$\phi(x, z, t) = \phi(x, t) \cos\left(\frac{\pi}{h} z\right) + \frac{z + h/2}{h} V \quad (24)$$

where $\phi(x, t)$ represent the longitudinal variation of the electric potential.

Using the polarization components in Equations (20) and (21), the electric potential in Equation (24), we obtain the nonlinear expression of the bending moment M , \tilde{M} and \tilde{N} , defined in Equations (11) to (14), in terms of the deflection w and the longitudinal potential ϕ . They are given by

$$M = -k_1 w'' + k_2 w'''' + \frac{2A d_{31}}{\pi a_{33}} \phi - \frac{A f_{14}}{a_{33}} \frac{V}{h} - \frac{d_{31} f_{14}}{a_{33}} \frac{A}{2L} \int_0^L w'^2 dx \quad (25)$$

$$N = \frac{\bar{E} A}{2L} \int_0^L w'^2 dx - \frac{d_{31} A}{a_{33}} \frac{V}{h} - \frac{2A}{a_{11} \pi} (d_{11} \phi' - f_{11} \phi'') + \frac{d_{11} f_{14} A k_2}{a_{33} \bar{E} I} w'''' \quad (26)$$

$$\tilde{M} = \frac{d_{11} f_{11} I}{a_{11}} w'' - k_2 w'''' \quad (27)$$

$$\tilde{N} = \frac{d_{11} d_{31} f_{11} f_{14} A}{a_{11} a_{33} \bar{E}} w'' - \frac{f_{14} d_{31} A k_2}{a_{33} \bar{E} I} w'''' - \frac{2 f_{11} A}{a_{11} \pi} \phi' - \frac{d_{11} f_{11}}{a_{11}} \frac{A}{2L} \int_0^L w'^2 dx \quad (28)$$

where k_1 and k_2 are given in the Appendix, $\bar{E} = (c_{11} - \frac{d_{11}^2}{a_{11}} - \frac{d_{31}^2}{a_{33}})$ and $I = \frac{bh^3}{12}$ is the second moment of area of the nanobeam's cross-section.

A nondimensional form of the equations is obtained by using the following variables:

$$\hat{w} = \frac{w}{h}, \quad \hat{\phi} = \frac{\phi}{\phi_0}, \quad \hat{x} = \frac{x}{L}, \quad \hat{z} = \frac{z}{h} \quad \text{and} \quad \hat{t} = \frac{t}{\tau} \quad (29)$$

where

$$\tau = \sqrt{\frac{m L^4}{k_1}} \quad \text{and} \quad \phi_0 = \frac{\pi k_1 a_{33}}{2 b L^2 d_{31}}$$

Following Baroudi and Najar [6], Equations (6) and (7) are used to calculate the associated mode shapes for the transverse displacement and the longitudinal potential. These mode shapes are used in a Galerkin procedure to obtain a reduced order model of the governing equations. For a single mode approximation based on the following expressions:

$$\hat{w}(\hat{x}, \hat{t}) = q(\hat{t}) \Psi(\hat{x}) \quad (30)$$

$$\hat{\phi}(\hat{x}, \hat{t}) = p(\hat{t}) \Phi(\hat{x}) \quad (31)$$

where the mode shapes functions Ψ and Φ are given in [6].

The modal equations are obtained by applying Equations (30) and (31) to Equations (6), (7) and (23). The result is given by

$$\ddot{q} + 2\mu\dot{q} + (\kappa_1 + \kappa_0 V)q + \kappa_3 q^3 = f \cos \Omega t \quad (32)$$

$$\dot{V} + \gamma_1 V + \gamma_2 q \dot{q} = 0 \quad (33)$$

where the p parameter has been eliminated between Equations (6) and (7), ω is the base excitation frequency and the other coefficients are given in the Appendix.

The mode shapes shown in Figures 2 are obtained for a BaTiO₃ material with the geometrical and physical properties given by Table 1. The characteristic nonlocal elastic length scale [5, 12] is defined as $l_0 = \sqrt{g_{11}/c_{11}} = 2\text{nm}$.

Table 1: Geometrical and physical properties of the BaTiO₃ with plane stress assumptions [13, 14, 15]

Length	L (nm)	400
Thickness	h (nm)	1
Width	b (nm)	20
Elastic Constant	c_{11} (GPa)	131
Dielectric constants	a_{11} (Vm/C)	0.89710
	a_{33} (Vm/C)	0.78810
Piezoelectric constants	d_{11} (V/m)	-18.52×10^8
	d_{31} (V/m)	1.87×10^8
Flexoelectric constants	f_{11} (V)	-0.013
	f_{14} (V)	5
Mass density	ρ (kg/m ³)	6.02×10^3
Resistance load	R	10^9 Ohm

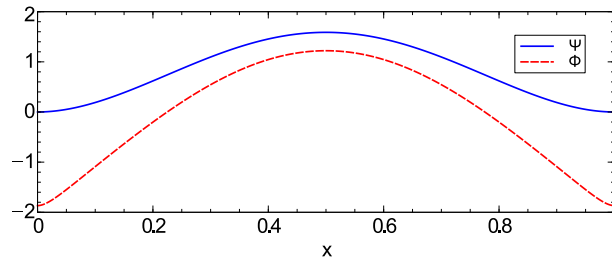


Figure 2: Transverse deflection and longitudinal electric potential mode shapes for a clamped-clamped nanobeam.

3 Energy harvesting from the nonlinear response of the nanobeam

In this section, we analyze the nonlinear dynamics of the nanobeam by numerically solving Equation (32) when a static component is present. The static component is introduced to simulate the presence of an initial deflection that can be observed in these nanosystems due to fabrication residual stresses. Consequently, the modal displacement $q(t)$ can be expressed as the sum of the static component around which a dynamic motions is achieved, that is,

$$q(t) = q_s + \eta(t) \quad (34)$$

Therefore, extracting the static equation expressed by $\omega_0^2 q_s + 3\kappa_3 q_s^3 = f_s$, Equation (32) is rewritten as

$$\ddot{\eta} + 2\mu\dot{\eta} + \omega_0^2 \eta + \kappa_0 V \eta + 3\kappa_3 q_s \eta^2 + \kappa_3 \eta^3 + \kappa_0 q_s V = f \cos \Omega t \quad (35)$$

$$\dot{V} + \gamma_1 V + \gamma_2 q_s \dot{\eta} + \gamma_2 \eta \dot{\eta} = 0 \quad (36)$$

here $\omega_0^2 = \kappa_1 + 3\kappa_3 q_s^2$.

Limit-cycle solutions of Equations (35) and (36) are obtained using the Finite Difference Method (FDM) [16, 17].

In Figure 3, the frequency-response curves of the transverse displacement of the clamped-clamped nanobeam are shown for different values of the thickness. As shown, the maximum deflection is obtained for the largest simulated thickness ($h = 10\text{nm}$), however in this case, the bandwidth is very small and a snap-through response is observed at 10nm of maximum displacement because of the imposed initial deflected configuration. The corresponding harvested voltage is displayed in Figure 4. As shown the maximum harvested voltage is also obtained for $h = 10\text{nm}$ with a small bandwidth and a snap-through response. It turns out that best performances are obtained for the 5nm thick nanobeam where very no jumps are observed for a 1.8MHz bandwidth.

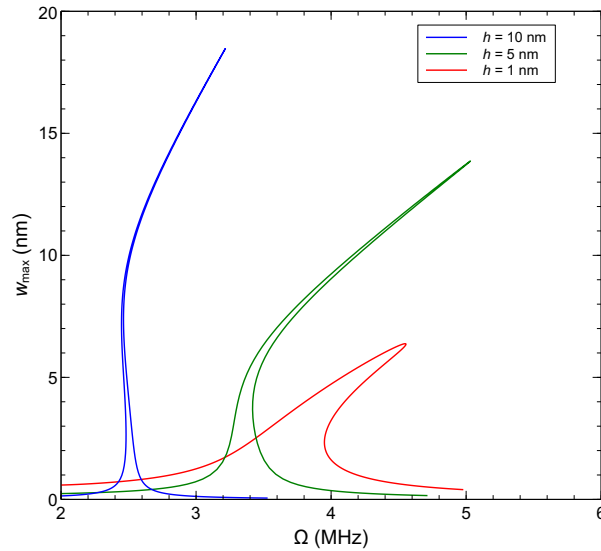


Figure 3: Frequency-response curves of the clamped-clamped nanobeam maximum deflection around the first mode, for different values of the thickness. $q_s = 0.5$ and $F = 100m$.

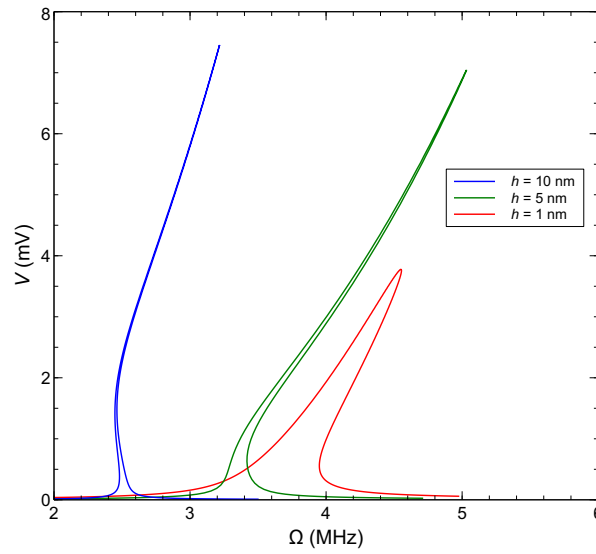


Figure 4: Frequency-response curves of the clamped-clamped nanobeam maximum harvested voltage around the first mode, for different values of the thickness. $q_s = 0.5$ and $F = 100m$.

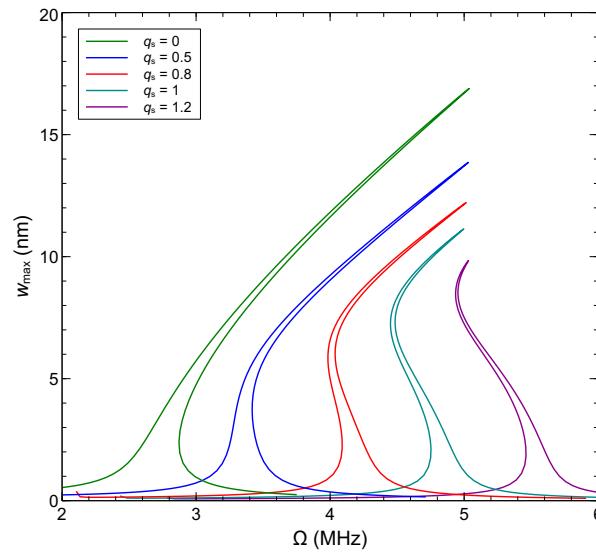


Figure 5: Frequency-response curves of the clamped-clamped nanobeam maximum deflection around the first mode, for different values of the thickness. $q_s = 0.5$ and $F = 100m$.

As long as the the initial deflected configuration can dramatically perturb the performance of the device, one can investigate their influence on the response of the nanobeam. In Figure 5 and 6, the maximum deflection and harvested voltage are shown for different values of the initial configuration parameter q_s . As depicted by these figures, the absence of initial deflection or when q_s is small (less than 0.5) no snap-through is observed and consequently the bandwidth response is very large (more than 2 MHz). Also, large harvested voltages can be achieved for large values of q_s however in this case the bandwidth is only around 0.5MHz. For intermediate values of q_s poor performance of the

energy harvester are observed. In these figures, one can also observe that the value of q_s can control the frequency-response hardening and softening behaviors and reduces the snap-through region.

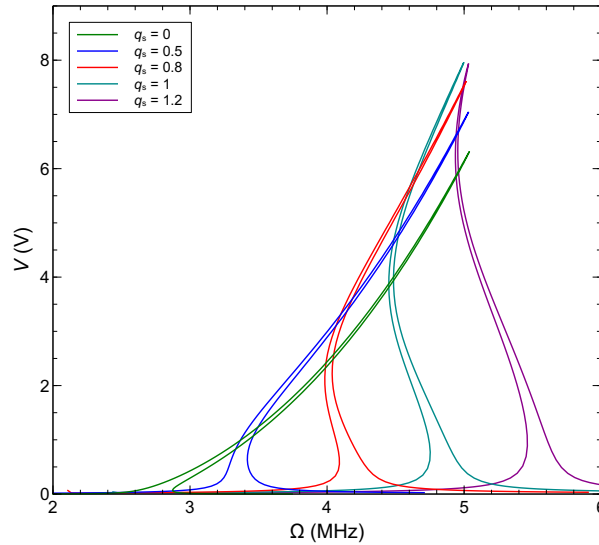


Figure 6: Frequency-response curves of the clamped-clamped nanobeam maximum harvested voltage around the first mode, for different values of the thickness. $q_s = 0.5$ and $F = 100m$.

4 Conclusion

An electromechanical model of a BaTiO₃ single layer clamped-clamped nanobeam is developed for energy harvesting applications. The coupled electromechanical model takes into accounting the piezoelectric and the flexoelectric effects for transverse and longitudinal polarization along with the presence of the nonlinear von Karman strain taking into account relatively large displacements. The model also incorporates residual stresses, due to fabrication, that can generate initial deflection of the nanobeam. The Galerkin approximation is used to discretize the space domain for the transverse displacement and the electric potential. The obtained reduced-order model is solved for limit-cycle solutions of the deflection of the nanobeam and the generated electrical voltage across a resistance load. The results depicted higher power density generation when the aspect ratio of the nanobeam is varied. It is found that if initial deflection is taking into account, intermediate values of the thickness gives better performance that high aspect ratio designs in terms of generated voltage and bandwidth. The effect of the initial deflection was also investigated in this work, the results showed that either small or large values can be used to increase the performance with a preference for the small deflections. Intermediate values revealed bad achievements of the device.

Appendix

We let $\Gamma(f, g) = \int_0^1 f g dx$:

$$\begin{aligned} \kappa_0 &= \frac{k_{11}L^2}{k_1h} \Gamma(\Psi', \Psi'), \quad \kappa_1 = J_1 + J_4 \frac{J_6}{J_5}, \quad \kappa_2 = J_2 + \frac{k_{12}L}{k_1} \Gamma(\Psi', \Psi') \frac{J_6}{J_5} \int_0^1 \Phi'_k(x) dx, \quad \kappa_3 = \frac{k_{13}h^2}{k_1} \Gamma(\Psi', \Psi')^2 \\ \Theta &= \frac{k_3L^2}{h^2k_1} \int_0^1 \Psi''(x) dx, \quad f = \frac{L^3}{k_1h} F \int_0^1 \Psi dx, \quad \gamma_1 = \frac{\tau}{bLRh}, \quad \gamma_2 = \frac{hd_{31}}{L^2a_{33}} \Gamma(\Psi', \Psi') \end{aligned}$$

where

$$J_1 = \Gamma(\Psi'', \Psi'') + \frac{k_2}{L^2 k_1} \Gamma(\Psi''', \Psi''') + \frac{k_4}{L k_1} \Gamma(\Psi'', \Psi'''), J_2 = \frac{3k_{10}h}{2k_1 L} \Gamma(\Psi', \Psi') \times \int_0^1 \Psi_k'''(x) dx$$

$$J_4 = -\frac{k_5 L^2}{k_1 h} \Gamma(\Psi'', \Phi) + \frac{k_6 L}{k_1 h} \Gamma(\Psi'', \Phi') + \frac{k_7 L}{k_1 h} \Gamma(\Psi''', \Phi'), J_5 = \Gamma(\Phi', \Phi') + \frac{k_9 L^2}{k_8}$$

$$J_6 = -\frac{k_5 h}{k_8} \Gamma(\Phi, \Psi'') - \frac{k_6 h}{k_8 L} \Gamma(\Phi', \Psi'') - \frac{k_7 h}{k_8 L^2} \Gamma(\Phi', \Psi''')$$

and

$$k_0 = \frac{d_{11} d_{31} f_{14}}{a_{11} a_{33} \bar{E}}, k_1 = \bar{E} I + \left(g_{11} - \frac{f_{14}^2}{a_{33}} \right) A - \frac{A d_{31}^2 f_{14}^2}{a_{33}^2 \bar{E}}, k_2 = \left(g_{11} - \frac{f_{11}^2}{a_{11}} \right) I$$

$$\bar{k}_2 = k_2 + \frac{A d_{31}^2 f_{14}^2}{a_{33}^2 \bar{E}^2} \left(g_{11} - \frac{f_{11}^2}{a_{11}} \right), k_3 = \frac{A f_{14}}{a_{33}} \left(1 + \frac{d_{31}^2}{a_{33} \bar{E}} \right), k_4 = -\frac{d_{11} f_{11}}{a_{11}} \left(I + \frac{A d_{31}^2 f_{14}^2}{a_{33}^2 \bar{E}^2} \right)$$

$$k_5 = -\frac{2d_{31}A}{\pi a_{33}}, k_6 = k_0 \frac{2A}{\pi}, k_7 = k_6 \frac{f_{11}}{d_{11}}, k_8 = -\frac{A}{4} \left(\epsilon + \frac{1}{a_{11}} \right), k_9 = -\frac{A \pi^2}{4h^2} \left(\epsilon + \frac{1}{a_{33}} \right)$$

$$k_{10} = k_0 f_{11} A, k_{11} = -\frac{A d_{31}}{a_{33}}, k_{12} = -\frac{2A d_{11}}{a_{11} \pi}, k_{13} = \frac{\bar{E} A}{2}, k_{14} = -\frac{A}{2} \left(\epsilon + \frac{1}{a_{33}} \right)$$

References

- [1] M.S. Majdoub, P. Sharma, and T. Çağın. Dramatic enhancement in energy harvesting for a narrow range of dimensions in piezoelectric nanostructures. *Physical Review B*, 78(12):121407, 2008.
- [2] S Baroudi, F Najar, and A Jemai. Static and dynamic analytical coupled field analysis of piezoelectric flexoelectric nanobeams: A strain gradient theory approach. *International Journal of Solids and Structures*, 135:110–124, 2018.
- [3] R. Maranganti, N.D. Sharma, and P. Sharma. Electromechanical coupling in nonpiezoelectric materials due to nanoscale nonlocal size effects: Green's function solutions and embedded inclusions. *Physical Review B*, 74(1):014110, 2006.
- [4] Jiashi Yang. A review of a few topics in piezoelectricity. *Applied Mechanics Reviews*, 59(6):335–345, 2006.
- [5] Qian Deng, Mejdi Kammoun, Alper Erturk, and Alper Sharma. Nanoscale flexoelectric energy harvesting. *International Journal of Solids and Structures*, 51:3218–3225, 2014.
- [6] S Baroudi and F Najar. Dynamic analysis of a nonlinear nanobeam with flexoelectric actuation. *Journal of Applied Physics*, 125(4):044503, jan 2019.
- [7] KF Wang and BL Wang. Non-linear flexoelectricity in energy harvesting. *International Journal of Engineering Science*, 116:88–103, 2017.
- [8] Anuruddh Kumar, Anshul Sharma, Rahul Vaish, Rajeev Kumar, and Satish Chandra Jain. A numerical study on flexoelectric bistable energy harvester. *Applied Physics A: Materials Science and Processing*, 2018.

- [9] E. F. Rojas, S. Faroughi, A. Abdelkefi, and Y. H. Park. Nonlinear size dependent modeling and performance analysis of flexoelectric energy harvesters. *Microsystem Technologies*, 2019.
- [10] Richard Toupin. The elastic dielectric. *Journal of Rational Mechanics and Analysis*, 5(6):849–915, 1956.
- [11] Ali H Nayfeh and P Frank Pai. *Linear and nonlinear structural mechanics*. John Wiley & Sons, 2008.
- [12] Harm Askes and Elias C Aifantis. Gradient elasticity in statics and dynamics: an overview of formulations, length scale identification procedures, finite element implementations and new results. *International Journal of Solids and Structures*, 48(13):1962–1990, 2011.
- [13] Z Yan and LY Jiang. Flexoelectric effect on the electroelastic responses of bending piezoelectric nanobeams. *Journal of Applied Physics*, 113(19):194102, 2013.
- [14] R Maranganti and P Sharma. Atomistic determination of flexoelectric properties of crystalline dielectrics. *Physical Review B*, 80(5):054109, 2009.
- [15] Alexander K Tagantsev and Alexander S Yurkov. Flexoelectric effect in finite samples. *Journal of Applied Physics*, 112(4):044103, 2012.
- [16] Hatem Samaali and Fehmi Najar. Design of a capacitive MEMS double beam switch using dynamic pull-in actuation at very low voltage. *Microsystem Technologies*, 23(12):5317–5327, dec 2017.
- [17] Ali H Nayfeh and Balakumar Balachandran. *Applied nonlinear dynamics: analytical, computational, and experimental methods*. John Wiley & Sons, 2008.

MECHATRONIC ROBOT ARM WITH ACTIVE VIBRATION ABSORBERS

Z. ŠIKA^{*}, K. KRAUS[†], P. BENEŠ[†], J. KRIVOŠEJ[†] AND T. VYHLÍDAL^{††}

^{*}[†] Department of Mechanics, Biomechanics and Mechatronics

^{††} Department of Instrumentation and Control Engineering

Faculty of Mechanical Engineering

Czech Technical University in Prague

Technická 4, Praha 6, 160 00 Prague, Czech republic

e-mail: Zbynek.Sika@fs.cvut.cz, web page: <https://www.fs.cvut.cz/en/home/>

Key words: Vibration suppression of robot, Active dynamic absorber, Multibody system.

Abstract. The serial robots are typically able to cover large workspace, but their mass/stiffness ratio does not allow to combine high accuracy and high dynamic of the end-effector operations. Widely spread usage of serial robots, even for tasks as drilling, leads to high accuracy demands through its workspace. Absolute measurement of the end-point for position feedback can be challenging due to objects or even workpiece in workspace, but mainly, inbuilt motors of the serial robot cannot response in frequency range high enough as vibration of the end-point is. Instead, additional spring-mass system is attached to the robot to suppress vibrations. Narrow frequency range of passive dynamical absorber can be extended with active elements between robot and absorber, which is also necessary due to robots eigenfrequencies and eigenvalues variability. As feedback input, for more robustness, relative sensing is considered, such as accelerometers or geophones for velocity. As an active absorber control algorithm, firstly, the LQR control with state observer has been designed. Finally, the prepared experimental demonstrators are presented.

1 INTRODUCTION

Vibration has negative effect in many engineering applications, whether we talk about drilling head vibration causing low workpiece surface quality, base vibration in precise instruments such as electron microscopes or about airflow induced vibration of complex structures reducing its lifetime. In robotics, there are types of manipulators such as serial robots or cable manipulators, that are typically able to cover large workspace, which usually implies high mass/stiffness ratio. Such robots are not capable of high accuracy while performing operations with high dynamic of the end-effector tool or external excitation. During last decades, there has been an intensive development of serial robots in order to increase their production efficiency, including their non-traditional usage e.g. for drilling [1].

The still open problem is what can be achieved through the accurate measurement of absolute end-effector motion and its subsequent use to compensate for control loop errors between robot motors and the end-effector. The first thing is difficulty of such a measurement, considering large workspace in complex industrial environment, end-point operation “inside” of the

workpiece or even obstacle created by robot's own body. Second thing is, that motors of those manipulators are not capable of operation in such high frequency range as the vibration is placed in. Consequently, more robust additional sensing and mechanical solution are important.

The usage of dynamic absorbers with active elements is one of the promising methods. Both, passive and active absorbers, have been widely used for vibration suppression and the benefit of mounting a passive vibration absorber on the primary structure with the objective of the amplitudes reducing has been known for decades [4]-[6]. The frequency band, where the classical passive absorber suppresses vibrations efficiently, is relatively narrow, being centered at the natural frequency of the absorber. Thus, the tunable [2] and especially the fully active absorbers can significantly improve the vibration suppression efficiency in a wide frequency band. Another reason for active additional structure is that robots operating in large workspaces usually have strong variability of eigenfrequencies and eigenmodes in different work positions.

Same reason also leads us to multi degree of freedom (multi-DoF) level of design, since tool high dynamics, external excitation or robot eigenvalues are rarely fixed to the local coordinates. One of the main questions for n -DoF mechanical resonator is, whether to design n single-DoF absorbers (n autonomous active spring-mass systems) or one n -DoF absorber with n (or more) active spring elements. From recent literature, let us point to passive multi-DoF tuned absorber investigated in [7], where 2-DoF and 3-DoF mass absorbers are tested on experimental demonstrator. This paper supports theory, that passive multi-DoF absorber is more capable of vibration suppression than multiple single-DoF absorbers with equal mass. After attaching 3-DoF absorber, main structure shows 86.5% amplitude reduction, which is improved about 29.5% then using 2-DoF absorber of equal mass. Vibration suppression for robotic machining in 3D using 1-DoF semi-active absorber attached to actual robotic arm with milling head is theoretically and experimentally tested in [8]. In this case, single-DoF mass-spring absorber was based on magnetorheological elastomers material and was designed for chatter occurring in around 7 to 20 Hz. Since there is only 1-DoF absorber, its direction has to be based on chatter direction of the robot, and roughness of milled surface is then improved by 30% (passive) or by 50% (semi-active). The application of two single-DoF passive absorbers is experimentally investigated in [9], where housing of the polishing tool attached to the serial robot is damped using two dynamical absorbers based on Eddy currents. There is about 60% acceleration amplitude reduction of the end-point compared to the case without absorbers.

Let us also point to vibration problematic in surgery robotics, where the precise motion is required [10], to an active absorber tuned by dual-loop controller and tested on a helicopter vibration suppression in [11] or to the multiple passive absorbers tuned for primary and secondary mode shapes of wind turbine to suppress the vibration [12], and many other uses.

In majority of applications the absorbers are considered as passive or semi-active, where the active elements adjust the absorber stiffness or damping. Even though they can reduce vibration substantially, they cannot achieve full suppression, thus, the absorber needs to be turned to an ideal absorber, which imitates zero damping and natural frequency equal to the excitation frequency. Although, the absorbing device should be as efficient as possible already in its passive form, without usage of the feedback control of actuators, which leads to the primary optimization of stiffness and mass properties and absorber placement.

The preliminary study [3] considered active 6-DoF cubic hexapod absorber mounted on 3D robot arm. Its results in simulation model are very promising in passive as well as in active form, as far as one fixed position of robot is externally excited. Further study leads to passive

optimization, active control algorithm design as well as to optimization of sensors placement, type and count. Since at most three of all the six spatial DoFs of the damping mass are available for controlling single translational vibration mode of the main structure [7], the 2D simulation model of robot arm and 3-DoF absorber will be used to optimize properties of such an absorber. Firstly, the LQR control with state observer has been designed, concerning sensing by accelerometers on end-effector and on absorber's body. Simultaneously with the optimization of mechanical design, sensing strategies and control algorithms, the appropriate demonstrators have been prepared, based on the voice coils AVM60-25 (Figure 5a) as actuators for testing.

2 SIMULATION MODEL

2.1 Structure

As mentioned above, target of this study are light structures with large workspace, but relatively bad ratio of mass/stiffness, e.g. cable structures or serial robotic arm (Figure 7b), which is also subject of our study. In order to simulate experiments, mathematical model of flexible 3-DoF serial robotic arm in 2D space was developed (Figure 1). It consists of three bodies attached with rotational joints to each other, where the last point of the last body is the end-point of the robot. This point is supposed to be kept still as well as (not necessarily) to be excited by external force, since those two usually collocate. The stiffness of individual bodies is achieved by cutting it into several elements joined elastically to each other and, also, by rotational stiffness between the post-joint element and rotor of the motor. Single-DoF or multi-DoF absorbers are then attached to elements using springs with dampers and actuators.

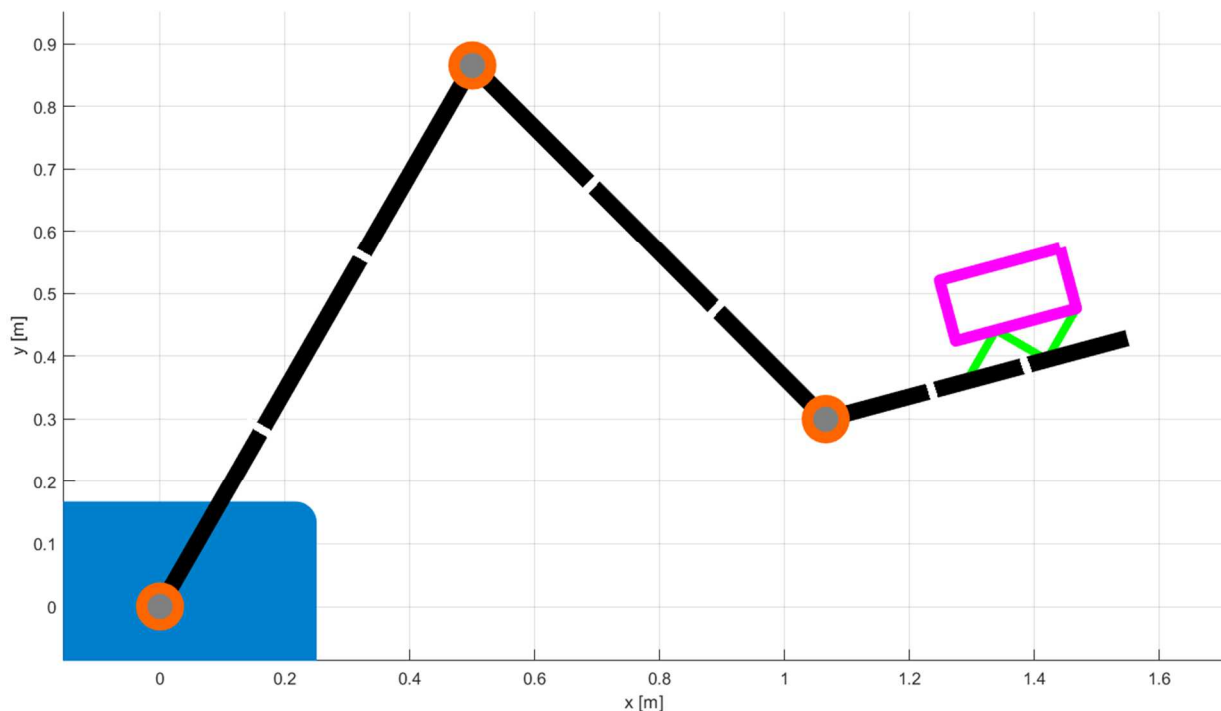


Figure 1: Simulation model with multi-DoF absorber

To prevent the model from computational inaccuracies, the whole system is described using independent variables only. Thus, as far as independent equations are considered, robotic arm is then divided into several types of subparts (**Figure 2**), which can be arbitrarily combined into resultant robot design: a) simple element (**Figure 2a**), which is single mass rigid body attached to previous and following elements with three springs (two translational and one rotational), and external forces can be applied to this element; b) joint set (**Figure 2b**), which consist of pre-joint element (3 equations), post-joint element (1 additional equation for rotation) and rotor mass with stiff gear-box (1 additional equation for rotation); c) single-DoF element (**Figure 2c**), which consists of simple element with one or more attached single-DoF absorbers (1 additional equation for each absorber) attached to the element using prismatic constraint; d) multi-DoF absorber (**Figure 2d**), which is single mass rigid body attached to robotic arm only using springs and actuators (no constraints), which in equations are represented only by external forces between absorber and relevant elements of the robotic arm (based on current state vector). Types b) and c) only (non-trivial) are described by matrix/vectors (2) and (3) respectively in mean of independent equations (1) below **Figure 2**.

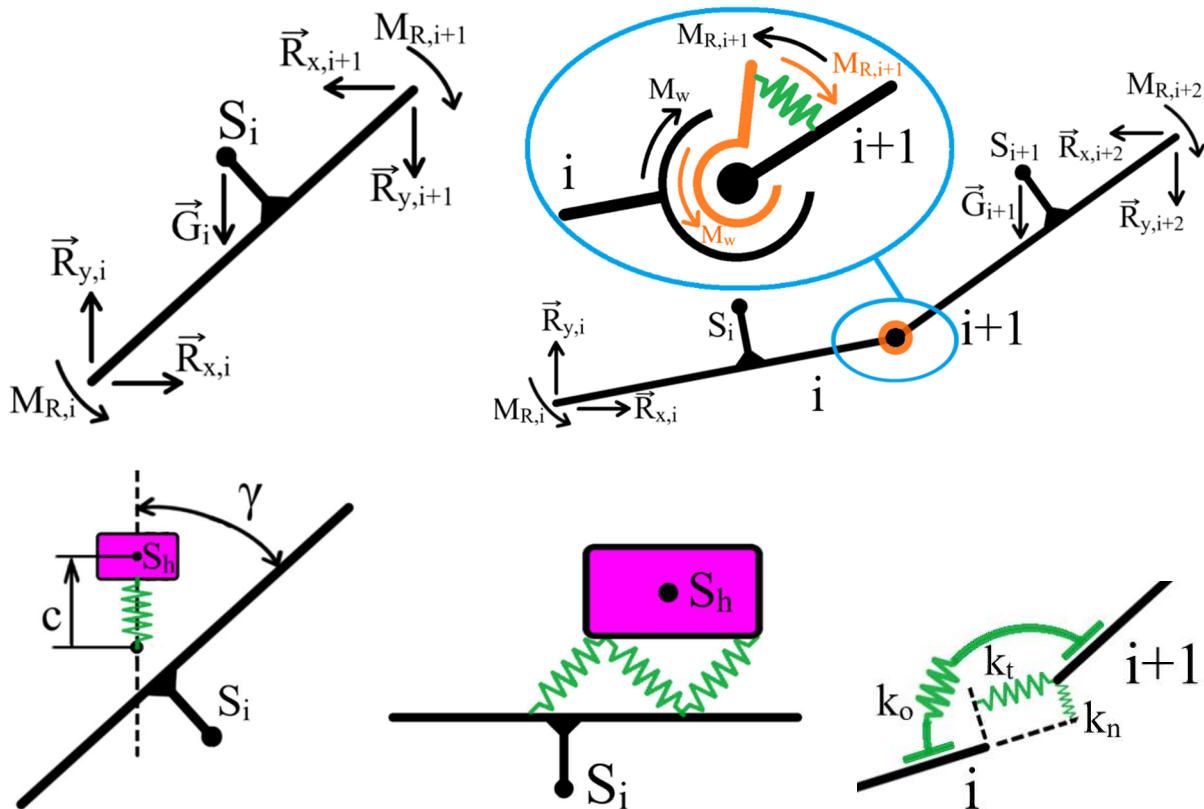


Figure 2: Types of elements of the robot simulation model (respectively):
a) simple element; b) joint set; c) single-DoF absorber; d) multi-DoF absorber; e) element cut

Newton-Euler equations of motion of simple element or multi-DoF absorber are trivial, thus are not displayed in following list. Firstly, list of variable description follows:

\vec{q}	vector of independent variables containing kinematics of robot and absorbers
$\mathbf{M}(\vec{q})$	mass matrix as a function of independent variables \vec{q}
$\vec{N}(\vec{q}, \dot{\vec{q}})$	vector of constraints as a function of independent variables \vec{q} and it's time derivative $\dot{\vec{q}}$
$\vec{f}(\vec{u}, \vec{q}, \dot{\vec{q}})$	vector of right sides of equations as a function of $\vec{q}, \dot{\vec{q}}$ and force inputs \vec{u}
m_i	mass of i-th element of the robot
\mathbf{m}_i	diagonal 2D matrix of mass m_i
$m_{w,k}$	mass of k-th motor of the robot
m_h	mass of the single-DoF absorber
$I_{S,i}$	moment of inertia of i-th element of the robot, with respect to its center of mass
$I_{w,k}$	moment of inertia of k-th motor of the robot
I_h	moment of inertia of single-DoF absorber
$\vec{r}_{SP,i}$	radius vector from center of mass of i-th element to previous element attachment point P, in global system
$\vec{r}_{SL,i}$	radius vector from center of mass of i-th element to following element attachment point L, in global system
$\vec{r}_{SH,i}$	radius vector from center of mass of i-th element to single absorber attachment point H, in global system
${}^i\vec{r}$	radius vector in i-th element local coordinate system
\vec{r}^\perp	radius vector perpendicular to original \vec{r} vector
φ_i	global rotation of i-th element of the robot
ω_i	angular velocity of i-th element of the robot
γ	angle between element's x-axis and motion axis of the single-DoF absorber
c	scalar distance of single-DoF absorber from its free position
\vec{R}	translational elastic force between i-th and previous element
$M_{R,i}$	rotational elastic force between i-th and previous element
\vec{F}_i	external translational force applied to the i-th element
M_i	external rotational force applied to the i-th element
\vec{G}_i	gravitational force acting on i-th element
$\vec{G}_{w,k}$	gravitational force acting on k-th motor of the robot
\vec{G}_h	gravitational force acting on single-DoF absorber
$\mathbf{S}_\varphi()$	rotational matrix

$$\mathbf{M}(\vec{q})\ddot{\vec{q}} + \vec{N}(\vec{q}, \dot{\vec{q}}) = \vec{f}(\vec{u}, \vec{q}, \dot{\vec{q}}) \quad (1)$$

$$\mathbf{M}(\vec{q})_i = \begin{bmatrix} m_i + m_{i+1} + m_{w,k} & (m_{i+1} + m_{w,k})\vec{r}_{SL,i}^\perp & -m_{i+1}\vec{r}_{SP,i+1}^\perp & \vec{0} \\ \vec{r}_{SL,i}^{\perp T}(m_{i+1} + m_{w,k}) & I_{S,i} + \vec{r}_{SL,i}^{\perp T}(m_{i+1} + m_{w,k})\vec{r}_{SL,i}^\perp & -\vec{r}_{SL,i}^{\perp T}m_{i+1}\vec{r}_{SP,i+1}^\perp & \emptyset \\ -\vec{r}_{SP,i+1}^{\perp T}m_{i+1} & -\vec{r}_{SP,i+1}^{\perp T}m_{i+1}\vec{r}_{SL,i}^\perp & I_{S,i+1} + \vec{r}_{SP,i+1}^{\perp T}m_{i+1}\vec{r}_{SP,i+1}^\perp & \emptyset \\ \vec{0}^T & \emptyset & \emptyset & I_{w,k} \end{bmatrix} \quad (2)$$

$$\begin{aligned}
 \vec{N}(\vec{q}, \dot{\vec{q}})_i &= \begin{bmatrix} \mathbf{m}_{i+1}(-\omega_i^2 \vec{r}_{SL,i} + \omega_{i+1}^2 \vec{r}_{SP,i+1}) - \mathbf{m}_{w,k} \omega_i^2 \vec{r}_{SL,i} \\ \vec{r}_{SL,i}^T \mathbf{m}_{i+1}(-\omega_i^2 \vec{r}_{SL,i} + \omega_{i+1}^2 \vec{r}_{SP,i+1}) + \vec{r}_{SL,i}^T \mathbf{m}_{w,k} \omega_i^2 \vec{r}_{SL,i} \\ \vec{r}_{SP,i+1}^T \mathbf{m}_{i+1}(-\omega_i^2 \vec{r}_{SL,i} + \omega_{i+1}^2 \vec{r}_{SP,i+1}) \\ \emptyset \end{bmatrix} \\
 \vec{f}(\vec{u}, \vec{q}, \dot{\vec{q}})_i &= \begin{bmatrix} \vec{R}_i + \vec{G}_i + \vec{F}_i - \vec{R}_{i+2} + \vec{G}_{i+1} + \vec{F}_{i+1} + \vec{G}_{w,k} \\ \vec{r}_{SP,i}^T \vec{R}_i + M_i + M_{R,i} - M_{w,k} + \vec{r}_{SL,i}^T (-\vec{R}_{i+2} + \vec{G}_{i+1} + \vec{F}_{i+1} + \vec{G}_{w,k}) \\ -\vec{r}_{SL,i+1}^T \vec{R}_{i+2} + M_{i+1} + M_{R,i+1} - M_{R,i+2} - \vec{r}_{SP,i+1}^T (-\vec{R}_{i+2} + \vec{G}_{i+1} + \vec{F}_{i+1}) \\ M_{w,k} - M_{R,i+1} \end{bmatrix} \\
 \mathbf{M}(\vec{q})_i &= \begin{bmatrix} \mathbf{m}_i + \mathbf{m}_h & \mathbf{m}_h \mathbf{S}_\varphi(\varphi_i) \begin{pmatrix} i_{SH,i}^T \\ \mathbf{S}_\varphi(\gamma) \end{pmatrix} \begin{bmatrix} 0 \\ 1 \end{bmatrix} & \mathbf{m}_h \mathbf{S}_\varphi(\varphi_i) \mathbf{S}_\varphi(\gamma) \begin{bmatrix} 1 \\ 0 \end{bmatrix} \\ m_h \begin{pmatrix} i_{SH,i}^T \\ \mathbf{S}_\varphi(\gamma) \end{pmatrix} \mathbf{S}_\varphi^T(\varphi_i) & I_{S,i} + I_H + m_h \begin{pmatrix} i_{SH,i}^2 + c^2 + i_{SH,i}^T \mathbf{S}_\varphi(\gamma) \begin{bmatrix} 0 \\ 2c \end{bmatrix} \end{pmatrix} & m_h \begin{bmatrix} 1 \\ 0 \end{bmatrix}^T \mathbf{S}_\varphi^T(\gamma) i_{SH,i}^T \\ m_h \begin{bmatrix} 1 \\ 0 \end{bmatrix}^T \mathbf{S}_\varphi^T(\gamma) \mathbf{S}_\varphi^T(\varphi_i) & m_h i_{SH,i}^T \mathbf{S}_\varphi(\gamma) \begin{bmatrix} 1 \\ 0 \end{bmatrix} & m_h \end{bmatrix} \quad (3) \\
 \vec{N}(\vec{q}, \dot{\vec{q}})_i &= \begin{bmatrix} \mathbf{m}_h \mathbf{S}_\varphi(\varphi_i) \left(-\dot{\varphi}^2 i_{SH,i}^T + \mathbf{S}_\varphi(\gamma) \begin{bmatrix} -\dot{\varphi}^2 c \\ 2\dot{\varphi} \dot{c} \end{bmatrix} \right) \\ m_h \left(2c \dot{c} \dot{\varphi} + i_{SH,i}^T \mathbf{S}_\varphi(\gamma) \begin{bmatrix} 0 \\ 2\dot{\varphi} \dot{c} \end{bmatrix} \right) \\ -m_h \left(i_{SH,i}^T \mathbf{S}_\varphi(\gamma) \begin{bmatrix} 0 \\ \dot{\varphi}^2 \end{bmatrix} + \dot{\varphi}^2 c \right) \end{bmatrix} \\
 \vec{f}(\vec{u}, \vec{q}, \dot{\vec{q}})_i &= \begin{bmatrix} \vec{R}_i + \vec{G}_i + \vec{F}_i - \vec{R}_{i+1} + \vec{G}_h \\ M_i + M_{R,i} - M_{R,i+1} + i_{SP,i}^T \mathbf{S}_\varphi^T(\varphi_i) \vec{R}_i - i_{SL,i}^T \mathbf{S}_\varphi^T(\varphi_i) \vec{R}_{i+1} + G_h^T \mathbf{S}_\varphi(\varphi_i) \begin{pmatrix} i_{SH,i}^T \\ \mathbf{S}_\varphi(\gamma) \end{pmatrix} \begin{bmatrix} 0 \\ 1 \end{bmatrix} + F_h^T \mathbf{S}_\varphi(\varphi_i) \mathbf{S}_\varphi(\gamma) \begin{bmatrix} 0 \\ 1 \end{bmatrix} \\ (G_h^T + F_h^T) \mathbf{S}_\varphi(\varphi_i) \mathbf{S}_\varphi(\gamma) \begin{bmatrix} 1 \\ 0 \end{bmatrix} \end{bmatrix}
 \end{aligned}$$

2.2 Kinematics and dynamics

Kinematics and dynamics of the simulation model is set as follows. The main bodies of the robot are meant to be prisms of length [1.0; 0.8; 0.5] m, so the workspace radius is around 2 m, and of weight [8; 7; 4] kg. Each of those bodies has its stiffness in all three axes – in both translations (axial and shear) and in rotation (bending) (as shown in **Figure 2e**) – and the values are set with respect to the size and cross-section of each body. Each stiff constrain has also its slight damping (around thousandths of stiffness value). Overall dynamics is designed in way, that the robot's eigenfrequencies in “neutral” position of the robot are placed into interval around 15 Hz and higher, taking “neutral” position to be in motor rotations of [60°; -105°; 60°] as shown in **Figure 1**. Since rigid bodies with only elasticity in joints is not sufficient enough to represent real structure behavior, all bodies are cut into several elements. Each element carries part of the body mass and stiffness of the body is spread over all elements in accordance to serial springs addition. Which means, that resultant stiffness of the elements-stacked body is same as before, only the corresponding count of higher extra eigenfrequencies occurs. Bode diagram (**Figure 3**) of the robot shows acceleration amplitude and phase of the end-point in all directions in response to the unit force in the global y axis applied in the same point (which is usually the case). As we can see, 4 of model eigenfrequencies are below the 100 Hz, which – considering voice-coil type of the actuators – is manageable limit for small amplitudes and loads. When mentioned slight damping (~1‰) is applied to the robot, some of the highest frequencies disappears due to overdamping (as can be seen in Bode diagram **Figure 1** in

following chapter), which has no influence in our study, since lower frequencies are subject of interest. Base of this study is then suppression of vibrations of the end-point when externally excited in the same point in area of first few eigenfrequencies of the robot.

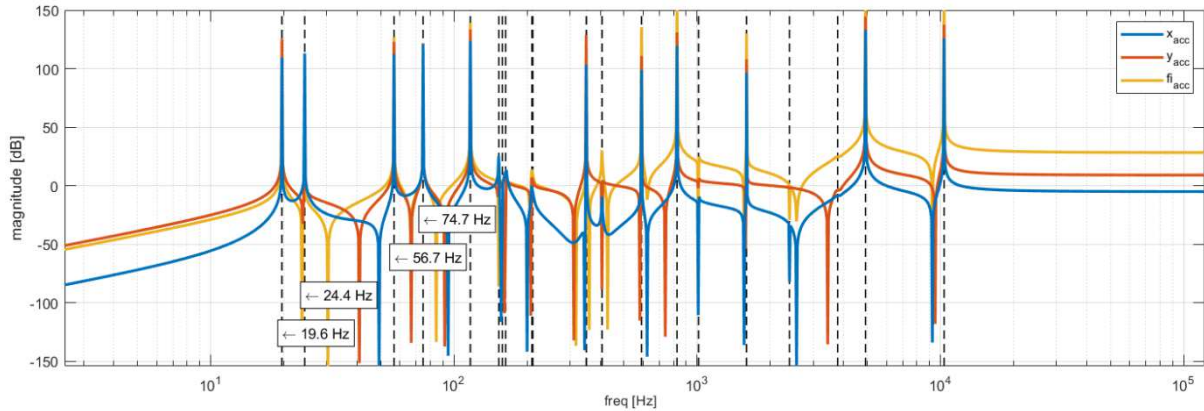


Figure 3: Bode diagram (end-point acceleration) - undamped model of the robot (without absorber)

3 ACTIVE ABSORBER DESIGN AND CONTROL

3.1 Absorber mechanical design

As mentioned in [7], most three of all the six spatial DoFs of the damping absorber are available for controlling single translational vibration mode of the main structure. Simulation in 2D is then planar reduction of such a case. Main attention of the study is focused to 3-DoF single mass absorber in order to lower mass and space requirements. It consists of the single main body with mass and inertia and is attached to the robot's arm with three linear springs arranged to be perpendicular to each other, as seen in **Figure 1**. Springs of the multi-absorber may be attached to various elements of the same robot body (**Figure 1**), if they are small enough compared to the absorber. Linear springs contains slight damping and, for further active control, colinear voice-coil actuators represented by raw force along those springs.

3.2 Passive absorber tuning

In order to perform active vibration suppression, it is important to begin with properly tuned passive absorber, which is able to damp some eigenfrequency at certain suppression level. Considering fix geometrical parameters, there are dynamical parameters left. Since the lowest eigenfrequency is usually the one with the highest amplitudes, the goal is to tune all three absorber's eigenfrequencies to this value – in our case it is 19.6 Hz. Both, global and local optimization methods were used to adjust mass, position of the center of mass, inertia and stiffness of springs to values 2.17 kg, [0 -0.033] m, 0.006 kg·m² and 2.14e4 N·m⁻¹ respectively. Comparison of both cases – before and after attaching of the absorber to the end-effector – is then shown in Bode diagram (**Figure 4**), represented by position amplitudes of the end-point in one direction (for better readability) in response to same direction external force input. Slight eigenfrequency redistribution can be seen, because another three eigenfrequencies were added to the system. Although we can retune absorber properties in order to suppress different

frequency interval or to be effective also in different robot positions, at this moment, there is no more we can do about variability of vibration suppression in general perspective. Therefore, active approach takes place from now on.

3.3 Active vibration suppression control design

Various control algorithms, such as LQR, PID regulator, fixed order H_∞/H_2 or DR, may be considered to actuate the absorber along with feedback from proper type and amount of sensors. The delayed resonator (DR) concept [13]-[18] has been researched in 1990s and is based on tuning of the absorber to the ideal absorber. Such an approach makes the absorber to mimic zero damping and it needs to be tuned to the excitation frequency. It is simple and effective concept with robust sensing of the structure based on single accelerometer, although, this analytical approach has been applied in 1D only so far.

In this paper, the LQR control with state observer is being designed, concerning sensing by accelerometers attached to the end-effector and, also, to the absorber's body. First of all, a proper linearization of whole system (robot with absorber) needs to be performed, which provides us with A B C and D state-space matrices. Another step is to include crucial problem of realistic robot sensing implementation in order to use an observer of the system state. The goal is to use as few of sensors as possible and the sensors to be robust, such as accelerometers or geophones – basically to avoid of any global absolute position measuring, which can be an unreachable requirement in industry environment. Firstly, it is convenient to include already existing robot sensors which is always known joints encoders of position and velocity. Secondly, to even be able to design an LQR we need to measure end-point kinematics. For sake of robustness, acceleration of the end-point in all axes is measured, since vibrations can be observed through acceleration measurement as well as through position measurement. Thus, this particular sensor can be also used for system observation. Thirdly, once an absorber is being designed, there may be placed sensors of body acceleration in all axes of the absorber and, also, encoders of spring elements for elongation (and its change) measurement. When all mentioned sensors are considered, the observation of the whole linear model is very few of all states. Even acceleration/velocity sensing of all robot's elements are not sufficient enough, until their global positions are unknown. Therefore, order reduction of the linear model is necessary for proper observer design.

Since the ability of actuators to work in certain frequency range, model order reduction (using Hankel singular numbers) is focused on the dynamics in this particular frequency range, which means up to approximately 100 Hz. The new state-space low-order model consists of matrices A_r B_r C_r and D_r , and original 51 states were reduced down to 14 states. Using pole placement method, an observer matrix L_{obsv} belonging to all measured outputs was created for observer to be as fast as possible. The whole system Bode diagram, when output-based observer LQR is considered, is shown in **Figure 4** as third line and it compares its amplitudes of one direction position of the end-point in response to the same direction force input to passive absorber and original system cases. Difference in frequency damping between passive and active approach is visible only in lower frequency range, since voice-coil actuators are able to effectively work in frequency range up to 100 Hz. In simulation design, these actuators are represented by the low-pass filter with time constant of 0.01 of second.

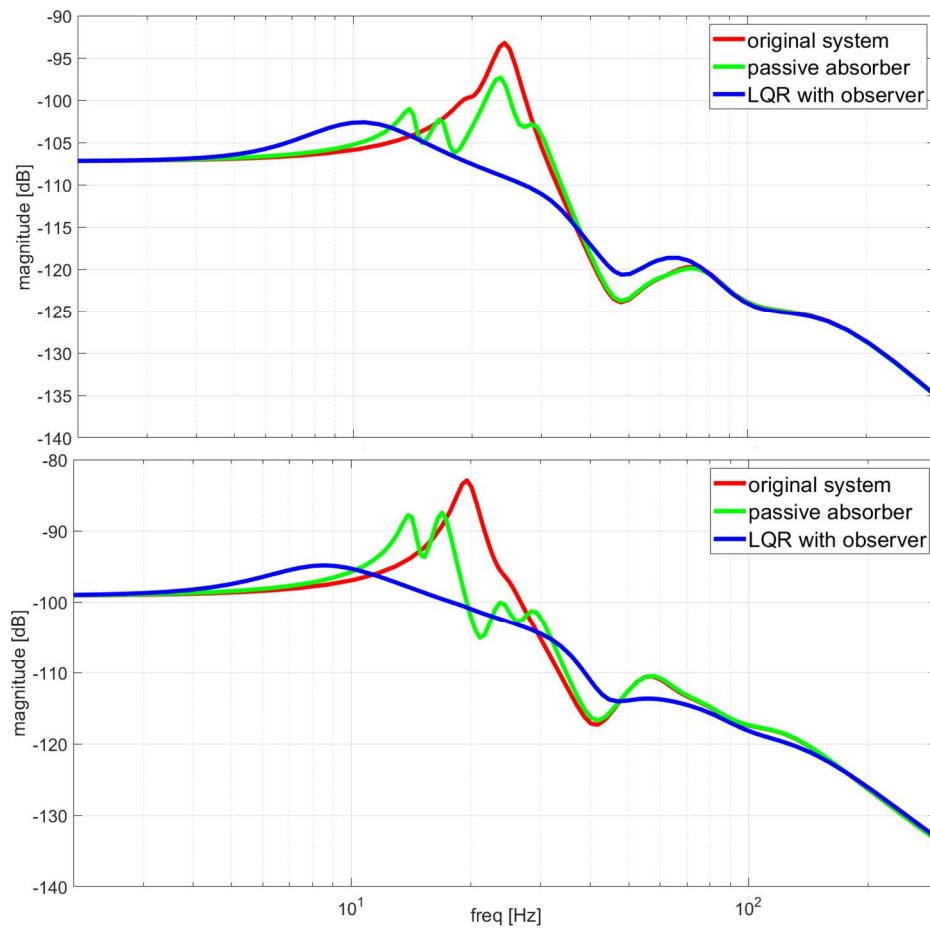
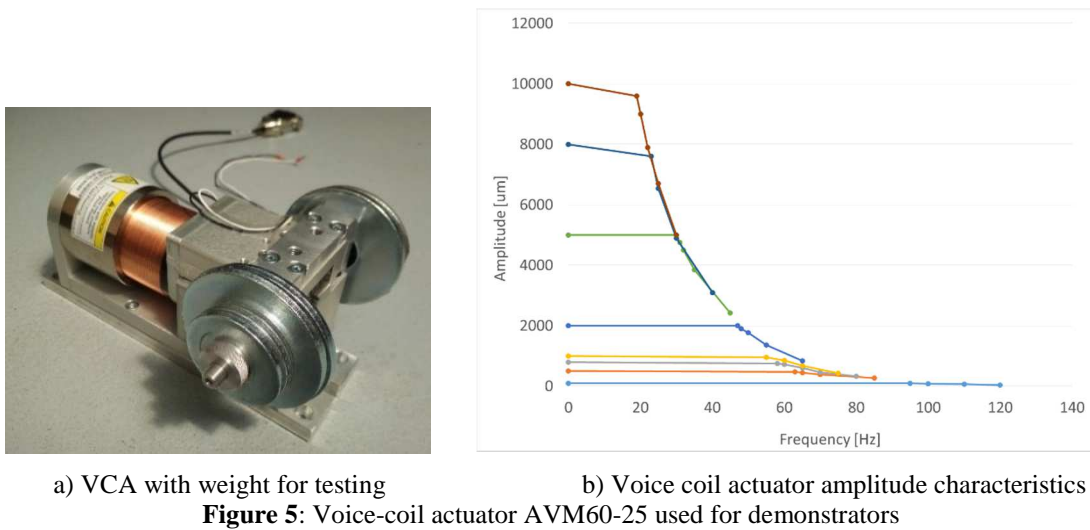


Figure 4: Bode diagram (end-point position), original robot vs. passive absorber vs. LQR with observer
 upper figure – x-force input to x-position lower figure – y-force input to y-position

4 PREPARATION OF EXPERIMENTAL DEMONSTRATORS

Two demonstrators are being prepared in order to experimentally verify functionality of the active vibration absorbers for multibody chains of robotic type. Different actuators can be used. The piezoactuators typically have a wide range of operating frequencies, but exhibit quite small range of strokes (dozens, at most hundreds of micrometers) and their inherent stiffness is high. The voice-coil actuators (VCA) (**Figure 5a**) are more suitable for the active absorbers because they have significantly larger range of strokes and almost zero inherent stiffness. Consequently, the modal properties of the absorber can be tuned not only by optimization of mass properties but also by tuning of stiffness of springs added in parallel to voice-coil actuators. The size of prepared demonstrators has been adapted to the available VCA AVM60-25 with 26N stable force and 110N peak force. The VCA amplitude characteristics are in **Figure 5b**.



The aim of the first demonstrator (**Figure 6**) is testing of dynamical properties of absorber “leg” including mounting spherical joints and translational guidance of voice coil actuator.

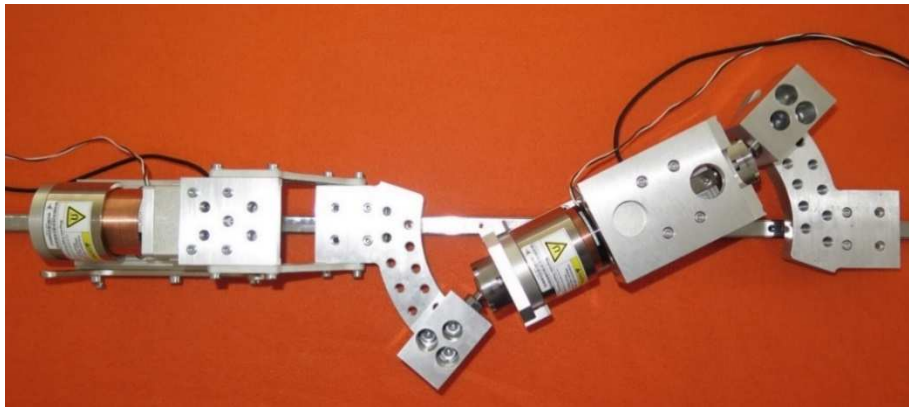
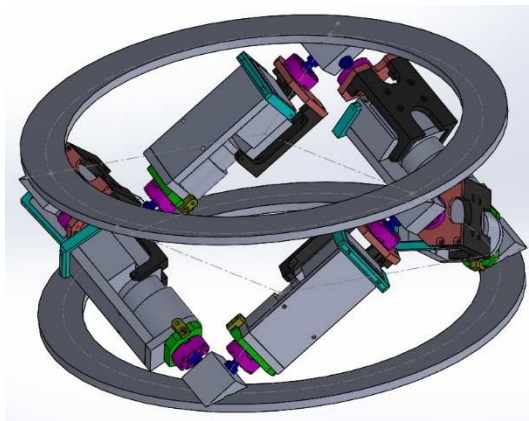


Figure 6: First demonstrator for vibrational testing of leg with spherical joints

The kinematics and other mechanical properties of spatial multi-DOF active absorber can be optimized in many ways. Taken into account that the modal properties of typical serial robot (**Figure 7b**) vary considerably and heterogeneously within the workspace, some regular architecture of absorber is an appropriate choice. The hexapod of cubic geometry created by actuators is considered (**Figure 7a**). The similar structure has been used also for 6 DOF active vibration isolation in [19]. The robot arm eigenmodes are typically geometrically complex including translations and rotations in several directions. The target of mechanical optimization of demonstrator of hexapod absorber is to achieve 6 identical eigenfrequencies equal to average value of the most critical (typically first) eigenfrequency of robot chain.



a) Basic design of cubic VCA architecture



b) Concept of use for serial robot

Figure 7: Demonstrator for testing of multi-DOF spatial active absorber concept

5 CONCLUSIONS

The concept of active dynamic absorbers for use on robotic mechanisms was introduced and formulated. Reducing the vibration of the robots by means of active absorbers has the advantage that it can only be realized with the help of local sensors, for example with accelerometers. In addition, the active absorbers allow the adaptation to the highly variable modal properties of the robot during motion in the workspace. The problem was primarily solved for the model of a flexible plane robot. The mechanical structure of the 3 DOF absorber has been designed so that it has a multiple eigenfrequency equal to the first eigenfrequency of the robotic arm. The control was implemented using the LQR method with observer considering accelerometers on the body of the absorber and on the robot arm. The research of the whole topic is still in progress, so, many questions remain opened. The experiments with both demonstrators equipped by the purchased voice-coils start just now. The currently considered active cubic hexapod structure with multiple natural frequency equal to average natural frequency of the most critical eigenmode seems to be the most suitable choice, however there are also other variants of implementation, namely the set of 1DOF absorbers spread over the arm of the robot.

ACKNOWLEDGEMENTS

The work has been supported by the Czech Science Foundation project GA17-20943S “Active multidimensional vibration absorbers for complex mechanical structures based on delayed resonator method”.

REFERENCES

- [1] T. Olsson, M. Haage, H. Kihlman and et al., "Cost-efficient drilling using industrial robots with high-bandwidth force feedback," *Robotics and Computer-Integrating Manufacturing*, vol. 26, no. 1, pp. 24-38, 2010.
- [2] C.A.M.Verbaan, P. Rosielle, M. Steinbuch, “Broadband damping of non-rigid-body resonances of planar positioning stages by tuned mass dampers”, *Mechatronics*, vol. 24, no. 6, pp. 712-723, 2014.

- [3] Z. Šika, K. Kraus, P. Beneš, T. Vyhliđal and M. Valášek, “Active Multidimensional Vibration Absorbers for Light Robots”, Proceedings of the 5th Joint International Conference on Multibody System Dynamics, pp. 1-12, June 24 – 28, 2018, Lisbon, Portugal, 2018.
- [4] Rana R, Soong TT., Parametric study and simplified design of tuned mass dampers, vol. 20(3), Engineering structures, 1998, pp. 193-204.
- [5] Lin G.L., Lin C.C., Chen B.C., Soong T.T., Vibration control performance of tuned mass dampers with resettable variable stiffness, vol. 83, Engineering Structures, 2015, pp. 187-197.
- [6] Verbaan C.A.M, Rosielle P.C.J.N, Steinbuch M., Broadband damping of non-rigid-body resonances of planar positioning stages by tuned mass dampers, vol. 24(6), Mechatronics, 2014, pp. 712-723.
- [7] W. Ma, Y. Yang and J. Yu, General routine of suppressing single vibration mode by multi-DOF tuned mass damper: Application of three-DOF, Mechanical Systems and Signal Processing, vol. 121, pp. 77-96, 2019.
- [8] L. Yuan et al, Mode coupling chatter suppression for robotic machining using semi-active magnetorheological elastomers absorber, Mechanical Systems and Signal Processing, vol. 117, pp. 221-237, 2019.
- [9] L. Chen et al, Contact force control and vibration suppression in robotic polishing with a smart end effector, Robotics and Computer Integrated Manufacturing, vol. 57, pp. 391-403, 2019.
- [10] H. Sang et al, A fuzzy neural network sliding mode controller for vibration suppression in robotically assisted minimally invasive surgery Int. J. of Medical Robotics and Comp. Assisted Surgery, 12(4), pp. 670-679, 2016.
- [11] Chesné S., Inquieté G., Cranga P., Legrand F., Petitjean B.: Innovative Hybrid Mass Damper for Dual-Loop Controller. Mechanical Systems and Signal Processing, 115 (2019), 514-23
- [12] Zuo H., Bi K., Hao H.: Using multiple tuned mass dampers to control offshore wind turbine vibrations under multiple hazards. Engineering Structures, 141 (2017), 303-15.
- [13] N. Olgac, B. Holm-Hansen, A novel active vibration absorption technique: delayed resonator, Journal of Sound and Vibration 176 (1) (1994), 93–104.
- [14] N. Olgac, H. Elmali, M. Hosek, M. Renzulli, Active vibration control of distributed systems using delayed resonator with acceleration feedback, J. of dyn. systems, measurement, and control, 119(3), (1997), 380–389.
- [15] N. Olgac, H. Elmali, S. Vijayan, Introduction to the dual frequency fixed delayed resonator, Journal of Sound and Vibration 189 (3) (1996) 355–367.
- [16] M. Hosek, N. Olgac, A single-step automatic tuning algorithm for the delayed resonator vibration absorber, IEEE/ASME Transactions on mechatronics 7 (2) (2002) 245–255.
- [17] D. Filipovic, N. Olgac, Torsional delayed resonator with velocity feedback, IEEE/ASME Transactions on Mechatronics 3 (1) (1998) 67–72.
- [18] A. S. Kammer, N. Olgac, Electromechanical delayed resonator implementation using piezoelectric networks, IFAC-PapersOnLine 49 (10), (2016), 71–76.
- [19] A. A. Hanieh, Active isolation and damping of vibrations via Stewart platform (Doctoral dissertation thesis), Université Libre de Bruxelles, Faculty of Applied Science, (2003).

MODELING OF SMART VIBRATION-BASED ENERGY HARVESTERS BASED ON THE PGD METHOD

**María Infantes*, Rafael Castro-Triguero*, Philippe Vidal[†], Laurent Gallimard[†] and
Olivier Polit[†]**

*Department of Mechanics, Universidad de Córdoba
Campus de Rabanales, 14071 Cordoba, Spain
e-mail: me2mainm@uco.es (M. Infantes, corresponding author)

[†] Laboratoire Energétique Mécanique Electromagnétisme (LEME), Université Paris Nanterre
50 rue de Sèvres, 92410 Ville d'Avray, France

Key words: Energy harvesting, PGD, Piezoelectric composite, Variable separation

Abstract. This study proposes a new strategy based on the proper generalized decomposition method to solve the forced vibration problem in bi-dimensional piezoelectric composite beams. The approach considers a classical harmonic space-frequency description of the problem and redefines it by approximating the coupled displacement and electric potential fields as a sum of separated functions of x (beam axis coordinate), z (thickness axis coordinate) and ω (mechanical load frequency). The methodology consists of an iterative algorithm that solves three one-dimensional problems at each iteration. The result is a 2D solution in frequency domain with 1D computational complexity. The main goal is to propose a new method to model vibration-based energy harvester devices reducing both the complexity of the model and the computational cost without losing accuracy.

1 INTRODUCTION

In recent years, energy harvesting (EH) devices are becoming an alternative to provide energy in many different low-powered applications. Among the several energy harvesting mechanisms, the vibration-based approach seems to be the most suitable one for engineering structures subject to continuous ambient vibration. Particularly, the piezoelectric energy conversion is a very versatile option able to harvest energy from different ambient sources. Most piezoelectric EH devices designs are based on cantilever beams, including unimorph, bimorph and functionally graded piezoelectric material (FGPM) beams configurations. The conventional approach to evaluate the performance of these devices is the use of simplified models (single degree of freedom systems, beam theory, etc.) or numerical techniques based on the finite element (FE) method. Equivalent Single Layer (ESL) models have been used for such problems: FSDT (First-order Shear Deformation Theory), HSDT (High-order Shear Deformation Theory) or refined theory in [1], [2] and [3], respectively. It should be also noted the systematic approach by Carrera, the so-called Carrera's Unified Formulation, that includes a wide family of models [4].

In order to reduce the computational cost without losing accuracy in the solution, the proper generalized decomposition (PGD) method [5] is used herein as a reduction model. Note that the method has been already applied to take into account the electro-mechanical coupling in [6]. Also in [7], the coupled

problem variables are decomposed into space, frequency and electrical load. In this last reference by Qin et al., the authors point out that the 3D spatial component dominates the performance of the simulation process. To reduce the computational cost, in the present approach both the displacements and the electric potential are written as a sum of products of unidimensional functions of spatial coordinates x and z (beam axis and thickness directions respectively) and frequency ω . Finally, the deduced non-linear problem implies the resolution of three linear problems alternatively. The main objective of this work is to develop a new PGD-based approach for the parametric study of energy harvesters to effectively reduce the complexity of the models and the CPU time.

2 REFERENCE PROBLEM DESCRIPTION

In the present study, a straight composite beam of length L with a rectangular uniform cross section of thickness h and depth b is considered. The beam consists of NC layers, piezoelectric or not, assumed to be orthotropic in the beam axes. The x axis is taken along the longitudinal beam axis whereas y and z are the two axes of symmetry of the rectangular cross section (see Figure 1).

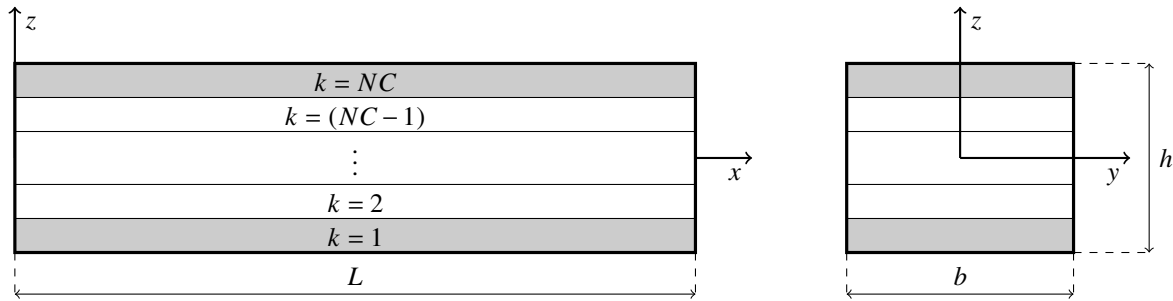


Figure 1: The laminated beam with embedded piezoelectric layers and coordinate system.

Hereafter, the y coordinate is neglected and the beam is considered in the (x, z) plane, i.e., in the domain $\Omega = \Omega_x \times \Omega_z = [0 \leq x \leq L] \times [-\frac{h}{2} \leq z \leq \frac{h}{2}]$. An additional step towards compactness in notation is achieved by renaming the coordinates such that $x \rightarrow x_1$, $y \rightarrow x_2$ and $z \rightarrow x_3$.

2.1 Governing equations

The formulation of the piezoelectric problem is based on the equations of motion of the elastodynamics and Gauss' law of the electrostatics, which are given by

$$\nabla \cdot [\sigma] + [b] = \rho \frac{\partial^2 [u]}{\partial t^2} \quad (1a)$$

$$\nabla \cdot [D] - q = 0 \quad (1b)$$

where $[\sigma]$ is the stress, $[b]$ is the prescribed body load, ρ is the density of the material, $[u]$ is the mechanical displacement, $[D]$ is the electric displacement and q is free electric volume charge. The two-dimensional formulation of the piezoelectric problem in absence of body loads and free electric volume charge can be reduced to

$$\frac{\partial \sigma_{11}}{\partial x_1} + \frac{\partial \sigma_{13}}{\partial x_3} = \rho \frac{\partial^2 u_1}{\partial t^2}, \quad \frac{\partial \sigma_{13}}{\partial x_1} + \frac{\partial \sigma_{33}}{\partial x_3} = \rho \frac{\partial^2 u_3}{\partial t^2}, \quad \frac{\partial D_1}{\partial x_1} + \frac{\partial D_3}{\partial x_3} = 0 \quad (2)$$

2.2 Constitutive relation

The constitutive equations with piezoelectric coupling for a layer k are

$$\begin{aligned} [\sigma^{(k)}] &= [C^{(k)}][\varepsilon] - [e^{(k)}]^\top [E] \\ [D^{(k)}] &= [e^{(k)}][\varepsilon] + [\epsilon^{(k)}][E] \end{aligned} \quad (3)$$

where $[\varepsilon]$ is the strain and $[E]$ is the electric field. Assuming plane stress in the xy -plane and vanishing out of plane electric displacement ($\sigma_{22} = \sigma_{12} = \sigma_{23} = D_2 = 0$), the constitutive equations read

$$\begin{aligned} \begin{bmatrix} \sigma_{11}^{(k)} \\ \sigma_{33}^{(k)} \\ \sigma_{13}^{(k)} \end{bmatrix} &= \begin{bmatrix} \bar{C}_{11}^{(k)} & \bar{C}_{13}^{(k)} & 0 \\ \bar{C}_{13}^{(k)} & \bar{C}_{33}^{(k)} & 0 \\ 0 & 0 & \bar{C}_{55}^{(k)} \end{bmatrix} \begin{bmatrix} \varepsilon_{11} \\ \varepsilon_{33} \\ \gamma_{13} \end{bmatrix} - \begin{bmatrix} 0 & \bar{e}_{31}^{(k)} \\ 0 & \bar{e}_{33}^{(k)} \\ \bar{e}_{15}^{(k)} & 0 \end{bmatrix} \begin{bmatrix} E_1 \\ E_3 \end{bmatrix} \\ \begin{bmatrix} D_1^{(k)} \\ D_3^{(k)} \end{bmatrix} &= \begin{bmatrix} 0 & 0 & \bar{e}_{15}^{(k)} \\ \bar{e}_{31}^{(k)} & \bar{e}_{33}^{(k)} & 0 \end{bmatrix} \begin{bmatrix} \varepsilon_{11} \\ \varepsilon_{33} \\ \gamma_{13} \end{bmatrix} + \begin{bmatrix} \bar{\epsilon}_{11}^{(k)} & 0 \\ 0 & \bar{\epsilon}_{33}^{(k)} \end{bmatrix} \begin{bmatrix} E_1 \\ E_3 \end{bmatrix} \end{aligned} \quad (4)$$

where the components of the constitutive matrices are expressed by

$$\bar{C}_{11}^{(k)} = C_{11}^{(k)} - \frac{C_{12}^{(k)2}}{C_{22}^{(k)}}, \quad \bar{C}_{13}^{(k)} = C_{13}^{(k)} - \frac{C_{12}^{(k)}C_{23}^{(k)}}{C_{22}^{(k)}}, \quad \bar{C}_{33}^{(k)} = C_{33}^{(k)} - \frac{C_{23}^{(k)2}}{C_{22}^{(k)}}, \quad \bar{C}_{55}^{(k)} = C_{55}^{(k)} \quad (5)$$

$$\bar{e}_{31}^{(k)} = e_{31}^{(k)} - e_{32}^{(k)} \frac{C_{12}^{(k)}}{C_{22}^{(k)}}, \quad \bar{e}_{33}^{(k)} = e_{33}^{(k)} - e_{32}^{(k)} \frac{C_{23}^{(k)}}{C_{22}^{(k)}}, \quad \bar{e}_{15}^{(k)} = e_{15}^{(k)} \quad (6)$$

$$\bar{\epsilon}_{11}^{(k)} = \epsilon_{11}^{(k)}, \quad \bar{\epsilon}_{33}^{(k)} = \epsilon_{33}^{(k)} + \frac{e_{32}^{(k)2}}{C_{22}^{(k)}} \quad (7)$$

being $C_{ij}^{(k)}$ the stiffness coefficients, $e_{ij}^{(k)}$ the piezoelectric constants and $\epsilon_{ij}^{(k)}$ the permittivity coefficients for the 3D problem.

For the analysis of piezoelectric problems it is useful to use the notation proposed by Barnett and Lothe [8]. With this notation, the mechanical displacement and electric potential, the strain and electric field, the stress and electric displacement, and the elastic and electric coefficients can be grouped for the 2D problem as

$$\begin{bmatrix} \sigma_{11}^{(k)} \\ \sigma_{33}^{(k)} \\ \sigma_{13}^{(k)} \\ D_1^{(k)} \\ D_3^{(k)} \end{bmatrix} = \begin{bmatrix} \bar{C}_{11}^{(k)} & \bar{C}_{13}^{(k)} & 0 & 0 & \bar{e}_{31}^{(k)} \\ \bar{C}_{13}^{(k)} & \bar{C}_{33}^{(k)} & 0 & 0 & \bar{e}_{33}^{(k)} \\ 0 & 0 & \bar{C}_{55}^{(k)} & \bar{e}_{15}^{(k)} & 0 \\ 0 & 0 & \bar{e}_{15}^{(k)} & -\epsilon_{11}^{(k)} & 0 \\ \bar{e}_{31}^{(k)} & \bar{e}_{33}^{(k)} & 0 & 0 & -\epsilon_{33}^{(k)} \end{bmatrix} \begin{bmatrix} \varepsilon_{11} \\ \varepsilon_{33} \\ \gamma_{13} \\ -E_1 \\ -E_3 \end{bmatrix} \quad (8)$$

In addition, using the Maxwell's law $[E] = -\nabla\phi$ to derive the electric field vector from the electric potential ϕ , and the kinematic relations $[\varepsilon] = 1/2\{\nabla[u] + \nabla[u]^\top\}$, the piezoelectric problem can be formulated only in terms of the generalized displacements defined as

$$[\hat{u}] = [u_1 \quad u_3 \quad \phi]^\top \quad (9)$$

2.3 Classical and new variational formulation of the boundary value problem

In the following, a single harmonic mechanical excitation, $[F_d(t)] = [f_d] e^{i\omega t}$, is assumed as a basic problem. The response of a linear solid in absence of body loads and free electric volume charge subjected to a harmonic excitation is presumed to have the same frequency as the applied load, $[u(M, t)] = [u(M)] e^{i\omega t}$ and $\phi(M, t) = \phi(M) e^{i\omega t}$, with $[u(M)]$ and $\phi(M)$ containing the displacements and electric potential amplitudes. Under these assumptions, the classical variational principle of a piezoelectric beam subjected to a mechanical harmonic load can be expressed as:

find $([u(M)], \phi(M)) \in U \times \Phi$ (space of admissible displacement and electric potential) such that

$$\int_{\Omega} [\varepsilon(\delta u)]^T [\sigma] dV - \int_{\partial_F \Omega} [\delta u]^T [f_d] dS = \omega^2 \int_{\Omega} \rho [\delta u]^T [u] dV, \quad (10a)$$

$$\int_{\Omega} [E(\delta \phi)]^T [D] dV = 0, \quad \forall ([\delta u], \delta \phi) \in \delta U \times \delta \Phi \quad (10b)$$

Eq. (10) can be solved for a given value of the load frequency ω so that the set of the load frequency within an interval $[\omega_{min}, \omega_{max}]$ involves the resolution of many problems. In order to avoid this iterative strategy, a new formulation as in [9] is proposed

find $([u(M, \omega)], \phi(M, \omega)) \in U \times \Phi$ (space of admissible generalized displacement) such that

$$\int_{\omega} \int_{\Omega} [\varepsilon(\delta u)]^T [\sigma] dV d\omega - \int_{\omega} \int_{\partial_F \Omega} [\delta u]^T [f_d] dS d\omega = \int_{\omega} \int_{\Omega} \omega^2 \rho [\delta u]^T [u] dV d\omega, \quad (11a)$$

$$\int_{\omega} \int_{\Omega} [E(\delta \phi)]^T [D] dV d\omega = 0, \quad \forall ([\delta u], \delta \phi) \in \delta U \times \delta \Phi \quad (11b)$$

To complete the boundary value problem, a prescribed displacement $[u(M, t)] = [u_d(t)]$ and electric potential $\phi(M, t) = \phi_d(t)$ are imposed on $\partial_u \Omega$ and $\partial_{\phi} \Omega$ respectively.

3 APPLICATION OF THE PGD METHOD

The Proper Generalized Decomposition (PGD) was first proposed in [5]. This method is based on an *a priori* construction of the solution in separate variables. In the literature, the PGD has been used in order to separate spatial variables and also to consider problem parameters as extra-coordinates. In this approach, the PGD is used to consider both the spatial variable separation and the introduction of the load frequency as an extra-coordinate in the solution of the electrodynamic problem in piezoelectric composites.

3.1 Separated representation

The unknowns of the problem, i.e. the generalized displacements, composed by the longitudinal and transversal displacements $[u] = [u_1 \quad u_3]^T$ and the electric potential ϕ are built as

$$\begin{bmatrix} u_1(x, z, \omega) \\ u_3(x, z, \omega) \end{bmatrix} = \sum_{i=1}^N g^i(\omega) \begin{bmatrix} f_1^i(z) v_1^i(x) \\ f_3^i(z) v_3^i(x) \end{bmatrix} \quad (12)$$

$$\phi(x, z, \omega) = \sum_{i=1}^N g_{\phi}^i(\omega) f_{\phi}^i(z) v_{\phi}^i(x) \quad (13)$$

where (g^i, g_ϕ^i) defined in $[\omega_{min}, \omega_{max}]$, (f_1^i, f_3^i, f_ϕ^i) defined in Ω_z and (v_1^i, v_3^i, v_ϕ^i) defined in Ω_x are functions which must be computed during the resolution process for each enrichment step $i = 1, 2, \dots, n, \dots, N$.

Eq. (12) can be written in a more compact way as

$$[u] = \sum_{i=1}^N g^i [F^i] [v^i] = \sum_{i=1}^N g^i [V^i] [f^i] \quad (14)$$

where

$$[v^i] = \begin{bmatrix} v_1^i(x) \\ v_3^i(x) \end{bmatrix}, \quad [V^i] = \begin{bmatrix} v_1^i(x) & 0 \\ 0 & v_3^i(x) \end{bmatrix}, \quad [f^i] = \begin{bmatrix} f_1^i(z) \\ f_3^i(z) \end{bmatrix}, \quad [F^i] = \begin{bmatrix} f_1^i(z) & 0 \\ 0 & f_3^i(z) \end{bmatrix} \quad (15)$$

This separated representation is also used in the following to express the virtual displacement δu and the virtual electric potential $\delta \phi$ used as test functions in Eq. (11)

$$[\delta u] = \delta g [F] [v] + g [V] [\delta f] + g [F] [\delta v] = \delta u_\omega + \delta u_f + \delta u_v \quad (16)$$

$$\delta \phi = \delta g_\phi f_\phi v_\phi + g_\phi \delta f_\phi v_\phi + g_\phi f_\phi \delta v_\phi = \delta \phi_\omega + \delta \phi_f + \delta \phi_v \quad (17)$$

3.2 The problem to be solved

Regarding the definition of the unknowns of the problem, an iterative procedure must be introduced to find the solutions for each enrichment step i . Assuming that the first $(n-1)$ functions have been already computed, the solution for iteration n can be expressed by

$$[u] = [\bar{u}] + g [V] [f] = [\bar{u}] + g [F] [v], \quad \phi = \bar{\phi} + g_\phi f_\phi v_\phi \quad (18)$$

where $([\bar{u}], \bar{\phi})$ are the displacement and potential solution at iteration $(n-1)$ defined by

$$[\bar{u}] = \sum_{i=1}^{n-1} [u^i] = \sum_{i=1}^{n-1} g^i [F^i] [v^i] = \sum_{i=1}^{n-1} g^i [V^i] [f^i], \quad \bar{\phi} = \sum_{i=1}^{n-1} \phi^i = \sum_{i=1}^{n-1} g_\phi^i f_\phi^i v_\phi^i \quad (19)$$

Taking into account the constitutive law and introducing Eqs. (16-17) in the weak form expressed by Eq. (11) the problem is decomposed into three pair coupled equations, which are

$$\begin{aligned} \int_\omega \int_\Omega \left([\varepsilon(\delta u_\omega)]^\top [C] [\varepsilon(\bar{u} + g F v)] - [\varepsilon(\delta u_\omega)]^\top [e]^\top [E(\bar{\phi} + g_\phi f_\phi v_\phi)] \right) dV d\omega \\ - \int_\omega \int_\Omega \omega^2 \rho [\delta u_\omega]^\top [\bar{u} + g F v] dV d\omega = \int_\omega \int_{\partial_F \Omega} [\delta u_\omega]^\top [f_d] dS d\omega \end{aligned} \quad (20a)$$

$$\int_\omega \int_\Omega \left([E(\delta \phi_\omega)]^\top [e] [\varepsilon(\bar{u} + g F v)] + [E(\delta \phi_\omega)]^\top [\epsilon] [E(\bar{\phi} + g_\phi f_\phi v_\phi)] \right) dV d\omega = 0 \quad (20b)$$

$$\begin{aligned} \int_\omega \int_\Omega \left([\varepsilon(\delta u_f)]^\top [C] [\varepsilon(\bar{u} + g V f)] - [\varepsilon(\delta u_f)]^\top [e]^\top [E(\bar{\phi} + g_\phi f_\phi v_\phi)] \right) dV d\omega \\ - \int_\omega \int_\Omega \omega^2 \rho [\delta u_f]^\top [\bar{u} + g V f] dV d\omega = \int_\omega \int_{\partial_F \Omega} [\delta u_f]^\top [f_d] dS d\omega \end{aligned} \quad (21a)$$

$$\int_\omega \int_\Omega \left([E(\delta \phi_f)]^\top [e] [\varepsilon(\bar{u} + g V f)] + [E(\delta \phi_f)]^\top [\epsilon] [E(\bar{\phi} + g_\phi f_\phi v_\phi)] \right) dV d\omega = 0 \quad (21b)$$

$$\begin{aligned} \int_{\omega} \int_{\Omega} \left([\varepsilon(\delta u_v)]^T [C] [\varepsilon(\bar{u} + g F v)] - [\varepsilon(\delta u_v)]^T [e]^T [E(\bar{\phi} + g_{\phi} f_{\phi} v_{\phi})] \right) dV d\omega \\ - \int_{\omega} \int_{\Omega} \omega^2 \rho [\delta u_v]^T [\bar{u} + g F v] dV d\omega = \int_{\omega} \int_{\partial_F \Omega} [\delta u_v]^T [f_d] dS d\omega \end{aligned} \quad (22a)$$

$$\int_{\omega} \int_{\Omega} \left([E(\delta \phi_v)]^T [e] [\varepsilon(\bar{u} + g F v)] + [E(\delta \phi_v)]^T [\epsilon] [E(\bar{\phi} + g_{\phi} f_{\phi} v_{\phi})] \right) dV d\omega = 0 \quad (22b)$$

From Eqs. (20),(21) and (22), a non-linear piezoelectric problem is defined. The simplest non-linear resolution strategy to solve these equations is the fixed point method. The iterative procedure is explained though the pseudo-code in Algorithm 1. The fixed point loop is iterated m times until reaching a fixed solution for each enrichment step n which composes the final solution.

Algorithm 1 Non-linear resolution strategy: PGD algorithm.

```

for  $n = 1$  to  $N$  do
  Initialize  $g^{(0)}, [f^{(0)}], f_{\phi}^{(0)}, g_{\phi}^{(0)}$  and compute  $[v^{(0)}], v_{\phi}^{(0)}$  from Eq. (22)
  for  $m = 1$  to  $m_{max}$  do
    Step 1:  $g^{(m)}, g_{\phi}^{(m)}$  satisfies Eq. (20) for functions set to  $[f^{(m-1)}], [v^{(m-1)}], f_{\phi}^{(m-1)}, v_{\phi}^{(m-1)}$ 
    Step 2:  $[f^{(m)}], f_{\phi}^{(m)}$  satisfies Eq. (21) for functions set to  $g^{(m)}, [v^{(m-1)}], g_{\phi}^{(m)}, v_{\phi}^{(m-1)}$ 
    Step 3:  $[v^{(m)}], v_{\phi}^{(m)}$  satisfies Eq. (22) for functions set to  $g^{(m)}, [f^{(m)}], g_{\phi}^{(m)}, f_{\phi}^{(m)}$ 
    Check for convergence
  end for
  Set  $g^n = g^{(m)}, [f^n] = [f^{(m)}], [v^n] = [v^{(m)}]$  and  $g_{\phi}^n = g_{\phi}^{(m)}, f_{\phi}^n = f_{\phi}^{(m)}, v_{\phi}^n = v_{\phi}^{(m)}$ 
  if  $n = 1$  then
    Set  $[u^n] = g^n [V^n] [f^n]$  and  $\phi^n = g_{\phi}^n f_{\phi}^n v_{\phi}^n$ 
  else
    Set  $[u^n] = [u^{n-1}] + g^n [V^n] [f^n]$  and  $\phi^n = \phi^{n-1} + g_{\phi}^n f_{\phi}^n v_{\phi}^n$ 
  end if
end for

```

3.3 Variational problem defined on load frequency domain: Step 1

In order to simplify the notation, the functions $[f^{(m)}], [v^{(m)}], f_{\phi}^{(m)}, v_{\phi}^{(m)}$, which are assumed to be known, will be denoted as $\tilde{f}, \tilde{v}, \tilde{f}_{\phi}, \tilde{v}_{\phi}$ (and subsequently \tilde{F}, \tilde{V} in matrix form) and the function $g^{(m+1)}, g_{\phi}^{(m+1)}$ to be computed will be denoted as g, g_{ϕ} . The functions $\bar{g}^i, \bar{f}^i, \bar{v}^i, \bar{g}_{\phi}^i, \bar{f}_{\phi}^i, \bar{v}_{\phi}^i$ are the solutions at the previous enrichment steps $i = 1, 2, \dots, (n-1)$. The strain and electric fields in Eq. (20) are defined in matrix notation as

$$[\varepsilon(g \tilde{F} \tilde{v})] = g [\Sigma_z(\tilde{f})] [\tilde{\mathcal{E}}_v], \quad [E(g_{\phi} \tilde{f}_{\phi} \tilde{v}_{\phi})] = g_{\phi} [\Sigma_z^{\phi}(\tilde{f}_{\phi})] [\tilde{\mathcal{E}}_{v_{\phi}}], \quad (23)$$

with

$$[\Sigma_z(\tilde{f})] = \begin{bmatrix} 0 & \tilde{f}_1 & 0 & 0 \\ 0 & 0 & \tilde{f}_3' & 0 \\ \tilde{f}_1' & 0 & 0 & \tilde{f}_3 \end{bmatrix}, \quad [\tilde{\mathcal{E}}_v] = [\tilde{v}_1 \ \tilde{v}_1' \ \tilde{v}_3 \ \tilde{v}_3']^T \quad (24)$$

$$[\Sigma_z^{\phi}(\tilde{f}_{\phi})] = \begin{bmatrix} 0 & -\tilde{f}_{\phi}' \\ -\tilde{f}_{\phi}' & 0 \end{bmatrix}, \quad [\tilde{\mathcal{E}}_{v_{\phi}}] = [\tilde{v}_{\phi} \ \tilde{v}_{\phi}']^T \quad (25)$$

where the prime (') stands for the classical derivation. Thus, the variational problem defined in Eq. (20) is then

$$k_{\omega}^{vv} g - k_{\omega}^{v\phi} g_{\phi} - \omega^2 m_{\omega} g = f_{\omega} + \omega^2 \sum_{i=1}^{n-1} \bar{g}^i \mu_{\omega}^i - \sum_{i=1}^{n-1} \bar{g}^i \sigma_{\omega}^{vv^i} + \sum_{i=1}^{n-1} \bar{g}_{\phi}^i \sigma_{\omega}^{v\phi^i} \quad (26a)$$

$$k_{\omega}^{\phi v} g + k_{\omega}^{\phi\phi} g_{\phi} = - \sum_{i=1}^{n-1} \bar{g}^i \sigma_{\omega}^{\phi v^i} - \sum_{i=1}^{n-1} \bar{g}_{\phi}^i \sigma_{\omega}^{\phi\phi^i} \quad \forall \quad \omega \in [\omega_{min}, \omega_{max}] \quad (26b)$$

being

$$\begin{aligned} k_{\omega}^{vv}(\tilde{f}, \tilde{v}) &= \int_{\Omega} [\tilde{\mathcal{E}}_v]^T [\tilde{\Sigma}_z]^T [C] [\tilde{\Sigma}_z] [\tilde{\mathcal{E}}_v] dV, & k_{\omega}^{v\phi}(\tilde{f}, \tilde{v}, \tilde{f}_{\phi}, \tilde{v}_{\phi}) &= \int_{\Omega} [\tilde{\mathcal{E}}_v]^T [\tilde{\Sigma}_z]^T [e]^T [\tilde{\Sigma}_z^{\phi}] [\tilde{\mathcal{E}}_{v_{\phi}}] dV, \\ k_{\omega}^{\phi v}(\tilde{f}, \tilde{v}, \tilde{f}_{\phi}, \tilde{v}_{\phi}) &= \int_{\Omega} [\tilde{\mathcal{E}}_{v_{\phi}}]^T [\tilde{\Sigma}_z^{\phi}]^T [e] [\tilde{\Sigma}_z] [\tilde{\mathcal{E}}_v] dV, & k_{\omega}^{\phi\phi}(\tilde{f}_{\phi}, \tilde{v}_{\phi}) &= \int_{\Omega} [\tilde{\mathcal{E}}_{v_{\phi}}]^T [\tilde{\Sigma}_z^{\phi}]^T [\epsilon] [\tilde{\Sigma}_z^{\phi}] [\tilde{\mathcal{E}}_{v_{\phi}}] dV \end{aligned} \quad (27)$$

$$\begin{aligned} \sigma_{\omega}^{vv^i}(\tilde{f}, \tilde{v}, \tilde{u}) &= \int_{\Omega} [\tilde{\mathcal{E}}_v]^T [\tilde{\Sigma}_z]^T [C] [\tilde{\Sigma}_z^i] [\tilde{\mathcal{E}}_v^i] dV, & \sigma_{\omega}^{v\phi^i}(\tilde{f}, \tilde{v}, \tilde{\phi}) &= \int_{\Omega} [\tilde{\mathcal{E}}_v]^T [\tilde{\Sigma}_z]^T [e]^T [\tilde{\Sigma}_z^{\phi^i}] [\tilde{\mathcal{E}}_{v_{\phi}}^i] dV, \\ \sigma_{\omega}^{\phi v^i}(\tilde{f}, \tilde{v}, \tilde{u}) &= \int_{\Omega} [\tilde{\mathcal{E}}_{v_{\phi}}]^T [\tilde{\Sigma}_z^{\phi}]^T [e] [\tilde{\Sigma}_z^i] [\tilde{\mathcal{E}}_v^i] dV, & \sigma_{\omega}^{\phi\phi^i}(\tilde{f}, \tilde{v}, \tilde{\phi}) &= \int_{\Omega} [\tilde{\mathcal{E}}_{v_{\phi}}]^T [\tilde{\Sigma}_z^{\phi}]^T [\epsilon] [\tilde{\Sigma}_z^{\phi^i}] [\tilde{\mathcal{E}}_{v_{\phi}}^i] dV \end{aligned} \quad (28)$$

$$m_{\omega}(\tilde{f}, \tilde{v}) = \int_{\Omega} [\tilde{v}]^T [\tilde{F}]^T \rho [\tilde{F}] [\tilde{v}] dV, \quad \mu_{\omega}^i(\tilde{f}, \tilde{v}, \tilde{u}) = \int_{\Omega} [\tilde{v}]^T [\tilde{F}]^T \rho [\tilde{F}^i] [\tilde{v}^i] dV \quad (29)$$

$$f_{\omega}(\tilde{f}, \tilde{v}) = \int_{\partial F \Omega} [\tilde{v}]^T [\tilde{F}]^T [f_d] dS \quad (30)$$

By using the system expressed by Eq. (26), the values of $g(\omega)$, $g_{\phi}(\omega)$ can be calculated explicitly for any ω considered in the range $[\omega_{min}, \omega_{max}]$. Note that there are specific values so-called natural frequencies ω_n for which resonance is detected.

3.4 Variational problem defined on Ω_z : Step 2

At this step the functions $g^{(m+1)}, [v^{(m)}], g_{\phi}^{(m+1)}, v_{\phi}^{(m)}$, assumed to be known, will be denoted as $\tilde{g}, \tilde{v}, \tilde{g}_{\phi}, \tilde{v}_{\phi}$ and the function $[f^{(m+1)}], f_{\phi}^{(m+1)}$ to be computed will be denoted as f, f_{ϕ} . The strain and electric field in Eq. (21) are defined in matrix notation as

$$[\mathcal{E}(\tilde{g} \tilde{V} f)] = \tilde{g} [\Sigma_x(\tilde{v})] [\mathcal{E}_f], \quad [E(\tilde{g}_{\phi} \tilde{v}_{\phi} f_{\phi})] = \tilde{g}_{\phi} [\Sigma_x^{\phi}(\tilde{v}_{\phi})] [\mathcal{E}_{f_{\phi}}], \quad (31)$$

with

$$[\Sigma_x(\tilde{v})] = \begin{bmatrix} \tilde{v}'_1 & 0 & 0 & 0 \\ 0 & 0 & 0 & \tilde{v}_3 \\ 0 & \tilde{v}_1 & \tilde{v}'_3 & 0 \end{bmatrix}, \quad [\mathcal{E}_f] = [f_1 \ f'_1 \ f_3 \ f'_3]^T \quad (32)$$

$$[\Sigma_x^{\phi}(\tilde{v}_{\phi})] = \begin{bmatrix} -\tilde{v}'_{\phi} & 0 \\ 0 & -\tilde{v}_{\phi} \end{bmatrix}, \quad [\mathcal{E}_{f_{\phi}}] = [\tilde{f}_{\phi} \ \tilde{f}'_{\phi}]^T \quad (33)$$

Introducing the above expression into Eq. (21), the variational problem defined on Ω_z is

$$\begin{aligned} \gamma_\omega \int_{\Omega_z} [\delta \mathcal{E}_f]^\top [k_x^{ff}] [\mathcal{E}_f] dz - \theta_\omega \int_{\Omega_z} [\delta \mathcal{E}_f]^\top [k_x^{f\phi}] [\mathcal{E}_{f\phi}] dz - \alpha_\omega \int_{\Omega_z} [\delta f]^\top [m_x] [f] dz = \\ \beta_\omega \int_{\partial_F \Omega_z} [\delta f]^\top [f_x] dz + \sum_{i=1}^{n-1} \left(\alpha_\omega^i \int_{\Omega_z} [\delta f]^\top [\mu_x^i] dz - \gamma_\omega^i \int_{\Omega_z} [\delta \mathcal{E}_f]^\top [\sigma_x^{ff^i}] dz \right. \\ \left. + \theta_\omega^{g\phi^i} \int_{\Omega_z} [\delta \mathcal{E}_f]^\top [\sigma_x^{f\phi^i}] dz \right) \quad (34a) \end{aligned}$$

$$\begin{aligned} \theta_\omega \int_{\Omega_z} [\delta \mathcal{E}_{f\phi}]^\top [k_x^{\phi f}] [\mathcal{E}_f] dz + \eta_\omega \int_{\Omega_z} [\delta \mathcal{E}_{f\phi}]^\top [k_x^{\phi\phi}] [\mathcal{E}_{f\phi}] dz = \\ - \sum_{i=1}^{n-1} \left(\theta_\omega^{g^i} \int_{\Omega_z} [\delta \mathcal{E}_{f\phi}]^\top [\sigma_x^{\phi f^i}] dz - \eta_\omega^i \int_{\Omega_z} [\delta \mathcal{E}_{f\phi}]^\top [\sigma_x^{\phi\phi^i}] dz \right) \quad (34b) \end{aligned}$$

where the coefficients integrated in the Ω_x domain are

$$\begin{aligned} [k_x^{ff}(\tilde{v})] &= \int_{\Omega_x} [\tilde{\Sigma}_x]^\top [C] [\tilde{\Sigma}_x] dx, & [k_x^{f\phi}(\tilde{v}, \tilde{v}_\phi)] &= \int_{\Omega_x} [\tilde{\Sigma}_x]^\top [e]^\top [\tilde{\Sigma}_x^\phi] dx, \\ [k_x^{\phi f}(\tilde{v}, \tilde{v}_\phi)] &= \int_{\Omega_x} [\tilde{\Sigma}_x^\phi]^\top [e] [\tilde{\Sigma}_x] dx, & [k_x^{\phi\phi}(\tilde{v}_\phi)] &= \int_{\Omega_x} [\tilde{\Sigma}_x^\phi]^\top [\epsilon] [\tilde{\Sigma}_x^\phi] dx \quad (35) \end{aligned}$$

$$\begin{aligned} [\sigma_x^{ff^i}(\tilde{v}, \tilde{u})] &= \int_{\Omega_x} [\tilde{\Sigma}_x]^\top [C] [\tilde{\Sigma}_x^i] [\tilde{\mathcal{E}}_f^i] dx, & [\sigma_x^{f\phi^i}(\tilde{v}, \tilde{\phi})] &= \int_{\Omega_x} [\tilde{\Sigma}_x]^\top [e]^\top [\tilde{\Sigma}_x^i] [\tilde{\mathcal{E}}_{f\phi}^i] dx, \\ [\sigma_x^{\phi f^i}(\tilde{v}_\phi, \tilde{\phi})] &= \int_{\Omega_x} [\tilde{\Sigma}_x^\phi]^\top [e] [\tilde{\Sigma}_x^i] [\tilde{\mathcal{E}}_f^i] dx, & [\sigma_x^{\phi\phi^i}(\tilde{v}_\phi, \tilde{u})] &= \int_{\Omega_x} [\tilde{\Sigma}_x^\phi]^\top [\epsilon] [\tilde{\Sigma}_x^i] [\tilde{\mathcal{E}}_{f\phi}^i] dx \quad (36) \end{aligned}$$

$$[m_x(\tilde{v})] = \int_{\Omega_x} [\tilde{V}]^\top \rho [\tilde{V}] dx, \quad [\mu_x^i(\tilde{v}, \tilde{u})] = \int_{\Omega_x} [\tilde{V}]^\top \rho [\tilde{V}^i] [\tilde{f}^i] dx \quad (37)$$

$$[f_x(\tilde{v})] = \int_{\partial_F \Omega_x} [\tilde{V}]^\top [f_d] dx \quad (38)$$

and the ones integrated in the load frequency domain are

$$\begin{aligned} \gamma_\omega = \int_{\omega} \tilde{g}^2 d\omega, \quad \gamma_\omega^i = \int_{\omega} \tilde{g} \tilde{g}^i d\omega, \quad \alpha_\omega = \int_{\omega} \omega^2 \tilde{g}^2 d\omega, \quad \alpha_\omega^i = \int_{\omega} \omega^2 \tilde{g} \tilde{g}^i d\omega, \quad \beta_\omega = \int_{\omega} \tilde{g} d\omega, \\ \theta_\omega = \int_{\omega} \tilde{g} \tilde{g}_\phi d\omega, \quad \theta_\omega^{g\phi^i} = \int_{\omega} \tilde{g} \tilde{g}_\phi^i d\omega, \quad \theta_\omega^{\phi g^i} = \int_{\omega} \tilde{g}_\phi \tilde{g}^i d\omega, \quad \eta_\omega = \int_{\omega} \tilde{g}_\phi^2 d\omega, \quad \eta_\omega^i = \int_{\omega} \tilde{g}_\phi \tilde{g}_\phi^i d\omega \quad (39) \end{aligned}$$

The variational problem defined by Eq. (34) is a linear expression that must be solved in the Ω_z domain.

3.5 Variational problem defined on Ω_x : Step 3

The problem in the Ω_x domain is analogous to the one presented in the previous section for the domain Ω_z . At this step, the functions $g^{(m+1)}, [f^{(m+1)}], g_\phi^{(m+1)}, f_\phi^{(m+1)}$, which are assumed to be known, will be denoted as $\tilde{g}, \tilde{f}, \tilde{g}_\phi, \tilde{f}_\phi$ and the functions $[v^{(m+1)}], v_\phi^{(m+1)}$ to be computed will be denoted as v, v_ϕ .

With the expression of the strain being $[\varepsilon(\tilde{g} \tilde{f} v)] = \tilde{g} [\Sigma_z(\tilde{f})][\mathcal{E}_v]$, and the electric field $[E(\tilde{g}_\phi \tilde{f}_\phi v_\phi)] = \tilde{g}_\phi [\Sigma_z^{\phi}(\tilde{f}_\phi)][\mathcal{E}_{v_\phi}]$, the variational problem defined on Ω_x becomes

$$\begin{aligned} \gamma_\omega \int_{\Omega_x} [\delta \mathcal{E}_v]^\top [k_x^{vv}] [\mathcal{E}_v] dx - \theta_\omega \int_{\Omega_x} [\delta \mathcal{E}_v]^\top [k_x^{v\phi}] [\mathcal{E}_{v_\phi}] dx - \alpha_\omega \int_{\Omega_x} [\delta v]^\top [m_x] [v] dx = \\ \beta_\omega \int_{\partial_v \Omega_x} [\delta v]^\top [v_x] dx + \sum_{i=1}^{n-1} \left(\alpha_\omega^i \int_{\Omega_x} [\delta v]^\top [\mu_x^i] dx - \gamma_\omega^i \int_{\Omega_x} [\delta \mathcal{E}_v]^\top [\sigma_x^{vv^i}] dx \right. \\ \left. + \theta_\omega^{g\phi^i} \int_{\Omega_x} [\delta \mathcal{E}_v]^\top [\sigma_x^{v\phi^i}] dx \right) \quad (40a) \end{aligned}$$

$$\begin{aligned} \theta_\omega \int_{\Omega_x} [\delta \mathcal{E}_{v_\phi}]^\top [k_x^{\phi v}] [\mathcal{E}_v] dx + \eta_\omega \int_{\Omega_x} [\delta \mathcal{E}_{v_\phi}]^\top [k_x^{\phi\phi}] [\mathcal{E}_{v_\phi}] dx = \\ - \sum_{i=1}^{n-1} \left(\theta_\omega^{\phi g^i} \int_{\Omega_x} [\delta \mathcal{E}_{v_\phi}]^\top [\sigma_x^{\phi v^i}] dx - \eta_\omega^i \int_{\Omega_x} [\delta \mathcal{E}_{v_\phi}]^\top [\sigma_x^{\phi\phi^i}] dx \right) \quad (40b) \end{aligned}$$

where the coefficients integrated in the load frequency domain are expressed by Eq. (39) and those integrated in the Ω_z domain are analogous to the ones presented before for Ω_x domain.

4 FINITE ELEMENT DISCRETIZATION

To numerically compute the solution, a discrete representations of functions $g, [f], [v], g_\phi, f_\phi, v_\phi$ is needed. For the load frequency domain, a uniform discretization of the interval $[\omega_{min}, \omega_{max}]$ is established. The size of the discrete functions g, g_ϕ associated with the mesh in the load frequency domain is denoted as n_ω . The trapezoidal rule is used for the approximation of the integrals involving these functions as in Eq. (39). On the other hand, a classical finite element approximation is used in domains Ω_x and Ω_z . The element vectors of degrees of freedoms (dofs) associated with the mesh in Ω_x and Ω_z are $[q_e^v], [q_e^{v\phi}]$ and $[q_k^f], [q_k^{f\phi}]$ respectively. The displacement field, the electric potential and also the derived strain and electric fields are expressed by

$$[v_e] = [N_x][q_e^v], \quad [\mathcal{E}_v^e] = [B_x][q_e^v], \quad [v_{\phi_e}] = [N_{\phi x}][q_e^{v\phi}], \quad [E_{v_\phi}^e] = [B_{\phi x}][q_e^{v\phi}] \quad (41)$$

$$[f_k] = [N_z][q_k^f], \quad [\mathcal{E}_f^k] = [B_z][q_k^f], \quad [f_{\phi_k}] = [N_{\phi z}][q_k^{f\phi}], \quad [E_{f_\phi}^k] = [B_{\phi z}][q_k^{f\phi}] \quad (42)$$

where the matrices $[N_x], [B_x], [N_z], [B_z], [N_{\phi x}], [B_{\phi x}], [N_{\phi z}], [B_{\phi z}]$ contain the shape functions, their derivatives and the Jacobian components. The total number of elements in $\Omega_x = \bigcup_{e=1}^{n_x} \Omega_x^e$ and $\Omega_z = \bigcup_{k=1}^{n_z} \Omega_z^k$ domains are denoted as n_x and n_z , respectively. The interpolation can be different for each domain and also for the mechanical and electric unknowns separately.

The introduction of the FE discretization in the Eq. (34) lead to the electro-mechanical linear system

$$\left(\begin{bmatrix} K_{ff} & -K_{ff\phi} \\ -K_{f\phi f} & -K_{f\phi\phi} \end{bmatrix} - \begin{bmatrix} M_f & 0 \\ 0 & 0 \end{bmatrix} \right) \begin{bmatrix} q^f \\ q^{f\phi} \end{bmatrix} = \begin{bmatrix} F_f \\ 0 \end{bmatrix} + \begin{bmatrix} R_f \\ R_{f\phi} \end{bmatrix} \quad (43)$$

where

- $[q^f], [q^{f\phi}]$ are the vector of dofs associated with the finite element mesh in Ω_z for the mechanical and electric unknowns respectively.
- $[K_{ff}], [K_{ff\phi}], [K_{f\phi f}], [K_{f\phi f\phi}]$ are the stiffness, electro-mechanical and electric matrices obtained by assembling the elementary matrices $[K_{ff}^k], [K_{ff\phi}^k], [K_{f\phi f}^k], [K_{f\phi f\phi}^k]$.

$$[K_{ff}^k(\tilde{v})] = \gamma_\omega \int_{\Omega_z^k} [B_z]^\top \left[\sum_{e=1}^{n_x} [k_x^{ff}(\tilde{v}_e)] \right] [B_z] dz \quad (44)$$

$$[K_{ff\phi}^k(\tilde{v}, \tilde{v}_\phi)] = \theta_\omega \int_{\Omega_z^k} [B_z]^\top \left[\sum_{e=1}^{n_x} [k_x^{f\phi}(\tilde{v}_e, \tilde{v}_{\phi_e})] \right] [B_{\phi z}] dz \quad (45)$$

$$[K_{f\phi f}^k(\tilde{v}, \tilde{v}_\phi)] = \theta_\omega \int_{\Omega_z^k} [B_{\phi z}]^\top \left[\sum_{e=1}^{n_x} [k_x^{\phi f}(\tilde{v}_e, \tilde{v}_{\phi_e})] \right] [B_z] dz \quad (46)$$

$$[K_{f\phi f\phi}^k(\tilde{v}_\phi)] = \eta_\omega \int_{\Omega_z^k} [B_{\phi z}]^\top \left[\sum_{e=1}^{n_x} [k_x^{\phi\phi}(\tilde{v}_{\phi_e})] \right] [B_{\phi z}] dz \quad (47)$$

- $[M_f]$ is the mass matrix obtained by assembling the elementary mass matrices $[M_f^k]$.

$$[M_f^k(\tilde{v})] = \alpha_\omega \int_{\Omega_z^k} [N_z]^\top \left[\sum_{e=1}^{n_x} [m_x(\tilde{v}_e)] \right] [N_z] dz \quad (48)$$

- $[F_f]$ is the load vector obtained by assembling the elementary load vectors $[F_f^k]$.

$$[F_f^k(\tilde{v})] = \beta_\omega \int_{\partial_F \Omega_z^k} [N_z]^\top \left[\sum_{e=1}^{n_x} [f_x(\tilde{v}_e)] \right] dz \quad (49)$$

- $[R_f], [R_{f\phi}]$ are the equilibrium and electric residuals respectively, obtained by assembling the elementary residual vectors $[R_f^k], [R_{f\phi}^k]$.

$$[R_f^k(\tilde{v}, \bar{u}, \bar{\phi})] = \sum_{i=1}^{n-1} \left(\theta_\omega^{g\phi^i} \int_{\Omega_z^k} [B_z]^\top \left[\sum_{e=1}^{n_x} [\sigma_x^{f\phi^i}(\tilde{v}_e, \bar{\phi})] \right] dz - \gamma_\omega^i \int_{\Omega_z^k} [B_z]^\top \left[\sum_{e=1}^{n_x} [\sigma_x^{ff^i}(\tilde{v}_e, \bar{u})] \right] dz + \alpha_\omega^i \int_{\Omega_z^k} [N_z]^\top \left[\sum_{e=1}^{n_x} [\mu_x^i(\tilde{v}_e, \bar{u})] \right] dz \right) \quad (50)$$

$$[R_{f\phi}^k(\tilde{v}_\phi, \bar{u}, \bar{\phi})] = \sum_{i=1}^{n-1} \left(\theta_\omega^{g\phi^i} \int_{\Omega_z^k} [B_{\phi z}]^\top \left[\sum_{e=1}^{n_x} [\sigma_x^{\phi f^i}(\tilde{v}_{\phi_e}, \bar{\phi})] \right] dz + \eta_\omega^i \int_{\Omega_z^k} [B_{\phi z}]^\top \left[\sum_{e=1}^{n_x} [\sigma_x^{\phi\phi^i}(\tilde{v}_{\phi_e}, \bar{u})] \right] dz \right) \quad (51)$$

Analogously, the introduction of the FE discretization in the Eq. (40) lead to the electro-mechanical linear system

$$\left(\begin{bmatrix} K_{vv} & -K_{vv\phi} \\ -K_{v\phi v} & -K_{v\phi v\phi} \end{bmatrix} - \begin{bmatrix} M_v & 0 \\ 0 & 0 \end{bmatrix} \right) \begin{bmatrix} q^v \\ q^{v\phi} \end{bmatrix} = \begin{bmatrix} F_v \\ 0 \end{bmatrix} + \begin{bmatrix} R_v \\ R_{v\phi} \end{bmatrix} \quad (52)$$

where the components of the linear system have an interpretation similar to that already presented.

5 MODELING ENERGY HARVESTER CONFIGURATION

The most popular energy harvester configuration is the bimorph cantilever connected to an electric load (usually a resistor) in series (see Figure 2). For this to be possible, very thin electrodes are deposited on the piezoelectric layers. The mechanical influence of these electrodes can be considered negligible but in the electric field they impose equipotential conditions. In order to incorporate circuit elements (e.g. the electric load) on the problem formulation, the *equivalent capacitance matrix* can be used as in [7]. This method consists on adding a so-called equivalent capacitance matrix to the dielectric matrix of the problem; the one that involves the dielectric matrix $[\epsilon]$. This new matrix is formulated as follows: for each circuit element l connected between the i th and j th components, define a vector $[V_l]$ of size of the electrical unknowns whose components are all null except the i th and j th whose values are 1 and -1 respectively. The equivalent capacitance matrix of element l is defined as $-j/\omega \tilde{Z}_l [V_l][V_l]^\top$, with j de imaginary number and $\tilde{Z}_l = -Z_l$ if l is a capacitor or $\tilde{Z}_l = Z_l$ if l is a resistor/inductor, being Z_l the impedance of l .

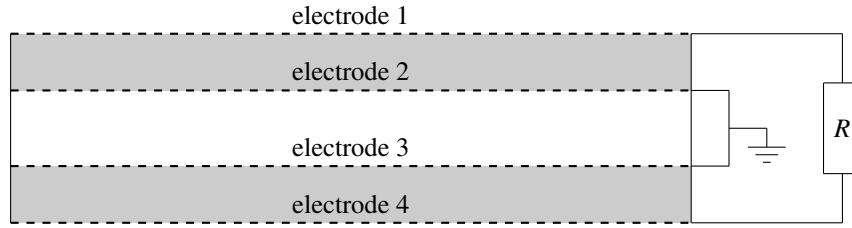


Figure 2: Energy harvester configuration: bimorph cantilever with a resistor in series.

For a classical energy harvester configuration connected to a single resistor in series, electrodes 2 and 3 are grounded, while a resistor of impedance R is connected between electrodes 1 and 4 as in Figure 2. As these conditions are established for a constant coordinate z , the equivalent capacitance matrix is introduced in Eq. (43), where $K_{f_\phi f_\phi}$ is redefined as $K_{f_\phi f_\phi} + \hat{K}_{f_\phi f_\phi}$, with

$$\hat{K}_{f_\phi f_\phi} = -\lambda_\omega \frac{j}{R} [V][V]^\top \quad (53)$$

where $\lambda_\omega = \int_\omega 1/\omega d\omega$.

6 CONCLUSIONS

This research work proposed a new methodology based on the PGD method to solve the forced vibration problem in bi-dimensional piezoelectric composite beams. A classical harmonic space-frequency description of the dynamic problem is considered and a variable separation in the spatial domain is introduced. For both spatial coordinates x (beam axis coordinate) and z (thickness coordinate), a finite element discretization is applied while a linear interpolation is proposed for the load frequency ω . The new approach is developed though an iterative algorithm in which the problem to be solved is split into three 1D problems: one associated to the load frequency ω , one associated with the z coordinate and the other associated to the x coordinate, . The number of dofs of the two last problems can be given as

- Problem on Ω_z : $Ndof_z^M = 2(n_z(N_z^M - 1) + 1)$, $Ndof_z^E = n_z(N_z^E - 1) + 1$.
- Problem on Ω_x : $Ndof_x^M = 2(n_x(N_x^M - 1) + 1)$, $Ndof_x^E = n_x(N_x^E - 1) + 1$.

where n_x, n_z are the total number of elements and $N_x^M, N_z^M, N_x^E, N_z^E$ are the number of nodes per element in Ω_x and Ω_z domains respectively. The superscripts M and E accounts for the interpolation of the mechanical and electrical unknowns. The total cost of the computation depends on the number of enrichment steps N used to represent the final solution. Furthermore, the proposed process requires, for each enrichment step, m iterations of the fixed point method which involves the resolution of one equation with n_ω unknowns and two linear systems of $Ndof_x$ and $Ndof_z$ dofs respectively. In contrast, in a classical layerwise FE approach, the calculation implies n_ω resolutions with $\frac{Ndof_x \times Ndof_z}{2}$ dofs. The advantages of the proposed approach in terms of the reduction of the computational cost become relevant when the number of numerical layers and the number of elements in axis direction is high. The most immediate future extensions of this document would involve parametric comparative studies of different laminates configurations for energy harvesting purposes to validate the proposed method.

REFERENCES

- [1] Behjat, B. Salehi, M. Sadighi, M. Armin, A. and Abbasi, M. Vibration Analysis and Transient Response of an FGPM Beam under Thermo-Electro-Mechanical Loads using Higher-Order Shear Deformation Theory. *Journal of intelligent material systems and structures* (2009) **20(13)**:1635–1646.
- [2] Doroushi, A., Eslami, M.R. and Komeili, A. Vibration Analysis and Transient Response of an FGPM Beam under Thermo-Electro-Mechanical Loads using Higher-Order Shear Deformation Theory. *Journal of intelligent material systems and structures* (2011) **22**:231–243.
- [3] Lezgy-Nazargah, M., Vidal, P. and Polit, O. An efficient finite element model for static and dynamic analyses of functionally graded piezoelectric beams. *Composite Structures* (2013) **104**:71–84.
- [4] Brischetto, S. and Carrera, E. Refined 2D models for the analysis of functionally graded piezoelectric plates. *Journal of intelligent material systems and structures* (2009) **20**:1783–1797.
- [5] Ammar, A., Mokdad, B., Chinesta, F. and Keunings R. A new family of solvers for some classes of multidimensional partial differential equations encountered in kinetic theory modeling of complex fluids. *Journal of non-Newtonian fluid Mechanics* (2006) **139(3)**:153–176.
- [6] Vidal, P., Gallimard, L. and O. Polit. Modeling of piezoelectric plates with variables separation for static analysis. *Smart Materials and Structures* (2016)**25(5)**: 055043.
- [7] Qin, Z., Talleb, H., Yan, S., Xu, X., and Ren, Z. Application of PGD on parametric modeling of a piezoelectric energy harvester. *IEEE Transactions on Magnetics* (2016) **52(11)**:1–11.
- [8] Barnett, D.M. and Lothe, J. Dislocations and line charges in anisotropic piezoelectric insulators. *Physica Status Solidi* (1975) **B76**:105–111.
- [9] Infantes, M., Vidal, P., Castro-Triguero, R., Gallimard, L., García-Macías, E. and Polit, O. Forced vibration analysis of composite beams based on the variable separation method. *Mechanics of Advanced Materials and Structures* (2019) 1–17.

MULTI-SECTION PNEUMATIC ARTIFICIAL MUSCLE CONTINUUM ROBOT ARM WITH OSSICLE-INSPIRED STRUCTURES

THOMAS E. PILLSBURY AND NORMAN M. WERELEY

Department of Aerospace Engineering
University of Maryland
College Park, MD 20742, USA
emails: tpills@umd.edu, wereley@umd.edu

Key words: Continuum robot, Pneumatic artificial muscles, Bio-inspired

Abstract. Continuum robotic manipulators are those that continuously bend to interact with unexpected objects in various orientations. These robots are typically extensions of hyper-redundant robot and more recently being built completely soft material, soft robots. Hyper-redundant robots by definition have a large number of joints and actuators, leading to heavy designs. Conversely, soft robots attempt to overcome this limitation, by using lightweight, low stiffness materials which deform to eliminate joints. The downside of these low stiffness materials, is a reduction in load capacity of these manipulator. This work studies a three section contractile pneumatic artificial muscles actuated manipulator. PAMs were chosen for their high force and stroke behavior. The arm is compared with a second version achieved by adding an ossicle-inspired structure similar to those found in the arms of sea-stars, with the goal of increasing the load capability of a multi-section pneumatic artificial muscle actuated manipulator. This work considers the planar projection of the workspace of the manipulator with and without ossicles. The pneumatic muscles are actuated in various loading conditions to determine the impact of load on the position of the end of the manipulator. With ossicles there is a benefit to the load carrying capability without sacrificing load performance.

1 INTRODUCTION

Soft robots are an emerging field of robotics which lack the rigid structure of traditional manipulators. Like hyper-redundant manipulators, soft robots are used for their flexibility and ability to conform to unexpected shapes. Soft robots have been used for crawling with smart material actuators [11] and grasping with pneumatic actuation such as the PneuNets [5] and pneumatic artificial muscles (PAMs) [7]. PAMs have been used in numerous rigid robot arms [15], legs [3], and non-robotic applications like trailing edge flaps [17].

Pneumatic artificial muscles are soft actuators composed of a braided sleeve surrounded by an elastomeric bladder, which either extends or contracts when pressurized [10]. The soft nature of PAMs makes them a natural choice for a soft robotic manipulator, having been used in soft robotic manipulators constructed of both extensile [12] and contractile [1] PAMs. Contractile PAMs were chosen in this work due to the higher force and work output that they achieve [13]. A tendency of PAM actuated soft robotics arms is to deform in less desirable ways as a result of the compliant nature of the inactive actuators. For example, the extensile PAM arm has points along the muscle groups connected to prevent this undesired

motion [12]. To achieve a similar goal, structures similar in function to the ossicles found on brittle stars are added to the contractile PAM manipulator and evaluated.

In soft robotics, there is interest in taking existing actuators and externally augmenting their structure to provide a new desired behavior [6]. Galloway et al. added an exterior sleeve to the bending fiber-reinforced actuators to control and limit the bending to a subset of shapes, which can approach joint-like structures with certain sleeve designs. These actuators were incorporated into a gripper that could more securely grasp desired shapes such as boxes [6]. Deimel and Brock present a tapered pneumatic fiber-reinforced actuator, PneuFlex, used on a soft hand which can complete a variety of different grasps with five finger and two palm actuators [4]. Additionally, Galloway et al. developed two soft grippers comprised of fiber-reinforced hydraulic actuators for deep sea sampling [5]. The first is an actuator that couples bending and twisting by incorporating a single fiber reinforcement to wrap around an object, and the second takes the PneuNet bellows actuators and incorporates fiber reinforcements to increase the pressure capability.

Soft robot modeling is based on the hyper-redundant robot modeling approximation as a continuum [2]. This can be applied as a geometrically exact continuous model [14] or there can be simplifying assumptions, such as constant curvature [18]. Tatlicioglu et al. calculated the planar dynamic model using the constant curvature assumption for a three-section PAM manipulator. The model developed includes gravitational energy as well as the energy to extend and bend a segment. The energies were integrated over each section of the arm to find the total energy and calculate the Lagrangian dynamics [16].

Constant curvature methods are calculated in terms of state variables of section curvature, bending plane, and length, but for a three actuator intrinsic manipulator, there is not direct control of these values. To develop models in terms of the control lengths and forces of the muscles, Godage et al. introduced shape functions based on the polynomial relationships between the length of the actuators for a PAM actuated continuum robot [8]. The expansions used in that work allow the mathematical singularity associated with a straight arm configuration to be avoided. This work was extended by considering the center of gravity of the section assuming uniform weight distribution. The formulation compared the total energy to both the integral and discretized formulations for a single section, applying a mass correction factor of $1/0.57$ [9].

This work investigates a three-section PAM manipulator and studies the effect of adding an ossicle-inspired backbone to the arm. For a single section the addition of ossicles has been shown to improve the load capabilities of a PAM actuated structure. The manipulator is tested through five different muscle combinations with five load conditions at each. The manipulator is also tested and modeled both with, and without, ossicles to evaluate the effect of adding this structure.

The ossicle structure was designed to interact and limit bending at approximately 45° , a similar model could be incorporated at angles above the design value to improve the model at high angles for the medial and distal sections. To improve modeling and reduce the effects of non-active PAMs, the ossicle structure could be sized such that the PAMs are contracted and pressurized when in a straight arm position, allowing the initial stiffness of the system to be tailored to the desired application. Additionally operation in environments which reduce gravitational impact, space or water, would be beneficial. One way to improve model fitting is improving PAM modeling in the low force and pressure regime. Solutions include a low and high pressure model, higher order PAM modeling or additional considerations of effects on PAM behavior, such as bending.

2 Constant Curvature Modeling

The manipulator modeled in this work has three bending sections connected at rigid plates, Fig 1. Each section has three PAMs which are offset by 120° . The section break between each section and at the end

of the arm is defined by the rigid PAM end fittings and the rigid plate to which the PAM are secured. These rigid section dividers also serve as a point of measurement for the poses at the beginning and end of a section. The modeling done in this work used the constant curvature assumption in each bending section, and then calculates the center of masses for the section as well as the rigid section breaks. The energies at these center of masses are calculated to find the Lagrangian dynamics with respect to the PAM lengths. This work assumed the weight of each section is evenly distributed throughout that section. The ossicle weight is assumed to be part of the bending section, but no additional influence of the ossicles is modeled.



Figure 1: Three section arm with ossicles installed.

Constant curvature kinematics appear in the review by Webster [18]. The constant curvature modeling equations are expressed for the position and orientation of section i , where section $i = 1$ is the proximal section. The rotation of the section is oriented so that the x-axis is in the same plane at the beginning and end of each section.

$$p_{CC_i}(s) = \begin{bmatrix} h_i \cos \phi_i \frac{1 - \cos \theta_i s}{\theta_i} \\ h_i \sin \phi_i \frac{1 - \cos \theta_i s}{\theta_i} \\ h_i \frac{\sin \theta_i s}{\theta_i} \end{bmatrix} \quad (1)$$

$$R_{CC_i} = \begin{bmatrix} \cos^2 \phi_i (\cos \theta_i - 1) + 1 & \sin \phi_i \cos \phi_i (\cos \theta_i - 1) & \cos \phi_i \sin \theta_i \\ \sin \phi_i \cos \phi_i (\cos \theta_i - 1) & \sin^2 \phi_i (\cos \theta_i - 1) + 1 & \sin \phi_i \sin \theta_i \\ -\cos \phi_i \sin \theta_i & -\sin \phi_i \sin \theta_i & \cos \theta_i \end{bmatrix} \quad (2)$$

Expressions for the section length, l , bending angle, θ , and plane of bending, ϕ . A 2D representation of the proximal section orientation is shown in Fig. 2 with a point mass after $s = 1$ representing the concentration of mass of the section plate. For the distal section this mass would also include any added mass during experimental testing.

The bending plane expression changes based on the orientation of the PAMs relative to the section definition. The derivation method of ϕ for different PAM orientations can be found in the Constant Curvature Review [18]. The first and third section have PAM $i1$ on the positive x-axis, and the second section has PAM $i2$ on the negative x-axis.

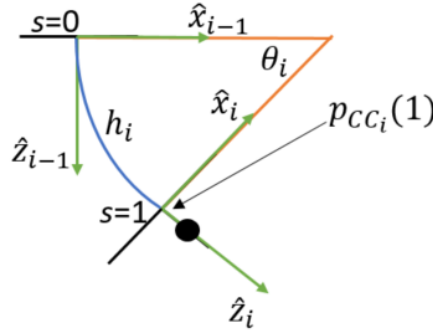


Figure 2: Single section orientation used in this work. Gravity acts in the positive \hat{z}_0 direction and ϕ_i is a rotation about \hat{z}_{i-1} .

$$h_i = h_{i0} + \frac{l_{i1} + l_{i2} + l_{i3}}{3} \quad (3)$$

$$\theta_i = \frac{2\sqrt{l_{i1}^2 + l_{i2}^2 + l_{i3}^2 - l_{i1}l_{i2} - l_{i1}l_{i3} - l_{i2}l_{i3}}}{3r_i} \quad (4)$$

$$\phi_{i=1,3} = \tan^{-1} \left(\frac{\sqrt{3}(l_{i2} - l_{i3})}{(l_{i2} + l_{i3} - 2l_{i1})} \right) \quad (5)$$

$$\phi_{i=2} = \tan^{-1} \left(\frac{\sqrt{3}(l_{i3} - l_{i1})}{(2l_{i2} - l_{i3} - l_{i1})} \right) \quad (6)$$

Identities for $\sin(\tan^{-1})$ and $\cos(\tan^{-1})$ can be used to rewrite the expressions in terms of PAM lengths and remove a number of the trigonometric functions from the expressions for position and orientation.

$$\sqrt{x_i^2 + y_i^2} = 2\sqrt{l_{i1}^2 + l_{i2}^2 + l_{i3}^2 - l_{i1}l_{i2} - l_{i1}l_{i3} - l_{i2}l_{i3}} = 3r_i\theta \quad (7)$$

$$p_{CC_i}(s) = \begin{bmatrix} \frac{h_i x_i}{3r_i} \frac{1 - \cos \theta_i s}{\theta_i^2} \\ \frac{h_i y_i}{3r_i} \frac{1 - \cos \theta_i s}{\theta_i^2} \\ h_i \frac{\sin \theta_i s}{\theta_i} \end{bmatrix} \quad (8)$$

$$R_{CC_i} = \begin{bmatrix} 1 + \frac{x_i^2}{9r_i^2} \frac{\cos \theta_i - 1}{\theta_i^2} & \frac{x_i y_i}{9r_i^2} \frac{\cos \theta_i - 1}{\theta_i^2} & \frac{x_i}{3r_i} \frac{\sin \theta_i}{\theta_i} \\ \frac{x_i y_i}{9r_i^2} \frac{\cos \theta_i - 1}{\theta_i^2} & 1 + \frac{y_i^2}{9r_i^2} \frac{\cos \theta_i - 1}{\theta_i^2} & \frac{y_i}{3r_i} \frac{\sin \theta_i}{\theta_i} \\ -\frac{x_i}{3r_i} \frac{\sin \theta_i}{\theta_i} & -\frac{y_i}{3r_i} \frac{\sin \theta_i}{\theta_i} & \cos \theta_i \end{bmatrix} \quad (9)$$

A Taylor expansion can be performed on the resulting functions of θ leaving the pose of the section in terms of only the PAM lengths. These expressions are differentiable and can be used to find the velocities of the center of gravities of the soft section as well as the rigid end plates.

The center of mass of a section can be found by integrating the position through the section, the integrals of these Taylor expandable functions can be used to find the position with a polynomial function of PAM lengths. The center of mass formulation is inspired by the work of Godage et al. [9], but this

work separates the effect of the break between sections where a large amount of the mass is located from the continuously bending lightweight PAM section.

$$\beta_i = \int_0^1 p_{CC_i} ds = \begin{bmatrix} \frac{h_i x_i}{3r_i} \int_0^1 \frac{1 - \cos \theta_i s}{\theta_i^2} \\ \frac{h_i y_i}{3r_i} \int_0^1 \frac{1 - \cos \theta_i s}{\theta_i^2} \\ h_i \int_0^1 \frac{\sin \theta_i s}{\theta_i} \end{bmatrix} \quad (10)$$

$$\frac{1 - \cos \theta_i s}{\theta_i^2} = -\frac{s^2}{2} + \frac{\theta_i^2 s^4}{24} - \frac{\theta_i^4 s^6}{720} + O(\theta_i^6 s^8) \quad (11)$$

$$\frac{\sin \theta_i s}{\theta_i} = s - \frac{\theta_i^2 s^3}{6} + \frac{\theta_i^4 s^5}{120} + O(\theta_i^6 s^7) \quad (12)$$

The positions of the center of masses of the bending sections, p_{β_i} , and non-bending section breaks, p_{M_i} can be found with the following equations, where p_i is the end of the i^{th} bending section and section divider, and $p_{M_{icli}}$ is the position of the end of the section divider with respect to the end of the previous section.

$$p_i = p_{CC_i}(1) + R_{CC_i} p_{M_{icli}} \quad (13)$$

$$p_{\beta_1} = \beta_1 \quad (14)$$

$$p_{\beta_2} = p_1 + R_{CC_1} \beta_2 \quad (15)$$

$$p_{\beta_3} = p_1 + R_{CC_1} p_2 + R_{CC_1} R_{CC_2} \beta_3 \quad (16)$$

$$p_{M_1} = p_{CC_1}(1) + \frac{1}{2} R_{CC_1} p_{M_{icli}} \quad (17)$$

$$p_{M_2} = p_1 + R_{CC_1} p_{CC_2}(1) + \frac{1}{2} R_{CC_1} R_{CC_2} p_{M_{icli}} \quad (18)$$

$$p_{M_3} = p_1 + R_{CC_1} p_2 + R_{CC_1} R_{CC_2} p_{CC_3}(1) + \frac{1}{2} R_{CC_1} R_{CC_2} R_{CC_3} p_{M_{icli}} \quad (19)$$

The partial derivatives with respect to the change in length can be taken to form the Jacobian relationship of the point velocity to the PAM velocities. The Jacobians can be used to find the gravity vector, G ,

$$G = \frac{\partial V_E}{\partial l} = (J_{\beta_1} m_1 + J_{\beta_2} m_2 + J_{\beta_3} m_3 + J_{M_1} M_1 + J_{M_2} M_2 + J_{M_3} M_3)^T \begin{bmatrix} 0 \\ 0 \\ g \end{bmatrix} \quad (20)$$

and can be related to the PAM force

$$G(l) = F(L_0, l, P) \quad (21)$$

the PAM force model is modeled according Pillsbury et al. [13]. Additional sources of potential energy not captured by the PAM force model such as the bending energy to bend pressurized PAMs could be further investigated to improve the model fit if necessary.

Dynamic validation will be required in the future, but as a initial step quasi-static validation of this model will be conducted using the arm with ossicles. The arm with ossicles will also be compared to an ossicle-free arm.

3 Testing of Ossicle Arm

The three section arm with three PAMs per section was experimentally evaluated with and without an ossicle-inspired structure running the length of each section. The arm was tested in five configurations that sweep out all the single muscle per section motions. For evaluating the performance, any additional single muscle combinations are mirrored by the ones tested in this study. The PAMs were manually pressurized beginning with the most distal section, then the medial section and finally the proximal section. The depressurization was done in the reverse order, proximal, medial, then distal. The order was chosen to minimize effects of unactuated PAMs in the more distal sections. The series of test were conducted with and without ossicles. The distal sections of the appendage have been previously compared by considering the angle achieved at the end of the section under load, but this comparison is complicated for multi-section appendages due to differences in the behavior of distal sections effecting the proximal sections. To compare the two cases the area traced by the tip will be compared at each load case. This captures the cumulative effect of the ossicles throughout the arm.

3.1 Model Validation

To validate the modeling techniques the average pressure versus angle was compared to the average modeled pressure for that angle. The average error was calculated separately for each section and load case and averaged over the five tests. The model output was calculated using the positions and PAM length determined from the experimental data. The model performs best for low loads and more distal sections, Fig. 3. Figure 4 shows the modeling results for the distal section with no weight the medial section with the max test load of 250 g, and the proximal section with 100 g.

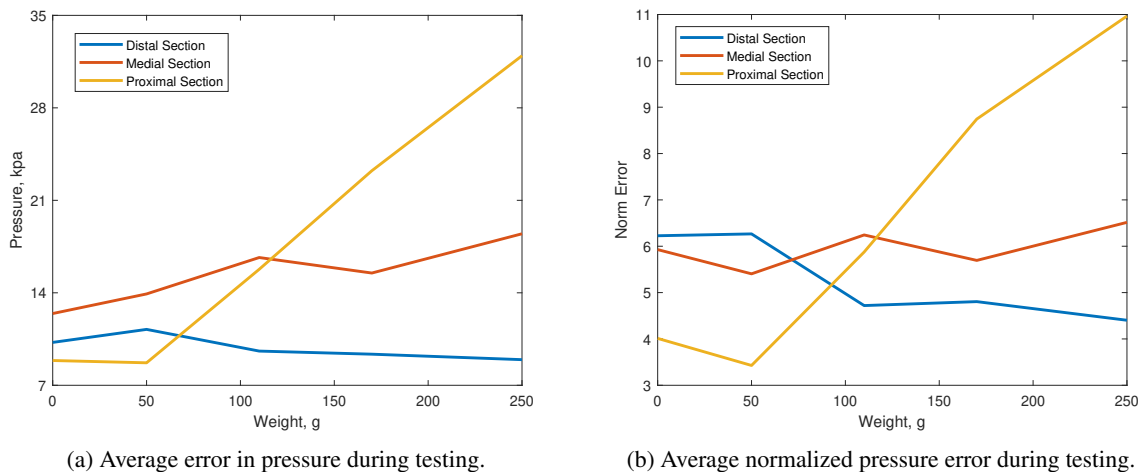
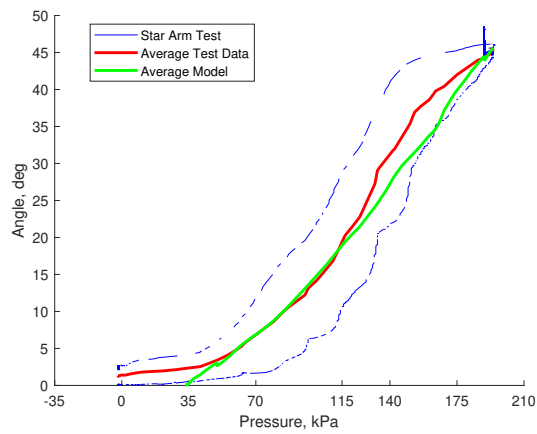
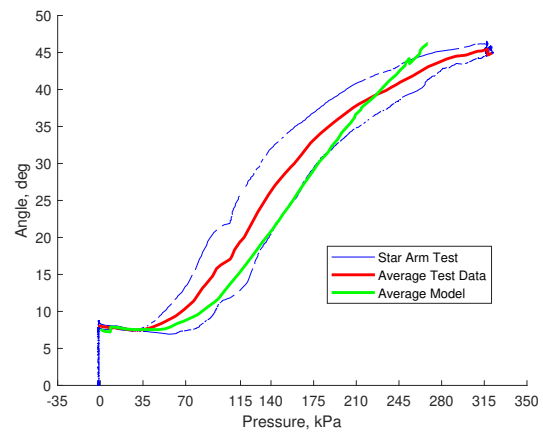


Figure 3: Modeling errors for all five test cases across all five loading conditions.

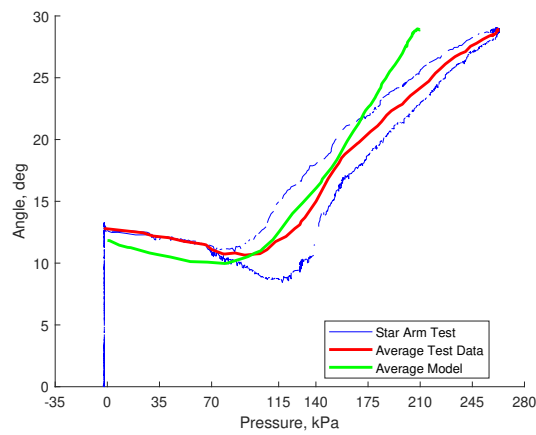
The ossicle structure was designed to interact and limit bending at approximately 45° , a similar model could be incorporated at angles above the design value to improve the model at high angles for the medial and distal sections. To improve modeling and reduce the effects of non-active PAMs, the ossicle structure could be sized such that the PAMs are contracted and pressurized when in a straight arm position, allowing the initial stiffness of the system to be tailored to the desired application. Additionally operation in environments which reduce gravitational impact, space or water, would be beneficial. One way to improve



(a) Distal section with no load.



(b) Medial section with 250 g of weight.



(c) Proximal section with 110 g of weight at the tip.

Figure 4: Angle pressure relationship modeling results for three test cases.

model fitting is improving PAM modeling in the low force and pressure regime. Solutions include a low and high pressure model, higher order PAM modeling or additional considerations of effects on PAM behavior, such as bending.

3.2 Effect of Ossicles

To study the effect of adding ossicles to the arm, the five motions that were tested can be rotated by 120° and 240° to represent the same combination of muscles for the other two proximal section PAMs. Four of the motions are non-planar and can be reflected about the plane of the proximal PAM, and then rotated for the remaining twelve motions. This procedure generates all 27 combinations of one active PAM per section. The procedure to track the tip position of the arm for a single motion is shown in a top down view in Fig. 5.

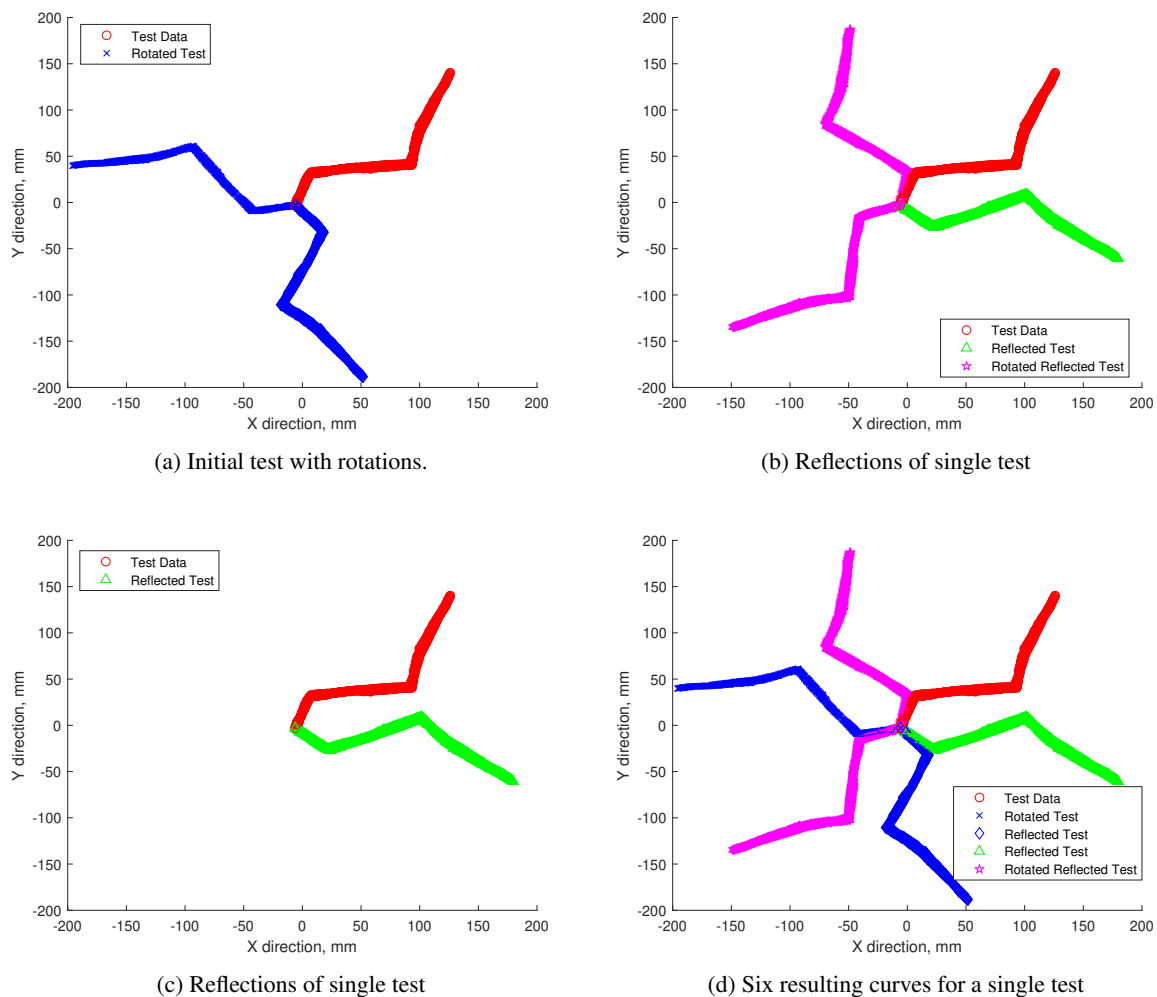


Figure 5: Procedure to construct other tip traces for untested muscle combinations.

This procedure was applied to both the ossicle and non-ossicle tests for each of the five loading conditions. Ossicles have been shown to improve the load capacity of a single section PAM soft robot. To

compare the cumulative effect of ossicles in each section, we consider the X-Y planar projection. This projection will be used to bound the area reached by the arm to compare the effect of adding ossicles. The boundary enclosing these curves were found using a shrink factor of $s = .091$. This shrink factor was chosen by performing a sweep of shrink factors from $s = 0$ to $s = 1$, where $s = 0$ represents a convex hull of the set of points. The chosen shrink factor provided the minimum area ratio for the unloaded test case. The planar projections for the zero load and 250 g load cases are shown in Fig. 6. The ratio of the areas comparing the effect of adding ossicles to the soft structure is shown for all five load cases in Fig. 7. The average area ratio in the no load case of the sweep conducted was 1.15.

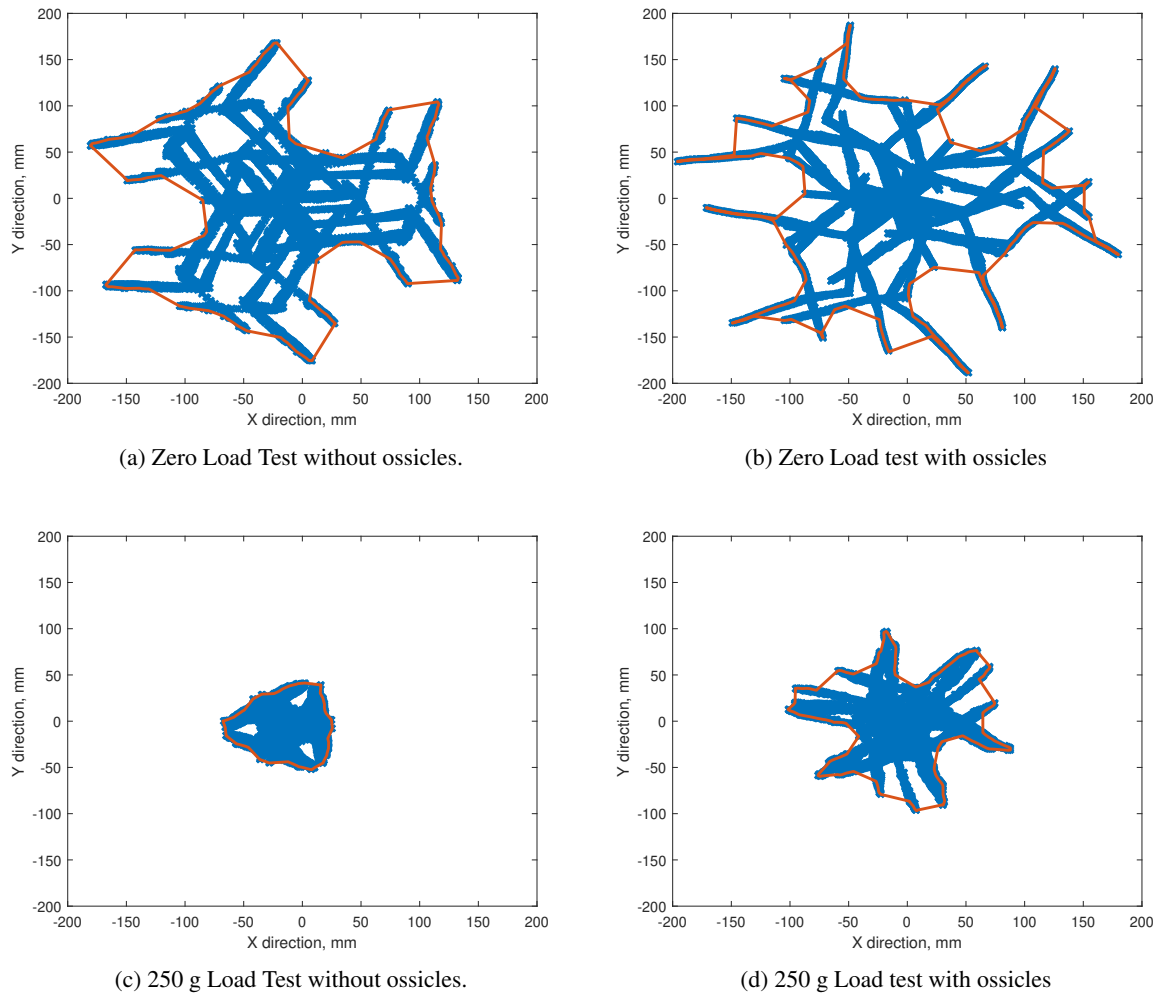
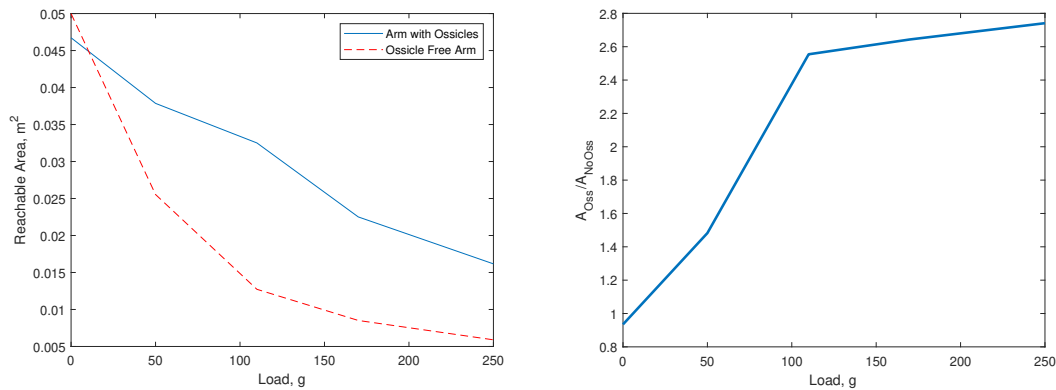


Figure 6: Planar view of test results for no load and highest load 250 g. Colors are consistent with Fig. 5, red is the boundary for the given shrink factor, blue is the processed data.

4 Conclusions

In this work a three section, nine PAM soft robotic manipulator constructed, modeled, and tested. This manipulator was tested with five different muscles combinations and five load cases to study the



(a) Bounded area for each load case with and without ossicles. (b) Ratio of bounded area of the ossicle test case compared to the no ossicle test case.

Figure 7: Effect of load on ossicle structure.

static model and effect of adding a bio-inspired ossicle structure. The constant curvature center of mass model developed was shown to work best at low loads and for the more distal sections. Improvements to PAM modeling and ossicle design should help improve the static modeling especially for the proximal section. Overall the addition of ossicles improved the ability of the manipulator to handle loads placed at the tip. When 250 g was hung from the end of the arm, the arm with ossicles was able to reach an area 2.6 times greater than that reached by the ossicle-free arm.

5 Acknowledgments

Research support was provided by the U.S. Office of Naval Research under a Basic Research Challenge grant, award no. N000141712063, entitled "SEA-STAR: Soft Echinoderm-Inspired Appendages for Strong Tactile Amphibious Robots." Additional support was provided to the first authors under a National Science Foundation Graduate Research Fellowship Program under Grant No. DGE 1322106. All opinions, findings, and conclusions or recommendations expressed herein are those of the authors.

REFERENCES

- [1] A. Bartow, A. Kapadia, and I. Walker. A novel continuum trunk robot based on contractor muscles. ... on *Signal Processing, Robotics, and ...*, pages 181–186, 2013.
- [2] G. S. Chirikjian. Hyper-redundant manipulator dynamics: a continuum approximation. *Advanced Robotics*, 9(3):217–243, jan 1994.
- [3] R. W. Colbrunn. *Design and control of a robotic leg with braided pneumatic actuators*. PhD thesis, Case Western Reserve University, 2000.
- [4] R. Deimel and O. Brock. A Novel Type of Compliant , Underactuated Robotic Hand for Dexterous Grasping. *Proceedings of Robotics: Science and Systems*, 2014.
- [5] K. C. Galloway, K. P. Becker, B. Phillips, J. Kirby, S. Licht, D. Tchernov, R. J. Wood, and D. F. Gruber. Soft Robotic Grippers for Biological Sampling on Deep Reefs. *Soft robotics*, 3(1):23–33, mar 2016.

- [6] K. C. Galloway, P. Polygerinos, C. J. Walsh, and R. J. Wood. Mechanically programmable bend radius for fiber-reinforced soft actuators. In *2013 16th International Conference on Advanced Robotics, ICAR 2013*, 2013.
- [7] N. Giri and I. Walker. Continuum robots and underactuated grasping. *Mechanical Sciences*, 2(1):51–58, feb 2011.
- [8] I. S. Godage, D. T. Branson, E. Guglielmino, and D. G. Caldwell. Pneumatic muscle actuated continuum arms: Modelling and experimental assessment. In *2012 IEEE International Conference on Robotics and Automation*, pages 4980–4985. IEEE, may 2012.
- [9] I. S. Godage, R. Wirz, I. D. Walker, and R. J. Webster. Accurate and Efficient Dynamics for Variable-Length Continuum Arms: A Center of Gravity Approach. *Soft Robotics*, 2(3):96–106, sep 2015.
- [10] C. S. Kothera, M. Jangid, J. Sirohi, and N. M. Wereley. Experimental characterization and static modeling of McKibben actuators. *Journal of Mechanical Design*, 131(9):091010, sep 2009.
- [11] S. Mao, E. Dong, H. Jin, M. Xu, S. Zhang, J. Yang, and K. H. Low. Gait Study and Pattern Generation of a Starfish-Like Soft Robot with Flexible Rays Actuated by SMAs. *Journal of Bionic Engineering*, 11(3):400–411, jul 2014.
- [12] W. McMahan, V. Chitrakaran, M. Csencsits, D. Dawson, I. Walker, B. Jones, M. Pritts, D. Dienno, M. Grissom, and C. Rahn. Field trials and testing of the OctArm continuum manipulator. In *Proceedings 2006 IEEE International Conference on Robotics and Automation, 2006. ICRA 2006.*, pages 2336–2341. IEEE, 2006.
- [13] T. E. Pillsbury, N. M. Wereley, and Q. Guan. Comparison of contractile and extensile pneumatic artificial muscles. *Smart Materials and Structures*, 26(9):095034, sep 2017.
- [14] F. Renda, M. Giorelli, M. Calisti, M. Cianchetti, and C. Laschi. Dynamic Model of a Multibending Soft Robot Arm Driven by Cables. *IEEE Transactions on Robotics*, 30(5):1109–1122, oct 2014.
- [15] R. M. Robinson, C. S. Kothera, R. M. Sanner, and N. M. Wereley. Nonlinear Control of Robotic Manipulators Driven by Pneumatic Artificial Muscles. *IEEE/ASME Transactions on Mechatronics*, 21(1):55–68, feb 2016.
- [16] E. Tatlicioglu, I. D. Walker, and D. M. Dawson. New dynamic models for planar extensible continuum robot manipulators. In *IEEE International Conference on Intelligent Robots and Systems*, 2007.
- [17] R. D. Vocke, C. S. Kothera, A. Chaudhuri, B. K. S. Woods, and N. M. Wereley. Design and testing of a high-specific work actuator using miniature pneumatic artificial muscles. *Journal of Intelligent Material Systems and Structures*, 23(3):365–378, jan 2012.
- [18] R. J. Webster and B. A. Jones. Design and Kinematic Modeling of Constant Curvature Continuum Robots: A Review. *The International Journal of Robotics Research*, 29(13):1661–1683, nov 2010.

WORKSPACE ANALYSIS OF MULTI-SECTION CONTINUUM PNEUMATIC ARM

Jacek Garbuliński and Norman M. Wereley

Department of Aerospace Engineering
University of Maryland
College Park MD 20742 USA
Email: jacek@umd.edu, wereley@umd.edu

Key words: Soft Robotics, Continuum Robotics, Pneumatic Artificial Muscle, Workspace

Abstract. Soft Robots achieve desired motion by deformation of their elastic links and offer the ability to adapt to unstructured environments and manipulate objects of varying sizes. Inherent elasticity and continuity allow for whole-arm operations such as grasping, wrapping, and lifting without damaging the manipulated object. In order to find the right base orientation and geometrical configuration of a continuum pneumatic arm (CPA) for tasks that require keeping the manipulated object at a fixed orientation, an approach to solve the forward kinematics and analyze the robot's workspaces is developed. The studied soft robotic arm is composed of multiple sections where each consists of three extensile pneumatic artificial muscles (PAMs) acting as both actuator and structure of the arm. The work includes analysis of the effective workspaces of the arm defined by points in space that the end-effector can reach, as well as fixed orientation workspaces (FOWs) defined by position of the end-effector at a given orientation. FOWs provide useful information for operations that require keeping manipulated object at constant angles such as in, e.g. boring, sealing, pushing/pulling handles or inserting bolts during on-site maintenance or repair of vehicles. The workspaces are characterized by metrics associated with their three-dimensional shape, volume and dexterity.

1 Introduction

Pneumatic artificial muscles (PAMs) are compliant actuators that offer high force-to-weight ratio and do not have any moving parts. PAMs are composed of elastomeric, tubular bladder surrounded by a braided sleeve and two end-fittings that seal the bladder and hold the sleeve's ends (Fig. 1). Once pressurized, PAMs contract or extend depending on the braid angle: contractile for angles larger than 35.26° , and extensile when the angles are smaller. Extensile PAMs (E-PAM) offer an advantage over contractile PAMs in terms of stroke. Theoretically, 200% extension can be achieved at the braid angle of 22° [12] although in practice for extensile McKibben muscles values up to 80% has been reported [6,8]. The exceptionally large stroke of extensile PAMs and relatively high force makes them a viable choice for continuum robots.

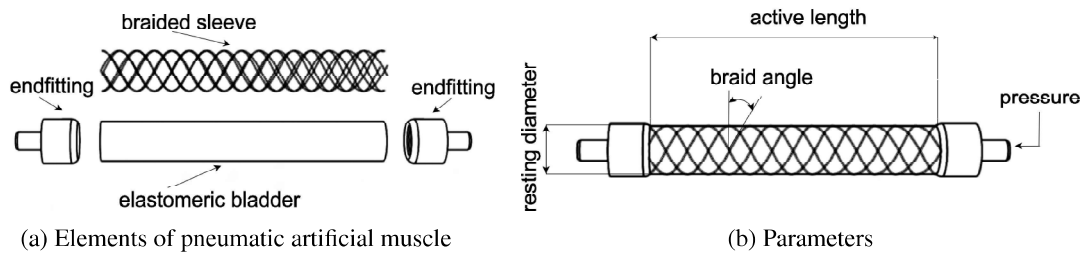


Figure 1: Overview of pneumatic artificial muscle

Continuum robots are bio-inspired robots which change their shape by contraction, extension and bending of actuators. So far, there have been numerous attempts to design a soft robotic arm that can grasp and lift objects. OctArm is one of the most comprehensively researched continuum pneumatic arms and it operates using three groups of pneumatic artificial muscles in order to move and be able to execute whole-arm operations [6]. An interesting extension of the continuum PAM-driven robot concept is to add ossicles [7] serving as a backbone-like structure which decrease required pressure to move loads and increase the maximum angle of section's curve (Fig. 2). One of the first tasks in the design process is to develop a robot's kinematics model. For continuum robots, some of the constant curvature models are: Jones Kinematic Model, Godage Kinematic Model, Allen Kinematic Model and Walker-Frazelle Approximation Model. Jones', Allen's, Walker-Frazelle assume piece-wise constant curvature of the robotic arm whereas Godage model approximates constant curvature with modal shape functions which makes the model numerically stable at all configurations [1,4]. Non-constant curvature models also exist, like those based on the Cosserat Rods theory [10]. When designing a continuum robot for a given set of tasks, it is important to know what moves the robot can conduct. At the time of writing, the OctArm has been one of few PAM-driven arms that have undergone dexterity and workspace analysis [9] or perhaps the only one. In this paper, we look into workspaces of a specific type of continuum robot that composes multiple sections where three PAMs drive each section. A general idea of our PAM-driven multisection continuum arm with ossicles can be drawn from Fig. 2.

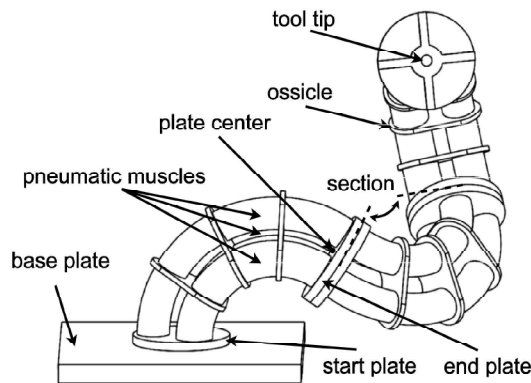


Figure 2: Overview of PAM driven multi-section robotic arm with ossicles

2 Kinematics

We developed a forward kinematic model for a multisection robotic arm. For one section the relationships for angles ϕ and θ as shown in Fig. 3 are:

$$\phi = \text{atan2} \left(\frac{\sin \frac{\pi}{3}}{\frac{L_3 - L_1}{L_2 - L_3} + \cos \frac{\pi}{3}} \right) \quad (1)$$

and

$$\theta = \frac{L_2 - L_3}{a \cdot \sin \phi} \quad (2)$$

where a is the distance between centers of the mounting points of actuators and L_1, L_2, L_3 are the active lengths of the PAMs. We can see that for the case when $L_2 = L_3$ there is a singularity in the expression for ϕ . We evade this by defining the angle at the point of singularity as $\phi = \frac{|L_1 - L_2|}{a \cdot \frac{\sqrt{3}}{2}}$. Identically to [5, 11], we get the transformation matrix for a point positioned on an arc of length L_i :

$$T = \begin{bmatrix} \cos(\phi) \cos(\theta) & -\sin(\phi) \cos(\phi) \sin(\theta) & \frac{L_i \cos(\phi) (1 - \cos(\theta))}{\theta} \\ \cos(\theta) \sin(\phi) & \cos(\phi) \sin(\phi) \sin(\theta) & \frac{L_i \sin(\phi) (1 - \cos(\theta))}{\theta} \\ -\sin(\theta) & 0 & \cos(\theta) \\ 0 & 0 & 1 \end{bmatrix} \quad (3)$$

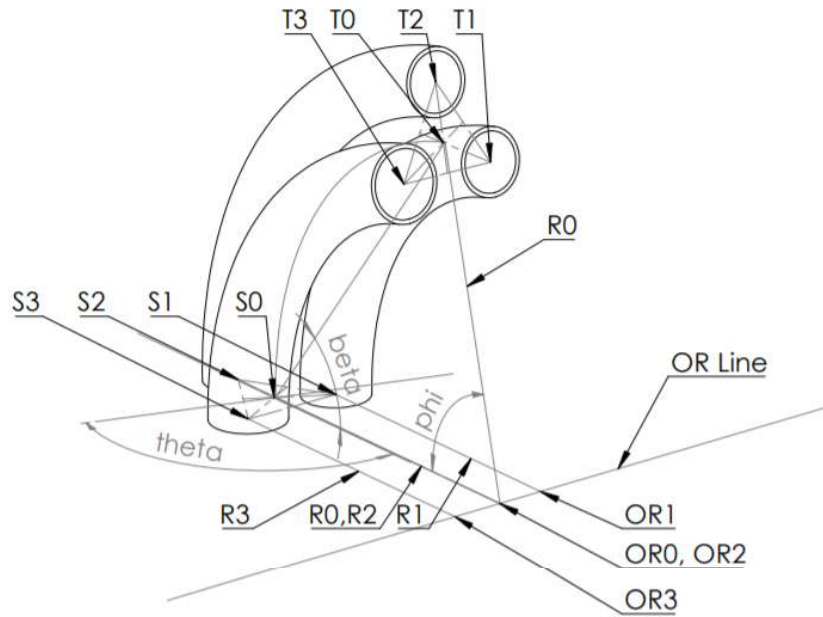


Figure 3: Section geometry

To calculate orientation and position of each section we define rotations as quaternions and take into account what the distances are between the active lengths of PAMs representing the rigid plate and endfittings. With this approach we also avoid singularity limitations of Euler angles [2–4]. We create a

quaternion q_k combining the angle of rotation of the next start plate relative to the preceding end plate and the rotations by angles θ and ϕ . For the end plate mounting point of X_{k-1} of $(k-1)^{th}$ section and x_{0k-1} being the vector along the thickness of the mounting plates we get the position of the next mounting point:

$$X_k = X_{k-1} + q_{k-1}x_{0k-1}q_{k-1}^{-1} \quad (4)$$

The above equations may involve more terms in addition if we specify a larger number of intermediate translations and rotations between given sections. This framework allows us to easily change the expressions in order to be able to study different types of section setups such as when a robot that has multiple sections in parallel as in Fig. 4.

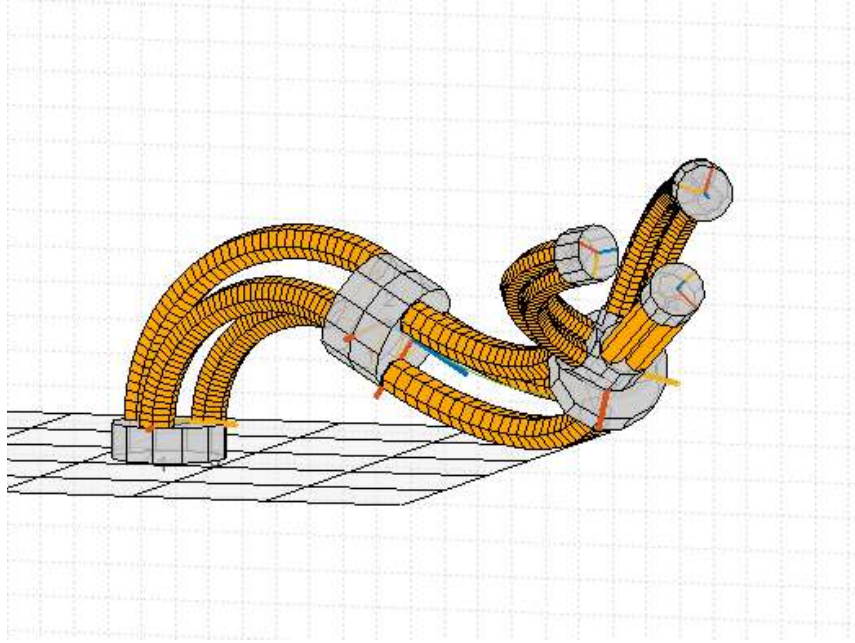
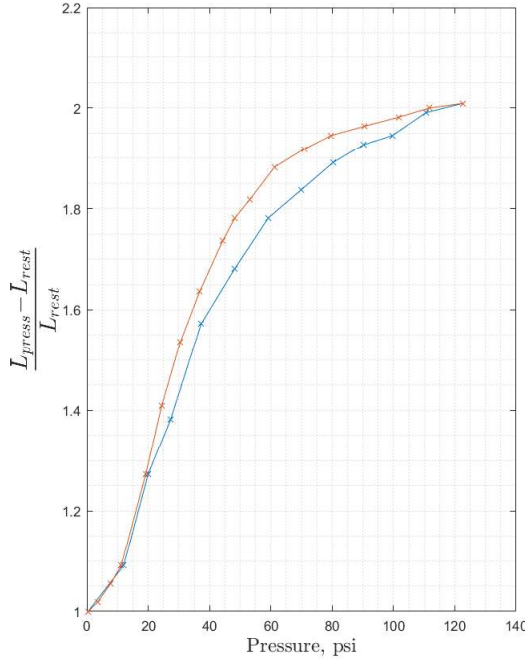


Figure 4: A graphic representation of kinematics model for continuum robot with multiple section in parallel which allows to use multiple tools using different distances and angles.

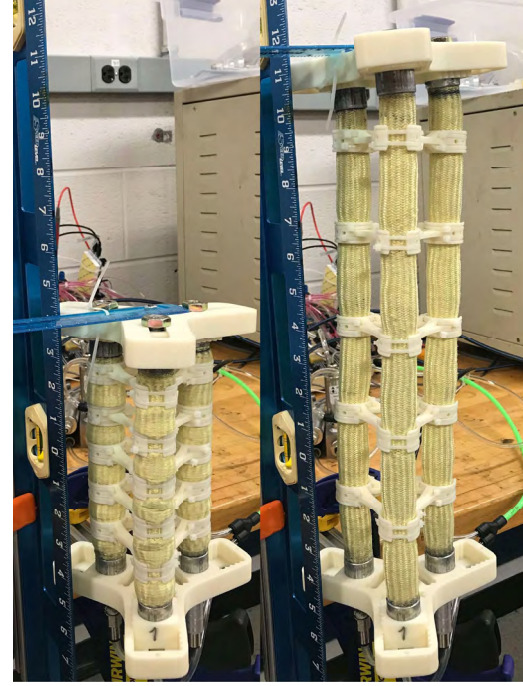
3 Workspace Analysis

3.1 Effective Workspace

Effective workspace is a volume created by all possible configurations of a robot in space. In this work, the approximation of a robot's workspace is obtained computationally. For our analysis, we assume that the extension ratio is defined as $ER = \frac{L_{press} - L_{rest}}{L_{rest}}$ and has a maximum value at 2 for our workspace analysis. L_{press} is the active length of the actuators in a section where each actuator is held at the same pressure. We assume that the maximum extension ratio is invariant of the robot's curvature. Fig. 5b presents data acquired for free extension of arm's section with ossicles.



(a) Pressure vs. Free-Extension relationship



(b) Continuum pneumatic arm's section.
Left: Resting; Right: Pressurized at 122 psi.

Figure 5: Pressure vs. Free-Extension relationship

We developed a computational algorithm that allows us to look at workspaces for different configurations of robots and assess their effective workspace shapes together with qualitative analysis of their workspace density. We define the workspace density as a measure of the quantity of points in an surrounding sphere weighted by function of their distance from the center of the sphere. We enclose the workspace in a cube of side length equal to twice the maximum absolute value of coordinates x, y, z defined as m . Then, an equal spaced 3D grid of n^3 points is created. For each point in the grid we look at the end-effector positions in its proximity which we defined as a sphere of radius r_{max} and compute the density score of the point. In this study we used $r_{max} = 10 \cdot m/n$. The density score for each point in the grid is a sum of gaussians defined as follows:

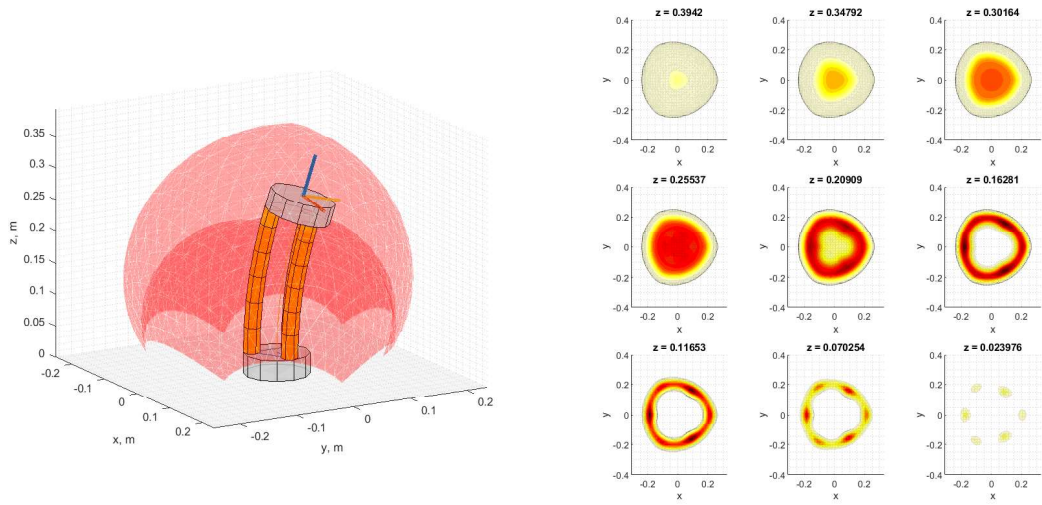
$$\rho_{score} = \sum_{i=1}^n \frac{1}{\sqrt{2 \cdot \pi \cdot r_{max}^2}} e^{-\frac{1}{2} \frac{r_i^2}{r_{max}^2}} \quad (5)$$

It allows us to create visual representation of the workspace shape and dexterity measure using density score. To generate a workspace approximation with points we compute a set of k configurations of the robotic arm by incrementally changing the actuators' lengths which gives us a set of points the end-effector can reach.

We decided not to use changes in pressure since our experimental robotic arm uses a new variant of extensible PAMs which has not been characterized extensively yet, hence, we use changes in actuator length to stay agnostic of the actuator characteristics. We also assume that the ossicles help in keeping

the robot shape close to the constant-curvature assumption and have minimal effect on the kinematics of a PAM-driven continuum robot.

For one section robotic arm, the workspace is characterized by the following shape and density score as the dexterity measure shown in Fig. 6. The light red surface is the boundary of the effective workspace of the section. Due to the fact that the workspace boundary is transparent, places where the surface overlaps are darker red. It can be observe that the workspace's shape resembles a closed tulip or Taj Mahal's dome. The workspace has been generated by computing 20^3 different configurations for a manipulator of one section with PAMs mounted at a distance of 6.7 cm from one another. The resting length for each PAM is 16.5 cm and the extension ratio is 2. The thicknesses of the plates (which include non-active elements: mounting plate and PAMs' endfittings) has been set to 3.2 cm.



(a) Effective workspace and an example of a one section robot's possible configuration.

(b) Slices of workspace volume characterized by p_{score} .

Figure 6: Effective workspace of a 1-section continuum robotic arm

For a two section robotic arm, the workspace is characterized by the shape and dexterity presented in Fig. 7. The Fig. 7a was computed for 13^6 possible configurations, whereas Fig. 7b used 7^6 possible configurations. The robotic arms composes of two sections which are identical to the one in the one-section example. An additional parameter in this case is the rotation of the second section relative to the first one. The second section start plate is rotated by 60° around the axis of symmetry of the first section end plate. The important thing is to note that there is a region inside the workspace where the arm cannot move. This can be observed in in the Fig. 7 where in the 3D the region is represented as the dark red area and in the dexterity plots where we can observe that the workspace resembles a an apple with some of its interior removed.

For three-section robotic arm, the workspace is characterized by the shape and dexterity presented in Fig. 8. The robotic arm composes of three sections which are identical to the one in the one-section example. An additional parameters in this case are the rotation of the second and third sections relative to the preceding ones. Both rotations are 60° around the axis of symmetry of the previous section end plate.

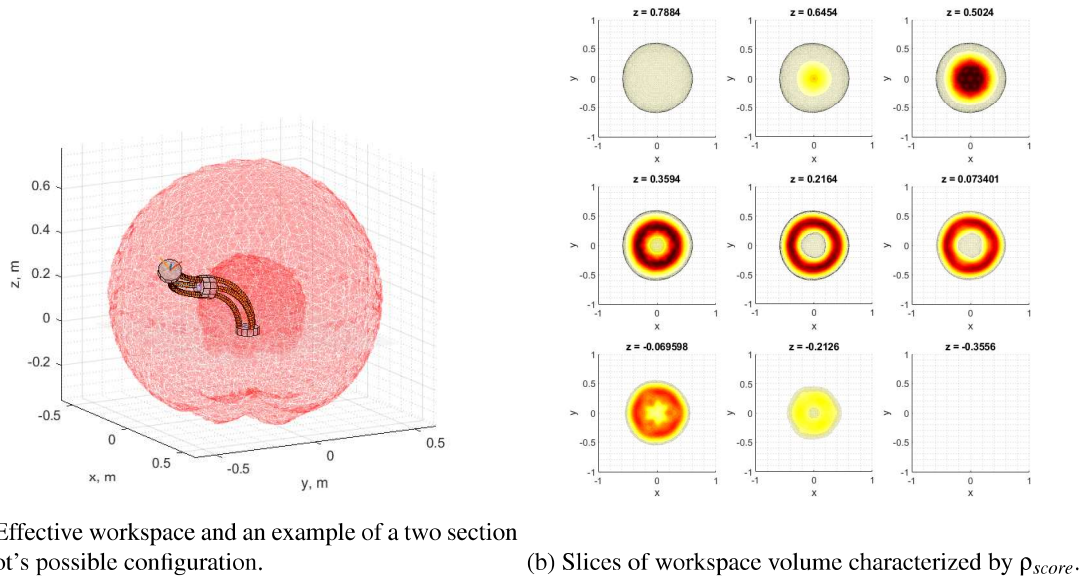


Figure 7: Effective workspace of a 2-section continuum robotic arm

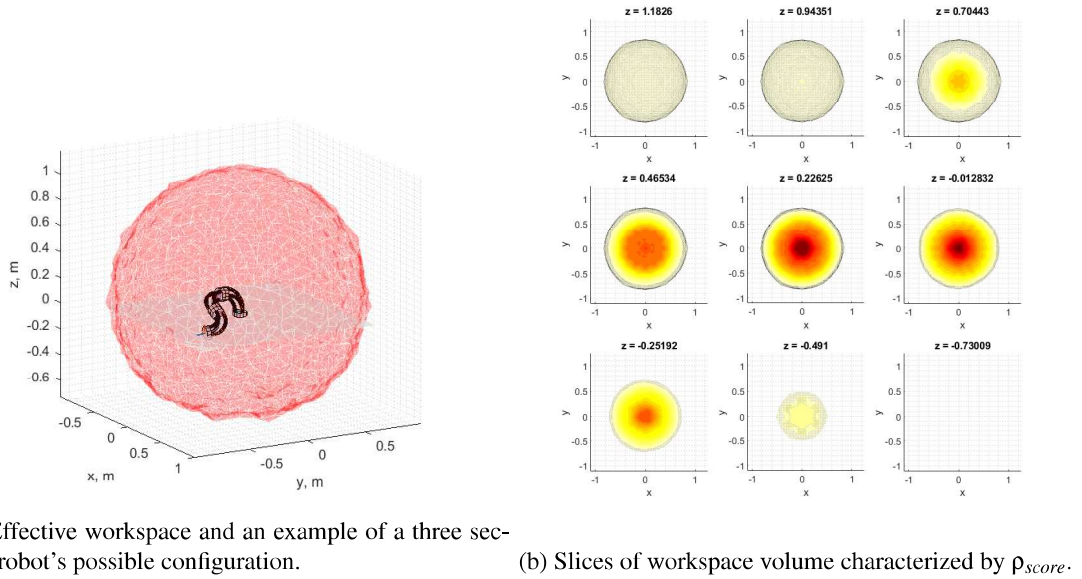


Figure 8: Effective workspace of a 3-section continuum robotic arm

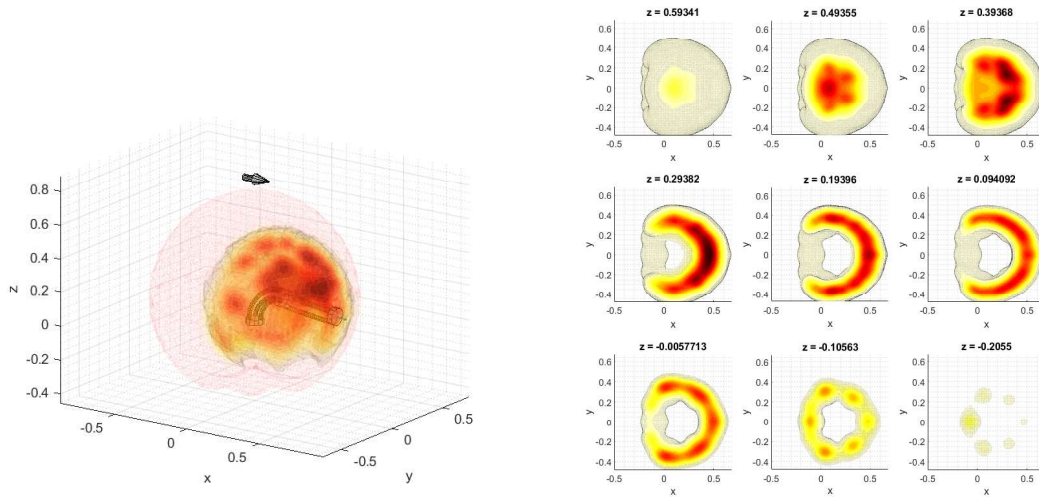
3.2 Fixed Orientation Workspace

As inherent to their flexible nature, continuum pneumatic arms (CPA) are superior for work in unstructured environments. Possible applications of CPAs are on-site maintenance including inspection

and repair of vehicles (reaching confined spaces), space robotics (high force-weight ratio), safer human-robot cooperation (compliance), crop harvesting and additive manufacturing of large structures (large and high-dexterity workspace). All of the applications mentioned above often involve tasks that require to move along lines or planes keeping the end-effector at a constant orientation. Those can be: pushing/pulling handles, spacecraft docking assistance, painting, serving food and drinks, fused filament fabrication or maintenance of surfaces. This is the reason why we aim to uncover qualitative trends for fixed-orientation arm configurations so that we have a better understanding of what are the capabilities of CPAs in terms of orienting its end effector.

The algorithm for fixed workspace generation is an extension of the algorithm we used for the effective workspaces. The only difference is that we constrain the end-effector to a subset of points where the orientation of the end-effector falls into a desired direction within some tolerance. In this paper the tolerance is defined as the apex angle of a cone created around the axis of a direction vector representing the fixed orientation. All the configurations for which the end-effector direction vector lands inside the cone belong to the workspace. Although for figures 9, 10 we chose an angle of 15° , it should be chosen taking into account the precision of a task a robot is to perform.

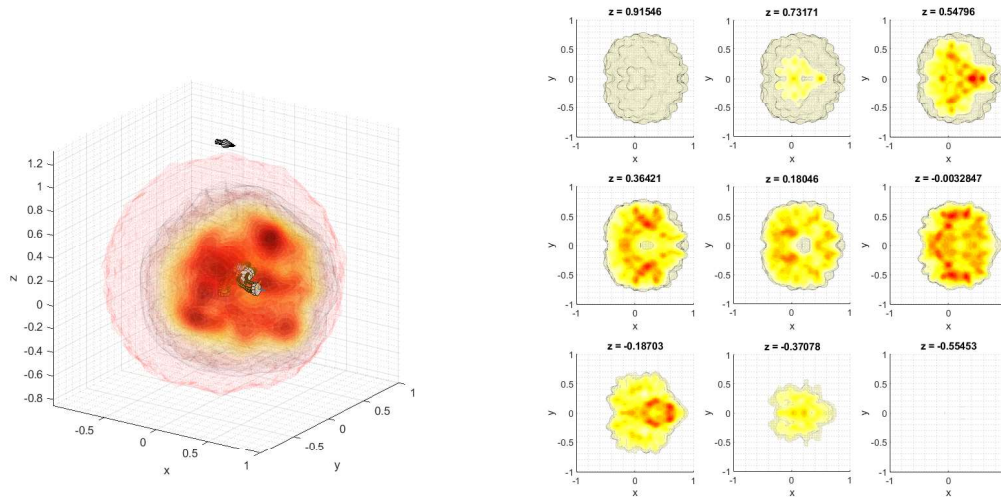
For two section robotic arm, the fixed orientation workspace in the gray arrow direction ($x = 1, y = 0, z = 0$) is characterized by the shape and dexterity presented in Fig. 9. The Fig. 9 was computed for 6^9 possible configurations and a grid of $50 \times 50 \times 50$ points for point density calculation. The arm used is the same as in the e.g. for the effective workspace of 2-section robotic arm. An additional parameter in this case is the rotation of the second section relative to the first.



(a) Fixed orientation workspace and an example of a three section robot's possible configuration. (b) Slices of workspace volume characterized by p_{score} .

Figure 9: Fixed orientation workspace of a two section robotic arm. For configurations constrained by the end-effector orientation represented by the gray arrow with 15° tolerance angle.

For three section robotic arm case as in Fig. 10, the arm is identical to the one in the e.g. of the effective workspace of 3-section robotic arm.



(a) Fixed orientation workspace and an example of a three section robot's possible configuration.

(b) Slices of workspace volume characterized by p_{score} .

Figure 10: Fixed orientation workspace of a three section robotic arm. For configurations constrained by the end-effector orientation represented by the gray arrow with 15° tolerance angle.

4 Conclusion

Kinematics model of a multi-section continuum robotic arm has been developed. An algorithm for computing shape and dexterity measure have been proposed and implemented. The work gives insight about the shape of workspaces of 1, 2 and 3-section robotic arms in one arbitrarily chosen orientation and provides information about the dexterity of the arms for constraints of the orientation of the end-effector. Some of the future work may involve quantitative analysis of fixed orientation workspaces. Having the idealized model of kinematics, it is essential to find out what is the gap between reality and the model for a continuum pneumatic robot arm with ossicles. A load at the end-effector will undoubtedly change the workspace of the robot and pose an exciting topic for future work.

Acknowledgments

The first author thanks the Polish-American Fulbright Commission for a Fulbright Scholarship to enable graduate studies at the University of Maryland. Additional research support was provided by the U.S. Office of Naval Research under a Basic Research Challenge grant, award no. N000141712063, entitled "SEA-STAR: Soft Echinoderm-Inspired Appendages for Strong Tactile Amphibious Robots." Any opinion, findings, and conclusions or recommendations expressed herein are those of the authors. The first author thanks Mr. Jon Chambers and Ms. Sabrina Tigik for sharing their knowledge and discussions during the course of this research.

REFERENCES

- [1] A. Chawla, C. Frazelle, and I. Walker. A comparison of constant curvature forward kinematics for multisection continuum manipulators. In *2018 Second IEEE International Conference on Robotic Computing (IRC)*, pages 217–223. IEEE, 2018.

- [2] E. Coutsias. The quaternions with an application to rigid body dynamics. *for Seminar on Dynamic and Stability Theory*, pages 1–16, 1999.
- [3] J. Diebel. Representing attitude: Euler angles, unit quaternions, and rotation vectors. *Matrix*, 58(15-16):1–35, 2006.
- [4] I. S. Godage and I. D. Walker. Dual quaternion based modal kinematics for multisection continuum arms. In *2015 IEEE International Conference on Robotics and Automation (ICRA)*, pages 1416–1422. IEEE, 2015.
- [5] A. D. Marchese and D. Rus. Design, kinematics, and control of a soft spatial fluidic elastomer manipulator. *The International Journal of Robotics Research*, 35(7):840–869, 2016.
- [6] W. McMahan, V. Chitrakaran, M. Csencsits, D. Dawson, I. D. Walker, B. A. Jones, M. Pritts, D. Di-enno, M. Grissom, and C. D. Rahn. Field trials and testing of the octarm continuum manipulator. In *Proceedings 2006 IEEE International Conference on Robotics and Automation, 2006. ICRA 2006.*, pages 2336–2341. IEEE, 2006.
- [7] T. Pillsbury. *Soft Robotic Appendages Using Pneumatic Artificial Muscles*. PhD thesis, University of Maryland, 2018.
- [8] T. E. Pillsbury, N. M. Wereley, and Q. Guan. Comparison of contractile and extensile pneumatic artificial muscles. *Smart Materials and Structures*, 26(9):095034, 2017.
- [9] D. Trivedi, D. Lesutis, and C. D. Rahn. Dexterity and workspace analysis of two soft robotic manipulators. In *ASME 2010 International Design Engineering Technical Conferences and Computers and Information in Engineering Conference*, pages 1389–1398. American Society of Mechanical Engineers, 2010.
- [10] D. Trivedi, A. Lotfi, and C. D. Rahn. Geometrically exact models for soft robotic manipulators. *Trans. Rob.*, 24(4):773–780, Aug. 2008.
- [11] R. J. Webster III and B. A. Jones. Design and kinematic modeling of constant curvature continuum robots: A review. *The International Journal of Robotics Research*, 29(13):1661–1683, 2010.
- [12] N. M. Wereley and J. M. Sater. *Plants and Mechanical Motion: A Synthetic Approach to Nastic Materials and Structures*. DEStech Publications, Inc, 2012.

BAYESIAN EVALUATION AND REDUCTION OF ECONOMIC RISK FOR STRUCTURAL HEALTH MONITORING USING WEIGHTED REGRESSION

A. IWASAKI^{*} AND S. SHIMIZU[†]

^{*} Division of Mechanical Science and Technology,
Gunma University
1-5-1 Tenjin-cho, Kiryu, 376-8515, Gunma, Japan
e-mail: aiwasaki@gunma-u.ac.jp

[†] School of Science and Technology,
Gunma University
1-5-1 Tenjin-cho, Kiryu, 376-8515, Gunma, Japan
email: t15302055@gunma-u.ac.jp

Key words: Statistical Analysis, Structural Reliability, Probability of Failure, Risk Analysis, Risk Based Maintenance, Bayesian Theorem

Abstract. This study outlines a method to numerically evaluate the probability of failure (PoF) and engineering risk using Bayesian theorem and the diagnostic results of real-time condition monitoring. Engineering risk is defined as the product of the PoF and consequences of failure. While a diagnostic result without any inspection error is ideal when conducting maintenance using real-time monitoring results. However, failure of structure is not caused even if the monitoring method overestimates to a few degree any small damage that can cause failure. Moreover, failure is not caused even if the method underestimates to a few degree any large damage., the inability to model failure dominates, Improving the accuracy of estimating specific damage levels is therefore important in reducing the PoF. Here a method for reducing the risk by improving the diagnostic accuracy of specific damage levels, which is achieved by controlling the sampling ratio of the training data with a weight function, is proposed. The consequences of the overestimation and underestimation of damage differ. The risk due to an underestimation is called failure risk and that due to an overestimation is called economic risk in this research. Here a numerical evaluation of the PoF using Bayesian theorem for each diagnostic result of real-time condition monitoring is proposed, and the effect of weighted regression on risk reduction is discussed. The proposed method is validated by employing it to identify delamination in a CFRP beam via the electric potential change method.

1 INTRODUCTION

The maintenance costs associated with aging infrastructure facilities has recently become an increasing concern. Temporary structures, such as the drainage plant at the Fukushima nuclear power plant, are of particular interest since there is a high degree of uncertainty in both the progression of corrosion and operating environment. Furthermore, inspection errors

are large since there is no established inspection method, and there are concerns regarding exposure during the inspection itself, highlighting the need to establish a risk evaluation method using remote monitoring data. Here we propose a method to evaluate the probability of failure (PoF) of structures using monitoring data and a Bayesian estimation.

It is possible to improve the damage evaluation method when the damage probability is quantitatively evaluated using a damage state evaluation and monitoring data, which reduces the damage probability. Here we consider a procedure that improves the damage evaluation method and also minimizes the risk. The engineering risk for infrastructure maintenance is expressed as the product of the PoF and consequence of failure (CoF). For example, risk-based maintenance [1,2], which takes the risks into account, has demonstrated that efficient facility maintenance can be achieved when considering the importance and urgency of the maintenance. It is possible to perform the appropriate degree of maintenance using damage identification estimation results if the damage is either significantly large or significantly smaller than the damage size determined by the distribution of the acting external force. Therefore, the method to reduce the risk by adjusting the estimation accuracy of a specific damage size is examined in this study.

Here the risk in the proposed method is reduced by using the weighting function, with the appropriate weighting function considered to be different for both the probability of occurrence of each damage size (PoO) and the assumed damage size that causes structural failure. The appropriate weighting functions for risk reduction under various conditions and the effectiveness of the risk reduction method using the weighting function are examined. The proposed method is validated by employing it to identify delamination in a CFRP beam via the electric potential change method [3–7].

2 FAILURE PROBABILITY EVALUATION PROCEDURE

2.1 Bayesian theorem

Bayesian theorem [8–11] is a simple mathematical theorem used for calculating conditional probabilities. In engineering, it is primarily used to assess the structural reliability of materials using small samples [12, 13] (e.g., RBM). Here the theorem is used to estimate the event probability of true damage due to an estimated damage size. Bayesian theorem is generally expressed as:

$$P(E_i | F) = \frac{P(E_i)P(F | E_i)}{\sum_j P(E_j)P(F | E_j)} \quad (i, j = 1, 2, \dots), \quad (1)$$

where $P(E_i)$ is the event probability of event E_i , $P(F | E_i)$ is the conditional probability that event F is caused by event E_i , and $P(E_i | F)$ is the “posterior probability” or the conditional probability that event E_i is caused by event F . When attempting to identify the damage sizes, the damage occurrence a_i is compared to the arbitrarily estimated results $EstA_k$, and the probability $P(EstA_k | a_i)$ that a_i leads to $EstA_k$ is determined. Eq. (1) can then be modified as follows:

$$P(a_i | EstA_k) = \frac{P(a_i)P(EstA_k | a_i)}{\sum_j P(a_j)P(EstA_k | a_j)} \quad (2)$$

where the left side is the posterior probability. Therefore, $P(a_i | EstA_k)$ is the event probability of $EstA_k$ for a true damage size a_i . The event probability distribution of a_i and $EstA_k$ can then be determined by estimating the event probability of each a_i value.

2.2 PoF Evaluation using an estimation of the true damage distribution

Figure 1 shows the PoF evaluation procedure. The learning data are first weighted, and a maximum likelihood estimation is performed using Gibbs sampling to estimate the damage parameter occurrence rate distribution, where the horizontal axis represents the estimated damage values, and the vertical axis represents the probability density function (PDF) (Figure 1; ①). Bayesian theorem is then employed to estimate the damage size event probability distribution and true damage parameter event probability, where the horizontal axis represents the true damage parameter value (Figure 1; ③). The residual strengths are estimated from the damage sizes, forming a residual strength distribution (Figure 1; ④), where the horizontal axis represents the residual strength. Finally, the PoF is evaluated (Figure 1; ⑤) since failure occurs when the external force exceeds the residual strength. Assumed external forces that could cause failure of structure at 15 (Chapter 3), 20, and 25 mm (Chapter 4) of damage in average are employed in this study.

The above-mentioned damage size occurrence distribution is the probability of occurrence of the damage sizes (PoO) that may occur in the target structure. An exponential distribution is used here, but Chapter 3 also examined cases with other distributions (chi-square, normal, Weibull, uniform).

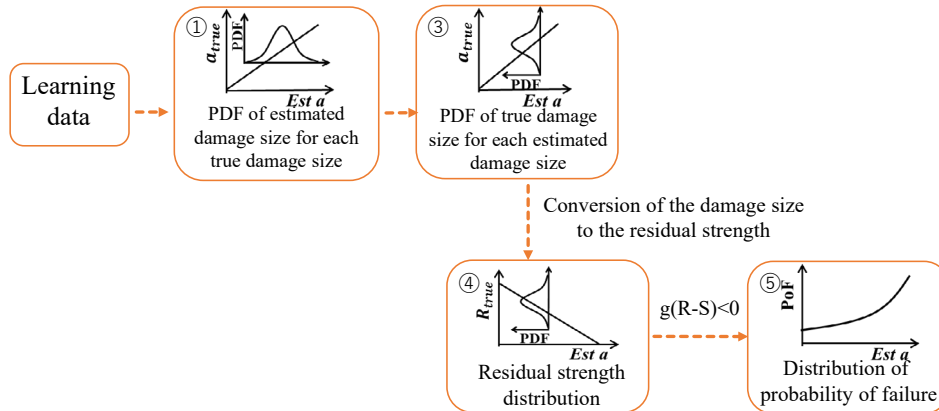


Figure 1: Procedure for estimating PoF.

2.2 Risk evaluation

Figure 2 shows the accidental and economic risks evaluated using the proposed method. Accidental risk is defined as the risk of failure due to an underestimation of the damage size, whereas the economic risk is defined as the risk of unnecessary maintenance costs due to an

overestimation of the damage size. The adjusted PoF (PDF of PoF versus PDF of PoO) is plotted on the vertical axis, and the estimated damage size is plotted on the horizontal axis. The accidental risk is evaluated as the area surrounded by the adjusted PoF and the maintenance threshold. The threshold is set as the accidental risk, and exhibits a constant value (0.03). The economic risk is evaluated as the area surrounded by the adjusted PoF, PoO, and maintenance threshold. This study aims to reduce the economic risk when the accidental risk is constant since the acceptable level of accidental risk is limited.

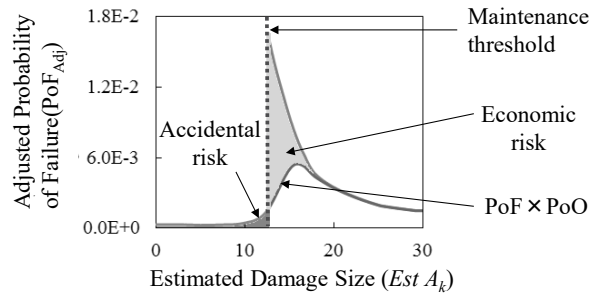


Figure 2: Accidental and economic risks from the estimated PoF.

3 EFFECTIVE WEIGHTED PEAK POSITION FOR RISK REDUCTION OF EACH PRIOR DISTRIBUTION

Figure 3 shows an example of the weighting function for a 5-mm peak position. The vertical axis is the probability density, and the horizontal axis is the damage size. This weighting function is used to evaluate the risk over the 3- to 15-mm peak position range. Figure 4 shows the results when an exponential distribution is used as the prior distribution. The vertical axis is the economic risk, and the horizontal axis is the peak position of the weight. The risk is reduced in both the small damage (4–5 mm) and increased PoF areas (10–11 mm).

The event probability of small damage is high and that of large damage decreases when an exponential distribution is used as the prior distribution. Risk evaluations were then conducted using a distribution with vertices (chi-square distribution ($k = 3$), normal distribution ($\mu = 5$, $\sigma^2 = 1.5$), and Weibull distribution (shape = 1.2, scale = 5)) as the prior distributions. Table 1 shows the appropriate weighting positions for risk reduction, with the chi-square distribution being the most effective. These risk evaluations indicate that it is possible to reduce the risk by locating a peak in either the small damage area or the increased PoF area.

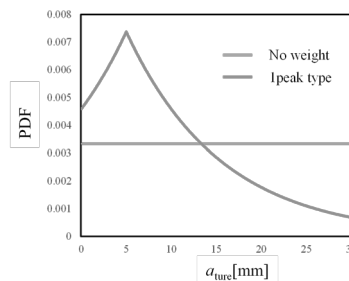


Figure 3: Example weighting function (5-mm peak).

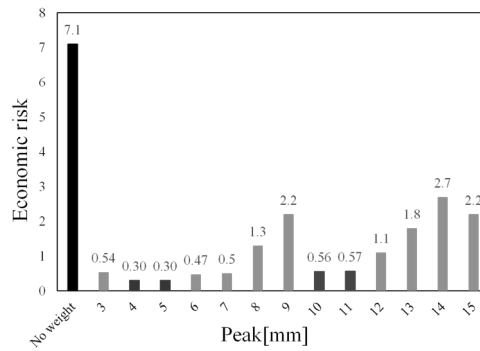


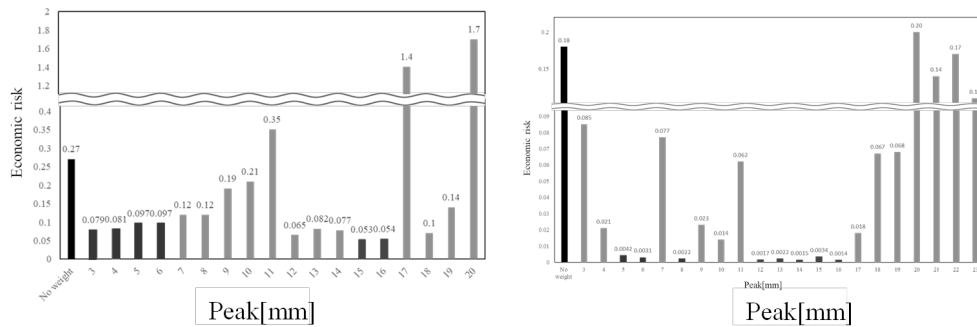
Figure 4: Economic risk at each peak location.

Table 1: Appropriate weighting positions for risk reduction.

	small damage size area	increasing PoF _{adj} area
Chi-square distribution	3	12
Normal distribution	5	11
Weibull distribution	3	11

4 INFLUENCE OF EXTERNAL FORCE ASSUMPTION

Figure 5 shows the results when the average failure size is increased to 20 and 25 mm. An exponential distribution is used as the prior distribution. The vertical and horizontal axes are the same as in Figure 4. The weighting in the small damage and increased PoF areas are effective for risk reduction in the tested damage size cases. Furthermore, the weighting in the increased PoF increase area becomes more effective as the average failure size increases.



(a) 20 mm

(b) 25 mm

Figure 5: Economic risk at each peak location.

5 CONCLUSION

- A method to evaluate the PoF of structures using monitoring data and a Bayesian estimation is proposed. This method reduces the risk by improving the diagnostic accuracy of specific damage levels, which is achieved by controlling the sampling ratio of the training data with a weight function.
- The weighting near the vertices is the most effective approach for risk reduction in

each distribution. It is possible to reduce the risk by locating a peak in either the small damage area or the increased PoF area.

- The weighting in both the small damage and increased PoF areas is effective for risk reduction in the tested damage size cases. Furthermore, the weighting in the increased PoF area becomes more effective as the average failure size increases.

REFERENCES

- [1] "API RP 581 Risk-Based Inspection Technology", API standards, American Petroleum Institute, 2016
- [2] "HPIS Z 107 Risk Based Maintenance Handbook", HPI Standard, High Pressure Institute of Japan, 2016
- [3] A.Iwasaki, A.Todoroki, Improvement of the Inverse Problem for the Damage Identification using Generalized Linear Mixed Model, Transactions of the JSME, A76(768), 1040-1047, 2010
- [4] A.Iwasaki, Delamination identification of CFRP structure using discriminant analysis via the support vector machine, Transactions of the JSME, 80(810), smm0020, 2014
- [5] A.Iwasaki, A.Todoroki, Statistical Evaluation of modified Electrical Resistance Change Method for Delamination Monitoring of CFRP Plate, Structural health monitoring, An International journal, 4, 2, 119-136, 2005
- [6] A.Iwasaki, A.Todoroki, S.Izumi, S.Sakai, Diagnostic Method for Delamination Monitoring of CFRP Plate using Kriging Interpolation Method, Key Engineering Materials, 353-358, 1422-1426, 2007
- [7] K.Takahashi, A.Todoroki, Y.Shimamura, A.Iwasaki, Statistical Damage Detection of Laminated CFRP Beam Using Electrical Resistance Change Method, Key Engineering Materials, 353-358, 1330-1333, 2007
- [8] H. Martz, R. Waller, "Bayesian reliability analysis", Krieger, 0894643959(1991)
- [9] T.Nakazuma, "Bayesian Statistics", Asakura, 4254295405(2007)
- [10] N.O.Siu, D.L. Kelly, Bayesian parameter estimation in probabilistic risk assessment, Reliability Engineering and System Safety, 62, pp. 89-116(1998)
- [11] J.Quigley, T.Bedford, L.Walls, Estimating rate of occurrence of rare events with empirical bayes: A railway application, Reliability Engineering and System Safety, 92, 619-627(2007)
- [12] S.Sakai, S.Okajima, S.Izumi, A.Iwasaki, Bayesian Inference of Fatigue Life Estimated by Inspection Data, J of the The Society of Materials Science Japan, 54-3, 308-313, 2005
- [13] S.Okajima, S.Sakai, S.Izumi, A.Iwasaki, Bayesian Estimation of Fatigue damage rate based on small sample, proc of 20th JSMS Symposium on Reliability Engineering and International Workshop, 60-65, 2004

Damage localization using controllable inputs: an experimental study

BA Qadri¹, MD Ulriksen¹, LB Klockmann¹ and PH Veis¹

¹*Dept. of Civil Engineering, Aalborg University, Niels Bohrs Vej 8, Esbjerg, Denmark*

Abstract

The recently proposed Shaped Damage Locating Input Distribution (SDLID) method locates structural damage by active interrogation with controllable inputs. The methodological premise is to shape these inputs such that certain steady-state vibration features (depending on the type of damage to be located) are rendered dormant in one subdomain at a time. As such, damage is localized when the vibration response induced by the shaped inputs in the damaged state corresponds to that stored for the reference state. Previously, the SDLID method, which operates free of system identification, has been tested through numerical simulations and, in this context, demonstrated its merits; namely, a low demand on output sensors, robustness towards noise, and conceptual simplicity. This paper presents an experimental application study, in which the SDLID method is used to locate different mass perturbations in a frame structure investigated using two actuators delivering harmonic excitation. Based on steady-state acceleration measurements, it is shown how the method succeeds in locating all the added mass perturbations.

Keywords: Structural Health Monitoring, Damage localization, Input shaping, Experimental study.

1 Introduction

Structural damage localization is conventionally handled by mapping shifts in vibration features, such as transfer functions or modal parameters, from the reference and damaged states to the structural domain [1]. This mapping can be conducted either directly, in which case we refer to the approach as *data-driven*, or by use of a theoretical model of the structure in question, implying that the approach is *model-based* [2]. Here, the theoretical model is typically established on the basis of a finite element (FE) formulation.

Numerous studies document successful model-based damage localization under both laboratory conditions [3, 4, 5] and in-situ settings [6, 7, 8], but it is evident that damage localization has yet to find the applicability level required for industrial use. One of the major issues is that the sensitivity to structural damage of the employed vibration features is typically lower than the features' sensitivity to noise and other variabilities [9].

Two approaches to (attempt to) resolve the noted sensitivity issue is 1) reducing the impact of noise and other variabilities [4, 10, 11] and 2) designing closed-loop systems with enhanced sensitivity to damage [12, 13, 14]. In the present study, we focus on the former path and investigate the Shaped Damage Locating Input Distribution (SDLID) scheme proposed by Ulriksen et al. [11]. The SDLID scheme employs inputs that are shaped by use of a theoretical model to “deactivate” the damage for determining its location. The idea is to operate with the

shaped inputs in a forward interrogation for damage of one structural subdomains at a time; with damage revealing itself when, under ideal conditions, the vibration signatures prior and posterior to damage coincide. In this way, the impact of noise is reduced since the SDLID scheme operates without calling for system identification to extract the damage features.

Besides circumventing system identification, the merits of the SDLID scheme include a user-defined spatial localization resolution (as postulated damage areas are selected), a low demand on output sensors (in principle, one may suffice), and conceptual simplicity. These merits have been highlighted through numerical application examples with simple structural systems [11] and an offshore jacket structure [2]. The scope of the present paper is therefore to further test the applicability of the SDLID scheme by applying it in an experimental context with a frame structure, which is analyzed in its reference state and “damaged” states with different mass perturbations.

The rest of the paper is organized as follows: in section 2, the SDLID method is reviewed, section 3 outlines the experimental setup, and section 4 presents the obtained damage localization results. A brief conclusion in section 5 closes the paper.

2 The SDLID method

The SDLID method interrogates for damage in a structural subdomain by applying a set of controllable inputs, $u(t)$, which, for each structural subdomain, is shaped to render dormant certain kinematic quantities [11]. If the subdomain containing the damage is suppressed, the steady-state vibration output will, under ideal circumstances, be the same in the damaged state and in the healthy one; given, of course, that the set of inputs is identical in the two states. The task of shaping the inputs can be resolved by numerous approaches; of which two are proposed in [11]. One of these two takes its outset in the Laplace domain and is, as such, useful when shaping harmonic inputs, while the second one operates in the time domain. Since the experimental study in the present paper employs harmonic excitation, we focus on the Laplace domain-based approach and refer the reader to [11] for a tutorial on the time domain-based approach.

Consider a structural domain that is discretized to n degrees of freedom (DOF) and subjected to p inputs that are collected in $u(t) \in \mathbb{R}^p$ and distributed spatially through $B_2 \in \mathbb{R}^{n \times p}$. The governing temporal equation reads

$$M\ddot{x}(t) + C\dot{x}(t) + Kx(t) = B_2u(t), \quad (1)$$

where M, C and $K \in \mathbb{R}^{n \times n}$ are the mass, damping and stiffness matrices, while, $x(t)$, $\dot{x}(t)$ and $\ddot{x}(t) \in \mathbb{R}^n$ are the nodal displacement, velocity and acceleration vectors. Assuming steady state and zero initial conditions, equation (1), with p shaped inputs acting solely in the DOF indexed by τ , can be expressed in the Laplace domain as

$$X(s) = (Ms^2 + Cs + K)^{-1}B_2U(s) = G(s)B_2U(s) = G_{\bullet,\tau}(s)U(s), \quad (2)$$

where $G_{\bullet,\tau}(s)$ is the transfer matrix containing the columns in which the shaped inputs are applied and $X(s) = \mathcal{L}(x(t))$ and $U(s) = \mathcal{L}(u(t))$ are the Laplace transforms of the output and the input.

For simplicity we assume that the structure is only affected by the p shaped inputs, hence implying that any other exogenous loading is neglected. The task therefore becomes to shape the amplitude and the phase angle of the harmonic inputs, such that some linear transformation of $X(s) \in \mathbb{C}^n$, denoted $\Gamma(s) \in \mathbb{C}^q$, is suppressed. That is,

$$\Gamma(s) = LG_{\bullet,\tau}(s)U(s) = 0, \quad (3)$$

where $LG_{\bullet,\tau}(s) \in \mathbb{C}^{q \times p}$ and with L being the transformation matrix. Provided that $p > q$ (that is, the number of shaped inputs is greater than the number of suppressed kinematic quantities), there exists a null space

$$U(s) = \text{null}(LG_{\bullet,\tau}(s)), \quad (4)$$

from where relative values of the amplitudes and phase angles are directly computed as the moduli and arguments of the chosen vector within the span of $\text{null}(LG_{\bullet,\tau}(s)) \in \mathbb{C}^{p \times (p-q)}$.

One gathers that the inputs are most conveniently shaped using a model of the healthy structure. By applying the inputs to the structure prior and posterior to damage, we capture the steady-state response, $y(t)$ and $\tilde{y}(t)$, where $(\tilde{\bullet})$ denotes a quantity from the damaged state. On the premise that $y(t)$ can contain displacements, velocities, accelerations, and so forth, the Euclidean distance of the steady-state response shift in frequency domain, that is,

$$\Xi_i = \sqrt{\sum_j (|Y_j(\omega)| - |\tilde{Y}_j(\omega)|)^2}, \quad (5)$$

is used as damage metric with the index i indicating the i th subdomain being interrogated. In this way, damage is located in the subdomain that yields the lowest metric.

In the present study, we focus on locating mass perturbations, thus, as proved in [11], steady-state accelerations must be suppressed. If, on the other hand, stiffness-related damage was to be located, one would suppress the steady-state strains. A further elaboration on this can be found in [11].

3 Experimental setup

A frame structure with 5 floors is assembled and used as a damage localization test bed in a controlled laboratory environment, see figure 1. The structure is assembled using aluminium beam elements, all connected by corner cubes, screws and threaded rods, see table (1) for the structural properties of a single aluminum beam element.

The structure is instrumented with two actuators that generate a horizontal load. Two load cells are attached to the structure that measure the input force from the actuators. The structural response is captured by 9 piezo-electric accelerometers, distributed on the frame structure. The structure is mounted on a HEB260 profile, which is reinforced with steel braces and bolted to the ground.

Table 1: Material properties of a single aluminum beam element.

Description	Symbol	Value	Unit
Cross-sectional area	A	$49 \cdot 10^{-6}$	$[\text{m}^2]$
Density	ρ	2900	$[\text{kg}/\text{m}^3]$
Modulus of elasticity	E	$68 \cdot 10^9$	$[\text{Pa}]$
Poisson's ratio	ν	0.33	$[-]$
Shear modulus	G	$25 \cdot 10^9$	$[\text{Pa}]$
Second moment of inertia	I_y/I_z	$495 \cdot 10^{-12}$	$[\text{m}^4]$
Polar moment of inertia	I_x	$991 \cdot 10^{-12}$	$[\text{m}^4]$

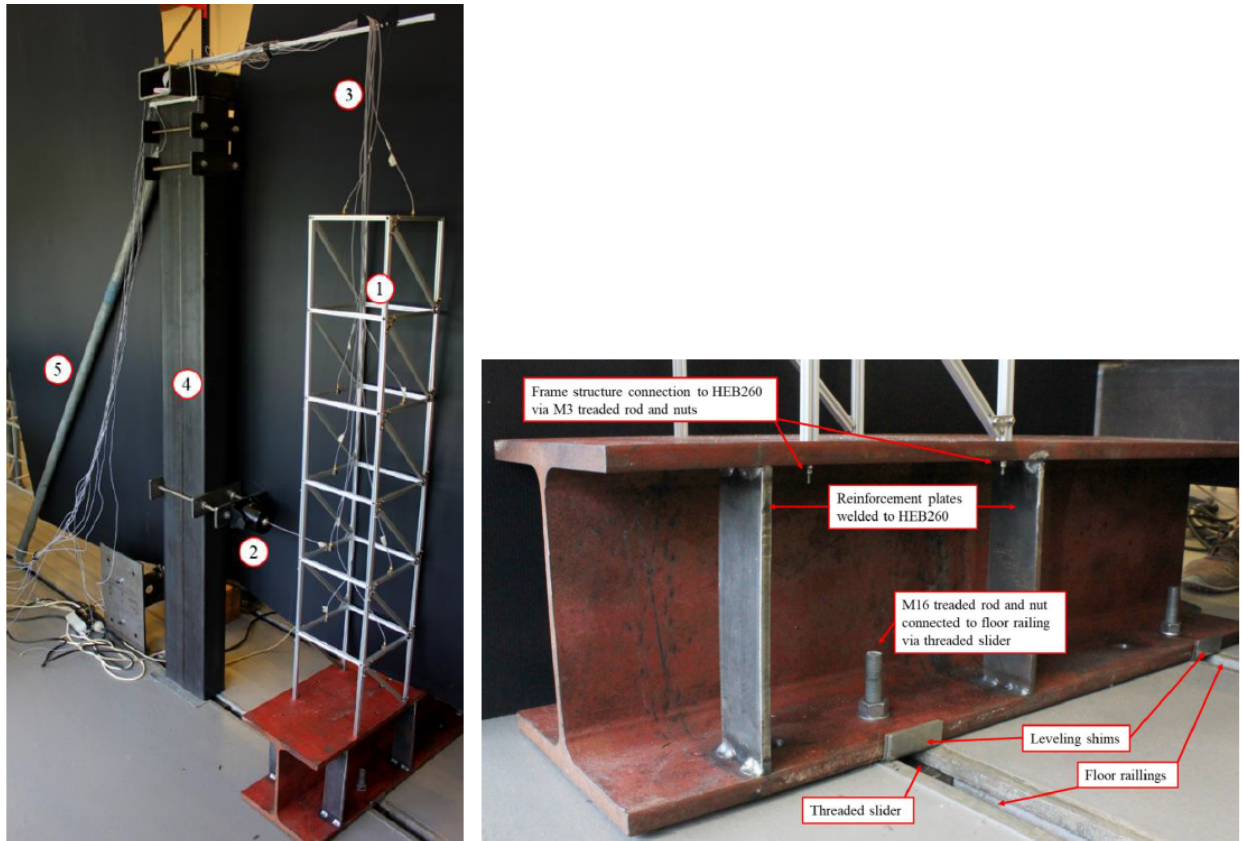


Figure 1: Experimental setup with indication of 1) frame structure, 2) actuator, 3) cables connecting the accelerometers, 4) steel column and 5) support cylinder for the steel column.

3.1 Damage emulation

The damage is introduced as a mass perturbation in different areas on the frame structure, see figure 2. The mass perturbation weighs 0.121 kg, which is approximately 6.31 % of the total mass of the frame structure. To appreciate the impact of adding the mass perturbation to the structure, we conduct an Experimental Modal Analysis (EMA) of the structure in its healthy configuration and with the mass perturbation added on the topmost level. The EMA is performed by use of a single actuator that delivers a sine sweep ranging from 0.1 Hz to 60 Hz, which ensures that the first three eigenmodes of the frame are excited. As observed from the resulting frequency response functions depicted in figure 3, the mass perturbation yields a clear damaged-induced shift in the eigenfrequencies.

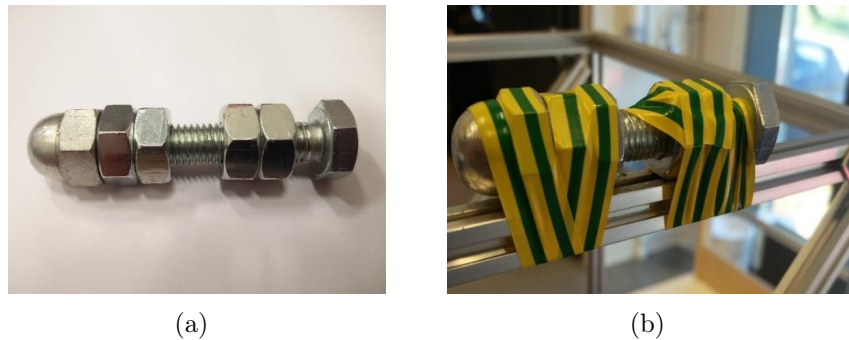


Figure 2: Pictures of a) bolt and nuts serving as mass perturbation and b) the perturbation applied to the structure.

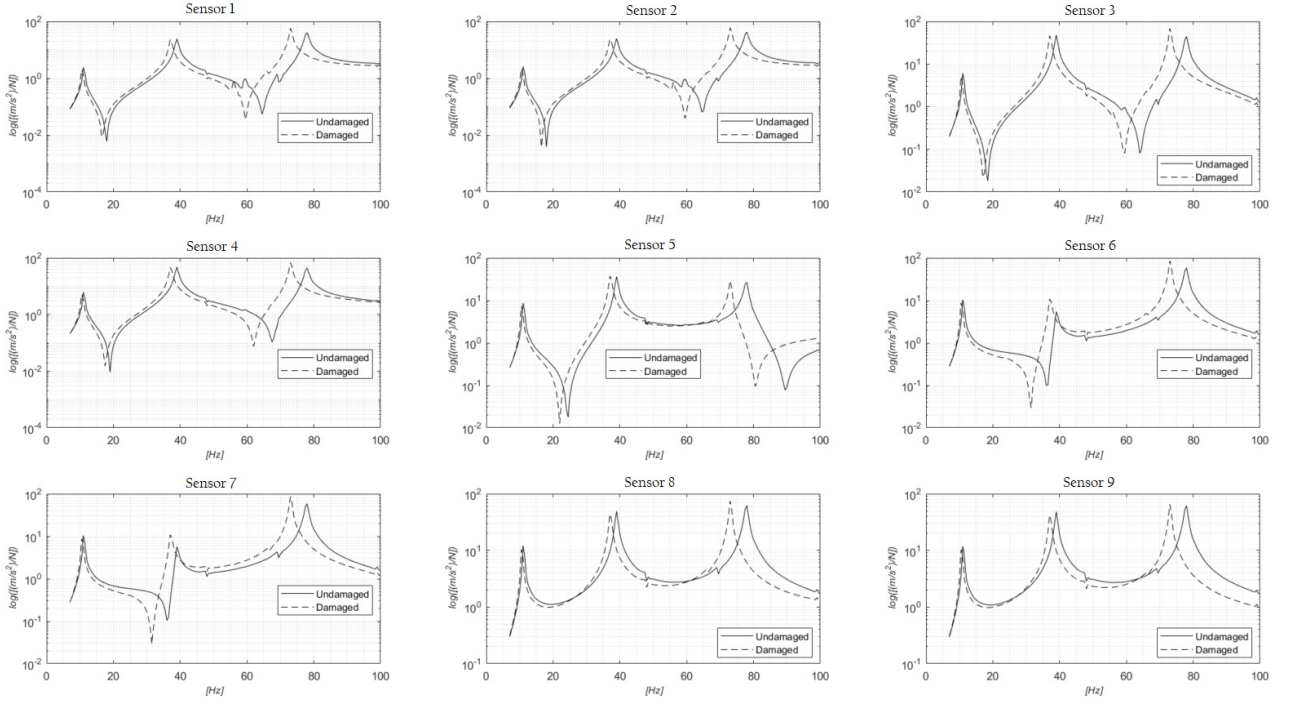


Figure 3: Frequency response functions for the structure in reference and damaged states.

4 Damage localization

As previously mentioned, the SDLID method is a model-based approach, meaning that a theoretical model must be used to shape the inputs. A finite element model consisting of 108

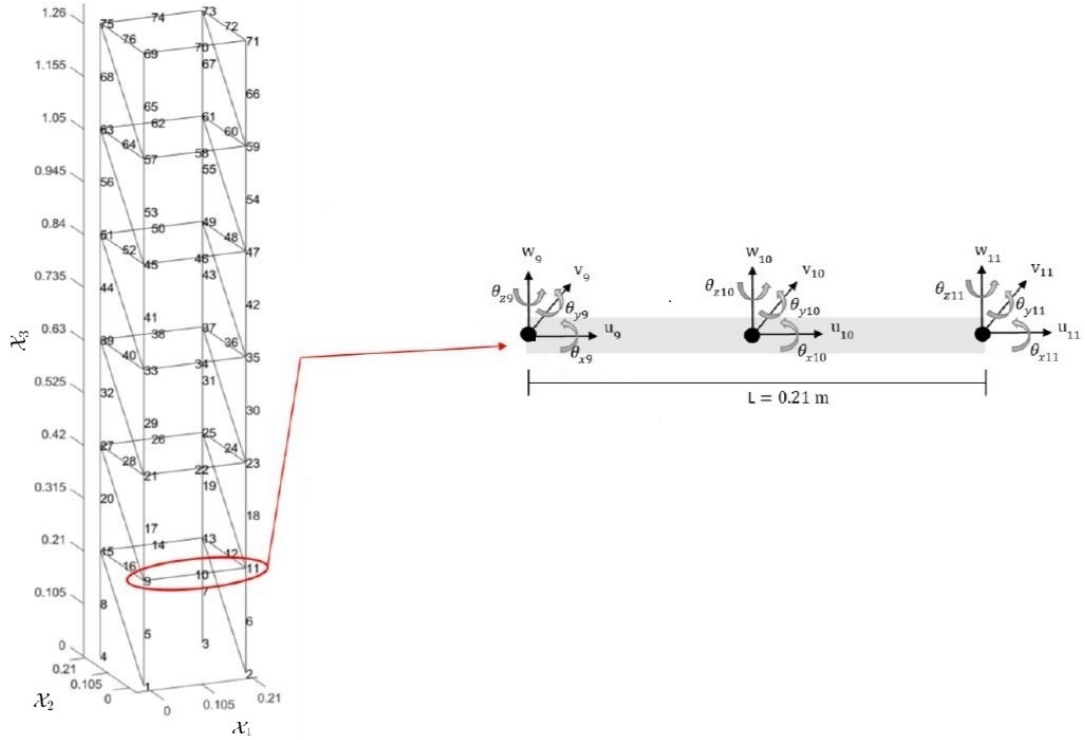


Figure 4: Finite element model of the frame structure and two highlighted beam elements, illustrated with the nodes and DOF.

Euler-Bernoulli elements has been established, see figure 4. The model has a total of 480 DOF of which 24 are fixed to represent the kinematic boundary conditions.

In the experimental study, two actuators are, as mentioned, attached to the frame structure to introduce a harmonic excitation; see figure 5, which also shows the positions of the accelerometers. The two harmonic inputs have a driving frequency of $\Omega = 0.7\omega_1$, where ω_1 is the first cyclic eigenfrequency, see figure 5 for the actuator positions. With two inputs, one gathers that the constraint of $p > q$ is violated if all six DOF in a node are to be suppressed. However, since the inputs only excite in one plane and the displacements and rotations are relatively small, suppressing just the translational DOF in the excitation direction is sufficient.

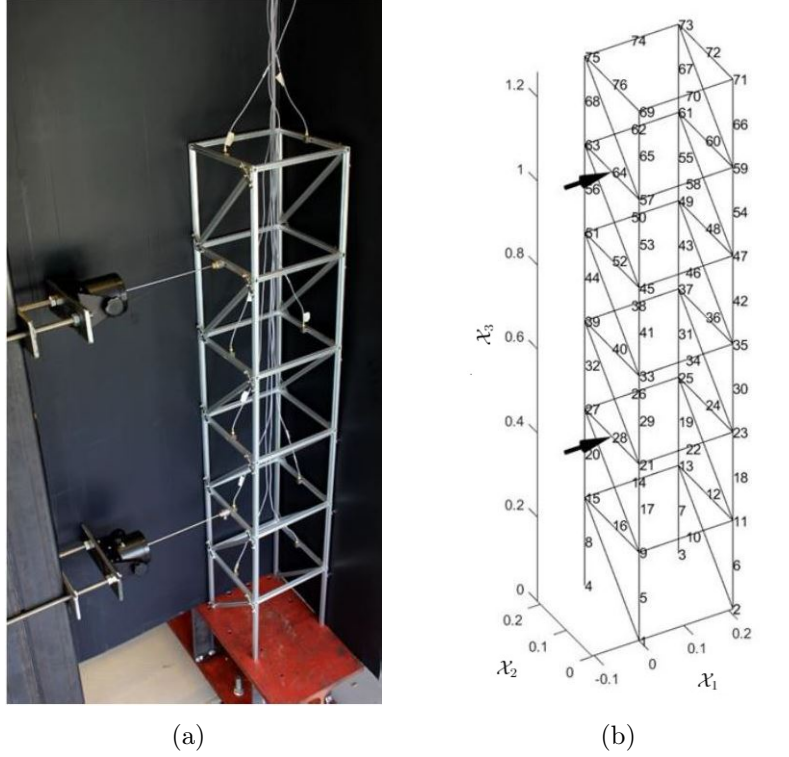


Figure 5: Frame structure in a) experimental setup with accelerometers and actuators and b) its numerical representation with the actuator positions.

The frame structure is tested in the healthy state and in five different damaged states, where the mass perturbation is located at node $\aleph = 12, 36, 52, 60$ or 76 . These nodes, which are indicated in figure 6, are also chosen as the subdomains to be interrogated consistently. The interrogations are conducted by suppressing steady-state accelerations in the excitation direction, and by doing so for each damaged state, we get the damage metrics—according to equation (4)—plotted in figure 6. As the red dot in each plot marks the damage location, it is evidenced how the SDLID method allows for successful localization of the mass perturbation in all damaged states.

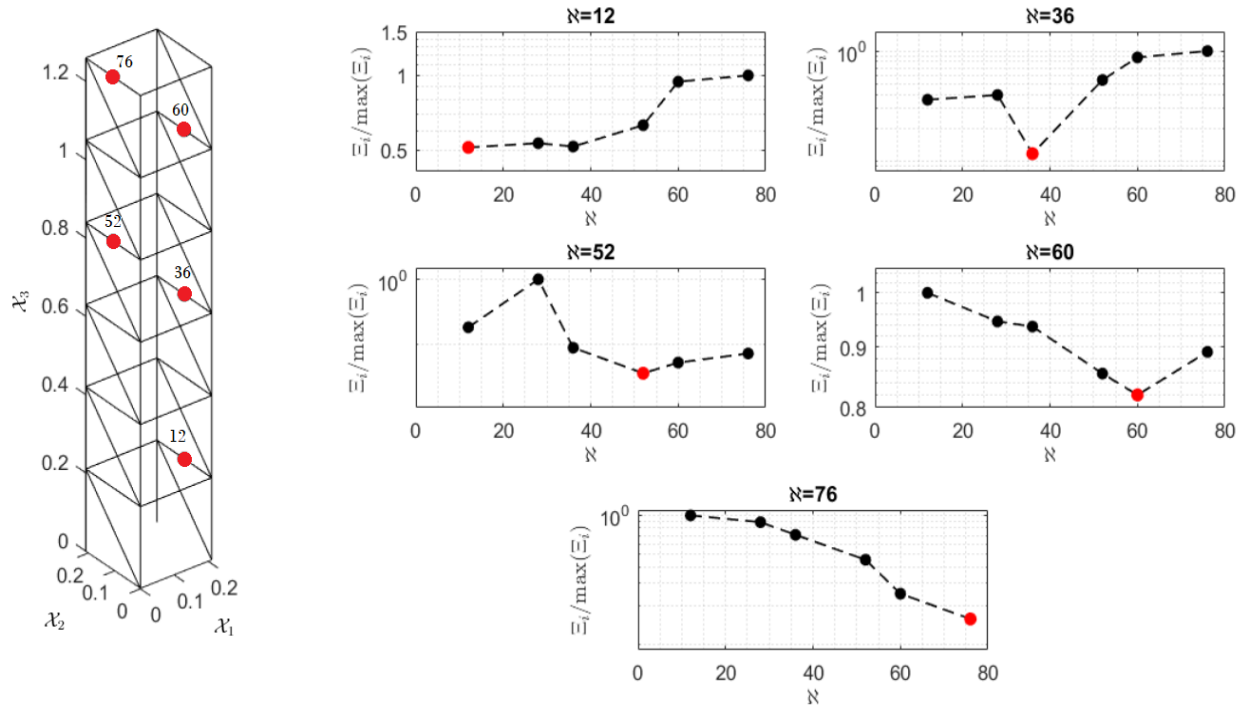


Figure 6: Damage localization results. The structure, depicted on the left side, illustrates the positions of the damage.

5 Conclusion

The principle of the SDLID method is to apply a set of inputs and then interrogate for damage by rendering dormant certain kinematic quantities (depending on the damage type to be located) in one structural subdomain at a time. Damage is, as such, located when the steady-state output governed by the shaped inputs is identical prior and posterior to the introduction of damage.

In the present paper, the SDLID method is tested in an experimental setup with a frame structure, which is subjected to two harmonic inputs and introduced to different mass perturbations. By shaping the available inputs to suppress steady-state accelerations in one subdomain at a time, it is found that the SDLID scheme succeeds in locating all the mass perturbations, albeit with rather poor resolution in some cases.

References

- [1] C. R. Farrar and K. Worden. *Structural Health Monitoring: A Machine Learning Perspective*. John Wiley & Sons, 1st edition, 2013.
- [2] M. D. Ulriksen, D. Bernal, M. E. Nielsen Nielsen, and Damkilde L. Damage localization in offshore structures using shaped inputs. *Procedia Engineering*, 199:2282–2287, 2017.
- [3] M. D. Ulriksen, D. Tcherniak, P. H. Kirkegaard, and L. Damkilde. Operational Modal Analysis and Wavelet Transformation for Damage Identification in Wind Turbine Blades. *Structural Health Monitoring*, 15(4):381–388, 2016.

- [4] L. H. G. Marin, M. Döhler, D. Bernal, and L. Mevel. Robust statistical damage localization with stochastic load vectors. *Structural Control and Health Monitoring*, 22(3):557–573, 2015.
- [5] R. J. Johansen, L. M. Hansen, M. D. Ulriksen, D. Tcherniak, and L. Damkilde. Damage localization in a residential-sized wind turbine blade by use of the sddlv method. *Journal of Physics: Conference Series*, 628:012069, 2015.
- [6] N. V. Hà and Jean-Claude Golinval. Localization and quantification of damage in beam-like structures using sensitivities of principal component analysis results. *Mechanical Systems and Signal Processing*, 24(6):1831–1843, 2010.
- [7] A. Teughels and G. De Roeck. Structural damage identification of the highway bridge z24 by fe model updating. *Journal of Sound and Vibration*, 278(3):589–610, 2004.
- [8] M. D. Ulriksen, D. Tcherniak, L. M. Hansen, R. J. Johansen, L. Damkilde, and L. Frøyd. In-situ damage localization for a wind turbine blade through outlier analysis of SDDLv-induced stress resultants. *Structural Health Monitoring*, 16(6):745–761, 2017.
- [9] C. Devriendt, W. Weijtjens, M. El-Kafafy, and G. De Sitter. Monitoring resonant frequencies and damping values of an offshore wind turbine in parked conditions. *IET Renewable Power Generation*, 8(4):433–441, 2014.
- [10] D. Bernal and M. D. Ulriksen. Subspace exclusion zones for damage localization. *Mechanical Systems and Signal Processing*, 114:120–127, 2019.
- [11] M. D. Ulriksen, D. Bernal, and L. Damkilde. Shaped input distributions for structural damage localization. *Mechanical Systems and Signal Processing*, 110:499–508, 2018.
- [12] L.R. Ray and L. Tian. Damage detection in smart structures through sensitivity enhancing feedback control. *Journal of Sound and Vibration*, 227(5):987–1002, 1999.
- [13] L. J. Jiang, J. J. Tang, and K. W. Wang. An optimal sensitivity-enhancing feedback control approach via eigenstructure assignment for structural damage identification. *Journal of Vibration and Acoustics*, 129(6):771–783, 2007.
- [14] D. Bernal and M. D. Ulriksen. Output feedback in the design of eigenstructures for enhanced sensitivity. *Mechanical Systems and Signal Processing*, 112:22–30, 2018.

EXAMINATION OF MODAL EXPANSION AND KALMAN FILTERING TECHNIQUES FOR VIBRATION ESTIMATION

MATHIAS W. PEDERSEN*, EMIL K. ANDERSEN*, MARTIN D. ULRIKSEN* AND
LARS DAMKILDE*

Dept. of Civil Engineering, Aalborg University

Niels Bohrs Vej 8, 6700 Esbjerg, Denmark

*e-mail: mwpe13@student.aau.dk, ekan14@student.aau.dk, mdu@civil.aau.dk & lda@civil.aau.dk

Key words: Vibration estimation, Modal expansion, Kalman Filter, Joint input-state estimation, Experimental testing

Abstract. State estimation is a well-established discipline within the field of modern control theory. In the context of vibration analysis, where application areas include damage prognosis and structural control with full state feedback, the topic has, however, emerged during the last couple of decades under the term *virtual sensing*. Here, the scope is to estimate physical quantities at both measured and unmeasured locations based on vibration signals captured in a limited set of sensors. This paper examines and compares three virtual sensing techniques, namely, modal expansion, direct Kalman filtering and a modified Kalman filter where the true value of the input is replaced by an optimal estimate. The performance of the three schemes is examined in an experimental setup with a cantilevered beam, which is subjected to different input types and installed with a limited set of accelerometers. Based on the experimental findings, some observations and particular recommendations on the use of the different schemes are provided.

1 INTRODUCTION

Within civil and mechanical engineering, it is common practice to use vibration measurements for structural monitoring and control purposes [1, 2, 3]. The vibrations are captured through an installed sensor network, which, in most applications, consists of a limited number of sensors due to the associated costs and the fact that there may be locations inaccessible for instrumentation. As such, virtual sensing can be utilized to estimate vibration responses at designated locations from response acquired by the installed sensor network [4].

The by far most applied virtual sensing approach within civil and mechanical engineering applications is to assume linearity and time invariance and then conduct modal expansion (ME). Here, an augmented basis consisting of measured and/or analytical mode shapes is used to solve an inverse problem resulting in vibration estimates in all the unmeasured degrees of freedom in the model of the structure in question [5, 6]. It follows directly that the inverse problem to be solved is underdetermined if the number of included modes exceeds the number of deployed sensors; a scenario that can easily occur in practice. Other virtual sensing methods include the direct Kalman filter (KF) algorithm [7] and a modified Kalman filter, namely, the joint input-state estimation (JISE) algorithm [8], which, in addition to estimating the full optimal state vector, also estimates the unknown input. In the present paper, the performance of these two schemes and ME is examined and compared in the context of an experimental setup with

a cantilevered beam, which is subjected to different input excitations, while a limited set of mounted accelerometers measure the output.

The paper is organized as follows: in Section 2, a brief overview of the prerequisite theory utilized in the three virtual sensing methods is provided, followed by the presentation of the methods in Section 3. Subsequently, in Section 4, the experimental setup is outlined and Section 5 provides a description of the required numerical model. In Section 6, the performance of the three schemes is examined and compared. Lastly, some concluding remarks are given in Section 7.

2 PREREQUISITE THEORY

Assuming linear, time-invariant (LTI) conditions for the structure of interest, which is spatially discretized with n degrees of freedom (DOF), the temporal equation of motion is given as

$$M\ddot{x}(t) + C\dot{x}(t) + Kx(t) = S_p f(t). \quad (1)$$

Here, $K, C, M \in \mathbb{R}^{n \times n}$ are the stiffness, damping and mass matrices, $x(t), \dot{x}(t), \ddot{x}(t) \in \mathbb{R}^n$ are the nodal displacements, velocities and accelerations, and $f(t) \in \mathbb{R}^p$ contains the p external inputs spatially distributed by $S_p \in \mathbb{R}^{n \times p}$. Assuming classical damping, Eq. (1) can be decoupled through the modal transformation

$$x(t) \approx \sum_{i \in \mathcal{A}} \phi_i q_i(t) = \Phi q(t) \quad (2)$$

where \mathcal{A} denotes a subset holding the indexes of the $m \leq n$ governing modes, $\Phi \in \mathbb{R}^{n \times m}$ is the truncated modal matrix containing mass-normalized mode shapes, and $q(t) \in \mathbb{R}^m$ is the truncated modal displacement vector. Let $(\tilde{\circ})$ denote a modal quantity, then it follows

$$\ddot{q}(t) + \tilde{C}\dot{q}(t) + \tilde{K}q(t) = \Phi^T S_p f(t) \quad (3)$$

where $\tilde{K} \in \mathbb{R}^{m \times m}$ is the spectral matrix and $\tilde{C} \in \mathbb{R}^{m \times m}$ is the modal damping matrix.

By defining the modal state vector, $\tilde{z}(t)^T = [q(t)^T \ \dot{q}(t)^T]^T \in \mathbb{R}^{1 \times 2m}$, and rewriting Eq. (3) into discrete state-space form, one has

$$\tilde{z}_{k+1} = \tilde{A}_d \tilde{z}_k + \tilde{B}_d f_k, \quad (4)$$

where $\tilde{z}_k = \tilde{z}(k\Delta t)$ and $f_k = f(k\Delta t)$ for $k \in [0, N-1]$, with N being the total number of samples and Δt the time increment. If the zero-order-hold rule is employed on the input, such that $\forall t \in [k\Delta t, (k+1)\Delta t] : f(t) = f_k$, the state-transition matrix, $\tilde{A}_d \in \mathbb{R}^{2m \times 2m}$, and the input matrix, $\tilde{B}_d \in \mathbb{R}^{2m \times p}$, are given as

$$\tilde{A}_d = \exp \left(\begin{bmatrix} 0 & I \\ -\tilde{K} & -\tilde{C} \end{bmatrix} \Delta t \right) \quad (5)$$

$$\tilde{B}_d = [\tilde{A}_d - I] \begin{bmatrix} 0 & I \\ -\tilde{K} & -\tilde{C} \end{bmatrix}^{-1} \begin{bmatrix} 0 \\ \Phi^T S_p \end{bmatrix}. \quad (6)$$

The s measured outputs are gathered in $y_k \in \mathbb{R}^s$ and defined as

$$y_k = \tilde{C}_d \tilde{z}_k + \tilde{D}_d f_k, \quad (7)$$

where $\tilde{C}_d = [S_d \Phi - S_a \Phi \tilde{K} \quad S_v \Phi - S_a \Phi \tilde{C}] \in \mathbb{R}^{s \times 2m}$ is the output matrix, $\tilde{D}_d = [S_a \Phi \Phi^T S_p] \in \mathbb{R}^{s \times p}$ is the input-output transmission matrix and $S_d, S_v, S_a \in \mathbb{R}^{s \times n}$ relate measured displacements, velocities and accelerations to the corresponding DOF in the numerical model.

3 VIRTUAL SENSING METHODS

The discrete system output is divided into two subsets: the s measurands, $y_k \in \mathbb{R}^s$, and the α response quantities to be estimated, $\mu_k \in \mathbb{R}^\alpha$.

3.1 Modal expansion (ME)

Let $\eta_k \in \mathbb{R}^m$ be the general notation for a modal kinematic quantity (depending on the nature of y_k), then the modal formulation is partitioned into

$$\begin{bmatrix} y_k \\ \mu_k \end{bmatrix} = \begin{bmatrix} \Phi_s \\ \Phi_\alpha \end{bmatrix} \eta_k \quad (8)$$

with $\Phi_s \in \mathbb{R}^{s \times m}$ and $\Phi_\alpha \in \mathbb{R}^{\alpha \times m}$ being the truncated modal matrices containing the corresponding s and α DOF, respectively. In this paper, it is chosen to use mode shapes from a finite element (FE) model, which is calibrated against modal parameters obtained from experimental modal analysis (EMA). From the first partition of Eq. (8),

$$y_k = \Phi_s \eta_k, \quad (9)$$

it is evident that a unique solution can only exist if the number of installed sensors, s , is no less than the number of considered modes, m . In cases where $s < m$, the measured output histories, y , should, if possible, be truncated or low-pass filtered such that at most s modes govern the signals.

The modal kinematics can be computed as

$$\eta_k = \Phi_s^\dagger y_k, \quad (10)$$

where $(\circ)^\dagger$ denotes the Moore-Penrose pseudo-inverse, which, in this case, minimizes $\|y_k - \Phi_s \eta_k\|_2$. When the modal kinematics are obtained, the physical response at the α desired locations can be readily estimated as

$$\mu_k = \Phi_\alpha \eta_k. \quad (11)$$

3.2 Kalman filter (KF) algorithm

The KF algorithm is a recursive algorithm, which estimates the full optimal state vector [7]. In the KF algorithm, the input is unknown and included in the process noise, $w_k \in \mathbb{R}^{2m}$ (and, as such, \tilde{w}_k), and measurement noise, $v_k \in \mathbb{R}^s$, such that Eqs. (4) and (7) become

$$\tilde{z}_{k+1} = \tilde{A}_d \tilde{z}_k + \tilde{w}_k \quad (12)$$

$$y_k = \tilde{C}_d \tilde{z}_k + v_k. \quad (13)$$

When accelerations are measured, a correlation between w_k and v_k is present [9]. Hence, to accommodate a general framework, w_k and v_k are assumed to be mutually correlated, zero mean, white signals with known covariance matrices, $Q \in \mathbb{R}^{2m \times 2m}$, $R \in \mathbb{R}^{s \times s}$ and $S \in \mathbb{R}^{2m \times s}$, given as

$$Q = \mathbb{E}[w_k w_k^T], \quad R = \mathbb{E}[v_k v_k^T], \quad S = \mathbb{E}[w_k v_k^T]. \quad (14)$$

The process noise covariance matrix, Q , indicates how accurate the algorithm considers the model to be, whereas the measurement noise covariance matrix, R , indicates the confidence put into the measured data. It is chosen to employ the approach outlined in [10], such that the triplet $\{Q, R, S\}$ is estimated as

$$\begin{bmatrix} Q & S \\ S^T & R \end{bmatrix} = \begin{bmatrix} \tilde{B}'_d \\ \tilde{D}'_d \end{bmatrix} U_{\text{in}} \begin{bmatrix} \tilde{B}'_d{}^T & \tilde{D}'_d{}^T \end{bmatrix} + \begin{bmatrix} 0 & 0 \\ 0 & U_{\text{out}} \end{bmatrix}, \quad (15)$$

Algorithm 1: The KF algorithm.

```

for  $k = 0$  to  $k = N - 1$  do
    Measurement update:
    (1)  $K_k = P_{k|k-1}^z \tilde{C}_d^T (\tilde{C}_d P_{k|k-1}^z \tilde{C}_d^T + R)^{-1}$ 
    (2)  $\hat{z}_{k|k} = \hat{z}_{k|k-1} + K_k (y_k - \tilde{C}_d \hat{z}_{k|k-1})$ 
    (3)  $P_{k|k}^z = P_{k|k-1}^z - K_k \tilde{C}_d P_{k|k-1}^z$ 
    Time update:
    (4)  $\hat{z}_{k+1|k} = \tilde{A}_d \hat{z}_{k|k}$ 
    (5)  $P_{k+1|k}^z = \tilde{A}_d P_{k|k}^z \tilde{A}_d^T + Q - \tilde{A}_d K_k S^T - S K_k^T \tilde{A}_d^T$ 
end
    
```

where $U_{\text{out}} = \sigma_{\text{out}}^2 I$ with σ_{out}^2 defined from known sensor characteristics or utilized as a tuning parameter, and $U_{\text{in}} = \sigma_{\text{in}}^2 I$ with σ_{in}^2 being the variance of the known input. If more than one input acts on the structure, σ_{in}^2 can, for example, be taken as the mean variance of the inputs. In Eq. (15), $\tilde{B}'_d \in \mathbb{R}^{2m \times n}$ and $\tilde{D}'_d \in \mathbb{R}^{s \times n}$ differ from $\tilde{B}_d \in \mathbb{R}^{2m \times p}$ and $\tilde{D}_d \in \mathbb{R}^{s \times p}$ as excitation in all DOF are assumed in the FE model; that is, $p = n$.

The KF algorithm is presented in Algorithm 1 according to [10], where $(\hat{\cdot})$ denotes an estimated quantity and $K_k \in \mathbb{R}^{2m \times s}$ is the Kalman gain, which is calculated such that the state estimate is minimum-variance and unbiased. Algorithm 1 is initialized using an initial state estimate vector, $\hat{z}_{0|-1}$, assumed independent of w_k and v_k , and its associated error covariance matrix, $P_{0|-1}^z$, defined as

$$P_{k|k}^z = \mathbb{E}[(\tilde{z}_k - \hat{z}_k)(\tilde{z}_k - \hat{z}_k)^T] \in \mathbb{R}^{2m \times 2m}. \quad (16)$$

After $\hat{z}_{k|k}$ is computed, the response can be estimated at desired locations using

$$\mu_{k|k} = \tilde{C}_{d,e} \hat{z}_{k|k}, \quad (17)$$

where the output matrix is redefined as

$$\tilde{C}_{d,e} = [S_{d,e} \Phi - S_{a,e} \Phi \tilde{K} \quad S_{v,e} \Phi - S_{a,e} \Phi \tilde{C}] \in \mathbb{R}^{\alpha \times 2m} \quad (18)$$

with subscript e referring to estimation and the distribution matrices, $S_{d,e}, S_{v,e}, S_{a,e} \in \mathbb{R}^{\alpha \times n}$, relating the estimated quantities to the designated locations.

3.3 Joint input-state estimation (JISE) algorithm

The JISE algorithm is an extension of the KF algorithm, as it jointly estimates both the input(s) and states from a limited number of sensor measurements [8]. Therefore, Eqs. (12) and (13) are extended to

$$\tilde{z}_{k+1} = \tilde{A}_d \tilde{z}_k + \tilde{B}_d f_k + \tilde{w}_k \quad (19)$$

$$y_k = \tilde{C}_d \tilde{z}_k + \tilde{D}_d f_k + v_k \quad (20)$$

in which it is assumed that w_k and v_k are correlated, zero mean and white noise signals. As such, Eqs. (14) and (15) still hold.

Algorithm 2: The JISE algorithm.

```

for  $k = 0$  to  $k = N - 1$  do
    Input estimation:
    (1)  $\hat{R}_k = \tilde{C}_d P_{k|k-1}^z \tilde{C}_d^T + R$ 
    (2)  $M_k = (\tilde{D}_d^T \hat{R}_k^{-1} \tilde{D}_d)^{-1} \tilde{D}_d^T \hat{R}_k^{-1}$ 
    (3)  $\hat{f}_{k|k} = M_k (y_k - \tilde{C}_d \hat{z}_{k|k-1})$ 
    (4)  $P_{k|k}^f = (\tilde{D}_d^T \hat{R}_k^{-1} \tilde{D}_d)^{-1}$ 

    Measurement update:
    (5)  $K_k = P_{k|k-1}^z \tilde{C}_d^T \hat{R}_k^{-1}$ 
    (6)  $\hat{z}_{k|k} = \hat{z}_{k|k-1} + K_k (y_k - \tilde{C}_d \hat{z}_{k|k-1} - \tilde{D}_d \hat{f}_{k|k})$ 
    (7)  $P_{k|k}^z = P_{k|k-1}^z - K_k (\hat{R}_k - \tilde{D}_d P_{k|k}^f \tilde{D}_d^T) K_k^T$ 
    (8)  $P_{k|k}^{zf} = (P_{k|k}^{fz})^T = -K_k \tilde{D}_d P_{k|k}^f$ 

    Time update:
    (9)  $\hat{z}_{k+1|k} = \tilde{A}_d \hat{z}_{k|k} + \tilde{B}_d \hat{f}_{k|k}$ 
    (10)  $N_k = \tilde{A}_d K_k (I - \tilde{D}_d M_k) + \tilde{B}_d M_k$ 
    (11)  $P_{k+1|k}^z = [\tilde{A}_d \quad \tilde{B}_d] \begin{bmatrix} P_{k|k}^z & P_{k|k}^{zf} \\ P_{k|k}^{fz} & P_{k|k}^f \end{bmatrix} \begin{bmatrix} \tilde{A}_d^T \\ \tilde{B}_d^T \end{bmatrix} + Q - N_k S^T - S N_k^T$ 
end
    
```

The JISE algorithm, presented in Algorithm 2 according to [10], is a three-step recursive filter, where $\hat{f}_{k|k}$ is the estimated input vector, $M_k \in \mathbb{R}^{p \times s}$ is the gain related to the input estimate and I is the identity matrix of appropriate size. The algorithm is, just like in the KF, initialized using an initial state vector, $\hat{z}_{0|-1}$, and its associated error covariance matrix, $P_{0|-1}^z$, defined in Eq. (16). After initialization, the algorithm recursively estimates the input and state vector. When the estimated state vector, $\hat{z}_{k|k}$, is computed, the response can be estimated at α desired locations by

$$\mu_{k|k} = \tilde{C}_{d,e} \hat{z}_{k|k} + \tilde{D}_{d,e} \hat{f}_{k|k}, \quad (21)$$

where $\tilde{C}_{d,e} \in \mathbb{R}^{\alpha \times 2m}$ is defined in Eq. (18) and $\tilde{D}_{d,e} = [S_{a,e} \Phi \Phi^T S_p] \in \mathbb{R}^{\alpha \times p}$ is the input-output transmission matrix.

Worth of explicit note regarding Algorithm 2 is that \hat{R}_k becomes rank deficient if $s > m$, while $\tilde{D}_d^T \hat{R}_k^{-1} \tilde{D}_d$ becomes rank deficient if $s > m$, $p > s$ or $p > m$. To prevent conditioning issues, the matrices can, as outlined in [11], be truncated using a singular value decomposition (SVD) procedure.

4 EXPERIMENTAL SETUP

The performance of the three virtual sensing methods is examined in an experimental context with a cantilevered beam, which is installed with nine uniaxial Brüel & Kjær (B&K) type 4507 piezoelectric accelerometers, see Fig. 1. The beam is treated in two different input settings; the first being an impulse

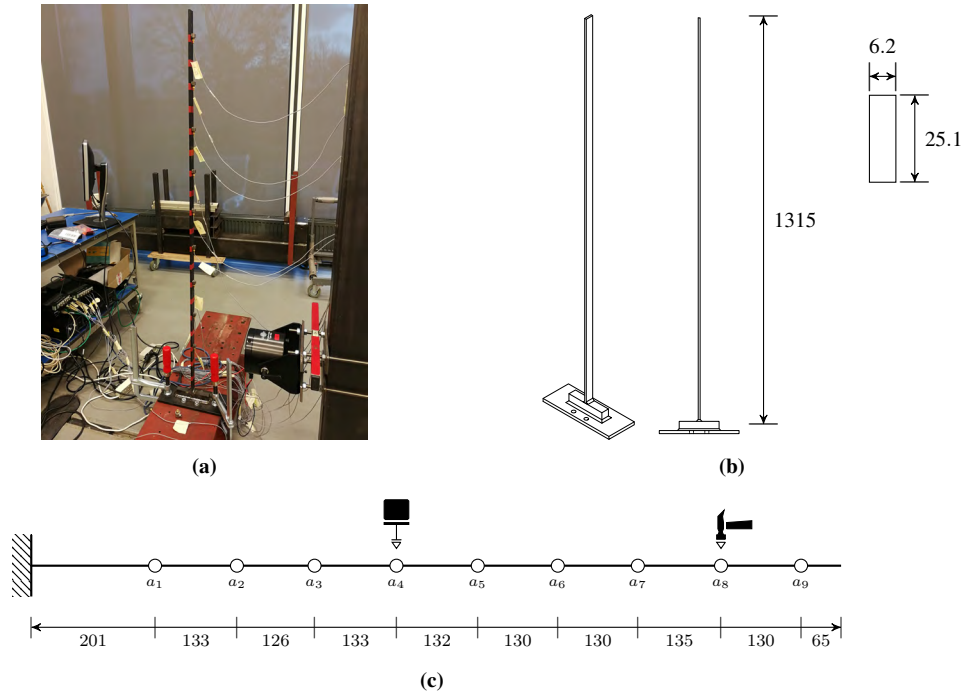


Figure 1: (a) Picture of the experimental setup with installed accelerometers on the cantilever beam, (b) illustration of the beam and its cross-section with dimensions and (c) spatial distribution of the accelerometers (denoted a_{1-9}), the pseudo-random input acting at a_4 and the impulse input applied at a_8 . All dimensions are in mm.

excitation with a B&K type 8206 impact hammer and the second being a pseudo-random excitation with a B&K type 4809 shaker. In Fig. 1c, the spatial distribution of the accelerometers is shown along with the input locations. The accelerations captured from the impulse excitation are low-pass filtered with a cut-off frequency of 250 Hz to include the first six in-plane bending modes, while the pseudo-random input acts within a frequency span of $[0, 100]$ Hz to include the first four in-plane bending modes.

5 NUMERICAL MODEL

The modal parameters of the first six in-plane bending modes are identified using a deterministic subspace state-space system identification algorithm [12]. Furthermore, the modulus of elasticity and mass density are from preliminary non-destructive tests found to be $E = 201$ GPa and $\rho = 7770$ kg/m³,

Table 1: Comparison of the identified and model-predicted eigenfrequencies and mode shapes. Furthermore, the identified modal damping ratios are shown.

Mode	$\bar{\omega}_{FE}$ [Hz]	$\bar{\omega}_{ID}$ [Hz]	$\frac{\bar{\omega}_{FE} - \bar{\omega}_{ID}}{\bar{\omega}_{ID}} 100$ [%]	ζ_{ID} [%]	MAC [–]
1	2.82	2.82	0.00	1.33	1.00
2	17.58	17.48	0.57	0.38	1.00
3	48.69	48.68	0.02	0.27	1.00
4	96.13	97.17	–1.08	0.33	0.99
5	161.21	161.77	–0.35	0.28	0.99
6	240.13	237.02	1.30	0.30	0.99

respectively. From the identified modal and material parameters, a FE model, discretized using 20 2D Euler-Bernoulli beams, is established. Subsequently, the FE model is calibrated against the identified undamped eigenfrequencies and mode shapes, where the percentage-wise eigenfrequency error and the modal assurance criterion (MAC) [13] are, respectively, minimized and maximized by adding point masses (from the equipment) and a rotational spring at the kinematic boundary condition. In Table 1, the identified modal parameters are compared with those of the calibrated FE model. As can be seen, the identified and numerical mode shapes are almost fully correlated with MAC values ≥ 0.99 for all modes, while the undamped eigenfrequencies deviate $\leq 1.30\%$.

6 COMPARATIVE ANALYSIS OF VIRTUAL SENSING METHODS

6.1 Assessment criteria for vibration estimation

To assess and compare the performance of the methods outlined in Section 3, the time response criterion (TRAC) [14] and the mean absolute error (MAE) are utilized. In this application, the former expresses the correlation at one DOF, i , between an estimated and a measured output signal, thus

$$\text{TRAC}_i = \frac{\left(\sum_{k=1}^N y_k^{(i)} \mu_k^{(i)}\right)^2}{\sum_{k=1}^N y_k^{(i)} y_k^{(i)} \sum_{k=1}^N \mu_k^{(i)} \mu_k^{(i)}} \in [0, 1]. \quad (22)$$

Here, a value of one implies full correlation, while a value of zero corresponds to no correlation. As the TRAC does not account for magnitude errors in the estimated signal, the MAE is introduced as the mean average error magnitude between an estimated and a measured signal at one DOF, i . As such,

$$\text{MAE}_i = \frac{1}{N} \sum_{k=1}^N |y_k^{(i)} - \mu_k^{(i)}| \in [0, \infty], \quad (23)$$

hence implying that $\text{MAE} = 0$ and $\text{TRAC} = 1$ indicate a perfect estimation.

6.2 Sensor configurations

From the nine installed accelerometers, see Fig. 1c, it is chosen to analyze 11 different subset of sensor configurations for both input types. In Fig. 2, an example of a sensor configuration—consisting of three accelerometers, namely, a_5 , a_7 and a_8 —is depicted along with the assumed virtual sensor, a_6 (marked with \bullet).

6.3 Impulse excitation

In Table 2, TRAC and MAE values for the 11 sensor configurations are presented for the case of a virtual sensor deployed instead of a_6 . The KF and JISE algorithms are initialized using $\hat{z}_{0|-1} = 0$ and $P_{0|-1}^z = 0$, as the initial state is known exactly. For the presented sensor configurations, the KF yields $\text{TRAC} \in [0.89, 0.99]$ and $\text{MAE} \in [0.09, 0.41] \text{ m/s}^2$ and JISE yields $\text{TRAC} \in [0.96, 1.00]$ and $\text{MAE} \in [0.09, 0.28] \text{ m/s}^2$. The ME scheme yields $\text{TRAC} \in [0.27, 1.00]$ and $\text{MAE} \in [0.08, 1.97] \text{ m/s}^2$, where

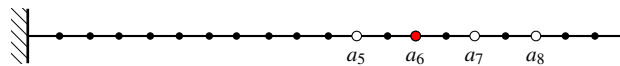


Figure 2: A sensor configuration with physical accelerometers (\circ) and a virtual sensor (\bullet).

Table 2: TRAC and MAE values for 11 sensor configurations. The beam is illustrated in the top with the chosen virtual sensor (●) and all the physical accelerometers (○). The impulse input is applied at a_8 and the first six bending modes are utilized in all configurations.

Config. no.	Considered accelerometers, a_i	TRAC [–]			MAE [m/s ²]		
		ME	KF	JISE	ME	KF	JISE
1	1,2,3,4,5,7,8,9	1.00	0.98	0.99	0.08	0.09	0.09
2	1,8,9	0.55	0.89	0.99	1.90	0.24	0.15
3	1,8	0.52	0.96	0.98	1.97	0.29	0.16
4	8,9	0.64	0.91	0.99	1.86	0.18	0.13
5	5,7,8	0.95	0.99	1.00	0.69	0.11	0.08
6	7,8	0.57	0.97	0.98	1.38	0.23	0.15
7	5,8	0.27	0.95	0.98	1.65	0.29	0.16
8	2,4,8	0.82	0.97	0.98	1.81	0.32	0.23
9	2,8	0.81	0.96	0.96	1.83	0.27	0.23
10	4,8	0.80	0.97	0.99	1.88	0.27	0.12
11	8	0.63	0.93	0.97	1.92	0.41	0.28

we note that the inconsistent performance is a consequence of having more modes than sensors in all configurations except no. 1.

To examine the performance when estimating at other locations than a_6 , virtual sensors are now deployed at the unmeasured locations for sensor configurations no. 5 and 8, see Figs. 3 and 4. It is observed that the KF and JISE schemes perform well for both configurations compared to ME, which—

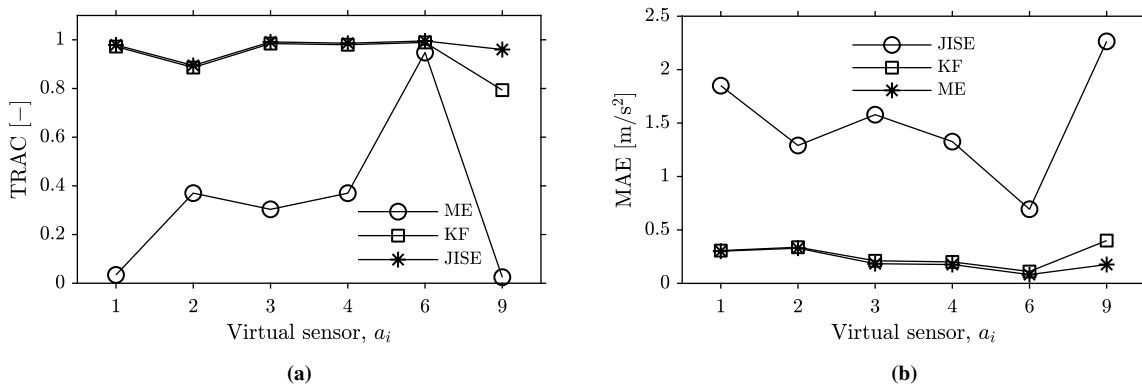


Figure 3: (a) TRAC and (b) MAE values for different virtual sensors using configuration no. 5 from Table 2.

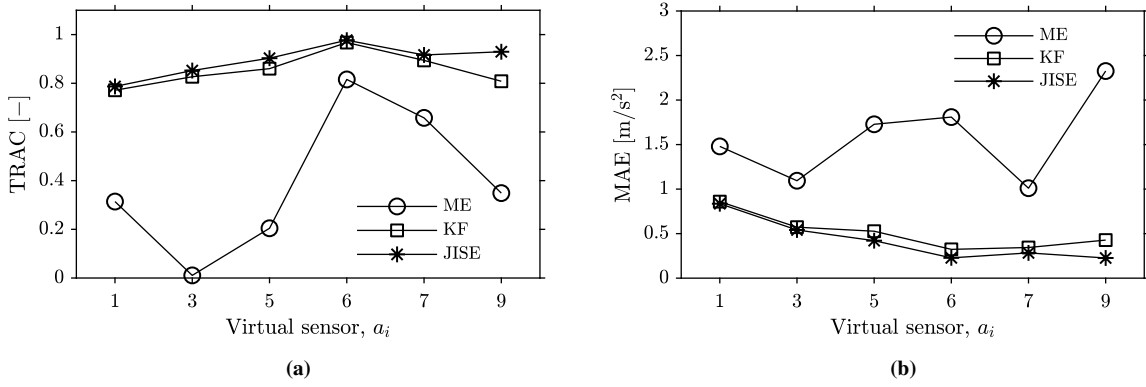


Figure 4: (a) TRAC and (b) MAE values for different virtual sensors using configuration no. 8 from Table 2.

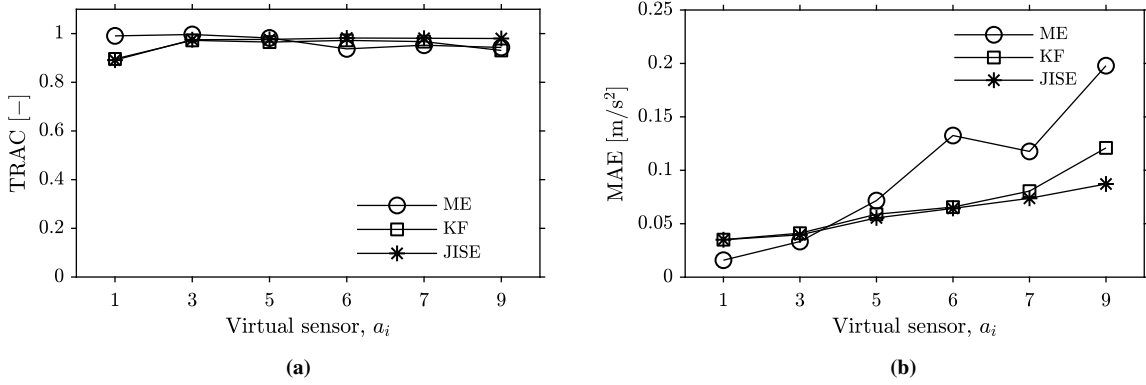


Figure 5: (a) TRAC and (b) MAE values for sensor configuration no. 8 from Table 2 using truncated data. Note that the interval on the second axis has changed from $[0, 3]$ to $[0, 0.25]$ m/s^2 compared to Fig. 4b.

in the underdetermined case where $s < m$ —is particularly sensitive to the placement of virtual sensors with respect to the specific physical sensor configuration. For instance, when utilizing configuration no. 5 for ME, the virtual sensor at a_6 yields $\text{TRAC} = 0.95$ and $\text{MAE} = 0.69 \text{ m/s}^2$, while a virtual sensor at a_9 yields $\text{TRAC} = 0.02$ and $\text{MAE} = 2.26 \text{ m/s}^2$, see Fig. 3. To exemplify the importance of having more sensors than modes in the ME scheme, some of the measured time histories for configuration no. 8 are removed such that $s \geq m$ is fulfilled. Hereby, we obtain the results depicted in Fig. 5, where it is seen that the performance of ME improves considerably when compared to Fig. 4. It is noted that ME improves for all configurations when $s \geq m$ is fulfilled.

6.4 Pseudo-random excitation

In Table 3, TRAC and MAE values for 11 sensor configurations are shown for the case of pseudo-random input and a virtual sensor deployed instead of a_6 . The KF and JISE algorithms are initialized with $\hat{z}_{0|-1} = 0$ and $P_{0|-1}^z = 0$, where JISE yields $\text{TRAC} \in [0.62, 0.98]$ and $\text{MAE} \in [0.40, 1.93]$, while the KF yields $\text{TRAC} \in [0.19, 0.87]$ and $\text{MAE} \in [1.15, 3.45]$. Correspondingly, ME provides $\text{TRAC} \in [0.01, 1.00]$ and $\text{MAE} \in [0.09, 3.84]$.

Configurations no. 7 and 10, which both fulfil $s \geq m$, are used to examine the performance when

Table 3: TRAC and MAE values for 11 sensor configurations. The beam is illustrated in the top with the chosen virtual sensor (●) and all the physical accelerometers (○). The pseudo-random input is applied at a_4 and the first four bending modes are utilized in all configurations.

Config. No.	Considered accelerometers, a_i	TRAC [–]			MAE [m/s^2]		
		ME	KF	JISE	ME	KF	JISE
1	1,2,3,4,5,7,8,9	0.99	0.80	0.98	0.29	1.40	0.44
2	1,4,8	0.07	0.20	0.91	2.98	3.45	0.98
3	1,4	0.02	0.19	0.81	3.48	3.44	1.34
4	1,4,7,8	0.98	0.80	0.97	0.43	1.38	0.57
5	4,5,7	0.99	0.83	0.98	0.39	1.31	0.43
6	4,7	0.73	0.87	0.94	1.59	1.15	0.73
7	4,5,7,8	1.00	0.85	0.98	0.09	1.21	0.40
8	2,4,7	0.98	0.80	0.97	0.65	1.40	0.53
9	2,4	0.01	0.22	0.82	3.61	3.36	1.30
10	1,2,4,7	0.31	0.81	0.81	3.84	1.37	1.44
11	4	0.04	0.32	0.62	3.40	3.01	1.93

virtual sensors are deployed at all unmeasured locations, see Figs. 6 and 7. Here, ME performs better than the KF and JISE at all locations for sensor configuration no. 7, while ME performs poorly when using sensor configuration no. 10. The latter is due to poor sensor placement, as a_1 and a_2 capture low modal amplitudes. When comparing configuration no. 10 with 4, where a_2 is changed with a_8 , one observes a considerable improvement in the performance of ME, see Fig. 8. The importance of

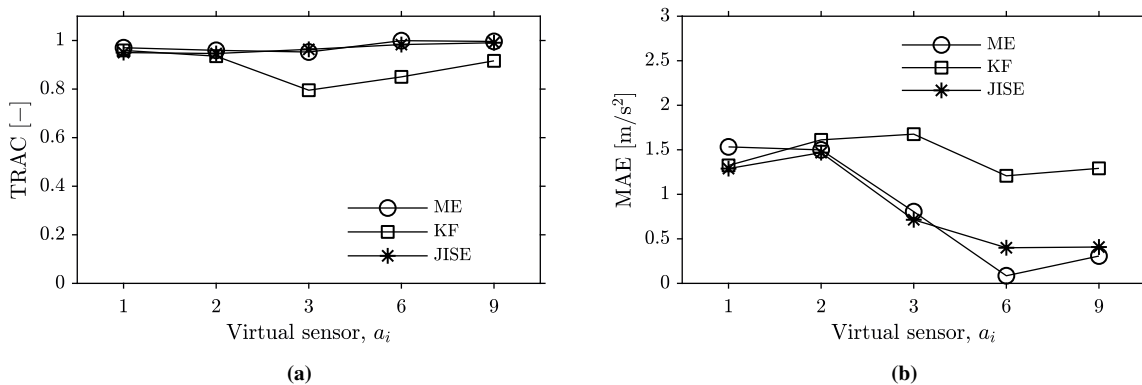


Figure 6: (a) TRAC and (b) MAE values for different virtual sensors using configuration no. 7 from Table 3.

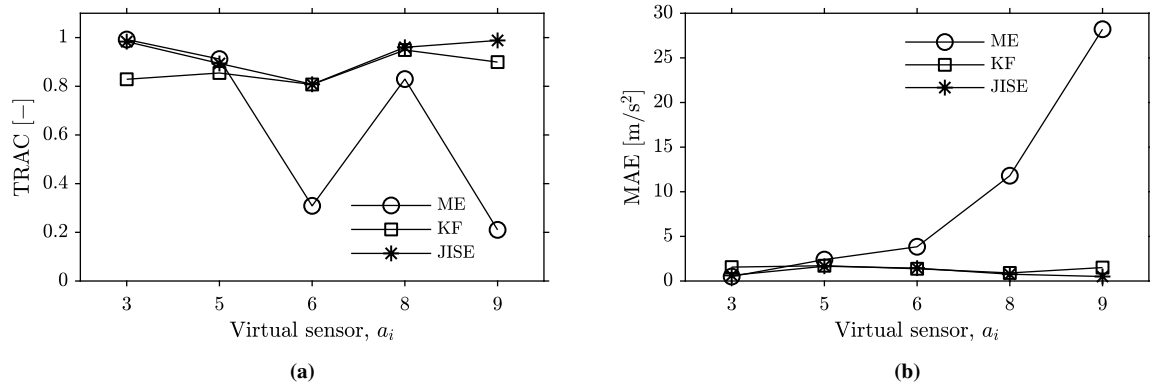


Figure 7: (a) TRAC and (b) MAE values for different virtual sensors using configuration no. 10 from Table 3.

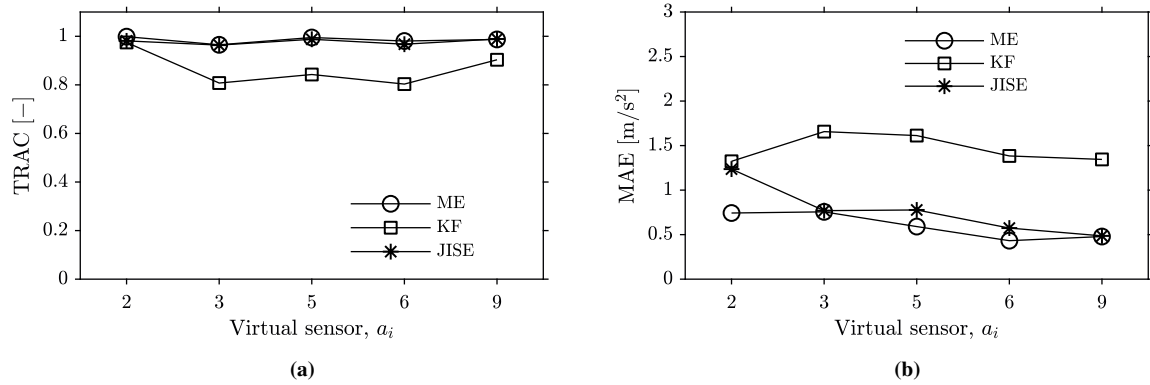


Figure 8: (a) TRAC and (b) MAE values for sensor configuration no. 4 from Table 3. Note that the interval on the second axis has changed from $[0, 30]$ to $[0, 3]$ m/s² compared to Fig. 7b.

well-placed sensors is elaborated by the authors in [15].

7 CONCLUSIONS

In the present paper, experimentally obtained vibration measurements are used to compare the performance of three vibration estimation schemes, namely, ME, KF and JISE. The comparative analysis is based on a cantilevered beam subjected to an impulse and a pseudo-random input. The findings suggest that if the number of installed sensors is no less than the number of considered modes, that is, $s \geq m$, ME is the preferable method. If $s \geq m$ is not fulfilled, JISE is the preferable method, as it generally outperforms ME and KF and demonstrates the lowest sensitivity to the sensor distribution.

Acknowledgment

The authors gratefully acknowledge the Danish Hydrocarbon Research and Technology Centre (DHRTC) for the financial support.

REFERENCES

- [1] W. Gawronski and K. B. Lim, “Balanced actuator and sensor placement for flexible structures,” *International Journal of Control*, vol. 65, no. 1, pp. 131–145, 1996.
- [2] C. R. Farrar and K. Worden, *Structural Health Monitoring: A Machine Learning Perspective*. John Wiley & Sons, 1st ed., 2013.
- [3] M. D. Ulriksen, D. Bernal, and L. Damkilde, “Shaped input distributions for structural damage localization,” *Mechanical Systems and Signal Processing*, vol. 110, pp. 499–508, 2018.
- [4] J. Kullaa, “Virtual sensing of structural vibrations using dynamic substructuring,” *Mechanical Systems and Signal Processing*, vol. 79, pp. 203–224, 2016.
- [5] E. Balmes, “Sensors, degrees of freedom and generalized modeshape expansion methods,” in *Proceedings of IMAC-XVII, A Conference & Exposition on Structural Dynamics*, 1999.
- [6] P. Avitabile, “Model reduction and model expansion and their applications - part 1: Theory,” in *Proceedings of IMAC-XXIII, A Conference & Exposition on Structural Dynamics*, 2005.
- [7] R. E. Kalman, “A new approach to linear filtering and prediction problems,” *Journal of Basic Engineering*, vol. 82, no. 1, pp. 35–45, 1960.
- [8] S. Gillijns and B. D. Moor, “Unbiased minimum-variance input and state estimation for linear discrete-time systems with direct feedthrough,” *Automatica*, vol. 43, no. 5, pp. 934–937, 2007.
- [9] B. D. O. Anderson and J. B. Moore, *Optimal filtering*. Prentice-Hall, 1979.
- [10] K. Maes, A. Iliopoulos, W. Weijtjens, C. Devriendt, and G. Lombaert, “Dynamic strain estimation for fatigue assessment of an offshore monopile wind turbine using filtering and modal expansion algorithms,” *Mechanical Systems and Signal Processing*, vol. 76-77, pp. 592–611, 2016.
- [11] E. Lourens, C. Papadimitriou, S. Gillijns, E. Reynders, G. D. Roeck, and G. Lombaert, “Joint input-response estimation for structural systems based on reduced-order models and vibration data from a limited number of sensors,” *Mechanical Systems and Signal Processing*, vol. 29, pp. 310–327, 2012.
- [12] P. V. Overschee and B. D. Moor, *Subspace identification for linear systems: theory - implementation - applications*. Kluwer Academic Publishers, 1st edition ed., 1996.
- [13] R. J. Allemang and D. L. Brown, “A correlation coefficient for modal vector analysis,” *International Modal Analysis Conference*, vol. 1, no. 1, pp. 110–116, 1982.
- [14] P. Avitabile and P. Pingle, “Prediction of full field dynamic strain from limited sets of measured data,” *Shock and Vibration*, vol. 19, no. 5, pp. 765–785, 2012.
- [15] E. K. Andersen, M. W. Pedersen, M. D. Ulriksen, and L. Damkilde, “Examination of sensor distribution schemes for vibration estimation,” in *Proceedings of IX ECCOMAS Thematic Conference on Smart Structures and Materials*, 2019.

EXAMINATION OF SENSOR DISTRIBUTION SCHEMES FOR VIBRATION ESTIMATION

EMIL K. ANDERSEN*, MATHIAS W. PEDERSEN*, MARTIN D. ULRIKSEN* AND LARS DAMKILDE*

Dept. of Civil Engineering, Aalborg University
Niels Bohrs Vej 8, 6700 Esbjerg, Denmark

*e-mail: ekan14@student.aau.dk, mwpe13@student.aau.dk, mdu@civil.aau.dk & lda@civil.aau.dk

Key words: Optimal sensor distribution, Vibration estimation, Effective independence, Driving point residue, Kinetic energy.

Abstract. The general outset in vibration analysis is that a sensor distribution is optimal if the utility of the deployed system is maximized; with system referring to, for example, an identification system if the sensors are deployed to facilitate modal parameter estimation or a monitoring system if damage detection is the target. While numerous studies have been presented in the context of system identification and structural health monitoring, few studies have addressed the sensor placement task for vibration estimation (also known as virtual sensing). Therefore, the present paper offers an examination of this by adapting four schemes—developed and widely used for optimal sensor placement in system identification and structural health monitoring—for placing sensors to estimate unmeasured vibrations from a limited number of output sensors. More specifically, we test the performance of the effective independence (EI) method, the driving point residue (DPR) method, a combination of the two (the EI-DPR method), and the kinetic energy (KE) method in the context of estimating unmeasured vibrations of a structural system of engineering interest.

1 INTRODUCTION

Within civil and mechanical engineering, it is common practice to use vibration measurements for structural monitoring and control purposes [1, 2, 3]. The vibrations are captured through an installed sensor network, which, in most applications, consists of a limited number of sensors due to the associated costs and the fact that there may be locations inaccessible for instrumentation. As such, virtual sensing can be utilized to estimate vibration responses at designated locations from response acquired by the installed sensor network [4, 5].

In [6], an experimental comparison study is conducted to assess the performance of three well-established virtual sensing methods, namely, modal expansion (ME) [7, 8], Kalman filtering [9] and a joint input-state estimation (JISE) algorithm [10], which, in addition to estimating the full optimal state vector, also estimates the unknown input. The findings reported in [6] aid to the general proposition that the performance of the virtual sensing methods is greatly affected by the number and distribution of sensors. While only a few studies have been put forth for optimal sensor placement for virtual sensing [11], the topic has been explored extensively in the context of system identification [12, 13, 14] and structural health monitoring [15, 16, 17]. Within both these application areas, a widely adopted approach is to, a

priori, select the type and number of sensors to install and then proceed by treating the task as a discrete optimization problem in which the sensor locations are the variables. What distinguishes each method is, as such, the cost function that must be minimized/maximized.

In this paper, we offer an examination of the virtual sensing applicability of four well-established sensor distribution schemes, which, albeit proposed for either system identification or structural health monitoring, all have cost functions with expected merit in the context of vibration estimation. Specifically, we test (1) the effective independence (EI) method [12], which places sensors to maximize the linear independence of the mode shapes, (2) the driving point residue (DPR) method [18], which places sensors to maximize the average modal amplitudes, (3) the EI-DPR method [19], which directly combines the EI and DPR methods, and (4) the kinetic energy (KE) method [20], which places sensors to maximize the kinetic energy. The methods are tested in a numerical framework with a finite element (FE) frame structure, where the ME technique and the JISE algorithm are utilized to estimate vibrations from the sensor networks deployed based on the four distribution schemes.

The paper is organized as follows: in Section 2, we present the prerequisite vibration theory that forms the basis for the vibration estimation techniques and sensor distribution methods outlined in Sections 3 and 4. Section 5 presents the numerical example in which the performance of the sensor distribution methods is examined and compared. Lastly, some concluding remarks are given in Section 6.

2 PREREQUISITE THEORY

Assuming the structure of interest is classically damped, can be adequately described with n degrees of freedom (DOF) and linear, time invariant (LTI) conditions hold, the temporal equation of motion is given as

$$M\ddot{x}(t) + C\dot{x}(t) + Kx(t) = S_p f(t). \quad (1)$$

Here, $K, C, M \in \mathbb{R}^{n \times n}$ are the stiffness, damping and mass matrices, $x(t), \dot{x}(t), \ddot{x}(t) \in \mathbb{R}^n$ are the nodal displacements, velocities and accelerations, and $f(t) \in \mathbb{R}^p$ contains the p external inputs distributed by $S_p \in \mathbb{R}^{n \times p}$. By introducing the modal transformation

$$x(t) \approx \sum_{i \in \mathcal{A}} \phi_i q_i(t) = \Phi q(t), \quad (2)$$

where \mathcal{A} denotes a subset holding the indexes of the $m \leq n$ governing modes and $\Phi = [\phi_1 \ \phi_2 \ \dots \ \phi_m] \in \mathbb{R}^{n \times m}$ is the truncated modal matrix containing mass-normalized mode shapes, Eq. (1) is transformed to modal coordinates as

$$\ddot{q}(t) + \tilde{C}\dot{q}(t) + \tilde{K}q(t) = \Phi^T S_p f(t), \quad (3)$$

with \tilde{C} being the modal damping matrix and \tilde{K} the spectral matrix.

By defining the modal state vector, $\tilde{z}(t)^T = [q(t)^T \ \dot{q}(t)^T]^T \in \mathbb{R}^{1 \times 2m}$, and rewriting Eq. (3) into discrete state-space form, one has

$$\tilde{z}_{k+1} = \tilde{A}_d \tilde{z}_k + \tilde{B}_d f_k, \quad (4)$$

where $\tilde{z}_k = \tilde{z}(k\Delta t)$ and $f_k = f(k\Delta t)$ for $k \in [0, N-1]$, with N being the total number of samples and Δt the time increment. Accepting a zero-order-hold, the state-transition matrix, $\tilde{A}_d \in \mathbb{R}^{2m \times 2m}$, and the input matrix, $\tilde{B}_d \in \mathbb{R}^{2m \times p}$, are given as

$$\tilde{A}_d = \exp \left(\begin{bmatrix} 0 & I \\ -\tilde{K} & -\tilde{C} \end{bmatrix} \Delta t \right) \quad (5)$$

$$\tilde{B}_d = [\tilde{A}_d - I] \begin{bmatrix} 0 & I \\ -\tilde{K} & -\tilde{C} \end{bmatrix}^{-1} \begin{bmatrix} 0 \\ \Phi^T S_p \end{bmatrix}. \quad (6)$$

The s measured outputs are gathered in $y_k \in \mathbb{R}^s$ and defined as

$$y_k = \tilde{C}_d \tilde{z}_k + \tilde{D}_d f_k, \quad (7)$$

where $\tilde{C}_d = [S_d \Phi - S_a \Phi \tilde{K} \quad S_v \Phi - S_a \Phi \tilde{C}] \in \mathbb{R}^{s \times 2m}$ is the output matrix, $\tilde{D}_d = [S_a \Phi \Phi^T S_p] \in \mathbb{R}^{s \times p}$ is the input-output transmission matrix and $S_d, S_v, S_a \in \mathbb{R}^{s \times n}$ relate measured displacements, velocities and accelerations to the corresponding DOF in the numerical model.

3 VIBRATION ESTIMATION TECHNIQUES

The discrete system output is partitioned into two subsets: the s measured vibration quantities, $y_k \in \mathbb{R}^s$, and the α vibrations quantities to be estimated, $\mu_k \in \mathbb{R}^\alpha$.

3.1 Modal expansion (ME)

Let $\eta_k \in \mathbb{R}^m$ be the general notation for a modal kinematic quantity (depending on the nature of y_k), then the modal formulation is rewritten as

$$\begin{bmatrix} y_k \\ \mu_k \end{bmatrix} = \begin{bmatrix} \Phi_s \\ \Phi_\alpha \end{bmatrix} \eta_k \quad (8)$$

with $\Phi_s \in \mathbb{R}^{s \times m}$ and $\Phi_\alpha \in \mathbb{R}^{\alpha \times m}$ being the truncated modal matrices containing the corresponding s and α DOF, respectively. From the first partition of Eq. (8),

$$y_k = \Phi_s \eta_k, \quad (9)$$

it is evident that a unique solution can only exist if the number of installed sensors, s , is no less than the number of considered modes, m . In cases where $s < m$, the measured output histories, y , should, if possible, be truncated or low-pass filtered such that at most s modes govern the signals.

The modal kinematics can be computed as

$$\eta_k = \Phi_s^\dagger y_k, \quad (10)$$

where $(\circ)^\dagger$ denotes the Moore-Penrose pseudo-inverse, which, in this case, minimizes $\|y_k - \Phi_s \eta_k\|_2$. When the modal kinematics are obtained, the physical response at the α desired locations can be readily estimated as

$$\mu_k = \Phi_\alpha \eta_k. \quad (11)$$

3.2 Joint input-state estimation (JISE)

The JISE algorithm [10] is a modified Kalman filter [9] where the input(s) and states are recursively estimated at each time step k from sensor measurements. Eqs. (4) and (7) are extended to

$$\tilde{z}_{k+1} = \tilde{A}_d \tilde{z}_k + \tilde{B}_d f_k + \tilde{w}_k \quad (12)$$

$$y_k = \tilde{C}_d \tilde{z}_k + \tilde{D}_d f_k + v_k, \quad (13)$$

where w_k (and, as such, \tilde{w}_k) and v_k are assumed mutually correlated, zero mean and white signals with covariance matrices, $Q \in \mathbb{R}^{2m \times 2m}$, $R \in \mathbb{R}^{s \times s}$ and $S \in \mathbb{R}^{2m \times s}$, given as

$$Q = \mathbb{E}[w_k w_k^T], \quad R = \mathbb{E}[v_k v_k^T], \quad S = \mathbb{E}[w_k v_k^T]. \quad (14)$$

The process noise covariance matrix, Q , indicates how accurate the algorithm considers the model to be, whereas the measurement noise covariance matrix, R , indicates the confidence put into the measured data.

The JISE algorithm is presented in Algorithm 1 according to [21], where $(\hat{\cdot})$ denotes an estimated quantity, $K_k \in \mathbb{R}^{2m \times s}$ is the Kalman gain, which is calculated such that the state estimate is minimum variance and unbiased, and $M_k \in \mathbb{R}^{p \times s}$ is the gain related to the input estimate. Algorithm 1 is initialized using an initial state vector, $\hat{z}_{0|-1}$, assumed independent of w_k and v_k , and its associated error covariance matrix, $P_{0|-1}^z$, defined as

$$P_{k|k}^z = \mathbb{E}[(\tilde{z}_k - \hat{z}_k)(\tilde{z}_k - \hat{z}_k)^T] \in \mathbb{R}^{2m \times 2m}. \quad (15)$$

When the estimated state vector, $\hat{z}_{k|k}$, is computed, the unmeasured response can be estimated by

$$\mu_{k|k} = \tilde{C}_{d,e} \hat{z}_{k|k} + \tilde{D}_{d,e} \hat{f}_{k|k}, \quad (16)$$

where $\tilde{C}_{d,e} = [S_{d,e}\Phi - S_{a,e}\Phi\tilde{K} \quad S_{v,e}\Phi - S_{a,e}\Phi\tilde{C}] \in \mathbb{R}^{\alpha \times 2m}$ is the redefined output matrix and $\tilde{D}_{d,e} = [S_{a,e}\Phi\Phi^T S_p] \in \mathbb{R}^{\alpha \times p}$ is the redefined input-output transmission matrix, with subscript e referring to estimation and the distribution matrices, $S_{d,e}$, $S_{v,e}$, $S_{a,e} \in \mathbb{R}^{\alpha \times n}$, relating the estimated quantities to the designated locations.

Algorithm 1: The JISE algorithm.

```

for  $k = 0$  to  $k = N - 1$  do
    Input estimation:
    (1)  $\hat{R}_k = \tilde{C}_d P_{k|k-1}^z \tilde{C}_d^T + R$ 
    (2)  $M_k = (\tilde{D}_d^T \hat{R}_k^{-1} \tilde{D}_d)^{-1} \tilde{D}_d^T \hat{R}_k^{-1}$ 
    (3)  $\hat{f}_{k|k} = M_k (y_k - \tilde{C}_d \hat{z}_{k|k-1})$ 
    (4)  $P_{k|k}^f = (\tilde{D}_d^T \hat{R}_k^{-1} \tilde{D}_d)^{-1}$ 

    Measurement update:
    (5)  $K_k = P_{k|k-1}^z \tilde{C}_d^T \hat{R}_k^{-1}$ 
    (6)  $\hat{z}_{k|k} = \hat{z}_{k|k-1} + K_k (y_k - \tilde{C}_d \hat{z}_{k|k-1} - \tilde{D}_d \hat{f}_{k|k})$ 
    (7)  $P_{k|k}^z = P_{k|k-1}^z - K_k (\hat{R}_k - \tilde{D}_d P_{k|k}^f \tilde{D}_d^T) K_k^T$ 
    (8)  $P_{k|k}^{zf} = (P_{k|k}^{fz})^T = -K_k \tilde{D}_d P_{k|k}^f$ 

    Time update:
    (9)  $\hat{z}_{k+1|k} = \tilde{A}_d \hat{z}_{k|k} + \tilde{B}_d \hat{f}_{k|k}$ 
    (10)  $N_k = \tilde{A}_d K_k (I - \tilde{D}_d M_k) + \tilde{B}_d M_k$ 
    (11)  $P_{k+1|k}^z = [\tilde{A}_d \quad \tilde{B}_d] \begin{bmatrix} P_{k|k}^z & P_{k|k}^{zf} \\ P_{k|k}^{fz} & P_{k|k}^f \end{bmatrix} \begin{bmatrix} \tilde{A}_d^T \\ \tilde{B}_d^T \end{bmatrix} + Q - N_k S^T - S N_k^T$ 
end
    
```

Worth of explicit note regarding Algorithm 1 is that \hat{R}_k becomes rank deficient if $s > m$, while $\tilde{D}_d^T \hat{R}_k^{-1} \tilde{D}_d$ becomes rank deficient if $s > m$, $p > s$ or $p > m$. To prevent conditioning issues, the matrices can, as outlined in [22], be truncated using a singular value decomposition (SVD) procedure.

4 SENSOR DISTRIBUTION METHODS

In the presentation of the four sensor distribution schemes, we distinguish between candidate sensor locations, l , and the final sensor locations, $s \subset l$. In this way, the former represents the set of all potential sensor locations, while the latter is the particular subset selected through the optimization.

4.1 The effective independence (EI) method

The EI method maximizes the linear independence of the considered mode shapes through an iterative process, where l candidate sensor locations are reduced to s locations. By defining the modal matrix, $\Phi_{\mathcal{B}} \in \mathbb{R}^{l \times m}$, adding white Gaussian noise, $u_k \in \mathbb{R}^l \sim \mathcal{N}(0, I\sigma)$, and rewriting Eq. (2) into discrete form, one has

$$x_k \approx \Phi_{\mathcal{B}} q_k + u_k. \quad (17)$$

The optimal estimate of q_k , denoted \hat{q}_k , is realized when the covariance matrix of the estimate errors, $J = \mathbb{E}[(q_k - \hat{q}_k)(q_k - \hat{q}_k)^T] \in \mathbb{R}^{m \times m}$, is minimized. In [12], it is shown that J can be written as

$$J = \left(\left(\frac{\partial x_k}{\partial q_k} \right)^T (\sigma^2)^{-1} \left(\frac{\partial x_k}{\partial q_k} \right) \right)^{-1} = \sigma^2 (\Phi_{\mathcal{B}}^T \Phi_{\mathcal{B}})^{-1} = \mathcal{F}^{-1}, \quad (18)$$

where $\mathcal{F} \in \mathbb{R}^{m \times m}$ is the Fisher information matrix (FIM). From Eq. (18), it is, given that $u_k \in \mathbb{R}^l \sim \mathcal{N}(0, I\sigma)$, seen how maximizing some suitable norm of the FIM, and, as such, $\Phi_{\mathcal{B}}^T \Phi_{\mathcal{B}}$, is tantamount to minimizing the covariance matrix of the estimate errors.

To determine which candidate sensor location to discard, one starts by solving the eigenvalue problem

$$(\Phi_{\mathcal{B}}^T \Phi_{\mathcal{B}} - \lambda I) \Psi = 0, \quad (19)$$

where $\Psi \in \mathbb{R}^{m \times m}$ contains the orthogonal eigenvectors and $\lambda \in \mathbb{R}^{m \times m}$ the associated eigenvalues. Worth of explicit note is that λ becomes rank deficient when $m > s$, which means that the amount of sensors utilized in the EI method can be no less than the number of considered modes. From the eigencharacteristics of $\Phi_{\mathcal{B}}^T \Phi_{\mathcal{B}}$, the EI coefficients at the l DOF are computed as

$$\mathcal{E} = (\Phi_{\mathcal{B}} \Psi) \otimes (\Phi_{\mathcal{B}} \Psi) \lambda^{-1} \mathcal{J} \in \mathbb{R}^l, \quad (20)$$

with \otimes denoting the Hadamard product (that is, term-by-term matrix multiplication) and $\mathcal{J} \in \mathbb{R}^m$ a vector with only ones. The procedure is to iteratively exclude the candidate sensor location associated with $\min\{\mathcal{E}\}$ and subsequently update Eqs. (19) and (20) until $l = s$.

4.2 The driving point residue (DPR) method

The DPR method selects a sensor distribution that yields the highest average modal amplitudes for the considered modes; that is, the s DOF with the largest DPR coefficients. The i th DPR coefficient is defined as

$$\mathcal{D}_i = \sum_{j=1}^m \frac{\phi_{ij}^2}{\bar{\omega}_j}, \quad (21)$$

where $\bar{\omega}_j$ and ϕ_{ij} are the undamped eigenfrequency and the i th eigenvector component of the j th mode.

By multiplying the i th EI coefficient, \mathcal{E}_i , with \mathcal{D}_i for $i \in [1, l]$, one can couple the two methods to the EI-DPR method and iteratively exclude $\min\{\mathcal{E}_i \mathcal{D}_i\}$ until $l = s$. Hence, it is possible to avoid placing sensors in DOF with low energy content.

4.3 The kinetic energy (KE) method

The KE method provides a measure of the average kinetic energy at the l candidate sensor locations for all considered modes. By defining

$$C = \Phi_B \otimes M_B \Phi_B \in \mathbb{R}^{l \times m}, \quad (22)$$

where $M_B \in \mathbb{R}^{l \times l}$ is the mass matrix truncated to l DOF, the i th KE coefficient is given as

$$\mathcal{K}_i = \frac{1}{m} \sum_{j=1}^m C_{ij}, \quad (23)$$

from which the s highest coefficients are chosen as sensor locations.

5 NUMERICAL EXAMPLE

The sensor distribution methods are tested on the FE frame model depicted in Fig. 1a. The model is discretized using 75 2D Euler-Bernoulli beam elements, with a uniform cross-section of 10×10 mm. The modulus of elasticity, mass density and Poisson's ratio are set to $E = 205$ GPa, $\rho = 7750$ kg/m³ and $\nu = 0.3$, and classical damping is assumed with damping ratios $\zeta_i = 0.02$. A pseudo-random input, which excites the first four bending modes, is applied, and acceleration outputs are captured with a sampling frequency of 2 kHz for a time duration of 20 s.

5.1 Assessment criteria for evaluating sensor distributions

To assess and compare the performance of the sensor distribution methods, the time response criterion (TRAC) [23] and the mean absolute error (MAE) are utilized. In this application, the former expresses

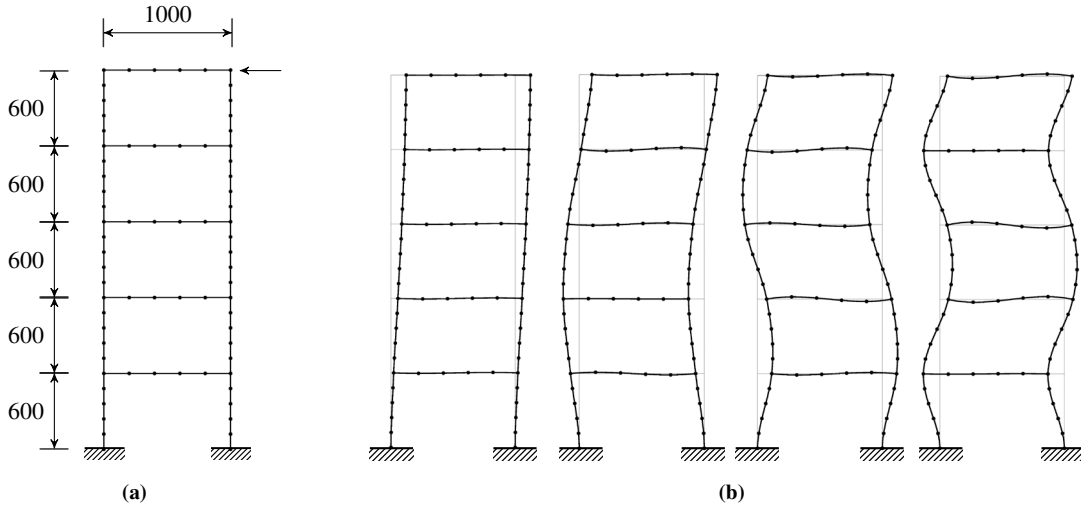


Figure 1: (a) FE frame model excited with a pseudo-random input at the top right corner (illustrated with an arrow). All dimensions are in mm. (b) The first four bending modes of the FE model.

the correlation between a measured and an estimated output signal, thus

$$\text{TRAC}_i = \frac{\left(\sum_{k=1}^N y_k^{(i)} \mu_k^{(i)} \right)^2}{\sum_{k=1}^N y_k^{(i)} y_k^{(i)} \sum_{k=1}^N \mu_k^{(i)} \mu_k^{(i)}} \in [0, 1] \quad (24)$$

for the i th DOF. Here, a value of one implies full correlation, while a value of zero corresponds to no correlation. As the TRAC does not account for magnitude errors in the estimated signal, the MAE is introduced as the mean average error magnitude between a measured and an estimated acceleration signal. As such,

$$\text{MAE}_i = \frac{1}{N} \sum_{k=1}^N |y_k^{(i)} - \mu_k^{(i)}| \in [0, \infty], \quad (25)$$

hence implying that $\text{MAE} = 0$ and $\text{TRAC} = 1$ indicate a perfect estimation.

5.2 Results of the sensor distribution methods

The sensor networks selected by the sensor distribution methods are exemplified with six sensors in Fig. 2. As seen, the DPR and KE approaches cluster the sensors at the top floor, while the EI and EI-DPR approaches select DOF at multiple levels. In Table 1, the TRAC and MAE values provided by the different sensor distributions from Fig. 2 are presented. Here, JISE yields $\text{TRAC} \in [0.96, 1.00]$ and $\text{MAE} \in [0.16, 1.13] \text{ m/s}^2$, while ME yields $\text{TRAC} \in [0.00, 1.00]$ and $\text{MAE} \in [0.17, 547] \text{ m/s}^2$. As expected, ME performs best when using the sensor network suggested by the EI approach, as the scheme maximizes the linear independence between the eigenvectors.

The performance of the sensor distribution methods are assessed for $s \in [1, 30]$, see Fig. 3. Here, it is seen that the ME technique is more sensitive towards the number and placement of sensors than the JISE algorithm. For ME, the sensor networks selected by the EI and EI-DPR approaches yield similar results when $s \geq 7$. By visual inspection of Figs. 3a and 3b, it is further noted that the KE scheme and the DPR scheme require, respectively, 19 and 27 sensors in the ME technique to achieve similar results as the EI scheme provides with four sensors. When using the JISE algorithm, it is seen in Figs. 3c and 3d how the sensor networks suggested by the EI, EI-DPR and KE approaches yield similar results when $s \geq 7$,

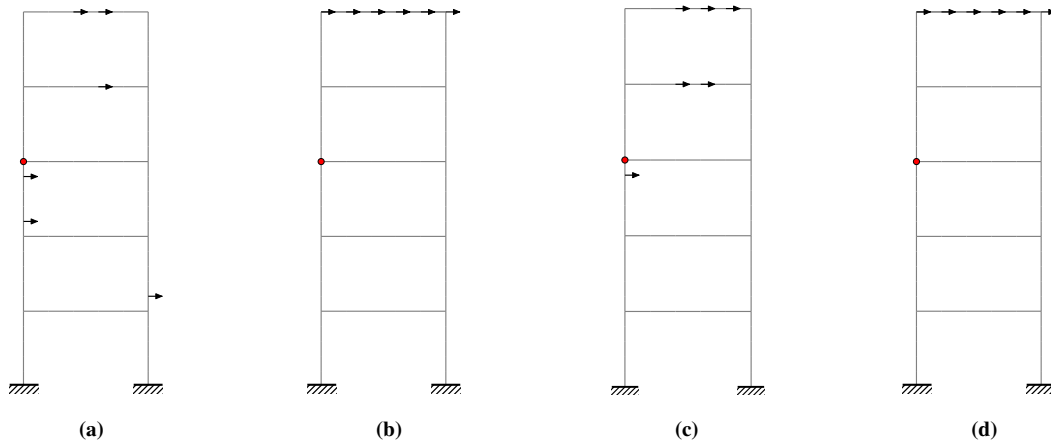


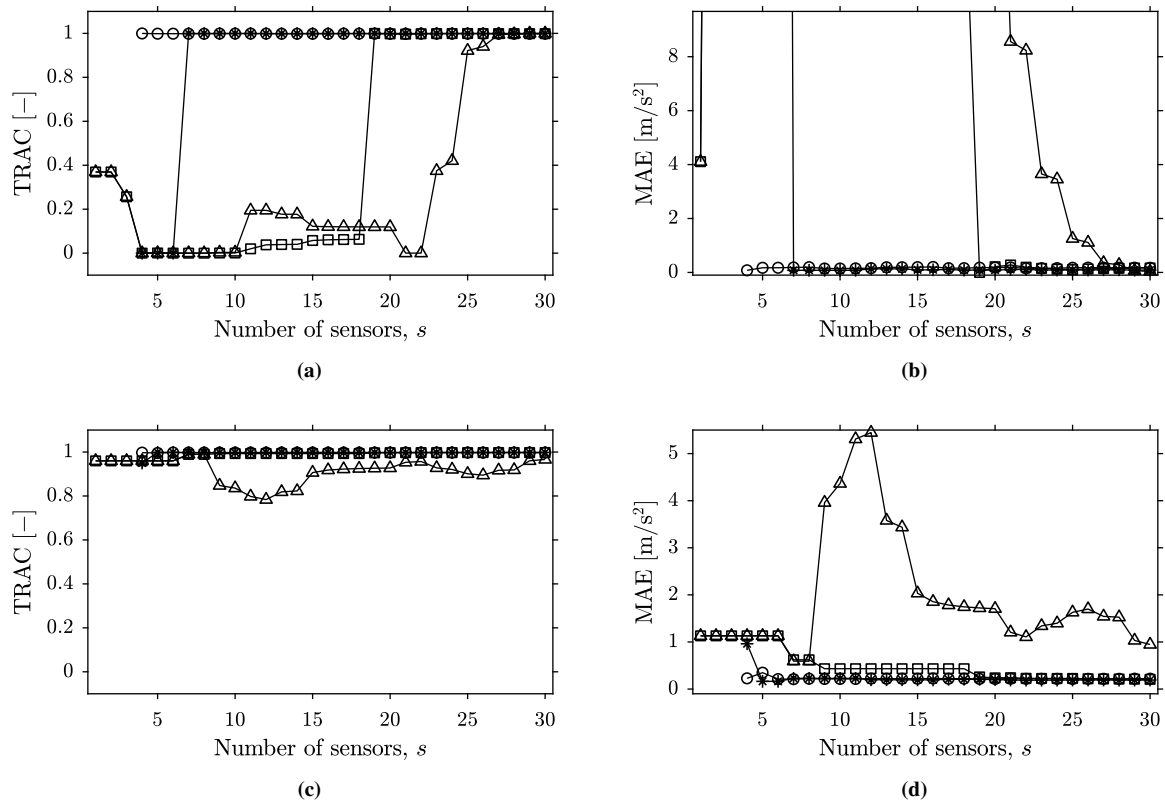
Figure 2: Distribution of six sensors when utilizing (a) the EI approach, (b) the DPR approach, (c) the EI-DPR approach and (d) the KE approach. The deployed virtual sensor is marked as (•) and the arrows indicate measurement in the horizontal direction.

Table 1: TRAC and MAE values for ME and JISE when utilizing six sensors distributed using the EI, DPR, EI-DPR and KE approaches, see Fig. 2.

Estimation method	TRAC [–]				MAE [m/s ²]			
	EI	DPR	EI-DPR	KE	EI	DPR	EI-DPR	KE
ME	1.00	0.00	0.00	0.00	0.17	547	129	547
JISE	1.00	0.96	1.00	0.96	0.21	1.13	0.16	1.13

while the MAE values are, more or less, equally good for the three methods. The best estimations are, in general, obtained utilizing the EI approach. It should, however, be recalled that the EI method (and, as such, the EI-DPR method) can only operate when $s \geq m$.

As the results in Fig. 3 are from ideal circumstances—that is, no model errors or measurement noise—a more realistic analysis setup is established. Here, model errors are introduced by assigning each element random perturbations such that eigenfrequency deviations up to 3.18 % and modal assurance criterion values ≥ 0.96 are observed. Furthermore, the outputs are polluted with 5 % white Gaussian noise. Hereby, the results depicted in Fig. 4 are obtained, where one observes the same tendencies as in


Figure 3: TRAC and MAE values for $s \in [1, 30]$ for (a, b) ME and (c, d) JISE. Note that the second axis in (b) is limited to 50 % of the maximum acceleration captured at the virtual sensor. The markers are assigned as follows: (O) EI, (Δ) DPR, (□) KE and (*) EI-DPR.

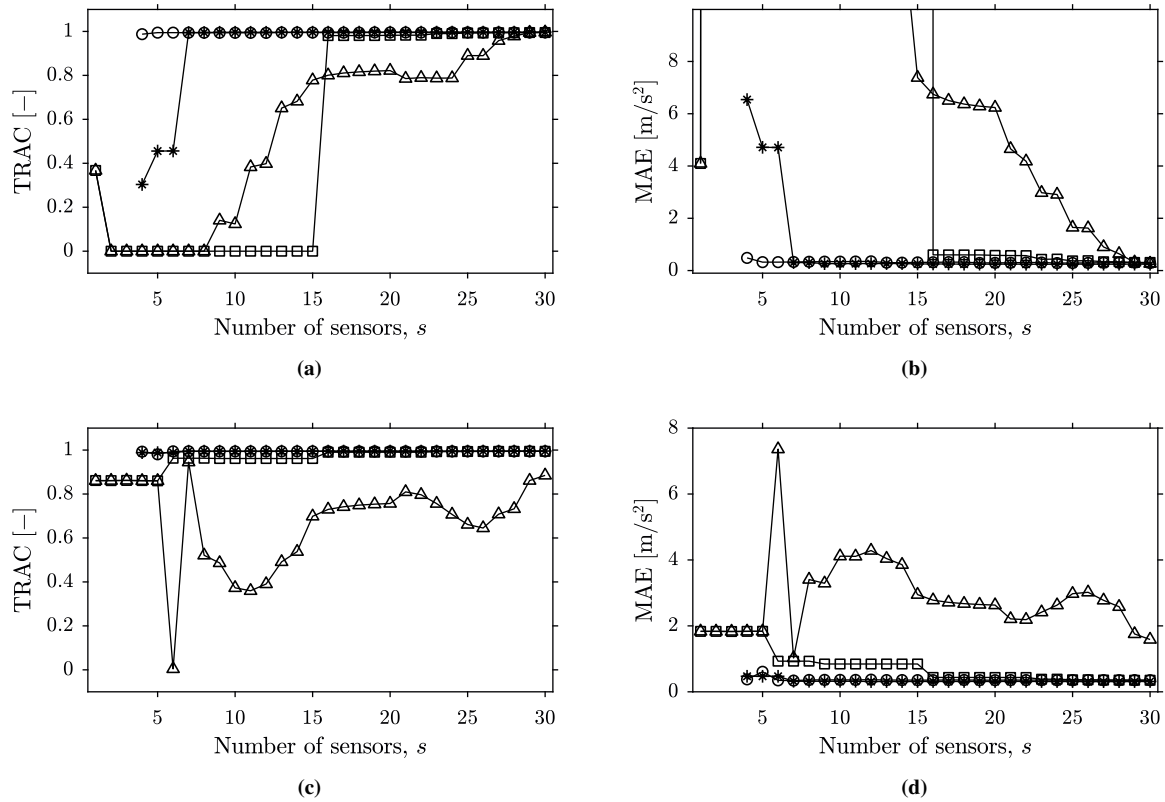


Figure 4: TRAC and MAE values for $s \in [1, 30]$ for (a, b) ME and (c, d) JISE. Note that the second axis in (b) is limited to 50 % of the maximum acceleration captured at the virtual sensor. The markers are assigned as follows: (○) EI, (△) DPR, (□) KE and (*) EI-DPR.

Fig. 3. It is worth of explicit note that, as seen in Figs. 4c and 4d, the performance of the DPR approach is impaired the most by model errors and noisy outputs.

6 CONCLUSIONS

In the present paper, the performance of different sensor distribution schemes, namely, EI, DPR, EI-DPR and KE is examined. The comparative analysis is based on a FE frame model subjected to a pseudo-random input, where accelerations at a designated location are estimated by means of the ME technique and JISE algorithm. The findings suggest in this particular application that when utilizing either ME or JISE for virtual sensing, the EI scheme is preferable for sensor placement, as it yields good results for all distributions when $s \geq m$. If utilizing JISE when $s < m$, the DPR and KE approach yield the exact same results for this particular application.

Acknowledgment

The authors gratefully acknowledge the Danish Hydrocarbon Research and Technology Centre (DHRTC) for the financial support.

REFERENCES

- [1] W. Gawronski and K. B. Lim, “Balanced actuator and sensor placement for flexible structures,” *International Journal of Control*, vol. 65, no. 1, pp. 131–145, 1996.
- [2] C. R. Farrar and K. Worden, *Structural Health Monitoring: A Machine Learning Perspective*. John Wiley & Sons, 1st ed., 2013.
- [3] M. D. Ulriksen, D. Bernal, and L. Damkilde, “Shaped input distributions for structural damage localization,” *Mechanical Systems and Signal Processing*, vol. 110, pp. 499–508, 2018.
- [4] J. Kullaa, “Virtual sensing of structural vibrations using dynamic substructuring,” *Mechanical Systems and Signal Processing*, vol. 79, pp. 203–224, 2016.
- [5] A. Iliopoulos, R. Shirzadeh, W. Weijtjens, P. Guillaume, D. V. Hemelrijck, and C. Devriendt, “A modal decomposition and expansion approach for prediction of dynamic responses on a monopile offshore wind turbine using a limited number of vibration sensors,” *Mechanical Systems and Signal Processing*, vol. 68-69, pp. 84–104, 2016.
- [6] M. W. Pedersen, E. K. Andersen, M. D. Ulriksen, and L. Damkilde, “Examination of modal expansion and kalman filtering techniques for vibration estimation,” in *Proceedings of IX ECCOMAS Thematic Conference on Smart Structures and Materials*, 2019.
- [7] E. Balmes, “Sensors, degrees of freedom and generalized modeshape expansion methods,” in *Proceedings of IMAC-XVII, A Conference & Exposition on Structural Dynamics*, 1999.
- [8] P. Avitabile, “Model reduction and model expansion and their applications - part 1: Theory,” in *Proceedings of IMAC-XXIII, A Conference & Exposition on Structural Dynamics*, 2005.
- [9] R. E. Kalman, “A new approach to linear filtering and prediction problems,” *Journal of Basic Engineering*, vol. 82, no. 1, pp. 35–45, 1960.
- [10] S. Gillijns and B. D. Moor, “Unbiased minimum-variance input and state estimation for linear discrete-time systems with direct feedthrough,” *Automatica*, vol. 43, no. 5, pp. 934–937, 2007.
- [11] J. Kullaa, “Bayesian virtual sensing in structural dynamics,” *Mechanical Systems and Signal Processing*, vol. 115, pp. 497–513, 2019.
- [12] D. C. Kammer, “Sensor placement for on-orbit modal identification and correlation of large space structures,” *Journal of Guidance, Control, and Dynamics*, vol. 14, no. 2, pp. 251–259, 1991.
- [13] C. Papadimitriou, “Optimal sensor placement methodology for parametric identification of structural systems,” *Journal of Sound and Vibration*, vol. 278, no. 4-5, pp. 923–947, 2004.
- [14] M. D. Ulriksen, D. Bernal, and L. Damkilde, “Sensor placement for modal parameter subset estimation: A frequency response-based approach,” in *8th European Workshop On Structural Health Monitoring (EWSHM 2016)*, (Madrid, Spain), 2016.
- [15] K. Worden and A. P. Burrows, “Optimal sensor placement for fault detection,” *Engineering Structures*, vol. 23, no. 8, pp. 885–901, 2001.

- [16] D. L. Parker, *Multi-objective design optimization framework for structural health monitoring*. Ph.D. thesis, Mississippi State University, Mississippi, USA, 2011.
- [17] M. D. Ulriksen and D. Bernal, “Sensor distributions for structural monitoring: a correlation study,” in *Proceedings of the International Conference on Structural Engineering Dynamics (ICEDyn 2017)*, (Ericeira, Portugal), 2017.
- [18] D. Kientzy, M. Richardson, and K. Blakely, “Using finite element data to set up modal tests,” *Sound and Vibration*, vol. 23, pp. 16–23, 1989.
- [19] M. Meo and G. Zumpano, “On the optimal sensor placement techniques for a bridge structure,” *Engineering Structures*, vol. 27, no. 10, pp. 1488 – 1497, 2005.
- [20] M. L. Wang, G. Heo, and D. Satpathi, “A health monitoring system for large structural systems,” *Smart Materials and Structures*, vol. 7, no. 5, pp. 606–616, 1998.
- [21] K. Maes, A. Iliopoulos, W. Weijtjens, C. Devriendt, and G. Lombaert, “Dynamic strain estimation for fatigue assessment of an offshore monopile wind turbine using filtering and modal expansion algorithms,” *Mechanical Systems and Signal Processing*, vol. 76-77, pp. 592–611, 2016.
- [22] E. Lourens, C. Papadimitriou, S. Gillijns, E. Reynders, G. D. Roeck, and G. Lombaert, “Joint input-response estimation for structural systems based on reduced-order models and vibration data from a limited number of sensors,” *Mechanical Systems and Signal Processing*, vol. 29, pp. 310–327, 2012.
- [23] P. Avitabile and P. Pingle, “Prediction of full field dynamic strain from limited sets of measured data,” *Shock and Vibration*, vol. 19, no. 5, pp. 765–785, 2012.

FAULT LOCALIZATION IN RING TYPE STRUCTURES WITH A SECOND-ORDER OUTPUT SPECTRUM BASED METHOD

Q. K. LI AND X. J. JING^{*}

^{*} Department of Mechanical Engineering
The Hong Kong Polytechnic University
Hung Hom, Kowloon, Hong Kong, China
e-mail: xingjian.jing@polyu.edu.hk, www.polyu.edu.hk

Key words: Ring Type, Nonlinear Fault, Damage Indicator, Fault Localization.

Abstract. In order to localize nonlinear faults in ring type structures, a novel second-order output spectrum (SOOS) based method is proposed in this paper. Along the vibration transmission paths in complex structures, the ring type structures are found and labeled by the sensor chains. The ring type multiple degree-of-freedom (MDOF) model and Volterra series are utilized to describe the nonlinear behavior of these ring type structures with nonlinear faults and inherent nonlinearity. With harmonic excitation analysis and local tuning approach (LTA), the properties of the SOOS of nonlinear ring type structure are derived and analyzed. Based on these properties, a novel SOOS based method with a local damage index is proposed for nonlinear fault localization. In the numerical study, the results of comparison between previous and novel methods demonstrate that the proposed local damage index can provide more correct information of fault positions, and hence the novel method can be used for multiple fault diagnosis in ring type structure with inherent nonlinearity.

1 INTRODUCTION

Bolt self-loosening frequently exists in complex structures like offshore platforms and bridges since these engineering structures are often subjected to various dynamic loads in their service process [1]. Some results in the literature demonstrate that structural failure caused by bolt-loosening will affect the smooth operation of structures and even cause some catastrophic accidents [2,3]. Therefore, evaluating the integrity of structures is a very important objective to minimize the downtime of structures and save maintenance costs. For this purpose, numerous fault diagnosis methods have been proposed [4-6]. Compared with others, vibration-based approaches provide more theoretical and operational simplicity [4]. The basic principle of this indirect method is that faults will change the structural properties (mass, damping and stiffness), which in turn will alter the vibration characteristics of the structure. Thus, the changes in vibration features can be used to evaluate the durability of structures [6]. Moreover, many structures with loose bolts behave in a nonlinear way [1,7]. For example, joint structures with loose bolts have nonlinear stiffness and damping [1]. Therefore, vibration-based methods utilizing the nonlinearity caused by bolt-loosening faults have been proposed and provide high sensitive damage indicators for fault diagnosis in complex structures [8].

Nonlinearity-based transmissibility (TF), defined as the ratio of output spectra between two

different response points of structures, is more available for the diagnosis of localized nonlinear damages since it considers nonlinearity due to faults and depends on structural zeros solely [9]. Considering the cubic nonlinear internal forces caused by loosen bolts, the properties of TF of multi-degree-of-freedom (MDOF) system were derived and then were applied for a rotorcraft fuselage [10]. Based on an efficient n th-order output spectrum estimation (n th-OSE) algorithm [11,12], the second order output spectrum (SOOS) was calculated through measured data directly, and the more sensitive SOOS based TF was defined to diagnose crack flaw in a beam-like structure [13], and then was applied to a satellite-like structure with bolt-loosening faults and inherent nonlinearity later [14]. The novel SOOS based methods provide higher sensitivity for local nonlinear faults in complex structures with inherent nonlinearity, while some problems should be further studied such as the MDOF model used to describe the behaviour of complex structures. In most previous fault diagnosis methods, the open chain type MDOF model with nonlinear connections is used for cantilever beams [15] and suspension systems of vehicle [16]. However, this MDOF model may not be suitable for other complex structures like pipelines [17] and steel frames [18].

To consider this issue, the nonlinear fault localization in ring type structures is studied in this paper. The main novelty of this paper is summarized below. (1) a more general ring type MDOF model with nonlinear restoring forces is built to describe the nonlinear behaviour of ring type structures. (2) Harmonic excitation analysis and local tuning approach (LTA) are utilized to derive the properties of the SOOS of nonlinear ring type structures. (3) A novel method with a local damage index, which is proposed based on the properties of the SOOS, can provide more position information of nonlinear faults in ring type structures even with inherent nonlinearity.

The rest of this paper is organized below. Section 2 introduces some basic theory about the model of ring type structures. Section 3 derives the properties of the SOOS of nonlinear ring type structure. In Section 4, a novel method based on the properties of the SOOS is proposed and is verified by numerical study. Conclusions and discussions are given in Section 5.

2 NONLINEAR MODEL OF RING TYPE STRUCTURES

2.1 Ring type structures

The vibration transmission paths in some complex structures such as pipeline and frame structures can form a closed loop. Thus, the closed ring type sensor chains should be targeted for exploring effective methods for fault localization.

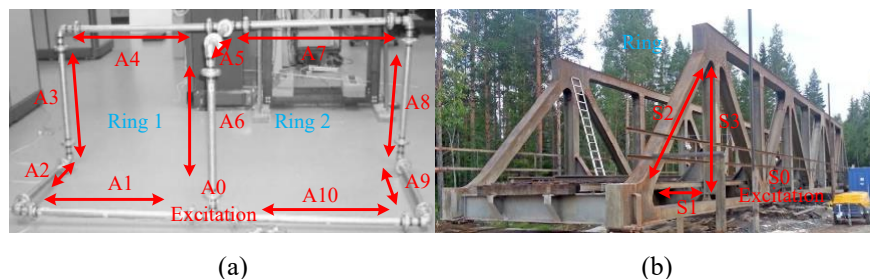


Figure 1: Ring type structures: (a) In a pipeline [17]; (b) In a steel frame [18]

Two typical examples of ring type structures are illustrated in Figure 1. When the pipeline structure (Figure 1(a)) is excited at A0, the closed vibration transmission paths (A0-A1-A2-A3-A4-A5-A6-A0 and A0-A6-A5-A7-A8-A9-A10-A0) can be regarded as two ring type structures, and can be used to detect and localize damaged bolted joints between pipes. Figure 1(b) shows a V-type planar truss which is formed by a series of triangles [18]. The nonlinear faults in beam members can be diagnosed through the dynamic output responses along the closed vibration transmission path labeled by a triangular sensor chain (S1-S2-S3-S1).

Overall, some pipeline and frame structures can be decomposed into some ring type structures, and the fault diagnosis of them can be performed by utilizing dynamic responses of these ring type structures.

2.2 Nonlinear MDOF model

According to the analysis above, a more general closed ring type MDOF model with nonlinear connections (Figure 2) is considered to describe the structural dynamic response of the ring type structure.

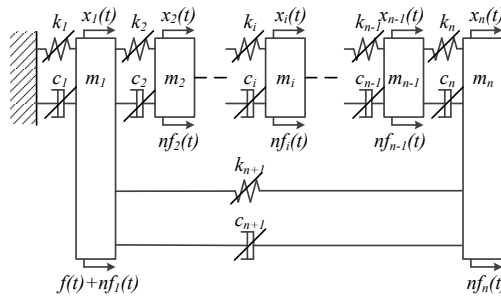


Figure 2: Ring type discretized MDOF model

The differential equation of motion can be written [8], as

$$[M]\{\ddot{x}\} + [C]\{\dot{x}\} + [K]\{x\} = \{f\} + \{nf\} \quad (1)$$

where $[M]$, $[C]$ and $[K]$ are mass, damping and stiffness matrices respectively. $\{\ddot{x}\}$, $\{\dot{x}\}$, $\{x\}$, $\{f\}$ and $\{nf\}$ are vectors of accelerations, velocities, displacements, external excitation forces and nonlinear restoring forces respectively.

To simulate the effects of inherent nonlinearity and nonlinear faults, the nonlinear restoring force vector $\{nf\}$, which is mainly a polynomial function of displacement and velocity responses [10], can be expressed, as

$$\{nf\} = \begin{Bmatrix} nf_1 \\ nf_2 \\ \vdots \\ nf_n \end{Bmatrix} = \begin{Bmatrix} nf_{-in-1} \\ nf_{-in-2} \\ \vdots \\ nf_{-in-n} \end{Bmatrix} + \begin{Bmatrix} nf_{-fa-1} \\ nf_{-fa-2} \\ \vdots \\ nf_{-fa-n} \end{Bmatrix}, i = 1, 2, \dots, n \quad (2a)$$

$$\begin{aligned}
 nf_{in_i} &= -\sum_{l=2}^{n^*} (c_{in_i,l} \dot{x}_i^l + k_{in_i,l} x_i^l); \\
 nf_{fa_i} &= \sum_{l=2}^{n^*} (c_{fa_i,l} \dot{S}_{i-1,i}^l + k_{fa_i,l} S_{i-1,i}^l) - \sum_{l=2}^{n^*} (c_{fa_i+1,l} \dot{S}_{i,i+1}^l + k_{fa_i+1,l} S_{i,i+1}^l); \\
 (\dot{S}_{i-1,i} &= \dot{x}_{i-1} - \dot{x}_i, S_{i-1,i} = x_{i-1} - x_i, \dot{x}_0 = \dot{x}_n, x_0 = x_n, \dot{x}_{n+1} = \dot{x}_1, x_{n+1} = x_1, c_{fa_1,l} = c_{fa_n+1,l}, k_{fa_1,l} = k_{fa_n+1,l})
 \end{aligned} \tag{2b}$$

where the term nf_{in_i} with nonlinear damping and stiffness parameters ($c_{in_i,l}$ and $k_{in_i,l}$) represents the nonlinear restoring force due to inherent nonlinearity, and the other term nf_{fa_i} with nonlinear damping and stiffness parameters ($c_{fa_i,l}$ and $k_{fa_i,l}$) represents the nonlinear restoring force caused by the i^{th} and/or the $(i+1)^{th}$ damaged damper-spring connections (nonlinear faults).

2.3 The Volterra model

The input-output relationship of above nonlinear MDOF structure can be expressed by the Volterra series up to order N^* [19-22], as

$$x_i(t) = \sum_{N=1}^{N^*} x_{i,N}(t) = \sum_{N=1}^{N^*} \int_{-\infty}^{\infty} \dots \int_{-\infty}^{\infty} h_{i,N}(\tau_1, \dots, \tau_N) \prod_{l=1}^N f(t - \tau_l) d\tau_l \tag{3}$$

where N^* is the maximum order of structure nonlinearity; $f(t)$ is the input; $h_{i,N}(\tau_1, \dots, \tau_N)$ and $x_i(t)$ are the N^{th} order Volterra kernel and output response of the i^{th} mass respectively.

Defining the N^{th} order generalized frequency response function (GFRF) as the multi-dimensional Fourier transform of the N^{th} order Volterra kernel gives [23]

$$H_{i,N}(j\omega_1, \dots, j\omega_N) = \int_{-\infty}^{\infty} \dots \int_{-\infty}^{\infty} h_{i,N}(\tau_1, \dots, \tau_N) e^{-j(\omega_1\tau_1 + \dots + \omega_N\tau_N)} d\tau_1 \dots d\tau_N \tag{4}$$

Then, (4) could be rewritten with the inverse Fourier transform of the N^{th} order GFRF [22], as

$$x_i(t) = \sum_{N=1}^{N^*} x_{i,N}(t) = \sum_{N=1}^{N^*} \frac{1}{2\pi} \int_{-\infty}^{\infty} \left[\frac{1}{(2\pi)^{N-1}} \underbrace{\int_{-\infty}^{\infty} \dots \int_{-\infty}^{\infty} \Xi_{i,N} d\omega_1 \dots d\omega_{N-1}}_{N-1} \right] e^{j\omega t} d\omega \tag{5}$$

where $\Xi_{i,N} = H_{i,N}(j\omega_1, \dots, j\omega_{N-1}, j(\omega - \omega_1 - \dots - \omega_{N-1})) F(j\omega_1) \dots F(j\omega_{N-1}) F(j(\omega - \omega_1 - \dots - \omega_{N-1}))$

Therefore, the nonlinear output spectrum of the MDOF structure can be expressed [22], as

$$X_i(j\omega) = \sum_{N=1}^{N^*} X_{i,N}(j\omega) = \sum_{N=1}^{N^*} \frac{1}{(2\pi)^{N-1}} \underbrace{\int_{-\infty}^{\infty} \dots \int_{-\infty}^{\infty} \Xi_{i,N} d\omega_1 \dots d\omega_{N-1}}_{N-1} \tag{6}$$

where $X_{i,N}(j\omega)$ is the N^{th} order output spectrum of the i^{th} mass.

3 ANALYSIS OF NONLINEAR RING TYPE STRUCTURES

3.1 Harmonic excitation with single frequency

If the structure (Figure 1) is excited by

$$f(t) = e^{j\omega_1 t} \quad (7)$$

The corresponding output response is

$$x_i(t) = Y_{i,1}(j\omega_1)e^{j\omega_1 t} + \text{other higher order terms} \quad (8)$$

Substituting (7) and (8) into (1), and equating the coefficients of $e^{j\omega_1 t}$ yields the equation of motion of the i^{th} mass in the frequency domain, as

$$A_i(j\omega_1)Y_{i,1}(j\omega_1) - B_i(j\omega_1)Y_{i-1,1}(j\omega_1) - B_{i+1}(j\omega_1)Y_{i+1,1}(j\omega_1) = 0 \quad (9)$$

where $A_i(j\omega_1) = -m_i\omega_1^2 + j\omega_1 c_i + k_i + j\omega_1 c_{i+1} + k_{i+1}$ and $B_i(j\omega_1) = j\omega_1 c_i + k_i$

Both sides of (9) divided by $Y_{i,1}(j\omega_1)$ gives

$$A_i(j\omega_1) = B_i(j\omega_1) \frac{Y_{i-1,1}(j\omega_1)}{Y_{i,1}(j\omega_1)} + B_{i+1}(j\omega_1) \frac{Y_{i+1,1}(j\omega_1)}{Y_{i,1}(j\omega_1)} \quad (10)$$

Define

$$\chi_{i-1,i}^1(j\omega_1) = \frac{Y_{i-1,1}(j\omega_1)}{Y_{i,1}(j\omega_1)}; \quad \chi_{i+1,i}^1(j\omega_1) = \frac{Y_{i+1,1}(j\omega_1)}{Y_{i,1}(j\omega_1)} \quad (11)$$

Equation (10) can be rewritten, as

$$A_i(j\omega) = B_i(j\omega)\chi_{i-1,i}^1(j\omega) + B_{i+1}(j\omega)\chi_{i+1,i}^1(j\omega), (\omega = \omega_1) \quad (12)$$

It is shown that parameters $B_i(j\omega)$ and $B_{i+1}(j\omega)$ are functions of the linear physical properties between mass m_{i-1} and m_{i+1} , and they will remain constant even though there are nonlinear faults and inherent nonlinearity in the structure. If an additional equation, which has the same form as (12) but different values of $\chi_{i-1,i}^1(j\omega)$ and $\chi_{i+1,i}^1(j\omega)$, exists, the left term in (12) can be eliminated and thus the ratio of $B_i(j\omega)$ to $B_{i+1}(j\omega)$ can be calculated to indicate the connection state between mass m_{i-1} and m_{i+1} in the structure.

To find a satisfactory equation, a local tuning approach (LTA), described in Appendix A, can be applied. The ring type MDOF structure is excited by excitation (7) again, new equation which is similar to (9) can be obtained, as

$$A_i(j\omega_1)Y'_{i,1}(j\omega_1) - B_i(j\omega_1)Y'_{i-1,1}(j\omega_1) - B_{i+1}(j\omega_1)Y'_{i+1,1}(j\omega_1) = 0 \quad (13)$$

where $Y'_{i,1}(j\omega_1)$ is the first order output spectra (FOOS) of the i^{th} mass when the LTA has been implemented.

Define

$$\chi_{i-1,i}^{\prime 1}(j\omega_1) = \frac{Y'_{i-1,1}(j\omega_1)}{Y'_{i,1}(j\omega_1)}; \quad \chi_{i+1,i}^{\prime 1}(j\omega_1) = \frac{Y'_{i+1,1}(j\omega_1)}{Y'_{i,1}(j\omega_1)} \quad (14)$$

Equation (13) can be expressed, as

$$A_i(j\omega) = B_i(j\omega)\chi_{i-1,i}^{r1}(j\omega) + B_{i+1}(j\omega)\chi_{i+1,i}^{r1}(j\omega), (\omega = \omega_1) \quad (15)$$

It can be seen that (15) and (12) have the same form but different values of $\chi_{i-1,i}^1(j\omega)$ and $\chi_{i+1,i}^1(j\omega)$. Therefore, the left term in (15) and (12) can be eliminated and one ratio $\gamma_i^{1,r}(j\omega)$ can be deduced, as

$$\gamma_i^{1,r}(j\omega) = \frac{\chi_{i+1,i}^{r1}(j\omega) - \chi_{i-1,i}^1(j\omega)}{\chi_{i-1,i}^{r1}(j\omega) - \chi_{i-1,i}^1(j\omega)} = -\frac{B_i(j\omega)}{B_{i+1}(j\omega)} \quad (16)$$

The ratio $\gamma_i^{1,r}(j\omega)$ is a function of the physical properties $B_i(j\omega)$ and $B_{i+1}(j\omega)$.

3.2 Harmonic excitation with dual frequencies

Exciting the structure (1) by the following input force.

$$f(t) = e^{j\omega_1 t} + e^{j\omega_2 t} \quad (17)$$

The obtained output response of the i^{th} mass is

$$x_i(t) = Y_{i,2}(j\omega_1, j\omega_2)e^{j(\omega_1 + \omega_2)t} + \text{other higher order terms} \quad (18)$$

Substituting (17) and (18) into (1) and equating the coefficients of $e^{j(\omega_1 + \omega_2)t}$, the equation of motion of the i^{th} mass can be written, as

$$A_i(j\omega_1 + j\omega_2)Y_{i,2}(j\omega_1, j\omega_2) = B_i(j\omega_1 + j\omega_2)Y_{i-1,2}(j\omega_1, j\omega_2) + B_{i+1}(j\omega_1 + j\omega_2)Y_{i+1,2}(j\omega_1, j\omega_2) + NF_{i,2}(j\omega_1, j\omega_2) \quad (19)$$

where $NF_{i,2}(j\omega_1, j\omega_2) = NF_{in_i,2}(j\omega_1, j\omega_2) + NF_{fa_i,2}(j\omega_1, j\omega_2)$ is the second-order nonlinear restoring force vector caused by inherent nonlinearity and nonlinear connections (nonlinear faults) between mass m_{i-1} and m_{i+1} .

Assuming that there is only inherent nonlinearity in the benchmark structure (i.e., structure is in reference state), (19) can be expressed, as

$$A_i(j\omega_1 + j\omega_2)Y_{i,2}^r(j\omega_1, j\omega_2) = B_i(j\omega_1 + j\omega_2)Y_{i-1,2}^r(j\omega_1, j\omega_2) + B_{i+1}(j\omega_1 + j\omega_2)Y_{i+1,2}^r(j\omega_1, j\omega_2) + NF_{in_i,2}(j\omega_1, j\omega_2) \quad (20)$$

Subtracting (20) from (19), a new equation can be obtained, as

$$A_i(j\omega_1 + j\omega_2)Y_{i,2}^{d-r}(j\omega_1, j\omega_2) = A_i(j\omega_1 + j\omega_2)(Y_{i,2}(j\omega_1, j\omega_2) - Y_{i,2}^r(j\omega_1, j\omega_2)) \\ = B_i(j\omega_1 + j\omega_2)Y_{i-1,2}^{d-r}(j\omega_1, j\omega_2) + B_{i+1}(j\omega_1 + j\omega_2)Y_{i+1,2}^{d-r}(j\omega_1, j\omega_2) + NF_{fa_i,2}(j\omega_1, j\omega_2) \quad (21)$$

Both sides of (21) divided by $Y_{i,2}^{d-r}(j\omega_1, j\omega_2)$ gives

$$A_i(j\omega_1 + j\omega_2) = B_i(j\omega_1 + j\omega_2)\frac{Y_{i-1,2}^{d-r}(j\omega_1, j\omega_2)}{Y_{i,2}^{d-r}(j\omega_1, j\omega_2)} + B_{i+1}(j\omega_1 + j\omega_2)\frac{Y_{i+1,2}^{d-r}(j\omega_1, j\omega_2)}{Y_{i,2}^{d-r}(j\omega_1, j\omega_2)} + \frac{NF_{fa_i,2}(j\omega_1, j\omega_2)}{Y_{i,2}^{d-r}(j\omega_1, j\omega_2)} \quad (22)$$

Define

$$\begin{aligned}\chi_{i-1,i}^{2,d-r}(j\omega_1, j\omega_2) &= \frac{Y_{i-1,2}^{d-r}(j\omega_1, j\omega_2)}{Y_{i,2}^{d-r}(j\omega_1, j\omega_2)}; \chi_{i+1,i}^{2,d-r}(j\omega_1, j\omega_2) = \frac{Y_{i+1,2}^{d-r}(j\omega_1, j\omega_2)}{Y_{i,2}^{d-r}(j\omega_1, j\omega_2)}; \\ n\chi_i^{2,d-r}(j\omega_1, j\omega_2) &= \frac{NF_{-fa-i,2}(j\omega_1, j\omega_2)}{Y_{i,2}^{d-r}(j\omega_1, j\omega_2)}\end{aligned}\quad (23)$$

Equation (22) can be rewritten, as

$$A_i(j\omega) = B_i(j\omega)\chi_{i-1,i}^{2,d-r}(j\omega) + B_{i+1}(j\omega)\chi_{i+1,i}^{2,d-r}(j\omega) + n\chi_i^{2,d-r}(j\omega), (\omega = \omega_1 + \omega_2) \quad (24)$$

Substituting (12) into (24) gives

$$0 = B_i(j\omega)(\chi_{i-1,i}^{2,d-r}(j\omega) - \chi_{i-1,i}^1(j\omega)) + B_{i+1}(j\omega)(\chi_{i+1,i}^{2,d-r}(j\omega) - \chi_{i+1,i}^1(j\omega)) + n\chi_i^{2,d-r}(j\omega) \quad (25)$$

Then, one ratio $\gamma_i^{2,d-r}(j\omega)$ can be defined, as

$$\begin{aligned}\gamma_i^{2,d-r}(j\omega) &= \frac{\chi_{i+1,i}^{2,d-r}(j\omega) - \chi_{i+1,i}^1(j\omega)}{\chi_{i-1,i}^{2,d-r}(j\omega) - \chi_{i-1,i}^1(j\omega)} = -\frac{B_i(j\omega)}{B_{i+1}(j\omega)} - \frac{n\chi_i^{2,d-r}(j\omega)}{B_{i+1}(j\omega)(\chi_{i-1,i}^{2,d-r}(j\omega) - \chi_{i-1,i}^1(j\omega))} \\ &= \gamma_i^{1,r}(j\omega) - \frac{n\chi_i^{2,d-r}(j\omega)}{B_{i+1}(j\omega)(\chi_{i-1,i}^{2,d-r}(j\omega) - \chi_{i-1,i}^1(j\omega))}\end{aligned}\quad (26)$$

The ratio $\gamma_i^{2,d-r}(j\omega)$ consists of the referenced ratio $\gamma_i^{1,r}(j\omega)$ and the second-order nonlinear restoring force term $n\chi_i^{2,d-r}(j\omega)$.

3.3 Properties of the SOOS

From (26), the properties of the SOOS among coordinates $x_{i-1}(t)$, $x_i(t)$ and $x_{i+1}(t)$ are summarized as follows.

Table 1: The properties

Coordinate	$1 < i < n$	
	Without nonlinear faults $n\chi_i^{2,d-r}(j\omega) = 0$	With nonlinear faults $n\chi_i^{2,d-r}(j\omega) \neq 0$
Relationship	$\gamma_i^{2,d-r}(j\omega) = \gamma_i^{1,r}(j\omega)$	$\gamma_i^{2,d-r}(j\omega) \neq \gamma_i^{1,r}(j\omega)$

The properties in Table 1 reveals that how the nonlinear faults between mass m_{i-1} and m_{i+1} affect the relationship between $\gamma_i^{2,d-r}(j\omega)$ and $\gamma_i^{1,r}(j\omega)$ in the nonlinear ring type structure. If the area between mass m_{i-1} and m_{i+1} is free from nonlinear faults (nonlinear connections), the nonlinear restoring force term $n\chi_i^{2,d-r}(j\omega)$ in (26) will be zero, and then $\gamma_i^{2,d-r}(j\omega)$ equals to $\gamma_i^{1,r}(j\omega)$.

4 APPLICATION TO NONLINEAR FAULTS DIAGNOSIS

4.1 A novel method

According to the properties of the SOOS of the ring type structure with nonlinear faults and inherent nonlinearity, a local damage index can be defined as the relative change between parameters $\gamma_i^{1,r}(j\omega)$ and $\gamma_i^{2,d-r}(j\omega)$, as

$$DI_i^{d-r}(j\omega) = \left| \frac{\gamma_i^{2,d-r}(j\omega) - \gamma_i^{1,r}(j\omega)}{\gamma_i^{1,r}(j\omega)} \right|, (1 < i < n) \quad (27)$$

Large value of $DI_i^{d-r}(j\omega)$ indicates that there are one or more nonlinear faults between mass m_{i-1} and m_{i+1} . Moreover, parameters $\gamma_i^{2,d-r}(j\omega)$ and $\gamma_i^{1,r}(j\omega)$ are just functions of the linear parameters $B_i(j\omega)$ and $B_{i+1}(j\omega)$. This means that $DI_i^{d-r}(j\omega)$ is a local fault indicator and can provide higher sensitivity for the positions of faults between mass m_{i-1} and m_{i+1} .

Based on the local damage index, a novel method can be proposed for nonlinear faults localization in ring type structures with inherent nonlinearity. The main merits of this method are summarized as follows:

- (1) A more general ring type MDOF model with nonlinear connections is used to describe the nonlinear behaviour of ring type structures;
- (2) This method considers the effect of nonlinearity caused by faults and inherent material or boundary nonlinearity;
- (3) The local damage index is decided only by the linear and nonlinear parameters in damaged area.

4.2 Procedures

The detailed procedures of this novel method are summarized here.

Step 1: The structure is in reference state

- (1) Choose the area to be investigated in the ring type structure and install sensors (S_{i-1} , S_i and S_{i+1});
- (2) Excite the structure with harmonic input at frequency ω_1 and $\omega_2 = 2\omega_1$ respectively. For each frequency, use the nth-OSE algorithm [11,12] to calculate the output spectra $\{Y_2^r(j2\omega_1)\}$ and $\{Y_1^r(j\omega_2)\}$ respectively.

Step 2: The structure is in reference state

- (1) Apply LTA to other parts of structure, which are away from the area between sensors S_{i-1} and S_{i+1} ;
- (2) Excite the structure with harmonic input at frequency $\omega_2 = 2\omega_1$ again. Use the nth-OSE algorithm [11,12] to calculate the output spectrum $\{Y_1^{rr}(j\omega_2)\}$;
- (3) Calculate the referenced ratio $\gamma_i^{1,r}(j2\omega_1)$ by (16) with $\{Y_1^r(j\omega_2)\}$ and $\{Y_1^{rr}(j\omega_2)\}$.

Step 3: The structure is in damaged state

(1) Excite the structure with harmonic input at frequency ω_1 . Use the nth-OSE algorithm [11,12] to calculate the output spectrum $\{Y_2^d(j2\omega_1)\}$;

(2) Calculate the diagnostic ratio $\gamma_i^{2,d-r}(j2\omega_1)$ by (26) with $\{Y_1^r(j\omega_2)\}$ and $\{Y_2^{d-r}(j2\omega_1)\} = \{Y_2^d(j2\omega_1)\} - \{Y_2^r(j2\omega_1)\}$.

Step 4: Fault diagnosis

(1) Calculate the damage index $DI_i^{d-r}(j2\omega_1)$ by (27) with $\gamma_i^{l,r}(j2\omega_1)$ and $\gamma_i^{2,d-r}(j2\omega_1)$;

(2) Decide where there are nonlinear faults between sensors S_{i-1} and S_{i+1} or not.

4.3 Numerical study

In this section, numerical case will be studied to verify the validity of proposed SOOS based method. As shown in Figure 3, a six DOF ring type structure with two nonlinear faults and inherent nonlinearity is considered. Mass m_1 is connected to the fixed boundary and is excited by harmonic excitation f . LTA will be applied to coordinate six (m_6). One fault is between mass m_1 and m_2 , and the other one is between mass m_5 and m_6 .

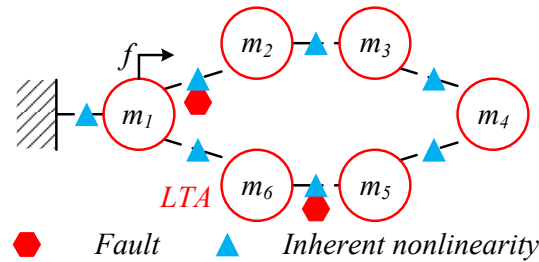


Figure 3: Schematic diagram of numerical case

The values of linear and nonlinear parameters used for simulation are shown in Table 2.

Table 2: Values of parameters

Parameters		i=1	i=2	i=3	i=4	i=5	i=6	i=7
Linear	m_i	1	1	1	1	1	1/20.5 ^a	
	c_i (1e2)	0.72	1.08	1.44	1.26	0.864	1.332	1.44
	k_i (1e4)	0.864	1.62	3.456	1.386	1.3824	2.9304	3.312
Inherent nonlinearity	$k_{in_i,2}$ (1e6)	1.296	2.592	3.888	5.184	6.48	7.776	-
Nonlinear faults	$k_{fa_i,2}$ (1e6)	0	2.592	0	0	0	6.48	0

^a An extra mass is applied to m_6 in LTA such that the value of m_6 is changed from 1 to 20.5.

For simplicity, only second-order stiffness nonlinearity in (2) is considered. Linear parameters are utilized to represent the structural model properties (mass, damping and stiffness). Nonlinear parameters ($k_{in_i,2}$) are used to simulate the inherent nonlinearity, and nonlinear parameters ($k_{fa_i,2}$) represent the nonlinear faults.

Following the procedures in section 4.2, data are proceed to calculate the local damage index. The results of the novel SOOS based method and previous SOOS transmissibility based method are shown below.

Table 3. The results of previous method [14]

Previous Method	i=1	i=2	i=3	i=4	i=5	i=6
$ \beta_{i,i+1}^{1,r}(j2\omega_1) $	0.94268	0.66408	0.84635	1.36967	1.44824	0.95147
$ \beta_{i,i+1}^{2,d}(j2\omega_1) $	0.77047	1.02797	1.06857	1.20290	1.04333	0.94145
$DI_{i,i+1}^d(j2\omega_1)^a$	0.18268	0.54794	0.26256	0.12175	0.27958	0.01052

$$^a DI_{i,i+1}^d(j2\omega_1) = \left| \left(\beta_{i,i+1}^{2,d}(j2\omega_1) - \beta_{i,i+1}^{1,r}(j2\omega_1) \right) / \beta_{i,i+1}^{1,r}(j2\omega_1) \right|$$

Table 4. The results of proposed method

Proposed Method	i=2	i=3	i=4	i=5
$ \gamma_i^{1,r}(j2\omega_1) $	0.52047	1.99557	1.15006	0.50673
$ \gamma_i^{2,d-r}(j2\omega_1) $	0.64944	1.99557	1.15006	0.44321
$DI_i^{d-r}(j2\omega_1)$	0.24780	2.28e-14	1.47e-14	0.12534

From the results in Table 3, it can be seen that the values of damage indexes for all coordinate pairs are larger than zero. Relatively large values of $DI_{i,i+1}^d(j2\omega_1)$ for $(i=1,2,...,5)$ indicate that faults may locate between m_1 and m_6 . Thus, the previous method can only give rough position information of faults, the reason is that this method, proposed based on open chain type MODF model, is not applicable for closed ring type structure. For the results of proposed method, the values of damage indexes $DI_3^{d-r}(j2\omega_1)$ and $DI_4^{d-r}(j2\omega_1)$ are about zero meaning that there is no fault between m_2 and m_5 , and that of damage indexes $DI_2^{d-r}(j2\omega_1)$ and $DI_5^{d-r}(j2\omega_1)$ are larger than zero indicate that one fault is located between mass m_1 and m_2 , and the other one fault is located between m_5 and m_6 . This diagnostic result is closer to the real situation of case setup. Therefore, the validity of proposed SOOS based method is proved by this numerical study.

5 CONCLUSIONS AND DISCUSSIONS

In this study, a new SOOS based method is proposed for the localization of nonlinear faults in a ring type structure. Some conclusions and discussions are outlined below.

(1) In some complex structures like pipeline and frame structures, closed sensor chains (i.e., the ring type structure) along the vibration transmission paths are found, and a more general closed ring type MDOF model is used to describe these structures' dynamic behavior.

(2) With the harmonic excitation analysis and LTA, the properties of the SOOS of the ring type structure with nonlinear faults and inherent nonlinearity are derived to reflect the relationship between nonlinear output spectra and nonlinear faults.

(3) Based on these properties, a novel fault localization method with local damage index is proposed to provide more local characteristics of faults in ring type structures. The results of

numerical study demonstrate that the novel method can localize the faults more precisely.

Furthermore, more local and sensitive damage indicator, which can provide more information of faults like the severity of faults, should be studied in the future.

6 ACKNOWLEDGEMENT

This work was supported in part by the GRF project (15206717) of Hong Kong RGC, and internal Research Grants of Hong Kong Polytechnic University.

APPENDIX A. LOCAL TUNING APPROACH

The main idea of LTA is that the local tuning operation on structure will only change the physical properties and/or boundary conditions away from the area between mass m_{i-1} and m_{i+1} . Then, the values of $\chi_{i-1,i}^1(j\omega)$ and $\chi_{i+1,i}^1(j\omega)$ in (12) are changed while the linear model parameters $B_i(j\omega)$ and $B_{i+1}(j\omega)$ between mass m_{i-1} and m_{i+1} remain constant.

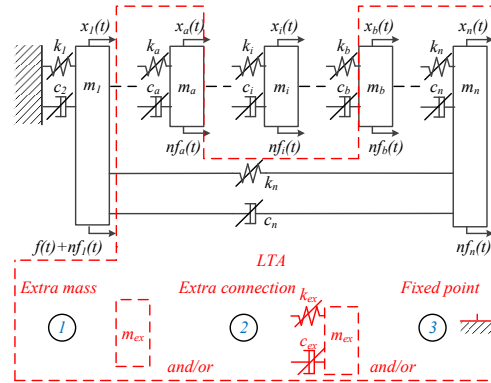


Figure 4: The local tuning approach

In practice, this LTA (Figure 4) can be performed by adding extra masse, damper and spring connection or fixed boundary condition to mass m_c ($c \neq i, i$). Moreover, to make a significant change of $\chi_{i-1,i}^1(j\omega)$ and $\chi_{i+1,i}^1(j\omega)$, more than one ways in Figure 4 can be applied to mass m_c and/or more than one masses can be applied the LTA.

REFERENCES

- [1] Bickford, J. H. and Nassar, S. *Handbook of bolts and bolted joints*, New York: Marcel Dekker, inc, (2009) 699-824.
- [2] Kaminskaya, V. and Lipov, A. Self-Loosening of Bolted Joints in Machine Tools During Service. *Metal Cut. Mach. Tools* (1990) 12: 81-85.
- [3] Helmreich, R. L. Culture and error in space: Implications from analog environments. *Aviation Space and Environmental Medicine* (2000) 71: 133-139.
- [4] Nikravesh, S. M. Y. and Goudarzi, M. A Review Paper on Looseness Detection Methods in Bolted Structures. *Latin American Journal of Solids and Structures* (2017) 14(12):

- 2153-2176.
- [5] Wang, T. Song, G. Liu S. and Li, Y. Review of bolted connection monitoring. *International Journal of Distributed Sensor Networks* (2013) 9(12): 871213.
 - [6] Carden, E. P. and Fanning, P. Vibration based condition monitoring: a review. *Structural health monitoring* (2004) 3(4): 355-377.
 - [7] Ewins, D. J. *Modal testing: theory, practice and application*. Research studies Pre, 2nd ed., 978-0863802188, (2000).
 - [8] Rytter, A. *Vibrational based inspection of civil engineering structures*. Doctoral dissertation, Dept. of Building Technology and Structural Engineering, Aalborg University (1993).
 - [9] Johnson, T. J. and Adams, D. E. Transmissibility as a differential indicator of structural damage. *Journal of Vibration and Acoustics* (2002) 124(4): 634-641.
 - [10] Johnson, T. J. Brown, R. L. Adams, D. E. and Schiefer, M. Distributed structural health monitoring with a smart sensor array. *Mechanical Systems and Signal Processing* (2004) 18(3):555-572.
 - [11] Jing, X. J. Truncation order and its effect in a class of nonlinear systems. *Automatica* (2012) 38: 2978–2985.
 - [12] Jing, X. J. Nonlinear characteristic output spectrum for nonlinear analysis and design. *IEEE/ASME Trans. Mech.* (2014) 19: 171–183.
 - [13] Jing, X. J. and Li, Q. K. A nonlinear decomposition and regulation method for nonlinearity characterization. *Nonlinear Dyn* (2016) 83: 1355–1377.
 - [14] Li, Q. K. and Jing, X. J. A second-order output spectrum approach for fault detection of bolt loosening in a satellite-like structure with a sensor chain,” *Nonlinear Dyn* (2017) 89: 587- 60.
 - [15] Sulaiman, M. S. A. Yunus, M. A. Bahari, A. R. and Rani, M. A. Identification of damage based on frequency response function (FRF) data,” *In MATEC Web of Conferences* (Vol. 90, p. 01025). EDP Sciences (2016).
 - [16] Haroon, M. and Adams, D. E. Time and frequency domain nonlinear system characterization for mechanical fault identification. *Nonlinear Dyn* (2007) 50(3):387-408.
 - [17] Airman, T. and Muleski, G. E. A review of the response of buried pipelines under seismic excitations. *Earthquake. Engineering and Structural Dynamics* (1981) 9:133–151.
 - [18] Xu, Z. D. and Wu, K. Y. Damage Detection for Space Truss Structures Based on Strain Mode under Ambient Excitation. *Journal of Engineering Mechanics* (2012) 138(10): 1215-1223.
 - [19] Schetzen, M. *The Volterra and Wiener theories of Nonlinear Systems*. Hoboken: John Wiley & Sons, Inc, (1980).
 - [20] Rugh, W. J. *Nonlinear System Theory: The Volterra/Wiener Approach*. The Johns Hopkins Univ. Press, (1981).
 - [21] Jing, X. J. Lang, Z. Q. and Billings, S. A. Output frequency properties of nonlinear systems. *International Journal of Non-Linear Mechanics* (2010) 45: 681-690.
 - [22] Jing, X. J. and Lang, Z. Q. *Frequency Domain Analysis and Design of Nonlinear Systems based on Volterra Series Expansion: A parametric characteristic approach*. Springer International Publishing Switzerland, (2015).
 - [23] George, D. A. *Continuous nonlinear systems*. MIT Research Lab. Electronics, Cambridge, (1959).

IMPROVING EFFICIENCY AND ROBUSTNESS OF STRUCTURAL HEALTH MONITORING TECHNIQUES BASED ON LAMB WAVE DETECTION

J. REBUFA*, G. JAUSSAUD*, M. FOURNIER*, M. LOGEAI*, N. BENCHEIKH*,
F. CLAEYSEN*, M. RÉBILLAT** AND M. GUSKOV**

* Cedrat Technologies S.A.
59 Chemin du Vieux Chêne - Inovallée - 38246 Meylan cedex – France
Email: jocelyn.rebufa@cedrat-tec.com, <https://www.cedrat-technologies.com>

** PIMM Laboratory, ENSAM-CNAM-CNRS-HESAM
151 Bd de l'Hôpital 75013 Paris - France
Email: marc.rebillat@ensam.eu - <https://artsetmetiers.fr/>

Key words: Structural health monitoring, Lamb waves, Pulse-echo, Piezo-electric arrays, High Frequency Power Amplifier

Abstract. Required improvements of piezoelectric elements actuation and measurement system efficiency and robustness are introduced as a critical feature for structural health monitoring (SHM) applications. An electronic module (Lamb wave detection system: LWDS) allowing to use each piezoelectric element in an array either in emission or reception mode is presented. The high commutation rate between these two states, for each transducer separately, is a key enhancement for SHM methods. The robustness of the sensor integration is also studied considering the patches size and bonding method. Coupled dispersion curve are introduced. Comparison of FEM simulation and experiments of the piezo-electric coupling are presented. This work takes part of the H2020 REMAP project about adaptive aircraft maintenance planning.

1 INTRODUCTION

Ultrasonic waves generated by piezo-electric patches offer a very promising way to perform Structural Health Monitoring (SHM) of composite aeronautic structures. Permanently bonded sensor arrays are interesting for on-demand interrogation of the structure in order to detect and localize damages (pits, disbonds), or to follow damage progression (cracks, delaminations). At the opposite of NDT techniques, SHM is independent from the operators.

Many applications have been reported for space applications [1], aircrafts [2] or civil engineering [3]. One can divide the piezoelectric elements applications between passive and active methods [4]. In passive methods piezoelectric elements array can be used to monitor acoustic emissions [5]. Active methods use signal generation on piezoelectric transducer to interact with the structure. Usual piezoelectric elements array are generally used to generate Lamb waves in plates [6]. The transmitted Lamb waves are received by another piezoelectric element in a pitch-catch mode, or by the same piezoelectric element in pulse-echo mode. The

wave generation can be controlled by phased array of various forms and distribution [4], [7]–[10]. Diverse signal processing methods can be used for damage monitoring with the signal measured with piezoelectric elements, such as transfer functions, time of flight analysis with cross correlation envelope [4], instantaneous baseline [11], time reversal [12], [13]. This can lead to an efficient damage localization mapping of the structure. However the positioning of the emitting and receiving piezoelectric elements, or the management of the commutation between these two states are of prior importance to ensure the covering of the whole structure as well as optimal signal quality.

Recently, Lamb waves detection techniques have been enhanced by developing a dedicated electronic system called Lamb Wave Detection System (LWDS) [8]. This module allows to use each piezoelectric element in an array either in emission or reception mode. Each sensor can not only be used in the usual pitch-catch method, (i.e. one sensor is emitting and the other sensors are receiving the propagated wave information), but also in pulse-echo (i.e. emitting a lamb wave and listening to the echo simultaneously on the same patch). This feature can drastically improve PZT network efficiency for SHM purposes as one additional information source (the signal received back by the exciter) is made available. All transducers can be used simultaneously to scan the structure, and directly listen to the structure response. It facilitates the use of advanced methods such as instantaneous baseline, beamforming in emission and reception, time reversal or other advanced algorithms.

Moreover the quality of signals is also highly impacted by the robustness of the sensor integration [14], [15]. Complex contributions such as the effects of temperature [16], or also adhesive nonlinearities [17] have been highlighted. The durability of sensor is also crucial for the proper application of SHM algorithms [18].

In order to overcome these difficulties and to improve SHM detection techniques, this paper presents a combination of an advanced electronic system with a robust piezo wafer integration within the host structure.

First, the electronics detection system is presented in detail. Commutation rates against capacitive loads of piezo patches is discussed, as well as Signal to Noise Ratio (SNR) improvement. Second, a focus is made on a fine study of coupling efficiency between the piezoelectric patches and Lamb wave propagation through so-called tuning curves. This feature helps in selecting the correct frequency range for ultrasonic SHM interrogation. These results are compared to FEM simulation on ATILA/GiD software. In the last part an experimental study is performed and the correlation with theory and simulation is discussed.

2 LAMB WAVE DETECTION SYSTEM & ELECTRONICS

The LWDS electronics is made for multi-channel Lamb wave excitation and measurement of thin structures.

From the hardware point of view, a channel suited for piezoelectric patches is described on Figure 1. This channel is typically composed of three analog functions:

- A power amplifier to drive the piezoelectric patches in order to emit the acoustic waves on the structure.
- A conditioner to be able to read the acoustic waves incoming on the piezoelectric

patches.

- A commutation function to be able to switch each piezoelectric patch between emission and reception modes.

The power amplifiers offer an unloaded wide bandwidth of 2.5 MHz with a current limit of 0.5 A peak, in order to reach the ultrasonic range and feature a high SNR (more than 70 dB). They are specifically designed to drive capacitive loads, since the piezo elements have a capacitive behavior.

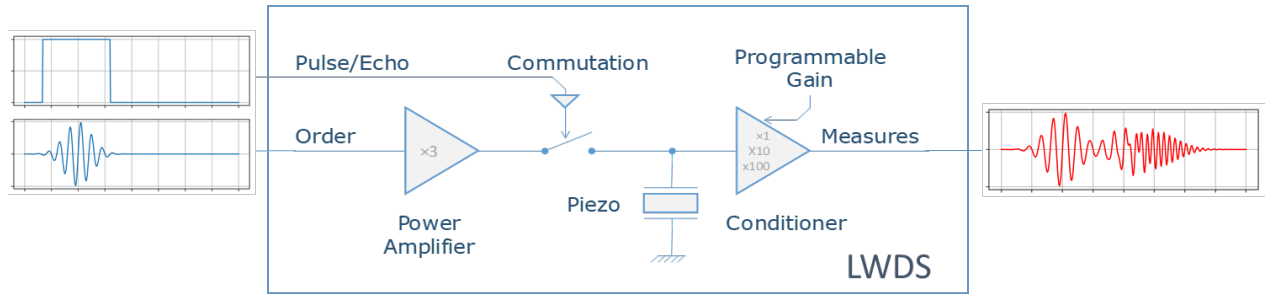


Figure 1 : High frequency commutation with LWDS

The conditioners offer a wide bandwidth to match the amplifier bandwidth and a very high SNR to be able to receive acoustic waves of low amplitude. If required, the conditioners can feature a variable amplifier gain up to 100, which is particularly interesting for laboratory setups. A picture of the LWDS module is presented on Figure 2 with 36 channels.

The switching function, allowing pulse-echo technique, offers the possibility to switch the patch between the two modes (emission or reception). This enables to emit a signal with a patch and to monitor the echo of the signal on the same patch, maximizing the detection ability for a given quantity of patches, cables and boards. It is thus a cost effective solution that reduces the complexity of the system. In order to take advantage of this function, the commutation time has to be short enough to be able to catch the echo. As an example a burst of 5 cycles at 1 MHz lead to a commutation time of 5 μ s. The LWDS allows commuting between emission and detection within 1 μ s. The echo can be caught even if the damage is very close from the patch.



Figure 2 : Up to 36 PZT channels simultaneously emitting or receiving signals with 1 μ s selective commutation

An example of emitted, reflected, and transmitted signals is shown on Figure 3. The upper

part of the figure shows the pulse signal applied by the emitting patch. The commutation signals enables the recording of the same patch for the reflected wave analysis. The center graph is a zoom on y-axis to observe reflected waves with around 20% of the emitted wave amplitude. The lower graph shows the signals measured by a second patch at the same order of magnitude as the echo signal.

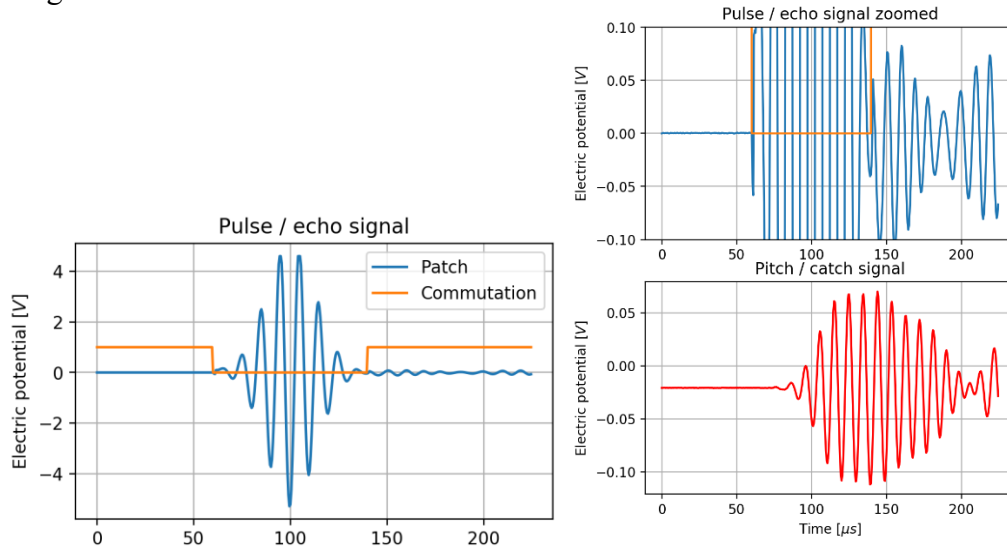


Figure 3- Pulse/echo and Pitch/catch signals

In addition to the previous functions, some generation and sampling functions are required to send the orders, and to record the received signals for analysis. This could be done with regular generators and with oscilloscopes or acquisition platforms. However, SHM applications often require specific equipment since multiple channels are required, as well as very high refresh rates. In order to reduce the time for acquisition and the complexity of the setup, dedicated generation and acquisition platforms are recommended. These platforms feature:

- Several synchronized input or output channels with refresh rates up to 10 MSps.
- High resolution to comply with the high SNR requirements of the SHM applications.
- Arbitrary generator channels so that the user can generate any waveform, to fit with his application.
- Interface with computers and dedicated GUI for loading the signals to be generated and recovering the recorded data

A picture of a full setup is presented on Figure 4.

The simultaneous excitation of all the piezo array with appropriate phase shifts allows beamforming for excitation [10] in excitation mode, as well as retro-propagation beamforming for acoustic wave field reconstruction [12] in listening mode.

The high frequency of commutation allows as correct patch selection to get closer to a defect and rapidly converge toward the spatial position of a damage.

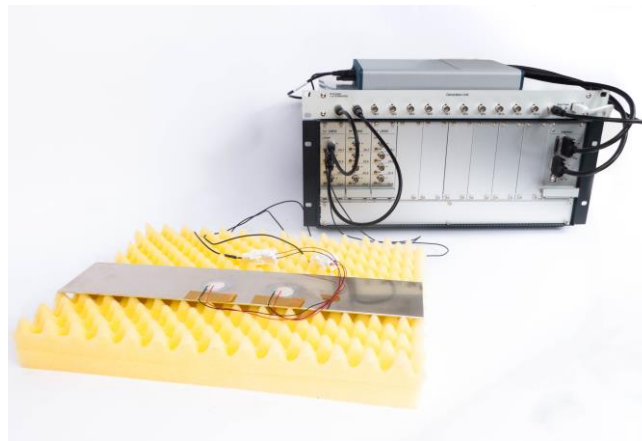


Figure 4 : Test bench of Lamb wave emission and acquisition with LWDS

3 PIEZO ELECTRIC PATCHES COUPLING MODELLING

In this part a focus is made on the definition of the piezo patches array, based on coupling efficiency, patch size, & material in order to get an efficient, reliable and robust SHM solution.

3.1 Dispersion curves

The detection of structural damages using Lamb Waves detection methods require some particular attention about the choice and the positioning of the piezo patches, and the frequency range to study. The dispersion curves are a useful tool to predict and understand the behavior of the sensorized structure and the patches signal output. These curves are based on analytical equations of waves propagation in frequency-wave number domain. They are function of the material and thickness of the structure. The material is considered as homogeneous and edge effects are not taken into account.

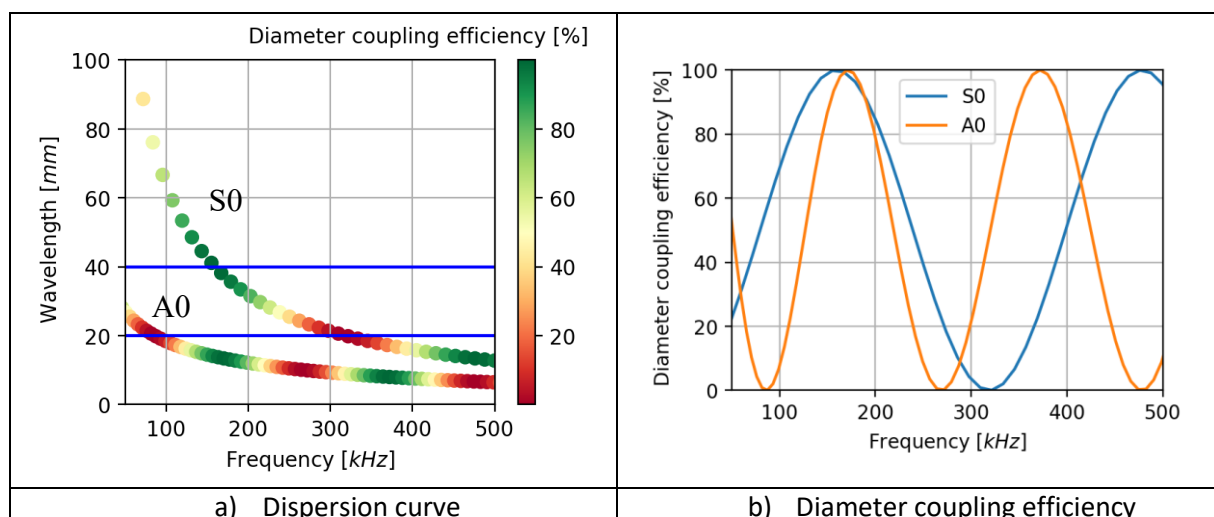


Figure 5 : Coupled dispersion curves of Lamb waves for a patch diameter 20 mm. Good coupling shown in green, low coupling in red

In ReMAP application the structure of the plate is defined: material is a multi-layer composite made of graphite-epoxy Hexcel IM7/8552 with 1.7mm thick. The computation of the equivalent homogeneous properties allows to plot the dispersion curves. Figure 5 shows the first symmetric and antisymmetric modes S0 and A0. A first criteria in SHM is to work in a frequency range where there is only the firsts mode to simplify the signal output analysis.

One cleverness of ReMAP approach is to add the information about the coupling between the piezo patches and the structure, in order to help in defining an efficient SHM solution.

Considering the diameter D_{PZT} of the piezo patch and λ the wave length of the considered mode, the coupled dispersion curve takes into account the facts that:

- If $D_{PZT} = n \cdot \lambda$, the patch cannot couple (excite or detect) the considered mode.
- If $D_{PZT} = (2n+1) \cdot \lambda/2$, the patch maximally couples (excites or detects) the considered mode.

Because the wave lengths of A0 and S0 modes are different for a given frequency, both modes are not equally coupled in general. So the coupled dispersion curve is a tool for choosing how to couple S0 or A0 modes by selecting the frequency and exhibits one role of the coupling.

The coupling aspect also manages the choice of the patch diameter with respect to the damage. The last point to study is to compare the size of the damage D_{Damage} with the wavelength. A damage will be better detected if its diameter is half of the wavelength, giving another design criteria

- If $D_{Damage} = \lambda/2$, the damage is optimally detected.

But this criteria is a more qualitative one than very predictive because of the different kinds and shapes of damages that the wave can encounter.

Besides, the material of the patches is selected to have a high value of d_{31} coefficient. This means that the voltage difference applied on the patch electrodes, implies a high in-plane deformation to the board, the polarization of the patch being orthogonal. Additionally, a low Q factor, a low aging and a thermally stable behavior are requested.

3.2 Finite element modelling

3.2.1 Wave propagation on a plate

A sample of composite plate $200 \times 40 \text{ mm}^2$ is modelled using finite element method. The modelling is performed on ATILA/GiD which enables to run transient analysis with piezoelectric coupling.

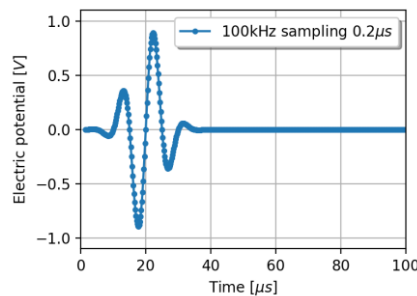


Figure 6 - Burst excitation at 100 kHz used in simulation

The plate is modelled in 3D with tetrahedral elements. It is sensorized with two Ø20mm

piezo-patches. A voltage is applied between the two faces of one patch. The voltage signal applied to the patch is a burst of a given frequency. The temporal signal is shown on Figure 6. The other patch has one electrode at 0V and the other free and is used in order to measure the voltage generated by the plate deformation. The plate is clamped at its two edges.

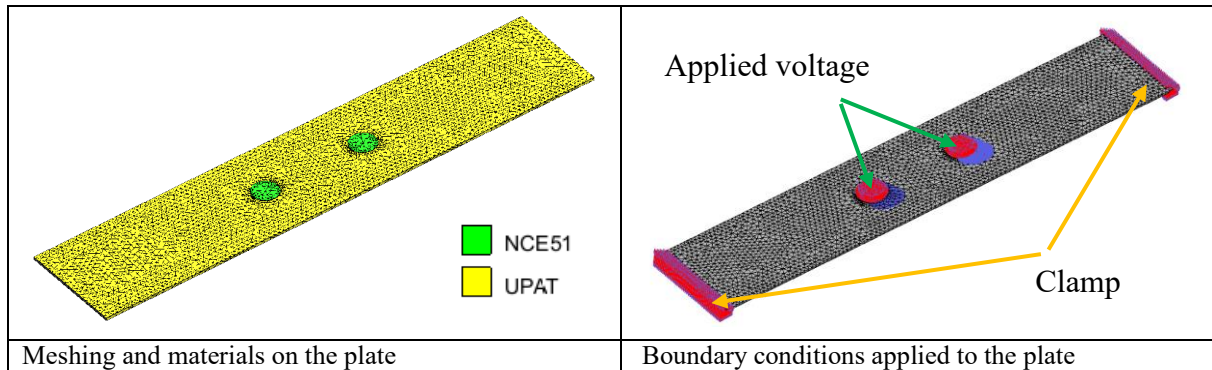


Figure 7 – FEM Simulation conditions in ATILA/GiD

A first modelling is performed with a coarse meshing (element size=4mm). For each frequency of the burst signal input, the convergence as a function of the mesh have to be carefully studied, particularly at high frequencies (>200 kHz). The meshing, materials and boundary conditions can be seen on Figure 7.

The transient displacement calculated for a burst at 100 kHz is given on Figure 8. The wave length is clearly visible and the displacement shape follow a cross repartition. That cross is representative of the fact that the material is orthotropic: the wave velocity is not the same in all directions.

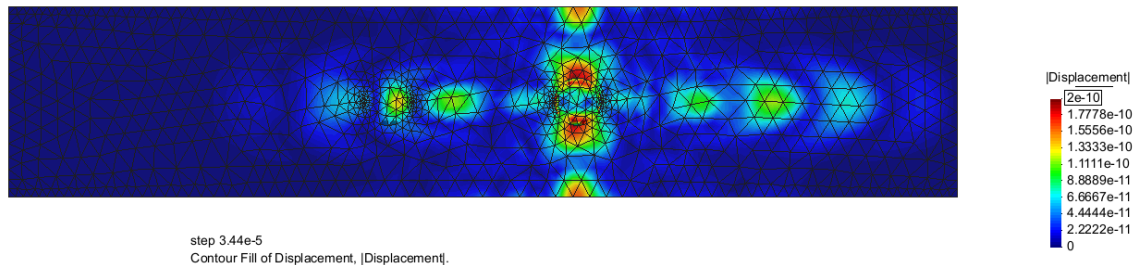


Figure 8 - Wave propagation in composite plate, 100 kHz

The same simulation is then performed considering an aluminum plate. In this case the distribution of the displacement is square. Close to the piezo patch the distribution is more circular like the patch shape. Then the square aspect can be explained by the edge effect.

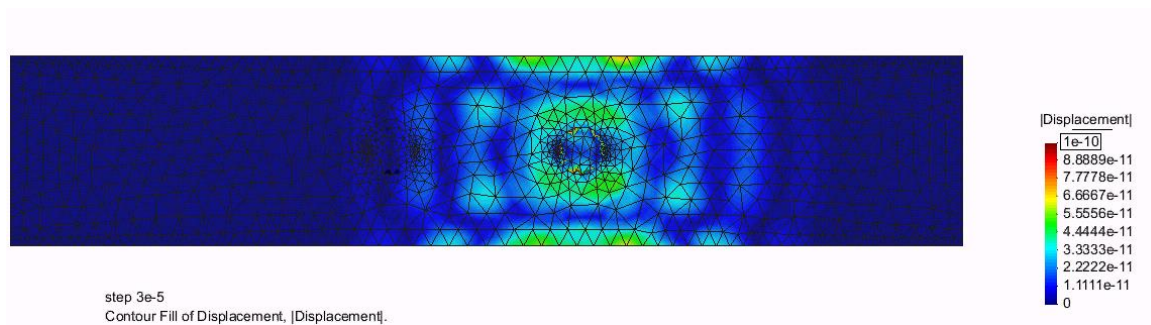


Figure 9 - Wave propagation in aluminum plate, 100 kHz

Using the plate made of composite material, the frequency of the burst is changed from 100 kHz to 200 kHz. For each signal the maximum displacement in the plate under the piezo patch is measured. The amplitude is plot in function of the frequency in Figure 10.

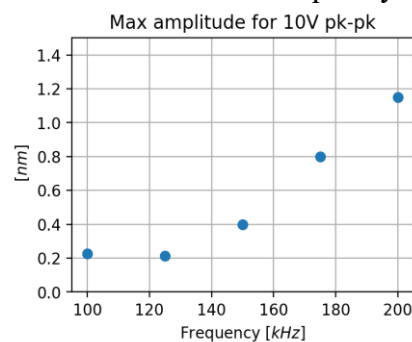


Figure 10 - Amplitude under the patch used in detection mode

We can see that the maximum of amplitude varies with the frequency of the signal. The amplitude is higher at 200 kHz than at 100 kHz which can be related to the coupling effect.

3.2.2 Damage detection

The finite element modelling is then performed using an aluminum plate with a local damage. The choice is made to represent the damage as a forced zero displacement in the damage zone. The goal of this computation is to study the wave propagation in the case which the wave encountered a damage. The material and boundary conditions are the same as previously described, we just changed the damage condition.

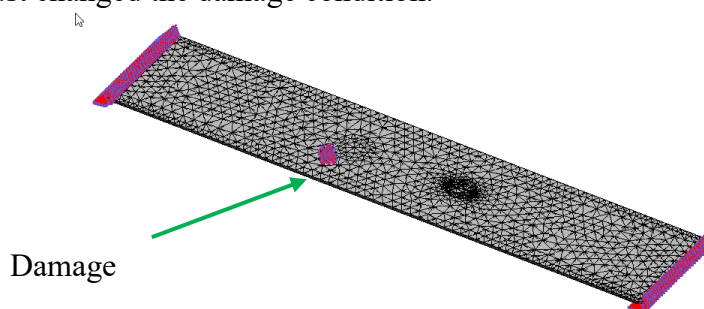


Figure 11 – Displacement clamping to simulate a damage

A MATLAB program is written to enable the comparison between two result distributions. Particularly, it's used to plot the displacement distribution difference between a perfect structure with homogeneous material and the structure with the damage. The displacement distribution into the two healthy and damaged structures, and the distribution difference, are shown on Figure 12.

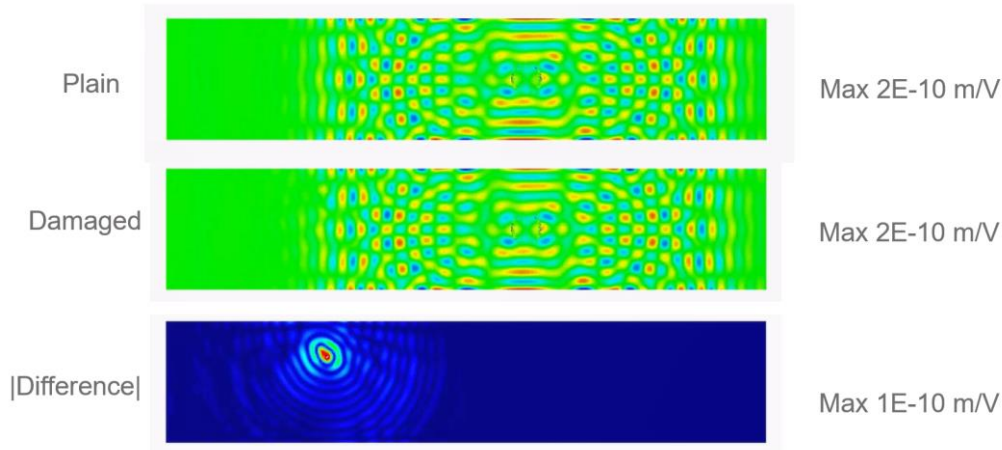


Figure 12 - Localization of the damage using Lamb Waves

The difference on displacement distribution clearly allows to establish the position of the damage. By varying the frequency on the signal we could study the quality of the detection, and compare these results with the dispersion curves and study the coupling. The transducer array could compute the difference in time with the emitting sensor synchronization. The fast commutation of the LWDS in this configuration is relevant for scanning the full structure quickly while keeping one additional measurement for virtual back-propagation.

4 EXPERIMENTAL VERIFICATIONS

In this part the LWDS electronics is used to compare coupling efficiency between pitch-catch mode and pulse-echo mode. Two samples are tested, equipped with two patches.

4.1 Gluing process

In the modelling we consider a perfect interface between the patches and the plate. In reality, the piezo patches are fixed on the plate by gluing. To ensure a good coupling between the patches and the plate another important point is the glue choice. In the frame of needs about reliability, the glue have to respect several criteria:

- Low thickness
- High shear modulus
- High thermal range
- High chemical resistance

Easy gluing process (cure at ambient temperature in aim at equipping large structures) According to these criteria, an epoxy glue have been chosen for the application. Then an accurate gluing process have been written to control the glue thickness and make the gluing as reproducible as possible. An overview of the gluing is available on Figure 13.

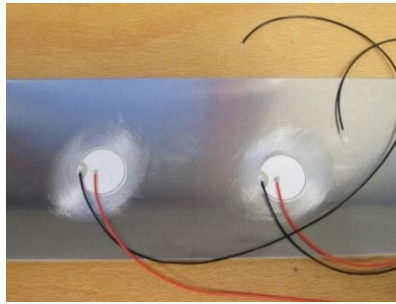


Figure 13- Overview of the patches gluing

4.2 Frequency tuning curve

In this section the comparison of the pulse echo and pitch catch modes are presented while varying the frequency of the burst excitation.

The Figure 14 shows two examples at 150 kHz and 250 kHz. One can notice a qualitative significant decrease in received signal amplitude.

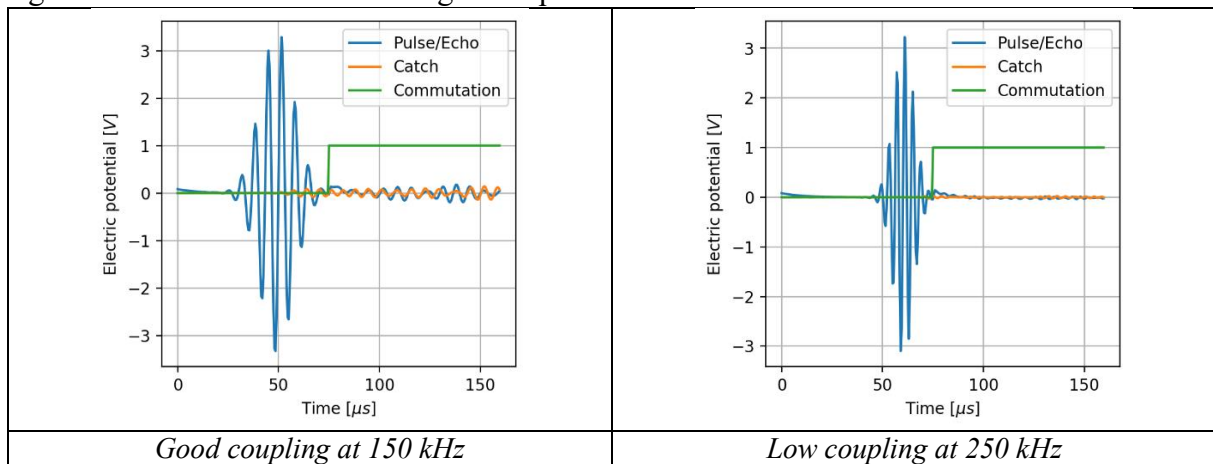


Figure 14- Comparison of different frequency for time signals

The amplitude ratio between excitation burst and reflected wave (coupling efficiency, in %) is compared between echo mode and catch mode in Figure 15. This picture shows relevant correlation between both transducers. It can be also correlated with coupled dispersion curves. The frequency 150 kHz shows a high coupling coefficient for the tested aluminum plate.

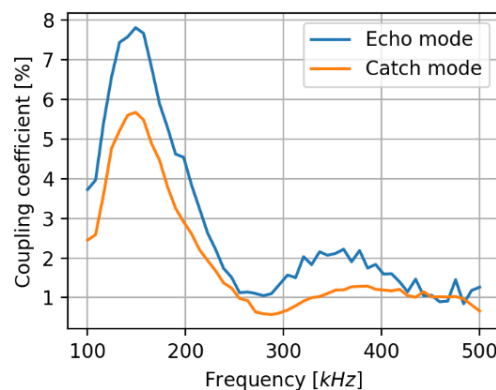


Figure 15- Comparison of pulse/echo and pitch/catch coupling coefficient

4.3 Toward robustness of SHM

In this section, four configuration are compared using two board samples and switching the emitting patch, and accordingly the pulse-echo mode and pitch catch mode. Figure 16 shows the results for the 2x2 configurations.

One can notice that the permutation of emitting and receiving patch in pitch catch mode shows very close results. For the pulse-echo mode, each transducer has its own coupling, but the trends are comparable for the 4 sensors. The variations between two different plates may be due to various factors such as gluing or piezo ceramics. These variations should be managed by software processing, for example by calibrations. The most important will be the time stability in order to clearly see any damage birth and growth.

So the future works should consider aging versus temperature cycles and time.

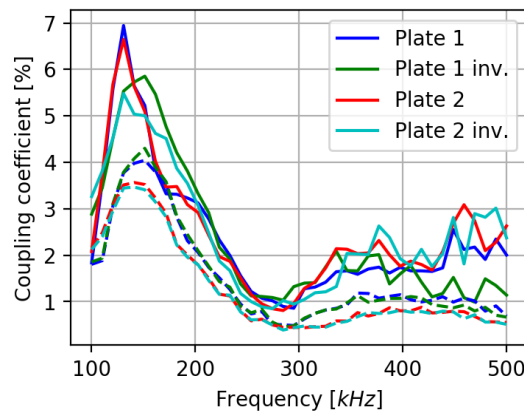


Figure 16- Reproducibility testing on patch coupling with two plates with two patches. Pulse/echo is represented by continuous lines, Pitch/catch by dotted lines

5 CONCLUSION

The baseline for the study of the robustness of SHM system has been detailed. The concept of coupled dispersion curves is introduced; Analytical, FEM simulation and experiments have been presented through examples to recall the notion of tuning and coupling in SHM systems. Different structural material have been tested including composites in the simulation campaign, illustrating the analytical results with spatial propagation analysis.

Experimental results showed good correlation with the well-known tuning curves. Apparent coupling coefficient is exposed for pulse-echo mode and pitch catch mode. The pulse echo mode shows an interesting behavior compared to pitch catch, showing that the commutation of sensor is relevant as an additional information to enhance the performance of SHM algorithm. The configuration discrepancy is analyzed on the coupling coefficient.

The synchronous difference of signals between a plain plate and a damaged plate has been illustrated through a 3D example and displacement mapping. Pulse-echo method can be relevant for increasing the efficiency of instantaneous baseline algorithm, or to decrease the number of patches to cover a whole structure.

As presented in the literature review there are many other algorithms such as time reversal and beamforming that are being develop to map structures and identify damages. The use of pulse echo method and the proper handling of transducer integration is likely to be key in future improvements.

ACKNOWLEDGEMENT

Most of the results have been achieved in the framework of H2020 ReMAP Project Grant n° 769288 : Real-time Condition-based Maintenance for Adaptive Aircraft Maintenance Planning, <https://h2020-remap.eu/>

REFERENCES

- [1] V. Giurgiutiu, B. Lin, G. Santoni-Bottai, et A. Cuc, « Space Application of Piezoelectric Wafer Active Sensors for Structural Health Monitoring », *J. Intell. Mater. Syst. Struct.*, vol. 22, n° 12, p. 1359-1370, août 2011.
- [2] K. Diamanti et C. Soutis, « Structural health monitoring techniques for aircraft composite structures », *Prog. Aerosp. Sci.*, vol. 46, n° 8, p. 342-352, nov. 2010.
- [3] D. Feng et M. Q. Feng, « Computer vision for SHM of civil infrastructure: From dynamic response measurement to damage detection – A review », *Eng. Struct.*, vol. 156, p. 105-117, févr. 2018.
- [4] L. Yu et V. Giurgiutiu, « Advanced signal processing for enhanced damage detection with piezoelectric wafer active sensors », *Smart Struct. Syst.*, vol. 1, n° 2, p. 185-215, avr. 2005.
- [5] Nihon-Hihakai-Kensa-Kyōkai, Éd., *Practical acoustic emission testing*. Tokyo: Springer, 2016.
- [6] Z. Sun, B. Rocha, K.-T. Wu, et N. Mrad, « A Methodological Review of Piezoelectric Based Acoustic Wave Generation and Detection Techniques for Structural Health Monitoring », *Int. J. Aerosp. Eng.*, vol. 2013, p. 1-22, 2013.
- [7] L. Yu et V. Giurgiutiu, « In situ 2-D piezoelectric wafer active sensors arrays for guided wave damage detection », *Ultrasonics*, vol. 48, n° 2, p. 117-134, avr. 2008.
- [8] T. Porchez, N. Bencheikh, et F. Claeysen, « Piezo-composite patches applied to the detection of defects using Lamb wave focusing », in *ResearchGate*, 2011.
- [9] W. Wang, H. Zhang, J. P. Lynch, C. E. S. Cesnik, et H. Li, « Experimental and numerical validation of guided wave phased arrays integrated within standard data acquisition systems for structural health monitoring », *Struct. Control Health Monit.*, vol. 25, n° 6, p. e2171, juin 2018.
- [10] P. Kudela, M. Radziński, W. Ostachowicz, et Z. Yang, « Structural Health Monitoring system based on a concept of Lamb wave focusing by the piezoelectric array », *Mech. Syst. Signal Process.*, vol. 108, p. 21-32, août 2018.
- [11] S. Park, S. R. Anton, J.-K. Kim, D. J. Inman, et D. S. Ha, « Instantaneous baseline structural damage detection using a miniaturized piezoelectric guided waves system », *KSCE J. Civ. Eng.*, vol. 14, n° 6, p. 889-895, nov. 2010.
- [12] R. Zhu, G. L. Huang, et F. G. Yuan, « Fast damage imaging using the time-reversal technique in the frequency–wavenumber domain », *Smart Mater. Struct.*, vol. 22, n° 7, p. 075028, juill. 2013.
- [13] J. He, C. A. C. Leckey, P. E. Leser, et W. P. Leser, « Multi-mode reverse time migration damage imaging using ultrasonic guided waves », *Ultrasonics*, vol. 94, p. 319-331, avr. 2019.
- [14] J. Agrahari et S. Kapuria, « Effect of Piezoelectric Transducer Bonding on Time Reversibility of Lamb Waves in Plates », in *Structural Health Monitoring 2015*, 2015.
- [15] S. Mustapha et L. Ye, « Bonding Piezoelectric Wafers for Application in Structural Health Monitoring–Adhesive Selection », *Res. Nondestruct. Eval.*, vol. 26, n° 1, p. 23-42, janv. 2015.
- [16] E. Balmès, M. GUSKOV, M. REBILLAT, et N. MECHEBAL, « Effects of temperature on the impedance of piezoelectric actuators used for SHM », in *14th Symposium on Vibration, Shock and Noise (VISHNO)*, France, 2014, p. 1–6.
- [17] S. Shan, L. Cheng, et P. Li, « Adhesive nonlinearity in Lamb-wave-based structural health monitoring systems », *Smart Mater. Struct.*, vol. 26, n° 2, p. 025019, févr. 2017.
- [18] H. Pfeiffer, F. Fransens, et M. Wevers, « Durability and Self-Testing of Sensor Bondings used in Structural Health Monitoring », présenté à EU Project Meeting on Aircraft Integrated Structural Health Assessment (AISHA), 2007.

MATERIAL INTRINSIC PHENOMENA USED FOR SMART STRUCTURAL HEALTH MONITORING

CHRISTIAN BOLLER^{*}, PETER STARKE^{**†}, RAMANAN SRIDARAN VENKAT^{*},
ALEXANDR LOZÁK^{*}, HAORAN WU^{**†}, VIKTOR LYAMKIN^{*} AND RUTH
ACOSTA^{*}

^{*} Chair of NDT and Quality Assurance (LZfPQ)
Saarland University
Campus Dudweiler, 66125 Saarbrücken, Germany
e-mail: c.boller@mx.uni-saarland.de, www.uni-saarland.de/en/lehrstuhl/boller/home.html

[†] Department of Materials Science and Materials Testing (WWHK)
University of Applied Sciences Kaiserslautern
Schoenstr. 11, 67659 Kaiserslautern, Germany
email: peter.starke@hs-kl.de, www.hs-kl.de

Key words: Fatigue; image processing; non-destructive testing; SteBLife; structural health monitoring; thermography

Abstract. Engineering structures are prone to damage when being under operation and under the process of ageing. Damage usually occurs locally such as in notches and/or material inhomogeneities and may then spread gradually around from those. A way on how to understand and model the phenomenon of damage is to transfer the material behaviour in the damage critical area onto a smooth specimen used for materials testing. This of course also requires the material behaviour itself to be understood, such as it is described in terms of fatigue behaviour as the material's related S-N curve. A way on how to get such a curve in a most efficient way has been proposed with the SteBLife approach, where a single close to unnotched specimen is divided into five sections with different gauge length diameters and through this each of the sections represents a source of the material's information being related to fatigue at different stress levels. This information is retrieved on the basis of parameters conventionally known from non-destructive testing (NDT) being related to temperature and magnetics at present, monitored with the respective sensors. This information, which can be even more sensitive than plastic strain being often used as a damage parameter for elastic-plastic materials, can be recorded along the life cycle of a material's fatigue test or even a component. Furthermore this information can virtually even be broken down to a pixel level with respect to the structure to be monitored, where histograms can be generated for each of the pixels. This may allow an ageing process of a material as well as the scattering of material properties to be described, all being an additional important information to reliably predict the residual life of a component in the end. Such a way of smart monitoring easily generates a large amount of data that has to be managed accordingly, using adequate data management

procedures. As a result techniques and technologies developed in the wider context of NDT including acoustics can be arranged in a ‘toolbox’ in a way that they can be combined to structural health monitoring (SHM) systems for smart monitoring in the longer term. The way on how to determine a material’s fatigue data on the basis of NDT-based parameters to configure an SHM-system on a possibly non-conventional but systematic way is indicated.

1 INTRODUCTION

SHM has now been around for at least a quarter of a century if not even more. It has been considered as the integration of sensors and possibly also actuators into structures to monitor changes in the structures’ condition using advanced signal processing. Much of the ideas and concepts for SHM have been explored and summarised in books (i.e. [1]). A vision has been around during that whole period, that a structure should become like a human body, monitored by billions of renewable sensors and controlled by a central ‘brain’, hence a computer or something similar. However, this more turns out to be an illusion since sensing in engineering is completely different to nature, as can be easily proven, not saying that bio-inspiration would not trigger new ideas in engineering. If SHM is ever to come into true application, then more pragmatic approaches need to be taken than the illusion described before.

A prerequisite for SHM is that a change in a structure’s condition has to be tolerated. This is provided through the damage tolerance design (DTD) principle where damage is allowed to exist in a structure as long as it does not become critical. This principle has now been applied for more than 70 years within aeronautics with success for designing structures becoming lighter weight. Recently civil engineering has also discovered the DTD principle, however, mainly in view of extending a structure’s operational life without compromising safety.

Damage in structures does principally not accumulate to become critical anywhere on a structure but rather at locations being specifically exposed to extreme loading, would the damage either be of a mechanical or corrosive nature. In the case of mechanical loading and its resulting impact, fatigue is possibly the most representative phenomenon currently represented in terms of crack propagation. Initiation and progression of fatigue cracking from a phenomenological point of view is a stochastic process. It is therefore difficult to predict when it occurs rather than where, because the latter is mainly driven by local stresses and strains distributed in an irregularly shaped structure, which can be determined numerically. Together with a damage accumulation rule, which in the case of the linearized Palmgren-Miner rule is rather incorrect, at least the damage critical locations can be determined. An additional numerical assessment has then to be made in which the allowable critical damage has to be configured in terms of shape and size. This preliminary work becomes the onset from where SHM starts and how an SHM system may have to be designed.

However, before getting an SHM system realised the material being considered needs to be understood. In the case of fatigue this can become rather laborious because S-N curves have to be generated, which traditionally require 15 fatigue experiments or even more. This is specifically true in the case of ageing infrastructure, where material conditions may have changed when compared to their pristine state and a structure’s residual life assessment may be ex-

posed to large uncertainties. To come around this problem so called Short Term Evaluation Procedures (STEP) [2], which in the ideal case require a single fatigue test to be performed only, can be of significant help. Another important aspect is the detection of the incubation of damage. Classical DTD is based on crack propagation only. Combined with an acoustics wave approach monitoring in the sense of SHM has become rather popular. However, the crack propagation life of a structure may be short when compared to the structure's pre-crack and crack initiation life and as such other parameters would have to hold in excess to the plastic strain being considered traditionally. Such alternative parameters can be found through techniques applied in NDT where electromagnetism and thermography are two techniques described in excess to the acoustic techniques used traditionally.

Finally, it needs to be mentioned that with the significant cost reduction and miniaturisation of sensors today the importance of the number of sensors used can become rather marginal. However, large amounts of data are to be easily generated when the number of sensors increases, of which the signals then need to be processed. Different of the emerging signal processing and visualisation tools may therefore be of invaluable help.

This article will first address STEP as a means to generate an S-N curve for fatigue life evaluation including the application of thermography and magnetism as NDT techniques from which micro-mechanic phenomena such as damage initiation and propagation patterns can be retrieved. Elements of those techniques can then be implemented into a 'toolbox' allowing appropriate SHM systems to be generated in the longer term.

2 SHORT TIME EVALUATION PROCEDURES (STEP)

Traditional testing of materials is based on the principle that a single result is retrieved from a single experiment. This makes it rather laborious in the case of a material's fatigue and the evaluation of S-N curves being required to assess a structure's residual fatigue life in the end. STEPs have therefore been around since a decade or slightly more as a means of enhanced determination of S-N curves reducing the effort to get those curves determined easily by a factor of 10 or more. The first approach considered was PhyBaL (physically based fatigue life calculation) [3], for which the logic is shown in Fig. 1 and which requires a load increase test (LIT) and two traditional constant amplitude tests (CAT) to be performed. The LIT starts at a load level usually below the so called fatigue limit (up to 2×10^6 cycles), where a decent number of fatigue cycles, often around 9000, is applied such that the material stabilizes cyclically, before the loading is then moved to a next higher level and the procedure of fatigue cycling is repeated again. This procedure is applied up to fracture of the specimen and generates the relationship between the controlling parameter (here the load) and a possible fatigue damage relevant but non-controlled parameter called the material response such as plastic strain as shown in the upper left of Fig. 1. This relationship between the controlled (stress) and the uncontrolled (material response) parameter obtained from the LIT is related to conventional CATs where one experiment is now performed close to the fatigue limit and another around the loading level where the LIT failed respectively. It is assumed that the well known Morrow equation

$$\sigma_a = K'_M(M)^{n'_M} \quad (1)$$

can be applied, where σ_a represents the stress applied and M the plastic strain measured respectively while K'_M and n'_M represent a coefficient and an exponent respectively. From the exponent n'_M the fatigue strength exponent b_M

$$b_M = \frac{-n'_M}{5 \cdot n'_M + 1} \quad (2)$$

is determined, describing the slope of the S-N curve in accordance to the Basquin equation

$$\sigma_a = \sigma'_f \cdot (2N_f)^{b_M} \quad (3)$$

where N_f represents the number of cycles to failure and σ'_f the fatigue strength coefficient describing the S-N curve respectively. With this an S-N curve of the material considered is determined on the basis of simply three experiments.

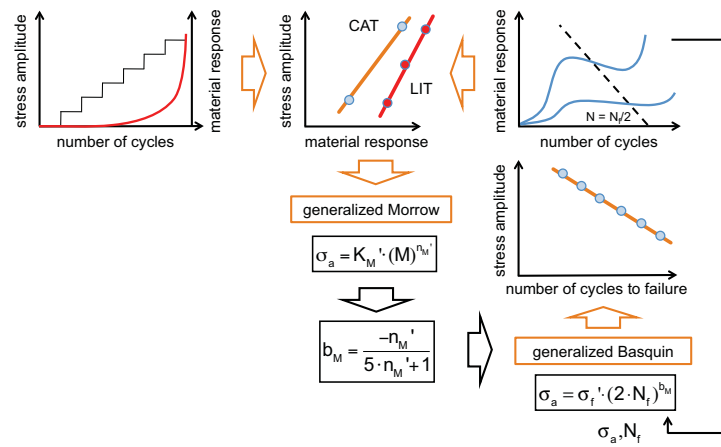


Figure 1: STEP for the evaluation of S-N curves

It is important to know that the above parameter M is by far not limited to plastic strain only but can be rather extended to any parameter describing a material's fatigue behaviour. Such parameters can be derived from NDT such as acoustics, temperature or electromagnetics driven parameters, to just name a few.

In the recently developed STEP StebLife [4] the evaluation of an S-N curve has been reduced to a single fatigue test only. This is achieved through a newly designed fairly smooth specimen, which is symmetric with regard to its minimum cross-section and consists of five sections of three different diameters \emptyset_1 , \emptyset_2 and \emptyset_3 respectively as can be seen from Fig. 2. Each of the sections represents a materials volume onto which a different stress depending on the diameter applies. As can be seen from Fig. 2 no LIT is now required and the material response is determined from a single CAT only. This CAT delivers the material response at the give loading including the fatigue life for the middle section with the minimum diameter only. The sections above and below the middle section only provide the material response up to the fatigue life of the middle section. However, the material response information retrieved from the sections other than the middle section can be well used for further evaluations in case the material response can be considered mainly stabilized which is true for most cases. Principal-

ly five data points are therefore made available that allow the loading versus material response relationship to be described in accordance to Eq. (1). The remaining procedure on how to determine the S-N curve is then identical to what has been explained before with regard to PhyBaL. Running more than one of those fatigue tests and this possibly at different load levels with respect to the fatigue life of the specimen immediately enhances the breadth of data sampling leading to the possibility to generate S-N data including their scatter bands possessing a remarkable level of confidence.

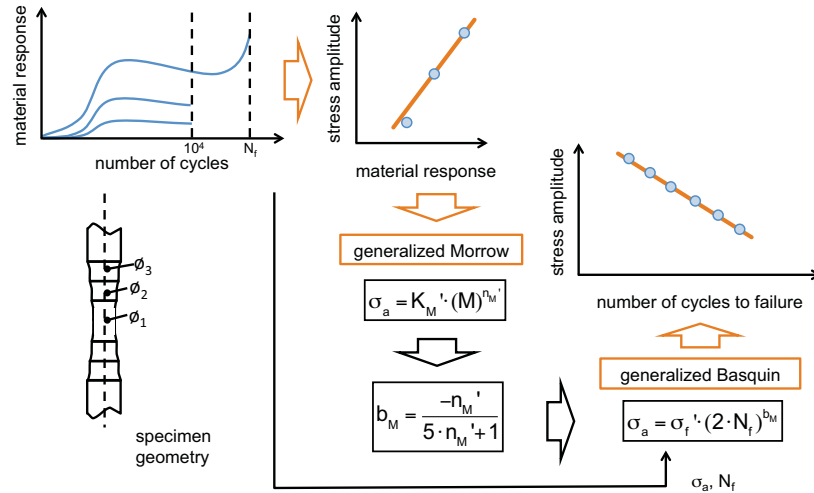


Figure 2: SteBLife as a STEP for the evaluation of S-N curves based on a single experiment

3 TEMPERATURE AS A MEANS FOR FATIGUE DAMAGE ASSESSMENT

As mentioned before the material response parameter M can be also chosen from an NDT technique where M should be sensitive to fatigue. In [4] results have been reported where thermographic data have been recorded in each of the sections of a SteBLife specimen using a commercial Micro-Epsilon type thermoIMAGER TIM 450 infrared camera. For temperature measurements, seven measurement fields with a size of 5×5 pixels were defined along the specimen within the infrared camera software, one in each gauge length (T_1 , $T_{2o/u}$, $T_{3o/u}$, ϕ : upper, u: lower), and two at each shaft ($T_{4o/u}$). The changes in temperature ΔT in the different specimen sections were calculated in accordance to Eq. (4) to Eq. (6):

$$\Delta T_1 = T_1 - 0.5 \times (T_{4o} + T_{4u}) \quad (4)$$

$$\Delta T_{2o/u} = T_{2o/u} - T_{4o/u} \quad (5)$$

$$\Delta T_{3o/u} = T_{3o/u} - T_{4o/u} \quad (6)$$

The diameter of the shafts is bigger than the diameters of the gauge lengths such that $T_{4o/u}$ can be considered as the elastic portion of the change in temperature as well as the environment. It is therefore subtracted from T_1 , $T_{2o/u}$, $T_{3o/u}$, which leads to the changes in temperature (ΔT_1 , $\Delta T_{2o/u}$, $\Delta T_{3o/u}$). ΔT_1 , $\Delta T_{2o/u}$, $\Delta T_{3o/u}$ are proportional to the plastic strain amplitude $\epsilon_{a,p}$ and are dedicated to the plastic deformations in the different gauge length sections. This temperature compensation allowed the elimination of external temperature effects to be maximised,

allowing thermal effects originating from the fatigue damaging process to be made available only. Fig. 3 shows the data recorded in terms of temperature based cyclic deformation curves and the material's response versus loading applied for a SAE 1045 (German designation C45E) medium carbon steel described in terms of Eq. (1). The resulting S-N curve added by the results of another four of those SteBLife fatigue tests can be seen in Fig. 4 which shows that even a statistical process having been applied to the five input values has allowed scatter bands to be described appropriately as can be seen from the different independent CAT results shown in Fig. 4. Those results as well as many others published can be considered as a proof that STEPs have become a most efficient means to assess a material's fatigue properties at a fraction of effort, time and cost making it ideal for the assessment of ageing infrastructure.

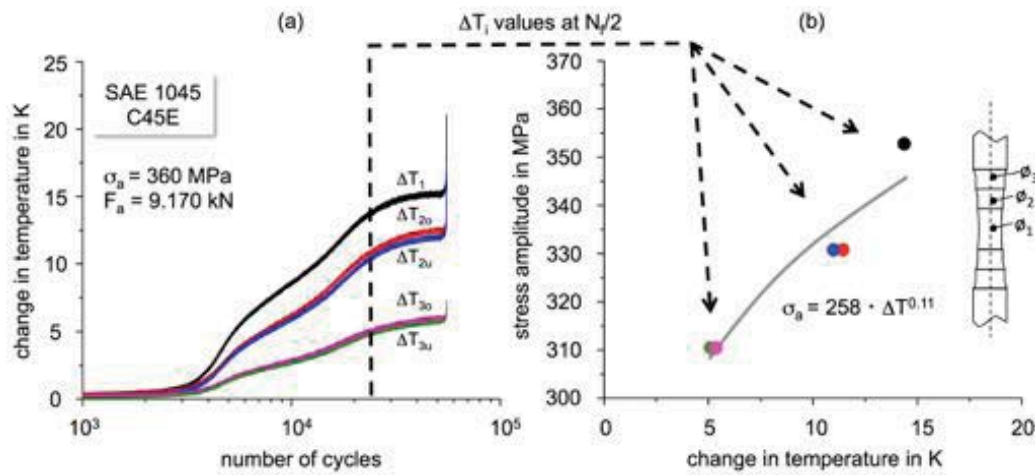


Figure 3: Temperature based cyclic deformation curves recorded from a constant amplitude loaded SteBLife specimen (left) and determined resulting Morrow function (right) for normalized SAE 1045

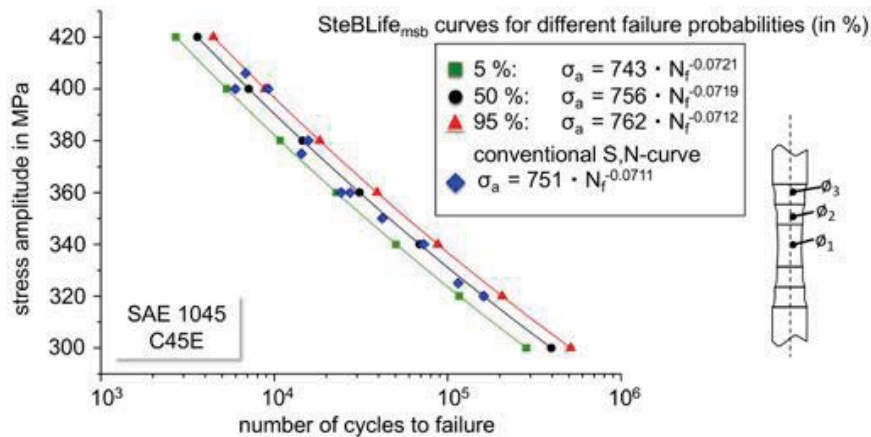


Figure 4: S-N curve and scatter band evaluated from five SteBLife experiments and compared to conventional determined S-N data for normalized SAE 1045

4 VISUALIZATION AND ANALYSIS OF RECORDED THERMOGRAPHIC DATA

Data can be recorded today with an increasing ease. This applies to most of the NDT tech-

niques applied would those be based on an acoustical/vibro-mechanical or electromagnetic/electro-mechanical basis. This easily leads to an interesting application in terms of digitized monitoring and visualization possibly followed by big data handling, advanced signal processing and deep learning. Many of the NDT techniques have been digitized the one way or the other would this be with digital radiography, phased array acoustics, laser vibrometry, laser speckle photometry or digital thermography, to just name a few. Such techniques allow data to be taken on a near to continuous basis and this over larger areas leading to histograms to be generated at virtually every location observed. Hence developments over the lifetime of a material and component can be visualized on a dynamic basis. Such a trend may lead to a material and component to be fully ‘pixelized’ and ‘digitized’ in the end.

A fatigue loaded SteBLife specimen as described under Fig. 2 made from SAE 4140QT and run at a loading frequency of 5 Hz has been fully recorded with a digital thermography camera, where Fig. 5 shows five stages along the fatigue life of the CAT performed. The displays show the topography of inertly generated accumulated energy appearing on the specimen’s surface. In the early phase within the fatigue process up to around 1000 s a fairly homogeneous and flat distribution is to be seen showing that fatigue accumulation has been rather constant up to that stage. At 1663 s or 67 % of the specimen’s fatigue life the rather homogeneous distribution of the accumulated thermal energy has been abandoned and some maxima have emerged indicating internal heat ‘generators’ resulting from some weakest links within the material not having appeared as cracks as such. It is then where it becomes clearly apparent where the final fracture is expected to occur and that the ‘heat generators’ identified earlier are indeed precursors of cracks to be initiated. A deeper look into these topographies and their development may be a source for further damage accumulation retrieval.

5 VISUALIZATION AND ANALYSIS OF OTHER RECORDED NDT DATA

What has been briefly performed and shown for thermography based data before can be principally also performed with electromagnetic measurements. However, here the digital image has been generated on measurements having been taken on a point to point basis although matrix sensors are gradually getting available in the meantime providing an additional option in this field. Principally scanning with a single sensor is possible as long as the sensor can be repeatedly positioned at the same position in a 3D space. With such an approach interesting first observations have been made such as the transformation to stress induced martensite and a relationship of magnetic measurement to plastic strain, which is shown for the example of a metastable austenitic steel AISI 347 in Fig. 6 and 7 respectively. In the case of martensite transformation a specifically designed magnetic force sensor (patent application pending) has been used in combination with a scanning device to scan the surface of a specimen having been fatigue loaded. This procedure could be done on a repetitive basis either by installing the sensor at the location of interest or scanning the specimen (i.e. component) at defined intervals. The information retrieved could be clearly localized and stored allowing some advanced signal processing to be performed in a next step. Fig. 6 shows a scanned image where locations of martensite generation, partially generated through hardness indentations, can be well recognized and this at a fairly high resolution [5].

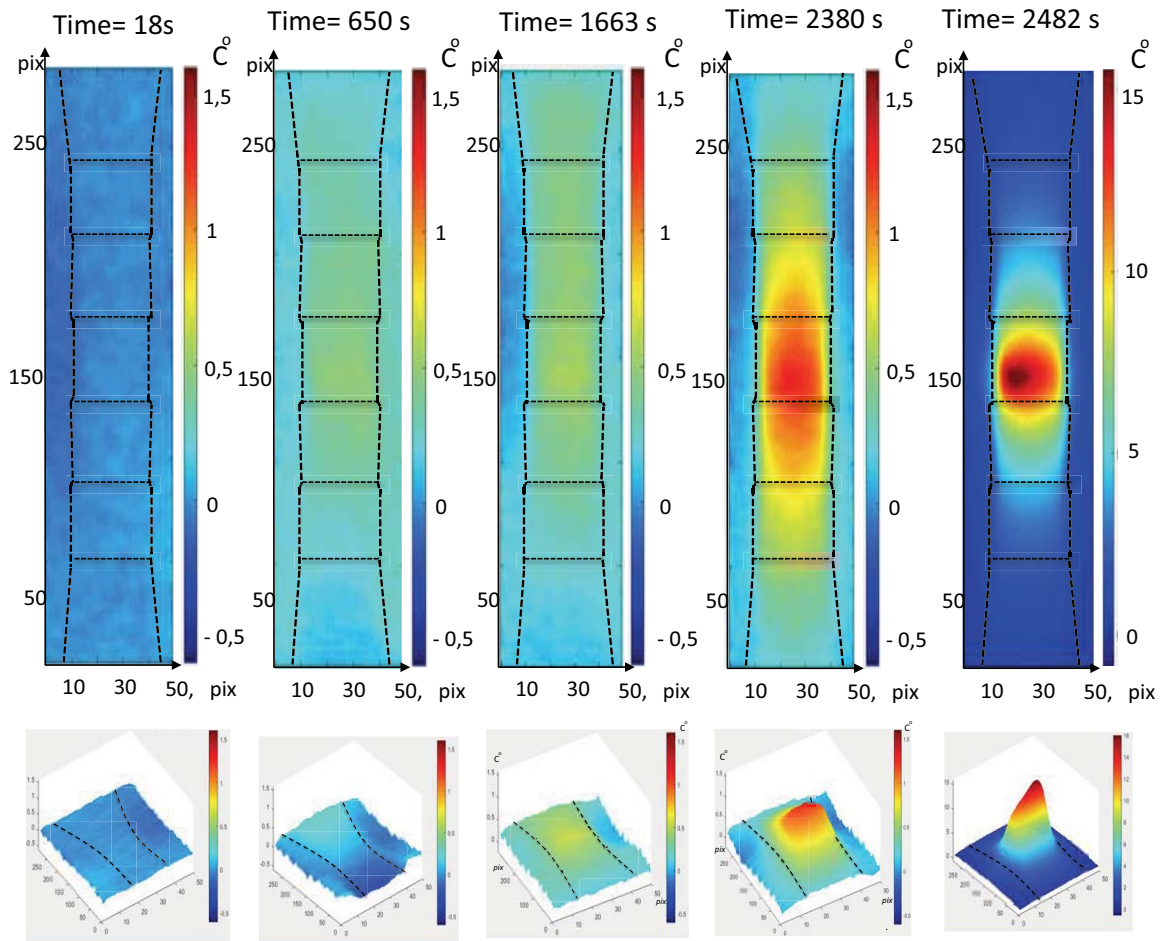


Figure 5: Topography of accumulated heat generation recorded along a constant amplitude fatigue test on a SteBLife specimen made of medium alloyed SAE 4140 QT

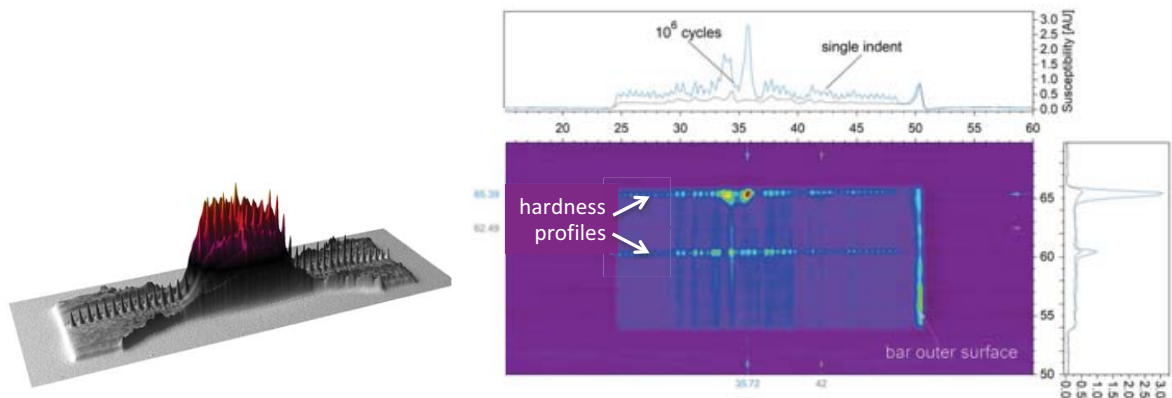


Figure 6: Distribution of stress induced martensite obtained through a scanning procedure for a metastable austenitic steel AISI 347

Magnetic sensors do also have the potential to identify other fatigue damage inducing phenomena such as plasticity as can be seen from the results shown in Fig. 7 below also for the

AISI 347 mentioned before [6]. Here a specimen has been magnetized and the normal and tangential magnetic field has been recorded with a Hall element based sensor in a test at ambient temperature. Although automation of this way of monitoring has still not been shown, the technique has all the potential to be done so in the longer term. This does also include the option in placing the sensing option in line with a strategy being based on continuous monitoring in the sense of SHM.

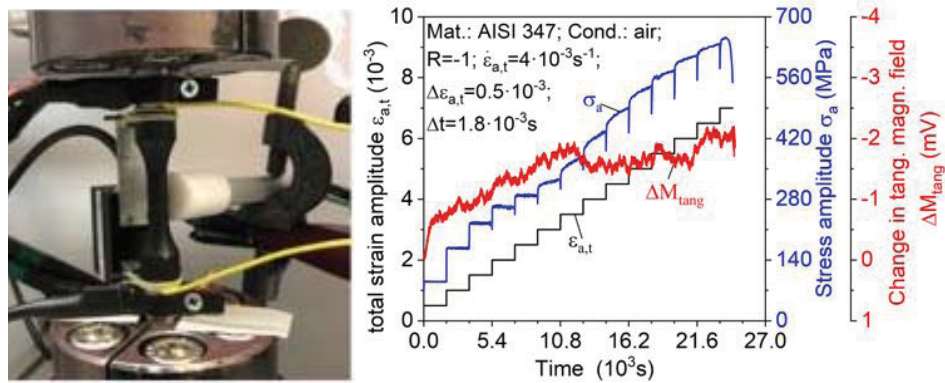


Figure 7: Experimental setup with magnetic sensor applied (left) and change in magnetic field obtained during a strain increase fatigue test (right) for a metastable austenitic steel AISI 347

One of the possibly most advanced techniques in NDT is ultrasonics, where sensing, signal and data processing as well as visualization is widely discussed when looking at the phased array developments including ray tracing and full matrix capture development. As can be schematically seen from Fig. 8 a phased array transducer with 16 elements is sending acoustic signals into a squared solid body of an either isotropic or even anisotropic material, which has been sectioned into individual elements (i.e. pixels), that can be considered as discrete data stocks of those elements. These elements can be considered as the elements of a 2D or even

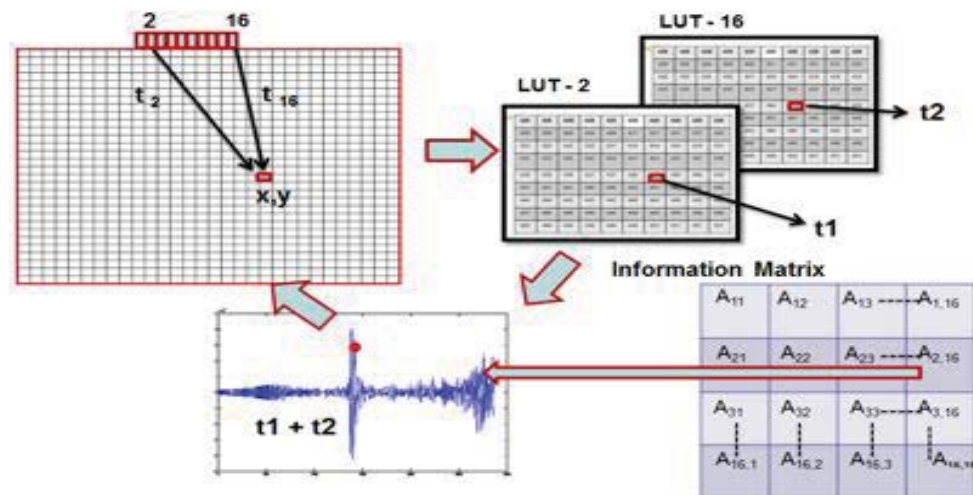


Figure 8: Ultrasonic phased array monitoring using ray tracing, SAFT and FMC for optimized monitoring

3D matrix of a structure. From each of the time domain signals recorded an allocation is made to each of those elements applying a ray tracing algorithm that identifies the relevant information then to be stored for each of those elements. The fact that specific features in the signal dominate allows an adaptation of the signals in terms of velocity, phase and even anisotropy to be made which has been known under the name of Synthetic Aperture Focusing Technique (SAFT) [7], Full Matrix Capture (FMC) [8] and Sampling Phased Array (SPA) [9]. The frame of such segmentations does allow NDT data to be managed and an ‘adaptive digital twin’ of the structure considered to be established that in the context of SHM could serve as an extension to improve an SHM system’s efficiency.

6 SMARTER SHM THROUGH NDT INHERITANCE

SHM has to be seen as an element within the frame of an engineering structure’s operational life. It is part of a process chain starting from the structure’s design expressed in terms of loads, geometry and material and is further broken down into strength, durability, integrity and inspection. Such a process has been drawn and discussed in further detail [10] and is shown in Fig. 9 below.



Figure 9: Design process chain for structural integrity assessment leading to SHM system generation

Structural integrity is directly associated with the expression of DTD which allows damage to be present in a structure as long as it does not become critical. DTD is a prerequisite for SHM. As such, a tolerable damage has to be defined, which needs to be detected by the SHM system reliably. To get this achieved, numerical simulation can be of invaluable help since it can allow locations to be identified where the tolerable damage would be monitored best. Much of the developments made in NDT are worth to be considered in the context of SHM. Acoustics has been the NDT technique most elaborated on in this regard over the past. To get those developments somehow placed in a logic order a trial has been made, which has been described in more detail in [11]. This trial is based on the fact that SHM requires simulation, data handling and a resulting hardware respectively. Fig. 10 shows how this can be configured in view of the design process chain shown in Fig. 9. Such a configuration has to be considered as a type of ‘toolbox’ for which a part of the scheme of the box is shown in Fig. 10 but the tools still need to be filled in. Filling such a toolbox is not a task to be done ‘overnight’ but rather a process to be continuously done and possibly never ending. However, it may provide some clarification and some new ideas with respect to SHM in view of a certain NDT inheritance. What is therefore tried is to fill the toolbox with some tools from the acoustics field point of view where more can be found in [11].

Fig. 11 shows the toolbox in terms of acoustics filled with some of the ‘tools’ made available. The scheme shown in Fig. 10 is now added by a fourth column, which makes reference to the various acoustics based NDT techniques available and serving as an input. All of those techniques may contain options with regard to simulation, data handling and hardware, which are worth to be broken up into the toolbox since they may be valuable tools in terms of gener-

ating new SHM solutions beyond the scope of what has been developed so far. This procedure of breaking up tools into the toolbox becomes specifically interesting when it comes to techniques other than acoustics and which have been considered less in the context of SHM. Electromagnetics looks to be one in that regard.

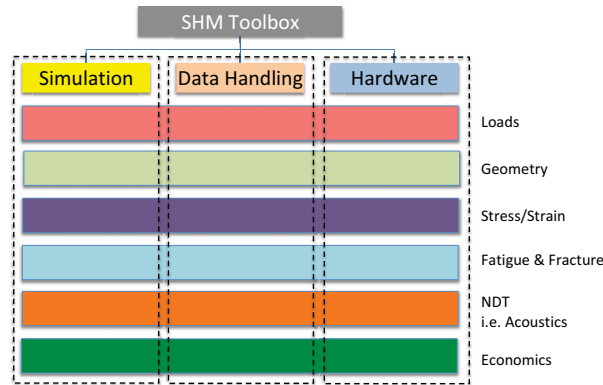


Figure 10: Upper level of a toolbox to configure SHM systems

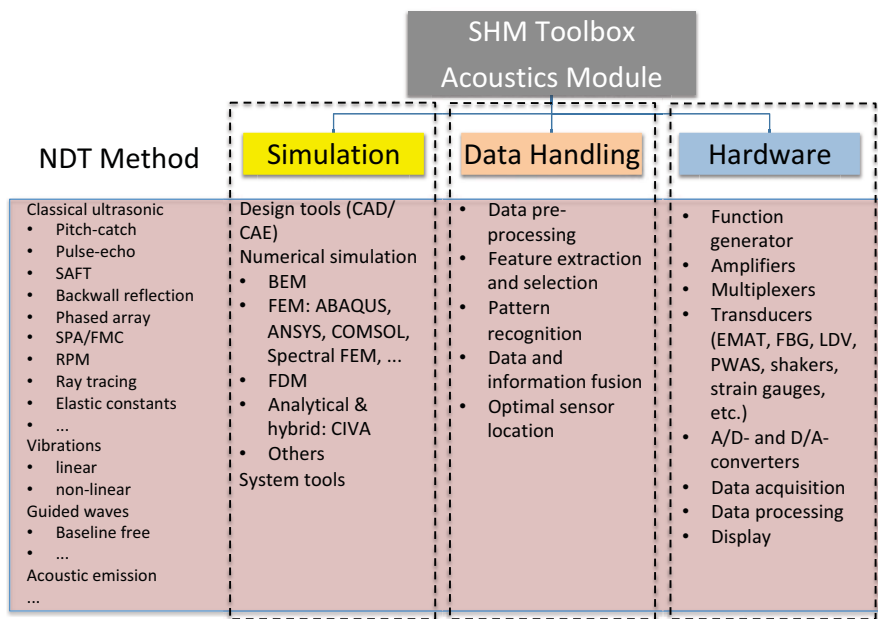


Figure 11: Acoustics based SHM systems design toolbox

7 CONCLUSIONS

SHM is a system's approach serving a structure's lighter weight design or longer operational life or possibly both of them. The longer operational life aspect requires a holistic view of a structure to be obtained including the design, operational and maintenance principles being applied. In many of those cases the SHM system's solution has to be specific and with this various input parameters have to be provided. This concerns the structural material's fatigue properties after ageing, which may have significantly changed and therefore may have to be

reassessed. Here STEPs are of an invaluable help since they allow a material's appropriate fatigue data to be determined at a reasonable effort. Along this assessment process damage relevant parameters can be recorded with sensing and possibly actuation options being beyond traditional strain measurement. Understanding the signal patterns of those sensors in view of structural damage can help to understand the measurement technique to be applied and as such build the basis to develop an SHM system being based on the respective technique and its parameters. This may not be an easy task as has been trying to be shown with regard to thermographic measurements, where influences not originating from the damaging phenomenon have to be eliminated. This may require an understanding of such phenomena that can be obtained through numerical simulation and may be further understood when imaging a measurement result. Such a process easily leads to a digital model of the structure considered if not to say to a 'digital twin' to be established already. This demonstrates the necessity of numerical simulation when efficiently designing an SHM system being an indispensable help to design an appropriate sensor network that reliably detects a damage considered to be tolerable. Getting the various NDT techniques being around broken down into a 'toolbox' can further serve to widen the scope of SHM and to make SHM further smart.

REFERENCES

- [1] Boller C., Chang F.-K., Fujino Y.: *Encyclopedia of Structural Health Monitoring*, J. Wiley & Sons, 5 Vols. (2009)
- [2] Boller C., Starke P., Enhanced assessment of ageing phenomena in steel structures based on materials data and non-destructive testing; *Mat.wiss. & Werkstofftechn.* 47, No. 10 (2016) 876-887,
- [3] Starke P., Eifler D., Boller C.: Fatigue assessment of metallic materials beyond strain measurement, *Int. J. Fat.* 82 (2016) 274-279.
- [4] Starke P., Wu H., Boller C.: SteBLife – The enhanced short-time evaluation procedure for materials fatigue data generation, *Materials Science Forum* 941 (2018) 2395-2400.
- [5] Lymakin V., Starke P., Boller C.: Cyclic indentation as an alternative to classic fatigue evaluation, *Proceedings, 7th Internat. Symp. on Aircraft Materials* (2018) 595-601.
- [6] Acosta R. et al.: Non-destructive testing derived parameters for microstructure-based residual service life assessment of ageing metallic materials in nuclear engineering; due to be submitted to *Materials Testing* (2019)
- [7] Schmitz, V., Müller, W., & Schäfer, G.: "Synthetic Aperture Focusing Technique- state of the art", *Journal of Acoustical Imaging*, Volume 19, 545-551, (1992)
- [8] Holmes C, Drinkwater BW, Wilcox PD. Post-processing of the full matrix of ultrasonic transmit-receive array data for non-destructive evaluation. *NDT&E Int*; (2005) 38(8):701–11
- [9] Bulavinov A.: *Der getaktete Gruppenstrahler*; Dissertation, Saarland University, (2005)
- [10] Boller C. et al.: Integration of Non-Destructive Evaluation- based Ultrasonic Simulation: A means for simulation in structural health monitoring, *Struct. Health Monit. - An Internat. J.*, (2017) 16, 611-629
- [11] Sridaran Venkat R.: *A Structural Health Monitoring Concept on Ultrasonic Based Assessment of Aged Structures with Isotropic and Anisotropic Material Properties*; Dissertation, Saarland University, (2018)

MODELLING OF DEFORMATION AND FRACTURE OF COMPOSITE STRUCTURES USING MONITORING DATA FROM OPTICAL FIBER STRAIN SENSORS

MIKHAIL A. TASHKINOV^{*}, VALERII P. MATVEENKO^{*†}

^{*} Faculty of Applied Mathematics and Mechanics
Perm National Research Polytechnic University
Komsomolsky Ave., 29, 614990 Perm, Russia
e-mail: m.tashkinov@pstu.ru, www.pstu.ru/en/

[†] Institute of Continuous Media Mechanics
Russian Academy of Science
Academician Korolev Street, 1, 614013 Perm, Russia
e-mail:.mvp@icmm.ru, www.icmm.ru/en/

Key words: Composite Structures, Elastic Constants Optimization, Optical Fiber Sensors, Bragg Gratings, Numerical Models.

Abstract. An iterative algorithm for refinement of elastic constant of composite laminates is offered. It comprises solution of the inverse problems in accordance with the data received from the fiber Bragg grating (FBG) sensors embedded into composite structure to ensure a match with a given precision of numerical and experimental results for strain values at the control points. The adjusted values of the constants allow to deliver more accurate simulation results using numerical models of mechanical behavior of the structures.

1 INTRODUCTION

The idea of creating materials that together with the basic functions allow to collect information about their condition is very relevant for polymeric composite laminates. The application fields of these materials are developing so rapidly that the current state of numerical and experimental methods for assessing their performance, strength and durability does not always meet the desired requirements. Therefore, it is important to enhance traditional methods for analysis of the mechanical state of composite laminates with new reliable approaches based on non-destructive solutions. One of the self-diagnostics concepts that can be implemented with regard to laminated composite structures involves optical fiber strain sensors [1–3]. The capabilities of such sensors to measure the mechanical state of the surrounding area are derived by using fiber Bragg gratings (FBGs), which provide periodic change in the refractive index of the core of an optical fiber subjected to external influence [4–6]. The operation principle of these sensors is based on a comparison of the wavelength of the light transmitted to and reflected from the Bragg grating.

There are many works devoted to the measurement of strains in composite materials with

the help of embedded or attached optical fiber sensors, with broad description of technical and methodological issues [6–12]. Embedded into composite laminates, optical fiber sensors have a wide range of advantages in comparison with the other structural health monitoring instruments. In particular, they are able to withstand strains comparable with strains of composite structures; are immune to electrical interference; are being integrated during the manufacturing process of the materials and allow to monitor the composite structure during both manufacturing and exploitation.

One of the specifics of composites is that, due to influence of manufacturing parameters, mechanical properties of the structure may not correspond exactly to the properties of the reference samples, even if they made of the same material. Increasing difference between final properties implemented in the structure and properties of testing samples sometimes makes it difficult to find correspondence between experimental and modelled behavior of composite structures.

This work is aimed at creating methods for evaluation of the mechanical state and prediction of mechanical properties of laminated composite structures using mathematical models which parameters are underpinned by the real-time monitoring data from the optical fiber strain sensors with Bragg gratings, integrated into the structures.

2 DEFINITION OF THE OPTIMIZATION PROBLEM

The principle of the proposed method is based on the comparison of the data of FBG sensors, placed in the predetermined control points in the composite structure, with the data of numerical finite element modelling of the same structure. The values of strains obtained from the sensors depend on the relative value of the resonance wave of the spectrum reflected by the Bragg grating, changes in the temperature of the optical fiber at location of the grating, strain and temperature coefficients. In the process of deformation of the sample, dependence of relative value of the resonance wavelength of the reflected spectrum of the optical fiber in the FBG location on the applied load is recorded at the control points. At the constant temperature, it is connected with strain tensor components ε_{ij} of the Bragg grating as follows [13]:

$$k = \Delta\lambda/\lambda = -\frac{n^2}{2}(p_{11} + p_{12})\varepsilon_{22} + \left(1 - \frac{n^2}{2}p_{12}\right)\varepsilon_{11}, \quad (1)$$

where n is refractive index of the optical fiber, p_{11} and p_{12} are the Pokkels coefficients of the strain-optical tensor.

Similar data, in terms of strain values later converted into the k coefficient, as in (1), is extracted from the simulation results. By the difference between the experimentally measured values $\Delta\lambda/\lambda$ and calculated values of k at the control points, a functional is constructed, which should be minimized:

$$M = \sum_{i=1}^N \left(k_i^{FBG}(F_i) - k_i^{FEM}(\mathbf{p}, \sigma_{ij}) \right)^2 \quad (2)$$

where $k_i^{FBG}(F_i)$ is relative value of the resonance wavelength of the reflected spectrum, obtained at the sample load F_i , $k_i^{FEM}(\mathbf{p}, \sigma_{ij})$ is computed with the same applied load F_i values of the coefficient k .

The optimization parameters are the elastic effective constants of the composite ply. Under plane stress conditions, only the values of $E_1, E_2, \nu_{12}, G_{12}$ and G_{13} are required to define an orthotropic material. Let's presume that the optical fiber is directed along the axis 1. The relations between strains and stress in the ply can be written in the following form:

$$\varepsilon_{11}^{FEM}(\mathbf{p}, \sigma_{ij}) = \frac{\sigma_{11}}{E_1} - \frac{\nu_{12}\sigma_{22}}{E_1} \quad (3)$$

$$\varepsilon_{22}^{FEM}(\mathbf{p}, \sigma_{ij}) = -\frac{\nu_{12}\sigma_{11}}{E_1} + \frac{\sigma_{22}}{E_2} \quad (4)$$

The regression function takes the form of Eq. (1) and is written using the constitutive relation for orthotropic media under conditions of plane stress state:

$$k^{FEM}(\mathbf{p}, \sigma_{ij}) = -\frac{n^2}{2}(p_{11} + p_{12})\left(-\frac{\nu_{12}\sigma_{11}}{E_1} + \frac{\sigma_{22}}{E_2}\right) + \left(1 - \frac{n^2}{2}p_{12}\right)\left(\frac{\sigma_{11}}{E_1} - \frac{\nu_{12}\sigma_{22}}{E_1}\right). \quad (5)$$

The stress values σ_{ij} depend on the applied sample load. Thus, the task is to find such values of the constants vector $\mathbf{p} = (E_1, E_2, \nu_{12})$, that will minimize the functional (2) and bring the results of the calculation $k_i^{FEM}(\mathbf{p}, \sigma_{ij})$ into conformity with the experimentally monitored values at a given load.

In the case of several control points, the multi-objective optimization problem is transformed into a single equation problem using the weighting coefficients w_i . Then the error estimation function is written as a sum:

$$G = \sum_{j=1}^N w_j M_j, \quad (6)$$

where N is the number of control points, M_j is the functional (2) for the control point j , the weighting factors w_j are chosen based on the parameters and initial conditions of the specific problems (for example, they can be related to the location of control points and closure of the critical zones).

The Levenberg-Marquardt (L-M) algorithm is used for the optimization, which presumes successive approximation of the given initial values of the parameters to the sought local optimum [14,15]. The initial value of the parameters vector $\mathbf{p} = (E_1, E_2, \nu_{12})$ corresponds to known or initially proposed values of the elastic constants of the ply. It is important, that if the

properties are unknown, zero initial vector of parameters can also lead to correct results with larger number of optimization steps required.

According to the Levenberg-Marquardt algorithm, the following formula is used to estimate the increment of the parameters vector $\Delta \mathbf{p}$:

$$\Delta \mathbf{p} = \left(J^T J + \lambda \text{diag}[J^T J] \right)^{-1} J^T \left(k_i^{FBG}(F_i) - k_i^{FEM}(\mathbf{p}, \sigma_{ij}) \right), \quad (7)$$

where parameter λ controls approximation speed, J is a Jacobian of $k^{FEM}(\mathbf{p}, \sigma_{ij})$ represented as a function of the current parameters values:

$$J = \begin{bmatrix} \frac{\partial k_1^{FEM}(\mathbf{p}, \sigma_{ij}(F_1))}{\partial p_1} & \dots & \frac{\partial k_1^{FEM}(\mathbf{p}, \sigma_{ij}(F_1))}{\partial p_3} \\ \dots & \dots & \dots \\ \frac{\partial k_n^{FEM}(\mathbf{p}, \sigma_{ij}(F_n))}{\partial p_1} & \dots & \frac{\partial k_n^{FEM}(\mathbf{p}, \sigma_{ij}(F_n))}{\partial p_3} \end{bmatrix} \quad (8)$$

Thus, as a result of the optimization problem solution, an optimal set of elastic constants can be found.

3 EXAMPLE OF IMPLEMENTATION

A test problem was considered in which optical fiber sensors were embedded in a composite sample with cutouts on the sides. The sample consisted of 14 0-oriented plies of fiberglass. The FBG sensors were placed in 4 control points on one optical fiber which was embedded between the 7th and 8th layer along axis 1 (coaxially with the direction of the applied load).

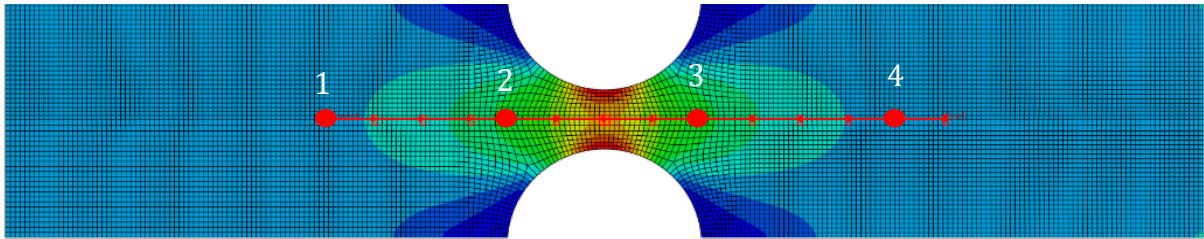


Figure 1: The numerical result of the calculation of the strain field ε_{11} and the location of control points (large red dots)

The calculated strain values ε_{11} obtained with (i) the finite-element model employing initial ply constants, (ii) FBG strain sensors and (iii) the finite-element model using optimized ply constants are presented in Fig. 2 for all control points located along axis 1. In the given example, using the proposed optimization algorithm, it was possible to achieve almost complete correspondence between the calculated and experimentally determined strain values. The

comparison of the values of the initial and optimized elastic constants for the lamina ply is presented in Table 1.

The Fig. 3 demonstrates the change in the values of the constants during implementation of the Levenberg-Marquardt optimization algorithm.

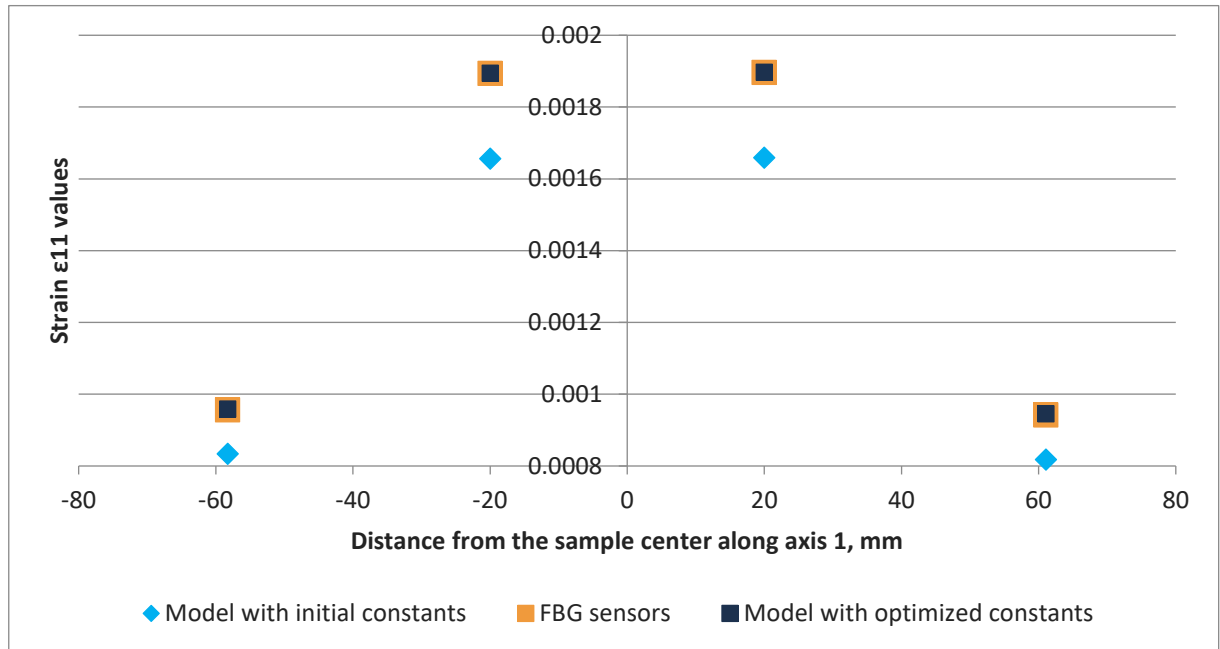


Figure 2: Comparison of strain values ε_{11} obtained using the model with initial constants (◆), FBG sensors (■) and model with optimized constants (■) depending on the distance from the center of the sample along its length

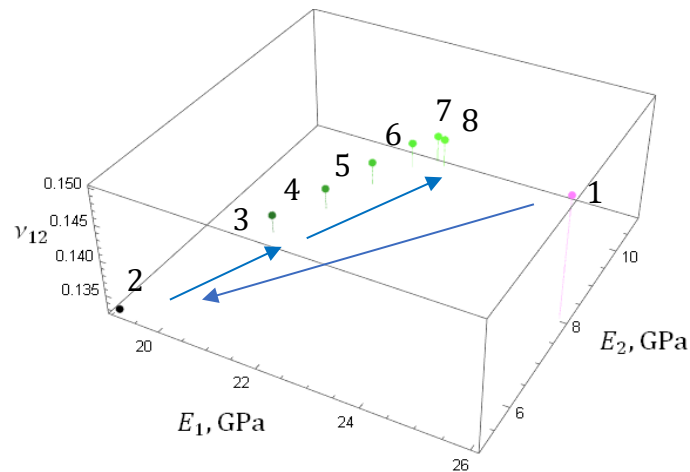


Figure 3: The values of the constants depending on a step of the optimization algorithm

Table 1: Initial and optimized properties of a fiberglass ply

	Young modulus E_1 , GPa	Young modulus E_2 , GPa	Poisson's ratio ν_{12}
Initial value	26,0	8,0	0,15
Adjusted value	22,05	10,81	0,137

The proposed method can be generalized for materials with higher anisotropy of properties or generalized strain-stress conditions. In such a case, it is necessary to experimentally measure several components of the strain tensor at the control points. To achieve this, the arrangement of optical fibers in the form of rosettes can be introduced, allowing to obtain measurements in different directions [16–18].

It should be noted that within the framework of this methodology, the measurements from FBG sensors should be considered reliable with the necessary precision. Since this area of research is actively developing at the moment, it is undoubtedly that recent advances will contribute to the development of FBG sensors as reliable tool for independent non-destructive monitoring of the state of composite structures.

4 CONCLUSIONS

- The method of assessment of the elastic constants of composite laminates is proposed based on the comparison of experimental measurements from the optical fiber sensors with Bragg gratings with the numerical results of finite element modelling.
- Numerical part of the proposed scheme is connected with finite element modelling of composite structures under quasi-static loading conditions. Experimental part is based on real-time measurement of strain values at the predetermined control points using FBG sensors.
- The regression function was constructed using constitutive relations for orthotropic media under conditions of plane stress state.
- The Levenberg-Marquardt algorithm is used for optimization of the effective elastic constants' values and their consequent application for validation of numerical modelling results.
- The proposed technique allows to estimate the elastic constants even if their initial values are unknown.
- Implementation of the proposed scheme is demonstrated on the test example.

ACKNOWLEDGEMENTS

The research was performed at the Perm National Research Polytechnic University with support of the Russian Science Foundation (project №15-19-00243).

REFERENCES

- [1] Staszewski W.J. Mahzan S. and Traynor R. Health monitoring of aerospace composite structures - Active and passive approach. *Compos. Sci. Technol.* (2009) **69**(11–12):1678–1685. doi:10.1016/j.compscitech.2008.09.034.

- [2] de Oliveira R. Frazão O. Santos J.. and Marques A.. Optic fibre sensor for real-time damage detection in smart composite. *Comput. Struct.* (2004) **82**(17):1315–1321. doi:10.1016/j.compstruc.2004.03.028.
- [3] Diamanti K. and Soutis C. Structural health monitoring techniques for aircraft composite structures. *Prog. Aerosp. Sci.* (2010) **46**(8):342–352. doi:10.1016/j.paerosci.2010.05.001.
- [4] Lau K.-T. Structural health monitoring for smart composites using embedded FBG sensor technology. *Mater. Sci. Technol.* (2014) **30**(13):1642–1654. doi:10.1179/1743284714Y.00000000608.
- [5] Kuang K.S.C. Kenny R. Whelan M.P. Cantwell W.J. and Chalker P.R. Embedded fibre Bragg grating sensors in advanced composite materials. *Compos. Sci. Technol.* (2001) **61**(10):1379–1387. doi:https://doi.org/10.1016/S0266-3538(01)00037-9.
- [6] Majumder M. Gangopadhyay T.K. Chakraborty A.K. Dasgupta K. and Bhattacharya D.K. Fibre Bragg gratings in structural health monitoring-Present status and applications. *Sensors Actuators, A Phys.* (2008) **147**(1):150–164. doi:10.1016/j.sna.2008.04.008.
- [7] Du W. Tao X.M. Tam H.Y. and Choy C.L. Fundamentals and applications of optical fiber Bragg grating sensors to textile structural composites. *Compos. Struct.* (1998) **42**(3):217–229. doi:10.1016/S0263-8223(98)00045-2.
- [8] Qiu Y. Wang Q.-B. Zhao H.-T. Chen J. and Wang Y.-Y. Review on composite structural health monitoring based on fiber Bragg grating sensing principle. *J. Shanghai Jiaotong Univ.* (2013) **18**(2):129–139. doi:10.1007/s12204-013-1375-4.
- [9] Matveenko V.P. Shardakov I.N. Voronkov A.A. Kosheleva N.A. Lobanov D.S. Serovaev G.S. Spaskova E.M. and Shipunov G.S. Measurement of strains by optical fiber Bragg grating sensors embedded into polymer composite material. *Struct. Control Heal. Monit.* (2018) **25**(3):e2118. doi:10.1002/stc.2118.
- [10] Yashiro S. Okabe T. Toyama N. and Takeda N. Monitoring damage in holed CFRP laminates using embedded chirped FBG sensors. *Int. J. Solids Struct.* (2007) **44**(2):603–613. doi:10.1016/j.ijsolstr.2006.05.004.
- [11] Hu H. Li S. Wang J. Wang Y. and Zu L. FBG-based real-time evaluation of transverse cracking in cross-ply laminates. *Compos. Struct.* (2016) **138**:151–160. doi:10.1016/j.compstruct.2015.11.037.
- [12] Di Sante R. Donati L. Troiani E. and Proli P. Reliability and accuracy of embedded fiber Bragg grating sensors for strain monitoring in advanced composite structures. *Met. Mater. Int.* (2014) **20**(3):537–543. doi:10.1007/s12540-014-3020-7.
- [13] Leduc D. Lecieux Y. Morvan P.A. and Lupi C. Architecture of optical fiber sensor for the simultaneous measurement of axial and radial strains. *Smart Mater. Struct.* (2013) doi:10.1088/0964-1726/22/7/075002.
- [14] Levenberg K. A Method for the solution of certain non-linear problems in least squares. *Q. Appl. Math* (1944) **11**(2):164–168.
- [15] Marquardt D. An Algorithm for Least-Squares Estimation of Nonlinear Parameters. *J. Soc. Ind. Appl. Math.* (1963) **11**(2):431–441. doi:10.1137/0111030.
- [16] Betz D.C. Thursby G. Culshaw B. Staszewski W.J. and Staszewski Wieslaw J. W.J. Structural damage location with fiber Bragg grating rosettes and Lamb waves. *Struct. Heal. Monit.* (2007) **6**(4):299–308. doi:10.1177/1475921707081974.
- [17] Chow H.L. and K.L. and L.C. and K. Embedded fibre Bragg grating sensors for non-

- uniform strain sensing in composite structures. *Meas. Sci. Technol.* (2005) **16**(12):2415.
- [18] Jin X.D. Sirkis J.S. Chung J.K. and Venkat V.S. Simultaneous Measurement of Two Strain Components in Composite Structures Using Embedded Fiber Sensor. *J. Compos. Mater.* (1999) **33**(15):1376–1389. doi:10.1177/002199839903301501.

THEORETICAL AND EXPERIMENTAL INVESTIGATION OF LAMB WAVES INDUCED BY BONDED AND DEBONDED PIEZOELECTRIC ACTUATORS IN A PLATE WITH A DELAMINATION

ALISA N. SHPAK*, MIKHAIL V. GOLUB*, ARTEM EREMIN*, INKA MUELLER[‡],
JENS KATHOL[†] AND CLAUS-PETER FRITZEN[†]

*Institute for Mathematics, Mechanics and Informatics, Kuban State University
350040 Krasnodar, Russian Federation
e-mail: alisashpak7@gmail.com, m_golub@inbox.ru; eremin_a.87@mail.ru

[‡] Department of Civil and Environmental Engineering, Ruhr-University Bochum
44801 Bochum, Germany
e-mail: inka.mueller@ruhr-uni-bochum.de

[†] Department of Mechanical Engineering and Center of Sensor Systems (ZESS)
University of Siegen, 57076 Siegen, Germany
e-mail: jens.kathol@uni-siegen.de; claus-peter.fritzen@uni-siegen.de

Key words: piezoelectric actuators, delamination, Lamb waves, hybrid approach, mode conversion

Abstract. This paper presents the results of theoretical and experimental investigations of Lamb wave propagation and scattering by a horizontal delamination in a layered elastic waveguide induced by a piezoelectric wafer active sensor (PWAS). The boundary integral equation method is used to simulate wave propagation and diffraction by a delamination. It is coupled with the frequency domain spectral element method, which is employed to model the dynamic behaviour of the PWAS considering possible debonding of the contact between the transducer and the multilayered waveguide. Experimental investigations of the debonded PWAS dynamic interaction with the layered plate, containing a horizontal delamination, conducted for several damage scenarios, are used to verify the obtained mathematical model. A good agreement between experimental and theoretical results is demonstrated. The developed mathematical model is employed to analyse alteration of the piezo-induced Lamb waves including modes' decomposition due to degradation of the contact conditions. The conversion and/or conservation of the Lamb waves due to delamination is investigated.

1 INTRODUCTION

Structural health monitoring (SHM) methods are of increasing importance since they enable the user to inspect the structure in an automated way in order to perform condition-based maintenance and prevent failure of the investigated system. A considerable amount of SHM techniques rely on elastic guided waves (GWs) as a physical principle for structural inspection [1]. Frequently, they employ a distributed network of surface-mounted piezoelectric wafer active sensors (PWAS) for GW excitation and detection. Since GWs are altered by all kinds of structural damages, the corresponding PWAS-recorded signals

after certain postprocessing are used for the estimation of the defect presence and might allow its localization and extent evaluation. To enhance these capabilities of SHM systems, preliminary numerical analysis of the corresponding wave phenomena is essential. Here, along with the investigation of single pure GW mode interaction with various defect types, studies of multimode PWAS-induced signal scattering are also important. Moreover, the PWAS itself might become a source of imperfections during the structure life-cycle, i.e., its cracking or partial debonding could have a non-negligible effect on the performance of the SHM system [2]. The latter should be also properly addressed in simulations. Thus, a reliable mathematical model simulating piezo-induced Lamb waves propagating and scattering from the delamination as well as PWAS' dynamic interaction with the structure is to be developed.

A combination of the boundary integral equation method (BIEM) and the frequency domain spectral element method (FDSEM), addressed as hybrid approach, is presented in the paper. The semi-analytical BIEM is an efficient tool for simulation of wave propagation in an elongated structure with an internal delamination [3, 4]. Moreover, this method allows investigating single pure Lamb wave mode propagation and scattering by the delamination and quantifying its conversion into other modes. The frequency domain spectral element method [5] is employed to discretize the complex-shaped PWAS in order to simulate its dynamic behaviour considering possible degradation of the contact between the transducer and the waveguide. These two methods are coupled in the contact area between the PWAS and the host structure on the basis of the continuity of the corresponding stresses and displacements. The proposed hybrid approach allows for a detailed parametric analysis of wave phenomena in an elongated structure due to partially debonded PWAS and in the presence of delamination.

2 STATEMENT OF THE PROBLEM

Let us consider an elastic layered structure with Lamé constants μ, λ and mass density ρ occupying the domain $\Omega_1 = \{|x_1| < \infty, -H \leq x_2 \leq 0\}$ with the surface bonded PWAS $\Omega_a = \{0 \leq x_1 \leq w_a, 0 \leq x_2 \leq h_a\}$ where h_a stands for the PWAS height and w_a denotes its width. The lower boundary of the PWAS is composed of the contact area S_c and the debonded area S_d . The horizontal delamination occupies the domain $\Omega_c = \{|x_1 - x_c| \leq l_c, x_2 = -d_c\}$, see Figure ??.

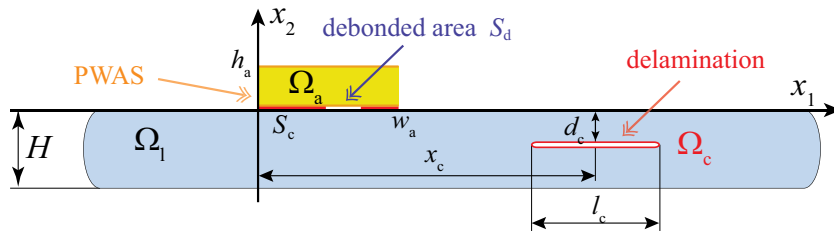


Figure 1: Statement for the mathematical problem

Governing equations defining time-harmonic vibrations of the PWAS Ω_a with angular frequency ω in the two-dimensional case (consider plane strain assumption) are written as follows:

$$C_{ijkl}u_{k,lj} + e_{kij}\phi_{,kj} + \rho\omega^2 u_i = 0, \quad (1)$$

$$e_{ikl}u_{k,li} - \epsilon_{ik}\phi_{,ki} = 0. \quad (2)$$

Here u_i are the components of the displacement vector, ϕ is electric potential; $u_{k,l}$ denotes differentiation $\frac{\partial u_k}{\partial x_l}$, while C_{ijkl} , e_{kij} and ϵ_{ij} are matrices of the elastic constants, piezoelectric constants and dielectric constants measured with zero strain respectively ($i, j, k, l = \overline{1, 2}$).

The electric potential $p(t)$ with the voltage $V = V_0$ is applied on the lower (S^+) surface of the PWAS:

$$\phi(\mathbf{x}, t) = p(t)V_0, \quad (\mathbf{x}) \in S^-, \quad (3)$$

while the upper (S^-) surface of the PWAS is grounded ($\phi(\mathbf{x}, t) = 0, (\mathbf{x}) \in S^+$) and the side boundaries of the PWAS are considered free of charge.

All boundaries of the piezoelectric structure Ω_a are stress-free except for the contact area S_c :

$$\sigma_{ij}\eta_j = 0, \quad \mathbf{x} \in \partial\Omega_a \setminus S_c, \quad (4)$$

here σ_{ij} – are components of the stress tensor and $\boldsymbol{\eta}$ is the normal vector.

The continuity of the stresses and displacements are assumed at the contact area S_c :

$$\boldsymbol{\tau}^a = \boldsymbol{\tau}^1, \quad (5)$$

$$\mathbf{u}^a = \mathbf{u}^1. \quad (6)$$

Components of the stress tensor hereinafter are expressed in terms of the traction vector $\boldsymbol{\tau} = \{\sigma_{12}, \sigma_{22}\}$.

Delamination boundaries are assumed being stress-free:

$$\boldsymbol{\tau} = 0, \quad \mathbf{x} \in \Omega_c. \quad (7)$$

3 HYBRID APPROACH

Application of the hybrid approach scheme is explained in detail in [9] for the case of the PWAS attached to a layered structure without delamination. The proposed method suggests solution of the problem in the frequency domain first and employment of the inverse Laplace transform to obtain a time domain solution afterwards. According to the FDSEM [6] the solution in the PWAS $\mathbf{y} = \{u_1, u_2, \phi\}$ can be approximated using Lagrange interpolation polynomials $C^I(x_1, x_2)$ at Gauss-Legendre-Lobatto points for each spectral element via a special index I :

$$\mathbf{y} = \sum_I y_I C^I(x_1, x_2). \quad (8)$$

In order to couple the PWAS with the waveguide at the contact area S_c , the unknown traction vector $\mathbf{q}(x_1)$ is introduced so that:

$$\mathbf{q} = \boldsymbol{\tau}^a = \boldsymbol{\tau}^1, \quad \mathbf{x} \in S_c. \quad (9)$$

The crack opening displacements (COD) $\mathbf{w}(x_1)$ for the delamination Ω_c are expanded via Chebyshev polynomials of the second kind with square root weight $p_n(x_1)$, see more details in [3]:

$$\mathbf{w}_k(x_1) = \sum_{n=0}^N \gamma_{kn} p_n(x_1). \quad (10)$$

The total wavefield in the elastic structure Ω_1 is obtained as sum of the wavefields excited by the PWAS \mathbf{u}^{in} and wavefields scattered by the crack \mathbf{u}^{sc} :

$$\mathbf{u}^1 = \mathbf{u}^{(in)} + \mathbf{u}^{(sc)}. \quad (11)$$

According to the BIEM [7, 8] displacements vector can be expressed as:

$$\mathbf{u}^{(in)}(\mathbf{x}) = \frac{1}{2\pi} \int_{\Gamma} \mathbf{K}(\alpha, x_2) \mathbf{Q}(\alpha) e^{-i\alpha x_1} d\alpha. \quad (12)$$

Here $\mathbf{K}(\alpha, x_2)$ is the Fourier transform of Green's matrix of the waveguide, $\mathbf{Q}(\alpha)$ is the Fourier transform of the surface load function $\mathbf{q}(x_1)$ with respect to x_1 coordinate, while Γ is the contour in the complex plane of the variable α along real axis surrounding poles of the integrand. Similar, the traction vector is expressed as:

$$\boldsymbol{\tau}^{(\text{in})}(\mathbf{x}) = \frac{1}{2\pi} \int_{\Gamma} \mathbf{T}(\alpha, x_2) \mathbf{Q}(\alpha) e^{-i\alpha x_1} d\alpha. \quad (13)$$

Here \mathbf{T} is matrix obtained after differential stress operator has been applied to representation (12). The scattered displacements vector is obtained in the same way:

$$\mathbf{u}^{(\text{sc})}(\mathbf{x}) = \frac{1}{2\pi} \int_{\Gamma} \mathbf{K}^{(c)}(\alpha, x_2) \mathbf{W}(\alpha) e^{-i\alpha x_1} d\alpha, \quad (14)$$

where $\mathbf{K}^{(c)}(\alpha, x_2)$ is the Fourier transform of Green's matrix and $\mathbf{W}(\alpha)$ is the Fourier transform of the unknown crack opening displacement $\mathbf{w}(x_1)$ for delamination Ω_c . Similar integral representations can be written for the traction vector:

$$\boldsymbol{\tau}^{(\text{sc})}(\mathbf{x}) = \frac{1}{2\pi} \int_{\Gamma} \mathbf{T}^{(c)}(\alpha, x_2) \mathbf{W}(\alpha) e^{-i\alpha x_1} d\alpha, \quad (15)$$

again, $\mathbf{T}^{(c)}$ is the matrix obtained after differential stress operator has been applied to representation (14).

The traction vector (9) is interpolated with the first order splines based on the nodal points χ_J at the contact area S_c . Employing the special index J , $\mathbf{q}(x_1)$ is expanded as follows

$$\mathbf{q}(x_1) = \sum_J \mathbf{q}^J s_J(x_1), \quad (16)$$

where $s_J(x_1)$ are the combinations of the first order splines.

Thus, a system of the linear algebraic equations with respect to the vector of unknowns

$$\mathbf{g} = \{y_1^J, y_2^J, y_3^J, q_1^J, q_2^J, \gamma_{1l}, \gamma_{2l}\}$$

can be written as follows

$$\begin{pmatrix} \mathbf{A}_{ij} & \mathbf{B}_{ik} & \mathbf{0} \\ \mathbf{C}_{lj} & \mathbf{D}_{lk} & \mathbf{F}_{lk} \\ \mathbf{0} & \mathbf{G}_{lk} & \mathbf{H}_{lk} \end{pmatrix} \cdot \begin{pmatrix} \mathbf{y} \\ \mathbf{q} \\ \boldsymbol{\gamma} \end{pmatrix} = \begin{pmatrix} \mathbf{V} \\ \mathbf{0} \\ \mathbf{0} \end{pmatrix}. \quad (17)$$

Matrices \mathbf{A}_{ij} and \mathbf{B}_{ik} are composed in accordance with the FDSEM, see more details in [9]. In order to satisfy boundary conditions (6) taking into account (11), the equations (12), (14) are substituted to (11) and afterwards the collocation method is applied to the solution at the nodal points. Thus matrices \mathbf{C}_{lj} , \mathbf{D}_{lk} , \mathbf{F}_{lk} are obtained:

$$C_{J'I;nj} = \delta_{J'I} \delta_{nj}, \quad (18)$$

$$D_{J'J;lk} = -\frac{1}{2\pi} \int_{\Gamma} K_{lk}(\alpha, 0) S_J(\alpha) e^{-i\alpha \chi_{J'}} d\alpha, \quad (19)$$

$$F_{J'n;lk} = -\frac{1}{2\pi} \int_{\Gamma} K_{lk}^{(c)}(\alpha, 0) P_n(\alpha) e^{-i\alpha \chi_{J'}} d\alpha. \quad (20)$$

Substitution of the representations (13), (15) to boundary conditions (7) and Bubnov-Galerkin scheme application results in the following expressions for the matrices G_{lk} , H_{lk} :

$$G_{n'J;lk} = -\frac{1}{2\pi} \int_{\Gamma} T_{lk}^{(0)}(\alpha, -d_c) S_J(\alpha) P_n^*(\alpha^*) d\alpha, \quad (21)$$

$$H_{n'n;lk} = -\frac{1}{2\pi} \int_{\Gamma} T_{lk}^{(c)}(\alpha, -d_c) P_n(\alpha) P_{n'}^*(\alpha^*) d\alpha. \quad (22)$$

The inverse Laplace transform is applied to the obtained time-harmonic solution $\mathbf{u}(\mathbf{x}, \omega)$ in order to calculate the time dependent solution.

The hybrid mathematical model can be used to investigate the elastic wave energy transfer from the PWAS into the waveguide and the amount of the wave energy carried by each Lamb wave. The application of the Cauchy's residue theorem and Jordan lemma allows to substitute integral representations (11)–(15) by sums of residues in the poles, which corresponds to propagating and attenuating Lamb waves [3]. Such analysis is based on the time-averaged power density vector $\mathbf{e}(\mathbf{x})$ or Umov-Poynting vector:

$$e_j = \frac{\omega}{2} \text{Im}(\sigma_{1j} u_1^* + \sigma_{2j} u_2^*). \quad (23)$$

The presence of the delamination in the waveguide results in a partial reflection of the GWs and, therefore, it is convenient to calculate transmission and reflection coefficients, which is also possible within the developed model. The wave energy distribution coefficients η_m^{\pm} (m corresponds to Lamb wave) are introduced via the integration of the horizontal component e_1 of the time-averaged power density vector along a certain cross-section of the waveguide in a far-field zone. The energy distribution coefficients $\eta_m^{\pm} = E_m^{\pm}/E^0$ are the ratios between the wave energy E_m^{\pm} carried by m -th Lamb wave in directions $x_1 \rightarrow \pm\infty$ and the wave energy transmitted by a PWAS:

$$E^0 = \frac{1}{2\pi} \int_{\Gamma} \mathbf{K}(\alpha, 0) \mathbf{Q}(\alpha) \mathbf{Q}^*(\alpha^*) d\alpha$$

or by a certain incoming Lamb wave

$$E^0 = \int_{-H}^0 e_1^{(\text{in})}(x_1, x_2) dx_2.$$

4 EXPERIMENT

Experimental investigations of the debonded PWAS dynamic interaction with the layered plate, containing a horizontal delamination, have been conducted for several damage scenarios. The scheme of the experiment specimen is shown in figure 2. Two rectangular piezoelectric transducers with sizes 10 mm×30 mm×1 mm have been glued one after another to the surface of the two-layered aluminum plate of dimensions 600 mm×100 mm with the thicknesses of the layers 1 mm and 2 mm. The interface horizontal delamination with the length $l_c = 10$ mm and center in $x_c = 155$ mm is located between the layers at the depth $d_c = 1$ mm. The Lamé constants $\lambda = 51.1$ GPa, $\mu = 26.3$ GPa and mass density $\rho = 2640$ kg/m³ are used in mathematical model for aluminum and the material of the PWAS is PIC 155 PI Ceramics production. Four different damage scenarios have been investigated, see Table 1. Within

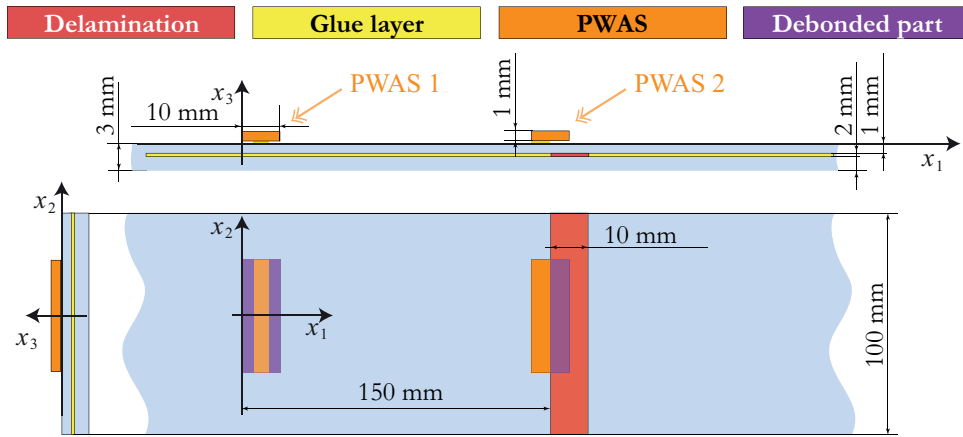


Figure 2: Design of the specimen

Table 1: Damage scenarios

Damage scenario	Transducer	Contact area S_c	PWAS x_1 coordinate
1	PWAS 1	$[0, 10]$	$[0, 10]$
2	PWAS 1	$[3, 7]$	$[0, 10]$
3	PWAS 2	$[0, 10]$	$[145, 155]$
4	PWAS 2	$[0, 5]$	$[145, 155]$

each damage scenario, only one transducer has been glued to the plate with the contact area S_c and particular distance to the crack. In that way, experimental results were obtained firstly for different bonding conditions and secondly for different mutual location between the PWAS and the delamination.

As input voltage signal $p(t)$ with the amplitude $V_0 = 40$ V is applied to the PWAS, Lamb waves are excited in the plate. The signal $p(t)$ has been used the same as was introduced in formula 53 in [9]. The velocities of the out-of-plane motion \dot{u}_2 have been measured at both sides of the plate $x_2 = 0$, $x_2 = -H$ with a 1D Laser Doppler vibrometer from OptoMET using a compact optical head with an infrared measurement laser of 1550 nm wavelength. In order to perform a comparison with the 2D mathematical model measurements have been taken along the line $x_2 = 0$, see Figure 2.

4.1 Verification of the model

In order to verify the developed mathematical model a comparison with the experimental signals and a standard FEM model has been performed. Comsol Multiphysics software has been used to calculate velocities of the piezo-induced motion at the surface of the plate with the standard finite element method. For the Comsol calculation 7921 (figures 3a, 3b) or 9176 (figures 3c, 3d) quadrilateral elements with quartic Lagrange interpolation polynomials have been used.

The results of the comparison for the damage scenario No 3 are shown in the figures 3a and 3b. The left plot presents velocities of the motion calculated and measured in the point $x_1 = 125$ mm which is located 20 mm from PWAS 2 on the left. The same data is shown in the right plot, but for the point $x_1 = 175$ mm, which is also located 20 mm from the PWAS 2 but on the right – where the delamination takes place (see Figure 2). All three methods provide similar results, though amplitudes of the calculated signals are slightly higher than the experimental data in the point $x_1 = 175$ mm. Additionally, it is

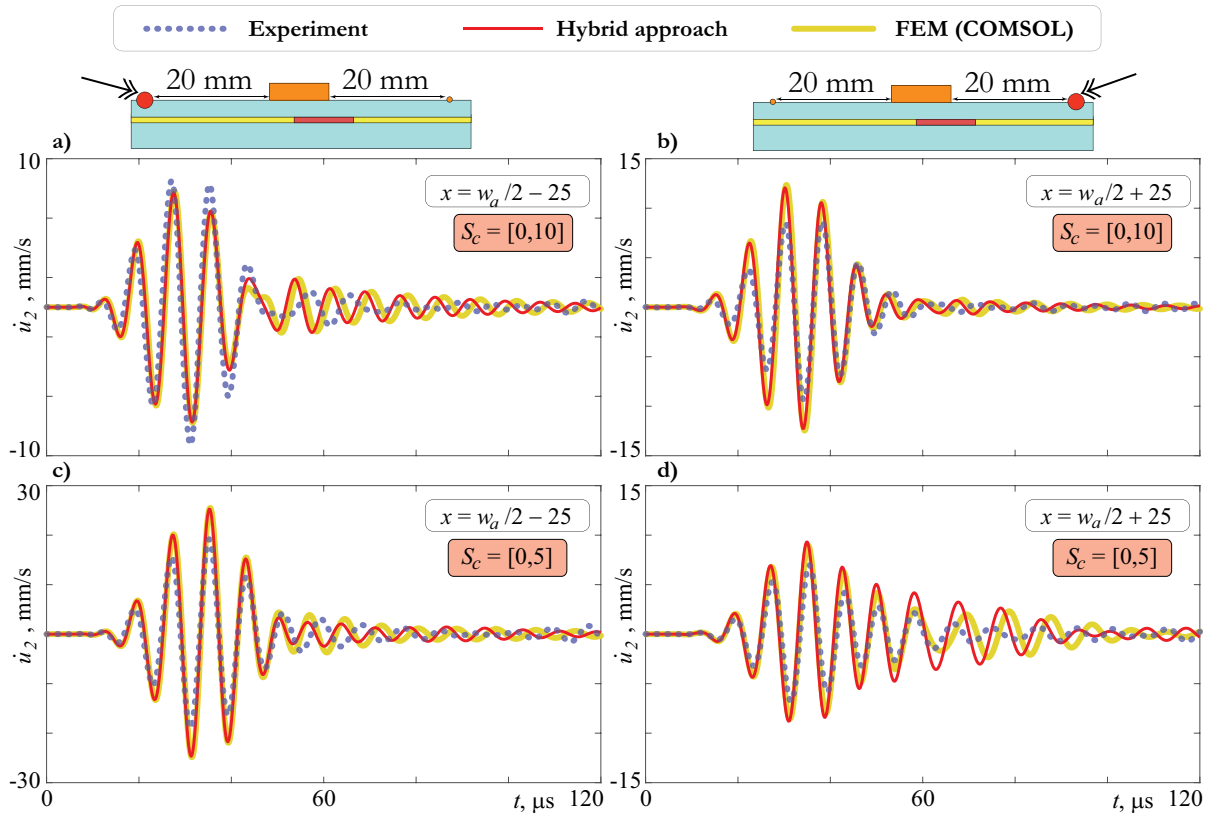


Figure 3: Velocities of the motion on the surface of the plate $u_2(125, 0, 0, t)$ (a,c) and $u_2(175, 0, 0, t)$ (b,d) measured and calculated with the central frequency $f = 120$ kHz for the perfectly bonded $S_c = [0, 10]$ (a,b) and partly debonded $S_c = [0, 5]$ (c,d) PWAS

observed that the amplitudes of the signal propagating over the delamination are slightly higher than the amplitudes of the signal propagating in the opposite of the delamination direction. The detailed analysis of transmission and reflection characteristics is provided in the section 4.2.

Figures 3c and 3d present results of the comparison at the same points measured and calculated with the partly debonded PWAS (damage scenario No 4). Again, agreement between the calculated and measured signals is very good. It is evident that in case of debonding, amplitudes of the signal propagating in the direction opposite to the delamination (figure 3c) are 2.8 times higher than the amplitudes measured at the point after the delamination (figure 3d). The proposed mathematical model predicts this effect accurately. Moreover, comparing figures 3b and 3d one can observe additional wave package, which is excited due to debonding.

4.2 Experimental investigation and analysis

The susceptance spectrum of the PWAS being the imaginary part of the admittance can be used to estimate PWAS structural health, including bonding conditions between the transducer and the waveguide [2]. It has been shown [2, 10] that the electro-mechanical impedance (EMI) spectrum is dependent on the contact conditions and various defects of the transducer. Electrical and mechanical parameters influence the EMI spectrum and therefore any structural alteration of the PWAS due to defect leads to an EMI spectrum change. The measurements of the EMI spectrum have been performed for four damage

scenarios with a Cypher C60 using 1024 points over a frequency range of 1kHz to 1MHz.

Figure 4 presents the measured susceptance spectrum for four PWAS conditions in dependence on frequency. The measured spectrum includes four eigenfrequencies leading to maxima in the susceptance spectrum in the following frequency ranges: 100kHz–260kHz; 410kHz–520kHz; 650kHz–780kHz and 910kHz–990kHz. Outside these frequency ranges susceptance spectrum does not depend neither on contact conditions nor on delamination existence and location. Two phenomena, which are explained in [2, 10] are visible here. The debonding leads to an elevated resonance phenomenon, as visible for the blue dotted line corresponding to the most debonded PWAS ($S_c = [3, 7]$, $w_a = 10\text{mm}$). Moreover there is a shift of the resonance to lower frequencies for the first resonance, which is highly influenced by the bonding conditions. To analyse the influence of the delamination it is proper to compare the yellow and red lines corresponding to the perfectly glued transducers, while the first one is far from the delamination (150 mm distanced) and the second one is located directly above the delamination. The difference in peaks is observed in the second and fourth frequency ranges, which leads to a conclusion that a delamination might influence susceptance spectrum as well. Though, more repetitions of similar experiments are needed to make a statistically proved resume.

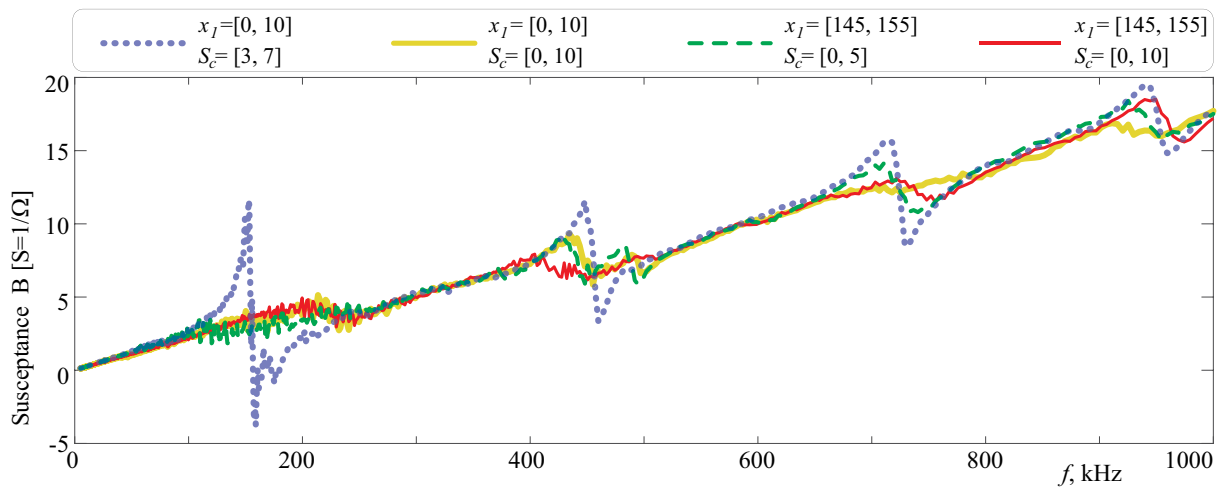


Figure 4: Susceptance spectrum

5 WAVE PHENOMENA ANALYSIS

The developed mathematical model allows to simulate distribution of the piezo-induced energy and quantify the conserved and/or converted energy due to delamination. Figure 5 presents the dependance of the energy E^0 on the excitation frequency for 4 damage scenarios and for the pristine PWAS glued to the waveguide with no delamination. It is visible, that the blue dotted and yellow solid lines oscillate, while the green dashed, red solid and brown solid lines are smooth. The reason for this effect lies in the method used to obtain E^0 – in the harmonic solution, the mutual influence between the delamination and the PWAS has no time dependence. And as long as the distance between the PWAS and delamination is rather big (145mm), the harmonic wavefields from both domains superimpose and the resulting E^0 plot oscillate. It is worthy to note, that E^0 excited in the waveguide with no delamination by the healthy PWAS (brown solid line) coincides with the same data, but with the delamination presence (yellow solid line). Thus, it can be concluded that the delamination has minor influence on the PWAS-excited energy if it is located in the far field.

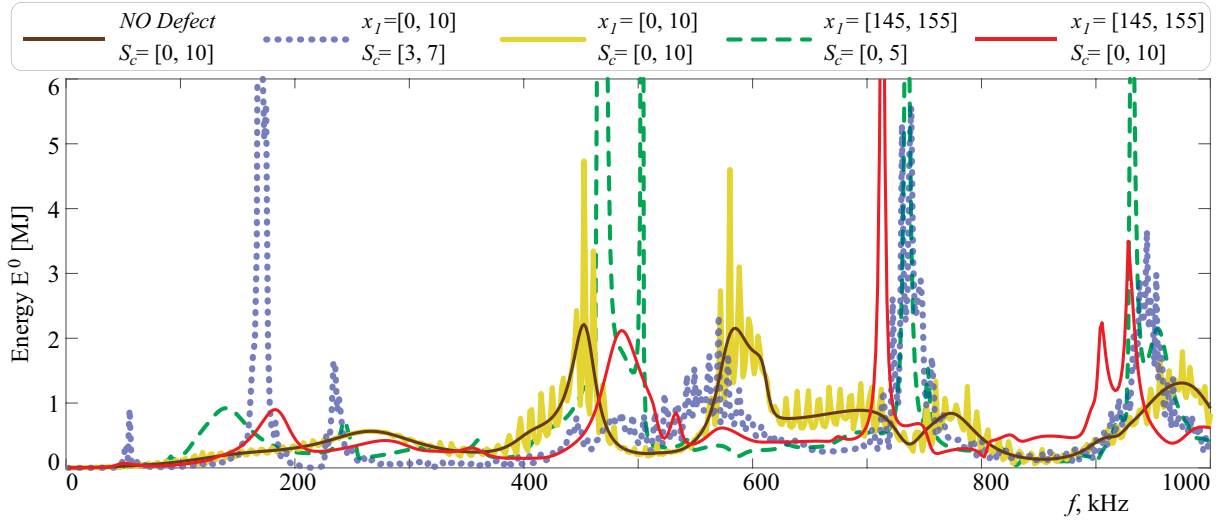


Figure 5: Wave energy E^0 excited by the PWAS in the plate with delamination $d_c = 1$ mm, $l_c = 5$ mm and $x_c = 155$ mm

It is observed that all maxima of the excited energy are located inside the same frequency diapasons determined during susceptance analysis. Moreover, all the peaks at the susceptance plot are in coincidence with peaks in the E^0 plot. For example the green dashed line indicating fourth damage scenario has two peaks at the susceptance plot ($f_1^B = 429\text{kHz}$ and $f_2^B = 489\text{kHz}$) and two similar peaks at the E^0 plot ($f_1^{E^0} = 464\text{kHz}$, $f_2^{E^0} = 502\text{kHz}$). The yellow solid line indicating the first damage scenario has no visible maximum in the third frequency range $650\text{kHz} - 780\text{kHz}$ at the susceptance plot and there is also no maxima at the E^0 plot in the same diapason. Such close correlation between the susceptance and elastic waves energy is due to both physical quantities are highly dependent on the eigen frequencies of the PWAS attached to waveguide. Nevertheless, there are additional maxima at the E^0 plot, in the additional frequency diapason $570\text{kHz} - 585\text{kHz}$, which have no counterpart at the susceptance plot. The nature of those peaks lies in the eigen characteristics of the coupled waveguide and PWAS.

A detailed analysis of the different modes of piezo-induced Lamb waves propagating in the waveguide with delamination has been performed. Figure 6 illustrates the modes' distribution over the excitation frequency for perfectly bonded (a) and debonded (b) PWAS located directly above the delamination (damage scenarios 3 and 4). Here parameter η_M^\pm indicates the share of the M mode in E^\pm , which is part of the PWAS-excited energy E^0 propagating in directions $x_1 \rightarrow \pm\infty$. It is observed that at lower frequencies (up to 250kHz) partial debonding results in increasing of the reflected energy. Thus, at frequency $f = 120\text{kHz}$ with the perfectly glued PWAS 44% of the energy is distributed to the right (33% A_0^+ , 11% S_0^+) and 56% of the energy is distributed to the left (20% A_0^- , 36% S_0^-). At the same time, with the half debonded PWAS only 26% of the energy is distributed to the right (2% A_0^+ , 24% S_0^+) and 74% of the energy is distributed to the left (25% A_0^- , 49% S_0^-). The same results are visible in the figure 3 – amplitudes of the velocities measured to the right and to the left from the PWAS are almost the same for the healthy PWAS (figures 3a and 3b) and differ in 2.8 times for the debonded PWAS (figures 3c and 3d).

In order to distinguish modes excited by the PWAS from converted modes due to delamination, the investigation of the modes' excitation in the waveguide without delamination has been performed. Figure 7 presents distribution of the modes in the excited wavefield by perfectly bonded (a) and partly debonded (b) PWASs. The contact conditions are chosen the same like in damage scenarios 1 and 2.

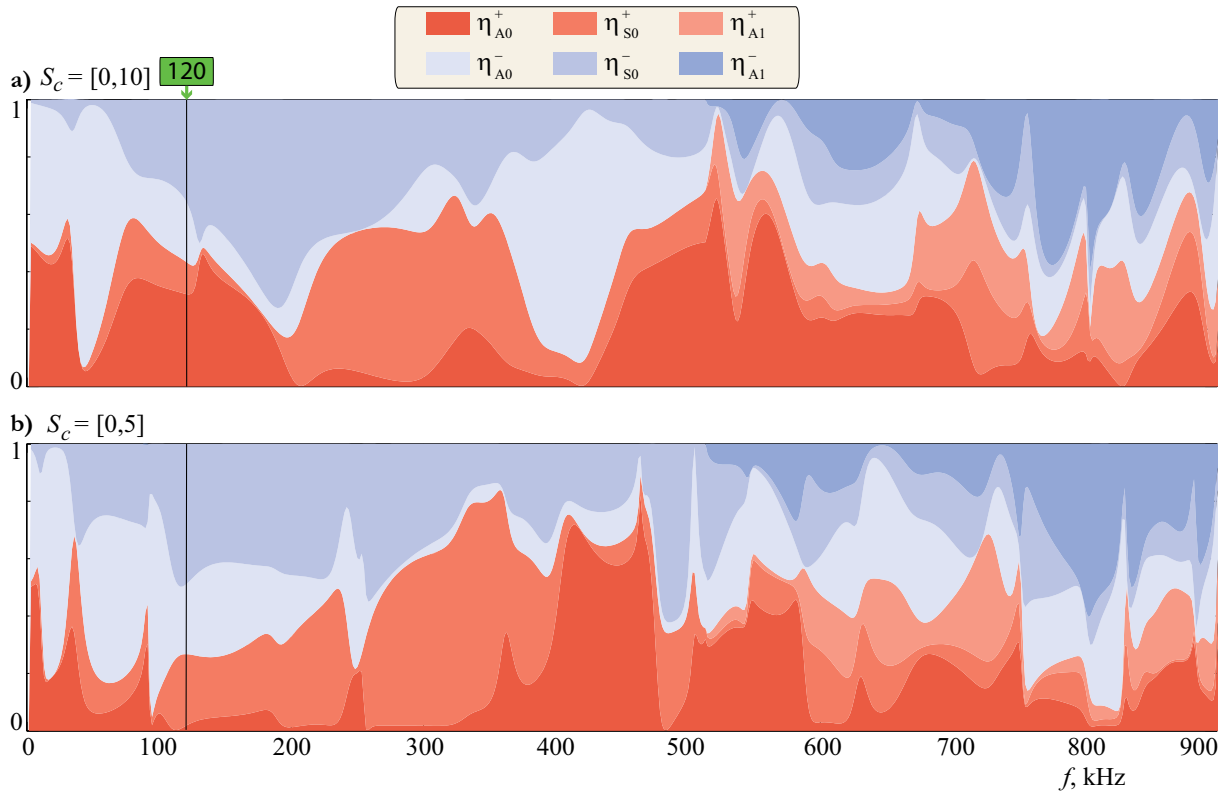


Figure 6: Wave energy modes distribution over frequency for (a) perfectly bonded ($S_c = [0, 10]$) and (b) debonded ($S_c = [0, 5]$) PWAS; $x_1 \in [145, 155]$

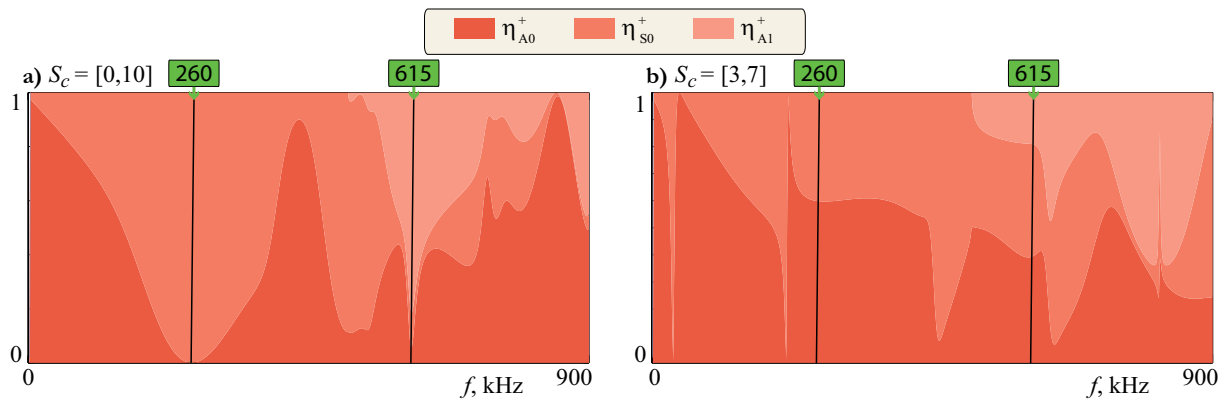


Figure 7: Decomposition of the piezo-induced Lamb waves over frequency for (a) perfectly bonded ($S_c = [0, 10]$) and (b) debonded ($S_c = [3, 7]$) PWAS in case of plate with no delamination

As the problem is symmetric, only the positive direction is shown. It is evident that even without the delamination, modes' distribution is strongly influenced by the PWAS debonding. For example, the healthy PWAS excites only the S_0 mode at the frequency $f = 260$ kHz and mostly A_1 mode (82%) at the frequency $f = 615$ kHz, but neither of these effects are visible if the PWAS is debonded. In that case, at $f = 260$ kHz share of the S_0 mode is only 38% and at $f = 615$ kHz share of A_1 mode is 18%. However, if one assumes that PWAS is healthy, such analysis might be quite useful for the practical applications. It is

possible to calculate modes' distribution for the PWAS of any size and choose appropriate combination of the PWAS size and frequency in order to select a so called sweet spot frequency to excite mainly the desired Lamb wave mode, interacting best with the presumed damage type.

In order to improve damage detection techniques, it is necessary to analyse how each Lamb wave interacts with every kind of defect. As illustrated in figure 7, either A_0 or S_0 are excited in the waveguide at frequencies up to 500kHz. Therefore, an analysis of the incident A_0 and S_0 modes interaction with the delamination is provided. Figure 8a presents Lamb waves energy distribution transmitted and scattered from the delamination. It is observed, that incident A_0 mode is reflected by the crack (A_0^-) and ratio between the transmitted and reflected waves depends on the frequency. Moreover, up to a frequency $f = 520\text{kHz}$ almost no mode conversion is visible; starting from $f = 520\text{kHz}$ firstly part of the A_0^+ is converted to A_1^+ and then to S_0^+ . The most interesting effect is observed at frequency $f = 440\text{kHz}$, where almost all incident A_0 wave is transmitted through the delamination without any reflection or conversion. Figure 8b demonstrates the same modes' distribution but for incident S_0 mode. It is evident, that the S_0 mode practically does not interact with delamination at the frequencies up to 580kHz. Starting from $f = 580\text{kHz}$, a small part of incident S_0 is converted to A_0 , the conversion-to-conservation ratio increases with the highest frequencies. But over the whole frequency range even at the higher frequencies, ratio of the reflected waves is insignificant. Thus, if a PWAS is used to induce Lamb waves at the frequency for example $f = 260\text{kHz}$, where only S_0 is excited, those GW most likely will not interact with the delamination and therefore the defect will not be detected. Evidently, such mode analysis is needed during development of the SHM system for the particular structure.

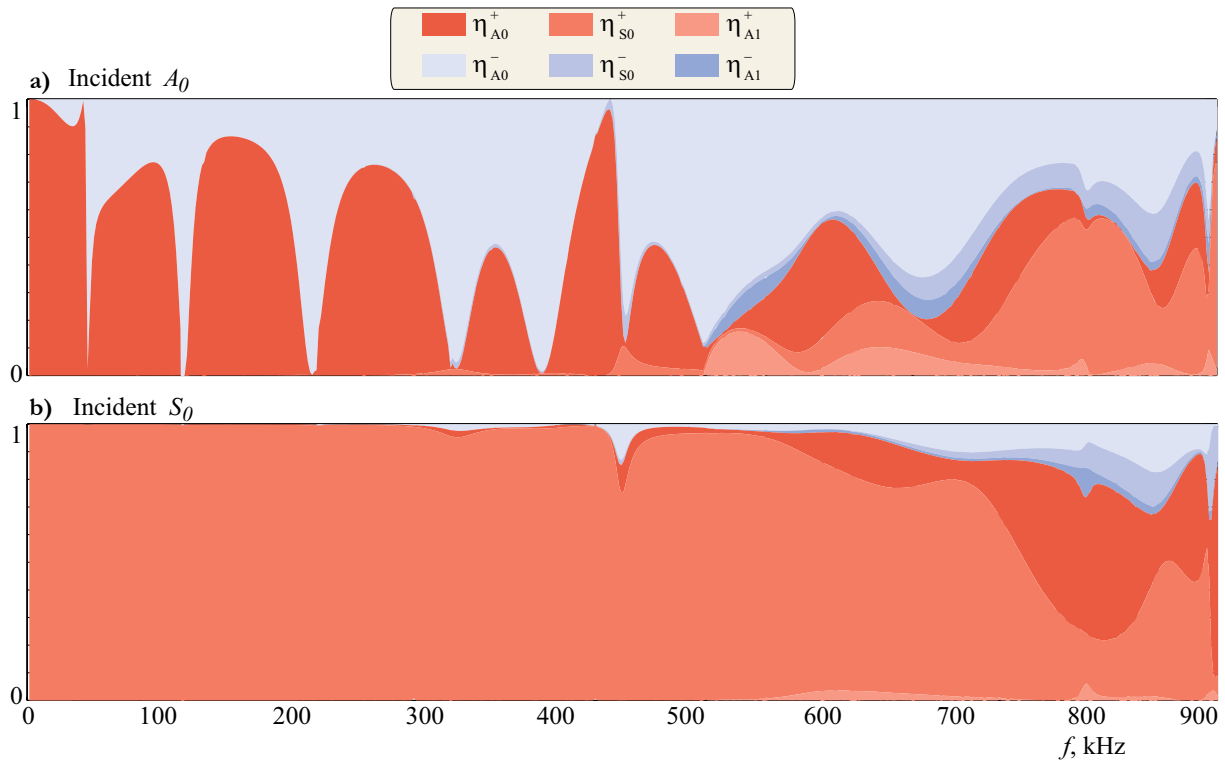


Figure 8: Wave energy distribution coefficients for A_0 and S_0 scattering by a delamination $l_c = 5\text{mm}$, $d_c = 1\text{mm}$

6 CONCLUSIONS

A mathematical model based on the combination of the BIEM and the FDSEM simulating piezo-induced Lamb waves propagation and scattering in a waveguide with a horizontal delamination has been obtained. Experiments with healthy and partially debonded PWASs glued to the layered waveguide with a delamination have been conducted. A good agreement between the calculated and measured signals has been demonstrated. A correlation between the susceptance value and energy of elastic waves induced in the waveguide has been revealed. It was shown that delamination does not influence the PWAS-induced energy, if the distance between the transducer and the delamination is considerable large. A detailed analysis of the Lamb waves transmission and/or reflection due to delamination including modal analysis has been performed. It was revealed that debonding of the PWAS leads to the significant changes in the modes' distribution in the excited wavefield. Incident A_0 and S_0 modes interaction with the delamination has been analysed. It was revealed that the A_0 mode is partly reflected by the delamination, while the S_0 interaction with the delamination is insignificant.

The work is supported by the Ministry of Science and Higher Education of the Russian Federation (Project No 9.1022.2017/4.6) and by the Deutscher Akademischer Austauschdienst (DAAD).

REFERENCES

- [1] Tian, Z., Yu, L. and Leckey, C. Delamination detection and quantification on laminated composite structures with Lamb waves and wavenumber analysis, *J. Intell. Material Syst. Struct.* 26 (13) (2015) 1723–1738.
- [2] Mueller, I. and Fritzen, C.-P. Inspection of Piezoceramic Transducers Used for Structural Health Monitoring, *Materials* 10 (1) (2017) 71.
- [3] Glushkov, E. Glushkova, N. Golub, M. V. and Zhang, C. Resonance blocking of travelling waves by a system of cracks in an elastic layer, *Acoust. Phys.* 55 (2009) 8–16.
- [4] Eremin, A.A., Golub, M. V., Glushkov, E. V. and Glushkova, N. V. Identification of delamination based on the Lamb wave scattering resonance frequencies, *NDT & E International*, 103 (2019) 145-153
- [5] Shi, L., Zhou, Y., Wang, J. M., Zhuang, M., Liu, N. and Liu, Q. H. Spectral element method for elastic and acoustic waves in frequency domain, *J. Comp. Phys.* 327 (2016) 19–38.
- [6] Priolo, E., Carlione, J. M., Seriani, G. Numerical simulation of interface waves by high-order spectral modeling techniques, *J. Acoust. Soc. Am.* 95(2) (1994) 681 – 693.
- [7] Glushkov, E. V. and Glushkova, N. V. On the efficient implementation of the integral equation method in elastodynamics, *J. Comput. Acoust.* 9(3) (2001) 889–898.
- [8] Glushkov, E. Glushkova and Eremin, A. Forced wave propagation and energy distribution in anisotropic laminate composites, *J. Acoust. Soc. Am.* 129 (5) (2011) 2923–2934.
- [9] Golub, M.V., Shpak, A.N. Semi-analytical hybrid approach for the simulation of layered waveguide with a partially debonded piezoelectric structure, *Appl. Math. Model.* Vol. 65 (2019) 234–255.
- [10] Mueller, I. Inspection of Piezoelectric Transducers used for Structural Health Monitoring Systems, *Siegen, Univ., Diss.* (2017) p. 206.

TUBULAR ULTRASONIC TRANSDUCER: MUST WITH AXIAL EXCITATION VERSUS CONVENTIONAL WITH RADIAL EXCITATION

NABIL BENCHEIKH, JOCELYN REBUFA AND FRANK CLAEYSSSEN

Cedrat Technologies
59 Chemin du Vieux Chêne - Inovallée - 38246 Meylan cedex – France

E-mail: nabil.bencheikh@cedrat-tec.com,

Key words: Ultrasonic transducer, Multiphysics problems, High power

Abstract. This paper presents comparison between two excitation solutions for tubular ultrasonic transducer. The axial excitation is widespread in conventional ultrasonic transducer. The radial excitation is proposed in order to have an uniform acoustic energy all along the tube. This excitation approach is also proposed to allow the modularity by adding several tubes.

1 INTRODUCTION

Ultrasonic transducers are commonly used for transmitting mechanical energy to several kinds of media: fluid, polymers. . . . in order to impact its properties.

Ultrasonic transducers are usually used for converting electrical energy to mechanical vibration. The Langevin solution is widely used for this conversion. This solution is based on two different masses at the ends of active material (typically piezoelectric material). Both masses are mechanically connected by a screw in order to preload and ensure the compression of the piezoelectric material during the vibration. The weight of both masses is different in order to favour the vibration in one direction. In order to increase the emitting surface, the ultrasonic transducers are connected to a large surface structure with adapted impedance in order to fit with the frequency resonance of the ultrasonic transducer. The most common cases are flat surfaces or tubular surface. For the flat surface, several ultrasonic transducers are required and the number of transducers is directly linked to the active power. The technological limitation for the tubular solution is the tube length. Tubes are convenient for some coating application if width is limited to typically less than 1 m. A new need addressed in H2020 PROTECT Eu project is to coat large textiles width using sonochemistry [<http://protect-h2020.eu/>]. For such a need, it is required to produce a uniform acoustic energy all along the textile widths. Similar acoustic uniformity requirements are also met in ultrasonic unclogging of cylindrical filters.

In order to overcome this technological limitation, several research activities have been performed. The wasted vibration issued from the Langevin ultrasonic transducer is recovered by connecting two tubes in both sides of the ultrasonic transducer [1]. The proposed solution is called wing type ultrasonic transducer. This architecture enables to increase the emitting surface through two tubes. Nevertheless, a non-vibration area remains at the piezoelectric stack location which means a non-uniform treatment all along the tube. So, another architecture is

proposed [2] by the by using two ultrasonic transducers at the two ends of the tube. This option enables to increase the length of the tube by 25 to 30 %. In the same way, the length of the tube is limited at 2 to 2.5 m. For longer tube, the attenuation of the vibration occurs in the middle of the tube. Such a solution is called a push-pull, ultrasonic transducer. This solution allows for increasing the length of the tube. Nevertheless, the modular approach seems more suitable for a longer tube. The modular approach is proposed [3] using the ultrasonic transducer connected in axial excitation. In this case, the diameter of the tube is higher compared to the diameter of the ultrasonic transducer. This approach allows connecting several tubes in serial from the mechanical point of view. So the ultrasonic transducer is located in the hollowed part of the previous tube. The entire tube is constituted by several tubes connected together by a welding process at the external diameters of the tube. In this case, the vibration is uniform all along the tube. This architecture allows having a longer tube with less dissipation of the vibration at the tube level. However, the ratio between the axial displacement of the ultrasonic transducer and the radial displacement at the tube lever is not favourable due to the difference between the diameter of the ultrasonic transducer and the diameter of the tube. Instead of using the ultrasonic transducer in the axial vibration, the approach of [4] is to use the strain generated in the radial direction of the ultrasonic transducer and transmitted to the tube through the internal diameter. This architecture is proposed to allow to pass the fluid (or the media) to treat inside the tube (instead of outside).

The approach proposed in this paper is to use a radial excitation in order to install the ultrasonic transducer within the tube. This configuration named MUST standing for Modular UltraSonic Transducer and patented by CTEC [5] is preferred in the perspective of providing a uniform acoustic energy along the transducer. It also offers a good potential for using the ultrasonic transducer in a modular approach, by stacking them to get a length of several meters.

2 CONVENTIONAL AXIAL EXCITATION

Tubular ultrasonic transducers are based on ultrasonic transducer (for the mechanical vibration generation) connected to one end of the tube. The second end of the tube is connected to an heavy mass (see Figure 1). The ultrasonic transducer is based typically on Langevin transducer. The aim of the tube is to increase the emitting surface through its external surface which is immersed in the media to treat.

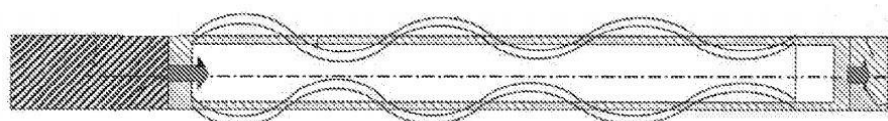


Figure 1: Tubular ultrasonic transducer approach

2.1 The transducer solution

The Langevin transducer which is typically made up of rear mass, head mass (emitter) and active material (stack of piezoelectric material) is depicted in Figure 2. The screw is used to preload the stack of the all the components constituting the ultrasonic transducer. In this way, the screw ensures that all the components stay connected during the vibration of the ultrasonic transducer.

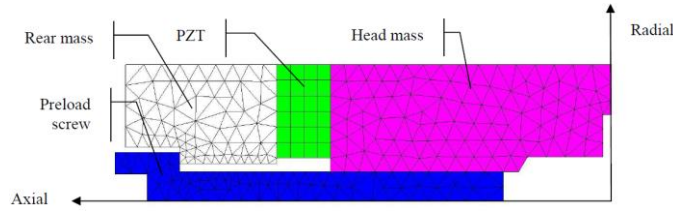


Figure 2: Typical Langevin, ultrasonic transducer (axisymmetric view)

The resonance frequency of such a system depends on the dimension and the material properties of the ultrasonic transducer components. The simplified formulation depicting this relation is given by the formulation given hereafter.

$$\text{wavelength } (\lambda) = \frac{1}{f} \times \sqrt{\frac{E}{\rho}} \quad (1)$$

With:

E: Young modulus [N/mm²]

ρ : Density of the material [Kg/m³]

f: Considered frequency [Hz]

Finite Element Method gives a more accurate prediction. The shape and the mapping of the axial and radial displacement are given the pictures below (Figure 3).

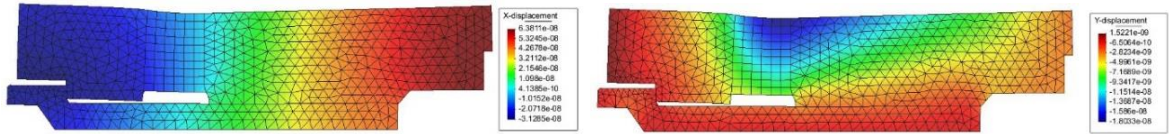


Figure 3: The axial and the radial displacement on the ultrasonic transducer

The displacement is considered in free-free consideration. The resonance frequency of the transducer is about 24.3 kHz with a coupling coefficient of 24 % at this frequency. The displacement depicted is given for 1 volt supply. The density of the rear mass is chosen in such a way to favour the emitting energy in the head mass side. The displacement of the transducer in the axial and radial all along the transducer is given in the curves below.

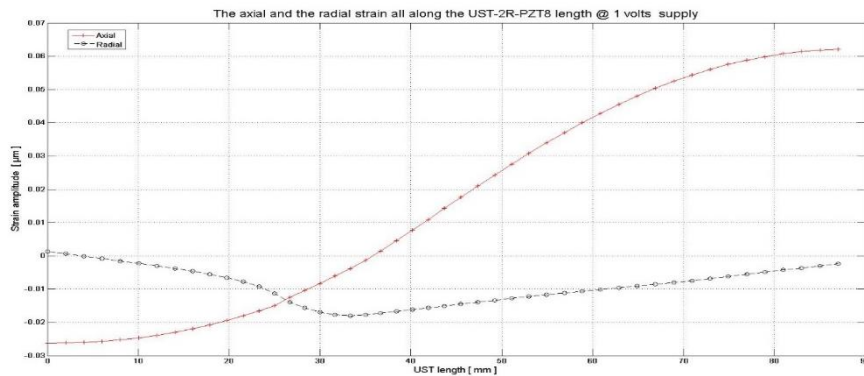


Figure 4: The axial and the radial displacement on the UST

In order to increase the emitting surface, the ultrasonic transducer is connected to the tube. The design of the tube is done in order to fit with the resonance frequency of the ultrasonic transducer. In such a configuration, the system is called ‘Tubular ultrasonic transducer’. This design is based on the previous equation above (equation 1).

2.2 The resonator behaviour

The assembly of the tube on the ultrasonic transducer is described below (Figure 5). The tubular part is designed in order to allow the maximum radial displacement while being compliant with the material fatigue.

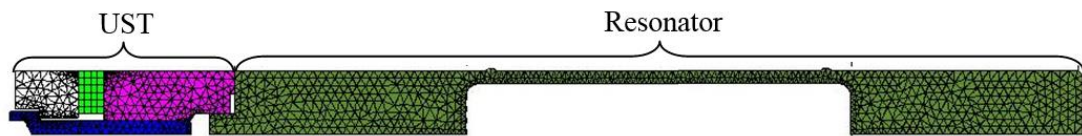


Figure 5: Tubular ultrasonic transducer with simple excitation

The analyses of the Eigen shape of the tube show two different shapes of deformation. The cylindrical shape corresponds to the increase of the tube diameter at a given position (Figure 6). The black lines correspond to the initial diameter of the tube, the red lines to the maximum position of the tube and the green line to the minimum position of the tube. For the elliptic shape, the diameter of the tube increases in one direction and decreases in the other direction at the given position (Figure 7). In the same approach, the black lines correspond to the initial diameter of the tube, the red lines to the maximum position of the tube and the green line to the minimum position of the tube.

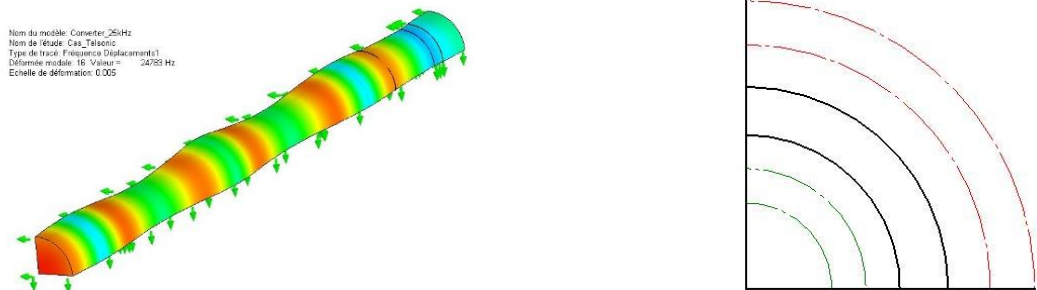


Figure 6: Tubular with the cylindrical deformation

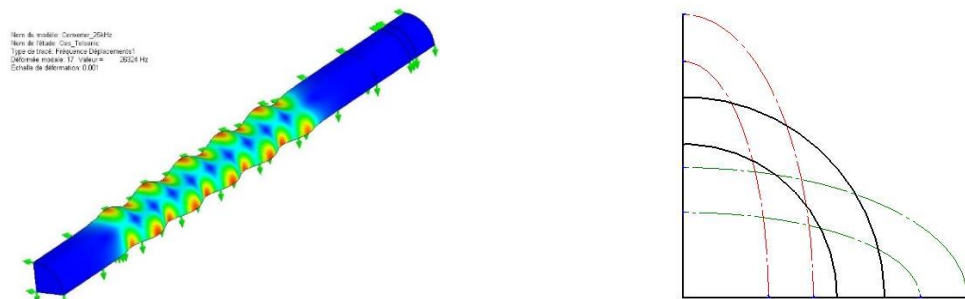


Figure 7: Tubular with the elliptic deformation

The cylindrical deformation of the tube occurs at 24.1 kHz 500 mm length of the hollowed part of the tube. The radial and the axial displacements all along the tube are given by Figure 8. The radial displacement at the hollowed part is lower by 50 % compare to the axial displacement.

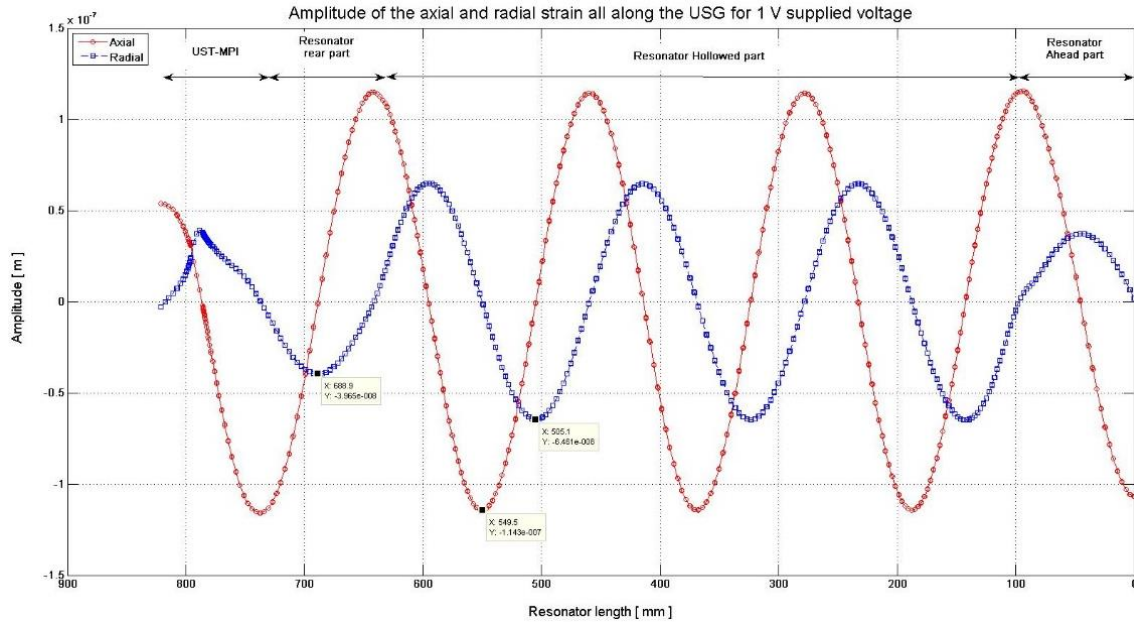


Figure 8: Tubular with the elliptic deformation

The impact of the vibration issued by the tube on the fluid has been studied. The mapping of the pressure generated by the transducer on the fluid (water in this case) is given below (Figure 9). The pressure is non-uniform all along the tube. The pressure is higher in the closer part of the tube to the generator and the pressure is attenuated at the farther part of the tube. This attenuation is due to the damping effect of the fluid. The maximum pressure is about 778 Pascal.

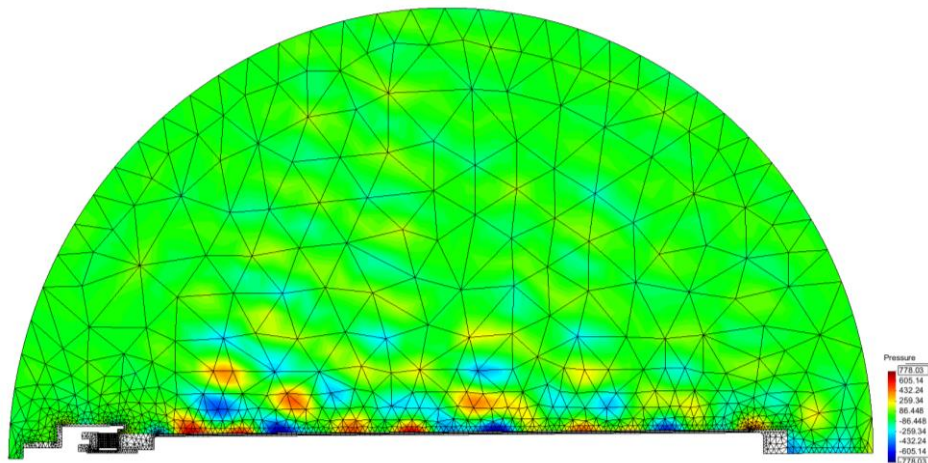


Figure 9: The generated pressure in the fluid (water) by the tubular ultrasonic transducer.

3 MUST WITH RADIAL EXCITATION

3.1 The transducer solution

For the MUST, the radial excitation ultrasonic transducer has been developed by Cedrat Technologies (Figure 10). The approach of this transducer is to install the head mass between both stacks of piezoelectric material and both rear masses on the other side of both piezoelectric stacks. Finally, a bolt connects the both rear masses. The activation piezoelectric material will compress the head mass of the ultrasonic transducer this will increase the diameter of the head mass.

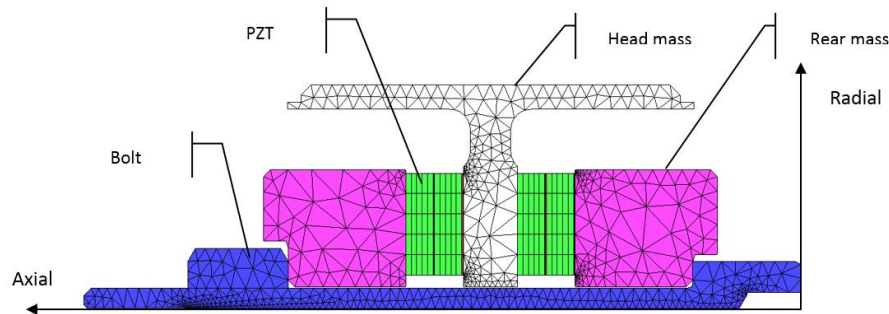


Figure 10: The ultrasonic transducer for radial excitation configuration (axisymmetric view)

The shape of the deformation of the radial excitation ultrasonic transducer is given below (Figure 11). The frequency resonance of the ultrasonic transducer is equal to 25.7 kHz with a coupling coefficient of 44.5 %. The displacement in the radial and axial displacement all along is also compared. The displacement in the radial direction is lower by 41 % compares to the axial direction. In the case of a hollowed preload screw, the amplification ratio decrease to 38 %.

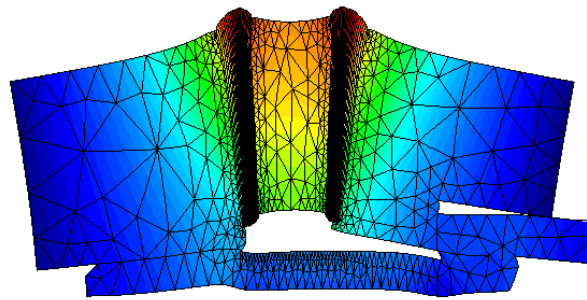


Figure 11: The ultrasonic transducer for radial excitation configuration

In the same way, the ultrasonic transducer is connected to the tube in order to increase the emitting surface of the transducer. The attachment isn't done with the same approach compare to the axial excitation solution.

3.2 The resonator behaviour

The mechanical connection between the ultrasonic transducer and the tube is obtained directly due to the shape of the monolithic part of the head mass (Figure 12).

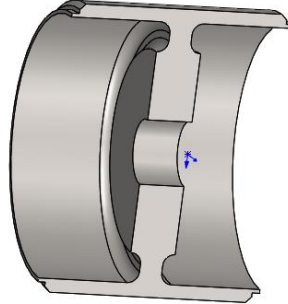


Figure 12: The head mass geometry for axial excitation configuration.

Once the ultrasonic transducer assembled (piezoelectric stack, rear mass and bolt) to the head mass, both tubular ends are connected mechanically to tubes.

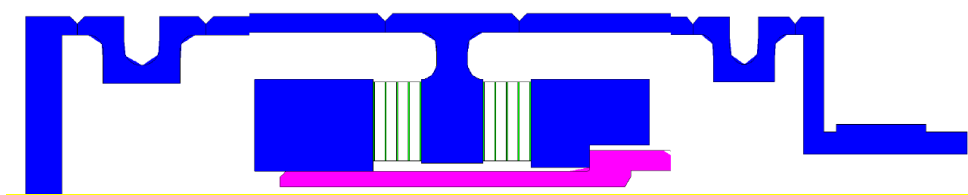


Figure 13: Tubular ultrasonic with the radial excitation

The frequency resonance of the ultrasonic transducer installed in the tube is equal to 25.0 kHz. The shape of deformation at the tube level corresponds to the cylindrical one (Figure 14). At both ends of the transducer, the geometry of the tube is changed in order to avoid the propagation of the vibration issued from the tube to the structure of the tank.

The wiring of both piezoelectric stacks comes out of the tube from the same side. (right side - Figure 13). The cable located in the left side goes through the hollowed preloading from the left to the right side of the tube.

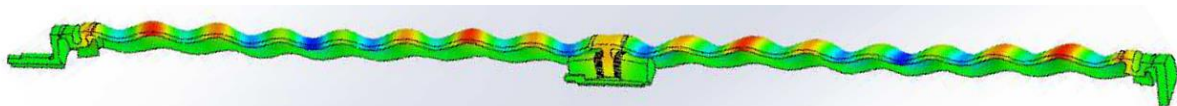


Figure 14: The tube deformation on the MUST transducer

The impact of the vibration issued by the tube on the fluid has been studied. The mapping of the pressure on the fluid (water in this case) is given below (Figure 15, to compare with figure 9). The pressure is uniform all along the tube, which is the main advantage of this transducer technology. The maximum pressure is about 6195 Pascal. The pressure level is

obtained at the same level of voltage as for ultrasonic transducer in axial excitation configuration.

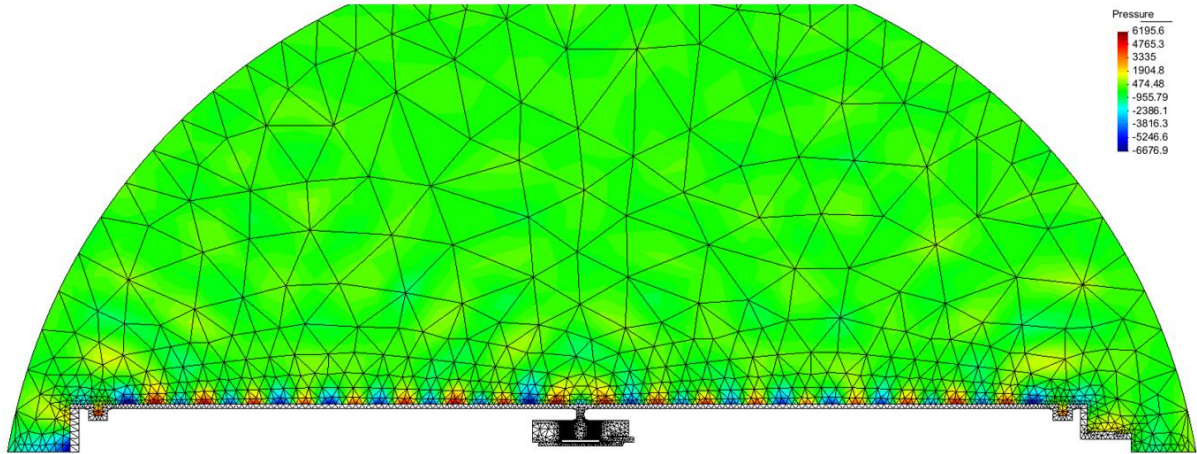


Figure 15: The generated pressure in the fluid (water) by MUST ultrasonic transducer

4 PROTOTYPING

An ultrasonic transducer with radial excitation prototype (Figure 16) has been manufactured in order to evaluate and compare the simulation and the experimental results. The stack of piezoelectric material and rear mass have been assembled.



Figure 16: The ultrasonic transducer for radial excitation assembly

A preliminary measurement has been performed in order to evaluate and compare the results to the simulation. The test has been done in two steps, the first one to measure the resonance frequency of the system (Figure 17 - a) and the second to measure the amplitude of displacement generated at the ultrasonic transducer level (Figure 17 – b).

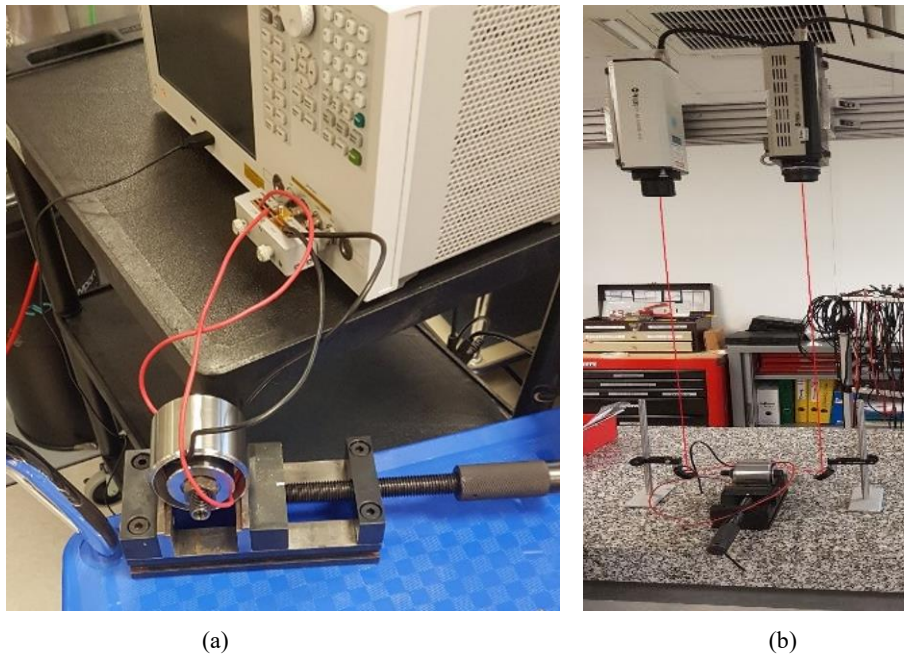


Figure 17: The ultrasonic transducer for radial excitation on test bench

The preliminary measurement on the prototype for the first test a variation of the frequency resonance from 25.7 kHz (simulation) to 22.1 kHz (measurement). The first analysis of such a variation of frequency could be generated due to the boundary condition which is not the same between the simulation and the test bench. For the second test, the displacement ratio as measured is about 45 % between the axial and the radial direction (for both cases of screws). The simulation shows a ratio of 41 % for standard screws and 38 for the hollowed screws. In the case of the standard screw, the coupling coefficient is about 37 % and 22 % in the case of the hollowed screw.

Two tubular ultrasonic transducers, one with axial and one with radial excitation approach have been manufactured (Figure 18) in order to evaluate their performances and to compare between both solutions. Further measurement and experimentation are planned in the near future. This test will include the performance measurement on immersed and also connected several MUST in order to increase the length of the tube (so the emitting surface) without losing vibration at the ends of the tube.



Figure 18: The MUST and conventional ultrasonic tube transducer

5 CONCLUSIONS

The comparison study between the axial and the radial excitation on the tubular ultrasonic transducers has been done in this paper. The radial excitation approach has been studied in order to improve the capability of such a solution for getting a homogeneous acoustic energy generation and higher tube length by staking. This has lead to a new Modular Ultra Sonic Transducer (MUST). Based on FEM simulation, its results show a higher coupling coefficient for the radial excitation with the same amplification ratio than conventional tube transducer using axial excitation. The pressure generated by the MUST is uniform all along the tube as wanted.

The experimental campaign is still in progress in order to have deeper information about the performance of MUST solution especial in the immersed configuration.

This activity takes parts on H2020 PROTECT project (GA 720851) targeting the textile sono-chemical treatment to get anti-bacteriologic property.

REFERENCES

- [1] Yang-Lae LeePil-Woo HeoSang-jin ParkJae-Yun KimEui-Su Lim, Daejeon-Si, Korea “*Wing type ultrasonic transducer*” Patent N° - US6342747B1 – Feb 2000.
- [2] Martin Walter, Dieter Weber, Karlsbad, Fed. Rep. of Germany, “*Ultrasonic transducer*”, Patent N° - US5200666A – Apr 1993.
- [3] Vladimir Abramov and Oleg Abramov, Moscow, Russia “*Device for transmitting ultrasonic energy to a liquid or part media*” Patent N° - US6429575 B1 – Apr 1986.
- [4] Andrew Shoh, Ridgefield, Conn, USA “*Sonic or ultrasonic processing apparatus*” Patent N° - US4011474 – Dec 1975.
- [5] NBE... CTEC Patent PCT ...

WIND TURBINE HEALTH MONITORING BASED ON ACCELEROMETER DATA

Yolanda Vidal*, José L. Rubias* and Francesc Pozo*

*Control, Modeling, Identification and Applications (CoDALab),
Department of Mathematics, Escola d'Enginyeria de Barcelona Est (EEBE),
Universitat Politècnica de Catalunya (UPC), Campus Diagonal-Besòs (CDB),
Eduard Maristany, 16, 08019 Barcelona, Spain
e-mail: yolanda.vidal@upc.edu, web page: <https://futur.upc.edu/CoDALab>

Key words: Offshore Wind Turbine, Structural Health Monitoring, Damage Detection, Damage Classification, Data Driven

Abstract. A structural health monitoring (SHM) system verifies the mechanical state of a structure to ensure its proper functioning and determines whether it needs some kind of maintenance. Thus, SHM for wind turbines (WT) in remote locations, as offshore, is crucial. Offshore wind farms are increasingly realized in water depths beyond 30 meters, where lattice support structures are an interesting option to withstand the severe environmental actions. In particular jackets appear to be a highly competitive substructure type with a wide range of applicability, from approximately 25 to 70 meters water depth. With no doubt, structural damage is a significant issue in these structures. Unlike on-shore structures or even shallow water structures, the access for regular monitoring and repair is not an easy option, in terms of both the cost and the accessibility. In this work, a methodology for the detection and classification of structural damages in offshore jacket-type WT is stated. The proposed method relies on the paradigm that any damage in the structure produces changes in the vibrational response. However, it is assumed that the only available excitation of the WT is the wind turbulence, so the input excitation is assumed to be unknown. Therefore, using only accelerometer information, a data driven approach for damage detection is developed. The scheme of the proposed method can be summarized in the following steps: (i) the wind excitation is simulated as a Gaussian white noise and the data coming from the WT is collected using a set of accelerometers; (ii) the raw data is arranged in matrix form and pre-processed using mean-centered group-scaling; (iii) principal component analysis (PCA) is selected as a technique to reduce the dimensionality of the data and the computing time of the next step; finally, (iv) the quadratic-kernel support vector machine (SVM) is used as a classifier. The 5-fold cross-validation technique is employed to estimate the overall accuracy and to avoid overfitting. In order to experimentally validate the proposed approach, the damage detection strategy is applied to different types of predefined damage in a small-scale structure—an experimental laboratory tower modeling an offshore-fixed jacked-type wind turbine—. The results that have been obtained for these predefined damages are included and discussed to demonstrate the reliability of the proposed approach.

1 INTRODUCTION

Offshore wind farms are seen as a key ingredient in renewable energy, and an important element in the battle against climate change. In the last ten years, the average offshore wind farm has increased in

size from 79.6 MW in 2007 to 561 MW in 2018, see [1]. Accordingly, the size of offshore wind turbines has also increased. Since 2014 the average rated capacity of newly installed wind turbines has grown at an annual rate of 16%. As an example, the largest turbine in the world to date was installed offshore in the United Kingdom in 2018: two V164-8.8 MW from MHI Vestas Offshore Wind, with a rotor diameter of 164 m, that were connected at the European Offshore Wind Development Centre (EOWDC) wind farm, see [2]. The extreme size of nowadays offshore wind turbines leads to the demand for structural health monitoring (SHM) solutions on its overall structure. However, the foundation of fixed offshore wind turbines, in particular, are subject to harsh conditions including environmental loadings (wave and current), a corrosive environment, and shifts in the seabed as scouring and water depth erosion. Besides, inspection of the submerged foundation is expensive due to the difficult access and sometimes impossible due to the environmental conditions. In this case, SHM is the crux of the matter to provide an early warning of degradation and diminish operation and maintenance costs.

SHM for offshore wind turbines remains a research topic which is slowly getting into the field deployment stage, see [5]. This is due to the early stage of the technology's deployment, the additional challenge that offshore environments pose to these technologies, and associated costs to operators for hardware installation and data processing.

There are different types of foundations, according to the depth at which the wind turbine will be installed. In general, monopiles are used in installations at depths below 15 meters, gravity foundations are preferred when depth is less than 30 meters, and jackets are the used option for greater depths. This work focuses on the jacket type. These are foundations with a lattice framework that feature three or four sea bed anchoring points, which increases the levels of safety when anchoring the towers. The top of the jackets features a transition piece that is connected to the turbine shaft, while the legs are anchored to the sea bed with piles. This work proposes a complete methodology for damage detection and classification in a laboratory jacket-type offshore-fixed wind turbine model. As in [3], it is supposed that the only available excitation of the WT is the wind turbulence, so the input excitation is assumed to be unknown. Therefore, the scheme of the proposed method can be summarized in the following steps: (i) the wind excitation is simulated as a Gaussian white noise and the data coming from the WT is collected using a set of accelerometers. It is worth remarking that only output data will be used to detect damage; (ii) the raw data is pre-processed using group-scaling to simplify the computation of the principal components; (iii) PCA is selected as a technique to reduce the dimensionality of the data and the computing time of the next step; finally, (iv) the quadratic SVM classifier is used. In the end, 5-fold cross-validation technique is employed to estimate the overall accuracy and to avoid overfitting. In order to validate the proposed approach in this work, the damage detection strategy is applied to different types of predefined damage in a small-scale structure—an experimental laboratory tower modeling an offshore-fixed jacked-type wind turbine—. The results that have been obtained for these predefined damages are included and discussed to demonstrate the reliability of the proposed approach.

2 LABORATORY TOWER MODEL

The real structure used in this work is a tower model, similar to those of a wind turbine. From Figure 1 it can be seen the components of the structure: jacket, tower and nacelle. As a whole, this structure is 2.7 m high. The tower is composed of three sections joined with bolts, while the jacket is composed with several sections, all of them joined with bolts, with a torque of 12 Nm. The different studied damages are introduced in one of these sections, see Fig. 1. The top piece is 1 m long and 0.6 m width. There a modal shaker is located that simulates the nacelle mass and the environmental effects of the wind over the whole structure. Applying an electrical signal to the shaker (white noise), the vibration needed to

excite the structure is created. The simulation of different wind speeds is also simulated with this shaker, by changing the amplitude of the input electrical signal, in particular multiplying it by the factor 0.5, 1, 2, and 3.

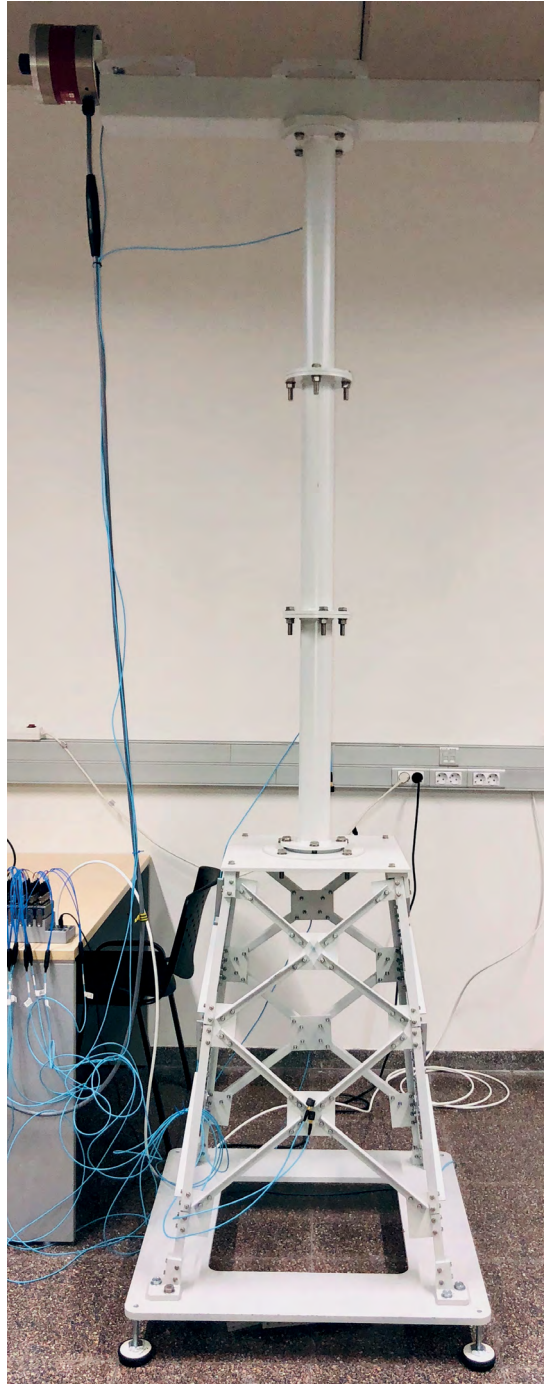


Figure 1: WT scaled tower model used in the experimental tests (off-shore fixed jacked-type platform).

Two types of damage are introduced at the jacket support: a 5 mm crack in one of the bars; and

loosening one of the bolts in the jacket. Also a healthy replica of the studied bar has been considered, as the proposed strategy should be able to detect and classify the studied faults, but also be robust to the replacement of one bar by a new healthy one (avoiding false alarms).

To analyze the structural response, eight triaxial accelerometers are placed in the tower and jacket. The method used to find the optimum location and amount of these sensors is given in [4]. Thus, data from 24 sensors is collected. The nomenclature used for each sensor is given in Table 1.

Table 1: Nomenclature used to refer to each available sensor. Note that $i = 1, \dots, 8$, as there are eight accelerometers.

Sensor	
A_i^x	Acceleration in x -direction for accelerometer number i
A_i^y	Acceleration in y -direction for accelerometer number i
A_i^z	Acceleration in z -direction for accelerometer number i

3 DAMAGE DETECTION AND CLASSIFICATION METHODOLOGY

3.1 Data collection

The time window for each experimental test is 60 seconds with a sampling frequency of 1651.6129 Hz. Thus, each experiment obtains $1651.6129 \times 60 = 99097$ data measurements from each of the 24 sensors.

In this work, a total of 25 experimental tests are conducted for each different white noise amplitude. In particular:

- (i) 10 tests with the original healthy bar.
- (ii) 5 tests with the replica bar.
- (iii) 5 tests with the 5 mm crack damaged bar.
- (iv) 5 tests with an unlocked bolt in the jacket.

That is 100 experiments in total, as there are 25 experiments for each one of the 4 different considered white noise amplitudes.

Given the k -th experimental test, the data is initially stored in a matrix $\mathbf{Y}^{(k)} \in \mathcal{M}_{99097 \times 24}(\mathbb{R})$ such that

$$\mathbf{Y}^{(k)} = \begin{pmatrix} y_{1,1}^{(k)} & y_{1,2}^{(k)} & \cdots & y_{1,24}^{(k)} \\ y_{2,1}^{(k)} & y_{2,2}^{(k)} & \cdots & y_{2,24}^{(k)} \\ \vdots & \vdots & \ddots & \vdots \\ y_{99097,1}^{(k)} & y_{99097,2}^{(k)} & \cdots & y_{99097,24}^{(k)} \end{pmatrix}, \quad (1)$$

where the number of rows is given by the number of time stamps in each experimental test and the number of columns is equal to the number of sensors. Note that data in the first column is related to sensor A_1^x , data in the second column is related to sensor A_1^y , third column is related to A_1^z , fourth column to A_2^x , and so on and so forth.

The data from the k -th experimental test stored initially in matrix $\mathbf{Y}^{(k)}$, see eq. (1), is reshaped into the matrix $\mathbf{Z}^{(k)} \in \mathcal{M}_{41 \times 2417 \cdot 24}$,

$$\mathbf{Z}^{(k)} = \begin{pmatrix} y_{1,1}^{(k)} & \cdots & y_{2417,1}^{(k)} & \cdots & y_{1,24}^{(k)} & \cdots & y_{2417,24}^{(k)} \\ y_{2418,1}^{(k)} & \cdots & y_{4834,1}^{(k)} & \cdots & y_{2418,24}^{(k)} & \cdots & y_{4834,24}^{(k)} \\ \vdots & \ddots & \vdots & \ddots & \vdots & \ddots & \vdots \\ y_{96681,1}^{(k)} & \cdots & y_{99097,1}^{(k)} & \cdots & y_{96681,24}^{(k)} & \cdots & y_{99097,24}^{(k)} \end{pmatrix}, \quad (2)$$

where each row (each sample) contains 2417 time stamps from each sensor.

Finally, the data matrix $\mathbf{X} \in \mathcal{M}_{(41 \cdot 100) \times (2417 \cdot 24)}(\mathbb{R})$ that contains the data from all the experiments is defined by:

$$\mathbf{X} = \begin{pmatrix} \mathbf{Z}^{(1)} \\ \vdots \\ \mathbf{Z}^{(k)} \\ \vdots \\ \mathbf{Z}^{(100)} \end{pmatrix} \quad (3)$$

that is, concatenating the data matrices coming from the 100 experiments.

3.2 Autoscaling

The main reason to autoscale the raw data is to simplify the computations for the multiway PCA decomposition. Autoscaling uses column-wise mean-centering followed by division of each column by the standard deviation of that column of matrix \mathbf{X} . The result is that each column of the new autoscaled matrix, $\tilde{\mathbf{X}}$, has a mean of zero and a standard deviation of one. The fact that $\tilde{\mathbf{X}}$ is a mean-centered matrix simplifies the empirical covariance matrix computation, needed for the PCA decomposition.

3.3 Principal component analysis

Recall that, before using a classifier, the data must be processed to obtain the most suitable features. In this work, after the autoscaling step, multiway PCA is selected as the main objective is to reduce computing time for the quadratic discriminant analysis classifier. In this work, the first 400 components of the PCA decomposition are used as they account for 85% of the variance. Thus, the transformed coordinates of the $\tilde{\mathbf{X}}$ data in the new basis given by the first 400 principal components are used as features by the quadratic SVM strategy. Thus, 400 features are used instead of 58008 variables, that is 0.69% of the data retains 85% of the variance.

3.4 Quadratic SVM

The scatter plots shown in Fig. 2 of the first feature versus the second and tenth features reveal a quadratic relationship. Therefore, the quadratic SVM classifier is adopted. For a detailed review on the SVM classifier see references [6], [7], and [8]. In this work the kernel scale is set to 10 and the box constraint level to 2.

Finally, in this work, the 5-fold cross-validation technique has been employed to estimate the overall accuracy and to avoid overfitting.

4 RESULTS

A comprehensive decomposition of the error between the true classes and the predicted classes is shown by means of the so-called confusion matrix, see Fig. 3 (an empty blank square means 0%). In this matrix, each row represents the instances in a true class while each column represents the instances in a predicted class (by the classifier). In particular, the first row (and first column) is labeled as 1 and corresponds to the healthy and replica bar. The next labels (for rows and columns) correspond to each fault (label 2 corresponds to crack damage, and label 3 to unlocked bolt type of damage).

As shown in Fig. 3 the true positive rate (TPR) for the healthy case is 99% and the false negative rate (FNR) only 1%. For the crack damaged bar a TPR of 96% is accomplished and for the unlocked bolt type of damage a TPR of 99% is obtained. The overall accuracy is 98.6%. The training time was 1080 seconds in a 3GHz Intel Core i7 with 16GB RAM computer. Finally, note that the proposed strategy can be deployed in real time as the prediction speed is 2100 observations per second.

5 CONCLUSIONS

In this work, using only accelerometer information, a data driven approach for damage detection in offshore jacket-type WT is developed. The proposed approach has been experimentally validated for different types of predefined damages in a small-scale structure—an experimental laboratory tower modelling an offshore-fixed jacked-type wind turbine—. The obtained results, with an overall accuracy of 98.6%, demonstrate the reliability of the proposed approach.

REFERENCES

- [1] Wind Europe Association. *Offshore Wind in Europe: Key Trends and Statistics 2018*. Via Internet (22.02.2019) <https://windeurope.org/wp-content/uploads/files/about-wind/statistics/WindEurope-Annual-Offshore-Statistics-2018.pdf>, (2019).
- [2] Onea, F. and Rusu, L. Evaluation of some state-of-the-art wind technologies in the nearshore of the black sea. *Energies* (2018) **11**(9):2452–2467.
- [3] Pozo, F. and Vidal, Y. Wind turbine fault detection through principal component analysis and statistical hypothesis testing. *Energies* (2016) **1**(3):1–20.
- [4] Zugasti Uriguen, E. Design and validation of a methodology for wind energy structures health monitoring. *PhD from Universitat Politècnica de Catalunya* (2014).
- [5] Martinez-Luengo, M. and Kolios, A. and Wang, L. Structural health monitoring of offshore wind turbines: A review through the Statistical Pattern Recognition Paradigm. *Renewable and Sustainable Energy Reviews* (2016) **64**:91–105.
- [6] Christianini, N., and J. Shawe-Taylor. *An Introduction to Support Vector Machines and Other Kernel-Based Learning Methods*. Cambridge University Press, (2000).
- [7] Smola, A. J. and Schölkopf, B. A tutorial on support vector regression. *Statistics and computing* (2004) **14**(3):199–222.
- [8] Hastie, T., R. Tibshirani, and J. Friedman. *The Elements of Statistical Learning*. Second edition, Springer, (2008).

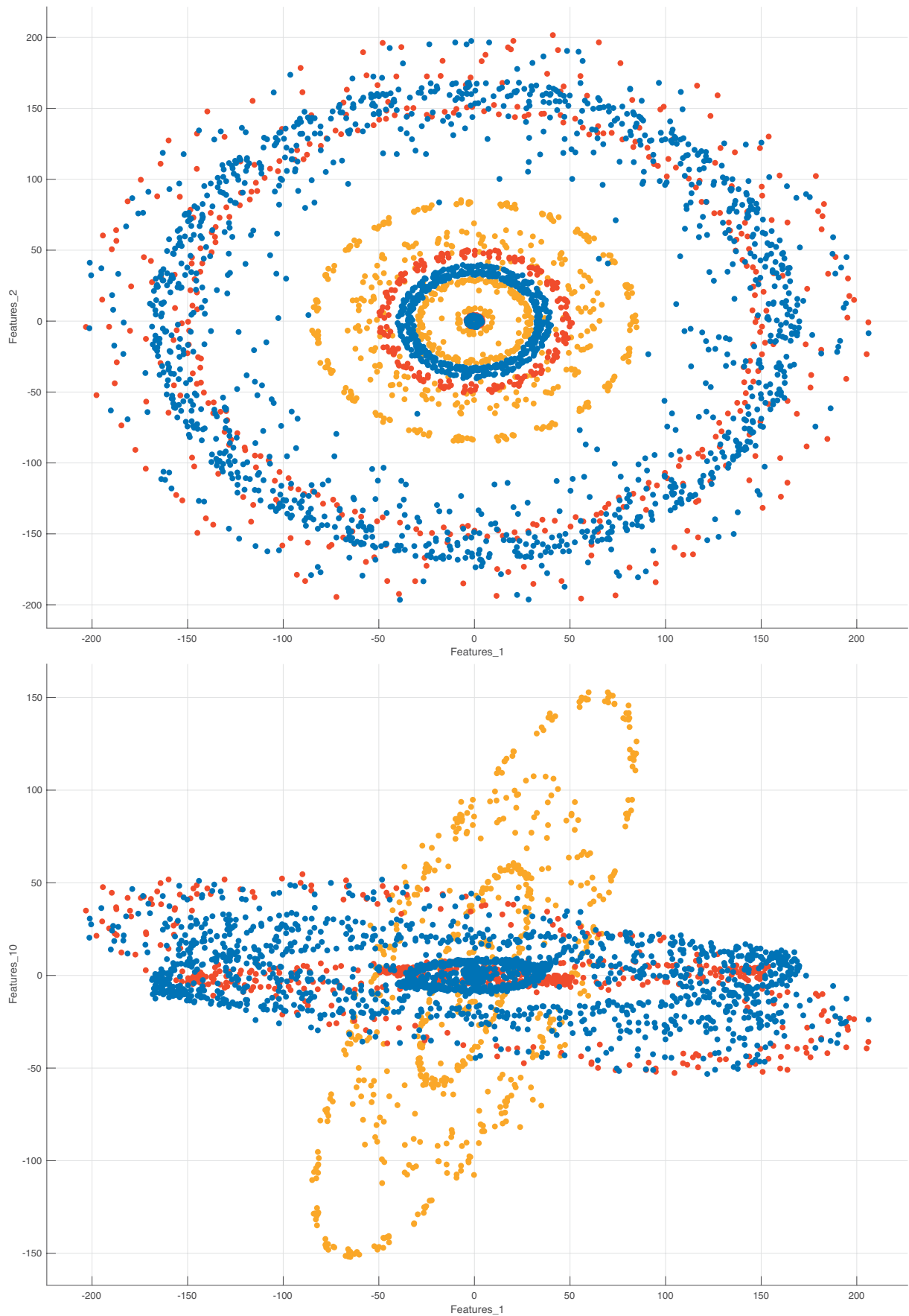


Figure 2: Scatter plots of the first versus the second feature (top) and the first versus the tenth feature (bottom). Blue dots represent healthy samples, red dots represent crack damage samples, and yellow dots represent unlocked bolt samples.

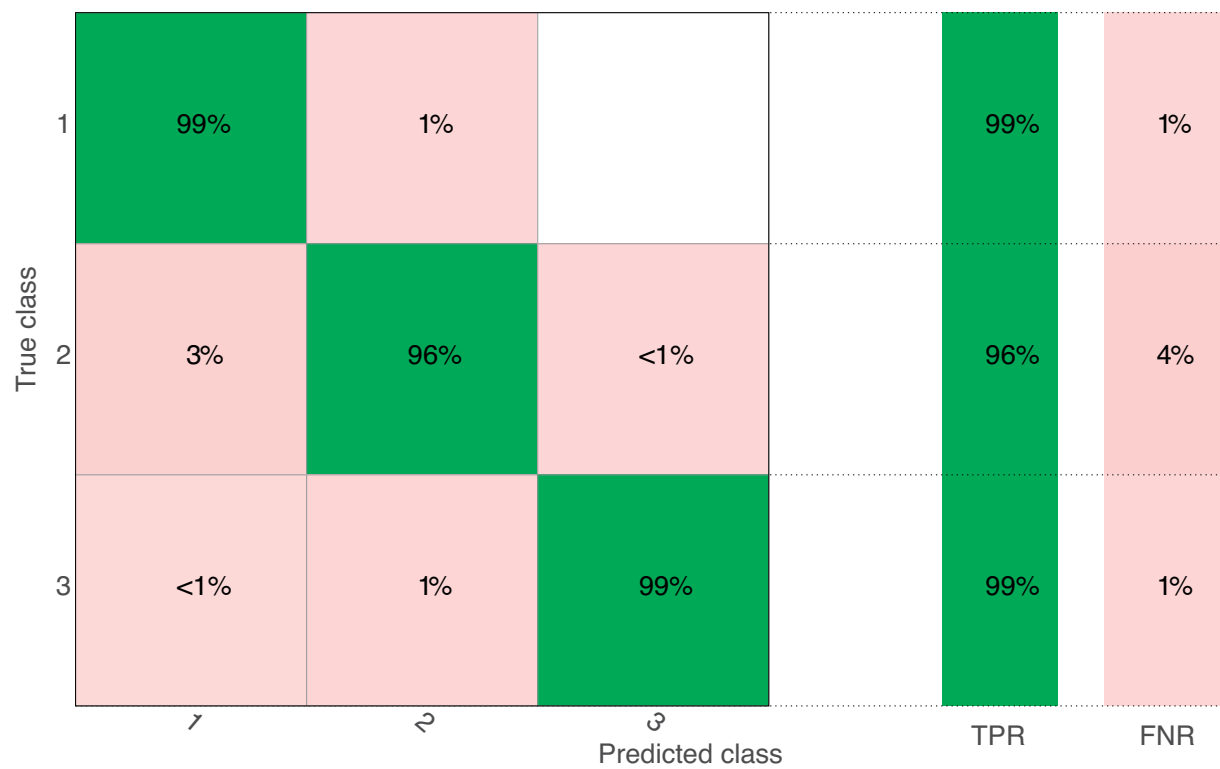


Figure 3: Confusion matrix. Label 1 corresponds to healthy, label 2 corresponds to crack damage, and label 3 to unlocked bolt type of damage.

WIRELESS NETWORK MONITORING SYSTEM FOR CULTURAL HERITAGE BUILDINGS

G. ZINI^{*}, M. BETTI AND G. BARTOLI

^{*} Department of Civil and Environmental Engineering (DICEA)
University of Florence
Via di Santa Marta 3, Florence, Italy
e-mail: giacomo.zini@unifi.it - Web page: <https://www.dicea.unifi.it/>

Key words: Cultural heritage, Wireless sensors network, Continuous Structural Health Monitoring, Stochastic Subspace Identification, Environmental Effects.

Abstract

This paper focuses on the use of wireless sensors networks (WSN) on cultural heritage buildings for long-term monitoring purposes. This technology is highly attractive because of both the reduced dimensions of the sensors and the absence of cables, that ensures a small visual impact. In this way, the need of a long-term monitoring is addressed without significant impact on the features of the cultural heritage. Nevertheless, this technology is still growing, and several issues still need to be addressed: wireless connection of signals is not even simple because of the thickness of the structural elements, size of the transmitted packages could not be too large, thus implying low frequency resolution and small length signals, etc.[1] [2]. In this emerging scenario, this paper discusses and reports on an automated procedure setting-up for the Modal Tracking (MT) of the Modal Parameters (MP) obtained from long-term monitoring data. The considered data were recorded through a WSN recently installed on a representative historic structure: an ancient masonry tower [3]. The monitoring system has been built with cheap devices, ensuring a wide applicability to the cultural heritage. As shown by several authors [4] [5], the tracking of the frequency across a suitable time span allows to identify possible structural anomalies and/or checking the effectiveness of a specific retrofitting. The results of the first six months are discussed in detail, showing performances and criticism of the monitoring system.

INTRODUCTION

The preservation of the Cultural Heritage (CH) is one of the biggest challenges for our generation to avoid the loss of priceless objects. The recent cases of partial or total collapses renewed the attention on that, topic showing how that structures that are exposed to hazardous events.

The Structural Health Monitoring (SHM) framework gives a powerful tool to analyze the evolution in time of the selected damage sensitive features. That operation, usually known as Modal Tracking (MT), is based on extraction of the Modal Parameters (MP) through an automated procedure. The major part of the automated procedure proposed in the last years are based on the Stochastic Subspace Identification algorithm [6], fed both with the data or with the covariance matrix. The capability of the technique in the modal identification under unknown input in operative conditions led to an increasing interest among the scientific community. The main issue was the high number of setting parameters needed for perform the modal identification. Indeed, in several works the Authors [7–10] proposed several semi or fully automated procedures based on the clustering analysis techniques.

Then the identified modes are tracked [11,12] over the time based on the distance in terms of frequency and Modal Assurance Criterion (MAC) index.

The most investigated damage sensitive feature is the frequency because of its numerical stability and for the limited number of accelerometers required for the identification. Even if the frequency is sensitive to the environmental effects such as temperature and humidity [13–15] that can be of the same measure of that produced by a damage. Then the environmental effects are compensated by ARX model, Multiple Linear Regression (MLR), the Principal Component Analysis (PCA) and the non linear models as the kernel PCA. The damage detection is then finalized through statistical tools called control charts [16].

In the recent years, many Authors [4,17] developed monitoring systems for the CH site, showing how the detection of damage can be successfully achieved with a limited number of accelerometers.

In the present paper is introduced an algorithm for the features extraction in the continuous dynamic monitoring system installed on a historic masonry tower from the recorded signals. The entire monitoring system is wireless, and the accelerometers are Micro Electro Mechanical Systems (MEMS) devices. Not so many cases of application of wireless long-term monitoring system to the CH, despite the advantages in terms of low invasiveness.

The results of the first six months of monitoring of an ancient masonry tower through a continuous (ten minutes of record every hour) wireless monitoring system and the features extraction algorithm are showed.

THE FEATURES EXTRACTION ALGORITHM

The Modal Parameter Identification (MPI) through automated procedures is still an open issue. The parametric techniques in the time allows the implementation of codes based on the identification of the system properties managing the data collected by the sensors. The calibration of the procedure allowing to distinguish among the real modes and the mathematical or spurious modes minimizing the variance of the identified modal parameters is one of the biggest issues that usually is underestimated.

Nevertheless, in the operative conditions the source of excitation is sometimes a colored noise

or a harmonic excitation and the hypothesis of a broadband process decays. In many cases the signals exhibit a low power respect to the ground noise leading to difficult modal identification. Considering all these problems the automated procedure should replace the judgment of an expertise selecting the recorded signals which lead to a higher accuracy in the identification of the MP. This procedure is effective if the monitoring system collect a high number of records for each day, enabling the Continuous Vibration-Based Structural Health Monitoring (CVB-SHM). Ceravolo [18] applied the CVB-SHM technique to a complex elliptical dome by selecting the input of the identification procedures exhibiting higher levels of root mean square. Then the Subspace-Stochastic Identification based on the data (SSI-data) is set guaranteeing the identification of a higher number of modes.

The algorithm herein proposed is based on the definition of statistical threshold through the analysis over a limited period (Calibration Phase) that affect all the phases of the automated procedure. Starting from the selection of the inputs, the setup of the modal order and the number of rows in the Henkel matrix and the definition of the threshold for each mode for the MT are set.

The input selection is based on the quality of the signals measured through the kurtosis and the rms and on the level of signal respect to noise measured as the signal to noise ratio [19] (SNR). The setup of the SSI based on the covariance matrix of the signal (SSI-cov) is made by means of a sensitivity analysis and then by the analysis of the obtained standard deviations of each mode in terms of frequency and damping ratio. Then the distance in terms of MAC and frequency is evaluated for each mode.

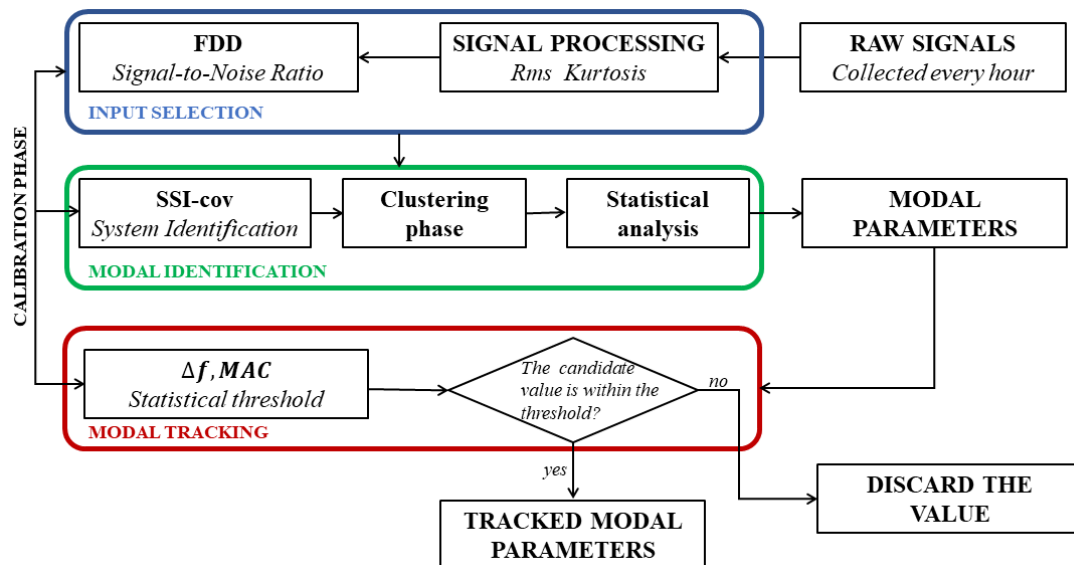


Figure 1: Block scheme of the proposed automated modal identification algorithm.

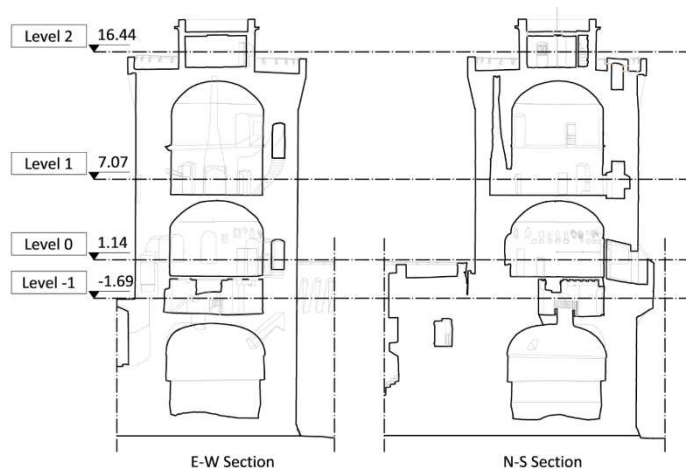
APPLICATION TO THE MATILDA'S TOWER

The Matilde Tower in the Livorno's harbor, is a round plan tower with a height of about 29 m and an external diameter of about 12 m. The masonry walls have a thickness of about 2,5 m with a spiral staircase embedded to connect the level zero with the upper two levels. The tower

has four levels mainly built by vaults that were reinforced with steel bars in the past centuries. In the upper level there is a round terrace with at the center another small round area with a flat slab.

The tower was erected as a free-standing structure probably in the late XII century with the purpose of ensuring a clear observation of the sea and the possibility of repelling the enemy attacks from all directions. With the passing of centuries, the structure was surrounded by the walls, becoming a complex fortress (the Old Fortress). The whole architectural complex shows a severe cracking pattern, probably due to several causes (foundation settlements, sea erosion, bombing of the second world war).

Within the MOSCARDO project, a research project funded by Tuscany Regional Administration in 2015-2018, the tower was listed in the relevant cases of study to analyze to develop a wireless monitoring system and a reliable post-processing algorithm. Indeed, the modal properties of the structure were extracted from preliminary dynamic tests [3]. The results of the preliminary dynamic tests campaign were also very useful to understand the characteristics of the dynamic excitations and their intensity levels. In the preliminary experimental campaign, the most relevant dynamic loads were the wind and the harmonic forces probably generated by the engines of the boats operating in the harbor.



(a)



(b)

Figure 2 (a) cross sections of the Matilda's tower. (b) Global view from inside the Old Fortress of the Matilde Tower in Livorno.

The monitoring system and the calibration of the MP extraction algorithm

The wireless sensor network installed on the tower is composed by seven MEMS accelerometers (three at the level 0 and four at the terrace level), two meteorological stations measuring the temperature and humidity (one inside the level 0 and one outside at the terrace level), one anemometer (at the top of the highest level) and two strain gauges on the steel chains of the level 0. The acquisition last for ten minutes for every daily hour with a frequency of acquisition of 50 Hz, the data are then sent to a server and the results can be visualized on the website (<http://www.moscardo.it/>).

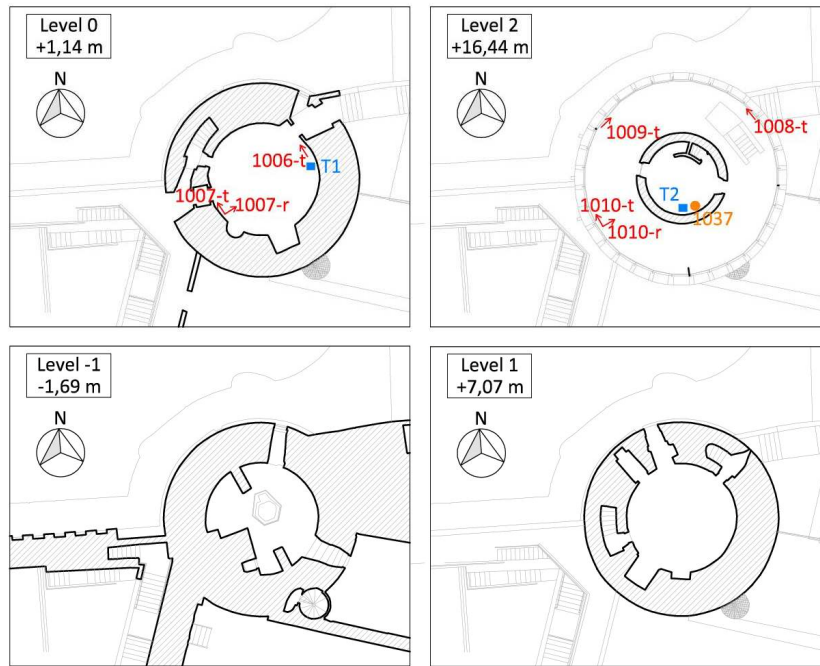


Figure 3 The sensor positions for the long-term monitoring of the Matilde Tower. The red arrows represent the direction of the accelerometers. In blue are represented the two meteorological stations (temperature and humidity). In yellow the anemometer measuring the wind speed and direction.

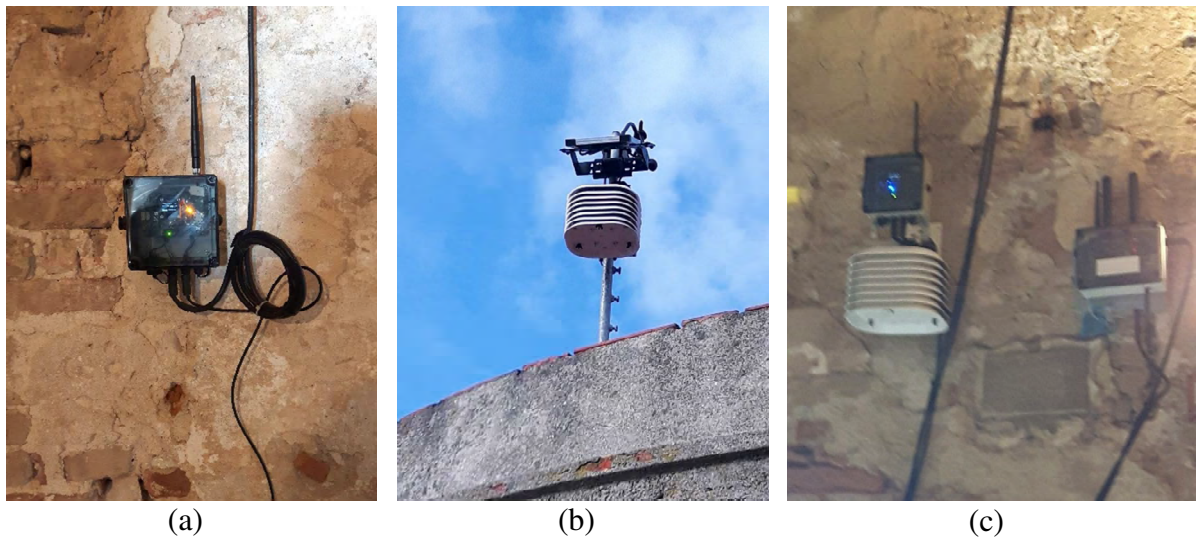


Figure 4 (a) The biaxial accelerometer at the node 1007. (b) The node 1037 with the anemometer and the meteorological station. (c) A node of the network at the level zero with the meteorological station a monoaxial accelerometer and the gateway.

The calibration of the algorithm is made over two distinct periods of one week. The first period #P1 (3/12/2018-7/12/2018) is when the tower is excited by the highest wind level and the second #P2 (15/02/2019-22/02/2019).

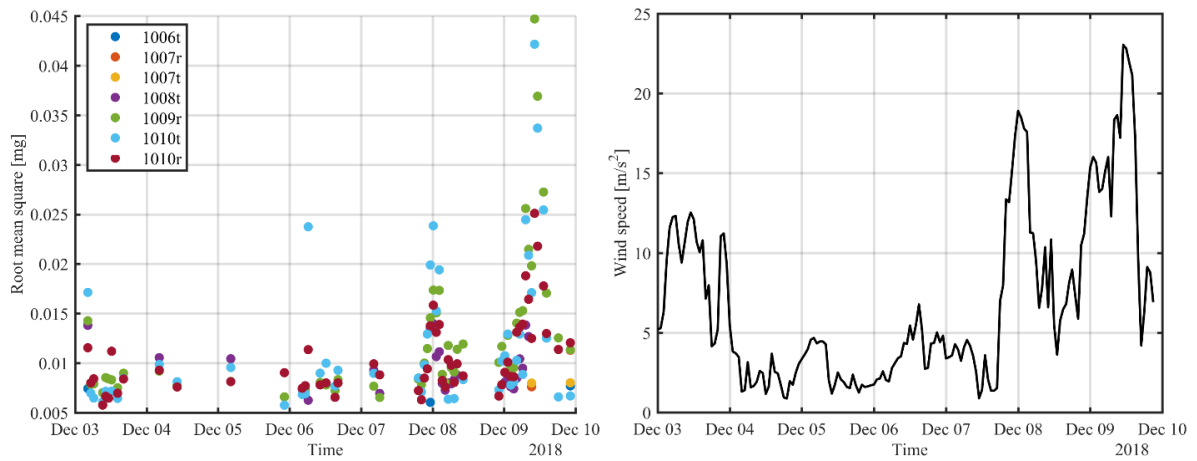


Figure 5 The results of the first calibration period (#P1) in terms of rms and average wind speed.

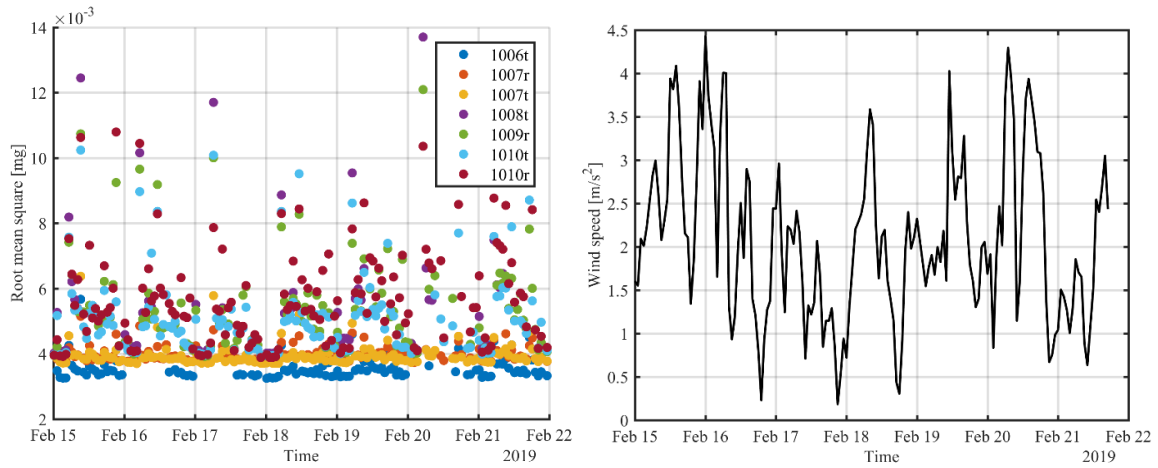


Figure 6 The results of the second calibration period (#P2) in terms of rms and average wind speed.

From the analysis of these two extreme events the threshold for the input selection are defined by means of an outlier analysis excluding the values outside 1,5 times the interquartile range. Then the minimum values evaluated from the two periods is selected in terms of rms and SNR and the maximum for the Kurtosis. Indeed, the first two thresholds guarantee a minimum input quality even if the external excitation is very low. Instead the Kurtosis gives a refined information about the tails of the pdf that can from anomalies in the signals or from non-gaussian process.

Table 1: Threshold values for the input selection

	SNR [dB]	RMS [mg]	Kurtosis
#P1	39,06	0,0075	118,67
#P2	34,72	0,0040	24,49
Threshold	34,72	0,0040	118,67

In the analysed case of study in the band of interest (0-10 Hz) are available the first three modes, that in many cases are not excited at the same time. The automated procedure for the modal identification based on the *SSI-cov* algorithm is set by means of a sensitivity analysis and a minimum number of elements for each cluster is chosen to avoid the selection of spurious and mathematical modes. In the calibration period it is evaluated the complexity of the mode shapes by means of the Mean Phase Deviation (MPD) and Mean Phase Collinearity (MPC) [20]. Both these indicators are normalized to give a result equal to one for perfect real modes and equal to zero for modes with the highest degree of complexity. Usually the physical modes exhibit a low degree of complexity, but in some cases some degree of complexity can arise from the structural non-linear behaviour [21]. For these reasons a statistical threshold is built for each mode in terms of MPC and MPD as the minimum value of the mean across the two calibration periods.

Table 2: Threshold values for the modal identification phase.

	MPC	MPD
#P1	0,90	0,77
#P2	0,73	0,78
Threshold	0,73	0,77

The MT of the identified modal parameters is made starting from a reference value for each mode in terms of frequency and mode shapes. During the calibration phase a hierarchical clustering algorithm is performed with two initial fixed threshold 5 % for the frequency and 0,7 for the MAC index. Then for each identified mode is computed the MAC distance for each value and the threshold value is obtained as the lower bound of the interquartile range. Then the maximum value among the two calibration periods is chosen for the MT of each mode during the whole monitoring period.

Table 3: Threshold values for the MT of the MP

	1st Mode	2nd Mode	3rd Mode
#P1	0,78	0,79	0,84
#P2	0,73	0,79	-
Threshold	0,78	0,79	0,84

This conservative choice is made to avoid the selection of some harmonic response of the structure near to the band of interest of each modal frequency.

The results of the first six months

The early results from the first six months (from the 19th of September 2018 to the 20th of March 2019) of long-term monitoring of the Matilda's tower obtained with the algorithm introduced in the previous section are described herein.

Despite some disconnections of instruments due to the initial trial period, the results can furnish some preliminary information on the working activity of the package WSN monitoring system and the feature extraction algorithm. The MT of the first three modes is successfully achieved, even if some offline periods (mid-November and mid-January) of some sensors cannot allow a continuous tracking over the monitoring period.

The first two modes seem to be less scattered than the third, implying a lower accuracy in the

modal identification. Moreover, the third mode cannot be identified in every session, probably requiring higher energy levels in the input.

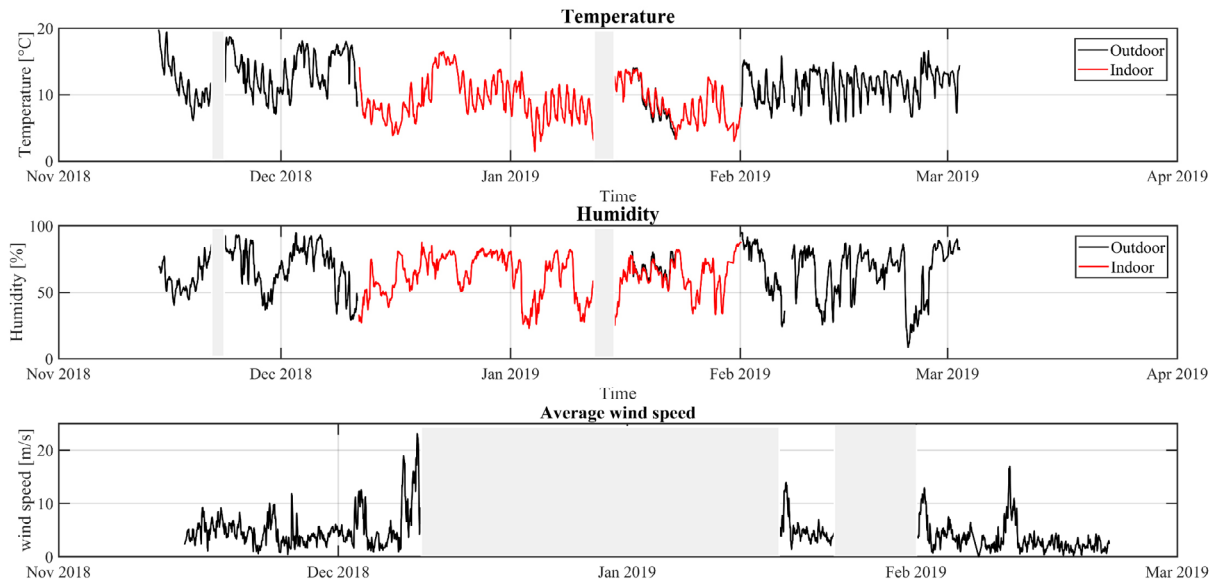


Figure 7 The variation of the environmental parameters in the first six months of monitoring period.

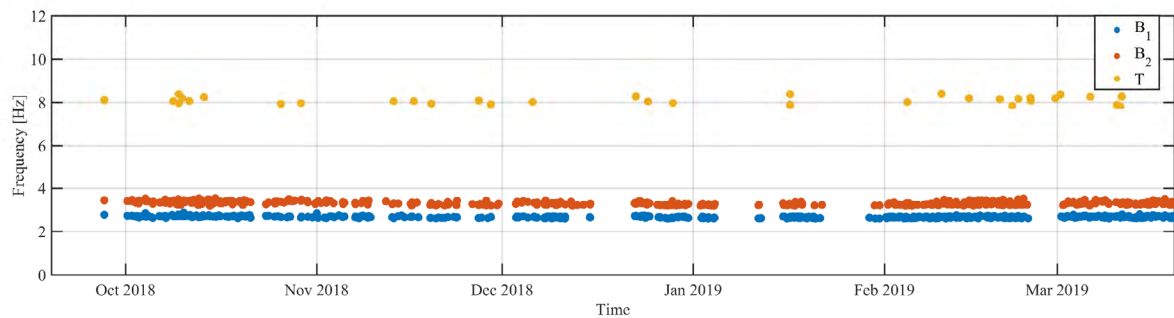


Figure 8 The modal tracking of the first three modes: The bending (B_1 , B_2) and the torsional (T).

CONCLUSIVE REMARKS

The presented monitoring system is based on a wireless network of sensors developed during the MOSCARDO project shows how it is possible to satisfying the requirements of low visual impact and low costs that are fundamental in the CH application.

The feature extraction algorithm for a CVB-SHM monitoring system is presented focusing on the calibration of the entire automated procedure to obtain good quality identification results that is crucial for the systems based on the tracking of the frequency. Enabling the damage detection (level 1 in the Rytter's scale [22]) for the monitored CH building.

Despite the presented algorithm is suitable for every kind of CH building, the preliminary dynamic identification and the calibration phase should be adopted to the operative conditions and to the dynamics of the monitored structure.

In the case of study presented herein the main dynamic excitation source was the wind, and the

calibration phases furnishes the input selection parameters in order to avoid outliers or low excited modes. In the modal identification phase through an automated *SSI-cov* procedure with the initial values are set by means of a sensitivity analysis. Then for the MT the MAC thresholds are defined for each mode by the results obtained in the calibration period. Instead the distance in terms of frequency is fixed relatively high to group together the MP represented the same mode with different environmental conditions.

To make further analysis, more data are required with different environmental conditions to understand the relationships among these values and the tracked modes.

ACKNOWLEDGEMENTS

The authors kindly acknowledge the Region of Tuscany which financially supported the MOSCARDO research project (theme FAS 2007-2013).

REFERENCES

- [1] A. Pierdicca, F. Clementi, D. Isidori, E. Concettoni, C. Cristalli, S. Lenci, Numerical model upgrading of a historical masonry palace monitored with a wireless sensor network, *Int. J. Mason. Res. Innov.* **1** (2016) 74–98.
- [2] F. Potenza, F. Federici, M. Lepidi, V. Gattulli, F. Graziosi, A. Colarieti, Long-term structural monitoring of the damaged Basilica S. Maria di Collemaggio through a low-cost wireless sensor network, *J. Civ. Struct. Heal. Monit.* **5** (2015) 655–676.
- [3] G. Zini, M. Betti, G. Bartoli, S. Chiostri, Frequency vs time domain identification of heritage structures, *Procedia Struct. Integr.* (2018).
- [4] N. Cavalagli, G. Comanducci, C. Gentile, M. Guidobaldi, A. Saisi, F. Ubertini, Detecting earthquake-induced damage in historic masonry towers using continuously monitored dynamic response-only data, *Procedia Eng.* **199** (2017) 3416–3421.
- [5] F. Lorenzoni, F. Casarin, C. Modena, M. Caldon, K. Islami, F. da Porto, Structural health monitoring of the Roman Arena of Verona, Italy, *J. Civ. Struct. Heal. Monit.* **3** (2013) 227–246.
- [6] B. Peeters, G. De Roeck, Stochastic System Identification for Operational Modal Analysis: A Review, *J. Dyn. Syst. Meas. Control.* **123** (2001) 659.
- [7] F. Magalhães, Á. Cunha, E. Caetano, Online automatic identification of the modal parameters of a long span arch bridge, *Mech. Syst. Signal Process.* **23** (2009) 316–329.
- [8] F. Ubertini, C. Gentile, A.L. Materazzi, Automated modal identification in operational conditions and its application to bridges, *Eng. Struct.* **46** (2013) 264–278.
- [9] E. Reynders, J. Houbrechts, G. De Roeck, Fully automated (operational) modal analysis, *Mech. Syst. Signal Process.* **29** (2012) 228–250.
- [10] E. Neu, F. Janser, A.A. Khatibi, A.C. Orifici, Fully Automated Operational Modal Analysis using multi-stage clustering, *Mech. Syst. Signal Process.* **84** (2017) 308–323.
- [11] P. Verboven, E. Parloo, P. Guillaume, M. Van Overmeire, Autonomous Structural Health Monitoring--Part I: Modal Parameter Estimation and Tracking, *Mech. Syst. Signal Process.* **16** (2002) 637–657.
- [12] A. Cabboi, F. Magalhães, C. Gentile, Á. Cunha, Automated modal identification and tracking: Application to an iron arch bridge, *Struct. Control Heal. Monit.* **24** (2017).
- [13] L.F. Ramos, L. Marques, P.B. Lourenço, G. De Roeck, A. Campos-Costa, J. Roque,

- Monitoring historical masonry structures with operational modal analysis: Two case studies, *Mech. Syst. Signal Process.* **24** (2010) 1291–1305.
- [14] F. Ubertini, G. Comanducci, N. Cavalagli, A. Laura Pisello, A. Luigi Materazzi, F. Cotana, Environmental effects on natural frequencies of the San Pietro bell tower in Perugia, Italy, and their removal for structural performance assessment, *Mech. Syst. Signal Process.* **82** (2017) 307–322.
 - [15] R.M. Azzara, G. De Roeck, M. Girardi, C. Padovani, D. Pellegrini, E. Reynders, The influence of environmental parameters on the dynamic behaviour of the San Frediano bell tower in Lucca, *Eng. Struct.* **156** (2018) 175–187.
 - [16] F. Magalhães, A. Cunha, E. Caetano, Vibration based structural health monitoring of an arch bridge: From automated OMA to damage detection, *Mech. Syst. Signal Process.* **28** (2012) 212–228.
 - [17] N. Cavalagli, G. Comanducci, F. Ubertini, Earthquake-Induced Damage Detection in a Monumental Masonry Bell-Tower Using Long-Term Dynamic Monitoring Data, *J. Earthq. Eng.* **22** (2018) 96–119.
 - [18] M.L. Pecorelli, R. Ceravolo, R. Epicoco, An Automatic Modal Identification Procedure for the Permanent Dynamic Monitoring of the Sanctuary of Vicoforte, *Int. J. Archit. Herit.* (2018):1-15.
 - [19] R. Brincker, C.E. Ventura, Introduction to Operational Modal Analysis, 2015.
 - [20] R.S. Pappa, K.B. Elliott, A. Schenk, Consistent-mode indicator for the eigensystem realization algorithm, *J. Guid. Control. Dyn.* **16** (1993) 852–858.
 - [21] M. Imregun, D.J. Ewins, Complex modes-origins and limits, *Proc. 13th Int. Modal Anal. Conf.* (1995) 496–506.
 - [22] A. Rytter, Vibrational Based Inspection of Civil Engineering Structures, Aalborg Universitet, (1993).

A NEW SMART APPROACH TO MONITOR THICKNESS REDUCTION IN METALLIC STRUCTURES

PIERVINCENZO RIZZO^{*,†}, BOWEN ZHENG^{*}, AMIR NASROLLAHI^{*}, HODA
JALALI^{*,†}

^{*}Laboratory for Nondestructive Evaluation and Structural Health Monitoring studies
Department of Civil and Environmental Engineering, University of Pittsburgh,
3700 O'Hara Street, Pittsburgh, PA, 15261, USA

[†] Corresponding author: Tel. +1-412-624-9575; E-mail: pir3@pitt.edu

Key words: Corrosion Detection, Solitary waves, Structural Health Monitoring, Smart Structures.

Abstract. Structural health monitoring methods based on the generation and detection of highly nonlinear solitary waves are emerging as a potential cost-effective technique for a variety of structures and materials. Meanwhile, outlier analysis is a statistic tool able to identify anomalies in data that diverge from a set of baseline data. In this paper the use of outlier analysis was explored to detect damage in metallic plates using the propagation and detection of highly nonlinear solitary waves. A thick steel plate was monitored with a solitary wave transducer placed above the plate, and damage was simulated in terms of a foreign object attached to the bottom of the plate. Three different masses located at an increasing distance from the transducer were considered. A few features were extracted from the experimental time waveforms, and then fed to a multivariate analysis that compared the testing data to a set of baseline data. The experimental results show that the outlier analysis significantly enhances the ability to detect damage using solitary waves.

1 INTRODUCTION

Structural health monitoring (SHM) and nondestructive evaluation (NDE) play a consolidate role in a wide range of industrial activities and are considered a vital component for the development and deployment of smart structures. In recent years, a novel SHM / NDE approach based on the propagation of highly nonlinear solitary waves (HNSWs) has emerged [1-5]. The overall principle of this novel method is rather straightforward: a chain made of spherical particles is in dry point-contact with the material or structure to be evaluated. An incident solitary wave (ISW) is induced at one end of the chain, which is in contact with the structure of interest. This compact non-dispersive compressive wave propagates along the chain and reaches the opposite end. Here, owing to principles discussed in several papers, including some by the authors, the single pulse gives rise to one or two reflected waves that are typically referred to as the primary and the secondary reflected solitary waves (PSW and SSW). Most of the studies reported in the scientific literature demonstrated that the amplitude and time-of-

flight (ToF) of these reflected pulses are dependent on some characteristics of the material/structure to be monitored/inspected.

Statistical approaches have been proven effective in SHM [6-10]; generally, these methods are based on the evaluation of certain damage-sensitive features which are measured on the structure of interest. One of these statistical approaches is based on outlier analysis (OA), which is a novelty detection method that establishes whether a new configuration of the system is discordant or inconsistent from the baseline configuration that consists of an existing set of data (or patterns) that describe the normal operative conditions.

The work presented in this article combines HNSWs and outlier analysis. A HNSW *transducer* is placed in contact with the structure of interest, in this case a metallic plate. To mimic damage a magnet is attached to the plate to simulate the change in local impedance. The solitary wave signals are stored and processed in order to extract a few features that are assumed to be damage-sensitive. The features are clustered into a vector to perform a multivariate analysis in order to determine whether a current feature is representative of damage or it is simply within the baseline, undamaged distribution.

It is noted here that the article presented here is a short version of an extended article currently under revision [11].

2 BACKGROUND

In monodisperse chains of spherical particles, the interaction among weakly compressed beads supports the generation and propagation of HNSWS [12-13]. The nonlinearity derives from the Hertzian contact law $F=k\delta^{3/2}$ between two adjacent beads. In this relationship, the force F is proportional to the deformation δ of the diameter connecting the centers of the interacting beads through the stiffness constant k equal to $E\sqrt{2R}/3(1-\nu^2)$. This stiffness contains the particles radius R , the Poisson's ratio ν , and the elastic modulus E of the particles material. As mentioned in the Introduction, several authors found that the acoustic energy distribution between the PSW and the SSW depends on the elastic modulus and geometry of the object in contact with the chain, and this can be used for SHM and NDE applications.

The OA is an unsupervised learning algorithm based on novelty detection. It establishes whether a new configuration of the system is discordant or inconsistent from the baseline configuration which consists of an existing set of data (or patterns) that describes the normal operative conditions. OA can be performed by using one or more parameters. In the analysis of one-dimensional elements, the detection of outliers is a straightforward process based on the determination of the discordancy between the one-dimensional datum and the baseline.

In the analysis of multi-dimensional elements (multivariate data), the Mahalanobis squared distance (MSD) D_ζ is often computed. This distance is a scalar defined as:

$$D_\zeta = \left(\{x_\zeta\} - \{\bar{x}\} \right)^T \cdot [K]^{-1} \cdot \left(\{x_\zeta\} - \{\bar{x}\} \right) \quad (1)$$

where $\{x_\zeta\}$ is the potential outlier vector, $\{\bar{x}\}$ is the mean vector of the baseline, $[K]$ is the covariance matrix of the baseline and T is the transpose symbol.

In order to determine whether a new datum is an outlier, the corresponding value of D_ζ has to be compared to a threshold computed from the baseline.

3 EXPERIMENTS

3.1 Setup

A straight HNSW transducer was assembled: it consisted of a chain of eight spheres 19.05 mm in diameter, a commercial electromagnet able to lift and release the first particle of the chain (typically indicated with the term *striker*), a sensor, and a frame. The sensing system consisted of a wafer transducer (PZT), embedded between two 6.05 mm thick, 19.05 mm diameter disks. The *transducer* was connected to and driven by a National Instruments PXI running in LabVIEW using a graphical user interface created *ad hoc* for the experiments. The waveforms were sampled at 4 MHz and stored for post-processing.

A $610 \times 610 \times 6.35$ mm³ simply-supported steel plate was monitored. The *transducer* sit at the center of the plate face (Fig. 1a). Defect was mimicked by attaching one of the magnets displayed in Fig. 1b below the plate. The magnets were labeled as small, medium and large and their mass was 20.0 g, 52.1 g and 199 g. Each object was attached to the plate at eight different locations, 10 mm apart, according to the scheme of Fig. 1c.

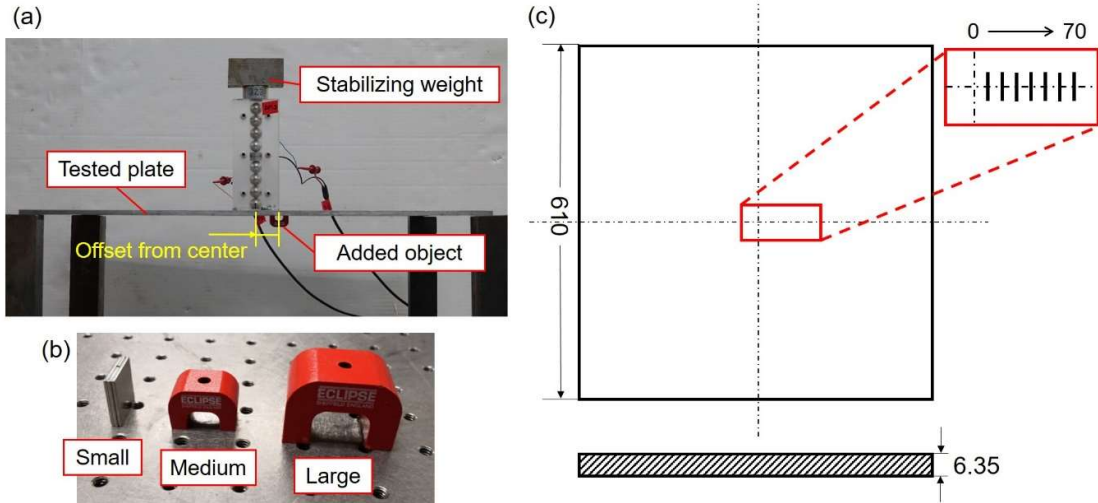


Figure 1: Test setup. (a) Photo of the sample with the transducer above the plate and a foreign object magnetically attached. (b) Photo of the small, medium, and large magnets used as foreign objects. (c) Scheme of the tested thick steel plate including the offset between the magnet and the *transducer*. (Dimensions in mm).

For convenience of discussion, the measurements taken with the *transducer* were grouped into five clusters. The first cluster includes two measurements of 15 waveforms each, taken with the pristine plate. Group 2 comprised the experiments with the small object, whose mass was only 0.09% of the total mass of the plate-transducer system. In this cluster, measurement numbers 3 through 10 identify the positions 0 through 7 shown in Fig. 1c, respectively. Position 0 indicates the object located right below the *transducer* whereas position 7 represents the magnet attached 70 mm away. For each measurement number, 15 recordings of the solitary waves were taken. Groups 3 and 4 follow the same scheme of Group 2, but represent the cases with the medium and the large magnet, respectively. The last group represents two sets of 15

measurements collected with the pristine plate after monitoring the plate with the large object. Based on the above, a total of 420 time waveforms were recorded and post-processed.

3.2 Results

Figure 2 shows one of the waveforms recorded when the small magnet was attached 40 mm away from the contact point. The ISW, PSW, and SSW are visible.

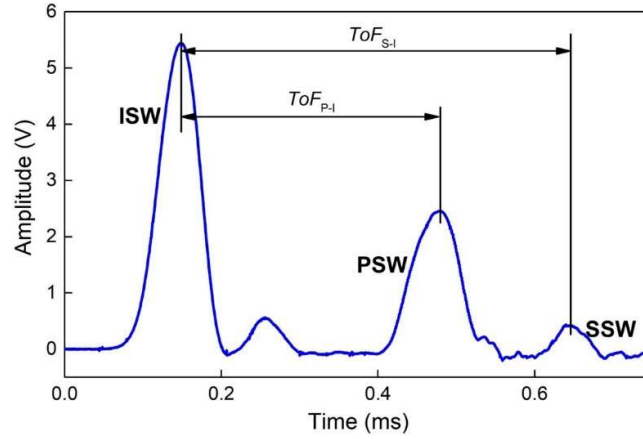


Figure 2: Experimental waveform recorded during the experiment.

The following features were extracted from the waveforms: (1) amplitude ratios A_P/A_I and A_S/A_I of the primary and secondary reflected waves; (2) time-of-flight ToF_{P-I} and ToF_{S-I} of the two reflected waves. Figures 3a to 3d show these features for the 28 sets of measurements.

The data in Fig. 3(a) represent the A_P/A_I feature, i.e. the amplitude of the PSW normalized with respect to the amplitude of the ISW. Here, the ratio remains between 0.45 and 0.50 for the pristine plate and the small magnet. An evident step-up is visible when the medium and the large masses were located close to the *transducer*. The region of influence, i.e. the distance from the *transducer* within which the foreign object was detected, was about 40 mm. Figure 3b shows that the amplitude of the secondary wave does not complement the primary reflection. Typically, when the PSW increases, the SSW is expected to decrease and vice versa. In the experimental data shown in Figs. 3a and 3b, both amplitudes increase when the medium and the large mass were added. The motivation of such behavior is related to the “local” increase of the thickness but also to local vibrations of the plate. Finally, both time-of-flights do not show uniform trend, and at the moment seems not effective at detecting any anomaly.

To validate the research hypothesis that the OA can enhance the ability to detect structural anomalies using solitary waves, the four features were the inputs of a multivariate analysis. The calculation of the confidence threshold values was based on measurement #1 and #2. The MSD was computed by considering all four solitary wave features. In the present study, since the potential outliers are always known *a priori*, both z_ζ and D_ζ were calculated exclusively without contaminating the statistics of the baseline data.

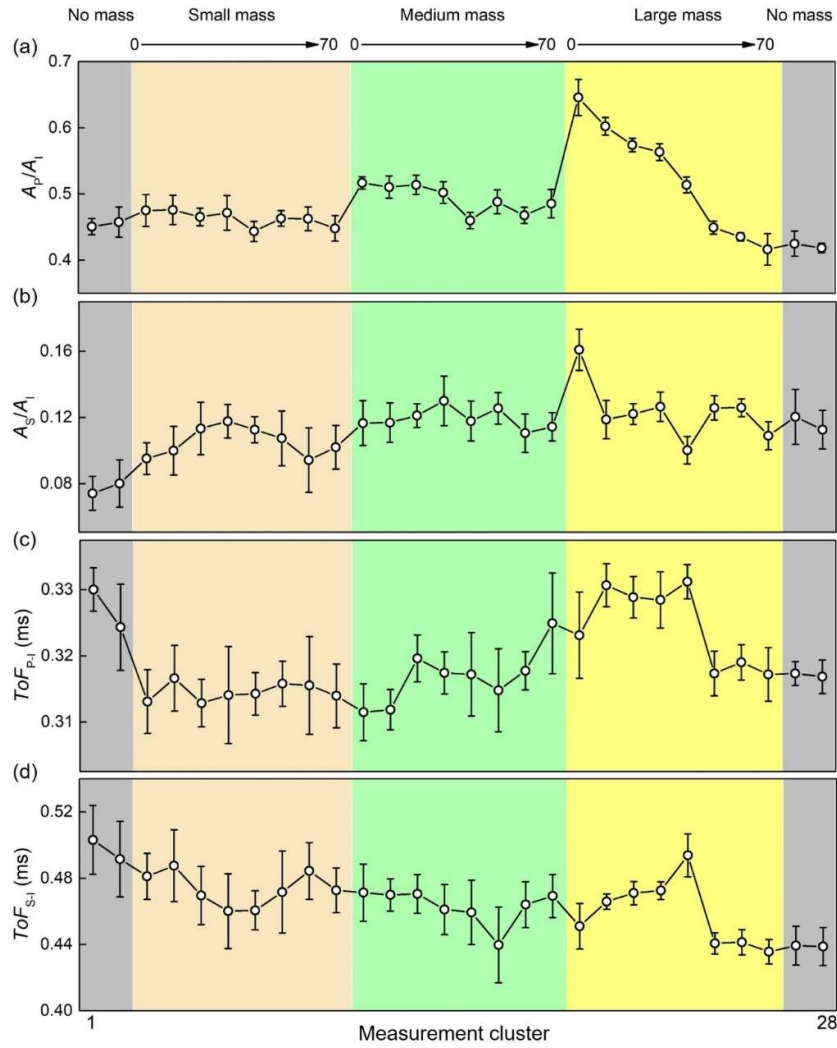


Figure 3: Solitary wave features associated with the PSW and SSW calculated at the 28 measurement points. The data are the average of the 15 measurement and the vertical bars are twice the corresponding standard deviation. The numbers on top of the figure refer to the offset distance in millimeter. (a) amplitude ratio A_p/A_1 ; (b) amplitude ratio A_s/A_1 ; (c) time flight of the primary wave; (d) time of flight of the secondary wave.

The results are presented in Fig. 4 where the MSD is plotted for all 420 measurements. The results show that the multivariate analysis properly classified most of the data. Only a few testing data were classified as false negatives.

All but one of these false negatives referred to the small mass. Surprisingly, the data associated with the last cluster, i.e. no mass, were labeled as outliers. These false positives confirm the existence of the aforementioned “hysteretic” behavior, and warrants an improvement of the *transducer* design for the future.

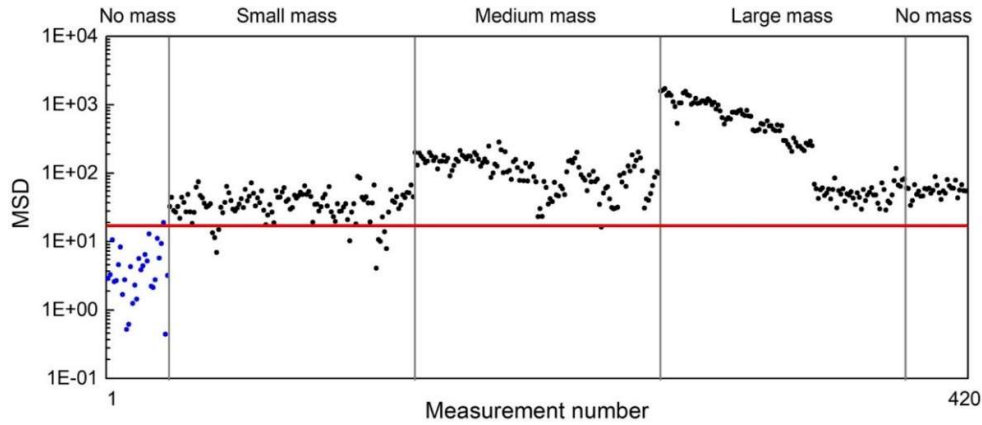


Fig. 4. Health monitoring of a thick plate. Mahalanobis squared distance (MSD) of a four-dimensional vector that contains the four features A_p/A_t , A_s/A_t , ToF_{P-I} , and ToF_{S-I} . The horizontal line is the value of 17.49 representing the 99.73% confidence threshold.

4 CONCLUSIONS

In this study, a HNSW-based defect detection strategy with the assistance of OA was established. The strategy consists of the use of a special transducer designed to trigger, sustain, and sense nonlinear solitary waves that interact dynamically with the structure to be monitored. The recorded waveforms are then processed with a multivariate statistics to label data that diverge significantly from a set of baseline data. The experiment presented in this article consisted of a transducer located at the center of a thick plate and damage simulated by adding magnetically a mass significantly smaller than the overall weight of the structure-transducer system. The results demonstrated that the proposed monitoring system was effective at detecting the presence of a defect as small as 0.25% of the mass of the structure. Although the sensitivity may not be as good as the one provided by an ultrasonic-based thickness gauge device, the proposed HNSW-based system may be suitable to be deployed when the structure to be monitored operates at high temperature and the use of piezoelectric transducers may not be feasible due to the Curie temperature of the piezoelectric crystal. Future studies should attempt to test the monitoring system at high-temperature and in presence of real corrosion.

ACKNOWLEDGMENTS

This work was supported by the U.S. National Science Foundation grants 1745232 and 1809932.

REFERENCES

- [1] Ni, X. and Rizzo, P. Use of highly nonlinear solitary waves in nondestructive testing. *Materials Eval.* (2012) **70**(5), 561-569.
- [2] Ni, X. and Rizzo, P. Highly nonlinear solitary waves for the inspection of adhesive joints.

- Exp. Mech.* (2012) **52**: 1493-1501.
- [3] Nasrollahi, A., Deng, W., Rizzo, P., Vuotto, A., and Vandenbossche, J.M. Nondestructive testing of concrete using highly nonlinear solitary waves. *Nondestr. Testing Eval.* (2017) **32**(4): 381-399.
- [4] Shelke, A., Uddin, A. and Yang, J. Impact identification in sandwich structures using solitary wave-supporting granular crystal sensors. *AIAA Journal* (2014) **52**(10): 2283-2290.
- [5] Kim, E., Restuccia, F., Yang, J., and Daraio, C. Solitary wave-based delamination detection in composite plates using a combined granular crystal sensor and actuator. *Smart Materials and Structures* (2015) **24**(12), 125004.
- [6] Farrar, C.R. and Worden, K. *Structural health monitoring: a machine learning perspective*. John Wiley & Sons, (2012).
- [7] Adams, D. *Health monitoring of structural materials and components: methods with applications*. John Wiley & Sons (2007).
- [8] Balageas, D. Fritzen, C.-P. and Güemes, A. *Structural health monitoring*. John Wiley & Sons, (2010).
- [9] Bagheri, A. Pistone, E. and Rizzo, P. Outlier Analysis and Artificial Neural Network for the Non-contact Nondestructive Evaluation of Immersed Plates. *RNDE* (2015) **26**(3): 154-173.
- [10] Rizzo, P. and Lanza di Scalea, F. Feature Extraction for Defect Detection in Strands by Guided Ultrasonic Waves. *Intl. J. SHM* (2006) **5**(3): 297-308.
- [11] Zheng, B. Rizzo, P. and Nasrollahi, A. Outlier Analysis of Nonlinear Solitary Waves for Health Monitoring Applications, *under review* (2019).
- [12] Nesterenko V.F. *Dynamics of heterogeneous materials*. Springer Science & Business Media, (2013).
- [13] Coste, C., Falcon, E. and Fauve, S. Solitary waves in a chain of beads under Hertz contact. *Physical review E* (1997) **56**: 6104.

DEVELOPMENT OF CONTROL STRATEGIES FOR VERTICAL MOBILITY OF ADAPTIVE TELESCOPIC HIGH-ALTITUDE AEROSTATS

C. GRACZYKOWSKI^{*}, L. KNAP[†], J. HOLNICKI-SZULC^{*} AND Z. WOŁEJSZA^{*}

^{*} Institute of Fundamental Technological Research
Polish Academy of Sciences

Pawińskiego 5B, 02-106 Warsaw, Poland

e-mail: cezary.graczykowski@ippt.pan.pl, web page: <http://www.ippt.pan.pl>

[†] Warsaw University of Technology

Faculty of Automotive and Construction Machinery Engineering

Narbutta 84, 02-524 Warsaw, Poland

Email: Lech.Knap@pw.edu.pl, web page: <http://www.simr.pw.edu.pl>

Key words: helium airship, control of vertical mobility, reduced energy consumption, optimal ascending and descending paths

Abstract. In this article we propose a new concept of adaptive telescopic high-altitude aerostat designed in a modular form which allows for sequential changes of volume during the flight. The proposed telescopic aerostat can be easily enlarged or contracted due to application of multi-segmented construction, controllable segments' couplings and precise adjustment of internal pressure obtained using additional gas tank, valve and compressor. Conducted changes of aerostat volume allow to precisely control generated lift force and to obtain desired paths of ascending and descending. The paper briefly presents development of control strategies aimed at: i) reaching the subsequent altitudes in the shortest period of time, ii) reaching these altitudes at the smallest cost defined as total work done by the compressor. The obtained results show high potential of the proposed innovative concept of the aerostat.

1 INTRODUCTION

Over the last 30 years, there have been a few projects conducted in different parts of the world, the purpose of which was to build numerous objects operating in the stratosphere in order to carry communications and monitoring equipment for intelligence, surveillance and reconnaissance missions (so-called HAPS - High Altitude Pseudo Satellites). Currently, more and more companies, mainly specializing in telecommunications or remote monitoring are working on development of technologies enabling applications of flying objects located 20-30 km above the sea level [1]. Ultimately, they are intended to be unmanned aircrafts powered by solar energy, having the ability to move both in the vertical and horizontal directions and which may persist in space for several months to 1-2 years without landing on the ground. In parallel to development of stratospheric airplanes, many countries are working on new generation of airships filled with hydrogen or helium, also with electric drive.

Such airships are usually built as classical systems in which the external volume of the airship is constant and does not change during its ascent from the ground to the level of the stratosphere. Examples of such solutions are, for example, US constructions HiSentinel and ISIS (see Fig. 1a and 1b), or French Stratobus (see Fig. 2).

As a rule, these are objects with very large dimensions - length from approx. 100 m to approx. 300 m and diameters from approx. 30 m to approx. 50 m. In this type of construction the required flight altitude is obtained by changing the mass and pressure of the gas (helium hydrogen or air) inside additional storage tanks located inside the airship. Another solution, where the external volume of the airship is changing during increasing of the altitude is, for example, the Russian proposal of the HAA Berkut airship (Fig. 3a), in which at the low altitude the airship has a small volume Fig. 3b, and in the stratosphere its volume is about 12 times larger - Fig. 3c. In this case, the elevation control is carried out by changing the gas pressure inside the airship

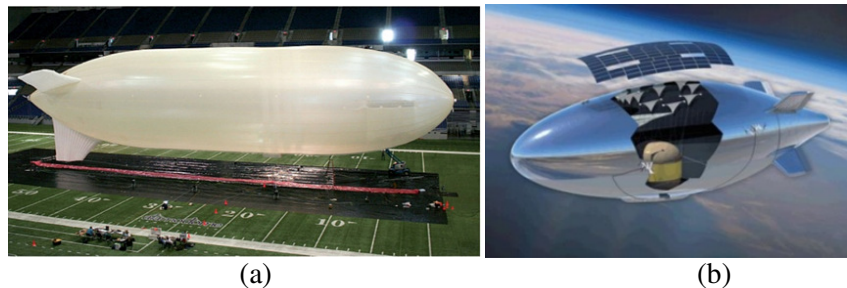


Figure 1: (a) – Airship HiSentinel 80 [2], (b) – Lockheed Martin's ISIS airship ISIS [3]

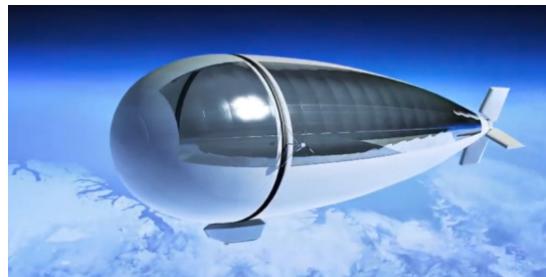


Figure 2: The airship of Thales Alenia Space – Stratobus [4]

Despite the large number of programs currently implemented in the world and huge expenses related to the construction of stratospheric airships, a number of technical problems still rise and some of them remain unresolved. Many research papers are dedicated to particular ultralight materials, technical solutions or development of airships design in which various solutions are used in order to reduce weight and to obtain required payload. In the case of airship with the electric propulsion one of the heaviest components reducing significantly available payload are electric batteries and solar panels which are needed to provide the airship the enough amount of energy. Therefore, the objective of our research is to show that proper control of aerostat's volume during the flight allows to noticeably decrease the amount of energy required for its operation and thus to reduce the total weight of the applied power system.

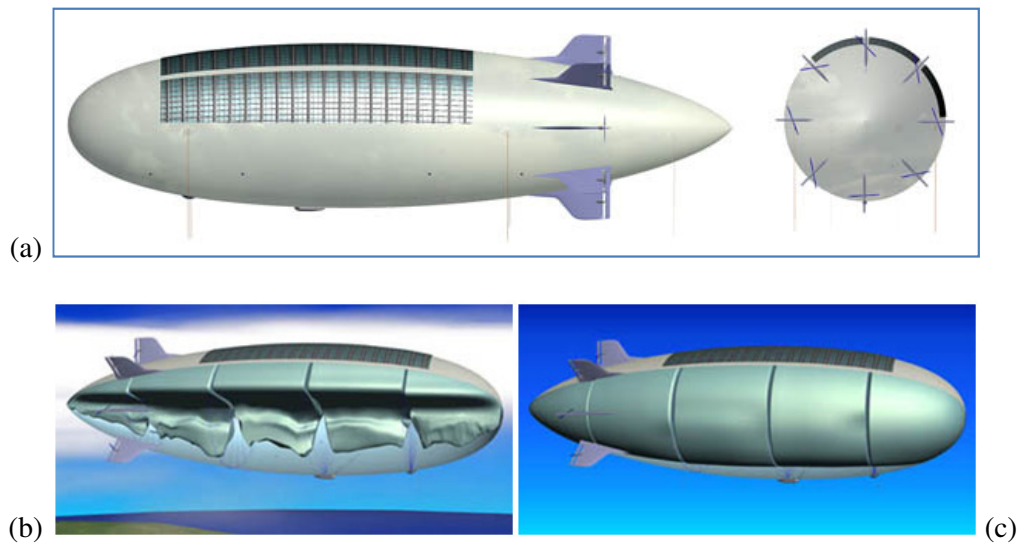


Figure 3: The concept of the Russian airship HAA Berkut [5]

In this paper we briefly present numerical analyses of vertical motion of the aerostat of innovative telescopic design. Conducted simulations, even though regarding the medium-altitude aerostat, reveal key problems and indicate factors that play crucial role in design and control of telescopic aerostats with reasonable payload. The first issue to be addressed is the requirement of obtaining maximal efficiency of the aerostat, understood as minimal time of ascending and descending. In turn, the second issue is minimization of the total cost required for controlling vertical mobility, understood as total amount of energy required for transfer of helium between storage tank and aerostat and vice versa. The corresponding control problems are formulated basing on previous research works [6,7]. The conducted numerical simulations show that both the time of ascending / descending and the amount of energy needed for the flight can be significantly reduced by proper control of HAPS volume and helium flow. In the latter case, the applied control strategy allows to reduce the mass of external energy sources, such as electric batteries or solar panels.

2 GENERAL IDEA OF TELESCOPIC HAPS

The proposed concept for vertical mobility is based the reversible, telescopic option for the aerostat volume modifications, in which the crucial feature is system composed of structural sections connected via controllable actuators fixing or releasing their relative movement and additional helium container (pressure tank) allowing controllable release or absorption of gas [8]. The design concept of the small HAPS module applied in further analyses of its mobility and load-carrying capacity is illustrated in Fig. 4. The construction consists of a cylindrical housing reinforced by axial and circumferential ribs. The HAPS offers a possibility of volume modification by changing the length of the cylindrical section from initial dimension of D to the maximal dimension of $2D$. It is possible due to the construction consisting of the inner (1) and outer segments (2), which are sliding along linear guideways (7). Relative motion of these guideways can be blocked by actuator (3), which creates the clamping mechanism providing control of the aerostat volume.

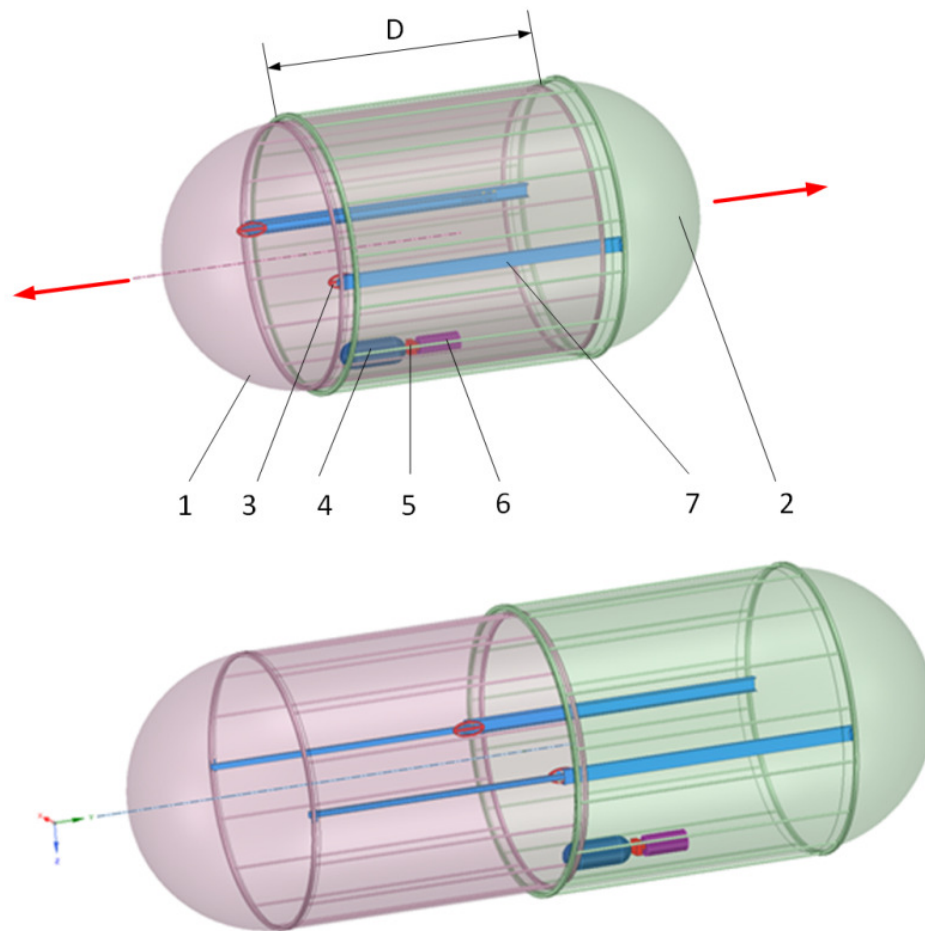


Figure 4: Scheme of the HAPS design: a) aerostat in initial form: 1 – inner segment, 2 – outer segment, 3 – piezoelectric actuator, 4 – additional helium tank, 5 – valve controlling helium flow, 6 – compressor, 7 – linear guideways; b) aerostat in extended form

In order to achieve a proper mobility the aerostat is equipped with an additional gas storage tank (4) with an additional amount of pressurised helium. This additional tank serves for the purpose of generating the pressure difference between aerostat and its environment. The created overpressure or underpressure is used to generate forces needed to fold and unfold the aerostat. In order to reduce helium losses caused by its release to atmosphere, the aerostat is equipped with a compressor (6) and a valve (5), which control the flow of helium from the aerostat back to the additional gas tank.

Application of the above described system composed of additional pressure tank, the compressor and the valve enables precise control the gas flow and actual pressure difference between the aerostat and the atmosphere during the ascending and descending process. This allows to control the process of folding and unfolding of the aerostat, to generate the required value of the lift force resulting from buoyancy and to obtain equilibrium position of the aerostat at desired altitude.

3 STRATEGY AIMED AT MAXIMIZATION OF VERTICAL MOBILITY EFFICIENCY

In the considered control problem we will analyze the process of aerostat ascending and descending of total duration of 12000 s. During the first part of the process, the aerostat should ascend from the ground level to initial equilibrium position located at $h_1=350$ m, next it should float to the target altitude $h_3=5000$ m with an intermediate stop at the altitude $h_2=3000$ m. Further, in the second part of the process, the aerostat should descend from the altitude $h_3=5000$ m back to altitude $h_5=350$ m, with the intermediate stop at the altitude of $h_4=3000$ m.

The first control problem is to find change of aerostat volume $V(t)$ and the corresponding required change of pressure difference between the aerostat and the atmosphere $\Delta p_{HAPS-atm}(t)$, which enable realization of the above defined aerostat ascending and descending sequence, simultaneously providing the shortest time of aerostat motion between the assume altitudes. Mathematically, the above problem of maximization of vertical mobility efficiency takes the form:

Find $V(t)$ and $\Delta p_{HAPS-atm}(t)$ such that:

1. $\{(h_1, 0), (h_2, 0), (h_3, 0), (h_4, 0), (h_5, 0)\} \subset \{x(t), \dot{x}(t)\}, t \in \langle 0, T \rangle$
2. $\Delta t_{h_1-h_2} + \Delta t_{h_2-h_3} + \Delta t_{h_3-h_4} + \Delta t_{h_4-h_5}$ is minimal
subject to condition of compressor maximal mass flow rate: $\dot{m}_h \leq q_{max}$

The first condition describes successful realization of the assumed flight scenario, which includes reaching the subsequent altitudes h_1 - h_5 with intermediate brief stops. The second condition defines the objective function, which is a sum of subsequent times of transfer between the altitudes. The intuitive solution of the above control problem is maximally fast change of pressure difference and step-wise change of aerostat volume at the beginning of each stage of ascending and descending. The corresponding plots of HAPS altitude and work done by compressor are presented in Fig. 5 and Fig. 6.

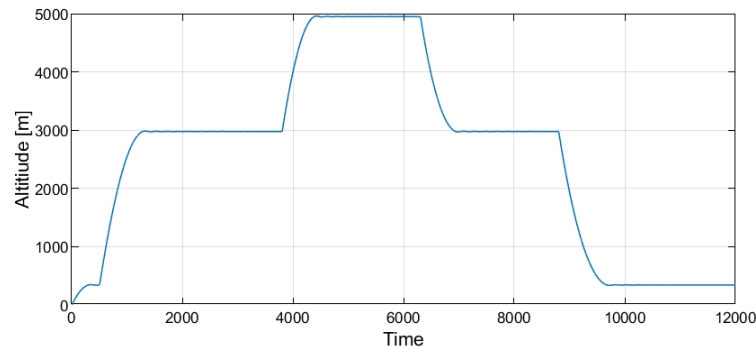


Figure 5: Strategy maximizing vertical mobility efficiency: change of aerostat altitude

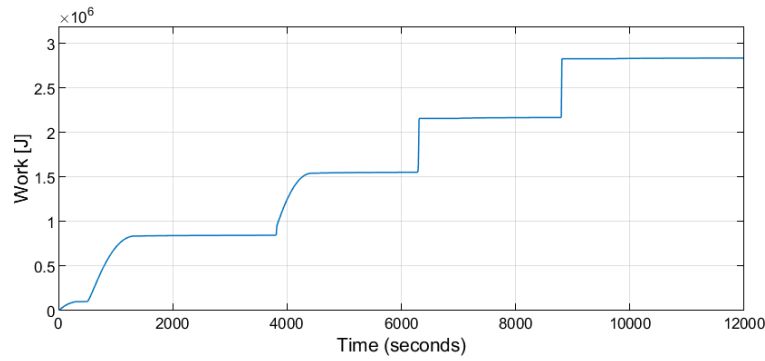


Figure 6: Strategy maximizing vertical mobility efficiency: work done during gas transfer

The conducted simulations indicate that for the assumed parameters of the aerostat the required altitudes can be achieved in time periods substantially shorter than initially assumed (Fig. 5). However, each stage of ascending and descending process is associated with large amount of work done by the compressor. In particular, large power consumption is required at the beginning of the descending stages, when large mass of helium has to be transferred back to storage tank (Fig. 6).

4 STRATEGY AIMED AT MINIMIZATION OF VERTICAL MOBILITY ENERGETIC COST

The second control problem is to find change of aerostat volume $V(t)$ and the corresponding required change of pressure difference between the aerostat and the atmosphere $\Delta p_{\text{HAPS-atm}}$, which enable realization of the above defined aerostat ascending and descending sequence, simultaneously providing minimization of the energy used for gas transfer between additional gas tank and aerostat. Mathematically, the above problem of minimization of vertical mobility energetic cost takes the form:

Find $V(t)$ and $\Delta p_{\text{HAPS-atm}}(t)$ such that:

1. $\{(h_1, 0), (h_2, 0), (h_3, 0), (h_4, 0), (h_5, 0)\} \subset \{x(t), \dot{x}(t)\}, t \in \langle 0, T \rangle$
2. $E_{\text{comp}} = \int_0^t \frac{\dot{m}_h}{\rho_h} (\Delta p_{\text{HAPS-tank}}) dt$ is minimal

subject to condition of compressor maximal mass flow rate: $\dot{m}_h \leq q_{\text{max}}$

Now, the second condition defines the objective function, which is work done by compressor during helium transfer and is a function of required mass flow rate of helium, its actual density and pressure difference between the additional storage tank and the aerostat. The intuitive solution of the above control problem is realization of the entire process in possibly slow manner, with minimal pressure difference between the aerostat and the storage tank. The corresponding plots of aerostat altitude and work by compressor are presented in Fig. 7 and Fig. 8.

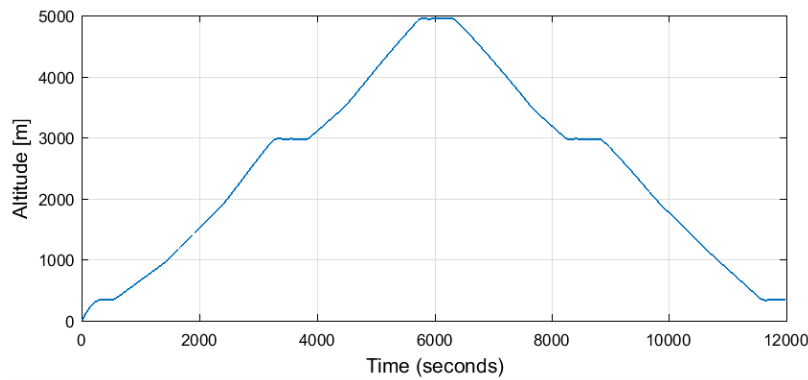


Figure 7: Strategy for minimization of vertical mobility energetic cost: change of aerostat altitude

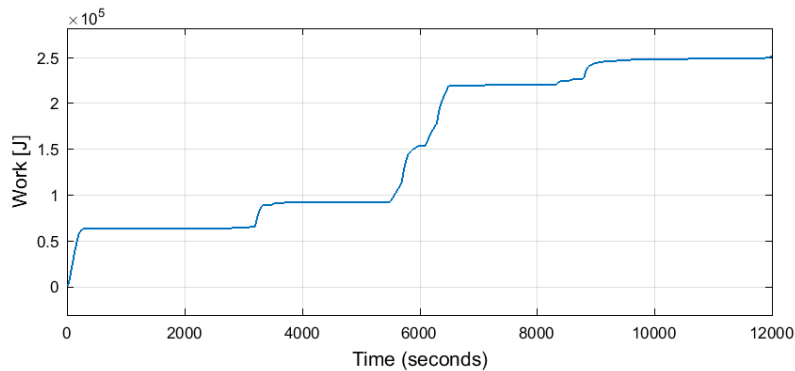


Figure 8: Strategy for minimization of vertical mobility energetic cost: work done during gas transfer

In the conducted simulations the change of aerostat volume during each stage of the process is not instantaneous but gradual and subsequent time periods of volume change are equal to the corresponding predefined time periods of ascending or descending (Fig. 7). In this strategy each stage of the process is associated with significantly smaller work done by compressor and, in particular, initial part of descending stages does not require excessive power consumption (Fig. 8). As a result, the total work done by compressor is almost ten times smaller than in previous control strategy (note the scale difference in Fig. 6 and Fig. 8).

5 CONCLUSIONS

The paper provides preliminary positive verification of the concept of adaptive telescopic stratospheric aerostats based on mechanism of volume change, application of additional pressure tank and compressor. The conducted simulations prove that adaptive telescopic HAPS can be adjusted to various operational conditions. Control of internal pressure can be used to achieve desired altitudes possibly fast or to operate in a slow mode providing significant reduction of energy consumption. It can be concluded that adaptive telescopic aerostats offer exceptional vertical mobility and thus they seem to be promising solution in many practical applications in the coming years.

ACKNOWLEDGMENT

Financial support of the National Science Centre, Poland, granted through the project “Application of the AIA concept (Adaptive Impact Absorption) in aeronautical and space engineering, AIA-AERO” (TANGO2/341494/NCBR/2017), is gratefully acknowledged.

REFERENCES

- [1] Lee M., Smith S. and Androulakis S. The high altitude lighter-than-air airship efforts at the US Army Space and Missile Defense Command/Army Forces Strategic Command. *Proceedings of the 18th AIAA Lighter-Than-Air Systems Technology Conference*, Seattle, USA (2009)
- [2] Smith S., Fortenberry M., Michael L. and Judy R. HiSentinel80: flight of a high altitude airship, *Proceedings of the 11th AIAA Aviation Technology, Integration, and Operations (ATIO) Conference*, Virginia Beach, USA (2011)
- [3] ElectronicsWeekly.Com. Airship set to become the ultimate eye in the sky; [accessed 2018 Jun 26]. <https://www.electronicsworld.com/news/business/information-technology/airship-set-to-become-the-ultimate-eye-in-the-sky-2011-08> (2018)
- [4] Thales. What’s up with Stratobus? [accessed 2018 Jun 26]. <https://www.thalesgroup.com/en/worldwide/space/news/whats-stratobus> (2018)
- [5] Augur RosAeroSystems High Altitude Airship "Berkut"; [accessed 2018 Jun 26]. <http://rosaerosystems.com/projects/obj687> (2018)
- [6] Zhao Y.J., Mueller J. and Garrard W., Benefits of trajectory optimization in airship flights, *AIAA Journal* (2004) **65**:27
- [7] Sun L. and Zheng Z., Nonlinear adaptive trajectory tracking control for a stratospheric airship with parametric uncertainty, *Nonlinear Dynamics* (2015) **82**:1-12
- [8] Holnicki-Szulc J., Faraj R., Pawłowski P., Wołajsza Z., Kaźmierczak K., and Hinc K., Deployable structure of stratospheric airship and method of volume change of deployable structure of stratospheric airship” (in Polish), Polish Patent Pending No. 419786, (2016).

FLUID-STRUCTURE INTERACTION ANALYSIS OF A FOUR-BAR FLAPPING WING MECHANISM

CAN BEKER^{*}, ALI E. TURGUT[†], KUTLUK B. ARIKAN[‡] AND D. FUNDA
KURTULUS[§]

^{*}METU Aerospace Engineering Department, 06800 Cankaya Ankara, Turkey
e-mail: can.beker@metu.edu.tr, web page: <http://ae.metu.edu.tr>

[†]METU Mechanical Engineering Department, 06800 Cankaya Ankara, Turkey
E-mail: aturgut@metu.edu.tr, web page: <http://me.metu.edu.tr>

[‡]TEDU Mechanical Engineering Department, 06420, Cankaya, Ankara, Turkey
E-mail: kutluk.arikan@tedu.edu.tr, web page: <https://me.tedu.edu.tr/en/me>

[§]METU Aerospace Engineering Department, 06800 Cankaya Ankara, Turkey
E-mail: kurtulus@metu.edu.tr, web page: <http://ae.metu.edu.tr/>

Key words: Flapping Wing Micro Air Vehicle, Fluid Structure Interaction, Four Bar Mechanism.

Abstract. In this paper, it is introduced to find net aerodynamic lift capacity of proposed flapping-wing micro air vehicle (FWMAV) by performing dynamical calculation and FSI (Fluid Structure Interaction) analysis of a flapping wing test system. In the flapping system, a single degree of freedom type four-bar mechanism which was used as a piezo-driven flapping wing mechanism in previous literature studies is implemented to create beating motion of the wings. For the wing structure, Calliphora Erythrocephala's wing is used which is presented by Konkuk University [1]. The flapping wing mechanism and wing structure are fabricated by 1 mm of plexiglass. In FWMAV applications, in order to produce enough force to levitate the flapping structure, the inertial forces are created by flapping wing mechanism should not dominate on aerodynamic lift capacity of the wings. In this framework, the real-time flapping test is performed by six degrees of freedom force transducer for a specific flapping frequency (11.2 Hz) to understand inertial and aerodynamic characteristics of the proposed mechanism and test results are presented. The theoretical approach is put forward by obtaining the dynamic model of the proposed flapping structure. The initial angular position, mass, and radius of rotation values of the major linkages of the flapping wing mechanism are presented. Tangential and centrifugal forces acting on major linkages of the four-bar flapping wing mechanism are found and total inertial characteristics of the proposed mechanism are obtained in different axes. FSI analysis of the proposed flapping wing mechanism is performed to understand how the elasticity of the wing effects of the aerodynamic lift capacity of the structure. The aeroelastic analysis is modelled based on the conditions are performed in the test phase. The Fluid-structure interaction model is created in two different domain using ABAQUS CAE and STARCCM+. ABAQUS CAE is used to create the

structural dynamics finite element model of the proposed flapping wing structure. A time-dependent dynamic implicit analysis step is created in finite element analysis (FEA) model and sinusoidal input is defined to the corresponding linkage and inertial results are shared. In this framework, the wing is modelled in STARCCM+ interface. The inertial force results belonging to FSI analysis is presented and compared with the theoretical model and experimental test results.

1 INTRODUCTION

In recent years, there has been growing interest in micro air vehicles (MAV) in military and civilian applications using the state of art technology of developed micro-sized mechanical and electronic devices. In literature, MAVs are categorized with respect to their wing types as fixed, rotary and flapping wing. Flapping wing micro air vehicles (FWMAV) have gained great attention in MAV category for their high maneuver capability, especially for indoor activities. Researchers are in this field still trying to enlighten how to use low Reynold flyer's such as birds and bats features in their design.

In FWMAV applications, some preliminary items emerge as aerodynamic and inertial forces for producing enough aerodynamic lift force to levitate the flapping wing structure. Flapping wing mechanisms are used to obtain beating motion of wings. During flapping motion, the flapping mechanism creates inertial forces in different axes. In this framework, the inertial forces created by the flapping wing mechanism must be investigated deeply. In literature, some preliminary real-time tests have been performed to find the generated inertial forces by four-bar flapping wing mechanisms [1]. However, this study is an experimental based study and does not present an inertial analysis. Senol et al. ([2]-[3]) presented inertial force analysis and compared with test results. But, in this study, the inertial analysis is carried out only based on the proposed wing, the inertial forces created by linkages and rotating parts are neglected.

To understand the inertial characteristic of the flapping wing based structures, the flapping test is performed using 6 DOF force/moment transducer. Flapping wing test bed gives extensive information about the aerodynamic characteristics of flapping wing structure. Khan et al. [4] performed force and moment measurements by use of 6 DOF force/moment transducer and correlate the measured force and moment values with the proposed dynamical flapping model. Jang et al. [5] improved a passive control mechanism for adjusting the mean angle of attack in hovering using 6 DOF transducer. Phan et al. [6] proved that clap and fling mechanism has a positive impact on aerodynamic lift capacity using a force sensor.

In FWMAV applications, the net lift capacity which is the combination of aerodynamic lift force and inertial force created by flapping wing mechanism determines whether the proposed FWMAV structure produce just enough lift to levitate the model or not. There are great numbers of computational studies are performed to understand the lift capacity of the presented FWMAV structure, mostly using computational fluid dynamics (CFD) technique for rigid bodies ([7], [8]). However, using CFD model for the rigid structures neglects the elasticity of the wing structure and does not take account into the inertial forces created by flapping wing mechanism and wing structure during beating motion.

Fluid-structure interaction analyses solve fluid and dynamic equations simultaneously for an elastic body and give a net force result in the desired direction. Some preliminary works are performed to understand aerodynamic characteristic using FSI technique. Cetraro et al. [9] implemented electro-active material on a wing membrane and used FSI analysis to show generating oscillations on wing membrane at a resonance frequency and an angle of attack increases aerodynamic lift force. Nakata et al. [10] performed FSI analysis to investigate the flexibility effect of the wings to the aerodynamic efficiency based on Hawkmoth *Agrius Convolvuli* insect wing. Nakata et al. [10] reported that using flexible wing enhances the aerodynamic efficiency in terms of the lift capacity, in contrast flexible wings require more power for flapping and creates more drag force since the deformation of the wings.

The goal of this study is to validate the test results using theoretical and computational approach and offer a design methodology for the proposed FWMAV structure. In this framework, a flapping wing mechanism is presented and a flapping test is performed. Based on the proposed mechanism and flapping conditions, dynamical calculations and some preliminary computational studies (FSI) are performed and compared with test results.

2 FLAPPING WING MECHANISM DESIGN

The flapping wing mechanism is responsible for transferring the actuation force to wings and creating flapping motion. For this study, a four-bar mechanism is designed based on the piezo-driven four bar mechanism designed in Ref. [1]. The position analysis is carried out and an amplification ratio is found between the input angle and the flapping angle. With the lengths of the four-bar mechanism selected as $l_0=38$ mm, $l_1=30$ mm, $l_2=8$ mm and $l_3=7.5$ mm, the maximum flapping angle (θ_3) is achieved as 24.9° whereas the minimum angle is -16.6° . The four-bar flapping wing mechanism flapping angle response is given in Figure 1.

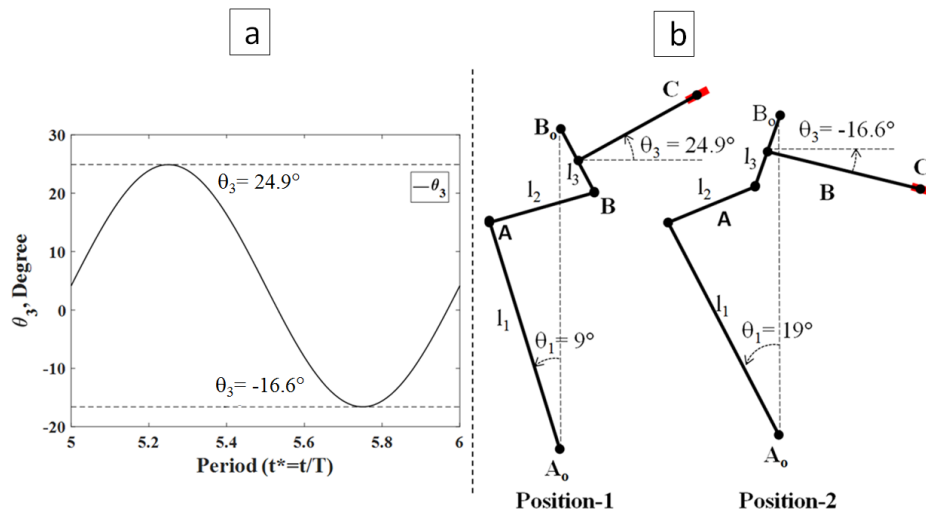


Figure 1: Kinematic relations a) Instantaneous flapping angle b) Position of the mechanism at the maximum up-stroke (position-1) and at the minimum down-stroke (position-2) during the flapping motion

3 EXPERIMENTAL SETUP

Experimental test is performed to measure total forces created by the designed and manufactured flapping wing mechanism in non-vacuum condition using ATI Nano17 6 DOF F/T (Force/Torque) transducer. The resolution of the ATI Nano F/T card is 3 mN of force and 16 μ Nm of moment. The flapping wing mechanism is driven by a servo motor. A sinusoidal input is defined in microcontroller as to run the servo motor. Its oscillation amplitude is 10° and its frequency is 11.2 Hz. The measured force data is transferred to DAQ/FT and its amplifier and the gathered data is visualized in Lab-View program in PC. The schematic view of the experimental setup is given in Figure 2.

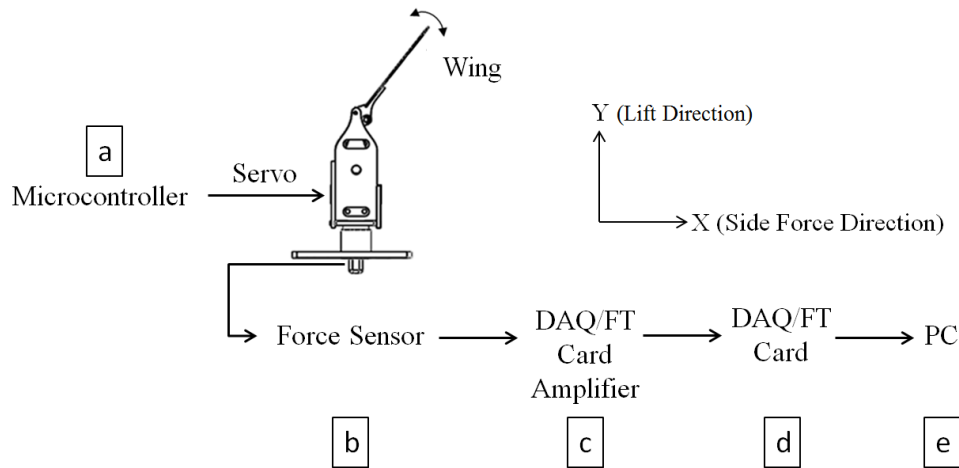


Figure 2 : Experimental Setup a) Microcontroller b) Force Sensor c) Data Acquisition Board (DAQ) Amplifier d) Data Acquisition Board e) Computer

The flapping test is performed with flapping frequency of 11.2 Hz and a flapping angle of 41.5° . Using acquired data, Fast-Fourier Transformation is performed using MATLAB and to eliminate white noise, 5th order Butterworth filter with a cut-off frequency of 33.54 Hz is used. In this study, since the lift capacity of the proposed flapping wing mechanism is investigated the forces in lift direction (y-axis) is studied in detail.

4 RIGID-BODY DYNAMICS CALCULATIONS

In this section, the inertial forces created by flapping wing mechanism are investigated. The majority of the inertial forces are created by linkages of the four-bar flapping mechanism and the Calliphora Erythrocephala's wing. In this framework, the forces acting on the major four-bar linkages and wing are found and inertial forces are presented in different directions. The proposed flapping wing mechanism and the obtained free-body diagram are given in Figure 3.

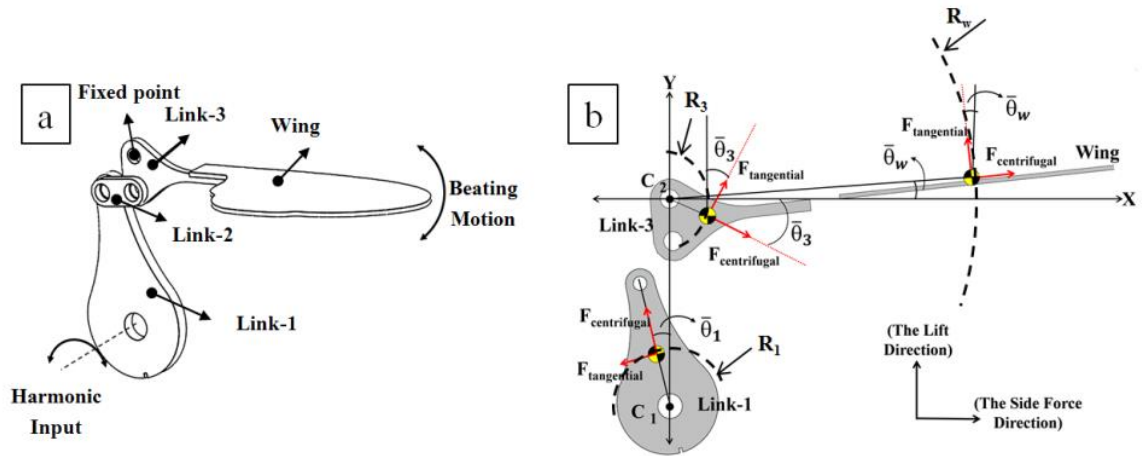


Figure 3: Schematic and exploded view of the proposed flapping wing mechanism a) Sections of the proposed flapping wing mechanism b) Forces acting on proposed flapping wing mechanism

The link-1 rotates around C_1 with R_1 (6.72 mm) radius of rotation whereas the wing and link-3 rotates about C_2 with R_w (6.72 mm) and R_3 (52.56 mm) radius of rotations respectively as given in Fig.3b. The mass, initial angular position of the center of mass and derived instantaneous angular position of the major linkages and wing are given in Table 1. The maximum angle obtained for the Link-1 is 19° with respect to y-axis whereas for the wing and link-3, the maximum angle is 20.75° with respect to x-axis. In Table 1, $\bar{\theta}_i$ (as shown in Fig.3b) represents instantaneous angle, $\bar{\theta}_{i-initial}$ represents the initial angular position of the center of mass, $\bar{\theta}_{i-max}$ represent the reached maximum angle of the corresponding part for $i=w, 1, 3$. In dynamical calculations, the link-2 is neglected since it has a small mass or 0.1 gram.

Table 1: The masses and radius of rotations of each part of the proposed flapping wing mechanism

Part name	Mass [gram]	Initial Angle, (Relevant axis) ($\bar{\theta}_{i-initial}$)	Maximum angle ($\bar{\theta}_{i-max}$)	Instantaneous Angular Positions
Wing	1.5	3.55 (x-axis)	3.55 (x-axis)	$\bar{\theta}_w = \bar{\theta}_{w-initial} + \bar{\theta}_{w-max} \sin(2\pi ft)$
Link-1	1.9	14 (y-axis)	14 (y-axis)	$\bar{\theta}_l = \bar{\theta}_{l-initial} + \bar{\theta}_{l-max} \sin(2\pi ft)$
Link-2	0.1	-	-	-
Link-3	0.3	-28.42 (x-axis)	-28.42 (x-axis)	$\bar{\theta}_3 = \bar{\theta}_{3-initial} + \bar{\theta}_{3-max} \sin(2\pi ft)$

After obtaining the instantaneous angular positions of the wing, link-1 and link-3, the instantaneous angular velocities and angular accelerations of the corresponding parts are obtained using Eq. (1) and Eq. (2) respectively.

$$w(t) = \frac{\partial \theta_i}{\partial t} \quad (1)$$

$$\alpha(t) = \frac{\partial w}{\partial t} \quad (2)$$

The obtained angular acceleration values are plugged into the centrifugal and tangential force terms in Eq. (3) and Eq. (4). Then the inertial forces generated in the x-axis and the y-axis are found using Eq. (5) and Eq. (6).

$$F_{i\text{-centrifugal}} = m_i w_i^2 R_i \quad (3)$$

$$F_{i\text{-tangential}} = m_i \alpha_i R_i \quad (4)$$

$$\Sigma F_{i-x} = \Sigma F_{i\text{-centrifugal}} + \Sigma F_{i\text{-tangential}} \quad (5)$$

$$\Sigma F_{i-y} = \Sigma F_{i\text{-centrifugal}} + \Sigma F_{i\text{-tangential}} \quad (6)$$

For $i = 1, 3, w$

Based on the dynamical calculations, the instantaneous angles of the center of mass of the each corresponding parts and total inertial forces in the x-axis and y-axis are given in Figure 4.

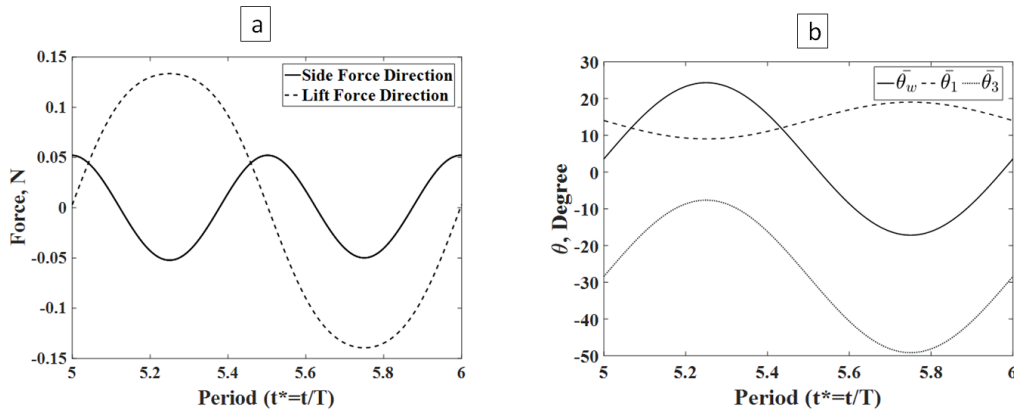


Figure 4 Dynamic calculations a) Forces during the 5th period in lift and side force directions b) Instantaneous angular positions for the wing, link-1 and link-3

5 COMPUTATIONAL METHOD

Fluid-structure interaction analysis (FSI) is performed to understand the inertial and aerodynamic lift characteristic of the proposed flapping wing mechanism. FSI analysis gives extensive results about how dynamically moving body is affected by fluid surround it. In FSI analysis, two types of computational domains work simultaneously and communicate with each other as the structural and fluid domain. Essentially, in this study, ABAQUS CAE 14.0 is used for the structural domain and STARCCM+ is used for the fluid domain. The simulation is ran with 5×10^{-4} seconds time increment.

A dynamic implicit analysis step is defined as the finite element analysis model. The linear-hexagonal element type is used for the created FEA model. The total node number of the FEA model is 7375, the total element number of the FEA model is 4830. The created finite element analysis (FEA) model of the proposed flapping wing mechanism is given in Fig. 5. Sinusoidal angular displacement rotation is defined from point C_1 in z-axis whereas fixed-type boundary condition is defined from point C_2 and the flapping wing mechanism is fixed from point C_1 (Figure 3).

The plexiglass material is defined for the whole parts of the proposed flapping wing mechanism. The modulus of elasticity, Poisson's ratio and density of the Plexiglass are defined as 3100 MPa, 0.3 and 1.4 kg/m³ respectively.

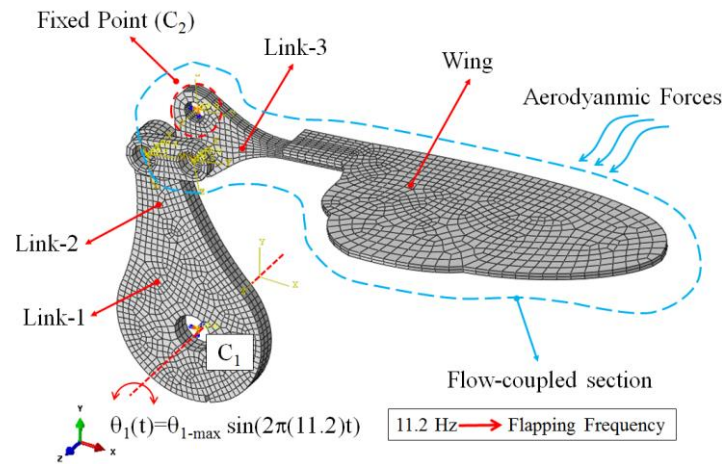


Figure 5 Finite element analysis model of the proposed flapping wing mechanism

CFD analysis only covers the flow coupled section as shown in Fig.5 and Fig. 6. The fluid domain and its dimensions are given in Figure 6. The property of air is defined for the fluid domain as 1.18 kg/m³. The section view of the fluid domain is also given in Figure 7.

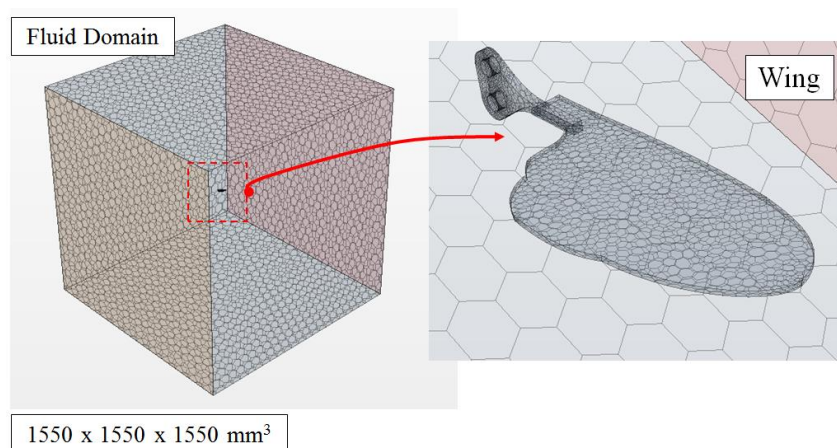


Figure 6: Fluid domain for the CFD analysis

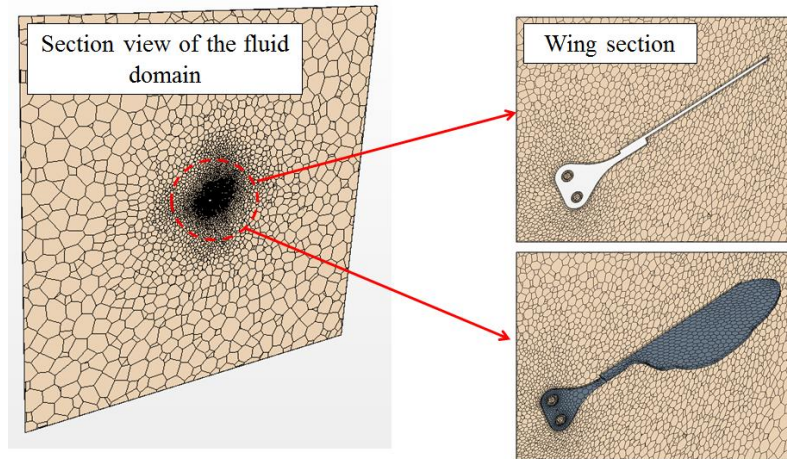


Figure 7 Mesh in the fluid domain

5 RESULTS

In this section, the theoretical, experimental, FSI (Fluid-structure interaction) and dynamic FEA (Finite element analysis) results of the proposed flapping wing mechanism are compared and the effect of the aero-elasticity is addressed. In the FSI analysis, the proposed flapping wing mechanism undergoes the body inertial force and aerodynamic effects simultaneously. However, in the FEA analysis, the effect of aerodynamics is not included and it simulates as the proposed flapping wing mechanism is in vacuum condition. As a result of this, different load and wing tip deflections occur between FSI and FEA results. Figure 8a, illustrates the wing tip deflection difference between the FSI and dynamic FEA for the proposed flapping wing mechanism. According to the Figure 8b, performing FSI analysis causes maximum 0.135 mm difference in the y-axis.

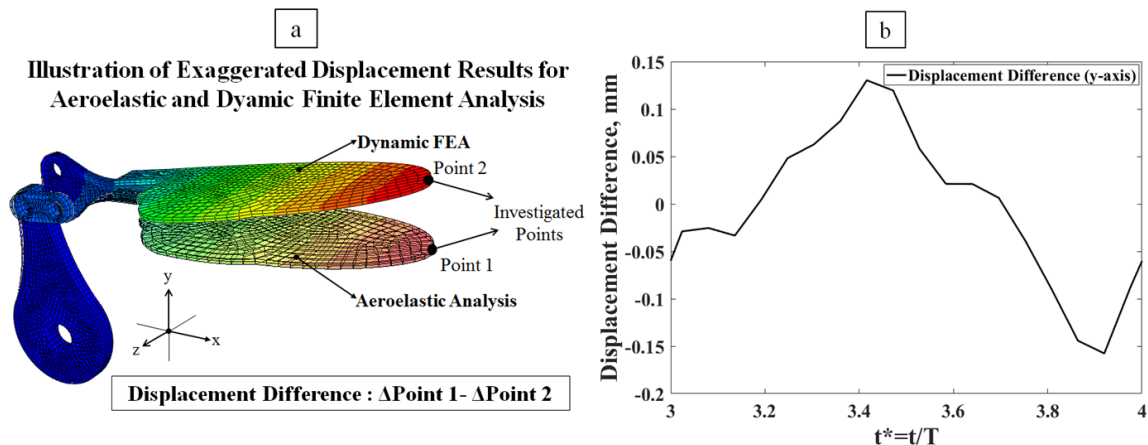


Figure 8: Tip displacement difference between FSI and dynamic FEA analysis in the y-axis

An experimental study is also conducted and compared with the theoretical, FEA and FSI results during the second period as it is given in Fig. 9.

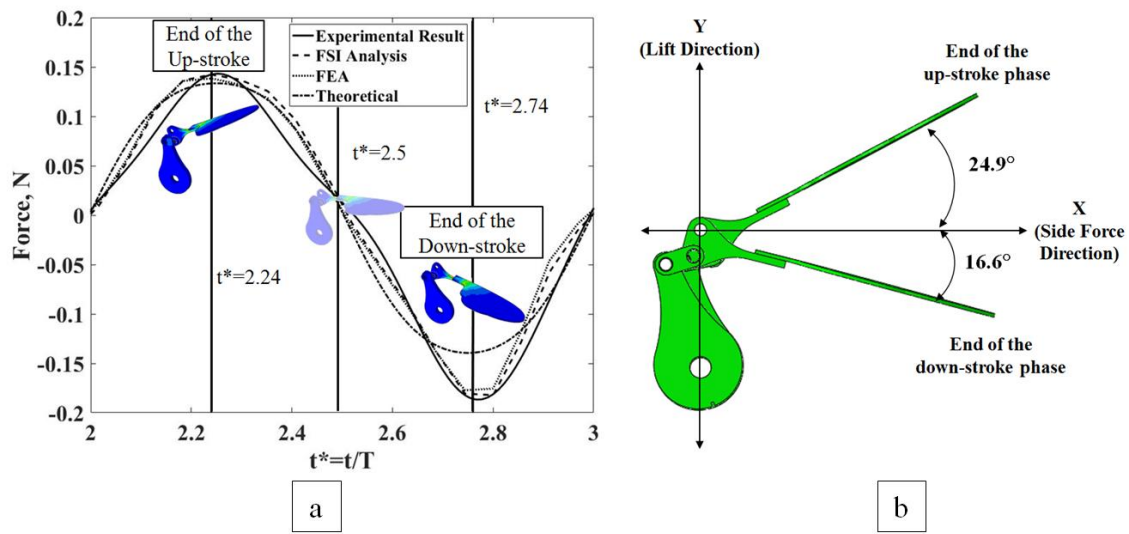


Figure 9: Comparison of the forces in y direction

The maximum and minimum inertial forces for the introduced methods are pin-pointed and given in Table 2.

Table 2: Inertial values at the end of the up-stroke and down-stroke

Method	End of the Up-stroke ($t^*=2.24$)	End of the Down-stroke ($t^*=2.74$)
Experiment	0.143	-0.186
FSI	0.142	-0.182
FEA	0.138	-0.177
Theory	0.133	-0.139

According to Table 2, the maximum and minimum inertial forces obtained in the experiment at the end of the up-stroke ($t^*=2.24$) and down-stroke ($t^*=2.74$) are 0.143 N and -0.186 N, respectively. From Fig. 9, it is evident that the FSI and FEA give the closest result to the experiment compared to the theoretical result. However, since FSI analysis result includes elastodynamics and aerodynamic effects in contradiction of the FEA result which only includes elastodynamics effect, the FSI analysis gives more realistic result to the experimental study as 0.142 N and -0.182 N at the end of the up and down-strokes respectively. During flapping motion, the wing sweeps different angles with respect to the x-axis between 24.9° and -16.6° (Fig. 9b). Thus, the introduced flapping wing mechanism is subject to instantaneous inertial loads. Based on the theoretical study results, the proposed flapping wing mechanism experiences more inertial load at the end of the down-stroke compared to the up-stroke as it is given in Table 2. As a result of this, different wing tip deflection occurs at the end of each stroke phase. In this study, the proposed theoretical formulation is derived based on rigid body dynamics and does not cover the inertial forces created by the elastic effects. It is also noted that, a significant difference is inspected in inertial forces between the theoretical

and experimental result as 7% and 25% for the end of the up-stroke and down-stroke, respectively.

6 CONCLUSIONS

- In this study, a single degree of freedom type four-bar flapping mechanism is introduced and the performed experimental force results are compared with the theoretical, FSI and FEA results. To find the inertial loads created by the proposed flapping wing mechanism theoretical, FEA and FSI analysis studies are conducted. In the theoretical approach, a rigid-body dynamics formulation is derived by finding out the tangential and centripetal forces on the Calliphora Erythrocephala's wing and linkages. Then the lift contribution of the corresponding force is investigated. For FEA, dynamic implicit step is defined and the total inertial forces are found in the lift direction. In FSI analysis, the dynamic structural analysis and CFD domain are created and performed together to find the inertial forces in the lift direction. 0.135 mm tip deflection difference is obtained between performed FSI analysis and FEA for the introduced flapping wing mechanism.
- According to the results obtained, each calculation method used to find the inertial loads in lift direction, the FSI analysis gives the closest result to the experiment result with 0.7% and 2.15% difference at the end of the upstroke and downstroke phases respectively whereas the theoretical result gives the worst result since it does not include elastic effect in its formulation.
- As a future work, the current mechanism is intended to be actuated by use of piezoelectric materials [11] instead of a servo motor to perform sinusoidal flapping motion.

ACKNOWLEDGMENTS

The current work is supported by TUBITAK Project No: 116M273.

REFERENCES

- [1] Syaifuddin, M., Park, H.C. and Goo, N.S., *Design and evaluation of a LIPCA-actuated flapping device*, Smart Materials and Structures, Vol. 15, No. 5, pp. 1225-1230, 2006.
- [2] Senol, G., Arikan, K. B. and Kurtulus, D. F., *Experimental and Numerical Results of a Flapping Wing Four Bar Mechanism*, 55th AIAA Aerospace Sciences Meeting, AIAA Scitech Forum, AIAA 2017-0498, January 9-13, 2017, Grapevine, Texas.
- [3] Senol M.G., Comez F. Y., Kurtulus D. F., Arikan K. B., *Testing of Flapping Wing Four-Bar Mechanism*, Workshop on Non-Intrusive Measurements of Unsteady Flows and Aerodynamics, Poitiers, France, 27-29 October 2015.
- [4] Khan, Z. A. and Agrawal, S.K., *Wing Force and Moment Characterization of Flapping Wings for Micro Air Vehicle Application*, American Control Conference, June 8-10, 2005, Portland, OR, USA.
- [5] Jang, J.H. and Yang, G.H., *Design of Wing Root Rotation Mechanism for Dragon-fly Inspired Micro Air Vehicle*, Appl. Sci., 8, 1868, October 10, 2018.
- [6] Phan, H.V., Au, T.K.L and Park, H.C., *Clap and Fling Mechanism in a Hovering Insect-*

- like Two Winged Flapping Wing Micro Air Vehicle*, R. Soc. Open Sci., 3: 160746, January 16, 2017.
- [7] Mayo, D.B., Lankford, J.L., Benedict and Chopra, I., *Experimental and Computational Analysis of Rigid Flapping Wing for Micro Air Vehicle*, Journal of Aircraft, Vol. 52, No. 4 (2015), pp. 1161-1178, January 20, 2015.
- [8] Qin, Y., Zhang, W., Chen, W., Liu, W., Li, H., Chi, P., Meng, K., Cui and Wu, X., *Flapping Mechanism Design and Aerodynamic Analysis for the Flapping Wing Micro Air Vehicle*, Advanced Materials Research Vols. 291-294, pp. 1543-1546, 2011.
- [9] Cetraro, G. and Sandberg, R. D., *Fluid Structure Interaction simulations of a membrane wing with variable compliance*, 54th AIAA Aerospace Sciences Meeting, AIAA Scitech Forum, AIAA 2016-1351, 4-8 January, 2016, San Diego, California, USA.
- [10] Nakata, T., Liu, H., *A fluid-structure interaction model of insect flight with flexible wings*, Journal of Computational Physics, Volume 231, Issue 4, p. 1822-1847, November 15, 2011.
- [11] Comez Y. F., Senol M.G., Kurtulus D. F., Arikan K.B., *Unsteady Aerodynamic Analysis of a Flapping Wing Actuated with PZT Material*, Workshop on Non-Intrusive Measurements of Unsteady Flows and Aerodynamics, Poitiers, France, 27-29 October 2015.

SEISMIC PERFORMANCE OF ROBOTIC BRIDGE USING SCISSORS SYSTEM

Y. CHIKAHIRO^{*}, S. ZENZAI^{*}, S. SHIMIZU^{*}, I. ARIO[†] AND M. NAKAZAWA[‡]

^{*}Department of Civil and Water Environment
Shinshu University
Wakasato 4-17-1, Nagano, Japan
e-mail: chikahiro@shinshu-u.ac.jp

[†]Department of Civil & Environmental Engineering
Hiroshima University
Kagamiyama 1-3-2, Higashi-Hiroshima, Japan
Email: mario@hiroshima-u.ac.jp

[‡]Department of Civil Engineering
Tohoku Gakuin University
Chuo 1-3-1, Tagajo, Japan
Email: naka@mail.tohoku-gakuin.ac.jp

Key words: Deployable bridge, Scissors-type of robotic bridge, Seismic performance.

Abstract. This paper presents a dynamic characteristics of robotic emergency bridge, called Mobile Bridge, which can be quickly constructed to recovery the damage after a natural disaster. The concept of the bridge is based on the application of a scissor mechanism, which enables its rapid deployment. From the point of to use the Mobile Bridge in disaster area, it is needed to investigate the dynamic behavior by the numerical simulation included both eigenvalue and seismic response analysis. From these results, it was possible to estimate basic mechanical characteristics of dynamic properties of the bridge including reduction of vibration by reinforcement technique. The conducted research allows for better and safer design of the structure of the Mobile Bridge.

1 INTRODUCTION

In recent years, the world has seen several types of natural disasters that have caused many critical situations in the lives of people by damage of an infrastructure. It is important to rebuild the damaged traffic routes immediately in such serious situations in order to facilitate quick relief and restoration activities. An emergency bridge is a specialized bridge designed for short time construction. Typical emergency bridges, for example, the Bailey bridge proposed by D. Bailey in 1943, are modularized truss bridges. It is possible to design different types of bridge configurations by the combination of modularized bridge panels [1]. However, prefabricated truss block type bridges require construction yards and heavy machinery on site. Even some erectable bridges which are possible to build up manually, require a number of

considerable skilled human resources, sometimes over a hundred workers.

Therefore the authors have proposed a rapidly and easily constructible emergency bridge using a deployable system, called Mobile Bridge (herein called MB). It is based on the concept of the Origami skill [2] and Multi-Folding Micro structures (MFM) theory [3]. The original structural form of the MB, in its patent [4], is similar to a scissor system [5] for its structural form. The design concept of the MB enables the reduction of construction time on site by deploying the structural frame directly over a damaged bridge or road. Research development of the MB began with a small footbridge as a prototype [6] which used patented technology. The expansion time depended on the person performing operation, and was approximately 2 mins. After the successful development of the footbridge, research focused on the live loading both pedestrian and vehicle. A prototype of the full-scaled MB was created, MB version 1.0 [7], The MB1.0 demonstrated its potential for the live loading of the traffic weight using a vehicle. Based on this experimental demonstration using the MB1.0, the current model, the MB4.0 with a length of approximately 20m and height of approximately 2m was created [8]. The expansion process can be easily controlled and it looks only 5 mins for the bridge to be fully deployed.

This presented research reviews fundamental dynamic analysis of the pedestrian type of the MB (herein called prototype). In the case of deployable structures, as well as the static analysis of different configurations, it is important to investigate dynamic behaviour of the system. The high compliance and flexibility of the scissors-type bridge may influence the comfort and safety of users in case of heavy dynamic loads such as human induced impacts, wind gusts, or earthquakes. Therefore, numerical simulation included both eigenvalue and seismic response analysis was performed. From these considerations, it was possible to estimate basic mechanical characteristics of dynamic properties of the bridge. The conducted research allows for better and safer design of the structure of the MB.

2 NUMERICAL MODEL

In case of the deployable structures which have completely different configurations by change of their structural forms, investigation of the dynamic behavior is so important due to their flexibility. Hence, we carried out numerical simulation and experimental testing for the prototype to find out the fundamental dynamics of the MB, that is natural frequency and vibration mode. Besides, the seismic response analysis is performed by assuming the use of the MB in the disaster area.

2.1 FE model

The prototype used in this research has a span of approximately 6.1m and a height of 0.5m. The main structural members of the bridge are fabricated using extruded aluminum alloy A6063. The material of the shafts connecting main frame is assumed to be same with scissors member, and the total mass of the bridge is less than 100kg. The FE numerical model is created using MSC Marc 2016 which is one of the major nonlinear finite element software. The model is represented in 3D by use of beam elements. The pivot part which is connecting two components is allowed to rotate without any friction. Besides, the damping of the bridge dynamics is assumed as Rayleigh damping model. Detail modeling method can be found

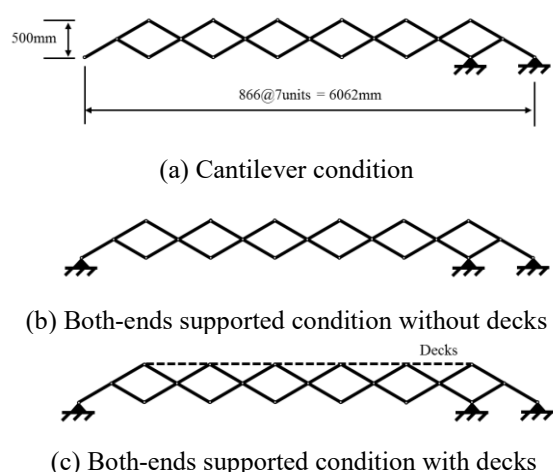


Figure 1: Change of boundary condition according to deployable action

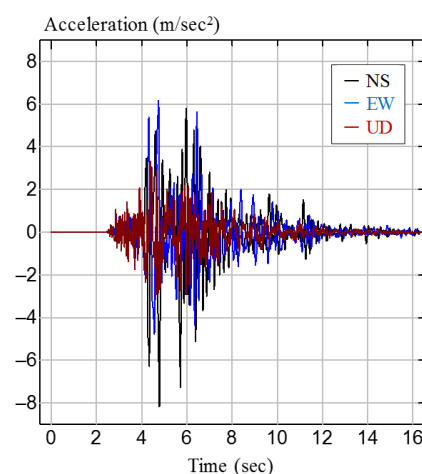


Figure 2: Acceleration response on time of Kobe earthquake

in our previous paper [7].

2.2 Boundary condition

This research examined the basic dynamic characteristics of the MB under two sets of boundary conditions. During the deployment phase, the bridge is supported only at one end resulting in cantilever boundary conditions (see **Figure 1** (a)). Once deployed, the bridge has two supports hence the deployed, second condition is the simply supported beam case, where the supports have horizontal and vertical displacement constraint (see **Figure 1** (b)). After finishing construction, the pedestrian bridge is set on the upper decks aligned at the line of top hinges (see **Figure 1** (c)).

2.3 Seismic load

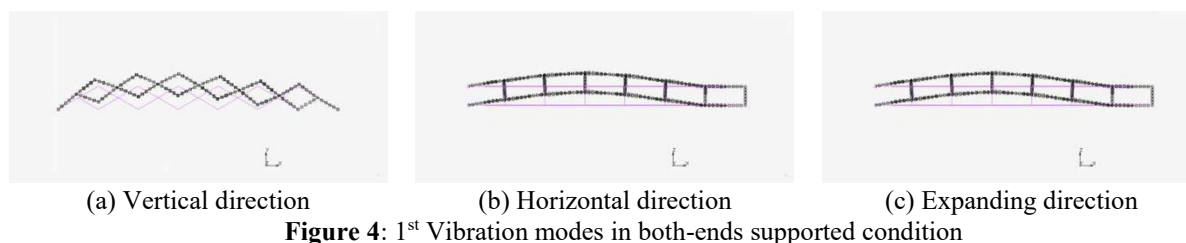
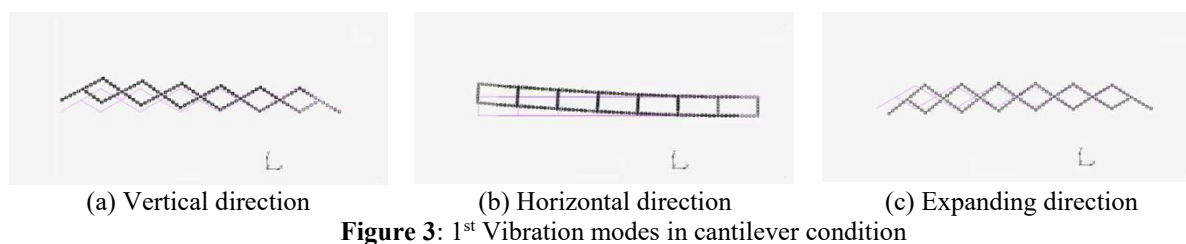
The dynamic data from the Kobe earthquake (1995) observed by the Japan Metrological Agency (JMA) was utilized to model the ground acceleration acting on the bridge as shown in **Figure 2**. In this research three directions, that is North-South (NS), East-West (EW) and Up-Down (UD) direction, are considered. A relatively high acceleration which resulted in severe damage to structures was observed in the North-South (NS) direction at approximately 5 sec., and it was equal to 8.2m/s^2 . These accelerations were applied to the considered FE model as seismic excitation.

3 NUMERICAL RESULT

Primary numerical results in cantilever and both-ends supported conditions without decks are described.

3.1 Eigenvalue analysis for natural frequency

The considered problem was the eigenvalue analysis aimed at finding the frequencies of free vibrations and the corresponding vibration modes. Although the MB has geometric



nonlinearity which affect to the stiffness of the bridge according to its expansion angle, in this paper, we present the results of the eigenvalue analysis for particular expanding angle as local linearization problem.

The numerical result for the prototype under cantilever condition showed that the frequencies for the 1st modes for the vertical direction, horizontal direction and expanding direction were 2.6Hz, 2.6Hz and 4.6Hz as shown in **Figure 3**. Similarly, the 1st modes under both-ends supported condition were 12.0Hz in the vertical direction, 12.6Hz in the horizontal direction and 19.0Hz in the vertical direction as shown in **Figure 4**. These results indicate that in the case of the prototype, the vibrations in the horizontal direction are stronger than those in the vertical and expanding direction. Besides, we can see that the vibration modes of the scissor bridge are generally similar to the beam structure. Therefore, special attention has to be paid to the in-plane vibrations when a pedestrian type of the MB is installed on-site.

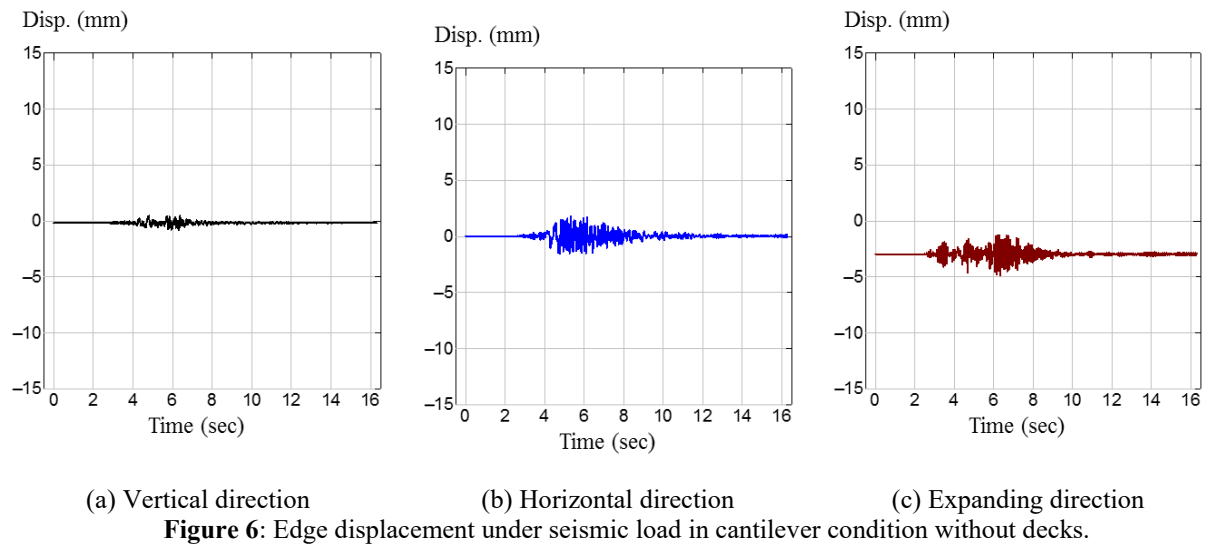
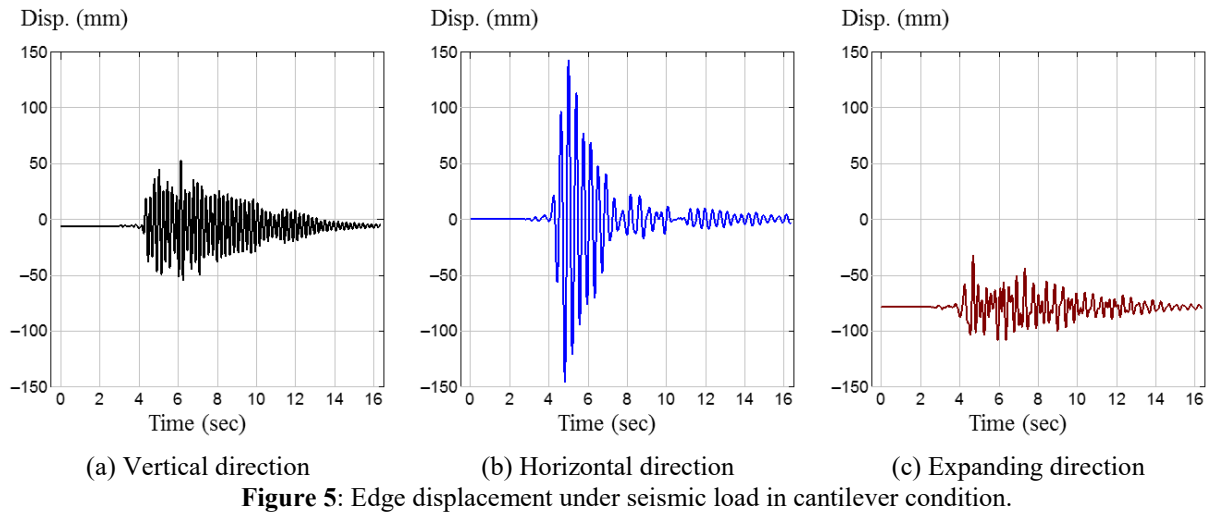
3.2 Seismic response analysis

The numerical results of time-displacement relationship under the earthquake are shown in **Figure 5** and **Figure 6**. **Figure 5** shows the result in fully deployment focused on the bottom hinge of the edge member. In this case, the vibration in horizontal direction has high response in comparison with the vertical and expansion direction. The maximum amplitude of the vibration for the horizontal direction is approximately 145mm, and this result is over 3 times higher than vertical direction and 4 times higher than expanding direction. **Figure 6** shows the result after finishing construction focused on the bottom hinge at the middle of the bridge. The central displacement is not so large value during the earthquake compared with the cantilever condition. The maximum amplitude of the vibration for the horizontal direction is approximately 2mm, and the value become less than 1/30 times than that of cantilever condition. Therefore the bridge should be careful during expanding case in design stage.

Further results including seismic behavior with decks and live load are presented in the conference.

4 CONCLUSIONS

This paper reviewed the dynamic characteristics of the MB based on the experimental



pedestrian bridge. The eigenvalue analysis revealed the basic vibration modes of the prototype and indicated that major vibration of the scissoring bridge was dependent on its boundary conditions.

Thus, it is more susceptible to vibration in the horizontal direction than in the vertical direction after installation. Besides, we found that the vibration modes of the longer scissor bridge are generally similar to the discreted beam structure. This tendency was also found from the seismic response analysis. The horizontal vibration of the prototype was dominant in both cantilever and both-ends supported conditions, and maximum vibration amplitude was 3 - 4 times higher than another direction. Therefore, special attention has to be paid for the in-plane vibrations when a pedestrian type of the MB is installed on-site, especially in fully deployment state. The conducted research allows for better and safer design of the MB. We would like to tackle to reduction and/or control of this flexible bridge by optimal reinforcement or using traditional mass damper in the future studies.

ACKNOWLEDGEMENT

This research has been partially supported by Grant-in-Aid for Early-Career Scientists JP18K13818 in 2018 – 2020 and Grant-in-Aid for Challenging Exploratory Research JP18K18888 in 2018 – 2020. The author wishes to thank my undergraduate students, Mr. Hayashi and Mr. Minami, for their continuous supports.

REFERENCES

- [1] Haskins, J. (1992). One more river to cross. New York: Scholastic Incorporated.
- [2] Hunt, G. W., & Ario, I. (2005). Twist buckling and the foldable cylinder: an exercise in origami. *International Journal of Non-Linear Mechanics*, 40(6), 833-843.
- [3] Holnicki-Szulc, J. (Ed.). (2008). Smart technologies for safety engineering. *John Wiley & Sons*.
- [4] Ario, I. (2006). Structure with the expanding and folding equipment as a patent (No.2006037668) registered in 2012, Japan.
- [5] Pinero, E. P. (1965). Three Dimensional Reticular Structure, United States Patent 3, 185, 164.
- [6] Ario, I., Nakazawa, M., Tanaka, Y., Tanikura, I., Ono, S. (2013). Development of a prototype deployable bridge based on origami skill. *Automation in Construction*, 32, 104-111.
- [7] Chikahiro, Y., Ario, I., Nakazawa, M., Ono, S., Holnicki-Szulc, J., Pawlowski, P., ... & Watson, A. (2016). Experimental and numerical study of full-scale scissor type bridge. *Automation in Construction*, 71, 171-180.
- [8] Hama, Y., Ario, I., Chikahiro, Y., Adachi, K., Watoson, A. (2017). Origami-inspired deployable & movable bridge for disaster relief, *proc. of FootBridge 2017 in Berlin*.

SHAPE MEMORY ALLOYS AS PIPE JOINTS: APPLICABILITY AS VIBRATION ATTENUATORS TO DRILL-STRINGS CONSIDERING UNCERTAINTIES

Raphael S. Silva^{*}, Thiago G. Ritto^{*} and Marcelo A. Savi[†]

^{*} Laboratory of Acoustics and Vibration (LAVI/COPPE)

Federal University of Rio de Janeiro (UFRJ)

Centro de Tecnologia, I-130, Cidade Universitária, Rio de Janeiro-RJ, Brazil

e-mail: raphaelsantana@poli.ufrj.br, web page: <http://www.lavi.coppe.ufrj.br>

^{*}e-mail: tritto@mecanica.ufrj.br, web page: <http://www.lavi.coppe.ufrj.br>

[†] Center for Nonlinear Dynamics (MECANON/COPPE)

Federal University of Rio de Janeiro (UFRJ)

Centro de Tecnologia, I-128D, Cidade Universitária, Rio de Janeiro-RJ, Brazil

Email: savi@mecanica.ufrj.br - Web page: <http://www.mecanon.coppe.ufrj.br>

Key words: Shape Memory Alloy, Drilling, Drill-string Joints, Uncertainties Quantification

Abstract. For decades, several researches with shape memory alloys focused on pipe coupling by taking advantage of shape memory effect in assembly. This application can avoid problems such as loosening on traditional threaded tool joints, but an added benefit on its dynamics was never discussed. This paper investigates the use of shape memory alloys as pipe joints on drill-string dynamics. The idea is to evaluate the hysteretic behavior's influence of the superelastic effect and the attenuation of severe torsional vibration, especially stick-slip oscillations. A simplified lumped parameter model is used to model the torsional dynamics of the drill-string, with imposed angular speed at the top and a nonlinear bit-rock interaction at the bottom. This simplified model is validated through finite element analysis. Thermomechanical behavior of SMA is described using a constitutive model proposed by Lagoudas. The numerical results show strong dependence of the system torsional oscillations on temperature and austenitic elastic modulus of the selected material in some drilling conditions as weight on bit and top angular speed. In order to evaluate the impact of SMA uncertainties on the system dynamic response, the material parameters are modeled as random variables, and Monte Carlo simulations are performed to estimate the statistics of permanent response. The random stability map is obtained for different values of weight on bit and top angular velocity. The stick-slip severity factor, which is a measure of the amplitude of the torsional vibration, is computed for this purpose. Overall, this work stands that the main variables in drilling operation can be improved by the introduction of an admissible length of SMA connection, and it brings new perspectives to smart material adoption in a very significant mechanical system.

1 INTRODUCTION

Over this century, mechanical systems have incorporated special materials capable of *smart* behavior. Among such metals, Ni-Ti and others shape memory alloys (SMAs) have close interest to the offshore industry such in applications as pipe joints¹ and actuators.² Particularly, the tubing solution also presented by Schlumberger® have not been completely studied for their impact on the dynamics.

For the SMA, this work is interested on the pseudoelastic effect, or also called superelasticity, which is a phenomenological effect that occurs above the austenitic temperature and comes from the transformation cycle between austenite - detwinned martensite - austenite.³ Fig. 1 illustrate this phenomenon by showing an experimental result where the hysteresis loop can be seen in force-displacement diagram of load-unload history.

Based on this matter, we focused on the application to drilling operation, where force and torque are transmitted from a drilling rig to the drill bit through a drill-string. In this system, torsional oscillations, such as stick-slip phenomenon caused by the bit-rock interaction⁴, may occur frequently and causes several damages to its tools. This can be catastrophic to the operation and must be avoided.

This work aims to combine the use of SMAs as a pipe joints¹ and the application in tubes⁵ which brought notice to SMA as torque tubes with high energy density and low mass density. As certain parameters could have huge impact in the system's response, uncertainties quantification of the drilling operation and the material characterization are explored by a stochastic evaluation.

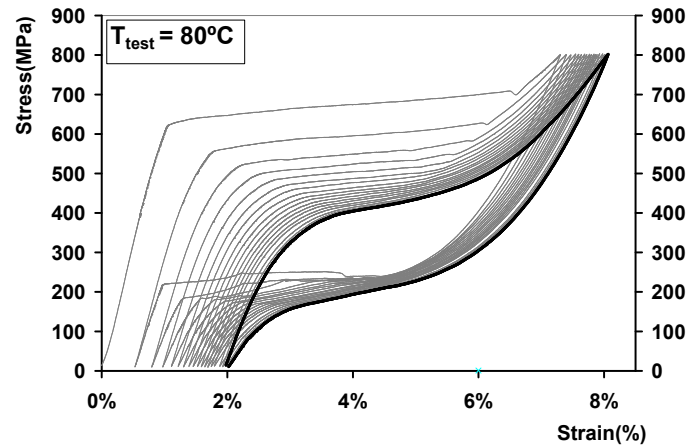


Figure 1: Experimental results for training via isothermal cycling of stress (Source: Hartl and Lagoudas³).

2 MATHEMATICAL MODEL

This work considers a lumped parameter approach of a drill-string and the obtained results are validated by a finite element analysis performed with ABAQUS. As for the shape memory alloy, we use a constitutive model to account for the pseudoelastic effect. Again, we validate it using the pseudoelasticity model present in ABAQUS, which is based in an alternative constitutive model.

2.1 SMA constitutive model

In 2012, Lagoudas et al.⁶ proposed a phenomenological model to describe the shape memory effect and the pseudoelasticity that has been used in several mechanical models including the previous

application analysis designed by UFRJ workgroup^{7,8}. In 2016, Enemark et al.⁹ presented a reduction for one dimensional shearing, so that the Lagoudas constitutive model can be expressed in terms of the stress-strain relationship as

$$\tau = G_{SMA} (\gamma - \gamma_t) \quad (1)$$

where τ is the shear stress; G_{SMA} is the shear modulus; γ is the engineering shear strain; and γ_t is the phase transformation strain. Fig. 2 depicts Eq. 1. Moreover, G and γ_t , which are time dependents, can be written as

$$G_{SMA} = (G_A + (G_M - G_A) \xi) \quad (2a)$$

$$\dot{\gamma}_t = \dot{\xi} \Lambda, \quad \Lambda = \begin{cases} \Lambda_f = \sqrt{3} \text{sgn}(\tau) H & , \dot{\xi} > 0 \\ \Lambda_r = \frac{1}{\tilde{\xi}} \tilde{\gamma}_t & , \dot{\xi} < 0 \end{cases} \quad (2b)$$

with G being the shear modulus and the subscript A and M standing for austenite and martensite phase, respectively; ξ is the martensite volume fraction (belonging to interval $0 \leq \xi \leq 1$); Λ is the phase transformation direction, with the subscripts, Λ_f and Λ_r , standing for the forward and reverse direction; $\text{sgn}(\tau)$ is the sign of τ ; H is the maximum transformation strain, considered constant in this investigation; and the dot notation, $\dot{\gamma}_t$ and $\dot{\xi}$, stands for evolution while the tilde notation, $\tilde{\gamma}_t$ and $\tilde{\xi}$, indicates that the value should be taken at change in phase transformation direction.

For the evolution equations, there are transformation functions for the forward and reverse transformation, that together with the Kuhn-Tucker conditions control whether phase transformations take place.

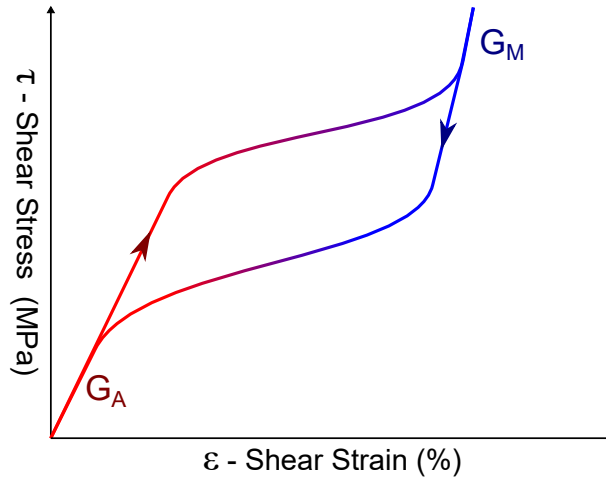


Figure 2: Stress-strain relationship for SMA pseudoelasticity effect in pure torsion.

2.2 Drill-string equations

The drill-string can be modeled as a linear torsional pendulum using lumped parameters.^{10,11} This simplification offers a low computational cost with great agreements to the continuum model. To include the nonlinear effect of the shape memory alloy, small modifications were made by adding the SMA stiffness in the joint. Figure 3 shows a schematic representation of the proposed model. The governing equations here presented in Eq. 3(a-h) were adapted from Navarro and Lopez¹² formulation and used for the case of constant angular velocity applied in the rotary table, at the top

$$\ddot{\phi}_r = 0 \quad (3a)$$

$$\ddot{\phi}_1 = \frac{c_{SMA} + c_{tc}}{I_c}(\dot{\phi}_r - \dot{\phi}_1) + \frac{k_{SMA} + k_{tc}}{I_c}(\phi_r - \phi_1) - \frac{c_t}{I_c}(\dot{\phi}_1 - \dot{\phi}_2) - \frac{k_t}{I_c}(\phi_1 - \phi_2) \quad (3b)$$

$$\ddot{\phi}_2 = \frac{c_t}{I_p}(\dot{\phi}_1 - \dot{\phi}_2) + \frac{k_t}{I_p}(\phi_1 - \phi_2) - \frac{c_{SMA} + c_{tc}}{I_p}(\dot{\phi}_2 - \dot{\phi}_3) - \frac{k_{SMA} + k_{tc}}{I_p}(\phi_2 - \phi_3) \quad (3c)$$

$$\vdots$$

$$\ddot{\phi}_{j-1} = \frac{c_{SMA} + c_{tc}}{I_c}(\dot{\phi}_{j-2} - \dot{\phi}_{j-1}) + \frac{k_{SMA} + k_{tc}}{I_c}(\phi_{j-2} - \phi_{j-1}) - \frac{c_t}{I_c}(\dot{\phi}_j - \dot{\phi}_{j-1}) - \frac{k_t}{I_c}(\phi_j - \phi_{j-1}) \quad (3d)$$

$$\ddot{\phi}_j = \frac{c_t}{I_p}(\dot{\phi}_{j-1} - \dot{\phi}_j) + \frac{k_t}{I_p}(\phi_{j-1} - \phi_j) - \frac{c_{SMA} + c_{tc}}{I_p}(\dot{\phi}_j - \dot{\phi}_{j+1}) - \frac{k_{SMA} + k_{tc}}{I_p}(\phi_j - \phi_{j+1}) \quad (3e)$$

$$\vdots$$

$$\ddot{\phi}_n = \frac{c_{tc} + c_{SMA}}{I_p}(\dot{\phi}_{n-1} - \dot{\phi}_n) + \frac{k_{tc} + k_{SMA}}{I_p}(\phi_{n-1} - \phi_n) - \frac{c_{tl}}{I_p}(\dot{\phi}_n - \dot{\phi}_l) - \frac{k_{tl}}{I_p}(\phi_n - \phi_l) \quad (3f)$$

$$\ddot{\phi}_l = \frac{c_{tl}}{I_l}(\dot{\phi}_n - \dot{\phi}_l) + \frac{k_{tl}}{I_l}(\phi_n - \phi_l) - \frac{c_{tb}}{I_l}(\dot{\phi}_l - \dot{\phi}_b) - \frac{k_{tb}}{I_l}(\phi_l - \phi_b) \quad (3g)$$

$$\ddot{\phi}_b = \frac{c_{tb}}{I_b}(\dot{\phi}_l - \dot{\phi}_b) + \frac{k_{tb}}{I_b}(\phi_l - \phi_b) - \frac{T_{ob}}{I_b} \quad (3h)$$

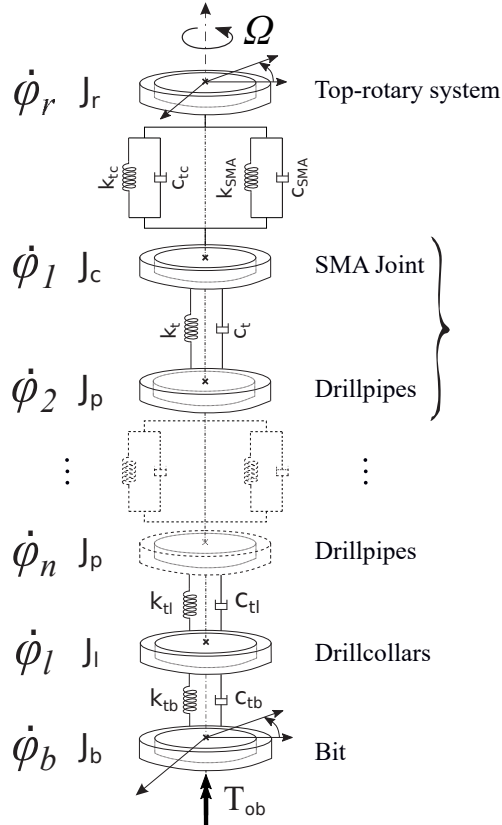


Figure 3: Drillstring schematics. SMA joint added to original Navarro-Lopez and Cortes¹² formulation.

where φ_i , $\dot{\varphi}_i$, $\ddot{\varphi}_i$ ($i \in \{r, 1, 2, \dots, j-1, j, \dots, n, l, b\}$) are the angular position, velocity and accelerations with the subscripts standing for: r , the top-rotary system; 1 to n , the drill-pipes parts; l , the drill collars; and, b , the bit. The inertias, I_i ($i \in \{c, p, l, b\}$), are in agreement with the locations of the drill-pipes, p , coupling components, c , the drill-collars, l , and the bit, b . These inertias are connected by linear torsional springs (k_t , k_{tl} and k_{tb}), nonlinear torsional springs (k_{SMA}) and viscous torsional dampers (c_t , c_{tl} , c_{tb} and c_{SMA}) in order to represent the dynamics as a mass-spring-damper of this rotating system.

For the nonlinear torsional stiffness, representing the SMA's pseudoelasticity, we can define the expression as

$$k_{SMA} = \frac{G_{SMA} J_c}{L_c} = \frac{J_c}{2L_c(1+\nu)} (E_A + (E_M - E_A)\xi) \quad (4)$$

where J_c is the polar moment of inertia of the cross-sectional area; and L_c is the length of the coupling. Again, the dependencies of G_{SMA} to the current temperature and phase transformation are implicit.

Additionally, n is an even number and, in this case, the system of $n + 3$ Degrees of Freedom (DOF), can be represented as a $2n + 6$ DOF set of first-order Ordinary Differential Equation (ODE) in the state-space representation. Moreover, by integration over time, using a MATLAB integrator, they can be solved for positions and velocities.

2.3 Bit-rock interaction

The bit-rock interaction is the second source of nonlinearity presented in the governing equations. In order to estimate it, several authors have tried to capture their essential dynamic properties of interest.^{11, 13} This work uses a simplified model based in a regularization on the classical Coulomb's dry friction model (as presented by Lin and Wang¹⁴, with regularization near to zero angular velocity) expressed in Eq. 5 which is a non-smooth but simple and continuous torque on bit model.

$$T_{ob} = W_{ob} r_b \begin{cases} \mu_s \frac{\dot{\varphi}_b}{\omega_{reg}} & , \dot{\varphi}_b \leq \omega_{reg} \\ \mu_c + (\mu_s - \mu_c) \exp(-d_c (\dot{\varphi}_b - \omega_{reg})) & , \dot{\varphi}_b > \omega_{reg} \end{cases} \quad (5)$$

where W_{ob} is the Weight on bit; ω_{reg} is the transition velocity between the regularized *stick* and *slip* zone r_b is the bit radius; μ_s is the static friction coefficient for the *stick* zone; μ_c is the kinetic friction coefficient for the *slip* zone; d_c is the exponential decay of transition between static and kinetic friction; and ω_{reg} is the regularization and defines the *stick* zone. All parameters must be calibrated from experimental or field data.

2.4 Stochastic evaluation

The stochastic evaluation of the deterministic results here presented tries to determine which parameters uncertainties could cause significant changes in the drill-string oscillatory dynamics. Preliminary results have showed that the martensite and austenite modulus of elasticity needed further investigation due to their uncertainties effect in the stick-slip mitigation.

For the elastic modulus, we can state that the support must be positive and nonzero, so $E_A, E_M \in (0, \infty)$. In addition, it's a usual procedure for stiffness to guarantee that its expectation must be positive and not infinity. Thus, we avoid the indetermination on the compliance tensor of division by zero.

Finally, we can address the probability distribution function (PDF), by means of the maximum entropy principle, as follows in Eq. 6(a-c).

$$E_A \sim \text{GAMMA}(100, 0.7) \quad (6a)$$

$$E_M \sim \text{GAMMA}(100, 0.3) \quad (6b)$$

These PDFs are used to perform a Monte Carlo's simulation for the parametric evaluation varying the weight on bit (W_{OB}) and Angular velocity at the top rotary table (Ω). Similar analysis was previously done by Nogueira and Ritto¹⁶, which presented the probability map we are interest in.

3 DETERMINISTIC RESULTS

The drill-string here considered is based on the same analyzed by Ritto et al.¹¹ The geometry and material properties are described in Tab. 1- 2. This choice was made due to the experimental data provided so the bit-rock interaction could be calibrated to match those data.

The system behavior is illustrated in Fig. 4 for three values of W_{ob} , with the same top angular velocity being prescribed constant, i.e., $\dot{\phi}_r = 100 \text{ rpm}$. At these three pairs, we can see that at $W_{ob} = 100 \text{ kN}$ we have an condition of great drilling operation from its torsional dynamics. However, at $W_{ob} = 150, 200 \text{ kN}$ we can observe torsional oscillations that are recurrent over time. This behavior is unwanted during operation because can cause failure over drill-string tools, resulting in a catastrophic rupture of pipes. To quantify it, authors have used an indicator of torsional vibration severity, also named as stick-slip severity, Eq. 7.

$$S_{SS} = \frac{\max(\dot{\phi}_b) - \min(\dot{\phi}_b)}{2\Omega} \cdot 100\% \quad (7)$$

Table 1: Drill-string geometry and drilling parameters

$J_r = 134 \text{ kg m}^2$	$J_c = 13 \text{ kg m}^2$	$J_p = 134 \text{ kg m}^2$	$J_l = 235 \text{ kg m}^2$
$J_b = 471.9698 \text{ kg m}^2$	$\omega_{reg} = 3 \text{ RPM}$	$W_{ob} = 120 \text{ kN}$	$\Omega = 100 \text{ RPM}$
$k_t = 3.08 \text{ kN m/rad}$	$k_{tc} = 0.31 \text{ kN m/rad}$	$k_{tl} = 38.55 \text{ kN m/rad}$	$k_{tb} = 687.41 \text{ kN m/rad}$
$c_t = 1.24 \text{ kN m s/rad}$	$c_{tc} = 0.12 \text{ kN m s/rad}$	$c_{tl} = 15.42 \text{ kN m s/rad}$	$c_{tb} = 274.87 \text{ kN m s/rad}$
$\mu_c = 0.65$	$\mu_s = 1.5$	$d_c = 0.5$	$r_b = 0.4 \text{ m}$

Table 2: Steel and shape memory alloy material parameters

$E_{steel} = 206.8 \text{ GPa}$	$\nu_{steel} = 0.28$	$\alpha = 0.05$	$\beta = 0.4$
$H = 0.04$	$E_A = 30 \text{ GPa}$	$E_M = 70 \text{ GPa}$	$\nu = 0.3$
$C_A = 6 \text{ MPa/K}$	$C_M = 7 \text{ MPa/K}$	$A_s = 30^\circ \text{ C}$	$A_f = 43^\circ \text{ C}$
$M_s = 30^\circ \text{ C}$	$M_f = 20^\circ \text{ C}$	$n_s = \{.1 \ .1 \ .2 \ .2\}^T$	

To compare the effect on drill-string dynamics of the SMA tool joint, we use the same pairs of W_{OB} and $\dot{\phi}_r$ presented earlier and the new results are presented in Fig. 5. We can see that the angular velocity amplitudes were decreased in each W_{ob} compared. In fact, for $W_{ob} = 150 \text{ kN}$, it attenuates torsional vibrations. These results were compared with a finite element analysis, modeled in ABAQUS.

For the SMA joint, we present in Fig. 6 the evolution of the martensite volume fraction and the stress-strain relationship for three positions in the drillpipes: one close to the top rotary table, one in middle and another one close to the BHA. Also, the results are shown for two conditions, one with large torsional amplitude vibration and other with stable velocity at the bit.

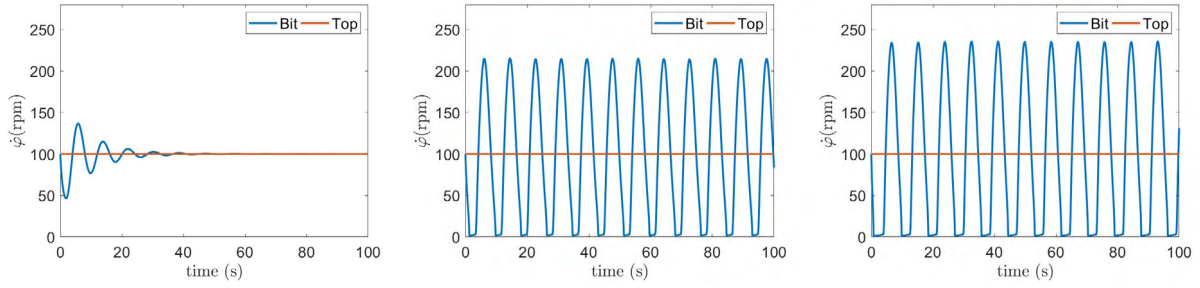


Figure 4: Deterministic results for drill-string angular velocities, ϕ_b and ϕ_r , without SMA joint. From left to right: $W_{ob} = 100, 150$ and 200 kN.

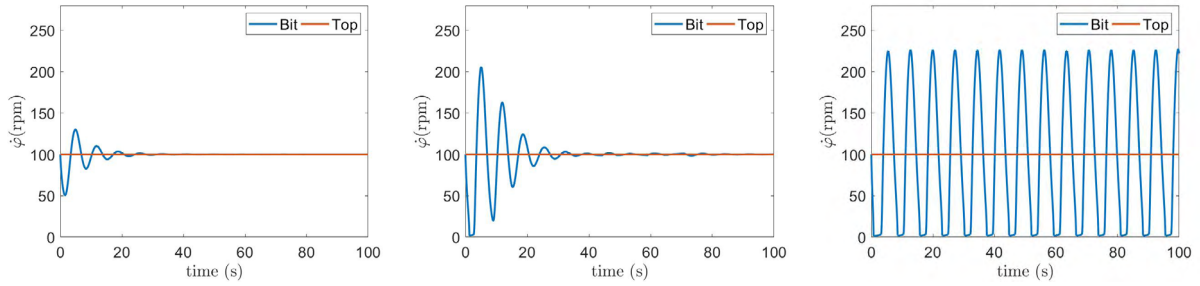


Figure 5: Deterministic results for a drill-string angular velocities, ϕ_b and ϕ_r , with SMA joint. From left to right: $W_{ob} = 150$ and 200 kN.

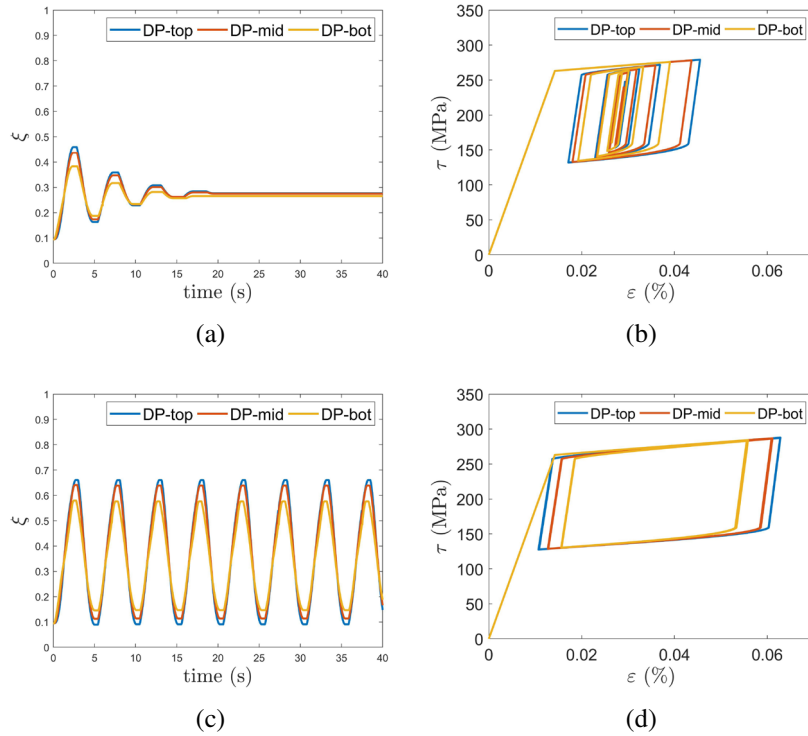


Figure 6: Deterministic results of the SMA joint, martensite volume fraction over time, $\xi(t)$, and stress-strain relationship, $\tau - \epsilon$, with SMA joint. For (a) and (b), $W_{ob} = 150$; and, for (c) and (d), $W_{ob} = 200$ kN.

The outcomes from Figs. 4-5 also led to a parametric investigation of SMA joint effect in different pairs of $(\dot{\phi}_r, W_{ob})$. This evaluation was done in Matlab due to lower computational cost when compared with ABAQUS. Fig. 7 presents the results for different parameters of drilling operation.

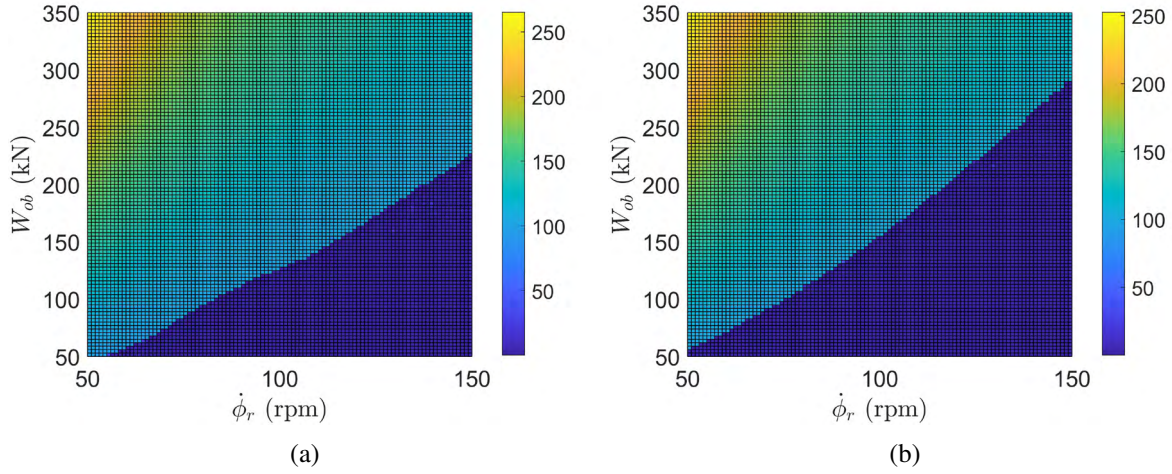


Figure 7: Parametric evaluation of torsional stability (a) without and (b) with SMA joint. Colors indicate the torsional vibration severity factor, S_{SS} .

4 STOCHASTIC RESULTS

For the stochastic evaluation, we run a Monte Carlo's simulations in a 40 by 40 grid of $(\dot{\phi}_r, W_{ob})$ pairs. We consider the uncertainties separately so we could assess the effects of austenite and martensite elastic modulus into the stability map. To determine the agreement of these simulations in the system response, for each point, we observe the convergence in quadratic mean for the angular velocity at the bit. For 50 simulations, we could see it converging. Therefore, Fig. 8 presents the probability of each point in the map to have stick-slip, i.e. $S_{SS} > 80$.

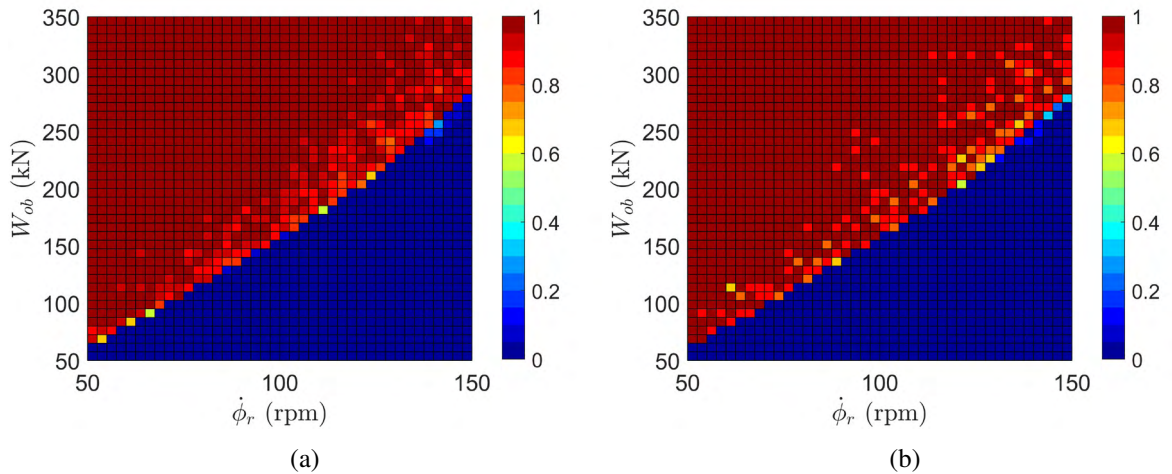


Figure 8: Stochastic parametric evaluation of drill-string's torsional vibrations with SMA joint. Analysis for (a) E_A and (b) E_M . Colors indicate the occurrence probability of large torsional oscillations.

From Fig. 8 we can see that occurrence zone of stick-slip, on this map in red, is the most altered zone in both stochastic analysis.

5 CONCLUSIONS

It follows from the deterministic and stochastic analyses here presented:

- The introduction of the SMA joint gives a broader spectrum of safe operation due to damping introduced by the SMA coupling. Fig. 7 shows that the effect into this verge varies different for each W_{ob} and $\dot{\phi}_r$.
- The choice of the shape memory alloy is important to the drilling system because the new drill-string dynamics depends on it. In this work, we chose the SMA as experimental data was available at our laboratory. Optimal material parameters could be determined in order to maximize the attenuation behavior introduced by hysteresis.
- The stochastic analysis presented the response dependency of SMA material parameters, by showing changes in the parametric evaluation of two random gamma distributions with coefficients of variation of only 15%. It suggests that, for different values of E_A or E_M , the verge dividing stability and stick-slip could be different, but, luckily, the effect could be to increase the safe region of torsional vibrations.

REFERENCES

- ¹ Lewis, P. and Vasquez, M. (2013) Shape Memory Alloy: Low-Cost Manufacturing for the Oil and Gas Industry. In *Offshore Technology Conference*. Offshore Technology Conference.
- ² Patil, D. and Song, G. (2016) Shape memory alloy actuated accumulator for ultra-deepwater oil and gas exploration. *Smart Materials and Structures*, **25**(4).
- ³ Hartl, D.J. and Lagoudas, D.C. (2007) Aerospace applications of shape memory alloys. *Proceedings of the Institution of Mechanical Engineers, Part G: Journal of Aerospace Engineering*, **221**(4): 535–552.
- ⁴ Lobo, D.M., Ritto, T.G. and Castello, D. A. (2017) Stochastic analysis of torsional drill-string vibrations considering the passage from a soft to a harder rock layer. *Journal of the Brazilian Society of Mechanical Sciences and Engineering*, **39**(6): 2341–2349.
- ⁵ Jardine, A. P. , Bartley-Cho, J. D. and Flanagan, J.S. (1999) Improved design and performance of the SMA torque tube for the DARPA Smart Wing program. In *Proc. SPIE 3674, Smart Structures and Materials 1999: Industrial and Commercial Applications of Smart Structures Technologies*, p. 260–269.
- ⁶ Lagoudas, D.C., Hartl, D., Chemisky, Y., Machado, L. and Popov, P. (2012) Constitutive model for the numerical analysis of phase transformation in polycrystalline shape memory alloys. In: *International Journal of Plasticity*. **32-33**: 155–183.
- ⁷ Leal, P.B.C. (2016) *Design and optimization of a bias SMA flap actuator in a fluid-structure application*. Master's dissertation, Federal University of Rio de Janeiro.
- ⁸ Silva, R.S. (2018) Analysis of morphing winglets using shape memory alloys. *Master's dissertation*, Federal University of Rio de Janeiro.
- ⁹ Enemark, S., Santos, I. F. and Savi, M.A. (2016). Modelling, characterisation and uncertainties of stabilised pseudoelastic shape memory alloy helical springs. In: *Journal of Intelligent Material Systems and Structures*, **27**(20): 2721-2743.

- ¹⁰ Navarro-López, E.M. and Cortés, D. (2007) *Sliding-mode control of a multi-DOF oilwell drillstring with stick-slip oscillations*. Proceedings of the American Control Conference, 3837–3842.
- ¹¹ Ritto, T.G., Aguiar, R.R. and Hbaieb, S. (2017) *Validation of a drill string dynamical model and torsional stability*. Meccanica, **52**(11-12): 2959–2967.
- ¹² Navarro-López, E.M. and Cortés, D. (2007) *Avoiding harmful oscillations in a drillstring through dynamical analysis*. Journal of Sound and Vibration, **307**(1-2): 152-171.
- ¹³ Real, F.F., Batou, A., Ritto, T.G., Desceliers, C. and Aguiar, R.R. (2018) *Hysteretic bit/rock interaction model to analyze the torsional dynamics of a drill string*. Mechanical Systems and Signal Processing, **111**: 222–233.
- ¹⁴ Lin, Y.Q. and Wang, Y.H. (1991) *Stick-Slip Vibration of Drill Strings*. Journal of Manufacturing Science and Engineering, **113**(1), 38.
- ¹⁵ Ritto, T.G., Soize, C., Sampaio, R. (2009). *Non-linear dynamics of a drill-string with uncertain model of the bit-rock interaction*. In: *International Journal of Non-Linear Mechanics*. **44**(8), 865-876.
- ¹⁶ Nogueira, B.F. and Ritto, T.G. (2018) *Stochastic torsional stability of an oil drill-string*. Meccanica, **53**(11-12): 3047–3060.

INSTRUCTIONS TO PREPARE A FULL PAPER FOR THE IX ECCOMAS THEMATIC CONFERENCE ON SMART STRUCTURES AND MATERIALS - SMART 2019

MARIA A. MUNITSYNA*

*Moscow Institute of Physics and Technology (MIPT)

e-mail: munitsyna@gmail.com

Key words: celt, friction, stability

Abstract. The problem of the motion of a celt on a fixed horizontal plane with viscous friction is considered. On the plane of the parameters of the problem, regions of stability of uniform rotations about the vertical are constructed. The dynamics of transient processes from unstable motions to stable ones is studied.

1 INTRODUCTION

The Celt is a convex solid body, one of its principal central axis of inertia being perpendicular to the surface of the body, and the directions of the principal curvatures of the surface at the point of intersection with this axis are not parallel to the other two principal axes. It is well known that the stability of the rotations of this body around the vertical axis depends from the direction of rotation. In most of the papers devoted to this property, the non-holonomic formulation of the problem is considered; it is assumed that the velocity of the point of contact between the body and the plane is zero (see, for example, [1], [2]). In the paper [4] the motion of the celt on a plane with friction is considered, and the consistency of this formulation of the problem with full-scale experiments is confirmed.

In the present paper, the investigation of [1] is continuing, in which it is assumed that the viscous friction force acts on the stone from the side of the plane. This model of friction allows us to carry out not only numerical, but also analytical studies in the problem. In addition, when the coefficient of viscous friction strives for infinity, the force of viscous friction is realized the non-holonomic constraint [3].

2 STATEMENT OF THE PROBLEM

We will introduce the following variables: \mathbf{v} is the velocity of the mass centre of the celt, ω is its angular velocity and γ is the unit vector of the rising vertical. The slipping velocity is given by the relation $\mathbf{u} = \mathbf{v} + [\omega, \mathbf{r}]$, where \mathbf{r} is the radius vector of the point of contact of the body with the plane, defined by the equation $\gamma = -\text{grad} f(\mathbf{r})/|\text{grad} f(\mathbf{r})|$.

A gravitational force $\mathbf{P} = -mg\gamma$, the normal component of the reaction of the support plane $\mathbf{N} = N\gamma$ and the friction force $\mathbf{F} = -mk\mathbf{u}$ (k is the coefficient of viscous friction) act on the celt. The equations of

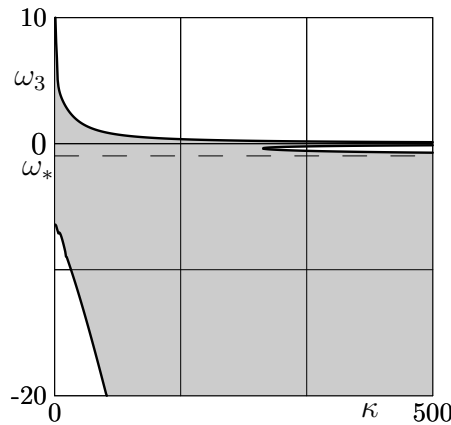


Figure 1: $A_1 = 3 \text{ kg} \cdot \text{m}^2$, $A_2 = 4 \text{ kg} \cdot \text{m}^2$, $A_3 = 5 \text{ kg} \cdot \text{m}^2$, $a_1 = 5 \text{ m}$, $a_2 = 4 \text{ m}$, $a_3 = 3 \text{ m}$, $m = 1 \text{ kg}$, $\delta = 0.75$; $J = 7 \text{ kg} \cdot \text{m}^2$, $\omega_* = -0.97 \text{ s}^{-1}$

its motion in the moving coordinates have the form

$$m\dot{\mathbf{v}} + [\boldsymbol{\omega}, m\mathbf{v}] = (N - mg)\boldsymbol{\gamma} + \mathbf{F} \quad (1)$$

$$\mathbf{J}\dot{\boldsymbol{\omega}} + [\boldsymbol{\omega}, \mathbf{J}\boldsymbol{\omega}] = [\mathbf{r}, N\boldsymbol{\gamma} + \mathbf{F}] \quad (2)$$

$$\dot{\boldsymbol{\gamma}} + [\boldsymbol{\omega}, \boldsymbol{\gamma}] = 0 \quad (3)$$

$$(\mathbf{v} + [\boldsymbol{\omega}, \mathbf{r}], \boldsymbol{\gamma}) = 0 \quad (4)$$

where $\mathbf{J} = \text{diag}(A_1, A_2, A_3)$ is the central inertia tensor or the celt. Eq. ((1)) is the theorem of the change of the momentum of the celt, Eq. (2) is the theorem of the change of the angular momentum, Eq. (3) is the condition for the vector $\boldsymbol{\gamma}$ to be constant in an absolute coordinates, and Eq. (4) is the condition for the celt to be in contact with the supporting plane. The system (1)–(4) is closed with respect to the variables \mathbf{v} , $\boldsymbol{\omega}$, $\boldsymbol{\gamma}$ and N . From this system, the normal reaction of the supporting plane is determined

$$N = m(g + ([\mathbf{r}, \dot{\boldsymbol{\omega}}] + [\dot{\mathbf{r}}, \boldsymbol{\omega}], \boldsymbol{\gamma})) + ([\boldsymbol{\omega}, \mathbf{r}], [\boldsymbol{\omega}, \boldsymbol{\gamma}]) \quad (5)$$

then the system (1)–(3), taking into account Eq. (5) is considered

The resulting system of equations has solutions of the form

$$v_1 = v_2 = v_3 = 0, \quad \gamma_1 = \gamma_2 = 0, \quad \gamma_3 = 1, \quad \omega_1 = \omega_2 = 0, \quad \omega_3 = \omega \quad (\omega \in \mathbb{R}). \quad (6)$$

They correspond to uniform rotations of the elt around the principal axis of inertia which is normal to its surface and coincides with the vertical. The equation of the body surface at $\gamma_3 = 1$ can be represented in the form

$$f(\mathbf{r}) = x_3 + a_3 - \frac{(x_1 \cos \delta + x_2 \sin \delta)^2}{2a_1} - \frac{(x_1 \sin \delta - x_2 \cos \delta)^2}{2a_2} + O_3(x_1, x_2),$$

where a_1 , a_2 – are the main radii of curvature of the body surface at the point of contact, a_3 – is the height of the center of mass, δ — is the angle between the vectors of principal curvatures and principal axes (for celt the relations are satisfied $A_1 \neq A_2$, $a_1 \neq a_2$, $\delta \neq 0 \pmod{\pi/2}$).

3 STABILITY CONDITIONS

Linearized equations of perturbed motion of the system in the neighborhood of solutions Eq. (6) and the corresponding characteristic equation are in [1]. In the case of non-holonomic statement of the

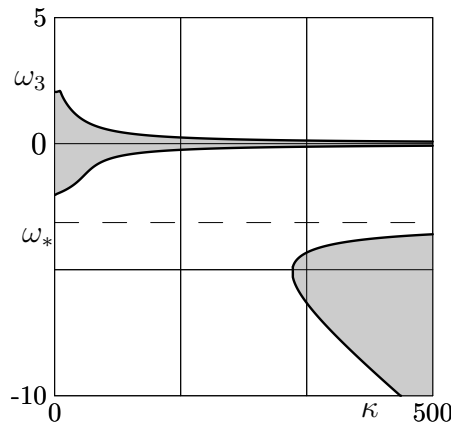


Figure 2: $A_1 = 3 \text{ kg} \cdot \text{m}^2$, $A_2 = 4 \text{ kg} \cdot \text{m}^2$, $A_3 = 5 \text{ kg} \cdot \text{m}^2$, $a_1 = 5 \text{ m}$, $a_2 = 4 \text{ m}$, $a_3 = 2 \text{ m}$, $m = 1 \text{ kg}$, $\delta = 0.75$; $J = 3 \text{ kg} \cdot \text{m}^2$, $\omega_* = -3.13 \text{ s}^{-1}$

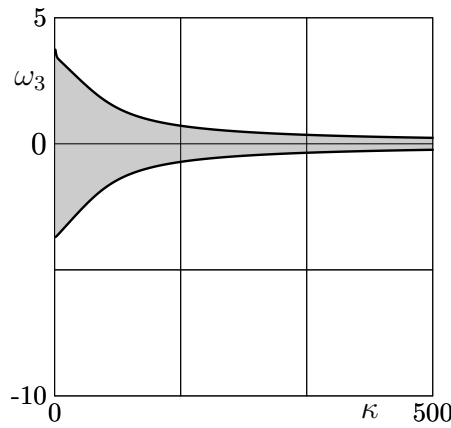


Figure 3: $A_1 = 3 \text{ kg} \cdot \text{m}^2$, $A_2 = 4 \text{ kg} \cdot \text{m}^2$, $A_3 = 5 \text{ kg} \cdot \text{m}^2$, $a_1 = 5 \text{ m}$, $a_2 = 4 \text{ m}$, $a_3 = 2 \text{ m}$, $m = 3 \text{ kg}$, $\delta = 0.75$, $J = -1 \text{ kg} \cdot \text{m}^2$

problem ($k \rightarrow +\infty$) the stability conditions have the form [1],[2]

$$A_1 < A_2 < A_3, \quad a_1 > a_2 > a_3, \quad 0 < \delta < \frac{\pi}{2} \quad (7)$$

$$J = (A_1 + A_2 - A_3) \left(\frac{a_1}{a_3} + \frac{a_2}{a_3} - 2 \right) - m a_3^2 \left(4 - 3 \left(\frac{a_1}{a_3} + \frac{a_2}{a_3} \right) + 2 \frac{a_1 a_2}{a_3^2} \right) > 0 \quad (8)$$

$$\omega < 0, \quad \omega^2 > \omega_*^2 = \frac{mg}{J a_3} (a_1 - a_3)(a_2 - a_3) \quad (9)$$

Eq. (7) means that the rotation occurs around the axis of the greatest moment of inertia, and the corresponding equilibrium ($\omega = 0$) is stable. Eq. (8) imposes constraints on geometric and dynamic parameters of the body. Eq. (9) means that only rotations in the negative direction and with a enough large angular velocity are stable.

In the case of an arbitrary coefficient of viscous friction, the linearized equations of the perturbed motion of the system in the neighborhood of the solutions Eq. (6) are rather cumbersome [1] and the analytical analysis of stability conditions is difficult. At Fig. 1, Fig. 2, Fig. 3 the stability regions for some parameters of the problem are given. In the case shown at Fig. 1, for sufficiently large friction

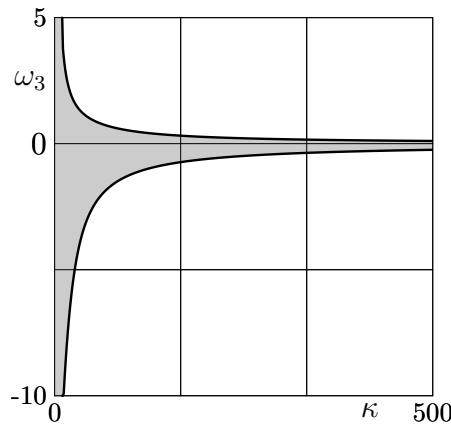


Figure 4:

coefficients, there are two regions of stability. One corresponds to a non-holonomic statement of the problem (below the dotted line), the second is located in a neighborhood of zero. As k decreases, these regions merge into one, containing almost all negative values of ω and a small range of positive values ω . At very small k the stability region has some symmetry with respect to the horizontal.

In the case shown at Fig. 2 (which differs from the previous only by the height of the center of mass), the stability region is divided into two parts: the region corresponding to the non-holonomic case and the region in the neighborhood of equilibrium. In the case shown at Fig. 3 (body mass increases) only the region of stability in the neighborhood of equilibrium remains.

4 NUMERICAL EXPERIMENTS

Numerical experiments were carried out for a celt with parameters

$$A_1 = 0.058 \cdot 10^{-3} \text{ kg} \cdot \text{m}^2, A_2 = 0.44 \cdot 10^{-3} \text{ kg} \cdot \text{m}^2, A_3 = 0.49 \cdot 10^{-3} \text{ kg} \cdot \text{m}^2 \\ a_1 = 0.661 \text{ m}, a_2 = 0.073 \text{ m}, a_3 = 0.0098 \text{ m}, m = 0.1 \text{ kg}, \delta = 0.1, J = -0.007 \text{ kg} \cdot \text{m}^2.$$

These parameters correspond to the model of a stone having the shape of an ellipsoid, and all obtained results of numerical experiments coincide with full-scale experiments.

The region of stability of permanent rotations for this model is presented at Fig. 4. Numerical experiments were carried out on a plane with a coefficient of friction $k = 50 \text{ s}^{-1}$. The initial conditions had the form

$$\gamma_2(0) = 0, \quad \omega_1(0) = \omega_2(0) = 0, \quad \mathbf{u}(0) = 0. \quad (10)$$

At Fig. 5 on the left are the results of experiments with different initial angular velocities of rotations with a very small initial deviation from the vertical ($\gamma_3(0) = 0.99999$), on the right for greater deviation ($\gamma_3(0) = 0.999$). The area of stability of rotations with a selected coefficient of viscous friction is highlighted in gray. As we see, stable rotations with a positive angular velocity of rotation have a very small region of attraction.

We note that in the non-holonomic statement of the problem for the chosen parameters there are no stable rotations ($J < 0$). In the case of the plane with friction and a small positive initial angular velocity of rotation, there is a change in the direction of rotation of the stone, with a subsequent exit to the stable uniform rotations.

The results of numerical experiments with sufficiently large initial angular velocities are presented at Fig. 6. Here such property of a stone, as the transition of rotational motions to vibrational motions

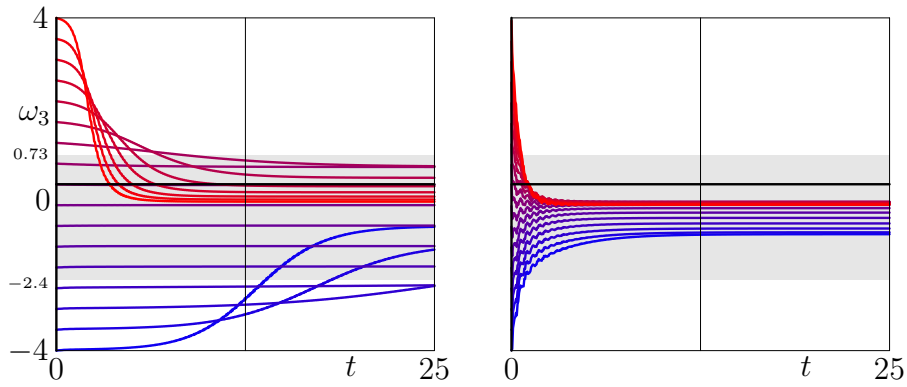


Figure 5: $\gamma_3(0) = 0.99999$ and $\gamma_3(0) = 0.999$

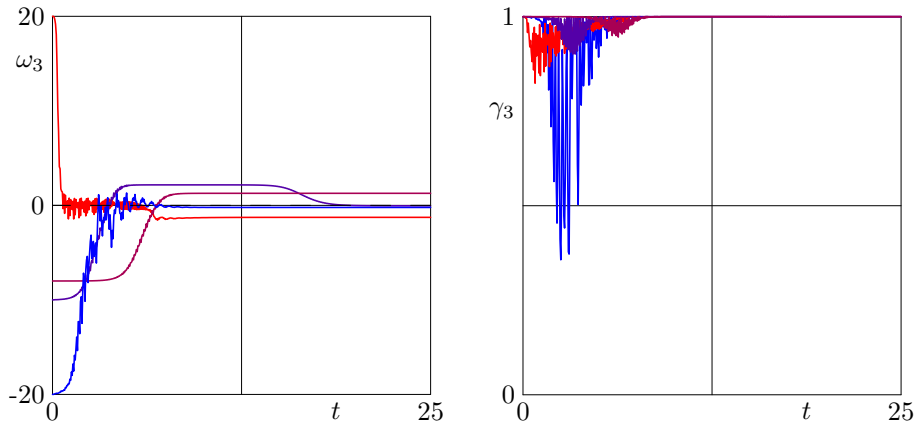


Figure 6:

and vice versa is observed. The final movement with a negative initial speed can be rotation in both the negative and positive directions.

5 TRANSIENT PROCESSES

For study the transient processes shown at Fig. 5 the equations (1)–(3) up to second-order terms in the variables $v_1, v_2, \omega_1, \omega_2, \gamma_1, \gamma_2$ are considered.

$$\dot{\mathbf{x}} = A(k, \delta, \omega_3)\mathbf{x} + \mathbf{b}(\mathbf{x}, k, \delta, \omega_3) + O_3(\tilde{\mathbf{x}}) \quad (11)$$

The changing of variables

$$v_1 = v \cos \psi, \quad v_2 = v \sin \psi, \quad \omega_1 = \rho_2 \cos \varphi_2, \quad \omega_2 = \rho_1 \sin \varphi_1, \quad \gamma_1 = \frac{\rho_1}{\xi_1} \cos \varphi_1, \quad \gamma_2 = \frac{\rho_2}{\xi_2} \sin \varphi_2$$

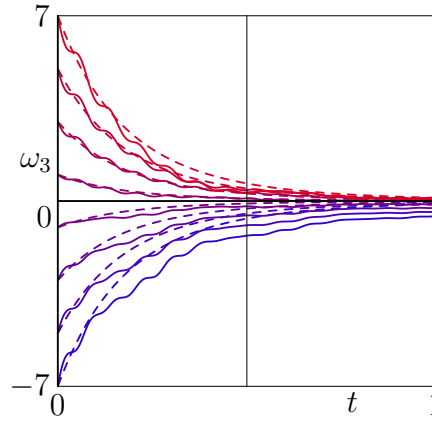


Figure 7: $\delta = 0$, $\gamma_3(0) = 0.999$

is performed, where $\xi_{1,2}^2 = mg(a_{1,2} - a_3)/A_{2,1}$. Averaging over variables ψ , φ_1 and φ_2 is carried out. Then the equations Eq. (11) have a view

$$\begin{aligned} \dot{v} &= -kv, \quad \dot{\rho}_1 = -k \frac{ma_3^2}{2A_2} \rho_1, \quad \dot{\rho}_2 = -k \frac{ma_3^2}{2A_1} \rho_2, \\ \dot{\omega}_3 &= -k \frac{m}{2A_3} \left(\frac{a_1^2 \cos^2 \delta - a_2^2 \sin^2 \delta}{\xi_1^2} \rho_1^2 + \frac{a_2^2 \cos^2 \delta - a_1^2 \sin^2 \delta}{\xi_2^2} \rho_2^2 \right) \omega_3 + \frac{mg}{2A_3} \sin 2\delta (a_1 - a_2) \left(\frac{\rho_1^2}{\xi_1^2} - \frac{\rho_2^2}{\xi_2^2} \right) \end{aligned} \quad (12)$$

For the case of the coincidence of the directions of the principal axes of the body with the directions of the principal curvatures ($\delta = 0$) the numerical solutions of the averaged system Eq. (12) (Fig. 7, dotted curves) and leanerized system (Fig. 7, solid curves) have a good coincidence. Solving the averaged system Eq. (12) for example, under the initial conditions Eq. (10), we have $v \equiv 0$, $\rho_1 = \rho_1(0) \exp(-mka_3^2 t / (2A_2))$, $\rho_2 \equiv 0$ and equality

$$\omega_3 = \omega_3(0) e^{\alpha_1(\rho_1^2 - \rho_1(0)^2)}, \quad \alpha_1 = \frac{a_1^2 A_2}{2a_3^2 A_3 \xi_1^2} \quad (13)$$

is fair. Under initial conditions differing only in the direction of rotation, the motions are completely analogous and differ only in sign ω_3 , and the corresponding curves $\omega_3(t)$ Fig. 7 are symmetrical with respect to the horizontal.

This property is not preserved for the Celt ($\delta \neq 0$), and the equality Eq. (13) takes the form

$$\omega_3 = \omega_3(0) e^{\alpha_1(\rho_1^2 - \rho_1(0)^2)} + \frac{g(a_1 - a_2) \sin 2\delta}{2k(a_1^2 \cos^2 \delta + a_2^2 \sin^2 \delta)} \left(1 - e^{\alpha_1(\rho_1^2 - \rho_1(0)^2)(a_1^2 \cos^2 \delta + a_2^2 \sin^2 \delta)/a_1^2} \right) \quad (14)$$

In this case, the solutions of the averaged system, differing only in the initial direction of rotation, are not symmetric with respect to the horizontal. However, the displacements arising in this case are sufficiently small, and, depending on the initial conditions, they can be directed both to the lower and upper half-planes. In this case, the solutions of the system Eq. (11) deviate significantly from the solutions of the averaged system (Fig. 8), but in reality the displacement is directed to the lower half-plane. The changing in the direction of rotation of the stone is explained by the deviations of the exact solution from the averaged solution, and the final value of the angular velocity of rotation is always in a small neighborhood of zero.

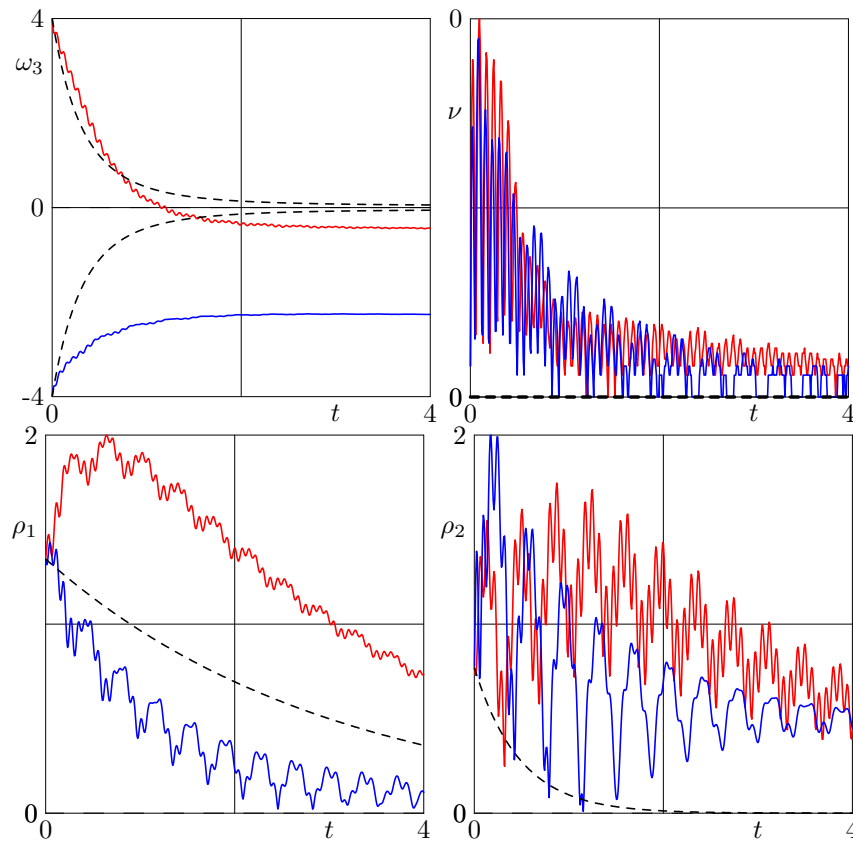


Figure 8:

The Full Paper must be written in English within a printing box of 16cm x 21cm, centered in the page. The Full Paper including figures, tables and references must have a minimum length of 6 pages and must not exceed 12 pages. Maximum file size is 4 MB.

6 CONCLUSIONS

REFERENCES

- [1] Karapetyan, A.V. Stability of steady motions, (in Russian) *Editorial URSS* (1998).
- [2] Markeev, A.P. The dynamics of the body osculating with a solid surface, (in Russian) *Institute of Computer Sciences* (1998).
- [3] Karapetyan, A.V. *On realizing nonholonomic constraints by viscous friction forces and celtic stones stability* Journal of Applied Mathematics and Mechanics (1981) **45**:30–36.
- [4] Zhuravlev, V.P. and Klimov, D.M. *Global motion of the celt* Mechanics of Solids (2008) **43**:320–327.

APPLICABILITY OF MAGNETIC HYSTERESIS MODELS FOR PREDICTING THE BEHAVIOUR OF MR DAMPERS

J. GOLDASZ*, B. SAPINSKI[†], L. JASTRZEBSKI[†] AND M. KUBIK[‡]

*Faculty of Electrical Engineering and Computer Science
Cracow University of Technology
ul. Warszawska 24, 31-155 Krakow, Poland
e-mail: jgoldasz@pk.edu.pl - Web page: <http://www.pk.edu.pl>

*BWI Technical Center
BWI Group, ul. Podgorki Tynieckie 2, 30-399 Krakow, Poland
Web page: <http://www.bwigroup.com>

[†] Department of Process Control
AGH University of Science and Technology
Al. Mickiewicza 30, 30-059 Krakow, Poland
e-mail: deep@agh.edu.pl - Web page: <http://www.agh.edu.pl>

[‡] Faculty of Mechanical Engineering
Brno University of Technology
Technická 2869/2, 616 69 Brno, Czechia
e-mail: Michal.Kubik@vutbr.cz - Web page: <http://www.vutbr.cz>

Key words: MR Damper, Magnetic Hysteresis, Magnetic Flux, Hysteretic Behaviour

Abstract. This study concerns modeling the magnetic hysteretic behaviour of magnetorheological (MR) dampers. Magnetic hysteresis is one of factors influencing the output of such actuators. The origin of magnetic hysteresis in the actuator's output is obvious - it is the inherent property of ferromagnetic materials which form the electromagnet's assembly of the actuator. Prior work on solenoid actuators indicates that hysteresis plays a major role in the flux generation mechanism, and it should be accounted for in the controls development process. So far less attention has been paid to studying the contribution of magnetic hysteresis on the output of MR dampers. Majority of studies on the hysteretic behaviour of MR dampers have virtually neglected that specific contributor. Instead, the hysteretic behaviour of MR actuators was studied by observing the relationships between the output (force/torque) and the inputs (current, velocity, position). Instead, in the present study we separate the magnetic hysteresis from the mechanical/hydraulic one by investigating the magnetic flux vs exciting current relationship of an exemplary MR damper subjected to sinusoidal current (voltage) loading. The resulting behaviour of the electromagnets is then examined using the nonlinear inductor approach with hysteresis. The performance of several hysteretic operators is then evaluated based on their ability to reproduce the magnetic flux output of the MR actuator.

1 INTRODUCTION

Magnetorheological (MR) fluids are well-known representatives of smart fluids. The material develops a yield stress when exposed to magnetic field [1]. The yield stress field-dependent change is of sufficient strength for the material to be used in commercial applications, namely, semi-active vehicle dampers or powertrain mounts [2].

It is well-known a typical MR flow-mode/shear-mode damper features an internal control valve in the form of an electromagnet with a fixed height flow channel. When supplied with an electric current in the coil it induces a magnetic field in the flow channel, thus activating the fluid. The result is a resistance-to-flow build-up manifested by changes in the output force or torque. The effect is reversible and fast. Various factors make the conversion process complicated [3, 4], namely, temperature, friction, material's liability to sedimentation, non-linear magnetisation characteristics of the materials forming the magnetic circuit of the damper, magnetic hysteresis, mechanical (hysteresis), driver dynamics, control coil dynamics, non-linear relationship between the magnetic flux and the field-dependent yield stress, etc. Generally, the contributors make the control algorithm development process a challenge.

In the present study we focus on the hysteretic behaviour of the MR damper's electromagnet. The hysteresis is present virtually in any ferromagnetic material although on a different scale. Although the electromagnetic circuit of MR valves are usually developed with soft magnetic alloys the flux's hysteresis should be accounted for in the damper design process or control algorithm development. In fact, the phenomenon has been subject to extensive research over the years [6]. In general, the existence of magnetic hysteresis in MR actuators is important for two reasons. First, it complicates the issue of controlling the output of such actuators. Second, it has an effect on the actuator's output force even at off-state conditions.

Briefly, magnetic hysteresis models can be classified into two groups [5]. The first one includes energy-based models of which the Stoner-Wohlfart (S-W) model or Jiles-Atherton (J-A) model are the most well-known representatives [7, 8]. The other category incorporates the so-called phenomenological models of Preisach [9], Duhem/ Hodgdon-Coleman [10] or Chua [11]. For this study we chose two representatives of the phenomenological group, namely, the Duhem model and the Bouc-Wen operator.

The significance of hysteresis on the force output of MR dampers has been recognized early on [14]. Since Spencer et al. numerous models have been developed and applied for the purpose of predicting the force/torque output of MR dampers [15]. However, few authors focused attempted to analyze the magnetic hysteresis independently of other hysteretic contributors [16, 17, 18, 19].

In general, the purpose of the research study is in examining the capabilities of two selected phenomenological models to copy the magnetic hysteretic behaviour of MR dampers. To accomplish the goal, we reconstruct the magnetic behaviour of a rotary MR brake (damper) from voltage and current measurements as in [3] to obtain the induced flux variation against the exciting current. Next, by employing the hysteretic non-linear inductor concept we examine the performance of each model. The sensorless flux estimation technique we use allows inspecting the damper behaviour without any knowledge of its internals.

Briefly, the paper is organized as follows. Section 2 contains the description of the lumped parameter model of the MR actuator's circuit. In Section 3 we explain the test setup and the hardware used. Next, Section 4 presents modeling results and a comparison of selected data against the hysteretic models. Finally, conclusion is presented in Section 5.

2 MODELING OF NONLINEAR INDUCTORS WITH HYSTERESIS

First, let us consider a nonlinear resistor-inductor model of the MR damper's circuit as in Figure 1. The model would include the input voltage source $u(t)$, the coil resistance R and the nonlinear inductance $L(i)$ in series with the resistor. The model equation is then as follows

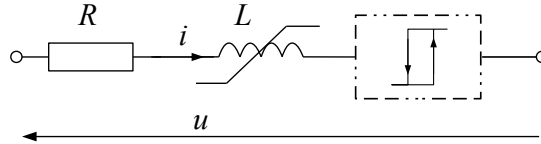


Figure 1: Nonlinear inductor – proposed model

$$u(t) = iR + \frac{d\lambda}{dt} \quad (1)$$

where i denotes the coil current, and $\lambda = L(i)i$ refers to the structure's magnetic flux linkage. Equation 1 represents the dynamics of a simple nonlinear inductor. The relationship $\lambda(i)$ incorporates a hysteretic operator, and it may be further extended for use with eddy current models.

For reasons already explained above we proceed further with the Duhem model and the Bouc-Wen hysteretic operator, respectively. Briefly, in the following sections we highlight an MR damper experiment based on which we extract the $\lambda - i$ relationship. Then, we execute a model identification study using the above mentioned operators, and discuss the obtained results.

2.1 Duhem hysteresis model

Using the Duhem hysteresis model, the relationship between the flux linkage λ and the coil current i can be described as follows

$$\frac{d\lambda}{dt} = a \left| \frac{di}{dt} \right| [f(i) - \lambda] + g(i) \frac{di}{dt} \quad (2)$$

We define the shape functions $f(i)$ and $g(i)$ in Equation 2 as

$$\begin{cases} f(i) = b_1 \tanh(b_2 i) \\ g(i) = c \end{cases} \quad (3)$$

The model incorporates four parameters (a, b_1, b_2, c) which can be identified from experimental data, for instance. Furthermore, we assume the parameters depend on the exciting current. In the limiting case ($a = 0$) the hysteresis is effectively eliminated and the inductor model reduces to that of a nonlinear one without hysteresis. As a result, an initial estimate of the parameter c can be provided from coil inductance calculations, for example.

The model parameter set can be then used for varying the hysteresis width and shape. In Figure 2 the authors reveal the impact that each parameter of the model has on the $\lambda - i$ normalized loop shape; the arrow in each figure shows how each parameter was increased.

In the presented form, the Duhem model has the advantage over the generic Bouc-Wen model, for example, of being less complex as it requires half of the parameters (that the Bouc-Wen model needs) as shown below.

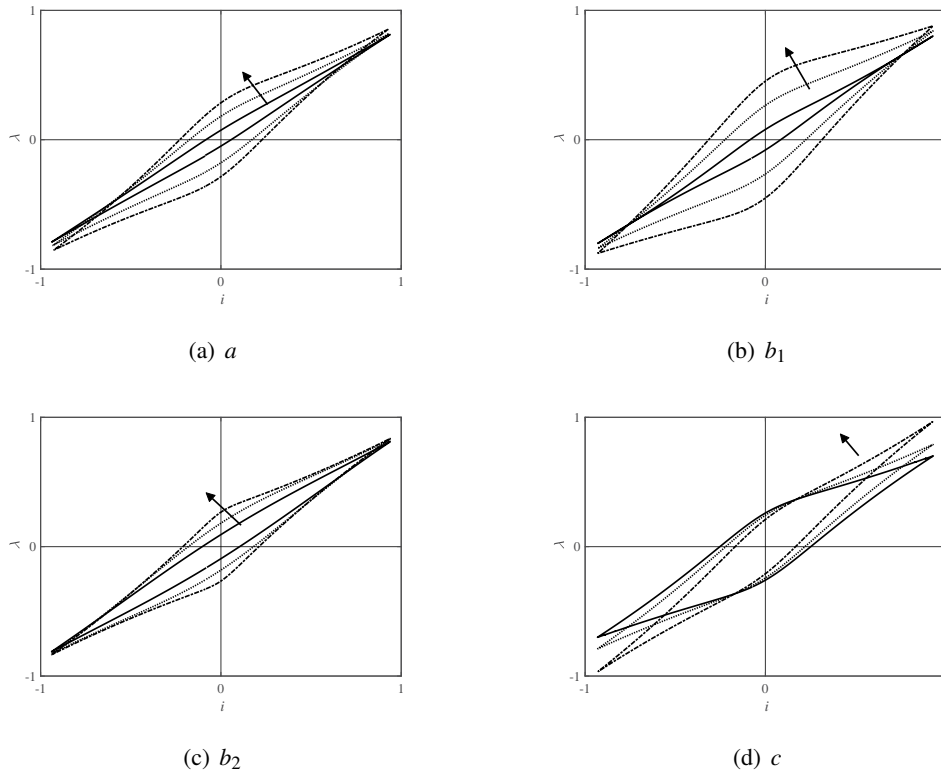


Figure 2: Duhem model: impact of the model parameters on the $\lambda - i$ loop

2.2 Bouc-Wen model

Considering the Bouc-Wen approach the relationship between the flux linkage and the circuit current can be implemented as follows

$$\begin{cases} \lambda = \alpha ki + (1 - \alpha)kDz \\ \frac{dz}{dt} = D^{-1} \left(A \frac{di}{dt} - \beta \frac{di}{dt} |z|^{n_1} - \gamma \left| \frac{di}{dt} \right| |z|^{n_2-1} \right) \end{cases} \quad (4)$$

where z - hysteretic operator, and A , α , β , γ , k , D , n_1 , n_2 control the hysteresis width and shape as illustrated in the normalized $\lambda - i$ plots in Figure 4. Here, the Bouc-Wen model is given in the form presented in [12, 13]. Again, it should be noted that in the limiting case ($\alpha = 1$) the model is effectively reduced to that of a nonlinear inductor without hysteresis. The parameter k is then equal to the circuit inductance $L(i)$. Also, if $\alpha < 1$, then the model's behaviour resembles that of elastic materials with hysteresis (see Figure 3), i.e. the $\lambda - i$ loop rotation is clockwise, otherwise it is counterclockwise for $\alpha > 1$. As in the Duhem model, the initial estimate of k can be obtained from coil inductance calculations or measurements.

3 TEST INPUTS, HARDWARE

In the research study we rely on the flux estimation technique illustrated in [3], and the reader should refer there for further details. In this specific case we carried out measurements of supply voltage and coil current using the test setup in Figure 5. Based on the data, the magnetic flux time histories were extracted through integration. In the study we examined the behaviour of one rotary (shear-mode) MR

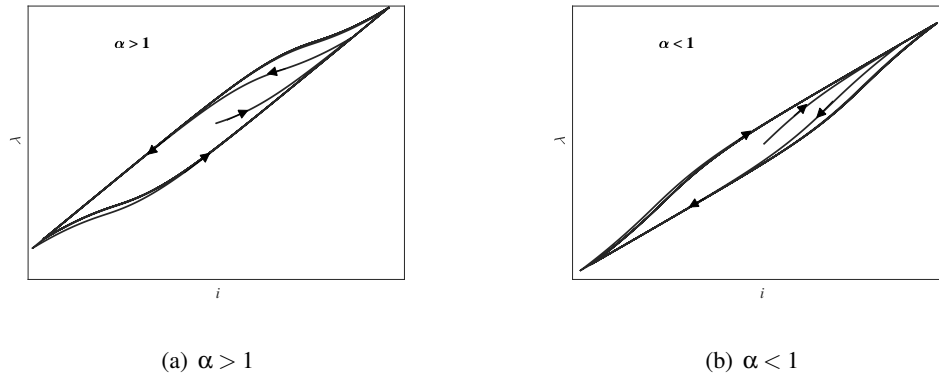


Figure 3: Bouc-Wen model: impact of the parameter α on the model hysteresis

damper. The hardware of choice was a shear-mode rotary brake no. RD-2028 by Lord Corp. The rotary damper's coil resistance is appr. 8.9Ω , and the device can be operated up to 1 A. In order to examine the $\lambda - i$ behaviour of the damper we subjected it to sinusoidal input voltage waveforms at low frequency ($f = 1$ Hz) (to reduce the contribution of eddy currents). The input voltage was adjusted to result in the peak coil currents $I = \{0.2, 0.4, 0.6, 0.8, 1.0\}$ A. The sampling frequency was 1 kHz.

4 RESULTS

The experimental and modeling results are highlighted in the sections below. The material in the respective sections highlights the data obtained for each hysteretic model. The results are presented as time histories of the flux linkage λ and plots of $\lambda - i$. As highlighted in the above section, the magnetic flux linkage was extracted from the measured data through integration, and then used in the model identification stage with the `fmincon` solver of the MATLAB's Optimization Toolbox using the loss function V_λ of the following form

$$V_\lambda = \frac{1}{N} \sum_{i=1}^N (\lambda_i - \hat{\lambda}_i)^2 \quad (5)$$

where N – number of samples, λ_i – measured flux linkage sample, $\hat{\lambda}_i$ – hysteresis model prediction (Duhem - Equation 2, Bouc-Wen - Equation 4).

4.1 Duhem model

Here, we show the results involving the Duhem model. The obtained data are illustrated in Figure 6 and Table 1 for the current levels 0.2, 0.4, 0.6, 1.0 A, respectively. Based on the presented data, it seems the model well copies the $\lambda - i$ characteristics of the damper both in terms of hysteresis width, magnitude and shape.

Next, observations of the Table 1 contents imply variation of the model's specific parameters against the current which confirms our initial assumptions. In particular, the magnitude of the estimate of the parameter c nearly double during the transition from the highest current input to the lowest one. The estimates of the parameters b_1 and b_2 vary by appr. 10 percent, whereas the parameter a estimate remains fairly constant anywhere except for the smallest current level.

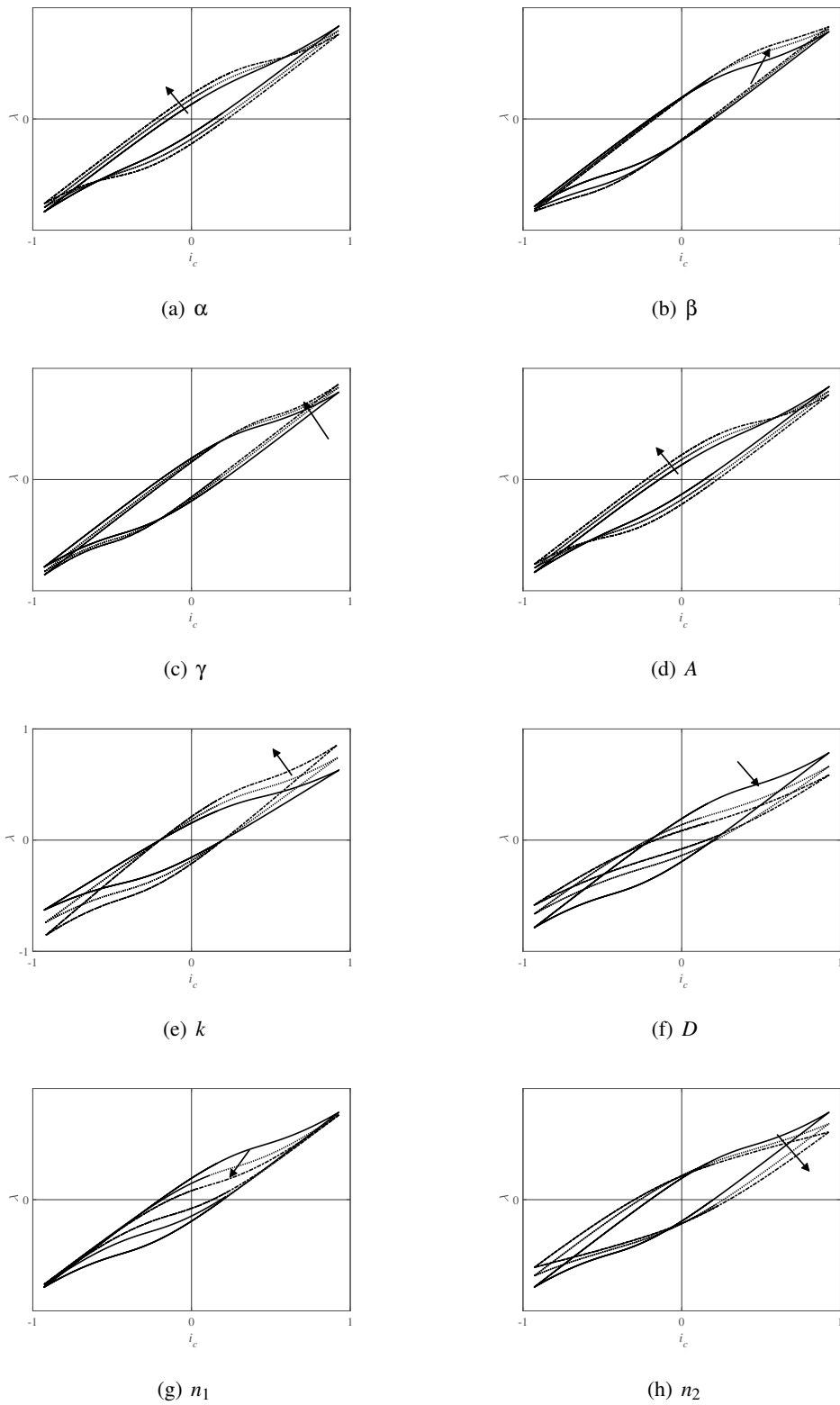


Figure 4: Bouc-Wen: impact of the model parameters on the $\lambda - i$ loop

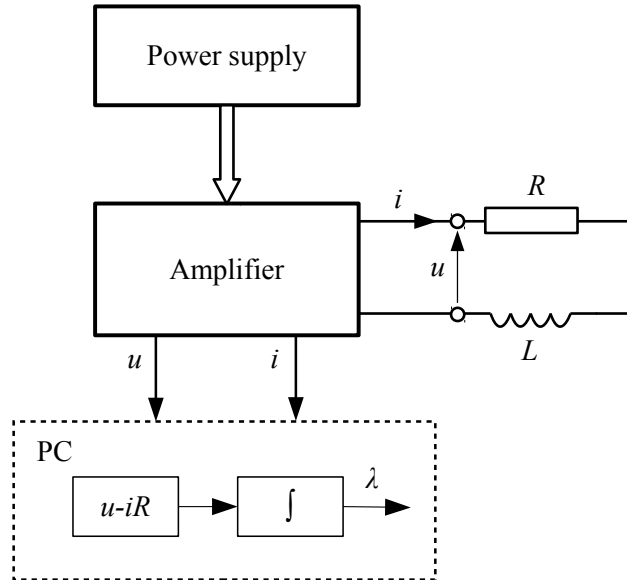


Figure 5: Test rig layout [3]

4.2 Bouc-Wen model

The results concerning the Bouc-Wen operator are presented in Figure 7 and Table 2 for the same current level range. Again, it seems the model well copies the $\lambda - i$ characteristics of the damper, however, inspecting the plots and the contents of the Table 2 shows that the Bouc-Wen model yields curve fits on the order of magnitude worse than the Duhem operator. Although the hysteresis width seems well predicted by the model the shape of the $\lambda - i$ loop predicted by the model is relatively poorly captured when compared against the Duhem based approach. That is most evident at the highest current levels – see Figures 7(g) and 7(h).

Similarly to the examined predecessor, the obtained estimates are current dependent and, except for the exponents n_1 and n_2 , they vary in a monotonous manner. This may explain the curve fitting problem at the highest current level as the exponents control the $\lambda - i$ shape. Note that the parameter k varies with the current similarly to the experimentally measured inductance of the rotary actuator in [3], although the identified variation range is different than that of the parameter c of the Duhem model.

5 SUMMARY

Magnetic hysteresis is one of the key factors affecting the output of MR dampers; it is an inherent property of the ferromagnetic material forming the damper electromagnetic circuit. As pointed out in previous study, it is of different nature than the mechanical (hydraulic) hysteresis of the devices as it does not vanish in the DC limit. It may present both control as well as engineering issues (off-state force increase due to the residual field).

As such, the present modeling study concerns the magnetic hysteresis only. It extends the concept of a

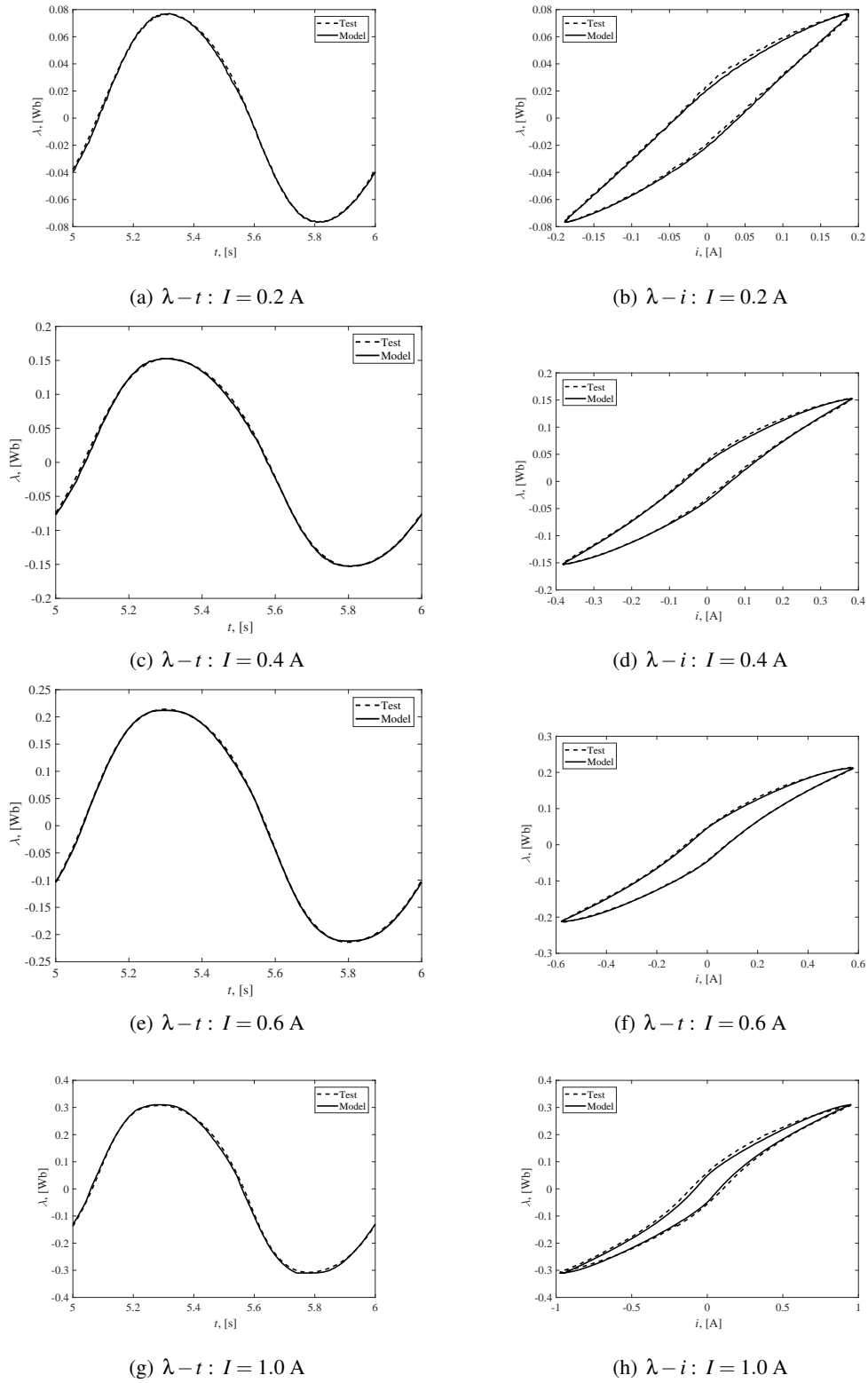
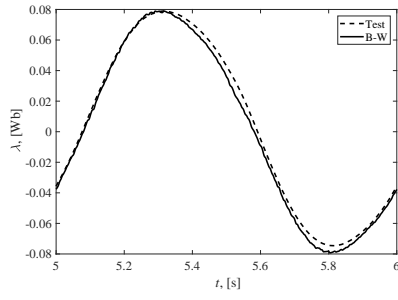
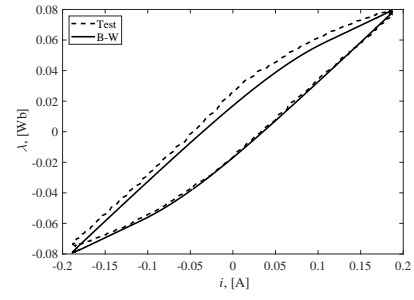


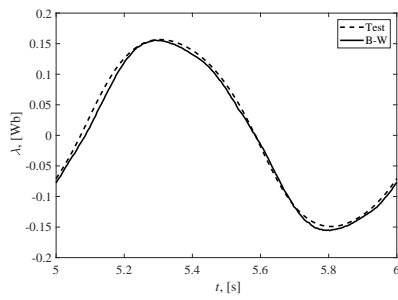
Figure 6: Duhem model vs test data, $f = 1$ Hz



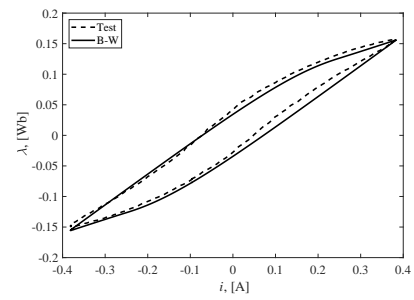
(a) $\lambda - t$: $I = 0.2$ A



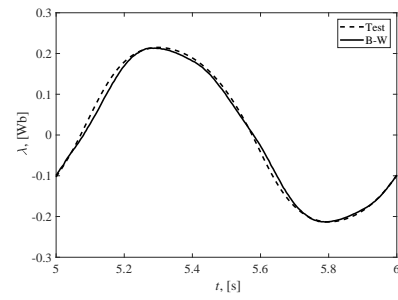
(b) $\lambda - i$: $I = 0.2$ A



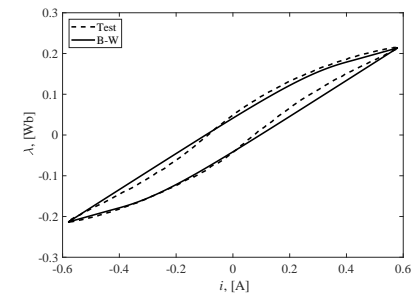
(c) $\lambda - t$: $I = 0.4$ A



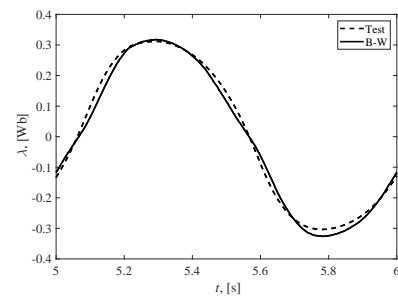
(d) $\lambda - i$: $I = 0.4$ A



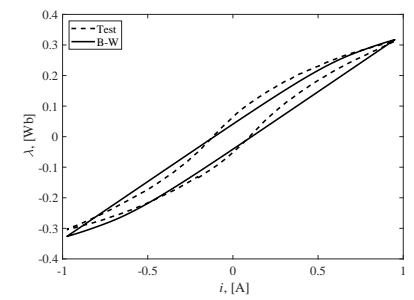
(e) $\lambda - t$: $I = 0.6$ A



(f) $\lambda - i$: $I = 0.6$ A



(g) $\lambda - t$: $I = 1.0$ A



(h) $\lambda - i$: $I = 1.0$ A

Figure 7: Bouc-Wen model vs test data, $f = 1$ Hz

Table 1: Duhem model parameter estimates

$I, [A]$	a	b_1	b_2	c	V_λ
0.2	7.370	0.367	0.792	0.311	1.82e-6
0.4	8.026	0.351	0.759	0.239	5.87e-6
0.6	7.972	0.344	0.741	0.171	4.08e-6
1.0	8.102	0.334	0.712	0.158	4.74e-5

Table 2: Bouc-Wen model estimated parameters

$I, [A]$	A	β	k	n_1	n_2	γ	α	D	V_λ
0.2	2.000	114.249	0.393	1.226	1.530	95.682	1.353	5.992	1.118e-05
0.4	2.252	122.928	0.378	1.301	1.219	96.141	1.339	11.302	5.590e-05
0.6	2.411	125.294	0.338	1.347	1.276	102.351	1.311	13.236	9.369e-05
1.0	2.277	127.938	0.303	1.224	1.356	112.282	1.246	21.569	3.415e-04

non-linear inductor with the magnetic hysteresis contribution. In the present form it captures the average flux variation in the structure, and it requires measurements of the damper's output. Therefore, it may be only used during a control algorithm development stage and is not suitable for, e.g. damper sizing studies. Of the two models which we examined the Duhem model's performance is clearly superior. The model captures all key features of the $\lambda - i$ loop. The Bouc-Wen operator is redundant in the analyzed form which may explain its poor performance at the highest current levels as the flux in the electromagnet approaches saturation. The authors intend to extend their use in transient studies by adopting a more complex and efficient inductor concept so that the effects of eddy currents and the hysteresis dependence on the excitation input frequency are well captured.

ACKNOWLEDGMENT

The authors wish to acknowledge the support of the grant no. PPI/APM/2018/1/00027/DEC/1 (NAWA – National Agency for Academic Exchange, Poland) and the statutory grant no. E3/611/2019/DS (Cracow University of Technology).

REFERENCES

- [1] Rabinow, J. Magnetic fluid torque and force transmitting device. U.S. Patent No 2,575,360, (1951).
- [2] Hopkins, P.N., Fehring, J.D., Lisenker, I., Longhouse, R.E., Kruckemeyer, W.C., Oliver, M.L. and Alexandridis, A.A. Magnetorheological fluid damper. US Patent No. 6,311,810, (2003).
- [3] Goldasz, J., Sapinski, B. and Jastrzebski, L. Assessment of the Magnetic Hysteretic Behaviour of MR Dampers through Sensorless Measurements. *Shock and Vibration* (2018) **2018**:3740208.
- [4] Strecker, Z., Roupec, J., Mazurek, I., Machacek, O., Kubik, M., and Klapka, M. Design of magnetorheological damper with short time response. *J. Intell. Mater. Syst. Struct.* (2015) **26(14)**:1951–1958.

- [5] Mazgaj, W. *Determining the magnetic field distribution in soft magnetic materials incl. hysteresis and anisotropy*. Wydawnictwo Politechniki Krakowskiej, Krakow, (2010).
- [6] Mayergoyz, I.D., Friedman, G. and Salling, C. Comparison of the classical and generalized Preisach hysteresis models with experiments. *IEEE Trans. Magn.* (1989) **25(5)**:3925–3927.
- [7] Jiles, D.C. and Atherton, D.L. Theory of ferromagnetic hysteresis. *J. Appl. Phys.* (1984) **55**:2115.
- [8] Mayergoyz, I. D. and Friedman, G. Generalized Preisach model of hysteresis. *IEEE Trans. Magn.* (1988) **24(1)**:212–217.
- [9] Mayergoyz, I. D. Mathematical models of hysteresis. *IEEE Trans. Magn.* (1986) **22(5)**:603–608.
- [10] Macki, J. W., Nistri, P. and Zecca, P. Mathematical models for hysteresis. *SIAM Rev.* (1993) **35(1)**:94–123.
- [11] Chua, L. and Stromsmoe, K. Lumped-circuit models for nonlinear inductors exhibiting hysteresis loops. *IEEE Trans. Circuit Theory* (1970) **17(4)**:564–574.
- [12] Ikhoulane, F., Manosa, V. and Rodellar, J. Dynamic properties of the hysteretic Bouc-Wen model. *Syst. Control Lett.* (2007) **56**:197–205.
- [13] Goldasz, J., Sapinski, B. and Jastrzebski, L. On the Application of Bouc-Wen Hysteresis Approach for Modeling of MR Actuators. *Proc. of the 16th International Conference on New Actuators, Bremen, DE.*, (2018).
- [14] Dyke, S. J., Spencer Jr, B. F., Sain, M. K. and Carlson, J. D. Modeling and control of magnetorheological dampers for seismic response reduction. *Smart Mater. Struct.* (1996) **5(5)**:565.
- [15] Wang, D.H. and Liao, W.H. Magnetorheological fluid dampers: a review of parametric modelling. *Smart Mater. Struct.* (2011) **20(2)**:023001.
- [16] An, J. and Kwon, D.S. Modeling of a magnetorheological actuator including magnetic hysteresis. *J. Intell. Mater. Syst. Struct.* (2003) **14(9)**:541–550.
- [17] Szczyglowski, J. Influence of eddy currents on magnetic hysteresis loops in soft magnetic materials. *J. Magn. Magn. Mater.* (2001) **223**:97–102
- [18] Zheng, J., Li, Y., Li, Z. and Wang, J. Transient multi-physics analysis of a magnetorheological shock absorber with the inverse Jiles-Atherton hysteresis model. *Smart Mater. Struct.* (2015) **24(10)**:105024.
- [19] Guo, P., Xie, J. and Guan, X. Dynamic model of MR dampers based on a hysteretic magnetic circuit. *Shock and Vibration* (2018) **2018**:2784950.

COMPARISON OF PASSIVE AND ACTIVE MITIGATION DEVICES FOR VIBRATION CONTROL IN SLENDER STRUCTURES

A. MAGDALENO^{*}, C. CASADO^{**}, JOSE M. SORIA[†], E. PEREIRA[‡], I. M. DIAZ[†]
AND A. LORENZANA^{*}

^{*} ITAP. Escuela de Ingenierías Industriales
Universidad de Valladolid
Paseo del Cauce 59, 47011 Valladolid, Spain
e-mail: alvaro.magdaleno@uva.es; ali@eii.uva.es

^{**} Fundación CARTIF
Parque Tecnológico de Boecillo, 47151 Valladolid, Spain
e-mail: carcas@cartif.es

[†] ETSI de Caminos, Canales y Puertos
Universidad Politécnica de Madrid
Calle del Profesor Aranguren 3, 28040 Madrid, Spain
e-mail: jm.soria@upm.es; ivan.munoz@upm.es

[‡] Escuela Politécnica Superior
Universidad de Alcalá de Henares
Campus Universitario, 28805 Alcalá de Henares, Spain
e-mail: emiliano.pereira@uah.es

Key words: Structural dynamics, Vibration control, Tuned Mass Damper, Active Mass Damper

Abstract.

This paper presents a comparative study including the theoretical modelling and the practical implementation of two types of well-known devices for structural vibration control. Firstly, a lab scale model for a two-storey building is dynamically identified. Then, a tuned mass damper (TMD) and an active mass damper (AMD) are described, modelled and assembled in the upper floor, both of them with similar effective mass. After coupling the dynamic equations, the experimental results are compared with the numerical ones and their performance is discussed.

For modelling purposes, an experimental comparison and the corresponding computational simulation is carried out. Resulting assembled systems will undergo the same loading, consisting on an initial condition away from the equilibrium position and then released. The performance of each device is evaluated in terms of the time free oscillations take to return to rest (with accelerations within a 10% and a 5% band with regard to their maximum value). This is a relevant loading case from which interesting engineering conclusions can be drawn about not only the practical implementation of each proposed mitigation device but also about the computing and simulation capabilities.

1 INTRODUCTION

Several engineering structures can exhibit vibration problems that need to be mitigated. For vibrations under, let's say, 10 Hz (typical in slender buildings and civil structures) the problem can be addressed using passive or active approaches [1]. Assuming that the structure cannot be stiffened (nor additional supports neither bracings) the only solution is to inertially act on it. Among the possible inertial systems, TMDs (tuned mass dampers) or AMDs (active mass dampers) are standard mitigation devices. The TMDs are passive systems consisting of a moving mass linked to a mounting frame by guides, springs and dampers. The AMDs are actuators capable of accelerating a heavy block according to the corresponding signals from a microcontroller, which depend on some input records (usually via accelerometers).

Although it is much more common (and affordable) to equip large structures with TMDs, it is not uncommon to find AMD in high-rising buildings, communication towers or large-scale bridge towers for reducing wind-induced vibration or earthquake-induced vibration [1,2]. Usually AMD control exhibit superior performance but, depending on the type of loading and considering engineering issues such as manufacturing cost, power consumption, operating threshold or maintenance cost, passive systems [3,4,5] are often the chosen option.

2 MODEL DESCRIPTION

In order to illustrate and compare the effects of both mitigation devices, a specific benchmark structure (distributed by Quanser® [6] and presented in several papers [2, 7, 8, 9, 10]) is going to be studied. As it can be seen in Figure 1a, it is a building model consisting of two thick plates (or floors, letters A, B) and several slender plates joining them (or columns, C, D). The TMD and AMD mounting frames are attached on the top floor (E, F respectively). The AMD moving mass (G) is removed when the TMD device is under study and, complementary, the TMD moving mass (H) is removed when only the AMD effect is the one to be considered. The shaking table (I) is not used in this work.

Although more information will be presented later, it is convenient to anticipate some data: the first mode is at 1.57 Hz, having a modal mass of 3 kg and 0.5% of modal damping ratio. Both TMD and AMD devices will be installed on the upper floor with a moving mass of 22% of the modal mass. TMD will be tuned to mitigate this first mode of vibration. As it is known, the performance of both systems depends on the moving mass involved. Nevertheless, TMD and AMD also require some fixed mass (mounting frame, supports, etc.) affecting the modal parameters of the structure. To eliminate the influence of these fixed masses, some additional mass will be added to the model so the structure will have the same dynamic properties when the moving mass of the mitigation devices is removed. Also, friction on both devices can be neglected as mechanical parts (rotational bearings, linear ball guides, etc.) are high quality ones.

The physical model can be represented by the conceptual discrete model shown in Figure 1b, where all the building mass is concentrated on the first and second floors. Both floors are joint together and to the ground through two plates which restrain the movement to one vertical plane and provide stiffness and structural damping. The corresponding equations of motion,

considering the two degrees of freedom shown in Figure 1b, are shown in Eq. 1. There, m_1 and m_2 are the masses of each floor, k_1 and k_2 are the equivalent stiffness values of both plates and c_1 and c_2 their corresponding equivalent viscous damping coefficients. F_2 represents a force applied on the second floor. Forces applied on the first floor do not appear in this study.

$$\begin{aligned} m_1 \ddot{x}_1 + (c_1 + c_2) \dot{x}_1 - c_2 \dot{x}_2 + (k_1 + k_2) x_1 - k_2 x_2 &= 0 \\ m_2 \ddot{x}_2 - c_2 \dot{x}_1 + c_2 \dot{x}_2 - k_1 x_1 + k_2 x_2 &= F_2 \end{aligned} \quad (1)$$

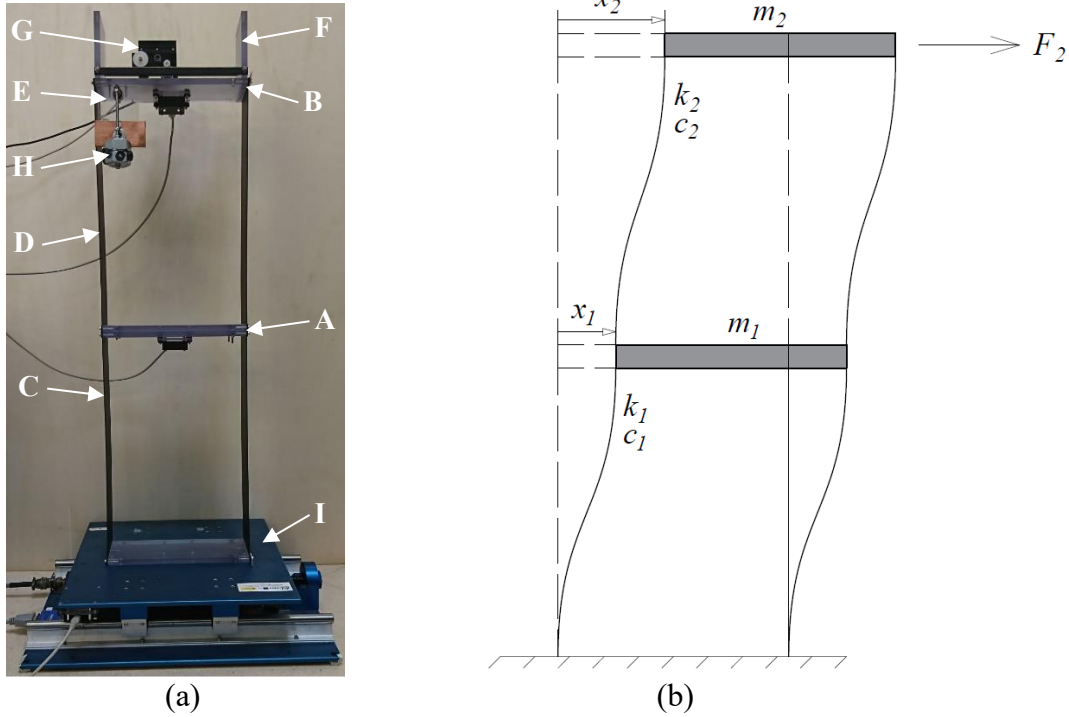


Figure 1: Real (a) and conceptual (b) building model

Bearing in mind control strategies, these equations are transformed into the equivalent state space model (Eq. 2). Considering as input $u = F_2$, the state vector containing both displacements and velocities ($x_0 = [x_1 \ x_2 \ \dot{x}_1 \ \dot{x}_2]^t$) and establishing as outputs the accelerations of both floors ($y_0 = [\ddot{x}_1 \ \ddot{x}_2]^t$), the state space matrices A_0 , B_0 , C_0 and D_0 in Eq. 3 are obtained.

$$\begin{cases} \dot{x}_0 = A_0 x_0 + B_0 u_0 \\ y_0 = C_0 x_0 + D_0 u_0 \end{cases} \quad (2)$$

A modal test has been performed in order to estimate the physical and modal properties of the model. Using an impact hammer, a measured force is applied on the second floor. The accelerations \ddot{x}_1 and \ddot{x}_2 are registered and correlated with the input force. In this way, two Frequency Response Functions (FRFs) are calculated using the H_v estimator and the two degree of freedom mathematical model is fit to them. For doing so, a routine has been scripted in

Matlab to minimize the squared error between both real and imaginary parts of the two FRFs. The built-in *fmincon()* function has been chosen as the solver. Results can be shown in Figure 2, comparing both the fitted FRFs and the time response of the building and the model subjected to the same initial conditions.

$$\begin{aligned} A_0 &= \begin{bmatrix} 0 & 0 & 1 & 0 \\ 0 & 0 & 0 & 1 \\ -\frac{k_1+k_2}{m_1} & \frac{k_2}{m_1} & -\frac{c_1+c_2}{m_1} & \frac{c_2}{m_1} \\ \frac{k_2}{m_2} & -\frac{k_2}{m_2} & \frac{c_2}{m_2} & -\frac{c_2}{m_2} \end{bmatrix} & B_0 &= \begin{bmatrix} 0 \\ 0 \\ 0 \\ 1/m_2 \end{bmatrix} \\ C_0 &= \begin{bmatrix} -\frac{k_1+k_2}{m_1} & \frac{k_2}{m_1} & -\frac{c_1+c_2}{m_1} & \frac{c_2}{m_1} \\ \frac{k_2}{m_2} & -\frac{k_2}{m_2} & \frac{c_2}{m_2} & -\frac{c_2}{m_2} \end{bmatrix} & D_0 &= \begin{bmatrix} 0 \\ 1/m_2 \end{bmatrix} \end{aligned} \quad (3)$$

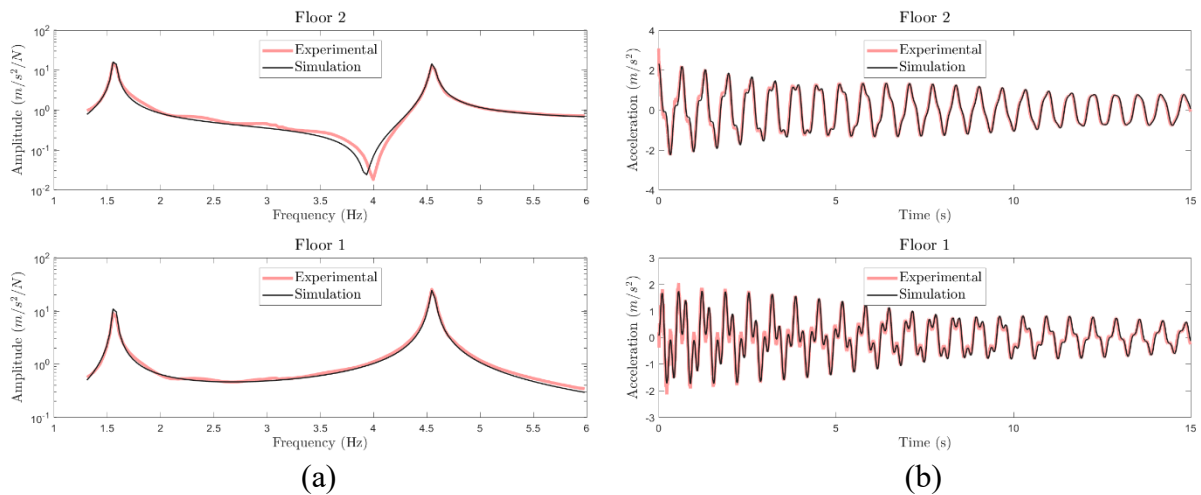


Figure 2: Frequency (a) and time (b) simulations of the bare building model

Table 1: Physical and modal properties of the model

		Floor 1 / Mode 1	Floor 2 / Mode 2
Physical properties	Mass (m_j)	1.89 kg	2.37 kg
	Stiffness (k_j)	491 N/m	662 N/m
	Damping (c_j)	0.651 Ns/m	≈ 0.00 Ns/m
Modal properties	Frequency (f_j)	1.57 Hz	4.56 Hz
	Damping ratio (ζ_j)	0.5 %	0.4 %
	Modal mass (\tilde{m}_j)	3.04 kg	2.67 kg

Finally, Table 1 summarizes the estimated physical and modal properties of the model. It must be noted that, with comparative aims, the mounting rigid frames of both mitigation devices and the different wires are considered as part of the structure and were present during all the tests carried out for this work.

3 VIBRATION MITIGATION DEVICES: TMD AND AMD

In this section both mitigation devices are described physically and mathematically. In both cases, the conceptual model, together with its mathematical model, is presented. Also, the FRFs and the response of the structure and the model subjected to the same initial conditions are depicted with and without the control device for comparison purposes.

3.1 TMD

The Tuned Mass Damper is composed by a moving mass joint to a point of the structure and contains an element sought to dissipate part of the energy the TMD receives. In this case, the device has been conceived as a pendulum (see Figure 1a, letter H), with no elastic members, so the restitution force is its own weight. For small amplitude displacements, the system can be linearized and an equivalent stiffness as well as a natural frequency and a modal damping ratio can be calculated. The damping is induced through a permanent magnet moving in front of a copper plate. The relative velocity between them induces magnetic forces and energy dissipation that oppose the movement, resulting in a simple system that can be modelled just like a viscous damping device [11]. The equation of motion of the resulting Single Degree of Freedom is shown in Eq. 4, where ω_t is the natural frequency of the pendulum (in rad/s) and ζ_t is its modal damping ratio. x_t represents its horizontal displacement (relative to the attachment point) and \ddot{x}_2 is the acceleration of the second floor, where it is installed.

$$\ddot{x}_t + 2\zeta_t\omega_t\dot{x}_t + \omega_t^2x_t = -\ddot{x}_2 \quad (4)$$

The linking force F_t between the TMD and the second floor can be calculated as stated in Eq. 5 (where m_t accounts for the device moving mass), and this, together with Eq. 4, can be combined in a state space model whose state vector is $\mathbf{x} = [x_t \ \dot{x}_t]^t$, the input is $u = \ddot{x}_2$ and the output is the force, $y = F_t$ resulting in the state space matrices shown in Eq. 6.

$$F_t = m_t(\ddot{x}_2 + \ddot{x}_t) = -m_t(2\zeta_t\omega_t\dot{x}_t + \omega_t^2x_t) \quad (5)$$

$$A_t = \begin{bmatrix} 0 & 1 \\ -\omega_t^2 & -2\zeta_t\omega_t \end{bmatrix} \quad B_t = \begin{bmatrix} 0 \\ 1 \end{bmatrix} \quad C_t = [-m_t\omega_t^2 \quad -2m_t\zeta_t\omega_t] \quad D_t = 0 \quad (6)$$

The properties of the TMD have been measured separately, resulting in a total moving mass of 0.66 kg with a natural frequency of 1.41 Hz and an equivalent modal damping ratio of 16%. Using these values and closing the loop as shown in Figure 3, a coupled model is built. This task is easily performed with Matlab thanks to its built-in *feedback()* function. In Figure 4a, the measured FRFs of the closed loop model are compared with the simulated ones and with the

original model (without any control device). This comparison is also done in the time domain (Figure 4b), comparing the responses of the three models subjected to the same initial conditions (0.011 m for the first floor and 0.019 m for the second one).

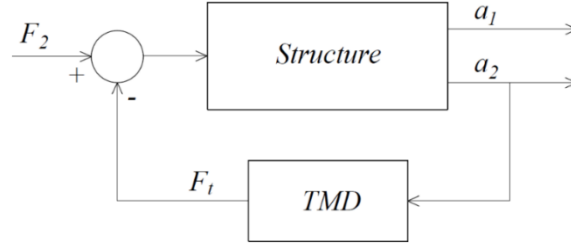


Figure 3: Feedback model of the structure with the TMD

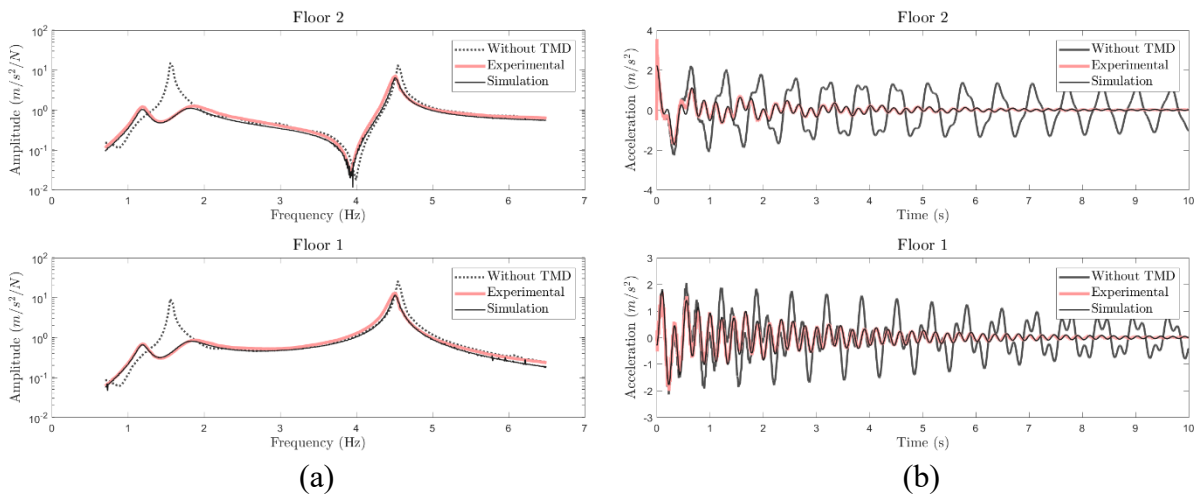


Figure 4: Frequency (a) and time (b) simulations of building model with the TMD

3.2 AMD

The Active Mass Damper system, from Quanser® [6], is composed by a linear actuator moving a 0.66 kg cart connected to a board which, in real-time conditions, measures two accelerometers, gives a voltage command to the actuator amplifier and measures its encoder to retrieve its relative position. The board is connected to a computer and the whole system is driven by Windows Real Time and a proprietary software named WinCon [6]. As the core of this technology, the selection of the best control algorithm is challenging. Although there are other alternatives [6] the traditional pole location control algorithm originally implemented by Quanser® is used.

The goal now is to command the linear actuator so the cart induces movements capable to mitigate the building vibrations. For this, the acceleration of both floors is measured in real-time and, by means of an observer, the state of the system is estimated. Finally, this state is fed back into the structure (which now contains the linear actuator) multiplied by a certain gain matrix. The closed loop system (Figure 5) should now have improved damping characteristics.

The actuator is composed by a guided moving mass, whose driving force is applied through

a DC motor, a planetary gearbox and a rack pinion mechanism to transform the rotary movement into linear displacement. The behavior of the whole system is expressed in terms of the properties of all these elements and the resulting driving force is shown in Eq. 7, where α and β are calculated from the electrical and mechanical parts of the cart, giving the values of 7.72 Ns/m and 1.72 N/V respectively. The driving force of the actuator has the same value than the force it produces on the second floor of the building, but in the opposite sense. In this way, the equation of motion associated to the second floor is modified as stated in Eq. 8 and a new equation of motion, Eq. 9, is added to the whole system to take into account the dynamics of the cart.

$$F_c = \beta V_m - \alpha (\dot{x}_c - \dot{x}_2) \quad (7)$$

$$m_2 \ddot{x}_2 + (c_2 + \alpha) \dot{x}_2 - c_2 \dot{x}_1 - \alpha \dot{x}_c + k_2 x_2 - k_2 x_1 = F_2 - \beta V_m \quad (8)$$

$$m_c \ddot{x}_c + (c_{eq} + \alpha)(\dot{x}_c - \dot{x}_2) = \beta V_m \quad (9)$$

To include the cart dynamics on the structure description, a new state space model must be built. The new inputs are the motor voltage and the external force applied to the second floor ($u = [V_m \ F_2]^t$). The state vector is $x = [x_c \ x_1 \ x_2 \ \dot{x}_c \ \dot{x}_1 \ \dot{x}_2]^t$ and the output signals are the three monitored magnitudes: $y = [x_c \ \ddot{x}_1 \ \ddot{x}_2]^t$, since the position of the cart can be registered thanks to its encoder. Such a model produces the state space matrices shown in Eq. 10.

$$\begin{aligned} A_c &= \begin{bmatrix} 0 & 0 & 0 & 1 & 0 & 0 \\ 0 & 0 & 0 & 0 & 1 & 0 \\ 0 & 0 & 0 & 0 & 0 & 1 \\ 0 & 0 & 0 & -\frac{c_{eq} + \alpha}{m_c} & 0 & \frac{c_{eq} + \alpha}{m_c} \\ 0 & -\frac{k_1 + k_2}{m_1} & \frac{k_2}{m_1} & 0 & -\frac{c_1 + c_2}{m_1} & \frac{c_2}{m_1} \\ 0 & \frac{k_2}{m_2} & -\frac{k_2}{m_2} & \frac{\alpha}{m_2} & \frac{c_2}{m_2} & -\frac{c_2 + \alpha}{m_2} \end{bmatrix} & B_c &= \begin{bmatrix} 0 & 0 \\ 0 & 0 \\ 0 & 0 \\ \frac{\beta}{m_c} & 0 \\ 0 & 0 \\ -\frac{\beta}{m_2} & \frac{1}{m_2} \end{bmatrix} \\ C_c &= \begin{bmatrix} 1 & 0 & 0 & 0 & 0 & 0 \\ 0 & -\frac{k_1 + k_2}{m_1} & \frac{k_2}{m_1} & 0 & -\frac{c_1 + c_2}{m_1} & \frac{c_2}{m_1} \\ 0 & \frac{k_2}{m_2} & -\frac{k_2}{m_2} & \frac{\alpha}{m_2} & \frac{c_2}{m_2} & -\frac{c_2 + \alpha}{m_2} \end{bmatrix} & D_c &= \begin{bmatrix} 0 & 0 \\ 0 & 0 \\ -\frac{\beta}{m_2} & \frac{1}{m_2} \end{bmatrix} \end{aligned} \quad (10)$$

Note that matrices B_c and D_c contain two columns, the first being associated with V_m and the second to F_2 . The next goal is to estimate a feedback gain matrix K so as the closed loop system satisfies some requirements. The input voltage is calculated just like $V_m = -Kx_c$, so the state equations are modified as shown in Eq. 11. The modal properties of the closed-loop system are the eigenvalues and eigenvectors of the state matrix $[A_c - B_{cV}K]$, where B_{cV} is the column from B_c associated to the input V_m .

$$\ddot{x}_c = A_c x_c + [B_{cV} \ B_{cF}]u = (A_c - B_{cV}K)x_c + B_{cF}F_2 \quad (11)$$

One way to calculate the matrix K is by placing the eigenvalues of the closed-loop state matrix $(A_c - B_{cV}K)$ in some appropriate values in order to satisfy the following conditions. In this case, the desired closed-loop eigenvalues are shown in Eq. 12. They limit the settling time of the free decay response to 1.5 s when initial conditions of 10 mm are applied to each floor [6]. In this sense, and using the *place()* function of Matlab, the matrix K is calculated and shown in Eq. 13.

$$CP = [-5.3 + 5.9j \quad -5.3 - 5.9j \quad -4.2 + 21.9j \quad -4.2 - 21.9j \quad -13.7 + 8.4j \quad -13.7 - 8.4j] \quad (12)$$

$$K = [51.74 \quad 159.3 \quad -500.1 \quad 4.930 \quad 30.60 \quad -25.42] \quad (13)$$

This closed loop system cannot be implemented yet, since the state of the system is not directly measurable. For overcoming this issue, an observer must be used. This observer will estimate the state of the system from the measurable magnitudes: V_m , x_c , \ddot{x}_1 and \ddot{x}_2 , which are one of the inputs and the output vector. The output of the observer is an estimation of the system state vector, x_o . The strategy followed in this work consists in using the same state space model that describe the dynamics of the structure but modified adding the measured output. According to Eq. 14, this output (y) and the observer output vector (y_o) form an error vector which is multiplied by a gain matrix G and modifies the dynamics of the observer.

$$\dot{x}_o = A_c x_o + B_{cV}V_m + G(y_o - y) \quad (14)$$

$$y_o = C_c x_o + D_{cV}V_m$$

$$y_{xo} = I_n x_o$$

$$\dot{x}_o = (A_c - GC_c)x_o + (B_{cV} - GD_{cV})V_m + Gy_o \quad (15)$$

$$y_{xo} = I_n x_o$$

After some manipulation, Eq. 15 is obtained, where it can be seen that the dynamics of the observer depend on the matrix $[A_c - GC_c]$. The matrix G should be designed in such a way that the resulting observer dynamics are fast and damped enough. The chosen eigenvalues for this work are shown in Eq. 16. Real eigenvalues in this case mean that the dynamics are critically damped ($\zeta_j = 100\%$ for all modes). Once again, using the *place()* function of Matlab the matrix G can be computed.

$$OP = [-40 \quad -45 \quad -50 \quad -55 \quad -60 \quad -65] \quad (16)$$

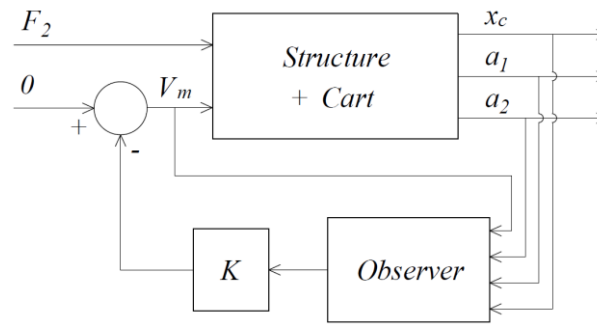


Figure 5: Feedback model of the structure with the AMD

After scripting the corresponding state space models, the loop can be easily closed as depicted in Figure 5 leaving one free input, F_2 , and three outputs (x_c , \ddot{x}_1 and \ddot{x}_2). Once again, FRFs have been experimentally estimated using the same procedure (impact hammer). A comparison between the experimental and simulated one is shown in Figure 6a. It is interesting to note a main difference between them around the first natural frequency. A peak at 1.37 Hz appears, which is probably due to the threshold value of the accelerometers used as input for control: for practical reasons, when accelerations are under 0.15 m/s^2 (estimated value) no output signal is generated. Due to this issue, the AMD does not interact for low accelerations so a residual movement, which is governed by the first mode of the structure, can only dissipate by the original structural damping, giving an appreciable peak around that frequency. The natural frequency (1.37 Hz) is lower than before (1.57 Hz, original model) because within the threshold the cart moves along with to the second floor of the structure, increasing its equivalent mass.

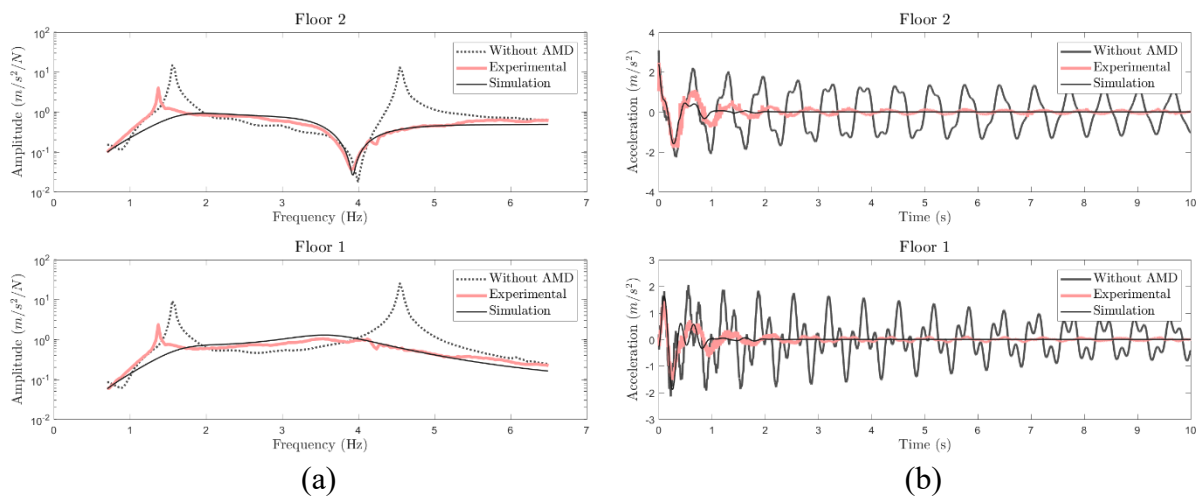


Figure 6: Frequency (a) and time (b) simulations of building model with the AMD

Also, a time comparison of the response of the system subjected to the same initial conditions is shown in Figure 6b. Here, more differences as before can be appreciated, mainly due to the aforementioned practical limitation together with the fact that an AMD system contains much more incertitude in its design and implementation.

4 DISCUSSION

To compare each system, two sets of results have been prepared. First, the plot in Figure 7 shows the poles and zeroes of the three treated models: the open loop uncontrolled system and the closed loop systems corresponding to the TMD and to the AMD. The horizontal axis represents the product $\omega_j \zeta_j$ of the corresponding eigenvalue whilst the vertical axis represents the product $\omega_j \sqrt{1 - \zeta_j^2}$.

As it can be easily seen, the uncontrolled structure (blue) has two natural modes (two pairs of poles) close to the vertical axis, which implies low damped modes (see Table 1). When adding the TMD (green), the first mode (the closest pair to the horizontal axis) is split into two new modes, one above and one below, which correspond to the two close peaks shown in Figure 4a. Both new pairs of poles are more damped than the original one, which translates into the damper effect of the device. When the AMD is considered, the original poles are notably moved to the left, which means an important increase of its modal damping. These results, theoretically, in an enormous increase of the damper effect and the efficiency of the system. However, as it has been mentioned and will be seen in Table 2, this is only true when the practical issues about the accelerometers measuring threshold are not considered.

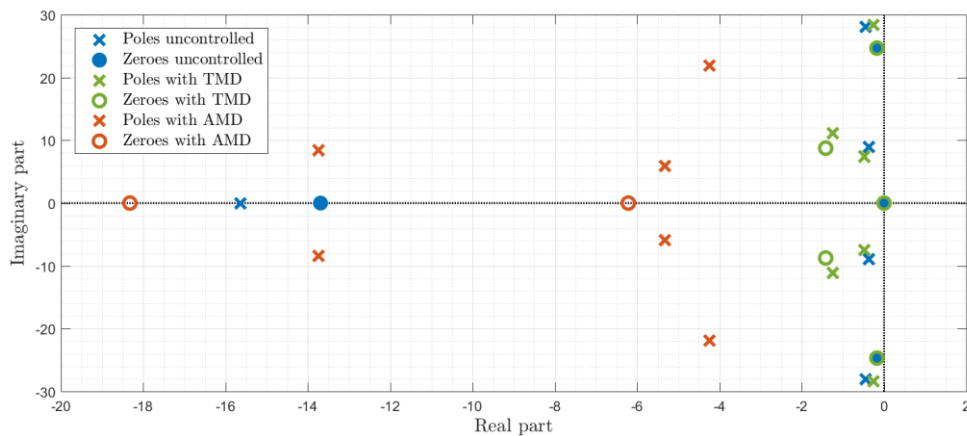


Figure 7: Poles and zeroes of the structure without control, with TMD and with AMD

Finally, a chart summarizing the value of some indicators is presented in Table 2. The maximum of the FRFs of Figures 2a, 4a and 6a are shown in the first two rows. Note that only the greatest maximum values between the first and the second floors has been considered. Also, the settling time (S.T.) of the free decay response (Figures 2b, 4b and 6b) has been estimated, first assuming a band of $\pm 10\%$ of the first maximum of the response (third row) and then assuming a band of $\pm 5\%$ (last row). These values are taken, once again, from the floor which produces the worst values. Every indicator is expressed in terms of its absolute value and also in percentage improvement.

As it can be seen, both damping devices have great and similar performance, being the AMD better to reach the $\pm 10\%$ band, as expected. However, in a more demanding case, to get the $\pm 5\%$ band, the AMD takes a little longer than the TMD. This is due to the fact that the accelerometers belonging to the control loop output a null value when the structure

accelerations are below a certain threshold (around 0.15 m/s^2). This causes the AMD to stop working which forces the residual movement to dissipate by itself, taking at the end longer time than the TMD to get the $\pm 5\%$ band.

Table 2: Indicators summary

	Uncontrolled	With TMD		With AMD	
Max. FRF1 [m/s ² /N]	14.7	1.2	91.8%	4.0	72.8%
Max. FRF2 [m/s ² /N]	24.4	12.9	47.1%	1.0	95.9%
S.T. 10% [s]	37.9 (p2)	5.7 (p1)	85.0%	4.0 (p2)	89.4%
S.T. 5% [s]	52.3 (p2)	7.2 (p1)	86.2%	11.7 (p2)	77.6%

5 CONCLUSIONS

As it can be seen from the results presented in this work, when compared with the same amount of moving mass both mitigation devices have great performance in mitigating oscillations on slender structures. It is also notable that both systems can be numerically simulated accurately. For the demanding loading scenarios presented in sections 3.1 and 3.2, the correspondence between experiments and simulation is very good. Also, as it is known [5], for the impulsive load under consideration, both affect very little to the first peak of the response (Figures 4b and 7b). After that, they both decrease the response levels to acceptable ranges. However, they present some important differences:

- The TMD is intended to deal with the contribution of one single mode of the structure. If the structure has more than one mode contributing significantly to its response, then more than one TMD should be installed. In this sense, the AMD is able to deal with a wider frequency band, mitigating the contribution of more than one mode at the same time. This conclusion is also applicable to the case of evolutionary structures whose frequencies can significantly change due to the occupation, thermal changes, etc.
- The TMD is a purely mechanical system. Its dynamics are coupled to the structural ones and, once tuned, if the mechanical moving parts have a good enough quality (to avoid friction and wearing effects), its good performance is ensured. The AMD, however, is an electro-mechanical system whose efficiency, apart from the aforementioned mechanical issues, depends on the power supply, programming and electronic performance (quality of sensors, real-time processing, etc.)
- For practical reasons (power consumption, maintenance, stability, mechanical gaps, sensor issues, etc.) the AMD exhibit a dead zone for low response levels while the TMDs, assuming that friction is negligible, work throughout the whole range.
- For the particular scenarios presented in sections 3.1 and 3.2, the settling time for a band of $\pm 10\%$ is 1.7 s shorter with the AMD but when a more demanding band ($\pm 5\%$)

is required, the TMD is 4.5 s quicker. Although these differences may not seem relevant, for loading cases (as vortex shedding, for example) where comfortability or serviceability conditions are compromised, it may be a factor to bear in mind.

Although other loading scenarios have to be considered, the results of this study show that the selection of the proper vibration control device is a hard task that depends on multiple factors. Being the performance a vital engineering factor, the durability, reliability and cost (including initial budget and operation and maintenance expenses) are also relevant issues.

ACKNOWLEDGEMENTS

The authors wish to acknowledge the *Ministerio de Ciencia, Innovación y Universidades*, Spanish Government, for the partial support through the RTI2018-098425 Research Project and the *Ministerio de Educación, Cultura y Deporte*, Spanish Government, for the FPU16/01339 predoctoral grant.

REFERENCES

- [1] Spencer Jr, B.F. and Nagarajaiah, S. State of the art of structural control. *ASCE Journal of Structural Engineering* (2003) **129**(7):845-56.
- [2] Zhang, C. and Ou, J. Modeling and dynamical performance of the electromagnetic mass driver system for structural vibration control. *Engineering Structures* (2015) **82**:93-103.
- [3] Elias, S. and Matsagar, V. Research developments in vibration control of structures using passive tuned mass dampers. *Annual Reviews in Control* (2017) **44**:129-156.
- [4] Ghassempour, M., Failla, G. and Arena, F. Vibration mitigation offshore wind turbines via tuned mass dampers. *Engineering Structures* (2019) **183**:610-636.
- [5] Casado, C., Munoz, I.M., Sebastian, J., Poncela, A. and Lorenzana, A. Implementation of passive and active vibration control on an in-service footbridge. *Structural Control and Health Monitoring* (2011) **20**:70-87.
- [6] Quanser Consulting Inc. Active mass damper. Two-floor (AMD-2), User Manual. (2002).
- [7] Ashashi-Sorkhabi, A., Malekghasemi, H. and Mercan, O. Implementation and verification of real-time hybrid simulation (RTHS) using a shake table for research and education. *Journal of Vibration and Control* (2013) **21**(8):1459-1472.
- [8] Tu, J., Lin, X., Tu, B., Xu, J. and Tan, D. Simulation and experimental tests on active mass damper control system based on Model References Adaptive Control algorithm. *Journal of Sound and Vibration* (2014) **333**(20):4826-4842.
- [9] Baratta, A., Corbi, I., Corbi, O., Carneiro Barros, R. and Bairrao, R. Shaking Table Experimental Researches Aimed at the Protection of Structures Subject to Dynamic Loading. *The Open Construction and Building Technology Journal* (2012) **6**:355-360.
- [10] Dyke, S.J., Truman, K.Z. and Gould, P.L. Current Directions in Earthquake Engineering Education: The University Consortium on Instructional Shake Tables. *Proceedings of the ASEE Annual Meeting, St. Louis, MO*, June 2000.
- [11] Irazu, L. and Elejabarrieta, M.J. Analysis and numerical modelling of eddy current damper for vibration problems. *Journal of Sound and Vibration* (2018) **426**: 75-89.

EDDY CURRENT DAMPED INTERCONNECTION FOR MITIGATION OF INTERNAL POUNDING IN A SEISMICALLY-ISOLATED BUILDING

FABIO MAZZA^{*} AND RODOLFO LABERNARDA[†]

^{*} Dipartimento di Ingegneria Civile
Università della Calabria
87036 Rende (Cosenza), Italy
e-mail: fabio.mazza@unical.it

[†] Dipartimento di Ingegneria Civile
Università della Calabria
87036 Rende (Cosenza), Italy
e-mail: rodolfo.labernarda@unical.it

Key words: Isolated R.C. Framed Building; Fixed-Base Steel Framed Elevator Shaft; Internal Pounding, Eddy Current Dampers, Nonlinear Seismic Analysis.

Abstract. Internal pounding effects between closely spaced structural parts (e.g. in the case of an insufficient gap between elevator and surrounding building) may be found in seismically isolated structures, due to notable displacement at the level of the isolation system under severe earthquakes. To study this poorly investigated question, a reinforced concrete (r.c.) building, with a hybrid isolation system including elastomeric and sliding bearings, is considered. The building, which is located in the Sicilian town of Augusta, is comprised of a basement and three storeys above the ground level, and is seismically isolated at the top of rigid columns in the basement, while a steel framed elevator shaft crosses the isolation level. A very common structural configuration is presented here, with a gap between the fixed-base elevator shaft and the building. Despite the gap, internal pounding may occur at all levels of the superstructure when the elevator with maximum load stops at the upper floors. To reduce pounding effects, a smart eddy current damped interconnection (ECDI) between adjacent corners of the elevator and the surrounding building at the floor level is proposed. This occupies less space than traditional passive dampers and transmits considerably less forces compared to a rigid link configuration. Specifically, an eddy current damper (ECD) consists of an outer cylindrical tube, as conductor, and an inner tube, equipped with an array of axially magnetized and ring-shaped permanent magnets separated by iron pole pieces, as mover. The relative motion between conductor and magnets, during seismic loading, induces an eddy current producing electromagnetic damping. Given that viscoelastic linear behaviour can be hypothesized for the ECDs, a simplified iterative design procedure of the ECDI is proposed. Finally, to evaluate the effectiveness of the ECDI, nonlinear seismic analysis is carried out with regard to five structural models: i.e. no connection (i), flexible links (ii), rigid links (iii), viscous damped links (iv), eddy current damped links (v).

1 INTRODUCTION

Internal pounding between a fixed-base elevator shaft and/or stairs crossing the isolation level and structural parts of the surrounding building may occur in seismically isolated buildings, due to the fact that the difference in the dynamic properties of independent units may lead to out-of-phase movements inducing structural interaction during an earthquake [1]. Previous studies showed that seismic pounding may lead to significant damage of the lighter structure (e.g. the elevator shaft), whereas the behaviour of the heavier structure (i.e. the main building) is only slightly influenced by collisions [2]. Moreover, the high deformability of an isolated structure may lead to amplification in the pounding under anomalous ground motions like those recorded near-faults [3, 4], where considerable displacement is expected under long-duration and high-amplitude velocity pulses [5]. Seismic codes provide the minimum design gap between independent units of the same building, depending on maximum horizontal displacement of the two units at the corresponding level under the design basis [6] and/or maximum considered [7] earthquakes. The simplest way to avoid or reduce internal pounding is to design a separation joint between the potentially colliding systems, but a wide gap may well conflict with practical considerations that may make the creation of a sufficiently wide internal gap problematic. One alternative is to minimize the effect of pounding through decreasing lateral motion at the level of the isolation system with a self-stopping mechanism [8] or a passive gap damper [9], but a substantial increase of the shear and drift demands of the superstructure represents the counterpart [10]. In-phase motion of adjacent structures is expected with rigid links placed at critical locations (e.g. floor levels), but an increase of base shear on the stiffer structure [11] and notably higher forces are reciprocally transmitted in comparison to damped links also increasing damping capacity [12].

With the aim of studying the effects of damped links to reduce internal pounding effects, a recent commercial building in the Sicilian town of Augusta (Italy) is considered as test structure. Specifically, an r.c. framed structure with rectangular plan, composed of a basement and three storeys above ground level, is seismically isolated with a hybrid system including sixteen elastomeric (i.e. High-Damping-Rubber Bearings, HDRBs) and sixteen sliding (i.e. Low-Friction-Sliding Bearings, LFSBs) bearings. An internal elevator shaft with a fixed-base steel framed structure crosses the isolation plane and emerges in the basement. In order to prevent mutual pounding under severe earthquakes, the idea of connecting two structures with different dynamic properties by using traditional passive devices was explored in early 70's. This paper proposes a major innovation in the form of a smart eddy current damped interconnection (ECDI) at the floor levels, between adjacent corners of the elevator and surrounding building, because it takes up less space than traditional damped links while allowing a damping of the same order as viscous dampers. An eddy current damper (ECD) produces an electromagnetic damping force by using an array of axially magnetized ring-shaped permanent magnets separated by iron pole pieces [13]. Stiffness and damping properties of the smart coupling and alternative traditional links are first designed through an iterative procedure where minima floor displacements of the elevator are selected as performance targets. A seismic gap is also designed to verify the possibility of displacement of the steel structure and deformation of the isolation system of the unconnected r.c. superstructure. The effectiveness of coupling with links placed only at top level and at all levels is checked by means of nonlinear dynamic analysis of the said building subjected to strong near-fault earthquakes.

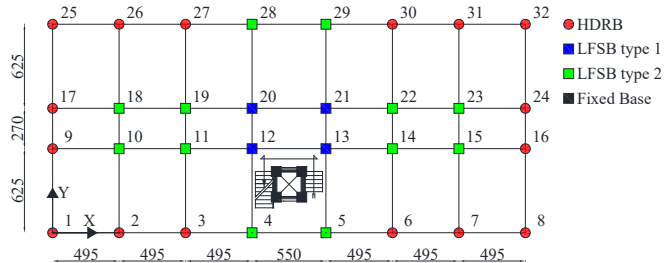
2 SEISMICALLY ISOLATED BENCHMARK BUILDING

An r.c. framed commercial building located in the Sicilian town of Augusta (Italy), composed of a basement and three storeys above ground level (Figure 1a), is considered as test structure. It is seismically isolated with a hybrid system including sixteen HDRBs and sixteen LFSBs inserted at the top of rigid columns in the basement (Figure 1b). The building plan is symmetrical with respect to the transversal (Y direction), but not with respect to the longitudinal (X direction) due to the presence of a steel framed elevator structure crossing the isolation level (Figures 1c,d).

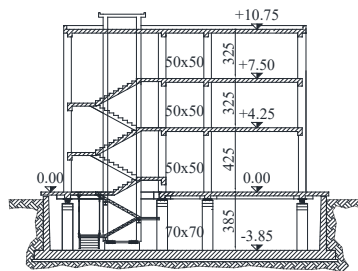
The design of the isolation system is carried out on the basis of the following assumptions for the horizontal seismic loads at the collapse prevention (CP) limit state: equivalent viscous damping of the isolation system $\xi_H=15\%$; high-risk seismic zone (peak ground acceleration on rock, $a_g=0.406g$); stiff subsoil (class B, with subsoil parameter $S_S=1.018$); topographic class T1 (stratigraphic parameter $S_T=1$); displacement demand $d_{dc}=270$ mm. The fundamental vibration period of the seismically-isolated structure is equal to $T_{1H}=2.38s$ [14], corresponding to a mass of the superstructure equal to 2400 tons and a horizontal stiffness of the isolation system of 16.45 kN/mm. The latter is divided between the sixteen HDRBs on the assumption that the stiffness contribution of the sixteen LFSBs is negligible. Type SI-N500/150 is selected for the HDRBs produced by FIP Industriale [15], corresponding to normal rubber compound with a shear modulus $G=0.8MPa$, assuming the geometrical and mechanical properties shown in Table 1: i.e. external diameter of the isolator (D); total thickness of the rubber (t_r); primary (S_1) and secondary (S_2) shape factors; equivalent horizontal (ξ_{eH}) and vertical (ξ_{eV}) viscous damping ratios; horizontal (K_{H0}) and vertical (K_{V0}) stiffnesses at the shear deformation $\gamma=1$; maximum vertical load (P_c) and displacement capacity (d_c) at the collapse prevention (CP) limit state.



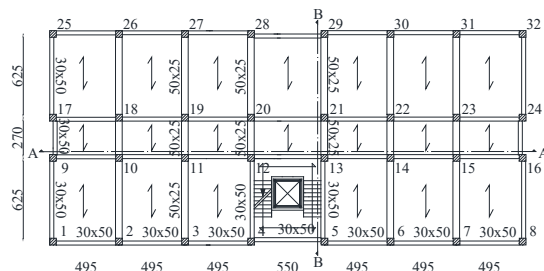
(a) Picture of the building



(b) Plan of the isolation level



(c) Transversal section A-A



(d) Plan of the first level

Figure 1: The Augusta building, Italy (units in cm)

Two types of LFSBs produced by the same company are placed in the building plan

depending on the maximum loading capacity (Figure 1b): i.e. type 1, VM 200/600/600, and type 2, VM 150/600/600, where the first number represents the vertical load capacity in tons (P_c) and the other two the permitted longitudinal and transversal movements in mm ($\pm d_c$). Moreover, a dynamic-fast friction coefficient $\mu_{fast}=1.7\%$ is the outcome of a calibration process.

Table 1: Geometrical and mechanical properties of the HDRBs (units in kN, mm and s)

D_b	t_r	S_1	S_2	ξ_{eH}	ξ_{eV}	K_{H0}	K_{V0}	P_c	d_c
500	150	20	3.2	15%	5%	1.05	1016	1200	300

The design of the superstructure is carried out at the ultimate life-safety (LS) limit state, under the corresponding horizontal seismic loads (i.e. $a_g=0.285g$ and $S_S=1.136$), assuming nearly elastic response (behaviour factor, $q=1.5$). The gravity loads used in the design are represented by dead- and live loads, equal to: 6.47 kN/m^2 and 4 kN/m^2 , for the first three levels; 5.27 kN/m^2 and 2 kN/m^2 , for the roof level. Perimeter masonry infills without openings are placed along the short side of the building, at the second storey, and in the central bay of the long side of the building, at the first and second storey, while additional masonry infills are placed around the staircase. A cylindrical compressive strength of 30 N/mm^2 for the concrete and a yield strength of 450 N/mm^2 for the steel are assumed as characteristic values for the r.c. cross sections. The length of the frame members is shown in Figure 1, where cross-sections of columns (Figure 1c) and beams (Figure 1d) are also reported.

The steel frame elevator shaft crosses the isolation plane and emerges in the basement where it is fixed-base and separated from the surrounding building by a gap (Figure 2a). The elevator shaft is classified as non-dissipative (i.e. behaviour factor $q=1$) and designed at the LS limit state. A dead load of 10 kN plus a live load of 10 kN , depending on the maximum number of persons allowed, are considered for the elevator. Moreover, a lightweight infill panel of the elevator shaft equal to 0.43 kN/m^2 is applied on three sides of its perimeter.

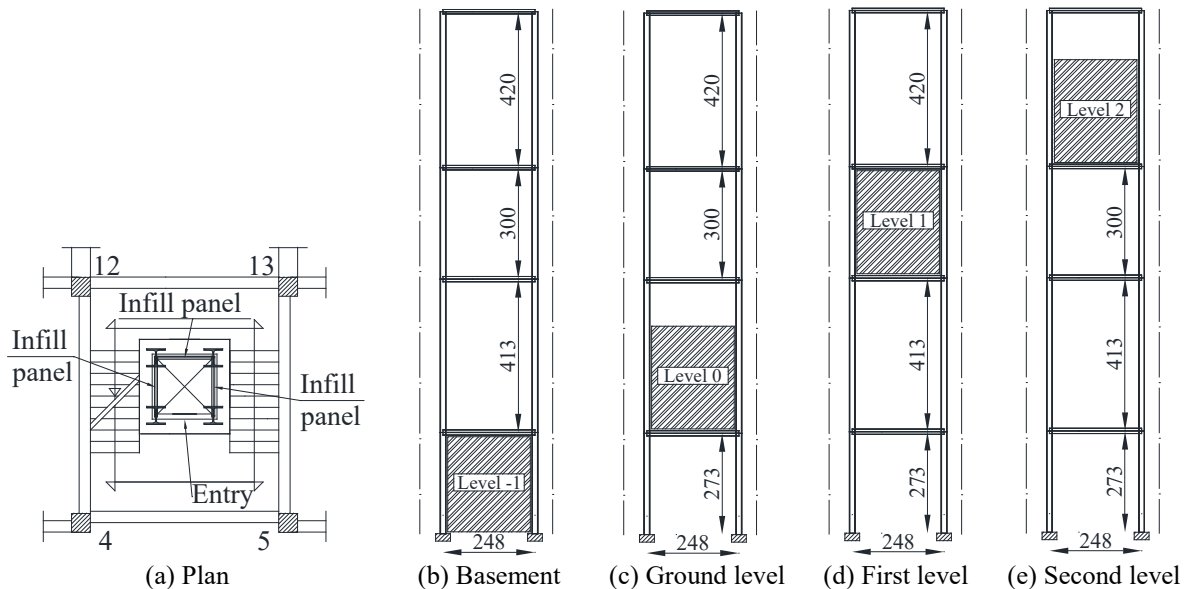


Figure 2: View of stairs and elevator shaft (units in cm)

For the elevator eight design scenarios are considered, assuming maximum ($W_{\text{elev.}}=20$ kN) and minimum (i.e. empty, $W_{\text{elev.}}=10$ kN) loads combined with four different vertical positions, corresponding to the basement (level -1) and three floors above (levels 0, 1 and 2 shown in Figures 2b-2e). The elevator shaft is designed to fulfil the full operational ($\Delta/h=0.33\%$, defined as interstorey drift (Δ) normalized by the storey height (h)) and operational ($\Delta/h=0.5\%$) deformability limit states, under the corresponding horizontal seismic loads (FO: $a_g=0.056g$ and $S_S=1.20$; OP: $a_g=0.076g$ and $S_S=1.20$), and ultimate LS limit states for strength and buckling. Cross-sections of steel frame members are assumed constant along the height and ductile, in line with class 1 (i.e. double-T steel sections type HEA 120 for beams) and 2 (i.e. double-T steel sections type HEA 160 for columns, with principal axis oriented as shown in Figure 2a) provided by the Italian seismic code [6]. Yield and ultimate strengths of 355 N/mm² and 510 N/mm² are assumed for the steel, respectively. Finally, the dynamic properties of the elevator shaft for different vertical positions of the elevator at maximum load are presented in Table 2: i.e. fundamental vibration periods ($T_{1,X}$ and $T_{1,Y}$) and effective masses ($m_{e1,X}$ and $m_{e1,Y}$) along the principal in-plan directions.

Table 2: Dynamic properties of the elevator shaft

Elevator at maximum load ($m_{\text{tot}}=8.16$ ton)				
Position of the elevator	$T_{1,X}$ (s)	$m_{e,X}$ (% m_{tot})	$T_{1,Y}$ (s)	$m_{e,Y}$ (% m_{tot})
-1	0.914	70.04	0.715	75.37
0	0.923	61.09	0.721	65.04
1	1.049	78.65	0.817	82.06
2	1.147	78.81	0.909	81.54

A three-spring-three-dashpot viscoelastic model can be adopted for an HDRB, consisting of an axial spring acting in parallel with a viscous dashpot both in the horizontal and vertical directions. Specifically, coupled nonlinear elastic springs in the horizontal ($F_{K,x}$, $F_{K,y}$) and vertical (P_K) directions proportional to horizontal and vertical displacement ($u_{H,x}$, $u_{H,y}$ and u_V), with a vertical displacement (u_V^*) taking into account the axial shortening or lengthening due to second order geometric effects, are assumed [4]

$$\begin{Bmatrix} F_{K,x} \\ F_{K,y} \end{Bmatrix} = \bar{K}_{H0} \cdot \left(I - \left(\frac{P}{P'_{cr}} \right)^2 \right) \cdot \begin{Bmatrix} u_{H,x} \\ u_{H,y} \end{Bmatrix} = K_{H0} \cdot [0.337 + 0.663 \cdot e^{-4.64 \cdot \gamma}] \cdot \left(I - \left(\frac{P}{P'_{cr}} \right)^2 \right) \cdot \begin{Bmatrix} u_{H,x} \\ u_{H,y} \end{Bmatrix} \quad (1a,b)$$

$$P_K = \bar{K}_{V0} \cdot u_V^* \cong \frac{K_{V0} \cdot \text{sgn}(u_V)}{1 + 48 \cdot \left(\frac{u_H}{\pi \cdot D_b} \right)^2} \cdot \left(|u_V| - \frac{16 \cdot \alpha_b}{\pi^2 \cdot D_b \cdot S_2 \cdot \alpha_{K0}} \cdot u_H^2 \right) \quad (1c)$$

where $\alpha_{K0}(=K_{V0}/K_{H0})$ is the nominal stiffness ratio, P'_{cr} is the reduced critical buckling load and $\alpha_b=h_b/t_r$, h_b being the total height of the bearing. It is worth noting that the horizontal stiffness is characterized by significant variation when shear deformation (γ) is lower than 1 and is practically constant for γ values greater than 1. On the other hand, taking into consideration that the equivalent viscous damping in the horizontal direction depends on the amplitude of displacement, the bearing is subjected to and, ultimately, on the amplitude of the shear strain [15], the following uncoupled damping axial forces ($F_{C,x}$, $F_{C,y}$ and P_C), proportional to the horizontal and vertical velocity ($\dot{u}_{H,x}$, $\dot{u}_{H,y}$ and \dot{u}_V), are assumed

$$\begin{Bmatrix} F_{C,x} \\ F_{C,y} \end{Bmatrix} = \bar{C}_{H0} \cdot \begin{Bmatrix} \dot{u}_{H,x} \\ \dot{u}_{H,y} \end{Bmatrix} = C_{H0} \cdot [0.543 + 0.457 \cdot e^{-2.843 \cdot \gamma}] \cdot \begin{Bmatrix} \dot{u}_{H,x} \\ \dot{u}_{H,y} \end{Bmatrix} \quad (2a,b)$$

$$P_C = C_{V0} \cdot \dot{u}_V \cong \frac{\xi_V \cdot K_{VI} \cdot T_{IV}}{\pi} \cdot \dot{u}_V \quad (2c)$$

with significant differences for low horizontal displacements and almost the same values when $\gamma > 1$ are obtained (see Equations 2a,b).

For sliding bearings with low values of the friction coefficient (i.e. steel-PTFE low friction flat sliding bearings, LFSBs), the force-displacement behaviour in the horizontal directions can be idealized as bilinear (rigid-plastic). In particular, variable axial load (i.e. $N = W \pm \Delta N$, W being the weight of the superstructure and ΔN the additional axial load, positive when compressive, due to the overturning moment produced by the horizontal ground acceleration) and constant value of the friction coefficient (i.e. μ equal to the dynamic fast value μ_{max}) can be represented by hysteretic model with biaxial interaction

$$\begin{Bmatrix} F_x \\ F_y \end{Bmatrix} = \mu \cdot N \cdot \begin{Bmatrix} Z_x \\ Z_y \end{Bmatrix} = \mu_{max} \cdot N \cdot \begin{Bmatrix} Z_x \\ Z_y \end{Bmatrix} = \mu_{max} \cdot N \cdot \begin{Bmatrix} \cos\theta \\ \sin\theta \end{Bmatrix}, \quad \theta = \arctan\left(\frac{\dot{u}_{H,y}}{\dot{u}_{H,x}}\right) \quad (3a,b)$$

where the dimensionless quantities Z_x and Z_y are governed by two coupled differential equations which account for the interaction between the x and y directions [4]. Furthermore, a gap element with infinitely rigid behaviour in compression is assumed in the vertical direction to account for the fact that a sliding bearing does not resist tensile axial loads and is thus free to uplift at any given moment during an earthquake

$$P = N \quad \text{for } u_V \geq 0 \quad \text{and} \quad P = 0 \quad \text{for } u_V < 0 \quad (3c)$$

neglecting the equivalent viscous damping in the vertical direction.

3 CONNECTION FOR MITIGATING OF INTERNAL POUNDING

A seismic gap (g_d) between the fixed-base elevator shaft (Es) and base-isolated surrounding building (Sb) (Figure 3a) is first designed on the basis of current Italian [6] and European [7] seismic codes. Specifically, three different thresholds are evaluated as function of the lateral load resisting system (i.e. base-isolated or fixed-base structure), the LS (i.e. $PGA_{LS} = 0.324$ g) and CP (i.e. $PGA_{CP} = 0.413$ g) limit states and the elevator height (i.e. $H = 14.06$ m): i.e. sum of the horizontal top displacements of both systems at the LS limit state (i.e. $g_{d,NTC18} = 33$ cm), no less than $2 \cdot H / 100 \cdot a_g \cdot S/g$; square root of the sum of the squares of the maximum top horizontal displacements of both systems, at the LS (i.e. $g_{d,EC8.1} = 24$ cm) and CP (i.e. $g_{d,EC8.2} = 35$ cm) limit states. To ensure that the seismic gap is large enough to cope with sizeable horizontal displacements induced by strong earthquakes, the Es-Sb relative displacements are evaluated along the in-plan X (i.e. $u_{Es,i}$ and $u_{Sb,i}$) and Y (i.e. $v_{Es,i}$ and $v_{Sb,i}$) directions

$$g_{X,i}(t) = u_{Es,i}(t) - u_{Sb,i}(t), \quad g_{Y,i}(t) = v_{Es,i}(t) - v_{Sb,i}(t), \quad i = 1-4 \quad (4a,b)$$

on the assumption that a positive value corresponds to a coordinate of the Es corner greater than that of the corresponding Sb corner (Figure 3b).

Then, the problem of connecting two different subsystems of the same structure is examined for four types of connection between the four couples of corner joints at each floor level (Figure

3c): i.e. flexible links (FLs); rigid links (RLs); viscous damped links (VDLs); eddy current damped links (ECDLs).

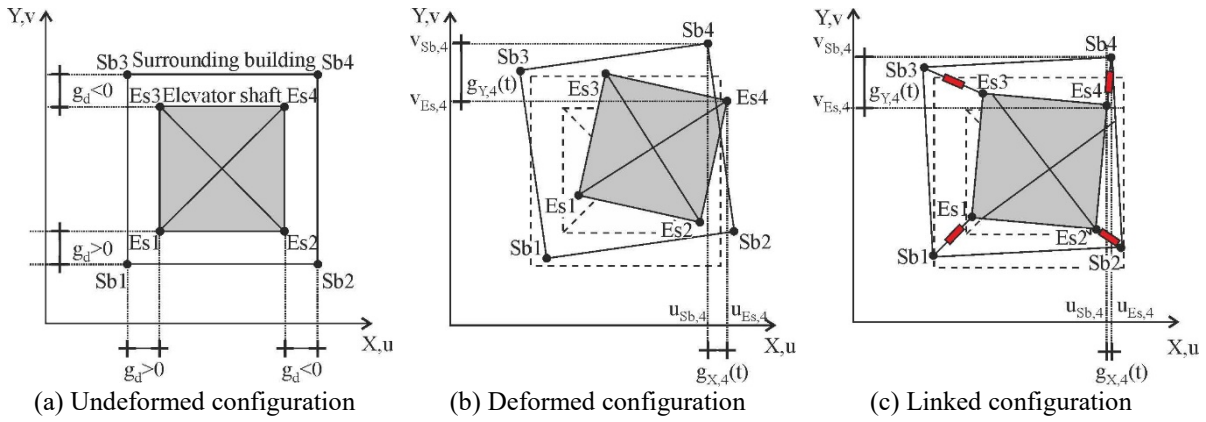


Figure 3: Internal pounding between the fixed-base elevator shaft and base-isolated surrounding building

Once selected the type of connection, the model of coupling between the base-isolated Sb and fixed-base Es is made under the following assumptions along both the principal in-plan directions (X and Y): i) mass, stiffness and damping of the Sb ($m_{Sb,j}$, $k_{Sb,j}$ and $c_{Sb,j}$) and Es ($m_{Es,j}$, $k_{Es,j}$ and $c_{Es,j}$) and stiffness and damping of the connective links ($k_{L,j}$ and $c_{L,j}$) can be varied along the height ($j=0-3$); ii) viscous damping of the Sb is considered only at the isolation level ($c_{Sb,0}$), while the contribution of the superstructure is not considered; iii) assuming an equivalent viscous damping ratio $\xi_{Es,H}=2\%$, the Rayleigh approach is used to evaluate the viscous damping of the Es; iv) the Sb and Es are modelled as shear- (r.c.) and flexible-type (steel) plane frames, respectively; v) classical damping simplification is assumed, given that the fundamental frequencies of Sb and Es are well separated; vi) floor elevations are the same for Sb and Es, without taking into account the extra head at top of the elevator shaft; vii) the Sb and Es are connected only at the top floor (case A, Figure 4a) or at all floors (case B, Figure 4b).

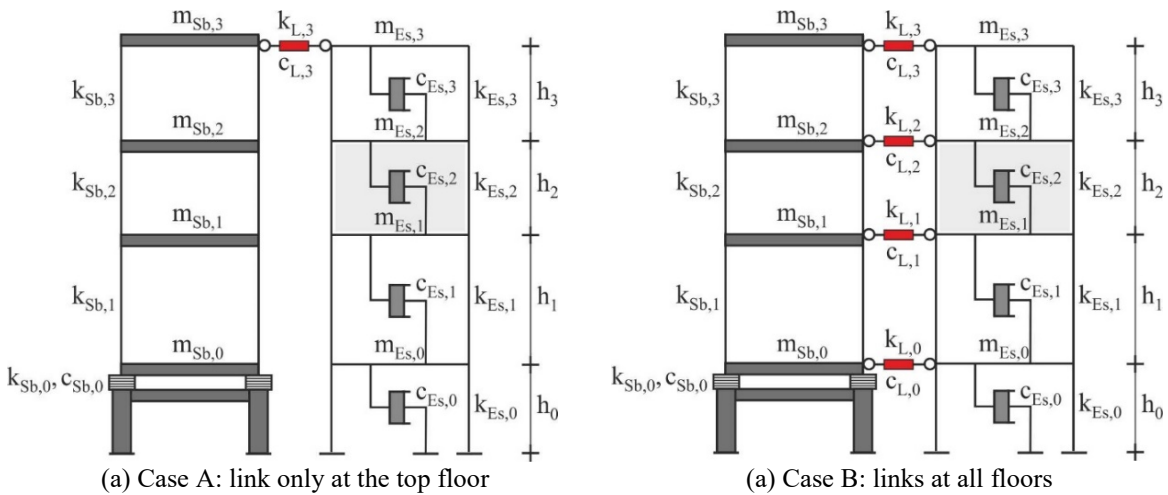


Figure 4: Model of coupling between surrounding building (Sb) and elevator shaft (Es)

The main properties of the surrounding building (Sb) and elevator shaft (Es) are reported in Table 3. It should be noted that Sb stiffness is the same for the principal X and Y directions, since all columns have a square section, while stiffness and damping of Es are not reported because a static condensation of the number of degrees of freedom reduces the number of free displacement to eight (i.e. four horizontal displacements for Sb and Es, respectively).

A design procedure of the links ($k_{L,j}$) is first developed to evaluate the distribution of vertical stiffness, with the aim of minimizing horizontal displacement of the elevator at all levels (u_j , $j=0-3$). In detail, a four-sweep-four-step iterative approach is adopted, in which the k -th sweep consists of four steps each with the aim of evaluating stiffness by reducing the horizontal displacement at one level at a time, for fixed values of stiffness at the other levels. Then, damping force of the dissipative links is evaluated based on a stiffness-proportional criterion, with equivalent viscous damping ratio $\xi_{DL,H}=25\%$. Results of the iterative procedure, in terms of the horizontal displacement ratio ($u_j/u_{j,max}$), are shown in Figure 5, with reference to both principal in-plan directions assuming that the most critical internal pounding condition occurs when the elevator with maximum load stops at the first level (Figure 4).

Table 3: Main properties of the model of coupling between Sb and Es

Floor level	h_i [m]	m_{Sb} [ton]	k_{Sb} [kN/m]	c_{Sb} [kNs/m]	m_{Es} [ton]
0	2.85	722	16450	1798	1.847
1	4.25	776	563670	-	1.660
2	3.12	631	1260500	-	3.939
3	3.12	271	212830	-	0.714

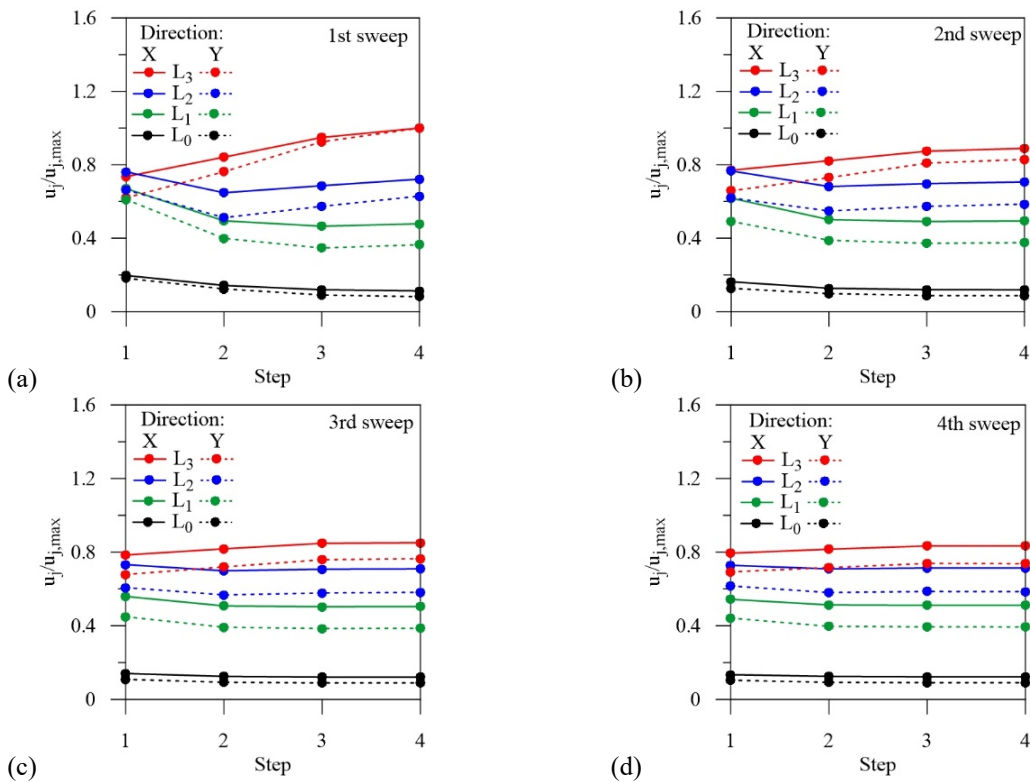


Figure 5: Results of the four-sweep-four step iterative design procedure of links

Note that maximum displacement (i.e. $u_j/u_{j,max}=1.0$) is obtained to step four of the first sweep along both the principal in-plan directions (Figure 5a). Moreover, gradual reduction of the ratio $u_j/u_{j,max}$ occurs at all four levels proving the effectiveness of the iterative procedure (Figure 5d). Finally, stiffness and damping properties of the links are summarized in Table 4 for cases A and B and both principal directions.

Table 4: Main properties of links (units in kN, m and s)

	Case A: X direction		Case A: Y direction		Case B: X direction		Case B: Y direction	
Floor level	k_L	c_L	k_L	c_L	k_L	c_L	k_L	c_L
3	56.47	5.55	80.00	6.58	56.47	5.55	80.00	6.58
2	0	0	0	0	40.00	3.93	58.59	4.85
1	0	0	0	0	24.00	2.36	45.00	3.70
0	0	0	0	0	26.67	2.62	54.74	4.50

A sketch of an Eddy Current Damped Link (ECDL) is shown in Figure 6, consisting of an outer cylindrical tube, as conductor, and an array of axially magnetized ring-shaped permanent magnets, separated by iron pole pieces, as a mover [13]. In detail, eddy currents are generated in the copper conductor following the relative motion from the magnets, where the direction of magnetization for each permanent magnet is indicated by bold arrows. It should be noted that these eddy currents produce an electromagnetic damping force proportional to the velocity of the conductor so that the ECDL acts as a viscous damper but with a significant improvement because it takes up less space. For the sake of brevity, only the main parameters of the ECDL are reported in Table 5, with reference to maximum values of stiffness and damping shown in Table 4 in the Y direction: i.e. t_c , conductor thickness; t_m , magnet thickness; t_p , pole thickness; r_m , annular magnet radius; r_r , cylindrical rod radius; air gap, a_g ; number of magnets (n_m) and poles (n_p); conductivity of copper, σ_c ; residual magnetic flux density, B_r .

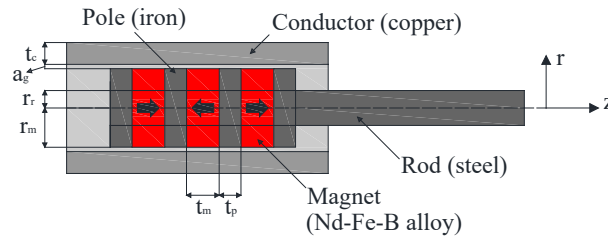


Figure 6: Sketch of an Eddy Current Damped Link [13]

Table 5: Main properties of the ECDLs (units in mm, S/m and T)

Floor level	t_c	t_m	t_p	r_m	r_r	a_g	n_m	n_p	σ_c	B_r
3	20	20	10	60	15	0.5	4	3	5.80×10^7	1.43
2	15	20	10	50	15	0.5	4	3	5.80×10^7	1.43
1	11	20	10	45	15	0.5	4	3	5.80×10^7	1.43
0	15	20	10	48	15	0.5	4	3	5.80×10^7	1.43

4 NUMERICAL RESULTS

To investigate the effectiveness of different types of connection between Sb and Es of the Augusta building for mitigating internal pounding, nonlinear dynamic analyses are carried out

considering the horizontal components of seven spectrum-compatible near-fault earthquakes characterized by forward directivity [4]. R.c. frame members of the superstructure are described by a lumped plasticity model, while an elastic-linear response consistent with the design hypotheses is adopted for the steel framed structure of the elevator shaft. On the other hand, the three-degrees-of-freedom model of the HDRBs and the simplified model of the LFSBs, previously described, are adopted for the hybrid isolation system. Preliminary analysis is carried out with a view to identifying the critical incidence angle of the selected bi-directional earthquakes (i.e. $\alpha=150^\circ$), then results are obtained as the mean of those for each pair of records.

Firstly, plots of the maximum internal pounding parameter (i.e. the relative displacements g_x and g_y between Sb and Es) along the building height are reported in Figure 7, for the adjacent corner joints n.1 (Figures 7a,b) and n.3 (Figures 7c,d) and both directions. Flexible (FL) and rigid (RL) links without dissipation are compared with viscous damped (VDL) and eddy current damped (ECDL) links, assuming connection only at the top floor (case A) or at all floors (case B). As shown, internal pounding is confirmed for the unlinked configuration, exceeding in some cases the EC8 upper and lower bound values (Figure 7b) and in others the NTC18 threshold (Figure 7c). In terms of mitigation of internal pounding, the best performance is attained when more than one connection is considered (case B). Moreover, coupling of stiffness and damping (i.e. ECDLs) is more effective than a viscous connection on its own (i.e. VDLs) or a flexible spring (i.e. FLs). With reference to rigid links, the observed performance highlights remarkable reduction of internal pounding.

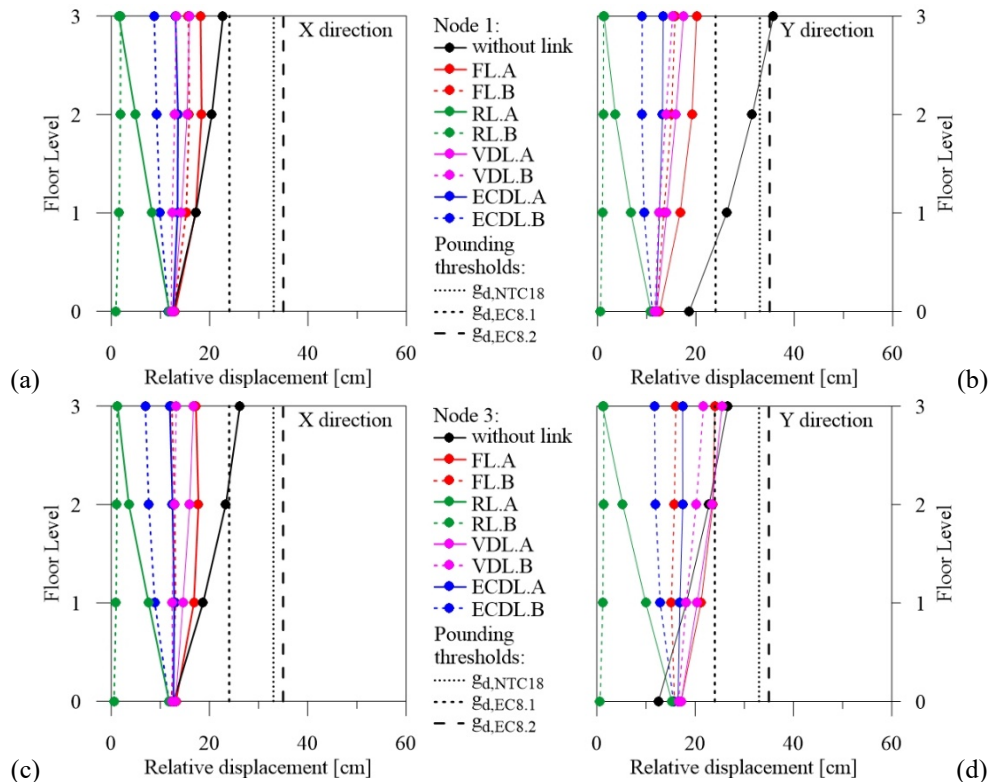


Figure 7: Internal pounding of Sb and ES along the building height

Graphs similar to the previous ones are shown in Figure 8, where maximum values of floor acceleration (Figures 8a,b) and storey drift (Figures 8c,d) of the elevator shaft at corner joint n. 2 are plotted, with a view to serviceability and damage conditions, respectively. It is interesting to note that ECDLs continue to prove the best coupling solution. On the contrary, FLs and RL.A correspond to accelerations comparable with those of the solution without link, while RL.B is ineffective at reducing storey drift, producing too high values at level 0 where the elevator shaft is forced to undergo the same displacement as the isolation system when connection at all levels is assumed.

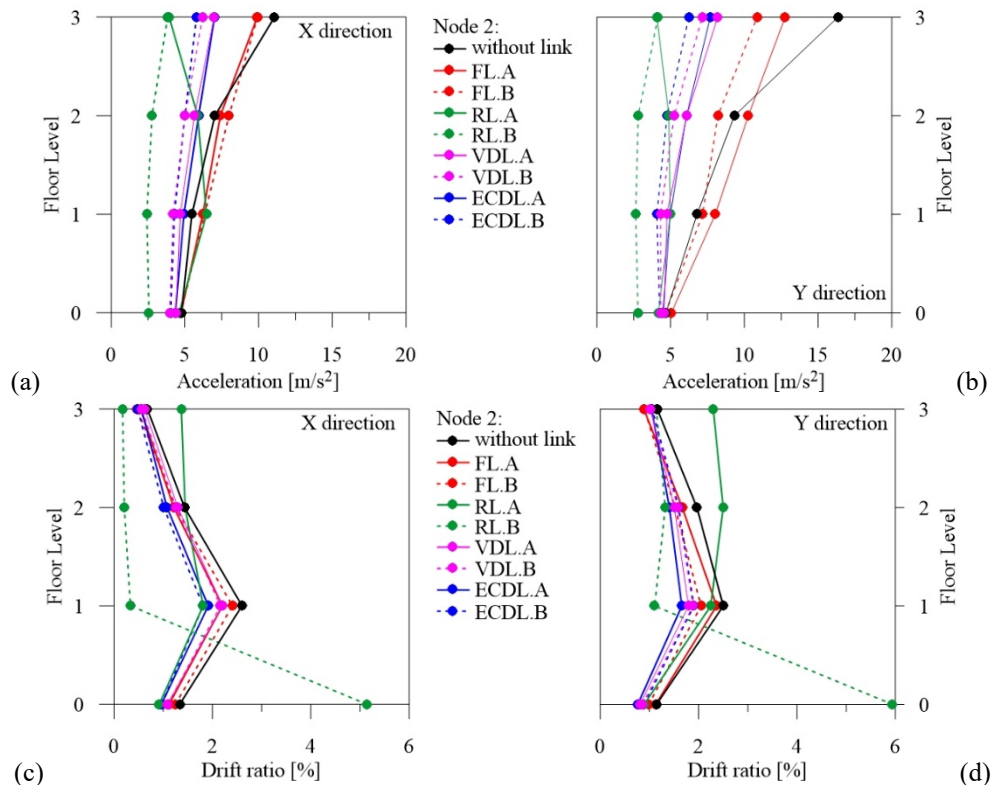


Figure 8: Floor acceleration (a, b) and storey drift (c, d) of the ES along the building height

5 CONCLUSIONS

The effectiveness of coupling between independent units of seismically isolated buildings located near an active fault for mitigating internal pounding is investigated here, through a case study of a four-storey r.c. framed structure in the Italian town of Augusta (Sicily). An elastomeric-friction hybrid isolation system at ground level, crossed by the steel framed structure of a fixed-base elevator shaft, is considered. First, a four-sweep-four-step iterative design procedure is proposed, to evaluate stiffness and/or damping properties of four types of connections between the four couples of corner joints, only at the top floor or at all floors: flexible links (FLs); rigid links (RLs); viscous damped links (VDLs); eddy current damped links (ECDLs). Then, nonlinear dynamic analysis is carried out to test their performance during spectrum-compatible near-fault earthquakes. The results show that the coupling of stiffness and damping (ECDLs) is always more effective than a viscous connection (VDLs) on its own, while

FLs and RL.A are ineffective because of accelerations comparable with those of the solution without link, and RL.B produces excessive storey drift, especially at isolation level.

ACKNOWLEDGEMENTS

The present work was financed by Re.L.U.I.S. (Italian network of university laboratories of earthquake engineering), in accordance with the “Convenzione D.P.C.–Re.L.U.I.S. 2019–2021, WP15, Code Revisions for Isolation and Dissipation”.

REFERENCES

- [1] Maison, B.F. and Kasai, K. Dynamics of pounding when two buildings collide. *Earthquake Engineering and Structural Dynamics* (1992) **21**:771-786.
- [2] Jankowski, R. Non-linear FEM analysis of earthquake-induced pounding between the main building and the stairway tower of the Olive View Hospital. *Engineering Structures* (2009) **31**(8):1851-1864.
- [3] Pant, D.R. and Wijeyewickrema, A.C. Influence of near-fault ground motions on the response of base-isolated reinforced concrete buildings considering seismic pounding. *Advances in Structural Engineering* (2013) **16**(12):1973-1988.
- [4] Mazza, F. and Labernarda, R. Effects of nonlinear modelling of the base-isolation system on the seismic analysis of r.c. buildings. *14th International Conference on Building Pathology and Constructions Repair, CINPAR*, (2018) Firenze, Italy, 20-22 June.
- [5] Chioccarelli, E. and Iervolino, I. Near-source seismic demand and pulse-like records: A discussion for L'Aquila earthquake. *Earthquake Engineering and Structural Dynamics* (2010) **39**(9):1039-1062.
- [6] Updating of the Technical Regulations for the Constructions (NTC18). Italian Ministry of the Infrastructures, D.M. 17-01-2018.
- [7] Eurocode 8 (EC8). Design of structures for earthquake resistance - Part 1: General rules, seismic actions and rules for buildings. C.E.N, European Committee for Stand. (2004).
- [8] Ismail, M. An isolation system for limited seismic gaps in near-fault zones. *Earthquake Engineering and Structural Dynamics* (2014) **44**(7):1115-1137.
- [9] Rawlinson T.A., Marshall, J.D., Ryan, K.L. and Zargar, H. Development and experimental evaluation of a passive gap damper device to prevent pounding in base-isolated structures. *Earthquake Engineering and Structural Dynamics* (2015) **44**(11):1661-1675.
- [10] Mazza, F. and Vulcano, A. Nonlinear response of rc framed buildings with isolation and supplemental damping at the base subjected to near-fault earthquakes. *Journal of Earthquake Engineering* (2009) **13**(5):690-715.
- [11] Westermo, B. The dynamics of interstructural connection to prevent pounding. *Earthquake Engineering and Structural Dynamics* (1989) **18**:687-699.
- [12] Licari, M., Sorace, S. and Terenzi, G. Nonlinear modeling and mitigation of seismic pounding between r/c frame buildings. *Journal of Earthq. Engineering* (2015) **19**:431-460.
- [13] Ebrahimi, B., Khamesee, M.B. and Golnaraghi, F. Permanent magnet configuration in design of an eddy current damper. *Microsystem Technologies* (2008) **16**: 19-24.
- [14] Oliveto, G., Athanasiou, A. and Granata, M. (2013). Blind simulation of full scale free vibration tests on a three story base isolated building. *Proceedings of the 10th International Conference on Urban Earthquake Engineering* (2018) Tokyo, Japan.
- [15] FIP Industriale S.p.A.. Elastomeric isolators-Series SI. <https://www.fipindustriale.it> (2018)

Hg(II)-IMPRINTED POLYMER GELS – SMART MATERIALS FOR MERCURY DETERMINATION AND SPECIATION

IVANKA G. DAKOVA AND IRINA B. KARADJOVA

Faculty of Chemistry and Pharmacy, University of Sofia “St. Kliment Ohridski”,
Sofia 1164, Bulgaria

e-mail: i.dakova@chem.uni-sofia.bg, t.yordanova@chem.uni-sofia.bg,
karadjova@chem.uni-sofia.bg, www.uni-sofia.bg

Key words: Hg(II)-imprinted polymer gels, Smart materials, Solid phase extraction, Mercury speciation, Cold vapor atomic absorption spectrometry.

Abstract. In this study, Hg(II) imprinted copolymer gels (Hg(II)-IIPs) are prepared and used as smart sorbents for selective solid phase extraction of mercury ions from surface water samples. Hg(II)-IIPs are synthesized by dispersion copolymerization of 1-vinylimidazole, methacrylic acid or 2-hydroxyethyl methacrylate as functional monomer, trimethylolpropane trimethacrylate as cross-linking agent and 2,2'-azoisobutyronitrile as initiator in the presence of a Hg(II)–1-(2-thiazolylazo)-2-naphthol (Hg(II)-TAN) complex. The structure and morphology of the prepared Hg(II)-IIPs are defined using scanning electron microscopy, and nitrogen adsorption–desorption measurements. The extraction efficiency (degree of sorption/desorption, selectivity, capacity) of the Hg(II)-IIPs toward inorganic mercury ion (Hg(II)) are studied using batch procedure. The optimal pH value for the quantitative sorption is 7, and full desorption is achieved by 0.1 mol/L thiourea in 0.1 mol/L HCl. The Hg(II)-IIPs exhibit excellent selectivity towards Hg(II) over methylmercury, Cd(II), Ni(II) and Pb(II), due to the introduced memory effect. The prepared copolymer gel with 1-vinylimidazole as a functional monomer has higher capacity and selectivity towards Hg(II). Adsorption process is characterized by Langmuir isotherm model. Analytical scheme for Hg speciation and enrichment in surface waters is developed based on the high selectivity of Hg(II)-IIPs toward Hg(II).

1 INTRODUCTION

Mercury and its compounds are considered extremely harmful and toxic environmental pollutants and according to the European legislation are identified as priority hazardous substances [1]. Although all mercury species have detrimental impact on the human and ecosystems health, their toxicity, mobility and bioavailability strongly depend on the particular chemical form. In general, organic Hg species, especially methylmercury (MeHg) are known to be much more toxic than inorganic (e.g. Hg(II) and Hg(I)) because of their lipid solubility which facilitates relatively easy passing through biomembranes and subsequent accumulation in living cells. Due to the significant differences between toxicity of Hg(II) and MeHg as well as their extremely low concentrations in the environment, a reliable procedure for enrichment and further speciation analysis is often required. Widely used approach in analytical practice is based on preliminary separation and preconcentration of the mercury species by solid-phase extraction (SPE) with ion imprinted polymers.

Ion imprinted polymers (IIPs) are a new generation synthetic “smart” materials combining the selective recognition properties for a template ionic species with the ability to respond to specific external stimuli (such as the presence of another ions, pH, magnetic field etc.) with consequent changes in their properties including the affinity of the polymeric matrix toward the template [2, 3]. Based on ion imprinting technology “smart materials” are created by integrating a template ion into the polymer network during the preparation of these polymeric materials. [4, 5]. In brief, the most commonly used synthetic scheme for the preparation of IIPs involves several stages: (i) complexation of a template species (metal ions or their complexes with specific ligands) with functional monomers, (ii) copolymerization of these monomers around the template ion with the help of a cross-linking agent in the presence of an initiator, and (iii) removal of the imprinted ion by extraction which leaves cavities with a size, shape, charge and chemical functionality complementary to those of the template ion species. Thus, ion level information is transferred from the template ion species to the polymers in the form of a three-dimensional “memory” of the template’s characteristics. IIPs have the advantage that they not only can respond to external stimuli, but they also have ion recognition ability for template ion species [5, 6]. Choosing the right functional monomer and chelating ligand is very important because this will determine, on one hand, the stability of the complex formed before and during the polymerization process and, on the other hand, the subsequent ability of the IIP to interact selectively with the target ion. Numerous studies on IIPs and their application for selective preconcentration and separation of Hg species have been reported [7-15]. Recently, our group reported an easy synthetic procedure for synthesis of Hg(II)-IIPs via dispersion copolymerization using methacrylic acid (MAA) as a monomer, trimethylolpropane trimethacrylate as a cross-linking agent and 1-(2-thiazolylazo)-2-naphthol (TAN) [8] or pyrrolidine dithiocarbamate [9] as specific Hg(II) ligands. According to authors’ knowledge, the effect of the type of functional monomer (basic, acidic or neutral) on the adsorption properties and selectivity of Hg(II)-IIPs has not been investigated yet.

In the present study, Hg(II)-IIPs were synthesized via dispersion copolymerization using three different functional monomers – MAA, 1-vinylimidazole (VIA) or 2-hydroxyethyl methacrylate (HEMA), trimethylolpropane trimethacrylate (TMPTMA) as a cross-linking agent, and TAN as a non-polymerizable chelating agent and Hg(II) as a template ion. Critical comparison between extraction efficiencies, adsorption capacities, and selectivities of Hg(II)-imprinted copolymer gels prepared on the basis of MAA, VIA or HEMA was presented. Finally, SPE procedure using Hg(II)-IIPs as sorbent and next subsequent cold vapor atomic absorption spectrometric (CV AAS) measurements were developed and applied for Hg speciation in water samples. The analytical scheme proposed consists of two steps: (1) selective determination of Hg(II) and (2) determination of total Hg as Hg(II) after water sample digestion. The content of methylmercury is defined as the difference between these two measurement results.

2 EXPERIMENTAL

2.1 Materials

1-Vinylimidazole (VIA), methacrylic acid (MAA), 2-hydroxyethyl methacrylate (HEMA), trimethylolpropane trimethacrylate (TMPTMA), 2,2'-azobisisobutyronitrile (AIBN), thiourea (TU) (Merck), 1-(2-thiazolylazo)-2-naphthol (TAN, Fluka)) and acetonitrile (ACN, Labscan)

were used to prepare the Hg(II) ion-imprinted and non-imprinted polymer sorbents. Stock standard solutions for Hg were: inorganic Hg(II), stock standard solution for AAS, Trace CEPT™, 998 µg/mL in 2 mol/L HNO₃, (Sigma-Aldrich). Methylmercury stock solutions (100 mg/L) were prepared by dissolving the appropriate amount of methylmercury(I) chloride (highly toxic, handle with care), PESTANAL®, analytical standard, Fluka (33368) in 5 mL of methanol and diluting to 100 mL with water. The exact concentration of this solution was defined against standards prepared from inorganic Hg(II). All stock solutions were stored in dark glass bottles at 4 °C. Working standard solutions for calibration were freshly (daily) prepared by successive dilution and contained reagents used for sample preparation or elution; e.g. 0.1 mol/L thiourea in 0.1 mol/L HCl. Reductant solutions of sodium tetrahydroborate(III) NaBH₄ (Merck) 0.04 % (m/V) and 0.4% (m/V) in 0.1 % (m/V) NaOH were prepared fresh daily and was used without filtration. The stock standard solutions for Cd(II), Ni(II) and Pb(II) (1000 µg/mL) were Titrisol (Merck), in 2 % HNO₃ (V/V).

All reagents were of analytical-reagent grade and all aqueous solutions were prepared in deionized water (DW).

2.2 Apparatus

CV AAS measurements were carried out with a Perkin Elmer AAnalyst 400 atomic absorption spectrometer (Perkin Elmer, USA) equipped with a MHS 15 Mercury Hydride System and externally heated quartz tube atomizer at room temperature for inorganic Hg(II) and in air/acetylene flame for MeHg. The optimal instrumental parameters for Hg species determination include: pre-reaction purge time 7 s, post reaction purge time 60 s. Solutions of NaBH₄ 0.04 % (m/V) and 0.4 % (m/V) were used as reductants for inorganic Hg(II) and MeHg respectively.

A scanning electron microscope (SEM, JEOL JSM-5500) was used for the determination of the microbead shape and morphology. Specific surface area and pore size distribution were measured through nitrogen adsorption–desorption isotherms at 77 K using a Brunauer–Emmett–Teller (BET) analyzer (Quantachrome NOVA 1200, Quantachrome). A microprocessor pH meter (Hanna Instruments) was used for pH measurements. A centrifuge EBA 20 (DJB Labcare) was used to separate micro particles and extracted metal ion solution in batch experiments.

2.3 Synthesis of the Hg(II) ion-imprinted and non-imprinted copolymer gels

The imprinted and non-imprinted copolymer gels were synthesized as described earlier with minor modification [16]. Reaction scheme for Hg(II)-IIPs preparation is shown in Fig. 1. As template the complex (0.046 mmol) of the imprinted ion Hg(II) with TAN was used. The Hg(II)-IIPs were prepared via a cross-linking dispersion copolymerization using three various functional monomer – VIA, MAA or HEMA (0.862 mmol), TMPTMA (0.373 mmol) as a cross-linking agent, AIBN (32 mg) as an initiator, and acetonitrile (10 mL) as a porogen solvent at temperature 60 °C for 24 h. The following types copolymer gels were prepared: (i) with VIA as a functional monomer (named Hg(II)-VIA-IIP); (ii) with MAA as a functional monomer (named Hg(II)-MAA-IIP); (iii) with HEMA as a functional monomer (named Hg(II)-HEMA-IIP); and (vi) non-imprinted polymers (named VIA-NIP, MAA-NIP and HEMA-NIP) synthesized in the same way as described above, in the absence of template. They were

recovered by centrifugation, washed with ACN to remove unreacted monomers and other ingredients.

Mercury was removed from the produced polymer networks by several, sequential elution steps using 4 mol/L HNO₃ and 0.5 mol/L TU in 0.5 mol/L HCl as eluents. This procedure was repeated until the Hg concentration (template ions) in the eluate solution is below the LOD as measured by CV AAS. Then IIPs were dried in a vacuum oven at 60 °C. The non-imprinted polymer gels were treated in the same way.

2.4 Solid-phase extraction of Hg(II)

A portion of the solution containing 0.1 µg Hg(II) was diluted to a 10 mL total volume and pH was adjusted with buffer solution to the desired value. Polymer microbeads of ca. 50 mg were added to this solution and stirred for 20 min. The sample was centrifuged (5000 rpm), the supernatant was removed and the polymer gel was washed twice with DW. In order to investigate the degree of Hg(II) sorption the supernatant was collected and analyzed by CV AAS as an effluat. The Hg(II) was eluted from the copolymer gels with 2 mL of various reagents for 30 min. The degree of Hg elution was determined in the eluate solutions by CV AAS.

The degree of sorption (D_S %) of Hg(II) ions is defined as:

$$D_S \% = [(A_i - A_{eff}) / A_i] \cdot 100, \quad (1)$$

The degree of elution (D_E %) of sorbed Hg(II) ions from loaded sorbent is defined as:

$$D_E \% = (A_{el} / (A_i - A_{eff})) \cdot 100, \quad (2)$$

where A_{el} [µg] is the amount of metal cations in solution after elution process.

2.5 Capacity and adsorption isotherms

The adsorption capacity (Q) was defined following the procedure: 50 mg of copolymer gels (imprinted or non-imprinted) were added to 10 mL solution with various concentrations of mercury ions (from 100 to 600 µmol/L) at pH 7. The mixtures were shaken for 20 min at temperature 25 °C. The total mercury ions sorbed was quantified by CV AAS after elution with mixture of 0.1 mol/L TU in 0.1 mol/L HCl. The adsorption capacity ($Q_{max,exp}$), the amount of Hg(II) adsorbed by 1 g of copolymer gel at equilibrium, was calculated according to the equation:

$$Q_{max,exp} = (C_0 - C_e) \cdot V / m, \quad (3)$$

where: $Q_{max,exp}$ is the mass of Hg(II) ions adsorbed per unit mass of the copolymer gel, µmol/g; V is volume of the solution; m is the mass of the sorbent, g; C_0 is concentration of Hg(II) ions in the initial solution, µmol/L; C_e is equilibrium concentration of Hg(II) in solution after adsorption, µmol/L.

2.6 Selectivity experiments

A 10 mL solutions containing model, metals mixture solution containing 5 ng Hg(II), 5 ng MeHg and 10 µg Pb(II) and Ni(II), Cd(II) were treated with the Hg(II)-IIPs or non-imprinted sorbents (50 mg) at pH 7 and shaken for 20 min with an electric shaker. The solutions were

centrifuged, sorbent particles were washed twice with deionized water and elution was performed with 10 mL 0.1 mol/L TU in 0.1 mol/L HCl for 30 min. The concentrations of Hg(II) and MeHg were measured by CV AAS and Cd(II), Ni(II), Pb(II) in the supernatant and eluate solutions were determined by flame AAS.

The distribution ratio (D) is defined as

$$D = (A_i - A_{eff}) / A_{eff} \quad (4)$$

The selectivity coefficient ($S_{Hg/Me}$) is

$$S_{Hg/Me} = D_{Hg} / D_{Me} \quad (5)$$

where D_{Hg} and D_{Me} are the distribution ratios for Hg(II) and Cd(II), Ni(II), Pb(II), and MeHg, respectively.

2.7 Analytical procedure for Hg(II) and MeHg determination in surface waters

Water sample 100 mL was shaken with 50 mg Hg(II)-VIA-IIP for 20 min. After centrifugation (5000 rpm) the supernatant was removed and polymer was washed twice with DW, finally Hg(II) was eluted with 2 mL 0.1 mol/L TU in 0.1 mol/L HCl. The eluate was transferred in 10 mL volumetric flask and diluted up to the mark with DW. Hg(II) was measured by CV AAS under optimal instrumental parameters. In a parallel procedure, 100 mL water sample was MW digested with concentrated nitric acid (in order to transform MeHg into Hg(II)) and then passed through the same already described analytical protocol. In this case the sum Hg(II) + MeHg was determined by CV AAS. Finally, MeHg content in the analyzed water sample was defined as a difference between two measured values.

3 RESULTS AND DISCUSSION

3.1 Synthesis of Hg(II)-IIPs and characterization studies

The functional monomer plays an important role in the adsorption performance of IIPs because from one side it has to interact with the template molecule and give a good polymerization performance with the crosslinking agent and from the other side do not influence the sorption activity of the sorbent. In this work, in order to get Hg(II)-IIPs with high adsorption capacity, selectivity and fast sorption/desorption rate, three different monomers, including VIA (basic), MAA (acidic) and HEMA (neutral) were synthesized and studied.

Hg(II)-IIPs were synthesized by “trapping” technique, i.e. complexes between target metal ion and non-vinylated chelating agent were trapped inside the polymer matrix during the polymer formation. Preparation of Hg(II)-IIPs included several steps (Fig. 1). The first one was formation of the prepolymerization complexes between template species (complex of Hg(II) ion with TAN) and the functional monomers (VIA, MAA or HEMA) in ACN. The second step was, the dispersion cross-linking copolymerization of these complexes with the TMPTMA as cross-linking agent producing copolymer network. Finally, Hg(II) ions were removed from copolymer gels prepared leaving behind some specific binding sites with functional groups in a predetermined orientation and cavities with special size of templates.

Scanning electron micrographs of the obtained Hg(II)-VIA-IIP and VIA-NIP copolymer particles are shown in Fig. 2. Analogous micrographs are obtained for Hg(II)-MAA-IIP, Hg(II)-HEMA-IIP, MAA-NIP and HEMA-NIP. As can be seen from Fig. 2, the shape of particles

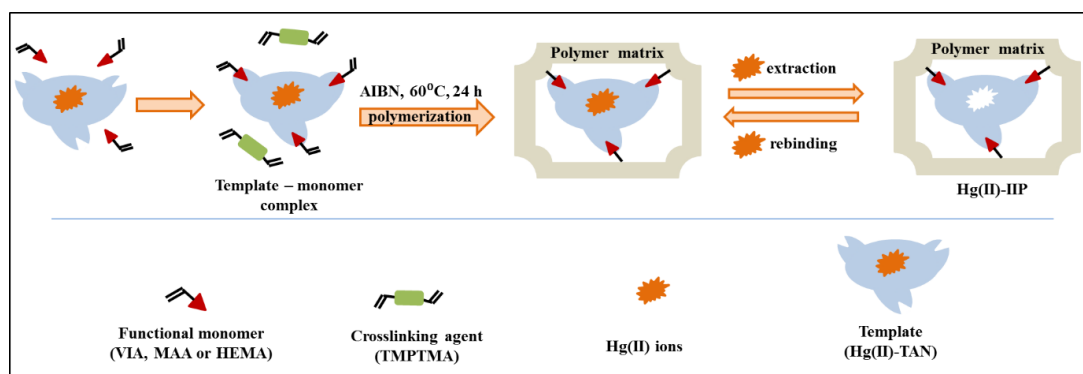


Figure 1: Scheme of the Hg(II)-IIPs preparation.

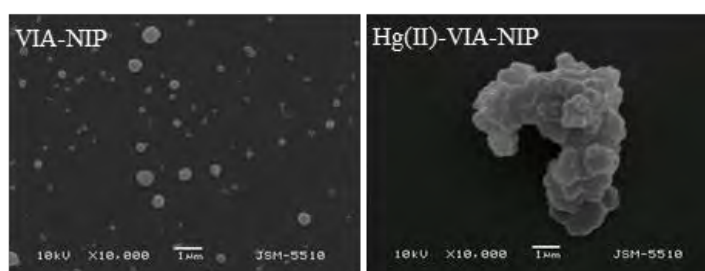


Figure 2: Scanning electron micrographs of Hg(II)-VIA-IIP and VIA-NIP at a 10 000× magnification.

of the non-imprinted copolymer gel is close to spherical. The surface structure and morphology of the particles of Hg(II)-imprinted sorbent is different – Hg(II)-VIA-IIP is in the form of bigger aggregates with irregular shape. Rough surface of ion imprinted polymers as compared to the non-imprinted polymer suggests that cavities were formed on the sorbent surface after template removal [17].

The specific surface area, total pore volume and average pore diameter, for the Hg(II)-IIPs and non-imprinted copolymer gels were determined from nitrogen adsorption–desorption isotherms. The three Hg(II)-imprinted copolymer gels have similar surface areas (Hg(II)-VIA-IIP: 4 m²/g; Hg(II)-MAA-IIP: 5 m²/g; and Hg(II)-HEMA-IIP: 3 m²/g) and average pore diameters (9 nm, 15 nm and 12 nm, respectively), while non-imprinted copolymer gels have higher surface area (VIA-NIP: 55 m²/g; MAA-NIP: 28 m²/g; and HEMA-NIP: 9 m²/g) and average pore diameters (15 nm, 28 nm and 18 nm, respectively). As it is evident, all the polymer gels studied could be described as a mesoporous structures. These typical results after imprinting are explained with the incorporation of Hg(II)-TAN complex in polymer network which causes a certain filling of the pores and reduced adsorption of N₂ [18].

3.2 Optimization of chemical parameters for quantitative sorption and desorption of Hg(II) with Hg(II)-imprinted and non-imprinted copolymer gels

The sorption of metal ions on the IIPs resulted from the combined effect of the chemistry of metal ions in aqueous solutions and their interactions with the chelating agent and the functional

groups present in the polymeric network. The extraction efficiency of three synthesized copolymer gels toward Hg(II) was studied at pH values in the range 3–8 (Section 2.4). The results obtained for the influence of pH on Hg(II) selective sorption are presented in Fig. 3. As can be seen the degrees of sorption for Hg(II)-MAA-IIP and Hg(II)-VIA-IIP were significantly higher than those of other studied sorbents. The quantitative sorption of Hg(II) ions on the Hg(II)-MAA-IIP and Hg(II)-VIA-IIP was achieved at pH 7, while for the sorbent imprinted with HEMA as a functional monomer the maximal degree of sorption was around 85%. Probably the neutral functional monomer HEMA could not form a stable prepolymerization complex with template molecule (Hg(II)-TAN complex) and the prepared copolymer gel had less amount of specific Hg(II) binding cavities [19]. In the same time, for the weak basic and acidic functional monomers VIA and MAA, the prepolymerization complex formed more stable structures, and the specific binding cavities could remain in the prepared IIPs, which provides quantitative sorption of the analyte and high adsorption capacity (see Section 3.3). The adsorption pattern for non-imprinted copolymer gels was found similar to Hg(II)-IIPs, but as might be expected in all cases lower degrees of sorption were observed (Fig. 3). This can be attributed to the non-specific interaction of Hg(II) with the functional groups in the polymer matrix and the lack of specific binding sites. Moreover, monomers aggregation leading to a suppressed number of binding sites in the NIPs additionally affected the adsorption efficiency [20].

The choice of the suitable eluent is important for the next application of sorbent in analytical procedure for solid phase extraction. In order to elute mercury adsorbed on the copolymer gels, different eluents were tested (HNO_3 , HCl , $\text{HCl} + \text{TU}$). Among the acids employed as eluents, HCl has been reported to have an enhanced performance due to its complexing abilities toward mercury. However in the present study the quantitative elution of Hg(II) could not be achieved even with 4 mol/L HCl . Quantitative elution of adsorbed Hg(II) was achieved using a combination of 0.1 mol/L thiourea in 0.1 mol/L HCl with minimum volume of 2 mL. The kinetics of both processes of sorption and desorption of Hg(II) were investigated by batch procedure with 50 mg of imprinted nanoparticles for 5–60 min. Quantitative sorption was reached for 20 min while for quantitative desorption 30 min has to be used.

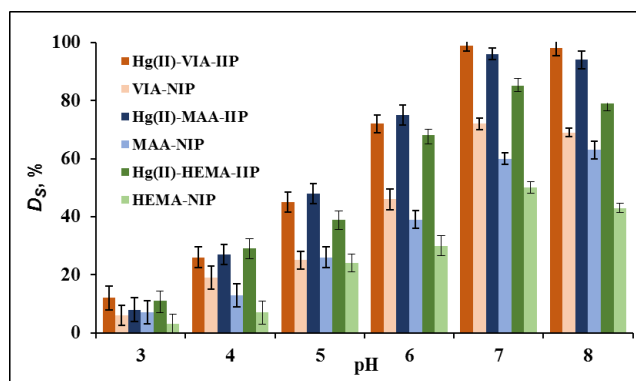


Figure 3: pH-dependence of the degree of sorption of Hg(II) ions onto Hg(II)-imprinted and non-imprinted copolymer gels (50 mg polymer gel, $T = 25\text{ }^{\circ}\text{C}$).

3.3 Capacity and adsorption isotherms

The maximum experimental sorption capacity ($Q_{max,exp}$) of the Hg(II)-MAA-IIP, Hg(II)-VIA-IIP, MAA-NIP and VIA-NIP was determined after saturation of the sorbents with mercury ions under optimum conditions at temperature 25 °C (Fig. 4a). For this purpose, increasing amounts of Hg(II) (100–600 $\mu\text{mol/L}$) were added to 50 mg copolymer gel and the equilibrium Hg(II) concentration after adsorption was measured by CV AAS. As can be seen in Fig. 4a, the amount of Hg(II) adsorbed per unit mass of sorbent increased with the initial concentration of Hg(II) and reach the plateau values, determining the adsorption capacity values. The determined $Q_{max,exp}$ of Hg(II)-MAA-IIP, Hg(II)-VIA-IIP, MAA-NIP and VIA-NIP are given in Table 1. As expected the adsorption capacity of Hg(II)-IIPs are higher versus non-imprinted polymer gels, indicating that the cavities created after removal of the template in Hg(II)-imprinted polymer gels are more complementary to the imprinted ion in size, shape, and chemical functionality. The results presented in Table 1 also show that the polymer gel containing the basic functional monomer VIA (78.0 $\mu\text{mol/g}$) has higher adsorption capacity than the polymer synthesized using acidic MAA (73.7 $\mu\text{mol/g}$).

τ **Table 1:** Adsorption parameters of the Langmuir isotherm model for the adsorption of Hg(II) ions onto the imprinted and non-imprinted polymer gels-at temperature 25°C

Copolymer gel	$Q_{max, exp}$ ($\mu\text{mol/g}$)	Adsorption parameters		
		Q_{max} ($\mu\text{mol/g}$)	b (L/ μmol)	R^2
Hg(II)-VIA-IIP	78.0	78.1	0.033	0.996
VIA-NIP	44.4	44.8	0.117	0.998
Hg(II)-MAA-IIP	73.7	73.5	0.145	0.994
MAA-NIP	38.4	38.1	0.308	0.997

Langmuir isotherm model was used for curve fitting in order to derive data describing adsorption process. According to the Langmuir isotherm theory [21] the sorption process occurs in a surface monolayer of homogenous sites which number is fixed. The expression of the linearized Langmuir isotherm (Eq. (6)) is

$$C_e/Q_e = C_e/Q_{max} + 1/(b \cdot Q_{max}) \quad (6)$$

where: C_e ($\mu\text{mol/L}$) is the equilibrium concentration of Hg(II) in the solution, Q_e ($\mu\text{mol/g}$) is the adsorption capacity of the adsorbed mercury ions onto the copolymer gel at equilibrium, Q_{max} ($\mu\text{mol/g}$) is the theoretical maximum adsorption capacity, b (L/ μmol) is the Langmuir constant that relates to the affinity of binding sites. The linearized Langmuir isotherm (Fig. 4b) and the isotherm parameters calculated from their analysis are presented in Table 2. The high R^2 value achieved for the adsorption of Hg(II) ions onto all copolymer gels show that the Langmuir equation gives very good mathematical fit to the adsorption isotherm. The slope of the curves (Fig. 4b) was used for the calculation of theoretical (monolayer) capacities (Q_{max}) of the Hg(II) on the Hg(II)-IIPs and non-IIPs. The experimental values of sorption capacity, determined according to the procedure described in paragraph 2.5 are very close to the calculated values by Langmuir model (Table 2). The sorption capacities of non-imprinted copolymer gels were lower than these obtained for imprinted particles.

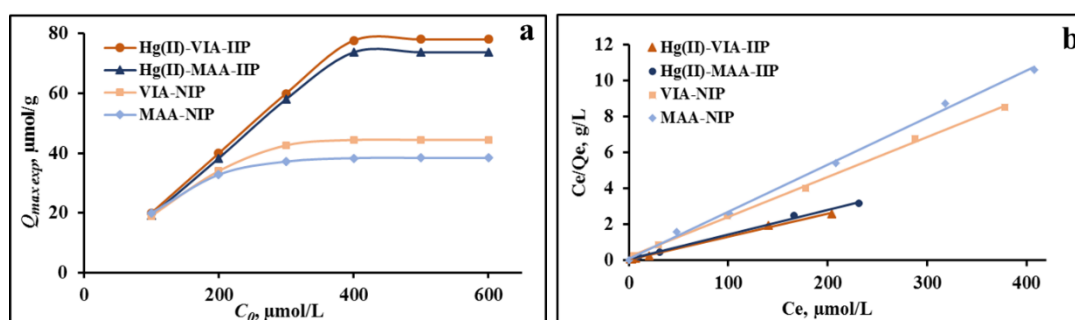


Figure 3: Experimental adsorption isotherms (a) and linearized form of Langmuir isotherm (b) of Hg(II) onto Hg(II)-MAA-IIP, Hg(II)-VIA-IIP, MAA-NIP and VIA-NIP (50 mg copolymer gel, pH 7, $T = 25^\circ\text{C}$).

3.4 Selectivity experiments

The high selectivity toward templated ion is an important characteristic of the imprinted polymers due to specific recognition sites created in the obtained three-dimensional polymer network. In order to confirm the selectivity of Hg(II)-IIPs, a competitive adsorption of Cd(II), Cu(II), Ni(II), Pb(II) and MeHg from their model mixture was studied as well. The experiments were carried out with Hg(II)-MAA-IIP, Hg(II)-VIA-IIP, MAA-NIP and VIA-NIP in batch mode at pH 7. The degrees of sorption (D_S) of cations, achieved by using copolymer gels are given in Fig. 5. The D_S values of Hg(II)-IIPs sorbent toward Hg(II) were highest and decreased in order $\text{Pb(II)} > \text{Cd(II)} \approx \text{Ni(II)} \gg \text{MeHg}$ most probably due to the selective coordination-geometry of the sorbent toward Hg(II) providing the ligand groups arranged in a suitable way required for best coordination of Hg(II) [22]. The greatest difference is established between degrees of sorption of Hg(II) and MeHg. The large size of MeHg probably hinders the ion diffusion and further interaction with functional groups resulting in a very low extraction efficiency of Hg(II)-IIPs toward MeHg and highest values for selectivity coefficients $S_{\text{Hg/Me}} = 4851$ for Hg(II)-VIA-IIP and 4625 for Hg(II)-MAA-IIP (Table 2). These results unambiguously confirm the very good selectivity of Hg(II)-MAA-IIP, Hg(II)-VIA-IIP toward the target (imprinted Hg(II)) ions and its applicability for Hg speciation.

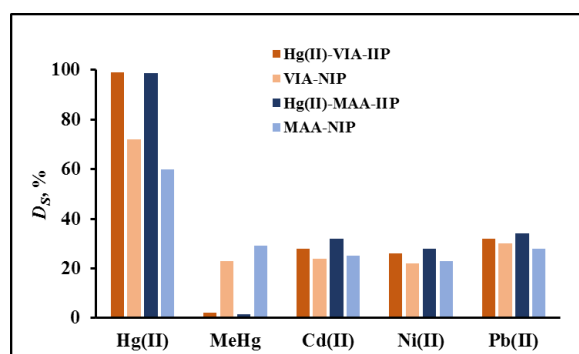


Figure 5: Degree of sorption of template and competitive ions upon SPE with Hg(II)-MAA-IIP, Hg(II)-VIA-IIP, MAA-NIP and VIA-NIP (50 mg copolymer gel, pH 7, $T = 25^\circ\text{C}$).

Table 2: Selectivity coefficients ($S_{Hg/Me}$) of Hg(II)-IIPs and non-IIP for Hg(II)

Copolymer gel	$S_{Hg/Me}$			
	MeHg	Cd(II)	Ni(II)	Pb(II)
Hg(II)-VIA-IIP	4851	254.6	282	210
VIA-NIP	9	8	9	6
Hg(II)-MAA-IIP	4625	136.7	131	131
MAA-NIP	4	5	5	4

3.5 Analytical application

Selective and quantitative sorption of Hg(II) on Hg(II)-VIA-IIP was used for the development of non-chromatographic solid phase extraction procedure for Hg speciation in surface waters. As a first step recovery studies were performed for the influence of water matrix on the selectivity and degree of sorption of Hg(II). Results obtained showed that recoveries in the range between 93-97% were obtained for Hg(II) in the presence of mineral, sea or river water. As a second step the selectivity of Hg(II)-VIA-IIP toward Hg(II) was studied in the presence of increased concentrations of MeHg in matrices like sea water and highly mineralized underground water. The results obtained show that independently of the matrix the selectivity of Hg(II)-VIA-IIP toward Hg(II) is very high. Even at 1:10 ratio between Hg(II) and MeHg the recoveries for MeHg are negligible while for Hg(II) they are close to 95-96%. Additional experiments for the sample volume breakthrough showed that volumes of about 100 mL might be used still ensuring quantitative sorption of Hg(II). As a final step analytical procedure was developed for Hg speciation in surface waters. Two parallel; water samples were prepared with pH adjusted to 7. One of the samples was mineralized and 50 mg of Hg(II)-VIA-IIP sorbent were added to both samples. After sorption the sorbents were recovered by centrifugation, the sorbents were washed with doubly distilled water and elute in a defined eluent mixture followed by Hg measurements by CV-AAS. Total Hg content is determined in mineralized sample and Hg(II) in a parallel nonmineralized one. The content of MeHg is obtained as a difference between these measurements. The analytical figures of merit were defined based on 10 parallel measurements of model solutions containing 5 µg/L of both Hg(II) and MeHg. The detection limits achieved based on 3σ criteria are 0.005 µg/L for Hg(II) and 0.006 µg/L for MeHg. Relative standard deviation varied for both Hg species between 4-9% for concentration range 1-10 µg/L content of Hg. The validity of developed procedure was confirmed by parallel analysis of certified reference material. Additionally, total Hg content determined by developed solid phase extraction procedure agreed very well with content measured by ICP-MS. In addition the sorbent is characterized with good mechanical stability and reusability (almost 50 sorption/desorption cycles with equal extraction efficiency).

4 CONCLUSIONS

In the present paper new Hg(II) imprinted copolymer gels microbeads were successfully synthesized by a dispersion crosslinking copolymerization with VIA, MAA or HEMA as functional monomers in the presence of Hg-TAN complexes as template species. All prepared Hg(II) imprinted copolymer gels are characterized with fast sorption/desorption kinetics and good chemical and mechanical stability. Better binding properties and highest selectivity toward Hg(II) was observed for imprinted copolymer gel based on VIA as monomer. The

application of Hg(II)-VIA-IIP for the determination of inorganic and methylmercury in surface waters samples was demonstrated.

Acknowledgements: The authors gratefully acknowledge the financial support provided by the Bulgarian National Scientific Foundation (Grant DN 19/10 SmartSpeciation).

REFERENCES

- [1] European Union Directive 2008/105/EC of the European Parliament and of the Council of 16 December 2008 on environmental quality standards in the field of water policy, amending and subsequently repealing Council Directives 82/176/EEC, 83/513/EEC, 84/156/EEC, 84/491/EEC, 86/280/EEC and amending Directive 2000/60/EC of the European Parliament and of the Council, Off. J. Eur. Union L348 (2008) 84–97.
- [2] Karadjova, I., Yordanova, T., Dakova, I. and Vasileva, P. *Smart Materials in Speciation Analysis*, in Handbook of Smart Materials in Analytical Chemistry, John Wiley & Sons, Vol. II, (2019).
- [3] Ge, Y., Butler, B., Mirza, F., Habib-Ullah, S. and Fei, D. Smart molecularly imprinted polymers. *Macromol. Rapid. Commun.* (2013) **34**:903-915.
- [4] Branger, C., Meouche, W. and Margaillan, A. Recent advances on ion-imprinted polymers. *React. Funct. Polym.* (2013) **73**:859-75.
- [5] Fu, J., Chen, L., Li, J. and Zhang, Z. Current status and challenges of ion imprinting. *J. Mater. Chem. A* (2015) **3**:13598-13627.
- [6] Lorenzo, R.A., Carro, A.M., Concheiro, A. and Alvarez-Lorenzo, C. Stimuli-responsive materials in analytical separation. *Anal. Bioanal. Chem.* (2015) **407**:4927-4948.
- [7] Liu, Y., Chang, X., Yang, D., Guo, Y. and Meng, S. Highly selective determination of inorganic mercury(II) after preconcentration with Hg(II)-imprinted diazoaminobenzene–vinylpyridine copolymers. *Anal. Chim. Acta.* (2005) **538**:85-91.
- [8] Dakova, I., Karadjova, I., Georgieva, V. and Georgiev G. Ion-imprinted polymethacrylic microbeads as new sorbent for preconcentration and speciation of mercury. *Talanta* (2009) **78**:523-529.
- [9] Yordanova, T., Dakova, I., Balashev, K. and Karadjova, I. Polymeric ion-imprinted nanoparticles for mercury speciation in surface waters. *Microchem. J.* (2014) **113**:42–47.
- [10] Dakova, I., Yordanova, T. and Karadjova, I. Non-chromatographic mercury speciation and determination in wine by new core-shell ion-imprinted sorbents. *J. Hazard. Mater.* (2012) **231–232**:49-56.
- [11] Rodríguez-Reino, M.P., Rodríguez-Fernández, R., Peña-Vázquez, E., Domínguez-González, R., Bermejo-Barrera, P. and Moreda-Piñeiro, A. Mercury speciation in seawater by liquid chromatography-inductively coupled plasma-mass spectrometry following solid phase extraction pre-concentration by using an ionic imprinted polymer based on methylmercury-phenobarbital interaction. *J. Chromatogr. A* (2015) **1391**:9-17.
- [12] Jiang, W., Jin, X., Yu, X., Wu, W., Xu, L. and Fu, F. Ion-imprinted magnetic nanoparticles for specific separation and concentration of ultra-trace methyl mercury from aqueous sample. *J. Chromatogr. A* (2017) **1496**(Supplement C):167-173.
- [13] Zhang, Z., Li, J., Song, X., Ma, J. and Chen, L. Hg²⁺ ion-imprinted polymers sorbents

- based on dithizone-Hg²⁺ chelation for mercury speciation analysis in environmental and biological samples. *RSC Adv.* (2014) **4**:46444-46453.
- [14] Liu, Y., Zai, Y., Chang, X., Guo, Y., Meng, S. and Feng, F. Highly selective determination of methylmercury with methylmercury-imprinted polymers. *Anal. Chim. Acta.* (2006) **575**:159-165.
- [15] Büyüktiryaki, S., Say, R., Denizli, A. and Ersöz, A. Mimicking receptor for methylmercury preconcentration based on ion-imprinting. *Talanta* (2007) **71**:699-705.
- [16] Dakova, I., Karadjova, I., Ivanov, I., Georgieva, V., Evtimova, B. and Georgiev, G. Solid phase selective separation and preconcentration of Cu(II) by Cu(II)-imprinted polymethacrylic microbeads. *Anal. Chim. Acta* (2007) **584**:196–203.
- [17] Mafu, T. and Msagati, B. Ion-imprinted polymers for environmental monitoring of inorganic pollutants: synthesis, characterization, and applications. *Environ. Sci. Pollut. Res. Int.* (2013) **20**:790-802.
- [18] Liu, Y., Qiu, J., Jiang, Y., Liu, Z., Meng, M., Ni, L., Qin, C. and Peng, J. Ce(III) ion imprinted polymer grafted on Fe₃O₄ nanoparticles supported by SBA-15 mesopores microreactor via surface-initiated RAFT polymerization. *Microporous Mesoporous Mater.* (2016) **234**:176-185.
- [19] Ren, Z., Kong, D., Wang, K. and Zhang, W. Preparation and adsorption characteristics of an imprinted polymer for selective removal of Cr(VI) ions from aqueous solutions. *J. Mater. Chem. A* (2014) **2**:17952-17961.
- [20] Yusof, N.F., Mehamod, F.S. and Suah, F.B.M. Fabrication and binding characterization of ion imprinted polymers for highly selective Co²⁺ ions in an aqueous medium. *J. Environ. Chem. Eng.* (2019) **7**:103007.
- [21] Langmuir, I. The constitution and fundamental properties of solids and liquids, *J. Am. Chem. Soc.* (1916) **38**:2221-2295.
- [22] Fang, G.-Z., Tan, J. and Yan, X.-P. An ion-imprinted functionalized silica gel sorbent prepared by a surface imprinting technique combined with a sol–gel process for selective solid-phase extraction of cadmium (II), *Anal. Chem.* (2005) **77**:1734-1739

PROCESS-INDUCED STRAIN MESUREMENT IN CONCRETE USING FIBER-OPTIC STRAIN SENSORS

NATALIA A. KOSHELEVA^{*}, GRIGORII S. SEROVAEV^{*} AND
GEORGII N. GUSEV^{*}

^{*} Institute of Continuous Media Mechanics Ural Branch Russian Academy of Science
(ICMM UB RAS)
1, Akademika Koroleva str., 614013, Perm, Russia
e-mail: kosheleva.n@icmm.ru

Key words: fiber-optic strain sensors, Bragg grating, process-induced strains, concrete.

Abstract. Strain evaluation in various objects is crucial for preventing accidents. Information about the mechanical state is usually collected by various sensors or using visual inspection methods, according to special maintenance schedule. Fiber-optic strain sensor (FOSS) discover new possibilities for measuring strain in materials. The greatest interest is connected with FOSS applications for materials, in particular concretes, in the volume of which the sensors can be embedded at the technological stage of manufacturing. The information obtained in real time from fiber-optic strain sensor (FOSS) can provide an early warning about the violation of the structure integrity and, thus, help to avoid serious losses. Such information is also useful for adapting and updating new and existing structures. The purpose of this study is to obtain experimental results that demonstrate the possibility of the application of FOSS based on Bragg gratings embedded in concrete to measure strains, including process-induced strains.

1 INTRODUCTION

Concrete structures are a significant part of all engineering structures. However, in many objects made of concrete, one can see serious wear after active use for several years. It is necessary to monitor the mechanical state over time to ensure the safety of such structures. Non-destructive methods are commonly used for structural health monitoring of concrete structures. These methods use a various electrical sensors, as well as sensing elements for displacements, rotations measurements at various points along the structure [1].

Cheaper production and consequently the wide distribution of fiber optics and fiber-optic sensors led to an increased interest in the use of this type of sensors. The first works on the use of fiber-optic strain sensors (FOSS) for assessing the mechanical state in concrete structures began to appear about twenty years ago. The authors of the study [2] showed that FOSS have several advantages compared with standard sensing elements. Various schemes have been developed for the application of FOSS based on fiber Bragg gratings (FBGs) for surface mounting and for embedding in concrete structures. Thus, the authors of [3] carried out a finite-element modeling and proposed a protection scheme for fiber-optic sensors mounted on the surface of the concrete structure. Also, experiments were carried out to confirm the operability

of FOSS to assess the condition of concrete cylinders. In a review paper [4], the main works on the use of FOSS based on Bragg gratings for various engineering structures were gathered. It should be noted that in most of the studies, where the FOSS is embedded inside the concrete, it is encapsulated by a steel tube. Since “pure” FBGs are very fragile in nature this additional steel shell of the FOSS is required to preserve the integrity of the sensor during structural monitoring, as well as to protect the sensor itself from the strong external alkaline environment of the cement. In the review authors also note that in most cases the sensitivity to strain of encapsulated FBG is significantly different from “pure” one. Therefore, calibration of the encapsulated FBG is necessary. This must be done before the sensor is used in the actual structure. In [5], protective coatings of embedded FBGs are considered in detail to determine the deformation of concrete structures. For one particular coating, optimal curing conditions were found that showed good repeatability. The response of the sensor under static load was compared with a surface-mounted electrical resistance strain gauge (ERSG) and an embedded fiber-optic EFPI sensor. Similar work was done by researchers in [6]. The study describes preliminary work of creating an economical and easy-to-use technology of protecting fiber optic sensors by resin using 3D printing methods to create a reliable, inexpensive sensor system usable with concrete structures for surface mounting and for embedding inside. In [7] a method of detection of corrosion cracking of reinforced concrete by FBG is presented. The effectiveness of the proposed method was confirmed experimentally. It is shown, that the crack detection technology using FBG is capable of tracking corrosion cracking in real time. The study [8] compares the readings obtained using FBG with the data obtained by the method of digital image analysis. The test results show that the digital image analysis method gives more accurate cracks development data on the surface area of the structure when compared with FBG. However, the authors showed that the high sensitivity of FBG sensors can be used at low levels of deformation to study very small strain changes that cannot be reliably detected by the digital image analysis method.

It can be noted from the review, that the embedded FOSS based on Bragg gratings in most cases are encapsulated by a metal tube, and, therefore, at least calibration is necessary to obtain reliable values. In addition, there is the danger of inaccurate strain transfer from material to FBG.

The authors have already tested a method for measuring process-induced strains in polymer composite materials using FOSS based on Bragg gratings [9]. This method allows to track the evolution of strain during the entire technological process of product manufacturing from a polymer composite material. In this paper, the authors propose to apply this technique for detection of the process-induced strains in the manufacturing of objects from granular composites, i.e. concrete products, using the embedded fiber-optic strain sensors based on Bragg gratings.

2 THE PRINCIPLE OF FBG OPERATION

A fiber Bragg grating is a section of a single-mode fiber optic core with a periodically varying refractive index. Figure 1 shows the principle of FBG operation: when an optical signal is transmitted through a fiber optic core in a given broadband wavelength range, a part of this signal is reflected on the Bragg grating.

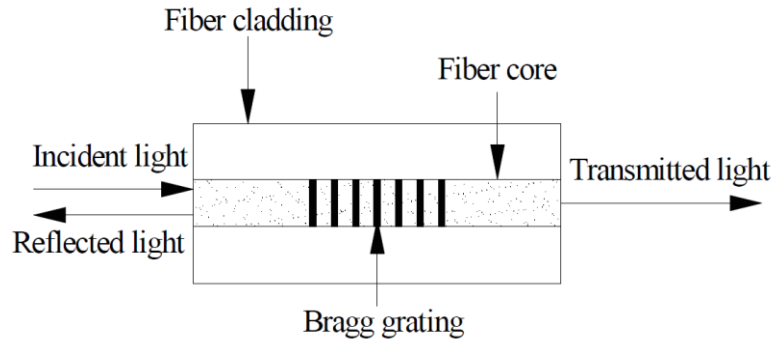


Figure 1: FBG principle [7].

The reflected optical signal has a central wavelength λ , the magnitude of which is directly proportional to the effective refractive index of the core n and the geometric length of the Bragg grating period L . This dependence can be described by the relation:

$$\lambda = 2nL \quad (1)$$

When FOSS interacts with a deformable material, a change in the Bragg grating length occurs, leading to a change in the wavelength of the reflected spectrum $\Delta\lambda$, which is recorded by the interrogator. Under the uniaxial stress state of the optical fiber, the change in the wavelength of the reflected spectrum is related with the strain of the fiber in the Bragg grating zone by the equation [10]:

$$\frac{\Delta\lambda}{\lambda^*} = \left(1 - \frac{n_1^2}{2} (p_{12} - \nu(p_{11} + p_{12})) \right) \varepsilon_3 \quad (2)$$

$$\text{or} \quad \varepsilon_3 = \frac{1}{k} \cdot \frac{\Delta\lambda}{\lambda^*} \quad (3)$$

where ε_3 – axial strain along the optical fiber, p_{11}, p_{12} – Pockels coefficients, ν – Poisson's ratio of the optical fiber.

In [11] it was found that for a silica glass optical fiber that does not interact at the location of the Bragg grating with other solids, the strain coefficient has the value $k \sim 0.78$. It should be noted that in the FOSS embedded in the material there will be a complex stressed state, and using the relation (3) will require additional conditions, for example, the use of calibration coefficients.

3 EXPERIMENT DESCRIPTION

To obtain experimental data and to achieve the objective of the study, an experimental stand was designed and created. An experimental stand is shown in figure 2. The studied problem involves monitoring of the shrinkage process of a test specimen made of concrete B15 for a long period of time. The duration of the experiment is determined by the stages of hardening and drying of the specimen. The duration of the experiment was defined as the time required for the test specimen under the current conditions of temperature and humidity until the shrinkage completely stops.



Figure 2: Experimental stand

The experimental stand is designed in such a way that the shrinkage of the test specimen placed on it passes under the control of all the necessary parameters, the analysis of which can give the information about the completion of the shrinkage process. The elements of the experimental stand include:

- Steel frame (1) with planar dimensions of 300x300 mm and height of 1000 mm, made of metal equal angle 35x35x3 mm. On the frame two movable brackets (2) are placed for laser position sensors at the top and bottom level of the sample. Also on the frame the mounting beam for fiber optic strain sensors line (3) is placed.
- Laser position sensor (4) with built-in microprocessor control system LS (manufactured by PRIZMA, Russia). The range of displacement measurement for the sensor is 10 mm with a resolution of 0.01%.
- Weight platform (5), equipped with two strain gauge strain sensors to control the sample weight. The strain gauges are assembled according to the “Wheatstone Full Bridge” scheme with thermal compensation on a separate part (strain gages produced by UK Sibtenzopribor, Russia).
- Sensor (6) for monitoring the sample temperature (immersion type) - DTS3105PT1000 (manufactured by OWEN, Russia).
- Sensor (7) for monitoring temperature and humidity of the environment - PVT10 (manufactured by OWEN, Russia).
- Sensor interrogation modules and interface converter for communication with a PC - MW110-224.4TD (8), MW110-224.8A (9), AC4 (10) (manufactured by OWEN, Russia).

The sample is a concrete cylinder with a diameter of 150 mm and a height of 400 mm, the formation and curing of which is carried out in a polypropylene tank of cylindrical shape with a bottom and a free top surface of the corresponding dimensions. At the beginning of the experiment, the tank not filled with concrete is placed inside the steel frame of the experimental stand (1) on the weighing platform (5). Inside the tank (through the bottom) on the beam of the stand (3) a fiber-optic strain sensors line is placed on the suspension in the center of the tank. After placing a line of fiber-optic strain sensors, layered (with compaction and vibration) filling of the tank with concrete mix to the level of the free surface is performed. A line of FOSS remains immersed in a concrete sample by means of a plumb with a predetermined pre-tension. Next, laser position sensors LS5 (4) are applied to the bottom of the tank and the upper free surface of the concrete mix to monitor the shrinkage of the sample. A temperature sensor DTS3105Pt1000 (6) is immersed in the sample to monitor its change at all stages of hardening and shrinkage. The change of temperature and humidity of the surrounding space is measured by means of a PVT10 sensor (7) located in the vicinity of the sample on the free surface level of the top of the tank. The weight of the sample is controlled by the weighing platform on which it is placed (5). The weighing platform is equipped with two strain gauge strain sensors assembled according to the “Wheatstone Full Bridge” scheme with thermal compensation on a separate element. All measuring equipment is commuted by means of the MV110-224.4TD (8), MB110-224.8A (9) interrogation modules and the AC4 interface converter (10). After filling the tank with a concrete mixture and setting up all measuring equipment, the stand with the sample is closed with a thermo-insulating casing made of extruded polystyrene foam.

The measurements of the sensors in the 24/7 mode with a frequency of 1 time per second are recorded in the database on a separate personal computer. In the same place, the process of sample hardening is periodically monitored via a graphical interface on the SCADA system. During the manufacture of the sample and throughout the entire technological mode, the data was recorded using the FOSS line with five FBG sensors and the FS 2100 interrogator. The readings from the FBG sensors were recorded 1 time per second for a week into the database on a separate personal computer. Figure 3a shows a scheme of the specimen with embedded FOSS. A fiber line with 5 FBGs spaced 10 mm apart was placed in the center of the sample. Figure 3b shows a photograph of an experimental sample with embedded FOSS based on Bragg gratings.

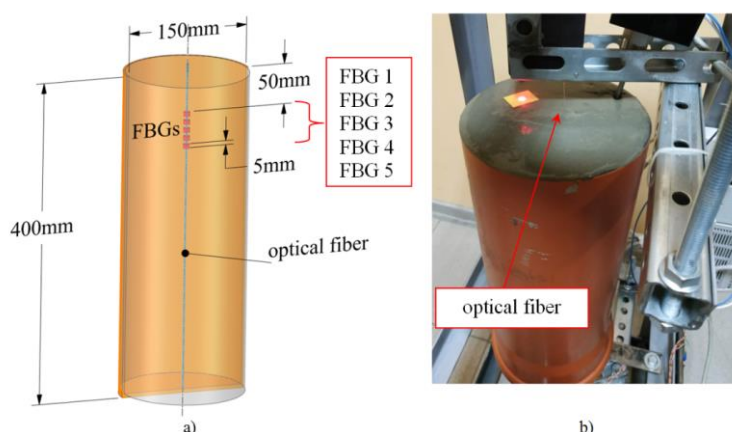


Figure 3: The scheme of a sample with five FBGs (a); Photo of an experimental sample with FBGs (b)

4 EXPERIMENTAL RESULTS ANALYSIS

Shrinkage of the sample of concrete mix occurs in three stages. The first stage is plastic or capillary shrinkage, which occurs as a result of the water evaporation from the concrete mixture prior to hardening. The second stage is autogenous shrinkage of concrete, associated with direct curing of the mixture and further “drying” as a result of cement hydration and water evaporation during cement exotherm. The third stage - shrinkage during the drying of the sample, associated with the removal of all remaining water, which did not enter into a hydration reaction and was not evaporated at the stage of autogenous shrinkage. Shrinkage during drying depends on the humidity and temperature of the ambient air, being reversible, unlike capillary and autogenous. The control of shrinkage processes, shown in figure 4, allows to determine the time interval after which the shrinkage processes do not lead to a change in the sample geometry. This interval is ~ 13 hours.

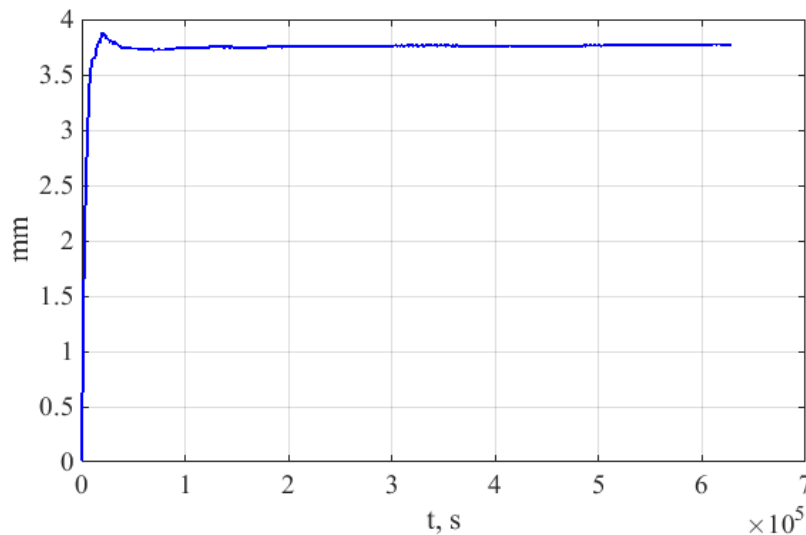


Figure 4: Registration of the shrinkage process in the sample

Figure 5 shows the change in process-induced strains recorded for 194 hours by FOSS, placed in the sample according to the scheme shown in figure 3. These results lead to the following conclusions. Process-induced strains in concrete begin to appear after the completion of shrinkage processes, which were controlled by changing the sample geometry. The level of process-induced strains increases with distance from its surface. The results of the change in process-induced strains over time give a qualitative and quantitative picture of relaxation processes in concrete and can serve as the basis for building models, which can quantitatively describe the concrete creep.

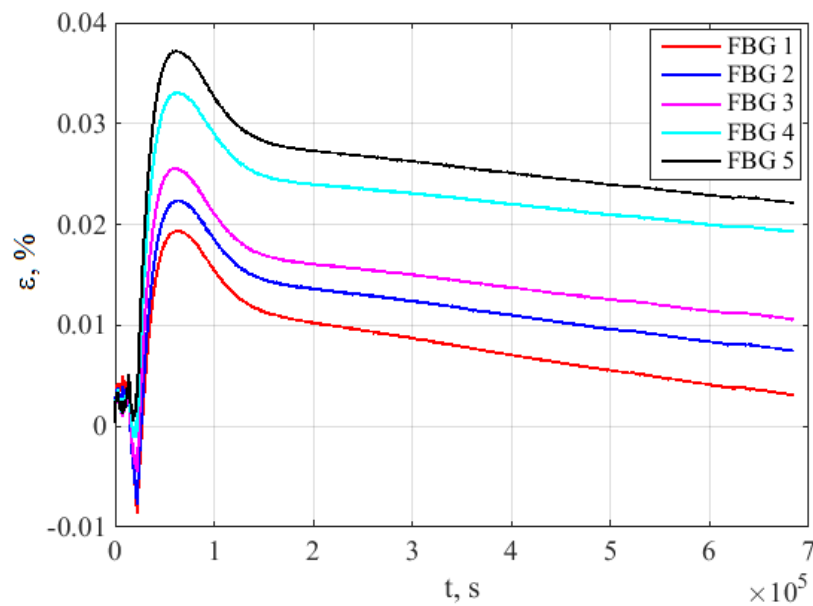


Figure 5: Registration of process-induced strains in the sample

5 CONCLUSIONS

- The paper describes the technological process of creating a concrete sample with embedded fiber-optic strain sensors based on Bragg gratings. An experimental stand was designed and built, equipped with the necessary sensors to monitor sample shrinkage.
- With the help of five fiber Bragg gratings, the entire history of process-induced strains arising during the sample fabrication process is recorded in real time and saved.
- A brief description of the principle of the FOSS operation is given, as well as relations for obtaining the strain values with the help of FBG.
- The information on process-induced strains in concrete is received, which allows to give a quantitative idea of their level, assess the non-uniform strain distribution in the volume and the information about the rheological behavior of concrete.

ACKNOWLEDGEMENTS

This work was supported by the grant of the President of Russian Federation for support of young Russian scientists and leading scientific schools (MK-2401.2019.1).

REFERENCES

- [1] Stepinski, T., Uhl, T. and Staszewski, W. *Advanced Structural Damage Detection: From Theory to Engineering Applications*. John Wiley & Sons, Ltd., 2013.
- [2] Leung, C. K. Y. Fiber optic sensors in concrete: The future? *NDT E. Int.* (2001) **34**:85-94.
- [3] Leng, J. S., Barnes, R. A., Hameed, A., Winter, D., Tetlow, J., Mays, G. C. and Fernando, G. F. Structural NDE of concrete structures using protected EFPI and FBG sensors. *Sensors*

- Actuators A Phys.* (2006) **126**:340–7.
- [4] Majumder, M., Gangopadhyay, T. K., Chakraborty, A. K., Dasgupta, K. and Bhattacharya, D. K. Fibre Bragg gratings in structural health monitoring—Present status and applications. *Sensors Actuators A Phys.* (2008) **147**:150–64
 - [5] Biswas, P., Bandyopadhyay, S., Kesavan, K., Parivallal, S., Sundaram, B. A., Ravisankar, K. and Dasgupta, K. Investigation on packages of fiber Bragg grating for use as embeddable strain sensor in concrete structure. *Sensors Actuators A Phys.* (2010) **157**:77–83.
 - [6] Scott, R. H., Chikermane, S., Vidakovic, M., McKinley, B., Sun, T., Banerji, P. and Grattan, K. T. V. Development of low cost packaged fibre optic sensors for use in reinforced concrete structures. *Meas.* (2019) **135**:617–24.
 - [7] Mao, J., Xu, F., Gao, Q., Liu, S., Jin, W. and Xu, Y. A Monitoring Method Based on FBG for Concrete Corrosion Cracking. *Sensors* (2016) **16**:1093.
 - [8] Kearsley, E. and Jacobsz, S. Condition assessment of reinforced concrete beams – Comparing digital image analysis with optic fibre Bragg gratings. *MATEC Web Conf.* (2018) **199**:06011.
 - [9] Matveenko, V. P., Kosheleva, N. A., Shardakov, I. N. and Voronkov, A. A. Temperature and strain registration by fibre-optic strain sensor in the polymer composite materials manufacturing. *Int. J. Smart Nano Mater.* (2018) **9**:99–110.
 - [10] Lammens, N., Luyckx, G., Degrieck, J. and De Waele, W. Experimental determination of the multi-axial strain transfer from CFRP-laminates to embedded Bragg sensor. *Smart Struct. Mater. 5th ECCOMAS Themat. Conf. Proc.* (2011) 482–5.
 - [11] Kablov, E. N., Sivakov, D. V., Gulyaev, I. N., Sorokin, K. V., Fedotov, M. Y., Dianov, E. M., Vasil'ev, S. A. and Medvedkov, O. I. Application of optical fiber as strain gauges in polymer composite materials. *Polym. Sci. Ser. D* (2011) **4**:246–51.

MESOSCOPIC MODELLING OF ZNO VARISTORS

KYLE A. TAYLOR*, ERION GJONAJ[†] AND HERBERT DE GERSEM

*Technische Universitaet Darmstadt

Schlossgartenstr. 8, 64291 Darmstadt, Germany

e-mail: taylor@temf.tu-darmstadt.de, web page: <http://www.temf.tu-darmstadt.de//>

[†]e-mail: gjonaj@temf.tu-darmstadt.de

Key words: Piezoelectricity, Semiconductors, Coupled Problems, Simulation

Abstract. This newly developed modelling framework for the simulation of electric current flow in ZnO varistors is based on an equivalent circuit representation of the varistor microstructure, where the grain boundaries are represented by nonlinear resistors in the circuit. The present approach extends similar models introduced earlier by including the effect of mechanical stress on the grain boundary conductivity. This effect is based on the coupling between the semiconducting and the piezoelectric properties of ZnO. The model used for the calculation of single grain boundary conductivities is based on the theories of Blatter et al. and Verghese et al.. It includes a self-consistent solution for the interface charge and for the potential barrier of the boundary, taking into account the local stress in the grain. 2D varistor models are constructed using appropriate Voronoi tessellations. The stress distribution within the material is calculated by FEM, and the electric current flow patterns within the microstructure are obtained by solving the nonlinear circuit equations for each applied voltage and stress condition of the sample. The simulated current-voltage characteristics reveal a significant sensitivity of the bulk electrical conductivity to stress. Furthermore, the simulations demonstrate the current concentration effect in the voltage breakdown region.

1 INTRODUCTION

Zinc oxide (ZnO) was one of the earliest functional materials to see extensive use in many engineering fields, and still plays an important role to this day. In single-crystal form, ZnO is utilised in UV and blue light emitting diodes [1], solar-blind photodetectors [2], transparent thin film transistors [3] and many other applications. Bulk ceramic ZnO is commonly employed as a varistor for voltage surge protection in power transmission lines [4] as well as in low voltage electronic circuits [5]. The capability of ZnO varistors to almost instantly absorb large amounts of electric energy is due to the diode-like current-voltage characteristic of the material. This characteristic is attributed to the double Schottky barriers that form at the boundaries between the individual ZnO grains with an effective electrical response corresponding roughly to that of a back-to-back pair of Zener diodes [6].

Recently, ZnO has attracted great interest as a tunable electromechanical material. The modulation of the electric conductivity of ZnO under applied mechanical stress is due to the piezotronic effect [7]. This effect has been recently studied for tunable ZnO nanowires [8], strain gated transistors [9] and photonic-strain mapping [10]. Specifically, the stress sensitivity of the electrical conductivity for ZnO

varistor ceramics was studied in [11, 12]. The authors observed huge gauge factors of up to 800 for conventionally manufactured ZnO varistor samples of several millimeters in size under applied uniaxial compressive stress of the order of 100 MPa. This clearly qualifies the material for macroscopic scale sensing applications.

The piezotronic effect occurs here due to the coupling between the semiconducting and piezoelectric properties of ZnO. The strain-induced piezoelectric polarization modifies the trapped interface charge distribution at the grain boundaries, thus changing the effective grain boundary potential barriers. This leads to a modification of the current-voltage switching characteristics of the material. Such a mechanism was originally proposed by Verghese et al. [13], where the effect of internal stress on the electrical conductivity of ZnO varistors was studied. However, it was not until very recently that the piezoelectric contribution to the grain boundary conductivity was experimentally verified. Raidl et al. [7] showed that the electrical conductivity for ZnO bicrystals depends on the reciprocal grain polarity as expected by Verghese's theory.

While the basic piezotronic effect at the grain boundaries is well understood, the electromechanical characterization of bulk materials remains a challenge. Macroscopic size varistor samples consist of a large number of grains of different sizes, shapes and crystallographic orientations. Due to these purely geometric factors, each grain boundary experiences a different mechanical stress. Thus, depending on the distribution of crystallographic orientations and the mechanical stress field within the material, the conductivity of some grain boundaries will increase, while that of others decreases. Furthermore, even if all grain boundaries were electrically identical, they operate at different working points along the current voltage characteristic and thus feature different conductivities. This causes the electric current to concentrate along a few conductive paths within the material [14]. The resulting current flow pattern in the material, and therefore its effective electrical conductivity, depend not only on the current voltage characteristics of any single grain boundary, but also on the details of the varistor microstructure.

In this paper, we introduce a modeling approach for the electro-mechanical characterization of ZnO varistors. The model extends on the equivalent circuit analysis for varistor ceramics originally proposed in [15]. In this approach, the grain boundaries are modeled as the current branches of a large nonlinear network representing the varistor microstructure. This enables the computation of the current flow patterns in the material by solving a global set of circuit equations. In addition to this, we compute the mechanical stress field in the material for different applied stresses using FEM, in order to take into account the piezotronic effect. The local stress at each grain boundary is then introduced into a self-consistent grain boundary model, describing the mechanical modulation of potential barriers due to piezoelectric polarization. Several simulations using 2D varistor models under different mechanical stress conditions are performed and the corresponding gauge factors of the material characteristics are computed.

2 THEORY

2.1 Grain Boundary Theory

A detailed description of the charge carrier transport through grain boundaries in polycrystalline semiconductors has been presented by Blatter et al. [16, 17]. The band bending at the grain boundary induced by an applied potential is calculated in the Schottky approximation by imposing consistency conditions with the deep trap states and the bulk Fermi level relative to the conduction band of the material. The solution for the electrostatic potential across the boundary resembles that of a potential barrier with height

$$\phi_B(V) = \frac{1}{4}V_c \left(1 - \frac{V}{V_c}\right)^2 + \frac{1}{q\gamma} \sum_{v=1}^n \gamma_v (\varepsilon_v - \varepsilon_\xi), \quad (1)$$

where q is the positive unit charge, V is the applied voltage, V_c is the switching voltage and ε_v and ε_ξ are, respectively, the deep trap positions and the bulk Fermi level relative to the conduction band. γ is the total charge in the deep traps defined as $\gamma = \sum_{v=1}^n qN_v/\varepsilon\varepsilon_0$ where N_v is the density of deep trap states and ε is the relative permittivity of the material.

Furthermore, the switching voltage V_c is related to the interface charge Q_i at the grain boundary by

$$V_c = \frac{1}{2\gamma} \left(\frac{Q_i}{\varepsilon\varepsilon_0} \right)^2. \quad (2)$$

where the interface charge is determined by the interface density of states, $N_i(E)$, assuming that the electron traps are filled up to the Fermi level ξ_i^n of the neutral interface:

$$Q_i = q \int_{\xi_i^n}^{\infty} N_i(E) f_i(E) dE, \quad (3)$$

with $f_i(E) = \frac{1}{1+e^{(E-\xi_i)/k_B T}}$, ξ_i the quasi Fermi level of the interface, k_B the Boltzmann constant and T the temperature.

In order to determine the interface charge in (3), however, the modification of the interface density of states, $N_i(E)$, due to the grain boundary potential must be taken into account. In other words, according to Blatter's theory [16], Q_i and ϕ_B are mutually dependent. When a bias V is applied to the junction, the interface states are shifted according to $N_i(E) = N_{i0}(E - \phi_B(V))$. Thus, given an assumption for the distribution of interface states $N_{i0}(E)$ in absence of a boundary potential, a self-consistent solution of (1)-(3) is required. Such a solution can only be obtained numerically as described in Section 3.1.

Finally, the electron current density emitted across the grain boundary is [16]

$$J = A^* T^2 \exp\left(\frac{-q\phi_B + \varepsilon_\xi}{k_B T}\right) \left[1 - \exp\left(\frac{-qV}{k_B T}\right)\right], \quad (4)$$

where A^* is the Richardson constant. In the following, the above relation is applied to determine a lumped nonlinear electrical resistance for each of the grain boundaries in the equivalent circuit model.

2.2 Piezoelectric Coupling

The coupling mechanism suggested in [13] is based on the piezoelectrically induced polarisation charges that emerge at the grain boundary when a mechanical stress is applied. These charges add to (or subtract from) the interface charge Q_i , resulting in an increase (or a decrease) of the barrier height. This effect can be expressed by a modification of the switching voltage as

$$V_c = \frac{1}{2\gamma} \left(\frac{Q_i + \mathbf{n} \cdot (\mathbf{P}_l - \mathbf{P}_r)}{\varepsilon\varepsilon_0} \right)^2, \quad (5)$$

where \mathbf{n} is the grain boundary normal and \mathbf{P}_l and \mathbf{P}_r are polarization vectors defined in the two grains on the left and on the right hand side of the boundary, respectively. The polarization vectors are obtained from the stress tensor field, $\boldsymbol{\sigma}$, and the piezoelectric tensor \mathbf{d} in the respective grain as $\mathbf{P} = \boldsymbol{\sigma} \cdot \mathbf{d}$. Thus, the effect depends on the reciprocal crystallographic orientations of the two grains sharing the boundary, as well as on the strength and orientation of the applied stress. Furthermore, it should be noted that the

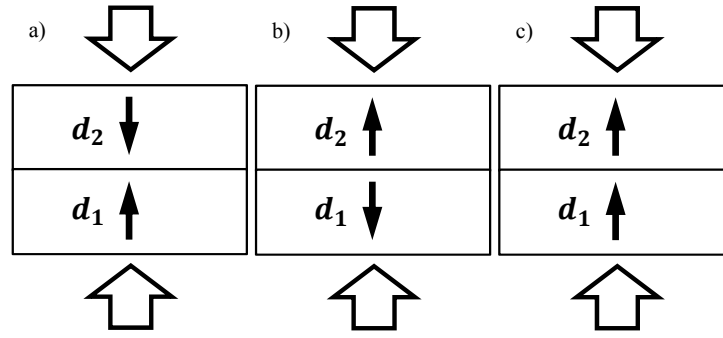


Figure 1: Schematic representation of head-to-head (a), tail-to-tail (b) and head-to-tail (c) reciprocal grain orientations.

barrier height, as well as the unbounded interface charge Q_i will depend on the mechanical stress seen by the grain boundary. This is a result of the complicated relationship between the two, that requires now the simultaneous solution of (1), (3) and (5).

An important special case, is that of a uniform uniaxial stress applied to two grains with aligned crystallographic orientations. This occurs in three main forms with head-to-head, tail-to-tail, or head-to-tail crystallographic orientations (see Fig. 1). Note, that in the head-to-tail case the piezoelectric charges induced at the boundary cancel and thus no piezoelectric coupling can occur. For a ZnO-bicrystal with such a grain alignment, Raidl et al. [7] observed that, indeed, in this case the grain boundary conductivity depends only very weakly on the applied mechanical stress.

3 THE BICRYSTAL

3.1 Grain Boundary Model

In the present model, a grain boundary is represented by the sub-circuit shown in Fig. 2. This approach is similar to the one used by Votja et al. [18]. It incorporates the nonlinear grain boundary resistance defined by (4), R_{gb} , a large Ohmic resistance, R_s , accounting for leakage currents across the boundary, as well as the contribution of the grain bulk resistivity to the total current denoted by R_g . Each grain center is associated with a voltage node, whereas the grain boundary is represented by a current branch of the circuit. Furthermore, we assume that the mechanical stress is uniformly distributed within the grains. For ZnO, this assumption is justified by the comparatively high stiffness of the crystal [19]. Thus, the mechanical condition of a grain boundary is uniquely defined by the two pairs (σ_1, d_1) and (σ_2, d_2) of the stress and piezoelectric tensors characterizing the two grains sharing the boundary, respectively.

In order to determine the grain boundary barrier, the coupled equations (1), (3) and (5) are solved using a symbolic computation package [20]. Typical parameters used in the calculation are displayed in Table 1. Here, we assume a single dominant bulk state energy, ϵ_v . Otherwise, the grain boundary parameters are similar to the ones given in [16, 15]. All energies are given relative to the valence band edge energy.

The obtained solutions for the grain boundary potential and interface charge are depicted in Fig. 3. The calculations are performed exemplarily for the case when the crystallographic orientations of the two neighboring grains are normal to the grain boundary and pointing in opposite directions in a head-to-head configuration (cf. Fig. 1). A uniaxial compressive as well as tensile mechanical stress field is assumed in the direction normal to the boundary. The results are similar to those reported previously in [16], with the only difference being that here the effect of mechanical stress is included. These results reveal the strong

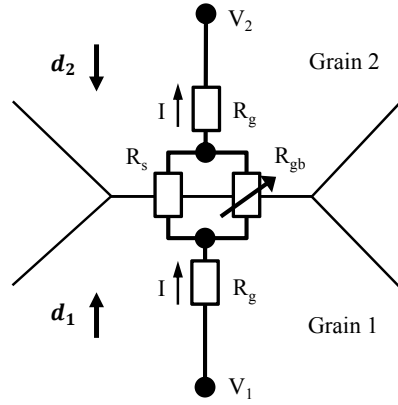


Figure 2: Lumped conductivity model using an equivalent electrical circuit for current flow at a grain boundary.

Table 1: Grain boundary parameters used in the model

$\varepsilon_{\xi}(\text{eV})$	$\varepsilon_{\xi_i}^n(\text{eV})$	$N_v(\text{cm}^{-3})$	$N_i(\text{cm}^{-2})$	$E_i(\text{eV})$	$\Delta E_i(\text{eV})$
3.133	0.0	9×10^{17}	9×10^{12}	2.2	0.15
$\varepsilon_v(\text{eV})$	$A_b(\text{m}^2)$	ε	$R_l(\Omega)$	$R_g(\Omega)$	
3.18	100	8.81	2×10^9	5×10^6	

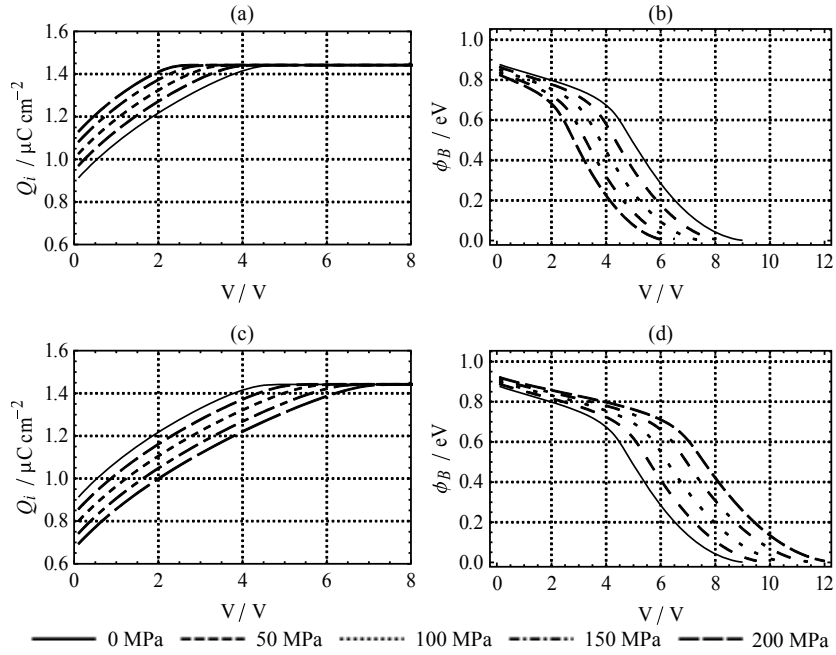


Figure 3: Potential barrier (b and d) and interface charge (a and c) solutions for a single grain boundary. This is shown first for compressive stress (a and b), and also for tensile stress (c and d).

impact of piezoelectric charges on the barrier height. As expected, in the compressive case, the barrier height is lowered with increasing stress whereas in the tensile case the barrier is increased. Nevertheless, this effect is strongly nonlinear as it depends on the electric voltage applied to the boundary.

In order to be able to consider general polycrystalline configurations and arbitrary mechanical stresses, the potential barrier solutions obtained by this procedure are tabulated with respect to voltage, V , and piezoelectric charge, Q_p . In the following simulations, these tables are incorporated into larger equivalent circuit models for more complicated varistor structures.

3.2 Mechanical Model

In the general case, with ZnO grains of arbitrary orientations, the mechanical stress is calculated by the Finite Element Method (FEM) using the software package Elmer [21]. We solve for the mechanical equilibrium condition in the crystal:

$$-\text{div} \cdot \boldsymbol{\sigma} = \mathbf{f}, \quad (6a)$$

$$\sigma_{ij} = \mathbf{C}^{ijkl} \epsilon_{kl} - \beta^{ij} (T - T_0). \quad (6b)$$

where \mathbf{f} is the applied force density, \mathbf{C} is the stiffness tensor, $\boldsymbol{\epsilon}$ the strain, $\boldsymbol{\beta}$ the thermal expansion tensor and T the temperature. Throughout the paper the stiffness tensor for a hexagonal type ZnO crystal in the Voigt two-index notation is assumed as [19],

$$\mathbf{C} = \begin{bmatrix} 210 & 120 & 105 & 0 & 0 & 0 \\ 120 & 210 & 105 & 0 & 0 & 0 \\ 105 & 105 & 211 & 0 & 0 & 0 \\ 0 & 0 & 0 & 43 & 0 & 0 \\ 0 & 0 & 0 & 0 & 43 & 0 \\ 0 & 0 & 0 & 0 & 0 & 44 \end{bmatrix} / \text{GPa}. \quad (7)$$

and the thermal expansion tensor for a ZnO crystal with principal axis pointing in the z -direction is

$$\boldsymbol{\beta} = \begin{bmatrix} 4.31 & 0 & 0 \\ 0 & 4.31 & 0 \\ 0 & 0 & 2.49 \end{bmatrix} / \mu\text{K}^{-1}. \quad (8)$$

3.2.1 Effect of Thermal Stress

To illustrate the coupled model, we consider the effect of internal thermal stress due to cooling in the simple bicrystalline structure shown in Fig. 4. The thermal stress is computed for cooling from a stress-free state at 1500 K to 300 K, given the known matrix of thermal expansion coefficients. The grains shrink upon cooling, which produces a mechanical stress at the interface. The mechanical stress and the piezoelectric vector in each grain is computed according to (6), using (7) and (8). The simulated thermal stress distribution in the bicrystal is shown in Fig. 4 (left). The resulting current-voltage characteristic and the non-linearity coefficient of the thermalised bicrystal and at room temperature after thermal treatment are shown in Fig. 4 (right). Obviously, the main effect of thermal stress, in this case, consists in shifting the switching voltage of the bicrystal to higher values by approximately 1V.

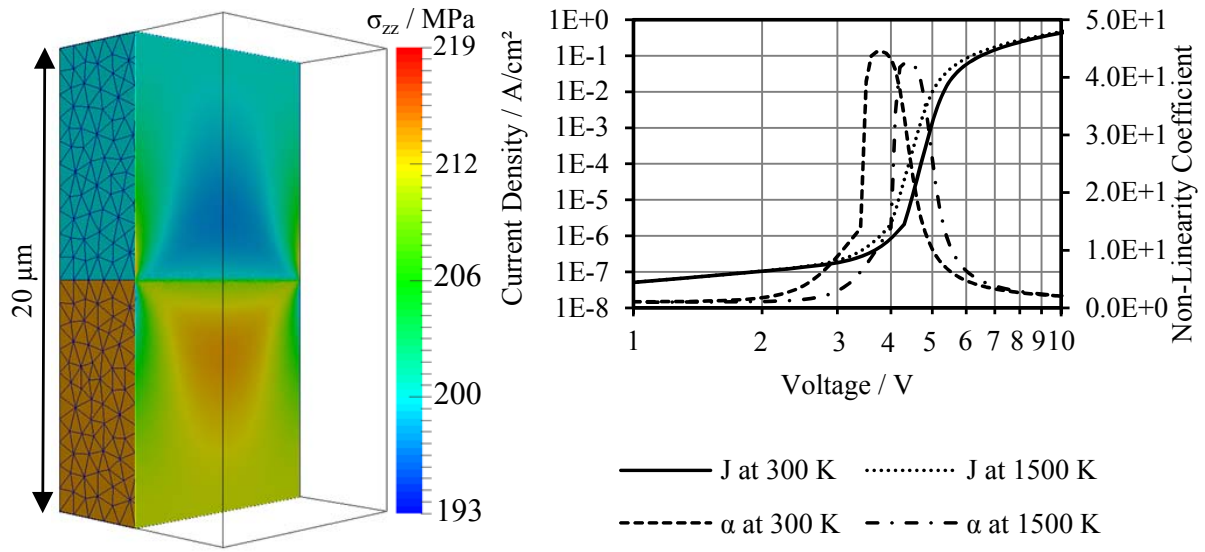


Figure 4: Distribution of residual thermal stress in the z -direction remaining in a $10 \mu\text{m} \times 10 \mu\text{m} \times 20 \mu\text{m}$ bicrystal after cooling from 1500 K (left) and the resulting current-voltage characteristic (right).

3.2.2 Applied Stress

In the following, we consider the effect of applied, compressive uniaxial stress on the bicrystal system. Three different bicrystal configurations are considered. In the first configuration, the grain's c -axis are oriented head-to-head as in Fig. 1(a). In the second configuration, the c -axis of one of the grains is rotated by 90 degrees with respect to the other grain. Finally, in the third configuration, the grains are oriented head-to-tail as in Fig. 1(c). As expected, in the latter case, no piezoelectric coupling occurs (see Fig. 5(c)). In the other two cases, a strong effect of the applied stress on the resulting current-voltage characteristics is observed. Hereby, it is important to note that piezoelectric coupling becomes important even when the grain orientations are not co-linear as is the case in the rotated grain configuration shown in Fig. 5(b). The effect of this coupling is two fold. First, the switching voltage of the barrier is shifted to lower values. Second, the nonlinearity degree of the characteristic curve is decreased. As seen in Fig. 5(a), for high applied stresses the electrical response becomes linear and the varistor property of the material is completely lost.

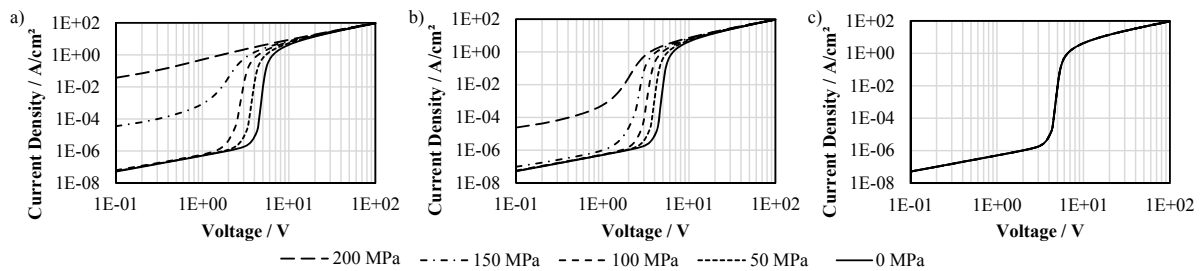


Figure 5: Current-voltage plots showing the stress sensitivity of a single grain boundary in a head-to-head orientation (a), grain orientations forming a 90° angle (b) and a head-to-tail orientation (c).

4 POLYCRYSTALLINE MODEL

For 2D polycrystalline structures, an equivalent electrical network is constructed, consisting of a large number of grain boundary sub-circuits (see Fig. 2) of different current-voltage characteristics depending on the local mechanical stress distribution. The polycrystalline microstructure is modeled using a Voronoi tessellation of the varistor sample as suggested in [14]. This is realised by means of the software package Neper [22]. The package provides, furthermore, a set of grain orientations randomly distributed within the sample volume.

Using such a description for the microstructure, an FEM mesh is generated with the open source program Gmsh [23] and the strain-stress equations (6) are solved numerically with Elmer [21]. Fig. 6 shows, exemplarily, the resulting Voronoi structure for a varistor sample of dimensions $200 \times 300 \mu\text{m}$ and an average grain size of $10 \mu\text{m}$. The computed stress distribution in the material for an applied uniaxial stress of 200 MPa in the vertical direction is depicted in Fig. 6(a). Furthermore, the current flow pattern within the sample resulting from the numerical solution of the circuit equations for an applied external voltage of 5 V is shown in Fig. 6(b). The well known current concentration effect for polycrystalline varistors [14] is hereby clearly observed.

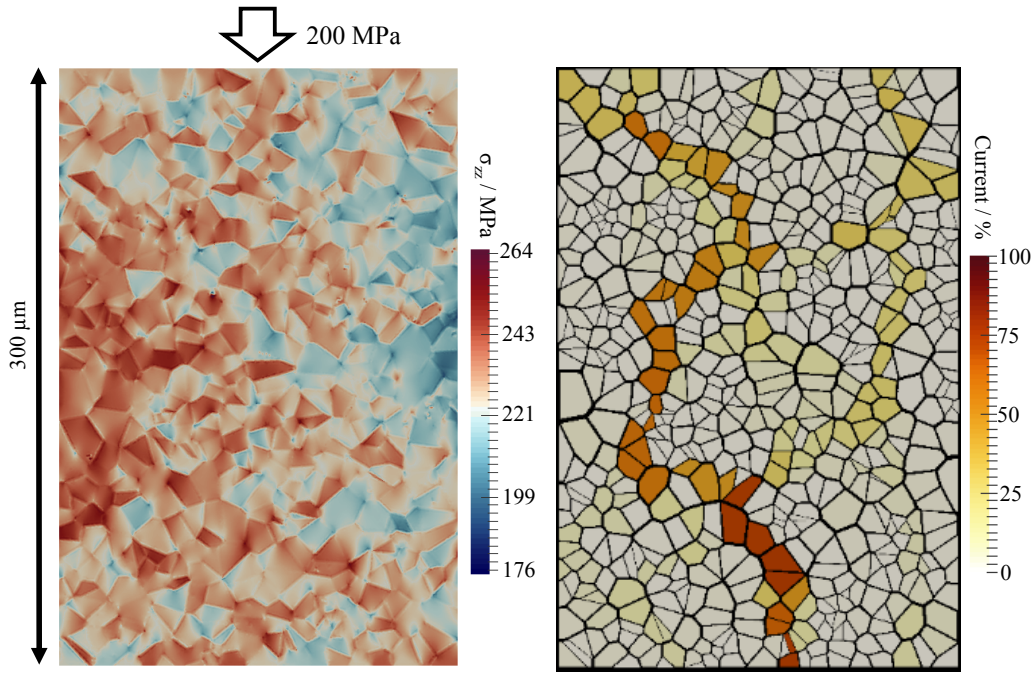


Figure 6: Mechanical stress distribution and current flow map for the non-linear region of a 2D polycrystal of size $200 \times 300 \mu\text{m}$ and average grain size of $10 \mu\text{m}$ when a uniaxial compressive stress of 200 MPa is applied (left). Electrical current pattern in the sample for an applied voltage of 5 V. The current in each grain is given relative to the total current flowing through the sample.

Current-voltage plots for network simulations based on Voronoi structures are shown in Fig. 7. Note that, as in the head-to-head bicrystalline case, a compressive stress results in a reduction in the switching voltage exhibited by the polycrystal, as shown by the progressive shift of the curves to the left along the voltage-axis. This is because, although grain boundaries with configurations close to tail-to-tail will exist, these are ignored by the current in favor of more conductive grain boundaries. Thus, the overall effect, is comparable to that of a single head-to-head grain boundary. Nevertheless, since the effect is the

result of current flow through many grain boundaries in series, few of which are likely to be of a perfect head-to-head orientation, this shift is less pronounced than for a bicrystal.

Also in Fig. 7, the gauge factor of the sample is shown. This is defined as the relative change of sample's resistivity with applied stress, $GF = \frac{\delta R/R}{\epsilon}$, where ϵ is the mechanical strain in the material and R is the effective resistance of the sample. In this case, gauge factors of more than 1800 are observed. The peak gauge values for a given mechanical stress are always retained in the corresponding switching voltage region of the varistor. Furthermore, the simulation reveals that the highest gauge sensitivity is obtained for lower applied stresses and at the corresponding moderate switching voltage values.

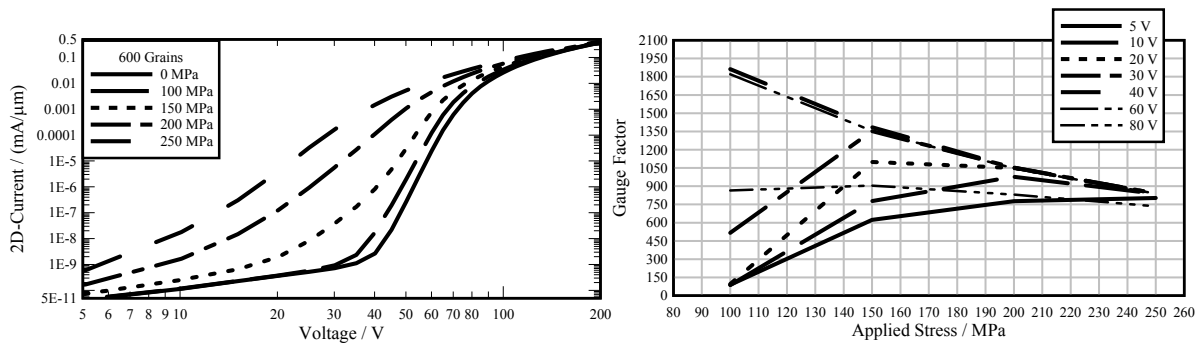


Figure 7: Electrical characteristics (left) and gauge factor (right) for the 2D polycrystal show in Fig. 6.

One important consideration is the effect of sample size on the effective current voltage characteristic of the material. In Fig. 8 simulations are performed for varistor samples of different sizes while keeping the average grain size constant. It can be seen that, for a varistor sample with 600 grains, a saturation occurs, after which edge effects from the sample no longer have an influence on the effective characteristics. This sample size is thus sufficient for the characterization of the bulk varistor material.

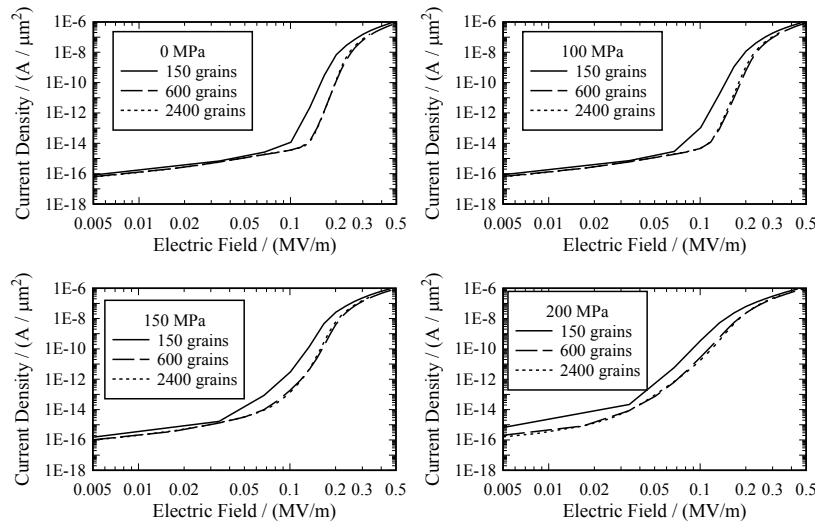


Figure 8: Stress dependent current-voltage characteristics for different sizes of the varistor sample. In all cases, the average grain size is $10\mu m$.

In Fig. 9, current flow maps, similar to the one presented in Fig. 6(b), are shown to illustrate the effect of applied stress on the current path pattern within the microstructure. The varistor sample considered is the same as the one examined in Fig. 6. It can be seen from the left-most column that, even when no external stress is applied, the varistor current flows through a single dominant path of high conductivity, emerging at a switching voltage of about 60 V. The topology of this path is determined essentially by the geometry of the microstructure (cf. [11]). When a compressive stress is applied to the material, three main effects are observed. First, the current concentration effect occurs already at lower (switching) voltages, corresponding to the lowering of the potential barriers for the conducting grain boundaries. Second, the location of the current paths is modified. The topology of current conducting paths depends now, in addition, on the mechanical stress distribution and the crystallographic orientations of the individual grains. Finally, the current concentration effect at higher applied stresses is less pronounced and the current distribution is more homogeneous. Two or more conductive paths within the sample can be observed. This corresponds to the overall lowering of the nonlinearity coefficient of the single grain boundary characteristics induced by the applied stress, as described in Section 3.2.2.

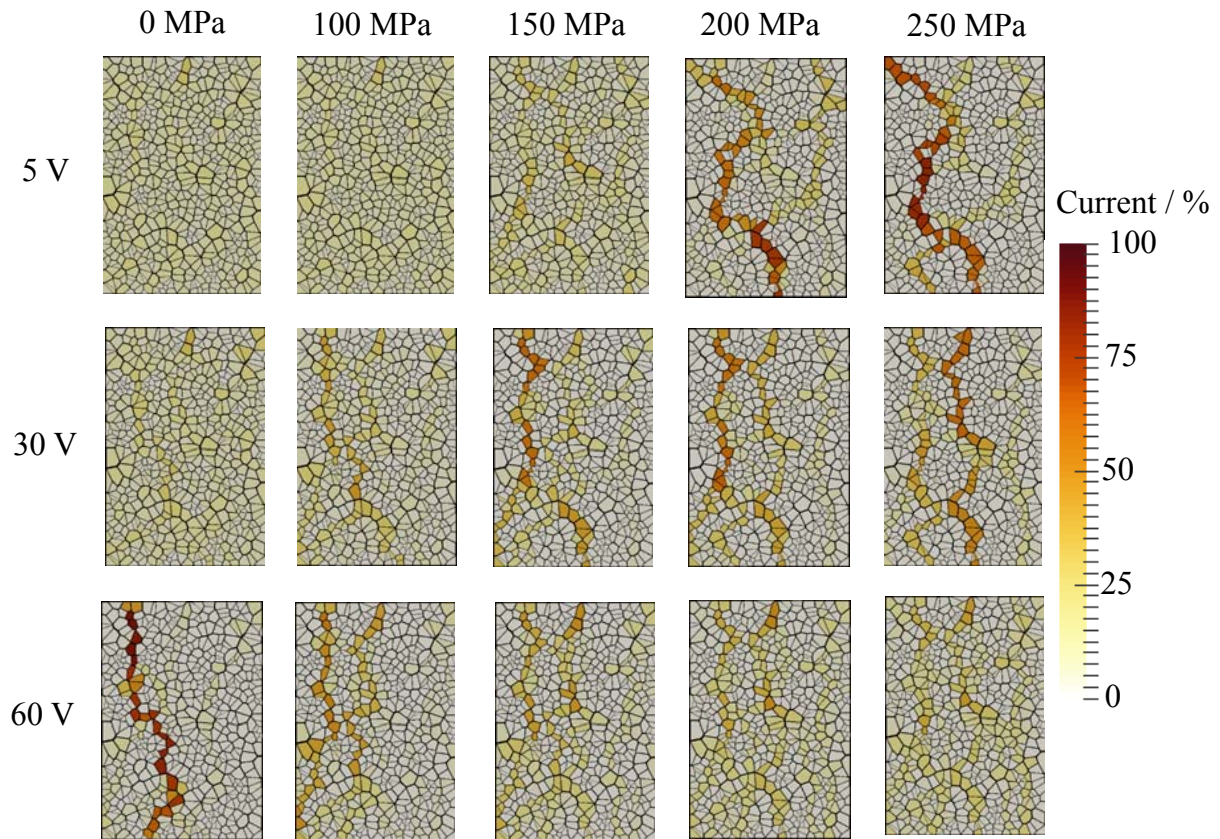


Figure 9: Current concentration for varying applied voltages and uniaxial compressive stresses in a 2D polycrystal of size $200 \times 300 \mu\text{m}$ and average grain size of $10 \mu\text{m}$. The current in each grain is given relative to the total current flowing through the sample.

5 CONCLUSIONS

A self-consistent coupled model for calculating the stress dependent grain boundary potential barriers, and thus the current-voltage characteristics of polycrystalline ZnO microstructures, has been developed. This model holds in both the context of externally applied stresses and those remaining within microstructures as a result of the thermal expansion anisotropy occurring in ZnO polycrystals. This method can be used for any given varistor sample described by its granular microstructure and the distribution of crystallographic grain orientations. The method provides, furthermore, insight into the current flow patterns within the material under the influence of mechanical stress. Based on these calculations, a stress induced reduction in the switching voltage of the polycrystal, as well as the decrease in the nonlinearity degree of the effective electrical characteristics under applied stress can be observed. This stress sensitivity can be quantified by use of the gauge factor, and doing so shows comparable values for ZnO polycrystals to those measured experimentally. Furthermore, the impact of system size on the model's output was investigated and assessed.

REFERENCES

- [1] X. W. Sun, and H. S. Kwok, *Optical Properties of Epitaxially Grown Zinc Oxide Films on Sapphire by Pulsed Laser Deposition*, J. Appl. Phys., 86, 408, 1999.
- [2] Z. G. Ju, C. X. Shan, D. Y. Jiang, J. Y. Zhang, B. Yao, D. X. Zhao, D. Z. Shen, and X. W. Fan, *Mg_xZn_{1-x}-based Photodetectors Covering the Whole Solar-Blind Spectrum Range*, Appl. Phys. Lett., 93, 173505, 2008.
- [3] K. Ellmer, A. Klein and B. Rech, *Transparent Conductive Zinc Oxide*, Springer, 2008.
- [4] D. R. Clarke, *Varistor Ceramics* J. Am. Ceram. Soc. 82, 485-502, 1999.
- [5] T. K. Gupta, *Application of Zinc Oxide Varistors*, J. Am. Ceram. Soc., 73, 18171840, 1990.
- [6] L. K. J. Vanadamme and J. C. Brugman, *Conduction Mechanisms in ZnO Varistors*, J. Appl. Phys., 51, 4240, 1980.
- [7] N. Raidl, P. Supancic, R. Danzer and M. Hofstaetter, *Piezotronically Modified Double Schottky Barriers in ZnO Varistors*, Adv Mater. 27, 2031-5, 2015.
- [8] R. Baraki, N. Novak, M. Hofstätter, P. Supancic, J. Rdel and T. Frmling, *Varistor piezotronics: Mechanically tuned conductivity in varistors*, J. Appl. Phys., 118, 85703, 2015.
- [9] W. Han, Y. Zhou, Y. Zhang, C. Y. Chen, L. Lin, X. Wang, S. Wang and Z. L. Wang, *Strain-Gated Piezotronic Transistors Based on Vertical Zinc Oxide Nanowires*, ACS Nano, 6, 3760-3766, 2012.
- [10] Y. Purusothaman, N. Alluri, C. Arunkumar, V. Vivekananthan and S. J. Kim, *Regulation of Charge Carrier Dynamics in ZnO Microarchitecture-Based UV/Visible Photodetector via Photonic-Strain Induced Effects*, Small, 01, 1703044, 2018.
- [11] R. Baraki, N. Novak, T. Frömling, T. Granzow and J. Rödel, *Bulk ZnO as Piezotronic Pressure Sensor*, Applied Physics Letters, 105, 111604, 2014.
- [12] P. Keil, R. Baraki, N. Novak, J. Rödel and T. Frömling, *Gauge Factors for Piezotronic Stress Sensor in Polycrystalline ZnO*, J. Phys. D: Appl. Phys., 50, 175106, 2017.

- [13] P. M. Verghese and D. R. Clarke, *Piezoelectric Contributions to the Electrical Behaviour of ZnO Varistors*, J. Appl. Phys., 87, 4430, 2000.
- [14] M. Bartkowiak and G. D. Mahan, *Nonlinear Currents in Voronoi Networks*, Phys. Rev. B, 51, 1082510832, 1995.
- [15] K. Bavelis, E. Gjonaj and T. Weiland, *Modeling of Electrical Transport in Zinc Oxide Varistors*, Adv. Radio Sci., 12, 2934, 2014.
- [16] G. Blatter and F. Greuter, *Carrier Transport Through Grain Boundaries in Semiconductors*, Phys. Rev. B, 33, 39523966, 1986.
- [17] F. Greuter, G. Blatter, *Electrical-properties of grain-boundaries in polycrystalline compound semiconductors*. Semicond Sci Technol., 5, 111-37, 1990.
- [18] A. Votja, Q. Wen and D. R. Clark, *Influence of Microstructural Disorder on the Current Transport Behavior of Varistor Ceramics*, Comp. Mater. Sci. 6, 51-62, 1996.
- [19] T. Yao and S. Hong, *Oxide and Nitride Semiconductors*, Springer, 2009.
- [20] Wolfram Research, Inc., Mathematica, Version 11.3, Champaign, IL, 2018.
- [21] M. Malinena and P. Råback, *Elmer finite element solver for multiphysics and multiscale problems*, Multiscale Model. Methods Appl. Mater. Sci., IAS Ser., 19, 101-113, 2013.
- [22] R. Quey, P. Dawson and F. Barbe, *Large-scale 3D random polycrystals for the finite element method: Generation, meshing and remeshing*, Comput. Methods Appl. Mech. Engrg., 200, 1729-1745, 2011.
- [23] C. Geuzaine and J. F. Remacle. *Gmsh: a three-dimensional finite element mesh generator with built-in pre- and post-processing facilities*, International Journal for Numerical Methods in Engineering 79, 1309-1331, 2009.

VIBRATION CONTROL OF A SEMI-ACTIVE SUSPENSION SYSTEMS USING MODEL PREDICTIVE CONTROL

MAI VAN NGOC, SEUNG-BOK CHOI, AND GI-WOO KIM*

Department of Mechanical Engineering
Inha University, Incheon, 22212, South Korea

* Email: gwkim@inha.ac.kr

Key words: Model Predictive Control (MPC), Physical Constraints, Semi- Active Suspension, Magneto-Rheological (MR) Damper

Abstract. This study presents vibration control performance of model predictive control (MPC) for a quarter car suspension system equipped with a MR damper suffering from the saturation on damping force of MR damper. The MPC controller is designed and then applied to the suspension system to take into account the constraints associated with MR damper. The performance of MPC controller is compared to a conventional control method where the constraint of control input is handled by using a saturation function. The effectiveness of the MPC controller is evaluated by using bump excitation in time domain.

1 INTRODUCTION

Suspension system plays an important role in vehicle vertical dynamics by enhancing the performances of the vehicle system in term of ride comfort and road handling . Among different types of suspension, the semi-active suspension system has received much attention because it provides the best compromise between control performance and energy consumptions compared to others including passive and active suspension system [1]. However, the main challenge faced by semi-active suspension control problems is how to deal with the dissipativity constraints of semi-active dampers which usually works as an actuator of the semi-active suspension system [2]. In practice, the most common semi-active damper used for the vehicle suspension system is magneto-rheological (MR) damper which uses MR fluids to provide controllablle damping force [3]. To date, a couple of control strategies have been developed for the semi-active suspension with semi-active damper [4]. Although lots of advanced control algorithms exist, only little can handle the dissipativity constraints of semi-active dampers in efficient way [5]. Model predictive control (MPC) is one of the promising control schemes which can meet the physical constraints on both control inputs and outputs while guarantee the control performance of the control system as semi-active suspension system [6]. It is obvious that the semi-active dampers as MR damper which has the dissipativity constraints can be handled elegantly within the MPC framework. However, since MPC has to solve an online constrained optimization problem at every sampling time, it usually requires high computational time for real time implementation.

In fact, several studies have employed the MPC control for the vehicle suspension system in

the literature. Many research has investigated the feasibility and performance of MPC controller for quarter car semi-active suspension system [7]. Some of works also proposed a methodology for optimal semi-active suspension system based on a fast MPC scheme for a quarter car model while a road profile preview is used by using expensive and not standard sensors [8]. In addition, MPC controller is also extendedly adapted to a half car [9] and full car [10] suspension model.

In this study, a practically implementable semi-active suspension MPC controller is developed for a quarter car system equipped with MR damper. The MPC controller is proposed for the semi-active suspension system which has physical constraint of 800 N on damping force of MR damper. As a first of step, the equations of motion of a quarter car suspension with MR damper are derived. The MPC controller is designed to satisfy the constraints on both control input and outputs and then applied to the suspension system. The performance of the proposed controller is also compared to the conventional optimal controller where the constraint of damping force is handled by using a standard saturation function which is not strong enough to deal with the physical constraint of control input. The effectiveness of the MPC controller is evaluated by using a bump excitation. As a result, MPC controller shows a much better vibration control performance compared with the other conventional controllers while meet the constraint on damping force of MR damper.

2 MODELING OF THE QUARTER CAR SUSPENSION SYSTEM

In this study, a two degree of freedom (2-DOF) quarter car suspension with a MR damper is considered for designing MPC controller as illustrated in Figure 1. It is assumed that the spring coefficient of the suspension and tire are linear, then the equation of motion (EOM) of the suspension system can be formulated as follows

$$\begin{aligned} m_s \ddot{z}_s &= -c_s (\dot{z}_s - \dot{z}_u) - k_s (z_s - z_u) - F_{MR} \\ m_u \ddot{z}_u &= c_s (\dot{z}_s - \dot{z}_u) + k_s (z_s - z_u) - k_t (z_u - z_r) + F_{MR} \end{aligned} \quad (1)$$

where m_s is the sprung mass, c_s denotes damping coefficient of the suspension, k_s is the stiffness of the suspension which includes the effective stiffness of the MR damper induced by air chamber, k_t indicates the stiffness of tire. Moreover, z_s , z_u , and z_r are the vertical displacements of sprung mass, unsprung mass and road disturbance, respectively. From Eq. (1), the state space equation of the quarter car suspension system with MR damper can be represented by

$$\begin{aligned} \dot{x}(t) &= Ax(t) + Bu(t) + Ew(t) \\ y(t) &= Cx(t) \end{aligned} \quad (2)$$

where

$$x(t) = [z_s \quad \dot{z}_s \quad z_u \quad \dot{z}_u]^T, u(t) = F_{MR}, w(t) = z_r \quad (3)$$

are state variables, control input and road disturbance, respectively.

$$\begin{aligned}
 A &= \begin{bmatrix} 0 & 1 & 0 & 0 \\ -k_s/m_s & -c_s/m_s & k_s/m_s & c_s/m_s \\ 0 & 0 & 0 & 1 \\ k_s/m_u & c_s/m_u & -(k_t+k_s)/m_u & -c_s/m_u \end{bmatrix} \\
 B &= \begin{bmatrix} 0 & -1/m_s & 0 & 1/m_u \end{bmatrix}^T, \quad E = \begin{bmatrix} 0 & 0 & 0 & k_t/m_u \end{bmatrix}^T \\
 C &= \begin{bmatrix} 1 & 0 & 0 & 0 \\ 0 & 0 & 1 & 0 \end{bmatrix}
 \end{aligned} \tag{4}$$

Table 1: Parameters of the quarter car suspension control system

Parameters	Value	Unit
Sprung mass (m_s)	315	kg
Unsprung mass (m_u)	41.5	kg
Stiffness coefficient (k_s)	21,000	N/m
Tire stiffness (k_t)	210,000	N/m
Damping coefficient (c_s)	1,400	Ns/m

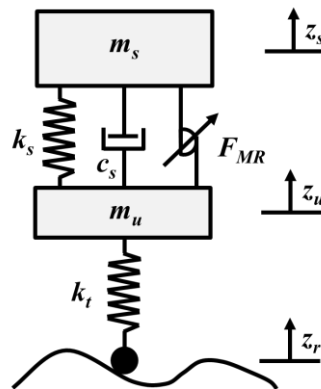


Figure 1: A quarter car suspension control system with MR damper

3 DESIGN AND CHARACTERISTIC OF MR DAMPER

3.1 Design of MR damper

In this study, a flow type MR damper is designed for the proposed quarter car suspension system. The schematic diagram of prototype MR damper is illustrated in Figure 2. The damping force of the MR damper consists of three components: viscous damping force, controllable

force, air force induced by the air chamber. It is assumed that the MR fluid is incompressible and that the pressure in one chamber is uniformly distributed. Then, the flow type Bingham damping force of an MR damper can be represented as follows

$$F_{MR} = F_{vis} + F_a + F_{air} \quad (5)$$

where F_{vis} denotes the viscous damping force of MR fluid, F_{MR} is the field-dependent damping force controlled by current applied to the coil, F_{air} indicates the air force induced by the air chamber when the piston is moved. According to the reference [11], the damping force induced by the MR damper can be derived as follows

$$F_{MR} = k_e x_p + \frac{6\mu L}{\pi d^3 R_d} (A_p - A_r)^2 \dot{x}_p + 2c \frac{L_p}{d} \tau_y (A_p - A_r) \text{sgn}(\dot{x}_p) \quad (6)$$

where

$$c = 2.07 + \frac{12Q_l \mu}{12Q_l \mu + 0.8\pi R_d d^2 \tau_y(B)} \quad (7)$$

$$Q_l = (A_p - A_r) \dot{x}_p$$

where x_p and \dot{x}_p are the displacement and velocity of piston, Q_l is the flow rate of the MR fluid; $\text{sgn}(\cdot)$ is the signum function, k_e is the stiffness coefficient related to gas pressure inside gas chamber; A_p and A_r are the area of the piston and piston rod; μ is its post-yield viscosity; L and L_p are the piston length and magnetic pole length; R_d and d are the average radius, and gap of MR fluid path; τ_y is the yield stress produced by applied magnetic field, B is the magnetic flux density dependent on the magnetic field, c is a coefficient that depends on the piston velocity.

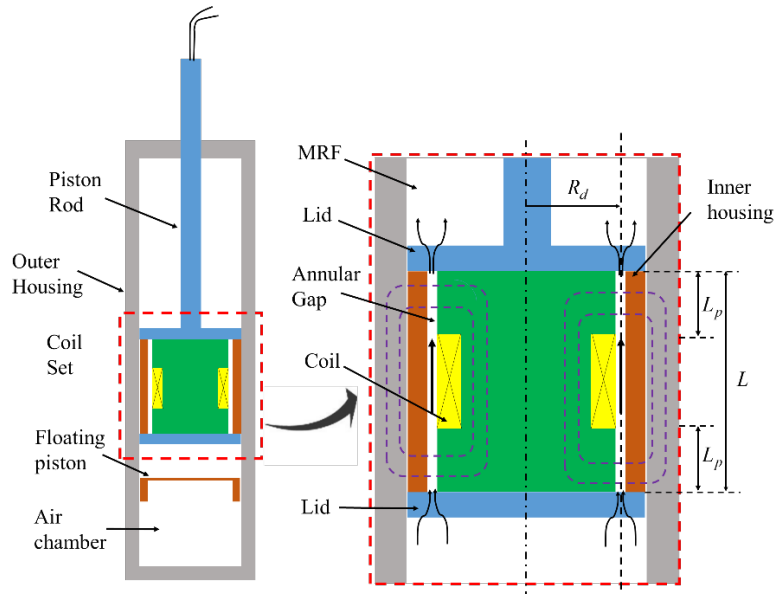


Figure 2: Configuration design of MR damper

3.2 Characteristics of MR damper

The characteristics of MR damper is estimated through simulation where MR fluid is modeled based on Bingham model. Figure 3 presents the measured field-dependent damping force of the MR damper. The maximum damping force is approximately 2300 N at input current of 1.5 A. It is obvious that the damping force is constrained at the maximum allowable input current. Even though the maximum of damping force reaches 2300 N at 1.5A through simulation but in practice we may be cannot use this maximum value of damping force because a maximum allowable power consumption should be required or the experimental results is not the same as the simulation results sometimes. In this study, the maximum allowable damping force is set as 800 N to validate the effectiveness of MPC controller with better output responses under constraint of actuator while reduce energy consumption of MR damper. Table 2 indicates design parameters of MR damper.

Table 2: Design parameters of the MR damper

Parameters	Value	Unit
Acceptable current (I)	1.5	A
Piston area (A_p)	0.0008668	m ²
Piston rod area (A_r)	0.00007854	m ²
Length of the piston (L)	0.031	m
Length of magnetic pole (L_p)	0.012	m
Circumference of inner core (b)	0.1078	m
Gap of MR fluid path (d)	0.0007	m

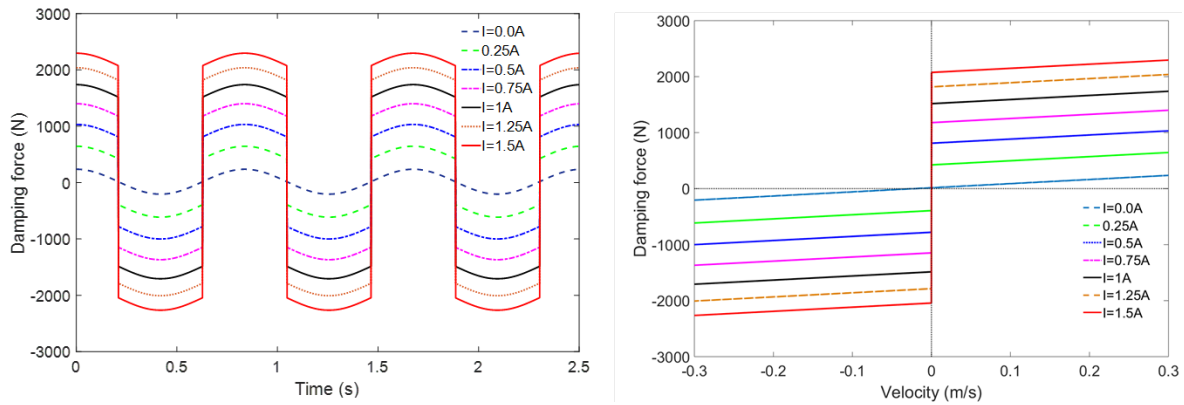


Figure 3: Characteristics of the prototype MR damper

4 MPC CONTROLLER DESIGN

To design MPC controller for the quarter car suspension, the continuous state equation of the semi-active suspension system should be formulated in discrete time domain with sampling time T_s (10 ms) as follows

$$\begin{aligned} x(k+1) &= (I + T_s A)x(k) + T_s B u(k) + T_s E w(k) \\ y(k) &= C x(k) \end{aligned} \quad (8)$$

where $A_d = I + T_s A$, $B_d = T_s B$, $E_d = T_s E$, $C_d = C$

The discrete time state equation can be rewritten as

$$\begin{aligned} x(k+1) &= A_d x(k) + B_d u(k) + E_d w(k) \\ y(k) &= C_d x(k) \end{aligned} \quad (9)$$

To establish an optimization problem, a cost function is defined as follows,

$$\begin{aligned} \min_{u_0, u_1, \dots, u_{N-1}} \quad & J = x_N^T P x_N + \sum_{k=0}^{N_p-1} x(k)^T \bar{Q} x(k) + \sum_{k=0}^{N_c-1} u(k)^T \bar{R} u(k) \\ \text{s.t.} \quad & x(k+1) = A_d x(k) + B_d u(k) \\ & y_{\min} \leq C_d x(k) \leq y_{\max} \\ & u_{\min} \leq u(k) \leq u_{\max} \end{aligned} \quad (7)$$

where x_N is the terminal states of each state variable which are determined as zeros for the suspension system. N_p and N_c are the length of prediction horizon and control horizon ($N_c \leq N_p$); $P > 0$ is defined to ensure the stability of the MPC control problem which is a solution to the Riccati equation

$$P = A_d^T P A_d + Q - A_d^T P B_d (R + B_d^T P B_d)^{-1} B_d^T P A_d \quad (8)$$

\bar{Q} and \bar{R} are symmetric and positive definite weighting matrices which is represented as

$$\bar{Q} = \begin{bmatrix} Q & 0 & \dots & 0 \\ 0 & Q & \dots & \vdots \\ \vdots & \vdots & \ddots & 0 \\ 0 & \dots & 0 & P \end{bmatrix}, \quad \bar{R} = \begin{bmatrix} R & 0 & \dots & 0 \\ 0 & R & \dots & 0 \\ \vdots & \vdots & \ddots & \vdots \\ 0 & \dots & 0 & R \end{bmatrix} \quad (9)$$

The positive definite matrix Q and R should be selected appropriately to minimize the performance index [1]. In this study, the weighting matrix Q and R are set as follows

$$Q = \text{diag}([6e9 \ 100 \ 100 \ 100]), \quad R = 0.12 \quad (10)$$

Performance index in Eq. (10) is a combination of sprung mass and unsprung mass displacements and velocities, respectively with the main object is to improve the ride comfort of the suspension system. The simulation parameters are represented in Table 3

Table 3: Simulation parameters for MPC controller

Parameters	Value	Unit
Prediction horizon (N_p)	10	--
Control horizon (N_c)	5	--
Sampling time (T_s)	10	ms
Constraint of damping force (F_{MR})	$-800 \leq F_{MR} \leq 800$	N

4 SIMULATION RESULTS

The performance of the MPC controller is evaluated by using a bump road profile as shown in Figure 4. In fact, the bump excitation is usually used to evaluate the transient characteristic in time domain. Figure 4 shows the output responses of the bump excitation to evaluate two controllers including the controller using saturation function and MPC controller. The sprung mass acceleration, suspension travel, damping force and unsprung mass acceleration are shown in Figures 4 (a), (b), (c), (d), respectively. It is obvious that two controllers show good performance, and the unwanted vibration induced from the bump excitation are remarkably attenuated. The output responses of the MPC controller are always less than the controller with saturation function.

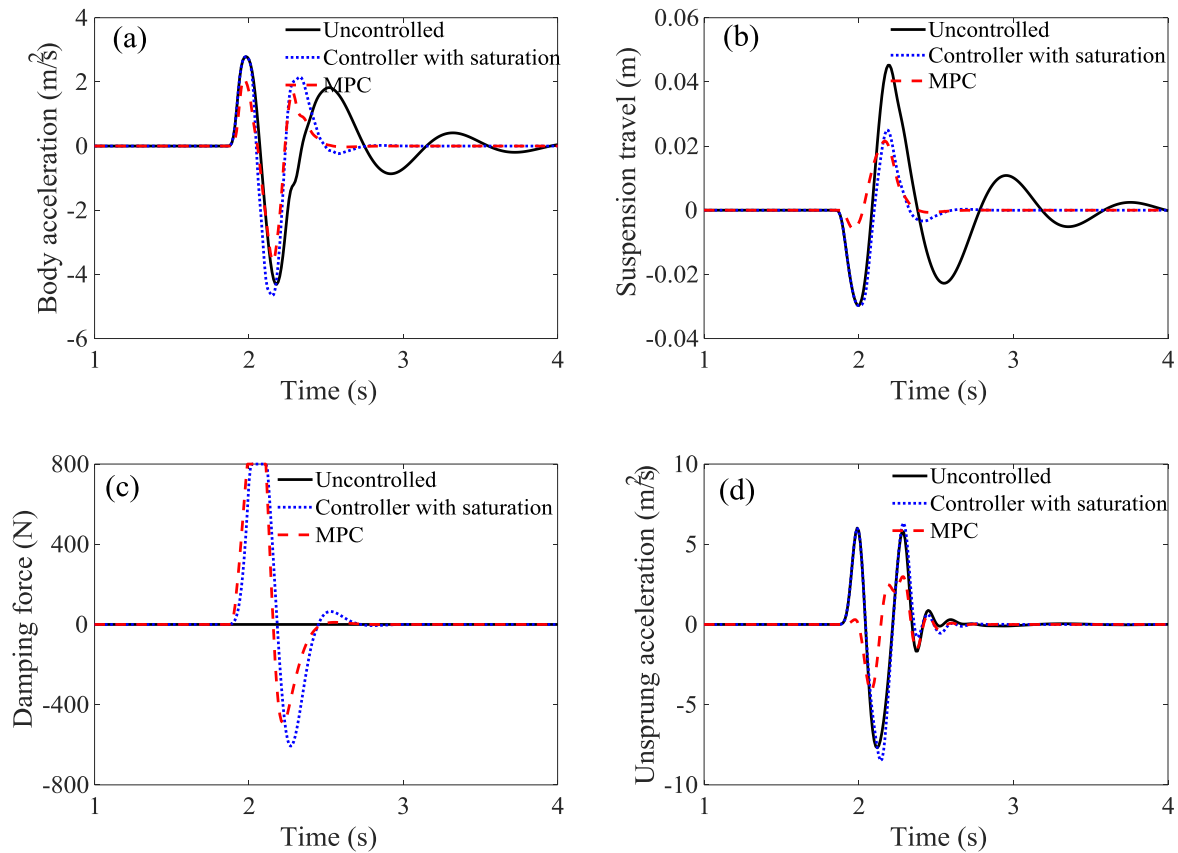


Figure 4: Output responses to bump excitation (a) sprung mass acceleration (b) suspension deflection (c) damping force (d) unsprung mass acceleration.

6 CONCLUSION

The MPC controller is applied for vibration control of a quarter car suspension with MR damper. An MR damper was designed based on the Bingham characteristics of the MR fluid, and its characteristics were experimentally evaluated to reveal the constraints of the controllable damping force. The vibration control performance of the MPC controller was investigated

under bump excitation in time domain. It is shown that the vibration of the suspension system is significantly reduced by applying the MPC controller compared to the controller which using a conventional saturation function. Especially, even though the damping force of MR damper is constrained, the ride comfort of the suspension system is remarkably improved.

REFERENCES

- [1] Savaresi S.M, Poussot-Vassal C, Spelta C, et al. *Semi-active suspension control design for vehicles*. Elsevier (2010).
- [2] Poussot-Vassal C., Sename O, Dugard L, et al. A new semi-active suspension control strategy through LPV technique. *Control Eng. Pract* (2008) **16**(12): 1519-1534.
- [3] Choi S. and Han Y. MR seat suspension for vibration control of a commercial vehicle. *Int. J. Veh. Des* (2003) **31**(2): 202-215.
- [4] Choi S., Li W, Yu M, et al. State of the art of control schemes for smart systems featuring magneto-rheological materials. *Smart Mater. Struct* (2016) **25**(4): 043001.
- [5] Giorgetti N., Bemporad A, Tseng HE, et al. Hybrid model predictive control application towards optimal semi-active suspension. *Int J Control* (2006) **79**(05): 521-533.
- [6] Mayne D.Q., Rawlings JB, Rao CV, et al. Constrained model predictive control: Stability and optimality. *Automatica* (2000) **36**(6): 789-814.
- [7] Brezas P., Smith MC and Houlst W. A clipped-optimal control algorithm for semi-active vehicle suspensions: Theory and experimental evaluation. *Automatica* (2015) **53**: 188-194.
- [8] C. Göhrle, A. Schindler, A. Wagner, et al. (2013) Model Predictive Control of semi-active and active suspension systems with available road preview. In: *2013 European Control Conference (ECC)* Anonymous , pp.1499-1504.
- [9] Canale M., Milanese M and Novara C. Semi-active suspension control using “fast” model-predictive techniques. *IEEE Trans. Control Syst. Technol* (2006) **14**(6): 1034-1046.
- [10] M. Q. Nguyen, M. Canale, O. Sename, et al. A Model Predictive Control approach for semi-active suspension control problem of a full car. *2016 IEEE 55th Conference on Decision and Control (CDC)* (2016): 721-726.
- [11] Oh J., Shin Y, Koo H, et al. Vibration control of a semi-active railway vehicle suspension with magneto-rheological dampers. *Adv Mech Eng* (2016) **8**(4): 1687814016643638.

OWN OSCILLATIONS OF THE FRAGMENT STANDS OF THE SPORTS COMPLEX “ARENA-OMSK” FROM THE NATURAL BACKGROUND

A. ZHIVAEV*, G. BOLDYREV†

* Penza state architecture and construction university 440028 Penza, Russia
e-mail: zhivaev@geoteck.ru, web page: <http://www.pguas.ru>

† Penza state architecture and construction university 440028 Penza, Russia
e-mail: g-boldyrev@geoteck.ru, web page: <http://www.pguas.ru>

Key words: grandstand structure, modal analysis.

Abstract. The article presents the results of measuring the natural vibration frequencies, mode shapes for the sports complex stands. Operational modal analysis based on the results of measurements was performed by ARTEMIS Extractor Pro. In work the equipment of firm Reftek was used. The results of identification of EFDD and SSI CVA with indication of confidence intervals (with a given confidence level of 95%) and corresponding coefficients of variation are presented. The measured frequency of the first form of natural oscillations is in the range of 3.61 ± 0.46 Hz (EFDD). Based on the analysis of the shape of the oscillations (all points of the structure synchronously to each other make vertical oscillations), this form of oscillations refers to the vibrations of construction-foundation system. As a result of measurements of the response of the tribune structure from the ambient vibrations, it was revealed that the first natural frequency of vertical oscillations of the investigated structures is higher than 6 Hz, which does not limit the operation of these structures for various measures according to the frequency criterion.

1 OBJECT DESCRIPTION

Ice arena “Arena-Omsk” has the following dimensions in plan 148.2 x 88.2 meters. Cross-section is shown on figure 1. Top of cover girders have level 19.35 meters. Building’s frame consists of reinforced concrete columns, hinged seated on them metal girders with span from 31 meters to 78 meters. Also frame contains reinforces concrete beams of grandstand structure implemented in monolith and precast variants. Spatial stiffness provided by vertical ties held on columns, stiffness diaphragms, vertical and horizontal ties on cover girders, and by spacers. Grandstand structure represents by slab-bar system consisted by prefabricated reinforced concrete columns, beams, tribune elements (shells) and slabs. Beams of grandstand has span from 5.5 meters to 12 meters. Tribune elements have span from 1 meter to 12 meters.

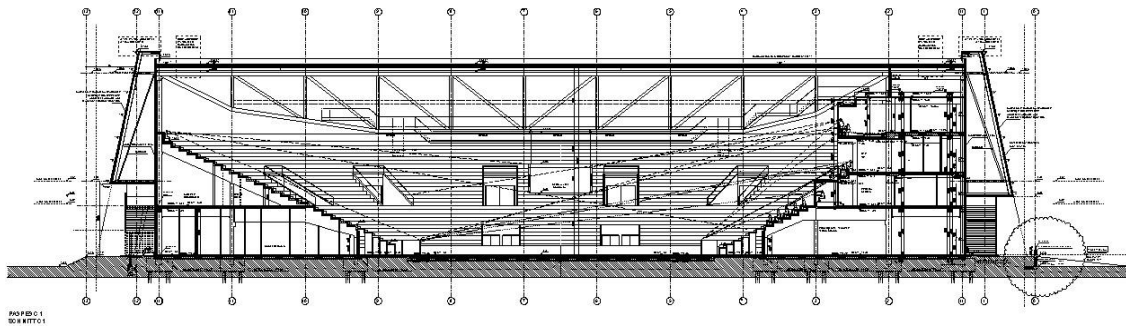


Figure 1: Cross-section of ice arena

2 SETTING GOAL

In life cycle of ice arena occurred requirement in provision not only sport events but also mass culture events. These events characterized by different activity of spectators, which seated or stayed on grandstand structure. Elements of grandstand structure must have required load bearing capacity for all variant of activity from spectators.

In this work authors of paper were followed by interim guidance on assessment and design for permanent grandstands [2]. Accordantly to this document significant dynamic load can be applied on tribune within process of music concerts by crowd that stomps to the beat of music. Moreover crowd can acts rhythmically within sports events, when people jumping on grandstand, and also swaying or applauding. When crowd suddenly jump up and then return, it also can apply significant dynamic loading. It should be noted that crowd can generate vertical and horizontal loadings.

Vertical dynamic loading can be applied due to crowd action with follow characteristics:

1. In frequency range 1.5-3.5 Hz from small group of people;
2. In frequency range 1.5-2.8 Hz for greater group of people (this frequency range is smaller due to synchronization problem).

Horizontal dynamic loading can be applied due to crowd action in frequency range 0.7-0.9 Hz.

Grandstand structure satisfied to requirements of dynamic comfort and strength when minimum natural frequency of vertical oscillations greater than 3.5 Hz for sports events and greater than 6 Hz for all events. Minimum natural frequency of horizontal oscillations is limited by 3 Hz.

The goal of current work was measurement of natural frequencies of grandstand fragments. In terms of advisory note [3] the goal we pursued was “type 1 tests” with natural frequencies measurement by AVS (ambient vibration survey). Bellow represented measurements results of grandstand structure free oscillations due to ambient vibration of sport arena “Arena-Omsk”.

3 WORK IMPLEMENTATION TECHNIQUE

3.1 Common information

All works divided on two series stages – field investigation and analytical works. All

stages were done in 2013 year.

Analytical works can split into follow parts:

1. Choosing adequate methods with following data processing.
2. Results assessment, making conclusions and recommendations.

Operational modal analysis was performed by ARTeMIS Extractor Pro [1] software.

Shown below figures with mode shapes were made by GNU Octave [5] software. Statistical calculations also were performed in GNU Octave.

Follow seismic measurement equipment made by RefTek are used [6]:

1. Two 1-axis accelerometers RefTek 131B-01/1 with sensitivity 1.6 V/g, measurement range $\pm 4g$, self noise $2 \mu g^2/Hz$, dynamic range 112 dB.
2. One 3-axis accelerometers RefTek 131B-01/3 with semi characteristics to RefTek 131B-01/1.
3. One seismic recorder RefTek 130-01 with 24-bit ADC, dynamic range 138 dB.

Current work is continuation of work [4]. Unlike previous work, the results of measurements on several grandstand elements are obtained here. Observed fragments as rule have the largest span. As a typical result of measurements outcomes for fragment in axes 11-11.1_G-H are shown bellow.

3.2 Statistical evaluation of data

For each measurement result of natural frequency follow calculations were done:

- mean values \bar{x} ;
- bounds of confidence intervals $\bar{x} - \delta$ and $\bar{x} + \delta$ for specified confidence level 95%;
- variation coefficients V , expressed as a percentage.

Bounds of confidence intervals were determined accordantly to ГOCT P 54859—2011 [7] with follow formulas:

$$(\bar{x} - \delta; \bar{x} + \delta), \delta = \mu\sigma \quad (1)$$

where \bar{x} - is a sample mean; σ - a standard deviations; μ - a parameter obtained by tables in applications in [7] for specified probability (it is a function of count of measurements and confidence level).

Variation coefficient is shown for relative assessments of natural frequencies obtained with different methods. Formula for variation coefficient calculation:

$$V = \frac{\sigma}{\bar{x}} 100 \% \quad (2)$$

4 NATURAL FREQUENCIES AND MODE SHAPES OF FRAGMENT 11-11.1_G-H

Accelerometers disposition scheme for measurements of natural frequencies and mode shapes for fragment 11-11.1_G-H is shown on figure 2 (a). Location of this grandstand fragment on plan is shown on figure 2 (b). In measurement experiments accelerometers were fixed to embedded plates – seating deck anchor bolts. One accelerometer RefTek 131B-01/1 was used as reference sensor and other accelerometers were rearranging in different points accordantly to shown on figure 2 (a) scheme.

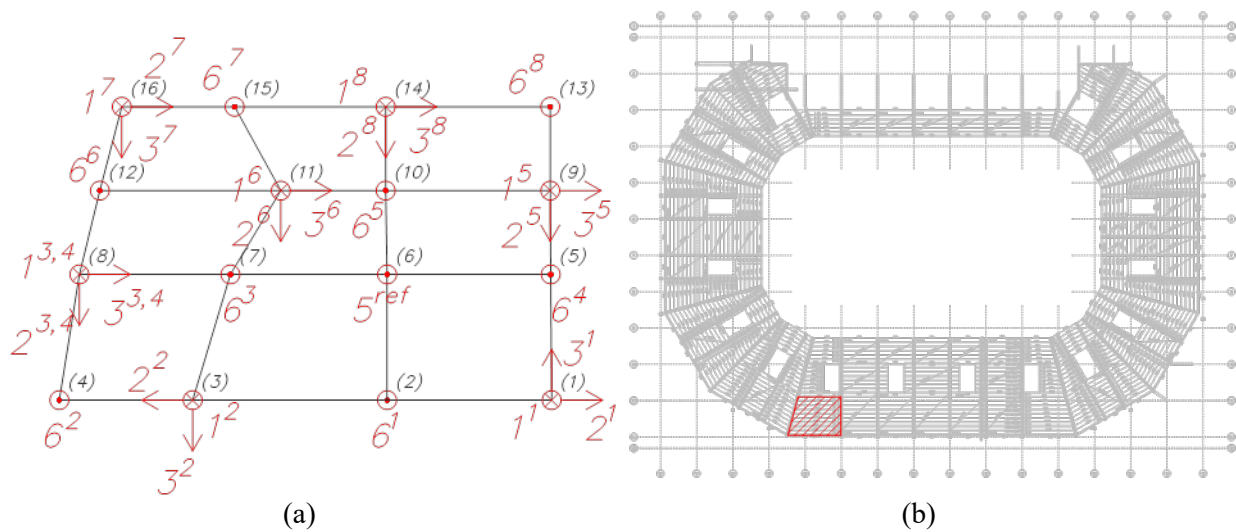


Figure 2: Accelerometers disposition scheme for fragment of grandstand structure in axes 11-11.1_G-H (a) and location of this fragment on plan (b)

Identification results by methods EFDD (enhanced frequency domain decomposition) and SSI CVA (stochastic subspace identification – canonical variate analysis) are shown on figure 3 and 4 respectively.

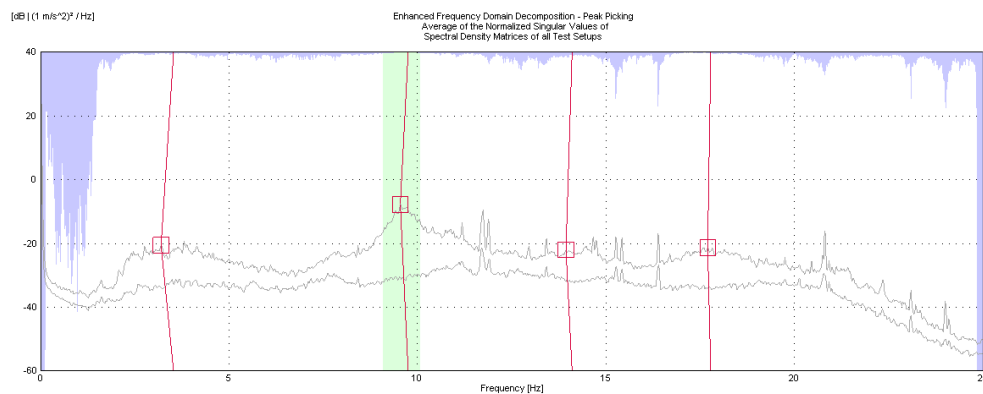


Figure 3: Average of the normalized singular values of spectral density matrices for fragment 11-11.1_G-H

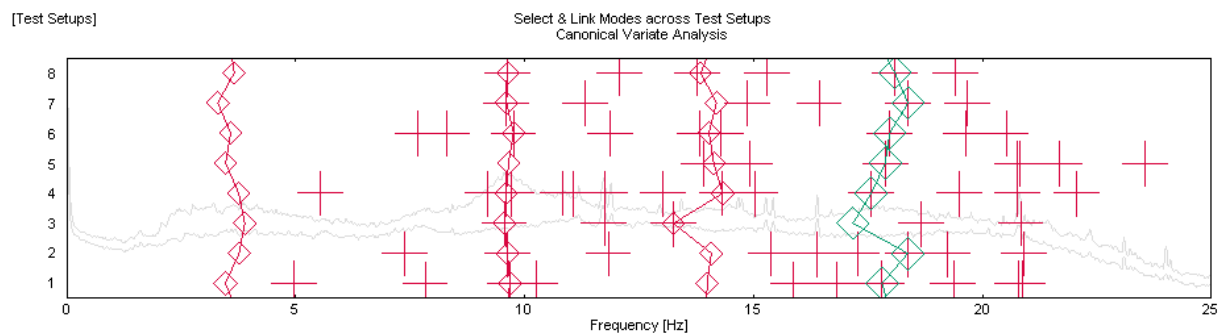


Figure 4: Poles SSI CVA for fragment 11-11.1_G-H

Natural frequencies obtained by EFDD and SSI CVA methods with confidence intervals (with specified confidence level 95%) and variations coefficients are shown in table 1. As shown in advisory note [3] for tests performed by AVS only natural frequencies and mode shapes can be measured. Damping coefficients determination for this type tests in this work was unreliable. Obtained variation coefficients for damping coefficients were significantly greater then variation coefficients for natural frequencies.

Table 1: Natural frequencies from EFDD and SSI CVA methods for fragment 11-11.1_G-H

EFDD				SSI CVA			
Frequency				Frequency			
$\bar{x} - \delta$, [Hz]	\bar{x} , [Hz]	$\bar{x} + \delta$, [Hz]	V , [%]	$\bar{x} - \delta$, [Hz]	\bar{x} , [Hz]	$\bar{x} + \delta$, [Hz]	V , [%]
2.63	3.53	4.44	10.83	3.15	3.61	4.07	5.35
8.86	9.75	10.65	3.89	9.49	9.64	9.78	0.63
12.69	14.10	15.51	4.23	13.21	13.98	14.75	2.34
17.37	17.78	18.19	0.97	16.95	17.90	18.85	2.25

MAC (modal assurance criterion) coefficients for mode shapes obtained by EFDD and SSI CVA methods are shown in table 2. Mode shapes are shown on figure 5.

Table 2: MAC coefficients

		SSI CVA			
		3.61 [Hz]	9.64 [Hz]	13.98 [Hz]	17.90 [Hz]
EFDD	3.53 [Hz]	0.593	0.667	0.021	0.140
	9.75 [Hz]	0.390	0.877	0.038	0.064
	14.10 [Hz]	0.019	0.067	0.290	0.101
	17.78 [Hz]	0.032	0.007	0.062	0.711

Natural frequencies for fragment 11-11.1_G-H with confidence intervals graphically are shown on figure 6.

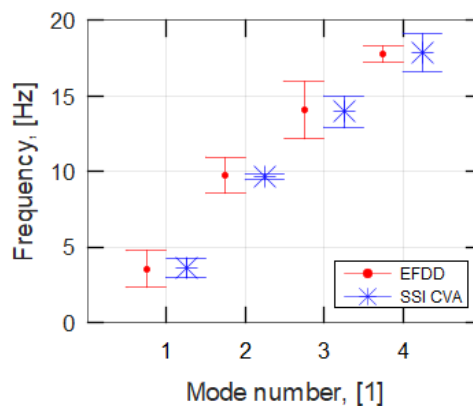


Figure 5: Confidence intervals for natural frequencies for fragment 11-11.1_G-H

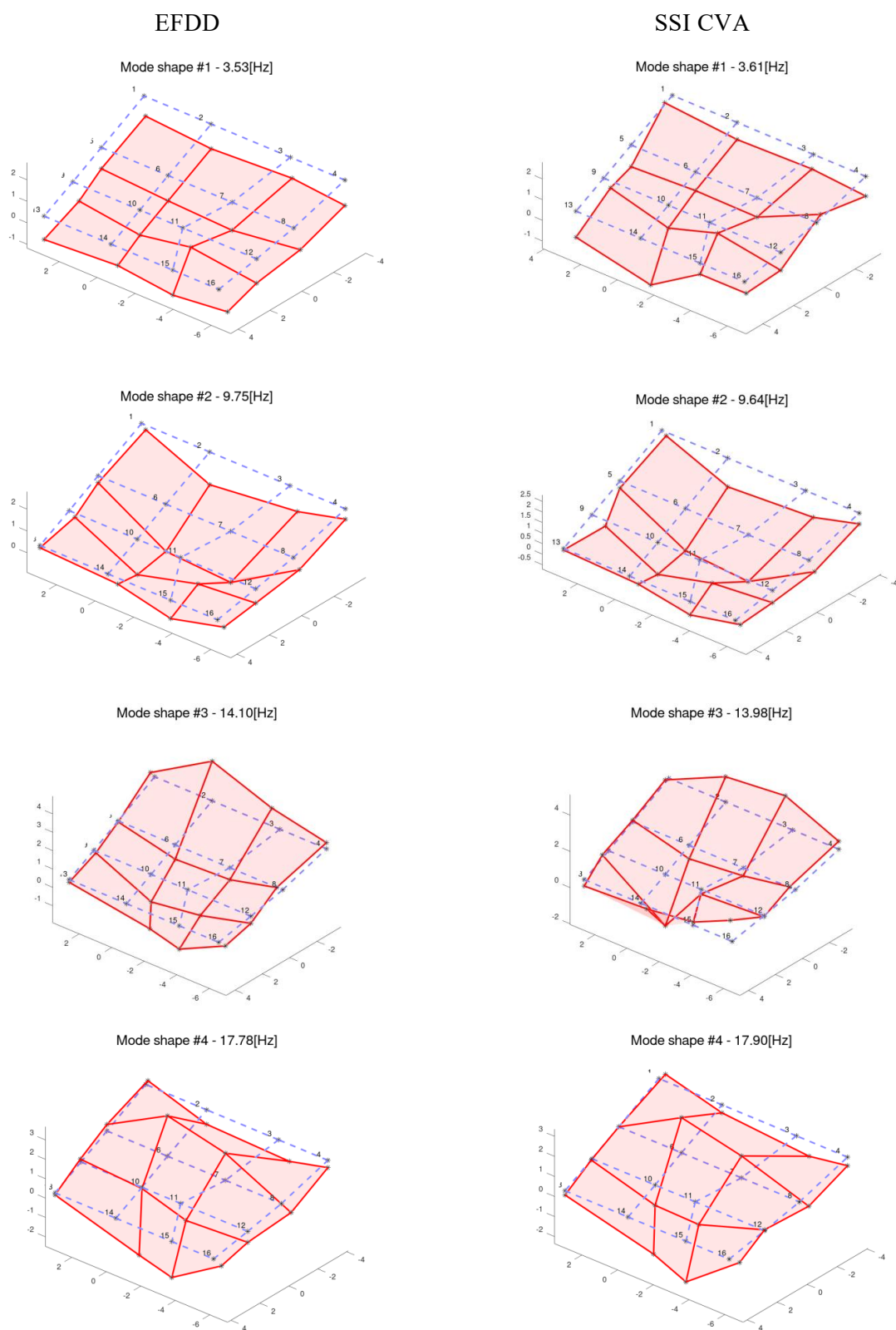


Figure 6: Mode shapes for fragment 11-11.1_G-H

5 CONCLUSION

1-st natural frequency for fragment 11-11.1_G-H was in interval 3.61 ± 0.46 Hz (EFDD). Corresponded mode shape is characterized by synchronous vertical deflections of all observed point – on tribune elements and on supports (columns). 1-st natural frequencies of other investigated grandstand fragments had similar values. It says that this mode shape refers to construction-foundation system.

2-nd mode shape was in interval 9.75 ± 0.9 Hz (EFDD). This mode shape refers to grandstand construction.

For all investigated grandstand fragments lowest natural frequency was greater than 6 Hz. Therefore there are not limitations for providing all sports and mass culture events according to frequency criterion [2].

REFERENCES

- [1] ARTeMIS Extractor - Operational Modal Analysis. Structural Vibration Solutions A/S [Electronic resource] - URL: <http://www.svibs.com/Products>.
- [2] Dynamic performance requirements for permanent grandstands subject to crowd action. Interim guidance on assessment and design. - London: The Institution of Structural Engineers, 2001 - 22p.
- [3] Dynamic testing of grandstands and seating decks. Advisory Note. – London, UK: The Institution of Structural Engineers, 2002 – 14 p.
- [4] Finite element model identification of arena stand. A.A. Zhivaev, G.G. Boldyrev. IWSHM, 2013.
- [5] GNU Octave - Scientific Programming Language. [Electronic resource] - URL: <https://www.gnu.org/software/octave/>.
- [6] REF TEK. Seismic and earthquake engineering systems. [Electronic resource] – URL: <http://reftek.com/>.
- [7] ГОСТ Р 54859—2011. Buildings and constructions. Determination of the parameters of the basic tone of free oscillations of buildings. Moscow, 2012.

RESEARCH AND DEVELOPMENT OF CIRCULAR PIPE PUMP USING EHD FLUID

TETSUHIRO TSUKIJI*

* Department of Engineering and Applied Sciences
Sophia University
7-1 Kioi-cho, Chiyoda-ku, 1028554 Tokyo, Japan
E-mail: t-tukiji@sophia.ac.jp

Key words: Smart Fluid, EHD Fluid, Fluid Mechanics, CFD Analysis, Pump.

Abstract. The EHD(Electro-hydro-dynamics) fluid is one of the smart fluid. The devices such as pumps using EHD fluid are developed and the researches especially about EHD ion-drag micro-pump have been performed to obtain the high performance. The circular pipe EHD pump with circular pipe electrodes unlike a pump shape developed in the past is proposed for the applications such as in small scale liquid cooling systems. The pumps are structurally simple, easy to fabricate, and the flow direction can be reversed by simply swapping the positive and negative electrodes. In the present study, the induced two-dimensional flow between electrodes is explained under application of the electric fields by the experimental flow visualization and CFD (Computational Fluid Dynamics) methods. The distributions of the velocity, the electric force and the charge density, which are obtained by the CFD method near the electrodes are shown and the numerical results are confirmed by the experimental flow visualization. In the next, the small pump based on cylindrical electrodes developed to utilize the flow analysis results and to induce one directional flow is explained. Furthermore we produced the pumps in which the electrode contains multiple holes to increase one-directional flow velocity and the load pressure. We measured the pressure-flow rate characteristics of the cylindrical electrode pump and the multi-holes electrode pair pumps, and compared their performances. As a result, the mechanism to induce one directional EHD flow near the electrodes under application of the voltage is understood clearly and the pressure-flow rate characteristics of the present pump based on cylindrical electrodes and the multi-holes electrodes are shown.

1 INTRODUCTION

The EHD fluid is one of the smart fluid. The flow of the EHD fluid is induced under the application of the electric field and the flow properties of the EHD flow such as pressure, flow velocity and flow rate can be controlled by the electric fields.

The development of the EHD pumps is conducted eagerly because those have no moving part and quite. In recent years, a review on EHD pumps is introduced and three different methods of EHD pumping such as ion-drag, induction and conduction are briefly outlined in the review paper [1]. It is pointed out that the ion-drag pumps show the higher flow rates compared with other two types of pumping in the paper. From the merit of the ion-drag pump

the researches about EHD ion-drag micro-pump have been performed [2-5]. However, it seems not to be led to practical use yet.

In the present study the EHD pump with circular pipe electrodes unlike a pump shape developed in the past is proposed for the applications such as in small scale liquid cooling systems. This small scale technology can be thought to be applied for microscale system. In the chapter 2 of the present paper, the induced flow between electrodes is explained under application of the electric fields using the experimental and the numerical flow visualizations. The velocity distributions obtained by the numerical method between electrodes are shown and the numerical results are confirmed by the experimental flow visualization. From the results, it is found that the one directional flow can be generated in some range of the electrode configuration. In the chapter 3, the small pump based on cylindrical electrodes developed to utilize previous research using liquid crystal [6] and to induce one directional flow is explained. Finally, we produced the pumps in which the electrode contains multiple holes to increase one-directional flow velocity and the load pressure [7]. In the present experiment the influence of the asymmetries of the electrode width on the relation between the flow rate and the pressure is examined. We measured the pressure-flow rate characteristics of multi-holes electrode pair pumps and compared their performances. Our pumps are structurally simple, easy to fabricate, and the flow direction can be reversed by simply swapping the positive and negative electrodes.

2 FLOW ANALYSIS OF EHD FLUID

The two-dimensional numerical simulation of EHD fluid flow in the simple flow channel is conducted when steady electric fields are generated through a direct current by two plate electrodes at the bottom of the flow channel.

2.1 Governing equations

The governing equations used in the present calculation are (1) Continuous equation, (2) Navier-Stokes equation, (3) Gauss' law and (4) Charge conservation law. The velocity vector, pressure, charge density and electric potential are unknown variables to solve the equations. The influence of the electric field on the flow is considered by the body force term in Navier-Stokes equation. We regard the coulomb force as the principal body force that generates the flow in the electric fields. HSMAC (Highly Simplified Marker and Cell method) is used to derive the velocity and Poisson equation is used to derive the pressure in the present calculation.

2.2 Flow field

In order to understand the EHD-induced flow velocity, the flow visualization was carried out. The flow channel and a plate electrode pair used in these measurements are illustrated in Fig.1(a). Each electrode plate EF, GH had a width of 1 mm and the gap between the two plates was 0.2 mm. The width of the channel perpendicular to the paper surface is 5mm. An electric field was generated at the bottom of the flow channel by applying a voltage to the plate electrode pair. Specifically, the cathode and anode of a DC power supply were connected to electrodes EF and GH, respectively. To enable visualization, the EHD fluid was first mixed with green fluorescent polymer microspheres (Duke Scientific Corporation Co., Ltd, particle diameter 8 μm), after which the mixture was introduced into the flow channel. The channel was placed on

a hot plate and the temperature of the mixture was maintained at 30 ± 1 °C. A voltage was then applied to the electrode pair to generate an electric field, thus initiating the fluid flow. A laser sheet was used to illuminate the center of the flow channel, and the flow behavior was observed from the front of the flow channel using a video camera. The flow was observed both above the electrode pair and in the entire channel during experiments, which were conducted at 1.5 kV. The experimental observed region ABCD is shown in Fig.1 (a). The calculated region A'B'C'D' is shown in Fig.1(b). The calculated region is reduced to save the computational time and the free boundary condition is applied at the boundaries B'C'D'A'.

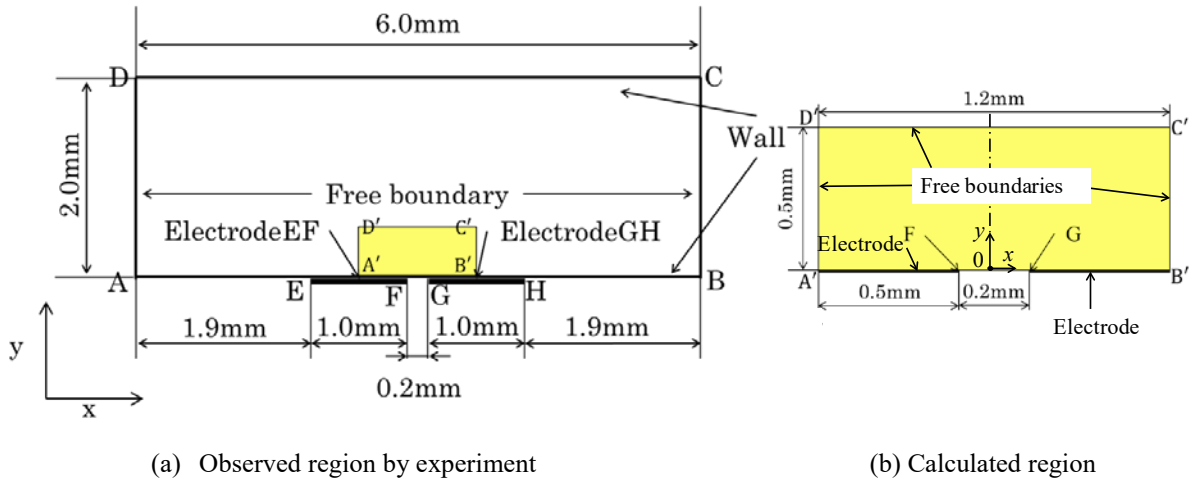


Figure 1: Flow field

2.3 Calculated results

The distributions of the electric potential and the electric field are shown in Figs.2(a) and (b) in the case of 1.5kV at $t=5.23 \times 10^{-5}$ s. The voltage is added at $t=0$ to the electrode GB' (GH) and the electrode A'F is ground. The distribution of the electric potential is symmetric for the axis of $x=0$. The large value of the electric field is concentrated near the points F and G of the electrodes. The direction of the electric field vectors is from the electrode GB' to the electrode A'F.

The distributions of the charge density and the electric force which is the coulomb force are shown in Figs.3 (a) and (b). The coulomb force is derived from the charge density times the electric field. The distribution of the charge density is shown in Fig.3(a). The positive charge density is generated and is diffused from the high electric potential electrode. The negative charge density is also generated from the ground electrode, however the generated region is small compared to the positive charge density region. The positive charge density region outside the negative region near the ground electrode can be seen. The positive region seems to be transported by the advection from the positive region and the all distribution of the charge density is asymmetric.

2.4 Comparison with experimental results

The visualization result is shown in Fig.4(a). The fluid called HFE-7100 (methoxy-

nonafluorobutane) is used as one of the EHD fluid. The sketched lines to indicate the flow direction clearly are shown. The vortex flow is indicated by white line and one directional flow from the boundary B'C' to the boundary A'D' is indicated by red line. It is recognized that the one directional flow is generated probably due to the asymmetric distribution of the charge density shown in Fig.3(a). The velocity distribution is shown in Fig.4(b). The magnitude of the velocity near the points F, G is large. The flow configuration such as the vortex upper the electrodes and the one-way streamline is very similar between the experimental observation and the simulated results.

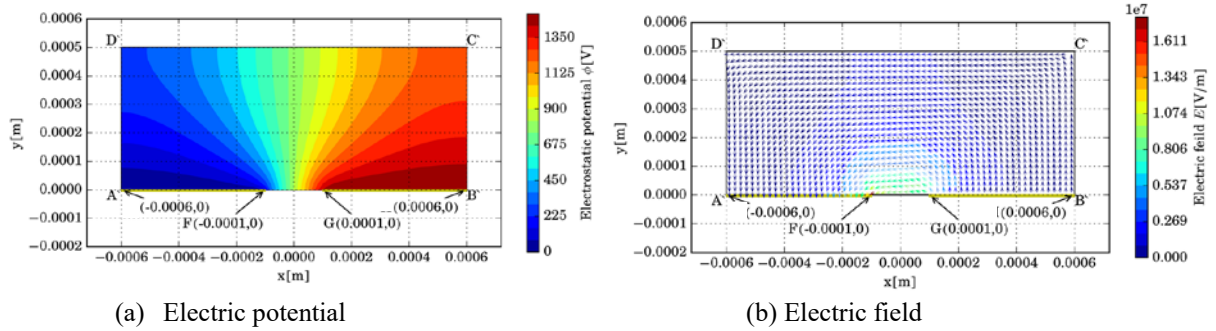


Figure 2: Calculated results for electric properties

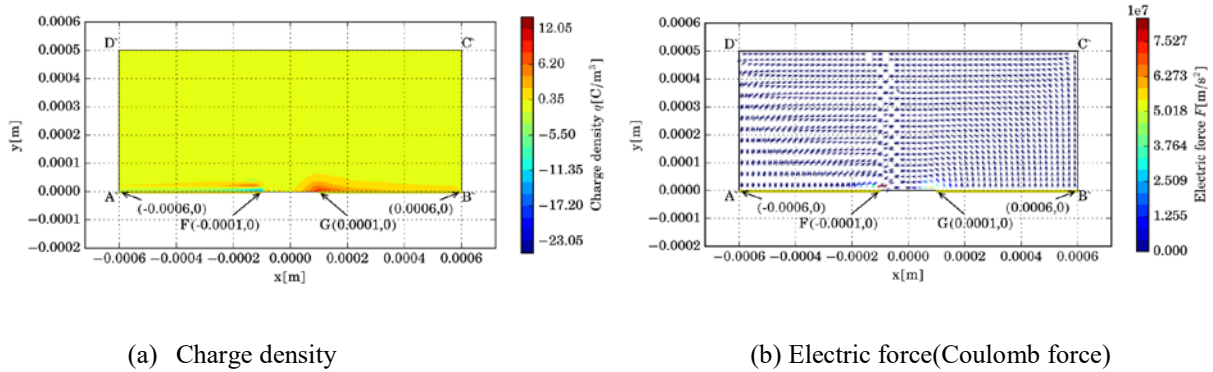


Figure 3: Calculated results for the coulomb force

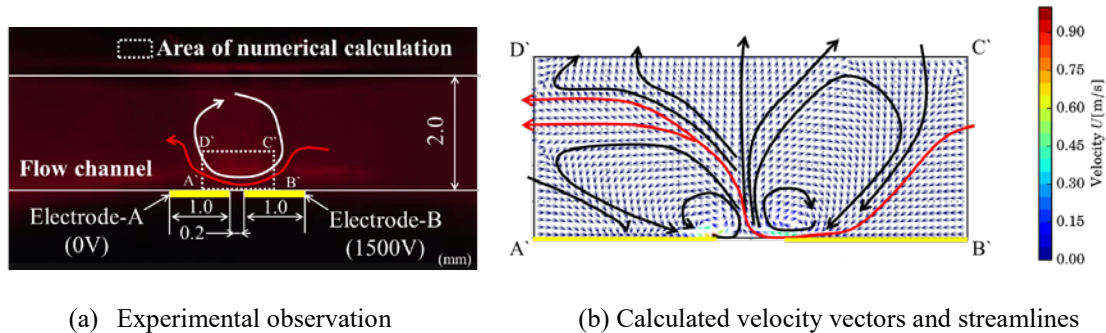


Figure 4: Flow visualization results

3 CIRCULAR PIPE PUMP

3.1 Pump based on cylindrical electrodes

The concept of the pump based on the cylindrical electrode pairs is shown in Fig. 5. The electrode material was copper plated with tin. An electric field was generated at the channel inside the cylindrical electrode pair by applying voltage. The one-directional flow generated by this electric field is caused by rotational flows, as shown in Fig. 4. The pump has a very simple structure and hence can be made easily. The cylindrical electrode pair is symmetric about a section perpendicular to its central axis, so the direction of the one-directional flow can be reversed by switching the anode and cathode.

The one of the pumps based on the cylindrical electrode pairs is shown in Fig.6(a). The pressure-flow rate characteristics plot in Fig.6(b) is approximately linear. Furthermore, the approximate line of the graph translates in the direction of decreasing pressure or flow rate when the applied voltage is decreased. Therefore, we concluded that the pressure and flow rate of the pump increase with the applied voltage. We also found that the pressure doubles when two pumps are connected in series.

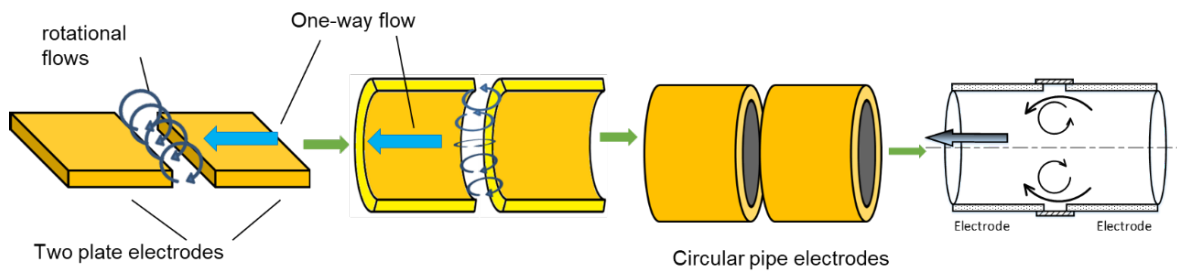
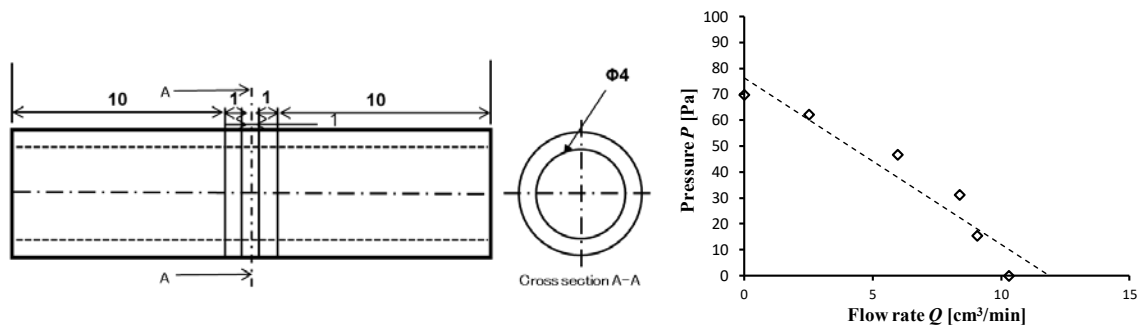


Figure 5: Pump based on cylindrical electrodes



(a) Pump based on the cylindrical electrode pairs

(b) Flow rate and pressure

Figure 6: Characteristics between flow rate and pressure

3.2 Pumps based on the electrode with the multiple holes

Four types of multi-holes electrode pumps, termed Types I ~IV which are illustrated in Fig. 7 respectively. The disk electrodes used in the Type I~IV pump contain nine holes (1 mm diameter). The distance between the electrodes is 1mm. The width of one electrode of the pump is changed from 0.25 to 1mm. The electrode material was copper and the flow channel between the electrodes was produced from transparent acrylic resin. An electric field was generated in the flow channel of the multi-hole electrode pair by connecting the cathode and anode of a DC power supply, respectively.

The flow rates are measured by measuring the flow velocity inside the pump after the pressure is given by setting up the difference of the high between inlet and outlet of the pump. One of the typical characteristics between the flow rate and the pressure is shown in Fig.8. The pumps are connected series and the voltage is 5.0kV. The results are almost linear as same as the pumps based on the cylindrical electrode pairs. The flow rate and the pressure of the type II whose electrode widths are 1 and 0.5mm are large compared to other pump.

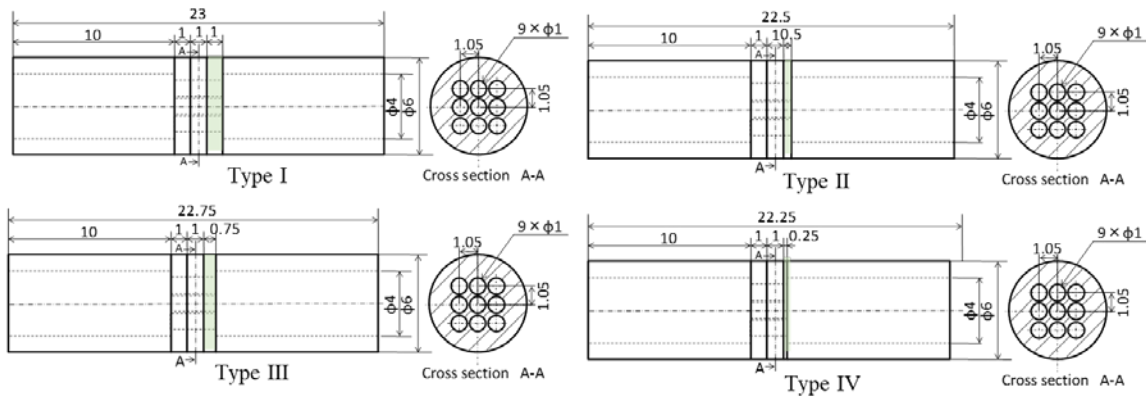


Figure 7: Pumps based on the electrode with the multiple holes

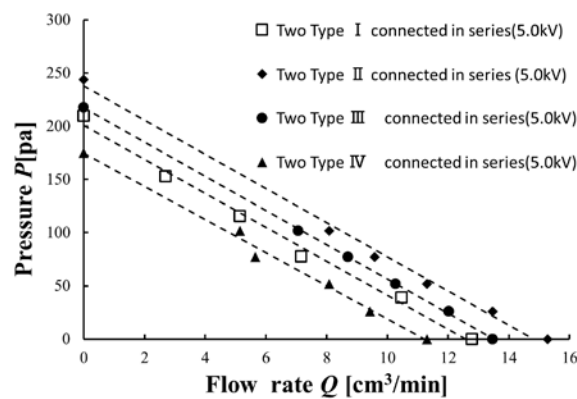


Figure 8: Relation between flow rate and pressure

4 CONCLUSIONS

The induced flow between electrodes was explained under application of the electric fields using CFD method and the flow observation technique. Especially it is found that the distributions of the charge density and the electric field are important because the coulomb force to induce the flow is affected by the charge density and the electric field. In addition it is found that the one directional flow can be generated by the asymmetry of the charge density distribution. For the characteristics of the pressure-flow rate of the EHD pump, the influence of the asymmetries of the electrode width on the relation between the flow rate and the pressure was examined and we found that both the pump pressure and flow rate can be increased by changing the widths of the electrode asymmetrically for the multi-holes electrode pair pumps.

5 ACKNOWLEDGEMENT

The author thanks Mr. Takahiro Shimizu, Taisei Tajima and Rei Suzuki for their generous support.

REFERENCES

- [1] Aryana, K., Ghiami, A. , Edalatpour, M. and Passandideh-Fard, M. A review on Electrohydrodynamic(EHD) pumps. *Proceedings of the 24th Annual International Conference on Mechanical Engineering-ISME2016*(2016) pp. 1–6.
- [2] Russel, M.K., Selvaganapathy, P.R. and Ching, C.Y. Ion drag electrohydrodynamic (EHD) micro-pumps under a pulsed voltage. *Journal of Electrostatics*(2016), vol. 82, pp. 48–54.
- [3] Russel, M.K., Selvaganapathy, P.R. and Ching, C.Y. Ion drag micropump with single walled carbon nanotube(SWCNT) electrodes. *Proceeding of the 4th micro and nano flows conference UCL*(2014), pp. 1–8.
- [4] Kazemi, P. Z., Selvaganapathy, P.R. and Ching, C.Y. Effect of electrode asymmetry on performance of electrohydrodynamic micropumps. *Journal of Microelectromechanical systems*(2009), vol.18, no. 3, pp. 271–350.
- [5] Lee, C.K., Robinson, A.J. and Ching, C.Y. Development of EHD ion-drag micropump for microscale electronics cooling. *Therminic 2007*(2007), pp. 1–6.
- [6] Tsukiji, T. and Miyahara, K. Study on pump using liquid crystalline flow under electric field. *Journal of Applied Electromagnetics and Mechanics*(2014), vol. 45, pp. 101–107.
- [7] Tsukiji, T. , Hamada, K. and Shimizu, S. Pump using EHD fluid. *Proceedings of the 10th JFPS International Symposium on Fluid Power*(2017).

SEISMIC BEHAVIOUR OF A CERTAIN TYPE OF TOWER CRANES

CARLOS S. OLIVEIRA^{*}, PEDRO M. B. CORREIA[†]

^{*} Instituto Superior Técnico (IST), CERis
Universidade de Lisboa
1049-001 Lisboa, Portugal
e-mail: csoliv@civil.ist.utl.pt

[†] Instituto Superior Técnico (IST)
Universidade de Lisboa
1049-001 Lisboa, Portugal
email: pedrombcorreia@hotmail.com

Key words: Tower Cranes, *In-situ* Measurements, Modal Analysis, Linear Dynamic Analysis, Seismic Vulnerability.

Abstract. Low to moderate size tower cranes used essentially in construction sites are very slender steel structures designed to carry high loads (1 to 3 tons) to distances up to 50 m around a central tower standing alone. They are required in many sites where working place is exiguous and easy to handle construction materials. Essentially they are composed by a tower with height varying according to the height of the construction and by an horizontal jib and counter-jib spanning a few tens of meters. We will analyse a particular tower crane with 33 m height and a jib with 35 m. These structures are very light, slender and flexible. Additionally they can be subjected to winds and earthquakes. Even though there are thousands of these structures all over the world specially in developing areas, there is very few published work for these type of structures. However, many disasters have occurred causing damage to people or urban equipment in the vicinity due to total or partial collapse of the structure. Wind has been in the past probably the most frequent cause of collapse, even though the jib is loose and can rotate freely around the tower axis. For earthquakes the main problem is the existence of large mass (a few tons) placed at a high position at an eccentric position. We developed a 3-D mathematical linear model of the structure with a finite element program SAP2000 and compared analytical frequencies with *in-situ* measurements. The maximum error for the 2 translation identified modes in X and Y direction was respectively 2.1%. Frequencies corresponding to the first modal shapes of this type of structure are very low (well below 0.5 Hz, depending on height of tower and counterweight). It has been found that the dynamic behaviour of the crane is largely dependent on the way its foundation is designed, which in this case is made of bogies supported on rails with concrete ballasts providing stability to the structure. Consequently the higher percentages of excited mass of the structure are associated with the more rigid vibration modes. We applied ground motion at the base to understand the dynamic 3-D behaviour of the whole system. The results indicate that a moderate ground motion ($PGA=1.5m/s^2$) shaking does not pose safety problems for this type of structure. However, caution should be exercised in order to maintain the concrete ballasts located at the foundation in place, to any type of seismic action.

1 FRAMEWORK AND DESCRIPTION OF THE STRUCTURE

This study focuses on the analysis of the dynamic behaviour of a tower crane and its vulnerability to a seismic action.

The subject in question is of great importance given the shortage of studies concerning the behaviour of this type of structures in the face of a moderate to intense seismic action and given the serious consequences inherent to their collapse [1].

During the research for this study it was found one of the few studies concerning this subject by Li-Jeng, et al [2] and also a regulatory document named as ISO 11031 [1].

Additionally, together with a growth of the construction in certain cities, there is a natural increase to use this type of structures.

The case study (Alto do Olival Crane) is located in Lisbon, Portugal.

The tower cranes are considered lightweight structures, essentially due to their geometry and the material used, steel, which although is not light (high volume weight), allows the application of slender profiles with adequate resistance.

In addition to this structural material, concrete ballasts are also used only as weight.

On the one hand, steel is used in the cross sections, the connections between profiles by means of bolts and welds and in the jib and counter-jib suspension cables.

On the other hand, concrete ballasts provide weight to the structure, ensuring its balance. In the present crane concrete ballasts serving as counterweight of about 3.9 tons are located at the end of the counter-jib and another group at the foundation for stabilization with 2x16 tons (see figure 1b)).

In the course of this chapter the crane is characterized sequentially from the ground to the top, starting from the foundation, the tower, and, finally, the jibs. This distinction is made on the basis of differences in terms of geometry, function, installation and functionality.

Firstly, the foundation is made of steel beams and is laid on rails, i.e. there is a possibility of changing the position crane if necessary. However, when it is in operation, four welded steel restrainers are placed on the rails to prevent the translation of this one. In addition, there are ballasts made of concrete with high mass, which accumulate on each side of the base a mass of 16 tons, providing stability to the tower crane.

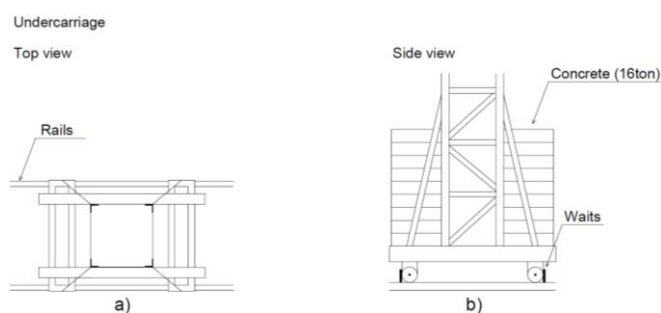


Figure 1: Bottom view (a) and side view (b) of the tower crane base

As far as the tower is concerned, it has a spiral arrangement, consisting of modules that are repeated in height with different dimensions and profiles. The steel profiles applied along the tower are characterized by L and U sections and are gradually smaller along the height (figure 2). The tower reaches a height till the jib of 33 m.

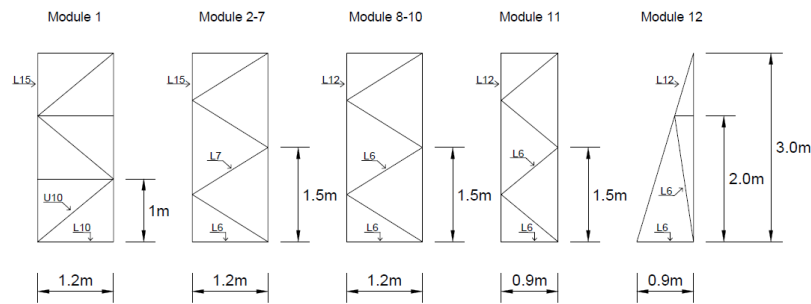


Figure 2: Tower crane modules

Finally, the jibs are divided into two types, the jib, a longer one with a length of about 35 m, which aims to lift and transport the loads in the perimeter of influence, and the counter-jib, a smaller one with a length of 13 m, which has the counterweight at its end, in order to provide a balancing force to the load on the jib. While the jib is attached to the tower by a steel suspension cable with a diameter of $\phi=5$ cm, the counter-jib is connected by two suspension cables with $\phi=2.5$ cm each (figure 3).

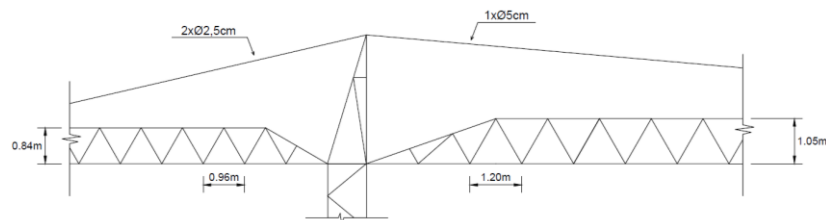


Figure 3: Zone of connection between the tower and jibs

Again, the jibs also contain modules that are repeated throughout their development. In these zones tubular profiles are used essentially with square or sometimes circular sections (RHS and CHS sections).

2 STRUCTURE MODELING

The structure under study was modeled using the finite-element analysis program SAP2000 [3].

The following table presents the constituent elements of the structure and the way in which they were modeled.

Table 1: Elements forming the structure

Elements	Model
Steel profiles	Frame
Steel suspension cables	Cable
Concrete slabs	Area with distributed load

As can be seen to ensure the correct behaviour of the various constituent parts of the structure, three types of elements were used.

In figure 4 we can see the wide application of the frame in the model.

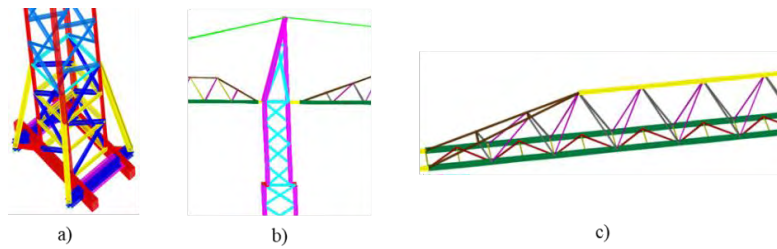


Figure 4: Application of the frame element in the model: a) base; b) tower-jibs connection and c) jib

Then, the effect of the concrete ballasts in the structure was counted through loads distributed in areas (shells) equivalent to the occupied size by these weights (Figure 6).

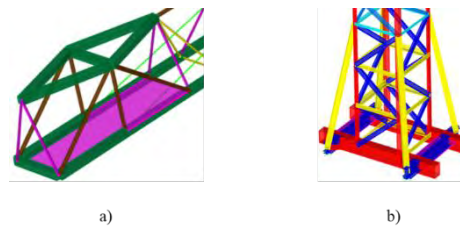


Figure 5: Application of the area element in the model: a) counter-weight e b) weights located in the base of the structure

Finally, in order to guarantee the correct behaviour of the suspension steel cables, which work only at tension, they were modeled as element “cable”.

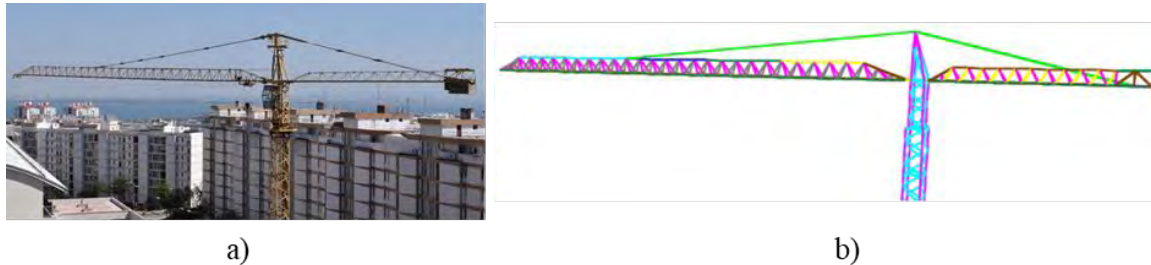


Figure 6: Application of the cable element in the model: a) photography of the real structure and b) model

After completing the modeling phase of the structure in geometric terms, the following numerical model was obtained (figure 7).

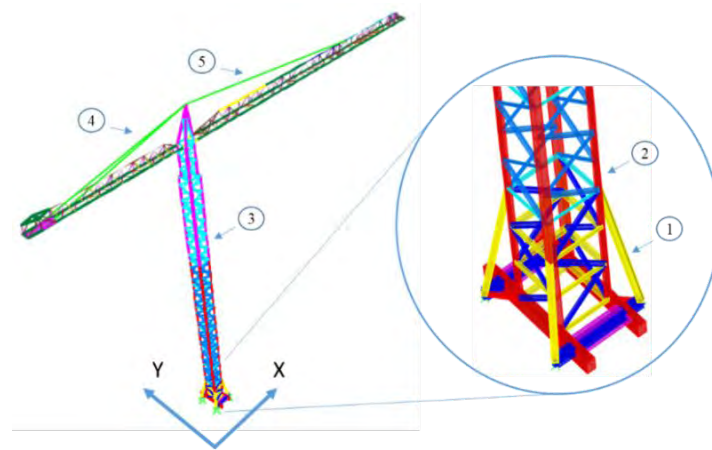


Figure 7: Numerical model of the case study with identification of steel elements under safety check

4 MODAL CHARACTERIZATION

4.1 *In situ* dynamic characterization

Not only to ensure a closer proximity between the numerical model and the actual structure, as well as to provide a greater credibility of the results exposed in this work, a dynamic identification test based on ambient vibrations was performed in the structure under analysis (figure 8).

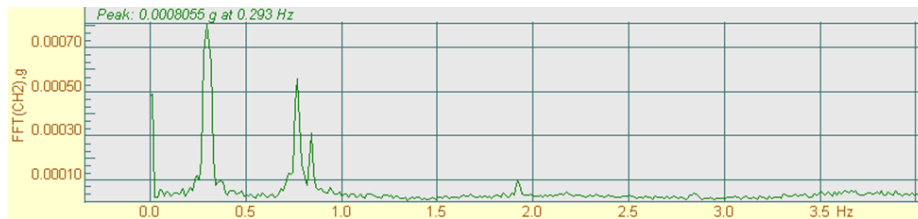


Figure 8: Frequencies according to the direction X (longitudinal) obtained through the dynamic identification test

From the analysis of this graphic it can be concluded that this type of structure is able to offer a wide range of results with great clarity and quality, thus facilitating the identification of the natural frequencies of the structure and, consequently, the calibration of the model.

Table 2: Frequencies obtained in the experimental test in the Y and X direction

f_y (Hz)	f_x (Hz)
0.32	0.29
-	0.78
0.83	0.82
1.90	1.90
2.35	-
2.80	2.80
3.10	-
3.51	-

It should be noted that in this test only the frequencies corresponding to the translation of the structure in the x and y direction, and not to torsional movements around were obtained. This is due to the location at which the accelerometer was placed (platform on the tower shaft of the structure), obtaining frequencies associated with torsional movements would require placing the apparatus at the tip of one of the jibs.

4.2 Modes of vibration

In this phase the vibration modes and respective dynamic characteristics of the structure under analysis are described.

It should be noted that the following table is composed of already adjusted and calibrated values, based on the results obtained in the dynamic identification test performed.

Table 3: Vibration modes and mass participation factors of the numerical model (orange color - most influential vibration modes, green color - cumulative mass participation factor of 90%)

Modes	T (s)	f (Hz)	Mass Participation Factors							
			U _x	ΣU _x	U _y	ΣU _y	U _z	ΣU _z	R _z	ΣR _z
1	6.859	0.146	0.00	0.00	0.00	0.00	0.00	0.00	0.97	0.97
2	3.343	0.299	0.12	0.12	0.00	0.00	0.00	0.00	0.00	0.97
3	3.219	0.311	0.00	0.12	0.23	0.23	0.00	0.00	0.00	0.98
4	1.508	0.663	0.16	0.28	0.00	0.23	0.00	0.00	0.00	0.98
5	1.148	0.871	0.00	0.28	0.05	0.28	0.00	0.00	0.00	0.98
6	0.679	1.474	0.00	0.28	0.00	0.28	0.15	0.15	0.00	0.98
7	0.528	1.892	0.00	0.28	0.00	0.28	0.00	0.15	0.00	0.98
8	0.405	2.470	0.00	0.28	0.00	0.28	0.00	0.15	0.00	0.98
9	0.372	2.687	0.00	0.28	0.00	0.28	0.01	0.16	0.00	0.98
10	0.296	3.375	0.00	0.28	0.00	0.28	0.00	0.16	0.00	0.98
11	0.253	3.952	0.00	0.28	0.04	0.32	0.00	0.16	0.00	0.98
12	0.233	4.301	0.04	0.33	0.00	0.32	0.00	0.16	0.00	0.98
-	-	-	-	-	-	-	-	-	-	-
30	0.057	17.569	0.00	0.33	0.00	0.32	0.58	0.74	0.00	0.98
-	-	-	-	-	-	-	-	-	-	-
41	0.042	23.657	0.00	0.36	0.14	0.51	0.00	0.95	0.00	0.98
42	0.042	23.950	0.00	0.36	0.39	0.90	0.00	0.95	0.00	0.98
-	-	-	-	-	-	-	-	-	-	-
89	0.018	55.359	0.45	0.85	0.00	0.99	0.00	0.99	0.00	0.99
-	-	-	-	-	-	-	-	-	-	-
91	0.018	55.804	0.04	0.94	0.00	0.99	0.00	0.99	0.00	0.99

As it is generally known, the overall response of the structure must be composed of all modes of vibration that contribute significantly. As such, in order for the sum of the mass participation factors of the structure to reach a minimum value of 90% of the total mass of the structure, a total of 91 vibration modes were recorded.

From the analysis of the vibration modes and its respective factors of mass participation, it highlights an interesting fact that must be evidenced.

As can be seen, the first twelve vibration modes of the structure do not generate high

percentages of excited mass ($\approx 33\%$), thus, the number of vibration modes under analysis has been widened in order to reach the minimum condition of 90% of excited mass of the structure. Consequently, it has been noted that the higher percentages of excited mass are associated with the translation of the base of the structure in each direction, x and y, which in turn concerns the more rigid modes of vibration.

The following table compares the results of the numerical model and the experimental test.

Table 4: Comparison of the model and *in situ* frequencies and error calculation

Direction	f (Hz)		Error (%)
	Model	<i>In situ</i> test	
x1	0.299	0.293	2.1
y1	0.311	0.317	-1.9
x2	0.663	0.770	-13.9
y2	0.871	0.830	4.9

From the analysis of the results it is concluded that the values obtained from the *in situ* test reveal a great quality, being close to three modes of vibration of the structure, thus proving a good approximation between the numerical model and the real structure.

From this comparison the lowest error obtained is around 1.9% and the maximum 13.9%, it should be noted that this maximum error is associated with a second mode of vibration in the y direction, and as such may possibly correspond to a less clear mode compared to the first two modes of translation vibration.

The following is a brief description of the most influential vibration modes in the behaviour of the structure.

4.2.1 1° Vibration mode

The first mode of vibration (figure 9) corresponds to a torsional mode with a period of 6.86 s and a mass participation factor of 97%.

As can be seen in the following figure, the movement of the structure occurs around the axis of the tower, guaranteeing a high percentage of excited mass.

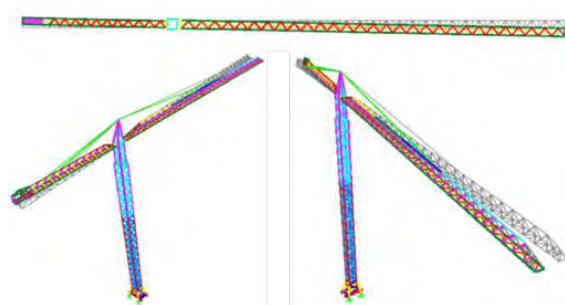


Figure 9: 1st Vibration mode - Torsion around the axis of the tower

4.2.2 2° Vibration mode

The second mode of vibration (figure 10) represents the vibration of the structure in the x

direction, that is, in the direction of the jibs, with a period of 3.34 s and a mass participation factor of 12%.

Unlike the first mode of vibration, this mode has a reduced percentage of excited mass.

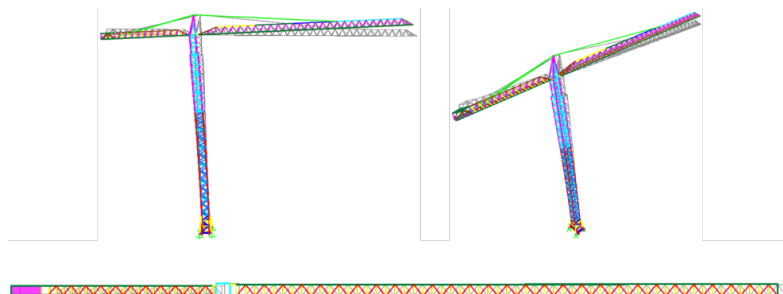


Figure 10: 2nd Vibration mode - Translation in the x direction

4.2.3 3^o Vibration mode

The third mode of vibration (figure 11) is characterized by a translation in the y direction, direction transverse to the length of the jibs, with a period of 3.22 s and a mass participation factor of 23%.

Once again, the percentage of excited mass is reduced.

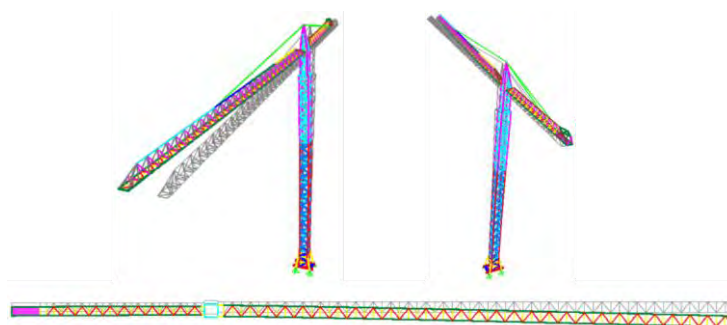


Figure 11: 3^o Vibration mode – Translation in the y direction

The following modes of vibration represent the modes with the greatest influence on the dynamic behaviour of the tower crane, since they concentrate mainly on the mass excitation located at the base of the structure. Of note, the high discrepancy between the mass of the base of the structure and the rest of it.

Thus, the dynamic behaviour of a crane is largely dependent on the way its base is designed.

4.2.4 4^o Vibration mode

This mode of vibration (figure 12) represents a translation of the base of the structure in the y direction with a period of 0.042 s and a mass participation factor of 39%.

As can be seen this is a rather rigid mode and with a considerable excited mass percentage.

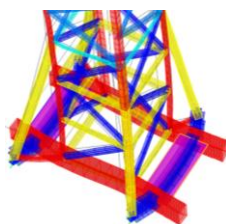


Figure 12: 42° Vibration mode - Translation of the base in the y direction

4.2.5 89° Vibration mode

This mode of vibration (figure 13) is characterized by a translation of the base of the structure in the x direction with a period of 0.018 s and a mass participation factor of 45%.

Once again a greater percentage of excited mass associated with a more rigid vibration mode is found.

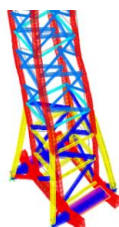


Figure 13: 89° Vibration mode - Translation of the base in the x direction

In this way, it is fundamental not to neglect the influence of these last rigid modes of vibration on the dynamic behaviour of the structure.

5 SAFETY CHECK

In the context of a security analysis and verification, it was decided to subject the structure not only to a seismic record characteristic of the earthquake that occurred in Portugal in the past (1969), which is considered a small earthquake, but with very low frequency content, but also to the seismic action by means of a response spectrum (CEN, 2013) [4]. In this analysis the structure was considered without any loading along the jib.

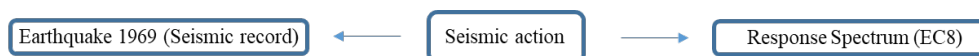


Figure 14: Seismic action applied to the structure

The structure is located in Lisbon and implanted on a soil type B. According to the National Annex [4] (portuguese version) for a type I and type II seismic action corresponds respectively a maximum reference acceleration of 1.5 m/s^2 and 1.7 m/s^2 (RP = 475 years).

Thus, based on each type of seismic action, it was intended to evaluate the tensions acting on the various elements, the reactions in the base and the resistance of the restrains that prevent the movement of the crane base. As previously mentioned the crane is supported on rails and, in order to prevent the translation of this was welded some profiles to the rails.

5.1 Stress analysis

In terms of tensions, it is observed that the axial stresses predominate in the various profiles that make up the structure and that the transverse stress and bending moment are practically negligible (figure 15)

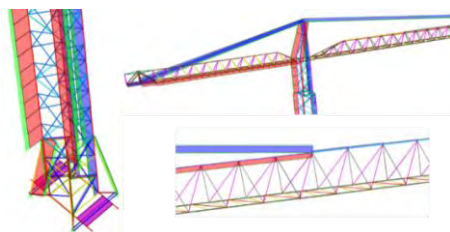


Figure 15: Axial stress in different zones of the structure (red and green – tension and blue – compression)

Therefore, we identified the most conditioning zones and compared the design loads with the design strength. In the case of a steel structure, the influence of the bending lengths and the reduction coefficients according to the possible directions must be taken into account. Fortunately, a tower crane consists of modules contemplating small lengths between profiles.

Table 5: Security check for certain profiles

Identification (from figure 8)	Designation	Seismic action	Ned (kN)	Nb,Rd (kN)	Check?
1	Base knee brace	Sismo 1 (X+0,3Y)	177,9	614,4	Yes
		S69-EW-UX	132,6		
2	Module 2 - L15	Sismo 1 (X+0,3Y)	222,1	1308,4	Yes
		S69-EW-UX	149,8		
3	Module 8 - L12	Sismo 1 (X+0,3Y)	166,3	847,0	Yes
		S69-NS-UX	116,7		
4	Jib – Suspension cable	Sismo 1 (X+0,3Y)	145,4	697,0	Yes
		S69-EW-UX	123,4		
5	Counter-jib – Suspension cable	Sismo 1 (X+0,3Y)	105,3	174,3	Yes
		S69-EW-UX	102,5		

It is concluded that the structure does not present problems due to the effects from both seismic actions.

5.2 Reactions on base and resistance of restraints

Then, the reactions in the base are quantified as a result of the seismic action applied in the structure, which makes it possible to analyze the resistance of the restraints and the capacity of the crane to maintain equilibrium.

Table 6: Base reactions due to the seismic record (Earthquake of 1969) and to the seismic action based on a response spectrum

Seismic action	Base reactions	
	R _x (kN)	R _y (kN)
S69 - EW-UX	12,5	19,0
Sismo II (0,3X+Y)	25,7	36,9
Sismo I (X+0,3Y)	28,8	27,1

From the analysis of this table it is verified that the application of the seismic record associated to the earthquake of 1969 brings results smaller than those obtained according to the seismic action regulating through a spectrum of response.

Thus, the values of the reactions in the base are compared with the resistance of the restraints provided by the welds. Safety was checked in the longitudinal direction of the welded section.

Table 7: Safety check of welded steel profiles on rails (restraints)

R _y (kN)	F _{w,rd} (kN)	Check?	Ratio (%)
36,9	1910	Yes	1,9

6 CONCLUSIONS AND FURTHER STUDIES

Thus, the most relevant issues are pointed out in the course of this study:

- In the first place, a collection of information was indispensable for the modeling of the structure in question. However, there was a lack of detailed information regarding the dimensions of the steel profiles and their connections, as such, field visits and photographic collections were carried out, which allowed to some extent reduce the uncertainties related to the characteristics of the structure.

- Next, it is with the realization of a dynamic identification test based on environmental vibrations that one has had the opportunity to calibrate the numerical model, thus approaching it of the real structure. Not only was a set of results obtained with great clarity through the test, but they also came close to a large part of the vibration periods characteristic of the model. A maximum error of 2.1% was thus obtained for the first two modes of translation vibration in the X and Y direction.

- In the next phase, the most relevant vibration modes of the structure and their dynamic characteristics were described. The most flexible vibration mode of the structure corresponds to a torsion mode around the tower axis with a period of 6.85 s.

- In general, the structure can be considered as flexible, taking into account the first modes of vibration with high vibration periods, however it was only in the higher frequency modes that there were higher percentages of excited mass. This is due to the concentration of most of the mass at the base of the structure. As such, the design of the base of a crane can greatly influence its dynamic behaviour.

- In order to verify the minimum condition of 90% of the excited mass of the structure, 91 modes of vibration were considered in the analysis of the results;

- In the analysis and safety check, the structure was requested to two types of seismic action, seismic action equivalent to the earthquake that occurred in Lisbon in 1969 through seismic records and a regulatory seismic action through a response spectrum. On the one hand, it was

verified that the earthquake of 1969 is less conditioning than the seismic action regulating and, on the other hand, the structure presents a good resistance to these actions both in terms of tensions and in terms of reactions in the base.

- As a recommendation, it is pointed out qualitatively that concrete ballasts located at the base of the structure are not properly confined, which may lead to the sliding of these during the seismic action.

- Consequently, this sliding would cause the collapse of the structure. To avoid this problem it is suggested to confine these concrete ballasts through a set of vertical and horizontal steel profiles, thus creating a containment box for these concrete ballasts.

Further studies include: (i) the study of performance of the crane for areas with higher seismic action and (ii) the analysis of other cranes of similar morphology but with other dimensions, to check if the present conclusions can be extended to other cranes. In Table 8 we present the main characteristics of a few cranes under study, for which *in-situ* measurements were already obtained, and in Figure 17 we show the correlation of the first longitudinal frequency with the total length of the crane (tower+jib).

Table 8: Main characteristics of several cranes already subjected to *in-situ* testing

Cranes	Supplier	Tower	Jib	Load (kg)	Tower	flong1 (Hz)	flong2 (Hz)	ftrans (Hz)
Location		Height (m)	Length (m)		Width (m)			
Alto Olival	Potain	33	37	3000	1,20	0,29	0,84	0,32
CM Pátria 1	Soima	24	21	2000	1,16	0,76	1,54	0,36
CM Pátria 2	GRU	40	39	3000	1,20	0,20	0,71	0,11
Entre-Campos	Potain	43	50	2500	1,60	0,18	0,61	0,18
Arco-Cego	Potain	37,5	60	-	1,60	0,14	0,65	0,22

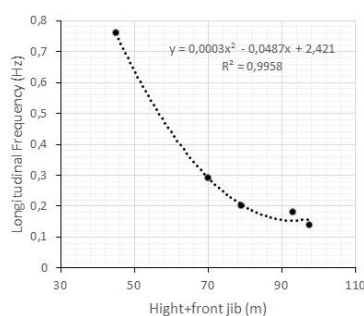


Figure 16: Correlation of longitudinal first frequencies with total length of Crane

REFERENCES

- [1] ISO 11031: (2016) Cranes -- Principles for seismically resistant design.
- [2] Li-Jeng, H.; Hong-Jie, S. (2014). Seismic Response Analysis of Tower Cranes Using SAP2000, *Procedia Engineering* 79, 513-522.
- [3] CSI, COMPUTER & STRUCTURES, INC (2013) – SAP2000: Finite Element Analysis and Design of Structures.
- [4] CEN, European Committee for Standardization (2009) ‘Eurocode 8: Design of structures for earthquake resistance - Part 1: General rules, seismic actions and rules for buildings’.

SELF-CORRECTING SOIL MODELS FOR NUMERICAL SIMULATION OF STRAIN RATE DEPENDENT ICE SCOUR IN SAND

A. NEMATZADEH*, R. AGHAKHANI† AND H. SHIRI‡

* Department of Civil Engineering
Memorial University of Newfoundland
Carew Building, FEAS, A1B3X5 St. John's, NL, Canada
e-mail: anematzadeh@mun.ca

† Department of Civil Engineering
Memorial University of Newfoundland
Carew Building, FEAS, A1B3X5 St. John's, NL, Canada
e-mail: raghakhani@mun.ca

‡ Department of Civil Engineering
Memorial University of Newfoundland
Carew Building, FEAS, A1B3X5 St. John's, NL, Canada
e-mail: hshiri@mun.ca

Key words: Ice Gouging, Mohr-Coulomb, Dense Sand, Coupled Eulerian-Lagrangian.

Abstract. The integrity of subsea pipelines in the Arctic regions is threatened by ice-related subsea geohazard. A common practice for physical protection of the pipelines against the ice loads is to bury them inside the subsea trenches. However, determining the minimum burial depth of the pipeline to minimize the construction cost is a challenging design aspect of Arctic offshore pipelines. This requires an in-depth understanding of the ice-soil-pipe interaction, which in turn is significantly affected by ice-soil interaction. Mohr-Coulomb soil model is conventionally used for continuum modeling of dense sand by adopting the constant friction and dilation angles. However, this approach neglects the pre-peak hardening and the post-peak softening behavior of dense sand. In this study, a smart self-correcting soil model was incorporated into an advanced Coupled Eulerian-Lagrangian (CEL) analysis to automatically update the shear strength parameters by the magnitude of plastic strains. The analysis was conducted using ABAQUS/ Explicit scheme incorporating the soil model that was coded into a user-defined subroutine. The soil strength parameters are self-corrected to model the nonlinear hardening, softening and pressure dependency behavior of dense sand by considering the ice keel bearing pressure and octahedral shear strain. The pre-peak hardening and post-peak softening behavior of dense sand were captured through a series of free-field ice gouging analysis. The sub gouge soil deformation and ice-soil contact pressure were extracted and compared with the results of the original Mohr-Coulomb model, the existing analytical solutions, and the published test data. The study showed the significance of incorporating the strain rate dependency of dense sand on seabed response to ice gouging. The methodology was found to be a strong but simple framework that can be used in daily engineering analyses. It was observed that the magnitude of the subgouge soil deformation is overestimated by the

conventional decoupled methods. Also, the required burial depth was found to be smaller than those recommended by conventional methods, which in turn can significantly reduce the construction effort.

1 INTRODUCTION

Ice scouring is one of the most hazardous challenges that the subsea pipeline has faced in the Arctic region. The most common way to protect the pipeline is to bury them under the seabed. Obtaining the minimum burial depth is a significant design aspect due to the dependency of the project cost and the uncertainties with the ice gouging features. A deep understanding of ice gouge process is needed to find the best burial depth, and it can be gained through proper modeling of this event. During the last two decades, many studies have been conducted on both cohesive and cohesionless soils to improve the offshore industries' prospects on ice gouging characteristics [1,2].

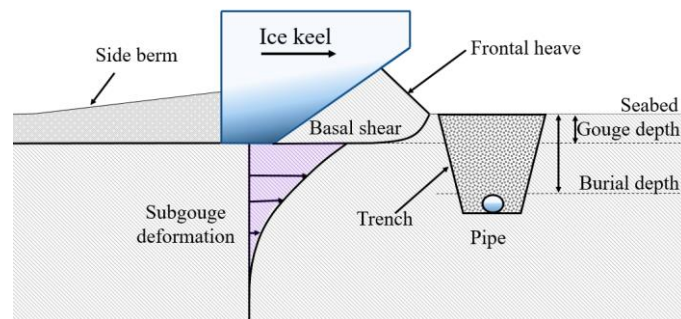


Figure 1: Ice gouging process and subgouge deformation

The conventional Mohr-Coulomb (MC) soil model considers the constant friction and dilation angles for the numerical modeling of the ice gouging in the sandy region; however, it does not consider the non-linear stress-strain characteristics of dense sand such as non-linear pre-peak hardening, post-peak softening, effects of density and confining pressure [3], and the type of shearing (triaxial or plane-strain condition) [4]. These simplifications cause inaccuracy in the predicting of the soil behavior within the gouging area.

In this study, a set of key aspects from some developed non-linear models were employed by a simplified approach to studying all the non-linear behavior associated with dense sand in an ice gouging event [e.g., 4,5]. A Coupled Eulerian-Lagrangian (CEL) model was developed in ABAQUS/Explicit to simulate the ice gouging process, and the soil model was tailored in a user-defined subroutine (VUSDFLD). In each time increment, the ABAQUS called the subroutine to update the shear strength parameters of the seabed through using accumulated plastic shear strain, loading condition, density and confining pressure.

The results of MC and Modified Mohr-Coulomb (MMC) models were conducted and also by published experimental investigations [6]. The outputs show that the MC model is not able to capture the results accurately and overestimated the sub gouge deformation, frontal mound, and the keel reaction forces. The MMC model fully captured the soil response and solved the problem of overestimation of the MC model, and its results were also well close to the test. The cyclic response of the keel was also captured which has been stated in the experimental results

and was not reported in any other previous numerical simulations in the past.

2 NUMERICAL MODELING

In this study, the free field ice gouging analysis was conducted using finite continuum element (FE) analysis. These type of research has been proven to be valuable in order to understand the soil behavior under the ice gouging load and then applying this behavior to the pipeline by using simple beam spring method to investigate the critical aspects of design [7-13]. Although this model is computationally effective, it suffers from the superposition errors and directional load decoupling influences during the discretized soil media [14].

ABAQUS/EXPLICIT has proven to be a powerful tool in capturing large deformation behavior of soil under the ice gouging load [15]. In this study, a half-space ice/soil model was simulated. The dimension of the soil media is $76 \times 22 \times 40$ m which are respectfully length, width and height. The seabed was implemented in Eulerian domain, and the boundaries of this domain were considered large enough to prevent any boundary effect and also allowed the material to flow freely inside the Eulerian body. The 8-noded linear reduced integration hexahedral elements were used for meshing the Eulerian part.

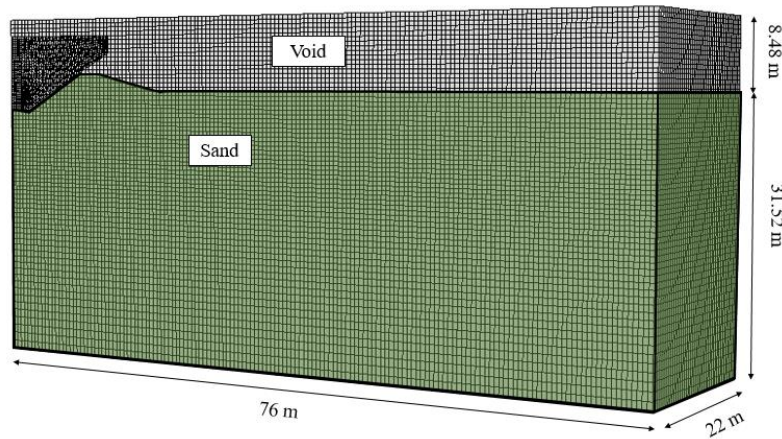


Figure 2: The constructed FE model configuration

The ice keel was modeled as a rigid body [16]. The void part in Figure 2 was considered to allow the material to move within the Eulerian mesh. Unlike the Lagrangian mesh, the nodes are not attached to the Eulerian mesh and material is able to move inside the mesh without distorting the mesh. The ABAQUS built-in “general contact” was used to simulate the ice/soil interaction. This feature of ABAQUS captures any contact between the Lagrangian body (ice) and Eulerian domain (soil) in a CEL model which enhance the accuracy of the model. The frictional behavior was defined as a penalty based contact with a friction coefficient of (μ) of 0.7 (i.e., $\tan(\varphi_\mu)$). The parameter φ_μ is the ice/soil friction angle and varies between $\varphi'_p/2$ and φ'_p of sand [17]. The “hard” pressure overclosure was used for normal surface contact. This feature controls the penetration of the slave body into the master body. Once the two surfaces become into contact, these relationships stop the tensile transfer at the interface of the contact surfaces [15].

For using the CEL method, the velocity or displacement boundary conditions of the Eulerian

body should be restricted to prevent the mesh from moving. The ice was free just to move forward and the vertical displacement and rotation boundaries were secured. To consider the soil column pressure, the geostatic stress was employed to the model [18]. An initial geostatic condition was defined while the gravity load was applied to the whole model in the first step. This step is crucial to mitigate the instabilities that applying the gravity load may cause. In the second step, the ice moved horizontally forward. To avoid causing any dynamic effects for the model, the velocity of ice was increasing gradually in a small part of the time from zero to the velocity of the test and then advanced with the same velocity. A finer mesh was used in gouging affected area, and a coarse mesh was applied for another area to minimize the computational cost of the simulation. Different tracer sets were defined to record the soil displacement and subgouge deformation. Moreover, both 2D and 3D tracer particles were planted in the model to visualize the subgouge mechanism.

3 SOIL MODEL

One of the most important factors in ice gouging modeling is the soil model which is employed in the model [e.g., 19]. Regards to the cohesionless material, Mohr-Coulomb soil model was proved to be approximately accurate and able to capture the desired behavior; however, the ABAQUS built-in Mohr-Coulomb model utilizes constant friction (φ') and dilation angle (ψ) which result in unrealistic results and dilation. This excessive dilation can affect an ice gouging model significantly. The subgouge deformation, reaction forces and frontal mound which are the most important results of an ice gouging simulation are dependent on the friction and dilation angles. Therefore, in this study, a modified Mohr Coulomb model was adopted after Roy et. al, (2015) to overcome these problems. In this soil model, the pre peak, post peak softening behavior of sand was applied by increasing the friction angle from and initial value (φ'_{in}) to a peak value (φ'_P) and then decrease it to a critical value (φ'_C). The same thing also happens for dilation angle (ψ) [5].

Bolton (1986) has come up with an equation for peak friction angle after investigating 17 sands sample [4].

$$\varphi'_P - \varphi'_C = A_\psi I_R \quad (1)$$

where φ'_P indicates the friction angle in the peak point and φ'_C is the critical friction angle. A_ψ is 3 for the triaxial condition and 5 for plain strain condition. $I_R = I_D(Q - \ln p') - R$ in which I_D is the relative density ($I_D = Dr(\%)/100$) and in $0 < I_R < 4$, $Q = 10$ and $R = 1$ are the best match to show the sand behavior [4].

As Bolton (1986) discussed, the peak dilation angle (ψ_P) is related to the φ'_C and φ'_P :

$$\varphi'_P - \varphi'_C = k_\psi \psi_P \quad (2)$$

k_ψ is equal to 0.5 for the triaxial and 0.8 for plain strain conditions [4].

$$\gamma_P^P = \gamma_C^P \left(\frac{p'}{p'_a} \right)^m \quad (3)$$

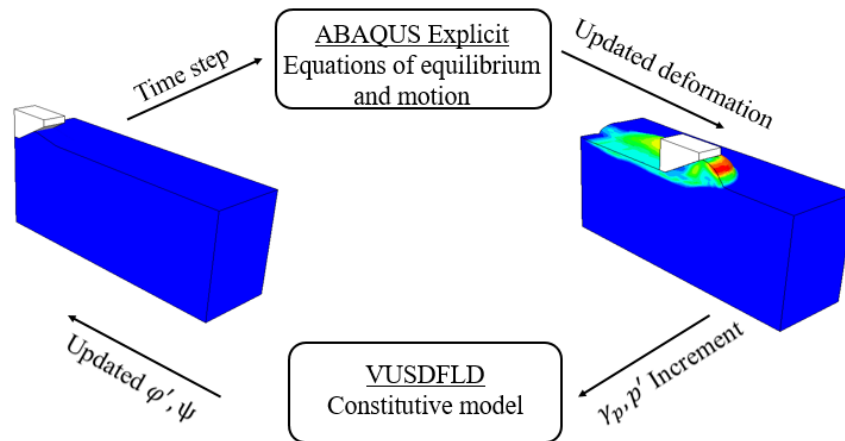
$$\gamma_C^P = C_1 - C_2 I_D \quad (4)$$

where γ_C^P is the softening parameter and p'_a is the atmospheric pressure. m , C_1 and C_2 are the

Table 1: Soil parameters for Mohr-Coulomb and developed model

Parameters		Values	
		Mohr-Coulomb	Modified Mohr-Coulomb
$\varphi'(^{\circ})$		$\varphi'_c = 35$	Eqs. 1-7
$\psi(^{\circ})$		6	Eqs. 1-7
Cohesion (kPa)		2	
Parameters of variation of φ' and ψ	A_{ψ}	3 [5]	
	k_{ψ}	0.5 [5]	
	φ_{in}	29 [5]	
	C_1	0.22 [5]	
	C_2	0.11 [5]	
	m	0.25 [5]	

The soil model was coded in VUSDFLD user subroutine to apply the nonlinear variation of the φ' and ψ with the plastic shear strain, mean effective stress, density. The stress components were called into the subroutine in each time increment using VGETVRM utility in the subroutine. Using the stress components, p' was calculated and stored as the first field variable FV1. VGETVRM is not able to call the principal plastic strains; therefore, the VSPRINC utility was used to call the principal plastic strains and the maximum principal plastic strain was deposited as major principal plastic strain component (ε_1^p) and the minimum one was deposited as minor principal plastic strain component (ε_3^p). The plastic shear strain (γ^p) was calculated as $\gamma^p = \varepsilon_1^p - \varepsilon_3^p$ and stored as the second field variable FV2. The γ^p was calculated during the time of analysis and accumulated. In the input file, the mobilized φ' and ψ were defined in a tabular table using the equation discussed before. During the analysis, this process happened in each time increment and the software updated the values of the φ' and ψ [5]. Figure 4 shows the VUSDFLD process in ABAQUS/EXPLICIT.

**Figure 2:** VUSDFLD in ABAQUS/EXPLICIT

4 FINITE ELEMENT MODEL VALIDATION

The last step in a finite element modeling is to validate the simulation with experimental results or other published numerical models. To be able to compare the numerical model with the physical tests, the developed model must match the test in regards to the dimension, soil material, and ice condition. Therefore, the model described before was similar to the centrifuge tests conducted by Yang (2009) as part of the Pipeline Ice Risk Assessment (PIRAM) project that was used for validation [6]. The test parameters have been shown in Table 2.

Table 2: The centrifuge tests parameters

Parameters		Values	
		PIRAM P06	PIRAM P07
Gouge Depth (m)		2.3	2.4
Ice Velocity		0.11 m/s	0.55 m/s
D_r		% 50.8	%39
Ice Keel	Speed (m/s)	0.11	0.55
	Attack Angle	30°	
Young Modulus (MPa)		26	
Poisson's Ratio		0.32	
Density (Kg/m ³)		1455	1421

The ice was planted in the centrifuge tests, and an initial mound was created by hand in front of it. In the numerical model, the exact thing happened which caused reaching to steady state sooner than penetrating to the ice down. Further, putting the ice in the gouge depth and applying an initial mound is also preventing the dynamic effects of pushing the ice down.

5 RESULTS AND DISCUSSION

Two comparisons between the conventional Mohr-Coulomb model and modified Mohr-Coulomb model are shown in the following. The reaction forces and subgouge deformation were obtained as the most important output results commonly study in ice gouging process. The test results are also provided to show the consistency of the proposed model with the physical test results.

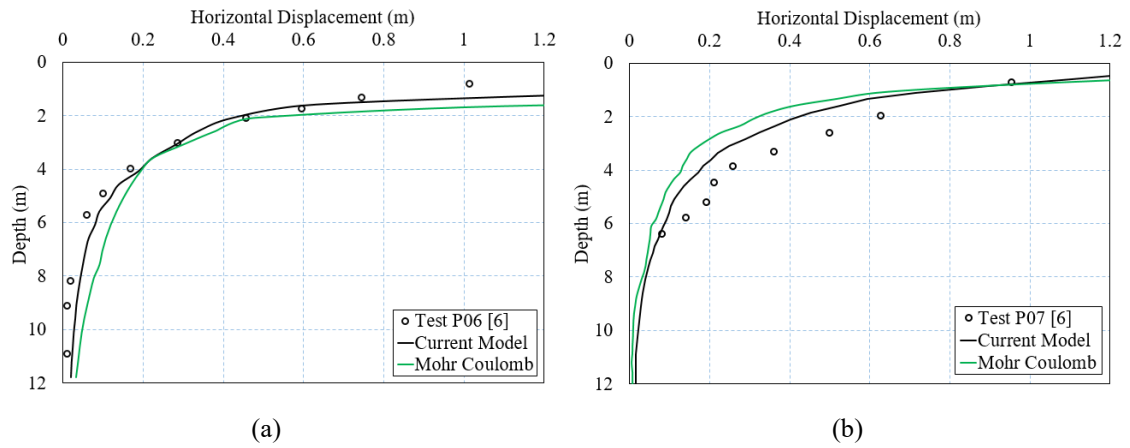


Figure 3: The comparison of the subgouge deformation, a., test P06, b., test P07

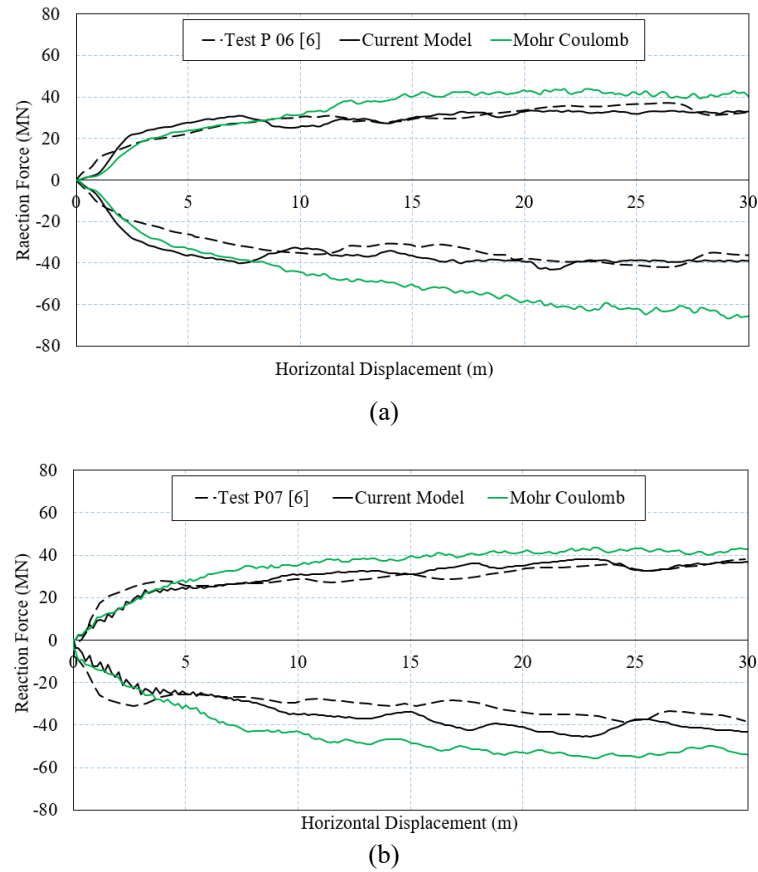


Figure 4: The comparison of reaction forces, a., test P06, b., test P07

Less subgouge deformation was observed in denser sand, and more subgouge deformation was seen in looser sand in MMC models which in all cases were in more consistency with the tests. Also, the reaction forces were smaller in both simulations and closer to the test. It can be concluded that the MC model overestimates the sand response to the ice gouging load (See Figures 5 and 6). The cyclic steady state is also seen in both tests and MMC models [6].

There are other soil models that can solve the excessive dilation problem of Mohr-Coulomb model such as Norsand model. However, this soil model associated with many parameters and difficulties in technical methodology for applying these parameters. The MMC model proved to be time efficient, simple to use and accurate for large models like ice gouging.

Figure 7 shows the excessive dilation caused by MC model in comparison to the MMC soil model. In addition, the current model predicts and visualizes the basal shear bands where the plastic shear strain is largely developed. This visualization cannot be conducted in a simple Mohr-Coulomb model in ABAQUS.

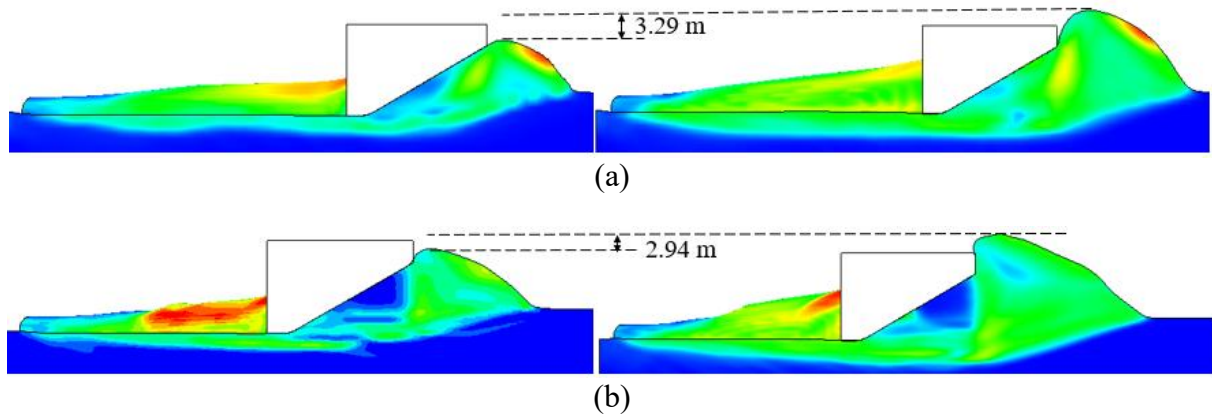


Figure 5: Comparison of the dilation of Mohr-Coulomb and Modified Mohr-Coulomb in test P06, a., Modified Mohr-Coulomb model, b., Mohr-Coulomb model

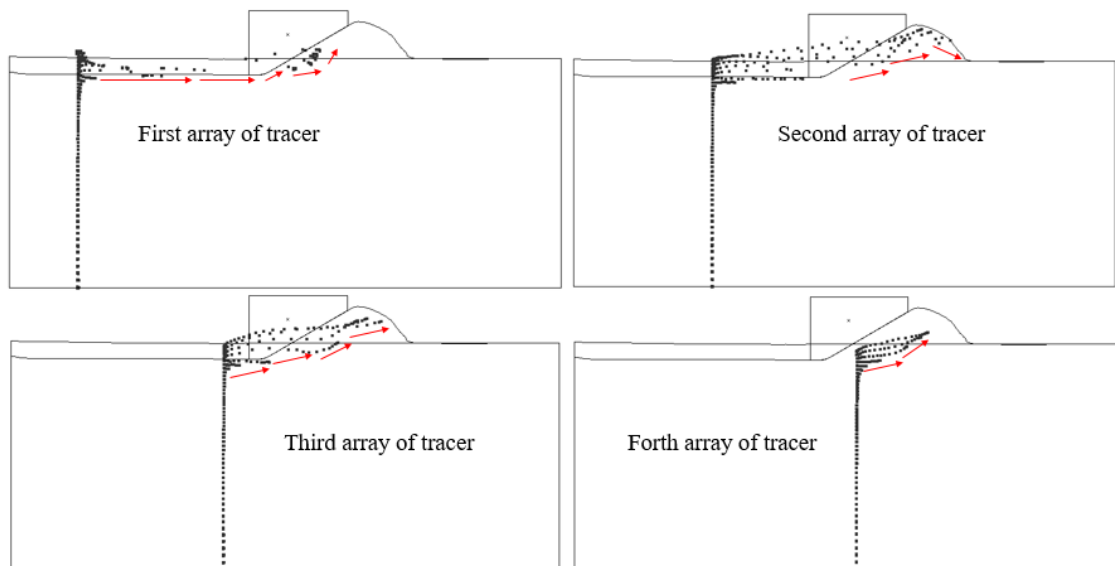


Figure 6: Tracer particles inside the developed model of the current model

The tracer particles were planted in the model as shown in Figure 8. These particles will show the trajectory of soil deformation from different views in the last stage of ice gouging in the current model.

6 CONCLUSION

Finite element analysis of the free field ice gouging in the sand was created. Coupled Eulerian-Lagrangian method was utilized for large deformation analysis. A modified Mohr-Coulomb was adopted and tailored in a user-defined subroutine to update the friction and dilation angles with maximum plastic shear strain and effective stress. The model simulated the pre-peak hardening and post-peak softening behavior of sand within the basal and other shear bands. The cyclic steady-state response of the keel was captured. It was concluded that the modified Mohr-Coulomb resulted in more accurate simulation and closer subgouge deformation and reaction forces to the physical experiments. This can lead to the less excavation and trenching depth requirement and therefore a more economical design. Further investigation is still conducting to study the performance of the model in coupled ice-soil-pipe interaction and the resultant stresses and strain in the buried subsea pipelines.

ACKNOWLEDGMENT

The authors gratefully acknowledge the financial support of “Wood” that established a Research Chair program in Arctic and Harsh Environment Engineering at Memorial University of Newfoundland, the “Natural Science and Engineering Research Council of Canada (NSERC)”, and the “Newfoundland Research and Development Corporation (RDC) (now InnovateNL)” through “Collaborative Research and Developments Grants (CRD)”. Special thanks are extended to Memorial University for providing excellent resources to conduct this research project.

REFERENCES

- [1] NRC-PERD (2014), Ice-Seabed Gouging Database: Review & Analysis of Available Numerical Models (Babae, M.H. and Sudom, D. (2014)); Physical Simulations of Seabed Scouring by Ice: Review and Database (Barrette, P. and Sudom, D. (2014)).
- [2] BSEE-WGK (2015). Ice Scour and Gouging Effects with Respect to Pipeline and Wellhead, Final Report, 100100.01.PL.REP.004, Rev0.
- [3] Hsu, S. T., & Liao, H. J. (1998). Uplift behaviour of cylindrical anchors in sand. *Canadian Geotechnical Journal*, 35(1), 70-80.
- [4] Bolton, M. D. (1986). Strength and dilatancy of sands. *Geotechnique*, 36(1), 65-78.
- [5] Roy, K., Hawlader, B., Kenny, S., & Moore, I. (2015). Effects of post-peak softening behavior of dense sand on lateral and upward displacement of buried pipelines. Paper presented at the ASME 2015 34th International Conference on Ocean, Offshore and Arctic Engineering, V001T10A011-V001T10A011.
- [6] Yang, W. (2009). Physical Modeling of Subgouge Deformations in Sand.
- [7] Barrette, P. (2011). Offshore pipeline protection against seabed gouging by ice: An overview. *Cold Regions Science and Technology*, 69(1), 3-20.
- [8] Been, K., Peek, R., Croasdale, K., & Verlaan, P. (2013). Subscour displacements for

- pipeline design: State of practice for kashagan project. Proceedings, Port and Ocean Engineering Under Arctic Conditions. Paper no. POAC-189.
- [9] Kenny, S., Phillips, R., McKenna, R., & Clark, J. (2000). Response of buried marine arctic pipelines to ice gouge events. Paper presented at the Proceedings, International Conference on Ocean, Offshore and Arctic Engineering. ASME. Paper no. OMAE-5001.
- [10] Kenny, S., Bruce, J., King, T., McKenna, R., Nobahar, A., & Phillips, R. (2004). Probabilistic design methodology to mitigate ice gouge hazards for offshore pipelines. Paper presented at the 2004 International Pipeline Conference, 1925-1933.
- [11] Kenny, S., Palmer, A. C., & Been, K. (2007b). Design challenges for offshore pipelines in arctic environments. Proceedings, IBC Oil and Gas in Arctic and Cold Waters.
- [12] Nixon, J., Palmer, A., & Phillips, R. (1996). Simulations for Buried Pipeline Deformations Beneath Ice Scour.
- [13] Woodworth-Lynes, C., Nixon, D., Phillips, R., & Palmer, A. (1996). Subgouge deformations and the security of arctic marine pipelines. Paper presented at the Offshore Technology Conference.
- [14] Pike, K., & Kenny, S. (2016). Offshore pipelines and ice gouge geohazards: Comparative performance assessment of decoupled structural and coupled continuum models. Canadian Geotechnical Journal, 53(11), 1866-1881.
- [15] Eskandari, F., Phillips, R., & Hawlader, B. (2011). Ice gouging analysis using NorSand critical state soil model. Paper presented at the Proceedings of the Pan-Am CGS Geotechnical Conference, 2-6.
- [16] Fadaifard, H., & Tassoulas, J. L. (2014). Numerical modeling of coupled seabed scour and pipe interaction. International Journal of Solids and Structures, 51(19-20), 3449-3460.
- [17] Yimsiri, S., Soga, K., Yoshizaki, K., Dasari, G., & O'Rourke, T. (2004). Lateral and upward soil-pipeline interactions in sand for deep embedment conditions. Journal of Geotechnical and Geoenvironmental Engineering, 130(8), 830-842.
- [18] Lele, S., Hamilton, J., Panico, M., Arslan, H., & Minnaar, K. (2011). 3D continuum simulations to determine pipeline strain demand due to ice-gouge hazards. Paper presented at the OTC Arctic Technology Conference.
- [19] Banneyake, R., Hossain, M. K., Eltaher, A., Nguyen, T., & Jukes, P. (2011). Ice-soil-pipeline interactions using coupled eulerian-lagrangian (CEL) ice gouge simulations-extracts from ice pipe JIP. Paper presented at the OTC Arctic Technology Conference.

SMART SYSTEM BASED ON RAFFINOSE-COATED SILVER NANOPARTICLES AS SELECTIVE AND SENSITIVE OPTICAL PROBE/SORBENT FOR CHROMIUM SPECIATION IN WATER SAMPLES

PENKA VASILEVA^{*}, LUBOMIR P. DJERAHOV[†], IRINA B. KARADJOVA^{*}

^{*} University of Sofia “St. Kliment Ohridski”

Faculty of Chemistry and Pharmacy, 1164 Sofia, Bulgaria

e-mail: pvasileva@chem.uni-sofia.bg, Karadjova@chem.uni-sofia.bg, www.uni-sofia.bg

[†] University of Mining and Geology “St. Ivan Rilski”

Department of Chemistry, 1700 Sofia, Bulgaria

e-mail: lubomirdjerahov@gmail.com, www.mgu.bg

Key words: Smart System, Silver Nanoparticles, Raffinose Coating, Solid Phase Microextraction, Optical sensor, Chromium Speciation

Abstract. In this study, raffinose-coated silver nanoparticles (Ag@Raff NPs) with narrow size distribution were synthesized by green ultrasound-assisted reduction method employing raffinose as both reducing and protecting reagent in alkaline reaction medium. UV-visible absorption spectrum of the light yellow aqueous nanoparticle dispersion showed surface plasmon resonance band at λ_{\max} of 411 nm. The electrostatic surface potential of Ag@Raff NPs was -47.2 ± 1.1 mV at pH 6.8. The polycrystalline solid product mainly consisted of quasi-spherical silver nanoparticles of mean diameter 27.2 ± 6.7 nm. Some polyhedral nanoparticles were also observed in the TEM micrographs. XRD analysis showed broad diffraction peaks with 2θ of 38.2° , 44.4° , 64.6° and 77.4° corresponding to the (111), (200), (220) and (311) planes, respectively, of the face-centered cubic (fcc) silver.

The analytical method developed for Cr(III) and Cr(VI) determination consists of two steps: (i) Addition of Ag@Raff NPs dispersion to water sample, containing Cr(III) and Cr(VI). Cr(III) is selectively sorbed on the nanoparticle surface under optimized chemical conditions and determined by using ETAAS; (ii) Addition of Ag@Raff NPs dispersion to parallel water sample, containing Cr(III) and Cr(VI); Cr(VI) was in-situ reduced by ascorbic acid to Cr(III) and determined through the sensitive and selective optical response of Ag@Raff NPs at optimized ratios between the components and optimal contact time. The proposed method was successfully applied for chromium speciation in surface water samples.

1 INTRODUCTION

Chromium is an element found in rocks, animals, plants, water and soil [1]. Chromium and its compounds are used in variety industries – chemical, medical/health care industry, leather tanning, textile dyes, and metallurgical technologies [2]. The most common forms of chromium in the environment are the trivalent form Cr(III) (chromium oxide and chromium

sulphate) and hexavalent form Cr(VI) (chromium trioxide, chromic acid and dichromate) [3]. The trivalent chromium is nontoxic and it is involved in several biochemical processes: glucose metabolism, enzymes reactions, body fat decrease [2]. The hexavalent chromium is toxic to the most living organisms and could be the cause of lung-cancer, dermatitis, allergies, kidney-damage [2, 4]. For these reasons, the quantification of chromium is really important in the control of environmental pollution.

Different methods have been developed for chromium detection: flame atomic absorption spectroscopy [5], graphite furnace atomic absorption spectroscopy [6], x-ray fluorescence spectrometry [7], chromatography [8], inductively coupled plasma, atomic emission spectrometry and inductively coupled plasma-mass spectroscopy [9]. Although these methods show high sensitivity and accuracy in the determination of total chromium, they are costly and time-consuming.

Nanoparticles and nanomaterials have attracted great attention from scientists in recent years due to their unique physical and chemical properties. Aragay et al. has been presented a comprehensive review about macro-, micro-, and nanomaterial-based tools and strategies for detection of heavy metal in the environment [10]. The application of noble metal nanoparticle for drinking water purification from different types of contaminants (halogenated organics including pesticides, heavy metals and microorganisms) has been presented [11]. Zhang and Fang presented the recent progress of detection and treatment of persistent organic pollutants and heavy metal by using nanomaterials and analytical nanotechnology [12]. El-Ansary and Faddah elucidated the possibility of using nanoparticles functionalized with antibodies as markers for proteins in their review [16]. Starch-stabilized silver nanoparticles were synthesized and used for optical sensor of hydrogen peroxide [13]. Colorimetric methods based on metal nanoparticles are extremely attractive, because they are rapidly, low-cost and can be easily read out with the naked eye. Many examples for using of noble nanoparticles (gold and silver) for colorimetric detection of heavy metal ions (e.g., Hg(II), Pb(II), Cu(II)) have been reported [14]. Ravindran et al. has been presented excellent results for selective colorimetric sensing of cysteine in aqueous solutions using silver nanoparticles and a presence of Cr³⁺ [15]. Lai and Tseng used 5-thio-(2-nitrobenzoic acid) modified gold nanoparticles for sensing of Cr(VI) [3].

The aims of this study were: (i) synthesis and characterization of raffinose-coated silver nanoparticles and (ii) investigations on the possibility of their application as both effective sorbent for solid phase microextraction of Cr(III) from aqueous solutions and optical probe in LSPR based sensing system for quantitative, selective and sensitive determination of Cr(VI). Silver nanoparticles have been already explored as sorbents/colorimetric probes for metal ions determination, but their capabilities for chromium speciation are still not reported.

2 MATERIAL AND METHODS

2.1 Apparatus

UV-Vis absorption spectra were recorded on an Evolution 300 spectrometer (Thermo Scientific, USA) within the 200–800 nm range using quartz cuvettes with 1 cm optical path length. High-purity water was used as a reference sample for background absorption. The formation of Ag@Raff NPs was further confirmed by X-ray diffraction (XRD). Briefly, 2 mL of Ag@Raff NPs dispersion (on portions of 100 µL) were placed on microscope glass and air-

dried. The XRD patterns of the dried samples were determined using X-ray powder diffractometer (Siemens D500) equipped with $\text{CuK}\alpha$ radiation ($\lambda = 1.54\text{\AA}$) in 2θ ranging from 15° to 80° . The morphology and particle sizes were examined using a high resolution transmission electron microscope (TEM, JEOL JEM-2100 operating at an accelerating voltage of 200 kV). Volume of 5 μl Ag@Raff NPs suspension was placed on a carbon-covered copper grid for TEM and air-dried. The histogram of Ag@Raff NPs size distribution and mean diameter of nanoparticles were determined by counting at least 200 nanoparticles from the different TEM images using Image J software. Some structural details of the nanoparticles were analysed using the high-resolution TEM image and SAED pattern. The zeta potential of nanoparticles was measured with a Zetasizer Nano ZS (Malvern) instrument.

ETAAS measurements were carried out on AAnalyst 400 spectrometer (Perkin Elmer) under optimal instrumental parameters. A microprocessor pH-meter (Hanna Instruments, Portugal) was used for pH measurements. Shaver, model "BOECO OS-20", Germany and centrifuge model "K-1000" KUBOTA Corporation, Japan were used sorption experiments.

2.2 Chemicals

All chemicals used were of analytical-reagent grade and all aqueous solutions were prepared in high-purity water (18 M Ω , Millipore Corp., Milford, MA, USA). Silver nitrate (AgNO_3 , 99.8 %), sodium hydroxide (NaOH , 99 %), nitric acid (HNO_3 , 65 %), salts of the different cations studied (NaCl , KCl , MgCl_2 , CaCl_2 , $\text{Pb}(\text{NO}_3)_2$, ZnCl_2 , CuCl_2 , NiCl_2 , CdCl_2 , CoCl_2 , FeCl_3) from Merck, Germany, pharmaceutical grade D-(+) raffinose from Alfa Aesar, Germany were used. The stock standard solutions for Cr were: Cr(III), Spex Certiprep 1000 mg/L in 2% HNO_3 and Cr(VI) Spex Certiprep 1000 mg/L in H_2O . Working standard solutions were prepared daily by appropriate dilution.

2.3 Synthesis and characterization of raffinose-coated silver nanoparticles

Raffinose-coated silver nanoparticles were prepared by one-step, one-phase "green" synthesis following the synthetic procedure described in our previous study [17]. Silver nanoparticles were obtained through a reduction reaction of silver nitrate with trisaccharide raffinose as both reducing and stabilizing agent in the presence of suitable sodium hydroxide amount as a reaction catalyst. Figure 1 shows the reaction scheme of preparation and coating of silver nanoparticles with raffinose.

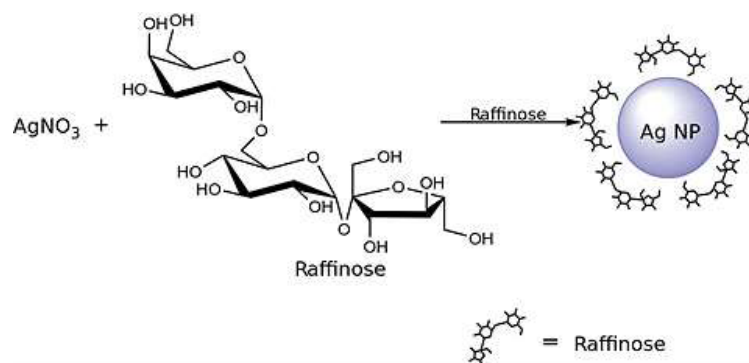


Figure 1. Reaction scheme for obtaining raffinose-coated silver nanoparticles

Briefly, 0.75 mL stock solution of AgNO_3 (0.1 mol/L) were diluted with 60.75 mL high-purity water and homogenised for 5 min in an ultrasonic bath (power 100 W, frequency 38 MHz). After that, 7.5 mL raffinose aqueous solution (0.1 mol/L) were added and left for at least 15 min to form a complex under ultrasonic treatment. The reaction was started by addition of 6 mL NaOH aqueous solution (0.1 mol/L) and continued for 1 h at constant temperature (30 ± 2 °C) in an ultrasonic bath to assure the homogeneous formation of the silver nanoparticles. A change of the solution color from colorless to pale brown and subsequently to yellow orange was observed, indicating nanoparticle formation.

The as-prepared Ag@Raff NPs dispersion with Ag concentration 1×10^{-3} mol/L (110 mg/L) was kept in a dark glass flask at room temperature and was used in the following experiments without any purification. Prior to each experiment, Ag@Raff NPs dispersion was homogenized by an ultrasonic bath for 30 min.

2.4 Evaluation of Ag@Raff NPs as a nanosorbent for the selective separation of Cr(III) and Cr(VI) species in aqueous solution

Volumes of 0.25 mL Ag@Raff NPs dispersion and 1.25 mL solution, containing both chromium chemical species (100 µg/L Cr(III) and 100 µg/L Cr(VI)), were mixed in 2 mL centrifuge tube. pH value of the resulting solution was adjusted with 10 mol/L NH_3 solution in the range 7-9. The analyte sorption was carried out under continuous stirring for contact time 0-30 min. The sample was centrifuged in ultra-centrifuge at 14 000 rpm. The effluent was decanted. The analyte, adsorbed on Ag@Raff NPs surface, was eluted/dissolved with 0.050 mL c. HNO_3 and diluted with 1 mL high-purity water. The Cr concentrations in the eluate (c_{el}) and the effluent ($c_{\text{supernatant}}$) were determined by ETAAS. The degree of analyte sorption was presented as $D, \% = [1 - (c_{\text{supernatant}}/c_{\text{ini}})] \cdot 100$, where c_{ini} is the initial concentration of the metal ion in the sorption solution.

2.5 Assessing the Ag@Raff NPs dispersion as an optical probe in LSPR based sensing system for Cr(VI)

An aliquot of 200 µL Ag@Raff NPs dispersion and 1400 µL high purity water were consecutively added into a small quartz cuvette, followed by addition of 150 µL of 5×10^{-3} mol/L solution of ascorbic acid. 500 µL The solution was vortexed for 30 s, and then 250 µL Cr(VI) solution with varying concentration were added and homogenized for 30 s. The concentration of Cr(VI) solution ranged from 1×10^{-6} mol/L to 1×10^{-4} mol/L. The pH of the solution was maintained in the range 3.5-4 with hydrochloric acid solution. After contact time in the range of 0-30 min, UV-Vis absorption spectrum was taken in the wavelength range 300-800 nm. In order to investigate the sensitivity of colorimetric assay towards other ions, raffinose-coated Ag NPs were allowed to interact separately under the same conditions with 50 µmol/L solutions of alkali, alkaline earth, and transition-metal ions (separately for each ion). Resulting solutions were monitored by UV-Vis absorption spectroscopy.

3 RESULTS AND DISCUSSION

3.1 Characterization of raffinose-coated silver nanoparticles

The optical properties of as synthesized raffinose-coated silver nanoparticles and after their

storage were examined by UV-Vis spectroscopy and shown in Figure 2.

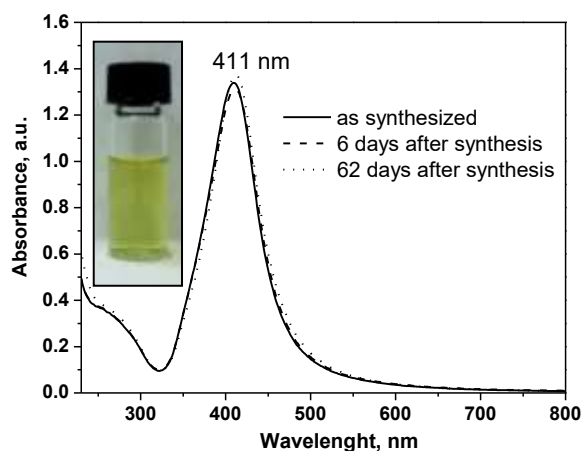


Figure 2. UV-Vis absorption spectra and photograph of raffinose-coated silver nanoparticles taken after nine-fold dilution of the aqueous dispersion immediately after synthesis, after one week, and after 2 months of storage

UV-Vis absorption spectrum of fresh synthesized aqueous dispersion shows the presence of single, narrow and high-intensive localized surface plasmon resonance (LSPR) band with λ_{max} of 411 nm, which indicates the formation of mainly spherical nanosized silver particles with a narrow size distribution [18]. The yellow color of silver nanoparticle aqueous dispersion (left in Figure 2) obtained by the synthesis procedure described is consistent with spectroscopic observation. Registered reproduction of the optical characteristics (wavelength of the surface-plasmon resonance peak and half-width of the band) after prolonged storage of aqueous nanoparticle dispersion indicates a high stability of raffinose-coated silver nanoparticles. The electrokinetic measurement of surface electrostatic potential (ξ) of silver nanoparticles shows a value of -47.2 ± 1.1 mV at pH 6.8, which is indicative of high electrostatic stabilization in addition to the steric nanoparticle stabilization due to the surface layer of raffinose. The negative value of ξ -potential is most likely due to the sorption of negatively charged oxidized forms of raffinose fragments (resulting from the alkaline raffinose degradation in the course of nanoparticle synthesis) onto nanoparticle surface [19].

The conclusion concerning the formation of silver nanoparticles with narrow size distribution and approximately spherical morphology (based on the shape and location of LSPR absorption band in the UV-vis spectrum of synthesized nanoparticle dispersion) is further confirmed by TEM/HRTEM observations (Figure 3a,b,c). TEM micrographs illustrate that quasi-spherical Ag@Raff NPs with narrow size distribution and average size of 27.2 ± 6.7 nm are obtained by the synthesis method developed. In addition to the nanospheres, some typical polyhedral nanoparticles (multiple twined nanocrystals) are also observed in the HRTEM images (Figure 3c). The diffused rings in SAED pattern of Ag@Raff NPs confirmed the polycrystalline nature of the synthesized nanoparticles (inset in Figure 3b).

The crystallinity of raffinose-coated silver nanoparticles was confirmed by XRD analysis. The XRD pattern of Ag@Raff NPs (Figure 3d) showed four relatively broad diffraction peaks with 2θ of 38.2° , 44.4° , 64.6° , and 77.4° corresponding to the (111), (200), (220) and (311)

planes respectively, of the face-centered cubic (fcc) silver (PDF 04-0783). The relatively broad diffraction peaks indicated either imperfect or fine nanocrystallite nature of the polycrystalline Ag@Raff NPs [20]. The results from XRD analysis are consistent with the SAED pattern obtained in TEM observations. Furthermore, the characteristic diffraction reflections of raffinose were not observed in the diffractogram of Ag@Raff NPs. This could be due to the formation of non-crystalline complexes of raffinose with silver nanoparticles [13]. The halo at reflection angles in the range 20–30° is due to the glass support, which used in the sample preparation. No impurity peaks were observed in the X-ray diffraction pattern of silver nanoparticles synthesized.

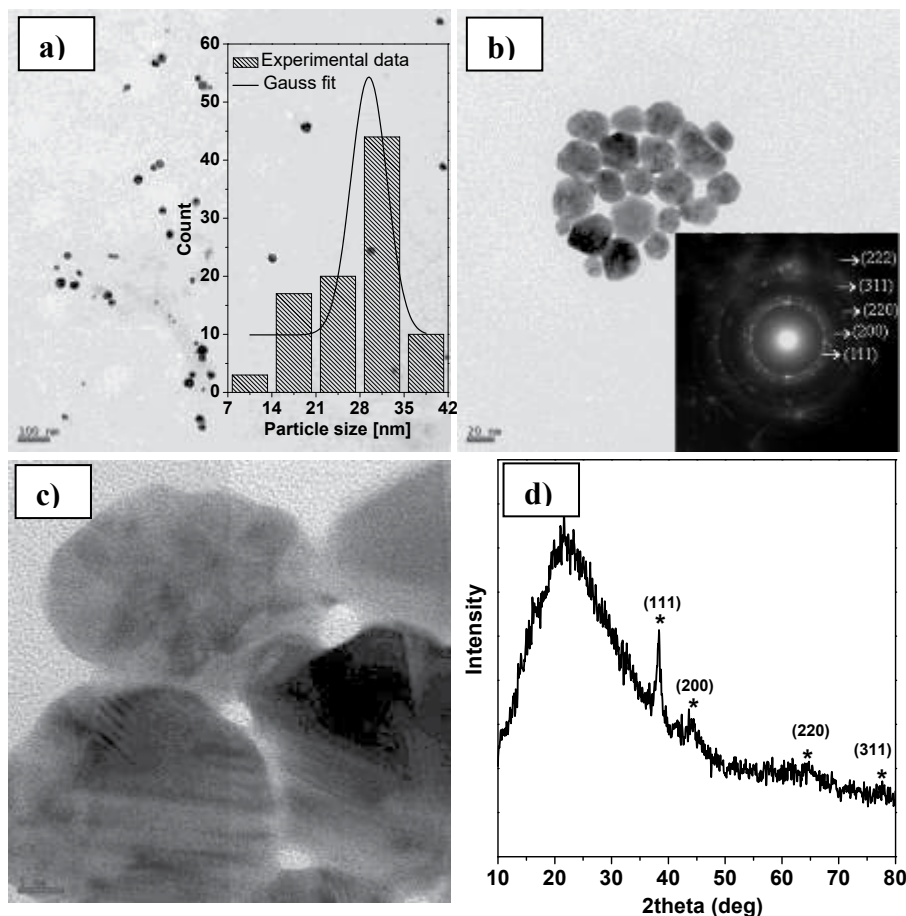


Figure 3. (a, b) TEM micrographs at different magnifications (insets: size distribution histogramme and SAED pattern, respectively); (c) HRTEM micrograph, and (d) X-ray diffraction pattern of Ag@Raff NPs

3.2 Optimization of extraction parameters of Ag@Raff NPs toward Cr(III)

Effect of pH and sorbent amount

The extraction efficiency of Ag@Raff NPs toward Cr(III) was examined at pH values in the range 6–9, achieved with 10 mol/L NH_3 solution, applying the sorption procedure described in Section 2.4. The results presented in Figure 4a show that quantitative sorption of Cr(III) is achieved at pH 8–9, whereas the sorption degree of Cr(VI) is 2%. Most probably, the

retention of Cr(III) is a combination of electrostatic attraction between the positively charged ammonium complexes of Cr(III) (formed in the presence of ammonia solution) and the negatively charged raffinose-coated silver nanoparticles, with further complexation between the analyte and the deprotonated functional groups of raffinose, while the negatively charged Cr(VI) species remain in the solution. This assumption is confirmed by the negative values of ξ -potential of silver nanoparticles at pH 7–9: -48.8 ± 1.5 mV (pH 6.9); -47.2 ± 1.1 mV (pH 7.8); -47.0 ± 1.9 mV (pH 8.8).

In a neutral, pH 7, or slightly acidic environment, pH 6, the resulting sorption degree is lower - about 70% or 10%, respectively. Probable reason for this drastic reduction in Cr(III) sorption degree below pH 7 is the electrostatic repulsion between the complexes $\text{Cr}(\text{H}_2\text{O})_5(\text{OH})^{2+}$ or $\text{Cr}(\text{H}_2\text{O})_4(\text{OH})_2^+$ (which are the predominant chemical forms of Cr(III) under these conditions [21]), and the partially protonated, positively charged functional groups of raffinose [22], in combination with a limited complexation potential of chromium, due to the inertness of its complexes ($\text{Cr}(\text{H}_2\text{O})_5(\text{OH})^{2+}$ and $\text{Cr}(\text{H}_2\text{O})_4(\text{OH})_2^+$). The insignificant Cr(VI) sorption, registered at the optimal pH 8.5 for Cr(III) sorption (achieved with ammonia solution), demonstrates the potential of Ag@Raff NPs to be used as an effective nanosorbent for chromium speciation analysis of water samples.

The experiments, performed with different amounts of Ag@Raff NPs (between 10 and 45 μg Ag as nanoparticle aqueous dispersion), showed that 22 μg Ag, contained in 0.2 mL Ag@Raff NPs dispersion, is the optimal silver amount for quantitative Cr sorption. The Cr(III) sorption with lower or higher volume of Ag@Raff NPs was below 80%, in the first case due to the lower density of negative charges, and in the second case most probably due to the blocking of raffinose functional groups.

Sorption kinetics

The sorption kinetics of both Cr(III) and Cr(VI) on the raffinose-coated silver nanoparticles was studied for time period of 2–40 min at pH 8.5 (procedure in Section 2.4). The samples were shaken on a shaking machine. As can be seen from the results presented on Figure 4b, at least 0.5 h is necessary for selective and quantitative sorption (> 99 %) of Cr(III) on the surface of Ag@Raff NPs, while Cr(VI) remains quantitatively in the solution. Relatively rapid sorption is most likely associated with the high nanoparticle contact surface in the aqueous dispersion.

Experiments for the influence of sample volume on the sorption degree of Cr(III) and Cr(VI) were performed with sample volume ranged between 10 and 50 mL using 0.2 mL Ag@Raff NPs dispersion. The experimental results defined 20 mL as an optimal sample volume ensuring a selective separation of both Cr species for 0.5 h sorption time. The adsorption capacity, achieved under these chemical conditions, is 10 mmol Cr(III)/mg sorbent. This capacity is completely sufficient for retention and separation of Cr(III) even in relatively polluted surface and ground waters.

Elution study

The effect of eluent concentration (HNO_3) on the Cr(III) desorption and regeneration of sorbent particles was studied at relatively soft conditions from 2 mol/L HNO_3 to 4 mol/L HNO_3 , taking into account chemical instability of Ag@Raff NPs in acidic solutions. The results obtained showed that HNO_3 with concentration 2 mol/L does not ensure a quantitative

elution of Cr(III), which does not allow complete nanoparticle regeneration for the next sorption cycle. More concentrated HNO₃ ensures complete Cr(III) desorption (Table 1), however the nanoparticles partially dissolve and again are not suitable for next sorption cycle. Consequently, the synthesized Ag@Raff NPs are not recyclable and new sorbent amount has to be used for each sorption cycle of Cr(III). Taking into account the simple synthesis procedure, this fact just ensures application of fresh sorbent for each sorption cycle and thus reproducible degree of sorption on the fresh nanoparticle surface.

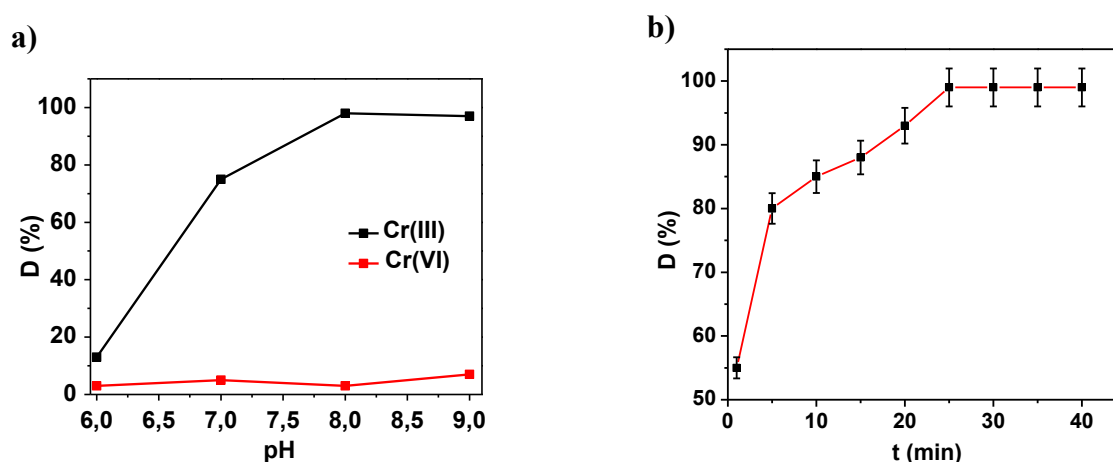


Figure 4. (a) Effect of pH on the degree of sorption of Cr(III) and Cr(VI) on Ag@Raff NPs (sample volume - 20 mL; contact time - 60 min); (b) Kinetics of Cr(III) sorption on Ag@Raff NPs (sample volume - 20 mL; volume of Ag@Raff NPs dispersion - 0.2 mL)

Table 1. Study of elution process of Cr(III), sorbed onto the surface of Ag@Raff NPs

Eluent; t, °C	2M HNO ₃ ; 20°C	4M HNO ₃ ; 20°C	c. HNO ₃ ; 20°C	c. HNO ₃ ; 80°C
Recovery, %	33±4	92±5	67±5	100±5

3.3 Optimization of chemical parameters for colorimetric detection of Cr(VI) using Ag@Raff NPs dispersion as optical probe

Several parameters were investigated systematically in order to establish optimal conditions for the colorimetric detection of Cr(VI), *in-situ* reduced to Cr(III) by ascorbic ratio (AA), in the presence of Ag@Raff NPs. As a first step, the pH value was adjusted taking into account the analysis of real samples and their preservation. The experiments performed showed that pH about 4, achieved by hydrochloric acid, ensured the highest sensitivity and could be accepted as an optimal sample medium. This acidity is obtained as a result of the following optimal volume ratios:

$$V(\text{Ag@Raff NPs dispersion, mL}):V(\text{Cr(VI) standart solution, mL}):V(\text{AA solution, mL}) = 0.20:0.25:0.15$$

In order to evaluate the optimal contact time, the kinetic of interaction between Ag@Raff NPs and *in situ* obtained Cr(III) by chemical reduction of Cr(VI) with ascorbic acid in a hydrochloric acid aqueous solution (pH 4), was followed within half hour by measurements of UV-Vis absorbance. Typical evolution of UV-Vis absorbance spectrum with time, due to the interaction of Ag@Raff with 5×10^{-5} mol/L Cr(VI), *in situ* reduced to Cr(III), is shown in

Figure 5a. For comparison, the kinetics of interaction between Ag@Raff NPs and Cr(III) was also studied at the same conditions and presented in Figure 5b.

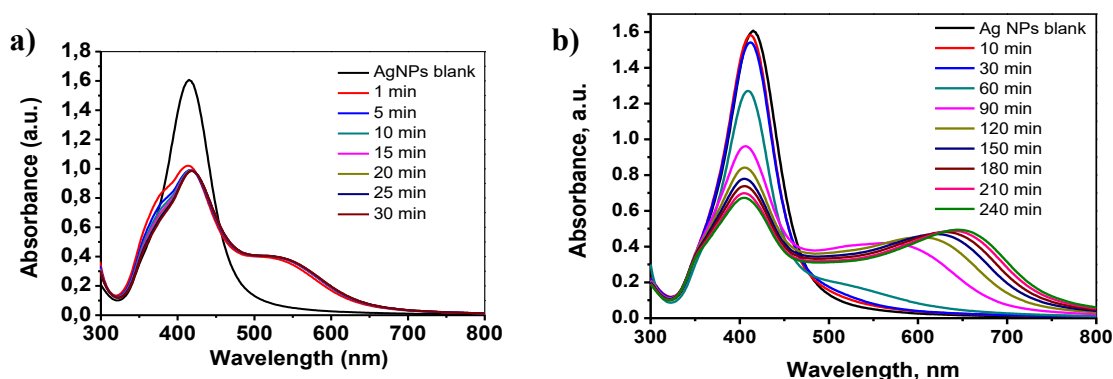


Figure 5. (a) Evolution of UV-Vis absorbance spectrum of Ag@Raff NPs upon the addition of 5×10^{-5} mol/L Cr(VI) reduced to Cr(III) by ascorbic acid at pH 4, and (b) upon the addition of 5×10^{-5} mol/L Cr(III)

It is seen that the sensor's response toward Cr(VI) is significant during the first five minutes of the contact time and a negligible change in the absorption intensity of Ag@Raff NPs at λ_{\max} is observed over this time in the presence of Cr(III). This fact allows selective analytical detection of Cr(VI) species within only five minutes. This difference in the response kinetics of developed optical probe to a standard aqueous solution of Cr(III) on the one hand and to Cr(III) obtained *in situ* by reduction of Cr(VI) with ascorbic acid could be explained by the extremely high inertness of complex $\text{Cr}(\text{H}_2\text{O})_6^{3+}$ in the standard solution.

As a next step, the sensitivity and applicability of Ag@Raff NPs for quantitative determination of Cr(VI) were studied under the defined optimal conditions. The colorimetric response and LSPR band behavior were monitored as a function of Cr(VI) concentrations in the range of 1.0–11.5 $\mu\text{mol/L}$ Cr(VI) (Figure 6a). As seen from the UV-Vis absorbance spectra (5-min contact time), a gradual decrease of the intensity of the characteristic plasmon band of the AgNPs at 411 nm is observed with increase of Cr(VI) concentration. In addition, a shoulder band appears at the wavelength range of 550–650 nm, which intensity increases accompanied by a slight blue shift along with decreasing intensity of the main plasmon absorbance band as a result of partial nanoparticle aggregation in the presence of freshly produced Cr(III) ions, which reaches varying degrees depending on the analyte concentration. This phenomenon is already reported and described as a change of the refractive index of the particles as a result of sorption of the positive Cr(III) produced by Cr(VI) reduction onto the negatively charged nanoparticle surface [23].

For quantitative determination of Cr(VI), the change of the intensity of LSPR band at 411 nm upon the addition of analyte with various concentrations was estimated as a ratio A_t/A_0 , where A_0 corresponds to the intensity of absorbance maximum of blank Ag@Raff NPs dispersion (without Cr(VI)) and A_t corresponds to the intensity of absorbance maximum of Ag@Raff NPs 5 min after the addition of Cr(VI) standard solutions at optimized conditions (Figure 6b). A linear correlation exists between the relative values of absorbance maximum intensity and the concentration of Cr(VI) over the concentration range 2.5–7.5 $\mu\text{mol/L}$:

$$A_r = 0.1019 \times c(\text{Cr(VI)}) - 0.1287 \quad R^2 = 0.9798$$

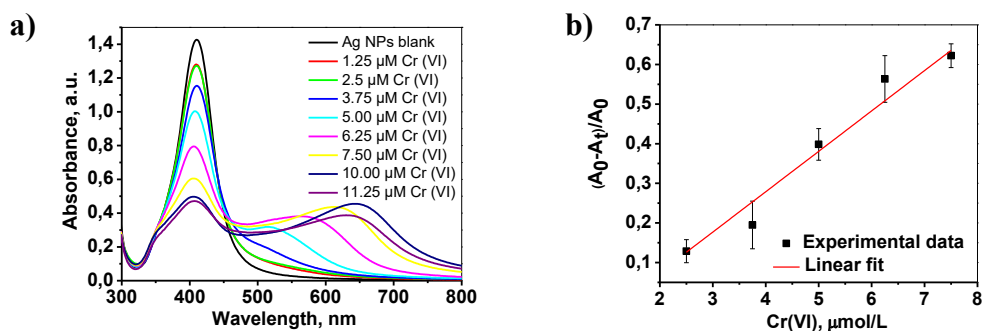


Figure 6. a) UV-Vis absorption responses of Ag@Raff NPs recorded 5 min after the addition of various concentrations of *in-citu* reduced Cr(VI) with ascorbic acid at pH 4; (b) Calibration curve

3.4 Analytical application

Analytical procedures for Cr speciation in surface waters was developed based on fast screening for Cr(VI) content using Ag@Raff NPs as efficient optical sensor or determination of both Cr(III) and Cr(VI) using selective sorption of Cr(III) on the sorbent Ag@Raff NPs and ETAAS measurement. Model experiments performed with various types of surface waters (river, lake and mineral) spiked with Cr(III) and Cr(VI) showed insignificant influence of water matrix on both optical sensor response or the degree of sorption of Cr(III) on Ag@Raff NPs (recoveries achieved varied between 94-97%) as well as on the selectivity in the presence of Cr(VI). Detection of Cr(VI) by optical sensing is an efficient way for fast and simple on site evaluation of the content of Cr(VI) in surface waters (see Figure 7a). Limit of quantification achieved 1.9 $\mu\text{mol/L}$ and relative standard deviation 3-5% fulfil the requirements for field studies for Cr(VI) content in surface waters.

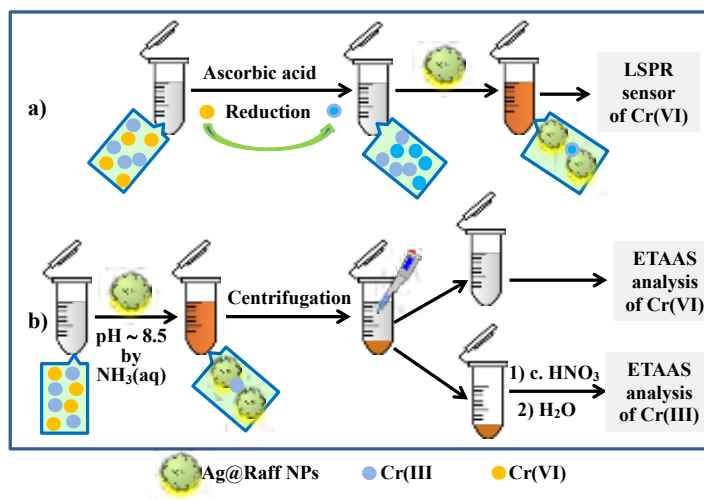


Figure 7. Schemes of analytical procedures for Cr speciation in surface waters: a) Ag@Raff NPs as selective sorbent for Cr(III) and b) Ag@Raff NPs as efficient optical sensor for Cr(VI)

Reliable quantitative determination of both Cr(III) and Cr(VI) is possible using ETAAS measurements: Sorbent, 200 μL Ag@Raff NPs dispersion, was added to 10 mL water sample

and shaken for 30 min. Sample solution is centrifuged and Cr(VI) was measured in the effluate, sorbent is washed with distilled water and dissolved in 2 mL c. HNO₃ (see Figure 7b), where Cr(III) is measured by ETAAS. Analytical figures of merit as well as validity studies of developed method were shown in Table 2. As can be seen, very good agreement was achieved for the sum of Cr species determined by proposed SPE procedure with total Cr content measured by direct ICP-MS. The values of detection limit were 0.01 µg/L and 0.05 µg/L for Cr(III) and Cr(VI), respectively; the relative standard deviation varied between 4-6 % for both Cr species in the range 0.1-50 µg/L.

Table 2. Analytical figures of merit and validity studies of developed method

Parameter	Cr(III), µg/L	Cr(VI), µg/L	Total Cr (by ICP-MS)
Maritsa river	4.8±0.2	0.82±0.06	5.73±0.06
Iskar Dam	2.7±0.2	0.19±0.02	2.65±0.05
Mineral water Bankia	0.15±0.03	<LOQ	0.16±0.01

4 CONCLUSIONS

- Raffinose-coated silver nanoparticles were successfully synthesized and their physicochemical characteristics were analyzed.
- Promising applications of Ag@Raff NPs were demonstrated as both effective sorbent for solid phase microextraction of Cr(III) from aqueous solutions and as optical probe in smart LSPR based sensing system for quantitative, selective and sensitive determination of Cr(VI).

ACKNOWLEDGEMENTS: The authors gratefully acknowledge the financial support provided by Bulgarian Scientific Fund, Grant DN19/10 “Smart Speciation”.

REFERENCES

- [1] Velma, V., Vutukuru, S.S. and Tchounwou, P.B. Ecotoxicology of hexavalent chromium in freshwater fish: A critical review. *Reviews on Environ. Health* (2009) **24**:129-145.
- [2] Bielicka, A., Bojanowska, I. and Wisniewski, A. Two Faces of Chromium – Pollutant and Bioelement. *Pol. J. Environ. Stud* (2005) **14**:5-10.
- [3] Lai, Y.J and Tseng, W.L. Role of 5-thio-(2-nitrobenzoic acid)-capped gold nanoparticles in the sensing. *Analyst* (2011) **136**:2712-2717.
- [4] Xiao, D., Wang, K. and Xiao, W. Synchronous fluorescence and absorbance dynamic liquid drop sensor for Cr(VI) determination at the femtomole level. *Analyst* (2001) **126**:1387-1392.
- [5] Afkhami, A. and Saber-Tehrani, M. Flame atomic absorption spectrometric determination of trace amounts of Pb(II) and Cr(III) in biological, food and environmental samples after preconcentration by modified nano-alumina. *Microchim. Acta* (2011) **172**:125-136.
- [6] Krzysik, M., Grajeta, H. and Prescha, A. Chromium content in selected convenience and fast foods in Poland. *Food Chem* (2008) **107**:208-212.
- [7] Marqui, E., Fontas, C., Toribio, M., Guillem, M., Hidalgo, M. and Queralt, I. Determination of water-soluble hexavalent chromium in clinker samples by wavelength-dispersive x-ray fluorescence spectrometry after concentration in activated layers. *Appl. Spectrosc* (2010) **64**:547-551.

- [8] Baralkiewicz, D., Pikosz, B., Belter, M. and Marcinkowska, M. Speciation analysis of chromium in drinking water samples by ion-pair reversed-phase HPLC-ICP-MS: validation of the analytical method and evaluation of the uncertainty budget. *Accred. Qual. Assur* (2013) **18**:391-401.
- [9] Hua, L., Chan, Y.C., Wu, Y.P., Wu, B.Y., Karabi, S. and Tan, S.C. A highly selective technique to determine hexavalent chromium in electronic and electrical products for RoHS compliance. Conf. paper (Polytronic-6th Int. Conf. on Polymers and Adhesives in Microelectronics and Photonics) (2007).
- [10] Aragay, G., Pons, J. and Merkoç, A. Recent trends in macro-, micro-, and nanomaterial-based tools and strategies for heavy-metal detection. *Chem. Rev* (2011) **111**:3433-3458.
- [11] Pradeep, T. and Anshup. Noble metal nanoparticles for water purification: A critical review. *Thin Solid Films* (2009) **517**:6441-6478.
- [12] Zhang, L. and Fang, M. Nanomaterials in pollution trace detection and environmental improvement. *Nano Today* (2010) **5**:128-142.
- [13] Vasileva, P., Donkova, B., Karadjova, I. and Dushkin, C. Synthesis of starch-stabilized silver nanoparticles and their application as a surface plasmon resonance-based sensor of hydrogen peroxide. *Colloids Surf. A Physicochem. Eng. Asp* (2011) **382**:203-210.
- [14] Wu, X., Hu, Y., Dong, Y., Jiang, X. and Zhu, N. Colorimetric determination of hexavalent of chromium with ascorbic acid capped silver nanoparticles. *Anal. Methods* (2013) **5**:560-565.
- [15] Ravindran, A., Mani, V., Chandrasekaran, N. and Mukherjee, A. Selective colorimetric sensing of cysteine in aqueous solutions using silver nanoparticles in the presence of Cr³⁺. *Talanta* (2011) **85**:533-540.
- [16] El-Ansary, A. and Faddah, L.M. Nanoparticles as biochemical sensors. *Nanotechnol. Sci. Appl.* (2010) **3**:65-76.
- [17] Chichova, M., Shkodrova, M., Vasileva, P., Kirilova, K. and Doncheva-Stoimenova, D. Influence of silver nanoparticles on the activity of rat liver mitochondrial ATPase. *J. Nanopart. Res* (2014) **16**:2243.
- [18] Hutter, E. and Fendler, J. Exploitation of localized surface plasmon resonance. *Adv.Mater* (2004) **16**:1685-1706.
- [19] Tongsakul, D., Wongravee, K., Thammacharoen, C. and Ekgasit, S. Enhancement of the reduction efficiency of soluble starch for platinum nanoparticles synthesis. *Carbohydr. Res* (2012) **357**:90-97.
- [20] Cooke, D. and Gidley, M. Loss of crystalline and molecular order during starch gelatinization: origin of the enthalpic transition. *Carbohydr. Res* (1992) **227**:103-112.
- [21] Vimala, K., Murali Mohana, Y., Samba Sivudu, K., Varaprasad, K., Ravinda, S., Narayana Reddy, N., Padma, Y., Sreedhar, B. and MohanaRahu, K. Fabrication of porous chitosan films impregnated with silver nanoparticles: A facile approach for superior antibacterial application. *Colloids Surf. B Biointerfaces* (2010) **76**:248-258.
- [22] Ščančar, J. and Milačič, R., A critical overview of Cr speciation analysis based on high performance liquid chromatography and spectrometric techniques. *J. Anal. At. Spectrom* (2014) **29**:427-443.
- [23] Homola, J., Present and future of surface plasmon resonance biosensors. *Anal. Bioanal. Chem* (2003) **377**:528-539.

BAYESIAN UPDATING FOR THE ASSESSMENT OF STRUCTURAL MODIFICATIONS BY MEANS OF SUBSPACE-BASED FAULT DETECTION METHODS: THE CASE STUDY OF THE S. MARIA DI COLLEMAGGIO BASILICA

ANGELO ALOISIO*, LUCA DI BATTISTA[†] RICCARDO CIRELLA* ROCCO ALAGGIO* ELENA ANTONACCI* MASSIMO FRAGIACOMO*

*Department of Civil, Construction-Architectural and Environmental Engineering, Università degli Studi dell'Aquila, Via G. Gronchi, 18, L'Aquila, 67100, Abruzzo, Italy

[†] Department of Information Engineering, Computer Science and Mathematics, Università degli Studi dell'Aquila, Via Vetoio, Coppito, 67100 L'Aquila, Abruzzo, Italy

Key words: Structural Health Monitoring, Bayesian Inference, Dynamic Identification, Damage Detection, Masonry structures

Abstract. The paper focuses on the development of an elementary Bayesian framework for the assessment of damage occurrence from subspace-based indicators. The proposed method is tested on real data, acquired by a complex monitoring system installed in a masonry monumental structure, the basilica of Santa Maria di Collemaggio in L'Aquila, Italy. The procedure is calibrated on two sets of data, measured from the façade accelerometers, before and after the CLT (Cross-Lam Timber) roof connection, interpreted as damage and reference states respectively. The application of Bayesian inference, based on two different damage indicators, for the assessment of the façade's structural modification, is presented and compared with the results of the χ^2 -tests by Dohler et al. The issue of the choice of the reference data set is further considered, providing a computation procedures for the built of a reference statistical model.

1 INTRODUCTION

The problem of detecting faults, interpreted as changes in the eigenstructure of a linear dynamical system, has been investigated following various approaches [1, 2, 3, 4, 5, 6, 7, 8]. During the last two decades there has been a growing interest in subspace-based linear system identification methods [9, 10]. Many have attempted to design fault detection algorithms based on subspace identification [11, 12, 6]. In particular several damage detection tests, which do not require the computation of modal parameters, so-called non-parametric damage tests, have been proposed [13, 14]. They compare output data measured during the structure's reference state to those coming from the possibly damaged state using a subspace-based residual function [15].

Following Rytter [16], the ultimate goal of SHM is to determine the four levels of damage identification at the earliest possible stage: (i) existence, (ii) location, (iii) severity of damage and (iv) remaining useful life. According to [6], the vibration-based structural health monitoring (SHM) problem could be considered as a double task problem; (i) detecting damages modelled as changes in the eigenstructure of a linear dynamic system, (ii) and localizing the detected damages within a finite element model (FEM) of

the monitored structure [6]. Besides, the assessment of the damage occurrence (1st task of both [16] and [6]), by means of subspace-based damage detection tests, shows to be quite complex, if proper criteria for the choice of the reference data are not adopted. Most vibration-based damage detection methods can in fact acquire satisfactory verification on analytical or numerical structures, but they may encounter problems when applied to real-world structures under varying environments [17, 18, 19].

In this paper, the performance of three damage indicators have been investigated against a masonry structure, the Santa Maria di Collemaggio basilica in L'Aquila, Italy.

So far, the basilica has represented an important case of study [20, 21, 22, 23, 24, 25, 26, 27, 28, 29, 30, 31, 32, 33, 34, 35].

It is a Romanesque masterpiece characterized by a dense, fascinating history and construction phases, which began in 1270, with many stratified interventions occurred across the centuries. The church, seriously damaged by the 2009 earthquake¹, was subjected to an extensive rehabilitation, ended in 2017. The observed seismic behaviour was characterized by the presence of specific damage patterns as well as collapse mechanisms in well-defined parts of the structure [36, 37]: the damage was in fact mainly related with the collapse of structural portions (macro-blocks), principally due to the lack of stiff floors able to provide diaphragmatic action, the so-called “box behaviour” [38].

The use of dynamic-based methods to detect the damage on this type of structures is an attractive, but complex tool [39]. Many methods and applications have been presented in the literature for damage identification based on vibration data, see e.g. [40, 41, 42, 43, 44, 45, 46, 47], but there are only a few papers related to masonry-like structures [39, 48]. Damage indicators reliability is highly affected by the lack of a thorough mechanical interpretation as well as by the sensitivity to damage severity, localization and variations in the excitation conditions: in fact, in a no-damage situation, which acquisition should be the most qualified candidate to represent the reference condition, under varying operational environments? It has been attempted to overcome the problem of the reference choice, by means of a general statistical model, detailed in the following sections.

The paper is organized as follows: in the first section an overview about subspace-based damage detection tests, implemented in the paper, is presented; in the second section an elementary Bayesian framework is outlined; In the third section the monitoring system in the Santa Maria di Collemaggio basilica is briefly described; In the last sections the application of Bayesian inference, based on two different damage indicators, for the assessment of the façade's structural modification is presented and commented.

2 DAMAGE DETECTION TESTS

Subspace-based damage detection tests, implemented in the current paper, are briefly reviewed.

2.1 State space representation

State-space representation for output-only vibration-based structural monitoring corresponds to the following discrete time model

$$\begin{aligned}x_{k+1} &= Ax_k + v_k \\ y_k &= Cx_k + w_k\end{aligned}\tag{1}$$

¹On April 6th, 2009, at 3:32 a.m. an earthquake (Richter Magnitude 5.9) struck L'Aquila (Central Italy): 309 victims, 65,000 displaced people. More than 10 billion Euro of estimated damage, about 100 churches uninhabitable for the major collapses, along with thousands of historic buildings in the old town centres.

with the states $x_k \in \mathbb{R}^n$, the outputs $y_k \in \mathbb{R}^r$, the state transition matrix $A \in \mathbb{R}^{n \times n}$ and the observation matrix $C \in \mathbb{R}^{r \times n}$, where r is the number of sensors and n is the system order. The excitation v_k is an unmeasured Gaussian white noise sequence with zero mean and constant covariance matrix $Q = E(v_k v_k^T) = Q\delta(k - k')$, where $E(\cdot)$ denotes the expectation operator and w_k is the measurement noise.

2.2 Residual matrices

In [5, 49] a residual function was proposed to detect changes in the system's eigenstructure from measurements y_k , without actually identifying the eigenstructure in the possibly damaged state. The considered residual is associated with a covariance-driven output-only subspace identification algorithm. Let $G = E(x_{k+1} y_k^T)$ be the cross-covariance between the states and the outputs, let $R_i = E(y_k y_{k-i}^T) = CA^{i-1}G$ be the theoretic output covariances and

$$H_{p+1,q} = \begin{bmatrix} R_1 & R_2 & \dots & R_q \\ R_2 & R_3 & \dots & R_{q+1} \\ \vdots & \vdots & \ddots & \vdots \\ R_{p+1} & R_{p+2} & \dots & R_{p+q} \end{bmatrix} = \text{Hank}(R_i) \quad (2)$$

be the theoretic block Hankel matrix. Using measured data $(y_k)_{k=1,\dots,N}$, a consistent estimate $\hat{H}_{p+1,q}$ is obtained from the empirical output covariances:

$$R_i = \frac{1}{N} \sum_{k=1}^n y_k y_{k-i}^T \quad (3)$$

$$H_{p+1,q} = \text{Hank}(R_i) \quad (4)$$

The residual function, originally proposed by [5, 49], compares the system's undamaged or reference state with the damaged or current one. The considered residual matrix writes

$$R_c = \hat{S}^T H_{p+1,q} \quad (5)$$

where \hat{S}^T is the left null space of the block Hankel matrix $H_{p+1,q}$ in the reference state and $H_{p+1,q}$ is the covariance block Hankel matrix in the current one.

In practice, the excitation covariance Q may change between different measurement sessions of the system due to different environmental factors, while the excitation is still assumed to be stationary during one measurement. A change in the excitation covariance Q leads to a change in the cross-covariance between states and outputs G and thus in the Hankel matrix. Dohler et al. [14, 15] proposed a new residual, which is robust to changing excitation. Let U_1 be the matrix of the left singular vectors obtained from an SVD of $H_{p+1,q}$. As U_1 is a matrix with orthonormal columns, it can be regarded as independent of the excitation Q , which qualifies its use for a residual function, that is robust to changes in the excitation covariance. Then, the residual matrix writes

$$R_r = \hat{S}^T U_1 \quad (6)$$

²The system parameters in terms of eigenvalues and eigenvectors in the reference and current states are respectively θ_0 and θ . [13] proposed a non-parametric version of the damage detection test, adopted in the current paper, where the system parameters θ_0 do not need to be known explicitly in the reference state. Instead of using the null space $S(\theta_0^T)$ on the parameterized observability matrix [5, 49], an empirical (non-parametric) null space \hat{S} is computed on an estimated block Hankel matrix from data in the reference state using e.g. an SVD.

As stated by [15], other residual matrices (see (5)) are not ideal candidates for structural damage detection, since the amplitude of the residues, resulting from erroneous definition of the system order or the amplitude's excitation, may mask the residues variation due to small structural damages.

2.2.1 Dohler et al. non parametric damage detection tests

Following a procedure used by Basseville et al. [5] and Fritzen et al. [50], the residual matrix (5), is rearranged in a vectorial form. The formulation adopted by [13] is followed³:

$$\xi_N^Q = \sqrt{N} \text{vec}(\hat{S}^T U_1) \quad (7)$$

The index Q of the residual vector ξ_N^Q indicates the excitation covariance of the system, corresponding to the measured data $(y_k)_{k=1,\dots,N}$ used for the computation. It is tested if this residual function is significantly different from zero. A non-parametric test to decide if ξ_N^Q is significantly different from zero or not, following the one reported by [13], is adopted by [14] for the new robust residual matrix. The mentioned non-parametric test boils to the following χ^2 -test:

$$\hat{\gamma}_N^2 = (\hat{\xi}_N^Q)^T \hat{\Sigma}_\xi^{-1} (\hat{\xi}_N^Q) \quad (8)$$

which should be compared to a threshold and where $\hat{\Sigma}_\xi$ is a consistent estimate of the asymptotic covariance of ξ_N^Q . The computation of the $\hat{\Sigma}_\xi^{-1}$ matrix is a numerically critical issue, as it involves the inversion of big low-rank matrices.

2.2.2 Yan et al. damage detection tests

Yan [15], clinging to the geometric interpretation of the residual matrix, as expression of a loss of orthonormality, proposed a damage indicator given by the maximal singular value of the matrix R_r

$$\bar{\sigma}_N^2 = \text{norm}(R_r) \quad (9)$$

where $\text{norm}(\cdot)$ is an operator giving the maximal singular value of a matrix.

3 BAYESIAN UPDATING

An elementary Bayesian framework is outlined in order to interpret results from damage detection tests.

Generally, the lack of a structural model does not allow an *a priori* definition of damage indicators thresholds, however, even without any information about the structure, the occurrence of damage or more properly of a structural modification could be assessed anyway. The deviation between the statistical model, representative of the indicators reference population, and that of the current population is in fact a sort of marker of the occurrence of a structural modification. In order to assess such deviation between the current statistical model and the reference one, over time, using incoming measurements, continuous Bayesian updating may be implemented.

Theoretically, for an overall appreciation of the modification of the statistical reference model over time, a number of thresholds I_T ⁴ could be defined with respect to certain probabilities of exceeding

³*vec* denotes the vectorization operator.

⁴The indicators thresholds I_T do not correspond to Damage Limit States or Damage thresholds.

(p_E) the probability distribution of the indicators reference population. p_E may change over time as the number of measurements increases: the (p_E -incoming measurements) curve will provide information about the effectiveness of the reference statistical model in predicting the current indicators statistics. Rates of change and the slope of such curve could be interpreted as markers of the deviations from the reference model, which may converge towards other statistical representations.

3.1 Multiparameter Bayesian updating

The issue of Bayesian updating damage detection tests may fall into the problem of updating normal distributions with unknown mean and variance, assuming the variance as a *nuisance parameter*. Let I_d be a certain damage indicator, the *a priori* or reference probability distribution writes

$$p(I_d) = N(\mu_0, \sigma_0^2) \quad (10)$$

Suppose a sample of independent and identically distributed damage indicators in both the reference and damaged state is measured, $y_i = (y_{i,1}, \dots, y_{i,n_0})$ $\dim(y_i) = n_0 \times 1$ and $y_d = (y_{d,1}, \dots, y_{d,n})$ $\dim(y_d) = n \times 1$ respectively, where the first represents initial information, I , and the latter actual data, D . Let σ^2 be the unknown damage indicator variance. The joint posterior density of I_d and σ^2 , given initial information I and actual data D , may be factored in [51]

$$p(I_d, \sigma^2 | D, I) \propto p(I_d, \sigma^2 | I) p(D | I_d, \sigma^2) \quad (11)$$

where $p(I_d, \sigma^2 | I)$ is the joint prior density and $p(D | I_d, \sigma^2)$ the likelihood function. The population mean, I_d , could be assumed as the estimand of interest, and so the objective of Bayesian analysis is the marginal posterior distribution of I_d , which can be obtained by integrating the joint posterior density over σ^2 .

$$p(I_d | D, I) \propto \int_0^\infty p(I_d, \sigma^2 | I) p(D | I_d, \sigma^2) d\sigma^2 \quad (12)$$

The cumulative probability associated to the occurrence a certain damage indicator threshold, given initial information and actual data, writes

$$p(I_d > I_{DLS} | D, I) \propto 1 - \int_{-\infty}^{I_{DLS}} \int_0^\infty p(I_d, \sigma^2 | I) p(D | I_d, \sigma^2) d\sigma^2 dI_d \quad (13)$$

As reported in Appendix A, the joint prior density could be factored in the marginal distribution of σ^2 , which is scaled inverse- χ^2 , and the conditional distribution of I_d given σ^2 , which is normal. Given the normal likelihood, the marginal posterior density is a t -distribution with the following parametrization [51]

$$\begin{aligned} p(I_d > I_{DLS} | D, I) &\propto \int_{-\infty}^{I_{DLS}} p(I_d | D, I) dI_d \\ &= \left(1 + \frac{k_n (I_d - \mu_n)^2}{v_n \sigma_n^2} \right)^{(v_n+1)/2} \\ &= \int_{-\infty}^{I_{DLS}} t_{v_n}(I_d | \mu_n, \sigma_n^2 / k_n) dI_d \end{aligned} \quad (14)$$

where $\mu_n = \frac{k_0}{k_0+n}\mu_0 + \frac{n}{k_0+n}\bar{y}_d$; $v_n\sigma_n^2 = v_0\sigma_0^2 + (n-1)s^2 + \frac{k_0n}{k_0+n}(\hat{y}_d - \mu_0)^2$; $k_n = k_0 + n$; $k_0 = n_0$; $\mu_0 = \frac{1}{n_0}\sum_{i=1}^{n_0}y_{i,i}$; $\sigma_0^2 = \frac{1}{n_0-1}\sum_{i=1}^{n_0}(y_{i,i} - \mu_0)^2$; $v_0 = n_0 - 1$; $\hat{y}_d = \frac{1}{n}\sum_{i=1}^n y_{d,i}$; $s = \frac{1}{n-1}\sum_{i=1}^n (y_{d,i} - \hat{y}_d)^2$;

The issue of Bayesian updating the damage indicators PDF in the reference state, given the actual possibly damaged state, represents the well-known problem of updating normal data with a conjugate prior distribution. By means of Bayesian inference, the prior state of knowledge about the presence of structural damage is updated and quantified in the light of actual data (14).

As new damage indicators are computed from incoming measurements, the sole likelihood function is affected. It follows that the sole mean, \hat{y}_d , and variance, s , are continuously updated. Continuous Bayesian estimation is the extension of (14) using incoming measurements. Let D_{k+1} be the set of actual data up to the $(k+1)$ -th measurement.

$$\begin{aligned} p(I_d, \sigma | D_{k+1}, I) &\propto p(I_d, \sigma | I) p(D_{k+1} | I_d, \sigma) \\ &= p(I_d, \sigma | I) p(D_k | I_d, \sigma) p(y_{d,k+1} | I_d, \sigma) \end{aligned} \quad (15)$$

As the likelihood function does not change except for its parameters, the continuous update of the marginal posterior distribution is obtained by updating the t-distribution parameters. The probability of exceeding a certain threshold writes

$$\begin{aligned} p(I_{d,k} > I_{DLS} | D_k, I) &\propto 1 - \int_{-\infty}^{I_{DLS}} p(I_{d,k} | D_k, I) dI_{d,k} \\ &= \int_{-\infty}^{I_{DLS}} t_{v_n}(I_{d,k} | \mu_k, \sigma_k^2/k_k) dI_{d,k} \end{aligned} \quad (16)$$

where $\mu_k = \frac{k_0}{k_0+k}\mu_0 + \frac{k}{k_0+k}\bar{y}_{d,k}$; $v_k\sigma_k^2 = v_0\sigma_0^2 + (k-1)s_k^2 + \frac{k_0k}{k_0+k}(\hat{y}_{d,k} - \mu_0)^2$; $k_k = k_0 + k$; $k_0 = n_0$; $\mu_0 = \frac{1}{n_0}\sum_{i=1}^{n_0}y_{i,i}$; $\sigma_0^2 = \frac{1}{n_0-1}\sum_{i=1}^{n_0}(y_{i,i} - \mu_0)^2$; $v_0 = n_0 - 1$; $\hat{y}_{d,k} = \frac{1}{k}\sum_{i=1}^k y_{d,i}$; $s = \frac{1}{k-1}\sum_{i=1}^k (y_{d,i} - \hat{y}_{d,k})^2$;

4 MONITORING SYSTEM

A permanent monitoring system was installed in the Santa Maria di Collemaggio basilica. The system consists of a network of sensors, supported by a service platform, which synchronizes, interrogates, transmits and manages the alarms from the different sensors.

The monitoring system acquires data from the sensors, according to two possible recording patterns: (i) following a time schedule or (ii) when a certain acceleration threshold is exceeded. The installed sensors are of two types, the ones for the measurement of dynamic quantities, the others for the measurement of static quantities⁵, Fig.1.

Both low-intensity tremors and strong-motion earthquakes can be effectively recorded.

5 APPLICATION OF DAMAGE DETECTION TESTS

A set of damage indicators is tested: accelerometric data from the façade macroelement, corresponding to two different structural conditions, have been compared: a first data set, recorded before the CLT-roof was connected to the façade, is assumed as the *actual or damaged state*; A second data set, recorded

⁵9 potentiometers crack measurement devices, 78 FBA accelerometers (2 triaxial 12 biaxial and 48 monoaxial), 14 inclinometers and 5 temperature/humidity sensors have been installed

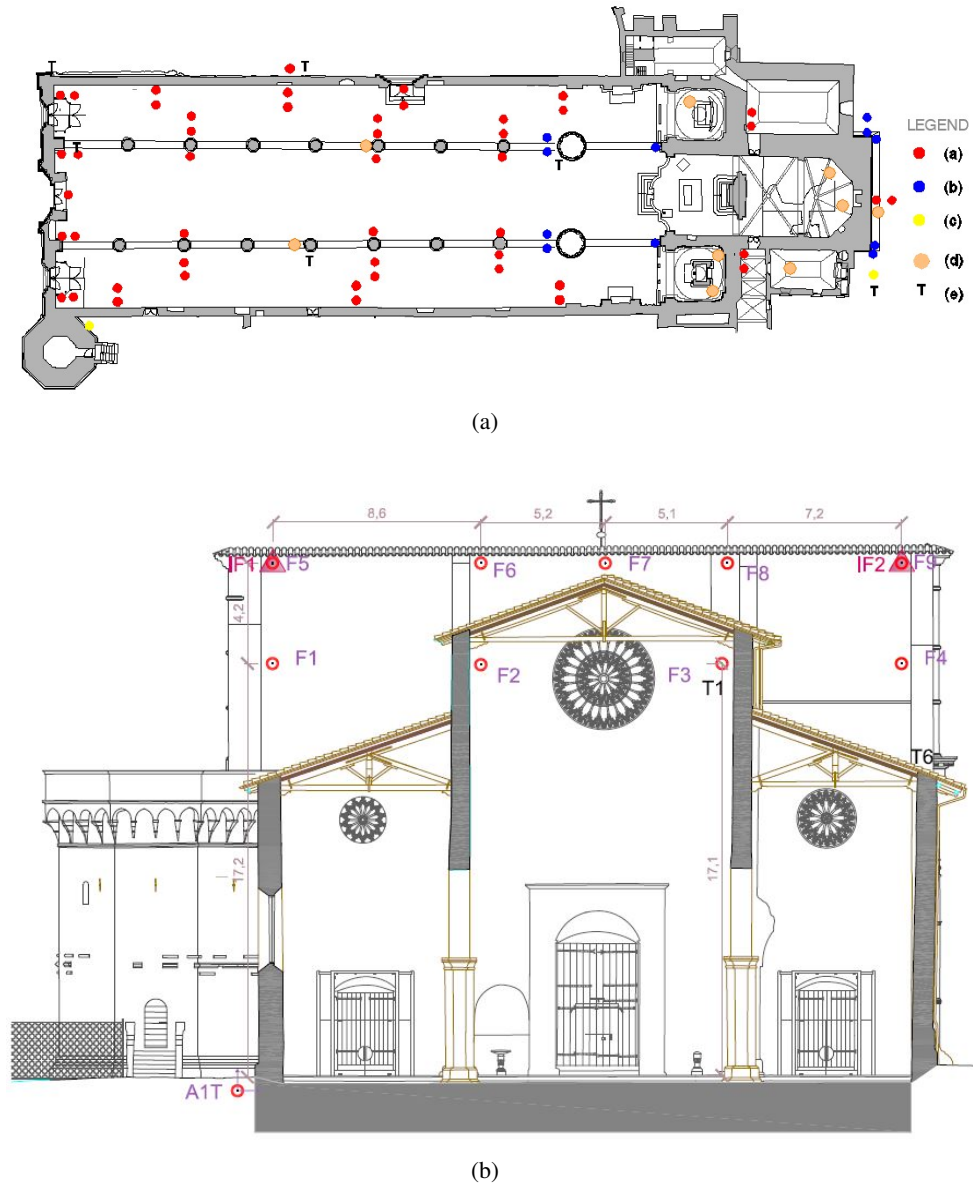


Figure 1: (a) Monitoring system layout, (a) monoaxial FBA (Force Balance Accelerometer), (b) biaxial FBA, (c) triaxial FBA, (d) inclinometers, (e) crack monitoring device, (f) temperature and humidity sensor; (b) Layout of the façade FBA;

after the CLT-roof was connected to the façade (Fig.2), is assumed as the *reference or un-damaged state*. 21 and 162 acquisitions, recorded from the façade FBA accelerometers, have been used as a first and

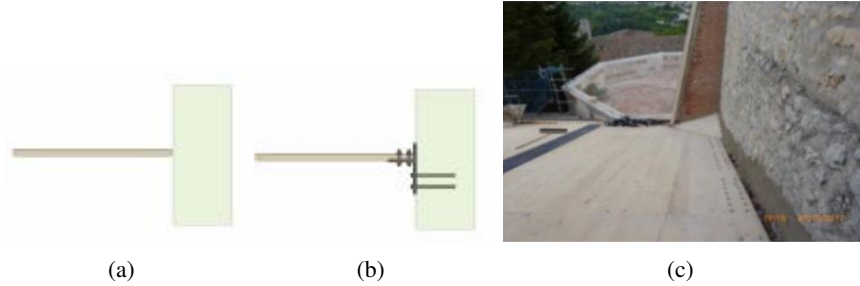


Figure 2: Detail of the connection between the facade and the CLT roof; Sketch of the roof-facade interaction before and after the connection, (a) and (b) respectively; Picture of the connection (c).

second data set. Three damage detection tests are implemented, the first (17) is from Yan et al. [15], the second (18) is the square of the Euclidean norm of the residual vector, the third (19) is the χ^2 -test itself [14].

$$I_{d,Y} = \hat{\sigma}_N^2 = \text{norm}(R_r) \quad (17)$$

$$I_{d,D} = (\hat{\xi}_N^Q)^T (\hat{\xi}_N^Q) \quad (18)$$

$$\chi^2\text{-test} = \hat{\gamma}_N^2 = (\hat{\xi}_N^Q)^T \hat{\Sigma}_\xi^{-1} (\hat{\xi}_N^Q) \quad (19)$$

5.1 Damage Indicators computation

Two different methods are followed for the computation of the reference and damage population of the three damage indicators. Let n_0 be the number of recordings during the un-damaged state and n the number of recordings during the damaged state.

- The first criterion assumes as reference population the indicators from all possible cross-comparison between data acquired during the reference condition, excluding self comparisons. The size of the reference population will be $n_0(n_0 - 1) = 26082$, while that of the damaged one will be $nn_0 = 3402$; It means that, following such criterion, every actual or damaged recording should be compared with all reference acquisitions.
- A sole recording is assumed as reference data set. The size of the reference population will be $n_0 - 1 = 161$, while that of the damaged one will be $n = 21$;

The first computation method comes from the assumption that the choice of a reference data set is extremely difficult and critical. It is often complex to discriminate changes in structural systems response, caused by damage, from those caused by environmental factors, whose effects might cover the actual presence of damage. Therefore, an effective damage detection procedure is required to be not only sensitive to damage but also insensitive to varying operational environments [17]. Acquisitions, recorded under different environmental conditions, will produce in fact a varied reference population. A way to include the environmental effects and to monitor the actual presence of damage in dynamic systems could be achieved by means of the proposed first criterion, since the variability of the indicator is embraced by the reference statistical model.

The second criterion may be considered more standard, since all data are compared with a single reference, accurately chosen according to disparate criteria [17, 41]. The results of the two computation methods are reported and compared in the following subsections.

5.2 First method

Following the first computation method two sets of damage indicators are evaluated, Fig.3. The vertical line, in Fig.5(a), 5(b) and 5(c), divides the reference population from the actual or damaged one. The $I_{d,Y}$ (17), $I_{d,D}$ (18) and χ^2 -test (8) visually belong to two different statistical models. The $I_{d,Y}$ (Fig.5(d)) population almost resembles a normal distribution, while that of $I_{d,D}$ (Fig.5(e)) is likely to gather around two different values, as if two statistical models were behind the system's dynamics. The χ^2 -test results seems to fit a chi-squared distribution Fig.5(f). In Fig.4 the PDF and CDF from the two data sets are

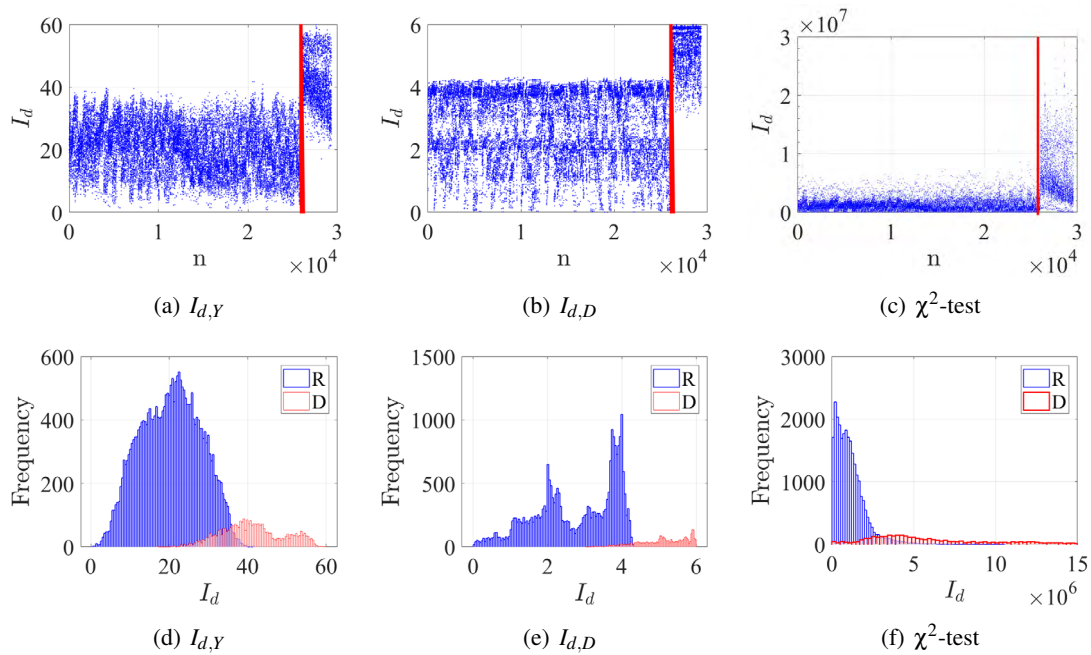


Figure 3: (a)-(c) General trend of the results of damage detection tests; The vertical line separates the reference population from the actual or damaged one; (d)-(f) Frequency histogram of the results of damage detection tests; "R" stands for Reference population, "D" for Damaged or Actual population.

reported: the curve (R) corresponds to the normal distribution associated with the reference population $p(I_{d,reference}) = N(\mu_0, \sigma_0^2)$ (10), the curve (D) indicates the normal distribution associated with the actual or damaged population $p(I_{d,damage}) = N(\hat{y}_d, s)$, the curve (B) indicates the marginal posterior density t-distribution (14) given actual data (actual population) and initial information (reference population). The t-distribution obtained from the Bayesian updating of the conjugate prior distribution, representative of the reference population, shows a negligible deviation from the R curve. While the χ^2 -test results seem to be very sensitive to the effects of the specific structural modification (Fig.3), the Bayesian treatment of data is not very effective, given the position of the D curve, representative of the actual population: the t-distribution seems to be reluctant to change. The causes are due to the different sizes of the reference and actual populations, 26082 vs 3402 respectively. The larger the size of the reference population, the larger the size of the damage population must be in order to significantly update the prior distribution.

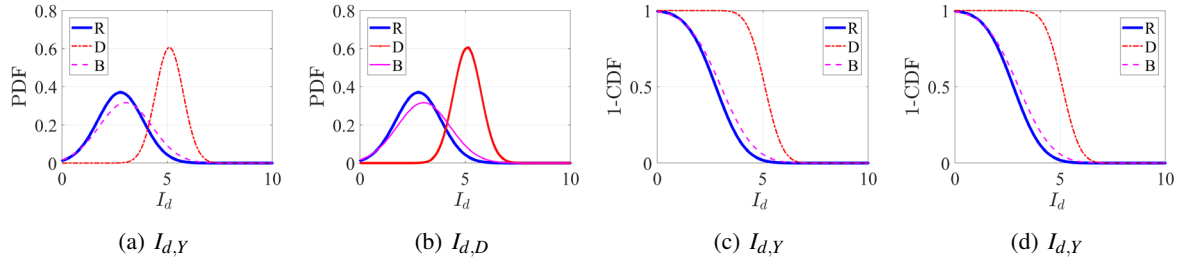


Figure 4: Results from the Bayesian updating of the reference population given the actual or damaged population in terms of PDF (a)-(b) and CDF (c)-(d). The curve (R) corresponds to the normal distribution associated with the reference population $p(I_{d,reference}) = N(\mu_0, \sigma_0^2)$ (10), the red (D) indicates the normal distribution associated with the actual or damaged population $p(I_{d,damage}) = N(\bar{y}_d, s)$, the curve (B) indicates the marginal posterior density t-distribution (14) given actual data (actual population) and initial information (reference population).

A size reduction of the reference population will increase the "reactivity" of the prior distribution to the effects of a structural change. For these purposes a proper truncation of the reference population could be adopted. Fig.5 shows the evolution of mean μ_0 and variance σ_0 of the reference population as the number of samples increases: they converge towards a certain value; Thus the size of the reference pop-

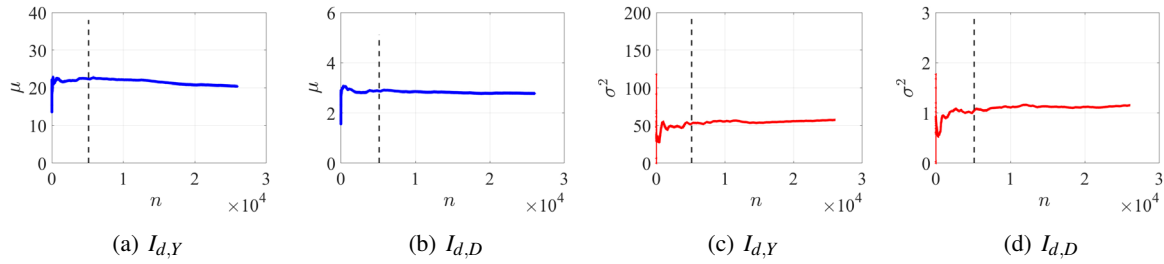


Figure 5: Evolution of mean μ_0 and variance σ_0 of the reference population as the number of samples increases.

ulation may be truncated as soon as the oscillation is contained within a certain threshold. The dotted line represents the truncation threshold adopted in the current application. Fig.6 reports the results of

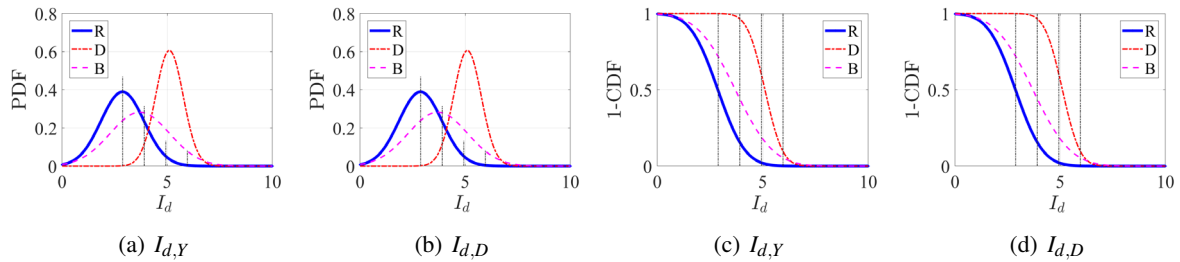


Figure 6: Results from the Bayesian updating of the reduced reference population given the actual or damaged population in terms of PDF (a)-(c) and CDF (d)-(f). The blue curve (R) corresponds to the normal distribution associated with the reference population $p(I_{d,reference}) = N(\mu_0, \sigma_0^2)$ (10), the red curve (D) indicates the normal distribution associated with the actual or damaged population $p(I_{d,damage}) = N(\bar{y}_d, s)$, the pink curve (B) indicates the marginal posterior density t-distribution (14) given actual data (actual population) and initial information (reference population).

the Bayesian updating from the reduced reference data set: the t-distribution markedly differs from the statistical model of the reference population, approaching the red curve. Four dashed lines are drawn over the probability distributions in Fig.6, corresponding to four thresholds arbitrarily chosen from the reference distribution, μ_0 , $\mu_0 + \sigma_0$, $\mu_0 + 2\sigma_0$, $\mu_0 + 3\sigma_0$ respectively. As new damage detection tests are performed, the t-distribution (16) is updated, so that the probability of exceeding p_E the indicator thresholds, I_T , changes with respect to the original p_E corresponding to the reference population, Fig.7. The

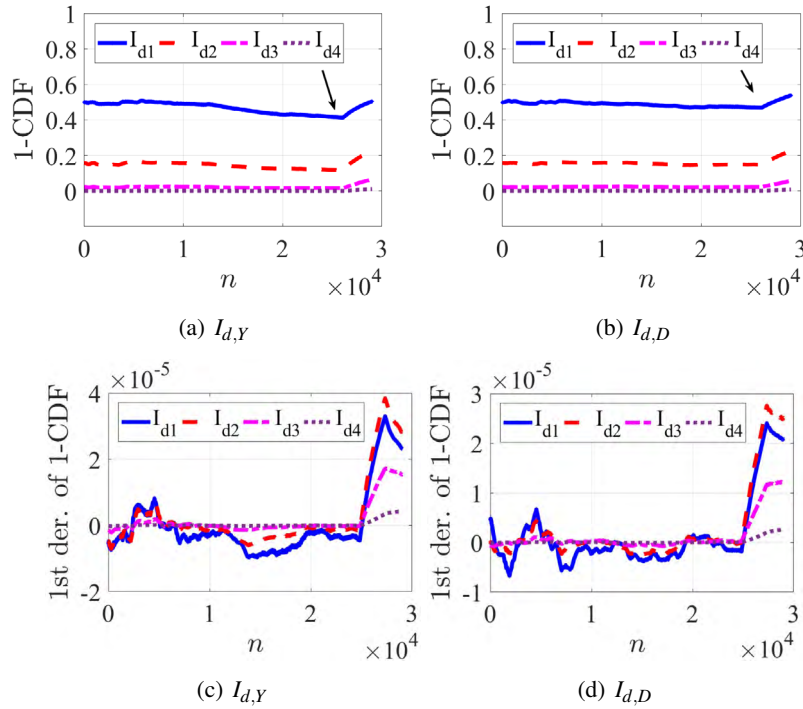


Figure 7: General trend of the probability of exceeding p_E four indicators' thresholds, reported in the legend, using incoming damage tests results ($I_{d1} = \mu_0$, $I_{d1} = \mu_0 + \sigma_0$, $I_{d1} = \mu_0 + 2\sigma_0$, $I_{d1} = \mu_0 + 3\sigma_0$). In (a)-(b) all damage indicators are representative of both the reference and actual condition, sequentially concatenated, in order to simulated a chronological evolution, while in (c)-(d) damage indicators are representative of the sole actual condition.

occurrence of a structural modification is significantly manifested by the $I_{d,Y}$ and $I_{d,D}$ indicators, Fig.7: a sudden change in the curve's slope testifies the occurrence of a modification of the statistical model representative of the actual condition under test. In order to amplify the effects of a structural modification, an approximation of the first derivative of (16) is estimated, Fig.9(c)-(d): the peaks manifest the occurrence of the structural modification.

5.3 Second method

Following the second computation method two sets of damage indicators are evaluated. Between the 162, the results from the tests referred to the 53rd reference acquisition, which best manifests the occurrence of damage, are reported in Fig.8: the results are shown in terms of the general trend of the indicators values, sequentially concatenated, in addition with the curves, which track the statistical model evolution from incoming measurements (16). The $I_{d,Y}$ and $I_{d,D}$ indicators seem to be less sensitive to the specific damage, Fig.10(d)-(e). There is not a marked variation in the curve's slope, as in Fig.9(a)-(b). A

satisfactory performance emerges from the χ^2 -test results, although the population's size in the damage state is too small to obtain a significant plot of the frequency distribution, Fig.10(f).

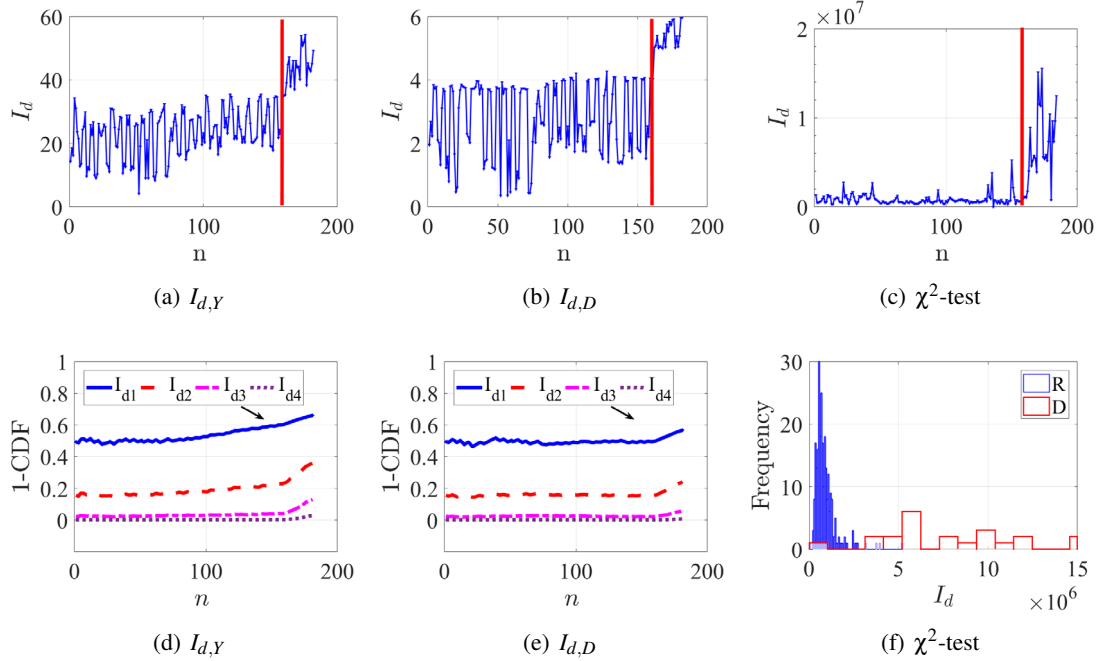


Figure 8: General trend of the results from damage detection tests, assuming the 53rd acquisition as reference data set (a)-(c); The vertical line separates the reference population from the actual or damaged one; In (d)-(e) the evolution of the probability of exceeding p_E four indicator thresholds, described in the legend ($I_{d1} = \mu_0$, $I_{d1} = \mu_0 + \sigma_0$, $I_{d1} = \mu_0 + 2\sigma_0$, $I_{d1} = \mu_0 + 3\sigma_0$), from incoming measurements (reported on the horizontal axis), starting from the p_E in the normal distribution representative of the reference population; In (f) the frequency histogram of the results of the χ^2 -test; "R" stands for Reference population, "D" for Damaged or Actual population.

5.4 COMMENTS

- In real case applications, the use of the robust residual (6) may not provide independence from ambient factors; The variability in the excitation conditions, between different measurement sessions, may not be modelled as a change in the covariance of a random Gaussian process. If the independence from operational environments is not obtained from the robust residual, it should be statistically achieved. The first method proposed for the building of the reference population attempts to capture all the variability of damage detection tests, induced by operational conditions, alternatively assuming each recording as a possible reference state. The so-built reference population will be represented by a statistical model, which may be more stable, since all the results variability may have been experienced in a first step. Hence any discrepancy from the reference statistical model could be more likely attributed to structural modifications, in successive analysis. For these reasons, the first method, proposed for the choice of the reference population, could to be more effective in detecting structural modifications, Fig.8 and Fig.9. Besides the $I_{d,D}$ indicator, Fig.8(b), in the reference state, seems to be more stable than the $I_{d,Y}$, Fig.8(a).
- The χ^2 -test, which was validated by Dohler et al. [14], seems to be effective in detecting the specific structural modification in a masonry structure despite the varying environmental factors.

Theoretically, the second computation method, for the estimate of the reference population, may be considered more rigorous, since each recording is compared with a single acquisition, assumed as reference state; However the χ^2 -test may benefit from the first computation method: the cross comparison between all data in the reference state explores all possible variability of the test results, thus accounting for varying environments in the built of an empirical chi-squared distribution.

- In the presented statistical framework, reference data, represented by the conjugate prior distribution, are not updated from incoming measurements. They express in fact a certain structural condition, estimated during a specific reference time interval. Actual data are instead continuously updated from incoming measurements: the sole likelihood function is affected by the continuous model updating.
- Other damage detection tests could be alternatively derived from the residual matrix and effectively implemented in the proposed Bayesian framework. The statistical treatment of data is not embedded in the damage test itself, as in the χ^2 -test, but it is achieved *a posteriori*, by manipulating data coming from an arbitrary indicator built on the residual (6). Non intrinsically robust indicators may acquire insensitivity to environmental factors by means of the proposed method.
- As only 21 acquisitions were recorded, before the CLT roof connection, the convergence of the test results towards the statistical model, representative of the damage state, cannot be fully appreciated.
- The proposed elementary Bayesian framework could represent an effective tool in tracking the evolution of a statistical reference model, for the purposes of SHM.

6 ACKNOWLEDGEMENTS

The authors thank *ENI* for having financed the structural rehabilitation and the monitoring system, giving back to the city of L'Aquila one of the most identifying monument.

7 CONCLUSIONS

An elementary Bayesian framework based on subspace-based damage detection tests is applied to a masonry structure, the Santa Maria di Collemaggio basilica, severely injured by the 2009 earthquake of L'Aquila, where a monitoring system is installed. So far, few damage detection methods have been proved to be effective for real-life structures owing to the fact that most of the existing damage features or indices are not immune to the field environmental effects that are more complicated than those appearing in analytical or well-controlled laboratory studies. An application of three damage detection tests is shown. Two computation methods, for the choice of the reference population of damage indicators, support an elementary Bayesian framework, which drives the comparison between two different data sets, representative of two structural conditions. The first method (i) assumes as reference population the indicators from all possible cross-comparisons between data, acquired during the reference condition, excluding self comparisons. In the second method (ii) a sole recording is assumed as reference data set. The first method seems to be more effective in assessing the occurrence of a specific structural modification (lack of the CLT roof connection to the basilica's facade). It is likely that the cross comparison (i) between all reference data could account for the variability of environmental factors, making the damage detection test more robust to varying operational environments. The occurrence of a structural modification is detected from the curve, which shows the probability of exceeding certain numerical values of the indicators, as new damage detection tests are performed from incoming measurements.

The change in the curve's slope marks the occurrence of a modification in the statistical model representative of the current state. The implementation of the proposed method could be effectively used for tracking the structural behaviour over time from incoming measurements. The correlation between the expected value of the indicator, the particular structural modification and the associated probability of failure could represent the ultimate goal of a monitoring system which aims to a general procedure for the structural reliability assessment, continuously performed over time; However relevant research and field application verification are, at present, lacking.

REFERENCES

- [1] A. S. Willsky, A survey of design methods for failure detection in dynamic systems, *Automatica* 12 (6) (1976) 601–611.
- [2] P. M. Frank, Fault diagnosis in dynamic systems using analytical and knowledge-based redundancy: A survey and some new results, *automatica* 26 (3) (1990) 459–474.
- [3] R. Patton, P. Frank, R.(eds.) clark. fault diagnosis in dynamic systems: Theory and application. englewood cliff (1989).
- [4] M. Basseville, I. V. Nikiforov, et al., Detection of abrupt changes: theory and application, Vol. 104, Prentice Hall Englewood Cliffs, 1993.
- [5] M. Basseville, M. Abdelghani, A. Benveniste, Subspace-based fault detection algorithms for vibration monitoring, *Automatica* 36 (1) (2000) 101–109.
- [6] M. Döhler, L. Mevel, Subspace-based fault detection robust to changes in the noise covariances, *Automatica* 49 (9) (2013) 2734–2743.
- [7] J. J. Gertler, Survey of model-based failure detection and isolation in complex plants, *IEEE Control systems magazine* 8 (6) (1988) 3–11.
- [8] R. Isermann, Process fault detection based on modeling and estimation methods—a survey, *automatica* 20 (4) (1984) 387–404.
- [9] P. Van Overschee, B. De Moor, N4sid: Subspace algorithms for the identification of combined deterministic-stochastic systems, *Automatica* 30 (1) (1994) 75–93.
- [10] P. Van Overschee, B. De Moor, Subspace algorithms for the stochastic identification problem, *Automatica* 29 (3) (1993) 649–660.
- [11] A. Benveniste, M. Basseville, G. Moustakides, The asymptotic local approach to change detection and model validation, *IEEE Transactions on Automatic Control* 32 (7) (1987) 583–592.
- [12] Q. Zhang, M. Basseville, A. Benveniste, Early warning of slight changes in systems, *Automatica* 30 (1) (1994) 95–113.
- [13] E. Balmès, M. Basseville, F. Bourquin, L. Mevel, H. Nasser, F. Treyssède, Merging sensor data from multiple temperature scenarios for vibration monitoring of civil structures, *Structural health monitoring* 7 (2) (2008) 129–142.
- [14] M. Döhler, L. Mevel, F. Hille, Subspace-based damage detection under changes in the ambient excitation statistics, *Mechanical Systems and Signal Processing* 45 (1) (2014) 207–224.

- [15] A.-M. Yan, J.-C. Golinval, Null subspace-based damage detection of structures using vibration measurements, *Mechanical Systems and Signal Processing* 20 (3) (2006) 611–626.
- [16] A. Rytter, Vibrational based inspection of civil engineering structures, Ph.D. thesis, Dept. of Building Technology and Structural Engineering, Aalborg University (1993).
- [17] Y. Lin, W. Ren, S. Fang, Structural damage detection based on stochastic subspace identification and statistical pattern recognition: II. experimental validation under varying temperature, *Smart Materials and Structures* 20 (11) (2011) 115010.
- [18] H. Sohn, Effects of environmental and operational variability on structural health monitoring, *Philosophical Transactions of the Royal Society A: Mathematical, Physical and Engineering Sciences* 365 (1851) (2006) 539–560.
- [19] B. Peeters, J. Maeck, G. De Roeck, Vibration-based damage detection in civil engineering: excitation sources and temperature effects, *Smart materials and Structures* 10 (3) (2001) 518.
- [20] D. Ranalli, M. Scozzafava, M. Tallini, Ground penetrating radar investigations for the restoration of historic buildings: the case study of the collemaggio basilica (l’aquila, italy), *Journal of cultural heritage* 5 (1) (2004) 91–99.
- [21] D. Oreni, R. Brumana, S. Della Torre, F. Banfi, M. Previtali, Survey turned into hbim: the restoration and the work involved concerning the basilica di collemaggio after the earthquake (l’aquila), *ISPRS Annals of the Photogrammetry, Remote Sensing and Spatial Information Sciences* 2 (5) (2014) 267.
- [22] C. Bartolomucci, *Santa Maria di Collemaggio: interpretazione critica e problemi di conservazione*, Palombi, 2004.
- [23] F. Redi, *Santa maria di collemaggio. archeologia di un monumento*.
- [24] S. Sfarra, A. Bendada, C. Ibarra-Castanedo, D. Ambrosini, D. Paoletti, X. Maldague, Santa maria di collemaggio church (l’aquila, italy): historical reconstruction by non-destructive testing techniques, *International Journal of Architectural Heritage* 9 (4) (2015) 367–390.
- [25] E. Antonacci, G. Beolchini, F. Di Fabio, V. Gattulli, The dynamic behaviour of the basilica s. maria di collemaggio, in: *Proc. of 2nd Int. Congress on Studies in Ancient Structures, SAS2001*, 2001.
- [26] E. Antonacci, G. Beolchini, F. D. F. V. Gattulli, Retrofitting effects on the dynamic behaviour of s. maria di collemaggio, *WIT Transactions on Modelling and Simulation* 30.
- [27] E. Antonacci, V. Gattulli, A. Martinelli, F. Vestroni, Analisi del comportamento dinamico della basilica di collemaggio per il progetto di un sistema di monitoraggio, *XIV Convegno di Ingegneria Sismica ANIDIS*.
- [28] G. D. Alaggio R., Antonacci E., Il monitoraggio della basilica di collemaggio a l’aquila, *Ingenio* 63 (1) (2018) 68–75.
- [29] V. Gattulli, E. Antonacci, F. Vestroni, Field observations and failure analysis of the basilica s. maria di collemaggio after the 2009 l’aquila earthquake, *Engineering Failure Analysis* 34 (2013) 715–734.

- [30] R. Brumana, S. Dellatorre, D. Oreni, M. Previtali, L. Cantini, L. Barazzetti, A. Franchi, F. Banfi, et al., Hbim challenge among the paradigm of complexity, tools and preservation: the basilica di collemaggio 8 years after the earthquake (l'aquila).
- [31] R. Brumana, S. Della Torre, M. Previtali, L. Barazzetti, L. Cantini, D. Oreni, F. Banfi, Generative hbim-modeling to embody complexity. surveying, preservation, site intervention. the basilica di collemaggio (l'aquila).
- [32] G. P. Cimellaro, A. M. Reinhorn, A. De Stefano, Introspection on improper seismic retrofit of basilica santa maria di collemaggio after 2009 italian earthquake, *Earthquake engineering and engineering vibration* 10 (1) (2011) 153–161.
- [33] P. Crespi, A. Franchi, N. Giordano, M. Scamardo, P. Ronca, Structural analysis of stone masonry columns of the basilica s. maria di collemaggio, *Engineering structures* 129 (2016) 81–90.
- [34] V. Arcidiacono, G. P. Cimellaro, J. A. Ochsendorf, Analysis of the failure mechanisms of the basilica of santa maria di collemaggio during 2009 l'aquila earthquake, *Engineering Structures* 99 (2015) 502–516.
- [35] E. Antonacci, V. Gattulli, A. Martinelli, F. Vestroni, Il crollo del transetto della basilica di collemaggio: analisi di vulnerabilità e meccanismo di collasso, in: *Atti del workshop: Sicurezza e conservazione dei beni culturali colpiti da sisma: Strategie e tecniche di ricostruzione ad un anno dal terremoto abruzzese*, 2010, pp. 8–9.
- [36] S. Casolo, S. Neumair, M. A. Parisi, V. Petrini, Analysis of seismic damage patterns in old masonry church facades, *Earthquake Spectra* 16 (4) (2000) 757–773.
- [37] P. B. Lourenço, Computations on historic masonry structures, *Progress in Structural Engineering and Materials* 4 (3) (2002) 301–319.
- [38] P. B. Lourenço, N. Mendes, L. F. Ramos, D. V. Oliveira, Analysis of masonry structures without box behavior, *International Journal of Architectural Heritage* 5 (4-5) (2011) 369–382.
- [39] L. F. Ramos, L. Marques, P. B. Lourenço, G. De Roeck, A. Campos-Costa, J. Roque, Monitoring historical masonry structures with operational modal analysis: two case studies, *Mechanical systems and signal processing* 24 (5) (2010) 1291–1305.
- [40] S. W. Doebling, C. R. Farrar, M. B. Prime, D. W. Shevitz, Damage identification and health monitoring of structural and mechanical systems from changes in their vibration characteristics: a literature review, Tech. rep., Los Alamos National Lab., NM (United States) (1996).
- [41] C. Farrar, S. Doebling, Damage detection and evaluation ii, in: *Modal analysis and testing*, Springer, 1999, pp. 345–378.
- [42] S. W. Doebling, C. R. Farrar, M. B. Prime, et al., A summary review of vibration-based damage identification methods, *Shock and vibration digest* 30 (2) (1998) 91–105.
- [43] S. Choi, S. Park, N. Stubbs, Nondestructive damage detection in structures using changes in compliance, *International Journal of Solids and Structures* 42 (15) (2005) 4494–4513.

- [44] O. Salawu, Detection of structural damage through changes in frequency: a review, *Engineering structures* 19 (9) (1997) 718–723.
- [45] P. C. Chang, A. Flatau, S. Liu, Health monitoring of civil infrastructure, *Structural health monitoring* 2 (3) (2003) 257–267.
- [46] D. Montalvao, N. M. M. Maia, A. M. R. Ribeiro, A review of vibration-based structural health monitoring with special emphasis on composite materials, *Shock and vibration digest* 38 (4) (2006) 295–324.
- [47] B. Peeters, System identification and damage detection in civil engineering.
- [48] L. F. Ramos, Damage identification on masonry structures based on vibration signatures, Ph.D. thesis (2007).
- [49] M. Basseville, L. Mevel, M. Goursat, Statistical model-based damage detection and localization: subspace-based residuals and damage-to-noise sensitivity ratios, *Journal of sound and vibration* 275 (3-5) (2004) 769–794.
- [50] C. Fritzen, G. Mengelkamp, A. Guemes, Elimination of temperature effects on damage detection within a smart structure concept, *Structural Health Monitoring* (2003) 15–17.
- [51] A. Gelman, H. S. Stern, J. B. Carlin, D. B. Dunson, A. Vehtari, D. B. Rubin, *Bayesian data analysis*, Chapman and Hall/CRC, 2013.
- [52] A. Extractor, *Structural vibration solutions*, Aalborg, Denmark.
- [53] B. Peeters, G. De Roeck, Reference-based stochastic subspace identification for output-only modal analysis, *Mechanical systems and signal processing* 13 (6) (1999) 855–878.
- [54] B. Peeters, G. De Roeck, Stochastic system identification for operational modal analysis: a review, *Journal of Dynamic Systems, Measurement, and Control* 123 (4) (2001) 659–667.
- [55] J. Brownjohn, F. Magalhaes, E. Caetano, A. Cunha, Ambient vibration re-testing and operational modal analysis of the humber bridge, *Engineering Structures* 32 (8) (2010) 2003–2018.

TRANSPARENT SENSORY FIBER-REINFORCED COMPOSITES

YAVUZ CAYDAMLI^{*†}, SABINE FRICK[†], MICHAEL R. BUCHMEISER^{*†}

^{*} Institute of Polymer Chemistry (IPOC)

Chair of Macromolecular Compounds and Fiber Chemistry

University of Stuttgart

Pfaffenwaldring 55, D-70569 Stuttgart

e-mail: michael.buchmeiser@ipoc.uni-stuttgart.de, <https://www.ipoc.uni-stuttgart.de/msf/index.html>

[†] German Institutes of Textile and Fiber Research (DITF)

Institute of Textile Chemistry and Chemical Fibers (ITCF)

Koerschtalstr. 26, D-73770 Denkendorf

Keywords: Optical transparency, Fiber-reinforcement, Sensor application, Polymer composites, Façade element.

Abstract. Transparent fiber-reinforced polymer composites are designed for high mechanical and sensory performance. In this study, it was aimed to elaborate optically transparent glass fiber-reinforced polymer composites as building components in futuristic architecture. E-glass fabric was used as fiber reinforcement. The polymeric matrix, which was designed to have the same refractive index value with glass fibers, was synthesized from a calculated ratio of styrene and methyl methacrylate comonomers and was used as the polymeric matrix of optically transparent fiber-reinforced composites with strain sensing capabilities. The synthesized polymer was first melt-pressed into a film structure; then two sheets of these films and glass fabric were melt-pressed together in a sandwich manner. Poly(ethylenedioxythiophene-poly(styrenesulfonic acid) (PEDOT:PSS) was used as conductive material. It was printed onto the finished composite, i.e. onto the surface of the polymer matrix. By matching the refractive index values of the thermoplastic matrix with those of the glass fabric and by using PEDOT:PSS, optically transparent polymer-based fiber-reinforced composite for sensory application were produced.

1 INTRODUCTION

A transparent composite with fiber reinforcement is a long-term studied topic. Firstly, one needs to understand how optical transparency can be obtained. The matrix material of the composite has to be either non-crystalline or the largest crystal of that material must be smaller than the wavelength of visible light. The reinforcement material of the composite (particles and fibers) should have exactly the same refractive index value than the matrix component. This way, the light will not be further refracted when passing through the reinforcement material. Another way to have fully transparent fiber-reinforced polymeric

composites is to have fiber diameter smaller than the wavelength of the visible light.[1] When the nano-additive is smaller than one-tenth of the wavelength of light, it cannot scatter the light and will be optically transparent though the additive is semi-crystalline.[2]

Transparent fiber-reinforced polymer composites are designed for high mechanical and thermal performance while having the optical transparency required for various applications. Generally, polymer composites are supposed to have a strength/weight ratio advantage compared to silica glass. Application candidates for transparent composites: high-impact resistance windshields [3], lightweight armor[3], opto-electronics[4-6], antibacterial[7], UV-protection[8], fire retardancy[9]

Fiber-reinforcement does not only give mechanical strength or toughness but also allows for an adjustment of the direction of the enforcement taking advantage of the anisotropy of the fibers. Anisotropy is the most important difference between fiber reinforcement compared to small particle improvements. Thus, self-reinforced poly(ethylene terephthalate) (PET) composites have a translucent structure with an elevated impact toughness due to anisotropy coming from the PET fibers.[10]

Decreasing the coefficient of thermal expansion is a major issue for polymer composites. Compared to inorganic materials like glass, polymeric materials have larger coefficients which make them thermally unstable for critical applications. Thus, glass fiber-reinforced composites need to be tested in terms of CTE performance as well. By using the difference in CTE, it is possible to design adaptive engineering materials, which are transparent in a temperature interval and opaque or translucent beyond that adjusted interval.

So far, major approaches to achieve this aim entailed, e.g., either the blending of a polymer matrix with small molecules or particles, which can tune the overall refractive index of the polymer matrix, the grafting of small molecules onto a polymer chain.[11] Krug et al. produced S-glass mat-reinforced epoxy composites. In order to match the refractive indices of the components, epoxy resin was mixed with epoxy-functionalized polyhedral oligomeric silsesquioxanes (POSS) molecules. [12] POSS molecules with a wide variety of functional groups can be tuned to match the targeted RI values. [13]

Velez et al. matched epoxy resin's refractive index with soda-lime glass ribbon and tested these composites with impact tests simulating bird crushes at the aircraft industry.[3, 14] Kagawa et al. blended a commercial epoxy resin with glass particles in order to adjust/decrease the coefficient of thermal expansion (CTE) while maintaining the transparency of the resin.[15]

As mentioned, when nanoparticles or nanofibers are used, they cannot scatter the light and will be inert in terms of refractive index matching. The critical issue is the possible agglomeration issues of these particles/fibers so they might start scattering the light. For such kind of nanocomposites, bacterial cellulose (BC) nanofibers based composites are important examples: They can have optical transparency due to nanometer size diameters of the fibers.[2, 16] Though the fibers are semi-crystalline and though they have distinctly different refractive index values[2] compared to the polymer matrix of the composite, fibers cannot reflect the light since they are smaller than the wavelength of the visible light.[2, 16-18] Also BC nanocomposites reduced the temperature-based refractive index change with the different polymer matrix.[18] Besides the mechanical and optical advantages, BC nanocomposites have low CTE.[2, 16] Nogi et al. acetylated BC nanofibers in order to reduce their hygroscopicity for optoelectronics applications, and showed that the high transparency, low CTE, but also

reduced hygroscopicity can be managed in a BC composite.[16] The same group tried various degree of substitution (DS) in terms of acetylation of BC and found the optimum level for high transparency, low CTE, low hygroscopicity, and lower refractive index.[19] Optimum wt. % of the BC nanofibers was decided in terms of their reduction in light transmittance and performance to decrease CTE.[20] By using 7.4 wt. % of BC nanofibers, composites lost only 2.4% in light transmittance, while CTE was successfully reduced for 56%.[20] Like bacterial cellulose attempts, nanofibers were produced by grinding wood pulp fibers, and their nanocomposites can be optically transparent even with 70 wt. % fiber content.[17, 21] Nanofibers made out of wood pulp fibers were effective to decrease the composites' coefficient of thermal expansion as well.[17, 21] As an alternative production way, transparent acrylic resins were deposited on to cellulose nanofiber sheet and independent from the difference in refractive indices transparency of the composites were achieved.[22]

For PMMA, at room temperature, relative humidity is in correlation with the refractive index.[23] Generally, an increase in temperature decreases the refractive index value of the polymers drastically.[23, 24] PMMA was reinforced with borosilicate glass fiber as they are matching in refractive index.[25-27] Besides mechanical evaluations[25], a strong dependence of refractive index on temperature changes[26, 27] was shown. Recently, Keaney et al. showed the optimum amount of fillers in a PMMA composite in order to have a high level of transparency.[28]

Optically transparent fiber-reinforced composites were made not only by using polymeric material. Iba et al. produced oxynitride glass fiber composites by hot-pressing different types of glass powders as matrix material.[29] Nanofibers made out of chrysolite, a natural mineral, had also 85% transparency when the refractive index of the resin is matched.[30, 31] Like other nanofibers or nanostructures [17, 32, 33], carbon nanotube-based composites showed also a high level of transparency.[34] Aloui et al. defined how the refractive index of the matrix polymer changes during photopolymerization.[35] As the conversion of monomers goes on, the material transforms from liquid to sol-gel, and eventually to solid state (glassy). Until it gets solidified refractive index increase, and thermo-optic coefficient decrease so its refractive index value gets more stable upon changes in temperature.[35]

In this study, it was aimed to elaborate optically transparent glass fiber-reinforced polymer composites as a building component of a futuristic architecture project. Also, an optically transparent fiber-reinforced material with sensory properties was to be realized.

2 MATERIALS AND METHODS

Styrene and methyl methacrylate monomers were purchased from Merck Millipore, Germany in order to synthesize the polymer matrix of the composites. Glass fabric (HexForce – 02116) was purchased from Hexcel Corporation, France. Its weight was 106 g/m² and plain-woven.

2.1. Polymer Synthesis

The polymer matrix of this study was synthesized by free radical copolymerization of styrene (100-42-5) and methyl methacrylate (80-62-6) and used after distillation to remove stabilizers. Azobisisobutyronitrile (AIBN) (Sigma Aldrich, 78-67-1) was used after recrystallization in methanol. The styrene/methyl methacrylate ratio was 51.15 – 48.85 wt.% and the AIBN amount was 0.1 mol% with respect to all monomers. Polymerization was accomplished in an ultrasonic bath at 80°C within 24 h.

2.2. Foil Production via Melt pressing

Polymer synthesis was done in reaction tubes. Due to the N₂ formation, a lot of bubbles were trapped in the polymer bars. After removing the reaction tubes, those bars were melt-pressed by using a Meyer press (Herbert Meyer GmbH, Germany) operated at 200°C and 6 bar for 20 minutes. As a result of this process, flat polymer foils without bubbles were produced. After individual polymer bars were transformed into the films, glass fabric was placed between two layers of those films and pressed together again at 200°C and 6 bars for 20 minutes. Just before this process, glass fabric was immersed into the styrene monomer to increase the affinity between the fabric surface and the copolymer. Since the surface morphology is critical to adjust the highest level of transparency, we decided to use polyimide (PI) foil purchased from Haufler GmbH, Germany. Generally, the surface that touches to the composite surface must be absolutely flat, have low thermal expansion constant, high thermal stability, and low affinity to the composite material. With high surface roughness, we can lose the light transmittance of a %100 non-crystalline material due to the light scattering of those surface features.

2.3. Screen Printing of PEDOT: PSS

In order to gain sensory properties, PEDOT:PSS (Clevios SV3; Heraeus Epurio, Germany) was applied to the composite surface via screen printing tools (Johannes Zimmer GmbH, Austria). For both pure polymer film, and to the final composite with fabric support 1 and 20 layers of printing was applied to observe the possible change in the electrical conductivity and also light transmittance.

2.4. Electrical Resistance Measurement

Four-point surface resistivity tests were accomplished using Fluke 8846A Multimeter (Fluke Corporation, USA)

2.5. Mechanical Tests

The tensile properties of the polymer film, glass fabric, and the fiber-reinforced composites were evaluated using a Zwick/Roell (Zwick Universal Typ 144503). The grip-to-grip distance was 5 cm. The width of all specimens was 3 cm and test speed was set as 5 mm/min. Each material was tested at least five times.

2.6. Refractive Index Measurement

The refractive index of the polymer film was measured with the aid of an Abbe Mark III refractometer (Reichert Analytical Instruments, USA). The refractive index of the glass fabric was evaluated using the standard refractive index liquids (Cargille Laboratories, USA) and Becke Line test was done under the optical microscope (Zeiss AG, Germany).

2.7. Transmission Intensity Measurement

The transparency level of the composites was evaluated by RC2 Ellipsometer (J.A. Woollam Co., Inc., USA) between the wavelengths of 210 – 1690 nm at normal incidence in a transmission configuration. In addition, Mueller matrix measurements were performed, in order to check the isotropy of the samples. The Mueller matrices showed no amplitude in the off-diagonal elements, which justifies the isotropy of the samples.

3 RESULTS AND DISCUSSION

Synthesized copolymer bars were successfully melt-pressed and films with smooth surface were produced (see Figure 1-a). Their average refractive index was 1.55, which perfectly matched the refractive index of the E-glass. The refractive index of the glass fabric was found to be ≈ 1.552 . Besides matching the refractive indices of two materials accurately, surface adhesion of the polymer to the glass is critical as well. If there is no good level of adhesion then air gaps might form at the interface of those materials and optical transparency will be impossible as the refractive index of the air is 1.0003. In fact, we observed this phenomenon, too. In order to overcome that, glass fabric was immersed into styrene monomer (refractive index 1.5471) just before the final melt-pressing it between two sheets of the polymer film. This step enhanced the adhesion, so overall the optical transparency of the composite (see Figure 1-b).



Figure 1: Materials of this study in front of the logo: (a) Pure poly(styrene)-*co*-poly(methyl methacrylate)-based polymer film, (b) polymer matrix with glass fabric, (c) only glass fabric, (d) polymer printed with single layer PEDOT:PSS, (e) polymer overprinted with 20 layers of PEDOT:PSS.

Tensile test results (see Figure 2 and Table 1) showed that the glass fabric almost doubled the tensile strain and significantly reduced the modulus of the polymer film. Both aspects are positive for the final application as a sensory material. In the final composites, the average glass fabric ratio to the polymer matrix was ≈ 29 wt.%.

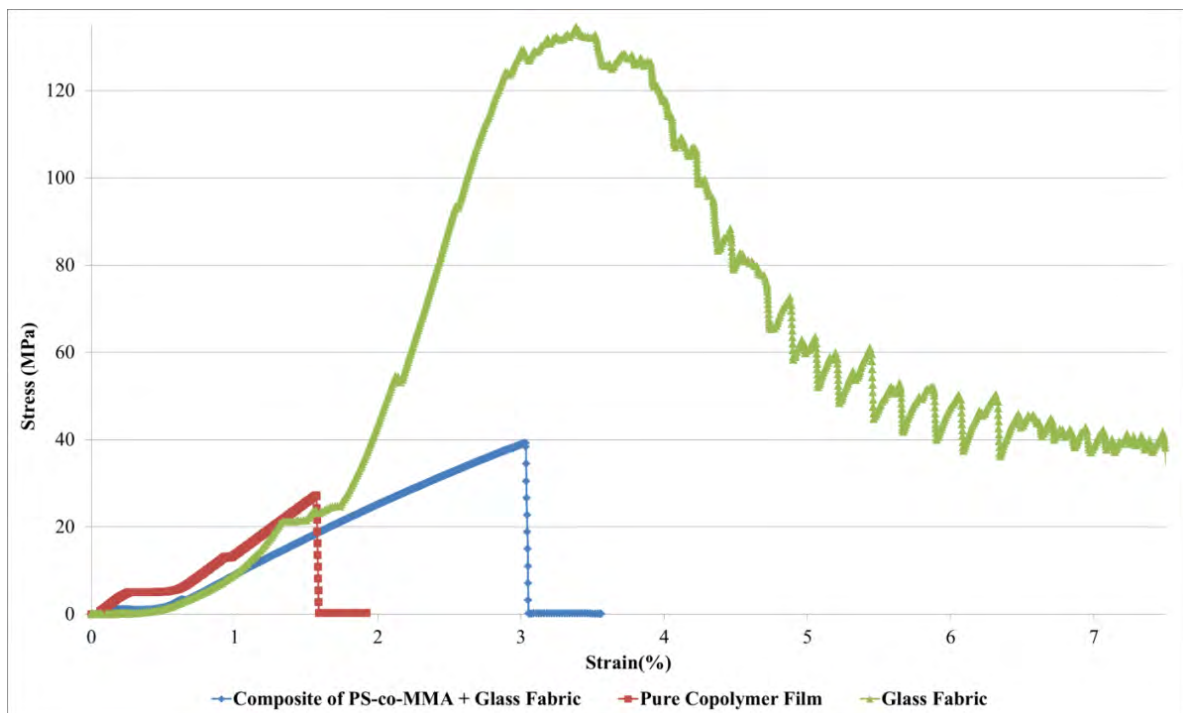


Figure 2: Comparison of the tensile tests, representative strain-stress diagrams of the composite and its components

Table 1: Summary of tensile test results.

	Composite	Copolymer Film	Glass Fabric
E_{mod} (GPa)	0.202 ± 0.08	1.847 ± 0.289	0.455 ± 0.015
Strain% at largest Stress	2.7±0.3	1.8±0.3	3.33±0.3
Maximum Stress (MPa)	44.2±6.2	27.1±3.7	124.1±4.9

Figure 3 displays the transmitted light intensity percentage through the materials. This is the ratio of the directly transmitted light, which was neither absorbed, reflected or refracted by the material components. It is obvious that glass fabric in the composite causes an important level of refraction. Screen printing of PEDOT:PSS causes less loss in transmission of light than the glass fabric, however, it is worth mentioning that PEDOT:PSS layers do allow infrared (IR) light to pass through the material when it is overprinted twenty times. In Figure 4, we compare the overprinting effect of PEDOT:PSS. It is clear that a single-layer of printing does not cause a big loss in transparency. Also, the response to infrared cannot be seen anymore. The maximum number of overprinted layers of PEDOT:PSS to fully block IR transmission are currently under investigation.

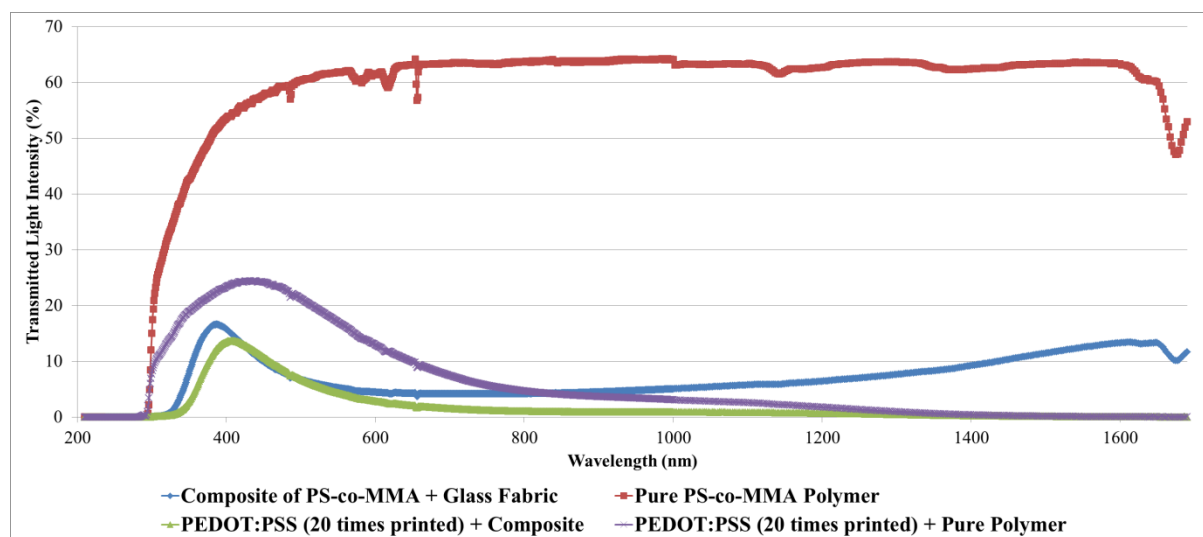


Figure 3: Comparison of the percentage of transmitted light intensity illustrating the effect of PEDOT:PSS printing and fabric composites.

It is important to discuss the electrical resistance values of the samples with PEDOT:PSS. Samples with single-layer printing have an average surface resistance of $\approx 240\text{k}\Omega/\text{sq}$, while it reduces to $\approx 150\text{k}\Omega/\text{sq}$ when PEDOT:PSS was overprinted 20 times. Considering the big loss in transmitted light intensity (See Figure 4), single layer printing is a better option since overprinting PEDOT:PSS does not provide a big advantage in the electrical conductivity but a relatively big loss in the transmitted light intensity.

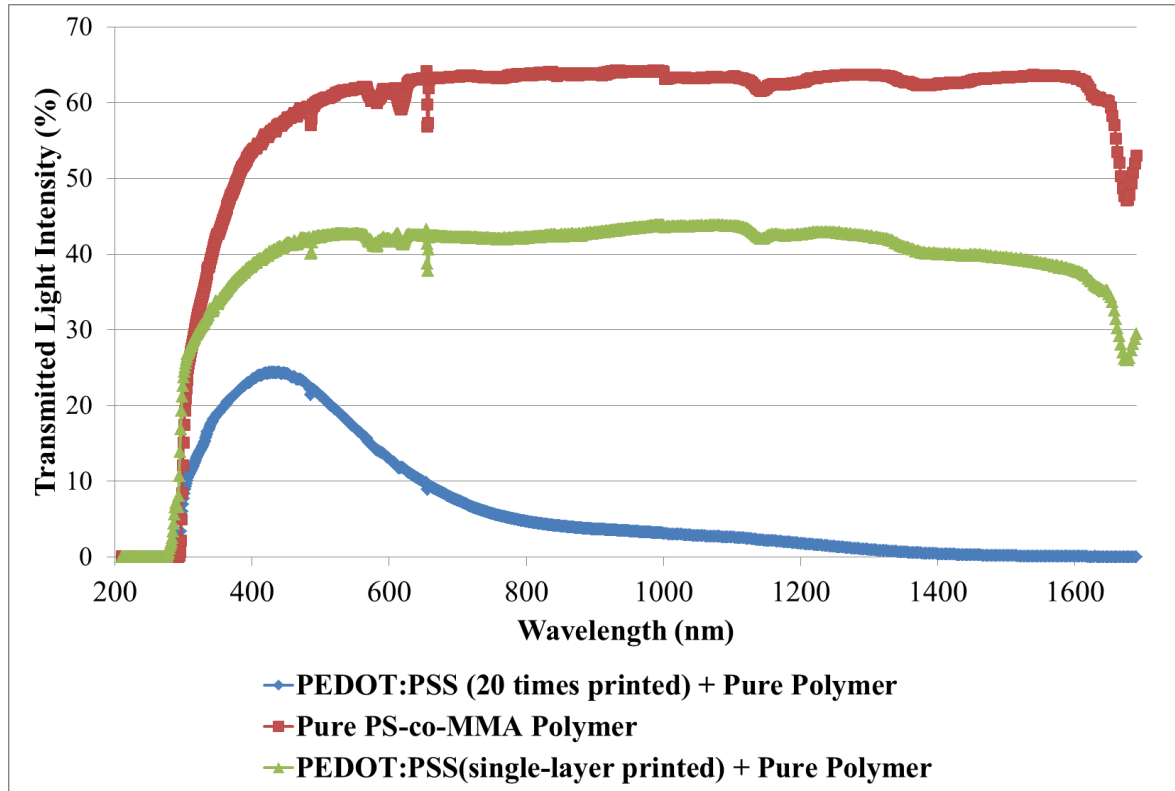


Figure 4: Comparison of transmitted light intensity (%) values between different times overprinted composites of PEDOT:PSS

4 CONCLUSIONS

In this study, optically transparent glass fiber-reinforced polymer composites as a building component of a futuristic architecture project were produced. The glass fabric ratio to the polymer matrix was ≈ 29 wt.%. Optimized products might be developed in terms of transmitted light intensity in case the refractive indices match perfectly to the fourth digit after the decimal point. Another alternative might be changing the surface chemistry of the glass fabric to increase the adhesion of the polymer matrix to the fiber. The performance of PEDOT:PSS, both in terms of changing the surface resistance and to light-transmittance was evaluated. It is concluded that single layer printing of PEDOT:PSS is good enough to test it in the final sensory applications. As the final step, these materials will be tested for the optimum sensory applications.

REFERENCES

- [1] Bergshoef, M.M. and G.J. Vancso, Transparent nanocomposites with ultrathin, electrospun nylon-4, 6 fiber reinforcement. *Adv. Mater.* (1999) **11**: 1362-1365.
- [2] Yano, H.; Sugiyama, J.; Nakagaito, A. N.; Nogi, M.; Matsuura, T.; Hikita, M.; Handa, K. Optically Transparent Composites Reinforced with Networks of Bacterial Nanofibers. *Adv. Mater.* (2005) **17**:153-155.
- [3] Velez, M.; Braisted, W. R.; Frank, G. J.; Phillips, P. L.; Day, D. E.; McLaughlin, M. D. Impact strength of optically transparent glass ribbon composites. *Journal of Composite Materials* (2011) **46**:1677-1695.
- [4] Beecroft, L. L.; Ober, C. K. Nanocomposite materials for optical applications. *Chemistry of materials* (1997) **9**:1302-1317.
- [5] Li, S.; Meng Lin, M.; Toprak, M. S.; Kim, D. K.; Muhammed, M. Nanocomposites of polymer and inorganic nanoparticles for optical and magnetic applications. *Nano reviews* (2010) **1**:5214.
- [6] Tsai, C.-L.; Yen, H.-J.; Liou, G.-S. Highly transparent polyimide hybrids for optoelectronic applications. *Reactive and Functional Polymers* (2016) **108**:2-30.
- [7] Mallakpour, S.; Behranvand, V. Nanocomposites based on biosafe nano ZnO and different polymeric matrixes for antibacterial, optical, thermal and mechanical applications. *European Polymer Journal* (2016) **84**:377-403.
- [8] Faure, B.; Salazar-Alvarez, G.; Ahniyaz, A.; Villaluenga, I.; Berriozabal, G.; De Miguel, Y. R.; Bergström, L. Dispersion and surface functionalization of oxide nanoparticles for transparent photocatalytic and UV-protecting coatings and sunscreens. *Science and technology of advanced materials* (2013) **14**:023001.
- [9] Vahabi, H.; Eterradosi, O.; Ferry, L.; Longuet, C.; Sonnier, R.; Lopez-Cuesta, J.-M. Polycarbonate nanocomposite with improved fire behavior, physical and psychophysical transparency. *European Polymer Journal* (2013) **49**:319-327.
- [10] Rojanapitayakorn, P.; Mather, P. T.; Goldberg, A. J.; Weiss, R. A. Optically transparent self-reinforced poly(ethylene terephthalate) composites: molecular orientation and mechanical properties. *Polymer* (2005) **46**:761-773.
- [11] Loste, J.; Lopez-Cuesta, J.-M.; Billon, L.; Garay, H.; Save, M. Transparent polymer nanocomposites: An overview on their synthesis and advanced properties. *Progress in Polymer Science* (2019) **89**:133-158.
- [12] Krug III, D. J.; Asuncion, M. Z.; Popova, V.; Laine, R. M. Transparent fiber glass reinforced composites. *Composites Science and Technology* (2013) **77**:95-100.
- [13] Asuncion, M. Z. K. I., D.J., Abu-Seir, H.W., Laine, R.M. Facile thiol-ene reactions of vinyl T10/T12 silsesquioxanes for controlled refractive indices for transparent fiber glass reinforced composites. *Journal of the Ceramic Society of Japan* (2015) **123**:725-731.
- [14] Velez, M.; Schuman, T. P.; Day, D. E. Optical properties of optically transparent glass-ribbon composites. *Journal of Composite Materials* (2013) **48**:3747-3754.
- [15] Kagawa, Y.; Iba, H.; Tanaka, M.; Sato, H.; Chang, T. Fabrication and optical/thermal properties of glass particle-epoxy optically transparent composites. *Acta Mater.* (1998) **46**:265-271.

- [16] Nogi, M.; Abe, K.; Handa, K.; Nakatsubo, F.; Ifuku, S.; Yano, H. Property enhancement of optically transparent bionanofiber composites by acetylation. *Applied Physics Letters* (2006) **89**:233123.
- [17] Iwamoto, S.; Nakagaito, A. N.; Yano, H.; Nogi, M. Optically transparent composites reinforced with plant fiber-based nanofibers. *Applied Physics A* (2005) **81**:1109-1112.
- [18] Nogi, M.; Handa, K.; Nakagaito, A. N.; Yano, H. Optically transparent bionanofiber composites with low sensitivity to refractive index of the polymer matrix. *Applied Physics Letters* (2005) **87**:243110.
- [19] Ifuku, S.; Nogi, M.; Abe, K.; Handa, K.; Nakatsubo, F.; Yano, H. Surface modification of bacterial cellulose nanofibers for property enhancement of optically transparent composites: dependence on acetyl-group DS. *Biomacromolecules* (2007) **8**:1973-1978.
- [20] Nogi, M.; Ifuku, S.; Abe, K.; Handa, K.; Nakagaito, A. N.; Yano, H. Fiber-content dependency of the optical transparency and thermal expansion of bacterial nanofiber reinforced composites. *Applied Physics Letters* (2006) **88**:133124.
- [21] Iwamoto, S.; Nakagaito, A. N.; Yano, H. Nano-fibrillation of pulp fibers for the processing of transparent nanocomposites. *Applied Physics A* (2007) **89**:461-466.
- [22] Nogi, M.; Yano, H. Optically transparent nanofiber sheets by deposition of transparent materials: A concept for a roll-to-roll processing. *Applied Physics Letters* (2009) **94**:233117.
- [23] Watanabe, T.; Ooba, N.; Hida, Y.; Hikita, M. Influence of humidity on refractive index of polymers for optical waveguide and its temperature dependence. *Applied Physics Letters* (1998) **72**:1533-1535.
- [24] Roy M. Waxler, D. H., and Albert Feldman. Optical and physical parameters of Plexiglas 55 and Lexan. *Applied Optics* (1979) **18**:101-104.
- [25] Olson, J. R.; Day, D. E.; Stoffer, J. O. Fabrication and Mechanical properties of an optically transparent glass fiber-polymer matrix composite. *Journal of Composite Materials* (1992) **26**:1881-1192.
- [26] Lin, H.; Day, D. E.; Stoffer, J. O. Optical and mechanical properties of optically transparent poly(methyl methacrylate) composites. *Polymer Engineering and Science* (1992) **32**:344-350.
- [27] Lin, H.; Day, D. E.; Stoffer, J. O. Aging behavior of optically transparent poly (methyl methacrylate) composites. *Polymer Composites* (1993) **14**:402-409.
- [28] Keaney, E.; Shearer, J.; Panwar, A.; Mead, J. Refractive index matching for high light transmission composite systems. *Journal of Composite Materials* (2018) **52**:3299-3307.
- [29] Iba, H.; Chang, T.; Kagawa, Y.; Minakuchi, H.; Kanamaru, K. Fabrication of Optically Transparent Short-Fiber-Reinforced Glass Matrix Composites. *J. Am. Ceram. Soc.* (1996) **79**:881-884.
- [30] Liu, K.; Zhu, B.; Feng, Q.; Duan, T. Novel transparent and flexible nanocomposite film prepared from chrysotile nanofibres. *Materials Chemistry and Physics* (2013) **142**:412-419.
- [31] Liu, K.; Zhu, B.; Duan, T.; Du, C.; Tan, Y.; Sheng, S. Transparency of chrysotile nanofiber-reinforced nanocomposite films: Effect of Rayleigh scattering. *Composites Science and Technology* (2015) **119**:68-74.

- [32] Yamamoto, K.; Otsuka, H.; Wada, S.-I.; Sohn, D.; Takahara, A. Transparent polymer nanohybrid prepared by in situ synthesis of aluminosilicate nanofibers in poly (vinyl alcohol) solution. *Soft Matter* (2005) **1**:372-377.
- [33] Kumar, A. K.; Jiang, J.; Bae, C. W.; Seo, D. M.; Piao, L.; Kim, S.-H. Silver nanowire/polyaniline composite transparent electrode with improved surface properties. *Materials Research Bulletin* (2014) **57**:52-57.
- [34] Havel, M.; Behler, K.; Korneva, G.; Gogotsi, Y. Transparent Thin Films of Multiwalled Carbon Nanotubes Self-Assembled on Polyamide 11 Nanofibers. *Advanced Functional Materials* (2008) **18**:2322-2327.
- [35] Aloui, F.; Lecamp, L.; Lebaudy, P.; Burel, F. Photopolymerization of an Epoxy Resin: Conversion and Temperature Dependence of its Refractive Index. *Macromolecular Chemistry and Physics* (2016) **217**:2063-2067.

VARIABLE STIFFNESS SYSTEM BASED ON RHEOLOGY PROPERTIES OF SHEAR THICKENING FLUID

HEIMIR TRYGGVASON^{*}, FELIX STARKER[†], CHRISTOPHE LECOMTE[†] AND
FJOLA JONSDOTTIR^{*}

^{*} School of Engineering and Natural Sciences,
University of Iceland
107 Reykjavik, Iceland
e-mail: fj@hi.is

[†] Össur
Grjóthálsi 5
110 Reykjavik, Iceland
email: clecomte@ossur.com

Key words: Discontinuous Shear Thickening, Variable Stiffness, Non-linear damping, Force response system.

Abstract. The unique rheological properties of discontinuous shear thickening fluids (STF) have been employed in various engineering applications in recent years. In a commercial aspect, this has most notably been body armor and protective equipment, but also specialized smart structures in damping and force-coupling applications. The topic of this work is the application of STF in a translational element for an articulating prosthetic foot. Connected in series and parallel to a spring system, the element can be used to affect the force transfer within the system and thereby influence the stiffness of the prosthetic foot dynamically over the gait cycle. The device described in this work is a STF filled piston/cylinder design. The objective is a velocity dependent force response over the translational motion. Ranging from dampened, compliant deflection at low velocity, to efficient force transfer (coupling) for energy storage and return in the spring system at higher speed. The rapid viscosity increase in the STF at a critical shear rate is used to produce a stepwise force response, thereby enabling adaptive response of the foot for different walking speeds and other various tasks, such as standing up from a seated position. The adaptive response results in a greater range of motion with easier rollover through stance phase for slow movement without sacrificing the energy return needed in faster walking.

1 INTRODUCTION

Modern passive prosthetic feet can be described mechanically as efficient and designated spring systems. The force reaction to deflection, follows a fixed curve that is aimed at imitating as closely as possible the reaction of the biological foot through the gait cycle [1]. Passive or controlled damping is also added in some models [2] and most standard prosthetic feet are used with a visco-elastic cover, that provides additional damping. It has been demonstrated that different tasks and conditions in ambulation would benefit from varying stiffness of the foot [3–5]. The aim of this research is to design a device that will provide variable stiffness to the spring system as a function of speed. Previous work has indicated that the stiffness of a certain model of a prosthetic foot can be changed dynamically with a non-linear, speed-dependent damping element [6]. The purpose of the element described in this work, is to provide a compliant, dampened force reaction at slow speeds. Then, at a certain speed of translational displacement of the element, the damping should increase rapidly, approaching force coupling function. The element is to be connected in parallel and series to the springs in the system so that, as the function changes from damping to coupling, the stiffness of the overall system changes. It is hypothesized here that the unique properties of shear thickening fluids (STFs) can be utilized to realize this element. Concentrated suspensions of solid particles are known to show a non-Newtonian change in viscosity with changing shear rate. The sharp increase in viscosity of several orders of magnitude, or discontinuous shear thickening (DST), observed in a jamming effect in certain colloidal suspensions [7] is of particular interest. The aim is to employ this property for the change of function from damping to coupling. The challenge is to design the device so that the speed at which the function changes can be adapted. Analysis of the application has revealed specific speeds at which the reaction forces are required to increase. The required force value requirements of the element have also been mapped.

STFs have been commercially utilized in a number of applications and are actively being researched [8,9]. One commercialized field of use is impact protection for various applications, e.g. personal protective equipment and protectors for sensitive devices [10,11]. Of similar category is the embedment of STF in textile, e.g. for puncture resistance of body-armor [12,13]. The use of STFs for damping in structures has also been a research topic. Guo et al. [14] used STF to dampen flange connections on pipe assemblies and Yeh et al. [15] proposed a STF filled piston damper designed for earthquake protection of buildings. Furthermore, Zhang et al. [16] and Zhou et al. [17] designed and built STF filled piston dampers. Devices working on the principles of STF properties have also been proposed in torque brakes [18].

The design proposed here is a linear piston damper, comparable to the ones referenced above but with the objective being, transition from damping to force coupling and control of the speed at which the transition occurs. The gap, between piston and cylinder in the damper, serves as the orifice. The dimension of the gap is varied to affect the reacting force as a function of velocity. Our results show that the forces realized in the prototype damper fulfill the requirements. The DST effect is apparent in the tests, but further modifications are required to the damper to obtain control of the transition speed. Testing of varying STF properties shows that reaction forces drop with reducing DST effect and that critical shear rate has little effect on transition speed of the damper.

2 METHODS

2.1 System characterization

The prosthetic foot model studied is a system of serial and parallel connected leaf springs, articulating around a pivot point. The design change involves replacing a rigid mechanical link with the adaptive STF damper and a serial connected spring. The effect is a more compliant pivoting movement, as a new translational joint is introduced in the system. Figure 1 shows schematically the functions as intended for speed dependent stiffness. At low velocity movement over the element, a dampened deflection will render a more compliant force reaction of the whole system. As the velocity of movement over the element reaches a critical value that translates to the DST of the STF, and particle jamming occurs, the piston will couple the force over the element. The intention is that this coupling will make the whole system response approach the effect of the original rigid link. The force in the element is compressive at heel strike and rolls over to extension as the weight is moved over the foot in roll over in the step.

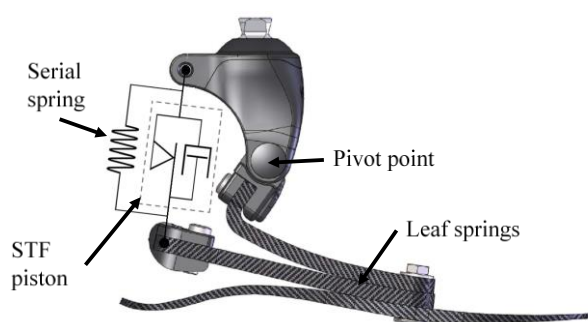


Figure 1: Schematic of a speed dependent stiffness system, connected in prosthetic foot model, replacing a rigid mechanical link.

The parameters of the design goals of the STF damper are determined by the results from simulation of the prosthetic foot system [6]. The compliant dampening forces prior to DST should be minimized while the coupling force after DST should exceed 2 kN. The critical shear rate of the fluid should translate to a speed of 5-8 mm/s linear movement of the piston. This critical speed should be adjustable to adapt the device to different users. This initial study aims at characterizing the piston design to approach these values.

2.2 Fluid properties

The STF material used is a commercially available suspension of silica particles in polyethylene glycol (STF Technologies, Delaware) [19]. The nominal particle size was determined ~200 nm with a scanning electron microscope. The silica content is not disclosed but stated in data sheet as 50-70 wt.% [20]. The shear thickening properties of the STF can be adjusted by diluting the suspension with carrier fluid. Viscosity of the STF, as stated by the supplier, is shown in figure 2. The dilution of the STF will result in a higher critical shear rate and a lower viscosity. Although it is not indicated in the chart, the viscosity is expected to drop quite rapidly after the maximum value is reached in the DST, as indicated in literature [21]. Measurements of varying gap dimensions are done on undiluted STF. To investigate the effect

of fluid properties, three mixtures are made for testing of diluted STF; 2.5 and 7.5 wt.% diluted.

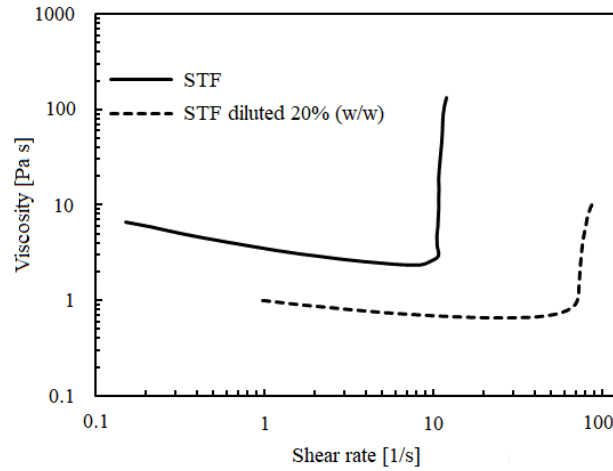


Figure 2: Viscosity of the STF [19].

2.3 Piston damper design

The STF damper design is a symmetric piston damper with an axial piston-rod, eliminating the need for a compensator; see Figure 3. The cylinder and endcaps are made of aluminum alloy but the piston/rod and seal/bearing insert are from stainless steel. Low friction seals and bearings are selected to minimize forces at low velocities. The cylinder inner diameter is 20 mm and the rod diameter is 12 mm. Four piston diameters were prepared; 19.50, 19.36, 19.16 and 18.56 mm. The piston length is $l = 16$ mm. These result in dimensions of the annular gap (orifice) between piston and cylinder, h ; 250, 320, 420 and 720 μm , respectively. The available piston stroke is 13 mm.

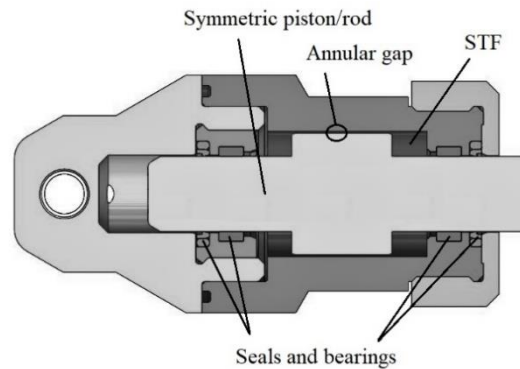


Figure 3: STF damper, section view.

2.4 Orifice flow case

As the piston is displaced forward at a velocity U_p , the piston pushes the STF back through the annular gap orifice. For an analytical model of the flow in the orifice, we consider the combined Couette-Poiseuille (pressurized Couette) flow between moving and fixed, parallel

plates. The velocity profile of the developed flow is a superposition of the linear profile due to the moving plate and the parabolic profile due to the pressure gradient. For all test setups of the piston damper; dimensions, velocity and fluid properties, the Reynold's-number for the orifice flow fulfills, $Re < 1$. Hence, laminar flow through the gap is assumed. Furthermore, it is assumed that for shear rates below the critical shear rate of DST, the flow is fully developed of homogenous properties and that entrance/exit effects can be neglected. Figure 4 shows a schematic representation of the two-dimensional, axis symmetric flow between the piston and cylinder wall.

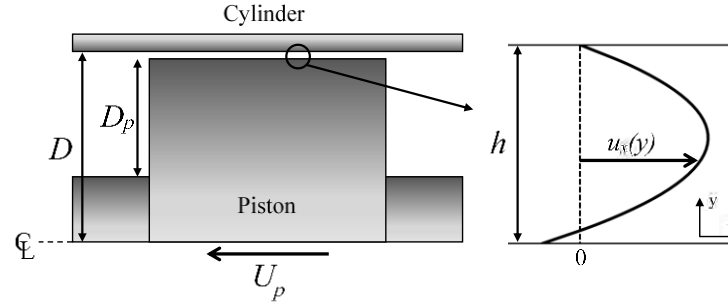


Figure 4: Schematic illustration of the Couette-Poiseuille flow case assumptions for the orifice gap.

The velocity profile $u_x(y)$, derived from the momentum equation and the no-slip boundary conditions, is well known and adapted here from [22]. The first term is due to the flow being driven by the pressure gradient in the x direction, P , and the second due to the wall driven flow,

$$u_x(y) = \frac{P}{2\mu}y(h-y) + U_p \frac{y}{h} \quad \text{where} \quad P = -\frac{dp}{dx} \quad (1)$$

where, μ is fluid viscosity.

The flow through the gap is the integral of the velocity profile over the full gap width. Assuming that the flow is incompressible and continuous, the flow equals the product of pushed area of the piston, D_p , and the piston speed.

$$Q = \int_0^h u_x(y) dy = \frac{Ph^3}{12\mu} + \frac{U_p h}{2} = D_p U_p \quad (2)$$

Solving for P and get,

$$P = \frac{12U_p\mu}{h^3} \left(D_p - \frac{h}{2} \right) \quad (3)$$

The force acting on the piston is a linear function of the pressure gradient, piston length and viscosity, so we can assume the force is dependent of the piston diameter and gap height in the form $F(D_p^2, h^{-3})$.

Of particular interest is the shear rate of the flow and relations to onset of DST.

$$\dot{\gamma}(y) = \frac{du_x}{dy} = \frac{P}{2\mu}(h-2y) + \frac{U_p}{h} \quad (4)$$

It is furthermore assumed that the DST phenomena initiates at the boundaries, ($y = 0$ and y

= h). Evaluating the shear rate for these, yields;

$$\dot{\gamma}(y) \Big|_{y=0}^{y=h} = \pm \frac{6U_p}{h^2} \left(D_p - \frac{h}{2} \right) + \frac{U_p}{h} \quad (5)$$

The onset of shear thickening at the critical shear rate is thus assumed to depend on the pushed area and gap thickness as $\dot{\gamma}(D_p, h^{-2})$. Attention is drawn to the dependency of force and shear rate on the thickness, h . The above indicates that decreasing gap dimension will affect the resulting damper-force more than the shear rate and therefore the velocity at which the DST will occur.

2.5 Force-displacement measurements

The force-displacement of the damper is measured with an electric dynamic testing machine, Instron ElectroPuls E3000 (Instron, Norwood). The control settings are displacement at constant speed. For each test, the piston is displaced for 17 runs at incrementing speeds. For each run the piston is pulled a displacement of 5 mm and then pushed back to the original position. After each displacement and between runs, the instrument is stopped for 1 s to allow the fluid to recover from thickened state. The speed is increased in 1 mm/s increments up to 14 mm/s, and thereafter; 16, 18, 20 mm/s. The displacement is done over the mid-range of the piston stroke length, to avoid end effects.

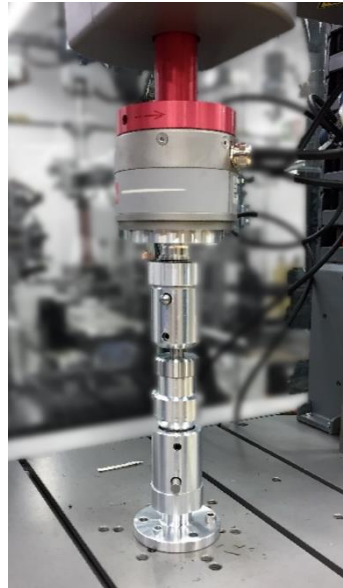


Figure 5: Test setup of the STF damper in an electro pulse dynamic test instrument.

The highly non-linear characteristics of the damper result in an increasing deviation from set velocity value, as the reaction forces increase, as shown in figures 6-8. The data is filtered in steps to clarify the plots. Data for negative direction (push) is filtered out as it is symmetric to the positive direction. Data for the initiation of each run is filtered out in terms of position, so the first 0.4 mm of each stroke are dismissed. Similarly, the last 0.2 mm of each stroke are

discarded. Runs for each set velocity are shown up to where the resulting force starts to increase due to DST. For higher forces, cycles for even number velocities are plotted. For the smaller gap dimensions, the force reaction of runs at higher speed, exceed the load capacity of the test machine, ~ 4 kN, so these are omitted.

3 RESULTS

3.1 Varying gap dimension

Results for different gap dimension of the piston damper are shown in figure 6. An increase in damping force and decrease in critical velocity is seen with decreasing gap dimension. The consecutive curves for runs of each test are plotted in same color (dots). Polynomial regression lines are plotted through the maximum force for each run after DST to capture the general trend.

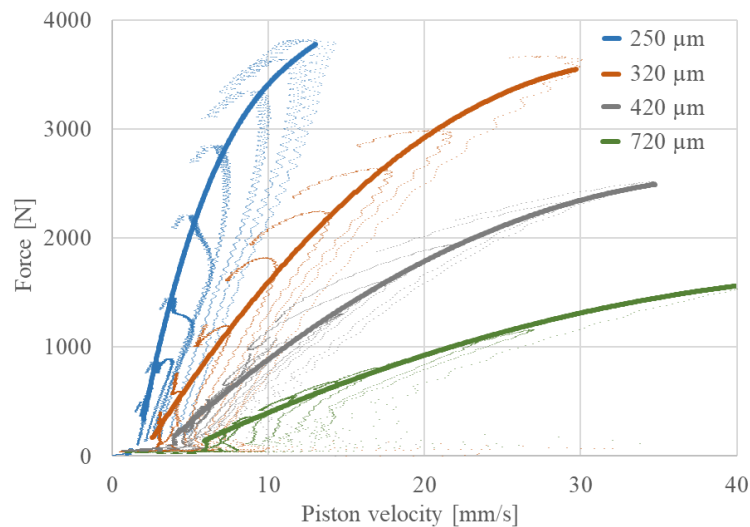


Figure 6: Damping force vs. piston velocity for different gap dimensions. Measured for each run (dots) and regression lines through maximum force for each test.

For the application studied, the 250 and 320 μm gap arrangements generate damping forces that meet the criteria of $F > 2$ kN in the velocity range stated. As detailed further in table 1. The transition for these occur at a piston velocity that is below required values (Section 2.1). Although the control parameters are fixed speed, the step-wise increase in viscosity at the DST results variation from set value and severe overshooting (100%), especially for the 420 and 720 μm gaps. Rapidly decreasing viscosity for shear rate, higher than critical shear rate, could also induce this overshooting. The force for each run, as the piston is accelerated, is lower than the force during deceleration, for same measured velocity. Therefore, each run shows hysteresis curve, indicating a time dependency of the force. Anti-thixotrophy in concentrated suspensions has been described by Mewis et al. [23] as time dependent increase in viscosity under steady shear. Whether this phenomenon is apparent in the above measurements or if this is due to a time effect in the development of the flow through the length of the orifice, is outside the scope of this study. However, this effect is beneficial for the intended application as it generates a more efficient force transfer.

For a closer look at the onset of DST, the data in figure 6 is plotted again as force vs. average fluid velocity in the orifice, calculated from $\bar{u}_x = Q/h$; see figure 7. The data is further filtered out of runs exceeding maximum forces above 600 N. Regression lines are plotted for the data set after DST. The evaluated critical velocities at DST of the measured piston velocity, U_p , and calculated fluid velocity, \bar{u}_x , are further presented in table 1.

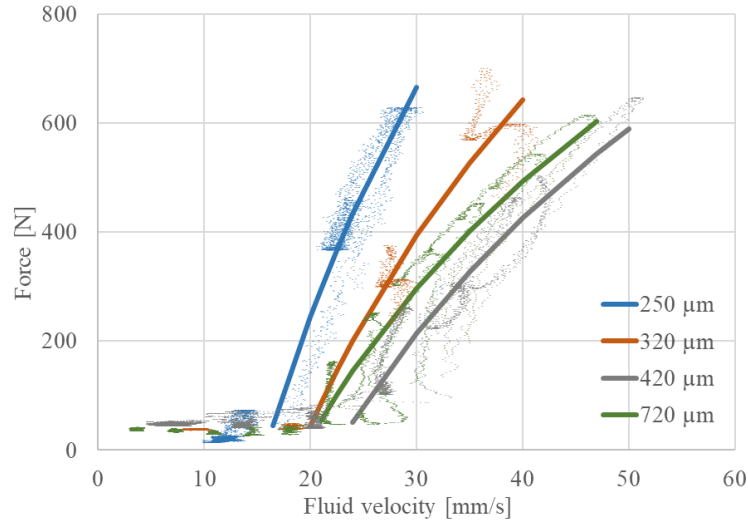


Figure 7: Damping force vs. average fluid velocity in orifice, for different gap dimensions. Regression lines for data sets above DST

A close look at the results of 720 μm gap at velocities below DST reveals a slight decrease of force with increasing fluid velocity. This is consistent with the shear thinning properties of the STF for shear below critical shear rate; see figure 2. The results in figure 7 indicate an independency of the DST to the average fluid velocity, as sudden rise in force gathers around a fixed fluid velocity value of ~ 20 mm/s. Further evaluation of the values in table 1, indicate that the critical U_p at transition is a linear function of h . This is in contrast with equations 4 and 5, where the shear rate is a function of gap height, $\dot{\gamma}(h^{-2})$. This indicates that the onset of DST is not only due to the shear stresses described by the Couette-Poiseuille model. Other effects in the actual flow case, like entrance/exit effects, could influence the propagation of DST.

Table 1: Critical velocities for different gap dimensions and ratio between them.

Gap dim. h [μm]	Piston velocity U_p [mm/s]	Piston area / gap area D_p/h [-]	Calc. fluid velocity \bar{u}_x [mm/s]
250	1,4	12,0	16,4
320	2,2	9,2	19,9
420	3,3	6,8	22,5
720	5,7	3,6	20,7

3.2 Fluid properties

To quantify the effect of shift in critical shear rate of DST in the fluid, the damper was further tested with varying dilutions of the STF. The force vs. piston velocity results for undiluted STF are compared to those from tests of fluid diluted 2.5 and 7.5 wt.%.. The tests were made with a piston of 19.16 mm diameter, or a gap of 420 μm . The results are shown in figure 8. The onset of DST occurs at a similar piston velocity for the three fluid mixtures, $U_p \sim 4 \text{ mm/s}$, and appears to be unaffected by dilution of the fluid. These results further imply that the onset of DST in the piston damper is initiated by other dynamics than the shear rate, derived from the Couette-Poiseuille flow equations.

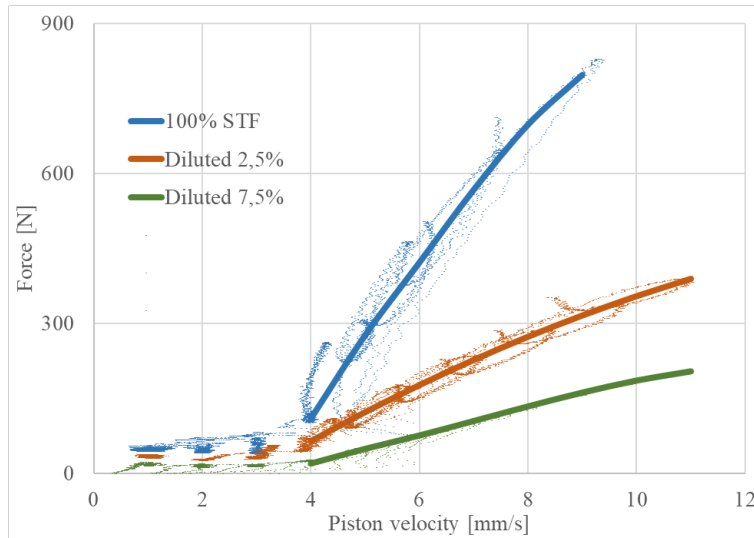


Figure 8: Damping force vs. fluid velocity for different STF dilutions

4 CONCLUSIONS

In this paper we described the design objectives and requirements for a bi-functional STF piston damper. The damper is intended as an active element in a variable stiffness system. The damper shows velocity dependent behavior that shifts from compliant damping to force transfer at critical value of speed, dependent on gap dimension. Testing of the prototype showed that reaction forces above 2 kN, for $h < 320 \mu\text{m}$, meeting the requirements. The transition from damping to coupling, for these gap dimensions, occurred at a piston velocity below the required range (5 – 8 mm/s).

The results indicate time dependency in the fluid flow, where forces for deceleration are higher than during acceleration of the linear displacement of the piston. Whether this time dependency originates from time dependent increase of viscosity or transition in the flow regime is inconclusive. It is noted that the effect will increase the force reaction for deceleration and therefore be beneficial to the force coupling intended for the application. It was demonstrated that the analytical model does not capture the full complexity of the onset of DST. Furthermore, it was shown that the onset of DST was unaffected by change in critical shear rate of the STF, further demonstrating the deviance to the simplified Couette-Poiseuille flow.

It is the result of this initial study that there is potential in use of STFs for velocity dependent

force transfer, as defined here. Future work will focus on the transition at critical shear rates and how it can be translated to the linear displacement. This will include further development of the piston geometry for both shift in the transition velocity as well as adaptability.

REFERENCES

- [1] Hansen A, Starker F. Handbook of Human Motion. Müller B, Wolf SI, editors. Springer International Publishing AG. 2016. 1343-1358 p.
- [2] De Asha AR, Munjal R, Kulkarni J, Buckley JG. Impact on the biomechanics of overground gait of using an ‘ Echelon ’ hydraulic ankle – foot device in unilateral trans-tibial and trans-femoral amputees. *Clin Biomech [Internet]. Elsevier B.V.*; (2014) **29**(1): 728–34. Available from: <http://dx.doi.org/10.1016/j.clinbiomech.2014.06.009>
- [3] Adamczyk PG, Roland M, Hahn ME. Sensitivity of biomechanical outcomes to independent variations of hindfoot and forefoot stiffness in foot prostheses. *Hum Mov Sci [Internet]. Elsevier*; (2017) **54**(August 2014): 154–71. Available from: <http://dx.doi.org/10.1016/j.humov.2017.04.005>
- [4] Shell CE, Segal AD, Klute GK, Neptune RR. Clinical Biomechanics The effects of prosthetic foot stiffness on transtibial amputee walking mechanics and balance control during turning. *Clin Biomech [Internet]. Elsevier*; (2017) **49**(August): 56–63. Available from: <http://dx.doi.org/10.1016/j.clinbiomech.2017.08.003>
- [5] Hansen AH, Childress DS, Miff SC, Gard SA, Mesplay KP. The human ankle during walking: Implications for design of biomimetic ankle prostheses. *J Biomech.* (2004) **37**: 1467–74.
- [6] Tryggvason H, Starker F, Lecomte C, Jonsdottir F. Modeling of stiffness characteristics in a prosthetic foot. *ASME 2017 Conf Smart Mater Adapt Struct Intell Syst SMASIS 2017.* (2017) **2**: 1–7.
- [7] Brown E, Jaeger HM. Shear thickening in concentrated suspensions: Phenomenology, mechanisms and relations to jamming. *Reports Prog Phys [Internet].* (2014) **77**(046602). Available from: <http://arxiv.org/abs/1307.0269v0>
<http://dx.doi.org/10.1088/0034-4885/77/4/046602>
- [8] Ding J, Tracey PJ, Li W, Peng G, Whitten PG, Wallace GG. Review on shear thickening fluids and applications. *Text Light Ind Sci Technol.* (2013) **2**(4): 161–73.
- [9] Tian T, Nakano M, Li W. Applications of shear thickening fluids : a review. *Int J Hydromechatronics.* (2018) **1**(2): 238–57.
- [10] Palmer RM, Green PC. Energy absorbing material [Internet]. US7381460B2, 2008. Available from: <https://patents.google.com/patent/US7381460>
- [11] D3O: Impact protection [Internet]. D3O. 2019. Available from: <https://www.d3o.com/>
- [12] Decker MJ, Halbach CJ, Nam CH, Wagner NJ, Wetzel ED. Stab resistance of shear thickening fluid (STF) - treated fabrics. *Recent Patents Mater Sci.* (2011) **4**: 565–78.
- [13] Wagner NJ, Brady JF. Shear thickening in colloidal dispersions. *Phys Today [Internet].* (2009) **62**(10): 27–32. Available from: <http://wrap.warwick.ac.uk/13885/>
<http://scitation.aip.org/content/aip/magazine/physics/article/62/10/10.1063/1.3248476>
- [14] Guo Y, Wei Y, Zou J, Huang C, Wu X, Liu Z, et al. Impact and usage of the shear

- thickening fluid (STF) material in damping vibration of bolted flange joints. *Smart Mater Struct.* (2018) .
- [15] Yeh F, Chang K, Chen T. Smart Viscous Dampers utilizing Shear Thickening Fluids with Silica Nanoparticles. In: *15 th World Conference on Earthquake Engineering*. 2012.
- [16] Zhang XZ, Li WH, Gong XL. The rheology of shear thickening fluid (STF) and the dynamic performance of an STF-filled damper. *Smart Mater Struct [Internet]*. (2008) **17**(3): 035027. Available from: <http://stacks.iop.org/0964-1726/17/i=3/a=035027?key=crossref.785c0f54ba20b5b0ad8eb791c8d78688>
- [17] Zhou H, Yan L, Jiang W, Xuan S, Gong X. Shear thickening fluid–based energy-free damper: Design and dynamic characteristics. *J Intell Mater Syst Struct [Internet]*. (2016) **27**(2): 208–20. Available from: <http://journals.sagepub.com/doi/10.1177/1045389X14563869>
- [18] Tian T, Nakano M. Design and testing of a rotational brake with shear thickening fluids. *IOP Publishing*; (2017) **26**(035038).
- [19] Data Sheet: STF SG - Standard.
- [20] Safety Data Sheet: STF. 2015.
- [21] Galindo-Rosales FJ, Rubio-Hernández FJ, Sevilla A. An apparent viscosity function for shear thickening fluids. *J Nonnewton Fluid Mech [Internet]*. Elsevier B.V.; (2011) **166**(5–6): 321–5. Available from: <http://dx.doi.org/10.1016/j.jnnfm.2011.01.001>
- [22] White FM. Viscous fluid flow. 2nd ed. Beamesderfer L, Morriss JM, editors. 1991. 118-119 p.
- [23] Mewis J, Wagner NJ. Thixotropy. *Adv Colloid Interface Sci.* (2009) **148**: 214–27.

AUTHORS INDEX

Abdelkefi, A.	1377, 1397	Bhalla, S.	223
Aboura, Z.	628	Blachowski, B.	284, 345
Ahrentorp, F.	866	Bodkhe, S.	433
Ahsani, S.	1076	Boehm, M.	90
Alaggio, R.	1795	Boldyrev, G.	1746
Aloisio, A.	1795	Boller, C.	1562
Aloui, O.	118	Bolson, N.	1371
Aloui, R.	1327	Bolzmacher, C.	527
Altay, O.	754	Borggaard, J.	65
Amberg, M.	515	Bouhaddi, N.	1085
Amoozgar, M.	452	Boukadia, R.	1066
Amoozgar, M.	473	Bouraoui, T.	787, 877
Andersen, E. K.	1515, 1527	Braghin, F.	1183, 1105
Anlas, G.	844	Briand, W.	1201
Anoshkin, A.	640	Broun, V.	991
Antonacci, E.	1795	Brune, K.	409
Araujo, A.L.	618, 580	Brzeski, P.	333, 373
Arbab Chirani, S.	855	Brüning, H.	409
Arikan, K. B.	1637	Buchmeiser, M.	1812
Ario, I.	1648, 243	Buroni, F. C.	592
Astolfi, J. A.	952	Bätge, M.	102
Auleley, M.	908	Böhm, M.	43
Avalishvili, G.	1349	Calloch, S.	855
Avalishvili, M.	1349	Cao, Z.	571
Baena, M.	200	Carlsson, R.	866
Bai, J.	1281	Carrera, E.	610
Balasubramaniam, K.	381	Casado, C.	1682
Balzani, C.	102	Castro-Triguero, R.	1468
Bareille, O.	1169, 1058, 1157, 1124, 1136	Caydamli, Y.	1812
Baroudi, S.	1446	Cazzulani, G.	1105, 1183
Barris, C.	200	Ceballes, S.	1377, 1397
Barrière, L.	1389	Chakraborty, T.	223
Bartoli, G.	1612	Chambers, J. M.	543
Beker, C.	1637	Chang, C. M.	169
Beliaev, F. S.	686	Chatzi, E.	1146
Bellelli, A.	764	Chellattoan, R.	1371
Belmonte, M.	1319	Chen, W.	571
Ben Ayed, S.	65	Chevalier, M.	1389
Ben Zineb, T.	877, 787	Chiang, H. F.	169
Benbara, N.	503, 527	Chikahiro, Y.	1648, 243
Bencheikh, N.	1594, 1550	Chirani, S. A.	877
Beneš, P.	1456	Choi, S. B.	1738
Berardengo, M.	364, 1014	Choi, Y.T.	1300, 1312
Bergamini, A.	433, 942	Chou, J. Y.	169
Berthelot, E.	1427	Chouchane, M.	1327
Bessaguet, C.	1389	Chrysochoidis, N. A.	973
Betti, M.	1612	Ciambella, J.	275

Cirella, R.	1795	Fournier, M.	1550
Claeys, C.	1076, 1066	Foutsitzi, G.	1037
Claeyssen, F.	1594, 1550	Fragiacomo, M.	1795
Cliff, E.	65	Franco, F.	1096, 1112, 1085, 1124, 1169
Colin, M.	1025	Frick, S.	1812
Collette, C.	930, 991	Friswell, M.	452, 473
Correia, P.	1760	Fritzen, C. P.	1582
Cross, E.	251	Fröhlich, B.	43
Cunha, A.	189	Fu, J.	1270, 1281
D'Almeida, O.	402	Furth, D.	1397
da Silva, S.	1213	Gallimard, L.	1468
Dai, Z.	1281	Gao, J.	571
Dakova, I. G.	1706	Garbuliński, J.	1491
Damkilde, L.	1527, 1515	Garcia-Sanchez, F.	592
Daniel, L.	1427	Gawlicki, M.	215
Dantras, E.	1389	Genco, T.	421
Darleux, R.	896	Georgopoulos-Bosinas, K.	973
de Acosta, R.	1562	Gerstmayr, J.	31
De Gersem, H.	1726	Ghaffari, S.	1377
De Rosa, S.	1096, 1169, 1112, 1085, 1124	Giaralis, A.	301
Deckers, E.	1157, 1076, 1066	Giraud, F.	515
Dekemele, K.	922	Giraud-Audine, C.	515, 908
Della Porta, G.	364	Givois, A.	1025, 709
Deraemaeker, A.	251, 930	Gjonaj, E.	1726
Dertimanis, V.	1146	Goldasz, J.	1671
Dervilis, N.	251	Goi, Y.	313, 177
Desmet, W.	1136, 1066, 1157, 1076	Golub, M.	1582
Deü, J. F.	896, 709, 1046, 952, 1037	Grabec, T.	1319
Di Battista, L.	1795	Graczykowski, C.	485, 1629
Diaz, I. M.	1682	Grundmann, N.	409
Djerahov, L.	1783	Guenfoud, N.	1157
Domenjoud, M.	1427	Guenther, J.	125
Dong, X.	816	Guillot, V.	1025
Doudard, C.	855	Guo, S.	1236
Droz, C.	1136, 1058, 1157	Guskov, M.	1201, 1550, 1224
Du, X.	1270	Hadjria, R.	402
Dumoulin, C.	251	Halevi, Y.	492
Eberhard, P.	43	Hamada, Y.	313
Elmquist, L.	866	Hansy-Staudigl, E.	650
Enferad, E.	515	Harder, N.	125
Eremin, A.	1582	Harizi, W.	628
Ermanni, P.	433	Hartl, D.	462
Errico, F.	1124	Hayashi, G.	177
Evard, M. E.	686	He, Y.	797
Fan, P.	571	Hegger, C.	1291
Fan, Z.	207	Hiemenz, G.	1300
Fang, G.	571	Hirooka, T.	177
Faraj, R.	485	Hoffmeyer, D.	158
Feng, C.	81	Holnicki-Szulc, J.	1629, 537, 485

Hoxha, E.	263	Kruisová, A.	1319
Huang, C.	1270	Kubik, M.	1671
Humer, A.	721, 650, 775, 674	Kulikov, G. M.	599, 696
Høgsberg, J.	884, 961, 158	Kulikov, M. G.	696
Ichchou, M.	1124, 1169, 1066, 1157, 1096, 1136, 1058	Kurtulus, D. F.	1637
Infantes, M.	1468	Labernarda, R.	1694
Israelsson, B.	866	Lagoudas, D.	462
Iurlov, M.	1337, 1002	Lamarque, C. H.	1025
Iurlova, N.	1002, 1337	Lammering, R.	421
Ivanov, D.	1058	Larbi, W.	1327
Iwasaki, A.	1501	Lazarek, M.	333, 373
Jacquemin, Q.	1435	Lecompte, C.	1823
Jagdish, A. K.	592	Legrand, V.	855
Jalali, H.	1622	Lemaire-Semail, B.	515
Jankowski, Ł.	345, 357, 485, 284, 323, 1076, 215	Li, Q. K.	1538
Jastrzębski, Ł.	1671	Li, X.	1224
Jaussaud, G.	1550	Lima, R.	985
Jayendiran, R.	825	Linke, M.	421
Jia, Z.	137	Liu, J.	1281
Jing, X. J.	1538	Liulchak, P. S.	686
Johannisson, P.	866	Loccufier, M.	922
Johansson, C.	866	Logeais, M.	1550
Jonsdottir, F.	1823	Lorenzana, A.	1682
Inocente-Junior, N.	1189	Lossouarn, B.	896, 1046, 952
Karadjov, M.	1706	Loutas, T.	1248
Karadjova, I.	1783	Lozák, A.	1562
Karadjova, I.	1706	Lubineau, G.	1371
Kathol, J.	1582	Lyamkin, V.	1562
Kaup, A.	754	Ma, N.	816
Kerschen, G.	991, 930, 1046	Maas, J.	1291
Khalil, W.	787	Mabe, J.	462
Khelif, A.	1112	Madeira, J. F. A.	618
Khellil, K.	628	Magdaleno, A.	1682
Kim, C. W.	313, 177, 291	Magliacano, D.	1112
Kim, D.	65	Mahé, H.	908
Kim, G. W.	1738	Malinowski, P.	381, 390
Kitagawa, S.	313	Mallik, N.	443
Klinkel, S.	754, 662	Mamontov, S. A.	696
Klockmann, L. B.	1507	Manzoni, S.	1014, 364
Knap, L.	1629	Marakakis, K.	1037
Koller, M.	1319	Marconi, J.	1183
Kondo, Y.	291	Masri, S.	1146
Kosheleva, N.	1718	Matveenko, V.	1574
Koutsianitis, P.	1037	Mayer, M.	409
Kraus, K.	1456	Mazza, F.	1694
Krivošej, J.	1456	Mazzeo, G.	1096
Krommer, M.	721, 650	McCullum, J. R.	562
		Mechbal, N.	503, 1236, 1435, 527, 1224, 1213, 1201

Megdiche, M.	877	Peng, F.	571
Meindlhumer, M.	775, 721, 674	Pereira, E.	1682
Melnik, R.	592	Perera, R.	200
Merkusheva, N. P.	599	Perlikowski, P.	373, 333
Meyer, Y.	628	Pernod, L.	952
Michon, G.	1389	Petrone, G.	1096
Mikułowski, G.	357	Petrovic, V.	102
Mikulowski, G.	323	Pieber, M.	31
Milanoski, D.	1248	Pierce, R. M.	1312
Mimasu, T.	177	Pillsbury, T. E.	1480
Miranzo, P.	1319	Pines, D. J.	562
Moharana, S.	55	Pisarski, D.	345
Montano, Z.	102	Plotnikova, S. V.	599, 696
Monteiro, E.	1224, 1435	Pluymers, B.	1136
Moumni, Z.	844	Polit, O.	1361, 1468
Moutinho, C.	189	Polniak, B.	373
Mueller, I.	1582	Poplawski, B.	323, 357
Munitsyna, M.	1664	Pozo, F.	263, 1604
Muramatsu, Y.	742	Praster, M.	662
Najar, F.	1446	Puchowski, B.	390
Nakazawa, M.	1648, 243	Qadri, B. A.	1507
Nasedkin, A. V.	551	Qi, M.	816
Nasrollahi, A.	1622	Qin, G.	797
Negi, P.	223	Quadrelli, D. E.	1105
Nematzadeh, A.	1772	Quiroga Cortes, L.	1389
Neuhaus, L.	102	Rao, J.	207
Ngoc, M.	1738	Raze, G.	991, 930
Nguyen, V.	805	Rebillat, M.	1224, 1236, 1201, 527
Nour, B.	825	Rebufa, J.	1550, 1594
Nóbrega, E.	1189	Rekatsinas, C.	973
Oei, M.	125	Reksowardojo, A.P.	72
Ohayon, R.	1037	Revalor, Y.	973
Oliveira, C.	1760	Rhode-Barbarigos, L.	118
Opitz, S.	102	Riemenschneider, J.	102
Oshima, Y.	291	Ritto, T.	1654
Oshmarin, D.	1337, 1002	Riva, E.	1105, 1183
Ostachowicz, W.	390	Rizzo, P.	1622
Ostrowski, M.	345	Robert, F.	930
Osée, M.	930	Rodriguez-Tembleque, L.	592
Ottavio, M.	1361	Román-Manso, B.	1319
Ouisse, M.	1085, 1112	Rubias, J. L.	1604
Ozerim, G.	844	Ruimi, A.	825
Paixão, J.	1213	Rébillat, M.	503, 1550, 1213
Paknejad, A.	991, 930	S. A, V.	55
Palumbo, R.	1058	Saeedifar, M.	1260
Pau, A.	275	Saez, A.	592
Pechstein, A.S.	674, 775, 721	Saint-Sulpice, L.	855
Pedersen, M. W.	1515, 1527	Sallami, A.	877, 787
Pelenev, K.	640	Samaali, H.	1446

Sampaio, R.	985	Testoni, O.	433
Sanches, L.	1389	Thiebaud, F.	877
Santos, R.	1189	Thomas, O.	1025, 1014, 709, 908
Sapiński, B.	1671	Thore, A.	866
Saravanos, D.	730	Thuau, D.	1435
Saravanos, D. A.	973	Tikhonova, A.	640
Saunders, B.	1377	Timorian, S.	1085
Savi, M.	1654	Toftekær, J. F.	961
Sawodny, O.	43, 125, 90	Tong, Y.	816
Scarpa, F.	1058	Torres, L.	200
Schaller, V.	866	Tryggvason, H.	1823
Schmied, J.	942	Tsukiji, T.	1753
Sedlák, P.	1319	Tufano, G.	1136
Sehitoglu, H.	837	Tuloup, C.	628
Seiner, H.	1319	Ture Savadkoohi, A.	1025
Senatore, G.	72	Turgut, A. E.	1637
Serovaev, G.	1718	Törnvall, M.	866
Sevodina, N.	1002, 1337	Ulriksen, M. D.	1507, 1527, 1515
Shaw, A.	473, 452	Unguran, R.	102
Shestakov, A.	1718	Van Torre, P.	922
Shih, M. H.	146	Vanali, M.	1014, 364
Shilo, D.	1414	Varelis, D.	730
Shimizu, S.	1501, 1648	Vasileva, P.	1783
Shimoda, M.	742	Veis, P. H.	1507
Shinoda, M.	313	Vestroni, F.	275
Shipunov, G.	640	Vidal, P.	1361, 1468
Shiri, H.	1772	Vidal, Y.	263, 1604
Shpak, A.	1582	Vieira, F.	580
Shustova, E.	640	Volkov, A.E.	686
Silva, R.	1654	Volkova, N. A.	686
Singh, P.	102	Voronkov, A.	640
Singh, R. P.	1169	Vyhlídal, T.	1456
Smith, I. F. C.	72	Wagner, J. L.	90
Soria, J. M.	1682	Wagner, J.L.	43
Souza, P.	1189	Wandowski, T.	381, 390
Spaggiari, A.	764	Wang, C.	473, 452
Sridaran Venkat, R.	1562	Wang, Y.	81
Starke, P.	1562	Wang, Z.	301
Starker, F.	1823	Wereley, N. M.	1480, 543, 1300,
Stavroulakis, G. E.	1037	1312, 1491, 562
Sung, W. P.	146	Werthen, E.	102
Suo, L.	1405	Wolejsza, Z.	1629
Swiercz, A.	284, 537	Woods, B.	452
Tairidis, G.K.	1037	Worden, K.	251
Takhirov, S.	233	Wu, H.	1562
Tashkinov, M.	1574	Wu, Z.	1405
Tauzowski, P.	284	Yaacoub, J.	837
Taylor, K.	1726	Yang, J.	81
Tencé-Girault, S.	1435	Yang, Z.	1281

Yao, H.	313
Yoffe, A.	1414
Yokotani, Y.	243
Yoo, B.	562
Yordanova , T. V.	1706
Yoshitome, K.	313
Yu, M.	1270, 1281
Yudhanto, A.	1371
Zaki, W.	805
Zappino, E.	610
Zarouchas, D.	1260
Zenzai, S.	1648
Zhang, J.	452, 473
Zhang, S.	797
Zhang, X.	137
Zhao, G.	991, 930
Zhao, Z.	81
Zheng, B.	1622
Zhivaev, A.	1746
Zielinski, T. G.	1076
Zine, A. M.	1136
Zini, G.	1612
Šika, Z.	1456



CIMNE^R
International Centre
for Numerical Methods in Engineering